CODEN: JASMAN

The Journal of the Acoustical Society of America

ISSN: 0001-4966

Vol. 125, No. 6 June 2009

JASA EXPRESS LETTERS

LETTERS TO THE EDITOR

GENERAL LINEAR ACOUSTICS [20]

NONLINEAR ACOUSTICS [25]

AEROACOUSTICS, ATMOSPHERIC SOUND [28]

(Continued)

CONTENTS—*Continued from preceding page*

UNDERWATER SOUND [30]

ULTRASONICS, QUANTUM ACOUSTICS, AND PHYSICAL EFFECTS OF SOUND [35]

TRANSDUCTION [38]

STRUCTURAL ACOUSTICS AND VIBRATION [40]

NOISE: ITS EFFECTS AND CONTROL [50]

(Continued)

CONTENTS—*Continued from preceding page*

(Continued)

CONTENTS—*Continued from preceding page*

(Continued)

CONTENTS—*Continued from preceding page*

Hidden Markov and Gaussian mixture models for automatic call classification

Judith C. Brown
Physics Department, Wellesley College, Wellesley Massachusetts 02481 and Media Laboratory, Massachusetts Institute of Technology Cambridge Massachusetts 02139
brown@media.mit.edu

Paris Smaragdis
Adobe Systems, Newton, Massachusetts
paris@adobe.com

Abstract: Automatic methods of classification of animal sounds offer many advantages including speed and consistency in processing massive quantities of data. Calculations have been carried out on a set of 75 calls of Northern Resident killer whales, previously classified perceptually (human classification) into seven call types, using, hidden Markov models (HMMs) and Gaussian mixture models (GMMs). Neither of these methods has been used previously for classification of marine mammal call types. With cepstral coefficients as features both HMMs and GMMs give over 90% agreement with the perceptual classification, with the HMM over 95% for some cases.

PACS numbers: 43.80.Ka, 43.80.Ev, 43.60.Uv [CM]
Date Received: December 17, 2008

1. Introduction

The automatic classification of marine mammal sounds is very attractive as a means of assessing massive quantities of recorded data, freeing humans, and offering rigorous and consistent output. Calculations on a set of vocalizations of Northern Resident killer whales using dynamic time warping were reported recently. (Brown and Miller, 2006, 2007). Since this method requires the time-consuming preprocessing measurement of the frequency contours, the methods of Gaussian mixture models (GMMs) and hidden Markov models (HMMs) have been explored. These calculations can be applied directly to the time-frequency decomposition of the recorded signals and have not been used previously for the classification of call types of marine mammals.

2. Background

2.1 Gaussian mixture models

The GMM is a commonly used estimate of the probability density function used in statistical classification systems. GMM classifiers (Duda *et al.*, 2001) are well known for their ability to model arbitrarily complex distributions with multiple modes and are effective classifiers for many tasks.

Although GMMs have found widespread use in speech research, primarily for speaker recognition (Reynolds and Rose, 1995 and references therein), and have been used in other fields, for example, for musical instrument identification (Brown, 1999 and Brown *et al.*, 2001), there is only one report in animal bioacoustic research (Roch *et al.*, 2007).

Roch *et al.* (2007) used GMMs to distinguish among three dolphin species obtaining 67%–75% accuracy. In this study they vary the number of mixtures from 64 to 512, in steps differing by a factor of 2. Best results were obtained with 256 mixtures using 64 cepstral coefficients as features on sounds of duration from 1 to 30 s.

The cepstrum is the Fourier transform of the log magnitude spectrum (Oppenheim and Schafer, 1975); it involves two transforms which makes it computationally more intensive than

fast Fourier transform (FFT) based calculations. The choice of cepstra as features has been particularly successful in characterizing the vocal tract resonances which identify individual speakers, speech, or vowels. See Rabiner and Schafer, 1978 and Rabiner and Huang, 1993 for a discussion of the use of cepstra for speech applications.

2.2 Hidden Markov models

The HMM is widely used in human speech processing and is described in tutorials by Rabiner and Juang (1986) and Rabiner (1989). An excellent introuction to HMMs can be found on the website of R. D. Boyle[1] with an introduction for animal bioacousticians in Clemins (2005). A HMM models temporal data in as a sequence of *states*. States are usually defined as separate GMMs, and their successive usage across time is governed by a *transition matrix*. The transition matrix is learned from training data and defines the probabilities of moving from one state to another, ensuring that the data are optimally explained. Ultimately, what the HMM does is create a sequence of GMM models to explain the input data, thus being sensitive to temporal changes.

HMMs have been used far more extensively than GMMs in the field of animal bioacoustics. The principal difference in the two methods is that the HMM takes account of the temporal progression of the sound and is thus able to describe the structure of the call. The GMM treats the entire sound as a single entity with unique spectral properties which characterize each class. Since the HMM takes account of the temporal structure of the call, it uses the temporal variation of the calls as additional information to disambiguate among call types. In comparison a GMM could not distinguish a call type from itself played backwards since it does not examine the temporal structure.

Weisburn *et al.* (1993) used a HMM for detecting bowhead whale notes with the three largest peaks in the FFT as features. Kogan and Margoliash (1998) compared the methods of HMM and dynamic time warping for automated recognition of bird song elements and found that the HMM was more robust. Mellinger and Clark (2000) compared spectrogram correlation to HMMs on the task of recognizing bowhead whale calls finding that the spectrogram worked marginally better. Datta and Sturtivant (2002) used HMMs to identify three different groups of dolphin whistles, finding that one group was very distinct from the other two.

More recently HMMs have been used for classification or detection of vocalizations by African elephants (Clemins *et al.*, 2005; Clemins and Johnson, 2006), red deer (Reby *et al.*, 2006), and the ortolan bunting (Trawicki *et al.*, 2005, Tao *et al.*, 2008). There have been no computations with HMMs or GMMs on automatic classification of call types of marine mammal sounds.

3. Calculations and results

The features chosen for all of the calculations were cepstral coefficients and their temporal derivatives. These were calculated with the program melcepst available with the MATLAB toolbox VOICEBOX.[2] The sample rate was 44 100 samples/s with each sound divided into 23 ms segments for the calculations. The HMM/GMM computations were carried out with software by Paris Smaragdis. The training set for all classifications consisted of all the sounds except the one being classified, called the "leave one out" method. Preliminary results were reported by Brown and Smaragdis (2008).

3.1 GMM results

Results for the GMM calculations are given in Fig. 1 with the number of Gaussians in the probability distributions varying from 1 to 6 and the number of cepstral coefficients from 8 to 30. The calculation diverges for more than 4 Gaussians with 18 or more features due to model overfitting.

Agreement with the perceptual (human classification) results were over 85% with 18–30 features. The calculation is not highly sensitive to the number of Gaussians. Best results were obtained for 30 features with two Gaussians and gave 92% agreement.

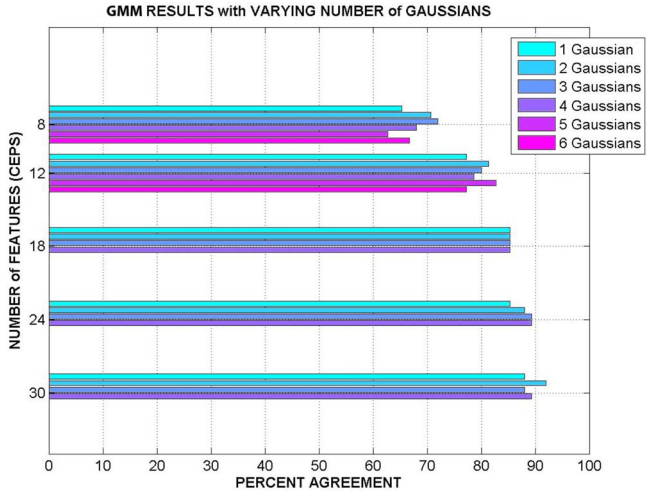

Fig. 1. (Color online) Gaussian mixture model results showing the dependence on the number of features (cepstral coefficients) and the number of Gaussians in the estimate of the probability density function.

3.2 HMM results

For the HMM classification, a left-to-right model was used, and there were three variable parameters rather than two. The number of Gaussians in the probability function was varied from 1 to 4 with the results consistently about 5% better for one Gaussian than two and from 3% to 10% better for two Gaussians than three. The number of states was varied from 5 to 17 and the number of features from 8 to 42 with results given in Fig. 2. Excellent agreement with the perceptual classification is obtained over a wide range of these paramters with over 90% for from 18 to 42 features and from 9 to 17 states. Truly outstanding agreement of over 95% was obtained for 24 to 30 features and 13 to 17 states.

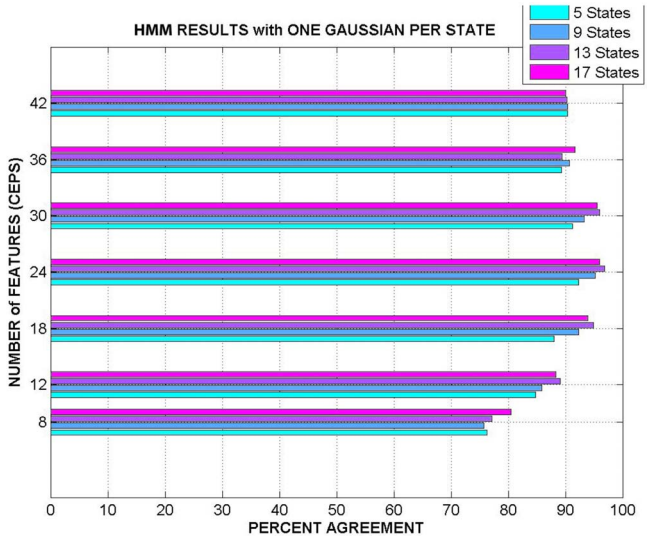

Fig. 2. (Color online) Hidden Markov model results showing the dependence on the number of features (cepstral coefficients) and the number of states in the model with one Gaussian in the estimate of the probability density function.

4. Conclusion

These results demonstrate that both GMMs and HMMs are highly successful in the task of automatic classification of killer whale call types, with the performance of the HMM being truly outstanding. Even more impressive is the wide range of parameters over which the calculations agree with the perceptual classification indicating a very robust calculation and great promise for successful extension to other data sets and other species.

Acknowledgments

We are very grateful to Patrick Miller for the killer whale sounds which made this study possible.

References and links

[1]"Hidden Markov models," http://www.comp.leeds.ac.uk/roger/HiddenMarkovModels/html_dev/main.html. Last viewed 5/6/2009.
[2]M. Brooks, "VOICEBOX: Speech processing toolbox for MATLAB," http://www.ee.ic.ac.uk/hp/staff/dmb/voicebox/voicebox.html. Last viewed 5/6/2009.

Brown, J. C. (**1999**). "Computer identification of musical instruments using pattern recognition with cepstral coefficients as features," J. Acoust. Soc. Am. **105**, 1933–1941.
Brown, J. C., and Miller, P. J. O. (**2006**). "Classifying killer whale vocalization using time warping," Acoust. Today **16**, 45–47.
Brown, J. C., and Miller, P. J. O. (**2007**). "Automatic classification of killer whale vocalizations using dynamic time warping," J. Acoust. Soc. Am. **122**, 1201–1207.
Brown, J. C., and Smaragdis, P. (**2008**). "Automatic classification of vocalizations with Gaussian mixture models and hidden Markov models," J. Acoust. Soc. Am. **123**, 3345.
Brown, J. C., Houix, O., and McAdams, S. (**2001**). "Feature dependence in the automatic identification of musical woodwind instruments," J. Acoust. Soc. Am. **109**, 1064–1072.
Clemins, P. J. (**2005**). "Automatic classification of animal vocalizations," Ph.D. thesis Marquette University, Milwaukee, WI.
Clemins, P. J., and Johnson, M. T. (**2006**). "Generalized perceptual linear prediction feature for animal vocalization analysis," J. Acoust. Soc. Am. **120**, 527–534.
Clemins, P. J., Johnson, M. T., Leong, K. M., and Savage, A. (**2005**). "Automatic classification and speaker identification of African elephant Loxodonta africana vocalizations," J. Acoust. Soc. Am. **117**, 956–963.
Datta, S., and Sturtivant, C. (**2002**). "Dolphin whistle classification for determining group identities," Signal Process. **82**, 251–258.
Duda, R. O., Hart, P. E., and Stork, D. G. (**2001**). *Pattern Classification*, 2nd ed. (Wiley, New York).
Kogan, J. A., and Margoliash, D. (**1998**). "Automated recognition of bird song elements from continuous recordings using dynamic time warping and hidden Markov models: A comparative study," J. Acoust. Soc. Am. **103**, 2185–2196.
Mellinger, D. K., and Clark, C. W. (**2000**). "Recognizing transient low-frequency whale sounds by spectrogram correlation," J. Acoust. Soc. Am. **107**, 3518–3529.
Oppenheim, A. V., and Schafer, R. W. (**1975**). *Digital Signal Processing* (Prentice-Hall, Inc., Englewood Cliffs).
Rabiner, L. R. (**1989**). "A tutorial on hidden Markov models and selected applications in speech recognition," Proc. IEEE **77**, 257–286.
Rabiner, L. R., and Juang, B. H. (**1986**). "An introduction to hidden Markov models," IEEE ASSP Mag. **3**, 4–16.
Rabiner, L. R., and Juang, B. H. (**1993**). *Fundamentals of Speech Recognition* (Prentice Hall, Englewood Cliffs).
Rabiner, L. R., and Schafer, R. W. (**1978**). *Digital Processing of Speech Signals* (Prentice-Hall, London).
Reby, D., Andr-Obrecht, R., Galinier, A., Farinas, J., and Gargnelutti, B. (**2006**). "Cepstral coefficients and hidden Markov models reveal idiosyncratic voice characteristics in red deer Cervus elaphus stage," J. Acoust. Soc. Am. **120**, 4080–4089.
Reynolds, D. A., and Rose, R. C. (**1995**). "Robust text-independent speaker identification using Gaussian mixture speaker models," IEEE Trans. Speech Audio Process. **3**, 72–83.
Roch, M. A., Soldevilla, M. S., Burtenshaw, J. C., Henderson, E. E., and Hildebrand, J. A. (**2007**). "Gaussian mixture model classification of odontocetes in the Southern California Bight and the Gulf of California," J. Acoust. Soc. Am. **121**, 1737–1748.
Tao, J., Johnson, M. T., and Osiejuk, T. S. (**2008**). "Acoustic model adaptation for ortolan bunting (Emberiza hortulana L.) song-type classification," J. Acoust. Soc. Am. **123**, 1582–1590.
Trawicki, M. B., Johnson, M. T., and Osiejuk, T. S. (**2005**). "Automatic song-type classification and speaker identification of Norwegian ortolan bunting Emberiza hortulana vocalizations," IEEE Workshop on Machine Learning for Signal Processing, Mystic, CT, pp. 277–282.
Weisburn, B. A., Mitchell, S. G., Clark, C. W., and Parks, T. W. (**1993**). "Isolating biological acoustic transient signals," IEEE ASSP Mag. **1**, 269–272.

Rhythmic structure in humpback whale (*Megaptera novaeangliae*) songs: Preliminary implications for song production and perception

Stephen Handel
University of Tennessee, Knoxville, P.O. Box 95, Hulls Cove, Maine 04644
stephen.handel@gmail.com

Sean K. Todd
College of the Atlantic, 105 Eden Street, Bar Harbor, Maine 04609
stodd@coa.edu

Ann M. Zoidis
Cetos Research Organization, 11 Des Isle Avenue, Bar Harbor, Maine 04609
ann@cetosresearch.org

Abstract: The hierarchical organization of the male humpback whale song has been well documented. However, it is unknown how singers keep these intricate songs intact over multiple repetitions or how they learn variations that occur sequentially during each mating season. Rather than focus on the sequence of sounds within a song, results presented here demonstrate that the individual sounds are organized into rhythmic groups that make the production and perception of the lengthy songs tractable by yielding a set of simple groups that, although arranged in rigid order, can be repeated multiple times to generate the entire song.

PACS numbers: 43.80.Ka, 43.80.Lb [CM]
Date Received: January 5, 2009 **Date Accepted:** March 25, 2009

1. Introduction

Roughly 40 years ago, Payne and McVay (1971) described the hierarchical repetitive "songs" produced by male humpback whales (*Megaptera novaeangliae*) on their mating grounds. The basic sound units are grouped into subphrases, these are grouped into phrases, and the phrases are grouped into themes (Payne *et al.*, 1983). In turn, the themes are organized into a repetitious pattern that recycles in a fairly rigid order. One complete cycle has been termed a song; the song may be repeated several times in a song session (Payne *et al.*, 1983).

Recent work (Miksis-Olds *et al.*, 2008; Suzuki *et al.*, 2006) has demonstrated that the sound sequence is highly constrained and hierarchically organized supporting (Payne and McVay, 1971). But, such analyses do not explain whether the production and perception of the songs should be understood in terms of the creation and transitions among the individual sounds or in terms of higher order phrases and themes.

We investigated whether the rhythmic structure defined by the durations of individual sounds and the duration of the silent intervals between pairs of sounds can expose some of the production constraints and/or reveal how the whale organizes the sounds into phrases and themes. In particular, by varying the duration of the sounds and/or the silent intervals between two sounds, the rhythm acts to segment the song into small groups of sounds physically separated in time from other individual sounds and other groups of sounds. To clarify the role of the rhythmic structure, we propose three processes that might control song organization.

(1) Each sound is articulated in isolation so that the duration of the sound and duration of the silent interval following that sound will be invariant regardless of the subsequent following sound, or its position within a phrase. The sounds are of short duration, separated by periods

of silence, and the songs are sung slowly, roughly one sound every 3.5 s, so that there would be no reason for adjacent sounds to affect each other. The rhythm would be determined solely by the articulation of individual sounds.

(2) The sounds are not produced independently; the following sound influences the temporal properties of the present sound. The production of successive sounds involves adjustments in the vocal tract, and some transitions between particular sounds are more natural and therefore quicker than others. The rhythmic timing would be local between successive sounds.

(3) The temporal properties of individual sounds are a function not only of the following sound but the overall composition of the phrase and theme. In this case, the timing between the pair of sounds AB would be different in ABB, ABC, BAB, or CAB. Furthermore, by analogy to music, we might expect at the transition from one theme to a different one, the duration of the silent interval between the last sound of the initial theme and the first sound of the next theme to increase (Krumhansl, 2000).

These three possibilities are not mutually exclusive. The difficulty of making any sound (No. 1) generates the basic timing unit. By reducing the interval between two or three sounds and increasing the interval between repetitions of those sounds, the whale organizes the sounds into rhythmic groups (No. 2), and by further varying the timing across larger numbers of sounds, the whale constructs phrases segregated in time (No. 3).

Consider the sequence AABCABBCDEDDE whereby each letter represents a sound. If there is no effect of sequence (No. 1), then the timing for A in the AA-AB pairs, the timing for B in the BB-BC pairs, and so on would be identical although the timings for each sound should differ due to the probable different production constraints. In contrast, if the sequence of the sounds influences the timing (No. 2), then all of the above pairs should differ. Finally if the phrase and theme structure also influence the timing (No. 3), then the AB timing should differ between ABC and ABB and if DEDDE represents a second theme then the duration of the silent interval between the C terminating phrase 1 and the D beginning phrase 2 should increase.

Although the song may be hierarchical, that does not determine how the song is organized into phrases and themes. For example, even the simple repetition AABBAABB could be organized as (AABB)(AABB), (BBAA)(BBAA), (BAAB)(BAAB), or (AA)(BB)(AA)(BB) among other possibilities. There is no way to derive the organization solely from the constraints in the element sequence. While it is possible to argue that one possible organization into phrases and themes is better in some formal sense than another or in terms of gestalt perceptual principles (e.g., similarity and good continuation), that does not prove that organization is used by the whales. Here we argue that it is the rhythmic structure that distinguishes among possibilities and serves both the singer and receiver as a framework to organize the sound units into phrases and themes. It minimizes memory requirements necessary to sing the song by segmenting the sounds into short rhythmic groups. In the highly variable ocean environment, the rhythm would be an invariant cue to phrases and themes, independent of random noise and the location of the singer and receiver.

2. Method

The humpback whale songs analyzed here, found in the MobySound archives (Mellinger and Clark, 2006), were recorded in March 1994 off the north coast of the island of Kauai, HI by Cetos Research Organization. Details of the recording procedure and the determination of the start- and end-time of each sound are detailed in Mellinger and Clark (2006).

Songs from three individual whales were identified in the MobySound archive based on field notes: whale 1: 940302-12:22 and 940302-12:37 (564 sounds), whale 2: 940302-13:22–940302-13:38 (307 sounds), and whale 3: 940305-09:37–940305-10:22 (1099 sounds). Using the recordings in the MobySound archive, spectrograms were made for each sound using the PRAAT analysis program (Boersma, 2001). Classification of the sounds was done aurally and visually and confirmed by a second acoustician. Here our results will focus on 5 of the roughly 20 different sounds, shown in Fig. 1, embedded in two of the major themes. The first theme, BA,

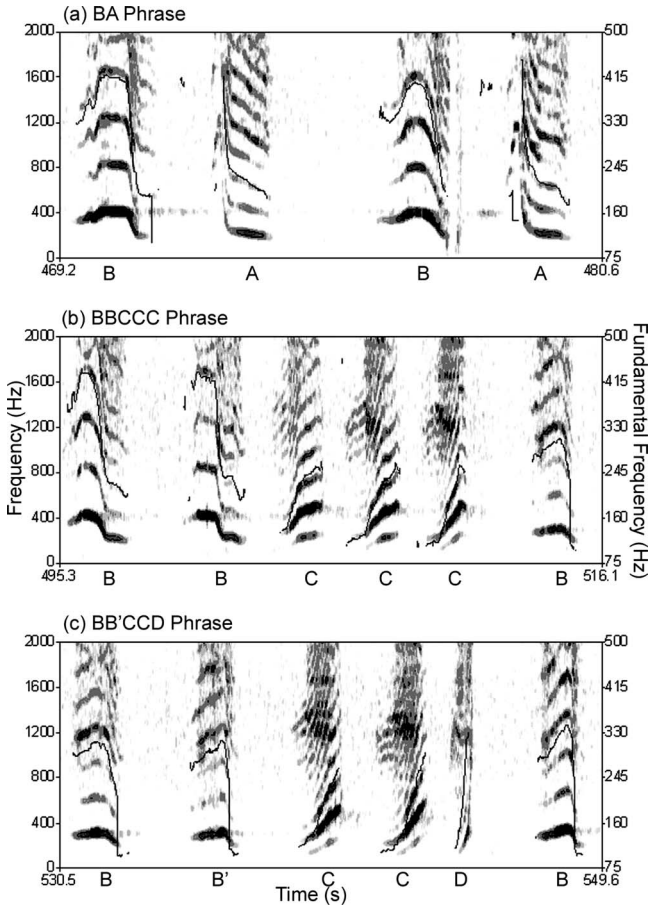

Fig. 1. The spectrogram representation of the phrases in the two themes. The B at the end of the two phrases BBCCD and BB′CCD begins another phrase of the same type. Each representation comes from the song 940302-12:22. The timing for each phrase is given along the *x*-axis and each sound is labeled. For each phrase, the frequency of each harmonic is given on the left margin. The solid line within each sound represents an estimate of the fundamental frequency given on the right margin (Boersma, 2001).

is composed of the repeating BA phrase, and the second theme, BCD, is composed of the two phrases BBCCD and BB′CCD.

3. Results

The role of rhythm in structuring the song into phrases can be illustrated by considering the timing of the same sounds in different phrases. Here, we will concentrate on findings related to two common themes only. The first is the BA theme, the strict alternation between sounds B and A, found for all three whales, accounting for 21% of the sounds produced for the entire song. The second is the BCD theme accounting for 11% of the sounds. For whales 1 and 2, the theme consists of two repetitions of BBCCD followed by one repetition of BB′CCD; for whale 3 only BB′CCD occurs. The BA theme and the two phrases of the BCD theme are shown in Fig. 1. The average duration (± standard deviation) of each sound, average duration (± standard deviation) of the silent interval between each pair of sounds, and the number of cases for each whale are presented in Table 1.

The BA phrase is identical for the three whales. The average duration of the silent interval between sounds B and A is 0.75 s while the average duration of the silent interval for the

Table 1. Means, standard deviations, and sample size (n) for each whale and sound. For each pair of sounds, the duration (in seconds) shown is that of the initial bolded sound, and the duration of the silent duration (in seconds) shown is that between the pair. Superscripts refer to comparisons in Sec. 3.

Sounds	Whale	Duration	Silent interval duration	n
		AB phrase		
A→B	1	1.58 ± 0.12	1.91 ± 0.26	57
	2	1.45 ± 0.18	2.17 ± 0.38	39
	3	1.71 ± 0.22	1.95 ± 0.16	130
B→A	1	2.18 ± 0.31 [a,b]	0.82 ± 0.24 [c,d]	58
	2	1.92 ± 0.25 [a,b]	0.94 ± 0.36 [c,d]	39
	3	2.10 ± 0.23 [a]	0.66 ± 0.39 [d]	130
		BBCCD phrase		
B→B	1	2.52 ± 0.10 [b]	1.95 ± 0.33 [c]	4
	2	2.35 ± 0.16 [b]	2.07 ± 0.28 [c]	7
B→C	1	2.36 ± 0.41 [e]	1.24 ± 0.39 [f]	5
	2	2.37 ± 0.33 [e]	1.05 ± 0.20 [f]	7
C→C	1	1.94 ± 0.29	0.87 ± 0.44 [g]	6
	2	1.99 ± 0.29	0.86 ± 0.30 [g]	10
C→C	1	2.13 ± 0.33	0.82 ± 0.41	6
	2	2.06 ± 0.29	0.75 ± 0.23	9
C→B	1	1.74 ± 0.16	2.08 ± 0.19	6
	2	1.70 ± 0.16	2.15 ± 0.21	9
		BB′CCD phrase		
B→B′	1	2.07 ± 0.10 [a]	2.21 ± 0.12 [d]	3
	2	1.94 ± 0.41 [a]	2.37 ± 0.37 [d]	4
	3	2.36 ± 0.21 [a]	2.10 ± 0.23 [d]	20
B′→C	1	1.79 ± 0.22 [e]	1.59 ± 0.12 [f]	3
	2	1.52 ± 0.13 [e]	2.06 ± 0.47 [f]	4
	3	2.26 ± 0.26	2.05 ± 0.26	20
C→C	1	1.99 ± 0.03	1.07 ± 0.06 [g]	3
	2	1.68 ± 0.03	1.32 ± 0.07 [g]	3
	3	1.93 ± 0.25	1.20 ± 0.32	20
C→D	1	1.96 ± 0.05	0.61 ± 0.07	3
	2	1.45 ± 0.06	0.77 ± 0.14	3
	3	2.26 ± 0.26	0.51 ± 0.11	20
D→B	1	1.07	1.80	1
	2	0.79 ± 0.31	2.05 ± 0.40	3
	3	1.27 ± 0.16	1.80 ± 0.22	15

return from A to B is 1.98 s. This creates a BA grouping rhythm, not AB, with each repeat of the BA group separated by silent intervals 2.5 times longer than the intervals within the group.

The low probability transition from sound A to the double or triple repetition of sound C creates the link to the BCD theme. If the rhythmic structuring is purely articulatory, then the timing between B and B or B and B′ in this second theme would equal that between B and A in the first theme. As shown in Table 1, the timing between sounds B and B or between B and B′ differs from that between B and A. The duration of B in the BA phrase and in the BB′CCD phrase was equal [$F(1,245)=0.001$], comparison a in Table 1, while the duration of the B in the BBCCC phrase was greater [$F(1,104)=10.4$, $p<0.002$] and the whale x duration interaction was nonsignificant [$F(1,104)=0.11$], comparison b. However, this difference was only 13%, 2.41–2.14 s. What is more important here is that the duration of the silent interval between B and B averaged 2.03 s and B and B′ averaged 2.22 s, roughly three times longer than the B to A transition in the first theme [$F(1,104)=225.8$, comparison c, and $F(1,245)=287.4$, comparison d, $p<0.001$ in both cases]. The whale x interval interaction was nonsignificant in both cases [$F(1,104)=0.631$, and $F(2,245)=0.110$], indicating that the difference in the duration of the silent intervals was similar for both whales. Thus, the following sound strongly affects the duration of the silent interval between the sounds.

For whales 1 and 2, differences in the rhythmic structure between phrases BBCCC and BB′CCD further illustrate that the rhythm is a function of the entire phrase. In comparison to the BBCCC phrase, for the BB′CCD phrase, the duration of the final B′ was significantly shorter, 1.66–2.37 s [$F(1,14)=18.9$, $p<0.001$], comparison e; the duration of the silent interval to sound C was significantly longer, 1.82–1.15 s [$F(1,15)=19.8$, $p<0.001$], comparison f, and the duration of the silent interval between the initial C and second C was significantly longer, 1.22–0.86 s [$F(1,18)=4.64$, $p<0.05$], comparison g. In all three comparisons, the whale x interval interaction was nonsignificant [$F(1,15)=4.5$; $F(1,14)=0.99$, $F(1,18)=0.77$], which is evidence that the differences in the durations were equivalent across whales. Regardless of the number of C repeats, the short silent interval among three successive C's or between the second C and D creates a CCC or CCD rhythmic group segmented from the initial double B's. The rhythmic function of sound B changes in the two themes. In the BA theme, B is the initial element in a single BA rhythmic group; in the BCD theme, B (or B′) is set off from the CCC and CCD groups (shown in Fig. 1).

To determine if the rhythmic structure segments themes, we considered sequences such as BB′CCDBB′CCDEDEDE (E is a short upward whistle-like sound). If so, then we might expect the timing to be either (BB′CCDBB′CCD) (EDEDE) or (BB′CCDBB′CC) (DEDEDE) whereby the parentheses indicate thematic breaks and resulting rhythmic groupings. However, this is not the case; the duration of the silent interval between D and E at thematic breaks does not differ from the duration of the silent interval between D and E within a phrase (0.88 ± 0.23 s to 1.23 ± 0.33 s, [$F(1,10)=4.5$, $p>0.05$]) and the silent interval duration between C and D at a break does not differ from the interval between C and D within a phrase (0.54 ± 0.16 s to 0.56 ± 0.13 s, [$F(1,21)=0.953$]).

4. Discussion

The rhythmic structure acts to group the sounds into the phrases and themes that make up the hierarchical humpback whale songs. While the duration of any sound is relatively constant probably due to the articulatory process, the duration of the silent interval between two sounds is strongly affected by the following sound and further affected by the other sounds within the phrase.

A fundamental question is how whales learn the intricate songs that may span at least 150 sound units. One possible explanation is that the rhythmic structuring that occurs within each phrase creates a repeating grouping pattern so that two or three sounds are heard together as a rhythmic unit, separated from other sounds in the phrase that are heard individually. The rhythm provides a set of timed slots, reference points, to which sounds can be attached. In all

cases, the rhythmic structuring makes the phrases more coherent, creating repeating units such as BA, CCC, or CCD that should be easy to sing, remember, repeat, and recognize. The end of a phrase or theme occurs at the end of a rhythmic unit.

It still is unclear why particular rhythmic groups form. At least for these sounds, the similarity between the frequency at the end of one sound and the frequency at the beginning of the next sound does not predict the length of the silent interval. The silent interval for the BA, BB, and BC pairs is independent of frequency separation. If that was the case, then the timing of A and B would be reversed because the ending frequency of A is more similar to the beginning frequency of B than vice versa. Thus, the rhythmic sequencing does not appear to be a function of ease of articulation.

Furthermore, it is unclear how whales organize the song. The sounds, phrases, and themes are not independent units that can be rearranged randomly. Miksis-Olds *et al.* (2008) and Suzuki *et al.*, (2006) showed that an empirical Markov model based on pair-wise sound adjacencies cannot predict the constraint found in the songs. Based on these preliminary results, the rhythmic groupings also are not simply based on pair-wise contingencies. For the BB′CCD and the BBCCC phrases, the timing of sounds B and C is a function of the entire phrase sequence. However, it does not appear that the rhythmic grouping extends beyond the phrase level based on this small set of songs.

In summary, the rhythmic grouping segments the sounds into repeating phrases separated in time that should simplify the production and determine the perception of the entire song. The same sound sequences with different rhythms are different songs.

Acknowledgments

The authors would like to thank Peyton Todd for his thoughtful comments on this article. The recordings were collected under NOAA Permit No. 1039-1699.

References and links

Boersma, P. (**2001**). "Praat, a system for doing phonetics by computer," Glot International **5**, 341–345.
Krumhansl, C. L. (**2000**). "Rhythm and pitch in music," Psychol. Bull. **126**, 159–179.
Mellinger, D. K., and Clark, C. W. (**2006**). "MobySound: A reference archive for studying automatic recognition of marine mammal sounds," Appl. Acoust. **67**, 1226–1242.
Miksis-Olds, J. L., Buck, J. R., Noad, M. J., Cato, D. H., and Stokes, M. D. (**2008**). "Information theory analysis of Australian humpback whale song," J. Acoust. Soc. Am. **124**, 2385–2393.
Payne, K., Tyack, P. L., and Payne, R. S., "Progressive changes in the songs of humpback whales (*Megaptera novaeangliae*): A detailed analysis of two seasons in Hawaii," in *Communication and Behavior of Whales*, edited by R. S. Payne (Westview, Boulder, CO, **1983**), Vol. **76**, pp. 9–58.
Payne, R. S., and McVay, S. (**1971**). "Songs of humpback whales," Science **173**, 585–597.
Suzuki, R., Buck, J. R., and Tyack, P. L. (**2006**). "Information entropy of humpback whale songs," J. Acoust. Soc. Am. **119**, 1849–1866.

A note on the effects of roughness on acoustic propagation past curved rough surfaces

Andrew Whelan
6B J Alsobrooks Dr., Carriere, Mississippi 39426
andrew.whelan83@gmail.com

James P. Chambers
National Center for Physical Acoustics, University of Mississippi, University, Mississippi 38677-1848
chambers@olemiss.edu

Abstract: Previous work on sound propagation past curved rough rigid surfaces demonstrated substantial changes in the insertion loss in the shadow zone due to the roughness ranging from +6 to −20 dB from their smooth counterparts. These previous data also lead to new propagation modeling efforts to incorporate the effects of roughness via an impedance model but the data and modeling efforts were limited to a narrow range of roughness and hill sizes. The current effort was designed to expand the range of roughness and hill sizes in order to explore the range of influence of the roughness. The work presented here confirms the effects of surface roughness as observed in previous work and indicates where the effects of roughness begin to emerge as well as where they transition between decreasing the insertion loss to increasing the insertion loss.

PACS numbers: 43.28.Fp, 43.20.Fn [VO]
Date Received: March 16, 2009 **Date Accepted:** April 11, 2009

1. Introduction

Acoustic detection systems offer the prospect of long range and non line of site detection and monitoring of targets or events such as tanks, cruise missiles, nuclear explosions, or chemical-biological weapons, which may be difficult to detect by other methods. In order to fully exploit acoustic signals, however, more work is needed to understand their propagation over realistic terrain. Much work has progressed on propagation past individual terrain features such as a barrier, a hill, or an earthen berm.[1] Similarly, work has progressed on propagation over rough but nominally flat surfaces[2,3] including attempts to model roughness as an effective impedance.[4–9] Less has been done on the combination of large scale and small scale terrain features such as roughness on a hill, which is the basis for the current work. Preliminary work in this area[7] indicated the presence of a so called creeping boundary wave that penetrated into the shadow zone of the curved rough surface increasing sound levels relative to an equivalent smooth surface at lower frequencies. At higher frequencies the effect of the roughness was to decrease sound levels. The effect was able to be modeled by means of treating the roughness as an effective impedance,[10] which should help propagation modeling efforts, but this initial work was for a limited range of frequency, roughness sizes, and radius of curvature. More recent work[11,12] has investigated an expanded range of frequency, roughness sizes, and radius of curvature and is the basis of the manuscript. While this effort is nominally directed at outdoor sound propagation, the scale model work reported here was conducted indoors to eliminate the complicating factors of meteorology, which will surely impact the results and ultimately needs to be incorporated into any realistic propagation scheme.

2. Experimental arrangement

A sketch of the geometry of the experimental arrangement is shown in Fig. 1. Data were recorded in the shadow zone, along the line of sight and along a vertical that traversed from the

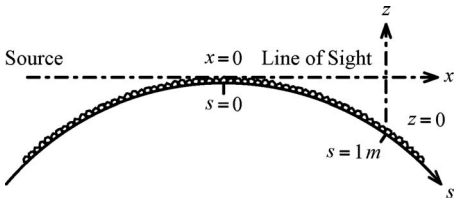

Fig. 1. Geometry of the problem.

shadow into the bright zone behind the hill. The source was elevated above the ground and could represent a source such as a helicopter or cruise missile. Data were collected at frequencies ranging from 2 to 20 kHz over curved surfaces with radii of curvature that ranged from 1.25 to 10 m. Four surface types, in order of increasing roughness size, were considered: (1) smooth varnished plywood, (2) sheets of Plexiglas light diffusers used in overhead lighting, (3) small ($\sim 1/4$ in.) pea gravel (small gravel), and (4) larger ($\sim 1/2$ in.) gravel (large gravel). The roughness metric of interest is the nondimensional roughness length scale $k\varepsilon$ where k is the acoustic wavenumber and ε is the roughness length parameter discussed originally by Tolstoy and Medwin, and more recently by Chambers and co-workers.[2–6,8–10] The roughness length parameter, ε, incorporates the mean height, rms height, and correlation length of boss such as protuberances embedded in an otherwise smooth surface. The mean height, standard deviation in height, and correlation length were determined by tracing the roughness profile onto a sheet of paper, which was scanned and digitized into a computer for analysis. These parameters yielded roughness values[2] for ε of 0.08, 0.9, and 2.0 mm for the plex, small gravel, and large gravel surfaces, respectively. This in turn provided roughness values of $k\varepsilon$ from 0.003 to 0.73. The topography size kR, with R being the radius of curvature of the hill, ranged from 44 to 3661 as shown in Table 1. It should be noted that the previous work of Refs. 7 and 10 incorporated a narrower range of surface features of $k\varepsilon$ from 0.09 to 0.22 and kR from 228 to 549.

The quantity of interest for comparative purposes is the insertion loss. Mathematically it is posed as

$$\mathrm{IL} = -20\log_{10}\frac{|P_{\mathrm{curved}}|}{P_{\mathrm{free\ field}}} = L_p(\mathrm{w/o\ \ hill}) - L_p(\mathrm{w/hill}), \tag{1}$$

where P_{curved} represents the sound pressure in the presence of the curved surface, $P_{\mathrm{free\ field}}$ represents the sound pressure in the absence of the curved surface, and L_p represents the sound

Table 1. Values of roughness scale and curvature used.

	f (Hz)						
	2000	3000	5000	8000	10 000	12 000	20 000
ε (mm)	$k\varepsilon$						
0.08	0.0029	0.0044	0.0073	0.012	0.015	0.02	0.03
0.90	0.033	0.049	0.082	0.13	0.16	0.20	0.33
2.00	0.07	0.11	0.18	0.29	0.37	0.44	0.73
R (m)	kR						
1.25	45.8	68.7	114.4	183.1	228.9	274.6	457.7
2.50	91.5	137.3	228.9	366.2	457.7	549.3	915.5
5.00	183.1	274.6	457.7	732.4	915.5	1 098.5	1 830.9
10.00	366.2	549.3	915.5	1464.7	1 830.9	2 197.1	3 661.8

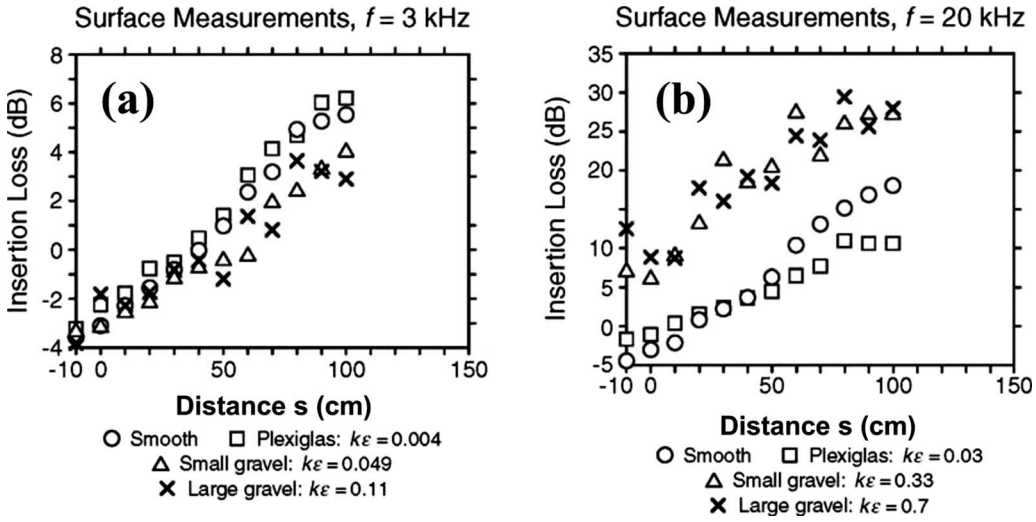

Fig. 2. Insertion loss along the surface in the shadow zone with $R=2.5$ m and (a) $f=3$ kHz and (b) $f=20$ kHz.

pressure level in decibels. Physically, the insertion loss represents the loss (or gain for IL <0) associated with the presence of the curved surface.

For these experiments, the peak to peak amplitude of the sound (tone burst) was measured at a point on or near the curved surface and compared to the sound that would have existed in the absence of the curved surface at the same point. This reference sound level was determined from a signal that was measured before the experiment and away from the surface. This reference signal was measured at 1 m and was then spherically corrected for each receiver position. The ratio of the signal in the field to the signal that would have existed in free space was used to determine the insertion loss via Eq. (1) where P_{curved} represents either the curved smooth surface or the curved rough surface.

Measurements were made along the surface, s, from a point 10 cm on the bright side of the apex, past the apex, and 1 m deep into the shadow zone as depicted in Fig. 1. Data for $f=3$ and 20 kHz are presented in Figs. 2(a) and 2(b) where 0 cm represents the apex and positive values of s are in the shadow zone and along the surface. As seen in Fig. 2(a), at low frequencies and small roughness ($k\varepsilon=0.004$ for the Plexiglas), there is little difference between propagation past a smooth surface and rough one. At more modest roughness sizes ($k\varepsilon=0.049-0.11$ for the two gravel sizes) there is a noted decrease in the insertion loss (added sound) of 2–3 dB. At the higher frequency shown in Fig. 2(b) one can observe a 6–7 dB decrease in the insertion loss for the small roughness whose nondimensional roughness size is now $k\varepsilon=0.03$. For the larger roughnesses, ($k\varepsilon=0.33-0.73$) one can observe an increase in the insertion loss of approximately 10 dB. This trend persisted across the data sets with no noticeable effect for extremely small roughnesses ($k\varepsilon<0.01$), a decrease in the insertion loss for small to modest roughness sizes ($0.01<k\varepsilon<0.1$), and an increase in the insertion loss for $k\varepsilon>0.2$. The decrease in insertion loss (added sound) is attributed to a creeping boundary wave[7] that penetrates into the shadow zone. It is analogous to a surface wave above a porous surface. The increase in insertion loss is attributed to incoherent scattering. The region $0.1<k\varepsilon<0.2$ represents a transition zone with a lower insertion loss in the deep portion of the shadow zone and a higher insertion loss near the apex. The data for this region, as well as a more complete review of all the data, can be found in Refs. 11 and 12.

A different view of the phenomena can be made looking at data along a vertical slice, z, across the shadow zone as depicted in Figs. 3(a) and 3(b) for $f=3$ and 10 kHz. The abscissa is the z axis as seen in Fig. 1 with 0 cm being on the surface at $s=1$ m deep in the shadow zone and extending into the bright zone. In Fig. 3(a), one can see a negligible difference in the inser-

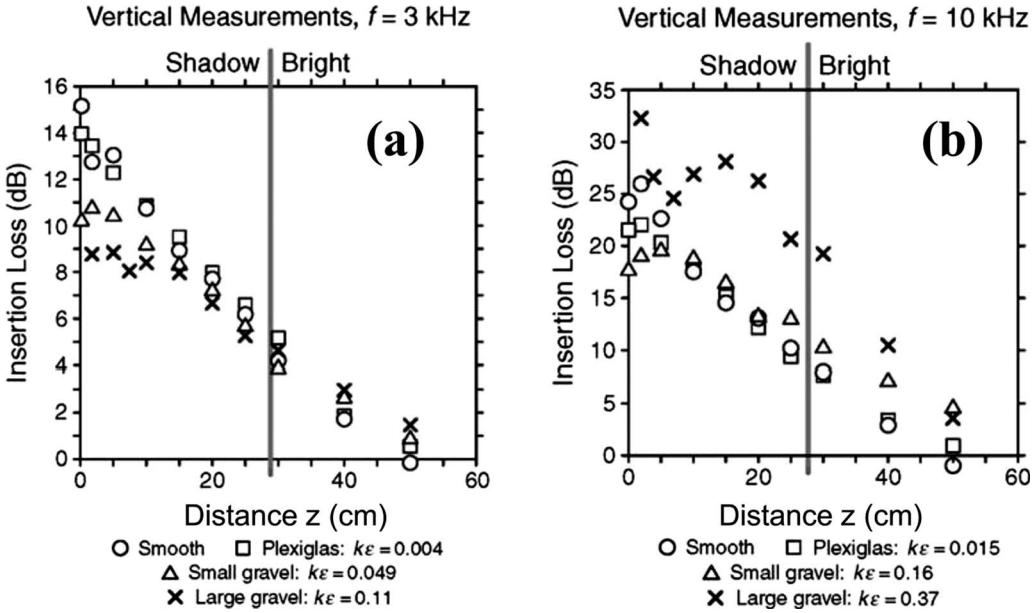

Fig. 3. Insertion loss along a vertical segment staring 1 m deep in the shadow zone with $R=1.25$ m and (a) $f=3$ kHz and (b) $f=10$ kHz.

tion loss between smooth and Plexiglas roughness surfaces ($k\varepsilon=0.004$). There is a 4 dB decrease in the small gravel surface ($k\varepsilon=0.049$) and a 5 dB decrease in the large gravel surface ($k\varepsilon=0.11$). This difference is confined near the surface as one might expect for a boundary/surface wave. At the higher frequency reported in Fig. 3(b), one can note a 2–3 dB decrease in the insertion loss for the Plexiglas ($k\varepsilon=0.015$), a 7–8 dB decrease in the small gravel ($k\varepsilon=0.16$), and a 5–10 dB increase in the insertion loss for the large gravel ($k\varepsilon=0.37$). The increase in the large gravel crosses the entire shadow and bright zone while the decrease in insertion loss for the Plexiglas and small gravel is mostly contained near the surface.

3. Conclusions

The work presented here confirms and expands on the effects of surface roughness as observed in previous work. For a sufficiently small roughness or low frequency ($k\varepsilon<0.01$) there is little effect as would be expected from common sense. If the roughness is small enough the surface appears smooth. As the roughness size or frequency is increased ($0.01<k\varepsilon<0.1$) there is a decrease in the insertion loss (increased sound level) as compared to a smooth surface near the surface boundary and in the deep shadow zone. As the roughness size or frequency is further increased ($k\varepsilon>0.2$) the insertion loss is higher than that for the smooth surface at all locations observed in the shadow zone. The region $0.1<k\varepsilon<0.2$ is a transition zone with decreased insertion loss (added sound) in the deep shadow zone and higher insertion loss in the bright zone. In addition, for most of the data, and even for $k\varepsilon>0.2$ where the insertion loss on rough surfaces is higher than on smooth surfaces, the insertion loss at the surface of the rough surface is often lower than just above the surface suggesting some type of ducted boundary effect such as a surface wave.

Acknowledgments

This work was supported by the corporate and computing center (Dr. Sandra Collier) under the auspices of the U.S. Army Research Office Scientific Services Program administered by Battelle (Delivery Order 327, Contract No. DAAD 19-02-D-0001).

References and links

[1]A. Berry and G. A. Daigle, "Controlled experiments on the diffraction of sound by a curved surface," J. Acoust. Soc. Am. **83**, 2047–2058 (1988).
[2]H. Medwin and G. D'Spain, "Near-grazing, low frequency propagation over randomly rough rigid surfaces," J. Acoust. Soc. Am. **79**, 657–665 (1986).
[3]I. Tolstoy, "The scattering of spherical pulses by slightly rough surfaces," J. Acoust. Soc. Am. **66**, 1135–1144 (1979).
[4]K. Attenborough and S. Taherzadeh, "Propagation from a point source over a rough finite impedance boundary," J. Acoust. Soc. Am. **98**, 1717–1722 (1995).
[5]J. P. Chambers, R. Raspet, J. M. Sabatier, and Y. H. Berthelot, "Incorporating the effects of roughness in outdoor sound propagation models," *Proceedings of the 1996 National Conference on Noise Control Engineering*, pp. 905–910 (1996).
[6]Y. H. Berthelot and J. P. Chambers, "On the analogy between sound propagation over a rough surface and sound propagation over a smooth surface with modified surface impedance," Proceedings of the Sixth Long Range Sound Propagation Symposia (1996).
[7]J. P. Chambers and Y. H. Berthelot, "An experimental investigation of the propagation of sound over a curved, rough, rigid surface," J. Acoust. Soc. Am. **102**, 707–714 (1997).
[8]P. Boulanger, K. Attenborough, and Q. Qin, "Effective impedance of surfaces with porous roughness: Models and data," J. Acoust. Soc. Am. **117**, 1146–1156 (2005).
[9]P. Boulanger, K. Attenborough, Q. Qin, and C. M. Linton, "Reflection of sound from random distributions of semi-cylinders on a hard plane: Models and data," J. Phys. D **38**, 3480–3490 (2005).
[10]J. P. Chambers and Y. H. Berthelot, "Utilizing a modified impedance analogy on sound propagation past a hard curved rough surface," J. Acoust. Soc. Am. **120**, 1186–1189 (2006).
[11]A. W. Whelan, "Examination on the diffraction and scattering of sound by curved, rough surfaces and experimental analysis into propagation around a spherical berm," MS thesis, University of Mississippi, University, MS (2007).
[12]A. W. Whelan and J. P. Chambers "An investigation of the effects of roughness on acoustic propagation past curved surfaces," Proceedings of the 12th International Long Range Sound Propagation Symposia (2008).

 [DOI: 10.1121/1.3129304] Published Online 14 May 2009

The use of fundamental frequency for lexical segmentation in listeners with cochlear implants

Stephanie Spitzer, Julie Liss, Tony Spahr, Michael Dorman, and Kaitlin Lansford
Department of Speech and Hearing Science, Arizona State University, P.O. Box 870102, Tempe, Arizona 85287-0102
spitzer@asu.edu, julie.liss@asu.edu, tony.spahr@asu.edu, michael.dorman@asu.edu, kaitlin.lansford@asu.edu

Abstract: Fundamental frequency (F0) variation is one of a number of acoustic cues normal hearing listeners use for guiding lexical segmentation of degraded speech. This study examined whether F0 contour facilitates lexical segmentation by listeners fitted with cochlear implants (CIs). Lexical boundary error patterns elicited under unaltered and flattened F0 conditions were compared across three groups: listeners with conventional CI, listeners with CI and preserved low-frequency acoustic hearing, and normal hearing listeners subjected to CI simulations. Results indicate that all groups attended to syllabic stress cues to guide lexical segmentation, and that F0 contours facilitated performance for listeners with low-frequency hearing.

PACS numbers: 43.71.Ky, 43.71.An [JH]
Date Received: January 30, 2009 **Date Accepted:** March 23, 2009

1. Introduction

Many studies have demonstrated a benefit to speech understanding when the electric stimulation provided by a cochlear implant (CI) is complemented by preserved low-frequency acoustic hearing (e.g., Ching *et al.*, 2004; Dorman *et al.*, 2008; Gantz and Turner, 2004; Kiefer *et al.*, 2004; Tyler *et al.*, 2002; von Ilberg *et al.*, 1999). It has been hypothesized that the availability of this low-frequency information allows for, among other things, higher quality fundamental frequency (F0) representation than when stimulation is wholly electric (Brown and Bacon, 2009; Chang *et al.*, 2006; Kong *et al.*, 2005; Qin and Oxenham, 2006; Turner *et al.*, 2004). On this view, access to the F0 contour may facilitate tracking of the speech signal, which leads to better speech intelligibility, especially in noise.

The present investigation examined the hypothesis that the presence of the F0 contour improves performance specifically by allowing a listener to better segment the acoustic stream into its component words. This task of lexical segmentation is central to speech understanding. Although it is conducted seemingly effortlessly in most listening situations, parsing speech that is degraded or unreliable requires attention to prosodic contrasts, including variations in vowel and syllable durations, F0, amplitude, and vowel quality (Cutler and Butterfield, 1992). In English and other so-called "stress-timed" languages, listeners tend to treat strong (stressed) syllables as word-onsets, a strategy that is effective because of the statistical probabilities of English in which most words begin with stressed syllables (Cutler and Carter, 1987). This strategy is particularly important when the speech signal is impoverished and the words cannot be immediately recognized in the acoustic stream (Liss *et al.*, 1998; Liss *et al.*, 2002; Mattys, 2004; Mattys *et al.*, 2005). Further, it has been demonstrated that normal hearing (NH) listeners flexibly use all available acoustic cues to syllabic stress, but that reductions in F0 variation are especially detrimental to the task of lexical segmentation of degraded speech (Spitzer *et al.*, 2007). If the performance benefit accrued from the presence of low-frequency information is due to improved F0 representation as a cue for lexical segmentation decisions, this will be apparent in the patterns of lexical boundary errors (LBEs) that are elicited when F0 is present and when it is not. Specifically, the proportion of predicted error types (e.g., erroneously inserting a lexical boundary before a strong syllable than before a weak syllable) should be greater when F0 contour information is available than when it is not.

The purpose of the present study was to determine whether acoustic F0 contour information is used to facilitate lexical segmentation by listeners fitted with CIs and a group of NH controls subjected to CI simulations. We examined two groups of CI listeners, with different capacities for representing low-frequency information: those with CIs, and those with implants and residual low-frequency acoustic hearing in the ear opposite the implant (EAS). All participants transcribed utterances in which the F0 contour was either unaltered (normal) or flattened. Participants with capabilities for low-frequency hearing (NH and EAS) transcribed these unaltered and flattened F0 phrases in an electric-only condition (a proxy for traditional CI, in which they were not provided with low-frequency acoustic information) and in an electric-acoustic condition (in which low-frequency acoustic information also was provided). It was hypothesized that F0 flattening would reduce the listeners' ability to discern strong and weak syllables for the purposes of lexical segmentation in all conditions in which F0 could be sufficiently represented. We predicted that, because F0 representation in the electric-only condition would be poor, F0 flattening would have little effect on the proportion of predicted versus nonpredicted LBEs in this condition for all three listener groups. However, EAS and NH listeners should show detrimental effects of F0 flattening in the electric-acoustic condition, with lower predicted-to-nonpredicted LBE ratios than would be elicited in the unaltered F0 condition. This finding would confirm the listeners' use of F0 variation for lexical segmentation, and provide a *source* of the intelligibility benefit associated with the presence of low-frequency hearing.

2. Method

2.1 Participants

Twelve listeners with CIs and ten NH listeners participated in this study. Six of the CI patients had conventional cochlear implants (CI). The other six possessed residual low-frequency hearing in the non-implanted ear (EAS). The averaged hearing thresholds obtained from the non-implanted ears of EAS subjects revealed a steeply sloping sensori-neural hearing loss, with thresholds of 30 dB hearing loss (HL) through 250 Hz, and 70 dB HL by 750 Hz. Only two conventional CI listeners had measurable auditory thresholds from the non-implanted ear of less than 115 dB sound pressure level (SPL). One had audiometric thresholds of 85 dB SPL at 250 Hz, and 115 dB SPL at 500 Hz. The other had a flat, severe sensori-neural hearing loss from 250 to 8000 Hz, and an earplug was used to attenuate any audible low-frequency information for this listener.

2.2 Speech stimuli

Eighty phrases were developed for LBE analysis in previous investigations (see Liss *et al.*, 1998 for details). Briefly, they each consisted of six syllables (three to five words) that alternated in syllabic stress (iambic or trochaic). A male speaker produced high fidelity digital recordings of the phrases. These phrases were presented to all listeners in normal (unaltered) F0 and F0-flattened conditions. F0 flattening was achieved by calculating the mean F0 (Hz) of each digitized phrase using the *pitch contour* function in Computerized Speech Laboratory (Computerized-Speech Lab (CSL), 2004). The F0 contour was then flattened to this mean value using the numerical editor function in Analysis Synthesis Laboratory (2004); see Spitzer *et al.*, 2007 for details. The F0-flattened phrases were perceptually monotonous, with no perceptible distortion.

CI simulations for the NH listeners were achieved by processing the phrases through a 15-channel vocoder (Litvak *et al.*, 2007). Acoustic information from 350–5600 Hz was divided into 15 logarithmically spaced analysis bands. The energy in each band was used to modulate the amplitude of 15 spectrally-shaped noise bands. The center frequency of each output was equal to the center frequency of the corresponding analysis band. All outputs had a spectral peak at the center frequency and rolled off at a rate of 30 dB/octave from center. The manipulation was intended to simulate the perceptual experience of listeners fitted with CIs.

Table 1. Examples of the four possible categories of LBEs, based on type (insertion or deletion) and location (before strong or weak syllables). The bolded text [insertions before strong (IS) and deletions before weak (DW)] are the categories predicted by the metrical segmentation strategy hypothesis (Cutler and Butterfield, 1992).

LBE	Before a strong syllable	Before a weak syllable
Insertion	**Target: "account for who could knock"** **Response: "he got so he could knock"**	"its harmful note abounds" "its hard to know abounds"
Deletion	Target: "and spoke behind her sin" Response: "and spoke behind person"	**"push her equal culture"** **"pressure equal culture"**

2.3 Procedures

Because of the different hearing modes among the three participant groups, data collection procedures varied accordingly. The phrases were presented in a free field or under headphone (distinctions described below) in a sound attenuated booth. Presentation amplitudes, regardless of mode, were set at a comfortable listening level (65 dB SPL). Phrases were presented one time each, without the opportunity for replay, using the ALVIN software program (Hillenbrand and Gayvert, 2005). Listeners were instructed to use the computer keyboard to type exactly what they heard, and they did not receive feedback about their response accuracy. Phrases were presented in blocks of 20.

All listeners transcribed blocks of unaltered and F0-flattened phrases. For the NH and EAS listeners, these were transcribed in both an electric-only condition and in an electric-acoustic condition. Obviously, it was not possible for the conventional CI participants to receive the latter condition.

In the electric-only condition, phrases were presented via loudspeaker to the implanted ear. A standard foam earplug was used to attenuate the signal in the non-implanted ear for the EAS participants (see Gifford *et al.*, 2008). CI simulated signals were presented to the NH listeners at the left ear via headphones.

In the electric-acoustic condition, phrases were presented free field to the EAS listeners. The NH listeners received the CI simulated phrases to the left ear to simulate electric hearing. The right ear received phrases that had been passed through a low-pass filter with a cutoff frequency of 500 Hz (sixth order Butterworth) to simulate residual low-frequency hearing.

2.4 Analysis

Listener transcripts were coded independently by two judges proficient in LBE analysis. As per standard consensus procedures, codes were compared and discrepancies were either resolved or omitted from the analysis (see Liss *et al.*, 2002 for details). Dependent variables included the total number of LBEs committed, and the type (insertion or deletion) and location (before strong or weak syllables) of LBEs. Thus, errors could be of one of four types: lexical boundary insertion or deletion occurring either before a strong or weak syllable (IS, IW, DS, and DW). Examples of each type are provided in Table 1. Based on predictions generated from the metrical segmentation strategy hypothesis (Cutler and Carter, 1987), if listeners attend to syllabic stress to segment the speech stream, they will be most likely to erroneously insert lexical boundaries before strong syllables (i.e., treat a strong syllable as a word-onset), and erroneously delete lexical boundaries before weak syllables (i.e., treat a weak syllable as the second, or greater, syllable of a word). Thus, IS and DW errors are of the predicted type. Ratios of predicted error types also were calculated (IS+DW/total errors); higher ratios indicate greater reliance on—and quality of—syllabic stress information to segment the phrases.

Pearson chi-square analyses were conducted to determine if LBEs were distributed differently across type (insertion/deletion) and location (before strong/weak syllables) within each of the pools of LBEs. Additional chi-square analyses were conducted to identify differences in distributions between unaltered and F0-flattened LBE pools within condition, whereby

Table 2. Performance values for all listener groups across listening conditions (electric-only or electric-acoustic) with unaltered or F0-flattened phrases. Data columns contain mean intelligibility (% words correct and standard error), the proportions of types of LBEs (insertions or deletions, before strong or before weak syllables), and the total number of LBEs per condition. The final two columns contain *p*-values for the χ^2 analyses conducted on each condition LBE pool, and differences between distributions derived from F0-flattened stimuli relative to unaltered for each condition.

Groups	Condition	Phrases	% words correct (SE)	% IS	% IW	% DS	% DW	Total LBE	($\chi^2 df=1$) *p*-value	($\chi^2 df=3$) *p*-value
EAS *N*=6	E-only	F0-flat	32 (4.3)	33	21	16	30	82	0.003	0.000
	E-only	Unaltered	4 (3.1)	51	9	14	26	78	0.000	
	E-A	F0-flat	50 (2.4)	52	25	10	13	63	0.03	0.000
	E-A	Unaltered	56 (3.2)	57	9	16	18	56	0.002	
CI *N*=6	E-only	F0-flat	25 (6.5)	49	20	10	21	72	0.000	0.08
	E-only	Unaltered	34 (6.5)	59	13	7	21	55	0.000	
NHL *N*=10	E-only	F0-flat	40 (3.7)	38	17	13	32	121	0.000	0.03
	E-only	Unaltered	43 (2.3)	46	9	15	30	134	0.000	
	E-A	F0-flat	48 (2.4)	45	28	10	17	109	0.03	0.000
	E-A	Unaltered	68 (3.5)	60	7	5	28	60	0.000	

the proportions of errors elicited by F0-*unaltered* were treated as the expected cell values, and the F0-*flattened* were the observed cell values. Significant differences were regarded as a rejection of the null hypothesis that the values were sampled from the same distribution. A *p*-value of 0.05 was selected for all analyses.

3. Results and discussion

Table 2 contains the group performance data across conditions, as well as the results of the chi-square analyses. The first novel observation is that all groups in all conditions produced patterns of LBEs that align with the metrical segmentation strategy for predicted errors, with ten significant chi-square tests confirming differential distributions across LBE type and location. In all cases, insertions errors occurred more frequently before strong than before weak syllables; and deletion errors occurred more often before weak than before strong. This is further exemplified in Fig. 1, which shows the total proportions of predicted LBEs across groups and conditions. The ratio values on the ordinate range from 0.5 (reflecting instances in which predicted and nonpredicted errors occur equally often) to a value of 1 (in which all errors are of the predicted type). This figure is important in showing that all values exceeded 0.5, which is consistent with the explanation that listeners attended to available syllabic stress cues to guide lexical segmentation, even when F0 was not among those cues. These cues likely include variations in syllable durations, dispersion of vowel formant frequencies, and amplitude envelope modulations. Thus, as for NH listeners, those fitted with CI appear to rely on syllabic stress cues for lexical segmentation and to flexibly use the cues that are available and reliable to accomplish this task.

All groups showed evidence of attending to syllabic stress, but the primary question of this study is whether the flattening of F0 made a difference in LBE distributions. The relative heights of the bars in Fig. 1 suggest this to be the case for all conditions. Recall that we expected to see differences *only* in instances in which F0 was adequately represented. Returning to the final column of Table 2, we see the chi-square results of pitting the F0-flattened LBE distributions against those generated by the unaltered phrases. As predicted, these distributions were not different for the CI group, and they were different for the EAS and NH in the electric-acoustic condition. However, we also see that the F0 flattening served to significantly reduce adherence

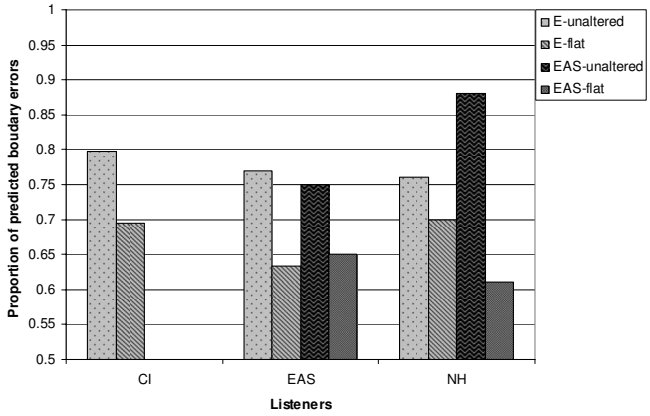

Fig. 1. Proportion of total LBEs that are of the predicted type (IS+DW/total LBE). The data are presented by listener group (CI, EAS, and NH listeners) and condition. The conditions include electric-only and electric-acoustic (EAS), in both the unaltered and F0-flattened conditions.

to the predicted error patterns for the EAS and NH groups in the electric-only condition as well. A likely explanation is that the electric-only condition did not effectively eliminate low-frequency and F0 information for these listeners who were capable of processing it. However, it also is of interest that, even though insignificant, the CI listeners showed the tendency for lower adherence to the predicted LBE patterns in the F0-flattened condition. It will be important to explore the possibility that even poorly represented F0 contour information can facilitate lexical segmentation.

These patterns of results support the hypothesis that syllabic stress information is exploited by listeners with CIs for the purposes of lexical segmentation, in much the same way that NH listeners deal with the CI simulation. Further, the presence of an F0 contour was shown to facilitate lexical segmentation decisions in EAS listeners, and this thereby points to a specific source of perceptual benefit afforded by the presence of low-frequency hearing.

4. Conclusion

Listeners fitted with CI appear to behave much like NH listeners in the deciphering of degraded speech in that they attend to syllabic stress cues to guide lexical segmentation. The present investigation provides evidence for the informative role of F0 as one of these cues. Specifically, F0 variation appears to be used, to the extent possible, to mark strong and weak syllables for the purposes of lexical segmentation. The data also provide preliminary support for the hypothesis that at least some of the performance benefit enjoyed by EAS listeners may be traceable to the availability of a high resolution F0 contour for facilitating lexical segmentation.

Acknowledgments

This research was supported by NIH Grant Nos. 5R01 DC6859 (J.L.) and R01 DC00654-18 (M.D.) from the National Institute on Deafness and Other Communication Disorders, and by a grant from Advanced Bionics Corp. (T.S.).

References and links

Analysis Synthesis Laboratory (**2004**). Software (KayPentax, NJ).

Brown, C. A., and Bacon, S. P. (**2009**). "Low-frequency speech cues and simulated electric-acoustic hearing," J. Acoust. Soc. Am. **125**, 1658–1665.

Chang, J. E., Bai, J. Y., and Zeng, F. G. (**2006**). "Unintelligible low-frequency sound enhances simulated cochlear-implant speech recognition in noise," IEEE Trans. Biomed. Eng. **53**, 2598–2601.

Ching, T. Y., Incerti, P., and Hill, M. (**2004**). "Binaural benefits for adults who use hearing aids and cochlear implants in opposite ears," Ear Hear. **25**, 9–21.

Computerized-Speech Lab (CSL) (**2004**). computer hardware (KayPentax, NJ).

Cutler, A., and Butterfield, S. (**1992**). "Rhythmic cues to speech segmentation: Evidence from juncture

misperception," J. Mem. Lang. **31**, 218–236.
Cutler, A., and Carter, D. M. (**1987**). "The predominance of strong syllables in the English vocabulary," Comput. Speech Lang. **2**, 133–142.
Dorman, M. F., Gifford, R., Spahr, A. J., and McKarns, S. (**2008**). "The benefits of combining acoustic and electric stimulation for the recognition of speech, voice and melodies," Audiol. Neuro-Otol. **13**, 105–112.
Gantz, B. J., and Turner, C. (**2004**). "Combining acoustic and electrical speech processing: Iowa/nucleus hybrid implant," Acta Oto-Laryngol. **124**, 344–347.
Gifford, R., Dorman, M., Spahr, A., Bacon, S., Skarzynski, H., and Lorens, A. (**2008**). "Hearing preservation surgery: Psychophysical estimates of cochlear damage in recipients of a short electrode array," J. Acoust. Soc. Am. **124**, 2164–2173.
Hillenbrand, J. M., and Gayvert, R. T. (**2005**). "Open source software for experimental design and control," J. Speech Lang. Hear. Res. **48**, 45–60.
Kiefer, J., Gstöettner, W., Baumgartner, W., Pok, S. M., Tillein, J., Ye, Q., and Von Ilberg, C. (**2004**). "Conservation of low-frequency hearing in cochlear implantation," Acta Oto-Laryngol. **124**, 272–280.
Kong, Y. Y., Stickney, G. S., and Zeng, F. G. (**2005**). "Speech and melody recognition in binaurally combined acoustic and electric hearing," J. Acoust. Soc. Am. **117**, 1351–1361.
Liss, J. M., Spitzer, S. M., Caviness, J. N., and Adler, C. (**2002**). "The effects of familiarization on intelligibility and lexical segmentation of hypokinetic and ataxic dysarthria," J. Acoust. Soc. Am. **112**, 3022–3031.
Liss, J. M., Spitzer, S. M., Caviness, J. N., Adler, C., and Edwards, B. W. (**1998**). "Syllabic strength and lexical boundary decisions in the perception of hypokinetic dysarthric speech," J. Acoust. Soc. Am. **104**, 2457–2466.
Litvak, L. M., Spahr, A. J., Saoji, A. A., and Fridman, G. Y. (**2007**). "Relationship between perception of spectral ripple and speech recognition in cochlear implant and vocoder listeners," J. Acoust. Soc. Am. **122**, 982–991.
Mattys, S. L. (**2004**). "Stress versus coarticulation: Towards an integrated approach to explicit speech segmentation," J. Exp. Psychol. Hum. Percept. Perform. **30**, 397–408.
Mattys, S. L., White, L., and Melhorn, J. F. (**2005**). "Integration of multiple segmentation cues: A hierarchical framework," J. Exp. Psychol. Gen. **134**, 477–500.
Qin, M. K., and Oxenham, A. J. (**2006**). "Effects of introducing unprocessed low-frequency information on the reception of envelope-vocoder processed speech," J. Acoust. Soc. Am. **119**, 2417–2426.
Spitzer, S. M., Liss, J. L., and Mattys, S. L. (**2007**). "Acoustic cues to lexical segmentation: A study of resynthesized speech," J. Acoust. Soc. Am. **122**, 3678–3687.
Turner, C. W., Gantz, B. J., Vidal, C., Behrens, A., and Henry, B. A. (**2004**). "Speech recognition in noise for cochlear implant listeners: Benefits of residual acoustic hearing," J. Acoust. Soc. Am. **115**, 1729–1735.
Tyler, R. S., Parkinson, A. J., Wilson, B. S., Witt, S., Preece, J. P., and Noble, W. (**2002**). "Patients utilizing a hearing aid and a cochlear implant: Speech perception and localization," Ear Hear. **23**, 98–105.
von Ilberg, C., Kiefer, J., Tillein, J., Pfenningdorff, T., Hartmann, R., Sturzebecker, E., and Klinke, R. (**1999**). "Electric-acoustic stimulation of the auditory system," ORL **61**, 334–340.

Rough surface scattering in a Born approximation from a two-way coupled-mode formalism

Steven A. Stotts and Robert A. Koch
Applied Research Laboratories, The University of Texas at Austin, P.O. Box 8029, Austin, Texas 78713-8029
stotts@arlut.utexas.edu, koch@arlut.utexas.edu

Abstract: Scattering from a rough surface in an ocean waveguide is described in a new derivation from a two-way coupled-mode representation. The general formalism, which contains scattering effects to all orders, is truncated to the first-order terms of an iterative (Born) expansion. Both two- and three-dimensional ocean waveguide geometries are discussed. By reducing the mode functions in terms of plane wave reflection coefficients, the off-diagonal components of the scattering kernel that is derived are shown to be consistent with a standard solution, but the diagonal components are different from the standard solution.

PACS numbers: 43.30.Bp, 43.30.Gv, 43.30.Hw, 43.20.Mv [JL]
Date Received: December 18, 2008 **Date Accepted:** March 19, 2009

1. Introduction

A two-way coupled-mode fomulation[1–3] is demonstrated to produce a kernel that describes the scattering from rough interfaces in ocean waveguides.[4,5] This approach to deriving the scattering kernel is new. A Born approximation solution of the coupled-mode equations to lowest order in the mean square roughness characterizes the scattering. The purpose of this paper is to discuss the details of this derivation beginning with the general solution to the two-way mode coupling equation and proceeding to the scattering kernel in the Born approximation. This work is motivated by recent workshops on reverberation modeling[6] in which issues concerning the representation and accuracy of the Born approximation have been examined with several models. The basic set of workshop problems was horizontally stratified environments in two- and three-dimensions with various scattering kernels for surface and/or bottom interfaces.

2. Coupled-mode formalism

In this section the formalism defined in Refs. 1–3 is used to derive the scattered field. The important steps to deriving the scattering kernel for both two- and three-dimensions are presented, beginning with the exact coupled-mode formalism.

The total pressure field $p(\boldsymbol{r},z,\omega)$ for an acoustic source in a fluid medium at a single frequency in $D=2$ or $D=3$ dimensions is given by the solution to the equation

$$\left[\nabla_{\boldsymbol{r}}^2+\frac{\partial^2}{\partial z^2}+k^2(\boldsymbol{r},z)\right]p=-QS(\omega)\,\delta(\boldsymbol{r}-\boldsymbol{r}_s)\,\delta(z-z_s), \tag{1}$$

where $Q\equiv Q_0|p_0|$ makes explicit the reference pressure amplitude $|p_0|$, typically 1 μPa, at reference range r_0, typically 1 m, for the source spectrum $S(\omega)$ relative to a point source in an infinite medium, i.e.,

$$Q_0 = \begin{cases} \dfrac{4}{|H_0^{(1)}(k_s r_0)|}, & D=2 \\ 4\pi r_0, & D=3. \end{cases} \tag{2}$$

In Eq. (1), the source is located at $(\boldsymbol{r}_s, z_s)$. The wavenumber is $k_s = \omega/c_s$, where the sound speed c_s and density ρ_s are the values at the source depth. The Fourier transform convention is $s(t) = (1/2\pi)\int_{-\infty}^{\infty} S(\omega) e^{-i\omega t} d\omega$. The solution $p = QS(\omega)G$ to Eq. (1) is obtained with the Green's function $G(\boldsymbol{r}, z, \boldsymbol{r}_s, z_s, \omega)$ given by

$$\left[\nabla_{\boldsymbol{r}}^2 + \frac{\partial^2}{\partial z^2} + k^2\right] G = -\,\delta(\boldsymbol{r} - \boldsymbol{r}_s)\,\delta(z - z_s). \tag{3}$$

For fluid layers both p and G satisfy continuity of pressure and normal displacement across interfaces. In terms of range dependent normal mode depth functions $\psi_n(\boldsymbol{r}, z)$ and the associated radial functions $R_n(\boldsymbol{r})$, the Green's function solution is

$$G = \sum_{n=1}^{\infty} R_n(\boldsymbol{r})\,\psi_n(\boldsymbol{r}, z). \tag{4}$$

Then, the coupled-mode radial equation is[1–3]

$$[\nabla_{\boldsymbol{r}}^2 + k_m^2(\boldsymbol{r})] R_m(\boldsymbol{r}) = -\frac{1}{\rho_s}\psi_m(\boldsymbol{r}, z_s)\,\delta(\boldsymbol{r} - \boldsymbol{r}_s) - \sum_n [\bar{\boldsymbol{B}}_{mn}(\boldsymbol{r}) \cdot \boldsymbol{\nabla}_{\boldsymbol{r}} + \bar{C}_{mn}(\boldsymbol{r})] R_n(\boldsymbol{r}). \tag{5}$$

The coupling coefficients are

$$\bar{\boldsymbol{B}}_{mn}(\boldsymbol{r}) = 2\int_0^{\infty} \frac{1}{\rho(z)}\psi_m(\boldsymbol{r}, z)\boldsymbol{\nabla}_{\boldsymbol{r}}\psi_n(\boldsymbol{r}, z)dz + I^B_{mn}(\boldsymbol{r}) \equiv \tilde{\boldsymbol{B}}_{mn} + I^B_{mn}, \tag{6}$$

$$\bar{C}_{mn}(\boldsymbol{r}) = \int_0^{\infty} \frac{1}{\rho(z)}\psi_m(\boldsymbol{r}, z)\nabla_{\boldsymbol{r}}^2\psi_n(\boldsymbol{r}, z)dz + I^C_{mn}(\boldsymbol{r}) \equiv \tilde{C}_{mn} + I^C_{mn}, \tag{7}$$

where $\bar{\boldsymbol{B}}_{mn}$ and $\bar{C}_{mn}$ are referred to as the first and second coupling coefficients, respectively, and where I^B_{mn} and I^C_{mn} are the interface coupling coefficients introduced by Fawcett[7] to ensure conservation of energy. To lowest order, with the coupling due explicitly to roughness on some interface at $H = h_0 + h(\boldsymbol{r})$, where h_0 is the mean depth of the relevant interface for which the modal eigenvalues are $\boldsymbol{k}_m(\boldsymbol{r}) = \bar{\boldsymbol{k}}_m = \text{const}$, the coupling coefficients are

$$\bar{\boldsymbol{B}}^{(0)}_{mn}(\boldsymbol{r}) = \tilde{B}^{(0)}_{mn}\boldsymbol{\nabla}_{\boldsymbol{r}}h(\boldsymbol{r}) = B^A_{mn}\boldsymbol{\nabla}_{\boldsymbol{r}}h(\boldsymbol{r}), \tag{8}$$

$$\bar{C}^{(0)}_{mn}(\boldsymbol{r}) = \tfrac{1}{2}\tilde{B}^{(0)}_{mn}\nabla_{\boldsymbol{r}}^2 h(\boldsymbol{r}). \tag{9}$$

The symmetric and antisymmetric parts of the first coupling coefficient are

$$\tilde{B}^{(0)}_{mn} = \tfrac{1}{2}(\tilde{B}^{(0)}_{mn} + \tilde{B}^{(0)}_{nm}) + \tfrac{1}{2}(\tilde{B}^{(0)}_{mn} - \tilde{B}^{(0)}_{nm}) \equiv B^S_{mn} + B^A_{mn}, \tag{10}$$

and $B^S_{mn} = -I^B_{mn}$.[1–3] In the Rutherford form of the coupling coefficients[2,8] $B^A_{mn} = 2(\sigma^A_{mn} - \nu^A_{mn})/(\bar{k}_m^2 - \bar{k}_n^2)$ for the off-diagonal components with

$$\sigma^A_{mn} = \psi^{(0)}_m(h_0)\psi^{(0)}_n(h_0)\left[\frac{1}{\rho_2}\left(\frac{\bar{k}_n^2 + \bar{k}_m^2}{2} - k_2^2\right) - \frac{1}{\rho_1}\left(\frac{\bar{k}_n^2 + \bar{k}_m^2}{2} - k_1^2\right)\right], \tag{11}$$

$$\nu_{mn}^{A} = \frac{\rho_2}{\rho_1}\frac{\partial\psi_m^{(0)}(h_0)}{\partial z}\frac{\partial\psi_n^{(0)}(h_0)}{\partial z}\left(\frac{1}{\rho_1}-\frac{1}{\rho_2}\right), \tag{12}$$

and

$$B_{mn}^{S} = -\psi_m^{(0)}(h_0)\psi_n^{(0)}(h_0)\left(\frac{1}{\rho_1}-\frac{1}{\rho_2}\right), \tag{13}$$

where $\psi_m^{(0)}(z)$ is the mode function for the environment with $H=h_0$. The subscripts 1 and 2 on the sound speed and density parameters in Eqs. (11)–(13) refer to the values on opposite sides of the rough interface. The conservation of energy[7,8] dictates that the diagonal components have the explicit forms $\bar{\boldsymbol{B}}_{mm}^{(0)}(\boldsymbol{r})=0$ and $\bar{C}_{mm}^{(0)}(\boldsymbol{r})=(1/2)B_{mm}^{S}\nabla_{\boldsymbol{r}}^2 h(\boldsymbol{r})$.

The radial Green's function $g_m(\boldsymbol{r},\boldsymbol{r}')$ satisfies $[\nabla_{\boldsymbol{r}}^2+k_m^2]g_m(\boldsymbol{r},\boldsymbol{r}')=-\delta(\boldsymbol{r}-\boldsymbol{r}')$and has the zeroth-order ($H=h_0, \boldsymbol{k}_m(\boldsymbol{r})=\bar{\boldsymbol{k}}_m=$const) solution

$$g_m^{(0)}(\boldsymbol{r},\boldsymbol{r}') = \begin{cases} -e^{i\bar{k}_m\cdot(\boldsymbol{r}-\boldsymbol{r}')}/(2i\bar{k}_m), & D=2 \\ iH_0^{(1)}[\bar{k}_m\cdot(\boldsymbol{r}-\boldsymbol{r}')]/4, & D=3. \end{cases} \tag{14}$$

In Eq. (14), as well as the remaining equations, for $D=2$ the radial vector $\boldsymbol{r}$ has only one component, $x\hat{i}$. For both $D=2$ and $D=3$ by convention $\bar{\boldsymbol{k}}_m \| \boldsymbol{r}-\boldsymbol{r}'$ in $g_m^{(0)}(\boldsymbol{r},\boldsymbol{r}')$.

In terms of the radial Green's function, Eq. (5) has the solution

$$R_m(\boldsymbol{r}) = \frac{1}{\rho_s}g_m(\boldsymbol{r},\boldsymbol{r}_s)\psi_m(\boldsymbol{r},z_s) + \int d^{D-1}r'\sum_n g_m(\boldsymbol{r},\boldsymbol{r}')[\bar{\boldsymbol{B}}_{mn}(\boldsymbol{r}')\cdot\nabla_{\boldsymbol{r}'}+\bar{C}_{mn}(\boldsymbol{r}')]R_n(\boldsymbol{r}'). \tag{15}$$

The first term on the right side of Eq. (15) is the direct blast component, and the second (integral) term is the scattered field from the rough interface.

The zeroth-order solution of the radial equation satisfies

$$[\nabla_{\boldsymbol{r}}^2+\bar{k}_m^2]R_m^{(0)}(\boldsymbol{r}) = -\frac{1}{\rho_s}\psi_m^{(0)}(z_s)\delta(\boldsymbol{r}-\boldsymbol{r}_s), \tag{16}$$

and is

$$R_m^{(0)}(\boldsymbol{r}) = g_m^{(0)}(\boldsymbol{r},\boldsymbol{r}_s)\frac{1}{\rho_s}\psi_m^{(0)}(z_s). \tag{17}$$

Substituting $R_m^{(0)}(\boldsymbol{r})$ for $R_m(\boldsymbol{r})$ in the right side of Eq. (15), and replacing all modal quantities by their values for $H=h_0$, produces the first-order correction for the radial wave function

$$R_m^{(1)}(\boldsymbol{r}) = \int d^{D-1}r'\sum_n g_m^{(0)}(\boldsymbol{r},\boldsymbol{r}')[\bar{\boldsymbol{B}}_{mn}^{(0)}(\boldsymbol{r}')\cdot\nabla_{\boldsymbol{r}'}+\bar{C}_{mn}^{(0)}(\boldsymbol{r}')]g_n^{(0)}(\boldsymbol{r}',\boldsymbol{r}_s)\frac{1}{\rho_s}\psi_n^{(0)}(z_s). \tag{18}$$

The derivative terms in Eq. (18) operating on the zeroth-order radial Green's functions (in asymptotic form for $D=3$) give $\nabla_{\boldsymbol{r}'}g_m^{(0)}(\boldsymbol{r},\boldsymbol{r}')=i\bar{\boldsymbol{k}}_m g_m^{(0)}(\boldsymbol{r},\boldsymbol{r}')$,and the derivative operators acting on the roughness $h(\boldsymbol{r})$ are integrated by parts and transferred to the Green's functions. For instance, with Eqs. (8)–(10), the first term in the square brackets in Eq. (18) becomes

$$\int d^{D-1}r' g_m^{(0)}(\boldsymbol{r},\boldsymbol{r}') B_{mn}^A \nabla_{\boldsymbol{r}'} h(\boldsymbol{r}') \cdot \nabla_{\boldsymbol{r}'} g_n^{(0)}(\boldsymbol{r}',\boldsymbol{r}_s)$$

$$= \int d^{D-1}r' \boldsymbol{k}_n \cdot (\boldsymbol{k}_n - \boldsymbol{k}_m) B_{mn}^A h(\boldsymbol{r}') g_m^{(0)}(\boldsymbol{r},\boldsymbol{r}') g_n^{(0)}(\boldsymbol{r}',\boldsymbol{r}_s). \tag{19}$$

Similarly, the second term in the square brackets in Eq. (18) is

$$\frac{1}{2}\int d^{D-1}r' \tilde{B}_{mn}^{(0)} \nabla_{\boldsymbol{r}'}^2 h(\boldsymbol{r}') g_m^{(0)}(\boldsymbol{r},\boldsymbol{r}') g_n^{(0)}(\boldsymbol{r}',\boldsymbol{r}_s)$$

$$= -\frac{1}{2}\int d^{D-1}r' (\boldsymbol{k}_n - \boldsymbol{k}_m) \cdot (\boldsymbol{k}_n - \boldsymbol{k}_m) \tilde{B}_{mn}^{(0)} h(\boldsymbol{r}') g_m(\boldsymbol{r},\boldsymbol{r}') g_n(\boldsymbol{r}',\boldsymbol{r}_s). \tag{20}$$

Thus,

$$R_m^{(1)}(\boldsymbol{r}) = \int d^{D-1}r' \frac{1}{\rho_s} g_m^{(0)}(\boldsymbol{r},\boldsymbol{r}') \sum_n g_n^{(0)}(\boldsymbol{r}',\boldsymbol{r}_s) \psi_n^{(0)}(z_s) \mathcal{I}_{mn} h(\boldsymbol{r}'), \tag{21}$$

where the scattering matrix is

$$\mathcal{I}_{mn} \equiv \left[\tfrac{1}{2} B_{mn}^A (\bar{\boldsymbol{k}}_n + \bar{\boldsymbol{k}}_m) \cdot (\bar{\boldsymbol{k}}_n - \bar{\boldsymbol{k}}_m) - \tfrac{1}{2} B_{mn}^S (\bar{\boldsymbol{k}}_n - \bar{\boldsymbol{k}}_m) \cdot (\bar{\boldsymbol{k}}_n - \bar{\boldsymbol{k}}_m)\right]. \tag{22}$$

For the off-diagonal terms, Eq. (22) can be written as

$$\mathcal{I}_{mn} = \frac{k_1^2}{\rho_1}\left\{\left[\left(\frac{1}{\rho} - 1\right)\frac{\bar{k}_m}{k_1}\frac{\bar{k}_n}{k_1}\cos\phi + \left(1 - \frac{\kappa^2}{\rho}\right)\right]\psi_m^{(0)}(h_0)\psi_n^{(0)}(h_0)\right.$$

$$\left. - \left[\frac{\partial\psi_m^{(0)}(h_0)}{\partial z}\frac{\partial\psi_n^{(0)}(h_0)}{\partial z}\frac{(\rho-1)}{k_1^2}\right]\right\} \equiv \frac{k_1^2}{\rho_1}\hat{\mathcal{I}}_{mn}, \tag{23}$$

and for the diagonal terms,

$$\mathcal{I}_{mm} = \frac{k_1^2}{\rho_1}\left\{\left(\frac{1}{\rho} - 1\right)(\cos\phi - 1)\frac{\bar{k}_m^2}{k_1^2}\right\}[\psi_m^{(0)}(h_0)]^2 \equiv \frac{k_1^2}{\rho_1}\hat{\mathcal{I}}_{mm}, \tag{24}$$

where $\kappa = k_2/k_1$, $\rho = \rho_2/\rho_1$, and $\phi = \cos^{-1}(\bar{\boldsymbol{k}}_m \cdot \bar{\boldsymbol{k}}_n / \bar{k}_m \bar{k}_n)$ is the azimuthal bistatic scattering angle. This form of the scattering matrix has several advantages that will be discussed at the end of this section. For convenience, incoming (n) and outgoing (m) mode source amplitudes, one for $z = z_s$ and one for $z = h_0$, can be defined by

$$P_j(\boldsymbol{r},\boldsymbol{r}') = \frac{Q_0 g_j(\boldsymbol{r},\boldsymbol{r}')\Psi_j}{\rho_j}, \tag{25}$$

where

$$\frac{\Psi_j}{\rho_j} = \begin{cases} \psi_n^{(0)}(z_s)/\rho_s, & j = n \\ \psi_m^{(0)}(z)/\rho_1, & j = m. \end{cases} \tag{26}$$

The total pressure $p = p_d + p_s$ is the sum of the direct blast and scattered components that can be written as

$$p_d(\boldsymbol{r},z,\omega) = QS(\omega)\sum_m \psi_m^{(0)}(z)\frac{1}{\rho_s}\psi_m^{(0)}(z_s) g(\boldsymbol{r},\boldsymbol{r}_s), \tag{27}$$

$$p_s(\boldsymbol{r},z,\omega) = |p_0|S(\omega)\sum_{mn} F_0\frac{k_1^2}{2}\hat{\mathcal{I}}_{mn}\frac{1}{(2\pi)^{(D-1)/2}}\int_0^\infty d^{D-1}r' P_m(\boldsymbol{r},\boldsymbol{r}')P_n(\boldsymbol{r}',\boldsymbol{r}_s)h(\boldsymbol{r}'), \tag{28}$$

where

$$F_0 = \begin{cases} \sqrt{\dfrac{\pi}{2}}|H_0^{(1)}(k_1 r_0)| \simeq \dfrac{1}{\sqrt{k_1 r_0}}, & D=2 \\ \dfrac{1}{r_0}, & D=3. \end{cases} \tag{29}$$

The right side of Eq. (28) describes the propagation to the receiver of the field in mode m from a source [referenced to Q_0, see Eq. (25)] at each position $\boldsymbol{r}'$ on the scattering interface. The mode m source at the scattering interface is produced by the field in mode n propagated to the interface at position $\boldsymbol{r}'$ in the direct blast from the source at $(\boldsymbol{r}_s,z_s)$ (also referenced to Q_0) and then scattered to mode m. The r_0 factor in F_0 comes from the Q_0 reference for the source at each $\boldsymbol{r}'$.

The scattered pressure time series is obtained by Fourier transforming Eq. (28) to the time domain. Let

$$X_{mn}(\boldsymbol{r}',t) = \frac{1}{2\pi}\int_{-\infty}^{\infty} d\omega S(\omega)e^{-i\omega t}|p_0|F_0\frac{k_1^2}{2}\hat{\mathcal{I}}_{mn}P_m(\boldsymbol{r},\boldsymbol{r}')P_n(\boldsymbol{r}',\boldsymbol{r}_s), \tag{30}$$

which is a real-valued function. Then, the time dependence of the scattered pressure is

$$P_s(t) = \sum_{mn}\frac{1}{(2\pi)^{(D-1)/2}}\int_0^\infty d^{D-1}r' X_{mn}(\boldsymbol{r}',t)h(\boldsymbol{r}'). \tag{31}$$

The scattered intensity time series averaged over an ensemble of interface roughnesses is

$$\langle P_s^2(t)\rangle = \sum_{mn}\sum_{m'n'}\frac{1}{(2\pi)^{D-1}}\int_0^\infty d^{D-1}r' d^{D-1}r'' X_{mn}(\boldsymbol{r}',t)X_{m'n'}(\boldsymbol{r}'',t)\langle h(\boldsymbol{r}')h(\boldsymbol{r}'')\rangle. \tag{32}$$

The ensemble average $\langle h(\boldsymbol{r}')h(\boldsymbol{r}'')\rangle$ of the product of the interface roughness at $\boldsymbol{r}'$ and $\boldsymbol{r}''$ can be related to the Fourier transform of the roughness power spectrum $W(\boldsymbol{\lambda})$ and to the spatial correlation $C(\boldsymbol{r}'-\boldsymbol{r}'')$ of the roughness,[4] i.e.,

$$\langle h(\boldsymbol{r}')h(\boldsymbol{r}'')\rangle = \int d^{D-1}\lambda W(\boldsymbol{\lambda})e^{-i\boldsymbol{\lambda}\cdot(\boldsymbol{r}'-\boldsymbol{r}'')} = \langle h^2\rangle C(\boldsymbol{r}'-\boldsymbol{r}''), \tag{33}$$

where $\langle h^2\rangle$ is the ensemble averaged mean square roughness. Then, the scattered intensity is

$$\langle P_s^2(t)\rangle = \frac{1}{(2\pi)^{D-1}}\int_{-\infty}^{\infty} d^{D-1}\lambda|\mathcal{K}(\boldsymbol{\lambda},t)|^2, \tag{34}$$

where

$$\mathcal{K}(\boldsymbol{\lambda},t) \equiv \sqrt{W(\boldsymbol{\lambda})}\sum_{mn}\int_{-\infty}^{\infty} d^{D-1}r' X_{mn}(\boldsymbol{r}',t)e^{-i\boldsymbol{\lambda}\cdot\boldsymbol{r}'}, \tag{35}$$

Furthermore, by applying Parseval's theorem the scattered intensity can be written as

$$\langle P_s^2(t)\rangle = \int_{-\infty}^{\infty} d^{D-1}r' K^2(\boldsymbol{r}',t). \tag{36}$$

The quantity $K(\boldsymbol{r}',t)$ is the Fourier transform of $\mathcal{K}(\boldsymbol{\lambda},t)$, i.e.,

$$K(\boldsymbol{r}',t) = \frac{1}{(2\pi)^{D-1}} \int_{-\infty}^{\infty} d^{D-1}\lambda e^{i\boldsymbol{\lambda}\cdot\boldsymbol{r}'} \mathcal{K}(\boldsymbol{\lambda},t)$$

$$= \sum_{mn} \frac{1}{(2\pi)^{D-1}} \int_{-\infty}^{\infty} d^{D-1}\lambda e^{i\boldsymbol{\lambda}\cdot\boldsymbol{r}'} \sqrt{W(\boldsymbol{\lambda})}\mathcal{X}_{mn}(\boldsymbol{\lambda},t) = \sum_{mn} X_{mn}(\boldsymbol{r}',t)\sqrt{W(\bar{\boldsymbol{k}}_m - \bar{\boldsymbol{k}}_n)}, \quad (37)$$

where

$$\mathcal{X}_{mn}(\boldsymbol{\lambda},t) \equiv \int_{-\infty}^{\infty} d^{D-1}r' X_{mn}(\boldsymbol{r}',t) e^{-i\boldsymbol{\lambda}\cdot\boldsymbol{r}'}, \quad (38)$$

and from Eqs. (14), (25), (26), and (30) $\mathcal{X}_{mn}(\boldsymbol{\lambda},t) \propto (2\pi)^{D-1}\delta(\boldsymbol{\lambda} - \bar{\boldsymbol{k}}_m - \bar{\boldsymbol{k}}_n)$.

Finally, the scattered intensity time series is

$$\langle P_s^2(t)\rangle = \left[\frac{1}{2\pi}\int_{-\infty}^{\infty} d\omega e^{-i\omega t}|p_0|S(\omega)\sum_{m,n} T_{mn}\int_{-\infty}^{\infty} d^{D-1}r' P_m(\boldsymbol{r},\boldsymbol{r}')P_n(\boldsymbol{r}',\boldsymbol{r}_s)\right]^2, \quad (39)$$

where the scattering kernel is

$$T_{mn}^2 = \frac{k_1^4}{4} F_0^2 \hat{\mathcal{I}}_{mn}^2 W(\bar{\boldsymbol{k}}_n - \bar{\boldsymbol{k}}_m). \quad (40)$$

In Eq. (40) the scattering kernel, through the r_0 dependence in F_0^2, has the correct dimensions of inverse length (area) for $D=2$ ($D=3$), which have been omitted in previous papers.[4,5,9] For bistatic scattering and $W(\bar{\boldsymbol{k}}_n - \bar{\boldsymbol{k}}_m) = W(|\bar{\boldsymbol{k}}_n - \bar{\boldsymbol{k}}_m|)$

$$|\bar{\boldsymbol{k}}_n - \bar{\boldsymbol{k}}_m|^2 = [\bar{k}_n - \bar{k}_m \cos\phi]^2 + (\bar{k}_m)^2 \sin^2\phi. \quad (41)$$

The representation of Eqs. (23)–(26) and Eqs. (39) and (40) in a model calculation is facilitated by a comparison with the usual modal expansion for the field on the bottom at $(\boldsymbol{r}', h_0)$ from a source with reference amplitude $Q_0|p_0|$ at $(\boldsymbol{r}, z_s)$, i.e., $p(\boldsymbol{r}', h_0, \boldsymbol{r}_s, z_s) = |p_0|\Sigma_n P_n(\boldsymbol{r}', \boldsymbol{r}_s)\psi_n^{(0)}(h_0)$. Similarly, the usual modal expansion for the field from a source with reference amplitude $Q_0|p_0|$ on the bottom at $(\boldsymbol{r}', h_0)$ to the receiver at $(\boldsymbol{r}, z)$ is $p(\boldsymbol{r}, z, \boldsymbol{r}', h_0) = |p_0|\Sigma_m P_m(\boldsymbol{r}, \boldsymbol{r}')\psi_m^{(0)}(h_0)$.

The Moe–Jackson (MJ) form of the scattering kernel[4,5] can be obtained from Eq. (40) by introducing Γ_m, the plane wave reflection coefficient for the interface at h_0, in terms of which

$$\frac{\partial\psi_m^{(0)}(h_0)}{\partial z} = \frac{i\gamma_{1,m}\psi_m^{(0)}(h_0)(1-\Gamma_m)}{(1+\Gamma_m)}, \quad (42)$$

where $\gamma_{1,m} = \sqrt{k_1^2 - \bar{k}_m^2}$ is the vertical wavenumber at the interface. Then, the off-diagonal components of the scattering kernel are

$$T_{mn}^2 = \left[\frac{\psi_m^{(0)}(h_0)\psi_n^{(0)}(h_0)}{(1+\Gamma_m)(1+\Gamma_n)}\right]^2 \sigma_{\mathrm{MJ}}(\theta_n, \theta_m), \quad (43)$$

where the arguments of σ_{MJ} are the mode angles, e.g., $\theta_m = \cos^{-1}(k_m/k_1)$. In terms of the mode angles with $\gamma_{1,m} = k_1 \sin\theta_m$, the MJ scattering kernel is

$$\sigma_{\mathrm{MJ}} = (k_1^4 F_0^2/4)\{[(1/\rho - 1)\cos\,\theta_m \cos\,\theta_n \cos\,\phi + (1 - \kappa^2/\rho)] \times (1+\Gamma_m)(1+\Gamma_n) + (\rho - 1)\sin\,\theta_m \sin\,\theta_n (1-\Gamma_m)(1-\Gamma_n)\}^2 W(\bar{\boldsymbol{k}}_n - \bar{\boldsymbol{k}}_m), \quad (44)$$

with the correct dimensions as derived for T_{mn}^2. The bracketed expression in Eq. (43) converts the mode function $\psi_n^{(0)}(h_0)$ $[\psi_m^{(0)}(h_0)]$ into the downgoing (upgoing) wave component that is incident on (scattered from) the rough surface, consistent with the derivations of scattering from plane waves.[4,5] For the diagonal components of the scattering kernel, the quantity in braces in Eq. (44) is replaced by $(1/\rho - 1)(1-\cos\,\phi)(1+\Gamma_m)^2 \cos^2\,\theta_m$, which differs from the MJ form because of the energy conservation requirements for the mode coupling coefficients.

There are several advantages in expressing the scattering kernel in terms of mode functions and mode function derivatives via Eqs. (23), (24), and (40), instead of mode angles and reflection coefficients with Eqs. (43) and (44). First, the scattering from a pressure release interface ($\psi_m = 0$, $\Gamma_m = -1$) is accounted for automatically, whereas the bracketed expression on the right side of Eq. (43) is indefinite. Indeed, for such interfaces, Eqs. (23) and (40) produce the usual result for the off-diagonal components of the acoustic scattering kernel from a rough sea surface.[5] Also, the scattering of attenuated or evanescent modes, for which $\gamma_{1,m}$ and θ_m are complex, is accounted for straightforwardly. Finally, the factor $(k_1^4 F_0^2/4)$ in the MJ scattering kernel [Eq. (44)] for two-dimensions is seen to be equal to $k_1^3/4r_0$ only asymptotically.[5]

The coupling coefficient $\bar{C}_{mn}$ produces significant contributions to the scattering kernel T_{mn}^2 and must be included to derive Eq. (40). This fact suggests that the assumption[8] in some mode coupling treatments that $\bar{C}_{mn}$ is higher order in $\boldsymbol{\nabla}_r h(\boldsymbol{r})$ compared to $\bar{\boldsymbol{B}}_{mn}$ needs to be re-examined.

3. Conclusion

The pressure field time series produced by scattering from a rough interface can be derived from a two-way coupled-mode formalism for two- or three-dimensional environments. The solution of the coupled range equation to lowest order in the mean square roughness produces a Born approximation for the scattering kernel in terms of the mode coupling coefficients. The derivation involves a spatial transform of the roughness into its power spectrum. The off-diagonal scattering kernel components derived thereby are equivalent to the off-diagonal components of the MJ scattering kernel with proper dimensions.

This derivation for the scattering kernel is valid for an arbitrary horizontal layering profile[2,3] and avoids the calculation of a reflection coefficient that is extraneous to a reverberation model constructed with propagated fields determined from modes that already incorporate reflection effects.

References and links

[1]D. P. Knobles, "Solutions of coupled-mode equations with a large dimension in underwater acoustics," J. Acoust. Soc. Am. **96**, 1741–1747 (1994).
[2]S. A. Stotts, "Coupled-mode solutions in generalized ocean environments," J. Acoust. Soc. Am. **111**, 1623–1643 (2002).
[3]S. A. Stotts, "Two-way coupled-mode solutions in the complex horizontal wavenumber plane," J. Comput. Acoust. **16**, 225–256 (2008).
[4]J. E. Moe and D. R. Jackson, "First-order perturbation solution for rough scattering cross section including the effects of gradients," J. Acoust. Soc. Am. **96**, 1748–1754 (1994).
[5]E. I. Thorsos and D. R. Jackson, "The validity of the perturbation approximation for rough surface scattering using a Gaussian roughness spectrum," J. Acoust. Soc. Am. **86**, 261–277 (1989).
[6]E. I. Thorsos and J. S. Perkins, "Overview of the reverberation modeling workshops," in *International Symposium on Underwater Reverberation and Clutter, Proceedings of a Symposium*, Villa Marigola, Lerici, Italy, 9–12 September, edited by P. Neilsen, C. H. Harrison, and J.-C. LeGac (NATO Undersea Research Centre, La Spezia, Italy 2008), pp. 3–14.
[7]J. A. Fawcett, "A derivation of the differential equations in coupled-mode propagation," J. Acoust. Soc. Am. **92**, 290–295 (1992).
[8]S. R. Rutherford and K. E. Hawker, "Consistent coupled mode theory of sound propagation for a class of nonseparable problems," J. Acoust. Soc. Am. **70**, 554–564 (1981).
[9]D. D. Ellis, "A shallow-water normal-mode reverberation model," J. Acoust. Soc. Am. **97**, 2804–2814 (1995).

LETTERS TO THE EDITOR

This Letters section is for publishing (a) brief acoustical research or applied acoustical reports, (b) comments on articles or letters previously published in this Journal, and (c) a reply by the article author to criticism by the Letter author in (b). Extensive reports should be submitted as articles, not in a letter series. Letters are peer-reviewed on the same basis as articles, but usually require less review time before acceptance. Letters cannot exceed four printed pages (approximately 3000–4000 words) including figures, tables, references, and a required abstract of about 100 words.

Anomalous signed passive fathometer impulse response when using adaptive beam forming (L)

Chris H. Harrison[a)]
NATO Undersea Research Centre, Viale San Bartolomeo, 400, 19126 La Spezia, Italy

(Received 19 January 2009; revised 8 April 2009; accepted 9 April 2009)

The impulse response of the seabed can be extracted from sea surface ambient noise by cross-correlating the time series from an upward and a downward steered beam. When the steering for each beam is standard minimum variance adaptive beam forming it has been found that the impulse response for significant echoes appears to have the same amplitude but opposite sign. A mathematical explanation is offered for this strange phenomenon. Crucial contributing factors are that the cross-spectral density matrix for the vertical array typically consists of the sum of a Toeplitz matrix and a much weaker Hankel matrix and that it is ill-conditioned.
 [DOI: 10.1121/1.3126345]

PACS number(s): 43.30.Pc, 43.30.Re, 43.30.Wi, 43.30.Nb [AIT] Pages: 3511–3513

I. INTRODUCTION

It has been shown that high fidelity sub-bottom profiles can be obtained from ocean ambient noise by cross-correlating the upward and downward steered beams of a drifting vertical array.[1,2] By using earlier theorems[3] one obtains an impulse response from the surface noise, which, through its sign, retains a faithful record of the sub-bottom impedance changes from layer to layer (see Figs. 5, 6, 11, and 14 of Ref. 2).

Recently adaptive beam forming (ABF) has been used instead of conventional beam forming[4] (CBF) on sub-sets of the data reported in Ref. 2. Evidently this provides, among other things, a high degree of robustness against interference from passing ships. When ABF is applied to both the experimental results and the simulated waveforms that were described in Ref. 2 there appears to be an anomalous sign difference between the CBF and the ABF solutions. That is to say that (despite the ABF's built in constraint that beam amplitude should equal plus one in the steer direction) the amplitude of the ABF-derived impulse response in the vicinity of significant echoes, in particular, the main seabed return, is almost exactly minus that of the CBF response. Elsewhere, although amplitudes are comparable, there are no particular similarities in detail. Figure 1 shows an example from an experiment with a moored array at Site 1 on the Malta Plateau[2] averaged over about 30 min. This paper gives an analytical explanation for this peculiar phenomenon.

[a)]Electronic mail: harrison@nurc.nato.int

II. THEORY

The time differential of the normalized cross-correlation of the two beam time series is equivalent to the impulse response of the seabed that would have been received with a point impulsive source at the array's center.[2] This process including filtering, beam forming, cross-correlation, and time differentiation can be written very efficiently in the frequency domain. The up-beam amplitude using conventional frequency domain beam forming is

$$U = \sum_{n}^{N} u_n^* x_n / N, \tag{1}$$

where u_n is the steering vector for the N hydrophones and x_n are the Fourier transforms of the time series for each hydrophone. Here the u_n are pure phase terms (complex with unit amplitude) and the N ensures unit response. Thus, defining the down beam D with steering vector d_n in the same way as in Eq. (1), the cross-spectral density (CSD) of the up and down beams is just $\langle U(\omega) \times D^*(\omega) \rangle$, and the cross-correlation is the inverse Fourier transform (IFT) of this. Note that " *" denotes complex conjugate and that the down beam is exactly the complex conjugate of the up beam. Clearly filtering (see Ref. 2) can be incorporated in this scheme and so can time differentiation since it corresponds exactly to multiplication by $-i\omega$ before the inverse transform; however, for clarity, they will be omitted in the following discussions. The result can also be normalized by the standard deviations of the up and down beam powers,[2] but this has no influence on the discussion here. To make comparisons with ABF it is convenient to write the CSD of the

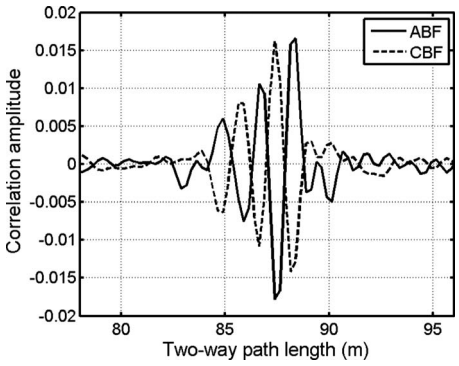

FIG. 1. An experimental example of adaptive (solid line) vs conventional (dashed) beam formed seabed impulse response derived from ambient noise. Typically the adaptive response has the same amplitude but opposite sign from the conventional.

up-down beams (steering vectors $\mathbf{u}$ and $\mathbf{v}$) in terms of the noise field's CSD matrix $\mathbf{R}$ and to remain in the frequency domain. Whereas the power in a conventional beam, say u, is given by $\mathbf{u}^{\dagger}\mathbf{R}\mathbf{u}/N^2$ (" †" meaning conjugate transpose), the CSD of the up-down conventional beams is

$$C_C(\omega) = \mathbf{d}^{\dagger}\mathbf{R}\mathbf{u}/N^2. \tag{2}$$

In contrast, the ABF minimum variance distortionless response[5] has optimum steering weights given by

$$\mathbf{w_o} = \frac{\mathbf{R^{-1}s}}{\mathbf{s}^{\dagger}\mathbf{R^{-1}s}}, \tag{3}$$

where $\mathbf{s}$ is the desired steer direction and "-1" denotes matrix inverse. Assuming no shading in the CBF, and assuming that the ABF up-down beams are formed independently, the ABF response is then

$$C_A(\omega) = \left(\frac{\mathbf{R^{-1}d}}{\mathbf{d}^{\dagger}\mathbf{R^{-1}d}}\right)^{\dagger}\mathbf{R}\frac{\mathbf{R^{-1}u}}{\mathbf{u}^{\dagger}\mathbf{R^{-1}u}} = \frac{\mathbf{d}^{\dagger}\mathbf{R^{-1}u}}{(\mathbf{d}^{\dagger}\mathbf{R^{-1}d})(\mathbf{u}^{\dagger}\mathbf{R^{-1}u})}, \tag{4}$$

where $\mathbf{d}$ and $\mathbf{u}$ are again pure phase terms. Because $\mathbf{R}$ is, by definition, Hermitian, its inverse must also be Hermitian and therefore positive-definite. So the two terms in the denominator are positive scalars (for each frequency), whereas the term in the numerator is complex. Therefore the problem is to find out why the scalar (at each frequency) $\mathbf{d}^{\dagger}\mathbf{R^{-1}u}$ has the opposite sign to $\mathbf{d}^{\dagger}\mathbf{R}\mathbf{u}$ and also to check the relative amplitudes.

There are three contributing factors to the problem, as we shall see: the symmetry of $\mathbf{R}$ vs the symmetry of the matrix $\mathrm{conj}(\mathbf{d})\mathbf{u}^{\mathbf{T}}$, the weak part of $\mathbf{R}$ that depends on the travel time to the seabed, and the fact that $\mathbf{R}$ is typically ill-conditioned.

Typical behavior of $\mathbf{R}$ is described in Refs. 6–8. Considering the direct and (once) bottom reflected paths from a noise source to hydrophone n the spatial coherence R_{nm} between a hydrophone pair contains four terms, which are weighted by noise directionality and integrated over all angles. The integrand is of the form

$$\begin{aligned}&\exp[ik(z_n - z_m)S] + VV^*\exp[-ik(z_n - z_m)S] \\ &\quad + V\exp[ik(Z - (z_n + z_m))S] \\ &\quad + V^*\exp[-ik(Z - (z_n + z_m))S],\end{aligned} \tag{5}$$

where V is the reflection coefficient, S is the modulus sine of the elevation angle, k is the acoustic wavenumber, z_n and z_m are hydrophone depths from array center, and Z is path length from array center to seabed and back. Note that the subsequent angle integration, time differentiation, and cross-correlation conspire to select just the vertically up and down components so angle dependence is of no concern here. Regarding these terms as elements of a matrix, the first two terms have Toeplitz symmetry but the third and fourth have Hankel symmetry (constant values running at right angles to the main diagonal). So $\mathbf{R}$ can be thought of as the sum of a Toeplitz and a Hankel matrix

$$\mathbf{R} = \mathbf{T} + \mathbf{H}. \tag{6}$$

Furthermore the crucial path length to the seabed Z only occurs in $\mathbf{H}$. The CBF response, Eq. (2), is a double sum over hydrophones, and it can also be seen as the sum of an element-by-element product of $\mathbf{R}$ with the matrix $\mathrm{conj}(\mathbf{d})\mathbf{u}^{\mathbf{T}}$. The latter matrix is Hankel because $\mathbf{d}$ is the conjugate of $\mathbf{u}$ and so the matrix contains terms of the form $\exp[ik(z_n + z_m)]$. It is therefore much more sensitive to the Hankel component of $\mathbf{R}$ than the Toeplitz component. The last term in Eq. (5), for instance, matches perfectly for all hydrophones, leaving only $V^*\exp[-ik(Z)]$ (after the hydrophone double sum). None of the other terms match (to beam forming accuracy). In addition, even residuals of these other terms will be eliminated by the final IFT since the only part of $\mathbf{R}$ that contains contributions near the time Z/c is $\mathbf{H}$. All contributions from $\mathbf{T}$ arrive at very early times comparable with travel across the array. Therefore the only significant contribution to the CBF CSD is

$$C_C(\omega) = \mathbf{d}^{\dagger}\mathbf{H}\mathbf{u}/N^2. \tag{7}$$

The ABF equivalent is seen by substituting Eq. (6) in Eq. (4) as follows:

$$C_A(\omega) = a \times \mathbf{d}^{\dagger}(\mathbf{T} + \mathbf{H})^{-1}\mathbf{u}, \tag{8}$$

where a is shorthand for the scalar denominator. Using the Woodbury identity[9] the inverse can be expanded in several ways, a convenient way being

$$\begin{aligned}\mathbf{R^{-1}} &= (\mathbf{T} + \mathbf{H})^{-1} = \mathbf{T^{-1}} - \mathbf{T^{-1}}\mathbf{H}(\mathbf{I} + \mathbf{T^{-1}}\mathbf{H})^{-1}\mathbf{T^{-1}} \\ &= \mathbf{T^{-1}} - \mathbf{T^{-1}}\mathbf{H}(\mathbf{T^{-1}}\mathbf{T} + \mathbf{T^{-1}}\mathbf{H})^{-1}\mathbf{T^{-1}} \\ &= \mathbf{T^{-1}} - \mathbf{T^{-1}}\mathbf{H}(\mathbf{T^{-1}}\mathbf{R})^{-1}\mathbf{T^{-1}} = \mathbf{T^{-1}} - \mathbf{T^{-1}}\mathbf{H}\mathbf{R^{-1}}.\end{aligned} \tag{9}$$

Thus

$$C_A(\omega) = a \times \mathbf{d}^{\dagger}(\mathbf{T^{-1}} - \mathbf{T^{-1}}\mathbf{H}\mathbf{R^{-1}})\mathbf{u}. \tag{10}$$

Now $\mathbf{T}$ is Hermitian and Toeplitz, so its inverse is also Hermitian but not quite Toeplitz, and we will return to this later. Furthermore for the same reason that $\mathbf{T}$ does not contain the two-way path length Z, neither does $\mathbf{T^{-1}}$. Therefore the IFT will contain no contribution from $\mathbf{T^{-1}}$ at time Z/c. We can

therefore write the relevant part of the CSD, i.e., the part that does contain the bottom reflection, as

$$C_A(\omega) = -a \times \mathbf{d}^\dagger \mathbf{T}^{-1} \mathbf{H} \mathbf{R}^{-1} \mathbf{u}. \quad (11)$$

Since Eq. (11) contains a negative sign and a positive number a, the difference between it and Eq. (7) depends on the behavior of $\mathbf{T}^{-1}$ and $\mathbf{R}^{-1}$. In this context $\mathbf{R}$ is almost identical to $\mathbf{T}$ because $\mathbf{H}$ is extremely small. [Remember that Eq. (5) has to be integrated over angle, and this eventually results in an extra term of order ikZ in the denominator of $\mathbf{H}$, with a much smaller term in the denominator of $\mathbf{T}$, resulting in $\mathbf{T}$ being much larger than $\mathbf{H}$.] It is easy to demonstrate, for instance, using the analytical form, Eq. (5) above (or from Refs. 6–8), or using simulations or experimental data that both $\mathbf{T}$ and $\mathbf{R}$ are typically ill-conditioned. This can be understood from a number of points of view, perhaps the simplest being that an upper limit to the number of conceivable pieces of information contained in $\mathbf{R}$ (essentially its rank) is the number of independent beams that can be formed. With only surface sources, N hydrophones, and frequencies f below the design frequency f_o, this number is $Nf/(2f_o)$, i.e., always less than N. The effect of this rank deficiency can be understood by considering the singular value decomposition of $\mathbf{R}=\mathbf{usv}^\dagger$ where since $\mathbf{R}$ is Hermitian the unitary matrices $\mathbf{u}$ and $\mathbf{v}$ are equal. The ill-conditioning means that the diagonal matrix $\mathbf{s}$ contains only a small number of significant singular values. Because the inverse of $\mathbf{R}$ can be expressed as $\mathbf{R}^{-1}=\mathbf{upv}^\dagger$ where $\mathbf{p}$ is also a diagonal matrix with elements equal to the reciprocal of those of $\mathbf{s}$ (but re-ordered), $\mathbf{p}$ has a large number of significant elements on the diagonal and therefore can be approximated by a constant times the identity matrix. Since $\mathbf{u}=\mathbf{v}$ and $\mathbf{u}$ is unitary $\mathbf{R}^{-1}=\mathbf{upv}^\dagger \cong b\mathbf{uu}^\dagger = b\mathbf{I}$ where b is a large number. The same argument applies to $\mathbf{T}^{-1}$ so Eq. (11) becomes

$$C_A(\omega) \cong -ab^2 \times \mathbf{d}^\dagger \mathbf{H} \mathbf{u}. \quad (12)$$

This establishes that the sign of $C_A(\omega)$ is opposite to that of $C_C(\omega)$ for all frequencies. By definition, a is the product of the denominators on the right of Eq. (4). Making use of the shape of $\mathbf{R}$ again we see that

$$\mathbf{d}^\dagger \mathbf{R}^{-1} \mathbf{d} \cong b \times \mathbf{d}^\dagger \mathbf{I} \mathbf{d} = b \times \mathbf{d}^\dagger \mathbf{d} = b \times N. \quad (13)$$

The similar result for $\mathbf{u}$ leads to $a=1/(bN)^2$ and substituting Eq. (7) in Eq. (12) we have

$$C_A(\omega) \cong -C_C(\omega). \quad (14)$$

Since this is true for all frequencies (below the design frequency) the ABF impulse response looks identical to the CBF one except that its sign is reversed, and note that CBF has the correct sign.[2] Q.E.D.

III. CONCLUSIONS

The performance of passive sub-bottom profiling by cross-correlating beams can be improved with ABF. In the adaptive case the derived seabed impulse response has been found by this author to have the opposite sign to the conventional beam formed impulse response in all experimental and simulated data to date. This paper has offered a mathematical explanation for this peculiar phenomenon. The proof relies on the fact that the noise's cross-spectral-density matrix consists of the sum of a Toeplitz matrix and a much weaker Hankel matrix, and that it is typically ill-conditioned. Although the proof is approximate, applying the ABF and CBF numerical algorithms to the analytical form given in Eq. (5) results in almost exact amplitude agreement, given the sign change. Evidently ABF works even though the noise CSD matrix is ill-conditioned. One suspects that this matrix becomes well-conditioned in the presence of interfering shipping, hence improving performance over CBF.

[1] M. Siderius, C. H. Harrison, and M. B. Porter, "A passive fathometer technique for imaging seabed layering using ambient noise," J. Acoust. Soc. Am. **120**, 1315–1323 (2006).
[2] C. H. Harrison and M. Siderius, "Bottom profiling by correlating beam-steered noise sequences," J. Acoust. Soc. Am. **123**, 1282–1296 (2008).
[3] R. L. Weaver and O. I. Lobkis, "Diffuse fields in open systems and the emergence of the Green's function," J. Acoust. Soc. Am. **116**, 2731–2734 (2004).
[4] M. Siderius, "Analysis of passive seabed imaging techniques (A)," J. Acoust. Soc. Am. **123**(5), 3629 (2008).
[5] S. Haykin, *Adaptive Filter Theory* (Prentice-Hall, Englewood Cliffs, NJ, 1996), pp. 225–226.
[6] B. F. Cron and C. H. Sherman, "Spatial correlation functions for various noise models," J. Acoust. Soc. Am. **34**, 1732–1736 (1962).
[7] M. J. Buckingham, "A theoretical model of ambient noise in a low-loss shallow water channel," J. Acoust. Soc. Am. **67**, 1186–1192 (1980).
[8] C. H. Harrison, "Formulas for ambient noise level and coherence," J. Acoust. Soc. Am. **99**, 2055–2066 (1996).
[9] W. W. Hager, "Updating the inverse of a matrix," SIAM Rev. **31**, 221–239 (1989).

Effect of a stack on Rayleigh streaming cells investigated by laser Doppler velocimetry for application to thermoacoustic devices (L)

Solenn Moreau, Hélène Bailliet, and Jean-Christophe Valière
Laboratoire d'Etudes Aérodynamiques (LEA) Université de Poitiers, ENSMA, CNRS, Bâtiment K-40, avenue du Recteur Pineau, 86022 Poitiers Cedex, France

(Received 15 September 2008; revised 8 April 2009; accepted 8 April 2009)

A preliminary study was conducted to observe the influence of a stack on the Rayleigh streaming pattern for application to thermoacoustic devices. The velocity field was estimated from laser Doppler velocimetry measurements in a resonator first without a stack; then a stack was placed at various positions along the resonator axis for various acoustic levels. It was observed that adding a stack locally modifies the streaming pattern and that new streaming vortices appear. When the stack position approaches the location of the streaming velocity maximum or when the acoustic velocity amplitude is increased, the amplitude of additional acoustic streaming vortices at the ends of the stack increases. © *2009 Acoustical Society of America.* [DOI: 10.1121/1.3126342]

PACS number(s): 43.25.Nm [RR] Pages: 3514–3517

I. INTRODUCTION

A schematic thermoacoustic refrigerator is basically composed of a closed tube, a resonator, in which a sinusoidal stationary plane wave of high amplitude is maintained and in which a stack is placed, as shown in Fig. 1. In this configuration, the length of the tube corresponds to a half-wavelength. The stack placed in the resonator is subjected to an oscillating flow due to the stationary acoustic wave. When the geometry and the material of the stack are suitably chosen, a temperature difference between the two ends of the stack is set up because of the thermoacoustic effect. To take advantage of the thermoacoustic effect, the ends of the stack are connected to heat exchangers.

The induced heat flow present along the stack is very sensitive to other possible flows in this region. Among potential sources of thermoacoustic heat flow disturbance, Rayleigh streaming (associated with local mass and thus heat flow) can have an important influence on the efficiency of thermoacoustic machines. "Acoustic streaming" refers to the second order steady velocity that is induced by and superimposed on the dominating first order acoustic velocity. Among the different kinds of streaming, Rayleigh streaming owes its origin to the viscous interaction between the sound field and a solid boundary. In a two-dimensional resonator with rigid walls in which a $\lambda/2$ standing wave is set up, streaming vortices are present on either sides of the central axis with a periodicity of $\lambda/4$ along this axis, as shown by Fig. 2(a), with $\lambda=c/f_{ac}$ the acoustic wave length, c the velocity of sound, and f_{ac} the acoustic frequency. Outer vortices are present in the core guide that is for $R-5\delta_\nu<r<-R+5\delta_\nu$, with R the tube radius, $\delta_\nu=\sqrt{2\nu/\omega}$ the boundary layer thickness, ν the kinematic viscosity of the fluid, and $\omega=2\pi f_{ac}$ the angular acoustic frequency. In the near wall region, the inner streaming vortices have directions of rotation opposite to those of the outer.

Streaming was first modeled by Rayleigh[1] in 1883 for wide channels (in which the boundary layer thickness is negligible in comparison to the channel width and the wavelength is big compared to the tube radius), his solution describes the outer streaming vortices. Streaming vortices are quite well characterized for slow streaming both theoretically[1–5] and experimentally[6–8] in the case of a $\lambda/2$ empty resonator but the effect of an obstacle has never been investigated before. The object of this study is to determine if Rayleigh streaming pattern is modified by setting an obstacle in the guide.

Streaming velocity field was investigated experimentally using laser Doppler velocimetry (LDV) in a half-wavelength cylindrical resonator first without stack; then a stack was placed at various positions along the wave guide axis for various acoustic levels. Section II provides an overview of the procedure and of the method used to calculate streaming velocity and Sec. III presents results of measurements together with their comparison to the available theoretical expectations.

II. PROCEDURE

A. Experimental apparatus

The setup used to observe the phenomenon of acoustic streaming is shown in Fig. 3 and consists in a cylindrical (two dimensional) tube connected at each end to a loudspeaker so that a $\lambda/2$ high level standing wave is sustained in the guide. Loudspeakers are connected to each end of the wave guide via connecting tubes designed empirically to avoid separation effect related to singularities when changing cross section, as shown by Fig. 4. The main part of the wave-

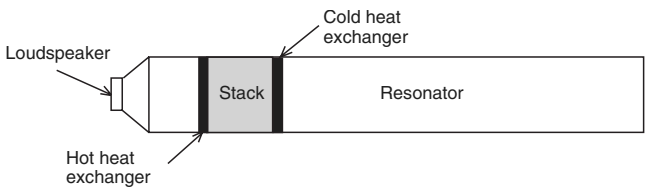

FIG. 1. Sketch of a basic thermoacoustic refrigerator.

 0001-4966/2009/125(6)/3514/4/$25.00

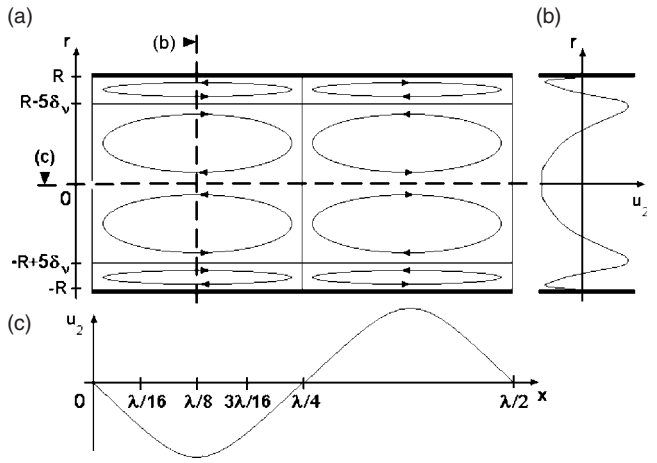

FIG. 2. Streaming velocity field for $R/\delta_\nu \approx 4$. In (a), the acoustic streaming vortices in a $\lambda/2$ resonator are depicted. In (b), the variation of axial streaming velocity with respect to the transverse coordinate r is depicted for $x=\lambda/8$. In (c), the variation of axial streaming velocity with respect to the axial coordinate x is depicted for $r=0$.

guide is a glass cylinder of inner radius $R=19.5$ mm that is simply surrounded by air. The waveguide itself is filled with atmospheric air. The total length of the wave guide is little bigger than $\lambda/2$ ($L=1.9$ m) and the resonant frequency f_{ac} is 88 Hz (with an adiabatic speed of sound taken to be $c=342$ m/s at 18 °C). Frequency of resonance was determined with signal of pressure given by microphone that is placed in the wall of the waveguide. Frequency of resonance corresponds to the frequency with the maximum of pressure. For this frequency, the boundary layer thickness δ_ν, of order of 0.23 mm, is a very small fraction of the acoustic wavelength λ. Because streaming vortices have a $\lambda/4$ periodicity, two Rayleigh streaming cells along the guide length are expected.

Wood smoke is introduced into the guide to render the flow visible. A wave generator provides the loudspeaker input signal, whose frequency and amplitude are controlled, as well as a trigger reference signal, used to synchronize the LDV system. The parameters of the LDV system are adjusted for sound measurements.[9] Preliminary LDV measurements were performed to determine the amplitude of acoustic particle velocity. The axial particle velocity is measured both along the centerline of the guide and across the cross section.

The stack introduced in the resonator consists of a ceramic monolith with square channels, as shown by Fig. 5. This thermally insulating material withstands repeated high-amplitude thermal cycling and large temperature gradients, making it useful in thermoacoustic machines. From a thermoacoustic point of view, the ceramics monolith with square channels offers the advantage of constituting a rigid and regular structure of small parallel channels, thus multiplying the surface offered to the thermoacoustic exchanges between the fluid and material. Note that in this preliminary study, no

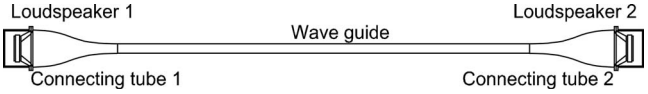

FIG. 3. Diagram of the experimental apparatus.

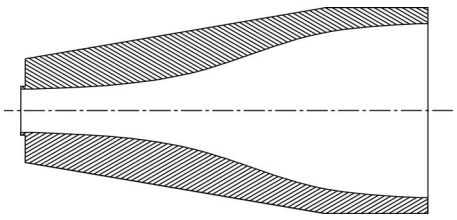

FIG. 4. Connecting tube.

heat measurements were performed in the system. The thickness of the channel partition is $e=0.12$ mm, the size of the square channel side is $d=0.92$ mm, and the length of the stack along the axis of the tube is $l_s=0.08$ m. In our case, the ratio $d/\delta_\nu \approx 4$, thus in each channel of the stack, viscous effects notably modify the profile of acoustic velocity in the section of the channel. To have a maximum temperature variation between the two ends of the stack, the stack position in the resonator must lie between a pressure antinode and a velocity antinode nearer a pressure antinode[10] thus between $\lambda/8$ and $\lambda/4$ on the experimental setup.

Particle velocity was measured by LDV for different positions of the stack along the wave guide axis and at different acoustic levels as given by Table I. In this table, A is the acoustic velocity amplitude and

$$\mathrm{Re}_{\mathrm{NL}} = \left(\frac{A}{c}\right)^2 \left(\frac{R}{\delta_\nu}\right)^2 \tag{1}$$

is the nonlinear Reynolds number. $\mathrm{Re}_{\mathrm{NL}}$ compares inertia and viscosity and determines the degree to which the streaming velocity field is distorted. The case $\mathrm{Re}_{\mathrm{NL}} \ll 1$ corresponds to slow streaming and the case $\mathrm{Re}_{\mathrm{NL}} \geq 1$ is referred to as "nonlinear streaming" or fast streaming. The thermoacoustic devices operate at fast streaming so that $\mathrm{Re}_{\mathrm{NL}} \geq 1$, but all theoretical studies available in the literature assume the streaming to be slow. For a given nonlinear Reynolds number, measurements in the centerline of the guide ($r=0$) are made for several position of the stack along the x-axis: $x_s=\lambda/4$, $x_s=7\lambda/32$, $x_s=5\lambda/32$, and $x_s=\lambda/8$, with x_s the position of the midpoint of the stack. For a given position of the stack, $x_s=5\lambda/32$, measurements in the centerline of the guide are made for two acoustic levels and thus for two nonlinear Reynolds numbers: $\mathrm{Re}_{\mathrm{NL}}=2$ and $\mathrm{Re}_{\mathrm{NL}}=4$. All the measurements were performed at this resonance frequency.

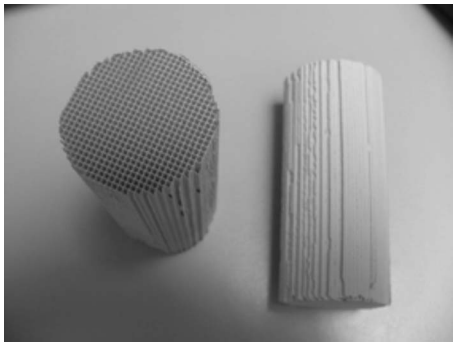

FIG. 5. Photograph of the stack.

TABLE I. Experiments characteristics (f_{ac}=88 Hz).

Position x_s	A (m/s)	Re_{NL}
$\lambda/4$	8.2	4.0
$7\lambda/32$	7.9	3.7
$5\lambda/32$	8.0	3.8
$\lambda/8$	8.2	4.0
$5\lambda/32$	5.3	1.7

B. Determination of axial streaming velocity

The axial velocity is estimated from LDV signal that is characterized by irregular sampling and nonuniform density over the acoustic period. Furthermore, in the adverse condition induced by the proximity of the wall, the signal is composed of very few data. A specific signal post-processing strategy is then proposed.[11] The first step of this method consists in bringing back the axial velocity issued from LDV measurement on one acoustic period $T_{ac}=1/f_{ac}$. Then the date points are sorted per growing time and averaged over regular time step on the acoustic period. The time step used for averaging is chosen to ensure the presence of at least one velocity measurement. Streaming axial velocity u_2 is then calculated by averaging the velocity points over the period.

Preliminary studies[12] show that measurements should be performed more than 26 min after the acoustic field is switched on so that streaming steady state is reached. Once the steady-state has been reached, it is important to evaluate how many samples are needed to ensure convergence of streaming velocity. Again, preliminary studies show that 40 000 samples or more are needed for streaming velocity to reach its convergence.

Finally, the influence of connecting tube on the streaming pattern[12] was studied, and it was shown that the stabilization distance for the streaming is 0.34 m (for $A<29$ m/s and $f_{ac}=88$ Hz).

III. RESULTS

Streaming velocity measurements are compared to the theoretical expression of Rayleigh that is valid for slow streaming ($Re_{NL}<1$):

$$u_{2,\mathrm{Rayleigh}}(x,r)=\frac{A^2}{4c}\left[\frac{1}{2}e^{-2R(1+\eta)/\delta_\nu}+e^{-R(1+\eta)/\delta_\nu}\times\cos\left(\frac{R(1+\eta)}{\delta_\nu}\right)+2e^{-R(1+\eta)/\delta_\nu}\times\sin\left(\frac{R(1+\eta)}{\delta_\nu}\right)+\frac{3}{4}-\frac{9\eta^2}{4}\right], \quad (2)$$

where x is the axial coordinate, k is the complex wave number, and $\eta=r/R$ with r the distance to the waveguide center. In previous works,[8,13] it was shown that for $Re_{NL}\simeq 1$ the value of the centerline streaming velocity is a little smaller than the prediction given by Rayleigh theory.

Figure 6 presents the axial streaming velocity measurements in the centerline of the guide ($r=0$), $u_{2,c}$, for $Re_{NL}=4$, without stack [Fig. 6(a)] and with stack at different positions: $x_s\approx\lambda/8$ [Fig. 6(b)], $x_s=5\lambda/32$ [Fig. 6(c)], $x_s=7\lambda/32$ [Fig. 6(d)], and $x_s=\lambda/4$ [Fig. 6(e)].

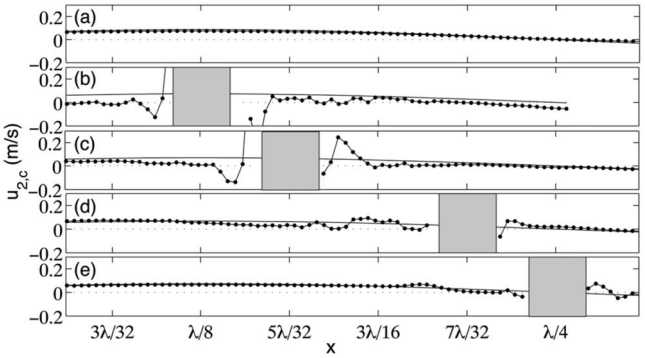

FIG. 6. Axial streaming velocity measurements in the centerline of the guide (●) for $Re_{NL}=4$ compared with the theoretical expression of Rayleigh (—) without stack (a) and with stack at the position $x_s\approx\lambda/8$ (b), $x_s=5\lambda/32$ (c), $x_s=7\lambda/32$ (d), and $x_s=\lambda/4$ (e). The gray zone corresponds to the stack.

For $Re_{NL}=4$, in the empty guide, the velocity in the centerline of the guide, $u_{2,c}$, is close to the Rayleigh theory [see Fig. 6(a)] in agreement with our previous experimental study of acoustic streaming in standing wave guides.[12] When the stack is introduced, the streaming centerline velocity is modified on both sides of the stack whatever the position of the stack in the waveguide. However, at this level ($Re_{NL}=4$), apart from the area close to the stack, the configuration of Rayleigh streaming is not fundamentally modified. The closest the stack gets to the maximum of streaming velocity (located at $\lambda/8$), the more disturbed the streaming velocity is. Because vortex edge is represented by zero crossing of the streaming velocity [see Fig. 2(c)], Fig. 6 shows that new vortices appear at the ends of the stack. This figure also shows that when the stack is moved toward $x_s=\lambda/8$, the amplitude of the vortices generated at the ends of the stack increases and the distance along which the measured velocity differs from the expectation increases too.

Figure 7 represents the measured acoustic streaming velocity in the centerline of the guide for a given position of the stack ($x_s=5\lambda/32$) and for two acoustic levels corresponding to two nonlinear Reynolds numbers: $Re_{NL}=2$ [Fig. 7(a)] and $Re_{NL}=4$ [Fig. 7(b)]. Figure 7 shows that when the Reynolds number Re_{NL} increases, the amplitude of the vortices

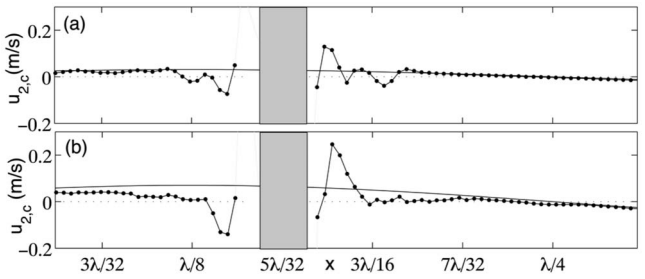

FIG. 7. Axial streaming velocity measurements in the centerline of the guide (●) compared with the theoretical expression of Rayleigh (—) with stack at $x_s=5\lambda/32$ for $Re_{NL}=2$ (a) and $Re_{NL}=4$ (b).

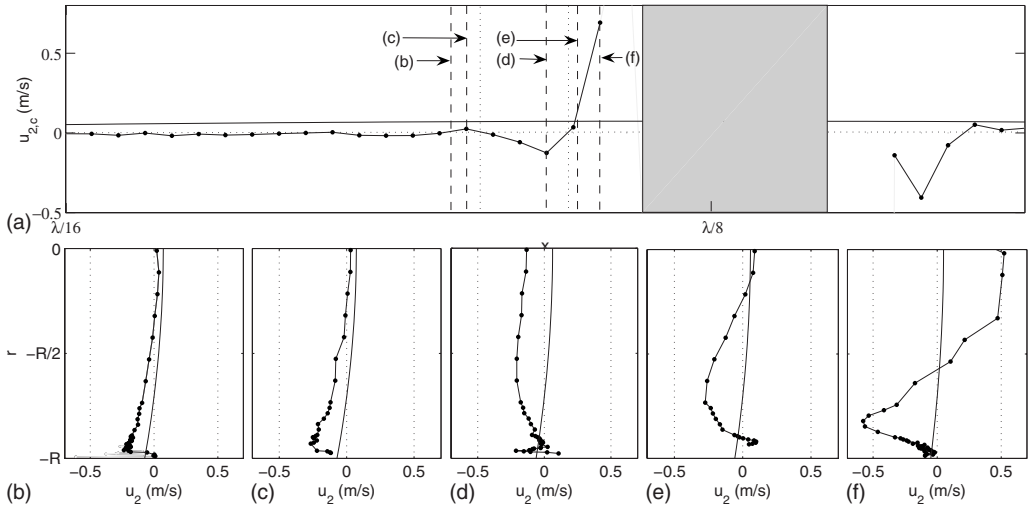

FIG. 8. Axial streaming velocity measurements (●) for $Re_{NL}=4$ compared with the theoretical expression of Rayleigh (—) with stack at the position $x_s \approx \lambda/8$ for $Re_{NL}=4$. In (a), the centerline axial streaming velocity according to the axis x is represented; ∷ end of a streaming vortex generated by the insertion of the stack. In (b)–(f), the axial streaming velocity is represented for positions defined on (a).

generated at the ends of the stack increases and the distance along which the measured velocity differs from the expectation increases too.

Figure 8 represents the streaming velocity measurements for $x_s \approx \lambda/8$ and $Re_{NL}=4$ in the centerline of the guide [Fig. 8(a)] and across the guide half section for different positions along the x axis [Figs. 8(b)–8(f)]. The vertical dotted lines in Fig. 8(a) represent the ends of vortices defined by the axial streaming velocity zero crossing [see Fig. 2(c)]. Therefore, the profiles given by Figs. 8(b) and 8(c) are along the same vortex. These two streaming velocity profiles have a similar overall shape with two outer vortices detected. Here also a streaming vortex is recognized by streaming velocity $u_2=0$ crossing, corresponding to the center of the vortex [see Fig. 2(b)]. The profiles given by Figs. 8(e) and 8(f) also correspond to a single vortex different from the one shown by Figs. 8(b) and 8(c) [they are separated by two dotted lines in Fig. 8(a)]. Compared to the profiles further away from the stack considered above [Figs. 8(b) and 8(c)], these profiles are even more different from theoretical expectation. These two streaming velocity profiles have also an overall similar shape. Figure 8(d) corresponds to another vortex and the shape of streaming velocity profiles is different from the previously mentioned ones. It is therefore possible to detect several vortices in the stack end region. The streaming velocity profiles have essentially the same shape within a single given vortex, but the profiles in two different vortices may be quite dissimilar.

IV. CONCLUSION

A preliminary study of the effect of a stack on Rayleigh streaming was carried out in order to understand streaming phenomena in thermoacoustic devices. A stack was introduced at various positions in a waveguide to study its effects on streaming vortices. It is observed that adding a stack in the streaming pattern modifies the latter and that new streaming vortices appear in the vicinity of the stack. When the stack position approaches a maximum of the streaming velocity, the amplitude of additional vortices at the ends of the stack increases and the stabilization length for streaming velocity on the both sides of the stack increases too. Similar tendencies were observed when the acoustic velocity amplitude was increased. Because streaming in the vicinity of the stack end is complex and has a high amplitude, heat effects can be expected to be important and complex at the ends of the thermoacoustic stack where heat exchangers are located.

[1] L. Rayleigh, "On the circulation of air observed in Kundt's tubes, and on some allied acoustical problems," Philos. Trans. R. Soc. London **175**, 1–21 (1884).
[2] N. Rott, "The influence of heat conduction on acoustic streaming," Z. Angew. Math. Phys. **25**, 417–421 (1974).
[3] H. Bailliet, V. Gusev, R. Raspet, and R. A. Hiller, "Acoustic streaming in closed thermoacoustic devices," J. Acoust. Soc. Am. **110**, 1808–1821 (2001).
[4] M. Hamilton, Y. Ilinski, and E. Zabolotskaya, "Acoustic streaming generated by standing waves in two-dimensional channels of arbitrary width," J. Acoust. Soc. Am. **113**, 153–160 (2003).
[5] L. Menguy and J. Gilbert, "Non-linear acoustic streaming accompanying a plane stationary wave in a guide," Acta Acust. **86**, 249–259 (2000).
[6] M. Campbell, J. A. Cosgrove, C. A. Greated, S. Jack, and D. Rockliff, "Review of LDA and PIV applied to the measurement of sound and acoustic streaming," Opt. Laser Technol. **32**, 629–639 (2000).
[7] M. Thompson and A. Atchley, "Simultaneous measurement of acoustic and streaming velocities in a standing wave using laser Doppler anemometry," J. Acoust. Soc. Am. **117**, 1828–1838 (2005).
[8] S. Moreau, H. Bailliet, and J. Valière, "Measurements of inner and outer streaming vortices in a standing waveguide using laser Doppler velocimetry," J. Acoust. Soc. Am. **123**, 640–647 (2008).
[9] S. Moreau, R. Boucheron, J. Valière, and H. Bailliet, "VLD and PIV measurements in acoustic boundary layers," in Proceedings of the 9e congrès francophone de vélocimétrie laser, Brussels, Belgium, 14–17 September 2004.
[10] S. Duffourd, "Thermoacoustic refrigerator: Analytical and experimental studies for miniaturization," Ph.D. thesis, Ecole Centrale de Lyon, France (2001).
[11] J. Valière, S. Moreau, and H. Bailliet, "Development of laser techniques for acoustic boundary layer measurements; Part I: LDV signal processing for high acoustic displacements," Acta Acust. In press (2009).
[12] S. Moreau, "Design of an experimental device and study of oscillating flow in a high acoustic level resonator for the characterization of nonlinear phenomena: Transition to turbulence and acoustic streaming," Ph.D. thesis, Université de Poitiers, France (2007).
[13] M. Thompson, A. Atchley, and M. Maccarone, "Influences of a temperature gradient and fluid inertia on acoustic streaming in a standing wave," J. Acoust. Soc. Am. **117**, 1839–1849 (2005).

A sound field separation technique based on measurements with pressure-velocity probes (L)

Yong-Bin Zhang[a] and Xin-Zhao Chen
Institute of Sound and Vibration Research, Hefei University of Technology, Hefei 230009, China

Finn Jacobsen
Department of Electrical Engineering, Acoustic Technology, Technical University of Denmark, Building 352, Ørsteds Plads, DK-2800 Kgs. Lyngby, Denmark

(Received 3 February 2009; revised 1 April 2009; accepted 10 April 2009)

It has recently been shown that statistically optimized near field acoustic holography based on measurement with an array of pressure-velocity transducers makes it possible to distinguish between sources on the two sides of the array and thus suppress the influence of a disturbing source [F. Jacobsen and V. Jaud, J. Acoust. Soc. Am. **121**, 1550–1558 (2007)]. However, the suggested technique uses a transfer matrix optimized for the source under test and may be expected to perform less well when the disturbing source is not placed symmetrically on the other side of the array, and this will usually be the case. In this letter, a modified method is presented.
 [DOI: 10.1121/1.3127128]

PACS number(s): 43.60.Sx, 43.60.Pt, 43.20.Rz [EGW] Pages: 3518–3521

I. INTRODUCTION

In conventional planar near field acoustic holography (NAH), it is a necessary condition that the sound sources are confined to half space (say, $z<0$), whereas the other half space is source-free and free-field conditions obtain.[1,2] However, in many realistic situations, this condition cannot be satisfied because of reflections or disturbing sources. If the disturbing sources cannot be removed, a sound field separation technique should be applied to eliminate the influence of the disturbing sound. Such sound field separation techniques based on double layer pressure measurements have been investigated for years.[3–6] An alternative single layer technique for separating the primary source from the disturbing source was recently proposed by Jacobsen and Jaud.[7] This method is based on the statistically optimized version of NAH (SONAH) developed by Hald *et al.*,[8,9] and requires measurement of both the sound pressure and the normal component of the particle velocity in the measurement plane. Yet another method for separating sound field contributions using pressure-velocity measurement has been proposed by Bi and Chen.[10] Their method combines the double layer technique with the equivalent source method, and the particle velocity is obtained from a finite difference approximation.

The transfer matrices employed by Jacobsen and Jaud's method have been optimized for the primary source.[7] Thus one might perhaps expect a reduced performance when the primary source and the disturbing source are not located symmetrically with respect to the measurement plane, as anticipated in Ref. 7. The purpose of this letter is to examine the matter and present an improvement to the method that extends it to the general case where the location of the disturbing source is arbitrary on the side of the measurement plane opposite to that of the primary source. The modified method is compared with the original method in a simulation study as well as experimentally.

II. THE SINGLE LAYER METHOD AND A MORE GENERAL VERSION

The so-called *p-u* method described in Ref. 7 combines a pressure-based SONAH prediction with a particle velocity-based prediction, the idea being that the two estimates should be identical if the sound is coming from the primary source but have an opposite sign if the sound is coming from a disturbing source located directly opposite to the measurement plane from the primary source because of the fact that the particle velocity is a vector whereas the pressure is a scalar. Thus the sound pressure in a grid of N points ($\mathbf{r}_{s,n}$) in the prediction plane ($z=z_s$) generated only by the primary source can be expressed as the average of a weighted sum of measured pressure and particle velocity signals measured at N positions ($\mathbf{r}_{h,n}$) in the hologram plane ($z=z_h$),

$$\mathbf{p}_1^T(\mathbf{r}_s) = \tfrac{1}{2}[\mathbf{p}^T(\mathbf{r}_h)\mathbf{C}_{pp} + \mathbf{u}_z^T(\mathbf{r}_h)\mathbf{C}_{vp}], \tag{1}$$

where T denotes matrix transpose, $\mathbf{p}_1(\mathbf{r}_s)$ is a column vector with the predicted pressures due to the primary source, and $\mathbf{p}(\mathbf{r}_h)$ and $\mathbf{u}_z(\mathbf{r}_h)$ are column vectors with the measured pressures and particle velocities generated both by the primary source and the disturbing source. The two $N\times N$ transfer matrices $\mathbf{C}_{pp}$ and $\mathbf{C}_{vp}$ are determined by requiring that an infinite set of propagating and evanescent elementary waves of the form

$$\Phi_m(\mathbf{r}) = e^{-j(k_{x,m}x+k_{y,m}y+k_{z,m}z)}, \quad m=1,2,\ldots,M, \quad M\to\infty, \tag{2}$$

originating from the primary source plane, satisfy Eq. (1) with optimal accuracy (with the $e^{j\omega t}$ sign convention). This implies that

[a]Author to whom correspondence should be addressed. Electronic mail: zybmy1997@163.com

 0001-4966/2009/125(6)/3518/4/$25.00

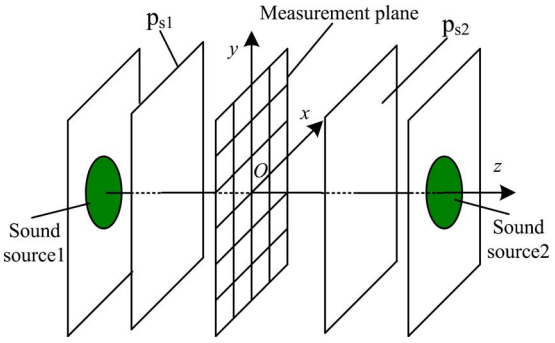

FIG. 1. (Color online) Configuration.

$$\mathbf{B} = \mathbf{A}\mathbf{C}_{pp}, \quad [\mathbf{A}]_{mn} = \Phi_m(\mathbf{r}_{h,n}), \quad [\mathbf{B}]_{mn} = \Phi_m(\mathbf{r}_{s,n}), \tag{3}$$

and that

$$-j\omega\rho \int \mathbf{B} dz_s = \mathbf{A}\mathbf{C}_{vp}, \tag{4}$$

from which the two transfer matrices are determined; see Refs. 7–9.

A modified version of this method is described in what follows. The configuration is shown in Fig. 1, where $\mathbf{p}_{s1}$ is the sound pressure generated only by the primary source in the prediction plane, which may coincide with the primary source plane or may be between the source and the measurement plane, and $\mathbf{p}_{s2}$ is the sound pressure generated only by the disturbing source on the other side of the measurement plane.

The pressure and the particle velocity generated by both sources in the measurement plane can be written as sums of two contributions:

$$\mathbf{p}^T(\mathbf{r}_h) = \mathbf{p}_{s1}^T\mathbf{C}_{pp1} + \mathbf{p}_{s2}^T\mathbf{C}_{pp2}, \tag{5}$$

$$\mathbf{u}_z^T(\mathbf{r}_h) = \mathbf{p}_{s1}^T\mathbf{C}_{pv1} - \mathbf{p}_{s2}^T\mathbf{C}_{pv2}, \tag{6}$$

where $\mathbf{C}_{pp1}$ and $\mathbf{C}_{pv1}$ are determined from

$$\mathbf{A} = \mathbf{B}\mathbf{C}_{pp1} \tag{7}$$

and

$$(-1/(j\omega\rho))(\partial\mathbf{A}/\partial z_h) = \mathbf{B}\mathbf{C}_{pv1}. \tag{8}$$

However, the transfer matrices for the disturbing source are different. They should be optimized for elementary waves coming from the disturbing source, and therefore they should be determined by another set of propagating and evanescent elementary waves:

$$\Psi_m(\mathbf{r}) = e^{-j(k_{x,m}x + k_{y,m}y - k_{z,m}z)}, \quad m = 1,2,\ldots,M, \quad M \to \infty. \tag{9}$$

The two transfer matrices $\mathbf{C}_{pp2}$ and $\mathbf{C}_{pv2}$ can now be determined in the same way as Eqs. (7) and (8) by replacing $\mathbf{A}$ and $\mathbf{B}$ with $[\mathbf{A}]_{mn}=\Psi_m(\mathbf{r}_{h,n})$ and $[\mathbf{B}]_{mn}=\Psi_m(\mathbf{r}_{s,n})$. Finally, combining Eqs. (5) and (6) gives the pressure generated by the primary source,

$$\mathbf{p}_{s1}^T = [\mathbf{u}_z^T(\mathbf{r}_h) + \mathbf{p}^T(\mathbf{r}_h)\mathbf{C}_{pp2}^{-1}\mathbf{C}_{pv2}](\mathbf{C}_{pv1} + \mathbf{C}_{pp1}\mathbf{C}_{pp2}^{-1}\mathbf{C}_{pv2})^{-1}. \tag{10}$$

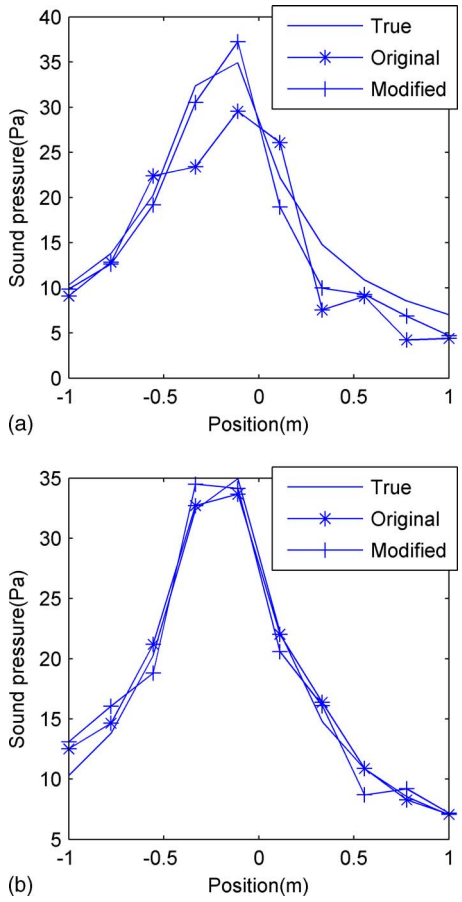

FIG. 2. (Color online) True and reconstructed undisturbed pressure along the x-axis at 500 Hz with the primary and secondary source placed nonsymmetrically (a) and placed symmetrically (b).

It should be mentioned that the Tikhonov regularization is needed when all transfer matrices are computed.

III. A SIMULATION STUDY

To examine the performance of the modified method, a simulation study has been carried out. A test case with two monopoles not located at symmetrical positions was examined. One monopole was regarded as the primary source and placed at $(-0.2, 0, -0.2)$ (x, y, z, coordinates in m), and the other one was regarded as the disturbing source and placed at $(0.2, 0, 0.1)$ on the other side of the measurement plane, which was located at $z=0$. The sound pressure and normal component of the particle velocity were "measured" in a grid of 10×10 points with dimensions 2×2 m^2, and noise was added to the measured data corresponding to a signal-to-noise ratio of 20 dB.

Figure 2(a) shows the "true" undisturbed sound pressure at 500 Hz along the x-axis in the measurement plane, and the reconstructed undisturbed pressure in the same plane determined using the original p-u method based on Eq. (1) and the new version based on Eq. (10). It can be seen that the new version of the p-u method gives much better results than the original version. Other test cases (not shown) have confirmed this observation.

Figure 2(b) shows the effect of moving the disturbing source to the position $(-0.2, 0, 0.2)$, which is symmetrical

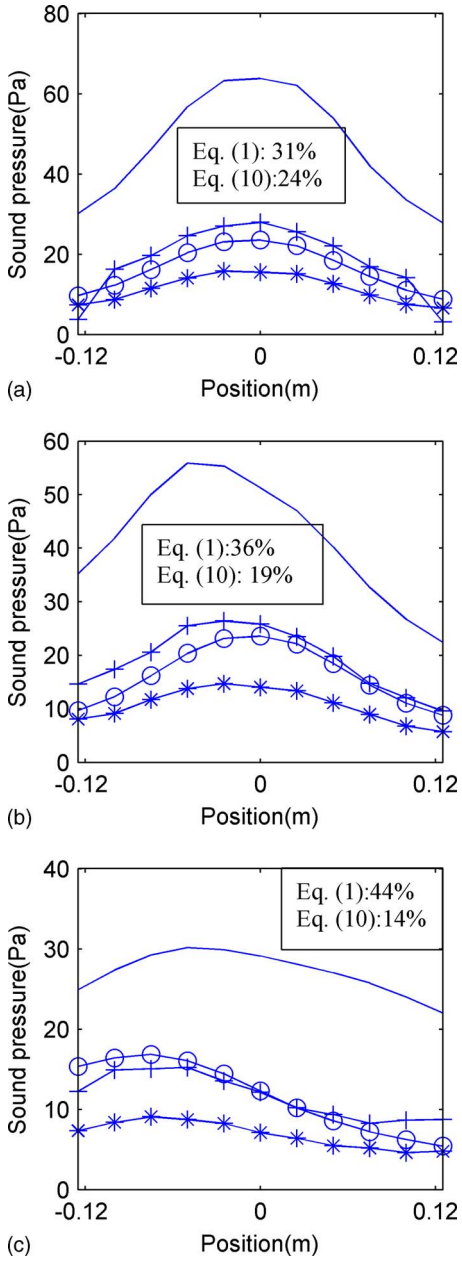

FIG. 3. (Color online) True and reconstructed pressure along the x-axis at 320 Hz in case 1 (a), case 2 (b), and case 3 (c). Solid line: total pressure; line with circles: true pressure generated by the primary source; line with crosses: reconstruction based on Eq. (10); line with stars: reconstruction based on Eq. (1). The global errors are also given.

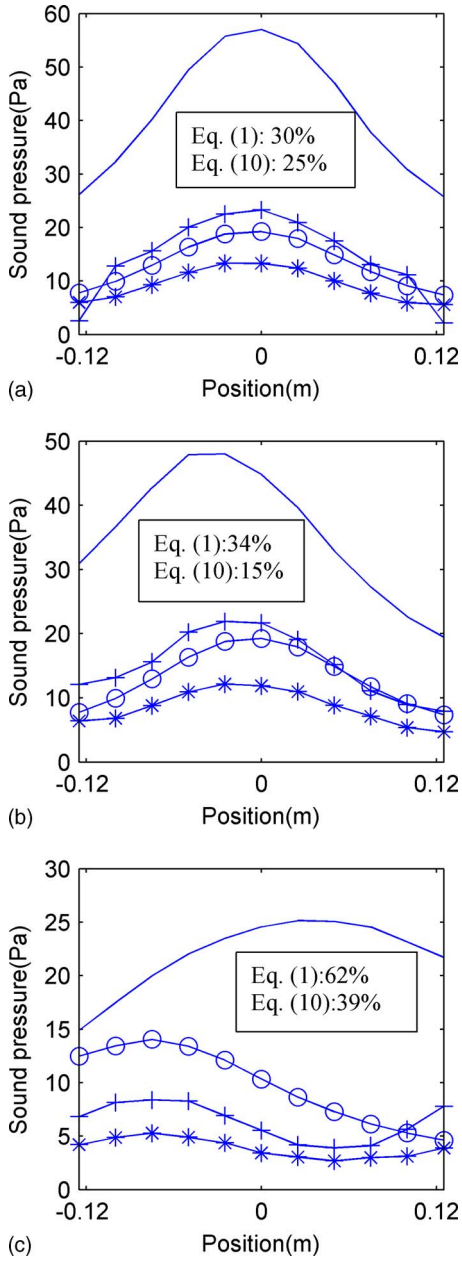

FIG. 4. (Color online) As in Fig. 3 but at 528 Hz.

with respect to the measurement plane. Not surprisingly, the original p-u method performs very well in this case, in fact, even slightly better than the alternative method.

IV. EXPERIMENTAL RESULTS

An experiment has been carried out in a large anechoic room at the Technical University of Denmark. A loudspeaker mounted in a sphere and an "experimental monopole" served as the primary source and the disturbing source, respectively. The latter device, described in Ref. 11, consists of a tube driven by a loudspeaker. The sound pressure and the particle velocity were measured at 11×11 points with a single 1/2 in. p-u sound intensity probe produced by Microflown. The measurement plane with dimensions 25×25 cm^2 was located at $z=0$, and the measurement was carried out with the two sources operating together and with only the primary source turned on. This plane also served as prediction plane. Three test cases were examined: a symmetrical case (1) with the primary source at $(0,0,-0.05)$ (coordinates in m) and the disturbing source at (0, 0, 0.05), a nonsymmetrical case (2) with the primary source at $(0,0,-0.05)$ and the disturbing source at $(-0.05, 0.05, 0.05)$, and yet another nonsymmetrical case (3) with the primary source at $(-0.075, 0, -0.08)$ and the disturbing source at (0.075, 0.05, 0.14).

Figures 3–5 show the pressure generated by two sources together, the undisturbed pressure generated by the primary source, reconstructed using the method based on Eq. (1), and reconstructed using the modified method based on Eq. (10), and relative errors between the undisturbed pressure and the reconstructed pressure obtained by Eqs. (1) and (10), at three

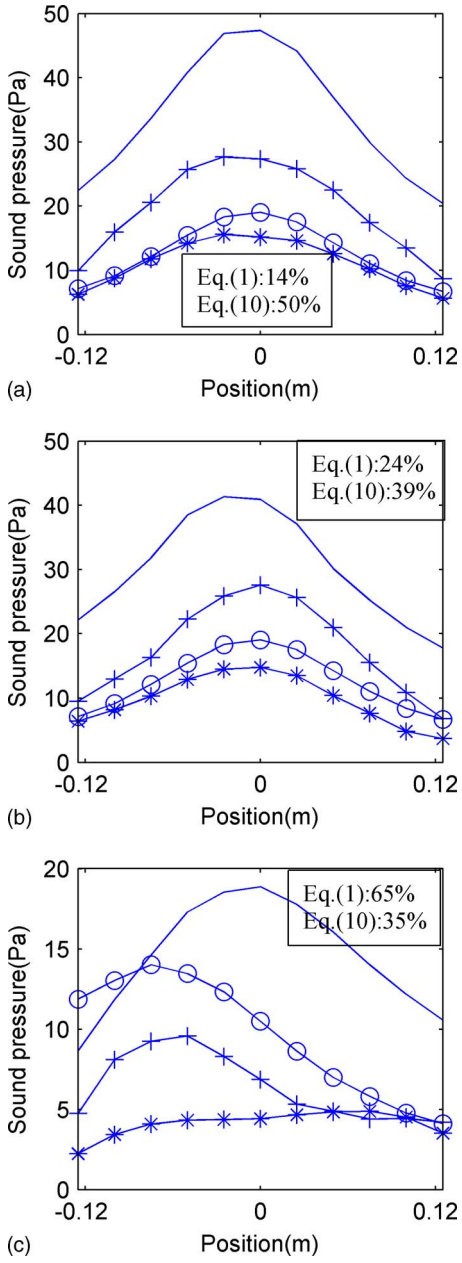

FIG. 5. (Color online) As in Fig. 3 but at 1016 Hz.

different frequencies, 320, 528, and 1016 Hz, respectively. In the symmetrical case 1, both methods perform reasonably well, although the original method is clearly better than the modified method at 1016 Hz. However, in the two nonsymmetrical cases (2 and 3), the method based on Eq. (10) is somewhat better than the original method based on Eq. (1), in particular, at low frequencies. It should finally be mentioned that the reconstructed phase has also been examined. The results, not shown, showed a similar tendency.

V. CONCLUSIONS

The single layer *p-u* method proposed by Jacobsen and Jaud can separate sound field contributions coming from the two sides of the measurement plane and performs well in some cases. However, the primary source and the disturbing source are usually not located symmetrically, and in such cases the alternative version described and examined in this letter somewhat performs better.

ACKNOWLEDGMENT

The authors would like to thank Microflown for lending us a *p-u* sound intensity probe. This work was supported by the National Natural Science Foundation of China (Grant Nos. 50675056 and 10874037) and Fok Ying Tung Education Foundation (Grant No. 111058). Additionally, the China Scholarship Council is acknowledged for financial support.

[1]J. D. Maynard, E. G. Williams, and Y. Lee, "Nearfield acoustic holography: I. Theory of generalized holography and the development of NAH," J. Acoust. Soc. Am. **78**, 1395–1413 (1985).
[2]W. A. Veronesi and J. D. Maynard, "Nearfield acoustic holography (NAH): II. Holographic reconstruction algorithms and computer implementation," J. Acoust. Soc. Am. **81**, 1307–1322 (1987).
[3]G. V. Frisk, A. V. Oppenheim, and D. R. Martinez, "A technique for measuring the plane-wave reflection coefficient of the ocean bottom," J. Acoust. Soc. Am. **68**, 602–612 (1980).
[4]M. T. Cheng, J. A. Mann III, and A. Pate, "Wave-number domain separation of the incident and scattered sound field in Cartesian and cylindrical coordinates," J. Acoust. Soc. Am. **97**, 2293–2303 (1995).
[5]J. Hald, "Patch holography in cabin environments using a two-layer handheld array with an extended SONAH algorithm," in Proceedings of Euronoise 2006, Tampere, Finland (2006).
[6]C.-X. Bi, X.-Z. Chen, and J. Chen, "Sound field separation technique based on equivalent source method and its application in nearfield acoustic holography," J. Acoust. Soc. Am. **123**, 1472–1478 (2008).
[7]F. Jacobsen and V. Jaud, "Statistically optimized near field acoustic holography using an array of pressure-velocity probe," J. Acoust. Soc. Am. **121**, 1550–1558 (2007).
[8]R. Steiner and J. Hald, "Near-field acoustical holography without the errors and limitations caused by the use of spatial DFT," Int. J. Acoust. Vib. **6**, 83–89 (2001).
[9]Y. T. Cho, J. S. Bolton, and J. Hald, "Source visualization by using statistically optimized nearfield acoustical holography in cylindrical coordinates," J. Acoust. Soc. Am. **118**, 2355–2364 (2005).
[10]C.-X. Bi and X.-Z. Chen, "Sound field separation technique based on equivalent source method using pressure-velocity measurements and its application in nearfield acoustic holography," in Proceedings of Inter-Noise, Shanghai, China (2008).
[11]S. Gade, N. Møller, J. Hald, and L. Alkestrup, "The use of volume velocity source in transfer measurements," in Proceedings of Inter-Noise 2004, Prague, Czech Republic (2004).

Greater sensitivity to prosodic goodness in non-native than in native listeners (L)

Anne Cutler[a)]
Max Planck Institute for Psycholinguistics, Nijmegen 6500 AH, The Netherlands and MARCS Auditory Laboratories, University of Western Sydney, NSW 1797, Australia

(Received 23 December 2008; revised 16 March 2009; accepted 16 March 2009)

English listeners largely disregard suprasegmental cues to stress in recognizing words. Evidence for this includes the demonstration of Fear *et al.* [J. Acoust. Soc. Am. **97**, 1893–1904 (1995)] that cross-splicings are tolerated between stressed and unstressed full vowels (e.g., *au-* of *autumn, automata*). Dutch listeners, however, do exploit suprasegmental stress cues in recognizing native-language words. In this study, Dutch listeners were presented with English materials from the study of Fear *et al.* Acceptability ratings by these listeners revealed sensitivity to suprasegmental mismatch, in particular, in replacements of unstressed full vowels by higher-stressed vowels, thus evincing greater sensitivity to prosodic goodness than had been shown by the original native listener group. © *2009 Acoustical Society of America.* [DOI: 10.1121/1.3117434]

PACS number(s): 43.71.Hw, 43.71.Es [RSN] Pages: 3522–3525

I. INTRODUCTION

Stressed and unstressed syllables in English differ both suprasegmentally and segmentally. Word recognition experiments in English have shown, however, that listeners attend primarily to the segmental structure, and to a great extent disregard suprasegmental cues to stress. Mis-stressing disrupts word identification only or principally when vowel quality is altered (Bond and Small, 1983; Cutler and Clifton, 1984; Slowiaczek, 1990), and the processing of minimal stress pairs where vowel quality does not differ, e.g., *insight/incite*, has in many differing experiments been shown to depend on contextual criteria rather than on assigned stress (Cutler, 1986; Slowiaczek, 1991; Small *et al.*, 1988; see Cutler, 2005, for a full review of the word recognition evidence).

A most telling finding was provided by Fear *et al.* (1995), who studied the production and perception of syllables varying in vowel quality (full, reduced) and stress. Vowel quality is the segmental reflection of English stress variation. Vowels bearing (primary or secondary) stress are always full, and reduced vowels are always unstressed. The reverse implications, though, do not hold; some full vowels do not bear stress, or conversely: some unstressed vowels are not reduced. English thus effectively has three syllable types: stressed with a full vowel (common), unstressed with a reduced vowel (common), and unstressed but with a full vowel (rare). Despite their rarity, the latter cases are crucial for understanding use of stress variation in speech perception.

The study of Fear *et al.* (1995) centered on sets of four vowel-initial words; each set comprised one word in which the initial vowel bore primary stress, one with an initial vowel bearing secondary stress (and primary stress on the third or fourth syllable), one with an unstressed initial vowel (and primary stress on the second syllable), and one with a reduced initial vowel. The four stimulus types can be referred to as P, S, U, and R, respectively, and an example set is *autumn, automation, automata, atomic*. Thus the initial vowel of *automata*, a U case, i.e., unstressed but with full vowel quality, is crucial; the central question of Fear *et al.* (1995) amounted to whether listeners treated U as more like R (because it was unstressed), as more like P or S (because it had a full vowel), or as a true separate case. Table I gives the sentence contexts for this set; it can be seen that phonetic and prosodic context was kept as similar as possible. The full set of materials is listed in Fear *et al.*, 1995.

In their study, 12 speakers produced all word sets in sentence context at two speech rates. Acoustic analyses showed that the four vowel types differed, at both rates. P and S differed in duration (P was longer) and these two stressed vowels as a class were distinct from U, and U from R, on duration, F0, intensity, and spectral quality. The acoustic foundation was thus in place for U vowels to function as cases different from either stressed (P/S) or R vowels.

To examine listeners' perception of (in particular) U vowels, the vowels were exhaustively cross-spliced within each word set, giving 16 stimuli per set. In shorthand terms in which each stimulus is referred to as a vowel (P, S, U, or R) followed by a body (from a word normally having P, S, U, or R vowel), the set for *autumn* would be PP, SP, UP, and RP, i.e., the P vowel (of *autumn*) or the S vowel (of *automation*), or the U vowel (of *automata*), or the R vowel (of *atomic*), each followed by the body of *autumn* (normally having an initial P vowel). The acceptability of these 16 item types was rated by listeners, who heard them either in a neutral environment, offering no contextual support regarding the identity of the word, or in a meaningful context, in which it was clear what each word should be (see Table I); the meaningful sentences were spoken at two speech rates: normal or fast.

Fear *et al.* (1995) distinguished four possible hypothesised outcomes of this perception test. The outcomes were principally distinguished by different patterns of statistical associations for the six stimulus types involving U vowels cross-spliced with another vowel. Two hypotheses assumed that U vowels would be treated as unlike either stressed or

[a)]Electronic mail: anne.cutler@mpi.nl

 0001-4966/2009/125(6)/3522/4/$25.00

TABLE I. Example stimulus set.

Initial syllable stress	Example word	Sentence context
P (primary)	*Autumn*	Summer is the time for berries, but autumn is the time for apples.
S (secondary)	*Automation*	The factory once employed 80, but automation reduced this by half.
U (unstressed)	*Automata*	The workers were treated as if they weren't humans, but automata to be programmed.
R (reduced)	*Atomic*	Armies used to be a country's main defense, but atomic weapons changed all that.

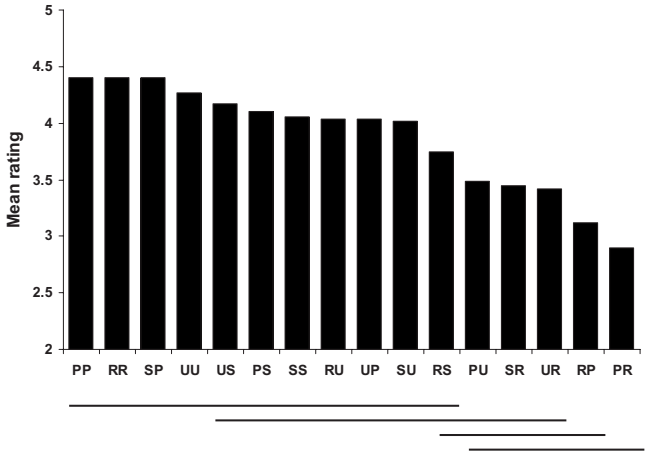

FIG. 1. Mean acceptability ratings (across participants and word sets) given by Dutch listeners to the 16 stimulus types, coded in vowel-body order (so, SP is a secondary-stressed vowel on the word body of the primary-stressed set member). Ratings were on a scale of 1–5, with maximum acceptability at 5. Ratings of word types linked by underlining do not differ statistically.

reduced vowels, and postulated a grouping linking US, SU, UP, PU, RU, and UR because they would all be perceived as mismatching. The other two hypotheses postulated a single category boundary, either based on vowel quality, with RU and UR items (different vowel quality expected versus realized) grouping distinctly from SU, US, PU, and UP (same quality), or on difference magnitude, with PU and UP (two steps apart) grouping distinctly from US, SU, UR, and RU (all one step apart). The results of Fear *et al.* (1995) most strongly supported a vowel-based categorical distinction. The acceptability ratings fell into distinct sets, linked by no statistical association, and overall SU, US, PU, and UP items were in one set, and RU and UR in the other. Further, correlation analyses of the listeners' ratings with acoustic properties of the stimuli showed the ratings to be more strongly related to measures of vowel quality than to any suprasegmental dimension. Fear *et al.* (1995) concluded that although the production data did not support a categorical distinction, listeners acted as if there were one anyway.

English stress is very similar to that in other Germanic languages such as Dutch and German (van der Hulst, 1999), but the vowel-based categoricality apparent in English listeners' responses is not seen in other Germanic languages for which listening evidence is plentiful. Mis-stressing in Dutch harms word identification even when vowel quality is unchanged (van Heuven, 1985), and suprasegmental information is used in the processing of Dutch minimal stress pairs (Cutler and van Donselaar, 2001). In both Dutch and German, word fragments cause inhibition of stress-mismatching words (van Donselaar *et al.*, 2005; Friedrich, 2002), whereas this inhibition is absent in English (Cooper *et al.*, 2002); thus *admi*-from *admiration* does not effectively inhibit *admiral*, whereas in Dutch, *domi*- of final-stress *dominant* ("dominant") does inhibit initially-stressed *dominee* ("pastor"). Sensitivity to suprasegmental cues to stress level is greater in German- or Dutch-speakers than in English-speakers.

When such speakers acquire English as a second language, the cues to stress level that they encounter and use in their native language will—as acoustic analyses of Fear *et al.* (1995) showed—also be available in the English they hear. Indeed, Cooper *et al.* (2002) found that Dutch listeners outperformed native English listeners in use of suprasegmental information. In the present study, Dutch listeners were exposed to the cross-spliced materials created by Fear *et al.* (1995), and their responses were compared with those of the native listeners in the original study.

II. METHOD

A. Materials

The stimuli of Fear *et al.* (1995) in the meaningful context, in which it was clear what each word should be, were selected for the present study. (Preliminary tests suggested that both the fast-speech condition and the neutral environment, offering no contextual cues to word identity, were difficult for non-native listeners.) There were 80 items: five word sets of four words each, each word occurring in four vowel versions. All versions contained the same word body in its sentence context, but differed in whether the initial vowel was original or was spliced in from another word of the same set. Thus in the example sentence "…but autumn is the time for apples," the word *autumn* could be, as described, a PP, SP, UP, or RP token. The test items were preceded, as in the original study, by a practice set of cross-spliced versions of *upper*, *upset*, *appeal* in sentence context.

B. Participants and procedure

Twenty-four Nijmegen University undergraduates, all native Dutch speakers with high proficiency in English, heard the sentences over Sennheiser headphones from disk, and followed written instructions (in Dutch) to rate the naturalness of the critical word specified for each sentence on a scale from 1 to 5, with 1 signifying that the word's prosodic form was completely wrong, 5 that it was completely right.

III. RESULTS

A. Acceptability ratings

Mean acceptability ratings were computed for each version of each word. The mean ratings for the 16 stimulus types (four words with four vowels each), averaged across the five word sets, are shown in Fig. 1 in order of rated

acceptability. As Figs. 5, 6, and 7 in Fear *et al.*, 1995 show, the original acceptability ratings plotted in this way showed a clear discontinuity, both in the meaningful context used here, as in the neutral environment, and overall. The present results are not discontinuous in this way, already suggesting that for the Dutch listeners no single over-riding cue is ascribed greatest weight in judging acceptability.

Statistical difference between these means was tested, as in the original study, by multiple comparisons; the association lines under the stimulus types in the figure link sets which are not statistically different from one another. In the original study, again, the multiple comparison results produced distinct sets; in both Fig. 7 of Fear *et al.*, 1995 for the meaningful context and Fig. 6 for the neutral context, despite differences in the precise ordering, the full set of 16 stimulus types always fell into two sets linked by no association lines. Here, this is not so; the four highest-rated stimuli are linked by no association lines to the five lowest-rated, but there is overlap across the seven stimulus types in between.

Of the four possible hypotheses set out by Fear *et al.* (1995), the two postulating a single category boundary are thus not supported by the present data. Instead, Fig. 1 shows a single association running from US to UR. Fear *et al.* (1995) predicted this if all cross-splicings involving U vowels were treated as mismatches, i.e., U vowels were treated as differing from both stressed and from reduced vowels.

B. Cross-experiment comparisons

Fear *et al.* (1995) conducted no analyses across participants, but in order to compare the response patterns of the present participant group with those of the original listeners, the raw data of Fear *et al.* (1995) was re-coded and mean ratings for each stimulus type were computed for each listener. The same values were computed for the present participants. Because the Dutch listeners' ratings were distributed over a different range than those of the native speakers, each group's ratings were converted to z-scores for a comparison across subjects via t-tests (uncorrelated means).

No effects of listener group were observed for most stimulus types. Just as the identity conditions were rated most highly by both listener groups, so the vowel quality differences were rated least highly by both. Significant differences emerged in exactly two conditions: U words with vowel replaced by a more highly stressed vowel (i.e., PU, SU). In each case ratings were significantly lower from the Dutch than from the native listeners ($t[46]=2.285$, $p=0.027$ for PU, $t[46]=2.292$, $p=0.027$ for SU).

C. Correlations of acceptability with acoustic factors

The acoustic properties of each stimulus token had been recorded by Fear *et al.* (1995), who conducted correlation analyses between their listeners' ratings for each token and measures of the difference between that token's original and substituted vowel in duration, intensity, F0, and spectral quality (expressed as the difference between F1 and F2 on a log scale). They found, as described, that the ratings were more strongly related to the vowel measure than to any of the suprasegmental measures (of which one, F0, was not related to the ratings at all, largely because the values for the speaker's tokens did not differ widely on this measure).

The same analyses were conducted for the present data. Again, the F0 measures did not predict listeners' ratings. There were significant correlations of rated acceptability with differences in duration ($r[59]=-0.483$, $p<0.001$) and intensity ($r[59]=-0.526$, $p<0.001$). In contrast to the native listener group, the present listeners did not show as systematic an effect of vowel quality difference; the correlation which had been the strongest for the native group did not reach significance here ($p=0.088$).

IV. DISCUSSION

The pattern of results found by Fear *et al.* (1995) with English listeners was not replicated here. The listener ratings of cross-spliced stimuli in Fear *et al.* (1995) were best described by a statistical model involving a vowel-based category distinction: stimuli in which vowel quality was preserved were statistically indistinguishable, and were rated significantly better than stimuli in which vowel quality was altered. Such a categorical division was not observed here; instead, there was a more gradient distribution across the ratings received by the stimulus types, with overlapping statistically motivated groupings, including one spanning the six cross-splicings involving U vowels. The responses of the original listeners correlated most strongly with a vowel quality measure, while the present responses correlated more strongly with acoustic measures of intensity and duration.

Direct comparisons between the two response sets showed that the differences principally occurred with words containing U vowels. Substitutions of a more stressed vowel (the PU and SU cases) were significantly less acceptable to the present Dutch listeners than to the original group.

Note that the converse of this finding is that in general, the ratings given by these non-native listeners were not significantly different from those of native listeners. Like listeners of Fear *et al.* (1995), the present group rated the items with an original vowel most highly, and the cross-spliced items where both segments and suprasegmentals mismatched least highly. The difference emerged precisely with the crucial case in which the mismatch was exclusively suprasegmental. By focusing on this case, using the paradigm devised by Fear *et al.*, (1995) it has been possible to discern a difference between these listener groups who are otherwise performing at an equivalently high level.

The findings suggest that Dutch listeners have a rather more refined appreciation of prosodic goodness than do English listeners. Specifically, they have a notion of what words with U (unstressed but full) vowels should sound like. There is good reason why they should have such a concept; U vowels are far more common in Dutch than they are in English. Cognate pairs abound to illustrate this: the first syllables of *cigar, parade, banana*, and the second syllables of *panda, cobra*, and *octopus* are all reduced in English, while the equivalent syllables in Dutch *sigaar, parade, banaan, panda, cobra*, and *octopus* all have full U vowels. Substitution of P or S vowels in place of the U vowel in such words would violate listeners' preconceptions. Cooper *et al.* (2002) found

that English syllables such as *mus-* from *music* versus *museum* could be more accurately attributed by Dutch than by English listeners, and the difference was greatest with the unstressed case (*mus-* from *museum*). English-speaking participants in that study actually performed significantly below chance with these cases. Dutch-speaking participants performed significantly above chance with the same items.

Another feature of the present results is also indicative of sensitivity to prosodic goodness. The present Dutch listener group produced a completely consistent response pattern with respect to direction of a mismatching cross-splice; mismatches in which the inserted vowel was less stressed than the original vowel were always rated more highly than mismatches in which a more highly stressed vowel replaced a less stressed (thus, as can be seen from Fig. 1, the rating for SP is above that for PS, UP above PU, US above SU, RP above PR, RS above SR, and RU above UR). This is in accord with what happens in natural speech—casual-speech processes lead to both suprasegmental and segmental reduction, so that citation forms are realised naturally in less stressed form. The reverse situation, i.e., higher stress than in the citation form, can also happen (in contrastive stress on morphemes, e.g., *He said IGnited not United*), but is far less likely.

This internal consistency, too, was absent from the responses found by Fear *et al.* (1995). For their English listeners, substitution of a more highly stressed vowel for a U vowel actually led to a higher rating than the reverse operation (with the same items as used here, SU was rated higher than US, and PU higher than UP). If, as Fear *et al.* (1995) proposed, the English listeners have internalized a vowel-based distinction (full versus reduced) only, then it may be that a P or S vowel better matches to their notion of what a full vowel should sound like than a U vowel does.

There are good reasons for English listeners to attend less to suprasegmental information in speech than listeners of other languages do. The payoff, in terms of reduction in the competitor population in spoken-word recognition, is significantly less in English than it is in Dutch and other languages (Cutler *et al.*, 2004; Cutler and Pasveer, 2006). English listeners can easily distinguish *parade* from *paradise* during the first syllable, because the vowels in the two words are different; Dutch listeners can distinguish the cognate words *parade* and *paradijs* as quickly as this only if they can use suprasegmental cues in the initial syllables, because even though the stress is different, the vowel quality is the same.

In comparison to native listeners, non-native listeners are in general disadvantaged. However, the present findings join those of Cooper *et al.* (2002) as evidence that listening skills encouraged by the native language might sometimes, when deployed in non-native listening, help to compensate for the disadvantages. The processing of stress is not the only case in which Dutch listeners to English appear to outdo native listeners; Broersma (2005, 2008) also observed that Dutch listeners can display more sensitivity than English listeners in distinguishing voicing contrasts at the end of English syllables. In that case, the native language, where voicing can contrast only syllable-initially, encouraged attention to cues within the consonant to distinguish the voicing feature. Dutch listeners could then use such cues also for English syllable-final contrasts, whereas for English listeners, vowel duration was an over-riding cue. In the stress case, the greater frequency of U vowels in Dutch has caused listeners to store knowledge of the acoustic differences between such vowels and vowels bearing stress. This knowledge can be deployed in recognizing Dutch words (e.g., to rule out *parade* during the *pa-* of *paradijs*). Even though the payoff is undoubtedly less in English than in Dutch, the same acoustic differences do obtain and hence the native listening skills can be transferred. In English, then, a Dutch listener could in principle call on these skills to determine, fractionally earlier than a native English listener, that *automatic* is being uttered, and not *automata*.

ACKNOWLEDGMENTS

Financial support was provided by the NWO SPINOZA project "Native and Non-native Listening." Thanks to Abeer Alwan for suggesting that this experiment would be likely to work, and to Sally Butterfield, Karly van Gorp, and Michael Tyler for unmissable assistance in making it happen.

Bond, Z., and Small, L. H. (**1983**). "Voicing, vowel, and stress mispronunciations in continuous speech," Percept. Psychophys. **34**, 470–474.
Broersma, M. (**2005**). "Perception of familiar contrasts in unfamiliar positions," J. Acoust. Soc. Am. **117**, 3890–3901.
Broersma, M. (**2008**). "Flexible cue use in nonnative phonetic categorization," J. Acoust. Soc. Am. **124**, 712–715.
Cooper, N., Cutler, A., and Wales, R. (**2002**). "Constraints of lexical stress on lexical access in English: Evidence from native and non-native listeners," Lang Speech **45**, 207–228.
Cutler, A. (**1986**). "Forbear is a homophone: Lexical prosody does not constrain lexical access," Lang Speech **29**, 201–220.
Cutler, A. (**2005**). "Lexical stress," in *The Handbook of Speech Perception*, edited by D. B. Pisoni and R. E. Remez (Blackwell, Oxford), pp. 264–289.
Cutler, A., and Clifton, C. (**1984**). "The use of prosodic information in word recognition," in *Attention and Performance X: Control of Language Processes*, edited by H. Bouma and D. G. Bouwhuis (Erlbaum, Hillsdale, NJ), pp. 183–196.
Cutler, A., and van Donselaar, W. (**2001**). "Voornaam is not (really) a homophone: Lexical prosody and lexical access in Dutch," Lang Speech **44**, 171–195.
Cutler, A., Norris, D., and Sebastián-Gallés, N. (**2004**). "Phonemic repertoire and similarity within the vocabulary," in Proceedings of Eighth International Conference on Spoken Language Processing, edited by S. H. Kim and D. H. Youn (Sunjin Printing Co., Seoul), Vol. **1**, pp. 65–68.
Cutler, A., and Pasveer, D. (**2006**). "Explaining cross-linguistic differences in effects of lexical stress on spoken-word recognition," in Proceedings of the Third International Conference on Speech Prosody, edited by R. Hoffman and H. Mixdorff (TUD, Dresden), pp. 250–254.
Fear, B. D., Cutler, A., and Butterfield, S. (**1995**). "The strong/weak syllable distinction in English," J. Acoust. Soc. Am. **97**, 1893–1904.
Friedrich, C. K. (**2002**). "Prosody and spoken word recognition—Behavioral and ERP correlates," Ph.D. thesis, University of Leipzig, Leipzig.
Slowiaczek, L. M. (**1990**). "Effects of lexical stress in auditory word recognition," Lang Speech **33**, 47–68.
Slowiaczek, L. M. (**1991**). "Stress and context in auditory word recognition," J. Psycholinguist. Res. **20**, 465–481.
Small, L. H., Simon, S. D., and Goldberg, J. S. (**1988**). "Lexical stress and lexical access: Homographs versus nonhomographs," Percept. Psychophys. **44**, 272–280.
van der Hulst, H. G. (**1999**). "Word accent," in *Word Prosodic Systems in the Languages of Europe*, H. G. van der Hulst (Mouton de Gruyter, Berlin), pp. 3–116.
van Donselaar, W., Koster, M., and Cutler, A. (**2005**). "Exploring the role of lexical stress in lexical recognition," Q. J. Exp. Psychol. A **58**, 251–273.
van Heuven, V. J. (**1985**). "Perception of stress pattern and word recognition: Recognition of Dutch words with incorrect stress position," J. Acoust. Soc. Am. **78**, S21.

A model for sound absorption by spheroidal particles

Alexander K. Hipp
Dow Chemical, 8810 Horgen, Switzerland

(Received 9 December 2008; revised 16 March 2009; accepted 25 March 2009)

This paper describes a mathematical model for the scattering of acoustic waves in dispersions of prolate or oblate non-spherical particles. Based on fundamental equations of change for mass, momentum, and energy, wave equations are derived and solved in spheroidal coordinates. The examination of the boundary-value problem of an aligned spheroidal particle in a continuous medium, excited by a plane wave, leads to a description of the viscoinertial, thermal, and diffractive phenomena. The model is analogous to the Epstein–Carhart–Allegra–Hawley theory for spherical particles, and suggests itself for studying non-sphericity in the acoustic analysis of industrial dispersions. © *2009 Acoustical Society of America.* [DOI: 10.1121/1.3119623]

PACS number(s): 43.20.Hq, 43.35.Bf [RR] Pages: 3526–3538

I. INTRODUCTION

Acoustic techniques for the analysis of dispersed system typically involve, first, capturing the response of the system to an acoustic signal and, second, interpretation of these data. The second part can cause considerable difficulty, as the information of interest is typically hidden in the measured data in a non-obvious way. Predictive models based on first principles can offer convenient data analysis without empirical calibration. Well-known models for dispersions of spherical particles or droplets include the model of Epstein–Carhart–Allegra–Hawley,[1,2] also referred to as ECAH theory, and coupled-phase models such as that of Dukhin and Goetz.[3,4] These models have found use, for example, in the determination of the solid content and particle size (and distribution) from acoustic attenuation spectra.[5–8]

To address the fact that industrial systems often involve non-spherical particles, this work implements an axisymmetric spheroidal particle geometry into the ECAH theory, as an approximation of the various shapes in real systems. As illustrated in Fig. 1, these objects are formed by rotation of an ellipse about its major (prolate spheroid) or minor axis (oblate spheroid). Alternative approaches toward the generalization of the ECAH framework to non-spherical geometries are reported, for example, for cylindrical obstacles[9,10] such as fiber suspensions, and by Datta and Shah[11] who used an ECAH type of model (yet without thermal transport) in spheroidal coordinates to derive solutions for the limiting cases of spheres and cylinders. Earlier work on acoustic scattering by spheroidal objects was narrower in scope and limited to rigid, elastic, soft, or penetrable scatterers without thermal transport mechanisms;[12–21] see also Ye's review paper.[22] Yet other ways of dealing with spheroidal scatterers are within the coupled-phase concept[23,24] or the transition matrix.[25] A similar separation-of-variables approach as in the ECAH theory was also used in spheroidal electromagnetic problems.[26–29]

This paper presents the background of the suggested spheroidal model, including its differential equations and assumptions, the corresponding wave equations, and the solution in prolate and oblate coordinates in terms of spheroidal wave functions by a separation of variables. The boundary conditions of a spheroidal particle in an infinite continuous medium, excited by a plane compressional wave, leads to a system of algebraic equations. This provides the model equations for the physical phenomena in and around the spheroid and thereby, for example, the attenuation imparted to an acoustic wave by a dispersion of spheroidal particles.

II. SPHEROIDAL COORDINATES

The particle under investigation is best described in spheroidal coordinates, where its surface corresponds to a constant value of the radial coordinate ξ. The definitions and the notation of Flammer[30] will be largely adopted throughout this work, where prolate coordinates $\{\eta,\xi,\psi\}$ are related to rectangular coordinates $\{x,y,z\}$ as follows:

$$x = a(1-\eta^2)^{1/2}(\xi^2-1)^{1/2}\cos\psi, \tag{1}$$

$$y = a(1-\eta^2)^{1/2}(\xi^2-1)^{1/2}\sin\psi, \tag{2}$$

$$z = a\,\eta\xi. \tag{3}$$

Oblate coordinates are defined in a similar way, except that (ξ^2+1) appears in place of (ξ^2-1) in Eqs. (1) and (2). The radial coordinate $\xi=1,\ldots,\infty$ (prolate) or $\xi=0,\ldots,\infty$ (oblate) defines the distance from the origin. The angles $\eta=-1,\ldots,1$ and $\psi=0,\ldots,2\pi$ are analogous to $\cos\theta$ and ψ in spherical coordinates. The constant a defines the semifocal distance of the spheroid, the z axis is its axis of revolution.

Instead of ξ and a, a spheroidal particle can also be characterized by its eccentricity ϵ (aspect ratio; ratio of the longest to the shortest axis) and the radius r_{eq} of a sphere of equivalent volume. The values of ξ and a can be recovered by

$$\xi = \begin{cases} \dfrac{\epsilon}{(\epsilon^2-1)^{1/2}} & \text{prolate} \\ \dfrac{1}{(\epsilon^2-1)^{1/2}} & \text{oblate}, \end{cases} \tag{4}$$

 0001-4966/2009/125(6)/3526/13/$25.00

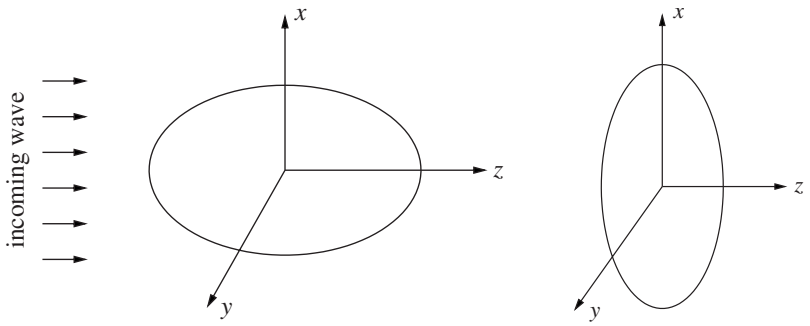

FIG. 1. A prolate (left) and an oblate spheroid (right) in a plane wave.

$$a = \begin{cases} \dfrac{r_{\mathrm{eq}}}{(\xi^3 - \xi)^{1/3}} & \text{prolate} \\ \dfrac{r_{\mathrm{eq}}}{(\xi^3 + \xi)^{1/3}} & \text{oblate}. \end{cases} \tag{5}$$

These relations follow from the half-axis lengths of the respective spheroid, which are $a\xi$ and either $a(\xi^2-1)^{1/2}$ (prolate) or $a(\xi^2+1)^{1/2}$ (oblate),[30] and its volume, which is $4\pi/3$ times the product of the three half-axes.

Except for Eqs. (4) and (5), the oblate and the prolate cases are analogous. This paper presents only the prolate equations. The oblate versions can be obtained at any time by replacing ξ and a in a prolate relation by $i\xi_{\mathrm{obl}}$ and $-ia_{\mathrm{obl}}$, where ξ_{obl} and a_{obl} are those of Eqs. (4) and (5).

For some vector operations used below, scale factors will be required, as defined by $h_\eta^2=(\partial x/\partial\eta)^2+(\partial y/\partial\eta)^2+(\partial z/\partial\eta)^2$, etc.[31] With Eqs. (1)–(3), this results in

$$h_\eta = \frac{a(\xi^2 - \eta^2)^{1/2}}{(1-\eta^2)^{1/2}}, \tag{6}$$

$$h_\xi = \frac{a(\xi^2 - \eta^2)^{1/2}}{(\xi^2-1)^{1/2}}, \tag{7}$$

$$h_\psi = a(1-\eta^2)^{1/2}(\xi^2-1)^{1/2}. \tag{8}$$

Using the coordinates in the order $\{\eta,\xi,\psi\}$ ensures a right-handed coordinate system.[30]

III. DIFFERENTIAL EQUATIONS

The model of this paper is based on the fundamental principles of mass, momentum, and energy conservation, simplified for linear acoustic waves and vanishing overall motion. Linearity implies small deviations of all variables (e.g., $\delta\rho$ for the density ρ) from their values at rest (e.g., ρ_0) and therefore $\delta\rho \ll \rho_0$ in $\rho=\rho_0+\delta\rho$. This allows writing the equations of change for mass, momentum, and energy without second-order terms such as $(\delta\rho)^2$,[31,32]

$$\rho^{-1}\frac{\partial\rho}{\partial t} = -(\boldsymbol{\nabla}\cdot\boldsymbol{v}), \tag{9}$$

$$\rho\frac{\partial\boldsymbol{v}}{\partial t} = -(\boldsymbol{\nabla}\cdot\boldsymbol{\tau}), \tag{10}$$

$$\rho\frac{\partial u}{\partial t} = -(\boldsymbol{\nabla}\cdot\boldsymbol{q}) - p(\boldsymbol{\nabla}\cdot\boldsymbol{v}), \tag{11}$$

where ρ is the density, t is the time, $\boldsymbol{v}$ is the velocity vector, $\boldsymbol{\tau}$ is the stress tensor, u is the internal energy, $\boldsymbol{q}$ is the heat flux, and p is the pressure. These relations can be transformed into an equivalent potential representation.[32,33] This transformation makes use of Helmholtz' theorem to express the velocity vector $\boldsymbol{v}$ in terms of a scalar potential Φ and a vector potential $\mathbf{A}$ by means of $\boldsymbol{v}=-i\omega(-\boldsymbol{\nabla}\Phi+\boldsymbol{\nabla}\times\mathbf{A})$, where the vector potential $\mathbf{A}$ is assumed to be non-divergent without loss of generality, thus $\boldsymbol{\nabla}\cdot\mathbf{A}=0$, and the scalar potential is split into a "compressional" and a "thermal" component, $\Phi=\Phi_c+\Phi_t$. By assuming harmonic oscillations with an angular frequency ω and thus an $e^{-i\omega t}$ dependence for all states, whereby time derivatives $(\partial/\partial t)$ become equivalent to $(-i\omega)$, and by assuming a linear stress–strain relation and Fourier's law for the heat transfer, the above equations can be transformed into the following scalar and vector equations:

$$(\boldsymbol{\nabla}^2 + k_c^2)\Phi_c = 0, \tag{12}$$

$$(\boldsymbol{\nabla}^2 + k_t^2)\Phi_t = 0, \tag{13}$$

$$(\boldsymbol{\nabla}^2 + k_s^2)\mathbf{A} = \mathbf{0}, \tag{14}$$

with the wavenumbers k_c (compressional), k_t (thermal), and k_s (shear),

$$k_c = \frac{\omega}{c} + i\alpha, \quad k_t = \left[\frac{i\omega\rho c_p}{\lambda}\right]^{1/2}, \quad k_s = \left[\frac{\rho\omega^2}{\mu}\right]^{1/2} \tag{15}$$

or in products with the semifocal distance a:

$$c_c = k_c a, \quad c_t = k_t a, \quad c_s = k_s a. \tag{16}$$

The symbols c (without subscript), α, c_p, and λ stand for the sound speed and attenuation in the medium under consideration, heat capacity, and thermal conductivity, respectively. μ is either the shear modulus G (for solids), or equal to $-i\omega$ times the shear viscosity (for liquids), or $G'-iG''$ (for viscoelastic materials).[34]

When focusing on a specific coordinate system, the scalar components of the vector equation (14) can be written out.[31,35] In the axisymmetric case, $\boldsymbol{\nabla}\cdot\mathbf{A}=0$ implies that $\mathbf{A}$ consists of only one non-vanishing component, $\mathbf{A}=[0\ 0\ A_\psi]$, which is also not a function of the azimuthal angle ψ, whereby two components of Eq. (14) vanish identically. In prolate coordinates, the third component of Eq. (14) becomes

$$\left[\nabla^2 + k_s^2 - \frac{1}{a^2(\xi^2-1)(1-\eta^2)}\right]A_\psi = 0. \tag{17}$$

Equations (12), (13), and (17) define a system of three scalar elliptic Helmholtz equations for the potentials Φ_c, Φ_t and $\mathbf{A}=[0\ 0\ A_\psi]$. A Helmholtz equation can be solved by separation of variables: using $R(\xi)S(\eta)T(\psi)$ for the potential and multiplying the equation with $(\xi^2-1)(1-\eta^2)(\xi^2-\eta^2)^{-1}(RST)^{-1}$ allow to identify parts that depend solely on ξ, η, or ψ, respectively; each part needs to be constant to be able to fulfill the equation for arbitrary values of the independent variables.

The part that depends on ψ, that is, $(1/T)\partial^2 T/\partial\psi^2$, can be set to $-m_c^2$ when solving Eq. (12), to $-m_t^2$ for Eq. (13), and to $1-m_s^2$ for Eq. (17). The solutions of this equation are $\cos(m_{c/t}\psi)$ and $\sin(m_{c/t}\psi)$ in the compressional and thermal cases, and $\cos((m_s^2-1)^{1/2}\psi)$ and $\sin((m_s^2-1)^{1/2}\psi)$ in the shear case. Because of the axial symmetry of the problem at hand, where the solution is not a function of ψ, it is clear that $m_c=m_t=0$ and $m_s=1$ (Ref. 36) and thus $T(\psi)=1$. The parts that depend on ξ or η can in turn be split into two independent ordinary differential equations using the eigenvalue λ_{mn} as separation constant. With the present choice of separation constants, this leads to the same pair of equations for the compressional, thermal, and the shear case:

$$\frac{\partial}{\partial\xi}\left[(\xi^2-1)\frac{\partial}{\partial\xi}R_{mn}(c,\xi)\right] - \left[\lambda_{mn} - c^2\xi^2 + \frac{m^2}{\xi^2-1}\right]R_{mn}(c,\xi) = 0, \tag{18}$$

$$\frac{\partial}{\partial\eta}\left[(1-\eta^2)\frac{\partial}{\partial\eta}S_{mn}(c,\eta)\right] + \left[\lambda_{mn} - c^2\eta^2 - \frac{m^2}{1-\eta^2}\right]S_{mn}(c,\eta) = 0. \tag{19}$$

The solution of these equations are the radial and angular spheroidal wave functions, respectively, usually denoted as R_{mn} and S_{mn}, or actually linear combinations thereof for all n and m. Both functions exist in two kinds, which are both a solution of the respective second-order differential equation. Both kinds need to be retained in the radial case, done here by $R_{mn}^{(3)}=R_{mn}^{(1)}+iR_{mn}^{(2)}$ and $R_{mn}^{(1)}$. In the angular case, the function of the second kind $S_{mn}^{(2)}$ is irregular at $\eta=\pm 1$ and is thus not considered. The remaining $S_{mn}^{(1)}$ (S_{mn} for simplicity) can be expanded in terms of orthogonal Legendre polynomials $P_n^m(\eta)$ and a coefficient $d_r^{mn}(c)$,[30]

$$S_{mn}(c,\eta) = \sum_{r=0}^{\infty} d_r^{mn}(c)P_{m+r}^m(\eta), \tag{20}$$

where $d_r^{mn}=0$ for $m+n+r=$odd or $r<0$; otherwise d_r^{mn} follows from a recurrence relation.[30] The associated Legendre polynomial is $P_r^m(\eta)\equiv(1-\eta^2)^{m/2}(d^m/d\eta^m)P_r^0(\eta)$.

A. General solution

Built according to $R(\xi)S(\eta)T(\psi)$ as defined above, the solutions of Eqs. (12), (13), and (17) can be written as

$$\Phi_c = \sum_{n=0}^{\infty}\sum_{r=0}^{\infty} i^n(2n+1)f_c d_r^{0n}(c_c)P_r^0(\eta), \tag{21}$$

$$\Phi_t = \sum_{n=0}^{\infty}\sum_{r=0}^{\infty} i^n(2n+1)f_t d_r^{0n}(c_t)P_r^0(\eta), \tag{22}$$

$$A_\psi = \sum_{n=0}^{\infty}\sum_{r=0}^{\infty} i^n(2n+1)f_s d_{r-1}^{1n}(c_s)P_r^1(\eta), \tag{23}$$

with, for convenience, the following shorthands:

$$f_c = A_n R_{0n}^{(3)}(c_c,\xi) + \bar{A}_n R_{0n}^{(1)}(c_c,\xi), \tag{24}$$

$$f_t = B_n R_{0n}^{(3)}(c_t,\xi) + \bar{B}_n R_{0n}^{(1)}(c_t,\xi), \tag{25}$$

$$f_s = C_n R_{1n}^{(3)}(c_s,\xi) + \bar{C}_n R_{1n}^{(1)}(c_s,\xi), \tag{26}$$

where A_n, $\bar{A}_n$, B_n, $\bar{B}_n$, C_n and $\bar{C}_n$ are integration constants to be defined by the boundary conditions. Note that a form of Eq. (20) with a shifted r was used in Eq. (23), $S_{mn}(c,\eta)=\sum_{r=1}^{\infty}d_{r-1}^{mn}(c)P_{m+r-1}^m(\eta)$, where the sum can be started at $r=0$ as in the original series because of $d_r^{mn}=0$ for $r<0$. Because of the arbitrarily introduced factor $i^n(2n+1)$, above potentials converge to the ECAH theory[1,2] in the spherical limit, where $\xi\to\infty$, $a\xi\to r^*$, $\eta\to\cos\theta$, and

$$R_{mn}^{(1)}(c,\xi) \xrightarrow{\text{spherical}} j_n(kr^*), \tag{27}$$

$$R_{mn}^{(3)}(c,\xi) \xrightarrow{\text{spherical}} h_n(kr^*), \tag{28}$$

$$S_{mn}(c,\eta) \xrightarrow{\text{spherical}} P_n^m(\cos\theta), \tag{29}$$

$$d_r^{mn}(c) \xrightarrow{\text{spherical}} \begin{cases} 1 & \text{for } r=n-m \\ 0 & \text{otherwise,} \end{cases} \tag{30}$$

with the spherical Bessel functions j_n and h_n.

B. Special forms of the solution

Equation (21) can represent a plane compressional wave. This can be seen from the general description of a plane wave with wavenumber k_c in prolate coordinates [Eq. (5.3.3) in Ref. 30]

$$\Phi_{c0} = \sum_{n=0}^{\infty}\sum_{m=0}^{\infty} 2i^n\frac{2-\delta_{0m}}{N_{mn}(c_c)}S_{mn}(c_c,\cos\theta_0)R_{mn}^{(1)}(c_c,\xi) \times S_{mn}(c_c,\eta)\cos m(\psi-\psi_0), \tag{31}$$

where δ_{0m} is the Kronecker delta. θ_0 and ψ_0 define the propagation direction of the plane wave. The time factor $e^{-i\omega t}$ is suppressed for readability. For propagation in positive z direction, $\theta_0=\psi_0=0$, in which case all terms with $m\neq 0$ vanish identically. This can be seen by rewriting $S_{mn}(c,1)$ with Eq. (20), and noting that $P_r^m(1)$ is zero for $m\neq 0$ (or unity for $m=0$). In this case, the normalization constant N_{0n} is $\sum_{r=0}^{\infty}[2(d_r^{0n})^2/(2r+1)]$ [Eq. (3.1.33) in Ref. 30], and the above equation simplifies to

$$\Phi_{c0} = \sum_{n=0}^{\infty} \frac{i^n \Sigma_{r=0}^{\infty} d_r^{0n}(c_c)}{\Sigma_{r=0}^{\infty} (d_r^{0n}(c_c))^2/(2r+1)} R_{0n}^{(1)}(c_c,\xi) S_{0n}(c_c,\eta). \tag{32}$$

This can be brought into the standard form of Eq. (21) by means of

$$f_{c0} = A_n^0 R_{0n}^{(1)}(c_c,\xi), \tag{33}$$

with

$$A_n^0 = \frac{(\Sigma_{r=0}^{\infty} d_r^{0n}(c_c))/(2n+1)}{\Sigma_{r=0}^{\infty} (d_r^{0n}(c_c))^2/(2r+1)}. \tag{34}$$

The index 0 was introduced to denote the incoming wave. Note that A_n^0 approaches unity in the spherical limit with Eq. (30).

Equations (21)–(26) can also represent "secondary" waves, e.g., as created inside and around a particle in response to a primary wave. Outside the particle (index 1 below), the potentials cannot contain $R_{mn}^{(1)}$, as this function (as its spherical analog j_n) becomes infinite for $\xi \to \infty$. This reduces Eqs. (24)–(26) to

$$f_{c1} = A_n R_{0n}^{(3)}(c_c,\xi), \tag{35}$$

$$f_{t1} = B_n R_{0n}^{(3)}(c_t,\xi), \tag{36}$$

$$f_{s1} = C_n R_{1n}^{(3)}(c_s,\xi). \tag{37}$$

Instead, within the particles (index 2 below), $R_{mn}^{(3)}$ cannot be used, as this function (as its spherical analog h_n) becomes infinite for $\xi \to 0$ and thus

$$f_{c2} = \bar{A}_n R_{0n}^{(1)}(\bar{c}_c,\xi), \tag{38}$$

$$f_{t2} = \bar{B}_n R_{0n}^{(1)}(\bar{c}_t,\xi), \tag{39}$$

$$f_{s2} = \bar{C}_n R_{1n}^{(1)}(\bar{c}_s,\xi). \tag{40}$$

Bars have been used for properties of the particles $(\bar{A},\bar{c})$ vs the continuous medium (A,c).

IV. MODEL EQUATIONS

The above framework is used below to describe a spheroidal particle in a compressional plane wave. Because of the different physical properties in the particle and the surrounding medium, secondary waves are created inside (index 2) and around the particle (index 1) as a response to the incident wave (index 0). The descriptors of these waves $[A_n, B_n, \ldots, \bar{C}_n$ of Eqs. (35)–(40)] are determined below from boundary conditions for the velocity, temperature, heat flux, and the stress at the particle surface. This will produce six equations for the determination of the six unknowns, Eqs. (44), (48), (54), (55), (59), and (63) below, in analogy to Eqs. (8a–f) in Ref. 2 for the spherical case.

A. Velocity in radial direction

The derivation starts from the definition of the velocity in terms of the potentials, $\boldsymbol{v} = (-i\omega)\ (-\boldsymbol{\nabla}\Phi + \boldsymbol{\nabla} \times \mathbf{A})$. By resolving the $\boldsymbol{\nabla}$-operators for general orthogonal coordinates using scale factors,[31] the ξ component of this vector relation can be written as follows:

$$v_\xi/(-i\omega) = -\boldsymbol{\nabla}_\xi \Phi + \boldsymbol{\nabla}_\xi \times \mathbf{A} = -\frac{1}{h_\xi}\frac{\partial \Phi}{\partial \xi} - \frac{h_\xi}{h_\eta h_\xi h_\psi}\frac{\partial (h_\psi A_\psi)}{\partial \eta}. \tag{41}$$

The scale factors are given by Eqs. (6)–(8), and noting that $\Phi = \Phi_c + \Phi_t$, the potentials can be expressed by Eqs. (21)–(23). This introduces terms in P_r^0 and P_r^1, which can be collected in P_r^0 using the recurrence relation $d/d\eta[(1-\eta^2)^{1/2} P_r^1(\eta)] = -r(r+1) P_r^0(\eta)$ [follows when rewriting Eq. (8.5.2) in Ref. 37 with the associated Legendre polynomial as defined after Eq. (20)]. This results in

$$v_\xi = \sum_{n=0}^{\infty}\sum_{r=0}^{\infty} \frac{(-i\omega) i^n (2n+1)}{a(\xi^2-\eta^2)^{1/2}} \cdot [-(\xi^2-1)^{1/2}(d_r^{0n}(c_c) f_c' + d_r^{0n}(c_t) f_t') + r(r+1) d_{r-1}^{1n}(c_s) f_s] P_r^0(\eta), \tag{42}$$

with $f' \equiv \partial f/\partial \xi$. This is a general relation between the potentials and the resulting radial velocity which can be used for the incoming wave (index 0) as well as for the secondary waves around (index 1) and inside the particle (index 2). Since the waves and the resulting velocities can be superimposed due to the linearity of the problem, the continuity in radial velocity requires $v_{\xi 0} + v_{\xi 1} = v_{\xi 2}$ at the particle boundary, and thus

$$\sum_{n=0}^{\infty} -(\xi^2-1)^{1/2}(d_r^{0n}(c_c)(f_{c0}' + f_{c1}') - d_r^{0n}(\bar{c}_c) f_{c2}' + d_r^{0n}(c_t) f_{t1}' - d_r^{0n}(\bar{c}_t) f_{t2}') + r(r+1)(d_{r-1}^{1n}(c_s) f_{s1} - d_{r-1}^{1n}(\bar{c}_s) f_{s2}) = 0 \quad \text{for } r = 0, \ldots, \infty. \tag{43}$$

Bars distinguish properties of the particulate phase from those of the continuous phase. Note that the summation over r has been dropped due to the orthogonality of the Legendre polynomials, which requires that each term in the series needs to vanish individually for every r $(0, \ldots, \infty)$ to achieve validity for arbitrary values of η. In turn, this allowed dropping $P_r^0(\eta)$, and the boundary condition is therefore now entirely independent of η. With Eqs. (33)–(40) for the shorthands f, Eq. (43) becomes

$$\sum_{n=0}^{\infty} A_n^0 d_r^{0n}(c_c) R_{0n}^{(1)\prime}(c_c,\xi) + A_n d_r^{0n}(c_c) R_{0n}^{(3)\prime}(c_c,\xi) + B_n d_r^{0n}(c_t) R_{0n}^{(3)\prime}(c_t,\xi) - C_n r(r+1) d_{r-1}^{1n}(c_s) R_{1n}^{(3)}(c_s,\xi)/(\xi^2-1)^{1/2} - \bar{A}_n d_r^{0n}(\bar{c}_c) R_{0n}^{(1)\prime}(\bar{c}_c,\xi) - \bar{B}_n d_r^{0n}(\bar{c}_t) R_{0n}^{(1)\prime}(\bar{c}_t,\xi) + \bar{C}_n r(r+1) d_{r-1}^{1n}(\bar{c}_s) R_{1n}^{(1)}(\bar{c}_s,\xi)/(\xi^2-1)^{1/2} = 0 \quad \text{for } r = 0, \ldots, \infty. \tag{44}$$

As opposed to the spherical case, the summation over n needs to be retained, as the expression does not contain an orthogonal function in n. Note that because of $d_r^{mn} = 0$ for $m+n+r = \text{odd}$ [see Eq. (20)], the terms in the sum vanish

identically for every other n. Even and odd modes are therefore coupled among themselves, but are decoupled from each other.

B. Velocity in tangential direction

The tangential velocity is handled along the same lines as the radial component. With $\boldsymbol{v}=(-i\omega)(-\boldsymbol{\nabla}\Phi+\boldsymbol{\nabla}\times\mathbf{A})$, the tangential velocity can be written out as follows:[31]

$$v_\eta/(-i\omega) = -\nabla_\eta\Phi + \nabla_\eta \times \mathbf{A} = -\frac{1}{h_\eta}\frac{\partial\Phi}{\partial\eta} + \frac{h_\eta}{h_\eta h_\xi h_\psi}\frac{\partial(h_\psi A_\psi)}{\partial\xi}. \tag{45}$$

With $\Phi=\Phi_c+\Phi_t$ and A_ψ from Eqs. (21)–(23), the scale factors from Eqs. (6)–(8), and by rewriting P_r^0 in terms of P_r^1 using the definition of the associated Legendre polynomial [see after Eq. (20)], one arrives at

$$v_\eta = \sum_{n=0}^{\infty}\sum_{r=0}^{\infty}\frac{(-i\omega)i^n(2n+1)}{a(\xi^2-\eta^2)^{1/2}}\left[-d_r^{0n}(c_c)f_c - d_r^{0n}(c_t)f_t + \frac{\partial}{\partial\xi}(\xi^2-1)^{1/2}d_{r-1}^{1n}(c_s)f_s\right]P_r^1(\eta). \tag{46}$$

The boundary condition $v_{\eta 0}+v_{\eta 1}=v_{\eta 2}$ at the particle surface, with the incoming (index 0) and the secondary waves (index 1 outside the particle, index 2 inside), then becomes

$$\sum_{n=0}^{\infty} -d_r^{0n}(c_c)(f_{c0}+f_{c1}) + d_r^{0n}(\bar{c}_c)f_{c2} - d_r^{0n}(c_t)f_{t1} + d_r^{0n}(\bar{c}_t)f_{t2} + \frac{\partial}{\partial\xi}(\xi^2-1)^{1/2}(d_{r-1}^{1n}(c_s)f_{s1} - d_{r-1}^{1n}(\bar{c}_s)f_{s2}) \quad \text{for } r=1,\ldots,\infty \tag{47}$$

and, with f from Eqs. (33)–(40),

$$\sum_{n=0}^{\infty} A_n^0 d_r^{0n}(c_c)R_{0n}^{(1)}(c_c,\xi) + A_n d_r^{0n}(c_c)R_{0n}^{(3)}(c_c,\xi) + B_n d_r^{0n}(c_t)R_{0n}^{(3)}(c_t,\xi) - C_n d_{r-1}^{1n}(c_s)(R_{1n}^{(3)\prime}(c_s,\xi)(\xi^2-1)^{1/2} + R_{1n}^{(3)}(c_s,\xi)\xi/(\xi^2-1)^{1/2}) - \bar{A}_n d_r^{0n}(\bar{c}_c)R_{0n}^{(1)}(\bar{c}_c,\xi) - \bar{B}_n d_r^{0n}(\bar{c}_t)R_{0n}^{(1)}(\bar{c}_t,\xi) + \bar{C}_n d_{r-1}^{1n}(\bar{c}_s)(R_{1n}^{(1)\prime}(\bar{c}_s,\xi)(\xi^2-1)^{1/2} + R_{1n}^{(1)}(\bar{c}_s,\xi)\xi/(\xi^2-1)^{1/2}) = 0 \quad \text{for } r=1,\ldots,\infty. \tag{48}$$

Regarding the summation over r and the dropping of the Legendre polynomial, the same comments apply as before Eq. (44). Also note that, as Eq. (46) vanishes identically for $r=0$ because of $P_0^1=0$, Eqs. (47) and (48) are invalid for $r=0$.

C. Temperature fluctuation and heat flux

In a similar way as the velocity, also the temperature fluctuation can be computed from the potentials. This relation can be written as $T=b_c\Phi_c+b_t\Phi_t$, which can be obtained in the derivation of the wave equations,[1,2,32] with

$$b_c = -\frac{\gamma}{c_1^2\beta}\left[\omega^2 - \left(\frac{c_1^2}{\gamma}+\frac{4\mu}{3\rho}\right)k_c^2\right], \tag{49}$$

$$b_t = -\frac{\gamma}{c_1^2\beta}\left[\omega^2 - \left(\frac{c_1^2}{\gamma}+\frac{4\mu}{3\rho}\right)k_t^2\right], \tag{50}$$

$$c_1^2 = c^2 - 4\,\mathrm{Re}(\mu)/(3\rho), \tag{51}$$

$$\gamma = c_p/c_v = 1 + c_1^2\beta^2 T_{\mathrm{abs}}/c_p, \tag{52}$$

where γ is the ratio of the specific heats, β is the thermal volumetric expansion, μ is the quantity defined after Eq. (16), c is the sound speed, c_1 is the modified sound speed as defined in Ref. 2, and T_{abs} the average absolute temperature in Kelvin. With Eqs. (21) and (22), the temperature can then be written as

$$T = \sum_{n=0}^{\infty}\sum_{r=0}^{\infty} i^n(2n+1)[b_c d_r^{0n}(c_c)f_c + b_t d_r^{0n}(c_t)f_t]P_r^0(\eta). \tag{53}$$

With Eqs. (33)–(40), the boundary condition $T_0+T_1=T_2$ for the superposition of the incoming wave (index 0) and those in the continuous phase (1) and the particle (2) results in

$$\sum_{n=0}^{\infty} A_n^0 b_c d_r^{0n}(c_c)R_{0n}^{(1)}(c_c,\xi) + A_n b_c d_r^{0n}(c_c)R_{0n}^{(3)}(c_c,\xi) + B_n b_t d_r^{0n}(c_t)R_{0n}^{(3)}(c_t,\xi) - \bar{A}_n\bar{b}_c d_r^{0n}(\bar{c}_c)R_{0n}^{(1)}(\bar{c}_c,\xi) - \bar{B}_n\bar{b}_t d_r^{0n}(\bar{c}_t)R_{0n}^{(1)}(\bar{c}_t,\xi) = 0 \quad \text{for } r=0,\ldots,\infty. \tag{54}$$

As before, the summation over r and thus also P_r^0 were dropped due to the orthogonality of the Legendre polynomials. The boundary condition for the radial component of the heat flux follows from Eq. (53) with Fourier's law $\boldsymbol{q}=-\lambda\boldsymbol{\nabla}T$:

$$\sum_{n=0}^{\infty} A_n^0\lambda b_c d_r^{0n}(c_c)R_{0n}^{(1)\prime}(c_c,\xi) + A_n\lambda b_c d_r^{0n}(c_c)R_{0n}^{(3)\prime}(c_c,\xi) + B_n\lambda b_t d_r^{0n}(c_t)R_{0n}^{(3)\prime}(c_t,\xi) - \bar{A}_n\bar{\lambda}\bar{b}_c d_r^{0n}(\bar{c}_c)R_{0n}^{(1)\prime}(\bar{c}_c,\xi) - \bar{B}_n\bar{\lambda}\bar{b}_t d_r^{0n}(\bar{c}_t)R_{0n}^{(1)\prime}(\bar{c}_t,\xi) = 0 \quad \text{for } r=0,\ldots,\infty. \tag{55}$$

D. Shear stress

The derivation of the stress tensor components is somewhat more involved than the above, although it follows the same principles. The reason is that the terms in the series are a more complicated function of the angle η than before. Whereas previously, the dependence on η was only through the orthogonal Legendre polynomial (which immediately justifies looking at every r individually and in turn allows dropping P_r^m and thus all η dependence), the present case necessitates the use of recurrence relations to remove η.

The starting point is Newton's law of viscosity for liquids, or analogous Hooke's law for solids, which both define a linear relation between material deformation and the resulting stress. Two components of the stress tensor are relevant in the present context: the η-directed shear stress in a plane perpendicular to the ξ axis, $\tau_{\xi\eta}$, and the normal stress in ξ direction, $\tau_{\xi\xi}$. In the first case, Newton's and Hooke's law can be written as $\tau_{\xi\eta}=-\mu[\boldsymbol{\nabla v}+(\boldsymbol{\nabla v})^{\mathrm{T}}]_{\xi\eta}/(-i\omega)$, where μ is the symbol in Eq. (15). The terms in the square bracket correspond to a rate of strain, and can be resolved as follows:[31]

$$[\boldsymbol{\nabla v}+(\boldsymbol{\nabla v})^{\mathrm{T}}]_{\xi\eta}=\frac{h_\xi}{h_\eta}\frac{\partial}{\partial\eta}\frac{v_\xi}{h_\xi}+\frac{h_\eta}{h_\xi}\frac{\partial}{\partial\xi}\frac{v_\eta}{h_\eta}. \tag{56}$$

With Eqs. (42) and (46) for v_ξ and v_η, and Eqs. (6) and (7) for the scale factors, an expression with infinite sums in n and r is obtained. In addition to applying the product rule for $d/d\eta$ and $d/d\xi$ [leaving either the terms before or after the opening square bracket of Eqs. (42) and (46) intact], one can also make use of $P_n^1(\eta)=(1-\eta^2)^{1/2}dP_n^0(\eta)/d\eta$ [see after Eq. (20)] to obtain

$$\begin{aligned}\tau_{\xi\eta}=\sum_{n=0}^{\infty}\sum_{r=0}^{\infty}\frac{(-\mu)i^n(2n+1)}{a^2(\xi^2-\eta^2)^2}\Big\{&(\xi^2-\eta^2)[-(\xi^2-1)^{1/2}(d_r^{0n}(c_c)f_c'+d_r^{0n}(c_t)f_t')+r(r+1)d_{r-1}^{1n}(c_s)f_s]P_r^1(\eta)\\&+2\eta(1-\eta^2)^{1/2}[-(\xi^2-1)^{1/2}(d_r^{0n}(c_c)f_c'+d_r^{0n}(c_t)f_t')+r(r+1)d_{r-1}^{1n}(c_s)f_s]P_r^0(\eta)+(\xi^2-\eta^2)(\xi^2-1)^{1/2}\Big[-d_r^{0n}(c_c)f_c'\\&-d_r^{0n}(c_t)f_t'+\frac{\partial^2}{\partial\xi^2}(\xi^2-1)^{1/2}d_{r-1}^{1n}(c_s)f_s\Big]P_r^1(\eta)-2\xi(\xi^2-1)^{1/2}\Big[-d_r^{0n}(c_c)f_c-d_r^{0n}(c_t)f_t+\frac{\partial}{\partial\xi}(\xi^2-1)^{1/2}d_{r-1}^{1n}(c_s)f_s\Big]P_r^1(\eta)\Big\}.\end{aligned} \tag{57}$$

As opposed to the previous cases, where the dependence on η was identical in all sums with only either $P_r^0(\eta)$ or $P_r^1(\eta)$, the present series contain also other dependencies on η:

$\eta^2 \quad d_r^{0n}\ P_r^1(\eta)\rightarrow$ Eq. (A8),

$\eta^2 \quad d_{r-1}^{1n}\ P_r^1(\eta)\rightarrow$ Eq. (A9),

$\eta^2 \quad r(r+1)d_{r-1}^{1n}\ P_r^1(\eta)\rightarrow$ Eq. (A10),

$\eta(1-\eta^2)^{1/2} \quad d_r^{0n}\ P_r^0(\eta)\rightarrow$ Eq. (A11),

$\eta(1-\eta^2)^{1/2}r(r+1)d_{r-1}^{1n}\ P_r^0(\eta)\rightarrow$ Eq. (A12).

With the identities in Appendix A (using the equations indicated above), the series in Eq. (57) can be replaced by equivalent ones that contain the dependence on η only through $P_r^1(\eta)$:

$$\begin{aligned}\tau_{\xi\eta}=\sum_{n=0}^{\infty}\sum_{r=0}^{\infty}\frac{\mu i^n(2n+1)}{a^2(\xi^2-\eta^2)^2}&[t_c^{t0}(c_c)f_c+t_c^{t1}(c_c)f_c'+t_c^{t0}(c_t)f_t\\&+t_c^{t1}(c_t)f_t'+t_s^{t0}(c_s)f_s+t_s^{t1}(c_s)f_s'+t_s^{t2}(c_s)f_s'']P_r^1(\eta).\end{aligned} \tag{58}$$

The expressions for t are given in Appendix B. As the t are independent of η, the only η dependence is now in terms of $P_r^1(\eta)$, which, however, cancels out in the usual way when building the boundary condition $\tau_{\xi\eta,0}+\tau_{\xi\eta,1}=\tau_{\xi\eta,2}$ at the particle boundary:

$$\begin{aligned}\sum_{n=0}^{\infty}&A_n^0\mu[t_c^{t0}(c_c)R_{0n}^{(1)}(c_c,\xi)+t_c^{t1}(c_c)R_{0n}^{(1)\prime}(c_c,\xi)]+A_n\mu[t_c^{t0}(c_c)R_{0n}^{(3)}(c_c,\xi)+t_c^{t1}(c_c)R_{0n}^{(3)\prime}(c_c,\xi)]+B_n\mu[t_c^{t0}(c_t)R_{0n}^{(3)}(c_t,\xi)\\&+t_c^{t1}(c_t)R_{0n}^{(3)\prime}(c_t,\xi)]+C_n\mu[t_s^{t0}(c_s)R_{1n}^{(3)}(c_s,\xi)+t_s^{t1}(c_s)R_{1n}^{(3)\prime}(c_s,\xi)+t_s^{t2}(c_s)R_{1n}^{(3)\prime\prime}(c_s,\xi)]-\bar{A}_n\bar{\mu}[t_c^{t0}(\bar{c}_c)R_{0n}^{(1)}(\bar{c}_c,\xi)\\&+t_c^{t1}(\bar{c}_c)R_{0n}^{(1)\prime}(\bar{c}_c,\xi)]-\bar{B}_n\bar{\mu}[t_c^{t0}(\bar{c}_t)R_{0n}^{(1)}(\bar{c}_t,\xi)+t_c^{t1}(\bar{c}_t)R_{0n}^{(1)\prime}(\bar{c}_t,\xi)]-\bar{C}_n\bar{\mu}[t_s^{t0}(\bar{c}_s)R_{1n}^{(1)}(\bar{c}_s,\xi)+t_s^{t1}(\bar{c}_s)R_{1n}^{(1)\prime}(\bar{c}_s,\xi)\\&+t_s^{t2}(\bar{c}_s)R_{1n}^{(1)\prime\prime}(\bar{c}_s,\xi)]=0\quad\text{for } r=1,\ldots,\infty.\end{aligned} \tag{59}$$

Note that as already in the case of the tangential velocity, this expression is not meaningful for $r=0$ because of $P_0^1=0$ in Eq. (58).

E. Normal stress

The stress in normal direction to the particle surface, $\tau_{\xi\xi}$, can be derived in a similar way as the tangential stress. The expressions are somewhat longer due to a more complicated form of Newton's and Hooke's law in this case,

$$\tau_{\xi\xi} = \mu(2k_c^2 - k_s^2)\Phi_c + \mu(2k_t^2 - k_s^2)\Phi_t - \mu[\boldsymbol{\nabla v} + (\boldsymbol{\nabla v})^{\mathrm{T}}]_{\xi\xi} \times(-i\omega), \tag{60}$$

where μ is the symbol in Eq. (15). The first two terms on the right-hand side represent contributions from the hydrodynamic pressure and the volumetric expansion,[32,33] whereas the last expression corresponds to the geometric strain of deformation. The latter is given by[31]

$$[\boldsymbol{\nabla v} + (\boldsymbol{\nabla v})^{\mathrm{T}}]_{\xi\xi} = \frac{2}{h_\xi}\left[\frac{\partial v_\xi}{\partial \xi} + \frac{v_\eta}{h_\eta}\frac{\partial h_\xi}{\partial \eta} + \frac{v_\psi}{h_\psi}\frac{\partial h_\xi}{\partial \psi}\right].$$

With Eqs. (42) and (46) for the velocities, the scale factors of Eqs. (6)–(8), and Eqs. (21) and (22) for the potentials, Eq. (60) then becomes

$$\tau_{\xi\xi} = \sum_{n=0}^{\infty}\sum_{r=0}^{\infty}\frac{-2\mu i^n(2n+1)}{a^2(\xi^2-\eta^2)^2}\Big\{-(\xi^2-\eta^2)^2(c_c^2 - c_s^2/2)f_c d_r^{0n}(c_c)P_r^0(\eta) - (\xi^2-\eta^2)^2(c_t^2 - c_s^2/2)f_t d_r^{0n}(c_t)P_r^0(\eta) + (\xi^2-\eta^2)(\xi^2-1)^{1/2}\frac{\partial}{\partial\xi}$$
$$\times[-(\xi^2-1)^{1/2}(d_r^{0n}(c_c)f_c' + d_r^{0n}(c_t)f_t') + r(r+1)d_{r-1}^{1n}(c_s)f_s]P_r^0(\eta) - \xi(\xi^2-1)^2[-(\xi^2-1)^{1/2}(d_r^{0n}(c_c)f_c' + d_r^{0n}(c_t)f_t') + r(r$$
$$+1)d_{r-1}^{1n}(c_s)f_s]P_r^0(\eta) - \eta(1-\eta^2)^{1/2}\left[-d_r^{0n}(c_c)f_c - d_r^{0n}(c_t)f_t + d_{r-1}^{1n}(c_s)\frac{\partial}{\partial\xi}(\xi^2-1)^{1/2}f_s\right]P_r^1(\eta)\Big\}. \tag{61}$$

As already for the shear stress, this expression contains numerous dependencies on η,

$$\eta^2 \quad d_r^{0n}\ P_r^0(\eta) \rightarrow \text{Eq. (A5)},$$

$$\eta^4 \quad d_r^{0n}\ P_r^0(\eta) \rightarrow \text{Eq. (A7)},$$

$$\eta^2 \quad r(r+1)\ d_{r-1}^{1n}\ P_r^0(\eta) \rightarrow \text{Eq. (A6)},$$

$$\eta(1-\eta^2)^{1/2} \quad d_r^{0n}\ P_r^1(\eta) \rightarrow \text{Eq. (A13)},$$

$$\eta(1-\eta^2)^{1/2} \quad d_{r-1}^{1n}\ P_r^1(\eta) \rightarrow \text{Eq. (A14)},$$

which need to be removed using the recurrence relations indicated above. The result is the following expression for the normal stress with the desired simple dependence on η through only the Legendre polynomial $P_r^0(\eta)$:

$$\tau_{\xi\xi} = \sum_{n=0}^{\infty}\sum_{r=0}^{\infty}\frac{-2\mu i^n(2n+1)}{a^2(\xi^2-\eta^2)^2}[t_c^{r0}(c_c)f_c + t_c^{r1}(c_c)f_c' + t_c^{r2}(c_c)f_c'' + t_c^{r0}(c_t)f_t + t_c^{r1}(c_t)f_t' + t_c^{r2}(c_t)f_t'' + t_s^{r0}(c_s)f_s + t_s^{r1}(c_s)f_s']P_r^0(\eta). \tag{62}$$

The shorthands t are independent of η, details can be found in Appendix B. This form of the normal stress allows the construction of the corresponding boundary condition $\tau_{\xi\xi,0} + \tau_{\xi\xi,1} = \tau_{\xi\xi,2}$ at the particle boundary (0=incoming wave, 1=wave around the particle, 2=wave inside the particle) as follows:

$$\sum_{n=0}^{\infty} A_n^0\mu[t_c^{r0}(c_c,c_s)R_{0n}^{(1)}(c_c,\xi) + t_c^{r1}(c_c)R_{0n}^{(1)\prime}(c_c,\xi) + t_c^{r2}(c_c)R_{0n}^{(1)\prime\prime}(c_c,\xi)] + A_n\mu[t_c^{r0}(c_c,c_s)R_{0n}^{(3)}(c_c,\xi) + t_c^{r1}(c_c)R_{0n}^{(3)\prime}(c_c,\xi)$$
$$+ t_c^{r2}(c_c)R_{0n}^{(3)\prime\prime}(c_c,\xi)] + B_n\mu[t_c^{r0}(c_t,c_s)R_{0n}^{(3)}(c_t,\xi) + t_c^{r1}(c_t)R_{0n}^{(3)\prime}(c_t,\xi) + t_c^{r2}(c_t)R_{0n}^{(3)\prime\prime}(c_t,\xi)] + C_n\mu[t_s^{r0}(c_s)R_{1n}^{(3)}(c_s,\xi)$$
$$+ t_s^{r1}(c_s)R_{1n}^{(3)\prime}(c_s,\xi)] - \bar{A}_n\bar{\mu}[t_c^{r0}(\bar{c}_c,\bar{c}_s)R_{0n}^{(1)}(\bar{c}_c,\xi) + t_c^{r1}(\bar{c}_c)R_{0n}^{(1)\prime}(\bar{c}_c,\xi) + t_c^{r2}(\bar{c}_c)R_{0n}^{(1)\prime\prime}(\bar{c}_c,\xi)] - \bar{B}_n\bar{\mu}[t_c^{r0}(\bar{c}_t,\bar{c}_s)R_{0n}^{(1)}(\bar{c}_t,\xi)$$
$$+ t_c^{r1}(\bar{c}_t)R_{0n}^{(1)\prime}(\bar{c}_t,\xi) + t_c^{r2}(\bar{c}_t)R_{0n}^{(1)\prime\prime}(\bar{c}_t,\xi)] - \bar{C}_n\bar{\mu}[t_s^{r0}(\bar{c}_s)R_{1n}^{(1)}(\bar{c}_s,\xi) + t_s^{r1}(\bar{c}_s)R_{1n}^{(1)\prime}(\bar{c}_s,\xi)] = 0 \quad \text{for } r = 0,\ldots,\infty. \tag{63}$$

In the usual way, the orthogonality of the Legendre polynomial allowed to consider each r in Eq. (62) individually, and in turn to drop P_r^0.

V. DISCUSSION

The model consists of Eqs. (44), (48), (54), (55), (59), and (63), providing six algebraic equations for the determination of A_n, B_n, C_n (waves in the continuous phase) and

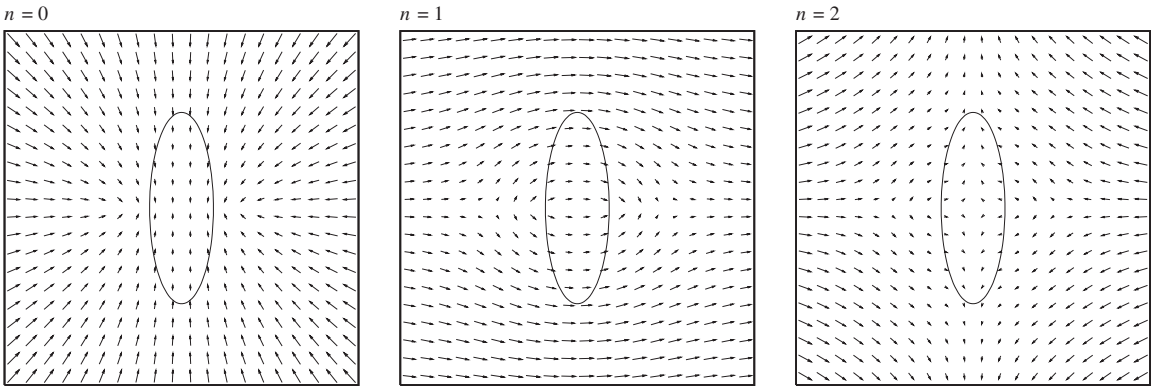

FIG. 2. Flow around an oblate spheroid (ϵ=3). The figure shows axisymmetric compression in the thermal mode (n=0), particle drag in the viscoinertial mode (n=1), and the first higher-order mode (n=2) for silica in water (Ref. 6), an equivalent-sphere diameter of 300 nm, 5 MHz, and ωt=93°.

$\bar{A}_n, \bar{B}_n, \bar{C}_n$ (waves within the particle). These equations are analogous to Eqs. (8a–f) in Ref. 2 for the spherical case and converge to those in the spherical limit. The zeroth-order coefficients C_0 and $\bar{C}_0$ are not used [as $d_r^{mn}=0$ for $n<m$ in Eq. (23)]; the parity between equations and unknowns is maintained by noting that Eqs. (48) and (59) are undefined for $r=0$. The system is completely determined by the size and shape of the spheroid [$\xi=\xi_{\text{pro}}$ and $a=a_{\text{pro}}$, or $\xi=i\xi_{\text{obl}}$ and $a=-ia_{\text{obl}}$, of Eqs. (4) and (5)] and the physical properties of the continuous phase and the particle.

In contrast to the spherical case,[2] where the model equations can be solved individually for every n, the spheroidal model equations are connected for different n because of the summation $n=0,\ldots,\infty$. This coupling is among all even modes $n=0,2,4,\ldots,\infty$ on the one hand, and all odd modes $n=1,3,5,\ldots,\infty$ on the other, as discussed after Eq. (44). It is therefore impossible to compute, e.g., A_0 without also computing A_2, A_4, etc.

In practice, thanks to the fact that the series converge for higher n, the evaluation can usually be restricted to some $n_{\max}$. The number of equations then follows from $r=0,\ldots,n_{\max}$. If sufficient accuracy is obtained when dropping, for example, all orders $n>5$, one obtains an 18×18 system of equations from $n=1,3,5$ and $r=1,3,5$ for the odd modes, and a 16×16 system from $n=0,2,4$ and $r=0,2,4$ for the even modes (where the zeroth-order mode contributes only a 4×4 subsystem). The convergence can be verified by augmenting $n_{\max}$ until the coefficients of interest converge to the desired accuracy. Larger values of the eccentricity ϵ typically require a higher $n_{\max}$.

A. Using the solutions

After solution of the model equations, the values of $A_n, B_n, \ldots, \bar{C}_n$ can, e.g., be used to produce the velocity field shown in Fig. 2. The underlying equation is $\boldsymbol{v}=-i\omega(-\boldsymbol{\nabla}\Phi+\boldsymbol{\nabla}\times\mathbf{A})$. At this point, it is important to introduce the time factor $e^{-i\omega t}$, a factor which is implicitly assumed in the wave equations but was omitted in the definition of the incident wave in Eq. (31). The real part of the resulting complex velocity is the actual physical quantity, $\boldsymbol{v}_{\text{actual}}=\text{Re}(-i\omega(-\boldsymbol{\nabla}\Phi+\boldsymbol{\nabla}\times\mathbf{A})e^{-i\omega t})$.[32]

The solution also leads to the attenuation of an acoustic wave by the particles in the system. Assuming that all particles in the system contribute in a linear way, the attenuation α is given by

$$\alpha=-\frac{3\phi}{2k_c^2 r_{\text{eq}}^3}\sum_{n=0}^{\infty}(2n+1)\text{Re}(A_n), \tag{64}$$

where ϕ is the volume fraction occupied by dispersed particles.[2,33] As the computation of attenuation is based on waves at a large distance from the particle, where the spheroidal wave functions approach their spherical counterparts with $\xi\to\infty$, see Eqs. (27)–(30), Eq. (64) is identical as in the spherical theory.

B. Model comparison

Figure 3 shows a comparison between the suggested model and that of Babick and Richter.[24] The attenuation spectra were produced for the limiting case of axisymmetric aligned prolate and oblate spheroids with an aspect ratio of 3 and an equal-sphere diameter of 1 μm. Aligning to the scope of Babick and Richter's coupled-phase model, the present

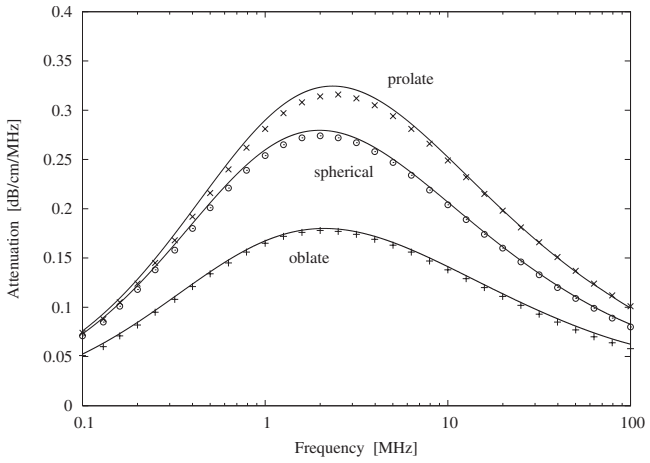

FIG. 3. Viscoinertial attenuation from the suggested model (lines) and that of Babick and Richter (symbols) (Ref. 24) for silica in water (Ref. 6), an equivalent-sphere diameter of 1 μm, an eccentricity of ϵ=3, and a particle concentration of 10 vol %. All terms but n=1 were dropped from Eq. (64) to restrict the model to viscoinertial effects.

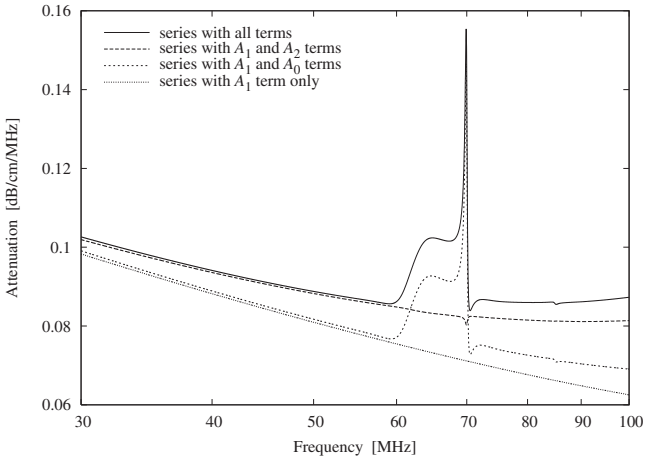

FIG. 4. As Fig. 3, but showing also modes other than $n=1$ for the oblate case.

model was restricted to viscoinertial losses by using only the $n=1$ term in Eq. (64). The figure shows good agreement between the two models, both for the prolate and oblate as well as the spherical case.

C. Modes

The contribution of the different modes is shown in Fig. 4. Although the viscoinertial losses ($n=1$) are dominant, the thermal losses ($n=0$) and higher-order modes (redirective scattering) become increasingly important at higher frequencies. This is particularly true for $n=0$ with peaks around 60–70 MHz, but also $n=2$ is significant. This suggests that the long-wavelength assumption, the basis of common simplifications such as the restriction to viscoinertial losses, breaks down relatively early for spheroidal scatterers.

The interpretation of $n=0$ as axisymmetric compressions and $n=1$ as viscoinertial drag, and their relative importance for systems of low and high density contrast, appears to be independent of particle shape. This is shown in Fig. 5. Regardless of the aspect ratio, and for prolate as well as oblate particles, $n=0$ dominates systems of low density contrast such as the polystyrene latex in Fig. 5(a), with a density of 1.05 g/cm^3 for polystyrene vs 1 g/cm^3 for water. This type of system is governed by local axisymmetric compressions ($n=0$ in Fig. 2) and the resulting thermal fluxes. Instead, systems of high density contrast such as the colloidal silica in Fig. 5(b), with 2.2 vs 1 g/cm^3, are dominated by the viscoinertial mode ($n=1$), where the overall particle motion and the resulting viscous drag ($n=1$ in Fig. 2) result in strong acoustic attenuation.

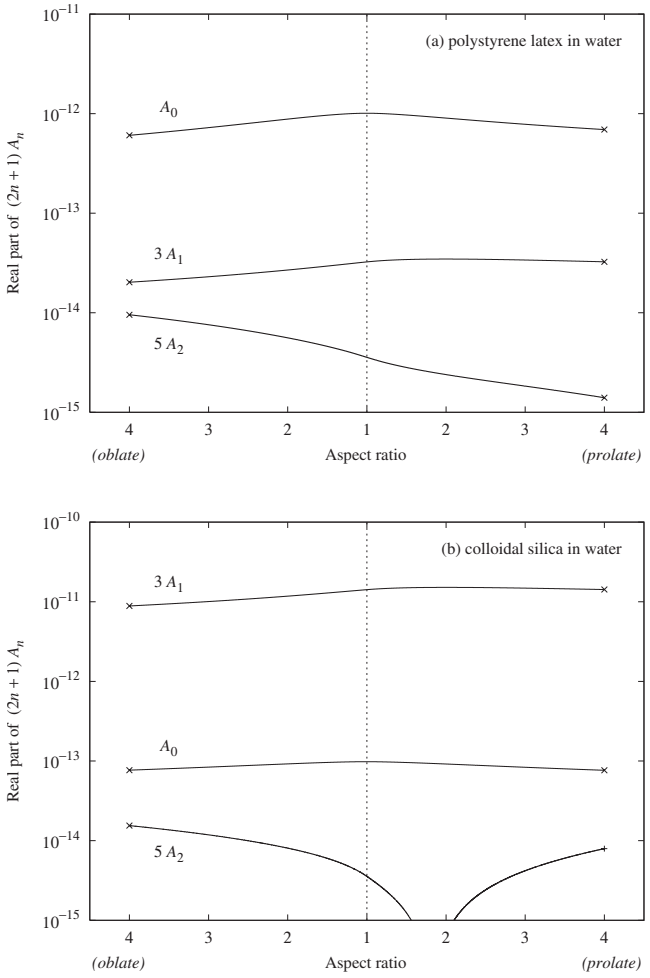

FIG. 5. The first three terms ($n=0,1,2$) in the series of Eq. (64). Regardless of the aspect ratio ϵ, and both for oblate and prolate spheroids, the attenuation is dominated by the thermal mode ($n=0$) for low density contrast (a) and by the viscoinertial mode ($n=1$) for high density contrast (b). The lines were computed for 1.5 MHz, an equivalent-sphere diameter of 300 nm and standard physical properties (Refs. 2 and 6). + denotes positive, and × negative values.

VI. CONCLUSIONS

A new model for the acoustic analysis of spheroidal suspended particles was presented. The wave equations for the compressional, thermal, and shear waves were solved in spheroidal coordinates and used to describe an aligned spheroid in an infinite embedding medium. The resulting model is a system of six algebraic equations, representing the continuity of velocity, stress, temperature, and heat flux at the particle boundary.

The spheroidal model is analogous to the spherical ECAH theory[1,2] and also converges to the latter in the spherical limit; however, its model equations and their solution are considerably more involved. The reason is that the angular spheroidal functions S_{mn} are not orthogonal, as opposed to the analogous Legendre polynomials P_n^m in the spherical case. The recurrence relations which are therefore needed for the elimination of the angular position η from the model equations introduce a cumbersome coupling among all even and among all odd modes.

The model predictions are in good agreement with Babick and Richter's viscoinertial model.[24] However, the suggested model offers a more comprehensive description of the transport phenomena and the resulting thermal, viscoinertial, and higher-order scattering losses. It is therefore not restricted to viscoinertial attenuation in high density-contrast

systems, and can be useful for the validation of simpler models, for example, to verify the validity of the common long-wavelength assumption.

ACKNOWLEDGMENTS

The present work was inspired by research initiated by Professor Massimo Morbidelli and Giuseppe Storti at the Swiss Federal Institute of Technology/ETH Zurich, Switzerland, on acoustic characterization of colloidal systems.[32] Thanks also go to Peter Falloon at the University of Western Australia for his help on spheroidal wave functions[38] and to Frank Babick at the Technical University Dresden for details on Figs. 3 and 4 of their publication.[24]

APPENDIX A: RECURRENCE RELATIONS

A number of recurrence relations for Legendre polynomials are used in the derivation of the stress tensor. They are based on the following identities:

$$\eta P_r^0 = \frac{r+1}{2r+1} P_{r+1}^0 + \frac{r}{2r+1} P_{r-1}^0, \tag{A1}$$

$$\eta P_r^1 = \frac{r}{2r+1} P_{r+1}^1 + \frac{r+1}{2r+1} P_{r-1}^1, \tag{A2}$$

$$(1-\eta^2)^{1/2} P_r^0 = \frac{1}{2r+1} P_{r+1}^1 - \frac{1}{2r+1} P_{r-1}^1, \tag{A3}$$

$$(1-\eta^2)^{1/2} P_r^1 = r P_{r-1}^0 - r\eta P_r^0. \tag{A4}$$

These identities follow from Eq. (8.5.3) in Ref. 37 with $\mu=0$ and 1, and Eq. (8.5.5) with $\mu=1$ and 0, keeping in mind the specific definitions of the associated Legendre polynomial P_r^m [see after Eq. (20) vs their Eq. (8.6.6)]. The argument η of all P_r^m is suppressed for readability.

In this work, the left-hand sides of Eq. (A1)–(A4) appear in series of $r=0,\ldots,\infty$. This allows to deduce more specific relations. A first relation is obtained by multiplying Eq. (A1) with ηd_r^{0n} and summing for $r=0,\ldots,\infty$:

$$\sum_{r=0}^{\infty} \eta^2 d_r^{0n} P_r^0 = \sum_{r=1}^{\infty} \eta d_{r-1}^{0n} \frac{r}{2r-1} P_r^0 + \sum_{r=-1}^{\infty} \eta d_{r+1}^{0n} \frac{r+1}{2r+3} P_r^0.$$

In the series on the right-hand side, a variable transformation $r_{\text{new}}=r_{\text{old}}+1$ or $r_{\text{new}}=r_{\text{old}}-1$, respectively, was used to obtain all polynomials with the same index. Noting r and $r+1$ in the numerators, the series on the right-hand side can be started at $r=0$ without loss of generality. By reinserting Eq. (A1) for ηP_r^0 on the right-hand side, and repeating the variable transformation to obtain the Legendre polynomials with the same index r, one obtains an expression without η on the right-hand side [except in $P_r^0(\eta)$]:

$$\sum_{r=0}^{\infty} \eta^2 d_r^{0n} P_r^0 = \sum_{r=0}^{\infty} \left[d_{r-2}^{0n} \frac{(r-1)r}{(2r-3)(2r-1)} + d_r^{0n} \frac{2r^2+2r-1}{(2r-1)(2r+3)} + d_{r+2}^{0n} \frac{(r+2)(r+1)}{(2r+5)(2r+3)} \right] P_r^0. \tag{A5}$$

Similar relations are obtained from Eq. (A1)–(A4) with this iterative procedure of summation, index shifting, and application of recurrence relations. For instance, when multiplying Eq. (A1) with $\eta r(r+1) d_{r-1}^{1n}$, this procedure leads to

$$\sum_{r=0}^{\infty} \eta^2 r(r+1) d_{r-1}^{1n} P_r^0 = \sum_{r=0}^{\infty} \left[d_{r-3}^{1n} \frac{(r-2)(r-1)^2 r}{(2r-3)(2r-1)} + d_{r-1}^{1n} \frac{r(r+1)(2r^2+2r-1)}{(2r-1)(2r+3)} + d_{r+1}^{1n} \frac{(r+3)(r+2)^2(r+1)}{(2r+5)(2r+3)} \right] P_r^0. \tag{A6}$$

A third relation is obtained from Eq. (A1) after multiplication with $\eta^3 d_r^{0n}$ and going through above procedure (however, several times due to the higher power of η):

$$\sum_{r=0}^{\infty} \eta^4 d_r^{0n} P_r^0 = \sum_{r=0}^{\infty} \left[d_{r-4}^{0n} \frac{(r-3)(r-2)(r-1)r}{(2r-7)(2r-5)(2r-3)(2r-1)} + d_{r-2}^{0n} \frac{2(2r^2-2r-7)(r-1)r}{(2r-5)(2r+3)(2r-1)(2r-3)} + d_r^{0n} \frac{3(2r^4+4r^3-6r^2-8r+3)}{(2r-3)(2r-1)(2r+5)(2r+3)} + d_{r+2}^{0n} \frac{2(2r^2+6r-3)(r+2)(r+1)}{(2r-1)(2r+3)(2r+7)(2r+5)} + d_{r+4}^{0n} \frac{(r+4)(r+3)(r+2)(r+1)}{(2r+9)(2r+7)(2r+5)(2r+3)} \right] P_r^0. \tag{A7}$$

The procedure can also be applied to Eq. (A2) instead of Eq. (A1). Multiplication of Eq. (A2) with ηd_r^{0n} yields

$$\sum_{r=0}^{\infty} \eta^2 d_r^{0n} P_r^1 = \sum_{r=0}^{\infty} \left[d_{r-2}^{0n} \frac{r-2}{2r-3} \frac{r-1}{2r-1} + d_r^{0n} \frac{2r^2+2r-3}{(2r-1)(2r+3)} + d_{r+2}^{0n} \frac{r+3}{2r+5} \frac{r+2}{2r+3} \right] P_r^1. \quad \text{(A8)}$$

Instead, upon multiplication of Eq. (A2) with ηd_{r-1}^{1n}, the procedure leads to

$$\sum_{r=0}^{\infty} \eta^2 d_{r-1}^{1n} P_r^1 = \sum_{r=0}^{\infty} \left[d_{r-3}^{1n} \frac{r-2}{2r-3} \frac{r-1}{2r-1} + d_{r-1}^{1n} \frac{2r^2+2r-3}{(2r-1)(2r+3)} + d_{r+1}^{1n} \frac{r+3}{2r+5} \frac{r+2}{2r+3} \right] P_r^1, \quad \text{(A9)}$$

whereas, upon multiplication of Eq. (A2) with $\eta r(r+1) d_{r-1}^{1n}$, the procedure leads to

$$\sum_{r=0}^{\infty} \eta^2 r(r+1) d_{r-1}^{1n} P_r^1 = \sum_{r=0}^{\infty} \left[d_{r-3}^{1n} \frac{(r-2)^2(r-1)^2}{(2r-3)(2r-1)} + d_{r-1}^{1n} \frac{r(r+1)(2r^2+2r-3)}{(2r-1)(2r+3)} + d_{r+1}^{1n} \frac{(r+2)^2(r+3)^2}{(2r+5)(2r+3)} \right] P_r^1. \quad \text{(A10)}$$

When multiplying Eq. (A3) with ηd_r^{0n}, the procedure of summation, index shifting, and insertion of Eq. (A2) leads to

$$\sum_{r=0}^{\infty} \eta (1-\eta^2)^{1/2} d_r^{0n} P_r^0 = \sum_{r=0}^{\infty} \left[d_{r-2}^{0n} \frac{1}{2r-3} \frac{r-1}{2r-1} + d_r^{0n} \frac{1}{(2r-1)(2r+3)} + d_{r+2}^{0n} \frac{(-1)}{2r+5} \frac{r+2}{2r+3} \right] P_r^1, \quad \text{(A11)}$$

whereas after multiplication of Eq. (A3) with $\eta r(r+1) d_{r-1}^{1n}$, the procedure leads to

$$\sum_{r=0}^{\infty} \eta (1-\eta^2)^{1/2} r(r+1) d_{r-1}^{1n} P_r^0 = \sum_{r=0}^{\infty} \left[d_{r-3}^{1n} \frac{(r-2)(r-1)^2}{(2r-3)(2r-1)} + d_{r-1}^{1n} \frac{r(r+1)}{(2r-1)(2r+3)} + d_{r+1}^{1n} \frac{(-1)(r+2)^2(r+3)}{(2r+5)(2r+3)} \right] P_r^1. \quad \text{(A12)}$$

Finally, two more relations are obtained from Eq. (A4). When multiplied with ηd_r^{0n}, the procedure leads to [with Eq. (A1)]:

$$\sum_{r=0}^{\infty} \eta (1-\eta^2)^{1/2} d_r^{0n} P_r^1 = \sum_{r=0}^{\infty} \left[d_{r-2}^{0n} \frac{(r-2)(r-1)(-r)}{(2r-3)(2r-1)} + d_r^{0n} \frac{r(r+1)}{(2r-1)(2r+3)} + d_{r+2}^{0n} \frac{(r+1)(r+2)(r+3)}{(2r+5)(2r+3)} \right] P_r^0. \quad \text{(A13)}$$

When Eq. (A4) is instead multiplied with ηd_{r-1}^{1n}, the procedure yields

$$\sum_{r=0}^{\infty} \eta (1-\eta^2)^{1/2} d_{r-1}^{1n} P_r^1 = \sum_{r=0}^{\infty} \left[d_{r-3}^{1n} \frac{(r-2)(r-1)(-r)}{(2r-3)(2r-1)} + d_{r-1}^{1n} \frac{r(r+1)}{(2r-1)(2r+3)} + d_{r+1}^{1n} \frac{(r+1)(r+2)(r+3)}{(2r+5)(2r+3)} \right] P_r^0. \quad \text{(A14)}$$

APPENDIX B: STRESS TENSOR COEFFICIENTS

The full expressions for the shorthands in the shear stress $\tau_{\xi\eta}$ [Eqs. (58) and (59)] are as follows:

$$t_c^{t0}(c) = d_r^{0n}(c) 2\xi(\xi^2-1)^{1/2}. \quad \text{(B1)}$$

$$t_c^{t1}(c) = 2(\xi^2-1)^{1/2} \left[d_{r-2}^{0n}(c) \frac{(r-3)(r-1)}{(2r-1)(2r-3)} + d_r^{0n}(c) \times \left(\frac{2(r-1)(r+2)}{(2r-1)(2r+3)} - \xi^2 \right) + d_{r+2}^{0n}(c) \frac{(r+2)(r+4)}{(2r+3)(2r+5)} \right]. \quad \text{(B2)}$$

$$t_s^{t0}(c) = d_{r-3}^{1n}(c) \left[\frac{1}{\xi^2-1} - (r-4)(r-1) \right] \frac{(r-2)(r-1)}{(2r-3)(2r-1)} + d_{r-1}^{1n}(c) \left[\xi^2 r(r+1) - \frac{2\xi^4-\xi^2}{\xi^2-1} + \frac{2r^2+2r-3}{\xi^2-1} - (2r^2+2r-5) r(r+1) \right] + d_{r+1}^{1n}(c) \times \left[\frac{1}{\xi^2-1} - (r+2)(r+5) \right] \frac{(r+2)(r+3)}{(2r+3)(2r+5)}. \quad \text{(B3)}$$

$$t_s^{t1}(c) = -2\xi\left[d_{r-3}^{1n}(c)\frac{(r-2)(r-1)}{(2r-3)(2r-1)} - d_{r-1}^{1n}(c)\frac{2r(r+1)}{(2r-1)(2r+3)} + d_{r+1}^{1n}(c)\frac{(r+2)(r+3)}{(2r+3)(2r+5)}\right]. \tag{B4}$$

$$t_s^{t2}(c) = -(\xi^2-1)\left[d_{r-3}^{1n}(c)\frac{(r-2)(r-1)}{(2r-3)(2r-1)} + d_{r-1}^{1n}(c)\times\left(\frac{2r^2+2r-3}{(2r-1)(2r+3)} - \xi^2\right) + d_{r+1}^{1n}(c)\frac{(r+2)(r+3)}{(2r+3)(2r+5)}\right]. \tag{B5}$$

The expressions in the normal stress $\tau_{\xi\xi}$ [Eqs. (62) and (63)] are

$$t_c^{r0}(c,\tilde{c}) = \left(c^2 - \frac{\tilde{c}^2}{2}\right)\left\{ - d_{r-4}^{0n}(c)\frac{(r-3)(r-2)(r-1)r}{(2r-7)(2r-5)(2r-3)(2r-1)} + d_{r-2}^{0n}(c)2(r-1)r\frac{\xi^2 - \frac{2r^2-2r-7}{(2r-5)(2r+3)}}{(2r-3)(2r-1)} - d_r^{0n}(c)\frac{(2r-1)(2r+3)\xi^4 - 2(2r^2+2r-1)\xi^2 + \frac{3(2r^4+4r^3-6r^2-8r+3)}{(2r-3)(2r+5)}}{(2r-1)(2r+3)} + d_{r+2}^{0n}(c)\frac{(r+1)(r+2)2\xi^2 - \frac{2(2r^2+6r-3)(r+2)(r+1)}{(2r-1)(2r+7)}}{(2r+3)(2r+5)} - d_{r+4}^{0n}(c)\frac{(r+4)(r+3)(r+2)(r+1)}{(2r+3)(2r+5)(2r+7)(2r+9)}\right\} - d_{r-2}^{0n}(c)\frac{(r-2)(r-1)r}{(2r-3)(2r-1)} + d_r^{0n}(c)\frac{r(r+1)}{(2r-1)(2r+3)} + d_{r+2}^{0n}(c)\frac{(r+1)(r+2)(r+3)}{(2r+3)(2r+5)}. \tag{B6}$$

$$t_c^{r1}(c) = \xi\left\{ d_{r-2}^{0n}(c)\frac{(r-1)r}{(2r-3)(2r-1)} + d_r^{0n}(c)\left[\frac{2r^2+2r-1}{(2r-1)(2r+3)} - 1\right] + d_{r+2}^{0n}(c)\frac{(r+1)(r+2)}{(2r+3)(2r+5)}\right\}. \tag{B7}$$

$$t_c^{r2}(c) = (\xi^2-1)\left\{ d_{r-2}^{0n}(c)\frac{(r-1)r}{(2r-3)(2r-1)} + d_r^{0n}(c)\left[\frac{2r^2+2r-1}{(2r-1)(2r+3)} - \xi^2\right] + d_{r+2}^{0n}(c)\frac{(r+1)(r+2)}{(2r+3)(2r+5)}\right\}. \tag{B8}$$

$$t_s^{r0}(c) = \frac{\xi}{(\xi^2-1)^{1/2}}\left\{ d_{r-3}^{1n}(c)\frac{(r-2)(r-1)r}{(2r-3)(2r-1)} - d_{r-1}^{1n}(c)\left[\frac{r(r+1)}{(2r-1)(2r+3)} + r(r+1)(\xi^2-1)\right] - d_{r+1}^{1n}(c)\frac{(r+1)(r+2)(r+3)}{(2r+5)(2r+3)}\right\}. \tag{B9}$$

$$t_s^{r1}(c) = -(\xi^2-1)^{1/2}\left\{ d_{r-3}^{1n}(c)\frac{(r-2)^2(r-1)r}{(2r-3)(2r-1)} + d_{r-1}^{1n}(c)\left[\frac{2r^2(r+1)^2}{(2r-1)(2r+3)} - r(r+1)\xi^2\right] + d_{r+1}^{1n}(c)\frac{(r+1)(r+2)(r+3)^2}{(2r+3)(2r+5)}\right\}. \tag{B10}$$

Note that all expressions produce the correct spherical limit. With $a\xi \to r^*$, $\eta \to \cos\theta$ (where r^* and θ denote the radial and angular spherical coordinates), d_r^{mn} of Eq. (30), and $\xi \to \infty$, Eq. (58) and (62) can be rewritten by resolving the infinite series in r. The terms in Eq. (58) then simplify to the expressions in the ECAH theory:[1,2,32]

$$\frac{\mu i^n(2n+1)}{a^2(\xi^2-\eta^2)^2} f\sum_{r=0}^{\infty} t_c^{t0}(c)P_r^1(\eta) \xrightarrow{\text{spherical}} \frac{2\mu i^n(2n+1)}{(r^*)^2} fP_n^1(\cos\theta),$$

$$\frac{\mu i^n(2n+1)}{a^2(\xi^2-\eta^2)^2}\frac{df}{d\xi}\sum_{r=0}^{\infty} t_c^{t1}(c)P_r^1(\eta) \xrightarrow{\text{spherical}} -\frac{2\mu i^n(2n+1)}{r^*}\frac{df}{dr^*}P_n^1(\cos\theta),$$

$$\frac{\mu i^n(2n+1)}{a^2(\xi^2-\eta^2)^2} f\sum_{r=0}^{\infty} t_s^{t0}(c)P_r^1(\eta) \xrightarrow{\text{spherical}} \frac{\mu i^n(2n+1)[n(n+1)-2]}{(r^*)^2} fP_n^1(\cos\theta),$$

$$\frac{\mu i^n(2n+1)}{a^2(\xi^2-\eta^2)^2}\frac{df}{d\xi}\sum_{r=0}^{\infty} t_s^{f1}(c)P_r^1(\eta) \xrightarrow{\text{spherical}} 0 \text{ (result} \propto \xi^{-1}),$$

$$\frac{\mu i^n(2n+1)}{a^2(\xi^2-\eta^2)^2}\frac{d^2f}{d\xi^2}\sum_{r=0}^{\infty} t_s^{f2}(c)P_r^1(\eta) \xrightarrow{\text{spherical}} \mu i^n(2n+1)\frac{d^2f}{(dr^*)^2}P_n^1(\cos\theta).$$

This is also true for the terms in Eq. (62):

$$\frac{-2\mu i^n(2n+1)}{a^2(\xi^2-\eta^2)^2}f\sum_{r=0}^{\infty} t_c^{r0}(c,c_s)P_r^0(\eta) \xrightarrow{\text{spherical}} \mu i^n(2n+1)(2k^2 - k_s^2)fP_n^0(\cos\theta),$$

$$\frac{-2\mu i^n(2n+1)}{a^2(\xi^2-\eta^2)^2}\frac{df}{d\xi}\sum_{r=0}^{\infty} t_c^{r1}(c)P_r^0(\eta) \xrightarrow{\text{spherical}} 0 \text{ (result} \propto \xi^{-2}),$$

$$\frac{-2\mu i^n(2n+1)}{a^2(\xi^2-\eta^2)^2}\frac{d^2f}{d\xi^2}\sum_{r=0}^{\infty} t_c^{r2}(c)P_r^0(\eta) \xrightarrow{\text{spherical}} 2\mu i^n(2n + 1)\frac{d^2f}{(dr^*)^2}P_n^0(\cos\theta),$$

$$\frac{-2\mu i^n(2n+1)}{a^2(\xi^2-\eta^2)^2}f\sum_{r=0}^{\infty} t_s^{r0}(c)P_r^0(\eta) \xrightarrow{\text{spherical}} \frac{2\mu i^n(2n+1)n(n+1)}{(r^*)^2}fP_n^0(\cos\theta),$$

$$\frac{-2\mu i^n(2n+1)}{a^2(\xi^2-\eta^2)^2}\frac{df}{d\xi}\sum_{r=0}^{\infty} t_s^{r1}(c)P_r^0(\eta) \xrightarrow{\text{spherical}} -\frac{2\mu i^n(2n+1)n(n+1)}{r^*}\frac{df}{dr^*}P_n^0(\cos\theta).$$

[1] P. S. Epstein and R. R. Carhart, "The absorption of sound in suspensions and emulsions. I. Water fog in air," J. Acoust. Soc. Am. **25**, 553–565 (1953).
[2] J. R. Allegra and S. A. Hawley, "Attenuation of sound in suspensions and emulsions: Theory and experiments," J. Acoust. Soc. Am. **51**, 1545–1564 (1972).
[3] A. S. Dukhin and P. J. Goetz, "Acoustic spectroscopy for concentrated polydisperse colloids with high density contrast," Langmuir **12**, 4987–4997 (1996).
[4] A. S. Dukhin, P. J. Goetz, and C. W. Hamlet, Jr., "Acoustic spectroscopy for concentrated polydisperse colloids with low density contrast," Langmuir **12**, 4998–5003 (1996).
[5] F. Alba, D. Higgs, R. Jack, and P. Kippax, "Ultrasound spectroscopy: A sound approach to sizing of concentrated particulates," in *Handbook on Ultrasonic and Dielectric Characterization Techniques for Suspended Particulates*, edited by V. A. Hackley and J. Texter (American Ceramic Society, Westerville, OH, 1998).
[6] A. K. Hipp, G. Storti, and M. Morbidelli, "Particle sizing in colloidal dispersions by ultrasound. Model calibration and sensitivity analysis," Langmuir **15**, 2338–2345 (1999).
[7] A. S. Dukhin and P. J. Goetz, *Ultrasound for Characterizing Colloids* (Elsevier, Amsterdam, 2002).
[8] R. E. Challis, M. J. W. Povey, M. L. Mather, and A. K. Holmes, "Ultrasound techniques for characterizing colloidal dispersions," Rep. Prog. Phys. **68**, 1541–1637 (2005).
[9] K. Attenborough and L. A. Walker, "Sound dissipation by a small cylindrical obstacle," J. Acoust. Soc. Am. **51**, 192–196 (1972).
[10] C. C. Habeger, "The attenuation of ultrasound in dilute polymeric fiber suspensions," J. Acoust. Soc. Am. **72**, 870–878 (1982).
[11] S. K. Datta and A. H. Shaw, "Axially symmetric waves in an elastic solid of revolution," J. Acoust. Soc. Am. **44**, 473–477 (1968).
[12] R. D. Spence and S. Granger, "The scattering of sound from a prolate spheroid," J. Acoust. Soc. Am. **23**, 701–706 (1951).
[13] T. B. A. Senior, "Scalar diffraction by a prolate spheroid at low frequencies," Can. J. Phys. **38**, 1632–1641 (1960).
[14] N. G. Einspruch and C. A. Barlow, "Scattering of a compressional wave by a prolate spheroid," Q. Appl. Math. **19**, 253–258 (1961).
[15] A. Silbiger, "Scattering of sound by an elastic prolate spheroid," J. Acoust. Soc. Am. **35**, 564–570 (1963).
[16] T. B. A. Senior, "The scattering from acoustically hard and soft prolate spheroids for axial incidence," Can. J. Phys. **44**, 655–667 (1966).
[17] J. E. Burke, "Low-frequency scattering by soft spheroids," J. Acoust. Soc. Am. **39**, 826–831 (1966).
[18] C. Yeh, "Scattering of acoustic waves by a penetrable prolate spheroid," J. Acoust. Soc. Am. **42**, 518–521 (1967).
[19] J. E. Burke, "Scattering by penetrable spheroids," J. Acoust. Soc. Am. **43**, 871–875 (1968).
[20] A. A. Kleshchev and L. S. Sheiba, "Scattering of a sound wave by ideal prolate spheroids," Sov. Phys. Acoust. **16**, 219–222 (1970).
[21] K. N. Rozhdestvenskii and L. A. Tolokonnikov, "Acoustic scattering by an elastic spheroid," Sov. Phys. Acoust. **36**, 515–516 (1990).
[22] Z. Ye, "Recent developments in underwater acoustics: Acoustic scattering from single and multiple bodies," Proc. Natl. Sci. Counc., Repub. China, Part A: Phys. Sci. Eng. **25**, 137–150 (2001).
[23] A. S. Ahuja, "Scattering of sound in suspensions of spheroidally shaped particles," J. Acoust. Soc. Am. **66**, 801–805 (1979).
[24] F. Babick and A. Richter, "Sound attenuation by small spheroidal particles due to visco-inertial coupling," J. Acoust. Soc. Am. **119**, 1441–1448 (2006).
[25] R. H. Hackman, "The transition matrix for acoustic and elastic wave scattering in prolate spheroidal coordinates," J. Acoust. Soc. Am. **75**, 35–45 (1984).
[26] S. Asano and G. Yamamoto, "Light scattering by a spheroidal particle," Appl. Opt. **14**, 29–49 (1975); **15**, 2028–2028 (1976).
[27] V. G. Farafonov, "Diffraction of a plane electromagnetic wave at a dielectric spheroid," Diff. Eq. **19**, 1319–1329 (1983).
[28] N. V. Voshchinnikov, "Electromagnetic scattering by homogeneous and coated spheroids: calculations using the separation of variables method," J. Quant. Spectrosc. Radiat. Transf. **55**, 627–636 (1996).
[29] V. G. Farafonov, V. B. Il'in, and T. Henning, "A new solution of the light scattering problem for axisymmetric particles," J. Quant. Spectrosc. Radiat. Transf. **63**, 205–215 (1999).
[30] C. Flammer, *Spheroidal Wave Functions* (Stanford University Press, Stanford, CA, 1957).
[31] R. B. Bird, W. E. Stewart, and E. N. Lightfoot, *Transport Phenomena*, 2nd ed. (Wiley, New York, 2007).
[32] A. K. Hipp, "Acoustic Characterization of Particulate Systems," Ph.D. thesis, ETH Zürich, Switzerland, 2001 (WVB Berlin, Germany, 2002).
[33] J. R. Allegra, "Theoretical and Experimental Investigation of the Attenuation of Sound in Suspensions and Emulsions," Ph.D. thesis, Harvard University, Cambridge, MA, 1971.
[34] A. K. Hipp, L. P. Adjadj, G. Storti, and M. Morbidelli, "Incorporating linear viscoelasticity into acoustic scattering theory," J. Acoust. Soc. Am. **111**, 1549–1551 (2002).
[35] P. Moon and D. E. Spencer, "The meaning of the vector Laplacian," J. Franklin Inst. **256**, 551–558 (1953).
[36] O. I. Grossman and A. A. Kleshchev, "On the separability of the vector wave equation," Sov. Phys. Acoust. **16**, 120–121 (1970).
[37] M. Abramowitz and I. A. Stegun, *Handbook of Mathematical Functions* (Dover, New York, 1972).
[38] P. E. Falloon, P. C. Abbott, and J. B. Wang, "Theory and computation of spheroidal wavefunctions," J. Phys. A **36**, 5477–5495 (2003).

Radiation force of a helicoidal Bessel beam on a sphere

Philip L. Marston[a)]
Department of Physics and Astronomy, Washington State University, Pullman, Washington 99164-2814, USA

(Received 14 October 2008; revised 24 March 2009; accepted 25 March 2009)

The partial-wave series for the scattering of an acoustic helicoidal Bessel beam by a sphere centered on the axis of the beam is applied to the calculation of the acoustic radiation force by the beam on the sphere in an inviscid fluid. The term "helicoidal" refers to a type of beam having an axial amplitude null and an azimuthal phase gradient. Such a beam is known as an acoustic vortex and only the case of a vortex having a unit magnitude topological charge is considered. There is no monopole contribution to the radiation force. Radiation force examples are computed for a soft sphere, a fixed rigid sphere, a movable rigid sphere, an aluminum sphere in water, and an acrylic sphere in water. Beam parameters are found for the rigid sphere and the aluminum and acrylic cases in which the radiation force is directed opposite the propagation direction of the beam. Negative radiation forces appear to be associated with relatively weak scattering into the backward hemisphere. Some aspects of the low frequency scattering of plane waves and helicoidal Bessel beams are examined for movable rigid spheres.
 [DOI: 10.1121/1.3119625]

PACS number(s): 43.25.Qp, 43.25.Uv, 43.80.Ev, 43.40.Fz [TDM] Pages: 3539–3547

I. INTRODUCTION

While there has been a long history of research into the acoustic radiation force on spheres caused by propagating waves,[1–3] there have been relatively few investigations of the radiation force caused by propagating acoustic beams.[3–6] The present investigation extends prior research[5,6] on the radiation forces produced by acoustic Bessel beams to the special case of an acoustic Bessel beam having an axial null in the amplitude and an $\exp(i\phi)$ phase factor where ϕ denotes the azimuthal angle. In this analysis the sphere is taken to be centered on the axis of the beam. The compact analytical expressions for the axial radiation force derived here make use of Marston's exact solution for the acoustic scattering for the case of a sphere in an inviscid fluid centered on the axis of the beam.[7] Since this analysis of the scattering and of the radiation force neglects the effects of viscosity, the results obtained may only be directly relevant for cases where the radius of the sphere is large in comparison to the oscillating thermal-viscous boundary layer produced by the incident wave in the vicinity of the sphere in real fluids.[5] This simplified analysis should assist the development of models that include viscous stresses. For a discussion of acoustic radiation forces on small spheres, see Ref. 8. For sufficiently large spheres viscous corrections are found experimentally to be small.[2,9]

The spatial part of the complex velocity potential for a generalized Bessel beam in an ideal fluid may be expressed as follows in cylindrical coordinates:[7,10]

$$\psi_{Bm}(z,R,\phi) = \psi_0 i^m \exp(i\kappa z + im\phi) J_m(\mu R), \tag{1}$$

where ψ_0 is an amplitude constant, m is an integer, z is the axial coordinate, R is the radial coordinate, ϕ is an azimuthal angle, J_m is a Bessel function of order m, $\mu/k=\sin\beta$, β is a beam parameter, and the factor i^m is included for convenience. The $\exp(-i\omega t)$ time convention is assumed and the axial wave vector κ is $k\cos\beta$ where $k=\omega/c_0$ where c_0 is the speed of sound in the surrounding fluid. The beam parameter $\beta=\arccos(\kappa/k)=\arcsin(\mu/k)$ has the geometric significance of a conic angle illustrated in Fig. 1 of Ref. 5 in Durnin's representation of a Bessel beam.[10–12] The first-order complex acoustic velocity of the beam is given by $\mathbf{u}_{Bm}=\nabla\psi_{Bm}$ and the complex first-order acoustic pressure is $p_{Bm}=i\omega\rho_0\psi_{Bm}$, where ρ_0 is the density of the surrounding fluid. The physical pressure of the generalized Bessel beam becomes the real part of $p_{Bm}(z,R,\phi)\exp(-i\omega t)$. For an ordinary Bessel beam, $m=0$ and the beam has an axial maximum. Marston's prior analysis of the axial radiation force concerns the $m=0$ beam case[13] and various examples: rigid spheres, fluid spheres, solid elastic spheres, and evacuated spherical shells.[5,6] The present paper concerns the axial radiation force for beams having $m=1$.

Bessel beams with an integer azimuthal index $m\neq 0$ in Eq. (1) are examples of an acoustic vortex,[14,15] also known as an acoustic helicoidal wave.[16] Such acoustic waves have an axial phase singularity where the index m is sometimes referred to as the topological charge[14] of the wave. The distinguishing feature of the helicoidal Bessel beam solution of the Helmholtz equation is that the beam propagates without spreading. There are other linear acoustical vortices having different radial and axial dependences but in all cases the amplitude vanishes on the axis of the beam.[14–16]

One remarkable property of the radiation force calculated for spheres placed on the axis of an ordinary Bessel beam (i.e., a beam having $m=0$), is that for some material properties and beam parameters, conditions have been found where the axial force is directed opposite to the direction of the beam propagation.[5,6] That condition is described as a

[a)]Electronic mail: marston@wsu.edu

negative radiation force. For non-absorbing spheres in a plane propagating wave in an ideal fluid, the radiation force is predicted to be non-negative.[5] Some predictions are given in the present analysis of negative radiation forces on lossless isotropic spheres placed on the axis of a helicoidal Bessel beam with $m=1$.

One of the reasons for giving attention to conditions for generating negative axial forces is that this condition suggests the feasibility of pulling a sphere toward the acoustic source in contrast to the usual case in which objects tend to be pushed away from the source of the sound (though exceptions are known for some diverging waves[3,17]). Other ways to acoustically pull an object closer to an acoustic source include reflecting some of the beam back toward a source so as to generate a quasistationary wave or by introducing a counter-propagating wave with a second source.[18] In that case, however, the direction of the force depends strongly on the axial position of the sphere.[19,20] In contrast to the quasistationary or dual-beam acoustic tweezers for the manipulation of small objects, the single acoustic beam case may have potential advantages. Consequently improved understanding of mechanisms for generating negative radiation forces in propagating acoustic beams should be helpful. Acoustic devices for manipulating small objects[15–21] are a potential alternative to the more widely used laser-based optical devices.[10,22,23]

Because analytical forms for the scattering by spheres illuminated by acoustic Bessel beams having $m=0$ and $m=1$ are only available when the sphere is placed on the beam axis, analytical results concerning the transverse stability of spheres in these beams are not available. When the sphere is on the beam's axis, the transverse force vanishes by symmetry. There has been some effort to apply elementary ray methods to the analysis of acoustic radiation forces on particles displaced from the axis of focused acoustic beams;[21] however in the opinion of the present author, a modified approach will likely be needed to account for resonances that appear to strongly influence the scattering[24] and radiation force[6] on some small objects. Electromagnetic resonances are also known to influence the optical radiation force on some small objects.[23,24] It has been possible to verify the analytical results for the acoustic radiation force on a sphere in the case of a beam with $m=0$ by applying the finite-element method (FEM) to compute the local first-order acoustic amplitudes needed in the evaluation of the second-order radiation stress tensor.[25] It may eventually be possible to use FEM to predict the radiation forces and stability of spheres displaced from the axis of acoustic beams; however, a FEM computation of that type is complicated by the lack of axial symmetry. Marston's force expression[5] based on far-field scattering has also been verified by the propagating wave limit of Mitri's near-field analysis of radiation stresses on spheres.[19] When considering the stability of dielectric spheres in optical beams, it is common to find that stability in beams having an axial intensity minimum[10,26,27] differs from the case of a Gaussian beam which has an axial maximum. For example, using a beam having an axial minimum, with a bright surrounding doughnut, Unger and Marston[26] were able to optically trap gas bubbles in water. That technique has been extended by various groups.[27–29] The relevance to the present investigation is that it is plausible that the transverse stability of spheres in *acoustic* Bessel beams will depend on the index m in Eq. (1).

Though the analysis here is limited to the case of an ideal Bessel beam, it is reasonable to expect that the results are relevant to spheres in acoustic beams generated with a transducer having a finite aperture provided that the distance of the sphere from the source transducer is somewhat less than $a_T/\tan\beta$, where a_T is the lateral radius of the source. Close-to and beyond the distance $a_T/\tan\beta$, it is known that the incident wave is no longer well approximated by a Bessel beam.[10–12]

Though the derivation given here is for beams described by Eq. (1) with $m=1$, the result for the radiation force also applies to beams described by Eq. (1) having $m=-1$. That is because for the isotropic spheres considered, the direction and magnitude of the force cannot depend on reversing the handedness of the acoustic beam.

While this paper concerns the axial acoustic radiation force on spheres, it is noteworthy that if a sphere absorbs acoustic energy, helicoidal waves should also generate an axial *radiation torque* on the sphere.[16] That prediction is consistent with prior research into the radiation torques on spheres produced by electromagnetic waves.[22,30] Though not specifically concerned with spheres, recent experiments have demonstrated radiation torques caused by helicoidal beams incident on symmetric objects.[31,32] The results in Sec. II may be used for beams described by ψ_{B1} in Eq. (1), to find the radiation force on an absorbing sphere for cases where the partial-wave scattering coefficients are known.

This paper is organized as follows. Section II gives the analysis of the radiation force in a way which closely parallels the prior analysis of the $m=0$ case.[5] Section III discusses the application to fixed rigid and perfectly soft spheres. Negative forces on a rigid sphere are found to be possible for a situation with reduced acoustic scattering into the backward hemisphere. Section IV discusses the radiation force and scattering for an acrylic sphere. Section V discusses the radiation force and scattering for an aluminum sphere in water and for a movable rigid sphere having the same density as aluminum. Section VI summarizes conclusions and discusses other examples and applications. Appendix A reviews the scattering by a helicoidal Bessel beam having $m=1$ and discusses the expansion of the beam in terms of spherical waves. Appendix B lists some relevant properties of Legendre functions and discusses the evaluation of certain integrals. Appendix C discusses scattering by movable rigid spheres and makes a comparison with the scattering of plane waves by an aluminum sphere. Some of the examples displayed in Secs. III and IV were selected because of related cases important in the history of research on acoustic radiation pressure.[1–3]

II. AXIAL RADIATION FORCE ON THE SPHERE

The following analysis involves the far-field scattering by the sphere. This approach uses the property of the radiation stress tensor $\mathbf{S}_T$ for an ideal fluid that $\nabla\cdot\mathbf{S}_T=0$. The

divergence theorem allows the integral for the radiation force on the object to be evaluated on a surface located a large distance from the object.[33,34] In the present case this surface is taken to be a spherical surface (designated as S_r) of radius r with $kr \gg 1$. In various cases it has been verified that when evaluating radiation forces on objects in ideal fluids, this far-field procedure predicts forces in agreement with near-field evaluations of the radiation stress.[19,25,35] The radiation force [Eq. (9) of Wei *et al.*[34]] is expressed in terms of the real-valued time-varying first-order pressure p and velocity $\mathbf{u}$ through the surface integrals:

$$\mathcal{F} = \oint_{S_r} \mathbf{S}_T \cdot d\mathbf{A} = -\oint_{S_r} \rho_0 \langle \mathbf{uu} \rangle \cdot d\mathbf{A} + \oint_{S_r} \left\{ \frac{\rho_0}{2} \langle |\mathbf{u}|^2 \rangle - \frac{1}{2\rho_0 c_0^2} \langle \mathbf{p}^2 \rangle \right\} d\mathbf{A},$$

where the area differential $d\mathbf{A}$ is directed radially outward and $\langle (\,) \rangle$ denotes a time average of the quantity in the brackets. The time average of the products in the above equation may be expressed as one-half of the real part of the product of the first corresponding complex quantity with the complex conjugate of the second corresponding complex quantity.[36] The quantities p and $\mathbf{u}$ each involve a superposition of incident and scattered amplitudes. The complex velocity potential of the scattering is given by Eqs. (A1) and (A2) and for the incident wave the partial-wave expansion of ψ_{B1} from Eq. (A5) is used. The expressions are simplified by taking the amplitude factor ψ_0 to be real. In prior applications of this method to radiation forces on spheres, the velocity potential ψ_S of the scattered wave had no dependence on azimuthal angle ϕ. In the present case, though ψ_S is proportional to $\exp(i\phi)$, the ratio of the azimuthal-to-radial first order velocity magnitude is $(r \sin\theta)^{-1} |\partial\psi_S/\partial\phi| / |\partial\psi_S/\partial r| = (kr \sin\theta)^{-1}$ in the far field. That ratio vanishes when $kr \to \infty$. [The dependence near $\theta = 0$ is unimportant because ψ_S vanishes as θ approaches 0 and π from the form of Eq. (A2).] It follows that there are no alterations to the form of the radiation stress integrals given by Marston.[5] These integrals of the axial radiation stress follow from Lee and Wang's expressions[33] by using the normalization for the scattering given in Eq. (A1) and by letting $w = \cos\theta$, where θ is the scattering angle relative to the axis of the beam (see Fig. 1 of Marston[5]). In the application of Lee and Wang's expressions for the stress integrals, the integrals which contain only the incident wave (without cross terms involving the scattered waves) may be omitted. That is because in the absence of a sphere, there is no scattering ($\psi_S = 0$) and the radiation force must vanish. A similar approach was used by Wei *et al.*[34,35] to simplify integrals for the radiation force on cylinders. Showing explicitly the azimuthal integration, the axial radiation force, Eqs. (3)–(6) of Marston,[5] becomes

$$\mathcal{F}_z = -\pi\rho_0 k^2 (I_1 + I_2 - I_3), \tag{2}$$

$$I_1 = (2\pi)^{-1} (\psi_0 a/2)^2 \int_0^{2\pi} \int_{-1}^{1} |F(w,\phi)|^2 w dw d\phi, \tag{3}$$

$$I_2 = (\psi_0 ra/4\pi) \mathrm{Re} \left[\int_0^{2\pi} \int_{-1}^{1} \psi_{B1}{}^* F(w,\phi) e^{ikr} w dw d\phi \right], \tag{4}$$

$$I_3 = (\psi_0 ra/4\pi k) \times \mathrm{Im} \left[\int_0^{2\pi} \int_{-1}^{1} (\partial\psi_{B1}/\partial z)^* F(w,\phi) e^{ikr} dw d\phi \right], \tag{5}$$

where a is the radius of the illuminated sphere and * denotes complex conjugation and Re and Im designate real and imaginary parts of a complex quantity. As explained in Appendix B, the integrals may be evaluated using the far-field partial-wave representations of the scattering F and of ψ_{B1} given in Appendix A and by using properties of the associated Legendre functions $P_n^m(w)$. As in the ordinary beam case, the integrals reduce to expressions involving the real and imaginary parts α_n and β_n of partial-wave coefficients which describe the scattering of plane waves by the sphere reviewed in Appendix A. Let $b = \cos\beta$ where β denotes the beam parameter discussed in Sec. I. From Appendix B the results for I_1 and $I_{23} = I_2 - I_3$ are

$$I_1 = (2\psi_0/k)^2 \sum_{n=1}^{\infty} (n+1)^{-1} (\alpha_n \alpha_{n+1} + \beta_n \beta_{n+1}) \times P_n{}^1(b) P_{n+1}{}^1(b), \tag{6}$$

$$I_{23} = 2(\psi_0/k)^2 \sum_{n=1}^{\infty} (n+1)^{-1} (\alpha_n + \alpha_{n+1}) P_n{}^1(b) P_{n+1}{}^1(b). \tag{7}$$

The expression for I_1 is similar in appearance to the corresponding expression in the $m=0$ case[5] with the factors $(n+1)P_n(b)P_{n+1}(b)$ replaced by $(n+1)^{-1}P_n{}^1(b)P_{n+1}{}^1(b)$. In addition, the term with $n=0$ is suppressed in I_1 and in I_{23}. That is expected since by symmetry[7] the helicoidal beam does not excite the partial wave in Eq. (A2) having $n=0$. It is convenient to express the axial radiation force using a dimensionless radiation force function $Y_p(ka,\beta)$ which is related to force as previously[5] by

$$\mathcal{F}_z = (\pi a^2)(I_0/c_0)(1/\cos\beta) Y_p(ka,\beta), \tag{8}$$

where in the present case $I_0 = (\rho_0 c_0/2)(k\psi_0)^2 \cos\beta$ becomes a quantity that has units of an acoustic intensity (in $\mathrm{W/m^2}$) that characterizes the intensity of the beam parallel to the z axis. The actual intensity in the z direction is only proportional to I_0 in the case of a beam having $m=1$. The factor $I_0/\cos\beta$ is given by $(\rho_0 c_0/2)(k\psi_0)^2$ in terms of the amplitude coefficient ψ_0. From Eq. (2) and Eqs. (6)–(8), it follows that

$$Y_P = -(2/ka)^2 \sum_{n=1}^{\infty} [\alpha_n + \alpha_{n+1} + 2(\alpha_n \alpha_{n+1} + \beta_n \beta_{n+1})] \times (n+1)^{-1} P_n{}^1(b) P_{n+1}{}^1(b). \tag{9}$$

This result has the same form as the $m=0$ case, Eq. (10b) of Ref. 5, with $(n+1)P_n(b)P_{n+1}(b)$ replaced by $(n+1)^{-1}P_n{}^1(b)P_{n+1}{}^1(b)$ and the omission of a term with $n=0$. When β is 90°, the product of $P_n{}^1(\cos\beta)P_{n+1}{}^1(\cos\beta)$ vanishes for all n so that Y_p and $\mathcal{F}_z$ vanish as expected from

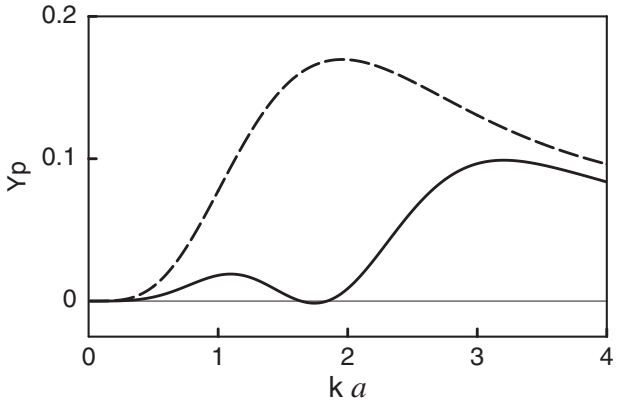

FIG. 1. The dimensionless radiation force function Y_p from Eq. (9) [which is for a helicoidal Bessel beam having $m=1$ in Eq. (1)] is plotted for the following spheres: a fixed rigid sphere (solid curve) and a perfectly soft sphere (dashed curve). The horizontal axis is the dimensionless frequency ka, where a denotes the radius of the sphere. The beam parameters are taken so that $\cos\beta=0.4$ ($\beta\approx 66.42°$). In the rigid case Y_p is negative near ka of 1.74.

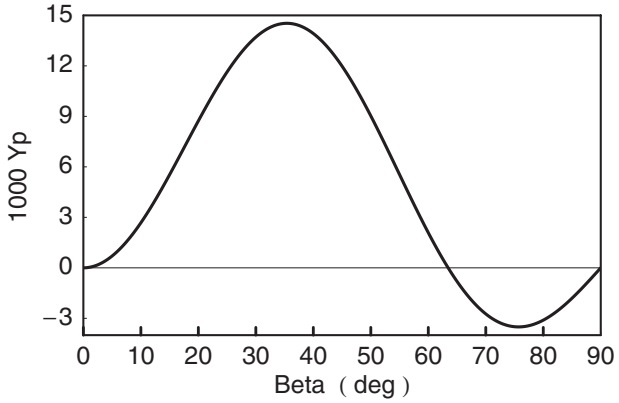

FIG. 2. The function Y_p scaled by a factor of 1000 plotted as a function of the beam parameter β for $ka=1.74$ for a fixed rigid sphere. When β is large, Y_p is negative so that the force is opposite the beam direction.

symmetry. Unlike the $m=0$ case, however, Y_p and $\mathcal{F}_z$ vanish when β vanishes since the product $P_n^1(\cos\beta)P_{n+1}^1(\cos\beta)$ also vanishes in that limit. Experience in evaluating Eqs. (9) and (A2) indicates that terminating the series with n in excess of[24] $1.6ka$ introduces a negligible error when $ka\gg 1$. When ka exceeds 4, for most cases it is more than sufficient to terminate the series when n exceeds $2+(1.5ka)$.

III. FORCE ON RIGID AND SOFT SPHERES

The coefficients in Eq. (9) are evaluated from the definitions in Eq. (A4) where the function $s_n(ka)$ is given by the solution for the plane-wave scattering, Eq. (A3). For a fixed rigid sphere[13] $s_n=-h_n^{(2)}(ka)'/h_n^{(1)}(ka)'$, where h_n is a spherical Hankel function of the indicated kind and primes denote differentiation. It is appropriate to investigate the rigid case since that sphere has no elastic vibration and the plane-wave radiation force[1,5] and scattering[13] are well known. Figure 1 shows Y_p from Eq. (9) for a beam having $m=1$ and $\cos\beta=0.4$. This value of β was selected because Y_p is negative in the region $1.64<ka<1.84$. This is an unanticipated result because for all cases investigated with an ordinary Bessel beam, beams having $m=0$ in Eq. (1), Y_p is non-negative for a fixed rigid sphere.[5] Furthermore, it has been demonstrated analytically[5] that Y_p is non-negative for plane-wave illumination of all spheres having $|s_n|=1$. For the situation in Fig. 1, the most negative value occurs with $(ka, Y_p)=(1.74, -0.001\,47)$. Increasing β causes the ka region having $Y_p<0$ to expand and the magnitude of the negative parts tend to grow for up to $\beta=76°$. Figure 2 shows the rigid sphere Y_p (scaled by a factor of 1000) for $ka=1.74$. While the peak magnitude in the negative region is less than the peak in the positive region, the general order of magnitude is similar to Y_p in the positive region.

Figure 1 also shows Y_p for the case of a perfectly soft sphere. In that case the α_n and β_n are evaluated by taking[11] $s_n=-h_n^{(2)}(ka)/h_n^{(1)}(ka)$. The resulting Y_p is non-negative and remains so for the whole range of the beam parameter β: $0<\beta<90°$. The behavior of the function Y_p in this case is important for understanding the response of gas-filled bubbles in liquids. The perfectly soft sphere provides a smooth background on which resonance features associated with the modes of bubbles are superposed. While for a complete description of the scattering by a gas bubble, it is essential to include the effects of thermal and viscous dissipation,[37] a correction which is sometimes neglected,[38] the smoothly varying behavior of Y_p of a perfectly soft sphere is relevant to applications in which helicoidal Bessel beams are used to manipulate bubbles.

As previously noted,[5,6] in the case of ordinary Bessel beams, the regions of negative Y_p are correlated with regions of (ka, β) for which the scattering is weak in the regions of the backwards hemisphere, that is, the scattering is weak for $90°<\theta\leq 180°$. It is instructive to examine the θ dependence of $|F|$ from Eq. (A2) for situations considered in Fig. 1. Figure 3 shows $|F|$ for the rigid and soft spheres with ka values selected to lie close to the condition of the extrema in Fig. 1. As a consequence of the symmetry of the sphere relative to the helicoidal beam,[7,16] F vanishes for $\theta=0°$ and 180°. The solid curve is the only case in which the scattering into the backward hemisphere is appreciably weaker than the scatter-

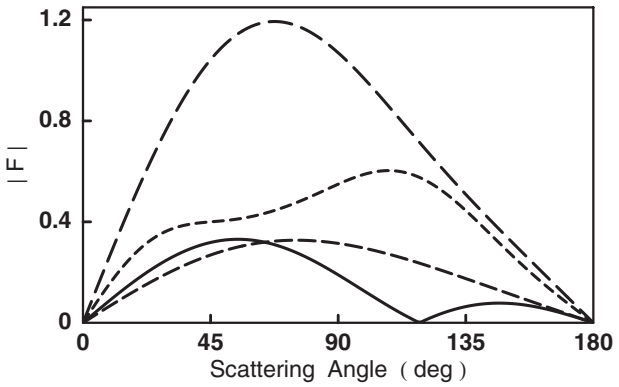

FIG. 3. The dependence of the far-field scattering $|F|$ on the scattering angle θ for a sphere illuminated by a beam with $\cos\beta=0.4$ and $m=1$ in Eq. (1) and ka selected as follows: solid curve (rigid sphere with $ka=1.74$); curve having long dashes (soft sphere with $ka=1.96$); curve with medium-length dashes (rigid sphere with $ka=1.1$); and the curve having short dashes (rigid sphere with $ka=3.2$). Inspection of Fig. 1 shows that $Y_p<0$ only in the case of the solid curve. The scattering on the beam axis vanishes (Refs. 7 and 16).

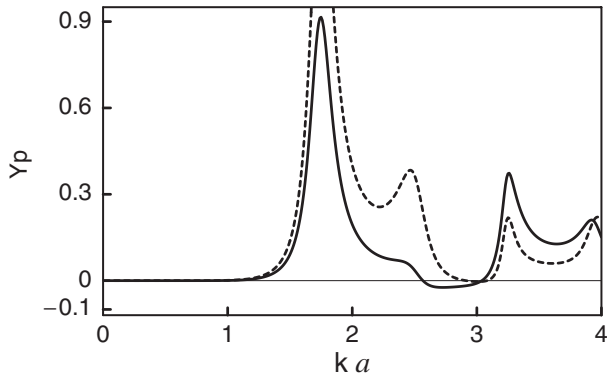

FIG. 4. The dimensionless radiation force Y_p for a non-absorbing acrylic sphere in water is plotted as a function of ka for beams with $\beta=60°$ (solid curve) and $\beta=50°$ (dashed curve). In both cases there is a region with $Y_p<0$.

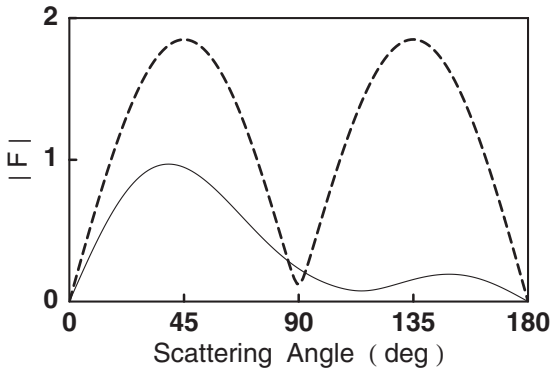

FIG. 5. The angular dependence of the far-field scattering $|F|$ for the acrylic sphere considered in Fig. 4 for a beam having $\beta=60°$ and $ka=2.74$ (solid curve) and 1.75 (dashed curve). From Fig. 4, the computed Y_p are, respectively, negative and positive in those cases.

ing into the forward hemisphere. It corresponds to the condition for the minimum in Fig. 1 with $Y_p<0$. The curve having short dashes corresponds to the peak in Y_p at $ka=3.2$ in the rigid sphere case. That corresponds to a condition for generating *enhanced scattering* into the backward hemisphere. While correlation of the sign of Y_p with the angular dependence of $|F|$ is only qualitative, these observations may be helpful for anticipating the sign of Y_p in other situations with illumination by propagating beams.

IV. FORCE ON AN ACRYLIC SPHERE IN WATER

This example was selected because for the material considered [polymethylmethacrylate (PMMA)], when the sphere is placed in water the low-frequency backscattering displays a sequence of regular spaced peaks when the sphere is illuminated by a plane wave.[39,40] Those features are associated with a weakly damped elastic wave guided by the surface of the sphere and are attributed to resonances in partial waves having $n\geq 2$. (Some authors[24,40] prefer to classify these waves as generalized Rayleigh waves as a consequence of the wave properties when the fluid loading is weak and ka is large; however, some authors[41] prefer the terminology, Scholte–Stoneley wave.) For the case of a solid lossless sphere the α_n and β_n are given by taking $s_n=-D_n^*/D_n$, where the functions $D_n(ka)$ are given in Appendix A of Marston.[24] The consequence of dissipation is neglected here since the resonance features are known to dominate the scattering by high-quality spheres in the region of ka considered.[40] The values of the material parameters and the surrounding water given by longitudinal wave velocity $c_L=2690$ m/s, transverse wave velocity $c_T=1340$ m/s, and density $\rho_E=1.19$ g/cm^3 for PMMA, and $c_0=1479$ m/s and $\rho_0=1.00$ g/cm^3 for water. These are the same as the values used in prior computations of scattering[24,40] and radiation force[6] on acryllic spheres. Figure 4 shows Y_p in this case for two values of the beam parameter β. The solid curve is for $\beta=60°$ and the dashed curve is for $\beta=50°$. For both curves there is a region of ka where $Y_p<0$: solid curve ($2.57<ka<3.04$) and dashed curve ($2.92<ka<3.08$). The negative extremum of the solid curve is at $(ka, Y_p)=(2.73, -0.0236)$. As in the case of a beam having[6] $m=0$, the dependence on ka is strongly influenced by the resonances of the elastic modes of the sphere. The peak in the solid curve at $ka=1.75$ is associated with the ka dependence of s_2.

Figure 5 shows the angular dependence of $|F|$ for $\beta=60°$ and ka of 2.74 (solid curve) and 1.75 (dashed curve). When $ka=2.74$, $Y_p=-0.0235$ and Fig. 5 shows that the scattering into the region $90°<\theta\leq 180°$ is relatively weak, as in Fig. 3 and other cases[6,7] having $Y_p<0$. The dashed curve, however, is nearly symmetric around $\theta=90°$. That is because when $ka=1.75$ (where Y_p is sharply peaked), the $n=2$ mode of the sphere is strongly excited and F in Eq. (A2) is dominated by the $n=2$ term. The scattering contains a phase factor $\exp(i\phi)$ and the mode excited corresponds to a wave that runs azimuthally around the sphere.

V. FORCE ON ALUMINUM AND MOVABLE RIGID SPHERES

In contrast to the case of the acrylic sphere considered in Sec. IV, the scattering by a solid aluminum sphere in water does not exhibit regularly spaced narrow resonances.[39] As explained in Appendix C, the low-frequency properties of the backscattering with plane-wave illumination are similar to those of a *movable* rigid sphere whose density corresponds to that of aluminum. As reviewed in Appendix C, the partial-wave series for the movable rigid sphere, as given by Hickling and Wang,[42] is given by modifying the dipole scattering according to Eq. (C1). By making that modification, it was possible to compute how Y_p for a movable rigid sphere depends on the density ρ_E of the sphere. The computation revealed that as the density was decreased below the fixed rigid sphere limit ($\rho_E/\rho_0=\infty$), the location of the valley in $Y_p(ka)$ in Fig. 1 shifts to smaller ka from 1.74 down to $ka=1.46$ for the density ratio appropriate for an aluminum sphere in water ($\rho_E/\rho_0=2.7$). Figure 6 shows Y_p, scaled as in Fig. 2, as a function of the beam parameter β for an aluminum sphere (solid curve) and a movable rigid sphere (dashed curve). For each curve $ka=1.46$ and the density ratio is $\rho_E/\rho_0=2.7$. The other material properties for the solid curve are $c_L=6420$ m/s, $c_T=3040$ m/s, and $c_0=1479$ m/s. The similarities of the two curves in Fig. 6 is evidence that it is the inertia of the aluminum sphere, not its elasticity, that governs the Y_p function for ka near 1.46. A movable rigid sphere

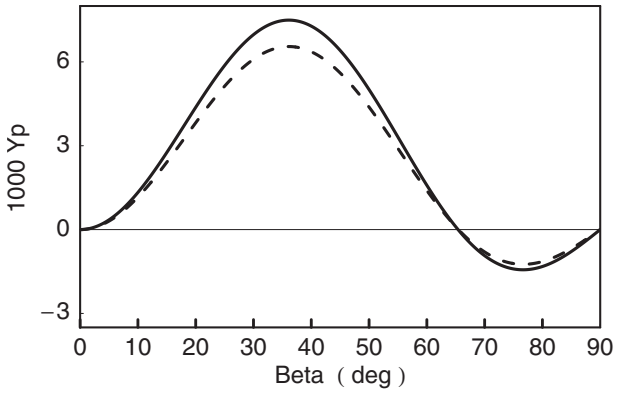

FIG. 6. The function Y_p (scaled by a factor of 1000) is plotted as a function of the beam parameter β for $ka=1.46$ for an aluminum sphere in water (solid curve) and a movable rigid sphere in water having the same density as aluminum (dashed curve). The similarity between the curves shows that the elastic response of the aluminum sphere is unimportant for this ka.

having the same mass as the aluminum sphere has the same translational inertia.

Figure 7 compares $|F|$ as a function of θ for $ka=1.46$ and $\cos\beta=0.4$. Three models are shown: the solid curve uses s_n for an aluminum sphere in water, the curve with short dashes is for a movable rigid sphere having a relative density $\rho_E/\rho_0=2.7$, the curve with long dashes is for a fixed rigid sphere. Since $\beta=66.42°$, inspection of Fig. 6 shows that $Y_p<0$ for the former two cases but inspection of Fig. 1 shows that for the fixed rigid sphere $Y_p>0$. Inspection of Fig. 7 shows not only are the angular dependence of $|F|$ in the aluminum and movable sphere cases similar, the scattering into the backward hemisphere is relatively weak in comparison with scattering into the forward hemisphere in agreement with other situations producing negative Y_p. For the fixed rigid sphere case, however, the pattern has a different appearance.

VI. DISCUSSION AND CONCLUSIONS

The dimensionless radiation force function was derived in Sec. II by generalizing the previous method[5] to the present case where the velocity potential of the acoustic beam is described by Eq. (1) with $m=1$. The examples shown in Secs. III–V illustrate some aspects of how Y_p depends on ka and the beam parameter β. The examples were selected to illustrate conditions having negative radiation forces (directed opposite to the propagation direction of the beam) as well as the more common case of positive radiation force. As with the prior investigation of spheres placed on the axis of a Bessel beam having $m=0$, when the radiation force is negative, the scattering by the sphere into the backward hemisphere is relatively weak. An especially noteworthy result is that for some values of ka and β, Y_p is negative for a fixed rigid sphere and for a movable rigid sphere in water having the density of aluminum.

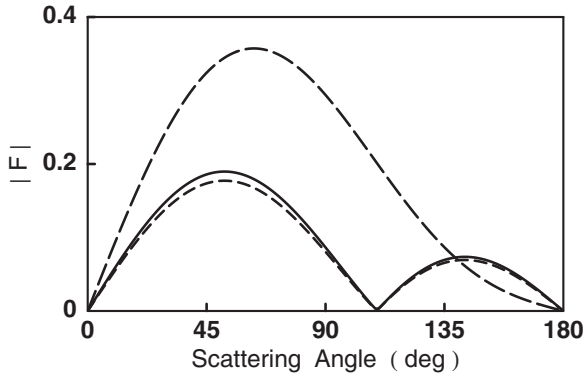

FIG. 7. The angular dependence of the far-field scattering $|F|$ for $ka=1.46$ and $\cos\beta=0.4$ for an aluminum sphere in water (solid curve), a movable rigid sphere with the density ratio corresponding to aluminum in water (curve with short dashes), and a fixed rigid sphere (curve having long dashes).

The derivation of Eq. (9) applies for any isotropic sphere in an ideal inviscid fluid provided the coefficients α_n and β_n are derived from the s_n of the corresponding plane-wave problem. Consequently, the derivation applies to evacuated shells. In the case of no dissipation within the shell, $s_n=-D_n^*/D_n$, where D_n depends on the shell parameters and on the surrounding fluid through the expressions given in Appendixes A and B of Ref. 24. In the case of an absorbing sphere or shell, $s_n\neq-D_n^*/D_n$ and it is necessary to use the full expression[39,40] for s_n in Eq. (A4); nevertheless Eq. (9) remains valid. Examples of Y_p for absorbing spheres were not evaluated. Hasegawa and Watanabe[43] computed that for acrylic spheres in water illuminated by plane waves, when $ka\leq3.9$ the peaks in Y_p are suppressed by $\leq10\%$. This is consistent with small alterations in the scattering.[40]

It has not been feasible to carry out a systematic search for beam parameters (ka,β) and material shell parameters that cause Y_p to be negative. The function Y_p has been evaluated for a few types of spheres and it is not uncommon to find regions with $Y_p<0$ provided β exceeds approximately 45°. For example, spherical hexane drops in water are predicted to have isolated islands in (ka,β) space where $Y_p<0$. The islands are qualitatively similar to islands found in the $m=0$ case (Fig. 7 of Ref. 5) except that the locations are displaced. When $m=1$, it is not known whether a combination of fluid parameters exists to cause $Y_p<0$ for small ka over an extended region, as illustrated in Fig. 8 of Ref. 5 in the $m=0$ case (where $\beta=60°$ and the ka region extends from 0 to 1.52). A few computations of Y_p were carried out for evacuated aluminum shells in water with the ratio (inner radius)/(outer radius) in the range 0.83–0.95 and in each case a region was easily found having $Y_p<0$.

In addition to the potential applications mentioned in Sec. I, Eq. (9) may be useful for estimating the axial radiation force of Bessel beams guided by a circular cylindrical waveguide. There has been renewed interest in particle manipulation in cylindrical waveguides.[44] Since the waveguide will reflect the sound scattered by a spherical particle back onto the particle, Eq. (9) will describe only part of the total radiation force. For waveguides made of stiff materials, when R is taken to be the inner radius of the cylinder, ordinarily[45] μ in Eq. (1) should be selected so that μR is close to a root of $dJ_m(\mu R)/dR=0$. Additional potential applications include alternative approaches to the manipulation of objects in reduced gravity,[46,47] translation of bubbles,[47,48] and localized drug delivery.[47–49] Because there is no mono-

pole contribution to Eq. (9), the dynamics of bubbles would be significantly altered on the axis of a helicoidal beam.

Mitri[50] recently published an analysis of the scattering of helicoidal Bessel beams by spheres where the incident wave is proportional to ψ_{Bm} in Eq. (1) with integer $m \neq 0$. Unfortunately the connection with the partial-wave coefficients in the plane-wave case [shown here by using (s_n-1)] is obscure in Mitri's notation. Nevertheless, $|F|$ computed using Eq. (A2) yields a curve like one given in Mitri's $m=1$ case when appropriate material properties and beam parameters are used.

ACKNOWLEDGMENT

This research was supported by NASA and by the Office of Naval Research. Likun Zhang and Dr. David B. Thiessen provided helpful comments.

APPENDIX A: PARTIAL-WAVE EXPANSIONS

Consider the scattering by a sphere having isotropic material properties centered on the Bessel beam at $z=0$ using the coordinate system shown in Fig. 1 of Ref. 5. For beams described by $\psi_{B1}$from Eq. (1), the far-field scattering is given by[7]

$$\psi_S(r,\theta,\phi) = \psi_0(a/2r)e^{ikr}F(\theta,\phi), \tag{A1}$$

$$F = (-i/ka)e^{i\phi}\sum_{n=1}^{\infty}(s_n-1)[(2n+1)/n(n+1)] \times P_n^{\,1}(\cos\theta)P_n^{\,1}(\cos\beta), \tag{A2}$$

where r is the radial coordinate in spherical coordinates centered on the sphere. Here (s_n-1), which depends on ka, is the same as the partial-wave coefficient for the dimensionless form function associated with scattering caused by plane-wave illumination:[7,13]

$$f(\theta) = (-i/ka)\sum_{n=0}^{\infty}(2n+1)(s_n-1)P_n(\cos\theta), \tag{A3}$$

where P_n is a Legendre polynomial. It is convenient for the purposes of the present paper to retain the notation previously used for the normalized partial-wave coefficient $\alpha_n + i\beta_n = (s_n-1)/2$, where

$$\alpha_n = [\mathrm{Re}(s_n)-1]/2, \quad \beta_n = \mathrm{Im}(s_n)/2 \tag{A4}$$

and Re and Im designate real and imaginary parts. The partial-wave series for ψ_{B1} is found by converting Stratton's spherical wave expansion of a cylindrical wave[51] into the notation of the present paper that gives

$$\psi_{B1} = \psi_0 \exp(i\phi)\sum_{n=1}^{\infty}(2n+1)[n(n+1)]^{-1}i^n j_n(kr) \times P_n^{\,1}(\cos\theta)P_n^{\,1}(b), \tag{A5}$$

where $b=\cos\beta$ and j_n is a spherical Bessel function. Numerical evaluation of Eq. (A5) verifies agreement with ψ_{B1} from Eq. (1) where $z=r\cos\theta$ and $R=r\sin\theta$. For $kr \gg 1$, j_n may be approximated to leading order in powers of $(2kr)^{-1}$ as follows:[36]

$$j_n(kr) \approx (2kr)^{-1}e^{ikr}i^{-(n+1)} + (2kr)^{-1}e^{-ikr}i^{n+1}. \tag{A6}$$

APPENDIX B: ASSOCIATED LEGENDRE FUNCTIONS AND INTEGRALS

Insertion of Eq. (A2) into Eq. (3) gives an integral of a product of two series. The integration over ϕ yields a factor of 2π. The remaining integration yields a double summation containing terms proportional to:

$$I_{nq} = \int_{-1}^{1} wP_n^{\,1}(w)P_q^{\,1}(w)dw, \tag{B1}$$

which may be evaluated using the relations[52,53]

$$(2n+1)wP_n^{\,1}(w) = nP_{n+1}^{\,1}(w) + (n+1)P_{n-1}^{\,1}(w), \tag{B2}$$

$$\int_{-1}^{1} P_n^{\,1}(w)P_q^{\,1}(w)dw = 2(2n+1)^{-1}n(n+1)\delta_{n,q}, \tag{B3}$$

where $\delta_{n,q}=1$ if $n=q$ and $\delta_{n,q}=0$ if $n \neq q$. It follows that

$$I_{nq} = R_n^{\,+}\delta_{q,n+1} + R_n^{\,-}\delta_{q,n-1}, \tag{B4}$$

$$R_n^{\,+} = 2(n+2)(n+1)n/[(2n+3)(2n+1)] = R_{n+1}^{\,-}, \tag{B5}$$

$$R_n^{\,-} = 2(n+1)n(n-1)/[(2n+1)(2n-1)]. \tag{B6}$$

Surviving terms in the integrated series contain factors of the form

$$(s_n-1)(s_{n+1}^{\,*}-1)/4 = \alpha_n\alpha_{n+1} + \beta_n\beta_{n+1} + i(\beta_n\alpha_{n+1} - \alpha_n\beta_{n+1}), \tag{B7}$$

$$(s_{n+1}-1)(s_n^{\,*}-1)/4 = \alpha_{n+1}\alpha_n + \beta_{n+1}\beta_n + i(\beta_{n+1}\alpha_n - \alpha_{n+1}\beta_n), \tag{B8}$$

such that I_1 in Eq. (3) reduces to Eq. (6).

To evaluate I_2 in Eq. (4), insertion of the partial-wave series for the Bessel beam, Eq. (A5), into Eq. (4) again gives an integral of a product of two series. The integration over ϕ yields a factor of 2π. Again the integration over $w=\cos\theta$ yields a double summation containing terms evaluated using Eqs. (B1)–(B6). The far-field form of $j_n(kr)$ in Eq. (A6) is used. The $\exp(-ikr)$ factor in one term in Eq. (A6) combines with the $\exp(ikr)$ factor in Eq. (4) to give unity. From the form of Eq. (B4), the double summation in the corresponding contribution to I_2 reduces to the following expression:

$$I_{21} = (\psi_0/k)^2\sum_{n=1}^{\infty}P_n^{\,1}(b)(n+1)^{-1}\alpha_{n+1}P_{n+1}^{\,1}(b) + (\psi_0/k)^2\sum_{n=1}^{\infty}P_n^{\,1}(b)n^{-1}\alpha_{n-1}P_{n-1}^{\,1}(b), \tag{B9}$$

where $P_0^{\,1}(b) \equiv 0$. Re-indexing the second summation with $n-1=n'$ and then replacing n' by n gives $I_{21}=I_{23}/2$, where I_{23} is given by Eq. (7). The term with an $\exp(ikr)$ factor in

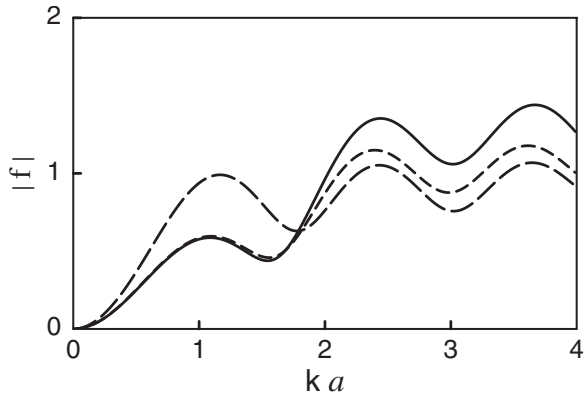

FIG. 8. For an acoustic plane-wave incident on three types of spheres, the backscattering amplitude $|f|$ [Eq. (A3) with $\theta=180°$] is plotted as a function of ka. The solid curve is for an aluminum sphere in water. The curve with long dashes is for a fixed rigid sphere. The curve with the short dashes is for a movable rigid sphere in water having the same density as aluminum.

Eq. (A6) gives a contribution to I_2 denoted by $I_{22}(kr)$ so that $I_2=I_{21}+I_{22}$.

The first step in the evaluation of Eq. (5) is to evaluate $\partial\psi_{B1}/\partial z$ using the partial-wave expansion, Eq. (A5), and note that $\partial\psi_{B1}/\partial z=\hat{z}\cdot\nabla\psi_{B1}$ where $\hat{z}$ is an axial unit vector. To leading order in powers of $(kr)^{-1}$, when kr is large, $\hat{z}\cdot\nabla\psi_{B1}\approx w\partial\psi_{B1}/\partial r$. Again the integration over ϕ yields a factor of 2π. The integration over w of the double summation contains terms evaluated using Eqs. (B1)–(B6). The resulting expression, which is again evaluated with $kr\gg1$, gives $I_3=-I_{21}+I_{22}$ so that $(I_2-I_3)=I_{23}$ does not depend on kr. Evaluations of radiation stresses based on far-field integrals often contain oscillating kr dependent terms that cancel when contributions to the total are summed.[30]

APPENDIX C: MOVABLE RIGID SPHERE AND ALUMINUM SPHERE COMPARISON

When a rigid sphere is mounted in such a way as to permit translation of its center-of-mass when the sphere is illuminated by a propagating plane acoustic wave, the scattering becomes a function of the ratio of the density of the sphere ρ_E to the density of the surrounding fluid ρ_0. Hickling and Wang[42] analyzed this dependence and found that it is necessary to modify the complex amplitude of only the dipole $(n=1)$ partial wave in Eq. (A3). In the notation of the present paper, the modification consists of taking $s_1=-D_1^*/D_1$, where

$$D_1=ka(\rho_E/\rho_0)h_1^{(1)}(ka)'-h_1^{(1)}(ka). \tag{C1}$$

It follows that for $ka\rho_E/\rho_0\to\infty$, $s_1\to-h_1^{(2)}(ka)'/h_1^{(1)}(ka)'$, which is the fixed rigid sphere limit and that for $\rho_E/\rho_0=0$, $s_1\to-h_1^{(2)}(ka)/h_1^{(1)}(ka)$, which is the soft sphere limit.

Figure 8 illustrates the value of the movable rigid sphere approximation when ka is small. Three curves for the far-field backscattering $|f|$ from Eq. (A3) are shown for plane-wave illumination. The solid curve is the exact result for an aluminum sphere in water computed as discussed in Sec. V with $\rho_E/\rho_0=2.7$. The curve with long dashes is for a fixed rigid sphere and that result overestimates the scattering when ka is small. The curve with short dashes is for a movable rigid sphere having $\rho_E/\rho_0=2.7$. The agreement with the aluminum sphere results for $ka<1.7$ suggests that in the case of an aluminum sphere, when $ka<1.7$ the backscattering is more strongly influenced by the inertia of the sphere than the details of the elastic moduli.

[1]L. V. King, "On the acoustic radiation pressure on spheres," Proc. R. Soc. London, Ser. A **147**, 212–240 (1933).
[2]T. Hasegawa and K. Yosioka, "Acoustic radiation force on fused silica spheres, and intensity determination," J. Acoust. Soc. Am. **58**, 581–585 (1975).
[3]X. C. Chen and R. E. Apfel, "Radiation force on a spherical object in an axisymmetric wave field and its application to the calibration of high-frequency transducers," J. Acoust. Soc. Am. **99**, 713–724 (1996).
[4]J. R. Wu and G. Du, "Acoustic radiation force on a small compressible sphere in a focused beam," J. Acoust. Soc. Am. **87**, 997–1003 (1990).
[5]P. L. Marston, "Axial radiation force of a Bessel beam on a sphere and direction reversal of the force," J. Acoust. Soc. Am. **120**, 3518–3524 (2006).
[6]P. L. Marston, "Negative axial radiation forces on solid spheres and shells in a Bessel beam," J. Acoust. Soc. Am. **122**, 3162–3165 (2007).
[7]P. L. Marston, "Scattering of a Bessel beam by a sphere: II. Helicoidal case and spherical shell example," J. Acoust. Soc. Am. **124**, 2905–2910 (2008).
[8]S. D. Danilov and M. A. Mironov, "Mean force on a small sphere in a sound field in a viscous fluid," J. Acoust. Soc. Am. **107**, 143–153 (2000).
[9]K. Yosioka, T. Hasegawa, and A. Omura, "Comparison of ultrasonic intensity from radiation force on steel spheres with that on liquid spheres," Acustica **22**, 145–152 (1969).
[10]D. McGloin and K. Dholakia, "Bessel beams: Diffraction in a new light," Contemp. Phys. **46**, 15–28 (2005).
[11]J. Durnin, "Exact solutions for nondiffracting beams. I. The scalar theory," J. Opt. Soc. Am. A **4**, 651–654 (1987).
[12]J. Durnin, J. J. Miceli, Jr., and J. H. Eberly, "Diffraction-free beams," Phys. Rev. Lett. **58**, 1499–1501 (1987).
[13]P. L. Marston, "Scattering of a Bessel beam by a sphere," J. Acoust. Soc. Am. **121**, 753–758 (2007).
[14]J.-L. Thomas and R. Marchiano, "Pseudo angular momentum and topological charge conservation for nonlinear acoustical vortices," Phys. Rev. Lett. **91**, 244302 (2003).
[15]R. Marchiano and J.-L. Thomas, "Synthesis and analysis of linear and nonlinear acoustic vortices," Phys. Rev. E **71**, 066616 (2005).
[16]B. T. Hefner and P. L. Marston, "An acoustical helicoidal wave transducer with applications for the alignment of ultrasonic and underwater systems," J. Acoust. Soc. Am. **106**, 3313–3316 (1999).
[17]T. Hasegawa, M. Ochi, and K. Matsuzawa, "Acoustic radiation force on a solid elastic sphere in a spherical wave field," J. Acoust. Soc. Am. **69**, 937–942 (1981).
[18]J. R. Wu, "Acoustical tweezers," J. Acoust. Soc. Am. **89**, 2140–2143 (1991).
[19]F. G. Mitri, "Acoustic radiation force on a sphere in standing and quasi-standing zero-order Bessel beam tweezers," Ann. Phys. **323**, 1604–1620 (2008).
[20]F. G. Mitri and Z. E. A. Fellah, "Theory of the acoustic radiation force exerted on a sphere by a standing and quasi-standing zero-order Bessel beam tweezers of variable half-cone angles," IEEE Trans. Ultrason. Ferroelectr. Freq. Control **55**, 2469–2478 (2008).
[21]J. W. Lee and K. K. Shung, "Radiation forces exerted on arbitrarily located sphere by acoustic tweezer," J. Acoust. Soc. Am. **120**, 1084–1094 (2006).
[22]T. A. Nieminen, V. L. Y. Loke, A. B. Stilgoe, G. Knöner, A. M. Branczyk, N. R. Heckenberg, and H. Rubinsztein-Dunlop, "Optical tweezers computational toolbox," J. Opt. A, Pure Appl. Opt. **9**, S196–S203 (2007).
[23]D. G. Grier, "A revolution in optical manipulation," Nature (London) **424**, 810–816 (2003).
[24]P. L. Marston, "Acoustic beam scattering and excitation of sphere resonance: Bessel beam example," J. Acoust. Soc. Am. **122**, 247–252 (2007).
[25]D. B. Thiessen and P. L. Marston, "Negative radiation forces on spheres illuminated by Bessel beams: Modeling using finite elements," J. Acoust. Soc. Am. **122**, 3025 (2007).
[26]B. T. Unger and P. L. Marston, "Optical levitation of bubbles in water by the radiation pressure of a laser beam: An acoustically quiet levitator," J. Acoust. Soc. Am. **83**, 970–975 (1988).

[27]K. T. Gahagan and G. A. Swartzlander, "Trapping of low-index microparticles in an optical vortex," J. Opt. Soc. Am. B **15**, 524–534 (1998).
[28]P. A. Prentice, M. MacDonald, T. Frank, A. Cuschier, G. Spalding, W. Sibbett, P. Campbell, and K. Dholakia, "Manipulation and filtration of low index particles with holographic Laguerre–Gaussian optical trap arrays," Opt. Express **12**, 593–600 (2004).
[29]V. Garbin, D. Cojoc, E. Ferrari, E. Di Fabrizio, M. L. J. Overvelde, S. M. van der Meer, N. de Jong, D. Lohse, and M. Versluis, "Changes in microbubble dynamics near a boundary revealed by combined optical micromanipulation and high-speed imaging," Appl. Phys. Lett. **90**, 114103 (2007).
[30]P. L. Marston and J. H. Crichton, "Radiation torque on a sphere caused by a circularly polarized electromagnetic wave," Phys. Rev. A **30**, 2508–2516 (1984).
[31]K. Volke-Sepúlveda, A. O. Santillán, and R. R. Boullosa, "Transfer of angular momentum to matter from acoustical vortices in free space," Phys. Rev. Lett. **100**, 024302 (2008).
[32]K. D. Skeldon, C. Wilson, M. Edgar, and M. J. Padgett, "An acoustic spanner and its associated rotational Doppler shift," New J. Phys. **10**, 013018 (2008).
[33]C. P. Lee and T. G. Wang, "Acoustic radiation force on a bubble," J. Acoust. Soc. Am. **93**, 1637–1640 (1993).
[34]W. Wei, D. B. Thiessen, and P. L. Marston, "Acoustic radiation force on a compressible cylinder in a standing wave," J. Acoust. Soc. Am. **116**, 201–208 (2004).
[35]W. Wei and P. L. Marston, "Equivalence of expressions for the acoustic radiation force on cylinders," J. Acoust. Soc. Am. **118**, 3397–3399 (2005).
[36]A. L. Fetter and J. D. Walecka, *Theoretical Mechanics of Particles and Continua* (Dover, Mineola, NY, 2003), pp. 265 and 548–553.
[37]A. Prosperetti, "Thermal effects and damping mechanisms in the forced radial oscillations of gas bubbles in liquids," J. Acoust. Soc. Am. **61**, 17–27 (1977).
[38]K. A. Sage, J. George, and H. Uberall, "Multipole resonances in sound scattering from gas bubbles in a liquid," J. Acoust. Soc. Am. **65**, 1413–1422 (1979).
[39]R. Hickling, "Analysis of echoes from a solid elastic sphere in water," J. Acoust. Soc. Am. **34**, 1582–1592 (1962).
[40]B. T. Hefner and P. L. Marston, "Backscattering enhancements associated with subsonic Rayleigh waves on polymer spheres in water: Observation and modeling for acrylic spheres," J. Acoust. Soc. Am. **107**, 1930–1936 (2000).
[41]A. Tesei, P. Guerrini, and M. Zampolli, "Tank measurements of scattering from a resin-filled fiberglass spherical shell with internal flaws," J. Acoust. Soc. Am. **124**, 827–840 (2008).
[42]R. Hickling and N. M. Wang, "Scattering of sound by a rigid movable sphere," J. Acoust. Soc. Am. **39**, 276–279 (1966).
[43]T. Hasegawa and Y. Watanabe, "Acoustic radiation pressure on an absorbing sphere," J. Acoust. Soc. Am. **63**, 1733–1737 (1978).
[44]G. Goddard and G. Kaduchak, "Ultrasonic particle concentration in a line-driven cylindrical tube," J. Acoust. Soc. Am. **117**, 3440–3447 (2005).
[45]J. B. Lonzaga, D. B. Thiessen, and P. L. Marston, "Uniformly valid solution for acoustic propagation in weakly tapered circular waveguides: Liquid jet example," J. Acoust. Soc. Am. **123**, 151–160 (2008).
[46]P. L. Marston and D. B. Thiessen, "Manipulation of fluid objects with acoustic radiation pressure," Ann. N.Y. Acad. Sci. **1027**, 414–434 (2004).
[47]J. O. Toilliez and A. J. Szeri, "Optimized translation of microbubbles driven by acoustic fields," J. Acoust. Soc. Am. **123**, 1916–1930 (2008).
[48]P. A. Dayton, J. S. Allen, and K. W. Ferrara, "The magnitude of radiation force on ultrasound contrast agents," J. Acoust. Soc. Am. **112**, 2183–2193 (2002).
[49]M. J. Shortencarier, P. A. Dayton, S. H. Bloch, P. A. Schumann, T. O. Matsunaga, and K. W. Ferrara, "A method for radiation-force localized drug delivery using gas-filled lipospheres," IEEE Trans. Ultrason. Ferroelectr. Freq. Control **51**, 822–831 (2004).
[50]F. G. Mitri, "Acoustic scattering of a high-order Bessel beam by an elastic sphere," Ann. Phys. **323**, 2840–2850 (2008).
[51]J. A. Stratton, *Electromagnetic Theory* (McGraw-Hill, New York, 1941), p. 413.
[52]M. Abramowitz and I. A. Stegun, *Handbook of Mathematical Functions* (Dover, Mineola, NY, 1965), pp. 331–341.
[53]J. D. Jackson, *Classical Electrodynamics*, 3rd ed. (Wiley, New York, 1999), Sec. 3.5, pp. 107–110.

Stirring and mixing of liquids using acoustic radiation force

Armen Sarvazyan
ARTANN Laboratories, Inc., 1459 Lower Ferry Road, Trenton, New Jersey 08618

Lev Ostrovsky
Zel Technologies/NOAA Earth Science Research Laboratory, University of Colorado, 325 Broadway, Boulder, Colorado 80305

(Received 29 October 2008; revised 20 February 2009; accepted 27 March 2009)

The possibility of using acoustic radiation force in standing waves for stirring and mixing small volumes of liquids is theoretically analyzed. The principle of stirring considered in this paper is based on moving the microparticles suspended in a standing acoustic wave by changing the frequency so that one standing wave mode is replaced by the other, with differently positioned minima of potential energy. The period-average transient dynamics of solid microparticles and gas microbubbles is considered, and simple analytical solutions are obtained for the case of standing waves of variable amplitude. It is shown that bubbles can be moved from one equilibrium position to another two to three orders of magnitude faster than solid particles. For example, radiation force in a standing acoustic wave field may induce movement of microbubbles with a speed of the order of a few m/s at a frequency of 1 MHz and ultrasound pressure amplitude of 100 kPa, whereas the speed of rigid particles does not exceed 1 cm/s under the same conditions. The stirring effect can be additionally enhanced due to the fact that the bubbles that are larger and smaller than the resonant bubbles move in opposite directions. Possible applications of the analyzed stirring mechanism, such as in microarrays, are discussed. [DOI: 10.1121/1.3124769]

PACS number(s): 43.25.Qp, 43.35.Mr, 43.80.Qf [OAS] Pages: 3548–3554

I. INTRODUCTION AND BACKGROUND

This paper discusses the physical basis for a new area of application of acoustics in biotechnology and microfluidics: stirring and mixing in small volumes of liquids. Stirring and mixing of liquids is a necessary part of many industrial, chemical, and pharmaceutical technological processes. The majority of these processes is carried out on macroscopic levels. However, it has been only in recent years that mixing of small quantities of liquids has become technologically relevant in the context of microfluidics and biotechnology since mixing is often crucial for effective functioning of devices manipulating small quantities of liquids (Nguyen and Werely, 2002). Microfluidic devices are useful in various biological and chemical applications, including such diverse fields as biochemical analysis, drug screening, genetic analysis, medical diagnostics, chemical synthesis, and environmental monitoring (Nguyen and Werely, 2002).

Achieving effective stirring and mixing in macroscopic volumes of fluids is a relatively straightforward task. Various conventional, mechanically or magnetically driven stirring elements may be employed. Alternatively, special geometries may be employed in flow channels to promote mixing without the use of moving elements. Stirring and mixing in small volumes is, however, difficult. Applying conventional mixing strategies to microfluidic volumes is generally ineffective. Various designs of micromixers have been proposed in recent years. There are several publications that comprehensively review mixing methods and devices developed for microfluidic applications (e.g., Campbell and Grzybowski, 2004; Ottino and Wiggins, 2004).

Some of the methods of stirring and mixing in microvolumes are based on acoustical principles. Liu *et al.* (2002, 2003) developed an approach to micromixing based on acoustic microstreaming around an array of small air bubbles resting at the top of the mixing chamber. When the bubbles were made to vibrate by a sound field, they created steady circular flows around them.

Ultrasound radiation force provides an efficient means of moving various microparticles in a solution, thus providing effective stirring. Manipulation of particles suspended in a fluid by standing acoustic waves is a well-known phenomenon effectively employed in numerous biomedical and industrial applications (Groschl, 1998; Coakley *et al.*, 2000; Hawkes *et al.*, 2004). The term "microparticles," as it is used here, includes various solid particles as well as microbubbles of various origins, such as simple gas bubbles, which disappear in less than 1 min after being injected into a liquid sample, or gases encapsulated in a shell known as ultrasound contrast agents (UCAs). Radiation force drives the particles to their local potential energy minima to create concentration regions that appear as clumps striated at half-wavelength separation (Nyborg, 1968; Wiklund and Hertz, 2006).

The range of currently explored applications of driving particles by acoustic radiation force is broad: targeted drug and gene delivery, increasing sensitivity of biosensors and immunochemical tests, and manipulating cells in suspensions, micro-stirring, and others. In this paper, we specifically focus on the use of radiation force in a standing ultrasonic wave field for inducing rapid motion of microparticles suspended in the liquid to facilitate various processes, which require mixing and stirring.

 0001-4966/2009/125(6)/3548/7/$25.00

In this work, using the known expressions for the radiation force acting on small objects (see references in Sec. III), we considered transient motion of microparticles from one equilibrium position to another in the field of standing waves (resonance modes), the amplitudes of which are decaying and increasing in the process of frequency switching, and made quantitative estimates for rigid particles and bubbles.

II. PHYSICAL BASIS FOR STIRRING LIQUIDS BY RADIATION FORCE IN A STANDING ACOUSTIC WAVE FIELD

By changing the frequency of the driving signal applied to the transducer of a standing wave chamber (resonator), various harmonics of the standing wave (resonator modes) can be generated. Upon achieving a resonance frequency, the ultrasound radiation force urges the microparticles to move toward the multitude of potential energy minima locations within the nodal pattern of the standing wave field. When the frequency of the ultrasound transducer is further changed to another resonance frequency, this destroys the previous nodal pattern of standing waves and creates a new nodal pattern corresponding to the new resonance frequency of the standing wave. Since the locations and the number of the second set of potential energy minima locations where particles tend to accumulate are substantially different from that of the first plurality, the microparticles are urged to move to the new plurality of locations. After enough time (in the range of milliseconds) has passed to allow the microparticles to move substantially to the second set of locations, the frequency of the ultrasound transducer is changed again to yet another resonance frequency or to the previous resonance frequency. This again urges the microparticles to change their location. The process of changing frequencies of the ultrasound transducer may be continued further so that vigorous movement of the microparticles throughout the resonator cell occurs causing intense mixing and stirring of the liquid contained therein.

The ultrasound frequency range necessary for stirring liquids with suspended microparticles using a variable frequency mode of sonification depends on several factors. One factor is related to the fact that the lower the frequency of ultrasound and the longer the distance between the nodal planes, the higher the ultrasound intensity should be needed to move a particle from one equilibrium position to another, but an increase intensity might produce unwanted effects in the treated liquid. On the other hand, if the distance between nodal planes is too short, the motion of particles will be greatly limited and will not provide efficient stirring. Another factor is that the volume of the liquid which needs to be stirred in most biotechnological applications is typically of the order of tens of microliters, and the characteristic dimensions of resonator cells typically lie in a range from about 0.5 to about 5 mm, whereas the number of pressure nodes in the liquid should preferably be in a range from 1 to about 10. Yet another factor is that, at higher frequencies, e.g., in the range of tens of megahertz and above, attenuation of ultrasound in aqueous solutions greatly increases, and the intensity of reflected waves is insufficient to generate standing waves. Based on all these factors, it can be estimated that the range of ultrasound wavelengths to be used for stirring liquids by manipulating microparticles in standing waves is typically in the 0.05–2.0 mm range, which corresponds to frequencies in about a 0.7–30 MHz range.

III. TRANSIENT DYNAMICS OF PARTICLES AND BUBBLES

A. Mode switching

There exists a wide range of literature on acoustic radiation force acting on small particles and bubbles, as well as on their motion in an acoustic field. For the early history of such studies we refer the reader to, e.g., Yosioka and Kawasima, 1955; Gor'kov, 1962; Nyborg, 1968; Crum, 1975. More recently, many papers have dealt with this problem, in relation to manipulating microparticles in liquids (e.g., Wiklund and Hertz, 2006; Kuznetsova and Coakley, 2007; Manneberg *et al.*, 2008). Here we explore the possibility of moving microparticles from one position to another by switching the frequency of exciting ultrasound in one-dimensional resonator (acoustic interferometer) formed by two parallel reflecting planes, so that one standing mode is replaced by the other, with differently positioned minima of the particle's potential energy. This causes the particles to be drawn from one equilibrium position to another and then back or to another equilibrium. The rate of stirring may depend not only on the particle motion speed but, in general, on the time of switching between the modes. The latter depends on wave dissipation in fluid filling the resonator: the higher the mode quality factor, the longer this mode field would increase and then attenuate to give way to the next excited mode. In what follows, we consider the transient dynamics of hard particles and bubbles in a field of two modes with variable amplitudes.

In the general case of a multimodal field in the resonator with an acoustic path L, the pressure is

$$P = \sum_{n=1}^{N} P_n(t) e^{i\omega t} \cos(k_m x), \quad k_m = \frac{n\pi}{L}, \tag{3.1}$$

where N is the number of significant modes and P_n are the complex amplitudes which can, in general, slowly (relative to the wave period) depend on time. The average radiation force is proportional to

$$F \propto \frac{\partial \langle P^2 \rangle}{\partial x} \quad \text{thus } F = \sum_{n=1}^{N} Q_n P_n P_n^* \sin(2k_n x). \tag{3.2}$$

Here the angular brackets denote time averaging, and the factors Q_n depend on modal frequencies and particle size.

As an example we consider multiple transitions between the standing fields at the third and fourth modes. Suppose that at $t<0$ a standing wave corresponding to mode 3 has been generated, and at $t=0$ its source is instantaneously turned off. Simultaneously, at $t=0$, the source at a frequency resonant with the fourth mode is abruptly started. It takes a certain amount of time (depending on the quality factor of the resonator) for the standing wave pattern to fade away and for a new one to be established. At this stage, the radiation force is

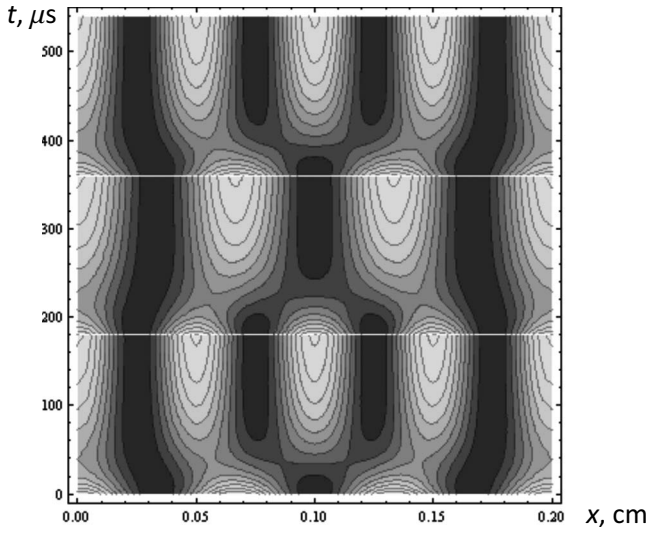

FIG. 1. Contour plot of radiation force for three subsequent switches between the third and fourth modes of a 2-mm-wide acoustic interferometer. Light areas correspond to the higher force.

$$F = \Psi_3 e^{-2b_3 t} \sin(2k_3 x) + \Psi_4 (1 - e^{-b_4 t})^2 \sin(2k_4 x), \quad (3.3)$$

where $\Psi_{3,4}$ are proportional to the squares of the peak amplitudes of the modes (see below) and $b_{3,4}$ are the damping rates (this can be due to internal losses in fluid and radiation through the resonator walls). Then, after time T, the process is inverted: the fourth mode is switched off and the third mode is switched on, etc. Thus, the force is

$$\begin{aligned} F \propto & [H(t) - H(t-T)] \cdot \{\Psi_3 e^{-2b_3 t} \sin(2k_3 x) + \Psi_4 (1 - e^{-b_4 t})^2 \\ & \times \sin(2k_4 x)\} + [H(t-T) - H(t-2T)] \\ & \cdot \{\Psi_4 (1 - e^{-b_4 T})^2 e^{-2b_4 (t-T)} \sin(2k_4 x) + \Psi_3 e^{-2b_3 T} \\ & \times (1 - e^{-b_3 (t-T)})^2 \sin(2k_3 x)\} + \ \ldots \ , \end{aligned} \quad (3.4)$$

where $H(t)$ is the Heaviside step function.

For estimates we take $L=2$ mm, so that, in the water, the frequency of the third resonance mode is 1.125 MHz and of the fourth mode, 1.5 MHz. The mode change time is $T=180$ μs. For simplicity, in this example it is supposed that $\Psi_3=\Psi_4$ and $b_3=b_4=0.035$ μs^{-1} (i.e., the resonator's quality factor is of the order of 100). Figure 1 presents a contour plot for three such changes: from the third mode to the fourth, back to the third and again to the fourth. It is seen that the transient times for decay and increase in the field are about a few dozen microseconds.

B. Motion of rigid particles

Based on the known expressions for the radiation force, here we consider again the sum of two transient modes with different spatial structures, so that the force has the form (3.3). The amplitude of period-average radiation force acting on a suspended particle in a plane standing wave can be written as (e.g., Kuznetsova and Coakley, 2007)

$$\Psi = -\frac{\pi V f P_0^2 \Phi}{2\rho_0 c_0^3}. \quad (3.5)$$

Here V is particle volume, f is frequency, ρ_0 and c_0 are density and sound velocity in a fluid, P_0 is sound pressure amplitude, and

$$\Phi = \left(1 - \frac{\rho_0 c_0^2}{\rho_p c_p^2}\right) + \frac{3(\rho_p - \rho_0)}{2\rho_p + \rho_0}, \quad (3.6)$$

where subscript p refers to the particle parameters. A more general, three-dimensional expression for the radiation force vector has been given by Manneberg *et al.* (2008).

Consider the motion of a small spherical particle under the action of the radiation force and Stokes friction. The corresponding equation for a period-average motion velocity $u(x,t)$ along the x axis is

$$\rho_p V \frac{du}{dt} = -6\pi\eta a u - F. \quad (3.7)$$

Here a is the particle radius and η is the dynamic viscosity of a fluid.

For the sizes and velocities of the microparticles considered here, the inertial term on the left-hand side of this equation is small compared to each term on the right-hand side. Hence, a quasi-static solution can be used. For a decaying single-mode field, it is

$$\begin{aligned} u = \frac{dx_p}{dt} &= -\Psi e^{-2bt} \sin(4\pi f x_p / c_0) \\ &= -\frac{\pi a^2 f P_0^2 \Phi}{9\rho_0^2 c_0^3 \nu} e^{-2bt} \sin(4\pi f x_p / c_0), \end{aligned} \quad (3.8)$$

and same but with $(1-e^{-bt})^2$ instead of e^{-2bt} for a mode with increasing amplitude.

In this section we consider a non-deformable particle, so that $\Phi=5/2$. To give an idea of particle velocity magnitude, Fig. 2(a) shows the maximum velocity according to Eq. (3.8) (reachable at $x_p=nc_0/8f$, $n=0,1,2,\ldots$) as a function of ul-

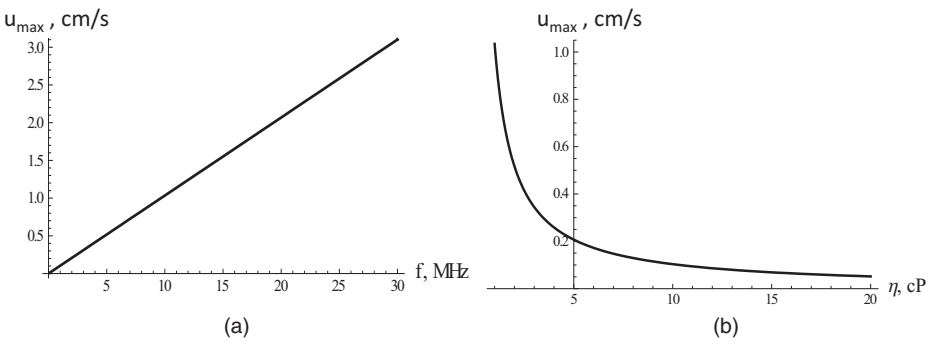

FIG. 2. (a) Dependence of maximal particle velocity, u_{max}, on ultrasound frequency for water ($\eta=\rho\nu=1$ cP, $c=1500$ m/s, $\rho=10^3$ kg/m^3) for a particle of radius $a=10$ μm at $P_0=200$ kPa. (b) Dependence of u_{max} on the viscosity of liquid at frequency $f=10$ MHz.

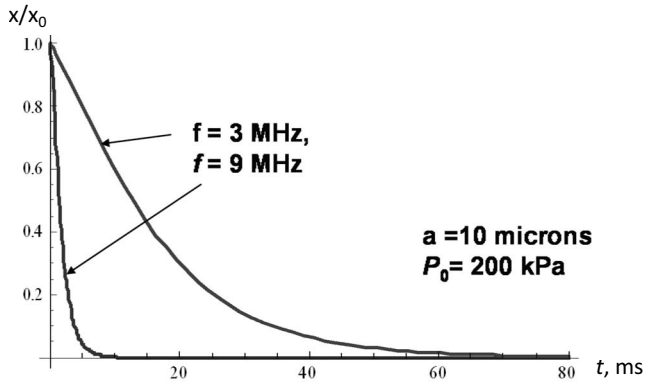

FIG. 3. Temporal variation of particle position upon switching to a frequency of 3 or 9 MHz from a distance of $x_0=0.15$ wavelength in a 2-mm long resonator.

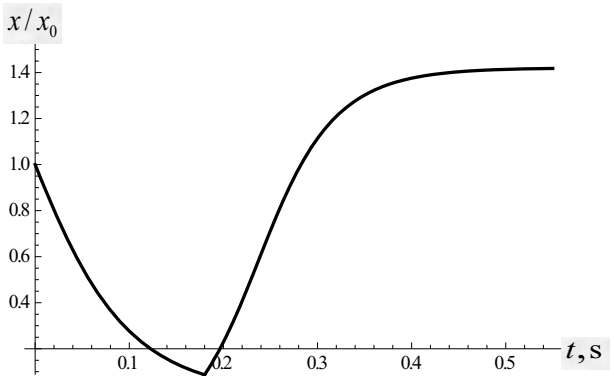

FIG. 4. Particle motion under the action of the third mode (1.125 MHz) switched to the fourth mode (1.5 MHz) in a 2-mm long resonator. Pressure amplitude is 200 kPa for each mode.

trasonic frequency. Figure 2(b) shows the velocity dependence on molecular viscosity beginning from "pure" water viscosity up to 20 times more, which covers a realistic range for biological fluids, such as solutions of biopolymers that need to be stirred or mixed.

To evaluate the time of shifting from one equilibrium to another after a fast frequency switching, we consider Eq. (3.8) as a differential equation for the particle coordinate x_p with an initial condition $x_p(t=0)=x_0$. For a single mode, analytical solutions can be obtained. At $b=0$ such a solution reads

$$x_p = \frac{1}{k_n}\arctan[\exp(-2k_n\Psi_n t + 2\ln\sqrt{\tan(kx_0)})], \qquad (3.9)$$

where $k=2\pi f/c_0$ is the wave number of the given mode and x_0 is the initial particle coordinate. If b is finite, then for an increasing mode and, separately, for a decaying mode we have, respectively,

$$x_p = \frac{1}{k_n}\arctan\{\exp[-b^{-1}(2bt + 4e^{-bt} + e^{-2bt} - 3)k_n\Psi_n]\tan(k_n x_0)\},$$

$$x_p = \frac{1}{k_n}\arctan\{\exp[-b^{-1}(1-e^{-bt})k_n\Psi_n]\tan(k_n x_0)\}. \qquad (3.10)$$

Figure 3 illustrates the motion of a particle initially displaced at a distance $x_0=0.15\lambda$ ($\lambda=2\pi/k$ is the wavelength) from the nearest equilibrium ($x=0$), for two frequencies, 3 and 9 MHz (8th and 12th modes of a 2-mm-long resonator). Other parameters are the same as above. The typical time scales for such motions are from several milliseconds to several dozen milliseconds, depending on frequency.

Figure 4 shows a cycle of switching from mode 3 to mode 4. The typical time scales for such motion are a few hundreds of milliseconds (which is larger than that in Fig. 3 due to the lower frequencies). Comparison with Fig. 1 shows that for a hard particle these time scales are much larger than those of the mode switching.

The above results refer to a hard, non-deformable particle the density of which and sound speed in which (and hence the acoustic impedance) significantly exceed these parameters in water. According to the factor Φ defined by Eq. (3.6), softer particles can move differently and even in an opposite direction. This is especially important for gas bubbles considered in Sec. III C.

C. Bubbles

Consider now the dynamics of a microbubble in a standing wave. As previously mentioned, whereas a hard particle in an acoustic field oscillates as a dipole, a small (compared with the wavelength) bubble most intensively pulsates as a monopole. The average motion of a bubble under the action of radiation force is determined by the interaction between its monopole and dipole motions. A theory of such a motion has been developed in, e.g., Yosioka and Kawasima, 1955; Watanabe and Kukita, 1993; Doinikov, 2002; Mettin and Doinikov, 2008; and, for collective, 3D bubble motions, in Kobelev and Ostrovsky, 1989.

Based on these works, radiation force acting on a bubble in a standing wave has a form similar to Eq. (3.2), namely,

$$F(x) = -\frac{3\pi a}{2\rho_0 c_0^2}\sum_n^N P_n^2 \frac{(1-\xi_n^2)}{(1-\xi_n^2)^2+\delta^2}\sin 2k_n x. \qquad (3.11)$$

Here δ is the bubble damping factor and $\xi=\omega_0/\omega$, where $\omega_0=(3\gamma p_0/\rho a^2)^{1/2}$ is the bubble resonance frequency (γ is the polytropic ratio of gas, p_0 is static pressure, and ρ is liquid density); for encapsulated bubbles, resonance frequency can be higher. Other notations are the same as above.

If, as above, inertia (in this case, virtual mass) is neglected and only the motion along x is considered (for the time intervals considered, buoyancy is also neglected, which is justified for small bubbles), then, balancing (3.11) with the Stokes force, we obtain the average translational velocity of a bubble:

$$u(x) = -\frac{1}{4\nu\rho_0^2 c^2}\sum_{n=1}^N \frac{P_n^2}{k_n}\frac{(1-\xi_n^2)}{(1-\xi_n^2)^2+\delta^2}\sin 2k_n x. \qquad (3.12)$$

Note that the Stokes force for a bubble is $4\pi\eta aU$ rather than $6\pi\eta aU$ taken above for a hard particle (Landau and Lifshits, 1993). Note also that in some works (Crum, 1975; Watanabe and Kukita, 1993) another expression for the drag

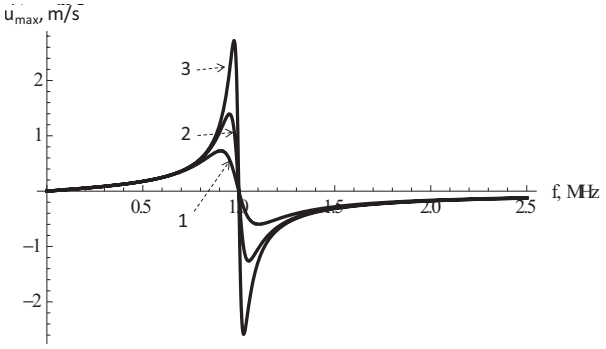

FIG. 5. Maximal average bubble velocity vs frequency at the following parameters: $P=100$ kPa, $\nu=1$ cP (water), $\omega_0=2\pi f_0=1$ MHz (for an air bubble without surfactants, resonance bubble radius is 3.26 μm), at different bubble damping factors: $1-\delta=0.2$, $2-\delta=0.1$, $3-\delta=0.05$.

force acting on a bubble was used. In these works, bubble motion with Reynolds numbers in the range of $\mathrm{Re}=1-200$ was considered. In our case typically $\mathrm{Re}\ll 1$ (except possibly in the case of exact resonance when Re can be of the order of unity), so that the use of Stokes force is better justified. We also neglect the integral "history" term (e.g., Lovalenti and Brady, 1993) which is small in the cases considered here.

As seen from Eq. (3.12), even for a single-mode field, the drift directions are different for bubbles that are larger or smaller than the resonance bubbles. Equilibrium points correspond to pressure nodes and peaks, which can be stable or unstable depending on the frequency and bubble radius.

Figure 5 shows the frequency dependence of the translational bubble velocity in the maxima of $\sin 2kx$ for bubbles resonant at 1 MHz, and different loss factors of a bubble which depend on the fluid viscosity (water and solutions of biopolymers) in a rather complicated manner (e.g., Naugolnykh and Ostrovsky, 1998). Comparison with Fig. 2 indicates the much faster motion of a bubble even for a lower frequency and smaller pressure amplitude. As mentioned previously, the direction of motion is different for bubbles larger and smaller than the resonance bubble, which can additionally enhance stirring capability.

Considering again Eq. (3.12) as a differential equation with respect to the bubble coordinate and integrating it, one can follow the bubble motion to its equilibrium. For the case of a single mode, the solutions (3.9) and (3.10) can be used, where now the magnitude Ψ is defined by Eq. (3.12). Figure 6 shows the transition from an initial displacement of $\lambda/8$ at two frequencies, one below and one above the resonance in a non-viscous fluid. Under the action of ultrasound at frequencies higher and lower than the resonant one, the bubble drifts to equilibrium positions $x=0$ and $x=\lambda/4$, respectively. This motion is approximately two orders of magnitude faster than that for a hard particle (see Fig. 4).

For bubbles, the time of motion to an equilibrium can be comparable with the time of acoustic mode decay. Figure 7 illustrates the effect of decay on bubble motion. At $b\neq 0$, the bubble does not return to the equilibrium position, and this factor may decrease the efficiency of stirring.

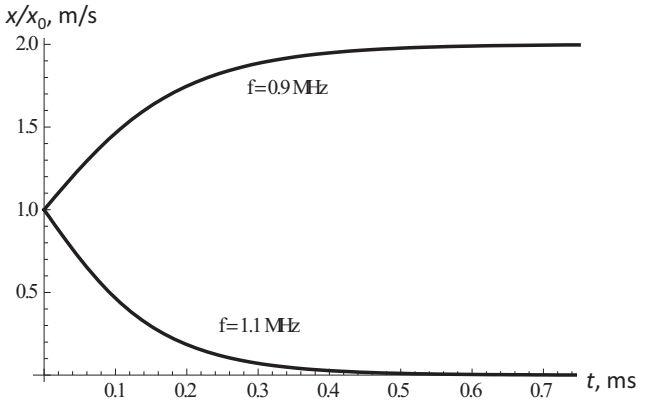

FIG. 6. Bubble position as a function of time from the initial point $x_0=0.15\lambda$, with respect to the nearest equilibrium, for two ultrasonic frequencies, 900 and 1100 kHz. Damping factor of a bubble is taken as $\delta=0.1$; this value can be considered as typical of contrast microbubbles (e.g., de Jong *et al.*, 2002).

IV. CURRENT AND PROJECTED BIOTECHNOLOGICAL AND BIOMEDICAL APPLICATIONS

Radiation force in an ultrasound standing wave has been employed mainly for manipulating (separating, washing, sorting, and isolating) biological cells and particles rather than for mixing and stirring liquids. Stirring of liquids in an ultrasonic resonator cell using the multi-mode standing wave method described in this paper was implemented in the study by Ossina *et al.* (2007a) on HIV antibody detection using an ultrasound particle agglutination method. In that study it was demonstrated that ultrasonic stirring can enhance the performance of bead-based immunoassays, such as the latex agglutination test (LAT) used for identification and quantification of analytes, biomolecules, and other substances of biological importance. LAT is widely used in point-of-care tests for diagnostic purposes, as well as in drug discovery/proteomics research and in food-industry quality controls due to its simplicity, low cost, and speed. Effective microstirring may enhance bead-based assay by destroying non-specifically bound aggregates and improving signal-to-noise ratio in quantitative assessment of the amount of immunochemically bound aggregates. In another study by the same group (Os-

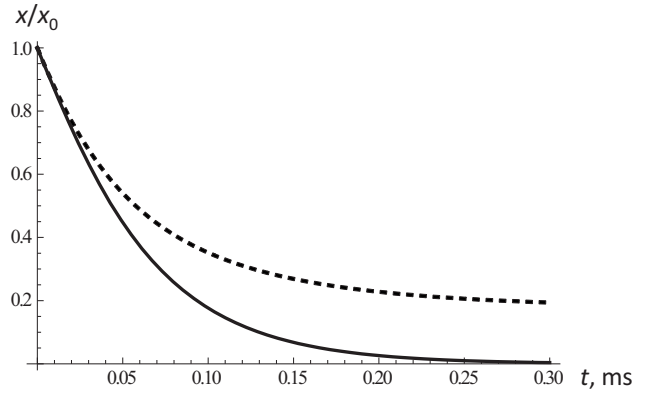

FIG. 7. Return of the bubble to the equilibrium from the initial point $x_0=0.15\lambda$, under the action of the field at frequency of 1.1 MHz; the bubble parameters are the same as in Fig. 6. (Solid line) non-damping mode; (Dashed) a mode with a damping factor $b=10$ ms^{-1}, see Eq. (3.10) (quality factor of the resonator is about 100).

sina *et al.*, 2007b), the proposed method of ultrasonic stirring was successfully implemented in the immuno-agglutination tests for food-borne pathogenic bacteria.

We hypothesize that the potential range of applications of acoustic radiation force as a tool for microstirring and mixing liquids is much wider than those limited applications described in the literature. There are numerous biotechnological applications in which diffusion is a main factor limiting the rate and efficiency of the process, such as in microarrays, which are widely used for identification of proteins, oligonucleotides, and other biologically important molecules. Microarray analysis became the basis for the recent advances in high-throughput technologies for studying genes and their function. The basic structure of a microarray is simple: a glass slide or membrane is spotted or "arrayed" with various molecules, such as DNA fragments or oligonucleotides that represent specific gene coding regions. One of the drawbacks of a microarray analysis is the long testing time, which could be in the range of hours. Effective microstirring of the sample tested by the microarray analysis may reduce diffusion limitation and may significantly improve the performance of the microarray method. Such microstirring as is necessary for accelerating the microarray analysis can be achieved by adding a small amount of microparticles to the test sample. Generating a varying nodal pattern of standing acoustic waves may greatly increase the rate of molecular processes involved in microarray analysis.

Ultrasonic stirring and mixing of fluids with added microparticles, including microbubbles, can be applicable to the processes occurring at the interface between a solid surface and a liquid when the effectiveness of these processes depends on diffusion rate. Examples of processes that can be enhanced by increasing diffusion rate include various chemical and biochemical reactions such as the polymerase chain reaction, binding of a substrate and a ligand, hybridization of nucleic acids and their fragments, interaction between antigen and antibody, etc.

The range of applications of the proposed method may be limited by the existing containers used in biotechnologies. Standard containers used for biological assays would be hard to integrate into conventional ultrasound standing wave devices, but there is a solution to that problem. Our preliminary observation showed that there is no need to have a regular plane-parallel or cylindrical resonator to stir liquids using suspended microparticles. When ultrasound in the swept-frequency mode is transmitted into any container with reflective boundaries, complex and greatly variable nodal patterns are formed, which should potentially be able to provide the motion of particles necessary for stirring and mixing. It is hard to generate traveling waves, but generation of some complex modes of standing waves occurs automatically when the frequency of ultrasound transmitted into a container is varied. Obviously, such a swept-frequency mode of stirring will require specific arrangements for coupling the container with the source of ultrasound, and in any particular application it would need separate consideration.

Other processes which can be enhanced by improved diffusion with the use of microparticles include extracting, separating, and sterilizing. A further process that can be improved by stirring the microparticles added to the investigated sample is thermostating, which is commonly used in numerous biotechnological applications. Enhanced convection caused by ultrasonically induced rapid motion of suspended microparticles in the thermostated liquid will accelerate the temperature equilibration in the treatment vessel.

The particles necessary for inducing stirring and mixing of liquids by standing acoustic waves include various microbeads made of an inert material not affecting the treated sample, as well as gas microbubbles encapsulated in a biocompatible shell, such as those that are currently used as an UCA. The wall-forming material could be a thermally denatured protein, a surfactant, a lipid, polysaccharide, or other membrane-forming substances. As was shown in this study, the microbubbles could be orders of magnitude more efficient in stirring liquids than solid particles such as latex beads. If there are no technological limitations for adding a small amount of UCA to the treated sample, then the microbubble will be the first choice for use in an ultrasonic standing wave method of stirring and mixing liquids.

An important technical aspect of the acoustical stirring of liquids is that there is significant flexibility in using different patterns of the standing wave field to optimally adapt this technology to a particular application. In applications where the volume containing the liquid that needs to be stirred is a tube, it could be beneficial to use cylindrical standing waves. An important advantage of cylindrical geometry is that it eliminates the need for accurate alignment of a transducer/reflector system, in contrast to the case of planar or confocal standing wave fields. If the vessel containing the liquid has a rectangular configuration, a two-dimensional (2D) standing wave pattern could be most efficient for stirring the liquid. Such a 2D pattern can be generated by the superposition of the orthogonally oriented standing waves (Oberti *et al.*, 2007; Manneberg *et al.*, 2008).

In biomedical applications, where the liquids which need to be stirred and mixed may contain biological cells and biopolymers, an important issue is the safety of the treatment. The stirring should be conducted without damaging the gentle biological components of the treated liquid. Numerous studies involving biological effects in an ultrasound standing wave field have clearly demonstrated that at the intensities of ultrasound sufficient for manipulating particles and biological cells, no measurable damaging biological effects are observed (Evander *et al.*, 2007; Haake *et al.*, 2005; Hultstrom *et al.*, 2007).

V. CONCLUSIONS

The theoretical analysis presented in this paper suggests that the use of radiation force in a standing ultrasonic field as a means for mixing and stirring small volumes of liquids (in the range of microliters) has significant potential in various biomedical and biotechnological applications. In numerous technologies and in microfluidics, where the volume of cells is on the order of tens of mm^3 and less, diffusion is the main factor limiting the rate and efficiency of the process, so that an efficient stirring can be of critical importance. As potential applications of standing acoustic waves for microstirring

of liquids are not yet sufficiently explored and implemented, thorough theoretical and experimental studies and efforts will be needed to make full use of the processes described in this paper.

Campbell, C. J., and Grzybowski, B. A. (**2004**). "Microfluidic mixers: From microfabricated to self-assembling devices," Philos. Trans. R. Soc. London, Ser. A **362**, 1069–1086.

Coakley, W. T., Hawkes, J. J., Sobanski, M. A., Cousins, C. M., and Spengler, J. (**2000**). "Analytical scale ultrasonic standing wave manipulation of cells and microparticles," Ultrasonics **38**, 638–641.

Crum, L. A. (**1975**). "Bjerknes forces on bubbles in a stationary sound field," J. Acoust. Soc. Am. **57**, 1363–1370.

de Jong, N., Bouakaz, A., and Frinking, P. (**2002**). "Basic acoustic properties of microbubbles," Echocardiogr. **19**, 229–240.

Doinikov, A. A. (**2002**). "Translational motion of a spherical bubble in an acoustic standing wave of high intensity," Phys. Fluids **14**, 1420–1425.

Evander, M., Johansson, L., Lilliehorn, T., Piskur, J., Lindvall, M., Johansson, S., Almqvist, M., Laurell, T., and Nilsson, J. (**2007**). "Noninvasive acoustic cell trapping in a microfluidic perfusion system for online bioassays," Anal. Chem. **79**, 2984–2991.

Gor'kov, L. P. (**1962**). "On the forces acting on a small particle in an acoustic field in an ideal fluid," Sov. Phys. Dokl. **6**, 773–775.

Groschl, M. (**1998**). "Ultrasonic separation of suspended particles—Part I: Fundamentals," Acust. Acta Acust. **84**, 432–447.

Haake, A., Neild, A., Kim, D. H., Ihm, J. E., Sun, Y., Dual, J., and Ju, B. K. (**2005**). "Manipulation of cells using an ultrasonic pressure field," Ultrasound Med. Biol. **31**, 857–64.

Hawkes, J. J., Barber, R. W., Emerson, D. R., and Coakley, W. T. (**2004**). "Continuous cell washing and mixing driven by an ultrasound standing wave within a microfluidic channel," Lab Chip **4**, 446–452.

Hultström, J., Manneberg, O., Dopf, K., Hertz, H. M., Brismar, H., and Wiklund, M. (**2007**). "Proliferation and viability of adherent cells manipulated by standing-wave ultrasound in a microfluidic chip," Ultrasound Med. Biol. **33**, 145–151.

Kobelev, Yu. A., and Ostrovsky, L. A. (**1989**). "Nonlinear acoustic phenomena due to bubble drift in a gas-liquid mixture," J. Acoust. Soc. Am. **85**, 621–627.

Kuznetsova, L. A., and Coakley, W. T. (**2007**). "Applications of ultrasound streaming and radiation force in biosensors," Biosens. Bioelectron. **22**, 1567–1577.

Landau, L. D., and Lifshits, E. M. (**1993**). *Fluid Mechanics* (Pergamon, Oxford).

Liu, R., Lenigk, R., Druyor-Sanchez, R. L., Yang, J., and Grodzinsk, P. (**2003**). "Hybridization enhancement using cavitation microstreaming," Anal. Chem. **75**, 1911–1917.

Liu, R. H., Yang, J., Pindera, M. Z., Athavale, M., and Grodzinski, P. (**2003**). "Bubble-induced acoustic micromixing," Lab Chip **2**, 151–157.

Lovalenti, P. M., and Brady, J. F. (**1993**). "The force on a bubble, drop, or particle in arbitrary time-dependent motion at small Reynolds number," Phys. Fluids A **5**, 2104–2116.

Manneberg, O., Svennenberg, H., Hertz, H. M., and Wiklund, M. (**2008**). "Wedge transducer design for two-dimensional ultrasonic manipulation in a microfluidic chip," J. Micromech. Microeng. **18**, 1–9.

Mettin, R., and Doinikov, A. A. (**2008**). "Translational instability of a spherical bubble in a standing ultrasound wave," Appl. Acoust. (in press).

Naugolnykh, K. A., and Ostrovsky, L. A. (**1998**). *Nonlinear Wave Processes in Acoustics* (Cambridge University Press, Cambridge).

Nguyen, N., and Werely, S. (**2002**). *Fundamentals and Applications of Microfluidics* (Artech House, Boston).

Nyborg, W. L. (**1968**). "Mechanisms for nonthermal effects of sound," J. Acoust. Soc. Am. **44**, 1302–1309.

Oberti, S., Neild, A., and Dual, J. (**2007**). "Manipulation of micrometer sized particles within a micromachined fluidic device to form two-dimensional patterns using ultrasound," J. Acoust. Soc. Am. **121**, 778–785.

Ossina, N., Ketema, F., Constantine, N., and Bystryak, S. (**2007a**). "HIV antibody detection using an ultrasound particle agglutination method," Proceedings of the 19th International Congress on Acoustics, Madrid, 2–7 September 2007; http://www.sea-acustica.es/WEB_ICA_07/fchrs/papers/ult-14-012.pdf. Last viewed 4/30/2009.

Ossina, N., Panikov, N., Sizova, M., and Bystryak, S. (**2007b**). "Ultrasonic immuno-agglutination tests for food-borne pathogenic bacteria," Proceedings of the 19th International Congress on Acoustics, Madrid, 2–7 September 2007; http://www.sea-acustica.es/WEB_ICA_07/fchrs/papers/ult-14-013.pdf. Last viewed 4/30/2009.

Ottino, J. M., and Wiggins, S. (**2004**). "Introduction: Mixing in microfluidics," Philos. Trans. R. Soc. London, Ser. A **362**, 923–935.

Watanabe, T., and Kukita, Y. (**1993**). "Translational and radial motions of a bubble in an acoustic wave field," Phys. Fluids A **5**, 2682–2688.

Wiklund, M., and Hertz, H. M. (**2006**). "Ultrasonic enhancement of bead-based bioaffinity assays," Lab Chip **6**, 1279–1292.

Yosioka, K., and Kawasima, Y. (**1955**). "Acoustic radiation pressure on a compressible sphere," Acustica **5**, 167–173.

Bistable and dynamic states of parametrically excited ultrasound in a fluid-filled interferometer

Isabel Pérez-Arjona, Víctor J. Sánchez-Morcillo, and Víctor Espinosa
Instituto de Investigación para la Gestión Integrada de las Zonas Costeras, Universidad Politécnica de Valencia, Carretera Natzaret-Oliva s/n, 46730 Grau de Gandia, Valencia, Spain

(Received 21 May 2008; revised 4 March 2009; accepted 25 March 2009)

In this paper the problem of parametric sound generation in an acoustic resonator filled with a fluid is considered, taking explicitly into account the influence of the nonlinearly generated second harmonic. A simple model is presented, and its stationary solutions were obtained. The main feature of these solutions is the appearance of bistable states of the fundamental field resulting from the coupling to the second harmonic. An experimental setup was designed to check the predictions of the theory. The results are consistent with the predicted values for the mode amplitudes and parametric thresholds. At higher driving values a self-modulation of the amplitudes is observed. This phenomenon is identified with a secondary instability previously reported in the frame of the theoretical model. © *2009 Acoustical Society of America.* [DOI: 10.1121/1.3119628]

PACS number(s): 43.25.Ts, 43.25.Rq [OAS] Pages: 3555–3560

I. INTRODUCTION

The development of nonlinear effects, and in particular the observation of parametric phenomena in acoustics, requires relatively high-intensity fields, for which high-quality resonators are most adequate. The knowledge of the field evolution in resonators in nonlinear regime is important both in its fundamental and applied aspects. One of the simplest configurations consists of two plane and parallel walls (an acoustic interferometer) where nearly one-dimensional standing waves are formed along the cavity axis. The system was the basis, 40 years ago, of the first experimental observation of acoustic parametric excitation in a fluid.[1,2] The phenomenon,[3] first observed by Faraday[4] and later described by Lord Rayleigh, consists in the emergence of oscillation modes at frequencies smaller than that of the driving when a parameter of the system is varied periodically in time. The phenomenon is universal and has been demonstrated in a variety of physical systems.[5] In the case of the acoustical interferometer, the length of the cavity (and thus the eigenfrequencies of the normal modes) is the time-dependent parameter, and the parametric excitation is achieved when the input energy is high enough to overcome the dissipative losses. The parametric fields usually appear as doublets, whose frequencies f_1 and f_2 add to match the driving frequency f_0, i.e., $f_0=f_1+f_2$, although in some circumstances the half-frequency mode is observed.

A theoretical description, based on the Mathieu equation, has been successfully applied to the description of these processes in an acoustical interferometer, allowing to predict the subharmonic spectrum and its excitation threshold.[5,6] This approach has, however, a restricted validity since it cannot describe the further evolution of the parametric fields above the threshold and, on the other hand, it ignores the unavoidable effects of the higher harmonics of the driving, which are the main signature of non- or weakly-dispersive acoustic systems.

The spectrum of higher harmonics can be controlled using additional dispersion mechanisms, such as bubbly fluids or walls with selective (frequency dependent) absorption.[7–10] Ostrovsky *et al.*[11] designed a waveguide cavity where dispersion is introduced by the lateral boundaries, and the higher harmonics could be completely inhibited. As a theoretical framework, a set of evolution equations for the triad of interacting modes was considered, resulting in an excellent agreement with the measured amplitudes above threshold.

This theory has been also applied to the interferometer case,[7,12–14] but the agreement with the experiment[7] was mainly qualitative. The discrepancies can be interpreted in terms of the influence of the first higher harmonics (those with non-negligible amplitudes) on the parametric process, introducing additional features that cannot be captured by the fully dispersive model, where higher harmonics of the pump are absent.

In this work we present a theoretical description of parametric sound generation in a fluid-filled interferometer, extending the previous models to include the coupling with the second harmonic. The stationary solutions both above and below the threshold are obtained and discussed. The solutions are compared with experimentally measured values, with an excellent agreement. The novel effects induced by the second harmonic (e.g., bistability or hysteresis) are discussed. Finally, we also report the existence of low frequency self-oscillations, occurring at pump values beyond the parametric instability threshold. This phenomenon is discussed in terms of secondary instabilities of the proposed model.

II. THEORY

The acoustical interferometer considered in this paper is composed by two parallel and solid walls, with thicknesses D and H, respectively, located at a distance L from each other, containing a fluid medium inside. Each medium involved in the model is acoustically characterized by its den-

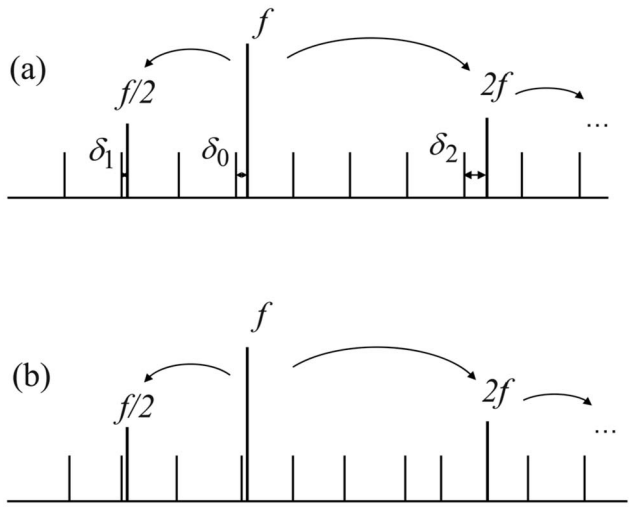

FIG. 1. Schematic representation of the field and cavity spectra in the cases of (a) ideal (lossless) cavity and (b) a real cavity with finite impedances. The generation of half- and second-harmonic frequencies is illustrated, together with their corresponding detunings.

sity ρ, bulk modulus κ, and sound velocity c, related as $c^2=\kappa/\rho$. The resonance modes (eigenfrequencies) of the resonator depend on these parameters, defining the acoustical impedances $z=\rho c$ of each section. In the ideal (lossless) case, corresponding to an infinite impedance of the walls, the resonance modes are equidistant and obey the equation

$$\tan(k_f L)=0, \tag{1}$$

or, equivalently, $k_f L=n\pi$, where $k_f=2\pi f/c_f$, with c_f being the sound velocity in the fluid. However, in a real system the impedances have finite values, and the spectrum of the resonator is no longer equidistant, but distributed according to the transcendental equation[7]

$$\tan(k_f L)=\frac{\mathcal{R}[\tan(k_w H)+\tan(k_w D)]}{\mathcal{R}^2\tan(k_w H)\tan(k_w D)-1}, \tag{2}$$

where $k_w=2\pi f/c_w$, with c_w being the sound velocity in the wall, and $\mathcal{R}$ is the quotient between wall and fluid impedances.

Now consider the driven system, assuming that one of the walls vibrates with frequency f_0. Then, above the parametric generation threshold the spectrum inside the resonator can be decomposed in two sets: the subharmonics resulting from the parametric instability and the higher harmonics of the driving nf_0, with n an integer number. Usually only harmonics with small n reach a signifficant amplitude. The amplitude of any of these harmonics decreases with the detuning, defined as the difference between the corresponding field frequency ω_n and the frequency of the closest mode, ω_n^c, i.e., $\delta_n=\omega_n-\omega_n^c$. The energy transfer into a harmonic is then more effective under resonance conditions. In an ideal cavity, a resonant driving implies that all higher harmonics are also resonant with a cavity mode, enhancing the cascade of energy from the driving into many higher frequency components. However, an initial detuning δ_0 implies that the detuning of the higher order modes increases linearly with the frequency [Fig. 1(a)]. As a consequence, the amplitude of these modes is reduced with respect to the resonant case. This situation can be more dramatic in a real system, where the mode distribution is non-equidistant and the detuning of the second and higher harmonics can be tuned to be much larger than that of the driving and the subharmonics, as shown in Fig. 1(b).

The above arguments suggest that a theoretical approach to parametric sound generation must take into account the effect of the second harmonic, whose amplitude is not negligible in general, but one can neglect the influence of the third and higher harmonics, assuming that they are sufficiently out of resonance. To simplify the analysis, we consider that the parametric generation is degenerated, i.e., the half harmonic of the driving is excited.

Under these assumptions, and following the technique described in detail in Ref. 13 for the dispersive resonators (where higher harmonic contributions were neglected), the following system of equations for the evolution of the slowly-varying amplitudes for each mode is obtained:

$$\frac{dP_0}{dt}=-(\gamma_0+i\delta_0)P_0-i\beta(P_1^2+P_2P_0^*)+\frac{c}{L}P_{\text{in}},$$

$$\frac{dP_1}{dt}=-(\gamma_1+i\delta_1)P_1-i\frac{\beta}{2}P_0P_1^*,$$

$$\frac{dP_2}{dt}=-(\gamma_2+i\delta_2)P_2-i\beta P_0^2, \tag{3}$$

corresponding to the fundamental (driving), subharmonic, and second harmonic, respectively. Other parameters are as follows: P_{in} is the driving amplitude (pump), $\gamma_n(n=0,1,2)$ are the decay rates of each mode in the cavity, $\beta=\omega_0/4\rho c^2(1+B/A)$ is related to the nonlinearity parameter B/A of the fluid, and $\delta_n=\omega_n-\omega_n^c$ are the detunings.

The dynamical system given by Eq. (3) can be reduced to a simpler, dimensionless form, defining the new variables $A_0=i(2\gamma_1/\beta)P_0$, $A_1=i(\sqrt{2\gamma_0\gamma_1}/\beta)P_1$, $A_2=i(\gamma_0/\beta)P_2$, and $E=i(2L\gamma_0\gamma_1/\beta)P_{\text{in}}$, and the parameters $\gamma=\gamma_1^2/\gamma_0\gamma_2$ and $\Delta_n=\delta_n/\gamma_n$. With these changes we obtain

$$\gamma_0^{-1}\frac{dA_0}{dt}=-(1+i\Delta_0)A_0+E-A_1^2-A_2A_0^*,$$

$$\gamma_1^{-1}\frac{dA_1}{dt}=-(1+i\Delta_1)A_1+A_0A_1^*,$$

$$\gamma_2^{-1}\frac{dA_2}{dt}=-(1+i\Delta_2)A_2+i\gamma A_0^2. \tag{4}$$

Equation (4) admits two different stationary solutions. When the pump amplitude E is below the parametric threshold, one can set $A_1=0$. Neglecting the temporal derivatives in Eq. (4) we obtain

$$E=|A_0|\left(1+\Delta_0^2+\frac{\gamma|A_0|^2(\gamma|A_0|^2+2(1-\Delta_0\Delta_2))}{1+\Delta_2^2}\right)^{1/2},$$

$$|A_2|=\frac{\gamma}{\sqrt{1+\Delta_2^2}}|A_0|^2. \tag{5}$$

The solution given in Eq. (5) reflects the fact that the amplitudes of both the fundamental and the second harmonic grow with the pump amplitude, as expected. The most interesting feature is, however, the emergence of multivalued solutions, i.e., the system shows a bistable or hysteretic behavior, when some conditions on the parameters are fulfilled. We note that the predicted hysteretic behavior occurs even in a medium with quadratic nonlinearity by means of a coupling between different harmonics, as will be discussed below. The condition for multivaluedness is found by imposing the existence of an inflection point in the S-shaped curve given by Eq. (5). This occurs when $d^2E/d|A_0|^2=0$, i.e., at

$$|A_0|^2 = -\frac{2(1-\Delta_0\Delta_2)}{3\gamma}. \tag{6}$$

Note that the existence of bistable solutions requires that $\Delta_0\Delta_2 > 1$, i.e., both detunings must have the same sign and exceed a certain critical value. Figure 2 shows the monostable (a), critical (b), and bistable (c) cases of the fundamental mode for different sets of parameters.

At a pump value given by

$$E_{\text{th}} = \sqrt{(1+\Delta_1^2)[(1+\tilde{\gamma})^2 + (\Delta_0 - \tilde{\gamma}\Delta_2)^2]}, \tag{7}$$

where we have defined $\tilde{\gamma} = \gamma(1+\Delta_1^2)/(1+\Delta_2^2)$, the solution given by Eq. (5) becomes unstable, denoting the threshold of the parametric instability. The new solution corresponds to a nonzero value of the subharmonic amplitude given by

$$|A_1|_{\pm}^2 = (-1+\Delta_0\Delta_1) - \tilde{\gamma}(1+\Delta_1\Delta_2) \pm \sqrt{E^2 - [\Delta_0 + \Delta_1 + \tilde{\gamma}(\Delta_1 - \Delta_2)]^2}. \tag{8}$$

Above the instability threshold, the fundamental mode saturates to a constant value

$$|A_0|^2 = 1 + \Delta_1^2, \tag{9}$$

and A_2 is given by Eq. (5).

Note that in the limiting cases of large second-harmonic detuning Δ_2 or large losses γ_2 (in both cases $\tilde{\gamma}$ tends to zero), the solutions (5)–(8) reduce to those obtained in previous works (see, e.g., Ref. 13) for the dispersive cavity. Physically a mode with large detuning or losses is strongly damped in the cavity, so in practice it can be neglected in the analysis.

The parametric instability can be either supercritical or subcritical, resulting in monostable or bistable subharmonic, respectively. As shown in Refs. 11 and 12 the bistability of the subharmonic is also present in the fully dispersive cavity in contrast to the bistability of the fundamental mode, which should be absent in this case.

Finally we note that, in order to observe the bistable regime of the fundamental mode, it must occur with precedence to the parametric instability. Combining Eqs. (6) and (9), we find that the fundamental mode presents bistability whenever

$$0 < \frac{2}{3\gamma}(\Delta_0\Delta_2 - 1) - \Delta_1^2 < 1.$$

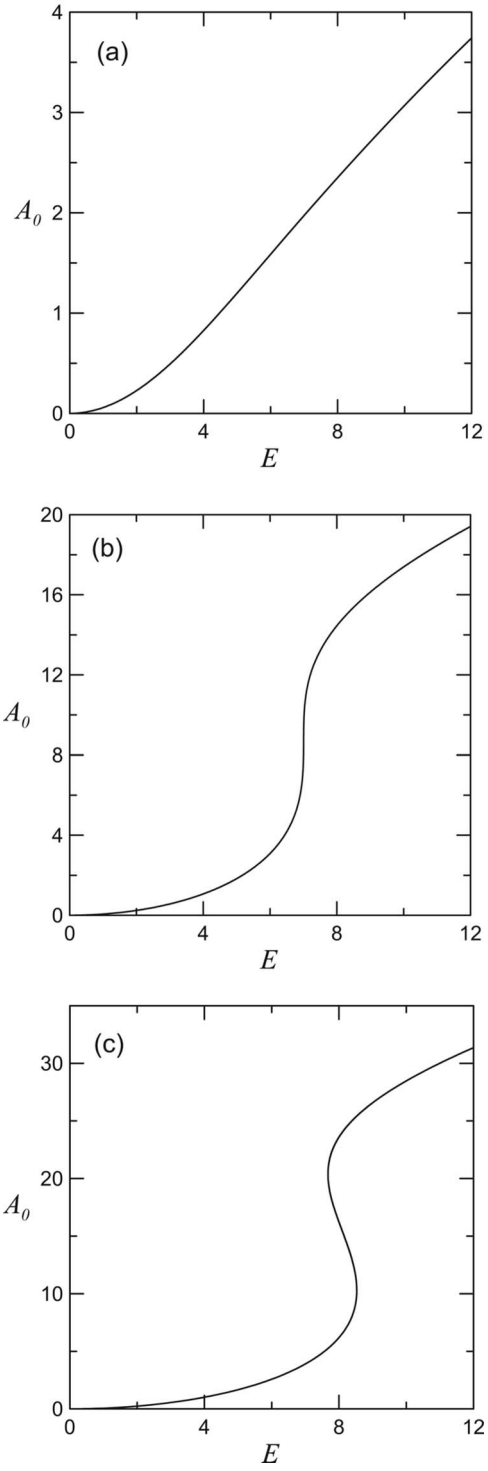

FIG. 2. Development of bistability of the fundamental mode as the second-harmonic detuning is varied. Parameters are $\gamma=1$, $\Delta_0=-2$, and $\Delta_2=1$ (a), $\Delta_2=0$ (b), and $\Delta_2=-1$ (c).

III. EXPERIMENT

A. Description

The resonator consists in two piezoceramic disks ($\rho = 7700$ kg/m^3 and $c=4400$ m/s) with radius of 1.5 cm and thicknesses of 1 and 2 mm (corresponding to resonance frequencies around 2 and 1 MHz, respectively), mounted in a Plexiglas tank containing distilled and degassed water ($\rho = 1000$ kg/m^3 and $c=1480$ m/s at $T=20$ °C). Both sides

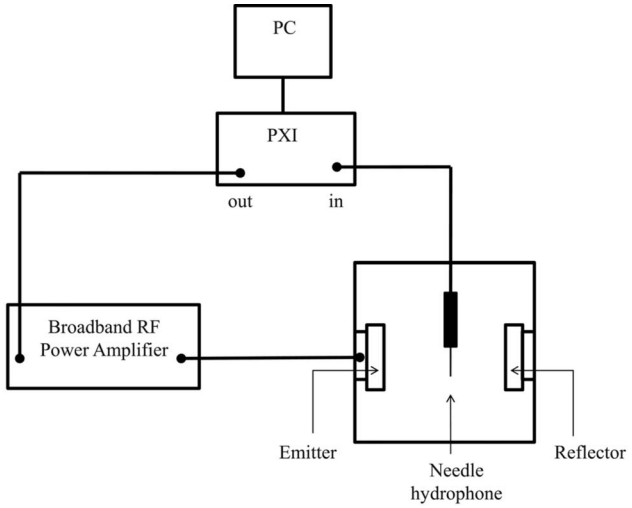

FIG. 3. Block diagram of the acoustic fluid-filled interferometer: The personal computer (PC)-based peripheral component interconnect extensions for instrumentation (PXI) platform consists in both a signal generation and a digital acquisition (oscilloscope) card. The generated signal is amplified by a rf broadband power amplifier to excite the piezoelectric emitter, while the acoustical field inside the interferometer is measured by means of a needle hydrophone with flat frequency response.

are located at a variable distance L, and its parallelism can be carefully adjusted to get a high-Q interferometer. One of the piezoceramics—that with resonance frequency around 2 MHz—is driven by the signal provided by a function generator (Agilent 33220) and a broadband rf power amplifier ENI 240L. The experimental setup is completed by a needle hydrophone (TNUA200 NTR Systems) to measure the intracavity pressure field. The hydrophone has a sensitive section of 0.2 mm. Since measurements are taken with the hydrophone placed vertically in the resonator, we measured previously the directivity factor at 90 deg with the emitter in free field operation. The wavelength varies from 0.75 mm for 2 MHz up to 3 mm for 0.5 MHz; therefore the fixed positioning along the stationary waves makes the hydrophone signal to be frequency dependent. We placed the hydrophone at an antinode of the excited fundamental frequency, and its absolute value was properly determined. In addition, the real amplitude of each frequency is affected by the detuning to the closest cavity mode. Consequently, the values of the subharmonic or superharmonic amplitudes and the curves describing their variation must be considered only qualitatively. The Fourier transform of the acquired signal allows to determine the spectral content of the acoustic field inside the resonator, which allows to quantify (with the mentioned restrictions) the amplitude of any frequency component. Figure 3 shows a block diagram of the experimental setup.

In this way, by changing the amplitude of the driving source, we are able to follow the bifurcation diagram of the resonator for a given set of parameters. Although the pump value and the decay rates γ_n can be unambiguously determined (the latter by measuring the line width of the cavity modes), the detuning parameters δ_n are difficult to control and, in general, vary from one set of measurements to the next. The reason is the dependence of the cavity resonances on the temperature of the medium, which changes with time

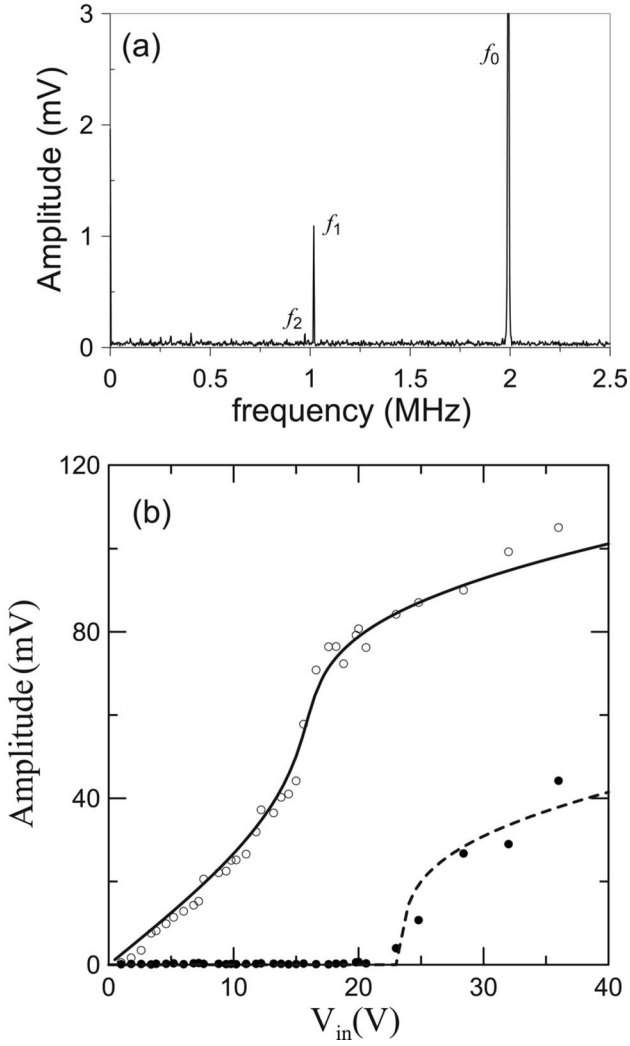

FIG. 4. (a) Spectral content of the acoustic field in the resonator obtained for a driving frequency $f_0=1.991$ MHz and an input voltage of $V_{in}=25$ V. (b) Experimental bifurcation diagram (symbols) obtained at the same driving frequency and different input voltages. Solid and dashed lines correspond to the fundamental and subharmonic amplitudes, as obtained from Eqs. (5) and (8) for $\Delta_0=-2.35$, $\Delta_1=3.25$, and $\Delta_2=-4$.

due to the external sources (heating of the driving transducer or ambient temperature variations). However, we have monitored the temperature variations to ensure that the detunings did not changed appreciably within one set of measurements, so we could apply the theory of Sec. II to the description of this problem.

B. Bifurcation diagrams

In the series of experiments we have obtained different bifurcation diagrams. They differ in the spectral content (frequency of the subharmonic pairs and amplitudes of the higher harmonics) corresponding to different sets of detunings, but also in the behavior of the individual amplitudes. We illustrate two of such cases in Figs. 4 and 5.

Figure 4 was obtained for a driving frequency $f_0=1.991$ MHz and $L=3.5$ cm. In this case a nearly-degenerated subharmonic pair, with frequencies $f_1=1.018$ MHz and $f_2=0.974$ MHz, is parametrically excited. As shown in Fig. 4(a), corresponding to a driving amplitude

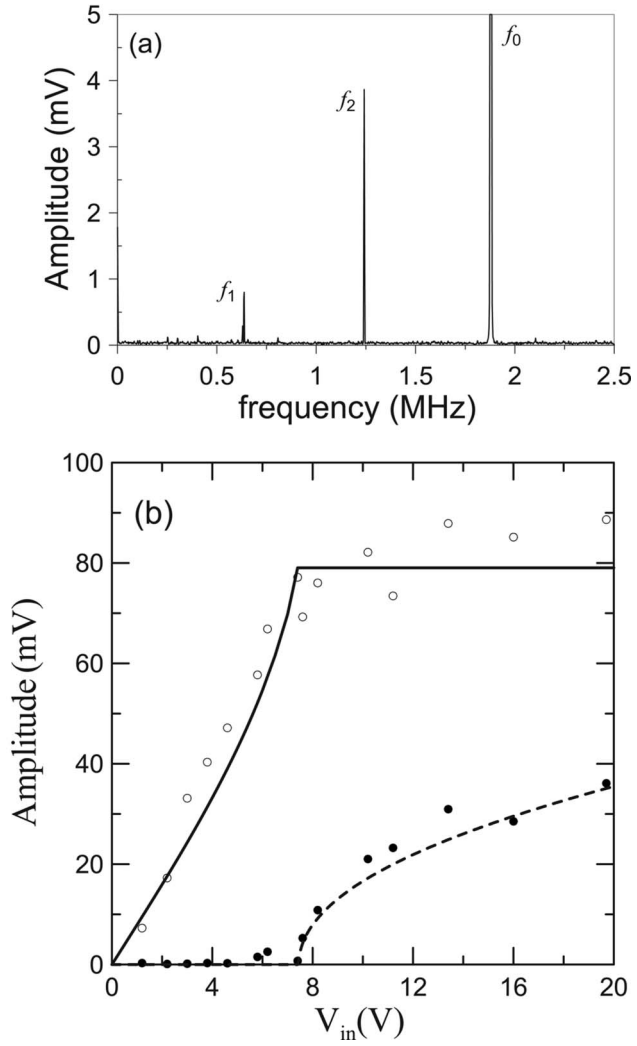

FIG. 5. (a) Spectral content of the acoustic field in the resonator obtained for a driving frequency $f_0=1.879$ MHz and an input voltage of $V_{in}=8$ V. (b) Experimental bifurcation diagram (symbols) obtained at the same driving frequency and different input voltages. Solid and dashed lines correspond to the fundamental and subharmonic amplitudes, as obtained from Eqs. (5) and (8) for $\Delta_0=1.35$, $\Delta_1=0.6$, and $\Delta_2=10$.

of 25 V, the pair is highly asymmetric, the amplitude of one of the components, f_2, being negligible with respect to f_1. This suggests the applicability of Eq. (3), where only one of the subharmonics is taken into account. The experimental bifurcation diagram is shown in Fig. 4(b) with symbols. Two features of this bifurcation diagram can be discussed. First, at $V_{in}=24$ V the threshold of parametric generation is reached, and for higher driving values the amplitude of the subharmonics grows monotonically with the pump. The existence of a threshold evidences the origin of subharmonics as the result of an instability in the system. Note that in Fig. 4(b) this amplitude is magnified five times for a better clarity.

A second feature of the diagram in Fig. 3(b), which also follows from the theoretical analysis of Sec. III A (see, e.g., Fig. 2), is the non-linear (pump dependent) growth rate of the fundamental mode amplitude as the driving amplitude V_{in} is increased: for sufficiently high excitation amplitudes, the fundamental harmonic amplitude grows faster than in the initial (small-amplitude) linear regime. This occurs despite the fact that the second harmonic creates an additional channel of the energy consumption since it additionally pumps out the energy from the fundamental component. This unexpected effect is a consequence of the nonlinear coupling of the fundamental with the second harmonic, already discussed in Eq. (4), which results in an effective amplitude-dependent detuning for the fundamental. Note that from Eq. (4) it follows that in a stationary regime $A_2 \sim A_0^2$, which results in the cubic term $A_2 A_0^* \sim |A_0|^2 A_0$ in the first of Eq. (4). As the coefficient of this term is complex, it represents an amplitude-dependent detuning.

Without this coupling the quadratic nonlinearity did not give the amplitude-dependent detuning due to self-action, whereas the second harmonic introduces this possibility. However, this can be observed only for sufficiently large initial detuning of the fundamental harmonic from the nearest resonance [see Eq. (5)]. Thus in the small-amplitude linear regime, the excitation of the fundamental harmonic is fairly far from optimal. With increased driving amplitude, the coupling with the second harmonic results in the effective compensation of the detuning for the fundamental harmonic. Consequently, the excitation conditions for the fundamental harmonic become more optimal and in this amplitude range, the fundamental harmonic grows faster than initially (up to creation of the inflection point in the amplitude dependence).

The solid lines represent the analytical stationary solutions given by Eqs. (5), (8), and (9). The theoretical amplitude and pump values have been scaled by respective numerical factors taking into account the efficiency of the transducer, the sensitivity of the hydrophone, and the additional normalizations leading to Eq. (4). We used the medium parameters $\rho=1000$ kg/m^3, $c=1480$ m/s, and $\beta=0.002$ s^{-1} Pa^{-1}. The decay rates were obtained by measuring the line width of the modes, resulting in $\gamma_n \sim 5000$ s^{-1}. Finally, the detunings have been chosen to get the best fit to the experimental data. In Fig. 4(b) we used $\Delta_0=-2.35$, $\Delta_1=3.25$, and $\Delta_2=-4$.

For a slightly different driving frequency $f_0=1.879$ MHz, we observed a different scenario, shown in Fig. 5. In this case pair frequencies $f_1=1.242$ MHz and $f_2=0.638$ MHz are excited above threshold. The pair is also clearly asymmetric in the amplitudes, as shown in Fig. 4(a) corresponding to a driving amplitude of 8 V. Different from the previous case a linear growth of the fundamental mode below threshold is observed in Fig. 5(b), saturating at a constant value above threshold (7 V in this case). As discussed in Sec. III A, this situation is typical of a highly detuned second harmonic, where the dispersive model represents a good approach. The theoretical bifurcation diagrams in Fig. 5(b) were obtained for the set of detunings $\Delta_0=1.35$, $\Delta_1=0.6$, and $\Delta_2=10$ and show a good agreement with the measured values.

C. Self-modulation

Further increasing the pump above the threshold the field components (both fundamental and subharmonics) often develop side band modes, characterized by a small frequency shift with respect to the original (central) mode, as

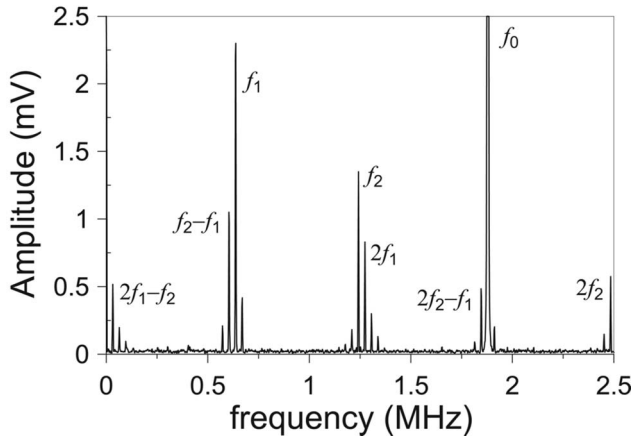

FIG. 6. Development of low-frequency side bands for the experimental conditions in Fig. 5 for a driving amplitude $V_{in}=17$ V.

shown in Fig. 6. The parameters are those corresponding to Fig. 4, and the pump parameter is nearly twice the parametric threshold value. In the temporal domain, the presence of the side bands implies a low frequency time modulation of the field amplitudes, indicating a transition from stationary to dynamic states. This phenomenon, also demonstrated in fluids[11] and solids,[15] is usually called self-modulation since the source amplitude is kept constant. Self-modulation can result from different mechanisms, as discussed in Ref. 16.

In Ref. 14 we considered the stability of the solutions of Eqs. (8) and (9), identifying the appearance of the self-modulation with a Hopf bifurcation of the stationary solutions under certain conditions. The frequency of the slow modulation predicted by the theory was of the order of several kilohertz for typical operation conditions. This value is in agreement with the experimentally observed side band frequency, $\Delta f=34$ kHz, in Fig. 6. A careful analysis of the spectrum allows to identify these new frequencies as the result of the mixing (sum and difference, $f_i \pm f_j$) between the fundamental and the subharmonics components, and with the second harmonics $2f_i$, owing to the quadratic nonlinearity of the medium. Some of these frequencies are correspondingly labeled in Fig. 6. The experiment also shows that the appearance of the low side band frequencies occurs once the pump reaches a critical value. This behavior of the spectrum is characteristic of a secondary instability of the Hopf type, in agreement with the analysis performed in Ref. 14.

IV. CONCLUSIONS

The different effects observed in the experiments of parametric sound generation in acoustic resonators cannot be completely explained by the previously proposed models. The first reasonable approach to this problem is to consider the role played by the first higher harmonics, whose magnitude is strongly dependent on the distance to the cavity resonances. The proposed model, which is a simple extension of previous (dispersive) models, considers the coupling of the fundamental field to its second harmonic. We demonstrate that the bifurcation diagrams predicted by the theory and observed in the experiment can be qualitatively different under different parameters and are very sensible to the experimental conditions (mainly the driving frequency and the temperature, both affecting the detuning values). Such model also predicts the emergence of secondary instabilities, leading to time self-modulated solutions, in agreement with the experimental observation at drivings beyond the threshold. We expect that, at even higher drivings, the dynamics of the system can be chaotic, as the theory predicts. Experimental work in the direction is in progress.

ACKNOWLEDGMENTS

The work has been financially supported by the MEC of the Spanish Government under Project No. FIS2005-0793-C03-02 and FIS2008-06024-C03-03. We gratefully acknowledge the unknown referee for suggesting the self-action mechanism as responsible for some of the effects observed in this work.

[1] A. Korpel and R. Adler, "Parametric phenomena observed on ultrasonic waves in water," Appl. Phys. Lett. **7**, 106–106 (1965).
[2] L. Adler and M. A. Breazeale, "Excitation of subharmonics in a resonant ultrasonic wave system," Naturwiss. **55**, 385–385 (1968).
[3] L. Adler and M. A. Breazeale, "Generation of fractional harmonics in a resonant ultrasonic wave system," J. Acoust. Soc. Am. **48**, 1077–1083 (1970).
[4] M. Faraday, "On a peculiar class of acoustical figures; and on certain forms assumed by particles upon vibrating elastic surfaces," Philos. Trans. R. Soc. London **121**, 299–340 (1931).
[5] L. Adler and M. A. Breazeale, "Parametric phenomena in physics," Am. J. Phys. **39**, 1522–1527 (1971).
[6] A. Teklu, M. S. McPherson, M. A. Breazeale, R. D. Hasse, and N. F. Declercq, "Measurement of the frequency dependence of the ultrasonic parametric threshold amplitude for a fluid-filled cavity," J. Acoust. Soc. Am. **120**, 657–660 (2006).
[7] N. Yen, "Experimental investigation of subharmonic generation in an acoustic interferometer," J. Acoust. Soc. Am. **57**, 1357–1362 (1975).
[8] L. A. Ostrovsky and I. A. Soustova, "Theory of parametric sound generators," Sov. Phys. Acoust. **22**, 416–419 (1976).
[9] F. V. Bunkin, Yu. A. Kravtsov, and G. A. Lyskhov, "Acoustic analogues of nonlinear-optics phenomena," Sov. Phys. Usp. **29**, 607–619 (1986).
[10] L. K. Zarembo and O. Y. Serdoboloskaya, "Parametric amplification and generation of acoustic waves," Sov. Phys. Acoust. **20**, 440–443 (1975).
[11] L. A. Ostrovsky, I. A. Soustova, and A. M. Sutin, "Nonlinear and parametric phenomena in dispersive acoustic systems," Acustica **39**, 298–306 (1978).
[12] V. J. Sánchez-Morcillo, "Spontaneous pattern formation in an acoustical resonator," J. Acoust. Soc. Am. **115**, 111–119 (2004).
[13] I. Pérez-Arjona and V. J. Sánchez-Morcillo, "Pattern formation in parametric sound generation," Phys. Rev. E **72**, 066202 (2005).
[14] V. J. Sánchez-Morcillo, V. Espinosa, J. Redondo, and J. Alba, "Nonlinear dynamics and chaos in parametric sound generation," Acta. Acust. Acust. **92**, 210–216 (2006).
[15] I. Solodov, J. Wackerl, K. Pfleiderer, and G. Busse, "Nonlinear self-modulation and subharmonic acoustic spectroscopy for damage detection and location," Appl. Phys. Lett. **84**, 5386–5389 (2004).
[16] L. Fillinger, V. Zaitsev, V. Gusev, and B. Castagnede, "Wave self-modulation in an acoustic resonator due to self-induced transparency," Europhys. Lett. **76**, 229–235 (2006).

The rumble sound generated by a tidal bore event in the Baie du Mont Saint Michel

Hubert Chanson[a)]
Department of Civil Engineering, The University of Queensland, Brisbane QLD 4072, Australia

(Received 24 November 2008; revised 27 March 2009; accepted 1 April 2009)

A tidal bore is a sharp rise in free-surface elevation propagating upstream in an estuarine system at the leading edge of the flood tide. It generates a powerful noise that was sometimes compared to the sounds of a horse cavalcade. Herein the sounds generated by a tidal bore event in the Baie du Mont Saint Michel were carefully recorded. The data showed three distinct periods. These were the incoming tidal bore when the sound amplitude increased with the approaching bore front, the passage of the tidal bore in front of the microphone where the impacts of the bore on the bank, rocks, or jetty generated powerful noises, and the upstream propagation of the bore when the flood flow motion caused additional loud noises. During the arrival of the tidal bore, the sound levels were less energetic and a lower-pitch sound was noted than during the subsequent record. For the breaking bore process, the analysis of the sound record indicated a dominant frequency around 76–77 Hz. The low-pitch rumble had a frequency comparable to the collective bubble oscillations, suggesting that air entrapment in the bore roller might play a major role in the acoustic signature.
 [DOI: 10.1121/1.3124781]

PACS number(s): 43.28.Ra, 43.28.Tc, 43.30.Nb, 43.30.Pc [KVH] Pages: 3561–3568

I. INTRODUCTION

A tidal bore is a sharp rise in free-surface elevation propagating upstream in an estuarine system as the tidal flow turns to rising. Also known as aegir, mascaret, or pororoca, a tidal bore forms typically during spring tide conditions with tidal ranges exceeding 4–6 m when the flood tide converges into a narrow funneled channel. Figure 1 illustrates a tidal bore event in the Baie du Mont Saint Michel (France), while Fig. 2(a) shows the promontory from where the photographs were taken. Figure 2(b) presents a map of the area.

A tidal bore creates a powerful sound. In China, the noise of the Qiantang River bore was compared to "the clamor of a hundred thousand troops" in a poem by Guo of the Tang dynasty and to "10 000 horses break out of an encirclement (Chen *et al.*, 1990), crushing the heavenly drum, while 56 huge legendary turtles turn over, collapsing a snow mountain" by the Chinese poet Yuan during the Yuan dynasty (Dai and Zhou, 1987). The sounds generated by a tidal bore were also called a "roar" (Darwin, 1897) or a "great destructive noise" and compared to the sound of locomotive train, of bass drums, of thunder, and of torrential flows. A Canadian composer, Monahan, created a musical piece that was a metaphorical interpretation of the tidal bore action, using sound recordings of water flow from the Bay of Fundy: "the tidal bore of the Maccan River" (Monahan, 1981).

The noise generated by a tidal bore combines sounds caused by the turbulence in the bore front and whelps, entrained air bubbles in the bore roller ("white waters"), sediment erosion beneath the bore front and of the banks, scouring of the sandbars, and impacts on obstacles (rocks and bridge piers). The bore rumble can be heard far away because low frequencies can travel over long distances. During his expedition in the Qiantang River mouth, Moore almost lost his survey ship and two steam cutters on 20 September 1888 when he inadvertently anchored in the Qiantang River estuary; he heard the first murmur of the bore 1 h before it reached his Pandora ship (Moore, 1888, p. 7). In the Baie du Mont Saint Michel, the writer heard often the tidal bore 25–30 min before the bore front reached him. Animals can be more sensitive to the tidal bore sounds than the human ear (Warfield, 1973; Fay, 1988; Encyclopædia Britannica, 2008). When the bore closes in, the rumbling noise disorientates some species. In the Baie du Mont Saint Michel, sheep have been outrun and drowned by the tidal bore. In Alaska, moose have tried unsuccessfully to outrun the bore (Molchan-Douthit, 1998). In each case, the animals were panicked with the deafening noise of the bore although they could run faster than the bore front.

A tidal bore is somehow a continuous breaking "wave," and passive acoustic techniques were used successfully to characterize to wind-generated wave breaking and the entrained air bubbles (Loewen and Melville, 1991; Manasseh *et al.*, 2006). The air bubble entrainment process is indeed fundamental to the air-sea interactions (Melville and Rapp, 1985; Wallace and Wirick, 1992; Chanson and Cummings, 1994). Most studies of wave breaking used underwater hydrophones (Felizardo and Melville, 1995; Manasseh *et al.*, 2006). Some investigated similar flow patterns to study specific features of the entire process (e.g., Nicholas *et al.*, 1993; Kolaini *et al.*, 1994). Passive acoustic techniques were also used successfully to investigate sediment transport under waves and in tidal flows (Thorne, 1986; Mason *et al.*, 2007).

Although there are numerous anecdotic observations, the acoustic properties of a tidal bore have not been investigated in detail until now. Herein, the atmospheric sounds of a tidal bore event were carefully recorded, and the passive acoustic

[a)]Electronic mail: h.chanson@uq.edu.au

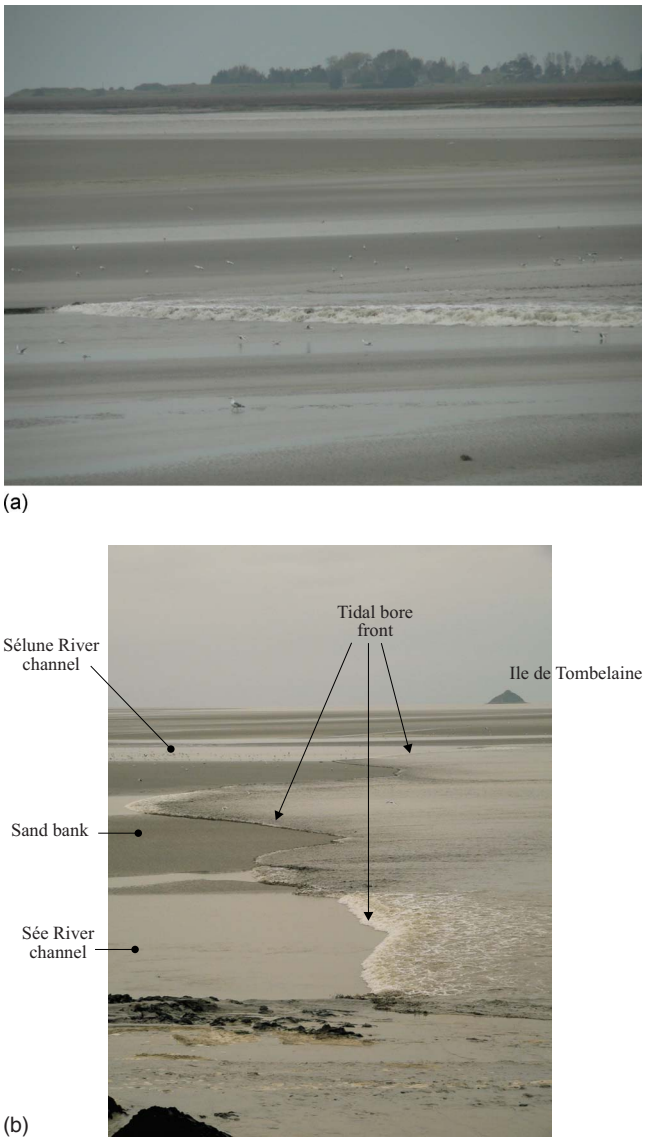

FIG. 1. (Color online) Tidal bores in the Baie du Mont Saint Michel (France) on 14 October 2008 evening. (a) Breaking bore of the Sée-Sélune River system North of Pointe du Grouin du Sud on 14 October 2008 evening. The photograph was taken shortly before the tidal bore divided into the Sée and Sélune River channels, with Bec d'Andaine in the upper left of the photograph. (b) Tidal bore of the Sée and Sélune Rivers at Pointe du Grouin du Sud on 14 October 2008 evening. Note the Sée River bore in the foreground with the rocky promontory of Pointe du Grouin du Sud (bottom left) and the Sélune River bore in the background with Ile de Tombelaine (top right).

characteristics were analyzed. The present work takes preliminary steps toward an acoustic signature technique for characterizing a tidal bore process.

II. STUDY SITE AND FIELD MEASUREMENTS

The Baie du Mont-Saint-Michel (France) in the English Channel (La Manche) is characterized a very large tidal range (up to 14 m) and fast advancing flood tides. The Baie is drained by three main rivers: the Couesnon, the Sélune, and the Sée [Fig. 2(b)]. In the past, the hydrodynamics and sedimentology of the Baie, including the access to the Mont Saint Michel, were mostly affected by the strong flows of the Couesnon and Sélune Rivers. The Sélune River is 70 km long with a catchment area of 1010 km^2, and it constitutes the most significant freshwater inflow into the Baie du Mont Saint Michel. At its mouth between Roche-Torin and Pointe du Grouin du Sud, the Sélune River joins the Sée River, and the waters merge at low tides.

During spring tides, the Baie du Mont Michel is subjected to several tidal bore processes. Larsonneur (1989) mentioned briefly a tidal bore near Pointe du Grouin du Sud propagating at about 2.5 m/s. Tessier and Terwindt (1994) discussed the effect of tidal bore on sediment transport downstream of the Sée and Sélune river mouths. Chanson (2005a, 2005b, 2008a) presented photographic evidences of the tidal bore processes and discussed their impact on the Baie.

Herein the tidal bore of the Sée-Sélune River system was observed at the Pointe du Grouin du Sud in the Baie du Mont Saint Michel on the 14 October 2008 early evening when photographs and video movies where taken (Fig. 1), and again at the next flood tide on 15 October 2008 early morning. It was a full moon and the tidal range was 12.55 m. During the latter event, the sounds were recorded with a digital video camcorder Canon MV500i equipped with a stereo electret condenser microphone. The microphone was fixed to the camera and its signal-to-noise ratio (SNR) setting is fixed for the duration of each recording. The audio signal pulse-code modulation (PCM digital sound: 16 bit, 48 kHz/2 channels) was separated from the video signal, and the WAV file is available in a digital appendix. Note that the audio recording was taken by the author alone. The closest livestock was 500 m away, and the nearest dwelling 1 km away.

The video camera and microphone were placed on the rocky promontory (Fig. 2). Its location was fixed (about 45–50 m from the western edge of the rocky promontory) but the microphone was moved to follow the tidal bore front for the whole duration of the record. Figure 2(a) indicates the exact location of the camcorder. A miniDV tape recorder digitized the signal at 32 kHz, implying a Nyquist frequency of about 16 kHz. The range of tidal bore conditions caused a difference in acoustic signal power of up to 20 dB corresponding to a factor of 10 in sound amplitude during the record. Since all data recorded on tape should have similar magnitudes to minimize distortion or loss of dynamic range, the entire record was sub-divided into three periods of comparable sound amplitude to deliver comparable recorded quality during the signal processing. The WAV recordings were processed with the software DPLOT™, Version 2.2.1.6. Fast Fourier transforms were taken. Each experimental data set was sub-sampled into sub-sets 2 s long to give a frequency span of 0–16 kHz.

Further details on the field study were reported by Chanson (2008a).

III. FIELD OBSERVATIONS

A. Presentation

On 15 October 2008, the tidal bore (*mascaret*) was seen in the morning darkness about 1 h before sunrise. The sky was cloudy and there were intermittent showers. The tidal bore arrived from the Sée-Sélune River channel [Figs. 1(a)

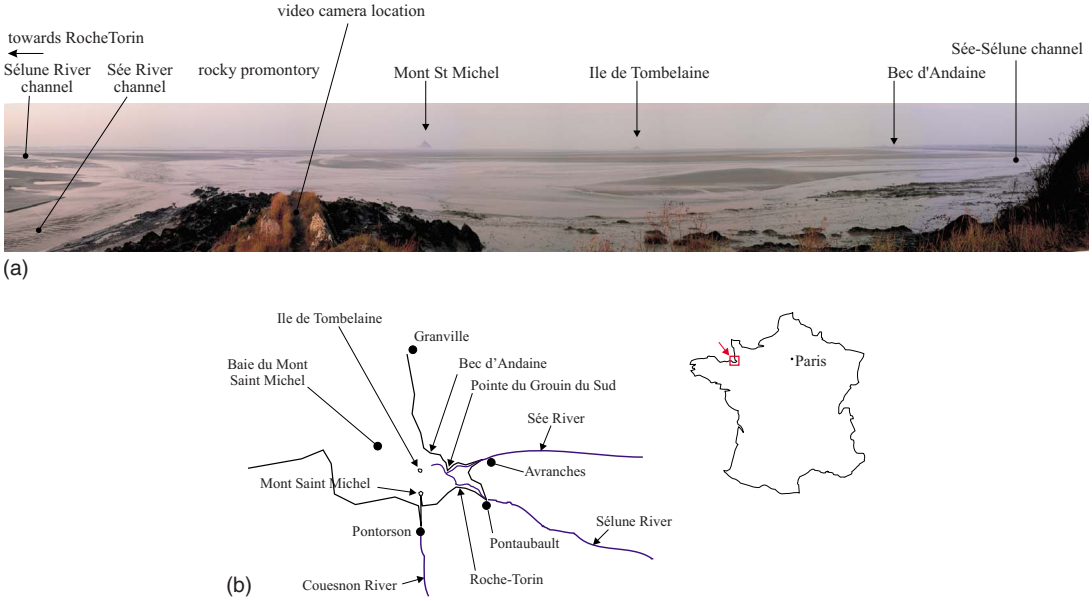

FIG. 2. (Color online) Photograph and sketch of the Baie du Mont Saint Michel (France). (a) Panoramic view of the Baie du Mont Saint Michel seen from the Pointe du Grouin du Sud on 19 October 2008 at 08:20 at sunrise and low tide. Note the rocky promontory of Pointe du Grouin du Sud in the foreground, the Mont Saint Michel and Ile de Tombelaine in the background, and the joint Sée-Sélune River system on the right of the photograph. (b) Sketch of the Baie du Mont Saint Michel and the Sée and Sélune Rivers.

and 2(a) right]. The bore front passed the rocky promontory of the Pointe du Grouin du Sud at 06:50. It entered into the Sée River channel while another tidal bore continued into the Sélune River channel toward Roche-Torin and Pontaubault [Fig. 2(a) left]. The entire process was a breaking bore, similar to the one photographed 12 h earlier (Fig. 1). In the darkness, the white waters of the breaking bore were clearly seen with a torch, but there was not enough light for photographic observations.

The sound measurements started at 06:48 and lasted for about 4 min (Fig. 3). The entire bore sound record may be sub-divided into three consecutive periods. From the first 95 s of the record, the tidal bore approached Roche-Torin and the sound amplitude gradually increased. For $95 < t < 130$ s, the tidal bore reached the rocky promontory seen in Figs. 1(b) and 2(a) and "crashed" onto the rocks, yielding loud and powerful noises. The tidal bore was just in front of the promontory in the same position as in Fig. 1(b) for $t = 100-102$ s (visual observation with a torch at 06:50). For $130 < t < 221$ s, the tidal bore continued into the Sée River channel toward Avranches and in the Sélune River channel toward Roche-Torin and Pontaubault. During this third period, the audio record was a combination of the sounds generated by the tidal bore in the Sée River channel that was in the foreground, the flood tidal flow past the rocky promontory of Pointe du Grouin du Sud, and the tidal bore in the Sélune River channel in the background (Fig. 2).

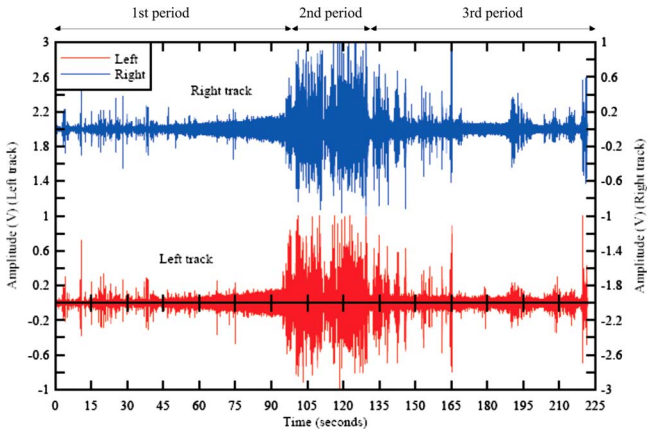

FIG. 3. (Color online) Audio signals of the tidal bore of the Sée-Sélune River at Pointe du Grouin du Sud on 15 October 2008 between 06:48 and 06:52.

The entire sound record is presented in Fig. 3, and the three distinct periods are highlighted.

The acoustic properties of the record were analyzed in terms of the absolute value of the sound pressure amplitude. Typical results are summarized in Table I (columns 5 and 6), showing the mean and standard deviation of the amplitude modulus. It is seen that the noises during the second period, when the tidal bore passed around the rocky promontory, were in average five times louder than during the first period (incoming bore). The quantitative data were supported by the personal observations during the event. The ratio of standard deviation to mean absolute value was typically between 1.1 and 1.5 for the complete study, nearly independent of the period.

A spectral analysis was conducted, and the basic properties are summarized in Table I (columns 7 and 8). The acoustic spectra are shown in Fig. 4 for each period of the sound record presented in Fig. 3. Each spectrum exhibited a minimum in energy below 5 Hz, indicating that the low-frequency rumbling noise of the tidal bore noise was above 5 Hz, within the entire audible range of sounds for a human ear (Encyclopædia Britannica, 2008). In each spectrum, a dominant frequency was observed, and the characteristic values are summarized in Table I (column 7). The dominant frequency ranged from 74 to 131 Hz depending on the period,

TABLE I. Acoustic properties of tidal bore sound record.

Reference	Record	Duration (s)	Audio track	Average sound amplitude modulus (V)	STD sound amplitude modulus (V)	Dominant frequency (Hz)	Integral of PSD function 0–16 kHz (V^2)	Remarks
Sée-Sélune River tidal bore, 15 Oct. 2008	Tidal bore (breaking)							From Pointe du Grouin du Sud (right bank)
	First period	95	Left	0.0159	0.0178	76.2	1.234	Incoming tidal bore
			Right	0.0143	0.0160	76.7	1.181	
	Second period	35	Left	0.0786	0.0851	130.9	3.625	
			Right	0.0840	0.0920	113.3	3.858	
	Third period	91	Left	0.0230	0.0326	92.3	1.356	Bore, whelps, and flood flow
			Right	0.0249	0.0379	73.8	1.501	
Sée-Sélune River, 15 Oct. 2008	Whelps							From Pointe du Grouin du Sud (right bank),
	Entire record	78	Left	0.0455	0.0502	125.4	1.663	3–5 min after
			Right	0.0414	0.0392	89.4	1.485	bore passage
Dordogne River, 18 Oct. 2005	Tidal bore (undular)							From Port de Saint Pardon (left bank)
	First period	22	Left	0.0328	0.0275	191.4	1.611	Incoming tidal bore
			Right	0.0141	0.0113	233.4	0.800	
	Second period	44	Left	0.0988	0.0789	246.6	6.186	Bore passage in
			Right	0.0676	0.0624	238.8	4.872	front of jetty

Note that Dordogne River data set was provided by Patrick Vialle, modulus is the absolute value, PSD is the power spectral density, and STD is the standard deviation.

and these values corresponded to a low-pitch sound, or rumble. Such a rumble frequency could be explicable by collective oscillations of bubble clouds entrapped in the bore roller and during wave breaking on the banks (Prosperetti, 1988; Kolaini *et al.*, 1994).

During the first period of the record, the tidal bore was a breaking bore advancing in the main channel and over sand banks and mudflats (Fig. 1). The low-frequency sound (76–77 Hz) may be considered to be a characteristic feature of the advancing roller, caused by the turbulence and entrained bubbles in the roller, sediment erosion beneath the advancing bore, and the scouring of channel edges, sand flats, sandbars, and shoals [Fig. 1(b)]. For the second period, the tidal bore impacted onto the rocky promontory, and the impact was an energetic process generating louder noises of a higher pitch, yielding a dominant frequency around 113–131 Hz. This is clearly seen in Fig. 4 where the higher acoustic energy illustrates a louder noise, as well as by the integral of the power spectral density function (Table I, column 8). During the third period, the sounds were a combination of the tidal bores leaving the Pointe du Grouin du Sud in the Sée and Sélune River channels, as well as the impact of the flood flow on the promontory rocks. This yielded a slightly flatter, broader acoustic spectrum (Fig. 4). Note that, since all peak frequencies were greater than the low-frequency noise found below 5 Hz, no high-pass filtering was required.

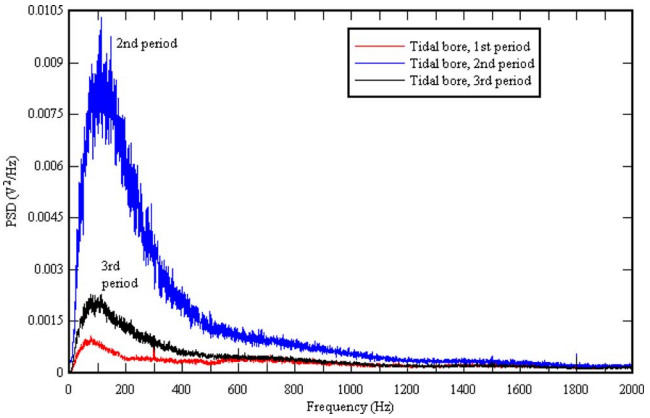

FIG. 4. (Color online) Acoustic spectra of the tidal bore event, Sée-Sélune River at Pointe du Grouin du Sud, Baie du Mont Saint Michel on 15 October 2008 between 06:48 and 06:52. Average of left and right sound track spectra.

B. Comparison with other tidal flows

The acoustic signature of the tidal bore event was compared with two other relevant sound records (Table I). One was the sound of the tidal bore whelps and flood flow measured at the Pointe du Grouin du Sud on 15 October 2008 between 06:54 and 06:56, about 4–5 min after the tidal bore passage at Pointe du Grouin du Sud. The data were recorded with the same microphone and at the same location as the tidal bore event, but the microphone was facing the Pointe du Grouin du Sud promontory for the entire recording. During this record, the sounds were a combination of the noises of the flood flow crashing on the rocks of the promontory, of the flood flow in the Sée River channel just below the Pointe du Grouin du Sud, and, in the far background, of the tidal bores in the Sée and Sélune River channels. The recorded sounds were powerful and quite violent.

The second record was taken from the left bank of the Dordogne River at Port de Saint Pardon on the 18 October 2005 during the passage of an undular tidal bore (Fig. 5). Figure 5 shows a photograph of the undular tidal bore of the Dordogne River at Port de Saint Pardon, but taken at a later

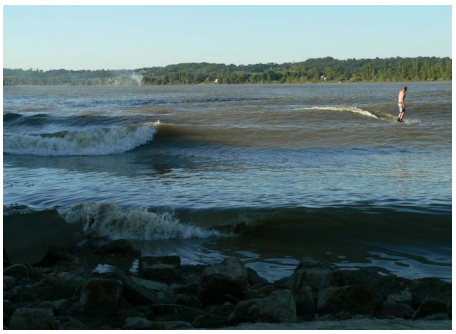

FIG. 5. (Color online) Undular tidal bore of the Dordogne River at Port de Saint Pardon on 22 July 2008 evening. Note the first wave crest breaking on the jetty in the foreground and the surfer riding on the third wave.

date. The microphone was located in the vicinity of the jetty. It pointed toward the river channel and was fixed for the duration of the record. That data set is presented in Fig. 6. It shows a first period of the record corresponding to the arrival of the tidal bore toward Port de Saint Pardon while the second part was dominated by the successive breaking of the undulations on the jetty during and after the bore passage. See the breaking of the Dordogne River tidal bore undulations on the jetty in Fig. 5 (foreground left). In Fig. 6, note the difference between the left and right sound tracks that resulted from the stationary position of the microphone on the left bank.

The characteristics of these two records are reported in Table I and compared with the tidal bore sound record in the Baie du Mont Saint Michel on 15 October 2008.

The acoustic spectrum of the whelps and flood flow at Pointe du Grouin du Sud is presented in Fig. 7 where it is compared with the tidal bore event data set. The comparison is relevant since all the sound data were recorded with the same microphone from the same location. In Fig. 7, both horizontal and vertical axes have a logarithmic scale. The plots illustrate the minimum in energy at roughly 1–5 Hz for all data, as well as maxima for frequencies between 76 and 131 Hz. While all data sets corresponded to low-frequency noises, the loudness of the tidal bore impact on the rocky

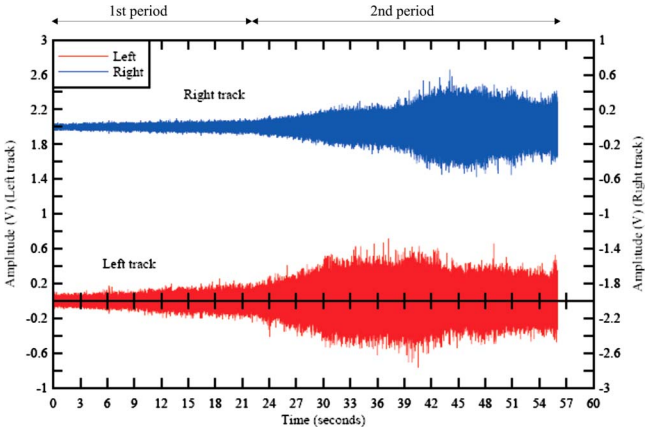

FIG. 6. (Color online) Audio signals of the tidal bore of the Dordogne River at Port de Saint Pardon on 18 October 2005.

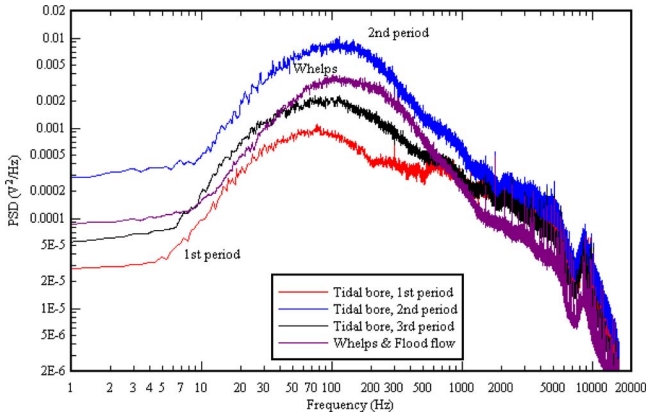

FIG. 7. (Color online) Comparison in acoustic spectra between the tidal bore (06:48–06:52), and its whelps and flood flow (06:53–06:55), at Pointe du Grouin du Sud, Baie du Mont Saint Michel on 15 October 2008. Average of left and right sound track spectra.

promontory of Pointe du Grouin du Sud is highlighted by its high acoustic energy (Fig. 7, tidal bore second period), and the second loudest sound record was that of the whelps and flood flow (Fig. 7).

The Dordogne and Sée-Sélune River tidal bores exhibited similar acoustic features during the first period of each record (Figs. 3 and 6). That is, an increasing sound level with increasing time, as well as a sound amplitude that was much lower than during the subsequent record sections. The acoustic spectra of the Sée-Sélune River and Dordogne River tidal bores showed some low-pitch sound frequency, with the Dordogne River tidal bore having a slightly higher dominant frequency (191–233 Hz) than that of the Sée-Sélune River tidal bore (Table I, column 7).

There were, however, some key differences between the two tidal bore events. First the Sée-Sélune River tidal bore was a breaking bore with a well-defined roller, while the Dordogne River tidal bore was an undular bore. It is believed that the turbulence and air bubble entrainment in the breaking bore roller in the Baie du Mont Saint Michel generated lower-frequency rumble sounds. Second, the Dordogne River tidal bore sound data were recorded with a fixed microphone, and there were a few background noises including voices. (The microphone was within 50 m from dwellings.) A limitation of the present analysis was indeed the quality in surrounding sounds. Because the sound amplitude falls off as $1/r$, and the sound power as $1/r^2$, where r is the radial distance to the microphone, sounds generated in the vicinity of the recording device contribute most to the measured sound. For example, people on the bank next to the microphone. On 15 October 2008, the sound recording in the Baie du Mont Saint Michel was conducted in the early morning in absence of spectators. This feature ensured a minimum level of background noise and a better characterization of the tidal bore acoustic signature, as shown by a comparison with the audio recoding of the tidal bore at the same location on 14 October 2008 evening [Fig. 8(a)]. Figure 8 presents a comparison of the audio records of the same tidal bore recorded with the same equipment from the same location: (a) on the evening of the 14 October when the camcorder was surrounded by

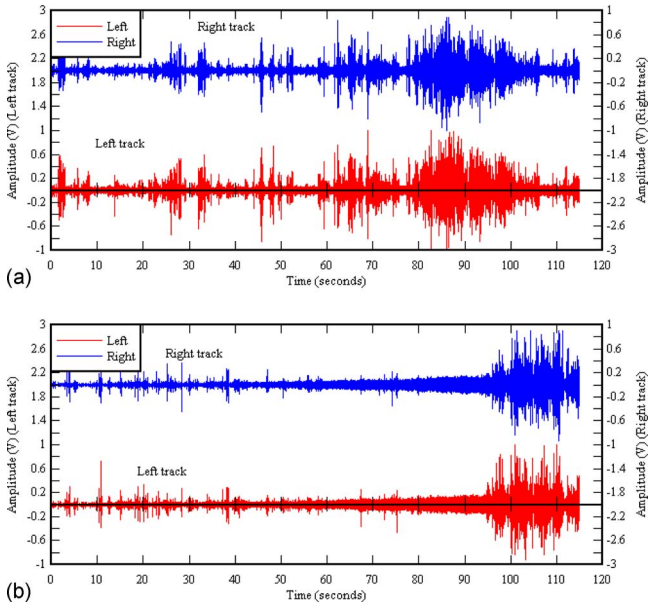

FIG. 8. (Color online) Audio signals of the tidal bore of the Sée River at Pointe du Grouin du Sud, Baie du Mont Saint Michel (France) during two successive tidal bore events. (a) On 14 October 2008 between 18:26 and 18:28. Tidal bore front passage at Pointe du Grouin du Sud: $t \sim 90$ s. (b) On 15 October 2008 between 06:48 and 06:52. Tidal bore front passage at Pointe du Grouin du Sud: $t \sim 100$ s.

several adults and children [Fig. 8(a)] and (b) on the early morning of 15 October when the closest livestock was 500 m away and the closest dwelling nearly 1 km away [Fig. 8(b)].

IV. DISCUSSION

In a breaking bore, large-scale vortical structures are generated at the roller toe and advected downstream (Hornung *et al.*, 1995; Koch and Chanson, 2009). The growth, advection, and pairing of these vortices are responsible for low-frequency oscillations of the turbulent velocity field in the bore roller. For example, some laboratory data yielded pulsation frequency F data corresponding to a Strouhal number $F \times d/V = 0.02$, where d is the initial water depth and V is the relative bore velocity, as seen a fluid particle traveling with the initial flow velocity (Chanson, 2008b). (Note that the findings are close for traveling bores and steady hydraulic jumps.) The bore roller is also characterized by some air bubble entrainment at the toe and advection in the roller (Fig. 9). Figure 9 illustrates the air bubble entrapment in the roller toe of an advancing breaking bore in laboratory. Using upon a conceptual model of a spilling breaker, Prosperetti (1988) showed that bubble generation at the roller toe can amplify the pressure oscillations induced by the large-scale turbulence. In a bubble cloud, the lowest natural frequency of the bubbly cloud is in first approximation

$$f_{\text{cloud}} = \frac{1}{L}\sqrt{\frac{P}{\rho\alpha}}, \quad (1)$$

where L is the bubble cloud characteristic length, P is the ambient pressure, ρ is the fluid density, and α is the void fraction (Prosperetti, 1988). The natural frequency of a bubble cloud is inversely proportional to $\alpha^{1/2}$ and to the cloud characteristic size. In a tidal bore, the bubbles are entrapped in large-scale vortical structure and a characteristic dimension is the roller height (Fig. 9). Equation (1) would imply that large tidal bores would generate lower-pitch sound than small ones. Considering a bore height between 0.7 and 1 m as seen in Fig. 1, the lowest natural frequency of the bubbly cloud would be about 30–140 Hz for void fractions between 1% and 10%. For comparison, the field measurements by Kolaini *et al.* (1994) showed collective oscillations of bubble clouds within 44–190 Hz (Table II). The result tends to suggest that the air bubbles entrapped in the large-scale eddies of the tidal bore roller might be acoustically active and play a dominant role in the rumble sound generation.

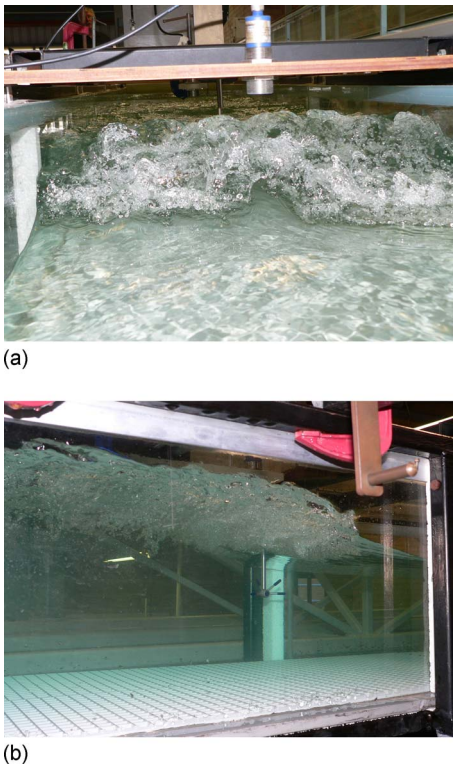

FIG. 9. (Color online) Photographs of breaking bore roller (shutter speed: 1/80 s). Laboratory data: $d = 0.14$ m, Fr = 1.5. (a) Looking at incoming bore roller. (b) Underside of the bore roller showing the entrained air bubble-bore propagation from left to right.

In tidal channels and under waves, sediment motion by bed load and saltation induced particle collisions that transmit an acoustic pulse to the water. The acoustic signature of sediment transport was previously studied, and experimental results showed that the sounds have a high pitch with characteristic frequencies between 1.5 and 400 kHz (Thorne 1986; Mason *et al.*, 2007). That is, sediment motion was unlikely to be the dominant cause of the tidal bore rumble noise, but it might explain the secondary peak about 8–10 kHz in Fig. 7.

Table II presents a comparative summary of the dominant frequencies of the low-pitch rumble of tidal bores and of other processes, including bubble clouds, sediment bed load motion, breaking waves, and music instruments. The comparison shows, for example, that the sounds generated by the breaking bore had a low-pitch comparable to the sound generated by collective oscillations of rising bubble

TABLE II. Comparison of dominant sound frequencies generated by tidal bores and other processes.

Type	Sub-type	Dominant frequency(ies) (Hz)	Remarks
		Atmospheric observations	
Approaching tidal bores	Breaking bore	76–77	Sée River tidal bore, 15 Oct. 2008
(First period)	Undular bore	191–233	Dordogne River, 18 Oct. 2005
Locomotive train	3000 Hp diesel locomotive	60	Measured at the engineer's ear in the cabin (Maguire 2004)
	Locomotive whistle	~400	
Drums	Concert bass	40–100	
	Kettle	8–150	
Piano	A0	27.5	Fundamental frequency
	A1	55	
	Middle C	246	
	A4	440	
		Underwater observations	
Unsteady plunging jet	Field/laboratory data	44–190	Kolaini *et al.* (1994)
Rising bubble clouds	Laboratory data	200–700	Nicholas *et al.* (1993)
Steady plunging jet	Laboratory data	1 200–4 000	Chanson and Manasseh (2003)
Wave breaking	Laboratory data	2 200–4 500	Loewen and Melville (1991)
Gravel transport under waves	Large-scale laboratory data	1 500–4 000	Mason *et al.* (2007); d_{50}=21 mm
Rain drops		8 000–14 000	Oguz and Prosperetti (1991)
Sediment bed load and saltation	Laboratory and field data	20 000–400 000	Thorne (1986); d_{50}=25 mm down to 0. 3 mm

clouds, bass drums, and trains. The latter may explain the "common analogy" between the sounds of breaking bores in the Qiantang River and Baie du Mont Saint Michel, and locomotive trains.

V. CONCLUSION

The sounds generated by a tidal bore event in the Baie du Mont Saint Michel were carefully measured. The sound record showed three distinct periods, and a similar feature was noted during another tidal bore event in the Dordogne River. These were (a) the incoming tidal bore when the sound amplitude increased with the approaching bore front, (b) the passage of the tidal bore in front of the microphone where the impacts of the bore on the bank, rocks, or jetty generated powerful noises, and (c) the upstream propagation of the bore when the whelps and flood flow motion caused additional loud noises. The distinction between periods was easily heard on site. Further the data highlighted the loudness of the noises generated during the whelps and flood flow several minutes after the tidal bore passage.

During the first period, the sounds generated by the incoming tidal bore were dominated by the bore front hydrodynamic processes including turbulence, air entrainment, breaking next to the banks, and sediment scour. A comparison between two tidal bore events illustrated both common features and differences. In each case, the approaching tidal bore generated an increasing sound with increasing time, and the sound levels were considerably lower than during the subsequent record sections. Both tidal events generated low-pitch sounds. For a breaking bore process, the audio record gave a lower-pitch sound (76–77 Hz) than during the undular bore event (191–233 Hz). It is likely that the difference in dominant sound frequencies resulted from some fundamental hydrodynamic differences between breaking and undular tidal bores (Chanson, 2008b; Koch and Chanson, 2009). The low-pitch rumble of the breaking bore had a dominant frequency comparable to the collective oscillations of bubble clouds [Eq. (1)], suggesting that air entrapment in the bore roller is likely to play a major role in the acoustic signature of the bore.

In the future, however, the surrounding sound conditions should be carefully monitored, as well as the location of the microphone relative to the channel edge.

ACKNOWLEDGMENTS

The author acknowledges the helpful comments of Dr. Eric Jones, Dr. Pierre Lubin, and Dr. Richard Manasseh, of the reviewers, and of the associate editor. He thanks the people who provided him with valuable information, including (in alphabetical order) Jean-Yves Cocaign, Nathanaëlle Eudes, and Patrick Vialle. He further acknowledges the help of Ya-Hui Chou, Bernard Chanson, Nicole Chanson. and André Chanson during the field observations.

NOMENCLATURE

d = initial water depth (m)
d_{50} = median sediment size (m)
Fr = surge Froude number
F = turbulence frequency (Hz)
f = sound frequency (Hz)
L = bubble cloud characteristic length
P = pressure
r = distance (m) to the microphone
t = time (s)
α = void fraction
ρ = water density (kg/m^3)

Chanson, H. (**2005a**). "Mascaret, aegir, pororoca, tidal bore. Quid? Where? When? How? Why?," Jl La Houille Blanche, **3**, pp. 103–114.
Chanson, H. (**2005b**). "Tidal bore processes in the Baie du Mont Saint Michel (France): Field observations and discussion," Proceedings of the 31st Biennial IAHR Congress, Seoul, Korea, edited by B. H. Jun, S. I. Lee, I. W. Seo, and G. W. Choi, Theme E.4, Paper No. 0062, pp. 4037–4046.
Chanson, H. (**2008a**). "Photographic observations of tidal bores (mascarets) in France," Hydraulic Model Report No. CH71/08, The University of Queensland, Brisbane, Australia.
Chanson, H. (**2008b**). "Turbulence in positive surges and tidal bores. Effects of bed roughness and adverse bed slopes," Hydraulic Model Report No. CH68/08, The University of Queensland, Brisbane, Australia.
Chanson, H., and Cummings, P. D. (**1994**). "Effects of plunging breakers on the gas contents in the oceans," Mar. Technol. Soc. J. **28**, 22–32.
Chanson, H., and Manasseh, R. (**2003**). "Air entrainment processes in a circular plunging jet. Void fraction and acoustic measurements," ASME Trans. J. Fluids Eng. **125**, 910–921.
Chen, J. Y., Liu, C. Z., Zheng, C. L., and Walker, H. J. (**1990**). "Geomorphological development and sedimentation in Qiantang Estuary and Hangzhou Bay," J. Coastal Res. **6**, 559–572.
Dai, Z., and Zhou, C. (**1987**). "The Qiantang bore," Int. J. Sediment Res. **1**, 21–26.
Darwin, G. H. (**1897**). "The tides and kindred phenomena in the solar system," *Lectures Delivered at the Lowell Institute, Boston* (Freeman, London, 1962).
Encyclopædia Britannica (**2008**). "Ear, human," Encyclopædia Britannica 2006 Ultimate Reference Suite DVD, 22 Oct.
Fay, R. R. (**1988**). *Hearing in Vertebrates: A Psychophysics Databook* (Hill-Fay Associates, Winnetka, IL.
Felizardo, F. C., and Melville, W. K. (**1995**). "Correlations between ambient noise and the ocean surface wave field," J. Phys. Oceanogr. **25**, 515–532.
Hornung, H. G., Willert, C., and Turner, S. (**1995**). "The flow field downstream of a hydraulic jump," J. Fluid Mech. **287**, 299–316.
Koch, C., and Chanson, H. (**2009**). "Turbulence measurements in positive surges and bores," J. Hydraul. Res. **47**, 29–40.
Kolaini, A. R., Roy, R. R., and Gardner, D. L. (**1994**). "Low-frequency acoustic emissions in fresh and salt water," J. Acoust. Soc. Am. **96**, 1766–1772.
Larsonneur, C. (**1989**). "The bay of Mont-Saint-Michel: A sedimentation model in temperate environment," Bull. Inst. Géol. Bassin d'Aquitaine, Bordeaux, **46**, 5–73.
Loewen, M. R., and Melville, W. K. (**1991**). "Microwave backscatter and acoustic radiation from breaking waves," J. Fluid Mech. **224**, 601–623.
Manasseh, R., Bababin, A. V., Forbes, C., Rickards, K., Bobevski, I., and Ooi, A. (**2006**). "Passive acoustic determination of wave-breaking events and their severity across the spectrum," J. Atmos. Ocean. Technol. **23**, 599–618.
Mason, T., Priestley, D., and Reeve, D. E. (**2007**). "Monitoring near-shore shingle transport under waves using a passive acoustic technique," J. Acoust. Soc. Am. **122**, 737–746.
Melville, W. K., and Rapp, R. F. (**1985**). "Momentum flux in breaking waves," Nature (London) **317**, 514–516.
Molchan-Douthit, M. (**1998**). *Alaska Bore Tales* (National Oceanic and Atmospheric Administration, Anchorage, AL).
Monahan, G. (**1981**). "The tidal bore of the Maccan river," Musical piece.
Moore, R. N. (**1888**). "Report on the Bore of the Tsien-Tang Kiang," Hydrographic Office, London.
Nicholas, M., Roy, A. A., Crumb, L. A., Oguz, H., and Prosperetti, A. (**1994**). "Sound emissions by a laboratory bubble cloud," J. Acoust. Soc. Am. **95**, 3171–3182.
Oguz, H. N., and Prosperetti, A. (**1995**). "Air entrapment by a falling water mass," J. Fluid Mech. **294**, 181–207.
Prosperetti, A. (**1988**). "Bubble-related ambient noise in the ocean," J. Acoust. Soc. Am. **84**, 1042–1054.
Tessier, B., and Terwindt, J. H. J. (**1994**). "An example of soft-sediment deformations in an intertidal environment—The effect of a tidal bore," C. R. Acad. Sci., Ser. II., **319**, 217–233.
Thorne, P. D. (**1986**). "Laboratory and marine measurements on the acoustic detection of sediment transport," J. Acoust. Soc. Am. **80**, 899–910.
Wallace, D. W. R., and Wirick, C. D. (**1992**). "Large air-sea gas fluxes associated with breaking waves," Nature (London), **356**, 694–696.
Warfield, D. (**1973**). in *Methods of Animal Experimentation*, edited by E. Gay (Academic, London), Vol. **IV**, pp. 43–143.

The vertical structure of shadow-zone arrivals at long range in the ocean

Lora J. Van Uffelen,[a] Peter F. Worcester, Matthew A. Dzieciuch, and Daniel L. Rudnick
Scripps Institution of Oceanography, University of California at San Diego, La Jolla, California 92093

(Received 6 October 2008; revised 21 January 2009; accepted 16 March 2009)

Multimegameter-range acoustic data obtained by bottom-mounted receivers show significant acoustic energy penetrating several hundred meters into geometric shadow zones below cusps (caustics) of timefronts computed using climatological databases [B. D. Dushaw *et al.*, IEEE J. Ocean. Eng. **24**, 202–214 (1999)]. This penetration is much larger than predicted by diffraction theory. Because these receivers are horizontal arrays, they do not provide information on the vertical structure of the shadow-zone arrivals. Acoustic data from two vertical line array receivers deployed in close proximity in the North Pacific Ocean, together virtually spanning the water column, show the vertical structure of the shadow-zone arrivals for transmissions from broadband 250-Hz sources moored at the sound-channel axis (750 m) and slightly above the surface conjugate depth (3000 m) at ranges of 500 and 1000 km. Comparisons to parabolic equation simulations for sound-speed fields that do not include significant internal-wave variability show that early branches of the measured timefronts consistently penetrate as much as 500–800 m deeper into the water column than predicted. Subsequent parabolic equation simulations incorporating sound-speed fluctuations consistent with the Garrett–Munk internal-wave spectrum at full strength accurately predict the observed energy level to within 3–4-dB rms over the depth range of the shadow-zone arrivals.
 [DOI: 10.1121/1.3117430]

PACS number(s): 43.30.Ft, 43.30.Re [JAC] Pages: 3569–3588

I. INTRODUCTION

Observations made during the Acoustic Thermometry of Ocean Climate (ATOC) project in the late 1990s found stable, resolved acoustic arrivals 500–1000 m into the geometric shadow zones below the predicted acoustic timefronts at the receiver locations (Dushaw *et al.*, 1999). These arrivals, referred to as shadow-zone arrivals, were seen in transmissions from a broadband 75-Hz source on Pioneer Seamount, off the coast of central California, to bottom-mounted receivers located well below the sound-channel axis at megameter ranges (Fig. 1). All of the shadow-zone arrivals occurred at the times of cusps (caustics) in the predicted timefronts (Fig. 2). The acoustic wavelength at 75 Hz is approximately 20 m. The observed arrivals are therefore 25–50 wavelengths into the geometric shadow, indicating that diffraction is unlikely to be adequate to account for their presence (Brekhovskikh and Lysanov, 2003).

The ATOC transmissions are not the only evidence of stable, resolved acoustic arrivals deep in the geometric shadow. A similar non-geometric arrival was seen many years earlier in an experiment performed during May and June of 1980 approximately 350-km west/southwest of San Diego (Worcester, 1981). A broadband 224-Hz source moored at a depth of 1375 m transmitted to a four-hydrophone array moored at approximately the same depth 215.2 km distant. Three distinct arrivals were evident in the data. The first two arrivals were consistent with ray predictions, but the third was non-geometric. The arrival pattern suggested that the third arrival might be associated with a caustic at a depth of 900 m, approximately 475 m above the receiver. Wentzel-Kramers-Brillouin-Jeffreys (WKBJ) calculations (Brown, 1982) showed that diffraction was inadequate to account for the observed arrival.

The obvious hypothesis is that scattering from internal-wave-induced sound-speed fluctuations is responsible for this vertical extension. Somewhat surprisingly, previous calculations, performed for the bottom-mounted receiver geometries utilized during the ATOC experiment, suggested that these fluctuations were inadequate to account for the observed vertical extent of the arrivals (Colosi and Dushaw, personal communication). At least two other hypotheses

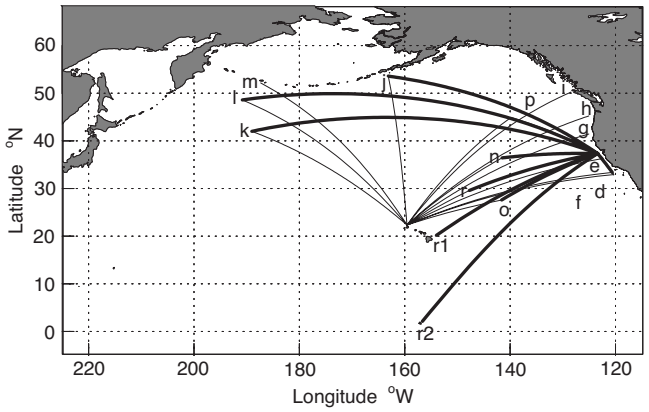

FIG. 1. Transmission paths from sources at Pioneer Seamount (heavy lines) and Kauai (light lines) to bottom-mounted receivers in the North Pacific Ocean. Figure from Dushaw *et al.* (1999).

[a]Author to whom correspondence should be addressed. Electronic mail: lvanuffe@ucsd.edu

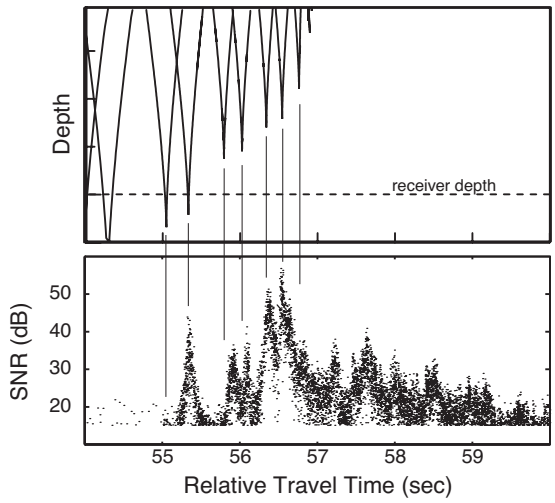

FIG. 2. Predicted timefronts (upper panel) and observed arrivals (lower panel) at receiver *n* for transmissions from a bottom-mounted source on Pioneer Seamount, off the coast of California. The observed arrivals occur at the times of cusps in the predicted timefronts, but have intensities that are not simply related to the depths of the cusps. The depth axis is not labeled because the depth of the bottom-mounted receivers is classified. Figure from Dushaw *et al.* (1999).

were subsequently proposed to account for shadow-zone arrivals. Dzieciuch *et al.* (2004) suggested that scattering from the sound-speed perturbations caused by density-compensated fine structure (spice) could contribute to scattering into the acoustic shadow. Rudnick and Munk (2006) suggested that the lower cusps of the early arrivals in the timefront will be deepened by reflections off the base of a tilted mixed layer. Acoustic rays steepen by twice the angle of inclination of the mixed layer base with each reflection, shifting the lower turning points of the rays to greater depths. Here, the internal-wave hypothesis is re-examined for a well-defined experimental geometry incorporating long vertical line array (VLA) receivers to investigate the vertical structure of the shadow-zone arrivals previously only observed on the bottom-mounted receivers.

In June 2004, two moorings with broadband 250-Hz sources and two VLA receivers were deployed in the North Pacific for the Spice Experiment (SPICEX) (Fig. 3). SPICEX was one component of the larger 2004 North Pacific Acoustic Laboratory (NPAL) experiment, which also included the Long-range Ocean Acoustic Propagation EXperiment (LOAPEX) and the Basin Acoustic Seamount Scattering EXperiment (BASSEX). Shadow-zone arrivals, analogous to those seen on the bottom-mounted receivers, were clearly seen on the Deep VLA (DVLA) receiver in SPICEX. In addition, upward scattering into the geometric shadow is observed at the end of the arrival pattern for the case of sources located well below the sound-channel axis. These arrivals are referred to as axial shadow-zone arrivals. Here, measured timefronts obtained in June 2004, shortly after deployment of the moorings, are compared with timefronts computed for sound-speed fields with and without internal-wave-induced sound-speed perturbations. Hydrographic environmental data collected at the time of deployment formed the basis for the sound-speed fields.

The SPICEX geometry and acoustic transmissions are described in Sec. II. Sec. III presents the acoustic data acquired during the experiment; Sec. IV describes how the environmental measurements were used to develop appropriate range-dependent sound-speed fields for propagation simulations. Section V describes the parabolic equation simulations that were performed and compares simulations based on the different sound-speed environments. The results are discussed in Sec. VI.

II. EXPERIMENT

Each of the two source moorings supported two broadband acoustic sources (Fig. 4). Hydroacoustics, Inc., HLF-5 sources with a center frequency of 250 Hz (Munk *et al.*, 1995) were located at about 750-m depth, approximately on the sound-channel axis. Webb Research Corporation (WRC) swept-frequency sources with a center frequency of 275 Hz (Morozov and Webb, 2003, 2007; Webb *et al.*, 2002) were located at about 3000-m depth, slightly above the estimated surface conjugate depth (Table I).

The transmissions were received on two autonomous VLA receivers deployed within a few kilometers of one another. Each VLA was constructed using quasi-independent subarrays of 20 hydrophones (High Tech, Inc. HTI-90-U series) at 35-m spacing and an overall length of 700 m (ATOC Instrumentation Group, 1995). One VLA receiver, referred to

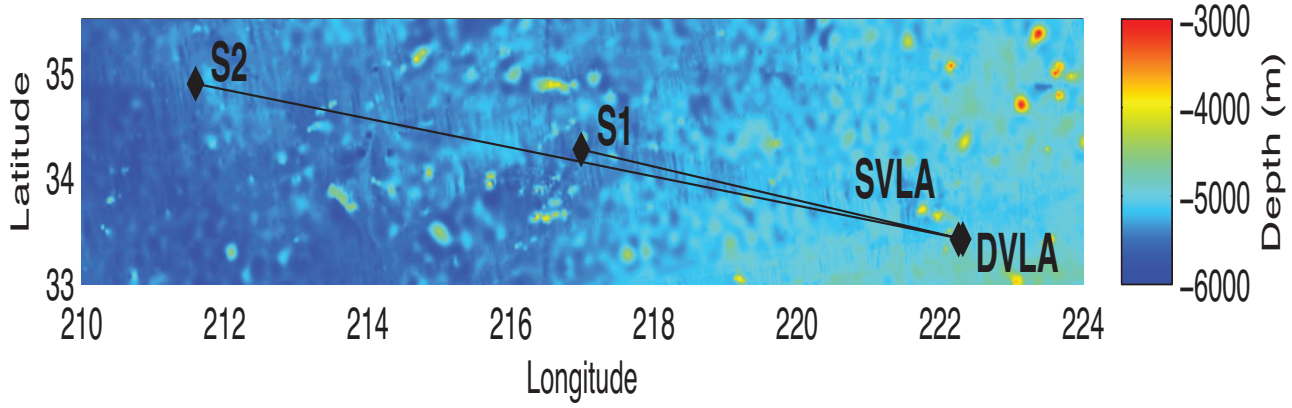

FIG. 3. Mooring locations for SPICEX. S1 (source 1) and S2 (source 2) are the locations of moorings with 250-Hz acoustic sources. SVLA and DVLA are the locations of two VLA receivers that are in close proximity.

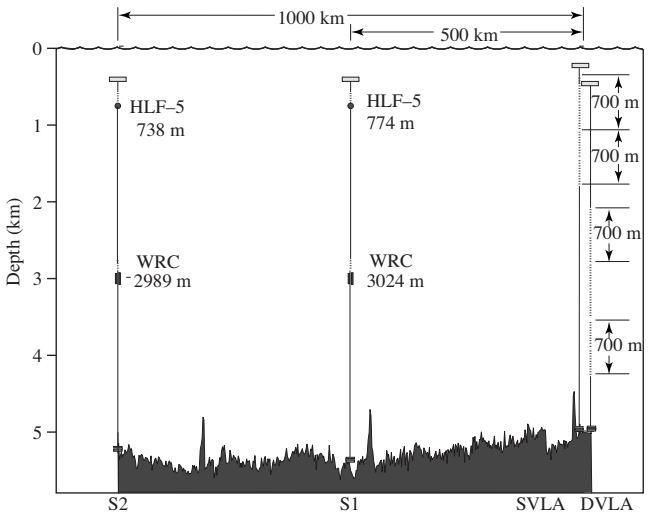

FIG. 4. SPICEX cross-sectional geometry overlaid on measured multibeam bathymetric data. Positions of SVLA and DVLA are not to scale due to their close proximity.

as the Shallow VLA (SVLA), spanned the sound-channel axis. It consisted of two subarrays, with a total of 40 hydrophones over the depth range 375.7–1739.3 m. The second VLA receiver, referred to as the DVLA, was designed to span the surface conjugate depth. It consisted of three subarrays. Unfortunately, the center subarray failed, leaving an upper subarray of 20 hydrophones over the depth range 2153.1–2819.6 m and a lower subarray of 20 hydrophones over the depth range 3575.3–4249.5 m. The hydrophone signals were amplified, bandpass filtered, and sampled at a 1000-Hz rate using 16-bit analog-to-digital converters.

The source and receiver positions were determined to within a few meters using Global Positioning System (GPS) navigation (Table II). The source moorings were approximately 500 km (S1) and 1000 km (S2) distant from the VLA receivers (Table III). The acoustic paths were nearly colinear. The source and VLA moorings were all deployed at approximately the same latitude in order to provide nearly zonal acoustic paths, with relatively range-independent sound-speed profiles.

Large time-bandwidth signals and pulse-compression techniques were used to improve the signal-to-noise ratio of the receptions. The two near-axial HLF-5 acoustic sources simultaneously transmitted 11 periods of a 1023-digit phase-coded *m*-sequence with a carrier frequency of 250 Hz (Munk *et al.*, 1995). Each digit contained 3 cycles of the carrier ($Q=3$). Each digit was then 12.0 ms in duration, each sequence period was 12.276 s long, and the transmission lasted for 135.0360 s. Ten of the 11 periods, beginning at the nominal arrival time of the middle of the first sequence, were recorded and coherently processed. The source level was approximately 192 dB with regard to 1 μPa at 1 m. The two deep WRC sources simultaneously transmitted linear frequency-modulated (FM) sweeps from 225 to 325 Hz lasting 135.000 s. The VLAs recorded for 155.000 s, beginning 10 s prior to the nominal arrival time of the signal. The source level in the horizontal was nominally 190 dB with regard to 1 μPa at 1 m. Each source transmitted six times a day every 4 days from the time of deployment in June 2004 until the end of November 2004.

TABLE I. Source depths (m), as determined using long-baseline acoustic navigation systems.

	S1	S2
HLF-5	774	738
WRC	3024	2989

TABLE II. SPICEX mooring locations and water depths.

Mooring	Latitude	Longitude	Depth
DVLA	33.41892°N	222.31753°E	5045
SVLA	33.41840°N	222.25907°E	5005
S1	34.26722°N	216.98292°E	5500
S2	34.88912°N	211.59197°E	5475

The HLF-5 and WRC sources were calibrated at the U.S. Navy Seneca Lake Sonar Test Facility. The source level of the HLF-5 sources was measured at full power. The source level of the WRC sources was measured at less than full power and extrapolated. The source level for the WRC sources may therefore not be quite as accurate. Intermittent receptions from the WRC sources, particularly toward the end of the transmission period, displayed significantly lower signal-to-noise ratios. Subsequent investigation of the sources found intermittent problems in the source hardware. All of the acoustic receptions presented here, however, possess typical signal-to-noise ratios.

The positions of the sources and the positions and shapes of the VLAs were measured once an hour throughout the deployment by long-baseline acoustic navigation systems. A net of four acoustic transponders was deployed on the ocean floor surrounding each source mooring. The SVLA and DVLA shared a network of six transponders. The source positions were determined to within about 1.5-m rms, using acoustic interrogators on the sources. The absolute positions of the hydrophones in the VLAs were also determined to within about 1.5-m rms, using acoustic interrogators in the center of each subarray. The navigation signals were received on six of the same hydrophones in each subarray as were used to receive the 250-Hz transmissions, distributed over the subarray aperture, as well as on the interrogation transducers. The relative positions of the hydrophones were determined to within about 0.2-m rms.

TABLE III. Source-receiver ranges (km) (WGS84).

	DVLA	SVLA	S1	S2
DVLA	0	5.438	502.562	1001.927
SVLA		0	497.262	966.628
S1			0	499.366
S2				0

Deep conductivity-temperature-depth (CTD) measurements were made at each mooring location at the time of deployment. High-resolution measurements of the upper ocean temperature and salinity fields along the acoustic path were obtained while the ship was in transit between mooring locations using the newly developed underway CTD (UCTD) (Rudnick and Klinke, 2007). Ninety-six UCTD casts sampled the upper 400 m of the acoustic path from S2 to the VLAs. In addition, Sea-bird temperature recorders (SBE 39) and MicroCAT (Conductivity And Temperature) sensors (SBE 37) were attached to the source and receiver moorings to collect data at the mooring locations throughout the duration of the acoustic transmissions.

A detailed multibeam bathymetric survey was performed at each of the mooring sites prior to deployment, and bathymetric data were collected along the acoustic path while the ship was in transit between mooring deployment sites. The ship's track during the leg from the VLAs to the S1 source mooring was slightly offset from the acoustic path because the location of the S1 mooring was adjusted southward by a few kilometers upon arrival at the mooring site due to the presence of a large seamount, with a maximum height of 3870 m. The seamount did not appear in the Smith–Sandwell bathymetry (Smith and Sandwell, 1997).

III. ACOUSTIC DATA

The SVLA captures the near-axial portion of the timefronts, while the DVLA extends below the surface conjugate depth in order to capture the deep portions of the timefronts (Fig. 5). The acoustic signals arrive at the SVLA several seconds before reaching the DVLA because the SVLA is 5.30 km closer to the source moorings. Previous comparisons of measured and predicted timefronts for broadband, long-range transmissions relied on VLA receivers that did not extend to sufficiently great depths to capture the deep, early arrivals (Sparrock, 1990; Worcester *et al.*, 1999, 1994).

Analyses of earlier experiments focused on comparisons of measured and predicted travel times. Here the comparisons emphasize the absolute intensities of the measured and predicted timefronts in order to assess whether or not internal-wave-induced scattering is adequate to account for the observed intensities of the shadow-zone arrivals. The SVLA and DVLA receivers were fully calibrated. The intensities of the measured receptions were calculated using the measured hydrophone sensitivity (−168 dB with regard to 1 V/μPa) and SVLA/DVLA system gain, taking account of the signal processing gains achieved using the large time-bandwidth signals with the assumption that the received signals are coherent over the duration of the transmission. Idealized *m*-sequence and linear FM-sweep signals were generated to emulate the signals transmitted by the HLF-5 and WRC sources and were subsequently processed using the same signal processing as used for the acoustic data to experimentally determine the gain resulting from the processing algorithms. This processing gain was removed from the signal to calculate the intensity in the absence of pulse compression.

The receptions from the near-axial HLF-5 sources display the well-studied "accordion" pattern consisting of well-defined and identifiable early arrivals and a highly scattered, near-axial finale. The early arrivals with well-defined lower cusps seen on the DVLA are from high-angle rays that sample the full water column, including the highly variable upper ocean. These cusps will be shown below to extend downward well into the geometric shadow zone.

Steep arrivals corresponding to rays that reflect from both the sea surface and seafloor are clearly evident in the receptions from the axial source on mooring S1 at 500-km range. These surface-reflected, bottom-reflected (SRBR) arrivals can be seen on the SVLA just prior to 336 s, overlapping the purely refracted arrivals, and near 337 s, following the near-axial finale. Three SRBR arrivals can also be seen on the DVLA between 339 and 340 s. There is even a suggestion of a SRBR arrival in the receptions from the axial source on mooring S2 at 1000-km range, appearing on the DVLA just prior to 676 s. The SRBR arrivals have intensities as large as 65 dB with regard to 1 μPa and can complicate the analysis of the purely refracted arrivals when the two overlap, but they will not otherwise be studied further here.

The receptions from the deep off-axis swept-frequency sources include well-defined and identifiable early arrivals, but not the near-axial finale, because the sources were located well below the sound-channel axis. In addition to shadow-zone arrivals associated with the lower cusps in the timefronts, these receptions will be shown below to include non-geometric arrivals extending upward toward the sound-channel axis, following the final geometric arrival. These shadow-zone arrivals are evident as the final branch of the timefronts extending upward toward the sound-channel axis from the last lower cusp.

IV. SOUND-SPEED FIELDS

Three representations of the sound-speed field on the acoustic path between the moored sources and the VLA receivers were constructed for use in generating predicted acoustic arrival patterns (Fig. 6). A relatively smooth range-dependent sound-speed field was first constructed using the UCTD and CTD data collected during June 2004 on the SPICEX mooring deployment cruise. This field was then averaged in range to create a range-independent sound-speed profile. Finally, realizations of range-dependent sound-speed fields including internal waves were constructed by adding internal-wave-induced sound-speed fluctuations to the range-average profile.

A. UCTD and CTD data

In order to construct a range-dependent sound-speed field, temperature and salinity fields were first constructed from the UCTD and CTD data by objective mapping. Sound speed was then computed using the sound-speed equation of Del Grosso (1974).

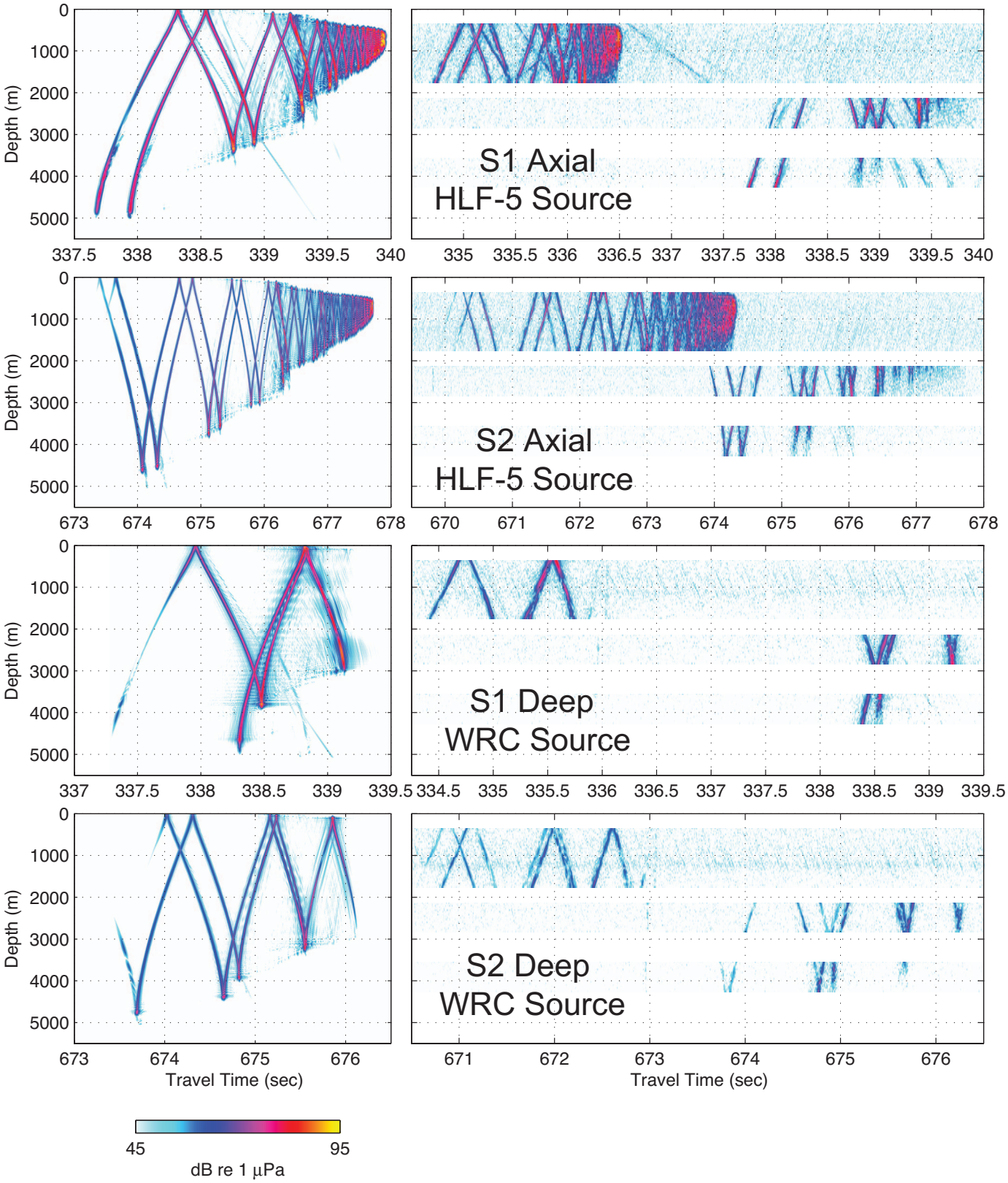

FIG. 5. Predicted (left column) and measured (right column) acoustic intensities (decibel with regard to 1 μPa) as a function of travel time and hydrophone depth for receptions from S1 axial HLF-5, S2 axial HLF-5, S1 deep off-axis WRC, and S2 deep off-axis WRC sources. The measured receptions are for transmissions at 1230 UTC (axial sources) and 1640 UTC (deep off-axis sources) on 15 June 2004 (yearday 167). The predicted timefronts are for the location of the DVLA and were calculated using the range-average sound-speed profile derived in Sec. IV .

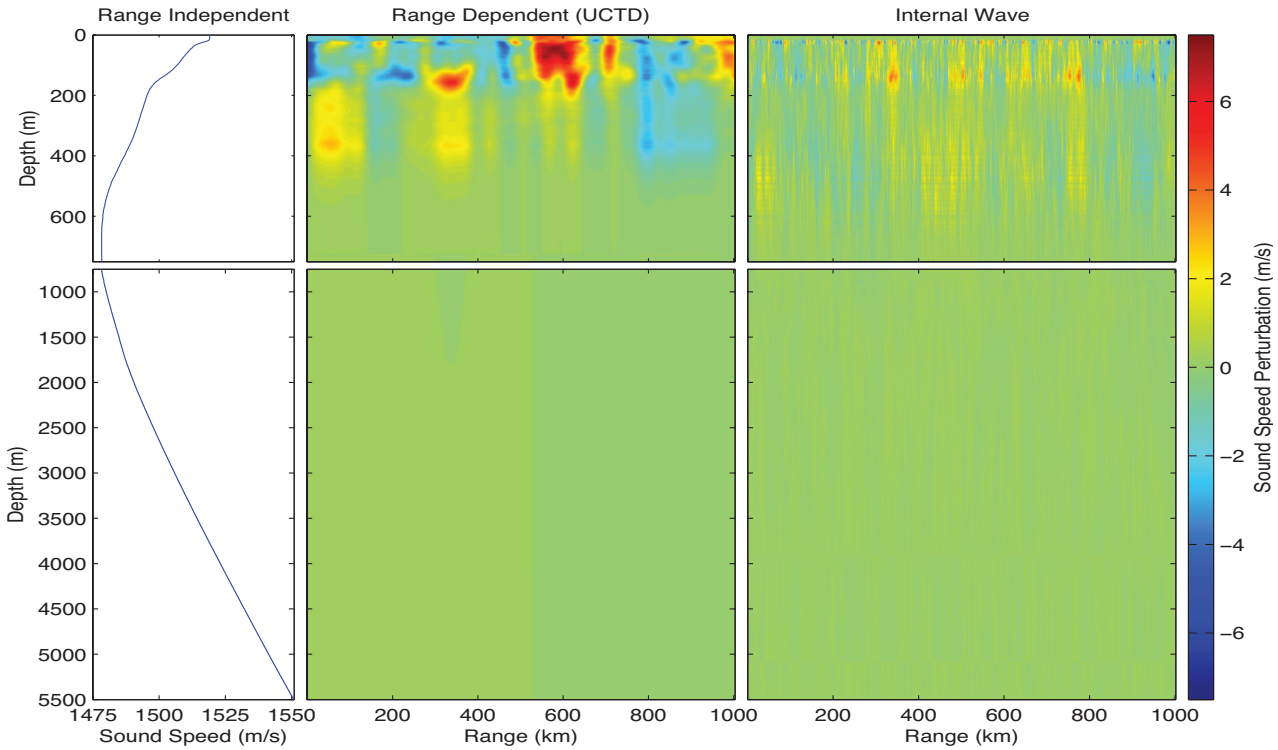

FIG. 6. Range-average sound-speed profile (left), sound-speed perturbations computed by subtracting the range-average sound-speed profile from objectively-mapped sound speeds derived from the UCTD/CTD data (center), and internal-wave-induced sound-speed perturbations computed for one realization of the GM internal-wave spectral model (right). The top (bottom) panels show sound speed above (below) 750 m.

To construct the maps, the temperature and salinity fields were expressed as range-dependent perturbation fields relative to mean temperature and salinity profiles obtained by averaging the three deep CTD profiles obtained at the mooring locations.

$$\Delta T(x_k,z) = \sum_{j=1}^{M} a_{jk}^T F_j^T(z), \tag{1}$$

$$\Delta S(x_k,z) = \sum_{j=1}^{M} a_{jk}^S F_j^S(z), \tag{2}$$

where a_{jk}^T, a_{jk}^S are the model parameters for temperature and salinity, respectively, at evenly-spaced intervals, k, along the acoustic path. The $F_j^T(z)$, $F_j^S(z)$ were chosen to be the eigenvectors of the vertical covariances of the temperature and salinity perturbations as a function of depth as estimated from the UCTD data, i.e., the empirical orthogonal functions (EOFs) for the UCTD data set.

For temperature, the lowest $M=8$ EOFs were retained, accounting for approximately 99% of the variance. To account for approximately 99% of the salinity variance, $M=13$ EOFs were required. Since relatively few UCTD casts extended much past 370 m, the EOFs were tapered smoothly to zero below this depth using an e-folding scale of 350 m to avoid sharp discontinuities in the temperature and salinity fields.

The coefficients a_{jk}^T, a_{jk}^S were computed by objective mapping, utilizing the Gauss–Markov minimum variance theorem, to minimize the differences between the temperature and salinity perturbations from the UCTD data and those computed from the ocean model (Wunsch, 1996). The resulting map had a horizontal resolution of 2.5 km in the horizontal and 1 m in the vertical. The objective mapping procedure substantially reduces internal-wave and other finescale variability, but retains mesoscale variability.

The sound-speed perturbation field shows maximum perturbations in the upper ocean of about ± 8 m/s. There is a thin mixed layer, perhaps 10–15 m thick, over most of the acoustic path. The sound-speed field is range-independent below a depth of about 500 m, where it is simply the mean of the three deep CTD profiles.

B. Internal waves

Simulated internal-wave-induced sound-speed fluctuations were added to the range-average sound-speed profile to generate stochastic realizations of range-dependent sound-speed fields that include internal waves. The simulated fields were generated to be consistent with the empirical Garrett–Munk (GM) spectral model (Garrett and Munk, 1979), using the method of Colosi and Brown (1998).

These perturbations to the sound-speed profile, δc, can be expressed as vertical displacements of a fluid parcel ζ,

$$\delta c = \left(\frac{\partial c}{\partial z}\right)_{\text{pot}} \zeta, \tag{3}$$

where $(\partial c/\partial z)_{\text{pot}}$ is the potential sound-speed gradient. The GM spectrum of internal-wave vertical displacement ζ as a function of range x and depth z for a frozen vertical slice is

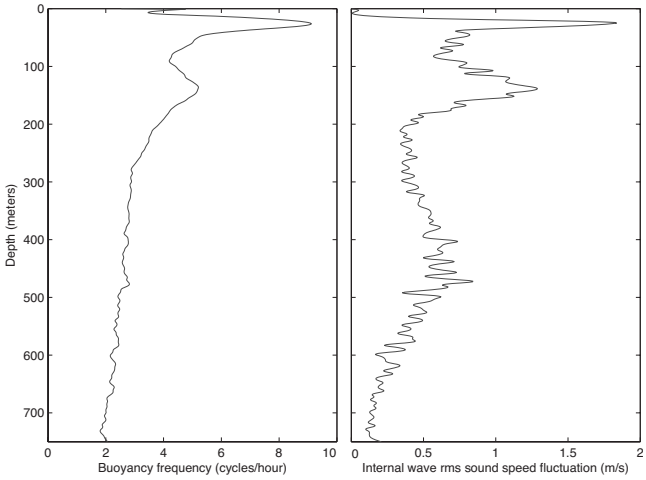

FIG. 7. The range-average buoyancy frequency profile used in the internal-wave calculations (left) and the internal-wave rms sound-speed fluctuation of one realization of the internal-wave field (right) for the upper 750 m of the ocean.

$$\zeta(x,z) = \mathrm{Re}\left[\frac{2B}{\pi}\left(\frac{E}{M}\right)^{1/2}\left(\frac{N_0}{N(z)}\right)^{1/2}(\Delta k_x)^{1/2}\cdots \times \sum_j \frac{\sin(j\pi\xi(z))}{(j^2+j_*^2)^{1/2}}\sum_{k_x}(I(j,k_x))^{1/2}G_j(k_x)e^{ik_x x}\right], \tag{4}$$

where

$$\xi(z) = \frac{1}{N_0 B}\int_{-h}^{z} N(z')dz' \tag{5}$$

and

$$I(j,k_x) = \frac{k_j}{k_x^2+k_j^2} + \frac{1}{2}\frac{k_x^2}{(k_x^2+k_j^2)^{3/2}}\ln\left(\frac{\sqrt{k_x^2+k_j^2}+k_j}{\sqrt{k_x^2+k_j^2}-k_j}\right). \tag{6}$$

In these simulations, G_j, a complex Gaussian random variable, was used in the place of the uniform random phase representation of Colosi and Brown (1998). Here $B=1135$ m is the thermocline depth scale, $E=6.3\times10^{-5}$ (for the reference internal-wave energy level referred to as 1 GM), M is the normalization constant for the sum over mode number, $M=\Sigma_{j=1}^{\infty}(j^2+j_*^2)^{-1}$, $j_*=3$ is an empirical constant, $k_j=\pi\omega_i j/N_0 B$, ω_i is the inertial frequency at the latitude of the internal waves, and $N_0=4.34$ cph is the reference buoyancy frequency. A single, range-independent buoyancy frequency profile, $N(z)$, was used to construct the internal-wave fields (Fig. 7). A range-dependent buoyancy frequency field was first computed from the objectively mapped temperature and salinity fields. This field was then averaged in range to create the range-independent buoyancy frequency profile. The lowest 100 internal-wave vertical modes were used to generate the internal-wave fields employed in parabolic equation simulations described in Sec. V. (The simulation results did not change significantly when only 30 modes were included.) Sound-speed perturbation fields were generated in domains that were twice the propagation range, with $\Delta x=0.2$ km. The step sizes in wave number space are then $\Delta k_x=2\pi/1000$ km^{-1} and $\Delta k_x=2\pi/2000$ km^{-1} for S1 and S2, respectively. Figure 7 shows the rms sound-speed fluctuation for one realization of the internal-wave sound-speed field.

V. PARABOLIC EQUATION SIMULATIONS

Broadband acoustic arrival patterns at the SVLA and DVLA were calculated for the range-independent, range-dependent, and internal-wave sound-speed fields using the split-step Padé solution to the parabolic equation (Collins, 1993, 1989). The parabolic equation (PE) simulations include diffractive effects. The earth-flattening transformation was first applied to the sound-speed fields to account for the curvature of the earth along the acoustic path. The PE simulations employed a grid spacing of 200 m in the horizontal and 0.5 m in the vertical. Six Padé coefficients were retained. An absorbent bottom was included with an attenuation coefficient of 5 dB/λ.

The solutions were also modified to include the frequency-dependent transmission loss (TL) due to volume attenuation (Fisher and Simmons, 1977):

$$\alpha(f) = 0.79A\frac{f^2}{0.8^2+f^2} + 36\frac{f^2}{5000+f^2}\ \mathrm{dB/km}, \tag{7}$$

where the frequency, f, is in kilohertz and $A=0.055$ for the North Pacific Ocean (Lovett, 1980). At 250 Hz, the volume attenuation is 0.0043 dB/km.

The source spectra needed for the broadband simulations were estimated by constructing idealized versions of the phase-coded m-sequence and linear FM signals transmitted by the HLF-5 and WRC sources. The idealized signals were processed using the same signal processing as used for the acoustic data. The results were then normalized to set the amplitudes of the processed signals to the values of pressure corresponding to the rms source levels of 192 and 190 dB with regard to 1 μPa at 1 m for the HLF-5 and WRC sources, respectively. This normalization removes the pulse-compression gain. Transforming to the frequency domain gives the idealized spectra of the transmitted signals (Fig. 8). The idealized FM signal has sharp cutoffs in frequency at 225 and 325 Hz, the start and stop frequencies, resulting in high sidelobes in the time domain. To reduce the strength of the sidelobes to better reflect the actual performance of the WRC source, the idealized spectrum was windowed with a Kaiser–Bessel window with $\beta=2$ (Fig. 8). The idealized m-sequence spectrum had very low sidelobes, which were removed using a rectangular window in the frequency band of the source. The windowed spectra were used in the broadband simulations.

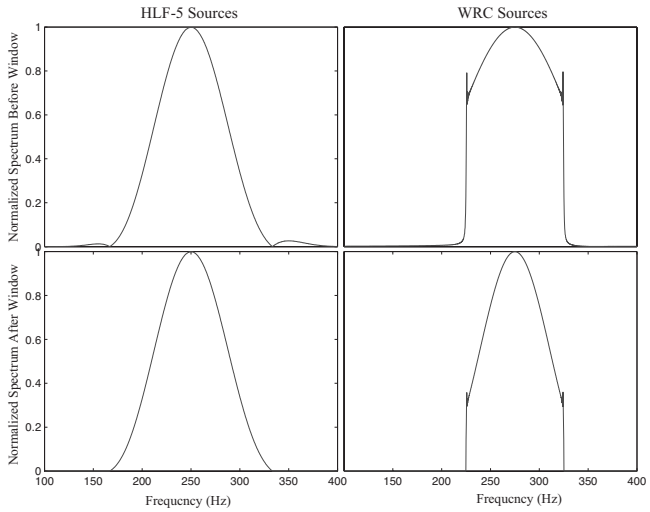

FIG. 8. Source spectra for the *m*-sequences transmitted by the HLF-5 sources and for the FM sweep transmitted by the WRC sources. Both idealized (top) and windowed (bottom) spectra are shown for each waveform.

The predicted pressures (P), and therefore intensities, of the receptions were derived from a simple algebraic manipulation of the standard TL equation

$$\mathrm{TL} = -20 \log_{10}\left(\frac{P}{P_o}\right), \tag{8}$$

utilizing the pressure at 1 m from the source (P_o) and TLs from the broadband parabolic equation simulations.

Parabolic equation simulations for transmissions from the S1 axial source to the SVLA using range-dependent sound-speed fields with internal waves give a highly scattered near-axial finale not present in the range-independent and range-dependent simulations [cf., Colosi *et al.* (1994)]. Comparison of Monte-Carlo calculations using internal-wave fields consistent with the GM spectrum (1 GM) and with half the energy of the GM spectrum (1/2 GM) shows that neither fully accounts for the amount of scattering seen in a daily average of the measured receptions; however, twice the energy of the GM spectrum (2 GM) produces more scattering than is evident in the measured data (Fig. 9).

The daily average of the measured receptions is an incoherent average of the intensities for the six transmissions occurring on 15 June 2004 (yearday 167), shortly after the deployment of the acoustic sources. This transmission day was selected to be nearly concurrent with the collection of the environmental data on the deployment cruise and, therefore, the sound-speed fields utilized in the simulations. Because the sources transmitted only every fourth day, a single-day average was employed to minimize changes in the ocean environment between transmissions.

The Monte-Carlo calculations are incoherent averages of the intensities of the arrival patterns computed from five independent realizations of the internal-wave field. The number of internal-wave simulations was selected to roughly coincide with the number of averaged receptions.

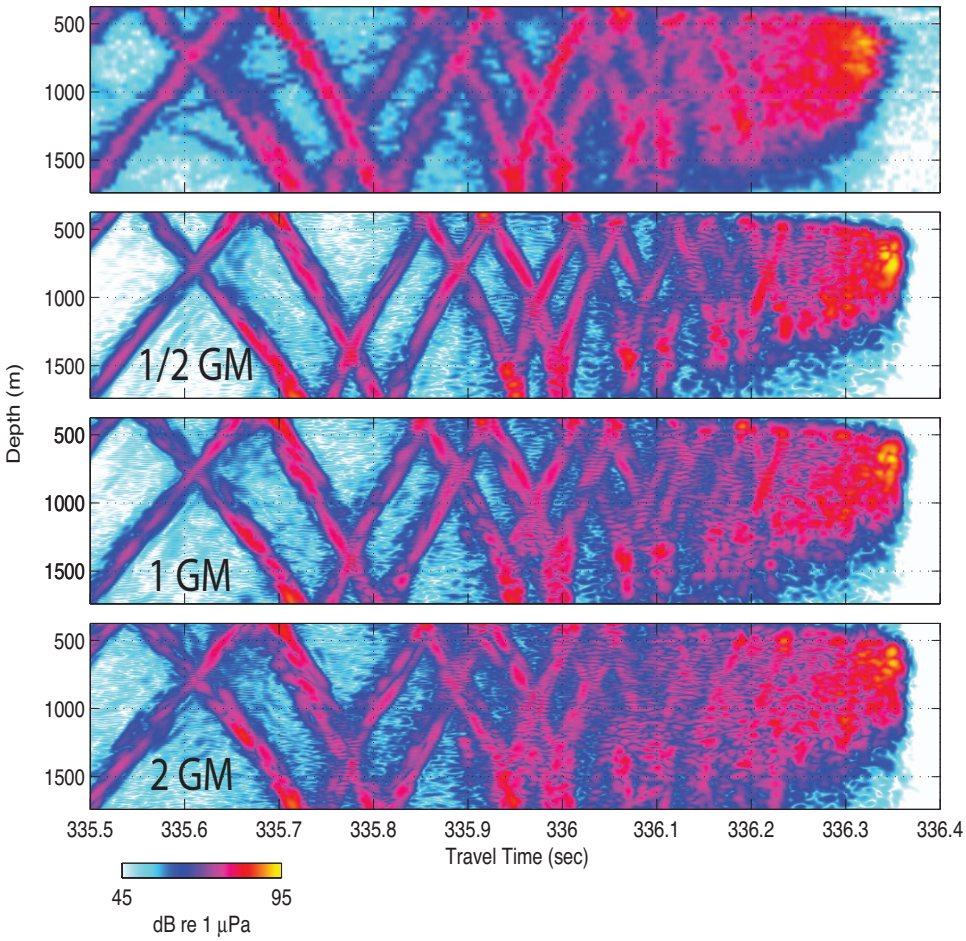

FIG. 9. Finale of the timefront for transmissions from the S1 axial source to the SVLA. The daily average of receptions on yearday 167 (top) is compared with parabolic equation simulations based on 1/2-, 1-, and 2-GM internal-wave energy levels.

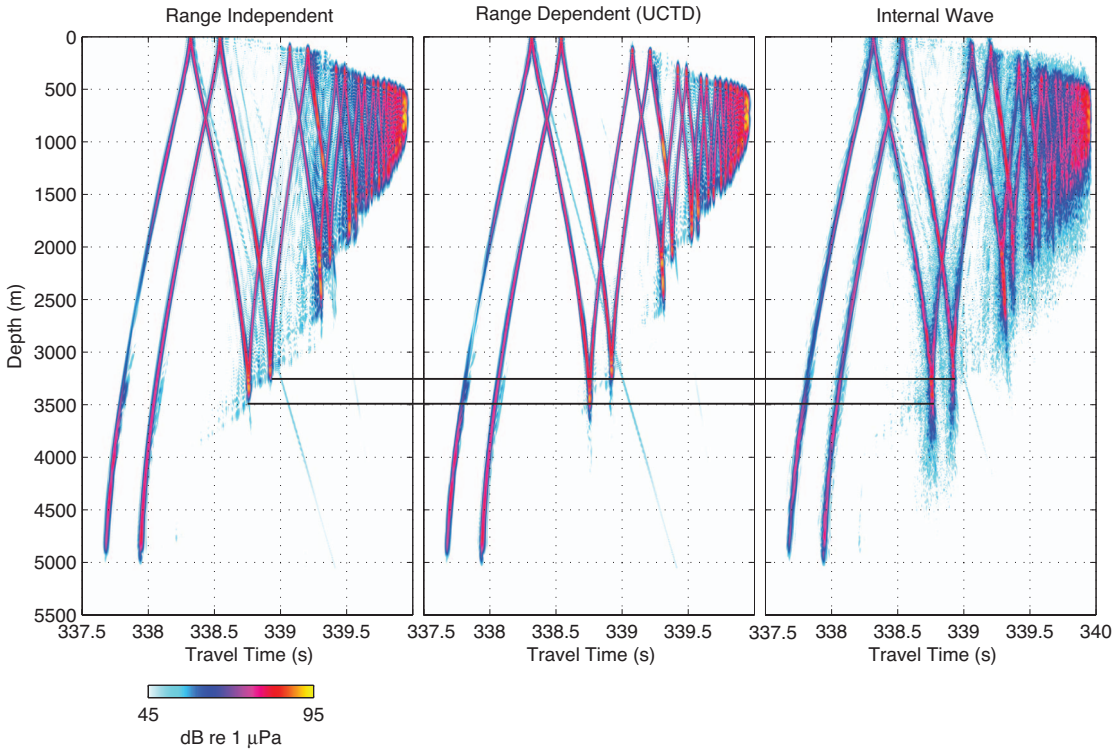

FIG. 10. Parabolic equation simulations for S1 axial source transmissions using the range-independent profile (left), range-dependent sound-speed field derived from the UCTD/CTD data (center), and stochastic internal-wave sound-speed field incorporating perturbations consistent with 1-GM internal-wave energy (right). The horizontal lines indicate the depths of the deepest pair of cusps for the range-independent case.

The 2-GM simulation exhibits more pronounced scattering in the earlier branches of the timefront and increased broadening, or flattening, of the near-axial finale than are present in the measured data. The 1/2-GM simulation exhibits distinguishable branches of the timefronts occurring after a travel time of 336.2 s, whereas the branches of the measured timefronts are more highly scattered and not discernible after about 336.1 s. Although not perfect, simulations using the full GM energy level best capture both the extent to which the branches of the timefronts are scattered and the broadening of the near-axial finale. All subsequent simulations in this paper that incorporate internal-wave-induced scattering will therefore use sound-speed perturbations consistent with the full GM spectrum.

Parabolic equation simulations for transmissions from the S1 axial source to the location of the DVLA using the range-independent and range-dependent sound-speed fields are quite similar (Fig. 10). The smoothed sound-speed field resulting from the construction of objective maps of the UCTD data results in predicted timefronts that show minimal scattering. The set of lower cusps arriving between 338.5 and 339 s barely extends to 3500 m for the range-independent case, as indicated by the horizontal black line. Although the range-dependent profile shows a slight deepening, the internal-wave profile causes significant scattering, reaching depths of almost 4500 m. This is a clear example of a shadow-zone arrival.

VI. DISCUSSION

Detailed intensity comparison between PE simulations incorporating range-independent, range-dependent, and internal-wave sound speed fields as well as comparisons between internal-wave simulations and acoustic data are presented in Figures 11–18. For completeness, each of the eight source-receiver pairs: S1 axial source to the SVLA (Fig 11) and DVLA (Fig 12), S2 axial source to the SVLA (Fig 13) and DVLA (Fig 14), S1 deep source to the SVLA (Fig 15) and DVLA (Fig 16), and S2 deep source to the SVLA (Fig 17) and DVLA (Fig 18) are included.

A. Axial finale arrivals

The vertical broadening of the axial finale due to the inclusion of internal-wave-induced sound-speed perturbations is evident from even the most superficial comparison of the arrival patterns in Fig. 10. This broadening is further displayed in the intensity vs travel time plots shown in Figs. 11 and 13. The final cutoff for all three simulated environments occurs approximately simultaneously at the near-axial depths of 691 and 1041 m, but the final cutoff time for the internal-wave simulation is significantly delayed at depths both above (376 m) and below (1390 and 1739 m) the sound-channel axis [Figs. 11(a) and 13(a)].

This delay in final cutoff is also present with comparable intensity in the daily averages of hydrophone data at the same depths [Figs. 11(b) and 13(b)]. This broadening of the axial finale was observed during the SLICE89 experiment and was described by Worcester *et al.* (1994), simulated by Colosi *et al.* (1994), and explained in terms of mode coupling by Colosi and Flatté (1996) and ray chaos by Beron-Vera *et al.* (2003). The effect was observed to be more significant below the axis than above, which is consistent with the observational data presented here.

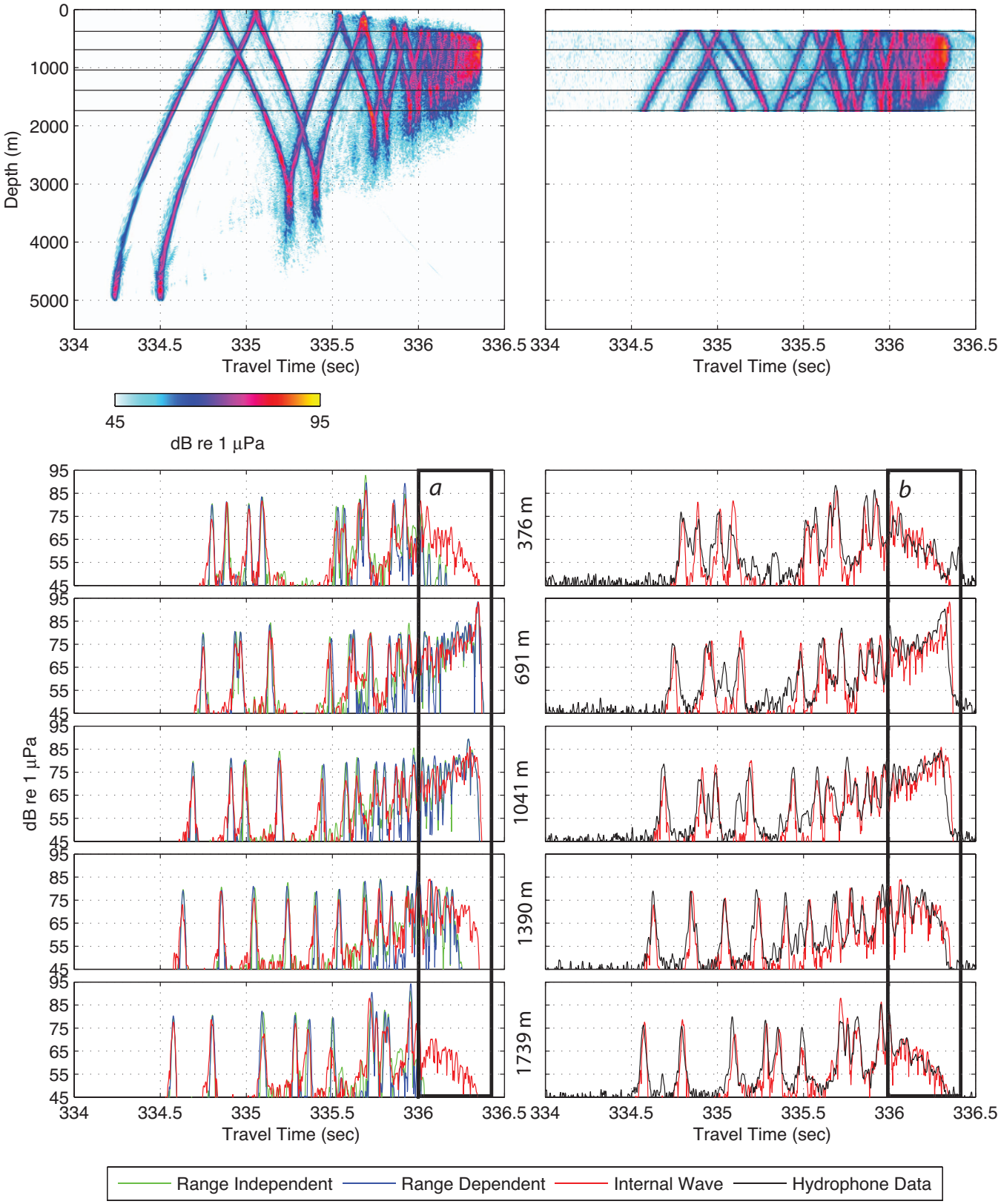

FIG. 11. Intensity-averaged PE simulations for the S1 axial source to SVLA acoustic path incorporating five realizations of 1-GM internal-wave fields (top left) and an intensity average of six receptions of acoustic data received on yearday 167 (top right). Horizontal black lines indicate depths where slices of the internal-wave PE simulation timefront are compared with similar range-dependent and range-independent predictions (lower left) and acoustic hydrophone data (lower right).

Although peak-to-peak comparisons between data and simulations are difficult due to the complex arrival pattern typical of the axial finale, the internal-wave simulations capture both the intensity level and the extent of the vertical scattering observed in the finale portion of the SVLA receptions for both the 500-km and 1000-km ranges.

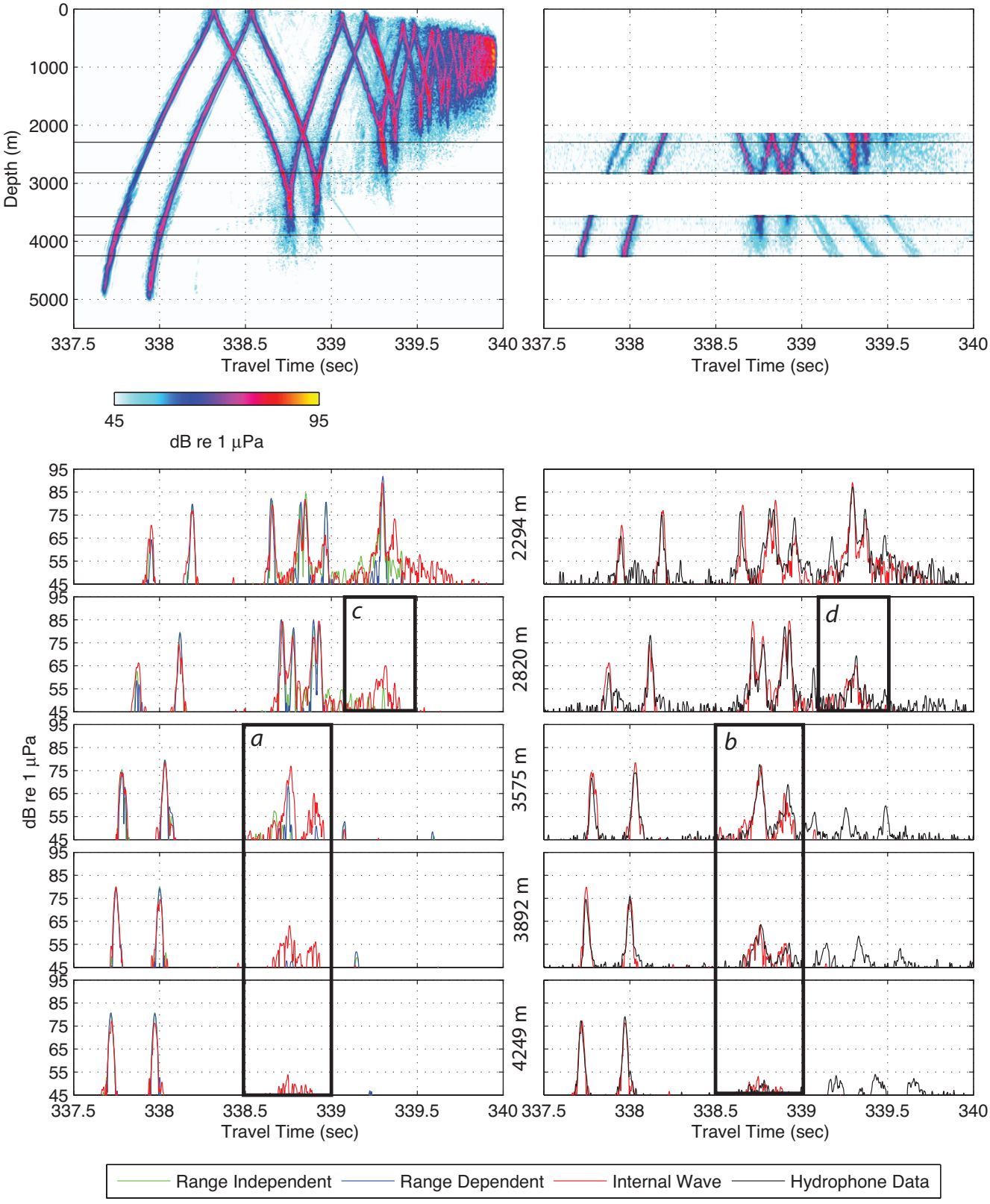

FIG. 12. Same as Fig. 11, except for the S1 axial source to DVLA acoustic path.

B. Early geometric arrivals

Comparisons of acoustic data and internal-wave propagation simulations show extraordinary agreement for early geometric arrivals. The leading timefront branches of the S1 axial source receptions both on the SVLA and DVLA depicted in Figs. 11 and 12, respectively, show good agreement, especially on the deepest phones, with the internal-wave predictions both in terms of intensity level and in the width of the peaks in travel time.

Clean, early geometric arrivals are also observable for

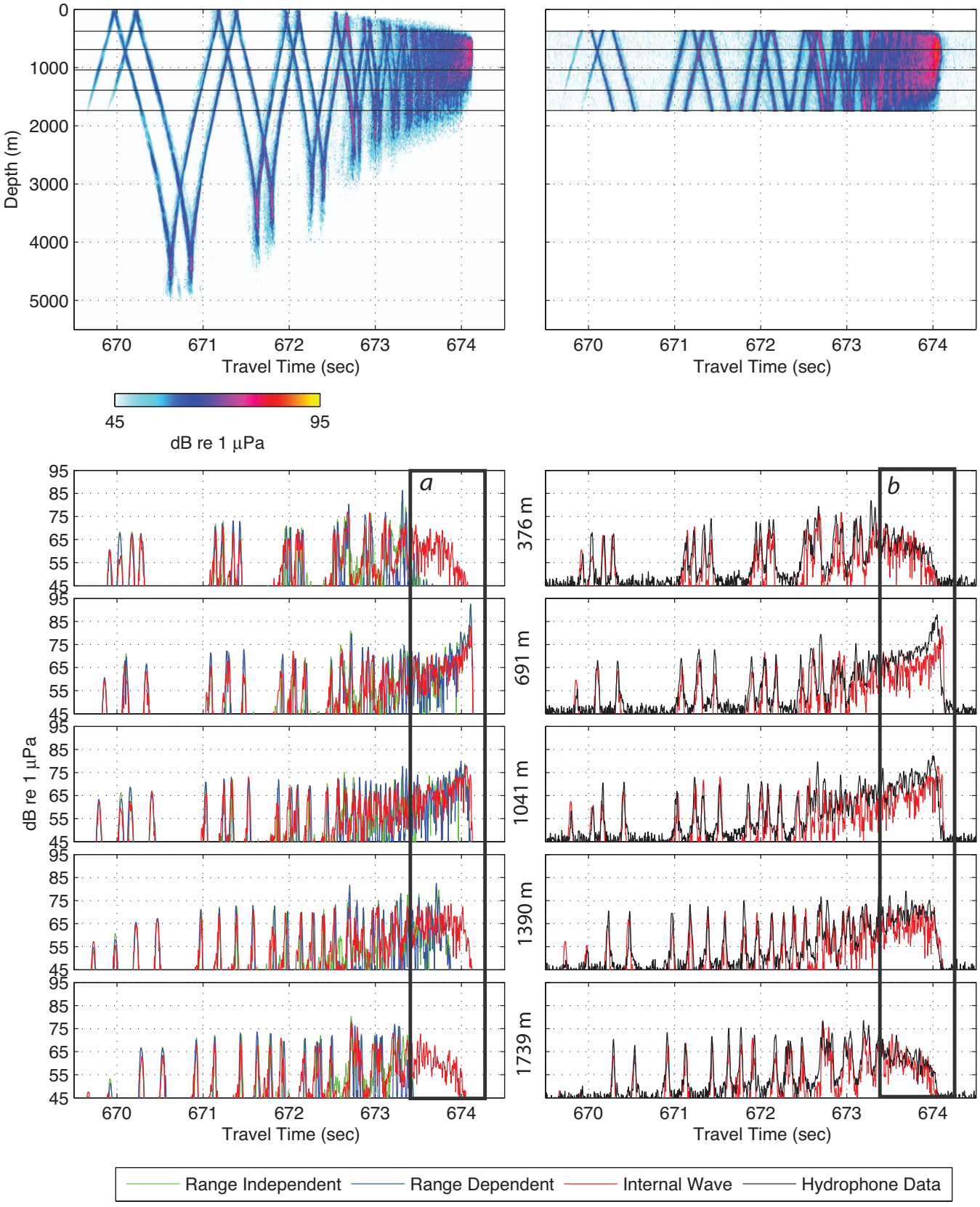

FIG. 13. Same as Fig. 11, except for the S2 axial source to SVLA acoustic path.

the portion of the S1 deep off-axis source arrival captured by the SVLA (Fig. 15). Interestingly, the measured intensity agrees well with the simulations for the upper hydrophones, decreases dramatically on the hydrophone located at 1739 m [Fig. 15(a)], and is absent on all of the phones of the DVLA (Fig. 16). This early branch of the timefront was predicted not only by the internal-wave simulation but also by both the range-independent and range-dependent simulations. Deep

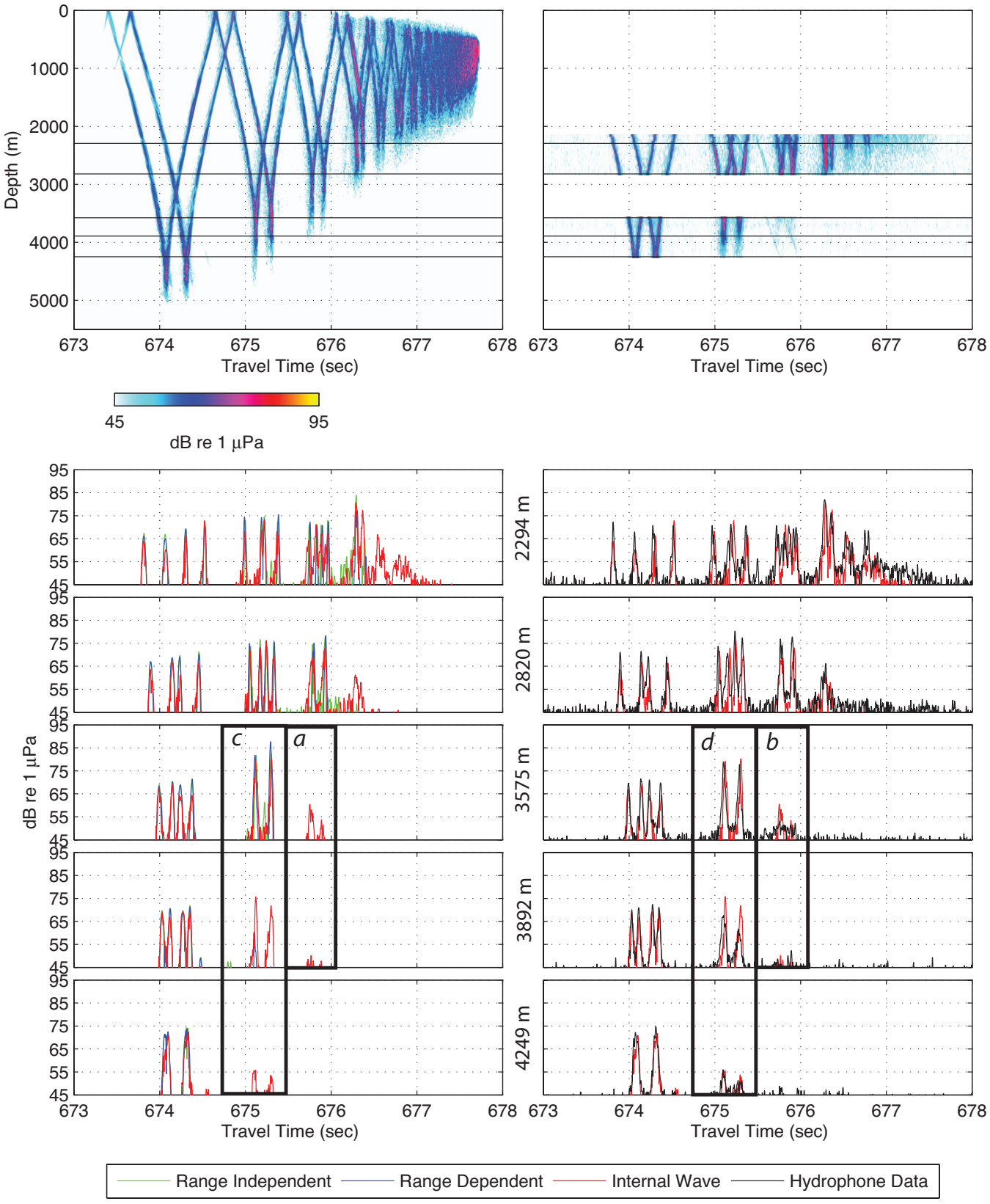

FIG. 14. Same as Fig. 11, except for the S2 axial source to DVLA acoustic path.

arrivals are similarly less intense than predicted in the earliest branches of the 1000-km range receptions for the deep off-axis source, particularly evident at the depth of 3575 m [Fig. 18(a)].

C. Deep shadow-zone arrivals

Scattering induced by the addition of internal-wave sound-speed fluctuations was shown in Sec. V to extend the lower cusps occurring between 338.5 and 339 s on the S1

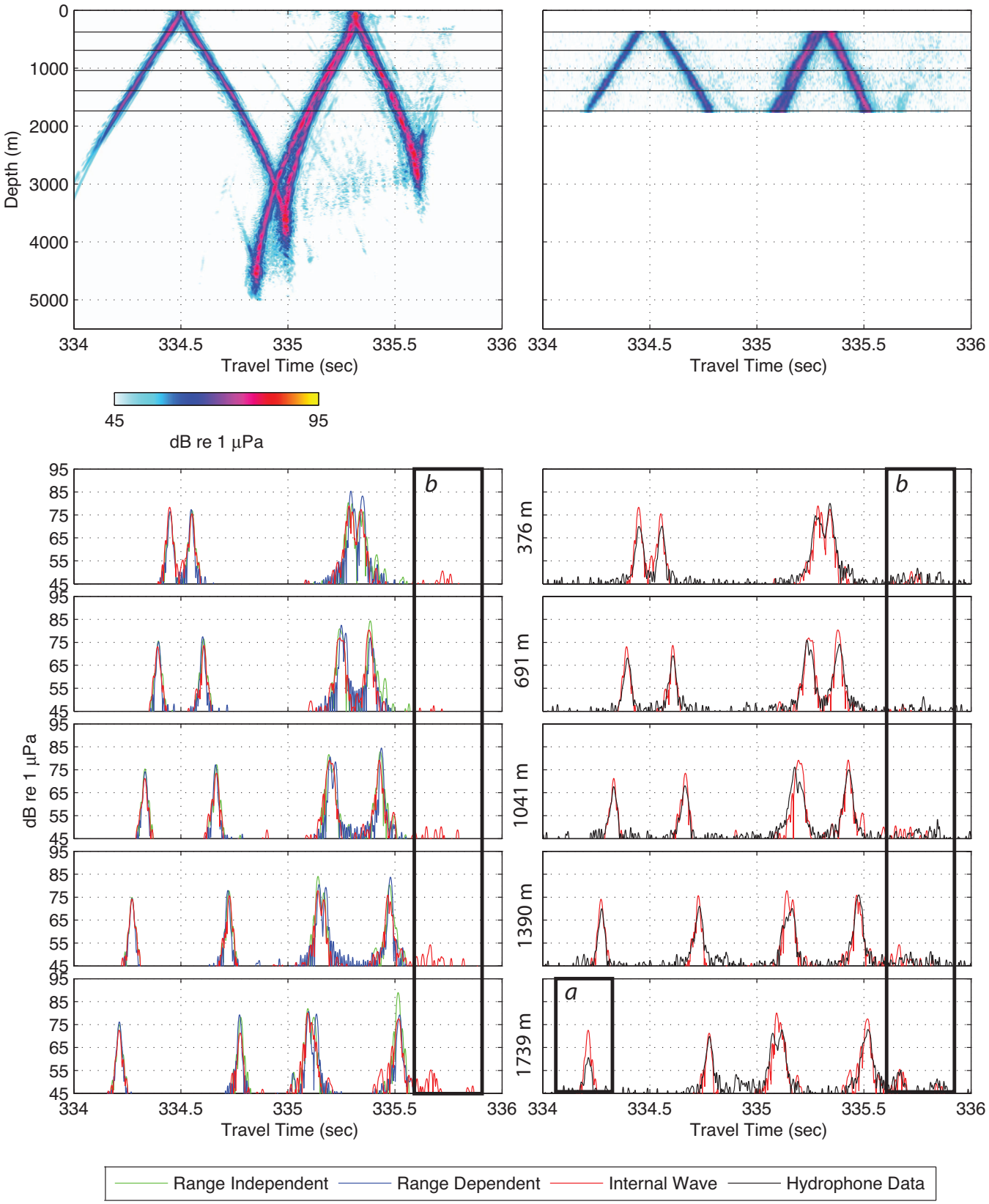

FIG. 15. Same as Fig. 11, except for the S1 deep off-axis source to SVLA acoustic path.

axial source to DVLA propagation path nearly 1000 m beyond the 3500-m depth predicted by a range-independent environment [Figs. 10 and 12(a)].

The lower cusps of the measured acoustic timefront extend to the deepest hydrophone depth of 4249 m, matching the extent and intensity of scattering into the shadow zone predicted by the internal-wave simulation [Fig. 12(b)].

Although the missing VLA segment obscures the full

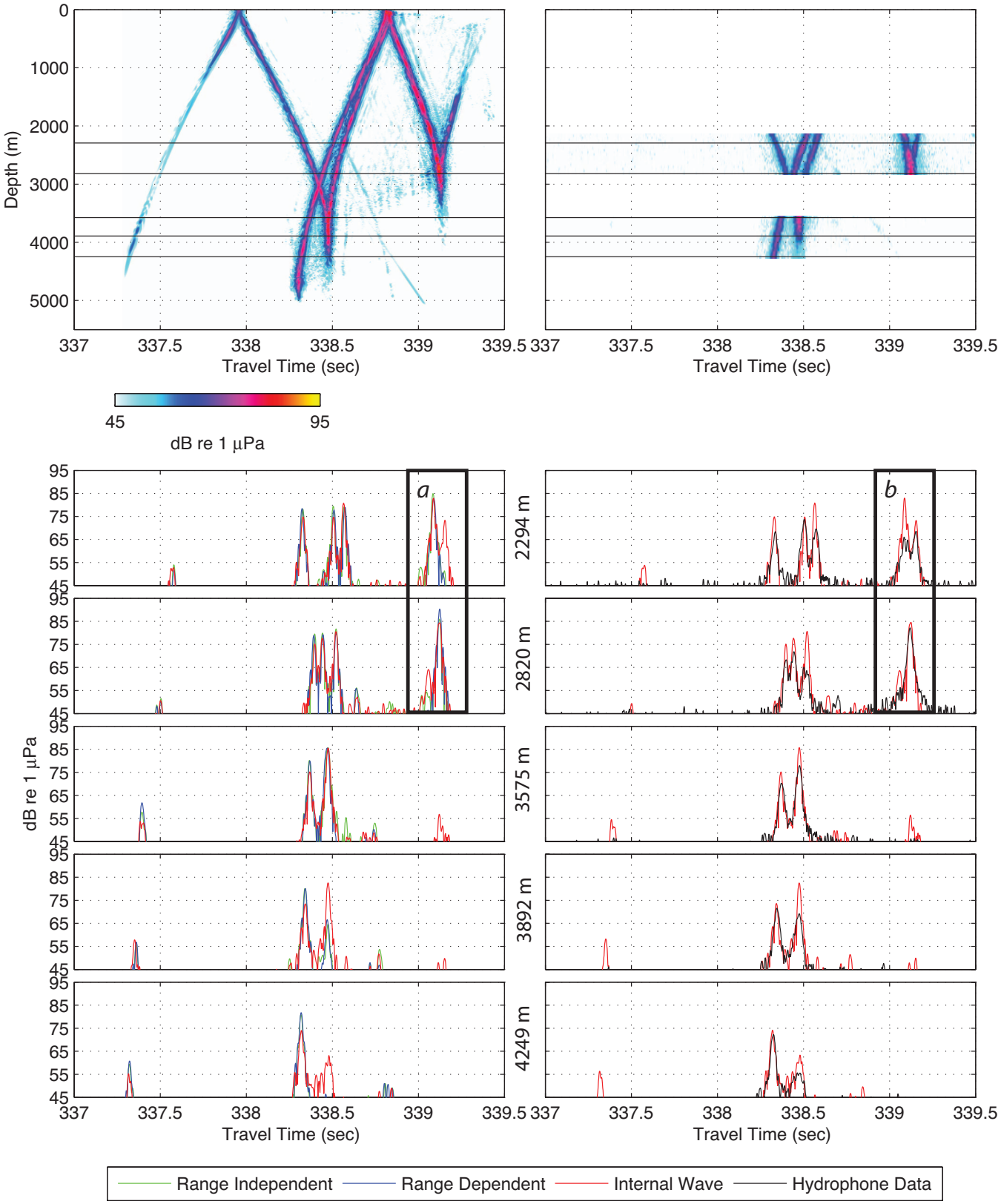

FIG. 16. Same as Fig. 11, except for the S1 deep off-axis source to DVLA acoustic path.

extent of the subsequent pair of lower cusps, arriving between 339 and 339.5 s, the portion that is captured has already extended into the acoustic shadow zone [Fig. 12(c)]. There is a clear arrival predicted by the internal-wave simulation at 2820 m, the depth of the lowest hydrophone on the upper segment of the DVLA, which is also present in the acoustic data, although it is somewhat obstructed by interfering SRBR arrivals [Fig. 12(d)].

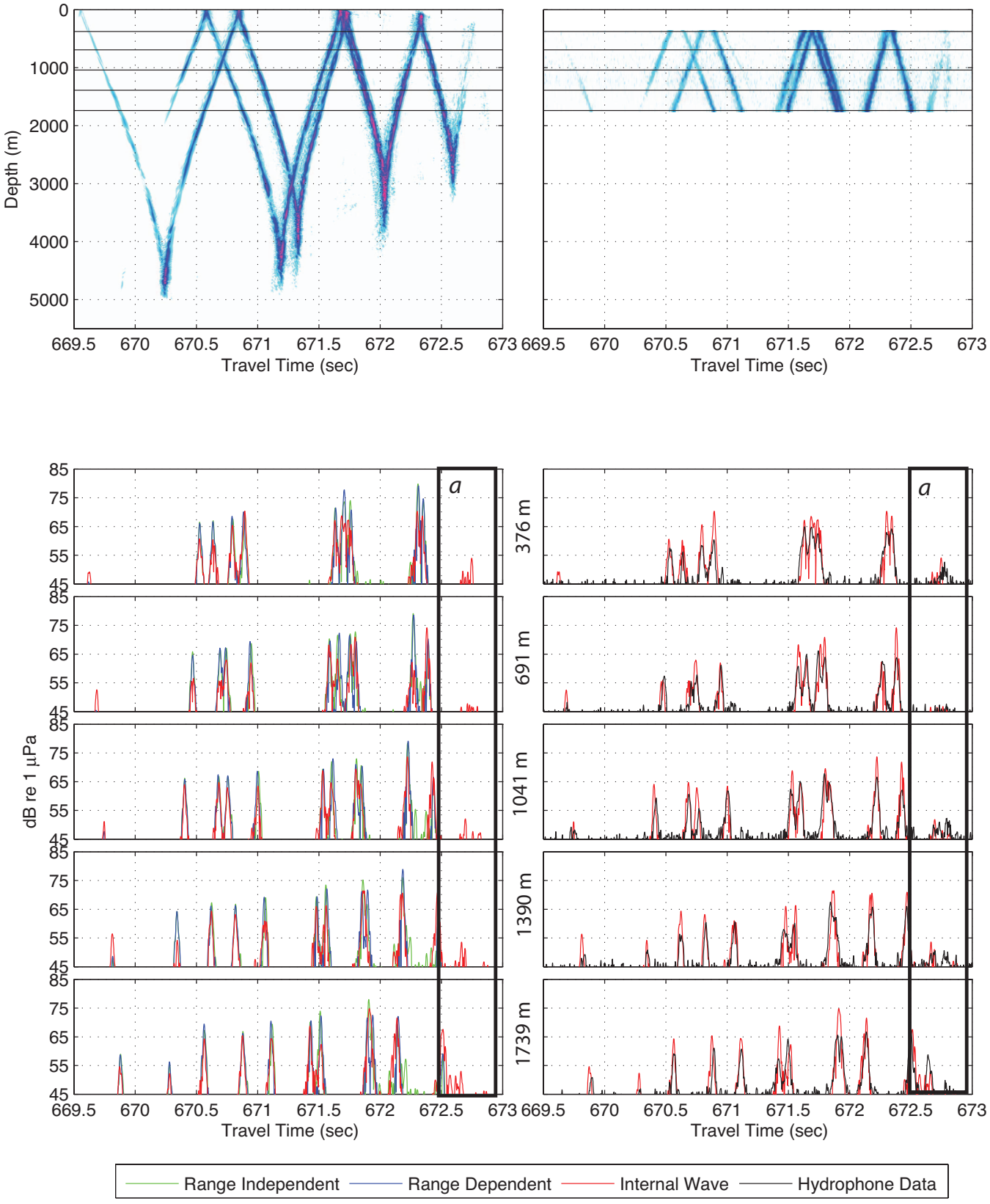

FIG. 17. Same as Fig. 11, except for the S2 deep off-axis source to SVLA acoustic path.

These SRBR arrivals, discussed in Sec. III, are not present in the PE simulations due to the addition of an absorptive layer which suppressed most of the bottom interaction.

The 1000-km propagation path from the S2 axial source to the DVLA renders several examples of shadow-zone extensions due to its extended arrival pattern (Fig. 14). The most prominent of these extensions are the second and third pairs of lower cusps.

The third pair of lower cusps, arriving just prior to the

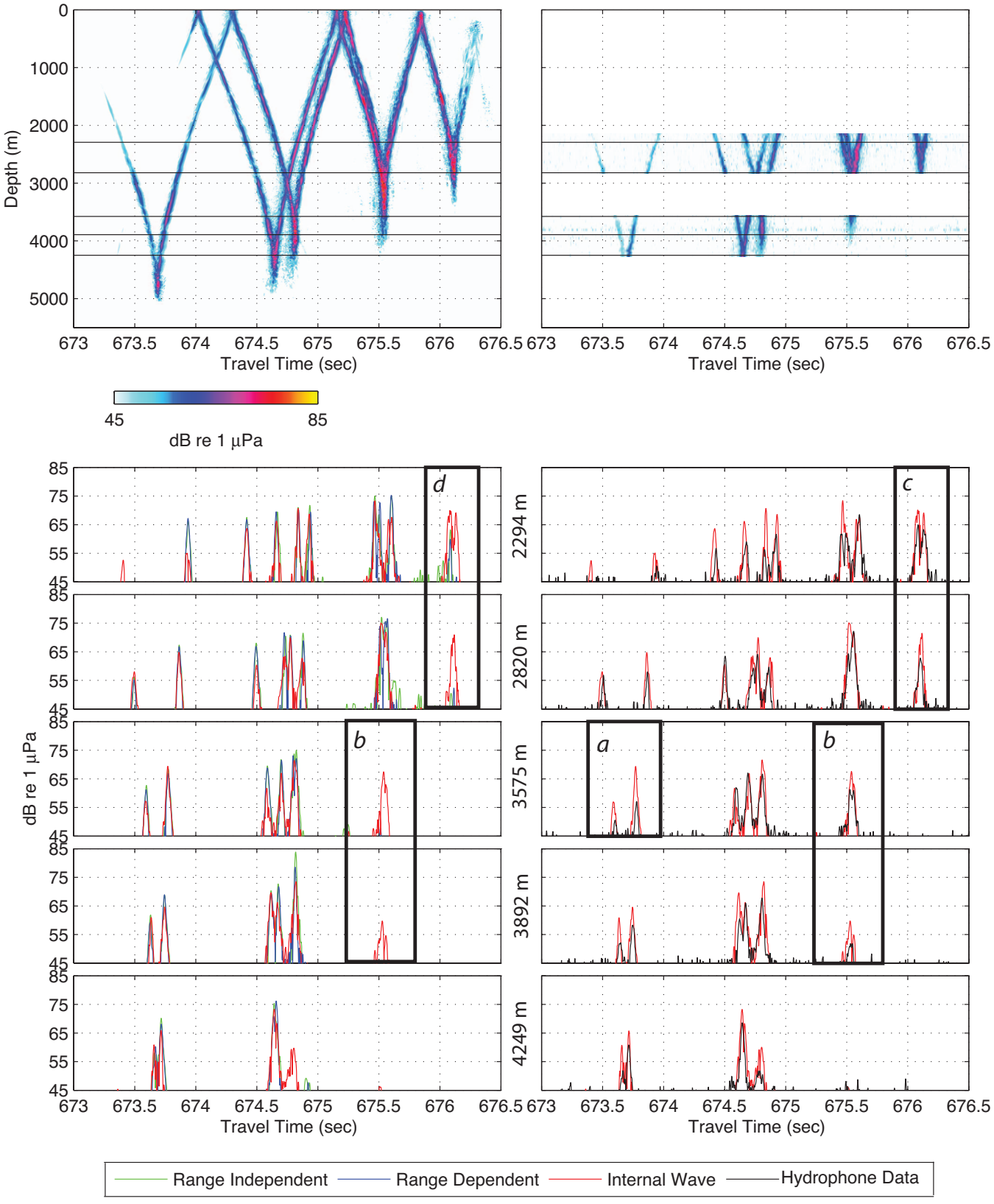

FIG. 18. Same as Fig. 11, except for the S2 deep off-axis source to DVLA acoustic path.

676-s mark, show no suggestion of an arrival in either the range-independent or range-dependent predictions at 3575 m, the shallowest hydrophone on the DVLA; however, the internal-wave prediction extends to the phone located at 3892 m [Fig. 14(a)]. The simulation predicts a somewhat sharper and more intense arrival at the 3575-m depth than is evident in the acoustic data [Fig. 14(b)].

The second pair of lower cusps, arriving immediately

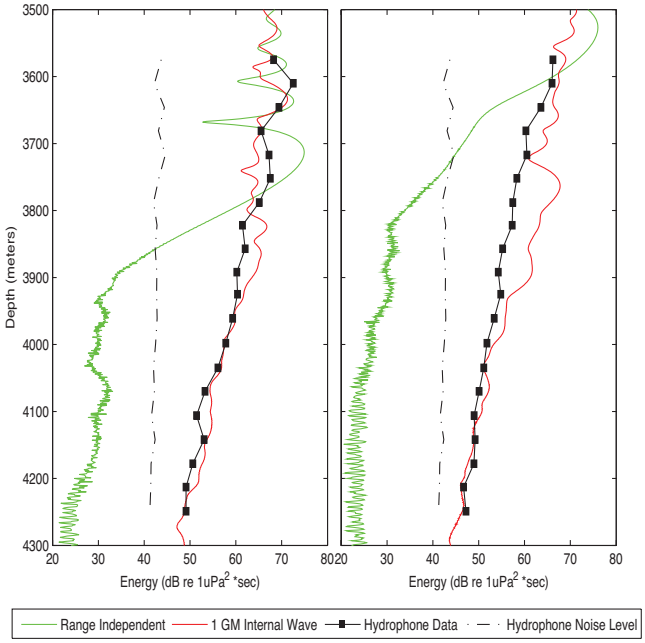

FIG. 19. Energy in the pair of lower cusps occurring after 675 s for the S2 axial source to DVLA propagation path (Fig. 14). Energy was calculated for a time window of 675.0–675.2 s for the first cusp (left) and 675.2–675.4 s for the second cusp (right). Hydrophone data and noise levels are shown for the 20 phones on the lower segment of the DVLA.

after 675 s, are perhaps a better example because the transition into the shadow zone occurs within the depth range of the lower segment of the DVLA. The range-independent prediction is consistent with the internal-wave prediction at 3575 m, but does not extend to the hydrophone at 3892 m. The internal-wave simulation, however, exhibits a 75-dB arrival at this depth for the first cusp of the pair, and both cusps reach the lowest limit of the DVLA [Fig. 14(c)]. Although the intensities compare well at the 3575- and 4249-m depths, the internal-wave scattering over-predicts the intensity of the shadow-zone arrival by approximately 8 dB when compared with the hydrophone data at the 3892-m depth [Fig. 14(d)].

This deviation is also clearly seen in Fig. 19, which displays a measure of the energy in the cusp as it extends into the acoustic shadow. The energy, E, is calculated by integrating the intensity, I, of a peak in a specified time window T:

$$E = \int_T I dt. \tag{9}$$

The hydrophone noise level was determined by calculating the energy in a time window where there was no acoustic arrival.

The upper limit of the shadow zone is indicated where the energy for the range-independent calculation rapidly decreases. The upper limit of the shadow for the first cusp is approximately 100 m deeper than for the second cusp. The internal-wave simulation appropriately describes both cusps with rms differences from the measured energy levels of 2.5 dB for the first cusp and 4.0 dB for the second cusp.

Receptions from the 1000-km range deep off-axis source illustrate the same deep shadow-zone arrivals as exhibited by the axial HLF-5 sources (Fig. 18). Conspicuous examples arrive at approximately 675.5 s on the lower segment of the DVLA [Fig. 18(b)] and just after 676 s on the upper segment of the DVLA [Figs. 18(c) and 18(d)].

D. Axial shadow-zone arrivals

The axial shadow-zone arrivals observed in receptions from deep off-axis sources are not predicted by the PE simulations for the range-independent environmental models, but internal-wave model results again show a penetration into the acoustic shadow, indicating that scattering into this shadow-zone region is also caused by fluctuations due to internal waves. It is not surprising that the same mechanism is responsible for the axial extensions, as they are essentially the same scattered energy. For the reciprocity condition to be satisfied, propagation from an axial source to a deep receiver is equivalent to propagation from a deep off-axial source to an axial receiver through the same ocean.

Figure 16 shows the structure of this scattering in the internal-wave PE simulation result. The upper portion of the DVLA displays a lower cusp turning back upward at the termination of the arrival pattern. The range-dependent and range-independent simulations show only a single peak after 339 s, whereas the arrival in the internal-wave solution is followed by a distinct second peak [Fig. 16(a)].

This scattering is also present in the acoustic data on the propagation path from the S1 deep off-axis source to the DVLA [Fig. 16(b)] and extends upward far enough to appear in the SVLA [Fig. 15(b)], although the arrival is diffuse and barely visible above the noise level. The same effect is observable at the end of the timefront at 1000-km range [Fig. 17(a)].

The final lower cusp exhibited in Fig. 18(c) can be classified as both an axial shadow-zone arrival and a deep shadow-zone arrival. The internal-wave prediction penetrates deeper than the range-dependent solution with an intensity at 2820 m which exceeds that of the range-independent solution by nearly 20 dB. The single peak at the 2820-m depth then scatters back upward into the axial shadow zone, displaying two distinct peaks at 2294 m [Fig. 18(d)].

The receptions from deep off-axis sources show that scattering occurs predominantly along acoustic timefronts not only for the deep shadow-zone arrivals but also at the end of the reception timefronts for off-axis sources. The prediction of these relatively narrow penetrations of several hundred meters into the shadow zone supports previous observations made during the SLICE89 experiment that internal-wave-induced scattering occurs predominantly along timefronts rather than across them (Beron-Vera and Brown, 2004; Flatté and Colosi, 2008; Godin, 2007; Virovlyansky, 2003).

VII. SUMMARY

The extensive VLAs employed in the SPICEX experiment enabled an examination of the vertical structure of shadow-zone arrivals first observed on bottom-mounted receivers during the ATOC experiment.

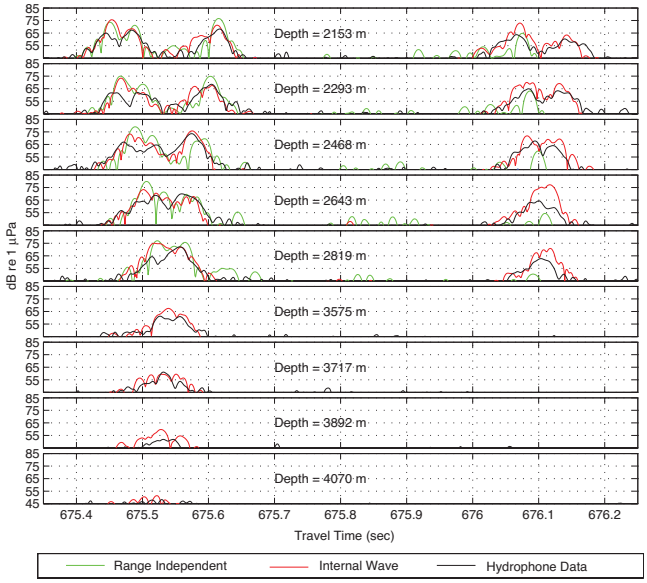

FIG. 20. Magnification of two lower cusps on the S2 deep off-axis source to DVLA propagation path displayed in Fig. 18. Simulations utilizing the range-independent and internal-wave environments are included along with the hydrophone data. Data are shown at the depths of nine hydrophones on the DVLA.

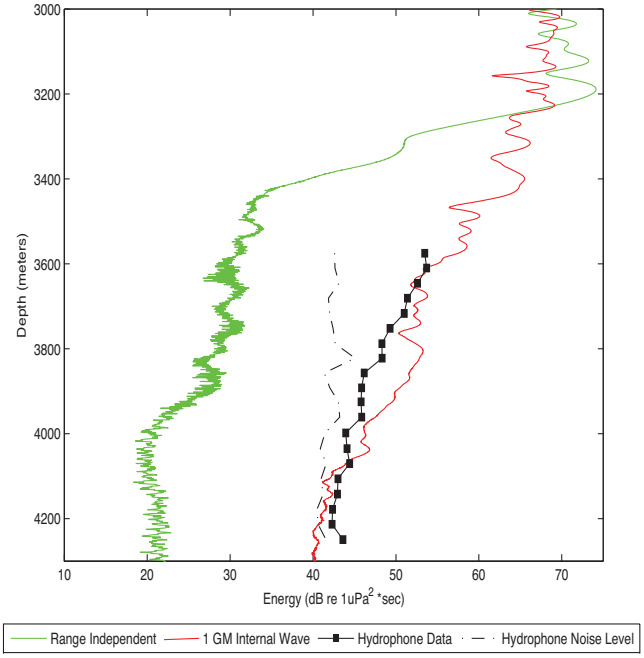

FIG. 21. Energy in the lower cusp occurring at 675.5 s for the S2 deep off-axis source to DVLA propagation path (Fig. 20). Energy was calculated for a time window of 675.4–675.65 s. Hydrophone data and noise levels are shown for the 20 phones on the lower segment of the DVLA.

Since travel time is the primary observable of interest in acoustic tomography experiments, intensities of the acoustic data have received little attention. Here, the acoustic array data were calibrated, and parabolic equation simulation results were transformed into units of intensity to facilitate direct comparisons between model and data. The intensity comparisons presented in this paper indicate that models incorporating scattering consistent with the Garrett-Munk internal-wave spectrum with an internal-wave energy of 1 GM are adequate to account for the structure and extent of measured acoustic shadow-zone arrivals.

Figure 20 summarizes the shadow penetration for the cusp at 675.5 s of the S2 deep off-axis source to DVLA transmission. At depths less than 3 km, measured intensities are in fair accord with the calculated intensities ignoring internal-wave scatter. Taking internal-wave scatter into account does not significantly change the theoretical intensities above 3 km, but increases the theoretical intensities substantially beneath 3 km, bringing them into accord with the measured intensities. Beneath 4 km both measured and computed intensities are negligible. From this, it can be concluded that the internal-wave perturbations can account for the penetration into the deep shadow zone.

The lower cusp of the range-independent prediction occurs in the gap between the hydrophones located at 2819 and 3575 m. Figure 21 shows the energy in the cusp as it decays into the sound shadow. The hydrophone data capture the shadow-zone arrival below 3575 m and are consistent with the internal-wave prediction, with a rms difference of 2.8 dB, as it approaches the noise threshold 800–1000 m below the cusp.

Figure 20 also demonstrates that internal-wave perturbations account for the axial shadow-zone extensions. The two arrival peaks at 676.1 s for the phones at 2293- and 2153-m depths clearly show the internal-wave simulation to concur with the hydrophone data in scattering back toward the axis along the timefront.

Other hypotheses have been offered to explain the deeply scattered arrivals. One such hypothesis is that oceanic spice could contribute to scattering into the acoustic shadow (Dzieciuch *et al.*, 2004). Since the GM internal-wave spectrum was based on empirical hydrographic measurements of oceanic variability (Garrett and Munk, 1979), the spectrum may include other types of oceanic variability, including spice, so that the internal-wave profile referred to in this paper may actually include effects due to oceanic spice.

It has also been suggested (Rudnick and Munk, 2006) that the lower cusps will deepen due to reflections off the base of a tilted mixed layer. Rudnick described a steepening of acoustic rays by twice the angle of inclination of the mixed layer base with each reflection off the base of the mixed layer. An experimental investigation of the effect of the mixed layer on acoustic shadow-zone arrivals would require acoustic transmissions in the presence of a pronounced mixed layer, typical of a spring profile in the North Pacific. Since acoustic data were only collected during the period from June to November, it is, unfortunately, not possible to explore the entire development of the mixed layer with the acoustic data at-hand.

The results presented here focus on a single day of acoustic transmissions at a time coinciding with the collection of the environmental data that formed the basis for the sound-speed profiles used in the simulations. The intent of this paper is to demonstrate that sound-speed fluctuations consistent with the Garrett–Munk internal-wave spectrum are adequate to describe the extent of the observed acoustic shadow-zone arrivals. The comparisons here are largely qualitative. A quantitative analysis of the statistics of the

shadow-zone extensions, as well as the characterization of their variability throughout the transmission period, will be left for future examination.

ACKNOWLEDGMENTS

The SPICEX data set which formed the basis of this paper is a product of the hard work of many individuals. The authors would especially like to thank L. Green, D. Horwitt, J. Kemp, and M. Norenberg as well as the crews of the *R/V Roger Revelle* and *R/V Thomas Thompson*. Bruce Cornuelle was instrumental in the implementation of the objective mapping techniques. The experiment was funded by the Office of Naval Research Grant No. N00014-03-1-0182. L.J.V.U. was also supported by the Office of Naval Research Graduate Traineeship Award No. N00014-07-1-0270.

ATOC Instrumentation Group (**1995**). "Instrumentation for the acoustic thermometry of ocean climate (ATOC) prototype Pacific Ocean network," Oceans'95 MTS/IEEE Conference Proceedings, San Diego, CA, 9–12 October **1995**, Vol. **3**, pp. 1483–1500 (ATOC Instrumentation Group: B. M. Howe, S. G. Anderson, A. B. Baggeroer, J. A. Colosi, K. R. Hardy, D. Horwitt, F. W. Karig, S. Leach, J. A. Mercer, K. Metzger Jr., L. O. Olson, D. A. Peckham, D. A. Reddaway, R. R. Ryan, R. P. Stein, K. von der Heydt, J. D. Watson, S. L. Weslander, and P. F. Worcester).

Beron-Vera, F., and Brown, M. (**2004**). "Travel time stability in weakly range-dependent sound channels," J. Acoust. Soc. Am. **115**, 1068–1077.

Beron-Vera, F., Brown, M., Colosi, J., Tomsovic, S., Virovlyansky, A. L., Wolfson, M., and Zaslavsky, G. (**2003**). "Ray dynamics in a long-range acoustic propagation experiment," J. Acoust. Soc. Am. **114**, 1226–1242.

Brekhovskikh, L., and Lysanov, Y. (**2003**). *Fundamentals of Ocean Acoustics*, 3rd ed. (Springer-Verlag, Berlin).

Brown, M. G. (**1982**). "Application of the WKBJ Green's function to acoustic propagation in horizontally stratified oceans," J. Acoust. Soc. Am. **71**, 1427–1432.

Collins, M. (**1993**). "A split-step Padé solution for the parabolic equation method," J. Acoust. Soc. Am. **93**, 1736–1742.

Collins, M. D. (**1989**). "A higher-order parabolic equation for wave propagation in an ocean overlying an elastic bottom," J. Acoust. Soc. Am. **86**, 1459–1464.

Colosi, J. A., and Brown, M. G. (**1998**). "Efficient numerical simulation of stochastic internal wave induced sound speed perturbation fields," J. Acoust. Soc. Am. **103**, 2232–2235.

Colosi, J. A., and Flatté, S. M. (**1996**). "Mode coupling by internal waves for multimegameter acoustic propagation in the ocean," J. Acoust. Soc. Am. **100**, 3607–3620.

Colosi, J. A., Flatté, S. M., and Bracher, C. (**1994**). "Internal-wave effects on 1000-km oceanic acoustic pulse propagation: Simulation and comparison with experiment," J. Acoust. Soc. Am. **96**, 452–468.

Del Grosso, V. A. (**1974**). "New equation for the speed of sound in natural waters," J. Acoust. Soc. Am. **56**, 1084–1091.

Dushaw, B. D., Howe, B. M., Mercer, J. A., Spindel, R. C., and the ATOC Group (**1999**). "Multimegameter-range acoustic data obtained by bottom-mounted hydrophone arrays for measurement of ocean temperature," IEEE J. Ocean. Eng. **24**, 202–214.

Dzieciuch, M., Munk, W., and Rudnick, D. L. (**2004**). "Propagation of sound through a spicy ocean, the SOFAR overture," J. Acoust. Soc. Am. **116**, 1447–1462.

Fisher, F., and Simmons, V. P. (**1977**). "Sound absorption in sea water," J. Acoust. Soc. Am. **62**, 558–564.

Flatté, S., and Colosi, J. (**2008**). "Anisotropy of the wavefront distortion for acoustic pulse propagation through ocean sound-speed fluctuations: A ray perspective," IEEE J. Ocean. Eng. **33**, 477–488.

Garrett, C., and Munk, W. (**1979**). "Internal waves in the ocean," Annu. Rev. Fluid Mech. **11**, 339–369.

Godin, O. (**2007**). "Restless rays, steady wave fronts," J. Acoust. Soc. Am. **122**, 3353-336.

Lovett, J. (**1980**). "Geographic variation of low-frequency sound absorption in the Atlantic, Indian, and Pacific Oceans," J. Acoust. Soc. Am. **67**, 338–340.

Morozov, A., and Webb, D. (**2003**). "A sound projector for acoustic tomography and global ocean monitoring," IEEE J. Ocean. Eng. **28**, 174–185.

Morozov, A., and Webb, D. (**2007**). "Underwater tunable organ-pipe sound source," J. Acoust. Soc. Am. **122**, 777–785.

Munk, W., Worcester, P., and Wunsch, C. (**1995**). *Ocean Acoustic Tomography* (Cambridge University Press, Cambridge).

Rudnick, D. L., and Klinke, J. (**2007**). "The underway conductivity-temperature-depth instrument," J. Atmos. Ocean. Technol. **24**, 1910–1923.

Rudnick, D. L., and Munk, W. (**2006**). "Scattering from the mixed layer base into the sound shadow," J. Acoust. Soc. Am. **120**, 2580–2599.

Smith, W., and Sandwell, D. (**1997**). "Global sea floor topography from satellite altimetry and ship depth soundings," Science **277**, 1956–1962.

Sparrock, R. (**1990**). "Stability of time fronts on a large vertical array at long range in the ocean," MS thesis, University of California, San Diego, La Jolla, CA.

Virovlyansky, A. (**2003**). "Ray travel times at long ranges in acoustic waveguides," J. Acoust. Soc. Am. **113**, 2523–2532.

Webb, D., Morozov, A., and Ensign, T. (**2002**). "A new approach to low frequency wide-band projector design," Oceans MTS/IEEE Conference Proceedings, Biloxi, MS, pp. 2342–2349.

Worcester, P. F. (**1981**). "An example of ocean acoustic multipath identification at long range using both travel time and vertical arrival angle," J. Acoust. Soc. Am. **70**, 1743–1747.

Worcester, P., Cornuelle, B., Dzieciuch, M., Munk, W., Howe, B., Mercer, J., Spindel, R., Colosi, J., Metzger, K., Birdsall, T., and Baggeroer, A. (**1999**). "A test of basin-scale acoustic thermometry using a large-aperture vertical array at 3250-km range in the eastern North Pacific Ocean," J. Acoust. Soc. Am. **105**, 3185–3201.

Worcester, P. F., Cornuelle, B. D., Hildebrand, J. A., Hodgkiss, W. S., Jr., Duda, T. F., Boyd, J., Howe, B. M., Mercer, J. A., and Spindel, R. C. (**1994**). "A comparison of measured and predicted broadband acoustic arrival patterns in travel time-depth coordinates at 1000-km range," J. Acoust. Soc. Am. **95**, 3118–3128.

Wunsch, C. (**1996**). *The Ocean Circulation Inverse Problem* (Cambridge University Press, Cambridge).

Attenuation and dispersion of antiplane shear waves due to scattering by many two-dimensional cavities

Jun Kawahara[a)]
Faculty of Science, Ibaraki University, 2-1-1 Bunkyo, Mito 310-8512, Japan

Taichi Ohno[b)]
Graduate School of Science and Engineering, Ibaraki University, 2-1-1 Bunkyo, Mito 310-8512, Japan

Kiyoshi Yomogida
Graduate School of Science, Hokkaido University, North 10 West 8, Kita-ku, Sapporo 060-0810, Japan

(Received 13 March 2008; revised 9 January 2009; accepted 1 April 2009)

Propagation and scattering of antiplane shear waves within media with two-dimensional cavities are numerically simulated, and the attenuation and phase velocities are experimentally determined. The results are compared with the predictions by the Foldy theory and its three corrected versions. If the cavity concentrations are small such as 0.02, the differences among the theoretical predictions are insignificant, and every theory is consistent with the experimental results. For higher concentrations such as 0.1, the differences become significant, but there are no objective grounds to say that any of the corrected versions of the Foldy theory works better than the original. If the error tolerance is as high as 10%, the simple Foldy formula may remain useful for concentrations up to about 0.1.
 [DOI: 10.1121/1.3124779]

PACS number(s): 43.35.Cg, 43.20.Jr, 43.20.Gp, 43.20.Bi [RAS] Pages: 3589–3596

I. INTRODUCTION

Wave propagation in a medium with distributed scatterers results in the attenuation and dispersion of coherent wave fields, even if each constituent is lossless. This phenomenon has been studied in a variety of research areas because of its wide applications. Examples are acoustic scattering in the ocean and in biological media,[1] ultrasonic nondestructive evaluation of materials,[2] and seismic scattering in the earth's lithosphere.[3] Many of such researches have been based on theoretical modeling or laboratory experiments as stated below. In contrast, the purpose of the present article is to approach the phenomenon by the use of a numerical method of wave simulations. Because of computational tractability, only a specific case of antiplane shear (SH) wave scattering due to two-dimensional (2D) cavities is treated, which enables the authors to achieve simulations with high accuracy at relatively low computational costs.

A large variety of theories has been proposed for the problem stated above. Among others, Foldy[4] established a category of theories (multiple scattering theories) about 60 years ago. He considered scalar wave propagation in media with randomly distributed three-dimensional (3D) isotropic scatterers and derived the following well-known formula:

$$K^2 = k^2 + 4\pi n f, \tag{1}$$

in which K is the effective wavenumber of mean (ensemble-averaged) wave fields, k is the wavenumber in the absence of scatterers, n is the number density of the scatterers, and f is the isotropic scattering amplitude of a single scatterer. This equation gives the solution K as a function of k, whose real and imaginary parts correspond to the phase velocity and attenuation, respectively. Foldy's theory is based on the assumption that the scatterers are distributed very sparsely and independently so that its validity is limited to sufficiently small n. Later, Lax[5] verified that Eq. (1) remains valid for anisotropic scatterers if f is replaced with the forward scattering amplitude $f(0)$:

$$K^2 = k^2 + 4\pi n f(0). \tag{2}$$

Many researchers tried to improve the theory in order that it may be valid for denser scatterer distributions by taking account of the multiple scattering more appropriately. Lax[6] proposed the quasicrystalline approximation, in which statistical information on the relative location of two scatterers is described by a pair-correlation function. Waterman and Truell[7] derived a formula alternative to Eq. (2) under the condition of non-overlapping scatterers with infinitesimal volumes. Despite its lasting popularity, the Waterman–Truell formula was shown to be incorrect by Lloyd and Berry,[8] who presented an alternative one. Other researchers applied more appropriate pair-correlation functions for scatterers with finite sizes.[9–12] Still other researchers proposed corrected versions of Foldy's theory not based on the quasicrystalline approximation. Examples are the works based on a diagram method[13,14] and the combinations of the Waterman–Truell formula and a self-consistent method.[15] Concerning other categories of theories on wave propagation in inhomogeneous media (such as self-consistent methods), see Ref. 16 and the references therein.

The above-mentioned theories, including Foldy's, have been exploited in order to describe the results of laboratory experiments on wave transmission in bubbly liquids, suspen-

a)Author to whom correspondence should be addressed. Electronic mail: junk@mx.ibaraki.ac.jp
b)Present address: OYO RMS Corp., 3-11-15 Akasaka, Minato-ku, Tokyo 107-0052, Japan.

sions, emulsions, particulate composites, and materials with cavities (see Refs. 11, 12, and 16–23 and the references therein). The predictions of all such theories coincide with each other up to the first order of n, and they are consistent with the experimental data for small volume concentrations of scatterers.[17,20] The limits of the concentrations below which the theories remain valid, however, vary among studies. One possible reason for this may be the factors that are not considered in the theories but essential in the experiments, such as viscous and thermal dissipation[20] and ill-controlled parameters such as scatterer sizes.[22] On one hand, incorporating such effects appropriately into the theories to bridge this gap is certainly an important task from the practical viewpoint.[18–20] On the other hand, using computer simulations of wave scattering free from those effects may be helpful in examining the validity of the theories more directly; though less practical than laboratory ones, numerical experiments could be configured more loyally to the assumptions made in the theories.[24–27] Another possible reason for the discrepancy among the experimental results may be the variation in the methods to measure the attenuation and phase velocities of coherent waves. Some researchers measured the amplitude changes and moving speeds of the peaks of transmitting pulses,[22–24] whereas others calculated their spectral changes.[12,17–21] Although the latter method has the advantage of high spectral resolution, the estimates thus obtained could be affected by the incoherent waves included within the pulses. Ensemble averaging of the waveform data was shown to be effective in reducing the incoherent waves as well as noises.[12,17,19,27]

In this article, multiple scattering theories of Foldy,[4,5] Waterman and Truell,[7] Lloyd and Berry,[8] and Ye and Ding[13] are compared with numerical-experimentally measured attenuation and phase velocities. To focus on the validity of the theories, numerical experiments are performed as mentioned earlier; antiplane shear wave scattering by 2D circular (or parallel cylindrical) cavities in elastic media are simulated with high accuracy, closely following Benites *et al.*[24] The attenuation and phase velocities are measured by applying the spectral ratio technique to averaged waveform data, as was successfully done by Suzuki *et al.*[27] Although the model scattering media in the present experiment are rather idealized, it would be a good analog of high-contrast particulate materials and media with small aspect ratio cavities (e.g., cracks).

In Sec. II, the 2D solutions of the above four theories are summarized. In Sec. III, the configuration of the numerical experiments and the data acquisition method are described. The experimentally determined attenuation and dispersion curves are shown in Sec. IV, in which they are compared with the theoretical predictions. The validity of the theories is thereby discussed.

II. MULTIPLE SCATTERING THEORIES

All of the theories considered here share the advantage of giving explicit solutions of K like Eq. (2), which in the 2D case are summarized in this section. It is worth noting that all of them are based on a point scatterer assumption. Treating scatterers with finite sizes will be possible by using a proper pair-correlation function, but then the solution K would be obtained only numerically.[9–12]

The 2D version of Foldy's formula (with Lax's correction) (2) can be found in, e.g., Linton and Martin.[28] It is written in the form

$$K^2 = k^2 - 4inf(0), \tag{3}$$

in which i is the imaginary unit. Here $f(\theta)$ is the 2D scattering amplitude for the scattering angle θ measured from the incident direction.

As stated in Sec. I, Waterman and Truell[7] took account of the effect of non-overlapping scatterers under the point scatterer assumption. This means that only the "perfect overlapping" of scatterers with finite sizes (or the overlapping of the centers of the scatterers) is excluded. The 2D version of their formula corresponding to Eq. (3) was given by Angel and Aristégui[29] as

$$K^2 = k^2 - 4inf(0) - \frac{4n^2}{k^2}[f(0)^2 - f(\pi)^2]. \tag{4}$$

Although this formula has been widely used,[15–17,21] Lloyd and Berry[8] pointed out that it is based on an incorrect pair-correlation function. According to them, the exclusive volume of a spherical scatterer (whose radius was finally allowed to become zero) actually imposed in the Waterman–Truell theory is not spherical but slablike, being perpendicular to the direction of wave propagation. Applying a correct pair-correlation function and taking the limit of point scatterers again, Lloyd and Berry derived an alternative formula, using a technique called the "resummation method" coming from nuclear physics. However, the Lloyd–Berry formula seems less popular than the Waterman–Truell formula. Linton and Martin[30] inferred that it is perhaps because the Lloyd–Berry formula is less simpler and its derivation seems suspect. Nevertheless, they obtained a new and clearer derivation of this formula. Linton and Martin[28] also developed its 2D version as

$$K^2 = k^2 - 4inf(0) + \frac{8n^2}{\pi k^2}\int_0^{\pi} \cot(\theta/2)\frac{d}{d\theta}f(\theta)^2 d\theta. \tag{5}$$

It has been clarified that Foldy's approach is equivalent to taking into account "successive scattering" only, whose paths do not touch any scatterers more than once.[1,13] Using a diagram method, Ye and Ding[13] incorporated into formula (1) the effect of triple scattering involving two scatterers, as depicted in Fig. 1. The result is that

$$K^2 = k^2 + 4\pi n(f + \Delta f), \tag{6}$$

in which Δf is the variation in the scattering amplitude of S1 due to the incidence of waves that are scattered by S1 and then scattered back by S2. This quantity is given by

$$\Delta f = nf^3 \int\int\int \left[\frac{e^{ikr}}{r}\right]^2 d\mathbf{r} = \frac{2\pi inf^3}{k}. \tag{7}$$

The 2D version of these equations may be inferred by replacing the term $f\exp(ikr)/r$, which represents a far-field single-scattered wave, by its 2D counterpart $fH_0^{(1)}(kr)$, in which

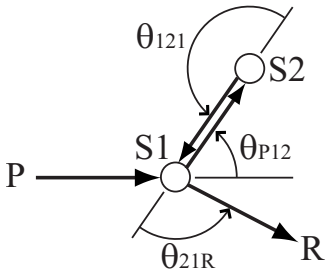

FIG. 1. Triple scattering involving two scatterers S1 and S2. Here P and R denote the source and receiver, respectively.

$H_0^{(1)}(\,)$ is the Hankel function of the first kind. The result in the 2D case is that

$$K^2 = k^2 - 4in(f + \Delta f), \tag{8}$$

$$\Delta f = nf^3 \int\int [H_0^{(1)}(kr)]^2 d\mathbf{r} = \frac{4nf^3}{\pi k^2}. \tag{9}$$

The extension of these relations to the case of anisotropic scattering may be achieved as follows. To be consistent with formula (3) to which only the forward scattering ($\theta=0$) contributes, it may be enough to consider only the contribution of the triple scattering depicted in Fig. 1 with the directions P→S1 and S1→R being the same. One can therefore let $\theta_{21R}=\pi-\theta_{P12}$. Moreover, the second scattering is always backward, that is, $\theta_{121}=\pi$. Thus the Ye–Ding formula in the case of 2D anisotropic scattering may be inferred as

$$K^2 = k^2 - 4in\left[f(0) + \frac{4nf(\pi)}{\pi^2 k^2}\int_0^{\pi} f(\theta)f(\pi-\theta)d\theta\right]. \tag{10}$$

Note that Henyey[14] pointed out that the Ye–Ding formula may overestimate the contribution of the triple scattering of the above type because it neglects the scattering attenuation during the first and second scattering processes. His corrected formula for 3D isotropic scattering, resulting in a cubic equation with respect to K, would give results falling between those by the theories of Foldy and Ye–Ding. The extension of the formula, however, to anisotropic scattering is not straightforward and hence it is not considered here.

For $K=K(k)$ given by any of the theories, the attenuation coefficient α and the phase velocity c of the mean (or coherent) waves are evaluated by the relations

$$\alpha = \mathrm{Im}\, K, \quad \frac{c}{c_0} = \frac{k}{\mathrm{Re}\, K}, \tag{11}$$

in which "Im" and "Re" denote the imaginary and real parts, respectively, and c_0 is the wave speed of a matrix surrounding scatterers. In the case of a cylindrical cavity with the radius a, $f(\theta)$ is expressed as the sum of an infinite series with the Bessel and Hankel functions[31]

$$f(\theta) = -\sum_{m=0}^{\infty} \frac{J_{m-1}(ka) - J_{m+1}(ka)}{H_{m-1}^{(1)}(ka) - H_{m+1}^{(1)}(ka)} \epsilon_m \cos m\theta, \tag{12}$$

in which $\epsilon_0=1$ and $\epsilon_m=2$ for $m \geqslant 1$.

III. NUMERICAL EXPERIMENTS

The configurations of the present numerical experiments follow those of Benites *et al.*,[24] which are explained below. First, N identical circular cavities are distributed inside a rectangular area with the horizontal size W and vertical one L. Here both the cavity diameter $d=2a$ and the wave speed of the matrix c_0 are chosen to be unity. It is also assumed that the cavities do not overlap, i.e., they are "impenetrable." Using a uniform random number series, the cavities are distributed inside the area randomly, except for the constraint that the interval between the centers of any pair of cavities must be greater than $1.1d$. Specifically, the cavity centers (x_i, y_i) $(i=1,\ldots,N)$ are randomly generated one by one; if a newly generated center (x_j, y_j) does not satisfy the constraint [i.e., if the distance between this and any of the preexisting centers (x_i, y_i) $(i<j)$ is smaller than $1.1d$], then it is eliminated and another one is newly generated. Here it is also imposed that the distance between any cavity center and the top end of the area must be greater than d. Hence the vertical size of the actual distribution area is regarded as $L'=L-0.5d$, and the cavity number density may be defined as $n=N/WL'$.

Second, 101 receivers are evenly arrayed along the top end of the area. Note that the distance between any receiver and any cavity boundary is not smaller than $0.5d$, according to the algorithm of distributing the cavities stated above. A plane Ricker wavelet with the dominant frequency f_C is vertically impinged on the bottom end from below, and then waveforms at the receivers are synthesized using the method of Benites *et al.*;[24] see their paper as for the source time function and the spectrum of the Ricker wavelet. Although time-domain waveforms are synthesized in the end, the basic calculations are performed in the frequency domain; that is, the responses at various frequencies are computed first, then a time-domain waveform is synthesized from their inverse Fourier transforms with the convolution of a source wavelet (the Ricker wavelet in this case). Note that four ends of the distribution area are transparent with respect to wave transmission. In order to suppress the effect of the scattered waves leaking through the both side ends, the waveforms at N_R receivers around the middle of the receiver array are used in the analysis. The value of N_R is chosen dependent on the size of the distribution area and the time interval of synthetic waveforms.

Third, the above-mentioned process is repeated for N_D different realizations of cavity distributions that are stochastically identical but are generated using different random number series. Then the $N_R \times N_D$ waveforms obtained are averaged to yield a "synthetic mean wave." This implies the assumption of ergodicity, that is, the equivalence of spatial and ensemble averaging. For sufficiently large $N_R \times N_D$, incoherent waves would be effectively removed.

Finally, α and c are evaluated from the spectral ratio of the primary parts of the mean wave to the initial wavelet. The time window for the analysis is centered on the arrival time of the central peak of the initial wavelet, with the interval of $4/f_C$; the choice of the interval would not significantly affect the results if the incoherent waves had been sufficiently removed. The evaluation of α and c is conducted for

TABLE I. Parameters of the cavity distribution models.

	N	W/d	L/d	C	N_R	N_D	$\max\|nf/k^2\|$
Model 1	50	80	30	0.017	61	5	0.013
Model 2	100	80	10	0.10	61	10	0.078
Model 3	100	40	10	0.21	41	15	0.16

the frequency band $0.75f_C-1.5f_C$ and is repeated for different initial wavelets with f_C=0.15, 0.3, 0.6, and 1.2 ($\times c_0/d$).

The success of the numerical experiments described above depends on the accuracy of the wave simulation method. The method of Benites *et al.*[24] adopted here can be categorized into boundary integral methods (or indirect boundary element methods), which probably dates back to Copley[32] and have been successfully applied to solve various types of elastodynamic problems in engineering and seismology.[33–38] The method of Benites *et al.* can accurately simulate wave fields in media with arbitrarily distributed cavities, including anisotropic scattering and every degree of multiple scattering; this is in contrast to the other methods based on the Born approximation or the parabolic one.[3,39] Note that similar methods were previously applied by Dravinski[34] and Benites and Aki[36] to one or two inclusions. Although the details of the method can be seen in the paper of Benites *et al.*,[24] the essence is that a scattered wave due to each cavity is expressed as the sum of waves radiated from fictitious line sources distributed behind (but close to) the cavity boundary. More specifically, the sources are evenly spaced along a circle with the radius $0.8a$, which is concentric with the circular boundary. The source strengths are determined in the least-square sense so as to satisfy the traction-free boundary condition, and thus the wave fields outside the cavities are synthesized. Here the number of the sources per cavity (or the interval between the sources) controls the accuracy of wave simulations. Benites *et al.*[24] checked the validity of their method on the basis of three different tests and demonstrated that it really produces sufficiently accurate wave fields if there exist at least four sources per wavelength measured along the cavity boundary (i.e., the number of the sources per cavity is not less than $4\pi d/\lambda$, in which λ is the minimum wavelength considered). Note that this criterion is consistent with the results of other researches on boundary integral methods.[33,35,36] In the present wave simulations, the number of the sources per cavity is chosen so as to satisfy the criterion. The authors also checked the stability of simulations by temporally increasing the number to large extent in some cases. This turned out not to change the results significantly (within a few percent at most), implying that the original number would be enough.

In Sec. IV, the results for three models of cavity distributions are shown. Table I summarizes the parameters of the models, in which the area concentrations $C=\pi na^2$ are shown instead of n. An example of the realizations for each model is depicted in Fig. 2. Model 1, representing the case of sparse distributions, is stochastically identical to the model examined by Benites *et al.*[24] In contrast, models 2 and 3 represent the cases of rather dense distributions. Here the denser distributions are realized partly by making the model areas

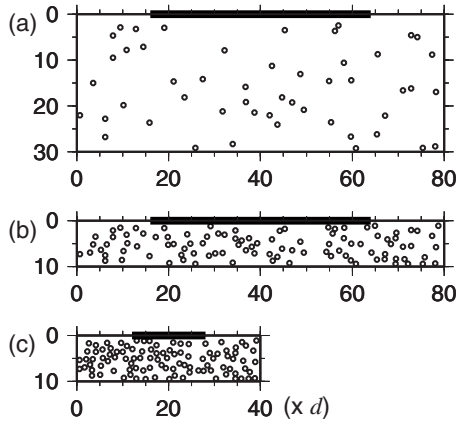

FIG. 2. Examples of the realizations for (a) model 1, (b) model 2, and (c) model 3. The thick bars along the top ends of the model areas designate the receiver arrays.

smaller in order to save the computational costs because the costs strongly depend on the numbers of cavities (more exactly, the numbers of fictitious sources). Note that the N_D values listed in Table I were actually determined as a result of repeated evaluation of α and c with the increasing number of the realizations for each model. The repetition was terminated when the addition of a new realization did not significantly change the results anymore, and then the final number of the realizations was defined as N_D. Consequently, N_D is not the same among the models; a smaller model area seems to need more representations for stable ensemble average. Note also that Table I includes the maximum value of $|nf(\theta)/k^2|$ for each model just for reference, which will be discussed later.

The results are to be compared in Sec. IV with the predictions of the theories stated in Sec. II, thus discussing their validity, mainly in terms of the distribution density of cavities. Other parameters that might also limit the validity of the theories will be also discussed there. Here C is employed instead of n as a measure of the distribution density, following the convention in laboratory experiments.[11,12,16–23] It may be worth mentioning, however, that the use of C may not be effective if the aspect ratios of scatterers are much deviated from unity. An example is distribution of highly oblate cavities (or cracks), for which C would remain negligibly small even for considerably large n; there "crack density" nr^3 (r is the major axis) is conventionally used instead.

IV. RESULTS AND DISCUSSION

The synthetic waveforms are exemplified in Fig. 3 in the case of model 1 (C=0.017) and f_C=0.3. In Fig. 3(a), the cloud of lines denotes the waveforms at the N_R receivers for a model realization. It is clearly illustrated that the waves keep their coherency around the first motion but lose them rapidly, resulting in the incoherent long wave trains composed of the scattered waves. The synthetic mean wave obtained from all of the waveforms is plotted in Fig. 3(b), in which the waveform in the absence of cavities (initial wavelet) is superimposed for comparison. Here the attenuation and delay of the mean wave are clearly recognized. In addition, it is a compact wavelet like the initial one and has no

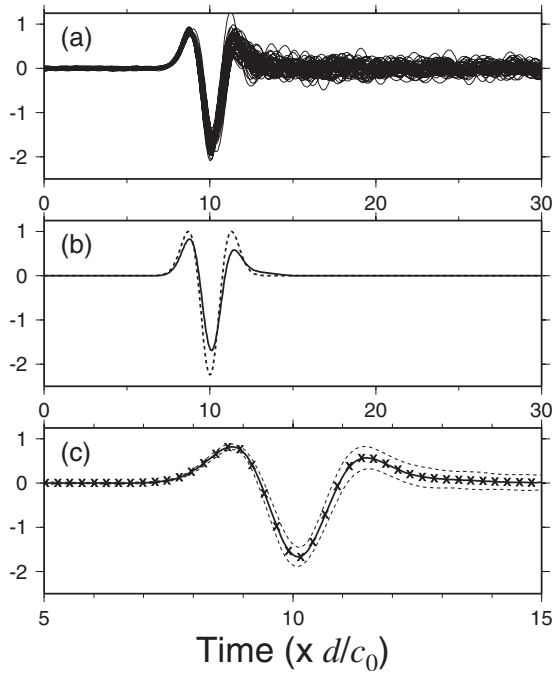

FIG. 3. (a) Synthetic waveforms for model 1 with f_C=0.3. (b) Synthetic mean wave (solid line) and the initial wavelet (dotted line). (c) Close-up of the primary part. The solid line and the two dotted ones denote the average and the standard deviation of the waveforms. The crosses indicate the mean wave predicted by Foldy formula (3).

long tail. This implies that the present averaging process is successful in removing the incoherent waves, validating the present experimental procedures. In Fig. 3(c), the mean wave predicted by Foldy formula (3) is also plotted; it is completely consistent with the synthetic mean wave. Similar consistency between the synthetic and predicted mean waves is observed also in the other dominant frequencies, suggesting high validity of formula (3) for such sparse scatterer distributions, as expected.

Figure 4 depicts the attenuation and dispersion of the synthetic mean waves for model 1 as functions of the normalized wavenumber ka. Here

$$Q^{-1} = \frac{c}{c_0}\frac{2\alpha}{k} = \frac{2\,\mathrm{Im}\,K}{\mathrm{Re}\,K} \tag{13}$$

is plotted instead of α in Eq. (11). Note that the inverse of quality factor Q^{-1}, preferably used in seismology, material mechanics, and electric circuits, represents attenuation per wavelength; a small difference in α leads to large one in Q^{-1} at $ka \sim 1$, at which Q^{-1} reaches a peak. Here are plotted the values of Q^{-1} and c determined for f_C=0.15, 0.3, 0.6, and 1.2 (corresponding to ka=0.47, 0.94, 1.88, and 3.77, respectively), together with the values predicted by the Foldy formula. Note that the predictions by the other formulas are not shown because the deviations from those by the Foldy formula are insignificant in the present case. The experimental values are closely followed by the predicted ones on the whole, as expected again. There exist, however, minor systematic discrepancies on Q^{-1} in the range $2 < ka < 3$. As will be discussed later, these discrepancies might be due to the effect of finite scatterer sizes.

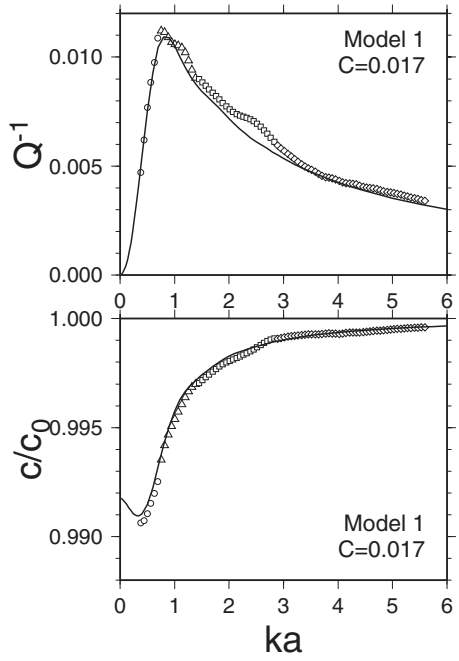

FIG. 4. Attenuation and dispersion curves for model 1. The open symbols with different shapes denote the experimental values for different f_C. The solid lines denote the values predicted by Foldy formula (3).

Figure 5 shows Q^{-1} and c obtained for model 2 (C=0.10) and for f_C=0.15, 0.3, and 0.6; the case of f_C=1.2 is omitted because of high computational costs. Now the predictions by all of the four theories are depicted. The differences among the theoretical values are remarkable in the present case, especially on Q^{-1} for $ka \sim 1$ and c for $ka < 1$. In the latter wavenumber range, the formulas of Lloyd–Berry (5) and Ye–Ding (10) give very close c values, between

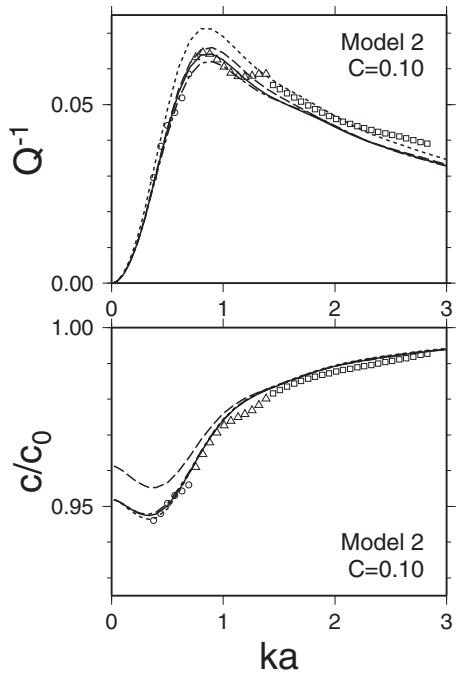

FIG. 5. Attenuation and dispersion curves for model 2. The open symbols denote the experimental values. The solid, dashed, dotted, and dash-dotted lines denote the predictions by the theories of Foldy, Waterman–Truell, Lloyd–Berry, and Ye–Ding, respectively.

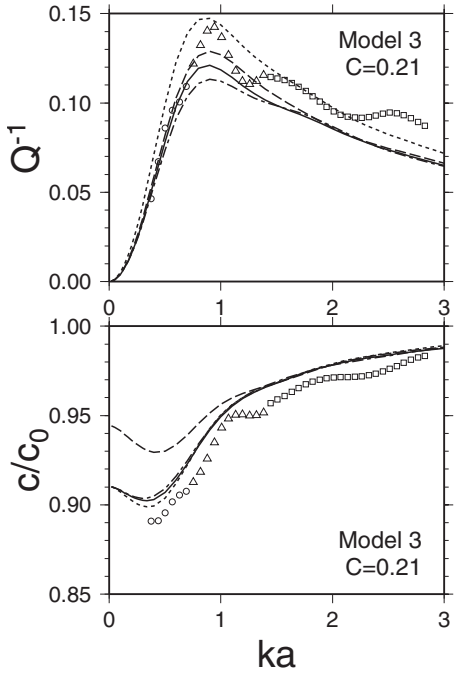

FIG. 6. Attenuation and dispersion curves for model 3. The open symbols denote the experimental values. The solid, dashed, dotted, and dash-dotted lines denote the predictions by the theories of Foldy, Waterman–Truell, Lloyd–Berry, and Ye–Ding, respectively.

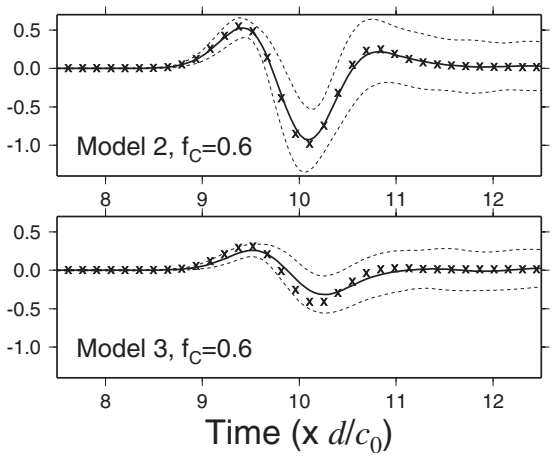

FIG. 7. The primary parts of the synthetic mean waves for models 2 and 3. The solid line and the two dotted ones denote the average and the standard deviation of the waveforms. The crosses indicate the mean waves predicted by the Foldy formula. Here f_C=0.6, for which the discrepancies between the synthetic and predicted mean waves are most remarkable in these models.

which lie those of Foldy formula; any of these values are consistent with the experimental ones. In contrast, the Waterman–Truell formula (4) obviously disagrees with the other three as well as the experimental results. As ka increases, however, the four theoretical values converge and equally follow the experimental ones. Concerning Q^{-1}, the formulas of Foldy, Waterman–Truell, and Ye–Ding give relatively similar values, whereas those by the Lloyd–Berry formula are somewhat larger. The experimental curve is located between the Waterman–Truell and Ye–Ding curves in the range $ka<1$. As ka increases, it begins to corrugate, and approaches and slightly exceeds the Lloyd–Berry curve.

The oscillating behavior of the experimental Q^{-1} curve is magnified in the case of a denser cavity distribution of model 3 (C=0.21; Fig. 6). In this case, the experimental Q^{-1} values considerably exceed all of the theoretical ones beyond $ka\sim2$. Oscillating behavior is clearly observed also on the experimental dispersion curve. Here the experimental c values are systematically smaller than any theoretical ones for any wavenumber considered.

Another noticeable feature of Figs. 5 and 6 is that the dispersion curves of the Foldy, Lloyd–Berry, and Ye–Ding formulas are nearly identical even in such cases of rather high concentrations, from which that of the Waterman–Truell is considerably deviated. The exceptional behavior of the latter might be due to the error in the Waterman–Truell theory claimed by Lloyd and Berry[8] and also Linton and Martin.[28,30] It would be worth mentioning that Ye[40] demonstrated that the Waterman–Truell formula does not satisfy the Kramers–Kronig relation. This might be also attributed to the incorrectness of the formula.

In summary, it is reconfirmed that the Foldy theory predicts the attenuation and dispersion very accurately for sufficiently low cavity concentrations (say, $C\sim0.02$). For $C\sim0.1$ and higher, the discrepancies between the Foldy predictions and experimental results are no more insignificant and are larger for the larger C, as may also be expected. In such situations, however, the other three theories also appear to be equally unsuccessful in describing the experimental results, despite the claim that they are corrected versions of the classical Foldy theory. None of the theories closely follows the experimental results on attenuation throughout the wavenumber range considered ($0.5<ka<3$). Concerning dispersion, the Waterman–Truell theory obviously disagrees with the experiments even for $C\sim0.1$; the other theories are consistent with the experiments for this concentration, but beyond it all of them systematically underestimate the magnitude of dispersion. Therefore it is hard to place one over the other, except for that the Foldy formula has the advantage of its high simplicity. Roughly speaking, the formula may be useful even for $C\sim0.1$ if the relative error tolerance is as high as, say, 10%. Indeed, the discrepancies between the synthetic mean waveforms and those predicted by the Foldy formula remain relatively small even for such a case, as demonstrated in Fig. 7(a). Figure 7(b) denotes, however, that it is not the case for $C\sim0.2$ (model 3).

As the distributions become denser, the experimental attenuation and dispersion curves show the oscillating (or resonant) behavior more clearly. None of the present theories explains this behavior. This does not indicate the resonance of one cavity which could occur even without the others; otherwise, similar oscillation would be always observed on the theoretical curves, which are obtained from the scattering amplitude of an isolated scatterer. It is unlikely to be due to the computational errors because of the care taken to assure the accuracy of the simulations, as mentioned in Sec. III. It may not be also related to the finiteness of the scatterer distribution areas that is not assumed in the theories because the "resonant wavelengths" are apparently not correlated to the area size. For example, the first and second peaks above ka=1 of the Q^{-1} curve in Fig. 6 occur at around ka=1.4 and 2.5, which correspond to the wavelengths 4.5a and 2.5a,

respectively, much smaller than $L'=9.5d=19a$. Since all of the theories are based on the point scatterer assumption as stated in Sec. II, the behavior might be attributed to the effect of finite scatterer sizes (more accurately, finite exclusive areas of scatterers), which would be stronger for denser scatterer distributions. Adopting a pair-correlation function properly describing the cavity distributions would be necessary to recover the agreement with the experiments. This inference may be supported by a theoretical result of Varadan *et al.*[11] In order to make comparison with a laboratory-experimental result, they derived dispersion curves for lead spheres of a finite size embedded in an epoxy matrix, using the quasicrystalline approximation and a realistic pair-correlation function. Their results were given for two cases with $C=0.05$ and 0.15, and the dispersion curve for the latter case shows oscillation much more noticeably than the former. Nevertheless, the oscillating behavior is observed even in Fig. 4 ($2<ka<3$), though slightly. This implies that the effect of finite scatterer sizes may not necessarily be negligible even for such a small C.

The validity of the theories has been discussed in terms of $C=\pi na^2$ for a specific type of scatterers (cavities) so far. From a general viewpoint, however, it would be also important to consider the effect of the scattering strength, which would depend on not only n but also the scattering amplitude of each scatterer $f(\theta)$. A possible measure of the strength might be $|nf(\theta)/k^2|$,[7] which seems to be assumed to be small, either explicitly or implicitly, in the present theories. As mentioned in Sec. III, the maximum value of $|nf(\theta)/k^2|$ for each model is given in Table I. It turns out that this value is fairly close to $C(\approx 0.75C)$ in the present cases. For model 3 for which any theory does not work, it is 0.16 and actually not so small compared with unity. In addition, if one assumes weak scattering

$$|nf(\theta)/k^2| \ll 1, \tag{14}$$

then Foldy formula (3) yields

$$|K^2/k^2 - 1| \ll 1, \tag{15}$$

that is, K is very close to k. Under this condition, both Q^{-1} and $|c/c_0-1|$, defined by Eqs. (11) and (13), respectively, are equally of the order of $|nf(\theta)/k^2|$. Hence these two quantities may also work as approximate measures of the scattering strength; if the actual values of Q^{-1} and $|c/c_0-1|$ were not so small as compared with unity, the theories would not reproduce their accurate values. This inference seems to be consistent with the present results; the maximum value of either Q^{-1} or $|c/c_0-1|$ exceeds 0.1 for model 3 (Fig. 6), like $\max|nf(\theta)/k^2|$ in this case. More convincing discussions would require further similar experiments on different types of scatterers. Another possible factor limiting the validity of the theories might be the propagation distance L', which was chosen not in a systematic manner in the present study. Loosely speaking, only cases of relatively short distance were treated here. It would be of interest to confirm whether the present theories remain valid for much more larger distance, though it would require the significant increase in computational costs.

V. CONCLUSION

In this article, the attenuation and phase velocities of antiplane shear waves due to scattering by 2D cavities were experimentally measured, using computer simulations based on the boundary integral method of Benites *et al.*[24] The results are then compared with the predictions by the classical Foldy theory and its three corrected versions: the theories of Waterman–Truell, Lloyd–Berry, and Ye–Ding. As long as the cavity concentrations remain small, the differences among the theoretical predictions are insignificant and any one is consistent with the experimental results. For higher concentrations (say, over 0.1), those differences become not negligible. In such situations, however, the experimental results show complicated dependence on wavenumbers, and none of the theoretical predictions matches the experimental results consistently. For example, all of the theories systematically underestimate Q^{-1} for $2<ka<3$ and $\Delta c/c_0$ for any ka, respectively. Nevertheless, even the simple Foldy formula seems to be useful for concentrations up to about 0.1 if the error tolerance is relatively high.

Future work should deal with other types of scatterers from the practical viewpoint, such as inclusions either harder or softer than the matrix. This would be also helpful to clarify the validity of multiple scattering theories in terms of scattering strength. Researches focusing on the dependence of the attenuation and dispersion on the wave propagation distance would be also valuable.

ACKNOWLEDGMENTS

The authors appreciate Dr. Rafael Benites for providing us with detailed information on his previous works. Discussions with Dr. Haruo Sato were helpful in the early stage of this study. The critical comments of two anonymous reviewers are valuable for improving the manuscript. The figures in this paper were generated using the GMT software of Wessel and Smith.[41] This study was supported partially by the Earthquake Research Institute Cooperative Research Program (1996-B-08, 2000-B-07, and 2001-B-02) and KAKENHI (11740254).

[1] A. Ishimaru, *Wave Propagation and Scattering in Random Media* (Academic, New York, 1978).
[2] S. M. Nair, D. K. Hsu, and J. H. Rose, "Porosity estimation using the frequency dependence of the ultrasonic attenuation," J. Nondestruct. Eval. **8**, 13–26 (1989).
[3] H. Sato and M. C. Fehler, *Seismic Wave Propagation and Scattering in the Heterogeneous Earth* (Springer-Verlag, New York, 1998).
[4] L. L. Foldy, "The multiple scattering of waves. I. General theory of isotropic scattering by randomly distributed scatterers," Phys. Rev. **67**, 107–119 (1945).
[5] M. Lax, "Multiple scattering of waves," Rev. Mod. Phys. **23**, 287–310 (1951).
[6] M. Lax, "Multiple scattering of waves. II. The effective field in dense systems," Phys. Rev. **85**, 621–629 (1952).
[7] P. C. Waterman and R. Truell, "Multiple scattering of waves," J. Math. Phys. **2**, 512–537 (1961).
[8] P. Lloyd and M. V. Berry, "Wave propagation through an assembly of spheres IV. Relation between different multiple scattering theories," Proc. Phys. Soc. London **91**, 678–688 (1967).
[9] V. Twersky, "Acoustic bulk parameters in distributions of pair-correlated scatterers," J. Acoust. Soc. Am. **64**, 1710–1719 (1978).
[10] L. Tsang, J. A. Kong, and T. Habashy, "Multiple scattering of acoustic waves by random distribution of discrete spherical scatterers with the qua-

sicrystalline and Percus-Yevick approximation," J. Acoust. Soc. Am. **71**, 552–558 (1982).
[11]V. K. Varadan, Y. Ma, and V. V. Varadan, "Scattering and attenuation of elastic waves in random media," Pure Appl. Geophys. **131**, 577–603 (1989).
[12]F. V. Meulen, G. Feuillard, O. B. Matar, and F. Levassort, "Theoretical and experimental study of the influence of the particle size distribution on acoustic wave properties of strong inhomogeneous media," J. Acoust. Soc. Am. **110**, 2301–2307 (2001).
[13]Z. Ye and L. Ding, "Acoustic dispersion and attenuation relations in bubbly mixture," J. Acoust. Soc. Am. **98**, 1629–1636 (1995).
[14]F. S. Henyey, "Corrections to Foldy's effective medium theory for propagation in bubble clouds and other collections of very small scatterers," J. Acoust. Soc. Am. **105**, 2149–2154 (1999).
[15]R.-B. Yang, "A dynamic generalized self-consistent model for wave propagation in particulate composites," J. Appl. Mech. **70**, 575–582 (2003).
[16]D. G. Aggelis, S. V. Tsinopoulos, and D. Polyzos, "An iterative effective medium approximation (IEMA) for wave dispersion and attenuation predictions in particulate composites, suspensions and emulsions," J. Acoust. Soc. Am. **116**, 3443–3452 (2004).
[17]J. Mobley, K. R. Waters, C. S. Hall, and J. N. Marsh, "Measurements and predictions of the phase velocity and attenuation coefficient in suspensions of elastic microsphere," J. Acoust. Soc. Am. **106**, 652–659 (1999).
[18]D. J. McClements, "Comparison of multiple scattering theories with experimental measurements in emulsions," J. Acoust. Soc. Am. **91**, 849–853 (1992).
[19]A. K. Holmes, R. E. Challis, and D. J. Wedlock, "A wide bandwidth study of ultrasound velocity and attenuation in suspensions: Comparison of theory with experimental measurements," J. Colloid Interface Sci. **156**, 261–268 (1993).
[20]A. K. Hipp, G. Storti, and M. Morbidelli, "On multiple-particle effects in the acoustic characterization of colloidal dispersions," J. Phys. D: Appl. Phys. **32**, 568–576 (1999).
[21]C. Layman, N. S. Murthy, R.-B. Yang, and J. Wu, "The interaction of ultrasound with particulate composites," J. Acoust. Soc. Am. **119**, 1449–1456 (2006).
[22]A. Richter, F. Babick, and S. Ripperger, "Polydisperse particle size characterization by ultrasonic attenuation spectroscopy for systems of diverse acoustic contrast in the large particle limit," J. Acoust. Soc. Am. **118**, 1394–1405 (2005).
[23]M.-F. Poujol-Pfefer, "Application of an homogenization model to the acoustical propagation in inhomogeneous media," J. Sound Vib. **184**, 665–679 (1995).
[24]R. Benites, K. Aki, and K. Yomogida, "Multiple scattering of SH waves in 2-D media with many cavities," Pure Appl. Geophys. **138**, 353–390 (1992).
[25]S. Biwa, S. Yamamoto, F. Kobayashi, and N. Ohno, "Computational multiple scattering analysis for shear wave propagation in unidirectional composites," Int. J. Solids Struct. **41**, 435–457 (2004).
[26]T.-K. Hong and B. L. N. Kennett, "Scattering of elastic waves in media with a random distribution of fluid-filled cavities: Theory and numerical modelling," Geophys. J. Int. **159**, 961–977 (2004).
[27]Y. Suzuki, J. Kawahara, T. Okamoto, and K. Miyashita, "Simulations of SH wave scattering due to cracks by the 2-D finite difference method," Earth, Planets Space **58**, 555–567 (2006).
[28]C. M. Linton and P. A. Martin, "Multiple scattering by random configurations of circular cylinders: Second-order corrections for the effective wavenumber," J. Acoust. Soc. Am. **117**, 3413–3423 (2005).
[29]Y. C. Angel and C. Aristégui, "Analysis of sound propagation in a fluid through a screen of scatterers," J. Acoust. Soc. Am. **118**, 72–82 (2005).
[30]C. M. Linton and P. A. Martin, "Multiple scattering by multiple spheres: A new proof of the Lloyd-Berry formula for the effective wavenumber," SIAM J. Appl. Math. **66**, 1649–1668 (2006).
[31]Y.-H. Pao and C.-C. Mow, *Diffraction of Elastic Waves and Dynamic Stress Concentrations* (Crane Russak, New York, 1973).
[32]L. G. Copley, "Integral equation method for radiation from vibrating bodies," J. Acoust. Soc. Am. **41**, 807–816 (1967).
[33]F. J. Sánchez-Sesma and E. Rosenblueth, "Ground motion at canyons of arbitrary shape under incident SH waves," Earthquake Eng. Struct. Dyn. **7**, 441–450 (1979).
[34]M. Dravinski, "Ground motion amplification due to elastic inclusions in a half-space," Earthquake Eng. Struct. Dyn. **11**, 313–335 (1983).
[35]G. D. Manolis and D. E. Beskos, *Boundary Element Methods in Elastodynamics* (Unwin Hyman, London, 1988).
[36]R. Benites and K. Aki, "Boundary integral-Gaussian beam method for seismic wave scattering: SH waves in two-dimensional media," J. Acoust. Soc. Am. **86**, 375–386 (1989).
[37]T. Pointer, E. Liu, and J. A. Hudson, "Numerical modelling of seismic waves scattered by hydrofractures: Application of the indirect boundary element method," Geophys. J. Int. **135**, 289–303 (1998).
[38]*Wave Analysis and Boundary Element Methods*, edited by S. Kobayashi (Kyoto University Press, Kyoto, 2000), in Japanese.
[39]J. M. Martin and S. M. Flatté, "Intensity images and statistics from numerical simulation of wave propagation in 3-D random media," Appl. Opt. **27**, 2111–2126 (1988).
[40]Z. Ye, "Acoustic dispersion and attenuation in many spherical scatterer systems and the Kramers-Kronig relations," J. Acoust. Soc. Am. **101**, 3299–3305 (1997).
[41]P. Wessel and W. H. F. Smith, "New, improved version of generic mapping tools released," EOS Trans. Am. Geophys. Union **79**, 579 (1998).

Resolving the shape of a sonoluminescence pulse in sulfuric acid by the use of streak camera

Wei Huang, Weizhong Chen,[a] and Weicheng Cui
The Key Laboratory of Modern Acoustics, Ministry of Education, and Institute of Acoustics, Nanjing University, Nanjing 210093, China

(Received 30 October 2008; revised 9 April 2009; accepted 10 April 2009)

A streak camera is used to measure the shape of sonoluminescence pulses from a cavitation bubble levitated stably in a sulfuric acid solution. The shape and response to an acoustic pressure field of the sonoluminescence pulse in 85% by weight sulfuric acid are qualitatively similar to those in water. However, the pulse width in sulfuric acid is wider than that in water by over one order of magnitude. The width of the sonoluminescence pulse is strongly dependent on the concentration of the sulfuric acid solution, while the skewed distribution of the shape remains unchanged.
 [DOI: 10.1121/1.3126943]

PACS number(s): 43.35.Hl, 43.35.Ei [RR] Pages: 3597–3600

I. INTRODUCTION

As the ultrasound passes through a liquid, the air dissolved in the liquid will form tiny bubbles, which could be visible to the naked eye. This phenomenon is called ultrasonic cavitation. Eighty years ago, light emitted from cavitation bubbles created by an ultrasonic wave was observed. This phenomenon is now called sonoluminescence (SL).[1] SL is caused by the remarkably high temperatures and pressures[2] inside the cavitation bubbles at the end of collapse.[3] The temperatures inside the bubble have been estimated on the order of thousands of kelvin. In 1990, Gaitan *et al.*[4] trapped a single, stationary SL bubble at the antinode of a standing acoustic wave. The SL bubble expands and collapses periodically with the frequency of sound. This phenomenon is called single bubble sonoluminescence (SBSL). A single, stationary bubble permits better measurement of the features of the collapse, such as sub-micron minimum bubble size,[5] high compression ratio of volume,[6] sub-nanosecond flash duration,[7] and high synchronicity of the SL pulse.[8] The cavitation bubble can emit light by focusing the acoustic energy by 12 orders of magnitude.[1,9] However, it is difficult to obtain experimentally precise information during the short final stages of the bubble's collapse, such as the width of the transitory SL flash. The SL flash is too short to be measured by some typical optical detectors, such as a photomultiplier tube (PMT). Barber *et al.*[7] compared the response of a micro-channel-plate PMT to the SL pulse with a 34 ps laser pulse and found that the SBSL pulse is shorter than 50 ps. In 1997 the pulse width was measured by using the technique of time-correlated single photon counting.[10] The precision of the pulse width measurement was improved with the aid of a streak camera. The streak camera images the incident light through a slit, getting a one dimensional image. This image is propagated along the second dimension of the image plane at a constant speed. The result is a picture of the time dependency of the incident light. Using this technique, the full width at half maximum (FWHM) of the SL pulse in water was 200–300 ps.[11] In 2005, Suslick and co-workers[12,13] observed a bright, moving SBSL in sulfuric acid (SA). In SA, SL is 2700 times brighter than that in water under argon,[12] and the bubble size in SA is larger than that in water.[13] Unfortunately the moving SBSL in SA always dithers around the antinode.[12–14] Moving SBSL bubble makes some measurements using streak camera impossible, because the light beam from the bubble cannot be collected by the camera through the entrance slit. As a result, the shape of the SL pulse is still lacking in SA. In fact, the moving SBSL bubble can be levitated in strictly degassing SA solution as stably as in water.[15,16] The harmonics of the driving sound can also help to trap the moving bubble.[17] A bright and steady SBSL makes the measurement of the shape of the SBSL pulse in SA possible. In this paper we report data on the shape of the SL pulse in SA obtained by using a streak camera and compare them with those obtained for water. The dependence of the SL pulses on the concentration of SA and on the driving pressure is also investigated.

II. EXPERIMENTAL SYSTEM

Figure 1 shows the experimental setup for the measurement of the shape of the SL pulse. A 100 ml spherical flask serves as a spherical resonator. A pair of piezoelectric transducers (PZTs) is bonded with epoxy to the wall on opposite sides. The flask, filled with 98% SA by weight, resonates at a frequency of 26.0 kHz. A flat quartz window of 15 mm diameter is used to avoid spherical distortion and reduce the UV absorption of the image. A single-frequency sinusoidal signal generated by a signal generator (Agilent 33250) was amplified by a power amplifier (B&K 2713), and used to drive the PZTs to generate the sound field in the flask. The host liquids are the SA solutions at different concentrations dissolved with argon gas under a pressure head of 30 $\times 133$ Pa (30 torr). To stably levitate the bubble all host liquids were thoroughly degassed before dissolving the argon gas. An air bubble was injected into the flask, and levitated at the antinode of the sound field. The bubble began to emit

[a]Author to whom correspondence should be addressed. Electronic mail: wzchen@nju.edu.cn

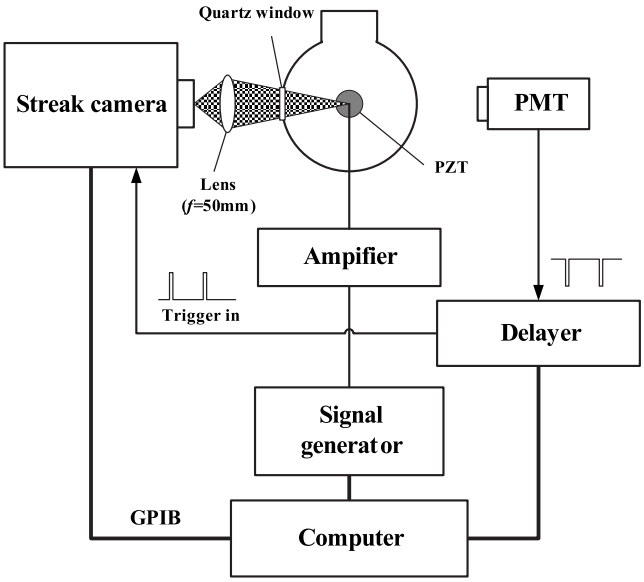

FIG. 1. The sketch of experimental setup. To reduce the error of measurement from the space instability of the bubble, the entrance slit of the streak camera was adjusted to 50 nm, near the narrowest possible.

light as the driving pressure increases. A streak camera (Hamamatsu C7700) was used to measure the shape of the SL pulse. It was triggered by the previous SL pulse collected by a PMT and delayed by a digital delayer (DG535). Although the streak camera can be triggered by other signals, such as the acoustic driving signal, the SL signal worked best in all of our attempts. The time window of the streak camera was set to 20 ns, which is about twice the pulse width of the SBSL in SA. A lens between the resonator and the streak camera was used to collect as much light as possible (see Fig. 1).

III. THE SHAPE OF SL PULSE IN CONCENTRATED SA

Because the SL flash is not strong enough to obtain a clear image of the shape of the SL pulse from a single shot of the streak camera, it was necessary to sum a number of single shots. In our experiment, 1000 single shots were recorded, and stored in the computer. Before summing, it was necessary to exclude some false single shots whose mass centers were out of the central region of 10 ns. About 98% effective single shots were summed by overlaying their mass centers, resulting in a jitter-corrected image. The estimated error in this summation method is less than 10%.[11]

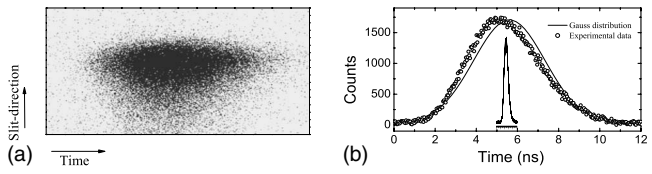

FIG. 2. The summed streak image and the shape of the SL pulses in SA. (a) The integrated streak image. (b) The histogram of (a) where the solid line is the best-fit Gaussian distribution. The inset in (b) shows the shape of SL flash in water (Ref. 11). The concentration of the SA solution used is 85% by weight. The bubble is driven by 1.40 Pa at 20.8 °C.

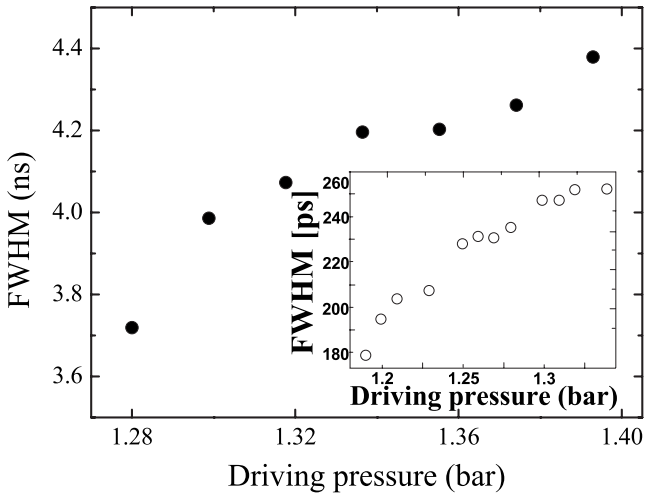

FIG. 3. The FWHMs of the SL pulses in 85% SA by weight under different driving pressures. The inset shows the FWHMs in water (Ref. 11).

Figure 2(a) is a typical summed steak image of the SL pulse in SA. Figure 2(b) is the histogram corresponding to the image in Fig. 2(a). It indicates that the FWHM of the pulse is 3.393 ns. Compared with the previous work in water[11] [see the inset of Fig. 2(b)], the SL pulse width in SA is much wider. Figure 3 shows that the FWHM of the SL pulse in SA increases with the driving pressure, which is the same as that in water, although the FWHM in SA is over one order of magnitude wider than that in water[11] (see the inset of Fig. 3).

Comparing the experimental shape of the SL pulse with the Gaussian distribution [see Fig. 2(b)] we find that the SL pulse shape in concentrated SA solution is asymmetric with a positively skewed distribution, which means the rise-time (10%–90%) t_r is shorter than the fall-time (10%–90%) t_f. In our experiment t_r=2.471 ns and t_f=3.479 ns, respectively. With different sound pressures both t_r and t_f are changed. The higher the sound pressure, the wider t_r and t_f are. Figure 4 shows the detailed results of t_r and t_f as functions of the driving pressure. We see that the rise-time t_r is always shorter than the fall-time t_f. Furthermore, the gap between them becomes larger with an increase in sound pressure, which means the skewness of photon distribution becomes larger with the driving pressure.

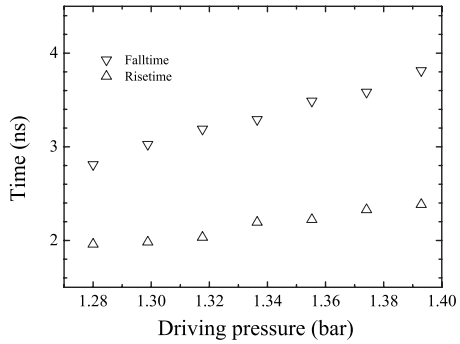

FIG. 4. The rise-time and fall-time of the SL pulse as functions of the driving pressure. The host liquid was the 85 wt % SA solution dissolved by 30×133 Pa argon gas.

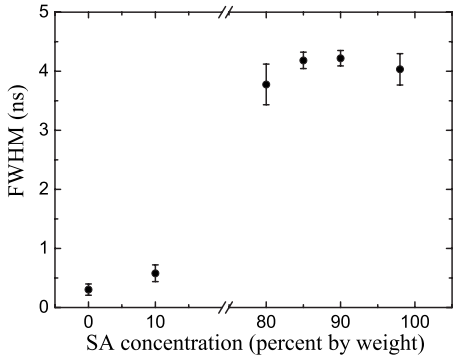

FIG. 5. The FWHMs of the SBSL pulses in SA solutions with different concentrations. All solutions have been dissolved with 30×133 Pa argon gas.

IV. THE DEPENDENCE OF SL SHAPE ON SA CONCENTRATION

The FWHM of the SL pulse as a function of SA concentration has been measured. The pulse width of water was used as reference. For the SA solutions with concentration from 10% to 80% by weight, the SL was very instable, leading to the failure of the bubble levitation. The FWHM's dependence on the SA concentration is shown in Fig. 5. The FWHM in concentrated SA is larger than that in water or diluted SA by an order of magnitude. However, the FWHM reaches its maximum, 4.222 ns, in 85% SA solution instead of 98%. Its brightness also reaches the maximum at 85%. A similar result has been observed in SA solutions dissolved with krypton gas.[16] The FWHM and brightness of the SL pulses are closely related to the bubble size. The dynamics of the bubbles levitated in SA solutions are measured using the integrated imaging technique under strobe illumination.[18] From these data, the ambient radii R_0 of the bubbles are obtained by fitting the experimental data of the radii to the Rayleigh–Plesset model.[19] Figure 6 shows the dependence of the ambient radii on SA concentration. The peak ambient radius occurs at 85% SA solution. Since larger bubbles emit the brighter and wider SL pulses, the brightest and widest pulse is at 85% SA solution.

To compare the shape of the SL pulse in water with that in SA solutions, we defined the ratio of the fall-time to rise-time t_f/t_r as the skewness of SL photon distribution. Figure 7 shows that with increasing SA concentration, the skewness

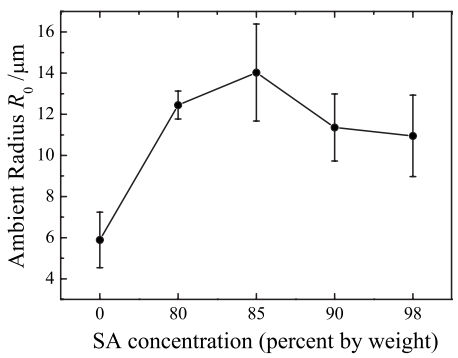

FIG. 6. The ambient radii of the bubbles levitated in experimental SA solutions.

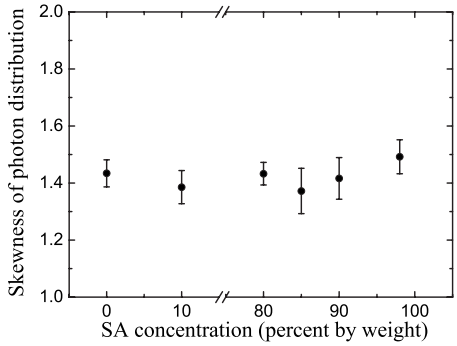

FIG. 7. Skewness of photon distribution (t_f/t_r) of SBSL under different driving pressures in SA solutions with different concentrations.

of photon distribution remains unchanged, $t_f/t_r\sim1.4$ in our experiment. This ratio can be changed from 1.2 to 1.6 if we change the driving pressure.

V. SUMMARY AND DISCUSSION

The SBSLs driven by different sound pressures in SA solutions having different concentrations have been systemically investigated by using a streak camera. The width, rise-time t_r, fall-time t_f, and skewness t_f/t_r of the SL photon distribution have been measured. The main results are as follows: (1) The width of the SL pulse in 85% by weight SA is wider than that in water by over one order of magnitude; (2) a positively skewed distribution of SL pulse, the rise-time being shorter than the fall-time $t_f/t_r>1$, deviates from the Gaussian distribution; (3) both the width and skewness increase with the driving pressure; and (4) the skewness is independent of the concentration of the SA solution although the width substantially increases in concentrated SA solutions. The concentrated SA solution can levitate the cavitation bubble with larger ambient radius, leading to both width and brightness of the SL pulse enlarged.

ACKNOWLEDGMENTS

This work was partly supported by the National Natural Science Foundation of China (Grant Nos. 10434070 and 10704037). The authors are grateful to Dr. David Palmer for his invaluable help in English writing.

[1]B. P. Barber, R. A. Hiller, R. Löfstedt, S. J. Putterman, and K. R. Weninger, "Defining the unknowns of sonoluminescence," Phys. Rep. **281**, 65–144 (1997).
[2]G. Vazquez, C. Camara, S. J. Putterman, and K. R. Weninger, "Blackbody spectra for sonoluminescing hydrogen bubbles," Phys. Rev. Lett. **88**, 197402 (2002).
[3]M. P. Brenner, S. Hilgenfeldt, and D. Lohse, "Single-bubble sonoluminescence," Rev. Mod. Phys. **74**, 425–484 (2002).
[4]D. F. Gaitan, L. A. Crum, C. C. Church, and R. Roy, "Sonoluminescence and bubble dynamics for a single, stable, cavitation bubble," J. Acoust. Soc. Am. **91**, 3166–3183 (1992).
[5]B. P. Barber, R. A. Hiller, R. Lofstedt, S. J. Putterman, and K. R. Weninger, "Pulsed Mie scattering measurements of the collapse of a sonoluminescing bubble," Phys. Rep. **281**, 65 (1997).
[6]D. F. Gaitan and R. G. Holt, "Experimental observations of bubble response and light intensity near the threshold for single bubble sonoluminescence in an air-water system," Phys. Rev. E **59**, 5495–5502 (1999).
[7]B. P. Barber, R. Hiller, K. Arisaka, H. Fetterman, and S. Putterman, "Resolving the picosecond characteristics of synchronous sonoluminescence," J. Acoust. Soc. Am. **91**, 3061 (1992).

[8]B. P. Barber and S. J. Putterman, "Observation of synchronous picosecond sonoluminescence," Nature (London) **352**, 318–320 (1991).
[9]L. A. Crum and R. A. Roy, "Sonoluminescence," Science **266**, 233–234 (1994).
[10]B. Gompf, R. Gunther, G. Nick, R. Pecha, and W. Eisenmenger, "Resolving sonoluminescence pulse width with time-correlated single photon counting," Phys. Rev. Lett. **79**, 1405–1408 (1997).
[11]R. Pecha, B. Gompf, G. Nick, Z. Q. Wang, and W. Eisenmenger, "Resolving the sonoluminescence pulse shape with a streak camera," Phys. Rev. Lett. **81**, 717–720 (1998).
[12]D. J. Flannigan and K. S. Suslick, "Plasma formation and temperature measurement during single-bubble cavitation," Nature (London) **434**, 52–55 (2005).
[13]S. D. Hopkins, S. J. Putterman, B. A. Kappus, K. S. Suslick, and C. G. Camara, "Dynamics of a sonoluminescing bubble in sulfuric acid," Phys. Rev. Lett. **95**, 254301 (2005).
[14]R. Toegel, S. Luther, and D. Lohse, "Viscosity destabilizes sonoluminescing bubbles," Phys. Rev. Lett. **96**, 114301 (2006).
[15]J. F. Xu, W. Z. Chen, X. H. Xu, Y. Liang, W. Huang, and X. X. Gao, "Investigation on the compositions and their evolutions inside a sonoluminescing bubble by spectra," Phys. Rev. E **76**, 026308 (2007).
[16]W. Z. Chen, W. Huang, Y. Liang, X. X. Gao, and W. C. Cui, "Time-resolved spectra of single-bubble sonoluminescence in sulfuric acid with a streak camera," Phys. Rev. E **78**, 035301(R) (2008).
[17]R. Urteaga and F. J. Bonetto, "Trapping an intensely bright, stable sonoluminescing bubble," Phys. Rev. Lett. **100**, 074302 (2008).
[18]W. Huang, W. Z. Chen, and Y. N. Liu, "Precise measurement technique for the stable acoustic cavitation bubble," Chin. Sci. Bull. **50**, 2417–2421 (2005).
[19]T. G. Leighton, *The Acoustic Bubble* (Academic, London, 1994).

A new safety parameter for diagnostic ultrasound thermal bioeffects: Safe use time

Irfan Karagoz[a] and Mustafa K. Kartal
Department of Electrical and Electronic Engineering, Gazi University, Maltepe, Ankara 06100, Turkey

(Received 26 September 2008; revised 7 April 2009; accepted 9 April 2009)

It is widely accepted that diagnostic ultrasound has the potential to elevate the temperature of tissue being scanned. Because both the maximum value of the temperature rise and the temporal profile of that rise are necessary to estimate the risk correctly, the temperature rise $[\Delta T(t)]$ at an observation point for an exposure condition is presumed to have two components, that is, $\Delta T(t)=\Delta T_{\max}X(t)$. The amplitude component $\Delta T_{\max}$ is the maximum value of $\Delta T(t)$, and the exposure time component $X(t)$ represents the time dependency of that $\Delta T(t)$. Ninety-six cases were investigated to obtain the proposed $\Delta T(t)$ model at six frequencies, four source diameters, and four f-numbers. Then, using the relative change in the rate of induction of a thermal effect due to ultrasound exposure that produces $\Delta T(t)$ different from a threshold exposure, the safe use time (SUT) model was constructed. SUT informs the user of the maximum duration of exposure in a region at a particular output level that would be no more hazardous than scanning at the threshold exposure. Using the SUT model, high power ultrasound can be applied for a short time so that the user can improve imaging performance while staying within safe limits. © *2009 Acoustical Society of America.* [DOI: 10.1121/1.3126525]

PACS number(s): 43.35.Wa, 43.80.Gx [CCC] Pages: 3601–3610

I. INTRODUCTION

Diagnostic ultrasound (DUS) has been used for more than 50 years in medical practice to obtain valuable information about the structure and function of tissues and organs (Wells, 2006). However, as a form of energy transmitted into the body, DUS has potential effects on living tissues, namely, thermal and nonthermal bioeffects (Barnett *et al.*, 1997). As the US propagates through tissue, a portion of its energy is absorbed and converted to heat, raising the temperature of the tissue (NCRP, 1992; Drewniak and Dunn, 1996; Ziskin and Bartnett, 2001). The increase in temperature $[\Delta T(t)]$ is dependent on (1) output characteristics of the acoustic source such as frequency, source dimensions, power, the duration of exposure, and wave shape; and (2) tissue properties such as attenuation, absorption, speed of sound, perfusion, and thermal diffusivity (NCRP, 1992; Barnett, 2001; Church and Miller, 2007). Acoustic cavitation is perhaps the most widely studied nonthermal mechanism (Church, 2002), and a variety of biological effects can be attributed to activity associated with acoustic cavitation (Dalecki, 2004). Nonthermal effects also include phenomena such as acoustic radiation pressure, force and torque, and acoustic streaming (Dalecki, 2004; Church *et al.*, 2008). However, it is important to note that no actual damage attributable to both thermal and nonthermal bioeffects by DUS has been described in the human medical literature (Abramowicz *et al.*, 2008; Church *et al.*, 2008). As stated above, there is more than one possible biological effect due to US in tissue, but only the thermal effects are discussed in the present study.

As the determination of tissue heating by DUS is of great importance for assessing risk, mathematical models that estimate the $\Delta T(t)$ in tissue have been produced by a number of groups; many of these, those by Nyborg (1988), Curley (1993), and O'Brien and Ellis (1996), make use of the bioheat transfer equation (Pennes, 1948). Moreover, two different sets of algorithms have been developed by the National Council on Radiation Protection and Measurements (NCRP, 1992) and the American Institute of Ultrasound in Medicine and the National Electrical Manufacturers Association (AIUM/NEMA, 1992) to aid in the prediction of ΔT in clinical applications of US. There has also been great interest in establishing experimental methods for predicting $\Delta T(t)$ (Fry and Fry, 1954a, 1954b; Drewniak *et al.*, 1989; Carstensen *et al.*, 1990; Bosward *et al.*, 1993, among others). Data from such theoretical and experimental studies have been used for the development of guidelines for the safe use of DUS (Barnett *et al.*, 2000).

The Food and Drug Administration (FDA) initiated a regulatory process for the control of acoustic output levels of DUS equipment and maintained the maximum application-specific intensity limits (FDA, 1985, 1987). Then, the FDA agreed to incorporate the AIUM/NEMA output display standard (ODS) into its pre-market approval process (AIUM/NEMA, 1992; FDA, 1993). However, since the ODS did not include upper limits, the FDA approved ODS stipulated regulatory upper limits of 720 $\mathrm{mW/cm^2}$ for the derated (0.3 dB/cm MHz) spatial-peak temporal-average intensity, $I_{\mathrm{SPTA.3}}$, and 1.9 for the mechanical index (MI) for all but ophthalmic ultrasound examinations (FDA, 1997). The ODS requires two safety indices, namely, the thermal index (TI) and MI, be displayed on the screen to enable the operator to apply the as low as reasonably achievable principle more easily to ultrasound exposure (Abbott, 1999). The MI is developed as a relative indicator of the potential for mechanical bioeffects (Abbott, 1999; Church, 2005), and TI is used to provide an indicator of potential bioeffects due to the thermal

[a]Author to whom correspondence should be addressed. Electronic mail: irfankaragoz@gazi.edu.tr

mechanism. Later, because of concern over the validity of the ODS indices as a reasonable indicator of potential bioeffects, it was deemed necessary to check the accuracy of these indices. Among others, O'Brien and Ellis (1996), Horder *et al.* (1998), Jago *et al.* (1999), O'Brien and Ellis (1999), Herman and Harris (1999), Lubbers *et al.* (2003), and O'Brien *et al.* (2004) showed that the ODS-defined TIs may not be a reasonable indicator of potential bioeffects due to US heating that could occur in some exposure conditions. Additionally, some researchers have made efforts to obtain a more accurate TI; for example, Lubbers *et al.* (2003), O'Brien *et al.* (2004), and Church (2007) showed the potential for improvement of the current TIs and proposed a new safety parameter. Recently, it was recommended that an appropriately representative and knowledgeable group evaluates the current TIs and, if needed, develop improved indices (AIUM, 2008; O'Brien *et al.*, 2008).

During the assessment of the risk of thermal bioeffects due to US, it is generally assumed that the maximum temperature rise is achieved instantaneously, intentionally ignoring the interval at lower temperature. This assumption ignores the fact that short exposures may present a risk very much lower than that estimated from an instantaneous temperature rise (Church, 2007). Therefore, it is necessary to know both the maximum value of the temperature increase that occurs and the time-dependent behavior of that rise in order to estimate the risk correctly (Church, 2007; Church and Miller, 2007). The present study was motivated particularly by this consideration. Initially, the temperature rise model $\Delta T(t)$ that takes into account both the maximum value of the temperature rise and temporal profile of that heating is constructed. Then, the calculated temperature rise obtained from this model is used to estimate the safe use time (SUT), which is the maximum duration of this US exposure that would be no more hazardous than scanning at the threshold exposure. In addition, the advantages and disadvantages of the SUT model are discussed.

II. MATERIAL AND METHOD

A. Ultrasound beam assumptions and the calculation of temperature rise

A circular focused transducer located with the front face at $(x,y,z)=(0,0,0)$ is considered. The z axis coincides with the beam axis and the quantity z will indicate the position of an observation point at which the temperature rise is to be calculated (see also Lubbers *et al.*, 2003 for geometry). It is assumed that the transducer generates a circular beam with homogeneous intensity over its cross section. All of the acoustic power W is defined to exist within the given beam width and to be zero outside the beam. This beam geometry is chosen to simplify the calculations (Nyborg 1988; Lubbers *et al.*, 2003). The attenuation of intensity by soft tissue between the transducer and the surroundings of the observation point is taken into account. The determinations are made of the intensity I within the beam and the heat source function q_v, as a function of depth z from the equations (NCRP, 1992)

$$I = \frac{W}{\pi d^2(z)/4}\exp(-2\alpha z) \tag{1}$$

and

$$q_v = 2\alpha I. \tag{2}$$

Here, W is the source output power, $d(z)$ is the local value of the beam width, and α is the acoustic attenuation coefficient. The width of the acoustic field as a function of depth z is obtained as follows (Curley, 1993):

$$d(z) = d + [D-d]|1-(z/F)|, \tag{3}$$

where d is the focal beam width, D is the source diameter, and F is the focal length. The focal beam width d is calculated according to the following equation: $d=\lambda F/D=\lambda f$-number. (Macovski, 1983; NCRP, 1992; Curley, 1993), where λ is the acoustic wavelength.

The temperature rise $\Delta T(t)$ at an observation point is estimated by summing the contributions of heated tissue elements around this point, using the algorithm described by Nyborg (1988) and Nyborg and Wu (1994). This algorithm was implemented in a simulation program called SPHERESUM (Lubbers *et al.*, 2003). The program calculates the temperature rise for an arbitrary ultrasonic field in four dimensions: x, y, z, and t. Lubbers *et al.* (2003) validated this program by repeating various calculations mentioned in literature. The starting point of the calculation is the point source solution of the bioheat transfer equation (Nyborg, 1988). $\Delta T(t)$ at an observation point due to the heating of a volume element dv with an energy q_v at a distance r is estimated from (Nyborg, 1988)

$$\Delta T(t) = (C/r)\{E[2-\mathrm{erfc}(t^*-R)]+E^{-1}\,\mathrm{erfc}(t^*+R)\}, \tag{4}$$

where

$$C = q_v dv/8\pi K, \tag{5}$$

$$E = \exp(-r/L), \tag{6}$$

$$L = \mathrm{sqrt}(\kappa\tau), \tag{7}$$

$$t^* = \mathrm{sqrt}(t/\tau), \tag{8}$$

$$R = r/\mathrm{sqrt}(4\kappa t), \tag{9}$$

and where K, τ, L, and κ are, respectively, the thermal conductivity, the time constant for perfusion, the perfusion length of tissue, and the thermal diffusivity of tissue. The total temperature rise at the observation point is found by integrating over all volume elements in space (Lubbers *et al.*, 2003). In this study, it is assumed that the soft tissue is homogeneous in terms of both acoustic and thermal properties. The tissue is characterized by the following constants: $K=0.6$ W m^{-1} °C^{-1}, $\tau=720$ s, $\alpha=0.3$ dB cm^{-1} MHz^{-1}, propagation speed $c=1540$ m/s, and $\kappa=0.0014$ cm^2 s^{-1}. These are the values used in the ODS (AIUM/NEMA, 1992) and the values used herein for the calculation of the temperature rise. However, it should be noted that any deviations from these values that occur in clinical practice cause the real temperature rise in tissue to be different from its estimated

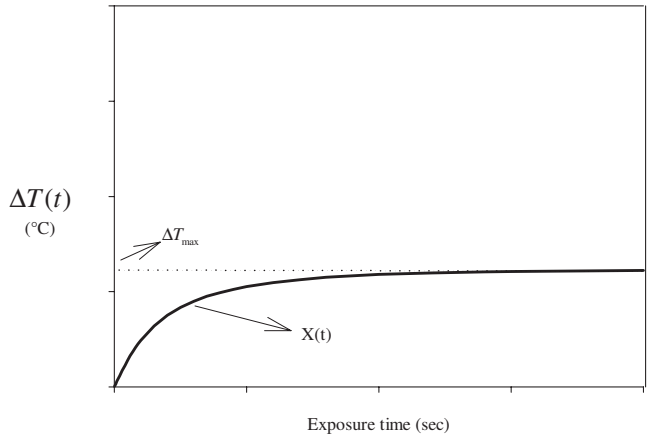

FIG. 1. A typical example of temperature rise due to DUS. The proposed multiplicative temperature rise model for a particular case: $\Delta T(t) = \Delta T_{\max} X(t)$, where $\Delta T_{\max}$ is the amplitude component and $X(t)$ is the exposure time component.

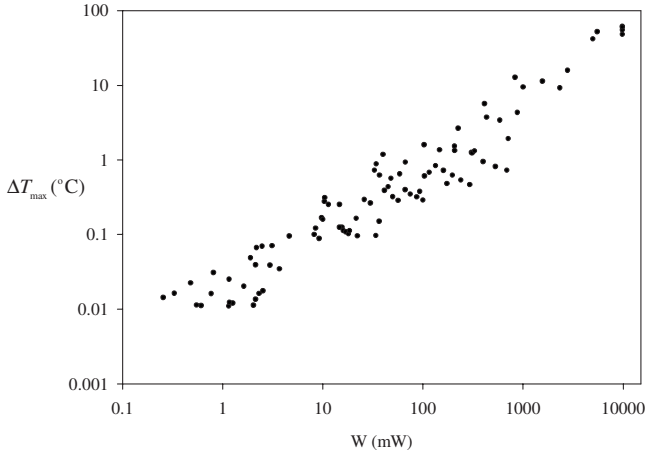

FIG. 2. The paired maximum steady-state temperature rise $\Delta T_{\max}$ vs source power W under the condition that the derated $I_{\mathrm{SPTA.3}}$ is 720 $\mathrm{mW/cm^2}$.

value. The transducer is presumed to operate in continuous wave mode and to be stationary. Further, it is assumed that no heat is transferred through the front face of the transducer. However, in clinical applications, the transducer itself is a substantial source of heat (Hekkenberg and Bezemer, 2004).

Ninety-six cases were investigated to obtain the temperature rise model values at six frequencies f (1, 3, 5, 7, 9, and 11 MHz), four source diameters D (1, 2, 3, and 4 cm), and appropriate focal length F to yield f-numbers ($=F/D$) of 1, 2, 3, and 4. Moreover, the acoustic powers are limited to the $I_{\mathrm{SPTA.3}}$ of 720 $\mathrm{mW/cm^2}$, the maximum value allowed by the FDA DUS equipment approval process. These values are chosen to provide sufficient detail to evaluate SUT in the DUS range (O'Brien and Ellis, 1999; O'Brien *et al.*, 2004; O'Brien, 2007). For each case, the values of ΔT are calculated at 31 insonation times: 1, 2, 5, 10 20, 30, 40, 50, 60, 70, 80, 90, 100, 150, 200, 250, 300, 350, 400, 450, 500, 600, 700, 800, 900, 1000, 1100, 1200, 1300, 1400, 1500, and 2000 s to determine the time dependency of that ΔT.

B. The proposed temperature rise model

The axial temperature rise profiles are determined for each case. It is assumed that $\Delta T(t)$ at an observation point for a particular exposure has two components, that is,

$$\Delta T(t) = \Delta T_{\max} X(t), \tag{10}$$

where the amplitude component $\Delta T_{\max}$ is the maximum value of $\Delta T(t)$ and the exposure time component $X(t)$ characterizes that $\Delta T(t)$ in time (Fig. 1). The following statements explain the determination of the $\Delta T_{\max}$ and $X(t)$ for an exposure condition. The maximum value of the axial steady-state temperature increase for that exposure is denoted $\Delta T_{\max}$. The location with the highest rate of temperature rise along the axial distance z for that exposure is considered during the calculation of time dependency. Then, the time dependency for this exposure is reported and expressed in terms of time required for the temperature to reach 50% of its steady-state temperature rise, where the time and temperature rise at that location are denoted by $t_{50\%}$ and $\Delta T_{50\%}$, respectively (Nyborg, 1988). Hence, the maximum axial steady-state temperature rise and the highest rate of temperature rise along the z-axis for this exposure are taken into account during the construction of the proposed $\Delta T(t)$ model. This approach corresponds to a worst-case scenario and the effect of this approach on the calculation will be discussed below.

It is well known that the value of $\Delta T_{\max}$ due to DUS depends on W, f, D, and F (O'Brien *et al.*, 2004). The following trends are generally observed for $\Delta T_{\max}$. As seen from Fig. 2, $\Delta T_{\max}$ increases as a function of W at an observation point. For the shorter-focus cases, the location of $\Delta T_{\max}$ is near the geometric focus. However, as the f-number increases for each frequency, the location of $\Delta T_{\max}$ moves toward the acoustic source (O'Brien and Ellis, 1999; O'Brien *et al.*, 2004). Therefore, the following model for $\Delta T_{\max}$ at an observation point is proposed (O'Brien *et al.*, 2004):

$$\Delta T_{\max} = A W^b f^c D^d F^e, \tag{11}$$

where $\Delta T_{\max}$ is the computed maximum value of the temperature rise, A is a constant, b is the source power exponent, c is the frequency exponent, d is the aperture diameter exponent, and e is the focal length exponent. The units for the indicated quantities are as follows: W in milliwatt, f in megahertz, and D and F in cm. The maximum value of axial $\Delta T_{\max}$ for an exposure condition is used in the statistical calculations.

The following conclusion is drawn for the time dependency of $\Delta T(t)$: After a short time, the temperature rise is small; with increasing exposure time, the temperature rise is larger. The rate of $\Delta T(t)$ during the beginning of the US examination is high and that rise reaches a stationary value after a sufficiently long exposure time. It is required that $X(t)$ provides satisfactory accuracy for both the long and short exposure times according to our model. Therefore, an exponential rise to the max function may be a candidate for $X(t)$. For the simplification of the calculation, $X(t)$ is chosen as follows:

$$X(t) = [1 - \exp(-\mathrm{sqrt}(t/\alpha))], \tag{12}$$

where t is the exposure time and α is the dependent variable. This selection of $[1-\exp(-\mathrm{sqrt}(t/\alpha))]$ is chosen so that $X(t)$

TABLE I. The parameter estimates and standard errors for the log ΔT_{max} model.

Variable	Parameter	Parameter estimate	Standard error	p-value
Constant	log A	−1.895	0.033	1.54×10^{-73}
log W	b	1.029	0.023	2.44×10^{-63}
log f	c	0.580	0.031	1.17×10^{-32}
log D	d	−0.497	0.081	2.00×10^{-8}
log F	e	−0.614	0.105	7.64×10^{-8}

exhibits suitable time-dependent behavior for $\Delta T(t)$ at any exposure time. Substituting Eq. (12) into Eq. (10) leads to

$$\Delta T(t) = \Delta T_{max}[1 - \exp(-\mathrm{sqrt}(t/\alpha))]. \quad (13)$$

Lubbers *et al.* (2003) illustrated the influence of the focal beam width on US heating. The rate of temperature rise depends strongly on the tissue model and on the focal beam width. With a wide beam, the steady-state temperature level is reached later than with a narrow beam. Furthermore, the effect of the beam width on the maximum value of the temperature rise can be observed by using Eqs. (1), (2), and (5). A higher steady-state temperature level with a narrow beam is calculated compared to a wide beam. The focal beam width depends on frequency f, diameter D, and focal length F [Eq. (3)]. Therefore, the dependent variable α in Eq. (12) can be modeled as

$$\alpha = Ef^g D^h F^i, \quad (14)$$

where E is a constant, g is the frequency exponent, h is the aperture diameter exponent, and i is the focal length exponent. The units for the indicated quantities are as follows: α in seconds, f in megahertz, and D and F in centimeters.

C. Statistical analysis for ΔT_{max} and α models

The multiplicative model for ΔT_{max} in Eq. (11) implies a linear regression model for the logarithm of ΔT_{max}. Expressing in logarithms (to base 10) and including a random error term, Eq. (11) is constructed in the form of

$$\log \Delta T_{max} = \log A + b \log W + c \log f + d \log D + e \log F + \mathrm{error}. \quad (15)$$

The parameters log A, b, c, d, and e are estimated by the method of least-squares by using SPSS for Windows (ver 16.0, SPSS Inc., Chicago, IL). The 96 maximum temperature rise data points are fitted by multiple linear regression to log ΔT_{max}. The 95% confidence interval based on the log ΔT_{max} model contains the true data point. The parameter estimates and standard errors of the log ΔT_{max} model are given in Table I. The goodness of fit of the regression is assessed from values of the square of the correlation coefficient (r^2), the standard error of fit, and the F-statistic (Church and O'Brien, 2007). The r^2 for Eq. (15) is 0.989, with all the effects being statistically significant ($p<0.001$). The standard error of fit and the F-statistic for this model are 0.103 and 2055.64, respectively. The exponents b and c are both positive, indicating that ΔT_{max} increases as either W or f increases. However, exponents d and e are both negative, indicating that ΔT_{max} decreases as either D or F increases.

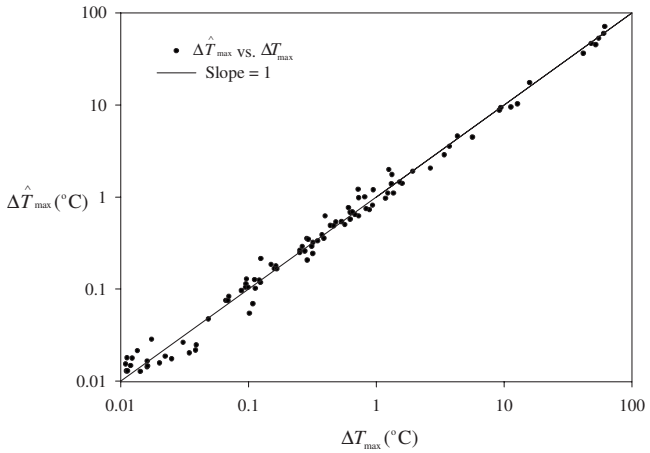

FIG. 3. The paired $\Delta\hat{T}_{max}$ vs ΔT_{max} for all cases under the condition that the $I_{SPTA.3}$ is 720 mW/cm^2. $\Delta\hat{T}_{max}$ and ΔT_{max} are, respectively, the predicted and observed maximum temperature rise.

The estimated coefficient for log W is large in magnitude relative to those for the other three effects. Because the associated probabilities of all exponents are small, they are strongly correlated with ΔT_{max}. A linear fit to the ΔT_{max} model using the constant and exponent estimates gives the following approximation:

$$\Delta\hat{T}_{max} = \frac{W^{1.029} f^{0.580}}{78.52 D^{0.497} F^{0.614}}, \quad (16)$$

where $\Delta\hat{T}_{max}$ is the prediction of ΔT_{max}. The quality of fit provided by this expression may be illustrated by plotting the predictions of Eq. (16), $\Delta\hat{T}_{max}$ vs the observed temperature rise ΔT_{max} as shown in Fig. 3. The diagonal line in Fig. 3 indicates equality between $\Delta\hat{T}_{max}$ and ΔT_{max}. Satisfactory agreement between the observed and predicted values is obtained except for the lowest points, but those deviations do not cause a significant error in SUT calculations, as discussed below. The exposure conditions with the higher ΔT_{max} values in Fig. 3 are exceptional cases and are most likely not combinations that occur clinically (e.g., $D=4$ cm and $F=16$ cm at $f=9$ MHz or $D=4$ cm and $F=16$ cm at $f=1$ MHz). Moreover, these higher values are obtained because of the worst-case assumption discussed above. ΔT_{max} is calculated according to the assumption of $d(z)$ [Eq. (3)], and a different assumption of $d(z)$ causes a deviation from the calculated ΔT_{max} here.

The temporal dependency of axial temperature increase is reported and expressed in terms of time ($t_{50\%}$) and $\Delta T_{50\%}$ as explained above. The $t_{50\%}$ value is generally observed during short exposure times (Fig. 4). This approach yields satisfactory accuracy for the short exposure times during the calculation of time dependency. When the insonation time equals $t_{50\%}$, the following equation holds:

$$0.5\Delta T_{max} = \Delta T_{max}[1 - \exp(-\mathrm{sqrt}(t_{50\%}/\alpha))]. \quad (17)$$

Equation (17) is satisfied when $t_{50\%}=0.48\alpha$. Therefore, Eq. (14) can be written as follows:

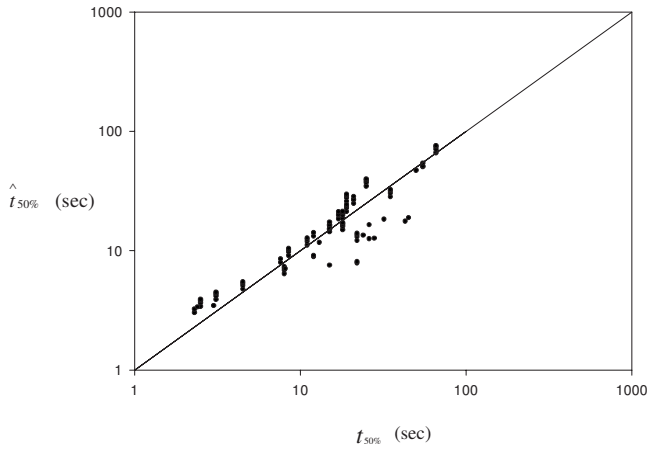

FIG. 4. The paired $\hat{t}_{50\%}$ vs $t_{50\%}$ for all cases. $\hat{t}_{50\%}$ and $t_{50\%}$ are, respectively, the predicted and observed time required for the temperature to reach 50% of its steady-state temperature rise. The diagonal line indicates equality between $\hat{t}_{50\%}$ and $t_{50\%}$.

$$2.08t_{50\%} = Ef^g D^h F^i. \tag{18}$$

Initially, $t_{50\%}$ and $\Delta T_{50\%}$ values for all exposure conditions are obtained from the results of the simulation program. Then, the parameters log E, g, h, and i for the $t_{50\%}$ model are estimated using SPSS as explained above. Finally, the α model is derived from the predicted $t_{50\%}$ model by using $t_{50\%}=0.48\alpha$. The multiplicative model for $t_{50\%}$ in Eq. (14) implies a linear regression model for the logarithm of $t_{50\%}$. Expressed in logarithms (to base 10) and including a random error term, Eq. (14) is constructed in the form of

$$\log t_{50\%} = \log E + g \log f + h \log D + i \log F + \text{error}. \tag{19}$$

The 96 $t_{50\%}$ data points are fitted by multiple linear regression to log $t_{50\%}$ The estimated values and standard deviations for the log $t_{50\%}$ model are given in Table II. The constant and exponent estimates are used to yield the $\hat{\alpha}$ model for all of the cases

$$\hat{\alpha} = \frac{25.2F^{1.228}}{D^{1.127}f^{0.581}}, \tag{20}$$

where $\hat{\alpha}$ is the prediction of α. Substituting the constant and exponent estimates of the model α in Eq. (12) leads to the following expression:

$$X(t) = \left[1 - \exp\left(-\text{sqrt}\left(\frac{D^{1.127}f^{0.581}t}{25.2F^{1.228}}\right)\right)\right]. \tag{21}$$

The assessment of the goodness of fit of regression for $t_{50\%}$ is performed in the same way as for $\Delta\hat{T}_{\max}$. Figure 4 shows the comparison of the predicted and observed values of $t_{50\%}$. Table II shows that all parameters are significantly ($p < 0.001$) different from 0. The r^2 value for the $t_{50\%}$ model (or α model) is 0.844. The standard error of fit and the F-statistic for this model are 0.151 and 166.04, respectively. The 95% confidence interval based on the log $t_{50\%}$ model contains the true data point.

TABLE II. The parameter estimates and standard errors for the log $t_{50\%}$ model.

Variable	Parameter	Parameter estimate	Standard error	p-value
Constant	log E	1.083	0.047	6.68×10^{-40}
log f	g	−0.581	0.044	6.76×10^{-23}
log D	h	−1.127	0.097	7.18×10^{-20}
log F	i	1.228	0.068	7.94×10^{-32}

The combination of $\Delta\hat{T}_{\max}$ and $\hat{\alpha}$ models yields the desired expression of the temperature rise

$$\Delta T(t) = \frac{W^{1.029}f^{0.580}}{78.52D^{0.497}F^{0.614}}\left[1 - \exp\left(-\text{sqrt}\left(\frac{D^{1.127}f^{0.581}t}{25.2F^{1.228}}\right)\right)\right]. \tag{22}$$

Therefore, this generalized formula takes into account both the maximum temperature increase at an observation point and the time-dependent behavior of that temperature rise at a specific setting of a circular acoustic source. Figure 5 shows the predicted and observed values of the temperature rise as a function of insonation time for different exposure conditions when the beam is stationary. Satisfactory agreement between $\Delta\hat{T}(t)$ and $\Delta T(t)$ is obtained for these exposure conditions. It is impossible to present the results with all exposure conditions but the same trends are exhibited in other cases. $\Delta T(t)$ obtained from Eq. (22) is used to develop the SUT model for an exposure condition as discussed in Sec. II D.

D. The rate of adverse events due to ultrasound heating and the SUT model

Because the SUT model incorporates the concept of rate of induction of an adverse event relative to a reference exposure condition, this concept will be discussed first. The principle is that the thermal damage to a biological system, Ω, which occurs regardless of the temperature of the system, may be modeled as a first-order chemical rate equation (Church, 2007). From the Eyring equation for reaction rates in condensed or mixed-phase materials, it is possible to show that (Carstensen *et al.*, 1974)

$$\frac{d\Omega}{dt} = k = A\exp(-E_a/R_gT(t)), \tag{23}$$

where A is an arbitrary constant proportional to the change in entropy, E_a is the activation energy for the damage process, R_g is the gas constant, and T is the temperature at time t. In Eq. (23), Carstensen *et al.* (1974) assumed that the damage rate is characterized by a single activation energy but recognized that this could be an oversimplification. It is further assumed that when the probability of occurrence of an adverse event, i.e., the prevalence rate (PR), for the event is small, PR is proportional to the amount of damage that occurred during heating interval t_h (Miller *et al.*, 2005). PR is thus the integral of Eq. (23) over the heating interval t_h (Miller *et al.*, 2005) as follows:

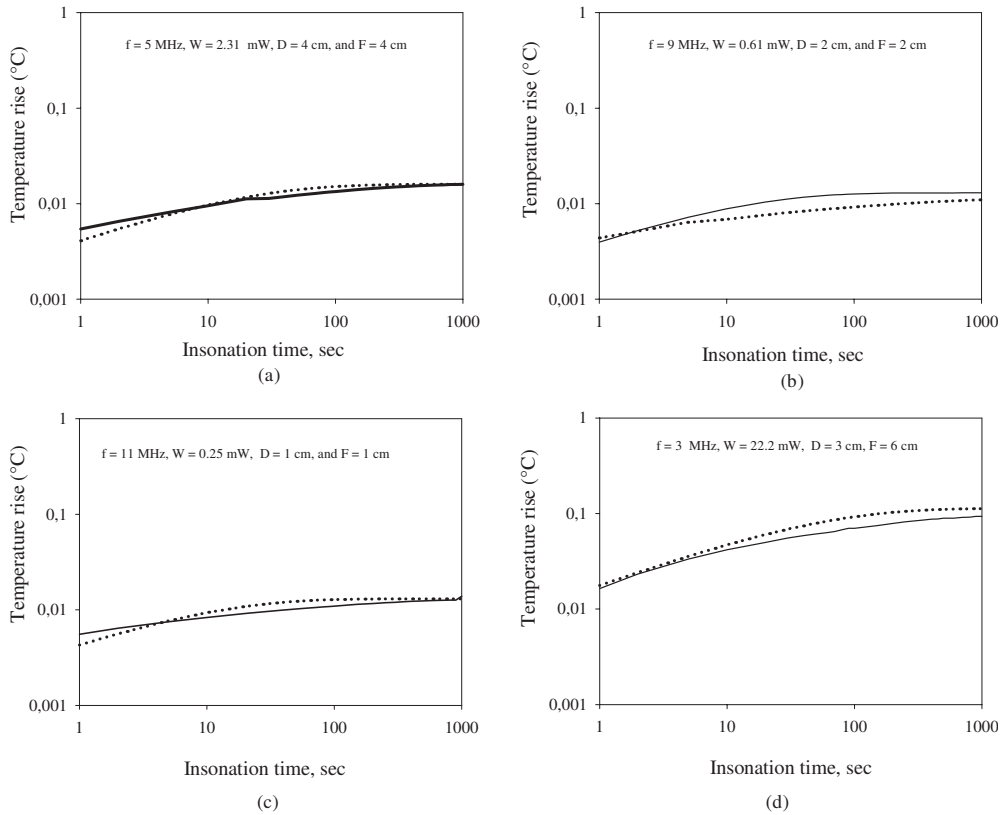

FIG. 5. The predicted and observed values of the temperature rise as a function of insonation time when (a) $f=5$ MHz, $W=2.31$ mW, $D=4$ cm, and $F=4$ cm; (b) $f=9$ MHz, $W=0.61$ mW, $D=2$ cm, and $F=2$ cm; (c) $f=11$ MHz, $W=0.25$ mW, $D=1$ cm, and $F=1$ cm; and (d) $f=3$ MHz, $W=22.2$ mW, $D=3$ cm, and $F=6$ cm. The solid and dotted lines, respectively, give the observed and predicted values.

$$\mathrm{PR} = C\int_{t_h} \exp(-E_a/R_g T(t))dt, \tag{24}$$

where C is a constant with units of t^{-1}. Equation (24) holds for all heating profiles, including normal physiological temperature, i.e., for $T(t)=T_o$ (Johnson and Pavelec, 1972a, 1972b). For a temperature increase ΔT of a few degrees above T_o, the PR for an adverse event relative to the background rate for the same event ΔPR is given by (Church, 2007)

$$\frac{\mathrm{PR}_1}{\mathrm{PR}_b} = \frac{1}{t_h}\int_{t_h} \exp\left(\frac{E_a \Delta T(t)}{R_g T_o[T_o + \Delta T(t)]}\right)dt. \tag{25}$$

The relative increase in the PR above the normal background rate, $\Delta\mathrm{PR}_1$, due to the temperature rise ΔT, is given by

$$\frac{\Delta\mathrm{PR}_1}{\mathrm{PR}_b} = \frac{1}{t_h}\int_{t_h} \exp\left(\frac{E_a \Delta T(t)}{R_g T_o[T_o + \Delta T(t)]}\right)dt - 1. \tag{26}$$

For two temperature rises depending on time, ΔT_1 and ΔT_2, the ratio of the corresponding increases in rates $\Delta\mathrm{PR}_1$ and $\Delta\mathrm{PR}_2$ is (Church, 2007)

$$\frac{\Delta\mathrm{PR}_2}{\Delta\mathrm{PR}_1} = \frac{\frac{1}{t_h}\int_{t_h} \exp\left(\frac{E_a C_T}{R_g T_0^2}\right)^{\Delta T_2/C_T} dt - 1}{\frac{1}{t_h}\int_{t_h} \exp\left(\frac{E_a C_T}{R_g T_0^2}\right)^{\Delta T_1/C_T} dt - 1}, \tag{27}$$

where $C_T=1$ K. Similar analysis was used to estimate the increase in the PR due to US heating (Germain *et al.*, 1985; Miller *et al.*, 2005). When the thermal normalization constant R is defined as (Dewey, 1994)

$$R = \exp(E_a C_T/R_g T_0^2), \tag{28}$$

Equation (27) becomes the following (Church, 2007):

$$\frac{\Delta\mathrm{PR}_2}{\Delta\mathrm{PR}_1} = \frac{\frac{1}{t_h}\int_{t_h} R^{\Delta T_2} dt - 1}{\frac{1}{t_h}\int_{t_h} R^{\Delta T_1} dt - 1}, \tag{29}$$

where $\Delta\mathrm{PR}_2$ is an estimate of the damage produced due to ΔT_2 ultrasound and $\Delta\mathrm{PR}_1$ is the estimated damage rate produced by a temperature rise of ΔT_1. This approach provides an expression for the relative change in the rate of induction of an effect as a result of ΔT_2 different from an arbitrarily chosen increase ΔT_1 (Church, 2007). Empirical values of R vary among species, tissues, temperature, and biological end points. In general, it is assumed that R values are fixed at

$R=2$ for $T>43$ °C and $R=4$ for $T<43$ °C (Sapareto and Dewey, 1984; Dewey, 1994).

To be considered potentially hazardous on thermal grounds, it appears that a DUS exposure must increase embryonic and fetal in-situ temperatures to 4° above the normal value for 4 min (Minister of Public Works and Government Services (Canada), 2001). Therefore, the reference exposure for our calculation is selected as 4 °C for 240 s. It is assumed in the present study that the thermal normalization constant R equals 4 because $T<43$ °C. It is because of this assumption that the present SUT model cannot be applied for $T>43$ °C. However, a new SUT model that takes into account the relative increase in the PR due to $T>43$ °C can be constructed. Therefore, for an ultrasound examination [induces $\Delta T_1(t)$] that produces an equal level of biological effect to this reference exposure, the following equation must hold:

$$\frac{1}{t_{\max}}\left(\int_0^{240} 4^4 dt + \int_{240}^{t_{\max}} 4^0 dt\right) = \frac{1}{t_{\max}}\left(\int_0^{t_h} 4^{\Delta T_1(t)} dt + \int_{t_h}^{t_{\max}} 4^0 dt\right), \tag{30}$$

where $t_{\max}$ is the maximum exposure time in clinical application of US, and t_h, that is, SUT, is the duration of scanning that would be no more hazardous than scanning at the reference output level. The heating profile is assumed to be 4 °C for an exposure time of 240 s except for the $(240-t_{\max})$ interval. For the rate of induction in relation to $\Delta T_1(t)$, it is assumed that the exposure time is in the range 0–SUT. Incorporating $t_{\max}$ into Eq. (30) results in the following expression:

$$\left(\int_0^{240} 4^4 dt + \int_{240}^{t_{\max}} 4^0 dt\right) = \left(\int_0^{\mathrm{SUT}} 4^{\Delta T_1(t)} dt + \int_{\mathrm{SUT}}^{t_{\max}} 4^0 dt\right), \tag{31}$$

$$61\ 200 = \left(\int_0^{\mathrm{SUT}} 4^{\Delta T_1(t)} dt - \mathrm{SUT}\right). \tag{32}$$

Equation (32) gives the SUT value of an exposure condition that produces heating of $\Delta T_1(t)$. The calculation given in Eq. (32) requires an integration that causes a computational burden. The calculation can be simplified by using the temperature rise value $\Delta T_1(\mathrm{SUT})$ at the end of SUT (Fig. 6). The integral in Eq. (32) is then replaced with the product of SUT and $4^{\Delta T_1(\mathrm{SUT})}$ as follows:

$$61\ 200 = \mathrm{SUT} \times 4^{\Delta T_1(\mathrm{SUT})} - \mathrm{SUT}. \tag{33}$$

For not very long values of SUT (say, below 3600 s), the "–SUT" term on the right side of Eq. (33) can be ignored. Hereinafter, the SUT value for an exposure condition is estimated by solving Eq. (33). Figure 6 shows a typical example of temperature rise induced by an US wave [see, for example, figures in Atkins and Duck (2003)]. Areas 2 and 3 under the curve are, respectively, the heating and cooling periods. The contributions of the temperature rise during both the heating and cooling periods have to be taken into account in the calculation of the relative increase in the PR. While Eq. (32) considers the sum of the contributions of areas 2 and 3, Eq. (33) takes into account the sum of the contributions of areas 1 and 2. High temperatures are present for a longer time in area 1 than in area 3. Therefore, the algorithm followed in this paper results in an additional safety margin because area 3 contributes less to SUT than area 1.

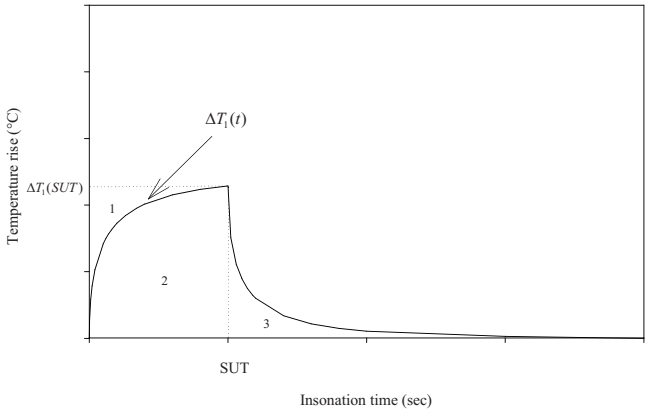

FIG. 6. A typical example of temperature rise due to DUS. The examination is terminated when $t=$SUT. The temperature rise in tissue at $t=$SUT is $\Delta T_1(\mathrm{SUT})$.

III. RESULTS AND DISCUSSION

To evaluate the effects of accuracy of the prediction and the worst-case assumption on the calculations, the thermal load (TL) is estimated by using the following equation:

$$\mathrm{TL} = t \times 4^{\Delta T_1(t)} - t. \tag{34}$$

Figure 7 shows the TL curves for 12 exposure conditions as a function of t and f-number. An insonation time at which a TL curve of a case intersects the "61 200" line is the SUT value for that case. Satisfactory agreement between the TL curves of the observed and predicted temperature rises is obtained except for a short exposure time (say, below 1000 s). These disagreements are observed because of the worst-case assumption discussed above. Although there is a relative higher error in the prediction of the lower $\Delta T_{\max}$, the predicted and observed SUT values for the corresponding exposure conditions are almost equal to each other [e.g., Fig. 7(a), f-number=1]. However, the prediction error in the higher $\Delta T_{\max}$ value (e.g., above 3 °C) is more important compared to that of the lower $\Delta T_{\max}$ during the calculation of the SUT [Fig. 7(b), f-number=4, $\Delta T_{\max}=3.414$ °C]. Therefore, the use of an additional safety margin is required, because the prediction is not on the safe side for all cases (Figs. 3 and 4) to which it can be applied. To examine the effect of the time dependency on the accuracy of the SUT, the calculation above is repeated with the assumption that $\Delta T_{\max}$ is achieved instantaneously, intentionally ignoring the interval at lower temperature. Table III shows the results from that the calculations for four exposure conditions. These results suggest no significant difference SUT values when maximum temperature rise <3 °C. However, ignoring the interval at lower

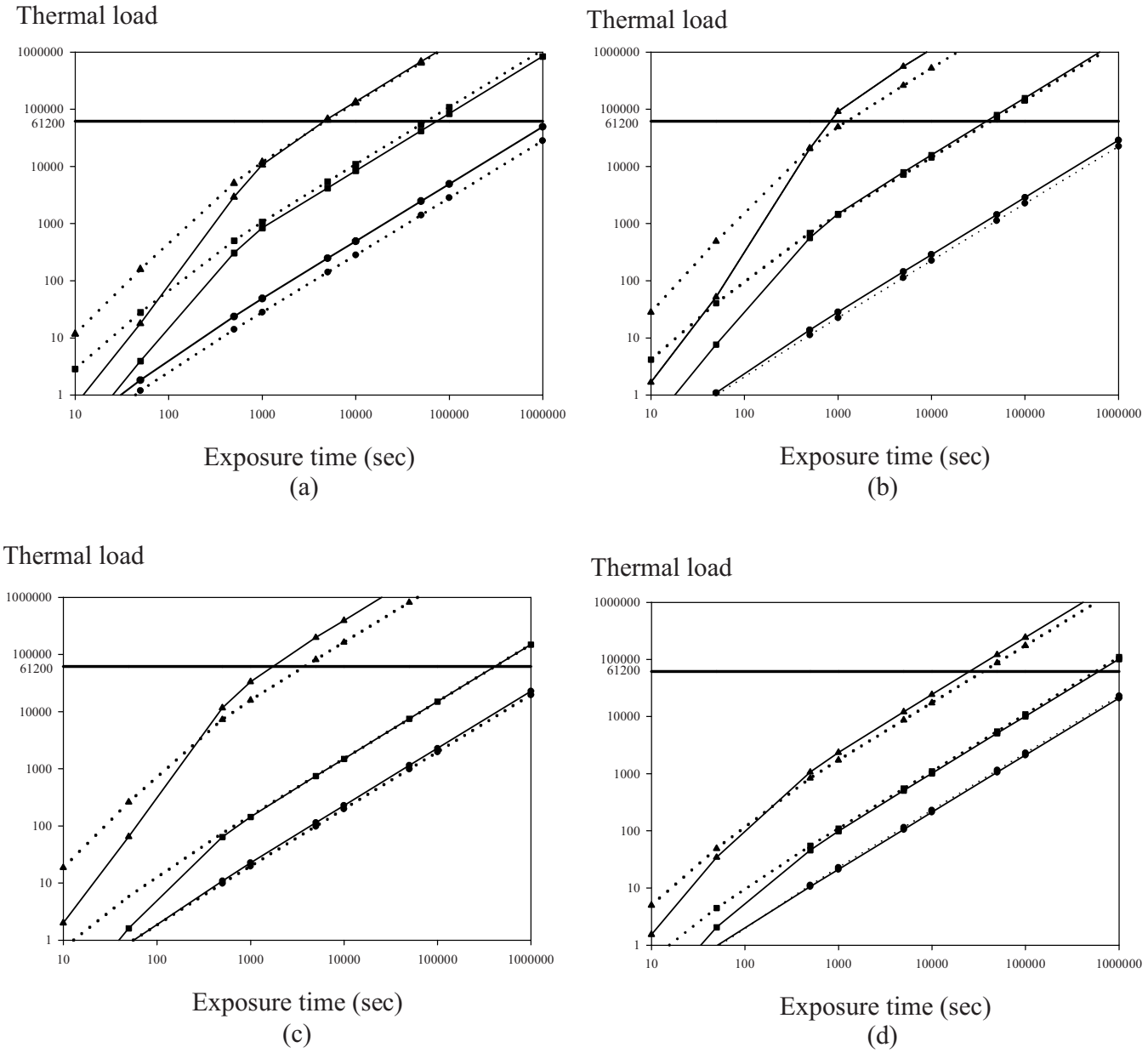

FIG. 7. The thermal load as a function of time and f-number when (a) $f=3$ MHz and $D=4$ cm, (b) $f=5$ MHz and $D=3$ cm, (c) $f=7$ MHz and $D=2$ cm, and (d) $f=9$ MHz and $D=1$ cm. The solid and dotted lines, respectively, show the observed and predicted values. The symbols ●, ■, and ▲ indicate f-number=1, f-number=3, and f-number=4, respectively.

temperature substantially affects the SUT value in the case of maximum temperature rise >3 °C.

Using the SUT model, it is possible to operate a DUS machine at the allowed maximum power W_a much higher than had been permitted previously power W under the FDA condition $I_{\mathrm{SPTA.3}}<720$ mW/cm^2 for a desired brief exposure time to enable the user to have better imaging quality while staying within safe limits. To determine W_a, it is as-

TABLE III. SUT values when considering and ignoring the interval at lower temperature for the four exposure conditions and the corresponding $\Delta\hat{T}_{\max}$ values.

Exposure condition	SUT value when considering the interval at lower temperature (s)	SUT value when ignoring the interval at lower temperature (s)	$\Delta\hat{T}_{\max}$ (°C)
$f=3$ MHz, $D=4$ cm, f-number=4	4750	4740	1.902
$f=5$ MHz, $D=3$ cm, f-number=4	1200	1150	2.869
$f=9$ MHz, $D=3$ cm, f-number=3	495	455	3.538
$f=7$ MHz, $D=4$ cm, f-number=3	200	109	4.570

TABLE IV. W, W_a, ΔT_{max}, and $\Delta \hat{T}_{max}$ values for the SUT=500 s.

Exposure condition	W (mW)	W_a based on the observed values (mW)	W_a based on the calculated values (mW)	ΔT_{max} (°C)	$\Delta \hat{T}_{max}$ (°C)
f=3 MHz, D=4 cm, f-number=4	712	1792	1424	1.932	1.902
f=5 MHz, D=3 cm, f-number=3	115.9	738	647	0.682	0.642
f=7 MHz, D=2 cm, f-number=1	0.77	173	190	0.016	0.014
f=9 MHz, D=1 cm, f-number=1	0.33	72	76	0.016	0.015

sumed that the user of the scanner wants to examine a region of interest for an exposure time of 500 s; hence SUT is selected as 500 s. Incorporating that SUT value into Eq. (33) leads to the following expression:

$$61\ 700 = 500 \times 4^{\Delta T_1(500)}. \tag{35}$$

For four exposure conditions, Table IV summarizes the corresponding power W, the observed and predicted values of a maximum temperature rise due to these conditions, and W_a values for SUT=500 s. These results suggest that the agreement between the observed and calculated values of W_a for an exposure condition is at the satisfactory level when the accurate temperature rise prediction is obtained. However, the TL value of calculated temperature rise is higher than that of the corresponding observed temperature rise for a case in which a deep focus is present because of the approach in the determination of the ΔT_{max} and $X(t)$ as stated above. Therefore, the proposed temperature rise model can conservatively calculate W_a for such a case (Table IV). The accuracy for a short exposure time has a substantial effect on the calculation of W_a because it is necessary to focus on short exposure times when the operator wants to use higher US power. Therefore, the present SUT model can be applied for brief exposure times [e.g., even lower than the reference exposure time (240 s)] by using an accurate model of the temperature rise.

The regression formulas in Eq. (22) are developed from results with SPHERESUM. The regression formulas are useful to perform a fast calculation for the case that the ODS tissue model applies, and are thus convenient to use in the SUT model. A more detailed calculation according to SPHERESUM is required in case one wants to deal with (possibly inhomogeneous) deviations from the ODS tissue model in an individual patient. Such a calculation to be used to accommodate variations in tissue properties in individual patients yields accurate results for the SUT model. Moreover, the SUT model can be applied to any beam and transducer geometries as well as any tissue model by using any method that estimates the temperature rise with satisfactory accuracy (e.g., Nyborg, 1988; O'Brien and Ellis, 1996; Curley, 1993; Lubbers *et al.*, 2003).

The procedure presented here for the construction of the temperature rise model is similar to that described by O'Brien *et al.* (2004) except for the consideration of exposure time. O'Brien *et al.* (2004) attempted to show the potential for improvement of the current TI model for a rectangular acoustic source. However, the SUT model is proposed to determine how long one piece of tissue can be insonated safely according to a threshold exposure. Church and O'Brien (2007) discussed the difficulties in the implementation of a time-dependent safety parameter. One of these is that the user of the US machine may be required to pay some attention to SUT rather than focusing on the patient. Another is that a detailed consideration associated with the occurrence of the change by the user in the ultrasonic field of transducers is required. The following expression can be used to calculate the SUT value for US exposure on a tissue sample in which the US field is changed $n(>1)$ times by the user as follows:

$$61\ 200 - t_1 4^{\Delta T_1(t_1)} + t_1 \cdots - (t_{n-1} - t_{n-2}) 4^{\Delta T_{n-1}(t_{n-1}-t_{n-2})} + (t_{n-1} - t_{n-2}) = (\mathrm{SUT} - t_{n-1}) 4^{\Delta T_n(\mathrm{SUT}-t_{n-1})} - (\mathrm{SUT} - t_{n-1}), \tag{36}$$

where the subscript indicates the nth examination period for that US exposure.

According to the SUT model, a sketch of the safety system can be given as follows. When the user of the machine starts the US examination for an observation point, the machine sets a SUT value depending on default settings of the selected transducer and application-specific reference exposure. When the ultrasonic field of transducers is altered during the examination of the same location, the system automatically sets a new value for SUT [Eq. (36)]. Additionally, when the user wants to examine another observation point far from the first point, the SUT value must be reset. However, it may not be clinically practical for the user to perform an additional action for this reset. The present authors consider that it is not necessary to reset the SUT even if the probe is moved to another tissue region. Therefore, this approach handles movement as an additional safety margin. At the end of the SUT, the user begins the new ultrasound examination after a brief waiting time (e.g., 1 or 2 min). SUT may be feasible but necessitates the measurement of the W, f, F, and D of an ultrasound probe by the manufacturer.

It is hoped that the real-time displaying of SUT enables the physician or sonographer to know the maximum duration of safe imaging. It is theoretically shown that SUT may be a more reliable indicator of potential bioeffects due to the thermal mechanism based on our tissue model. A number of experiments are required for validation of the SUT model. The present authors think that SUT may be sufficient for performing an appropriate risk-to-benefit judgment in applying diagnostic US, after carrying out a detailed study about the aforementioned difficulties.

Abbott, J. G. (**1999**). "Rationale and derivation of MI and TI—A review," Ultrasound Med. Biol. **25**, 431–441.

Abramowicz, J. S., Barnett, S. B., Duck, F. A., Edmonds, P. D., Hynynen, K. H., and Ziskin, M. C. (**2008**). "Fetal thermal effects of diagnostic ultrasound," J. Ultrasound Med. **27**, 541–559.

AIUM (**2008**). "AIUM consensus report on potential bioeffects of diagnostic ultrasound," J. Ultrasound Med. **27**, 503–515.

AIUM/NEMA (**1992**). *Standard for Real-Time Display of Thermal and Mechanical Indices on Diagnostic Ultrasound Equipment* (AIUM/NEMA, Laurel, MD and Rosslyn, VA).

Atkins, T. J., and Duck, F. A. (**2003**). "Heating caused by selected pulsed Doppler and physiotherapy ultrasound beams measured using thermal test objects," Eur. J. Ultrasound **16**, 243–252.

Barnett, S. B. (**2001**). "Intracranial temperature elevation from diagnostic ultrasound," Ultrasound Med. Biol. **27**, 883–888.

Barnett, S. B., Haar, G. R. T., Ziskin, M. C., Rott, H. D., Duck, F. A., and Maeda, K. (**2000**). "International recommendations and guidelines for the safe use of diagnostic ultrasound in medicine," Ultrasound Med. Biol. **26**, 355–366.

Barnett, S. B., Rott, H. D., Haar, G. R. T., Ziskin, M. C., and Maeda, K. (**1997**). "The sensitivity of biological tissue to ultrasound," Ultrasound Med. Biol. **23**, 805–812.

Bosward, K. L., Barnett, S. B., Wood, A. K. W., Edwards, M. J., and Kossoff, G. (**1993**). "Heating of guinea-pig fetal brain during exposure to pulsed ultrasound," Ultrasound Med. Biol. **19**, 415–424.

Carstensen, E. L., Child, S. Z., Norton, S., and Nyborg, W. L. (**1990**). "Ultrasonic heating of the skull," J. Acoust. Soc. Am. **87**, 1310–1317.

Carstensen, E. L., Miller, M. W., and Linke, C. A. (**1974**). "Biological effects of ultrasound," J. Biol. Phys. **2**, 173–192.

Church, C. C. (**2002**). "Spontaneous, homogeneous nucleation, inertial cavitation and the safety of diagnostic ultrasound," Ultrasound Med. Biol. **28**, 1349–1364.

Church, C. C. (**2005**). "Frequency, pulse length, and the mechanical index," ARLO **6**, 162–168.

Church, C. C. (**2007**). "A proposal to clarify the relationship between the thermal index and the corresponding risk to the patient," Ultrasound Med. Biol. **33**, 1489–1494.

Church, C. C., Carstensen, E. L., Nyborg, W. L., Carson, P. L., Frizzell, L. A., and Bailey, M. R. (**2008**). "The risk of exposure do diagnostic ultrasound in postnatal subjects," J. Ultrasound Med. **27**, 565–592.

Church, C. C., and Miller, M. W. (**2007**). "Quantification of risk from fetal exposure to diagnostic ultrasound," Prog. Biophys. Mol. Biol. **93**, 331–353.

Church, C. C., and O'Brien, W. D., Jr. (**2007**). "Evaluation of the threshold for lung hemorrhage by diagnostic ultrasound and a proposed new safety index," Ultrasound Med. Biol. **33**, 810–818.

Curley, M. G. (**1993**). "Soft tissue temperature rise caused by scanned, diagnostic ultrasound," IEEE Trans. Ultrason. Ferroelectr. Freq. Control **40**, 59–66.

Dalecki, D. (**2004**). "Mechanical bioeffects of ultrasound," Annu. Rev. Biomed. Eng. **6**, 229–248.

Dewey, W. C. (**1994**). "Arrhenius relationships from the molecule and cell to the clinic," Int. J. Hyperthermia **10**, 457–483.

Drewniak, J. L., Carnes, K. I., and Dunn, F. (**1989**). "In vitro ultrasonic heating of fetal bone," J. Acoust. Soc. Am. **86**, 1254–1258.

Drewniak, J. L., and Dunn, F. (**1996**). "An experimentally obtainable heat source due to absorption of ultrasound in biological media," J. Acoust. Soc. Am. **100**, 1250–1253.

FDA (**1985**). *501(k) Guide for Measuring and Reporting Acoustic Output of Diagnostic Ultrasound Medical Devices* (Center for Devices and Radiological Health, US FDA, Rockville, MD).

FDA (**1987**). *Diagnostic Ultrasound Guidance Update* (Center for Devices and Radiological Health, US FDA, Rockville, MD).

FDA (**1993**). *Revised 510(k) Diagnostic Ultrasound Guidance for 1993* (Center for Devices and Radiological Health, US FDA, Rockville, MD).

FDA (**1997**). "*Information for Manufacturers Seeking Marketing Clearance of Diagnostic Ultrasound Systems and Transducers*," (Center for Devices and Radiological Health, US FDA, Rockville, MD).

Fry, W. J., and Fry, R. B. (**1954a**). "Determination of absolute sound levels and acoustic absorption coefficients by thermocouple probes—Theory," J. Acoust. Soc. Am. **26**, 294–310.

Fry, W. J., and Fry, R. B. (**1954b**). "Determination of absolute sound levels and acoustic absorption coefficients by thermocouple probes—Experiments," J. Acoust. Soc. Am. **26**, 311–317.

Germain, M. A., Webster, W. S., and Edwards, M. J. (**1985**). "Hyperthermia as a teratogen: Parameters determining hyperthermia-induced head defects in the rat," Teratology **31**, 265–272.

Hekkenberg, R. T., and Bezemer, R. A. (**2004**). "On the development of a method to measure the surface temperature of ultrasonic diagnostic transducers," J. Phys.: Conf. Ser. **1**, 84–89.

Herman, B. A., and Harris, G. R. (**1999**). "Theoretical study of steady—State temperature rise within the eye due to ultrasound insonation," IEEE Trans. Ultrason. Ferroelectr. Freq. Control **46**, 1566–1574.

Horder, M. M., Barnett, S. B., Vella, G. J., Edwards, M. J., and Wood, K. W. (**1998**). "In vivo heating of the guinea-pig fetal brain by pulsed ultrasound and estimates of thermal index," Ultrasound Med. Biol. **24**, 1467–1474.

Jago, J. R., Henderson, J., Whittingham, T. A., and Mitchell, G. (**1999**). "A comparison of AIUM/NEMA thermal indices with calculated temperature rises for a simple third-trimester pregnancy tissue model," Ultrasound Med. Biol. **25**, 623–628.

Johnson, H. A., and Pavelec, M. (**1972a**). "Thermal injury due to normal body temperature," Am. J. Pathol. **66**, 557–564.

Johnson, H. A., and Pavelec, M. (**1972b**). "Thermal noise in cells. A cause of spontaneous loss of cell function," Am. J. Pathol. **69**, 119–130.

Lubbers, J., Hekkenberg, R. T., and Bezemer, R. A. (**2003**). "Time to threshold (TT), a safety parameter for heating by diagnostic ultrasound," Ultrasound Med. Biol. **29**, 755–764.

Macovski, A. (**1983**). *Medical Imaging System* (Prentice-Hall, Englewood Cliffs, NJ), pp. 190–191.

Miller, M. W., Miller, H. E., and Church, C. C. (**2005**). "A new perspective on hyperthermia-induced birth defects: The role of activation energy and its relation to obstetric ultrasound," J. Therm. Biol. **30**, 400–409.

Minister of Public Works and Government Services (Canada) (**2001**). "Guidelines for the safe use of diagnostic ultrasound," 01-HECS-255.

NCRP (**1992**). "Exposure criteria for medical diagnostic ultrasound: I. Criteria based on thermal mechanism," Report No. 113, NCRP Publications, Bethesda, MD.

Nyborg, W. L. (**1988**). "Solutions of the bio-heat transfer equation," Phys. Med. Biol. **33**, 785–792.

Nyborg, W. L., and Wu, J. (**1994**). "Solution of the linear bio-heat transfer equation," Phys. Med. Biol. **39**, 924–926.

O'Brien, W. D., Jr. (**2007**). "Ultrasound–biophysics mechanisms," Prog. Biophys. Mol. Biol. **93**, 212–255.

O'Brien, W. D., Jr., Deng, C. X., Harris, G. R., Herman, B. A., Merritt, C. R., Sanghvi, N., and Zachary, J. F. (**2008**). "The risk of exposure to diagnostic ultrasound in postnatal subjects," J. Ultrasound Med. **27**, 517–535.

O'Brien, W. D., Jr., and Ellis, D. S. (**1996**). "Comparison of the output display standard's TIS estimates with independently determined maximum temperature increase calculations," Proc.-IEEE Ultrason. Symp. **2**, 1171–1175.

O'Brien, W. D., Jr., and Ellis, D. S. (**1999**). "Evaluation of the unscanned soft-tissue thermal index," IEEE Trans. Ultrason. Ferroelectr. Freq. Control **46**, 1459–1476.

O'Brien, W. D., Jr., Yang, Y., and Simpson, D. G. (**2004**). "Evaluation of unscanned-mode soft-tissue thermal index for rectangular sources and proposed new indices," Ultrasound Med. Biol. **30**, 965–972.

Pennes, H. H. (**1948**). "Analysis of tissue and arterial blood temperatures in the resting human forearm," J. Appl. Physiol. **1**, 93–122.

Sapareto, S. A., and Dewey, W. C. (**1984**). "Thermal dose determination in cancer therapy," Int. J. Radiat. Oncol., Biol., Phys. **10**, 787–800.

Wells, P. N. T. (**2006**). "Ultrasound imaging," Phys. Med. Biol. **51**, R83–R98.

Ziskin, M. C., and Barnett, S. B. (**2001**). "Ultrasound and the developing central nervous system," Ultrasound Med. Biol. **27**, 875–876.

A Fabry–Pérot fiber-optic ultrasonic hydrophone for the simultaneous measurement of temperature and acoustic pressure

Paul Morris[a)]
Department of Medical Physics and Bioengineering, University College London, Gower Street, London WC1E 6BT, United Kingdom

Andrew Hurrell
Precision Acoustics Ltd., Hampton Farm Business Park, Higher Bockhampton, Dorchester DT2 8QH, United Kingdom

Adam Shaw
Quality of Life Division, National Physical Laboratory, Hampton Road, Teddington, Middlesex TW11 0LW, United Kingdom

Edward Zhang and Paul Beard
Department of Medical Physics and Bioengineering, University College London, Gower Street, London WC1E 6BT, United Kingdom

(Received 9 October 2008; revised 11 March 2009; accepted 16 March 2009)

A dual sensing fiber-optic hydrophone that can make simultaneous measurements of acoustic pressure and temperature at the same location has been developed for characterizing ultrasound fields and ultrasound-induced heating. The transduction mechanism is based on the detection of acoustically- and thermally-induced thickness changes in a polymer film Fabry–Pérot interferometer deposited at the tip of a single mode optical fiber. The sensor provides a peak noise-equivalent pressure of 15 kPa (at 5 MHz, over a 20 MHz measurement bandwidth), an acoustic bandwidth of 50 MHz, and an optically defined element size of 10 μm. As well as measuring acoustic pressure, temperature changes up to 70 °C can be measured, with a resolution of 0.34 °C. To evaluate the thermal measurement capability of the sensor, measurements were made at the focus of a high-intensity focused ultrasound (HIFU) field in a tissue mimicking phantom. These showed that the sensor is not susceptible to viscous heating, is able to withstand high intensity fields, and can simultaneously acquire acoustic waveforms while monitoring induced temperature rises. These attributes, along with flexibility, small physical size (OD ~ 150 μm), immunity to Electro-Magnetic Interference (EMI), and low sensor cost, suggest that this type of hydrophone may provide a practical alternative to piezoelectric based hydrophones.
 [DOI: 10.1121/1.3117437]

PACS number(s): 43.35.Yb, 43.35.Wa, 43.30.Xm [TDM] Pages: 3611–3622

I. INTRODUCTION

Ultrasonic hydrophones are widely used to characterize diagnostic and therapeutic medical ultrasound fields. In both cases there are stringent measurement requirements to be met.[1] The increasing prevalence of higher frequency ultrasound in diagnostic imaging devices, such as very high frequency ocular and intravascular scanners, calls for measurement bandwidths that extend to several tens of megahertz. In addition, to minimize spatial averaging errors at these frequencies, an element size smaller than the acoustic wavelength (≈75 μm at 20 MHz in water) is desirable. Although piezoelectric polyvinylidene (PVdF) needle and membrane hydrophones can readily meet the bandwidth requirement, achieving element sizes on this scale with adequate sensitivity is problematic as sensitivity decreases with decreasing element area.

Characterizing therapeutic ultrasound fields poses a somewhat different measurement challenge. The hydrophone bandwidth and element size requirements are often less demanding than for diagnostic ultrasound measurements since the fundamental frequencies used tend to be in the low megahertz range. The greater challenge lies in withstanding the hostile environment that can be produced, particularly where high amplitude or high intensity focused beams are employed, such as in extracorporeal lithotripsy or high-intensity focused ultrasound (HIFU) therapy. In the latter case, for example, the cavitational activity and temperature rises induced at clinical intensities can readily damage PVDF hydrophones. A further requirement for procedures that exploit thermal effects to provide a therapeutic benefit is measurement of the induced temperature rise within the sound field. This is most commonly achieved using wire thermo-

a)Author to whom correspondence should be addressed. Electronic mail: psmorris@medphys.ucl.ac.uk

couple probes. These are acoustically robust, sensitive, and small enough to be inserted into tissue or a tissue mimicking phantom for *in-situ* measurements.[2,3] However, they can suffer from significant measurement errors due to viscous self-heating induced by the ultrasound field.[4] Although the thin-film thermocouple[5–7]does not suffer from this limitation, its large size prevents it from being used *in-situ*. Furthermore, it is fragile and susceptible to damage by high intensity fields. It would also be advantageous if both the temperature rise and the acoustic pressure could be measured simultaneously at the same location. This would enable the two measurands to be correlated in order to study the relationship between acoustic and thermal effects, for example, to elucidate the role that cavitation plays in enhancing heating in HIFU therapy. To our knowledge, this type of dual measurement capability has not previously been demonstrated using non-optical methods.

Fiber optic hydrophones offer the prospect of overcoming some or all of the above limitations. The most practically applicable type of fiber-optic hydrophone is the extrinsic type. This employs a fiber-optic downlead to deliver light to and from an optical sensor, or some transducing mechanism, at the end of the fiber. In principle, the sensitive region is defined by the spot size of the incident illumination. This, in turn, is given by the fiber core diameter which is typically a few microns for a single mode optical fiber. This offers the prospect of providing acoustically small element sizes at frequencies of tens of megahertz. Other generic advantages include the small fiber diameter ($\approx$150 μm), a flexible probe type configuration, robustness, low cost, immunity to EMI, and in some cases the ability to measure temperature as well as pressure. Several types of extrinsic fiber-optic hydrophone have been investigated for measurement applications in medical ultrasound. The simplest is based on the detection of pressure-induced changes in the Fresnel reflection coefficient at the tip of an optical fiber.[8–11] This approach offers very low sensor cost, technical simplicity, and the potential for exceptionally wide bandwidth, limited by the wavelength of light and thus potentially extending to several hundred megahertz. Furthermore, there is the potential to measure ultrasound-induced heating since the Fresnel reflection coefficient is dependent on temperature as well as pressure. The fundamental disadvantage, however, is low acoustic sensitivity with a broadband noise-equivalent-pressure (NEP) typically of the order of 1 MPa. This limits its application to the measurement of temporally stable signals that can be signal averaged over many cycles or the output of high amplitude sources, such as shockwave lithotripters.[9,12,13]

Higher detection sensitivities, comparable to those of PVDF hydrophones, have been obtained by exploiting interferometric methods. A promising approach that has been explored for medical ultrasound metrology is based on the detection of acoustically-induced changes in the optical thickness of a solid Fabry–Pérot interferometer (FPI) located at the tip of an optical fiber. Two variants of this approach, distinguished by the materials and methods used to fabricate the FPI, have been demonstrated. One involves sputtering onto the fiber tip, a multilayer dielectric sensing structure comprising a central SiO_2 spacer sandwiched between two stacks of alternating SiO_2 and Nb_2O_5 layers—the latter form the mirrors of the FPI.[14] The small thickness of the multilayer structure (typically a few microns) enables bandwidths extending to several hundred megahertz to be achieved.[15] Although this type of sensor has not been evaluated for the purpose of measuring ultrasound-induced heating, its potential for measuring temperature has been demonstrated by detecting laser-induced thermal transients.[16] The second approach employs a different design, one in which the spacer between the two FPI mirrors is a polymer.[17–20] The lower Young modulus of polymers compared to relatively hard dielectrics such as SiO_2 results in larger acoustically-induced phase shifts and thus higher sensitivity for a given FPI finesse.[21] The thickness of the spacer tends to be larger (10–100 μm) than the SiO_2 spacer referred to above providing bandwidths in the tens of megahertz range. It also results in a smaller free spectral range, thereby reducing the required wavelength tuning range for the interrogating laser. An early laboratory prototype hydrophone system based on this type of sensor has been demonstrated previously.[20] This system employed a free space 850 nm distributed Bragg reflector (DBR) laser diode as the interrogation source (the wavelength of which was manually adjusted in order to optimally bias the FPI) and provided a bandwidth of 25 MHz and a peak NEP of 10 kPa (over a 25 MHz measurement bandwidth). This type of sensor has also been used to detect laser-induced thermal transients[22] and a preliminary study has been undertaken to evaluate its ability to measure ultrasound-induced heating.[23]

In this paper, we provide a detailed account of a system based on this approach but incorporating several key technical developments. These include modifying the design of the sensor and the system detection optoelectronics to extend the acoustic bandwidth to 50 MHz and the use of a computer controlled discretely tunable "telecom" laser to interrogate the sensor. The latter significantly enhances the practical utility of the concept as it enables the FPI biasing procedure to be fully automated. Furthermore, because the laser is fiber-coupled, stability problems associated with coupling free-space beams into single mode fibers are eliminated. A major advance has been the development and implementation of a sensor interrogation algorithm that enables simultaneous measurements of temperature and acoustic pressure to be made for the first time.

Section II A describes the acoustic and thermal transduction mechanisms of the sensor and the interrogation scheme used to recover pressure and temperature simultaneously. Sections II B–II D describe the procedure used to fabricate the sensor, the design of the instrumentation required to interrogate it, and the practical implementation of the interrogation scheme. In Sec. III, the acoustic performance in terms of sensitivity, linearity, frequency response, and directivity are discussed, and in Sec. IV the thermal sensitivity and response time are described. The dual measurement capability of the system, demonstrated by making measurements of ultrasound-induced heating in a tissue phantom, is discussed in Sec. V.

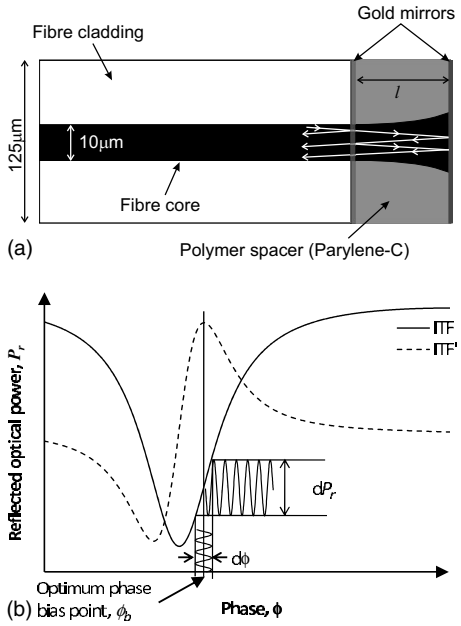

FIG. 1. (a) Schematic of FPI sensor. (b) Phase (ITF) and its first derivative (ITF′). Operation at optimum phase bias point ϕ_b for the linear detection of a small acoustically-induced phase modulation $d\phi$ is illustrated.

II. THE FABRY–PÉROT FIBER OPTIC HYDROPHONE

A. Principles of operation

A schematic of the tip of the fiber-optic hydrophone is shown in Fig. 1(a). The sensing element is a FPI which comprises a thin ($l \approx 10$ μm) Parylene-C polymer film spacer sandwiched between a pair of gold mirrors. Light emitted by a tunable laser is incident on the FPI and is multiply reflected from both mirrors and interferes as it re-enters the fiber. Acoustically- or thermally-induced changes in the optical thickness of the polymer spacer produce a corresponding phase shift between the light reflected from the two mirrors. This is demodulated to obtain a measure of pressure or temperature. In Secs. II A 1 and II A 2, the transduction mechanisms for each measurand are described.

1. Acoustic transduction mechanism

The variation in reflected optical power, P_r, from a FPI as a function of phase ϕ is termed the phase interferometer transfer function (ITF) where ϕ is given by

$$\phi = \frac{4\pi nl}{\lambda}, \tag{1}$$

where n and l are the refractive index and thickness of the polymer spacer, respectively, and λ is the optical wavelength. For a plane parallel FPI formed with non-absorbing mirrors and illuminated with a collimated beam, the phase ITF takes the form of the Airy function, an example of which is shown in Fig. 1(b) along with its derivative. In order to make an acoustic measurement, the laser wavelength is adjusted so that $\phi = \phi_b$, where ϕ_b is the phase corresponding to the peak derivative of the phase ITF. At this wavelength, the sensitivity and linearity are at a maximum and the FPI is said to be optimally biased. Under these conditions, a small acoustically-induced phase shift $d\phi$ can be regarded as being linearly converted to a corresponding change in the reflected optical power, dP_r.

The sensitivity, the reflected optical power modulation per unit acoustic pressure, at ϕ_b is given by

$$\frac{dP_r}{dp} = \frac{dP_r}{d\phi}\frac{d\phi}{dp}, \tag{2}$$

where p is the acoustic pressure. $dP_r/d\phi$ is the first derivative of the ITF at ϕ_b and is termed the optical phase sensitivity. It is dependent on the incident optical power and the finesse of the FPI. The finesse is in turn defined by the mirror reflectivities and the phase dispersion due to the divergence of the incident beam and non-uniformities in the spacer thickness.

$d\phi/dp$ is termed the acoustic phase sensitivity and represents the magnitude of the optical phase shift produced per unit pressure. The change in phase arises from a change in the optical thickness of the spacer and may be caused by two mechanisms, a change in physical thickness or a change in refractive index. In general, the acoustic phase sensitivity can be written as

$$\frac{d\phi}{dp} = \frac{4\pi}{\lambda}\left(n_0\frac{dl}{dp} + l\frac{dn}{dp}\right)P_l(k), \tag{3}$$

where dl is a small change in the spacer thickness and dn is a small change in the refractive index. $P_l(k)$ is a frequency modifying term that accounts for the spatial variation of stress within the spacer that occurs when an acoustic wave is incident on the sensor and is dependent on the geometry, structure, and physical properties of the fiber tip.[24] Equation (3) indicates that $d\phi/dp$ depends on the elasto-mechanical and elasto-optic properties of the spacer, although for the polymer (Parylene-C) spacers used in the sensors described in this study, the elasto-optic effect can be neglected.[25] Equation (3) can therefore be written as

$$\frac{d\phi}{dp} = \frac{4\pi n}{\lambda}\frac{l}{E}P_l(k), \tag{4}$$

where E is the Young modulus of the spacer. Equation (4) shows that the sensitivity is proportional to the thickness of the spacer and inversely proportional to the Young modulus of the material. Thus a sensor with a thicker spacer will have a higher sensitivity but reduced bandwidth since the sensor responds to the spatial average of the stress over its sensitive volume.

2. Thermal transduction mechanism

When subjected to a change in temperature, the optical thickness of the FPI spacer will change due to thermal expansion and the change in refractive index (the thermo-optic effect). In principle, the resulting phase shift could be recovered by optimally biasing the FPI and measuring the reflected optical power modulation as described in Sec. II A 1. Indeed, such an approach has been employed previously to make temperature measurements using FPIs.[16,22,26,27] However, this method has several limitations. First, it is expected that for a polymer spacer, even a relatively small temperature change of only few degrees will induce a phase shift that

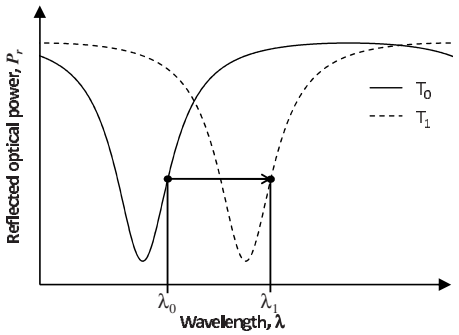

FIG. 2. Effect of temperature on the wavelength ITF. A change in temperature from T_0 to T_1 produces a linear shift in the optimum bias wavelength from λ_0 to λ_1.

exceeds the phase range over which the ITF is linear around the optimum bias point ϕ_b. As well as compromising the linearity of the temperature measurement, a phase shift of this magnitude will shift the bias point to the extent that it no longer corresponds to the peak derivative of the ITF thus reducing the acoustic sensitivity. This will clearly be problematic if simultaneous acoustic and temperature measurements are required. In addition, unlike acoustic measurements, the relatively long timescale (milliseconds to seconds) of thermal excursions makes temperature measurements susceptible to low frequency noise such as that due to fluctuations in the laser output power. For these reasons, the following alternative interrogation scheme which relies on tracking the optimum bias wavelength has been implemented.

Figure 2 shows the reflected optical power as a function of wavelength. This is termed the wavelength interferometer transfer function. At temperature T_0, an optimum bias wavelength, λ_0, can be found which corresponds to ϕ_b, the phase bias at the peak derivative of the phase ITF in Fig. 1(a). Thus we can write

$$\phi_b = \frac{4\pi(nl)_0}{\lambda_0}, \tag{5}$$

where $(nl)_0$ is the optical thickness at temperature T_0. If the wavelength ITF is measured at a different temperature, T_1, a different wavelength, λ_1, is now found to correspond to ϕ_b and we can write

$$\phi_b = \frac{4\pi(nl)_1}{\lambda_1}, \tag{6}$$

where $(nl)_1$ is the optical thickness at T_1. From Eqs. (5) and (6), it can be seen that the change in the optimum bias wavelength, $\Delta\lambda = \lambda_1 - \lambda_0$, which occurs for a temperature change $\Delta T = T_1 - T_0$, is given by

$$\Delta\lambda = \frac{4\pi}{\phi_b}\Delta(nl), \tag{7}$$

where $\Delta(nl)$ is the change in optical thickness caused by the temperature change. Providing $\Delta(nl)$ is directly proportional to the change in temperature, the shift in the optimum bias wavelength will also be proportional to the temperature change. This wavelength shift could, in principle, be measured by continually sweeping the laser wavelength and tracking the wavelength ITF as it shifts along the horizontal axis with temperature. If temperature alone is being measured, this approach would be feasible provided that the time to sweep the laser wavelength is small compared to the timescale of the temperature change. However, since the FPI is only transiently at the optimum phase bias point, ϕ_b, it would be difficult to make simultaneous ultrasound measurements with this method.

For this reason, an alternative interrogation scheme was developed. This requires initially tuning the laser output to the optimum bias wavelength and thereafter continuously monitoring the reflected optical power P_r. As soon as P_r changes due to a temperature-induced phase shift, the laser wavelength is immediately re-tuned so as to return P_r to its initial value. By continually re-adjusting the laser wavelength to maintain a constant P_r, the thermally-induced shift in the optimum bias wavelength, and therefore the temperature change, can be tracked over time. Providing the laser wavelength is rapidly re-tuned (before the thermally-induced phase shift becomes appreciable), the system will always be operating at, or close to, ϕ_b thus allowing an acoustic measurement to be made. In this way ultrasound waveforms can be acquired at the same time that the temperature is being monitored.

The sensitivity of the temperature change measurement using this method is dependent on several factors: first, the thermo-mechanical and thermo-optic properties of the Parylene spacer. The phase change, $d\phi$, induced by a temperature change, dT, can be written as

$$\frac{d\phi}{dT} = \frac{4\pi l}{\lambda}\left(n_0\alpha + \frac{dn}{dT}\right), \tag{8}$$

where α is the coefficient of (linear) thermal expansion and n_0 is the refractive index at T_0. For Parylene-C,[28] $\alpha = 3.5 \times 10^{-5}\ ^\circ\mathrm{C}^{-1}$ but no data exist for the thermo-optic coefficient dn/dT. However, Zhang *et al.*[29] proposed an empirical formula for the calculation of dn/dT of polymers based on the value of α. Using this, a value of $6 \times 10^{-5}\ ^\circ\mathrm{C}^{-1}$ is obtained. Unlike the elasto-optic effect, the thermo-optic cannot therefore be neglected. Second, the optical phase sensitivity $(dP_r/d\phi)$ influences the thermal sensitivity since it defines the minimum detectable reflected power variation, which is used to determine when it is necessary to re-tune the laser to maintain a constant P_r. In addition, the minimum detectable temperature change depends on the wavelength tuning resolution of the laser.

B. Sensor fabrication

The sensors were fabricated in batches of 32 as follows. A 2 m length of 1550 nm single mode optical fiber (outer diameter of 125 μm and core diameter of 9 μm) is cleaved using an ultrasonic fiber cleaver (PK technology FK11). The fibers are then loaded into a mount for the deposition of the reflective coatings and polymer spacer. Thin gold films are used for the reflective coatings, with the reflectivity of the coating being controlled by the thickness of the film. A numerical model of the ITF was developed in order to inform

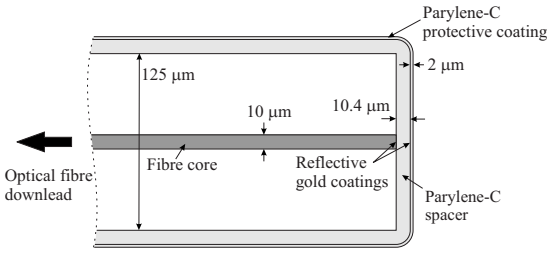

FIG. 3. Schematic of the FPI sensing structure deposited at the tip of the optical fiber.

the choice of mirror reflectivity.[24] It was found that a front mirror reflectivity of approximately 75% and a back mirror reflectivity of 98% (the maximum achievable with gold between 1500 and 1600 nm) were optimal. The gold coatings are deposited onto the tip of the optical fiber via a standard dc sputtering process. The polymer spacer was formed by vapor deposition of Parylene-C, poly(chloro-*para*-xylene).[20] Sensors were fabricated according to the process outlined above with a spacer thickness of 10.4 μm. In order to protect the sensing element, a second Parylene layer 2 μm thick was deposited over the tip of the fiber, as shown in Fig. 3.

There are several advantages of the above fabrication process. The use of a vapor phase deposition process to form the polymer spacer enables a highly conformal coating with excellent surface finish, good optical clarity, and uniformity of thickness to be achieved. These attributes allow a high quality FPI with good fringe visibility and finesse to be produced. The thickness can also be precisely controlled ($<$0.1 μm) to design sensors with specific free spectral ranges and acoustic bandwidths. Furthermore, the use of all vacuum deposition methods allows batch fabrication of large quantities of sensors with high repeatability at low unit cost.

C. The interrogation unit

Figure 4(a) shows a schematic of the system used to interrogate the sensor. The components within the dotted box make up the interrogation unit which has been developed into a fully integrated portable prototype [Fig. 4(b)]. The sensor downlead is terminated with an FC/APC connector which is inserted in the front panel of the interrogation unit. Light from a tunable laser is delivered to the downlead by means of a 2×2 fiber-optic coupler. Light reflected from the FPI is then routed to an InGaAs photodiode again via the coupler. A second photodiode is used to monitor the direct output from the laser. The photodiode measuring the light reflected from the sensor has both ac and dc coupled outputs. The dc coupled output is connected to an analog to digital data acquisition device which is connected to a control personal computer (PC) via a universal serial bus (USB) interface. This allows measurement of the reflected optical power from the sensor in order to measure the ITF and monitor temperature changes. The ac coupled output (-3 dB cut-off frequency: 50 kHz) is connected to an oscilloscope for measurement of acoustic waveforms.

The laser used in the system is an AltoWave 1100 tunable laser from Intune Technologies Ltd. The laser has a 40 nm tuning range in the telecoms C-band (1528–1568 nm)

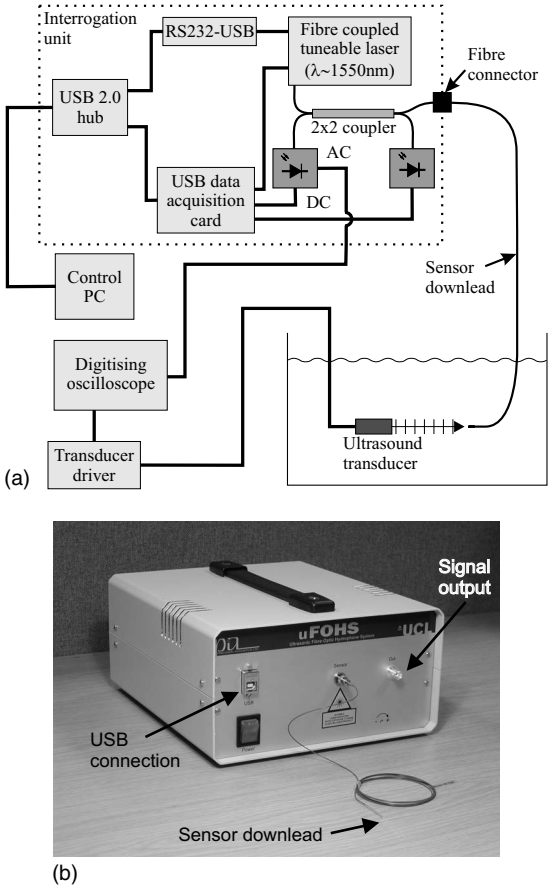

FIG. 4. (a) Schematic of the fiber-optic hydrophone system. The components contained in the dotted box form the interrogation unit shown in the photograph (b).

and is based on the sampled-grating (SG) DBR design. SG-DBR lasers are monolithically integrated semiconductor lasers and have no moving parts. This allows rapid, electronic wavelength tuning which is controlled via an RS232 communications interface. The AltoWave 1100 has an optical output power of approximately 8 mW, which is constant over its tuning range ($\pm$0.2 dB). It is tunable over 600 discrete wavelength channels, separated by a constant optical frequency of 8.33 GHz ($\approx$0.06 nm increment in wavelength) and can perform a linear sweep through all 600 channels in a time of 120 ms. It is also capable of random channel to channel tuning in approximately 200 μs although in practice this is limited to approximately 2 ms due to the time taken to communicate with the PC via the RS232 interface.

D. Implementation of sensor biasing scheme

The following describes the practical implementation of the interrogation schemes described in Secs. II A 1 and II A 2.

1. Acoustic measurement

To acquire an acoustic waveform, it is necessary to bias the FPI, as described in Sec. II A 1. In principle, this can be achieved by sweeping the laser through its 40 nm wavelength range and measuring the reflected optical power P_r. Since the laser channels are separated by a constant optical

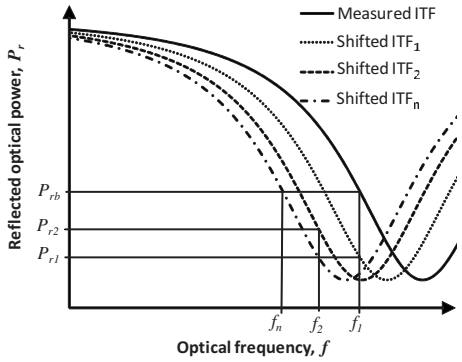

FIG. 5. Iterative scheme to optimally bias the FPI in the presence of self-heating.

frequency, and frequency is proportional to phase, plotting P_r as a function of channel provides a direct measure of the phase ITF. The latter can then be differentiated and the laser can be tuned to the wavelength that corresponds to the peak phase derivative. However, it was found that this approach was compromised by the heating of the FPI due to absorption of the laser light. This self-heating effect corrupts the measurement of the ITF since the optical thickness of the FPI varies during the wavelength sweep. To mitigate this, the ITF was obtained as rapidly as possible by performing a single sweep through the 40 nm wavelength range of the laser at the maximum tuning speed. Since the FPI is illuminated for only 120 ms, the self-heating is negligible enabling an accurate measurement of the ITF to be obtained. However, a difficulty was then found to arise when the laser wavelength was subsequently tuned to the optimum bias point. The FPI is now illuminated for an extended period and this results in a temperature rise large enough to cause the ITF to shift. The FPI is then no longer optimally biased.

To overcome this, an alternative interrogation scheme that relies on iteratively tuning the laser wavelength in order to search for P_{rb}, the reflected optical power at the optimum bias point, was implemented. This procedure is illustrated in Fig. 5. First, the ITF is measured by sweeping the laser through its 40 nm tuning range sufficiently quickly that significant self-heating does not occur as described above. From the ITF measured in this way (denoted "Measured ITF" in Fig. 5), the frequency f_1 and reflected power P_{rb} corresponding to the optimum bias point are identified. The laser frequency is then tuned to f_1. As a consequence, the reflected power measured by the photodiode is momentarily equal to P_{rb}. However, self-heating at f_1 immediately causes the ITF to shift, (becoming "shifted ITF_1") and so the reflected power now decreases from P_{rb} to P_{r1}. In an attempt to return the reflected power to P_{rb}, the laser is tuned to f_2. This results in a further (but smaller) shift in the ITF which now becomes "shifted ITF_2." At f_2, the reflected power P_{r2} is still less than P_{rb} so the laser is tuned yet again in order to approach P_{rb}. This procedure is repeated a number of times. With each iteration, the additional temperature rise due to self-heating becomes progressively smaller and therefore so too does the shift in the ITF. Eventually, after n iterations, the FPI attains a constant temperature, the position of the ITF no longer changes, and the system converges on P_{rb} which corresponds to the optimum bias point f_n. In practice, the iteration is terminated when the measured reflected optical power lies within 2% of the value obtained in the previous iteration. The system is then ready to make an acoustic measurement. The entire procedure including acquiring the ITF takes approximately 1 s. In practice, this procedure is implemented as an initialization routine when the system is switched on. Thereafter, the reflected power is monitored and if it changes by more than 2% the laser is retuned so as to maintain a constant value of P_r.

2. Temperature measurement

Assume that the system has been optimally biased as described above and that the sensor is now subjected to an external source of heat which produces a temperature rise over some time interval. As the temperature begins to increase, the reflected power P_r will change. If P_r changes by more than a small amount (2%), the laser wavelength is automatically adjusted by the control software so as to return P_r to P_{rb}, thus returning the system to the optimum bias point. As the temperature continues to rise, this procedure is repeated. In this way, the time course of the temperature rise is discretely sampled by tracking the changes in the bias wavelength as described in Sec. II A 1. Since the FPI is always maintained at the optimum bias point, ultrasound waveforms can be acquired at the same time the temperature is being monitored.

III. ACOUSTIC CHARACTERISTICS

The acoustic performance of the sensor was measured using a substitution calibration method[30] at Precision Acoustics Ltd., Dorchester, UK. This was carried out using a calibrated 0.4 mm (diameter) PVDF membrane hydrophone (Precision Acoustics Ltd., Dorchester, UK) that acted as a reference against which the fiber-optic hydrophone measurements were compared. The acoustic field was generated in water by a 1 MHz planar transducer producing a 25 cycle tone burst with an approximate peak to peak pressure of 1 MPa at the transducer face. Due to the non-linear propagation of the acoustic field in the water tank, integer harmonics of the fundamental up to at least 60 MHz are generated. This arrangement was used to measure the sensitivity, frequency response, and directivity of the hydrophone.

A. Sensitivity

Figure 6 shows a typical measurement of the shocked wave tone-burst as measured by both the reference membrane hydrophone [Fig. 6(a)] and the fiber-optic hydrophone [Fig. 6(b)]. In both cases the signals were acquired without signal averaging. The calibration sensitivities of the membrane hydrophone and fiber-optic hydrophone were 50 and 580 mV/MPa, respectively, at 5 MHz. Comparison of the signals shows that the signal-to-noise ratio of the fiber-optic hydrophone is comparable to that of the membrane hydrophone. The comparison also reveals significant structure in the signal from the fiber-optic hydrophone; this is due to the probe-type geometry of the sensor that causes radial resonances and edge waves that propagate across the tip of the

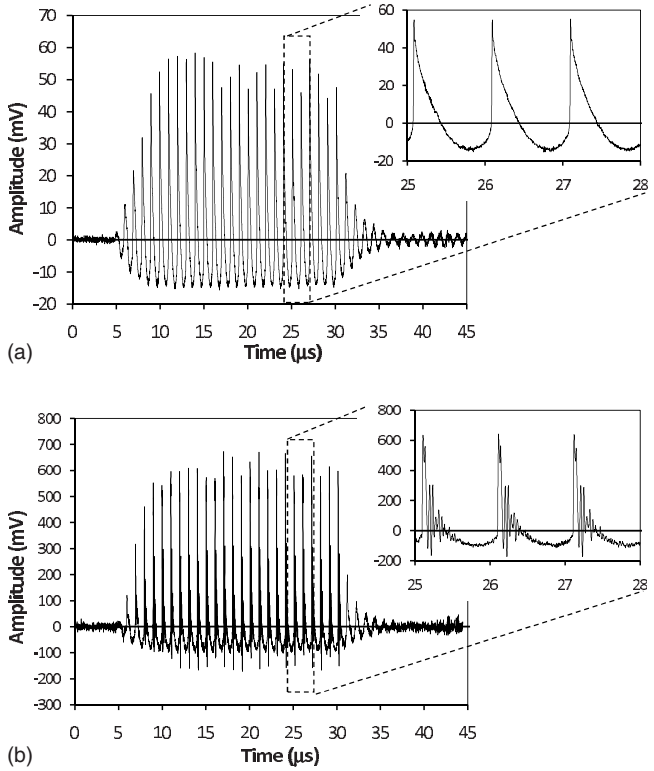

FIG. 6. Comparisons of the outputs of (a) a 0.4 mm PVDF membrane hydrophone and (b) the fiber-optic hydrophone in response to a "shocked" 1 MHz toneburst. Insets show expanded timescale (in μs).

fiber. These are then detected by the sensor as they cross the active area after the initial acoustic wave has passed. This will be described in more detail in Sec. III C.

The NEP, is defined as the acoustic pressure which provides a signal to noise ratio of 1. The NEP was obtained by recording the output of the photodiode over a 20 MHz bandwidth in the absence of an acoustic signal. The rms value of the noise voltage was then computed and multiplied by a factor of 3 to obtain the peak value. The peak noise voltage was then converted to an equivalent pressure by dividing by the calibration sensitivity (580 mV/MPa) of the hydrophone. This gave a peak NEP of 15 kPa (at 5 MHz) over a 20 MHz measurement bandwidth. By comparison, the peak NEP of the membrane hydrophone was 10 kPa and that of a 75 μm PVDF needle hydrophone (Precision Acoustics Ltd.) was 28 kPa under the same measurement conditions. Note that the peak rather than rms noise figures are quoted since the former provides a more realistic indication of the smallest signal that can be detected when measuring broadband signals in the time domain.

B. Linearity

Assuming the elastic limits of the polymer spacer are not exceeded, the upper limit of linear acoustic detection is determined by the phase range over which the gradient of the ITF is nearly constant at the bias point and the acoustic phase sensitivity. The linearity is determined by calculating the equation of the straight line which passes through the optimum bias point with a gradient equal to the peak derivative of the phase ITF. The difference between the ITF and the straight line is then calculated and the range of phase over which the difference is less than 5% and 10% determined.[20] The linear pressure range is then given by multiplying this phase range by the acoustic phase sensitivity. A value for the latter has been determined experimentally in a previous study.[20] This was found to be 0.075 rad/MPa for a sensor with a film thickness of 25 μm at a laser wavelength of 850 nm. Since $d\phi/dp$ is proportional to l/λ, this must be converted to the appropriate value for a sensor 10 μm in thickness interrogated by a laser wavelength of 1550 nm. The acoustic sensitivity can be found from

$$\left(\frac{\delta\phi}{\delta p}\right)_{(\lambda_2,l_2)} = \left(\frac{\delta\phi}{\delta p}\right)_{(\lambda_1,l_1)} \left(\frac{\lambda_1}{l_1}\right)\left(\frac{l_2}{\lambda_2}\right). \tag{9}$$

Noting that, in this case $\lambda_1 = 850$ nm, $\lambda_2 = 1550$ nm, $l_1 = 25$ μm, and $l_2 = 10$ μm, give

$$\left(\frac{\delta\phi}{\delta p}\right)_{(1550\ \text{nm},10\ \mu\text{m})} = 0.016\ \text{rad/MPa}. \tag{10}$$

The linear pressure range (to within 5%) of the fiber-optic hydrophone used to obtain the waveform shown in Fig. 6(b) is -4 MPa to 7.5 MPa. If a reduced linearity of 10% can be tolerated, this range becomes -6 MPa to 10 MPa. The pressure range is not symmetric as the ITF is not symmetrical about the bias point. The ITF reflectance minimum is also asymmetric, due to the use of metallic reflective coatings in the FPI. These metallic coatings introduce additional phase changes on reflection and transmission leading to the asymmetry in the ITF. As a result, the peak positive phase derivative is smaller than the peak negative derivative.

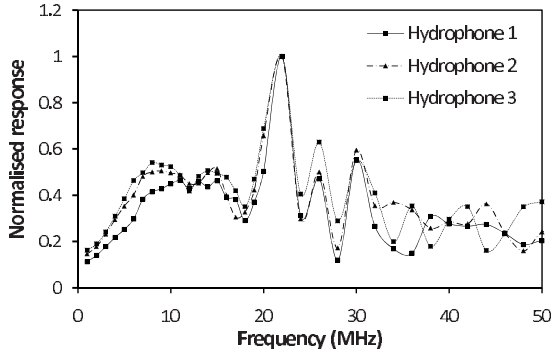

FIG. 7. Measured frequency responses of three typical fiber-optic hydrophones.

C. Frequency response

Figure 7 shows the frequency responses of three nominally identical fiber-optic hydrophones—the responses are normalized for ease of comparison. The calibration sensitivities of each hydrophone (hydrophones 1–3) at 5 MHz are 209, 255, and 580 mV/MPa, respectively—the variation in sensitivity is due to the fact that the output power of the laser was set to a different value for each hydrophone. The uncertainties associated with these measurements are as follows: 1–15 MHz, 14%; 16–20 MHz, 18%; 22–30 MHz, 23%; and 30–50 MHz, 40%, based on combined systematic and random uncertainties. It should be noted that the frequency re-

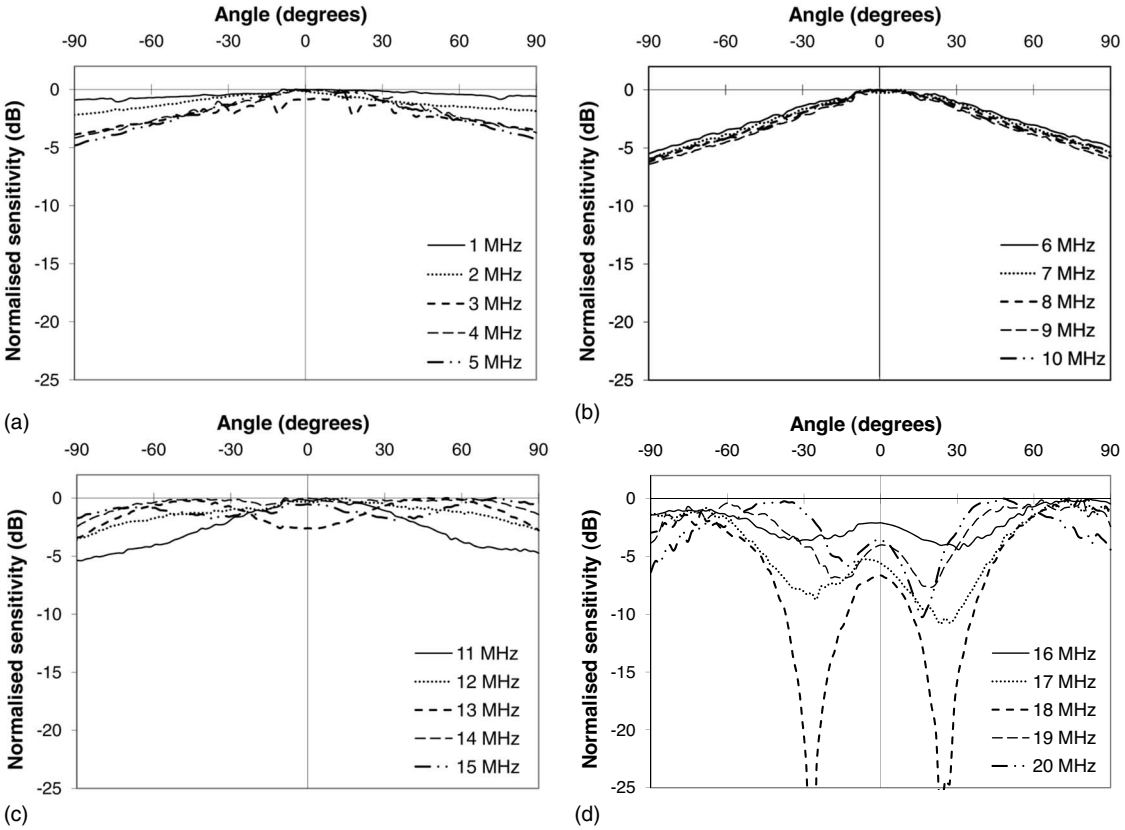

FIG. 8. Directional response of a fiber-optic hydrophone. Response shown for frequencies: (a) 1–5 MHz, (b) 6–10 MHz, (c) 11–15 MHz, and (d) 16–20 MHz.

sponses shown in Fig. 7 are those of the hydrophone system and thus include the finite bandwidth of the photodiodes (−3 dB bandwidth ≈50 MHz). Thus, while the response of the hydrophone decreases toward 50 MHz, the intrinsic response of the sensors is expected to extend beyond this. The responses of all three sensors are in close agreement up to 25 MHz indicating good sensor-to-sensor uniformity. Above this frequency, there is greater variation which is consistent with the higher uncertainty in the measurement. The variation may also be due to small differences in the geometries of the fiber tips, which will have greater influence at higher frequencies.

Figure 7 also shows that the frequency response of the hydrophone is significantly non-uniform. A detailed investigation of the frequency response, including a comparison using a finite difference simulation, has shown that the non-uniformities in the response arise from diffraction of the acoustic wave at the tip of the sensor.[24] The diffraction causes multiple edge waves to propagate and reverberate across the tip of the sensor. The presence of two diffracting boundaries (that of the fused silica fiber and Parylene spacer) leads to waves propagating with more than five different wave speeds: longitudinal in water, longitudinal and shear in the Parylene, and longitudinal and shear in the fused silica fiber as well as several interface wavespeeds. It is the frequency dependent interaction of all of these waves that is responsible for the complex structure in the frequency response.

D. Directivity

The directional response of a fiber-optic hydrophone was measured up to a frequency of 20 MHz at 1 MHz intervals, as shown in Fig. 8. The multitude of wave types that interact within the sensor and contribute to its output means that the directivity inevitably differs from that of an ideal rigid disk receiver. It can be seen that for frequencies up to 10 MHz, the directional response is well behaved with the sensitivity decreasing with increasing angle and the variation across the angular range increasing with increasing frequency. At 10 MHz, the sensitivity drops approximately 6 dB for a 90° angle of incidence. Above 10 MHz the behavior changes significantly. The measurement at 13 MHz shows that the maximum sensitivity is no longer obtained at normal incidence, but at approximately ±45°. At 15 MHz, the sensitivity appears to oscillate as a function of angle, but with a maximum drop in sensitivity of just 1.8 dB across the full 180° range. As the frequency is increased to 18 MHz, two large drops in sensitivity of greater than 25 dB appear in the response at approximately ±30°. At 20 MHz, the nulls have reduced in magnitude but occur closer to normal incidence.

IV. THERMAL CHARACTERISTICS

The thermal performance of the sensor was characterized in terms of its sensitivity, linearity, and response time.

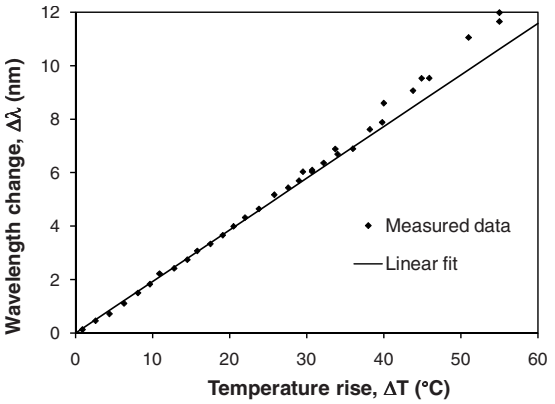

FIG. 9. Change in optimum bias wavelength as a function of temperature change.

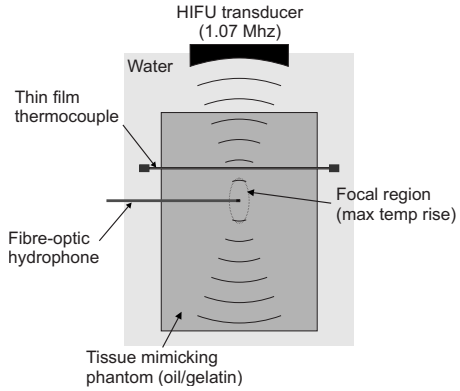

FIG. 10. Experimental setup for making simultaneous pressure and temperature measurements in a HIFU field.

A. Sensitivity

The sensitivity was measured by placing the tip of the fiber in a water bath at room temperature, T_0. The sensor was then placed into a second water bath held at second temperature, T_1, while the change in the optimum bias wavelength, $\Delta\lambda$, was recorded. The temperature change, $\Delta T = T_1 - T_0$, was measured using a pair of thermocouple probes in a differential measurement configuration. This was repeated for a range of values of T_1, from 25 °C to 80 °C, and the results can be seen in Fig. 9. In the linear region of the graph (up to $\Delta T = 45$ °C), a change of 1 nm in the bias wavelength corresponds to a temperature change of 5.18 °C. The photodiode noise-equivalent optical power is much less than the change in reflected power that occurs over a single wavelength tuning step. Hence, the temperature measurement resolution is determined largely by the minimum wavelength step by which the laser can be tuned, approximately 0.06 nm, which leads to a temperature resolution of approximately 0.34 °C.

B. Linearity and dynamic range

The calibration data in Fig. 9 show that the response of the hydrophone to temperature is linear up to a temperature change of approximately 45 °C, which in this case corresponds to a temperature of 70 °C. Above this, there is an increase in the gradient of the curve. This is consistent with a glass transition in the Parylene spacer. Below the glass transition temperature, T_g, the Parylene is in a hard, glassy state and acts elastically. In this state, the thermal expansion of the polymer is linear and reversible. Above T_g, the Parylene is in transition between glassy and rubbery moduli and viscoelastic losses are significant.[31] Hence the sensor is currently limited to measuring temperatures up to 70 °C.

C. Response time

The intrinsic thermal response time of the sensor, based on the time it takes for heat to diffuse across a 12 μm thick Parylene spacer, is approximately 850 μs.[22] However, the rate at which the system can measure temperature changes is limited by a combination of two factors: first, the acquisition rate of the USB A-D module which is used to sample the photodiode output, and second the overhead involved in communicating with the laser via the RS232 interface. These factors result in a system sampling rate of 200 samples/s for the temperature measurements. Since the system is only capable of measuring temperature in steps corresponding to the tuning resolution of the laser, there is a maximum temporal temperature gradient which the sensor can accurately measure. Since tuning one channel corresponds to a temperature change of approximately 0.34 °C, the maximum rate of temperature change which can be measured is approximately 67 °C s^{-1}.

V. MEASUREMENTS OF ULTRASOUND INDUCED HEATING

In order to demonstrate the applicability of the sensor for the measurement of ultrasound-induced heating, it was used to record the temperature rise produced at the focus of a HIFU transducer in a tissue mimicking phantom. These measurements were made at the National Physical Laboratory (NPL), Teddington, UK.

A. Experimental setup

The sensor was embedded in a tissue mimicking phantom based on an oil-gelatin emulsion,[5] as shown in Fig. 10. To provide a reference for the temperature measurement, a thin-film thermocouple (TFT) was also embedded within the phantom approximately 1 cm below the fiber-optic hydrophone. The TFT was developed at the UK's NPL in order to make accurate measurements of ultrasound-induced temperature rises.[5,6] The structure of the TFT renders it immune to heating artifacts such as viscous heating, to which wire thermocouples are susceptible.[4] The fiber-optic hydrophone was positioned such that the axis of the fiber was perpendicular to the acoustic axis. This removed the fiber mount from the acoustic path, thereby eliminating acoustic reflections from the mount. In order to compare the output of each device, a measurement was first made with the TFT at the focus. The system was then realigned (including changing the distance to the transducer) so that the fiber-optic hydrophone was at the focus and a second measurement made. The heating was induced by the output of a 1.07 MHz HIFU transducer with a focal length of 117 mm and a focal spot 3–4 mm in diameter and 4–5 cm in length (−6 dB). The heating was con-

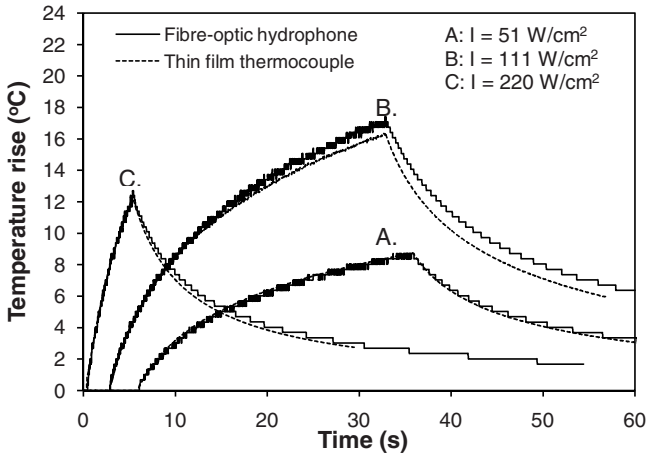

FIG. 11. Comparison of temperature-time curves obtained by the fiber-optic hydrophone and the thin-film thermocouple.

trolled by setting the intensity and duration of the (cw) insonation. It should be noted that intensity values quoted in the results below are based on values measured in water only. Thus they provide only an approximate indication of the values within the phantom.

B. Comparison of temperature-time curves measured by the fiber-optic hydrophone and thin-film thermocouple

In the first instance, a comparison of temperature-time curves obtained by both the fiber-optic hydrophone and the TFT, for a variety of acoustic output settings, was made. Figure 11 shows three temperature-time curves for acoustic intensities of 51, 111, and 220 W cm^{-2} (≈2.5, 3.7, and 5.4 MPa peak-to-peak pressures, respectively). The insonation at 220 W cm^{-2} was limited to 5 s in order to minimize the risk of damage to the TFT. It can be seen that the shape of the temperature-time curves measured by the fiber sensor closely match those measured by the TFT. This implies that there are no significant viscous heating artifacts in the measurement by the fiber-optic hydrophone. It can also be seen that in the case of the 111 W cm^{-2}, 30 s insonation, the maximum temperature measured by the sensor is slightly higher than that measured by the TFT. This is attributed to a slight error in the alignment of each sensor in the focal region of the beam. The overall shape remains a good match even in this case.

Additional measurements were made at a range of intensities as high as 700 W cm^{-2} (≈12 MPa peak-to-peak) which approaches clinical intensity levels. No damage or change in performance was observed at this intensity.

C. Simultaneous acquisition of ultrasound waveforms and a temperature-time curve

The arrangement shown in Fig. 10 was also used to demonstrate the ability of the system to conduct simultaneous acoustic and thermal measurements. The results can be seen in Fig. 12, which shows a temperature-time curve for a 30 s insonation with an acoustic intensity (I_{spta}—spatial peak, temporal average intensity) of 220 W cm^{-2} and several acoustic waveforms taken at different times during the insonation period. The temperature-time curve is of the same overall shape as those obtained for lower insonation intensities or shorter heating periods (Fig. 11) with the exception

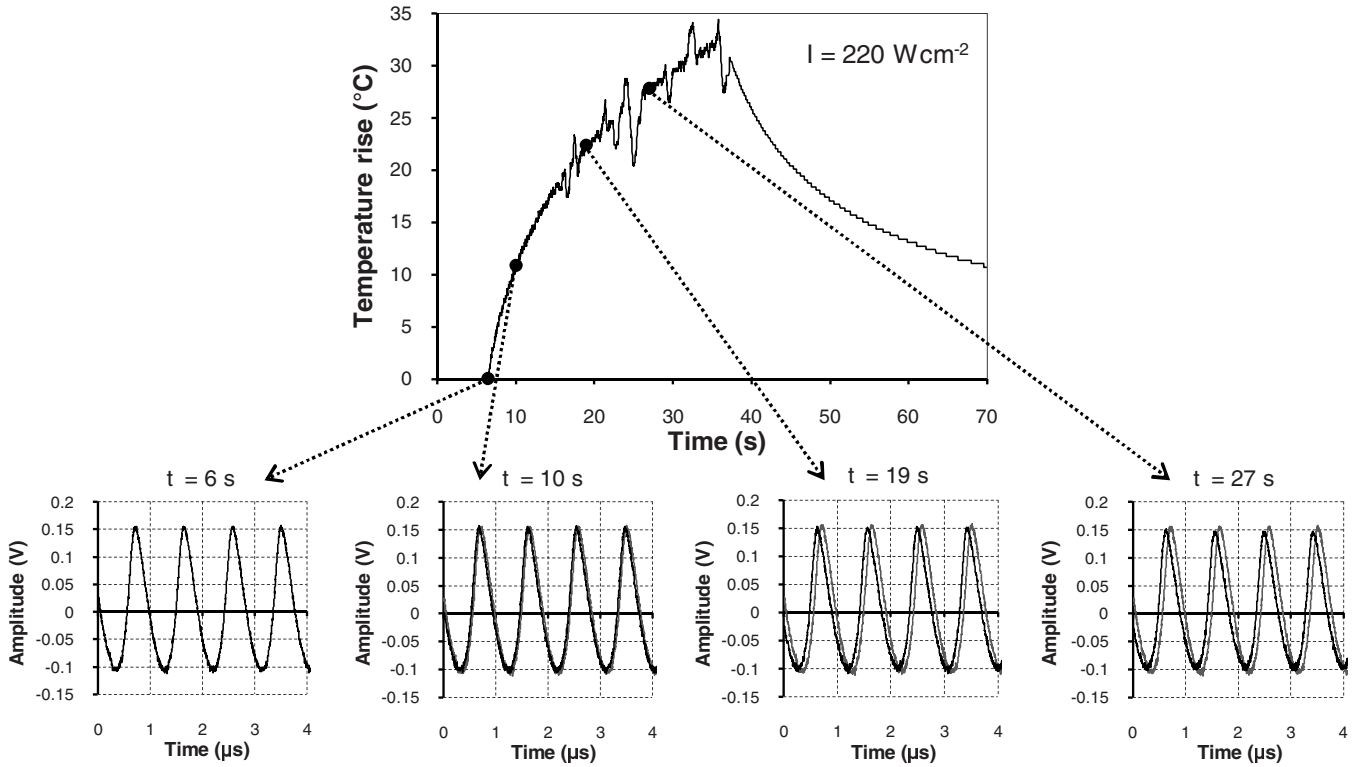

FIG. 12. Simultaneous acquisition of a temperature-time curve (top) and acoustic waveforms (lower row) captured at four different times during a 30 s insonation (cw). For the acoustic waveforms obtained at $t=10$, 19, and 27 s, the waveform captured at $t=6$ s (gray line) is also shown in order to illustrate the phase shift due to the thermally-induced change in sound speed.

that several rapid temperature fluctuations can be seen over the heating period. One possible explanation is that these fluctuations are related to the presence of cavitational activity close to the tip of the sensor. If bubbles form between the fiber-optic hydrophone and the transducer, some of the acoustic energy from the transducer will be reflected away from the sensor; this would lead to a temporary reduction in temperature. Similarly, if bubbles form behind the sensor, they may reflect some of the acoustic beam back toward the sensor thus increasing the local temperature. Cavitational activity close to the tip may also convert more acoustic energy to heat, thereby increasing the temperature temporarily while the activity persists.

The set of acoustic waveforms accompanying the temperature-time curve shows that as the temperature rises, the speed of sound increases slightly. The waveforms shift to the left of the trace, and the amplitude of the signal decreases slightly. These effects are expected since, in general, sound speed increases with temperature; thus the time-of-flight of the wave will be reduced. In addition, as the sound speed and the acoustic properties of the phantom change with temperature, the focal point of the transducer may move; thus the sensor will no longer be at the focus and the amplitude may decrease.

A limitation of the current system is that the acoustic waveforms were captured on a digitizing oscilloscope and transmitted to the control PC via a general purpose interface bus interface. With this method, it took approximately 2 s to instruct the scope to capture a waveform and download it to the PC. Thus, during the 30 s insonation used to obtain the data shown in Fig. 12, a maximum of only 15 acoustic waveforms could be captured. Unfortunately, none of these coincided with the rapid fluctuations in the temperature-time curve so it was not possible to test the above hypothesis that cavitational activity (which may have been evident from the acoustic waveforms) is responsible for these fluctuations. This limitation could be overcome by using an oscilloscope or PC digitizing card with an on-board segmented memory architecture. This would allow a large number of successive waveforms to be captured in real time, concatenated in a single segmented record, and the whole record downloaded to the PC in a single step as described in Ref. 32. A much higher waveform acquisition rate could then be achieved, enabling an acoustic waveform to be acquired for each measurement point on the temperature-time curve.

VI. CONCLUSIONS

A practical wideband (50 MHz) fiber-optic hydrophone system for characterizing diagnostic and therapeutic medical ultrasound fields has been demonstrated. In terms of acoustic performance, its principal advantage is that it can provide a small element size with significantly higher sensitivity than can be achieved with PVDF hydrophones of comparable element dimensions. As well as measuring acoustic pressure, the ability to measure temperature changes produced by ultrasound-induced heating has been demonstrated. There are two distinguishing features of this capability. First the measurement is free of errors due to viscous self-heating that afflict wire thermocouples conventionally used to make such measurements. Second, it is possible to acquire ultrasound waveforms while simultaneously monitoring the temperature. This unique dual measurement capability provides a means of directly correlating temperature rises with acoustic field parameters. For example, it could be employed to help understand the role that cavitation plays in enhancing tissue heating in HIFU therapy. A further advantage is that, unlike PVDF hydrophones, the fiber-optic hydrophone appears to be able to withstand the hostile environment produced by a HIFU field at clinical intensity levels. Even if it should fail, the ability to batch fabricate the sensors at low unit cost using all vacuum deposition techniques means that the sensor can be inexpensively replaced. Other advantages include small physical size and flexibility, biocompatibility, and electrical passivity, attributes that suggest the sensor could be used as an implantable probe for making *in-vivo* measurements.

Future work will be directed toward improving both the acoustic and thermal performance of the hydrophone. Preliminary experimental and theoretical studies suggest that there is significant scope to obtain a more uniform frequency response by appropriately shaping the tip of the optical fiber to reduce the influence of diffraction.[24] This also offers the prospect of producing an improved directional response, particularly at higher frequencies where the fluctuations in angular sensitivity are most apparent. Although the current NEP of 15 kPa is sufficient for many medical ultrasound measurement applications, there is significant scope to increase sensitivity if required. The noise performance of the current system is limited by the relatively high phase noise of the SG-DBR interrogation laser. It has previously been shown that the use of an external cavity laser as the interrogation source, which has significantly narrower linewidth and therefore lower phase noise, can provide a NEP of 3 kPa.[33] There is further potential to reduce the NEP by replacing the gold coatings currently used to form the mirrors of the FPI with dielectric coatings. These are significantly less absorbing enabling a higher finesse FPI to be obtained. A NEP of 0.21 kPa has been achieved with free-space illuminated sensors fabricated in this way.[34]

The sensor is currently limited to making temperature measurements up to 70 °C and the thermal resolution is limited by the wavelength tuning resolution of the laser. The former may be improved by using an alternative material to form the spacer, such as the Parylene variant Parylene-HT. This material offers similar optical and acoustic properties to Parylene-C but with a higher glass transition temperature. The thermal resolution may be increased by monitoring the variation in the reflected power and using this data, along with knowledge of the ITF, to interpolate between successive wavelength tuning steps. It should then be possible to achieve a resolution limited by the photodiode noise voltage rather than tuning resolution of the laser.

In summary, it is considered that the wide bandwidth, small element size, and high sensitivity of this type of sensor, along with its ability to measure temperature, offers a potentially useful new measurement tool for characterizing medical ultrasound fields.

ACKNOWLEDGMENTS

This work was funded by the UK Engineering and Physical Sciences Research Council (EPSRC). The authors acknowledge the support of the National Measurement System Programme Unit of the UK Department for Innovation, Universities and Skills (DIUS) for the work carried out at NPL.

[1]G. Harris, "Progress in medical ultrasound exposimetry," IEEE Trans. Ultrason. Ferroelectr. Freq. Control **52**, 717–736 (2005).
[2]W. J. Fry and R. B. Fry, "Determination of absolute sound levels and acoustic absorption coefficients by thermocouple probes—Theory," J. Acoust. Soc. Am. **26**, 294–310 (1954).
[3]C. C. Coussios, C. H. Farny, G. T. Haar, and R. A. Roy, "Role of acoustic cavitation in the delivery and monitoring of cancer treatment by high-intensity focused ultrasound (HIFU)," Int. J. Hyperthermia **23**, 105–120 (2007).
[4]H. Morris, I. Rivens, A. Shaw, and G. ter Haar, "Investigation of the viscous heating artefact arising from the use of thermocouples in a focused ultrasound field," Phys. Med. Biol. **53**, 4759–4776 (2008).
[5]D. R. Bacon and A. Shaw, "Experimental validation of predicted temperature rises in tissue-mimicking materials," Phys. Med. Biol. **38**, 1647–1659 (1993).
[6]A. Shaw, N. M. Pay, R. C. Preston, and A. D. Bond, "Proposed standard thermal test object for medical ultrasound," Ultrasound Med. Biol. **25**, 121–132 (1999).
[7]IEC, "IEC62306 Ultrasonics-field characterization-test objects for determining temperature elevation in diagnostic ultrasound fields," International Electrotechnical Commission, Geneva, 2006.
[8]R. L. Phillips, "Proposed fiberoptic acoustical probe," Opt. Lett. **5**, 318–320 (1980).
[9]J. Staudenraus and W. Eisenmenger, "Fiberoptic probe hydrophone for ultrasonic and shock-wave measurements in water," Ultrasonics **31**, 267–273 (1993).
[10]C. Wurster, J. Staudenraus, and W. Eisenmenger, "The fiber optic probe hydrophone," Proc.-IEEE Ultrason. Symp. **2**, 941–944 (1994).
[11]P. A. Lewin, S. Umchid, A. Sutin, and A. Sarvazyan, "Beyond 40 MHz frontier: The future technologies for calibration and sensing of acoustic fields," J. Phys.: Conf. Ser. **1**, 38–43 (2004).
[12]J. E. Parsons, C. A. Cain, and J. B. Fowlkes, "Cost-effective assembly of a basic fiber-optic hydrophone for measurement of high-amplitude therapeutic ultrasound fields," J. Acoust. Soc. Am. **119**, 1432–1440 (2006).
[13]V. A. Leitao, W. N. Simmons, Y. F. Zhou, J. Qin, G. Sankin, F. H. Cocks, J. Fehre, B. Granz, R. Nanke, G. M. Preminger, and P. Zhong, "Comparison of light spot hydrophone (LSHD) and fiber optic probe hydrophone (FOPH) for lithotripter field characterization," Renal Stone Disease **900**, 377–380 (2007).
[14]V. Wilkens and C. Koch, "Fiber-optic multilayer hydrophone for ultrasonic measurement," Ultrasonics **37**, 45–49 (1999).
[15]V. Wilkens, "Characterization of an optical multilayer hydrophone with constant frequency response in the range from 1 to 75 MHz," J. Acoust. Soc. Am. **113**, 1431–1438 (2003).
[16]V. Wilkens, C. Wiemann, C. Koch, and H. J. Foth, "Fiber-optic dielectric multilayer temperature sensor: In situ measurement in vitreous during Er:YAG laser irradiation," Opt. Laser Technol. **31**, 593–599 (1999).
[17]P. C. Beard and T. N. Mills, "Extrinsic optical-fiber ultrasound sensor using a thin polymer film as a low-finesse Fabry–Pérot interferometer," Appl. Opt. **35**, 663–675 (1996).
[18]P. C. Beard and T. N. Mills, "Miniature optical fibre ultrasonic hydrophone using a Fabry–Pérot polymer film interferometer," Electron. Lett. **33**, 801–803 (1997).
[19]Y. Uno and K. Nakamura, "Pressure sensitivity of a fiber-optic microprobe for high-frequency ultrasonic field," Jpn. J. Appl. Phys., Part 1 **38**, 3120–3123 (1999).
[20]P. Beard, A. Hurrell, and T. Mills, "Characterization of a polymer film optical fiber hydrophone for use in the range 1 to 20 MHz: A comparison with PVDF needle and membrane hydrophones," IEEE Trans. Ultrason. Ferroelectr. Freq. Control **47**, 256–264 (2000).
[21]J. M. Vaughan, *The Fabry–Pérot Interferometer: History, Theory, Practice and Applications* (Hilger, London, 1989).
[22]J. G. Laufer, P. C. Beard, S. P. Walker, and T. N. Mills, "Photothermal determination of optical coefficients of tissue phantoms using an optical fibre probe," Phys. Med. Biol. **46**, 2515–2530 (2001).
[23]P. Morris, P. Morris, A. Hurrell, E. Zhang, S. Rajagopal, and P. Beard, "A Fabry–Pérot fibre-optic hydrophone for the measurement of ultrasound induced temperature change," Proc.-IEEE Ultrason. Symp. , 536–539 (2006).
[24]P. Morris, "A Fabry–Pérot fibre-optic hydrophone for the characterisation of ultrasound fields," Ph.D. thesis, University College London, London (2008).
[25]B. T. Cox and P. C. Beard, "The frequency-dependent directivity of a planar Fabry–Pérot polymer film ultrasound sensor," IEEE Trans. Ultrason. Ferroelectr. Freq. Control **54**, 394–404 (2007).
[26]P. C. Beard, F. Perennes, E. Draguioti, and T. N. Mills, "Optical fiber photoacoustic-photothermal probe," Opt. Lett. **23**, 1235–1237 (1998).
[27]K. Nakamura and K. Nimura, "Measurements of ultrasonic field and temperature by a fiber optic microprobe," J. Acoust. Soc. Jpn. E **21**, 267–269 (2000).
[28]SCS, "Parylene properties," www.scscoatings.com (2008), URL http://www.scscoatings.com/docs/coatspec.pdf (date last viewed 4/20/09).
[29]Z. Y. Zhang, P. Zhao, P. Lin, and F. G. Sun, "Thermo-optic coefficients of polymers for optical waveguide applications," Polymer **47**, 4893–4896 (2006).
[30]R. A. Smith and D. R. Bacon, "A multiple-frequency hydrophone calibration technique," J. Acoust. Soc. Am. **87**, 2231–2243 (1990).
[31]R. O. Ebewele, *Polymer Science and Technology* (CRC, Boca Raton, FL, 1996).
[32]E. Z. Zhang and P. Beard, "Broadband ultrasound field mapping system using a wavelength tuned, optically scanned focused laser beam to address a Fabry–Pérot polymer film sensor," IEEE Trans. Ultrason. Ferroelectr. Freq. Control **53**, 1330–1338 (2006).
[33]P. Morris, P. Beard, and A. Hurrell, "Development of a 50 MHz optical fibre hydrophone for the characterisation of medical ultrasound fields," Proc.-IEEE Ultrason. Symp. **3**, 1747–1750 (2005).
[34]E. Zhang, J. G. Laufer, and P. Beard, "Backward-mode multiwavelength photoacoustic scanner using a planar Fabry–Pérot polymer film ultrasound sensor for high resolution three-dimensional imaging of biological tissues," Appl. Opt. **47**, 561–577 (2008).

Excitation and scattering of guided waves: Relationships between solutions for plates and pipes

Alexander Velichko[a] and Paul D. Wilcox
Department of Mechanical Engineering, University of Bristol, Bristol BS8 1TR, United Kingdom

(Received 10 December 2008; revised 5 March 2009; accepted 16 March 2009)

The detection of localized defects such as cracks and corrosion in pipes using guided elastic waves is now an established non-destructive testing procedure. However, the prediction of guided wave excitation and scattering in pipes is a complex three-dimensional (3D) problem with many parameters that can generally only be solved using numerical methods. In many important industrial applications, the diameter of a pipe is much larger than wall thickness. In this case an approximate theory is applicable, when a pipe is considered as an unwrapped isotropic plate. In this paper, a technique for obtaining pipe mode amplitudes in terms of the solution to the forced 3D problem on a plate is presented. The same principle is extended to relate guided wave scattering from defects in plates to scattered circumferential modal amplitudes from defects in pipe. This is of practical benefit as the scattering of guided waves by defects in a plate is a much simpler problem than that in a pipe, and one that, in some cases, can be solved using analytical methods. Results are shown that illustrate the application of the method to reflection from through-thickness circumferential cracks in pipes.
 [DOI: 10.1121/1.3117441]

PACS number(s): 43.35.Zc, 43.20.Bi, 43.20.Mv, 43.35.Cg [YHB] Pages: 3623–3631

I. INTRODUCTION

Ultrasonic guided waves provide a highly efficient technique for rapid pipe inspection.[1,2] The design of guided wave NDT systems and the interpretation of results require the ability to predict the radiated guided wave field of a transmitting transducer and reflected guided wave field of a defect in a pipe. The process of guided wave propagation in a pipe and their interaction with defects are extremely complicated. The majority of guided wave modeling in pipes is based, therefore, on direct numerical methods such as the finite element method.[1,3] However, these methods are time consuming and provide little understanding of mechanics of wave processes.

In many industrial applications, the radius of a pipe is much larger than the pipe thickness. The wave propagation in pipes of such geometry can be described by a simplified theory, where a pipe is considered as an unwrapped isotropic plate and the transducer is replaced by a periodic array of transducers with inter-element distance equal to the pipe circumference.[2,4] This approach provides a fast technique for modeling of wave phenomena in a pipe.

In this paper, the relation between forced solutions in pipes and plates is presented. The relationship between circumferential mode amplitudes in a pipe and the directivity function of a transducer on a plate is obtained. The approximate solution is compared with the exact solution for a hollow cylinder and the applicability range of the approximation is discussed.

Quantitative prediction of reflection of guided waves from defects in pipes is of practical importance since it allows defect characterization and sizing based on measured reflected signals to be performed. The complexity of the scattering process limits the application of analytical methods to this problem. Ditri[5] derived the general analytical expression for the scattering coefficients of wave modes in a pipe using the *S*-parameter formalism.[6] However, in order to calculate the scattering parameters the wave field on the defect surface must be known. This requires numerical modeling or some approximation methods to be applied.

In this paper, scattered circumferential modal amplitudes from defects in pipe are related to guided wave scattering from defects in plates. This makes it possible to apply known results of guided waves reflection from defects in plates to the corresponding diffraction problem in a pipe. The technique is illustrated by the calculation of mode-converted guided waves reflected from a through-thickness crack in a pipe.

II. EXCITATION OF GUIDED WAVES

A. Formulation of excitation problem

A hollow cylinder of radius R and wall thickness h is considered with cylindrical coordinate system θ, y, z defined with y axis normal to the pipe surface, as shown in Fig. 1(a). An arbitrary time harmonic load $\mathbf{q}e^{-i\omega t}$ is applied to the outer surface of the cylinder. In this paper, the guided waves modes are classified, as proposed in Ref. 7. The total harmonic displacement field due to surface load can be represented as the superposition of axisymmetric longitudinal modes $L(0,m)$, non-axisymmetric flexural modes $L(n,m)$ $(n \neq 0)$, and torsional modes $T(n,m)$:

$$\mathbf{u}(\theta,y,z) = \sum_{n,m} \mathbf{u}_m^n(y) e^{in\theta} e^{ik_m^n z}, \tag{1}$$

where $\mathbf{u} = \{u_\theta, u_y, u_z\}^T$ is the displacement field and k_m^n is the wavenumber of the mth mode of the nth circumferential order.

[a]Author to whom correspondence should be addressed. Electronic mail: a.velichko@bristol.ac.uk

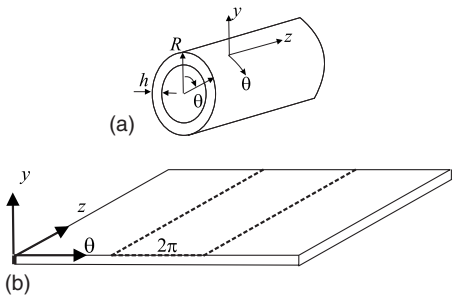

FIG. 1. System geometry. (a) Pipe geometry. (b) A pipe is replaced by an infinite plate.

In formula (1) it is assumed that the domain of the variable θ is limited by 0 and 2π. The modal amplitudes a_m^n can be obtained, for example, by the normal mode expansion method.[5,6] However, from the wave analysis point of view, an alternative wave field representation is useful.[4] According to this approach, a pipe is considered as unbounded in the θ direction. The physical solution to a pipe excitation problem must be periodic in the θ direction with a period of 2π. Therefore, the displacement field u in a pipe under some particular excitation condition can be written as a superposition of displacements in an unbounded structure in the circumferential direction θ with a period of 2π:

$$\mathbf{u}(\theta,y,z) = \sum_{l=-\infty}^{+\infty} \mathbf{u}_{\mathrm{unb}}(\theta + 2\pi l, y, z), \tag{2}$$

where $\mathbf{u}_{\mathrm{unb}}$ is the solution to the problem of excitation of guided waves in an unbounded structure due to excitation forces that are nonzero only for values θ between 0 and 2π and the index l is an integer. This concept is illustrated schematically in Fig. 1(b).

When the wall thickness h is much less than the pipe radius R,

$$h \ll R, \tag{3}$$

various approximate shell theories can be applied. As shown in Ref. 4 in this case the governing equations for the unbounded medium are associated with the equations for some anisotropic medium and the wave field u_{pl} can be calculated using the integral transforms technique.

Condition (3) means that the curvature of the pipe is approximately constant through the pipe thickness. If in addition to Eq. (3) the wavelength λ is much less than the pipe circumference,

$$\lambda \ll 2\pi R, \tag{4}$$

the effect of the curvature of the pipe on wave propagation becomes negligibly small. In this case the unbounded isotropic pipe can be formally regarded as an unbounded flat isotropic plate of the same thickness. Instead of angle θ, the new variable x can be defined as $x = \theta R$ and Eq. (2) can be written in the form

$$\mathbf{u}(x,y,z) = \sum_{l=-\infty}^{+\infty} \mathbf{u}_{\mathrm{pl}}(x + 2\pi R l, y, z), \tag{5}$$

where the function $\mathbf{u}_{\mathrm{pl}}$ represents the displacement field in a flat infinite isotropic plate due to excitation in the region $x = 0$ to $2\pi R$ only.

B. Excitation of guided waves in a plate

The wave field in a plate due to surface load can be calculated by using multiple integral transforms.[8,9] The displacement, $\mathbf{u}_{\mathrm{pl}}$, can be written in terms of its two-dimensional (2D) Fourier transform with respect to the in-plane coordinates x and z:

$$\mathbf{u}_{\mathrm{pl}}(x,y,z) = \frac{1}{4\pi^2} \int\int \mathbf{U}_{\mathrm{pl}}(k_x,k_z,y) e^{ik_x x} e^{ik_z z} dk_x dk_z, \tag{6}$$

where the function $\mathbf{U}_{\mathrm{pl}}(k_x,k_z,y)$ is the amplitude of straight-crested waves propagating in the direction given by the components (k_x,k_z) of the wave vector.

The polar coordinate system r,φ on the x-z plane is defined as

$$x = r \sin \varphi, \quad z = r \cos \varphi. \tag{7}$$

If the propagation distance from the source, r, is large compared with the wavelength then integral (6) can be evaluated using the residues technique.[10] The wave field u_{pl} is expressed as a sum of circular crested modes:

$$\mathbf{u}_{\mathrm{pl}}(x,y,z) = \sum_m \mathbf{u}_m \frac{e^{ik_m r}}{\sqrt{r}}, \tag{8}$$

where the vector of modal displacements, $\mathbf{u}_m$, is given by

$$\mathbf{u}_m(\varphi,y) = \sqrt{\frac{k_m}{2\pi}} e^{i\pi/4} \operatorname{res} \mathbf{U}_{\mathrm{pl}}(k \sin \varphi, k \cos \varphi)|_{k=k_m}, \tag{9}$$

and the poles, k_m, of the function $\mathbf{U}$ are associated with the mode wavenumbers.

In an isotropic media, the function $\mathbf{U}_{\mathrm{pl}}(k_x,k_z,y)$ has the following structure:

$$\mathbf{U}_{\mathrm{pl}}(k_x,k_z,y) = \frac{\mathbf{W}(k_x,k_z,y)}{D(k)}, \quad k = \sqrt{k_x^2 + k_z^2}, \tag{10}$$

where $\mathbf{W}(k_x,k_z,y)$ is the analytical function of the variables k_x,k_z. The poles of the function $\mathbf{U}_{\mathrm{pl}}$ correspond to the roots of the denominator $D(k)$. The real roots represent the propagating waves while the complex roots represent nonpropagating waves that decay exponentially with propagating distance from the source. In this paper, only the contribution from real roots is considered. For a single root corresponding to a first order pole, the vector $\mathbf{u}_m$ using representation Eq. (10) can be written as

$$\mathbf{u}_m(\varphi,y) = \sqrt{\frac{k_m}{2\pi}} e^{i\pi/4} \frac{\mathbf{W}(k_m \sin \varphi, k_m \cos \varphi, y)}{D'(k_m)}. \tag{11}$$

Note that at some isolated frequencies the function $D(k)$ may have double roots giving rise to a second order pole. The mode at these frequencies has zero group velocity that leads to the energy accumulation in the finite volume of the

waveguide.[10,11] Such resonance phenomena can be important in practice.[12] Below it is assumed that the mode wavenumbers k_m correspond to the non-resonant frequencies.

C. Relation between plate and pipe forced solutions

The representation (1) of the wave field in a pipe can be regarded as the Fourier series of $\mathbf{u}$ which is a periodic function of the circumferential angle θ. On the other hand, the function $\mathbf{u}$ represented by the sum (5) is a periodic function with respect to the circumferential variable x with a period of $2\pi R$ and also can be expanded into a Fourier series:

$$\mathbf{u}(x,y,z) = \sum_n \mathbf{A}_n(y,z)e^{inx/R}. \tag{12}$$

In this section, the expansion of the coefficients $\mathbf{A}_n$ in terms of plate modes will be derived. As a result the function $\mathbf{u}$ given by the sum (5) takes the same form as the pipe solution (1). This allows the relationship between the circumferential mode in a pipe, $\mathbf{u}_m^n$, and the guided wave mode in a plate, $\mathbf{u}_m$, to be obtained.

The nth Fourier coefficient, $\mathbf{A}_n$, is defined as

$$\mathbf{A}_n = \frac{1}{2\pi R}\int_0^{2\pi R} \mathbf{u}(x,y,z)e^{-inx/R}dx$$

$$= \frac{1}{2\pi R}\sum_{l=-\infty}^{+\infty}\int_0^{2\pi R} \mathbf{u}_{\mathrm{pl}}(x+2\pi Rl,y,z)e^{-inx/R}dx. \tag{13}$$

Using the change of variable $x'=x+2\pi Rl$ in the integral in the sum (13), the expression for the coefficient $\mathbf{A}_n$ can be rewritten as

$$\mathbf{A}_n = \frac{1}{2\pi R}\sum_{l=-\infty}^{+\infty} e^{i2\pi ln}\int_{2\pi Rl}^{2\pi R(l+1)} \mathbf{u}_{\mathrm{pl}}(x',y,z)e^{-inx'/R}dx'. \tag{14}$$

By taking into account that indices n and l are integers, expression (14) reduces to

$$\mathbf{A}_n = \frac{1}{2\pi R}\int_{-\infty}^{+\infty} \mathbf{u}_{\mathrm{pl}}(x,y,z)e^{-inx/R}dx. \tag{15}$$

Note that this relationship can be obtained directly from the properties of a discrete Fourier transform (DFT).[13] The series (12) represents a DFT of a function $\mathbf{A}(\alpha), \mathbf{A}(n) \equiv \mathbf{A}_n$. In this case Eq. (12) can be calculated in the form of the sum (5) with the spectrum of the function $\mathbf{A}$ instead of $\mathbf{u}_{\mathrm{pl}}$. This leads to the relationship (15).

Using the integral representation (6) for the plate solution and the identity

$$\int_{-\infty}^{+\infty} e^{ikx}dx \equiv 2\pi\delta(k), \tag{16}$$

coefficient $\mathbf{A}_n$ can be written in the form

$$\mathbf{A}_n = \frac{1}{4\pi^2 R}\int \mathbf{U}_{\mathrm{pl}}\left(\frac{n}{R},k_z,y\right)e^{ik_z z}dk_z. \tag{17}$$

By using the residues technique, the integration in Eq. (17) can be reduced to the sum of residuals:

$$\mathbf{A}_n = \sum_m \mathbf{u}_m^n(y)e^{ik_m^n z}, \quad \mathbf{u}_m^n(y) = \frac{i}{2\pi R}\mathrm{res}\,\mathbf{U}_{\mathrm{pl}}\left(\frac{n}{R},k_z,y\right)\Big|_{k_z=k_m^n}. \tag{18}$$

where the poles, k_m^n, represent axial wavenumbers of pipe modes.

Expression (10) shows that the poles, k_m^n, of the function $\mathbf{U}_{\mathrm{pl}}(n/R,k_z,y)$ as a function of the variable k_z correspond to the zeros of the function $D(\sqrt{n^2/R^2+k_z^2})$. As it has been shown in Sec. II B, the zeros, k_m, of the function $D(k)$ are associated with the wavenumbers of the guided wave modes in a plate. Hence,

$$k_m^n = \sqrt{k_m^2 - \frac{n^2}{R^2}}. \tag{19}$$

Using expression (10) the residue of the function $\mathbf{U}_{\mathrm{pl}}(n/R,k_z,y)$ at the point $k_z=k_m^n$ can be written as

$$\mathrm{res}\,\mathbf{U}_{\mathrm{pl}}\left(\frac{n}{R},k_z,y\right)\Big|_{k_z=k_m^n} = \mathbf{W}\left(\frac{n}{R},k_m^n,y\right)\left(\frac{\partial D(k)}{\partial k_z}\right)^{-1}_{k_z=k_m^n}, \tag{20}$$

and, therefore, the vector $\mathbf{u}_m^n$ is given by

$$\mathbf{u}_m^n(y) = \frac{i}{2\pi R}\frac{\mathbf{W}\left(\frac{n}{R},k_m^n,y\right)}{D'(k_m)}\frac{k_m}{k_m^n}. \tag{21}$$

This expression can be rewritten in terms of plate mode displacements, $\mathbf{u}_m$. The function $\mathbf{u}_m$ is defined by the formula (11). The comparison of expressions ((21) and (11) enables the following relation between plate and pipe modes to be obtained:

$$\mathbf{u}_m^n(y) = e^{i\pi/4}\frac{1}{k_m^n R}\sqrt{\frac{k_m}{2\pi}}\mathbf{u}_m(\varphi_m^n,y). \tag{22}$$

Here the angle φ_m^n is defined by

$$\varphi_m^n = \arcsin\left(\frac{n}{k_m R}\right). \tag{23}$$

D. Relation between guided wave modes in pipe and plate

In the Appendix, it is shown that the displacements of a guided wave mode in a plate, $\mathbf{u}_m$, can be expressed in terms of a modal directivity function, $f_m(\varphi)$ [formula (A5)]. So, expression (22) for pipe mode can be rewritten in the form

$$\mathbf{u}_m^n(y) = a_m^n \mathbf{w}_m(\varphi_m^n,y), \tag{24}$$

where $\mathbf{w}_m(\varphi_m^n,y)$ is the power normalized displacements of the mth plate mode propagating in the φ_m^n direction, and the mode amplitude a_m^n is related to the directivity function of the plate mode as

$$a_m^n = e^{i\pi/4}\frac{1}{k_m^n R}\sqrt{\frac{k_m}{2\pi}}f_m(\varphi_m^n). \tag{25}$$

Expression (24) leads to the simple analogy between guided wave modes in pipe and plate. Index m defines the set of guided wave modes in a pipe which corresponds to the

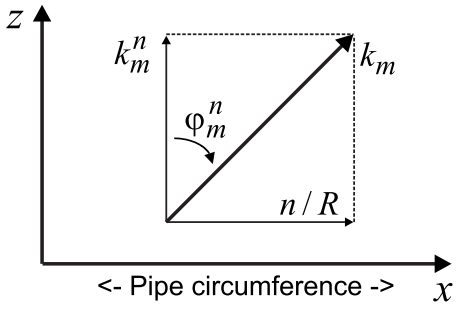

FIG. 2. Relation between pipe modes and direction of propagation of plate modes.

particular guided wave mode in a plate. If the index m is fixed then the circumferential order n of pipe mode corresponds to specific directions of propagation, φ_m^n, of the plate mode, as shown in Fig. 2. The axial wavenumber of the pipe mode, k_m^n, given by formula (19), is the projection of plate wavenumber, k_m, into the axial direction z.

The similarities between dispersion characteristics of guided waves in pipes and plates were studied earlier by Nishino *et al.*[7] and Li and Rose.[2] It was shown that longitudinal and flexural modes $L(n,m)$ in a pipe correspond to Lamb modes in a plate and torsional modes $T(n,m)$ in a pipe correspond to shear horizontal modes SH_m in a plate. For example, the $L(n,1)$ and $L(n,2)$ cylindrical modes correspond to the A_0 and S_0 Lamb wave modes.

III. ESTIMATION OF APPROXIMATION ERROR

The approximation theory given by the formulas (24) and (25) ignores the effect of curvature of a pipe on wave propagation. This effect becomes small for pipes with large radius to thickness ratio at higher frequencies. In this section, numerical calculations are performed to make quantitative estimation of approximation errors.

A. Comparison between dispersion characteristics

From formula (19) it follows that the approximate phase velocity of the pipe mode is given by

$$v_m^n = \frac{v_m}{\sqrt{1-\left(\frac{n}{k_m R}\right)^2}}, \tag{26}$$

where v_m is the phase velocity of the corresponding plate mode. This expression shows that the phase velocity of the pipe mode, v_m^n, given by the approximation theory, asymptotically approaches v_m at high frequencies. On the other hand, the same high frequency behavior of the phase velocities is revealed by the numerical calculations of dispersion curves for exact theory.[2,7] Therefore, the relative error of phase velocity decreases with the frequency and always tends to zero for any radius to thickness ratio of pipe.

Figure 3(a) shows the relative error of the phase velocity for the $T(n,1)$ modes as a function of frequency in steel pipes with radius to wall thickness ratio of 15. Dispersion curves for a plate and a pipe were calculated using the program DISPERSE (Imperial College, London).[14] For each circumferential mode, the error monotonically decreases with frequency. At a fixed frequency, the error increases with the circumferential order of the mode, n. This can be explained by the fact that pipe modes with larger circumferential orders propagate at larger angles φ_m^n relative to the axial direction of the pipe, and hence, these modes are more affected by the curvature of the pipe.

Note that the approximate expression (26) for the phase velocity depends on the radius of the pipe, R. Consider the difference between phase velocities calculated for the inner radius, $R=R_{\text{in}}$, and the outer radius, $R=R_{\text{out}}=R_{\text{in}}+h$. If the pipe thickness is small compared with the pipe radius, then this difference can be written as

$$v_m^n(R_{\text{out}}) - v_m^n(R_{\text{in}}) = v_m^n(R_{\text{in}})\left(1+\frac{h}{R_{\text{in}}}\frac{1}{1-\left(\frac{k_m R_{\text{in}}}{n}\right)^2}\right). \tag{27}$$

So, the relative error has the order h/R_{in}, but the approximate theory has the same order of accuracy itself. Hence, formally, any value of the radius R between R_{in} and R_{out} in the calculations will result in the approximation error of the same order.

However, at a fixed frequency, the value of the approximation error depends on the choice of R. In Fig. 3(a) calculations were performed using R equal to the mean radius,

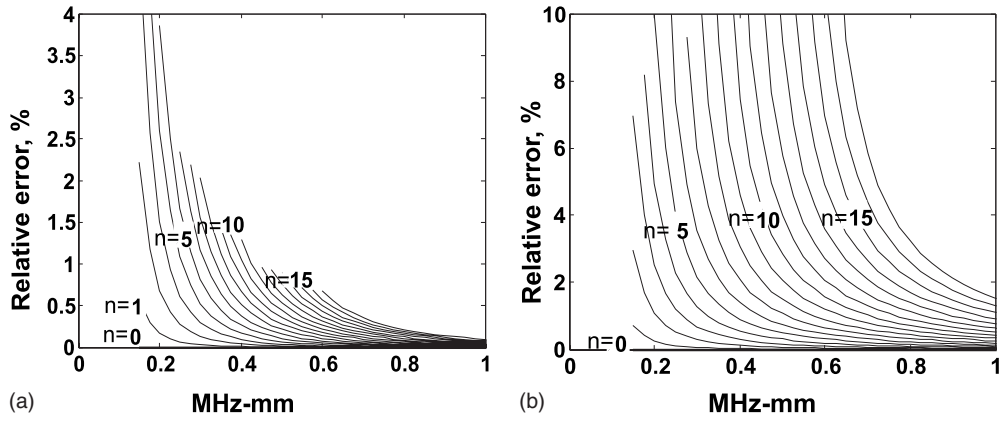

FIG. 3. Relative error of phase velocity calculated by the approximate theory for $T(n,1)$ modes in a pipe with inner radius/wall thickness ratio as 15 using radius value equal to the (a) mean radius and (b) outer radius.

R_{mean}. For comparison, Fig. 3(b) shows the error in phase velocities of the $T(n,1)$ modes in a pipe with $R_{\text{in}}/h=15$ calculated using $R=R_{\text{out}}$. It can be seen that for a fixed frequency the error corresponding to $R=R_{\text{mean}}$ is approximately ten times smaller then the error corresponding to $R=R_{\text{out}}$.

Note that the similarities between dispersion characteristics of circumferential guided waves in thin shells and plates were discussed by Liu and Qu.[15] The circumferential waves propagate in the circumferential direction θ only and can be described by expression (1), where $k_m^n \equiv 0$ and $n=kR_{\text{out}}$, k is the wavenumber. It was shown that in the limit of $h/R \to 0$, the dispersion curves of the circumferential modes in a pipe are identical to the guided wave modes in a plate of the same thickness regardless of frequency. This is different from the considered case where the approximation error is a function of frequency.

B. Comparison between modal solutions of the forced problem

A solution to the problem of generation of guided waves by a surface load can be expressed in terms of the convolution of the Green's matrix with this load [formula (A1) in the Appendix]. Therefore, in order to assess the approximation error in the forced case, it is enough to compare the Green's matrices given by the approximate and exact theories.

Using formulas (22), (A3), and (A4), the approximate Green's matrix, $\mathbf{g}_m^n$, can be written in the form

$$\mathbf{g}_m^n = \frac{i\omega}{4}\frac{1}{2\pi R\cos\varphi_m^n}\mathbf{w}_m(\varphi_m^n,y)\cdot\mathbf{w}_m^{*T}(\varphi_m^n,R_{\text{out}}). \tag{28}$$

On the other hand, the exact pipe modal solution can be obtained by the normal mode expansion method[5] and the result is given by

$$\mathbf{g}_{(\text{pipe})m}^n = \frac{i\omega}{4}\mathbf{w}_m^n(y)\cdot\mathbf{w}_m^{n*T}(R_{\text{out}}), \tag{29}$$

where $\mathbf{w}_m^n(y)$ is the power normalized pipe mode displacements.

Formulas (28) and (29) were used for numerical calculations of the modal solutions. In formula (28) the mean radius $R=R_{\text{mean}}$ was taken. Mode shapes and dispersion curves for a plate and a pipe were calculated using the program DISPERSE (Imperial College, London).[14] At each thickness value y, the relative error was estimated as the operator norm of the matrix $\|\mathbf{g}_{(\text{pipe})m}^n - \mathbf{g}_m^n\|$. The relative error was calculated according to

$$\epsilon_m^n = \max_y\left(\frac{\|\mathbf{g}_{(\text{pipe})m}^n(y)-\mathbf{g}_m^n(y)\|}{\|\mathbf{g}_{(\text{pipe})m}^n(y)\|}\right). \tag{30}$$

Note that the mode Green's matrices $\mathbf{g}_{(\text{pipe})m}^n$ and $\mathbf{g}_m^n$ are Hermitian matrices. For Hermitian matrix $\mathbf{g}$, the operator norm is given by

$$\|\mathbf{g}\| = \max_i|\lambda_i|, \tag{31}$$

where λ_i are eigenvalues of matrix g.

Figure 4 shows the relative error of the modal solutions for $T(n,1)$ modes as a function of frequency. It can be seen

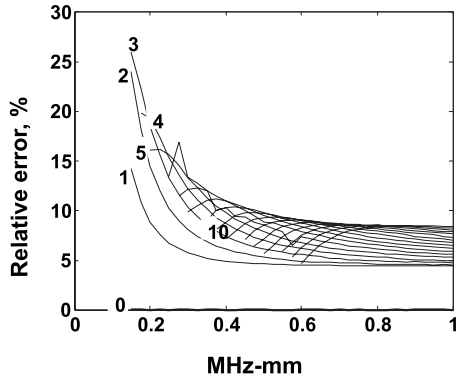

FIG. 4. Relative error of modal solutions for $T(n,1)$ modes calculated by the approximate theory in a pipe with inner radius/wall thickness ratio as 15 using radius value equal to the mean radius.

that the qualitative behavior is similar to that of the error of phase velocities. The error of modal amplitudes decreases with frequency and increases with the circumferential order of the mode. However, at high frequencies the error tends to some nonzero value of the order of h/R.

This fact can be explained by comparing the normalized mode shapes for plate and pipe modes. If $\mathbf{u}_m$ and $\mathbf{u}_m^n$ are mode displacements for guided wave mode in the plate and pipe, respectively, then the power normalized displacements are given by

$$\mathbf{w}_m = \frac{\mathbf{u}_m}{\sqrt{P_m}}, \quad \mathbf{w}_m^n = \frac{\mathbf{u}_m^n}{\sqrt{P_m^n}}. \tag{32}$$

Here P_m is the average power flow of the plate mode in the direction of mode propagation, and P_m^n is the average power flow of the pipe mode in the axial z direction:

$$P_m = \frac{\omega}{2}\text{Im}\int_{-h}^{0}(\mathbf{T}_m\mathbf{u}_m^*(0,y))\mathbf{e}_z dy,$$

$$P_m^n = \frac{\omega}{2}\frac{1}{2\pi}\text{Im}\int_{R_{\text{in}}}^{R_{\text{out}}}(\mathbf{T}_m^n\mathbf{u}_m^{n*})\mathbf{e}_z y dy. \tag{33}$$

where $\mathbf{T}_m$ and $\mathbf{T}_m^n$ are the stress tensors for plate and pipe modes, respectively.

If the pipe curvature can be neglected (i.e., $h/R \to 0$) then in formulas (32) and (33) the mode displacements $\mathbf{u}_m^n$ can be substituted by the plate mode displacements $\mathbf{u}_m(\varphi_m^n,y)$. Using the fact that the plate mode Poynting vector is in the direction of the mode propagation, it can be seen that expression (29), as expected, is converted to formula (28) of the approximation theory. For the finite ratio h/R from expression (33), it follows

$$\mathbf{g}_{(\text{pipe})m}^n = \mathbf{g}_m^n\left[1+O\left(\frac{h}{R}\right)\right]. \tag{34}$$

In other words, the approximate theory gives a relative error of the order of wall thickness to radius ratio for all frequencies.

IV. SCATTERING OF GUIDED WAVES FROM DEFECTS IN PIPES AND PLATES

A. Relation between plate and pipe scattered solutions

The approximate theory for guided wave excitation in pipe developed in Sec. II can be extended to relate guided wave scattering from defects in plates to scattered circumferential modal amplitudes from defects in pipe.

It is assumed that guided waves are excited and detected in the far-field of a defect. The incident wave field in the pipe is given by the sum of circumferential modes (1). The defect acts as a secondary source and the reflected signal consists of all possible combinations of mode-converted guided waves:

$$\mathbf{u} = \sum_{l,q} \left(\sum_{n,m} \mathbf{u}_{mq}^{nl}(y) \right) e^{il\theta} e^{-ik_q^l z}, \tag{35}$$

where each reflected mode $\mathbf{u}_{mq}^{nl}$ is caused by the incident $\mathbf{u}_m^n$ mode.

Expression (24) for the mode displacement vector $\mathbf{u}_m^n$ shows that, in the framework of the plate approximation, pipe mode $\mathbf{u}_m^n$ represents the straight-crested mth plate mode with amplitude a_m^n propagating in φ_m^n direction. Consider the interaction of this wave with the defect in the plate. Similar to Eq. (A5), the far-field reflected signal can be expressed in terms of mode-converted guided waves as

$$\mathbf{u} = \sum_q \mathbf{u}_{mq} \frac{e^{ik_q r}}{\sqrt{r}}, \quad \mathbf{u}_{mq} = a_m^n S_{mq}(\varphi_m^n, \varphi) \mathbf{w}_q(\varphi, y), \tag{36}$$

where the function $S_{mq}(\varphi_{\text{in}}, \varphi_{\text{sc}})$ is the scattering matrix of the defect depending on the incident φ_{in} and scattering φ_{sc} angles.

Using formulas (36) and (24), the displacement vector $\mathbf{u}_{mq}^{nl}$ of the scattered circumferential mode in the pipe can be written as

$$\mathbf{u}_{mq}^{nl}(y) = a_m^n S_{mq}^{nl} \mathbf{w}_q(\varphi_q^l, y), \tag{37}$$

where S_{mq}^{nl} is the scattered modal amplitude. Formula (25) leads to the following relationship between S_{mq}^{nl} and the scattering matrix S_{mq} in a plate:

$$S_{mq}^{nl} = e^{i\pi/4} \frac{1}{k_q^l R} \sqrt{\frac{k_q}{2\pi}} S_{mq}(\varphi_m^n, \varphi_q^l). \tag{38}$$

Formula (38) is obtained under the assumption that receiver is in the far-field from the defect, $r \gg d, r \gg \lambda$. It is possible to show that this relationship also holds if only the second condition is satisfied. It is supposed that the waves scattering by the defect can be described by some equivalent surface and bulk forces applied to a defect-free structure. If condition $r \gg \lambda$ is satisfied then relationships (37) and (38) are valid for the pipe and plate Green's matrices. The total scattered field in the pipe is given by the convolution of the pipe Green's matrix with the force distribution and may also be written in the forms (37) and (38). Note that expression (35) for the wave field in the pipe represents plane waves superposition. The function S_{mq} in this case is expressed as the convolution integral (A6), which is the definition of the defect's scattering matrix.

B. Approximate model for through-thickness crack scattering in plate

Equation (38) is the approximate scattering formula for scattering of guided wave modes in pipes. In order to calculate scattered modal amplitudes, the scattering matrix S_{mq} for a plate must be known. The general problem of diffraction of guided waves by arbitrary defects in plates can be solved only by time consuming direct numerical methods (e.g., finite elements, boundary elements, or finite differences). However, in some cases, a simplified model can be applied.

At relatively low frequency-thickness values, the normal stress, σ_y, corresponding to the S_0 mode, is small compared with the in-plane stresses, σ_z and σ_x, and can be neglected. Here $\sigma_j = \mathbf{T}\mathbf{e}_j$, $j = x, y, z$ and $\mathbf{T}$ denotes the stress tensor. For example, at 0.5 MHz mm for the S_0 mode propagating in the z direction $|\sigma_y|/|\sigma_z| < 0.018$. Note that for the SH_0 mode the normal stress is identically zero. Therefore, the propagation of these modes in a plate can be modeled using a plane stress approximation. The plate is replaced by a 2D infinite elastic media in-plane stress and the displacement vector $\mathbf{u}$ can be considered as a 2D vector with the components (u_z, u_x). The longitudinal (L) and shear (S) bulk waves in these media correspond to the S_0 and SH_0 modes in the plate. A similar approach has been used before for finite element modeling of the S_0 mode in a plate.[16]

This simplified approach can also be used for modeling of the scattering from a through-thickness defect with a constant profile through the plate thickness. Such a defect is fully described by its 2D shape in the x-z plane and the mode conversion occurs between S_0 and SH_0 modes only. Therefore, the three-dimensional (3D) problem of diffraction of guided waves in a pipe reduces to the problem of longitudinal and shear bulk wave scattering in infinite 2D media. For example, in the case of a circular hole, the known analytical solution can be used.[17]

If the defect is a crack then this problem can be solved by the semi-analytical method, developed in Ref. 8, which is based on the boundary integral equation method. In this case the scattering matrix depends on the crack length, d, and frequency, ω. From expression (36), it follows that dimension of scattering matrix is $(\text{length})^{1/2}$. The only parameter with the dimension of length is a wavelength λ of the mode of interest (longitudinal of shear). Hence,

$$S(\varphi_{\text{in}}, \varphi_{\text{sc}}, d, \omega) = \sqrt{\lambda} \tilde{S}\left(\varphi_{\text{in}}, \varphi_{\text{sc}}, \frac{d}{\lambda} \right), \tag{39}$$

where dimensionless scattering matrix $\tilde{S}$ depends on dimensionless crack length d/λ. Figure 5 shows the amplitudes of the calculated scattering matrices for the shear (S) wave incident on the crack of λ_S length in steel. The zero angle corresponds to the normal direction to the crack surface.

C. Scattering of guided waves in pipes

If the scattering matrix S_{mq} for a plate is known, then the first step in calculating the scattered modal amplitudes in a pipe is the evaluation of equivalent propagation angles φ_m^n and φ_l^q of plane waves in a plate for different pipe modes.

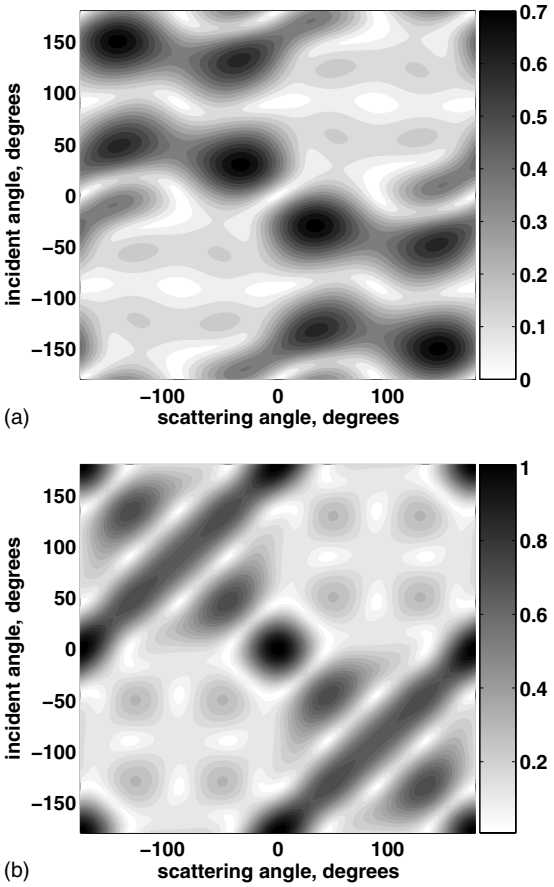

FIG. 5. Dimensionless scattering matrices for the shear (S) wave incident on the crack of λ_S length in steel. (a) Shear to longitudinal wave reflection. (b) Shear to shear wave reflection.

Then the pipe modal amplitudes are obtained by substituting the corresponding values of matrix S_{mq} into expression (38).

To illustrate the application of the proposed approximate theory, a 12 in. diameter, schedule 10S steel pipe ($R_{\text{out}}=161.95$ mm, $h=4.58$ mm, and $R_{\text{mean}}/h=34.8$) at 100 kHz is considered. The reflection coefficients of the $L(n,2)$, $n=0,1,2$ modes for axisymmetric $L(0,2)$ mode incident on a through-thickness circumferential crack with varying extents are shown in Fig. 6. These results are in good agreement with the results by a finite element modeling and experiment obtained in Ref. 1.

The scattered modal amplitudes S can also be presented

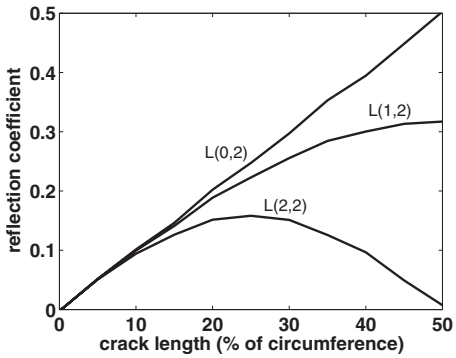

FIG. 6. Variation of scattered amplitudes of $L(n,2)$, $n=0,\ldots,4$ modes with circumferential extent of a through-thickness crack in a 12 in. diameter pipe, $L(0,2)$ mode incident.

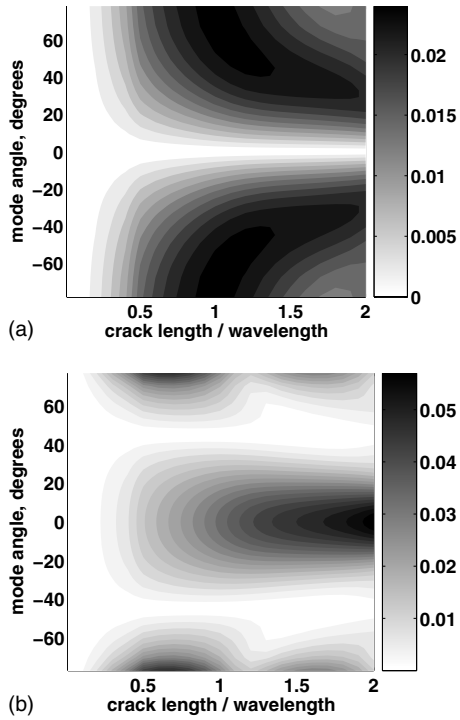

FIG. 7. Scattering coefficients for the $T(0,1)$ mode incident on the circumferential crack in 12 in. diameter steel pipe, wavelength=$\lambda_{T(0,1)}$. (a) $T(0,1)$ to $L(n,2)$ mode conversion. (b) $T(0,1)$ to $T(n,1)$ mode conversion.

in the form of 2D color map of the isolines of the 3D function $S(\varphi_n,d)$, where φ_n is the angle of propagation of nth scattered mode and d is a length of the crack. In Fig. 7 scattering amplitudes of the $L(n,2)$ and $T(n,1)$ modes for the $T(0,1)$ mode incident on the circumferential crack are shown. This corresponds to the SH_0-S_0 and SH_0-SH_0 mode conversion in a plate.

These results can be easily extended to through-thickness cracks inclined with respect to the pipe circumferential direction. In this case in formula (38) different angles φ_m^n and φ_l^q in matrix S_{mq} must be taken.

V. DETECTABILITY OF DEFECTS IN PIPES

Recently the common source method (CSM) for pipe imaging has been introduced.[18,19] In this section, the approximate model developed above will be applied to estimate the minimal crack size that can be detected using the CSM.

The detectability of the imaging method is characterized by a detectability map. Such a map represents the amplitude of the defect in an image relative to the biggest reflector as a function of defect parameters. For a through-thickness crack, these parameters are crack length and crack orientation. As a reference reflector, a pipe end is taken.

The same configuration of system as in Ref. 18 is considered. An axisymmetric $T(0,1)$ mode is excited and reflected $T(l,1)$ modes are detected by 24 shear transducers located around the circumference of an 8 in. nominal diameter schedule 40 steel pipe ($R_{\text{out}}=109.55$ mm, $h=8.18$ mm, and $R_{\text{mean}}/h=12.9$). The transmitted signal used is a 5 cycle Hanning windowed toneburst with a center frequency of 50 kHz. Note that the $T(n,1)$ modes correspond to the SH_0 mode in a plate.

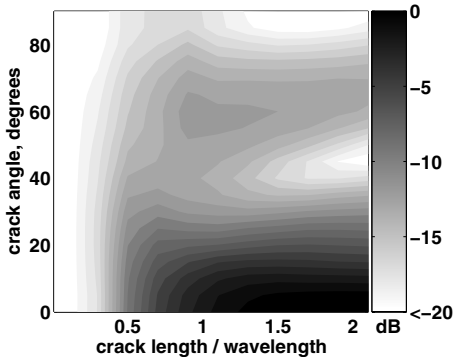

FIG. 8. Image amplitude of a though thickness crack relative to the image amplitude of a pipe end wall as a function of crack length and crack orientation.

The imaging algorithm consists of the extraction of scattering mode amplitudes, back-propagation of each circumferential mode to a given axial position, and conversion of the back-propagated modes from the circumferential wavenumber domain to the circumferential spatial domain.[18] The approximate model was applied to obtain the scattered data for cracks up to 2λ length and any orientation. Here λ =65.2 mm is a wavelength of the SH_0 mode at 50 kHz. The function $f(\varphi)=\cos\varphi$ was taken as the directivity function of the transducer.

The results given in Refs. 18 and 19 show that the noise in an experimental image is at about –20 dB level relative to an end wall reflection. This means that any defect with the image amplitude greater than −20 dB relative to a pipe end can be detected. The detectability map is shown in Fig. 8. It can be seen that the CSM allows the detection of through-thickness cracks over 0.4λ(26 mm) length and up to 80° orientation. It interesting to note that detectability map has narrow "valley" for cracks greater than 1.5λ length inclined at about 45°. This implies that even cracks with significant length have very small amplitudes in this orientation and, therefore, are undetectable.

VI. CONCLUSION

A technique for obtaining pipe mode amplitudes in terms of the solution to the forced 3D problem on a plate has been developed. The amplitude of a particular circumferential mode in a pipe is related to the amplitude of a corresponding plate mode propagating in some specific direction. The comparison of approximate and exact solutions for a pipe has been performed and limitations of the approximation have been discussed. A relation between modal scattering coefficients in a pipe and plate has been obtained. The semi-analytical model of through-thickness crack diffraction in a plate has been implemented and applied to the problem of guided wave scattering from a through-thickness crack in a pipe. The results of calculation of mode-converted guided waves in a pipe have been presented.

ACKNOWLEDGMENTS

This work was supported by the UK Engineering and Physical Sciences Research Council (EPSRC, GR/T11449/01) through the UK Research Centre in NDE and by BNFL, Nexia Solutions, DSTL, and British Energy.

APPENDIX: DIRECTIVITY FUNCTION OF GUIDED WAVES IN A PLATE

An isotropic plate is considered with Cartesian coordinate system x,y,z defined with the y axis normal to the plate, as shown in Fig. 1(a). It is assumed that wave field is generated by some distributions of surface load, $\mathbf{q}$, applied to the upper surface at $y=0$, and volume forces, $\mathbf{F}$. The displacements $\mathbf{u}$ are related to $\mathbf{q}$ and $\mathbf{F}$ by the 3D Green's function $\mathbf{g}$:

$$\mathbf{u}(x,y,z)=\int \mathbf{g}(x-x',z-z',y,0)\mathbf{q}(x',z')dx'dz' + \int \mathbf{g}(x-x',z-z',y,y') \times \mathbf{F}(x',z',y')dx'dz'dy'. \tag{A1}$$

As it has been shown in Ref. 9, in the far field from the location of the sources, the Green's function $\mathbf{g}(x,z,y,y')$ can be written in the form

$$\mathbf{g}=\sum_m \mathbf{E}_m^{(3)}(\varphi,y,y')\frac{e^{ik_m r}}{\sqrt{r}}, \tag{A2}$$

where cylindrical coordinates (r,φ,y) are used and the 3D modal excitability matrix, $\mathbf{E}_m^{(3)}$, is given by

$$\mathbf{E}_m^{(3)}(\varphi,y,y')=e^{-i\pi/4}\sqrt{\frac{k_m}{2\pi}}\mathbf{E}_m^{(2)}(\varphi,y,y'). \tag{A3}$$

The function $\mathbf{E}_m^{(2)}$ is the 2D modal excitability matrix and can be expressed in terms of mode shape as[6]

$$\mathbf{E}_m^{(2)}(\varphi,y,y')=\frac{i\omega}{4}\mathbf{w}_m(\varphi,y)\cdot\mathbf{w}_m^{*T}(\varphi,y'), \tag{A4}$$

where ω is the circular frequency, * denotes complex conjugation, and T represents transpose. The vector $\mathbf{w}_m(\varphi,y)$ is the power normalized displacements for mth mode propagating in the φ direction. Note that the vector $\mathbf{w}_m(\varphi,y)$ is formed by the rotation of the vector $\mathbf{w}_m(0,y)$ about axis y by the angle φ.

Using Eqs. (A1) and (A4), the following far-field expression for the total displacement field $\mathbf{u}$ can be obtained:

$$\mathbf{u}=\sum_m \mathbf{u}_m\frac{e^{ik_m r}}{\sqrt{r}},\quad \mathbf{u}_m=f_m(\varphi)\mathbf{w}_m(\varphi,y), \tag{A5}$$

where f_m is the modal directivity function, which is given by

$$f_m(\varphi)=\frac{e^{i\pi/4}}{4}\omega\sqrt{\frac{k_m}{2\pi}}\left[\int \mathbf{w}_m^*(\varphi,0)\mathbf{q}(x',z') \times e^{-ik_m(x'\cos\varphi+z'\sin\varphi)}dx'dz' + \int \mathbf{w}_m^*(\varphi,y')\mathbf{F}(x',z',y') \times e^{-ik_m(x'\cos\varphi+z'\sin\varphi)}dx'dz'dy'\right]. \tag{A6}$$

[1]M. J. S. Lowe, D. N. Alleyne, and P. Cawley, "The mode conversion of a guided wave by a part-circumferential notch in a pipe," ASME J. Appl. Mech. **65**, 649–656 (1998).
[2]J. Li and J. L. Rose, "Natural beam focusing of non-axisymmetric guided waves in large-diameter pipes," Ultrasonics **44**, 35–45 (2006).
[3]A. Demma, P. Cawley, M. Lowe, A. Roosenbrand, and B. Pavlakovic, "The reflection of guided waves from notches in pipes: A guide for interpreting corrosion measurements," NDT Int. **37**, 167–180 (2004).
[4]A. D. Pierce and H.-G. Kil, "Elastic wave propagation from point excitations on thin-walled cylindrical shells," J. Vibr. Acoust. **112**, 399–406 (1990).
[5]J. J. Ditri, "Utilization of guided elastic waves for the characterization of circumferential cracks in hollow cylinders," J. Acoust. Soc. Am. **96**, 3769–3775 (1994).
[6]B. A. Auld, *Acoustic Fields and Waves in Solid*, 2nd ed. (Krieger, Malabar, FL, 1990).
[7]H. Nishino, S. Takashina, F. Uchida, M. Takemoto, and K. Ono, "Modal analysis of hollow cylindrical guided waves and applications," Jpn. J. Appl. Phys., Part 1 **40**, 364–370 (2001).
[8]E. Glushkov, N. Glushkova, A. Ekhlakov, and E. Shapar, "An analytically based computer model for surface measurements in ultrasonic crack detection," Wave Motion **43**, 458–473 (2006).
[9]A. Velichko and P. D. Wilcox, "Modeling the excitation of guided waves in generally anisotropic multilayered media," J. Acoust. Soc. Am. **121**, 60–69 (2007).
[10]V. A. Babeshko, E. V. Glushkov, and N. V. Glushkova, "Energy vortices and backward fluxes in elastic waveguides," Wave Motion **16**, 183–192 (1992).
[11]L. Brevdo, "Wave packets, signaling and resonances in a homogeneous waveguide," J. Elast. **49**, 201–237 (1997).
[12]A. Gibson and J. Popovics, "Lamb wave basis for impact-echo method analysis," J. Eng. Mech. **131**, 438–443 (2005).
[13]J. W. Goodman, *Introduction to Fourier Optics* (McGraw-Hill, New York, 1996).
[14]B. Pavlakovic, M. Lowe, D. Alleyne, and P. Cawley, in *Review of Progress in Quantitative NDE*, edited by D. Thompson and D. Chimenti (Plenum, New York, 1997), Vol. **16**, pp. 185–192.
[15]G. Liu and J. Qu, "Guided circumferential waves in a circular annulus," ASME J. Appl. Mech. **65**, 424–430 (1998).
[16]O. Diligent, T. Grahn, A. Bostrom, P. Cawley, and M. J. S. Lowe, "The low-frequency reflection and scattering of the S_0 Lamb mode from a circular through-thickness hole in a plate: Finite element, analytical and experimental studies," J. Acoust. Soc. Am. **112**, 2589–2601 (2002).
[17]R. J. Brind, J. D. Achenbach, and J. E. Gubernatis, "High-frequency scattering of elastic waves from cylindrical cavities," Wave Motion **6**, 41–60 (1984).
[18]J. Davies and P. Cawley, "The application of synthetically focused imaging techniques for high resolution guided wave pipe inspection," in *Review of Progress in Quantitative NDE*, edited by D. O. Thompson and D. E. Chimenti (Melville, New York, 2007), Vol. **26A**, pp. 681–688.
[19]J. Davies and P. Cawley, "Synthetic focusing for high resolution guided wave pipe inspection: Further results and robustness studies," in *Review of Progress in Quantitative NDE*, edited by D. O. Thompson and D. E. Chimenti (Melville, New York, 2008), Vol. **27A**, pp. 139–146.

Electroacoustic analysis of an electret loudspeaker using combined finite-element and lumped-parameter models

Mingsian R. Bai,[a] Rong-Liang Chen, and Chun-Jen Wang
Department of Mechanical Engineering, National Chiao-Tung University, 1001 Ta-Hsueh Road, Hsin-Chu 300, Taiwan

(Received 1 May 2008; revised 11 March 2009; accepted 12 March 2009)

An unconventional type of electrostatic loudspeaker is presented in this paper. The loudspeaker made of thin, light, and flexible electret material lends itself well to the space-concerned applications. Electrical impedance measurement reveals that the coupling between the electrical system and the mechanical system is weak, which renders conventional parameter identification based on electrical impedance measurement impractical. A different approach is thus employed to model the electret loudspeaker. To predict the loudspeaker's dynamic response, finite-element analysis (FEA) is conducted on the basis of a simple model and a full model. In the simple model, FEA is applied to model the electret membrane, leaving the rest of system as rigid parts. In the full model, FEA is applied to model the entire membrane-spacer-back plate assembly. Velocity response of the membrane subject to a uniformly distributed force is calculated using FEA harmonic analysis. Mechanical impedance is then calculated with the velocity response. The acoustical impedance due to the back cavity, pores, and the radiation loading at the front side is calculated by theoretical formulas. The volume velocity of the membrane and the resulting on-axis sound pressure level are predicted with electrical-mechanical-acoustical analogous circuits. The response data predicted by the simulation compare very well with experimental measurements.
 [DOI: 10.1121/1.3117377]

PACS number(s): 43.38.Bs, 43.38.Ja, 43.40.Dx [AJZ] Pages: 3632–3640

I. INTRODUCTION

A flat type of loudspeaker based on electret technology is presented in this paper. The loudspeaker is made of thin, light, and flexible electret material, which lends itself very well to space-concerned applications as demanded by many 3C (computer, communication, and consumer electronics) products. This paper aims to model the electret loudspeaker and assess the acoustical performance using a combined finite-element and lumped-parameter model. Being able to simulate the response of the transducer is crucial to optimizing the performance of this special type of transducer.

The principle of the electret loudspeaker resembles that of electrostatic loudspeakers. An electrostatic loudspeaker exploits the varying electrostatic force generated between two charged plates separated by an air gap. In the 1930s, there were a number of practical electrostatic loudspeakers invented.[1] McLachlan[2] conducted theoretical investigations of sound power and pressure at resonant and non-resonant frequencies on a stretched-membrane electrostatic loudspeaker. On the other hand, electret is a dielectric material that has a quasi-permanent electric charge or dipole polarization. An electret generates internal and external electric fields, and is the electrostatic equivalent of a permanent magnet. There is a similarity between electrets and the dielectric layer used in capacitors; the difference being that dielectrics in capacitors possess an induced polarization that is only transient, dependent on the potential applied on the dielectric, while dielectrics with electret properties exhibit quasi-permanent charge storage or dipole polarization in addition. Paajanen *et al.*[3] modeled the electret film using a simplified model involving multiple parallel air gaps. Reciprocity of the sensor and actuator is demonstrated experimentally using the model. Mellow and Karkkainen[4] calculated the free-space radiation of a tensioned circular membrane. Near-field and far-field pressure responses and efficiency were calculated based on the diaphragm impedance. The on-axis pressure response calculated using this method was compared with that obtained using a finite-element model. Medley *et al.*[5] analyzed an electrostatic transducer analytically and numerically. The frequency response of the transducer with layered construction was calculated and compared with experimental data.

Electret transducers have advantage over conventional electrostatic transducers to enable simple and compact electroacoustic construction without external polarization circuit and power supply. A celebrated example is the electret condenser microphone invented at Bell laboratories in 1962 by Sessler and West,[6] using a thin metalized Teflon foil. Rather than the well established microphone technology, the reciprocal application of electret material to loudspeakers is attempted in this paper. Over the past years, various polymer materials such as polyethylene, polystyrene, polyurethane, polyethyleneterephtalate, Teflon (FEP and PTFE), polyvinylidene fluoride, and polypropylene (PP) have been used as electret materials.[7,8] These are usually homogeneous solid materials. Paajanen *et al.*[8] suggested a new multipurpose material, electromechanical film (EMFi). The EMFi is a thin, cellular, biaxially oriented PP film that can be used as an

[a]Author to whom correspondence should be addressed. Electronic mail: msbai@mail.nctu.edu.tw

electret. Having a special voided internal structure and high resistivity, it is capable of storing large permanent charge. EMFi can be applied to sensors, switches, loudspeakers, special transducers, etc. Saarimaki *et al.*[9] developed heat-resistive sensors and actuators using electromechanical cyclo-olefin-based polymer films. They described in detail the manufacturing of electromechanical and electrostatic transducers used in the audible frequency range. Recently, Chiang and Chen[10] proposed a new flexible electret loudspeaker using nano-technology. The electret diaphragms are fabricated using fluoro-polymer with nano-meso-micro pores precharged by the corona method. Heydt *et al.*[11] measured the acoustical response produced by electrostrictive polymer film loudspeakers. Measurements of harmonic distortion are also shown, accompanied with results demonstrating reduced harmonic distortion achieved using a square-root wave shaping technique.

This paper aims at establishing a simulation platform for electret loudspeakers with the main structure consisting of a membrane, a spacer grid, and a back plate. Due to the effect of the spacer grid, the membrane is rigidly constrained at the grid such that the motional impedance presented in the terminal electrical impedance is almost negligible. As we shall see later in the presentation, the characteristics of the mechanical system are not present in the electrical domain and the effective electrical impedance resembles that of a capacitor. Electrical impedance measurement reveals that the coupling between the electrical system and the mechanical system is weak, which renders conventional parameter identification based on electrical impedance measurement[12–14] impractical in the case of electret loudspeakers. In this paper, a different approach is thus employed to model the electret loudspeaker by taking advantage of the fact that the electrical and the mechanical systems are weakly coupled. Specifically, the electrical response is treated as a capacitor without considering the mechanical loading, whereas the mechanical response is calculated by using the unloaded electrical response as the input to the mechanical systems. Finite-element analysis (FEA) is employed in a simple model as well as a full model to predict the loudspeaker's dynamic response. The FEA model is tuned by matching the resonance frequency predicted by a single-cell model with the velocity response measured by a laser vibrometer. The mechanical impedance is estimated by the average velocity response subjected to a uniformly distributed force. Furthermore, the acoustical impedance due to the back cavity, pores, and the radiation loading at the front side is calculated by the theoretical formulas. Using this hybrid model, the volume velocity of the membrane and the on-axis sound pressure level (SPL) can be calculated with accuracy.

II. OPERATING PRINCIPLES OF AN ELECTRET LOUDSPEAKER

A sample of electret loudspeaker with length 101 mm and width 41 mm is shown in Figs. 1(a) and 1(b). The main structure of the loudspeaker includes a membrane (nanoporous fluoro-polymer), a spacer grid, and a perforated back plate (stainless steel) with 24.15% perforation ratio. The gap between the membrane and the back plate is 100 μm. Figure

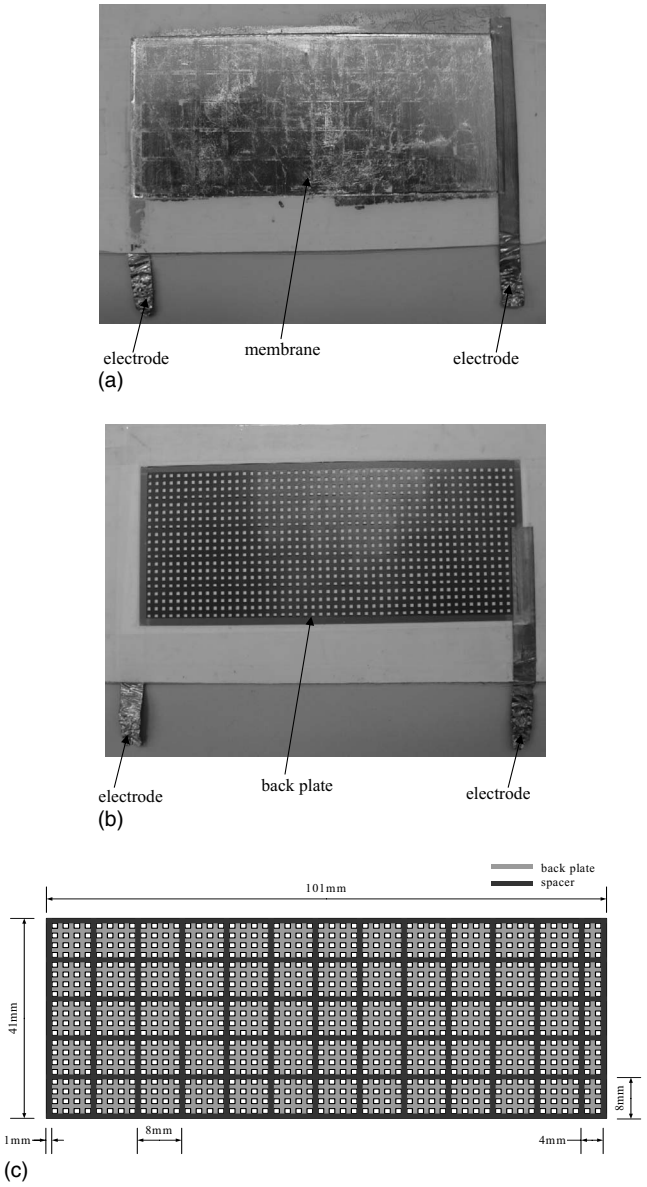

FIG. 1. The electret loudspeaker. (a) Photo (front view). (b) Photo (rear view). (c) Schematic showing the perforated back plate and the spacer grid.

1(c) is the top-view of the loudspeaker structure, where the arrangement of the spacer grid is shown. The time-varying attraction force between the back plate and the membrane gives rise to the motion of the membrane. The device *per se* is a capacitor with capacitance varying with the distance between the membrane and the back plate, as shown in Fig. 2(a). The static attraction force (Coulomb force) between the membrane and the back plate can be calculated using the following formula:

$$F_0 = \frac{\varepsilon S}{2}\frac{E_0^2}{d^2}. \tag{1}$$

The dielectric constant ε is given by

$$\varepsilon = \frac{C_0 d}{S}, \tag{2}$$

where S is the area of action, E_0 is the effective dc bias voltage due to the precharged electret, d is the distance be-

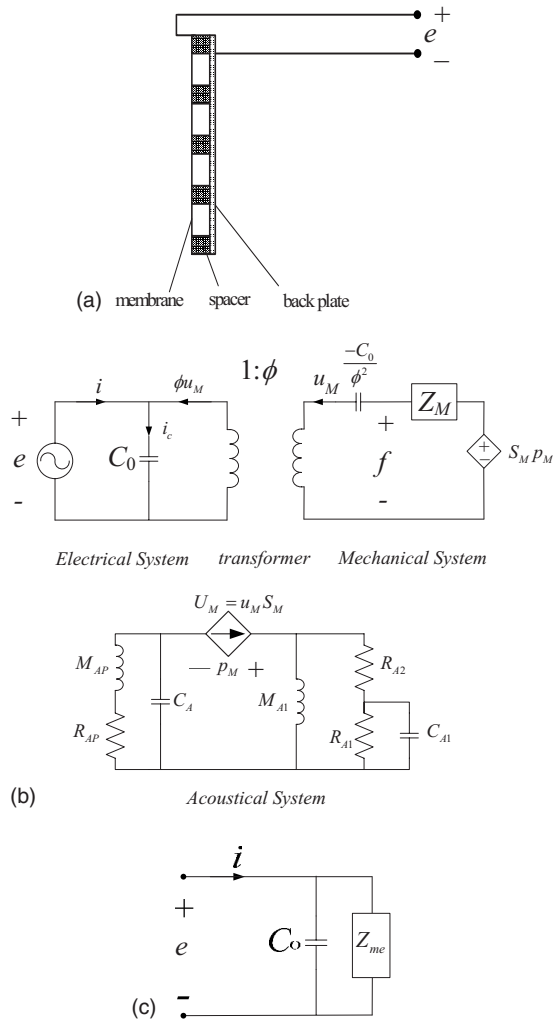

FIG. 2. The electret loudspeaker. (a) Cross-section. (b) Electroacoustic analogous circuit. (c) Analogous circuit reflected to the electrical domain.

tween the membrane and the back plate, and C_0 is the static capacitance. Assume that the membrane motion is small and the gap between the membrane and the back plate is nearly constant. The dynamic attraction force produced by the driving voltage can be approximated as

$$f = \varepsilon S \frac{E_0 e}{d^2}, \tag{3}$$

where e is the driving voltage. The electret loudspeaker can be modeled with the electroacoustic analogous circuit in Fig. 2(b). The linearized ac dynamic equation can be expressed as follows:

$$e = Z_E i + \frac{1}{j\omega C_{EM}} u_M, \tag{4}$$

$$f = \frac{1}{j\omega C_{EM}} i + Z_M u_M, \tag{5}$$

where

$$Z_E = \frac{1}{j\omega C_0}, \tag{6}$$

$$C_{EM} = \frac{\varepsilon S}{q_0}, \tag{7}$$

i is the current, u_M is the membrane velocity, Z_M is the (open-circuit) mechanical impedance of the diaphragm, Z_E is the (blocked) electrical impedance, q_0 is the static charge, and C_0 is the static capacitance. Equations (4) and (5) can also be expressed in matrix form

$$\begin{bmatrix} e \\ f \end{bmatrix} = \begin{bmatrix} Z_E & \frac{1}{j\omega C_{EM}} \\ \frac{1}{j\omega C_{EM}} & Z_M \end{bmatrix} \begin{bmatrix} i \\ u_M \end{bmatrix}. \tag{8}$$

The fact that the impedance matrix is symmetric indicates that the device is a reciprocal transducer (XDCR) with an associated transduction factor ϕ

$$\phi = \frac{C_0 E_0}{d} = \frac{C_0}{C_{EM}}. \tag{9}$$

Equations (4) and (5) can be rewritten as

$$e = \frac{1}{j\omega C_0} i_c, \tag{10}$$

$$f = \frac{\phi}{j\omega C_0} i_c + Z_{ms} u_M, \tag{11}$$

where

$$i_c = i + \phi u_M, \tag{12}$$

$$Z_{ms} = Z_M - \frac{1}{j\omega C_0/\phi^2}. \tag{13}$$

Z_{ms} is the short-circuit mechanical impedance, which is the sum of the open-circuit mechanical impedance Z_M and a negative capacitor $(-C_0/\phi^2)$. The negative capacitor can be removed if controlled sources are used in lieu of the transformer coupling.

Figure 2(c) shows the circuit with the mechanical system reflected to the electrical domain. Z_{me} is the motional impedance reflected to the electrical domain from mechanical system.

$$Z_{me} = \frac{Z_{ms}}{\phi^2}. \tag{14}$$

Since the transduction factor (ϕ) is very small, the mechanical impedance reflected to the electrical domain effectively becomes an open circuit. This is why the mechanical characteristics would not appear in the electrical impedance. In the following, we shall verify this point by using a practical measurement and FEA.

The terminal electrical impedance is measured from 400 Hz to 10 kHz using a 1.5 Vrms sweep-sine input. Figure 3(a) shows the experimental arrangement for the measurement, with symbols defined in the figure

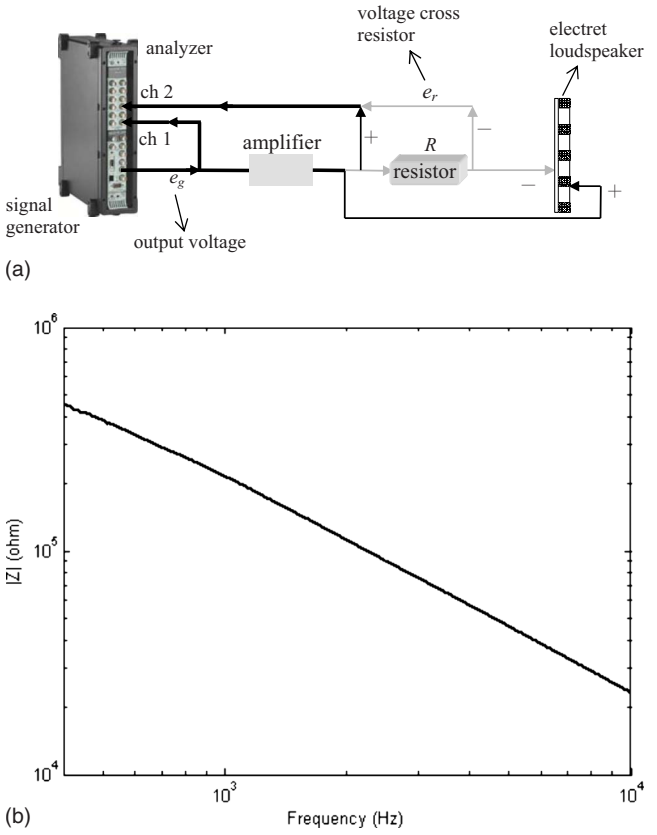

FIG. 3. (Color online) The electrical impedance measured at the terminals of the electret loudspeaker. (a) Experimental arrangement. (b) The frequency response of the measured electrical impedance.

$$Z_e = \frac{e_g G - e_r}{e_r} R, \tag{15}$$

where G is the gain of the voltage amplifier and Z_e is the terminal electrical impedance. The measured electrical impedance is shown in Fig. 3(b). It can be observed from the figure that the measured electrical impedance fits very well with the impedance of an ideal capacitor because the electromechanical coupling is weak enough to conceal the motional impedance.

$$|Z_e| = \frac{1}{\omega C_0}. \tag{16}$$

Although the mechanical parameters cannot be extracted from the measured electrical impedance, the static capacitance (C_0) can still be estimated as follows:

$$\log C_0 = -\log \omega - \log|Z_e|. \tag{17}$$

Using this formula, the static capacitance (C_0) can be estimated from the impedance log-log plot to be 7.9577×10^{-10} F. For the electret loudspeaker sample under test, the effective dc bias voltage (E_0) is approximately 600 V, the gap between the membrane and back plate is 0.1 mm, and the applied voltage (e) is 20 Vrms. Thus, the dielectric constant (ε) is estimated by Eq. (2) to be 1.9217×10^{-11}. The transduction factor (ϕ) calculated using Eq. (9) is 0.0048. The static and dynamic attraction forces estimated using Eqs. (1) and (3) are 1.4324 N and 0.0955 Nrms, respectively.

III. THE MODEL OF THE ELECTRET LOUDSPEAKER

As mentioned previously, the electrical impedance of the electret loudspeaker is predominantly capacitive without being influenced by the motional impedance, meaning the electromechanical coupling is extremely weak. Therefore, the parameter identification based on electrical impedance measurement is not applicable to the electret loudspeaker. An alternative approach for modeling the electret loudspeaker will be presented next.

A single-cell model, a simple model, and a full model based on FEA are developed to model the electret loudspeaker. Specifically, FEA is applied to a single-cell on the membrane in the single-cell model, and FEA is applied to the membrane in the simple model, leaving the rest of system as rigid parts, whereas FEA is applied to the entire membrane-spacer-back plate assembly in the full model. The FEA is carried out with the aid of ANSYS®.[15] In the single-cell model, the natural frequencies and the mode shapes of the membrane are calculated by the FEA modal analysis. This FEA result combined with the laser vibrometer measurement determines the material constants of the membrane. To evaluate the mechanical impedance of the membrane, the displacement frequency response of the membrane is calculated and converted into velocity by using the FEA harmonic analysis. The ratio of the external force to the mean velocity of diaphragm in mechanical system is defined as the open-circuit mechanical impedance Z_M. In order to facilitate the integration of the mechanical system, the open-circuit mechanical impedance (Z_M) defined in the following lumped-parameter two-port formalism is calculated using the complex velocity response.

$$Z_M = \frac{F}{\bar{u}}, \tag{18}$$

where F is an external force applied in the finite-element model and $\bar{u}$ denotes the mean of the complex velocity, which is obtained by the FEA harmonic analysis. Moreover, the impedance Z_{me} that is reflected from the mechanical domain to the electrical domain can be calculated by Eq. (14). Figure 4 compares $|Z_{me}|$ and the electrical impedance $|Z_E|$. It can be observed from the figure that $|Z_{me}|$ is much greater than $|Z_E|$. Therefore, the mechanical impedance reflected to the electrical domain effectively becomes an open circuit. The mechanical characteristics would not appear in the electrical impedance. This justifies the weak coupling assertion between the electrical and the mechanical systems.

The FEA simulation is based on both the simple and the full models. The mechanical impedances are calculated using harmonic analysis of FEA. The mean velocity u_M can be obtained by solving the electrical-mechanical-acoustical analogous circuits of Fig. 2(b). From a membrane with effective area S_D, the on-axis pressure at a far field distance r can be calculated using the simple source model

$$p(r) = \frac{j\rho_0 \omega U_M}{2\pi} \frac{e^{-jkr}}{r}, \tag{19}$$

where $U_M = S_D u_M$ is the volume velocity, ρ_0 is the density of air ($\rho_0 = 1.21$ kg/m^3), and k is the wave number.

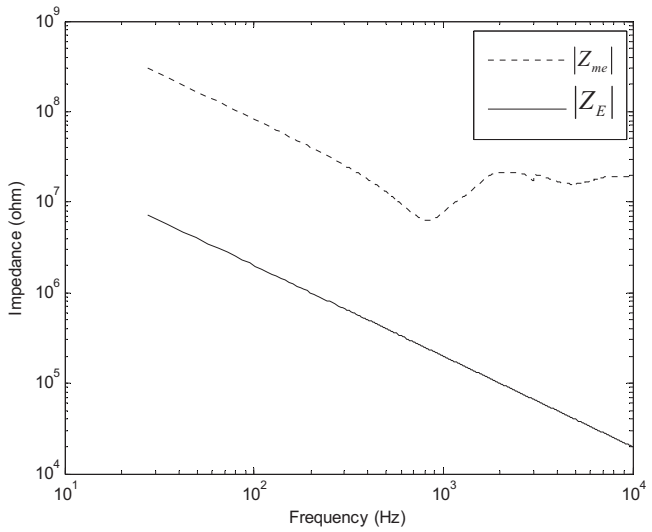

FIG. 4. The comparison between the frequency response functions of Z_{me} and Z_E.

The FEA simulation is based on both simple and full models.

A. The single-cell model and the simple model

In the simple model, it is assumed that the back plate and the spacer are rigid, while the FEA models only the flexible membrane of the electret loudspeaker. The membrane is modeled with the element "shell 41," which is a three-dimensional element allowing membrane (in-plane) stiffness but no bending (out-of-plane) stiffness. The element has four nodes and three degrees of freedom (U_x, U_y, and U_z) at each node.

TABLE I. Material properties of the electret loudspeaker.

Parameters	Spacer and back plate	Membrane
Young's modulus (N/m^2)	201×10^9	82×10^9
Poisson's ratio	0.28	0.3
Density (kg/m^3)	8000	700
Thickness (m)	17×10^{-3}	32×10^{-6}

We begin with tuning the single-cell FEA model with reference to the laser velocity response measurement. The mesh used in the finite-element model of a single-cell is shown in Fig. 5. The boundary conditions are selected such that all degrees of freedom for the outer edge of the single-cell and the displacements at the spacer are zero. Using this approach, the determined material constants of the membrane are summarized in Table I.

Next, the simple FEA model and the associated mesh of the membrane are shown in Fig. 5. The boundary conditions are selected such that all degrees of freedom for the outer edge of the membrane and the displacements at the spacer are set to be zero. The complex velocity and mechanical impedance are calculated using the FEA harmonic analysis.

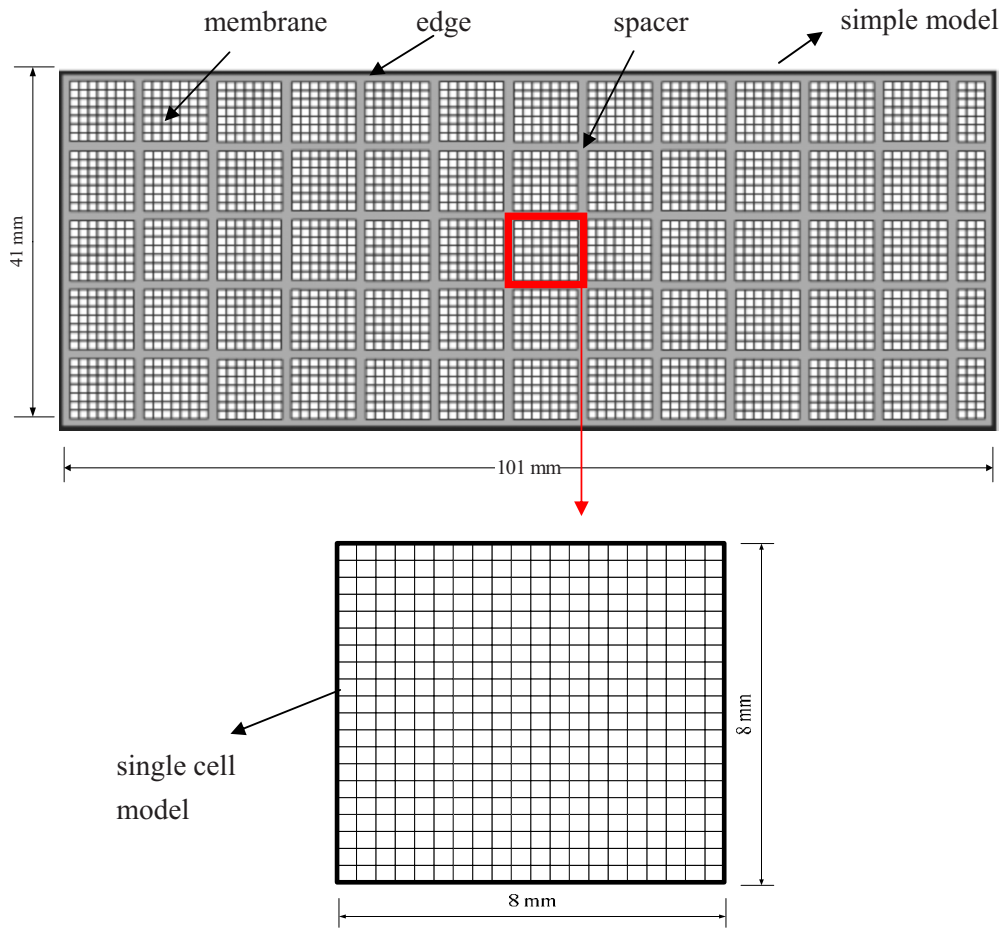

FIG. 5. (Color online) The mesh plot of the simple FEA model and single-cell FEA model of the membrane.

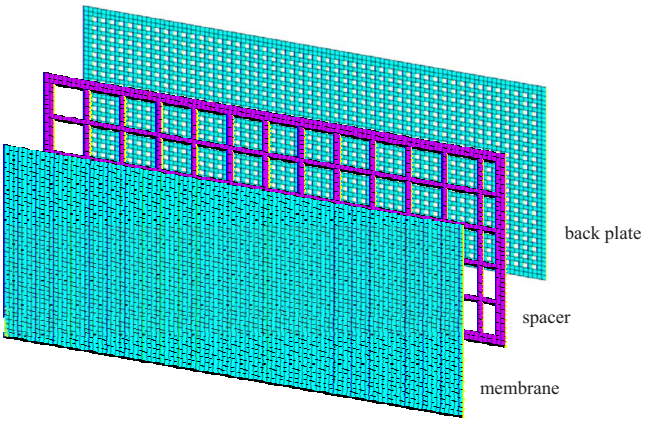

FIG. 6. (Color online) The full FEA model of the electret loudspeaker.

B. The full FEA model

In the full model, FEA is applied to the whole structure of the electret loudspeaker consisting of the membrane, the spacer grid, and the back plate.[16] The material constants assumed in the FEA are those obtained in the single-cell model (Table I). The membrane, the spacer, and the back plate are modeled using "shell 41," "solid 45," and "shell 63," respectively. The solid 45 element has eight nodes and three degrees of freedom (U_x, U_y, and U_z) at each node. The shell 63 element has four nodes and six degrees of freedom, (U_x, U_y, U_z, ROT_x, ROT_y, and ROT_z) at each node. The finite-element mesh is shown in Fig. 6. The boundary conditions are selected such that all degrees of freedom for the outer edge of the electret loudspeaker are zero. The attraction forces between the back plate and membrane are calculated using Eqs. (3) and (4). The effective mechanical impedance of the loudspeaker can also be established via the FEA harmonic analysis, as that of the simple model.

C. Modeling of the acoustical enclosure

Apart from the electrical and the mechanical systems, the modeling of the electret loudspeaker takes into account the acoustical loading resulting from the perforation of the back plate and the cavity between the back plate and the membrane. The back plate has 1000 square holes uniformly distributed over the metal sheet (perforation ratio=24.15%). The acoustical impedance of the perforation can be written as[14]

$$Z_{AP} = R_{AP} + j\omega M_{AP}, \tag{20}$$

$$R_{AP} = \frac{\rho_0}{N\pi a_h^2}\sqrt{2\omega\mu}\left[\frac{t_p}{a_h} + 2\left(1 - \frac{\pi a_h^2}{b^2}\right)\right], \tag{21}$$

$$M_{AP} = \frac{\rho_0}{N\pi a_h^2}\left[t_p + 1.7a_h\left(1 - \frac{a_h}{b}\right)\right], \tag{22}$$

where N is the number of holes of the back plate, μ is the kinematic coefficient of viscosity ($\mu = 1.56 \times 10^{-5}$ m^2/s), a_h is the equivalent radius of the hole, b is the spacing between the center of the adjacent holes, and t_p is the thickness of the back plate. The cavity can be modeled as acoustic compliance

$$C_A = \frac{V}{\rho_0 c^2}, \tag{23}$$

where V is the volume of cavity and c is the speed of sound ($c \approx 345$ m/s at the room temperature). The analogous circuit of the acoustical system of the electret loudspeaker is shown in Fig. 2(b). In particular, the circuit parameters to approximate radiation impedance are given by[14]

$$M_{A1} = \frac{8\rho_0}{3\pi^2 a_h}, \tag{24}$$

$$R_{A1} = \frac{0.4410\rho_0 c}{\pi a_h^2}, \tag{25}$$

$$R_{A2} = \frac{\rho_0 c}{\pi a_h^2}, \tag{26}$$

$$C_{A1} = \frac{5.94a_h^3}{\rho_0 c^2}. \tag{27}$$

The FEA-based simulation procedure for the electret loudspeaker can be summarized as follows.

(1) Obtain the resonance frequencies and velocity response from the single-cell FEA model of membrane.
(2) Measure the membrane velocity by a laser vibrometer and compare the data with the FEA results. Tune the FEA model with the experimental data.
(3) Using the simple FEA model, obtain the complex velocity response of the membrane via FEA harmonic analysis.
(4) Using the full FEA model, obtain the complex velocity response of the membrane via FEA harmonic analysis.
(5) Calculate the mechanical impedance (Z_M) based on the complex velocity response.
(6) Calculate the acoustical impedance (Z_A) due to the perforated back plate and the cavity by the theoretical formulas and combine the mechanical impedance and the acoustical impedance to form a coupled lumped-parameter model.
(7) Calculate the volume velocity using the coupled model. Calculate the on-axis pressure based on the volume velocity response.
(8) Compare the measured on-axis pressure with the response simulated using the simple and full FEA models.

IV. NUMERICAL AND EXPERIMENTAL INVESTIGATIONS

Experimental investigation was undertaken to validate the proposed simulation models of the electret loudspeaker. The experimental arrangement for an electret loudspeaker sample is shown in Fig. 7. The electret loudspeaker is mounted on a baffle of length 1650 mm and width 1350 mm according to the standard AES2-1984 (R2003).[17] On-axis SPL and total harmonic distortion (THD) of the electret loudspeaker are measured using this setup. A 20 Vrms swept-sine signal is used to drive the electret loudspeaker in the fre-

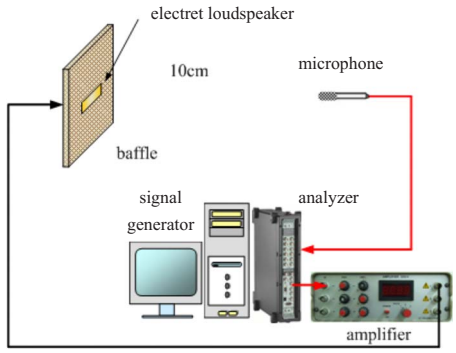

FIG. 7. (Color online) Experimental arrangement of the on-axis SPL measurement for the electret loudspeaker.

quency range 20 Hz–20 kHz. The on-axis SPL is measured by using a microphone positioned at 10 cm away from the loudspeaker.

A. Comparison of the measured and the simulated responses

Simulation of the membrane response was carried out using the single-cell finite-element model. The fundamental resonance frequency predicted by the FEA modal analysis is 849.43 Hz, with the associated mode shape shown in Fig. 8(a). Using the FEM harmonic analysis, complex displacement is calculated and converted into the velocity. The fundamental resonance frequency of the velocity response measured using the laser vibrometer is 818.75 Hz, which is in close agreement with the foregoing FEA result. Figure 8(b) compares the velocity responses obtained from the experiment and simulation. Except for some minor discrepancies at high frequencies, the simulated responses (dotted lines) compare well with those of the measured results (solid lines). Some peaks of the measured frequency response may correspond to unmodeled high-order modes of the membrane. Those modes cannot be predicted by the single-cell model.

On the basis of the material constants determined in the single-cell model, simulation can be conducted for the electret loudspeaker using the simple and the full models. FEA modal analysis reveals that the fundamental resonance frequency of the simple model is 811.6 Hz, with the associated mode shape shown in Fig. 9(a). In the fundamental mode, a drumming motion appears locally in phase at every cell of the membrane. The fundamental resonance frequency found in the full model is 789.3 Hz, with the associated mode shape shown in Fig. 9(b). Clearly visible is that the entire membrane-spacer-back plate assembly moves in phase collectively in this fundamental mode.

Next, the mechanical impedance of the membrane is calculated with the aid of the FEA harmonic analysis. Combining the mechanical impedance and the acoustical impedances due to the cavity and radiation enables the estimation of the volume velocity produced by the electret loudspeaker, with which the on-axis SPL can be calculated. Figure 10 compares the on-axis SPL obtained from the simulation and the experiment, respectively. The FEA simulation is based on both the simple and the full models. It can be observed that in lower frequencies the on-axis SPL response predicted by

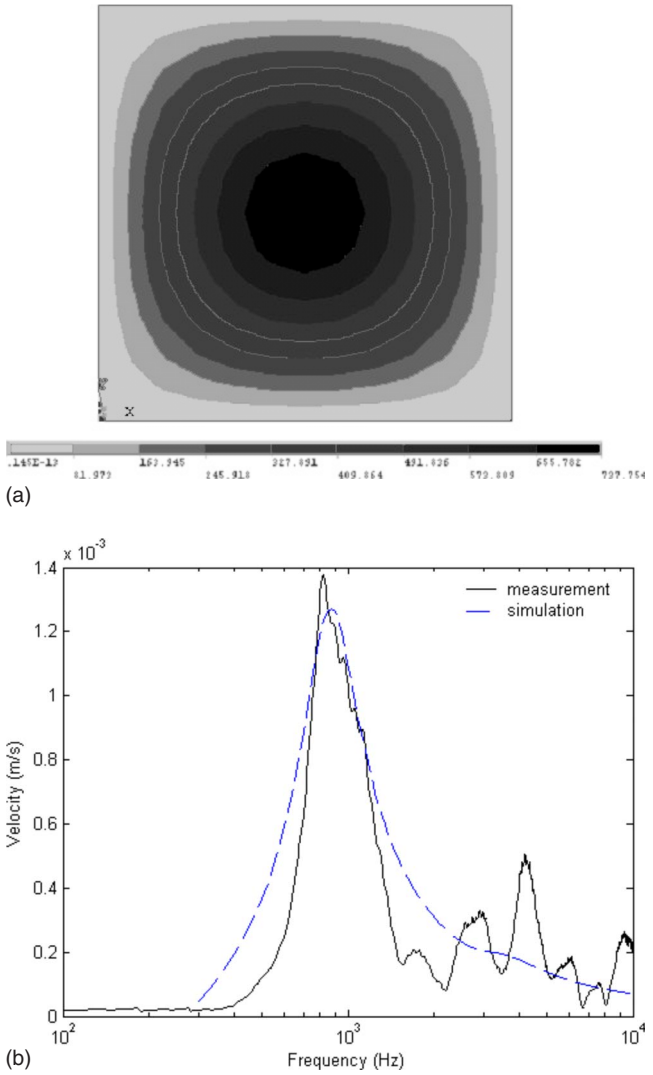

FIG. 8. (Color online) The simulation results obtained using the single-cell FEA model. (a) The fundamental mode shape of membrane. (b) Comparison of the simulated velocity response with the measured response.

the FEA simple model is in good agreement with the measurement. The discrepancy between the measured low-frequency response and the FEA full model could be due to the effect of the spacer and the back plate, which may induce some unmodeled low-frequency motions. In high frequencies, however, the simple model fails to capture the response due to the flexural modes of the structure. By contrast, the FEA full model seems to have predicted the high-frequency response better than the simple model. The on-axis SPL response calculated using the full FEA model matches reasonably well the measured response.

B. Nonlinear distortion

In order to assess the nonlinear distortion of the electret loudspeaker, THD is calculated from the measured frequency response of the on-axis SPL.[18]

$$\mathrm{THD} = \frac{\sqrt{p_{2f}^2 + p_{3f}^2 + \cdots + p_{nf}^2}}{p_{1f}} \times 100\,\%\,, \tag{28}$$

where p_{nf} is the sound pressure magnitude of the nth harmonic in the spectrum and p_{1f} is the sound pressure magni-

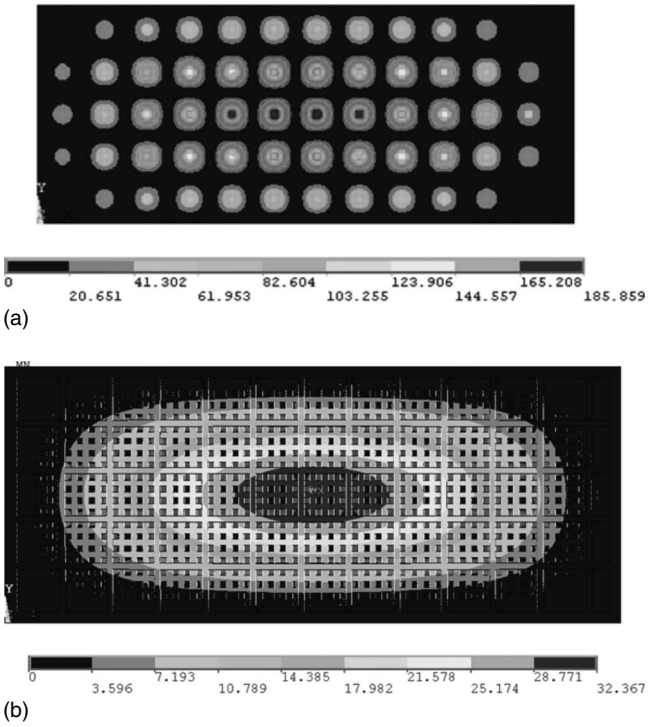

FIG. 9. The fundamental mode of the electret loudspeaker. (a) Result obtained using the simple FEA model. (b) Result obtained using the full FEA model.

tude of the input fundamental frequency. The measured THD of the electret loudspeaker sample is shown in Fig. 11. It can be observed that the average THD is about 17% and the THD is greater than 10% in the frequency range above the fundamental resonance frequency. The maximum THD even reaches about 20% in the range 2–3 kHz. It may be caused by the structural resonance of the loudspeaker. Informal listening tests revealed that ringing artifact is audible for some music signals involving percussion instruments.

V. CONCLUSIONS

A simulation technique for an electret loudspeaker based on the FEA alongside electroacoustical modeling has been presented in this paper. As an early attempt for the transducer of this kind, the loudspeaker element has an extremely low sensitivity. The coupling from the mechanical to the electrical circuit was simply too low to make parameter measurements based on electrical impedance measurements. Due to the weak coupling between the electrical and the mechanical systems, the electrical impedance-based parameter identification procedure is not applicable to the electret loudspeaker. An alternative approach has been presented in the paper to model the electret loudspeaker. FEA was exploited for modeling the loudspeaker with a simple model and a full model. The mechanical impedance, the volume velocity of membrane, and the on-axis pressure can be predicted using the coupled electroacoustical model.

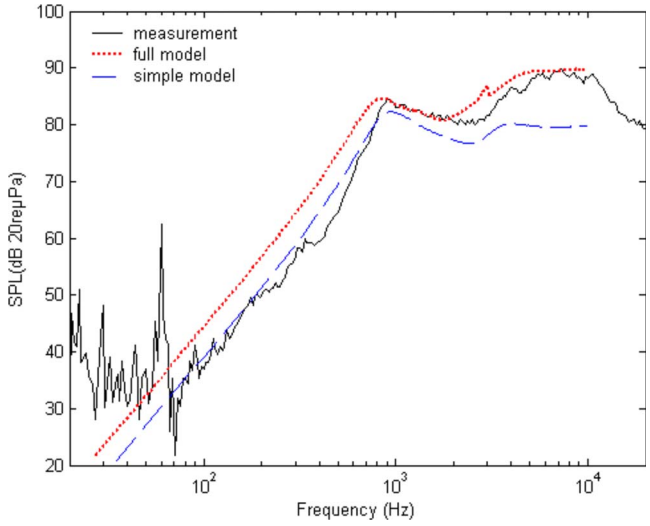

FIG. 10. (Color online) Comparison of the on-axis SPL responses of the electret loudspeaker obtained from the simulation and the experiment.

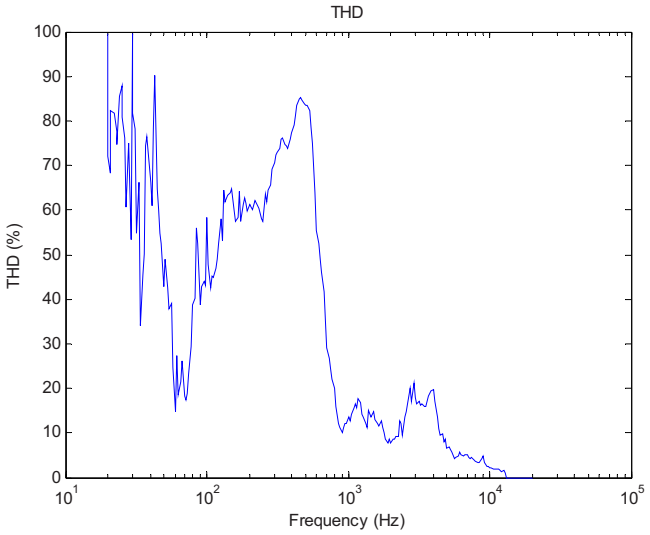

FIG. 11. (Color online) The measured THD of the electret loudspeaker.

ACKNOWLEDGMENTS

The work was supported the National Science Council in Taiwan, under Project No. NSC 95-2221-E-009-009-MY2. Special thanks also go to the Electronics and Optoelectronics Research Laboratories, Industrial Technology Research Institute in Taiwan.

[1]I. M. Charles, "A wide-range electrostatic loudspeaker," J. Audio Eng. Soc. **7**, 47–54 (1959).
[2]N. W. McLachlan, "The stretched membrane electrostatic loudspeaker," J. Acoust. Soc. Am. **5**, 167–171 (1933).
[3]M. Paajanen, J. Lekkala, and H. Valimaki, "Electromechanical modeling and properties of the electret film EMFI," IEEE Trans. Dielectr. Electr. Insul. **8**, 629–636 (2001).
[4]T. Mellow and L. Karkkainen, "On the sound field of a circular membrane in free space and infinite baffle," J. Acoust. Soc. Am. **120**, 2460–2477 (2006).
[5]A. P. Medley, D. R. Billson, D. A. Hutchins, and L. A. Davis, "Properties of an electrostatic transducer," J. Acoust. Soc. Am. **120**, 2658–2667 (2006).
[6]G. M. Sessler and J. E. West, "Self-biased condenser microphone with high capacitance," J. Acoust. Soc. Am. **34**, 1787–1788 (1962).
[7]J. Lekkala and M. Paajanen, "EMFi—New electret material for sensors and actuators," IEEE Tenth International Symposium on Electrets, Athens, Greece, (1999).
[8]M. Paajanen, J. Lekkala, and K. Kirjavainen, "Electromechanical film (EMFi)—A new multipurpose electret material," Sens. Actuators, A **84**, 95–102 (2000).
[9]E. Saarimaki, M. Paajanen, A. M. Savijarvi, and H. Minkkinen, "Novel

heat durable electromechanical film processing: Preparations for electromechanical and electret applications," IEEE Trans. Dielectr. Electr. Insul. **13**, 963–972 (2006).
[10]D. M. Chiang and J. L. Chen, "A novel flexible loudspeaker driven by an electret diaphragm," AES 121st Convention, San Francisco, CA (2006).
[11]R. Heydt, R. Pelrine, J. Joseph, J. Eckerle, and R. Kornbluh, "Acoustical performance of an electrostrictive polymer film loudspeaker," J. Acoust. Soc. Am. **107**, 833–839 (2000).
[12]H. Olson, *Acoustical Engineering* (Van Nostrand, New York, 1957); *ibid.*, reprinted (Professional Audio Journals, Philadelphia, PA, 1991).
[13]L. L. Beranek, *Acoustics* (Acoustical Society of America, Melville, NY, 1996).
[14]W. M. Leach, Jr., *Introduction to Electroacoustics and Audio Amplifier Design* (Kendall-Hunt, Dubuque, IA, 2003).
[15]Swanson Analysis Systems, ANSYS User's Manual, Philadelphia, PA (2005).
[16]G. S. Brady, H. R. Clauser, and J. A. Vaccari, *Materials Handbook* (McGraw-Hill, New York, 2002).
[17]Audio Engineering Society Inc., AES Recommended Practice Specification of Loudspeaker Components Used in Professional Audio and Sound Reinforcement, AES2-1984, NY (2003).
[18]M. R. Bai and R. L. Chen, "Optimal design of loudspeaker systems based on sequential quadratic programming (SQP)," J. Audio Eng. Soc. **55**, 44–54 (2007).

Design optimization of condenser microphone: A design of experiment perspective

Chee Wee Tan
Micromachines Centre, School of Mechanical and Aerospace Engineering, Nanyang Technological University, 50 Nanyang Avenue, Singapore 639798, Singapore and Center for Environmental Sensing and Modeling (CENSAM) IRG, Singapore-MIT Alliance for Research and Technology (SMART) Centre, 3 Science Drive 2, Singapore 117543, Singapore

Jianmin Miao[a)]
Micromachines Centre, School of Mechanical and Aerospace Engineering, Nanyang Technological University, 50 Nanyang Avenue, Singapore 639798, Singapore

(Received 18 March 2009; revised 1 April 2009; accepted 2 April 2009)

A well-designed condenser microphone backplate is very important in the attainment of good frequency response characteristics—high sensitivity and wide bandwidth with flat response—and low mechanical-thermal noise. To study the design optimization of the backplate, a 2^6 factorial design with a single replicate, which consists of six backplate parameters and four responses, has been undertaken on a comprehensive condenser microphone model developed by Zuckerwar. Through the elimination of insignificant parameters via normal probability plots of the effect estimates, the projection of an unreplicated factorial design into a replicated one can be performed to carry out an analysis of variance on the factorial design. The air gap and slot have significant effects on the sensitivity, mechanical-thermal noise, and bandwidth while the slot/hole location interaction has major influence over the latter two responses. An organized and systematic approach of designing the backplate is summarized.
 [DOI: 10.1121/1.3125322]

PACS number(s): 43.38.Kb, 43.38.Bs, 43.38.Ar, 43.58.Ta [AJZ] Pages: 3641–3649

I. INTRODUCTION

Microphones are acoustic transducers that convert an incident pressure into a corresponding output voltage. The condenser (or capacitive) type of microphones stands out due to high sensitivity, excellent noise immunity, good stability, and flat frequency response. A deformable elastic diaphragm, which detects pressure variations, and a perforated rigid backplate constitute a pair of sensing electrodes, which behaves like a variable capacitor. Fine arrangement of perforated holes in the backplate weakens the air damping effect, which ensures a flat frequency response and reduces the mechanical-thermal noise[1] as well. For condenser microphones, an optimized viscous damping value has its origin in a well-designed backplate structure.[2] Thus, other than the function of an electrode, the backplate also has an important task in shaping the frequency response characteristics and determining the mechanical-thermal noise of the microphone.

The condenser microphone is a complex acoustical electromechanical system, which consists of tightly coupled acoustical, electrical, and mechanical elements. A common modeling approach to evaluate the microphone performance is the lumped-element method.[3,4] In this method, via simple analytical expressions, mass, compliance, and damping have their equivalent electrical counterparts in inductance, capacitance, and resistance, respectively. Another modeling approach is the finite element method.[5,6] An accurate, but more complicated, modeling approach has been described by Zuckerwar[7,8] and verified with very good accuracy.[7–9] This approach also provides an accurate expression for the air resistance term due to mechanical losses in the air gap, slot, and holes.

In this paper, a systematic investigation into the design optimization of the microphone backplate is carried out based on the comprehensive modeling approach of Zuckerwar via the design of experiment (DOE) technique. The DOE technique is particularly helpful to learn more about a specific process or system with the ultimate aim of further optimization and has already demonstrated its capability in many engineering applications.[10,11] So far, to the best of our knowledge, a detailed systematic optimization of the backplate parameters has not been reported. For previous reported work,[3–6] the backplate parameters are determined on the basis of simple analytical expressions and the prior experience of the authors. However, with a systematic design methodology in place, any design optimization work can be simplified greatly.

A factorial design[12] is an effective method to study and screen out the main effects and interactions of several factors in an experiment setting. In a typical factorial design, every possible combination run of all involved factors can be investigated. One important special class of the factorial design is the 2^k factorial design, in which there are k factors at only two levels each. The 2^k factorial design is particularly useful in the initial stages of the research work, where there are

[a)]Author to whom correspondence should be addressed. Electronic mail: mjmmiao@ntu.edu.sg

many unknowns, to screen out the important factors for further optimization work. However, since there are only two levels for each factor, the assumption of almost linearity over the range of the factor levels may not be valid. In addition, any interaction terms can only contribute a little curvature to the response surface function. Thus, in some cases, the second-order quadratic effects may have to be considered. Very often, limited resources only justify a single replicate of the design combination to be run. Then, a special case of the 2^k factorial design (unreplicated factorial design) occurs, in which only a single replicate is allowed in every run, with the assumption that the random error (or noise) in the system is reasonably small. Since there is only one replicate, there is no internal estimate of error.

In this work, which is a more in-depth study of our previous ones,[2,9] since the primary objective is to study the design optimization of the backplate by identifying the main effects and any significant interactions via the 2^k factorial design, it is not strictly a must to consider the potential effect of non-linearity. And since the 2^k factorial design is carried out on analytical expressions, there are no random errors during the factorial run. Thus, the single replicate of the 2^k factorial design approach is the most appropriate for this design optimization work. If a main effect of an unreplicated 2^4 factorial design is not significant and all interactions involving that effect are negligible, then that main effect can be removed from the design so that it becomes a 2^3 factorial design with two replicates. Then, an analysis of variance (ANOVA) can be performed on the remaining main effects and interactions. Thus, this concept of projecting an unreplicated factorial design into a replicated one with fewer factors is very useful in the factorial design.

II. CONDENSER MICROPHONE THEORY

The theory of the condenser microphone will be briefly described, which follows the modeling approach of Zuckerwar.[7,8] The theoretical considerations are based on a circular diaphragm of radius a.

A. Microphone sensitivity

The open-circuit sensitivity[7,8] of the condenser microphone can be expressed by

$$M_{oc} = M_e M_m = \frac{E_o}{h_o}\left(1 - \frac{b^2}{2a^2}\right)\left(\frac{1}{TK^2}\frac{J_2(Ka)}{J_0(Ka) + D(\omega)}\right), \quad (1)$$

where M_e is the electrical sensitivity, M_m is the mechanical sensitivity, h_o is the average air gap distance between the diaphragm and the backplate due to the electrostatic deflection caused by the polarization voltage E_o, b is the backplate radius, a is the diaphragm radius, T is the diaphragm tension, ω is the angular frequency, and $J_0(Ka)$ and $J_2(Ka)$ are the zero- and second-order Bessel functions of Ka, respectively, while K, which is the wave number of sound in the diaphragm, and $D(\omega)$, which is the air layer damping term (a dimensionless quantity), can be expressed, respectively, by

$$K = \omega\left(\frac{\sigma_M}{T}\right)^{1/2}, \quad (2)$$

where σ_M is the mass surface density of the diaphragm and

$$D(\omega) = \frac{j4\omega\rho_o J_o(Ka)}{\pi T J_2(Ka)}\sum_{m=0}^{\infty}\left[-j\omega\left(\frac{y_m}{y_o}\right) + \sum_{s=1}^{q}\left(\frac{f_s}{y_o}\right)s_s\Gamma_m J_o(\xi_m a_s)\right] \times \frac{1}{T_m J_0(\xi_m a)}\left\{\frac{J_2(Ka)\delta(m)}{4K^2a^2} + \frac{J_1(Ka)[1-\delta(m)]}{2Ka(K^2a^2 - \xi_m^2 a^2)}\right\}, \quad (3)$$

where ρ_o is the static air density (1.205 $\mathrm{kg/m^3}$) and $J_1(Ka)$ is the first-order Bessel function of Ka. For further reading, the detailed mathematical derivation of $D(\omega)$ can be found in Refs. 7 and 8.

B. Mechanical-thermal noise

The background noise of a microphone is one of the most important design specifications because it imposes a restriction on the microphone sensitivity. The mechanical-thermal noise, together with other sources of background noise,[13–15] establishes the lowest possible limit of acoustic pressure[16,17] that can be picked up by the microphone. Well below the first resonant frequency of the diaphragm, the air resistance[7,8] can be expressed as

$$R_A(\omega) = \frac{8\pi T\,\mathrm{Im}(D)}{\omega(\pi a^2)^2}, \quad (4)$$

where $\mathrm{Im}(D)$ is the imaginary part of $D(\omega)$. The air resistance R_A, which is due to the viscous damping losses in the air gap,[18] slot, and holes,[19] accounts for the mechanical-thermal noise and it is frequency dependent. The background noise pressure level (A-weighted) of the mechanical-thermal noise[9] can be expressed by

$$N_T = \sqrt{\int_{f_1}^{f_2} 4k_B T R_A(f) A^2(f) df}, \quad (5)$$

where k_B is the Boltzmann constant (1.38×10^{-23} J/K), T is the absolute temperature (K), $A(f)$ is the function of the A-weighted filter, and f_1 and f_2 are 10 Hz and 20 kHz, respectively. Therefore, the mechanical-thermal noise of the microphone is dependent on the amount of viscous damping that is present in the mechanical structure.

C. C_A/C_M ratio

Well below the first resonant frequency of the diaphragm, the diaphragm compliance[7,8] and air layer compliance[7,8] can be expressed, respectively, as

$$C_M = \frac{(\pi a^2)^2}{8\pi T}, \quad (6)$$

TABLE I. Assignment of factors and backplate parameters in the 2^6 factorial design.

Parameters	Assigned factor	−	+
Air gap	A	20 μm	25 μm
Slot	B	Presence	Absence
Hole location	C	0.55 mm	1.2 mm
Hole number	D	4	8
Hole radius	E	40 μm	80 μm
Backplate thickness	F	150 μm	300 μm

$$C_A(\omega) = \frac{(\pi a^2)^2}{8\pi T\,\mathrm{Re}(D)}, \tag{7}$$

where $\mathrm{Re}(D)$ is the real part of $D(\omega)$. Therefore, the C_A/C_M ratio can be expressed as

$$\frac{C_A}{C_M} = \frac{1}{\mathrm{Re}(D)}. \tag{8}$$

This ratio determines whether the diaphragm or the underlying air layer controls the microphone sensitivity. The diaphragm is the better choice as the air layer is much more temperature sensitive and less stable. For this to be realized, C_A should be larger than C_M.

III. DESIGN OF EXPERIMENT

Table I tabulates the factor assignment of the six selected backplate parameters—air gap (A), absence or presence of a slot (B), hole location (C), hole number (D), hole radius (E), and backplate thickness (F)—and their respective assigned values. The hole location is defined by one radius ring from the backplate center. Other microphone parameters[9,20] used for the factorial design are listed in Table II. From Table II, a diaphragm value of 170 N/m is selected so that an analysis can be performed on a workable microphone design.[20] For the 2^6 factorial design, a total of 64 single-replicate simulation runs have been performed as tabulated partially in Table III. The four desired responses are the open-circuit sensitivity (250 Hz), A-weighted mechanical-thermal noise, bandwidth (±3 dB), and C_A/C_M ratio (250 Hz).

TABLE II. Other microphone parameters used for the factorial design.

Parameters	Symbol	Value
Diaphragm radius	a	1.95 mm
Diaphragm thickness	d	0.5 μm
Diaphragm mass surface density	σ_M	0.0015 kg/m^2
Diaphragm tension	T	170 N/m
Backplate radius	b	1.4 mm
Backchamber volume	V	7.6×10^{-8} m^3
Polarization voltage	E_o	200 V
Preamplifier input capacitance	C_i	0.4 pF
Stray capacitance	C_s	5.1 pF

A. Open-circuit sensitivity

Figure 1 illustrates the normal probability plot of the effect estimates for the open-circuit sensitivity for the single-replicate 2^6 factorial design. Negligible effects, which are normally distributed, tend to lie along a straight line while significant effects are far away from it. Thus, the normal probability plot is an excellent method to identify and isolate the main effects and any important interactions of the factorial design. From Fig. 1, the significant effects are the main effects of A (−2.450) and B (−3.350) without any significant interactions. Figure 2 illustrates the main effects of A and B and both are negative. Therefore, a high sensitivity can be attained when A and B are at the low level.

Since the main effects of C, D, E, and F are not significant and all interactions involving them are negligible, they can be discarded from the 2^6 factorial design so that it becomes a 2^2 factorial design in A and B with 16 replicates. Table IV tabulates the open-circuit sensitivity data (rearranged from Table III) of the 2^2 factorial design in A and B with 16 replicates. As Table IV only tabulates the average sensitivity data of the 16 replicates, it does not reveal that all 16 replicates of each run have the same value. However,

TABLE III. Partial list of data of the single-replicate ($N=1$) 2^6 factorial design.

Run No.	Factor A	Factor B	Factor C	Factor D	Factor E	Factor F	Run label	Open-circuit sensitivity (dB ref. 1 V/Pa)	Bandwidth (kHz)	Mechanical-thermal noise [dB(A)]	C_A/C_M ratio
1	−	−	−	−	−	−	(1)	−33.2	15.0	23.0	16.1
2	+	−	−	−	−	−	a	−35.6	20.0	19.8	16.1
3	−	+	−	−	−	−	b	−36.5	2.5	30.6	16.1
4	+	+	−	−	−	−	ab	−39.0	5.0	27.4	16.3
5	−	−	+	−	−	−	c	−33.2	7.5	25.7	16.2
6	+	−	+	−	−	−	ac	−35.6	12.0	22.6	16.2
:	:	:	:	:	:	:	:	:	:	:	:
59	−	+	−	+	+	+	bdef	−36.5	2.5	30.4	15.9
60	+	+	−	+	+	+	abdef	−39.0	6.0	27.1	16.1
61	−	−	+	+	+	+	cdef	−33.2	10.0	25.4	16.1
62	+	−	+	+	+	+	acdef	−35.6	18.0	22.0	16.1
63	−	+	+	+	+	+	bcdef	−36.5	10.0	25.6	16.1
64	+	+	+	+	+	+	abcdef	−39.0	16.0	22.4	16.2

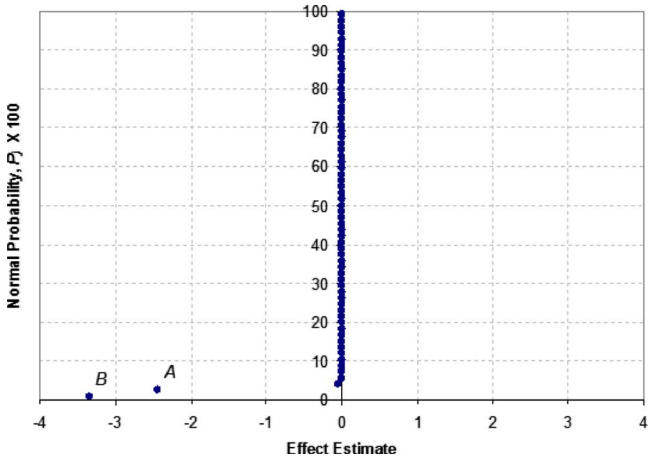

FIG. 1. (Color online) Normal probability plot of the effect estimates for the open-circuit sensitivity for the single-replicate 2^6 factorial design.

these are revealed upon closer inspection of Table III under the sensitivity data column, in which the four values of −33.2, −35.6, −36.5, and 39.0 keep repeating themselves in a cycle. The ANOVA for the data after the projection of the unreplicated factorial design into a replicated one with two factors is summarized in Table V. Table V cannot be completed—F_0 values cannot be computed—because the sum of squares of the error is zero. This can be attributed to all 16 replicates of each of the four runs in Table IV sharing similar value as noted above. Nevertheless, by looking at the mean square values in Table V, the significant effects are the main effects of *A* and *B* without any significant interaction, a similar conclusion that is also revealed by the normal probability plot of Fig. 1.

B. *A*-weighted mechanical-thermal noise

Figure 3 illustrates the normal probability plot of the effect estimates for the *A*-weighted mechanical-thermal noise for the single-replicate 2^6 factorial design. From Fig. 3, the significant effects are the main effects of *A* (−3.188) and *B* (4.006) and the *BC* interaction (−3.613). Figure 4 illustrates the main effects of *A*, *B*, and *C* and the interaction effect of *BC*. The main effect of *C* is relatively insignificant (−0.937) when compared to that of *A* and *B*. From Fig. 4(b), there is a significant interaction between *B* and *C*. When there are significant interactions, examination of the main effects alone is insufficient. As a result, both the main effects and the inter-

TABLE IV. Open-circuit sensitivity data of 2^2 factorial design in *A* and *B* with 16 replicates.

Run No.	Factor *A*	Factor *B*	Average open-circuit sensitivity (dB ref. 1 V/Pa) (N=16)
1	−	−	−33.2
2	+	−	−35.6
3	−	+	−36.5
4	+	+	−39.0

TABLE V. ANOVA for the open-circuit sensitivity in *A* and *B*.

Source of variation	Sum of squares	Degrees of freedom	Mean square	F_0
A (air gap)	96.04	1	96.04	−
B (slot)	179.56	1	179.56	−
AB	0.04	1	0.04	−
Error	0	60	0	
Total	275.64	63		

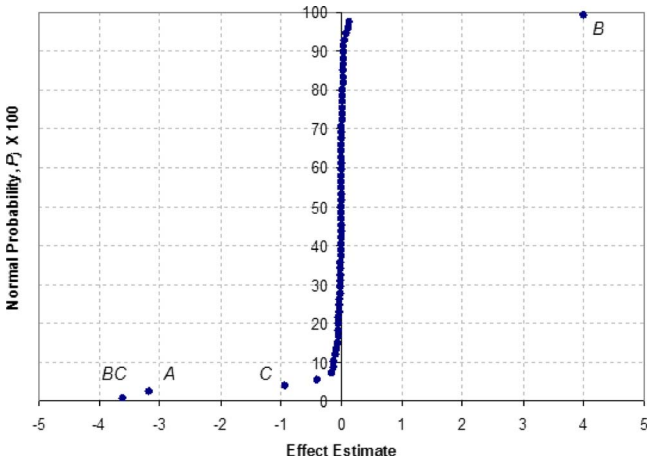

FIG. 3. (Color online) Normal probability plot of the effect estimates for the *A*-weighted mechanical-thermal noise for the single-replicate 2^6 factorial design.

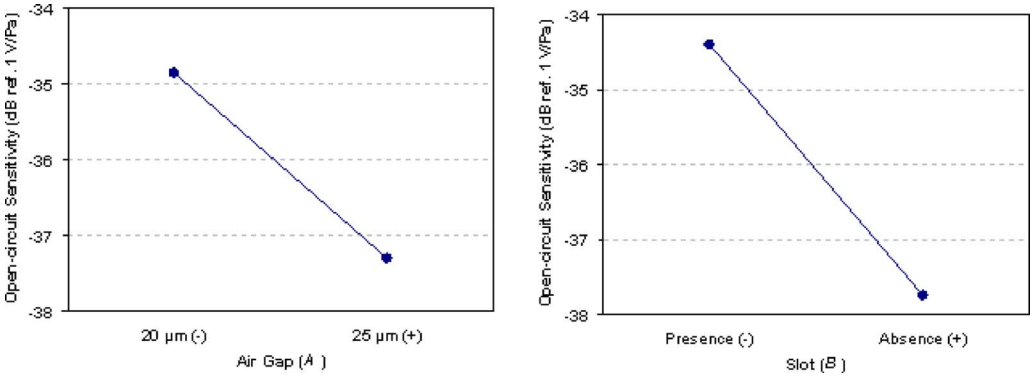

FIG. 2. (Color online) Main effect plots for the open-circuit sensitivity.

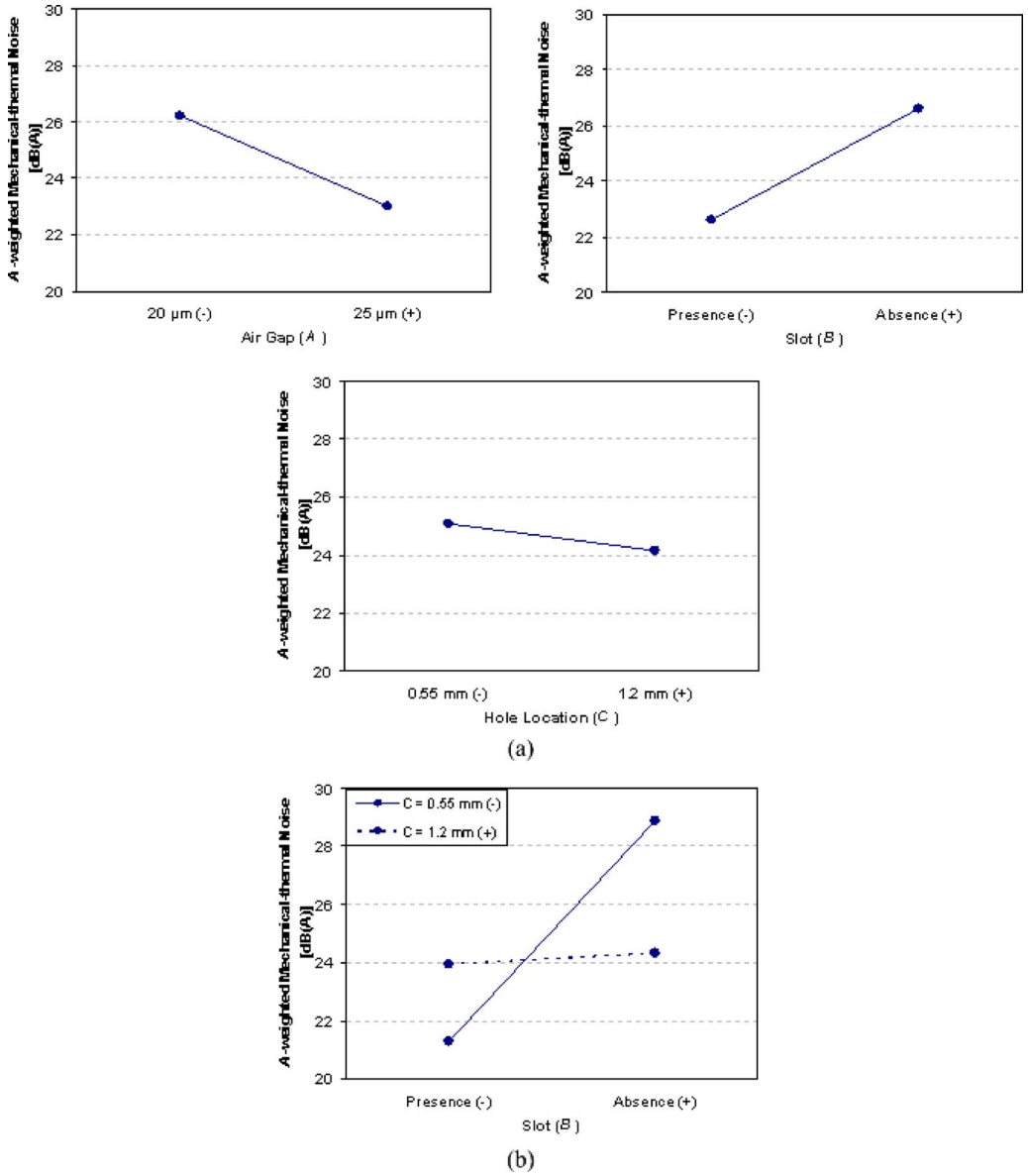

FIG. 4. (Color online) Main effect and interaction plots for the *A*-weighted mechanical-thermal noise: (a) *A*, *B*, and *C* and (b) *B*-*C* interaction.

actions have to be considered together. Therefore, a low mechanical-thermal noise can be attained when *A* is at the high level and *B* and *C* are at the low level.

Since the main effects of *D*, *E*, and *F* are not significant and all interactions involving them are negligible, they are discarded from the 2^6 factorial design so that it becomes a 2^3 factorial design in *A*, *B*, and *C* with eight replicates. Table VI tabulates the *A*-weighted mechanical-thermal noise data of

TABLE VI. *A*-weighted mechanical-thermal noise data of 2^3 factorial design in *A*, *B*, and *C* with eight replicates.

Run No.	Factor *A*	Factor *B*	Factor *C*	Average mechanical-thermal noise [dB(A)] (N=8)
1	−	−	−	22.9
2	+	−	−	19.6
3	−	+	−	30.5
4	+	+	−	27.3
5	−	−	+	25.6
6	+	−	+	22.3
7	−	+	+	25.9
8	+	+	+	22.8

TABLE VII. ANOVA for the *A*-weighted mechanical-thermal noise in *A*, *B*, and *C*.

Source of variation	Sum of squares	Degrees of freedom	Mean square	F_0
A (air gap)	162.56	1	162.56	2032.00
B (slot)	256.80	1	256.80	3210.00
C (hole location)	14.06	1	14.06	175.75
AB	0.09	1	0.09	1.13
AC	0.05	1	0.05	0.63
BC	208.80	1	208.80	2610.00
ABC	0.02	1	0.02	0.25
Error	4.71	56	0.08	
Total	647.09	63		

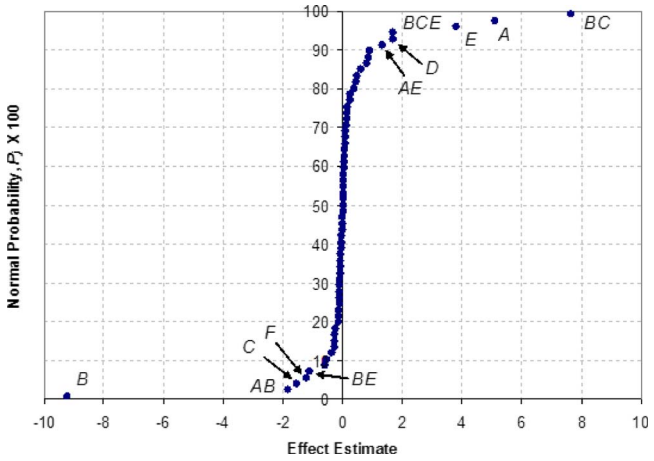

FIG. 5. (Color online) Normal probability plot of the effect estimates for the bandwidth for the single-replicate 2^6 factorial design.

the 2^3 factorial design in A, B, and C with eight replicates. The ANOVA for the data after the projection of the unreplicated factorial design into a replicated one with three factors is summarized in Table VII. From Table VII, since $F_{0.05,1,56} \approx 4.02$, the significant effects are the main effects of A and B and the BC interaction, which are also verified by the normal probability plot of Fig. 3.

C. Bandwidth

Figure 5 illustrates the normal probability plot of the effect estimates for the bandwidth for the single-replicate 2^6 factorial design. From Fig. 5, the most significant effects are the main effects of A (5.117), B (−9.227), and E (3.820) and the BC interaction (7.648) while the least significant effects are the main effects of C (−1.539), D (1.680), and F (−1.195) and the interaction effects of AB (−1.820), AE (1.352), BE (−1.117), and BCE (1.695). Figure 6 illustrates

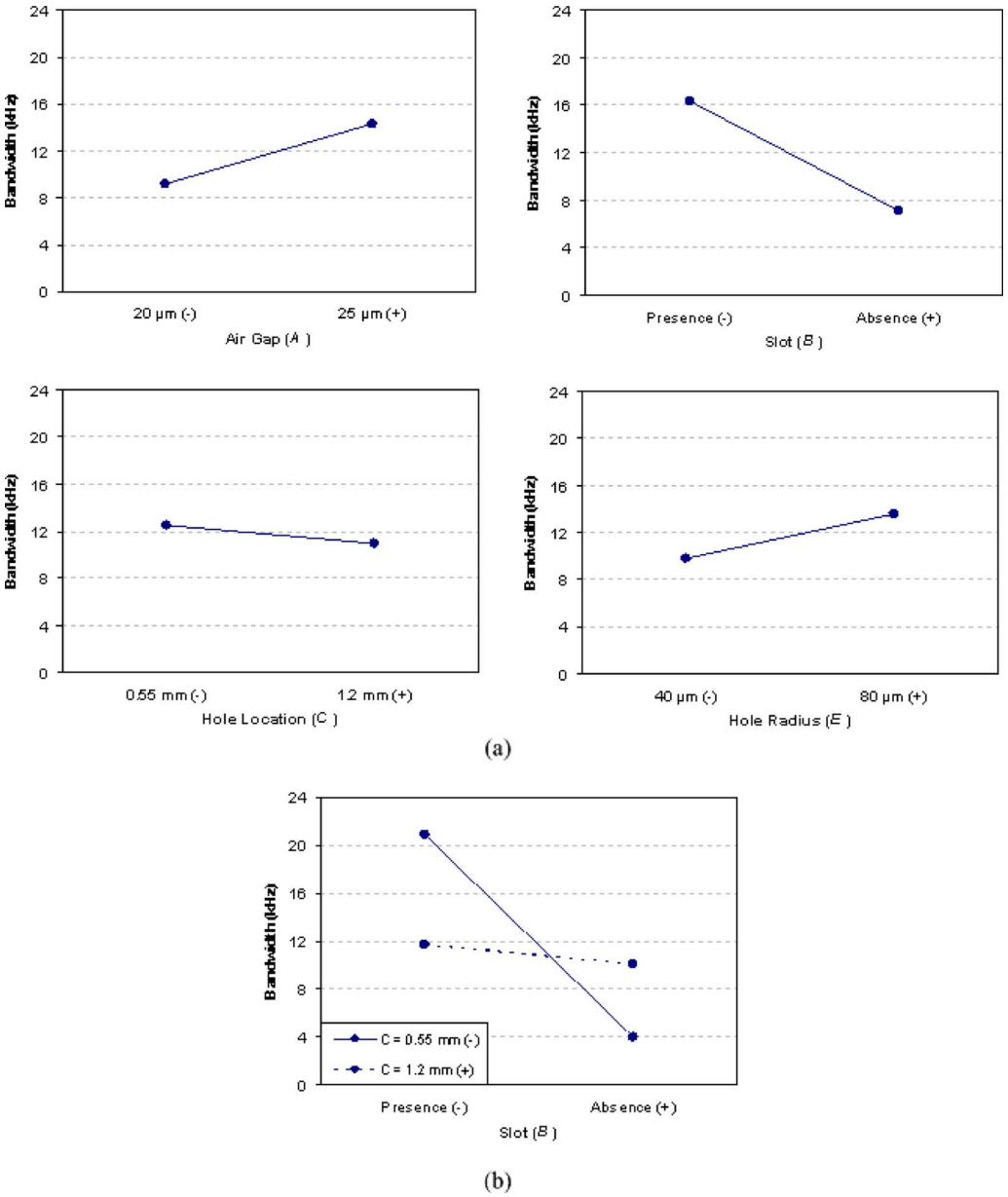

FIG. 6. (Color online) Main effect and interaction plots for the bandwidth: (a) A, B, C, and E and (b) B-C interaction.

TABLE VIII. Bandwidth data of 2^4 factorial design in A, B, C, and E with four replicates.

Run No.	Factor A	Factor B	Factor C	Factor E	Average bandwidth (kHz) (N=4)
1	−	−	−	−	14.9
2	+	−	−	−	20.8
3	−	+	−	−	2.5
4	+	+	−	−	5.0
5	−	−	+	−	7.5
6	+	−	+	−	12.3
7	−	+	+	−	6.8
8	+	+	+	−	8.7
9	−	−	−	+	19.1
10	+	−	−	+	28.9
11	−	+	−	+	2.6
12	+	+	−	+	6.0
13	−	−	+	+	9.9
14	+	−	+	+	17.3
15	−	+	+	+	9.9
16	+	+	+	+	15.3

the main effects of A, B, C, and E and the interaction effect of BC. The main effect of C is the least significant of all four factors while the main effects of A and B are larger than that of E. Therefore, a large bandwidth can be attained when A and E are at the high level and B and C are at the low level.

Since the main effects of D and F are not significant and all interactions involving them are negligible, they are discarded from the 2^6 factorial design so that it becomes a 2^4 factorial design in A, B, C, and E with four replicates. Table VIII tabulates the bandwidth data of the 2^4 factorial design in A, B, C, and E with four replicates. The ANOVA for the data after the projection of the unreplicated factorial design into a replicated one with four factors is summarized in Table IX. From Table IX, since $F_{0.05,1,48} \approx 4.05$, the most significant effects are the main effects of A, B, and E and the BC interaction while the least significant effects are the main effects of C, D, and F and the AB, AE, BE, and BCE interactions.

TABLE IX. ANOVA for the bandwidth in A, B, C, and E.

Source of variation	Sum of squares	Degrees of freedom	Mean square	F_0
A (air gap)	418.97	1	418.97	163.02
B (slot)	1362.07	1	1362.07	529.99
C (hole location)	37.90	1	37.90	14.75
E (hole radius)	233.52	1	233.52	90.86
AB	53.02	1	53.02	20.63
AC	1.06	1	1.06	0.41
AE	29.23	1	29.23	11.37
BC	935.98	1	935.98	364.19
BE	19.97	1	19.97	7.77
CE	3.17	1	3.17	1.23
ABC	6.09	1	6.09	2.37
ABE	1.20	1	1.20	0.47
ACE	0.43	1	0.43	0.17
BCE	45.99	1	45.99	17.89
$ABCE$	3.63	1	3.63	1.41
Error	123.17	48	2.57	
Total	3275.40	63		

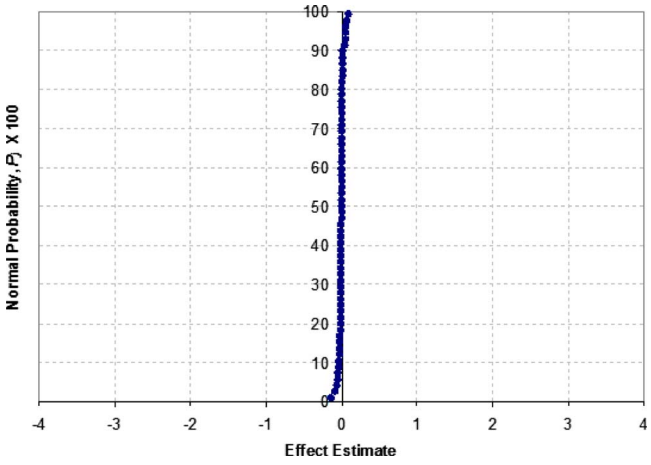

FIG. 7. (Color online) Normal probability plot of the effect estimates for the C_A/C_M ratio for the single-replicate 2^6 factorial design.

D. C_A/C_M ratio

From Table III, the C_A/C_M ratio is around 16 for all simulation runs, which indicate that the diaphragm controls the sensitivity. Figure 7 illustrates the normal probability plot of the effect estimates for the C_A/C_M ratio for the single-replicate 2^6 factorial design. From Fig. 7, there are no significant main effects and interactions. As such, the ANOVA on the C_A/C_M ratio data is not necessary.

IV. DISCUSSION

Table X illustrates a summary of the main effects and interactions for the open-circuit sensitivity, A-weighted mechanical-thermal noise, and bandwidth. For best microphone performance, the backplate parameters should be set to $A-$ and $B-$ for sensitivity; $A+$, $B-$, and $C-$ for mechanical-thermal noise; and $A+$, $B-$, $C-$, and $E+$ for bandwidth. Upon closer examination, a design conflict involving the air gap (A) is clearly observed. A smaller air gap ($A-$) is required for higher sensitivity but it is at the expense of narrower bandwidth and higher mechanical-thermal noise. On the contrary, a larger air gap ($A+$) is desired for lower mechanical-thermal noise and wider bandwidth but it is at the expense of lower sensitivity. In addition, if the air gap is too large, a resonant peak can be observed at the resonant frequency coupled with further loss in sensitivity. Thus, there appears to be an optimized air gap value to ensure a good performance compromise between the sensitivity, mechanical-thermal noise, and bandwidth.[9] From Table X, it is obvious that the presence of a slot ($B-$) around the circumference of the backplate enhances both the sensitivity and bandwidth and lowers the mechanical-thermal noise.[9]

As illustrated in Table X, the BC interaction is significant for both the mechanical-thermal noise and bandwidth but the main effect of C is relatively insignificant for both cases. Although C is least significant as compared to A and B, it does play an important role in both the mechanical-thermal noise and bandwidth by virtue of its interaction with

TABLE X. Summary of the main and interaction effects for the open-circuit sensitivity, *A*-weighted mechanical-thermal noise, and bandwidth.

Performance parameters	Most significant main effects	Least significant main effects	Most significant interactions	Least significant interactions	Factor level for best performance
Open-circuit sensitivity	*A* (−2.450) *B* (−3.350)	⋯	⋯	⋯	*A*− *B*−
Mechanical-thermal noise	*A* (−3.188) *B* (4.006)	*C* (−0.937)	*BC* (−3.613)	⋯	*A*+ *B*− *C*−
Bandwidth	*A* (5.117) *B* (−9.227) *E* (3.820)	*C* (−1.539) *D* (1.680) *F* (−1.195)	*BC* (7.648)	*AB* (−1.820) *AE* (1.352) *BE* (−1.117) *BCE* (1.695)	*A*+ *B*− *C*− *E*+

B. Figures 8(a) and 8(b) illustrate the effect of the *BC* interaction on the frequency response and the mechanical-thermal noise voltage spectrum density plots, respectively. From Fig. 8, the *B*−*C*− factor combination presents the best performance characteristics—highest sensitivity, widest bandwidth, and lowest mechanical-thermal noise—of all four *BC* factor combinations. With reference to the *B*−*C*− factor combination, for the *B*−*C*+ factor combination, a significant increase in mechanical-thermal noise and a significant reduction in bandwidth are observed while the sensitivity remains unchanged. Thus, when the hole location is shifted further away from the backplate center, the performance deteriorates. Also clearly shown in Fig. 8, the *B*+*C*− factor combination results in the worst performance characteristics with the lowest sensitivity, narrowest bandwidth, and highest mechanical-thermal noise. Based on the results of the *B*−*C*− and *B*−*C*+ factor combinations, one would expect that the performance characteristics of the *B*+*C*+ factor combination will be worse than those of the *B*+*C*− factor combination when the hole location is shifted outwards from the backplate center. However, on the contrary, only the reverse situation is true as shown in Fig. 8. Therefore, the *BC* interaction is an important consideration in the backplate design.

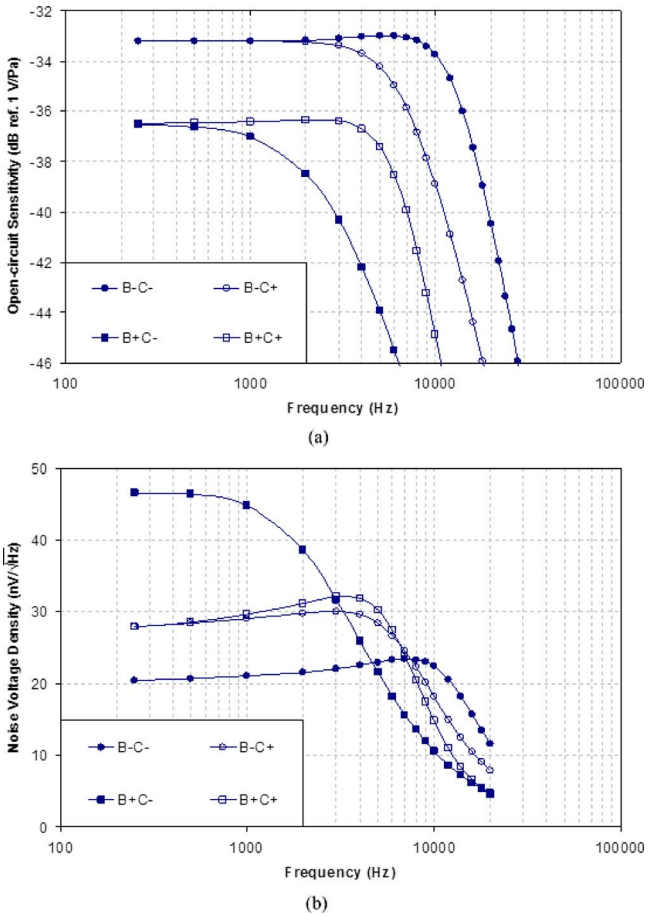

FIG. 8. (Color online) Effect of the *BC* interaction on (a) the frequency response and (b) the mechanical-thermal noise voltage spectrum density plots.

It should be apparent by now that Table X presents an organized and systematic methodology of optimizing the backplate design. As shown, the main effects of *A* (air gap) and *B* (slot) appear to exert a significant influence on all three performance parameters while the *BC* (slot/hole location) interaction affects the mechanical-thermal noise and bandwidth only. The main effect of *E* (hole radius) also has an influence over the bandwidth but it is not as significant as *A* and *B*. After the determination of the microphone size (i.e., diaphragm size), the air gap thickness (*A*) and the slot width (*B*) are determined next to achieve the desired open-circuit sensitivity. For the slot width, there is an optimum size criterion,[8,21] which states that the ratio of the backplate radius to the diaphragm radius is 0.82. For the air gap thickness, although a small air gap is desired for high sensitivity (bearing in mind that a small air gap is detrimental to both the mechanical-thermal noise and bandwidth), it must not be so small that both the mechanical-thermal noise and bandwidth enhancements cannot be made by exploiting the other remaining main effects. Thus, the selected air gap thickness should be a good design compromise between the sensitivity, mechanical-thermal noise, and bandwidth. In order to make further enhancement to the mechanical-thermal noise after the determination of the air gap thickness and the slot width, the main effect of *C* (hole location) should be optimized due

to the significant BC interaction. The remaining parameters of D, E, and F have negligible influence on the mechanical-thermal noise.

Likewise, the bandwidth enhancement can also be simultaneously made with the mechanical-thermal noise enhancement by manipulating the main effect of C. After the main effect of C, further enhancement to the bandwidth can be achieved by optimizing the remaining main effects of D, E, and F. The order of parameter optimization is suggested by their effect estimates as tabulated in Table X. Since the main effect of E (hole radius) has the highest effect estimate (3.820) of all, it should be given the first priority for optimization. By this reasoning, the next in line for optimization is the main effect of D (hole number) (1.680) and, finally, F (backplate thickness) (-1.195).

To summarize, first, the main effects of A and B are used to maximize the open-circuit sensitivity with due consideration given to the detrimental effect of a narrow air gap on the mechanical-thermal noise and bandwidth. Second, for the enhancement of both the mechanical-thermal noise and bandwidth, the main effect of C is manipulated next by virtue of the BC interaction. Finally, the main effects of E, D, and F, in that order, are used to fine-tune the bandwidth to a desired value.

V. CONCLUSION

A 2^6 factorial design with a single replicate has been carried out on a comprehensive condenser microphone model on the basis of six backplate design parameters and four output responses. By eliminating the insignificant parameters via normal probability plots of the effect estimates, a replicated factorial design is obtained so that an ANOVA on the factorial design can be performed. The main effects of air gap and slot are found to have significant influences over the sensitivity, mechanical-thermal noise, and bandwidth while the slot/hole location interaction has significant effects on the latter two responses. The remaining main effects of hole number, hole size, and backplate thickness have only minor influences over the bandwidth. For the C_A/C_M ratio, there are no significant main effects and interactions. The DOE optimization approach also demonstrates the robustness of the condenser microphone modeling approach of Zuckerwar. Finally, an organized and systematic approach of designing the backplate is summarized.

[1] T. B. Gabrielson, "Mechanical-thermal noise in micromachined acoustic and vibration sensors," IEEE Trans. Electron Devices **40**, 903–909 (1993).
[2] C. W. Tan, Z. H. Wang, J. M. Miao, and X. F. Chen, "A study on the viscous damping effect for diaphragm-based acoustic MEMS applications," J. Micromech. Microeng. **17**, 2253–2263 (2007).
[3] W. Kühnel and G. Hess, "A silicon condenser microphone with structured back plate and silicon nitride membrane," Sens. Actuators, A **30**, 251–258 (1992).
[4] P. R. Scheeper, W. Olthuis, and P. Bergveld, "Improvement of the performance of microphones with a silicon nitride diaphragm and backplate," Sens. Actuators, A **40**, 179–186 (1994).
[5] J. Bergqvist and F. Rudolf, "A silicon condenser microphone using bond and etch-back technology," Sens. Actuators, A **45**, 115–124 (1994).
[6] X. Li, R. Lin, H. S. Kek, J. Miao, and Q. Zou, "Sensitivity-improved silicon condenser microphone with a novel single deeply corrugated diaphragm," Sens. Actuators, A **92**, 257–262 (2001).
[7] A. J. Zuckerwar, "Theoretical response of condenser microphones," J. Acoust. Soc. Am. **64**, 1278–1285 (1978).
[8] A. J. Zuckerwar, in *AIP Handbook of Condenser Microphone: Theory, Calibration and Measurements*, edited by G. S. K. Wong and T. F. W. Embleton (AIP, New York, 1995), Chap. 3, pp. 37–69.
[9] C. W. Tan and J. M. Miao, "Analytical modeling for bulk-micromachined condenser microphone," J. Acoust. Soc. Am. **120**, 750–761 (2006).
[10] L. P. Yeo, Y. H. Yan, Y. C. Lam, and M. B. Chan-Park, "Design of experiment for optimization of plasma-polymerized octafluorocyclobutane coating on very high aspect ratio silicon molds," Langmuir **22**, 10196–10203 (2006).
[11] Z. W. Zhong, Z. F. Wang, and Y. H. Tan, "Chemical mechanical polishing of polymeric materials for MEMS applications," Microelectron. J. **37**, 295–301 (2006).
[12] D. C. Montgomery, *Design and Analysis of Experiments* (Wiley, New York, 1997).
[13] T. B. Gabrielson, "Fundamental noise limits in miniature acoustic and vibration sensors," J. Vibr. Acoust. **117**, 405–410 (1995).
[14] A. J. Zuckerwar, T. R. Kuhn, and R. M. Serbyn, "Background noise in piezoresistive, electret condenser and ceramic microphones," J. Acoust. Soc. Am. **113**, 3179–3187 (2003).
[15] A. J. Zuckerwar and K. C. T. Ngo, "Measured 1/f noise in the membrane motion of condenser microphones," J. Acoust. Soc. Am. **95**, 1419–1425 (1994).
[16] V. Tarnow, "Thermal noise in microphones and preamplifiers," B&K Technical Review **3**, 3–14 (1972).
[17] V. Tarnow, "The lower limit of detectable sound pressure," J. Acoust. Soc. Am. **82**, 379–381 (1987).
[18] J. B. Starr, "Squeeze-film damping in solid-state accelerometers," IEEE Workshop in Solid-State Sensor and Actuator Fourth Technical Digest (1990), pp. 44–47.
[19] Z. Škvor, "On the acoustical resistance due to viscous losses in the air gap of electrostatic transducers," Acustica **19**, 295–299 (1967).
[20] P. R. Scheeper, B. Nordstrand, J. O. Gulløv, B. Liu, T. Clausen, L. Midjord, and T. Storgaard-Larsen, "A new measurement microphone based on MEMS technology," J. Microelectromech. Syst. **12**, 880–891 (2003).
[21] M. S. Hawley, F. F. Romanow, and J. E. Warren, in *AIP Handbook of Condenser Microphone: Theory, Calibration and Measurements*, edited by G. S. K. Wong and T. F. W. Embleton (AIP, New York, 1995), Chap. 2, pp. 8–34.

The mode shapes of a tennis racket and the effects of vibration dampers on those mode shapes

Nicholas Timme[a] and Andrew Morrison
Illinois Wesleyan University, P.O. Box 2900, Bloomington, Illinois 61702

(Received 7 August 2008; revised 7 April 2009; accepted 8 April 2009)

The vibrational behavior of a tennis racket was studied using a speckle-pattern interferometry system. Specifically, the first 12 mode shapes of a racket are shown and discussed. In addition, the speckle-pattern interferometry system was used to compare the effects of four commercially available vibration damping systems. It was found that these vibration dampers produce a variety of effects on the vibrational behavior of the racket, though these effects may not be noticeable during play. © *2009 Acoustical Society of America.* [DOI: 10.1121/1.3126343]

PACS number(s): 43.40.At, 43.20.Ks [TDR] Pages: 3650–3656

I. INTRODUCTION

A great deal of research has been performed concerning the mechanical behavior of the tennis racket.[1–8] The purpose of this project with regard to tennis rackets was twofold: to observe the vibrational behavior of a tennis racket using a speckle-pattern interferometry (SPI) system and to test the effects of various commercially available vibrational damping systems on the vibrational behavior of a tennis racket using that SPI system. While some publications have discussed specifically the vibrational behavior of the tennis racket,[7,8] as far as the author is aware, no research has employed SPI to directly observe the vibrational behavior of a tennis racket and no research has yielded detailed information regarding the first 12 mode shapes. In addition, several authors studied the effects of vibration dampers on the mechanical performance of the tennis racket,[9–12] but again no research has directly studied the changes in vibrational behavior caused by vibration dampers. The vibration damping systems, of which there are several distinct designs, are advertised as lessening uncomfortable high frequency vibrations in the racket that lead to a bad "feeling" in the racket as experienced by the player. The purpose of this paper is not to directly assess the claimed performance of the vibration damping systems with regard to the feeling experienced by the player; rather the goal is to observe what effects, if any, these systems have on the mode shapes and vibrational amplitude of a tennis racket.

II. SPI SYSTEM

SPI represents a relatively low cost, real time, nondestructive method for measuring the vibrations of various surfaces. Moore, Lokberg, and Rosvold presented generally equivalent, though differently phrased, overviews of the theory involved in SPI.[13–17] The SPI setup used in these experiments can be found in Fig. 1.

A laser beam (in this case a 532 nm HLaser OptoTech) is divided by a beam splitter into a reference and object beam. The object beam strikes an object and is partially reflected into a camera. The reference beam is directed to a charge coupled device camera (Unibrain Fire-I firewire) through a beam splitter that serves to recombine the object and reference beams. The optical system was designed such that the size of an individual speckle seen by the camera was approximately equal to the size of a pixel of the camera. In order to minimize background vibration, the system is mounted on a Newport RS 4000 floating optical table.

To produce interferograms in traditional SPI systems, one image is taken prior to the onset of vibration and subsequent images of the object during vibration are subtracted from the initial image. However, this method will fail as the beam decorrelates. Thus, in the setup used by this experiment interferograms were produced by continually taking and subtracting pairs of images during vibration, as was suggested by Moore.[18] This process was accomplished with a LABVIEW program.

The irradiance of a pixel in an interferogram produce by the SPI system is given by Eq. (1).[15,16]

$$I_{mn} = \left| A_{mn} J_0 \left[\frac{4\pi \Delta z}{\lambda} \right] \right|. \quad (1)$$

In Eq. (1) m and n refer to the nth image subtracted from the mth image, A_{mn} is a proportionality constant for all pixels, Δz refers to the vibrational amplitude of an individual speckle on the object, λ is the wavelength, and J_0 is a zero-order Bessel function of the first kind. Therefore, on interferograms, regions of no vibration (nodes) appear white and increasing vibrational displacement results in a sequence of alternating light and dark fringes as a result of the oscillation of the Bessel function. The sequence of fringes is similar to a contour plot in that densely arranged fringes imply large changes in displacement. Using 1 a direct measurement of the maximum vibrational amplitude can be made by counting fringes. The white area of nodes corresponds to zero vibrational amplitude, the light area of the first fringe corresponds to the next maximum in 1 (given a wavelength of 532 nm this is approximately 42 nm), the second fringe corresponds to approximately 85 nm, and so forth. Depending

[a]Present address: Indiana University, 727 E. Third St., Bloomington, IN 47405-7105. Author to whom correspondence should be addressed. Electronic mail: nmtimme@umail.iu.edu

 0001-4966/2009/125(6)/3650/7/$25.00

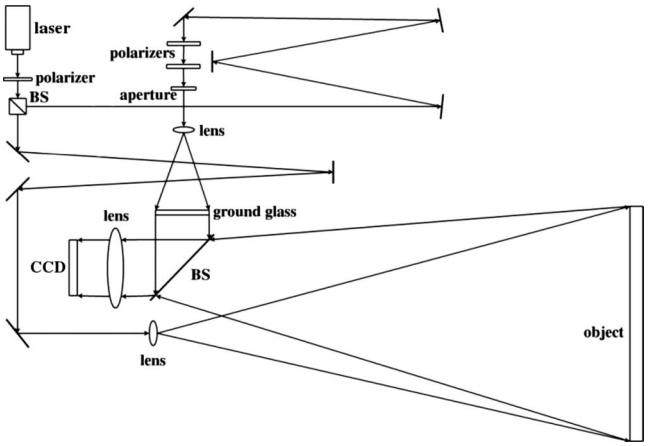

FIG. 1. The optical design of the SPI system used to study the vibrational behavior of a tennis racket.

on the quality of the interferogram, the process of counting fringes can be difficult. This process is made even more difficult in this particular experiment by the very small reflecting area of the strings. In order to compensate for this difficulty, this study employed a large estimated uncertainty: 0.25 fringes (roughly 10 nm) were applied to modes that possessed less than two fringes and one fringe (roughly 42 nm) was applied to modes that possessed more than two fringes.

III. EXPERIMENTAL SETUP

The following observations of the vibrational behavior of a tennis racket were performed using a Pro-Kennex Reach Precept 110 tennis racket with the factory string tension. The method of securing the racket was of crucial importance to this study and there has been discussion in the literature regarding this topic.[19,20] For instance, Brody determined that the vibrational behavior of a racket rigidly clamped at the handle following the impact of a tennis ball is significantly different from the vibrational behavior of a hand held racket following the impact of a tennis ball. Brody found that the vibration decay time in the rigidly clamped racket is significantly longer than the decay times for a hand held racket. He also found that several low frequency vibrations are not present following impacts with hand held rackets, while these vibrations are present following impacts with rigidly clamped rackets. However, in this study the racket is not being struck by a tennis ball and vibration decay is not being studied, so these concerns are not pertinent to this experiment. Furthermore, rigidly clamping the racket at the handle is a necessity in order to employ the SPI system. The racket must be stationary within a few nanometers between sequential images in order to obtain useful interferograms.

The racket was mounted using two test tube clamps on magnetic posts, as can be seen in Fig. 2. The clamps were on the handle of the racket approximately 8 cm apart. The test tube clamps were chosen because they wrapped partly around the handle and because their rubber covers prevented damage to the racket handle. The racket was mounted so that the whole racket face was perpendicular to the object beam

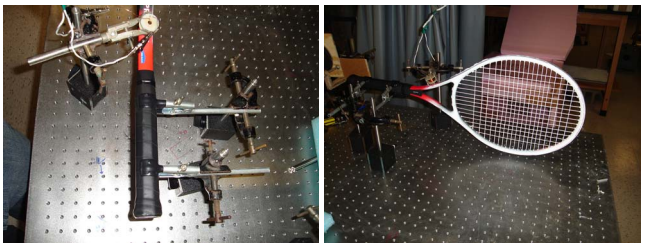

FIG. 2. (Color online) Image of racket on optical table: (a) view of mounting structure (b) front view of the racket.

of the SPI. The racket was sprayed with false frost (Chase Products' Santa SnowFrost) in order to increase the reflectivity of the strings.

In this study the racket was driven by two methods: acoustic and electromagnetic. When driven with an electromagnet, a small magnet was attached to one of three points on the racket: the throat of the racket (the electromagnet for this method is in place in Fig. 2), at the center of the face of the racket at an intersection between strings, and approximately 8 cm off center of the face of the racket at an intersection between strings. These locations can be seen in Fig. 3. The magnet was then driving by passing an alternating current through a solenoid near the magnet. When driven acoustically, a speaker (approximately 5 in. in diameter) was placed behind the face of the racket near to the throat and also driven with an ac current. This can also be seen in Fig. 3.

Both the speaker and the electromagnet were driven using a Hewlett-Packard 3325A Signal Generator and controlled using a LABVIEW program. The driving amplitude controlled by the LABVIEW program was recorded in order to ensure consistent driving force (see Sec. V C).

IV. THE MODES OF A TENNIS RACKET

In order to best understand the vibrational mode shapes of a tennis racket, the racket was vibrated with the electromagnet at all three locations and acoustically. The resulting interferograms were then compared in an attempt to understand the overall vibrational behavior of the racket. The frequency found for each mode shape when vibrating the racket acoustically is assumed to be the closest to the actual mode frequency because acoustic vibration does not require applying the vibration to a specific point on the racket nor adding

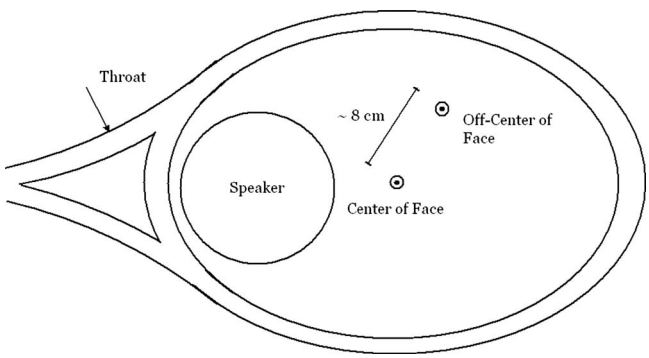

FIG. 3. Diagram of vibration methods (strings not shown, vectors indicate magnet vibration axis).

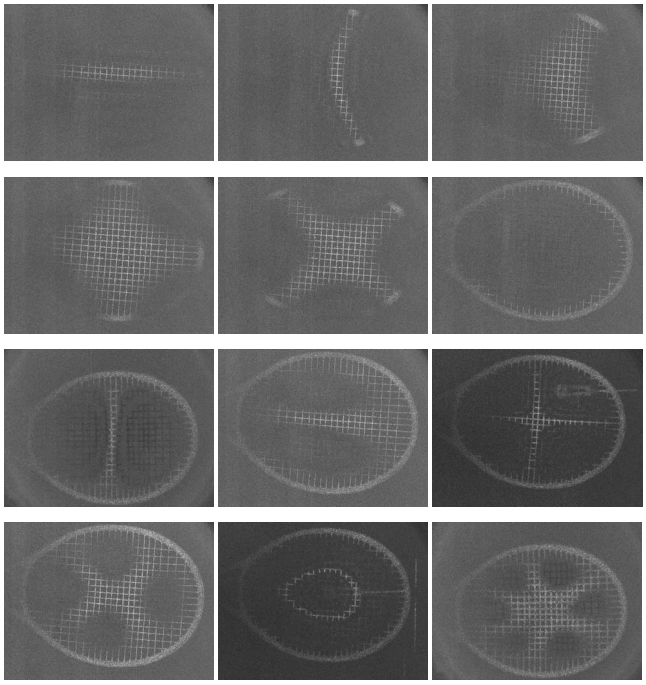

FIG. 4. The mode shapes of a tennis racket (a) $(1a,0)$: Acoustic 67 Hz (b) $(1b,0)$: Acoustic 114 Hz (c) $(1c,0)$: Acoustic 205 Hz (d) $(2a,0)$: Acoustic 349 (e) $(2b,0)$: Acoustic 432 (f) (0,1): Acoustic 562 Hz (g) $(1a,1)$: Throat 895 Hz (h) $(1b,1)$: Acoustic 909 Hz (i) $(2a,1)$: Off center 1154 Hz (j) $(2b,1)$: Acoustic 1186 Hz (k) (0,2): Center 1270 Hz (l) (3,1): Throat 1476 Hz.

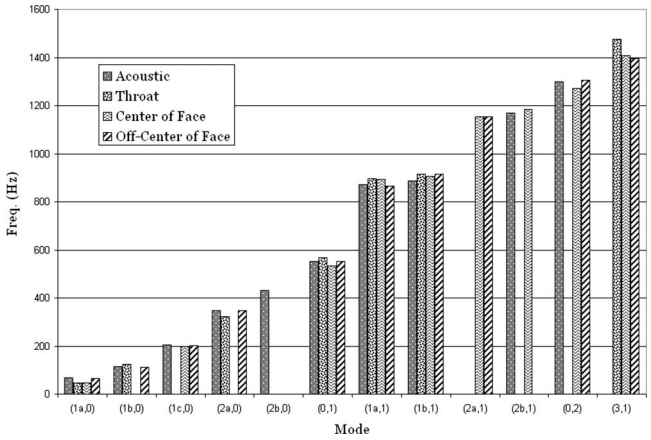

FIG. 5. The mode frequencies of a tennis racket vibrated by four differing methods.

mass to the racket as was the case with the electromagnetic method. However, by vibrating the racket at the two points on the face, we can gain useful information regarding the vibrational response of the racket to vibrations applied to those specific regions. From these measurements, we were able to identify the first 12 mode shapes. In naming the modes, we have adopted a notation similar to the notation used in the naming of the modes of circular plates. Thus, the modes are named by an ordered pair (x,y), where x is the number of nodal diameters and y is the number of nodal circles. In addition, modes with the same number of nodal diameters and nodal circles but possessing different shapes are noted by a letter following the number of nodal diameters. A representative interferogram for each mode shape can be seen in Fig. 4.

Some modes were not seen for each method of vibration and the modes that were observed appeared at slightly different frequencies depending on the method of vibration (see Fig. 5). The uncertainty for the mode frequencies is, relative to the overall frequency, very small at only 3 Hz. For this reason, error bars are not included in Fig. 5.

It was also observed that several mode shapes differed slightly between methods of vibration. For instance, when the racket was vibrated acoustically, the nodal line in the $(1a,1)$ mode was rotated approximately 30° counterclockwise. Also, for the $(1c,0)$ mode, the nodal arc was distorted when the racket was vibrated at both positions on the face of the racket.

The mode shapes in Fig. 4 can be divided into two general regimes: high frequency [mode (0,1) and higher] and low frequency [mode $(2b,0)$ and lower]. For the high frequency regime, the racket appears to behave like a clamped elliptical membrane. For these modes the racket frame is always a node and the lowest frequency mode is the (0,1), as is the case for a clamped elliptical membrane. As the mode frequency increases nodal diameters and nodal circles appear, as is the case for a clamped elliptical membrane. Thus, in this regime vibration only occurs in the strings. For the low frequency regime complicated behavior is observed. Modes $(1b,0)$ and $(1c,0)$ are similar to a cantilever. Thus, the strings and frame behave as one body. However, modes $(1a,0)$, $(2a,0)$, and $(2b,0)$ are similar to the modes seen for a free elliptical membrane. Thus, for these modes the frame vibrates, but the frame and strings do not behave as one body as they did for the $(1b,0)$ and $(1c,0)$ modes. Therefore, in the low frequency regime the frame and string interact in a complicated fashion, but for the high frequency regime the racket is consistently similar to a clamped elliptical membrane. This interesting behavior underscores the complexity of the interaction between the strings and the frame in the tennis racket system as a whole.

A. The sweet-spot controversy

There has been some disagreement within the literature regarding the "sweet spot" of a tennis racket.[3,5,6,8,12,20] Tennis players generally refer to the sweet spot as the region of the racket face where, if the ball is struck there, the hit "feels good" or "feels effortless" to the player and the ball travels large distances. This project did not hope to address the feel associated with ball-racket impacts on various parts of the racket, nor the relationship between the ability of the racket to impart a large velocity on the ball and the location of the impact. However, several authors considered the possibility that the sweet spot is a node of a particularly strong low frequency mode of vibration.[3,5,6,8,12,20] By using SPI, this project has been able to clearly identify the nodal regions of the low frequency modes. Furthermore, several authors noted that the average impact time of a tennis ball (approximately 5 ms) is roughly one-half of 1 cycle of vibration for modes near 100 Hz.[6,8] Thus, when the ball is struck in the nodal region, less energy is spent in stretching the racket face and more energy is imparted to the ball than if the ball had struck

an anti-node. There is some ambiguity regarding precisely which mode is responsible for this behavior. For instance, Brody claimed that the main mode responsible for this behavior is the arc shaped mode [the $(1b,0)$ and $(1c,0)$ modes as they are being referred to here] and that this is the fundamental mode.[12] Regardless of precisely which mode is responsible, from the mode shapes observed here it is apparent that the nodes of the lowest five modes all overlap in roughly the area of the center of the face. Thus, an impact in this area may be expected to excite these modes less than an impact in another region of the face, resulting in a larger amount of energy input to the ball for impacts in the center of the face in comparison to impacts in other regions of the face. Indeed, when the racket was vibrated at the center of the face the $(1b,0)$, $(2a,0)$, and $(2b,0)$ modes were not seen and the $(1a,0)$ mode was shifted approximately 30% lower, as can be seen in Fig. 5. In addition, four of the lowest five modes were seen unshifted when the racket was vibrated off the center of the face (i.e., away from the possible sweet spot). Thus, using SPI, we are able see a clear difference in vibrational behavior based on the location of vibration on the face and this behavior seems to correlate with the sweet spot behavior.

V. THE EFFECTS OF VIBRATION DAMPERS

A. Vibration damping systems

There are several vibration damping systems commercially available today. In this paper a sample of four such models were studied: the Wilson Vibra-Fun (specifically the rectangular model), the Prince NXG Silencer, the Head Smartsorb, and the Babolat RVS. All of these models cost around five dollars and claim to offer a low cost way to improve racket feel by diminishing uncomfortable high frequency racket vibrations. All four models of vibration dampers attach to the racket near the bottom of the racket head. All models supplied rudimentary directions about how to attach the device to the racket and these were followed explicitly. The models attached to the racket can be seen in Fig. 6.

All four models are made primarily of flexible rubberlike materials. The Prince and Wilson models are similar in that they attach to the racket by wedging between several strings. In this way, they are in contact with several strings, though the Prince model is in contact with several more than the Wilson model. The Head model winds between several strings in such a way that for each string, the vibration damper crosses the string on the opposite side compared to the lowest perpendicular string. It is also pressed up against this perpendicular string. The Babolat model is wedged between several strings, similar to the Prince model, but it also rests against the frame and has attached to it a small metal weight. The masses of the four models were (Wilson) 2.32 g, (Prince) 5.92 g, (Head) 2.43 g, and (Babolat) 6.71 g.

B. Comparison mode frequencies

For the purposes of comparing the effects of the vibration dampers on the vibrational behavior of the racket, the lowest eight modes, mode $(2b,1)$, and mode (0,2) were observed by vibrating the racket acoustically. The acoustic method was used because it produced the most mode shapes and because it did not require adding mass to the racket or vibrating the racket at a specific point, as was the case with the electromagnetic method. The mode frequencies observed in this comparison can be seen in Fig. 7. As before, at 3 Hz the uncertainty for the mode frequencies is relatively very small compared to the mode frequency. Therefore, error bars are not included in Fig. 7. Also, there were several modes that were heavily distorted [mode $(2a,0)$ for the Prince model, $(2b,0)$ for the Prince, Head, and Wilson models, and modes $(1a,1)$ and $2b,1$ for the Head model] that are included in Fig. 7, but which will be specifically addressed (see Sec. V D).

From the results in Fig. 7, it is apparent that the vibration dampers have a relatively small effect on the lower mode frequencies, but that they do significantly affect the higher mode frequencies. For instance, the Head model shifted the mode (0,1) and $(1a,1)$ frequencies significantly lower than when the racket was undamped. Also, the $(1a,1)$ and $(1b,1)$ mode frequencies were switched when the Wil-

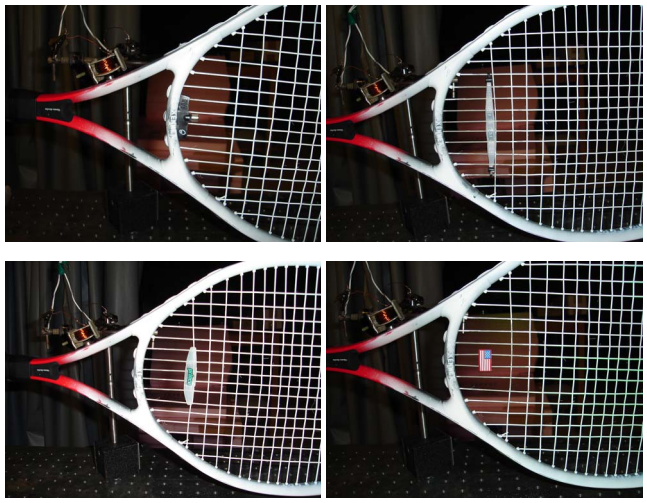

FIG. 6. (Color online) The vibration dampers attached to the racket (electromagnet vibration method shown, but not employed): (a) Babolet model, (b) Head model, (c) Prince model, and (d) Wilson model.

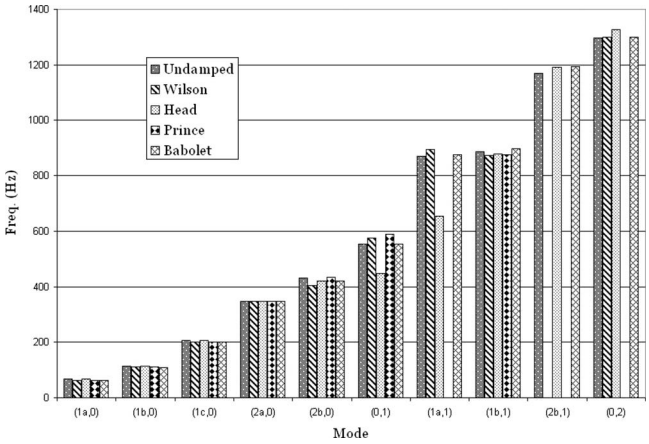

FIG. 7. The mode frequencies of a tennis racket undamped and with dampers in place.

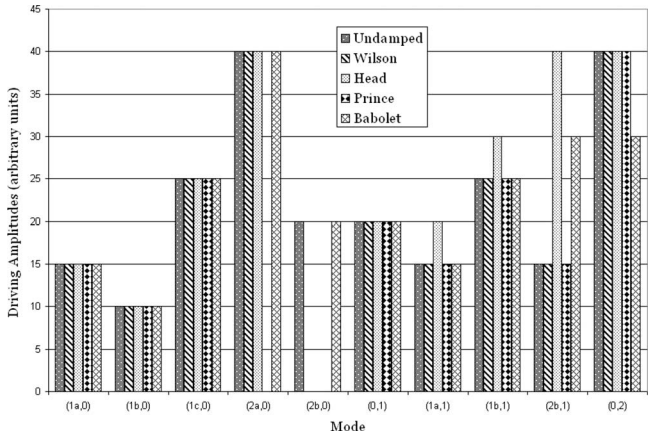

FIG. 8. The driving amplitude applied to the racket.

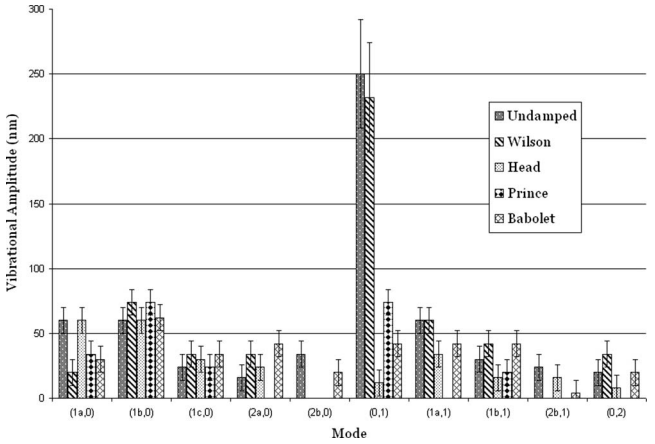

FIG. 9. The maximum vibrational amplitude with and without vibration dampers in place.

son vibration damper was in place. Mode frequencies were not only shifted lower. For instance, the Wilson model shifted the $(1a,1)$ and (0,1) mode frequencies higher. Finally, several modes were eliminated entirely as will be further discussed in Sec. V D.

C. Driving amplitude

In order to maintain consistency between measurements, all racket interferograms involved in the comparison between the racket with vibration dampers in place and the undamped racket were taken on the same day with no changes being made to the clamping system or the method of vibration. In addition, every attempt was made to compare modes using the same driving amplitude for each damper in order to gain an accurate measure of the change in vibrational amplitude. Different driving amplitudes were used for different modes in order to produce the best possible interferogram. Some modes were more difficult to excite than others and thus required a larger driving amplitude. As stated in Sec. III, the driving amplitude from the LABVIEW program was recorded in order to maintain consistent driving forces between dampers. The driving amplitudes can be found in Fig. 8.

The modes missing in Fig. 8 represent special cases of distortion that will be addressed specifically in Sec. V D. For the first six modes, the driving amplitudes applied to the racket are identical for all damper models for a given mode. For the last four modes different driving amplitudes were required to obtain the best possible interferograms. Differences in driving amplitudes should be considered when comparing the vibrational amplitude of the racket in Sec. V D.

D. Comparison of mode shapes

The primary goal of comparing the effects of vibration dampers is to examine the changes in vibrational amplitude produced by the vibration dampers. Following the process outlined in Sec. II, the maximum vibrational amplitude of the racket modes with the dampers in place and undamped were measured and are presented in Fig. 9.

As can be seen in Fig. 9, the (0,1) mode possesses by far the largest maximum vibrational amplitude despite the fact that the driving amplitude applied to the racket for the (0,1) mode is near to or less than all other driving amplitudes applied to the racket (see Fig. 8). Furthermore, we can see directly that this dominate mode is greatly reduced by the Head, Prince, and Babolet models.

In order to better evaluate the performance of the vibration dampers, the relative maximum vibrational amplitude of the maximum vibrational amplitude with the dampers in place in comparison to the undamped maximum vibrational amplitude was computed. If the relative maximum vibrational amplitude is greater than 1, then the maximum vibrational amplitude is increased with the damper in place. If the relative maximum vibrational amplitude is less than 1, then the maximum vibrational amplitude is decreased with the damper in place. The relative maximum vibrational amplitude can be found in Fig. 10.

In Fig. 10 several modes are missing because they possessed large distortions that require dedicated discussion. The modes whose maximum vibrational amplitude was completely eliminated by a vibration damper still possess error bars in Fig. 10. The large error bars in Fig. 10 [particularly modes $(1c,0)$ and $(2a,0)$] result from the low maximum vibrational amplitude of those modes (see Fig. 9) and the relatively large (in comparison to the maximum vibrational amplitude) estimated uncertainty of 10 nm. These facts combined with the large driving amplitude required to produce

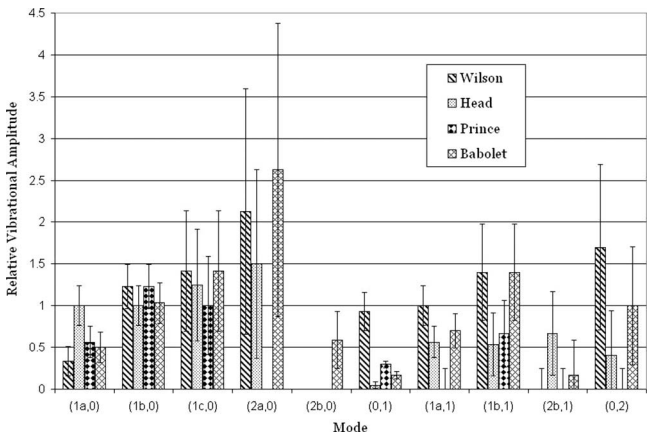

FIG. 10. The relative vibrational amplitude of several vibration dampers in comparison to undamped vibrations.

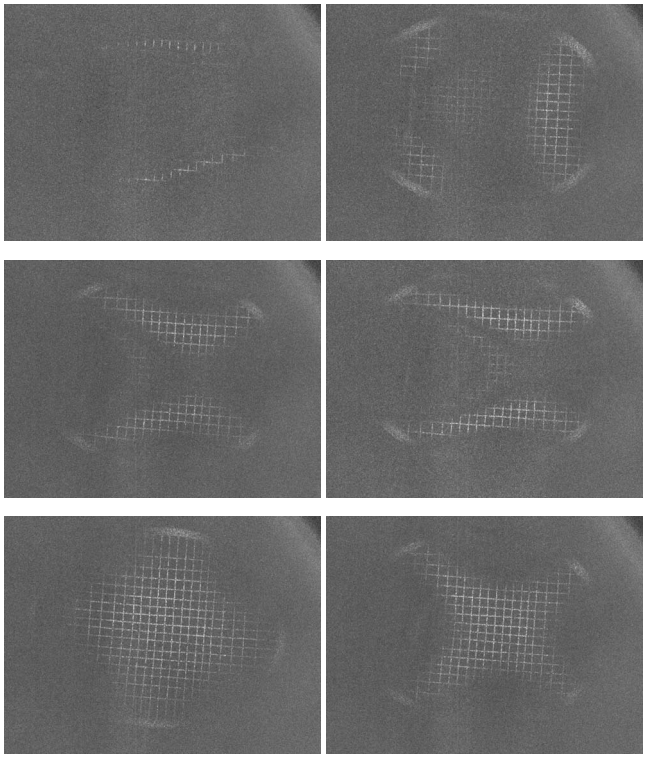

FIG. 11. Distorted modes shapes with vibration dampers and the corresponding undistorted undamped mode shapes.

these modes imply that large uncertainties in the change in maximum vibrational amplitude for these modes are not significant.

From the relative maximum vibrational amplitude, several conclusions can be drawn. The Wilson model only appreciably decreased the maximum vibrational amplitude for the $(1a,0)$ mode. The Head model left the lower four modes relatively unaltered, but decreased the maximum vibrational amplitude of the highest five modes. The Prince model greatly decreased the highest five modes and the $(1a,0)$ mode, while leaving the $(1b,0)$ and $(1c,0)$ modes essentially unaltered. The Babolet model generally decreased the maximum vibrational amplitude with some noticable increases that are within uncertainty of unity.

The $(2a,0)$ mode was significantly distorted for the Prince model and the $(2b,0)$ mode was also significantly distorted for the Prince, Head, and Wilson models. These mode shapes along with the undamped mode shapes can be seen in Fig. 11. Note that the driving amplitudes for these mode shapes were identical to the undamped driving amplitude.

All of the mode shapes in Fig. 11 possess a greater maximum vibrational amplitude than the amplitude seen in the undamped case. It was unexpected that attaching a vibration damper would increase the maximum vibrational amplitude. In addition to the dramatic distortions seen in Fig. 11, some small distortions were seen in some higher frequency modes with the Head model: the $(2b,1)$ mode was distorted so that either the mode shape was rotated to appear as the $(2a,1)$ mode or the $(2a,1)$ mode became excitable with the acoustic method when the Head model was in place and the $(1a,1)$ mode was shifted 25% lower (see Fig. 7) and was distorted such that one anti-node became much larger than the other.

E. Discussion of the effects of vibration dampers

The vibration dampers studied produced a variety noteworthy effects on the vibrational behavior of the tennis racket. Several high frequency modes were eliminated entirely and several others exhibited reduced vibrational amplitude when a vibration damper was in place. The (0,1) mode was the most dominate and its vibrational amplitude was decreased by values near 75%–90% for the Head, Prince, and Babolet models. The Wilson model on the other hand did not greatly reduce the (0,1) mode. The $(2a,0)$ mode was significantly distorted for the Prince model and the $(2b,0)$ mode was also significantly distorted for the Prince, Head, and Wilson models. For all four of these distorted modes, the distortion increased the maximum vibrational amplitude. This is certainly a curious result that requires further investigation. Many mode frequencies were shifted higher or lower. For instance, the Head model shifted the (0,1) and $(1a,1)$ mode frequencies lower, while the Wilson model shifted those mode frequencies higher. It was expected that the presence of the vibration dampers would lower mode frequencies due to the additional mass of the vibration damper. Further work should be conducted to understand why the frequency is shifted higher in some cases.

While these findings are not in direct opposition with the findings of other research, they certainly draw interesting contrasts. For instance, Brody *et al.* found that the vibration dampers did not affect the time it takes for vibrations to die out following an impact, nor do they affect the frequency of the racket vibrations.[11,12] In this project, the time taken for cessation of vibration following an impact was not studied, so no comparison can be made. With regard to the frequency of vibration, perhaps the higher modes that were found to be more affected by the dampers in this project do not contribute largely to the overall vibrations seen in a racket following an impact. Stroede found that vibration dampers have no effect on the feel of the racket as experienced by the player.[9] Li found that vibration dampers do not reduce the vibrations felt by the hand and arm with regard to the approximately 120 Hz resonance of their racket.[10] This project did not measure the vibrations felt by the hand, so again, perhaps the mainly higher modes that were damped in this project do not contribute largely to the vibrations felt by the hand following an impact. This conclusion is supported by the lower maximum vibrational amplitude found in the higher frequency modes (see Fig. 9) and the lack of vibration in the frame for the higher frequency modes (see Fig. 4). Therefore, while it may be true that vibration dampers reduce some vibrations, these reduced vibrations most likely do not significantly alter the overall vibrational behavior of the racket. In order to better address the past studies, it would be worthwhile to construct a clamping system that better models the human hand and is able to detect vibration. Also, with the addition

of a high speed camera to the SPI system, the vibrations of a tennis racket following an impact with a tennis ball could be observed and studied using SPI.

In connection with the discussion in Sec. IV A, it is interesting to note the distortion of the $(2a,0)$ mode by the Prince model and the $(2b,0)$ mode by the Prince, Head, and Wilson models. All of these distortions remove a node from the center of the racket near the supposed sweet spot. If the sweet spot is indeed the result of the presence of the nodes in the center of the racket, then these models of vibration dampers may actually weaken the sweet spot.

VI. CONCLUSIONS

It has been demonstrated that the vibrational behavior of a tennis racket can be studied using SPI. As a result of this study, the first 12 mode shapes of a tennis racket have been shown and analyzed. In addition, the SPI system was utilized to examine the effects of vibration dampers on the vibrational behavior of a tennis racket. It was found that the vibration dampers do reduce vibrations for some mode frequencies, though these effects may not be significant in play. In addition, the vibration dampers were observed to alter some mode frequencies and mode shapes.

ACKNOWLEDGMENTS

We would like to thank the IWU students Tom Traynor, Alex Boecher, Sawyer Campbell, and Kristy Streu for their efforts in constructing the SPI system and LABVIEW programs. In addition, we would like to thank Dr. Thomas Moore of Rollins College for his advice about the SPI system setup.

[1] J. Kotze, "The role of the racket in high speed tennis serves," Sports Eng. **3**, 67 (2000).
[2] R. Cross, "Center of percussion of hand-held implements," Am. J. Phys. **72**, 622 (2004).
[3] R. Cross, "The sweet spots of a tennis racket," Sports Eng. **1**, 63 (1998).
[4] H. Brody, "The physics of tennis: III the ball-racket interaction," Am. J. Phys. **65**, 981 (1997).
[5] H. Brody, "The physics of the tennis racket: II the "sweet spot"," Am. J. Phys. **49**, 816 (1981).
[6] S. J. Haake, "The dynamic impact characteristics of tennis balls with tennis rackets," J. Sports Sci. **21**, 839 (2003).
[7] J. E. Oh, "A study on the dynamic characteristics of tennis racket by modal analysis," Bull. JSME **29**, 2228 (1986).
[8] M. Brannigan, "Mathematical modeling and simulation of a tennis racket," Med. Sci. Sports Exercise **13**, 44 (1981).
[9] C. L. Stroede, "The effect of tennis racket string vibration dampers on racket handle vibrations and discomfort following impacts," J. Sports Sci. **17**, 379 (1999).
[10] F. X. Li, "String vibration dampers do not reduce racket frame vibration transfer to the forearm," J. Sports Sci. **22**, 1041 (2004).
[11] H. Brody, "Vibration damping of tennis rackets," Int. J. of Sports Biomechanics **5**, 451 (1989).
[12] H. Brody, R. Cross, and C. Lindsey, *The Physics and Technology of Tennis* (Racquet Tech Publishing, Solana Beach, CA, 2002).
[13] O. J. Lokberg, "Use of chopped laser light in electronic speckle pattern interferometry," Appl. Opt. **18**, 2377 (1979).
[14] O. J. Lokberg, "Interferometric comparison of displacements by electronic speckle pattern interferometry," Appl. Opt. **20**, 2630 (1981).
[15] T. R. Moore, "A simple design for an electronic speckle pattern interferometer," Am. J. Phys. **72**, 1380 (2004).
[16] T. R. Moore, "Interferometric studies of a piano soundboard," J. Acoust. Soc. Am. **119**, 1783 (2006).
[17] G. O. Rosvold, "Effect and use of exposure control in vibration analysis using tv holography," Appl. Opt. **32**, 684 (1993).
[18] T. R. Moore, "Imaging vibrations and flow using electronic speckle pattern inteferometry (a)," J. Acoust. Soc. Am. **120**, 3364 (2006).
[19] H. Brody, "Models of tennis racket impacts," Int. J. of Sports Biomechanics **3**, 293 (1987).
[20] R. Cross, "The dead spot of a tennis racket," Am. J. Phys. **65**, 754 (1997).

Graph theory applied to noise and vibration control in statistical energy analysis models

Oriol Guasch[a] and Lluís Cortés
GTM Grup de recerca en Tecnologies Mèdia, La Salle, Universitat Ramon Llull, C/Quatre Camins 2, Barcelona 08022, Catalonia, Spain

(Received 6 September 2008; revised 10 February 2009; accepted 3 April 2009)

A fundamental aspect of noise and vibration control in statistical energy analysis (SEA) models consists in first identifying and then reducing the energy flow paths between subsystems. In this work, it is proposed to make use of some results from graph theory to address both issues. On the one hand, linear and path algebras applied to adjacency matrices of SEA graphs are used to determine the existence of any order paths between subsystems, counting and labeling them, finding extremal paths, or determining the power flow contributions from groups of paths. On the other hand, a strategy is presented that makes use of graph cut algorithms to reduce the energy flow from a source subsystem to a receiver one, modifying as few internal and coupling loss factors as possible. © *2009 Acoustical Society of America.* [DOI: 10.1121/1.3125324]

PACS number(s): 43.40.At, 43.50.Jh [RLW] Pages: 3657–3672

I. INTRODUCTION

Statistical energy analysis (SEA) has become a widely acknowledged method to deal with vibroacoustic complex problems in the high frequency range. A quick approach to the subject can be found in Ref. 1, while the seminal monograph[2] is still the classic to consult. Concerning SEA applied to building acoustics, Ref. 3 provides a friendly and complete approach to the subject.

SEA is nowadays used as a prediction tool in several sectors such as aerospace, naval, railway, automotive, or building. A large number of different physical processes are involved in the interactions between subsystems appearing in the SEA models for these fields. Consequently, much research in SEA has been devoted to the key issue of finding the coupling loss factors that characterize these interactions by means of experiments, analytic developments, or using numerical methods. A vast amount of literature exists on these topics which will not be cited here. Another fundamental question concerns whether a particular problem can be addressed by means of SEA, given that it relies on a set of hypotheses that a system should satisfy for the method to be applied to it. Interesting attempts to mathematically formulate these hypotheses[4] as well as to analyze the involved statistics are being carried out.[5–8] Hybrid or new approaches to cover the gap between low frequency deterministic prediction methods (e.g., finite element methods) and high frequency statistical methods such as SEA constitute also another active field of research.[9–13]

This paper focuses on noise and vibration control in SEA models, i.e., on identifying power flow transmission paths from source subsystems to receiver ones and modifying them so as to reduce the energy level at a desired target subsystem. Energy attenuation along a path in a SEA model was first defined in Ref. 14, whereas contributions from groups of paths were analyzed in Ref. 15. SEA path analysis applications can be found in many areas. For example, the subject has recently acquired much importance in building acoustics, where the need to correctly predict the contributions of flanking paths has become mandatory with the development of new European noise regulations and standards. Several experimental and numerical SEA path analyses in building acoustics have been performed to test and improve the predictions of these regulations.[16–19]

However, it is quoted in Ref. 20, that "usually the path-by-path analysis is done by selecting the dominating paths based on experience or intuition and comparing them," while in Ref. 21 (cf. Ref. 20), it is concluded that "more intelligent path identification and assessment algorithms are needed." The aim of this paper is to propose some basis and a few possible steps toward some aspects of this ambitious goal. This is done by resorting to graph theory.

On the one hand, SEA graphs (closely resembling SEA models) are introduced and characterized by means of their adjacency matrices. The application of linear and path algebras[22] to these matrices provide a general mathematical framework where many SEA transmission path problems can be posed, e.g., having information on the existence of paths between subsystems, counting and labeling them, finding extremal paths, or finding the contributions from groups of paths. Well-known results on the subject are recovered as particular cases. On the other hand, the question of how to reduce the energy at a target or receiver subsystem (not to surpass a desired threshold value) by modifying the SEA system internal and coupling loss factors is also addressed. Actually, it is to be noted that the somehow naive approach of directly minimizing the target subsystem energy with respect to the whole system internal and coupling loss factors could probably result in having to change a large amount of them. This may become totally infeasible from a practical point of view. An interesting option may be that proposed in Ref. 20, where a sensitivity analysis of the SEA system is carried out by means of a Taylor expansion of the subsystem

[a]Author to whom correspondence should be addressed. Electronic mail: oguasch@salle.url.edu.

energies at the maximum values of the coupling loss factors. This could provide the factors that have more influence on a particular subsystem energy and modifications could be only attempted on them. In this paper, an alternative procedure is proposed based again on graph theory. The idea is to make use of graph cut algorithms[23–25] to locate the minimum *s-t* cut[26] in the SEA graph that separates a source subsystem from a target one. Then, it is expected that increasing the internal loss factors and diminishing the coupling loss factors of this *cutset* (maximum allowed variations will be considered in this paper) can result in a large amount of reduction in the target subsystem energy (given that all transmission paths cross the cutset). In the case that the desired energy reduction is not attained with these initial modifications, the immediately higher sized cutset is selected, and so on until the threshold energy level at the receiver is reached.

Finally, maybe it is worthwhile to mention that finding and establishing the contributions of transmission paths is the main goal of several noise and vibration control techniques, such as the force transmission path analysis method[27–30] or the method of direct transfer functions.[31–35]

The paper is organized as follows. Section II first contains a reminder of the basic SEA matrix equations. It presents the series development to analyze the contributions of groups of paths in a general nonsymmetric SEA model, and an analogous development is derived for the case of symmetric loss factor matrices. Then, basic results from graph theory are reviewed in order to make the paper more self-contained. Key definitions are given as well as an introduction to path algebras and related issues. Notation for subsequent sections is also provided. In Sec. III, SEA graphs are introduced and various algebras are used to extract information from the powers of the SEA graph adjacency matrix. A benchmark numerical example is also given to help clarify all concepts. In Sec. IV, the strategy based on graph cut algorithms to diminish the energy at a target subsystem due to transmission from a source subsystem is presented. A numerical example is again included to illustrate its behavior and potentiality. The asymptotic cases of low damping and high damping dominated systems are also addressed and a comparison with the Monte Carlo approach to the problem is carried out. Finally, conclusions are drawn in Sec. V.

II. SEA AND GRAPH THEORY BASIC CONCEPTS

A. SEA basic matrix equations

Throughout this work, we will deal with a general SEA model characterized by a coupling loss factor matrix $\mathcal{H}$. The *a priori* unknown subsystem energies, E_i, will be the entries of the energy vector $\boldsymbol{E}$ and the vector $\boldsymbol{W}$ will contain minus the external subsystem power inputs, W_i, per radian frequency ω. These quantities are related by means of the linear system[2,3]

$$\mathcal{H}\boldsymbol{E} = -\frac{1}{\omega}\boldsymbol{W} \equiv \boldsymbol{E}^0, \tag{1}$$

where the right hand side of the equation has been redefined as an external energy input vector. The elements in $\mathcal{H}$ are given by

$$\mathcal{H}(i,j) = \begin{cases} \eta_{ji}, & i \neq j \\ -\eta_i & i = j, \end{cases} \tag{2}$$

with η_{ij} standing for the *coupling loss factors* and η_i standing for the *total loss factors*. The latter are related to the former and to the *internal loss factors* η_{id} through $\eta_i = \eta_{id} + \Sigma_j \eta_{ij}$.

An alternative symmetric form for Eqs. (1) and (2) consists of multiplying each term by the modal density ratio $(n_i/n_i=1)$ so that Eq. (1) becomes[3]

$$\mathcal{H}_{\text{sym}}\boldsymbol{E}_n = \boldsymbol{E}^0, \tag{3}$$

with

$$\mathcal{H}_{\text{sym}}(i,j) := \begin{cases} n_i\eta_{ij}, & i \neq j \\ -n_i\eta_i, & i = j, \end{cases} \tag{4}$$

$$E_n(i) := E_i^0/n_i, \tag{5}$$

and where use has been made of the *consistency relation* $n_i\eta_{ij} = n_j\eta_{ji}$ to attain a symmetric matrix. Equations (3) and (4) are sometimes preferred to Eqs. (1) and (2) as they yield faster numerical algorithms to compute the system solution.

Path by path analysis in a SEA model was introduced in Ref. 14 (see also Ref. 3). A kth order path between any pair of subsystems u_i and u_j is defined as a set of k pairs of subsystems (u_{h_i}, u_{h_j}) linking u_i with u_j. The energy attenuation through such a path is provided by

$$\frac{\eta_{ih_1}}{\eta_{h_1}}\frac{\eta_{h_1h_2}}{\eta_{h_2}}\cdots\frac{\eta_{h_{k-1}j}}{\eta_j}. \tag{6}$$

To analyze the contributions from groups of paths, it was lately proposed[15] to divide each row of Eq. (1) by $-\eta_i$. Then $\mathcal{H}$ can be rewritten as $\mathcal{H} = \mathcal{I} - \mathcal{S}$ with $\mathcal{S}(i,j) := (\eta_{ji}/\eta_i)(1-\delta_{ij})$, $\eta_{ii} \equiv \eta_i$. It then follows that the solution of the SEA system $\mathcal{H}\boldsymbol{E} = \boldsymbol{E}^0$ can be obtained by means of the series expansion

$$\boldsymbol{E} = (\mathcal{I}-\mathcal{S})^{-1}\boldsymbol{E}^0 = \left(\sum_{k=0}^{\infty}\mathcal{S}^k\right)\boldsymbol{E}^0 = (\mathcal{I}+\mathcal{S}+\mathcal{S}^2+\ldots)\boldsymbol{E}^0, \tag{7}$$

with the external energy vector elements being now given by E_i^0/η_i. The kth power matrix $\mathcal{S}^k$ contains information on the kth order path contributions linking any pair of subsystems. For example, $\mathcal{S}^3(1,3)$ provides the ratio of energy attenuation from subsystem 1 to subsystem 3 due to all third-order paths connecting them (see Refs. 3 and 15 for details). Actually, similar information to that provided by the terms in the series expansion (7) was already known in graph theory path problems, and we will see in Sec. III how additional information and more precise definitions can be inferred from it.

It is worthwhile noting that the information obtained from the series expansion (7) could have also been derived from the step-by-step outputs of an iterative numerical scheme[3] to solve the SEA system (1). From a mathematical point of view, the condition for the series to converge is that the eigenvalues λ_i of the generating matrix $\mathcal{S}$ fulfill $|\lambda_i| < 1$.

From physical considerations, this accounts for the system to have some damping; otherwise the energy will grow indefinitely. It is to be mentioned that for such cases other standard methods to solve (1) (e.g., Gaussian elimination) will also fail given that the condition number of $\mathcal{H}$ will strongly increase as the damping diminishes, making the system solution totally unreliable.

On the other hand, a similar expansion to Eq. (7) can be obtained when working with the symmetric systems (3) and (4). If we premultiply $\mathcal{H}_{\text{sym}}$ by $-\mathcal{D}^{-1/2} \equiv \text{diag}(\{1/\sqrt{n_i \eta_i}\})$ and postmultiply by $\mathcal{D}^{-1/2}$, we obtain

$$-\mathcal{D}^{-1/2}\mathcal{H}_{\text{sym}}\mathcal{D}^{-1/2} = \mathcal{I} - \mathcal{S}_{\text{sym}}, \tag{8}$$

with

$$\mathcal{S}_{\text{sym}}(i,j) = n_i \eta_{ij}(1-\delta_{ij})/\sqrt{n_i \eta_i n_j \eta_j}. \tag{9}$$

Taking into account Eq. (8), the linear system (3) can be rewritten as

$$-\mathcal{D}^{1/2}(\mathcal{I} - \mathcal{S}_{\text{sym}})\mathcal{D}^{1/2}\boldsymbol{E}_n = \boldsymbol{E}^0. \tag{10}$$

If we next define the energy vector $\boldsymbol{E}_\eta := \mathcal{D}^{1/2}\boldsymbol{E}_n$ and redefine the external energy input vector as $\boldsymbol{E}^0 \equiv -\mathcal{D}^{-1/2}\boldsymbol{E}^0$, the solution for $\boldsymbol{E}_\eta$ can be obtained from the series expansion

$$\begin{aligned}\boldsymbol{E}_\eta &= (\mathcal{I} - \mathcal{S}_{\text{sym}})^{-1}\boldsymbol{E}^0 = \left(\sum_{n=0}^{\infty} \mathcal{S}_{\text{sym}}^n\right)\boldsymbol{E}^0 \\ &= (\mathcal{I} + \mathcal{S}_{\text{sym}} + \mathcal{S}_{\text{sym}}^2 + \cdots)\boldsymbol{E}^0,\end{aligned} \tag{11}$$

which is nothing but the symmetric counterpart of Eq. (7). [Note that it is possible to directly obtain the solution $\boldsymbol{E}_n = -\mathcal{D}^{-1/2}(\mathcal{I}-\mathcal{S}_{\text{sym}})^{-1}\mathcal{D}^{-1/2}\boldsymbol{E}^0$ from Eq. (10) but the above procedure is preferred to make the analogy with Eq. (7) easier and more meaningful from a physical point of view.]

B. Some basic graph theory definitions

Let us remember that a *graph* $G=(U,E)$ is a mathematical structure consisting of a set $U=\{u_1,u_2,\ldots,u_n\}$ whose elements are called *vertices* or *nodes*, and a subset $E \subset U \times U$ of unordered pairs $(u_i,u_j) \in E$ known as *edges*. We can think of the former as points (nodes) in a d-dimensional space ($d=2,3$) joined by a set of segments (edges). In the case of the graph edges being *directed*, i.e., $(u_i,u_j) \neq (u_j,u_i)$ we will have a *directed graph* or *digraph* (think of it as a graph having nodes connected by arrow segments). If this is not the case, we will have an *undirected graph*.

An algebraic structure that will prove very useful to address path issues in SEA is that of a *path algebra*.[22] A path algebra, $\mathfrak{P}$, is an idempotent semiring, i.e., a set P equipped with two binary operations, the *join* operation, $\vee$, and the *multiplication* operation, $*$, such that $\vee$ is idempotent, commutative, and associative [$\forall x,y \in P$ it follows that $x \vee x = x$, $x \vee y = y \vee x$, and $(x \vee y) \vee z = x \vee (y \vee z)$], whereas $*$ is associative and distributes over $\vee$ [$\forall x,y \in P$ it follows that $(x*y)*z = x*(y*z)$, $x*(y \vee z) = (x*y) \vee (x*z)$, and $(y \vee z)*x = (y*x) \vee (z*x)$]. Moreover, zero $\varnothing$ and unit e elements exist such that $\varnothing \vee x = x$, $\varnothing * x = \varnothing = x * \varnothing$, and $e*x = x = x*e$. Henceforth, a path algebra on a set P will be referred as $\mathfrak{P} \equiv (P, \vee, *)$, while the standard elementary linear algebra on $\mathbb{R}$ will be designated by $\mathfrak{R} \equiv (\mathbb{R}, +, \cdot)$. Detailed properties of path algebras can be found in Ref. 22.

Path algebras naturally extend to the set of all $n \times n$ matrices $M_n(P)$ whose elements belong to P. That is, $\mathfrak{P}_n \equiv (M_n(P), \vee, *)$ is also a path algebra. Given any $\mathcal{C}, \mathcal{D} \in M_n(P)$, the *join matrix* $\mathcal{X} = \mathcal{C} \vee \mathcal{D}$ will contain elements

$$\mathcal{X}(i,j) = \mathcal{C}(i,j) \vee \mathcal{D}(i,j), \tag{12}$$

whereas the elements of the *product matrix* $\mathcal{Y} = \mathcal{C} * \mathcal{D}$ will be

$$\mathcal{Y}(i,j) = \bigvee_{k=1}^{n} \mathcal{C}(i,k) * \mathcal{D}(k,j). \tag{13}$$

Examples of path algebras applied to SEA systems will be provided in Sec. III. In what concerns notation, $\mathfrak{R}_n \equiv (M_n(\mathbb{R}), +, \cdot)$ will denote the standard linear algebra on squared matrices.

A graph $G=(U,E)$ is said to be *labeled* or *weighted* with an algebra $\mathfrak{P}$ (or $\mathfrak{R}$), when each edge of G is assigned some element of P (or $\mathbb{R}$), other than its zero element $\varnothing$. The *label* or *weight* of each edge (u_i,u_j) will be designed by w_{ij}. The *total weight* of a kth order path on G defined by the edge set $\alpha^k_{i_0 i_k} := \{(u_{i_0},u_{i_1}),(u_{i_1},u_{i_2}),\ldots,(u_{i_{k-1}},u_{i_k})\}$ is given by[22]

$$w(\alpha^k_{i_0 i_k}) = w_{i_0 i_1} * w_{i_1 i_2} * \cdots * w_{i_{k-1} i_k}. \tag{14}$$

Although not optimal from an implementation point of view, graphs can be represented by matrices. This allows to gain insight on some conceptual aspects as well as to make use of linear matrix algebra to derive some results. A labeled graph $G=(U,E)$ can be described by means of its *adjacency* matrix $\mathcal{A} \in M_n(P)$ (or $M_n(\mathbb{R})$) whose entries are

$$\mathcal{A}(i,j) = \begin{cases} w_{ij} & \text{if } (u_i,u_j) \in E \\ \varnothing & \text{if } (u_i,u_j) \notin E. \end{cases} \tag{15}$$

The adjacency matrix powers, $\mathcal{A}^k$, have special interest. For path algebras, $\mathcal{A}^0 \equiv \mathcal{E}$, with $\mathcal{E}$ standing for the unit matrix of $\mathfrak{P}_n$, and $\mathcal{A}^k = \mathcal{A}^{k-1} * \mathcal{A}$ (equivalent results in $\mathfrak{R}_n$ are well-known). For $k>0$, a typical element, $\mathcal{A}^k(i,j)$ of $\mathcal{A}^k$ can be computed as

$$\mathcal{A}^k(i,j) = \bigvee_{h_1 \ldots h_{k-1}} w_{i h_1} * w_{h_1 h_2} * \ldots * w_{h_{k-1} j} \tag{16}$$

with $\vee_{h_1 \cdots h_{k-1}}$ denoting the join extended over all n^{k-1} possible values of the indices. That is, $\mathcal{A}^k(i,j)$ contains the join of the weights of all kth order paths connecting u_i and u_j, as expressed by Eq. (14). On the other hand, we will use $\mathcal{A}^{[h]}$ to designate the join $\mathcal{A}^{[h]} = \vee_{k=0}^{h} \mathcal{A}^k$.

We remark that many path algebra issues can be set as problems of solving matrix systems of the type $\boldsymbol{Y} = \mathcal{A} * \boldsymbol{Y} \vee \boldsymbol{B}$ (e.g., finding all shortest paths from any node in the graph to a particular one). These systems can be solved by means of direct and iterative algorithms quite analogous to those developed for linear matrix systems. However, this issue will be not pursued here and the interested reader is referred to Ref. 22 for extensive information.

Next, for a graph $G=(U,E)$ consider two *proper* subsets of U, U_s, and U_t, with a source node $s \in U_s$ and a target one $t \in U_t$. Let $\{U_s, U_t\}$ be a partition of U i.e., $U = U_s \cup U_t$ with $U_s \cap U_t = \varnothing$. The set of edges with initial nodes at U_s and end

nodes at U_t is termed an *s-t* cutset (or simply an *s-t-cut*) of G. An *s-t*-cut will be denoted by $\langle U_s, U_t\rangle := \{(u_i,u_j)\in E \,|\, u_i \in U_s, u_j \in U_t\}$. If the cardinality of the *s-t*-cut is L, we talk of an *s-t* L-cut or an *s-t*-cut of *size* L. Its weight is given by the sum of the weights of its edges, i.e., $\omega(\langle U_s, U_t\rangle)=\sum_{l=1}^{L}\omega_{ij}$ with $(u_i,u_j)\in\langle U_s,U_t\rangle$. If $\omega_{ij}=1\ \forall i,j$, the weight of the cut coincides with its cardinality.

Finally, for any pair of nodes in the graph, u_i and u_j, we define their *local edge-connectivity* $\lambda(u_i,u_j,G)$ as the minimum of all u_i-u_j cutset weights. The *global edge-connectivity* of a graph $\lambda(G)$ is given by the weight of the *minimum cut* in G (the *minimum cut* is the cut of minimum weight that partitions G). In other words, $\lambda(G):=\min\{\lambda(u_i, u_j,G),\ \forall u_i,u_j\in U\}$. Finally, for a designated node z, its *z-connectivity* $\lambda_z(G)$ is the minimum local edge-connectivity of any two nodes different from z, i.e.,[25] $\lambda_z(G)=\min\{\lambda(u_i, u_j,G)\,|\,u_i,u_j\in U-z\}$.

In Sec. III, our goal will be to see how different algebra operations on adjacency matrices describing SEA models provide a general framework from which a lot of information on transmission paths can be inferred.

III. SEA GRAPHS AND ADJACENCY MATRIX POWERS

A. SEA graphs

In this section, we will focus on a general SEA model represented by a linear system with solution (7) and, as mentioned, originally obtained by dividing each row of Eqs. (1) and (2) by $-\eta_i$. As a *SEA graph* corresponding to this model, we will chose a digraph with no self-loops, and with each node representing a subsystem. Edges will exist between those subsystems that have non-null coupling loss factors in the original SEA model. Note that the adjacency matrix corresponding to such a SEA graph will have zero elements in the diagonal.

B. Adjacency matrix powers for path problems

We next aim at solving several path problems between subsystems in the SEA graph. In particular, we would like to know about the existence of any *k*th order path connecting two arbitrary nodes in the graph, to count the number of these paths, to see which is their contribution in terms of coupling loss factors, to determine the extremal (minimum and maximum) paths, and to be able to label them. We will show how all these issues can be posed by means of different path algebras and how well-known SEA results can be recovered in this way. Resorting to path algebras allows to make use of their powerful general mathematical framework and gain insight in many aspects. In what follows, the theoretical grounds will be first stated, while in Sec. III C, the hereafter exposed results will be applied to a numerical example for a better comprehension.

Existence of paths. The problem can be solved by means of the *two-element Boolean algebra*[22] that is a path algebra with $P\equiv P_1=\{0,1\}$, $w_i\vee w_j\equiv\max\{w_i,w_j\}$, $w_i * w_j \equiv \min\{w_i,w_j\}$, $\varnothing\equiv 0$, and $e=1$. We can write it for short as $\mathfrak{P}_1\equiv(P_1,\max,\min)$. The adjacency matrix $\mathcal{A}_1$ for the SEA graph will have entries

$$\mathcal{A}_1(i,j)=\begin{cases}1 & \text{if } (u_i,u_j)\in E\\ 0 & \text{if } (u_i,u_j)\notin E.\end{cases} \tag{17}$$

Using the matrix path algebra $\mathfrak{P}_{n1}\equiv(M_n(P_1),\max,\min)$ and according to Eqs. (14) and (16), it becomes easy to check that the element $\mathcal{A}_1^k(i,j)$ of the *k*th power adjacency matrix $\mathcal{A}_1^k$ will be 1 if there exists a *k*th order path connecting u_i and u_j, and 0 otherwise.

Counting paths. In this case we just need to use standard linear algebra defined on $\mathbb{N}_0$ ($\mathbb{N}_0$ stands for the ensemble of positive integers), i.e., $\mathfrak{N}\equiv(\mathbb{N}_0,+,\cdot)$. The adjacency matrix is also given by Eq. (17) but its powers $\mathcal{A}_1^k$ will be totally different from those of the previous case. From Eq. (16), it is apparent that the matrix entry $\mathcal{A}_1^k(i,j)$ will now contain the number of *k*th order paths connecting u_i and u_j (the product of all weights in a single *k*th order path is 1). An equivalent approach was followed in Ref. 15 by setting to one all entries in matrix $\mathcal{S}$, Eq. (7).

Maximum paths. We now consider finding the most problematic paths (maximum power flow transmission) of any order in the SEA model. It is possible to do so by means of a path algebra given by $\mathfrak{P}_2\equiv(\mathbb{R}_0^+,\max,\cdot)$. The zero element for this case will be $\varnothing\equiv 0$ and the unit element $e=1$. The adjacency matrix $\mathcal{A}_2$ will have non-negative real entries given by

$$\mathcal{A}_2(i,j)=\begin{cases}\eta_{ji}/\eta_i & \text{if } (u_i,u_j)\in E\\ 0 & \text{if } (u_i,u_j)\notin E.\end{cases} \tag{18}$$

Note that Eq. (18) is nothing but matrix $\mathcal{S}$ in Eq. (7). On the other hand, and according to Eq. (16), the elements of $\mathcal{A}_2^k$ will be given by

$$\mathcal{A}_2^k(i,j)=\max_{h_1\ldots h_{k-1}}\left\{\frac{\eta_{jh_1}}{\eta_{h_1}}\frac{\eta_{h_1h_2}}{\eta_{h_2}}\cdots\frac{\eta_{h_{k-1}i}}{\eta_i}\right\}, \tag{19}$$

hence providing the most powerful path of order k linking subsystems u_i and u_j. It is clear from Eq. (19) that the attenuation through a single *k*th order path starting at u_i and ending at u_j is provided by Eq. (6), a result already derived in Refs. 3 and 14 using different lines of argument.

It has been mentioned by the end of Sec. II B that it is possible to build algorithms to solve systems involving the join and multiplication operations very similar to the ones derived to solve standard linear algebraic systems. For the $\mathfrak{P}_2\equiv(\mathbb{R}_0^+,\max,\cdot)$ algebra, the solution of such algorithms directly gives the contribution of the most dominant path linking any pair of subsystems in the SEA graph, and the corresponding paths (sequence of subsystems) as well.[22] Consequently there is no need to compute all paths and then select the maximum ones to find the most dominant paths in a SEA system.

Minimum paths. This case is analogous to the previous ones but now takes the algebra $\mathfrak{P}_3\equiv(\mathbb{R}^+\cup\{\infty\},\min,\cdot)$ with $\varnothing\equiv\infty$ and $e=1$. The adjacency matrix $\mathcal{A}_3$ has positive real

entries

$$\mathcal{A}_3(i,j)=\begin{cases}\eta_{ji}/\eta_i & \text{if} \quad (u_i,u_j)\in E\\ \infty & \text{if} \quad (u_i,u_j)\notin E,\end{cases} \tag{20}$$

and the expression analogous to Eq. (19), providing now the shortest kth order paths between u_i and u_j, becomes

$$\mathcal{A}_3^k(i,j)=\min_{h_1\ldots h_{k-1}}\left\{\frac{\eta_{jh_1}}{\eta_{h_1}}\frac{\eta_{h_1h_2}}{\eta_{h_2}}\cdots\frac{\eta_{h_{k-1}i}}{\eta_i}\right\}. \tag{21}$$

Groups of paths. This is the case analyzed in Eq. (7) by means of standard linear matrix algebra $\mathfrak{R}_n\equiv(M_n(\mathbb{R}),+,\cdot)$. The adjacency matrix $\mathcal{A}_4$ coincides with $\mathcal{A}_2$ in Eq. (18), which as mentioned corresponds to matrix $\mathcal{S}$ in Eq. (7). However, the elements $\mathcal{A}_4^k(i,j)$ of the kth power of the adjacency matrix have the expression

$$\mathcal{A}_4^k(i,j)=\sum_{h_1\ldots h_{k-1}}\frac{\eta_{jh_1}}{\eta_{h_1}}\frac{\eta_{h_1h_2}}{\eta_{h_2}}\cdots\frac{\eta_{h_{k-1}i}}{\eta_i} \tag{22}$$

instead of Eq. (19). They provide the overall energy attenuation of all kth order paths linking subsystems u_i and u_j.

Labeling of paths. Finally, we can use path algebras to list all kth order paths between subsystems. To do so we consider any *alphabet* K and denote by K^* the set of all words over K. The subsets of K^* are called *languages* and they all belong to its *power set* $\mathcal{P}(K^*):=\{X|X\subseteq K^*\}$. It follows that $\mathfrak{K}\equiv(\mathcal{P}(K^*),\cup,\circ)$ is also a path algebra (this is the algebra termed P_6 in Ref. 22). For any two languages X and Y, their join operation is given by $X\vee Y=X\cup Y$, with $\cup$ being the union operation, while the product operation is identified with the *concatenation* operation. That is, for any two *words* $x\in X$, $y\in Y$, $X*Y\equiv\{x\circ y|x\in X,y\in Y\}$, with $x\circ y$ standing for the concatenation of these two words. On the other hand, the zero element will be the *null language* or *null set* $\varnothing$ and the unit element becomes the set $\Lambda=\lambda$, where λ stands for the empty word.

We can then define the adjacency matrix $\mathcal{A}_5$ as

$$\mathcal{A}_5(i,j)=\begin{cases}'(u_i,u_j)' & \text{if} \quad (u_i,u_j)\in E\\ \varnothing & \text{if} \quad (u_i,u_j)\notin E.\end{cases} \tag{23}$$

where $'(u_i,u_j)'$ is the *word* for the edge linking nodes u_i and u_j [e.g., $'(u_3,u_4)'\equiv(u_3,u_4)$]. Then, the entry $\mathcal{A}_5^k(i,j)$ of the kth power adjacency matrix will provide the list of all edges of all kth order paths connecting u_i with u_j:

$$\begin{aligned}\mathcal{A}_5^k(i,j)&=\bigcup_{h_1\ldots h_{k-1}}{}'(u_i,u_{h_1})'\circ'(u_{h_1},u_{h_2})'\circ\ldots\circ'(u_{h_{k-1}},u_j)'\\&=\bigcup_{h_1\ldots h_{k-1}}(u_i,u_{h_1})(u_{h_1},u_{h_2})\ldots(u_{h_{k-1}},u_j).\end{aligned} \tag{24}$$

C. Numerical example

Let us next apply the above derived results to a numerical example. We have chosen the case shown in Ref. 3 (p. 152, Fig. 6.1), see Fig. 1, which can represent, for example, two cavities separated by a wall and also connected through a non-rigid flanking wall.

The linear system (1) corresponding to the SEA model in Fig. 1 is given by

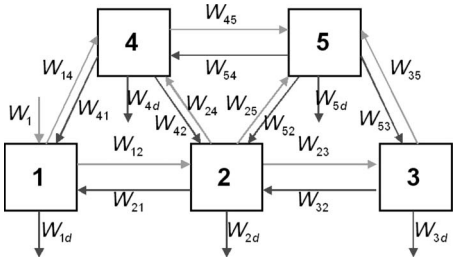

FIG. 1. Benchmark SEA model.

$$\begin{pmatrix}-\eta_1 & \eta_{21} & 0 & \eta_{41} & 0\\ \eta_{12} & -\eta_2 & \eta_{32} & \eta_{42} & \eta_{52}\\ 0 & \eta_{23} & -\eta_3 & 0 & \eta_{53}\\ \eta_{14} & \eta_{24} & 0 & -\eta_4 & \eta_{54}\\ 0 & \eta_{25} & \eta_{35} & \eta_{45} & -\eta_5\end{pmatrix}\begin{pmatrix}E_1\\E_2\\E_3\\E_4\\E_5\end{pmatrix}=\begin{pmatrix}-W_1/\omega\\0\\0\\0\\0\end{pmatrix}, \tag{25}$$

while its symmetric counterpart (3) becomes

$$\begin{pmatrix}-n_1\eta_1 & n_2\eta_{21} & 0 & n_4\eta_{41} & 0\\ n_1\eta_{12} & -n_2\eta_2 & n_3\eta_{32} & n_4\eta_{42} & n_5\eta_{52}\\ 0 & n_2\eta_{23} & -n_3\eta_3 & 0 & n_5\eta_{53}\\ n_1\eta_{14} & n_2\eta_{24} & 0 & -n_4\eta_4 & n_5\eta_{54}\\ 0 & n_2\eta_{25} & n_3\eta_{35} & n_4\eta_{45} & -n_5\eta_5\end{pmatrix}\begin{pmatrix}E_1/n_1\\E_2/n_2\\E_3/n_3\\E_4/n_4\\E_5/n_5\end{pmatrix}=\begin{pmatrix}-W_1/\omega\\0\\0\\0\\0\end{pmatrix}. \tag{26}$$

Matrix $\mathcal{S}_{\text{sym}}$ in the series development (11) is now given by

$$\mathcal{S}_{sym}=\begin{pmatrix}0 & \frac{n_1\eta_{12}}{\sqrt{n_1\eta_1n_2\eta_2}} & 0 & \frac{n_1\eta_{14}}{\sqrt{n_1\eta_1n_4\eta_4}} & 0\\ \frac{n_1\eta_{12}}{\sqrt{n_1\eta_1n_2\eta_2}} & 0 & \frac{n_2\eta_{23}}{\sqrt{n_2\eta_2n_3\eta_3}} & \frac{n_2\eta_{24}}{\sqrt{n_2\eta_2n_4\eta_4}} & \frac{n_2\eta_{25}}{\sqrt{n_2\eta_2n_5\eta_5}}\\ 0 & \frac{n_2\eta_{23}}{\sqrt{n_2\eta_2n_3\eta_3}} & 0 & 0 & \frac{n_3\eta_{35}}{\sqrt{n_3\eta_3n_5\eta_5}}\\ \frac{n_1\eta_{14}}{\sqrt{n_1\eta_1n_4\eta_4}} & \frac{n_2\eta_{24}}{\sqrt{n_2\eta_2n_4\eta_4}} & 0 & 0 & \frac{n_4\eta_{45}}{\sqrt{n_4\eta_4n_5\eta_5}}\\ 0 & \frac{n_2\eta_{25}}{\sqrt{n_2\eta_2n_5\eta_5}} & \frac{n_3\eta_{35}}{\sqrt{n_3\eta_3n_5\eta_5}} & \frac{n_4\eta_{45}}{\sqrt{n_4\eta_4n_5\eta_5}} & 0\end{pmatrix}. \tag{27}$$

On the other hand, the SEA graph corresponding to the SEA model in Fig. 1 is represented in Fig. 2. A path analysis for this graph reveals the following results.

Existence of paths. The adjacency matrix for the SEA graph in Fig. 2 together with its second and third powers are

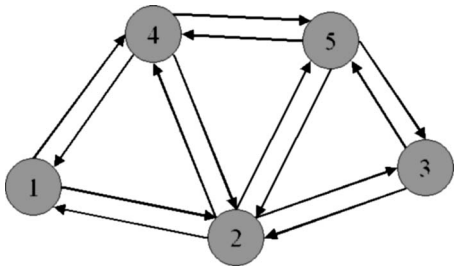

FIG. 2. SEA graph for the SEA model in Fig. 1.

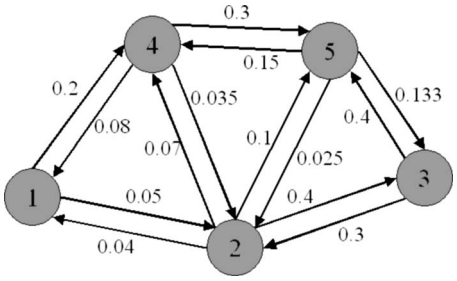

FIG. 3. SEA graph weights used for extremal and group of paths analysis.

given by

$$\mathcal{A}_1 = \begin{pmatrix} 0 & 1 & 0 & 1 & 0 \\ 1 & 0 & 1 & 1 & 1 \\ 0 & 1 & 0 & 0 & 1 \\ 1 & 1 & 0 & 0 & 1 \\ 0 & 1 & 1 & 1 & 0 \end{pmatrix}, \quad \mathcal{A}_1^2 = \begin{pmatrix} 1 & 1 & 1 & 1 & 1 \\ 1 & 1 & 1 & 1 & 1 \\ 1 & 1 & 1 & 1 & 1 \\ 1 & 1 & 1 & 1 & 1 \\ 1 & 1 & 1 & 1 & 1 \end{pmatrix},$$

$$\mathcal{A}_1^3 = \begin{pmatrix} 1 & 1 & 1 & 1 & 1 \\ 1 & 1 & 1 & 1 & 1 \\ 1 & 1 & 1 & 1 & 1 \\ 1 & 1 & 1 & 1 & 1 \\ 1 & 1 & 1 & 1 & 1 \end{pmatrix}. \tag{28}$$

Note that $\mathcal{A}_1$ expresses the fact that there is no first-order connection, e.g., between subsystems 1 and 5 ($\mathcal{A}_1(1,5)=0$), but this connection exists, e.g., between subsystems 1 and 2 ($\mathcal{A}_1(1,2)=1$). $\mathcal{A}_1^2$ expresses the fact that any pair of subsystems in the graph can be linked by means of a 2nd order path, the same being true for 3rd order paths. Actually, $\mathcal{A}_1$ is a *stable* matrix with *stability index* 2, i.e., for any $q \geq 2$ it follows that $\mathcal{A}_1^{[q]} = \mathcal{A}_1^{[q+1]}$.

Counting paths. The adjacency matrix is the same one as the previous case but now use is made of the standard linear algebra on natural numbers $\mathfrak{N} \equiv (\mathbb{N}_0, +, \cdot)$ extended to matrices to perform all operations. It follows that

$$\mathcal{A}_1 = \begin{pmatrix} 0 & 1 & 0 & 1 & 0 \\ 1 & 0 & 1 & 1 & 1 \\ 0 & 1 & 0 & 0 & 1 \\ 1 & 1 & 0 & 0 & 1 \\ 0 & 1 & 1 & 1 & 0 \end{pmatrix}, \quad \mathcal{A}_1^2 = \begin{pmatrix} 2 & 1 & 1 & 1 & 2 \\ 1 & 4 & 1 & 2 & 2 \\ 1 & 1 & 2 & 2 & 1 \\ 1 & 2 & 2 & 3 & 1 \\ 2 & 2 & 1 & 1 & 3 \end{pmatrix},$$

$$\mathcal{A}_1^3 = \begin{pmatrix} 2 & 6 & 3 & 5 & 3 \\ 6 & 6 & 6 & 7 & 7 \\ 3 & 6 & 2 & 3 & 5 \\ 5 & 7 & 3 & 4 & 7 \\ 3 & 7 & 5 & 7 & 4 \end{pmatrix}. \tag{29}$$

Having a look at Fig. 2, it can be easily checked how elements $\mathcal{A}_1^2(i,j)$ and $\mathcal{A}_1^3(i,j)$, respectively, give the number of second- and third-order paths connecting subsystems u_i and u_j. Obviously, as $n \to \infty$ $\mathcal{A}_1^n(i,j) \to \infty$.

Maximum paths. To find maximum paths, we have to assign some weights to the adjacency matrix corresponding to the loss factors quotients η_{ji}/η_i in Eq. (18). These weights have been chosen arbitrarily but they fulfill the consistency relation (we have taken the modal densities as $n_1=1$, $n_2=0.8$, $n_3=0.6$, $n_4=0.4$, and $n_5=0.2$). They are given in Fig. 3. The adjacency matrix together with its second and third-order powers computed according to $\mathfrak{P}_2 \equiv (\mathbb{R}_0^+, \max, \cdot)$ becomes

$$\mathcal{A}_2 = \begin{pmatrix} 0 & 0.05 & 0 & 0.2 & 0 \\ 0.04 & 0 & 0.4 & 0.07 & 0.1 \\ 0 & 0.3 & 0 & 0 & 0.4 \\ 0.08 & 0.035 & 0 & 0 & 0.3 \\ 0 & 0.025 & 0.1\hat{3} & 0.15 & 0 \end{pmatrix},$$

$$\mathcal{A}_2^2 = 1 \times 10^{-2} \begin{pmatrix} 1.6 & 0.7 & 2 & 0.35 & 6 \\ 0.56 & 12 & 1.\hat{3} & 1.5 & 16 \\ 1.2 & 1 & 12 & 6 & 3 \\ 0.14 & 0.75 & 4 & 4.5 & 3.5 \\ 1.2 & 4 & 1 & 0.17 & 5.\hat{3} \end{pmatrix},$$

$$\mathcal{A}_2^3 = 1 \times 10^{-3} \begin{pmatrix} 0.28 & 6 & 8 & 9 & 8 \\ 4.8 & 4 & 48 & 24 & 12 \\ 4.8 & 36 & 4 & 4.5 & 48 \\ 3.6 & 12 & 3 & 0.53 & 16 \\ 1.6 & 3 & 16 & 8 & 4 \end{pmatrix}. \tag{30}$$

Entries in $\mathcal{A}_2^2$ give the maximum second-order paths linking any pair of subsystems in the graph. For instance, the element $\mathcal{A}_2^2(1,5)$ is computed as $\mathcal{A}_2^2(1,5) = \max\{0\times 0, 0.05 \times 0.1, 0\times 0.4, 0.2\times 0.3, 0\times 0\} = 6\times 10^{-2}$ and corresponds to the path $(u_1,u_4)(u_4,u_5)$ linking subsystems 1 and 5 through subsystem 4 (see Fig. 3). In the case of subsystem 1 having energy E_1, the energy transmitted to 5 by this path would have been $6\times 10^{-2} E_1$, whereas only $5\times 10^{-3} E_1$ would have been transmitted through the path $(u_1,u_2)(u_2,u_5)$. Hence, $\mathcal{A}_2^2$ provides the contributions of the second-order most critical paths in the model. $\mathcal{A}_2^3$ gives the same results but for third-order paths, and so on with $\mathcal{A}_2^n$. However, note that in this case $\mathcal{A}_2^n \to 0$ for $n \to \infty$.

Minimum paths. This case is opposite to the previous one. Matrices $\mathcal{A}_3$, $\mathcal{A}_3^2$, and $\mathcal{A}_3^3$ have the following values:

$$\mathcal{A}_3 = \begin{pmatrix} \infty & 0.05 & \infty & 0.2 & \infty \\ 0.04 & \infty & 0.4 & 0.07 & 0.1 \\ \infty & 0.3 & \infty & \infty & 0.4 \\ 0.08 & 0.035 & \infty & \infty & 0.3 \\ \infty & 0.025 & 0.13\hat{} & 0.15 & \infty \end{pmatrix},$$

$$\mathcal{A}_3^2 = 1 \times 10^{-2} \begin{pmatrix} 0.2 & 0.7 & 2 & 0.35 & 0.5 \\ 0.56 & 2 & 1.3\hat{} & 0.8 & 2.1 \\ 1.2 & 1 & 5.3\hat{} & 2.1 & 3 \\ 0.14 & 0.4 & 1.4 & 0.25 & 0.35 \\ 0.1 & 0.53 & 1 & 0.18 & 0.25 \end{pmatrix},$$

$$\mathcal{A}_3^3 = 1 \times 10^{-3} \begin{pmatrix} 0.28 & 0.1 & 0.6\hat{} & 0.4 & 0.7 \\ 0.08 & 0.28 & 0.8 & 0.14 & 0.2 \\ 0.4 & 0.6 & 4 & 0.7 & 1 \\ 0.16 & 0.07 & 0.46\hat{} & 0.28 & 0.4 \\ 0.14 & 0.05 & 0.3\hat{} & 0.2 & 0.53 \end{pmatrix}. \quad (31)$$

As expected $\mathcal{A}_3^2(i,j) \leq \mathcal{A}_2^2(i,j)$, $\mathcal{A}_3^3(i,j) \leq \mathcal{A}_2^3(i,j)$ $\forall i,j$ and it also follows that $\mathcal{A}_3^n \to 0$ for $n \to \infty$. Note, for example, that $\mathcal{A}_3^2(1,5) = 5 \times 10^{-3}$ corresponding to the path $(u_1,u_2)(u_2,u_5)$ instead of the strongest one $(u_1,u_4)(u_4,u_5)$ of the previous case. It should also be observed that some elements in $\mathcal{A}_2^2$ and $\mathcal{A}_3^2$ coincide, for instance, $\mathcal{A}_3^2(1,2) = \mathcal{A}_2^2(1,2) = 0.7 \times 10^{-2}$. This is not surprising since there is only one second-order path, $(u_1,u_4)(u_4,u_2)$, connecting subsystems 1 and 2.

Groups of paths. In this case the kth powers of the adjacency matrix will give the total attenuations of all kth order paths connecting any pair of nodes. Consequently, it must happen that $\mathcal{A}_4^k(i,j) \geq \mathcal{A}_2^k(i,j) \geq \mathcal{A}_3^k(i,j)$ $\forall i,j$. Effectively

$$\mathcal{A}_4 \equiv \mathcal{S} = \begin{pmatrix} 0 & 0.05 & 0 & 0.2 & 0 \\ 0.04 & 0 & 0.4 & 0.07 & 0.1 \\ 0 & 0.3 & 0 & 0 & 0.4 \\ 0.08 & 0.035 & 0 & 0 & 0.3 \\ 0 & 0.025 & 0.13\hat{} & 0.15 & 0 \end{pmatrix},$$

$$\mathcal{A}_4^2 = 1 \times 10^{-2} \begin{pmatrix} 1.8 & 0.7 & 2 & 0.35 & 6.5 \\ 0.56 & 12.6 & 1.3\hat{} & 2.3 & 18.1 \\ 1.2 & 1 & 17.3\hat{} & 8.1 & 3 \\ 0.14 & 1.15 & 5.4 & 6.34 & 3.5 \\ 1.3 & 4.53 & 1 & 0.18 & 10.1 \end{pmatrix},$$

$$\mathcal{A}_4^3 = 1 \times 10^{-3} \begin{pmatrix} 0.56 & 8.6 & 11.46 & 13.84 & 9.75 \\ 6.92 & 9.61 & 74.92 & 37.16 & 24.93 \\ 6.88 & 56.19 & 8 & 7.6 & 94.63\hat{} \\ 5.54 & 18.58 & 5.07 & 1.61 & 41.78 \\ 1.95 & 6.23 & 31.54 & 20.89 & 9.05 \end{pmatrix}. \quad (32)$$

Matrix $\mathcal{A}_4$ fulfills $\mathcal{A}_4^n \to 0$ for $n \to \infty$. On the other hand, note, for instance, that $\mathcal{A}_4^2(1,5) = \mathcal{A}_3^2(1,5) + \mathcal{A}_2^2(1,5) = 6.5 \times 10^{-2}$. This is so because there exist only two second-order paths connecting subsystems 1 and 5, one being the maximum and the other one the minimum.

Labeling of paths. Finally, we can know the sequence of subsystems in a kth order path linking any two nodes in the SEA graph we are considering. We can do so by means of the previously introduced path algebra $\mathfrak{K} \equiv (\mathcal{P}(K^*), \cup, \circ)$. The adjacency matrix $\mathcal{A}_5$ becomes

$$\mathcal{A}_5 = \begin{pmatrix} \varnothing & (u_1,u_2) & \varnothing & (u_3,u_4) & \varnothing \\ (u_2,u_1) & \varnothing & (u_2,u_3) & (u_2,u_4) & (u_2,u_5) \\ \varnothing & (u_3,u_2) & \varnothing & \varnothing & (u_3,u_5) \\ (u_4,u_1) & (u_4,u_2) & \varnothing & \varnothing & (u_4,u_5) \\ \varnothing & (u_5,u_2) & (u_5,u_3) & (u_5,u_4) & \varnothing \end{pmatrix}. \quad (33)$$

Providing all terms in $\mathcal{A}_5^2$ and $\mathcal{A}_5^3$ would prove very long. Hence, only some of their entries will be presented. For instance, the term $\mathcal{A}_5^2(1,5)$ already analyzed with other algebras is given by

$$\mathcal{A}_5^2(1,5) = \{(u_1,u_4)(u_4,u_5),(u_1,u_2)(u_2,u_5)\}, \quad (34)$$

i.e., it contains the two second-order paths linking subsystems 1 and 5. The term $\mathcal{A}_5^3(3,4)$ has to be different from $\varnothing$ according to Eq. (28) and contain three paths as stated by $\mathcal{A}_1^3(3,4) = 3$ in Eq. (29). Effectively, we get

$$\mathcal{A}_5^3(3,4) = \{(u_3,u_2)(u_2,u_5)(u_5,u_4),(u_3,u_2)(u_2,u_1)(u_1,u_4),$$
$$(u_3,u_5)(u_5,u_2)(u_2,u_4)\}. \quad (35)$$

The individual attenuations of these three paths can be easily computed by means of Eq. (6), while their total attenuation is given by $\mathcal{A}_4^3(3,4) = 7.6 \times 10^{-3}$ in Eq. (32). The maximum of these paths has an attenuation of $\mathcal{A}_2^3(3,4) = 4.5 \times 10^{-3}$ [see Eq. (30)] and its label is given by the first line in Eq. (35). The minimum path is labeled by the last line in Eq. (35) and has a value of $\mathcal{A}_3^3(3,4) = 0.7 \times 10^{-3}$ [see Eq. (31)]. For the remaining path [central line in Eq. (35)], Eq. (6) yields $0.3 \times 0.04 \times 0.2 = 2.2 \times 10^{-3}$ (see Fig. 3).

IV. GRAPH CUTS TO REDUCE ENERGY FLOW BETWEEN SUBSYSTEMS

A. The source-receiver transmission path problem

In Sec. III, it has been shown how path algebras applied to SEA graphs have proved useful to answer several questions regarding transmission paths in SEA systems. In view of these results, one could wonder whether other aspects of graph theory could be helpful in solving further SEA issues. Indeed, this seems to be the case.

Consider a typical SEA model representing, e.g., the vibroacoustic behavior of a railway coach at a given high frequency band. In such a model, we will have several subsystems where external energy is input (*source* subsystems). These could be, e.g., the wheels that vibrate due to the interaction of their roughness with the rail one. The generated noise (*rolling* noise) will be transmitted to the interior of the coach via airborne paths. Moreover, the wheel vibration will be also transmitted to the interior via the bogies (structure-

TABLE I. Pseudocode for the energy reduction strategy at the target subsystem.

begin
  Build the SEA undirected graph with Boolean weights
  Assign the goal value E_t^g and the bounds η_{ij}^{low} and η_{id}^{up}
  Compute SEA graph *s-t* cuts $\{\langle U_s, U_t\rangle_k\}$ up to desired size M
  Set $l=\min\{\text{card}\langle U_s, U_t\rangle_k\}$
  while $E_t^r > E_t^g$ **or** $l \leq M$ **do**
    Compute the number R of possible disjoint unions $\{\cup_k\langle U_s, U_t\rangle_k\}|\text{card}\{\cup_k\langle U_s, U_t\rangle_k\}_r=l$
    Set $r=1$
    while $E_t^r > E_t^g$ **and** $r \leq R$ **do**
      Compute $\{\cup_k\langle U_s, U_t\rangle_k\}_r$
      Set $\eta_{ij} \rightarrow \eta_{ij}^{\text{low}}$ and $\eta_{id} \rightarrow \eta_{id}^{\text{up}}$ in $\{\cup_k\langle U_s, U_t\rangle_k\}_r$ and compute E_t^r
      $r=r+1$
    end
    $l=l+1$
  end
  output: $E_t^{\min}$ and $\{\cup_k\langle U_s, U_t\rangle_k\}_{\min}$
end

borne paths) and will result in the generation of interior noise. If we wish to diminish the noise at several locations inside the coach (*target* subsystems) we may wonder how we could do so by introducing minor changes in the train design (in other words, changing the minimum number of coupling loss factors in the SEA model). Obviously, the best way to proceed would consist in directly acting on the source subsystems but this is not always feasible. For instance, the coach wheels can only be smoothed from time to time. In such situations, changes can only be made in the transmission paths to obtain a noise reduction at the target subsystems. Consequently, it would be worthwhile to have some methodology to find a small number of subsystems, whose loss factor modifications result in the desired noise reduction at the targets. In what follows, we will develop such a strategy, which will rely on the use graph cut algorithms.

However, rather than focusing on a general SEA model with multiple sources and targets, we will limit to the easier case of transmission from one single source subsystem to a single target subsystem. This will be useful to explain pedagogically the proposed strategy. Its possible extension to address the multiple source multiple target case will be outlined at the end of Sec. IV B. As it will be explained, the fundamentals are already present in the easier problem presented below. Let us first state it in a clear way.

Consider the case of an n-dimensional SEA system where external power is inputted at the source subsystem with energy E_s and transmitted to the target subsystem. If the resulting energy at the target E_t is excessive, we may wonder how we could manage to decrease its level. Obviously, we would need to do so according to some premises. First, and as already mentioned, it would be worthwhile to make changes in the minimum possible number of subsystems. Second, it would not be feasible to arbitrarily reduce the coupling loss factors and increase the internal loss factors associated with these subsystems, η_{ij} and η_{id}, as much as we want, but we will have some lower and upper bounds on them ($\eta_{ij}^{\text{low}} \leq \eta_{ij}, \eta_{id} \leq \eta_{id}^{\text{up}}$). Third, we could wonder if diminishing E_t may result in a strong increment of other subsystem energies, so that the process should be done with a constraint on them, $E_i \leq E_i^{\text{up}}\ \forall i \neq t$. Initial numerical tests seem to indicate that the latter is not the case so we will focus hereafter on the first two points (see details below).

B. Strategy for energy reduction at the target

The proposed strategy to diminish the energy at the target subsystem is built from the following general steps (an algorithmic description is shown in Table I).

Building the SEA graph. An undirected SEA graph with weights given by Eq. (4), or alternatively by Eq. (9), is built. Then, the user selects the source and target subsystems and defines the goal value for the energy at the latter, E_t^g. Next, the user introduces the set of loss factors that are able to be modified, setting the values for η_{ij}^{low} and η_{id}^{up}.

Cutset algorithm. Once the SEA graph is built, the following step consists of making use of an algorithm to find the minimum *s-t* cutset$\langle U_s, U_t\rangle$ separating the source and target subsystems (the algorithm works on the SEA graph weighted with a Boolean algebra to find the cuts). We will consider a sorted collection of $\{\langle U_s, U_t\rangle_k\}$ in ascending order according to the cutset cardinality (in the case of two cutsets with identical number of edges we will first consider the one having maximum total weight). Given that all transmission paths between the source and the receiver cross the edges in the cutsets $\langle U_s, U_t\rangle$, it is expected that modifying the coupling loss factors of their edges starting with the minimum *s-t* cutset, as well as the internal loss factors of the nodes they link, could result in a large reduction in E_t. Effectively, from Eq. (7) we observe that the energy at the target can be expanded as the summation of the contributions of the paths of various orders. As all these paths will cross the cutset, we can sort them depending on the cutset edge they cross. The weight of every edge in the cutset will be a common factor of all the transmission paths going through it, and its modification (new loss factors) will consequently diminish the energy transmitted through this set of paths. Given that this applies to any edge in the cutset, any path that transmits energy from the source to the receiver becomes modified.

The effectiveness of such an approach will be shown in Sec. IV C.

It is not the purpose of this paper to provide a full detailed description of graph cut algorithms but to show how we can benefit from such algorithms to address our SEA problem. Hence, only a brief generic description of the subject will be given next, with some emphasis on the herein used algorithm. Traditionally, algorithms to find the minimum *s-t*-cut in a graph have been based on max-min duality theorems, most of them being variations of Menger's theorem.[36] In its edge form, the theorem essentially states[26] that *given a graph G*, the minimum number of edges needed to separate s and t equals the maximum size of a set of edge-disjoint *s-t* paths in G. Probably the most celebrated algorithm that solves this problem is the Ford–Fulkerson algorithm,[37] based on this max-flow-min-cut duality. Most algorithms for finding minimum cuts in graphs without specified vertices have also been based on the latter.

However, in the 1990s the first deterministic algorithms not based on flow algorithms were developed.[23,24,38,39] In this work we have made use of the algorithm in Ref. 25, intended to find all small cuts in an undirected network of weights less than a chosen value, α. The algorithm is divided in two main procedures. The first one decomposes the original graph $G \equiv G_n$ into a set of size reduced graphs $G_i, i \leq n$, until G_i consists of a single *reference* vertex $\{G_1\}$. At each step, the procedure isolates the node with less neighbor vertices from G_i. The algorithm to isolate vertices is based on the *edge-splitting* operation, which can reduce the size of a graph while preserving its edge-connectivity. Edge-splitting diminishes the weights of the edges between the designated node to be isolated, s, and two of its neighbor vertices, u and v, by a factor δ. The repeated application of edge-splitting yields isolation of node s. A set Q_s of triplets (u,v,δ) needed to isolate each graph vertex is stored during the process and used in the second procedure of the algorithm. This second procedure is based on the existing relation between the cuts in G_i and the cuts in G_{i-1}, which allow to obtain the former from the latter using the triplets Q_s, derived at the ith isolation step. In this way, and starting from the reference node $\{G_1\}$, the cutsets of any reduced graph G_i can be found recursively until the cutsets in the original graph $G_n \equiv G$ are finally derived. The cutsets of different size separating the source and the target subsystems in the SEA graph can then be selected and sorted. This is the output of this step of the proposed strategy, a list with all cutsets of the SEA graph sorted in ascending order.

Loop to compute the minimum energy at the target. Once we have the list of *s-t* cutsets, we begin by considering those of minimum cardinality $l = \min\{\mathrm{card}\langle U_s, U_t\rangle_k\}$. This is so because we aim at modifying as few subsystems as possible. Let us index them starting with $r=1$ and substitute the weights of this initial cutset by the new admissible values η_{ij}^{low} and the internal dissipation of its corresponding nodes by η_{id}^{up}. The resulting new energy at the target system E_t^r is computed and compared to the goal value E_t^g. If $E_t^r > E_t^g$ we increase $r = r+1$ and consider the next cutset with cardinality l. If none of them results in the expected energy reduction at the target, the cardinality of the cutsets is increased to $l = l+1$. Then, we compute the number of all possible combinations of disjoint unions of cutsets, $\{\cup_k \langle U_s, U_t\rangle_k\}$, such that their total cardinality coincides with the new value. We again sort them starting from $r=1$, the first r-values corresponding to those cutsets that directly have the new cardinality (in this way no combination needs to be considered for the initial attempts). If the goal energy is not achieved, we continue by considering combinations of disjoint cutsets with the specified total cardinality. In the case of E_t^r still being larger than E_t^g, we increase again the cardinality and proceed similarly until $E_t^r \leq E_t^g$ is reached (or the maximum cardinal value chosen for the cutsets, M, is surpassed).

It is to be noted at this stage that only combinations of disjoints cutsets are being considered in the above described loop. The reason for this is that the computational cost becomes considerably reduced in this way, although there is then no guarantee that the most optimum cut to achieve E_t^g with minimum modifications is found. However, the so far performed numerical tests (see Sec. IV C) seem to indicate that rather good solutions are obtained in this way. In addition, and as mentioned before, at each step we could have also considered starting a minimization routine for E_t^r with respect to η_{ij} and η_{id}, including an additional constraint on the remaining subsystem energies $E_i \leq E_i^{\mathrm{up}}\ \forall i \neq t$. This option could be valid but, again, computationally expensive. Moreover, the performed numerical tests indicate that a large energy reduction in decibels can be reached at the target subsystem, with only a small increment in decibels of the remaining subsystem energies (due to energy redistribution when only coupling loss factors are modified) and that energy reductions at almost all subsystems are obtained if the internal loss factors are allowed to change (see Sec. IV C). Consequently, we have postponed this minimization possibility for the moment.

Therefore, we could say that the above proposed strategy somehow balances finding a good solution that involves a small number of loss factors, with the computational cost this represents. Further insight on these topics would be worthwhile investigating in the future, especially when applying the energy reduction strategy to real, large SEA models.

Discussion. In this section, we have developed a particular strategy (see Table I) to address the single source single target transmission problem, but we note that other options may have been considered in the framework of graph theory. On the other hand, we note that the extension of the proposed methodology to more realistic SEA models involving multiple source and multiple target subsystems could be addressed in the present scheme introducing some modifications. For instance, for every frequency band of analysis we could work with cutsets separating all sources and targets and establishing some criteria for the admissible energy reduction at the latter (e.g., iterate until the goal energy for each individual target is achieved or give weights to them and iterate until a certain mean value for the goal energy at the targets is achieved). Moreover, given that the SEA model will change with frequency, the cutsets will be also different for each frequency band. The final modifications to be made to the whole system when considering all frequency bands

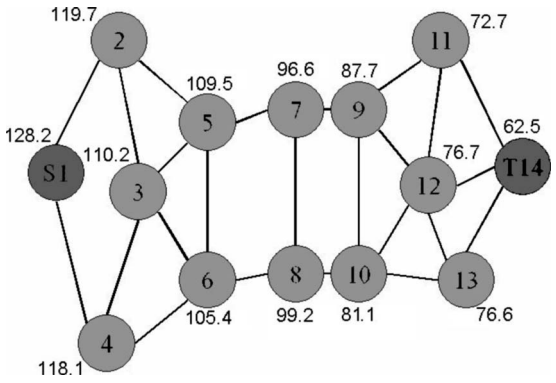

FIG. 4. SEA graph with initial subsystem energy levels in decibels.

will be provided by the union of all the cutsets found for every particular frequency. If only an overall rms value is assumed as the target goal energy, a certain spectral distribution can be assumed for it in order to apply the proposed strategy.

It is apparent from the previous reasoning (see also Sec. IV C) that the graph approach can be very useful if the structure under analysis has some *bottle neck* as it will be automatically detected. However, even when dealing with more standard and symmetric configurations represented by SEA matrices having a sparse structure, the presented strategy proves useful (see Sec. IV C). This is so because it detects the cutset that provides the largest energy reduction at the target and because, contrary to the Monte Carlo approach, the subsystems to be modified become localized in a limited area of the analyzed structure, instead of presenting a quite random distribution over it. Finally, we note that in practical situations it may happen that it becomes easier to change the design of many subsystems (isolators' thickness and panel stiffness) rather than a limited number of subsystems. This will pose no severe difficulty to the proposed strategy because it is possible to initially define those groups of subsystems that are to be changed together. For each analyzed cutest, one can then check if any of its edges belongs to one of these groups. If this is the case, the loss factors of all the members in the group become modified, together with the ones corresponding to the subsystems belonging to the cut. If this is not the case, only the loss factors of the subsystems in the cutset become modified.

C. Numerical example

1. A benchmark problem

We next consider a numerical example to illustrate how the above described energy reduction strategy works. We focus on the undirected SEA graph shown in Fig. 4 with coupling, internal loss factors and modal densities given in Table II. The graph has 14 subsystems linked by means of 24 edges. In Fig. 4, S1 stands for the source subsystem and T14 for the target one. The initial energy in decibels for every subsystem is also shown in the figure and corresponds to the application of a unit external input at the source subsystem. Our goal is to diminish 20 dB the energy at T14, i.e., $E_t^g = 42.5$ dB. To do so, it is assumed that the SEA model coupling loss factors are allowed to be reduced by an amount $\Delta\eta_{ij}$, so that $\eta_{ij}^{\text{low}} = \eta_{ij} - \Delta\eta_{ij}$, and that the internal loss factors are allowed to be increased by $\Delta\eta_{id}$ giving $\eta_{id}^{\text{up}} = \eta_{id} + \Delta\eta_{id}$ (see Table II).

TABLE II. Values used for the numerical example. $\eta_{ij}^{\text{low}} = \eta_{ij} - \Delta\eta_{ij}$, $\eta_{id}^{\text{up}} = \eta_{id} + \Delta\eta_{id}$.

(u_i, u_j)	η_{ij} $(\times 10^{-3})$	$\Delta\eta_{ij}$ $(\times 10^{-3})$	u_i	η_{id} $(\times 10^{-3})$	$\Delta\eta_{id}$ $(\times 10^{-3})$	n_i
(u_1, u_2)	17.1	7.9	u_1	105	92	4.5
(u_1, u_4)	28.8	13.8	u_2	77.3	71.5	4.3
(u_2, u_3)	22.1	11.4	u_3	142	184	4.7
(u_2, u_5)	18	15.9	u_4	306	187	3.8
(u_3, u_4)	0.1	0.1	u_5	112	131	5.2
(u_3, u_5)	11.1	6.3	u_6	237	148	5.1
(u_3, u_6)	28.8	21.4	u_7	245	26	4.9
(u_4, u_6)	12.6	10.2	u_8	19.7	45.6	2.7
(u_5, u_6)	15	10.9	u_9	259	153	4.5
(u_5, u_7)	14.3	11.6	u_{10}	140	130	5.2
(u_6, u_8)	3.3	1.9	u_{11}	360	94.6	5.4
(u_7, u_8)	16.5	7.9	u_{12}	390	143	5.2
(u_7, u_9)	42.2	19.9	u_{13}	29.1	28.9	4.9
(u_8, u_{10})	2.9	1.2	u_{14}	244	113	3.4
(u_9, u_{10})	20.9	10.6				
(u_9, u_{11})	14.2	1.8				
(u_9, u_{12})	37.5	18.6				
(u_{10}, u_{12})	11.3	8.8				
(u_{10}, u_{13})	15.1	8.9				
(u_{11}, u_{12})	2	1.5				
(u_{11}, u_{14})	3	0.9				
(u_{12}, u_{13})	16.8	5.3				
(u_{12}, u_{14})	3.8	3				
(u_{13}, u_{14})	1.5	0.8				

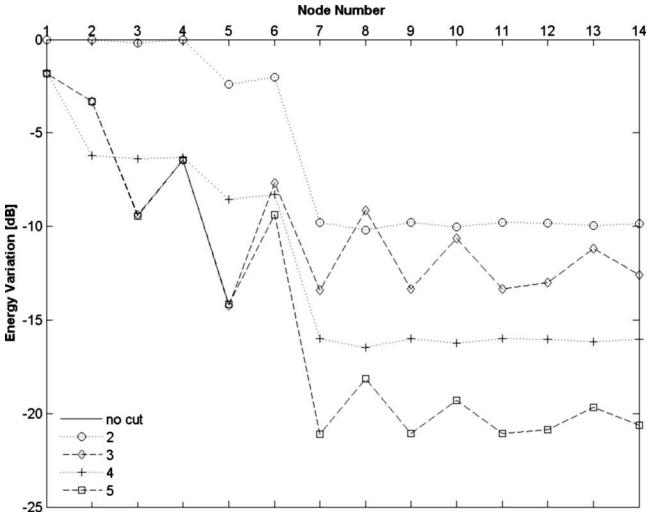

FIG. 5. Energy reduction in decibels at all subsystems.

The results of applying the graph cut strategy summarized in Table I are provided in Fig. 5. In this figure the energy variation of all graph subsystems in terms of the cutsets of various sizes is plotted. As observed, not only the expected energy reduction of 20 dB is achieved at the target subsystem but energy also considerably diminishes at several other subsystems. This is especially apparent for cutsets with cardinality equal or higher than 3.

The situation in Fig. 5 gets clarified if one has a look at the outputs of the various iterations of the strategy in Table I. These results are presented in Figs. 6(a)–6(c), where we show in dashed lines the best cuts (those giving maximum reduction at the target for a given size of the cutset) of sizes from 2 to 5. The figures also contain the energy reduction achieved at each node by replacing $\eta_{ij} \rightarrow \eta_{ij}^{\text{low}}$ in those edges belonging to the cutset and by setting $\eta_{id} \rightarrow \eta_{id}^{\text{up}}$ in the nodes they link. The energy reductions achieved at the target for the best 2-, 3-, 4-, 5-cutsets are respectively 9.8, 12.6, 16, and 20.6 dB. Given that for the best 5-cutset $E_t < E_t^g$ the strategy stops here. Consequently, for this particular example we observe that the goal has been achieved with the only modification of 5 of the 24 SEA graph edges. On the other hand, we note that for those nodes belonging to U_s (i.e., the source side of the graph partition) almost no energy is reduced. This

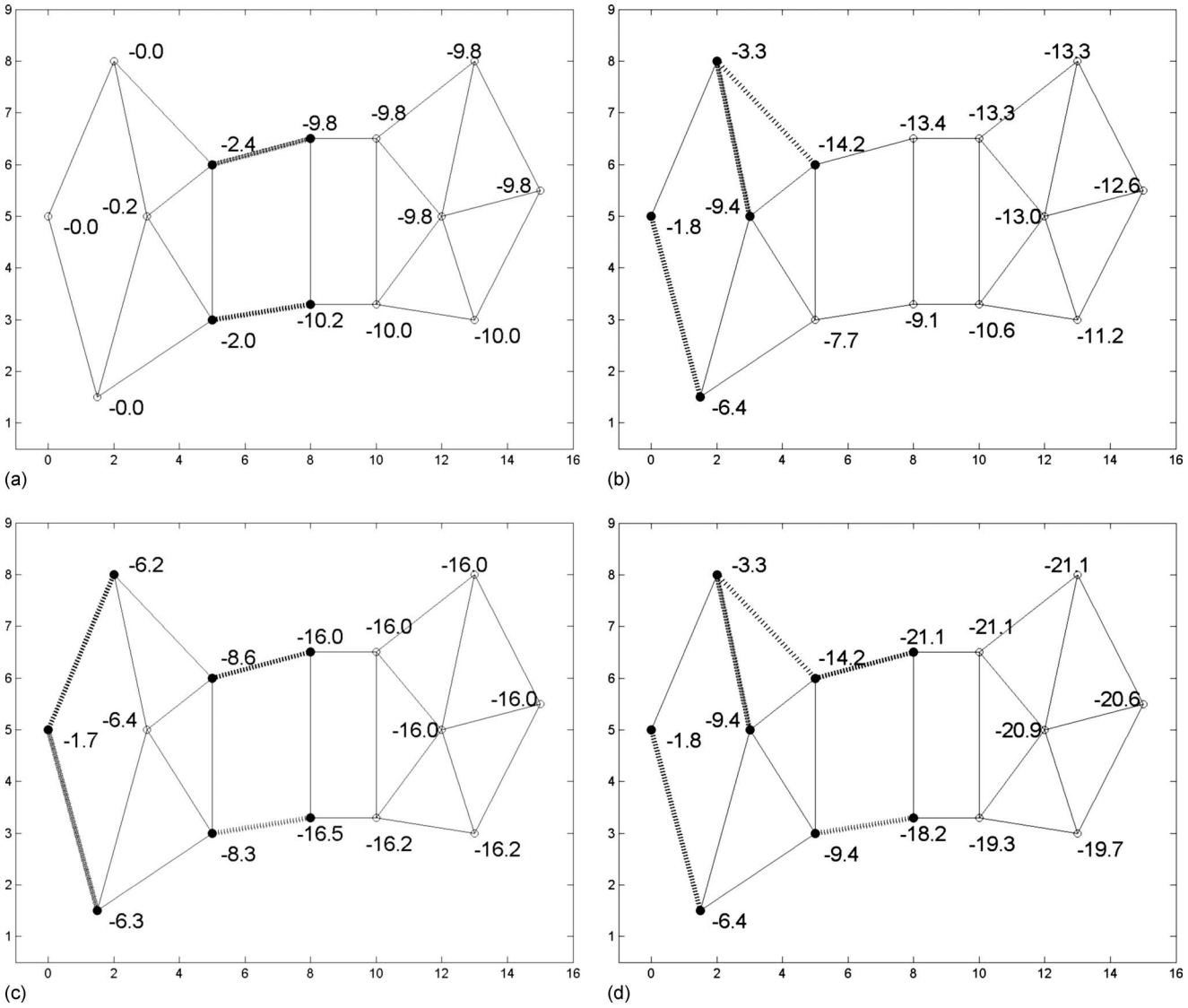

FIG. 6. *s-t* cutsets for the benchmark problem (dashed lines) with energy reduction achieved at each subsystem in decibels.

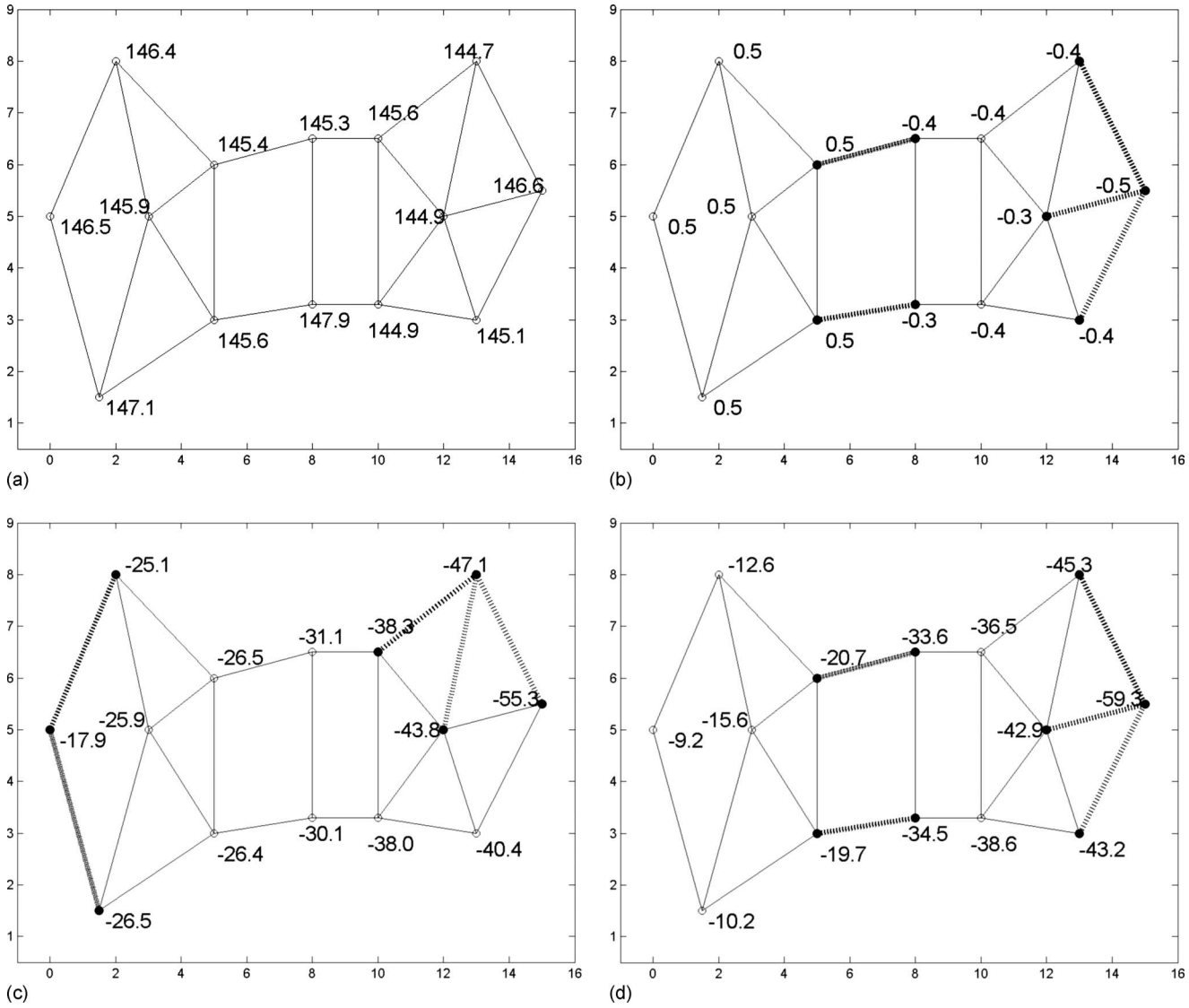

FIG. 7. Results for the low damping (energy equipartition) case. Energy reduction achieved at each subsystem in decibels.

is clearly observed for the best 2-cutset that shows negligible energy reduction for nodes $\{S_1, u_2, u_3, u_4\}$ (see Fig. 4) as Figs. 5 and 6(a) indicate. Logically if the cutset is placed very near the source a lot of energy reduction can be achieved at almost all subsystems in the SEA graph. This is, in fact, the case for the cutsets with sizes from 3 to 5, as clearly appreciated in Figs. 5 and 6(b)–6(d).

2. Asymptotic behavior

Let us next consider the behavior of the graph cut strategy when applied to two asymptotic cases, namely, a low damped SEA system, which results in energy equipartition at all subsystems, and a highly damped SEA system. For both cases we have considered the SEA benchmark graph of Sec. IV C 1. We have kept all parameters equal (see Table II) except for the internal loss factors that have been diminished by a factor 10^3 for the low damping case. For the high damping case, the internal loss factor of every subsystem has been assigned a value of 0.8 and we have multiplied the possible variations $\Delta\eta_{id}$ by a factor 10^{-1}, to avoid that any modified internal loss factor becomes higher than unity. Three different possibilities have been analyzed for each case, consisting of only modifying the subsystem coupling loss factors η_{ij} of the graph cutsets, only modifying the internal loss factors η_{id} of the subsystems linked by the cutset edges, and changing both the coupling and the internal loss factors. The graph cut strategy has been applied for cutsets up to size 5 so that the results for the best 5-cutset in the graph will be presented for each case.

The results for the low damping case are shown in Fig. 7. Figure 7(a) presents the graph with the initial energies of all subsystems. Given that the system has a very low damping, the energy almost equipartitions among them. In Fig. 7(b) we present the energy reduction for every subsystem in the graph for the best s-t 5-cutset, when only the coupling loss factors are allowed to be modified. As there is no means to dissipate energy with the sole modification of the coupling loss factors, energy can only redistribute, and this is what is observed in the figure. The subsystems located at the left of the graph bottle neck slightly increase their energy, whereas the opposite happens for the subsystems at the right side of the bottle neck. The energy at the target only diminishes in

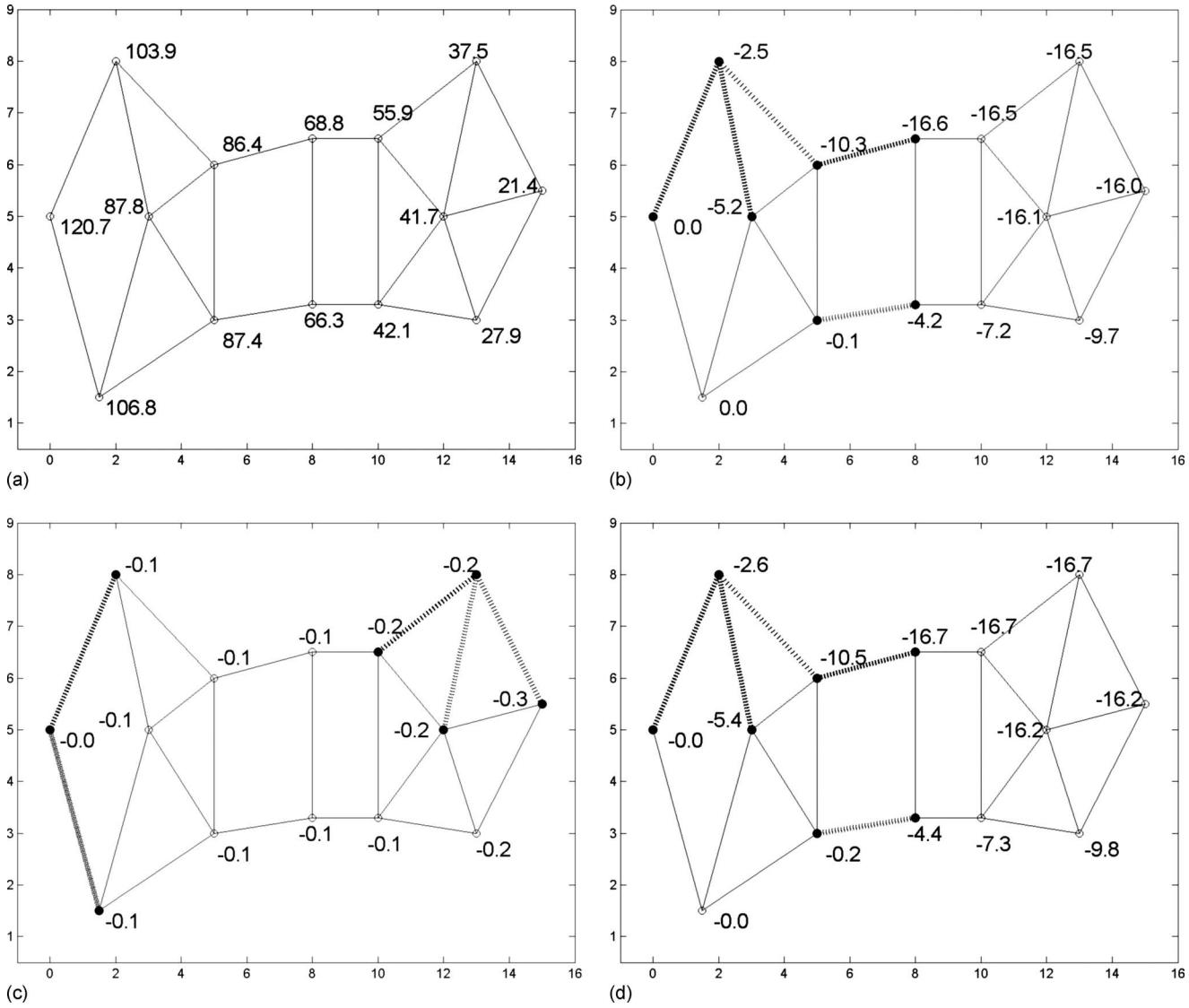

FIG. 8. Results for the strong damping case. Energy reduction achieved at each subsystem in decibels.

0.5 dB. However, the situation drastically changes when the system is allowed to dissipate energy. This is clearly observed in Fig. 7(c), where we show the results for the case in which only the internal loss factors become changed. As it can be appreciated, a large amount of energy reduction (55.3 dB) is achieved at the target. Moreover, many subsystems strongly decrease their energy given that two edges of the cutset have the source subsystem as an end point. If we finally allow both the internal and coupling loss factors to vary, the energy at the target still diminishes in 4 dB yielding a final energy decrease of 59.3 dB [see Fig. 7(d)]. We note, however, that the energy reduction at several of the remaining subsystems is weaker than the one obtained with the sole modification of the internal loss factors. This is due to the fact that the edges of the cutset in Fig. 7(d) are not located so close to the source subsystem.

The situation for the high damping case is somewhat opposite to the previous one. In Fig. 8(a) we present the initial energies of the subsystems in the SEA graph. A large difference is observed between the energy at the source and the energy at the target. Whereas they were equal for the low damping case, they now present a difference of 99.3 dB. Hence, a large amount of energy is already dissipated before reaching the target subsystem. If we next apply the energy reduction strategy with the sole modification of the coupling loss factors, we observe [see Fig. 8(b)] that the energy is redistributed in such a way that is more effectively dissipated. On the contrary, if we only allow the internal loss factors to be modified almost no energy reduction is achieved [see Fig. 8(c)]. This is due to the fact that the subsystem internal loss factors already have a very high value and cannot be substantially augmented to dissipate more energy. If both the internal and coupling loss factors become modified [see Fig. 8(d)], the result is almost equal to the one obtained with the sole modification of the coupling loss factors, for the reason just explained.

3. Comparison with the Monte Carlo approach

In this section, the proposed energy reduction strategy in Table I is compared with the performance of the Monte Carlo approach to the problem. To do so, a more complex example

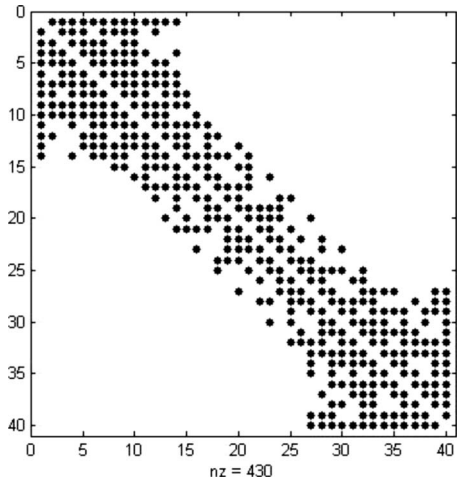

FIG. 9. SEA graph adjacency matrix for comparison with the Monte Carlo approach.

has been built consisting of a SEA graph of 40 nodes linked by means of 215 edges. The weights of the graph have been generated randomly yielding values for η_{ij} and η_{id} similar to those in Table II. The variations allowed for the coupling and internal loss factors have been also chosen to be of the same of order of those in Table II. The structure of the SEA graph adjacency matrix is provided in Fig. 9. As observed, the matrix has a sparse structure more typical of real SEA systems. The source subsystem has been identified with node 1 while the target subsystem corresponds to node 40.

The energy reduction strategy has been applied computing all cuts with size less or equal than 20. The first line in Table III indicates the sizes of the cutsets of the SEA graph, i.e., the number of edges in every cutset. As seen, the minimum cut involves 11 edges while the maximum cutset logically has 20 edges. The number of nodes linked by the edges in every cutset is given in the second line of Table III, while the overall number of cuts of any size is provided in the third line of the table.

In what concerns the Monte Carlo approach, the following procedure has been adopted: for every cutset of size L involving M nodes, we have randomly chosen L coupling loss factors and M internal loss factors to be modified in the original system. Then, we have computed the new SEA system energies by replacing these loss factors by their allowed modified values. An overall of 10^4 samples have been considered for every cutset size.

The comparison between both approaches is given in Table III, where we have listed the energy reduction achieved at the target subsystem. As observed, the graph approach performs slightly superior to the Monte Carlo one in every case except for the 11-cut. This is no surprising since there exists only one cutset of size 11. However, even for this case only 0.05% of the Monte Carlo solutions have proved superior to the one provided by the single 11-cut (see the last line of Table III where the percentage of the random samples performing better than the graph solution is given). On the other hand, there is a fundamental difference between the solutions provided with the graph approach and the Monte Carlo one. This can be clearly observed in Fig. 10, where we have plotted the elements in the SEA adjacency matrix that are involved in the 15- and 16-cuts and their corresponding best Monte Carlo solutions. Whereas the elements are located in a reduced area for the graph case [Figs. 10(a) and 10(b)], they present a large dispersion in the Monte Carlo case. That is to say, in practice the graph solution will imply acting on a bounded, located area of a structure to reduce the energy at a target, while the Monte Carlo solution may imply acting on several disconnected locations of the structure.

It should also be noted that increasing the cutset cardinality does not guarantee that the energy at the target will necessarily decrease. This is observed in Table III where, e.g., the reduction of the 15-cut is worst than the one provided by the 14-cut. The same happens for the Monte Carlo solutions. However, it is expected that as long as the sizes of the cuts increase, the general tendency will be to obtain better and better solutions in the mean, given that the number of involved modified loss factors will clearly grow. On the other hand, it is to be mentioned that the use of hybrid methods consisting on finding a cutset and then randomly exploring the improvement of the solution if some *extra* loss factors are randomly modified may be worth testing in the future. Finally, and in what concerns the CPU time expended for every method in the present example, the graph cut strategy has run eight times faster than the Monte Carlo approach.

V. CONCLUSIONS

In this work, a first attempt to address some noise and vibration control problems in SEA models using results from graph theory has been presented. It has been shown that it is possible to combine the so-called path algebras with standard linear matrix algebra to derive several transmission paths results for SEA graphs, in a general mathematical framework. Moreover, a strategy that makes use of graph cut algorithms has been developed to reduce the energy at a target subsystem, modifying as few system loss factors as possible. This may make the strategy very useful from an engineering point of view.

The herein derived results have been applied to some benchmark numerical problems to show their performance.

TABLE III. Comparison between the energy reduction strategy and the Monte Carlo approach

Cutset size (No. of edges)	11	13	14	15	16	17	18	19	20
No. of nodes in the cut	11	12	12	13	13	14	14	15	15
No. of cuts	1	5	8	5	7	7	17	27	51
Graph cut reduction	6.2	6.9	9.6	8.7	9.8	8.8	9.7	9.5	10
Monte Carlo reduction	6.3	6.8	7.4	7.1	7.5	8	7.8	8.2	8
% Monte Carlo to graph	0.05	0	0	0	0	0	0	0	0

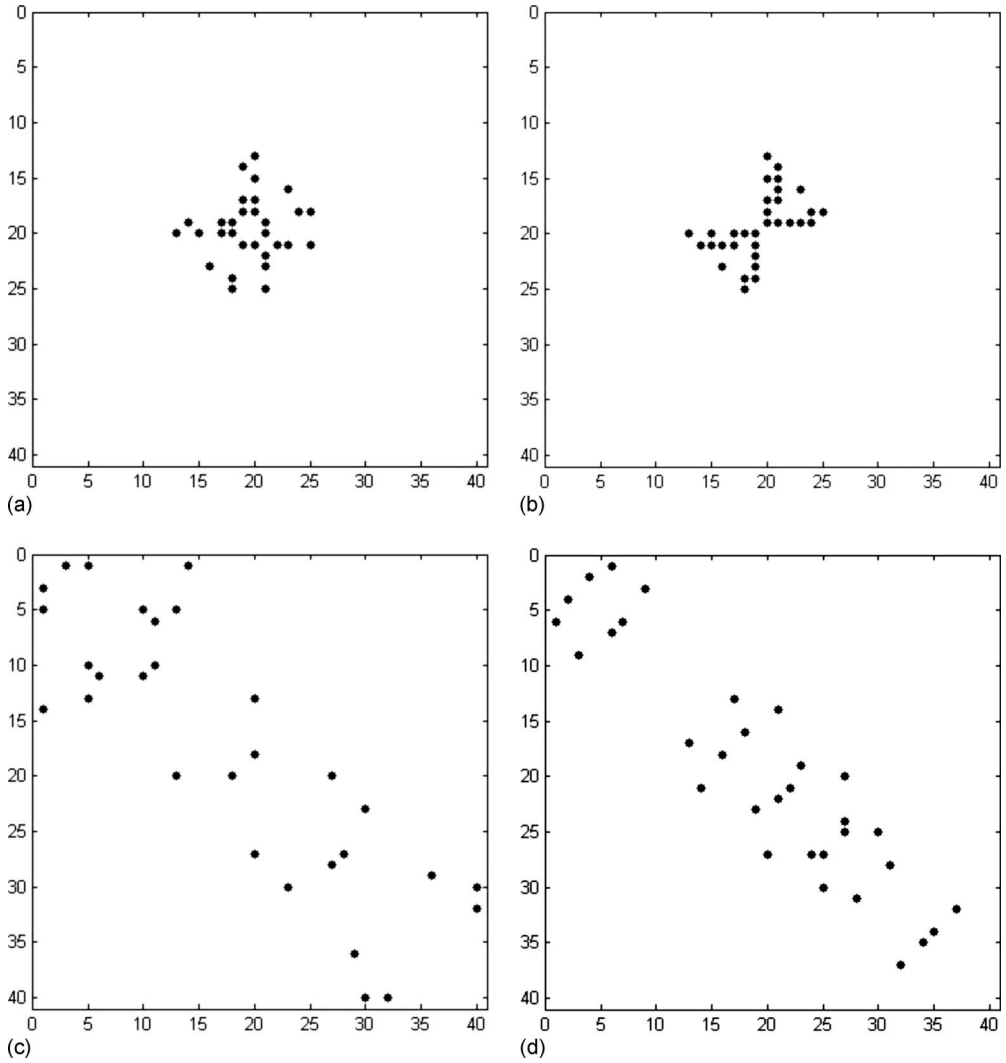

FIG. 10. Comparison of Monte Carlo and graph cut strategy solutions. Location of modified coupling loss factors.

Future work may involve, among other issues, implementing algorithms to find extremal paths in SEA graphs making use of path algebras, applying the energy reduction strategy to more realistic SEA models with multiple sources and targets, testing hybrid graph-random approaches, or taking into account the statistical nature of SEA, to check the robustness of the cutsets found by the graph cut algorithm.

[1]F. Fahy, "Statistical energy analysis: A critical overview," in *Statistical Energy Analysis: An Overview With Applications in Structural Dynamics*, edited by A. Keane and W. Price (Cambridge University Press, New York, 1997).
[2]R. Lyon, *Statistical Energy Analysis of Dynamical Systems: Theory and Applications* (MIT, Cambridge, MA, 1975), Vol. 1.
[3]R. Craik, *Sound Transmission Through Buildings Using Statistical Energy Analysis* (Gower, London, 1996).
[4]A. Culla and A. Sestieri, "Is it possible to treat confidentially SEA the wolf in sheep's clothing?" Mech. Syst. Signal Process. **20**, 1372–1399 (2006).
[5]R. Langley and A. Brown, "The ensemble statistics of the energy of a random system subjected to harmonic excitation," J. Sound Vib. **275**, 823–846 (2004).
[6]R. Langley and A. Brown, "The ensemble statistics of the band-averaged energy of a random system," J. Sound Vib. **275**, 847–857 (2004).
[7]B. Mace, "Statistical energy analysis, energy distribution models and system modes," J. Sound Vib. **264**, 391–409 (2003).
[8]B. Mace, "Statistical energy analysis: Coupling loss factors, indirect coupling and system modes," J. Sound Vib. **279**, 141–170 (2005).
[9]W. Zhang, A. Wang, N. Vlahopoulos, and K. Wu, "High-frequency vibration analysis of thin elastic plates under heavy fluid loading by an energy finite element formulation," J. Sound Vib. **263**, 21–46 (2003).
[10]Y. Park and S. Hong, "Hybrid power flow analysis using coupling loss factors of sea for low-damping system—Part I: Formulation of 1-D and 2-D cases," J. Sound Vib. **299**, 484–503 (2007).
[11]E. Wester and B. Mace, "Wave component analysis of energy flow in complex structures—Part I: A deterministic model," J. Sound Vib. **285**, 209–227 (2005).
[12]P. Shorter and R. Langley, "On the reciprocity relationship between direct field radiation and diffuse reverberant loading," J. Acoust. Soc. Am. **117**, 85–95 (2005).
[13]V. Cotoni and P. Shorter, "Numerical and experimental validation of a hybrid finite element-statistical energy analysis method," J. Acoust. Soc. Am. **122**, 259–270 (2007).
[14]R. Craik, "The noise reduction of the acoustic paths between two rooms interconnected by a ventilation duct," Appl. Acoust. **12**, 161–179 (1979).
[15]F. Magrans, "Definition and calculation of transmission paths within a SEA framework," J. Sound Vib. **165**, 277–283 (1993).
[16]R. Craik, "The contribution of long flanking paths to sound transmission in buildings," Appl. Acoust. **62**, 29–46 (2001).
[17]M. Kim, H. Kim, and J. Sohn, "Prediction and evaluation of impact sound transmission in apartment building structures by statistical energy analysis (SEA)," Appl. Acoust. **62**, 601–616 (2001).
[18]T. Nightingale and I. Bosmans, "Expressions for first-order flanking paths in homogeneous isotropic and lightly damped buildings," Acta. Acust. Acust. **89**, 110–112 (2003).
[19]L. Galbrun, "The prediction of airborne sound transmission between two

rooms using first-order flanking paths," Appl. Acoust. **69**, 1332–1342 (2008).
[20]R. Büssow and B. Petersson, "Path sensitivity and uncertainty propagation in SEA," J. Sound Vib. **300**, 479–489 (2007).
[21]E. Davis, "By air by sea," in Noise-Con 04, 2008 National Conference on Noise Control Engineering, Dearborn, MI (2008).
[22]B. Carré, *Graphs and Networks*, Oxford Applied Mathematics and Computing Science Series (Oxford University Press, Oxford, 1979).
[23]A. Subramanian, "Two recent algorithms for the global minimum cut problem," ACM SIGACT News **26**, 78–87 (1995).
[24]M. Stoer and F. Wagner, "A simple min-cut algorithm," J. ACM **44**, 585–591 (1997).
[25]H. Nagamochi, K. Nishimura, and T. Ibaraki, "Computing all small cuts in an undirected network," SIAM J. Discrete Math. **10**, 469–481 (1997).
[26]J. Gross and J. Yellen, *Graph Theory and Its Applications*, Discrete Mathematics and Its Applications (CRC, Boca Raton, FL, 1999).
[27]A. Thite and D. Thompson, "The quantification of structure-borne transmission paths by inverse methods. Part 1: Improved singular value rejection methods," J. Sound Vib. **264**, 411–431 (2003).
[28]A. Thite and D. Thompson, "The quantification of structure-borne transmission paths by inverse methods. Part 2: Use of regularization techniques," J. Sound Vib. **264**, 433–451 (2003).
[29]O. Guasch and F. Magrans, "A compact formulation for conditioned spectral density function analysis by means of the LDLH matrix factorization," J. Sound Vib. **277**, 1082–1092 (2004).
[30]A. Inoue, R. Singh, and G. Fernandes, "Absolute and relative path measures in a discrete system by using two analytical methods," J. Sound Vib. **313**, 696–722 (2008).
[31]F. Magrans, "Method of measuring transmission paths," J. Sound Vib. **74**, 321–330 (1981).
[32]F. Bessac, L. Gagliardini, and L. Guyader, "Coupling eigenvalues and eigenvectors: A tool for investigating the vibroacoustic behaviour of coupled vibrating systems," J. Sound Vib. **191**, 881–899 (1996).
[33]O. Guasch and F. Magrans, "The global transfer direct transfer method applied to a finite simply supported elastic beam," J. Sound Vib. **276**, 335–359 (2004).
[34]F. Magrans and O. Guasch, "The role of the direct transfer function matrix as a connectivity matrix and application to the Helmholtz equation in two dimensions: Relation to numerical methods and free field radiation example," J. Comput. Acoust. **13**, 341–363 (2005).
[35]O. Guasch, "Direct transfer functions and path blocking in a discrete mechanical system," J. Sound Vib. **321**, 854–874 (2009).
[36]K. Menger, "Zur allgemeinen Kurventheorie (On the general theory of curves)," Fundam. Math. **10**, 96–115 (1927).
[37]L. Ford and D. Fulkerson, "Maximal flow through a network," Can. J. Math. **8**, 399–404 (1956).
[38]H. Nagamochi and T. Ibaraki, "A linear-time algorithm for finding a sparse k-connected spanning subgraph of a k-connected graph," Algorithmica **7**, 583–596 (1992).
[39]H. Nagamochi and T. Ibaraki, "Computing edge-connectivity in multigraphs and capacitated graphs," SIAM J. Discrete Math. **5**, 54–66 (1992).

Modeling the dynamics of a vibrating string with a finite distributed unilateral constraint: Application to the sitar

Chandrika P. Vyasarayani,[a] Stephen Birkett, and John McPhee
Department of Systems Design Engineering, University of Waterloo, Waterloo, Ontario N2L 3G1, Canada

(Received 27 July 2008; revised 13 January 2009; accepted 27 March 2009)

The free vibration response of an ideal string impacting a distributed parabolic obstacle located at its boundary has been analyzed, the goal being to understand and simulate a sitar string. The portion of the string in contact with the obstacle is governed by a different partial differential equation (PDE) from the free portion represented by the classical string equation. These two PDEs and corresponding boundary conditions, along with the transversality condition that governs the dynamics of the moving boundary, are obtained using Hamilton's principle. A Galerkin approximation is used to convert them into a system of nonlinear ordinary differential equations, with lower mode-shapes parametrized with respect to the location of the moving boundary as basis functions. This system is solved numerically and the behavior of the string studied from simulations. The advantages and disadvantages of the proposed method are discussed in comparison to the penalty approach for simulating wrapping contacts. Simulations with bridge-string parameters consistent with the configuration of a real sitar show that any degree of obstacle wrapping may occur during normal playing. Finally, the model is used to investigate the mechanism behind the generation of the buzzing tone in a sitar. © *2009 Acoustical Society of America.*
[DOI: 10.1121/1.3123403]

PACS number(s): 43.40.Cw, 43.75.Gh, 43.40.At [NHF] Pages: 3673–3682

I. INTRODUCTION

The sitar (Fig. 1) is an Indian musical instrument[1] with plucked strings that can interact with a shallow curved ledge situated underneath the vibrating length of the string at one of its boundaries. The bridge, which includes the ledge, as well as grooves to constrain the strings in their correctly spaced lateral positions for playing, is typically carved from a piece of bone and rests on small wooden feet in contact with the soundboard of the instrument (Fig. 2). The tone of the sitar, and other instruments of Indian origin with a similar bridge design, such as the veena and tambura,[1] is markedly different from that of Western plucked stringed instruments such as a guitar. The interaction of the string with the obstacle generates high frequency components and creates a characteristic buzzing sound.

This mechanism is also not unknown in Western instruments. The Medieval and Renaissance bray harp, for example, has small bray-pins which provide a metal surface for the vibrating string to impact close to one end, increasing the upper partial content in the tone and providing a means for the harp to be audible in larger spaces and in ensemble with other instruments.[2] The arpichordium stop common on some virginals (a plucked string keyboard instrument) imitates the bray harp by soft metal (lead or brass) pins that can be bent so as to lie close to the vibrating strings about 15 mm from the termination point.[3]

The phenomenon common to all of these instruments is caused by the presence of a physical obstacle which alters the behavior of a vibrating string by interacting with it close to one of the termination points. Raman[4] gave a detailed description of bridge geometry for the sitar, veena, and tambura. He noted that even though a veena string may be plucked at a node the corresponding vibration mode appears in the response. Raman concluded that this phenomenon is a consequence of the interaction of the string with the bridge. Various approaches for modeling the interaction between a vibrating string and an obstacle have been presented in the literature. Amerio and Prouse,[5] Schatzman,[6] Burridge *et al.*,[7] and Cabannes[8–10] used the method of characteristics and energy conservation for simulating the impact between a string and a rigid obstacle. Cabannes[10] noted that modeling the case of a string not initially at rest is an open problem. Ahn [11] used a finite element approach and Newton's kinetic coefficient of restitution to simulate the string and its impact with the bridge. Han and Grosenbaugh[12] and Taguti[13] simulated the impact using a penalty approach combined with finite difference discretization for string motion, while Vyasarayani *et al.*[14] used the penalty approach with a modal representation of string motion. A different direction was taken by Krishnaswamy and Smith[15] who considered the curved sitar-bridge as a point obstacle and applied digital wave-guides and finite difference methods to obtain the solution for a rigid impact. Velette[16] analyzed the tambura string interaction with a distributed obstacle modeled as a unilateral point constraint considering completely plastic impact.[17]

When the obstacle is located near the termination of the vibrating continuum, it is possible to model the dynamics using a moving boundary problem. Fung and Chen[18] proposed this method and studied perfect wrapping of a flexible cantilever beam on a circular rigid foundation as a moving boundary problem. The sitar-bridge-string problem is closely related to this work, but differs from it in several respects: (i)

[a]Author to whom correspondence should be addressed. Electronic mail: cpvyasar@engmail.uwaterloo.ca

FIG. 1. Sitar, a stringed instrument of Indian origin.

the vibrating continuum is a string instead of a beam; (ii) the string can have a non-point contact length at static equilibrium; (iii) the contacting boundary is of finite length, thus limiting the maximum amount of wrapping around the obstacle; and (iv) the obstacle geometry is closer to a parabola than a circle.

The present paper describes a new modal formulation for solving the string contact problem for a finitely terminated parabolic obstacle, obtaining the equation of motion of the string during wrapping motion from Hamilton's principle. The developed model is used to study the general behavior of the string motion. Advantages and disadvantages of the proposed method for simulating wrapping contacts are discussed in comparison to the penalty approach. The parameter space for which the simulation model approximates the sitar-bridge-string interaction is analyzed and the mechanism behind the generation of the buzzing tone in a sitar is investigated.

II. MATHEMATICAL MODELING

A schematic representation of the bridge-string geometry is shown in Fig. 3. The bridge is a finite obstacle defined by a parabolic surface for X values between Γ_1 and Γ_2. The string has fixed termination points on the X-axis at $X=L$, and on the parabola at $X=\Gamma_1$.

String motion can be divided into three distinct phases: phase-I motion occurs when there is no contact with the obstacle; partial wrapping on the obstacle is called phase-II motion; a completely wrapped string is considered to be in phase-III motion. In this section we assume, for simplicity and without loss of generality, that $\Gamma_1=0$ and $\Gamma_2=B$. The equation of motion governing the dynamics of the string during each of the three phases is derived, as well as the corresponding switching conditions as the string passes between the phases. This approach is more general than that of Burridge *et al.*[7] who only considered phase-II motion because the parabola extends indefinitely below the string.

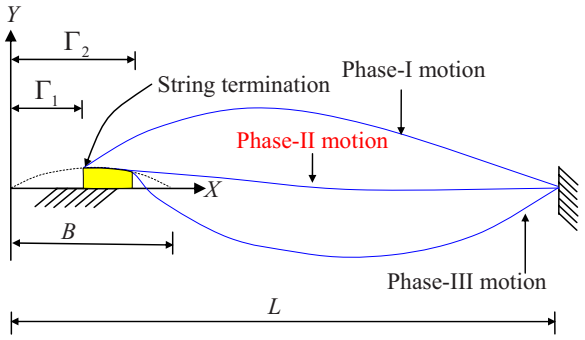

FIG. 3. (Color online) Bridge-string geometry and different phases of string motion (exaggerated for clarity). The right string termination lies on the X-axis; the left termination lies on the parabolic bridge surface as shown.

A. Phase-I motion

During phase-I motion the string is governed by the classical string equation given as follows:

$$\rho\Lambda\frac{\partial^2 Y_1}{\partial t^2} - T\frac{\partial^2 Y_1}{\partial X^2} = 0, \tag{1}$$

with boundary conditions

$$Y_1(0,t) = Y_1(L,t) = 0, \tag{2}$$

where Y_1 is the transverse displacement of the string, L is the length of the string, T is the string tension, ρ is the density, A is the cross-sectional area, X is the co-ordinate along the length, and t is the time. The shape of the obstacle is assumed to be a parabola as in the work of Burridge *et al.*[7] and the geometry can be analytically represented as

$$Y_B(X) = A_P X(B - X). \tag{3}$$

We substitute the following non-dimensional parameters into the equation of motion to facilitate analysis:

$$y_1 = \frac{Y_1}{h}, \quad x = \frac{X}{L}, \quad \tau = t\sqrt{\frac{T}{\rho A L^2}}, \tag{4}$$

where $h=A_P B^2/4$ is the height of the obstacle. The equation of motion after substituting the non-dimensional variables is as follows:

$$\frac{\partial^2 y_1}{\partial \tau^2} - \frac{\partial^2 y_1}{\partial x^2} = 0, \tag{5}$$

with boundary conditions

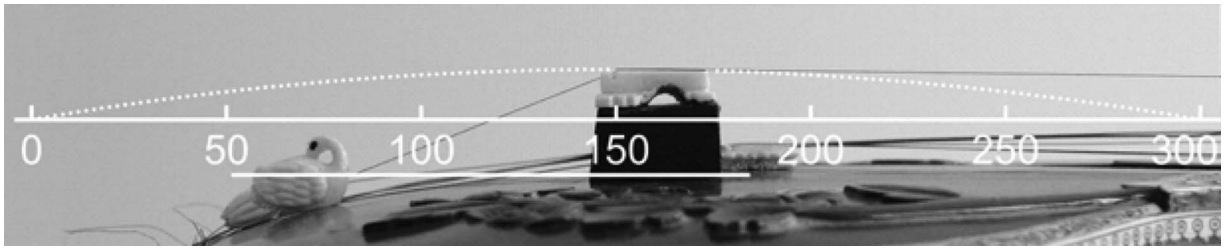

FIG. 2. Sitar-bridge. The profile can be approximated by a parabolic curve. The base of the parabola defines the x-axis passing through the far string termination point and parallel to the reference line shown, which runs along the neck of the instrument. See text for detailed dimensions.

$$y_1(0,\tau) = y_1(1,\tau) = 0. \tag{6}$$

A solution to Eq. (5) is assumed to be of the form

$$y_1(x,\tau) = \sum_{j=1}^{\infty} \phi_j(x)\,\eta_j(\tau). \tag{7}$$

In Eq. (7), $\phi_j(x) = \sqrt{2}\sin(j\pi x)$ are mass-normalized mode-shapes of the string and $\eta_j(\tau)$ are modal co-ordinates. Substituting Eq. (7) into Eq. (5), multiplying by $\phi_k(x)$, integrating over the domain, and simplifying the resulting equation by using orthogonality relations result in a set of uncoupled ordinary differential equations of the following form:

$$\ddot{\eta}_j(\tau) + \omega_j^2 \eta_j(\tau) = 0, \tag{8}$$

where $\omega_j = j\pi$ are the natural frequencies of the string. The modal initial conditions corresponding to physical initial conditions of $y_1(x,0)$ and $\dot{y}_1(x,0)$ are as follows:

$$\eta_j(0) = \int_0^1 y_1(x,0)\,\phi_j(x)dx \quad \text{and}$$

$$\dot{\eta}_j(0) = \int_0^1 \dot{y}_1(x,0)\,\phi_j(x)dx. \tag{9}$$

After specifying the system parameters and initial conditions, the modal equations of motion given by Eq. (8) can be numerically integrated using any standard numerical scheme. When the string starts to contact the obstacle, the equation of motion given by Eq. (8) is no longer valid. In Sec. II B we derive the equation of motion during wrapping motion of the string around the obstacle by using Hamilton's principle with a moving boundary.

B. Phase-II motion

The Hamiltonian with the distributed spatial constraint[18] can be written as follows:

$$H = \delta\int_{t_1}^{t_2}\left[\int_0^{\Gamma_-}(\Pi + \lambda(X)G(X))dX + \int_{\Gamma_+}^{L}\Pi dX\right]dt = 0, \tag{10}$$

where Π is the Lagrangian density function defined as

$$\Pi = \frac{1}{2}\rho A\dot{Y}_2(X,t)^2 - \frac{1}{2}T\left(\frac{\partial Y_2(X,t)}{\partial X}\right)^2, \tag{11}$$

and $G(X)$ is the gap function defined as $G(X) = Y_2(X,t) - Y_B(X)$ and Γ is the wrapped string length. Y_2 is the displacement of the string during wrapping motion and $\lambda(X)$ is the distributed constraint force. Substituting Eq. (11) into the Hamiltonian [Eq. (10)] and simplifying

$$\begin{aligned} H = {} & \delta\int_{t_1}^{t_2}\int_0^{\Gamma_-}\left(\frac{1}{2}\rho A\dot{Y}_2(X,t)^2\right)dXdt \\ & - \delta\int_{t_1}^{t_2}\int_0^{\Gamma_-}\left(\frac{1}{2}T\left(\frac{\partial Y_2(X,t)}{\partial X}\right)^2\right)dXdt \\ & + \delta\int_{t_1}^{t_2}\int_0^{\Gamma_-}(\lambda(X)G(X))dXdt \\ & + \delta\int_{t_1}^{t_2}\int_{\Gamma_+}^{L}\left(\frac{1}{2}\rho A\dot{Y}_2(X,t)^2\right)dXdt \\ & - \delta\int_{t_1}^{t_2}\int_{\Gamma_+}^{L}\left(\frac{1}{2}T\left(\frac{\partial Y_2(X,t)}{\partial X}\right)^2\right)dXdt = 0. \end{aligned} \tag{12}$$

After evaluating the variations in Eq. (12),

$$\begin{aligned} H = {} & \int_{t_1}^{t_2}\int_0^{\Gamma_-}\left(T\frac{\partial^2 Y_2(X,t)}{\partial X^2} - \rho A\frac{\partial^2 Y_2(X,t)}{\partial t^2} + \lambda(X)\right) \\ & \times \delta Y_2(X,t)dXdt + \int_{t_1}^{t_2}\int_0^{\Gamma_-}(\delta\lambda(X)G(X))dXdt \\ & + \int_{t_1}^{t_2}\int_{\Gamma_+}^{L}\left(T\frac{\partial^2 Y_2(X,t)}{\partial X^2} - \rho A\frac{\partial^2 Y_2(X,t)}{\partial t^2}\right)\delta Y_2(X,t)dXdt \\ & + \int_{t_1}^{t_2}\left(T\frac{\partial Y_2(\Gamma_+,t)}{\partial X}\delta Y_2(\Gamma_+,t)\right)dt \\ & - \int_{t_1}^{t_2}\left(T\frac{\partial Y_2(\Gamma_-,t)}{\partial X}\delta Y_2(\Gamma_-,t)\right)dt \\ & + \int_{t_1}^{t_2}\left(T\frac{\partial Y_2(0,t)}{\partial X}\delta Y_2(0,t)\right)dt \\ & - \int_{t_1}^{t_2}\left(T\frac{\partial Y_2(L,t)}{\partial X}\delta Y_2(L,t)\right)dt = 0. \end{aligned} \tag{13}$$

It should be noted that the virtual variables $\delta Y_2(\Gamma,t)$ and $\delta\Gamma$ are unspecified, but they are related due to the presence of the geometrical constraint. After some tedious algebra, the relation between the virtual variables can be shown to be

$$\delta Y_2(\Gamma,t) = 2A_P(B - 2\Gamma)\delta\Gamma. \tag{14}$$

The reader can find a more detailed derivation on relating the virtual variables in the work of Fung and Chen,[18] for a similar problem. Substituting Eq. (14) into Eq. (13), and utilizing the fact that the virtual variables are arbitrary and must vanish at the boundaries results in the following equations of motion that must be satisfied at all time:

$$T\frac{\partial^2 Y_2(X,t)}{\partial X^2} - \rho A\frac{\partial^2 Y_2(X,t)}{\partial t^2} + \lambda(X) = 0, \quad 0 < X < \Gamma_-, \tag{15}$$

$$T\frac{\partial^2 Y_2(X,t)}{\partial X^2} - \rho A\frac{\partial^2 Y_2(X,t)}{\partial t^2} = 0, \quad \gamma_+ < X < L, \tag{16}$$

with the boundary conditions

$$Y_2(0,t) = 0, \quad Y_2(\Gamma_-,t) = A_P\Gamma_-(B - \Gamma_-), \tag{17}$$

$$Y_2(L,t) = 0, \quad Y_2(\Gamma_+,t) = A_P\Gamma_+(B - \Gamma_+), \tag{18}$$

since $\delta\Gamma = \delta\Gamma_- = \delta\Gamma_+$. The transversality condition can be written as

$$\frac{\partial Y_2(\Gamma(t),t)}{\partial X} = A_P(B - 2\Gamma(t)). \tag{19}$$

The transversality condition is the necessary condition that must be satisfied for the variations to vanish at the free boundary γ. The physical implication of the transversality condition is the enforcement of the string slope to be equal to that of the slope of the parabola at the point of separation (Γ). We substitute the same non-dimensional parameters given in Eq. (4) along with $\gamma=\Gamma/L$, $b=B/L$, and $\alpha=4L^2/B^2$ into Eqs. (15)–(19). It should be noted that the solution of Eq. (15) is the geometry of the parabola, as the string in the domain $0<x<\gamma_-$ perfectly wraps around the obstacle. So we have to solve for the motion of the string in the domain $\gamma_+<x<1$; thus the equation of motion reduces to the following moving boundary problem:

$$\frac{\partial^2 y_2(x,\tau)}{\partial x^2} - \frac{\partial^2 y_2(x,\tau)}{\partial \tau^2} = 0, \quad \gamma_+ \le x \le 1, \tag{20}$$

$$y_2(\gamma_+,\tau) = \alpha\gamma_+(b-\gamma_+), \quad y_2(1,\tau) = 0. \tag{21}$$

We need one further equation that should be solved for obtaining the separation point (moving boundary), which comes from the tranversality condition

$$\frac{\partial y_2(\gamma,\tau)}{\partial x} = \alpha(b - 2\gamma). \tag{22}$$

To transform the non-homogenous boundary conditions given by Eq. (21) into homogenous boundary conditions, the following transformation defining y_3 is substituted into Eqs. (20)–(22):

$$y_2(x,\tau) = y_3(x,\tau) + s(x,\tau), \tag{23}$$

where

$$s(x,\tau) = \frac{\alpha\gamma_+(b-\gamma_+)}{(\gamma_+ - 1)}(x-1). \tag{24}$$

The transformed equations are shown below:

$$\frac{\partial^2 y_3(x,\tau)}{\partial x^2} - \frac{\partial^2 y_3(x,\tau)}{\partial \tau^2} = -\frac{\partial^2 s(x,\tau)}{\partial \tau^2}, \quad \gamma_+ < x < 1, \tag{25}$$

with boundary conditions

$$y_3(\gamma_+,\tau) = 0, \quad y_3(1,\tau) = 0. \tag{26}$$

The transversality condition now becomes

$$\frac{\partial y_3(\gamma_+,\tau)}{\partial x} = \alpha(b - 2\gamma_+) - \frac{\alpha\gamma_+(b-\gamma_+)}{(\gamma_+ - 1)}. \tag{27}$$

Substituting a solution of the following form:

$$y_3(x,\tau) = \sum_{i=1}^{N} \psi_i(x,\tau)\beta_i(\tau) \tag{28}$$

into Eq. (25), where $\psi_i(x,\tau)$ are the mass-normalized mode-shapes parametrized with respect to the moving boundary $\gamma_+(\tau)$. They are obtained by solving for the mode-shapes of Eq. (25):

$$\psi_i(x,\tau) = \sqrt{\frac{2}{(1-\gamma_+)}}\sin\left(j\pi\frac{(x-\gamma_+)}{(1-\gamma_+)}\right). \tag{29}$$

The partial differential equation (25) after substituting the solution (28) and using the orthogonality property of ψ_j reduces to the following coupled ordinary differential equations with time dependent coefficients:

$$\ddot{\beta}_i(\tau) + \left[\sum_{j=1}^{N} 2C_{ij}(\gamma_+,\dot{\gamma}_+)\right]\dot{\beta}_i(\tau) + \left[\left(\frac{j\pi}{(1-\gamma_+)}\right)^2 + \sum_{j=1}^{N} D_{ij}(\gamma_+,\dot{\gamma}_+,\ddot{\gamma}_+)\right]\beta_i(\tau) = -E_{ij}(\gamma_+,\dot{\gamma}_+,\ddot{\gamma}_+). \tag{30}$$

In the above equation, C_{ij}, D_{ij}, and E_{ij} are defined as follows:

$$C_{ij}(\gamma_+,\dot{\gamma}_+) = \int_{\gamma_+}^{1} \psi_i(x,\tau)\dot{\psi}_j(x,\tau)dx = J_{1ij}(\gamma)\dot{\gamma}, \tag{31}$$

$$D_{ij}(\gamma_+,\dot{\gamma}_+,\ddot{\gamma}_+) = \int_{\gamma_+}^{1} \psi_i(x,\tau)\ddot{\psi}_j(x,\tau)dx = J_{1ij}(\gamma)\ddot{\gamma} + J_{2ij}(\gamma)\dot{\gamma}^2, \tag{32}$$

$$E_{ij}(\gamma_+,\dot{\gamma}_+,\ddot{\gamma}_+) = \int_{\gamma_+}^{1} \ddot{s}_i(x,\tau)\psi_j(x,\tau)dx = J_{3ij}(\gamma)\dot{\gamma}^2 + J_{4ij}(\gamma)\ddot{\gamma}, \tag{33}$$

where J_{1ij}, J_{2ij}, J_{3ij}, and J_{4ij} are functions of γ only. The transversality condition [Eq. (27)], after substituting the solution given by Eq. (28), becomes

$$\sum_{i=1}^{N} i\pi\sqrt{2}\beta_i(\tau) = (1-\gamma_+)^{3/2}\left(\alpha(b-2\gamma_+) - \frac{\alpha\gamma_+(b-\gamma_+)}{(\gamma_+ - 1)}\right). \tag{34}$$

Differentiating the above equation twice, we get

$$\sum_{i=1}^{N} i\pi\sqrt{2}\ddot{\beta}_i(\tau) = H_1(\gamma_+)\ddot{\gamma}_+(t) + H_2(\gamma_+)\dot{\gamma}_+^2, \tag{35}$$

where H_1 and H_2 are functions of γ. Equations (30) and (35) can be solved simultaneously for $\beta_i(\tau)$ and $\gamma(\tau)$ to predict the motion of the string during the contact phase. The above method of satisfying the second derivative of the displacement constraint instead of displacement constraint directly, thus converting the constraint equation into a differential equation, is a very well known procedure in the field of multibody dynamics.[19]

C. Switching conditions between phase-I and phase-II motions

Let τ_{c1} be the time at which the string in phase-I comes in contact with the obstacle. The string in phase-I motion contacts the obstacle when the slope of the string at $x=\gamma_+=0$ matches with the slope of the obstacle. At the event of contact, we have

$$y_1(x,\tau_{c1}) = y_2(x,\tau_{c1}), \tag{36}$$

which can be further written as follows:

$$\sum_{i=1}^{N} \eta_i(\tau_{c1})\phi_i(x) = \sum_{i=1}^{N} \psi_i(x,\tau_{c1})\beta_i(\tau_{c1}) + \frac{\alpha\gamma_+(b-\gamma_+)}{(\gamma_+-1)}(x-1). \tag{37}$$

Since $\gamma_+=0$ at $\tau=\tau_{c1}$ and $\phi_i(0)=\psi_i(0,\tau_{c1})=0$, we have

$$\eta_i(\tau_{c1}) = \beta_i(\tau_{c1}). \tag{38}$$

Since the velocity distributions in phase-I motion and phase-II motion should also be equal at transferring time τ_{c1}, we have

$$\sum_{i=1}^{N} \dot{\eta}_i(\tau_{c1})\phi_i(x) = \sum_{i=1}^{N} (\dot{\psi}_i(x,\tau_{c1})\beta_i(\tau_{c1}) + \psi_i(x,\tau_{c1}) \times \dot{\beta}_i(\tau_{c1})) - b\alpha(x-1)\dot{\gamma}_+. \tag{39}$$

Multiplying both sides of Eq. (39) with $\psi_j(x,\tau_{c1})$ and integrating over the domain result in the following:

$$\begin{aligned}\dot{\eta}_i(\tau_{c1})\sum_{i=1}^{N}\int_0^1 \phi_i(x)\psi_j(x,\tau_{c1})dx &= \beta(\tau_{c1})\sum_{i=1}^{N}\int_0^1 \dot{\psi}_i(x,\tau_{c1})\psi_j(x,\tau_{c1})dx \\ &+ \dot{\beta}_i(\tau_{c1})\sum_{i=1}^{N}\int_0^1 \psi_i(x,\tau_{c1})\psi_j(x,\tau_{c1})dx \\ &- b\alpha\dot{\gamma}_+\int_0^1 (x-1)\psi_j(x,\tau_{c1})dx.\end{aligned} \tag{40}$$

After some simplifications using orthogonality relations, the above equation reduces to

$$\dot{\eta}_i(\tau_{c1}) = \dot{\beta}_i(\tau_{c1}) + \left[\beta(\tau_{c1})\sum_{j=1}^{N} J_{1ij}(0) + \sqrt{2}\left(\frac{b\alpha}{i\pi}\right)\right]\dot{\gamma}_+. \tag{41}$$

The above set of N equations contain $N+1$ unknowns, so we need one further equation to solve for $\dot{\gamma}_+$ which can be obtained by differentiating the transversality condition given by Eq. (34) with respect to time

$$\sum_{i=1}^{N} i\pi\sqrt{2}\dot{\beta}_i(\tau) = H_1(\gamma_+)\dot{\gamma}_+ \tag{42}$$

at transferring time $\tau=\tau_{c1}$. The above equation becomes

$$\dot{\gamma} = \frac{1}{H_1(0)}\sum_{i=1}^{N} i\pi\sqrt{2}\dot{\beta}_i(\tau_{c1}). \tag{43}$$

The above algebraic equations (41) and (43) can be solved to obtain $\dot{\beta}_i(\tau_{c1})$ and $\dot{\gamma}_+$. The time of switching can be obtained through the transversality condition as shown below:

$$\sum_{i=1}^{N} i\pi\sqrt{2}\eta_i(\tau_{c1}) = \sum_{i=1}^{N} i\pi\sqrt{2}\beta_i(\tau_{c1}) = \alpha b. \tag{44}$$

Standard event detection algorithms can be used in the simulation to detect the time at which Eq. (44) holds.

D. Phase-III motion

The phase-III motion is the same as phase-I motion except that the string is completely wrapped around the obstacle and vibrates between $x=\gamma_+=b$ and $x=1$. The dimensionless equation of motion of the string during phase-III can be written as

$$\frac{\partial^2 y_4(x,\tau)}{\partial x^2} - \frac{\partial^2 y_4(x,\tau)}{\partial \tau^2} = 0, \quad b \leqslant x \leqslant 1, \tag{45}$$

$$y_4(b,\tau) = 0, \quad y_4(1,\tau) = 0, \tag{46}$$

substituting a solution of the following form:

$$y_4(x,\tau) = \sum_{j=1}^{\infty} \varphi_j(x) r_j(\tau) \tag{47}$$

into Eq. (45) and performing standard modal analysis, we get the following uncoupled ordinary differential equations:

$$\ddot{r}_j(\tau) + \omega_{4j}^2 r_j(\tau) = 0, \tag{48}$$

where $\varphi_j(x)=\sqrt{2/(1-b)}\sin(j\pi(x-b)/(1-b))$ are the mass-normalized mode-shapes of the string, $r_j(\tau)$ are the generalized coordinates, and $\omega_{4j}=j\pi/(1-b)$ are the natural frequencies of the string.

E. Switching conditions between phase-II and phase-III motions

Once the slope of the string at $x=\gamma=b$ matches with the slope of the obstacle the string enters into phase-III motion. Let τ_{c2} be the instant of switching. The displacement and velocity distributions of the string during the last instant of phase-II will be transferred to the phase-III. This can be mathematically represented as

$$\beta_i(\tau_{c2}) = r_i(\tau_{c2}) \tag{49}$$

and

$$\dot{\beta}_i(\tau_{c2}) = \dot{r}_i(\tau_{c2}). \tag{50}$$

The transfer time τ_{c2} between phase-II and phase-III can be again obtained from the transversality condition as shown below:

$$\sum_{i=1}^{N} i\pi\sqrt{2}\beta_i(\tau) = (1-\gamma_+)^{3/2}\left(\alpha(b-2\gamma_+) - \frac{\alpha\gamma_+(b-\gamma_+)}{(\gamma_+-1)}\right). \tag{51}$$

Substituting $\tau=\tau_{c2}$ and $\gamma_+=b$, we get

$$\sum_{i=1}^{N} i\pi\sqrt{2}\beta_i(\tau_{c2}) = -\alpha b(1-b)^{3/2}. \tag{52}$$

F. Switching conditions between phase-III and phase-II motions

The switching conditions between phase-III and phase-II are similar to that of phase-I and phase-II. Let τ_{c3} be the transfer time, once the phase-III motion is initiated after time τ_{c2} the string vibrates downwards between the boundaries b and 1. Once the string starts to move upwards the slope of the string $x=\gamma=b$ matches with the slope of the obstacle and the string enters in to phase-II motion, and then it tries to unwrap itself thus again performing a phase-II motion. Now we try to relate the initial conditions between phase-III and phase-II motions. Following similar procedure as in Sec. II C, we get the following relations:

$$r_i(\tau_{c3}) = \beta_i(\tau_{c3}), \tag{53}$$

$$\dot{r}_i(\tau_{c3}) = \dot{\beta}_i(\tau_{c1}) + \left[\beta(\tau_{c1})\sum_{j=1}^{N} J_{1ij}(b) + \sqrt{2}\left(\frac{b\alpha}{i\pi}\right)\right]\dot{\gamma}_+, \tag{54}$$

$$\dot{\gamma}_+ = \frac{1}{H_1(b)}\sum_{i=1}^{N} i\pi\sqrt{2}\dot{\beta}_i(\tau_{c3}). \tag{55}$$

Equation (55) can be substituted into Eq. (54) to eliminate $\dot{\gamma}_+$ and that can be solved for $\dot{\beta}_j(t)$. Once $\dot{\beta}_j(t)$ are known they can be re-substituted into Eq. (55) to get $\dot{\gamma}_+$. The transferring time $\tau=\tau_{c3}$ can again obtained from the transversality condition as shown below:

$$\sum_{i=1}^{N} i\pi\sqrt{2}\beta_i(\tau_{c3}) = -\alpha b(1-b)^{3/2}. \tag{56}$$

Equations (53)–(55) relate the initial conditions between phase-III and phase-II.

G. Switching conditions between phase-II and phase-I motions

The switching conditions between phase-II and phase-I are similar to that of phase-II and phase-III. Let τ_{c4} be the switching time between phase-II and phase-I motions. When the string completely unwraps from the obstacle during phase-II motion the slope of the string at $x=\gamma=0$ matches with the slope of the obstacle and again phase-I motion gets initiated. Following similar procedure as in Sec. II E, we get the following relations:

$$\beta_i(\tau_{c4}) = \eta_i(\tau_{c4}), \tag{57}$$

$$\dot{\beta}_i(\tau_{c4}) = \dot{\eta}_i(\tau_{c4}). \tag{58}$$

The transfer time τ_{c4} between phase-II and phase-III can be again obtained from the transversality condition as shown below:

$$\sum_{i=1}^{N} i\pi\sqrt{2}\beta_i(\tau_{c4}) = \alpha b. \tag{59}$$

H. Summary of formulation

Now we have the equations governing the dynamics of the string during the three phases of motion given by Eqs. (8), (30), and (48). The switching conditions between phase-I and phase-II are given by Eqs. (38) and (43). The event of switching can be obtained from Eq. (44). The switching conditions between phase-II and phase-III motions are given by Eqs. (49) and (50). The event of switching can be obtained from Eq. (52). During upward motion of the string, the switching conditions between phase-III and phase-II and the event of switching can be obtained from equations (53)–(56). Finally, the switching condition between phase-II and phase-I and the event of switching are given by Eqs. (57)–(59). In Sec. III, we discuss the results obtained by numerical simulations of the formulated equations.

III. RESULTS AND DISCUSSION

In this section, we discuss the behavior of the string motion from simulations. For computational simplicity, we consider only a single mode representation of the string. It will be evident shortly that even a one mode approximation of the moving boundary formulation can capture the physics of the problem. This approximation requires the string to be plucked at the center of its unwrapped length.

A. General behavior of string motion

As we have introduced dimensionless quantities in the equation of motion, the natural frequencies of the completely unwrapped string are integer multiples of π. For a simulation we need two dimensionless quantities: the relationship between the bridge and string given by $b=B/L$, and the modal amplitude of the initial string configuration given by $\beta_1(0)$. The contact length $\gamma=1-\sqrt{(1-b)}$ for the string at static equilibrium on the parabolic obstacle can be obtained from the transversality condition [Eq. (34)] by setting $\beta_1(0)=0$; the string shape at static equilibrium, a straight line from the contact point to right termination, is given by Eqs. (23) and (24) with $y_3=0$.

Transitions between phases are controlled by two factors: (i) the location of the bridge terminations, as determined by γ_1 and γ_2; and (ii) the pluck amplitude, as given by the initial condition $\beta_1(0)$. The value of γ_1 constrains the left boundary of the vibrating string and shortens the effective speaking length at the phase-I transition, and γ_2 constrains the potential extent of the string wrapping before it enters into phase-III motion. For each defined pair of bridge terminations, limiting values of the initial condition such that the string only vibrates in phase-II motion can be obtained from the transversality condition [Eq. (34)]:

$$\frac{(1-\gamma_2)^{3/2}}{\sqrt{2}\pi}\left(\alpha(b-2\gamma_2) - \frac{\alpha\gamma_2(b-\gamma_2)}{(\gamma_2-1)}\right) < \beta_1(0) < \frac{(1-\gamma_1)^{3/2}}{\sqrt{2}\pi}\left(\alpha(b-2\gamma_1) - \frac{\alpha\gamma_1(b-\gamma_1)}{(\gamma_1-1)}\right). \tag{60}$$

The significance of these inequalities for sitar-bridge design will be demonstrated subsequently. A parabolic bridge that

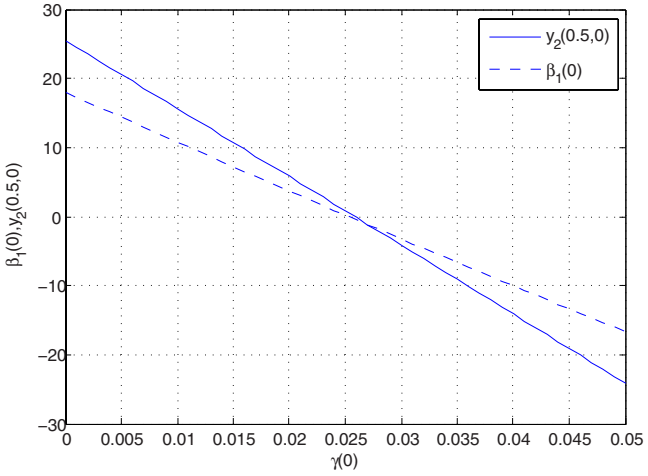

FIG. 4. (Color online) Variation of initial condition with initial contact length.

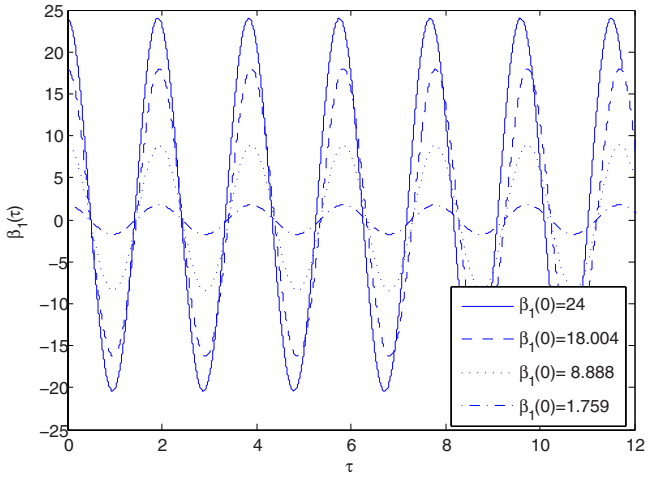

FIG. 5. (Color online) Variation of modal amplitude β_1 with time for four different initial conditions. Bridge terminations given by $\gamma_1=0$ and $\gamma_2=b=0.05$.

extends to the x-axis on both sides, as used in the derivation of equations of motion and switching conditions in Sec. II, corresponds to $\gamma_1=0$ and $\gamma_2=b$, in which case the inequalities constraining the string to phase-II motion simplify to $-4(1-b)^{3/2}/\sqrt{2\pi b}<\beta_1(0)<1/\sqrt{2\pi b}$. The bridge configuration in Ref. 7 corresponds to $\gamma_1=0$ and $\gamma_2\to\infty$.

Figure 4 shows the variation of initial condition $\beta_1(0)$ against initial contact length $\gamma(0)$ for a string in phase-II configuration with $b=0.05$, the same as considered by Burridge *et al.*[7] The corresponding midpoint deflection $y_2(0.5,0)$ is also shown. Interestingly the initial conditions seem to vary almost linearly with contact length. For this bridge configuration, the phase transitions occur when $\gamma(0)$ is 0 or 0.05, giving $\beta_1(0)$ values of 18.0 and −16.7, and corresponding midpoint deflections of 25.5 and −24.1; these demand very large amplitude initial conditions if the string is to vibrate in phase-I or phase-III motion. Increasing γ_1 will constrain the $\gamma(0)$ value on the left for the phase-I transition; decreasing γ_2 will constrain the $\gamma(0)$ value on the right giving the phase-III transition. In this way bridge termination can be used to control the string amplitude required for the phase transitions.

Now we study the free vibrations of the string about the equilibrium state. The equations of motions were solved numerically using MATLAB with ode 23s solver. The in-built event detection algorithm in MATLAB was used for detecting events for switching between the three phases of motion. An absolute and relative tolerance of 10^{-9} was used in the numerical simulations. Figure 5 shows the variation of modal coordinate $\beta_1(t)$ with time for four different initial conditions. The corresponding phase space plots are given in Fig. 6. The first initial condition is $\beta_1(0)=24>1/\sqrt{2\pi b}$ and thus the string starts its motion in phase-I; the string eventually vibrates in all the three phases of motion, but the asymmetry seen in the phase plot should be noted. All the other initial conditions shown satisfy the inequalities $-4(1-b)^{3/2}/\sqrt{2\pi b}<\beta_1(0)<1/\sqrt{2\pi b}$ and the initial string condition is in phase-II; in this case, the string remains only in phase-II motion; however, this cannot be concluded in general due to asymmetry. Figure 5 shows that the string starting in phase-I has a higher oscillation frequency than that starting in phase-II, since some motion in phase-III with the highest frequency occurs during a cycle. The frequency of oscillation for all cases that remain in phase-II motion is essentially the same, possibly due to the near linear relationship of $\beta_1(0)$ and $\gamma(0)$, as shown in Fig. 4. The period of oscillation with no obstacle is 2, and it can be seen that this is increased due to the presence of the bridge.

In order to understand how the natural frequency of the system changes while it wraps around the obstacle, an instantaneous natural frequency can be defined by taking a square root of the coefficient of $\beta_1(\tau)$ in Eq. (30) and by dropping rate dependent terms. Figure 7 shows the variation of instantaneous natural frequency for the same four initial conditions. It is clear that the natural frequencies are time dependent.

To validate our results with the moving boundary formulation, we compared them to those obtained by the penalty approach[14] and found good agreement when 100 modes were retained in the penalty method. Moreover, the moving

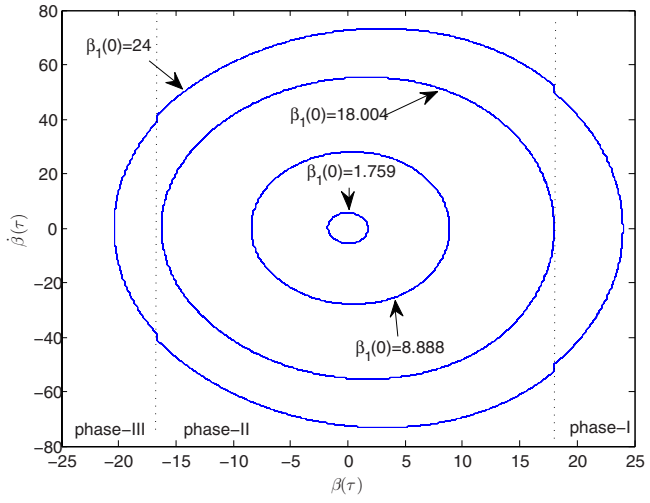

FIG. 6. (Color online) Phase space for β_1 and $\dot{\beta}_1$ for four different initial conditions. Bridge terminations given by $\gamma_1=0$ and $\gamma_2=b=0.05$.

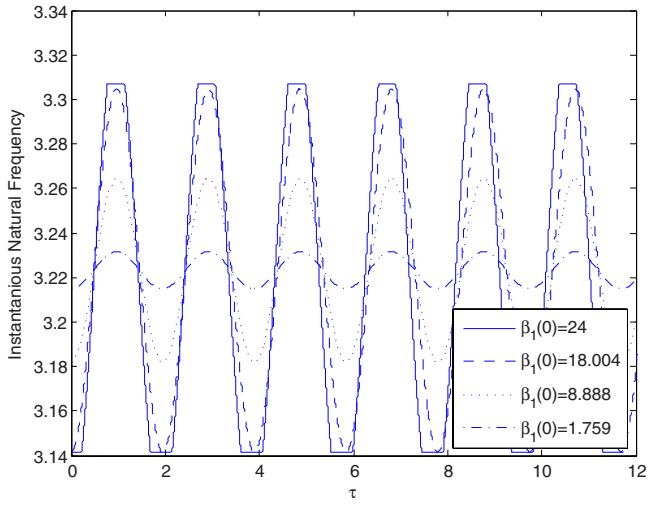

FIG. 7. (Color online) Variation of instantaneous natural frequency with time.

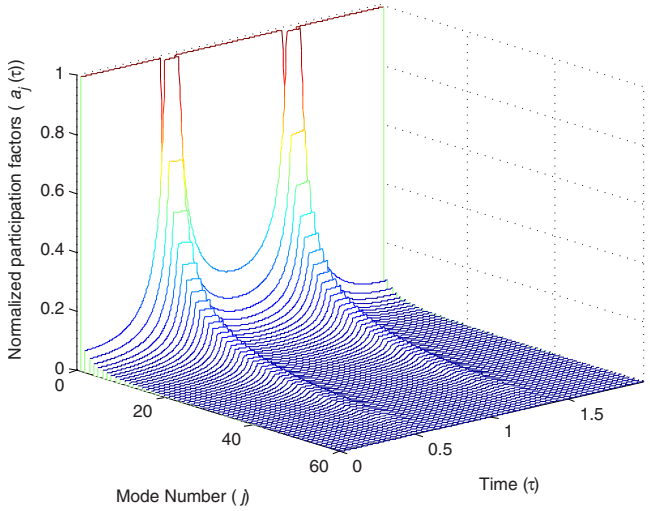

FIG. 9. (Color online) Waterfall plot showing the variation of string shape frequency components with time for motion in phase-II only.

boundary formulation simulated the string motion 50 times faster than the penalty approach. During phase-III the slope of the string at $\gamma=b$ is discontinuous, except at the beginning and end configuration. This non-smooth behavior in the string shape at $\gamma=b$ is exactly captured by the formulation and its discontinuous slope is shown in Fig. 8. This particular non-smooth behavior in string slope cannot be captured if the impact is modeled using a penalty approach,[14] for which method the obstacle is assumed as a linear continuum of distributed springs. Usually a series solution in terms of normal modes of the classical string is sought and it is well known that the series solution converges very slowly in the presence of non-smooth displacements and is prone to Gibbs phenomena.[20] Capturing such discontinuities in derivatives of the spatial displacement exactly is still a challenging problem with a sparse modeling literature.[20–22]

In order to investigate the frequency components present in the string shape during phase-II motion, the shape of the string during its entire motion (obtained by solving the moving boundary problem) is projected on the normal modes of the classical string. Mathematically,

$$y(x,t) = \sum_{j=1}^{N} a_j(t)\sin(j\pi x) \tag{61}$$

represents the shape of the string including both the wrapped and unwrapped portions. The series in Eq. (61) can also be interpreted as the series solution of the penalty approach, for which[14] the $a_j(t)$ are obtained by solving the differential equations

$$\ddot{a}_j(\tau) + \omega_j^2 a_j(\tau) = \Psi f(a_1, a_2, \ldots, a_N), \quad j = 1,2,\ldots,N, \tag{62}$$

with penalty parameter Ψ and penetration function $f(a_1, a_2, \ldots, a_N)$. The moving boundary approach of the present paper is the limiting case of the penalty method for $\Psi \to \infty$ and penetration function tending to zero corresponding to a rigid obstacle. Both the methods should give identical results in the limiting case.

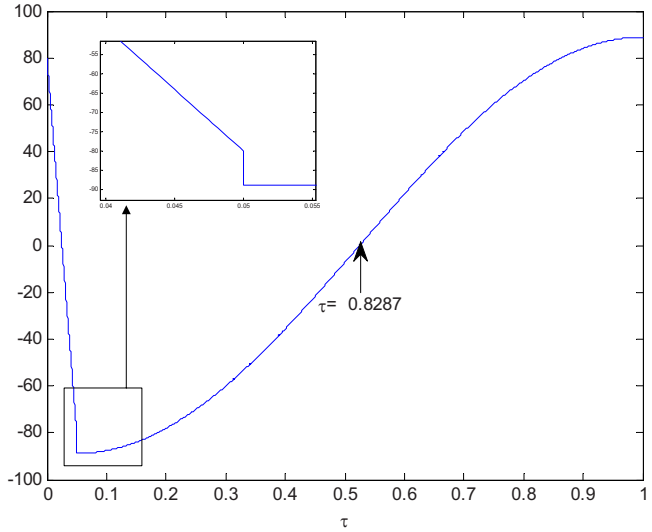

FIG. 8. (Color online) Slope of the string during phase-II and III motions.

Figure 9 is a waterfall plot obtained from Eq. (61) showing the variation of normalized participation factors $a_j(t)$ with time for the initial condition $\beta_1(0)=1.8$ with string motion constrained to phase-II only. The presence of a particular $a_j(\tau)$ in the waterfall plot means that the corresponding modal oscillator in Eq. (62) must participate in the response if the problem is solved using a penalty approach, and automatically its frequency component will be present in the time response. Figure 9 clearly shows the participation of higher modes during phase-II motion. Considerably more terms in the series [Eq. (61)] are needed around $\tau=0.5$ and $\tau=1.5$ when the shape of the string demands higher mode participation. It can be seen that Eq. (30) is highly coupled and during phase-II motion the modes can exchange energy. As time progresses higher modes will start participating and eventually lead to multiple distributed impacts between the bridge and the string, which will violate the perfect wrapping assumption required in the moving boundary method. The

authors believe that these multiple impacts are responsible for the distinct tone of the sitar. Future work will address this by developing a detailed simulation model that can handle spatial string motions with multiple impacts and friction.[23]

B. Simulation approximating the configuration of a sitar

An initial string deflection of 24 times the height of the bridge is required for phase-I string motion with the bridge-string configuration used in the above simulations, which is the same as that of Burridge *et al.*[7] This scenario is clearly impractical for a real sitar, if only because the resulting large amplitude string vibrations would have to pass through the back of the instrument. In reality, the geometry of a sitar-bridge, as shown in Fig. 2, is quite different in several respects: (i) the bridge is terminated on the left at its apex, with downbearing from string back length keeping it fixed there; (ii) the bridge is terminated on the right at a level considerably higher than that of the far string termination; and (iii) the slope of the bridge is very shallow, so the bridge surface remains very close to the string.

Measurements obtained from the sitar shown in Fig. 1 give the following dimensions: $B=300$ mm, $\Gamma_1=150$ mm, $\Gamma_2=173$ mm, and $L=1060$ mm (effective speaking length is 910 mm). We choose the straight neck of the instrument to define the horizontal direction. The x-axis for simulations (Fig. 3) is parallel to this and passes through the far string termination which is 14 mm above the neck reference line. The apex of the bridge at 27 mm above the neck reference line gives $h=13$ mm. Figures 2 and 3 show how the simulation configuration relates to the real sitar-bridge.

The tops of the frets at 11 mm above the neck reference line constrain the maximum vertical displacement of the string if it is to avoid hitting them. The normal plucking point is about 200 mm from the bridge apex, giving a plucking ratio or about 2:9. A typical pluck moves the string about 15 mm horizontally and 2–3 mm vertically.

This sitar string-bridge configuration is approximated for simulations using the following non-dimensional parameters: $L=1$, $b=0.283$, $\gamma_1=b/2=0.142$, and $\gamma_2=0.163$. The initial condition for a one mode solution requires a mid-string plucking point for which the $\beta_1(0)$ value of 0.25 is used. This corresponds to a string raised slightly above the horizontal between the bridge termination and the pluck point, a state that is easily achieved in normal playing.[24] Substituting the non-dimensional parameters in Eq. (60) gives phase transitions for β_1 values of 0.209 (phase-I to phase-II) and −0.172 (phase-II to phase-III), corresponding to midpoint defections of 0.890 and 0.329, respectively. It can be seen that string motion in all three phases can easily be achieved for the configuration of a real sitar in normal playing, as a result of the geometry of the bridge and its terminations. The results of simulations with the above conditions, shown in the phase plot of Fig. 10 should be contrasted with those shown in Fig. 6.

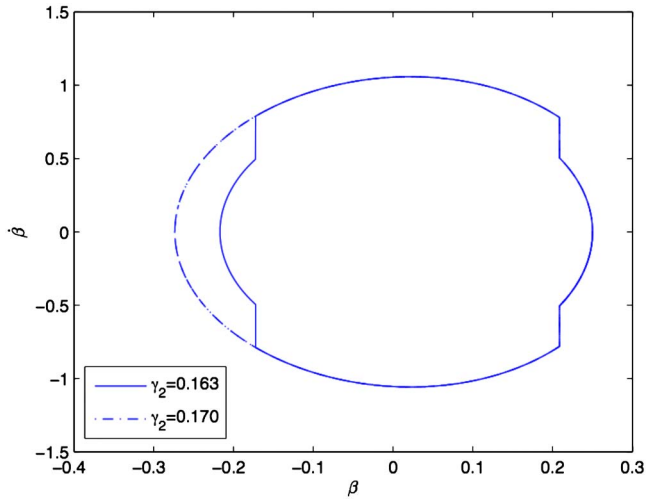

FIG. 10. (Color online) Phase space for β_1 and $\dot{\beta}_1$ with two initial conditions and simulation parameters approximating those for a sitar: $b=0.283$, and bridge terminations $\gamma_1=0.142$, $\gamma_2=0.163$. Also shown are results for extra wide 30 mm bridge surface with $\gamma_2=0.170$.

IV. CONCLUSIONS

A mathematical model of the string wrapping against obstacle at its boundary has been formulated using a moving boundary approach. The formulation includes the distributed behaviour of a rigid bridge obstacle which may be terminated at arbitrary locations on either side. Equations of motion have been provided for the three phases of motion corresponding to the string completely (phase-III), partially (phase-II), or not at all (phase-I) wrapped on the bridge. It is shown that a single mode moving boundary approach can reveal much of the underlying physics, including capturing the non-smooth string shape during phase-II motion. As many as 60 natural frequency components of the string are present in the wrapped string, in particular, during phase-II motion. Thus the model captures the characteristic buzzing behavior of the sitar tone. In the simulations given the string motion has been reasonably well represented using only a single mode, requiring solution of only a single ordinary differential equation (ODE) in phase-I and phase-III, or two coupled ODEs in phase-II. This suggests the applicability of the method to physics-based sound synthesis algorithms. The following conclusions can be drawn on phase-II motion:

- The modal amplitude $\beta_1(\tau)$ decreases as the contact length $\gamma(\tau)$ increases.
- The frequency of oscillation of the string initially in phase-I is higher than that initially in phase-II.
- The frequency of oscillation in phase-II remains constant irrespective of initial amplitude given by modal amplitude $\beta_1(0)$.

[1]B. C. Deva, *Musical Instruments of India: Their History and Development*, 2nd ed. (Munshiram Manoharlal, New Delhi, India, 1987).
[2]C. Fulton, "Playing the late medieval harp," in *A Performer's Guide to Medieval Music*, edited by R. Duffin (Indiana University Press, Bloomington IN, 2002), pp. 346–354.
[3]G. O'Brien, *Ruckers: A Harpsichord and Virginal Building Tradition* (Cambridge University Press, Cambridge, England, 1990).
[4]C. V. Raman, "On some Indian stringed instruments," Proceedings of the Indian Association for the Cultivation of Science **7**, 29–33 (1922).

[5]L. Amerio and G. Prouse, "Study of the motion of a string vibrating against an obstacle," Rend. Mat. **2**, 563–585 (1975).
[6]M. Schatzman, "A hyperbolic problem of second order with unilateral constraints: The vibrating string with a concave obstacle," J. Math. Anal. Appl. **73**, 138–191 (1980).
[7]R. Burridge, J. Kappraff, and C. Morshedi, "The sitar string, a vibrating string with a one-sided inelastic constraint," SIAM J. Appl. Math. **42**, 1231–1251 (1982).
[8]H. Cabannes, "Motion of a string in the presence of a straight rectilinear obstacle," C.R. Acad. Sc. Paris, Series II **295**, 637–640 (1982).
[9]H. Cabannes, "Motion of a vibrating string in the presence of a convex obstacle: A free boundary problem," C.R. Acad. Se. Paris, Series II **301**, 125–129 (1985).
[10]H. Cabannes, "Presentation of software for movies of vibrating strings with obstacles," Appl. Math. Lett. **10**, 79–94 (1997).
[11]J. Ahn, "A vibrating string with dynamic frictionless impact," Appl. Numer. Math. **57**, 861–884 (2007).
[12]S. M. Han and M. A. Grosenbaugh, "Non-linear free vibration of a cable against a straight obstacle," J. Sound Vib. **273**, 337–361 (2004).
[13]T. Taguti, "Dynamics of simple string subject to unilateral constraint: A model analysis of sawari mechanism," Acoust. Sci. & Tech. **29**, 203–214 (2008).
[14]C. P. Vyasarayani, S. Birkett, and J. McPhee, "Free vibration response of a plucked string impacting against a spatial obstacle," in Proceedings of the International Conference on Theoretical, Applied, Computational and Experimental Mechanics, Kharagpur, India (2007).
[15]A. Krishnaswamy and J. O. Smith, "Methods for simulating string collisions with rigid spatial obstacles," in IEEE Workshop on Applications to Signal Processing to Audio and Acoustics. (2003), pp. 233–236.
[16]C. Valette, "The mechanics of vibrating strings," in *Mechanics of Musical Instruments*, edited by J. Kergomard and G. Weinreich (Springer-Verlag, Vienna, 1995), pp. 115–183.
[17]In the literature, a perfectly wrapped string is often described as a completely plastic impact.
[18]R. Fung and Y. Chen, "Free and forced vibration of a cantilever beam contacting with a rigid cylindrical foundation," J. Sound Vib. **202**, 161–185 (1997).
[19]F. Pfeiffer and C. Glocker, *Multibody Dynamics With Unilateral Contacts* (Wiley, New York, 1996).
[20]A. V. Pesterev and L. A. Bergman, "An improved series expansion of the solution to the moving oscillator problem," ASME J. Vibr. Acoust. **122**, 54–61 (2000).
[21]W. D. Zhu and C. D. Mote, "Dynamics of the pianoforte string and narrow hammers," J. Acoust. Soc. Am. **96**, 1999–2007 (1994).
[22]S. Bilbao, "Conservative numerical methods for nonlinear strings," J. Acoust. Soc. Am. **118**, 3316–3327 (2005).
[23]C. P. Vyasarayani, S. Birkett, and J. McPhee, "A vibrating sitar string: Modeling the 3d dynamics of a plucked string impacting a spatial obstacle with friction," in Acoustics Paris '08 (2008).
[24]These comments refer to an open string. Fretting the string shortens its length and lowers the far termination about 2 mm, making only a minor difference to the vertical displacement at the normal plucking point.

Lamb mode spectra versus the Poisson ratio in a free isotropic elastic plate

Daniel Royer, Dominique Clorennec, and Claire Prada
Laboratoire Ondes et Acoustique, ESPCI, Université Paris 7, CNRS UMR 7587, 10 rue Vauquelin, 75231 Paris Cedex 05, France

(Received 23 December 2008; revised 20 March 2009; accepted 20 March 2009)

The variation, with material parameters, of Lamb modes is investigated. Vibration spectra of traction-free elastic plates are generally presented, for a given isotropic material, as a set of dispersion curves corresponding to the various Lamb mode branches. Here, the spectrum variations, with the Poisson ratio ν, are plotted in a dimensionless co-ordinate system in the form of a bundle of curves for each Lamb mode. Except for the fundamental anti-symmetric mode A_0, this representation highlights the same behavior for all Lamb modes. V_T denoting the shear wave velocity, the (ω,k) plane can be divided into two angular sectors separated by the line of slope $V_T\sqrt{2}$. In the upper one, corresponding to a phase velocity $V=\omega/k$ larger than $V_T\sqrt{2}$, dispersion curves are very sensitive to the plate material parameters. In the lower sector $(V<V_T\sqrt{2})$ all the branches, whatever the value of the Poisson ratio $(0\leq\nu<0.5)$, are gathered into a thin pencil. Moreover, curves of a given bundle cross the boundary line at coincidence points equally spaced. These properties and a specific behavior observed for $\nu=0$ are explained in terms of Lamé wave solutions of the characteristic equations of Lamb modes.
 [DOI: 10.1121/1.3117685]

PACS number(s): 43.40.Dx, 43.20.Mv [YHB] Pages: 3683–3687

I. INTRODUCTION

The characteristic equations governing the propagation of symmetric (S_n) and anti-symmetric (A_n) modes in a free isotropic plate was derived by Rayleigh.[1] First numerical solutions were obtained for the phase velocity V of the lowest modes by Lamb.[2] The propagation of these guided waves can be represented by a set of dispersion curves giving the angular frequency $\omega=2\pi f$ of each modes versus the wave number $k=2\pi/\lambda$. Plots of dispersion curves, numerically calculated for various materials, can be found in many textbooks.[3–6] They show the complexity of Lamb waves frequency spectra as a result of the coupling of shear waves (velocity V_T) and longitudinal waves (velocity V_L) at the traction-free surfaces.

Before the extensive use of computers, crossings of Lamb mode branches were investigated as a guide for sketching Lamb wave spectra without numerical calculations. Due to mode orthogonality,[7] curves of the same family never intersect. Crossing points between symmetric and anti-symmetric curves were first studied by Mindlin.[8] This author developed a method based on mixed boundary conditions for which shear and dilatational waves are uncoupled. The grid of intersecting dispersion curves for a plate subjected to these artificial boundary conditions forms a series of bounds for the dispersion curves of Lamb modes. Using dimensionless variables, Lamb wave frequency spectra only depend on the bulk wave velocity ratio V_L/V_T or Poisson's ratio ν. Extending Mindlin's method, Freedman[9] studied the variation of Lamb mode spectra over the full range of Poisson's ratio $(-1<\nu<0.5)$. This author also showed that coincidences of branches of like symmetry modes occur at intersection of bounds and for a ratio of the wave number k to the shear wave number in the plate material $(k_T=\omega/V_T)$ equal to $2^{-1/2}$. In a companion paper,[10] the special behavior of Lamb modes at $\nu=0$ was investigated in terms of Mindlin rules. In a third paper,[11] Freedman examined the variation of individual branches of lower order Lamb modes over the complete range of Poisson ratio.

In Freedman's papers, the dispersion curves are generally presented on an unusual plot of k/k_T versus d/λ_T (d denoting the plate thickness) and figures are schematic illustrations of the variations of Lamb branches. Additionally, a large number of accurate frequency spectra can be found in the literature on Lamb waves. However, each spectrum, computed for a given material or a fixed value of the Poisson ratio, is composed of many branches corresponding to various modes. From the juxtaposition of these families of dispersion curves, it is not easy to conclude on the evolution of Lamb modes with the mechanical properties of the plate material. It is thus desirable to reach a clear insight on the variations of the lower order Lamb mode branches with material parameters.

The objective of the present paper is to clarify the manner in which the frequency spectrum of Lamb waves varies with the Poisson ratio. For this purpose, the dispersion curves are presented in a co-ordinate system giving the normalized frequency $F=fd/V_T$ versus the normalized wave number $K=kd/2\pi=d/\lambda$. Moreover, we present the spectrum in the form of a bundle of curves for a selected Lamb mode. These plots show general trends and clearly highlight the specific behavior of Lamb modes at points where they consist solely of shear waves propagating at 45° to the plate surfaces.

II. NUMERICAL RESULTS

In a homogeneous isotropic plate, Lamb waves are either symmetric or anti-symmetric. For each family the angular frequency and the wave number satisfy a characteristic or frequency equation.[3] When the faces of the plate are free of tractions, no energy leakage occurs. Then, for any real k, the secular equation yields an infinite number of real roots in ω. The dispersion curves of these propagating modes, guided by the plate, is represented by a set of branches in the (ω,k) plane. Many frequency spectra can be found in the literature. Each of them, computed for a given material, testifies the complexity of Lamb wave propagation.

Elastic properties of an isotropic material are characterized by two constants c_{11} and c_{66}, related to longitudinal and shear wave velocities, respectively, V_L and V_T. The use of dimensionless frequency $F=fd/V_T$ and wave number $K=kd/2\pi$ allows us to express Lamb wave propagation in terms of only one material parameter, the bulk wave velocity ratio $\kappa=V_L/V_T$ or the Poisson ratio ν:

$$\nu=\frac{\kappa^2-2}{2(\kappa^2-1)} \tag{1}$$

and

$$\kappa=\frac{V_L}{V_T}=\sqrt{\frac{2(1-\nu)}{1-2\nu}}. \tag{2}$$

The advantage of Poisson's ratio is that this coefficient remains finite. With very few special exceptions, isotropic materials exhibit positive Poisson ratio. Therefore, the study is limited to the usual range, i.e., from the rigid solid ($\nu=0 \rightarrow \kappa=\sqrt{2}$) to the fluid ($\nu=0.5 \rightarrow \kappa=\infty$).

Numerical calculations have been performed in order to determine the normalized frequency F versus normalized wave number K. Dispersion curves were plotted for $0\leq K\leq 5$ and $0\leq F\leq 6$ and for 11 values of the Poisson ratio ν from 0 to 0.49. The first ten values are separated by a step equal to 0.05. The limiting case of a fluid, with $V_T=0$ and $\nu=0.5$, is not considered here. Results are presented in Fig. 1 for the first four anti-symmetric modes and in Fig. 2 for the first four symmetric modes. In these graphs, a straight line of unit slope corresponds to a phase velocity $V=\omega/k$ equal to V_T. This representation highlights some conclusions on the behavior of Lamb modes versus the plate material properties.

For a given mode, the lower curve of a bundle corresponds to $\nu=0$ and the upper one to $\nu=0.49$. This continuous evolution of the frequency spectrum observed for all the Lamb modes can be easily explained. Equation (2) shows that the bulk wave velocity ratio $\kappa=V_L/V_T$ increases with the Poisson ratio. Thus, in a co-ordinate system where the frequency thickness product is normalized to the shear wave velocity V_T, the dispersion curves are pulled toward high normalized frequencies when the longitudinal wave velocity V_L increases.

Except for the fundamental anti-symmetric mode A_0, the (ω,k) plane can be divided in two angular sectors. In the upper sector, corresponding to a phase velocity $V=\omega/k$ larger than $V_T\sqrt{2}$, dispersion curves are very sensitive to the material parameters. In the lower sector ($V<V_T\sqrt{2}$) all the

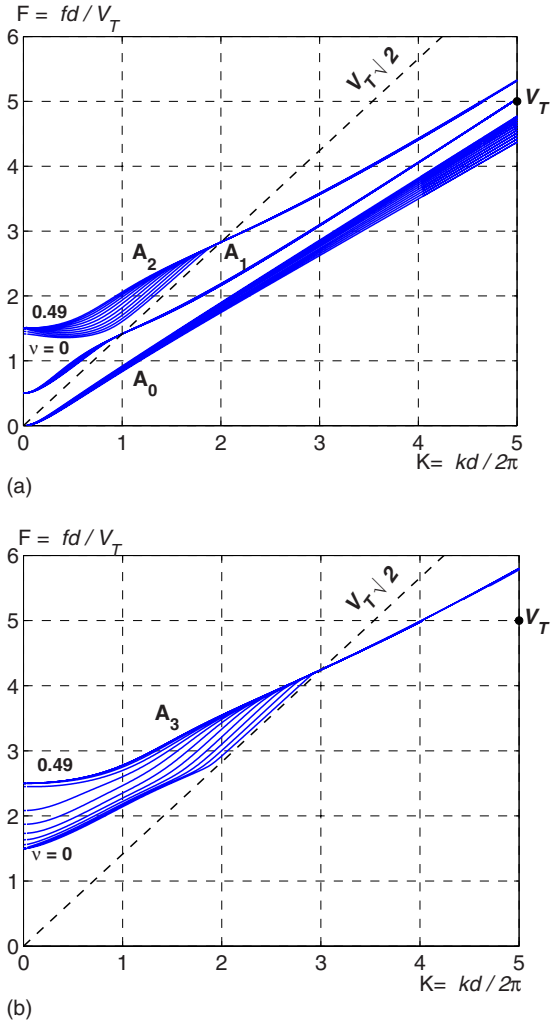

FIG. 1. (Color online) Variation, with Poisson's ratio in the range $0\leq\nu\leq 0.49$, of anti-symmetric Lamb modes in an isotropic free plate of thickness d. Bundle of dispersion curves for (a) A_0, A_1, and A_2 modes, and (b) A_3 mode. For each mode, the lower curve corresponds to $\nu=0$ and the upper one to $\nu=0.49$.

curves, whatever the value of Poisson's ratio, are gathered into a thin pencil. It should be noted that this velocity $(V_T\sqrt{2})$ represents the lowest possible value of the longitudinal bulk wave velocity V_L reached at zero Poisson ratio. Thus in the lower sector, for any material, the phase velocity is smaller than V_L, which dramatically reduces the influence of bulk wave velocity ratio and Poisson ratio on Lamb mode dispersion curves. For large values of kd, i.e., $d\gg\lambda$, the non-zero order symmetric and anti-symmetric branches tend asymptotically toward a unit slope, corresponding to a phase velocity equal to V_T. Lamb modes are often used to characterize material properties in platelike structures.[12] This remark indicates that for high order modes $(n\geq 1)$ the sensitivity to material parameter ν or $\kappa=V_L/V_T$ is much larger in the upper sector.

Branches of a given Lamb mode cross the line corresponding to the phase velocity $V_T\sqrt{2}$ at a fixed point independent of the Poisson ratio. These points are equally spaced on this line and their abscissa kd are equal to $(2n+1)\pi$ for the symmetric mode S_n $(K=n+1/2)$ and $2n\pi$ for the anti-symmetric mode A_n $(K=n)$, respectively. Curves of a given

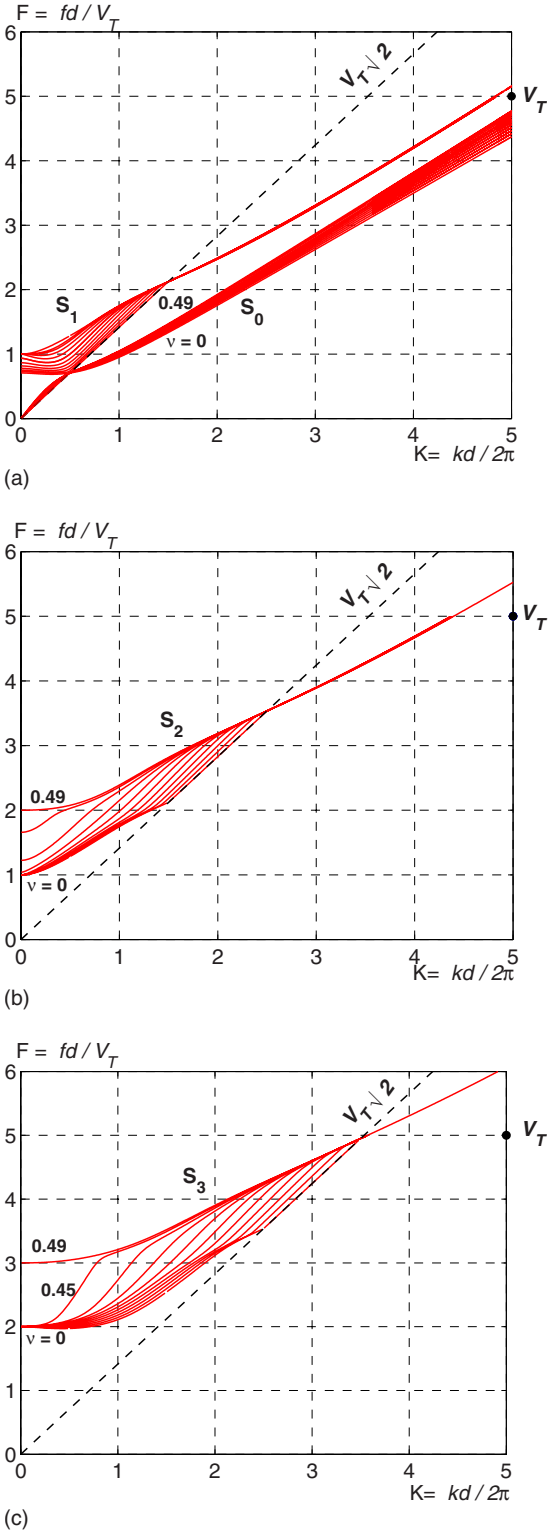

FIG. 2. (Color online) Variation, with Poisson's ratio in the range $0 \leqslant \nu \leqslant 0.49$, of symmetric Lamb modes in an isotropic free plate of thickness d. Bundle of dispersion curves for (a) S_0 and S_1 modes, (b) S_2 mode, and (c) S_3 mode. For each mode, the lower curve corresponds to $\nu=0$ and the upper one to $\nu=0.49$.

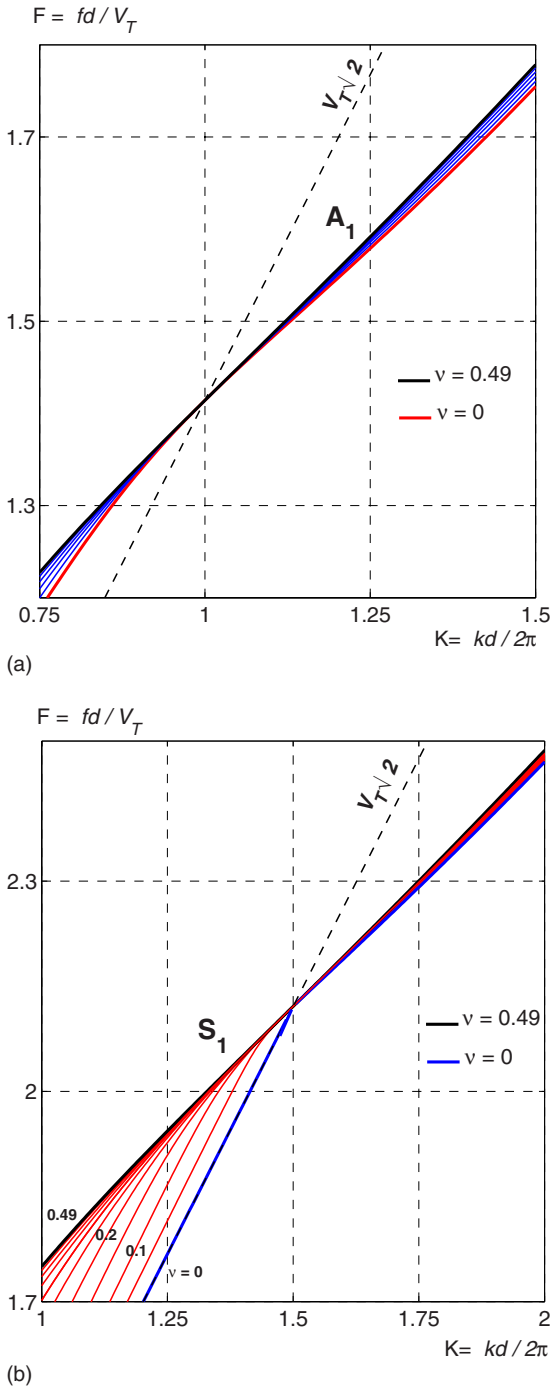

FIG. 3. (Color online) Behavior of dispersion curves over the coincidence points. (a) A_1 mode and (b) S_1 mode. Dispersion curves of a given mode cross the line $F=\sqrt{2}K$ with the same slope.

bundle do not intersect each other. Figure 3 illustrates this behavior for modes A_1 and S_1, showing that dispersion curves cross the line $F=\sqrt{2}K$ at the common point with the same slope. All branches of a bundle pass through the line so tangentially that their order does not change at the coincidence point. This property is valid for all the symmetric and anti-symmetric modes.

In the case of a rigid solid ($\nu=0$), Fig. 4(a) shows that symmetric Lamb modes exhibit a particular behavior. It appears that all the segments of the line $F=\sqrt{2}K$ belong to successive symmetric modes. The change from mode S_n to mode S_{n+1} occurs at the coincidence point of abscissa $kd=(2n+1)\pi$, giving rise to a discontinuity of the slope and thus of the group velocity $V_g=d\omega/dk$. These remarks are not valid for the anti-symmetric modes [Fig. 4(b)].

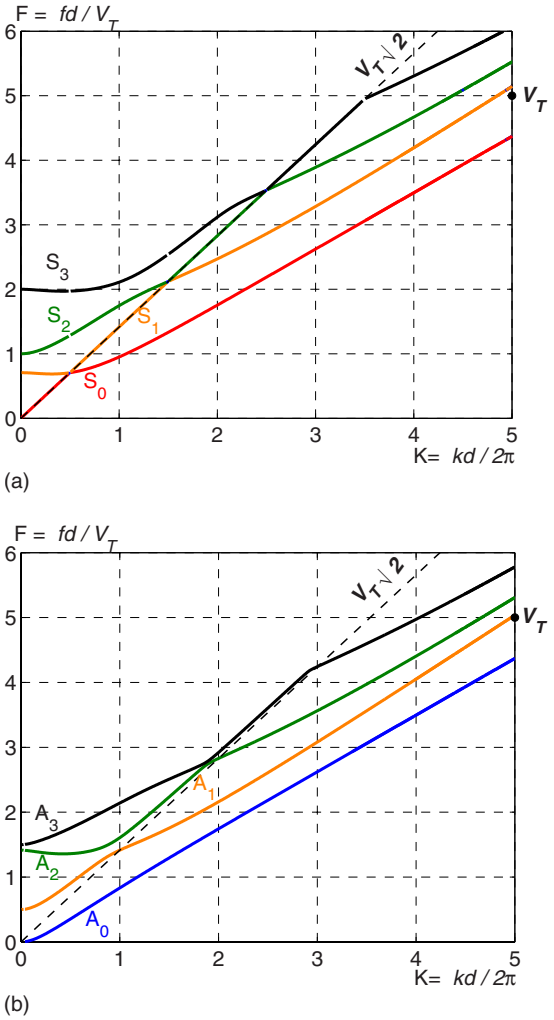

FIG. 4. (Color online) Special behavior at $\nu=0$ (rigid solid). (a) Symmetric Lamb modes: segments of the Lamé line belong to successive modes. The change from mode S_n to mode S_{n+1} occurs at the coincidence point of abscissa $K=n+1/2$ and gives rise to a discontinuity of the slope. (b) This discontinuous behavior is not observed on anti-symmetric branches.

In the following part, most of the features observed on Lamb mode frequency spectra are explained from the specific conditions for which the modes propagating in the free isotropic plate are Lamé modes, consisting solely of shear waves, or a degenerate Lamé mode, consisting of a purely longitudinal wave.[13]

III. INTERPRETATION IN TERMS OF LAMÉ MODES

The characteristic equations of Lamb modes result from the traction-free boundary conditions on the surfaces, located at $x_2=\pm h$ for a plate of thickness $d=2h$. Using classical notations:[5,6]

$$q^2=k_T^2-k^2 \quad \text{and} \quad p^2=k_L^2-k^2, \tag{3}$$

boundary conditions may be expressed, for the symmetric modes ($\alpha=0$) and the anti-symmetric modes ($\alpha=\pi/2$), as

$$(k^2-q^2)B\cos(ph+\alpha)+2ikqA\cos(qh+\alpha)=0 \tag{4}$$

and

$$2ikpB\sin(ph+\alpha)+(k^2-q^2)A\sin(qh+\alpha)=0. \tag{5}$$

A and B are the amplitudes of the vector and scalar displacement potentials, respectively.

Lamé modes are particular solutions of these equations for $k_T^2=2k^2$, i.e., for a phase velocity V equal to $V_T\sqrt{2}$. With

$$q^2=k^2 \quad \text{and} \quad p^2=-\frac{\nu}{1-\nu}k^2, \tag{6}$$

boundary conditions are satisfied with $kh=(n+1/2)\pi$ for the symmetric modes ($\alpha=0$) and $kh=n\pi$ for the anti-symmetric modes ($\alpha=\pi/2$). In both cases the amplitude B of the scalar potential vanishes, giving rise to a pure shear wave reflecting at 45° on the plate boundaries for which no mode conversion into longitudinal waves occurs.[14] The resulting guided wave propagates along the axis of the plate at the phase velocity $V=V_T\sqrt{2}$. These solutions exist for any positive value of ν and the normalized co-ordinates of their representative points are the equally spaced values:

$$K=m/2 \quad \text{and} \quad F=m/\sqrt{2}, \tag{7}$$

where m is an odd (even) integer for the symmetric (anti-symmetric) modes. Moreover, the acoustic energy is carried at a velocity equal to the projection of the shear wave velocity on the plate axis. Thus, the group velocity $V_g=d\omega/dk$ of Lamé modes is equal to $V_T/\sqrt{2}$, i.e., half the phase velocity.

Since positions and slopes of Lamé modes are independent of the Poisson ratio, each Lamb mode of a given bundle passes through the Lamé line $F=\sqrt{2}K$ at the same point with the same slope. This behavior is observed in Figs. 1 and 2 for all the Lamb modes, except for the anti-symmetrical mode A_0 whose phase velocity is less than the Rayleigh wave velocity V_R, thus less than V_T.

For the special case $\nu=0\rightarrow p=0$ and for the symmetric modes, another solution of Eqs. (4) and (5) exists with $A=0$ and a non-zero scalar potential ($B\neq 0$). In a rigid solid, the Lamé solutions correspond to a constant longitudinal displacement propagating at the velocity $V_L=V_T\sqrt{2}$. Conversely to the non-degenerate Lamé modes, the boundary conditions are satisfied for any wave number k. Thus, as shown in Fig. 4(a), the Lamé line is a locus for the roots of the Rayleigh–Lamb equation. Segments of the Lamé line belongs to successive symmetric modes, the change from modes S_n to S_{n+1} occurring at the coincidence point of abscissa $kd=(2n+1)\pi$. At this point, the S_n branch changes direction giving rise to a discontinuity of the group velocity from $V_T\sqrt{2}$ to $V_T/\sqrt{2}$. The inverse change occurs for the mode S_{n+1}. As predicted, Fig. 4(b) shows that this behavior is specific to symmetric modes.

IV. CONCLUSION

Although the propagation of elastic waves in an isotropic plate has been widely investigated, the influence of plate material properties on Lamb mode spectra was not easy to derive from the uncountable frequency spectra found in the literature. Using a dimensionless co-ordinate system, the way individual Lamb mode branches vary with the Poisson ratio ν was investigated. A representation in the form of a bundle of dispersion curves shows that the normalized frequency

increases continuously with the Poisson ratio and also highlights some feature common for all Lamb modes, except for the fundamental anti-symmetric one A_0. The (ω,k) plane can be divided in two angular sectors separated by a line of slope equal to the phase velocity $V_T\sqrt{2}$ of the Lamé modes. In the upper one, corresponding to a phase velocity V larger than $V_T\sqrt{2}$, the frequency spectrum is very sensitive to Poisson's ratio. In the lower sector $(V<V_T\sqrt{2})$, all curves in a bundle are gathered into a thin pencil, with a weak dependence on Poisson's ratio. Moreover, all the dispersion curves of a given Lamb mode cross the boundary line at a fixed point with the same slope. These coincidence points are equally spaced: their abscissa are such that $kd=2n\pi$ for the anti-symmetric mode A_n and $kd=(2n+1)\pi$ for the symmetric mode S_n. In the case of a rigid solid $(\nu=0)$, a specific behavior is observed: segments of the Lamé line belong to successive symmetric modes. The change from modes S_n to S_{n+1} occurs at the coincidence point of abscissa $kd=(2n+1)\pi$.

[1]Lord Rayleigh, "On the free vibrations of an infinite plate of homogeneous isotropic elastic matter," Proc. London Math. Soc. **20**, 225–234 (1889).
[2]H. Lamb, "On waves in an elastic plate," Proc. R. Soc. London, Ser. A **93**, 114–128 (1917).
[3]I. A. Viktorov, *Rayleigh and Lamb Waves: Physical Theory and Applications* (Plenum, New York, 1967).
[4]B. Auld, *Acoustic Fields and Waves in Solids II* (Wiley Interscience, New York, 1973).
[5]J. D. Achenbach, *Wave Propagation in Elastic Solids* (North-Holland, Amsterdam, 1980).
[6]D. Royer and E. Dieulesaint, *Elastic Waves in Solids 1: Free and Guided Propagation* (Springer, Berlin, 1999).
[7]W. B. Fraser, "Orthogonality relation for the Rayleigh–Lamb modes of vibration of a plate," J. Acoust. Soc. Am. **59**, 215–216 (1976).
[8]R. D. Mindlin, "Mathematical theory of vibrations of elastic plates," in Proceedings of 11th Annual Symposium on Frequency Control (U.S. Army Signal Engineering Laboratories, Fort Monmouth, NJ, 1957), pp. 1–40.
[9]A. Freedman, "The variation, with the Poisson ratio, of Lamb modes in a free plate, I: General spectra," J. Sound Vib. **137**, 209–230 (1990).
[10]A. Freedman, "The variation, with the Poisson ratio, of Lamb modes in a free plate, II: At transitions and coincidence values," J. Sound Vib. **137**, 231–247 (1990).
[11]A. Freedman, "The variation, with the Poisson ratio, of Lamb modes in a free plate, III: Behaviour of individual modes," J. Sound Vib. **137**, 249–266 (1990).
[12]W. Gao, C. Glorieux, and J. Thoen, "Laser ultrasonic study of Lamb waves: Determination of the thickness and velocities of a thin plate," Int. J. Eng. Sci. **41**, 219–228 (2003).
[13]V. Pagneux, "Revisiting the edge resonance for lamb waves in a semi-infinite plate," J. Acoust. Soc. Am. **120**, 649–656 (2006).
[14]*Elastic Waves in Solids 1: Free and Guided Propagation* (in Ref. 6), p. 321.

Stability of monitoring weak changes in multiply scattering media with ambient noise correlation: Laboratory experiments

Céline Hadziioannou, Eric Larose,[a] Olivier Coutant, Philippe Roux, and Michel Campillo
Laboratoire de Géophysique Interne et Tectonophysique, CNRS and Université J. Fourier, BP53, 38041 Grenoble, France

(Received 13 January 2009; revised 7 April 2009; accepted 7 April 2009)

Previous studies have shown that small changes can be monitored in a scattering medium by observing phase shifts in the coda. Passive monitoring of weak changes through ambient noise correlation has already been applied to seismology, acoustics, and engineering. Usually, this is done under the assumption that a properly reconstructed Green function (GF), as well as stable background noise sources, is necessary. In order to further develop this monitoring technique, a laboratory experiment was performed in the 2.5 MHz range in a gel with scattering inclusions, comparing an active (pulse-echo) form of monitoring to a passive (correlation) one. Present results show that temperature changes in the medium can be observed even if the GF of the medium is not reconstructed. Moreover, this article establishes that the GF reconstruction in the correlations is not a necessary condition: The only condition to monitoring with correlation (passive experiment) is the relative stability of the background noise structure.
 [DOI: 10.1121/1.3125345]

PACS number(s): 43.40.Ph, 43.60.Tj, 43.40.Le, 43.20.Fn [RLW] Pages: 3688–3695

I. INTRODUCTION

In order to image a complex medium the impulse response, or Green function (GF), of that medium is needed. Classically, the impulse response is retrieved by active means: A signal generated at one point (e.g., an earthquake) is recorded at another (a passive receiver such as a seismic station), and this record is treated as the band-pass filtered GF. Over the past 15 years, developments in helioseismology[1] and in acoustics[2,3] showed that information about a medium can be extracted from diffuse (coda) waves or ambient background noise. Since then, seismologists turn to this *passive imaging* technique.[4] In this latter case the seismic coda[5] or seismic noise[6] is correlated with reconstructing the GF, either by averaging over space, time, or both. Passive imaging requires some assumptions: One needs uniformly distributed noise sources and/or long enough record duration to get the correlation function to converge to the GF.

Monitoring dynamic media is a separate issue and, as we will see, is based on different (and weaker) assumptions. In the 1980s, Poupinet *et al.*[7] proposed to use coda waves to monitor velocity changes in scattering media (the aforementioned *doublet* technique). At first glance, coda waves might appear as a jumbled mess of wave arrivals. In fact, they consist of the waves which have described long, scattered paths through the medium, thereby sampling it thoroughly. As a result, these scattered waves are more sensitive to small variations than the ballistic waves. For this reason, the information in the coda can be exploited to monitor small changes in a medium. This technique, analogous to diffuse wave spectroscopy[8] in optics, was later named *coda wave interferometry*.[9] It tracks the tiny phase changes in the coda that are caused by velocity changes in the medium. A major issue of the doublet technique is that it requires stable reproducible sources, which are hardly available in seismology. Thus, a more recent idea was to combine noise-based passive imaging with the doublet technique.[10–13] First, one correlates the background noise between two receivers. Second, one analyzes small phase changes at large lapse times (coda) in the correlations. This forms the basis of passive monitoring (or passive image interferometry[11]) with seismic noise. Noise-based passive monitoring seems to simultaneously require two conditions: first, a homogeneous distribution of sources in space and, second, temporal stability of these sources.

In seismology, most of the noise (between 0.01 and 1 Hz) generated in the oceans[14,15] shows strong spatio-temporal variabilities. This feature is in favor of passive imaging as long as records are long enough (duration of the order of 1 year) to average over a large distribution of sources. But to *passively monitor* dynamic phenomena over a few days or less, this feature seems very unfavorable. In this paper, we investigate the effect of these non-ideal conditions on the reliability of *passive* monitoring. We will also examine if the GF reconstruction in the correlation is a necessary condition to perform passive monitoring. To that end, we test the passive monitoring technique under degraded conditions in a controllable (laboratory) environment. In Sec. II of the present paper, we describe the experimental setup and our motivations to do small-scale seismology. In Sec. III, we compare two different data processing procedures to extract velocity variations from the coda wave. One is the doublet technique introduced 20 years ago. The other, referred to as *stretching*, was developed more recently.[11,16,17] Advantages and drawbacks of both procedures are discussed. We also investigate the robustness of these procedures when noise is

[a]Author to whom correspondence should be addressed. Electronic mail: eric.larose@ujf-grenoble.fr

 0001-4966/2009/125(6)/3688/8/$25.00

TABLE I. Comparison of the physical parameters between seismology and ultrasound.

	Seismology	Ultrasound
Wavelength	km	mm
Frequency	mHz–Hz	MHz
Total size	10^3 km	m
Total duration	month–year	min

introduced in the signal. In Sec. IV, we investigate if passive monitoring is still possible when the GF is not properly reconstructed in the correlations. Finally, in Sec. V, we test the robustness of passive monitoring in the case of temporally changing distribution of sources.

II. METHODOLOGY

A. Motivations for doing analogous laboratory experiments

Seismology is based on the observation and processing of natural vibrations. In a passive field experiment where seismic waves originate from earthquakes, scientists face two simultaneous problems. They neither know the source location with sufficient precision, the source mechanism, nor the medium of propagation. It is therefore very complex to image the source and the medium at the same time. By reproducing some features of the seismic propagation in the laboratory and employing controlled sources and sensors, we can focus our efforts on the physics of the wave propagation and develop new methods more comfortably. In laboratory-scale seismology, we control, for instance, the size of the medium, the scattering properties, and the absorption. We are then able to adjust one parameter at a time and test the physical models and imaging techniques we develop. But the main reason for carrying out analogous ultrasonic experiments is more tactical: It is related to the order of magnitude of the physical parameters as recalled in Table I. Ultrasonic wavelengths are on the order of a millimeter, meaning that experiments are physically easy to handle. Additionally, the duration of a single ultrasonic experiment is very short (1 min) compared to seismology where we have to wait for earthquakes (year). This characteristic allows us to achieve many more experiments in the laboratory, and test many parameters over a wide range of magnitudes. In the view of testing processing technique to monitor weak changes, it is also of first importance to perfectly control the origin of the change in the medium. This is quite convenient in the laboratory, but almost impossible in a natural environment. These are the reasons why several seismology laboratories have decided to develop analogous experiments for methodological developments.[9,18–20] Our article presents one analogous ultrasonic experiment not only devoted to the study of the physics of wave propagation in heterogeneous media, but also to the development of new techniques applicable to seismic waves in geosciences.

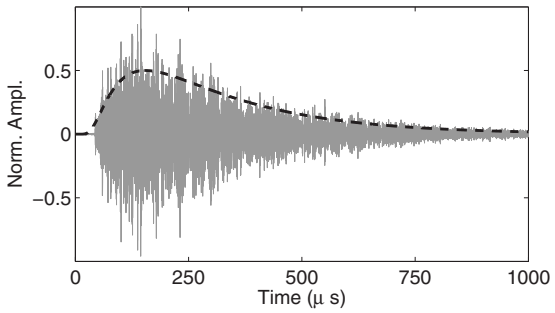

FIG. 1. Gray line: acoustic field transmitted through the 64 mm thick bubble-gel mixture (in normalized amplitude). Black broken line: 2D diffusion equation for $\ell^\star = 3.5$ mm and $\ell_a = 200$ mm.

B. Scattering properties of the medium

We perform the experiment on an 80×64 mm^2 block of agar-agar gel, which consists of 95% water and 5% agar (by weight). 8.5% of the volume of the gel consists of small air bubbles, with diameters between 100 μm and 1 mm. These bubbles render the medium multiply scattering. The source emits a pulse at 2.5 MHz (100% frequency bandwidth). For simplicity, we neglect the electronic noise in the experiment. Since shear waves are strongly attenuated, we assume that only *P*-waves propagate in the medium and are eventually recorded. To estimate the scattering properties of the medium, we performed several experiments in the transmission configuration for several medium thicknesses. From the attenuation of coherent plane wave, we obtain an estimation of the elastic scattering mean free path averaged in the working frequency band: $\ell_e \approx 3.5$ mm. Since the scatterers' size is smaller or of the order of the wavelength, scattering is isotropic and we expect a transport mean free path $\ell^\star$ of the same order. In Fig. 1 we plot an example of a diffuse record transmitted through 64 mm of our heterogeneous medium. A theoretical fit is obtained from the two-dimensional (2D) diffusion equation (including reflections from the sides) and plotted as a broken black line. The diffusion constant is $D = v_P \ell^\star / 2$ and we assume $\ell_e \approx \ell^\star$. The absorption length ℓ_a is the fit parameter, and the best fit is obtained for $\ell_a = 200$ mm. This corresponds to an absorption three times stronger than in pure water,[21] which is due to dissipation by the agar material.

III. COMPARISON OF DATA PROCESSING TECHNIQUES

Two processing techniques have been proposed in literature to estimate relative velocity changes dV/V in the diffuse coda. The first one, called the seismic doublet technique, was developed for geophysical purposes about 20 years ago.[7] The idea is to measure a time-shift between two different records in limited time-windows centered at t in the coda. By repeating this procedure at different times t, it is possible to plot the delay δt versus t. The velocity variation is simply the average slope of $\delta t(t)$: $dV/V = -\delta t/t$. Doing so, we implicitly assume that the time-shift is constant within the considered time-window, which might be not the case. This processing

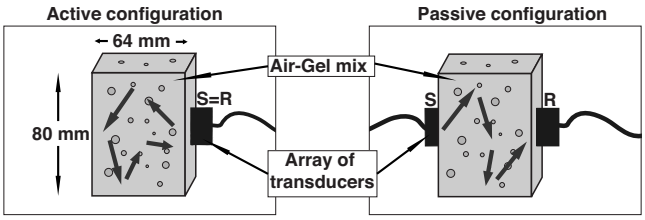

FIG. 2. Experimental setup. Left: the active experiment in the pulse-echo configuration. Right: the passive experiment in the transmission configuration before autocorrelation.

found remarkable applications in geophysics, including recent developments in volcano eruption prediction[13] and active fault monitoring.[22]

Another idea[11,16] is to interpolate the coda at times $t(1-\varepsilon)$ with various relative velocity changes ε. This corresponds to stretching the time axis. The actual velocity change is obtained when the interpolated coda best fits the original data. Because we do not assume a constant time-shift in the considered time-window $[0\ T]$, we can process the whole data at once, which is expected to result in a more stable, and thus more precise, estimation of dV/V. One drawback is that this latter processing assumes a linear behavior $\delta t(t)$ versus t, or a constant relative velocity change $dV/V=\varepsilon$, which is sometimes not the case in complex heterogeneous media. No quantitative comparison between these two techniques has been established in literature. In Sec. III A, we propose to test both techniques on the same data set, and analyze their sensitivity to the signal-to-noise ratio (SNR) of the records.

A. Active experiment: High quality data

In this experiment, we attach a set of transducers on one side of the gel, which act as both sources and receivers of the signal (Fig. 2, left). The source emits a 2.5 MHz pulse. The signal is collected on the same transducer (R) in the pulse-echo configuration. This procedure is repeated on seven different channels. As the gel contains a large amount of scatterers, the emitted waveform is multiply scattered before reaching the transducer again. A typical ultrasonic record is plotted in Fig. 1. Note that the early 5 μs are muted for technical reasons. This record is composed of the GF of the air-gel mix sample $G(R,R,t)$ and the source wavelet $e(t)$ as follows:

$$h_0(t) = G_0(R,R,t) \otimes e(t), \tag{1}$$

where $\otimes$ stands for convolution. This experiment is repeated four times while the temperature of the medium slowly increases by about 0.8 °C, as measured by a digital thermometer placed beneath the gel. We assume that the first effect of a temperature change is to stretch the record in time by $\varepsilon_k = dV/V$, and to additionally slightly distort it.[16] This weak distortion, noted $f(t)$, is not studied here, although it contains precious information about the medium and its evolution. An example of two records is displayed in Fig. 3. After a (small) temperature change, the record rewrites

$$h_k(t) = G_k(R,R,t) \otimes e(t) \tag{2}$$

$$= [G_0(R,R,t(1+\varepsilon_k)) + f(t)] \otimes e(t). \tag{3}$$

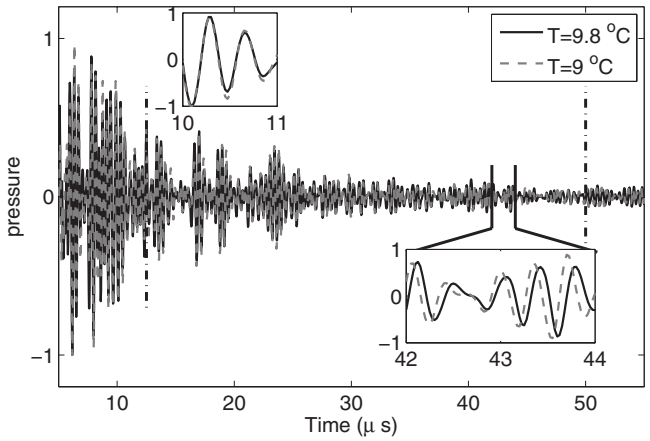

FIG. 3. Example of two records $h_0(t)$ and $h_3(t)$ acquired at the same position (same transducer) but at two different dates. Between the two acquisitions, the temperature has increased by 0.8 °C, which is hardly visible in the early part of the record (inset between 10 and 11 μs) but very clear in the late coda (inset between 42 and 44 μs).

For each temperature k, the record $h_k(R,R,t)$ is compared to the reference waveform $h_0(R,R,t)$ to evaluate the relative velocity change in the gel sample. Two processing techniques have been proposed in literature to estimate dV/V: the doublet technique and the stretching technique.

1. Doublet technique

The doublet technique, also known as cross-spectral moving-window technique (CSMWT),[23] computes the phase shift between records for consecutive, overlapping time-windows. For a given window, the time-shift is assumed to be constant and is estimated in the frequency domain by measuring the Fourier cross-spectrum phase. This estimator uses an accurate, unbiased Wiener filter technique[24] and produces an estimate whose confidence interval is controlled by the coherence values in the frequency band used for the analysis. The method can then measure arbitrary time-shifts between two records with enough similarity (or coherence). The key parameter in this analysis is the Fourier transform window length. The length choice is a trade-off between shift estimate accuracy, and the time resolution of possible temporal variations.

We use this doublet technique to compute the time-shift between the records. The time-shift between the two different records is measured in the coda between 12.5 and 50 μs. If the velocity changes homogeneously in the medium, the propagation time will vary proportionally to the propagation distance, producing a phase shift between records varying linearly with lapse time. The relative velocity change can be retrieved by measuring the slope of the phase shift as a function of lapse time, as shown in Fig. 4.

2. Stretching interpolation technique

In the stretching technique, the coda $h_k(R,R,t)$ is interpolated at times $t(1-\varepsilon)$ with various relative velocity changes, ε, in the $[t_1-t_2]$ time-window. ε_k is therefore the ε that maximizes the cross-correlation coefficient

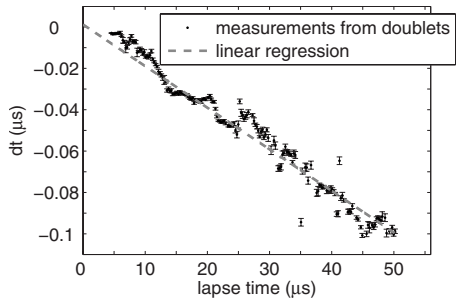

FIG. 4. Delay time evaluated for different lapse times in the coda from the doublet code. The broken line is the linear trend whose slope yields dV/V between $k=0$ and $k=3$.

$$\mathrm{CC}_k(\varepsilon) = \frac{\int_{t_1}^{t_2} h_k[t(1-\varepsilon)]h_0[t]dt}{\sqrt{\int_{t_1}^{t_2} h_k^2[t(1-\varepsilon)]dt \,.\, \int_{t_1}^{t_2} h_0^2[t]dt}}. \tag{4}$$

An example of correlation coefficient is plotted in Fig. 5. If we assume that h_0 and h_k are stationary waveforms[25] and are well described by Eqs. (1) and (2), we have a theoretical estimation of CC as

$$\mathrm{CC}_k(\varepsilon) = \frac{A}{\int_{\Delta\omega}\rho(\omega)d\omega}\int_{\Delta\omega}\frac{\rho(\omega)\sin(\omega\varepsilon t_2)-\sin(\omega\varepsilon t_1)d\omega}{\omega\varepsilon(t_2-t_1)} + B(\varepsilon), \tag{5}$$

which in the simple case of $t_1=0$ and $t_2=T$ simply reduces to

$$\mathrm{CC}_k(\varepsilon) = A\frac{\int_{\Delta\omega}\rho(\omega)\mathrm{sinc}(\omega(\varepsilon-\varepsilon_k)T)d\omega}{\int_{\Delta\omega}\rho(\omega)d\omega} + B(\varepsilon) \tag{6}$$

with ω the pulsation, $\Delta\omega$ the bandwidth, and $\rho(\omega)$ the power spectrum density. The constant A depends on the variance of G, noted $\langle G^2\rangle$, and the variance of the additional fluctuations, noted $\langle f^2\rangle$,

$$A = \frac{\sqrt{\langle G^2\rangle}}{\sqrt{\langle G^2\rangle + \langle f^2\rangle}}. \tag{7}$$

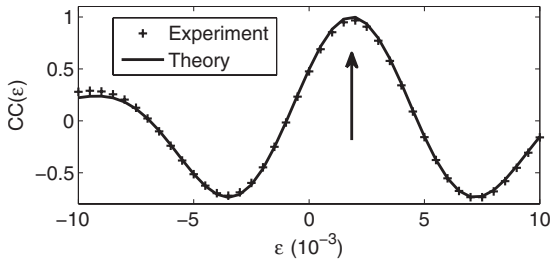

FIG. 5. The correlation coefficient CC(ε) is evaluated at two temperatures for $k=0$ and 3 in the 12.5–50 μs range. The maximum, obtained for a relative velocity change of $\varepsilon_3 = 1.86\times10^{-3}$, is indicated by the vertical arrow. It corresponds to an increase in temperature of 0.8 °C. Theory is from Eq. (5).

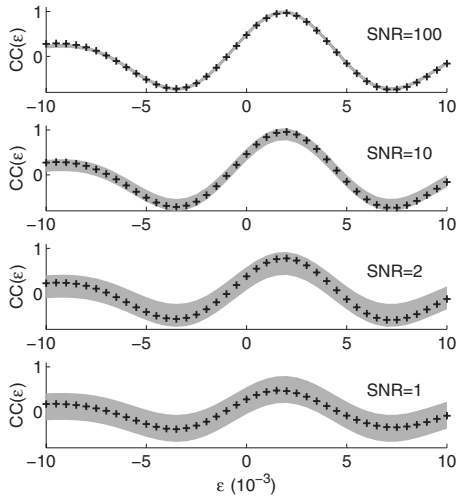

FIG. 6. The correlation coefficient CC(ε) is evaluated at two temperatures $k=0$ and 3 in the 12.5–50 μs range, for various SNRs. Crosses indicate experimental data. The gray background indicates expected fluctuations [Eq. (11)] around the theory [Eq. (10)]. The proper velocity change ε_3 is found in all cases, though a slight difference is visible for SNR=1.

$B(\varepsilon)$ is a random process of zero mean and standard deviation (see EPAPS Ref. 26)

$$\sqrt{\langle B^2\rangle} = \sqrt{\frac{2\pi}{T\Delta\omega}}\frac{\sqrt{\langle f^2\rangle}}{\sqrt{\langle G^2\rangle + \langle f^2\rangle}}. \tag{8}$$

The term containing the sinc function is represented by the crosses in Fig. 5 and 6, and the fluctuations ($\sqrt{\langle B^2\rangle}$) around this average are in gray. If the amplitude of the sinc function is much greater than the fluctuations, $A \gg \sqrt{\langle B^2\rangle}$, the maximum of the cross-correlation coefficient CC_k is obtained for $\varepsilon=\varepsilon_k$, which provides the relative velocity change for the given state k. It is interesting to note that the peak of the sinc function is visible even if the distortion $f(t)$ [or electronic noise noise $n(t)$; see Sec. III B] is strong. In such a case, increasing the integration time T or the frequency bandwidth $\Delta\omega$ can reduce the fluctuations B. This is a crucial advantage of the present technique compared to the doublet technique in the case of noisy or distorted data.

B. Active experiment: low quality data

To mimic a practical situation where data include additional noise (instrumental or electronic), we add a random δ-correlated noise $n(t)$ of zero mean to the signals $h(t)$ in Eqs. (1) and (2). For simplicity, we neglect the distortion f_k in the considered time-window, and assume a stationary noise

$$\langle n_0^2\rangle = \langle n_k^2\rangle = \langle n^2\rangle, \tag{9}$$

then we get a similar expressions as Eqs. (7) and (8), with

$$A = \frac{\langle h^2\rangle}{\langle h^2\rangle + \langle n^2\rangle} \tag{10}$$

and

$$\sqrt{\langle B^2\rangle} = \sqrt{\frac{2\pi}{T\Delta\omega}}\frac{\sqrt{\langle n^2\rangle + 2\langle n^2\rangle\langle h^2\rangle}}{\langle h^2\rangle + \langle n^2\rangle}. \tag{11}$$

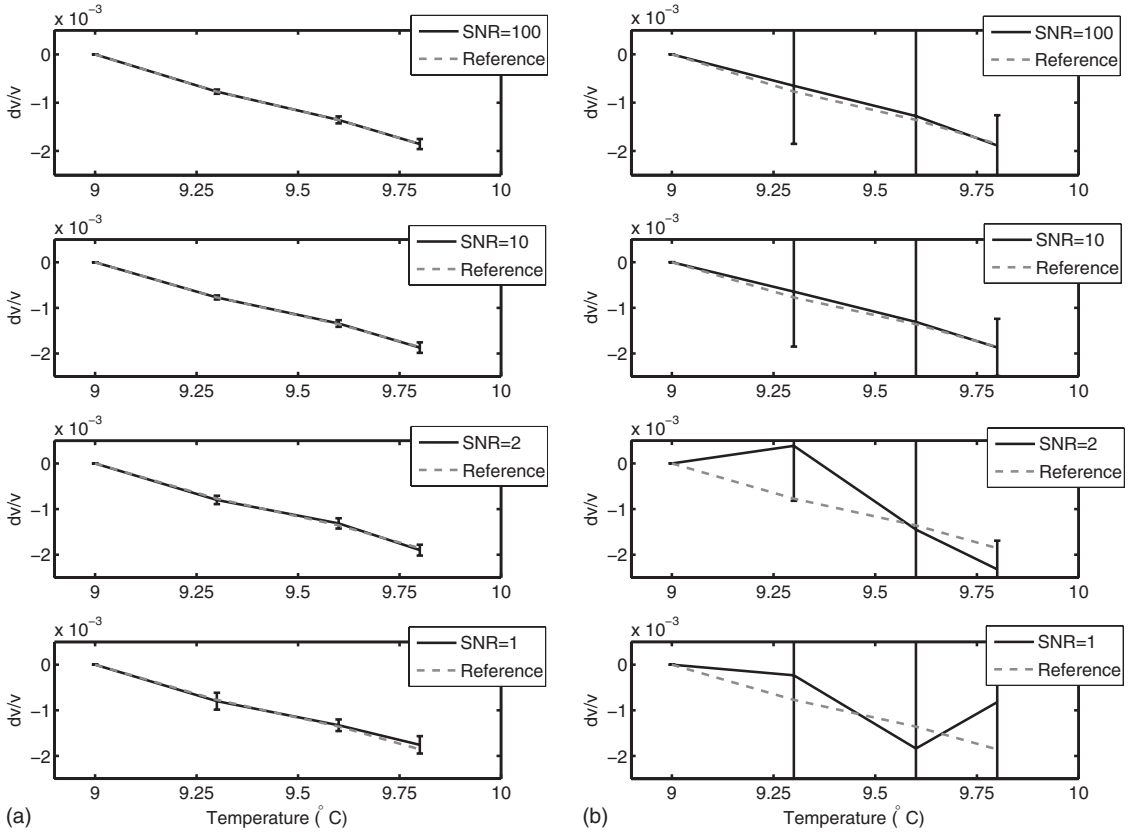

FIG. 7. Relative velocity changes evaluated from the stretching (left) and for the doublet (right) technique for various SNRs. The actual dV/V is satisfyingly retrieved for any SNR ≥ 1 with the first technique, not with the second.

The velocity change is measured again for SNR ranging from 1 to 100 (Fig. 7). For SNRs of 100 and 10, we find the same results for the stretching and for the doublet technique. However, if the SNR is decreased to 2, the velocity variations measured from the doublet technique are not accurate at all, while they remain relevant with the stretching technique. This establishes the stretching technique as a more stable processing procedure for noisy records. Note that the connection between the fluctuation of the waveforms and the error in the estimation of $dV/V=\varepsilon$ will be subject to a separate communication. Nevertheless, this error can be visually estimated by the gray area around the theoretical curve (crosses) in Fig. 6.

C. Advantages and drawbacks of both techniques

The doublet technique (CSMWT) has been used successfully for more than 20 years to efficiently retrieve small velocity changes in the medium.[7,9,13] This technique does not suffer from change in amplitude of the waveform, including the coda decay, and the processing is very fast. It also manages clock errors in origin time without further processing, which is a central issue in active and passive field experiments.[27] It also allows to select a given time-window in the data.

The stretching technique is more recent. It is based on a grid-search for ϵ, and is found to be slightly more time consuming in terms of computer processing. A noticeable disadvantage of this latter technique is also that it assumes a linear stretching of the waveform, which is not valid for media with heterogeneous changes (including Earth). The main interest of the stretching technique versus the doublet one is its stability toward fluctuations (noise) in the data, as mentioned in Sec. III B and demonstrated by Fig. 7. This provides an opportunity to increase the sensitivity of detection of weak changes in Earth's crust with seismic waves.[13,22]

IV. ACTIVE AND PASSIVE EXPERIMENT: MONITORING WITH THE CORRELATION?

Most previous authors suggested that monitoring weak changes in Earth with ambient seismic noise correlation is based on the assumption that those correlations yield the actual GF of the medium. Thus, the late part of the correlation is interpreted as the coda of the reconstructed impulse response. Is this assumption actually necessary to monitor the changing Earth with good accuracy? We address the question in the present section by comparing relative velocity changes measured either in the autocorrelations of records from distant noise sources (the passive experimental setup) or in pulse-echo data (the active experimental setup).

In the passive experiment, transducers are attached at opposite sides of the gel (Fig. 2, right). On one side, 16 sources (S) act to mimic a distribution of noise sources. Impulse responses are recorded by the seven receiving transducers (R) and consecutively convolved by a white noise to mimic acoustic (or seismic) ambient noise. Then they are autocorrelated at each receiver. Note that the precise knowledge of the noise source position is unnecessary: The source position has no effect on the velocity change estimation. If

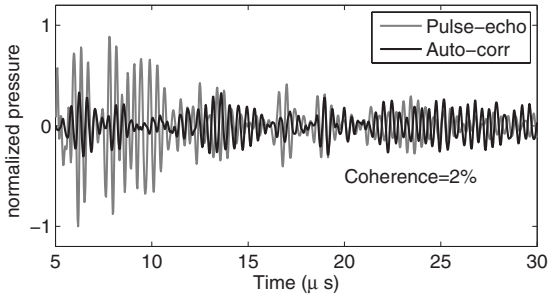

FIG. 8. Comparison of the pulse-echo data $h(R,R,t)$ obtained in the active experiment and the average autocorrelation $\partial_t h(S,R,t) \times h(S,R,t)$.

the noise sources were uniformly distributed and the coda records long enough, these correlations averaged over sources should result in the GF for the medium.[2] However, the records used in this experiment are of finite duration, and the autocorrelation has not converged to the GF yet. This can be seen visually in Fig. 8, where the autocorrelation is plotted alongside the (time derivative of the) reference GF obtained in the active experiment. The fact that the two signals are uncorrelated is confirmed by the low value of the coherence between them (2%).

The noise signals from each source are emitted at consecutive times. To emulate a signal coming from multiple sources at once, the signals recorded from each source i are stacked as follows:

$$h_k(t) = \sum_i G_k(S_i,R,t) \otimes n_i(t), \tag{12}$$

where the subscript k holds for temperature. The velocity variations are then computed using the autocorrelation of this total signal.

$$C_k(t) = h_k(t) \times h_k(t). \tag{13}$$

The velocity variations for each execution k of these experiments are displayed in Fig. 9, alongside those found with the active experiment. The acquisitions run over about 25 min, over which the temperature has increased by about 0.8 °C. Within the errors, the velocity variations found with the autocorrelation are the same as those found with the reference GF.

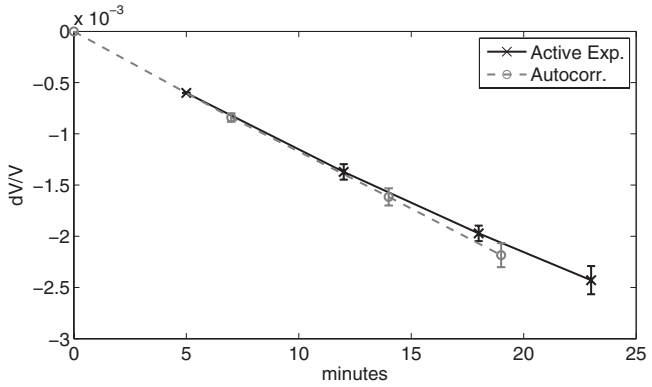

FIG. 9. Relative velocity changes evaluated from the active (pulse-echo with $S=R$) and the passive (autocorrelation with $S \neq R$) setup.

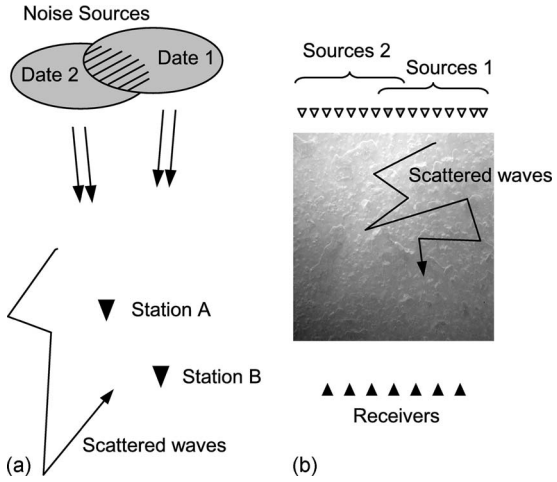

FIG. 10. (a) The seismic noise source structure changes from one date to another. (b) Analogous laboratory experiment: Two sets of sources are chosen at two different dates.

Until now, the analysis was based on the assumption that the autocorrelation used in the passive experiment closely resembles the GF of the medium if there are enough sources, and these sources are stable. In our experiment, the GF is not reconstructed in the autocorrelation. Nevertheless, Fig. 9 demonstrates[28] that it is still possible to retrieve correct information about small changes in the medium properties with the resulting autocorrelation. This is a very promising observation that supports the idea that correlation of seismic noise will give the opportunity to monitor weak changes in Earth with good reliability even when the correlations have not converged to the GF. Indeed, in both *active* and *passive* experiments, we measure the acoustic/seismic signatures of the medium, which naturally include its weak variations.

Nevertheless, in order to achieve a proper comparison between our laboratory-scale experiment and seismology, we have to take into account another phenomenon. Indeed, on Earth, the seismic noise sources' location smoothly changes from one week to another. The question addressed in Sec. V is the following: What will happen to our monitoring technique when the background noise is no longer stable, i.e., the source distribution changes spatially?

V. INFLUENCE OF NOISE SOURCE STABILITY

The change in background noise structure is simulated by averaging the autocorrelations for a number of simultaneous uncorrelated sources i. The same is done for a slightly different selection of sources a few instants later, then we calculate the relative velocity change dV/V between the two autocorrelations. A simple picture of this is given in Fig. 10. Imagine, for instance, that at date $k=0$, sources 1 and 2 are active, and at date $k=1$ sources 2 and 3. For three sources, the decorrelation of the signals can be analyzed theoretically. For the first experiment ($k=0$), the record is

$$h_0 = G(S_1,R,t) \otimes n_1(t) + G(S_2,Rt) \otimes n_2(t) \tag{14}$$

and its autocorrelation reads

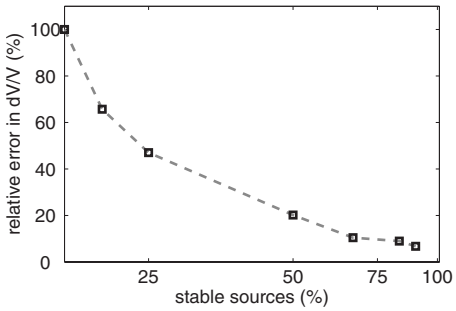

FIG. 11. Relative error in the estimation of $\varepsilon = dV/V$, versus the ratio of unchanged-to-total amount of noise sources (x-axis in logarithmic scale).

$$C_0 = h_0 \times h_0 \tag{15}$$

or

$$C_0 = G(S_1,R,t) \times G(S_1,R,t) \otimes n_1(t) \times n_1(-t) \tag{16}$$

$$+ G(S_2,R,t) \times G(S_2,R,t) \otimes n_2(t) \times n_2(-t) \tag{17}$$

$$+ 2G(S_1,R,t) \times G(S_2,R,t) \otimes n_1(t) \times n_2(-t). \tag{18}$$

Since $n_1(t) \times n_2(t)$ is almost zero, we neglect the third term. For simplicity, we shorten the notation

$$G(S_i,R,t) \times G(S_i,R,t) \otimes n_i(t) \times n_i(-t) = AC_i(t), \tag{19}$$

which leads to

$$C_0(t) = AC_1(t) + AC_2(t). \tag{20}$$

Similarly, for the second experiment ($k=1$), in which the signal is stretched due to the velocity change and the sources used are numbered 2 and 3, we get

$$C_k = AC_2(t[1-\varepsilon]) + AC_3(t[1-\varepsilon]). \tag{21}$$

The objective is to find the ε_k that maximizes the cross-correlation coefficient CC_k defined in Eq. (4). The terms AC_1 and AC_3 are decorrelated waveforms that play the role of fluctuations [Eq. (2)] and will contribute to the term B in Eq. (5). Assuming that the variance of AC_k is constant: $\langle AC_1^2 \rangle = \langle AC_2^2 \rangle = \langle AC_3^2 \rangle$, we find $A = \frac{1}{2}$ and the standard deviation of B simplifies as $\sqrt{\langle B^2 \rangle} = \sqrt{3}\sqrt{2\pi}/2\sqrt{T\Delta\omega}$. From this latter equation, we deduce that a proper estimation of dV/V is carried out if we process a sufficiently large amount of data: $\sqrt{T\Delta\omega} \gg \sqrt{3}\sqrt{2\pi}$. This figure is valid for two sets of sources that have 50% of sources in common. The same calculation can be carried out for any ratio of unchanged-to-total amount of uncorrelated sources.

As an example, we report in Fig. 11 the relative experimental error in the estimation of dV/V for various unchanged-to-total source amount ratios. The velocity evolution retrieved through the autocorrelation, as shown in Fig. 9, is used as a reference. For different ratios of spatially unchanged sources, the velocity changes are computed again, and the deviation with respect to the reference is considered the error. In Fig. 11 the relative error estimation is shown for different ratios of unchanged-to-total sources. When half the sources remain stationary, the relative error is ~20%, meaning that we have access to a rough (but relevant and interpretable) estimate of the velocity change. With the given experimental coda duration and bandwidth, we observe that a satisfying estimation of dV/V is obtained if 50% of the sources are unchanged.

In this framework, we conclude more generally that the spatial instability of the source distribution is not a limitation for noise-based correlation monitoring as long as at least part of the noise spatial distribution is stable. The smaller the stable area, the harder the dV/V estimation, and similar to the conclusion of Sec. III, a larger integration time T or bandwidth $\Delta\omega$ is required.

VI. DISCUSSION AND PERSPECTIVES

In this paper we conducted laboratory experiments with ultrasonic waves to monitor weak velocity changes in the medium. To that end, we employed and compared several procedures that process small phase shift in the diffuse coda waves. These phase shifts correspond to change in arrival time in the waveforms, which were due to small temperature changes in the medium.

The paper began with an active (pulse-echo) experiment (Sec. III), in which we compared the doublet (or CSMWT) technique to the more recent stretching technique. The former is based on Fourier analysis in multiple time-windows. The latter is based on the interpolation of the whole waveform and on a grid-search optimization. The latter was found to require more computing power, but was also found to be more stable toward noise in the data. In the second part of the paper (Sec. IV), we processed the autocorrelation of noise records acquired in the same medium. Active (pulse-echo) and passive (autocorrelations) data were processed using exactly the same processing procedure: The relative velocity changes in the medium were deduced from the late arrivals using the stretching technique. Very similar results were found in both cases, although autocorrelations had not at all converged to the GF. We therefore demonstrated that, contrary to prior belief, passive monitoring with ambient noise remains possible even when the correlation has not converged to the GF. In other words, noise-based monitoring requires weaker assumptions than noise-based imaging. In the last part of the present document (Sec. V), we tested the robustness of the noise-based monitoring technique in the case of unstable distributions of noise sources. We demonstrated that, as long as a certain portion of the sources is stable, velocity variations can still be retrieved.

Even though we consider a laboratory experiment in this paper, in practice the results can be extended to different scales, among which seismology is of particular interest. Note that the idea that the coda of the correlations contains precious information has been recently demonstrated by studying the correlation of the coda of the correlation (C3).[29] In previous monitoring studies along the San-Andreas fault-line at Parkfield, CA,[22] there were some doubts as to whether or not the GF was properly reconstructed in the correlations. This was due to (i) the imperfect source distribution in the ocean, (ii) the short time-series over which correlations were performed, and (iii) the low quality data for frequencies below 1 Hz. Nevertheless, it was still possible to observe small variations in the coda of the correlations. From our labora-

tory experiment, we can confirm that these latter changes are actual physical observations that can be interpreted by velocity changes in the crust. On a somewhat smaller scale, passive monitoring can be applied to seismic prospecting on reservoirs. On such reservoirs, the technique could, for instance, be used to follow the effect of fluid flows as oil or gas. During production, we indeed expect relative changes in velocity in the reservoir of the order of a few percent,[30] which seems to be observable by the method presented here. It might also be possible to detect the velocity variations caused by stress changes following subsidence. This monitoring could either be performed with reproducible active sources or with background seismic noise.

ACKNOWLEDGMENTS

This work was partially funded by the Department of TUNES, University J. Fourier, the CNRS-INSU AIPI program, and the ANR SISDIF grant (Grant No. JC08_313906). The authors acknowledge R. L. Weaver, A. Verdel, and F. Brenguier for scientific discussions and comments, and B. Vial for technical help in designing and setting up the experiment.

[1]T. L. Duvall, S. M. Jefferies, J. W. Harvey, and M. A. Pomerantz, "Time-distance helioseismology," Nature (London) **362**, 430–432 (1993).
[2]R. L. Weaver and O. I. Lobkis, "Ultrasonics without a source: Thermal fluctuation correlations at MHz frequencies," Phys. Rev. Lett. **87**, 134301 (2001).
[3]O. I. Lobkis and R. L. Weaver, "On the emergence of the Green's function in the correlations of a diffuse field," J. Acoust. Soc. Am. **110**, 3011–3017 (2001).
[4]E. Larose, L. Margerin, A. Derode, B. van Tiggelen, M. Campillo, N. Shapiro, A. Paul, L. Stehly, and M. Tanter, "Correlation of random wavefields: An interdisciplinary review," Geophysics **71**, SI11–SI21 (2006).
[5]M. Campillo and A. Paul, "Long range correlations in the diffuse seismic coda," Science **299**, 547–549 (2003).
[6]N. M. Shapiro and M. Campillo, "Emergence of broadband Rayleigh waves from correlations of the ambient seismic noise," Geophys. Res. Lett. **31**, L7–L614 (2004).
[7]G. Poupinet, W. L. Ellsworth, and J. Frechet, "Monitoring velocity variations in the crust using earthquake doublets: an application to the Calaveras Fault, California," J. Geophys. Res. **89**, 5719–5731 (1984).
[8]D. J. Pine, D. A. Weitz, P. M. Chaikin, and E. Herbolzheimer, "Diffusing-wave spectroscopy," Phys. Rev. Lett. **60**, 1134–1137 (1988).
[9]R. Snieder, A. Grêt, H. Douma, and J. Scales, "Coda wave interferometry for estimating nonlinear behavior in seismic velocity," Science **295**, 2253–2255 (2002).
[10]K. G. Sabra, P. Roux, P. Gerstoft, W. A. Kuperman, and M. C. Fehler, "Extracting coherent coda arrivals from cross-correlations of long period seismic waves during the Mount St. Helens 2004 eruption," Geophys. Res. Lett. **33**, L06313 (2006).
[11]C. Sens-Schönfelder and U. C. Wegler, "Passive image interferometry and seasonal variations of seismic velocities at Merapi Volcano, Indonesia," Geophys. Res. Lett. **33**, L21302 (2006).
[12]C. Sens-Schoenfelder and E. Larose, "Temporal changes in the lunar soil from correlation of diffuse vibrations," Phys. Rev. E **78**, 045601 (2008).
[13]F. Brenguier, N. M. Shapiro, M. Campillo, V. Ferrazzini, Z. Duputel, O. Coutant, and A. Nercessian, "Toward forecasting volcanic eruptions using seismic noise," Nature geosciences **1**, 126–130 (2008).
[14]J. Rhie and B. Romanowicz, "Excitation of Earth's continuous free oscillations by atmosphere-ocean-seafloor coupling," Nature (London) **431**, 552–556 (2004).
[15]L. Stehly, N. Shapiro, and M. Campillo, "A study of the seismic noise from its long-range correlation properties," J. Geophys. Res. **111**, B10306 (2006).
[16]O. I. Lobkis and R. L. Weaver, "Coda-wave interferometry in finite solids: Recovery of p-to-s conversion rates in an elastodynamic billiard," Phys. Rev. Lett. **90**, 254302 (2003).
[17]E. Larose and S. Hall, "Monitoring stress related velocity variation in concrete with a 2.10^{-5} relative resolution using diffuse ultrasound," J. Acoust. Soc. Am. **125**, 1853–1856 (2009).
[18]Y. Fukushima, O. Nishizawa, H. Sato, and M. Ohtake, "Laboratory study on scattering characteristics of shear waves in rock samples," Bull. Seismol. Soc. Am. **93**, 253–263 (2003).
[19]K. van Wijk, M. Haney, and J. A. Scales, "1d energy transport in a strongly scattering laboratory model," Phys. Rev. E **69**, 033611 (2004).
[20]E. Larose, A. Derode, D. Clorennec, L. Margerin, and M. Campillo, "Passive retrieval of Rayleigh waves in disordered elastic media," Phys. Rev. E **72**, 046607 (2005).
[21]J. A. Zagzebski, *Essentials of Ultrasound Physics* (Mosby-Yearbook Inc., St. Louis, 1996).
[22]F. Brenguier, M. Campillo, C. Hadziioannou, N. M. Shapiro, R. M. Nadeau, and E. Larose, "Postseismic relaxation along the San Andreas fault at Parkfield from continuous seismological observations," Science **321**, 1478–1481 (2008).
[23]J. Frechet, L. Martel, L. Nikolla, and G. Poupinet, "Application of the cross-spectral moving-window technique (CSMWT) to the seismic monitoring of forced fluid migration in a rock mass," Int. J. Rock Mech. Min. Sci. Geomech. Abstr. **26**, 221–233 (1989).
[24]G. M. Jenkins and D. G. Watts, *Spectral Analysis and Its Applications* (Holden-Day, San Francisco, CA, 1969).
[25]The stationary assumption is done for the sake of simplicity of the calculation. Nevertheless, the main conclusions of the article also apply to non-stationary waveforms as decaying coda.
[26]See EPAPS Document No. E-JASMAN-125-051906 for a detailed calculation. For more information on EPAPS, see http://www.aip.org/pubservs/epaps.html.
[27]L. Stehly, M. Campillo, and N. M. Shapiro, "Traveltime measurements from noise correlation: Stability and detection of instrumental time-shifts," Geophys. J. Int. **171**, 223–230 (2007).
[28]Note that the systematic deviation of the passive experiment from the active one is in part due to a small spatial variability of the temperature change. The autocorrelation ($S \neq R$) is sensitive to the whole medium whereas the pulse-echo wavefield ($S=R$) is more sensitive to the vicinity of the receiver.
[29]L. Stehly, M. Campillo, B. Froment, and R. L. Weaver, "Reconstructing Green's function by correlation of the coda of the correlation (c^3) of ambient seismic noise," J. Geophys. Res. **113**, B11306 (2008).
[30]S. J. Ellison, M. G. Imhofz, C. Çoruhz, A. D. Fuqua, and S. C. Henry, "Modeling offset-dependent reflectivity for time-lapse monitoring of water-flood production in thin-layered reservoirs," Geophysics **69**, 25–36 (2004).

Homogeneous and sandwich active panels under deterministic and stochastic excitation

J. Rohlfing[a] and P. Gardonio
Institute of Sound and Vibration Research, University of Southampton, Southampton SO17 1BJ, United Kingdom

(Received 26 August 2008; revised 5 March 2009; accepted 27 March 2009)

In this paper an element-based model is used to predict the structural response and sound radiation of two smart panels excited by (a) an acoustic plane wave, (b) a stochastic acoustic diffuse field, and (c) a turbulent boundary layer. The first panel is made of aluminum, while the second is a composite sandwich panel with equivalent static stiffness but four times lower mass per unit area. The panels are equipped with 16 decentralized velocity feedback control loops using idealized point force actuators. In contrast to previous studies on smart panels, the analysis is extended to the upper end of the audio frequency range. In this frequency region the response and sound radiation of the panels strongly depend on the spatial characteristics of the excitation field and the sound radiation properties with respect to the bending wavelength on the panels. Considerable reduction in structural response and sound radiation is predicted for the low audio frequency range where the panel response is dominated by well separated resonances of low order structural modes. It is also found that some reduction can be achieved around acoustic and convective coincidence regions.
 [DOI: 10.1121/1.3123405]

PACS number(s): 43.40.Vn, 43.50.Ki [KAC] Pages: 3696–3706

I. INTRODUCTION

Environmental and economic considerations increase the demand for weight-optimized structural design. This often conflicts with the requirements for noise control and acoustical comfort. Various active control approaches have been shown to enhance the sound attenuation through a panel at low frequencies where the structural response is dominated by discrete resonant modes with low modal overlap. Very appealing approaches are those of active structural acoustic control and active vibration control where actuators and sensors are integrated with the structure to create "smart panels."[1–4]

For many practical vibro-acoustic problems, the excitation is not deterministic. Common examples of stochastic excitations are acoustic diffuse fields (ADFs)[5] or turbulent boundary layers (TBLs),[6,7] which are often encountered in transportation vehicles such as aircraft, high speed trains, and cars.[8,9] These disturbances can be described by analytical formulations for the statistical properties of the resulting excitation field on a panel surface. An important characteristic of such disturbances is the projection of periodic pressure fluctuations onto the panel surface. In the case of acoustic disturbances this depends on the acoustic wavelength and angle of incidence;[3] for a TBL disturbance this depends on the convective wavelength and the direction of the flow.[6,10] Frequencies at which the convective or projected acoustic wavelength are the same as the transverse wavelength on a structure are known as coincidence frequencies. Coupling between excitation wavelengths, transverse structural wavelength, and acoustic wavelength has a significant influence on the sound transmission through a partition. For thin aluminum panels, the lowest acoustic coincidence or critical frequency[3] falls into the upper end of the audio frequency range. The convective coincidence frequency is typically much lower and affects the panel response in the mid audio frequency range. Composite sandwich panels feature a high stiffness to mass ratio and therefore become increasingly popular in the design of lightweight vehicles. However, for stiff lightweight sandwich panels, the convective and acoustic coincidences shift toward lower frequencies and may cause noise transmission problems.

The objective of this paper is twofold. First, to investigate and contrast the structural response and the sound radiation in the audio frequency range produced by homogeneous and lightweight sandwich panels subject to deterministic and stochastic distributed excitations. Second, to study and compare the control effects produced by an array of idealized velocity feedback control loops on homogeneous and lightweight sandwich panels.

An element approach[4,11,12] is used to predict the structural response and sound radiation of the two smart panels excited by (a) an acoustic plane wave (APW), (b) a stochastic ADF, and (c) a TBL. The first panel is made of aluminum while the second is a composite sandwich panel with equivalent static stiffness but four times lower mass per unit area. The panels are equipped with 16 decentralized velocity feedback control loops using idealized point force actuators and collocated idealized velocity sensors.[4,13] In this way the intrinsic limits of the decentralized feedback control are investigated independently of the electrodynamic response of the control units.

[a]Author to whom correspondence should be addressed. Electronic mail: v06jr@isvr.soton.ac.uk

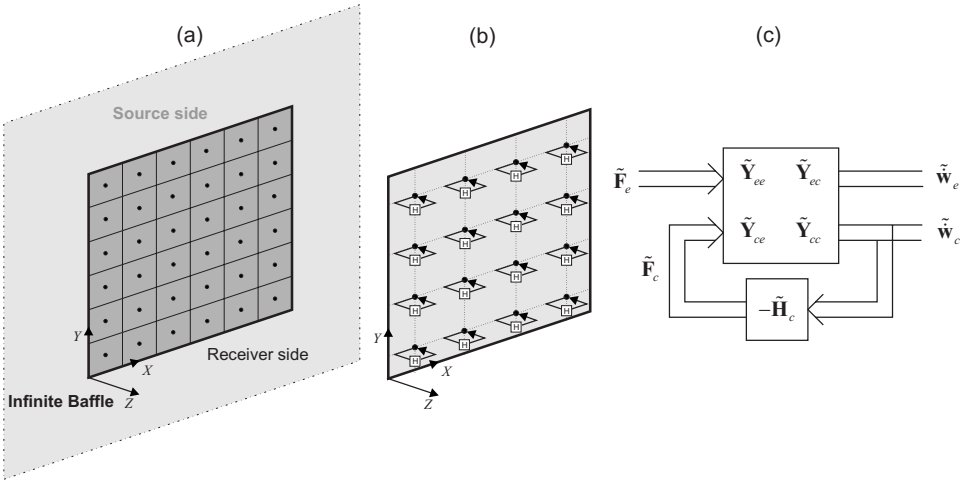

FIG. 1. Schematic of the panel model. (a) Panel in infinite baffle subdivided into a grid of elements. (b) Panel with 16 direct velocity feedback loops. (c) "Two-port" block diagram for panel model with decentralized multichannel feedback control.

II. PANEL MODEL

A. Mobility model

Figure 1 shows the geometry of the smart panels, which are assumed to be simply supported in an infinite baffle. They are equipped with 16 decentralized ideal velocity sensor and actuator pairs to illustrate the effects of decentralized velocity feedback control.[4,13] On the source side the panels are exposed to a surface pressure fluctuation induced by different types of deterministic and stochastic disturbances. On the receiver side the panels radiate into an infinite half space. Both panels have the dimensions $l_x=278$ mm and $l_y=247$ mm. The properties of the surrounding media on the source and the receiving sides of the panel are chosen as those of air with a mass density $\rho=1.21$ kgm^{-3} and characteristic sound speed $c_0=343$ ms^{-1}. Fluid loading effects and radiation losses have been neglected; this is a reasonable assumption for excitation and radiation into air.[3,14]

The steady state response is derived assuming time-harmonic excitation at angular frequency ω. For brevity the time-harmonic term $\exp(j\omega t)$ will be omitted in the formulation, which will be given in complex form. Therefore, the time-harmonic velocity $\dot{w}(t)=\mathrm{Re}\{\tilde{\dot{w}}\exp(j\omega t)\}$ and force $F(t)=\mathrm{Re}\{\tilde{F}\exp(j\omega t)\}$ fluctuations will be replaced with the complex velocity and force phasors $\tilde{\dot{w}}$ and $\tilde{F}$, respectively. Throughout the paper $\tilde{}$ will be used to identify complex, frequency dependent functions. As shown in Fig. 1(a), the panel is subdivided in a grid of elements so that the excitation forces and velocity response of the panel are determined at the elements' center coordinates. As shown in Fig. 1(b) the decentralized feedback control system is formed by a 4×4 grid of velocity feedback loops using collocated and dual point velocity sensor and point force actuators. The closed loop response of the panel can be modeled with the "two-port" block diagram in Fig. 1(c), assuming the system is linear. This indicates that the responses at the elements' centers and at the control positions result from the linear superposition of two components of vibration. The primary excitation is produced by the pressure field over the surface on the source side of the panel. The secondary excitation is produced by the control point forces, and depends on the control velocities via the feedback control gains.[2] Thus, the velocity response at the centers of the panel elements is given by

$$\tilde{\mathbf{w}}_e=\tilde{\mathbf{Y}}_{ee}\tilde{\mathbf{F}}_e+\tilde{\mathbf{Y}}_{ec}\tilde{\mathbf{F}}_c, \tag{1}$$

where $\tilde{\mathbf{w}}_e=[\tilde{\dot{w}}_{e_1},\tilde{\dot{w}}_{e_2},\ldots,\tilde{\dot{w}}_{e_{N_e}}]^T$ is the $[N_e\times1]$ dimensional vector of complex element velocities, $\tilde{\mathbf{F}}_e=[\tilde{F}_{e_1},\tilde{F}_{e_2},\ldots,\tilde{F}_{e_{N_e}}]^T$ is the $[N_e\times1]$ dimensional vector of excitation forces due to the pressure field incident on the source side of the elements, $\tilde{\mathbf{F}}_c=[\tilde{F}_{c_1},\tilde{F}_{c_2},\ldots,\tilde{F}_{c_{N_c}}]^T$ is the $[N_c\times1]$ dimensional vector of feedback forces, $\tilde{\mathbf{Y}}_{ee}$ is the $[N_e\times N_e]$ dimensional matrix of point and transfer mobilities between the centers of the panel elements, and $\tilde{\mathbf{Y}}_{ec}$ is the $[N_e\times N_c]$ dimensional matrix of transfer mobilities from the control locations to the panel element centers. The mobility functions in the matrices $\tilde{\mathbf{Y}}_{ee}$ and $\tilde{\mathbf{Y}}_{ec}$ are derived in terms of a modal summation as given in Ref. 15. As shown in the block diagram in Fig. 1(c), for direct velocity feedback control, the vector of control forces is given by

$$\tilde{\mathbf{F}}_c=-\tilde{\mathbf{H}}_c\tilde{\mathbf{w}}_c, \tag{2}$$

where $\tilde{\mathbf{H}}_c$ is the $[N_c\times N_c]$ dimensional diagonal matrix of control gains and $\tilde{\mathbf{w}}_c=[\tilde{\dot{w}}_{c_1},\tilde{\dot{w}}_{c_2},\ldots,\tilde{\dot{w}}_{c_{N_c}}]^T$ is the $[N_c\times1]$ dimensional vector of velocity sensor outputs at the control locations. According to the two-port block diagram in Fig. 1(c), the vector of control point velocities is given by

$$\tilde{\mathbf{w}}_c=\tilde{\mathbf{Y}}_{ce}\tilde{\mathbf{F}}_e+\tilde{\mathbf{Y}}_{cc}\tilde{\mathbf{F}}_c=(\mathbf{I}_c+\tilde{\mathbf{Y}}_{cc}\tilde{\mathbf{H}}_c)^{-1}\tilde{\mathbf{Y}}_{ce}\tilde{\mathbf{F}}_e, \tag{3}$$

where $\tilde{\mathbf{Y}}_{cc}$ is the $[N_c\times N_c]$ dimensional matrix of point and transfer mobilities at the control locations. The control force $\tilde{\mathbf{F}}_c$ in Eq. (2) can subsequently be reformulated to yield

$$\tilde{\mathbf{F}}_c=-\tilde{\mathbf{H}}_c(\mathbf{I}_c+\tilde{\mathbf{Y}}_{cc}\tilde{\mathbf{H}}_c)^{-1}\tilde{\mathbf{Y}}_{ce}\tilde{\mathbf{F}}_e. \tag{4}$$

TABLE I. Cross-section geometry and physical properties of the homogeneous aluminum panel.

Parameter	Symbol	Value	Unit
Thickness	h	1.6	mm
Mass density	ρ	2720	kg m^{-3}
Young's modulus	E	70	GPa
Poisson's ratio	ν	0.33	⋯
Loss factor	η	0.02	⋯

Substituting Eq. (4) into Eq. (1) gives the vector of element velocities as

$$\tilde{\mathbf{w}}_e = \tilde{\mathbf{G}}_{ee}\tilde{\mathbf{F}}_e, \tag{5}$$

where $\tilde{\mathbf{G}}_{ee}=\tilde{\mathbf{Y}}_{ee}-\tilde{\mathbf{Y}}_{ec}\tilde{\mathbf{H}}_c(\mathbf{I}_c+\tilde{\mathbf{Y}}_{cc}\tilde{\mathbf{H}}_c)^{-1}\tilde{\mathbf{Y}}_{ce}$ is the panel element mobility matrix with active control.

B. Wavenumbers and modeshapes

The response of the aluminum panel is modeled as that of a thin, homogeneous, and isotropic plate with all sides simply supported. The formulations for the natural frequencies and natural modes are taken from Ref. 15. The panel cross-section geometry and material properties are given in Table I.

The response of the composite sandwich panel is modeled using a basic theory,[3,16] which considers pure bending of the cross-section and the faceplates and transverse shear of the core only. The panel is assumed to have the same material properties in the x- and y-directions. The relationship between the transverse wavenumber k and the wavenumbers corresponding to pure bending and to pure shear of the composite sandwich panel is given by

$$1+\left(\frac{k_s}{k_b}\right)^2\left(\frac{k}{k_b}\right)^2-\left(\frac{k}{k_b}\right)^4-\left(\frac{k_b}{k_{bf}}\right)^4\left(\frac{k_s}{k_b}\right)^2\left(\frac{k}{k_b}\right)^6=0, \tag{6}$$

where $k_s^2=m''\omega^2/Gd$ gives the shear wavenumber in the absence of transverse bending forces, $k_b^4=m''\omega^2/D_1$ gives the overall cross-section bending wavenumber in the absence of shear distortion, and $k_{bf}^4=m''\omega^2/2D_2$ gives the bending wavenumber for faceplate bending alone. In these equations m'' is the panel mass per unit area, G is the core shear modulus, and, as shown in Fig. 2, d is the distance between the neutral axis of the faceplates. Also $D_1=Ed^2h_f/2(1-\nu^2)$ is the bending stiffness of the cross-section and $D_2=Eh_f^3/12(1-\nu^2)$ is the bending stiffness of an individual faceplate. The physical parameters used to model the sandwich panel are given in Table II. These parameters are chosen to yield a panel with equal static stiffness but four times lower mass per unit area

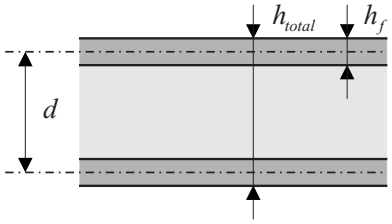

FIG. 2. Sketch of the sandwich cross-section geometry.

TABLE II. Cross-section geometry and physical properties for the composite sandwich panel.

Parameter	Symbol	Value	Unit
Thickness of faceplate	h_f	0.3	mm
Core depth	d	3	mm
Mass density faceplates	ρ_f	1000	kg m^{-3}
Mass density core	ρ	180	kg m^{-3}
Panel mass per unit area[a]	m''	1.086	kg m^{-2}
Young's modulus faceplates	E	17.7	GPa
Poisson's ratio	ν	0.33	⋯
Shear modulus core	G	80	MPa
Loss factor	η	0.02	⋯

[a] $m''=2h_f\rho_f+(d-h_f)\rho_c$.

than that of the homogeneous 1.6 mm thick aluminum panel. Equation (6) has one real and two imaginary pairs of axis symmetric solutions. For simplicity the honeycomb panel is assumed to have the same modeshapes as a corresponding thin, simply supported panel, considering an equivalent, frequency dependent bending stiffness, which is derived from the real (propagating) wavenumber solutions only. The imaginary wavenumber solutions to Eq. (6) correspond to decaying near field waves, which are neglected. This basic model captures the principal characteristics of a sandwich panel and is thought to be suitable for an initial comparison between the structural response and radiated sound power of homogeneous and sandwich active panels.

C. Deterministic excitation model

Acoustic plane waves are an example of a distributed deterministic disturbance. A plane wave excitation is characterized by its sound pressure amplitude, its angles of incidence θ, measured from the z-axis, normal to the panel, and the angle φ, in the x, y-plane, measured from the x-axis. Assuming time-harmonic pressure fluctuations, the incident sound pressure acting on the source side of the panel is given as $p(x,y,t)=\mathrm{Re}\{\tilde{p}(\omega)\exp j(\omega t-k_x x-k_y y)\}$, where $\tilde{p}(\omega)$ is the pressure phasor of the incident sound wave. The wavenumbers in the x- and y-directions of the panel are given by $k_x(\omega)=k_0(\omega)\sin\theta\cos\varphi$ and $k_y(\omega)=k_0(\omega)\sin\theta\sin\varphi$, where $k_0=\omega/c_0$ is the acoustic wavenumber and $c_0=343$ m/s is the speed of sound in air. The pressure excitation on a single panel element is approximated as a point force acting on the element center

$$\tilde{F}_{e_i}(\omega)=2A_e\hat{p}(\omega)\exp(-j(k_x x_i+k_y y_i)), \tag{7}$$

where A_e is the area of an element and the factor 2 accounts for the assumption of blocked forces on the panel surface, which causes a doubling of pressure. The incident forces for all elements are cast into a $[N_e\times 1]$ dimensional vector, which is then used as the excitation term in Eq. (5).

Panel kinetic energy. The response of the panel is assessed in terms of its total kinetic energy, which gives an indication of the spatially-averaged vibration and also of the near field sound radiation. Assuming time-harmonic excitations, the time-averaged kinetic energy of the panels is approximated from the sum over the squared element velocities

and the mass of the elements.[3] Utilizing matrix algebra this summation can be calculated from the inner Hermitian product of the element velocity vectors. This yields the total kinetic energy as[3]

$$E(\omega) = \frac{m_e}{4}\tilde{\mathbf{w}}_e^H(\omega)\tilde{\mathbf{w}}_e(\omega), \tag{8}$$

where ^{H} denotes the Hermitian transpose, m_e is the mass of an individual panel element, and the additional factor 1/2 arises from the conversion from peak to rms values.

Radiated sound power. The sound radiation by the panel is expressed in terms of the total sound power radiation, which gives an indication of the far field, spatially-averaged, sound radiation. In the elemental approach the time-averaged far field total sound power radiated to one side of the panel is given by[3]

$$P_{\text{rad}}(\omega) = \tilde{\mathbf{w}}_e^H(\omega)\mathbf{R}_{\text{rad}}(\omega)\tilde{\mathbf{w}}_e(\omega),$$

where $\mathbf{R}_{\text{rad}}(\omega)$ is the $[N_e \times N_e]$ dimensional element radiation matrix defined as[4]

$$R_{\text{rad}_{i,j}} = \frac{\omega^2 \rho_0 A_e^2}{4\pi c_0}\frac{\sin(k_0 r_{i,j})}{k_0 r_{i,j}}. \tag{9}$$

In this equation k_0 is the acoustic wavenumber on the receiving side of the panel and $r_{i,j} = \sqrt{(x_i - x_j)^2 + (y_i - y_j)^2}$ is the distance between two elements. The distance $r_{i,i}$ is zero; thus the radiation terms $R_{\text{rad}_{i,i}}$ on the main diagonal of the radiation matrix are undefined. However, using L' Hôpital's rule it is found that $\lim_{r\to 0} \text{sinc}(k_0 r) = 1$.

D. Stochastic excitation model

For many practical vibro-acoustic problems, the excitation is not deterministic. For instance, ADFs (Ref. 5) or TBL[6,7] pressure fields produced by the interaction of a turbulent flow of fluid and a structure are often encountered in transportation vehicles such as aircraft, high speed trains, and cars. Analytical formulations for the statistical properties of the excitation fields produced by the ADF and the TBL have been derived.[5–7] These formulations describe disturbances in terms of time-averaged power spectral density and spatial correlation functions. The response and sound radiation induced by such random excitation fields are also expressed in terms of power spectral densities. Considering the elemental formulation presented in Sec. II, the spectral density for the total kinetic energy can be formulated to give[11,17]

$$S_{EE}(\omega) = \frac{m_e}{2}\text{tr}[\tilde{\mathbf{G}}_{ee}^H \tilde{\mathbf{S}}_{ff} \tilde{\mathbf{G}}_{ee}], \tag{10}$$

where $\tilde{\mathbf{S}}_{ff}$ is the $[N_e \times N_e]$ dimensional matrix of power and cross-spectral density functions of the excitation forces on the elements, and $\tilde{\mathbf{G}}_{ee}$ is the panel element point and transfer mobility matrix as defined in Eq. (5) and tr[ ] is the trace of the matrix between square brackets. The matrix of spectral densities of the elemental excitation due to a general stationary stochastic excitation has the form

$$\tilde{\mathbf{S}}_{ff}(\omega) = A_e^2 \Phi \tilde{\mathbf{C}}_{ee}, \tag{11}$$

where Φ is the time-averaged power spectrum of the excitation and $\tilde{\mathbf{C}}_{ee}$ is the $[N_e \times N_e]$ dimensional spatial cross correlation matrix of the excitation forces calculated at the element center locations. The sound radiation is expressed in terms of the power spectral density of the sound power radiated into an infinite half space on the receiving side of the panel, which in the elemental approach is given by[11,17]

$$S_{PP}(\omega) = 2\ \text{tr}[(\tilde{\mathbf{G}}_{ee}^H \tilde{\mathbf{S}}_{ff} \tilde{\mathbf{G}}_{ee})\mathbf{R}_{\text{rad}}], \tag{12}$$

where $\mathbf{R}_{\text{rad}}$ is the element radiation matrix as defined in Eq. (9).

ADF is a widely used model to describe the excitation produced by random acoustic plane waves incident on a surface for all angles. The power spectral density of an ADF is $\Phi_{\text{ADF}}(\omega) = 4E[\tilde{p}\tilde{p}^*] = 4\overline{\langle \tilde{p}^2 \rangle}$ where $\tilde{p}$ denotes the complex acoustic pressure[5,18] and E indicates the expected value. The factor 4 arises from the pressure doubling at a rigid surface and from the relationship between the pressure magnitude and mean square value. The spatial correlation function for an ADF on the surface of a rigid infinite plane is given by[5,18]

$$C_{\text{ADF}_{i,j}}(\omega) = \frac{\sin(k_0 r_{i,j})}{k_0 r_{i,j}}, \tag{13}$$

where k_0 is the acoustic wavenumber on the source side of the panel and $r_{i,j}$ is the distance between the centers of the elements i and j. It is interesting to note that the correlation function for an ADF disturbance has the same spatial characteristics as the radiation matrix in Eq. (9).

TBL models are widely used to describe the excitation produced on a surface by a turbulent fluid flow.[6,7] The most common expression for the TBL cross-spectral density is given by Corcos.[19] The flow direction is assumed parallel to the y-axis. The spatial correlation function in the x-direction (spanwise) and y-direction (streamwise) is given by

$$\tilde{C}_{\text{TBL}_{i,j}}(\omega) = \exp\left(\frac{-|r_{x_{i,j}}|}{L_x(\omega)} + \frac{-|r_{y_{i,j}}|}{L_y(\omega)} + \frac{-j\omega r_{y_{i,j}}}{U_c}\right),$$

where $|r_{x_{i,j}}| = |x_i - x_j|$ and $|r_{y_{i,j}}| = |y_i - y_j|$ are the distances between two elements in the x- and y-directions and $L_x = \alpha_x U_{\text{conv}}/\omega$ and $L_y = \alpha_y U_{\text{conv}}/\omega$ are the correlation lengths in x and y. The empirical constants $\alpha_x = 1.2$ and $\alpha_y = 8$ are adopted from Refs. 11 and 20. The convection velocity $U_{\text{conv}} = U_\infty \times 0.6$ is approximated as a fixed fraction of the free flow velocity U_∞, which is taken as $U_\infty = 225$ m/s. This approximation results in an overestimation of the correlation length at very low frequency. A comprehensive review on the TBL excitation models is given by Cousin.[10] The power spectral density of the surface pressure fluctuations due to a TBL is a function of frequency and depends on multiple parameters describing the flow surface interaction. In general the power spectral density decreases with increasing frequency. The results presented in this paper do not reflect this frequency dependence but only compare the panel response to the different types of disturbances with respect to their frequency dependent spatial correlation.

E. Element resolution

The required spatial element mesh density depends on (a) the disturbance characteristics, (b) the flexural response of the panel, and (c) the radiation properties of the panels, which are given by the radiation matrix. For frequencies below the convective and lowest acoustic coincidence frequencies the bending wavelength is shorter than the acoustic wavelength; thus the required mesh density is determined by the bending wavelength $\lambda_b = c_b(f)/f$ on the panels. For frequencies above the acoustic critical frequency, it is the acoustic wavelength that is shorter than the bending wavelength on the panel; therefore the element density is determined by the acoustic wavelength $\lambda_0 = c_0/f$. For TBL disturbance, the element density in the streamwise direction for frequencies above the convective coincidence is determined by the convective wavelength $\lambda_{conv} = U_{conv}/f$. In the spanwise x-direction the correlation function is exponentially decaying; thus a low element resolution results in an overestimation of the structural response but does not change its general characteristics. At least two elements per shortest wavelength are required to avoid spatial aliasing. However, the simulation results presented in this paper are obtained using four elements per shortest wavelength to ensure convergence at the higher end of the observed frequency range.[14]

F. Dispersion curves and coincidence frequencies

Figure 3 shows the positive propagating bending wavenumber as a function of frequency for (a) the aluminum panel and (b) the composite sandwich panel. The black and white circles represent the modal wavenumber components in the x- and y-directions, respectively. The wavenumber components satisfy the relationship $k_n = \sqrt{k_{x,n}^2 + k_{y,n}^2}$. The convective and acoustic wavenumbers are given by $k_{conv} = \omega/U_{conv}$ and $k_0 = \omega/c_0$, respectively. For a given frequency the wavenumber of a thin panel is proportional to $\sqrt[4]{m''/D}$. Thus, at frequencies below 1 kHz, the bending wavenumber on the aluminum panel, shown in Fig. 3(a), is $\sqrt{2}$ higher than that of the four times lighter composite sandwich panel shown in Fig. 3(b). The bending stiffness and modal density of the thin aluminum panel are constant with frequency. The equivalent bending stiffness of the sandwich panel model is only constant for low frequencies, where it is determined by the bending stiffness of the sandwich cross-section. With increasing frequency the transverse shear effects of the core cause a reduction in the overall bending stiffness, which results in an increase in the modal density. At very high frequencies the transverse wavelength is determined by the bending stiffness of the faceplates, which is much lower than that of the homogeneous aluminum panel. At about 11 kHz both panel models produce similar transverse wavelength, and equal total mode count.

In the transition region from pure cross-section bending to pure faceplate bending the transverse wavenumber of the sandwich panel is dominated by the core shear distortion[3] so that $k = k_s$. If the phase speed in the core shear dominated region $\sqrt{Gd/m''}$ is the same as the speed of sound c_0 then the coincidence region is extremely wide. If $\sqrt{Gd/m''}$ is much less than the speed of sound, coincidence should not occur until very high frequencies. Thus composite sandwich structures must be carefully designed to obtain acceptable acoustic performance. However, this might not be the highest design priority in many engineering applications. A convective coincidence occurs when the transverse wavenumber on the panel in the direction of the flow equals the convective wavenumber of the TBL. For the aluminum panel the convective coincidence occurs at 1169 Hz and the lowest acoustic coincidence occurs at 7544 Hz. The lower wavenumbers on the composite sandwich panel at low frequencies result in a shift of the coincidence frequencies toward lower frequencies; the convective coincidence occurs at 609 Hz and the lowest acoustic coincidence occurs at 5489 Hz.

III. STRUCTURAL RESPONSE AND SOUND RADIATION

At first the structural response and sound radiation of the aluminum and the composite sandwich panels are investigated for deterministic and stochastic disturbances without active control. Significant differences in the panel response and sound radiation are observed for different types of disturbances. Figure 4 shows the frequency spectrum of panel kinetic energy (left hand side) and radiated sound power (right hand side) of the aluminum panel (solid line) and composite sandwich panel (faint line) for a plane wave excitation. Three different angles of incidence are considered:

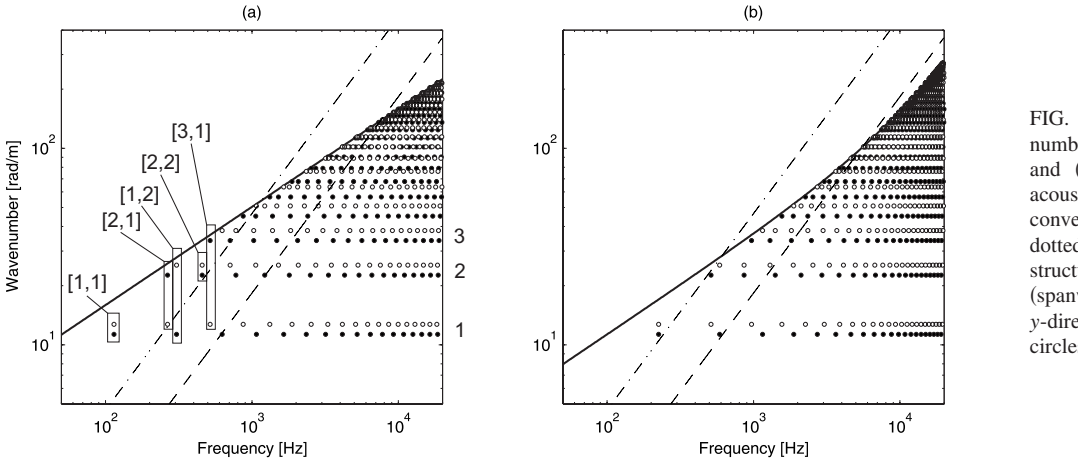

FIG. 3. Propagating bending wavenumbers (solid) of the (a) aluminum and (b) composite sandwich panel; acoustic wavenumber (dashed) and convective wavenumber (dashed-dotted). Wavenumber components of structural modes in the x-direction (spanwise) (black circles) and in the y-direction (streamwise) (white circles).

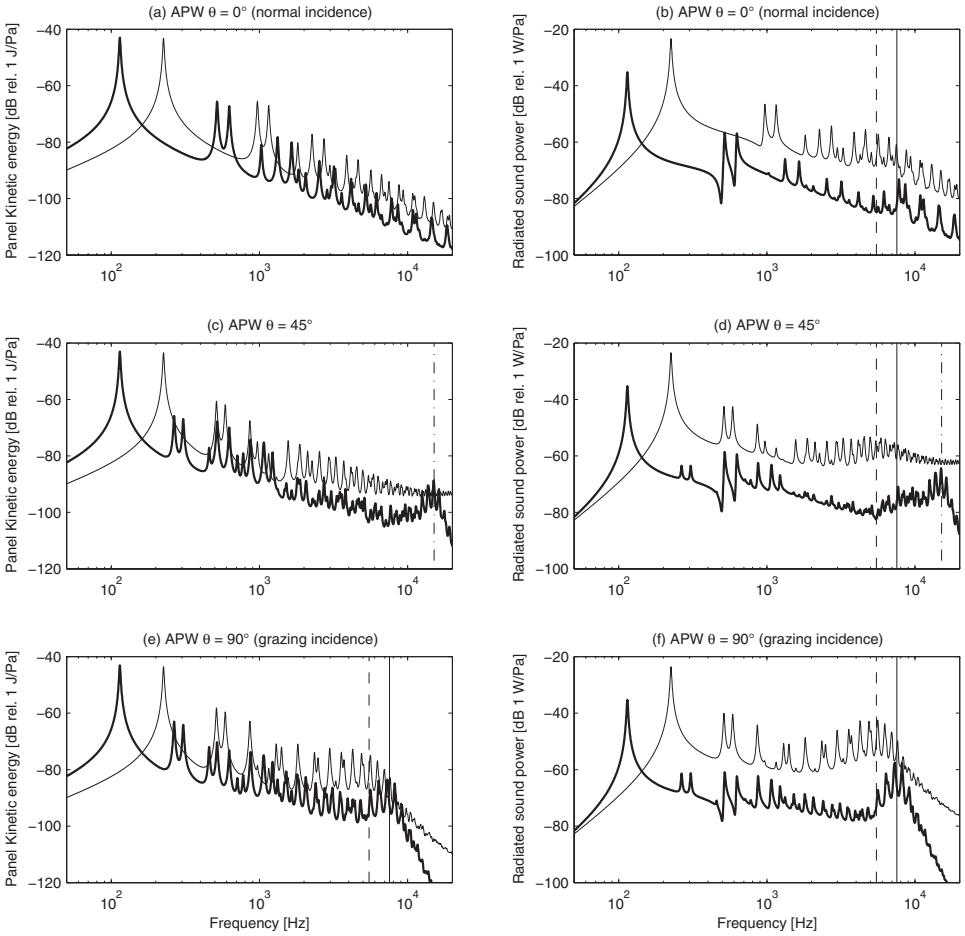

FIG. 4. Panel kinetic energy and radiated sound power of the aluminum panel (solid) and the composite sandwich panel (faint) for an APW incident at θ=0°, 45°, and 90°. Vertical lines mark the acoustic critical frequency of the aluminum panel (solid), sandwich panel (dashed), and the θ=45° coincidence frequency for the aluminum panel (dashed-dotted).

θ=0° (normal incidence), θ=45°, and θ=90° (grazing incidence). The excitation angle in the x, y-plane is φ=45° for all cases. Figure 5 shows the predicted panel kinetic energy and radiated sound power for ADF and TBL disturbance. All spectra are normalized to the power spectral densities of equivalent acoustic plane waves with a pressure amplitude of 1 Pa at all frequencies. It is interesting to note that for acoustic excitation, at low frequencies, the spectra of the radiated sound power of the aluminum panel are characterized by resonance and anti-resonance effects. This occurs in between two resonances of structural modes that interfere destructively, causing a cancellation of the modal contributions to the radiated sound power.

APW with θ=0° (normal *incidence).* Figures 4(a) and 4(b) show the structural response and radiated sound power of both panels for a plane wave excitation at normal inci-

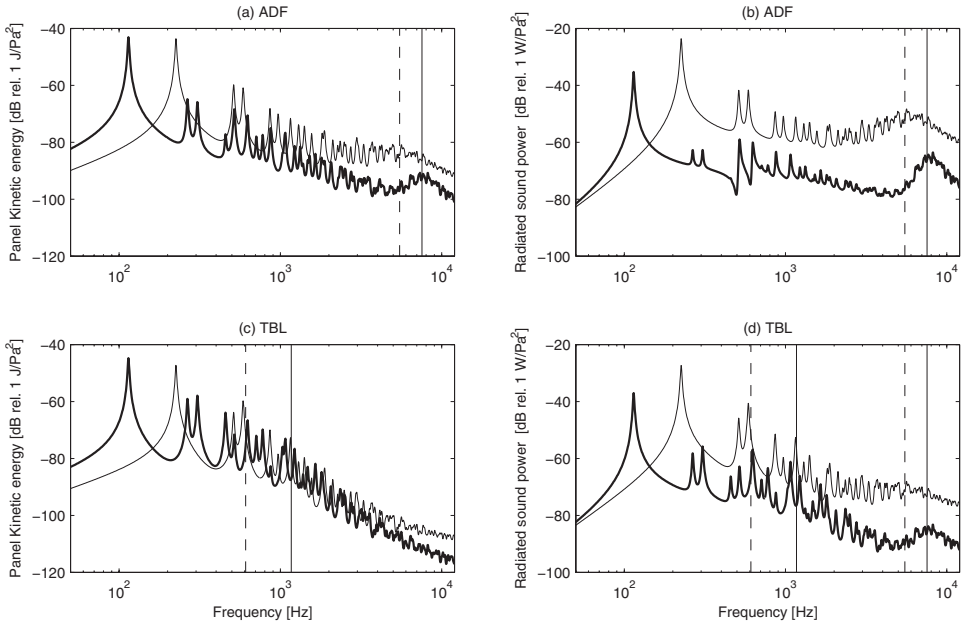

FIG. 5. Panel kinetic energy and radiated sound power for the aluminum panel (solid) and the composite sandwich panel (faint) for an ADF and a TBL disturbance. Vertical lines mark the acoustic critical and convective coincidence frequency of the aluminum panel (solid) and the sandwich panel (dashed).

dence. Even structural modes are not excited. This is because the excitation field is uniform over the surface of the panel. Odd modes, however, are efficiently excited. Since the plane wave is incident normal to the panel surface, no coincidence effects are present in the kinetic energy spectra. Above the first resonance, the panel kinetic energy follows the mass law[3] and rolls off at a rate of 6 dB/octave, i.e., 20 dB/decade. Because of its four times lower mass the panel kinetic energy of the composite panel is about 6 dB higher than that of the aluminum panel. Figure 4(b) shows that, for frequencies well below the first panel resonance frequency, the radiated sound power for both panels is the same. This is because, in this frequency region, the radiated sound power is determined by the static bending stiffness, which is equal for both panels. Above the first panel resonance frequency the radiated sound power is mass controlled up to the acoustic coincidence region. In the mass-controlled region the radiated sound power of the composite sandwich panel is 12 dB higher than that of the heavier aluminum panel. Around the acoustic critical frequency the radiated sound power of the panel increases because of the radiation properties of the panels. This coincidence effect occurs for frequencies above 5 kHz for the aluminum panel and for frequencies above 2 kHz for the composite panel. Because of the transition from bending to shear response of the sandwich panel a wider range of modes resonates at coincidence.

APW with $\theta=45°$. Figures 4(c) and 4(d) show the panel response and radiated sound power for a plane wave incident at an angle $\theta=45°$. At this angle all structural modes are efficiently excited. Above the first resonance, the structural response of the aluminum panel follows the mass law up to about 10 kHz. The projection of the acoustic wave onto the panel surface for an angle $\theta=45°$ is $\sqrt{2}$ longer than the acoustic wavelength. Thus, since the bending wavenumber is proportional to $\sqrt{f}$, the excitation coincidence effect occurs at twice the critical frequency, which is about 15 kHz. In this frequency region the response of the panel is dominated by efficiently excited modes and controlled by structural damping. Above this coincidence frequency band the panel response is stiffness and mass controlled and rolls off rapidly at a rate of 36 dB/octave. The structural response of the composite sandwich panel does not exhibit this excitation coincidence effect. This is because the phase speed on the sandwich panel in the shear transition region $\sqrt{Gd/m''}$ is smaller than $\sqrt{2}c_0$; therefore the excitation coincidence frequency is shifted up to 190 kHz for this angle of incidence, and is thus outside the observed frequency range. The response of the composite sandwich panel at high frequencies exhibits mass-controlled behavior. However, because of the increase in the modal density, the roll off rate is lower than 6 dB/octave. In comparison to the kinetic energy spectra in Fig. 4(c), some resonant peaks are significantly reduced in the spectrum of radiated sound power. This is because the surface pressure fluctuations caused by even modes counteract each other and are not efficiently radiated into the far field.[3] The radiated sound power of the aluminum panel shows the combined effect of the acoustic coincidence at 7.5 kHz, which is due to the radiation characteristics, and the excitation coincidence at 15 kHz. The radiated sound power spectra of the composite sandwich panel exhibit the acoustic coincidence effect due to the radiation characteristics around 5.5 kHz.

APW with $\theta=90°$ (grazing incidence). Figures 4(e) and 4(f) show the panel response and radiated sound power for a plane wave incident at an angle $\theta=90°$ (grazing incidence). At this angle the plane wave excites all structural modes. For grazing incidence the excitation coincidence frequency equals the acoustic critical frequency. This is because the acoustic wavelength projects directly onto the panel surface. The response around the coincidence frequency is dominated by discrete efficiently excited modes and controlled by structural damping. Above coincidence the panel response is stiffness and mass controlled and rolls off rapidly. The response of the aluminum panel rolls off at a rate of 36 dB/octave. The response of the composite sandwich panel rolls off at a lower rate of about 16 dB/octave. This is caused by the shear distortion in the transverse wavenumber and hence increasing modal density for the composite sandwich panel. For frequencies up to 1 kHz the radiated sound power spectra of both panels are similar to those for the plane wave incident at $\theta=45°$, shown in Fig. 4(d). For higher frequencies both panels show the effect of the acoustic coincidence.

ADF. Figures 5(a) and 5(b) show the structural response and radiated sound power of the aluminum panel and the composite sandwich panel for an ADF disturbance. As a comparison with Figs. 4(c) and 4(d) shows, the low frequency structural response and radiated sound power of both panels up to 1 kHz are very similar to the response to an acoustic plane wave with an incidence angle $\theta=45°$ and $\varphi=45°$. Figure 5(a) shows that, at higher frequencies, the structural responses of the aluminum and composite sandwich panels are characterized by the acoustical coincidence effect at 7.5 and 5.5 kHz, respectively. The panel response in the coincidence region is characterized by resonating modes, but the response of individual modes is less pronounced than for the cases of APW excitation, shown in Fig. 4. Above the coincidence region the kinetic energy spectrum of both panels rolls off at a lower rate than for the cases of APW excitation. These differences in the response spectra can be explained by the fact that the ADF excitation is formed by acoustic waves at arbitrary random angles of incidence. As for the acoustic plane wave excitation at grazing incidence in Fig. 4(e), the spectrum of radiated sound power in Fig. 5(b) shows the combined effect of acoustic excitation coincidence and radiation coincidence, which causes a considerable increase in the radiated sound power.

TBL. Figures 5(c) and 5(d) show the structural response and radiated sound power of both panels for the TBL disturbance. In the frequency range below 2 kHz the response of both panels is dominated by resonances of low order modes. For the aluminum panel the convective coincidence occurs at 1169 Hz, while for the composite sandwich panel it occurs at 609 Hz. The panel response therefore depends on how efficiently specific modes are excited by the TBL disturbance. Above the convective coincidence region, the response of the aluminum panel drops off at a rate of 9 dB/octave. The roll off rate for the sandwich panel is slightly lower, which is due to the increase in modal density above 2 kHz.

TABLE III. Modes efficiently excited by TBL.

Aluminum panel			Composite sandwich panel		
Mode	Frequency (Hz)	Order (n_x,n_y)	Mode	Frequency (Hz)	Order (n_x,n_y)
1	114	**(1,1)**	1	225	**(1,1)**
2	266	(2,1)	3	588	**(1,2)**
3	306	(1,2)	4	862	(2,2)
4	457	(2,2)	6	1155	**(1,3)**
6	626	**(1,3)**			
7	710	(3,2)			
8	777	(2,3)			
[10 12]	[1029 1073]	[**(3,3)** (1,4)]			
13	1224	**(2,4)**			
16	1477	(3,4)			
18	1648	**(1,5)**			
19	1800	(2,5)			
26	2351	(1,6)			

In considering the response of low order structural modes to TBL disturbance, it is necessary to recall the properties of the correlation function for the TBL. Since the correlation function for the TBL in the x-direction (spanwise) is characterized by a monotonically decaying exponential function, there are no coincidence effects along the x-axis of the panels. Therefore only the responses of structural modes whose modal wavenumber component in the y-direction is close to the convective wavenumber are characterized by a coincidence effect. Table III gives the panel modes that are efficiently excited by coincidence with the TBL convective field at their resonance frequency. Mode orders shown in bold indicate efficiently radiating modes, and modes in square brackets indicate a group of modes that cannot be distinguished as individual resonance peaks in Figs. 5(c) and 5(d). Comparison between the two panels shows that for the aluminum panel more modes are efficiently excited at resonance by the TBL disturbance than for the composite sandwich panel. A comparison of the results in Table III with Fig. 3 shows that efficiently excited modes indeed have a wavenumber component in y-direction (streamwise), which is close to the convective wavenumber. The radiated sound power spectrum in Fig. 5(d) shows that odd order modes in Table III radiate sound efficiently. The even (2,4) mode of the aluminum panel and the (1,2) mode of the composite sandwich panel also show high resonant peaks in the radiated sound power spectra in Fig. 5(d). Comparison with Fig. 3 shows that both modes have a wavenumber component in the x-direction, which is close to the acoustic wavenumber, which results in a high radiation efficiency.

IV. DECENTRALIZED VELOCITY FEEDBACK CONTROL

In this section the structural response and sound radiation of the aluminum and composite sandwich panels for a deterministic APW excitation with $\theta=45°$ and stochastic ADF and TBL disturbances with active structural control are considered. As shown in Fig. 1(b), the panels are fitted with 16 decentralized ideal velocity feedback control loops. Figures 6 and 7 show the spectra of structural response and total radiated sound power for the aluminum panel (left hand side) and the composite sandwich panel (right hand side) with feedback gains in the range from 5 to 80. Velocity feedback control introduces active damping, which allows the control of the response of modes at resonance.[4,13] In the off-resonance regions, active damping is not effective. For low feedback gains the resonant peaks are initially damped and anti-resonances in the radiated sound power spectra disappear. In the high frequency region the control is limited by the large number of modes that contribute to the response at each frequency. For increasing feedback gains new resonance behavior starts to develop at low frequencies. For the composite sandwich panel this occurs for gains above 20 and for the aluminum panel for gains above 40; this difference is caused by the higher structural impedance of the aluminum panel. On the other hand, for low feedback gains, higher control performance is achieved with the composite sandwich panel. For low order modes, a factor of 2 higher feedback gains for the aluminum panel are required to achieve equal reductions as for the composite sandwich panel. For all disturbances, the controllable frequency range produced with the composite sandwich panel extends to higher frequencies than with the aluminum panel. This is predominantly due to the lower modal density on the sandwich panel at low audio frequencies but also to the lower convective and acoustic coincidence frequencies. At coincidence, the response of the panels is dominated by the response of discrete resonant modes, which can be effectively reduced by means of active velocity feedback.

Figures 6(a), 6(c), and 6(e) show that considerable reductions in the structural response of the aluminum panel can be achieved up to about 1.5 kHz for the APW ($\theta=45°$), up to 2 kHz for the ADF, and up to 3 kHz for the TBL disturbance. For the structural response of the composite sandwich panel, shown in Figs. 6(b), 6(d), and 6(f), considerable reductions can be achieved for frequencies up to twice as high. Figures

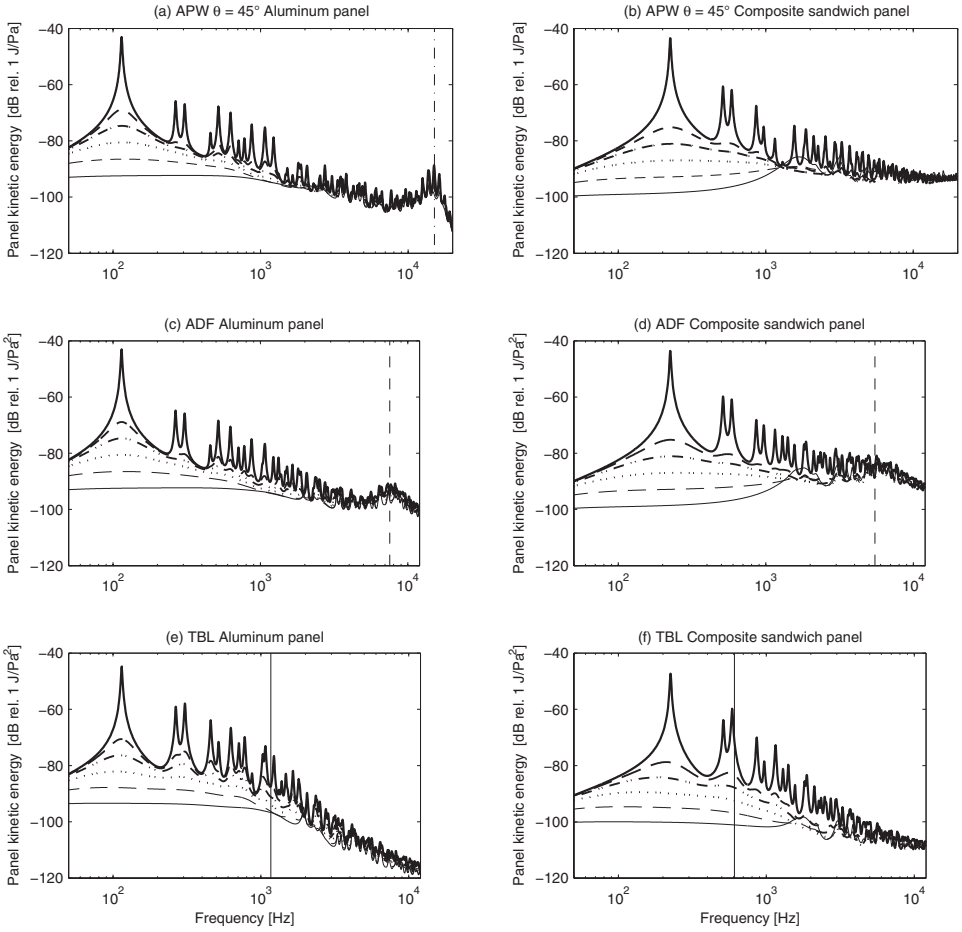

FIG. 6. Kinetic energy of the aluminum panel (left column) and the composite sandwich panel (right column) with 16 discrete idealized velocity feedback loops for an APW (θ=45°), an ADF, and a TBL disturbance. Passive panel (solid), and feedback gains of 5 (dashed), 10 (dashed-dotted), 20 (dotted), 40 (faint-dashed), and 80 (faint). Vertical lines mark the acoustic coincidence and critical frequencies (dashed and dashed-dotted) and convective coincidence frequencies (faint).

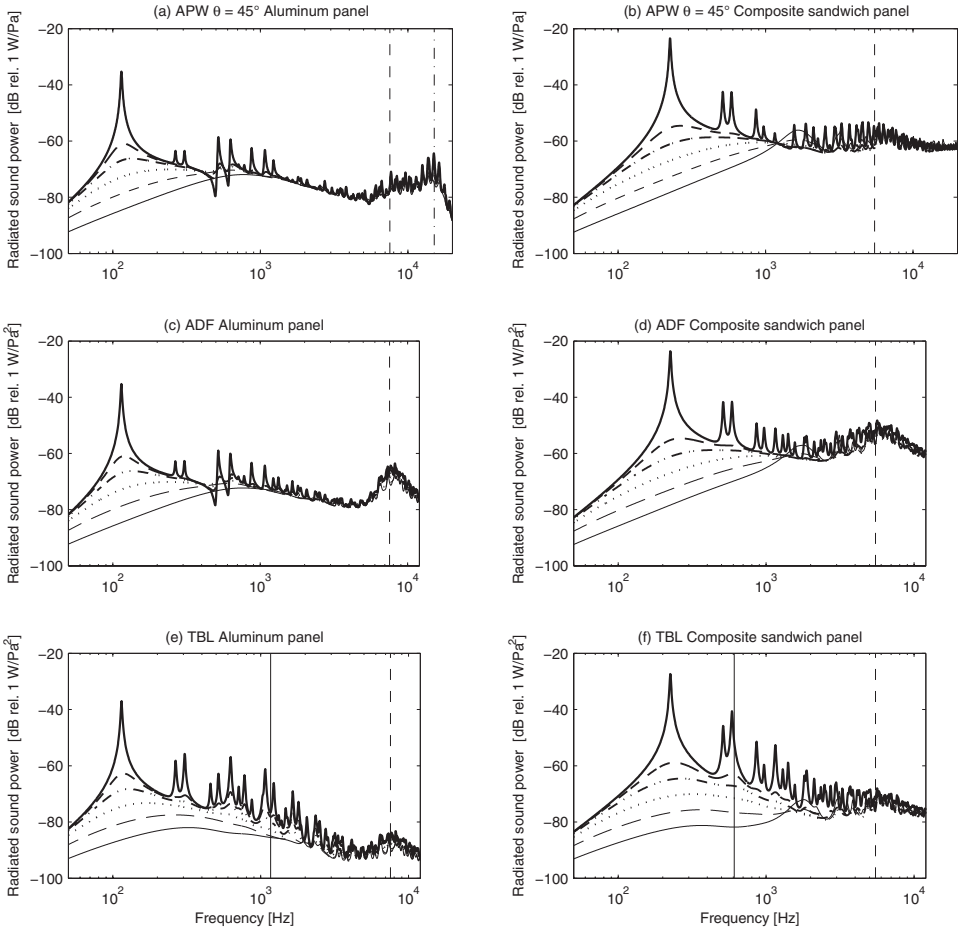

FIG. 7. Radiated sound power from the aluminum panel (left column) and the composite sandwich panel (right column) with 16 discrete idealized velocity feedback loops for APW (θ=45°), ADF, and TBL disturbance. Passive panel (solid), and feedback gains of 5 (dashed), 10 (dashed-dotted), 20 (dotted), 40 (faint-dashed), and 80 (faint). Vertical lines mark the acoustic coincidence and critical frequencies (dashed and dashed-dotted) and convective coincidence frequencies (faint).

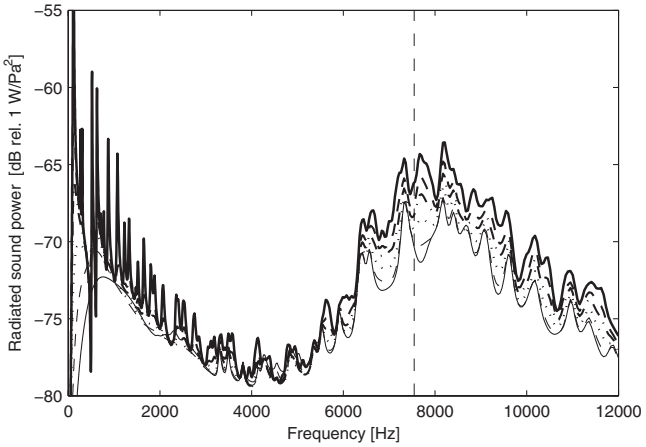

FIG. 8. Radiated sound power of the aluminum panel with 16 control loops for an ADF disturbance and feedback gains of 5 (dashed), 10 (dashed-dotted), 20 (dotted), 40 (faint-dashed), and 80 (faint). The vertical line marks the acoustic critical frequency (dashed).

7(a), 7(c), and 7(e) show that noticeable reductions in radiated sound power of the aluminum panel can be achieved up to 1 kHz for the APW (θ=45°) and ADF disturbances, while for the TBL disturbance considerable reductions are achieved up to 3 kHz. Figures 7(b), 7(d), and 7(f) show that the controllable frequency range for the radiated sound power from the sandwich panel is extended to higher frequencies for all three types of disturbance.

The control performance for the structural response and radiated sound power for the TBL disturbance is much higher than that for acoustic excitation. This is because the kinetic energy and radiated sound power spectra are dominated by a smaller number of resonant modes, for which the k_y component wavenumber coincides with the convective wavenumber of the TBL disturbance. The response and sound power radiation for APW and ADF disturbances are instead characterized by a large number of efficiently excited resonant modes, for which either the k_x or k_y wavenumber components coincide with the acoustic wavenumber. Thus a large number of feedback control units would be required to obtain the same control frequency bandwidth as for the TBL excitation.

Figure 8 shows the spectrum of the radiated sound power of the aluminum panel excited by an ADF disturbance on a linear frequency scale. In the coincidence region around 7.5 kHz reductions of up to 7 dB can be achieved with a feedback gain of 80. At these high frequencies, the bending wavelength on the panel is much shorter than the distance between the control loops. Therefore the control performance for individual modes will depend on the location of the control units with respect to the shape of efficiently excited modes. However, for stochastic disturbances, a range of structural modes is excited at coincidence so that some reductions may be expected for even distributions of control units.

V. CONCLUSIONS

Two different types of smart panel with 16 decentralized velocity feedback control loops using idealized point force actuators have been considered in this simulation study. One is a homogeneous aluminum panel while the second is a composite sandwich panel with equivalent static stiffness but four times lower mass per unit area. First, the panels' structural response and radiated sound power due to (a) an acoustic plane wave, (b) an ADF, and (c) a TBL disturbance have been discussed. Second, the response of the panels with applied active control has been studied. In contrast to previous studies on smart panels, the analysis has been extended to the upper end of the audio frequency range. Due to the low modal density and lower convective coincidence and acoustic critical frequencies, the response of the composite sandwich panel is dominated by discrete resonant modes over a wide range of audio frequencies. It has been demonstrated that for low feedback gains discrete active velocity feedback shows a better control performance for the smart sandwich panel than for the heavier smart homogeneous panel. This is particularly the case for TBL excitation where the structural response is dominated by low order resonant modes. The results of this simulation study suggest that decentralized velocity feedback control is efficient in reducing the structural response and radiated sound power of a smart sandwich panel up to the mid and high audio frequencies. In this case the benefits of active control systems could offset the additional costs and additional installed mass. In this paper basic structural models and ideal velocity sensor actuator pairs have been considered to evaluate the intrinsic control limits of decentralized velocity feedback. Further work is required to evaluate the control performance considering the dynamic response of the panels and actuator units in more detail.

[1]C. R. Fuller, S. J. Elliott, and P. A. Nelson, *Active Control of Vibration* (Academic, London, 1996).
[2]R. L. Clark, W. R. Saunders, and G. P. Gibbs, *Adaptive Structures: Dynamics and Control*, 1st ed. (Wiley-Interscience, New York, NY, 1998).
[3]F. J. Fahy and P. Gardonio, *Sound and Structural Vibration: Radiation, Transmission and Response*, 2nd ed. (Academic, Oxford, 2007).
[4]P. Gardonio and S. J. Elliott, "Smart panels for active structural acoustic control," Smart Mater. Struct. **13**, 1314–1336 (2004).
[5]D. Pierce, *Acoustics: An Introduction to Its Physical Principles and Applications* (Acoustical Society of America, Woodbury, NY, 1989).
[6]W. K. Blake, "Complex flow-structure interactions," *Mechanics of Flow-Induced Sound and Vibration* (Academic, Orlando, FL, 1986), Vol. **II**.
[7]M. S. Howe, *Acoustics of Fluid-Structure Interactions* (Cambridge University Press, Cambridge, 1998).
[8]J. S. Mixson and J. S. Wilby, "Interior noise," in *Aeroacoustics of Flight Vehicles, Theory and Practice*, edited by H. H. Hubbard (NASA Langley Research Center, Hampton, VA, 1995), pp. 271–335.
[9]D. J. Thompson and J. Dixon, "Vehicle noise," in *Advanced Applications in Acoustics, Noise and Vibration*, edited by F. Fahy and J. Walker (Spon, London, 2004), pp. 236–291.
[10]G. Cousin, "Sound from TBL induced vibrations," Royal Institute of Technology KTH, Stockholm, Department of Vehicle Engineering, The Marcus Wallenberg Laboratory for Sound and Vibration Research MWL, trita-fkt 1999:35 (1999).
[11]C. Maury, S. J. Elliott, and P. Gardonio, "Turbulent boundary-layer simulation with an array of loudspeakers," AIAA J. **42**, 706–713 (2004).
[12]M. E. Johnson and S. J. Elliott, "Active control of sound radiation using volume velocity cancellation," J. Acoust. Soc. Am. **98**, 2174–2186 (1995).
[13]S. J. Elliott, P. Gardonio, T. C. Sors, and M. J. Brennan, "Active vibroacoustic control with multiple local feedback loops," J. Acoust. Soc. Am. **111**, 908–915 (2002).
[14]J. Rohlfing and P. Gardonio, "Active control of sound transmission through panels with flexible boundaries under deterministic and stochastic excitation," University of Southampton, Institute of Sound and Vibration Research, ISVR Technical Memorandum No. 977 (2007).
[15]P. Gardonio and M. J. Brennan, "Mobility and impedance methods in structural dynamics," in *Advanced Applications in Acoustics, Noise and*

Vibration, edited by F. Fahy and J. Walker (Spon, London, 2004), pp. 389–447.
[16]G. Kurtze and B. G. Watters, "New wall design for high transmission loss or high damping," J. Acoust. Soc. Am. **31**, 739–748 (1959).
[17]J. Rohlfing and P. Gardonio, "Comparison of active structural acoustic control on homogeneous and composite sandwich panels under deterministic and stochastic excitation," University of Southampton, Institute of Sound and Vibration Research, ISVR Technical Memorandum No. 984 (2009).
[18]P. J. Shorter and R. S. Langley, "On the reciprocity relationship between direct field radiation and diffuse reverberant loading," J. Acoust. Soc. Am. **117**, 85–95 (2005).
[19]G. M. Corcos, "The resolution of pressures in turbulence," J. Acoust. Soc. Am. **35**, 192–199 (1963).
[20]S. J. Elliott, C. Maury, and P. Gardonio, "The synthesis of spatially correlated random pressure fields," J. Acoust. Soc. Am. **117**, 1186–1201 (2005).

Acoustical model and theory for predicting effects of environmental noise on people

Karl D. Kryter[a)]
School of Speech, Language, and Hearing Sciences, College of Health and Human Services, San Diego State University, San Diego, California 92182

(Received 21 March 2008; revised 13 January 2009; accepted 2 April 2009)

The Schultz [(1978). J. Acoust. Soc. Am. **64**, 377–405]; Fidell *et al.* [(1991). J. Acoust. Soc. Am. **89**, 221–233] and Finegold *et al.* [(1994). Noise Control Eng. **42**, 25–30] curves present misleading research information regarding DENL/DENL levels of environmental noises from transportation vehicles and the impact of annoyance and associated adverse effects on people living in residential areas. The reasons are shown to be jointly due to (a) interpretations of early research data, (b) plotting of annoyance data for noise exposure from different types of transportation vehicles on a single set of coordinates, and (c) the assumption that the effective, as heard, levels of noise from different sources are proportional to day, night level (DNL)/day, evening night level (DENL) levels measured at a common-point outdoors. The subtraction of on-site attenuations from the measured outdoor levels of environmental noises used in the calculation of DNL/DENL provides new metrics, labeled EDNL/EDENL, for the calculation of the effective exposure levels of noises perceived as equaling annoying. Predictions of judged annoyance in residential areas from the noises of transportation vehicles are made with predicted errors of <1 dB EDNL/EDENL, compared to errors ranging from ~ 6 to ~ 14 dB by DNL/DENL. A joint neurological, physiological, and psychological theory, and an effective acoustical model for the prediction of public annoyance and related effects from exposures to environment noises are presented.
 [DOI: 10.1121/1.3125320]

PACS number(s): 43.50.Ba, 43.50.Rq, 43.50.Qp [BSF] Pages: 3707–3721

I. INTRODUCTION

Starting in the early 1940s, civilian and government scientific agencies have been attempting to formulate acoustical measurements of noises (unwanted sounds) found in residential neighborhoods that are correlated with the annoyance perceived by the residents. Of particular concern has been the effects of daily, or near daily, throughout the year of non-impulsive noise events from vehicles of transportation, industrial, construction activities, etc. The USA Noise Control Act (1972) mandated that scientifically based Federal guidelines and regulations be prepared in order to protect, with a margin of safety, public health and welfare from adverse effects of environmental noise pollution.

To that end, Schultz (1978), under contract with various Federal government agencies, published a synthesis of the data from international research studies of the prevalence and degrees of public annoyance as a function of annualized day and night exposure-level (DNL) of the noise from street/road, railway, or aircraft traffic. Schultz (1978) concluded that a single monotonic curve fits the annoyance data, regardless of the type of vehicular source. Fidell *et al.* (1991) and Finegold *et al.* (1994) re-examined the data used by Schultz (1978), plus additional new data, and concluded that regardless of source the single Schultz curve is essentially correct.

The Schultz curve of annoyance as a function of DNL has been, and continues to be, a "guidance-standard" by the USA National Academy of Sciences (1977), Environmental Protection Agency (EPA) (1978), Federal Interagency Committee on Urban Noise (FICUN) (1980), and Federal Interagency Committee on Noise (FICON) (1992). In the European Union, curves of annoyance as a function of day, evening, night level (DENL) exposure levels of street, railway, or aircraft noise are used for similar purposes. However, data and conceptual models for the assessment and prediction of the effects of these noises have been controversial over that period of time and continue to the present day. The research findings and procedures for the acoustical measurement of noise and the prediction of its affects on people are confined to so-called non-impulsive noise. The measurements and effects of impulsive noises (events with durations of less than 0.5 s) are outside the scope of the present paper.

II. THE INDEPENDENT NOISE-DOSAGE VARIABLE

A. DNL/DENL noise-dosage

In the protocols of research studies of the psychological and physiological effects of a given non-impulsive environmental noise on people, the independent variable is generally identified as the *A*-weighted exposure levels of a sound, or noise, event measured outdoors at a free-field point near a house. Sound level meters integrate the sound energy in successive 1 s intervals during a given noise event and convert the sum to decibels. The product is labeled SENEL (single event noise exposure level). As a practical matter, the duration of a noise event is defined as the energy sum of 1 s

[a)]Electronic mail: kdkryter@cox.net

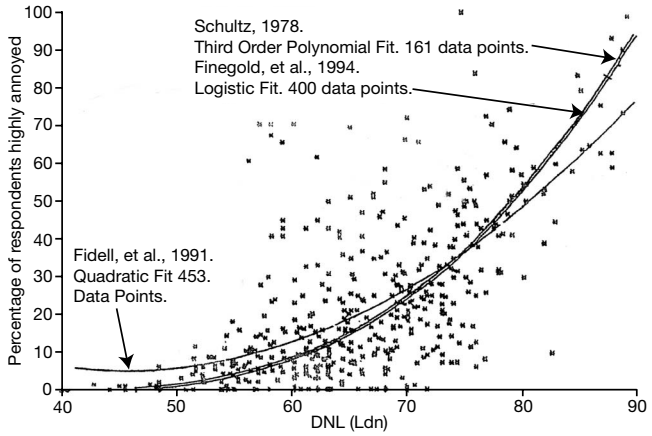

FIG. 1. Showing, as function of DNL, synthesized percentages of exposed people highly annoyed by aircraft, street traffic, and railway traffic noise. After Schultz, 1978; Fidell *et al.*, 1991; Finegold *et al.*, 1994.

intervals between the maximum 1 s energy level and the 10 dB lower 1 s levels occurring before and after the maximum 1 s level of the event.

The energy sum of daily SENEL's of a given environmental noise over a calendar year is averaged by dividing the sum by 315 360 000, the number of seconds in a year, converted to decibels:

$$(10 \log_{10}(\text{anti-log } 315\,360\,000/10)) = 49.4 \text{ dB}$$

and labeled as DNL/DENL, dB. In this paper, unless otherwise specified, decibels, will refer to *A*-weighted frequency spectra.

In the calculation of DNL a 10 dB "penalty" is added to the SENEL's of given events occurring in the 10 PM–7 AM daily time period. In the calculation of DENL, a 5 dB penalty is added to the SENEL's of events occurring during the 7–11 PM, and a 10 dB penalty during the 11 PM–7 AM daily time periods.

TABLE I. Max dBA levels of noise at two hoses near airport. After Ortega and Kryter, 1982.

Av. 2 Event Each Veh.	Front Yard	Back Yard	Front-Back
Aircraft	77.1	76.8	0.3
Car	71.5	52.3	19.2

B. The dependent annoyance variables

In the derivation of the Schultz curve, the up-dated curves of Fidell *et al.* (1991) and Finegold *et al.*, (1994) the data for street, railway, and aircraft traffic noises were plotted on a single set of DNL vs annoyance coordinates, see Fig. 1. The investigators in Fig. 1 implicitly presumed that the acoustical dosage of as measured or calculated DNL's of noise from the different types of vehicles were proportional to the levels present at a common free-field point outdoors near houses.

Schultz (1978), Fidell *et al.* (1991), and Finegold *et al.* (1994) removed data from studies that did not, in their opinion, closely enough cluster around a single curve. Some of the exclusions were justified because of difficulties in interpretations of multi-language semantics and noise measurements, but some of the exclusions are questionable, see Kryter, 1982, 1983, 1985, 1994. Also, the magnitudes of calculated sound transmission attenuations due to geometrical spherical divergence, see Fig. 2, and house-barrier attenuation as measured in Table I, showed that these attenuations

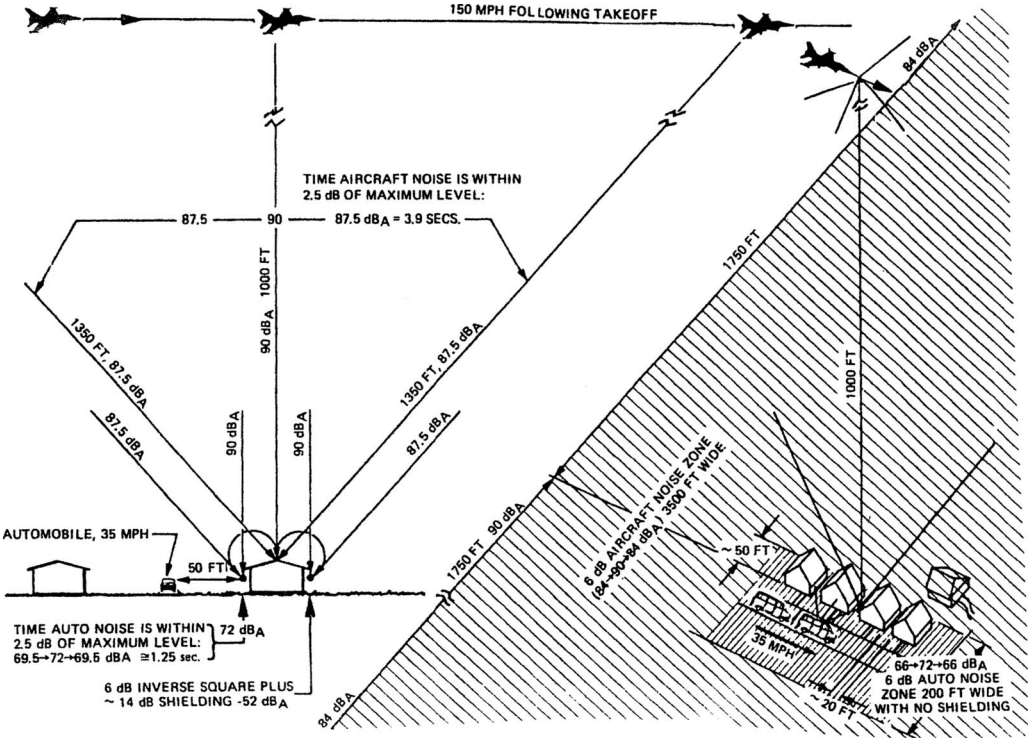

FIG. 2. Schematic diagram of acoustical factors that affect noise levels measured in and around houses from aircraft and ground vehicles. From Kryter, 1982.

TABLE II. Decibel differences in DNL/DENL when people highly annoyed by transportation noises. Note all differences in DNL with equal annoyance based on visual interpolations of grided enlargements of DNL vs equal annoyance curves for each cited synthesis or research study.

		Section 2 Aircraft-Street			Section 3				Section 4 Single Sources		
DNL	Section 1 Schultz, '78; Fidell*et al.*, '91; Finegold *et al.* '94[a]	Ollerhead, '80[b]	Av., Hall; Fidell, '81[b]	Kryter, 1982[b]	DNL/ DENL	Airc. Str.	Aircraft-Railway	Railway-Street	Airc.	Str.	Rail.
							Miedema and Oudshoorn, 2001[c]				
50	0	10	10	5	50	5	8	3	8	3	0
55	0	10	10	9	55	7	11	4	13	6	2
60	0	10	10	10	60	9	16	7	20	11	4
65	0	10	10	10	65	10	22	12	30	20	8
70	0	10	10	12	70	10	25	15	40	30	15
Average	0	10	10	9	Aver.	8	16	8	22	14	6

[a]No differences in DNL's between street, railway, and aircraft noise.
[b]Differences: Ollerhead, 1980; average of Hall *et al.*, 1981, and Fidell *et al.*, 1981; Kryter, 1982.
[c]Corrected here, see Fig. 3 on re-analysis of Miedema and Oudshoorn, 2001 (post-Kryter, 1982).

differ for the noise from ground-based compared to aircraft vehicles of noise.

Over the past 30 years several "pools" of research findings have been published regarding the relations between (a) the magnitudes of the independent annualized DNL/DENL exposures to environmental noise from transportation vehicles and (b) the dependent variable, the percentages of people living in thusly noise-exposed houses reporting given degrees of subjective annoyance.

One pool, consisting, as discussed, of three syntheses (Schultz, 1978; Fidell *et al.*, 1991; Finegold *et al.*, 1994) shows that over the range of 50–70 dB DNL, there are, in effect, 0 dB differences between equal magnitudes of annoyance from street, railway, or aircraft noise, see data column 1, Section I, Table II.

A second pool consisting of (a) individual studies (Ollerhead, 1980), (b) the average of studies by Hall *et al.* (1981) and Fidell *et al.* (1981), and (c) syntheses by Kryter (1982) of a number of studies shows the equivalent decibel exposure-level differences averaged over the range of 50–70 dB DNL/DENL. Section II, Table II shows the results when the noises from the different types of vehicles were judged to be equally annoying.

The Miedema and Oudshoorn (2001) synthesis, see Fig. 3 and Sections III and IV of Table II, is chosen for examination herein as the best state-of-art synthesis of attitude surveys of annoyance from street, railway, and aircraft vehicles of transportation. It is more inclusive than any of the other syntheses. All together for the three types of vehicles, Schultz (1978) synthesized a total of 12 separate studies; Kryter (1982) also employed the 12 separate studies used by Schultz (1978); Fidell *et al.* (1991) and Finegold *et al.* (1994) used the 12 studies included in the Schultz synthesis plus additional studies, or parts thereof, for a total of 15 separate studies. Miedema and Oudshoorn, (2001), however, used 20 aircraft, 14 street, and 9 railway traffic noise studies, a total of 43 separate studies.

Figure 3 shows, as a function of the DNL/DENL of street/road, railway, and aircraft traffic noise, the percentages of people living in urban residential areas who are (a) 0%–

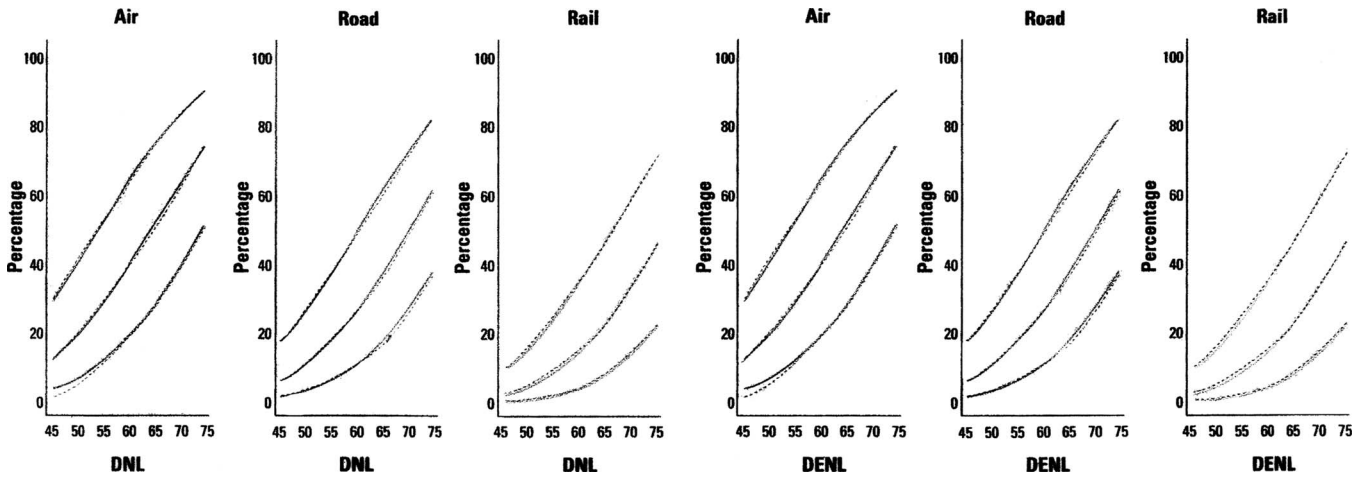

FIG. 3. Estimated curves (solid lines) of lowest curve, "at least a little annoyed;" middle curve, "annoyed;" and upper curve, "highly annoyed;" and their polynomial approximations (dashed lines) as function of DNL and DENL. From Miedema and Oudshoorn (2001).

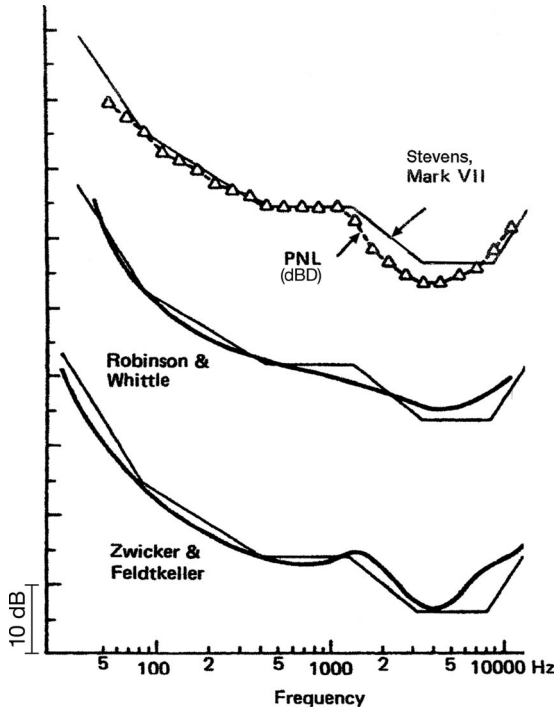

FIG. 4. Comparisons of equal loudness contours, solid curves, dB Phons, Zwicker and Feldtkeller (1967); Robinson and Whittle (1964); Stevens (1972), Stevens and Davis (1938), and perceived noisiness level contour triangles, dBD PNL. Kryter, 1970.

28% "little annoyed," (b) 29%–71% "annoyed," and (c) 72%–100% "highly annoyed." Note that in a number of the questionnaire surveys analyzed in the Miedema and Oudshoorn (2001) synthesis somewhat different verbal terms were used for categorizing degrees of annoyance, but were converted to be consistent with the Miedema and Oudshoorn (2001) category cutoff percentage points.

C. *A*, *D*, and Phon weightings for frequency spectra

The judgments of the loudness and perceived annoyance of noises in the audible spectrum correlate reasonably well with each other, see Fig. 4. However, the loudness and perceived noisiness of sounds/noises having somewhat different spectra correlate significantly better with exposure levels measured with PNL (dB D), and Phon spectra weightings than with *A*-weighting, see Fig. 5.

This is illustrated by a case study of unsolicited complaints of annoyance from exposures to narrow, tonal, frequency bands of "noise" with *A*-weighted octave levels of high-frequency church-bells in one neighborhood and low-frequency ceremonial drums in another neighborhood. The peak levels of the religious ceremonial drum noise in one neighborhood were several decibels below, and the religious ceremonial bell noise in a different neighborhood, were ~1 dB above the city's specified "tolerable" dBA octave band noise exposure-level ordinance. However, and consistent with complaints of annoyance, the respective octave bands each exceeded by several decibels the low- and high-frequency segments of the "equally-annoyance-tolerable" *D*-weighted octave bands levels, see Fig. 6.

The measured-on-the-ground "backblast" noise from jet

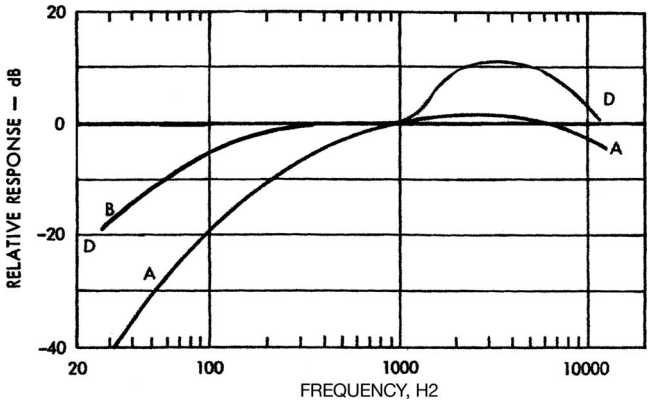

FIG. 5. Standardized *A*-weighted equal loudness (ANSI, 1983) and *D*-weighted equal noisiness contours for equal annoyance (Kryter, 1970).

aircraft during start and take-off roll has exceedingly more intense components in frequencies below ~315 Hz than are present in the on-the-ground flyover noise after take-offs of B-727 and B-757 aircraft, see Fig. 7. As a result, people in residential areas about 2 miles behind the main take-off runway at the San Francisco International Airport report feelings of annoyance greater than is predicted by *A*-weighted DNL. Similar cases of the lack of accuracy of the *A*-weighting for estimating the annovance impact in residential areas of general environmental noises have been reported (Goodfriend, 1991, 2006).

D. Proposed alternative un-solicited noise complaints and geo-DNL display method

Fidell (2003) presented a history of the early development of the Schultz curve and a discussion of his perspectives for further research and policies for the governing of

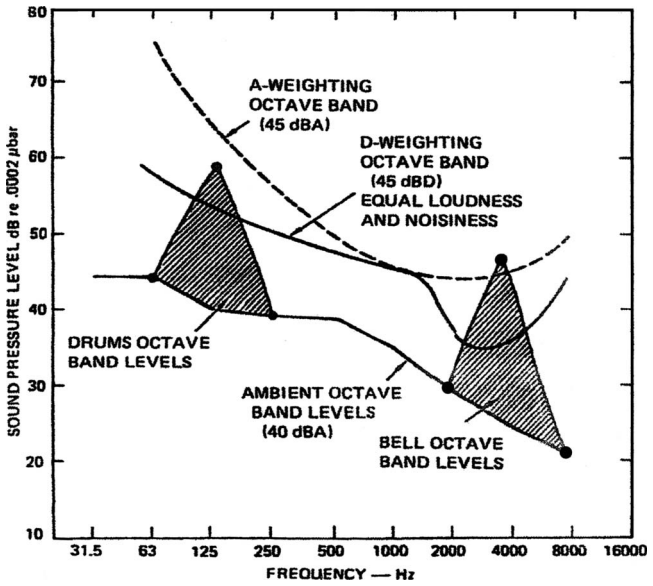

FIG. 6. Octave band levels of (a) ceremonial drums heard in one residential neighborhood and (b) ceremonial bells heard in a different residential neighborhood plus (c) average *A*- and *D*-weighted ambient background noise levels. Sound level meter measurements made by Darby-Ebieu Associates, Inc., Kaiwa, HI.

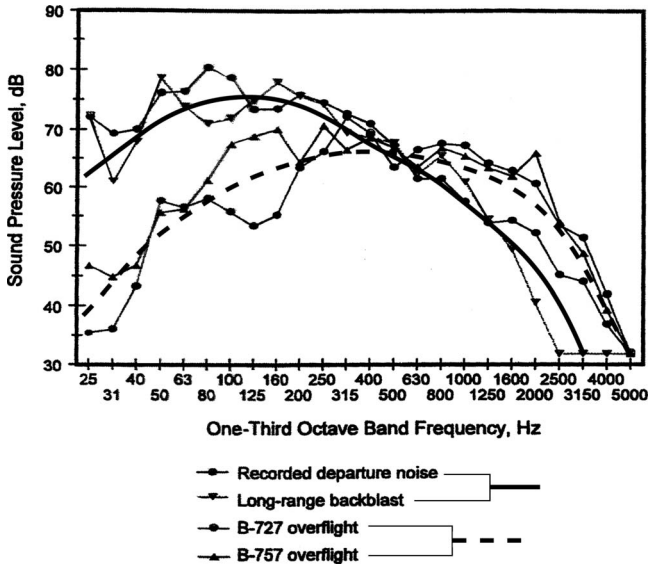

FIG. 7. Plots of spectra of recorded noise signals from on-the-ground noise from aircraft flying at typical altitudes over residential areas and on-the-ground "backblast" noise at San Francisco International Airport during departure take-offs. After Pearsons *et al.*, 2000.

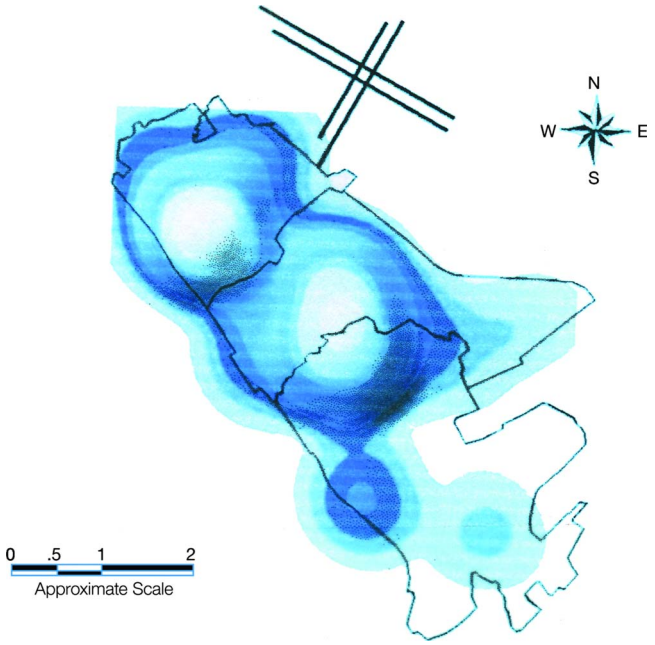

FIG. 8. (Color online) Rendering of complaint density as pseudo-terrain in color or shades of black-coded false elevation behind main departure runway at San Francisco International Airport. Total distance scale equals 2 miles. From Fidell, 2003.

environmental noise in residential living areas. Points of interest for the present paper are Fidell's statement and recommendation, p. 3014, that: *"The increased interpretability of noise complaints made possible by computer-based record keeping and geo-information software suggests a more prominent role in the future for complaint rate information in the design of aircraft noise mitigation projects and impact assessments."; and recommends "formal recognition of geographic distributions of (volunteered) noise complaints as an alternative (to attitude surveys) indication of actual community reaction to transportation noise."*

The subject computer-driven geographic displays of DNL footprints of aircraft noise around airports depict concentrations of volunteered complaints about aircraft noise as pseudo-terrain elevation peaks coded in brightness and/or color the relative numbers of volunteered complaints, see Fig. 8. Fidell (2003) suggested that such displays might provide insights into why DNL exposure levels do not uniformly correlate with attitude surveys of annoyance from transportation noises.

Note that, as presently portrayed, the numbers of volunteered complaints by pseudo-elevation peaks in DNL loci need not show the actual differences in the percentages of exposed people having different degrees of annoyance. Indeed, geographic areas exposed to aircraft noises of the same DNL could be displayed as having little or no volunteered complaints because some of the those geographic loci or areas happen to be unpopulated, or relatively less, people populated. Variable people density-populated areas around the San Francisco airport, as shwon in Fig. 8, could, on point, be such a case.

E. Non-auditory biases in judged perceived noisiness of noises of equal DNL/DENL levels

Job (1988) analyzed data from numerous attitude surveys of relations between noise exposure from a variety of sources and annoyance reactions, such as those in Fig. 1 and Table II. Job (1988) concluded that (p. 991) *"Only a small (typically less than 20%) of the variation in individual reaction is accounted for by noise exposure."…. "Variables, such as attitude to the noise source and sensitivity to noise, account for more variation in reaction than does noise exposure."*

Fidell and Green (1991) reason that such differences in degrees of annoyance from equal DNL exposure levels to noise from street, railway, or aircraft traffic could be attributed to psychological biases on the part of individual listeners, to quote (p. 23.3): "*Civic action groups, political or media attention, and other factors can make the residents of the quieter community more likely to describe themselves as highly annoyed even by relatively low noise exposure.*

Among the many non-acoustical factors that may affect the prevalence of noise-induced annoyance in communities are: (1) various attitudes towards noise sources and their operators (approval, fear, distrust, etc.), (2) socioeconomic levels of individuals, and (3) economic dependence on operations of noise sources. All these influences are reflected in response bias."

However, the correlations of DNL/DENL with noise annoyance reactions as found by Job (1988) are based on multiple-correlation analyses using (a) misleading DNL/DENL's as the independent variable and (b) using a host of un-quantified non-acoustical hypothetical "biasing" factors as serving as, in effect, statistically spurious dependent variables. This is to say that, as will be discussed latter, behavioral reactions based on cognitive decisions may unjustifiably be interpreted as causing biases in judgments of surveyed noise annoyance.

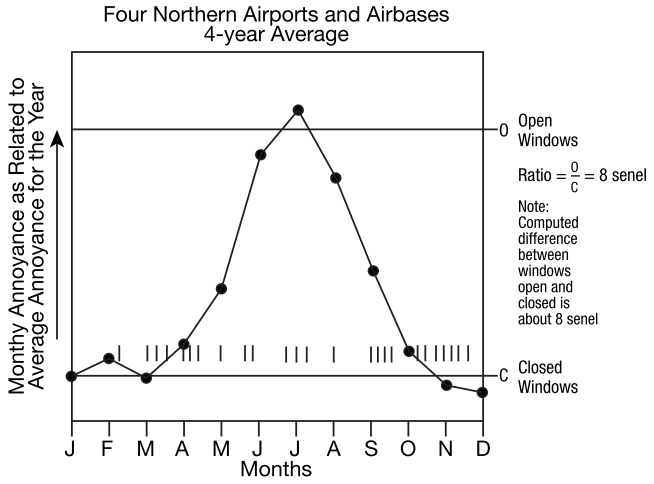

FIG. 9. Total monthly volunteered, via telephone, annoyance complaints over a 4-year period by residents near four airports in northeastern quarter of the United States. After Beranek *et al.* (1959). Tick marks above abscissa indicate approximate months of the year of representative attitude surveys used in the Schultz (1978) and Miedema and Oudshoorn (2001) syntheses.

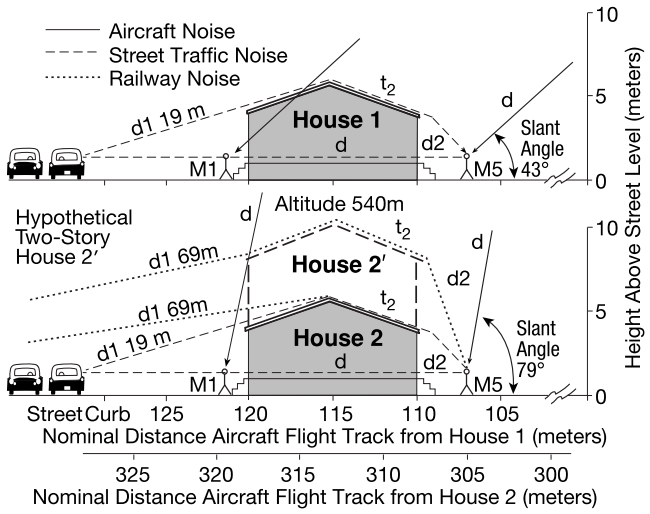

FIG. 10. Schematic showing House 1 and House 2 and hypothetical two-story House 2, slant angels, slant ranges to M1, front yard and M5, rear yard microphones. From Kryter, 2007.

III. ANNOYANCE AS FUNCTION OF EDNL/EDENL OF ENVIRONMENTAL NOISE

A. Fallacies of DNL/DENL metrics

Note that DNL/DENL's are generally measured or calculated for noise events from a given source that will occur during each, or nearly each, day during a year regardless of the seasonal-date of their occurrences. While this procedure is approximately appropriate for the outdoor noise measurements in DNL/DENL calculations for predicting annualized subjective annoyance, it is not appropriate for EDNL/EDENL. Since more open-window living during the 6 warmer months compared to more closed-window living during the colder 6 months of a calendar year, the subjective monthly annoyance impact of aircraft noise is equivalent to ~0 dB up to a peak of ~8 dB DNL during the warmer six months of the calendar year, see Fig. 9. For this reason, the annualized effective DNL of aircraft flyover noise equals the as-presently-calculated 12 monthly DNL/DENL level plus the increase up to ~8 dB in effective annoyance-causing noise energy during the warmer 6 months of the year, that is,

$$\mathrm{DNL}_x + (\mathrm{DNL}_x + (5\log_{10}(8\ \mathrm{dB}/4\ \mathrm{dB})) = 2\ \mathrm{dB},$$

where 4 in the (8 dB/4 dB) term reflects a halving of energy due to the "haystack" nature of the six warmer months of exposures (Fig. 9), and $5\log_{10}$ is adjustment for a moving sound-source [Eq. (3.18), Piercy and Daigle, 1991].

More importantly, established acoustical and auditory sensory principles dictate that different degrees of attenuations are imposed on the noise from different types of transportation vehicles during transmission from source to houses or housing sites. For examples, as shown, for one-story houses: (a) street traffic noise is 6 dB more attenuated than aircraft noise due to geometric spherical divergence between the front to rear yards, and vice-versa, see Fig. 2, and (b) as shown in Table I, street traffic noise is 19 dB more attenuated than aircraft noise due to house-barrier attenuation.

B. Measurements and calculations of on-site attenuations of street traffic and aircraft noise

Kryter (2007) had physical measurements made of on-site attenuations of street traffic and aircraft noise at two one-story houses. Using established acoustic algorithms, on-site attenuations were calculated for those houses and for a hypothetical two-story house, see Fig. 10. Differences in on-site outdoor and indoor attenuations of transportation vehicle noises at one- and two-story houses are shown in Table III. Formulas and terms used in the calculations are given in footnotes on Table III.

The attenuations in Table III are as follows.

(1) Attenuation due to geometric spherical divergence of sound waves as a function of the distance between the source and receiver, herein labeled *A*div(ergence).
(2) Attenuation due to a "thick" barrier, such as a house, of sound waves during transmission from the front yard to the rear yard (or vice-versa) of the house, herein labeled *A*bar(rier);
(3) Absorption attenuation and reflection of sound energy during transmission over ground, herein labeled *A*gro(und);
(4) Differences in the magnitudes of attenuations due to (a) differences in the relative sizes of façade and roof areas of houses that are the most accessible to the noises from different types of transportation vehicles and (b) their transmissibility into the interior areas of the houses, herein labeled *A*acc(ess)/trans(mission).
(5) Equivalent attenuation of the noises due to sensory fatigue and/or a diminution of loudness and perceived noisiness of a sound event as a function of its duration, herein labeled *A*adapt, see Fig. 11, and discussions in Small, 1963.

Note that the magnitude of on-site attenuation by air-absorption of typical street, railway, or aircraft traffic noise is negligible, <0.5 dB, for the field measurements at hand, see Eq. (3.3) in Piercy and Daigle, 1991.

TABLE III. Average calculated on-site decibel attenuations (*A*'s) and sums of street, railway, and aircraft noise. After Table IV, Kryter, 2007.

m(eter) source-measure points[a]	Averages of on-site attenuations for two one-story houses and a hypothetical two-story house																	
	Street 15/27/37 *Adiv*[a]	Street M1-M5 *Abar*[b]	Street 15 m *Agro*[c]	Street M1-M[d] *Aacc/tran*[d]	Street 6s *Aadapt*[e]	Street Sum *A*'s	Rail 53/65/75 *Adiv*	Rail M1-M5 *Abar*	Rail 53 m *Agro*	Rail M1-M[d] *Aacc/trar*	Rail 20s *Aadapt*	Rail Sum *A*'s	Airc. 458 m *Adiv*	Airc. M5-1 *Abar*	Airc. 0 m *Agro*	Airc. M5-M[d] *Aacc/tran*	Airc. 10s *Aadapt*	Airc. Sum *A*'s
Indoors	3	0	0	27	14	44	1	0	4	27	20	51	0	0	0	24	18	42
Outdoors	4	24	0	0	14	41	1	24	4	0	20	49	0	2	0	0	18	20

[a]Str, *Adiv* 15 m to front, 27 m rear wall, 37 m rear patio; rail: 53 m front, 65 m rear wall, 75 m rear patio. Eq. (3.18): $L_{eq\,ref} - 10\log_{10}(r/r_{ref})$ in Piercy and Daigle (1991).
[b]Abar: Measured M1-M5 street, presumed same for railway noise, M5-M1 for aircraft noise. Equations (3.14), (3.13), and (3.14) in Piercy and Daigle (1991).
[c]Agro: Front yrd. 15 m sreet noise, 53 m rail noise. Oct. band 500 Hz, source 0.3 m above grass. See Table 3.2, in Piercy and Daigle, 1991.
[d]Aacc/trans: diff. in size of house facades and roof areas exposed to aircraft vs street/railway noise (diff. of ~1/2 overall of street/railway vs airc.). Measured diff. indoor levels street/railway vs aircraft noise levels outdoors=Str. M1-(av. M2, 3, 4); Airc.=M5 -(av M2,3,4).
[e]Aadapt: loudness/noisiness diminution due to duration of noise event. Equivalent, decibel basis, exposure level of noise event.

FIG. 11. Relative effect of duration on the perceived attenuation of loudness and noisiness of a sound/noise event. From Kryter, 2007.

C. Real-life factors affecting the measurement and calculation of DNL

To test the premise that differences between calculated indoor and outdoor attenuations of street, railway, and aircraft traffic noise are important factors for correctly predicting annoyance, it is first necessary to estimate the equivalent on-site attenuations that occur in real-life at-home living. The joint reasons being (a) that in temperate climates people generally spend more time indoors than outdoors of their homes and (b) the effective attenuations of indoor compared to outdoor listening differ.

Table IV shows that the bold-typed average decibel differences in attenuations (*A*'s) for ratios of 80%/20%, 75%/25%, and 70%/30% for indoors vs outdoor listening locations are equivalent to (a) 7 dB for street vs aircraft, (b) 14 dB railway vs aircraft, and (c) 8 dB railway vs street noises. Note that the average differences between the >80% and higher indoor and the <20% and lower outdoor ratios are, respectively, smaller or larger than the selected average of 75%/25% indoor vs outdoor ratios. An exception is for railway-street, where the difference is a constant 8 dB. An average annualized temperate climate is presumed to be the general case (75% indoor/25% outdoor ratio) for the attitude surveys used in the Miedema and Oudshooorn (2001) synthesis.

The 90% indoor/10% outdoor ratio-attenuations shown in Table IV could be applicable in estimating the impact of environmental noises annoyance in frigid climates. The average of the 60% indoor/40% outdoor to 10% indoor/90% outdoor attenuation ratios could, as estimated, be applicable in tropical climates.

D. Formulas for ESENEL and EDNL/EDENL metrics for predicting annoyance

It has been postulated that to predict perceived noisiness, DNL/DENL levels should be corrected for on-site acoustical and equivalent sensory/perceptual attenuations of the noise during transmission from their source to positions near the ears of residents (Kryter, 2007). Metrics for that purpose were proposed and labeled EDNL/EDENL.

The following formula differs somewhat from those used by the author in 2007 because of the use herein of (a)

TABLE IV. Av. one- and two-story houses. Indoor and outdoor calculated ratios of on-site attenuations (A's) and differences between sources. See Table III. Note the 1 dB "error" in a few additions due to decimal roundings.

Listeners	Street Sum A's[a]	Rail Sum A's[a]	Aircraft Sum A's	Street-Aircraft[b]	Rail.-Aircraft[b]	Rail.-Street[b]
100% indoors	44	51	42	2	9	7
100% outdoors	41	49	20	21	29	8
90% indoors	40	46	38	2	8	6
10% outdoors	4	5	2	2	3	1
		dB attenuation: % ind.+% out.=		4	11	7
80% indoors	35	41	34	2	7	6
20% outdoors	8	10	4	4	6	2
		dB attenuation: % ind.+% out.=		6	13	8
75% indoors	33	38	32	2	7	6
25% outdoors	10	12	5	5	7	2
		dB attenuation: % ind.+% out.=		7	14	8
70% indoors	31	36	29	2	6	5
30% outdoors	12	15	6	6	9	3
		dB attenuation: % ind.+% out.=		8	15	8
		Aver.: 80%-20%; 75%-25%; 70%-30%=		7	14	8
60% indoors	26	31	25	1	5	4
40% outdoors	16	20	8	8	12	3
		dB attenuation: % ind.+% out.=		9	17	7
50% indoors	22	26	21	1	5	4
50% outdoors	21	25	10	11	15	4
		dB attenuation: % ind.+% out.=		12	19	8
40% indoors	17	20	17	0	4	3
60% outdoors	25	29	12	13	17	5
		dB attenuation: % ind.+% out.=		13	21	8
30% indoors	13	15	13	0	2	3
70% outdoors	29	34	14	15	20	5
		dB attenuation: % ind.+% out.=		19	27	8

[a]Decibel sums based on anti-logs.
[b]Decibel differences arithmetic.

solely the Miedema and Oudshoorn (2001) synthesis of noise annoyance research data and (b) the movement of the −2 dB correction to DNL/DENL's for "summer" vs "winter" open-window-outdoor living conditions from the second term of Eq. (1) (Kryter, 2007) to the first term of herein Eq. (1).

Mathematical equation for $\mathrm{EDNL}_x/\mathrm{EDENL}_x$, where x is a given environmental noise is as follows:

$$\begin{aligned}&\mathrm{EDNL}_x/\mathrm{EDENL}_x\\&\quad=((\mathrm{DNL}_x/\mathrm{DENL}_x-2\ \mathrm{dB})\\&\quad-(\text{arithmetic sum decibels, } A_x\text{'s})\\&\quad-(\text{arithmetic sum decibels, } A\text{'s}_{\mathrm{Aircraft,Ref.}})),\end{aligned}\qquad(1)$$

where the arithmetic average of noise over the range of 50–70 dB from ground-based sources are judged to be equally annoying to the arithmetic average of aircraft noise over the range of 50–70 dB: 22 dB; street, 14 dB; railway, 6 dB (see Section IV, Table II), and the −2 dB is an adjustment for the greater noise-annoyance measured in the about 6 warmer months compared to the about colder 6 months of the calendar year with $\mathrm{DNL}_x/\mathrm{DENL}_x$ exposure levels measured on an annualized monthly basis.

Note 1. EDNL_x can be transformed to EDENL_x by adding individually thereto: 0.6 dB for aircraft, 0.2 dB for street traffic, and 0 dB for railway noise (p. 415, Miedema and Oudshoorn 2001).

Note 2. $\mathrm{EDNL}_x/\mathrm{EDENL}_x$ is calculated from A_x's based on annoyance studies in Miedema and Oudshoorn (2001) synthesis that are presumed to have been conducted primarily in temperate climates with an average of 75% indoor/25% outdoor listening ratio, see Table IV, and mostly conducted in urban neighborhoods near commercial airports.

Note 3. EDNL/EDENL do not disturb the numerical relations between published DNL/DENL's and annoyance effects data but serve as a means of converting DNL/DENL into more realistic, as heard, noise-dosage levels.

Note 4. It is recommended that spectrum D-weighting be used in the process because of its more accurate reflection of the perceived noisiness and loudness of a wider spectrum variety of environmental noises than does A-weighting.

TABLE V. Calculated on-site attenuations and measured equal annoyance in equivalent decibels between sources. Average for one- and two-story houses.

Section	1 DNL[a]	2 DENL-DNL[b]	3 EDNLstr.-EDNLair.	4 EDENLstr.-EDENLair.	5 EDNL-EDENL
Street-aircraft traffic noise					
Calculated attenuations[c]			7.0	7.0	
Measured equal annoyance[d]	0.0	0.4	6.0	6.4	0.4
		Difference	1.0	0.6	
Railway-aircraft traffic noise					
Calculated attenuations[c]			14.0	14.0	
Measured equal annoyance[d]	0.0	0.0	14.0	14.0	0.0
		Difference	0.0	0.0	
Street-railway traffic noise					
Calculated attenuations[c]			8.0	8.0	
Measured equal annoyance[d]	0.0	0.2	8.0	8.2	0.2
		Difference	0.0	−0.2	0.2
		Sum attenuations	29.0	29.0	
		Sum measured equal annoyance	28.0	28.6	
		Sum atten.- sum meas. equal annoyance	1.0	0.4	
		Aver. diff.: str.-air.;rail.-air.; str-rail.	0.3	0.1	

[a]Schultz, 1978; Fidell *et al.*, 1991; Finegold *et al.*, 1994.
[b]Miedema and Oudshoorn, 2001.
[c]See Table IV: Indoor 80%–70%: Outdoor 20%–30%.
[d]Based on Table II and Eq. (1).

Note 5. In order to make comparison of the relative annoyance from EDNL/EDENL's of an aircraft source, A_x, other than $A's_{\text{Aircraft,Ref.}}$, i.e., per FAA specified aircraft operations, as herein discussed, may not be appropriate, see second term in Eq. (1). The $A's_{\text{Aircraft,Ref.}}$ is chosen as a reference anchor because aircraft noise is the single most environmental noise studied in attitude surveys of noise annoyance.

Table V shows the following.

(1) Schultz (1978), Fidell *et al.* (1991), and Finegold *et al.* (1994) found ~0 dB DNL differences between source-pairs of transportation vehicle noise (street vs aircraft, railway vs aircraft, and railway vs street noise), when judged to be equally annoying, see data column 1, Table V.
(2) Based on Miedema and Oudshoorn (2001) findings (p. 415) between source-pairs of transportation vehicle noise that cause equal annoyance, see columns 2 and 5, Table V, are DENL−DNLstr.−air.=0.4 dB; EDENL−EDNLstr.−air.=0.4; DENL−DNLrail.−air.=0.0 dB; DENL−DNLstr.−rail.=0.2 dB.
(3) Calculated differences in on-site attenuations, *A*'s, of source-pairs, see columns 3 and 4, Table V, are 7.0 dB EDNLstr.−EDNLair.; 14.0 dB; EDENLrail.−EDENL.air.; 8.0 dB EDENLstr.−EDENLrail..
(4) Measured differences in annoyance between source-pairs of transportation vehicle noise are, see columns 3 and 4, Table V, the equivalent of 6.0 dB EDNLstr.−EDNLair. and 6.4 dB EDENLstr.−EDENL.air.; 14.0 dB EDNLrail.−EDNLair.; 14.0 dB EDENLrail.−EDENLair.; 8.0 EDNLstr.−EDNL−rail.; 8.2 dB EDENLstr.−EDENLrail..
(5) The bottom data line of Table V shows that the average of the numerical sums of the differences between calculated decibels of on-site attenuations and the equivalent exposure levels for people reporting being equally annoyed from street-aircraft, railway-aircraft, and railway-street traffic noises are 0.3 EDNL dB, and 0.1 EDENL dB.

E. Impacts transportation noises on tolerable annoyance and numbers of housing-sites

Schultz (1978) prepared a "decision-maker's tool" for evaluating the relative "costs," in terms of annoyance and real-estate values to the general public from exposures to street, railway, and aircraft noises. FICUN and FICON thereby imply a criterion for residential land: that land exposed, or to be exposed, to noise that would cause more than 15% of the exposed people to be highly annoyed should be zoned as being unacceptable for typical detached housing.

Because of the averaging of the data for the different sources of noise, the Schultz curve *decreases* the estimated percentage of people highly annoyed by aircraft noise by averaging it with the estimated lesser percentages of people highly annoyed by equal DNL levels of street and railway traffic noise. Conversely, this process *increases* the apparent percentage of urban sites to be considered as incompatible for residential housing because of noise from transportation vehicles. An additional reason for the lesser differences of noise condemnation of USA urban housing sites from street compared to aircraft noise for a given DNL exposure level is that there are more urban house sites exposed to street traffic than to aircraft noise by a factor of approximately 3, see Fig. 12.

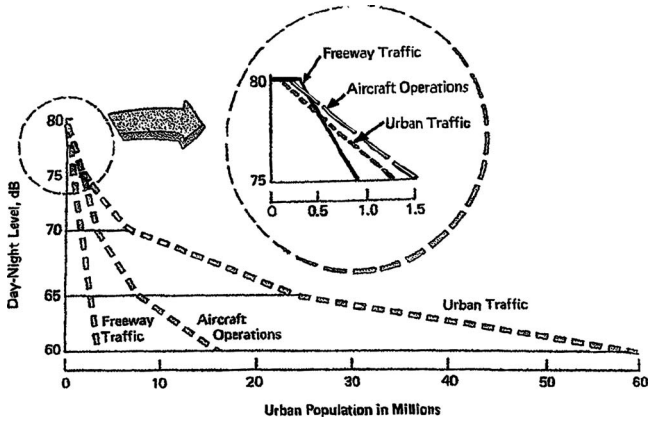

FIG. 12. Cumulative number of people in USA urban areas exposed to outdoor DNL from aircraft operations, and street and freeway traffic. Total estimated, 1978, urban population 138×10^6. Figure 6 in EPA Report, with extrapolations to DNL 50 dB for aircraft and 40 DNL 40 dB for street traffic noise.

Figure 13(a) shows that with 55 dB DNL street, railway, or aircraft noise ~4% of the exposed people would be highly annoyed, and 100% of the house building sites would be unsuitable for residential housing. With 65 dB DNL ~15% of exposed people would be highly annoyed (the FICON/FICUN maximum annoyance criterion percentage) and ~30% of USA house building sites would be unsuitable for residential housing.

Figure 13(b) shows that with 53 dB EDNL (55 DNL) exposure level, the percentages of exposed people highly annoyed would be ~15% aircraft, ~8% street, or 2% railway noise, and the percentages of urban building sites unsuitable for residential housing would be ~45% aircraft and 17% street traffic noise. With 63 dB EDNL (65 DNL) exposure level, the percentage of exposed people who would be highly annoyed would be ~35% aircraft and ~15% street traffic noise, and the percentages of urban house building sites unsuitable for residential housing would be ~4% aircraft and 17% street traffic noise. To the authors knowledge, no data are available as to the number of USA urban house-sites as a function of level of railway noise.

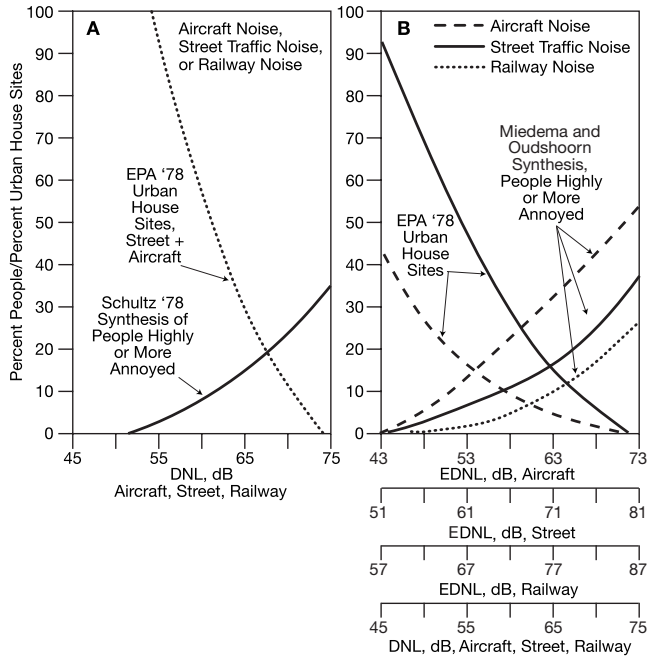

FIG. 13. (A) Showing as a function of DNL: (1) percent of residents highly annoyed by aircraft, street, or railway traffic noise according to Schultz (1978), Fidell *et al.* (1991), and Finegold *et al.* (1994) and (2) percent of USA urban house sites thusly exposed to street and aircraft noise based on extrapolations of EPA data in Fig. 12. (B) Showing (1) as functions of EDNL, percent of residents highly annoyed by aircraft, street, and railway traffic noise according to Miedema and Oudshoorn (2001) and (2) as a function of DNL, percent of USA urban exposed to aircraft or street traffic noise based on data Fig. 12, EPA.

F. Generality of the reliability and validity of EDNL/EDENL for predicting annoyance

While fallacies in the basic premise of the DNL/DENL methods for quantifying the levels of environmental noise as heard in homes may seem obvious, the accuracy in those regards by EDNL and EDENL, with average prediction errors of <1 dB, seems too good to be true. The following four factors may help explain the apparent generality, reliability, and validity of the EDNL/EDENL, compared to the DNL/DENL metrics:

(1) Most of the research on annoyance and other adverse effects of transportation noise on people have been centered in urban neighborhoods near commercial jet airports. These neighborhoods consist, by and large, of one- and two-story houses located on lots of approximately one-sixth of an acre (~640 sq m). The setbacks of the front facade of houses to the center of the street are typically ~15 m (47 ft) and 3.2 m (10 ft) between houses. Similar distances are promulgated in many international building codes for urban residential housing.
(2) Because of FAA (1993) "fixed" minimum allowable altitudes, ~1500 ft (968 m), and maximum allowable on-the-ground SENEL of ~65 dB, for aircraft flying over residential areas after take-off operations, the slant range angles between aircraft flyovers, following takeoffs, and the closest houses to each sided of flight paths must not be less than ~75°. At lesser slant angles the on-the-ground-directly-under the flight path noise level can exceed the FAA tolerable 65 dB SENEL level. Because of reduced engine-power during approach to landing operations, on-the-ground SENEL's in residential areas are generally below tolerable levels.
(3) On-site attenuations for noises having broad frequency bands, e.g., noises of transportation vehicles, should, within limits, be approximately the same regardless of the materials, architectural design, or building codes used in the construction of houses. However, note that the proposed EDNL/EDENL procedures can be tailored to fit urban and suburban neighborhoods having different lot-sizes, number of stories or building heights, house construction codes, different climates, and different ratios of indoor and outdoor listening positions. The procedure would, as needed for noise from different sources, be calculated in accordance with formulas in notes on Table III, on-site house attenuations (*A*div,

*A*bar, *A*gro, *A*cc/trans, and *A*adapt for indoor and outdoor listening conditions, see Table IV, and seasonal climate changes, see Fig. 9).

(4) The most important factors behind the EDNL/EDENL functions are (a) the synthesis by Miedema and Oudshoorn (2001) of data from thousands of people in industrialized countries who served as subjects in surveys of annoyance due to the environmental noise of transportation vehicles and (b) except for the DNL/DENL levels of transportation noises, the separate surveys were conducted in randomly selected residential neighborhoods. That is, appreciable differences in possible effects, if any, on noise annoyance due to different social, cultural, and idiosyncratic factors in different residential areas are averaged-out.

IV. NOISE ANNOYANCE AS FUNCTION OF AUDITORY SYSTEM STIMULATION

A. The adequate stimulus for hearing

It is a given that the adequate acoustical signal for stimulation of hearing is the sound energy present at or near the entrance to ear canals. As discussed above, it is important that the energy in a sound or noise be measured or estimated to be present at or close to that point in order to represent the adequate stimulus for hearing, i.e., EDNL/EDENL.

It is a given that the so-called equal energy concept is valid. That is, sound energy in a nonimpulsive noise event is, within limits of auditory fatigue-effects, the sum of its duration in seconds, regardless of duration, and the magnitude of the integrated instantaneous squared sound pressures during the noise event. Also important is the fact that the human auditory system is a *par excellence* sound frequency analyzer and level meter. It is capable in near-real time to (a) spectrum and intensity analyze and perceive sound/noise events.

B. Auditory sensations, perceived noisiness and associated psycho/physiological stress

Loudness is defined as the primary auditory sensation of the magnitude of the acoustical intensity of a sound event. Perceived noisiness is defined as the perception of the annoyance (synonymous with unwantedness, disturbance, and noisiness) of an unwanted familiar sound event or events because (a) they interfere with, mask, a simultaneously occurring wanted sound signal due to hydro-mechanical and neural commingling in the cochlea of sound energies from the wanted signal and the noise signals and/or (b) the arousal of the body from wanted relaxation and sleep.

The commonness, when it occurs, of judged loudness and perceived noisiness as a function of exposure levels does not mean that the sensation of loudness is necessarily equivalent to or useful for the prediction of noise annoyance. For example, as the duration of a sound or noise continues at a given exposure level, its loudness will remain about the same, but the possibility of its causing annoyance due to masking of wanted sounds and causing arousal from sleep and rest increases.

Perceived noise annoyance is also determined by the relative intensities of simultaneously occurring wanted auditory vs unwanted acoustical signals. The upper abscissa on Fig. 14 shows that the loudness level of noise presented at a steady level of 65 dBA will remain about the same during a given duration. But the correct understanding of sentences drops from 90% to 0% as the levels of spoken sentences are simultaneously presented at given lower levels ranging from 47 to 35 dBA. In short, as the speech level drops, masking of the speech signals increases and perceived annoyance will increase.

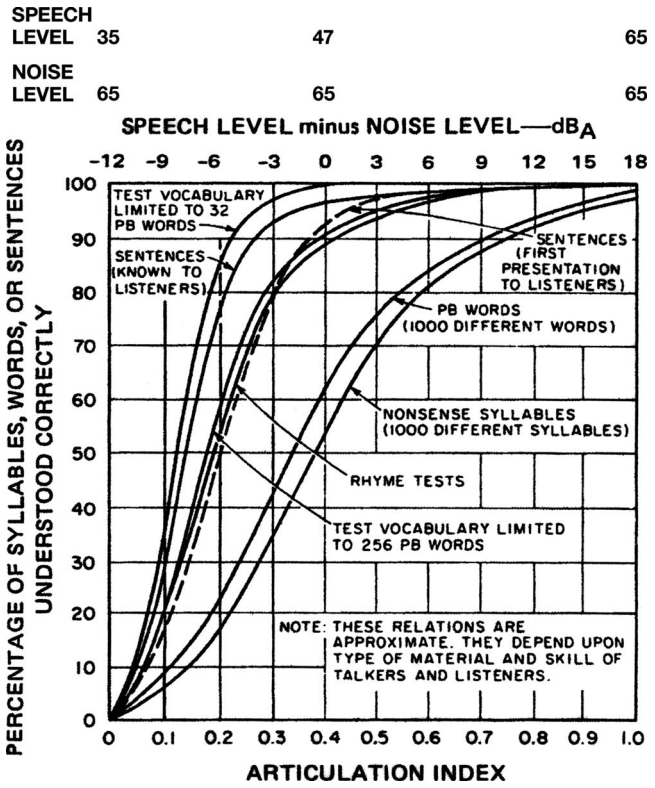

FIG. 14. Relations between correct understanding of speech signals: (1) articulation index (AI), bottom abscissa, and (2) upper abscissas of speech level, noise level and speech-noise levels. After Kryter, 1962.

The importance of cochlear masking for perceived annoyance flows from the fact that the presence of competing wanted sound signals and unwanted noise signals in the cochlea effectively "shuts down" hearing processes. It is theorized that perceived noisiness is perhaps largely an epiphenomenon attributable to (a) the noise masking of wanted auditory signals that are necessary for safe locomotion and avoidance of moving and stationary objects, and the successful performance and behavior in one's work and general living environments; (b) sounds can cause via whole-body systems the arousal from, or prevention of, rest and sleep.

The noisiness of a sound event is a perception that can cause changes in cardio-vascular and gastro-intestinal activities. Conventional physiological theory holds that the autonomic-glandular system prepares the body to "flee or fight" the noisy source or situation. As shown in Fig. 15, these processes can be initiated throughout the body because the peripheral cochlear system is directly connected to the autonomic nervous/glandular system, the auditory reticular system (upper spinal cord colliculi and mid-brain geniculate neural centers), and higher-brain centers.

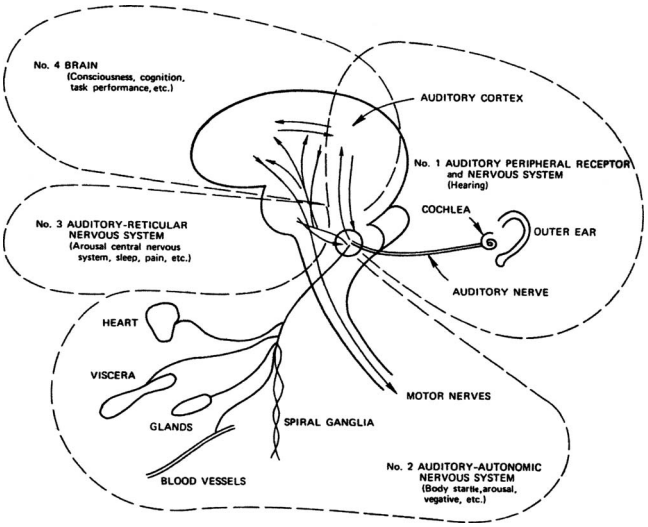

FIG. 15. Interconnections between (1) auditory cochlear and neural systems, (2) autonomic neural/glandular system, (3) mid-brain centers, and (4) high-brain centers and motor nerves to the body. After Fig. 9.1, Kryter, 1994.

It is to be noted that the neuro-anatomy of the auditory system is such that the threshold of hearing sensitivity in cats (which have auditory systems similar to that of humans) remains the same with severance or ablation of the neural connections to brain centers higher than spinal-cord collicular centers and mid-brain mediate-geniculate neural centers, see Fig. 16. The autonomic/glandular system monitors and controls homeostatic conditions in organs and mechanisms of the body without the direct involvement of high-brain center cognition. These autonomic system activities serve to effect physiological adjustments that are appropriate to the protection of the integrity of systems of the body, nourishment, and sleep-recuperation of the body from fatigue.

C. Non-auditory stress and cognitive behavioral variables

Examples of some non-auditory behavioral reactions that may bias stress and perceived noise annoyance are

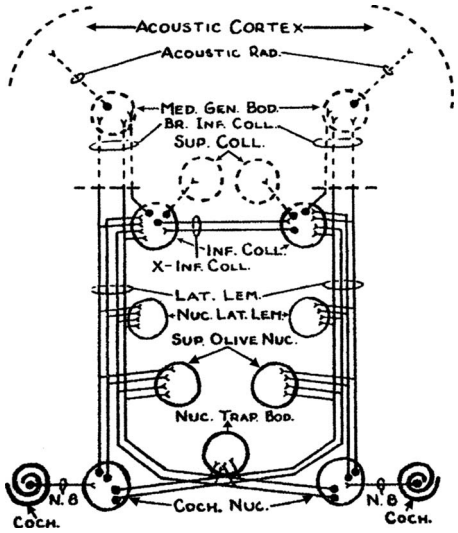

FIG. 16. Diagram of cochlear, upper spinal cord, mid-brain, and high-brain, cortical, neural centers of the cat's auditory system. Dashed segments show severances and ablations made in cats that were tested for thresholds of hearing sensitivity before and after recovery from the surgical interventions. From Kryter and Ades, 1943.

TABLE VI. People with high blood pressure.

Aircraft DNL Knipschild (1977)		Street Traffic Lercher and Kofler, 1993	
50	6%	DNL	0%
55	9%	50	0%
60	12%	59	0%
65	15%	64	0%
70	19%	65	0%

shown in Table VI, Figs. 17 and 18.

(1) It is seen in Table VI that the percentages of people with high blood pressure increases with DNL exposures to aircraft noise levels greater than ~55 dB, but not with exposures to street/road traffic noise DNL 55–65 dB. Note that this 10 dB differential between DNL for these two types of noise-sources is, as aforediscussed, consistent with their judged perceived noisiness and, as predicted, by EDNL/EDENL.
(2) It is seen in Fig. 17 that when the DNL in residential

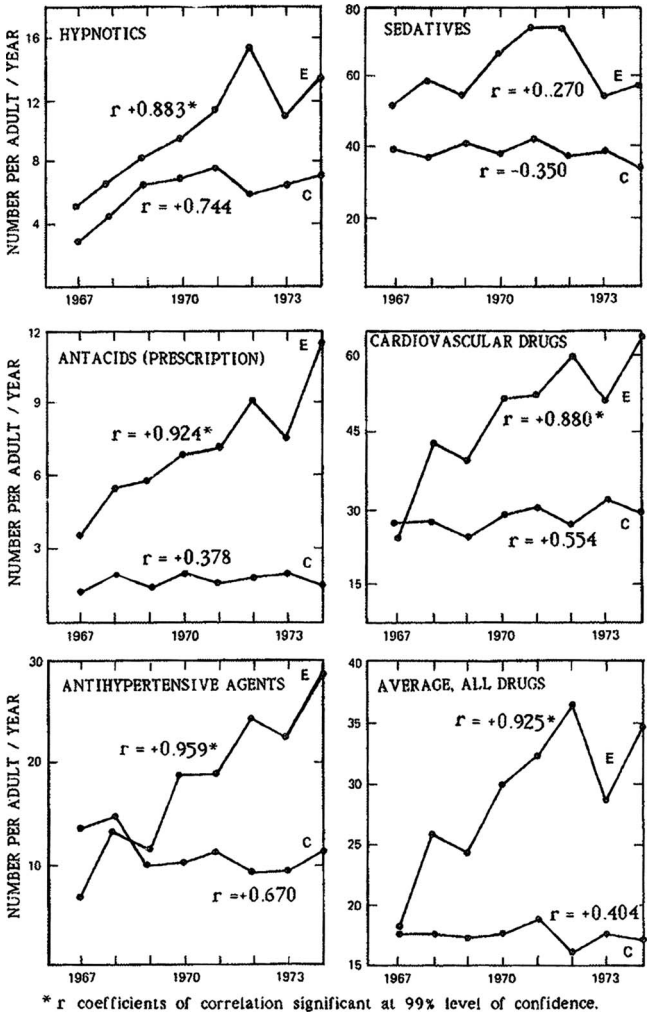

FIG. 17. Number of certain prescription drugs per adult per year. Area C, DNL < 51 dB; area E, DNL < 51 dB, 1967–1969 and DNL > 1969–1974, near Amsterdam Schiphol Airport. In 1972 there was an interruption of a nighttime curfew of aircraft take-off operations. From Knipschild and Oudshoorn, 1977.

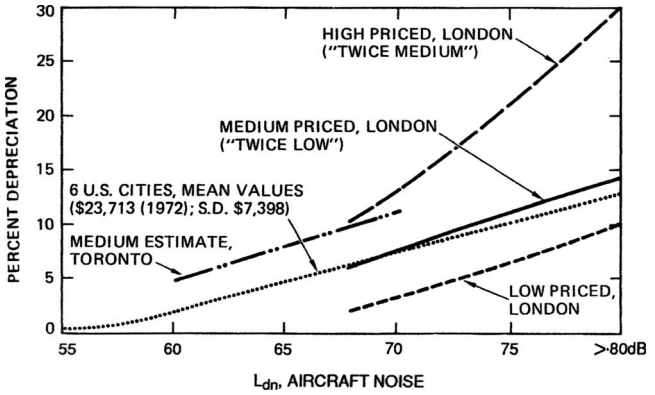

FIG. 18. Depreciation of house values as function of aircraft noise near London (Commission on the Third London Airport, 1970); near U.S. cities (San Francisco, St. Louis, Cleveland, San Diego, and Buffalo Nelson, 1979); and near Toronto, Canada (Mieszkowski and Saper, 1978). After Fig. 10.23, Kryter, 1994.

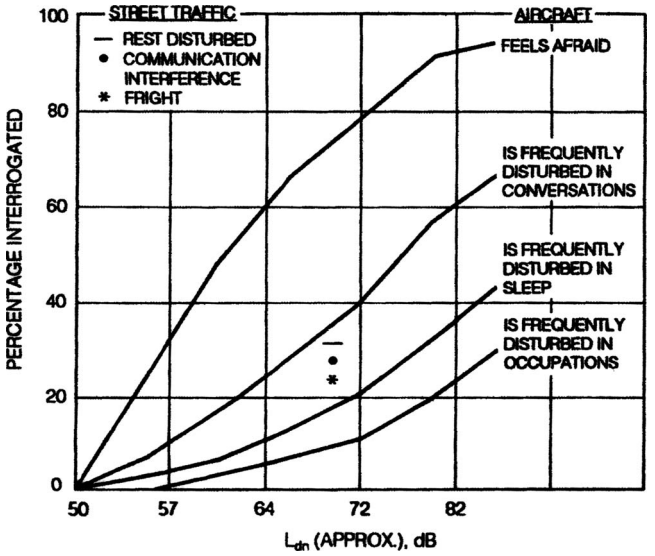

FIG. 19. Results of community survey in the Netherlands on effects of aircraft noise by Bitter (1968), as reported by Galloway and Bishop (1979), and the effects of street traffic noise in surveys in four Swiss cities by Nemecek *et al.*, 1981. After Fig. 10.3, Kryter, 1994.

neighborhoods near Amsterdam International Airport was increased from 51 dB DNL to >64 dB DNL, the use of prescription drugs for stress and sedation also increased.

(3) Figure 18 shows that lesser affluent people will apparently accept higher levels of aircraft noise and attendant annoyance from aircraft in exchange for lower costs of housing than will more affluent people.

(4) Jonson and Sorensen (1967) found that 54% of a group of citizens who were sent positively worded information regarding aircraft noise from training activities of the Royal Swedish Air Force reported "inconvenience" due to aircraft noise, whereas 79% of citizens from the same neighborhood, but not given this information, indicated inconvenience due to aircraft noise.

A research question is whether the magnitudes of annoyance and physiological stress differ for given EDNL/EDENL exposure levels of noises as separate or joint functions because of (a) the type of source of the noise, (b) less and more affluent listeners, (c) less and more "patriotic" persons, or (d) social or idiosyncratic factors. For example, it can be studied whether or not perceived annoyance from different acoustical levels of noise exposure appears to be readily distinguishable, as herein argued, from non-auditory cognitively and emotionally associated "biases" to the noise.

It is seen in Fig. 19 that (a) ~75% of people feeling fright or fear with exposures to DNL 70 dB aircraft noise, but only ~25% feel fright with exposures to DNL 70 dB street traffic noise, but (b) ~25% of people find sleep and speech communication disturbed by DNL 70 dB aircraft noise and ~25% of people are disturbed by DNL 70 dB street traffic noise. That is, the noise masking effects speech communication and rest/sleep arousal were seemingly judged independently of feelings of fright from the noise. These relations are not completely dispositive in that two different survey studies are involved.

D. Adaptation to noises expected as normal in given living environments

Annoyance is significantly greater from exposures to unexpected or new noise events in a residential environment than to equal EDNL/EDENL levels of familiar, chronic noise events. The adaptation is attributable to diminished annoyance as the noise becomes an understood and familiar part of one's living environment. Attitude surveys of annoyance from environmental noise indicate that some months of living in a new environment are generally required before reactions to the noises stabilize, see Borsky, 1961.

V. RECENT ANALYSES OF AUDITORY AND NON-AUDITORY FACTORS

A. Effect of background noise on annoyance from aircraft noise

In a recent publication Lim *et al.* (2008) compared the percentages of people living in detached brick houses in a rural, agriculture area of "rice fields," who were highly annoyed by aircraft noise with the percentages of people living in ferroconcretes apartment buildings in an urban area who were also highly annoyed by aircraft noise. Aircraft noise was from ~55 to ~65 dB DNL/DENL in both areas. However, the urban area had about 10 dBA higher levels of background, presumably street traffic noise, than did the rural area. Note that Lim *et al.* (2008) measured aircraft noise exposures in dB WECPLN, a metric that somewhat differently weight day, evening, and night-time occurring noise events than does dB DNL/DENL. However, the effects of differences should be small and DNL/DENL will be used in the present discussions of the Lim *et al.*, (2008) data.

Figure 6 in Lim *et al.* (2008) shows that ~35% of people reporting high annoyance were the equivalent of ~8 dB DNL/DENL lower in the urban than rural areas. Such a finding would seem to indicate that the ~10 dBA higher levels of background noise in the urban area than in the rural area somewhat inured the residents in the urban area to the annoying effects of aircraft noise.

Another plausible explanation is that because of differences in on-site attenuation, the DNL levels of background

TABLE VII. On-site attenuation, background, and aircraft noise. See Table IV.

Indoors average % 50%	Outdoors time spent 50%	Energy sum attenuation	Indoors average % 75%	Outdoors time spent 25%	Energy sum attenuation
	Rural[a] aircraft noise			Urban[b] aircraft noise	
21 dB	10 dB	21 dB	32 dB	5 dB	32 dB
	Rural background noise			Urban Background noise	
22 dB	21 dB	24 dB	33 dB	10 dB	33 dB
Energy sum, ind.+outd.		26 dB			34 dB
Diff. sums rural back.+air. noise-sums urban back.+airc.noise					8 dB

[a]Residential rural area, herein estimated, 100 daily number street traffic noise events at 42 dBA, per Lim *et al.*: =52 dB DNL/DENL plus, on an energy basis, aircraft noise per Lim *et al.*

[b]Residential urban area, herein estimated 800 daily number street traffic noise events at 42 dBA per Lim *et al.* =~61 dB DNLDENL plus, on an energy basis, aircraft noise per Lim *et al.* Estimates based on residental street traffic data furnished by Santa Barbara, CA city government.

and aircraft noises differently differ from their as-actually-heard levels. Table VII, which is based on Table IV, shows that (a) if the people in the rural area on average spend, say, 50% of the day working and living outdoors and 50% of the day working and living indoors, the sum of on-site attenuation of the background noise as heard indoors and outdoors in rural areas is 26 dB, and (b) if the people in the urban area on average spend on, say, 75% of the day working and living indoors, and 25% of the day working and living outdoors, the sum of on-site attenuation of aircraft noise as heard indoors and outdoors in the urban area sum is 34 dB.

Table II, Section IV, shows that when an equal percentage of exposed percentage of people are highly annoyed over the exposure range of 50–70 db DNL, there is an average difference of equivalent 8 dB difference (22–14 dB) exposure levels between street traffic and aircraft and noise. And Section III in Table V shows that over the same range of exposures and with equal percentages of people highly annoyed, the equivalent decibels of on-site attenuation between street traffic and aircraft noise is 7 dB. In short, the equivalent 7 dB DNL difference found by Lim *et al.* (2008) between background and aircraft noise exposures in the rural versus urban areas for equal annoyance is comparable to the summed on-site attenuations of ~8 dB used for correcting DNL to EDNL.

B. Structural equation analysis model of aircraft noise annoyance

Kroesen *et al.* (2008) tested a theory of aircraft noise annoyance, further developed a "structural equation analysis model," and reviewed related research findings. The investigators found that "concern about negative health and pollution (0.59)," and "perceived disturbance (0.56)" were the heaviest contributing factors and that acoustical noise exposure level, DNL, was a negligible (0.02) factor. Such findings appear to be similar to ratings found in the aforediscussed analyses by Job (1988). However, both analyses may be contaminated by the invalidity of the independent DNL/DENL noise measurements used in underlying research studies.

VI. CONCLUSIONS

A. DNL/DENL and EDNL/EDENL

DNL/DENL are invalid metrics for specifying the adequate stimulus for hearing sound and noise events, namely, the level of acoustical energy at or near the ears of a listener. The prediction errors, as found in the Miedema and Oudshoorn (2001) synthesis of annoyance attitude surveys of noise from transportation vehicles, are the equivalent of ~6 to ~22 dB DNL/DENL compared to <1 dB EDNL/EDENL.

B. Theory of noise annoyance as a sensory/autonomic-glandular/neural system perception

It is postulated that (a) the perception of the annoyance (synonymous with unwantedness, disturbance, and noisiness) of an unwanted sound event or events is as follows: (a) they interfere with, mask, a simultaneously occurring wanted sound signal due to hydro-mechanical and neural commingling in the cochlea of sound energies from the wanted signal and the noise signals and/or (b) the arousal of the body from wanted relaxation and sleep.

It is postulated that perceived noisiness is based on physiologically mechanisms and processes that are largely independent of biasing by higher-brain cognitive considerations. The anatomy and operation of the auditory and related bodily systems provides a foundation for such a theory.

C. Noise annoyance as a function of non-auditory factors

The misconceived acoustical DNL/DENL outdoor method of measuring and calculating the exposure levels of environment noise contaminates attempted multiple-correlations between DNL/DENL exposure levels and dependent hypothecated non-auditory causal variables. It is concluded that the most practical and accurate available method for the management and control of environmental noise to protect public health and welfare is to specify their exposure levels in terms of EDNL/EDENL metrics.

ACKNOWLEDGMENT

The author is grateful to the Paul S. Veneklasen Research Foundation, Santa Monica, CA for funds to complete and publish this paper.

ANSI (**1983**). S1.4-1971. American National Standard Specification for Sound Level Meters. American National Standards Institute, New York.

Beranek, L. L., Kryter, K. D., and Miller, L. N. (**1959**). "Reaction of people to exterior aircraft noise," Noise Control **5**, 23–31.

Bitter, C. (**1968**). "Noise annoyance due to aircraft," Colloq., *Hum. Demands with Respect to Noise*, Paris, Pap. Int. Gezondheidstech., TNO, Netherlands.

Borsky, P. N. (**1961**). "Community reaction to Air Force noise. I. Basic concepts and preliminary methodology; II. Data on community studies and their interpretation," Report No. TR 60-689, National Opinion Research Center, University of Chicago, Chicago, IL.

Environmental Protection Agency (EPA) (**1978**). "Protective Noise Levels, Condensed Version of EPA Levels," Report No. EPA 550/9-79-100, U.S. Environ. Protect. Agency, Washington, DC.

Federal Aviation Administration (FAA) (**1993**). Section 91.119 of Title 14, Code of Regulation: Minimum safe altitudes, General., Washington, DC.

Federal Interagency Committee on Urban Noise (FICUN) (**1980**). Guidelines for Considering Noise in Land Use Planning and Control. Washington, DC.

Federal Interagency Committee on Noise (FICON) (**1992**). Federal Agency Review of Selected Airport Noise Analysis Issues. Washington, DC.

Fidell, S. (**2003**). "The Schultz curve 25 years later: A research perspective," J. Acoust. Soc. Am. **114**, 3008–3015.

Fidell, S., and Green, D. M. (**1991**). "Noise induced annoyance of individuals and communities," *Handbook of Acoustical Measurements and Noise Control*, edited by C. M. Harris, McGraw-Hill, New York, Chap. 23.

Fidell, S., Barber, D. S., and Schultz, T. J. (**1991**). "Updating a dosage-effect relationship for the prevalence of annoyance due to general transportation noise," J. Acoust. Soc. Am. **89**, 221–233.

Fidell, S. R., Mills, J., Horornjeff, R., Baldwin, E., Teffeteller, S., and Pearsons, K. S. (**1981**). "Community sensitivity to changes in aircraft noise exposure," NASA Contractor Report No. 3490, NASA Langley Research Center, Langley, VA.

Finegold, L. S., Harris, S., and von Gierke, H. (**1994**). "Community annoyance and sleep disturbance: Updated criteria for assessing the impacts of general transportation noise on people," Noise Control Eng. J. **42**, 25–30.

Galloway, W. J., and Bishop, D. E. (**1970**). "Noise exposure forecasts: Evolution, evaluation, extensions, and land use interpretations," Report No. FAA-NO-70–9, Federal Aviation Administration, Washington, DC.

Goodfriend, L. S. (**1991**). "Re-evaluating use of the A-weighted sound level meter for environmental noise impact assessment," in Noise Control Engineering Proceedings, Noise Control Foundation

Goodfriend, L. S. (**2006**). "Inappropriateness of the A-weighted level for environmental noise assessment," J. Sound Vib. **49**, 5–6.

Hall, F. L., Birnie, S. E., Taylor, S. M., and Palmer, J. E. (**1981**). "Direct comparison of community response to road traffic noise and to aircraft noise," J. Acoust. Soc. Am. **70**, 1690–1698.

Job, R. F. S. (**1988**). "Community response to noise: A review of factors influencing the relationship between noise exposure and reaction," J. Acoust. Soc. Am. **83**, 991–1001.

Jonson, E., and Sorenson, S. (**1967**). "On the influence of attitudes to the source on annoyance reactions to noise," Nord. Hyg. Tidskr **48**, 35–45.

Knipschild, P. (**1977**). "Medical effects of aircraft noise. Community cardiovascular survey," Int. Arch. Occup. Environ. Health **40**, 185–190.

Knipschild, P., and Oudshoorn, N. (**1977**). "Medical effects of aircraft noise: Drug survey," Int. Arch. Occup. Environ. Health **44**, 185–190.

Kroesen, M., Molin, J. E., and van Wee, B. (**2008**). "Testing a theory of aircraft noise annoyance: A structural equation analysis," J. Acoust. Soc. Am. **123**, 4250–4260.

Kryter, K. D. (**1962**). "Methods for the calculation and use of the articulation index," J. Acoust. Soc. Am. **34**, 1659–1697.

Kryter, K. D. (**1970**). "Possible modifications to the calculation of perceived noisiness," NASA Report No. CR 1936, NASA Langley Research Center, Hampton, VA.

Kryter, K. D. (**1970**). *The Effects of Noise on Man* (Academic, New York); (**1985**). 2nd edition (Academic, New York).

Kryter, K. D. (**1982**). "Community annoyance from aircraft and ground vehicle noise," J. Acoust. Soc. Am. **72**, 1222–1242.

Kryter, K. D. (**1983**). "Rebuttal by K. D. Kryter to Comments by T. J. Schultz," J. Acoust. Soc. Am. **72**, 1253–1257.

Kryter, K. D. (**1994**). *The Handbook of Hearing and the Effects of Noise*, 2nd ed. (Academic, New York).

Kryter, K. D. (**2007**). "Acoustical, sensory, and psychological research data and procedures for their use in predicting effects of environmental noises," J. Acoust. Soc. Am. **122**, 2601–2614.

Kryter, K. D., and Ades, H. W. (**1943**). "Studies on the function of the higher acoustic nervous centers in the cat," Am. J. Psychol. **56**, 501–536.

Leercher, P., and Kofler, W. (**1993**). "Adaptive behavior to road noise in Noise as a Public Health Problem," in Proceedings of the Sixth International Congress I'NRETS, France, Vol. **2**, pp. 465–468.

Lim, C., Kim, J., and Lee, S. (**2008**). "Effect of background noise levels on community annoyance from aircraft noise," J. Acoust. Soc. Am. **123**, 766–771.

Miedema, H. M. E., and Oudshoorn, C. (**2001**). "Annoyance from transportation noise: Relationships with exposure metrics DNL and DENL and their confidence intervals," J. National Institute of Environmental Health Sciences **109**, 409–416.

Mieszkowski, P., and Saper, A. M. (**1978**). "An estimate of the effects of airport noise on property values," J. Urban Econ. **5**, 425–440.

National Academy of Sciences (**1977**). "Guidelines for preparing environmental impact statements on noise," Working Grouping 69, Comm. on Hearing and Bioacoustics, Washington, DC.

Nelson, J. P. (**1979**). "Aircraft noise and the market for residential: Empirical results for seven selected airports," Report No. DOT/RSPA/DPB-50/78.

Nemecek, L., Wehrli, B., and Turrian, V. (**1981**). "Effects of the noise of street traffic in Switzerland: A review of four surveys," J. Sound Vib. **78**, 223–234.

Noise Control Act (**1972**). Public Law 92-574, 92 Congress, HR 11021, October 27, 1972.

Ollerhead, J. B. (**1980**). "Accounting time of day and mixed source effects in the assessment of community noise exposure," ASHA Report. No. 10, Am. Speech-Lang.-Hearing. Assoc., Rockville, MD.

Ortega, J. C., and Kryter, K. D. (**1982**). "Comparison of aircraft and ground vehicle noise levels in front and backyards of residences," J. Acoust. Soc. Am. **71**, 216–217.

Pearsons, K., Fidell, S., Silvati, L., Sneddon, M., and Howe, R. (**2000**). "Study of the levels, annoyance and potential mitigation of backblast noise at San Francisco International Airport," BBN Report No. 8257, BBN Technologies, Canoga Park, CA.

Piercy, J. E., and Daigle, D. A. (**1991**). "Sound propagation in the open air," in *Handbook of Acoustical Measurements and Noise Control*, edited by C. M. Harris (McGraw-Hill, New York), Chap. 3.

Robinson, D. W., and Whittle, L. S. (**1964**). "The loudness of octave bands of noise," Acustica **14**, 24–35.

Schultz, T. J. (**1978**). "Synthesis of social surveys on noise annoyance," J. Acoust. Soc. Am. **64**, 377–405.

Small, A. M. (**1963**). "Auditory adaptation," in *Modern Developments in Audiology*, edited by J. Jerger (Academic, New York), Chap. 8.

Stevens, S. S., and Davis, H. (**1938**). *Hearing, Its Psychology and Physiology* (Wiley, New York).

Stevens, S. S. (**1972**). "Perceived level of Mark VII and decibels (E)," J. Acoust. Soc. Am. **51**, 575–601.

Zwicker, E., and Feldtkeller, R. (**1967**). *Das Ohr als Nachrichtenempfanger (The Ear as a Communication Receiver)*, Auflage. S. Hirzel, Stuttgart.

The objective measurement of individual earplug field performance

Jérémie Voix[a] and Frédéric Laville
École de technologie supérieure, Université du Québec, Montreal, Quebec H3C 1K3, Canada

(Received 4 June 2008; revised 8 April 2009; accepted 8 April 2009)

This paper presents a field-microphone-in-real-ear (MIRE) method for the objective measurement of individual earplug field attenuation. This development was made possible by using a recently designed instrumented expandable custom earplug. From the measurement of the noise reduction (NR) through the earplug, this method predicts the attenuation that would be experienced by the wearer and that would be measured using the real-ear attenuation at threshold (REAT) method. Formulations presented include establishing the relationship between NR, insertion loss, and REAT, as well as defining the laboratory and field calibration procedures required to determine the correction factors to be applied to the measured NR. This method was validated experimentally by comparing the predicted field-MIRE attenuation values to the REAT values measured on a group of test-subjects. This method offers fast and accurate measurement of earplug field performance on an individual basis and could lead to further developments for effective hearing protection practices as well as for hearing protection device rating and labeling.
 [DOI: 10.1121/1.3125769]

PACS number(s): 43.50.Hg, 43.38.Kb, 43.50.Yw [KA] Pages: 3722–3732

I. INTRODUCTION

For several already well-documented reasons,[1–4] current standardized methods[5] dramatically fail to predict the attenuation of *hearing protection devices* (HPDs) for individual users in on-site applications. As recommended by the National Institute for Occupational Safety and Health (NIOSH) and many researchers, substantial efforts have been deployed to "find a laboratory method to estimate the noise attenuation obtained with hearing protectors worn in the field."[6] As a result, recent standards[7–9] now include a "subject fit" method[10–12] that provides a better estimate of the attenuation obtained in the field, even if some discrepancies still arise between laboratory and field attenuation values.[13,14]

However, even if such laboratory methods better predict the average group field performance, it is still impossible to relate the individual field attenuation to this population-based, statistically-derived, laboratory-driven attenuation estimate. One solution to this fundamental problem, as Berger[13] mentioned, would be to perform "individual fit testing" as it would provide the most accurate assessment for an individual user and could also afford an excellent opportunity to train and motivate the employee in appropriate HPD use and fitting.

Very few field measurement methods are currently available (see Ref. 15 for a recent review), despite the many attempts to adapt laboratory methods for field measurement use (see Ref. 16 or Ref. 17). The FitCheck™ (Refs. 18 and 19) system is probably the most used and documented[20] field measurement method. It relies on the real-ear attenuation at threshold (REAT) test, that is, the difference between open and occluded-ear hearing thresholds as measured on human subjects. The REAT test, sometimes referred to as the "gold standard" since it was first standardized in 1957,[21] is now part of many worldwide standards[5,7,22,23] and takes into account all relevant sound paths to the inner ear. Unfortunately, REAT testing is not only time-consuming and very sensitive to the ambient background noise (making it often incompatible with practical field usage), but it is also hampered by two limitations: the first one is the well-known low-frequency masking error (caused by *physiological noise*), which leads to an overestimation of the low-frequency attenuation,[24] and the second one is the variability of the subjective response, i.e., the ability of a subject to track his or her hearing threshold levels. The authors' experience is that a human subject will rarely report twice the same hearing threshold (even when tested at 5 dB steps) and hence there is inherently large variability in the REAT protocol since it requires two complete audiograms in order to determine real-ear attenuation.

Among the various laboratory methods available to measure HPD attenuation (see Refs. 25 and 26 for an extensive list), there is one method that would overcome these limitations and still enable individual measurement: the microphone-in-real-ear (MIRE) technique. It consists of inserting a miniature microphone (either wired or in a probe-tube form) in the ear to measure the actual sound pressure level at a given location, usually close to the tympanic membrane. The difference between two of these measurements on a given individual at the same location in open and occluded-ear conditions gives the classical insertion loss (IL). MIRE measurements techniques have been used successfully for earmuff IL (see Ref. 27 for a comprehensive review) and are now standardized for supra-aural or circumaural HPDs.[28,29] Even if they cannot account for the bone conduction sound

[a]Author to whom correspondence should be addressed. Electronic mail: jvoix@jerevox.com

 0001-4966/2009/125(6)/3722/11/$25.00

path, these laboratory MIRE techniques are fast, efficient, and reliable and do not suffer from the physiological noise bias.

A field method based on the MIRE approach has been developed for use in the fitting of hearing aids which may be adaptable to HPD attenuation measurements. The method is used to determine the so-called "insertion gain" and is sometimes referred to as the "substitution method" (see Ref. 30). However, existing measurement devices used to measure the insertion gain rely on a microphone probe inserted around the device and usually cannot be used when measuring IL for HPDs, as the soft tube of the probe microphone is not protected against outside noise contamination (i.e., the measurement is affected by the sound source itself, an effect sometimes described as "flanking pathway"[26]), and the probe tube usually breaks the acoustic seal of the HPD.[26] Recent studies conducted on the use of MIRE as a field measurement device for earmuffs[27,31,32] or for earplugs[17] show promising results for in-field implementation of alternative attenuation tests. However, as mentioned by Mauney,[27] up to now, the equipment used was delicate laboratory equipment unsuited for regular field use and the procedure was complex, requiring that the subject be fitted and the microphone placed by a professional to avoid misplacement or tympanic injury. It is therefore necessary to develop more robust field-ready equipment and a simple procedure including HPD fitting by the subject.

This paper describes the development of a field-MIRE method for measuring HPD attenuation. This development was made possible by using the recent design[33,34] of an instrumented expandable custom earplug by Sonomax Hearing Healthcare Inc. (Montreal, Canada). This custom earplug has two main features: first, it is molded *in situ* by a trained technician and takes in a few minutes the shape of the wearer's ear through silicone injection, which increases physical comfort, and, second, it includes a sound-bore that can be used either for field-MIRE measurements or the insertion of filters to improve the wearer's auditory comfort, by letting a controlled amount of acoustical energy go through the earplug (see Ref.s 35 and 36 for details on the custom earplug filtered with acoustical dampers). Because custom earplugs are used, the need for a field-MIRE method could be questioned on the basis that custom earplugs have often been considered to be less prone to mis-fit by users, and it has even been suggested that they would not suffer from the discrepancies usually observed between laboratory and field performance. These assumptions do not withstand closer scrutiny and even if custom earplugs have some advantages over traditional HPD (like the fact that they provide increased comfort for some users and that they will fit certain earcanals that other plugs may not), they still require individual field attenuation measurements because they typically show the same inter-subject attenuation variability as other earplug types (pre-molded or roll-down foam plugs), as reported by Berger *et al.*[3] or more recently by Murphy *et al.*[37]

The instrumented expandable custom earplug is described in Sec. II. The proposed approach for the measuring of individual earplug field performance is formulated in Sec. III. An experimental validation follows in Sec. IV and conclusions are given in Sec. V.

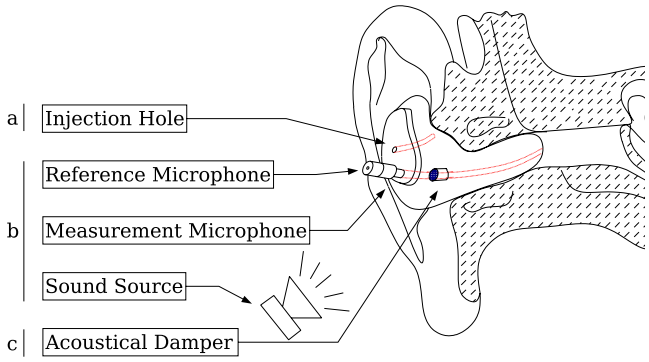

FIG. 1. (Color online) The custom earplug: (a) instantly-fitted by the injection of silicone; (b) instrumented with a dual microphone probe (external and internal pressure microphones with an extended probe tube inside the sound-bore) as well as the reference sound source; (c) filtered with acoustical damper for adapted protection.

II. THE DEVICE USED: AN INSTRUMENTED EXPANDABLE CUSTOM EARPLUG

As mentioned in Sec. I and as illustrated in Fig. 1, the earplug developed and used in this study is a re-usable custom earplug that is fitted *in situ* to the user's ear in a few minutes.

A hole through the core of the earplug is used for the injection of a soft medical-grade thermosetting two-part silicon rubber between the rigid core—of generic shape—and the soft envelope that will expand to take the precise shape of the earcanal. Below the injection hole, a sound-bore through the earplug is used first for the field-MIRE measurements and then for the insertion of an acoustical damper. To perform field-MIRE measurement, a miniature microphone is temporary inserted within the generic rigid core to measure sound pressure levels in the residual earcanal portion between the HPD and the eardrum. Attached to the back of this internal pressure microphone is an external pressure microphone so that sound pressure level difference across the earplug, noise reduction (NR), can be measured in the presence of loud pink noise generated from an outside reference sound source (frontal incidence, median plan). The two microphone elements used in the microphone probe assembly are miniature electret condenser pressure microphones manufactured by Knowles Electronics (Itasca, IL) and typically used in the hearing aid industry. These microphones offer a flat frequency response (within 0.1 dB) up to 10 kHz with omnidirectional directivity pattern. The NR measurement will be performed by the trained technician after the end-user removes and replaces the custom earplug in order to perform a "subject-fit" test. This subject-fit NR measurement will later be used to check the proper fit of the earplug and to predict the attenuation the user will achieve in an on-site situation (see Sec. III F). Finally, after the field-MIRE measurement, the microphone probe is removed and an acoustical damper (acoustic resistance resulting from a mesh of plastic fibers) is inserted in the earplug's sound-bore, for regular use.

The field-MIRE measurement device, dubbed the "SonoPass™System,"[38,39] is a proprietary DSP-based spectrum analyzer that measures the octave-band sound pressure levels (auto-spectrum's) from both microphones and calculates NR (using the magnitude of the transfer function (TF) between the external "reference" and internal "measurement" microphones) as well as the coherence function while generating a loud broadband sound (pink noise) through a loudspeaker. It can operate either connected to a computer or as a stand-alone unit (with LED indicators) and has successfully been used in the field since 2002.[40]

III. FORMULATION OF THE PROPOSED OBJECTIVE MEASUREMENT OF INDIVIDUAL EARPLUG FIELD PERFORMANCE

The proposed approach relies on the objective measurement of NR to predict the REAT equivalent value. The general relationships between NR, IL, and REAT are derived in Sec. III A. The expression of REAT is then formulated, in Sec. III B, as the sum of two terms: the corrected NR (the raw NR value modified by several corrections specific to the test procedure) and a compensation term (that accounts for sound pressure TFs between the open and the occluded-ear as well as psycho-physiological effects, such as the physiological noise). These corrections on the raw NR value are obtained from laboratory and field measurements, as presented in Sec. III C. The procedure to obtain an equivalent binaural NR is presented in Sec. III D.

The compensation value is obtained statistically, detailed in Sec. III E, based on the fact that many of the corrections involved vary according to the geometry and dimensions of the human head; they can therefore be properly represented by a normal distribution. For example, the use of a statistically averaged TF of the outer ear (TFOE) value rather than an individual one has the advantage of avoiding the cumbersome and delicate measurement of tympanic sound pressure levels. It also makes such an approach highly compatible with practical field usage, as suggested by Mauney,[27] even though it increases the uncertainty associated with the prediction.

In a traditional hearing conservation program, the expected NR of a protector is determined through measurement REAT for a population of subjects to determine the noise reduction rating (NRR) defined by EPA (Ref. 41) based on attenuation measurements performed according to ANSI standard[5] or the single number rating (SNR) as described in the ISO standard.[42] In the proposed approach, the estimated NR is determined by individual NR measurement and determination of the predicted personal attenuation rating (PPAR); its formulation is provided in Sec. III F.

A. Relationship between NR, IL, and REAT

Figure 2 illustrates the pressure variables at different locations in the open and occluded-ear (the "prime" symbol is used in this latter case). Index 1 is not used in the current paper but is presented for reference, since it has been associated to the sound pressure at the earcanal entrance point.

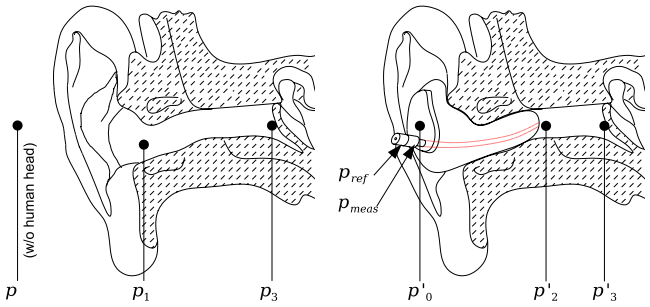

FIG. 2. (Color online) Schematics illustrating sound pressure variables at various locations for an open ear (left) and for an occluded-ear fitted with instrumented earplug (right)

The IL is defined as a ratio of the open tympanic sound pressure p_3 over the occluded-ear tympanic sound pressure p_3':

$$\mathrm{IL} = 20 \log_{10}\left(\frac{p_3}{p_3'}\right). \tag{1}$$

Since IL usually represents a physical "loss," it is usually a positive value (greater than zero); however, it can also be plotted as a negative one.

The theoretical noise reduction (NR_0) is defined as the ratio of the free field sound pressure p (at the tympanic membrane location, in the absence of a human subject) over the occluded-ear tympanic sound pressure p_3':

$$\mathrm{NR}_0 = 20 \log_{10}\left(\frac{p}{p_3'}\right). \tag{2}$$

NR_0 is also a positive value often plotted as a negative one.

The TFOE is defined as

$$\mathrm{TFOE} = 20 \log_{10}\left(\frac{p_3}{p}\right). \tag{3}$$

A direct relation between these three figures is

$$\mathrm{IL} = \mathrm{NR}_0 + \mathrm{TFOE}. \tag{4}$$

Such an expression for IL is commonly used when objectively measuring the attenuation of HPDs at suprathreshold levels. Indeed, for extremely high sound pressure levels (impulse or stationary), the HPD attenuation can no longer be considered to be linear or level independent (either purposely because of the non-linearity of the HPD's design or unintentionally because of the intrinsic non-linearity of the HPD material for very high amplitude acoustical waves). Many studies[25,32,43,44] rely on such two-part measurements where NR is measured on the device worn by an in-field user and TFOE is measured at a different time on the wearer in the laboratory to assess the overall HPD attenuation.

The REAT that would be measured on a subject is derived from the IL by adding the hearing threshold masking caused by the physiological noise (PN):

$$\mathrm{REAT} = \mathrm{IL} + \mathrm{PN} \tag{5}$$

PN is device-related[45,46] and depends on the earplug insertion depth and on the residual occluded-ear volume past the HPD. In our case, PN is considered a correction to be

applied for each frequency (even if it mostly occurs in the lower frequencies) on an individual basis. Using Eqs. (4) and (5), we obtain

$$\mathrm{REAT} = \mathrm{NR}_0 + \mathrm{TFOE} + \mathrm{PN}. \tag{6}$$

Equation (6) does not take into account the fact that the REAT measurements are affected by some bone-conduction (BC) pathways that flank the earplug and transmit energy to the inner ear, because those pathways are not modeled or measured with the field-MIRE approach described here. Though this is not necessary for the custom earplug of this study, it is conceptually part of the correction to be applied to the predicted REAT by representing the BC as a concurrent pathway to the earplug. In a recent implementations of the field-MIRE method[47] on high attenuation non-custom earplugs, an additional correction is applied to the prediction of the REAT of earplugs. For those high attenuation earplugs, the field-MIRE data need to be corrected by including an estimated BC pathway. The hypothesis behind this model is that the earplug and the BC are two independent paths (resulting in noncoherent sound pressures contributions at p_3') and that no interference (resonance/anti-resonance) occur between them; hence that the sound pressure p_3' can be expressed as an energy summation of the earplug and BC sound pathways. Such model has already been developed by the authors[36] for the prediction of the attenuation of the custom earplug filtered with the damper. When required, the "BC limited" REAT attenuation, $\mathrm{REAT}_{\mathrm{BCL}}$ can be derived from REAT using the following equation:

$$\mathrm{REAT}_{\mathrm{BCL}} = -10\log_{10}(10^{-\mathrm{REAT}/10} + 10^{-\mathrm{BC}/10}), \tag{7}$$

where BC is the attenuation of the BC sound pathway of the human skull, available in the literature.[48] Equation (7) shall be used twice, once to correct the measured REAT values used for the calculation of compensation in Eq. (16) and another time in Eq. (14) to correct the predicted REAT values.

B. Required corrections for the expression of REAT from the measured NR

Unfortunately, direct measurement of NR_0 in the field is problematic: it requires the measurement of p_3' very close to the tympanic membrane and the measurement of p in the absence of a human subject. A practical alternative is to measure the NR between the outer and inner faces of the earplug, at pressure locations p_0' and p_2', respectively. In practice, the device measures p_{ref} instead of p_0' with the *reference microphone* located 19.5 mm away from the outer face of the earplug [i.e., approximately 20 mm from the ear reference point defined in ISO 11904 (Ref. 29)] and measures p_{meas} instead of p_2' with the *measurement microphone* located at the aperture of a 18 mm long, semi-rigid (0.8 mm inside diameter) probe tube inserted into the sound-bore of the earplug. The NR that is practically measured (denoted NR_*) is therefore defined as

$$\mathrm{NR}_* = 20\log_{10}\left(\frac{p_{\mathrm{ref}}}{p_{\mathrm{meas}}}\right). \tag{8}$$

Three corrective factors need to be added to NR_* to obtain the previously mentioned NR.

- The use of p_{ref} instead of p requires the correction (p/p_{ref}) that will account mainly for head and torso diffraction and the pinna effect.
- The use of p_{meas} instead of p_3' requires the correction (p_{meas}/p_3') that will account for the occluded-ear canal shifted resonance, the microphone probe, and sound-bore tubing effects. This latter correction (p_{meas}/p_3') can be split in two terms: a first term (p_{meas}/p_2') that would account for the microphone probe-tube effect and a second one (p_2'/p_3') that would account for the occluded-ear canal resonance.

The NR expressed as a function of these correction terms is expressed as

$$\begin{aligned}\mathrm{NR}_0 = \mathrm{NR}_* &+ 20\log_{10}\left(\frac{p_{\mathrm{meas}}}{p_2'}\right)\\ &+ 20\log_{10}\left(\frac{p_2'}{p_3'}\right) + 20\log_{10}\left(\frac{p}{p_{\mathrm{ref}}}\right).\end{aligned} \tag{9}$$

Equation (9) is intentionally presented on three lines: the first line contains the measurement performed in the field, the second line represents the corrections associated with the measurement device, which can be determined in laboratory (i.e., probe-tube effect, etc.), while the third line contains the corrections related to human factors (i.e., morphology of the ear and psycho-physiological specificities of an individual's hearing). This three-line writing convention shall be used throughout this paper.

Equation (6) can now be re-written using Eq. (9) and the same aforementioned three-line presentation convention.

$$\begin{aligned}\mathrm{REAT} = \mathrm{NR}_* &+ 20\log_{10}\left(\frac{p_{\mathrm{meas}}}{p_2'}\right)\\ &+ \mathrm{TFOE} + \mathrm{PN} + 20\log_{10}\left(\frac{p}{p_{\mathrm{ref}}} \times \frac{p_2'}{p_3'}\right).\end{aligned} \tag{10}$$

The first line of Eq. (10) is the measured NR_*, assuming the use of an ideal microphone probe for which both cells of the dual microphone probe are perfectly equal in sensitivity and frequency response. However, in practical situations, the microphone cells, although very similar, do not absolutely have the same sensitivity, nor is their individual frequency response constant over time due to sensitivity to ambient atmospheric conditions and other factors. In order to take such differences into account, the uncalibrated values are included in the equations and denoted with a tilde symbol above them to distinguish them from corrected values. The calibration factors required for the uncalibrated measurements $\widetilde{\mathrm{NR}}_*$ are determined using, in the field, system *I* illustrated at the bottom of Fig. 3.

The quantity NR_* defined in Eq. (8) is rewritten as the ratio of two measured pressure values for the earplug (index *III*) in the wearer's ear, multiplied by a correction ratio ob-

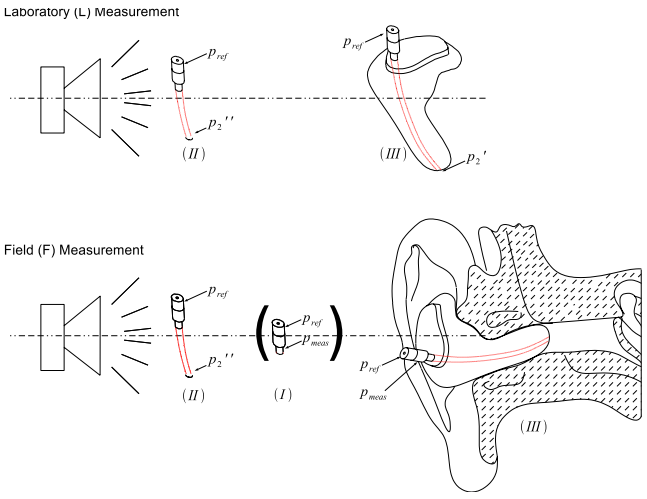

FIG. 3. (Color online) Scenario implemented to determine the sound-bore length and microphone sensitivity corrections. Top: Overview of the laboratory measurement of corrections $(\tilde{p}_{\mathrm{ref}}/\tilde{p}_{\mathrm{meas}})_{LII}$ and $(p_{\mathrm{ref}}/p_2')_{LIII}$. Bottom: Overview of the field measurement of $(\tilde{p}_{\mathrm{meas}}/\tilde{p}_{\mathrm{ref}})_{FII}$, $(\tilde{p}_{\mathrm{meas}}/\tilde{p}_{\mathrm{ref}})_{FI}$ (between brackets because not used in actual correction calculation), and $(\tilde{p}_{\mathrm{meas}}/\tilde{p}_{\mathrm{ref}})_{FIII}$.

tained by submitting the two microphone cells to the same pressure field the same day that the field measurement (index *F*) takes place, as illustrated at the bottom of Fig. 3:

$$\mathrm{NR}_* = \left(\frac{p_{\mathrm{ref}}}{p_{\mathrm{meas}}}\right)_{III} = \left(\frac{\tilde{p}_{\mathrm{ref}}}{\tilde{p}_{\mathrm{meas}}}\right)_{FIII} \times \left(\frac{\tilde{p}_{\mathrm{meas}}}{\tilde{p}_{\mathrm{ref}}}\right)_{FI} = \widetilde{\mathrm{NR}}_* \times \left(\frac{\tilde{p}_{\mathrm{meas}}}{\tilde{p}_{\mathrm{ref}}}\right)_{FI}. \tag{11}$$

The second line of Eq. (10) is the sound-bore length correction (p_{meas}/p_2'); it is a fixed correction that depends solely on the overall length of the sound-bore and microphone probe tube. In order to measure this sound-bore correction, three different systems were set up in front of the speaker: system *I* is simply the microphone pair, system *II* is the microphone pair with the probe-tube, and system *III* is the microphone pair with the probe-tube inserted into the earplug, as illustrated in Fig. 3.

Three scenarios were studied[49] to determine the correction required for the first two lines of Eq. (10), in order to obtain the corrected NR, called NR_C, that represents the difference in sound pressure levels between the inner and outer faces of the earplug.

The *first scenario* would consist in performing the measurement of the microphone pair TF on a daily basis $(\tilde{p}_{\mathrm{meas}}/\tilde{p}_{\mathrm{ref}})_{FI}$ and obtaining NR_*. The sound-bore length correction (p_{meas}/p_2') would be determined in the laboratory by placing the earplug in an acoustical field giving the same acoustic pressure at both microphone duct openings in free space. This first scenario is unfortunately not well adapted for field usage, since the two microphone cells that are used in the dual microphone probe cannot be easily dismounted on a daily basis for the field measurement of the microphone pair TF.

The *second scenario* requires no laboratory measurement, as the sound-bore length correction (p_{meas}/p_2') would be determined by means of a field measurement conducted by inserting the dual microphone probe in the earplug and positioning the instrumented earplug in a homogeneous sound field. This approach is straightforward but unfortunately not adapted for field usage because of the following three practical limitations: first, it should be performed on every size of each earplug to be measured (the Sonomax SonoCustom™earplug use to be available in three core sizes); second, the positioning of the relatively large instrumented earplug on the speaker grid was found to disturb the acoustical field in the vicinity of the loudspeaker; third, the orientation of the instrumented earplug in relation to the speaker is critical and difficult to achieve consistently because of the asymmetry of the earplug with respect to the sound-bore aperture. Consequently, it is not feasible to perform such measurement on a daily basis within subject.

The *third scenario* was implemented because it did not have the practical limitations of the two others. This scenario is a variation of the second scenario where the field measurement is performed on the dual microphone probe before its insertion into the earplug. Because of its simple geometry and its small size, the probe is easy to position precisely and does not disturb the acoustical field in any critical fashion. However, it requires two additional laboratory measurements. One measurement is required of the earplug to address the sound-bore compensation, and the other of the probe alone to correct for microphone sensitivities that change with time. The measurement setups are illustrated in Fig. 3. The expression of the sound-bore length correction (p_{meas}/p_2') is

$$\left(\frac{p_{\mathrm{meas}}}{p_2'}\right)_{III} = \left(\frac{\tilde{p}_{\mathrm{meas}}}{\tilde{p}_{\mathrm{ref}}}\right)_{LIII} \times \left(\frac{\tilde{p}_{\mathrm{meas}(FII)}}{\tilde{p}_{\mathrm{meas}(LII)}} \times \frac{\tilde{p}_{\mathrm{ref}(LII)}}{\tilde{p}_{\mathrm{ref}(FII)}}\right) \times \left(\frac{\tilde{p}_{\mathrm{ref}}}{\tilde{p}_{\mathrm{meas}}}\right)_{FI}. \tag{12}$$

where

$$\left(\frac{\tilde{p}_{\mathrm{meas}(FII)}}{\tilde{p}_{\mathrm{meas}(LII)}} \times \frac{\tilde{p}_{\mathrm{ref}(LII)}}{\tilde{p}_{\mathrm{ref}(FII)}}\right) = \left(\frac{\tilde{p}_{\mathrm{meas}}}{\tilde{p}_{\mathrm{ref}}}\right)_{FII} \times \left(\frac{\tilde{p}_{\mathrm{ref}}}{\tilde{p}_{\mathrm{meas}}}\right)_{LII}.$$

As in the case of the second scenario, this approach eliminates the need for a microphone pair TF evaluation as the last term in Eq. (12) cancels the last term in Eq. (11) (this is the reason why the *FI* system has been placed between brackets in Fig. 3). Experience with this scenario has confirmed that the measurement of the dual microphone probe response $(\tilde{p}_{\mathrm{meas}}/\tilde{p}_{\mathrm{ref}})_{FII}$ when clipped near the loudspeaker is a simple and repeatable measurement to cross-check laboratory and field measurements. First, it consists of simply using the "bare" dual microphone probe as used in practice without any specific preparation. Second, positioning of the dual microphone probe is fast and reliable: a "clip" similar to a fuse holder maintains the dual microphone probe in a vertical position onto the loudspeaker grid at a precise location. Third, such measurement of dual microphone probe response $(\tilde{p}_{\mathrm{meas}}/\tilde{p}_{\mathrm{ref}})_{FII}$ clipped near the loudspeaker is not susceptible to ambient noise nor the room's acoustics.

Equation (10) can be rewritten using Eq. (12) using the same three-line writing convention, with the field NR measurement and its *field correction* on the first line, all the

laboratory corrections on the second line, and a *compensation* on the third line:

$$\mathrm{REAT} = \widetilde{\mathrm{NR}}_{*} + 20\log_{10}\left(\frac{\tilde{p}_{\mathrm{meas}}}{\tilde{p}_{\mathrm{ref}}}\right)_{FII} + 20\log_{10}\left(\frac{\tilde{p}_{\mathrm{meas}}}{\tilde{p}_{\mathrm{ref}}}\right)_{LIII} + 20\log_{10}\left(\frac{\tilde{p}_{\mathrm{ref}}}{\tilde{p}_{\mathrm{meas}}}\right)_{LII} + \mathrm{TFOE} + \mathrm{PN} + 20\log_{10}\left(\frac{p}{p_{\mathrm{ref}}} \times \frac{p_2'}{p_3'}\right). \quad (13)$$

The measurement of the NR field correction $(\tilde{p}_{\mathrm{meas}}/\tilde{p}_{\mathrm{ref}})_{FII}$ is performed prior to the use of the measurement device, to discard any bias that would be introduced by small differences in the microphone sensitivity and frequency response during the measurement of the field noise reduction NR_{*}.

Given that the REAT method has been the "gold standard" for the past 50 years and in order to maintain consistency with current attenuation estimation protocols and standards, the proposed attenuation method aims to predict the attenuation value that would be measured on a human subject tested using the REAT method, for a given fit of a given HPD. In order to predict the REAT value, the previous equation (13) can be re-written as the sum of two terms:

$$\hat{\mathrm{REAT}} = \mathrm{NR}_{C} + \mathrm{COMP}. \quad (14)$$

The first term, NR_{C}, is the corrected NR, composed of the measured field NR and its field correction (first line) and laboratory correction terms (second line). The second term is the compensation factor COMP, and it is composed of the terms in the third line of Eq. (13). This term is detailed in Sec. III E.

Finally, this estimation of REAT attenuation is a monaural value. Since the NR measurement is performed on both earplugs, a binaural estimation of REAT is performed, with the "equivalent binaural approach" presented in Sec. III F.

C. Measurement of the field NR and its associated field and laboratory corrections

1. Measurement of the field NR

The NR values at octave-band index i, denoted $\widetilde{NR}_{*}^{i}$, are obtained from 1/3-octave bands filtered signals centered on the 125, 250, 500, 1000, 2000, 4000, and 8000 Hz frequencies. Such use of 1/3-octave band signals at octave-band center frequencies is common practice in the hearing protection measurement community, since the narrow band noise sources used for hearing threshold determination have precisely a 1/3-octave bandwidth (see Ref. 5 or Ref. 50).

2. Measurement of the NR field correction

The measurement in the acoustic near-field of the correction $(\tilde{p}_{\mathrm{meas}}/\tilde{p}_{\mathrm{ref}})_{FII}$ is performed prior to any use of the measurement device in the field and is part of a daily calibration check procedure. This procedure requires that the dual microphone probe be clipped to the center of the reference sound source speaker grid (ensuring the same acoustical pressure on both microphones), and that a TF measurement be performed between both microphones while the sound source is generating a moderate level pink noise (as shown at the bottom of Fig. 3). This procedure also serves two additional purposes, prior to any use of the measurement device: first to check that the sound source is functioning properly (since the sound pressure level measured at the reference microphone must be in a given range of levels), second to check that both microphones are working correctly and that the microphone probe is not clogged, altered in any way or incorrectly positioned on the speaker grid, since the measured TF magnitude must be within given bounds.

3. Measurement of the NR laboratory corrections

The acoustical length of the overall sound-bore depends on the type of earplug used: for example, at the time of writing, the earplug was available in three different sizes for the core. Consequently, the overall sound-bore length was set for a given earplug size. The associated correction was determined using the laboratory setup illustrated in Fig. 3: the TF $(\tilde{p}_{\mathrm{meas}}/\tilde{p}_{\mathrm{ref}})_{LIII}$ is measured in an anechoic chamber with the microphone probe placed into the earplug 2 ft away from the loudspeaker, and the TF $(\tilde{p}_{\mathrm{ref}}/\tilde{p}_{\mathrm{meas}})_{LII}$ is measured while the dual microphone probe is clipped onto the speaker grid.

D. Estimation of the equivalent binaural NR

The estimated REAT obtained from Eq. (14) is a monaural estimation, while the measured REAT is a binaural value. In order to estimate a binaural REAT value, an approach based on the protected hearing threshold has been successfully developed:[49] it considers that the test subject is able to detect the audio stimulus (that is, the test signal used for the hearing threshold determination) through the ear that is presenting a combination of the lowest HPD attenuation and the best hearing level. In practice, this approach consists of computing the protected hearing threshold for each ear by adding the respective right and left hearing thresholds level A_R and A_L of the test subject to the right and left corrected NR denoted $\mathrm{NR}_{C(R)}$ and $\mathrm{NR}_{C(L)}$; the equivalent binaural NR value to be used, denoted $\mathrm{NR}_{C(B)}$, is the one that corresponds to the weakest protected threshold:

$$\begin{aligned}
&\mathrm{NR}^{i}_{C(B)} = \mathrm{NR}^{i}_{C(L)} \quad \text{if } (\mathrm{NR}^{i}_{C(L)} + A^{i}_{(L)}) < (\mathrm{NR}^{i}_{C(R)} + A^{i}_{(R)}),\\
&\mathrm{NR}^{i}_{C(B)} = \mathrm{NR}^{i}_{C(R)} \quad \text{if } (\mathrm{NR}^{i}_{C(L)} + A^{i}_{(L)}) > (\mathrm{NR}^{i}_{C(R)} + A^{i}_{(R)}),\\
&\mathrm{NR}^{i}_{C(B)} = \min(\mathrm{NR}^{i}_{C(L)}, \mathrm{NR}^{i}_{C(R)}) \quad \text{if } (\mathrm{NR}^{i}_{C(L)} + A^{i}_{(L)}) = (\mathrm{NR}^{i}_{C(R)} + A^{i}_{(R)}). \quad (15)
\end{aligned}$$

E. Compensation calculation

Assuming the subject-related correction terms on the third line of Eq. (13) are all uncorrelated, their combining in a single compensation term COMP should lead to a normal distribution for large groups with average value $\overline{\mathrm{COMP}}$ and standard deviation σ_{COMP}. Such an assumption, validated in

Sec. IV A, is supported by the fact that all the terms included on the third line of Eq. (13) originate from morphological or psycho-physiological variables.

Based on Eq. (14), the following expression of COMP can be obtained for each octave-band (index i):

$$\mathrm{COMP}^i = \mathrm{REAT}^i - \mathrm{NR}^i_{C(B)}, \tag{16}$$

where REAT^i is the REAT attenuation measured on the human subject tested, while $\mathrm{NR}^i_{C(B)}$ is the equivalent binaural corrected NR [detailed in Eq. (15)] as measured on the same subjects, in the same fitting conditions.

The experimental protocol for COMP^i determination includes six steps repeated for each of the 20 subjects.

(1) Measurement of the octave-band REAT values according to ANSI S12.6-A.[5]
(2) Measurement of $\mathrm{NR}^i_{C(R)}$ and $\mathrm{NR}^i_{C(L)}$; since the test-subjects are instructed not to touch the HPD after the audiometric tests, and the NR measurement is performed immediately after the REAT tests, the fit of the earplug can be considered to be the same except for the slight effect of the insertion of the microphone probe (probably enhancing the quality of the fit, as the strength applied to insert the probe is toward the ear canal and tympanic membrane). The same "bias" is introduced by the microphone insertion for every earplug tested, and consequently, such systematic error is automatically canceled later in the compensation computation, as detailed in Ref. 49.
(3) The equivalent binaural $\mathrm{NR}_{C(B)}$ is then computed per octave-band using Eq. (15).
(4) The difference, per octave-band and per subject between the reported REAT attenuation values and the objectively measured $\mathrm{NR}_{C(B)}$, will provide the compensation values using Eq. (16).
(5) Repetition of steps 1–4 for a second test trial, leading to a second determination of REAT and $\mathrm{NR}_{C(B)}$ on each subject.
(6) This per-subject compensation can then be presented, per octave-band index, as a normal distribution $\mathcal{N}(\overline{\mathrm{COMP}^i}, \sigma^i_{\mathrm{COMP}})$; hence this compensation can be given with a confidence interval that is useful in determining the uncertainty associated with the proposed field-MIRE measurement.

F. Predicted personal attenuation rating

The PPAR is computationally very similar to the existing NRR and SNR: it is a single number, expressed in decibels, that represents the attenuation achieved by the user for a given HPD. While the NRR and the SNR are obtained from a subjective REAT measurement on a sample of individuals under laboratory conditions, the PPAR is obtained from an objective NR measurement, on a particular user wearing the hearing protector under more realistic conditions (since the HPD is fitted by the user). Furthermore, the NRR is a percentile value that is computed, according to EPA requirements,[41] by subtracting a two-standard deviation correction from the mean REAT attenuation values in order to estimate the "minimum NR theoretically achieved by 98% of the laboratory subjects."[4] The PPAR_x is the value that the user will obtain from his own HPD with a given protection performance x, where x, based on the definition of ISO 4869 standard,[42] represents the percentage of situations for which the effective personal attenuation is greater than or equal to the predicted value. Just like the SNR_x, defined in ISO 4869, is the minimal attenuation value that $x\%$ of a group should meet or exceed, the PPAR_x is the individual lower bound on the individual attenuation value such that $x\%$ of individual's attenuation in a group will meet or exceed their own PPAR_x value.

Although the PPAR is a personal value, the uncertainty that will be used to compute the PPAR_x value comes from the prediction error obtained on a group of subjects. Per octave-band i (from $i=1$ for 125 Hz to $i=7$ for 8000 Hz), Eq. (14) can be written as

$$\hat{\mathrm{REAT}}^i = \mathrm{NR}^i_C + \mathrm{COMP}^i, \tag{17}$$

where COMP^i is the octave-band compensation factor, detailed in Sec. III E.

The equivalent binaural predicted attenuation can be expressed, respectively, by

$$\hat{\mathrm{REAT}}^i_{(B)} = \mathrm{NR}^i_{C(B)} + \mathrm{COMP}^i. \tag{18}$$

The PPAR is essentially the REAT value obtained in Eq. (19) reduced by an uncertainty factor that is the product of the prediction uncertainty $u^i_{\hat{\mathrm{REAT}}}$ and the coefficient α:

$$\mathrm{PPAR}^i_x = \hat{\mathrm{REAT}}^i_{(B)} - \alpha \times u^i_{\hat{\mathrm{REAT}}}. \tag{19}$$

The coefficient α is a constant associated with a given protection performance, values of which are given in ISO 4869.[50]

The overall PPAR value is obtained in a very similar manner as the existing NRR or SNR, by taking the difference between the C-weighted overall exposure level and the A-weighted overall protected exposure level, for a theoretical pink noise with a 100 dB in each octave-band:

$$\mathrm{PPAR}_x = 10\log_{10}\sum_{i=1}^{7} 10^{(100+C^i)/10} - 10\log_{10}\sum_{i=1}^{7} 10^{(100+A^i-\mathrm{PPAR}^i_x)/10}, \tag{20}$$

where A^i and C^i are, respectively, the C- and A-weighting coefficients.

Alternatives to the computation presented in Eq. (20) are possible: for example, instead of using a pink noise spectrum and computing the C-A' attenuation value like the NRR (where the prime symbol represents the protected level), the PPAR could be computed on the basis of the noise level reduction statistics (NRS_A) from the recent ANSI S12.68-2007 (Ref. 51) standard: the personal attenuation rating would hence be computed from the difference between A-weighted exposure values and A-weighted protected values for real industrial spectrums (see Ref. 52 for details).

IV. EXPERIMENTAL VALIDATION OF THE PROPOSED APPROACH

The validation of the measurement device has been successfully completed, by assessing its electrical floor noise, dynamic range, linearity, and time stability, and the current paper will focus in this section on the validation of the proposed method by comparing predicted and reported attenuation values.

The prediction method is validated using results of tests conducted by a third-party research laboratory.[53] Two groups, denoted α and β of 20 subjects, were tested with the instrumented expandable custom earplug (presented in Sec. II). The compensation for group α is evaluated according to Eq. (16) and the experimental procedure described in Sec. III E, on 17 of the 20 subjects. For three subjects the dual microphone probe was impossible to insert properly inside the sound-bore with the earplug in the ear (whereas in the usual measurement, the probe would be inserted in the sound-bore with the earplug outside the ear) because a pronounced bend of the earplug canal portion had distorted the sound-bore.

Then, the same measurement and calculation (as described in steps 1–5 in Sec. III E) are performed on the 20 subjects of the validation group β (no subject was discarded in this validation group). Using the compensation values COMP_{α} determined on the two trials of the first group α and the equivalent binaural $\mathrm{NR}_{C(B)}$ computed with the second group β, the attenuation $\hat{\mathrm{REAT}}^{i}$ are predicted for each of the two test trials of group β.

These prediction values for group β are then compared to the REAT reported value for group β in order to evaluate the prediction error. The prediction error is presented in Sec. IV B, once the assumption of normality for compensation distribution is validated (Sec. IV A).

A. Validation of the assumption of normality for the distribution of the compensation values

The accuracy of fit of the compensation factor to a normal distribution was successfully validated at a significance level of 5% using the Jarque–Bera[54] tests of goodness-of-fit test of composite normality for both the first and second test trials of group α.

The normal probability plot for the compensation (from the first trial of group α) is presented in Fig. 4 together with the result of the statistical test ($H=0$ indicates that the null hypothesis "the data is normally distributed" cannot be rejected at the 5% significance level) and the p-value. The purpose of a normal probability plot of a physical quantity is to graphically assess whether this quantity could come from a normal distribution. If the data are normal the plot is linear. Other distribution types will introduce curvature in the plot. The plots in Fig. 4 provide a visual indication that the COMP function is a normal distribution although some outliers at high frequencies (2–8 kHz) can be observed. The normality hypothesis of Sec. III E is valid for the first trial of α data set at all octave-bands except 4 kHz at a significance level of 5%. A similar result is obtained by using the second trial of the α group.

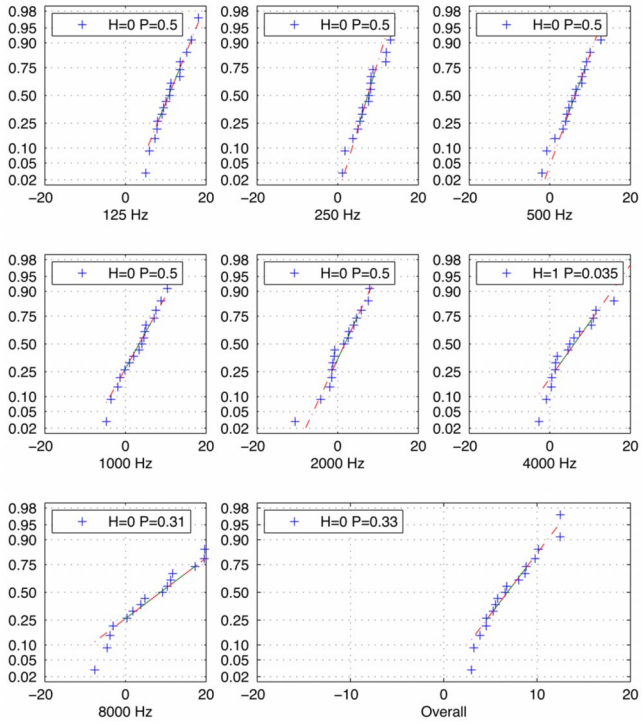

FIG. 4. (Color online) Normal probability plot of the Compensation for the first trial of α data set of experimental data ($n=17$). The abscissa coordinates are the unimodal Gaussian quantiles. The ordinate coordinates are the probability of the cumulative distribution.

B. Predicted vs observed attenuation

In Fig. 5, it can be seen that the average values predicted for the first trial of group β with the proposed field-MIRE approach are close to the REAT values in each octave-band and are less than 0.1 dB apart for the overall values. It can be seen that the standard deviation appears to be significantly lower in most octave-bands in the case of the field-MIRE than the one obtained from the REAT test. Given that the standard deviation primarily reflects the variability of the earplug attenuation in the group and does also include the

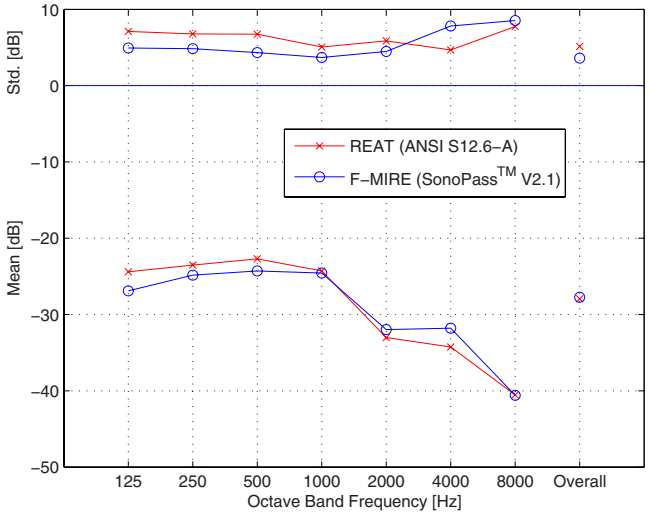

FIG. 5. (Color online) Mean and standard deviation of the attenuation measured, on the first trial test of group β, with the REAT and field-MIRE methods on the 20 subjects.

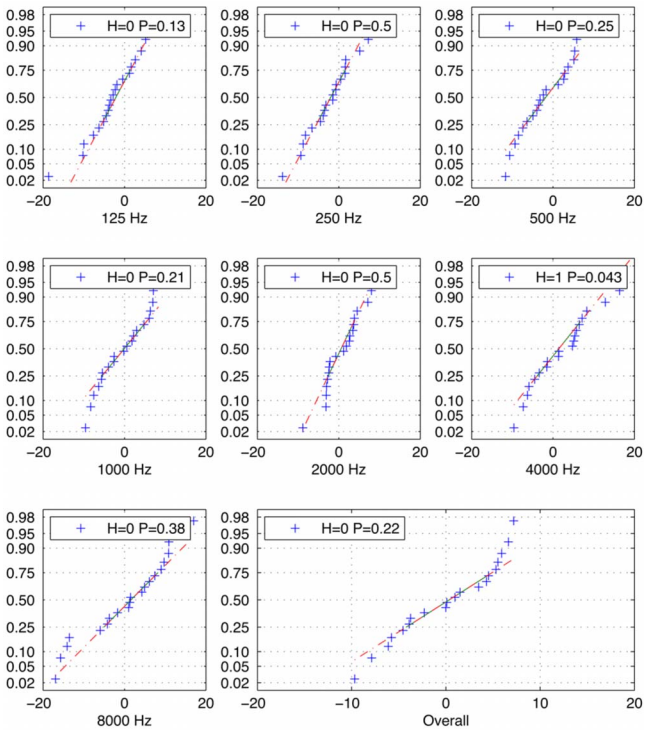

FIG. 6. (Color online) Normal probability plot of the observed prediction error ϵ^i per octave-bands and as an overall value for the first trial in the β data set ($n=20$).

variability associated with the measurement device itself, one could think that the proposed field-MIRE method is indeed introducing less variability (from 125 to 2000 Hz) than the REAT measurement approaches. Furthermore, the low-frequency octave-bands, where the field-MIRE shows less variability, are also the most critical for the assessment of the overall earplug attenuation, as it has already been demonstrated that the mere use of the 500 and 1000 Hz could be a good predictor of the overall attenuation.[16]

The observed prediction errors is defined as

$$\epsilon = \mathrm{REAT} - \hat{\mathrm{REAT}}, \tag{21}$$

where the measured REAT is considered the "true" attenuation value and $\hat{\mathrm{REAT}}$ is the predicted one. If the observed prediction errors appear to behave randomly, this suggests that the model fits the data well. On the other hand, if a non-random structure is evident in the observed prediction errors, this is a clear sign that the model fits the data poorly. It can be observed by the normal probability plot of the observed prediction errors in Fig. 6 that the distribution of the observed prediction errors for the "first" trials is very close to a normal distribution for the whole frequency range.

The Jarque–Bera hypothesis test of composite normality for the first trials indicates that for all octave-bands (at the exception of 4 kHz), the null hypothesis ("the data are normally distributed") cannot be rejected at the 5% significance level. The normality test is passed for 4 kHz by lowering the significance level to 4%. For the "second" trial, the normality test is passed at all frequencies at a significance level of 5%.

Overall, the assumption of a normally distributed observed prediction error is verified, which validates the model. In addition, it becomes possible to evaluate the uncertainty which is associated with the proposed measurement approach, as described in the first author doctorate thesis.[49]

V. CONCLUSIONS

To meet the need to improve earplug field performance prediction accuracy, average group performance prediction was replaced by individual performance prediction on a recently designed instrumented expandable custom earplug. The individual earplug field performance was objectively obtained using a field-MIRE method based on the field measurement of the NR through the earplug. Individual attenuation first resulted in a set of values for each octave-band center frequency and these values were then combined into a single value, the PPAR, which takes into account the measurement uncertainty. This PPAR is the equivalent of the "individual" NRR obtained from the traditional REAT attenuation testing. The method was validated experimentally on an ATF and using third party REAT testings on two groups of 20 subjects.

For effective hearing protection practices, the benefits of the proposed approach are threefold: (a) Fast and reliable measurement: the effective performance of the earplug can be measured quickly using a field-ready, durable, and robust measurement device. (b) The adaptation of earplug attenuation is now possible. If the earplug attenuation is known, it becomes possible to use acoustical filters to match the wearer's hearing protection needs. This will allow the wearer to more easily discriminate between noise and speech or warning signals and will maximize speech and warning signals perception. (c) Quick field tests are possible by adopting portions of the testing protocol described herein that could be performed in little time. A quick field test device could potentially be used to greatly facilitate user motivation and training: such a measurement device could be installed at the entrance of a noisy plant so that exposed wearers could check the fit and efficiency of their HPD prior to sound exposure.

An immediate improvement in HPD rating and labeling would come from updating standards and regulations with this new approach. Easy access to personal measurement of earplug performance on the wearer could completely supersede the current use of a single number rating (like the NRR) as the individual PPAR values are inherently superior to the population-based, statistically-derived, laboratory-driven NRR estimation. A proposal has been written and submitted to the ANSI S12 Working Group WG11: the HPD product would be rated with average and standard deviation on a laboratory panel, as currently done in ANSI S12.6—Method B, and the field measurement device would be rated in terms of the uncertainty that is associated with the individual measurement. A new rating and labeling paradigm would therefore contain the typical attenuation value that users can achieve (using a "subject-fit" REAT attenuation measurement), the variability observed on a panel group and the uncertainty associated with the field measurement device.[55]

A more long term improvement in HPD rating and labeling could come from the fact that the proposed field-

MIRE approach shows an equivalent or better uncertainty as compared to the current "gold standard" REAT and may be considered as a possible alternative for HPD attenuation measurement in the laboratory. In such cases, the IL could be used as an objective attenuation metric, rather than trying to predict a subjective REAT value that is also biased in several ways. Such an approach would bring the benefits of an objective measurement (lower measurement uncertainty) while keeping the human factor effect (variation in HPD fit with individuals). It could be integrated into current MIRE or ATF related standards [i.e., ANSI S12.42 (Ref. 28)] or could even be—when the remaining challenges associated with the instrumentation of all HPD will have been overcome—used instead of the current REAT method in a standard to measure the real-ear attenuation of hearing protectors [such as the current ANSI S12.6 (Ref. 7)].

Future research should address the need for an engineering design of a less intrusive dual microphone probe for reduced probe insertion variability and the need for computing compensation on an individual basis from an identification scheme rather than on a group basis from a statistical model. Individual compensation could be derived from the NR measurement in the occluded-ear using the identification of some individualized dimensions and characteristics from which it would be possible to reconstruct the required corrections (TF) that are part of COMP. For example, the computational process could identify the exact frequency of the occluded-ear canal resonance, then determine the length and area of the occluded residual ear canal, from which it would be possible to model the TF of the occluded-ear canal, as an acoustical duct. Such refinement could be beneficial for the precise and accurate prediction of an individual REAT-like attenuation but could also benefit the future measurement approaches presented in the previous paragraph, the prediction of the individual ILs.

ACKNOWLEDGMENTS

The support of Sonomax Hearing Healthcare Inc., IRSST (Quebec Occupational Health and Safety Research Institute) and Natural Sciences and Engineering Research Council of Canada (NSERC, CRDPJ 249345-01) is gratefully acknowledged.

[1]E. H. Berger, in *Noise-Con 81*, edited by F. D. Hart, L. H. Royster, and N. D. Stewart (Noise Control Foundation, New York, NY, 1981), pp. 147–152.
[2]E. H. Berger, "Can real-world hearing protector attenuation be estimated using laboratory data?," Sound Vib. **22**, 26–31 (1988).
[3]E. H. Berger, J. R. Franks, and F. Lindgren, "International review of field studies of hearing protector attenuation," *Scientific Basis of Noise-Induced Hearing Loss*, edited by A. Axlesson, H. Borchgrevink, R. P. Hamernik, P. Hellstrom, D. Henderson, and R. J. Salvi (Thieme Medical Pub., Inc., New York, NY, 1996), pp. 361–377.
[4]E. H. Berger, "EARLog #20—The naked truth about NRRs" (E-A-R Hearing Protection Products, Indianapolis, IN, 1993).
[5]American National Standards Institute, ANSI S3.19-1974 (R 1990), American National Standard Methods for the measurement of real-ear protection of hearing protectors and physical attenuation of earmuffs (1974).
[6]NIOSH, Criteria for a recommended standard—Occupational noise exposure (1998).
[7]American National Standard Institute, ANSI S12.6-1997 (R2002), American National Standard Methods for measuring the real-ear attenuation of hearing protector New York (1997).
[8]Australian/New Zealand Standard, AS/NZS1270:2002, Acoustics—Hearing protectors, Sydney, NSW (2002).
[9]International Organization for Standardization, ISO/TS 4869–5:2006, Acoustics—Hearing protectors—Part 5: Method for estimation of noise reduction using fitting by inexperienced test subjects, Switzerland (2006).
[10]E. H. Berger, J. R. Franks, A. Behar, J. G. Casali, C. Dixon-Ernst, R. W. Kieper, C. J. Merry, B. T. Mozo, C. W. Nixon, D. Ohlin, J. D. Royster, and L. H. Royster, "Development of a new standard laboratory protocol for estimating the field attenuation of hearing protection devices. Part III. The validity of using subject-fit data," J. Acoust. Soc. Am. **103**, 665–672 (1998).
[11]J. D. Royster, E. H. Berger, C. J. Merry, C. W. Nixon, J. R. Franks, A. Behar, J. G. Casali, C. Dixon-Ernst, R. W. Kieper, B. T. Mozo, D. Ohlin, and L. H. Royster, "Development of a new standard laboratory protocol for estimating the field attenuation of hearing protection devices. Part I. Research of Working Group 11, Accredited Standards Committee S12, Noise," J. Acoust. Soc. Am. **99**, 1506–1526 (1996).
[12]E. H. Berger, "In search of meaningful measures of hearing protector effectiveness," in 21st Annual Conference of the National Hearing Conservation Association, San Francisco, CA (1996).
[13]E. H. Berger, "EARLog #21—Hearing protector testing—Let's get real [Using the new ANSI Method-B data and the NRR(SF)]" (E-A-R Hearing Protection Products, Indianapolis, IN, 1999).
[14]E. H. Berger and R. W. Kieper, "ANSI S12.6-1997 Method-B testing of custom earmolds and its effect on the testing of other earplugs," Technical Report E-A-R 04-15/HP Version 2.1, EAR/Aearo Company, Indianapolis, IN, 2005.
[15]J. R. Franks, W. J. Murphy, D. A. Harris, J. L. Johnson, and P. B. Shaw, "Alternative field methods for measuring hearing protector performance," Am. Ind. Hyg. Assoc. J. **64**, 501–509 (2003).
[16]E. H. Berger, "Exploring procedures for field testing the fit of earplugs," in *Industrial Hearing Conservation Conference* (University of Kentucky, Lexington, KY,1989).
[17]A. Kusy and A. Damongeot, "Mesure des performances acoustiques des bouchons d'oreille. Essai d'application de la technique MIRE (Microphone in the real ear)," Technical Report ND 2023, Cahier de notes documentaires no. 164, Institut National de Recherche et de sécurité, Paris, France, 1996, pp. 287–292.
[18]K. Michael, "Measurement of insert-type hearing protector attenuation on the end-user: A practical alternative to relying on the NRR," Spectrum—National Hearing Conservation Association (NHCA) Publications **16**, pp. 13–17 (1998).
[19]K. Michael and D. C. Byrne, "Current state of insert-type hearing protector fit-testing: Follow-on measurements in the steel industry and fit-testing in a mobile environment," Spectrum—National Hearing Conservation Association (NHCA) Publications **19**, pp. 14–16 (2002).
[20]W. J. Murphy, J. R. Franks, and D. A. Harris, "Evaluation of a FitCheck ™hearing protector test system," J. Acoust. Soc. Am. **106**, 2263 (1999).
[21]ANSI, (1957). "Method for the Measurement of Real-Ear Attenuation of Ear Protectors at Threshold," American National Standards Institute, Z24.22–1957 (R1971), New York.
[22]Canadian Standards Association, CSA Z94.2-02, Hearing Protection Devices—Performance, Selection, Care, and Use, Toronto, ON (2002).
[23]International Standard Organization, ISO 4869-1 (1990), Acoustics—Hearing protectors—Part 1: Subjective method for the measurement of sound attenuation (1990).
[24]E. H. Berger, "Techniques for Measuring Hearing Protector Attenuation and the correct answer is…?," in *30th Annual NHCA Hearing Conservation Conference* (NHCCS Association, Tucson, AZ, 2005).
[25]E. H. Berger, "Review and tutorial—methods of measuring the attenuation of hearing protection devices," J. Acoust. Soc. Am. **79**, 1655–1687 (1986).
[26]E. H. Berger, "Preferred methods for measuring hearing protector attenuation," InterNOISE 2005, Rio de Janeiro, Brazil (2005).
[27]D. W. Mauney, "Investigation of physical and psychological methods for the attenuation measurement of circumaural hearing protectors with implications for field use," Ph.D. thesis, Virginia Polytechnique Institute and State University, Blacksburg, VA (1994).
[28]ANSI S12.42–1995 (R2004), American National Standard microphone-in-real-ear and acoustic test fixture methods for the measurement of insertion loss of hearing protection devices, American National Standard Institute, New York (1995).
[29]International Organization for Standardization, ISO 11904-1 (2002), Acoustics—Determination of sound emission from sound sources placed

close to the ear. Part 1: Technique using a microphone in the real ear (MIRE) technique, Switzerland (2000).
[30]P. B. Madsen, "Insertion gain optimization," Hearing Instruments **37**, 28–32 (1986).
[31]J. G. Casali, D. W. Mauney, and J. A. Burks, "Physical versus psychophysical measurement of hearing protector attenuation—a.k.a. MIRE vs. REAT," Sound Vib. **29**, 20–27 (1993).
[32]J. Pretzschner and A. Moreno, "Field evaluation of ear-muffs: Which is more suitable-insertion loss or transmission loss?," Appl. Acoust. **24**, 129–143 (1988).
[33]J. Voix and F. Laville, "Expandable Earplug With Smart Custom Fitting Capabilities," *InterNOISE 2002*, Dearborn, MI (2002).
[34]J. G. Casali and S. Gerges, "Hearing in noise: Effects upon, protection, and enhancement," in *Review of Human Factors*, Review of Human Factors, edited by R. C. Williges (Human Factors and Ergonomics Society, Santa Monica, CA, 2005).
[35]J. Voix, F. Laville, and J. Zeidan, "Filter selection to adapt earplug performances to sound exposure," Can. Acoust. **30**, 122–124 (2002).
[36]J. Voix and F. Laville, "Prediction of the attenuation of altered custom earplug," Appl. Acoust. **70**, 935–944 (2009).
[37]W. Murphy *et al.*, EPHB Survey Report 312–11a in Advanced Hearing Protector Study: Conducted at General Motors Metal Fabrication Division, Flint Metal Center, Flint, Michigan, 2006. U.S. Department of Health, Education and Welfare, Public Health Service, Center for Disease Control, National Institute for Occupational Safety and Health (NIOSH).
[38]J. Voix and F. Laville, "Method and apparatus for determining in situ the acoustic seal provided by an in-ear device," U.S. Patent No. 6,687,377 (2004).
[39]J. Voix and F. Laville, "Method and apparatus for customizing in situ an in-ear device," U.S. Patent No. 2,000,123,146 (2005).
[40]J. Voix and F. Laville, "New method and device for customizing in situ a hearing protector," Can. Acoust. **32**, 86–87 (2004).
[41]EPA, *Noise Labeling Requirements for Hearing Protectors* (Environmental Protection Agency, Washington, DC, 1979).
[42]International Organization for Standardization, ISO 4869-2 (1994), Acoustics—Hearing protectors—Part 2: Estimation of effective A-weighted sound pressure levels when hearing protectors are worn (1994).
[43]P. Hamery, A. Dancer, and G. Evrard, "Étude et réalisation de bouchons d'oreilles perforés non-linéaires (study and development of non-linear perforated earplugs)," Technical Report No. R128/97, Institut Franco-Allemand de recherches de Saint-Louis, France, 1997.
[44]R. Pääkkönen, S. Savolainen, J. Myllyniem, and K. Lehtomäki, "Ear plug fit and attenuation—An experimental study," Acust. Acta Acust. **86**, 481–484 (2000).
[45]J. Schroeter and C. Poesselt, "The use of acoustical test fixtures for the measurement of hearing protector attenuation. Part II: Modeling the external ear, simulating bone conduction, and comparing test fixture and real-ear data," J. Acoust. Soc. Am. **80**, 505–527 (1986).
[46]E. H. Berger and J. E. Kerivan, "Influence of physiological noise and the occlusion effect on the measurement of real-ear attenuation at threshold," J. Acoust. Soc. Am. **74**, 81–94 (1983).
[47]E. H. Berger, J. Voix, and R. W. Kieper, "Methods of developing and validating a field-MIRE approach for measuring hearing protector attenuation," Spectrum—National Hearing Conservation Association (NHCA) Publications **24**, Supplement 1, p. 22 (2007).
[48]E. H. Berger, R. W. Kieper, and D. Gauger, "Hearing protection: Surpassing the limits to attenuation imposed by the bone-conduction pathways," J. Acoust. Soc. Am. **114**, 1955–1967 (2003).
[49]J. Voix, "Mise au point d'un bouchon d'oreille "intelligent" (Development of a "smart" earplug)," Ph.D. thesis, École de Technologie Supérieure, Montréal, Canada (2006).
[50]International Organization for Standardization, ISO 4869-3:2007 Acoustics—Part 3: Measurement of insertion loss of hearing protectors, Switzerland (2007).
[51]ANSI, ANSI S12.68-2007, Methods of estimating effective *A*-weighted sound pressure levels when hearing protectors are worn, American National Standard Institute, New York (2007).
[52]J. Voix and L. D. Hager, "Individual fit testing of hearing protector devices," in First European Forum on Effective Solutions for Managing Occupational Noise, Noise at Work 2007, Lille, France (2007).
[53]General dynamics advanced information engineering services, real-ear attenuation at threshold (REAT), Test Report for Sonomax Hearing Healthcare Inc. (2004).
[54]C. M. Jarque and A. K. Bera, "A test for normality of observations and regression residuals," Int. Statist. Rev. **55**, 1–10 (1987).
[55]J. Voix, F. Laville, and J. Zeidan, "In-situ personal assessment of hearing protector performance-recommendations for an updated standard," J. Acoust. Soc. Am. **117**, 2480 (2005).

Comparing two methods to measure preferred listening levels of personal listening devices

Darrin A. Worthington[a)]
Roxelyn and Richard Pepper Department of Communication Sciences and Disorders, Northwestern University, Evanston, Illinois 60208

Jonathan H. Siegel and Laura Ann Wilber
Roxelyn and Richard Pepper Department of Communication Sciences and Disorders and The Hugh Knowles Center, Northwestern University, Evanston, Illinois 60208

Benjamin M. Faber
Faber Acoustical, LLC., Santaquin, Utah 84655

Kathleen T. Dunckley
Roxelyn and Richard Pepper Department of Communication Sciences and Disorders, Northwestern University, Evanston, Illinois 60208

Dean C. Garstecki and Sumitrajit Dhar[b)]
Roxelyn and Richard Pepper Department of Communication Sciences and Disorders and The Hugh Knowles Center, Northwestern University, Evanston, Illinois 60208

(Received 9 September 2008; revised 7 April 2009; accepted 8 April 2009)

The potential risk to hearing that mass-storage personal listening devices (PLDs) pose remains unclear. Previous research in this area has either focused on maximum outputs of these devices or on ear-canal measurements of listening levels that could not be compared to standards of occupational noise exposure. The purpose of this study was to compare two standard measurement protocols [ISO 11904-1 (2002), Switzerland; ISO 11904-2 (2004), Switzerland] for the measurement of preferred listening levels of PLD. Noise measurements, behavioral thresholds, and oral interviews were obtained from 30 (18–30 years) PLD users. Preferred listening levels for self-selected music were determined in quiet and background noise using a probe microphone, as well as in the DB-100 ear simulator mounted in KEMAR. The ear-canal measurements were compensated for diffuse-field. Only one of the subjects was found to be listening at hazardous levels once their reported daily usage was accounted for using industrial workplace standards. The variance across subjects was the smallest in the ear-canal measurements that were compensated for diffuse-field equivalence [ISO 11904-1 (2002), Switzerland]. Seven subjects were found to be listening at levels above 85 dBA based on measurements obtained in the KEMAR and then compensated for diffuse-field equivalence.
 [DOI: 10.1121/1.3125798]

PACS number(s): 43.50.Hg, 43.50.Qp, 43.38.Lc, 43.50.Yw [BLM] Pages: 3733–3741

I. INTRODUCTION

The potential risk to hearing from mass-storage personal listening devices (PLDs) has been the subject of recent interest in the popular as well as in the scientific press (Nature Neuroscience, 2007; Kenna, 2008). However, the data on which this concern is based are not straightforward to interpret as listening levels are often measured in the ear canal and then have to be compared with standards created for the risk of occupational sound exposures measured in the free field. Here we report preferred listening levels from PLD of 30 college-age individuals and compare measurements made using two methods based on two ISO standards.

The exact number of at-risk PLD users notwithstanding, the scale of the issue with over 100×10^6 PLD being sold annually world wide is undeniable. The perceived importance of this potential problem has led the Council of Science and Public Health of the American Medical Association to issue a specific report and resolution on PLDs and Noise-Induced Hearing Loss (CSAPH, 2008). Arguments in support of this predicted risk include the potential for users to listen more frequently and for longer durations due to the longer battery life, mass-storage capabilities, and perhaps most importantly, the high maximum output levels (MOLs) achievable in many of these devices (Reuters Press, 2005). Many popular PLDs are capable of generating diffuse-field equivalent MOL of 91–121 dBA (Fligor and Cox, 2004) or estimated listener sound levels between 79 and 125 dBA (Keith *et al.*, 2008). Recent measures of listening levels, sampled randomly from individuals passing by on a public street using MP3 players, reveal a wide range of listening

[a)]Present address: North Chicago VA Medical Center, North Chicago, IL.
[b)]Author to whom correspondence should be addressed. Electronic mail: s-dhar@northwestern.edu

levels from 73.7 to 110.2 dBA (mean=86.1; SD=7.9) (Williams, 2005). More recent work by Hodgetts *et al.* (2007) has documented preferred listening levels in quiet and in background noise measured near the tympanic membrane for different types of headphones to be in the same approximate range.

The threat of these high outputs becomes obvious when compared against the *damage risk criteria* of 85 and 90 dBA advocated by the National Institute of Occupational Safety and Health (NIOSH) and the Occupational Safety and Health Administration (OSHA), respectively, for the length of a typical 8 h working day. The OSHA specifies 90 dBA time-weighted average (TWA) as the "permissible exposure level" but 85 dBA TWA as the "action level." All individuals exposed to levels greater than 90 dBA TWA during a workday must use hearing protection devices. On the other hand, hearing protection devices are required to be made available to individuals exposed to levels between 85 and 90 dBA TWA. These individuals must also receive annual audiograms and counseling as necessary. These individuals must also begin to use hearing protection devices if significant threshold shifts are detected after adjusting for age-related changes in hearing. However, the appropriateness of applying *occupational* risk criteria with *recreational* noise exposure remains problematic for three reasons. First, these standards were developed specifically for spectrally dense industrial noise with limited dynamic range and their application to music can be questionable. Second, the standards were developed based on free-field measurements whereas measurements of listening levels are obtained using a probe microphone placed near the tympanic membrane. Finally, the standards were developed as an exposure dose for an 8 h workday. Two international standards describe methods of measuring sound levels generated by sources close to the ear by either using a probe microphone [microphone in real ear (MIRE); ISO, 2002] or a manikin (ISO, 2004). Our goal is to compare measurements made using these two recommended procedures and then derive an index of personal music-related exposure based on reported daily usage.

Early research in this area focused on the maximum outputs from various types of headphones (Wood and Lipscomb, 1972; Katz *et al.*, 1982). Findings from these studies reported maximum output levels exceeding 120 dBA but were flawed because of the following: (i) diffuse-field equivalents were not calculated, an important conversion needed to compare findings to occupational risk criteria (Fligor and Cox, 2004); and (ii) the relationship between MOLs and preferred listening levels in quiet and in background noise remained uncertain. Multiple studies were conducted to examine if users of personal cassette players (PCPs) were operating these devices at harmful levels. Objective measurements of listening levels, incorporating the appropriate conversion factor and user accounts of listening habits, have shown the use-practices of the vast majority of users to be *safe*. Rice *et al.* (1987a) found only 5% of the users of PCPs to be at risk for noise-induced hearing loss. These results were supported by Wong *et al.* (1990) and again by Turumen-Rise *et al.* (1991a).

To make the OSHA and NIOSH standards more applicable, some researchers have carefully selected music with characteristics approximating that of industrial noise. For example, Hodgetts *et al.* (2007) made their measurements using the same song with all subjects. The song was chosen for its limited dynamic range thereby approximating (relatively) steady state industrial noise. Similarly, Farina (2007) used the signal specified by the IEC 60268-1 standard as well as a signal resembling the average spectrum of 30 GB of music popular with Italian teenagers to make measurements of listening levels. In the choice of music lies a paradox; choosing a piece of music for the listener may help in relating the results to established damage risk criteria but may not prompt the listener to set the volumes to habitual levels. Alternately, allowing the listener to choose music used during the measurements should lead to a more realistic volume setting. However, comparisons with industrial standards have to be made with caution.

Finally, individuals listen to music for different durations (hours/day) and with different frequencies (e.g., days/week). Standard computations for industrial noise exposure, however, are based on an 8 h exposure period. Appropriate modifications can be made to such calculations for exposures of other durations. One approach to accommodate this aspect has been to provide guidelines of maximum exposure duration based on listening level (Fligor and Cox, 2004). An alternate would be to combine measured listening levels and reported listening duration to then compute the best-estimated exposure dose for a given individual.

With annual worldwide sales already greater than 100×10^6 units and projected growth rates of as much as 40% through 2010 (In-Stat, 2007), a sizable proportion of the global population will soon be using these devices. Accurate measurement techniques that provide realistic estimates of probable hearing damage need to be established. The goal of this research was to establish a benchmark protocol to measure preferred listening levels of mass-storage PLD users along with a set of preliminary data to demonstrate its validity. Our approach was to make empirical measurements of *preferred* listening levels using multiple techniques from a group of college students and use their reported daily listening durations to compute individual exposures comparable to OSHA and/or NIOSH standards.

II. METHODS

A. Subjects

Thirty subjects, 12 male and 18 female, between 18 and 30 years of age (mean=22, SD=3.44) were recruited using fliers posted around the Chicago and Evanston campuses of Northwestern University. Advertisement fliers stated that subjects would be answering questions about the typical use of their PLD and that measurements of preferred listening level would be taken. Subjects were required to have normal hearing sensitivity (<20 dB HL re: ANSI, 2004) between 250 and 8000 Hz, normal middle ear function as measured through tympanometry, and negative history for otologic problems ascertained through an interview. Subjects who failed the hearing screening were excluded to avoid any po-

tential confound of listening levels being affected by the presence of a hearing loss. The Institutional Review Board for Protection of Human Subjects at Northwestern University approved this study. All subjects signed informed consent agreements and were compensated ($10) for their time.

23 out of 30 subjects (77%) reported a history of infrequent noise exposure (i.e., music concerts and clubs). The last reported exposure was no sooner than 14 h before the time of testing. The remaining seven subjects did not report any exposure to loud noises. Measurements were made from alternating left and right ears. Every subject screened qualified to participate in the study.

B. General methods

Measurements of hearing function as well as listening level were conducted in a double-walled IAC booth at the Northwestern University Hearing Clinic on the Evanston Campus. Admittance data were recorded using a Maico MI 26 Tympanometer/Audiometer combination unit (Maico Diagnostics, Inc.). Behavioral hearing thresholds were estimated using custom tracking software following Levitt (1971) using 2 dB steps.

Subjects were orally interviewed regarding mass-storage PLD use as well as previous PLD use (e.g., compact disc player, cassette player, etc.). All answers were recorded on a standard data sheet (Appendix A). During the initial interview no questions of hearing loss from PLD use were asked to try to reduce subject bias. All subjects were read identical instructions for each portion of the study including directions for setting the volume level for their PLD (Appendix B). Preferred sound pressure levels were measured in subjects' ear canals (MIRE technique; ISO, 2002) as well as in a Knowles Electronics DB100 ear simulator mounted on a KEMAR (ISO, 2004).

Subjects were asked to choose a preferred musical selection and adjust their ideal listening level in a quiet environment on their own device and headphones. Musical selection and genre were recorded on the data sheet. A 3 min sample was recorded in the subject's ear canal using a Knowles Electronics ER-7C probe microphone with the probe inserted within 2 mm of the tympanic membrane, confirmed using otoscopic inspection. A second 3 min recording of the same sample was made in the DB100 on a KEMAR. These recordings (in quiet) were then repeated in the presence of background noise (described below). Subjects were asked to adjust their preferred listening level to the previously identified musical selection in the presence of a digitally recorded environmental noise stimulus delivered via sound field speakers, with the subjects seated at 45° azimuth to the speakers. The level of the noise delivered to the subjects fluctuated from 78 to 81 dB sound pressure level (SPL) (81 dB SPL L_{eq}, SD=2.12) during the 3 min recording. These recordings were obtained in the ear canal and verified in KEMAR in the noise condition.

In-ear measurements were made using an Etymotic Research ER-7C probe-tube microphone with 0 dB gain at the pre-amplifier. Measurements in KEMAR were made by coupling the subjects' headphones to standard adult size artificial external pinnae. The DB-100 ear simulators of KEMAR were fitted with 0.5 in. occluding microphones (Etymotic Research ER-11, 0 dB gain). The diffuse-field inverse (DFI) filter on the ER11 pre-amplifier, enabled during these measurements, is an inverse filter of KEMAR's ear canal to diffuse-field response. Applying this inverse filter results in the diffuse-field equivalent of the recorded signal (Killion, 1979). The microphones (ER-7C or ER-11) were connected through their respective preamplifiers to an M-Audio Fast Track Pro, four-channel, 24 bit, firewire input/output device with a sampling rate of 48 000 Hz. Customized software (Electroacoustics Toolbox, Faber Acoustical Services and Technologies) controlled the digital recording of the signal and calculated noise dose, equivalent sound level (L_{Aeq}), measurements for the 3 min recording, with an exchange rate of 3 dB and using the *A*-weighting scale.

All recordings through the ER-7C and the ER-11 were stored and recordings from 23 of the 30 subjects could be processed offline to establish diffuse-field equivalence. A spectral average over the entire duration of each recorded sound file was measured using SysRes (Neely and Stevenson, 2002). With a sample rate of 44.1 kHz and an averaging buffer size of 2048 points, 3800 spectral averages were required to sample each 3 min recording. The power in each one-third octave band was weighted by the appropriate *A*-weighting factor and the total *A*-weighted sum of spectral energy was calculated. The DFI filter transfer function of the ER11 preamplifier was measured using SysRes and chirp excitation delivered through an ear-bud style earphone (SR =44.1 kHz, 100 averages into a 2048 point buffer), first with the DFI filter switched in, then with it switched out. This transfer function was used either to add or remove DFI filtering from the spectral averages of the ER-7C recordings prior to calculating *A*-weighted levels. This yielded measurements comparable to exposure standards developed for diffuse-field conditions. The recordings from the remaining seven subjects had been lost during data transfer between computers and hence could not be processed for this analysis.

The environmental noise was recorded using a Roland EDIROL R-1 portable digital recorder (24 bit, linear WAV file). The acoustic sensitivity of the recorder was calibrated using a 1000 Hz pure tone delivered via sound field speakers. The sound pressure level near the recorder's microphones was measured using a Quest Technologies 1800 Integrating sound level meter set to flat frequency weighting. Recordings and sound level measurements were made during rush hour on the Blue Line of the Chicago Transit Authorities (CTA) train system while going through the underground section, seated in the center of the train car, a common environment where PLDs are used in Chicago. The spectrum of the recorded noise is displayed in Fig. 1. The noise was played back at the level (81 dB SPL) measured in the train car at the time of the recording.

Following the recordings, subjects were interviewed regarding potential risk to hearing from using their mass-storage PLD. They were also asked whether they experience tinnitus following PLD use. Descriptive statistics were performed on the data set in the statistical computing environ-

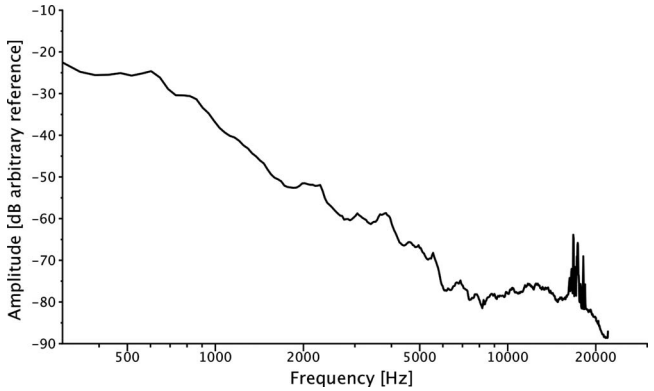

FIG. 1. Spectrum of noise recorded on a CTA train and played back at 80 dB SPL as the background noise.

ment R (R Development Core Team, 2006). A multiway-analysis of variance was also performed with L_{Aeq} measured in quiet and in noise as the dependent variables and gender, device, headphone type, and genre of music as the independent variables.

III. RESULTS

A. Listening Habits

23 subjects (77%) reported infrequent noise exposure (music concerts less than 2 times a year), and 7 subjects (23%) reported no exposure to noise in their everyday lives. Of the 23 subjects who reported infrequent noise exposure, only 4 (17% of the exposed subgroup; 13% of entire subject pool) reported routinely wearing some form of hearing protection while in noise, while an additional 4 (17% of exposed subgroup; 13% of entire subject pool) reporting infrequent use of hearing protection. 15 of the 23 subjects (65% of exposed subgroup; 50% of entire subject pool) reported not using any form of hearing protection while in noisy environments.

"Rock" was the most popular genre amongst our subjects followed by "Pop" and "Alternative Rock." Eighteen subjects (60%) used various models of an Apple iPod with several other devices being represented in approximately equal proportion with one subject (3%) using a multipurpose personal digital assistant as their device of choice. Subjects reported using the device on which measurements were made for an average of 13.2 months (SD=8.37; range =11 days to 36 months). All subjects reported using another type of PLD with headphones (cassette player, compact disc player, and/or another MP3 player) prior to acquiring the current device, with 19 subjects (63%) reported using two or more of these devices frequently in the past. Headphone style, make, and model were similarly varied with a large proportion of the subjects using "earbud" style headphones (73%) and none of the subjects using noise-isolating headphones. Reported use per week ranged from 1 day to 7 days with an average of 4.06 days (SD=1.99) (Fig. 2, bottom panel). Daily use ranged from 15 min to 4 h per day with an average of 1.68 h per day (SD=1.04) (Fig. 2, top panel). Thus, the group of subjects used their devices an average of 6.8 h per week (SD=5.89).

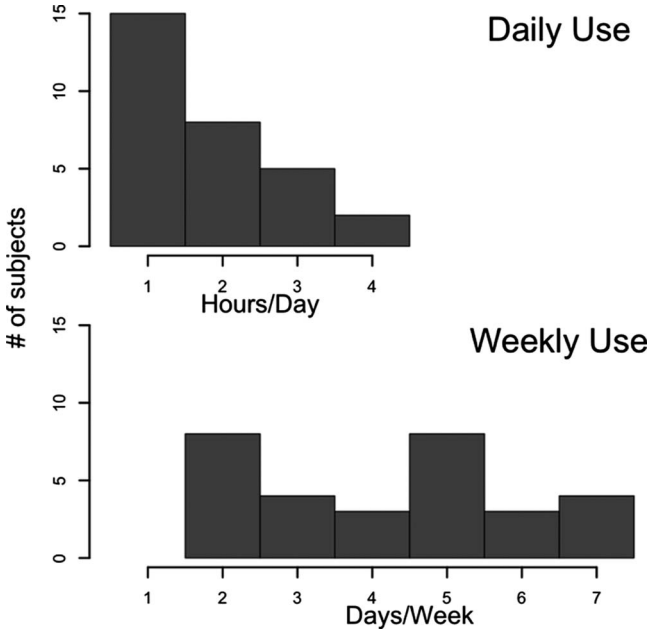

FIG. 2. Histograms of PLD use in hours/day (upper panel) and days/week (lower panel) for the 30 subjects.

B. Objective measurements

The A-weighted equivalent continuous noise level (L_{Aeq}) measured in the subjects' ear canal and in KEMAR in quiet is displayed in Fig. 3 along with a measure of exposure adjusted for the reported daily listening duration for each subject. L_{Aeq} is calculated as follows:

$$L_{eq} = 10 \log_{10}\left\{\left[(1/T)\int_{t1}^{t2} p_A^2(t)dt\right]/p_o^2\right\},$$

where $p_A^2(t)$ is the square of the instantaneous A-weighted sound pressure, in Pascals, as a function of time t for an averaging interval starting and ending at times t_1 and t_2, respectively, and p_o^2 represents the reference sound pressure of 20 μPa. If the exposure measurements are to be compared with NIOSH or OSHA standards, a transformation is necessary. In our application, we used the reported daily use for each subject to compute an L_{dpme} (daily personal music exposure) as follows:

$$L_{dpme} = L_{Aeq}(\text{in dBA}) + 10 \log[T/8],$$

where T is the reported use per day (in hours). Since we measured L_{Aeq} and then essentially used a 3 dB exchange rate to compute L_{dpme}, the values reported here are most applicable to the NIOSH risk criteria. In its derivation, L_{dpme} is identical to the computation for $L_{Aeq,d}$, where d is a duration other than 8 h. We choose to use the music-specific term L_{dpme} to emphasize the limitation of our measurement and computation to exposure related solely to the use of PLDs.

The box and whiskers in Fig. 3 represent the interquartile range with the whiskers extending to the greater of the range or 1.5 times the interquartile range. The symbols represent measurements from individual subjects with the open and closed symbols representing measurements below and above 85 dBA, respectively. The circles represent data from all 30 subjects while the squares represent the data from the

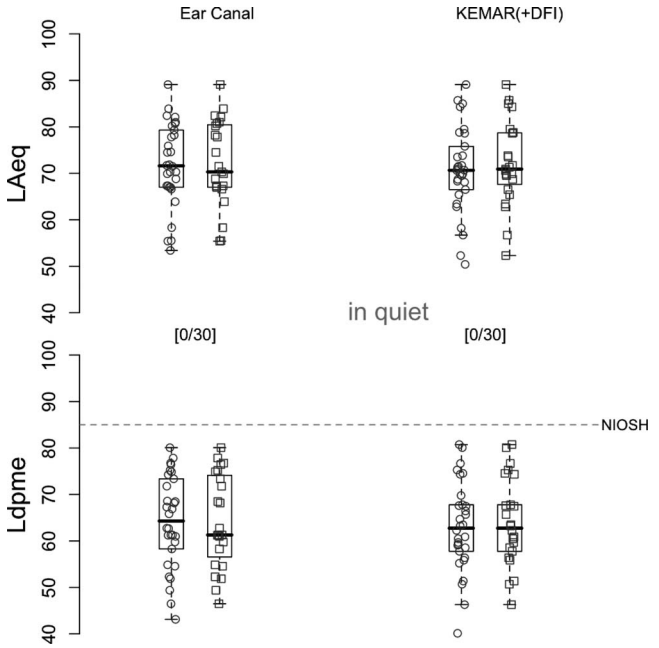

FIG. 3. Box-and-whisker plots comparing L_{Aeq} (top) and L_{dpme} (bottom) *in quiet* measured in the ear canal of individual subjects (left), and in KEMAR (right). The boxes span the interquartile range of the data with the whiskers extending to the greater of the range or 1.5 times the interquartile range. The solid line inside each box is the median. The dashed horizontal line in the bottom panel marks the limit of 85 dBA. See text for details on computation of L_{dpme}. The numbers in square brackets beside each data set show the number of subjects whose preferred listening level was equal to or greater than 85 dBA using that particular method of measurement (filled symbols). All open symbols represent data from subjects whose preferred listening level was lower than 85 dBA. The open and closed squares for each measure and measurement condition represent data from 23 of the 30 subjects, which were available for compensation for diffuse-field equivalent values. The circles, on the other hand, represent data from all 30 subjects.

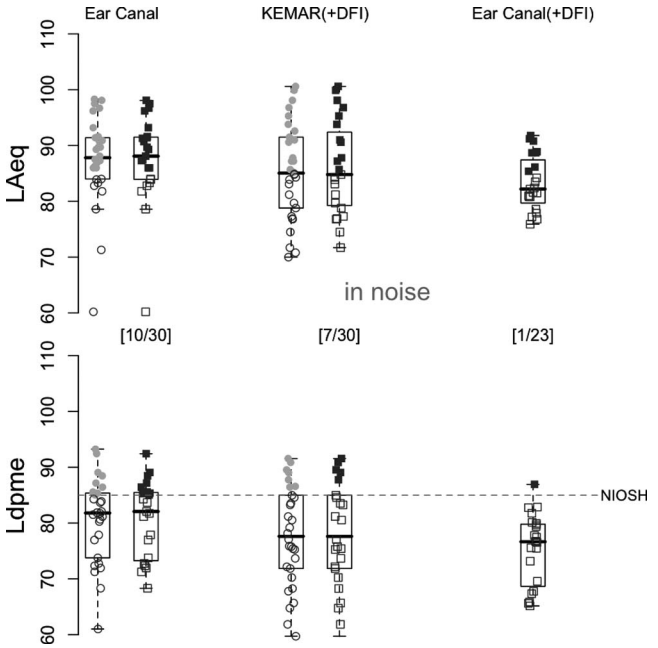

FIG. 4. Data similar to those in Fig. 3 but measured in noise. Measurements made in the ear canal and in KEMAR with DFI are presented with circles. Additionally, the ear-canal data from 23 subjects are presented in the rightmost column after equivalent diffuse-field compensation. This limited data set are for the ear-canal and KEMAR measurements are also presented in squares. Closed symbols represent preferred listening levels equal to or greater than 85 dBA. Circles and squares present data from all 30 subjects and the 23 subjects whose data were available for transformation, respectively.

limited set of 23 subjects whose ear-canal recordings were available for transformation to diffuse-field-equivalent values.

Measured L_{Aeq} in quiet (top left) ranged from 53.4 dBA to 89.1 dBA with a mean of 71.9 dBA (SD=8.9). One subject had L_{Aeq} values greater than or equal to 85 dBA. L_{Aeq} measured in KEMAR with DFI compensation are reported in the top right quadrant of Fig. 3. The data are presented in the same format as described for the ear-canal measures. L_{Aeq} in quiet in KEMAR ranged from 50.4 to 89.1 dBA with a mean of 70.7 dBA (SD=9.2). Three subjects had L_{Aeq} values greater than or equal to 85 dBA. Neither of these sets of measures is comparable to regulatory standards as listening duration is not taken into account, a hurdle in reporting personal damage risk in previously published work (Hodgetts *et al.*, 2007; Ahmed *et al.*, 2007).

Measured L_{dpme} in quiet are presented in the bottom panels of Fig. 3 for both ear-canal and KEMAR measurements. The ranges of L_{dpme} were 36.3–76.0 dBA and 39.3–76.08 dBA with mean (and standard deviations) of 57.5 (8.9) and 56.3 (9.8) dBA in the ear canal and the KEMAR, respectively. Although the measurements made in the KEMAR were lower than those made in individual ear canals (not DFI compensated) in the vast majority of our subjects, these differences were not found to be significantly different. The average L_{dpme} values (accounting for reported listening durations) were lower than the L_{Aeq} values by approximately 14 dB. The ear-canal measurements would have been lower (~6–8 dB estimate from our measurements) had we compensated them to express their diffuse-field equivalents.

Results of objective measurements made *in noise* are presented in Fig. 4. The format of the figure is similar to that of Fig. 3. In addition to the ear-canal and KEMAR data, the ear-canal data compensated for diffuse-field equivalence are presented in the right column. For the L_{Aeq} measurements (top row), mean (and standard deviation) values were 87.5 (7.8), 85.4 (8.5), and 82.01 (8.4) dBA for the ear canal, KEMAR, and DFI-compensated ear-canal recordings, respectively. For the L_{dpme} measurements (bottom row), mean (and standard deviation) values were 79.9 (9.1), 77.75 (8.9), and 74.14 (9.5) dBA for the ear canal, KEMAR, and compensated ear-canal recordings, respectively. The numbers of subjects at risk for L_{dpme} measured using each technique (ear canal, KEMAR, or DFI-compensated ear canal) are presented in square brackets in the bottom panel of Fig. 4. The portion of our subjects found to be at risk while listening in background noise varied greatly depending on the measurement used. 33% of our subjects were found to be at risk based on the L_{dpme} measured in the ear canal. In contrast, one (4%) of the subjects were found to be at risk based on the L_{dpme} computed after transforming the ear-canal recording to diffuse-field equivalence.

We have presented the data from the subset of 23 subjects for all conditions to demonstrate that the range and/or variance of the data set was not affected significantly due to the omission of the 7 subjects whose data were not available

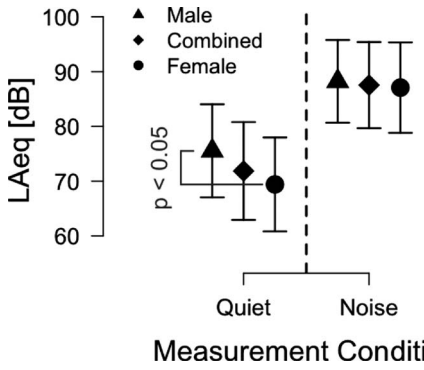

FIG. 5. Mean L_{Aeq} values in quiet (left) and in noise (right) for the entire subject pool and those for the male and female subjects. The error bars represent ±1 standard deviation.

for transformation to free-field equivalence. It is notable that the variance in the data is significantly reduced for the ear-canal data once compensated for diffuse-field equivalence.

The L_{Aeq} in the male participants was found to be 6.1 dB higher than the females in the quiet condition, and this difference was statistically significant ($p<0.05$) in a general linear model where gender, genre, device, and headphone types were all included as predictor variables without any interaction terms (Fig. 5). The main effect of gender was, however, not statistically significant ($p=0.06$) when the order of variables was changed on the right-hand-side of the model or when gender was used in isolation. A test of power revealed that a sample size of 32 in each gender-group would be needed to attain an effect size of 0.80 (confidence interval=95%) for gender if the difference between the two means (6.1 dB) and the standard deviation in the two samples (~8.5 dB) remained unchanged. The difference in L_{Aeq} between male and female subjects was smaller and not statistically significant in the noise condition. Similarly, no significant differences between male and female subjects were observed for L_{dpme}. The introduction of the background noise caused an average increase in L_{Aeq} by 15.7 dB.

IV. DISCUSSION

The possibility of increased incidence of hearing loss due to PLD use has been of recent interest in the popular media. Audiologists and other hearing health care professionals are often sought out as experts in this area. It is our responsibility to provide a realistic estimate of the potential problem and such estimates have to be based on accurate ecologically relevant measurements. Such empirical measurements then should be related to criteria for possible hearing damage for public consumption. Unfortunately, the only standards that allow any determination of damage risk were developed specifically for industrial noise and their application to music is not straightforward.

Previous work had time and again estimated that a vast majority of users of portable devices listen to them at safe levels (Rice *et al.*, 1987b; Wong *et al.*, 1990; Turumen-Rise *et al.*, 1991b). However, the alarm regarding the recent generation of PLDs was perhaps justified based on the capability of these devices to store more music and play the music back at hazardously high sound pressure levels (Fligor and Cox, 2004, Keith *et al.*, 2008). Objective measurements of preferred listening levels using modern-day PLDs have been missing from the debate. One peer-reviewed publication put 25% of the population "at risk" of listening at hazardous levels based on measurements made in KEMAR after randomly seeking participants from the street and not allowing the participants to adjust the volume control of their device prior to the measurement (Williams, 2005). Hodgetts *et al.* (2007) made similar measurements near the tympanic membrane of 38 individuals but could not relate their findings to NIOSH or OSHA standards as their measurements were not converted to their diffuse-field equivalent values. Further, one piece of music, limited in dynamic range to mimic industrial noise, was used for all subjects. While this approach makes the measures (when converted to diffuse-field equivalents) more comparable to NIOSH and OSHA standards, whether the volume setting is an accurate representation of an individual's habitual listening level is questionable. For example, a listener may "turn it up" for music they like but "turn it down" when the music is chosen by someone else and not liked as well. We deliberately chose to allow the individual to select the music thereby reducing the possibility of a bias towards lower listening levels. While this probably allowed greater accuracy in characterizing habitual listening levels, it makes comparison with OSHA and NIOSH standards less transparent.

Individual use over time (L_{dpme} rather than L_{Aeq}) and diffuse-field equivalency have been accounted for in this study to estimate the at-risk population. These estimates were based on standards-based measurement techniques and self-reported duration of use. Once these essential accommodations were made, one (4%) of the participants was found to be at risk *when listening in noise* using the stricter NIOSH benchmark for occupational noise exposure. In contrast, 7 of the 30 (23%) subjects would be categorized to be at risk if the measurements made in the KEMAR and then compensated for free-field equivalency. Our results are most directly comparable to, and in close agreement with those of Williams (2005). Williams (2005) reported an average L_{Aeq} of 86.1 dB measured in a manikin in the presence of background noise, comparable to the 85.4 dB reported here. Similarly, Williams (2005) reported an average value of 79.8 dB after accommodating for individual listening durations, comparable to the average L_{dpme} of 77.75 measured in the KEMAR in this data set. None of the participants would be considered at risk when listening in quiet, either with KEMAR or ear-canal recordings.

It was remarkable that the variance was significantly reduced in our free-field equivalent measures from the ear canal (MIRE technique, ISO, 2002). This transformation was only possible in 23 of the 30 subjects due to loss of data between computers. However, it is clear that the reduced variance is *not* a sampling error as the range of this reduced set is equivalent to the complete data set as seen by comparing the circles and squares for any measurement in Figs. 3 and 4. This would suggest that the subjects adjusted the listening levels to compensate for individual ear-canal acoustics, earphone frequency response, and fit and program material. The preferred listening level was relatively consistent

between subjects. It should also be noted that the transformation to diffuse-field equivalence does not scale all measures by a constant but rather is dependant on the spectrum of the music. The significant and important differences between the measurements made in KEMAR with the DFI filter activated (ISO, 2004) and the DFI-compensated ear-canal measurements (ISO, 2002) suggest that the latter is clearly the superior measure when assessing exposure from PLDs even with the use of an average transfer function, rather than individually measured ones. Our results seem to suggest that listeners choose a listening level from a relatively narrow range of levels which was by and large safe for our subjects, given their reported duration of use.

Given our small sample size and a biased population of a group of university students, our estimates of population at risk should not be extended to the general population. Caution has to be exercised in interpreting results from studies such as this one and projecting probable incidence of hearing loss from them. Even after the measurement is made using an appropriate diffuse-field compensation and an estimate of the daily listening duration is incorporated in computations, the comparison made is with standards developed specifically for industrial noise. Further, the use of specific types of background noise cannot be easily generalized to all listening situations. Perhaps most importantly, the bias introduced by participating in an experiment and selecting a preferred listening level knowing that an objective measurement is forthcoming cannot be accounted for. Finally, any additional exposure from other sources of noise is not accounted for in these computations, and hence may underestimate the true daily exposure of an individual.

Male participants were listening to the PLDs at a significantly higher level than female participants in quiet ($p < 0.05$). No gender-based difference was detected when the measurements were made in background noise. The difference in preferred listening level between male and female subjects was approximately 5 dB in our data set—in close alignment with other reports (Williams, 2005; Hodgetts *et al.*, 2007). No significant effects of gender were found on age and hearing thresholds, thus making the 5 dB difference between males and females an interesting yet unexplained phenomenon. The identification of physiological and psychological factors defining individuals who prefer to listen to music at levels higher than the general population may be an interesting and important area of research.

In the exit interview, close to three-quarters of our subjects were certain that they were not using their PLDs at levels harmful to their hearing and indeed they were not. However, 17% reported that they believed that they were using their devices at harmful levels. Encouragingly, an overwhelming majority of our subjects said that they would reduce their listening level or shorten their listening session if asked by a professional. These reported trends suggest that at least in a population equivalent in education and socioeconomic status to our subject pool, public awareness and education can play a very important role in preventing hearing loss due to over exposure from music delivered by PLDs.

V. CONCLUSIONS

Audiology and other professions related to hearing health care have received tremendous attention in the recent past with regard to PLD and the potential hazard they pose. Following a standardized and accepted protocol for accurate and consistent measurements that can be related to standards of damage risk is essential. We have demonstrated that the estimation of the population at risk varies significantly with the method used for measuring preferred listening levels. After comparing three methods of measurement, we recommend measurements made in the ear canal and then compensated for free-field equivalence, as described in ISO 11904-1 (ISO, 2002), as the method of choice. Further, we recommend incorporating daily listening durations, as we have done in our L_{dpme} computation, in risk assessment. We hope that such ecologically valid and accurate characterizations of listening levels will become the basis of risk projection and counseling.

ACKNOWLEDGMENTS

The research reported here was conducted as a Capstone project in the partial fulfillment of the Au.D. degree at Northwestern University (DW). The authors would like to thank Brian Fligor, Sc.D., for helpful discussions on topics related to his paper. They also thank the clinical staff at the Northwestern Hearing Clinic (Evanston) for the use of their testing suites, the members of the Auditory Research Laboratory at Northwestern University for their support. The Au.D. program at Northwestern University provided financial support to the project. The project was also partially supported by the NIH/NIDCD, Grant No. DC005692-04 to S.D.

APPENDIX A: DATA RECORDING SHEET

DATA SHEET
Subject ID#: _____ Date: _____
Filename: _____ Tester Initials: ___
Subject Demographics:
Age:_____
Sex: _____
Hearing History:

(1) Do you have any concerns with your hearing?
(2) History of ear infections?
(3) Have you ever been exposed to loud noises for long periods of time?
(4) In what environment?
(5) Do you wear hearing protection?
(6) Are you on any ototoxic medications (Aspirin, etc.)?
(7) Any ringing in your ears?
(8) Any head or neck surgeries within the last year?

Transducers: Make: _____
Model #: _____
Type:
☐ Circumaural
☐ Supra Aural
☐ Earbuds
☐ Ear Inserts

☐ Noise-Isolating
☐ Other

Initial Oral Interview:

(1) How long have you been using this particular device?
(2) On average for how many hours a day do you use your device under headphones?
(3) On average how many days a week do you use your device under headphones?
(4) What genre(s) of music do you generally listen to a majority of the time under headphones?
(5) In what situation do you listen to the device under headphones the majority of the time (e.g., home, train, while exercising, etc.)
(6) Do you listen to music through speakers? (i.e., computer speakers and stereo system)
(7) Have you previously used any of the following PLDs?:
☐ Personal cassette player
☐ Portable compact disc player
☐ Personal AM/FM Radio that required the use of headphones
☐ Other

Exit Oral interview:

(1) Can loud sounds cause damage to your hearing?
(2) Have you ever been educated on the risks to hearing from loud sounds?
(a) If so, when?
(b) Were you ever taught in middle or high school health class?

(3) Do you wish that you could turn your device up louder at anytime?
(a) If yes, when?

(4) Have you ever experienced a ringing (tinnitus) in your ears after using your device?
(a) If yes, how long did it last?

(5) Do you feel that you listen to your device at harmful levels?
(6) Do you feel that you are harming your hearing by using this device?
(a) If yes, do you plan to continue using this device?

(7) Do you feel that manufacturers should put a warning label about the potential risk to hearing from the maximum outputs of these devices?
(8) If you were warned that you are listening to your device under headphones at harmful levels and advised to turn it down/limit your daily use would you?

APPENDIX B: INSTRUCTIONS TO SUBJECTS

1. TRACKING

This test you will hear some tones. Once you begin to hear them, press and hold the mouse button. When you can no longer hear them, release the mouse button. Once you begin hearing them again, press and hold the mouse button until you can no longer hear them. Follow this pattern until you hear a bell, we will then move on to another tone. Do you have any questions?

2. CONDITION 1

You will set your preferred listening volume to your preferred musical selection. Please let me know the song title, band, and genre of music you will be selecting. I will be making a 3 min recording while your music is playing. During that time it is important that you do not talk. After the recording has ended, pause your selection and do not change the volume. I will take your device and place it on the manikin and make another 3 min recording. Any questions?

3. CONDITION 2

We will do the same thing again, but this time I will be playing train noise through the speakers. Again, set your preferred listening volume to your previously used musical selection. The recording will last 3 min. After the recording has ended, pause your selection and do not change the volume. I will make another recording on the manikin. Any questions?

Ahmed, S., Fallah, S., Garrido, B., Gross, A., King, M., Morrish, T., Pereira, D., Sharma, S., Zaszewska, E., and Pichora-Fuller, K. (**2007**). "Use of portable audio devices by university students," Can. Acoust. **35**, 35–52.

American National Standards Institute (ANSI) (**2004**). "Standards for audiometers," Standsard S3.6–2004.

Farina, A. (**2007**). *A Study of Hearing Damage Caused by Personal MP3 Players* (Audio Engineering Society, New York).

Fligor, B. J., and Cox, L. C. (**2004**). "Output levels of commercially available portable compact disc players and the potential risk to hearing," Ear Hear. **25**, 513–27.

Hodgetts, W. E., Rieger, J. M., and Szarko, R. A. (**2007**). "The effects of listening environment and earphone style on preferred listening levels of normal hearing adults using an MP3 player," Ear Hear. **28**, 290–297.

In-Stat (**2007**). "MP3 player market to reach 286 million units by 2010," In-Stat Market Track Research Press Release, http://www.instat.com/press.asp?ID=1648&sku=IN0603155ID (Last viewed May 24, 2006).

ISO (**2002**). "Acoustics—Determination of sound immission from sound sources placed close to the ear Part 1: Technique using a microphone in a real ear (MIRE technique)," ISO 11904-1, Switzerland.

ISO (**2004**). "Acoustics—Determination of sound immission from sound sources placed close to the ear Part 2: Technique using a manikin," ISO 11904-2, Switzerland.

Katz, A. E., Grestman, H. L., Sanderson, R. G., and Buchanan, R. (**1982**). "Stereo earphones and hearing loss," N. Engl. J. Med. **307**, 1460–1461.

Keith, S. E., Michaud, D. S., and Chiu, V. (**2008**). "Evaluating the maximum playback sound levels from portable digital audio players," J. Acoust. Soc. Am. **123**, 4227–4237.

Kenna, M. A. (**2008**). "Music to your ears: Is it a good thing?," Acta Paediatr. **97**, 151–152.

Killion, M. C. (**1979**). "Equalization filter for eardrum-pressure recording using a KEMAR manikin," J. Audio Eng. Soc. **27**, 13–16.

Levitt, H. (**1971**). "Transformed up-down methods in psychoacoustics," J. Acoust. Soc. Am. **49**, 467.

Nature Neuroscience (**2007**). "More noise than signal," Nat. Neurosci. **10**, 799.

Neely, S. T., and Stevenson, R. (**2002**). *SysRes* (Boys Town National Research Hospital, Omaha, NE), Technical Memo No. 19.

R Development Core Team (**2006**). "R: A language and environment for statistical computing," R Foundation for Statistical Computing, http://www.R-project.org (Last viewed September 10, 2008).

Reuters Press (**2005**). "Limit use of iPod earbuds to protect your ears," MSNBC Online, http://www.msnbc.msn.com/id/10648715/ (Last viewed May 26, 2006).

Rice, C. G., Breslin, M., and Roper, R. G. (**1987a**). "Sound levels from personal cassette players," Br. J. Audiol. **21**, 273–278.

Rice, C. G., Rossi, G., and Olina, M. (**1987b**). "Damage risk from personal cassette players," Br. J. Audiol. **21**, 279–288.

Turumen-Rise, I., Flottorp, G., and Tvete, O. (**1991a**). "Personal cassette players ('walkman'). Do they cause noise-induced hearing loss?," Scand. Audiol. **20**, 239–244.
Turumen-Rise, I., Flottorp, G., and Tvete, O. (**1991b**). "A study of the possibility of acquiring noise-induced hearing loss by the use of personal cassette players (walkman)," Scand. Audiol. **34**, 133–144.
Williams, W. (**2005**). "Noise exposure levels from personal stereo use," J. Acoust. Soc. Am. **44**, 231–236.
Wong, T. W., Van Hasselt, C. A., Tang, L. S., and Yiu, P. C. (**1990**). "The use of personal cassette players among youths and its effects on hearing," Public Health **104**, 327–330.
Wood, W. S. and Lipscomb, D. M. (**1972**). "Maximum available sound pressure levels from stereo components," J. Acoust. Soc. Am. **52**, 484–487.

Active noise control in a pure tone diffuse sound field using virtual sensing

D. J. Moreau,[a] J. Ghan, B. S. Cazzolato, and A. C. Zander
School of Mechanical Engineering, The University of Adelaide, Adelaide, South Australia 5005, Australia

(Received 19 June 2008; revised 22 March 2009; accepted 27 March 2009)

Local active noise control systems generate a zone of quiet at the physical error sensor using one or more secondary sources to cancel acoustic pressure and its spatial derivatives at the sensor location. The resulting zone of quiet is generally limited in size and as such, placement of the error sensor at the location of desired attenuation is required, which is often inconvenient. Virtual acoustic sensors overcome this by projecting the zone of quiet away from the physical sensor to a remote location. The work described here investigates the effectiveness of using virtual sensors in a pure tone diffuse sound field. Stochastically optimal virtual microphones and virtual energy density sensors are developed for use in diffuse sound fields. Analytical expressions for the controlled sound field generated with a number of control strategies are presented. These expressions allow the optimal control performance to be predicted. Results of numerical simulations and experimental measurements made in a reverberation chamber are also presented and compared.
 [DOI: 10.1121/1.3123404]

PACS number(s): 43.50.Ki [KAC] Pages: 3742–3755

I. INTRODUCTION

Local active noise control systems reduce the sound field at a number of points within the acoustic domain to create localized zones of quiet at the error sensors. While significant attenuation is achieved at the error sensor locations, the zone of quiet is generally small and impractically sized. Elliott *et al.*[1] investigated the spatial extent of the zone of quiet generated at the error sensor when controlling pressure with a single secondary source in a pure tone diffuse sound field. The zone of quiet generated at the microphone was found to be defined by a sinc function with the primary sound pressure level reduced by 10 dB over a distance of $\lambda/10$, where λ is the excitation wavelength. In an attempt to broaden the zone of quiet, Elliott and Garcia-Bonito[2] extended previous theory to the control of both pressure and pressure gradient in a diffuse sound field with two secondary sources. Minimizing both the pressure and pressure gradient along a single axis produced a 10 dB zone of quiet over a distance of $\lambda/2$ in the direction of pressure gradient measurement. This is a significant size increase in comparison to the zone of quiet obtained by canceling pressure alone.

Virtual acoustic sensors are used in active noise control systems to shift the zone of quiet to a desired location that is remote from the physical sensor. Garcia-Bonito and Elliott[3] and Garcia-Bonito *et al.*[4] investigated the performance of virtual sensors in a diffuse sound field using the virtual microphone arrangement.[5] The virtual microphone arrangement projects the zone of quiet away from the physical microphone using the assumption of equal primary pressure at the physical and virtual locations. A preliminary identification step is required in this virtual sensing method in which models of the transfer functions between the secondary source and microphones located at the physical and virtual locations are estimated. Garcia-Bonito *et al.*[4] investigated the performance of the virtual microphone arrangement in a local active headrest in a diffuse sound field. At low frequencies, below 500 Hz, the attenuation achieved at the virtual location with the virtual microphone arrangement is comparable to directly minimizing the signal of a physical microphone located there. At higher frequencies, however, limited attenuation is achieved at the virtual location due to the assumption relating to the similarity of the primary field at the physical and virtual locations being invalid. The remote microphone technique[6] is an extension to the virtual microphone arrangement that uses an additional filter to compute an estimate of the primary pressure at the virtual location from the primary pressure at the physical microphone location. The forward-difference extrapolation technique[7–14] is an alternative virtual sensing method that has several advantages. First the assumption of equal primary pressure at the physical and virtual locations does not have to be made but also preliminary identification is not required, nor are FIR filters or similar to model the complex transfer functions between the error sensors and the sources. Furthermore, this is a fixed gain prediction technique that can adapt to physical system changes, such as observer head movement, that may alter the complex transfer functions between the errors sensors and the control sources.

In this paper, the performance of virtual sensors is explored in a diffuse sound field. Stochastically optimal virtual microphones and virtual energy density sensors that use both pressure and pressure gradient sensors are developed specifically for use in pure tone diffuse sound fields. Of considerable significance is that this stochastically optimal virtual sensing technique, like the forward-difference extrapolation technique, does not require a preliminary identification stage nor models of the complex transfer functions between the error sensors and the sources.

[a]Author to whom correspondence should be addressed. Electronic mail: danielle.moreau@mecheng.adelaide.edu.au

TABLE I. Summary of research on local control strategies in a pure tone diffuse sound field.

Control strategy	Analytical analysis	Numerical analysis	Experimental analysis
1. Canceling the pressure at a point with one control source	Elliott *et al.*[a]	Elliott *et al.*[a] and Garcia-Bonito and Elliott[b]	Garcia-Bonito and Elliott[b,c]
2. Canceling the pressure and pressure gradient at a point with two control sources	Elliott and Garcia-Bonito[d] and Garcia-Bonito and Elliott[e]	Elliott and Garcia-Bonito[d] and Garcia-Bonito and Elliott[e,f]	
3. Canceling the pressures at two closely spaced points with two control sources	Elliott and Garcia-Bonito[d]	Elliott and Garcia-Bonito[d] and Garcia-Bonito and Elliott[e]	Miyoshi and Kaneda[g]
4. Canceling the pressures and pressure gradients at two closely spaced points with four control sources			
5. Canceling the pressures at four closely spaced points with four control sources			
6. Canceling the pressure at a virtual location with one control source using the pressure and pressure gradient at a point	Garcia-Bonito *et al.*[h]	Garcia-Bonito and Elliott[e] and Garcia-Bonito *et al.*[h]	Garcia-Bonito *et al.*[h]
7. Canceling the pressure at a virtual location with one control source using the pressures at two closely spaced points			
8. Canceling the pressure and pressure gradient at a virtual location with two control sources using the pressures and pressure gradients at two closely spaced points			
9. Canceling the pressure and pressure gradient at a virtual location with two control sources using the pressures at four closely spaced points			

[a]References 1 and 15.
[b]Reference 16.
[c]Reference 3.
[d]Reference 2.
[e]Reference 3.
[f]Reference 17.
[g]Reference 18.
[h]Reference 4.

The nine local control strategies analyzed in this paper are listed in Table I. The analytical expressions for the controlled sound field generated with these control strategies can be found in Ref. 19 or derived using the procedure outlined in Sec. II. For brevity, only the analytical expressions for control strategies 1, 6, and 8 are included in this paper. These expressions predict the optimal control performance obtained in a pure tone diffuse sound field and thus set performance limits for the maximum achievable attenuation for each of the sensing and control strategies. The optimal expressions for the controlled sound field generated with all nine control strategies are validated in numerically simulated and post-processed experimental control.

Table I also provides a summary of prior research conducted in a pure tone diffuse sound field, including analytical, numerical, or experimental analysis of any of the nine control strategies. This paper compares all nine control strategies using all three analysis methods. As shown in Table I, expressions for the controlled sound field generated with control strategies 1, 2, and 3 have been previously derived, and control strategies 1 and 3 have been experimentally validated. Also, control strategy 6 has been previously derived using the virtual microphone arrangement; however, it is investigated in this paper using the derived stochastically optimal virtual sensing method for pure tone diffuse sound fields. As shown in Table I, this paper validates and extends previous research to analytically, numerically, and experimentally analyze a broader range of local control strategies in a pure tone diffuse sound field. On a final note, a diffuse sound field is the most complex sound field to control and hence provides a lower limit on the performance that can be expected in practice,[2] and the results presented here provide a guide to the minimum control performance that is likely to be achieved in any sound field.

II. THEORETICAL BACKGROUND

This section presents the background theory required for deriving the analytical expressions for the controlled sound field generated with any of the nine control strategies listed in Table I. Analytical expressions for the controlled sound field generated with control strategies 1, 6, and 8 are presented in Secs. II A–II C. The analytical expressions for the controlled sound field generated with the remaining control strategies can be found in Ref. 19 or derived using the procedure outlined here. Derivations of the stochastically opti-

mal diffuse field virtual sensing technique for control strategies 6 and 8 are also presented in Secs. II B and II C.

For the present study, the primary acoustic field is considered diffuse and the sound field contributions due to each of the secondary sources are modeled as uncorrelated single diffuse acoustic fields. The secondary acoustic sound fields may be modeled as diffuse if each of the secondary sources is several wavelengths away from the cancellation region and remote from all other sources.[5]

In the following, a single diffuse acoustic field is denoted by the subscript i and the total acoustic field, given by superposition of each of the single diffuse acoustic fields, is indicated by a lack of subscript. The pressure at a point $\mathbf{x}$ in a single diffuse acoustic field is given by $p_i(\mathbf{x})$ and the x-axis component of pressure gradient at a point $\mathbf{x}$ in this field is given by $g_i(\mathbf{x})$.

For a displacement vector, $\mathbf{r}=r_x\mathbf{i}+r_y\mathbf{j}+r_z\mathbf{k}$, the following functions are defined:

$$A(\mathbf{r}) = \mathrm{sinc}(k|\mathbf{r}|), \tag{1}$$

$$B(\mathbf{r}) = \frac{\partial A(\mathbf{r})}{\partial r_x} = -k\left(\frac{\mathrm{sinc}(k|\mathbf{r}|)-\cos(k|\mathbf{r}|)}{k|\mathbf{r}|}\right)\left(\frac{r_x}{|\mathbf{r}|}\right), \tag{2}$$

$$C(\mathbf{r}) = \frac{\partial^2 A(\mathbf{r})}{\partial r_x^2} = -k^2\left[\mathrm{sinc}(k|\mathbf{r}|)\left(\frac{r_x}{|\mathbf{r}|}\right)^2 + \left(\frac{\mathrm{sinc}(k|\mathbf{r}|)-\cos(k|\mathbf{r}|)}{(k|\mathbf{r}|)^2}\right)\left(1-3\left(\frac{r_x}{|\mathbf{r}|}\right)^2\right)\right]. \tag{3}$$

The correlations between the pressures and pressure gradients at two different points $\mathbf{x}_j$ and $\mathbf{x}_k$ separated by $\mathbf{r}$ are given by[2]

$$\langle p_i(\mathbf{x}_j)p_i^\star(\mathbf{x}_k)\rangle = A(\mathbf{r})\langle|p_i|^2\rangle, \tag{4}$$

$$\langle p_i(\mathbf{x}_j)g_i^\star(\mathbf{x}_k)\rangle = -B(\mathbf{r})\langle|p_i|^2\rangle, \tag{5}$$

$$\langle g_i(\mathbf{x}_j)p_i^\star(\mathbf{x}_k)\rangle = B(\mathbf{r})\langle|p_i|^2\rangle, \tag{6}$$

$$\langle g_i(\mathbf{x}_j)g_i^\star(\mathbf{x}_k)\rangle = -C(\mathbf{r})\langle|p_i|^2\rangle, \tag{7}$$

where $\langle\cdot\rangle$ denotes spatial averaging and $\star$ indicates complex conjugation. In the case that $\mathbf{x}_j$ and $\mathbf{x}_k$ are at the same point, the limits of $A(\mathbf{r})$, $B(\mathbf{r})$, and $C(\mathbf{r})$ as $\mathbf{r}\to 0$ must be taken, yielding

$$\langle p_i(\mathbf{x}_j)p_i^\star(\mathbf{x}_j)\rangle = \langle|p_i|^2\rangle, \tag{8}$$

$$\langle p_i(\mathbf{x}_j)g_i^\star(\mathbf{x}_j)\rangle = 0, \tag{9}$$

$$\langle g_i(\mathbf{x}_j)p_i^\star(\mathbf{x}_j)\rangle = 0, \tag{10}$$

$$\langle g_i(\mathbf{x}_j)g_i^\star(\mathbf{x}_j)\rangle = (k^2/3)\langle|p_i|^2\rangle. \tag{11}$$

If there are m sensors in the field, then define $\mathbf{p}$ as an $m\times 1$ matrix whose elements are the relevant pressures or pressure gradients measured by the sensors. The pressure and the pressure gradient at any point in the diffuse sound field can be expressed as the weighted sum of the m components, each of which are perfectly correlated with a corresponding element of $\mathbf{p}_i$, and a component that is perfectly uncorrelated with each of the elements. In a single diffuse acoustic field, the pressure and pressure gradient at each position $\mathbf{x}$ can be written as[1]

$$p_i(\mathbf{x}) = \mathbf{H}_p(\mathbf{x})\mathbf{p}_i + p_{i,u}(\mathbf{x}), \tag{12}$$

$$g_i(\mathbf{x}) = \mathbf{H}_g(\mathbf{x})\mathbf{p}_i + g_{i,u}(\mathbf{x}), \tag{13}$$

where $\mathbf{H}_p(\mathbf{x})$ and $\mathbf{H}_g(\mathbf{x})$ are matrices of real scalar weights, which are functions of the position $\mathbf{x}$ only and $p_{i,u}(\mathbf{x})$ and $g_{i,u}(\mathbf{x})$ are perfectly uncorrelated with the elements of $\mathbf{p}_i$. It can be shown, by postmultiplying the expressions for $p_i(\mathbf{x})$ and $g_i(\mathbf{x})$ by $\mathbf{p}_i^{\mathrm{H}}$ and spatially averaging, that

$$\mathbf{H}_p(\mathbf{x}) = \mathbf{L}_p(\mathbf{x})\mathbf{M}^{-1}, \tag{14}$$

$$\mathbf{H}_g(\mathbf{x}) = \mathbf{L}_g(\mathbf{x})\mathbf{M}^{-1}, \tag{15}$$

where

$$\mathbf{L}_p(\mathbf{x}) = \frac{\langle p_i(\mathbf{x})\mathbf{p}_i^{\mathrm{H}}\rangle}{\langle|p_i|^2\rangle}, \tag{16}$$

$$\mathbf{L}_g(\mathbf{x}) = \frac{\langle g_i(\mathbf{x})\mathbf{p}_i^{\mathrm{H}}\rangle}{\langle|p_i|^2\rangle}, \tag{17}$$

$$\mathbf{M} = \frac{\langle \mathbf{p}_i\mathbf{p}_i^{\mathrm{H}}\rangle}{\langle|p_i|^2\rangle}. \tag{18}$$

$\mathbf{L}_p(\mathbf{x})$, $\mathbf{L}_g(\mathbf{x})$, and $\mathbf{M}$ can be determined using Eqs. (4)–(11) and therefore weight matrices $\mathbf{H}_p(\mathbf{x})$ and $\mathbf{H}_g(\mathbf{x})$ can also be found.

By postmultiplying the expression for $p_i(\mathbf{x})$ in Eq. (12) by its adjoint and spatially averaging, it can be shown that the uncorrelated component of pressure at the position $\mathbf{x}$ is

$$\langle|p_{i,u}(\mathbf{x})|^2\rangle = (1-\mathbf{L}_p(\mathbf{x})\mathbf{M}^{-1}\mathbf{L}_p^{\mathrm{H}}(\mathbf{x}))\langle|p_i|^2\rangle, \tag{19}$$

where $\mathbf{M}$ is self-adjoint. The total acoustic field, produced by superposition of the primary acoustic field and the acoustic field contributions due to each of the secondary sources, is

$$p(\mathbf{x}) = \sum_i p_i(\mathbf{x}) = \mathbf{H}_p(\mathbf{x})\mathbf{p} + \sum_i p_{i,u}(\mathbf{x}). \tag{20}$$

If the secondary sources are used to drive each of the elements of $\mathbf{p}$ to zero, then only the uncorrelated components remain and the resulting acoustic field is given by

$$p(\mathbf{x}) = p_u(\mathbf{x}) = \sum_i p_{i,u}(\mathbf{x}). \tag{21}$$

The uncorrelated components of each of the diffuse acoustic fields are uncorrelated with each other if the assumption is made that the secondary sources are all several wavelengths apart. Therefore the mean squared pressure at the point $\mathbf{x}$ can be expressed as

$$\begin{aligned}\langle|p(\mathbf{x})|^2\rangle &= \sum_i \langle|p_{i,u}(\mathbf{x})|^2\rangle \\ &= (1-\mathbf{L}_p(\mathbf{x})\mathbf{M}^{-1}\mathbf{L}_p^{\mathrm{H}}(\mathbf{x}))\sum_i\langle|p_i|^2\rangle \\ &= (1-\mathbf{L}_p(\mathbf{x})\mathbf{M}^{-1}\mathbf{L}_p^{\mathrm{H}}(\mathbf{x}))\langle|p|^2\rangle,\end{aligned} \tag{22}$$

where $\langle|p|^2\rangle$ is the mean squared pressure after control.

A. Control strategy 1: Canceling the pressure at a point with one control source

Control strategy 1 involves canceling the pressure at a point with a single control source. The pressure at a single location $\mathbf{x}_1$ is to be sensed and therefore the matrix $\mathbf{p}$ is given by

$$\mathbf{p} = [p(\mathbf{x}_1)]. \tag{23}$$

When a single control source is used to drive $p(\mathbf{x}_1)$ to zero, applying Eq. (22) and using Eqs. (4) and (8) to find $\mathbf{L}_p(\mathbf{x})$ and $\mathbf{M}$ give the mean squared pressure at the point $\mathbf{x}$ as

$$\begin{aligned}\langle|p(\mathbf{x})|^2\rangle &= (1 - A^2(\mathbf{x} - \mathbf{x}_1))\langle|p|^2\rangle \\ &= (1 - \mathrm{sinc}^2(k|\mathbf{x} - \mathbf{x}_1|))\langle|p|^2\rangle,\end{aligned} \tag{24}$$

which is the same as that previously derived by Elliott *et al.*[1]

The mean squared pressure of the total acoustic field, $\langle|p|^2\rangle$, is given by the sum of the mean squared pressure of the primary diffuse acoustic field, $\langle|p_p|^2\rangle$, and the mean squared pressure of the secondary diffuse acoustic field, $\langle|p_s|^2\rangle$. The distribution of the random variable $\beta = \langle|p_s|^2\rangle / \langle|p_p|^2\rangle$ is the $f_{2,2}$ distribution,[20] if the source and cancellation points are randomly selected, as previously shown by Elliott *et al.*[1] The increase in mean squared pressure of the acoustic field after control, α, is

$$\alpha = \frac{\langle|p|^2\rangle}{\langle|p_p|^2\rangle} = \frac{\langle|p_p|^2\rangle + \langle|p_s|^2\rangle}{\langle|p_p|^2\rangle} = 1 + \beta. \tag{25}$$

By substituting $\beta = \alpha - 1$ into the $f_{2,2}$ distribution, α has probability density and cumulative distribution functions given by

$$f_{\alpha_1}(\alpha) = \frac{1}{\alpha^2}, \quad \alpha \geq 1, \tag{26}$$

$$F_{\alpha_1}(\alpha) = \frac{\alpha - 1}{\alpha}, \quad \alpha \geq 1. \tag{27}$$

The relative change in mean squared pressure at the point $\mathbf{x}$, as a function of α, is therefore given by

$$\begin{aligned}\frac{\langle|p(\mathbf{x})|^2\rangle}{\langle|p_p(\mathbf{x})|^2\rangle} &= (1 - \mathrm{sinc}^2(k|\mathbf{x} - \mathbf{x}_1|))\frac{\langle|p|^2\rangle}{\langle|p_p|^2\rangle} \\ &= (1 - \mathrm{sinc}^2(k|\mathbf{x} - \mathbf{x}_1|))\alpha.\end{aligned} \tag{28}$$

B. Control strategy 6: Canceling the pressure at a virtual location with one control source using the pressure and pressure gradient at a point

Instead of canceling the measured quantities (pressure and pressure gradient), control strategy 6 involves minimizing the pressure at a virtual location $\mathbf{x}_0$ with a single control source. To create a virtual microphone, the pressure at the virtual location, $p(\mathbf{x}_0)$, must be estimated from measured quantities, in this case $p(\mathbf{x}_1)$ and $g(\mathbf{x}_1)$. The matrix $\mathbf{p}$ is given by

$$\mathbf{p} = [p(\mathbf{x}_1)g(\mathbf{x}_1)]^T. \tag{29}$$

As stated in Eq. (12), the pressure at any point $\mathbf{x}$ is given by

$$p(\mathbf{x}) = \mathbf{H}_p(\mathbf{x})\mathbf{p} + p_u(\mathbf{x}). \tag{30}$$

Therefore the pressure at any point $\mathbf{x}$ can be expressed as the sum of two components, one of which is perfectly correlated with the elements of $\mathbf{p}$, and a perfectly uncorrelated component. If only the measured quantities $p(\mathbf{x}_1)$ and $g(\mathbf{x}_1)$ are known, the best possible estimate of $p_u(\mathbf{x})$ is zero since it is perfectly uncorrelated with the measured signals. Therefore, the best estimate of the pressure, $p(\mathbf{x})$, is given by the component perfectly correlated with the elements of $\mathbf{p}$. Subsequently the best estimate of the pressure at the virtual location, $\mathbf{x}_0$, is

$$\hat{p}(\mathbf{x}_0) = \mathbf{H}_p(\mathbf{x}_0)\mathbf{p}. \tag{31}$$

The matrix of weights $\mathbf{H}_p(\mathbf{x}_0)$ is found to be

$$\mathbf{H}_p(\mathbf{x}_0) = \mathbf{L}_p(\mathbf{x}_0)\mathbf{M}^{-1} = \left[A(\mathbf{x}_0 - \mathbf{x}_1) - \frac{3}{k^2}B(\mathbf{x}_0 - \mathbf{x}_1)\right], \tag{32}$$

where Eqs. (4)–(11) have been used to find matrices $\mathbf{L}_p(\mathbf{x})$ and $\mathbf{M}$. The best estimate of the pressure at the virtual location, $\mathbf{x}_0$, is therefore given by

$$\hat{p}(\mathbf{x}_0) = A(\mathbf{x}_0 - \mathbf{x}_1)p(\mathbf{x}_1) - \frac{3}{k^2}B(\mathbf{x}_0 - \mathbf{x}_1)g(\mathbf{x}_1). \tag{33}$$

This diffuse field extrapolation method fits a sinc type function to the known data unlike the traditional forward-difference virtual microphone prediction technique that fits a polynomial to the measured quantities.

As the distance between $\mathbf{x}_0$ and $\mathbf{x}_1$ increases, the pressure estimate, $\hat{p}(\mathbf{x}_0)$, approaches zero. This is because the pressure at the virtual location and the known quantities become uncorrelated as the distance between $\mathbf{x}_0$ and $\mathbf{x}_1$ increases. This is the case for any virtual sensor in a diffuse sound field. If none of the distances between the virtual location and the physical sensors are small, then the pressure and pressure gradient at the virtual location will be uncorrelated with the measured quantities and the best estimate of the pressure and pressure gradient at the virtual location will be close to zero.

When the estimate of the pressure at the virtual location, $\hat{p}(\mathbf{x}_0)$, given in Eq. (33), is canceled in a pure tone diffuse sound field, the total complex pressure at a position $\mathbf{x}$, where $\mathbf{x} = \mathbf{x}_0 + \boldsymbol{\Delta}\mathbf{x}$, is given by $p(\mathbf{x})$. The total complex pressure, $p(\mathbf{x})$, can be decomposed into two components. The first is a component perfectly spatially correlated with the estimate of the pressure at the virtual location, $\hat{p}(\mathbf{x}_0)$, and the second is a component perfectly spatially uncorrelated with $\hat{p}(\mathbf{x}_0)$. The total complex pressure at any point $\mathbf{x}$ is the sum of these two components and may be written as

$$p(\mathbf{x}) = h_{pp}(\mathbf{x})\hat{p}(\mathbf{x}_0) + p_{uu}(\mathbf{x}), \tag{34}$$

where $h_{pp}(\mathbf{x})$ is a function of the distance $\mathbf{x}$ and $p_{uu}(\mathbf{x})$ is perfectly uncorrelated with $\hat{p}(\mathbf{x}_0)$. By postmultiplying the ex-

pression for $p(\mathbf{x})$ by $\hat{p}^{\star}(\mathbf{x}_0)$ and spatially averaging, it can be shown that

$$\langle p(\mathbf{x})\hat{p}^{\star}(\mathbf{x}_0)\rangle = h_{pp}(\mathbf{x})\langle|\hat{p}(\mathbf{x}_0)|^2\rangle. \tag{35}$$

Using Eqs. (4) and (5), the correlation between the total complex pressure at $\mathbf{x}$ and the estimate of the pressure at the virtual location can be written as

$$\langle p(\mathbf{x})\hat{p}^{\star}(\mathbf{x}_0)\rangle = \left(A(\mathbf{x}_0-\mathbf{x}_1)A(\mathbf{x}-\mathbf{x}_1) + \frac{3}{k^2}B(\mathbf{x}_0-\mathbf{x}_1)B(\mathbf{x}-\mathbf{x}_1)\right)\langle|p|^2\rangle. \tag{36}$$

Using Eqs. (8)–(11) and (33), it can be shown that the mean squared pressure estimate at the virtual location is related to the total mean squared pressure by

$$\langle|\hat{p}(\mathbf{x}_0)|^2\rangle = \left(A^2(\mathbf{x}_0-\mathbf{x}_1) + \frac{3}{k^2}B^2(\mathbf{x}_0-\mathbf{x}_1)\right)\langle|p|^2\rangle. \tag{37}$$

By substituting Eqs. (36) and (37) into Eq. (35), the weight function $h_{pp}(\mathbf{x})$ is found to be

$$h_{pp}(\mathbf{x}) = \frac{A(\mathbf{x}_0-\mathbf{x}_1)A(\mathbf{x}-\mathbf{x}_1) + \frac{3}{k^2}B(\mathbf{x}_0-\mathbf{x}_1)B(\mathbf{x}-\mathbf{x}_1)}{A^2(\mathbf{x}_0-\mathbf{x}_1) + \frac{3}{k^2}B^2(\mathbf{x}_0-\mathbf{x}_1)}. \tag{38}$$

The space-average mean squared pressure at $\mathbf{x}$, which is uncorrelated with $\hat{p}(\mathbf{x}_0)$, is obtained by multiplying both sides of Eq. (34) by their conjugates and spatially averaging. Using Eqs. (37) and (38), the space-average uncorrelated pressure may be written as

$$\langle|p_{uu}(\mathbf{x})|^2\rangle = \left(1 - \frac{\left(A(\mathbf{x}_0-\mathbf{x}_1)A(\mathbf{x}-\mathbf{x}_1) + \frac{3}{k^2}B(\mathbf{x}_0-\mathbf{x}_1)B(\mathbf{x}-\mathbf{x}_1)\right)^2}{A^2(\mathbf{x}_0-\mathbf{x}_1) + \frac{3}{k^2}B^2(\mathbf{x}_0-\mathbf{x}_1)}\right)\langle|p|^2\rangle. \tag{39}$$

If $\hat{p}(\mathbf{x}_0)$ is canceled with a single secondary source, the residual pressure at $\mathbf{x}$ is, according to Eq. (34), $p_{uu}(\mathbf{x})$ only. Therefore, the mean squared pressure at a position $\mathbf{x}$ in the controlled sound field is given by Eq. (39). When the pressure at the virtual location, $\mathbf{x}_0$, estimated using the pressure and pressure gradient at the point $\mathbf{x}_1$, is canceled with a single secondary source, the relative change in mean squared pressure at a point $\mathbf{x}$ in the controlled sound field is given by

$$\frac{\langle|p(\mathbf{x})|^2\rangle}{\langle|p_p|^2\rangle} = \left(1 - \frac{\left(A(\mathbf{x}_0-\mathbf{x}_1)A(\mathbf{x}-\mathbf{x}_1) + \frac{3}{k^2}B(\mathbf{x}_0-\mathbf{x}_1)B(\mathbf{x}-\mathbf{x}_1)\right)^2}{A^2(\mathbf{x}_0-\mathbf{x}_1) + \frac{3}{k^2}B^2(\mathbf{x}_0-\mathbf{x}_1)}\right)\alpha. \tag{40}$$

If $\mathbf{x}_0=\mathbf{x}_1$, then $\hat{p}(\mathbf{x}_0)=p(\mathbf{x}_1)$ and this control strategy is equivalent to control strategy 1, minimizing the pressure at a point with a single control source.

C. Control strategy 8: Canceling the pressure and pressure gradient at a virtual location with two control sources using the pressures and pressure gradients at two points

Control strategy 8 involves minimizing the pressure and pressure gradient at a virtual location $\mathbf{x}_0$, generating a virtual energy density sensor. In order to do this, the pressure, $p(\mathbf{x}_0)$, and pressure gradient, $g(\mathbf{x}_0)$, at the virtual location must be estimated from measured quantities, in this case $p(\mathbf{x}_1)$, $p(\mathbf{x}_2)$, $g(\mathbf{x}_1)$, and $g(\mathbf{x}_2)$. The matrix $\mathbf{p}$ is given by

$$\mathbf{p} = [p(\mathbf{x}_1)p(\mathbf{x}_2)g(\mathbf{x}_1)g(\mathbf{x}_2)]^T. \tag{41}$$

With reference to Eqs. (12) and (13), the pressure and pressure gradient at the virtual location $\mathbf{x}_0$ can be expressed as the sum of two components, one of which is perfectly correlated with the elements of $\mathbf{p}$, and an uncorrelated component. If only the measured quantities $p(\mathbf{x}_1)$, $p(\mathbf{x}_2)$, $g(\mathbf{x}_1)$, and $g(\mathbf{x}_2)$ are known, the best possible estimates of $p_u(\mathbf{x})$ and $g_u(\mathbf{x})$ are zero since they are perfectly uncorrelated with the measured signals. Therefore, the best estimates of the pressure and pressure gradient at the virtual location are given by

$$\hat{p}(\mathbf{x}_0) = \mathbf{H}_p(\mathbf{x}_0)\mathbf{p}, \tag{42}$$

$$\hat{g}(\mathbf{x}_0) = \mathbf{H}_g(\mathbf{x}_0)\mathbf{p}. \tag{43}$$

Weight matrices $\mathbf{H}_p(\mathbf{x}_0)$ and $\mathbf{H}_g(\mathbf{x}_0)$ can be found as

$$\begin{aligned}\mathbf{H}_p(\mathbf{x}_0) &= \mathbf{L}_p(\mathbf{x}_0)\mathbf{M}^{-1} \\ &= [\mathrm{H}_{pp1}(\mathbf{x}_0)\mathrm{H}_{pp2}(\mathbf{x}_0)\mathrm{H}_{pg1}(\mathbf{x}_0)\mathrm{H}_{pg2}(\mathbf{x}_0)],\end{aligned} \tag{44}$$

$$\begin{aligned}\mathbf{H}_g(\mathbf{x}_0) &= \mathbf{L}_g(\mathbf{x}_0)\mathbf{M}^{-1} \\ &= [\mathrm{H}_{gp1}(\mathbf{x}_0)\mathrm{H}_{gp2}(\mathbf{x}_0)\mathrm{H}_{gg1}(\mathbf{x}_0)\mathrm{H}_{gg2}(\mathbf{x}_0)],\end{aligned} \tag{45}$$

where matrices $\mathbf{L}_p(\mathbf{x}_0)$, $\mathbf{L}_g(\mathbf{x}_0)$, and $\mathbf{M}$ are found using Eqs. (4)–(11). Weight matrices $\mathbf{H}_p(\mathbf{x}_0)$ and $\mathbf{H}_g(\mathbf{x}_0)$ can be used in Eqs. (42) and (43) to give estimates of the pressure and pressure gradient at the virtual location.

When the estimates of the pressure and pressure gradient at $\mathbf{x}_0$ are canceled in a pure tone diffuse sound field, the total complex pressure at a position $\mathbf{x}$, where $\mathbf{x}=\mathbf{x}_0+\Delta\mathbf{x}$, is given by $p(\mathbf{x})$. The total complex pressure, $p(\mathbf{x})$, can be decomposed into three components. The first is a component perfectly spatially correlated with the estimate of the pressure, $\hat{p}(\mathbf{x}_0)$, the second is a component perfectly spatially correlated with the estimate of the pressure gradient, $\hat{g}(\mathbf{x}_0)$, and the third is a component perfectly spatially uncorrelated with both $\hat{p}(\mathbf{x}_0)$ and $\hat{g}(\mathbf{x}_0)$, $p_{uu}(\mathbf{x})$. The total complex pressure at any point $\mathbf{x}$ is the sum of these three components and may be written as

$$p(\mathbf{x}) = h_{pp}(\mathbf{x})\hat{p}(\mathbf{x}_0) + h_{pg}(\mathbf{x})\hat{g}(\mathbf{x}_0) + p_{uu}(\mathbf{x}), \tag{46}$$

where the weight functions $h_{pp}(\mathbf{x})$ and $h_{pg}(\mathbf{x})$ are functions of the distance $\mathbf{x}$, and may be found using the procedure outlined in Sec. II B, and are given by

$$h_{pp}(\mathbf{x}) = \frac{P_{px}}{P_0}, \tag{47}$$

$$h_{pg}(\mathbf{x}) = \frac{P_{gx}}{G_0}, \tag{48}$$

where

$$\begin{aligned}P_{px} = {} & \mathrm{H}_{pp1}(\mathbf{x}_0)A(\mathbf{x}-\mathbf{x}_1) + \mathrm{H}_{pp2}(\mathbf{x}_0)A(\mathbf{x}-\mathbf{x}_2) \\ & - \mathrm{H}_{pg1}(\mathbf{x}_0)B(\mathbf{x}-\mathbf{x}_1) - \mathrm{H}_{pg2}(\mathbf{x}_0)B(\mathbf{x}-\mathbf{x}_2),\end{aligned} \tag{49}$$

$$\begin{aligned}P_{gx} = {} & \mathrm{H}_{gp1}(\mathbf{x}_0)A(\mathbf{x}-\mathbf{x}_1) + \mathrm{H}_{gp2}(\mathbf{x}_0)A(\mathbf{x}-\mathbf{x}_2) \\ & - \mathrm{H}_{gg1}(\mathbf{x}_0)B(\mathbf{x}-\mathbf{x}_1) - \mathrm{H}_{gg2}(\mathbf{x}_0)B(\mathbf{x}-\mathbf{x}_2),\end{aligned} \tag{50}$$

and

$$\begin{aligned}P_0 = {} & (\mathrm{H}_{pp1}(\mathbf{x}_0)\mathrm{H}_{pp2}(\mathbf{x}_0) + \mathrm{H}_{pp2}(\mathbf{x}_0)\mathrm{H}_{pp1}(\mathbf{x}_0))A(\mathbf{x}_2-\mathbf{x}_1) \\ & + (\mathrm{H}_{pp2}(\mathbf{x}_0)\mathrm{H}_{pg1}(\mathbf{x}_0) - \mathrm{H}_{pg2}(\mathbf{x}_0)\mathrm{H}_{pp1}(\mathbf{x}_0))B(\mathbf{x}_1-\mathbf{x}_2) \\ & + (\mathrm{H}_{pp1}(\mathbf{x}_0)\mathrm{H}_{pg2}(\mathbf{x}_0) - \mathrm{H}_{pg1}(\mathbf{x}_0)\mathrm{H}_{pp2}(\mathbf{x}_0))B(\mathbf{x}_2-\mathbf{x}_1) \\ & - \mathrm{H}_{pg1}(\mathbf{x}_0)\mathrm{H}_{pg2}(\mathbf{x}_0)C(\mathbf{x}_2-\mathbf{x}_1) \\ & - \mathrm{H}_{pg2}(\mathbf{x}_0)\mathrm{H}_{pg1}(\mathbf{x}_0)C(\mathbf{x}_1-\mathbf{x}_2) + \mathrm{H}_{pp1}^2(\mathbf{x}_0) \\ & + \mathrm{H}_{pp2}^2(\mathbf{x}_0) + \frac{k^2}{3}(\mathrm{H}_{pg1}^2(\mathbf{x}_0) + \mathrm{H}_{pg2}^2(\mathbf{x}_0)),\end{aligned} \tag{51}$$

$$\begin{aligned}G_0 = {} & (\mathrm{H}_{gp1}(\mathbf{x}_0)\mathrm{H}_{gp2}(\mathbf{x}_0) + \mathrm{H}_{gp2}(\mathbf{x}_0)\mathrm{H}_{gp1}(\mathbf{x}_0))A(\mathbf{x}_2-\mathbf{x}_1) \\ & + (\mathrm{H}_{gp2}(\mathbf{x}_0)\mathrm{H}_{gg1}(\mathbf{x}_0) - \mathrm{H}_{gg2}(\mathbf{x}_0)\mathrm{H}_{gp1}(\mathbf{x}_0))B(\mathbf{x}_1-\mathbf{x}_2) \\ & + (\mathrm{H}_{gp1}(\mathbf{x}_0)\mathrm{H}_{gg2}(\mathbf{x}_0) - \mathrm{H}_{gg1}(\mathbf{x}_0)\mathrm{H}_{gp2}(\mathbf{x}_0))B(\mathbf{x}_2-\mathbf{x}_1) \\ & - \mathrm{H}_{gg1}(\mathbf{x}_0)\mathrm{H}_{gg2}(\mathbf{x}_0)C(\mathbf{x}_2-\mathbf{x}_1) \\ & - \mathrm{H}_{gg2}(\mathbf{x}_0)\mathrm{H}_{gg1}(\mathbf{x}_0)C(\mathbf{x}_1-\mathbf{x}_2) + \mathrm{H}_{gp1}^2(\mathbf{x}_0) \\ & + \mathrm{H}_{gp2}^2(\mathbf{x}_0) + \frac{k^2}{3}(\mathrm{H}_{gg1}^2(\mathbf{x}_0) + \mathrm{H}_{gg2}^2(\mathbf{x}_0)).\end{aligned} \tag{52}$$

The space-average mean squared pressure at $\mathbf{x}$, which is uncorrelated with both $\hat{p}(\mathbf{x}_0)$ and $\hat{g}(\mathbf{x}_0)$, is obtained by multiplying both sides of Eq. (46) by their conjugates and spatially averaging. Using Eqs. (47) and (48), the space-average uncorrelated pressure is found to be

$$\langle|p_{uu}(\mathbf{x})|^2\rangle = \left(1 - \left(\frac{P_{px}^2}{P_0} + \frac{P_{gx}^2}{G_0}\right)\right)\langle|p|^2\rangle. \tag{53}$$

If $\hat{p}(\mathbf{x}_0)$ and $\hat{g}(\mathbf{x}_0)$ are both canceled with two secondary sources, the residual pressure at a point $\mathbf{x}$ is, according to Eq. (46), $p_{uu}(\mathbf{x})$ only. Therefore, the mean squared pressure at a position $\mathbf{x}$ in the controlled sound field is given by

$$\langle|p(\mathbf{x})|^2\rangle = \left(1 - \left(\frac{P_{px}^2}{P_0} + \frac{P_{gx}^2}{G_0}\right)\right)\langle|p|^2\rangle. \tag{54}$$

When the pressure and pressure gradient at the virtual location, $\mathbf{x}_0$, estimated using the pressures and pressure gradients at the points $\mathbf{x}_1$ and $\mathbf{x}_2$, are canceled with two secondary sources, the relative change in mean squared pressure is given by

$$\frac{\langle|p(\mathbf{x})|^2\rangle}{\langle|p_p|^2\rangle} = \left(1 - \left(\frac{P_{px}^2}{P_0} + \frac{P_{gx}^2}{G_0}\right)\right)\alpha. \tag{55}$$

III. DIFFUSE FIELD SIMULATIONS

The performance of the nine local active noise control strategies was evaluated using a MATLAB simulation. Quadratic optimization[21] was used to simulate control, giving the limit on the maximum achievable feedforward control performance. The objective of quadratic optimization is to calculate the optimal control source strengths required to minimize a desired cost function, in this case the total physical or virtual quantities measured at the sensors.

The acoustic field was simulated using the analytical model described by Bullmore *et al.*[22] This analytical model assumes that the pressure at any point in the acoustic enclosure can be calculated using a finite modal summation. The complex pressure amplitude at any point $\mathbf{x}$ is given by

$$p(\mathbf{x},\omega) = \sum_{n=0}^{N} \psi_n(\mathbf{x})a_n(\omega) = \mathbf{\Psi}^T\mathbf{a}, \tag{56}$$

where the summation consists of N normal modes with normalized mode shape functions $\psi_n(\mathbf{x})$ and complex modal amplitudes $a_n(\omega)$. Nth order vectors of these quantities are given by $\mathbf{\Psi}$ and $\mathbf{a}$, whose nth order components are $\psi_n(\mathbf{x})$ and $a_n(\omega)$, respectively. The vector $\mathbf{a}$ can be considered as a linear superposition of contributions from a primary source

and a series of M secondary sources. Therefore $\mathbf{a}$ may be written as

$$\mathbf{a} = \mathbf{a}_p + \mathbf{B}\mathbf{q}_s, \tag{57}$$

where $\mathbf{a}_p$ is the vector of complex modal amplitudes $a_{pn}(\omega)$ due to the primary source, $\mathbf{q}_s$ is the Mth order vector of complex secondary source strengths $q_{sm}(\omega)$, and $\mathbf{B}$ is the $N \times M$ matrix of modal excitation coefficients $B_{nm}(\omega)$, connecting the excitation of the nth mode to the mth secondary source.

Morse's solution[23] was used to describe the form of the sound field in the rectangular enclosure. The normalized mode shape functions are given by

$$\psi_n(\mathbf{x}) = \sqrt{\varepsilon_{n_1}\varepsilon_{n_2}\varepsilon_{n_3}}\cos(n_1\pi x_1/L_1)\cos(n_2\pi x_2/L_2) \times \cos(n_3\pi x_3/L_3), \tag{58}$$

where n_1, n_2, and n_3 are integer modal indices and L_1, L_2, and L_3 are the enclosure dimensions. The normalization factors are $\varepsilon_\nu = 1$ if $\nu = 0$ and $\varepsilon_\nu = 2$ if $\nu > 0$, so that $\int_V \psi_n^2 dV = V$, where V is the enclosure volume. In the computer simulation, the primary and secondary sources are assumed to be point monopoles at positions $\mathbf{y}_p$ and $\mathbf{y}_s$, respectively. Therefore the complex amplitude of the nth mode due to the primary source, with source strength q_p, is

$$a_{pn}(\omega) = \frac{\rho V}{c}\frac{\omega}{2\xi_n\omega_n\omega - j(\omega_n^2 - \omega^2)}\psi_n(\mathbf{y}_p)q_p, \tag{59}$$

and the modal excitation coefficients of the mth secondary source are given by

$$B_{nm}(\omega) = \frac{\rho V}{c}\frac{\omega}{2\xi_n\omega_n\omega - j(\omega_n^2 - \omega^2)}\psi_n(\mathbf{y}_{sm}), \tag{60}$$

where ρ and c are the density and speed of sound in the medium and ξ_n and ω_n are the damping ratio and natural frequency of the nth mode, respectively.

The enclosure model used in this simulation was that described by Elliott *et al.*[1] and was rectangular in shape with dimensions $\pi \times e \times 1$ m^3. The constant damping ratio was set to be 0.0014 and the Schroeder frequency[24] was calculated as 400 Hz. An excitation frequency of 1.5 kHz was used and all modes with natural frequencies below 2 kHz were included so that the total number of modes was approximately 8000. A number of sources (dependent on the control strategy) were randomly located within the enclosure such that they were not within a wavelength of one another, or the enclosure walls. The average mean squared pressure[1] of the total controlled pressure field was computed over 200 source configurations at various distances in the x-direction from the point of cancellation. The results from these simulations are presented in Sec. V A.

IV. DIFFUSE FIELD EXPERIMENTS

Experiments were also conducted to validate the analytical expressions and the numerical simulations. Post-processed control was implemented computationally using transfer functions experimentally measured in the reverberation chamber in the School of Mechanical Engineering at the University of Adelaide. The chamber has dimensions $6.840 \times 5.660 \times 4.720$ m^3, a volume of 183 m^3, and a Schroeder frequency[24] of 391 Hz. In the chamber, a condenser microphone and a Microflown, to measure pressure and pressure gradient, respectively, were mounted to a stepper-motor traverse. This enabled measurement over a $465 \times 360 \times 320$ mm^3 volume, with the target zone of quiet being approximately located at the center of the volume. Six loudspeakers located near the corners of the room and sufficiently far apart as to produce uncorrelated sound fields were used to either generate the primary sound field or to act as control sources. Such an arrangement allowed for a large number of combinations of primary and secondary sources to be used. The sources were driven with a multi-tonal signal containing tones from 800 to 3000 Hz in 50 Hz increments using a dSpace DS1104 card. For each speaker acting as the source in turn, the sound field in the room was allowed to stabilize, then the complex transfer functions between each of the sources and the sensors were measured. The average diffuse field zone of quiet was estimated by calculating the mean squared average of the controlled sound fields over a number of data sets (dependent on control strategy) and dividing it by the mean squared average of the primary fields. To obtain a large number of data sets to provide the spatial average, a number of different points in the field were selected as the sensor location, while ensuring that the relative arrangement of sensors remained constant. At each of the sensor locations, one of the loudspeakers was selected as the primary source and then a suitable number of secondary sources (dependent on control strategy) were selected from the remaining loudspeakers. This process was repeated for a large number of primary and secondary source combinations at each sensor location.

V. RESULTS

Figures 1 and 2 show the control profiles obtained with each of the nine control strategies in a pure tone diffuse sound field. The zones of quiet generated in numerically simulated and post-processed experimental control are shown, together with the analytical expressions for the relative change in mean squared pressure after control. In Figs. 1 and 2 the solid vertical lines indicate the positions of the physical sensors while the dashed vertical line indicates the virtual location. Using control strategy 6 as an illustrative case, the control profiles obtained in analytical, numerically simulated, and post-processed experimental controls are shown in Fig. 1(b), where a single secondary source has been used to minimize the pressure at the virtual location, estimated using the pressure and pressure gradient at a point. The analytical zone of quiet in this figure has been generated using Eq. (40) for the relative change in mean squared pressure after control. The numerically simulated and post-processed experimental control profiles have been generated using Eq. (33) to estimate the pressure at the virtual location.

A. Numerically simulated results

Figure 1(a) shows the relative change in the mean squared pressure of the sound field when the pressure at a

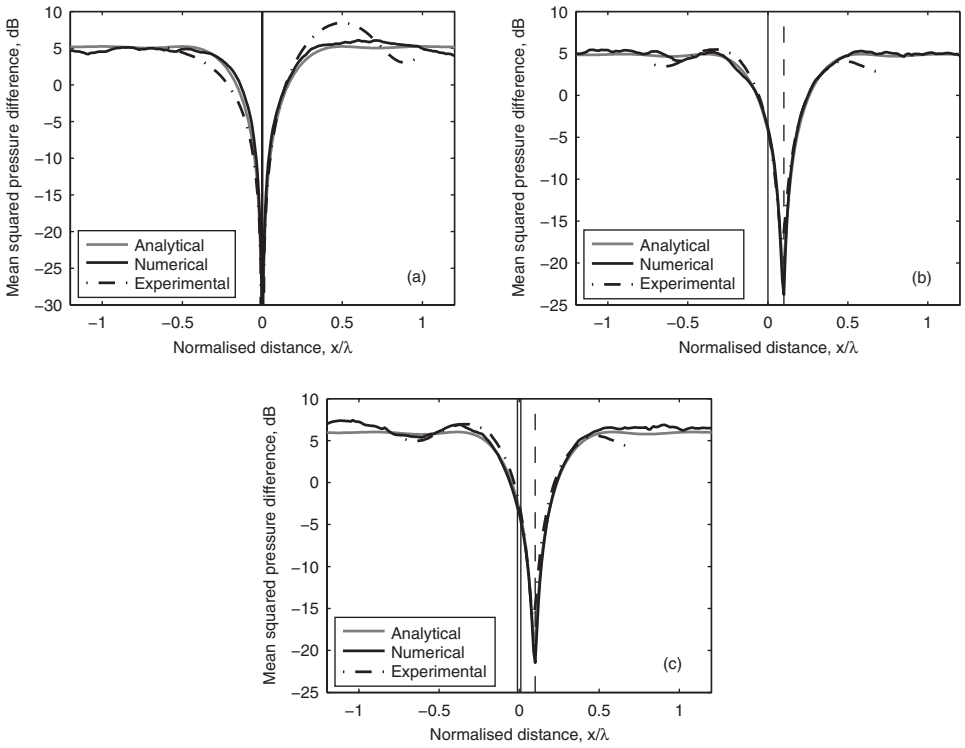

FIG. 1. Control profiles achieved in analytical, numerically simulated, and post-processed experimental control with control strategies employing a single source and error sensor: (a) Control strategy 1. (b) Control strategy 6. (c) Control strategy 7. Solid vertical lines indicate the positions of the physical sensors while the dashed vertical line indicates the virtual location.

point is canceled with a single control source. The mean squared pressure change is plotted against the distance from the point of pressure cancellation, for a value $\alpha=2$, the 50th percentile value of α obtained in the numerical simulation. Figure 1(a) reveals that the simulated results close to the point of cancellation are a good fit to the analytical function. When minimizing the pressure at a point with a single control source, the random variable α has the cumulative distribution given in Eq. (27). Such a distribution means that the increase in space-average mean squared pressure after control does not have a finite mean value. However, in practice, the strength of the secondary source is limited, which will prevent α from having a theoretically infinite mean value. Figure 3 shows the cumulative distribution function of the random variable α observed in the numerical simulation compared to the analytical distribution function. The distribution computed from 600 simulations is seen to be a good fit to the analytical function and indicates that sufficient modes have been included in the simulations. The 50th percentile value of α is approximately 2 for cancellation of pressure at a point with a single control source as seen in Fig. 3. For a value of $\alpha=2$, the 10 dB zone of quiet observed in the simulation is a sphere of approximately $\lambda/10$, as shown in Fig. 1(a). The same result was found by Elliott *et al.*[1]

Figure 2(a) illustrates the control profile achieved with an energy density sensor (pressure and pressure gradient) and two control sources in a diffuse sound field, for a value of $\alpha=3.4$. The analytical function clearly gives a good prediction of the zone of quiet obtained in the numerical simulation. The distribution of the random variable α observed in the numerical simulation, when two control sources are used, is shown in Fig. 4(a). Again, α does not have a finite mean value; however, in practice, the mean squared pressure after control will be limited by the secondary source strengths. The 50th percentile value of α observed in the numerical simulation is approximately 3.4 for cancellation of pressure and pressure gradient at a point with two control sources. For a value of $\alpha=3.4$, the 10 dB zone of quiet observed in the simulation has a diameter of $\lambda/2$ in the direction of pressure gradient cancellation. The same result was found by Elliott and Garcia-Bonito[2] and Garcia-Bonito and Elliott.[3] This is a fivefold increase in the size of the zone of quiet compared to that obtained by canceling pressure alone. Similar control performance is achieved by minimizing the pressures at two points with two control sources as shown in Fig. 2(b). Again, this is the same result found by Elliott and Garcia-Bonito[2] and Garcia-Bonito and Elliott.[3]

Superior control performance is achieved using energy density sensors at two points with four control sources, as shown in Fig. 2(c), for a value of $\alpha=5.6$. Again, numerically simulated results close to the point of cancellation are a good fit to the analytical function. When four control sources are used, the random variable α has the distribution shown in Fig. 4(a). Similarly to the previous two distributions, it does not have a finite mean value, but will in practice be limited by the strengths of the secondary sources. The 50th percentile value of α observed in the numerical simulation is approximately 5.6 for cancellation of pressure and pressure gradient at two points with four control sources. For a value of $\alpha=5.6$, the 10 dB zone of quiet observed in the simulation has a diameter of λ in the direction of pressure gradient measurement, as shown in Fig. 2(c). This is a tenfold increase compared to using a single microphone with one control source or a doubling compared to using a single energy density sensor with two control sources. The same result can be achieved by minimizing the pressures at four points with four control sources, as shown in Fig. 2(d).

Control with a virtual microphone, using the measured

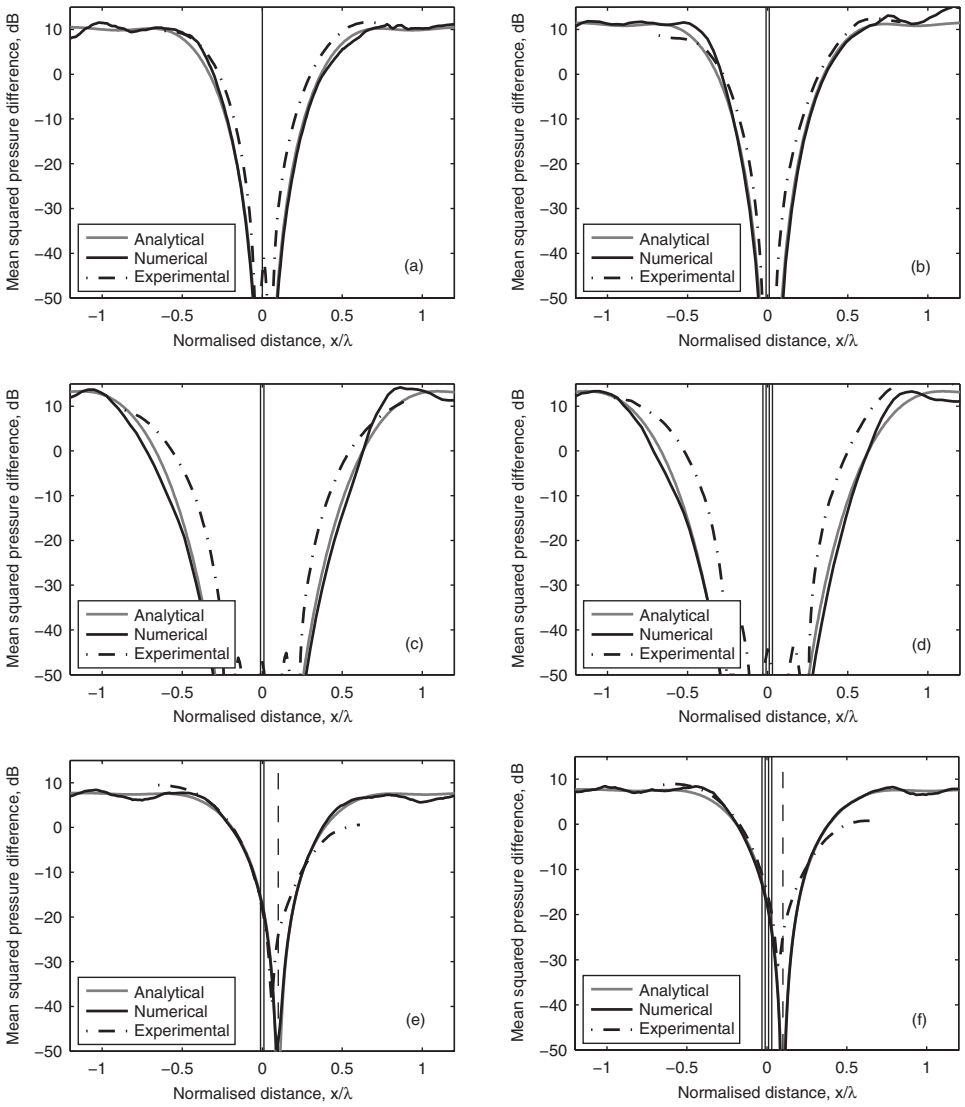

FIG. 2. Control profiles achieved in analytical, numerically simulated, and post-processed experimental control with control strategies employing multiple sensors and secondary sources: (a) Control strategy 2. (b) Control strategy 3. (c) Control strategy 4. (d) Control strategy 5. (e) Control strategy 8. (f) Control strategy 9. Control profiles obtained with post-processed experimental data are generated by removing any ill-conditioning. Solid vertical lines indicate the positions of the physical sensors while the dashed vertical line indicates the virtual location.

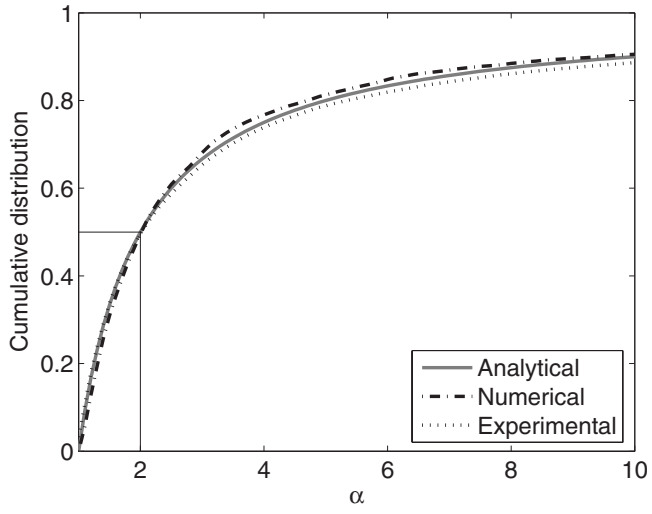

FIG. 3. Cumulative distributions for α obtained in numerically simulated and post-processed experimental control when using control strategy 1 compared to the analytical $F_{2,2}$ distribution. The 50th percentile value of α is indicated by a solid vertical line.

pressure and pressure gradient at a point, is shown in Fig. 1(b), for a value of $\alpha=2$. Figure 1(b) reveals that the numerically simulated results close to the point of cancellation are a good fit to the analytical function. The distribution of the random variable α, observed in the simulation of virtual microphone control, is equal to the $F_{\alpha,1}$ distribution given in Eq. (27) as demonstrated in Fig. 4(b). For the 50th percentile value of $\alpha=2$, a maximum attenuation of 24 dB and a 10 dB zone of quiet with diameter of approximately $\lambda/10$ are generated at the virtual location in the simulation. Figure 1(c) shows that similar control performance can be obtained using the pressures at two points to estimate the pressure at a virtual location. In comparison to the performance of conventional control strategies, a virtual microphone achieves higher attenuation at the virtual location than a single microphone and one control source or an energy density sensor and two control sources. Conventional control strategies employing four control sources achieve significantly higher attenuation at the virtual location than a virtual microphone and a single control source. The increase in attenuation at the virtual location achieved with four secondary sources is, however, most likely accompanied by an increase in sound pressure level away from the point of cancellation. This is

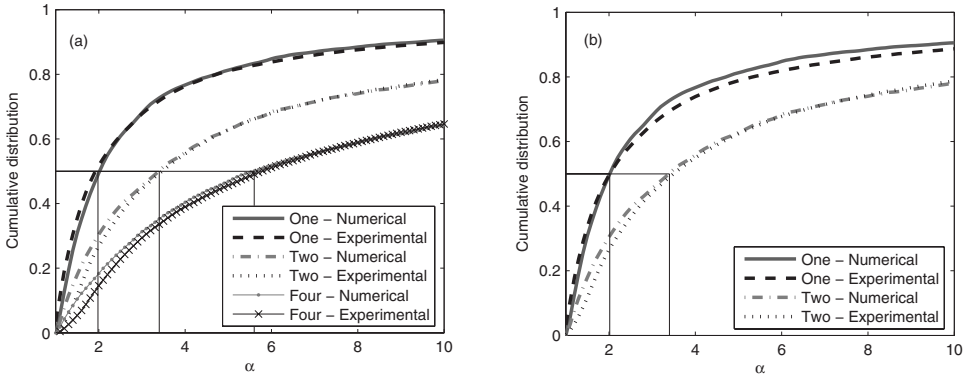

FIG. 4. Cumulative distributions for α obtained in numerically simulated and post-processed experimental control: (a) Conventional control strategies 1 (one control source), 2 or 3 (two control sources), and 4 or 5 (four control sources). (b) Virtual control strategies 6 or 7 (one control source) and 8 or 9 (two control sources). 50th percentile values of α are indicated by solid vertical lines.

indicated by the median (50th percentile) value of α being only 2 for a single control source and 5.6 for four control sources. As found in previous research, the size of the 10 dB zone of quiet achieved at the virtual location with the stochastically optimal diffuse field virtual sensing method and the virtual microphone arrangement is similar at low frequencies. However, at frequencies above 500 Hz, the stochastically optimal diffuse field virtual sensing method outperforms the virtual microphone arrangement because the assumption of equal sound pressure at the physical and virtual locations is no longer valid and the zone of quiet achieved at the virtual location with the virtual microphone arrangement is severely reduced.[3,4]

Control with a virtual energy density sensor and two control sources produces a superior control profile to that achieved with a virtual microphone and a single control source. This is indicated by the zone of quiet in Fig. 2(e), for a value of $\alpha=3.4$, where the pressure and pressure gradient at a virtual location are estimated using the measured pressures and pressure gradients at two points. Again, numerically simulated results close to the point of cancellation are a good fit to the analytical function. A maximum attenuation of 50 dB and a 10 dB zone of quiet with diameter of approximately $\lambda/2$ are achieved at the virtual location in the simulation. A similar result is obtained using the pressures at four points to estimate the pressure and pressure gradient at the virtual location as shown in Fig. 2(f). The distribution of the random variable α, when using two control sources and a virtual energy density sensor, is shown in Fig. 4(b). This figure indicates that the distribution for α is equal when using either a physical or virtual energy density sensor and two control sources. Comparison of Figs. 4(a) and 4(b) illustrates that the distribution of α is only dependent on the number of control sources and not on the control strategy. In comparing the performance of virtual energy density sensors to that of conventional control strategies, a virtual energy density sensor achieves significantly higher attenuation at the virtual location than a single microphone and one control source or an energy density sensor and two control sources. Conventional control strategies employing four control sources achieve similar levels of attenuation at the virtual location to a virtual energy density sensor and two control sources. The increase in mean squared pressure after control will, however, most likely be higher when four control sources are used compared to only two control sources. This is indicated by the median (50th percentile) value of α being approximately 3.4 for two control sources and 5.6 for four control sources.

B. Experimental results

Figure 1 shows the performance of control strategies employing a single error sensor and control source, for a value of $\alpha=2$. Using the post-processed experimental data, minimizing either the measured or estimated pressure generates a zone of quiet with diameter of $\lambda/10$ at the physical and virtual locations, respectively. This agrees well with the analytical and the numerically simulated results presented earlier. The distributions of the random variable α observed in post-processed experimental control are shown in Figs. 3 and 4. The distributions are seen to be a good fit with those observed in the simulations.

In comparison to previous experimental results, Garcia-Bonito and Elliott[3,16] also found that the 10 dB zone of quiet obtained by minimizing the pressure at a physical microphone is a sphere with a diameter of $\lambda/10$ in a pure tone diffuse sound field at high frequencies. It was also shown that minimizing the pressure at the surface of a rigid object tends to extend the zone of quiet beyond that achieved in the absence of the diffracting object.[3,16] As stated previously, minimizing the pressure estimated at the virtual location with the stochastically optimal diffuse field virtual sensing method generates a zone of quiet the same size as that achieved by minimizing the measured pressure. The same experimental result was observed at low frequencies by Garcia-Bonito *et al.*[4] for the virtual microphone arrangement. The attenuation achieved at the virtual location with the virtual microphone arrangement is, however, severely reduced at higher frequencies due to the assumption of equal sound pressure at the physical and virtual locations being invalid.

While the performance of control strategies employing a single error sensor and control source is as expected, control strategies employing multiple sensors and secondary sources achieve poorer experimental control than expected from the analytical and numerically simulated results. An example of the poor experimental performance of control strategies employing multiple sensors and secondary sources is shown in Fig. 5. With the raw experimental post-processed data, minimizing the pressure and pressure gradient at a point with two control sources generates a zone of quiet with a diameter of

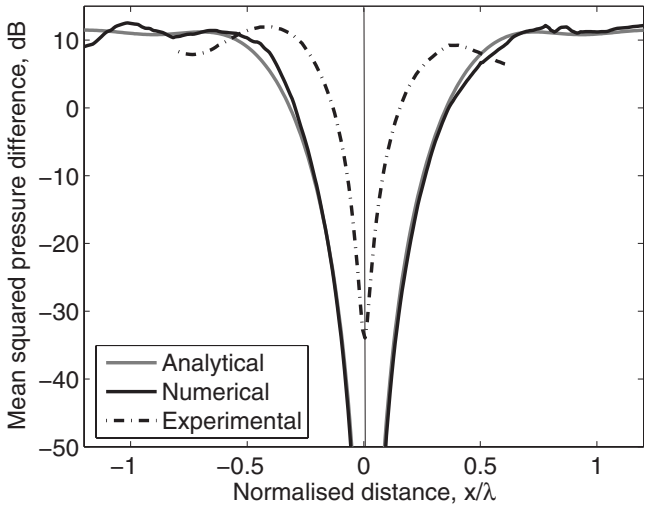

FIG. 5. Example of the effect of ill-conditioning in post-processed experimental results using control strategy 2. The solid vertical line indicates the position of the physical sensors.

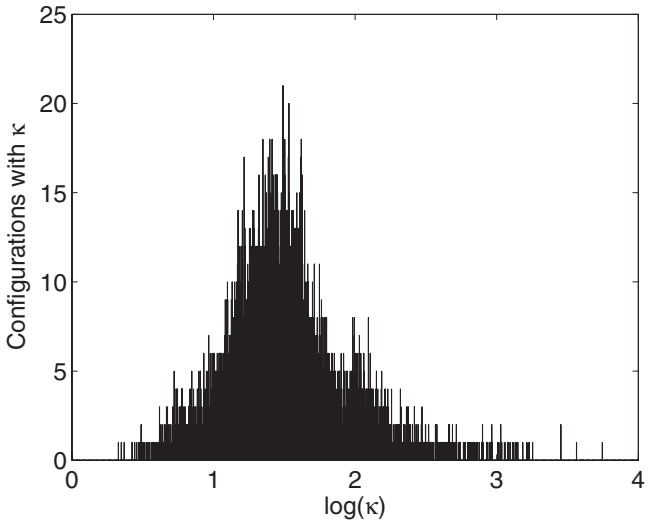

FIG. 6. Distribution of the condition number, κ, for control strategy 2.

$\lambda/5$ in the direction of pressure gradient measurement. This is significantly smaller than the zone of quiet with diameter of $\lambda/2$ obtained in analytical and numerically simulated results. A 15 dB reduction in maximum attenuation can also be seen at the sensor location in post-processed experimental results.

1. Improving conditioning

The poor experimental performance of strategies employing multiple sensors and secondary sources is attributed to ill-conditioning. Quadratic optimization was used to calculate the optimal secondary source strengths required to minimize the quantities measured at the physical or virtual sensors. As all control strategies employ the same number of secondary sources as sensors, the system is said to be fully-determined. In this case, the optimal set of secondary source strengths for which the value of the cost function is zero is[21]

$$\mathbf{q}_c = -\mathbf{Z}^{-1}\mathbf{p}_p, \tag{61}$$

where $\mathbf{Z}$ is the secondary transfer matrix and $\mathbf{p}_p$ is the primary sound field measured at the sensors. Calculation of the optimal source strengths therefore requires inversion of the secondary transfer matrix $\mathbf{Z}$. When minimizing the pressure at the physical or virtual location with a single secondary source, $\mathbf{Z}$ is scalar and hence the control source strength can be evaluated perfectly provided the impedance matrix is nonzero. All remaining control strategies, however, employ multiple sensors and secondary sources, and the accuracy of the calculated secondary source strengths can be attributed to the conditioning of matrix $\mathbf{Z}$. Distributions of the condition number, κ, of matrix $\mathbf{Z}$ have been examined for all control strategies employing multiple sensors and secondary sources. The spread of all condition number distributions is very wide and it is evident that certain configurations of secondary sources and sensors result in a high condition number and hence inaccurately calculated secondary source strengths. For the example of pressure and pressure gradient control given in Fig. 5, the median condition number is $\kappa_{\text{mean}}=53$ and the spread of all condition numbers is between $\kappa_{\text{min}}=2$ and $\kappa_{\text{max}}=5012$, as shown in Fig. 6. The ill-conditioning may be attributed to coherences less than unity in the measured transfer functions, thus introducing magnitude and more importantly phase errors.

To improve the poor experimental performance of control strategies employing multiple sensors and secondary sources, ill-conditioning was addressed in two ways. First, poorly conditioned data sets were removed from calculation of the mean squared pressure. Only samples of controlled sound field with a condition number below a certain threshold value were used in data averaging. The threshold value for each control strategy was selected to achieve the desired accuracy with the largest number of samples. For pressure and pressure gradient minimization, as shown in Fig. 5, the threshold value used was $\kappa=25$ and therefore 42% of the total number of data sets were included in calculation of the mean squared pressure (where the total number of data sets was 3600). The alternative technique used to improve the conditioning was to add one more control source than necessary to the active control system. When a greater number of control sources than error sensors are present, the system is said to be underdetermined. In this case, the optimal secondary source strengths are found by applying an additional constraint on the control effort.[25] Both of these methods for improving conditioning have been investigated and were found to produce essentially equivalent control profiles.

Figure 2 shows the experimental performance of control strategies employing multiple sensors and secondary sources with ill-conditioned data removed. By removing ill-conditioning, post-processed control with an energy density sensor and two control sources generates a zone of quiet of diameter 0.45λ as shown in Fig. 2(a). This is an agreeable fit with the analytical and numerically simulated results in which a quiet zone of size $\lambda/2$ is achieved. Minimizing the pressures at two points generates a similar sized zone of quiet to that with an energy density sensor and two control sources as shown in Fig. 2(b). The experimental results achieved here by minimizing the pressures at two points are

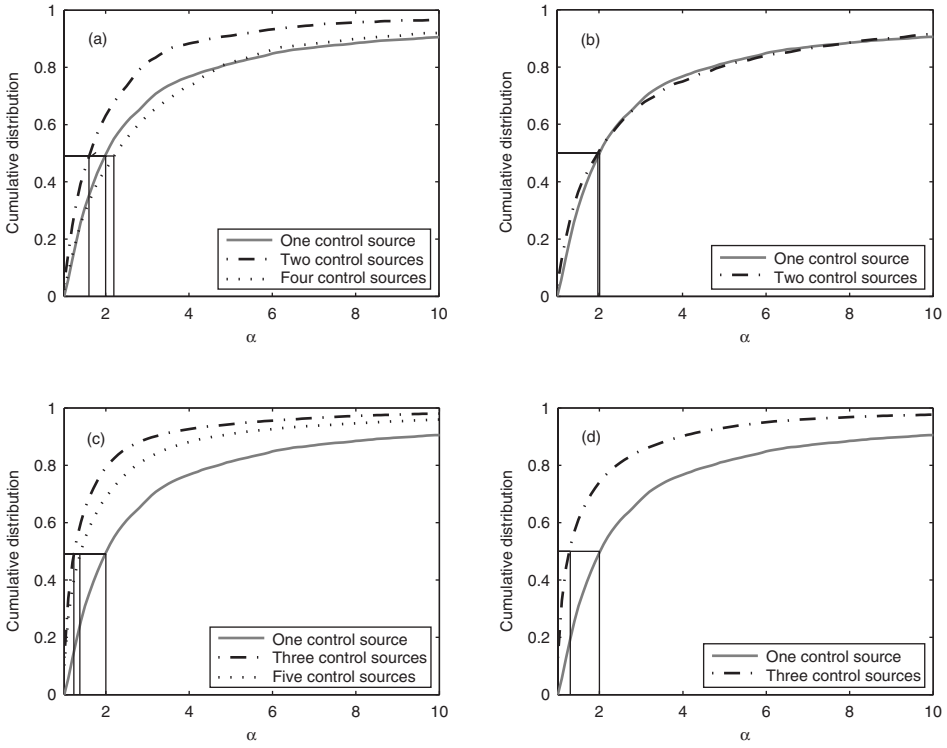

FIG. 7. Post-processed experimental cumulative distributions for α for control strategies employing multiple sensors and secondary sources when conditioning is improved. (a) Conventional control strategies 2 or 3 (two control sources) and 4 or 5 (four control sources) when ill-conditioning is removed. Distribution for control strategy 1 (single control source) is shown for comparison. (b) Virtual control strategies 8 or 9 (two control sources) when ill-conditioning is removed. Distribution for control strategies 6 or 7 (single control source) is shown for comparison. (c) Conventional control strategies 2 or 3 (three control sources) and 4 or 5 (five control sources) when one more control source than necessary is added. Distribution for control strategy 1 (single control source) is shown for comparison. (d) Virtual control strategies 8 or 9 (three control sources) when one more control source than necessary is added. Distribution for control strategies 6 or 7 (single control source) is shown for comparison. 50th percentile values of α are indicated by solid vertical lines.

in agreement with those obtained by Miyoshi and Kaneda;[18] however, they plotted zones of quiet using contours of 6 dB and 14.5 dB attenuations.

The superior control performance achieved with four control sources is indicated by the larger zones of quiet in Figs. 2(c) and 2(d). By removing ill-conditioning, a zone of quiet of diameter 0.9λ is obtained. This is a good fit with the analytical and numerically simulated results in which the quiet zone has a diameter of λ.

Control with a virtual energy density sensor is shown in Fig. 2(e), where the pressure and pressure gradient at a virtual location are estimated using the measured pressure and pressure gradient at two points. By removing ill-conditioning, this virtual control strategy results in a 10 dB zone of quiet with longest diameter approximately $\lambda/2$, which is a good fit with the analytical and numerically simulated results. A reduction in maximum attenuation is seen in post-processed control with 39 dB of attenuation achieved at the virtual location compared to 50 dB in the simulation. A similar level of control can be obtained using the pressures at four points to estimate the pressure and pressure gradient at the virtual location, as shown in Fig. 2(f).

Figure 7 shows the distributions of the random variable α observed in post-processed control when any ill-conditioning is removed or when one more control source than necessary is added to the control system. With the conditioning improved, the increase in mean squared pressure away from the point of cancellation is likely to be much smaller. This is indicated by the 50th percentile α values in Fig. 7 being significantly smaller than those discussed in Sec. V A. Figure 7 shows that a smaller increase in mean squared pressure away from the point of cancellation can be expected when conditioning is improved by adding an extra control source instead of by removing any ill-conditioning. The distributions corresponding to the removal of ill-conditioning shown in Figs. 7(a) and 7(b) can be improved and made to closely match those for addition of an extra control source, as shown in Figs. 7(c) and 7(d), by reducing the threshold value of κ. However, reducing the threshold value means that fewer data sets are included in calculation of the mean squared pressure after control, leading to an inaccurate estimate of the average control performance in a diffuse sound field.

VI. CONCLUSIONS

By considering the pressure and pressure gradient to have components perfectly spatially correlated and perfectly uncorrelated with the measured quantities in a diffuse sound field, prediction algorithms for stochastically optimal virtual sensors in a pure tone diffuse sound field have been derived. Analytical expressions for the controlled sound field generated with each of the nine local active noise control strategies have also been derived and these expressions were validated using numerical simulations and experimental results in a reverberation chamber. Results of numerically simulated and post-processed experimental control demonstrated that increasing the number of quantities to be minimized and the number of control sources not only generates larger zones of quiet at the physical or virtual locations but also increases the mean squared pressure away from the point of cancellation.

It was shown that stochastically optimal virtual sensors can accurately predict the pressure and pressure gradient at a location that is remote from the physical sensors and are therefore capable of projecting the zones of quiet to a virtual location. In the numerically simulated and post-processed experimental results, both virtual microphones and virtual

energy density sensors achieve higher attenuation at the virtual location than conventional control strategies employing their physical counterpart. Control with four secondary sources has been shown to achieve similar levels of attenuation at the virtual location to a virtual energy density sensor and outperform a virtual microphone. The pressure level after control away from the point of cancellation will, however, most likely be significantly higher when four control sources are used compared to only one control source with a virtual microphone or two control sources with a virtual energy density sensor.

In post-processed experimental results, the performance of control strategies employing multiple sensors and control sources was adversely affected by ill-conditioning. Conditioning was improved in two ways: first, by removing poorly conditioned data sets from calculation of the mean squared pressure after control; and second, by adding one more control source than necessary to the control system. Both methods significantly improved experimental control performance so that results of post-processed experimental control agreed with the analytical and numerically simulated results.

It is worth noting that in a pure tone diffuse sound field, perfect control may be achieved at the virtual location using the deterministic remote microphone technique,[6] provided a perfect estimate of the pressure at the virtual location is obtained in the preliminary identification stage. Although greater control is achieved at the virtual location with the remote microphone technique, the stochastically optimal diffuse field technique is much simpler to implement because it is a fixed scalar weighting method requiring only sensor position information. The remote microphone technique requires recalibration of the transfer functions between the sources and the sensors when the sensor or source locations are altered, compared to the stochastically optimal diffuse field method, which is independent of the source or sensor locations within the sound field. The weight functions only need to be updated if the geometric arrangement of physical and virtual locations changes with respect to each other.

In many real world applications it is likely that the sound field is not perfectly diffuse. Consequently, the experimental performance of stochastically optimal virtual sensors is currently being investigated in a modally dense three-dimensional cavity. Experimental results obtained to date in a sound field that is not perfectly diffuse indicate that this virtual sensing method performs as predicted by diffuse field theory. Also the subject of future investigation is the extension of this virtual sensing method to broadband noise.

On a final note, possible practical implementation of the stochastically optimal virtual sensing method is in a local active headrest. A number of authors have implemented virtual sensors in local active headrests in the past including Garcia-Bonito *et al.*,[4] Rafaely *et al.*,[26,27] Holmberg *et al.*,[28] and Pawelczyk.[29–31] It has been shown that implementing a virtual sensing method in a local active headrest significantly increases the attenuation generated at the occupant's ear.

ACKNOWLEDGMENTS

The authors gratefully acknowledge the financial support for this work provided by the Australian Research Council.

[1] S. Elliott, P. Joseph, A. Bullmore, and P. Nelson, "Active cancellation at a point in a pure tone diffuse sound field," J. Sound Vib. **120**, 183–189 (1988).

[2] S. Elliott and J. Garcia-Bonito, "Active cancellation of pressure and pressure gradient in a diffuse sound field," J. Sound Vib. **186**, 696–704 (1995).

[3] J. Garcia-Bonito and S. Elliott, "Strategies for local active control in diffuse sound fields," in Proceedings of Active 95, Newport Beach, CA (1995), pp. 561–572.

[4] J. Garcia-Bonito, S. Elliott, and C. Boucher, "Generation of zones of quiet using a virtual microphone arrangement," J. Acoust. Soc. Am. **101**, 3498–3516 (1997).

[5] S. Elliott and A. David, "A virtual microphone arrangement for local active sound control," in Proceedings of the First International Conference on Motion and Vibration, Yokohama, Japan (1995), pp. 1027–1031.

[6] A. Roure and A. Albarrazin, "The remote microphone technique for active noise control," in Proceedings of Active 99, Fort Lauderdale, FL (1999), pp. 1233–1244.

[7] B. Cazzolato, "Sensing systems for active control of sound transmission into cavities," Ph.D. thesis, School of Mechanical Engineering, The University of Adelaide, Australia (1999).

[8] C. Kestell, B. Cazzolato, and C. Hansen, "Virtual energy density sensing in active noise control systems," in *Proceedings of the Seventh International Congress on Sound and Vibration* (Garmisch-Partenkirchen, Germany, 2000).

[9] C. Kestell, B. Cazzolato, and C. Hansen, "Active noise control in a free field with virtual sensors," J. Acoust. Soc. Am. **109**, 232–234 (2001).

[10] C. Kestell, C. Hansen, and B. Cazzolato, "Active noise control with virtual sensors in a long narrow duct," Int. J. Acoust. Vib. **5**, 63–76 (2000).

[11] C. Kestell, C. Hansen, and B. Cazzolato, "Virtual sensors in active noise control," J. Acoust. Soc. Am. **29**, 57–61 (2001).

[12] J. Munn, B. Cazzolato, and C. Hansen, "Virtual sensing: Open loop versus adaptive LMS," in Proceedings of the Annual Australian Acoustical Society Conference, Adelaide, Australia (2002).

[13] J. Munn, C. Kestell, B. Cazzolato, and C. Hansen, "Real time feedforward active noise control using virtual sensors," in 2001 International Congress and Exhibition on Noise Control Engineering, Hague, The Netherlands (2001).

[14] J. Munn, C. Kestell, B. Cazzolato, and C. Hansen, "Real time feedforward active noise control using virtual sensors in a long narrow duct," in Australian Acoustical Society Annual Conference, Adelaide, Australia (2001).

[15] S. Elliott, P. Joseph, and P. Nelson, "Active control in diffuse sound fields," in Proceedings of the Institute of Acoustics, Cambridge, UK (1988), Vol. **10**, pp. 605–614.

[16] J. Garcia-Bonito and S. Elliott, "Local active control of diffuse sound fields," J. Acoust. Soc. Am. **98**, 1017–1024 (1995).

[17] J. Garcia-Bonito and S. Elliott, "Active cancellation of acoustic pressure and particle velocity in the near field of a source," J. Sound Vib. **221**, 85–116 (1999).

[18] M. Miyoshi and Y. Kaneda, "Active control of broadband random noise in a reverberant three-dimensional space," Noise Control Eng. J. **36**, 85–90 (1991).

[19] D. Moreau, J. Ghan, B. Cazzolato, and A. Zander, Technical Report, School of Mechanical Engineering, The University of Adelaide, Adelaide, Australia (2008), http://www.mecheng.adelaide.edu.au/avc/publications/techreport/2008.moreau_Internal_Report.pdf.

[20] R. Yeh, *Modern Probability Theory* (Harper and Row, New York, 1973).

[21] S. Elliott, *Signal Processing for Active Control* (Academic, San Diego, CA, 2001).

[22] A. Bullmore, P. Nelson, A. Curtis, and S. Elliott, "The active minimisation of harmonic enclosed sound fields, Part II: A computer simulation," J. Sound Vib. **117**, 15–33 (1987).

[23] P. Morse, *Vibration and Sound* (McGraw-Hill, New York, 1948).

[24] M. Schroeder and K. Kuttruff, "On frequency response curves in rooms, comparison of experimental, theoretical and Monte Carlo results for average frequency spacing between maxima," J. Acoust. Soc. Am. **34**, 76–80 (1962).

[25] P. Nelson and S. Elliott, *Active Control of Sound* (Academic, San Diego, CA, 1992).

[26]B. Rafaely, S. Elliott, and J. Garcia-Bonito, "Broadband performance of an active headrest," J. Acoust. Soc. Am. **106**, 787–793 (1999).
[27]B. Rafaely, J. Garcia-Bonito, and S. Elliott, "Feedback control of sound in headrest," in Proceedings of Active 97, Budapest (1997), pp. 445–456.
[28]U. Holmberg, N. Ramner, and R. Slovak, in *Proceedings of Active 02* (ISVR, Southampton, UK, 2002), pp. 1243–1250.
[29]M. Pawelczyk, "Multiple input-multiple output adaptive feedback control strategies for the active headrest system: Design and real-time implementation," Int. J. Adapt. Control Signal Process. **17**, 785–800 (2003).
[30]M. Pawelczyk, "Noise control in the active headrest based on estimated residual signals at virtual microphones," in Proceedings of the Tenth International Congress on Sound and Vibration, Stockholm, Sweden (2003), pp. 251–258.
[31]M. Pawelczyk, "Adaptive noise control algorithms for active headrest system," Control Eng. Pract. **12**, 1101–1112 (2004).

Flow noise from spoilers in ducts

Cheuk Ming Mak[a] and Jia Wu
Department of Building Services Engineering, The Hong Kong Polytechnic University, Hung Hom, Kowloon, Hong Kong, China

Chao Ye
Department of Building Services Engineering, The Hong Kong Polytechnic University, Hung Hom, Kowloon, Hong Kong, China and State Key Laboratory of Acoustics, Institute of Acoustics, Chinese Academy of Sciences, Beijing 100080, China

Jun Yang
State Key Laboratory of Acoustics, Institute of Acoustics, Chinese Academy of Sciences, Beijing 100080, China

(Received 17 April 2008; revised 28 March 2009; accepted 10 April 2009)

Measurements of flow noise produced by strip spoilers in the air duct of a ventilation system and radiated from an open exhaust termination unit into a reverberation chamber have been made. The results agree with the previous work of Nelson and Morfey [J. Sound Vib. **79**, 263–289 (1981)]. Prediction of flow noise produced by multiple spoilers requires the values of the ratio of the mean drag forces that act on the spoilers, the phase relationship between the fluctuating drag forces that act on the spoilers, and the coherence function of the noise sources. The latter is empirically derived from the measured results, where the predicted results agree well with the experimental results within 3 dB at most frequencies except for very high frequencies.
 [DOI: 10.1121/1.3127129]

PACS number(s): 43.50.Nm, 43.50.Ed, 43.50.Cb, 43.28.Ra [JWP] Pages: 3756–3765

I. INTRODUCTION

Flow noise is produced by in-duct elements such as dampers, sensors, bends, transition pieces, duct corners, branch points, or even splitter attenuators. At long distances from the fans in an air duct, flow noise produced by in-duct elements can be very serious. Our objective is to enable the prediction of the level and spectral content of the flow noise that is produced by the multiple elements in the air duct of a ventilation system.

The current design guides that are usually adopted, such as the ASHRAE handbook[1] and the CIBSE guide,[2] provide design methods for the prediction of flow noise only from a single, isolated in-duct element in an air ductwork system. Wilson and Iqbal[3] observed that these methods seriously underestimate the levels of flow noise in practical systems.

Measured data that have been reported in previous studies[4–9] can only be used with confidence on systems that incorporate the same configurations and carry the same airflows. Attempts[10–12] based on simplified theories that have been made using the limited data and equations are not applicable to systems with very different configurations.

Gordon[13,14] conducted a series of experiments and produced a free-field scaling law radiation model relating the sound power radiated from an element to the geometrical and flow parameters involved to collapse his measured sound power data into a "generalized spectrum." However, the experimental results he obtained were at low Strouhal numbers and high Mach numbers that are different from the air duct flow in a ventilation system (at high Strouhal numbers and low Mach numbers). Heller and Widnall[15] clarified the acoustical significance of the duct that encloses the noise source.

A method for predicting flow noise was produced and verified experimentally (at high Strouhal numbers and low Mach numbers) by Nelson and Morfey.[16] Oldham and Ukpoho[17] then rewrote the Nelson–Morfey equations. They determined the appropriate values of the open area ratio and of the characteristic dimension to be applied to a flow spoiler in a circular or a square duct. They focused on the sound field that is due to a single duct element such as a strip spoiler. Flow noise can be produced by the interaction of a moving fluid with a single duct element or a combination of duct elements. Ukpoho and Oldham[18] experimented with two sound sources (in-duct spoilers) to find that the flow noise increases when two duct elements are considered and that this increase is frequency-dependent. The latter conclusion shows that it is intuitively the same as the two sources in the active control of the sound in an air duct. Owing to the flow interaction between the duct elements,[19] the random (partially coherent) field case is likely to be the general case in ventilation systems. Mak and Yang[20,21] applied a model of partially coherent sources to formulate the sound power level due to duct spoilers. This model considers the acoustic interaction of two in-duct spoilers based on the earlier work of Nelson and Morfey.[16] Mak[22] later modified the Mak–Yang equations to determine the sound power radiated by the interaction of more complicated spoilers in circular ducts. He assumed a coherence function and compared the measured

[a]Author to whom correspondence should be addressed. Electronic mail: becmmak@polyu.edu.hk

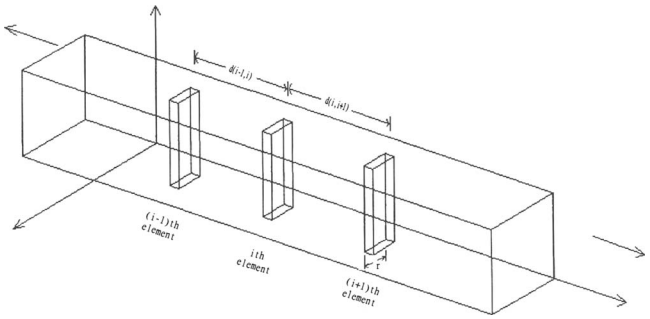

FIG. 1. Three in-duct elements in an infinite air duct.

values of Ukpoho and Oldham[18] with the predicted values of the modified Mak–Yang equations and found that these predicted values agreed well with the general trend of the measured values. Mak and Oldham's[23,24] approach was later used to modify the Mak–Yang equations to produce a turbulence-based prediction technique for flow noise.[25] Recent work by Mak and Au[26] has confirmed the usefulness of the approach. Mak[27] then extended Mak and Yang's prediction method to the prediction of multiple flow noise sources.

Airflow, acoustic, and force measurement data are collapsed into normalized spectra with the aid of these derived predictive equations. This is a prediction technique for the flow-generated noise produced by multiple spoilers in the air duct of a ventilation system.

II. THEORY AND PREDICTIVE EQUATIONS OF NOISE PRODUCED BY IN-DUCT FLOW SPOILER(S)

Mak adopted the concept of partially coherent sound fields to formulate the sound powers that are produced by the interaction of multiple spoilers at frequencies below and above the cut-on frequency of the lowest transverse duct mode. An example of three flow spoilers in an infinite air duct is shown in Fig. 1.

Two equations were obtained to determine the sound power that is generated by the interaction of multiple spoilers, one of which corresponds to frequencies, f_c, below the cut-on frequency, f_0, and one of which corresponds to frequencies above it. For N $(N>2)$ elements, the following are derived. For $f_c<f_0$,

$$\Pi_N = K^2(S) \times \Gamma_1 \times I_1. \tag{1}$$

For $f_c>f_0$,

$$\Pi_N = K^2(S) \times \Gamma_2 \times I_2. \tag{2}$$

The power term Γ_1 from the first spoiler below the cut-on frequency is

$$\Gamma_1 = \{\rho_0 A[\sigma^2(1-\sigma)]^2 C_D^2 U_c^4/16c_0\}.$$

The power term Γ_2 from the first spoiler above the cut-one frequency is

$$\Gamma_2 = \{\rho_0 \pi A^2(S)^2[\sigma^2(1-\sigma)]^2 \times [C_D^2 U_c^6/24c_0^3 r^2] \times [1+(3\pi c_0/4\omega_c)(a+b)/A]\}.$$

The interaction term I_1 below the cut-on frequency is

$$I_1 = \left\{ \sum_{i=1}^{N} \zeta_i^2 + 2\sum_{i=1}^{N-1}\sum_{j=1}^{N-2} \left[\sqrt{\gamma_{i(i+1)}^2} \times \cos(\omega_c d_{i(i+1)}/c_0)\cos[\phi_{i(i+1)}(\omega_c)]\zeta_i\zeta_{i+1} + \sqrt{\gamma_{(i-1)(i+j)}^2} \times \cos(\omega_c d_{(i-1)(i+j)}/c_0) \times \cos[\phi_{(i-1)(i+j)}(\omega_c)]\zeta_{i-1}\zeta_{i+j} \right] \right\}.$$

The interaction term I_2 above the cut-on frequency is

$$I_2 = \left\{ \sum_{i=1}^{N} \zeta_i^2 + 2\sum_{i=1}^{N-1}\sum_{j=1}^{N-2} \left[\sqrt{\gamma_{i(i+1)}^2} Q_{i(i+1)} \times \cos[\phi_{i(i+1)}(\omega_c)]\zeta_i\zeta_{i+1} + \sqrt{\gamma_{(i-1)(i+j)}^2} Q_{(i-1)(i+j)} \cos[\phi_{(i-1)(i+j)}(\omega_c)]\zeta_{i-1}\zeta_{i+j} \right] \right\},$$

where $N>2$, N, i, and j are integers and $j=1,2,\ldots,(N-2)$.

In the above equation, a value is ignored if any one of its subscripts is zero or greater than N. $Q_{i(i+1)}$ is given by $Q_{i(i+1)}=\Omega_{i(i+1)}/\Psi_{i(i+1)}$, where

$$\Omega_{i(i+1)} = \frac{k^2ab}{6\pi}3\left[\frac{\sin e}{e} + \frac{2\cos e}{e^2} - \frac{2\sin e}{e^3}\right] + \frac{k(a+b)}{8}2\left[J_0(e) - \frac{J_1(e)}{e}\right],$$

$$\Psi_{i(i+1)} = \left[\frac{k^2ab}{6\pi} + \frac{k(a+b)}{8}\right],$$

and $e=kd_{i(i+1)}$.

$Q_{(i-1)(i+j)}$ is given by $Q_{(i-1)(i+j)}=\Omega_{(i-1)(i+j)}/\Psi_{(i-1)(i+j)}$, where

$$\Omega_{(i-1)(i+j)} = \frac{k^2ab}{6\pi}3\left[\frac{\sin e}{e} + \frac{2\cos e}{e^2} - \frac{2\sin e}{e^3}\right] + \frac{k(a+b)}{8}2\left[J_0(e) - \frac{J_1(e)}{e}\right],$$

$$\Psi_{(i-1)(i+j)} = \left[\frac{k^2ab}{6\pi} + \frac{k(a+b)}{8}\right],$$

and $e=kd_{(i-1)(i+j)}$.

d_{ij} is the distance between the ith spoiler and the jth spoiler; k is the wave number; J_0 and J_1 are the zero-and first-order Bessel's functions, respectively; a and b are the duct cross-section dimensions; r is a characteristic dimension of the element; A is the area of the duct cross-section by $A=(a\times b)$; A_c is the area of the duct constriction by $A_c=(a\times b-r\times b)$; U_c is the flow velocity in the constriction that is provided by the spoiler and is defined by the volume flow rate q and the area of the duct constriction A_c, such that $U_c=q/A_c=UA/A_c$; U is the mean duct flow velocity; σ is the open area ratio determined by $\sigma=A_C/A$. The Strouhal number for this duct and flow is $S=f_c r/U_c$; the factor $K(S)$ is the ratio of fluctuating to steady-state drag forces on the spoilers;

P_N is the infinite-duct values of the radiated sound power; f_0 is the cut-on frequency of the first transverse duct mode (i.e., the least non-zero value of the cut-on frequency is defined by $f_0=(c_0/2\pi)\sqrt{(m\pi/a)^2+(n\pi/b)^2}$, where $m,n=0,1,\ldots$); c_0 is the ambient speed of sound; ρ_0 is the ambient air density; γ_{ij}^2 is the coherence function of the ith spoiler and the jth spoiler; ω_c is the center radiant frequency of the measurement band; $\phi_{ij}(\omega_c)$ is the phase of the cross-power spectral density of the source volume of the ith sound source and the jth sound source; ζ_i is a constant ratio of the mean drag forces acting on the ith spoiler and the first spoiler; ΔP_S is the static pressure drop across a spoiler (Pa); and C_D is the drag coefficient determined by

$$C_D = \frac{\Delta P_s}{\frac{1}{2}\rho_0 U_c^2 \sigma^2 (1-\sigma)}. \tag{3}$$

Comparing the above expressions with those obtained by Nelson and Morfey[16] for the sound power generated by an in-duct spoiler, the interaction factor β_N can be defined as follows:

$$\beta_N = \begin{cases} I_1, & f_c < f_0, \\ I_2, & f_c > f_0. \end{cases} \tag{4}$$

Furthermore, if the sound power that is due to an in-duct spoiler is denoted as Π_S, a simple relationship between Π_N, the sound power that is due to multiple (N) spoilers and that due to a single spoiler, is then obtained as follows:

$$\Pi_N = \Pi_S \times \beta_N, \tag{5}$$

where Π_S can be obtained by using the prediction method provided by Nelson and Morfey,[16] and β_N can be determined by experiments.

We define ζ_i as the constant ratio of the mean drag forces acting on the ith spoiler and the first spoiler. The first spoiler is closest to the inlet of the air flow:

$$\zeta_i = \frac{\bar{F}_{z1}}{\bar{F}_{zi}}, \tag{6}$$

where $\bar{F}_{zi}$ is the mean drag force acting on the ith spoiler counted from the inlet of the air flow, and $\bar{F}_{z1}$ is the mean drag force acting on the first spoiler. The mean drag force acting on the ith spoiler can be expressed as $F_{zi}=A\Delta P_s$.

Han *et al.*[28] and Han and Mak[29] suggested that the phase of the cross-power spectral density of the source volume of the ith sound source and the jth sound source, $\phi_{ij}(\omega_c)$, can be given by

$$\phi_{ij}(\omega_c) = \delta_{ij} - kM\overline{d_{ij}}, \tag{7}$$

where δ_{ij} is the difference between the phases of the total fluctuating drag forces acting on the ith spoiler and the jth spoiler: $\delta_{ij}=\theta_j(\omega)-\theta_i(\omega)$, where $\theta_i(\omega)$ and $\theta_j(\omega)$ are the phases of the fluctuating drag force acting on the ith spoiler, respectively. k is the wave number, $M=U/c_0$, and $\bar{d}_{ij}=d_{ij}/(1-M^2)$.

The coherence functions, γ_{ij}^2, of the noise sources are obtained as follows.

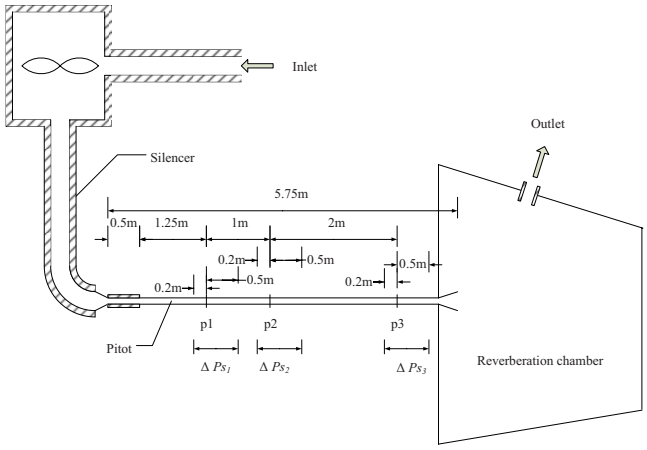

FIG. 2. (Color online) A schematic diagram of the test rig (plan view). (ΔP_{S1}, ΔP_{S2}, and ΔP_{S3}=a static pressure drop across the first spoiler, the second spoiler, and the third spoiler, respectively; p1=position at which the first test spoiler was inserted; p2=position at which the second test spoiler was inserted; and p3=position at which the third test spoiler was inserted.)

III. EXPERIMENTAL PROCEDURE

A. Design of the experimental rig

The test rig used for the determination of the sound power generated by flat plate spoiler(s) and their interactions are shown in Fig. 2. Air flow was provided by a centrifugal fan driven by a variable speed motor. The fan was vibration-isolated by springs and was enclosed in a lined acoustic enclosure of $1.22\times1.22\times1.22$ m^3. Fan noise was attenuated on both the upstream and downstream sides by silencers and acoustically lined elbows. The 0.1 m^2 test duct was made of steel and was enclosed by 25-mm-thick absorptive lining to reduce breakout noise from the duct. This arrangement yielded a quiet, fully developed air flow at the first test piece counted from the inlet of air flow, which was situated approximately 1.75 m from the duct entrance section. The total length of the duct was 5.45 m. The duct was passed into a 70 m^3 reverberation chamber with an outlet cone of 0.16×0.16 m^2 and a length of 0.3 m for acoustic measurements. The reverberation chamber was provided with lined outlet ducts that allowed air to escape without allowing noise from outside to penetrate. The entire system was located in another 200 m^3 reverberation chamber with a closed door so that the level of sound that was measured in the system was always well above the background noise level.

B. The spoilers used in the experiment

The spoilers used in the experiment, as shown in Fig. 3, were selected to test the validity of Mak's[27] prediction method for multiple flow spoilers. The spoiler plates were made from 1-mm-thick steel plate. These plates were fixed by springs and force transducers between the flanges of two adjoining sections of the test duct. The gap was sealed with compressed foam rubber. The spoilers provided a rigid obstruction to the flow in the duct and were not able to vibrate significantly in the air stream. Six different spoiler geometries were tested, each with at least four duct flow velocities. Three of the spoilers were vertical strips of plate placed centrally in the air stream. Their height was that of the test duct,

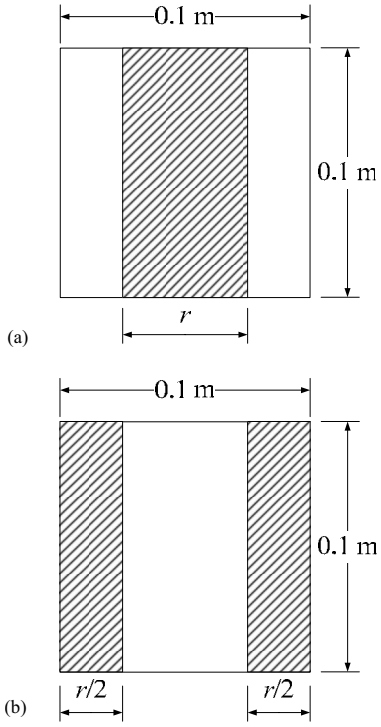

FIG. 3. Cross-section of the duct with two main types and various sizes of the flat plate strip spoilers used (shaded area). (a) Centrally placed strip spoilers; r=0.025, 0.05, 0.075 m. (b) The geometries consisted of trip plates protruding symmetrically from both sides of the duct, leaving a central vertical strip of the duct open; r=0.025, 0.05, 0.075 m.

and their widths were 0.025, 0.05, and 0.075 m, respectively. The other three geometries consisted of plates that protruded symmetrically from both sides of the duct, leaving a central vertical strip of the duct open. Again, the plates had the same height as the duct, and the widths of the two side plates were equal. The total widths in the three configurations were 0.025, 0.05, and 0.075 m, respectively. Eleven tests were conducted, as shown in Table I. In Tests 1–4, only a single spoiler was inserted into position p1. In Tests 5–9, two spoilers were inserted at two different positions p1 and p2. In Tests 10 and 11, three spoilers were inserted at three different positions p1, p2, and p3. The three spoiler positions are shown in Fig. 2.

C. Airflow measurements

The velocity profile in the empty test duct was measured.[30] A pitot tube was used to sample the dynamic pressure at specified points in the duct cross-section at the position shown in Fig. 4. Plots of the duct velocity profile at several test velocities at the 0.1 m side are shown in Fig. 5. The slight asymmetry of the velocity profiles that were measured is due to the non-symmetric inlet conditions and is not regarded as serious in the experiments. This procedure was used to calculate the mean duct velocity over the 5.4 m length at five duct velocities. The mean velocity calculated for each of the five velocities was found to have a linear relationship with the velocity measured at the "calibrated" position at the center of the duct (as shown in Fig. 6). Value of the mean duct velocity was determined by using this single calibrated position of the pitot tube. The pitot tube was removed from the duct when undertaking acoustic measurements.

TABLE I. Eleven spoiler configurations tested. See Fig. 2. (p1=position at which the first test spoiler was inserted, p2=position at which the second test spoiler was inserted, and p3=position at which the third test spoiler was inserted.)

LEGEND: Spoiler area, A_s; Air flow area, A_c

No.	Spoiler(s) used in the experiments	Mean flow velocities
1	r=0.025m at p1	10,15,20,25,30
2	r=0.05m at p1	10,14,18,22,26
3	r=0.025m at p1	15,20,25,30,35
4	r=0.05m at p1	10,15,20,25,30
5	r=0.025m at p1 r=0.025m at p2	10,15,20,25,30
6	r=0.025m at p1 r=0.05m at p2	10,14,18,22,26
7	r=0.05m at p1 r=0.05m at p2	10,13,16,19,22
8	r=0.075m at p1 r=0.075m at p2	10,11,12,13,14
9	r=0.025m at p1 r=0.025m at p2	10,14,18,22,26
10	r=0.025m at p1 r=0.025m at p2 r=0.025m at	10,13,16,19,22
11	r=0.05m at p1 r=0.05m at p2 r=0.05m at p3	10,12,14,16,18

The static pressure drop across the various spoilers that were tested was measured using two piezometric rings located at the positions p1, p2, and p3 shown in Fig. 2. Each ring consisted of four static pressure tappings, one in each

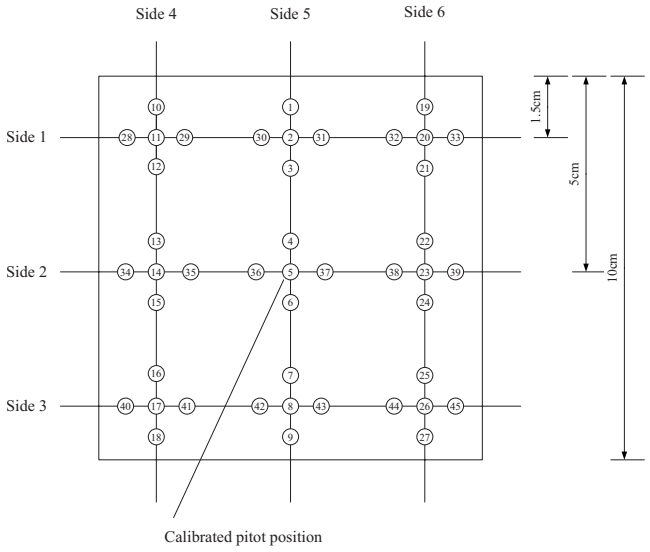

FIG. 4. Positions in the duct cross-section at which a pitot tube was used to sample the dynamic pressure.

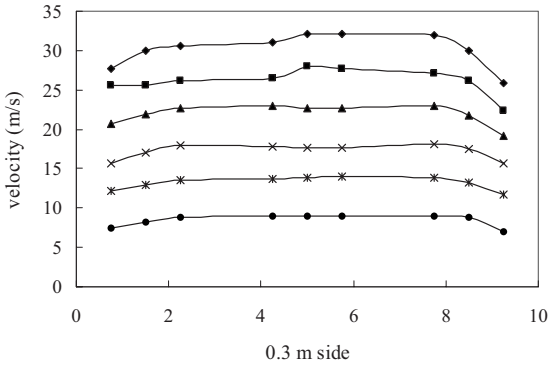

FIG. 5. (Color online) A linear relationship between the mean velocity calculated for each of the five velocities and the velocity measured at the calibrated position.

duct face. The downstream ring was far enough away (five times the duct dimensions) from the test spoiler to ensure that full static pressure recovery could take place in the wake of the flow obstructions under test.

D. Acoustic measurements

The temperature and relative air humidity in the reverberation chamber were measured with a sling psychrometer. During the measurements, the temperature ranged from 26.5 to 27.8 °C, and the relative humidity ranged from 53% to 59%. The reverberation time (RT) was measured by the impulse response method of the mean-length sequence (MLS), as shown in Fig. 7. This MLS signal was generated internally by DIRAC software installed on a notebook computer and fed to the omni-directional source B&K-type 4241, a dodecahedron loudspeaker that was placed at the corner of the chamber. A B&K-type sound level meter, which was connected to the computer through an external sound card, was located at 1.20 m above the floor at the predetermined positions. The door of the chamber was closed, and there were no personnel inside the chamber during the measurement process. Six different microphone positions were used for the frequencies between 200 and 10 kHz. All of the measured positions were located at least 1 m away from the chamber walls. The distance between the two microphones was larger than the half a wavelength of sound under consideration. The geometric mean of the measured RTs and the sound pressure

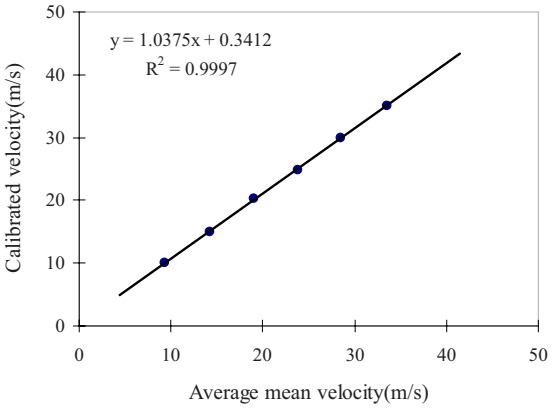

FIG. 6. Test duct velocity profile.

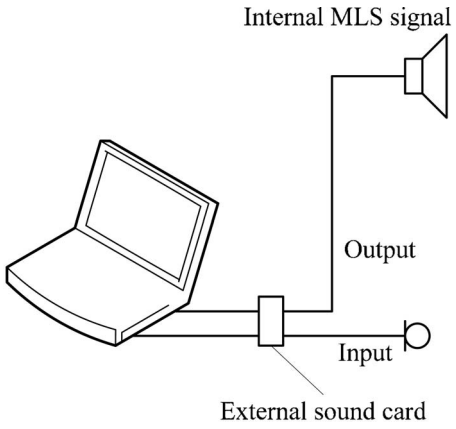

FIG. 7. A schematic diagram of the impulse response method using a MLS signal.

levels (SPLs) were based on the measured RT and the measured SPLs at the six different randomly selected positions, respectively. About 50 sampled averaged RTs and averaged SPLs were obtained so that the mean of the averaged RTs and the averaged SPLs and the standard deviation, S_D, of the variation of the averaged RTs and averaged SPLs could be calculated, respectively. Assuming that the measured value of S_D is the true standard deviation of a normal distribution of averaged RTs and averaged SPLs, it is found that the 95% confidence limits for the mean of the distribution estimated from n_s samples (n_s=50) are then given by $\pm 1.96 S_D/\sqrt{n_s}$. The error is $\pm 1.96 S_D/\sqrt{50}$, and the geometrical mean of the RTs and the SPLs should be around 1–3 s and ±1.5 dB, respectively. The geometrical mean of the measured RT is shown in Fig. 8. The 95% confidence limits for the mean SPL are shown in Fig. 9. The results are better than those measured by Nelson and Morfey,[16] as can be seen by the smaller errors at all frequencies (see Fig. 9). A sufficiently diffuse field was established in the middle of the frequency range so that more reliable results could be obtained. At high frequencies, the accuracy decreases again as the absorption in the room increases and the direct field of the duct exit encroaches on the reverberant field. The sound power level

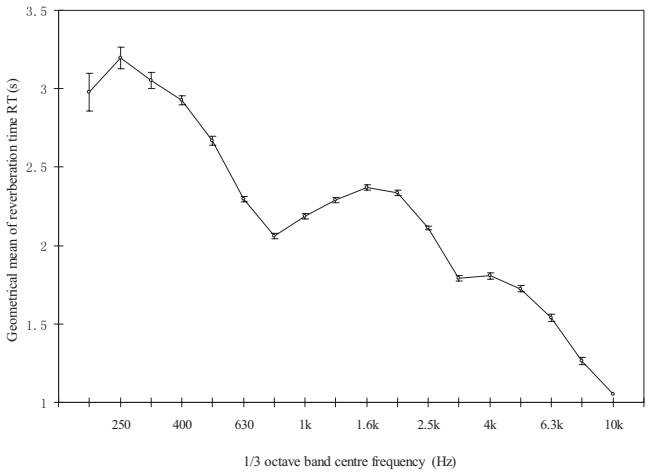

FIG. 8. Measured RTs for the test chamber and the geometrical mean of the RTs for the test chamber. Six microphone positions were used for 200 Hz–10 kHz. The error bars denote the spread of results.

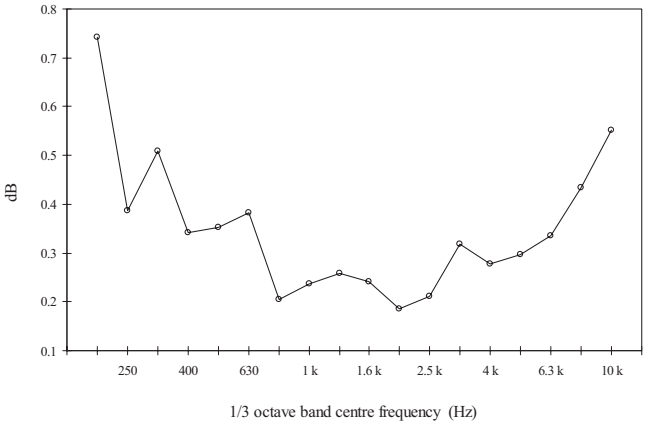

FIG. 9. The 95% confidence limits for an estimate of the mean SPL in the test chamber from the six microphone positions.

that radiated from the duct exit was then calculated from

$$\mathrm{SWL} = \mathrm{SPL} + 10\log_{10} V_R - 10\log_{10} \overline{\mathrm{RT}} - 14,$$

where V_R is the room volume (70 m^3), $\overline{\mathrm{RT}}$ is the geometrical mean of the reverberation time(s), and SPL is the space-averaged sound pressure level in the chamber (dB).

The background noise due to the flow in the empty duct was monitored at five test velocities. The ambient background noise level was also measured after each test. The measured noise levels were kept at least 10 dB above the ambient level, and the background flow noise level at the given test velocity in the duct.

E. Force measurements

The arrangement of springs and force transducers is shown in Fig. 10. The plates were fixed by springs and force transducers between the flanges of the two adjoining sections of the duct, and the gap sealed with a compressed foam rubber seal. For the centrally placed strip spoiler, two transducers mounted on the duct supporting flanges were required to measure the total fluctuating drag force. For the two side strip spoilers, four transducers on the duct supporting flanges

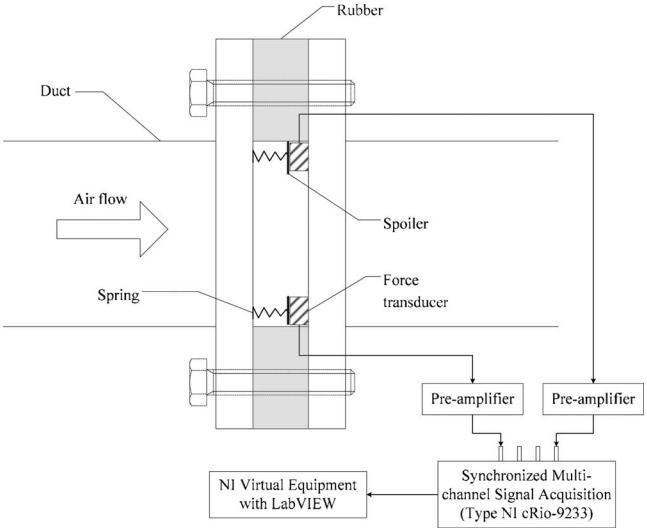

FIG. 10. A schematic diagram of the force-measuring system.

were required to measure the total fluctuating drag force. The springs used to provide support for the plates were selected to have stiffness sufficient to place the mechanical resonant frequency well below 200 Hz, the lowest 1/3 octave band measuring frequency of the reverberation chamber of 70 m^3, and also below 50 Hz, which is the frequency of the alternating current supply in Hong Kong. The frequency response of the force transducers was flat over the measuring frequency range. Their sensitivity was 11 mV/N. The force transducers were connected to NI LABVIEW equipment via a synchronized multi-channel signal acquisition of type NI cRio-9233 through pre-amplifiers, as indicated in Fig. 10. The magnitude and phases of the total fluctuating forces acting on the spoilers at various duct flow velocities were measured in real time and converted into a frequency domain by the NI equipment.

IV. ANALYSIS AND DISCUSSION OF THE RESULTS

A. Normalization of the experimental results for a single flow spoiler

The results measured for the sound power that radiated from the end of the duct for a single spoiler can be normalized according to Nelson and Morfey.[16] Their equations, and those of Mak[27] and Mak and Yang,[20,21] were developed for an infinite duct. The duct used, however, was of finite length with a considerable length-absorbent lining upstream of the test duct. It has been assumed that the spoiler is transparent to the waves reflected back upstream from the duct terminations. The radiated sound power measurement has therefore been interpreted on the basis that the test duct is semi-infinite, and no compensation has been made for any subsequent re-reflection of sound arriving from the duct exit. The sound power radiated by the spoilers down one direction of the infinite duct was corrected by a power transmission loss at the duct outlet.

The drag coefficient, C_D, used in the normalization of the results for the single spoilers was evaluated from the measurements of the static pressure drop across the spoilers based on Eq. (3). The values of C_D for each spoiler were found by averaging the values calculated from the measurements of ΔP_s and U_c, at each test velocity. For most of the spoilers tested, the calculated values of C_D varied by around 0.5%–5% over the range of the test velocities used.

The result for one of the single spoilers tested, normalized[16] with the measured values of C_D used and the sound power levels is shown in Fig. 11, which denotes $120 + 20\log_{10} K(S)$ and relates to the infinite-duct values of the radiated sound power Π_N in Eqs. (1) and (2). In view of the vastly different forms of the two equations for frequencies above and below the cut-on frequency of the first transverse duct mode, the collapse of the experimental data for all of the single spoilers tested is good in view of the widely differing drag coefficients associated with the various spoilers. Nelson and Morfey[16] reported that there was an error in their original normalized spectrum and that their trend lines need to be displaced vertically downwards by 6 dB. The scatter associated with the experimental points of Fig. 11 is comparable with the range of corrected trend lines in their normal-

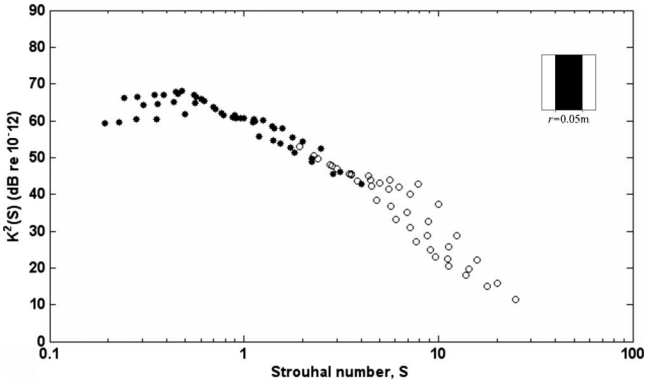

FIG. 11. Normalized 1/3 octave band results for strip spoilers in Test 2 (r =0.05 m). Values of the characteristic dimension (i.e., the total strip width) r and the drag coefficient C_D, as follows. Test 2: r=0.05 m, C_D=12.0.

ized spectrum. This suggests that the results reported here agree well with their corrected trend lines; Fig. 12 shows a comparison of the values of the normalized results for all of the single spoilers tested and a trend line based on simple linear relationships over the range of measurements. Scattering was observed at low Strouhal numbers (or low frequencies), which was also seen in the work of Oldham and Ukpoho.[17]

B. Determination of the coherence function of noise sources

The assumptions used in the determination of the coherence function, γ_{ij}^2, are as follows:

(1) The values of the coherence function should be between 0 and 1, i.e., $0 \leq \gamma_{ij}^2 \leq 1$. If γ_{ij}^2 takes the value of 1 at certain frequencies, then this means that the ith and jth sound sources are fully coherent at those frequencies. If γ_{ij}^2 is equal to zero at certain frequencies, then this means that the ith and jth sound sources are incoherent at those frequencies.
(2) The coherence function should be dependent on the magnitude and phases of the fluctuating drag forces acting on each spoiler at various frequencies.
(3) The coherence function is inversely related to the distance between the ith and jth spoilers. When one flow spoiler is far away from another, the coherence function between the flow noise sources should be small when the other parameters are fixed.
(4) The coherence function should be dependent on the mean duct flow air velocity.

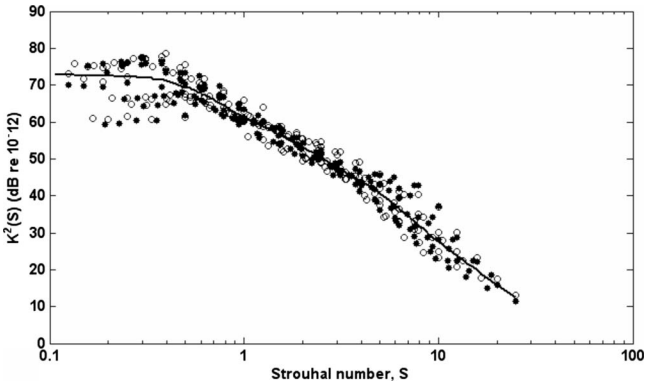

FIG. 12. The overall collapse of the normalized data for all tested single spoilers (Tests 1–4). The overall collapse of the normalized data for all single spoilers: (●) centrally placed strip spoiler; (○) plates protruding symmetrically from both sides of the duct; (—) trend line.

The experimental data for the two flow spoilers in Test 5 were used to obtain $\sqrt{\gamma_{ij}^2}$ in the predictive equations for multiple spoilers. The relationship between $\sqrt{\gamma_{ij}^2}$ and the other parameters, such as the phases and magnitude of the fluctuating drag forces, F, acting on the spoilers, the distance between the two noise sources, d_{ij}, and the mean flow air velocity, U, were analyzed by the Statistical Package for the Social Sciences (SPSS). The square of $\sqrt{\gamma_{ij}^2}$ will give the coherence function γ_{ij}^2, and the value of $\sqrt{\gamma_{ij}^2}$ will therefore also be between 0 and 1.

It was found from the SPSS analysis of the data that there was an approximately linear relationship between $\sqrt{\gamma_{ij}^2}$ and $\log(|F_j(\omega)/F_i(\omega)\cos(\theta_j(\omega)-\theta_i(\omega))|)$ with a correlation coefficient of 0.84 between them. It was therefore assumed that $\sqrt{\gamma_{ij}^2}$ may be a logarithmic function that contains the factor of $|F_j(\omega)/F_i(\omega)\cos(\theta_j(\omega)-\theta_i(\omega))|$. $F_i(\omega)$ and $F_j(\omega)$ are the magnitudes of the fluctuating drag force acting on the ith and jth spoilers, respectively. To ensure that the value of the coherence function was between 0 and 1, the following preliminary formula was obtained:

$$\gamma_{ij}^2 = \log_{10}^2\left(1 + \frac{15}{Ud_{ij}}\left|\frac{F_j(\omega)}{F_i(\omega)}\right|^2 \cos^2(\theta_j(\omega) - \theta_i(\omega))\right),$$

where $F_i(\omega)$ and $\theta_i(\omega)$ are the magnitude and phases, respectively, of the fluctuating drag force acting on the ith spoiler.

Together with the values of the other parameters, such as the phases of the cross-power spectral density of the source volumes and the ratio of the mean drag forces, the interaction factor β_N in the predictive equations can be obtained.

C. Comparison between predicted and measured results

Mak's predictive equations for multiple flow spoilers were used to predict the sound power levels produced by two or three flow spoilers in Tests 5–11. The predicted and measured results of the sound wave levels in the seven tests at a particular flow velocity are shown in Figs. 13–19. The error between the predicted and measured results was ±0–3 dB at most frequencies at a particular mean flow velocity. The deviation between the predicted and measured results at certain frequencies at or above 4 kHz at a particular flow may have been due to high frequency vibration modes of the flow spoiler or the duct system.

These predictive equations developed are useful for predicting the level and spectral contents of the flow-generated noise from multiple in-duct flow spoilers at the design stage. This prediction provides a normalized spectrum, using a table of parameters derived from experimental model measurements.

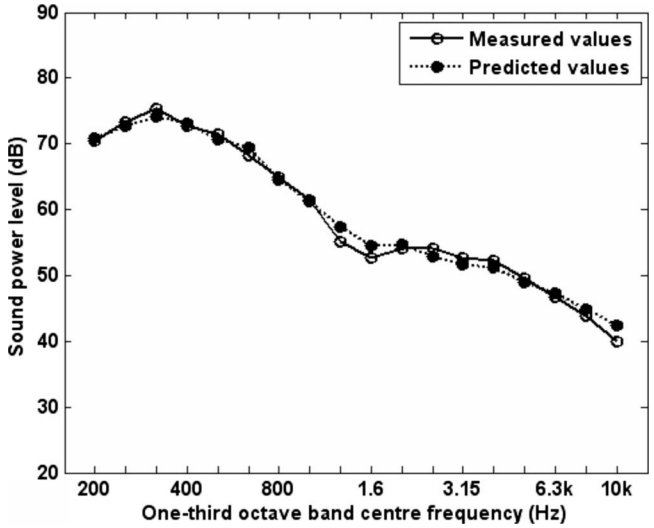

FIG. 13. Comparison of the measured values and predicted values of the SPL in Test 5 at $U=20$ m/s.

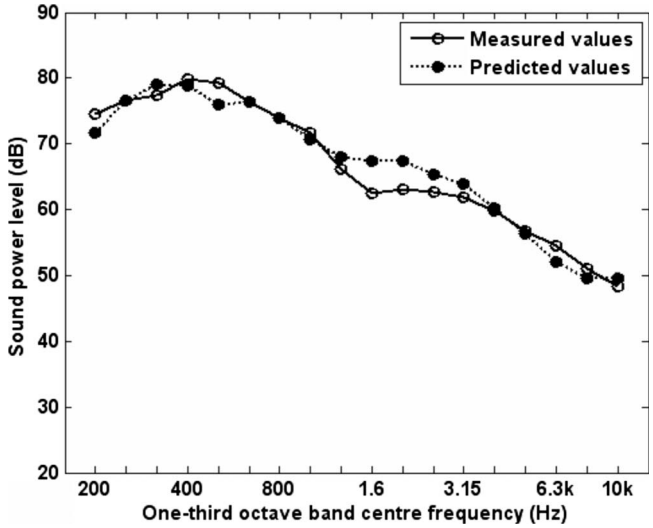

FIG. 16. Comparison of the measured values and predicted values of the SPL in Test 8 at $U=11$ m/s.

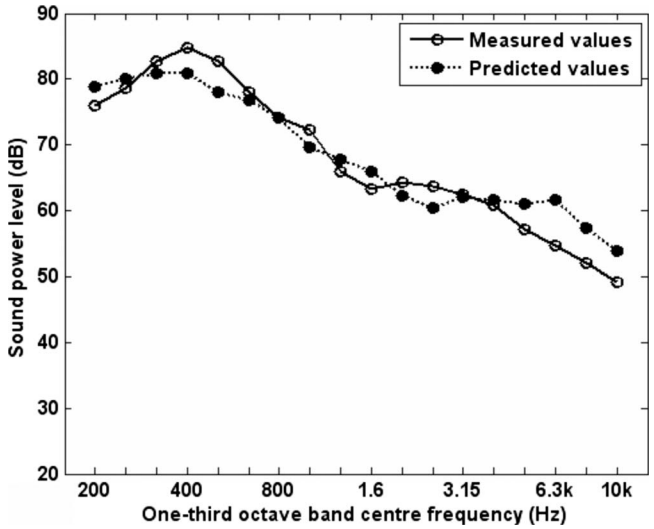

FIG. 14. Comparison of the measured values and predicted values of the SPL in Test 6 at $U=22$ m/s.

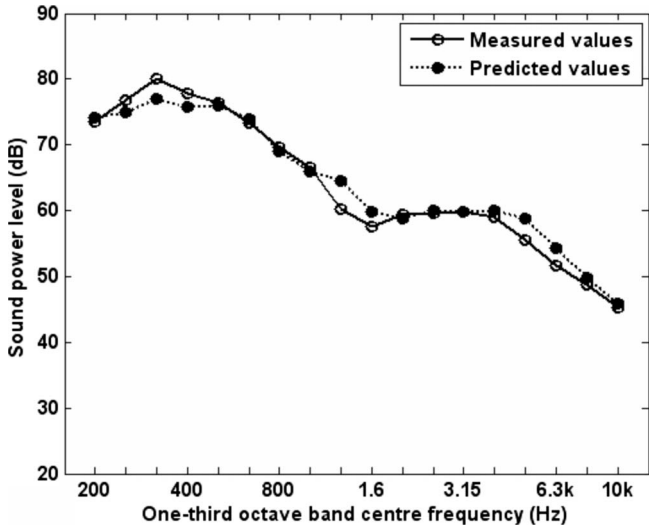

FIG. 17. Comparison of the measured values and predicted values of the SPL in Test 9 at $U=18$ m/s.

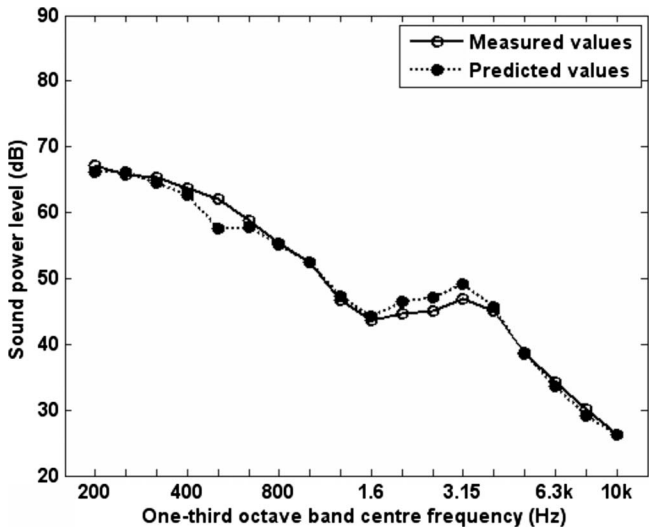

FIG. 15. Comparison of the measured values and predicted values of the SPL in Test 7 at $U=10$ m/s.

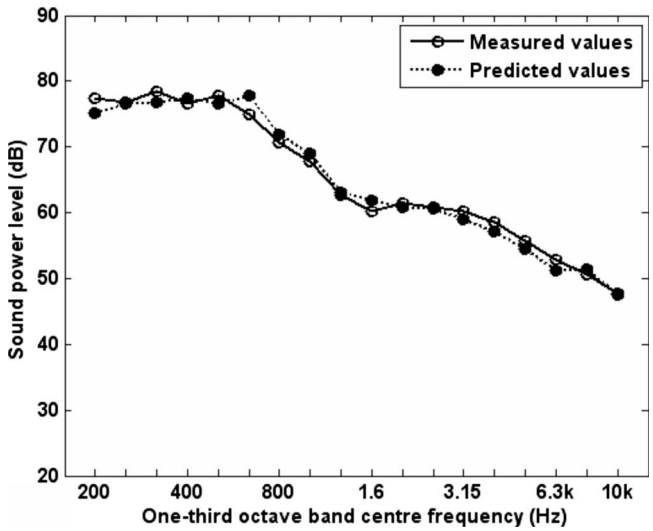

FIG. 18. Comparison of the measured values and predicted values of the SPL in Test 10 at $U=19$ m/s.

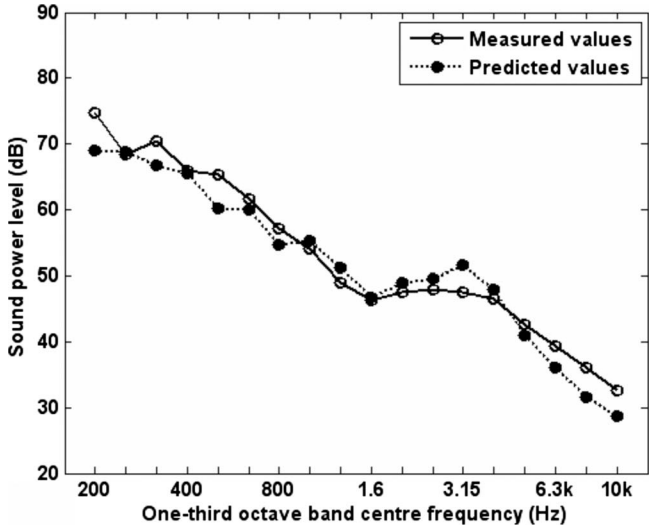

FIG. 19. Comparison of the measured values and predicted values of the SPL in Test 11 at $U=10$ m/s.

V. CONCLUSION

The collapse of the data found with single flow spoilers is similar to that observed by Nelson and Morfey[16] and Oldham and Ukpoho.[17] Together with the normalized spectrum and the coherence function, Mak's predictive equations[27] for multiple flow spoilers, one can now predict the sound power levels produced by two or three flow spoilers at most frequencies at various mean duct flow velocities.

It is suggested that the line trends reported in this study, together with the coherence function of the noise sources, the phase relationship between the fluctuating spoiler drag forces, and the ratio of the mean drag forces provide the basis of a generalized predictive technique. Further work is required to extend the work to the interactions of practical duct discontinuities such as bends and transition pieces.

ACKNOWLEDGMENTS

The work described in this paper was fully supported by a grant from the Research Grants Council of the Hong Kong Special Administrative Region, China (Project No. PolyU 5229/05E).

NOMENCLATURE

a,b = duct cross-section dimensions (m)
A = area of the duct cross-section determined by $A=(a\times b)$ (m^2)
A_s = face area of flat plate spoiler (m^2)
A_c = area of the duct constriction determined by $A_c=(a\times b-r\times b)$ (m^2)
c_0 = ambient speed of sound (m/s)
C_D = drag coefficient
d_{ij} = distance between the ith spoiler and the jth spoiler (m)
f_c = center frequency of measurement band (Hz)
f_0 = cut-on frequency of the first transverse duct mode (Hz) defined by $f_0=(c_0/2\pi)\sqrt{(m\pi/a)^2+(n\pi/b)^2}$, where $m,n=0,1,\ldots$
$F_i(\omega)$ = magnitude of the fluctuating drag force acting on the ith spoiler (N)
$\bar{F}_{zi}$ = mean drag force acting on the ith spoiler counted from the inlet of the air flow (N)
$\bar{F}_{z1}$ = mean drag force acting on the first spoiler (N)
i,j = integers
I_1,I_2 = Interaction terms below and above the cut-on frequency
J_0,J_1 = zero- and first-order Bessel's functions
k = wave number
$K(S)$ = ratio of fluctuating to steady-state drag forces on the spoilers
$K^2(S)$ = square of the ratio $K(S)$
m,n = integers
M = Mach number given by $M=U/c_0$
N = number of in-duct spoilers or in-duct elements
P_S = static pressure (Pa)
ΔP_S = static pressure drop across a spoiler (Pa)
q = volume flow rate (m^3/s)
r = characteristic dimension of the in-duct element (m)
RT = reverberation time (s)
$\overline{\mathrm{RT}}$ = geometrical mean of reverberation time (s)
S = Strouhal number determined by $S=f_c r/U_c$
S_D = standard deviation
SPL = sound pressure level (dB)
SWL = sound power level radiated from the duct exit (dB)
U = mean duct flow velocity (m/s)
U_c = flow velocity in the constriction (m/s) determined by $U_c=q/A_c=UA/A_c$
V_R = room volume of the reverberation chamber (m^3)
ω_c = center radiant frequency of the measurement band (rad/s)
Π = sound power (W)
Π_N = infinite-duct values of the radiated sound power due to multiple (N) spoilers (W)
Π_S = infinite-duct values of the radiated sound power due to an in-duct spoiler (W)
Γ_1,Γ_2 = power terms from the first spoiler below and above the cut-on frequency (W)
ρ_0 = ambient air density (kg/m^3)
σ = open area ratio determined by $\sigma=A_C/A$
γ_{ij}^2 = coherence function of the ith spoiler and the jth spoiler
$\phi_{ij}(\omega_c)$ = phase of the cross-power spectral density of the source volume of the ith sound source and the jth sound source
ζ_i = constant ratio of the mean drag forces acting on the ith spoiler and the first spoiler
β_N = interaction factor

$\phi_{ij}(\omega_c)$ = phase of the cross-power spectral density of the source volume of the ith sound source and the jth sound source

δ_{ij} = difference between the phases of the total fluctuating drag forces acting on the ith spoiler and the jth spoiler determined by $\delta_{ij} = \theta_j(\omega) - \theta_i(\omega)$, where $\theta_i(\omega), \theta_j(\omega)$ phases of the fluctuating drag force acting on the ith spoiler and the jth spoiler, respectively.

[1]ASHRAE (American Society of Heating, Refrigerating and Air-Conditioning Engineers) Handbook, HVAC Applications SI Edition, 47.7–47.10 (American Society of Heating, Refrigerating and Air-Conditioning Engineers, Inc., 2007).

[2]CIBSE (The Chartered Institution of Building Services Engineers) guide B5 Noise and Vibration Control for HVAC, 7–9 (The Chartered Institution of Building Services Engineers London, May 2005).

[3]T. K. Wilson and A. Iqbal, "Computer-aided analysis of airflow systems noise," Build. Services Eng. Res. Technol. **1**, 54–57 (1980).

[4]U. Ingard, A. Oppenheim, and M. Hirschorn, "Noise generation in ducts," ASHRAE Trans. **74** (1968).

[5]W. W. Soroka, Refrig. Eng. **37**, 393 (1939).

[6]W. W. Soroka, "Experimental study of high velocity air discharge noise from some ventilating ducts and elbows," Appl. Acoust. **3**, 309–321 (1970).

[7]W. F. Kerka, "In high velocity system duct parts create sound as well as suppress it," ASHRAE J. **429**, 49–54 (1960).

[8]J. H. Watson, "Acoustical characteristics of mitre bends with lined turning vanes," Australian Refrigeration, Air Conditioning & Heating **22**, 30–33 (1968).

[9]H. Brockmeyer, "Flow acoustic study of duct fittings of high velocity air conditioning systems," Ph.D. dissertation for degree of Dr.-Ing. Carolo Wilhelmina, Technical University, Braunschweig, HVRA (The Heating & Ventilating Research Assoc.) Translation 195, 1968.

[10]J. B. Chaddock, "Ceiling air diffuser noise," Technical Information Report No. 45. Bolt Beranek and Newman Inc., Boston, MA, 1957.

[11]M. Hubert, "Noise development in ventilation plant," Larmbekompfung **46–51**, 29–33 (1969).

[12]M. J. Holmes, "Air flow generated noise Part II: Bends with turning vanes," Proceedings of the Institute of Acoustics, Laboratory Report No. 78, The Heating & Ventilating Research Association, Blacknell, UK, 1973.

[13]C. G. Gordon, "Spoiler-generated flow noise. I: The experiment," J. Acoust. Soc. Am. **43**, 1041–0148 (1968).

[14]C. G. Gordon, "Spoiler-generated flow noise. II: Results," J. Acoust. Soc. Am. **45**, 214–223 (1969).

[15]H. H. Heller and S. E. Widnall, "Sound radiation from rigid flow spoilers correlated with fluctuating forces," J. Acoust. Soc. Am. **47**, 924–936 (1970).

[16]P. A. Nelson and C. L. Morfey, "Aerodynamic sound prediction in low speed flow ducts," J. Sound Vib. **79**, 263–289 (1981).

[17]D. J. Oldham and A. U. Ukpoho, "A pressure-based technique for predicting regenerated noise levels in ventilation systems," J. Sound Vib. **140**, 259–272 (1990).

[18]A. U. Ukpoho and D. J. Oldham, "Regenerated noise levels due to closely spaced duct elements," Proceedings of Institute of Acoustics **13**, 461–468 (1991).

[19]M. M. Zdravkovich, "Review of flow interference between two circular cylinders in various arrangements," J. Fluids Eng. **99**, 618–633 (1977).

[20]C. M. Mak and J. Yang, "A prediction method for aerodynamic sound produced by closely spaced elements in air ducts," J. Sound Vib. **229**, 743–753 (2000).

[21]C. M. Mak and J. Yang, "Flow-generated noise radiated by the interaction of two strip spoilers in low speed flow ducts," Acta. Acust. Acust. **88**, 861–868 (2002).

[22]C. M. Mak, "Development of a prediction method for flow-generated noise produced by duct elements in ventilation systems," Appl. Acoust. **63**, 81–93 (2002).

[23]C. M. Mak and D. J. Oldham, "The application of computational fluid dynamics to the prediction of flow generated noise in low speed ducts. Part 1: Fluctuating drag forces on a flow spoiler," Build. Acoust. **5**, 123–141 (1998).

[24]C. M. Mak and D. J. Oldham, "The application of computational fluid dynamics to the prediction of flow generated noise in low speed ducts. Part 2: Turbulence-based prediction technique," Build. Acoust. **5**, 199–213 (1998).

[25]C. M. Mak, "Prediction methods for regenerated noise produced by two elements in an air duct," Build. Acoust. **8**, 187–192 (2001).

[26]C. M. Mak and W. M. Au, "A turbulence-based prediction technique for flow-generated noise produced by in-duct elements in a ventilation system," Appl. Acoust. **70**, 11–20 (2009).

[27]C. M. Mak, "A prediction method for aerodynamic sound produced by multiple elements in air ducts," J. Sound Vib. **287**, 395–403 (2005).

[28]N. Han, X. J. Qiu, and C. M. Mak, "A further study of the prediction method for aerodynamic sound produced by two in-duct elements," J. Sound Vib. **294**, 374–380 (2006).

[29]N. Han and C. M. Mak, "Prediction of flow-gaenerated noise produced by acoustic and aerodynamic interactions of multiple in-duct elements," Appl. Acoust. **69**, 566–573 (2008).

[30]ASTM (American Society for Testing and Materials) Standard: D 3154 Standard test method for average velocity in a duct (Pitot tube method), An American National Standard (ASTM, November 2000).

Underwater noise from three types of offshore wind turbines: Estimation of impact zones for harbor porpoises and harbor seals

Jakob Tougaard[a] and Oluf Damsgaard Henriksen
Department of Arctic Environment, National Environmental Research Institute, Aarhus University, Frederiksborgvej 399, DK-4000 Roskilde, Denmark

Lee A. Miller
Institute of Biology, University of Southern Denmark, DK-5230 Odense M, Denmark

(Received 26 August 2008; revised 11 March 2009; accepted 17 March 2009)

Underwater noise was recorded from three different types of wind turbines in Denmark and Sweden (Middelgrunden, Vindeby, and Bockstigen-Valar) during normal operation. Wind turbine noise was only measurable above ambient noise at frequencies below 500 Hz. Total sound pressure level was in the range 109–127 dB re 1 μPa rms, measured at distances between 14 and 20 m from the foundations. The 1/3-octave noise levels were compared with audiograms of harbor seals and harbor porpoises. Maximum 1/3-octave levels were in the range 106–126 dB re 1 μPa rms. Maximum range of audibility was estimated under two extreme assumptions on transmission loss (3 and 9 dB per doubling of distance, respectively). Audibility was low for harbor porpoises extending 20–70 m from the foundation, whereas audibility for harbor seals ranged from less than 100 m to several kilometers. Behavioral reactions of porpoises to the noise appear unlikely except if they are very close to the foundations. However, behavioral reactions from seals cannot be excluded up to distances of a few hundred meters. It is unlikely that the noise reaches dangerous levels at any distance from the turbines and the noise is considered incapable of masking acoustic communication by seals and porpoises. © *2009 Acoustical Society of America.* [DOI: 10.1121/1.3117444]

PACS number(s): 43.50.Rq, 43.80.Nd [WWA] Pages: 3766–3773

I. INTRODUCTION

Noise levels in the oceans have increased considerably since engine powered shipping was introduced in the late 18th century. Until World War II it was not possible to measure absolute noise levels, so only post-World War II recordings of ambient noise are available for comparative studies (Urick, 1983). In a now classic comparative study Ross (1993) found a 15 dB increase in the low frequency ocean ambient noise level between 1950 and 1975. A more recent study shows that the noise level at the continental shelf off the coast of California has increased by 3–10 dB in the frequency range from 20 to 300 Hz from the mid-1960s to the turn of the century (Andrew *et al.*, 2002). Both studies conclude that the most significant source of the increased noise level is increased shipping activity.

Other sources of anthropogenic noise in the ocean include offshore installations to which offshore wind farms have recently been added. Few recordings of noise from wind turbines exist [reviewed by Wahlberg and Westerberg (2005) and Madsen *et al.* (2006)] and little is known about the reactions of marine life to this noise. The possible effects of wind turbine noise on marine mammals and the extent of zones of impact (*sensu* Richardson *et al.*, 1995) are considered in general by Madsen *et al.* (2006). The conclusion was that the zones were small, with audible ranges out to a few kilometers from the turbines under most favorable conditions.

Wind turbine noise has two main sources: air flow and turbulence noise from the wings and machinery noise. The machinery noise stems mainly from the gear box and generator located in the top of the wind turbine tower, the nacelle. The well known whoosh sounds from the wings are the main contributor to in-air noise, whereas machinery noise is the main contributor to underwater noise. Vibrations from the machinery are transmitted from the nacelle through the steel tower into the foundation from which it is radiated into the water column and into the seabed. The air borne noise is almost completely reflected from the water surface, and does not contribute significantly to the underwater noise level. The noise from gearbox and generator contain strong spectral peaks, which are generated from the repetitive contact between gear teeth. Since the turbines are maintained at a constant rate of revolution independent of wind speed, only the height of the peaks and not their location on the frequency axis is affected by increased wind speed.

Known underwater noise levels emitted from operating offshore wind farms are low by any standard (Madsen *et al.*, 2006), but as the offshore wind industry rapidly expands this does not imply that they are necessarily insignificant. High intensity noise sources in the ocean such as noise from individual ships, sonars, and seismic exploration are mostly transient in nature. On the other hand, the lifetime of an offshore wind farm is expected to be at least 20–30 years and associated noise emissions thus constitute an almost permanent

[a]Author to whom correspondence should be addressed. Electronic mail: jat@dmu.dk

 0001-4966/2009/125(6)/3766/8/$25.00

source of noise year round for many years. As offshore wind power is a new and expanding industry, there is a need to evaluate the possible effects of underwater turbine noise on marine mammals, and a first requirement for this assessment is the availability of good noise recordings from wind turbines.

Richardson *et al.* (1995) provided a common framework for noise impact assessment in the marine environment by introducing the concept of four zones of influence on marine mammal behavior and hearing. These zones are "zone of audibility," "zone of responsiveness," "zone of masking," and "zone of hearing loss, discomfort, and injury." Even though the methods for establishing these four zones for different species and noise sources are not standardized, the concept has resulted in better and more uniform noise related impact assessments. The spatial extensions of the four zones are by their nature very different as they describe different aspects of noise related influences, from the faintest sounds that are just perceptible by the animal to immediately lethal high intensity shock waves. The size of each zone differs from species to species, from individual to individual, and sometimes even for the same individual depending on the physical and behavioral status of the animal.

The zone of audibility is defined as the area where an animal can hear the sound or noise above the background noise level. The extent of this zone is easily defined and thus in principle easy to calculate as it can be found from knowledge of the hearing capabilities of the target species, background noise levels, and sound transmission patterns. In practice, however, lack of accurate measurements of one or more of these parameters may introduce considerable error in estimating the size of the zone of audibility.

Within the zone of responsiveness a target animal will react to a sound or noise with altered behavior. This can be a positive behavior (attraction, investigation, etc.), negative behavior (evasion and startle), or simply changes in ongoing behavior without obvious direction (altered breathing pattern, heart rate changes, etc.). As the zone of responsiveness is related to behavioral reactions by the target species it can only be established using behavioral observations, which in many cases are difficult to obtain. Practical measurements are further complicated by the fact that most animals will display different reactions to noise depending on previous exposure experiences and on the behavioral and physiological states of the animal during noise exposure.

The zone of masking is the area around a noise source where the noise reduces detection of other sounds that are important to the animal in question, such as communication sounds, sounds from prey or predators, and sounds used in orientation and navigation. Masking is defined in psychophysics as an elevation of thresholds for the detection or discrimination of particular sounds without a general effect on the sensitivity of the auditory system. Masking is thus separated from other phenomena such as accommodation (stapedius reflex) and temporary threshold shifts (TTSs) that cause a general reduction in auditory sensitivity following exposure to loud sounds. Accommodation should be considered a behavioral or physiological response, whereas TTS is a commonly adopted criterion defining the extent of the zone of hearing loss, discomfort, or injury (see below).

The zone of hearing loss, discomfort, or injury is usually a small zone close to very loud sound sources where the sound pressures are sufficiently high to inflict temporary or permanent damage to animals, either in their auditory system or in the form of other physiological effects. TTSs of the auditory system have been adopted in recent years as a practical and conservative measure of the lower limit of damaging sound pressures to marine mammals (Kastak *et al.*, 1999; Schlundt *et al.*, 2000; Nachtigall *et al.*, 2003; NMFS, 2003; National Research Council, 2003). Recently, however, Southall *et al.* (2007) suggested the adoption of permanent threshold shift (PTS) as a criterion for defining the zone of injury.

The last three zones, "responsiveness," "masking," and "hearing loss, discomfort, and injury," are of particular interest in the context of management as these describe effects of a noise source and can form the basis for judgments regarding short-term and long-term negative impacts on a particular species. Despite this, the zone of audibility is often used in impact assessment studies to describe worst-case scenarios, partly because this zone can be assessed with the least effort. However, if worst-case scenarios are used uncritically there is a risk of grossly overestimating the size of the zone where sound has a significant impact on the animals in question.

Our study focuses on the extent of impact zones for three different types of offshore wind turbines during normal operation. We discuss the possible effects of wind turbine noise on the hearing of harbor seals (*Phoca vitulina*) and harbor porpoises (*Phocoena phocoena*), which are the most common marine mammal species in the North Sea, the inner Danish waters, and the Baltic Sea.

II. MATERIALS AND METHODS

Underwater noise was recorded from three different types of wind turbines, denoted as locations 1–3; two Danish and one Swedish offshore wind farm. At location 1 (Middelgrunden, Denmark) underwater noise was recorded at two different wind speeds (1a and 1b). The locations and types of wind turbine are shown in Table I.

A. Noise measurements and analysis

Broadband digital recordings (100 Hz–150 kHz) of underwater wind turbine noise were made in a preliminary study. As no energy above the background noise was found for frequencies above 10 kHz, broadband recordings were not included in this study.

Portable standard digital audio tape (DAT) recording equipment with appropriate hydrophones and amplifiers were used for noise measurements. Briefly, a sensitive, calibrated hydrophone with a build-in preamplifier (a Brüel & Kjær 8101 or a Reson TC4032) was connected through a low-noise amplifier (B&K Nexus 2693A or an Etec HA01A) to a portable DAT recorder (SONY TCD-D8 or a HHP PDR 1000). Frequency responses of the recording chains were flat (within 3 dB) from 10 Hz to 20 kHz. The distances between

TABLE I. Description of the three wind farms.

Name	Position		Turbine type	No. of turbines
	Latitude	Longitude		
Middelgrunden offshore wind farm	55° 40′ N	12° 40′ E	Bonus 2 MW	20
Bockstigen-Valar offshore wind farm	56° 59′ N	16° 08′ E	WindWorld 500 kW	5
Vindeby offshore wind farm	54° 58′ N	11° 08′ E	Bonus 450 kW	11

the hydrophones and the foundations were measured using either Leica or Bushnell laser binoculars (distometers) and varied between 14 and 40 m. Recording depth was half-way between surface and bottom, i.e., 2.5, 5, and 2 m for locations 1, 2, and 3, respectively.

The complete recording setup was calibrated with a Brüel & Kjær 4223 pistonphone calibrator prior to each recording. The calibration signal was recorded on all DAT-tapes. Recorded sound levels could thus be converted to absolute levels by direct comparison with the reference signal. All other wind turbines within a range of approximately 1000 m were shut down during measurements of noise from a specific wind turbine. Background noise was measured at the same position but with all wind turbines shut down.

The audio range recordings were analyzed on a Hewlett Packard 35670A frequency analyzer (using the analog connection from the DAT recorder) and presented as 1/3-octave levels (TOLs) in dB_{rms} re 1 μPa. Each recording was divided into one section with the wind turbine active, denoted as "turbine noise," and one section with the wind turbine stopped, denoted as "background noise." Turbine and background noise recordings were subjected to identical analysis. The thirty 1/3-octave bands spanning the center frequencies from 12.5 Hz to 10 kHz were analyzed simultaneously. Unless otherwise stated, all references to frequencies in the following refer to 1/3-octave center frequencies.

The recordings from location 1 (a and b) were analyzed with multiple replicates with averaging times of 15 s [the shortest averaging time that can be used for analyzing 20 Hz white Gaussian noise with 95% confidence limits of ± 1 dB is 8 s (Brüel & Kjær, 1985)] and separated by at least 1 min in order to obtain independence between the averages. Wind turbine noise contains small periodical fluctuations due to varying load on the machinery. The period of these is one-third of the rotational speed, due to three wings of the turbines, and is approximately 1 Hz. Several cycles are thus covered within one 15-s averaging period. The total duration of recordings used for analysis at location 1 was 2.25 min at 6 m/s wind speed and 10 min at 13 m/s. Recordings from locations 2 and 3 were analyzed with averaging times of several minutes without replicates.

Statistical analysis was only applied to data from recordings at locations 1a and 1b, as measurements from locations 2 and 3 did not contain multiple replicates. The wind turbine noise levels in 1/3-octave bands were tested against the background noise levels pairwise for all bands (t-test, one-sided, equal variance). *P*-values were Dunn–Sidak-corrected for multiple comparisons (Sokal and Rohlf, 1995).

For all measurements the total sound pressure level of the turbine noise was calculated by addition of TOLs across all 1/3-octave bands.

B. Estimating the zone of audibility

Noise must be analyzed as "critical band levels" in order to be directly comparable with hearing thresholds for pure tones (Erbe, 2002), where critical bandwidths of the target species are taken into account. As few actual estimates of critical bandwidth are available for marine mammals, and almost none at very low frequencies, the common practice of using 1/3-octave bandwidths as an approximation was adopted (Madsen *et al.*, 2006). This introduces a degree of uncertainty in the estimates, but as turbine noise contains strong tonal components, generated in the gearbox machinery, the critical band levels are not strongly affected by changes in analysis bandwidth.

The zone of audibility was defined based on either the audiogram or the background noise level, depending on which of the two was limiting for detection.

The pure tone audiogram for the harbor seal was taken from the study by Kastak and Schusterman (1998) while that for the harbor porpoise was taken from Kastelein *et al.* (2002). Low frequency hearing for both marine mammals was extrapolated using a slope of approximately 35 dB per decade (Stebbins, 1983; Au, 1993) (see the discussion for further comments).

The turbine noise+background noise in a particular 1/3-octave band was used for calculating the zone of audibility if the combined level was higher than background noise alone in the same band. If the hearing sensitivity was above the background noise in a particular 1/3-octave band, then the zone of audibility was estimated by extrapolating from actual measurements out to the distance at which the turbine noise plus the background noise just equaled the auditory threshold. If the background noise was limiting, the zone of audibility was estimated by extrapolating from measurements out to the range at which the turbine noise equaled the background noise in the particular 1/3-octave band, corresponding to the point where the sum of the turbine noise and the background noise was 3 dB above background noise alone.

A suitable model for transmission loss is critical to both calculations. Due to lack of actual measurements a range was calculated. Upper end of the range was found from a cylindrical spreading loss model (transmission loss equal to $10 \log r$) and lower range was found using transmission loss equal to hyperspherical spreading ($30 \log r$) equal to the

only value for transmission loss actually measured for this type of noise (Madsen *et al.*, 2006).

III. RESULTS

Measurements of underwater noise (TOLs) from the three different wind turbines and background noise measurements are shown in Fig. 1. Common for all four recordings is that the turbine noise was only detectable above background noise levels at frequencies below 315–500 Hz. Maximum measured noise level was 126 dB re 1 μPa TOL at 25 Hz recorded at location 3 (Vindeby) at a distance of 14 m from the foundation. Maximum overall turbine noise level measured (summed across all 1/3-octave bands) was 127 dB re 1 μPa (rms) also at location 3 (Table II). The 25 Hz peak in Fig. 1(A) was clearly audible as machinery noise from the wind turbine.

Two measurements at different wind speeds were made at position 1 (Middelgrunden) and from those a pronounced effect of wind speed on noise level was observed. In both spectra a peak is present at 125 Hz, but the sound pressure level was 11 dB higher at 13 m/s wind speed, compared to 6 m/s wind speed [114 dB re 1 μPa (rms) TOL vs 103 dB re 1 μPa (rms) TOL]. The increase in intensity with wind speed, but constant frequency of the noise, is consistent with the fact that the turbines operate at a constant rate of revolution, irrespective of wind speed.

The strong peak at 25 Hz in the 6 m/s wind speed measurement was not visible in the measurement made at 13 m/s wind speed. This was likely due to a significantly higher background noise at low frequencies in the 13 m/s wind speed recording. The background noise below 50 Hz in recording B at location 1 [Fig. 1(B)] was dominated by heavy shipping noise (clearly audible in the recording) from a nearby deep water shipping lane. The measurements taken at the same position during recording A at location 1 [Fig. 1(A)] were from an unusually quiet day with little shipping traffic in the area. Furthermore the hydrophone used during recording B at location 1 was submerged from a surface float instead of a bottom mount due to rough weather. This is likely to have added to the low frequency noise due to wave-induced motion of the hydrophone.

The noise was not constant over the duration of recordings. For the recordings at position 1 it was possible to calculate percentiles of the noise intensity. 10%, 50%, and 95% percentiles for the noise at 25 Hz and at a wind speed of 6 m/s were 101 dB re 1 μPa (rms) TOL, 105 dB re 1 μPa (rms) TOL, and 109 dB re 1 μPa (rms) TOL. Similar percentiles at 125 Hz and 6 m/s wind speed were 100 dB re 1 μPa (rms) TOL, 102 dB re 1 μPa (rms) TOL, and 107 dB re 1 μPa (rms) TOL. At 25 Hz and 13 m/s these were 113 dB re 1 μPa (rms) TOL, 114 dB re 1 μPa (rms) TOL, and 116 dB re 1 μPa (rms) TOL, respectively.

The zone of audibility can be determined from the results shown in Fig. 1. Together with the turbine noise, audiograms for the harbor seal and the harbor porpoise are shown in Fig. 1. For each 1/3-octave band, the largest difference between turbine noise source level and the audiogram or the background noise, whichever is higher, was determined for

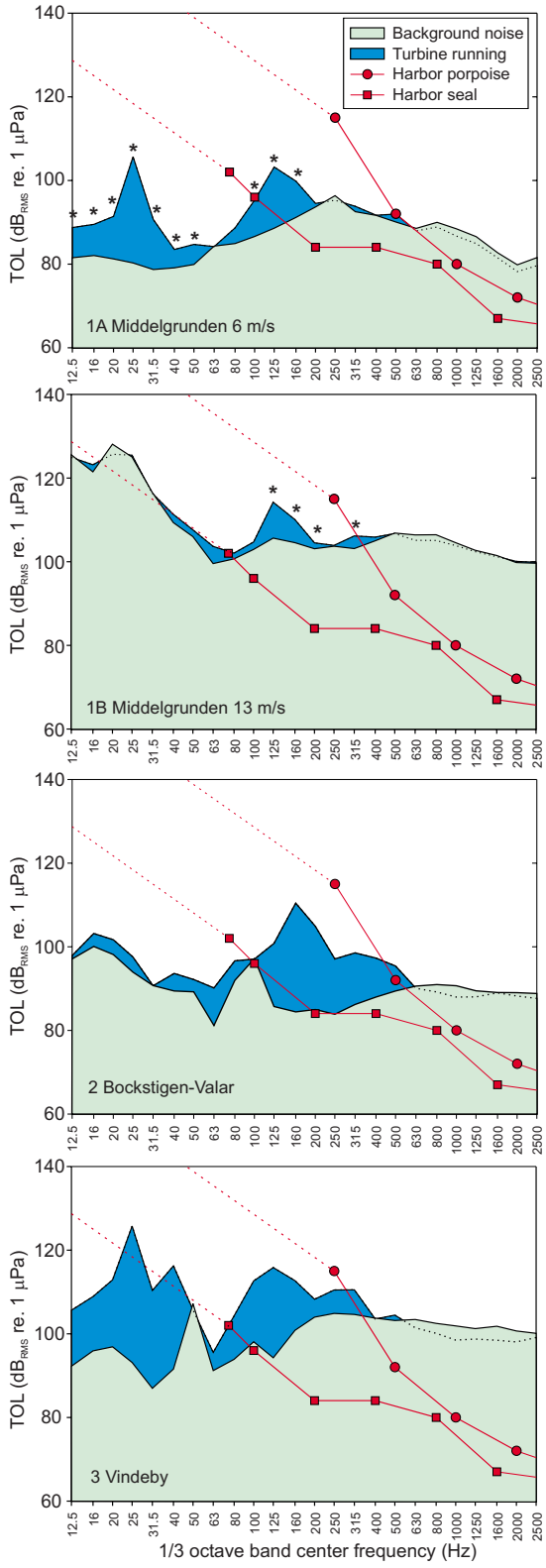

FIG. 1. (Color online) Noise recorded from three different offshore wind turbines given as 1/3-octave levels (TOLs). Background noise was measured at the same position as turbine noise but with the turbine stopped. Turbine and background noise at location 1 were measured at two different wind speeds on two different occasions. * in (A) and (B) indicate 1/3-octave bands where turbine noise was significantly higher than the background noise ($P<0.05$). Further details on recordings are given in Table II. Included in the figures are the underwater audiograms of a harbor seal and a harbor porpoise (Kastak and Schusterman, 1998; Kastelein *et al.*, 2002). Audiograms were extrapolated to low frequencies with 35 dB/octave (see text).

TABLE II. Summary of wind turbine noise measurements. Shown are the measuring distance, the wind speed, 1/3-octave bandwidths in which noise was measured, the center frequency of the 1/3-octave band containing the most energy followed by the maximum sound pressure in that band, and the overall sound pressure level of the turbine noise summed over all frequency bands. For each animal, the center frequency of the 1/3-octave band with most audible turbine noise is given (see text for further explanation). This is followed by the decibel difference above background noise, or above the detection threshold of the animal, which ever is largest. The last column for each species shows the extreme values calculated for maximum detection distance range, assuming cylindrical and hyperspherical spreading losses, respectively.

								Harbor seal			Harbor porpoise		
Location	Distance (m)	Depth (m)	Wind (m/s)	1/3-octave bands with turbine noise (Hz)	Overall sound pressure (dB re 1 μPa_{rms})	Peak band (Hz)	Sound pressure (dB re 1 μPa_{rms})	Center frequency (Hz)	Noise level (dB)	Detection distance[a] (m)	Center frequency (Hz)	Noise level (dB)	Detection distance[a] (m)
1a (Middelgrunden)	20	5	6	12.5–500	109	25	106	125	11	60–460	500	−5	19–20
1b (Middelgrunden)	40	5	13	40–400	122[b]	125	114	125	8[c]	70–250	315	−4	25–34
2 (Bockstigen-Valar)	20	10	8	12.5–500	113	160	110	160	26	140–6400	500	2	31–73
3 (Vindeby)	14	4	13	12.5–500	127	25	126	125	22[b]	70–2000	315	2	21–47

[a]Upper and lower estimates calculated by assuming cylindrical and hyperspherical spreading losses, respectively (see text).
[b]Likely overestimated due to high level of shipping noise.
[c]Limited by background noise rather than hearing threshold.

the harbor seal and the harbor porpoise. These values were used to calculate a range of maximum distance of detection (Table II) under two extreme assumptions regarding transmission loss (3 and 9 dB per doubling of distance, respectively).

The noise from all three turbines is predicted to be barely audible to harbor porpoises in all four recordings. In all cases, the turbine noise just exceeds the pure tone threshold. Thus the maximum predicted detection range is only marginally larger than the actual distance at which the recordings were obtained (Table II).

All turbines are predicted to be clearly audible to harbor seals at the locations where measurements were made as turbine noise in the 1/3-octave band best audible to the seals in all cases were ~10–20 dB above either the pure tone threshold or the background noise, whichever was the highest. The largest zone of audibility for the harbor seal was found at location 2 (Bockstigen-Valar), where the wind turbine TOL at 160 Hz exceeded the audiogram threshold by 26 dB. The predicted range of audibility in this 1/3-octave band is somewhere between 140 m and 6.4 km, strongly depending on assumptions of transmission loss.

IV. DISCUSSION

Underwater noise from the three different turbines was clearly identifiable above background noise at the distances at which measurements were obtained (14–40 m from foundations). Absolute noise levels were low, however, ranging between 109 and 127 dB re 1 μPa (rms) for total noise levels up to 20 kHz.

Based on audiograms from harbor seals and harbor porpoises the noise is predicted to be just audible to porpoises at the distances where measurements were made and audible to harbor seals at distances up to somewhere between several hundred meters to a few kilometers, depending critically on assumptions behind calculations of transmission loss. As discussed below, the noise has, due to the low intensity and the low frequency emphasis, limited if any capability to injure the animals or mask other signals of importance to seals and porpoises. Behavioral reactions to noise from the three turbines are not expected for porpoises and seals unless the animals are in the immediate vicinity of the foundation.

A. Zone of audibility

The zone of audibility for harbor seals and harbor porpoises was estimated to be between 2.5–10 km and 8–63 m, respectively (Table II), depending on critical bandwidths and under assumption of smallest transmission loss (cylindrical spreading) and for the worst of the four locations studied (Bockstigen-Valar). Harbor seals are thus able to detect the wind turbine noise at considerably longer distances than are harbor porpoises, a reflection of their significantly better low frequency hearing. It is worth noting that the greatest zone of audibility was not found around the most noisy wind turbine (location 3, Vindeby), but rather at location 2 (Bockstigen-Valar). The high source level at location 3 was caused by strong winds (and resulting heavy load on the turbine). The strong winds, however, also increased the wave induced background noise level leaving the extent of the zone of audibility around the wind turbine largely unaffected, as turbine noise to background noise level remains largely unaffected.

1. Transmission loss and near field effects

Assumptions on transmission loss are central to the calculation of the zone of audibility. In the above calculations an upper and a lower value for the extent of the zone were calculated. The upper extreme was based on a worst case assumption of cylindrical transmission loss (3 dB attenuation per distance doubled). However, true cylindrical spreading is rarely realized under natural conditions and actual measurements at a wind farm not included in this study (Utgrunden offshore wind farm, Madsen *et al.*, 2006) indicated a transmission loss as high as 9 dB per distance doubled. Until more measurements of transmission loss of turbine noise are available, there is thus good reason to consider the upper limit of the audibility ranges in Table II as unrealistic worst case scenarios.

Additional complications in calculating the audibility ranges could arise from the fact that noise measurements had to be made at short distances from the turbines, probably within the acoustic near field. Transmission loss in the near field is unpredictable due to the large size of the sound producing surface (entire foundation of turbines) and possibly also to Lloyd mirror effects caused by the shallow water. Lloyd mirror effects, however, are probably of minor importance as the sound did not radiate from a point but from the entire turbine foundation, and measurements were made under windy conditions, where the sea surface was rough and thus did not create strong specular reflections. The Fresnel near field generated by the large transducer area may extend out to several times the size of the foundation, i.e., out to distances of several tens of meters. An extension of the Fresnel near field beyond the measuring point would mean that simple geometric spreading cannot be assumed from the measuring point and hence an underestimation of the zone of audibility.

2. Auditory sensitivity: Hearing curve extrapolations

Few studies have dealt with hearing at very low frequencies in marine mammals and no thresholds are available for the lowest frequencies found in the turbine noise. In order to access the audibility of the noise, an extrapolation of existing audiogram data is needed. One low frequency audiogram is available for harbor seal (Kastak and Schusterman, 1998). It spans the frequency range from 75 to 6400 Hz, which only partially overlaps with the frequency range of the wind turbine noise. Likewise, a single audiogram with information on low frequency hearing is available for harbor porpoise (Kastelein *et al.*, 2002), covering the frequency range down to 250 Hz. Mammalian audiograms, including those of marine mammals, have in common a characteristic gradual increase in thresholds for low frequencies, with a slope of approximately 35 dB per decade (Stebbins, 1983; Au, 1993). Thus, the audiograms of harbor seal and harbor porpoise were extrapolated by a straight line with a slope of 35 dB per decade for frequencies below 75 Hz for the harbor seal and 250 Hz for the harbor porpoise (Fig. 1). This extrapolation is critical, and especially for species where no data on auditory sensitivity are available, the assumptions regarding audiograms are of utmost importance in estimating the zones of audibility.

3. Critical bandwidths

In order to compare broadband noise to an audiogram, the noise level must be stated in critical band levels, describing sound power per critical bandwidth (as done by Erbe and Farmer, 2000), instead of using the standard expression of sound power per 1 Hz bands. Assumptions on the width of the critical bands will affect calculations of the zone of audibility. Narrow critical bands, which may be seen as an adaptation to high-resolution frequency discrimination (Au, 1993), will result in less sensitivity to broadband noise whereas the opposite is true for wide critical bands (Au *et al.*, 2004). Good estimates of critical bandwidths are thus necessary when estimating the possible impact from man-made noise on marine mammals. Not much is known about the critical bandwidths of harbor porpoises and harbor seals at the low frequencies considered in this study. The harbor seal critical bandwidth has been measured by Terhune and Turnbull (1995), and the harbor porpoise estimated indirectly by Popov *et al.* (2006). The critical bandwidth for harbor seals has only been measured for frequencies above 4 kHz, and changes from 1/3-octave at 4 kHz to approximately 1/6-octave at 30 kHz. The critical bandwidth for ringed seals (*Phoca hispida*) (Terhune and Ronald, 1975) and northern fur seal (*Callorinus ursinus*) (Moore and Schusterman, 1987) is less than 1/6-octave in the frequency range between 2 and 30 kHz. Common for these two species is that the critical bandwidth increases for lower frequencies, increasing the sensitivity to broadband noise. Based on these data it is assumed that the critical bandwidth for harbor seals has a pattern similar to the two other pinnipeds and thus is between 1/6- and 1/3-octave wide in the frequency range below 1000 Hz.

Critical bandwidth measurements for cetaceans below 1 kHz are only available for the beluga (*Delphinapterus leucas)* (Johnson *et al.*, 1989). It varies from 1/12-octave at 1 kHz to approximately 2/3-octave at 200 Hz. The critical bandwidth of harbor porpoises was assessed by Popov *et al.* (2006) using auditory brainstem responses with pure-tones both as signals and maskers. In contrast to what is known for all other mammals, the bandwidth of the auditory filters in the harbor porpoise and the Finless porpoise (*Neophocoena phocaenoides*) was found to be approximately constant on a linear scale (constant bandwidth with increasing center frequency). Other mammals, including odontocetes such as bottlenose dolphin (*Tursiops truncatus*) (Johnson, 1968; Au and Moore, 1990) and False killer whale (*Pseudorca crassidens*) (Thomas *et al.*, 1990), have auditory filter bandwidths that are approximately constant on a logarithmic scale (constant ratio of bandwidth to center frequency). The measurements of Popov *et al.* (2006) indicate a constant filter bandwidth of around 3–4 kHz, irrespective of the center frequency in the range 20–150 kHz. Extrapolating to lower frequencies indicates that the critical bandwidth could be as much as several octaves in the frequency range of the turbine noise. As the main energy in the turbine noise is localized at a few prominent tonal peaks, broader filter bandwidths in this range would mean that the turbine noise would be masked by the broadband background noise and thus, if anything, would be harder to detect for the porpoises than the predictions in Table II, based on an assumption of 1/3-octave filter bands.

B. Zone of responsiveness

As described in the Introduction, the zone of responsiveness is not as straightforward to define and estimate as the zone of audibility and the zone of masking, but must be estimated based on actual observations. A number of studies have addressed the effect of various sound sources on the behavior of seals and porpoises, both in captivity and in the wild (most of these are summarized in Southall *et al.*, 2007). It is difficult to generalize from these studies to the turbine

noise of this study, but in general no studies have demonstrated significant behavioral reactions at received levels below about 100 dB re 1 μPa rms for odontocetes and about 140 dB re 1 μPa rms for pinnipeds. Due to the poor hearing capabilities of harbor porpoises within the turbine noise frequency range behavioral effects are unlikely, even at close range, simply because they cannot hear the noise, unless very close to the turbine. Harbor seals on the other hand have better hearing, but as summarized by Southall *et al.* (2007) they are more tolerant to underwater noise than odontocetes and it is questionable whether they would experience levels exceeding 140 dB re 1 μPa rms, even if they were next to the foundation. For the three turbines in this study the extent of the zone of responsiveness is thus considered small and insignificant. Other turbines, however, may produce louder noise or more importantly peak energies at higher frequencies. In this case the zones of responsiveness would be larger, but until a better general knowledge of underwater noise for other types of turbines is available, the possibility of behavioral effects should not be dismissed.

C. Zone of masking

In order for a signal to be masked by noise there must be an overlap between the frequencies of the signal and those of the noise. For a broadband signal to be masked by broadband noise it is reasonable to assume that the noise has to be at the same intensity as the signal (Green, 1969) and if the signal contains strong tonal components, even higher noise levels are needed (Au and Moore, 1990). Harbor seals are very social animals and are known to use a wide variety of communication sounds. Hanggi and Schusterman (1994) and Bjørgesæter *et al.* (2004) reported numerous different underwater sounds, several of which have components in the frequency range below 1000 Hz. All of these display sounds overlap with the wind turbine noise and they could potentially be masked to some degree. However, the broadband nature of the harbor seal sounds, as well as the low intensity of the turbine noise, makes it unlikely that communication signals are masked unless either the calling or the listening seal is located immediately next to the turbine foundation. The zone of masking is thus considered insignificant for harbor seals.

Harbor porpoises use ultrasound for echolocation and communication. Their signals have a peak frequency about 130 kHz and contain virtually no energy below 100 kHz (Møhl and Andersen, 1973; Teilmann *et al.*, 2002). Thus, the reception of these sounds cannot be affected by the turbine noise, which has energy at very low frequencies. The low sensitivity of porpoise hearing at low frequencies (as compared to seals) suggests that passive listening for sounds below 1000 Hz does not play a significant role for the porpoises. Zone of masking is thus considered to be zero for porpoises.

D. Zone of hearing loss, discomfort, and injury

As described in the Introduction, there is common agreement that the intensity of sounds eliciting TTSs can be used as the lower limit for defining the zone of damage (however, see Southall *et al.*, 2007 on the application of PTSs in impact assessment). TTS elicited by continuous noise exposure has been measured in harbor seals (Kastak *et al.*, 1999). It was found that 20 min of exposure to octave band white noise, 60 dB above the harbor seal hearing threshold at 100, 500, and 1000 Hz center frequencies (i.e., approximately 155, 144, and 140 dB re 1 μPa, respectively) resulted in an average 4.8 dB temporary decrease in hearing sensitivity. These levels are considerably higher than those to which a seal or porpoise will be exposed to when close to wind turbine, and animals remaining even very close to the foundation are unlikely to experience any hearing damage (temporary or permanent). For the types of turbines studied here there is thus no zone in which seals or porpoises are exposed to dangerously high levels of noise.

ACKNOWLEDGMENTS

Thanks to Rune Dietz, Jonas Teilmann, Peter T. Madsen, Magnus Wahlberg, Charlotte Boesen, and Pernille Holm Skyt for comments and advice; Uffe Degn, Rene Lützen, and Chris Maxon from Ødegaard & Danneskiold-Samsøe A/S for cooperation in the field and the laboratory; and Jakob Rye Hansen, Kenneth Kragh Jensen, and Marie Wandel for assistance in the field. The study was funded by the Danish Energy Authority, DONG Energy A/S, and SEAS' Center for Wind Power. Jakob Tougaard was funded during part of the study by the Danish National Research Foundation (Centre for Sound Communication, Institute of Biology, University of Southern Denmark). Financial support from the Danish Council for Strategic Research is also acknowledged.

Andrew, R. K., Howe, B. M., and Mercer, J. A. (**2002**). "Ocean ambient sound: Comparing the 1960s with the 1990s for a receiver off the California coast," ARLO **3**, 65–70.

Au, W. (**1993**). *The Sonar of Dolphins* (Springer, New York).

Au, W. W. L., Ford, J. K. B., Horne, J. K., and Allman, K. N. (**2004**). "Echolocation signals of free-ranging killer whales (*Orcinus orca*) and modelling of foraging for Chinook salmon (*Onchorynchus tshawytscha*)," J. Acoust. Soc. Am. **115**, 901–909.

Au, W. W. L., and Moore, P. W. B. (**1990**). "Critical ratio and critical bandwidth for the Atlantic bottle-nosed-dolphin," J. Acoust. Soc. Am. **88**, 1635–638.

Bjørgesæter, A., Ugland, K. I., and Bjørge, A. (**2004**). "Geographic variation and acoustic structure of the underwater vocalization of harbour seal *(Phoca vitulina)* in Norway, Sweden and Scotland," J. Acoust. Soc. Am. **116**, 2459–2468.

Brüel & Kjær (**1985**). *Noise and Vibration—Pocket Handbook* (Brüel & Kjær, Copenhagen).

Erbe, C. (**2002**). "Underwater noise of whale-watching boats and potential effects on killer whales *(Orcinus orca)*, based on an acoustic impact model," Marine Mammal Sci. **18**, 394–418.

Erbe, C., and Farmer, D. M. (**2000**). "A software model to estimate zones of impact on marine mammals around anthropogenic noise," J. Acoust. Soc. Am. **108**, 1327–1331.

Green, D. M. (**1969**). "Masking with continuous and pulsed sinusoids," J. Acoust. Soc. Am. **46**, 939–946.

Hanggi, E. B., and Schusterman, R. J. (**1994**). "Underwater acoustic displays and individual variation in male harbour seals, *Phoca vitulina*," Anim. Behav. **48**, 1275–1283.

Johnson, C. S. (**1968**). "Masked tonal thresholds in the bottlenosed porpoise," J. Acoust. Soc. Am. **44**, 965–967.

Johnson, C. S., McManus, M. W., and Skaar, D. (**1989**). "Masked tonal hearing thresholds in the beluga whale," J. Acoust. Soc. Am. **85**, 2651–2654.

Kastak, D., and Schusterman, R. J. (**1998**). "Low-frequency amphibious hearing in pinnipeds: Methods, measurements, noise, and ecology," J. Acoust. Soc. Am. **103**, 2216–2228.
Kastak, D., Schusterman, R. J., Southall, B. L., and Reichmuth, C. J. (**1999**). "Underwater temporary threshold shift induced by octave-band noise in three species of pinnipeds," J. Acoust. Soc. Am. **106**, 1142–1148.
Kastelein, R. A., Bunskoek, P., Hagedoorn, M., Au, W. W. L., and de Haan, D. (**2002**). "Audiogram of a harbour porpoise (*Phocoena phocoena*) measured with narrow-band frequency-modulated signals," J. Acoust. Soc. Am. **112**, 334–344.
Madsen, P. T., Wahlberg, M., Tougaard, J., Lucke, K., and Tyack, P. L. (**2006**). "Wind turbine underwater noise and marine mammals: Implications of current knowledge and data needs," Mar. Ecol.: Prog. Ser. **309**, 279–295.
Møhl, B., and Andersen, S. (**1973**). "Echolocation: High-frequency component in the click of the harbour porpoise (*Phocoena p.* L.)," J. Acoust. Soc. Am. **54**, 1368–1372.
Moore, P. W. B., and Schusterman, R. J. (**1987**). "Audiometric assessment of northern fur seals, *Callorhinus ursinus*," Marine Mammal Sci. **3**, 31–53.
Nachtigall, P. E., Pawloski, D. A., and Au, W. W. L. (**2003**). "Temporary threshold shifts and recovery following noise exposure in the Atlantic bottlenosed dolphin (*Tursiops truncatus*)," J. Acoust. Soc. Am. **113**, 3425–3429.
National Research Council (**2003**). *Ocean Noise and Marine Mammals* (National Academies Press, Washington, DC).
NMFS (**2003**). "Taking marine mammals incidental to conducting oil and gas exploration activities in the Gulf of Mexico," Fed. Regist. **68**, 9991–9996.
Popov, V. V., Supin, A. Y., Wang, D., and Wang, K. (**2006**). "Nonconstant quality of auditory filters in the porpoises, *Phocoena phocoena* and *Neophocoena phocaenoides* (Cetacea, Phocoenidae)," J. Acoust. Soc. Am. **119**, 3173–3180.
Richardson, W. J., Greene, C. R., Malme, C. I., and Thomson, D. H. (**1995**). *Marine Mammals and Noise* (Academic, San Diego, CA).
Ross, D. (**1993**). "On ocean underwater ambient noise," Acoust. Bull. **18**, 5–8.
Schlundt, C. E., Finneran, J. J., Carder, D., and Ridgway, S. H. (**2000**). "Temporary shift in masked hearing thresholds of bottlenose dolphins, *Tursiops truncatus*, and white whales, D*elphinapterus leucas*, after exposure to intense tones," J. Acoust. Soc. Am. **107**, 3496–3508.
Sokal, R. R., and Rohlf, F. J. (**1995**). *Biometry*, 3rd ed. (Freeman, New York).
Southall, B. L., Bowles, A., Ellison, W. T., Finneran, J. J., Gentry, R. L., Greene, C. R., Kastak, D., Ketten, D. R., Miller, J. H., Nachtigall, P. E., Richardson, W. J., Thomas, J. A., and Tyack, P. L. (**2007**). "Marine mammal noise exposure criteria: Initial scientific recommendations," Aquat. Mamm. **33**, 411–521.
Stebbins, W. (**1983**). *The Acoustic Sense of Animals* (Harvard University Press, Cambridge, MA).
Teilmann, J., Miller, L. A., Kirketerp, T., Madsen, P. T., Nielsen, B. K., and Au, W. W. L. (**2002**). "Echolocation characteristics of a harbour porpoise during target detection," Aquat. Mamm. **28**, 275–284.
Terhune, J. M., and Ronald, K. (**1975**). "Masked hearing thresholds of ringed seals," J. Acoust. Soc. Am. **58**, 515–516.
Terhune, J. M., and Turnbull, S. (**1995**). "Variation in the psychometric functions and hearing thresholds of a harbour seal," in *Sensory Systems of Aquatic Mammals*, edited by R. Kastelein, J. A. Thomas, and P. E. Nachtigall (De Spil, Woerden, Holland), pp. 81–93.
Thomas, J. A., Pawlovski, J. L., and Au, W. W. L. (**1990**). "Masked hearing abilities in a false killer whale (Pseudorca crassidens)," in *Sensory Abilities in Cetaceans. Laboratory and Field Evidence*, edited by J. A. Thomas and R. A. Kastelein (Plenum, New York), pp. 395–404.
Urick, R. J. (**1983**). *Principles of Underwater Sound*, 3rd ed. (Peninsula, Los Altos Hills, CA).
Wahlberg, M., and Westerberg, H. (**2005**). "Hearing in fish and their reactions to sounds from offshore wind farms," Mar. Ecol.: Prog. Ser. **288**, 295–309.

Hole distribution in phononic crystals: Design and optimization

V. Romero-García and J. V. Sánchez-Pérez[a)]
Centro de Technologías Físicas: Acústica, Universidad Politécnica de Valencia, Camino de Vera s/n, 46022 Valencia, Spain

L. M. García-Raffi
Instituto Universitario de Matemática Pura y Aplicada, Universidad Politécnica de Valencia, Camino de Vera s/n, 46022 Valencia, Spain

J. M. Herrero, S. García-Nieto, and X. Blasco
Department of Systems Engineering and Control, Universidad Politécnica de Valencia, Camino de Vera s/n, 46022 Valencia, Spain

(Received 10 July 2008; revised 10 April 2009; accepted 10 April 2009)

An exhaustive study has been made into the potential improvement in attenuation and focusing of phononic crystal arrays resulting from the deliberate creation of vacancies. Use is made of a stochastic search algorithm based on evolutionary algorithms called the epsilon variable multi-objective genetic algorithm which, in conjunction with the application of multiple scattering theory, enables the design of devices for effectively controlling sound waves. Several parameters are analyzed, including the symmetries used in the distribution of holes and the optimum number of holes. The validity and utility of the general rules obtained have been confirmed experimentally.
 [DOI: 10.1121/1.3126948]

PACS number(s): 43.55.Ev, 43.20.El, 43.20.Hq, 43.40.Sk [KA] Pages: 3774–3783

I. INTRODUCTION

During the past decade, new materials for controlling sound waves have been successfully designed and used. Devices formed by arrays of scatterers embedded in another medium with a periodical modulation of the physical properties between them have been shown to be useful alternatives to homogeneous materials. The behavior of phononic crystals (PCs) formed from periodic arrays of cylinders in the range of wavelengths larger than the separation between the scatterers is a topic of increasing interest. In the ranges of frequencies related to the periodicity of the array formed, these systems present spectral band gaps where the propagation of sound is forbidden. A considerable effort has been made studying their physical properties,[1–4] and this research has lead to the development of acoustic devices based on these materials.[5–8]

In recent years, there has been a growing interest in increasing and optimizing the sonic properties of these materials. The main motivation has been the development of technology for controlling sound. Some studies show performance improvements by means of varying the physical properties of the scatterers used: scatterers with resonant acoustic properties[9–12] or acoustic absorption.[13] Other possibilities include using scatterers with different shapes,[14,15] or varying the position of the scatterers in order to change the properties of the array. In this context, some authors analyzed the use of high-symmetry quasicrystals as acoustic lenses.[16]

The properties of defect modes and their application as waveguides and acoustic filters have attracted a great deal of interest for many years,[17–24] but the discussion of this mechanism and its properties are outside the scope of this work. Nevertheless, one of the strategies often used in the enhancement of the properties of PCs is based on the creation of defects in the starting array. Some authors demonstrated the possibility of increasing the attenuation capability of these materials by creating a periodic distribution of defects in the array.[25] Other authors used the creation of vacancies in conjunction with optimization algorithms, such as the genetic algorithm, as a method to increase the attenuation properties or to create lenses based on PCs.[26–29] There are clear advantages in using this method in the design of devices based on PCs, and this seems a suitable method for designing devices that are lighter and cheaper than complete PCs. Moreover, in some cases, as in the case of acoustic barriers, these new devices could be more competitive—both acoustically and economically—than the classical screens currently used. However, a study to analyze and systematize the best strategy for the mechanism that creates the holes seems necessary.

In this paper, we investigate the optimization of the acoustic properties of these materials using the mechanism for the creation of vacancies (subsequently referred to as "holes") in starting and complete two-dimensional (2D) PCs. Our aim is to provide general rules regarding (i) the optimum number of vacancies and (ii) how these vacancies should be distributed inside the crystal. Our approach to this problem consists of optimizing several acoustic properties simultaneously by means of a search algorithm. This situation is usually known as a multi-objective problem and may be solved with an optimization algorithm called the multi-objective evolutionary algorithm.[30] In this work, we have used a new implementation of this tool based on genetic

[a)]Author to whom correspondence should be addressed. Electronic mail: jusanc@fis.upv.es

algorithms, termed the epsilon variable multi-objective genetic algorithm (evMOGA),[31,32] in conjunction with a multiple scattering theory (MST).[33] A parallel implementation of the evMOGA method is used here, and the execution time of the optimization process is drastically reduced. This approach has not been previously used in 2D PC design due to the fact that, until now, the optimization of the sonic properties of these materials has been considered as a single objective problem.[26–29] The rest of the paper is arranged as follows. In Sec. II, we define the method of calculation. The results and discussion are developed in Sec. III. The experimental results that support our conclusions are presented in Sec. IV. Finally, we explain our conclusions in Sec. V.

II. METHOD OF CALCULATION

A. MST

Several mathematical methods have been used in recent years to study the physical behavior of PCs. These methods can be classified as theoretical or phenomenological. The former are based either on mathematical functions with a fixed symmetry or on a numerical resolution of the wave equation.[34,35] Phenomenological methods are based on experimental data obtained in specific situations.[36] In this paper, we have used a theoretical method called MST.

When an incident sound wave travels inside a PC, a multiple scattering process is produced due to the periodicity of the scatterers in the array. MST (Refs. 34–37) is based on the well-known Korringa–Kohn–Rostoker theory[38,39] and is a self-consistent theoretical method for calculating acoustic pressure. It includes all orders of scattering for mixed and high contrast composites. In this work, we have used a 2D MST for rigid cylinders with Neumann boundary conditions. The total acoustic pressure incident around the nth cylinder is the combined effect of the total acoustic incident pressure and the scattered pressure. Then,

$$P_{\text{in}}^{n}(\boldsymbol{r}) = P_0(\boldsymbol{r}) + \sum_{j=1, j\neq 1}^{N} P_s(\boldsymbol{r}, \boldsymbol{r}_j). \tag{1}$$

We can express the total acoustic pressure incident around the jth cylinder as

$$P_{\text{in}}^{n}(\boldsymbol{r}) = \sum_{q=-\infty}^{q=\infty} B_q^n J_q(k|\boldsymbol{r} - \boldsymbol{r}_n|) e^{iq\theta_{r-r_n}}. \tag{2}$$

The incident pressure from the source with respect to the coordinates centered at $\boldsymbol{r}_i$ is

$$P_0(\boldsymbol{r}) = \sum_{q=-\infty}^{q=\infty} S_q^n J_q(k|\boldsymbol{r} - \boldsymbol{r}_n|) e^{iq\theta_{r-r_n}}, \tag{3}$$

and the scattered pressure is

$$P_s(\boldsymbol{r}, \boldsymbol{r}_n) = \sum_{q=-\infty}^{q=\infty} \sum_{l=-\infty}^{l=\infty} i\pi A_l^j H_{l-q}(k|\boldsymbol{r}_n - \boldsymbol{r}_j|) e^{i(l-q)\theta_{r_n - r_j}} J_q(k|\boldsymbol{r} - \boldsymbol{r}_n|) e^{iq\theta_{r-r_n}}. \tag{4}$$

Using Eqs. (2)–(4) in Eq. (1), we obtain the following coefficient equation:

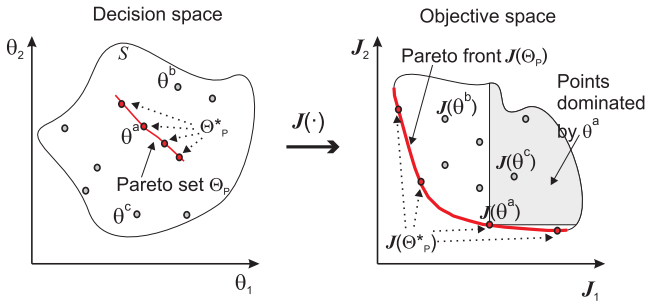

FIG. 1. (Color online) Example of a multiobjective optimization problem with 2D decision and objective space.

$$B_q^n = S_q^n + \sum_{j=1, j\neq 1}^{N} \sum_{l=-\infty}^{l=\infty} i\pi A_l^j H_{l-q}(k|\boldsymbol{r}_n - \boldsymbol{r}_j|) e^{i(l-q)\theta_{r_n - r_j}}. \tag{5}$$

To solve Eq. (5), we have to relate the coefficients B_q^j and A_q^j. This can be achieved with the Neumann boundary condition:

$$\left.\frac{\partial P_{\text{ext}}}{\partial n}\right|_{r=r_0} = 0, \tag{6}$$

where n represents the normal direction of the boundary surface. The coefficients A_q^j can then be obtained, and the acoustic pressure at any point outside the cylinders is

$$P(\boldsymbol{r}) = i\pi H_0^{(1)}(k|\boldsymbol{r}|) + \sum_{l=1}^{N} \sum_{q=-\infty}^{q=\infty} i\pi A_q^l H_q(k|\boldsymbol{r} - \boldsymbol{r}_l|) e^{iq\theta_{r-r_l}}, \tag{7}$$

where N is the number of cylinders with radius r located at $\boldsymbol{r}_l$ (with $l=1, \ldots, N$), k is the wave number, i is the imaginary unit, $H_0^{(1)}$ the zeroth order first-type Hankel function, $\theta_{\mathbf{r}-\boldsymbol{r}_l}$ the azimuthal angle of the vector $\boldsymbol{r}-\boldsymbol{r}_l$ to the positive x-axis, A_{lq} are the coefficients of the series expansion of the pressure, and H_{lq} is the qth order first-type Hankel function.

Although MST can be used to calculate accurately the dispersion relation of mixed composites where the contrast between the material parameters of scatterers and the host is very high,[40] the MST method presents some problems from the point of view of its use in classical optimization methods due to the large set of parameters involved: the type of dependencies, the size of the decision space (number of possible configurations of structures, i.e., PCs with or without holes), and the computational time show the complexity of the problem. The coefficients of the series expansions in the MST, A_q^l, are determined numerically from the equations obtained using the boundary conditions, and their values are related to both the frequency and the parameters defining the PC. As a consequence, the acoustic pressure, Eq. (7), depends simultaneously on discrete and continuous variables and is difficult to optimize.

An optimization method looks for the best solution in the decision space (also known as search space, see Fig. 1), that is, the space occupied by all the possible configurations of structures in our problem. Each structure is characterized by a vector of dimension N, where each coordinate is related with a position in the starting PC, so that the value of each

coordinate represents the existence of a cylinder, or a hole, in each position of the starting PC. Then, the dimension of the decision space is N and the size is 2^N. We also have to take into account that the computational time to calculate A_q^l increases to the third power of the number of cylinders (dimension of the decision space), N^3. So, the large existing number of cylinders in the designed devices implies considerable computational time. Finally, difficulty is added by the fact that the pressure calculated by MST depends on several variables of different types (real, integer, etc.). Therefore, the use of classical optimization methods is not feasible. Fortunately, the parallel implementation of the evMOGA method used in this work enables us to overcome these problems.

B. Multi-objective evolutionary algorithm

Decisions about optimal design in many scientific or engineering areas involve searching for compromises between different objectives. It is natural to look for the best solution to each objective. However, if objectives are in conflict, an improvement in one, or more, objectives means a worsening in one, or more, of the other objectives. The difficulty is the absence of a single optimal solution. Problems where several conflicting objectives have to be optimized simultaneously are known in the literature as multi-objective optimization problems. For this type of problem, the optimal solution is a set called the Pareto set Θ_p. The main characteristic of the members of this set is that any of the solutions is better than the other solutions for some of the objectives—meaning that all solutions are optimal in some sense. Basic concepts for these kinds of problems are illustrated in Fig. 1 for a minimization problem with two objectives (J_1 and J_2) and two decision variables (θ_1 and θ_2). The problem is set as

$$\min J(\theta) = \min[J_1(\theta), J_2(\theta)] \text{ subject to } \theta = [\theta_1, \theta_2] \in S. \tag{8}$$

One of the important definitions in this tool is the concept of dominance: a point $\theta^x = [\theta_1^x, \theta_2^x]$ is dominated by another point $\theta^y = [\theta_1^y, \theta_2^y]$ if at least one of the objectives of θ^x $[J_1(\theta^x)$ or $J_2(\theta^x)]$ is worse than the corresponding θ^y objective $[J_1(\theta^y)$ or $J_2(\theta^y)]$. This is true providing the rest of the objectives are equal.

Figure 1 shows, as an example, a situation where θ^a dominates θ^c, but not θ^b. The gray area represents all the points (in the objective space) dominated by θ^a.

We can define the Pareto set (and its corresponding Pareto front) as the set of nondominated points. The Pareto set in Fig. 1 is referred to as Θ_p and the Pareto front as $J(\Theta_p)$.

Solving a multi-objective optimization problem by obtaining the Pareto optimal solution (Pareto set and Pareto front) is not a trivial problem. For instance, some problems present an infinite number of points, and these problems must be solved by means of classical multi-objective optimization algorithms.[41] In essence, the aim of these algorithms is to obtain a discrete approximation of the Pareto set Θ_p^* and Pareto front $J(\Theta_p^*)$ in a distribution near $J(\Theta_p)$, while ensuring that solutions are not too near each other (since they would then be more or less the same) and attempting to characterize all of the Pareto front (see Fig. 1). However, classical algorithms are sometimes not the best option in problems where the shape of the Pareto front is complicated and shows problems of discontinuity.

An interesting alternative for solving multi-objective optimization problems is based on the use of evolutionary algorithms, which enable the simultaneous generation of several elements of the Pareto optimal set in parallel and in a single run. Evolutionary algorithms (or evolutionary computations) are inspired by biological evolution: reproduction, mutation, recombination, and selection.[30] An initial population (a set of possible solutions) evolves by applying genetic operators that combine the characteristics of some of the individuals of the population. At each iteration of the algorithm, the population changes and tries to converge to the optimal solution Θ_p, $J(\Theta_p)$.

A number of authors have developed different operators or strategies for converting the original single objective evolutionary algorithms into multi-objective optimization evolutionary algorithms that converge toward the Pareto optimal set with a set that is sufficiently discrete and diverse to be able to characterize it.[42] The good results obtained with this type of algorithm, together with their ability to handle a wide variety of problems with differing degrees of complexity, explains their increasing use in many situations.[43]

The algorithm used in this work is one of the most recent developments in MOGA. The evMOGA is an elitist multi-objective evolutionary algorithm based on the concept of epsilon-dominance.[44] A complete and detailed version of the evMOGA algorithm is described in Refs. 31 and 32. The evMOGA algorithm obtains a discrete approximation of the Pareto set, Θ_p^*, that converges toward the Pareto optimal set Θ_p in a smart way (in this type of distribution the more sloped a zone of the Pareto front, then the more points that are used to characterize the zone), and using limited memory resources.

One of the limitations of multi-objective optimization evolutionary algorithms is their high computational cost. For each individual of the chosen population, the objective functions have to be computed, and in most cases, this represents the costly part of the algorithm. Improvements in execution time have been obtained with a parallel implementation of evMOGA. Several alternatives for parallelization are possible,[45] and we have chosen the master-slave configuration. In this architecture, one processor works as master, executing the evolutionary tasks of evMOGA, while the other processors evaluate the objective function (see Fig. 2).

The master has to send a point in the decision space (or a set of points) to each slave, which then perform an objective function evaluation, and returns the results to the master. The master works synchronously, waiting for all the objective function values from each slave. After receiving all the values, the master performs the evolution to produce the next iteration and then sends the new population to the slaves for evaluation. This type of implementation is the simplest and does not change evMOGA operators or behavior. Thus, the optimization process is divided into three main procedures: evolution, communication between master-slaves, and the objective function evaluation. If the evolution and the

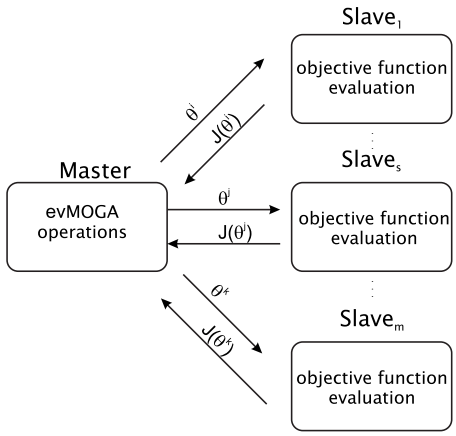

FIG. 2. Master-slave architecture for parallel evMOGA.

master-slave communication do not have a high computational cost, the overall time is theoretically divided by the number of slaves. So, the master-slave configuration offers a significant saving of time.

C. Starting conditions: Strategies in the creation of holes

In this paper, we seek to improve the acoustic properties of 2D PCs formed by isolated and rigid cylinders in air. We chose a starting PC containing 73 (4 cm diameter) cylinders, positioned in seven rows in a triangular pattern with a lattice constant $a=6.35$ cm. We have calculated, by means of MST, the acoustic pressure of the optimized samples for a predetermined range of frequencies, at a point located 1 m from the middle of the PC and in the ΓX direction (Fig. 3).

The optimized structures are obtained by means of the creation of vacancies, i.e., removing cylinders in the starting PC. To design these structures, we have used four strategies in the creation of vacancies by taking into account the symmetry axis of the starting PC (Fig. 3): (i) symmetry around the X axes (sym$X$), (ii) symmetry around the Y axes (sym$Y$), (iii) symmetry around both the X and Y axes (symXY), and (iv) random (nosym).

D. Characterization of the devices obtained

Due to the nature of multi-objective problems, the optimized solution is represented by a set of structures (Pareto set, see Sec. II B). It seems necessary to define suitable tools to characterize these optimized structures. Moreover, these

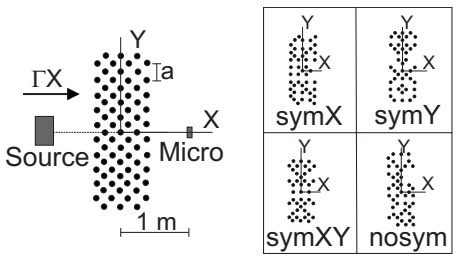

FIG. 3. Starting conditions for the analysis. The inset shows an example of each of the different strategies used in the creation of vacancies in the starting PC.

tools will enable a comparison among the different optimized samples. We have defined both optimizing and structural tools. The former help arrange the resulting samples as a function of their acoustic properties. These tools are Pareto front (PF), optimizing factor (O_f), and area of the spectrum (AS). Structural tools help establish the best arrangement of the vacancies for enhancing the acoustic properties of the resulting devices. These parameters are fraction of vacancies (F_v) and asymmetry (A). These tools are defined as follows.

Pareto front (PF). As we have mentioned above, in the approach to multi-objective optimization problems, the notion of optimized structures changes because the solution is a good compromise between the objectives involved in an optimization process. Thus, we do not normally obtain a single solution, but a set of solutions called the Pareto optimal set, which is mapped by the objective functions of the Pareto front (see Fig. 1). All points representing the PF correspond to optimum solutions. However, in our case, with two objective functions, we can see in Fig. 1 that an optimal solution with respect to one of the objective functions implies a low optimization with respect to the other function. Therefore, we need to define some decision criteria to choose the most suitable solution. This solution is characterized by the definition of the $\boldsymbol{Q}$-vector that is a point of the PF. If we consider k objective functions, the $\boldsymbol{Q}$-vector is defined in such a way that its distance to the origin is minimal in the objective space,

$$\boldsymbol{Q}/\min\left\{\sqrt{\sum_{i=1}^{k} J_i(\boldsymbol{Q})^2}\right\}. \tag{9}$$

This point is a compromise between all the objective functions optimized, and offers the best stability with respect to the optimization procedure.

Optimizing factor (O_f). This parameter helps determine how much better each optimization is with respect to the other optimizations, quantifying the improvement of the optimization process. Given several Pareto fronts for the same optimization problem, we define the optimization factor (O_f) as the Euclidean distance between the points $\boldsymbol{Q}$ of any two different PFs. Thus, if we consider $\boldsymbol{Q}_1$ and $\boldsymbol{Q}_2$ as two PF $\boldsymbol{Q}$-vectors, then

$$O_f = \sqrt{\sum_{i=1}^{N} (Q_{1i} - Q_{2i})^2}. \tag{10}$$

An important parameter used to measure the improvement obtained by the Pareto fronts is the so-called ideal point.[46] The ideal point is defined as the vector formed by the lowest components among all points in the PF. That is, the first components of the ideal point are the minimum value of all first components of the points in the PF; the second component is obtained in the same way. Distances to the ideal point, measured in the objective space, are one of the classical solution quality indices in multi-objective optimization. However, the ideal point is not easy to find in practice. The $\boldsymbol{Q}$-vector that corresponds to a real structure is easy to find in practice, and it is near to the value of the ideal point in our optimization problem. In addition, $\boldsymbol{Q}$-vector provides infor-

mation about the goodness of the optimization results.

Area of spectrum (AS). This is an important parameter based on the acoustic spectrum generated by the considered sample. It is defined as the area enclosed between the positive range of spectra, and the 0 dB threshold line in the range of selected frequencies. This parameter measures the sonic capability of the considered structure, and increasing its value means an improvement in sonic properties. This parameter has been used in previous works for attenuation cases.[29]

Fraction of vacancies (F_v). This structural parameter provides information about the number of existing vacancies in the resulting sample. We define this parameter as the number of vacancies with respect to the total number of cylinders:

$$F_v = \frac{N_v}{N}, \tag{11}$$

where N_v is the number of created vacancies, and N is the total number of cylinders in the starting PC. F_v belongs to the interval [0, 1].

Asymmetry (A). This structural parameter enables the distribution of the created vacancies in the resulting samples to be determined—taking into account the asymmetry of the existence of each vacancy with respect to the symmetry axes of the starting PC (X and Y). We define this parameter as

$$A = \frac{A_x + A_y}{2}, \tag{12}$$

where A_i $(i=x,y)$ represents the asymmetry with respect to the i-axis, which is defined as

$$A = \frac{\sum_{j=1} N\gamma_A(b_j - b'_j)}{2N_v}, \tag{13}$$

b_j and b_j take the values 1 or 0—depending on the existence, or not, of the cylinder in position j, or in the symmetrical j, with respect to a symmetry axis of the starting PC. N_v is again the number of created vacancies. The parameters b and b' are binary vectors with dimensions equal to the total number of cylinders N. Thus, we have defined the asymmetry distribution function γ_A as

$$\gamma_A(x) = \begin{cases} 1 & \text{if } x \neq 0 \\ 0 & \text{if } x = 0. \end{cases} \tag{14}$$

With these definitions, A belongs to the interval [0, 1].

General rules for building optimized devices for each sonic application based on these tools is given in Sec. III.

III. RESULTS AND DISCUSSION

In this section, we discuss the improvement of two main PC sonic properties by means of the creation of vacancies. Specifically, we want to independently increase their attenuation and their focusing properties. In each case, we are interested in optimizing, several spectrum properties. Because of this, we have considered these situations as multiobjective optimization problems to be resolved using the evMOGA method. The methodology followed involves the generation of vacancies in a starting PC using four different symmetry strategies, as explained above, so that the optimized samples present fewer cylinders than the starting PC.

evMOGA works by minimizing the functions under study (objective functions). Two objective functions based on the pressure values obtained by the MST have been used in both attenuation and focusing cases. The resulting samples that present the best values of the two objective functions are selected by evMOGA when forming the Pareto front. The analysis of the PF, and the other tools defined above, will enable us to approach the best strategy.

Multiple execution of evMOGA has been performed to increase the reliability of the results. Four runs were made for each of the analyzed symmetries. The first execution starts with differing constraints and initial populations, but takes into account the starting PC. The following runs start with the best structures found in the previous runs.

A. Attenuation sound devices

The first step in our attenuation study consists of defining the objective functions chosen for optimizing the acoustic attenuation of the starting PC, in a predetermined point of measurement, for a range of frequencies ($f=[2300,3700]$ Hz analyzed at intervals of $\Delta f=50$ Hz) and in the ΓX direction. We are interested in maximizing the acoustic attenuation level and stability. In other words, we want to obtain a high attenuation level in a predetermined range of frequencies, with the least possible fluctuation in the attenuation spectrum.

Acoustic attenuation at a point (x,y), due to an incident plane wave of frequency f traveling through a PC formed by an array of scatterers of radius r_l placed at $(X_{\text{cyl}}, Y_{\text{cyl}})$ coordinates, is defined as

$$\text{Attenuation(dB)} = 20\log\left\{\frac{1}{|p(x,y,X_{\text{cyl}},Y_{\text{cyl}},f,r_l)|}\right\}, \tag{15}$$

where p is the value of the acoustic pressure and is obtained by means of the MST. Attenuation is normalized for an incident acoustic pressure equal to unity. From Eq. (15), it is easy to conclude that maximizing sound attenuation means minimizing acoustic pressure. Taking into account this fact, we have defined two objective functions, J_1 and J_2, representing the mean pressure and the mean deviation, respectively, in the range of frequencies considered,

$$J_1(\mathbf{x}) = \bar{p} = \frac{\sum_{i=1}^{N_f} |p_i(\mathbf{x})|}{N_f}, \tag{16}$$

$$J_2(\mathbf{x}) = \sqrt{\frac{\sum_i (|p_i(\mathbf{x}) - \bar{p}|)^2}{N_f^2}}, \tag{17}$$

where N_f represents the number of frequencies considered in the range under study ($N_f=29$, in our case) and $\mathbf{x}=(X_{\text{cyl}}, Y_{\text{cyl}})$ represents the variable under study, meaning the position of the existing cylinders in the sample. Minimizing these functions implies obtaining a maximum for the acoustic attenuation in the chosen range of frequencies. J_1 is related with the attenuation level in Eq. (16), and J_2 represents

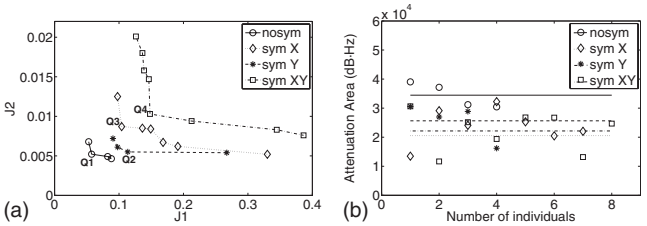

FIG. 4. (a) Pareto fronts for the different symmetries of generation of vacancies used for attenuation effect; (b) attenuation area for each analyzed symmetry.

the stability of the attenuation level in the range of considered frequencies in Eq. (17). We consider the attenuation level as the truly important function in this study—stability being a refinement of the obtained results, as shown below.

Figure 4(a) shows the Pareto fronts for the results obtained by evMOGA with the four vacancy generation strategies used. Their position in the plot implies the improved capability of the obtained attenuation properties. The closer the Pareto fronts are to the origin of the coordinates, the better the optimization. This is due to the fact that a low J_1 implies a high attenuation level through Eq. (16), and a low J_2 represents lower mean deviation. We can arrange the strategies used as a function of the results shown: nosym $>$ sym$Y$ $>$ sym$X$ $>$ symXY. It can be seen that the nosym strategy presents the highest optimization levels for the objective functions, and symXY seems the worst.

Moreover, we can compare the acoustic attenuation level for both the optimized samples and the starting PC. To do this, we will use the optimizing factor parameter. Taking into account that the $\boldsymbol{Q}$-vector for the PF corresponding to the nosym strategy is $(J_1, J_2)=(0.0575, 0.0052)$, and the values for the starting PC are $J_1=0.4633$ and $J_2=0.056$, we can obtain the value of the optimizing factor, $O_f=0.4090$. It seems that the attenuation level (J_1) is the truly important function in our study. Because for both cases, the difference between their values is similar to the O_f value. So, it seems that J_2 plays a secondary role in our attenuation study, representing the stability of the attenuation level. Finally, the value of O_f indicates that, physically, the creation of vacancies in a starting PC seems a suitable strategy for improving the attenuation characteristics of PCs. Thus, the value of O_f means that, in acoustic terms, there is a difference in the attenuation capacity between the starting PC and the best sample of the nosym strategy value at 18.5 dB.

After looking at Fig. 4(a), it seems possible to quantify the differences between the acoustic attenuations obtained among the four considered strategies. Regarding the $\boldsymbol{Q}$-vectors of the best (nosym) and the worst (symXY) strategies, the value of the O_f parameter is $O_f=0.0907$. This value represents an attenuation difference of 8.2 dB between both optimized samples.

To quantify how much better each strategy of vacancy generation is when compared to the others, we have analyzed the area of spectrum (AS) parameter, called in this case, attenuation area (AA). This parameter has been calculated for the spectra of all the optimized samples shown in Fig. 4(a). The points in Fig. 4(b) represent the value of the AA

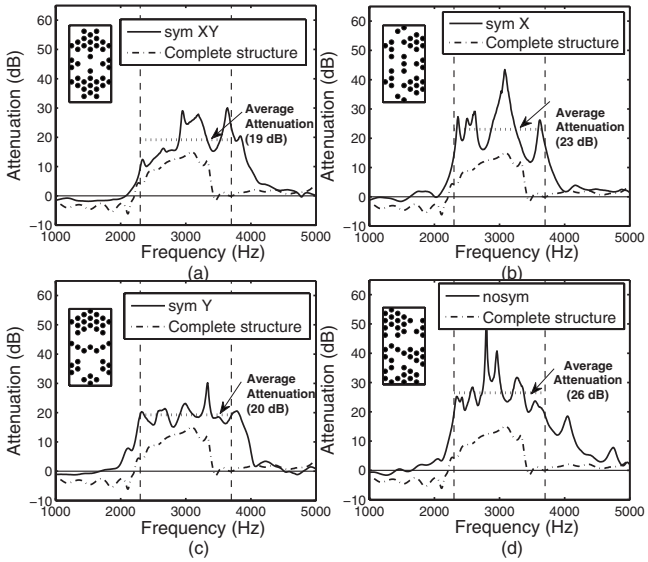

FIG. 5. Spectra of the resulting optimized samples: (a) Q1, (b) Q2, (c) Q3, and (d) Q4 shown in Fig. 4(a) (continuous line), and of the starting PC (dotted line). The range of frequencies optimized is delimited by two vertical dashed lines. The attenuation average level in the optimized range of frequencies for each of the symmetries used is represented (horizontal dotted line). Configurations of the optimized samples corresponding to each $\mathbf{Q}$-vector are included as an inset.

parameter for each resulting optimized structure in each of the symmetries of vacancies used, and the lines represent each average value of the parameter. The biggest AA corresponds to the nosym strategy, and this fact means that the resulting optimized samples obtained with this strategy show the best improvement in their attenuation properties.

Figure 5 can help us understand Figs. 4(a) and 4(b). Here, we present the attenuation spectra of the resulting samples marked in Fig. 4(a) as Q_1, Q_2, Q_3, and Q_4, corresponding to the $\boldsymbol{Q}$-vectors of each strategy of vacancy generation—analyzed together with that corresponding to the starting PC. The best average, as we have mentioned above, corresponds to the nosym strategy. Note that the values of the objective functions for the resulting samples shown in Fig. 4(a) are in very good agreement with the MST spectra simulations shown in Fig. 5. Thus, we can compare the improvement of both J_1 (mean pressure) in Fig. 4(a) and the average attenuation in Fig. 5. In Fig. 4(a), it can be seen that $J_1^{Q4} > J_1^{Q2} > J_1^{Q3} > J_1^{Q1}$, and this is in good agreement with the results obtained in Fig. 5: nosym $>$ sym$Y$ $>$ sym$X$ $>$ symXY. It can also be observed that the improvement of J_2 in the process is not as significant as the improvement of J_1. In Fig. 5 the predominance of the attenuation level criterion in the attenuation spectra of the resulting samples can be seen.

In short, taking into account the results obtained for the optimizing tools defined in Sec. II D (PF, SA, and O_f), the nosym strategy for creating vacancies in a starting PC seems the most suitable method for improving the acoustic attenuation properties of PCs. A possible explanation may be that evMOGA produces an optimized combination of holes; therefore, the multiple scattering process is able to increase the acoustic attenuation. To attenuate a range of frequencies, a large combination of distances between scatterers inside the PC is necessary to obtain an acoustic attenuation greater

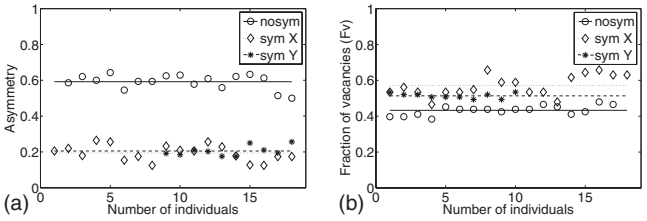

FIG. 6. (a) Asymmetry parameter and (b) fraction of vacancies for each analyzed symmetry. The points represent the value of the parameter for each of the optimized structures obtained, and the line represents their average value.

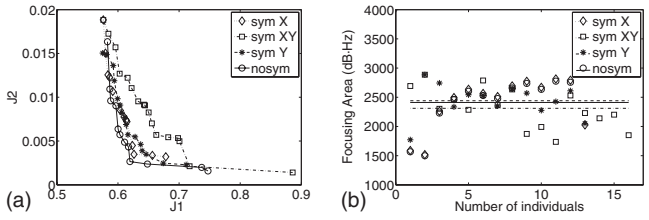

FIG. 7. (a) Pareto fronts for the different vacancy generation symmetries used for focusing effect; (b) focusing area for each analyzed symmetry. The points represent the value of the parameter for each of the optimized structures obtained and the line represents their average value.

than that corresponding to the starting PC modulating the phase. Among the four analyzed symmetries, the random symmetry presents more varying distances and, consequently, more attenuated frequencies.

The next step consists in obtaining some general rules about the number of vacancies and their distribution on the starting PC, as required to obtain structures with optimized attenuation properties. This has been achieved using the structural tools defined in Sec. II D: the fraction of vacancies (F_v) and asymmetry (A). In Fig. 6(a), we show the values of the asymmetry parameter for each of the analyzed symmetries in the creation of vacancies. In the case of the nosym strategy, it can be seen that the optimized value of the asymmetry is around 60%. This result indicates the method to create vacancies in the starting PCs to optimize attenuation properties, according to the definition of asymmetry. Note that the corresponding value of this parameter for the symXY vacancies is $A_{\text{sym}XY}=0$ due to the definition of asymmetry. Moreover, taking into account the Pareto fronts shown in Fig. 4(a), symXY becomes the worst strategy to increase the attenuation properties of PCs; therefore, the value of the A parameter is in good agreement with the results obtained with the PF. Accordingly, only the three remaining symmetries have been analyzed.

Figure 6(b) shows the results of the study of the fraction of vacancies. This parameter gives us the optimum number of vacancies for each of the considered strategies. It can be seen that for the best strategy (nosym) obtained above, the value of this parameter is the highest, and it is around 43% of the total number of cylinders in the starting PC. We have shown in this section, by means of the use of both optimization and structural parameters, that (i) the creation of vacancies is a suitable method for increasing the acoustic attenuation properties of PCs and (ii) the nosym strategy seems the best method for creating vacancies. Moreover, we have obtained general rules for creating random (nosym) vacancies in a PC based on the structural parameters defined. The optimal values of A and F_v to build an optimal structure should be 59% of asymmetry and 43% of vacancies. These values correspond to the best devices in terms of improved acoustic attenuation.

B. Focusing sound devices

This section examines the optimization of the focusing properties of PCs by means of the creation of vacancies in a starting PC. Specifically, the aim is to increase the focusing properties of these materials, in a predetermined point of measurement, for a range of frequencies ($f=[1400,2000]$ Hz, analyzed at intervals of $\Delta f=50$ Hz) and in the ΓX direction. Note that the chosen range of frequencies is just below the first band gap, that is, inside the first transmission band. As in the case of attenuation optimization, we have defined two objective functions, taking into account that the aim is to maximize the acoustic pressure at the predetermined point. The acoustic focusing level is defined as

$$\text{Focalization(dB)} = 20\log\{|p(x,y,X_{\text{cyl}},Y_{\text{cyl}},f,r_l)|\}, \quad (18)$$

where p again means acoustic pressure calculated by MST. As in the case of acoustic attenuation, the objective is to obtain a high pressure level with a small fluctuation of the pressure spectrum. Thus, the objective functions J_3 and J_2 to minimize are defined as

$$J_3(\boldsymbol{x}) = \frac{1}{\bar{p}} = \frac{N_f}{\sum_{i=1}^{N_f}|p_i(\boldsymbol{x})|}, \quad (19)$$

$$J_2(\boldsymbol{x}) = \sqrt{\frac{\sum_i (|p_i(\boldsymbol{x})-\bar{p}|)^2}{N_f^2}}, \quad (20)$$

where $\boldsymbol{x}=(X_{\text{cy}},Y_{\text{cy}})$ and N_f are defined as in the attenuation case. Note that J_2 is the same objective function used in the optimization case explained above, and this means the stability of the pressure level is in the range of the considered frequencies. The minimization of J_3 implies a high level pressure (focusing effect). Again, the pressure level has been considered as the main parameter in this study, pushing stability into the background of the obtained results.

Figure 7(a) shows the Pareto fronts with the optimization results using the four strategies for creating vacancies obtained by evMOGA for the focusing case. Here, as in the case of the attenuation analysis, the same order can be seen in the strategies used as a function of the obtained optimization: nosym > sym$Y$ > sym$X$ > symXY. Figure 7(a) shows that the nosym strategy offers higher optimization levels for the objective functions, and symXY offers the worst strategy. However, due to the small separation between all the Pareto fronts, it can be concluded that the vacancy creation strategy chosen to optimize the focusing properties of the PCs is unimportant. This result is in agreement with the reasoning and the strategy followed by several authors[25] in the case of focusing optimization. Moreover, the creation of vacancies

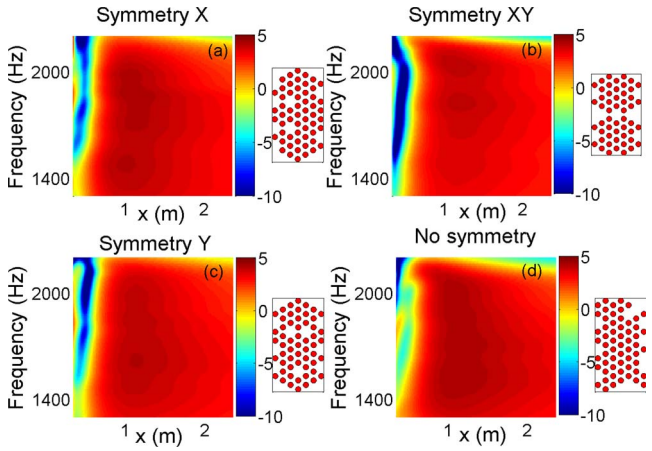

FIG. 8. (Color online) Acoustic level in the acoustic focus zone. On the *OX* axis, the distance along the direction of the incident wave is shown, and frequencies for the four strategies analyzed on the *OY* axis are also shown. The color bar represents the acoustic level in decibels. The corresponding samples are also included.

seems less efficient in the optimization of the focusing than in the case of attenuation. Again, we can evaluate the optimization process by comparing the values of the O_f parameter between the nosym strategy and the starting PC. The $\boldsymbol{Q}$-vector for the nosym strategy is $(J_3,J_2)=(0.6196,0.0027)$ and the corresponding objective function for the starting PC is $J_3=0.6428$, $J_2=0.0437$. The calculated value of the optimizing factor is $O_f=0.0471$. This means an improvement in the focusing properties equal to 0.4280 dB. In this case, O_f means a low optimization level compared with that obtained in the attenuation case ($O_f=0.4090$ meaning 18.5 dB) in the focusing properties of the PC.

To support these results, we can analyze the area of spectrum (AS) tool, refered to as the focusing area (FA). This optimization parameter has been calculated in the same way as the attenuation case. Figure 7(b) shows the FA for the analyzed strategies, and the similarity between the average values for all the strategies used can be seen.

Figure 8 enables the above results to be collaborated. This figure shows increases in the acoustic level in the range of frequencies under study, and for the predetermined point of measurement of the coordinates (1, 0). It can be clearly seen that the difference in acoustic level between the analyzed symmetries is smaller when compared with the acoustic attenuation case.

We have studied the behavior of the structural tools in order to provide some general rules about the number of vacancies and their distribution on the starting PC when intending to optimize focusing properties.

Figure 9(a) shows the variation of the asymmetry parameter for each of the analyzed strategies. As in the attenuation case, the value for the nosym symmetry is around 0.6, and for other symmetries it is between 0.38 and 0.45. Figure 9(b) shows the results regarding the fraction of vacancies necessary to optimize the focusing properties of PCs. For all cases, this parameter is around 20% of the total number of cylinders in the starting PC.

Taking into account the results obtained using both optimization and structural parameters, it can be concluded that

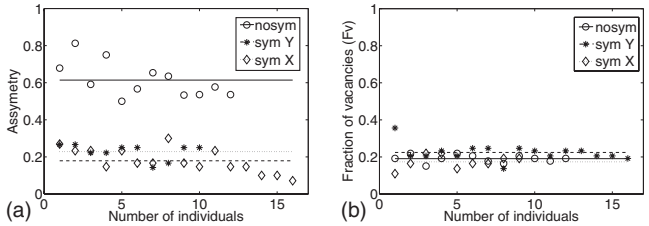

FIG. 9. (a) Asymmetry parameter and (b) fraction of vacancies for the analyzed symmetries. The points represent the value of the parameter for each of the optimized structures obtained, and the line represents their average value.

although the creation of vacancies provides an improvement in the focusing properties of PCs, this increase is smaller than that obtained in the attenuation case. Moreover, the strategy of vacancy creation does not seem a decisive factor in this optimization process.

IV. EXPERIMENTAL RESULTS

We have shown that the sonic properties of PCs can be increased by creating vacancies. We have provided general rules for optimizing the attenuation and focusing behavior of these materials at a predetermined point and for ΓX direction (0 of incidence). Both the mean pressure and the mean deviation of the sonic pressure are specifically used as objective functions. This section experimentally confirms the applicability and the robustness of the optimization rules obtained in Secs. II and III. To achieve this, we have designed the following random acoustic attenuation experiment. We have built a starting PC with an external shape and number of cylinders that differ from the PC used in the theoretical development. In this PC, we have created vacancies by removing a predetermined number of cylinders each time. We then measured the sound attenuation spectrum (the difference between the sound level recorded at the same point with and without the sample—usually called insertion loss) in the ΓX direction (0). We also calculated the AA, F_v, and A parameters for each of the resultant samples obtained. The experiments were performed in an anechoic chamber using a directional white noise sound source. Specifically, we used a PC with a honeycomb external shape, made from 397 cylinders of hollow aluminum with 4 cm diameters, 1 m long, and placed in a triangular array with parameter $a=6.35$ cm (Fig. 10). Ten samples were created as we created vacancies by removing 40 cylinders each time.

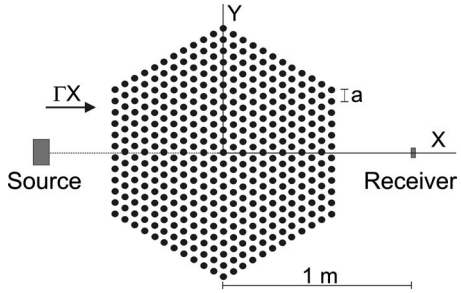

FIG. 10. Experimental measurement setup. The starting PC consists of hollow aluminum rods 1 m long and 4 cm in diameter arranged in a triangular pattern with constant lattice $a=6.35$ cm. There are 397 cylinders.

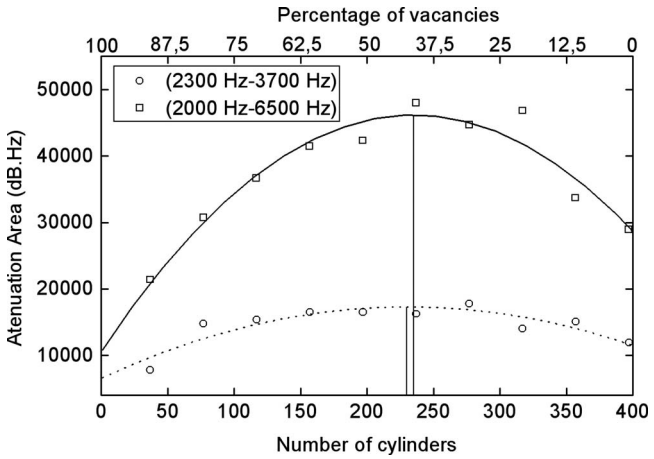

FIG. 11. Attenuation area versus number of cylinders for both analyzed cases.

In Fig. 11 we show the value of the AA parameter as a function of the number of cylinders, and for the two ranges of frequencies analyzed (2300–3700 Hz and 2000–6500 Hz). In both cases, it can be seen that there is a maximum of AA for a percentage of the existing vacancies of around 40% of the total cylinders of the starting PC. This value agrees with the value obtained in the optimization process.

The variation of the asymmetry parameter of the samples as a function of the number of vacancies is plotted in Fig. 12. It can be seen that the asymmetry is near 60% for the optimum number of vacancies corresponding to the best samples (around 40%) obtained in both analyzed cases. Again, this value is in good agreement with the theoretical result obtained in the optimization study.

Attenuation spectra for the best optimized sample (larger AA) and the complete starting PC are plotted in Fig. 13—corresponding to the range of frequencies from 2300 to 3700 Hz in Fig. 13(a) and from 2000 to 6500 Hz in Fig. 13(b). The best sample is also shown in each inset. In both cases, the increase of the AA when compared to the starting PC can be seen in those samples with vacancies.

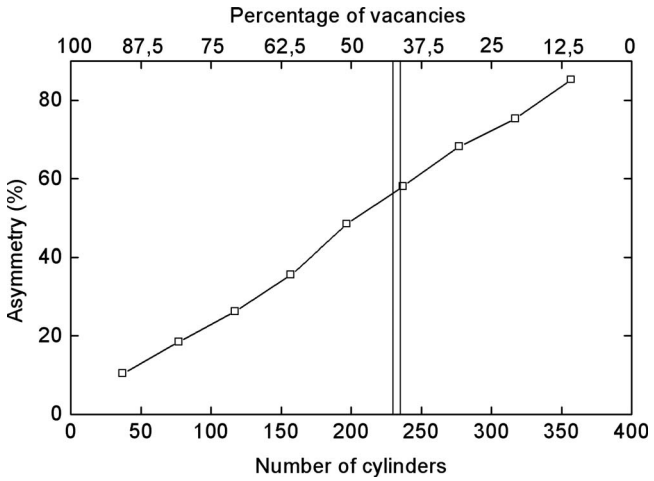

FIG. 12. Variation of the asymmetry of the nine obtained structures as a function of the vacancies created. Vertical lines represent the optimum number of vacancies for both analyzed cases.

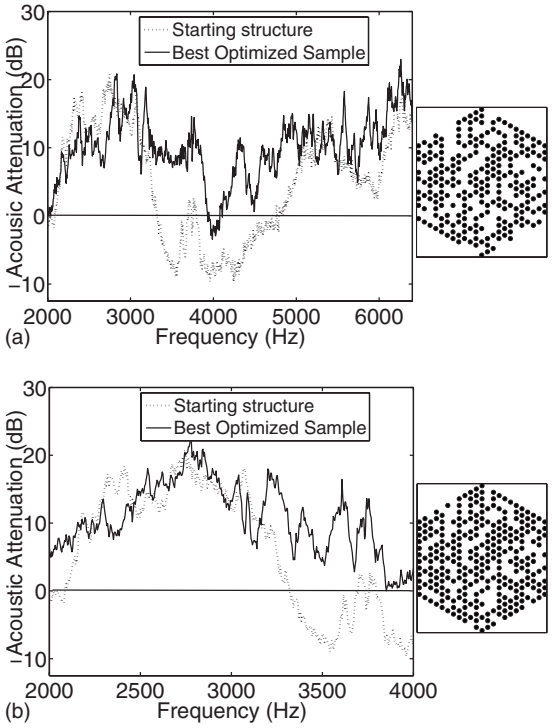

FIG. 13. Comparison of attenuation spectra corresponding to the starting PC, and the best sample obtained by means of the creation of vacancies: (a) (2300–3700 Hz); (b) (2000–6500 Hz). The corresponding best structure obtained is shown in the inset.

In short, the validity of the general rules obtained has been experimentally shown in our theoretical research on optimization. Moreover, the devices built by means of the creation of vacancies in the starting PC, when taking into account the theoretical general rules obtained, offer the best attenuation capability—in the predetermined range of frequencies analyzed theoretically; and also in a wider range.

V. SUMMARY

Based on the numerical results obtained by means of evMOGA in conjunction with MST, we have analyzed a mechanism for the creation of vacancies in a starting PC as a tool for increasing acoustic properties. The PC is formed by isolated cylinders surrounded by air. Specifically, we have studied the optimization of the attenuation and focusing properties of these materials and interesting conclusions have been obtained. First, these acoustic phenomena are not the same from the optimization point of view. Therefore, the creation of vacancies seems a suitable method for the improvement of attenuation capability, but not for improving focusing properties. Second, we have presented general rules for constructing attenuation devices based on PCs in an optimal approach: (i) the strategy used in the creation of vacancies seems an important factor and we have concluded that the random strategy is best; (ii) the optimal number of created vacancies is around 40% of the total number of cylinders in the starting PC, and the optimal asymmetry, i.e., the approach for distributing the vacancies, is near 60%. Moreover, we have experimentally demonstrated the validity of these theoretical rules and we have shown that the obtained results are independent of the PC characteristics (external

shape and number of cylinders) and the acoustic parameters to optimize (range of frequencies). Finally, due to the range of applicability of the wave crystal theory, the obtained results could be used as a guide for constructing devices in several wave fields.

ACKNOWLEDGMENTS

This work was partially supported by MEC (Spanish Government) and FEDER funds: Project Nos. 419DPI2005-07835, and MAT2006-03097 and Generalitat Valenciana Project Nos. GV06/026 and 420 GV/2007/191. The authors would like to thank John Rawlins (associate member of the Institute of Translation and Interpreting (No. 9743) of UK, and "Certified PRO" of ProZ according to the EN 15038) for his help with the use of English.

[1]J. Sánchez-Pérez, D. Caballero, R. Martínez-Sala, C. Rubio, J. Sánchez-Dehesa, F. Meseguer, J. Llinares, and F. Glvez, "Sound attenuation by a two-dimensional array of rigid cylinders," Phys. Rev. Lett. **80**, 5325–5328 (1998).
[2]W. M. Robertson and J. F. Rudy III, "Measurement of acoustic stop bands in two-dimensional periodic scattering arrays," J. Acoust. Soc. Am. **104**, 694–699 (1998).
[3]M. Sigalas and E. Economou, "Attenuation of multiple-scattered sound," Europhys. Lett. **36**, 241–246 (1996).
[4]F. Cervera, L. Sanchis, J. Sánchez-Prez, R. Martínez-Sala, C. Rubio, F. Meseguer, C. Lopez, D. Caballero, and J. Sánchez-Dehesa, "Refractive acoustic devices for airborne sound," Phys. Rev. Lett. **88**, 023902 (2001).
[5]M. Kushwaha, "Stop-bands for periodic metallic rods: Sculptures that can filter the noise," Appl. Phys. Lett. **70**, 3218–3220 (1997).
[6]J. Sánchez-Pérez, C. Rubio, R. Martínez-Sala, R. Sánchez-Grandia, and V. Gómez, "Acoustic barriers based on periodic arrays of scatterers," Appl. Phys. Lett. **81**, 5240–5242 (2002).
[7]L. S. Chen, C. H. Kuo, and Z. Ye, "Acoustic imaging and collimating by slabs of sonic crystals made from arrays of rigid cylinders in air," Appl. Phys. Lett. **85**, 1072–1074 (2004).
[8]J. Bravo-Abad, T. Ochiai, and J. Sánchez-Dehesa, "Anomalous refractive properties of a two-dimensional photonic band-gap prism," Phys. Rev. B **67**, 115116 (2003).
[9]Z. Liu, X. Zhang, Y. Mao, Y. Zhu, Z. Yang, C. Chan, and P. Sheng, "Locally resonant sonic materials," Science **289**, 1734–1736 (2000).
[10]M. Hirsekorn, P. Delsanto, N. Batra, and P. Matic, "Modelling and simulation of acoustic wave propagation in locally resonant sonic materials," Ultrasonics **42**, 231–235 (2004).
[11]M. Hirsekorn, "Small-size sonic crystal with strong attenuation bands in the audible frequency range," Appl. Phys. Lett. **84**, 3364–33676 (2004).
[12]X. Hu and C. Chan, "Two-dimensional sonic crystals with Helmholtz resonators," Phys. Rev. E **71**, 055601(R) (2005).
[13]O. Umnova, K. Attenborough, and C. Linton, "Effects of porous covering on sound attenuation by periodic arrays of cylinders," J. Acoust. Soc. Am. **119**, 278–284 (2006).
[14]W. Kuang, Z. Hou, and Y. Liu, "The effects of shapes and symmetries of scatterers on the phononic band gap in 2D phononic crystals," Phys. Lett. A **332**, 481–490 (2004).
[15]R. Min, Fugen Wu, L. Zhong, H. Zhong, S. Zhong, and Y. Liu, "Extreme acoustic band gaps obtained under high symmetry in 2D phononic crystals," J. Phys. D: Appl. Phys. **39**, 2272–2276 (2006).
[16]X. Zhang, "Universal non-near-field focus of acoustic waves through high-symmetry quasicrystals," Phys. Rev. B **75**, 024209 (2007).
[17]R. James, S. Woodley, C. Dyer, and V. Humphrey, "Sonic bands, band-gaps, and defect states in layered structures-theory and experiment," J. Acoust. Soc. Am. **97**, 2041–2047 (1995).
[18]M. Sigalas, "Elastic wave band gaps and defect states in two-dimensional composites," J. Acoust. Soc. Am. **101**, 1256–1261 (1997).
[19]M. Sigalas, "Defect states of acoustic waves in a two dimensional lattice of solid cylinders," J. Appl. Phys. **84**, 3026–3030 (1998).
[20]F. Wu, Z. Hou, Z. Liu, and Y. Liu, "Point defect states in two-dimensional phononic crystals," Phys. Lett. A **292**, 198–202 (2001).
[21]J. Munday, C. Brad Bennett, and W. Robertson, "Band gaps and defect modes in periodically structured waveguides," J. Acoust. Soc. Am. **112**, 1353–1358 (2002).
[22]A. Khelif, A. Choujaa, B. Djafari-Rouhani, M. Wilm, S. Ballandras, and V. Laude, "Trapping and guiding of acoustic waves by defect modes in a full-band-gap ultrasonic crystal," Phys. Rev. B **68**, 214301 (2003).
[23]A. Khelif, M. Wilm, V. Laude, S. Ballandras, and B. Djafari-Rouhani, "Guided elastic waves along a rod defect of a two-dimensional phononic crystal," Phys. Rev. E **69**, 067601 (2004).
[24]F. Wu, J. Liu, Y. Liu, and Y. Liu, "Splitting and tuning characteristics of the point defect modes in two-dimensional phononic crystals," Phys. Rev. E **69**, 066609 (2004).
[25]D. Caballero, J. Sánchez-Dehesa, R. Martínez-Sala, C. Rubio, J. V. Sánchez-Pérez, L. Sanchis, and F. Meseguer, "Suzuki phase in two-dimensional sonic crystals," Phys. Rev. B **64**, 064303 (2001).
[26]A. Hakansson, J. Sánchez-Dehesa, and L. Sanchis, "Acoustic lens design by genetic algorithms," Phys. Rev. B **70**, 214302 (2004).
[27]A. Hakansson, F. Cervera, and J. Sánchez-Dehesa, "Sound focusing by flat acoustic lenses without negative refraction," Appl. Phys. Lett. **86**, 054102 (2005).
[28]A. Hakansson, J. Sánchez-Dehesa, and F. Cervera, "Experimental realization of sonic demultiplexing devices based on inverse designed scattering acoustic elements," Appl. Phys. Lett. **88**, 163506 (2006).
[29]V. Romero-García, E. Fuster, L. M. García-Raffi, E. A. Sánchez-Pérez, M. Sopena, J. Llinares, and J. V. Sánchez-Pérez, "Band gap creation using quasiordered structures based on sonic crystals," Appl. Phys. Lett. **88**, 174104 (2006).
[30]T. Back, *Evolutionary Algorithms in Theory and Practice: Evolution Strategies, Evolutionary Programming, Genetic Algorithms* (Oxford University Press, New York, 1996).
[31]J. Herrero, X. Blasco, M. Martínez, C. Ramos, and J. Sanchis, "Robust identification of a greenhouse model using multi-objective evolutionary algorithms," Biosyst. Eng. **98**, 335–346 (2007).
[32]J. Herrero, M. Martínez, J. Sanchis, and X. Blasco, "Well-distributed pareto front by using the epsilon-moga evolutionary algorithm," Lect. Notes Comput. Sci. **4507**, 292–299 (2007).
[33]V. Twersky, "Multiple scattering of radiation by an arbitrary configuration of parallel cylinders," J. Acoust. Soc. Am. **24**, 42–46 (1951).
[34]Y. Chen and Z. Ye, "Theoretical analysis of acoustic stop bands in two-dimensional periodic scattering arrays," Phys. Rev. E **64**, 036616 (2001).
[35]D. García-Pablos, M. Sigalas, F. M. de Espinosa, M. Torres, M. Kafesaki, and N. García, "Theory and experiments on elastic band gaps," Phys. Rev. Lett. **84**, 4349–4352 (2000).
[36]E. Fuster-Garcia, V. Romero-García, J. V. S. Pérez, L. M. García-Raffi, and E. A. S. Pérez, "A phenomenological model for sonic crystals based on artificial neural networks," J. Acoust. Soc. Am. **120**, 636–641 (2006).
[37]M. Kafesaki and E. Economou, "Multiple scattering theory for three-dimensional periodic acoustic composites," Phys. Rev. B **60**, 11993 (1999).
[38]J. Korringa, "On the calculation of the energy of a Bloch wave in a metal," Physica (Amsterdam) **13**, 392–400 (1947).
[39]W. Kohn and N. Rostoker, "Solution of the Schrodinger equation in periodic lattices with an application to metallic lithium," Phys. Rev. **94**, 1111–1120 (1954).
[40]L. Sanchis, F. Cervera, J. Sánchez-Dehesa, J. V. Sánchez-Pérez, C. Rubio, and R. Martínez-Sala, "Reflectance properties of two-dimensional sonic band gap crystals," J. Acoust. Soc. Am. **109**, 2598–2605 (2001).
[41]K. Miettinen, *Nonlinear Multiobjective Optimization* (Kluwer Academic, Boston, 1998).
[42]C. Coello, D. Veldhuizen, and G. Lamont, *Evolutionary Algorithms for Solving Multiobjective Problems* (Kluwer Academic, Dordrecht, 2002).
[43]C. Coello and G. Lamont, *Applications of Multiobjective Evolutionary Algorithms* (Wold Scientific, Singapore, 2004).
[44]M. Laumanns, L. Thiele, K. Deb, and E. Zitzler, "Combining convergence and diversity in evolutionary multi-objective optimization," Evol. Comput. **10**, 263–282 (2002).
[45]R. Ursem, "Models for evolutionary algorithms and their applications in systems identification and control optimization," Ph.D. thesis, University of Aarhus, Denmark (2003).
[46]M. Ehrgott and D. Tenfelde-Podehl, "Computation of ideal and Nadir values and implications for their use in MCDM methods," Eur. J. Oper. Res. **151**, 119–139 (2003).

Ensemble averaged surface normal impedance of material using an *in-situ* technique: Preliminary study using boundary element method

Toru Otsuru,[a] Reiji Tomiku, and Nazli Bin Che Din
Department of Architecture and Mechatronics, Oita University, 700 Dannoharu, Oita 870-1192, Japan

Noriko Okamoto
Venture Business Laboratory, Oita University, 700 Dannoharu, Oita 870-1192, Japan

Masahiko Murakami
Shinryo Corporation, 2-4 Yotsuya, Shinjuku-ku, Tokyo 160-8510, Japan

(Received 6 August 2008; revised 31 March 2009; accepted 4 April 2009)

An *in-situ* measurement technique of a material surface normal impedance is proposed. It includes a concept of "ensemble averaged" surface normal impedance that extends the usage of obtained values to various applications such as architectural acoustics and computational simulations, especially those based on the wave theory. The measurement technique itself is a refinement of a method using a two-microphone technique and environmental anonymous noise, or diffused ambient noise, as proposed by Takahashi *et al.* [Appl. Acoust. **66**, 845–865 (2005)]. Measured impedance can be regarded as time-space averaged normal impedance at the material surface. As a preliminary study using numerical simulations based on the boundary element method, normal incidence and random incidence measurements are compared numerically: results clarify that ensemble averaging is an effective mode of measuring sound absorption characteristics of materials with practical sizes in the lower frequency range of 100–1000 Hz, as confirmed by practical measurements. © *2009 Acoustical Society of America.* [DOI: 10.1121/1.3125327]

PACS number(s): 43.55.Ev, 43.55.Ka, 43.58.Bh [NX] Pages: 3784–3791

I. INTRODUCTION

With the rapid progress of computer technology, numerical simulations based on wave equations, such as finite element method and boundary element method, have become powerful tools for conducting acoustical investigations and carrying out design processes.[1] Although the boundary conditions of such simulations are generally modeled using surface impedance, insufficient impedance databases might have been supplied to date. What is contradictory is that in many rooms and environmental acoustic problems within the lower frequency range—roughly less than 1000 Hz—wave-based considerations are required, whereas various *in-situ* impedance measurements frequently encounter difficulties because of the wave characteristics of the sound.

To overcome that situation, the authors proposed a method using a two-microphone technique and environmental anonymous noise: the "EA-noise method."[2] In the original method, the sound source was intended for use only with diffuse ambient noise that exists around the specimen to be measured. However, in the case where it is insufficient, a supplemental noise source(s) can be added to improve the result, which is designated as the "pEA-noise method.[3]

On the other hand, numerous methods have been proposed to measure the absorption characteristics of materials.[4–12] Allard *et al.*[6–9] focused on a transfer function method using two microphones located near the surface. Their method enables *in-situ* measurement of a sample area. However, the required sample size increases as the frequency decreases. Meanwhile, Garai[10] proposed a method to measure the absorption coefficient *in-situ* using maximum length sequential (MLS) as a test signal to improve background noise immunity. Nevertheless, some problems remain, e.g., low frequency limitation. Moreover, Mommertz[11] described an improved PC-based method of measuring the reflecting coefficient in combination with subtraction technique. This method requires an appropriate window function to gate out parasitic reflection from other surfaces, and a diffracted wave comes from the edge of the sample. The time length of the window is so short that the frequency resolution becomes insufficient when a practical measurement is conducted in the low frequency range.

Among the reports in the relevant literature, Nocke[12] proposed an area-averaged effective impedance to measure a material's absorption characteristics using a free field transfer function method with a MLS signal. The difference of the two concepts on averaging, those of Nocke and of the authors, is clarified in Secs. II–IV, but what we propose herein is time-space averaging over sound sources: neither the definitions nor the measuring techniques differ from conventional ones, including that of Nocke.

Meanwhile, a particle velocity sensor, i.e., Microflown™, recently developed by de Bree,[13] has presented new modes for direct measurements of impedance, acoustic inten-

[a]Author to whom correspondence should be addressed. Electronic mail: otsuru@cc.oita-u.ac.jp

 0001-4966/2009/125(6)/3784/8/$25.00

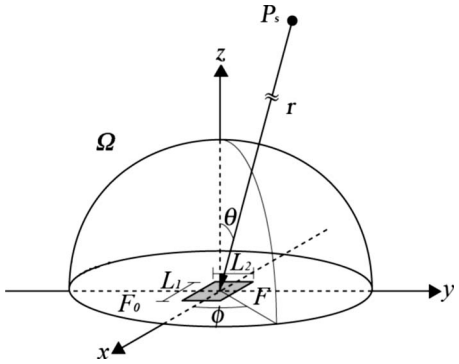

FIG. 1. System geometry and coordinates for a sound source P_s incident on a specimen F with the area of $L_1 \times L_2$ bounded by an infinitely flat hard-plane F_0.

sity, and other particle-velocity-related quantities;[14–17] the authors also described the use of a pu-sensor, a particle velocity sensor with a microphone, in the EA-noise method.

Sections II and III address pertinent concepts of ensemble averaged impedance and a basic technique to measure it using a pu-sensor. Simulations using the boundary element method (BEM) and a limited number of corresponding measurements are conducted as a preliminary study.

II. PROBLEM CONFIGURATION

A. General geometry and EA-noise method

The geometry of the system under consideration is depicted in Fig. 1. Here, $\Omega,(x,y,z)$ and (r,θ,ϕ), respectively, signify the upper half space, Cartesian, and polar coordinate systems and a point source P_s and a specimen F with the area of $L_1 \times L_2$ are assumed to be as portrayed in the figure. An infinite hard-plane F_0 is also assumed to surround the specimen: in cases where the specimen has a thickness T, it might be a plane such as $z=-T$, $z=0$, etc.

The setup of EA-noise method using two microphones (pp-sensor) is presented in Fig. 2. The method is based on measurement of the transfer function between the microphones using a spectrum analyzer [fast-Fourier-transform (FFT)]. Ambient noise around the specimen is used as the sound source; if the noise is insufficient, the supplemental sound source can be added to improve the signal-to-noise ratio. The FFT resolution is set to 1.0 Hz and a Hamming window is employed. Measured data are averaged 30 times. The specimen to be measured is backed by a rigid wall.

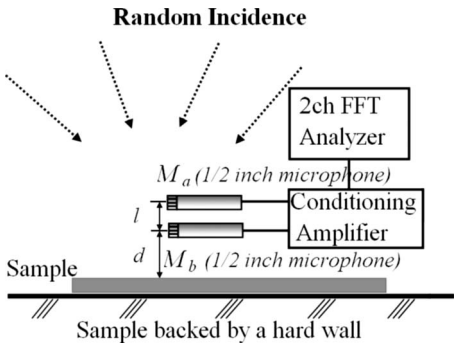

FIG. 2. Schematic diagram of the measurement setup with a pp-sensor.

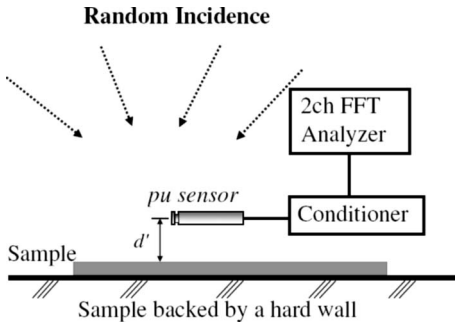

FIG. 3. Schematic diagram of the measurement setup with a pu-sensor.

As the first stage of our study, the objective of the previous paper[2] was set to carry out simple and stable measurement for absorption characteristics of materials *in-situ*.

For this study, measurements of the impedance of glass wool and rock wool have been made using method in various sound fields. Then, the repeatability and wide applicability of the method were demonstrated by comparing the results of measurements in one room with different noise conditions and in three other environments (corridor, cafeteria, and terrace).

On the other hand, if a pu-sensor is located at the material surface (Fig. 3), and if p_{surf} and $u_{n,\mathrm{surf}}$, respectively, signify the sound pressure and particle velocity normal to the specimen's surface, then the surface normal impedance at a point $(x,y,0)$ is defined simply as Eq. (1):

$$Z_n(x,y) = \frac{p_{\mathrm{surf}}(x,y)}{u_{n,\mathrm{surf}}(x,y)}. \tag{1}$$

Hereinafter, the expression (x,y) is omitted.

B. Ensemble averaged surface normal impedance at random incidence

We next introduce an impedance $\langle Z_n \rangle$, ensemble averaged impedance, over such a sufficient number of incoherent sound sources $P_S(r,\theta,\phi)$ that random incidence can be expected. The impedance can be expressed as Eq. (2a) and (2b):

$$\langle Z_n \rangle = \left\langle \frac{p_{\mathrm{surf}}}{u_{n,\mathrm{surf}}} \right\rangle, \tag{2a}$$

$$\langle Z_n \rangle = \frac{\langle p_{\mathrm{surf}} \rangle}{\langle u_{n,\mathrm{surf}} \rangle}, \tag{2b}$$

where $\langle \cdot \rangle$ denotes the ensemble average. The two equations become identical if the system is ergodic and the statistical randomness both in time and space is achieved at every instance. In practical cases, however, especially in measurements, achieving randomness requires time-windowing with some sufficient length as well as some amount of averaging numbers. Therefore, it might be safer to adopt the latter equation for the definition of $\langle Z_n \rangle$ at this stage.

The corresponding absorption coefficient $\langle \alpha \rangle$ is calculated as

$$\langle \alpha \rangle = 1 - \left| \frac{\langle Z_n \rangle - \rho c}{\langle Z_n \rangle + \rho c} \right|^2. \tag{3}$$

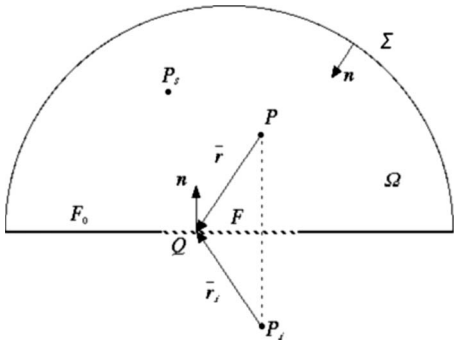

FIG. 4. Schematic drawing of random incidence model of the system for the construction of boundary integral equation. The point source is P_s: receiving points P are located in Ω. In addition, P_i denotes the image of P with respect to F and F_0.

In a practical measurement, to achieve the enough averaging, we propose the following equation:

$$\langle Z_n \rangle = \frac{1}{N} \sum_N \frac{\langle \tilde{p} \rangle}{\langle \tilde{u}_n \rangle}. \tag{4}$$

III. MATH-PHYSICAL MODEL AND NUMERICAL CONFIRMATION USING BOUNDARY ELEMENT METHOD

Kawai proposed and conducted a numerical simulation using a boundary integral equation to investigate the area effect of sound-absorbent surfaces at the random incidence condition. It is summarized below.

A. Brief summary of Kawai's method

In Kawai's[18] method (see Fig. 4), the thickness T of specimen F is set to zero. Its surface is assumed to be locally reactive; consequently, the following equation stands:

$$\frac{\partial \mathbf{\Phi}}{\partial n} = -ikA\mathbf{\Phi} \quad \text{on } F, \tag{5}$$

therein, $\mathbf{\Phi}$, k, and $A(=1/(Z_n/\rho c))$, respectively, represent the velocity potential, wave constant, and the specific admittance of F. The time factor $\exp(-i\omega t)$ is omitted hereinafter. Considering the image point P_i of a receiving point P with respect to F and F_0, a fundamental solution using Green's function in Eq. (6) is used to derive an integral equation in Eq. (7).

$$G(P,Q) = \frac{\exp(ik\bar{r})}{4\pi\bar{r}} + \frac{\exp(ik\bar{r}_i)}{4\pi\bar{r}_i}. \tag{6}$$

In Eq. (6), $\bar{r}=\overline{PQ}$ and $\bar{r}_i=\overline{P_iQ}$, where Q denotes a point source on F.

Then, considering (1) the normal component of particle velocity vanishes on F_0, (2) $\partial G/\partial n=0$ on F and F_0, and (3) Sommerfeld's radiation condition, and letting $\mathbf{\Phi}(P)$ denote the velocity potential at P and $\mathbf{\Phi}_D(P)$ be the direct wave at P, the following equation can finally be reduced:

$$\mathbf{\Phi}(P) = \mathbf{\Phi}_D(P) + \mathbf{\Phi}_D(P_i) + \frac{ikA}{2\pi} \int\int_F \mathbf{\Phi}(Q) \frac{\exp(ik\bar{r})}{\bar{r}} dS \quad (P \in \Omega, F, F_0). \tag{7}$$

When P is located on F, the BEM can give its solution numerically as

$$p = -i\omega\rho\mathbf{\Phi}, \qquad u = -\frac{\partial \mathbf{\Phi}}{\partial n}. \tag{8}$$

Using Eq. (8), Kawai conducted numerical simulations on absorption coefficients α of glass wool of two sizes. The numerical calculations were conducted for m plane waves that are incident on the specimen's surface from equally distributed directions on the semi-sphere Σ ($m=213$ in the case) to simulate random incidence noise. The admittance of a specimen F to be simulated is measured using the tube method prior to the simulation; it is given into Eq. (8) as the initial admittance condition A of F. The resulting sound pressure and particle velocity calculated by simulation include the effect of A spread over F together with those of direct and image sources. Consequently, Kawai finally obtained the sound absorption coefficient of the specimen from the ratio of the summation of the incident and absorption energies. The incident energy, or intensity, is calculable from the incident sound pressure and particle velocity, whereas absorption energy can be obtained using the sound pressure and particle velocity on the absorbent surface.

B. Math-physical model for ensemble averaged impedance

We follow Kawai's method and simulate the phenomena by which ensemble averaged impedance is to be measured using the procedure described above to clarify whether ensemble averaging makes any sense. Unlike Kawai's procedure, we do not calculate any energy: rather we calculate a series of sound pressure p_{surf} and particle velocity $u_{n,\text{surf}}$ using commercial BEM software (WAON, Version 3.1; Cybernet Systems Co. Ltd.),[19] then corresponding $\langle Z_n \rangle$ can be reduced using Eq. (2b).

1. Normal incidence simulation

Initially, rather simple normal incidence ($\theta=0$) cases for three isotropic materials are simulated and resulting $Z_{n,0}$ and corresponding α_0 are compared to those derived from Miki's empirical equations for an infinite porous material[20] (Z_{emp} and α_{emp}, respectively). To realize the plane wave incidence, a point source P_s is located at (0, 0, 500), or $r=500$ m distance.

Three sizes of glass wool were used, with $L(=L_1=L_2)=1,2,$ and 4 m, all having 32 kg/m^3 density and 10000 N s/m^4 flow resistivity. They are designated as specimen F. The thickness T is set to zero in the BEM's geometrical configurations. However, simultaneously, $T=0.05$ m is

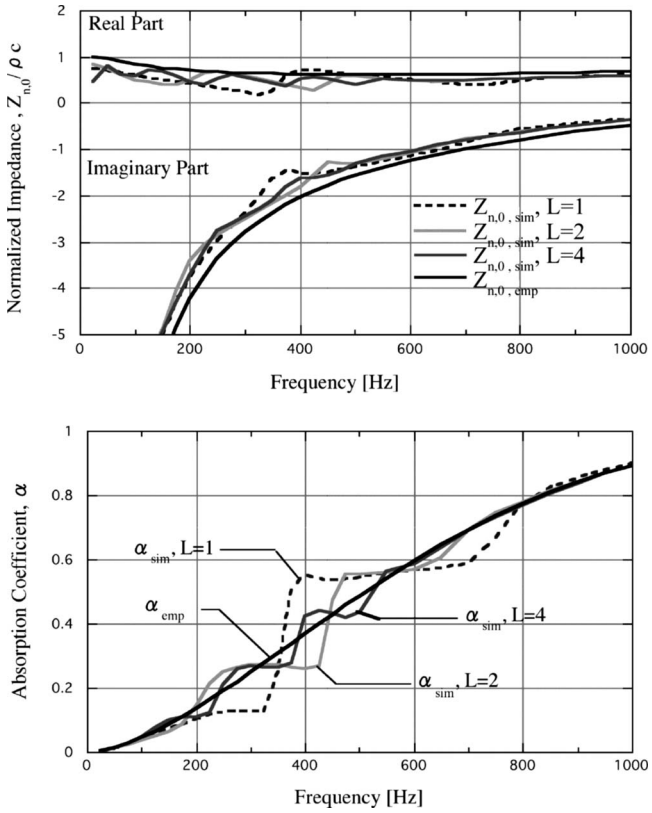

FIG. 5. Comparisons of absorption characteristics of glass wools at normal incidence, simulated ($L=1$, 2, and 4 m) vs empirical (infinite): (upper) normalized surface normal impedances $Z_{n,0}/\rho c$ and $Z_{emp}/\rho c$; (lower) corresponding absorption coefficients, α_0 and α_{emp}.

assumed for all three glass wool specimens to determine Z_{emp}. The determined Z_{emp} is assigned as the impedance condition A of F in the BEM simulation to be conducted.

Then, the surface impedance $Z_{n,0}$ at the center of the specimen is calculated using Eqs. (8) and (1). The calculated $Z_{n,0}$ is based on the assigned Z_{emp} as an initial impedance condition, but it includes the effects originating from the geometrical configuration of the system. Here, to verify the effects including that of d', the distance d' is set to 1 cm. Then both pressure and particle velocity at the point (0, 0, 0.01) are calculated in the frequency domains of 25–500 Hz at a 25 Hz interval and 500–1000 Hz at 50 Hz interval.

The results are portrayed in Fig. 5: the intermediate lines of both simulated $Z_{n,0}$ and corresponding α_0 agree well with Z_{emp} and α_{emp}, respectively, provided that the wavelike fluctuations are omitted. It is noteworthy that the absorption coefficient of a specimen with a finite size can be approximated using the method to fit that of the same material with infinite size. However, the effect of $d'=1$ cm portrayed in Fig. 5 might not be readily apparent because the wavelike fluctuations are unavoidable, but one can expect better results if wavelike fluctuations could be eliminated.

Nonetheless, discrepancies exist: wavelike fluctuations at frequencies of 100– 800 Hz. The discrepancies are thought to result from the interference between direct waves and diffracted waves from the edges around the specimen. Following the fundamental physics according to equation derived by Spandöck,[21] in-phase and out-of-phase frequencies that cause interference, f_{in} and f_{out}, respectively, can be estimated easily using Eqs. (9) and (10) on the condition of $r \gg L$ and λ, i.e., wavelength.

$$f_{in} = \frac{c}{\Delta L} \times n, \tag{9}$$

$$f_{out} = \frac{c}{\Delta L} \times \frac{2n-1}{2}. \tag{10}$$

In those equations, $\Delta L = L/2$, which is the path length difference between the direct sound wave and a representative reflected sound wave, and $n=1,2,\ldots$. The specimens have rectangular shapes. Therefore, ΔL lies between $L/2$ and $\sqrt{2}L/2$. The frequencies for the cases of both $\Delta L=(L/2+\sqrt{2}L/2)/2$ and $c=340$ m/s are calculated and listed in Table I.

The frequencies around which the wavelike fluctuations are portrayed in Fig. 5 coincide well with the in-phase and out-of-phase frequencies presented in Table I. Therefore, the issues that can be reduced to sound absorption characteristics might be measured using such a method with a sound source, but the wavelike fluctuations resulting from interference might be unavoidable.

The larger the specimen, the more numerous but smaller in amplitude the wavelike fluctuation becomes. However, because it is usual for buildings to use such a material as with $L \simeq 1$ m, an *in-situ* absorption measurement of the material using some reflection method will interfere.

Figure 5 also shows that, in the case where the material has $L=4$ m size, good results without distinct fluctuation can be expected only for frequencies higher than 700 Hz, whereas wavelike distortions are unavoidable below that frequency.

2. Random incidence simulation

Next, the same BEM calculations with the exception of the sound source condition are conducted for the same glass wool ($L=1$ m). Point sources are located at equally distrib-

TABLE I. In-phase (○) and out-of-phase (●) frequencies with respect to the specimen's size derived from Eqs. (9) and (10).

Specimen size L (m)	Frequency (Hz)													
	70.4	140.8	211.2	181.7	352.1	422.5	492.9	563.3	633.7	704.2	774.6	845.0	915.4	985.8
1	…	…	…	○	…	…	…	●	…	…	…	○	…	…
2	…	○	…	●	…	○	…	●	…	○	…	●	…	○
4	○	●	○	●	○	●	○	●	○	●	○	●	○	●

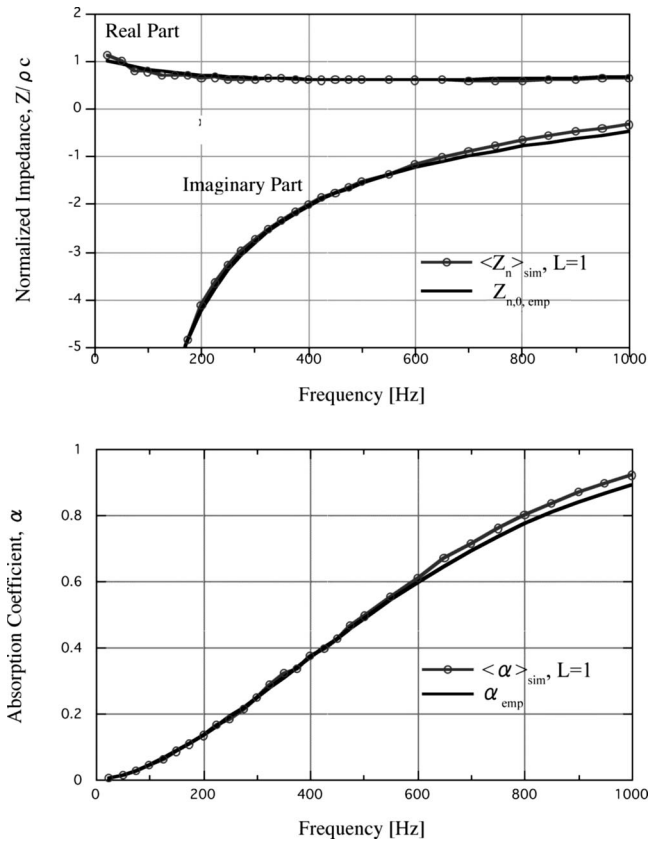

FIG. 6. Comparisons of absorption characteristics of the glass wool, simulated ($L=1$ m, random incidence, ensemble averaged) vs empirical (infinite, normal incidence): (upper) normalized surface normal impedances $\langle Z_n \rangle / \rho c$ and $Z_{\mathrm{emp}}/\rho c$; (lower) corresponding absorption coefficients $\langle \alpha \rangle$ and α_{emp}.

uted $m=206$ points on the sphere with radius $r=500$ m. The sound source number is slightly less than that of Kawai's model, but we conducted several preliminary simulations and confirmed that the difference is negligible.

A series of BEM calculations was performed changing the sound source simultaneously: the phases and amplitudes of the sound sources are randomized to average. A series of random numbers that follow a Gaussian distribution $N(\mu, \sigma^2)$ with mean μ and variance σ^2 is generated for the modeling of sound source amplitude. Similarly, a series of random numbers follows the uniform distribution $[-\pi, \pi]$ for the phase. The values of μ and σ that correspond, respectively, to 120 and 20 dB are assigned, and with a set of calculated p_{surf} and $u_{n,\mathrm{surf}}$, ensemble averaged impedances are calculated using Eq. (2b).

Actually, Fig. 6 shows that the wavelike fluctuations found in the normal incident simulations (Fig. 5) can be flattened. The figure also shows that the simulated $\langle Z_n \rangle$ and corresponding $\langle \alpha \rangle$ agree fairly well, respectively, with assigned Z_{emp} and corresponding α_{emp}. The result alleviates the second issue that the ensemble averaged surface normal impedance gives an excellent approximation of surface normal impedance of the material with no distinct fluctuation caused by the interference. Even if the specimen's size is $L=1$ m, the equation $\langle Z_n \rangle \simeq Z_{\mathrm{emp}}$ stands.

IV. EXPERIMENTAL CONFIRMATION

A. Measurement outline and comparison with simulation

Measurements of two types were conducted to support the issues inferred from results of the BEM simulations: one in an anechoic room with the volume of 58 m^3, the other in a reverberation room with non-parallel walls and with 165 m^3. Both rooms are at the Computing Center of Oita University. The measurements followed the basic procedure described in a previous paper[2] except that is not a pp-sensor: instead, it is a pu-sensor. In addition, calibration of the pu-sensor is made in an impedance tube with selected frequency range to determine the correction of amplitude and phase response.[22,23]

The environment noises inside are insufficient in such rooms. Therefore, an additional speaker(s) generating incoherent pink noise is (are) used as follows: in the anechoic room, a loudspeaker (10 cm single-cone speaker in a box) is located at $r=2$ m distance normal to the glass wool to realize a normal incidence condition. In the reverberation room, seven loudspeakers including a subwoofer generating incoherent pink noise are distributed over the floor to realize a random incidence condition.

In each room, glass wool with dimensions of $0.9 \times 0.9 \times 0.05$ m^3 and density of 32 kg/m^3 is laid on the floor. The four sides of the glass wool are covered with thin aluminum plates. In the anechoic room, the glass wool is laid on a 0.02 m acrylic plate, whereas in the reverberation room it is laid on the concrete floor directly. The glass wool size ($L=0.9$ m) is not exactly identical to that of the simulated one in Sec. III ($L=1$ m), but we expected to have sufficient validity for fundamental discussion at this stage.

Then a pu-sensor (PT0406-7; Microflown Technologies) is placed at the center of the glass wool with $d'=1$ cm, and the sensor's outputs are plugged into a two channel FFT instrument (SA-78; Rion Co. Ltd.). The FFT resolution is set to 1.25 Hz and a Hanning window with 0.8 s time length is used. Measured data are averaged 120 times. The FFT instrument settings we used differ slightly from those used with original method,[2] but we conducted several preliminary measurements and confirmed that they do not give any essential effect onto the results.

1. Comparison at normal incidence

In Fig. 7, the normalized surface normal impedances and corresponding absorption coefficients of the glass wool at normal incidence condition obtained using the measurement were compared to those obtained by simulation. The measurement is conducted in the anechoic room, and the simulated values are those of $L=1$ m case shown in Fig. 5. Again, the wavelike fluctuations are readily apparent in the measured data.

The experimental result also supports the first issue: the wavelike fluctuations are unavoidable for a measuring method with a normal incidence sound source. The measurement is conducted in a rather small anechoic room. The distance r or the distance from the specimen to the ceiling or

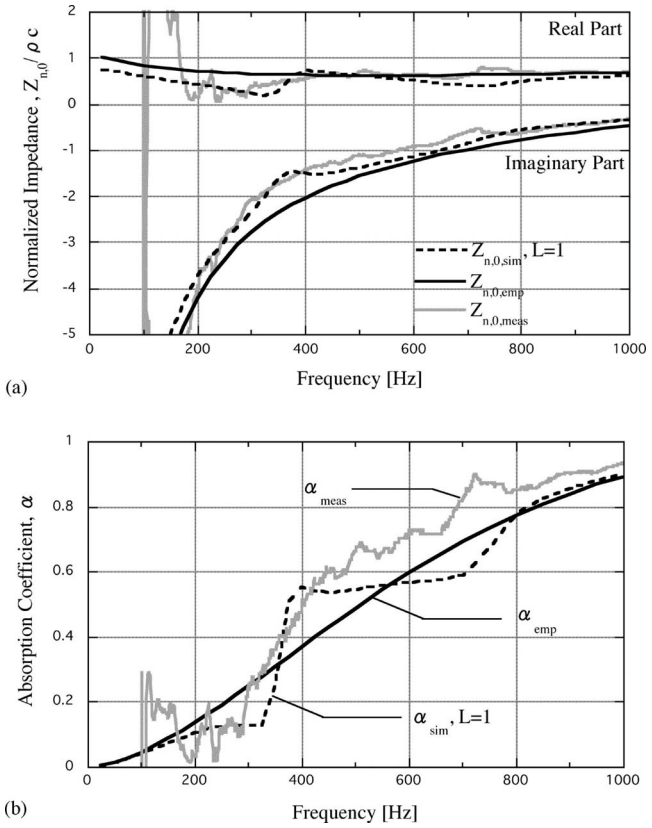

FIG. 7. Impedances and absorption coefficients of glass wool at normal incidence. Comparisons of measured (L=0.9 m), simulated (L=1 m), and empirical (infinite): (upper) normalized surface normal impedances, $Z_{n,0}/\rho c$ (Z_{meas} vs Z_{sim} and Z_{emp}); (lower) corresponding absorption coefficients, α_0 (α_{meas} vs α_{sim} and α_{emp}).

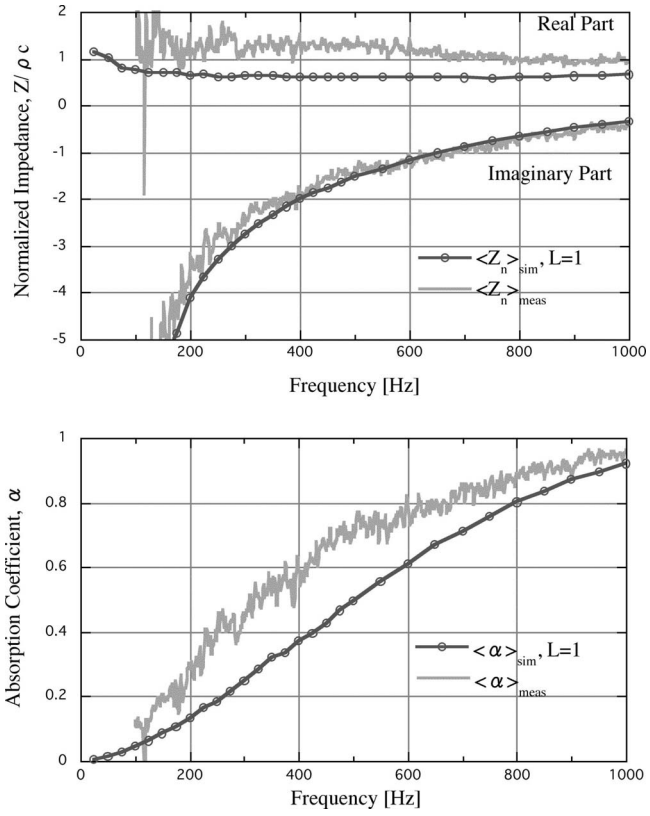

FIG. 8. Ensemble averaged impedances and absorption coefficients of glass wool at random incidence. Comparisons of measured (L=0.9 m) and simulated (L=1 m): (upper) normalized surface normal impedances $\langle Z_n\rangle/\rho c$ (Z_{meas} vs Z_{sim}); (lower) corresponding absorption coefficients $\langle\alpha\rangle$ (α_{meas} vs α_{sim}).

side walls is not sufficiently great that there might be reflections or some more interference effects to disturb the measurement.

Additionally, in the lower frequency range of less than 200 Hz, many distortions are apparent in the measured values, both Z_n and α, which suggests that the sound energy in the range might be insufficient. Treatment of the spherical wave might be necessary to improve the accuracy in the frequency range.[12]

2. Comparison at random incidence

The sound absorption characteristics of the glass wool are measured in the reverberation room for comparison to the BEM simulation using ensemble averaging. In the upper part of Fig. 8, the measured and simulated normalized surface normal impedances $\langle Z_n\rangle$ at random incidence conditions are compared. The lower part of Fig. 8 depicts a comparison of the corresponding absorption coefficients $\langle\alpha\rangle$. No distinct fluctuation is observed in measured $\langle Z_n\rangle$ or in measured $\langle\alpha\rangle$, which supports the second issue that ensemble averaging is sufficiently effective to reduce the wavelike fluctuations in the resulting absorption characteristics.

However, a non-negligible discrepancy remains between the measured and simulated data at frequencies of 100–900 Hz. Comparison of the results between normal and random incidence conditions shows a discrepancy in results from anisotropy of the glass wool which is not incorporated in the math-physical model above.

B. Improved simulation with anisotropy consideration

1. Consideration of anisotropy of glass wool into BEM simulation

For glass wool, angular-dependent normal impedance $Z_{n,\theta}$ can be estimated using Eq. (11) which was given by Allard *et al.*[24] and originated by Pyett.[25] Knowing the planar and normal wavenumbers k_p and k_n in the glass wool,

$$Z_{n,\theta} = (k_n Z_n/k_q)\coth(\gamma_q T). \tag{11}$$

The quantities k_q and γ_q are equal to

$$k_q^2 = k_n^2\{1 - (k_0/k_p)^2 \sin^2\theta\}, \tag{12}$$

$$\gamma_q = ik_q, \tag{13}$$

where k_0 is the wavenumber in air.

A series of procedures described by Allard *et al.*[7] is conducted to determine the k_p and k_n. First, several preliminary measurements using an acoustic tube were conducted and a normal flow resistivity, σ_n, of 10 000 N s/m^4 was chosen for the glass wool to fit the predicted normal surface impedances given by the empirical equations.[20,26] Next, the anisotropy parameter $s=\sigma_p/\sigma_n$ was inferred to be equal to 0.6, in

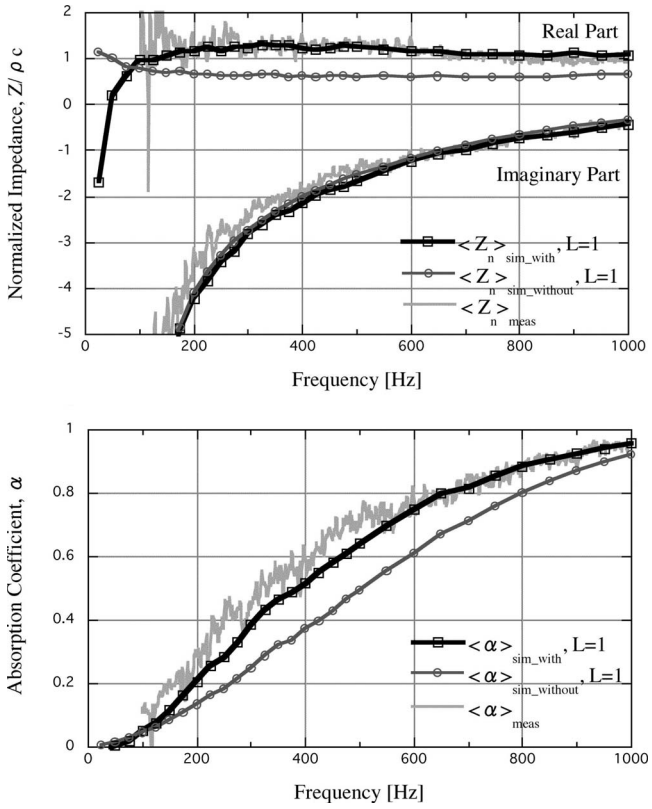

FIG. 9. Improvement of simulation by considering anisotropy of glass wool: (upper) normalized surface normal impedances $\langle Z_n \rangle / \rho c$ ($Z_{\text{sim\_with}}$ vs $Z_{\text{sim\_without}}$ and Z_{meas}); (lower) corresponding absorption coefficients $\langle \alpha \rangle$ ($\alpha_{\text{sim\_with}}$ vs $\alpha_{\text{sim\_without}}$ and α_{meas}).

which σ_p denotes the planar flow resistivity. Finally, k_p and k_n are calculated as propagation constants using empirical equations.[7,27] Thereby, $Z_{n,\theta}$ is obtainable.

To consider the anisotropy of the glass wool in the BEM simulation at random incidence that is described in Sec. III B 2, $Z_{n,\theta}$ is obtained following the procedure described above. In addition, $1/(Z_n/\rho c)$ is given as the initial admittance condition A of F into BEM calculation for each of the 206 sound sources. Except for the initial admittance condition, the remainder of the treatments in the improved BEM simulation is the same as those of the original BEM simulation, and ensemble averaged impedance with anisotropy consideration of glass wool is obtainable using the improved BEM simulation.

2. Comparison with measurement

The impedance and corresponding absorption coefficient obtained using the improved BEM simulation with anisotropy consideration of the glass wool ($L=1$ m) are compared with those by the original BEM simulation and with those by the measurement in Fig. 9 (the latter two values are shown in Fig. 8).

In Fig. 9, in the frequency range of 150–1000 Hz, the absorption coefficients obtained using the improved BEM simulation exceed those obtained using the original BEM simulation. Moreover, the agreement between the simulated and the measured absorption coefficients is improved remarkably by considering anisotropy in the BEM simulation. Similar improvement is apparent in the agreement of the real parts of the impedances between the improved simulation and the measurement. Although the imaginary parts of the simulated impedance do not show distinct change, we consider that, on the whole, the agreement is sufficient for the BEM simulation to investigate the phenomena at this stage of our study.

V. CONCLUSIONS

The pertinent concept of ensemble averaged surface normal impedance to be measured using an *in-situ* technique and its math-physical model was presented. Several BEM simulations of glass wool both at normal and at random incidences demonstrate that ensemble averaging decreases the interference effect caused mainly by the specimen's edges and that the ensemble averaged surface normal impedance at random incidence gives an appropriate expected value of the surface normal impedance of the material. Measurements in experimental rooms of two types were conducted for comparison with the simulations, yielding plausible agreement to support the issues. Further numerical and experimental investigations are now being pursued intensively.

ACKNOWLEDGMENTS

This research was partially supported by a Ministry of Education, Culture, Sports, Science and Technology Grant-in-Aid for Exploratory Research, Contract No. 19656143, 2007–2008, and was conducted as one Research Project (A) of the Venture Business Laboratory in Oita University.

[1] T. Okuzono, T. Sueyoshi, T. Otsuru, N. Okamoto, and R. Tomiku, "Time domain finite element sound field analysis of rooms using iterative methods and parallelization," Proceedings of the Inter-Noise 2006 Congress, Honolulu, HI, 2006.
[2] Y. Takahashi, T. Otsuru, and R. Tomiku, "*In situ* measurements of surface impedance and absorption coefficients of porous materials using two microphones and ambient noise," Appl. Acoust. **66**, 845–865 (2005).
[3] T. Otsuru, N. Okamoto, T. Okuzono, and Y. Takahashi, "Impedance measurement of materials using ambient noise for computational acoustics," Proceedings of the Inter-Noise 2006 Congress, Honolulu, HI, 2006.
[4] A. F. Seybert and D. F. Ross, "Experimental determination of acoustic properties using a two-microphone random-excitation technique," J. Acoust. Soc. Am. **61**, 1362–1370 (1977).
[5] J. Y. Chung and D. A. Blaser, "Transfer function method of measuring in-duct acoustic properties. I. Theory," J. Acoust. Soc. Am. **68**, 907–912 (1980).
[6] Y. Champoux, J. Nicolas, and J. F. Allard, "Measurement of acoustic impedance in a free field at low frequencies," J. Sound Vib. **125**, 313–323 (1988).
[7] J. F. Allard, Y. Champoux, and J. Nicolas, "Pressure variation above a layer of absorbing material and impedance measurement at oblique incidence and low frequencies," J. Acoust. Soc. Am. **86**, 766–770 (1989).
[8] J. F. Allard and Y. Champoux, "*In situ* two-microphone technique for the measurement of the acoustic surface impedance of materials," Noise Control Eng. J. **32**, 15–23 (1989).
[9] J. F. Allard, C. Depollier, and P. Guignouard, "Free field surface impedance measurements of sound-absorbing materials with surface coatings," Appl. Acoust. **26**, 199–207 (1989).
[10] M. Garai, "Measurement of the sound-absorption coefficient *In situ*: The reflection method using periodic pseudo-random sequences of maximum length," Appl. Acoust. **39**, 119–139 (1993).
[11] E. Mommertz, "Angle-dependent in-situ measurements of reflection coefficients using a subtraction technique," Appl. Acoust. **46**, 251–263 (1995).
[12] C. Nocke, "In-situ acoustic impedance measurement using a free-field transfer function method," Appl. Acoust. **59**, 253–264 (2000).

[13]H.-E. de Bree, P. Leussink, T. Korthorst, H. Jansen, T. Lammerink, and M. Elwenspoek, "The μ-flown: A novel device for measuring acoustical flows," Sens. Actuators, A **54**, 552–557 (1996).
[14]H.-E. de Bree, E. Tijs, and T. Basten, "Two complementary Microflown based methods to determine the reflection coefficient in situ," Proceedings of the ISMA2006 Conference, Leuven, Belgium, 2006.
[15]F. Jacobsen and H.-E. de Bree, "A comparison of two different sound intensity measurement principles," J. Acoust. Soc. Am. **118**, 1510–1517 (2005).
[16]D. Nutter, T. Leishman, S. Sommerfeldt, and J. Blotter, "Measurement of sound power and absorption in reverberation chambers using energy density," J. Acoust. Soc. Am. **121**, 2700–2710 (2007).
[17]T. Iwase, Y. Murotuka, K. Ishikawa, and K. Yoshihisa, "Measurements of acoustic impedance and their data application to calculation and audible simulation of sound propagation," Acoust. Sci. & Tech. **29**, 21–35 (2008).
[18]Y. Kawai and H. Meotoiwa, "Estimation of area effect of sound absorbent surfaces by using a boundary integral equation," Acoust. Sci. & Tech. **26**, 123–127 (2005).
[19]WAON, Version 3.1 User's Manual (Cybernet Systems Co. Ltd., 2008).
[20]Y. Miki, "Acoustical properties of porous materials modifications of Delany–Bazley models," J. Acoust. Soc. Jpn. (E) **11**, 19–24 (1990).
[21]V. F. Spandöck, "Experimentelle Untersuchung der akustischen Eigenschaften von Baustoffen durch die Kurztonmethode (Experimental investigation of the acoustic characteristics of building materials using the short tone method)," Ann. Phys. **412**, 328–344 (1934).
[22]F. Jacobsen and V. Jaud, "A note on the calibration of pressure-velocity sound intensity probes," J. Acoust. Soc. Am. **120**, 830–837 (2006).
[23]H.-E. dBree, *The Microflown E-Book* (Microflown Technologies, Arnhem, 2009), Chap. 4A.7, pp. 12–14, available from http://www.microflown.com/data/books/EBook_Microflown/Ebook_4A_standard_calibration_techniques.pdf (Last viewed January, 2009).
[24]J. F. Allard, R. Bourdier, and A. L'Espérance, "Anisotropy effect in glass wool on normal impedance in oblique incidence," J. Sound Vib. **114**, 233–238 (1987).
[25]J. S. Pyett, "The acoustic impedance of a porous layer at oblique incidence," Acustica **3**, 375–382 (1953).
[26]M. E. Delany and E. N. Bazley, "Acoustical properties of fibrous absorbent materials," Appl. Acoust. **3**, 105–116 (1970).
[27]K. Attenborough, "Acoustical characteristics of rigid fibrous absorbents and regular materials," J. Acoust. Soc. Am. **73**, 785–799 (1983).

The personal papers of Wallace C. Sabine

Leo L. Beranek[a)]
776 Boylston Street, Apartment E10A, Boston, Massachusetts 02199

(Received 25 February 2009; revised 3 April 2009; accepted 3 April 2009)

The notebooks of Wallace Clement Sabine were discovered in 1975, and his consulting files were discovered in 1979. Both findings were reported [J. Acoust. Soc. Am. **61**, 629–639 (1977); J. Acoust. Soc. Am. **69**, 1–7 (1981)]. By chance, his personal papers were discovered recently and highlights from them are presented here with emphasis on his European activities from 1906 to 1917. © *2009 Acoustical Society of America.* [DOI: 10.1121/1.3125326]

PACS number(s): 43.55.Fw, 43.10.Sv [NX] Pages: 3792–3794

I. BACKGROUND

In June 1921, Professor Theodore Lyman wrote in the preface to *Collected Papers on Acoustics by Wallace Clement Sabine*,[1] "…these papers [suggested in Sabine's publications] were either never written or else were destroyed by their author; no trace of them can be found…The severity of the criticism which Professor Sabine always applied to his own productions increased with time, and it is to this extreme self-criticism and repression that we must ascribe the loss of much invaluable scientific material." In 1975 in an unused closet at the Riverbank Acoustical Laboratories in Geneva, IL, 12 notebooks containing the research of Sabine from 1886 to 1918 were discovered. These were sent to this author for review, indexing, and publication, and now rest in the Harvard University Archives.[2] In 1979 in another closet 22 consulting correspondence files of Sabine were discovered. These were studied and highlights were published by Beranek and Kopec.[3] Photocopies of those documents are also in the Harvard Archives. Having had access to these notebooks and consulting files, the author longed to get to any papers that he might have kept in his home.

II. DISCOVERY OF SABINE'S PERSONAL PAPERS

Mrs. Wallace Sabine's maiden name was Jane Kelly. She studied medicine at Northwestern University where she received her M.D. degree. She and Wallace were married in August 1900, just before Boston Symphony Hall opened. Two daughters were born, Janet in 1903 and Ruth in 1906. Ruth died in 1922. My story here involves Janet, the older daughter.

In the fall of 1986, I had the pleasure of a discussion with Mrs. William Thompson, a long time resident of Boston. I happened to mention my interest in Wallace Sabine's work. She said that she was aware of Professor Sabine because she had known his secretary. A musical marathon, called "Salute to Symphony," was, until recently, held every year at Boston Symphony Hall. Over a period of 3 days, radio station WCRB in Boston carried a series of musical events live from Symphony Hall which was interspersed with requests for monetary contributions. A battery of volunteers answered telephone calls, received pledges of donations, and wrote down the names and addresses on cards for use in billing. On one of the evenings, Mrs. Thompson was driving to her suburb home near Boston and had her car radio tuned to WCRB. She heard the announcer say, "We have just received a pledge from Janet Wallace Ley of Williamstown, Massachusetts, who said she is the granddaughter of the man who designed Boston Symphony Hall--did the acoustics." On reaching home, Mrs. Thompson telephoned me with the news. The next day I called the Hall and Mrs. Ruth Hertz told me that it was nearly impossible to find a pledge card because each was handed to a typist who, after typing a bill to be mailed to the donor, threw the card into a barrel. She said it would be very time consuming to try and find it among the thousands there. She added, maybe next summer when she had time, she would have a try.

Only few days later, March 20, 1987, I received a letter from Ms. Hertz saying, "Janet Wallace Ley's card jumped up at me while I was looking for another pledge card…I hope it will help you in your research." I called Janet Wallace Ley a few days later and learned that indeed she had Sabine's personal papers. I arranged to visit their home. During my visit, I learned that Janet Sabine, Wallace Sabine's older daughter, married Frederic A. Ley. One of their daughters was Janet Wallace Ley who married a Lt. Col. Fred Bess. After hearing this, I said, "Your names are now Ley, not Bess." She replied, "My husband changed his name."

III. NEW FINDINGS FROM SABINE'S PERSONAL PAPERS

The papers are located in the Ley's home at 1521 Green River Road, Williamstown, MA 01267. There is an immense quantity of material to review. The items of interest to this author were those that tell more about Sabine's life. Things at the Ley home that were new are presented here.

A correspondence between Sabine, Charles McKim, the architect for Boston Symphony Hall, Henry Lee Higginson, the owner of the Boston Symphony Orchestra, and chairman of the building committee. Some of this correspondence was also given to me by Professor Emily Thompson of Princeton University who had studied McKim's papers which are in the archives of the New York Historical Society.

Letter of 26 January 1899. Higginson informed McKim for the first time that Sabine had studied the plans for the hall

[a)]Electronic mail: beranekleo@ieee.org

 0001-4966/2009/125(6)/3792/3/$25.00

and had opinions that Higginson was passing on. Sabine reportedly said that the design of the hall was altogether too long; that a second balcony should be introduced to shorten the length, and that the orchestra should be put in a stage house so that more seats can be put on the main floor where McKim had previously located the stage. McKim was unhappy with these changes and Higginson sent Sabine to New York to discuss them. Sabine spent 2 h with McKim, the only time he was ever with the architect.

Letter written just after the meeting: Sabine reported that McKim was happy with the changes and "…takes pleasure and interest in the architectural problem because of the difficulties and restrictions to be overcome." His report continued, "…The interview yesterday was both pleasant and satisfying."

Letter of 27 February, 1899. Architect McKim reported to Higginson that Sabine and McKim had gone "over the plans and in a thorough consideration of the unsettled points. I was much impressed by the force and reasonableness of Sabine's arguments, and by the modest manner in which they were presented, and have confidence that the acoustics of the hall will have greatly benefitted by his counsel and advice." Sabine's recommendations were incorporated into the official building plans. It is the author's opinion that McKim gave in so easily to these requests due to two considerations: (1) he probably felt that Higginson would be intractable and (2) the deadline for opening the hall was October 1900 and that was only 18 months away.

Letter of 8 March 1900. Sabine writes to Higginson. "Should the hall at any time fail of an audience—of a full house—the kind of seats will make a great deal of difference. I hope that they may be upholstered at least as well as in the old house…May I suggest that in order to compare the two halls it would be well if the first few concerts next year should be of music that had been heard in the old hall. I am anxious that the comparison should be a decisive one and such comparison would be better with strong and well liked music…"

Symphony Hall opened October 15, 1900 with a gala concert. The hall has since achieved world renowned for its excellent acoustics.[4] But, we may ask, what happened in Sabine's life after Symphony Hall?

IV. THE SABINES GO TO EUROPE

Wallace Sabine became Dean of the Scientific School at Harvard in 1906, a position that he did not want but which was put on him by Harvard's President Charles Eliot. Among Sabine's ideas for the school, one was to establish a course in Naval Engineering, which demanded that a testing-tank be built. He went off to Europe to study tanks, where he saw tanks at the German Naval Base and at the British Admiralty Base at Gosport, Stokes Bay.

On arriving home, Sabine was given a different assignment. He was placed in charge of diplomatic negotiations that led to a merger of the engineering departments at Harvard with those of the Massachusetts Institute of Technology. This meant a transfer to MIT of all of Harvard's instruction and research in engineering and applied science. In addition, Harvard was to contribute three-fifths of the funds derived from the enormous McKay Trust funds at Harvard's disposal as well as some other property. All administration was to be at MIT and 14 Harvard men would be involved in the transfer.

The agreement was actually put into operation in 1915, which meant the termination of Sabine's title as Dean of the Scientific School. The testing-tank was to be built at MIT so that Sabine's participation in that enterprise terminated. But, this merger did not last. Alumni at both Harvard and MIT objected to the merger, and 2 years later the Massachusetts Supreme Judicial Court ruled against it with the opinion that it did not satisfy the intention of the donor, Gordon McKay. At that time America entered World War One and Sabine wished to offer his services to his country.

The Sabine family had been spending summers in France and Berlin and the family went there in July 1914. On August 3, they had to flee from Berlin on an over-crowded train and, after traversing the English Channel, they arrived in London just as the August 4 newspapers were announcing that England had declared war on Germany. They departed for the United States on September 10.

Sabine was invited to give lectures in the Sorbonne at the University of Paris in the fall of 1916. Harvard appointed him "Exchange Professor to France for the first half of the 1916–17 year, with full pay." Sabine went to Paris the first of October intending to prepare for the Sorbonne lectures. But trouble developed. In mid-October he became seriously ill, so serious was his condition that the doctors feared for his life. Mrs. (Dr.) Sabine arrived in Paris in early November, unaware of his illness and within 24 h had arranged for a top surgeon to attend to him. But, before the surgeon arrived, the kidney abscess broke and drained naturally. To recuperate, it was decided that he should go to Dr. Rollier's Clinique Miremont in Leysin, Switzerland. While recovering, he prepared the lectures there.

Sabine went from Switzerland to Paris in early February 1917 and his lectures at the Sorbonne began late in the month and ran until the first of May. In addition to the lectures, which were well attended, mainly by professors and architects and students from the Ecole des Beaux Arts, he spoke before the French Academy of Science and the French Society of Architects. The architects presented him with a medal.

V. SABINE'S WORLD WAR I ACTIVITIES

Sabine's lectures at the Sorbonne came to the attention of the French Government. He was invited to investigate and to give his conclusions on telephone and other acoustical equipment in use by the French army and navy. In May 1917 he left for the Front with members of the American Scientific Commission and French scientists engaged in war problems. In a letter dated May 14, 1917, he wrote, "I have just had a most interesting trip along the whole Front from Reims to Verdun where I was shown every process of waging war. At Verdun I lunched with the Commander in the Citadel, and then was taken to Fort Douaumont…There not a vestige of a tree trunk, not a twig of a bush, not a blade of grass. All

blown to atoms…one continuous stretch of shell-holes—the little town of Fleury completely disappeared. Unexploded shells and hand-grenades and bombs everywhere, so that we had to pick our steps…arms shrieking out of the powdered ground and legs and skulls; and overall the odor of decaying flesh…It had been a quiet day, and the Commander of the Fort said I might go up on the rampart and look off toward the German lines and Dead Man's Hill. I had been up there hardly a moment, stooping low…when suddenly I heard the whistle of a shell and I fell flat. The next instant the shell buried itself in the powder not fifteen feet from me, and exploded. Another shell followed instantly. I rolled down into the Fort." Sabine's clothes were ripped and bits of shrapnel had to be removed from his face and hands. His biographer, William Dana Orcutt, wrote,[5] "Out of this experience came his own invention of a highly successful sound-device for locating artillery, which was soon used by the Allied Armies."

In July 1917, Sabine wrote, saying that he went to Toulon for direct experience on submarine problems, to Italy to the Italian Front, back to Paris, then again to the French Front, and finally back to Paris to report. Biographer Orcutt wrote,[5] "Sabine's most far-reaching service to England and Italy was his success in arranging conferences between the aeronautical departments of the two countries."

Sabine kept busy. He was of service to the French, British and Italian Governments as well as to the United States Government. He returned to America after having spent 17 months on war matters in Europe.

But Sabine was not well and he should have sought medical attention. Instead, upon his return, he spent only one day in Cambridge and was off to Washington to deliver some papers that had been given to him for delivery by the foreign offices. He was appointed the Director of a new Department of Technical Information in the Bureau of Aircraft Production where he was to obtain, put together, and distribute scientific data from a number of sources, including the British, French, and Italian war missions and the scientific attaches in the U.S. embassies. He also worked jointly with the National Advisory Committee for Aeronautics (NACA, predecessor of NASA). Soon, President Wilson appointed him as a member of NACA.

Also, immediately on arriving back in the United States from Europe, he was appointed by Harvard as Acting Director of the Jefferson Physical Laboratory. This tremendous load should have worried Sabine, who maintained an impossible schedule of Friday through Monday in Washington, taking the midnight train arriving in Cambridge at 8 am Tuesday and returning Thursday night on the midnight train to Washington. He taught his usual classes and even added a course on Aviation Ballistics. In the summer of 1918, he seldom saw his family because he slept in a hammock at the laboratory. With President Lowell's help, he obtained a permanent room in Washington because the hotels there were so crowded that he often had to go to Baltimore to sleep. His family saw that his health was worsening, but he refused to get medical help. The Armistice came on November 11, 1918 and he immediately sent his formal resignation to the Secretary of War in Washington.

Between then and January, Sabine not only taught several courses at Harvard but he threw himself into nighttime research on the transmission of sound through walls. He became absentminded; he would leave the table thinking he had eaten when he had only just sat down. He never complained about his pain although he knew that he was very ill. His wife urged him to take his physicians advice and have surgery to remove whatever was wrong. So long as he could stand he did his work. In December 1918, he underwent a preliminary operation in the Peter Bent Brigham Hospital in Boston. That indicated a cancerous kidney, but then he contracted influenza. As soon as the influenza subsided he underwent a major operation, but it was too late, he passed away on January 10, 1919.

[1]W. C. Sabine, *Collected Papers on Acoustics* (Penninsula Press for the Acoustical Society of America, Melville, NY, 1993).
[2]L. L. Beranek, "The notebooks of Wallace C. Sabine," J. Acoust. Soc. Am. **61**, 629–639 (1977).
[3]L. L. Beranek and J. W. Kopec, "Wallace C. Sabine, acoustical consultant," J. Acoust. Soc. Am. **69**, 1–7 (1981).
[4]R. P. Stebbins, *The Making of Symphony Hall* (Boston Symphony Orchestra, Boston, MA, 2000).
[5]W. D. Orcutt, *Wallace Clement Sabine: A Study in Achievement* (Harvard University, Cambridge, MA, 1933).

The directivity of the sound radiation from panels and openings[a)]

John L. Davy[b)]
School of Applied Sciences, RMIT University, GPO Box 2476V, Melbourne, Victoria 3001, Australia

(Received 18 January 2008; revised 22 March 2009; accepted 23 March 2009)

This paper presents a method for calculating the directivity of the radiation of sound from a panel or opening, whose vibration is forced by the incidence of sound from the other side. The directivity of the radiation depends on the angular distribution of the incident sound energy in the room or duct in whose wall or end the panel or opening occurs. The angular distribution of the incident sound energy is predicted using a model which depends on the sound absorption coefficient of the room or duct surfaces. If the sound source is situated in the room or duct, the sound absorption coefficient model is used in conjunction with a model for the directivity of the sound source. For angles of radiation approaching 90° to the normal to the panel or opening, the effect of the diffraction by the panel or opening, or by the finite baffle in which the panel or opening is mounted, is included. A simple empirical model is developed to predict the diffraction of sound into the shadow zone when the angle of radiation is greater than 90° to the normal to the panel or opening. The method is compared with published experimental results.
 [DOI: 10.1121/1.3117687]

PACS number(s): 43.55.Rg, 43.50.Jh, 43.55.Ti, 43.50.Gf [LMW] Pages: 3795–3805

I. INTRODUCTION

This paper describes a method for predicting the directivity of the sound radiated from a panel or opening excited by sound incident on the other side. This directivity needs to be known when predicting the sound level at a particular position due to the sound radiation from a factory roof, wall, ventilating duct, or chimney flue. The dependence on angle of incidence of the sound insulation of windows, doors, walls, and roofs also needs to be known in order to predict the internal noise due to an external noise source.

The method described in this paper is mainly two dimensional. The directivity is modeled as being that of a line source whose phase of vibration is determined by the angle of incidence of the incident sound. The angular distribution of the incident sound energy is a function of the sound absorption coefficient of the walls of the room or the duct, and the directivity of the sound source. The directivity of the sound source is modeled as being that of a line source of constant phase. The diffraction caused by the finite size of the opening or panel, and any baffle that it is mounted in, is also modeled. An empirical model is used to predict the diffraction of sound into the shadow zone. In some cases a correction is made for the effects of "background" scattering.

A number of authors report experimental measurements of the directivity of openings and panels in the external wall of a room. Rindel (1975) measured the directivity of openings and single and double leaf panels mounted in the wall of a scale model room mounted in an anechoic room. His measurements are from outside to inside the scale model room. It should be noted that Rindel (1975) measured and removed the sound pressure increase on the surface of the panel due to diffraction from his experimental results. The diffraction theory developed in this paper is based partly on Rindel's (1975) measurements of the sound pressure increase on a panel due to diffraction. Oldham and Shen (1982) made anechoic room measurements of the directivity of openings in the wall of a scale model room in the opposite direction. Roberts (1983) conducted measurements of the directivity of openings in the wall of a room from inside to outdoors. Shen and Oldham (1982) and Oldham and Shen (1983) extended their earlier anechoic room measurements to the directivity of single panels in the wall of their scale model room. Rowell and Oldham (1996) carried out near field acoustical holography measurements of the directivity of homogeneous, profiled, and composite single leaf panels in the wall of a room. Stead (2001) measured the directivity of a single panel in the wall of a room from outdoors to inside.

In addition to experimental measurements, a number of theoretical and numerical models for predicting the directivity of panels and openings in the external wall of a room are also reported in the literature. Rindel (1975) developed a theory for the directivity of openings and panels in the wall of a room. Oldham and Shen (1982) developed a computer model with experimentally determined corrections to predict the directivity of an opening in a room wall. Shen and Oldham (1982) presented a numerical model for the directivity of a panel in the wall of a room. Oldham and Shen (1983) developed an empirical model for the directivity of a panel in the wall of a room from their experimental data. The model presented in this paper is primarily a theoretical analytic model, although it does include some empirical equations and does involve one linear integral which needs to be inte-

[a)]Portions of this work were presented and published in a series of conference papers and theses by the author and his students, which are referred to in the Introduction and references.

[b)]Electronic mail: john.davy@rmit.edu.au. Also at CSIRO Materials Science and Engineering, P.O. Box 56, Highett, Victoria 3190, Australia.

grated numerically. It is an extension of Rindel's (1975) theory, but is different from Shen and Oldham's (1982) theories. The model in this paper extends Rindel's (1975) theory in a number of ways. It uses an analytic model for the radiation efficiency rather than an interpolation from a table of numerically calculated values. An empirical analytic model for the sound pressure increase on the surface of a panel due to diffraction replaces Rindel's (1975) measurements. A theoretical model for the directivity of the sound which excites the panel replaces Rindel's (1975) assumption of a reverberant field.

In the case of the opening at the end of a duct, a number of authors have published measurements and prediction methods for the directivity. Wells and Crocker (1953) made measurements on models and a prototype of an exhaust stack. Watters *et al.* (1955) and Björk (1994) conducted similar measurements on full scale and model exhaust stacks. Beranek (1954) presented measured directivity patterns for the inlet of a ventilating fan, while Allen (1960), Sharland (1972), and Woods (1972) gave graphs or tables for estimating the directivity of duct openings in rooms.

Bies and Hansen (2003) gave directivity curves for the radiation of sound from the end of a duct based on measurements in an anechoic room by Croft (1979) and Sutton (1990). These anechoic room measurements are continued by Dewhirst (2002) and Li (2005). Hansen supplied Dewhirst's (2002) and Li's (2005) data to the author of this paper in machine readable form. Neish (1997) and Potente *et al.* (2006) measured the directivity of a duct end in the open air. (Day supplied the author of this paper with all his test data in machine readable form, including some unpublished data.)

The classical theoretical paper on the directivity of an unflanged circular duct end is Levine and Schwinger (1948). Unfortunately, because it assumes plane wave propagation in the duct, it overestimates the experimentally observed duct directivity and can only be used up to the cut on frequency of the first cross mode. Joseph and Morfey (1999) extended the theory into the cross mode region. Wells and Crocker (1953) also calculated the directivity of circular and square cross section duct ends assuming plane wave propagation.

In a series of conference papers and theses, the author of this paper and his students gradually develop the method described in this paper. The derivation of the necessary results on the radiation efficiency of finite size flat panels is given by Davy (2004). Pavasovic (2006) and Davy and Pavasovic (2006) presented the first version of this model which assumes a cosine squared angular distribution of the incident sound energy. Davy and Kannanaikkel John (2006) replaced this cosine squared distribution with a physical model for the angular distribution of the incident sound energy which depends on the sound absorption coefficient of the side walls of the room or duct. They also introduced a simple line source directivity model for a sound source in a duct or room. Fisher (2006) compared the cosine squared and sound absorption coefficient models for the angular distribution of incident sound energy against the experimental directivity of openings and panels in the wall of a room. He introduced an automated method of determining the optimum value of the weighting angle which is used in the cosine squared model and an experimentally determined diffraction correction term. Fisher (2006) also showed that the models are not successful at predicting the directivity of cavity walls such as double glazing. Davy (2007) developed a model for predicting the diffraction on a finite flat surface as a function of angle of incidence and surface size. Davy (2007) and Davy and Kannanaikkel John (2007) introduced this diffraction model into the directivity model. This paper and Davy (2008) extended the diffraction model into the shadow zone and introduced a rule for calculating the average length of the line source which models the directivity of sound sources in ducts or rooms. The comparisons in this paper and Davy (2008) are based on a larger range of experimental results than the earlier papers. The purpose of this paper is to make the details of the directivity model easily and widely available.

II. THEORY

A. Radiation efficiency and transmitted sound pressure

The effective impedance $Z_e(\phi)$ of a finite panel in an infinite baffle to a plane sound wave incident at an angle of ϕ is (Rindel, 1975)

$$Z_e(\phi) = Z_{wfi}(\phi) + Z_{wft}(\phi) + Z_{wp}(\phi), \tag{1}$$

where $Z_{wfi}(\phi)$ is the wave impedance of the fluid as experienced by the finite panel in an infinite baffle, whose vibration is due to a plane sound wave incident at an angle of ϕ, on the side from which the plane sound wave is incident (this is the fluid loading on the incident side); $Z_{wft}(\phi)$ is the wave impedance of the fluid as experienced by the finite panel in an infinite baffle, whose vibration is due to a plane sound wave incident at an angle of ϕ, on the side opposite to which the sound is incident (this is the fluid loading on the non-incident or transmitted side); and $Z_{wp}(\phi)$ is the wave impedance of the finite panel in an infinite baffle to a plane sound wave incident at an angle of ϕ, ignoring fluid loading.

It is assumed that the fluid wave impedances on both sides are the same, and the imaginary part of the fluid wave impedance is ignored (Rindel, 1975). That is,

$$Z_{wfi}(\phi) = Z_{wft}(\phi) = \rho c \sigma(\phi), \tag{2}$$

where ρ is the density of the fluid, c is the speed of sound in the fluid, and $\sigma(\phi)$ is the radiation efficiency into the fluid of one side of the finite panel in an infinite baffle, whose vibration is due to a plane sound wave incident at an angle of ϕ.

Reflections at the panel edges are ignored (Rindel, 1975). The normal velocity $v(\phi)$ of the panel due to a plane sound wave incident at an angle of ϕ which exerts a pressure $p_i(\phi)$ is

$$v(\phi) = \frac{p_i(\phi)}{2\rho c \sigma(\phi) + Z_{wp}(\phi)}. \tag{3}$$

The transmitted sound pressure $p_t(\theta, \phi)$ which is radiated by the panel on the non-incident side to a receiving point which is at an angle of θ to the normal to the center of the panel and a large distance from the panel (see Fig. 1) is (Davy, 2004)

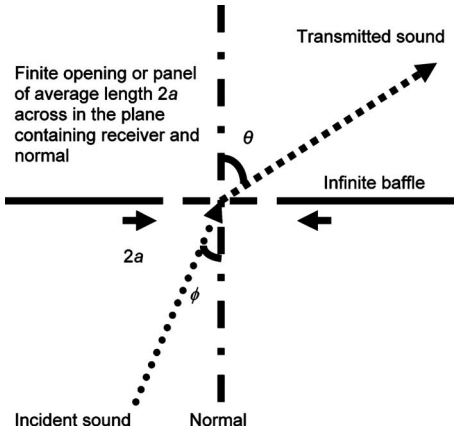

FIG. 1. Sound incident at an angle of ϕ to the normal to a panel or opening and radiated at an angle of θ to the normal.

$$p_t(\theta,\phi) \propto v(\phi)\frac{\sin[ka(\sin\theta-\sin\phi)]}{ka(\sin\theta-\sin\phi)}, \tag{4}$$

where k is the wave number of the sound and $2a$ is the average length across the panel or opening in the plane containing the receiver and the normal to the panel or opening. Thus

$$p_t(\theta,\phi) \propto \frac{p_i(\phi)}{2\rho c\sigma(\phi)+Z_{wp}(\phi)}\frac{\sin[ka(\sin\theta-\sin\phi)]}{ka(\sin\theta-\sin\phi)}. \tag{5}$$

The case where the incident sound is generated by a sound source in a room or duct is now considered. It is assumed that the sound pressure waves are incident at different angles ϕ with random phases and mean squared sound pressures which are proportional to a weighting function $w(\phi)$.

$$|p_i(\phi)|^2 \propto w(\phi). \tag{6}$$

The weighting function is to account for the fact that sound waves at grazing angles of incidence will have had to suffer more wall collisions and therefore be more attenuated before reaching the panel. The total mean square sound pressure $|p_T(\theta)|^2$ at the receiving point is

$$|p_T(\theta)|^2 \propto \int_{-\pi/2}^{\pi/2}\frac{w(\phi)}{|2\rho c\sigma(\phi)+Z_{wp}(\phi)|^2}\times\left\{\frac{\sin[ka(\sin\theta-\sin\phi)]}{ka(\sin\theta-\sin\phi)}\right\}^2 d\phi. \tag{7}$$

The case when sound is incident from a source in a free field at an angle θ to the normal to the panel and the panel radiates at all angles ϕ into a room or duct is also of interest. In this case the weighting function $w(\phi)$ is to account for the fact that sound waves radiated at grazing angles will have had more wall collisions and therefore be more attenuated before reaching the receiving position which is assumed to be a reasonable distance from the panel or opening which is radiating the sound. In this second case, it is necessary to integrate over all angles of radiation ϕ because of the reverberant nature of the sound. For this case, the impedance terms in the integral are functions of θ rather than ϕ and can be taken outside the integral. However, in this study both

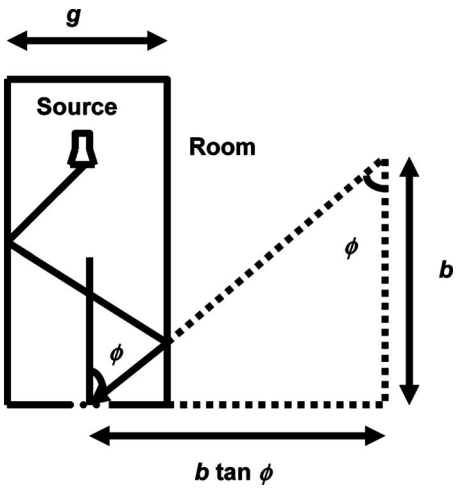

FIG. 2. Calculating the number of wall reflections before sound hits the panel or opening at an angle of ϕ to the normal.

cases are calculated using the formula for the first case which is shown above. This is because both cases should be the same by the principle of reciprocity and it is not clear which form of the formula is more appropriate.

For large values of ka, the two cases of the formula are similar. If ka is much greater than 1, the function

$$\left\{\frac{\sin[ka(\sin\theta-\sin\phi)]}{ka(\sin\theta-\sin\phi)}\right\}^2 \tag{8}$$

has a sharp maximum at $\phi=\theta$ and is symmetrical in both θ and ϕ about the point $\phi=\theta$. These facts are exploited by evaluating the impedance terms for the first case at $\phi=\theta$ and taking them outside the integral. This gives the formula for the second case.

To derive the angular weighting function, it is assumed that the sound source is a distance b from the surface of the room containing the panel or opening and that the room width is g in the plane containing the incident sound ray (see Fig. 2). If the sound ray is incident at an angle of ϕ to the normal to the panel or opening, it travels a minimum distance of $b\tan\phi$ parallel to wall containing the panel or opening before hitting the wall. The sound which travels this minimum distance hits the wall approximately

$$n=\frac{b}{g}\tan\phi \tag{9}$$

times before reaching the panel or opening, where n is allowed to be a real number rather than an integer in order to give a smooth weighting function. If the sound absorption coefficient of the walls of the room is α, the sound intensity incident at an angle of ϕ to the normal is proportional to

$$w(\phi)=(1-\alpha)^n=(1-\alpha)^{(b/g)\tan|\phi|}. \tag{10}$$

Equation (10) gives the weighting function $w(\phi)$. If α is zero, a uniform diffuse field will be obtained. If α is not known, the use of the empirical value $\alpha=0.05$ is suggested for hard walled rooms and ducts since this value gives reasonable agreement when the theory is compared to experiment. In a room or a straight unobstructed duct, b should be set equal to the perpendicular distance of the source from the

plane containing the opening or panel. For other ducts b should be set equal to the perpendicular distance of the closest bend or obstruction to the duct opening. For the comparisons made with ducts in this paper, the duct sound sources were assumed to be at the opposite end of the duct to the duct opening. This was approximately true for all the ducts considered in this paper.

In this study the radiation efficiency of a panel or opening of length $2a$ and width $2d$ is used. It is approximated with the following equation (Davy, 2004):

$$\sigma(\phi) = \begin{cases} \dfrac{1}{\dfrac{\pi}{2k^2ad} + \cos\phi} & \text{if } |\phi| \le \phi_l \\ \dfrac{1}{\dfrac{\pi}{2k^2ad} + \dfrac{3\cos\phi_l - \cos\phi}{2}} & \text{if } \phi_l < |\phi| \le \dfrac{\pi}{2}, \end{cases} \tag{11}$$

where

$$\phi_l = \begin{cases} 0 & \text{if } ka \le \dfrac{\pi}{2} \\ \arccos\left(\sqrt{\dfrac{\pi}{2ka}}\right) & \text{if } ka > \dfrac{\pi}{2} \end{cases} \tag{12}$$

and k is the wave number of the sound and $2a$ is the length of the panel in the direction of the receiver. Note that in Davy (2004) the width is assumed to be equal to the length.

For an opening with no panel in an infinite baffle, $Z_{wp}(\phi)=0$. For a finite panel in an infinite baffle, the infinite panel result for $Z_{wp}(\phi)$ is used.

$$Z_{wp}(\phi) = m\omega\left\{ j\left[1 - \left(\frac{\omega}{\omega_c}\right)^2 \sin^4(\phi) \right] + \eta\left(\frac{\omega}{\omega_c}\right)^2 \sin^4(\phi) \right\}, \tag{13}$$

where m is the surface density (mass per unit area) of the panel, η is the damping loss factor of the panel, ω_c is the angular critical frequency of the panel, and ω is the angular frequency of the sound. This result is expected to be the correct result when averaged over frequency because this approach gives the correct result for point impedances when averaged over frequency and position on a finite panel (Cremer and Heckl, 1973). However, comparisons between theory and experiment show that it does not work particularly well at and above the coincidence frequency.

The directivity of the sound source is also included when it is in the duct or room. The sound source is modeled as a line source of length $2r$, where r is the radius of the sound source. The directivity of the sound source is proportional to

$$\left[\frac{\sin(kr\sin\phi)}{kr\sin\phi}\right]^2, \tag{14}$$

where k is the wave number.

B. Diffraction due to the finite size of the baffle

To correctly model the directivity, it is necessary to include the effect of diffraction due to the finite size of the baffle in which the panel or opening is mounted, or the finite size of the panel or opening if it is not mounted in a baffle. $p(\theta)$ is the ratio of the increased sound pressure to the sound pressure without the baffle for an angle of incidence or radiation of θ. The baffle is of length $2L$ in the plane containing the receiver (or source) and the normal to the baffle and of width $2W$ in the direction at right angles to the above mentioned plane. Note that in Davy (2007), the length and width of the baffle are assumed to be equal.

Two cases are considered. The first is when the sound is incident internally on a panel or an opening mounted in the wall of a room or the end of a duct over a range of angles of incidence due to a sound source operating inside the room or the duct. In this first case, the receiver is a large distance away at a specified radiation angle. The second case is when the sound is incident externally on a panel or an opening mounted in the wall of a room or the end of a duct at a specified angle of incidence from a sound source external to the room or the duct which is a large distance away. In this second case, the sound reaches a receiver inside the room or the duct after being radiated over a range of angles. By the principle of reciprocity, these two cases should give the same directivity as a function of the specified angle of radiation or the specified angle of incidence.

Because the panel or opening may be mounted in a baffle, such as the external wall of a building, the average effects of diffraction over the whole of the rigid surface or over an area near the center of the rigid surface need to be known. The theoretical model is developed by considering experimental and theoretical results for the second case.

1. High frequencies

Consider the case of an infinite plane wave traveling in an infinite half space bounded by an infinite rigid plane. There is a discontinuity in the sound pressure on the surface of the rigid plane as a function of the angle of incidence. The sound pressure on the bounding infinite plane is double the sound pressure of the incident wave except when the angle of incidence is $\pi/2$ rad. In this exceptional case, the sound pressure on the bounding infinite rigid plane is equal to the sound pressure of the incident wave.

What happens when the rigid plane is finite in size? To answer this question for the high frequency case when the finite rigid planes are relatively large in terms of the wavelength, the experimental results for diffraction for the second case in Rindel (1975) are analyzed. For third octave bands with center frequencies from 200 Hz to 20 kHz, Rindel (1975) gave level recorder plots of the sound pressure level (SPL) of a flush mounted microphone at the center of a finite rigid plane as a function of angle of incidence from slightly less than $-\pi/2$ rad to slightly greater than $\pi/2$ rad. Rindel (1975) made measurements with two sizes of finite rigid plane. The larger finite rigid plane measures $2L=3800$ mm in the plane of the angle incidence and $2W=3100$ mm at right angles to the plane of the angle of incidence. The

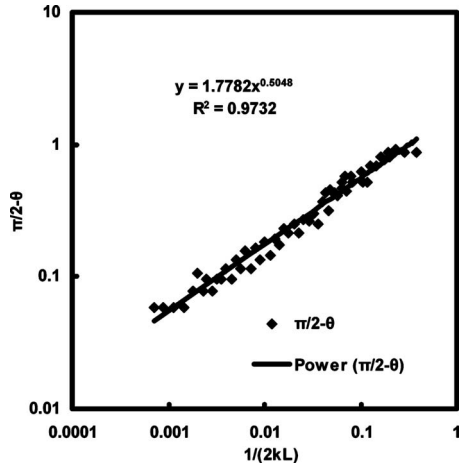

FIG. 3. Best fit of $y=\pi/2-|\theta_m|$ rad versus $x=1/(2kL)$.

smaller finite rigid plane is the wall of Rindel's (1975) experimental box and measures $2L=1360$ mm in the plane of the angle incidence and $2W=1110$ mm at right angles to the plane of the angle of incidence.

Except for planes which are relatively small in terms of the wavelength, Rindel's (1975) experimental results are approximately constant from a frequency dependent negative angle of incidence $-\theta_m$ rad to a frequency dependent positive angle of incidence θ_m rad. Because the magnitudes of the experimental values of these two angles of incidence are not exactly equal, their two magnitudes are averaged to give an experimental estimate of the frequency dependent magnitude θ_m rad. For planes which are relatively small in terms of the wavelength, $-\theta_m(\theta_m)$ rad is measured as the angle of incidence closest to $-\pi/2(\pi/2)$ rad at which the sound pressure is double the sound pressure at $-\pi/2(\pi/2)$ rad.

Below (above) an angle of incidence of $-\theta_m(\theta_m)$ rad, the sound pressure decreases linearly as a function of the (cosine of the) angle of incidence, becoming, at an angle of incidence of $-\pi/2(\pi/2)$ rad, half the sound pressure in the constant region.

Rindel's (1975) results are extended to finite rigid planes which are smaller in size compared to the wavelength by using results from Sivian and O'Neil (1932). Sivian and O'Neil (1932) made measurements at 13 different frequencies between 500 Hz and 13.5 kHz on a disk with a diameter of $D=120$ mm for angles of incidence from 0 to π rad. For the lowest two frequencies, there are no angles of incidence at which the sound pressure is double the sound pressure at an angle of incidence of $\pi/2$ rad. For the 11 highest frequencies from 1 to 13.5 kHz the value of θ_m rad is measured from their graphs. The value of $2L$ is set equal to the average distance across the disk in the direction of measurement. This means that $2L=D\pi/4$. Sivian and O'Neil (1932) also made measurements on a $2L=115$ mm square plate at frequencies of 7 and 10 kHz at angles of incidence from 0 to π rad. θ_m rad also is measured from the two graphs of these experimental results.

The variable y is set equal to $\pi/2-|\theta_m|$ rad and the variable x is set equal to $1/(2kL)$, where k rad/m is the wave number of the sound. A linear regression of $\ln(y)$ against $\ln(x)$ is used to fit the relationship $y=bx^m$ to the experimental data set, as shown in Fig. 3. The value of m is 0.505 with 95% confidence limits of ± 0.023 and the value of b is 1.78 with 95% confidence limits of ± 0.17. The value of r^2 is 0.973. Since $\sqrt{\pi}=1.77$, these experimental results suggest that m is equal to 0.5 and b is equal to $\sqrt{\pi}$. Since $\pi/2-|\theta_m|$ is equal to the second order expansion of $\cos(|\theta_m|)$ about $|\theta_m|=\pi/2$ rad, approximate and replace $\pi/2-|\theta_m|$ with $\cos(|\theta_m|)$. Because $\cos(|\theta_m|)$ is symmetrical about $\theta_m=0$, and $\cos(|\theta_m|)=\cos(\theta_m)$, this gives the limiting angle θ_m below which the sound pressure does not vary with angle of radiation (or incidence) as

$$\theta_m=\begin{cases} 0 & \text{if } kL\le\dfrac{\pi}{2} \\ \arccos\left(\sqrt{\dfrac{\pi}{2kL}}\right) & \text{if } kL>\dfrac{\pi}{2}, \end{cases} \tag{15}$$

where θ_m is set equal to zero for values of kL less than $\pi/2$ so that it is defined sensibly for all values of kL. The regression is repeated with the variable y set equal to $\cos(\theta_m)$. In this case, the value of m is 0.485 with 95% confidence limits of ± 0.022 and the value of b is 1.60 with 95% confidence limits of ± 0.15. The value of r^2 is 0.973.

It should be noted that ϕ_l [see Eq. (12)] is equal to θ_m for a strip of length $2L$. Thus both ϕ_l and θ_m indicate the angle of incidence or radiation at which the finite size of the panel starts to have an effect. Also note that both ϕ_l and θ_m have the correct limit of $\pi/2$ rad for a rigid infinite plane.

2. Low frequencies

For sound incident at a grazing incident angle, the sound pressure is equal to the sound pressure of the incident sound pressure wave. Note that this is different from the grazing incidence sensitivity of a condenser microphone which decreases at high frequencies because of the variation in the phase of the incident sound pressure wave across the microphone diaphragm once the diaphragm becomes comparable to or greater than the wavelength. Thus the average SPL due a grazing incident sound wave of unit sound pressure is set to be unity.

$$p\left(\frac{\pi}{2}\right)=1. \tag{16}$$

The low frequency theory is based on the work of Muller *et al.* (1937) and Brüel and Rasmussen (1959). If a plane wave is incident normally on the end of an infinite rigid half cylinder of diameter Dm, the SPL at the center of the end of the finite half cylinder reaches a maximum of 10 dB above the SPL of the incident sound wave as the frequency is increased. The SPL at the center of the end of the infinite half cylinder then proceeds to oscillate between 0 and 10 dB above the SPL of the incident sound wave as the frequency is increased further. However, when the sound pressure increase all over the end of the finite half cylinder is multiplied by the sensitivity of an equivalent condenser microphone diaphragm at that radial position and averaged, the net increase in SPL at and above the first maximum is be-

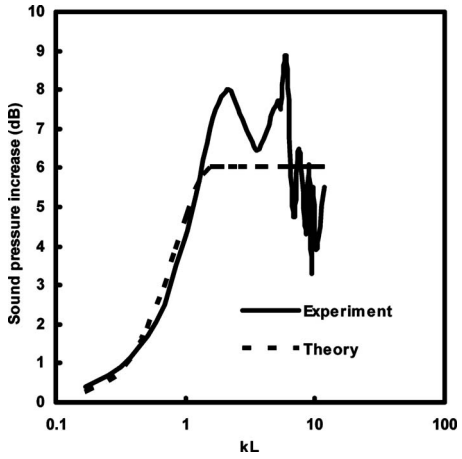

FIG. 4. Comparison of the experimentally determined sound pressure increase for normally incident sound on the diaphragm of a 1 in. condenser microphone without grid (Brüel and Rasmussen, 1959) with the theory of Eqs. (17)–(19).

tween 3 and 9 dB. Thus the assumption of a constant 6 dB increase in SPL above the frequency when the increase first becomes 6 dB is accurate to within 3 dB.

The SPL increase for normally incident sound waves on the diaphragm of a condenser microphone of diameter D without grid first reaches 6 dB for a value of kL of 1.33 where $2L=D\pi/4$. Although this somewhat less than the value of $kL=\pi/2=1.57$ for which θ_m becomes equal to zero, the average sound pressure p_0 on a panel of average dimensions $2L\times 2W$ due to a normally incident sound pressure wave of unit sound pressure is approximated using

$$p(0) = 1 + p_W p_L, \tag{17}$$

where

$$p_W = \begin{cases} \sin(kW) & \text{if } kW \le \dfrac{\pi}{2} \\ 1 & \text{if } kW > \dfrac{\pi}{2} \end{cases} \tag{18}$$

and

$$p_L = \begin{cases} \sin(kL) & \text{if } kL \le \dfrac{\pi}{2} \\ 1 & \text{if } kL > \dfrac{\pi}{2}. \end{cases} \tag{19}$$

These equations are compared with the sound pressure increase for normally incident sound on the diaphragm of a 1 in. condenser microphone without grid in Fig. 4.

3. Sound pressure increase

The average ratio over the baffle of the sound pressure to the incident sound pressure for angles of incidence between $-\pi/2$ $(\pi/2)$ and $-\theta_m(\theta_m)$ rad is estimated by linear interpolation of the sound pressure ratio as a function of the (cosine of the) angle of incidence between 1 at $-\pi/2(\pi/2)$ rad and $p(0)$ at $-\theta_m(\theta_m)$ rad.

The average sound pressure on a finite rigid plane due to a plane sound wave of unity amplitude which is incident at an angle of θ rad relative to the normal to the plane is given by

$$p(\theta) = \begin{cases} p(0) & \text{if } \cos(\theta) \ge \cos(\theta_m) \\ \dfrac{p(0)\cos(\theta) + p\left(\dfrac{\pi}{2}\right)(\cos(\theta_m) - \cos(\theta))}{\cos(\theta_m)} & \text{if } \cos(\theta_m) > \cos(\theta) \ge 0, \end{cases} \tag{20}$$

where interpolation in the cosine domain is used.

By reciprocity, this equation also gives the sound pressure radiated by a point source on a finite rigid plane at an angle of θ rad relative to the normal to the plane compared to the sound radiated in the absence of the plane. The value is averaged over all positions on the finite rigid plane. In Davy (2007), the interpolation in Eq. (20) is performed in the angle of incidence domain. In this paper and Davy (2008), the cosine of the angle of incidence is used. It should be noted that although this section has discussed rigid panels, the method is also used for openings.

C. Directivity of the sound radiation

The relative SPL $L(\theta)$ in the direction θ is

$$L(\theta) = 10\log_{10}(|p_T(\theta)|^2 p^2(\theta)) - 10\log_{10}(|p_T(0)|^2 p^2(0)). \tag{21}$$

If the transmission is into the shadow zone, that is, $\pi/2 < |\theta| \le \pi$, then the above calculations are carried out for $\theta=\pi/2$ and the product $|p_{T\mathrm{rms}}(\pi/2)|^2 p^2(\pi/2)$ in Eq. (21) is multiplied by the following diffraction correction:

$$D(\theta) = \frac{1}{1 - kz\cos(\theta)}, \tag{22}$$

where

$$z = \frac{1}{\dfrac{1}{L} + \dfrac{1}{W}}. \tag{23}$$

Fluctuations in the shadow zone can be large. Equations (22) and (23) approximate the average trend of the experimental data (Sutton, 1990; Neish, 1997; Dewhirst, 2002; Li, 2005; and Potente *et al.*, 2006).

In practical situations, scattering from turbulence and other objects places a lower limit on the relative SPL. Let $L_{\max}$ be the maximum value of $L(\theta)$. It is assumed that the scattered sound level is L_S dB below $L_{\max}$. The predicted observed relative SPL $L_O(\theta)$ is

$$L_O(\theta) = 10\log_{10}(10^{L(\theta)/10} + 10^{(L_{\max}-L_S)/10}). \tag{24}$$

L_S is usually expected to be greater than 20 dB. To predict the shadow zone data in Stead (2001), a value of L_S equals 22 dB is used.

III. COMPARISON WITH EXPERIMENTAL RESULTS FOR DUCTS

The theory developed in this paper is primarily two dimensional. If the dimensions of the opening, panel, or baffle are not constant parallel to and perpendicular to the plane in which the directivity is measured, it is necessary to calculate an average dimension in the two directions. In this paper, for a circular opening, panel, or baffle, the length and width are set equal to the $\pi/4$ times the diameter. The theoretical results for ducts given in this section are computed using a wall absorption coefficient of 0.05.

Most of the initial comparisons between the experimental results and the theory described in this paper were for the case of openings and panels mounted in the wall of a room where the sound source was external to the room and the microphone was inside the room. In these experiments the sound source was always rotated so that its direction of maximum sound radiation was directed toward the opening or the panel. In this situation, the directivity of the sound source had no effect on the results. The microphone in the room was relatively omnidirectional and thus its directivity also did not need to be considered. Thus there was no need to use Eq. (14).

However, when the directivity of the sound radiated from the opening at the end of a duct was considered, it became apparent that the directivity of the sound source at the other end of the duct needed to be included and Eq. (14) was introduced into the theoretical model. It was initially thought that the $2r$ in Eq. (14) should be set equal to the diameter of the sound source if this value was known. However, it was observed that this did not always produce the best agreement between theory and experiment.

For each duct and each frequency, $2r$ was set equal to value that made the average value over the angle of radiation of the difference between experiment and theory equal to zero or as close to zero as possible. These values of $2r$ varied over a wide range. However, somewhat surprisingly, it was observed that the values of $2r$ tended to decrease with increasing frequency. The average value of $2r$ over a large number of experimental results was approximately the wavelength λ of sound in air. This made the average value of kr approximately equal to π.

One of the reasons for this strange result is that smaller sound sources have to be used as the frequency is increased in order to achieve constant sound power output. Second as the frequency increases, loudspeakers only radiate efficiently from a decreasing area around the center of their cones because of wave motion in their cones. Thus the physics tends to require the use of constant kr sound sources.

The range of the kr values was investigated further by setting kr for each duct equal to value that made the average value over all angles of radiation and all frequencies of the differences between experiment and theory equal to zero. The standard deviation over all angles of radiation and all frequencies of the differences between experiment and theory was determined as an estimate of the goodness of agreement between theory and experiment.

Table I shows the values of kr and the standard deviations for ten outdoor measurements on circular ducts with diameters ranging from 305 to 1220 mm (Neish, 1997; Potente *et al.*, 2006). The values of kr range from 1.55 to 3.3. The standard deviations range from 1.7 to 4.6 dB. An example of the results used to calculate Table I is shown in Fig. 5.

TABLE I. Values of kr and standard deviations over all angles of radiation and all frequencies of the differences between the experimental directivity [(a) Neish (1997) and (b) Potente *et al.* (2006)] and the theoretical directivity for ten outdoor measurements on circular ducts.

Diameter of duct (mm)	Length of duct (m)	Measurement distance (m)	kr	Standard deviation (dB)
305 (b)	3	1	3.3	2.3
305 (b)	3	3	2.1	2.3
400 (a)	8	2	1.55	1.7
610 (b)	3	2	3.25	2.5
610 (b)	6	4	2.6	3.6
914 (b)	4.8	3	2.3	4.5
914 (b)	7.8	3	1.8	3.6
914 (b)	7.8	6	2.65	3.3
1220 (a)	12	3	1.55	2.8
1220 (a)	12	6	2.2	2.4

Table II shows the values of kr and the standard deviations for 18 anechoic measurements on ducts with cross sectional dimensions ranging from 40 to 240 mm (Croft, 1979; Sutton, 1990; Dewhirst, 2002; Li, 2005). The values of kr range from 2.75 to 13 for ducts driven with third octave bands of random noise which are unflanged except for the thickness of their wall sound insulation. The flanged duct has a kr of 20 and the duct driven with a pure tone has a kr of 30. The standard deviations range from 1.1 to 8.0 dB. The three biggest standard deviations were for three of Li's (2005) four measurements. Li (2005) measured at angles of 1° increments. His measurements may have picked up more deviations than the other coarser angular measurements. An example of the results used to calculate Table II is shown in Fig. 6.

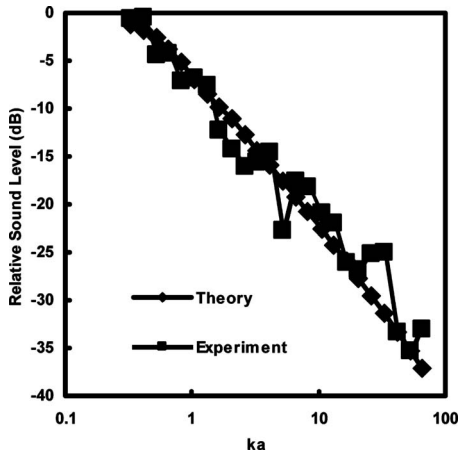

FIG. 5. Experimental (Potente *et al.*, 2006) and theoretical SPL relative to that at 0° for a 914 mm diameter 7800 mm long duct measured 3000 mm from the center of the duct end opening at an angle of radiation relative to the normal of 105° as a function of ka.

TABLE II. Values of kr and standard deviations over all angles of radiation and all frequencies of the differences between the experimental directivity [(a) Croft (1979), (b) Sutton (1990), (c) Dewhirst (2002), and (d) Li (2005)] and the theoretical directivity for 18 anechoic room measurements on ducts.

Duct cross section (mm)	kr	Standard deviation (dB)
85 diameter (b)	4.1	2.9
85 diameter (b)	5	3.1
80×80 (b)	3.7	2.8
120×40 (b)	2.75	2.7
40×120 (b)	4.6	1.7
80×40 (b)	4.1	2.9
40×80 (b)	6	3.0
85 diameter pure tone excitation (b)	30	4.3
112 diameter (a)	3.37	1.1
120×120 (c)	8	2.9
80×160 (c)	8	2.5
160×80 (c)	3.2	3.1
80×240 (c)	16	3.2
240×80 (c)	3.05	3.9
130 diameter 260 diameter flange (d)	20	8.0
130 diameter (d)	13	6.5
80×160 (d)	6	5.1
160×80 (d)	2.8	3.8

IV. COMPARISON WITH EXPERIMENTAL RESULTS FOR ROOMS

For the scale model anechoic room and near field acoustical holography measurements considered in this section, the procedure described at the start of Sec. III was repeated. The average value of kr was 1.78, and this value is used for the theoretical calculations in this section.

Oldham and Shen (1982), Shen and Oldham (1982), and Oldham and Shen (1983) conducted scale model investigations of the sound radiation from an opening or panel mounted in the wall of a room. They used a box with external dimensions of $0.5\times0.5\times0.5$ m^3 which they rotated in an anechoic room. The internal dimensions of their box are approximately $0.3\times0.3\times0.3$ m^3, but "two of the inner walls were inclined in order to improve the diffusion of the sound field. Four piezo-electric tweeters having a frequency range extending to 40 kHz were placed in the four lower corners of the model room with their axes inclined to the walls. 1/3 octave band filtered white or pink noise was supplied to the loudspeakers to produce a reverberant field inside the model room. Spherical diffusers of diameter about 4 cm were hung from the ceiling in order to improve the diffusion of the sound field." No reverberation times are given, so the absorption coefficient of the internal walls of the box is assumed to be 0.05 for the theoretical calculations in this section.

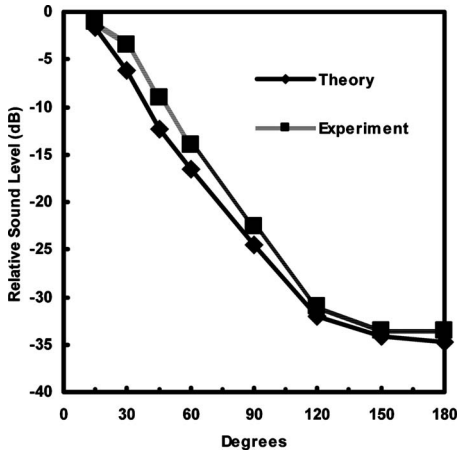

FIG. 6. Experimental (Sutton, 1990) and theoretical SPL for an 80 mm square cross section 750 mm long duct as a function of angle of radiation relative to the normal when $ka=11.6$.

TABLE III. The averages and standard deviations over all angles of radiation and all frequencies of the differences between the experimental directivity [(a) Oldham and Shen (1982), (b) Shen and Oldham (1982), and (c) Oldham and Shen (1983)] and the theoretical directivity for 12 anechoic room measurements on openings and panels in the wall of a model room.

Material and thickness (mm)	Size (mm)	Damping loss factor	Average difference (dB)	Standard deviation (dB)
Opening (a)	100×50		−0.1	1.6
Opening (a)	100×100		0.7	2.2
Opening (a)	50×100		−1.6	2.3
Opening (a)	Average		0.8	1.4
Concrete 5 (b)	200×150	0.01	1.0	6.2
Aluminum 0.5 (b)	100×50	0.1	1.5	2.0
Plexiglas 1 (c)	300×100	0.23	0.4	1.6
Plexiglas 2 (c)	200×200	0.23	0.4	4.0
Aluminum 0.5 (c)	100×50	0.1	1.3	2.6
Plexiglas 6 (c)	100×300	0.23	3.0	6.0
Plexiglas 6 (c)	300×100	0.23	4.1	7.3
Plexiglas 8 (c)	300×200	0.23	5.3	7.4

Table III shows the averages and standard deviations over all angles of radiation and all frequencies of the differences between the experimental directivity and the theoretical directivity. The first length of the two aperture dimensions is the length of the opening or panel in the plane of measurement. Oldham and Shen (1982) observed that their results for an opening depended mainly on the value of the product of the frequency with the length of the opening in the plane of measurement. They averaged all of their results which have the same values of this product. The difference between their average results and the theoretical results is also shown in Table III. An example of the results used to calculate Table III is shown in Fig. 7.

The general trend is for both the magnitudes of the average differences and the standard deviations of the differences to become greater as the panel thickness increases and decreases the critical frequency. To obtain theoretical values at the coincidence peaks which are in reasonable agreement with the experimental peaks, damping loss factors of 0.23 for Plexiglas and 0.1 for aluminum are assumed. These values are about 100 times greater than the typical values of 0.002 and 0.001. Also the value of the damping loss factor used for the concrete panel is 0.01 which is at the upper end of the expected *in-situ* range.

The problem appears to be the inadequacy of Eq. (13) to properly model the wave impedance of a finite panel in the vicinity of and above the critical frequency of the panel.

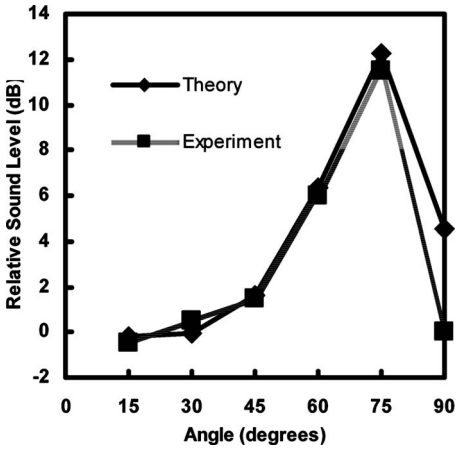

FIG. 7. Experimental (Oldham and Shen, 1983) and theoretical SPL relative to that at 0° for a 1 mm thick Plexiglas panel in the wall of a room as a function of angle of radiation relative to the normal when $ka=87$.

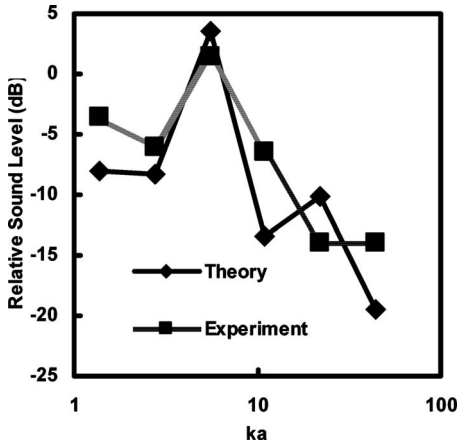

FIG. 8. Experimental (Rowell and Oldham, 1996) and theoretical SPL relative to that at 0° for a quasi-sinusoidally corrugated 0.5 mm thick steel panel measured in a plane parallel to the corrugations at an angle of radiation relative to the normal of 90° as a function of *ka*.

There have been some suggestions of this in previous comparisons made by the author on thin panels whose critical frequencies are near the high frequency end of the measured frequency range. It is much more obvious for a thick panel whose critical frequency is near the low frequency end of the measured frequency range.

Equation (13) is only strictly valid for the forced wave in an infinite panel. Ljunggren (1991) pointed out that one of the problems with Eq. (13), when it is applied to a finite panel, is the spatial rise length. It can take a considerable distance from the edge of the panel for the forced bending wave to reach the velocity implied by Eq. (13). It is possible for this distance to be much greater than the dimensions of the panel. A second problem is that the waves reflected from the edges of the panel propagate with the free bending wavelength rather than the trace wavelength forced by the airborne sound. An attempt was made to model the vibration of the 5 mm thick concrete panel as the forced wave in an infinite limp panel and the rest of the vibration as free bending waves. Unfortunately this approach made the disagreement worse. It produced an average difference of −2.6 dB and a standard deviation of 8.3 dB.

Rowell and Oldham (1996) used near field acoustical holography to measure the directivity of the sound insulation of homogeneous, profiled, and composite panels for the octave band frequencies from 125 Hz to 4 kHz. They also gave the results of far field measurements on a 6 mm thick aluminum panel measuring 2400×1200 mm^2 in one-third octave frequency bands from 2 to 6.3 kHz. The averages and standard deviations of the differences between their experimental results and the theoretical results over angles and frequencies are shown in Table IV. An example of the results used to calculate Table IV is shown in Fig. 8. A damping loss factor of 0.23 is used for the 6 mm thick aluminum panels. The use of such a large loss factor is required because the experimen-

TABLE IV. The averages and standard deviations over all angles of radiation and all frequencies of the differences between the experimental directivity (Rowell and Oldham, 1996) and the theoretical directivity for 14 near field acoustical holography measurements on panels in the wall of a room. The results for the third aluminum panel are from far field measurements.

Material thickness (mm) direction	Size (mm)	Corrugation	Damping loss factor	Average difference (dB)	Standard deviation (dB)
Aluminum 6	920×1200		0.23	−1.0	2.6
Aluminum 6	1200×920		0.23	−0.6	3.6
Aluminum 6	2400×1200		0.23	−0.1	6.1
Steel 0.5 across	805×1200	Quasi-sinusoidal	0.0004	0.3	3.5
Steel 0.5 parallel	1200×805	Quasi-sinusoidal	0.0004	0.3	4.7
Steel 0.7 across	920×1200	Trapezoidal	0.0004	0.8	4.1
Steel 0.7 parallel	1200×920	Trapezoidal	0.0004	−2.2	7.1
Steel 0.7 across	920×1200	Trapezoidal	0.0004	−0.5	4.7
Steel 0.7 parallel	1200×920	Trapezoidal	0.0004	−0.8	6.3
Steel 0.7 across	882×1200	Trapezoidal	0.0004	0.2	3.1
Steel 0.7 parallel	1200×882	Trapezoidal	0.0004	2.3	8.6
Sandwich panel	1200×1200		0.008	−0.9	5.7
Sandwich panel	1200×1200		0.008	0.3	5.2
Sandwich panel	1200×1200		0.008	−1.8	4.8
Sandwich panel	1200×1200		0.008	−2.5	4.5

tal coincidence peaks are not as large as expected and tend to disappear altogether at higher frequencies. This is discussed by Rowell and Oldham (1996).

The profiled panels measured are a quasi-sinusoidally corrugated 0.5 mm thick steel panel and three trapezoidally corrugated 0.7 mm thick steel panels. The directivity of the sound insulation was measured in both a plane at right angles to the corrugations and in a plane parallel to the corrugations. The damping loss factor used for all the theoretical calculations on the profiled panels is 0.0004 which is in the normal range for steel. The magnitudes of the averages and the standard deviations in a plane parallel to the corrugations were equal to or larger than those in a plane at right angles to the corrugations. This is believed to be due to the much lower critical frequency parallel to the corrugations and the problems with Eq. (13) at and above the critical frequency.

The composite panels consisted of a layer of thermally insulating polyurethane material sandwiched between and bonded to two slightly profiled steel panels. The directivity of the sound insulation was measured in two planes at right angles to each other. The damping loss factor used for the theoretical calculations on the composite panels was 0.008. The critical frequencies used for the two panels were 500 and 700 Hz, respectively.

The mean and the root mean square of the differences between experiment and theory for the 55 sets of data summarized in Tables I–IV are 0.2 and 4.4 dB. Thus the theory does a reasonable job of predicting the average trend of the experimental data, but the variation in the experimental data about the theoretical data is large. It must be remembered that the experimental measurements are difficult to make accurately because of breakout noise through the walls of the duct or room and residual reflections from other objects. It should also be noted that the 4.4 dB is relatively small compared with the possible 60 dB range of values from +20 to −40 dB. Nevertheless, it is believed that Eq. (13) does not adequately model the impedance of a finite panel in the vicinity of and above the critical frequency.

V. CONCLUSION

For a panel or opening excited by sound which is incident from the opposite side, the model presented in this paper can be used to predict the SPL radiated at a particular angle to the normal of the panel or opening, relative to the SPL radiated in the direction of the normal. The model includes a theory to predict the angular distribution of the incident sound based on the sound absorption coefficient of the walls of the room or the duct. A line source directivity model is also used when the sound source is inside the room or duct. On average, the length of this line source model has been experimentally determined to be the wavelength of the sound for loudspeaker sound sources in a duct. For a sound source in a room kr is set equal to 1.78 where $2r$ is the length of the line source model.

The model also includes an empirical method for predicting the diffraction effect of the finite size of the baffle in which the panel or opening is mounted as a function of angle of radiation or incidence up to 90° to the normal. Another empirical diffraction model is used for radiation into or diffraction from the shadow zone where the angle of radiation or incidence is greater than 90° to the normal.

The model is developed for the transmission of sound from a room wall or duct end via a panel or opening into a free field space. However, by the principle of reciprocity, it can also be used for transmission in the other direction. In some situations it is necessary to consider the effects of scattering from atmospheric turbulence and other objects and the effects of noise which breaks out through the duct or room walls.

The average difference between experiment and theory is only 0.2 dB. However, the experimental results show significant variability about the theoretical predictions. The root mean square of the differences between experiment and theory is 4.4 dB. The differences will be greater when the theory is compared with other experimental data because the theoretical sound source directivity used in this paper has been adjusted to minimize the differences. The agreement is worse when the critical frequency of the panel decreases as the thickness of the panel increases. This is believed to be due to the inadequacy of the model for the wave impedance of a panel at and above the critical frequency of the panel. It should be noted that the experimental difficulties also increase as the sound insulation of the panel increases with increasing thickness.

ACKNOWLEDGMENTS

Doug Growcott suggested the directivity problem considered in this paper as a suitable topic for research because of the paucity of information available in the literature for use by acoustical consultants. Matthew Stead, Jens Rindel, Colin Hansen, Xun Li, David Luck, and Athol Day provided experimental data and reports to the author. The experimental data were often in machine readable form. Vlad Pavasovic, Thomas Kannanaikkel John, and Kai Fisher worked on this research problem while students of the author.

Allen, C. H. (**1960**). "Noise control in ventilation systems," in *Noise Reduction*, edited by L. L. Beranek (McGraw-Hill, New York).

Beranek, L. L. (**1954**). *Acoustics* (Republished by the American Institute of Physics, New York).

Bies, D. A., and Hansen, C. H., (**2003**). *Engineering Noise Control: Theory and Practice*, 3rd ed. (Spon, London).

Björk, E. A. (**1994**). "Experimental study of measures to reduce noise radiated from power-station exhaust stacks," Noise Control Eng. J. **42**, 171–178.

Brüel, P. V., and Rasmussen, G. (**1959**). "Free field response of condenser of condenser microphones," Brüel and Kjær Technical Review, Part 1, No. 1–959, pp. 12–17, Part 2, No. 2–1959, pp. 1–15.

Cremer, L., and Heckl, M. (**1973**). *Structure-Borne Sound* (Springer-Verlag, New York).

Croft, G. J. (**1979**). "Noise Directivity of Exhaust Stacks," Honors thesis, University of Adelaide, Adelaide, Australia. This thesis has been lost and Croft's results only exist as a graph in Dewhirst (2002).

Davy, J. L. (**2004**). "The radiation efficiency of finite size flat panels," *Acoustics 2004, Transportation Noise and Vibration—The New Millennium*, *Proceedings of the Annual Conference of the Australian Acoustical Society*, Gold Coast, Australia, 3–5 November, edited by M. J. Mee, R. J. Hooker, and I. D. M. Hillock (Australian Acoustical Society, Castlemaine, Victoria, Australia), pp. 555–560.

Davy, J. L. (**2007**). "A model for predicting diffraction on a finite flat surface as a function of angle of incidence and surface size," *Global Approaches to Noise Control*, *Proceedings of the Inter-Noise 2007, The 36th*

International Congress and Exhibition on Noise Control Engineering, Istanbul, Turkey, 28–31 August (Turkish Acoustical Society, Istanbul), Paper No. 21.
Davy, J. L. (**2008**). "The directivity of the forced radiation of sound from panels and openings including the shadow zone," *Proceedings of the Acoustics'08*, Paris, 29 June–4 July 2008). [J. Acoust. Soc. Am. **123**, 3499]; 2008) Acta. Acust. Acust. **94**, S531.
Davy, J. L., and Kannanaikkel John, T. (**2006**). "The angular distribution of sound incident on a panel or opening (A)," J. Acoust. Soc. Am. **120**, 3187.
Davy, J. L., and Kannanaikkel John, T. (**2007**). "The directivity of the forced radiation of sound from panels and openings," Proceedings of the 14th International Congress on Sound and Vibration (ICSV14), Cairns, Australia, 9–12 July, edited by B. Randall, Paper No. 7.
Davy, J. L., and Pavasovic, V. (**2006**). "The directivity of sound radiated from a panel or opening excited by sound incident from the other side," Proceedings of the Acoustics 2006, Noise of Progress, First Australasian Acoustical Societies' Conference, Christchurch, New Zealand, 20–22 November, edited by T. McMinn, pp. 133–140.
Dewhirst, M., *"Exhaust stack directivity*," Final Year Project Report (University of Adelaide, Adelaide, Australia, **2002**).
Fisher, K. R. (**2006**). "Directivity of the sound transmission through finite sized apertures and panels," Honors dissertation, RMIT University, Melbourne, Australia, available at Arup Acoustics, Melbourne, Australia or the author of this paper.
Joseph, P., and Morfey, C. L. (**1999**). "Multimode radiation from an unflanged, semi-infinite circular duct," J. Acoust. Soc. Am. **105**, 2590–2600.
Levine, H., and Schwinger, J. (**1948**). "On the radiation of sound from an unflanged circular pipe," Phys. Rev. **73**, 383–406.
Li, X. (**2005**). "Milestone report for determination of the duct directivity in an anechoic chamber," University of Adelaide, Adelaide, Australia.
Ljunggren, S. (**1991**). "Airborne sound insulation of thin walls," J. Acoust. Soc. Am. **89**, 2324–2337.
Muller, G. G., Black, R., and Davis, T. E. (**1938**). "The diffraction produced by cylindrical and cubical obstacles and by circular and square plates," J. Acoust. Soc. Am. **10**, 6–13.
Neish, M. J. (**1997**). "Predicting sound directivity at a ventilation duct termination," Final year project, School of Mechanical Engineering, The University of Technology, Sydney, Australia.
Oldham, D. J., and Shen, Y. (**1982**). "A scale model investigation of sound radiation from a large aperture in a building," J. Applied Acoustics **15**, 397–409.
Oldham, D. J., and Shen, Y. (**1983**). "A scale model investigation of sound radiation from building elements," J. Sound Vib. **91**, 331–350.
Pavasovic, V. (**2006**). "The radiation of sound from surfaces at grazing angles of incidence," MS dissertation, RMIT University, Melbourne, Australia, available for download from the Australian Digital Theses Program: http://adt.lib.rmit.edu.au/adt/public/adt-VIT20060911.115939 (Last viewed September, **2009**).
Potente, D., Gauld, S., and Day, A. (**2006**). "Directivity loss at a duct termination," Proceedings of the Acoustics 2006, Noise of Progress, First Australasian Acoustical Societies' Conference, Christchurch, Australia, 20–22 November, edited by T. McMinn, pp. 283–289.
Rindel, J. H. (**1975**). "Transmission of traffic noise through windows—Influence of incident angle on sound insulation in theory and experiment," Report No. 9, Technical University of Denmark, Lyngby, Denmark.
Roberts, J. (**1983**). "The prediction of directional sound fields," Transactions of the Institution of Engineers, Australia, Mechanical Engineering **ME8**, 16–22.
Rowell, M. A., and Oldham, D. J. (**1996**). "Determination of the directivity of a planar noise source by means of near field acoustical holography, Part III: Measurements on homogeneous, profiled and composite panels," J. Sound Vib. **189**, 369–398.
Sharland, I. (**1972**). *Woods Practical Guide to Noise Control* (Woods of Colchester, Colchester).
Shen, Y., and Oldham, D. J. (**1982**). "Sound radiation from building elements," J. Sound Vib. **84**, 11–33.
Sivian, L. J., and O'Neil, H. T. (**1932**). "On sound diffraction caused by rigid circular plate, square plate and semi-finite screen," J. Acoust. Soc. Am. **3**, 483–510.
Stead, M. (**2001**). "Sound reduction for reverberant, direct and diffracted sound through single isotropic glass panels of finite size," MS dissertation, Monash University, Melbourne, Australia.
Sutton, M. (**1990**). "Noise directivity of exhaust stacks," Honors thesis, University of Adelaide, Adelaide, Australia.
Watters, B. G., Labate, S., and Beranek, L. L. (**1955**). "Acoustical behavior of some engine test cell structures," J. Acoust. Soc. Am. **27**, 449–456.
Wells, R. J., and Crocker, B. E. (**1953**). "Sound radiation patterns of gas turbine exhaust stacks," J. Acoust. Soc. Am. **25**, 433–437.
Woods, R. I. (**1972**). *Noise Control in Mechanical Services* (Sound Attenuaters Ltd. and Sound Research Laboratories Ltd., Colchester).

A double-panel active segmented partition module using decoupled analog feedback controllers: Numerical model

Jason D. Sagers
Department of Mechanical Engineering, Brigham Young University, Provo, Utah 84602

Timothy W. Leishman
Department of Physics and Astronomy, Brigham Young University, Provo, Utah 84602

Jonathan D. Blotter
Department of Mechanical Engineering, Brigham Young University, Provo, Utah 84602

(Received 17 July 2008; revised 11 March 2009; accepted 20 March 2009)

Low-frequency sound transmission has long plagued the sound isolation performance of lightweight partitions. Over the past 2 decades, researchers have investigated actively controlled structures to prevent sound transmission from a source space into a receiving space. An approach using active segmented partitions (ASPs) seeks to improve low-frequency sound isolation capabilities. An ASP is a partition which has been mechanically and acoustically segmented into a number of small individually controlled modules. This paper provides a theoretical and numerical development of a single ASP module configuration, wherein each panel of the double-panel structure is independently actuated and controlled by an analog feedback controller. A numerical model is developed to estimate frequency response functions for the purpose of controller design, to understand the effects of acoustic coupling between the panels, to predict the transmission loss of the module in both passive and active states, and to demonstrate that the proposed ASP module will produce bidirectional sound isolation. © *2009 Acoustical Society of America.* [DOI: 10.1121/1.3117682]

PACS number(s): 43.55.Rg, 43.50.Ki, 43.40.Vn [LMW] Pages: 3806–3818

I. INTRODUCTION

There has long been interest in the use of partitions to reduce sound transmission into noise-sensitive environments. A particular need for improvement exists at lower frequencies, where their passive sound isolation is inadequate. This is the case in both single- and double-leaf partitions wherein the transmission loss (TL) is severely degraded at lower frequencies due to resonance effects.[1] A common passive method to reduce sound transmission is to add mass to the partition. The normal-incidence mass law indicates that a 6 dB increase in the TL is possible for every doubling of the mass of the partition.[2,3] However, this solution is not feasible for many situations wherein extra weight cannot be tolerated, such as in aerospace vehicles, large ceiling structures of buildings, walls and ceilings of high-rise buildings, etc. A promising solution to the problem involves the use of active control of lightweight partitions.

Two active control strategies that have been utilized to improve the sound isolation performance of partitions at low frequencies include active structural acoustic control[4] (ASAC) and active segmented partitions (ASPs).[5] The ASAC approach typically involves actuating a continuous panel in such a way as to reduce the efficiency of acoustic radiation into the receiving space. This approach has been explored thoroughly.[4,6–15] It is typically implemented by locating several actuators over the continuous panel and by locating the sensors either on the panel or in the receiving space. A control algorithm is then used which either alters the radiating mode shapes of the panel (i.e., to make the panel a less efficient acoustic radiator) or reduces the vibration amplitudes of the existing mode shapes. The performance of the control scheme is typically quantified by using microphones to measure the attenuation in sound pressure level at several locations in the receiving space. In general, receiving-side attenuations produced by ASAC have been small, with typical results ranging from 5 to 10 dB in narrow frequency bands. However, a concise summary of ASAC performance results is difficult because the measurement techniques reported in the literature are inconsistent. The major challenges of the ASAC approach include large numbers of fully-coupled controllers, the frequent (but not exclusive) use of microphones as error sensors in the receiving space, the spatial control spillover that inevitably results when using a continuous transmitting panel, and the minimal attenuation achieved in narrow frequency bands.

The alternative classification of ASPs includes active control approaches wherein a partition is subdivided into an array of small modules that are both acoustically and mechanically segmented. The segmentation has several potential advantages. First, it allows independent control of each module, thus eliminating the impracticality of a large number of fully-coupled controllers. Second, it simplifies the active control problem by allowing the long-wavelength limit to be used with exposed module surfaces and within module cavities. If the acoustic wavelength is much larger than the module spatial dimensions, the acoustic field variables become relatively uniform over its extent. Simpler actuation, sensing, and control schemes result that may be used to increase sound isolation. Finally, the approach facilitates the placement of error sensors inside the partition (as has been occasionally tried in continuous double-leaf partitions), thus eliminating the common need for microphones in the acoustic space outside of the partition.

 0001-4966/2009/125(6)/3806/13/$25.00

An effective double-panel ASP has been implemented by Leishman and Tichy.[5,16–19] Several designs for individual ASP modules were published in 2005; analytical models were used to explore two single-panel designs and two double-panel designs.[5] Experimental embodiments followed.[18,19] The single-panel analytical models included an actuator, a transmitting diaphragm, and surrounding interstitial supports between adjacent modules. One of the models assumed that the transmitting diaphragm vibrated snugly but without friction within a surrounding interstitial structure with finite impedance and considerable exposed width in the plane of the partition. The other included a resilient surround between the diaphragm and a surrounding interstitial structure that was assumed to be rigid and very thin in the plane of the partition. In both cases, the transmitting diaphragm was forced directly by the actuator. The investigations found that both designs would produce modest actively controlled TL at some frequencies but they were unable to provide much TL near the resonances of either the wide interstitial structure or the surround.

The double-panel designs used an active composite panel on the source side of the module and a passive panel on the transmitting side of the module. The active composite panel consisted of a circular control loudspeaker mounted in a larger, square, aluminum honeycomb sandwich panel. The loudspeaker acoustically actuated the module to minimize the vibration of the transmitting panel. It was found that this was accomplished through a significant reduction in the volume velocity into the cavity. An individual double-panel ASP module and a digital feed-forward controller produced experimental TL results near 80 dB over a band of 40 Hz–1.0 kHz.[18] Two different error-sensing schemes were investigated: an acoustic microphone located in the cavity and an accelerometer mounted to the transmitting panel. Similar TL results were obtained in both cases.

Although the double-panel module and controller produced very high TL, it also had several limitations, as noted by the authors. First, the digital feed-forward controller required a time-advanced reference signal. Second, it could only attenuate narrowband disturbances (i.e., it lacked broadband random noise control capabilities). Third, it had a slow convergence rate and a difficult time tracking swept-sine disturbances. Finally, the module was unidirectional and could not produce TL in both directions. Despite these limitations, the double-panel module represented a unique lightweight active partition element that exhibited such high TL capabilities over a broad bandwidth, including very low frequencies. The authors concluded that additional work would be required to assess the normal-incidence TL characteristics of other individual module configurations and multiple modules mounted in ASP arrays.

The authors began the process of addressing the second half of this recommendation by constructing two ASP arrays with four double-panel modules, each with its own digital feed-forward controller.[19] The array was tested using both centralized and decentralized controls. Centralized control was implemented by using four multiple-input/multiple-output (MIMO) controllers while decentralized control was implemented by using four single-input/single-output (SISO) controllers. The experimental ASP array under SISO control produced TL results near 55 dB over a band of 40–300 Hz. This approached the maximum measurable TL of the experimental measurement system. Surprisingly, the SISO controllers produced an average TL that was about 6 dB higher than the MIMO controllers. The result emphasized the fact that the acoustic segmentation within the double-panel ASP allowed decoupled controllers to function with an array of modules. The same limitations manifested by the individual ASP modules were evident in the array.

By way of suggestion, a practical active partition (be it an ASAC or ASP partition) should satisfy a few important criteria. First, it should be bidirectional for many applications, being capable of providing sound isolation in both directions through the partition. Second, it should be capable of controlling both tonal and broadband random disturbances. Third, it should be self-contained, meaning that all necessary sensing and actuation hardware should be located on or within the partition. Finally, the partition should provide global attenuation of acoustic energy in the receiving space.

The purpose of this paper is to introduce a new ASP module and control scheme with pertinent analytical and numerical modeling. The model will include key components of the system, including panels, sensors, actuators, and controllers. It will be used to (1) estimate the plant frequency response functions (FRFs), (2) understand the effects of acoustic coupling between the panels, (3) predict the TL of the module in both passive and active states, and (4) demonstrate that the module design will produce bidirectional sound isolation. This paper will thus demonstrate the potential of the module and its satisfaction of the design criteria. Sections II–V address the module design, its analogous circuit representation, the development of its governing equations, and various modeling predictions.

II. DESIGN CONSIDERATIONS OF THE NEW MODULE

The new ASP module incorporated choices in both the design of the physical configuration and the active control method. These two aspects are described in Secs. II A and II B.

A. Physical description

The proposed design for the module includes a stiff, lightweight panel on its source side and one on its transmitting side, separated by an air volume, as shown in Fig. 1. Each panel is connected around its perimeter to a thin, lightweight structure through a resilient connection or surround. The enclosing structure, which acts as an interstice between adjacent modules in an ASP array, is considered to be a motionless rigid body in this investigation. However, if the structure were to vibrate to some degree, as it would in a constructed partition array, it would radiate inefficiently and the resilient surrounds would allow the panels to vibrate or be controlled with substantial independence. Mechanical coupling would be reduced between the two panels in a given module and between panels of any two modules in the array, thus enhancing the possibility of successful decoupled

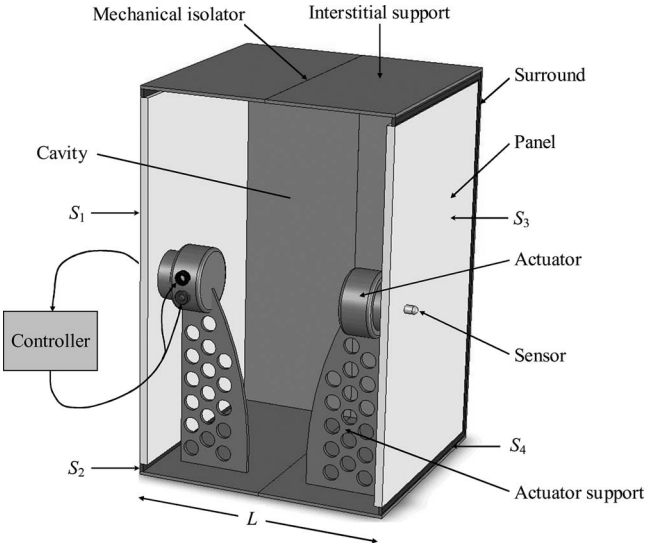

FIG. 1. Cutaway view of the double-panel ASP module.

controllers. As a further means of reducing mechanical coupling between panels in a module, and from one side of an array to the other, a resilient airtight mechanical isolator is also included between the two halves of the interstice.

An actuator and sensor pair is connected to each panel in the module. The actuators are contained inside the cavity, and the sensors can be mounted on either side of their respective panels. The actuators may be configured as inertial devices or connected to the interstitial structure by means of lightweight supports if the effects of reactive motor forces on the supports and structure are deemed insignificant. Other actuation schemes, including the use of inertial actuators, are also possible. The output of each sensor is fed into its respective controller as an error signal. The output of the controller is fed into the corresponding actuator (shown schematically for the leftmost panel in Fig. 1). Although not shown in the figure, the necessary electronics for the controllers could be compactly designed so that they are contained within the module. The remainder of the cavity is filled with fibrous acoustically absorbent material (not shown in the figure) to help improve the passive sound isolation performance of the module at higher frequencies (above the active control bandwidth).

Different types of actuators such as piezoelectric devices, inertial shakers, or moving-coil drivers could be used in the module. The actuators modeled in this paper are moving-coil drivers with magnets attached rigidly to the interstitial structure enclosing the module. Different types of sensors could likewise be used in the module. Ideal accelerometers are assumed in this paper. Although the types of actuators and sensors could be changed in a different design, it is critical to the validity of the model that all of the important dynamics of the panels, surrounds, actuators, and sensors are included.

B. Active control description

An analog feedback controller was selected for this module because of its potential for broadband control as well as its relative ease of implementation, low cost, and low

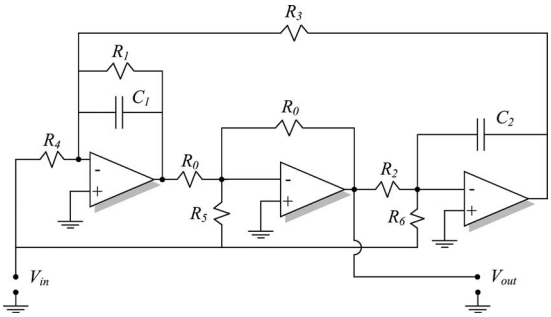

FIG. 2. Electrical schematic of a second-order Fleischer–Tow biquad circuit.

mass. Two independent controllers whose complex FRFs are represented by H_1 and H_2 were used (one for each panel). For this work, the controllers were second-order, analog Fleischer–Tow biquad circuits,[20–22] which use resistors, capacitors, and operational amplifiers to create desired transfer functions between their input and output voltages. The shape of a transfer function is determined by choosing the values of the resistors and capacitors. The electrical schematic of the controller is shown in Fig. 2.

The output voltage signal from the accelerometer becomes the input voltage to the controller (V_{in}). The output voltage from the controller (V_{out}) becomes the input voltage to the actuator. The Laplace domain transfer function between the input and output voltages of the controller is then given by the expression

$$\frac{V_{\text{out}}}{V_{\text{in}}} = -\frac{\frac{R_0}{R_5}s^2 + \frac{1}{R_1C_1}\left(\frac{R_0}{R_5} - \frac{R_1}{R_4}\right)s + \frac{1}{R_3R_6C_1C_2}}{s^2 + \frac{1}{R_1C_1}s + \frac{1}{R_2R_3C_1C_2}}. \quad (1)$$

Two important physical design choices made it possible to use a controller that was only second-order. First, it was important that collocated sensor and actuator pairs were used to eliminate undesirable delay in the plant due to acoustic propagation. Second, the airspace between the two panels was filled with absorptive material to dampen high-frequency cavity resonances which could unnecessarily complicate the control scheme.[23]

III. ANALOGOUS CIRCUIT REPRESENTATION

An analogous circuit model provides a multiple-domain (electrical, mechanical, and acoustical) representation of a system and yields a straightforward way to write its governing equations. Analogous circuit modeling techniques are used in this paper to develop the numerical model for the new ASP module. A discussion of these techniques can be found in the literature[24,25] and will not be repeated here, except as necessary to highlight specific areas of interest.

A. Physical schematic

A schematic drawing of the module is shown in Fig. 3. Each half of the module incorporates a two degree of freedom (DOF) mechanical system that resembles a moving-coil loudspeaker driver. The first DOF is contained in the motion of the panel (diaphragm), while the second DOF is contained

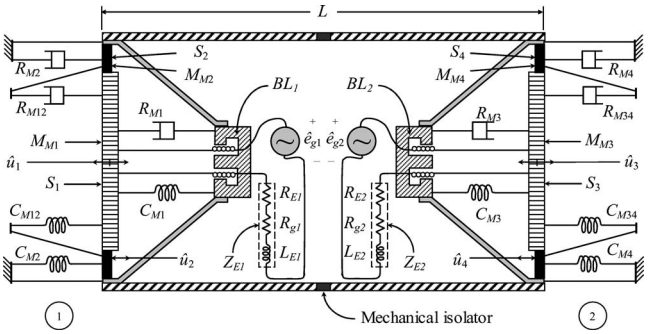

FIG. 3. Schematic view of the ASP module.

in the motion of the surround. Since the "classical" model of a loudspeaker[24,26] characterizes only a single DOF for the radiating surface, the loudspeaker model used in this paper is referred to as an "enhanced" model.

Because the two halves of the module contain identical components, only a detailed discussion of the left half will be given here. The mass of the panel is represented by M_{M1} and the mass of the surround is represented by M_{M2}. The panel and the surround each act as radiating surface areas S_1 and S_2, respectively. They are assumed to vibrate with uniform complex velocity amplitudes $\hat{u}_1$ and $\hat{u}_2$. This assumption is only valid at low frequencies as higher-order modal patterns will begin to appear in both the panel and surround at higher frequencies.

The connection between the surround and the interstitial support is modeled with a resistance and a compliance (R_{M2} and C_{M2}, respectively) as is the connection between the surround and the panel (R_{M12} and C_{M12}, respectively). These lumped elements are assumed to be distributed uniformly around the perimeter of the module face. Because of the possible asymmetry in surround properties at its inner and outer edges, R_{M2} and R_{M12} are generally not assumed to be equal, nor are C_{M2} and C_{M12}. Finally, the secondary suspension or spider of the moving-coil driver is modeled with its own resistance and compliance values R_{M1} and C_{M1}, respectively.

The moving-coil driver has intrinsic electrical properties which also describe its behavior. They have been converted to the mechanical mobility domain as an ideal flow source, with a value of $(\hat{e}_{g1}BL_1)/Z_{E1}$, in parallel with its internal mobility $Z_{E1}/(BL_1)^2$. The complex control voltage supplied by the controller as the input to the actuator is represented by $\hat{e}_{g1}$.

The benefit of using the enhanced model shown in Fig. 3 is that it allows the surround to vibrate as a lumped element, with its own DOF. As a result, it can better predict the TL that will occur if the panel vibration is reduced by the active control scheme while the surround is still permitted to vibrate. It is anticipated that any residual vibration of the surround can significantly degrade the TL performance of the module.

One of the difficulties with the enhanced model is that it requires the determination of the additional mechanical mass, resistance, and compliance values of the surround. Measurement methods exist to determine the composite parameters of the classical model,[27–38] but the individual values shown in Fig. 3 are more difficult to ascertain. To solve this problem, the authors developed a laser-based measurement method from which the unknown parameters (M_{M1}, M_{M2}, C_{M1}, C_{M2}, C_{M12}, R_{M1}, R_{M2}, R_{M12} and M_{M3}, M_{M4}, C_{M3}, C_{M4}, C_{M34}, R_{M3}, R_{M4}, R_{M34}) could be extracted. Details of the method are given elsewhere in the literature.[39]

As mentioned previously, the airspace between the two panels of the module was to be filled with a porous material to provide acoustic absorption. The attenuation coefficient α of such a material may be readily determined using a plane-wave tube,[40–42] and the resulting values may be used in the complex wave number $\tilde{k}$ of the model.

B. Analogous circuit schematic

The multiple-domain analogous circuit representation of the ASP module is shown in Fig. 4. The left and right halves of the module are represented in the left and right sides of the circuit, respectively. Eight gyrator elements were used in the circuit to couple the acoustic impedance domain and the mechanical mobility domain at various locations. The electrical components of the moving-coil driver have already been transferred from the electrical impedance domain to the mechanical mobility domain. A one-dimensional waveguide network is used in the center of the circuit to acoustically couple the left and right halves of the module and account for axial wave effects. Appropriate mechanical and acoustical grounds are represented by G_M and G_A, respectively.

Constant incident acoustic pressure sources are modeled on each side of the module with complex amplitudes $\hat{p}_{i1}$ and $\hat{p}_{i2}$. Disturbance pressures are allowed to impinge upon the device from the left (side 1), right (side 2), or both sides simultaneously. It should be noted that the analogous circuit

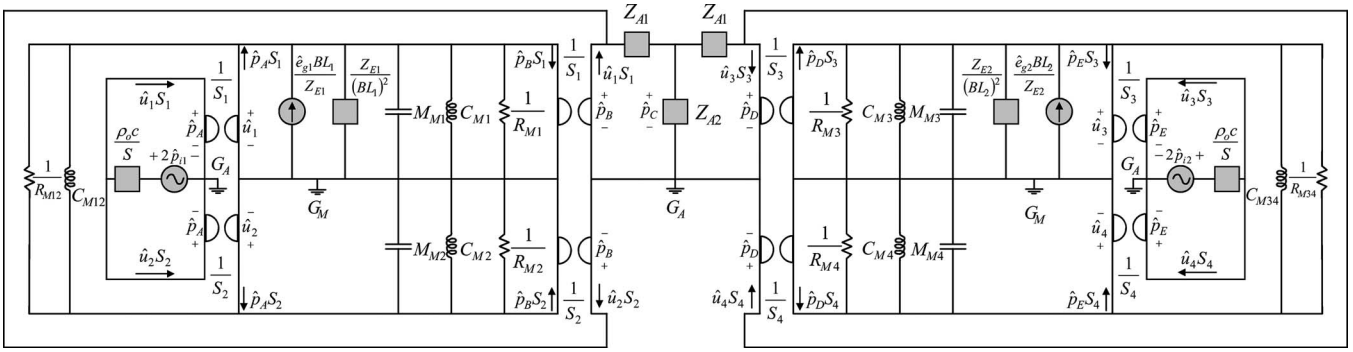

FIG. 4. Multiple-domain analogous circuit representing the ASP module.

is limited to one-dimensional modeling, as it assumes normal plane-wave incidence and transmission with respect to each panel. It also assumes steady-state time-harmonic excitation and control. However, as has been shown elsewhere, the TL predictions that result from such a circuit are well suited for comparison with classical normal-incidence TL formulations and related experimental measurements.[5,16–19]

IV. EQUATION DEVELOPMENT

Nodal analysis was used to write nine equations in nine unknowns ($\hat{u}_1$, $\hat{u}_2$, $\hat{u}_3$, $\hat{u}_4$, $\hat{p}_A$, $\hat{p}_B$, $\hat{p}_C$, $\hat{p}_D$, and $\hat{p}_E$) for the circuit:

$$\frac{\hat{e}_{g1}BL_1}{Z_{E1}} + (\hat{p}_A - \hat{p}_B)S_1 - (\hat{u}_1 - \hat{u}_2)Z_{M12} - \hat{u}_1 Z_{M1} = 0, \tag{2}$$

$$(\hat{p}_A - \hat{p}_B)S_2 + (\hat{u}_1 - \hat{u}_2)Z_{M12} - \hat{u}_2 Z_{M2} = 0, \tag{3}$$

$$\hat{p}_A = 2\hat{p}_{i1} - \hat{U}_1 \frac{\rho_0 c}{S}, \tag{4}$$

$$\hat{U}_1 - \frac{(\hat{p}_B - \hat{p}_C)}{Z_{A1}} = 0, \tag{5}$$

$$\frac{(\hat{p}_B - \hat{p}_C)}{Z_{A1}} - \frac{(\hat{p}_C - \hat{p}_D)}{Z_{A1}} - \frac{\hat{p}_C}{Z_{A2}} = 0, \tag{6}$$

$$\frac{(\hat{p}_C - \hat{p}_D)}{Z_{A1}} - \hat{U}_2 = 0, \tag{7}$$

$$\frac{\hat{e}_{g2}BL_2}{Z_{E2}} + (\hat{p}_D - \hat{p}_E)S_3 - (\hat{u}_3 - \hat{u}_4)Z_{M34} - \hat{u}_3 Z_{M3} = 0, \tag{8}$$

$$(\hat{p}_D - \hat{p}_E)S_4 + (\hat{u}_3 - \hat{u}_4)Z_{M34} - \hat{u}_4 Z_{M4} = 0, \tag{9}$$

$$\hat{p}_E = 2\hat{p}_{i2} - \hat{U}_2 \frac{\rho_0 c}{S}. \tag{10}$$

Six mechanical impedance substitutions (Z_{M1}, Z_{M2}, Z_{M3}, Z_{M4}, Z_{M12}, and Z_{M34}) are used in the above equations and are defined in the Appendix. The nine nodal equations can be reduced to four coupled equations of motion with $\hat{u}_1$, $\hat{u}_2$, $\hat{u}_3$, and $\hat{u}_4$ as the unknown variables. The solution to the equations of motion for these variables required careful algebraic reduction by means of impedance substitutions. The full solution is much too lengthy to include in this paper. Instead, the primary governing equations are presented in the body of the paper and all of the algebraic impedance substitutions are defined in the Appendix. The impedance definitions were created and labeled sequentially (with subscripts) during the solution process with the following letter order: *B*, *C*, *D*, and *F* (the letters *A* and *E* were skipped to avoid confusion with acoustic and electrical impedance definitions). The reader should be aware that the impedance substitutions are not intended to have specific physical significance, but are primarily used to enable the presentation of a compact solution.

Several quantities of interest can be obtained from the model. It will first be used to predict both plant FRFs. The plant FRFs can be used to design a new controller or to evaluate the stability margins of an existing controller. Second, the model is used to estimate the acoustic coupling strength between the two panels. This is accomplished by looking at the FRF between the control voltage of one actuator and the acceleration of the other panel. (It is expected that an acoustic coupling path will exist between the panels, but that its effect will not require coupled feedback controllers.) Third, the model is used to predict the unidirectional TL through the module. This is accomplished by letting $\hat{p}_{i1}$ equal 1 Pa while $\hat{p}_{i2}$ is set to zero for the left-to-right TL and vice versa for the right-to-left TL. Finally, the model is used to predict the bidirectional capabilities of the module. This is accomplished by letting both $\hat{p}_{i1}$ and $\hat{p}_{i2}$ be arbitrarily defined over different frequency bands.

A. Plant FRFs

Knowledge of the plant FRF *P* allows for the design of an appropriate controller. Two plants exist in this model (one for each panel) and are defined here as the frequency response from the input control voltage of an actuator to the output of the error-sensing accelerometer:

$$P(f) = \frac{\text{accelerometer output}}{\text{actuator input}}. \tag{11}$$

The voltage output of the panel-mounted accelerometer was used as the error signal for the feedback controller. The solution of the equations of motion yields the normal surface velocity for each panel:

$$\hat{u}_1 = 2\hat{p}_{i1}Z_{D1} + 2\hat{p}_{i2}Z_{D7} + \hat{e}_{g1}BL_1 Z_{D2} + \hat{e}_{g2}BL_2 Z_{D3}, \tag{12}$$

$$\hat{u}_3 = 2\hat{p}_{i1}Z_{F1} + 2\hat{p}_{i2}(Z_{F4} - Z_{F5}) + \hat{e}_{g1}BL_1 Z_{F3} + \hat{e}_{g2}BL_2 Z_{F2}. \tag{13}$$

The acceleration of each panel can then be found by using the simple relationships

$$\hat{a}_1 = j\omega\hat{u}_1, \tag{14}$$

$$\hat{a}_3 = j\omega\hat{u}_3. \tag{15}$$

The accelerance FRF of the first plant (between $\hat{e}_{g1}$ and $\hat{a}_1$) is readily found from Eqs. (12) and (14) by setting $\hat{p}_{i1}$, $\hat{p}_{i2}$, and $\hat{e}_{g2}$ equal to zero:

$$P_{11} = \frac{\hat{a}_1}{\hat{e}_{g1}} = j\omega BL_1 Z_{D2}. \tag{16}$$

Similarly, the accelerance FRF of the second plant (between $\hat{e}_{g2}$ and $\hat{a}_3$) can be found from Eqs. (13) and (15) by setting $\hat{p}_{i1}$, $\hat{p}_{i2}$, and $\hat{e}_{g1}$ equal to zero:

$$P_{22} = \frac{\hat{a}_3}{\hat{e}_{g2}} = j\omega BL_2 Z_{F2}. \tag{17}$$

The output voltages of the ideal accelerometers are considered to be equivalent to $\hat{a}_1$ and $\hat{a}_3$.

B. Acoustic coupling FRFs

The two halves of the module in this analysis are assumed to be structurally isolated from one another so that the only physical coupling path between them is through the air cavity. The magnitude of the acoustic coupling FRF will be large when resonances exist. A qualitative measure of the strength of this coupling path is the FRF between the acceleration of one panel due to an excitation of the other panel. It can be found by using Eqs. (12)–(15) and by solving for the cross FRFs, meaning the acceleration of one panel due to a control voltage on the other actuator (after $\hat{p}_{i1}$, $\hat{p}_{i2}$, and the uninvolved control voltage is set to zero):

$$P_{21} = \frac{\hat{a}_1}{\hat{e}_{g2}} = j\omega BL_2 Z_{D3}, \tag{18}$$

$$P_{12} = \frac{\hat{a}_3}{\hat{e}_{g1}} = j\omega BL_1 Z_{F3}. \tag{19}$$

C. TL

The TL of the module is defined in terms of the time-averaged incident sound power, $\langle \Pi_i \rangle_t$, and the time-averaged transmitted sound power $\langle \Pi_t \rangle_t$:[43]

$$\mathrm{TL} = 10 \log\left(\frac{\langle \Pi_i \rangle_t}{\langle \Pi_t \rangle_t}\right). \tag{20}$$

Since the total surface area of side 1 is the same as the total surface area of side 2 (i.e., $S=S_1+S_2=S_3+S_4$) and since plane-wave propagation is assumed, Eq. (20) can be reduced to

$$\mathrm{TL} = 10 \log\left(\left|\frac{\hat{p}_{in}}{\hat{p}_{tm}}\right|^2\right), \tag{21}$$

where $\hat{p}_{in}$ is the incident pressure on side n and $\hat{p}_{tm}$ is the transmitted pressure on side m due to $\hat{p}_{in}$. For the left-to-right TL through the module, $\hat{p}_{in}$ is $\hat{p}_{i1}$ and $\hat{p}_{tm}$ is $\hat{p}_{t2}$. For the normal one-dimensional field, the pressure $\hat{p}_{t2}$ is equal to the product of the total volume velocity of side 2, $\hat{U}_2$, and the acoustic impedance $\rho_0 c/S$ seen by the module on side 2 (assumed to be anechoic). Manipulation of the analogous circuit equations presented at the beginning of Sec. IV yields the left-to-right TL through the module:

$$\mathrm{TL}_{12} = 10 \log_{10}\left(\left|\frac{\hat{p}_{i1}S}{(\rho_0 c)\left[2\hat{p}_{i1}(Z_{A2}Z_{B1})(S_1Z_{D1}-S_2Z_{D4})+2\hat{p}_{i2}[Z_{A2}Z_{B1}(S_1Z_{D7}-S_2Z_{D8})-Z_{B1}]+\hat{e}_{g1}BL_1(Z_{A2}Z_{B1})(S_1Z_{D2}-S_2Z_{D5})+\hat{e}_{g2}BL_2\left[Z_{A2}Z_{B1}(S_1Z_{D3}-S_2Z_{D6})+\frac{Z_{B2}}{Z_{E2}}\right]\right]}\right|\right). \tag{22}$$

If $\hat{p}_{i2}$ were zero, the equation would reduce to the unidirectional left-to-right (side 1 to side 2) TL through the module based solely on the disturbance pressure $\hat{p}_{i1}$. The presence of $\hat{p}_{i2}$ acts to reduce the "measurable," though perhaps not "perceived," TL through the module because an observer on side 2 may not distinguish the time-harmonic sound pressure transmitted through the module due to $\hat{p}_{i1}$ from the time-harmonic sound pressure at the same frequency reflected from panel 2 due to $\hat{p}_{i2}$. Equation (22) can also predict the TL of the module in its passive configuration (with both $\hat{e}_{g1}$ and $\hat{e}_{g2}$ set equal to zero and both Z_{E1} and Z_{E2} set to infinity to represent open-circuit actuator terminals). It can further predict the TL of a configuration with only a single-panel active (either $\hat{e}_{g1}$ or $\hat{e}_{g2}$ equal to zero and either Z_{E1} and Z_{E2} set to infinity, respectively) or a configuration with both panels active (both $\hat{e}_{g1}$ and $\hat{e}_{g2}$ nonzero and $Z_{En}=R_g+R_{En}+j\omega L_{En}$). Alternatively, the right-to-left TL through the module is given, using the defined impedance substitutions, by the expression

$$\mathrm{TL}_{21} = 10 \log_{10}\left(\left|\frac{\hat{p}_{i2}S}{(\rho_0 c)[2\hat{p}_{i1}(S_1Z_{D1}-S_2Z_{D4})+2\hat{p}_{i2}(S_1Z_{D7}-S_2Z_{D8})+\hat{e}_{g1}BL_1(S_1Z_{D2}-S_2Z_{D5})+\hat{e}_{g2}BL_2(S_1Z_{D3}-S_2Z_{D6})]}\right|^2\right). \tag{23}$$

The control voltages in Eqs. (22) and (23) are given by the products of the panel accelerations and the FRFs of the control circuits:

$$\hat{e}_{g1} = j\omega H_1 \hat{u}_1, \tag{24}$$

$$\hat{e}_{g2} = j\omega H_2 \hat{u}_3. \tag{25}$$

One can substitute Eqs. (12) and (13) for $\hat{u}_1$ and $\hat{u}_2$ in these expressions, then the resulting expressions can be solved simultaneously for the control voltages $\hat{e}_{g1}$ and $\hat{e}_{g2}$ in terms of

the incident pressures. The appropriate terms need to be set equal to zero or infinity for the specific control configuration. For example, if only panel 1 is actively controlled and there is only a single disturbance source $\hat{p}_{i1}$, then $\hat{p}_{i2}$ and $\hat{e}_{g2}$ in Eq. (12) would be set to zero and Z_{E2} would be set to infinity. Equations (12) and (24) would then yield the following control voltage:

$$\hat{e}_{g1} = \frac{2\hat{p}_{i1} j\omega H_1 Z_{D1}}{1 - j\omega H_1 B L_1 Z_{D2}}. \tag{26}$$

Control voltages for the other configurations can be determined in a similar fashion. In each case, $\hat{e}_{g1}$ and $\hat{e}_{g2}$ represent the actual electrical voltages that drive the actuators. They do not necessarily represent control voltages that will completely force $\hat{u}_1$ and $\hat{u}_3$ to be zero.

D. Bidirectional TL

The equations presented in Sec. IV C can also predict the "bidirectional" TL through the module. In this context, the term bidirectional refers to the situation in which disturbance pressures are simultaneously incident on each side of the module. One must therefore speak in terms of the "measurable" TL because the ability to observe and separate the incident, reflected, and transmitted pressures depends on the nature of the disturbances. For example, the TL can be observed as usual when $\hat{p}_{i1}$ and $\hat{p}_{i2}$ contain different frequencies or when they contain the same frequencies but at dramatically different amplitudes. However, the second disturbance source will reduce the measurable TL through the module when both $\hat{p}_{i1}$ and $\hat{p}_{i2}$ possess the same frequencies with similar amplitudes. This is because one cannot readily separate the pressure that is transmitted through the module (from disturbance source 1) from the reflected pressure (from disturbance source 2).

V. MODEL PREDICTIONS

The predictive capabilities of the model may be illustrated using representative numerical module parameters. Table I lists several feasible values for the enhanced loudspeaker model, with the assumption that both halves of the module use identical components ($BL_1 = BL_2$, $L_{E1} = L_{E2}$, etc.). It also lists a frequency-dependent attenuation coefficient α, given in Np/m, for hypothetical damping within the cavity. The damping is then included in the model through the complex wave number. The module cavity depth L is chosen to be 15 cm and its total cross-sectional area S is chosen to be 33 cm^2.

TABLE I. Enhanced model parameters and frequency-dependent attenuation coefficient used in the numerical analysis.

Parameter	Value	Units
BL_1, BL_2	3.54	Tm
L_{E1}, L_{E2}	0.23	mH
R_{E1}, R_{E2}	6.48	Ω
R_{g1}, R_{g2}	0.10	Ω
S_1, S_3	30.0	cm^2
S_2, S_4	3.00	cm^2
M_{M1}, M_{M3}	7.21	g
M_{M2}, M_{M4}	0.15	g
C_{M1}, C_{M3}	2300	μm/N
C_{M2}, C_{M4}	448	μm/N
C_{M12}, C_{M34}	272	μm/N
R_{M1}, R_{M3}	0.57	kg/s
R_{M2}, R_{M4}	0.30	kg/s
R_{M12}, R_{M34}	0.30	kg/s

Frequency band	α (Np/m)
$f \leq 500$ Hz	0.1
$500 < f \leq 1000$ Hz	0.4
$1000 < f \leq 1300$ Hz	0.9
$f > 1300$ Hz	1.0

A. Predicted plant FRFs

The normalized accelerance FRF P_{11} predicted by Eq. (16) is shown in Fig. 5. This curve represents the acceleration seen by panel 1 due to an actuator excitation voltage $\hat{e}_{g1}$. Since panel 2 has the same parameters as panel 1, P_{22} is identical to P_{11}. The first peak seen near 80 Hz is the primary mechanical resonance of the panel with its attached moving-coil actuator. The magnitude of the FRF falls off at 12 dB per octave below this frequency. The second peak near 185 Hz is the mass-air-mass resonance frequency of the double-panel partition. The magnitude of the FRF is relatively flat above the mass-air-mass resonance frequency until it begins to roll off at high frequencies due to the inductance of the actuator voice coil.

The accelerance FRF can be used to design a controller or to test the stability margins of an existing controller. For the control circuit described earlier, the resistor and capacitor values were chosen to position the cutoff frequencies of the control filter and thus maximize attenuation while maintaining desired stability margins.[20–22] The selected values are given in Table II, and the frequency response of the resulting controller is shown in Fig. 6. The controller is primarily a low-pass filter, with an asymptotic attenuation approaching 20 dB above 20 kHz. A notch was also designed into the controller that can be strategically placed at a desired panel resonance (through selected resistor and capacitor values) to

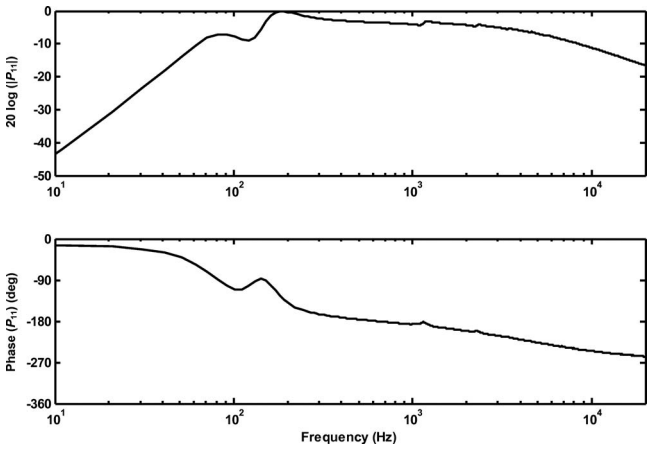

FIG. 5. Normalized accelerance FRF for the module.

TABLE II. Resistor and capacitor values used in the analog controller.

Parameter	Value	Units
R_0	10 000	Ω
R_1	430	Ω
R_2	13 120	Ω
R_3	1 000	Ω
R_4	452	Ω
R_5	10 000	Ω
R_6	1 300	Ω
C_1	0.047	μF
C_2	0.047	μF

allow the closed-loop response of the system to become smoother. Figure 6 shows the notch centered at 3 kHz.

B. Predicted acoustic coupling FRFs

The cross-coupling FRF P_{12} between the acceleration of one panel due to the input excitation of the other is shown in Fig. 7. The mass-air-mass resonance is evident at 185 Hz and represents the strongest coupling from one panel to the other. The axial cavity resonances are also clearly evident with the first resonance occurring near 1.1 kHz. However, the magnitude of the first cavity resonance is nearly 20 dB down from the mass-air-mass resonance. The P_{21} cross-coupling FRF is identical to the one shown in Fig. 7.

The effect of the cavity depth L on the acoustic coupling strength was investigated to explore its impact. The results for three different cavity depths are shown in Fig. 8. The peak magnitude of the acoustic coupling FRF increased by roughly 3 dB per halving of distance. The magnitude was independent of L at frequencies well below the mass-air-mass resonance. The general trend of P_{12} was also independent of L at frequencies far above the first axial cavity resonance (excluding, of course, the frequency-dependent location of the peaks that varied with L). The cross-coupling FRFs indicate that the acoustic coupling between the panels is weak at all frequencies other than the mass-air-mass resonance frequency.

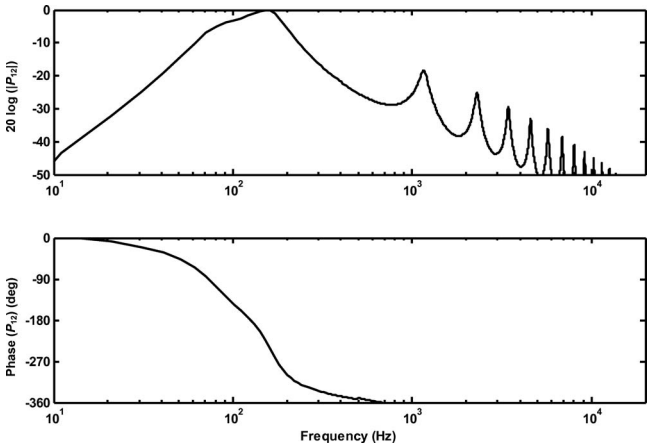

FIG. 7. Cross-coupling accelerance FRF.

C. Predicted TL

The unidirectional TL (e.g., from left-to-right) through the module is plotted in Fig. 9 for three control configurations. The passive configuration exhibits the characteristic response of a double-panel partition.[1] The TL increases at 18 dB per octave immediately above the mass-air-mass resonance frequency while the slope decreases slightly to 12 dB per octave at higher frequencies. The axial cavity resonances are also clearly seen.

The prediction for single-panel control is also shown in the figure and is the same regardless of whether panel 1 or panel 2 is actively controlled while the other panel remains passive. The controllers were designed such that the module transitions to a completely passive state at frequencies higher than about 1 kHz. The maximum increase in TL for this configuration is 27 dB at 165 Hz. The arithmetic average increase from 50 to 500 Hz is 18 dB. This represents a considerable improvement in low-frequency TL, even with only a single controlled panel. The control does not completely eliminate the TL effect caused by the strong acoustic coupling between panels at the mass-air-mass resonance frequency. Any uncontrolled residual vibration that exists on the first panel is readily transmitted to the second panel in the vicinity of the resonance.

The predicted TL increases further in the third control configuration when both panels are controlled independently

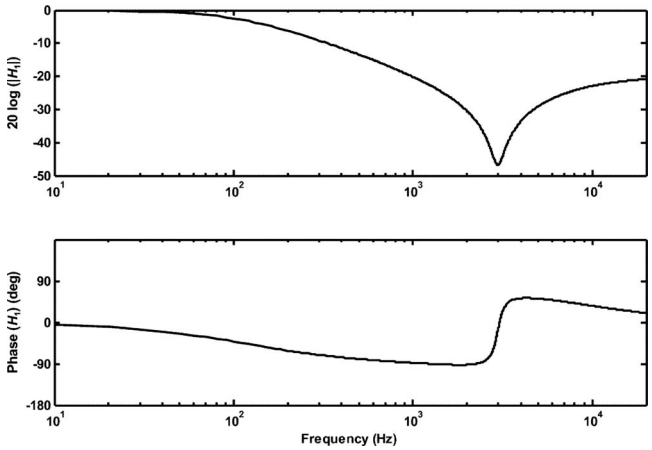

FIG. 6. Predicted FRF of the controller.

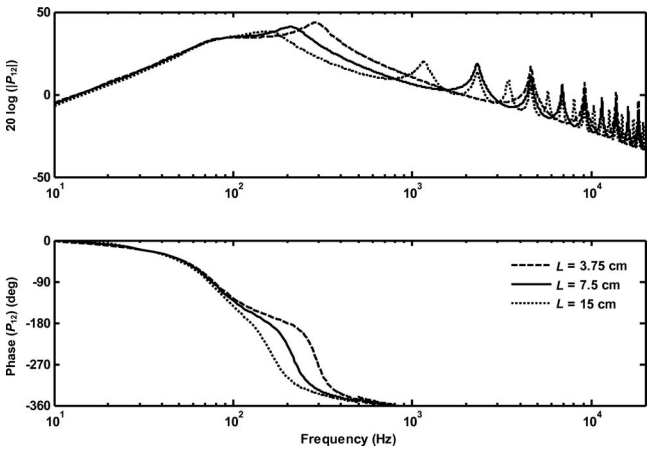

FIG. 8. Cross-coupling accelerance FRFs for three different cavity depths.

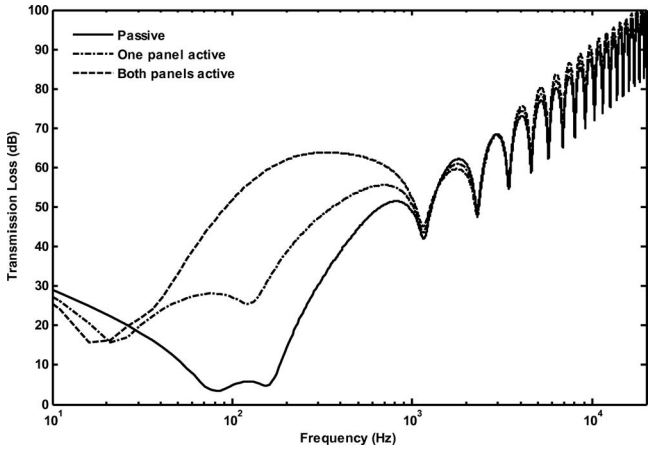

FIG. 9. Predicted unidirectional TL through the module.

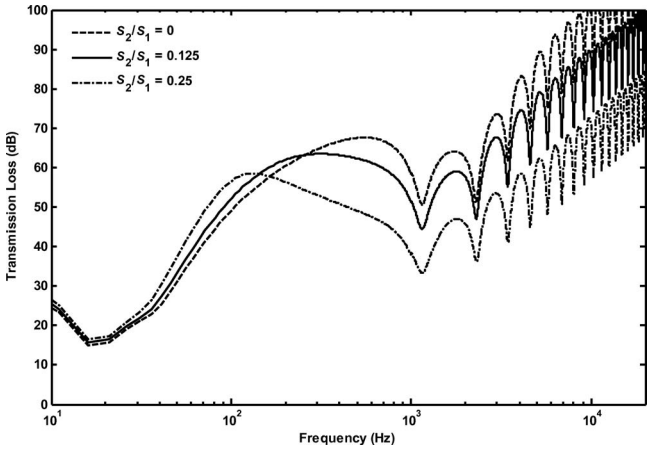

FIG. 10. Effect of the area ratio S_2/S_1 on TL when both panels are actively controlled.

but simultaneously. The maximum increase is 55 dB at 165 Hz. The average increase in the TL from 50 to 500 Hz is 36 dB—twice that produced by the single-panel control. The effect of the mass-air-mass resonance is no longer apparent.

The TL for both active cases was slightly lower than the passive case between 10 and 25 Hz. The dips in the TL curves in this region are an effect of the feedback controller, as these frequencies are near the lower instability point of the closed-loop feedback control system. At these frequencies, the control signal is nearly in phase with the disturbance signal, resulting in a slight degradation in the TL.

One should recall that the enhanced loudspeaker model permits the surround to respond with an additional DOF not represented in the classical model. It is conceivable that a surround could thus vibrate freely at some frequency even when its associated panel is not vibrating. The effect of the ratio of surround area to panel area on TL was explored with this effect in mind. Three different ratios of S_2/S_1 (and likewise S_4/S_3) were examined for the case when both panels were actively controlled. The total cross-sectional area of the module S was kept at 33 cm^2 and the ratio of S_2/S_1 was varied to produce ratios of 0, 0.125, and 0.250. The results are shown in Fig. 10. The degradation of the TL when S_2 is increased is substantial above 150 Hz. The TL prediction from the classical model of the loudspeaker is the same as the $S_2/S_1=0$ curve (i.e., no surround area). To obtain the best overall TL, the areas that are not directly actuated (S_2 and S_4) should be minimized while maintaining sufficient resilience for isolation of interstitial structures and adjacent panels.

The effect of cavity depth on TL was also explored. It was shown earlier that the acoustic coupling strength increases in the vicinity of the mass-air-mass resonance as the space between the panels is diminished. This reduces the TL that can be achieved in the control bandwidth. The predicted TL for three different cavity depths is shown in Fig. 11. It was found that the average achievable TL in the control bandwidth (20 Hz–1 kHz) increases by approximately 6 dB each time the cavity depth (L) is doubled. The low- and high-frequency regions of the TL curve remain essentially unaffected by the depth (although the cavity resonances shift in frequency).

The right-to-left unidirectional TLs for the module are exactly the same as the results presented above. This represents a significant advancement over other active methods. The physical configuration and independent controllers enable the module to exhibit the same unidirectional TL in both directions.

D. Predicted bidirectional TL

The final performance test of the ASP module explores how the TL is affected when pressure disturbances $\hat{p}_{i1}$ and $\hat{p}_{i2}$ exist simultaneously on both sides. (Section V C showed the results for the unidirectional TL that results when only $\hat{p}_{i1}$ or $\hat{p}_{i2}$ was present.) Suppose the primary disturbance source is $\hat{p}_{i1}$ and impinges on the left side of the module. The TL from left-to-right through the module is given in Eq. (22). If the pressure $\hat{p}_{i2}$ on the right side of the module is zero, then the equation reduces to the left-to-right unidirectional TL. The measurable left-to-right TL of the module becomes degraded if $\hat{p}_{i2}$ is nonzero. The degradation only occurs at frequencies contained in $\hat{p}_{i2}$, and the amount of degradation depends on the amplitude of $\hat{p}_{i2}$ relative to $\hat{p}_{i1}$.

For the sake of illustration, suppose $\hat{p}_{i1}$ has a real value of 1 Pa at all frequencies and $\hat{p}_{i2}$ is zero everywhere outside the arbitrary bandwidth of 200–400 Hz, but is allowed to take on various real values within that bandwidth: 0, 0.1, 1.0, and 10 Pa. The apparent TL with both panels actively con-

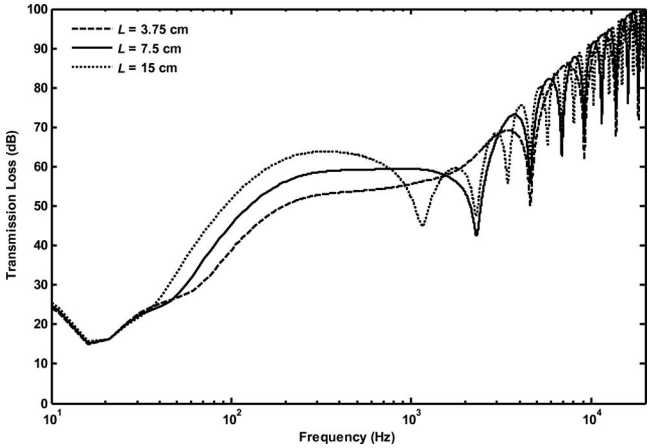

FIG. 11. Effect of cavity depth L on TL when both panels are actively controlled.

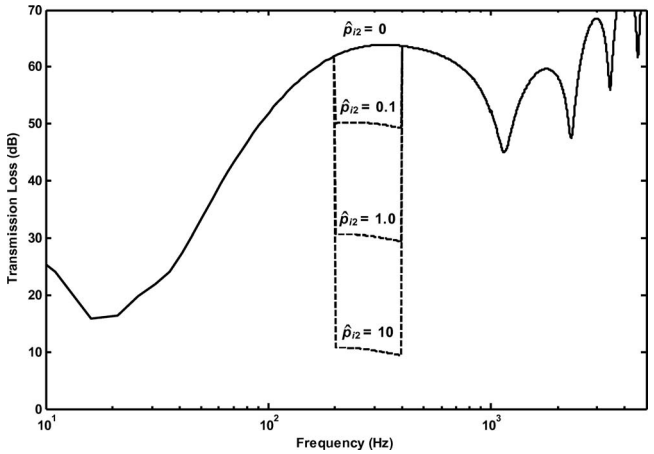

FIG. 12. Apparent left-to-right TL through the module when a second disturbance source of different amplitude is present.

trolled is shown in Fig. 12. It is apparent from this example that the measurable TL is reduced when a second disturbance source is present on the receiving side of the module, but the reduction depends on the relative amplitude of the source. It is not affected outside of the bandwidth of $\hat{p}_{i2}$. The controlled module is actually attenuating the sound energy passing through it from left to right, but the presence of a second source on the receiving side inhibits the ability to quantify the TL. In many cases, acoustic observation in a common excitation bandwidth and on a given side of the module could be dominated by the acoustic source that resides on that side.

VI. CONCLUSION

The performance of a feedback-controlled double-panel ASP module was examined using analytical tools and numerical calculations. An enhanced model of a loudspeaker was used to model each half of the ASP module, wherein the surround possessed an additional DOF. Equations were developed to estimate the plant FRFs, understand the effects of acoustic coupling between the panels, predict the TL of the module in both passive and active states, and demonstrate that the module design produces bidirectional TL.

It was shown that the TL for the passive double-panel module exhibited the classical resonance effects at low frequencies. Active feedback control of a single panel produced an average TL boost of 18 dB from 50 to 500 Hz. However, the mass-air-mass resonance dip was still apparent in the predicted TL curve due to the strong acoustic coupling in the cavity near its center frequency. Simultaneous active feedback control of both panels produced an average boost in the TL of 36 dB from 50 to 500 Hz. It also eliminated the TL dip at the mass-air-mass resonance frequency.

The enhanced model of the loudspeaker illustrates the effect of having an uncontrolled vibrating surface area as part of the panel. The surround of the panel is still permitted to vibrate even if the vibration of the panel is reduced. The residual vibration of the surround permits flanking around the panel and degrades its TL performance. This effect can be reduced by minimizing the area of the surround.

The cavity depth also affects the maximum achievable TL. Smaller cavity depths intensify the acoustic coupling between the panels. On average, the achievable TL in the control bandwidth is reduced by 6 dB every time the cavity depth is cut in half. The TL at frequencies well below the mass-air-mass resonance is not affected, nor is the general TL trend affected at sufficiently high frequencies above the control bandwidth.

The ASP module design and analysis presented in this paper demonstrate that simultaneous feedback control of each panel in a double-panel configuration provides an effective way to actively increase TL at low frequencies. The design transitions to passive TL control at higher frequencies, which is inherently effective for sound isolation. It also enables bidirectional TL capabilities over all frequencies. For future research, an experimental embodiment of the module should be constructed and tested. An array of such modules should also be constructed and tested as a complete partition between adjacent three-dimensional spaces.

ACKNOWLEDGMENTS

The authors gratefully acknowledge financial support from the Department of Mechanical Engineering at Brigham Young University as well as the NASA Rocky Mountain Space Grant Consortium.

Nomenclature

$\hat{a}_n$ = normal complex acceleration amplitude of the nth panel
BL_n = force factor of the nth moving-coil actuator
c = speed of sound in the fluid medium
c_{ph} = phase speed of sound in a dissipative medium
C_n = electrical capacitance of the nth capacitor in the control circuit
C_{Mn} = effective mechanical compliance of the nth module element
C_{Mmn} = effective mechanical compliance coupling the mth and nth module elements ($m=n$)
$\hat{e}_{gn}$ = complex control voltage amplitude driving the nth moving-coil driver
f = frequency
G_A = acoustical ground (ambient reference pressure)
G_M = mechanical ground (zero reference velocity)
H_n = complex FRF of the nth controller
$\tilde{k}$ = complex acoustic wave number, $=\omega/c_{\mathrm{ph}} - j\alpha$
L = effective cavity length of the module
L_{En} = electrical inductance of the voice coil in the nth moving-coil actuator
m = integer index value
M_{Mn} = effective mechanical mass of the nth module element
n = integer index value
$\hat{p}_q$ = complex acoustic pressure amplitude at location q in the analogous circuit

$\hat{p}_{in}$ = normally incident complex acoustic pressure amplitude on the nth side of the module

$\hat{p}_{tm}$ = normal transmitted complex acoustic pressure amplitude on the mth side of the module

P_{mn} = plant or coupling FRF from the side m actuator input to the side n error sensor output

R_n = electrical resistance of the nth resistor in the control circuit

R_{En} = electrical resistance of the voice coil in the nth moving-coil actuator

R_g = output resistance of the electrical control source

R_{Mn} = effective mechanical resistance of the nth module element

R_{Mmn} = effective mechanical resistance coupling the mth and nth module elements $(m \neq n)$

S = total cross-sectional area of the module, $=S_1+S_2=S_3+S_4$

s = Laplace domain frequency variable

S_n = cross-sectional area of the nth module element

TL = normal-incidence sound transmission loss

$\hat{u}_n$ = complex normal velocity amplitude of the nth module element

$\hat{U}_n$ = complex volume velocity amplitude on the nth side of module, e.g., $\hat{U}_1=\hat{u}_1S_1+\hat{u}_2S_2$

Z_{A1} = acoustic impedance substitution for waveguide network, $=j(\omega\rho_o/\tilde{k}S)\tan(\tilde{k}L/2)$

Z_{A2} = acoustic impedance substitution for waveguide network, $=-j(\omega\rho_o/\tilde{k}S)\csc(\tilde{k}L)$

Z_{En} = total electrical impedance of the nth moving-coil actuator, $=R_g+R_{En}+j\omega L_{En}$

α = attenuation coefficient of the absorptive material used in the cavity (Np/m)

ρ_0 = ambient density of the fluid medium

ω = angular frequency $=2\pi f$

Π = acoustic sound power

APPENDIX: IMPEDANCE DEFINITIONS

Mechanical impedance substitutions:

$$Z_{M1} \equiv \frac{(BL_1)^2}{Z_{E1}} + R_{M1} + \frac{1}{j\omega C_{M1}} + j\omega M_{M1}, \tag{A1}$$

$$Z_{M2} \equiv R_{M2} + \frac{1}{j\omega C_{M2}} + j\omega M_{M2}, \tag{A2}$$

$$Z_{M3} \equiv \frac{(BL_2)^2}{Z_{E2}} + R_{M3} + \frac{1}{j\omega C_{M3}} + j\omega M_{M3}, \tag{A3}$$

$$Z_{M4} \equiv R_{M4} + \frac{1}{j\omega C_{M4}} + j\omega M_{M4}, \tag{A4}$$

$$Z_{M12} \equiv R_{M12} + \frac{1}{j\omega C_{M12}}, \tag{A5}$$

$$Z_{M34} \equiv R_{M34} + \frac{1}{j\omega C_{M34}}, \tag{A6}$$

$$Z_{M1.PR} \equiv Z_{M1} + Z_{M12}, \tag{A7}$$

$$Z_{M2.PR} \equiv Z_{M2} + Z_{M12}, \tag{A8}$$

$$Z_{M3.PR} \equiv Z_{M3} + Z_{M34}, \tag{A9}$$

$$Z_{M4.PR} \equiv Z_{M4} + Z_{M34}. \tag{A10}$$

Acoustic impedance substitutions:

$$Z_{AA} \equiv \frac{\rho_0 c}{S} + Z_{A1} + Z_{A2}, \tag{A11}$$

$$Z_{AB} \equiv Z_{AA}. \tag{A12}$$

B impedance substitutions:

$$Z_{B1} \equiv \frac{S_3^2 Z_{M4.PR} + 2S_3S_4Z_{M34} + S_4^2 Z_{M3.PR}}{S_3^2 Z_{AB}Z_{M4.PR} + S_4^2 Z_{AB}Z_{M3.PR} + Z_{M3.PR}Z_{M4.PR} + 2S_3S_4Z_{AB}Z_{M34} - Z_{M34}^2}, \tag{A13}$$

$$Z_{B2} \equiv \frac{S_3Z_{M4.PR} + S_4Z_{M34}}{S_3^2 Z_{AB}Z_{M4.PR} + S_4^2 Z_{AB}Z_{M3.PR} + Z_{M3.PR}Z_{M4.PR} + 2S_3S_4Z_{AB}Z_{M34} - Z_{M34}^2}. \tag{A14}$$

C impedance substitutions:

$$Z_{C1} \equiv S_1^2 Z_{A2}^2 Z_{B1} - S_1^2 Z_{AA} - Z_{M1.PR}, \tag{A15}$$

$$Z_{C2} \equiv S_1S_2Z_{A2}^2 Z_{B1} + Z_{M12} - S_1S_2Z_{AA}, \tag{A16}$$

$$Z_{C3} \equiv S_2^2 Z_{A2}^2 Z_{B1} - S_2^2 Z_{AA} - Z_{M2.PR}. \tag{A17}$$

D impedance substitutions:

$$Z_{D1} \equiv \frac{Z_{E1}Z_{E2}(S_1Z_{C3} - S_2Z_{C2})}{Z_{E1}Z_{E2}(Z_{C2}^2 - Z_{C1}Z_{C3})}, \tag{A18}$$

$$Z_{D2} \equiv \frac{Z_{E2}(Z_{C3})}{Z_{E1}Z_{E2}(Z_{C2}{}^2 - Z_{C1}Z_{C3})}, \tag{A19}$$

$$Z_{D3} \equiv \frac{Z_{E1}Z_{A2}Z_{B2}(S_1Z_{C3} - S_2Z_{C2})}{Z_{E1}Z_{E2}(Z_{C2}{}^2 - Z_{C1}Z_{C3})}, \tag{A20}$$

$$Z_{D4} \equiv \frac{Z_{E1}Z_{E2}(S_1Z_{C2} - S_2Z_{C1})}{Z_{E1}Z_{E2}(Z_{C2}{}^2 - Z_{C1}Z_{C3})}, \tag{A21}$$

$$Z_{D5} \equiv \frac{Z_{E2}(Z_{C2})}{Z_{E1}Z_{E2}(Z_{C2}{}^2 - Z_{C1}Z_{C3})}, \tag{A22}$$

$$Z_{D6} \equiv \frac{Z_{E1}Z_{A2}Z_{B2}(S_1Z_{C2} - S_2Z_{C1})}{Z_{E1}Z_{E2}(Z_{C2}{}^2 - Z_{C1}Z_{C3})}, \tag{A23}$$

$$Z_{D7} \equiv \frac{Z_{E1}Z_{E2}Z_{A2}Z_{B1}(S_2Z_{C2} - S_1Z_{C3})}{Z_{E1}Z_{E2}(Z_{C2}{}^2 - Z_{C1}Z_{C3})}, \tag{A24}$$

$$Z_{D8} \equiv \frac{Z_{E1}Z_{E2}Z_{A2}Z_{B1}(S_2Z_{C1} - S_1Z_{C2})}{Z_{E1}Z_{E2}(Z_{C2}{}^2 - Z_{C1}Z_{C3})}. \tag{A25}$$

F impedance substitutions:

$$Z_{F1} \equiv \frac{(S_1Z_{D1} - S_2Z_{D4})(S_3Z_{A2}Z_{E2}Z_{M4.PR} + S_4Z_{M34}Z_{A2}Z_{E2})}{Z_{E2}(S_3{}^2Z_{AB}Z_{M4.PR} + S_4{}^2Z_{AB}Z_{M3.PR} + Z_{M3.PR}Z_{M4.PR} + 2S_3S_4Z_{AB}Z_{M34} - Z_{M34}{}^2)}, \tag{A26}$$

$$Z_{F2} \equiv \frac{(S_1Z_{D3} - S_2Z_{D6})(S_3Z_{A2}Z_{E2}Z_{M4.PR} + S_4Z_{M34}Z_{A2}Z_{E2}) + (S_4{}^2Z_{AB} + Z_{M4.PR})}{Z_{E2}(S_3{}^2Z_{AB}Z_{M4.PR} + S_4{}^2Z_{AB}Z_{M3.PR} + Z_{M3.PR}Z_{M4.PR} + 2S_3S_4Z_{AB}Z_{M34} - Z_{M34}{}^2)}, \tag{A27}$$

$$Z_{F3} \equiv \frac{(S_1Z_{D2} - S_2Z_{D5})(S_3Z_{A2}Z_{E2}Z_{M4.PR} + S_4Z_{M34}Z_{A2}Z_{E2})}{Z_{E2}(S_3{}^2Z_{AB}Z_{M4.PR} + S_4{}^2Z_{AB}Z_{M3.PR} + Z_{M3.PR}Z_{M4.PR} + 2S_3S_4Z_{AB}Z_{M34} - Z_{M34}{}^2)}, \tag{A28}$$

$$Z_{F4} \equiv \frac{(S_1Z_{D7} - S_2Z_{D8})(S_3Z_{A2}Z_{E2}Z_{M4.PR} + S_4Z_{M34}Z_{A2}Z_{E2})}{Z_{E2}(S_3{}^2Z_{AB}Z_{M4.PR} + S_4{}^2Z_{AB}Z_{M3.PR} + Z_{M3.PR}Z_{M4.PR} + 2S_3S_4Z_{AB}Z_{M34} - Z_{M34}{}^2)}, \tag{A29}$$

$$Z_{F5} \equiv \frac{Z_{E2}(S_3Z_{M4.PR} + S_4Z_{M34})}{Z_{E2}(S_3{}^2Z_{AB}Z_{M4.PR} + S_4{}^2Z_{AB}Z_{M3.PR} + Z_{M3.PR}Z_{M4.PR} + 2S_3S_4Z_{AB}Z_{M34} - Z_{M34}{}^2)}. \tag{A30}$$

[1] F. Fahy, *Sound and Structural Vibration: Radiation, Transmission, and Response* (Academic, London, 1985).
[2] L. L. Beranek and I. L. Vér, *Noise and Vibration Control Engineering: Principles and Applications* (Wiley, New York, 1992).
[3] D. A. Bies and C. H. Hansen, *Engineering Noise Control: Theory and Practice* (Unwin Hyman, London, 1988).
[4] C. R. Fuller, C. H. Hansen, and S. D. Snyder, "Active control of sound radiation from a vibrating rectangular panel by sound sources and vibration inputs: An experimental comparison," J. Sound Vib. **148**, 355–360 (1991).
[5] T. W. Leishman and J. Tichy, "A theoretical and numerical analysis of vibration-controlled modules for use in active segmented partitions," J. Acoust. Soc. Am. **118**, 1424–1438 (2005).
[6] B. Bingham, M. J. Atalla, and N. W. Hagood, "Comparison of structural-acoustic control designs on an active composite panel," J. Sound Vib. **244**, 761–778 (2001).
[7] C. R. Fuller and R. J. Silcox, "Acoustics 1991: Active structural acoustic control," J. Acoust. Soc. Am. **91**, 519 (1992).
[8] P. Gardonio, E. Bianchi, and S. J. Elliott, "Smart panel with multiple decentralized units for the control of sound transmission. Part I: Theoretical predictions," J. Sound Vib. **274**, 163–192 (2004).
[9] P. Gardonio, E. Bianchi, and S. J. Elliott, "Smart panel with multiple decentralized units for the control of sound transmission. Part II: Design of the decentralized control units," J. Sound Vib. **274**, 193–213 (2004).
[10] S. M. Hirsch, N. E. Meyer, M. A. Westervelt, P. King, F. J. Li, M. V. Petrova, and J. Q. Sun, "Experimental study of smart segmented trim panels for aircraft interior noise control," J. Sound Vib. **231**, 1023–1037 (2000).
[11] S. M. Hirsch, J. Q. Sun, and M. R. Jolly, "Analytical study of interior noise control using segmented panels," J. Sound Vib. **231**, 1007–1021 (2000).
[12] M. E. Johnson and S. J. Elliott, "Active control of sound radiation using volume velocity cancellation," J. Acoust. Soc. Am. **98**, 2174–2186 (1995).
[13] B. Petitjean, I. Legrain, F. Simon, and S. Pauzin, "Active control experiments for acoustic radiation reduction of a sandwich panel: Feedback and feedforward investigations," J. Sound Vib. **252**, 19–36 (2002).
[14] R. L. St. Pierre, Jr., G. H. Koopman, and W. Chen, "Volume velocity control of sound transmission through composite panels," J. Sound Vib. **210**, 441–460 (1998).
[15] D. R. Thomas, P. A. Nelson, S. J. Elliott, and R. J. Pinnington, "Experimental investigation into the active control of sound transmission through stiff light composite panels," Noise Control Eng. J. **41**, 273–279 (1993).
[16] T. W. Leishman, *Active Control of Sound Transmission Through Partitions Composed of Discretely Controlled Modules* (The Pennsylvania State University, University Park, PA, 2000).
[17] T. W. Leishman and J. Tichy, "A fundamental investigation of the active control of sound transmission through segmented partition elements," INCE Conference Proceedings **103**, 137–148 (1997).
[18] T. W. Leishman and J. Tichy, "An experimental investigation of two module configurations for use in active segmented partitions," J. Acoust. Soc. Am. **118**, 1439–1451 (2005).
[19] T. W. Leishman and J. Tichy, "An experimental investigation of two active segmented partition arrays," J. Acoust. Soc. Am. **118**, 3050–3063 (2005).
[20] P. E. Fleischer and J. Tow, "Design formulas for biquad active filters using three operational amplifiers," Proc. IEEE **61**, 662–663 (1973).
[21] K. L. Su, *Analog Filters* (Kluwer Academic, Norwell, MA, 2002).
[22] M. Herpy and J.-C. Berka, *Active RC Filter Design* (Elsevier, New York, 1986).
[23] P. D. Wheeler, *Voice Communications in the Cockpit Noise Environment—*

The Role of Active Noise Reduction (Southampton University, Southampton, 1986).
[24]L. L. Beranek, *Acoustics* (McGraw-Hill, New York, 1954).
[25]M. Leach, *Introduction to Electroacoustics and Audio Amplifier Design* (Kendall-Hunt, Dubuque, IA, 2003).
[26]H. F. Olson, *Elements of Acoustical Engineering* (Van Nostrand, New York, 1940).
[27]B. E. Anderson, *Derivation of Moving-Coil Loudspeaker Parameters Using Plane Wave Tube Techniques* (Brigham Young University, Provo, UT, 2003).
[28]J. R. Ashley and M. D. Swan, "Experimental determination of low-frequency loudspeaker parameters," J. Audio Eng. Soc. **17**, 525–531 (1969).
[29]J. R. Ashley and M. D. Swan, "Improved measurement of loudspeaker parameters," in Convention of the Audio Engineering Society (1971).
[30]H. Blind, A. Phillips, and E. Geddes, "Efficient loudspeaker parameter estimation—An extension," in Convention of the Audio Engineering Society, San Francisco, CA (1992).
[31]R. C. Cabot, "Automated measurements of loudspeaker small-signal parameters," in Convention of the Audio Engineering Society, 1986, Los Angeles, CA.
[32]D. Clark, "Precision measurement of loudspeaker parameters," J. Audio Eng. Soc. **45**, 129–141 (1997).
[33]E. Geddes and A. Phillips, "Efficient loudspeaker linear and nonlinear parameter estimation," in Convention of the Audio Engineering Society, New York, NY (1991).
[34]R. Gomez-Meda, "Measurement of the Thiele-Small parameters for a given loudspeaker, without using a box," in Convention of the Audio Engineering Society, New York, NY (1991).
[35]W. J. J. Hoge, "The measurement of loudspeaker driver parameters," in Convention of the Audio Engineering Society, New York, NY (1977).
[36]D. B. J. Keele, "Sensitivity of Thiele's vented loudspeaker enclosure alignments to parameter variations," J. Audio Eng. Soc. **21**, 246–255 (1973).
[37]M. H. Knudsen, J. G. Jensen, V. Julskjaer, and P. Rubak, "Determination of loudspeaker driver parameters using a system identification technique," J. Audio Eng. Soc. **37**, 700–708 (1989).
[38]J. N. Moreno, "Measurement of loudspeaker parameters using a laser velocity transducer and 2-channel FFT analysis," J. Audio Eng. Soc. **39**, 243–249 (1991).
[39]J. D. Sagers, "Analog feedback control of an active sound transmission control module," MS thesis, Brigham Young University, Provo, UT (2008).
[40]J. Y. Chung, "Cross-spectral method of measuring acoustic intensity without error caused by instrument phase mismatch," J. Acoust. Soc. Am. **64**, 1613–1616 (1978).
[41]J. Y. Chung and D. A. Blaser, "Transfer function method of measuring in-duct acoustic properties, Part I: Theory," J. Acoust. Soc. Am. **68**, 907–913 (1980).
[42]J. Y. Chung and D. A. Blaser, "Transfer function method of measuring in-duct acoustic properties, Part II: Experiment," J. Acoust. Soc. Am. **68**, 914–921 (1980).
[43]A. D. Pierce, *Acoustics: An Introduction to Its Physical Principles and Applications* (McGraw-Hill, New York, 1981).

Accuracy of acoustic ear canal impedances: Finite element simulation of measurement methods using a coupling tube

Sebastian Schmidt[a] and Herbert Hudde
Institute of Communication Acoustics, Ruhr University Bochum, D-44780 Bochum, Germany

(Received 21 January 2009; revised 7 April 2009; accepted 7 April 2009)

Acoustic impedances measured at the entrance of the ear canal provide information on both the ear canal geometry and the terminating impedance at the eardrum, in principle. However, practical experience reveals that measured results in the audio frequency range up to 20 kHz are frequently not very accurate. Measurement methods successfully tested in artificial tubes with varying area functions often fail when applied to real ear canals. The origin of these errors is investigated in this paper. To avoid mixing of systematical and other errors, no real measurements are performed. Instead finite element simulations focusing on the coupling between a connecting tube and the ear canal are regarded without simulating a particular measuring method in detail. It turns out that realistic coupling between the connecting tube and the ear canal causes characteristic shifts of the frequencies of measured pressure minima and maxima. The errors in minima mainly depend on the extent of the area discontinuity arising at the interface; the errors in maxima are determined by the alignment of the tube with respect to the ear canal. In summary, impedance measurements using coupling tubes appear questionable beyond 3 kHz.
 [DOI: 10.1121/1.3125344]

PACS number(s): 43.58.Bh, 43.64.Ha, 43.20.Ye, 43.20.Mv [BLM] Pages: 3819–3827

I. INTRODUCTION

Acoustic impedances at the entrance of the ear canal can be measured by a great variety of methods. Møller (1960) described the usage of "calibrated sound sources" as a means for measuring impedances. This principle is up-to-date nowadays as well. Actually it was applied in most measurements at the ear canal (Rabinowitz, 1981; Keefe *et al.*, 1992; Larson *et al.*, 1993; Voss and Allen, 1994; Hudde *et al.*, 1996; Sanborn, 1998). For calibration, Norton or Thevenin equivalent sources of the used measuring devices are determined by use of several known load impedances. After calibration of the sound source the ear canal entrance impedance is calculated from a single pressure measurement. In other studies the transfer function method, which relies on the influence of the termination impedance on pressure transfer functions in the duct, was applied (e.g., Ciric and Hammershøi, 2007).

Usually a robust and predictable coupling of the device outlet and the ear canal is required. Such a coupling can be realized by individually cast ear molds (e.g., Sanborn, 1998) or foam plugs (e.g., Keefe *et al.*, 1992) which are used to fix insert earphones and microphone probes in the canal. To avoid the area discontinuity between external sound tubes and the ear canal entrance area, alternatively the ear canal itself can be used as measuring duct (Hudde, 1983; Voss and Allen, 1994; Farmer-Fedor and Rabbitt, 2002). In principle, there is a third alternative of measuring impedances, namely, using impedance probes which contain separated pressure and volume velocity sensors (the method is illustrated in Lanoye *et al.*, 2006). If such devices are applied, the main problem is the strong disturbance of sound field at the measuring position. In this paper we consider exclusively measurement techniques using external tubes coupled to the ear canal entrance.

Input impedances of ear canals can be used for middle ear diagnostics, for instance. For this application the measured impedance has to be transformed to the eardrum position. However, results are often inaccurate. It is the central aim of this paper to elucidate the origin of possible errors in measurement and transformation. For frequencies higher than the main middle ear resonance, i.e., above 3 kHz, the eardrum can be assumed to be almost rigid (Hudde and Engel, 1998a; Hudde and Engel, 1998b). Therefore the frequencies of minimum and maximum input impedances are mainly affected by the ear canal length and its cross-sectional area function. This gives the opportunity to derive the ear canal shape from its input impedance by inverse procedures. Methods developed for geometry estimation of the vocal tract (Schroeder, 1967; Sondhi and Gopinath, 1971) were applied to the ear canal as well (e.g., Hudde *et al.*, 1999). The calculated cross-sectional area function can be used to estimate the required transformation of the impedance (and additionally of the sound pressure) to the eardrum. The eardrum sound pressure is useful as a reference signal that is independent of the individual ear canal (for instance, in psychoacoustic experiments). It should be mentioned that simple estimations of the ear canal transformation based on impedance or pure pressure measurements are possible as well (Larson *et al.*, 1993; Siegel, 1994; Schmidt and Hudde, 2008), but are not considered in this paper.

The mentioned methods of estimating ear canal area functions basically evaluate the frequencies of impedance extrema which are characteristically shifted compared to the equidistant extremal frequencies of homogeneous tubes. If

[a]Author to whom correspondence should be addressed. Electronic mail: sebastian.schmidt@rub.de

the area variation in the investigated canal is small, primarily the impedance minima are shifted. Actually, evaluating exclusively the minima can provide fairly good estimates of the ear canal transformation (Hudde *et al.*, 1999). Nevertheless the knowledge of maximum frequencies improves the estimate. Thus it is interesting to examine the impact of the coupling between connecting tube and ear canal for minima and as well for maxima arising at the ear canal entrance.

When external sound canals are attached to the ear canal entrance, a cross-sectional area discontinuity between device and ear canal cannot be avoided. At this interface, higher order modes are excited (Hudde and Letens, 1985; Brass and Locke, 1997; Fletcher *et al.*, 2005; Stinson and Daigle, 2007), but these modes decay within a short distance from the discontinuity. The acoustical waves in the homogeneous connecting tube are planar except very close to the orifice. In contrast, the waves in the ear canal are slightly curved due to the area function and, in particular, due to the curved shape of the ear canal. Additionally, in the ear canal strong local deviations from regular wave fronts that are only slightly curved are found (Stinson and Daigle, 2005; Hudde and Schmidt, 2009). Such findings suggest studying the structure of sound fields at the interface in order to get insight into the origin of systematical measuring errors. In this investigation, finite element (FE) models which simulate the acoustical condition appearing in impedance measurements are used.

II. MODELING EAR CANAL IMPEDANCE MEASUREMENTS

The models consist of connecting tubes, the ear canal, the eardrum, and the middle ear. The connecting tube is simultaneously used as measuring tube, primarily for determining the impedance at its orifice. The model is constructed as simple as possible for the given examination. In particular, it is aimed at getting insight to general characteristics of the sound field structure, not at the most accurate approximation of real sound fields in natural ear canals. Therefore the connecting tubes and the ear canal are assumed to be rigidly walled. The sound propagation in the tube and the ear canal are calculated without taking losses into account. The ear canal is "manually" constructed including features that can be found in natural ear canals. The cross-sectional area varies in size and shape over the canal length; its middle axis shows two prominent bendings. The ear canal is terminated by an inclined elastic eardrum which is loaded by the middle ear ossicles.

The geometry of ear canal, eardrum, and middle ear is kept constant throughout the calculations. The models only differ with respect to shape and alignment of the connecting tube (Fig. 1). The effect of the area discontinuity is examined by variation in the tube diameter. Three tubes with different cross-sectional areas were utilized. Two of the circular tubes have diameters of 2 mm ("thin") and 4 mm ("medium"). The third model provides a flush connection between connecting tube and ear canal. For that purpose, the entrance area of the ear canal model is extruded along its normal. By this means a maximally smooth transition is constructed. Such a tube is not very realistic, but is used as an "ideal" device because field disturbances at the interface are widely reduced. The

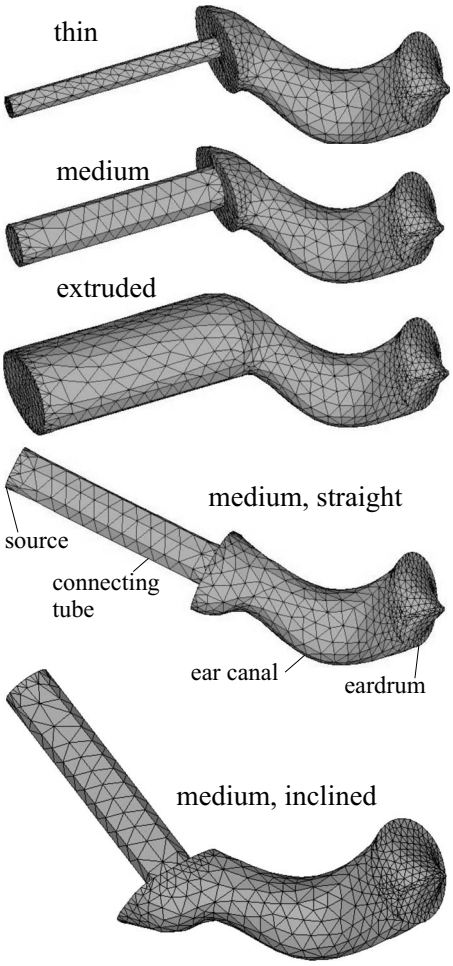

FIG. 1. Investigated impedance measurement models. The connecting tubes have different diameters and (for the medium tube) different adjustments with respect to the ear canal. The middle ear model is not shown in the plots, although taken into account in the calculations.

cross-section of the extruded canal corresponds to a circular tube diameter of about 9.3 mm. The position of the coupling area is the same in each of the three cases. At first, all the three connecting tubes are aligned with the surface normal of the cross-sectional area at the ear canal entrance.

In practice, however, the alignment of the connecting tube is not at all unique. To examine its influence, two models with inclined connecting tubes were generated, however exclusively for the medium diameter tube because it is the most practicable. To obtain other orientations, the tube is rotated about the center of its orifice area, which keeps the resulting ear canal length constant. As the "original" medium tube as given in the second place in Fig. 1 exhibits a significant inclination with respect to the axis of the foremost part of the ear canal, one of the two variations is constructed aiming at a straight continuation ("medium, straight") of this axis. The "medium, inclined" case is another variation which is rotated by 30 deg referred to the original position.

The models are generated using CAD software. Meshing and calculation of the resulting sound fields are performed using commercial FE software (ANSYS). The mean nodal distance of the mesh is generally adjusted to 1.5 mm. Thus, approximately 15 elements cover one wavelength at 16 kHz. Near the coupling tube orifice, particularly in the case of

large area discontinuities, the spatial variations within the sound field at the interface are much larger than at some distance away from the interface. Here the nodal distance needs to be increased accordingly. The necessary resolution was checked by increasing the node density until no significant differences in the calculated sound fields were observed. Frequencies are chosen in equidistant steps of 160 Hz up to 16 kHz.

III. SIMULATION OF IMPEDANCE MEASUREMENTS

The simulation of impedance measurements is intended to demonstrate the effects arising at the interface between connecting tube and ear canal. However, the measurement method itself should be as ideal as possible. Therefore a fully absorbing sound source in a sufficient distance from the end of the tube is simulated using a vibrating cross-sectional surface ("piston") of impedance equivalent with the wave impedance $Z_w=\rho c$. The absorption avoids reflections at the source which would yield strong transmission line resonances because the eardrum is highly reflecting. Such resonances can degrade the numerical accuracy of computations. In real measurements damping material, placed near the driving transducer, is necessary as well to avoid increasing errors near resonances.

The impedance is "measured" using the calibrated source method. It relies on the simple fact that the pressure excited by a known source allows the load impedance to be calculated. For a volume velocity source q_0 having an internal admittance Y_0 the load admittance Y_x is determined from the measured pressure p_x as

$$Y_x = \frac{q_0}{p_x} - Y_0. \tag{1}$$

In the case simulated with FE the internal admittance equals the tube wave admittance $Y_0=Y_{\mathrm{tw}}=A/Z_w=A/(\rho c)$, where A denotes the cross-section of tube and piston. The volume velocity of the source is derived from the applied piston displacement ξ according to $q_0=j\omega\xi A$. The pressure p_x is determined at the central node of the piston which can be considered as virtual microphone position. To calculate the impedance Z_{out} at the orifice of the connecting tube, the admittance Y_x has to be transformed according to

$$Z_{\mathrm{out}} = Z_{\mathrm{tw}} \frac{\cos(\beta L_t) - jY_x Z_{\mathrm{tw}} \sin(\beta L_t)}{Y_x Z_{\mathrm{tw}} \cos(\beta L_t) - j \sin(\beta L_t)}. \tag{2}$$

The product βL_t of wave number and tube length is perfectly known because the speed of sound and the dimension of the tube are specified as FE model parameters. The lossless transformation underlying Eq. (2) accurately matches the conditions simulated.

Usually it is assumed that the impedance at the orifice of the measuring tube equals the input impedance of the subsequent duct, i.e., the ear canal input impedance. Impedances measured under this assumption are displayed in Fig. 2 [the curves indicated by "(c)" are discussed later]. The impedances are normalized to the tube wave impedance of a cylindrical tube of 8 mm diameter. Obviously the utilized connecting tubes have considerable impact on the measured impedance. The most striking effect takes place in impedance minima. There is a systematical shift of measured minimum frequencies to lower values if the cross-section of the connecting tube is reduced. In contrast, the impedance maxima are much less affected.

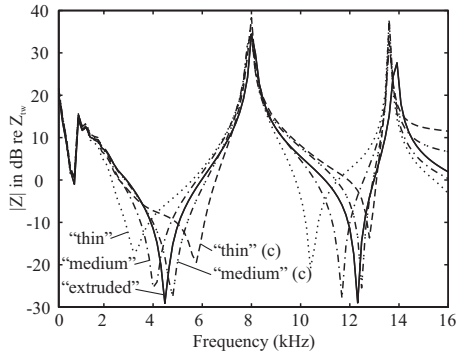

FIG. 2. Ear canal impedances measured by simulation of three different connecting tubes (cases thin, medium, and extruded according to Fig. 1) and corrected according to Karal's (1953) mass impedance at the discontinuity. Corrected impedances are indicated by (c). For the extruded tube no correction is applied because no discontinuity exists. The dip at low frequencies is no fault. It is caused by resonances of the eardrum and the middle ear.

Shifting of characteristic frequencies due to spatial sound field structures at tube orifices is well known. In some cases corrections are possible which approximate the three-dimensional effect in terms of the one-dimensional model, of course, only for sufficiently low frequencies. A tube acoustically coupled to a general sound field appears a little longer than it is. The physical background of such a length correction is the acoustical mass vibrating just behind the orifice of the tube. For the special case of an area discontinuity occurring in a circular cylindrical duct an approximate formula for the acoustical mass can be used (Karal, 1953). Karal's (1953) approximation provides a good estimate of the effective mass except for small area ratios at the discontinuity (Hudde and Letens, 1985). However, in the case of a small discontinuity the correction itself is small and therefore of low significance. Thus, Karal's (1953) correction can be expected to improve the measured impedances.

According to the corresponding equivalent circuit, Karal's (1953) acoustical mass impedance simply adds to the actual input impedance of the ear canal. Therefore the mass impedance is subtracted to obtain the corrected versions of the impedances [impedances denoted with "(c)" in Fig. 2]. It can be expected that the extruded case will give the best approximation of the correct impedance because an area discontinuity is completely avoided. The corrected results are disappointing: the minima are shifted in excess of the correct frequency which is close to that calculated for the extruded tube. For the cases regarded in Fig. 2 half of Karal's (1953) mass would yield better results. However, the mass correction is not always overestimated. Thus it is not reasonable to use a certain factor reducing the correction to a more accurate amount. For instance, Karal's (1953) correction applies fairly well if an axisymmetric circular duct with discontinuity is considered. Actually, the correct mass is critically dependent on the shape of the ear canal input area and on the

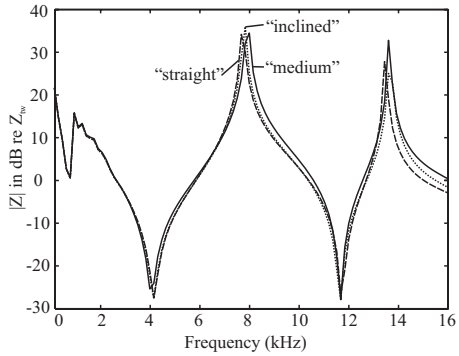

FIG. 3. Ear canal impedances measured by simulation of three different coupling angles using the medium tube (cases medium, "straight," and "inclined" according to Fig. 1).

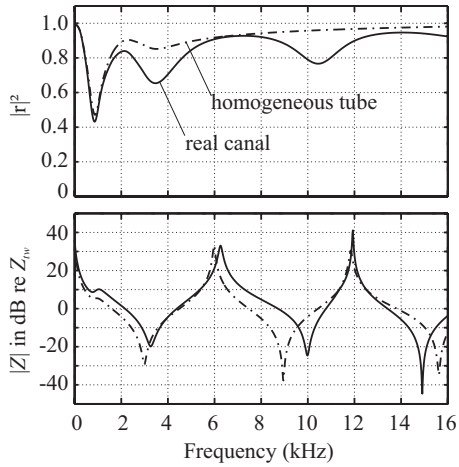

FIG. 4. Power reflectances and impedance magnitudes computationally obtained at the ear canal entrance. The same eardrum impedance is transformed via a lossless homogeneous tube and via a lossless ear canal having the same length, but taking into account a typical variation in the cross-sectional area.

area function and curvature of the section just behind the interface. No simple solution can be found to estimate the mass correction more accurately.

Under the perspective of the mass correction the missing frequency shift in impedance maxima is easily understood: subtracting the small mass impedance from the large entrance impedance near maxima has little effect, but the correction has high impact if it is in the order of the measured values. According to Fig. 2 the mass correction changes the result significantly in a fairly broad frequency range around the minima. Even impedance magnitudes larger than the tube wave impedance (over 0 dB in Fig. 2) are considerably altered.

In practice, another systematical error arises. Frequently the connecting tube cannot be correctly aligned with the orientation of the ear canal because parts of the pinna, in particular, the tragus, obstruct the direct access. Then the tube axis differs from the normal vector of the ear canal input area at the location of the tube orifice. Measuring errors due to such misalignment are considered in Fig. 3. The effect of different tube alignments appears generally smaller than the effect of discontinuities. Changes are stronger in impedance maxima than in minima.

In many publications, reflectances instead of impedances are considered (e.g., Stinson, 1990; Rabbitt and Dragicevic, 1991; Keefe *et al.*, 1993; Voss and Allen, 1994; Burns *et al.*, 1998; Farmer-Fedor and Rabbitt, 2002; Feeney and Sanford, 2004). The reflectance has the advantage that its magnitude is far less dependent on the measuring location than the magnitude of the impedance. Therefore the reflectance at the ear canal entrance is sometimes considered as a rough estimate of the reflectance at the tympanic membrane. Frequently, the power reflectance, the square of the reflectance magnitude, is provided. Thus it is interesting to consider the effect of the measurement errors on the reflectances as well. The reflectance is obtained from the input impedances Z_E according to

$$r = \frac{Z_E - Z_{\mathrm{tw}}}{Z_E + Z_{\mathrm{tw}}}. \tag{3}$$

Herein $Z_{\mathrm{tw}} = \rho c / A_{ecE}$ denotes the tube wave impedance at the entrance which has a cross-sectional area A_{ecE}.

The characteristics of the reflectance transformation from the tympanic membrane to the ear canal entrance are elucidated in Fig. 4 using two simple one-dimensional models. One model duct is shaped like a natural ear canal (taken from Stinson and Lawton, 1989), the other is a homogeneous circular cylinder. Since a homogeneous (lossless) tube does not alter the reflectance magnitude, the power reflectance at the entrance of the duct is identical to the eardrum power reflectance. It can be observed that the alteration of the power reflectance is small at low frequencies, but noticeable at higher frequencies, particularly near the frequencies of impedance minima. The amount of reflectance variation does not only depend on the area function of the ear canal but also on the eardrum reflectance itself. An eardrum reflectance having unity magnitude is not changed at all. Smaller reflectances are altered to a stronger extent because the reflections due to variation in the area function become more significant.

The eardrum impedance data underlying the calculations shown in Fig. 4 are taken from Hudde and Engel (1998b). The reflectances measured close to the eardrum of temporal bone preparations tend to be a little higher than the results of many in-vivo measurements. As we have seen, the deviations between entrance and eardrum reflectances would be greater for smaller power reflectances at the tympanic membrane.

The results of the FE simulation, now represented as power reflectances, are given in Fig. 5. Aside from the first sharp dip which corresponds to the main middle ear resonance and further weaker middle ear and tympanic membrane resonances, the minima of the power reflectance exhibit some similarity with the curves given in Fig. 4. The frequencies of the reflectance minima correspond to the impedance minima. The smallest dips are calculated for the almost ideal measuring tube, the "extruded" measuring tube. Minima of considerable depth arise if a thin coupling tube is used.

Obviously, measuring errors systematically increase the apparent depth of power reflectance minima. This immediately corresponds to the decreased depth of the impedance minima as represented in Fig. 2. Great care has to be taken to

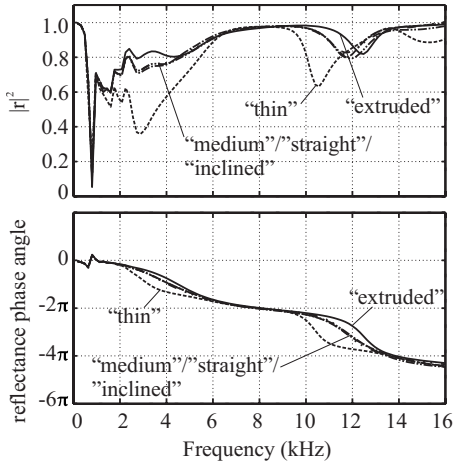

FIG. 5. Power reflectances and the phase of the (not squared) reflectance belonging to the uncorrected impedances of Figs. 2 and 3.

avoid overestimating the dips of the power reflection in frequency ranges around impedance minima at the ear canal entrance (roughly at 3 and 12 kHz, depending on the ear canal length). Maybe some published power reflectances are influenced by such measuring errors. It has to be noted, however, that many reflectance measurements are performed using a calibrated source directly in the ear canal, i.e., avoiding a coupling tube. Measuring errors occurring in this case are not covered by our current investigations, but will be examined soon.

The reflectance phase represented in Fig. 5 shows maximum deviations in the same frequency ranges. If the complete information about the acoustical system behind the measuring location is of interest, the reflectance phase is important as well. It can be used, for instance, to estimate the area function of the ear canal (Hudde *et al.*, 1999). The simulations reveal that also the phase is considerably disturbed if the area discontinuity at the ear canal entrance is not kept sufficiently small.

In the following the impact of the tube size and adjustment on the accuracy of measured impedances is investigated by considering the sound fields occurring near the interface.

IV. SOUND FIELD STRUCTURE AT THE INTERFACE

The three-dimensional structure of sound fields is usually visualized by surfaces of equal sound pressure ("isosurfaces") for given frequencies. Mostly, surfaces of equal magnitude of the complex pressure phasors are considered. The associated velocity field is completely determined by the complex sound pressure. Thus it provides no additional information, in principle. However, it is often very instructive to look at the velocity field as well because it can considerably enhance the insight into the sound field geometry. The visualization of the velocity field in the frequency domain, i.e., using phasors, is unfavorable because due to the vector property of velocities a comprehensive representation would have to include the three spatial components separately. However, such a representation does not contribute to an intuitive understanding of the actual velocity field. It is much more illuminative to consider instantaneous velocity vectors as arrows at meaningfully chosen points in time ("snapshots"). In Figs. 6 and 7 only one snapshot per condition is provided. The snapshots are always taken at the moment when the vector length at the location of highest velocity is maximal.

With varying frequency the minima and maxima of sound pressures and velocities are shifted in the connecting tube and the ear canal as well. At the position of pressure maxima, volume velocity minima arise, and vice versa. The most striking deviations from fundamental modes occur near the interface between connecting tube and ear canal. The errors of measured impedances as given in Figs. 2 and 3 suggest that the strongest deviations should be found if the orifice of the connecting tube lies in a pressure minimum of the ear canal. In pressure maxima smaller sound field distortions, but a higher sensitivity to differing adjustments of the connecting tube, can be expected in general. Therefore the conditions for both extremals are examined in the following.

Figures 6 and 7 show details of the sound fields calculated for different connecting tubes and adjustments under the conditions of the first pressure minimum (left) and the first maximum (right) appearing at the interface area. In these cases distinct spatial sound field structures are observed. The isosurfaces belong to 20 equidistant pressure magnitudes. The pressure and velocity amplitudes are separately normalized for each case. Hence, the gray shading of the isosurfaces and the length of the velocity vectors are not comparable between the panels. The dynamic range $D = 20 \log_{10}|p_{\max}/p_{\min}|$ of the pressure arising in ear canal and connection tube is given in the figures.

First, the pressure minimum is considered. Under the conditions examined the frequency of the first pressure minimum ranges from 3200 Hz for the thin connecting tube up to 4480 Hz for the extruded tube (Fig. 6, left; compare Fig. 2). As expected the isosurfaces close to an area discontinuity strongly deviate from regular, almost planar shapes that arise in the posterior part of the ear canal and even more in the connecting tubes. The isosurfaces obtained for the extruded tube also exhibit some change during transition to the ear canal, but these changes are generally small.

In the pressure minimum the velocity becomes maximal. The ear canal has an acoustic length of about a quarter wavelength and therefore low input impedance. The pressure isosurfaces and the velocity vectors as well reveal that the sound transmission from the smaller diameter tube to the ear canal has the character of radiation into the ear canal. The velocity vectors at the orifice spread into the space behind the discontinuity. After a small distance, the vectors rearrange and form the regular ear canal field, where the vectors are widely directed parallel to the walls again. The velocity flow lines which run close to the ear canal walls are considerably curved just behind the interface; therefore the traveling distance of sound waves is longer than the middle axis through tube and ear canal. Thus the mean distance from the tube orifice to the end of the ear canal is extended compared to a tube without discontinuity. Hence the ear canal appears longer than it is. The detour becomes longer if the discontinuity increases, i.e., if the tube diameter decreases. If the

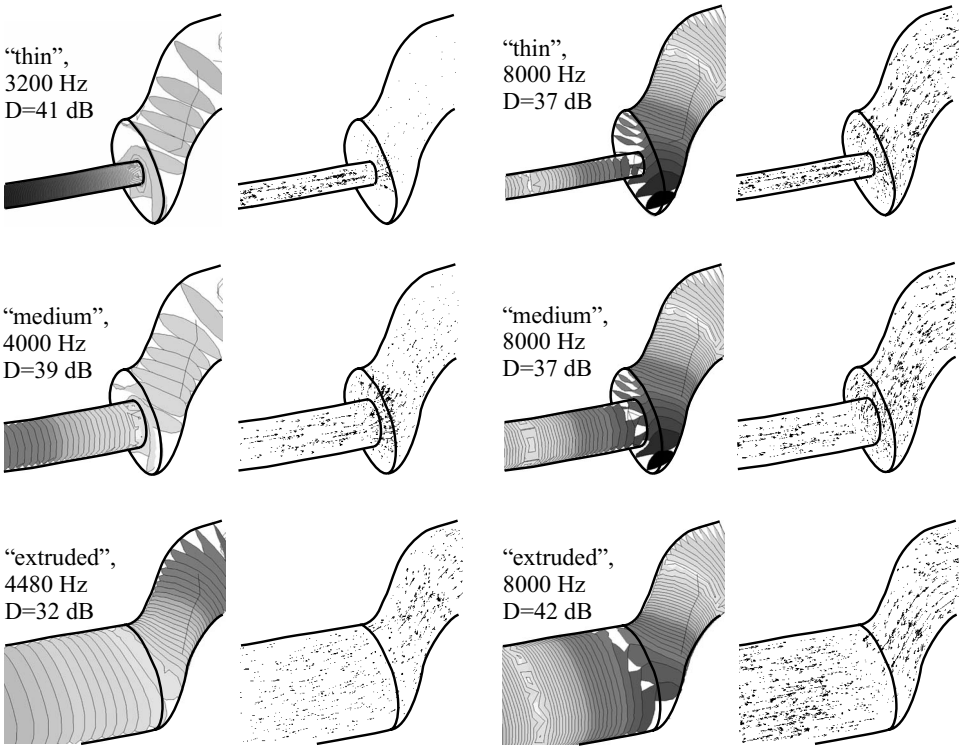

FIG. 6. Isosurfaces of pressure magnitude and instantaneous velocity vectors calculated for different connecting tubes at the interface between tube and two different acoustical conditions at the interface between tube and ear canal. Left: pressure minimum at the interface; right: pressure maximum at the interface. The frequency values denote the extremal frequencies within the resolution applied in the FE calculations (multiples of 160 Hz).

cross-sectional area of the connecting tube is identical to the entrance area of the ear canal, no extension effect takes place. Therefore the extruded tube produces impedance results which are close to the correct input impedance. However, it is hardly feasible in practice to use connection tubes which are matched to individual ear canal cross-sections. On the other hand, even the extruded connecting tube gives rise to errors. This item will be discussed at the end of this section.

Next, the sound fields near pressure maxima at the interface are examined. According to Fig. 2 the measured frequencies of the first pressure maximum are almost identical for the different connecting tubes. Now the ear canal is half a wavelength long which results in a high input impedance. Obviously, the sound fields arising for minima and maxima at the interface are fundamentally different (Fig. 6). The sound fields in the connecting tube and the ear canal appear widely decoupled in a pressure maximum, whereas the two fields are strongly coupled at the interface when a pressure minimum occurs. This is observed in both the pressure isosurfaces and the velocity field in the right panel of Fig. 6. For all the connecting tubes the velocities on both sides of the interface are in opposite phase, which is simply explained by the fact that the velocity runs through a minimum. In the

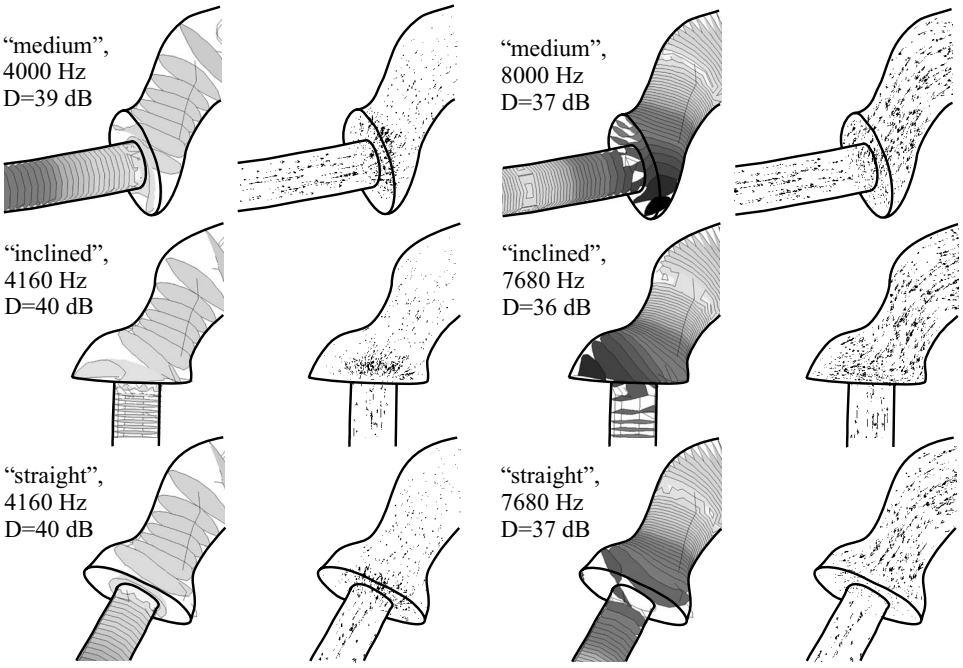

FIG. 7. Pressure isosurfaces and velocity vectors for connecting tube angle variation. Left: pressure minimum at the port area, right: pressure maximum at the port area. The frequency values denote the extremal frequencies within the resolution applied in the FE calculations (multiples of 160 Hz).

case of a highly reflecting termination the minimum of the velocity amplitude is close to zero, which is associated with a change in sign. The almost vanishing velocity at the interface decouples the sound fields in measurement tube and ear canal, whereas the large velocity occurring in a pressure minimum couples the fields. The spatial orientation of the velocity vectors on the left and the right of the interface is fairly independent from each other as well.

Nevertheless, the isosurfaces at 8000 Hz reveal that a weak coupling exists. The isosurfaces in both ducts are always aligned perpendicular to the walls. Therefore the structures are very different in both parts, particularly at large discontinuities. Here the rigid wall at the interface forms an essential part of the guidance of the acoustic wave. This leads to a distinct break of the isosurfaces pattern at the interface. However, the isosurfaces in the ear canal protrude a little into the connecting tube. This indicates the weak coupling. At the end of the connecting tube the isosurfaces are no longer approximately planar.

In the case of the extruded connecting tube, complicated isosurface structures as already described in Hudde and Schmidt (2009) occur. The loose coupling of sound fields keeps measuring errors low. In particular, the apparent extension of the ear canal as observed in pressure minima does not take place in the pressure maxima. In the panel for the extruded case at 8000 Hz, some isosurfaces form a set of domes arching over a certain point near the interface area. As they are oriented to one side of the ear canal wall, they are denoted "one-sided isosurfaces" in the following. Such structures occur when local pressure maxima arise in bends of wave ducts. The maxima are moved to the concave side of the duct as the pressure is here a little higher than on the opposite convex side due to reflections at the wall. One-sided isosurfaces are not conforming to sound waves propagating along a middle axis and cannot be represented in terms of fundamental modes. It can be shown, however, that one-sided isosurfaces follow the principle of minimum field energy in a weakened form. Hence, transformations over field regions containing one-sided isosurfaces yield only minimal error.

The small frequency variation in the pressure maximum is determined by details of the pressure distribution in the ear canal. In Fig. 6 the pressure maxima in the three regarded cases are rather similar in position (darkest part of the isosurfaces). This results in almost identical maximum frequencies. In contrast, the pressure maxima displayed in the right panel of Fig. 7 vary their position to some extent. In this figure the effect of varying angles between connecting tube and ear canal is examined for the tube of medium diameter. To leave the actual ear canal length untouched, the connecting tube is rotated about a fixed point when different coupling angles are modeled. The coupling angle changes the input area of the ear canal accordingly. As can be observed in Fig. 7, a variation in the angle changes the position of the pressure maximum near the interface and thereby the apparent length of the ear canal. The corresponding shift of the maximum frequency has already been observed in Fig. 3.

In the impedance minimum the differences of the minimum frequencies due to changes in the coupling angle are small (Fig. 7, left). As in the cases considered above the ear canal appears a little longer due to the lengthened velocity vectors occurring just behind the discontinuity. However, the minimum frequencies are shifted by almost the same amount if the utilized tubes have identical cross-section. The effect of the coupling angle on the minimum frequencies turns out to be low. Due to the strong coupling between tube and ear canal in pressure minima the pressure distribution in the ear canal is less variable than in the case of a pressure maximum (compare the sound fields in Fig. 7).

In conclusion, the amount of area discontinuity mainly takes effect on the frequency of measured impedance minima, whereas it hardly alters the frequencies of measured impedance maxima. In contrast, the coupling angle between tube and ear canal mainly influences the measured impedance maxima, whereas the impact on impedance minima is low.

So far the extruded tube has been considered as impractical, but also the best solution for the impedance measurement. However, the extruded tube does not provide perfect coupling as well. The ideal connecting tube is given by the requirement that the shape of isosurfaces in the sound field must not be altered compared to the open ear canal. This allows the necessary condition to be specified more exactly. First, the coupling has to take place at a position where the field structure is independent of the external sound source. Actually, such a position can be found. The foremost position is referred to as beginning of the "core region" of the ear canal or as "ear canal entrance" (Farmer-Fedor and Rabbitt, 2002; Hudde and Schmidt, 2009). In the core region a fundamental acoustic wave exists in the audio frequency range. Except at the already mentioned one-sided isosurfaces the field in the core region is regular, i.e., its isosurfaces are only slightly curved, perpendicular to a "middle axis," and almost independent of frequency. If these requirements are met, the shapes of the isosurfaces are the same for incident and reflected waves in the ear canal and therefore not depending on the termination of the ear canal.

The ideal connecting tube must not alter the core region of the ear canal. Hence it has to continue the ear canal outward without changing the orientation or shape of the isosurface at the interface. This means that the orifice of the connecting tube must perfectly match the isosurface at the desired location within the core region. Furthermore the tube must form an outward continuation of the ear canal which avoids any noticeable discontinuity including discontinuities in the course of the middle axis. Of course, this is not realistic. Any real connecting tube will disturb the sound pressure on the coupling surface to some extent.

To keep errors small, the ideal case should be approached as well as possible. Therefore a variety of connecting tubes are necessary to cope with individual ear canals. Discontinuities of any kind have to be avoided. In addition, the coupling should approximate calculable geometries and has to be free of leakage. These requirements make accurate impedance measurements very intricate and time-consuming.

V. SUMMARY AND CONCLUSIONS

If any acoustical measuring device is coupled to the ear canal, the problem arises how to realize a robust and predictable connection keeping measuring errors as small as possible. Practical experience reveals that it is very demanding to measure accurate impedances except at low frequencies when the complete ear canal behaves as lumped element. At frequencies beyond 3 kHz the input impedance mainly reflects the ear canal, to a lesser extent the terminating middle ear. Above the middle ear resonances, which arise between 700 Hz and 2 kHz, the eardrum forms a rather stiff termination guiding the sound waves to the rearmost point in the tympanomeatal corner. Thus ear canal impedance measurements in the frequency range above 3–4 kHz basically contain information on the ear canal geometry. Hence impedance measurements can be used as a means to derive the ear canal geometry (Hudde *et al.*, 1999). Whereas the method just quoted works well in artificial inhomogeneous, but straight ear canals, it often fails in real ear canals. Actually this failure gave rise to the investigations of this paper.

The ear canal area function shifts zeros and poles of the input impedance in a characteristic manner on the frequency scale. Thus it is of highest importance to measure the extremal frequencies correctly. Unfortunately, the present paper demonstrates that the extremal frequencies, in particular, the frequencies of impedance minima, can undergo considerable shifts if no special care is taken to avoid errors due to the coupling between measuring device and ear canal. The biggest effect on the resulting errors stems from the unavoidable discontinuity between the connecting tube and the ear canal. For circular cylinders the errors can be compensated fairly well using an appropriate acoustical mass formula (Karal, 1953). However, the correction turned out to be not satisfying in the case of discontinuities as arising under realistic measuring conditions. The reflectance (or power reflectance) at the ear canal entrance which is widely used as estimate for the reflectance at the tympanic membrane is affected by the described impedance measurement errors as well. The only way to reduce such errors is the usage of connecting tubes which widely fit the individual ear canal conditions. Further deviations, which are predominant in impedance maxima, arise if the adjustment of the connecting tube is not aligned with the normal vector of the input surface of the ear canal. A correct alignment is often not possible in practice. The errors due to misalignment are smaller than typical errors due to the area discontinuity, but nevertheless unacceptable if the ear canal shape is to be estimated.

All the investigations of this paper are based on FE simulations, not on real measurements. With respect to the impedance measurements this has the advantage to avoid mixing of errors due to the utilized equipment and unavoidable systematical errors due to the coupling between connecting tube and ear canal. Moreover the FE method allows the sound fields at the interface to be studied in detail. The sound fields near the interface between connecting tube and ear canal as arising in pressure minima and maxima are opposed to each other. In pressure minima the velocity is high. This yields a strong coupling between tube and ear canal. Therefore the effect of different adjustments of the connecting tube is comparably small in pressure minima, but due to the extension of velocity lines at the interface the ear canal appears extended as well. This produces the shift of minimum frequencies which cannot be successfully corrected taking Karal's (1953) acoustic mass into account. In pressure maxima the velocity is low and therefore the coupling as well. As a consequence the sound field at the interface is altered if the conditions are slightly changed. Thus the sensitivity to the adjustment of the connecting tube is high, which results in noticeable shifts of the maximum frequencies.

In conclusion, accurate measurements of ear canal input impedances are very problematic beyond 3 kHz. Below this frequency no pressure minimum occurs at the ear canal entrance. Hence measurement errors due to the coupling between measuring tube and ear canal are not significant, at least if the tube orifice is not much smaller than the ear canal. This allows measurements for diagnostic purposes up to 3 kHz. At higher frequencies the measurement of ear canal impedances for diagnostic aims is very questionable in any case because the transformation to the eardrum position is too inaccurate to estimate the high impedance at the eardrum.

ACKNOWLEDGMENTS

This work was supported by the Deutsche Forschungsgemeinschaft (DFG) in the project Hu 352/8. The authors would like to acknowledge the valuable comments and suggestions made by John J. Rosowski and an anonymous reviewer. This has considerably improved the manuscript.

Brass, D., and Locke, A. (**1997**). "The effect of the evanescent wave upon acoustic measurements in the human ear canal," J. Acoust. Soc. Am. **101**, 2164–2175.

Burns, E. M., Keefe, D. H., and Ling, R. (**1998**). "Energy reflectance in the ear canal can exceed unity near spontaneous otoacoustic emission frequencies," J. Acoust. Soc. Am. **103**, 462–474.

Ciric, D., and Hammershøi, D. (**2007**). "Acoustic impedances of ear canals measured by impedance tube," Proceedings of the 19th International Congress on Acoustics-ICA07, Madrid, Spain, 2–7 September.

Farmer-Fedor, B. L., and Rabbitt, R. D. (**2002**). "Acoustic intensity, impedance and reflection coefficient in the human ear canal," J. Acoust. Soc. Am. **112**, 600–620.

Feeney, M. P., and Sanford, C. A. (**2004**). "Age effects in the human middle ear: Wideband acoustical measures," J. Acoust. Soc. Am. **116**, 3546–3558.

Fletcher, N. H., Smith, J., Tarnopolsky, A. Z., and Wolfe, J. (**2005**). "Acoustic impedance measurements—correction for probe geometry mismatch," J. Acoust. Soc. Am. **117**, 2889–2895.

Hudde, H. (**1983**). "Measurement of the eardrum impedance of human ears," J. Acoust. Soc. Am. **73**, 242–247.

Hudde, H., and Engel, A. (**1998a**). "Measuring and modeling basic properties of the human middle ear and ear canal. Part I: model structure and measuring techniques," Acust. Acta Acust. **84**, 720–738.

Hudde, H., and Engel, A. (**1998b**). "Measuring and modeling basic properties of the human middle ear and ear canal. Part III: Eardrum impedances, transfer functions and model calculations," Acust. Acta Acust. **84**, 1091–1109.

Hudde, H., Engel, A., and Lodwig, A. (**1996**). "A wide-band precision acoustic measuring head," Acust. Acta Acust. **82**, 895–904.

Hudde, H., Engel, A., and Lodwig, A. (**1999**). "Methods for estimating the sound pressure at the eardrum," J. Acoust. Soc. Am. **106**, 1977–1992.

Hudde, H., and Letens, U. (**1985**). "Scattering matrix of a discontinuity with a nonrigid wall in a lossless circular duct," J. Acoust. Soc. Am. **78**, 1826–1837.

Hudde, H., and Schmidt, S. (**2009**). "Sound fields in generally shaped curved ear canals," J. Acoust. Soc. Am. **125**, 3146–3157.
Karal, F. C. (**1953**). "The analogous acoustical impedance for discontinuities and constrictions of circular cross section," J. Acoust. Soc. Am. **25**, 327–334.
Keefe, D. H., Bulen, J. C., Arehart, K. H., and Burns, E. M. (**1993**). "Ear-canal impedance and reflection coefficient in human infants and adults," J. Acoust. Soc. Am. **94**, 2167–2638.
Keefe, D. H., Ling, R., and Bulen, J. C. (**1992**). "Method to measure acoustic impedance and reflection coefficient," J. Acoust. Soc. Am. **91**, 470–485.
Lanoye, R., Vermeir, G., Lauriks, W., Kruse, R., and Mellert, V. (**2006**). "Measuring the free field acoustic impedance and absorption coefficient of sound absorbing materials with a combined particle velocity-pressure sensor," J. Acoust. Soc. Am. **119**, 2826–2831.
Larson, V. D., Nelson, J. A., Cooper, W. A., Jr., and Egolf, D. P. (**1993**). "Measurements of acoustic impedance at the input to the occluded ear canal," J. Rehabil. Res. Dev. **30**, 129–136.
Møller, A. R. (**1960**). "Improved technique for detailed measurements of the middle ear impedance," J. Acoust. Soc. Am. **32**, 250–257.
Rabbitt, R. D., and Dragicevic, J. (**1991**). "Measurement of acoustic energy reflection by the human ear," Third USA-China-Japan Conference on Biomechanics, Atlanta, GA, 25 August.
Rabinowitz, W. M. (**1981**). "Measurement of the acoustic input immittance of the human ear," J. Acoust. Soc. Am. **70**, 1025–1035.
Sanborn, P.-E. (**1998**). "Predicting hearing aid response in real ears," J. Acoust. Soc. Am. **103**, 3407–3417.
Schmidt, S., and Hudde, H. (**2008**). "Measurement of equal-loudness contours using eardrum pressure as reference signal," Proceedings of the Acoustics'08 SFA, ASA, EAA Conference, Paris.
Schroeder, M. R. (**1967**). "Determination of the geometry of the human vocal tract by acoustic measurements," J. Acoust. Soc. Am. **41**, 1002–1010.
Siegel, J. H. (**1994**). "Ear-canal standing waves and high-frequency sound calibration using otoacoustic emission probes," J. Acoust. Soc. Am. **95**, 2589–2597.
Sondhi, M. M., and Gopinath, B. (**1971**). "Determination of vocal tract shape from impulse response at lips," J. Acoust. Soc. Am. **49**, 1867–1873.
Stinson, M. R. (**1990**). "Revision of estimates of acoustic energy reflectance at the human eardrum," J. Acoust. Soc. Am. **88**, 1773–1778.
Stinson, M. R., and Daigle, G. A. (**2005**). "Comparison of an analytic horn equation approach and a boundary element method for the calculation of sound fields in the human ear canal," J. Acoust. Soc. Am. **118**, 2405–2411.
Stinson, M. R., and Daigle, G. A. (**2007**). "Transverse pressure distributions in a simple model ear canal occluded by a hearing aid test fixture," J. Acoust. Soc. Am. **121**, 3689–3702.
Stinson, M. R., and Lawton, B. W. (**1989**). "Specification of the geometry of the human ear canal for the prediction of sound-pressure level distribution," J. Acoust. Soc. Am. **85**, 2492–2503.
Voss, S. E., and Allen, J. B. (**1994**). "Measurement of acoustic impedance and reflectance in the human ear canal," J. Acoust. Soc. Am. **95**, 372–384.

Synchronized time-reversal focusing with application to remote imaging from a distant virtual source array

S. C. Walker,[a] Philippe Roux, and W. A. Kuperman
Marine Physical Laboratory of the Scripps Institution of Oceanography, University of California San Diego, La Jolla, California 92093-0238

(Received 31 December 2007; revised 10 March 2009; accepted 12 March 2009)

Time-reversing the transfer function between a time-reversal mirror (TRM) and a distant probe source location generates an acoustic spatio-temporal focus at the location. It is shown that a TR focus behaves as a "virtual" source (in the far-field limit) in the outbound direction with respect to the TRM. By extension, a collection of TRM-to-probe source transfer functions constitutes a virtual source array (VSA) that can serve as a remote platform for active imaging methods such as beam-steering and other coherent wavefront techniques. As a demonstration, a set of a-priori sampled TRM-to-VSA transfer functions are steered to coherently focus at a selected location beyond the VSA for which the transfer function is not known a-priori. In this case the VSA acts as a lens that refocuses the TRM field to the target location. Under proper conditions, the resolution is comparable to that of standard TR. While the specific application of active focusing is presented as a validation of the concept, the relationship between coherent focusing and the transfer function implies that the virtual array concept may find use in a range of imaging methods, both active and passive. Possible applications are discussed, and simulation and experimental results are presented. [DOI: 10.1121/1.3117374]

PACS number(s): 43.60.Ek, 43.60.Gk, 43.30.Vh, 43.30.Wi [DRD] Pages: 3828–3834

I. INTRODUCTION

In acoustic array imaging, an array of acoustic send-receive elements is used to extract information about features and/or targets embedded in the propagation medium, or even about the propagation medium itself. In the context of array processing, imaging may involve any combination of active,[1] passive,[2] and/or model based[3] algorithms that map (or image) a set of measured array signals via an acoustic propagation model to another set of parameters that characterize the acoustic properties of the medium, including information about any sources or scattering features. In a simple medium, where the propagation model is sufficiently accessible, imaging is straightforward. For example, passive source or active scatterer localization imaging in free space require nothing more than time-delay beam-steering. As the propagation medium (and hence the choice of propagation model) becomes more complex, more sophisticated array processing techniques are needed.

One solution to imaging and communications in complex media is time-reversal (TR) processing. In the TR paradigm, the field between an array of source-receive elements, often referred to as a time-reversal mirror (TRM),[4] and a remote probe source is sampled. Broadcasting the time-reversed probe source-to-TRM signal from the TRM results in a coherent acoustic focus at the original probe source location.[5] Rather than attempt to formulate a propagation model based on a-priori knowledge of the medium, in the TR paradigm, the propagation model is measured directly (it is the transfer function between the probe source element location and the TRM). Thus the process is completely self-adaptive, requiring only that the propagation medium be static (bear in mind that in a static medium, the field is reciprocal, so the sampling from probe source-to-TRM is equivalent to sampling from TRM-to-probe source). The TR paradigm then shifts the cost from that of characterizing the medium a-priori to that of experimentally directly measuring the propagation model, i.e., the transfer functions.

The main limitation to TR imaging is that it requires a probe source. This paper introduces the notion of using a collection of a-priori sampled transfer functions between the TRM and the locations of an initial set of probe source elements as the basis for imaging the medium beyond the initial probe source locations. In analogy with the guide-star technique used in astrophysics and adapted to the shallow ocean by Siderius *et al.*,[6] the set of measured transfer functions projects the TRM to the probe source locations. For the purposes of array processing, the collection of measured transfer functions constitutes an array of virtual acoustic elements at the initial probe source locations.

As a demonstration and validation of the theory and conceptual foundations of a TR generated virtual array, this paper considers the straightforward example of active line-of-sight (LOS) time-delay beam-steering applied in conjunction with a virtual source array (VSA) comprising a set of measured TRM-to-probe source transfer functions. The discussion considers the case of a shallow ocean waveguide where, due to boundary interactions, the acoustic field (and by extension the transfer functions) is complicated by multi-path arrivals. As suggested by Jackson and Dowling,[2] an active TR focusing event results in a wave that diverges from the focal location. Here it is shown that a TR focusing event can be considered to be a coherent virtual point source at the

[a]Author to whom correspondence should be addressed. Electronic mail: shane@physics.ucsd.edu

 0001-4966/2009/125(6)/3828/7/$25.00

original probe source location (in the outbound direction with respect to the TRM). Extending the virtual source equivalence to a spatially extended aggregation of TRM-to-probe source fields results in a VSA that serves as a platform for imaging remote locations beyond the VSA that are not accessible by a probe source. By projecting time-delay synchronizations[7] over the virtual source elements, the VSA effectively serves as a lens that coherently refocuses the TRM-to-VSA field to a selected unsampled target location. In a two-dimensional geometry, any (non-near-field) imaging techniques that can be deployed from a physical array can be applied from the virtual array (within the resolution limits relating the TRM and the virtual array that are discussed below). While it is not specifically treated here, the conceptual framework developed for the two-dimensional case is easily extended to imaging from a virtual array in three-dimensional geometries in conjunction with a curtain TRM (a TRM that is planar).

While the presented application can be used to ensonify new locations, the ability to focus remotely has broader imaging implications. Bearing in mind the relationship between a coherent focus and the transfer function, the resulting synchronized TRM-to-VSA field represents a good estimate of the transfer function between the TRM and the selected focal location, and thus is useful on its own as a propagation model for imaging and communications applications. Conceptually, then, the virtual array is similar to a physical array in terms of its potential for array processing strategies. Any number of imaging and communications strategies, active and passive can be applied to the VSA: for example, mono- and multi-static sonar techniques, beam-steering, spectral analysis,[8] matched field methods,[9] etc. Though the method is here demonstrated in the context of an ocean waveguide, it can be implemented in any static medium where TR processing is applicable. The virtual array concept is particularly suited to reverberant media, where the complexity introduced to the acoustic field by refraction, scattering, and boundary interactions actually serves to enhance TR performance.[10]

Section II demonstrates the equivalence between the field from a TR focusing event and that from a physical probe source. Section III introduces the concept of the VSA and presents simulation and experimental results for focusing from a linear geometry VSA. Possible applications for the VSA concept are discussed in Sec. IV with concluding remarks presented in Sec. V.

II. THE TR FOCUS AS A VIRTUAL POINT SOURCE

Consider the case that a TRM fully samples the radiative component of the field generated by a spatial point source (i.e., the TRM is spatially continuous and completely encloses the source) at location $\boldsymbol{r}=\boldsymbol{r}_n$ in a static, isotropic, free-space medium of sound speed c. For a source signal time dependence described by function $F(t-t_n)$, where t_n represents a reference delay, the time-reversed field, given by[2,11]

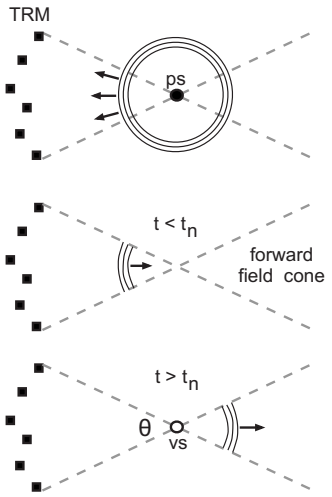

FIG. 1. TR focusing as a virtual source schematic. Though the probe source (solid black circle indicated by ps) radiates in all directions, TR returns only that part of the original field that is sampled by the TRM (solid black squares). The black circles and semi circles represent the probe source and TR fields, with the arrows indicating the direction of travel. At times less than the time of the focusing event, $t<t_n$, the TR field is converging to the source location. For points within the forward field cone, it is as if a virtual source exists at the TR focus location.

$$\psi_{\mathrm{tr}}(\boldsymbol{r},t)=\frac{1}{4\pi R_n}(F(t_n-T_n-t)-F(t_n+T_n-t)) \tag{1}$$

(with $R_n\equiv|\boldsymbol{r}-\boldsymbol{r}_n|$ and $T_n\equiv R_n/c$), describes a focusing event where waves converge to (for $t<t_n$) then diverge from (for $t>t_n$) the focal point at location $\boldsymbol{r}=\boldsymbol{r}_n$. Assuming the original field sampled by the TRM comprises only far-field contributions (always the case for the idealized construct of a spatial point source), the focusing event is diffraction limited.[2] In the case that the TRM also includes near-field contributions (i.e., the source is spatially extended and the TRM is within the near-field), the focus resolution may exceed the diffraction limit.[12,13]

At times $t>t_n$, the outbound TR field approximates the field originally sent by the active probe source, the main difference being that the field is time reversed. In this sense, the TR focus event can be considered a virtual source. Indeed, the outbound field from a TR virtual source approaches that emitted by the original active probe source (with its time-dependence reversed) in the high frequency, far-field limit. In the case that the TRM does not completely surround the source, the TR virtual source field comprises only components subtended by the TRM. As presented schematically in Fig. 1, for points located in the outbound region, or forward field cone (for $t>t_n$), the TR field is similar to the radiative component of the field generated by an active source at the TR focal point, $\boldsymbol{r}_n$. A simulated demonstration is shown in Fig. 2.

Considering the more general problem of TR focusing in an arbitrary static medium from a collection of N point sources synchronized to emit at times $t=t_n$ from locations $\boldsymbol{r}=\boldsymbol{r}_n$, the TR field is given by

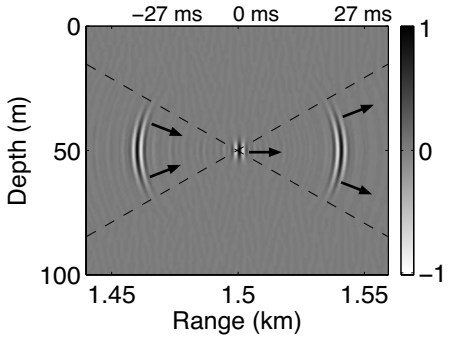

FIG. 2. TR focus simulation. Here three snap-shots of the field in the vicinity of a TR focusing event are superposed on the same figure with the corresponding snap-shot times indicated along the top. In this case the TR focusing event occurs at time $t=0$. The arrows indicate the direction of the acoustic intensity vector. The dashed lines delineate the aperture of the TRM (off to the left not shown). The field converges to, and then passes through the focal point. For points within the forward field cone, it is as if a virtual source exists at the TR focus location.

$$\psi_{\mathrm{tr}}(\boldsymbol{r},t)=\sum_{n=1}^{N}F(t-t_n)\bigstar\mathcal{G}_n, \tag{2}$$

where $\mathcal{G}_n=\mathcal{G}(\boldsymbol{r},\boldsymbol{r_n},t)$ is the time reversal operator (TRO) between the TRM and the source at location $\boldsymbol{r}=\boldsymbol{r_n}$ and ★ indicates the correlation operation.

III. IMAGING FROM A LINEAR GEOMETRY VIRTUAL ARRAY IN THE OCEAN WAVEGUIDE

One particular area of interest where the concept of a VSA might find immediate application is in shallow ocean acoustics where numerous interactions of the acoustic field with the surface and sediment complicate imaging strategies. The VSA concept combines a pair of imaging methods, TR and time-delay beam-steering, which have each proven effective at imaging in the ocean. TR methods have proven effective at generating acoustic focusing in even the most complex of multi-path shallow ocean environments.[1,2] One of the main advantages of TR is that it can be completely self-adaptive, requiring no a-priori knowledge about the propagation medium and no modeling. The main limitation is that TR methods require a probe source at the selected focal location. In contrast, time-delay beam-steer algorithms, while not well suited to complex environments, perform quite well in simple media[14] where LOS techniques are applicable. By combining an appropriate beam-steer algorithm with the concept of a VSA, it becomes possible to steer a collection of measured TRM-to-VSA fields to coherently focus at a selected location beyond the VSA. Most notably, the focusing is implemented without the need for a probe source at the selected location.

A. Theory of active focusing from a linear geometry VSA

Consider the cylindrically symmetric, range-independent shallow ocean case depicted in Fig. 3, where the fields between the elements [at locations (r_n,z_n)] of a passive array and a TRM (at $r=0$) are known, either by direct measurement or otherwise. Employing the (frequency domain) expression of Eq. (2), the frequency domain synchronized TR focusing field is given by[15]

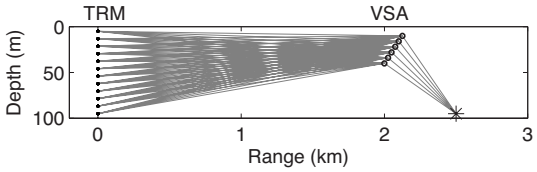

FIG. 3. Schematic of coherent focusing from a virtual array in the shallow ocean. By properly synchronizing the fields between a TRM (black dots) and a passive receive array (open circles), it is possible to ensonify a selected outbound location (denoted by *). The gray lines denote that the virtual array serves to redirect the TRM field to the selected location (boundary reflections are neglected in this schematic).

$$\tilde{\psi}_{\mathrm{tr}}(\boldsymbol{r},\omega)\approx\frac{\tilde{F}^{*}(\omega)e^{-i\omega t_n}}{8\pi\rho_n^2}\sum_{m=1}^{M}\frac{\phi_m(z_n)\phi_m(z)e^{ik_mR_n}}{k_m\sqrt{r_n}\sqrt{|R_n|}}, \tag{3}$$

where the time-frequency Fourier transform of the expression for the TRO specific to the shallow ocean waveguide has been substituted. In this expression ω represents angular frequency, and $\tilde{F}^{*}(\omega)e^{-i\omega t_n}$ is the complex conjugate of the Fourier transform of the time domain signal originally transmitted between the TRM and the nth element. The quantities $\phi_m(z)$ and k_m denote the mode m depth function and propagating wavenumber, respectively, while $R_n=r_n-r$ is the displacement between the nth element and the field point. The medium density at the depth z_n is denoted by ρ_n. The approximation symbol has been used to emphasize that this expression is valid in the far-field limit. Except for an extra factor related to cylindrical spreading, the nth focusing event describes the field from a virtual source (in the far-field limit) at location (r_n,z_n) that is outbound for times $t>t_n$ (the field being inbound from the TRM for $t<t_n$). Notice that the virtual source is time-reversed with respect to the original signal.

Applying the relationship between a TR focusing event and a virtual source, the synchronized TR focusing described by Eq. (3) defines a time-delay beam-steer operation over the VSA. For example, as with an array of physical sources, the basic LOS time-delay synchronization

$$t_n=\sqrt{(r_x-r_n)^2+(z_x-z_n)^2}/c \tag{4}$$

applied over the virtual sources results in an coherent focus at the point (r_x,z_x). As would be the case for a physical array, this assumes a homogenous medium with sound speed c between the array and the selected location. In addition to the homogenous medium assumption, the synchronization requires that the relative positions of the VSA elements be known. Neither of these requirements turn out to be overly restrictive. Simple LOS focusing techniques are quite robust with respect to errors in the positions of the sources. As well, in the shallow ocean where sound speeds vary at most by a few percent, refraction plays a very minimal role over the short distances relevant to LOS focusing.[14]

More important are the resolution considerations of the VSA. In a direct sense, the virtual array is conceptually equivalent to a virtual lens that focuses the field from the

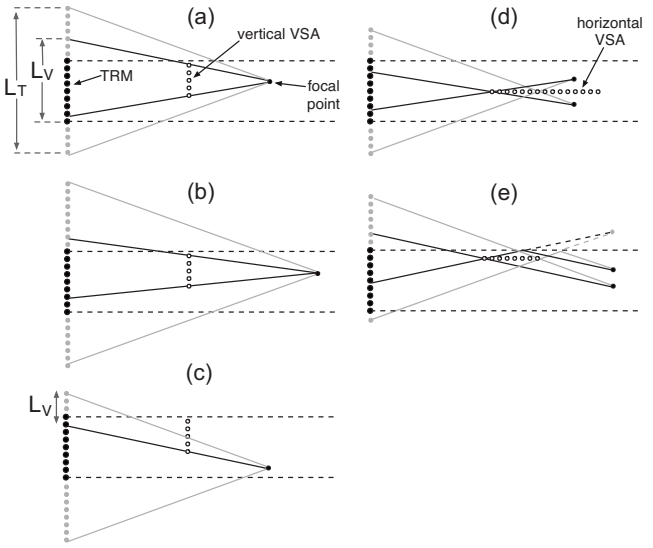

FIG. 4. Focusing and resolution of a linear geometry VSA in combination with a TRM in a waveguide. (a) At long distances, the waveguide geometry (denoted by dashed black lines) increases the effective aperture (solid gray circles), L_T, of the TRM (solid black circles). As a reminder, the critical angle determines the effective aperture of the TRM. The solid gray lines indicate the full TRM aperture available for focusing at the point indicated by the lone solid dark circle. To focus at the same location, the aperture of the VSA (open black circles), L_V, indicated by the solid black lines, is less than that of the TRM. (b) While the f-number, and hence the resolution, of the TRM remains constant with range, the f-number, and hence the resolution, of the VSA decreases with range between the VSA and the focal point. (c) The effective aperture of the VSA is limited to within the aperture of the TRM (in this case the critical angle of the waveguide), as in the example shown here for the case of off-axis focusing. To indicate this, one of the black lines denoting the VSA aperture has been omitted because it is coincident with one of the gray lines that indicate the TRM aperture. (d) Because the time-reversed field passes in both directions through a horizontal geometry VSA, a pair of foci exists. (e) The location of one or both of the foci generated by a horizontal geometry VSA may depend on boundary reflections. For panels (d) and (e) two of the black lines indicating the VSA aperture have been omitted because each is coincident with a gray line denoting the TRM aperture. Also for panels (d) and (e), only the portion of the effective aperture of the TRM relevant to the effective aperture of the VSA is shown. As a result, two of the gray lines indicating the full effective aperture of the TRM have been omitted.

TRM to a remote location. In accordance with the principles of geometric acoustics, the focal resolution of the VSA is dictated by its aperture. The only complication results from the attenuation of the waveguide. In the ocean waveguide, where field components traveling at greater than the critical angle are strongly attenuated, the effective aperture of the TRM, and by extension the angle subtended by the forward field cone (see Fig. 1), is limited to the critical angle. As a result, in cases where the virtual array is a great distance from the TRM (so that the TR field does not include any near-field components), the ability to perform LOS focusing is limited to within the critical angle cone. Thus, in the shallow ocean waveguide, it is not possible to focus at locations that fall outside the critical angle cone.

Figure 4 presents a schematic depiction of the relation between the resolution associated with the effective aperture of the TRM and the resolution expected from the virtual array alone, i.e., as if the virtual array were an isolated lens. Panels (a)–(c) of Fig. 4 demonstrate the effect of range and angle on the apertures of the TRM and the VSA. In a range-independent ocean waveguide, the effective aperture of the TRM is determined by the critical angle. Because the effective aperture of the TRM increases linearly with the range[16] to the focal spot (thus preserving the critical angle), the f-number, or the ratio of aperture to focal distance, is independent of range. Consequently, the focal resolution remains nearly constant as a function of range. On the other hand, because the VSA acts as a free-space lens, its f-number, and hence its focal resolution, decreases as the horizontal distance between the VSA and the selected focal spot increases. As a result, in combination with the TRM, the realizable resolution of the VSA is always less than or, at most, equal to the resolution associated with the effective aperture of the TRM. There is an added complication that must be considered in the case of a horizontal (or nearly so) geometry VSA. In this case it is useful to revisit the analogy between the VSA and a lens. For a vertical geometry VSA [panels (a)–(c)], the TR field transits the lens in only one direction (outbound with respect to TRM). In contrast, in the horizontal geometry case [panels (d) and (e)], even though the field is only outbound, it is still possible for field components to transit through both sides of the VSA. As a result, any LOS focusing operation applied to the VSA results in a pair of acoustic foci.

B. Simulated active focusing from a linear geometry VSA

A simulated demonstration of the method is presented in Fig. 5. Here the field from a TRM is focused by a vertically oriented VSA in order to ensonify a selected outbound location. The geometry of the VSA, the TRM, and the waveguide, as well as the region of the field visualized in the simulation is shown schematically in panel (a). The visualization in panel (b) shows a superposition of a series of snapshots of the TRM-to-VSA field. The beam-steering operation results in a curved front emanating from the location of the VSA that focuses at the selected location. Time $t=0$ has been set arbitrarily to coincide with the occurrence of the TR focusing event at location of the deepest VSA element. The first snap-shot shows the field just before it reaches the VSA location. The second snap-shot corresponds to the field just after it has passed the VSA. The third snap-shot shows the field between the VSA and the focal point. The fourth snap-shot shows the field just as it reaches the selected focal location. The final snap-shot shows the field as it continues past the focal spot.

The visualized field progression nicely demonstrates the analogy between the VSA concept and an actual physical array. Beyond the VSA location, the steered TRM-to-VSA field closely approximates the LOS focusing that would result from a physical source array at the VSA location. The main difference is that the TRM-to-VSA field lacks the near-field and field components that propagate at an angle greater than the critical angle. However, as these missing field components do not contribute to LOS focusing (to locations within the critical angle cone with respect to the VSA), the focal resolution of the steered TR-to-VSA focus field approaches the diffraction limit (with respect to the aperture of

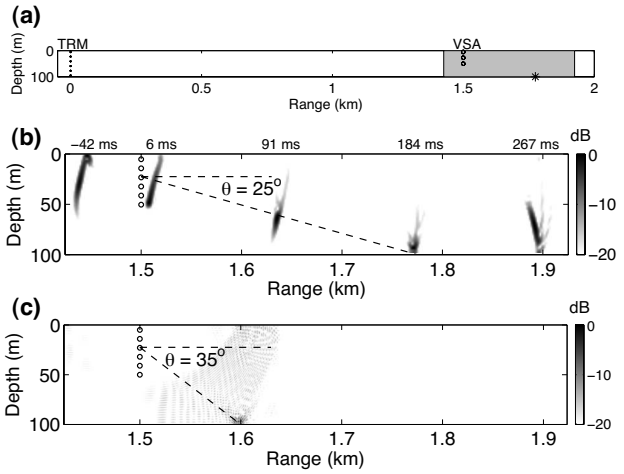

FIG. 5. Simulated coherent focusing from a linear geometry VSA in an ocean waveguide. Panel (a) shows the simulation set-up to scale. The TRM (dark circles) generated a VSA (open circles) from which to perform LOS focusing at the selected focal spot (indicated by *). The gray area indicates the region visualized in the simulation of panels (b) and (c). In (b), realizations of the TR field (dark features) at five different times have been superimposed with the corresponding times indicated above. Cylindrical spreading has been removed so that each snap-shot is shown in units of dB with respect to its own maximum. Open circles denote the location of the VSA. Time $t=0$ has been set to coincide with the TR focusing event at the deepest VSA element location. The location of the selected focal spot ($r=1775$ m, $z=95$ m) is at declination of $\theta=25°$ with respect to the VSA. The dashed line indicates the direct LOS from the VSA to the focal point. For comparison, panel (c) shows a single snap-shot (at the moment of maximal focusing) of the field for the case where the focal spot ($r=1600$ m, $z=95$ m) is oriented at a declination ($\theta=35°$) beyond the critical angle ($\theta_c=30°$). The simulation was carried out using a $\Delta f=500$ Hz bandwidth signal at carrier frequency $f_c=500$ Hz) in a Pekeris waveguide with water and sediment sound speeds of $c=1500$ m/s and $v_b=1732$ m/s, respectively. The TRM was vertical and full-spanning comprising 66 evenly spaced elements at intervals $dz=1.5$ m ($dz=\lambda/2$). The vertical VSA comprised 16 evenly spaced elements at intervals $dz=3$ m ($dz=\lambda$) spanning depths between 5 and 50 m.

the VSA). In the end, application of the VSA concept facilitated coherent focusing at the selected location without the need for a probe source element.

For the cases shown, the VSA aperture is similar to the effective aperture of the TRM. Thus the achieved resolution approaches the resolution that results from standard TR focusing using a probe source element at the selected focal point. Indeed, the results are similar enough that there is no need to present the simulated TR focusing benchmark that results from doing standard TR using a probe source at the selected location. However, a visualized benchmark comparison is presented in the experimental results. It is important to note that the selected focal location, which is oriented at an angle of $\theta=25°$ with respect to the VSA, falls within the critical angle cone ($\theta_c=30°$). As a demonstration of the limitation on LOS focusing from the VRA posed by the critical angle, panel (c) provides a visualization of a LOS beam-steer to a selected location outside the critical angle cone ($\theta=35°$). As shown, because the waveguide does not support propagation outside the critical angle cone, it is not possible to coherently focus to the selected location.

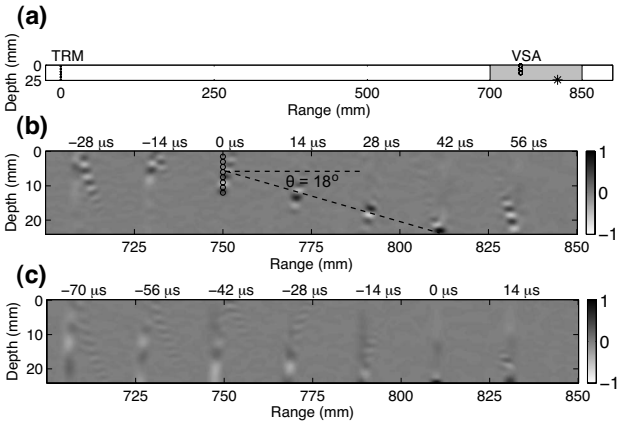

FIG. 6. Experimental coherent focusing from a linear geometry VSA in a laboratory waveguide. Panel (a) shows the experimental set-up to scale. The TRM (dark circles) generated a VSA (open circles) which was used to perform LOS focusing to a selected focal spot (indicated by *). The gray area indicates the region visualized in panels (b) and (c). Panel (b) visualizes the focus from the VSA, while, for comparison, panel (c) visualizes standard TR focusing to the same focal location. In the visualizations, measured realizations of the corresponding fields (light and dark features) at seven different times have been superimposed with the corresponding times indicated above. The visualizations are normalized in units of the absolute maximum of the aggregation of the superimposed fields. In panel (b), the open circles denote the location of the VSA. Time $t=0$ has been set to coincide with the TR focusing event at the deepest VSA element location. The location of the selected focal spot ($r=810$ mm, $z=24$ mm) is at declination of $\theta=18°$ with respect to the VSA. The dashed line indicates the direct LOS from the VSA to the focal point. In panel (c), time $t=0$ has been set to coincide with the TR focusing event at the focal location.

C. Experimental active focusing from a linear geometry VSA

Figure 6 shows the results of a VSA beam-steer focusing experiment in the ultrasonic regime. The geometry of the VSA, the TRM, and the waveguide, as well as the region of the field depicted in Fig. 6, are shown schematically in panel (a). The experiment was conducted in a laboratory waveguide comprising 25 mm of fresh water, ($c\approx1487$ m/s) over a flat steel bottom ($v_b\approx5000$ m/s). The waveguide, being very nearly range-independent and having a high boundary sound speed, is well modeled as an ideal waveguide, though knowledge of the environment is not required to implement the focusing.

To begin, the field between the TRM and the VSA at range $r=750$ mm was sampled using an ultra-broadband signal. The signal was a 1.5 MHz bandwidth Hanning modulated pulse centered on frequency $f_c=1.5$ MHz corresponding to a characteristic wavelength of $\lambda_c\approx1$ mm. The TRM comprised 51 piezo-electric acoustic transducer elements equally spaced at $dz=0.5$ mm ($dz\approx\lambda_c/2$) intervals. The VSA spanned the top half of the water column, comprising 25 elements spaced at intervals $dz=0.5$ mm. A piezo-electric hydrophone was placed at each of the VSA element locations to sample the TRM-to-VSA fields. The sampled fields were then synchronized in order to ensonify the point ($r=810$ mm, $z=24$ mm), summed together, time-reversed, and broadcast from the TRM. In order to measure the resulting ensonification, the TR field was finely sampled in both range and depth in the vicinity of the VSA and expected focal spot.

Panel (b) of Fig. 6 shows snap-shots of the sampled TR

field over all depths between ranges 700 mm $< r <$ 850 mm. While the sampling interval was $dz = 0.5$ mm $= \lambda_c/2$ in the z-direction, in range it was $dr = 1$ mm $= \lambda_c$. As a result, the field is spatially aliased in the r-direction so that the visualized field appears to be of a longer wavelength than it actually was. As with the simulated result above, the time $t = 0$ was arbitrarily chosen to coincide with occurrence of the TR focusing event at location of the deepest VSA element.

While the waveguide is nearly ideal, implying a large effective aperture (infinite in the ideal waveguide corresponding to a critical angle of 90°), in practice, the effective aperture is limited by the directionality of the individual TRM transducer elements. The working critical angle is approximately $\theta_c \approx 30°$. Consequently, as demonstrated in panel (b), the waveguide clearly supports the field that focuses at the selected focal spot which is oriented at an angle of $\theta = 18°$ with respect to the VSA. In order to benchmark the focal resolution of the VSA result, it is useful to compare the result to standard TR focusing, i.e., TR focusing achieved using a probe source element at the selected focal location, ($r = 810$ mm, $z = 24$ mm). Panel (c) shows a series of snapshots of the standard TR focusing field (time $t = 0$ coincides with the TR focusing event). In light of the discussion of Sec. III, one expects the resolution of the VSA focus to be less than the standard TR result. In this case the effective VSA aperture is about one-third the effective aperture of the waveguide. Comparing panels (b) and (c), it is clear that the resolution of the VSA focusing compares favorably with the resolution of the standard TR result. Thus, it was experimentally possible to use synchronized TRM-to-VSA fields to coherently focus at the selected location for which the transfer function was not known. Similar VSA focusing results were obtained for all locations attempted within the critical angle cone.

IV. POSSIBLE APPLICATIONS FOR THE VSA METHOD

One issue that arises concerning the practical utility of VSA implementations is the question of how the TRM-to-VSA transfer functions are obtained. This is a valid concern and, particularly in ocean applications, potentially the main limitation to VSA implementations. For example, consider the case where the transfer functions are sampled using a second receive array in conjunction with the TRM. An immediate question that arises is why would this VSA technique be useful if there are already physical array elements at the VSA location which could be used directly for active focusing. In this scenario, the main advantage of the VSA method is that it allows for the second receive array to be acoustically passive. It samples the field from the TRM, then transmits the received field to the TRM (perhaps, via electromagnetic transmissions originating from an antenna above the surface). Consequently, all transmissions, both the transfer function measurements and the VSA imaging fields, originate on the TRM. This is advantageous because a passive array tends to be less expensive, more easily deployable, and more maneuverable than a dedicated active TRM. As discussed, taking only a single measurement of transfer functions, the TRM can be projected to the location of the VSA and image the medium beyond. Once the measurement is taken the passive array may be transferred to a new location while the TRM images the selected region. In addition to towed and drifting passive line arrays, other possibilities include the deployment of GPS enabled sonobuoys or the generation of a synthetic aperture using an underwater autonomous vehicle (UAV).

As an example, consider a mine detection scenario in an azimuthally symmetric (with respect to the TRM) ocean environment where the goal is to ensonify a target in an unknown environment. The passive array is deployed in the vicinity of the target and the TRM-to-VSA transfer functions measured and transmitted (electromagnetically above the ocean surface) back to the TRM which then ensonifies the target location. In addition to the flexibility provided by the maneuverability of the passive array, the method provides an added layer of safety in that the TRM itself can be maintained at a large stand-off distance. Keeping in mind that the method performs well for arbitrary VSA geometries, a silent, navigated UAV could be used to generate a synthetic aperture VSA of any geometry by sampling the TRM-to-VSA fields as it moves over the area of the target. Because the UAV is highly maneuverable, it can periodically retrace its path to refresh the transfer functions (useful in highly dynamic environmental conditions) or visit new locations. Additionally, an UAV provides the capability to construct a synthetic curtain array that would be required for applying the technique in a azimuthally asymmetric environment.

While the preceding discussion concentrates on active focusing, the virtual array concept can be applied passively as well. With the transfer functions in hand, the same beamforming techniques can be passively applied to signals measured on the TRM to localize an active target beyond the VSA. In the case that a dedicated passive array (or a collection of sonobuoys) is used there is no advantage to performing the localization on the TRM data, as, presumably the localization can be applied directly on the passive array (or sonobuoys). In the silent UAV scenario, however, passive localization on the TRM becomes quite advantageous. Though the location of the TRM will may be compromised because it must initially broadcast once to obtain the transfer functions, the UAV can maintain a high measure of stealth.

As another possible application unrelated to ocean acoustics, consider the case of medical ultrasonics where the goal is to image a location for which the transfer function cannot be measured, perhaps because it is in a difficult location for a probe source to access. Assuming it is possible to determine the transfer functions to other nearby locations, then it might be possible to improve imaging of the location in question. Consider a case where the target is located in delicate internal tissue shielded by the rib cage. In fact, methods for steering a field through rib structures has been proposed.[17] As well, the relative positions of the rib structures are easily determined through diagnostics such as x-ray and magnetic resonance imaging. Such methods could possibly be adapted to determine the transfer function between the ultrasonic source array and the rib structures. By constructing a VSA from the rib structures, the TRM can be projected past the ribs, making it possible to ensonify the soft

tissue target. Once past the rib cage, the sound speed of the internal tissues may be uniform enough that it is possible to apply a simple time-delay synchronization method for steering ultrasound to the selected location. In fact, there have been several methods proposed for determining the transfer functions to scattering features in the human body.[18,19] While such scattering features are often viewed as an impediment to imaging, in the context of the VSA method, they may actually enhance imaging by serving as virtual sources from which to perform imaging to other locations.

V. SUMMARY

It has been demonstrated that a TR focusing event can itself be used as a virtual acoustic source. By extension, given a collection of transfer functions between a TRM and probe sources at different locations, it is possible to construct a virtual element array. It has been argued that such a virtual array can serve as a platform for imaging the adjacent medium in the TRM-VSA direction. The virtual array concept has been demonstrated through simulation and validated experimentally in a laboratory waveguide where a linear geometry VSA was deployed to direct the field from a TRM to coherently focus on a distant selected location with high focal resolution. In this application, in analogy with geometric optics the virtual array acts as a lens to direct the TRM field to the selected location. Because it is based on TR, the method is self-adaptive so that it may be applied generally in static media: free-space, multiple-scattering, waveguides, etc. Possible applications to ocean acoustics and medical ultrasonics have been presented.

ACKNOWLEDGMENTS

This work was sponsored by the Office of Naval Research.

[1]W. Kuperman, W. Hodgkiss, H. Song, T. Akal, C. Ferla, and D. R. Jackson, "Phase conjugation in the ocean: Experimental demonstration of an acoustic time-reversal mirror," J. Acoust. Soc. Am. **103**, 25–40 (1998).
[2]D. Jackson and D. Dowling, "Phase conjugation in underwater acoustics," J. Acoust. Soc. Am. **89**, 171–181 (1991).
[3]A. Baggeroer, W. Kuperman, and P. Mikhalevsky, "An overview of matched field methods in ocean acoustics," Ocean Eng. **18**, 401–424 (1993).
[4]M. Fink, "Time-reversal mirrors," J. Phys. D: Appl. Phys. **26**, 1333–1350 (1993).
[5]M. Fink, C. Prada, F. Wu, and D. Cassereau, "Self focusing in inhomogeneous media with time reversal acousticmirrors," in Ultrasonics Symposium (1989), pp. 681–686.
[6]M. Siderius, D. Jackson, D. Rouseff, and R. Porter, "Multipath compensation in shallow water environments using a virtual receiver," J. Acoust. Soc. Am. **102**, 3439–3449 (1997).
[7]D. Turnbull and F. Foster, "Beam steering with pulsed two-dimensional transducer arrays," Ultrasonics **38**, 320–333 (1991).
[8]M. Alam, J. McClellan, and W. Scott, "Spectrum analysis of seismic surface waves and its applications in seismic landmine detection," J. Acoust. Soc. Am. **121**, 1499–1509 (2007).
[9]A. Asif, Q. Bai, and J. Moura, "Time reversal matched field processing: An analytical justification," in 2006 IEEE International Symposium on Signal Processing and Information Technology (2006), pp. 81—86.
[10]L. Borcea, G. Papanicolaou, C. Tsogka, and J. Berryman, "Imaging and time reversal in random media," Inverse Probl. **18**, 1247–1279 (2002).
[11]M. Fink, D. Cassereau, A. Derode, C. Prada, P. Roux, M. Tanter, J. Thomas, and F. Wu, "Time-reversed acoustics," Rep. Prog. Phys. **63**, 1933–1996 (2000).
[12]E. Williams and J. Maynard, "Holographic imaging without the wavelength resolution limit," Phys. Rev. Lett. **45**, 554–557 (1980).
[13]S. Conti, P. Roux, and W. Kuperman, "Near-field time-reversal amplification," J. Acoust. Soc. Am. **121**, 3602–3606 (2007).
[14]A. Thode, W. Kuperman, G. D'Spain, and W. Hodgkiss, "Localization using Bartlett matched-field processor sidelobes," J. Acoust. Soc. Am. **107**, 278–286 (2000).
[15]T. Folégot, C. Prada, and M. Fink, "Resolution enhancement and separation of reverberation from target echo with the time reversal operator decomposition," J. Acoust. Soc. Am. **113**, 3155–3160 (2003).
[16]S. Kim, G. Edelmann, W. Kuperman, and W. Hodgkiss, "Spatial resolution of time-reversal arrays in shallow water," J. Acoust. Soc. Am. **110**, 820–829 (2001).
[17]H. Yao and E. Ebbini, "Refocusing dual-mode ultrasound arrays in the presence of strongly scattering obstacles," in Ultrasonics Symposium (2004), pp. 239–242.
[18]G. Montaldo, M. Tanter, and M. Fink, "Real time inverse filter focusing through iterative time reversal," J. Acoust. Soc. Am. **115**, 786–773 (2004).
[19]J. Robert and M. Fink, "Green's function estimation in speckle using the decomposition of the time reversal operator: Application to aberration correction in medical imaging," J. Acoust. Soc. Am. **123**, 866–877 (2008).

Non-linear, adaptive array processing for acoustic interference suppression

Elizabeth Hoppe[a] and Michael Roan
Department of Mechanical Engineering, Virginia Polytechnic Institute and State University, 131 Durham Hall, Blacksburg, Virginia 24060

(Received 9 December 2008; revised 9 April 2009; accepted 9 April 2009)

A method is introduced where blind source separation of acoustical sources is combined with spatial processing to remove non-Gaussian, broadband interferers from space-time displays such as bearing track recorder displays. This differs from most standard techniques such as generalized sidelobe cancellers in that the separation of signals is not done spatially. The algorithm performance is compared to adaptive beamforming techniques such as minimum variance distortionless response beamforming. Simulations and experiments using two acoustic sources were used to verify the performance of the algorithm. Simulations were also used to determine the effectiveness of the algorithm under various signal to interference, signal to noise, and array geometry conditions. A voice activity detection algorithm was used to benchmark the performance of the source isolation. © *2009 Acoustical Society of America.* [DOI: 10.1121/1.3126925]

PACS number(s): 43.60.Jn, 43.60.Fg [EJS] Pages: 3835–3843

I. INTRODUCTION

Sound source localization is an important and widely studied problem in acoustics.[1–4] One of the most fundamental and widely used spatial processing tools is phased array beamforming. Algorithms for beamforming range from simple, narrow-band, delay and sum beamformers,[5] which are completely data independent and nonadaptive, to more complex adaptive algorithms, such as minimum variance distortionless response (MVDR) beamforming.[6,7] One of the main challenges in any beamforming technique is to suppress sidelobe contributions to the beamformer output. MVDR, for example, attempts to accomplish this by minimizing the variance of the beamformer output under a distortionless constraint. In cases where the bearing angle to an interferer is known, a fixed null beamformer[8,9] can be used to suppress contributions to the beamformer output from that specific direction. In most applications however, the locations of interfering sources are not known a priori. In 1969, Capon introduced a beamforming technique that adaptively suppresses non-look direction interferers based on the covariance of the received array data.[6] Although a large set of algorithms exists to mitigate the effects of interferers, they mostly focus on adaptively placing nulls in the directions of interferers or minimizing sidelobe height.[10]

Another large body of work exists in the area of time or frequency domain blind source separation (BSS).[11,12] These techniques do not typically exploit spatial information about the signals. Where spatial information has been used is in attempt to solve the BSS permutation ambiguity problem.[13–16] In this paper, we bring together methods from BSS and phased array processing to create a unique approach to interference suppression. This method suppresses contributions to the spatial processor output from non-Gaussian interferers using a combination of beamforming and independent component analysis (ICA) techniques. The new method is less sensitive to errors in the array manifold vector than the MVDR method. In addition, the new method does not depend on estimates of the signal covariance, which is often problematic in application of the MVDR beamformer. However, an estimation of the probability density function (pdf) of the signal amplitude distribution is required.

The high-level operation of the new algorithm is as follows: Beamforming is used to correct for time delays caused by the propagation of wavefronts arising from the spatial distribution of sources. The FastICA algorithm is applied to these delay-corrected signals. Spatial knowledge is also used to resolve the permutation ambiguity problem inherent in the ICA algorithm. Individual signals that are retrieved from the ICA algorithm are then filtered from the mixed signals in all channels and the remaining signals are processed spatially for display.

II. BACKGROUND

A. MVDR beamforming

The MVDR beamforming strategy is to minimize the variance of noise in the look direction (sometimes called the signal protection constraint[17]), so that the response of the array is constant in the signal look direction regardless of the choice of weights (i.e., 1). One limitation of addition of this constraint is that the beamformer is limited to nulling m-2 interferers, where m is the number of sensors. The weights are adaptively calculated, based on the signal covariance matrix, to coherently sum the signal of interest, while simultaneously minimizing the noise variance of the output. The derivation begins with a set of spatially compact acoustic sources in a free field with amplitudes $\mathbf{s}(t)=[s_1(t), s_2(t),\ldots,s_n(t)]^T$. The sources are assumed to be narrow band and Gaussian distributed. The signals $x(t)$ at the output of the array at time t are

[a]Author to whom correspondence should be addressed. Electronic mail: ehoppe@vt.edu

$$\mathbf{x}(t) = \mathbf{a}(\theta)\mathbf{s}(t) + \mathbf{n}(t), \tag{1}$$

where $\mathbf{x}(t)$ is the output of the array, $\mathbf{a}(\theta)$ is the array manifold vector, $\mathbf{s}(t)$ is the source signal vector that lies in direction θ_s, and $\mathbf{n}(t)$ is a vector of noise that represents the undesired signals including background noise and interferers. The combined beamformer output of the MVDR process is given by[6]

$$\mathbf{y}(t) = \mathbf{W}^*\mathbf{x}(t) = \mathbf{W}^*\mathbf{a}(\theta)\mathbf{s}(t) + \mathbf{W}^*\mathbf{n}(t), \tag{2}$$

with $\mathbf{W}$ as a vector of array weights. The goal is to choose $\mathbf{W}$ to extract $\mathbf{s}(t)$ by minimization of the effects of $\mathbf{n}(t)$ in Eq. (2). The variance of the noise is quantified by the noise covariance matrix, $\mathbf{R}_n = E\{\mathbf{nn}^*\}$, and the variance of the beamformer output when the beamformer is steered to θ_s is given by

$$\sigma_n^2 = E\{\mathbf{W}^*\mathbf{nn}^*\mathbf{W}\} = \mathbf{W}^*\mathbf{R}_n\mathbf{W}. \tag{3}$$

The distortionless constraint is expressed as the requirement that $\mathbf{W}^*\mathbf{a}(\theta) = 1$. Therefore, $\mathbf{W}$ is given as the optimal solution to the LaGrange problem

$$\min \mathbf{W}^*\mathbf{R}_n\mathbf{W} \text{ subject to } \mathbf{W}^*\mathbf{a}(\theta) = 1. \tag{4}$$

In the MVDR method, the noise is typically unknown, and the matrix $\mathbf{R}_n$ is replaced by the sample covariance matrix $\mathbf{R}_y$. Replacing $\mathbf{R}_n$ with $\mathbf{R}_y$ in Eq. (4) and solving produces the analytical MVDR solution[6]

$$\mathbf{W} = \frac{\mathbf{R}_y^{-1}\mathbf{a}(\theta)}{\mathbf{a}^*(\theta)\mathbf{R}_y^{-1}\mathbf{a}(\theta)}. \tag{5}$$

The MVDR equation (5) shows that the weights depend on the covariance matrix and the presumed array manifold vector. As a consequence, the beamformer is sensitive to inaccuracies in the manifold vector. This is often a problem for towed array sonar where the shape of the array is often unknown due to the motion of the submarine causing bending of the array.[18] In some instances, the performance of the MVDR beamformer can degrade below the performance of the standard non-adaptive techniques. The advantage of the MVDR beamformer is that the locations of the interferers do not need to be known a priori, the beamformer suppresses contributions from all sources not lying along the steering direction θ_s up to m-2 degrees of freedom.

MVDR and other nulling beamforming techniques perform interference suppression through minimizing the response of the array in non-look direction through the placing of nulls in those directions. Another widely used technique to extract signals from a mixture using multiple measurements is BSS. These techniques typically use information theoretic measures such as entropy maximization as criteria for source extraction. A brief review of the more widely used techniques is given in Sec. I B in order to provide a basic review and introduce notation.

B. BSS

BSS is an algorithm based on ICA that attempts to extract statistically independent sources from a set of mixed signals using multiple independent measurements. Bell and Sejnowski[19] developed a method for BSS based on minimizing the mutual information between sensor outputs using arguments based on entropy. The information content of the signal is represented by the entropy of the sensor outputs, given by

$$H(y) = -E\{\ln p_y(y)\}, \tag{6}$$

where $p_y(y)$ is the pdf of the sensor output y, and $E\{.\}$ denotes expectation. Under the assumption of statistically independent sources, maximizing the joint entropy minimizes the mutual information between the channels. To maximize entropy in a constrained fashion (i.e., not just simply endlessly increasing the variance), a nonlinear "squashing function," $g(x)$, is used to bound the pdf of the output signal. If $g(x)$ is a monotonically increasing function, the pdf of the array output can be written as a function of the pdf of the source signals x, according to

$$p_y(y) = \frac{p_x(x)}{|J|}, \tag{7}$$

where $|J|$ is the absolute value of the Jacobian of $g(x)$. Substituting Eq. (7) into Eq. (6) gives the final entropy function to be

$$H(y) = E\{\ln|J|\} - E\{\ln p_x(x)\}. \tag{8}$$

To minimize the mutual information, only the first term in Eq. (8) needs to be minimized. An online stochastic gradient descent learning rule for the Infomax method is used to determine the optimal weight set, W, to separate the sources. Other more robust methods using the natural gradient have also been developed.[20] The learning rule for Infomax is

$$\Delta W \propto \frac{\partial H(y)}{\partial W} = [W^T]^{-1} - 2yx^T. \tag{9}$$

Hyvärinen[21] moved the mutual information minimization approach from the time domain to the frequency domain which resulted in a faster BSS algorithm called FastICA. The FastICA algorithm is based on the differential entropy, or negentropy, which is defined as

$$J(y) = H(y_{\text{Gauss}}) - H(y) \tag{10}$$

where J is the negentropy, $H(.)$ is the entropy, and y_{Gauss} is a Gaussian random vector of the same covariance matrix as y. This provides a measure of non-Gaussianity that is always non-negative and only zero for a signal of Gaussian distribution. The FastICA algorithm seeks to find a direction, w, such that the projection, w^Tx, maximizes the negentropy. An approximation of the negentropy of Eq. (10) is

$$J(w^Tx) \propto [E\{g(w^Tx)\} - E\{g(\nu)\}]^2, \tag{11}$$

where g is any non-quadratic function and ν is a Gaussian variable of zero mean and unit variance. The FastICA algorithm chooses w as the solution to the optimization problem

$$\max[E\{g(w^Tx)\} - E\{g(\nu)\}]^2 \text{ subject to } E\{(w^Tx)^2\} = \|w\|^2 = 1. \tag{12}$$

Similar to the Infomax method, only the first term in Eq. (12) is dependent on updated values of w. Using Newton's methods and algebraic simplification, the stabilized fixed point algorithm can be solved as

$$w^+ = E\{xg(w^T x)\} - E\{g'(w^T x)\}w. \tag{13}$$

An initial value of the weight vector, w, is chosen and w^+ is calculated. This updated value of the weight vector is normalized to unit length and compared to the previous weight vector. If the two vectors have a dot product of zero, they define the same direction and the algorithm has converged. A typical choice of nonlinear function is the hyperbolic tangent, which is ideal for separating super-Gaussian sources, such as voice signals.

One of the main limitations of these BSS techniques is that the mixing is assumed to be linear, a condition that does not exist in a convolutive mixing problem. When processing signals that are measured using multiple sensors, the geometry of the sources and sensors causes relative delays in the measured signals. The net result is that the mixing is convolutive mixing in most situations of interest. Therefore, some preprocessing must be performed on the array data to remove the convolutive mixing before it can be used in the FastICA algorithm.

C. Voice activity detection

An important application where both BSS and spatial processing can have a large impact is in voice activity detection[22,23] (VAD) in the presence of interference. VAD algorithms are key tools for communications systems where conserving power is important (i.e., mobile telephones) and where transmitting noise (as in military communications) is to be avoided. The VAD algorithm used in this paper to quantify the signal enhancement capabilities of the proposed algorithm uses the higher order statistics of the signal to distinguish between active voice frames and noise frames.[24] Every 10 ms, the second-, third-, and fourth-order moments are calculated as

$$M_{k,x} = \frac{1}{N}\sum_{n=0}^{N-1}[x(n)]^k, \tag{14}$$

where $x(n)$ is the signal, k is the moment order, and N is the number of samples in $x(n)$. Using these moments, the unbiased normalized skewness (SK) and the unbiased kurtosis (KU) are calculated using

$$\mathrm{SK} = \frac{M_{3,x}}{\sqrt{\frac{15v_g^3}{N}}}, \quad \mathrm{KU} = \left(1+\frac{2}{N}\right)M_{4,x} - 3(M_{2,x})^2, \tag{15}$$

where ν_g is the noise energy. The measure for SK and KU are normalized by the signal energy to give

$$\gamma_3 = \frac{\mathrm{SK}}{M_{2,x}^{1.5}}, \quad \gamma_4 = \frac{\mathrm{KU}}{M_{2,x}^2}. \tag{16}$$

The noise power is estimated from any frame declared as non-speech. For initialization, the first three frames are automatically declared as non-speech and used to initialize the noise energy. Whenever a frame is declared as non-speech, its energy is used to update the estimate for the noise energy according to an autoregressive averaging

$$v_g(k) = (1-\beta)v_g(k-1) + \beta M_{2,x}, \tag{17}$$

where k is the iteration index, and β is 0.1 Prob[Noise] (the probability of a frame being noise). Prob[Noise] is based on the value of KU_b, which is the unit-variance version of the KU defined as

$$\mathrm{KU}_b = \frac{\mathrm{KU}}{\sqrt{\frac{3v_g^4}{N}\left(104+\frac{452}{N}+\frac{596}{N^2}\right)}}, \tag{18}$$

where N is the number of samples in the frame. Using this value and the value of SK from Eq. (15), the probability of the frame being noise is

$$\mathrm{Prob[Noise]} = \frac{\mathrm{erfc(SK)} + \mathrm{erfc}(\mathrm{KU}_b)}{2}. \tag{19}$$

The final parameter calculated is the signal to noise ratio (SNR). The SNR of the frame is

$$\mathrm{SNR} = \mathrm{Pos}\left[\frac{M_{2,x}}{v_g} - 1\right], \tag{20}$$

where $\mathrm{Pos}[x]=x$ for $x>0$ and 0 otherwise. The values of γ_3, γ_4, Prob[Noise], and SNR are used with thresholds to determine the state of the current frame. If the Prob[Noise] is below its threshold value, and the SNR is greater than its threshold value, the frame is declared as speech state. A noise state is indicated by a Prob[Noise] greater than its threshold, and values for γ_3 and γ_4 above their respective thresholds. For extensive details on the VAD algorithm, see Ref. 24.

In Section IV G the relative performances of the proposed algorithm, the MVDR beamformer, and unmodified FastICA are compared and provide a quantitative performance enhancement provided by the proposed algorithm. The structure of the proposed algorithm is the subject of Sec. III.

III. PROPOSED ALGORITHM

This section describes the proposed algorithm that uniquely combines spatial and BSS processing streams. The FastICA algorithm assumes instantaneous mixing; however, when multiple sources are spatially distributed, this condition does not exist. The spatial processing portion of the new algorithm aligns the signals in time. This allows application of FastICA (or other ICA techniques for linear/simultaneous mixing) because the mixing is no longer convolutive. As Secs. III A–III C will show, the new algorithm's performance is only limited by the SNR and signal to interferer ratio (SIR).

A. Strategy and motivation

A block diagram of the proposed new algorithm is provided in Fig. 1. Assuming that there are m sensors and n sources, the goal is to remove j sources from each array channel. In this way, signals such as loud interferers can be

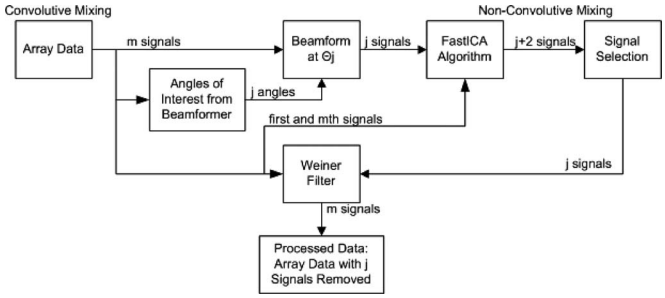

FIG. 1. Processing strategy for the combination of beamforming and ICA processing to suppress interferers.

removed, leaving behind the $(n-j)$ signals of interest. The inputs to the algorithm are the measured microphone array signals, and the output is the set of signals of interest. The m array signals are beamformed, which is used to estimate the direction of arrival (DOA) of the k signals. These angles are used to steer the array and extract signals from the k directions of interest. These signals, along with two unaltered array sensor signals, are passed to the FastICA algorithm, which separates the signals as explained in Sec. II B. A Weiner filter is used to cancel the interfering signals from the mixture of signals in each channel (least mean squares approaches can also be used).

One advantage of using this new method is that interferer rejection is not spatially based or null beamforming as in MVDR. As an interferer moves closer to the signal of interest, beamformers cannot distinguish the signal of interest from the interferer because they are spatially indistinct. This is especially true for compact arrays (i.e. low m), where the main beam lobe is very wide. In the new method, the higher order statistics of the signal are used for separation in addition to the spatial location and interfering signals can still be suppressed in spatially indistinct mixtures. While the algorithm's performance is degraded in this region, interferer suppression is still possible.

B. Correcting for delays

For simplicity of derivation, a linear array with m microphone elements is used. The n sound sources are all assumed to be in front of the array, with the source DOAs ranging from −90° to +90°. Figure 2 provides the scenario geometry and a definition of the delays appearing in Eqs. (21) and (22). Each array sensor sees a mixture of delayed versions of each of the n sources according to the model

$$x_i(t) = \sum_{k=1}^{n} A_{ki} s_k(t - \tau_{ki}) + n_i(t), \quad \tau_{ki} \equiv \frac{d_k}{c},$$

$$\text{for } i = 1,2, \ldots, m, \tag{21}$$

where x_i is the response of the ith sensor of the array, A_{ki} is the linear mixing component, s_k is the kth source, τ_{ki} is the delay from the kth source to the ith sensor based on the distance between the two, and n_i is the noise associated with the ith sensor. The time delays caused by the sensor and source geometry must be removed before FastICA can be applied. Electronic steering of the array is used to compensate for the delays. Once corrected using beamforming, the

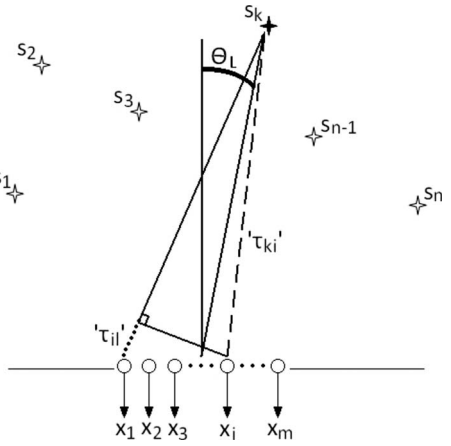

FIG. 2. The geometry of the sensors and sources assumed for algorithm development is shown. The array is a linear microphone array and all sources are in front of the array. The time delays introduced in Eqs. (21) and (22) are due to the corresponding distances indicated with the dashed and dotted line segments.

signals are linearly mixed and therefore can be processed by the FastICA portion of the algorithm.

In this paper, the steering is accomplished using a traditional narrow-band delay and sum beamformer. Other more sophisticated techniques could be used in this step; however, the narrow-band delay and sum beamformer is used for convenience due to its ease of implementation and processing speed. The weights for this beamformer are data independent and can be calculated in advance. The relative delays between sensors for each signal are given by

$$b_l(t) = \sum_{i=1}^{m} x_i(t - \tau_{il}) = \sum_{i=1}^{m} \sum_{k=1}^{n} A_{ki} s_k(t - \tau_{ki} - \tau_{il}) + n_i(t - \tau_{il})$$

$$\text{for } l = 1,2, \ldots, n$$

$$\tau_{il} = \frac{d_e}{c}(i-1)\sin\theta_k, \tag{22}$$

where b_l is the lth beamformed signal, τ_{il} is the delay from the delay-and-sum beamformer, and θ_k is the DOA of the kth source. The beamformed outputs, combined with the unaltered first and mth array signals, form the set of mixed signals for the ICA algorithm. The first and mth array signals are included to introduce additional unaltered information (beamforming distorts signals away from the steering angle) about the mixed signals into the FastICA algorithm to aid in the separation process. Although not a requirement of FastICA, inclusion of these undistorted mixed signals improves the separation result.

C. ICA and signal selection

The mixed signal set generated by the beamforming process contains $(j+2)$ signals. The FastICA algorithm will also produce $(j+2)$ outputs, j of which will contain unmixed signals. The other two are a residual mixture of all the signals and Gaussian noise. The FastICA algorithm has a permutation ambiguity in the outputs, so additional postprocessing is necessary to identify the separated sources. The unmixed sig-

nals must be classified as either the signal of interest, interferers, or residual mixtures. This task is accomplished using the coherence between the beamformed signals and the FastICA outputs. The interferer signals are chosen as the FastICA output channel with the highest coherence with the beamformer output at the DOA of the interferers. The interferer signals are used as the "noise" sample input into a Weiner filter, which cancels these from each channel in the array. Using this approach, a technique can be implemented where, starting with the loudest, interferers can be canceled from displays such as bearing time recorder (BTR) displays leaving behind successively more quiet sources. Examples of this technique are provided via both simulation and experiment in Sec. IV.

IV. SIMULATIONS

A. Simulation parameters

For the simulations presented in Secs. IV B–IV F, the data contains two voice signals; one signal of interest and one interferer signal. The sources used are digitally recorded files of voices, which are artificially placed at various locations in the environment with respect to the array. The data in the simulation in Sec. IV G contains one voice signal and one broadband interferer signal. In order to simulate the DOA, the source signals are up-sampled to five times their sampling frequencies and then shifted by the appropriate number of samples corresponding to the DOA delay. This method is not frequency dependent and creates minimal distortion in the signal.

All of the simulations assume an anechoic environment, where the speed of sound is 343 m/s. A linear array is used in all cases, where the element spacing is constant. The number of elements and the elemental spacing varies depending on the simulation. For each case, the sampling frequency is 11025 Hz, which is a standard sampling frequency used in wav audio files. The frequency of interest used for simulations is 3250 Hz, which was chosen based on the frequency content of the simulated signals. Unless stated otherwise, the two signals are at equal power, equidistance from the array, and there is no additional non-correlated background noise.

B. Effect of the algorithm on unmixing

To quantify the performance of the new algorithm, a comparison was done to compare unmixing performance under the conditions of linear mixing, convolutive mixing, and corrected convolutive mixing. The signal of interest is located at +5°, while the interferer is located at −10°. A 35 channel array is used with an element spacing of 0.035 m. For the convolutive mixing case, the first and *m*th array signal are passed directly to the FastICA algorithm. The corrected convolutive mixing case uses the beamforming technique to correct the time delays (as described above). Figure 3 shows the coherence between the original and unmixed signal for the three cases. While the linear mixing case has a coherence of nearly 1 for all frequencies, the other two cases show degradation of the signal after separation. However, the new algorithm shows much better performance for most of the frequencies considered.

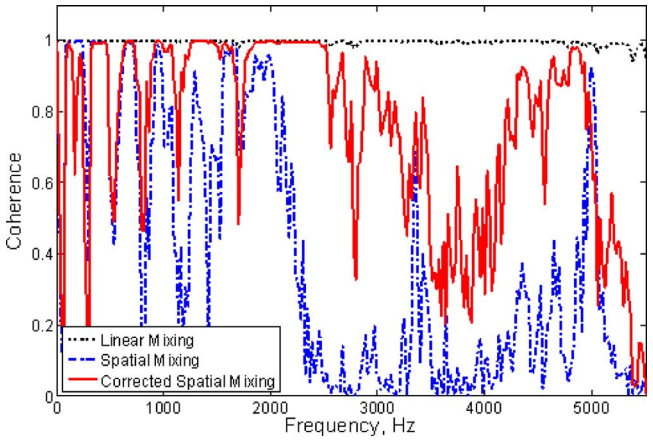

FIG. 3. (Color online) Coherence between the original signal and the unmixed signal for three cases: linear mixing with FastICA separation, convolutive mixing with FastICA separation, and convolutive mixing with time delay correction via beamforming and FastICA separation.

C. Two voices with equal signal strength

A simulation with two voice signals (one stationary, one moving) was done in order to examine the algorithm's performance with respect to a variety of spatial situations. The interferer remains stationary at +5°, while the signal of interest is moved from −20° to +20° at a rate of 1°/s. All sources are assumed to be in the far-field and have equal power. The data are simulated for a 35 channel linear array with an inter-microphone spacing of 0.035 m. Figure 4 shows the time-angle plot using a standard narrowband delay-and-sum beamformer. Each horizontal slice in Fig. 4 is the magnitude of the beamformer output calculated using one second of data. The two sources are clearly seen. The interferer appears as the vertical signature appearing at +5°. The signal of interest is the signature that crosses diagonally from −20° to +20°.

MVDR beamforming is used in this paper to provide a comparison or the new algorithm with spatial null forming techniques. The result of MVDR processing can be seen in

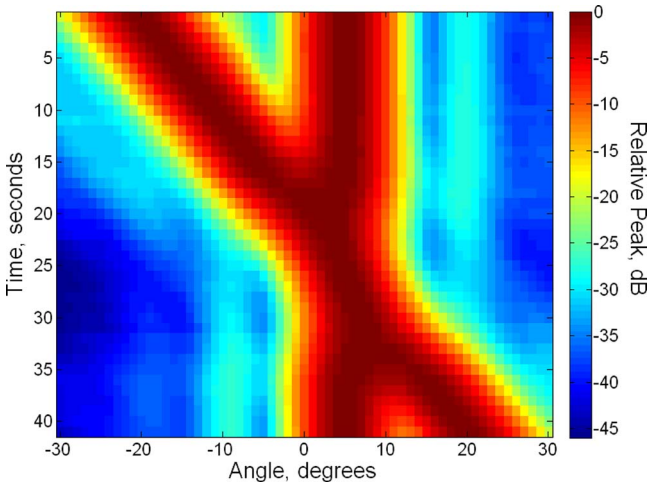

FIG. 4. (Color online) Bearing track recorder plot using a narrow-band delay and sum beamformer for two signals having equal power. One signal is located at +5°, while the other signal moves from −20° to +20° at a rate of 1°/s.

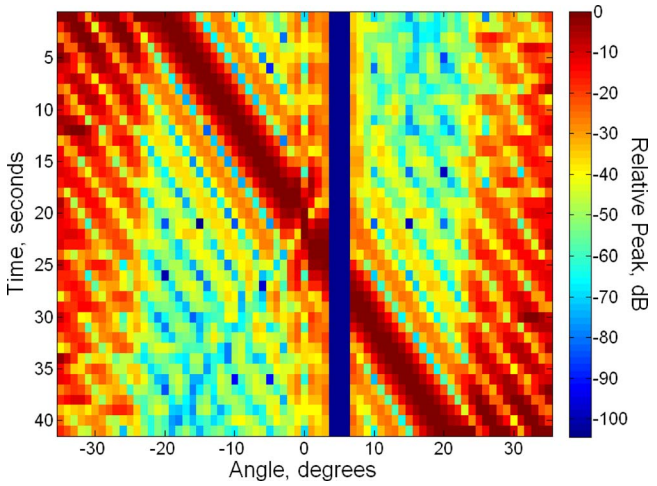

FIG. 5. (Color online) Bearing track recorder plot using MVDR beamforming. The undesired, stationary source at +5° has been nulled in all time steps, but numerous sidelobes in the beampattern obscure the bearing track recorder display.

the time-angle plot of Fig. 5. Over the entire duration of the simulation, the MVDR beamformer has placed a null in the direction of the interferer at +5°. While the MVDR algorithm has good performance with regard to the interferer suppression at +5°, as the signal of interest passes near the interferer, both signals are suppressed by the null at +5°. This is one of the shortcomings of null based interference suppression, such as MVDR. The beampattern has numerous sidelobes that distort the bearing track of the signal of interest. Figure 6 shows the results of applying the new algorithm to the simulated data. The interferer at +5° is suppressed in all time steps, while the signal of interest is clearly visible in all the time steps.

The beamformer output shows the reduction in power from the interferer direction with the application of the new algorithm. In Fig. 7, the algorithm's effect on coherence between the original signal of interest and the output of the algorithm is shown. For each second of data, instead of plotting the beamformer output as in Fig. 6, the coherence is plotted. When the angular separation is less than 3°, the coherence across the frequencies of interest is greater for the algorithm output than for the unmixed array data. For angular separation less than 3°, the coherence increases with application of the new algorithm, but not as significant as for greater angular spacing. In these cases, the sources are not spatially distinct, and the beamforming stage does not contribute new information to the algorithm. In these cases, the mixing matrix tends to be ill conditioned and the FastICA stage cannot completely separate the sources.

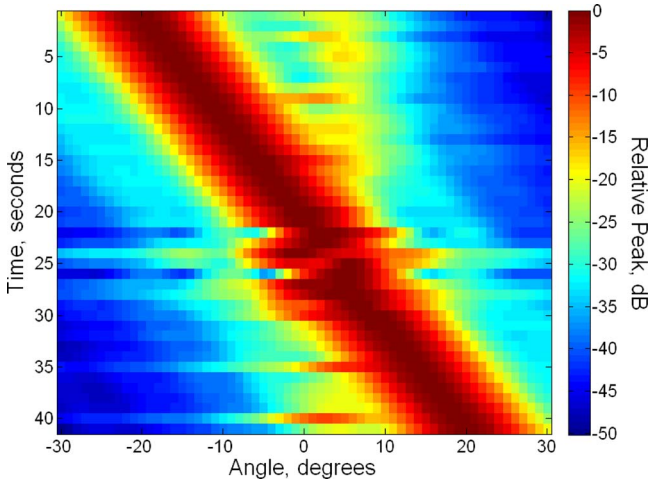

FIG. 6. (Color online) Bearing track recorder plot using a narrow-band delay and sum beamformer after application of the proposed algorithm. The undesired, stationary source at +5° has been suppressed in all time steps without significant suppression of the moving source.

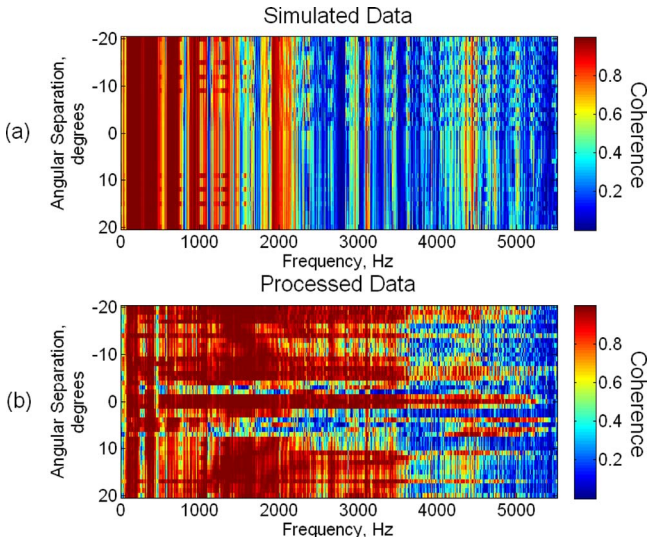

FIG. 7. (Color online) The algorithm's interference suppression performance as a function of the angular spacing between the interferer and the signal of interest is examined. (a) The coherence between the algorithm input data and the signal of interest. (b) The coherence between the algorithm output and the signal of interest.

D. Two voice signals with unequal signal strengths

The results presented previously are for the case where the signal of interest and the interferer have equal power. Next, in order to test the robustness of the new algorithm in terms of the SIR, cases were generated where the signal of interest and interferer powers are not equal. The SIR is given by

$$\mathrm{SIR} = 10 \log_{10} \frac{P_{\mathrm{signal}}}{P_{\mathrm{int}}}, \tag{23}$$

where P_{signal} and P_{int} are the power of the signal of interest and interferer, respectively. For all cases, the signal of interest was positioned at +5°, while the interferer was at −10°. Again, a 35 channel array with element spacing of 0.035 m is used. Figure 8 illustrates the impact of SIR on the new algorithm's performance. For all values of SIR greater than −15 dB, the signal of interest is clearly visible at +5° while the interferer at −10° is suppressed. When the SIR values falls below −15 dB, the signal of interest is completely masked by the interferer. However, even beyond −15 dB, the interfering signal sees nearly 20 dB of suppression as a result of the algorithm's application.

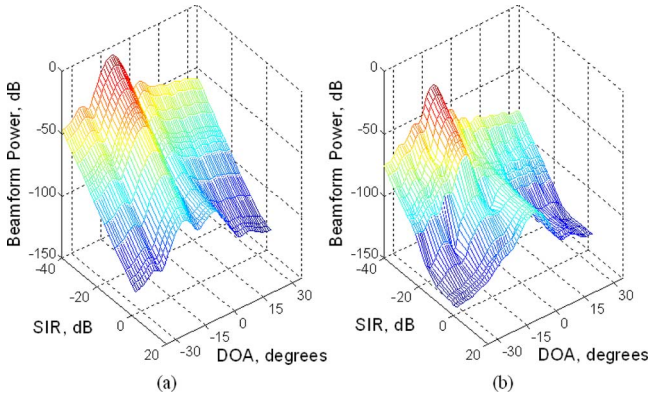

FIG. 8. (Color online) The effect of SIR on the performance of the new algorithm. (a) The beampattern of the algorithm input using a narrow-band delay and sum beamformer. This signal of interest is positioned at +5° and the interferer is at −10°. (b) The beampattern of the algorithm output using a narrow-band delay and sum beamformer. The interferer has been suppressed by 20 dB in all cases, and the signal of interest remains visible until SIR drops below −15 dB.

E. Two voices with equal signal strengths and the addition of noise

All of the cases previously presented contain no additional noise. To further test the performance of the new algorithm, cases were generated where the signal of interest and interferer are at equal power and additional white Gaussian noise is added to the system. The SNR is given by

$$\mathrm{SNR} = 10 \log_{10} \frac{P_{\mathrm{signal}}}{P_{\mathrm{noise}}}, \tag{24}$$

where P_{signal} is the power of the signal of interest. Since the signal of interest and the interferer have the same power, the SNR could also be calculated using P_{int} instead of P_{signal} in Eq. (24). For all cases, the signal of interest was positioned at +5°, while the interferer was positioned at −10° and a 35 channel array with 0.0.35 m spacing is used. Figure 9 shows a plot of the effect of SNR on the new algorithm's performance. A standard delay and sum beamformer was applied to the raw data, and the result is shown in Fig. 9(a), while Fig. 9(b) shows the results of applying the new algorithm.

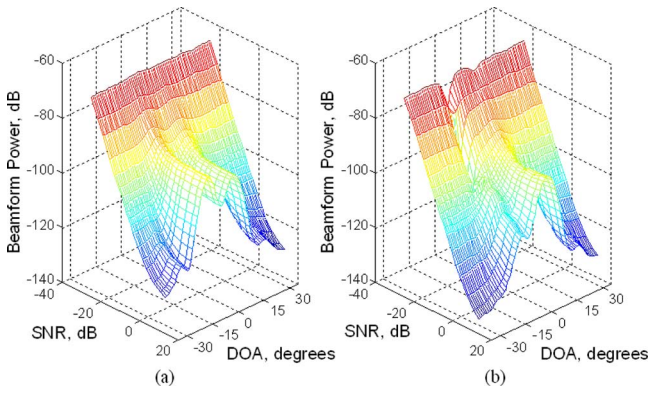

FIG. 9. (Color online) The effect of SNR on the algorithm. (a) The beampattern of the algorithm input using a narrow-band delay and sum beamformer. This signal of interest is positioned at +5° and the interferer is at −10°. (b) The beampattern of the algorithm output using a narrow-band delay and sum beamformer. The interferer is suppressed in all cases and the signal of interest remains visible until SNR drops below −18 dB.

Peaks in the beamformer output are identified as sources. Any peak that rises above a selected threshold on the beamformer output is considered a source. This threshold value is dependent on the data processed, especially on the background noise. For Fig. 9(a), two distinct signal peaks are apparent in the beamformer output when the SNR value is above −18 dB. After the application of the new algorithm, the signal of interest is a distinct peak for all values of SNR greater than −18 dB. When the SNR value falls below −18 dB, the signal of interest is not distinguishable from the background noise, but there is still some suppression at −10°. The breakdown of the algorithm beyond a SNR of −18 dB is comparable to the performance of other spatial techniques.

F. VAD for one voice with one interferer

The VAD algorithm was used to further quantify the performance of the algorithm and its ability to separate signals. For this simulation, the signal of interest is a voice signal at +5°, while the interferer is a white Gaussian noise source at −10°. Three different SIRs were tested: 5, 0, and −6 dB. A 35 channel array with element spacing of 0.035 m is used. The VAD technique was applied to the data before and after it was passed through the proposed algorithm as well as after MVDR processing. Figure 10 shows the results of the application of VAD to the data. Each box encloses a time segment that the VAD identified as an active voice frame. The left column shows the frames identified as active voice frames in the original simulated data for the three SIR cases. The middle column shows the active voice frames after the data were processed using MVDR, while the right column shows the active voice frames after the data have been passed through the separation algorithm. As the SIR drops, the VAD algorithm is unable to correctly identify the active speech sections of the signal in the unprocessed data. Application of the MVDR algorithm increases the VAD algorithm's ability to identify the active voice frames, especially in the lower SIR cases. However, for the lower SIR cases, some of the active voice frames are not identified. After application of the new separation algorithm, the VAD algorithm is able to identify all the active voice frames. Even in the lowest SIR case, it is able to identify the active voice frames.

V. EXPERIMENTS

A. Two voices with equal signal strength

Experiments were performed in an anechoic chamber. A 24 element linear array was used to collect the data. The array had an inter-elemental spacing of 0.75 in. and was sampled at 50 kHz. The signals were two voices. The signal of interest is a voice located at 0° and the interferer is moved from −20° to +20°. Both sources were located 15 ft away from the center of the array at all time steps. The frequency of interest for the experiments is 3250 Hz. Figure 11 shows the time-angle plot of the beamformed data collected during in-chamber testing. The signal of interest was a male voice, while the interferer is a female voice. As seen in Fig. 11, the male voice is barely visible in most instances, while the interferer is always easily observable.

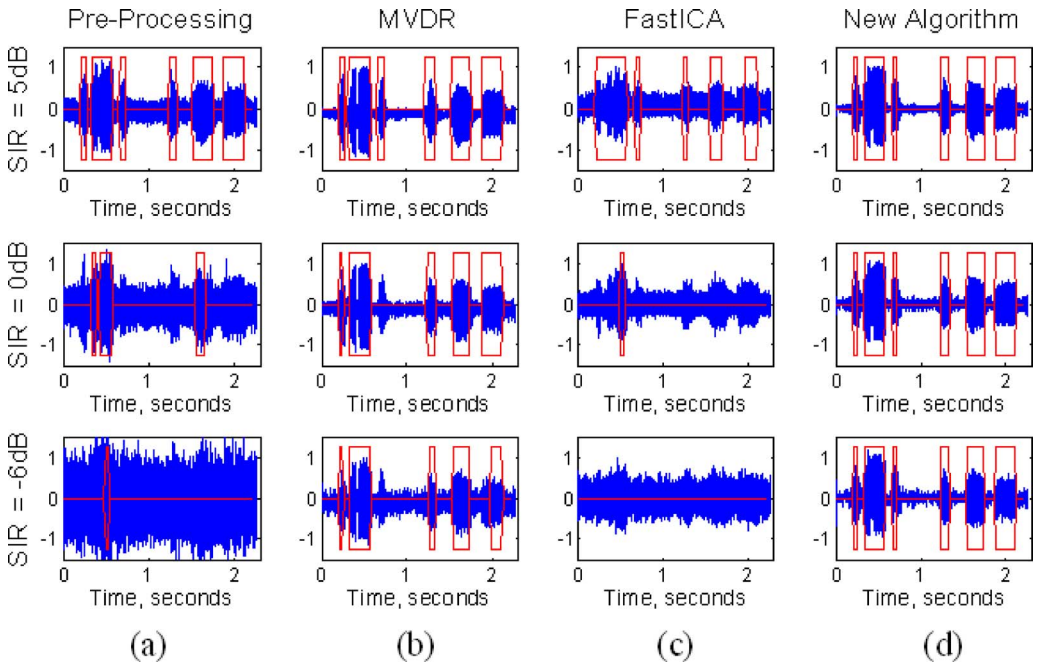

FIG. 10. (Color online) VAD on data containing one voice signal of interest and one white Gaussian interferer. The three rows show the results at varying SNR values. The active voice frames are enclosed with boxes. Column (a) shows the VAD results before the application of the new algorithm, column (b) shows the VAD results after MVDR, column (c) shows the VAD results after FastICA, and column (d) shows the VAD results after the new algorithm application.

The new algorithm was used to process the experimental data. To illustrate the performance of the algorithm in removing a slowly moving interferer, the crossing signal was chosen to be the interferer (opposite to the simulation cases). The result of the application of the new algorithm is shown in Fig. 12. In almost every time step, the signal of interest is now visible while the interferer is significantly suppressed when compared to Fig. 11. This supports the results from the simulation testing.

VI. CONCLUSION

This paper introduces a new method for interferer suppression based on a combination of spatial and ICA-based techniques. The new method has the capability to suppress non-Gaussian interferers, ideal for telecommunication applications speech processing applications. The new algorithm allows for the separation of signals that are not simultaneously mixed. In addition, the introduction of spatial processing allows the permutation ambiguity of the output of the FastICA algorithm to be solved. Using the location of a source, we can associate that source with an output of the FastICA algorithm using cross-correlations.

Simulations showed the capabilities of the new algorithm in suppressing interferers in a variety of conditions. During the simulations, the interferer was suppressed while the signal of interest saw little suppression for 0 dB SIR. Even when the signals become spatially indistinct, the algorithm was still able to partially suppress the interferer. This is not possible using spatial nulling techniques. Anechoic ex-

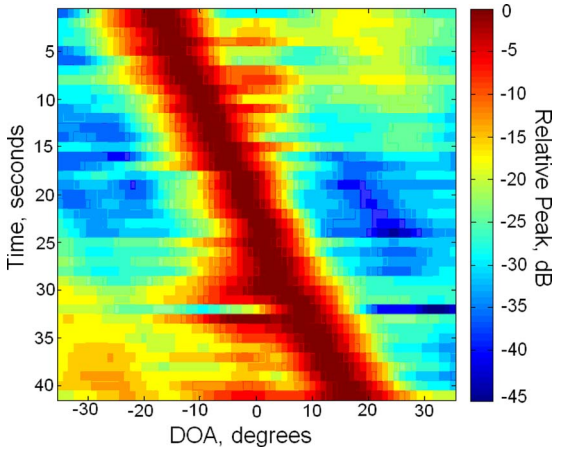

FIG. 11. (Color online) Bearing track recorder plot using a narrow-band delay and sum beamformer for the anechoic chamber testing. One signal is located 0°, while the other signal moves from −20° to +20° at a rate of 1°/s.

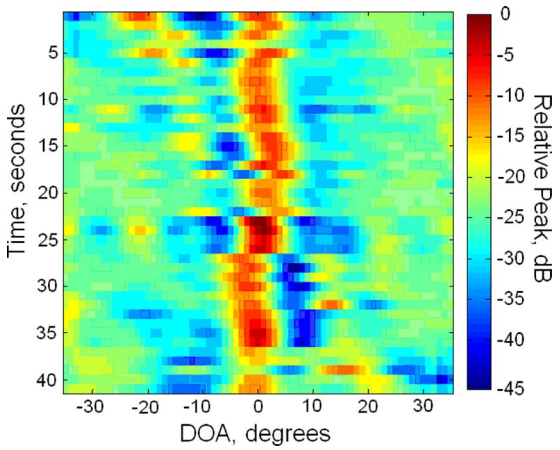

FIG. 12. (Color online) Bearing track recorder plot using a narrow-band delay and sum beamformer after the anechoic chamber data has been processed using the new algorithm. The moving interferer has been removed, and the signal of interest at 0° is visible.

perimental results confirmed the results obtained in the simulations. Although the signal of interest was not visible in many of the time steps of the original BTR, the new algorithm was able to increase its visibility by removing the interferer. The algorithm showed 20 dB of suppression of broadband interferers, even when the SIR dropped to −30 dB. In addition, the algorithm was shown to have good performance for SNR values above −18 dB, which is comparable to other spatial techniques. The performance of the new algorithm as a front-end to a VAD processor was shown to be superior to MVDR in the cases studied; however, future work will include a statistical performance on this enhancement using many types of voice signals and many more geometries.

[1]J. C. Chen, K. Yao, and R. E. Hudson, "Acoustics source localization and beamforming: Theory and practice," EURASIP J. Appl. Signal Process. **4**, 359–370 (2003).

[2]L. T. Fialkowski, M. D. Collins, J. S. Perkins, and W. A. Kuperman, "Source localization in noisy and uncertain ocean environments," J. Acoust. Soc. Am. **101**, 3539–3545 (1997).

[3]Steven J. Spencer, "The two-dimensional source location problem for time differences of arrival at minimal element monitoring arrays," J. Acoust. Soc. Am. **121**, 3579–3594 (2007).

[4]V. Best, S. Carlile, C. Jin, and A. van Schaik, "The role of high frequencies in speech localization," J. Acoust. Soc. Am. **118**, 353–363 (2005).

[5]H. L. Van Trees, *Optimum Array Processing: Detection, Estimation, and Modulation Theory* (Wiley, New York, 2002), Part IV.

[6]J. Capon, "High resolution frequency-wavenumber spectrum analysis," Proc. IEEE **57**, 1408–1418 (1969).

[7]R. G. Lorenz and S. P. Boyd, "Robust minimum variance beamforming," IEEE Trans. Signal Process. **53**, 1684–1696 (2005).

[8]P. J. Kootsookos, D. B. Ward, and R. C. Williamson, "Imposing pattern nulls on broadband array responses," J. Acoust. Soc. Am. **105**, 3390–3398 (1999).

[9]P. Jordan, J. A. Fitzpatrick, and C. Meskell, "Beampattern control of a microphone array to minimize secondary source contamination," J. Acoust. Soc. Am. **114**, 1920–1925 (2003).

[10]P. J. Bevelacqua and Constantine A. Balanis, "Minimum sidelobe levels for linear arrays," IEEE Trans. Antennas Propag. **55**, 3442–3449 (2007).

[11]B. C. Ihm and D. J. Park, "Blind separation of sources using higher-order cumulants," Signal Process. **73**, 267–276 (1998).

[12]J. F. Cardoso, "Blind signal separation: statistical principles," Proc. IEEE **86**, 2009–2025 (1998).

[13]H. Saruwatari, S. Kurita, and K. Takeda, "Blind source separation combining frequency domain ICA and beamforming," IEEE Trans. Audio, Speech, Lang. Process. **14**, 666–678 (2006).

[14]C. M. Coviello and L. H. Sibul, "Blind source separation and beamforming: algebraic technique analysis," IEEE Trans. Aerosp. Electron. Syst. **40**, 221–234 (2004).

[15]S. Araki, S. Makimo, Y. Hinamoto, R. Mukai, T. Nishikawa, and H. Sarwatari, "Equivalence between frequency-domain blind source separation and frequency-domain adaptive beamforming for convolutive mixtures," EURASIP J. Appl. Signal Process. **11**, 1157–1166 (2003).

[16]L. C. Parra and C. V. Alvino, "Geometric source separation: Merging convolutive source separation with geometric beamforming," IEEE Trans. Speech Audio Process. **10**, 352–362 (2002).

[17]S. Haykin, *Adaptive Filter Theory* (Prentice-Hall, Upper Saddle River, NJ, 1996).

[18]M. E. G. D. Colin, J. Groen, and B. A. J. Quesson, "Experimental comparison of bearing estimation techniques for short passive towed sonar arrays," in *OCEANS*, '04 Vol. **2**, pp. 608–612.

[19]A. J. Bell and T. J. Sejnowski, "An information-maximization approach to blind separation and blind deconvolution," Neural Comput. **7**, 1129–1159 (1995).

[20]S.-i. Amari, "Natural gradient works efficiently in learning," Neural Comput. **10**, 251–276 (1998).

[21]A. Hyvärinen, "Fast and robust fixed-point algorithms for independent component analysis," IEEE Trans. Neural Netw. **10**, 626–634 (1999).

[22]K. Li, M. N. S. Swamy, and M. Omair Ahmad, "An improved voice activity detection using higher order statistics," IEEE Trans. Speech Audio Process. **13**, 965–974 (2005).

[23]S. G. Tanyer and H. Ozer, "Voice activity detection in nonstationary noise," IEEE Trans. Speech Audio Process. **8**, 478–482 (2000).

[24]Project Group 841, "Robust Voice Activity Detection and Noise Reduction Mechanism Using Higher-order Statistics," Department of Communication Technology, Institute of Electronic Systems, Aalborg University, 2005.

Truncated aperture extrapolation for Fourier-based near-field acoustic holography by means of border-padding

Rick Scholte,[a] Ines Lopez, N. Bert Roozen, and Henk Nijmeijer
Department of Mechanical Engineering, Technische Universiteit Eindhoven, 5600 MB Eindhoven, The Netherlands

(Received 21 July 2008; revised 31 March 2009; accepted 10 April 2009)

Although near-field acoustic holography (NAH) is recognized as a powerful and extremely fast acoustic imaging method based on the inverse solution of the wave-equation, its practical implementation has suffered from problems with the use of the discrete Fourier transformation (DFT) in combination with small aperture sizes and windowing. In this paper, a method is presented that extrapolates the finite spatial aperture before the DFT is applied, which is based on the impulse response information of the known aperture data. The developed method called linear predictive border-padding is an aperture extrapolation technique that greatly reduces leakage and spatial truncation errors in planar NAH (PNAH). Numerical simulations and actual measurements on a hard-disk drive and a cooling fan illustrate the low error, high speed, and utilization of border-padding. Border-padding is an aperture extrapolation technique that makes PNAH a practical and accurate inverse near-field acoustic imaging method.
 [DOI: 10.1121/1.3126994]

PACS number(s): 43.60.Sx, 43.60.Pt, 43.60.Jn, 43.60.Uv [EGW] Pages: 3844–3854

I. INTRODUCTION

In conventional planar near-field acoustic holography (PNAH), there are two impediments when a proper implementation of inverse near-field acoustic imaging is concerned: first, the anti-leakage and anti-signal-deterioration measures on spatial data before discrete or fast Fourier transformation (DFT and FFT, respectively) and, second, regularization of inversely propagated *k*-space data before inverse DFT or FFT. The latter topic is extensively discussed in, for example, Refs. 1 and 2; however, the focus of this work lies on the first mentioned subject.

Use of near-field information for inverse determination of waveform patterns by means of holography was first introduced into the field of acoustics by Williams and Maynard in the 1980s.[3,4] This NAH method is applicable to general form source areas, including planar, cylindrical, and spherical sources (see Ref. 5 for a thorough discussion of these three configurations). The use of two-dimensional (2D) FFT allows a straightforward multiplication with an inverse propagation matrix based on Green's functions, which results in an extremely fast calculation of the source distribution on the area of interest, contrary to the two-dimensional spatial convolution with the sound propagation kernel required without 2D FFT. For large aperture sizes with many sensors PNAH is well applicable. On the other hand, spatial windowing on small apertures with a lower number of sensors accounts for increasingly larger errors with respect to *k*-space leakage, source deformation, and location, especially near the aperture edges.

These major disadvantages of the FFT-based NAH methods triggered a number of developments to counter them or to provide alternative methods. One of these methods is to avoid *k*-space and FFT processing entirely;[6] others use zero-padding and *k*-space regularization to iteratively extrapolate the measurement aperture or hologram.[7,8] The latter are iterative methods based on zero-padding of the measured aperture followed by *k*-space filtering to suppress high wavenumber leakage and smooth the result. The original hologram is then inserted into the extrapolated data, which is fed into the 2D FFT again until a pre-defined threshold is met in order to stop the iterative process. This results in a good performance for well-defined cases in a perfectly known and controllable environment, yet problems arise when the sources of interest are unknown together with the amount and type of noise or disturbance, which is often the case in more practical and industrial situations. Further developments on bandlimited approaches were described in Ref. 9 followed by a non-iterative method.[10] Statistically optimal NAH (SONAH) (Ref. 6) avoids the FFT entirely and calculates the inverse propagation from the hologram to the source plane by a spatial convolution. This method is one of the most popular procedures to deal with the leakage problems concerning the FFT. Besides a number of spatial advantages like the arbitrary spacing of measurement points, major drawbacks include the long computation times due to the spatial convolution required to determine the inverse solution and the sensitivity to sensor noise and positioning errors.[11]

In this paper, the relative simplicity, accuracy, and processing speed of FFT-based NAH is acknowledged; thus a method is introduced that makes the application of FFT-based NAH possible, also outside carefully regulated surroundings on well-defined sources. The general idea is to extend the finite aperture before the FFT is applied, while ensuring minimal deterioration near the edges of the hologram and maintaining maximum leakage reduction in *k*-space. This is achieved by extrapolating the finite aperture

[a]Author to whom correspondence should be addressed. Electronic mail: r.scholte@tue.nl

by a newly introduced method called border-padding, which is, in fact, a method that pads the acoustic data from the borders of the hologram outward, while the actual measured data within the finite aperture is kept unaltered.

The paper is organized as follows: First, in Sec. II, the use of windows and zero-padding in PNAH is discussed. The discrete planar inverse solution in k-space is given and the significant influence of leakage on this process is illustrated. Leakage is generally reduced by application of spatial window,[12] yet the evanescent character of increasingly higher wavenumbers possibly causes problems for the inverse solution. Zero-padding the windowed hologram improves the solution power of the FFT, thus resulting in a k-space spectrum with a smaller wavenumber stepsize. However, this does not mean an increase in wavenumber resolution; it is merely an interpolation. Section III first introduces the basic border-padding operation, followed by a more thorough introduction of linear predictive border-padding. Linear predictive border-padding is based on a physical model of the measured data, written in impulse responses of a given order. These impulse responses are then fed into a infinite impulse response (IIR) filter together with data at the aperture border and zero-valued extrapolation points, which results in filtered extrapolation points that naturally fit the aperture border. Alternatively, a border-padding algorithm based on (non-physical) spline extrapolation is derived. These border-padded apertures are processed by FFT with considerably less leakage and signal deterioration as a result. To illustrate and compare the proposed methods, the different implementations of border-padding and the basic windowing followed by zero-padding as a reference are compared in two numerical cases in Sec. IV. The practicability and accuracy are finally shown with a measured case of an idle spinning hard-disk drive and a cooling fan in Sec. V. Finally, some concluding remarks are given in Sec. VI.

II. THE USE OF WINDOWS AND ZERO-PADDING IN PNAH

A. Discrete solution for PNAH

In practice, it is impossible to measure sound quantities continuously neither in space nor in time. The finite measurement plane is best represented by a rectangular or truncation window, which basically is one at a given interval of time or space and zero outside. The spatial interval function in x-direction, $\sqcap_X(x)$, is defined by

$$\sqcap_X(x) = \begin{cases} 1, & |x| < X/2, \\ \frac{1}{2}, & |x| = X/2, \\ 0, & |x| > X/2. \end{cases} \tag{1}$$

Besides time discretization sampling, discrete acoustic image processing requires spatial sampling in the form of a limited number of sensor positions within the chosen spatial interval. The sampling function for the spatial domain x-direction is represented in the form of a Dirac comb function,

$$\sqcup(x) = \sum_{n=-\infty}^{\infty} \delta(x - x_n). \tag{2}$$

For reasons of simplicity the pressure $\tilde{p}(x,y,z,\omega)$ observed at a distance z and a given angular frequency ω, is written as $\tilde{p}_z(x,y)$. Spatially sampling a bounded plane $\tilde{p}_z(x,y)$ by applying Eqs. (1) and (2) is mathematically described as

$$\tilde{p}_z(x_n,y_m) = \tilde{p}_z(x,y)\sqcap_X(x)\sqcap_Y(y)\sqcup(x)\sqcup(y). \tag{3}$$

Without taking any precautions with respect to leakage and aliasing and taking the finite boundaries of the plane into account, the fully discretized pressure counterpart in k-space at the hologram plane $\hat{\tilde{p}}_d$ is written as

$$\hat{\tilde{p}}_d(k_{x_n},k_{y_m}) = \sum_{n=-N/2}^{N/2-1} \sum_{m=-M/2}^{M/2-1} \tilde{p}_d(x_n,y_m) e^{-2\pi j(k_{xnn/N}+k_{ymm/M})}, \tag{4}$$

with N and M the number of samples in x- and y-directions, respectively. The discrete solution of the wave-equation in k-space of an unknown, steady state pressure distribution $\tilde{p}_z(k_x,k_y)$ in a source-free half-space, $z>0$, is defined as[3]

$$\hat{\tilde{p}}_d(k_{xn},k_{ym},z) = \hat{\tilde{p}}_d(k_{xn},k_{ym},z_h) e^{jk_z(z-z_h)}, \tag{5}$$

where $z=z_h$ is the hologram distance. From Eq. (5) it follows that we need to determine k_z from the wavenumbers in both x- and y-directions, i.e., k_x and k_y, and the acoustic wavenumber k that follows from ω and c_0. In k-space k_z is determined by $k_z = \pm\sqrt{k^2-k_x^2-k_y^2}$ of which three types of solutions to this equation, with k already known, can be found:

$$k_x^2 + k_y^2 = 0, \quad \text{plane wave in } z\text{-direction}, \tag{6}$$

$$0 < k_x^2 + k_y^2 \leqslant k^2, \quad \text{propagating waves}, \quad k_z \text{ real}, \tag{7}$$

$$k_x^2 + k_y^2 > k^2, \quad \text{evanescent waves}, \quad k_z \text{ complex}. \tag{8}$$

The radiation circle lies exactly at $k^2=k_x^2+k^2$ and is denoted as k_r, outside this circle waves are evanescent, whereas inside waves are propagating. Applying Eq. (5) to propagating waves [Eqs. (6) and (7)] results in a phase shift, evanescent waves (8) are multiplied in k-space by an exponential power of increasing strength with increasing k_z. Before this operation in k-space is possible, the spatial data are first preprocessed before the FFT is applied. A widely used method in signal processing, and thus also in acoustic image processing, is the application of windows in order to reduce leakage. It is shown below that especially the higher wavenumbers are very vulnerable to leakage and signal distortion by the FFT.

B. 2D spatial anti-leakage windows

The finite aperture of a sensor array measurement is observed spatially as a truncation window. Outside the measured aperture there exists no directly sampled knowledge of the sound field, thus the 2D k-space is determined from a coarse, spatially sampled and finite aperture. The application of a window is observed as a procedure to reduce the order of the discontinuity at the border of the periodic extension of

the aperture in the FFT processing. This is realized by smoothly attenuating the data near the edges to zero. If, from another point of view, a basis set of wavenumbers for a given interval N is defined, and there exists a signal in this set with a wavenumber not exactly fitting on one of these basis wavenumbers, then the window application transforms this signal to the basis wavenumber closest to the original wavenumber of the signal (leakage). In other words, the wavenumber or k-space resolution of the spectrum is too low.

Leakage is caused by processing finite aperture data, not by the spatial sampling. A discontinuous edge at the aperture indicates the presence of non-fitting periodic signals and thus causes leakage to a large number of wavenumbers.

A large number of one-dimensional windows suitable for harmonic analysis is discussed in Ref. 12, which is also applicable to 2D spatial aperture processing. Unlike digital audio processing and spectral analysis, which often includes many thousands of samples, acoustic array measurements generally exhibit several tens of sensors in one direction at most. This means only coarse aperture data are available, which requires a careful process to determine the proper k-space with as much preserved spatial information as possible. Often this implies a trade-off between k-space leakage and loss of acoustic information, especially near the edges of the aperture. A good compromise is often made by the application of a Tukey window,[12] which is defined as

$$w(n) = \begin{cases} \frac{1}{2}\left[1+\cos\left(\frac{2\pi}{\alpha}\frac{(n-1)}{(N-1)}-\pi\right)\right], & n < \frac{\alpha}{2}(N-1)+1, \\ 1, & \frac{\alpha}{2}(N-1)+1 \leqslant n \leqslant N-\frac{\alpha}{2}(N-1), \\ \frac{1}{2}\left[1+\cos\left(\frac{2\pi}{\alpha}-\frac{2\pi}{\alpha}\frac{(n-1)}{(N-1)}-\pi\right)\right], & N-\frac{\alpha}{2}(N-1) < n, \end{cases} \tag{9}$$

where $n=1-N$ and α between 0 and 1. In the lower limit of $\alpha=0$, the Tukey window equals the rectangular window, while it evolves to the Hanning window as α increases to become $\alpha=1$. In between these extremes, the Tukey window is a combination of a cosine tapering near the edges and a non-attenuated area near the center of the aperture. Application of this window is a compromise between attenuation of acoustic data near the aperture border and the amount of leakage in k-space. The 2D Tukey window follows from the transpose vector of the window from Eq. (9) in y-direction multiplied with the row vector of the window in the x-direction:

$$w(n,m) = w(m)^T w(n). \tag{10}$$

In Fig. 1 a comparison is made between a number of settings for α in the Tukey window, including the rectangular ($\alpha=1$, lightest gray) and Hanning window ($\alpha=0$, black) settings, to determine the influence of leakage on the inverse process of PNAH. It is clear that increasing α causes the leakage sidelobes to become higher, when the exponential inverse propagation curve for k-space is multiplied with the window transform the threat of leakage becomes visible, since the sidelobes are amplified by the inverse propagator.

Window compensation after the complete inverse propagation process is an option, yet due to the applied window the wavenumbers have shifted and results near the edges are heavily affected. The inverse propagation and the discrimination of strengths between individual wavenumber bins are too varied to compensate with an inverse window. The promising alternative is to pre-process the data before the FFT is applied.

C. Zero-padding

By zero-padding it is possible to interpolate between the basis wavenumbers within the spectrum. If a finite aperture is considered, with edge values and all orders of the derivative near the edge equal to zero, and a FFT is applied on the spatially sampled data, then the resulting k-space spectrum is free of spectral leakage as discussed in Sec. II C. However, due to the finite number of sampling points in this perfect aperture, only a discrete number of wavenumber bins are available to map the data on. The discrete k-space is only a representation or mapping of the continuous spectrum on the set of basis wavenumbers. Wavenumbers present in the spatial data remain hidden in k-space if their periods do not exactly match the discrete wavenumbers. This finite resolution in k-space is due to the finite length of the spatial aperture, which is visible in the DFT of such an aperture.

If the spatial aperture is increased while padding the new samples with zero value, the solution power of the DFT increases, resulting in an optimal interpolation in k-space. Every single bin increase above the aperture size increases the number of bins in k-space: $\Delta k=2\pi/N+\upsilon$, $\upsilon=0,1,2,\ldots$. In order to maintain the original wavenumber bins, the aperture size is expanded by an integer number of the original aperture size: $\Delta k=2\pi/wN$, $w=1,2,3,\ldots$. Now, a greater number of wavenumbers are distinguished from the spectrum. However, zero-padding does not increase spectral resolution in k-space.

Another practical consideration for zero-padding is the calculation speed advantage that is accomplished by expanding the total number of samples in either direction to a power of two, resulting in $N \log N$ operations.[13] Careful investiga-

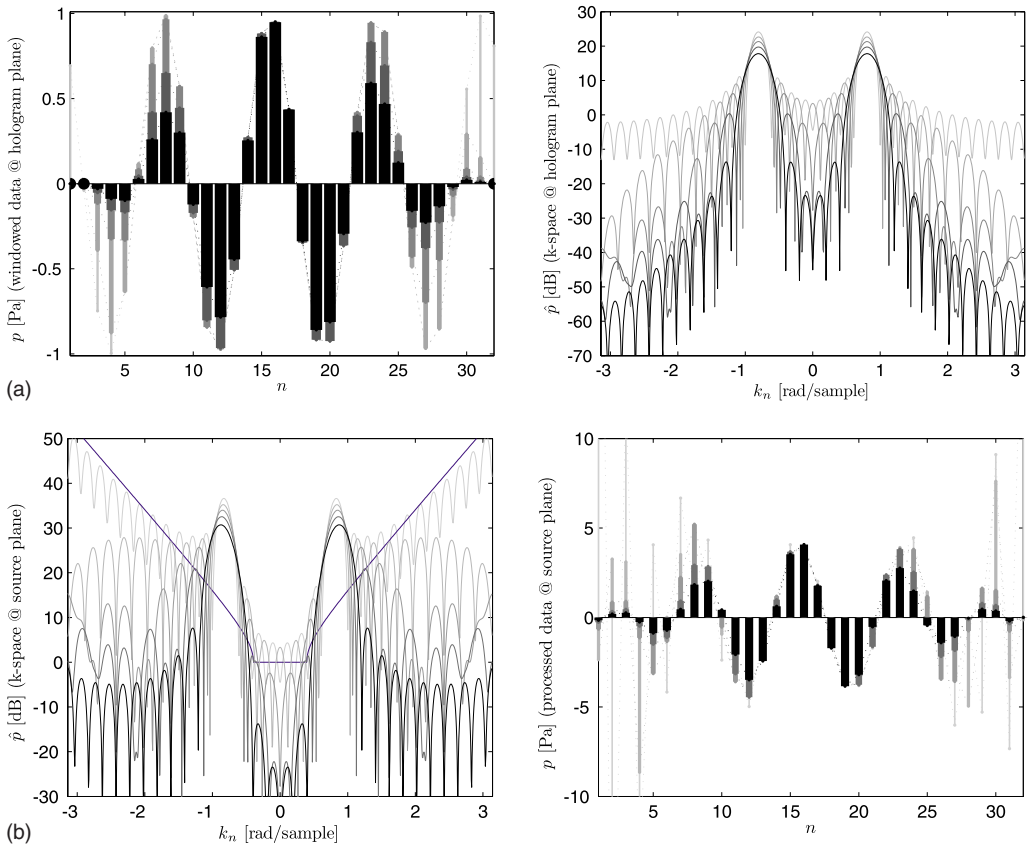

FIG. 1. (Color online) Signal leakage and influence on spatial data due to Tukey windowing with $\alpha=0$ (black), 0.25,…,1 (lightest gray) on a cosine with $k_n=(8.2/N)\pi$ at $z_h=0.02$ m sampled at $N=32$ points with 0.01 m spacing in between and a radiation wavenumber at $k_r=\frac{1}{4}\pi$.

tion of the characteristics of windowing and zero-padding has lead to the development of border-padding, which maintains good characteristics of the these methods while improving the negative aspects.

III. TRUNCATED APERTURE EXPANSION

A. Basic border-padding

Due to the above-described windowing methods, a significant part of the edges of the data get affected and large errors are introduced. In practice, while using these windowing methods, it is necessary to enlarge the measured aperture and make sure the interesting sources are not situated near the border. Another alternative is to use a direct method without using the Fourier transform.[6] The main idea of basic border-padding is to avoid sharp edges and make smooth transitions without losing information from the original hologram aperture.

Border-padding deals with these problems as follows. Instead of padding the added samples with zeros, the values of the samples at the edge or border of the signal are padded, filling up the added samples. After spatial extrapolation, a spatial window on the complete set of data, including the border-padded part, is applied. The Tukey window is especially fitted for this purpose since the constant part of the window is placed exactly over the original aperture, while the cosine-tapered part covers the border-padded region. In this way the spatial window does not affect the acoustic information and leakage is reduced as well. Basic border-padding is expressed as

$$\tilde{p}_b(n_b)=\begin{cases}\frac{1}{2}\tilde{p}(1)\left[1+\cos\left(2\pi\frac{(n_b-1)}{\left(\frac{N_b-N}{2}-1\right)}-\pi\right)\right], & n_b\leqslant\frac{N_b-N}{2},\\ \tilde{p}(n), & \frac{N_b-N}{2}<n_b\leqslant N_b-\frac{N_b-N}{2},\\ \frac{1}{2}\tilde{p}(N)\left[1+\cos\left(\pi-2\pi\frac{(n_b-1)}{\left(\frac{N_b-N}{2}-1\right)}\right)\right], & n_b>N_b-\frac{N_b-N}{2},\end{cases} \tag{11}$$

where $\tilde{p}_b(n_b)$ is the border-padded aperture, for $n_b = 1, \ldots, N_b$ with N_b the border-padding length. The fully border-padded aperture includes the original aperture $\tilde{p}(n)$, which is placed in the center of the border-padded aperture, with $n=1, \ldots, N$ and $N_b > N$. The 2D aperture is naturally border-padded by first applying Eq. (11) to every row followed by the resulting columns, or vice versa.

Still, this form of border-padding causes leakage, which is due to the used Tukey window and the cross-over area between aperture and padded area where the derivatives of the data across the edge are often discontinuous. Especially the discontinuous first derivative at the border introduces errors near this point, leaking back into the original aperture and thus causing errors in the determined acoustic source strengths and shapes.[14]

B. Linear predictive border-padding

Linear predictive filtering is a method that determines samples outside a hologram aperture by an approximation based on a chosen number of previous samples. For a finite spatial aperture, first, one row or column of data is used to calculate the impulse response coefficients. Second, a digital filter is implemented with the impulse response coefficients. Finally, a zero-valued vector, which covers the eventual border-padded width to either side of the aperture, is fed into the filter. Both ends of the finite aperture are extrapolated by this procedure. After every row or column is padded, the same sequence is applied in the other direction, including the border-padded parts. This results in a fully border-padded hologram, which is fitted for 2D FFT. To make sure no leakage from the outer edges is generated a wide Tukey window is applied that applies a cosine tapering far from the measured hologram, thus leaving the measurement data unchanged.[14]

1. Linear predictive filter

Take a measured acoustic pressure series $\tilde{p}(x_n, z)$ over a single line of the holographic aperture, which is N samples in size and $z > 0$ in a source-free half-space. The vector $\tilde{\mathbf{p}}(x_n) = [\tilde{p}(x_1), \tilde{p}(x_2), \tilde{p}(x_3), \ldots, \tilde{p}(x_N)]$ is expanded outside this interval, creating border-padded samples to the right $[\tilde{p}(x_{N+1}), \tilde{p}(x_{N+2}), \tilde{p}(x_{N+3}), \ldots]$ or to the left $[\ldots, \tilde{p}(x_{-2}), \tilde{p}(x_{-1}), \tilde{p}(x_0)]$ of the aperture. Ideally, a number of prediction "filter" coefficients predicts these samples perfectly, i.e., with zero prediction error, based on Q previous samples. Note that the linear predictive filter is used to determine samples outside the hologram aperture before the FFT and the inverse calculation is performed. The newly acquired sample is denoted as $p(x_s)$, a linear description of such a filter is written as

$$\tilde{p}(x_s) = \sum_{i=1}^{Q} h_i \tilde{p}(x_{s-i}), \tag{12}$$

where h_i are the prediction filter coefficients.

The measured, noisy data used for practical NAH are far from perfect and the analytical solution for $\mathbf{h}(h_{-\infty}, \ldots, h_{\infty})$ only exists in theory. The real world requires an iterative method based on the determination of a linear prediction error coefficients $\mathbf{a} = [1, a_1, a_2, \ldots, a_v]$, which are converted to impulse response coefficients by

$$\mathbf{h} = [h_1, h_2, \ldots, h_Q] = [-a_1, -a_2, \ldots, -a_v]. \tag{13}$$

Several methods exist to determine a fitting model to the signal, yet the Burg method[15] is both minimum-phase (i.e., all roots of the corresponding transfer function polynomials of the filter remain within the unit circle in the complex plane) and suitable for few observed samples (which is often the case in NAH measurements). The Burg method was initially introduced for estimating power density spectra of stationary time series, and provides good practical results in digital time series audio processing and extrapolation.[16,17] Additionally, the spatial domain is a viable area for implementation, since time-frequency processing is in many respect equivalent to space-wavenumber processing. The Burg method is used to fit an autoregressive (AR) model on $\tilde{p}(x_n)$, $n = 1, 2, \ldots, N$.

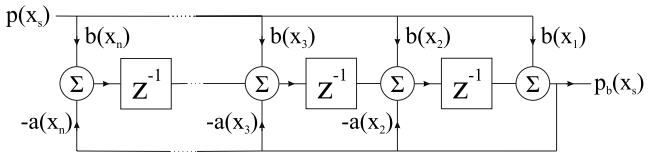

FIG. 2. Infinite impulse response filter direct form II realization, $p(x_s)$ is the unknown pressure outside the original aperture and $p_b(x_s)$ the border-padded prediction of the pressure on this position.

2. Implementation

The general form difference function for a direct form IIR filter[18] is defined for spatial sound pressure as

$$\sum_{i=0}^{v} a_i \tilde{p}_b(x_{s-i}) = \sum_{i=0}^{w} b_i \tilde{p}(x_{s-i}), \tag{14}$$

where a_i and b_i represent the filter coefficients, which are part of the coefficient vectors with lengths $v+1$ and $w+1$, respectively, $\tilde{p}_b(x_s)$ is the unknown sound pressure outside the aperture, and $\tilde{p}(x_s)$ is the initializing value that serves as input to the IIR filter. The direct form II realization of this filter is illustrated in Fig. 2. The value for the initialization $\tilde{p}(x_s) = 0$ for all s, thus the output in Eq. (14) is

$$\tilde{p}_b(x_s) = -\frac{1}{a_0} \sum_{i=1}^{v} a_i \tilde{p}_b(x_{s-i}). \tag{15}$$

This implementation for the IIR filter based interpolation equals the convolution product from Eq. (12) when $a_0 = 1$, which defines the filter causality, $a_i = -h_i$, $b_i = 1$ and $w = 0$, and results in the final IIR difference equation:

$$\tilde{p}_b(x_s) = \sum_{i=1}^{v} h_i \tilde{p}_b(x_{s-i}) + \tilde{p}(x_s). \tag{16}$$

The filter order is bounded by the number of available samples in the finite aperture, yet the choice of the optimal

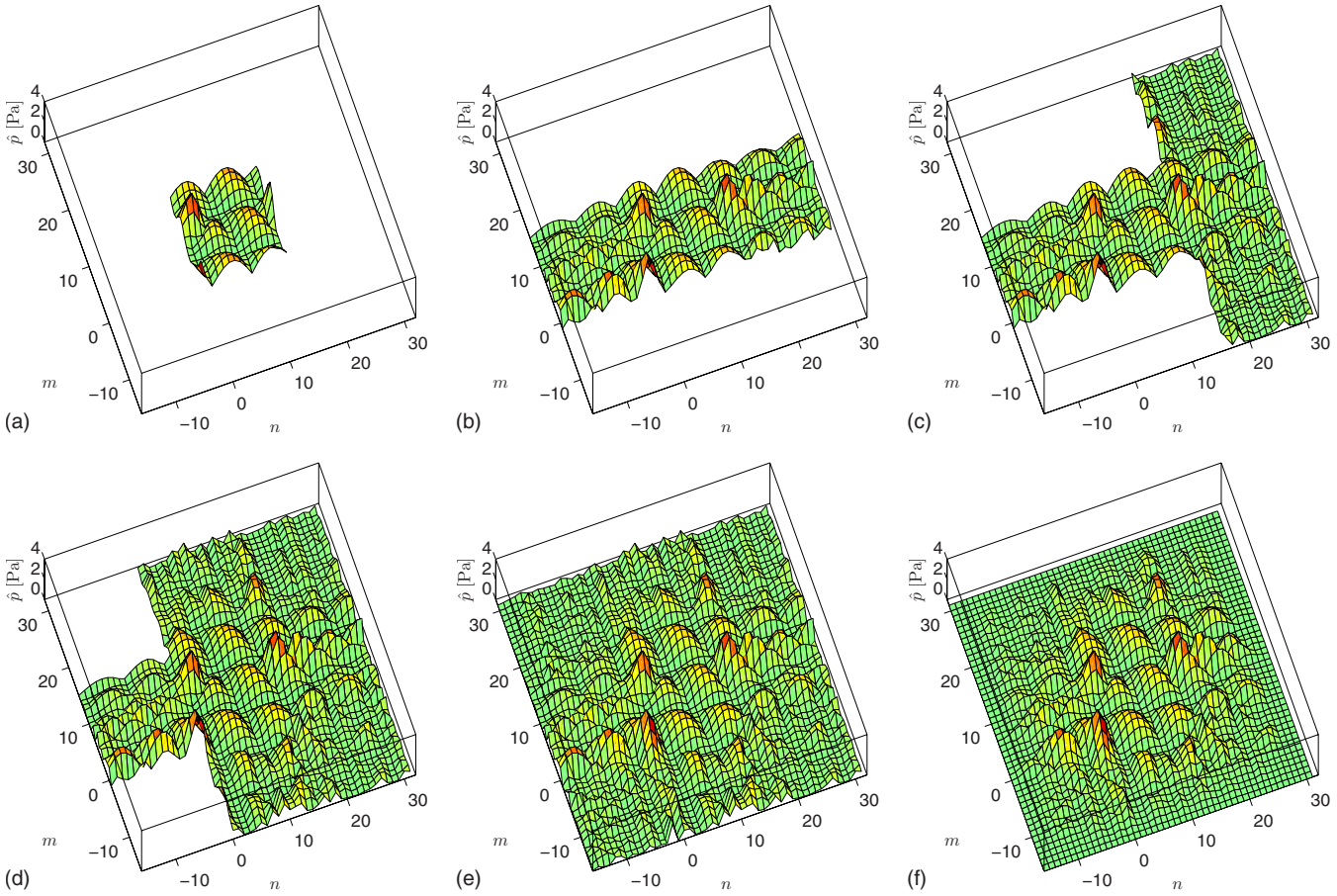

FIG. 3. (Color online) Border-padding a truncated holographic aperture in two dimensions: start with the original aperture (a), followed by x-direction expansion (b), y-direction expansion [(c) and (d)], resulting in a fully padded aperture (e), and finalized by a spatial window (f).

order is not entirely straightforward. The presence of high wavenumbers in the aperture data requires a higher order description, yet also noise is present at these higher wavenumbers which potentially causes problems for the inverse solution of a finite, discrete aperture. The k-space low-pass filter is also of influence, since an applied filter with a significantly lower cut-off than half the sampling wavenumber already lowers the relevant order of the linear predictive filter.

The implementation provided above extrapolates only one row to the right of a hologram aperture, thus an extended, 2D implementation is required. First, the 2D hologram measurement data $\tilde{p}_h(x_n, ym)$ is border-padded in the positive and negative x-direction, as illustrated in Fig. 3(b). Subsequently, the partly border-padded data are extrapolated in the positive and negative y-direction, also including the previously non-existing, border-padded parts. The illustrations from Figs. 3(b)–3(e) show that this process fills up a full array of data consisting of originally measured signals and surrounding, fully border-padded data.

From windowing theory, it is clear that data near the edges of the extended aperture are bound to go to zero for a number of derivatives. This is also the case for border-padded data, and thus a certain type of windowing or tapering is required. There are two clear options for border-padding: the first option is the application of a standard type window and, second, the connection of the negative with the positive aperture end of the data. The implemented version discussed in this work includes a 2D Tukey window with a cosine tapering applied to one-third of the extrapolated data, as shown in Fig. 3(f).

IV. NUMERICAL ANALYSIS OF BORDER-PADDING

A. Source reconstruction errors

In a numerical analysis on extrapolation of a limited aperture for an inverse method, consideration of a wide wavenumber band is appropriate. Naturally, discussion of modal waveforms is relevant, yet considering point sources or sharp edges in the hologram provides more information on the quality of inverse data-processing methods. The point sources contain energy over a broader k-space band, which causes more problems for the FFT. Therefore, not only modal or sine-shaped sources are considered in this numerical analysis but also point sources. Influence of noise is not considered here, since purely the influence of windowing or extrapolation is investigated. The two full-sized hologram (left) and source (right) apertures for the numerical analysis are shown in Figs. 4(a) and 4(b). The hologram data are determined with Rayleigh's second integral formula.

In order to test windowing and border-padding, a small portion of a large hologram aperture is selected. The small selection is then border-padded and both holograms are inverse propagated to the source. The border-padded inverse is

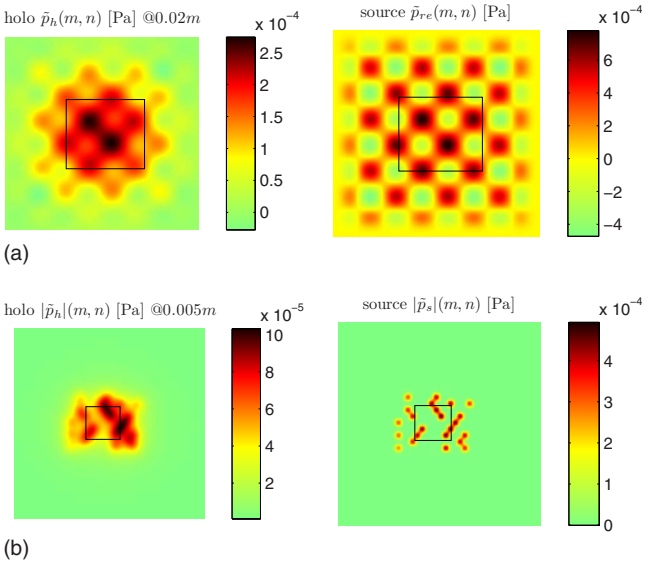

FIG. 4. (Color online) Modal source (a) with a hologram plane 0.02 m away from the source with a combined 1×1 and 8×8 mode, the height and width of the aperture measures 0.3 m with 128 spatial samples at a sound frequency of $f=1$ kHz; point sources (b) under test, the height and width of the aperture measures 0.1 m with 128 spatial samples at a sound frequency of $f=1$ kHz.

truncated and compared with a selection of the fully inverse calculated source, which corresponds to the selected area. These results provide much insight into the quality of the method. Besides this qualitative comparison, a quantitative measure is calculated in the form of a root mean squared reconstruction error (RMSRE):

$$\mathrm{RMSRE} = 100\,\% \cdot \sqrt{\frac{1}{MN}\sum_{n=1}^{N}\sum_{m=1}^{M}\frac{(|\tilde{p}_{\mathrm{ex}}(m,n)-\tilde{p}_{\mathrm{re}}(m,n)|)^2}{|\tilde{p}_{\mathrm{ex}}(m,n)|^2}}, \tag{17}$$

where $\tilde{p}_{\mathrm{ex}}(m,n)$ is the exact pressure on the source and $\tilde{p}_{\mathrm{re}}(m,n)$ the reconstructed pressure over the selected small aperture.

Various extrapolations of the same aperture are illustrated in Figs. 5 and 6 for three types of border-padding and basic spatial windowing. The third border-padding form is based on cubic spline extrapolation, which is implemented as a (non-physical) reference to the linear predictive extrapolation. Here, a number of piecewise polynomials based on the measured data are determined to extrapolate the field with. The selected finite aperture is marked by the rectangle in the hologram images. Two different filter orders are used to illustrate the influence of the order in linear prediction border-padding. For every case the left-most image is the hologram generated by the extrapolation method, which is easily compared to the exact holograms in Figs. 4(a) and 4(b), the center image is the exact solution and the right-most image is the resulting solution at the source for the extrapolated case. L-curve regularization is used to determine a fixed cut-off for a modified exponential filter[2] applied to the large hologram aperture, which is then used for every windowing or aperture extrapolation method for proper comparison.

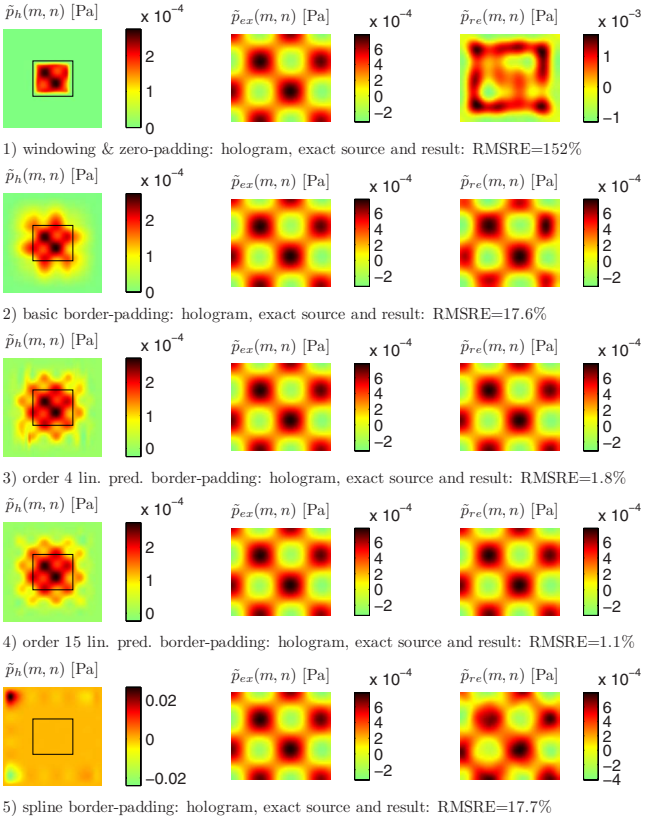

FIG. 5. (Color online) Results of five types of data extrapolation in combination with PNAH processing for the modal source under test, a fixed $k_{\mathrm{co}}=209$ rad/m is applied for all cases.

From the results of the modal case, it is clear that linear predictive border-padding outperforms the other three methods. The windowed case shows, as expected, very high quantitative as well as qualitative errors, introducing higher wavenumbers near the aperture edge due to the window slope. The field near the aperture edge in Fig. 5(1) is overestimated, since the higher wavenumbers are amplified more by the inverse propagator than the original modal content. Both the basic [Fig. 5(2)] and spline [Fig. 5(5)] border-padding show equal results, which are far better than the windowed version both in RMSRE and qualitatively. However, the linear predictive border-padding results both show an optically flawless comparison to the exact source distribution, while the RMSREs are between 1% and 2%.

For the point source case, the difference between linear predictive border-padding and the other three methods increases drastically. The windowed [Fig. 6(1)], basic border-padded [Fig. 6(2)], and spline border-padding [Fig. 6(5)] reconstructions of the source pattern are unrecognizable and also quantitatively incorrect. Although basic border-padding results in a fair RMSRE, the large errors near the aperture edges are not satisfying. The difference between the low and higher order linear predictive border-padding is interesting in comparison with the modal case. Order 4 linear predictive border-padding in Fig. 6(3) is clearly better, both qualitatively and quantitatively, compared to order 15 linear predictive border-padding in Fig. 6(4).

From the above it is clear that the point source case is much more challenging for the finite aperture extrapolation

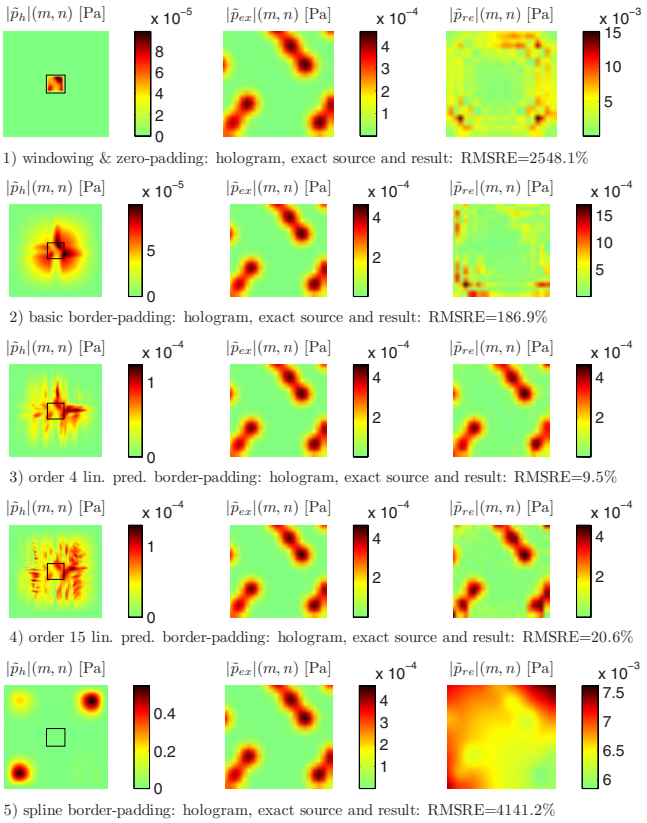

FIG. 6. (Color online) Results of five types of data extrapolation in combination with PNAH processing for the point sources under test; a fixed k_{co} = 1484 rad/m is applied for all cases.

algorithms. The linear predictive border-padding is the only tested method capable of handling both cases well. One downside of the higher order algorithm is the increased processing time compared to a lower order one. Also, higher order border-padding for cases with high wavenumber content possibly causes numerical errors due to the finite and discrete character of the data. This behavior is not exactly clear, yet errors occur when data consisting of high wavenumbers close to the Nyquist wavenumber are processed with a high order of the linear predictive filter. Section IV B discusses the trade-off between processing speed, RMSRE, and order.

B. Comparison of processing speeds

Besides accuracy considerations, another important factor is processing speed. Especially in situations where large numbers of frequencies are processed, or in-stationary sources are observed with an array. In these cases inverse solutions from many different hologram data-sets are required. Thus, limiting the processing time of the border-padding algorithm is necessary.

In order to illustrate the processing speed in comparison with the accuracy, a range of linear predictive border-padding applications varying in order from 1 to 20 are applied to the modal and point sources introduced in Sec. IV A. The processing speed test for the linear predictive border-padding algorithm is implemented in a MATLAB™ 7 environment on an average speed PC system (Pentium IV 2.8 GHz, with 1 Gbyte of memory).

From the results for the modal sources in Fig. 7 it is clear that the order has a small influence on the error from order 5 onwards. However, the speed linearly increases as we improve the order. For the modal case, an order 5 linear predictive filter would suffice. When observing the results for the point sources in Fig. 8, it shows minimum errors between orders 4 and 10. The processing speed of the practicable order between orders 4 and 10 is hardly an issue, since this average system shows speeds of a few tens of a second for a full 16384 point aperture.

V. PRACTICAL SOURCE EXPERIMENTS

A. Measurement set-up

In a practical situation the source distribution is generally unknown, which requires a robust extrapolation method that is able to deal with many different circumstances, source distributions, and noise. To illustrate the applicability of border-padding two highly practical cases are considered: a hard-disk drive and a cooling fan. In the case of the hard-disk drive, a frequency is observed where the source distribution mainly contains lower wavenumbers lying just outside the radiation circle. On the other hand, the cooling fan is observed at the rotational frequency where the total number of blades (seven) are observed at the source image. In the latter

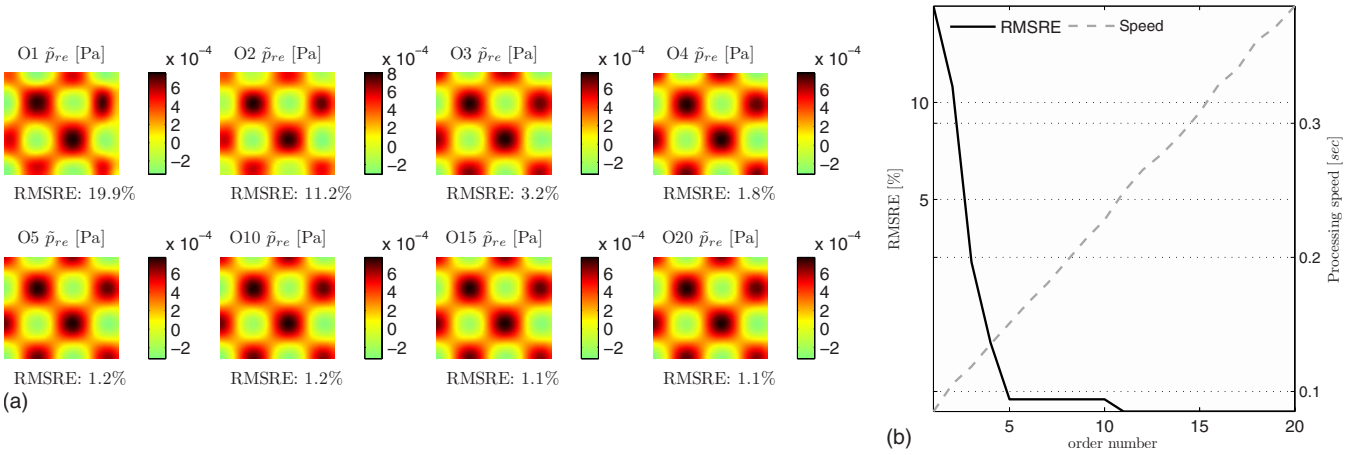

FIG. 7. (Color online) Influence of linear predictive border-padding order on resulting error of the modal source case after PNAH (a) and corresponding processing speed and error versus border-padding order (b); a fixed k_{co}=209 rad/m is applied for all cases.

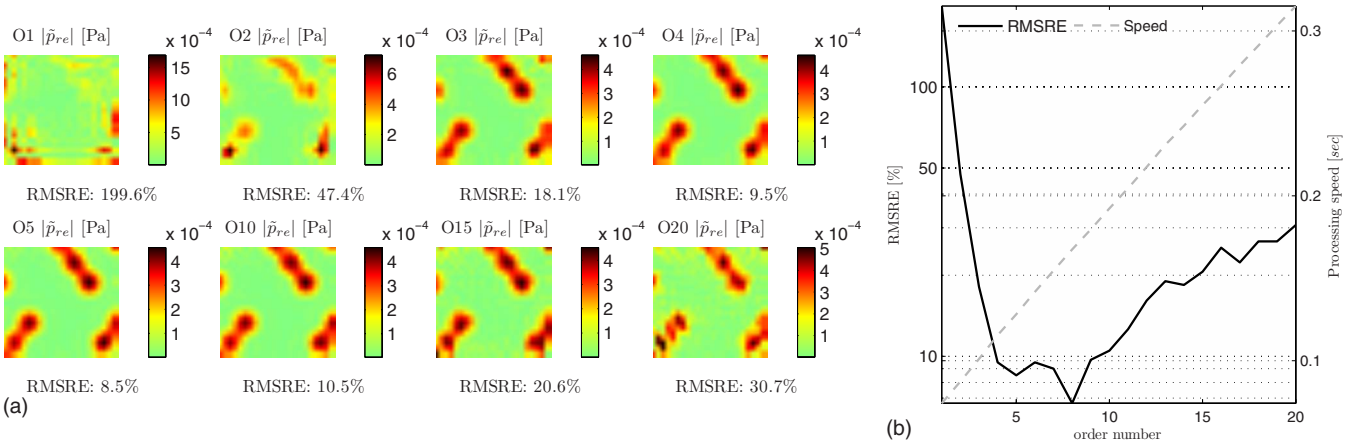

FIG. 8. (Color online) Influence of linear predictive border-padding order on resulting error of the point sources case after PNAH (a) and corresponding processing speed and error versus border-padding order (b); a fixed $k_{co}=1484$ rad/m is applied for all cases.

case, the wavenumbers that contain source information are much higher than the hard-disk drive case and the sources originating from the blades are rotating in the aperture plane.

The hard-disk drive under test is a Quantum Fireball LCT10, mounted in a vertical position with the top cover facing forward, driven in idle mode. The sensor, a Sonion 8002 microphone that is generally used in hearing aids, is placed on a triple axis *xyz*-robot. The sensor is traversed to pre-defined measurement grid points which results into a hologram of sound pressure when a spatially fixed reference microphone is used. The measured equidistant grid counts 21 rows by 17 columns with 0.01 m inter-sensor distance at 0.02 m from the source plane. The hologram at one of the peak-frequencies of 1075 Hz is shown in Fig. 9(a). For the cooling fan a grid of 32×32 is used at a hologram distance of 0.02 m and an inter-sensor distance of 0.002 m. The hologram at the peak-frequency of 722 Hz, which is equal to the rotational speed of the fan, is shown in Fig. 9(b). The cooling fan is blowing away from the measurement plane.

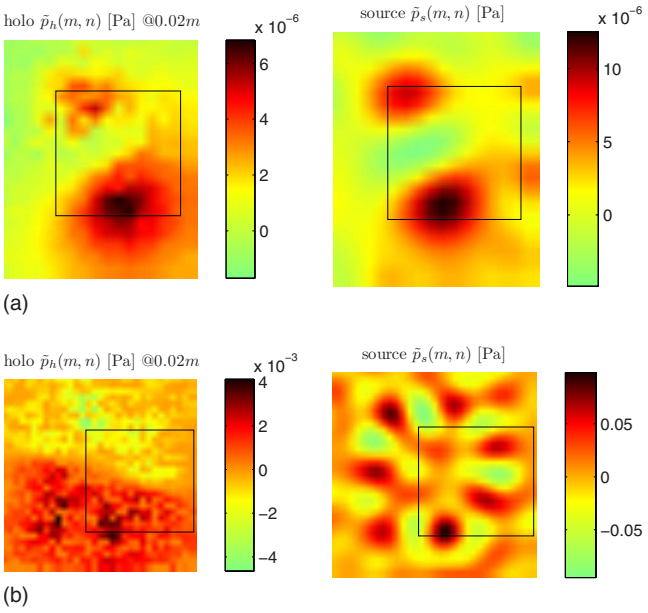

FIG. 9. (Color online) Acoustic images of the measured hologram at 1075 Hz (left) of the hard-disk drive and the PNAH result at the source plane (right) for a fully processed aperture (a) and the measured hologram at 722 Hz (left) of the cooling fan and the PNAH result at the source plane (right) for a fully processed aperture.

In both cases the modified exponential filter[2] is used, with the L-curve criterion to determine the filter cut-offs for the large original holograms. Obviously, in case of the hard-disk drive a different cut-off is chosen for the filter compared to the one used in the cooling fan case, yet once a cut-off is chosen for a single case it is used for all applied border-padding methods in order to compare them under equal circumstances.

B. Discussion

The practical results mainly show the same trend as the numerical analysis, although the errors are somewhat larger due to the presence of measurement noise in both holograms. The hard-disk drive case shows lowest errors due to the lower wavenumber content and amount of measurement noise. The difference between linear predictive border-padding on one side and basic border-padding and windowing on the other side is significant, both qualitative and error-wise. An interesting observation is the near equal RMSRE of both the windowing [Fig. 10(1)] and the basic border-padding [Fig. 10(2)] results and the clearly better qualitative result for basic border-padding. This difference illustrates the fact that low quantitative errors can occur, yet the usefulness for proper source identification is questionable. The cooling fan case shows much higher wavenumber content, especially along the borders of the chosen aperture. Here all three types of border-padding perform well, even basic border-padding [Fig. 11(2)] which failed in the numerical high wavenumber case [Fig. 6(2)]. The good performance of basic border-padding is very dependent on the aperture choice in this example, since the data near the border fit the cosine tapering very well. Overall, basic border-padding performs worse than linear predictive border-padding and at some point, at high wavenumber content, the numerical errors become too large and blow up the result after the inverse propagation.

In both cases the higher order prediction filter is bound to extrapolate more noise near the border, resulting in more leakage. This is also the reason of the relatively good perfor-

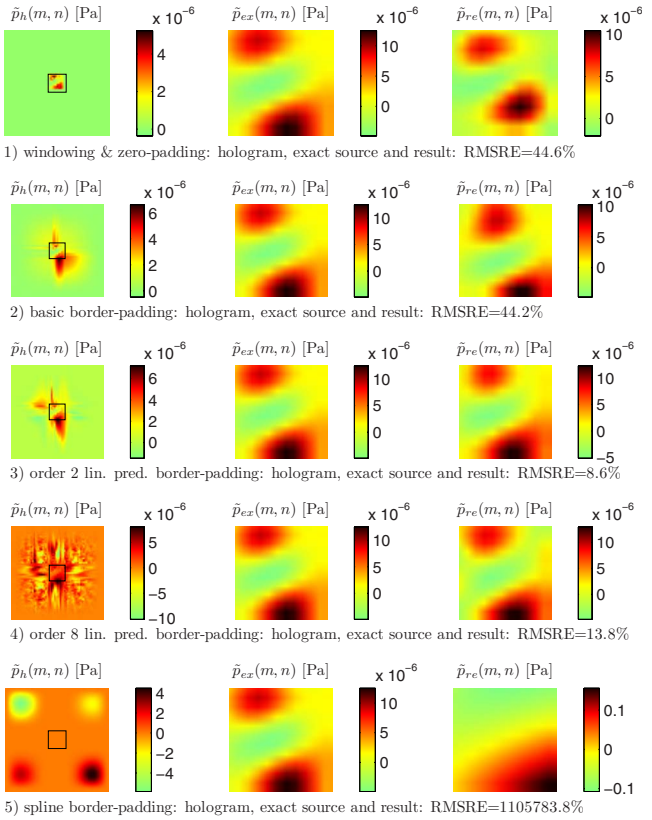

FIG. 10. (Color online) Five types of data extrapolation on measurements of the hard-disk drive and processed with PNAH, the rectangles mark the selected, smaller aperture that is border-padded; a fixed k_{co}=98 rad/m is applied for all cases.

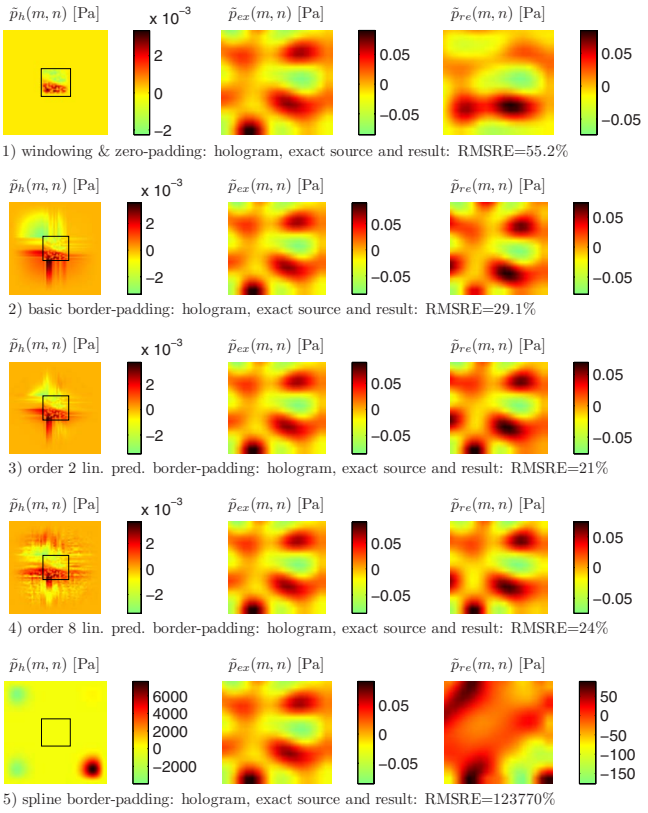

FIG. 11. (Color online) Five types of data extrapolation on measurements of the cooling fan and processed with PNAH, the rectangles mark the selected, smaller aperture that is border-padded; a fixed k_{co}=275 rad/m is applied for all cases.

mance by the basic border-padding algorithm compared to the numerical simulations, since it is less sensitive to noisy behavior within the aperture itself. The other alternative, spline border-padding, is highly sensitive to noise and although it shows reasonably good results in the numerical modal case, it fails in both practical applications, as shown in Figs. 10(5) and 11(5). The standard windowing and zero-padding method shows fairly good RMSREs, yet the qualitative results in Figs. 10(1) and 11(1) are very poor, which makes this method inappropriate for this kind of source identification.

From these results on actual measured holograms of real-life cases, the practicability of border-padding is visualized. Even in the presence of noise and only a very limited number of data points, still good and reliable results follow from applying either basic or linear predictive border-padding. A broader research on the influence of noise and the size of the border-padded aperture is required to give a distinct conclusion on a practically optimal choice of the filter order in linear predictive border-padding. However, based on these results both the second and eighth order descriptions provide good qualitative and quantitative results in the test and are both good standard orders to implement in practise.

VI. CONCLUSIONS

Border-padding is a fast, efficient and accurate extrapolation method that adds practical relevance to the standard FFT-based NAH methods based on k-space inverse propagation of the sound-field. The strategy to pre-process the spatial acoustic data before the FFT is applied is robust and minimizes leakage and distortion of the acoustic field. By decoupling the spatial pre-processing from inverse propagation and regularization, a highly versatile method without any pre-knowledge of noise color and variance resulted. The use of measured data to form a physically relevant filter implementation to extrapolate the finite aperture shows great improvements compared to standard windowing and other forms of data extrapolation.[19]

The numerical experiments on the modal source show very good results for filter orders of 5 and higher, yet the lower orders still show reasonably good results in comparison with basic border-padding, windowing, and spline extrapolation. The numerical point sources case shows equal results for low orders, although for high orders the RMSRE is steadily increasing, also resulting in qualitatively decreasing results. In a practical situation where sources are unknown, a filter order between orders 5 and 10 suffice. Also in the presence of noise in the actual measured cases it is shown that border-padding is a well-applicable method in real-life cases.

Besides extrapolation of the aperture edges outward, border-padding is also applicable to fill gaps in the hologram aperture. This allows the use of several patches along the area of interest without equidistant rectangular measurement grids, since border-padding permits coupling of the separate patches to form a rectangular grid. Also, the processing

speed of PNAH with border-padding allows processing of a very large number of connecting apertures of different sizes and shapes, a conclusion which also followed from Ref. 20.

The applied algorithm first treats the data in one dimension completely, followed by the other dimension, which probably results in sharp edges and thus high wavenumbers. This possibly poses a problem when the border-padded aperture is inverse propagated, yet this phenomenon only emerges relatively far away from the measured aperture, not causing any problems in the truncated result. Yet, a fully 2D method could increase the possibilities of border-padding.

ACKNOWLEDGMENT

This research is supported by the Dutch Technology Foundation (STW).

[1]E. G. Williams, "Regularization methods for near-field acoustical holography," J. Acoust. Soc. Am. **110**, 1976–1988 (2001).
[2]R. Scholte, I. Lopez, N. B. Roozen, and H. Nijmeijer, "Wavenumber domain regularization for near-field acoustic holography by means of modified filter functions and cut-off and slope iteration," Acta. Acust. Acust. **94**, 339–348 (2008).
[3]E. G. Williams and J. D. Maynard, "Holographic imaging without the wavelength resolution limit," Phys. Rev. Lett. **45**, 554–557 (1980).
[4]J. D. Maynard, E. G. Williams, and Y. Lee, "Nearfield acoustic holography: I. Theory of generalized holography and the development of NAH," J. Acoust. Soc. Am. **78**, 1395–1413 (1985).
[5]E. G. Williams, *Fourier Acoustics: Sound Radiation and Nearfield Acoustical Holography* (Academic, London, 1999).
[6]R. Steiner and J. Hald, "Near-field acoustical holography without the errors and limitations caused by the use of spatial DFT," Int. J. Acoust. Vib. **6**, 83–89 (2001).
[7]K. Saijyou and S. Yoshikawa, "Reduction methods of the reconstruction error for large-scale implementation of near-field acoustical holography," J. Acoust. Soc. Am. **110**, 2007–2023 (2001).
[8]E. G. Williams, "Continuation of acoustic near-fields," J. Acoust. Soc. Am. **113**, 1273–1281 (2003).
[9]M. Lee and J. S. Bolton, "Reconstruction of source distributions from sound pressures measured over discontinuous regions: Multipatch holography and interpolation," J. Acoust. Soc. Am. **121**, 2086–2096 (2007).
[10]M. Lee and J. S. Bolton, "A one-step patch near-field acoustical holography procedure," J. Acoust. Soc. Am. **122**, 1662–1670 (2007).
[11]R. Scholte, I. Lopez, and N. B. Roozen, "Improved data representation in NAH applications by means of zero-padding," in Proceedings of the Tenth International Congress on Sound and Vibration, Stockholm, Sweden (2003).
[12]F. J. Harris, "On the use of windows for harmonic analysis with the discrete Fourier transform," Proc. IEEE **66**, 51–83 (1978).
[13]J. W. Cooley and J. W. Tukey, "An algorithm for the machine calculation of complex Fourier series," Math. Comput. **19**, 297–301 (1965).
[14]J. W. Tukey, "An introduction to the calculations of numerical spectrum analysis," Proc. IEEE **66**, 61–83 (1978).
[15]J. P. Burg, *Maximum Entropy Spectral Analysis* (Stanford University, Stanford, CA, 1975).
[16]I. Kauppinen and J. Kauppinen, "Reconstruction method for missing or damaged long portions in audio signal," J. Audio Eng. Soc. **49**, 1167–1180 (2001).
[17]S. Haykin, *Adaptive Filter Theory*, 3rd ed. (Prentice-Hall, Upper Saddle River, NJ, 1996).
[18]A. V. Oppenheim and R. W. Schafer, *Digital Signal Processing* (Prentice-Hall, Englewood Cliffs, NJ, 1975).
[19]J. S. Bendat and A. G. Piersol, *Measurement and Analysis of Random Data* (Wiley, New York, 1966).
[20]A. Sarkissian, "Method of superposition applied to patch near-field acoustic holography," J. Acoust. Soc. Am. **118**, 671–678 (2005).

Analysis of parameters for the estimation of loudness from tone-burst otoacoustic emissions

Michael Epstein[a)]
Department of Speech-Language Pathology and Audiology, Auditory Modeling and Processing Laboratory, Communications and Digital Signal Processing Center, Northeastern University, 360 Huntington Avenue, Boston, Massachusetts 02115

Ikaro Silva
Department of Electrical and Computer Engineering, Auditory Modeling and Processing Laboratory, Communications and Digital Signal Processing Center, Northeastern University, 360 Huntington Avenue, Boston, Massachusetts 02115

(Received 4 November 2008; revised 28 February 2009; accepted 4 March 2009)

There is evidence that tone-burst otoacoustic emissions (TBOAEs) might be useful for estimating loudness. However, within-listener comparisons between loudness and TBOAE measurements are an essential prerequisite to determine appropriate analysis parameters for loudness estimation from TBOAE measurements. The purpose of the present work was to collect TBOAE measurements and loudness estimates across a wide range of levels in the same listeners. Therefore, TBOAEs were recorded for 1- and 4-kHz stimuli and then analyzed using a wide range of parameters to determine which parameter set yielded the lowest mean-square-error estimation of loudness with respect to a psychoacoustical, cross-modality-matching procedure and the inflected exponential (INEX) loudness model. The present results show strong agreement between 1-kHz loudness estimates derived from TBOAEs and loudness estimated using cross-modality matching (CMM), with TBOAE estimation accounting for almost 90% of the CMM variance. Additionally, the results indicate that analysis parameters may vary within a reasonable range without compromising the results (i.e., the estimates exhibit some parametric robustness). The lack of adequate parametric optimization for TBOAEs at 4 kHz suggests that measurements at this frequency are strongly contaminated by ear-canal resonances, meaning that deriving loudness estimates from TBOAEs at this frequency is significantly more challenging than at 1 kHz.
 [DOI: 10.1121/1.3106531]

PACS number(s): 43.66.Cb, 43.64.Jb [BLM] Pages: 3855–3864

I. INTRODUCTION

Typical procedures for the estimation of loudness growth require active participation by listeners giving subjective responses to stimuli. An alternative methodology for estimating loudness objectively would be very valuable in clinical populations that are unable to provide subjective responses. Schlauch *et al.* (1998) and Buus and Florentine (2001) showed compelling evidence that, for pure tone stimuli, loudness growth is proportional to the square of basilar-membrane velocity. This indicates that measures of cochlear activity may be useful for estimating loudness, at least for pure tones. A number of investigators have examined the general relationship between otoacoustic emissions and cochlear gain control, intensity, or loudness. Many of these studies have utilized distortion-product otoacoustic emissions (DPOAEs) and found at least some relationship between loudness and DPOAE input/output functions (Muller and Janssen, 2004; Janssen *et al.*, 2006; Neely *et al.*, 1997; Neely *et al.*, 2003; Buus *et al.*, 2001; Johannesen and Lopez-Poveda, 2008), but there has typically been difficulty selecting parameters that are suitable for estimating loudness over a wide range of levels in a diverse set of listeners. Despite evidence that tone-burst otoacoustic emissions (TBOAEs) might be useful for loudness estimation (Epstein *et al.*, 2004; Epstein and Florentine, 2005a), there is a dearth of measurements directly examining loudness estimates coupled with TBOAEs over a wide range of levels in a single group of listeners. In particular, there is some evidence that TBOAEs might be useful for estimating loudness at regional sites, as the response for a narrow-band stimulus is likely generated at around a characteristic location along the cochlea (Norton and Neely, 1987; Shera *et al.*, 2002) and OAEs are useful for estimating the peak of the traveling wave (Zweig and Shera, 1995). With the limited data in the literature, however, it is difficult to determine appropriate analysis parameters to be used for such an estimation procedure. The present work seeks to determine parameters that minimize the error in the loudness estimation from TBOAEs. Additionally, these parameters should be robust to small individual variations in optimality. For the present study, TBOAEs were recorded in response to 1- and 4-kHz tone bursts and then analyzed using a wide range of parameters to determine which parameter set yielded the average least-squares error estimation of loudness in reference to loudness functions derived using a cross-modality matching (CMM) procedure and the inflected exponential (INEX) loudness model (Florentine and Epstein, 2006). If TBOAEs are to be used for loudness estimation, it is important and desired that the esti-

[a)]Author to whom correspondence should be addressed. Electronic mail: m.epstein@neu.edu

mation procedure is insensitive to small variations in parametric choices in order to allow a robust procedure that accounts for anatomical and physiological variability across listeners. In addition, great care must be taken to avoid the linear, non-cochlear portion of the response that results from ear-canal resonances and other trivial acoustic reflections within the auditory system (Ravazzani *et al.*, 1996), which are particularly prevalent around 4 kHz.

II. METHODS

A. Listeners

Six listeners with normal hearing (four females, two males), ages 19–31, participated in both TBOAE and loudness measurements. No listener had a history of hearing difficulties, and their audiometric thresholds did not exceed 15 dB hearing level (HL) at octave frequencies from 250 Hz to 8 kHz (ANSI, 1996). Additionally, all listeners had their middle-ear function evaluated via a clinical exam. Measurements were also made in a coupler to further verify when the measurement parameters resulted in stimulus artifact contamination.

B. Stimuli

The tone bursts used in all parts of the experiment were 2-cycle-up-2-cycle-down pure tones multiplied by Gaussian windows. Two frequencies were tested: 1 and 4 kHz. The 1-kHz tone had a 4-ms duration and the 4-kHz tone had 1-ms duration. This 2-cycle-up-2-cycle-down tone duration ensured energy consistency between the two different frequencies (Hall, 2007). The windowed tone was then end-padded with silence to generate a stimulus length of 41.7 ms. The stimulus levels varied from 25 to 100 dB sound pressure level (SPL) in steps of 5 dB. The measurements at 25 and 30 dB SPL were omitted from analysis and presentation due to limited success getting both TBOAE and CMM measurements at these levels. Levels matched the specifications of the voltage-to-level conversion provided by Etymotic Research for the ER-10c apparatus.

For the CMM procedure, each stimulus presentation consisted of 12 concatenated 41.7-ms intervals in order to generate a train of tone bursts that lasted approximately 0.5 s. This train was presented in place of a single tone-burst in order to minimize any potential temporal integration effects (Buus *et al.*, 1997; Florentine *et al.*, 1996; Zwicker and Fastl, 1999). Levels were determined by a pressure-proportional voltage-to-level conversion based on calibration levels measured in a coupler.

C. Apparatus

The stimuli were generated in MATLAB (2007b running on Windows 2000 for CMM and Ubuntu for TBOAEs) and converted from digital (48-kHz sampling frequency) to analog using a 32-bit Lynx Two Soundcard. The analog signal was then passed through either a Tucker-Davis Technologies (TDT) HB6 (CMM) or a TDT HB7 (TBOAEs) headphone buffer and presented monaurally via Sony MDR-V6 headphones (CMM) or the two transducers of the Etymotic ER-10C (TBOAEs) to a listener inside a double-walled sound-attenuating booth. During the TBOAE measurements, the recordings from the ER-10C were converted from analog to digital (48-kHz sampling frequency) via a Lynx Two soundcard. Routine calibration for each system was performed at the beginning of each session to test for proper wiring and ER-10C output in a plastic syringe coupler provided by Etymotic. In order to perform calibration, the signal was sent through the system and both the electrical signal and the acoustic signal from the coupled ER-10C were measured to be within 1 dB of the expected level. For the TBOAEs, all levels were determined using the rms of the windowed signal relative to the specifications which were provided by Etymotic and verified by doing an actual in ear measurement for a single listener using a Fonix 6500-CX real-ear system.

D. TBOAE recordings

Stimuli were presented in blocks of 1000 trials (about 41.7 ms per trial, at a presentation rate of about 24 Hz). Each block of trials was repeated eight times for each level yielding 8000 recordings per level. For each level, two averages of TBOAE recordings were made. The first average consisted of a weighted mean (Elberling and Wahlgreen, 1985) of all the trials in the first half of each of the eight blocks (total of 4000 trials), and the second average consisted of a weighted mean of all the trials in the second half of each of the eight blocks (total of 4000 trials). These averages were the basis for the loudness estimation procedure described in Sec. II G. Additionally, a separate analysis was done on the results recorded in a plastic coupler with the approximate size of a normal ear canal in order to yield a stable reference and an artificial approximation of the acoustic response of the ear canal.

E. CMM

Listeners were presented with six repetitions of each level in random order and asked to cut a string to be "as long as the sound is loud." After the listener cut each string, they taped it into a notebook and turned the page. Two blocks of trials were run separately, one for each of the two test frequencies. If a particular stimulus was not heard, no string was cut. Levels were omitted if fewer than four out of the six repetitions were heard. All listeners provided at least four strings for levels at 35 dB SPL and higher. The loudness estimate for each level was the transformed geometric mean of the string lengths produced for that level. The transformation was performed in response to the finding that CMM, although it provides access to the details of the shape of the loudness function for individual listeners, yields functions with shallower slopes than other procedures (Epstein and Florentine, 2005b). As such, a string-length multiplicative correction factor was determined by using a least-squares fit to match the average group data to a power function with an exponent equal to 0.3, widely used as a simple first approximation of the general form of the loudness function (Hellman and Zwislocki, 1963; Stevens and Guirao, 1964; Stevens, 1955; Stevens, 1957; Stevens, 1961). This correction factor was then applied to the individual data. While it is

also known that the CMM string-length procedure may have edge effects at low levels, as listeners have a difficult time cutting very small string sizes, the string-length CMM procedure has been shown to yield reliable individual data for a wide range of levels (Epstein and Florentine, 2005b; Epstein and Florentine, 2006). A number of other similar cross-modal line-length methods have also been used to estimate loudness functions with consistent results (Hellman, 1999; Teghtsoonian and Teghtsoonian, 1983; Thalmann, 1965; Serpanos and Gravel, 2000, 2004; Serpanos *et al.*, 1998). The final loudness-growth curve was subtracted by an offset in order to yield a zero-mean loudness curve for comparison with loudness curves obtained through other modalities. The comparative parameters of interest and meaning are the slopes of the functions. Thus, the offsetting was performed on individual data sets. Because the scales differ, the vertical offsets between TBOAEs and CMM measurements are arbitrary.

F. INEX loudness model

The INEX loudness model was used only for comparisons with group average data and not for any individual fitting or parameter optimization. The INEX model is described in full in Florentine and Epstein (2006). It is a simple set of modifications to the classical power function that includes the subtle variations in slope as a function of level observed in a number of studies by a variety of investigators (Buus and Florentine, 2001; Buus *et al.*, 1998, 1997; Hellman and Zwislocki, 1961; Robinson, 1957; Stevens, 1972; Zwislocki, 1965). The plotted INEX used here is computed by the following equation:

$$\log_{10}(N) = 1.7058 \times 10^{-9}L^5 - 6.587 \times 10^{-7}L^4 + 9.7515 \times 10^{-5}L^3 - 6.6964 \times 10^{-3}L^{2+}0.2367L - 3.4831,$$

where N is the loudness in sones (Stevens, 1936) and L is the level in dB SPL. Because this model is designed for longer-duration sounds on the order of around 200–500 ms, the function was then adjusted by 28.75 dB to account for the difference in sensation level between the very brief tone bursts used in the present study and longer-duration sounds used in most psychoacoustical experiments (Epstein and Florentine, 2005b; Epstein and Florentine, 2006; Florentine *et al.*, 1996, 2001). This is the equivalent of replacing L in the equation with $(L+28.75)$. This value was determined by calculating a psychometric function from the number of responses to the CMM stimuli and determining the level at which, on average, 50% of trials were detected.

G. Estimation of loudness from TBOAEs

The procedure used to estimate a loudness function from the two averaged TBOAE waveforms at each level is similar to that of Epstein and Florentine (2005a). For the present study, four parameters were allowed to vary: window delay from the stimulus onset (from 0 to 39 ms in 1 ms steps), window size (2.5, 10, 20, or 30 ms), window type (rectangular or Hanning), and frequency bandwidth of the analysis region (F-ratio=1, 1.5, 2, or 3). Combinations in which the sum of window delay and window size exceeded the duration of the recording (41.7 ms) were omitted from analysis. F-ratio is defined here as the ratio by which the lower and upper bounds of the frequency bandwidth of the analysis region are related to the center frequency. An F-ratio of 1 indicates that only the single fast-Fourier-transform (FFT) bin nearest to the center frequency is used. An F-ratio of 2 indicates that the lower bound of analysis is one-half of the center frequency and the upper bound of analysis is two times the center frequency. For instance, with a 1-kHz tone-burst, an F-ratio of 2 corresponds to an analysis band from 500 Hz to 2 kHz (i.e., an octave-wide analysis region on each side of the center frequency).

While varying these parameters, loudness for each level was estimated using three steps. First, each of the two averaged waveforms (weighted, point-by-point means of 4000 trials) was windowed using the window delay, window type, and window size selected. In the second step, FFTs of the two individual averages were calculated and the real components of the cross-spectrum between the two averages determined. Instead of using the FFT absolute magnitude, the real components of cross-spectra were used in order to minimize noise artifacts by including only the portions of the wave that are synchronized in the two averages. In the third and final step, loudness is estimated by taking the logarithm of the sum of the positive, real components of the cross-spectrum within the frequency region specified by the F-ratio. The final loudness-growth curve was subtracted by an offset in order to yield a zero-mean loudness curve for comparison with loudness curves obtained through the other methods utilized.

H. Peak TBOAE latency estimation

The peak latencies of the recorded responses were also estimated as a function of level and stimulus frequency. The recordings at each level were filtered using an octave-wide filter with a center frequency equal to the stimulus frequency. The filter was generated in MATLAB as an eighth-order Butterworth infinite impulse response filter. The filtering was performed off-line in conjunction with the function FILTFILT in order to ensure that the filtered response had no phase shifts. The envelopes of these filtered responses were then estimated by passing the magnitude of the Hilbert transform of the filtered signals through a low-pass eighth-order Butterworth filter with cut-off frequency set to 200 Hz (again in conjunction with the FILTFILT function). The latency of the peak OAE in each condition was the maximum value of the filtered Hilbert transform observed between 2 ms after stimulus offset and 25 ms after the stimulus onset. The initial delay from the stimulus offset was chosen to help reduce the likelihood that the latency observed actually resulted from trivial acoustic artifacts in the ear canal rather than OAEs.

III. RESULTS AND DISCUSSION

A. Cross-modality measurement correction factor

The CMM measurements for 1 and 4 kHz were independently scaled by a fixed correction factor to ensure that the

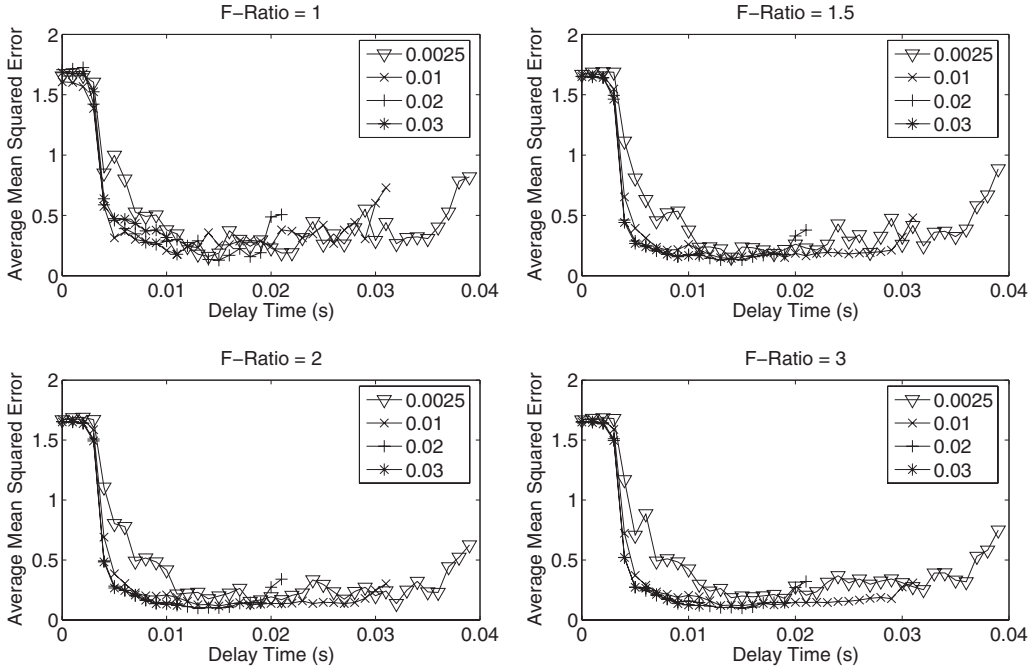

FIG. 1. AMSE between loudness measured using CMM and loudness estimated from TBOAEs in response to 1-kHz tone bursts using a rectangular analysis window. The plots show AMSE as a function of window delay, with each curve representing different window sizes and each plot representing a different *F*-ratio.

resulting functions were similar to the expected form of the loudness function (i.e., power function exponent equal to 0.3). The same scaling factor, 1.67, was used for all subjects based on the average data. The 1- and 4-kHz scale-factors were calculated separately, but agreed exactly to three decimal places, so the same value was used for both. This is consistent with the expectation that loudness functions for tones at different frequencies are parallel on a log scale within a relatively wide range of frequencies (Hellman, 1976).

B. Loudness Estimation from TBOAEs at 1 kHz

Figure 1 shows the averaged mean squared error (AMSE) across subjects between loudness measured using CMM (after scaling) and loudness estimated from TBOAEs in response to 1-kHz tone bursts using a rectangular analysis window. The measures are compared directly on an arbitrary normalized logarithmic scale with both functions vertically shifted to zero mean. An increase of 1 unit on this scale corresponds to the scaled string length multiplied by 10 and a change of 10 dB in TBOAE level. The plots show AMSE as a function of window delay, with each curve representing a different window size and each panel representing a different *F*-ratio. Figure 2 is identical to Fig. 1 except that the TBOAE loudness estimation was instead performed using a Hanning analysis window. All of the loudness estimations shown in both figures exhibit a similar pattern. Regardless of other parameters, when window delay is very short, the window captures stimulus artifact or the linear reflections within the auditory system. As the delay gets longer, the AMSE improves, indicating that the effects of the stimulus artifact diminish and the non-linear cochlear response becomes more pronounced. At very long delays, the window fails to capture the TBOAE at a level strong enough to overcome the background noise.

The Hanning window (Fig. 2) appears more robust than the rectangular window (Fig. 1) and results in near-optimal AMSE for a larger range of delays. In addition, the Hanning window reaches optimality sooner because it de-emphasizes the early portion of the signal more. It is thus important to note that the Hanning window has a total area equal to half of the rectangular window. As such, the Hanning window is more localized in time, resulting in an increased side-lobe attenuation in the spectral domain, which can improve spectral estimation and reduce any leakage artifacts (Harris, 1978). The AMSE curve is approximately flat for delays of 13–20 ms, similar to the findings of Epstein *et al.* (2004) in which no significant effect of window delay was found in that range. It is noteworthy that the apparatus and the duration of the stimulus differ somewhat between the two experiments and the results are still in agreement.

Each of the curves in Figs. 1 and 2 are for different window sizes. The shortest window size (0.0025 ms) tends to yield high variance estimates as a function of delay. This short window size is very sensitive to local variations in background noise because of the small number of points being collected. In addition, because the window is so short, it has a smaller range of near-optimal delays. At short delays, in particular, this window will place a lot of emphasis on the stimulus itself resulting in a poor loudness estimate. The loudness estimate becomes more robust as the window size increases (i.e., a classical trade-off between recording time and susceptibility to noise in measurements). The 20-ms and

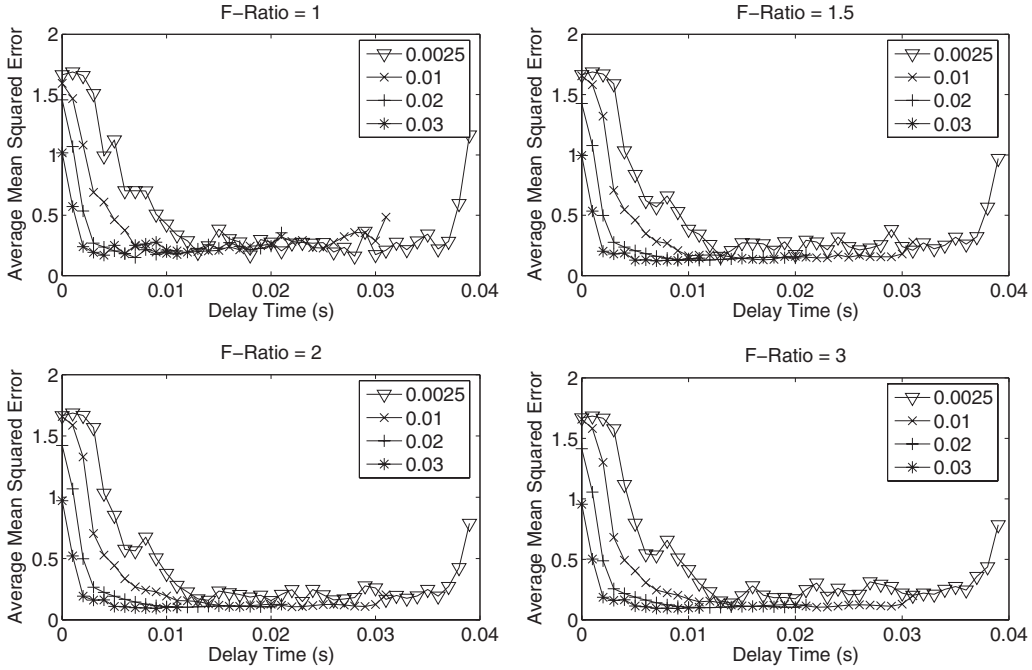

FIG. 2. AMSE between loudness measured using CMM and loudness estimated from TBOAEs in response to 1-kHz tone bursts using a Hanning analysis window. The plots show AMSE as a function of window delay, with each curve representing different window sizes and each plot representing a different *F*-ratio.

30-ms windows perform approximately equally well. As a result, a 20-ms window was arbitrarily chosen for subsequent loudness estimation.

The *F*-ratios of 2 and 3 result in lower optimal AMSEs (AMSE=0.10 for both) than *F*-ratios of 1 or 1.5 (AMSE =0.15 and 0.13, respectively). As the AMSEs for *F*-ratios of 2 and 3 are approximately equal, an *F*-ratio of 2 will be used for subsequent loudness estimation. The combination of parameters that provides the lowest AMSE is a Hanning window with a window delay of 10 ms, a window size of 20 ms, and an *F*-ratio of 2.

C. Loudness estimation from TBOAEs at 4 kHz

It is known that it is difficult to measure TBOAEs at 4 kHz due to ear-canal resonance and signal artifacts (Ravaz-

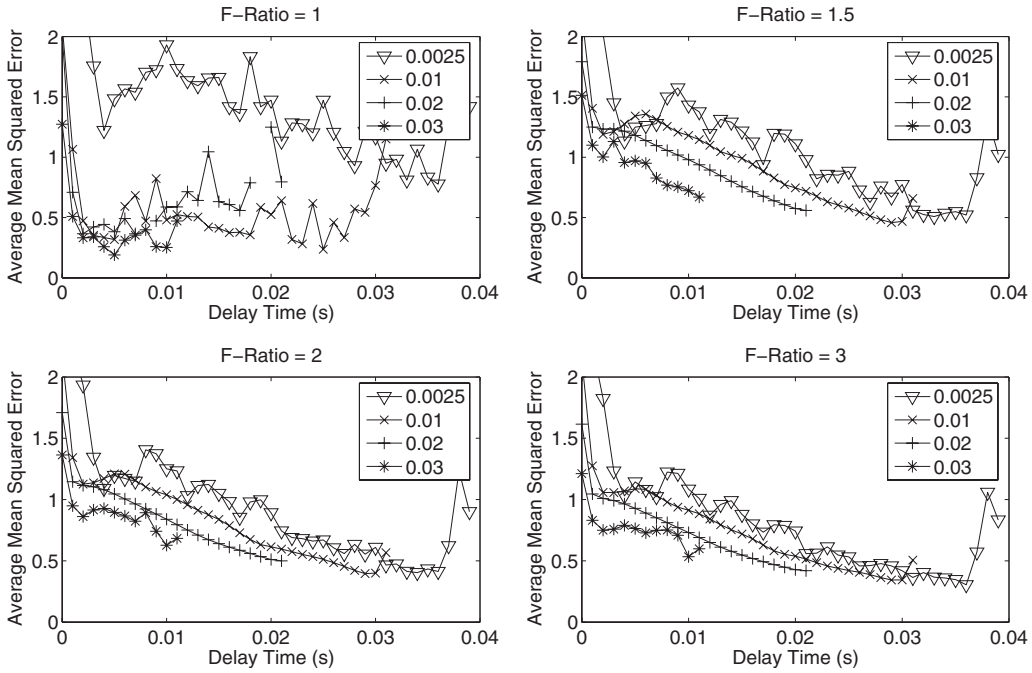

FIG. 3. AMSE between loudness measured using CMM and loudness estimated from TBOAEs in response to 4-kHz tone bursts using a Hanning analysis window. The plots show AMSE as a function of window delay, with each curve representing different window sizes and each plot representing a different *F*-ratio.

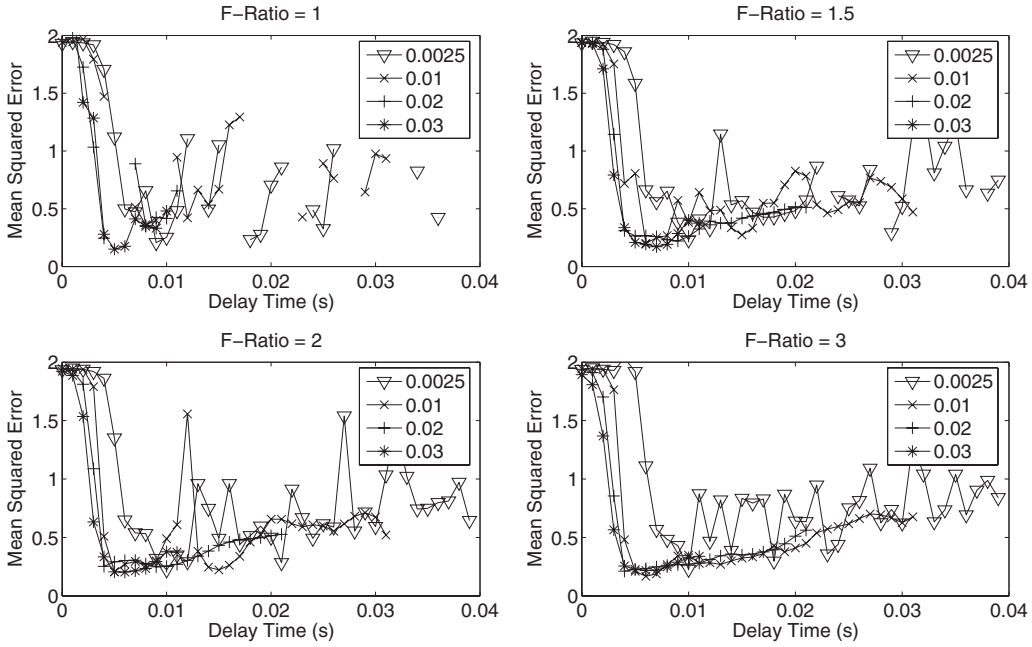

FIG. 4. MSE between loudness measured using CMM and loudness estimated from the response of the coupler to 1-kHz tone bursts using a Hanning analysis window. The plots show AMSE as a function of window delay, with each curve representing different window sizes and each plot representing a different *F*-ratio.

zani and Grandori, 1993; Whitehead *et al.*, 1994). Identical sets of analyses were performed for the responses to 4-kHz tone bursts to determine whether the current procedure could be used to estimate loudness of 4-kHz tone bursts using any possible combination of parameters. Although neither window produced particularly good results, both the Hanning and rectangular windows yielded roughly the same results, with the Hanning window providing a slightly more robust response. Therefore, only the Hanning-window results are shown in Fig. 3.

None of the parametric combinations resulted in AMSE approaching the values measured at 1 kHz. As the window delay increases and less of the stimulus resonance is captured, the error decreases. However, it seems like the linear response of the ear-canal resonance overpowers any possible non-linear cochlear response. The results support reports of difficulty making measurements at 4 kHz and support the claim that most of the 1-kHz responses are true non-linear responses and not simple linear reflections. The small number of missing data points resulted from noisy data that did not contain any positive real components in the cross-spectrum (see Sec. II G).

D. Coupler measurements

The goal of all of these analyses was not only to determine the parameters that minimize the error in the loudness estimation but also to identify a possible spurious relationship with stimulus artifacts. To this end, Fig. 4 shows the MSE comparing the results from the human listeners' average CMM and the loudness-estimation procedure in response to 1-kHz tone bursts compared to measurements in a coupler using a Hanning window as a function of window delay. These results exhibit a relatively clear MSE minimum despite the fact that the coupler generated no TBOAEs. However, this minimum still has a higher absolute estimation error than any of the minima measured using 1-kHz tones in real ears. Additionally, the lowest values of the MSE result immediately after the stimulus offset. As the CMM function has been shifted to have a zero mean, the MSE is then essentially just a sum of the squares of the logarithmic values of string length after the shift. This pattern is in great contrast with the results measured in the real ears, which show a relatively wide range of stable delays and lower MSE (see Fig. 2).

Identical measurements at 4 kHz in the coupler, shown in Fig. 5, exhibit a long, but asymptotic, decrease in MSE as the ringing diminishes (clearly, a much longer ringing decay time than for the 1-kHz stimulus). The optimal case results in a MSE much higher than the 1-kHz real-ear response (Fig. 1), but results that are not much worse than the 4-kHz real-ear responses (see Fig. 3). Again, this supports the idea that the 4-kHz measurements fail to capture the non-linear response, but that the 1-kHz non-linear response cannot be explained by simple resonance or linear reflections from the ear canal.

E. Comparison between TBOAE loudness estimates and CMM loudness measurements

In Figs. 6–8, functions were allowed to vary by a single parameter in order to adjust the location of the curve on the plot to have to zero-mean. Figure 6 shows estimates of loudness in response to 1-kHz tone bursts as a function of level derived from TBOAEs and CMM. Several loudness estimates are plotted, each for a different window delay to demonstrate the robustness of the estimation procedure and to show the contrast of the zero-delay stimulus response. There is excellent agreement between the TBOAE loudness estimates and the direct measure of loudness, except at the low-

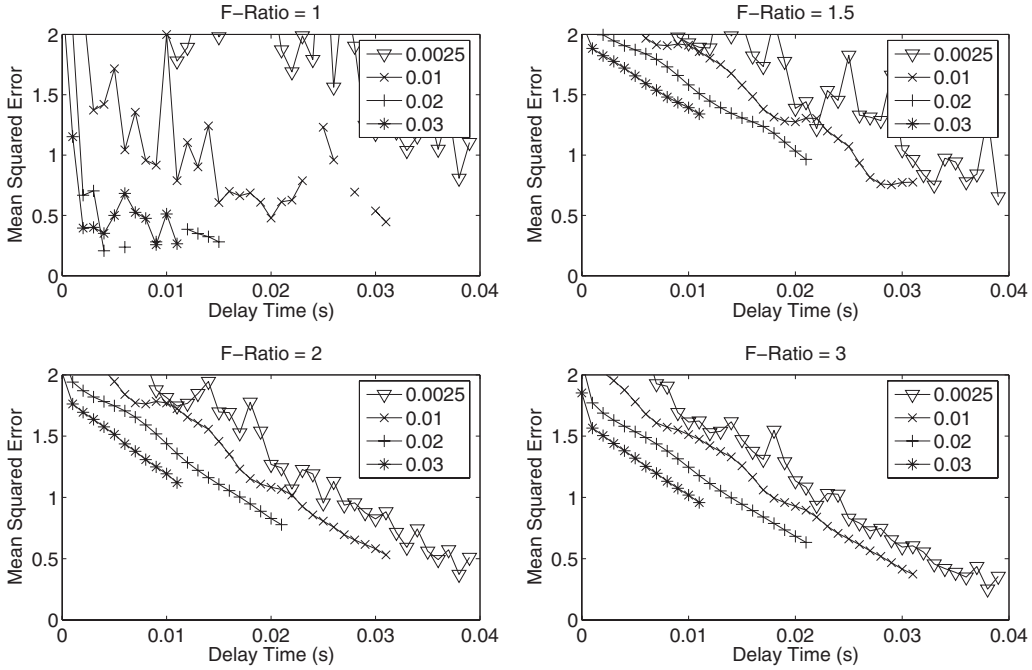

FIG. 5. MSE between loudness measured using CMM and loudness estimated from the response of the coupler to 4-kHz tone bursts using a Hanning analysis window. The plots show AMSE as a function of window delay, with each curve representing different window sizes and each plot representing a different *F*-ratio.

est levels. This is consistent with loss of steepness at low levels resulting from edge effects in the CMM procedure (Hellman and Meiselman, 1988). It is noteworthy that the analysis results in a nearly linear response when the window delay is set to zero and the stimulus itself is included in the analysis.

Figure 7 is identical to Fig. 6 for the 4-kHz tone bursts. The estimates derived from TBOAEs at 4 kHz are all far too steep and serve as very poor fits to the CMM function. In fact, they are more likely to match the linear response obtained when the window delay is set to zero. This is due to the difficulty in avoiding ear-canal resonances. The resulting OAEs contained too great a linear component to remove by simple windowing and averaging. As these results match those seen in the coupler, they are unlikely to arise from actual cochlear processing. In contrast, the OAEs in response to the 1-kHz tone bursts differed dramatically from the coupler recordings, indicating that these measurements did indeed result from cochlear processes.

Figure 8 shows a summary of all of the average functions in optimal parametric conditions. It is particularly noteworthy that the CMM functions at the two frequencies correspond quite closely, indicating that the psychoacoustical loudness functions are consistent across frequency. The INEX and the loudness function derived from TBOAEs at 1 kHz show excellent correspondence across the entire range.

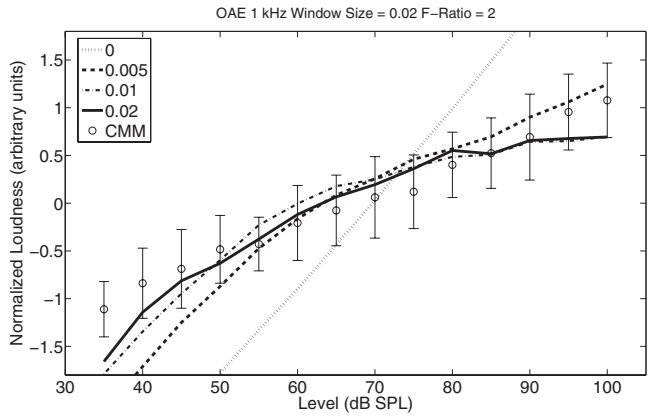

FIG. 6. Loudness resulting from 1-kHz tone bursts as a function of level for estimates derived from TBOAEs and for direct loudness measurements using CMM. Several loudness estimates for the TBOAEs are plotted, each for a different window delay. This analysis was performed with a 20-ms Hanning window and an *F*-ratio of 2. Error bars show ±1 standard deviation.

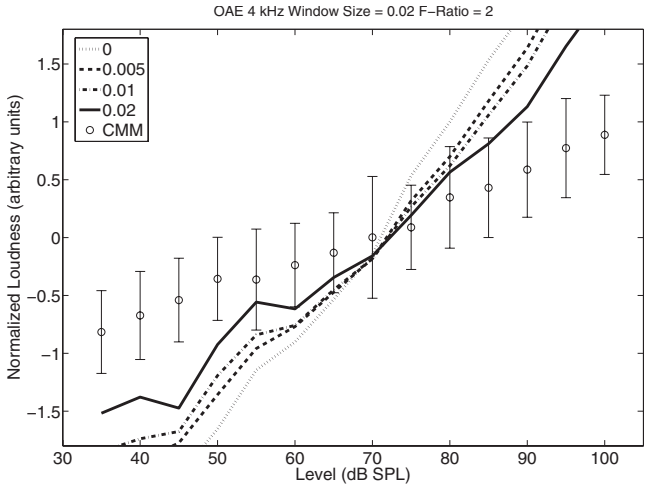

FIG. 7. Loudness resulting from 4-kHz tone bursts as a function of level for estimates derived from TBOAEs and for direct loudness measurements using CMM. Several loudness estimates for the TBOAEs are plotted, each for a different window delay. This analysis was performed with a 20-ms Hanning window and an *F*-ratio of 2. Error bars show ±1 standard deviation.

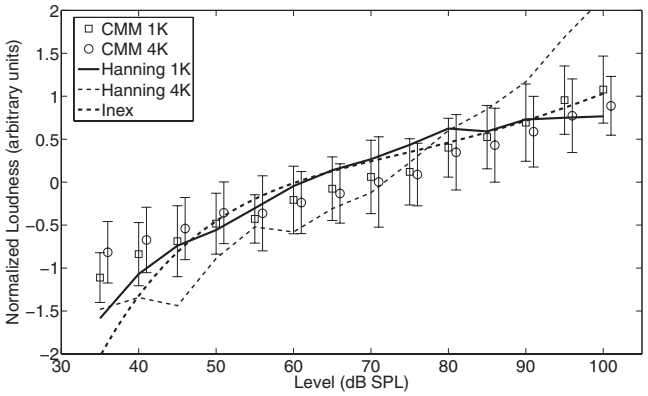

FIG. 8. Loudness as a function of level derived from CMM and Hanning-windowed TBOAEs in response to 1- and 4-kHz stimuli (The 4-kHz CMM data points are offset by 1 dB so that the error bars are visible). In addition, the INEX model loudness function is plotted for comparison with loudness measurements in the literature. Error bars show ±1 standard deviation.

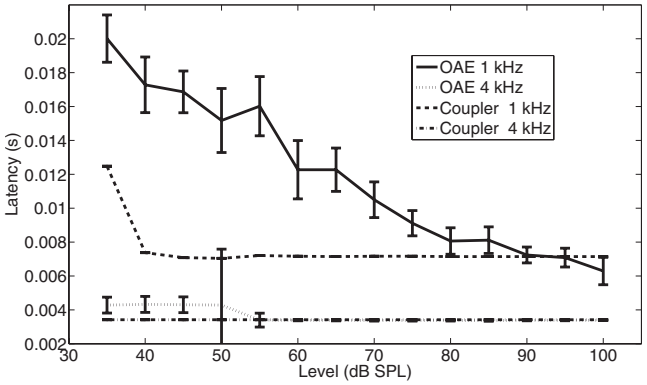

FIG. 9. TBOAE latency estimates as a function of level for both the real ears and coupler in response to 1- and 4-kHz stimuli. Error bars show ±1 standard deviation.

This indicates that TBOAE functions may be closely related to loudness measured using longer tones for an average of a group of listeners.

F. Latency/level relationship

Figure 9 shows the estimate of latency as a function of level for both the real ears and coupler at 1 and 4 kHz. For OAE measurements in real ears at 1 kHz, the results show a relatively smooth decrease in latency as a function of level, ranging from about 20 ms at 35 dB SPL to 6.3 ms at 100 dB SPL. Although this result differs somewhat from other reports of TBOAE latency (Hoth and Weber, 2001; Brass and Kemp, 1991; Schairer *et al.*, 2006; Sisto and Moleti, 2007), it is not surprising, since the methodologies for estimating OAE latency, the window sizes and shapes, and the definition of latency differ substantially among studies.

The present real-ear results are in agreement with the fact that the latency measured in the coupler at 1 kHz remains constant as a function of level. This indicates that the coupler recordings show a peak response at the biggest peak of the trivially reflected waveform, observed here to be close to 7 ms. In contrast, the acoustic ringing at 4 kHz was significant enough to render the procedure invariant to the initial delay chosen (i.e., the maximum would always occur at the beginning of the selected time region in both the real ears and the coupler). In this case, the latency was estimated at approximately 3.4 ms for both the real ears and the coupler. Even when the start of the observation window was delayed by several more milliseconds, the real ears and coupler produced identical, flat latency curves with latencies adjusted to match the start time of the window.

G. Analysis

Additional numerical analyses were performed by first assuming a "correct" loudness function and then determining the error (Model−Data) between the model and each of the other functions. Two analyses were performed: in one the correct model was the INEX function, and in the other the correct model was the CMM data at 1 kHz. The variability accounted for by the model function is then quantified by

$$1 - [\text{Variance}(\text{Model} - \text{Data})/\{\text{Variance}(\text{Model} - \text{Data}) + \text{Variance}(\text{Model})\}].$$

This method is more useful than a simple correlation analysis because it does not heavily weight trends that are simply in the same linear direction, but rather looks at whether the functions deviate from each other. Table I shows the variability accounted for by each data set given a specific model. It is noteworthy that the INEX resulted from a relatively large quantity of data, but none of the data or listeners in the present study.

When the CMM 1*k* function was used as the ideal function, the CMM 4*k* function was found to correspond closely. This indicates that the average loudness functions at these different frequencies are consistent. Other measurements of loudness have shown similar results (e.g., Hellman, 1976). Additionally, the Hanning-windowed 1 kHz OAE input/output function also closely matched the CMM 1*k* function. This supports the idea that TBOAE measurements at 1 kHz are related to loudness. This idea is further supported by the second comparison, performed with the INEX model as the "ideal" function. If the INEX is assumed to be a good average loudness function, CMM is then an acceptable, but not ideal measure of loudness based on the variance accounted for by the CMM functions when using the INEX as the

TABLE I. Variance accounted for by using the CMM 1-kHz data and INEX function as models of the results of CMM and TBOAEs.

Model		CMM 1*k*	CMM 4*k*	INEX	OAE Hann. 1*k*	OAE Hann. 4*k*	OAE Rect. 1*k*	OAE Rect. 4*k*
CMM 1*k*	Variance accounted	⋯	0.96	0.82	0.89	0.63	0.80	0.45
INEX	Variance accounted	0.88	0.76	⋯	0.96	0.72	0.95	0.60

model. In fact, the 1-kHz TBOAE loudness models matched the INEX function better than CMM, despite the fact that the analysis parameters were optimized to fit the CMM function. This indicates that TBOAEs may actually be a better measure of loudness than CMM. As expected, the 4-kHz TBOAE functions did not serve as very good models of either ideal function.

In order to examine potential viability for use as an individual metric for the assessment of loudness growth, the same analysis was performed comparing individual CMM at 1 kHz and loudness estimated using Hanning-window analysis on 1-kHz TBOAEs. The group average variance accounted for in this condition was 0.89 in the earlier analysis. The mean of the individual accounted variances was 0.80 with a standard deviation of 0.11. Of the six listeners, two estimates matched relatively poorly with variances accounted of 0.62 and 0.68. In both cases, the individuals for whom the variance accounted was lower had particularly shallow CMM slopes indicating that much of the problem may have arisen as a result of unreliable CMM data rather than unreliable OAE data.

The remaining listeners had variances accounted of 0.83, 0.86, 0.89, and 0.90. This indicates that, at least for two-thirds of the listeners, the two methods resulted in roughly the same estimates of loudness.

IV. CONCLUSIONS AND FUTURE WORK

These results indicate that there is significant potential for using tone-burst otoacoustic emissions for estimating loudness in response to 1-kHz stimuli across a wide range of levels in normal-hearing listeners. However, at frequencies near to ear-canal resonance, a simple reflection analysis procedure may not be sufficient to eliminate acoustic artifacts for loudness estimation. Tone-burst OAEs seem to be free from the complex interactions that occur with high-level DPOAEs, but the results of TBOAE measurements may not be as robust to ear-canal resonance as DPOAEs. If loudness functions could be estimated rapidly from TBOAEs at all audiometric frequencies in hearing-impaired listeners, this would provide an easy means for performing more advanced hearing-aid fitting using not only threshold but also loudness-growth functions. However, it remains to be seen if this measurement can be made across a wide enough range of frequencies and a separate strategy would likely need to be used for frequencies near the ear-canal resonances. More work still needs to be done to examine the frequency-specific applicability of TBOAEs for measuring loudness growth within the full range of audiometric frequencies. If the type of response measured at 1 kHz can be extended throughout the full frequency range, TBOAEs could be very useful clinically for performing improved hearing-aid fitting.

ACKNOWLEDGMENTS

The authors wish to thank Mary Florentine for helpful comments on an earlier version of this manuscript. The editor and two anonymous reviewers also provided helpful comments. This research was supported by The Capita Foundation.

ANSI (**1996**). "American National Standard Specification for Audiometers," ANSI S3.6-1996.

Brass, D., and Kemp, D. T. (**1991**). "Time-domain observation of otoacoustic emissions during constant tone stimulation," J. Acoust. Soc. Am. **90**, 2415–2427.

Buus, S., and Florentine, M. (**2001**). "Modifications to the power function for loudness," in *Fechner Day 2001*, edited by E. Sommerfeld, R. Kompass, and T. Lachmann (Pabst, Berlin).

Buus, S., Florentine, M., and Müsch, H. (**1998**). "Loudness function for tones at low levels derived from loudness summation," in *Psychophysical and Physiological Advances in Hearing*, edited by A. R. Palmer, A. Rees, A. Q. Summerfield, and R. Meddis (Whurr, London).

Buus, S., Florentine, M., and Poulsen, T. (**1997**). "Temporal integration of loudness, loudness discrimination, and the form of the loudness function," J. Acoust. Soc. Am. **101**, 669–680.

Buus, S., Obeling, L., and Florentine, M. (**2001**). "Can basilar-membrane compression characteristics be determined from distortion-product otoacoustic-emission input-output functions in humans?," in *Physiological and Psychophysical Bases of Auditory Function*, edited by D. J. Breebaart, A. J. M. Houtsma, A. Kohlrausch, V. F. Prijs, and R. Schoonhoven (Shaker, Maastricht, Netherlands).

Elberling, C., and Wahlgreen, O. (**1985**). "Estimation of auditory brainstem response, ABR, by means of Bayesian inference," Scand. Audiol. **14**, 89–96.

Epstein, M., Buus, S., and Florentine, M. (**2004**). "The effects of window delay, delinearization, and frequency on tone-burst otoacoustic emission input/output measurements," J. Acoust. Soc. Am. **116**, 1160–1167.

Epstein, M., and Florentine, M. (**2005a**). "Inferring basilar-membrane motion from tone-burst otoacoustic emissions and psychoacoustic measurements," J. Acoust. Soc. Am. **117**, 263–274.

Epstein, M., and Florentine, M. (**2005b**). "A test of the equal-loudness-ratio hypothesis using cross-modality matching functions," J. Acoust. Soc. Am. **118**, 907–913.

Epstein, M., and Florentine, M. (**2006**). "Loudness of brief tones measured by magnitude estimation and loudness matching," J. Acoust. Soc. Am. **119**, 1943–1945.

Florentine, M., Buus, S., and Poulsen, T. (**1996**). "Temporal integration of loudness as a function of level," J. Acoust. Soc. Am. **99**, 1633–1644.

Florentine, M., and Epstein, M. (**2006**). "To honor Stevens and repeal his law (for the auditory system)," in *Fechner Day*, edited by D. E. Kornbrot, R. M. Msetfi, and A. W. MacRae (International Society for Psychophysics, St. Albans, England).

Florentine, M., Epstein, M., and Buus, S. (**2001**). "Loudness functions for long and short tones," in *Fechner Day 2001*, edited by E. Sommerfeld, R. Kompass, and T. Lachmann (Pabst, Berlin).

Hall, J. W. (**2007**). *Handbook of Auditory Evoked Responses* (Allyn & Bacon, Boston, MA).

Harris, F. J. (**1978**). "On the use of windows for harmonic analysis with the discrete Fourier transform," Proc. IEEE **66**, 51–84.

Hellman, R. P. (**1976**). "Growth of loudness at 1000 and 3000 Hz," J. Acoust. Soc. Am. **60**, 672–679.

Hellman, R. P. (**1999**). "Cross-modality matching: A tool for measuring loudness in sensorineural impairment," Ear Hear. **20**, 193–213.

Hellman, R. P., and Meiselman, C. H. (**1988**). "Prediction of individual loudness exponents from cross-modality matching," J. Speech Hear. Res. **31**, 605–615.

Hellman, R. P., and Zwislocki, J. J. (**1961**). "Some factors affecting the estimation of loudness," J. Acoust. Soc. Am. **33**, 687–694.

Hellman, R. P., and Zwislocki, J. J. (**1963**). "Monaural loudness function at 1000 cps and interaural summation," J. Acoust. Soc. Am. **35**, 856–865.

Hoth, S., and Weber, F. N. (**2001**). "The latency of evoked otoacoustic emissions: Its relation to hearing loss and auditory evoked potentials," Scand. Audiol. **30**, 173–183.

Janssen, T., Niedermeyer, H. P., and Arnold, W. (**2006**). "Diagnostics of the cochlear amplifier by means of distortion product otoacoustic emissions," ORL **68**, 334–339.

Johannesen, P. T., and Lopez-Poveda, E. A. (**2008**). "Cochlear nonlinearity in normal-hearing subjects as inferred psychophysically and from distortion-product otoacoustic emissions," J. Acoust. Soc. Am. **124**, 2149–2163.

Muller, J., and Janssen, T. (**2004**). "Similarity in loudness and distortion product otoacoustic emission input/output functions: Implications for an objective hearing aid adjustment," J. Acoust. Soc. Am. **115**, 3081–3091.

Neely, S. T., Gorga, M. P., and Dorn, P. A. (**1997**). "Distortion product and

loudness growth in an active, nonlinear model of cochlear mechanics," in Symposium on Recent Developments in Auditory Mechanics, Sendai, Japan.
Neely, S. T., Gorga, M. P., and Dorn, P. A. (**2003**). "Cochlear compression estimates from measurements of distortion-product otoacoustic emissions," J. Acoust. Soc. Am. **114**, 1499–1507.
Norton, S. J., and Neely, S. T. (**1987**). "Tone-burst-evoked otoacoustic emissions from normal-hearing subjects," J. Acoust. Soc. Am. **81**, 1860–1872.
Ravazzani, P., and Grandori, F. (**1993**). "Evoked otoacoustic emissions: Nonlinearities and response interpretation," IEEE Trans. Biomed. Eng. **40**, 500–504.
Ravazzani, P., Tognola, G., and Grandori, F. (**1996**). "'Derived nonlinear' versus 'linear' click-evoked otoacoustic emissions," Audiology **35**, 73–86.
Robinson, D. W. (**1957**). "The subjective loudness scale," Acustica **7**, 217–233.
Schairer, K. S., Ellison, J. C., Fitzpatrick, D., and Keefe, D. H. (**2006**). "Use of stimulus-frequency otoacoustic emission latency and level to investigate cochlear mechanics in human ears," J. Acoust. Soc. Am. **120**, 901–914.
Schlauch, R. S., DiGiovanni, J. J., and Ries, D. T. (**1998**). "Basilar membrane nonlinearity and loudness," J. Acoust. Soc. Am. **103**, 2010–2020.
Serpanos, Y. C., and Gravel, J. S. (**2000**). "Assessing growth of loudness in children by cross-modality matching," J. Am. Acad. Audiol. **11**, 190–202.
Serpanos, Y. C., and Gravel, J. S. (**2004**). "Revisiting loudness measures in children using a computer method of cross-modality matching (CMM)," J. Am. Acad. Audiol. **15**, 486–497.
Serpanos, Y. C., O'Malley, H., and Gravel, J. S. (**1998**). "Cross-modality matching and the loudness growth function for click stimuli," J. Acoust. Soc. Am. **103**, 1022–1032.
Shera, C. A., Guinan, J. J., Jr., and Oxenham, A. J. (**2002**). "Revised estimates of human cochlear tuning from otoacoustic and behavioral measurements," Proc. Natl. Acad. Sci. U.S.A. **99**, 3318–3323.
Sisto, R., and Moleti, A. (**2007**). "Transient evoked otoacoustic emission latency and cochlear tuning at different stimulus levels," J. Acoust. Soc. Am. **122**, 2183–2190.
Stevens, J. C., and Guirao, M. (**1964**). "Individual loudness functions," J. Acoust. Soc. Am. **36**, 2210–2213.
Stevens, S. S. (**1936**). "A scale for the measurement of a psychological magnitude: Loudness," Psychol. Rev. **43**, 405–416.
Stevens, S. S. (**1955**). "The measurement of loudness," J. Acoust. Soc. Am. **27**, 815–827.
Stevens, S. S. (**1957**). "Concerning the form of the loudness function," J. Acoust. Soc. Am. **29**, 603–606.
Stevens, S. S. (**1961**). "To honor Fechner and repeal his law: A power function, not a log function, describes the operating characteristic of a sensory system," Science **133**, 80–86.
Stevens, S. S. (**1972**). "Perceived level of noise by Mark VII and decibels (E)," J. Acoust. Soc. Am. **51**, 575–601.
Teghtsoonian, M., and Teghtsoonian, R. (**1983**). "Consistency of individual exponents in cross-modal matching," Percept. Psychophys. **33**, 203–214.
Thalmann, R. (**1965**). "Cross-modality matching in the study of abnormal loudness functions," Laryngoscope **75**, 1708–1726.
Whitehead, M. L., Stagner, B. B., Lonsbury-Martin, B. L., and Martin, G. K. (**1994**). "Measurement of otoacoustic emissions for hearing assessment," IEEE Eng. Med. Biol. Mag. **13**, 210–226.
Zweig, G., and Shera, C. A. (**1995**). "The origin of periodicity in the spectrum of evoked otoacoustic emissions," J. Acoust. Soc. Am. **98**, 2018–2047.
Zwicker, E., and Fastl, H. (**1999**). *Psychoacoustics: Facts and Models*, Springer Series in Information Sciences (Springer, New York), Vol. **22**.
Zwislocki, J. J. (**1965**). "Analysis of some auditory characteristics," in *Handbook of Mathematical Psychology*, edited by R. D. Luce, R. R. Bush, and E. Galanter (Wiley, New York).

Interaural correlation and the binaural summation of loudness[a)]

Barrie A. Edmonds[b)] and John F. Culling[c)]
School of Psychology, Cardiff University, Tower Building, Park Place, Cardiff CF10 3AT, United Kingdom

(Received 14 March 2008; revised 16 March 2009; accepted 26 March 2009)

The effect of interaural correlation (ρ) on the loudness for noisebands was measured using a loudness-matching task in naïve listeners. The task involved a sequence of loudness comparisons for which the intensity of one stimulus in a given comparison was varied using a one-up-one-down adaptive rule. The task provided an estimate of the level difference (in decibels) for which two stimulus conditions have equal loudness, giving measures of loudness difference in equivalent decibel units (dB_{equiv}). Concurrent adaptive tracks measured loudness differences between $\rho=1$, 0, and -1 and between these binaural stimuli and the monaural case for various noisebands. For all noisebands, monaural stimuli required approximately 6 dB higher levels than $\rho=1$ for equal loudness. For most noisebands, $\rho=1$ and $\rho=-1$ were almost equal in loudness, with $\rho=-1$ being slightly louder in the majority of measurements, while $\rho=0$ was about 2 dB_{equiv} louder than $\rho=1$ or $\rho=-1$. However, noisebands with significant high-frequency energy showed smaller differences: for 3745–4245 Hz, $\rho=0$ was only about 0.85 dB_{equiv} louder than $\rho=\pm1$, and for 100–5000 Hz it was non-significantly louder (perhaps 0.7 dB_{equiv}).
 [DOI: 10.1121/1.3120412]

PACS number(s): 43.66.Cb, 43.66.Pn, 43.66.Ba [RYL] Pages: 3865–3870

I. INTRODUCTION

When a sound is presented binaurally it is perceived to be louder than when it is presented to one ear only (monaurally) at the same sound level. This effect is called binaural summation of loudness (Reynolds and Stevens, 1960). The increase in loudness in the diotic case (i.e., for a stimulus with $\rho=1$) is well established for a range of stimuli and sound levels. Early estimates suggested that a sound presented diotically would be heard as being twice as loud (approximately equivalent to a 10-dB increase in sound level) as the same sound presented monaurally (Fletcher and Munson, 1933; Stevens, 1955). More recent estimates (Zwicker and Zwicker, 1991; Sivonen and Ellermeier, 2006; Whilby *et al.*, 2006) have placed the diotic-monaural loudness ratio at somewhat less than 2:1 and equivalent to an increase in sound level of only 3–8 dB. However, data on the effect of presenting a sound dichotically (for instance, with independent noise at each ear) are sparse.

The only previous studies to directly examine the effects of ρ on loudness (Dubrovskii and Chernyak, 1969; Dubrovskii *et al.*, 1972; Eichenlaub *et al.* 1996) used a loudness-matching paradigm to measure the effect of ρ on the loudness of wide-band noises. The listener adjusted the intensity of one stimulus until it matched the loudness of a second with a different ρ. They found that there was no effect of ρ on binaural loudness.

Notwithstanding this negative outcome, other evidence suggests that an effect might be found. For instance, Zwicker and Zwicker (1991) provided some indirect evidence using magnitude estimation. They showed that a 20% increase in the loudness estimate of a continuous monaural noise is produced by rapidly alternating the stimulus from one ear to the other. While this is not a direct manipulation of, ρ at high alternation rates, this stimulus will have a ρ of around zero within a finite temporal analysis window, provided that this window is longer than the period of alternation. Zwicker and Zwicker (1991) found their effect at alternation rates of 7 Hz and over, which is consistent with the 50–200-ms duration of binaural temporal windows reported in the literature (Kollmeier and Gilkey, 1990; Culling and Summerfield, 1998; Holube *et al.*, 1998; Akeroyd and Summerfield, 1999). In addition, Perrott and Buell (1982) showed that interaural correlation can affect the "sound volume" of a noise presented over headphones. Due to the obvious ambiguities in using the word "volume," participants were asked to report the apparent "size" of the sound they heard, and this metric was found to be affected by interaural correlation, by stimulus duration, and by stimulus intensity. The overlapping influence of correlation and intensity upon the same reported metric suggests some degree of perceptual interaction between these stimulus properties.

Moreover, one might also expect ρ to affect loudness from a theoretical standpoint. Several studies have demonstrated that the rate of loudness growth with increasing intensity is greater for tones presented in the NoSo than in the NoSπ binaural configuration (Hirsh, 1948; Townsend and Goldstein 1972; Soderquist and Shilling, 1990; Zwicker and Henning, 1991) or in NoSo than in NoSm (Marks, 1987). It is assumed by those authors and in this article that the signal is perceived as a separate entity from the background noise

[a)]Portions of this work were presented at the International Symposium on Hearing, Cloppenburg, Germany, and appeared in Hearing: From Sensory Processing to Perception (Springer, Heidelberg, 2007).
[b)]Present address: MRC Institute of Hearing Research, University Park, Nottingham NG7 2RD, United Kingdom.
[c)]Author to whom correspondence should be addressed. Electronic mail: cullingj@cf.ac.uk

and possesses its own partial loudness. Detection of the signal in broadband noise is then simply the starting point of measurable growth in the partial loudness of that signal. Given these assumptions, the differing rate of loudness growth is, in a sense, logically inevitable. At detection threshold NoSo and NoSπ tones may differ widely in intensity, but be equal in their partial loudness. However, if intensity is then increased for both tones by, say, 20 dB, to a point where the noise becomes relatively insignificant, their difference in intensity leads to a very clear difference in partial loudness (Soderquist and Shilling, 1990). As intensity increases, therefore, a greater rate of increase in loudness occurs for the So tone than for the Sπ tone. At the same time, a number of authors have pointed out that stimuli in the NoSπ binaural configuration have reduced ρ at the signal frequency, which may act as a cue to tone detection (Osman, 1971; Durlach *et al.*, 1986). Combining these two observations leads to the predictions, first, that equivalent manipulation of ρ for a narrow sub-band of an otherwise diotic noise should create the impression of an equally detectable tone embedded within the noise (Jain *et al.*, 1991) and, second, that an inverse relation should exist between ρ in the manipulated band and the partial loudness of the perceived tone (Culling *et al.*, 2001, 2003). Both of these predictions have been fulfilled, although there is some doubt whether ρ is the exact statistic employed by the binaural system in binaural unmasking or whether it merely covaries with the residue from cancellation produced by an equalization-cancellation mechanism (Durlach, 1963; 1972; Van de Par *et al.*, 2001; Culling, 2007). In any case, the relation between ρ and loudness should still hold.

Strictly speaking, this theoretical argument applies only to situations in which the conditions of broadband binaural unmasking are simulated. For instance, where reduction in ρ is band-limited to the frequency region around the tone frequency and a diotic noise fills other frequency regions. However, the signal in NoSπ might also be a complex sound, such as speech, present at a number of different frequencies, and so resulting in more widespread reduction in ρ. The profile of ρ across frequency may then encode the spectral characteristics of the signal (Culling and Summerfield, 1995; Culling *et al.*, 2001). In the present investigation, we consider what happens to the loudness when ρ is manipulated across the entire stimulus spectrum, as though the signal and masker are identical bands of noise.

The effect of ρ on the binaural loudness of narrow- and wide-band noises was measured using a loudness-matching paradigm. Such an approach serves three purposes. First, the use of a loudness-matching paradigm makes the data obtained much more comparable to studies in the literature on the binaural summation of loudness than the loudness discrimination technique used by Culling *et al.* (2001, 2003). Second, assessing the loudness of noises at various bandwidths allows for a comparison of the contrasting results of Jain *et al.* (1991), Culling *et al.* (2001), and Culling *et al.* (2003) using narrow sub-bands of noise with those of Dubrovskii *et al.* (Dubrovskii and Chernyak, 1969; Dubrovskii *et al.*, 1972) using broadband noise. Third, by ensuring that the bandwidths chosen for investigation span above and below the region important for binaural unmasking one can investigate whether or not the effect of ρ on binaural loudness is linked to the binaural unmasking mechanism.

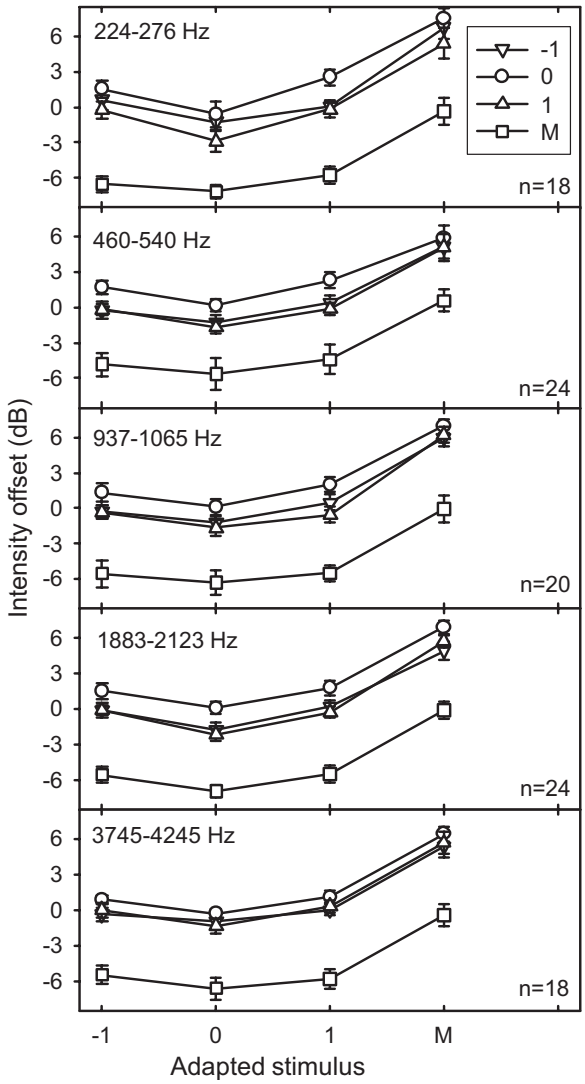

FIG. 1. Intensity offsets needed to match the loudness of noises in different interaural configurations for 1-ERB-wide noise bands at five center frequencies (250, 500, 1000, 2000, and 4000 Hz. Binaural configurations are diotic (1), uncorrelated (0), anticorrelated (−1), and monaural (*M*). Intensity offset is shown for each binaural configuration of reference stimulus as a function of the binaural configuration of the adapted stimulus. Error bars are 95% confidence intervals. The number of participants contributing data (*n*) is indicated on the appropriate panel.

II. METHOD

A. Participants

Between 14 and 24 paid participants were recruited for each bandwidth condition from the Cardiff University student population using the School of Psychology's participant panel (see Figs. 1 and 2 for exact numbers). Each participant contributed data to only one bandwidth condition. Normal hearing was a specified condition for participation.

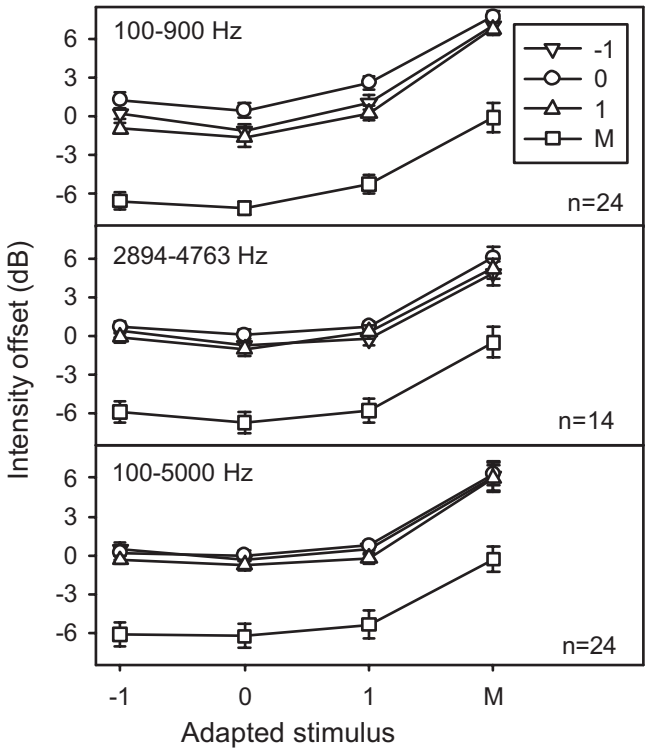

FIG. 2. As Fig. 1, but for the 100–900-, 2894–4763-, and 100–5000-Hz noisebands.

B. Stimuli

Stimuli were generated online using MATLAB. Broadband noises with a 20-kHz sampling frequency and 500-ms duration were generated digitally and band-pass filtered in the frequency domain by setting the amplitude of all frequencies outside the passband to zero. In order to assess the influence of frequency, five of these bands were 1 ERB wide (Moore and Glasberg, 1983) and centered at 250, 500, 1000, 2000, and 4000 Hz (i.e., 224–276, 460–540, 937–1065, 1883–2123, and 3745–4245). Three other, wider bands were also investigated. These were a low-frequency band of 100–900 Hz (11.5 ERBs wide), a high-frequency band of 2894–4763 Hz (4 ERBs wide, centered at 26 ERBs), and a still wider band of 100–5000 Hz (25.4 ERBs wide), encompassing both of these regions. These band-pass filtered noises were presented to listeners in four interaural configurations. Monaural (M) noise consisted of a single noise presented to either the left or right ear. Interaurally correlated ($\rho=1$) noise was generated by presenting the same noise to both ears. Anti-correlated ($\rho=-1$) noise was created by presenting a noise to the left ear and a phase-inverted copy of that noise to the right ear. Finally, uncorrelated ($\rho=0$) noise was generated by presenting independent noises at each ear.

The stimuli were presented over Sennheiser HD 590 headphones in a single-walled IAC sound-attenuating booth within a sound-treated room. Digital-to-analog conversion was performed by an Edirol UA20 soundcard and amplified by an MTR HPA-2 headphone amplifier. The intensity of reference stimulus was kept constant at 70-dB SPL, and the adapted stimulus was varied relative to that level.

C. Procedure

A two-interval, two-alternative, forced choice adaptive matching paradigm was used to measure the difference in intensity needed to equate in loudness a reference stimulus (M, 1, −1, or 0) with an adapted stimulus (M, 1, −1, or 0). The order of presentation of the reference and the adapted stimulus was randomly determined on each trial (the listener was unaware of the order of presentation). The intensity of the adapted stimulus was adjusted in accordance with a one-up/one-down rule (Levitt, 1971), producing a staircase pattern of intensity values over the course of the experiment.

Participants were asked to judge which interval contained the louder stimulus. If the participant judged the interval containing the adapted stimulus to be the louder interval, then the intensity of the adapted stimulus on the next trial of that staircase would be less intense. However, if the participant judged the interval containing the reference to be the louder interval then the intensity of the adapted stimulus was increased on the next trial of that staircase. The amount by which the adapted stimulus was adjusted (up or down) was dependent on the number of reversals made while traversing the staircase. The adjustment was ±2 dB for the first two reversals and then ±1 dB on subsequent reversals. Each individual staircase was considered complete after 12 reversals using the smaller step size[1] and was limited overall to 50 trials. This limit was included to limit the overall duration of the experiment if one adaptive track was slow to complete. Subsequent trials were therefore populated by the remaining staircases. A participant's loudness-matched-intensity offset in each of the 16 conditions was taken to be the mean intensity (in decibels) of the adapted stimulus over the last four reversals in each of the corresponding staircases.

Half of the listeners started all staircases with the adapted stimulus 3 dB more intense than the reference stimulus and the other half started each staircase with the adapted stimulus 3 dB less intense than the reference. Sixteen adaptive staircases were run concurrently in order to obtain 16 loudness matches (i.e., all pair-wise comparisons of the four interaural configurations with each serving as both reference and adapted stimulus). Trials for different staircases were interleaved at random.

III. RESULTS

A. 1-ERB bands

Mean intensity offsets at loudness match for each of the five center frequencies (250–4000 Hz) are shown in separate panels in Fig. 1. Each panel shows offsets for the four different interaural configurations of reference stimulus for each interaural configuration of adapted stimulus. An offset of zero indicates that the two interaural configurations did not differ in loudness.

These data were analyzed with separate two-way (reference × adapted) within-subjects analyses of variance. Each of the five analyses of variance showed rather similar patterns of results. Analyses for each bandwidth indicated significant main effects of both reference and adapted stimulus types ($p<0.0001$, in each case). Both of these results indicate that there is an effect of interaural configuration.

There was an interaction only for the lowest frequency [$F(9,153)$, $p<0.02$], which may be neglected after correction of α for multiple tests. It thus made no difference to the results which of the interaural configurations was the adapted stimulus. Tukey HSD *post-hoc* analyses showed, for both the reference and adapted stimuli, that all levels differed significantly ($p<0.001$) except for $\rho=1$ vs $\rho=-1$, which was only significant ($p<0.01$) for the 224–276-Hz band. These differences reflected an effect of binaural summation (M intensity must be increased to match the loudness of $\rho=1$) averaging[2] 5.6 dB, and an effect of ρ ($\rho=1$ and $\rho=-1$ intensities must be increased to match the loudness of $\rho=0$) averaging[2] 2 dB. It is noteworthy, however, that the latter effect reduced to 1.3 dB for the 4000-Hz center frequency.

B. Wider bands

Mean intensity offsets at loudness match for each of the three wider bandwidths are shown in Fig. 2 in the same format as in Fig. 1. Each panel shows data for bandwidths of 100–900, 2894–4763, and 100–5000 Hz, respectively. These data were also analyzed with separate two-way analyses of variance. Once again, each analysis produced significant main effects of both the reference and the adapted stimulus ($p<0.0001$, in each case). However, the pattern of results was now somewhat different across the three cases.

Tukey *post-hoc* analyses indicated that for the low band (100–900 Hz) and for the high band (2894–4763 Hz), the pattern was similar to the 1-ERB bands; after correction for multiple tests, each level differed significantly from every other except for $\rho=1$ vs $\rho=-1$. Thus, monaural stimuli must be more intense to match the loudness of $\rho=1$ and $\rho=-1$, while $\rho=0$ must be less intense to match them. The only exception was for the 2894–4763-Hz band, where the −1 and 0 levels were significant only at $\alpha=0.05$. Although this outcome may spring from reduced power in this condition (only 14 listeners were used), the size of the effect was also reduced to 0.9 dB. For the broadest band (100–5000 Hz), on the other hand, the only levels to differ significantly were monaural vs binaural contrasts ($p<0.001$, in each case).

IV. DISCUSSION

A. Implications for models of loudness

Across all of the results, there is a clear effect of ρ on loudness. Current loudness models take no account of ρ (e.g., Zwicker and Scharf, 1965; Moore *et al.*, 1999). Indeed, the current ANSI standard for loudness (ANSI, 2007) is essentially monaural, providing binaural loudness through a simple sum of the monaural responses. However, even in the diotic case the summation of loudness for broadband sounds across the ears is less than perfect and is level-dependent; Reynolds and Stevens (1960) reported that a binaural-to-monaural loudness ratio of 2 (i.e., a doubling of loudness) only occurs at relatively high intensity levels (~90-dB SPL). A recently revised loudness model (Moore and Glasberg, 2007) provides better predictions for the loudness of diotic and dichotically presented sounds, where interaural intensity or frequency differences may exist between the two ears. These predictions are not further affected by changes in ρ of a stimulus. The evidence presented here suggests that models of loudness need modification in order to account for binaural loudness,[3] particularly in order to model the effect of ρ on loudness at low-frequencies.

Although the effect of ρ may be regarded as small for broadband sounds, it seems likely that this reflects a diluting effect produced by a predominance of high-frequency sound in broadband white noise (see below). In a wide variety of contexts, environmental sound tends to have a predominance of energy at low-frequencies (e.g. Busch-Vishniac *et al.*, 2005; Tang, 1997), making the 2-dB effect more likely to be applicable in practice. Moreover, there are many everyday situations in which one might expect ρ to be low. This may particularly occur in reverberant rooms and in complex listening environments with multiple sounds sources. The effect of ρ may thus be important to consider when assessing levels of noise pollution and in adjusting hearing-aid gain for such situations.

B. Relation to binaural unmasking

Consistent with expectations based on theories of binaural unmasking, $\rho=0$ was found to be louder than $\rho=1$. This difference is expected on the basis that ρ is reduced when a tone is added in NoSπ, and as the tone increases in level, the resulting increase in loudness may be encoded via a further reduction in ρ. Reduction in ρ across the entire stimulus spectrum would occur if the signal was a sound of equal bandwidth to the masker.

It was also found that $\rho=0$ was louder than $\rho=-1$. Indeed, $\rho=1$ and $\rho=-1$ were found to produce approximately equal loudness. This result can also be accommodated by binaural unmasking theory. If one assumes that ρ is detected after the application of a compensating internal interaural delay within each frequency channel (Durlach, 1963, 1972, Colburn, 1973, 1977; Culling and Summerfield, 1995), then an external correlation of −1 results in an internal correlation, after the compensating delay, that is close to 1. As the level of the tone in NπSo is increased, this high internal correlation is again reduced. If the experiment is modeled using a 500-Hz gamma-tone filter from the filterbank of Patterson *et al.* (1987, 1988), an internal correlation of 0.98 is predicted for the −1 case. These predictions led Culling *et al.* (2003) to successfully predict that a ρ of 1 and −1 should be difficult to distinguish in circumstances where their obvious differences in laterality are obscured by flanking bands of noise. For the present data, it is noteworthy that $\rho=-1$ displayed a non-significant trend toward being slightly louder than $\rho=1$, consistent with the slightly lower internal correlation.

Binaural unmasking theory thus provides a viable framework for interpreting the effect of ρ on loudness. However, there are some details of the data which are difficult to fully reconcile with binaural unmasking theory, and binaural unmasking provides only one framework for interpreting this pattern of results. Other possibilities exist (see below).

The difference in loudness between $\rho=0$ and $\rho=1$ is consistently equivalent to only around 2 dB in intensity. This difference is small in relation to other measurements of sen-

sitivity to ρ. In particular, Culling *et al.* (2001) found a cumulative d' of around 6 for sensitivity to changes in ρ within a 1.3-ERB sub-band of otherwise-correlated broadband noise. While the two measures are not equivalent, the fact that jnds for intensity discrimination tends to be not much below 1 dB suggests that the d' for detecting a 2-dB change would be only 2 or, at most, 3. A possible explanation of this discrepancy is that listeners are much more sensitive to changes in the spectral profile of ρ, as measured by Culling *et al.* (2001) than to changes in overall ρ, as measured in the current study. This interpretation would suggest that discrimination of ρ mirrors the difference between absolute intensity discrimination and profile analysis, where listeners can display a smaller Weber fraction (Green and Mason, 1985).

The results with narrow (1-ERB) bands of noise indicate that the effect is largely independent of frequency. This result is broadly consistent with findings from narrowband binaural unmasking experiments, which show that a large BMLD ($\approx$25 dB) can occur over a wide range of frequencies (McFadden and Pasanen, 1978), although only some listeners appear able to achieve this performance (Koehnke *et al.*, 1986; Bernstein *et al.*, 1998). However, the salient perceptual cue that listeners report in a narrowband BMLD task is intracranial image width rather than the loudness percept which was investigated here, complicating any direct comparison of these findings. Conceivably, increased loudness is not so directly related to binaural unmasking as suggested above. Loudness might occur as a side effect of changes in perceived width. Such an explanation would still be fairly consistent with the pattern of data across different values of ρ because a ρ of -1, while certainly being perceived as wider than a ρ of 1, is usually reported as having much less image width than a ρ of 0 (Blauert and Lindemann, 1986); the rank ordering of the conditions, at least, is consistent. This interpretation may be supported by Perrott and Buell's (1982) data on perceived volume of broadband noise. They asked listeners to rate the size of broadband noises presented over headphones and found that listeners' ratings were similarly ordered with respect to correlation as in the current study (ρ=0 being the largest), while at the same time being positively related to stimulus intensity. Correlation and intensity thus contributed to a common construct which must at least be correlated with "loudness." The direction of influence between the constructs of image width, size, and loudness cannot be directly inferred from current data.

The effect of ρ on broader bands shows a marked (2.1 dB) difference in loudness between 1 and 0 for the low-frequency (100–900 Hz) band. This effect is much reduced (0.74 dB) for the broadband (100–5000 Hz) case. The simplest explanation for this outcome, and one consistent with the binaural unmasking theory, is that unmasking processes are much reduced for broadband stimuli at frequencies higher than about 1500 Hz, consistent with interaural processing being limited to the use of envelope cues (Bernstein and Trahiotis, 1992). The reduced binaural unmasking of the 1500–5000-Hz region may have diluted the overall effect of ρ on the broadband noise. Indeed, if the effective level in the region up to 1500 Hz increases by 2.1 dB, and no increase occurs elsewhere, the overall effective level increase is 0.68 dB, very close to the observed figure of 0.74. Thus, if the high-frequencies show little effect of ρ on loudness, binaural unmasking theory can account for the negative results of Dubrovskii and Chernyak (1969) and Dubrovskii *et al.* (1972) since their stimuli extended up to at least 5000 Hz.[4] The only problem for this interpretation is that the 4-ERB-wide, high-frequency band (2894–4763 Hz) displayed an increase in loudness equivalent to 0.86 dB. The effect is somewhat larger than the 0.74-dB effect observed for the 100–5000 Hz, which is inconsistent with an account based purely on dilution.

V. SUMMARY

These experiments provide the first direct evidence that interaural correlation can have an effect on the loudness of a binaural stimulus, which can be offset by a compensating difference in physical intensity. The difference in loudness produced by interaural correlation is most apparent at frequencies in the binaural dominance region; the intensity offset required to match in loudness noises that have different interaural correlations at these frequencies is as follows:

(1) Binaural-monaural loudness matches produced mean matched-intensity offsets of about 6 dB, which were consistent with the literature on binaural summation for moderate sound levels.
(2) Noises with an interaural correlation of 0 are louder than noises with interaural correlations of 1 or -1, the difference being equivalent to about 2 dB in signal energy in cases for which low-frequencies dominate.
(3) Noises with an interaural correlation of 1 and -1 are closely matched in loudness. Listeners judged anticorrelated noise to be only slightly (and nonsignificantly) louder than correlated noise.

ACKNOWLEDGMENTS

We would like to thank the reviewers for their help and advice in refining this article. Pilot data for this project were collected by Sonya Ginty. This work was supported by UK EPSRC.

[1]In the 500-Hz narrowband condition, only ten trials were used, but this was subsequently extended to 12 for all other data collected.
[2]Averages are across listeners, frequency bands, and the two measurements made with each of the interaural configurations (e.g., 0 and *M*) as the adapted stimulus.
[3]There are also data indicating that interaural time delay has some influence on binaural summation (Algom *et al.*, 1988).
[4]Dubrovskii *et al.* (1972) employed broadband noise limited only by the frequency response of the Russian TD6 audiological headphones they used. They assumed that the response of these headphones rolled off at about 5 kHz. However, measurements by Robinson (1971) show that those headphones have a substantial response up to at least 8 kHz with a peak in response at around 6 kHz.

Akeroyd, M. A., and Summerfield, A. Q. (**1999**). "A binaural analog of gap detection," J. Acoust. Soc. Am. **105**, 2807–2820.
Algom, D., Adam, R. Cohen-Raz, L. (**1988**). "Binaural summation and lateralization of transients: A combined analysis," J. Acoust. Soc. Am. **84**, 1302–1315.
ANSI (**2007**). *ANSI S3.4-2007. Procedure for the Computation of Loudness*

of Steady Sounds (American National Standards Institute, New York).
Bernstein, L. R., and Trahiotis, C. (**1992**). "Discrimination of interaural envelope correlation and its relation to binaural unmasking at high frequencies," J. Acoust. Soc. Am. **91**, 306–316.
Bernstein, L. R., Trahiotis, C., and Hyde, E. L. (**1998**). "Inter-individual differences in binaural detection of low-frequency or high-frequency tonal signals masked by narrow-band or broadband noise," J. Acoust. Soc. Am. **103**, 2069–2078.
Blauert, J., and Lindemann, W. (**1986**). "Spatial mapping of intracranial auditory events for various degrees of interaural coherence," J. Acoust. Soc. Am. **79**, 806–813.
Busch-Vishniac, I. J., West, J. E., Barnhill, C., Hunter, T., Orellana, D., and Chivukula, R. (**2005**). "Noise levels in Johns Hopkins Hospital," J. Acoust. Soc. Am. **118**, 3629–3645.
Colburn, H. S. (**1973**). "Theory of binaural interaction based on auditory nerve data I: General strategy and preliminary results on interaural discrimination," J. Acoust. Soc. Am. **54**, 1458–1470.
Colburn, H. S. (**1977**). "Theory of binaural interaction based on auditory nerve data II: Detection of tones in noise," J. Acoust. Soc. Am. **61**, 525–533.
Culling, J. F. (**2007**). "Evidence specifically favoring the equalization-cancellation theory of binaural unmasking," J. Acoust. Soc. Am. **122**, 2803–2813.
Culling, J. F., Colburn, H. S., and Spurchise, M. (**2001**). "Interaural correlation sensitivity," J. Acoust. Soc. Am. **110**, 1020–1029.
Culling, J. F., and Edmonds, B. A. (**2007**). "Interaural correlation and loudness," in *Hearing: From Sensory Processing to Perception*, edited by B. Kollmeier, G. Klump, V. Hohmann, U. Langemann, M. Mauermann, S. Uppenkamp, and J. Verhey (Springer, Heidelberg).
Culling, J. F., Hodder, K. I., and Colburn, H. S. (**2003**). "Interaural correlation discrimination with spectrally-remote flanking noise: Constraints for models of binaural unmasking," Acta. Acust. Acust. **89**, 1049–1058.
Culling, J. F., and Summerfield, Q. (**1995**). "Perceptual separation of concurrent speech sounds: Absence of across-frequency grouping by common interaural delay," J. Acoust. Soc. Am. **98**, 785–797.
Culling, J. F., and Summerfield, Q. (**1998**). "Mearurement of the binaural temporal window using a detection task," J. Acoust. Soc. Am. **103**, 3540–3553.
Dubrovskii, N. A., and Chernyak, R. I. (**1969**). "Binaural summation under varying degrees of noise correlation," Sov. Phys. Acoust. **14**, 468–473.
Dubrovskii, N. A., Chernyak, R. I., and Shapiro, V. M. (**1972**). "Binaural summation of differently correlated noises," Sov. Phys. Acoust. **17**, 468–473.
Durlach, N. I. (**1963**). "Equalization and cancellation theory of binaural masking-level differences," J. Acoust. Soc. Am. **35**, 1206–1218.
Durlach, N. (**1972**). "Binaural signal detection: Equalization and cancellation theory," in *Foundations of Modern Auditory Theory*, edited by J. V. Tobias (Academic Press, New York), pp. 369–462.
Durlach, N. I., Gabriel, K. J., Colburn, H. S., and Trahiotis, C. (**1986**). "Interaural correlation discrimination: II. Relation to binaural unmasking," J. Acoust. Soc. Am. **79**, 1548–1557.
Eichenlaub, C., Chouard, N., and Weber, R. (**1996**). "On the influence of interaural correlation on binaural loudness for broadband noise," in Proceedings of the Internoise '96, pp. 2227–2230.
Fletcher, H., and Munson, W. A. (**1933**). "Loudness, its definition, measurement and calculation," J. Acoust. Soc. Am. **5**, 82–108.
Green, D. M. and Mason, C. R. (**1985**). "Auditory profile analysis: Frequency, phase, and Weber's Law," J. Acoust. Soc. Am. **77**, 1155–1161.
Hirsh, I. J. (**1948**). "The role of interaural phase in loudness," J. Acoust. Soc. Am. **20**, 761–766.
Holube, I., Kinkel, M., and Kollmeier, B. (**1998**). "Binaural and monaural auditory filter bandwidths and time constants in probe tone detection experiments," J. Acoust. Soc. Am. **104**, 2412–2425.
Jain, M., Gallagher, D. T., Koehnke, J., and Colburn, H. S. (**1991**). "Fringed correlation discrimination and binaural detection," J. Acoust. Soc. Am. **90**, 1918–1926.
Koehnke, J., Colburn, H. S., and Durlach, N. I. (**1986**). "Performance in several binaural-interaction experiments," J. Acoust. Soc. Am. **79**, 1558–1562.
Kollmeier, B., and Gilkey, R. H. (**1990**). "Binaural forward and backward masking: Evidence for sluggishness in binaural detection," J. Acoust. Soc. Am. **87**, 1709–1719.
Levitt, H. (**1971**). "Transformed up-down methods in psychoacoustics," J. Acoust. Soc. Am. **49**, 467–477.
Marks, L. E. (**1987**). "Binaural versus monaural loudness: Supersummation of tone partially masked by noise," J. Acoust. Soc. Am. **81**, 122–128.
McFadden, D., and Pasanen, E. G. (**1978**). "Binaural detection at high frequencies with time-delayed waveforms," J. Acoust. Soc. Am. **63**, 1120–1131.
Moore, B. C. J., and Glasberg, B. R. (**1983**). "suggested formulae for calculating auditory-filter bandwidths and excitation patterns," J. Acoust. Soc. Am. **74**, 750–753.
Moore, B. C. J., and Glasberg, B. R. (**2007**). "Modeling binaural loudness," J. Acoust. Soc. Am. **121**, 1604–1612.
Moore, B. C. J., Glasberg, B. R., and Vickers, D. A. (**1999**). "Further evaluation of a model of loudness perception applied to cochlear hearing loss," J. Acoust. Soc. Am. **106**, 898–907.
Osman, E. (**1971**). "A correlation model of binaural masking level differences," J. Acoust. Soc. Am. **50**, 1494–1511.
Patterson, R. D., Nimmo-Smith, I., Holdsworth, J., and Rice, P. (**1987**). "An efficient auditory filterbank based on the gammatone function," paper presented to the IOC Speech Group on Auditory Modelling at the Royal Signal Research Establishment, 14–15 December.
Patterson, R. D., Nimmo-Smith, I., Holdsworth, J., and Rice, P. (**1988**). "Spiral vos final report, Part A: The auditory filter bank," Cambridge Electronic Design Contract Report No. APU 2341.
Perrott, D. R., and Buell, T. N. (**1982**). "Judgements of sounds volume: Effects of signal duration level and interaural characteristics on the perceived extensity of broadband noise," J. Acoust. Soc. Am. **72**, 1413–1417.
Reynolds, G. S., and Stevens, S. S. (**1960**). "Binaural summation of loudness," J. Acoust. Soc. Am. **32**, 1337–1344.
Robinson, D. W. (**1971**). "A review of audiometry," Phys. Med. Biol. **16**, 1–24.
Sivonen, V. P., and Ellermeier, W. (**2006**). "Directional loudness in an anechoic sound field, head-related transfer functions, and binaural summation," J. Acoust. Soc. Am. **119**, 2965–2980.
Soderquist, D. R., and Shilling, R. D. (**1990**). "Loudness and the binaural masking level difference," Bull. Psychon. Soc. **28**, 553–555.
Stevens, S. S. (**1955**). "The measurement of loudness," J. Acoust. Soc. Am. **27**, 815–829.
Tang, S. K. (**1997**). "Performance of noise indices in air-conditioned landscaped office," J. Acoust. Soc. Am. **102**, 1657–1663.
Townsend, T. H., and Goldstein, D. P. (**1972**). "Suprathreshold binaural unmasking," J. Acoust. Soc. Am. **51**, 621–624.
Van de Par, S., Trahiotis, C., and Bernstein, L. R. (**2001**). "A consideration of the normalization that is typically included in correlation-based models of binaural detection," J. Acoust. Soc. Am. **109**, 830–833.
Whilby, S., Florentine, M., Wagner, E., and Marozeau, J. (**2006**). "Monaural and binaural loudness of 5-and 200-ms tones in normal and impaired hearing," J. Acoust. Soc. Am. **119**, 3931–3939.
Zwicker, E., and Henning, G. B. (**1991**). "On the effect of interaural phase differences on loudness," Hear. Res. **53**, 141–152.
Zwicker, E., and Scharf, B. (**1965**). "A model of loudness summation," Psychol. Rev. **72**, 3–26.
Zwicker, E., and Zwicker, U. T. (**1991**). "Dependence of binaural loudness summation on interaural level differences, spectral distribution, and temporal resolution," J. Acoust. Soc. Am. **89**, 758–764.

Self-masking: Listening during vocalization. Normal hearing

Erik Borg,[a] Christina Bergkvist, and Dan Gustafsson
Ahlsén Research Institute, University Hospital of Örebro, 701 85 Örebro, Sweden

(Received 13 June 2008; revised 20 March 2009; accepted 30 March 2009)

What underlying mechanisms are involved in the ability to talk and listen simultaneously and what role does self-masking play under conditions of hearing impairment? The purpose of the present series of studies is to describe a technique for assessment of masked thresholds during vocalization, to describe normative data for males and females, and to focus on hearing impairment. The masking effect of vocalized [a:] on narrow-band noise pulses (250–8000 Hz) was studied using the maximum vocalization method. An amplitude-modulated series of sound pulses, which sounded like a steam engine, was masked until the criterion of halving the perceived pulse rate was reached. For masking of continuous reading, a just-follow-conversation criterion was applied. Intra-session test-retest reproducibility and inter-session variability were calculated. The results showed that female voices were more efficient in masking high frequency noise bursts than male voices and more efficient in masking both a male and a female test reading. The male had to vocalize 4 dBA louder than the female to produce the same masking effect on the test reading. It is concluded that the method is relatively simple to apply and has small intra-session and fair inter-session variability. Interesting gender differences were observed.
 [DOI: 10.1121/1.3124773]

PACS number(s): 43.66.Dc, 43.70.Mn, 43.71.Rt, 43.72.Dv [AL] Pages: 3871–3881

I. INTRODUCTION

Acoustic language—speech—is an important channel for inter-human communication and part of a communicative system with complicated interactions. These interactions contain feedback functions, which can be roughly divided into three levels.

(1) A behavioral-social level, where the dialog and turn-taking initiate and finish participants' speech and language activities and are challenged by overlaps, simultaneous talking and listening.
(2) A message level, where the subject listens to his/her own utterances, discovers errors and flaws in logic and (may) correct or terminate presentation.
(3) A signal level, where the physical/physiological effects of sound production, motor, and sensory activities of the speech and hearing system interact with numerous feedback loops to control and adjust sound production and auditory processing.

The two higher levels [(1) and (2) above] will not be further dealt with here; the focus will be on the signal level. The significance of sensory information for control of speech production and speech development has been reviewed by Borden (1980), e.g., the role of auditory feedback in speech intelligibility.

One example of the role of the perception of the voice in speech pathology is the influence of delayed feedback on the fluency of speech production. Stephen and Haggard (1980) found (as others before them) that a 100 ms speech feedback delay disrupted the speech production of normal hearing, non-stuttering subjects. On the other hand, the speech of stutterers was partly ameliorated both by delayed speech and by a low frequency masker modulated by the speech signal envelope.

A special aspect of the role of perception of one's own voice in language acquisition has been pointed out by Howell and Dworzynski (2001). They found that people in vulnerable language situations, e.g., when using a second language, were more susceptible to altered auditory feedback. The German accent of Germans speaking English was increased more in conditions of frequency shifting during delayed auditory feedback than under normal conditions.

Adaptation of the voice to environmental communication demands is largely caused by auditory feedback. The relationship between one's own sound production and one's own hearing is important in at least two respects.

First of all, in most realistic environments, there is a background noise or a requirement to be heard at a distance. In the latter case, what occurs is an adaptation of the voice so that it can be heard by the distant person. Therefore, there is an adjustment of one's own voice intensity and quality in relation to the perception—or expectation—of the acoustic environment. One example is the so-called Lombard effect (Lombard reflex), where an ambient background noise causes an increase in the intensity of the vocalized sound (e.g., Lamprecht, 1988). A situation related to the Lombard effect is singing in a choir. According to Ternström (1994), the relationship between the level of the singer's own voice and the sound of the rest of the choir was +3.9 dB (range +1.5 to +7.3 dB). The preferred relation of the level of the self-produced relation to the voice level of others was on the average 6.1 dB (Ternström, 1999). A detailed acoustic and perceptual analysis of speech in realistic noise environments has recently been presented by Södersten *et al.* (2005). The

[a]Author to whom correspondence should be addressed. Electronic mail: erik.borg@orebroll.se

noise was balanced by increased vocal effort and thereby an increase in the first formant frequency and a general increase in the high frequency components (tilt of the spectrum); this has also been found by Rostolland (1982) and Tranmüller and Eriksson (2000). A special condition is seen in many occupational situations, for instance, in airplanes where the cockpit personnel must communicate in high noise levels. Nixon *et al.* (1998) found that the intelligibility of female speech was unacceptable in military aircrafts at the highest tested noise level, 115 dB sound pressure level (SPL), and that it was slightly poorer for female than for male voices. Södersten *et al.* (2005) also found that females rated themselves significantly lower than males on the question: "Did you make yourself heard?" when reading in background noise of various types.

Second, the dialog, postulated as part of the social interaction, requires a perception of communicative signals, speech, and other sounds from communication partners, or events in the environment, even when one produces sound oneself (primarily talks). This aspect of sound perception requires a sophisticated relationship between the self-produced and the externally produced sounds in order to optimize communication.

The focus of the present study is on the ability to hear external sounds during one's own sound production. Successful management of this task may also, in our opinion, depend on processes at three levels (a three-level model).

(1) The social level, turn-taking. Each subject stops talking and leaves space for other persons. This works well in a small group, but less well in lively communication situations with several partners.
(2) A linguistic-cognitive aspect. With a large working memory capacity, small fragments of the received message are more easily interpreted, which may facilitate the ability of simultaneously listening and talking (Lyxell *et al.*, 2003).
(3) An auditory-physiological level. The masking effect of one's own speech on one's own ear and the role of possible control mechanisms at the level of the ear, middle ear muscles and olivo-cochlear efferents, and descending control in the auditory pathway (discussed, e.g., by Howell, 1985 and Borg and Counter, 1989).

The focus of the present study is on the third level, the masking effect of one's own speech on one's own ear. Cognitive and language factors (level 2) are also involved if the masked sound is speech, such as when using the just-follow-conversation (JFC) method (Borg *et al.*, 1998). Under the present experimental conditions, where the subjects vocalized a sustained [a:] without pauses, the cognitive effects were kept at a minimum.

The first studies of the effect of one's own voice on one's own hearing were conducted in the 1930s by Dunn and Farnsworth (1939). Well-known studies were also made by von Bekesy (1960). He found that the strength of the bone-conducted and air-conducted sound components of one's own voice was about equal. It is now generally accepted that there are three routes of auditory feedback (direct air conduction, reflected air conduction, and bone conduction), which have been reviewed, e.g., by Howell (1985). In later studies, Pörschmann (2000) used direct acoustic measurements and psycho-acoustic threshold determinations with an unvoiced [s:] and a voiced [z:] consonant. He estimated the bone conduction component by measuring the masked threshold when the air conduction component had been attenuated. The bone-conducted sound was most important at lower frequencies and for frequencies between 700 and 1200 Hz, bone conduction dominated perception of the person's own voice. Above 1200 Hz, air conduction was predominant.

Very little research has been done on self-masking by vocalization. Gauffin and Sundberg (1974) were probably the first to measure the masking effect of a self-produced sound. They used one voice-trained subject, who listened to an amplitude-modulated series of tone-bursts. The subjects adapted their own voice level so the perceived pulse rate was halved, i.e., the voice level fell in between the high and the low pulses. The tests were judged as demanding and required experience and good voice control. Shearer (1978) continued and compared the masking effect of self-produced vowels ([a], [u], [i]) and the same vowels recorded with a microphone 15 cm in front of the mouth. He found that the masking effect, primarily for the high frequencies, was greater when subjects listened to the recorded sounds than during actual vocalization. He trained 16 normal hearing persons to vocalize with a constant sound level at the same time as he or she adjusted a narrow-band noise to reach a threshold criterion. The frequency of the noise was swept between 50 Hz and 10 kHz. Whether the method could give reproducible results also for untrained subjects was not investigated. Issues such as gender effects were also not analyzed. Pörschmann's (2000) studies also included determination of masked thresholds, but only for the bone-conducted component.

The overall goal of the present ongoing project is to analyze the interference between the emitted and received sound in a simplified laboratory situation. The approach is based on a clinical audiological perspective, addressing the situation for normal hearing (the present study) and hearing impaired individuals (a forthcoming study).

The aim of the present study is

(1) to describe a method for studying the masking effect of one's own voice and
(2) to present normal masked thresholds for male/female voice on male and female speech and narrow-band noise in the frequency range 250–8000 Hz.

II. MATERIAL AND METHODS

Except for a description of experimental set-up, technical and experimental procedures, the present section contains an analysis of methods and a presentation of intra- and inter-session test-retest variability (presented in Secs. II G–II I).

A. Subjects

Twenty-two subjects with normal hearing participated in the study. Their audiometric thresholds were better than 20 dB hearing level (HL) at frequencies between 125 and 4000 Hz. Their age ranged from 21 to 64 years; 15 were females,

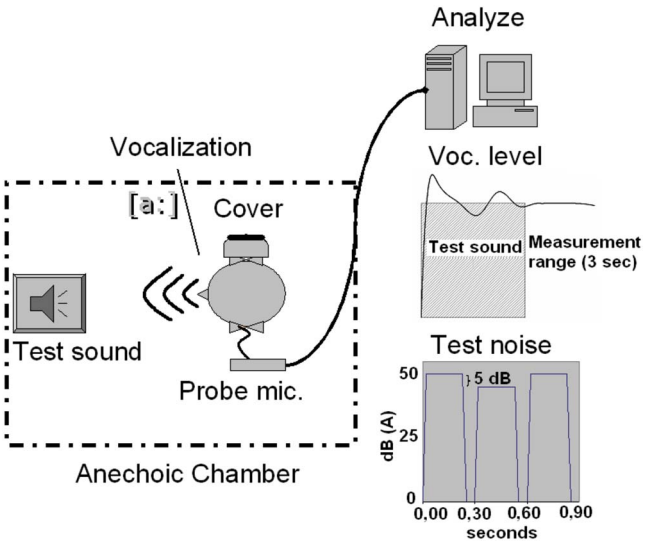

FIG. 1. (Color online) Experimental set-up. A test subject was placed in an anechoic chamber with a probe microphone in one ear and the other ear covered. The test sound, amplitude-modulated noise, or a test reading was presented via a loudspeaker in front of the subject. The masking effect was produced by a vocalized [a:]. The level of the [a:] was raised to cover the test sound and then adjusted to make the test sound just audible or just possible to follow. The vocalization level was measured immediately after the subject indicated that the masking effect was according to the criteria.

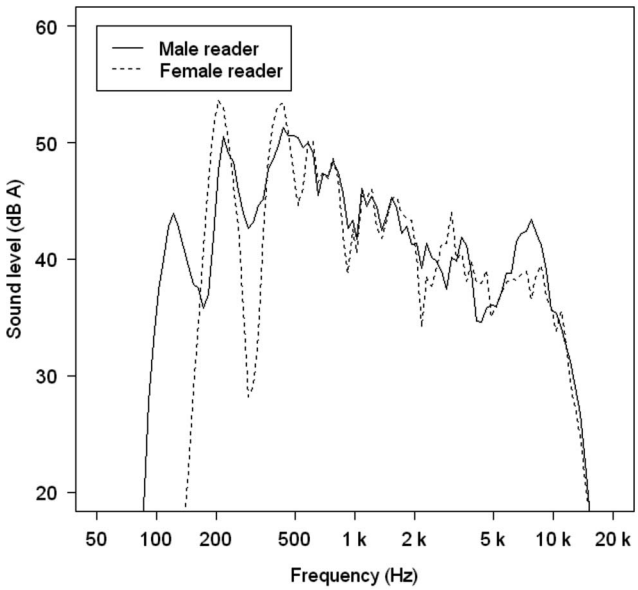

FIG. 2. Average 1/3-octave band spectra [sound level (dBA)] of a 2 min reading from "The Wonderful Adventures of Nils Holgersson" by a male reader, continuous line, and female reader, broken line.

7 were males. Six were singers or in music education (2 females, 4 males). All subjects had academic professions. Test-retest investigation was performed in 10 of the subjects (6 females, 4 males).

B. Experimental set-up

The measurements were made in an anechoic chamber equipped with 12 loud speakers (Tannoy System 800) at the acoustic ecological laboratory of the Ahlsén Research Institute. Two sound sources were used in the present study: external test sounds from the loud speaker straight ahead (zero degrees azimuth) and the internal masking sound: the subject's own voice (Fig. 1). One ear was protected with an earmuff [Peltor H9A; attenuation: 22.0 dB (at 250 Hz), 33.7 dB (at 500 Hz), 39.7 dB (at 1000 Hz), 36.5 dB (at 2000 Hz), 40.1 dB (at 4000 Hz), and 40.6 dB (at 8000 Hz)].

Two external test sounds were used: a narrow-band noise and a text reading. The first external sound, the narrow-band noise, had a band width of 1/3-octave and 60 dB/octave slopes and was presented at the frequencies of 250, 500, 1000, 2000, 4000, and 8000 Hz. The noise consisted of a series of 250-ms-long bursts (rise and fall times 25 ms and a 50 ms inter-burst interval) with a 5 dB difference in amplitude giving the impression of a steam engine train. The other external sound was a continuous text from Selma Lagerlöf's "The Wonderful Adventures of Nils Holgersson" (henceforth called "Holgersson"), which is regularly used for determination of speech perception thresholds using the JFC method. Two versions were tested: a male and a female test reader. Both were experienced newsreaders in the Swedish Radio. The long-term spectra (first 3 min) of the male and female test readings are shown in Fig. 2. Except for the difference in fundamental frequency, the spectral shapes are similar. The internal source was the subject's own vocalization of an [a:], using as constant a musical pitch as possible.

We chose the method of keeping the target sound, noise bursts, or "Holgersson" at a constant level and having the subject vary his/her vocalized [a:] to the criterion level: just being able to follow the Holgersson reading or just perceiving when the steam engine train decreased its speed to one-half, i.e., when the lower-level noise bursts were masked (maximum vocalization method).

The three types of signals were measured with an insert microphone (ER7C probe microphone system, Etymotic Research) placed 2 cm inside the outer ear canal. The level was continuously recorded and the spectrum fast Fourier transform (FFT) was determined at 2 s intervals. The 1/3-octave band spectra with dBA-weighting were evaluated. The vocalization level was monitored for 3 s after the end of the target sound (Fig. 1). The measurement was accepted if the voice level was kept constant within 2 dB during this period. The spectra and level measurements of the voice were taken from this 3 s period for further evaluation.

C. Calibration

The 1/3-octave spectra were made using filters with a 63 dB/octave slope. The amplitude-modulated noise was calibrated for the high-level bursts in the ear canal of each subject. The produced vocal sound was measured in the ear canal with the probe after the test sound had been turned off (see Fig. 1). The dBA-weighting was consistently used.

D. Procedure

The subjects (who all had normal hearing) were first trained and practiced producing a stable [a:] and adjusting the level to just cover the low intensity part of the amplitude-modulated noise, i.e., the steam engine train decreased speed to one-half or to just follow the Holgersson text reading. This

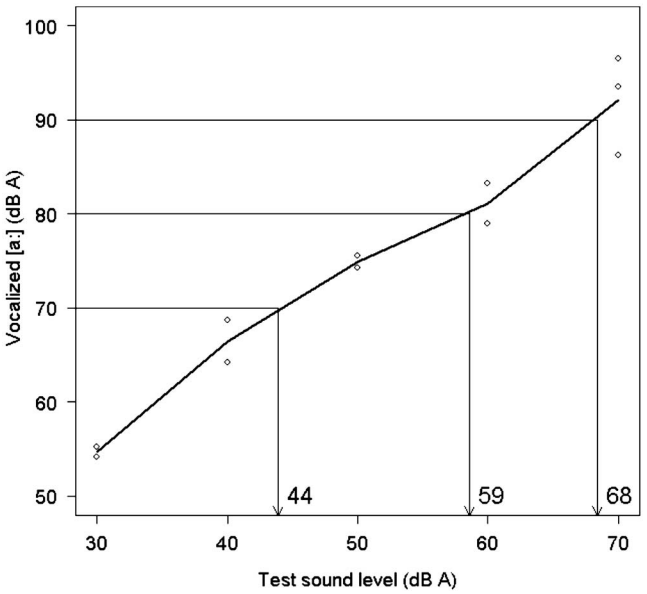

FIG. 3. Derivation of masked threshold values on the basis of measured values (○) of the vocalization needed to allow the amplitude-modulated noise to be just audible (the higher-level parts of the amplitude modulation). The masked threshold values for 70, 80, and 90 dBA vocalizations are in this example 44, 59, and 68 dBA, respectively. Data from one subject.

variant was adopted from Gauffin and Sundberg (1974) and modified as described above and is here named "the maximum vocalization method." The voice level should first be raised to completely mask the target, then gradually lowered to reach the criteria and/or repeatedly varied until the subject felt secure about the threshold. The level of the target (noise or male or female Holgersson) was varied in 5 or 10 dB steps from the lowest level that the subject could mask with his/her own voice to the highest level that could be masked by the subject's maximum vocalization effort. Thereafter the target level was decreased again. Two measurements were thus made at each level of the target. The mean value was used in further data treatment, provided the difference was 5 dB or less. If the difference was more than 5 dB, a third or fourth measurement was made and the mean value was used in further analyses. The different noise frequencies were tested in random order. The order of the noise target and the Holgersson target was randomized. The duration of the experimental session was up to 1.5 h.

E. Masked threshold

In the experimental situation, the test signal was presented at a fixed level and the subjects adjusted their voice. It is more appropriate to present the data in terms of masked thresholds, but with fixed voice level as the parameter. Therefore, the primary data had to be recalculated. Figure 3 shows an example from one subject. The open circles show the measured data values. The heavy lines connect the mean values (see above) representing the primary results for each level of the masked signal. The masked threshold value for each specific vocalization level was derived, as shown by the construction lines (horizontal and vertical) and the arrow in Fig. 3. Corresponding masked threshold curves are shown, for instance, in Figs. 5 and 6.

F. Statistical methods

To test the differences between conditions and the effects of factors the Student's t-test and normal regression with the Wald test for coefficients were used. A Bland–Altman plot (Bland and Altman, 1986) was used for evaluation of test-retest variability. All calculations and graphs were made with the statistical package R.

G. Analysis of methods

The tests turned out to be easy to perform, although all subjects could not vocalize the full number of times required for a complete test series. The maximum vocal effort also varied between subjects. Therefore the number of subjects for each data point varies. The numbers are indicated in the tables at the bottom of Fig. 8. The spectrum of the vocalized [a:] was not constant across the range of vocal effort. Figure 4(a) shows a series of average (7 males) spectral curves for vocalized [a:] with increasing test sound level (50, 60, and 70 dBA) and for three frequencies of the noise bursts (250, 1000, and 4000 Hz). It is to be noted that the analysis of the voice was performed immediately after the termination of the target signal. An increase in the higher frequency components of the voice at higher vocal effort is seen. In addition, an increase in the spectral peak at 3000 Hz is seen (less obvious in women). An analysis of individual spectra and average spectra for the whole group of subjects showed that the spectrum was involuntarily slightly changed upon presentation of noise bursts with different frequencies. The 4000 Hz target sound gave a 6 dB higher level for the 4000 Hz 1/3-octave band in the vocalization [male and female together: $p<0.001$, degrees of freedom (d.f.)=21] than did the 250 Hz target sound.

H. Male-female vocalization

The male vocalization showed a consistent pattern both when masking the target noise and Holgersson. For noise targets (at the lowest target levels 30–40 dBA), the [a:] spectrum was dominated by the fundamental partial at (F_0). This pattern was more evident in females and occurred also at higher levels, 50 and 60 dBA noise target sounds. For the Holgersson target, this gender difference was not seen and the average spectra for male and female can therefore be directly compared [Fig. 4(b)]. We do not know whether the described difference is a gender difference [relatively stronger fundamental partial (at F_0) at low vocal level] or an individual difference, which happened to be more prominent among females than males in the present material. One possible reason for the gender/individual difference is the existence of a possible gender/individual difference in bone/air components in the subjects' vocalizations. No corroborative data exist, but von Bekesy (1960) (p. 187) showed a 6 dB difference in the bone component between his four tested subjects, pointing toward a substantial individual variability.

I. Test-retest variability

Two repeatability conditions were evaluated: intra- and inter-session test-retest variabilities.

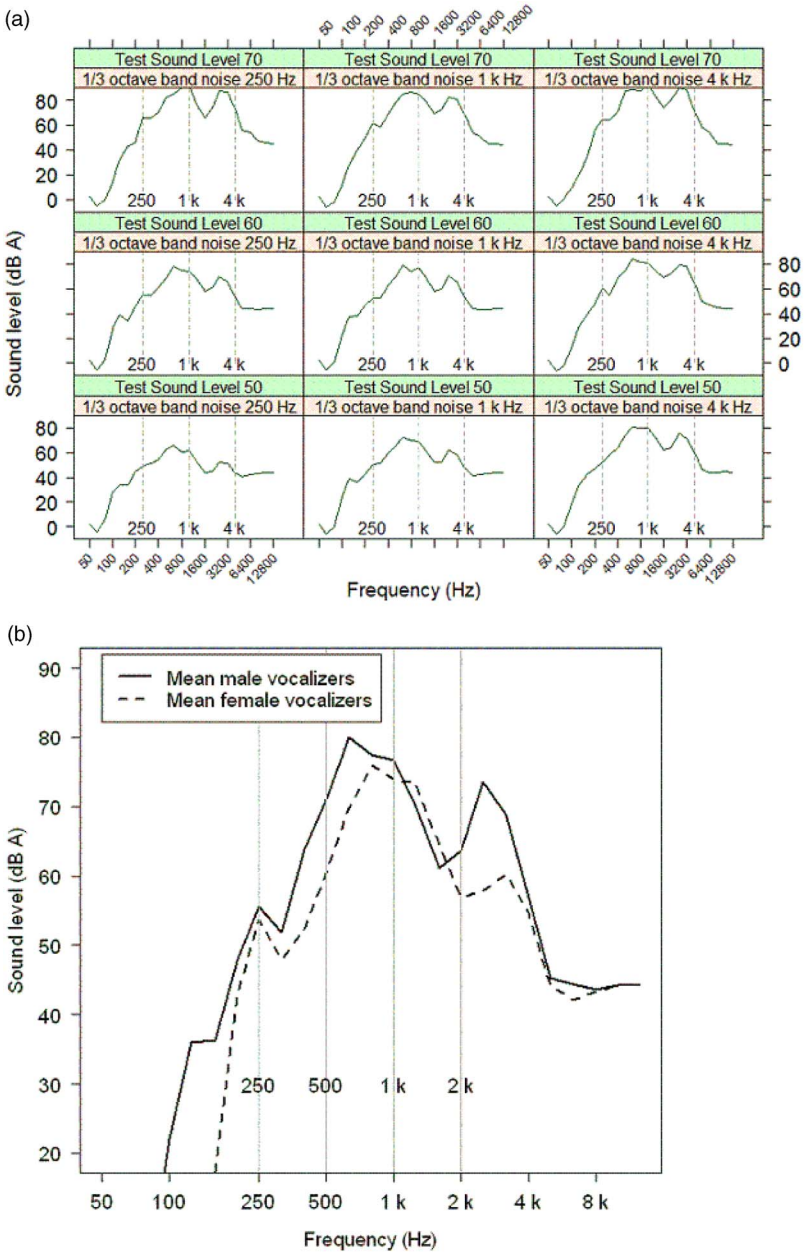

FIG. 4. (Color online) (a) 1/3-octave spectra of a vocalized [a:] for male subjects ($n=7$) at three different test sound intensities, 50, 60, and 70 dBA, and for three different test sound frequencies, 250, 1000, and 4000 Hz. (b) 1/3-octave spectra of a vocalized [a:] masking of 7 male (—) and 15 female (---) vocalizers on test reading from "The Wonderful Adventures of Nils Holgersson" by a female reader presented at 60 dBA. Probe microphone in the ear canal.

1. Intra-session variability

Each masked threshold was determined at least twice in each session. If the difference between the first two tests of a specific frequency and level of the test sound was more than 5 dB, an additional measurement was performed. Only 14% of the 830 presentations had to be supplemented with an extra test.

Sources of variation in vocalization level needed to mask a noise burst or speech include test sound, test sound level, and vocalizing person. If these sources are considered fixed at each measurement, thus assuming measurement error as the only random error source, we calculated the standard deviation of vocalization level to 2.7 dBA. Assuming different measurement error within test sounds gives the following set of estimates for the standard deviation for vocalization level (Table I).

If the standard deviation is large for a specific test sound, more measurements per person are required to maintain equal measurement precision of vocalization level across test sounds. A 95% confidence interval of ±3 dB at 250, 2000, and 8000 Hz thus requires four, two, and five measure-

TABLE I. Estimates of standard deviation of intra-session vocalization level differences.

Test sound	Standard deviation
The Wonderful Adventures of Nils Holgersson, female reader	2.84
The Wonderful Adventures of Nils Holgersson, male reader	2.76
Third octave band noise 250 Hz	2.97
Third octave band noise 500 Hz	2.62
Third octave band noise 1000 Hz	2.41
Third octave band noise 2000 Hz	1.90
Third octave band noise 4000 Hz	2.29
Third octave band noise 8000 Hz	3.48

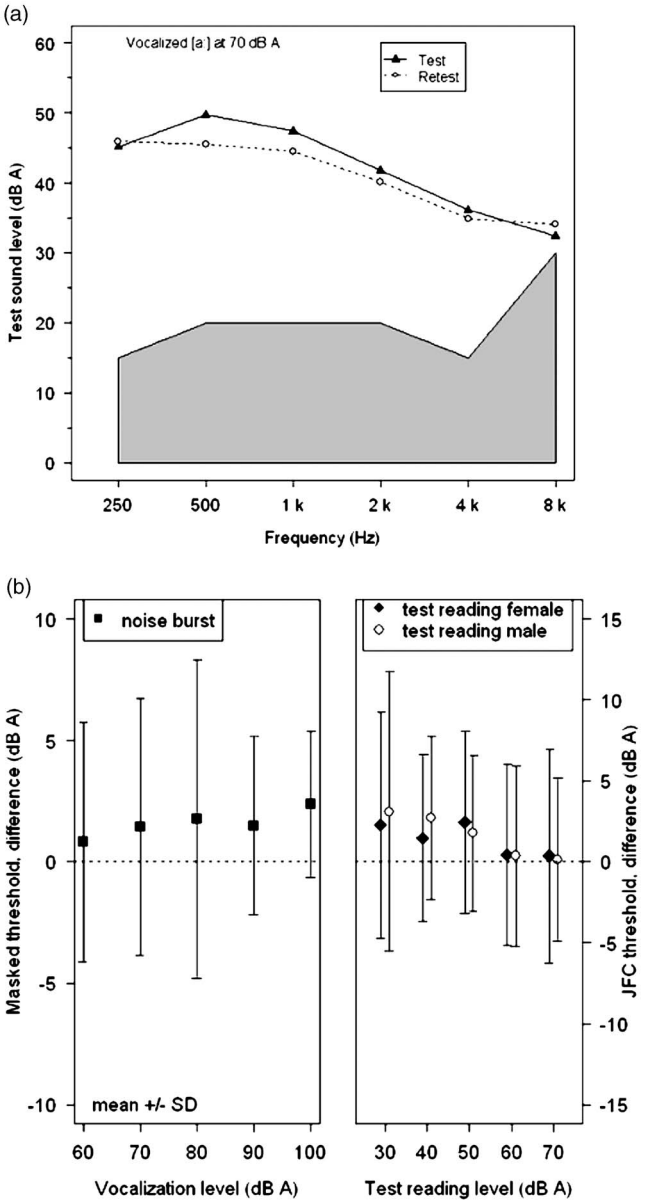

FIG. 5. Inter-session test-retest variability of the masking effect of a vocalized [a:] on an amplitude-modulated narrow-band noise at different frequencies. The upper border of the shaded area shows the binaural free field-hearing threshold. (a) Two individual masked thresholds of a female vocalizer recalculated to correspond to an [a:] at 70 dBA. (b) Mean test-retest difference (±SD) for amplitude-modulated noise test sound (left) and test reading of a female and a male reader (right). There are small average differences indicating a small training effect for the retest, but no differences are statistically significant.

ments, respectively. The spoken test sound (Holgersson) requires approximately three measurements to obtain a confidence interval of ±3 dB.

2. Inter-session variability

A complete test-retest investigation was performed in ten of the subjects with at least 1 week interval between the two sessions.

Test results from reproducibility analysis are shown in Fig. 5. Figure 5(a) shows two masked threshold determinations in one female subject at two sessions, and Fig. 5(b) shows mean and standard deviation of inter-session test-retest differences for masking of noise burst (pooled 250–8000 Hz) and continuous discourse (Holgersson). No mean difference values are significant.

The inter-session repeatability of vocalization level was assessed using Bland and Altman (1986) plots. Possible systematic measurement bias was seen at 500 and 8000 Hz, with inter-session differences (95% CI) of −5.3 to −0.7 dBA and −4.7 to −1.3 dBA, respectively. The differences in vocalization level were calculated within subjects across all test sound levels.

The standard deviation for the difference in vocalization level ranged from 4.3 to 7.4 dBA (Table II). A power calculation with an 80% power and a 5% significance level showed that 25–70 subjects in total were required to detect a 5 dB difference in all test sounds between two groups of normal hearing subjects. Thus at least 35 subjects in each group are required if we disregard the problem of decreasing confidence with multiple statistical tests. When making within-subject comparisons, e.g., with and without disturbing noise, the required sample size decreases to 8.

III. RESULTS

A. Individual data

The procedure of determining masked thresholds at the different vocalization effort levels is illustrated in Fig. 3. A representative example of the vocal level needed to change the perception of the noise bursts train is shown as a function of presented noise level (calibrated for the high-level burst). The masked threshold is obtained from the graph. The desired vocalization level is selected and the corresponding, just audible noise level is determined by interpolation on the abscissa. This is repeated for all test frequencies and generates the curves of Fig. 5(a) for one female subject at one vocalization level and Fig. 6 for one male subject at several vocalization levels. The binaural hearing threshold is shown by the upper border of the shaded area.

It is seen in Fig. 6 that the masking spreads to the higher frequencies when the vocal level is increased from 60 to 100 dBA, which is compatible with the change in the spectra of the [a:] shown in Fig. 4(a).

The effect of voice masking on the target speech sound (test reading) is shown in Fig. 7(a), with one male subject vocalizing, and in Fig. 7(b), with one female subject vocal-

TABLE II. Estimates of standard deviation of inter-session vocalization level differences.

Test sound	Standard deviation
The Wonderful Adventures of Nils Holgersson, female	5.8
The Wonderful Adventures of Nils Holgersson, male	5.8
Third octave band noise 250 Hz	4.8
Third octave band noise 500 Hz	5.6
Third octave band noise 1000 Hz	4.5
Third octave band noise 2000 Hz	4.3
Third octave band noise 4000 Hz	7.4
Third octave band noise 8000 Hz	7.1

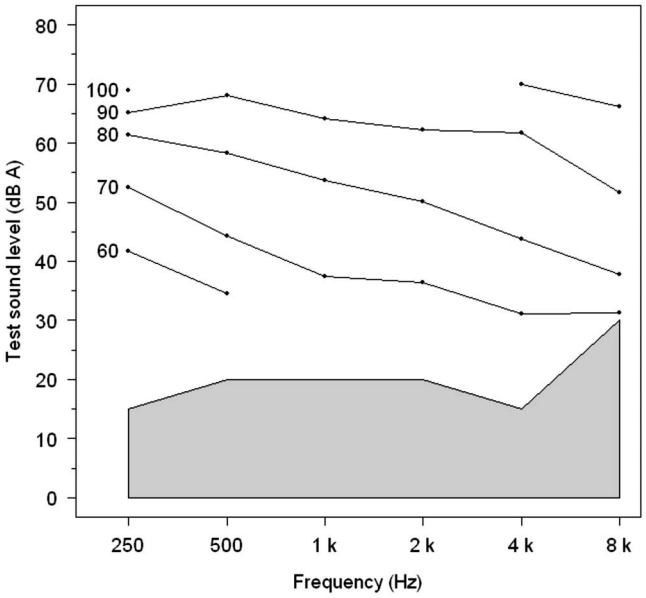

FIG. 6. Masking produced by a vocalized [a:] on amplitude-modulated noise at different frequencies for one male subject. The upper border of the shaded area shows the subject's binaural free field threshold curve in dBA. Masked thresholds for five vocalization levels (60–100 dBA) are shown.

izing. The masked signal was the Holgersson text with a male reader (continuous line) and a female reader (broken line). It is seen that there is very little difference between the masking effect on the male and female test reading.

B. Group data

The mean masked threshold values (±standard error of the mean, SEM) are shown in Fig. 8. The data are from the 22 subjects, and each point is represented by at least six subjects (see tables in the lower part of Figs. 8(a)–8(c), which show the number of subjects for each presented mean threshold value). Figure 8(a) illustrates the pooled data of male and female subjects, Fig. 8(b) vocalizing females, and Fig. 8(c) vocalizing males. The mean curves are produced by different numbers of subjects. This causes an artificial, misleading higher masked threshold at low vocalization level due to missing data. Data at low vocalization level could not be obtained since few subjects could maintain a sufficiently stable voice at the lowest levels. It is seen that there is a substantial masking effect even up to 8000 Hz.

There is a tendency for the increase in masking to be more than 10 dB upon a 10 dB increase in vocal sound level at higher test frequencies. This nonlinear increase can represent an upward spread of masking. However, this effect is not particularly pronounced. There is, on the other hand, a marked difference in the shape of the masked threshold curves between the female [Fig. 8(b)] and the male [Fig. 8(c)] vocalizing subjects. The males have more steeply sloping masking curves toward higher frequency than the females do. The female voices mask the high frequencies more efficiently than the male voices do. The masked threshold was significantly higher for female vocalization than male vocalization for a majority of measured values at 1000, 2000, 4000, and 8000 Hz for vocalization levels of 70, 80, and 90

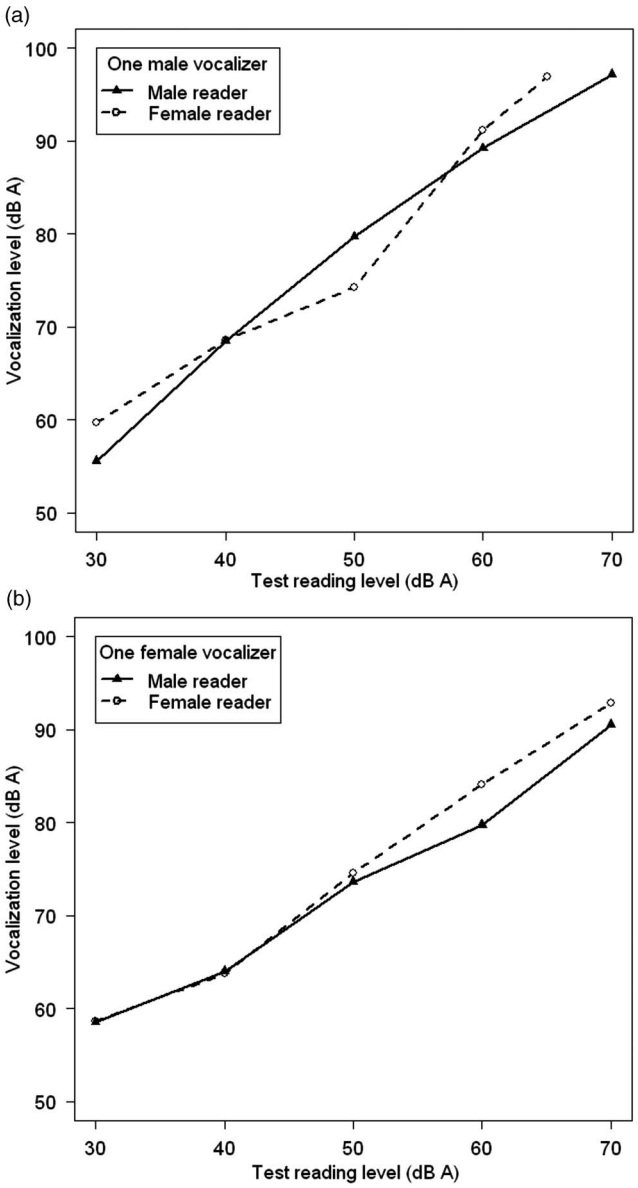

FIG. 7. (a) Maximum vocalization level allowing the test reading (The Wonderful Adventures of Nils Holgersson) to be just possible to follow (JFC) for a male vocalizing [a:] if the reading is done by a female test reader (broken line) and a male test reader (continuous line). (b) Maximum vocalization level allowing the test reading (The Wonderful Adventures of Nils Holgersson) to be just possible to follow (JFC) for a female vocalizing [a:] if the reading is done by a female test reader (broken line) and a male test reader (continuous line).

dBA. This difference was significant at the 1% level for 70 dBA at 1000 (d.f.=19) and 4000 Hz (d.f.=16) and for 80 dBA vocalization at 2000 (d.f.=18), 4000 (d.f.=19), and 8000 Hz (d.f.=17). It was significant at the 5% level for 60 dBA 500 Hz (d.f.=15), for 70 dBA vocalization at 500 Hz (d.f.=20), for 80 dBA vocalization at 1000 Hz (d.f.=14), and for 90 dBA vocalization at 2000 (d.f.=10) and 8000 Hz (d.f.=12). The male voice gave higher vocalization levels for most measurements at 250 Hz, but not significantly higher.

By comparing the Holgersson spectrum (Fig. 2) and the average masked threshold curves of Fig. 8 one can see that the Holgersson spectrum is steeper than the masked threshold during female vocalization [Fig. 8(b)], in particular. This

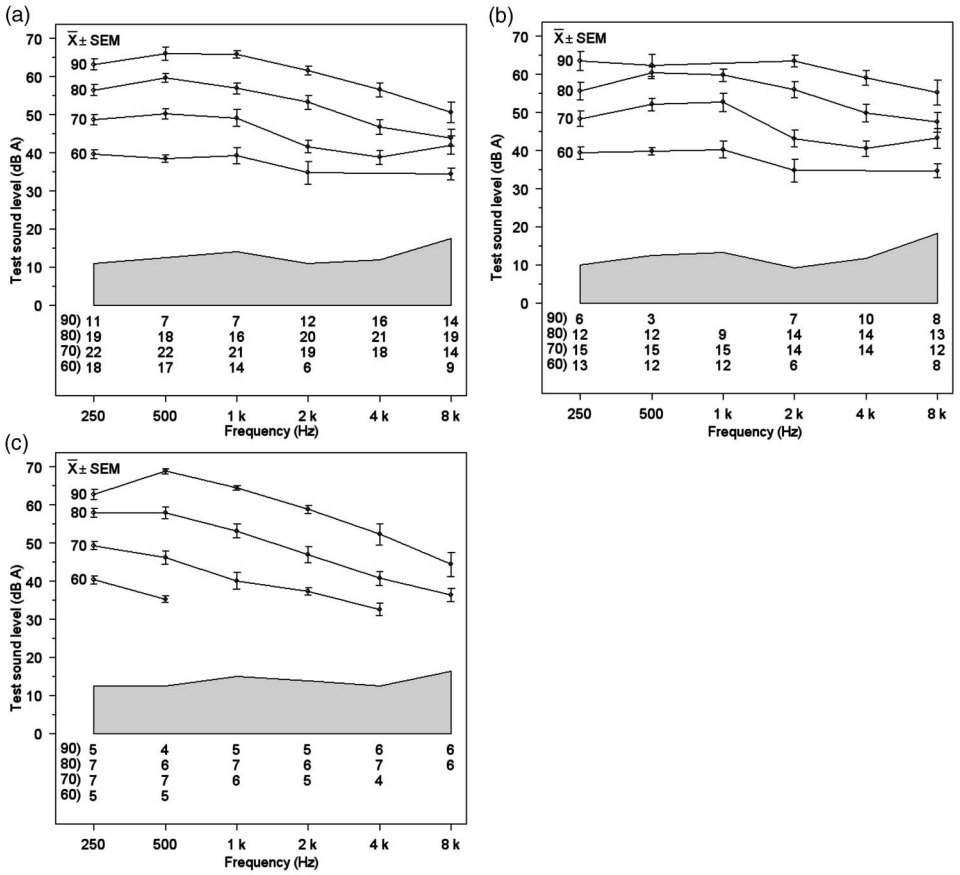

FIG. 8. (a) Average (±SEM) of masked thresholds for 1/3-octave noise bursts during own vocalization. Maximum vocalization method. Normal hearing subjects. Upper border of shaded area shows average hearing threshold (dBA). Male ($n=7$) and female ($n=15$) vocalizers. (b) Mean masked threshold for normal hearing female vocalizers. (c) Mean masked threshold for normal hearing male vocalizers. The number of subjects for each mean masked threshold value is indicated by the table below the graphs.

may mean that the high frequencies of speech are masked while low frequency components are still above threshold.

The level of the vocalized [a:] that is needed for the JFC criterion for the Holgersson reading is shown in Fig. 9. The male and female subjects are separated; the male reader of Holgersson is indicated by the continuous lines and the female by the broken lines. Heavy lines indicate male vocalizer, thin lines female vocalizer. It is seen that a certain test sound is masked by a lower vocalization level for females than for males. A signal-to-noise ratio can be estimated, −25 to −30 dB for men and −20 to −25 dB for women, with slightly lower values for high levels of the Holgersson reading. The difference between female and male masking effects in Fig. 9 can be explained by the data of Fig. 8. The female voice is more efficient in masking the higher frequencies. This means that the weaker but highly important high frequency components (for most consonants) are masked more efficiently by the female than by the male voice. In accordance with Fig. 8, the female voice is more efficient in masking the important frequency components (the higher frequencies) of the test speech sounds than is the male vocalization.

Using a regression model the gender difference was estimated to be 4.1 dBA (Wald test, $p<0.05$, $r^2=0.71$, d.f. $=448$) controlling for spoken test sound and test sound level. Also, a mean and median difference of 3.1 and 4.3 dB, respectively, were calculated by taking the differences between genders within each test sound and test sound levels.

C. Summary of results

The technique is easy to perform also for subjects who are not trained singers and shows adequate reproducibility: intra-session standard deviation of 1.9–3.5 dBA and inter-session standard deviation of 4.3–7.4 dBA. The masking effect covers the whole frequency range up to 8000 Hz. There is a weak tendency toward an upward spread of masking, slightly more at high vocal efforts. There is a gender effect: Female vocalization masks more efficiently at high frequencies. The female vocalization was 4 dB more efficient in

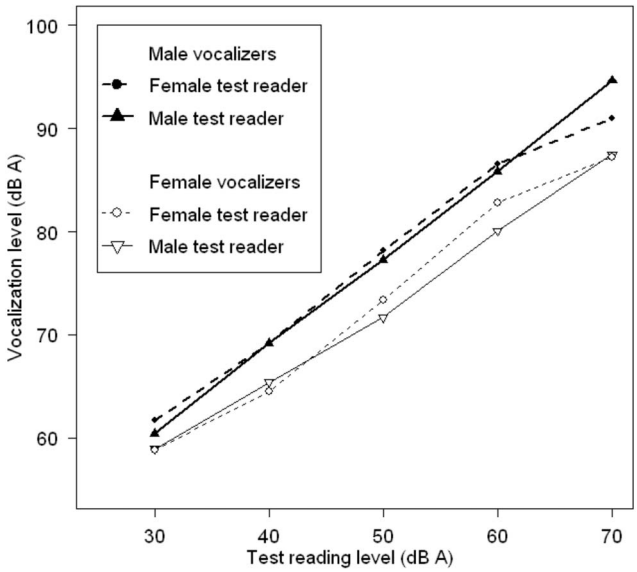

FIG. 9. The highest vocalization level allowing a test reading (maximum vocalization method. The Wonderful Adventures of Nils Holgersson) to be just possible to follow (JFC) for male and female test readers (continuous lines and broken lines, respectively) and for male and female vocalizers (heavy lines and thin lines, respectively).

masking a continuous discourse, both with a female and a male reader. The signal-to-noise ratio for male vocalization was −25 to −30 dB and for female −20 to −25 dB.

IV. DISCUSSION

A. Methodological aspects

One of the previous studies looking at the masking effect of one's own voice, Gauffin and Sundberg (1974), used a technique similar to that used in the present study for narrow-band noise masked signal (maskee) keeping the maskee constant and adjusting the voice (masker). One professionally trained subject participated. Shearer (1978) trained non-professionals to mask pure tones with their own voice. They kept voice level stable and adjusted the masked signal. None of the studies have tested speech as a masked signal. In earlier studies (unpublished), we found it extremely difficult to have subjects focus both on producing a stable vocalization and on adjusting a target speech sound. The experience was from studies in 1960s on speech perception in subjects with Bell's palsy. We trained subjects to vocalize at a certain level. During the vocalization, we presented phonetically balanced words, which were to be repeated. These experiments were difficult to conduct. On the one hand, the subject heard the target word and "reflexively" stopped vocalizing. Then they heard most of the word unmasked. On the other hand, they did not hear any external test sound at all and they just continued vocalizing. Changing the procedure to a JFC paradigm improved the possibility of obtaining reliable results. The present method of keeping the maskee constant while controlling the voice (maximum vocalization method) was easy to learn and required practically no training to achieve fair intra-session and inter-session reproducibilities. None of the present participants and only one subject of 20 among the hearing impaired group failed to perceive the change in the target noise sound (steam engine train) (Borg *et al.*, in preparation).

The within-session reproducibility was reasonably good. This means that short-term experiments can be carried out with fair confidence. On the other hand, comparisons between two sessions are questionable for single individuals. Measurement precision information is vital when describing new measurement techniques because it is used in a power analysis for controlling the type I and type II statistical inference errors when planning a second study. A power analysis was made to facilitate new research in the area. For instance, we calculated that a 5 dB difference in masked thresholds between two groups requires 35 subjects in each group or that a 5 dB difference within a group requires eight subjects.

The test readings were produced by one male and one female experienced newsreader at the Swedish Radio. We found that their spectra were quite similar, except for F_0. We could have chosen to record other readers as well in order to select subjects with larger differences. Our choice was not to do so, as these persons were primarily selected for their voice quality and oral presentation skills. Certainly, by selecting extreme voices, we would have seen differences in spectra and in masking effects on the male and female text readers, but we regard these subjects to be sufficiently normal and representative.

The masking patterns obtained are valid in the sense that they represent actual vocalization produced to mask a certain sound. However, the normal situation is often the reversed. A person talks at the same time as he/she has an interest in perceiving what is going on in the environment. Furthermore, the temporal and spectral variations in natural speech are not considered in the present test situation and have to be focused on in future studies. When a time varying masker (words or sentences) is used, cognitive factors (e.g., short-term memory and linguistic competence) become more important than in the present experimental design (constant [a:]). This means that factors at level 2 (in the schedule presented in the Introduction) have to be taken into consideration. For constant maskers, as in the present study, such effects are minimized even for the JFC test. The role of factors at levels 1 and 2 has to be investigated in further studies.

A tilt of the voice spectrum when vocal effort is increased is practically unavoidable for lay people. The tendency toward a change in spectrum upon change in target signal frequency (the noise bursts) was not expected. Such a frequency shift increases the masking efficiency of the voice, as a lower total dBA is required for a certain masking effect, particularly at the high frequencies. This frequency shift is one possible explanation for the shallow tails of the masked threshold curves toward high frequencies in addition to the previously mentioned statistical bias due to drop-outs (some subjects could not lower their voice so much that the threshold criteria of the low-level noise bursts were reached). Thereby some of the lower values were missing, and the mean values were spuriously somewhat too high.

B. Vocal effort and vocalization spectra

The normal use of voice for vocal communication involves at least four different sound production manners: whispering (no phonation), normal talk, shouting (including high-level talk), and singing. These different manners have acoustic correlates, which are at least partly understood. Ternström *et al.* (2006) found a shift in the spectral balance between low and high frequency components, indicating an increase in the high frequencies at strong vocal effort, but a less marked emphasis at the highest tested level (probably comparable to shouting). There is a general trend toward an increase in the fundamental frequency (F_0) as well as the first formant (F_1) with increased vocal effort. Professional male singers have a singer's formant around 3 kHz. The present material shows an inconsistent pattern across individuals. Some subjects show a very clear F_3 around 2–3 kHz, which also increases relative to F_1, whereas others show minimal F_3. This difference may correspond to a different degree of singing practice, but it is questionable whether it is a true singer's formant (Sundberg, 2001). However, no such evaluations were made.

In the present study, the 1/3-octave spectra of the vocalized [a:] picked up by the probe microphone in the ear canal showed some interesting features. In accordance with previ-

ous studies, there was an increase in the high frequency components when vocal level was raised. There was also an increase in the high frequency vocal spectra when masking 4000 Hz bursts compared to 250 Hz bursts. If the subjects had been able to maintain their voice at a totally constant spectrum, then we would have seen a slightly lower masked threshold for the high frequencies than that found in Figs. 6 and 8 because an [a:] at a certain dBA-level would have had less high frequency components and therefore masked the high frequency test noise less effectively.

The voice spectrum changed shape for the lowest vocalization levels, the fundamental dominated, and the overtones were relatively undeveloped, particularly in female vocalizers. This has also been seen occasionally in females earlier, e.g., by Nordenberg and Sundberg (2004). In addition, some of the female subjects managed to mask the test noise bursts even when they were of higher intensity, 50 or 60 dBA. This pattern was not seen among the males. This observation may be an expression of a gender difference or it may be purely an individual difference that happened to be more common among the females in this sample. There are several possible explanations for the large masking effect of the female voice at low vocal effort despite the fact that there is little energy at high frequencies at low vocal effort. First of all, we think we can rule out the response criterion as the main reason. The argument is that the difference between the male and the female masked thresholds is not constant across frequencies, it even crosses. The females have higher masked thresholds at high frequencies and lower at low frequencies than the males do.

Another possible explanation relates to the two components of the speaker's own voice, the air-conducted and the bone-conducted component. There are, to our knowledge, no data on gender differences in the relationship between the air-conducted and bone-conducted components. However, von Bekesy's (1960) data show an up to 6 dB difference in the bone-conducted signal among his sample of four test subjects, which indicates substantial individual variability. It can also be noted that Stenfelt and Reinfeldt (2007) showed a ± 10 dB difference in the occlusion effect, indicating great individual variability in bone conduction features.

The third possible explanation is that the individuals who succeed to mask even with low-level voice have either a pronounced upward spread of masking from their fundamental or managed to place a strong overtone close to the target noise frequency. This is in accordance with the observation that low-level vocalizations were only seen during masking of noise bursts and not of speech. The upward spread of masking is expected to be more pronounced for the approximately 250 Hz female fundamental than for the approximately 125 Hz male fundamental, which could explain part of the gender difference. This interesting question has to be addressed in further studies.

C. Gender differences

The female vocalization was 4 dB more efficient in masking a continuous discourse both with a female and a male reader, and the signal-to-noise ratio for the Holgersson was 5 dB better (more negative) when masked by a male than by a female vocalization. Except for the well-established gender differences in fundamental frequency (F_0), the characteristics of the voice at increased level also show some gender differences. First of all, the maximum level (total SPL) is about 5 dB higher for males than females in loud speech (Ternström *et al.*, 2006; Södersten *et al.*, 2005) when reading in background noise. Females also have a higher proportion of high frequency energy at the highest vocal levels, probably due to the higher frequency of the F_1 peak. It is interesting to note that the female subjects in the present study more efficiently masked both the male and the female text reader than the male vocalizers did. The difference was about 4 dB, which corresponds well to the higher maximal level for loud speech in noise for males than females (Ternström *et al.*, 2006). At high effort the masking effect on external speech thereby becomes about equal for males and females. One possible explanation for the higher masking effect of the female voice as compared to the male voice is that the higher frequencies (consonants in the Holgersson reading) carry more information than do the low frequency components. The slightly higher frequency emphasis of the female voice is therefore likely to mask these information-carrying components of the Holgersson material more efficiently than the male voice. The higher masked threshold for the high frequency noise bands during masking with the female as compared to the male voice is in accordance with the gender difference in the masking effect on the Holgersson reading. The female voice may be weak, but it is masking the own ear efficiently.

D. Application and future research

The present results concern primarily the fundamental physiological level of the three-level model presented in Introduction. Of course, cognitive and linguistic factors (level 2) are always involved in psycho-acoustic tests, particularly those involving speech signals. Such factors have been minimized by using a constant masker (a sustained [a:]). In order to understand the interaction both at level 1 (social) and level 2 (linguistic, cognitive), one must establish what is actually heard. Because the low frequency components are stronger in external speech, they are less likely to be masked during one's own vocalization. The resulting situation may be the following. During one's own vocalization, one can hear that someone is talking but not perceive what is said. In a vivid discussion, this may be a technique for dominance in that one is not distracted by the arguments of others. On the other hand, the robust hearing of the low frequency components of external speech may facilitate turn-taking. The present findings may help us understand social interaction, particularly in larger groups.

Future research could focus on more valid speech maskers such as repeated phonemes, words in sentences, and finally running speech. The vocalization methods used here certainly contain a component of singing and/or shouting at the higher levels and are therefore not entirely representative of running speech. Considering the difficulties and the sophisticated analysis method that Ternström *et al.* (2006) used

to develop acoustical measurement of various components of running speech, it will be very difficult to assess the masking effect of different components in running speech in clinical applications. The cognitive difficulties (informational masking) cannot easily be circumvented, as the test subject has to produce running speech at the same time as he/she tries to interpret the external target speech signal. A way for continued research could possibly be to use a non-speech signal as the target and repeated sequences of running speech as the masker.

One obvious application and focus for the study is how different types of hearing impairment affect self-masking. First of all, the focus is on peripheral hearing disorders where conductive and sensorineural impairments might have different effects due to different effects on the air-conducted and bone-conducted components of both the self-produced masker and the external target signals. The influence of different types of sensorineural impairment is the focus of a forthcoming article (Borg *et al.*, submitted). An interesting continuation also concerns the role of cognitive disturbances and central auditory disorders in the ability to conduct a rapid dialog in which talking and listening are more or less simultaneous. In this way, the analysis is extended from level 3 to level 2 in the three-level model.

V. SUMMARY AND CONCLUSIONS

A technique for assessment of masking effects of one's own vocalization has been found to be easy to perform, also for untrained subjects, and it shows adequate reproducibility: intra-session standard deviation of 1.9–3.5 dBA and inter-session standard deviation of 4.3–7.4 dBA. The masking effect of a vocalized [a:] is pronounced, extending over the whole frequency range (250–8000 Hz), and interferes substantially with perception of speech. There is a weak tendency toward an upward spread of masking, slightly more at high vocal efforts. There is a gender effect: A female vocalization masks more efficiently than a male vocalization at high frequencies. In accordance with this, a female vocalization was found to be more efficient (4 dB) in masking external speech, both with a female and a male reader. The signal-to-noise ratio for female vocalizers was −20 to −25 dB and for male vocalizers −25 to −30 dB, as measured in the ear canal. The importance of self-masking for social interaction in groups, particularly for persons with hearing impairment, is pointed out as well as the importance of cognitive and linguistic abilities.

ACKNOWLEDGMENT

The present study was supported by grants from Örebro University Hospital, Nyckelfonden, FAS (Swedish Council for working life and social research), Tysta skolan, and The Swedish Institute of Disability Research. Thanks to Professor Johan Sundberg, Department of Speech Music Hearing, Royal Institute of Technology, Stockholm, Sweden, for valuable suggestions and comments.

Bland, J. M., and Altman, D. G. (**1986**). "Statistical methods for assessing agreement between two methods of clinical measurement," Lancet **1**, 307–310.

Borden, G. J. (**1980**). "Use of feedback in established and developing speech," in *Speech and Language, Advances in Basic Research and Practice*, edited by N. J. Lass (Academic, New York), Vol. **3**, pp. 223–242.

Borg, E., and Counter, S. A. (**1989**). "The middle-ear muscles," Sci. Am. **260**, 74–80.

Borg, E., Wilson, M., and Samuelsson, E. (**1998**). "Towards an ecological audiology: Stereophonic listening chamber and acoustic environmental tests," Scand. Audiol. **27**, 195–206.

Dunn, H. K., and Farnsworth, D. W. (**1939**). "Exploration of pressure field around the human head during speech," J. Acoust. Soc. Am. **10**, 184–199.

Gauffin, J., and Sundberg, J. (**1974**). "Masking effect of one's own voice," QPSR Quarterly Progress and Status Report No. 035-041, Department of Speech, Music and Hearing, The Royal Institute of Technology, Stockholm, Sweden.

Howell, P. (**1985**). "Auditory feedback of the voice in singing," in *Musical Structure and Singing*, edited by P. Howell, I. Cross, and R. West (Academic, London), pp. 259–286.

Howell, P., and Dworzynski, K. (**2001**). "Strength of German accent under altered auditory feedback," Percept. Psychophys. **63**, 501–513.

Lamprecht, A. (**1988**). "Changes of the voice in the Lombard reflex (German)," Laryngol., Rhinol., Otol. **67**, 350–354.

Lyxell, B., Andersson, U., Borg, E., and Olsson, I. S. (**2003**). "Working-memory capacity and phonological processing in deafened adults and individuals with a severe hearing impairment," Int. J. Audiol. **42**, S86–S89.

Nixon, C. W., Morris, L. J., McCavitt, A. R., McKinley, R. L., Anderson, T. R., McDaniel, M. P., and Yeager, D. G. (**1998**). "Female voice communications in high levels of aircraft cockpit noises—Part 1: Spectra levels and microphones," Aviat., Space Environ. Med. **69**, 675–683.

Nordenberg, M., and Sundberg, J. (**2004**). "Effect on LTAS of vocal loudness variation," Logoped. Phoniatr. Vocol. **29**, 183–191.

Pörschmann, C. (**2000**). "Influences of bone conduction and air conduction on the sound of one's own voice," Acustica **86**, 1038–1045.

Rostolland, D. (**1982**). "Acoustic features of shouted voice," Acustica **50**, 118–125.

Shearer, W. M. (**1978**). "Self-masking effects from live and recorded vowels," J. Aud. Res. **18**, 213–219.

Södersten, M., Ternström, S., and Bohman, M. (**2005**). "Loud speech in realistic environmental noise: Phonetogram data, perceptual voice quality, subjective ratings and gender differences in healthy speakers," J. Voice **19**, 29–46.

Stenfelt, S., and Reinfeldt, S. (**2007**). "A model of the occlusion effect with bone-conductive stimulation," Int. J. Audiol. **76**, 595–608.

Stephen, S. C., and Haggard, M. P. (**1980**). "Acoustic properties of masking/delayed feedback in the fluency of stutterers and controls," J. Speech Hear. Res. **23**, 527–538.

Sundberg, J. (**2001**). "Level and center frequency of the singer's formant," J. Voice **15**, 176–186.

Ternström, S. (**1994**). "Hearing myself with others: Sound levels in choral performance with separation of one's own voice from the rest of the choir," J. Voice **8**, 293–302.

Ternström, S. (**1999**). "Preferred self-to-other ratios in choir singing," J. Acoust. Soc. Am. **105**, 3563–3574.

Ternström, S., Bohman, M., and Södersten, M. (**2006**). "Loud speech over noise: Some spectral attributes, with gender differences," J. Acoust. Soc. Am. **119**, 1648–1665.

Tranmüller, H., and Eriksson, A. (**2000**). "Acoustic effects of variation in vocal effort by men, women, and children," J. Acoust. Soc. Am. **107**, 3438–3451.

von Bekesy, G. (**1960**). *Experiments in Hearing* (McGraw-Hill, New York).

Gaussian-noise discrimination and its relation to auditory object formation

Tom Goossens[a)]
Eindhoven University of Technology, P.O. Box 513, NL-5600 MB Eindhoven, The Netherlands

Steven van de Par
Philips Research, High Tech Campus 36, NL-5656 AE Eindhoven, The Netherlands

Armin Kohlrausch
Philips Research, High Tech Campus 36, NL-5656 AE Eindhoven, The Netherlands and Eindhoven University of Technology, P.O. Box 513, NL-5600 MB Eindhoven, The Netherlands

(Received 3 April 2008; revised 20 March 2009; accepted 25 March 2009)

This study used a same/different experiment to assess the ability of human listeners to discriminate Gaussian-noise tokens with a spectral range of 350–850 Hz and a duration of 50 ms. For this duration, discrimination ability is high. However, when an identical 200-ms noise fringe with the same statistical properties as the 50-ms target tokens is appended to the end of the two target tokens, listeners show very poor discrimination. It was investigated whether altering the properties of the fringes with respect to those of the target improved the ability to discriminate the target tokens. This method was used to investigate the influence of changing fringe properties such as spectral range, level, interaural level difference, and interaural time delay on discrimination performance for the target. Spectral and temporal separation showed the strongest improvements, whereas no effect was found for doubling the fringe bandwidth, 5-dB level increases or decreases, or 10 dB interaural level differences. In the second experiment, subjects were asked to indicate whether they perceived one or two auditory objects for these stimuli. The results of the two experiments indicate that perceiving two objects is a necessary but not sufficient condition for good target discrimination.
 [DOI: 10.1121/1.3119626]

PACS number(s): 43.66.Fe, 43.66.Ba, 43.66.Lj, 43.66.Mk [RLF] Pages: 3882–3893

I. INTRODUCTION

In his work on auditory scene analysis, Bregman (1990) distinguished between acoustic events, auditory streams, and auditory units. An acoustic event is a happening in the physical world, causing vibrations that can be picked up by our hearing system. Examples include the acoustic events caused by walking in the streets or rain falling. In everyday situations, many such acoustic events occur in rapid succession. We perceive these acoustic events with our auditory system where the two waveforms arriving at our eardrums are analyzed and divided into several separate perceptual entities, often called auditory streams, e.g., a stream containing the footsteps of somebody walking and a stream of the sound of rain. The process of auditory scene analysis is the segregation and organization of acoustic information into separate auditory streams. The auditory streams can be a combination of several smaller auditory entities, which can be named auditory objects, or units in the nomenclature of Bregman (1990), e.g., the sound of the individual footsteps of the person walking in the streets or of the drops of rain splashing into a puddle.

We can, to a certain extent, direct our attention deliberately to either one of these auditory streams (Alain and Arnott, 2000). In their study on selective attention for auditory objects, Alain and Arnott (2000) adopted the definition of Bregman (1990) that an auditory object "[…] is the percept of a group of sounds as a coherent whole seeming to emanate from a single source." Much effort has been put into studying the principles that govern the grouping of auditory objects into perceptual streams, e.g., by van Noorden (1975). Reviews of the literature can be found in Bregman (1990), Yost and Sheft (1993), and Darwin and Carlyon (1995). Van Noorden (1975) found that the perceived relation of successive tones in a sequence depends on their temporal and spectral distance. He used sequences of alternating tones, in the form of an *ABAB* pattern, for which he varied their frequency and intertone interval. When their spectral distance was sufficiently close, they were inevitably perceived as a single auditory stream. However, for some combinations of spectral and temporal distance, the tones were segregated into two separate auditory streams, an *AA* and a *BB* stream. The *A*'s and *B*'s in these patterns can be considered to be the previously mentioned auditory objects, or units, of which the streams consist.

Yost (1991) distinguished at least seven physical parameters that contribute to the formation of auditory objects: spectral separation, intensity profile, harmonicity, spatial separation, temporal separation, common temporal onsets and offsets, and coherent slow temporal modulation. For example, several studies (e.g., Buell and Hafter, 1991; Woods and Colburn, 1992) showed that when one of the components in a harmonic tone complex had an asynchronous onset

[a)]Author to whom correspondence should be addressed. Electronic mail: tomgoos@gmail.com

with respect to the other components, two sound objects were reported instead of one when the components had synchronous onsets. This indicates that harmonic tones are likely to be fused into a single auditory object, but it is possible that they are segregated into different objects when there is evidence, e.g., an asynchronous onset of one of the components, indicating that they were not caused by the same physical event.

Object formation has been suggested to be an important factor that influences the ability to discriminate between Gaussian-noise tokens (Goossens *et al.*, 2008). These authors investigated the ability of human listeners to discriminate between Gaussian-noise tokens with bandwidths varying from 50 to 3000 Hz and durations varying from 1.6 to 409.6 ms. In agreement with the literature, it was found that performance increases with duration up to approximately 40 ms (Hanna, 1984; Heller and Trahiotis, 1995). For longer noise stimuli, discrimination decreases. Goossens *et al.* (2007) and Goossens (2008) modeled this duration effect by assuming a fixed capacity for retaining or processing an auditory object, independent of the duration of the object. Therefore, more information was lost in the internal representation of the longer stimulus than in the internal representation of the shorter stimulus. This difference in information loss caused a maximum performance at around 40-ms duration.

Goossens *et al.* (2007) and Goossens (2008) extended both Gaussian-noise target tokens in a trial with an identical piece of Gaussian noise. These were called uninformative fringes since, being identical, they could not contribute to the discrimination. When a fringe was concatenated without fringe alteration (i.e., the fringe had similar bandwidths, levels, interaural differences, etc., as the target) to one of the to-be-discriminated target noises, discrimination ability dropped substantially. The interpretation was that listeners were not able to listen to a subpart of an auditory object (noise token) and that the retention or processing capacity needed to be attributed to the whole auditory object, leading to much poorer discrimination performance. The correspondence between their model simulations and behavioral data supports this interpretation.

The assumption by Goossens *et al.* (2007) and Goossens (2008) that auditory objects are processed as inseparable units raises the question as to what stimulus properties are needed to create an auditory object. More specifically, one would expect that when target stimuli have an added fringe, as described above, introducing perceptual cues in the noise fringe, which enable the segregation of target and fringe, should improve the ability to discriminate the target noises compared to the situation where no such cues are present. This would provide a new method for assessing the importance of particular segregation cues in creating auditory objects consisting of Gaussian noise.

Several examples are known where segregation influences the perception of low level cues. The formation of auditory objects is sometimes investigated by presenting cyclic or continuous patterns to the listener (e.g., Royer and Robin, 1986; Crum and Bregman, 2006). Royer and Robin (1986), as mentioned above, found that the repetition rate of a sound-burst pattern influences the way the bursts are integrated into auditory objects. Crum and Bregman (2006) showed that a gradual timbre change in a continuous sound is detected more easily when silences are inserted, which cause unit boundaries, than when the sound is presented continuously without silences or when the silences are filled with loud noise bursts.

In the current study we investigate the influence of segregation cues on discrimination thresholds, rather than detection thresholds, in a non-cyclic paradigm. A number of spectral, temporal, intensity, and spatial cues are used to assess their influence on the discrimination of target noise tokens. Each trial consisted of the presentation of two Gaussian target noises of 50-ms duration with a spectral range of 350–850 Hz that could be identical or independently generated. For this combination of duration and bandwidth, discrimination performance is good. The task of the listener was to decide whether these targets were the *same* or *different*. In most conditions, an identical fringe was appended to the two targets in a trial. It was hypothesized that the ability to discriminate would be low when the fringe was perceptually fused with the target into a single auditory object and high when the fringe and target were perceptually segregated into two auditory objects.

II. METHOD

A *same/different* task was used for measuring discrimination performance. In each trial, two stimulus intervals were presented to the listener, both containing a target noise and a backward-fringe, i.e., an uninformative noise. The exception was for the baseline condition in which no fringes were presented. The targets could be identical or independent. These stimulus intervals were separated by an interonset interval (IOI) of 800 ms (unless stated otherwise). The trials were presented in blocks of 100, of which half had identical (same) target noises and the other half had independent (different) target noises. Same and different trials were presented in random order. The fringes of the two intervals were always identical and, thus, uninformative for the discrimination task. The listeners' task was to decide whether the *target* tokens were the same or different.

Conditions differed in the type of cue that was present in the fringe, which could potentially enable listeners to segregate the target from the fringe. For each experimental condition, four successive blocks of trials were presented, of which the first block was discarded. Listeners were allowed to take a break after a succession of four blocks if desired. Sensitivity indices, d', were calculated from the results for the last three blocks.

A d' value was obtained by calculating percentages correct for the same trials and the different trials. These percentages correct were converted to z-scores. Finally, d' was calculated by adding the z-scores for the same and the different trials. At chance performance, the d' value equals zero. Above-chance performance results in positive d' values; e.g., 69% correct for both same and different trials results in a d' value of approximately 1, and 84% correct results in a d' value of approximately 2.

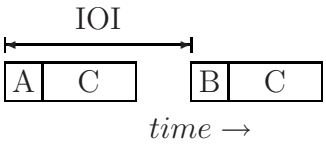

FIG. 1. A schematic representation of a discrimination trial. A trial contained two stimulus intervals, each containing a 50-ms target (A and B) followed by a 200-ms fringe (c). The targets could be identical (same) or independent (different) across the two trials. The fringes were always identical. The IOI was 800 ms (unless stated otherwise).

In most figures, the d' values of the individual subjects were normalized with their individual performance in the baseline conditions measured in Sec. IV. The baseline conditions consisted of one condition where only the targets (no fringe, NF) were presented and one condition where the targets had fringes that were appended without fringe alteration (fringe, F). Discrimination values for these conditions were obtained once at the beginning and once at the end of the experiment. The mean values for the session at the *beginning* of the experiment were used for normalization. The normalized d' will be called the *effect* and was obtained for a condition X using

$$\text{effect} = \frac{d'_X - d'_F}{d'_{NF} - d'_F}. \quad (1)$$

This maps the performance for condition F to an effect of zero and the performance for condition NF to an effect of 1, normalizing differences in baseline performances of different listeners. Note that in the across-subject means, the individual results were first normalized using the individual baseline performances before pooling the data.

Four normal hearing subjects, including the first (subject S3) and second authors (subject S2), who were all experienced in psychoacoustical experiments participated in this study. Their ages ranged from 28 to 41. First, the baseline conditions (see Sec. IV) were repeated until stable performance was achieved before continuing with the rest of the conditions. During the training, at least 16 blocks of 100 trials were presented. The stimuli were generated on a PC and were presented, through an RME DIGI96/8PAD 24 bit PCI Digital audio card, a TDT S3 HB7 headphone driver, and a PA5 programmable attenuator, on Beyerdynamic DT 990 Pro headphones.

III. STIMULI

Each stimulus interval contained a target and a fringe (see Fig. 1). The targets were Gaussian-noise tokens with a duration of 50 ms with 10-ms raised cosine onset and offset ramps, which were applied after bandpass filtering to a bandwidth of 500 Hz with a center frequency of 600 Hz. In each trial, new noise was generated for both target and fringe tokens. The targets were presented diotically with a spectrum level of 50 dB SPL (where SPL means sound pressure level). The target noise properties were never altered throughout the experiment.

The fringes were Gaussian-noise tokens with a duration of 200 ms with 10-ms raised cosine onset and offset ramps which were applied after bandpass filtering. Unless stated otherwise, the fringes were bandpass filtered to a bandwidth of 500 Hz with a center frequency of 600 Hz and were presented diotically, like the target.

The filtering was done with a digital fast Fourier transform (FFT) filter that transformed the signal (of 44 100 samples at 44 100 Hz sample rate) to the frequency domain, where all frequency components lying outside the specified bandwidth were set to zero. This signal was transformed back to the time domain with the inverse FFT operation.

The fringes always followed the target, and their onset and offset ramps overlapped such that the temporal envelope at the overlap was constant (unless stated otherwise). Moreover, it was made sure that during the 10-ms overlap, the fringe was identical to the target, also in a "different" condition, in order not to introduce indentation in the temporal envelope that could serve as a discrimination cue.

IV. BASELINE CONDITIONS

The baseline conditions consisted of one condition where the targets were presented without fringe, i.e., the condition for which the highest performance was expected, and a condition with fringe which had no audible cue that could lead to the segregation of target and fringe, i.e., the condition for which the lowest performance was expected. The two baseline conditions were tested twice, once at the beginning of the experiments and once at the end of all discrimination experiments, which provided information on whether the subjects were influenced by a training effect. In the remainder of this study, the individual baseline conditions of the first session were used to normalize the data of each subject (see Sec. III) which enabled the comparison of data across subjects. The properties of the targets and fringes were as specified in Sec. III.

A. Results

Figure 2 shows the results for the baseline conditions. In the conditions labeled NF (no fringe), only the target was presented. In the conditions labeled F (fringe), a fringe was added, which had the same bandwidth as the target (no fringe alteration). The conditions with a subscript b were obtained before all other conditions, and those with a subscript e were obtained after all other conditions. The mean sensitivity index d' across the different retests of each condition is shown on the ordinate. The error bars indicate the standard error of the mean across the different retests.

Table I shows the results of pairwise t-tests with Bonferroni correction with a significance level of $\alpha = 0.05$. This test showed no significant difference between the conditions at the start and at the end of the experiment for either the baseline condition without a fringe (NF) or the baseline condition with a fringe (F). This shows that we do not need to take a learning effect into account. Additional comparisons showed that there was a highly significant difference between the conditions without a fringe and the condition with a fringe at the beginning of the experiments ($d'_{NF_b} - d'_{F_b} = 2.0$) as well as at the end of the experiments ($d'_{NF_e} - d'_{F_e} = 1.7$) (see Table I).

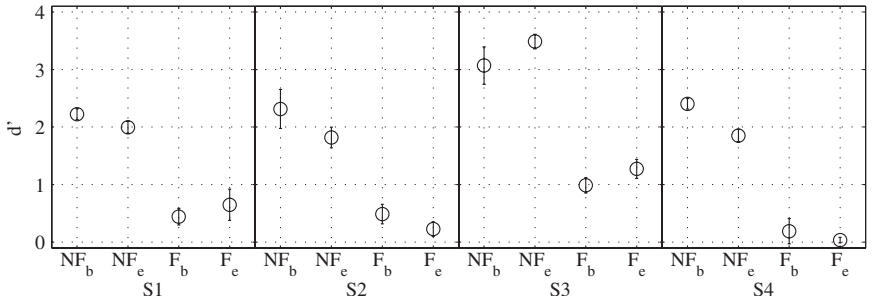

FIG. 2. Results for the baseline conditions. Mean d' values of individual subjects are shown. In condition NF (no fringe), only the target was presented. In condition F, both a target and fringe, without fringe alteration, were presented. The conditions with subscript b were obtained at the beginning of the experiment, and those with a subscript e were obtained at the end. The error bars indicate the standard error of the mean across the different retests.

B. Discussion

The results showed that performance for the condition where a fringe was appended to the target without fringe alteration (F) was significantly lower than that for the condition where no fringe was present (NF). One explanation for the poor performance in the fringed condition compared to the target-only condition is that the memory for the target suffers from interference by the succeeding fringe because of the new stimulus information that enters the periphery. In the absence of a fringe, the target is not degraded by memory interference, and performance is higher. A second explanation is that the target and fringe are combined into a single auditory object, and the discrimination is influenced by interference within this auditory object.

These two alternative explanations cannot be distinguished based on the data shown in Fig. 2. However, they make different predictions for conditions in which the fringe presented after the target is perceived as a separate object. According to the latter explanation, the ability of listeners to discriminate the targets should increase in a condition where the listener is able to perceptually segregate target and fringe into two distinct objects. For the former explanation, the mere presence of the fringe should be sufficient to lead to a poor performance. To evaluate these two alternatives, in the following experiment temporal gaps of varying duration were introduced between target and fringe in order to increase the likelihood that they would be perceived as two separate objects.

V. GAP DURATION

A. Stimuli

The properties of the targets and fringes were as specified in Sec. III, with the exception that a temporal gap was inserted between target and fringe with a duration of 0, 20, 40, 80, 160, or 320 ms. This gap duration was defined as the temporal distance between the middle of the offset ramp of the target and the middle of the onset ramp of the fringe. The IOI was always 800 ms, except for the 320-ms gap, where it was 960 ms.

These experiments resemble one of the experiments of Hanna (1984) (Exp. 2a), which was basically the same, except that he added a fringe with a temporal gap of 100 ms to only one of the targets in each trial, whereas in the current experiment a fringe was added to both targets. As an additional condition, we replicated his condition where a fringe was added to the end of the first target only, but with a temporal gap of 160 ms instead of 100 ms, to enable comparison with the two-fringe/160-ms condition.

TABLE I. Pairwise t-tests with Bonferroni correction with a significance level of $\alpha=0.05$ for the baseline conditions. The table also denotes the value of the test statistic (t), the degrees of freedom of the test (df), and the p value.

Condition 1	Condition 2	t	df	p	Significantly different
NF_b	NF_e	1.36	33	0.183	No
F_b	F_e	−0.12	33	0.906	No
NF_b	F_b	12.51	33	<0.001	Yes
NF_e	F_e	11.03	33	<0.001	Yes

B. Results

The normalized results for two fringes are shown by circular symbols in Fig. 3. The triangle symbols indicate the additional condition with only one fringe added to the end of the first target with a 160-ms temporal gap. The abscissa shows the gap duration in milliseconds, and the ordinate shows the effect. The label F on the abscissa indicates performance for the condition with a temporal gap of 0 ms, which was the baseline condition with a fringe from the experiment described in Sec. IV. An effect of 1 indicates that performance was the same as in the baseline condition containing only the targets. An effect of zero indicates that performance was the same as in the baseline condition containing a fringe without fringe alteration (see Sec. II). The error bars indicate the standard error of the mean across the different retests.

Both the individual results and the across-subject means show an increased effect with increasing gap duration. Pairwise t-tests on the across-subject data of the 0-ms gap condition (baseline condition F) with each of the other conditions showed that the conditions with a gap duration of 80 ms or longer were significantly different from the 0-ms condition at a 5% significance level with Bonferroni correction. The size of the effect ranged from 0.27 at a gap duration of 80 ms to 0.68 at a gap duration of 320 ms. Listeners performed significantly worse for the extra condition where only one fringe was added with a temporal gap of 160 ms ($160_{\text{one fringe}}$ in Table II or triangles in Fig. 3) compared to the original 160-ms gap condition (160). The difference in

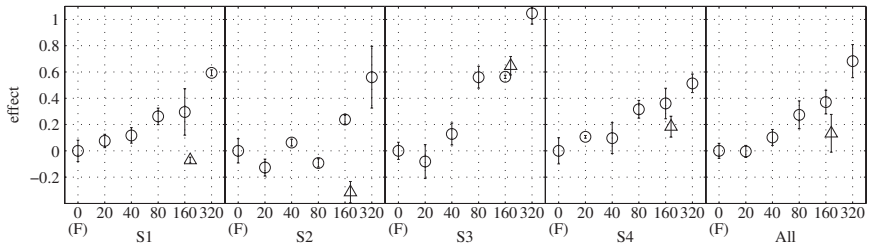

FIG. 3. Effect of gap duration. Mean effects of individual subjects are shown in the left four panels, and panel 5 shows the mean effect. Label F on the abscissa indicates the baseline condition, i.e., without temporal gap. The other labels on the abscissa give the gap duration in milliseconds. The circles indicate the conditions with a fringe added to both targets; the triangles indicate the conditions where only one fringe was added to the end of the first target token. The error bars indicate the standard error of the mean across the different retests.

effect was 0.24 (see triangle symbols in Fig. 3). It must be noted though that there were large across-subject differences; e.g., subject S3 performed the same for the two conditions, while subject S2 performed lower than his individual baseline condition (hence the negative effect). This is comparable to the findings of Hanna (1984). Although he did not report d'_{NF}, he stated in footnote 1 that it was very difficult to perform discrimination without a gap. Therefore the size of the effect in his study must have been smaller than or equal to 0.24. Also Hanna (1984) reported large across-subject differences. Condition $160_{\text{one fringe}}$ did not differ significantly from baseline condition F in our experiments. The results of this pairwise *t*-test are shown in Table II.

C. Discussion

The increased performance for target discrimination when a gap of 80 ms or more was introduced between target and fringe is not in line with the explanation of interference due to the mere presence of new stimulus information because the amount of interference would be expected to be considerable for all temporal gap conditions. The increased performance is, however, in line with an object-based explanation in which the temporal separation enables the listener to segregate the target and fringe into separate auditory objects.

In broadband noise, a gap is detectable for gap durations as short as approximately 3 ms (Penner, 1977). For 600-Hz wide noise bands, thresholds are about 10 ms (Eddins *et al.*, 1992). Thus, the mere presence of a perceivable temporal gap was not sufficient for the segregation of target and fringe. In the case of a 20-ms gap, i.e., well above this threshold, the presence of the gap did not lead to an improvement of discrimination ability, maybe because the gap was perceived as a feature of the auditory object containing the target and fringe rather than as a cue for segregation.

TABLE II. Effect of gap duration: pairwise *t*-tests with Bonferroni correction with a significance level of $\alpha=0.05$. The table also denotes the value of the test statistic (t), the degrees of freedom of the test (df), and the p value.

Condition 1	Condition 2	t	df	p	Significantly different
20	F	−0.05	66	0.962	No
40	F	1.21	66	0.232	No
80	F	3.24	66	0.002	Yes
160	F	4.38	66	<0.001	Yes
320	F	8.06	66	<0.001	Yes
$160_{\text{one fringe}}$	F	1.58	66	0.120	No
160	$160_{\text{one fringe}}$	2.81	66	0.007	Yes

VI. SPECTRAL SEPARATION

In the previous experiment, the *temporal* separation between target and fringe was shown to have a large effect on the ability to discriminate the targets. Another dimension in which the target and fringe can be separated is the spectral dimension. In the next experiment a *spectral* separation between target and fringe was introduced to determine its influence on the ability to discriminate the target.

A. Stimuli

The properties of the targets and fringes were as specified in Sec. III, except that the spectral bandpass range of the fringes was varied. In each condition the bandwidth of the fringes was constant on the ERB-rate scale (Glasberg and Moore, 1990) and the Equivalent Rectangular Bandwidth was 5.8, but the center frequencies were distributed such that there were five adjacent bandpass ranges. The bandpass ranges were 81–349 Hz (condition 1), 350–850 Hz (baseline condition F), 851–1783 Hz (condition 1), 1783–3520 (condition 2), and 3520–6757 (condition 3). The bandpass range of the targets was always 350–850 Hz.

B. Results

Figure 4 shows the results. The labels on the abscissa indicate the separation between the center frequencies of target and fringe. The label F indicates the baseline condition with fringe (from the experiment described in Sec. IV), which had no spectral separation between target and fringe. The ordinate shows the effect of the fringe manipulation with respect to the baseline conditions. Panels show the individual and mean results. The error bars indicate the standard error of the mean across the different retests.

Pairwise *t*-tests on the across-subject data for the baseline condition F with each of the other conditions showed that all conditions were significantly different from condition F at a 5% significance level with Bonferroni correction. The results of these pairwise *t*-tests are shown in Table III. On average, as the spectral separation between target and fringe increased, the ability to discriminate increased. For the largest spectral separation (labeled 3), three out of four listeners showed an effect of more than 0.8, which is close to perfor-

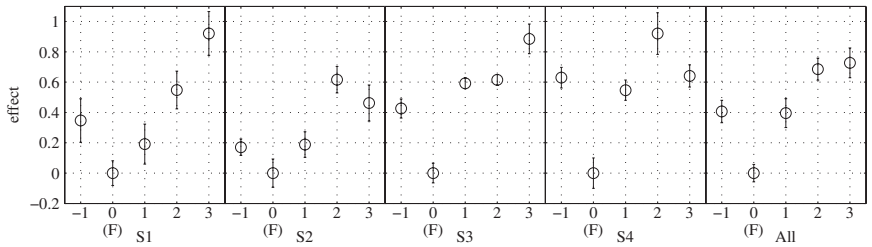

FIG. 4. Effect of spectral separation. Mean effects of individual subjects and the across-subject mean effect are shown. Label F on the abscissa indicates the baseline condition, i.e., without spectral gap. The other labels on the abscissa indicate the spectral separation between the center frequencies of target and fringe in number of bandwidths ($5.8\mathrm{ERB}_N$). The error bars indicate the standard error of the mean across the different retests.

mance for the baseline condition without a fringe. The size of the effect for a spectral separation of 1 (labeled −1 and 1) was 0.40.

C. Discussion

This experiment showed that spectral separation also had a large effect on the ability to discriminate the target noises. The ability to discriminate the targets increased with spectral distance. For three out of four subjects, an effect of more than 0.8 was observed, which was almost the same as performance for the baseline condition where the targets were presented without fringe. Spectral separation seems to be a salient cue for enabling the listener to access information from the target.

This section addressed situations where the target and the fringe had discontinuous spectral ranges. From a Gestalt theory point of view, it is likely that the targets and fringes originated from separate physical events since their spectra did not adhere to the rule of good continuity. More specifically, the end of the target within one spectral range and the start of the fringe in a completely disjoint region are difficult to reconcile with good continuity. Section VII addresses the situation where the spectral ranges of target and fringe overlap, and thus part of the stimulus adheres to the rule of good continuity.

VII. BANDWIDTH

In this experiment the center frequencies of the target and fringe spectra were identical. However, the *bandwidth* of the fringes was either double or half the bandwidth of the targets. Hence, the spectral ranges of the targets and the fringes were not discontinuous but overlapping, allowing for the interpretation that the stimulus part with the narrower bandwidth continues in the part with the wider bandwidth.

TABLE III. Effect of spectral gap: pairwise *t*-tests with Bonferroni correction with a significance level of $\alpha=0.05$. The table also denotes the value of the test statistic (t), the degrees of freedom of the test (df), and the p value.

Condition 1	Condition 2	t	df	p	Significantly different
−1	F	5.38	44	<0.001	Yes
1	F	5.25	44	<0.001	Yes
2	F	9.08	44	<0.001	Yes
3	F	9.63	44	<0.001	Yes

A. Stimuli

The properties of the targets and fringes were as specified in Sec. III, with the exception that the bandpass range of the fringes was either doubled to a bandpass range of 100–1100 Hz or halved to a bandpass range of 475–725 Hz. The spectral level of the stimuli was left unaltered, and thus the overall sound pressure level varied with different bandwidths. The center frequency was 600 Hz, which was the same as the center frequency of the targets. In addition, these conditions were presented with and without a temporal gap of 40 ms.

B. Results

Figure 5 shows individual and mean results. The ordinate shows the effect of the fringe manipulations with respect to the baseline conditions. The error bars indicate the standard error of the mean across the different retests.

In the conditions labeled 2, the fringe bandwidth was doubled compared to the target bandwidth, and in the conditions labeled 1/2 it was halved. The conditions labeled with subscript 40 had a temporal gap between target and fringe with a duration of 40 ms in addition to the bandwidth change. For comparison, the data for the 40-ms gap condition without bandwidth changes from the experiment described in Sec. V were included in the figure with the label 1_{40}.

Table IV shows the results of pairwise *t*-tests with Bonferroni correction with a significance level of $\alpha=0.05$ for several pairs of the bandwidth data. Comparing baseline condition F (including a fringe without fringe alteration) with each of the other conditions showed that the conditions where the fringe bandwidth was half the target bandwidth ($1/2$ and $1/2_{40}$) were significantly different from condition F (sizes of effects were 0.21 and 0.40, respectively). Other significantly different pairs were condition 1/2 compared to $1/2_{40}$ (difference of effect size was 0.19) and condition $1/2_{40}$ compared to 1_{40} (difference of effect size was 0.30). The conditions where the fringe bandwidth was double the target bandwidth (2 and 2_{40}) were not significantly different from condition F nor from one another. Condition 2_{40} was also not significantly different from condition 1_{40}.

C. Discussion

This experiment showed that doubling the bandwidth of the fringe with respect to the target bandwidth did not result

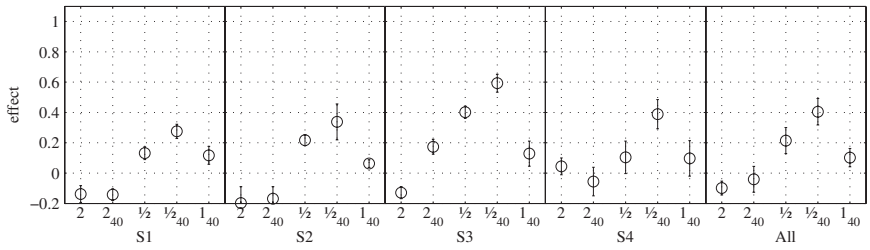

FIG. 5. Effect of bandwidth. Mean effects of individual subjects and the across-subject mean effect are shown. Label 2 on the abscissa indicates the conditions where the fringe bandwidth was doubled to 1000 Hz. Label 1/2 on the abscissa indicates the conditions where the fringe bandwidth was halved to 250 Hz. The conditions with subscript 40 had an additional temporal gap between target and fringe. For comparison, the temporal gap condition with a duration of 40 ms and the same bandwidth as the target was included (1_{40}). The error bars indicate the standard error of the mean across the different retests.

in an improvement in discrimination of the target token, even when combining this cue with a 40-ms temporal gap. Halving the bandwidth, however, resulted in a modest but significant effect of approximately 0.2. Combined with a 40-ms temporal gap, this effect was 0.4. Thus, the combination of a temporal gap with half bandwidth caused an extra improvement in effect of 0.2. This improvement was more than the effect of the temporal gap in isolation, which was a nonsignificant effect of 0.1.

VIII. LEVEL AND ILD

The next experiment investigated if changing the level or the interaural level difference (ILD) of the fringes leads to better discrimination of the targets.

A. Stimuli

The properties of the targets and fringes were as specified in Sec. III, except that the spectrum level of the fringes was varied. In one condition, the spectrum level of the fringe was 55 dB SPL, i.e., 5 dB higher than that for the target. In another condition, the spectrum level of the fringe was 45 dB SPL, i.e., 5 dB lower than that for the target. In the third condition, the spectrum level of the fringe was 45 dB SPL in the left ear and 55 dB SPL in the right ear, realizing a 10-dB ILD. This condition was also presented with a temporal gap of 40 ms. A final condition had a monaural fringe that was presented only in the right ear with a spectrum level of 50 dB SPL.

TABLE IV. Effect of bandwidth: pairwise *t*-tests with Bonferroni correction with a significance level of $\alpha=0.05$. The table also denotes the value of the test statistic (t), the degrees of freedom of the test (df), and the p value.

Condition 1	Condition 2	t	df	p	Significantly different
2	F	−1.66	55	0.102	No
2_{40}	F	−0.69	55	0.494	No
1/2	F	3.64	55	0.001	Yes
$1/2_{40}$	F	6.86	55	<0.001	Yes
2_{40}	2	0.98	55	0.333	No
$1/2_{40}$	1/2	3.23	55	0.002	Yes
2_{40}	1_{40}	−2.42	55	0.019	No
$1/2_{40}$	1_{40}	5.14	55	<0.001	Yes

B. Results

The results of the level conditions are shown in Fig. 6. The ordinate shows the effect of the fringe manipulations with respect to the baseline conditions. The error bars indicate the standard error of the mean across the different retests.

The conditions where the fringe level was 5 dB higher than the target level are labeled +5, and the conditions where it was 5 dB lower are labeled −5. The condition with a 10-dB ILD is labeled ±5, and when this condition included a 40-ms gap it is labeled $\pm 5_{40}$. The condition with the monaural fringe is labeled M. For comparison, the 40-ms gap condition from the experiment described in Sec. V is included in the figure with the label 0_{40}.

Table V shows the results of pairwise *t*-tests with Bonferroni correction with a significance level of $\alpha=0.05$ for several pairs of the level and ILD data. Comparing baseline condition F with each of the other conditions showed that only the monaural fringe condition (M) was significantly different from condition F (size of the effect was 0.35). Performance for the condition where the fringe had a combination of a 10-dB ILD with a 40-ms temporal gap ($\pm 5_{40}$) was not significantly different from performance for the condition where the fringe had only a 40-ms temporal gap (0_{40}).

C. Discussion

The level and ILD conditions only showed a significant effect for the condition with a monaural fringe. Apparently the influence of level cues and ILD cues in the fringe on the ability to discriminate the targets was very small or nonexistent, except for the extreme ILD case where the fringe was presented to only one ear.

In the individual data, it is striking that subject S1 performed more poorly for the $\pm 5_{40}$ condition containing the combination of a 40-ms temporal gap and a 10-dB ILD than for the 40-ms temporal gap condition and the 10-dB ILD condition in isolation. On the other hand, these combined cues seemed to have an additive effect on the performance of subject S3. For the other two subjects, there was little difference between these three conditions. This may hint at individual differences in listeners' ability to use the cues in the discrimination task.

Overall, presenting the fringe monaurally led to the best performance in this experiment, possibly because it consti-

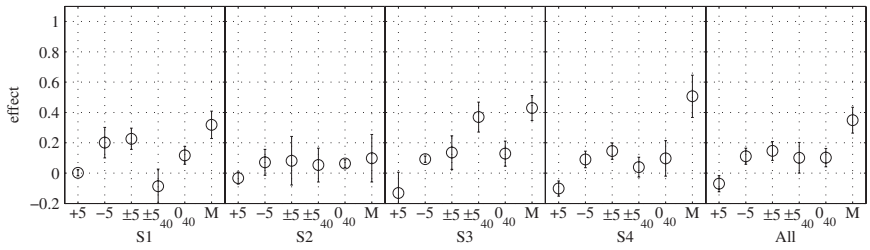

FIG. 6. Effect of level and ILD. Mean effects of individual subjects and the across-subject mean effect are shown. Label +5 on the abscissa indicates the condition where the spectrum level of the fringe increased by 5 dB. Label −5 indicates the condition where the spectrum level of the fringe decreased by 5 dB. Label ±5 indicates the conditions where the fringe was lateralized to the right with an ILD of 10 dB. The conditions with subscript 40 had an additional temporal gap between target and fringe. For comparison, the temporal gap condition with a duration of 40 ms and same level as the target was included with label 0_{40}. Label M indicates the monaural condition where the fringe was presented only to the right ear. The error bars indicate the standard error of the mean across the different retests.

tutes the largest ILD. An alternative explanation is that listeners may have focused on the ear without the fringe in the monaural condition.

IX. INTERAURAL TIME DELAY

The previous experiment showed that only for the monaural condition could we find a statistically significant improvement for discrimination of the targets. In the next experiment, the fringes were lateralized using an interaural time delay (ITD).

A. Stimuli

The properties of the targets and fringes were as specified in Sec. III, with the exception that a fine structure ITD of 0.5 ms was applied to the fringes before the 10-ms onset and offset ramps were applied, causing a lateralization to the right. Therefore, the temporal envelopes of the fringes were not delayed (only ongoing ITDs). In additional conditions, this ITD was combined with a 5-dB increase in spectrum level, a 5-dB decrease in spectrum level, or a temporal gap of 40 ms.

B. Results

The results are shown in Fig. 7. The ordinate shows the effect of the fringe manipulations with respect to the baseline conditions. The conditions with an ITD of 0.5 ms are labeled 0.5. The condition with a 5-dB spectrum level increase is labeled $.5_{+5}$, and the condition with a 5-dB spectrum level decrease is labeled $.5_{-5}$. The condition with a temporal gap of 40 ms is labeled $.5_{40}$. For comparison the 40-ms gap, the 5-dB increase, and the 5-dB decrease conditions from the experiments described in Secs. V and VIII are included in the figure using triangle symbols.

Table VI shows the results of pairwise *t*-tests with Bonferroni correction with a significance level of $\alpha=0.05$ on several pairs of the ITD data. Baseline condition F was significantly different from the ITD-only condition 0.5 (size of effect was 0.17). Comparison of the three ITD conditions which were combined with level cues or a temporal gap of 40 ms ($.5_{+5}$, $.5_{-5}$, and $.5_{40}$) to the ITD-only condition (0.5) showed that only the condition where the fringe had an ITD plus a 5-dB level decrease ($.5_{-5}$) was significantly different from the ITD-only condition (0.5) (difference in effect size was 0.19). In addition, performance for these three combined conditions was significantly higher than when they were presented without an ITD ($\text{effect}_{.5_{+5}}-\text{effect}_{+5}=0.25$, $\text{effect}_{.5_{-5}}-\text{effect}_{-5}=0.25$, $\text{effect}_{.5_{40}}-\text{effect}_{40}=0.18$).

C. Discussion

This experiment showed that discrimination of the target could be significantly improved by giving the fringe an ITD of 0.5 ms, although the size of the effect was modest (0.17). Listeners' ability to discriminate the target improved further, with an *added* effect of 0.19, by combining the ITD with a level decrease of 5 dB. Combining the ITD with a level increase of 5 dB or a temporal gap of 40 ms did not further improve the ability to discriminate the targets. Discrimination ability in these combined conditions, however, was significantly higher than that in the corresponding conditions without an ITD.

TABLE V. Effect of level and ILD: pairwise *t*-tests with Bonferroni correction with a significance level of $\alpha=0.05$. The table also denotes the value of the test statistic (t), the degrees of freedom of the test (df), and the p value.

Condition 1	Condition 2	t	df	p	Significantly different
+5	F	−1.00	66	0.319	No
−5	F	1.60	66	0.115	No
±5	F	2.10	66	0.039	No
±5$_{40}$	0$_{40}$	−0.01	66	0.992	No
0$_{40}$	F	1.46	66	0.148	No
M	F	5.01	66	<0.001	Yes

TABLE VI. Effect of ITD: pairwise *t*-tests with Bonferroni correction with a significance level of $\alpha=0.05$. The table also denotes the value of the test statistic (t), the degrees of freedom of the test (df), and the p value.

Condition 1	Condition 2	t	df	p	Significantly different
.5	F	2.83	77	0.006	Yes
$.5_{+5}$	5	0.12	77	0.909	No
$.5_{-5}$	5	3.09	77	0.003	Yes
$.5_{40}$	5	1.72	77	0.090	No
$.5_{+5}$	+5	4.07	77	<0.001	Yes
$.5_{-5}$	−5	4.11	77	0.001	Yes
$.5_{40}$	40	2.89	77	0.005	Yes

X. NUMBER OF PERCEIVED OBJECTS

In the previous experiments, it was shown that target discrimination can improve when a fringe alteration is introduced. The size of the effect depended on the type of fringe alteration. The working hypothesis at the end of Sec. I stated that discrimination would be low when the fringe was perceptually fused with the target and high when the fringe and target were segregated into separate auditory objects.

To further explore this hypothesis, the next experiment investigated if there is a direct relation between target discrimination and the number of perceived auditory objects. Listeners were asked directly how many auditory objects they perceived when listening to the stimuli used in the previous experiments.

A. Method and stimuli

In this experiment listeners were presented in each trial with only *one* stimulus interval containing a target and a fringe token. They were asked to respond how many auditory objects they perceived. The conditions were the same as in the experiments described above; the stimuli were generated identically. There were 20 trials for each condition. The trials were presented in random order. The same four subjects participated.

B. Results

The second column of Table VII shows the mean number of perceived objects across subjects for each of the conditions. The last column shows the effect of the fringe alterations from the previous experiments for comparison. These results are shown in Fig. 8 as a scatter plot. The conditions that are either spectrally or temporally discontinuous (marked with an * in Table VII) are plotted with a plus symbol; the other conditions are plotted with a circle.

The correlation coefficient R for the number of perceived objects and the effect for all the conditions is 0.55. For the spectrally or temporally discontinuous conditions R equals 0.53, and for the other conditions R equals 0.74.

C. Discussion

The results of this experiment show that there is a moderate positive correlation between the effect for fringe alterations and the number of perceived objects. The number of perceived objects is however not a very close predictor of the change in discrimination performance.

It appears that all conditions lie approximately on or below the line connecting the lower left corner (no effect, one object) and the upper right corner (maximum effect, two objects). For our conditions this indicates that perceiving more than one object, i.e., object segregation, is a necessary but not a sufficient condition for high target discrimination performance.

XI. GENERAL DISCUSSION

Hanna (1984) and Goossens (2008) showed that discrimination performance for noise tokens is substantially impaired when a noise fringe (a piece of uninformative noise) is placed either before or after one of the target tokens, while the same amount of useful information was present. The current study showed that this impairment can be strongly reduced by introducing cues into the fringe that may help to segregate the fringe and the target.

The ability to discriminate Gaussian-noise target tokens in a same/different discrimination paradigm was further explored. Of particular interest was the effect of adding an uninformative backward-fringe to *both* 50-ms target tokens. This fringe had the same statistical properties as the target, and its duration was 200 ms. Again, while the same amount of useful information was present, the ability to discriminate the targets decreased substantially when a fringe was added to the targets without fringe alteration. If, however, the properties of the fringes were altered, the influence of the fringes on the ability to discriminate the targets could be reduced, and, hence, discrimination performance for the targets could improve. The type of fringe alteration determined whether discrimination performance improved and determined the size of the effect.

The largest effects were found when a spectral or temporal separation was introduced between target and fringe. In some of these conditions, some listeners improved their performance to nearly the discrimination performance that was achieved in absence of a fringe. Modest effects were found for halving the bandwidth of the fringe, introducing a 0.5-ms ITD, or presenting the fringe to only one ear. No effect was found for doubling the fringe bandwidth, 5-dB level increases or decreases, or 10-dB ILDs. However, combining a 5-dB level decrease with a 0.5-ms ITD resulted in an addi-

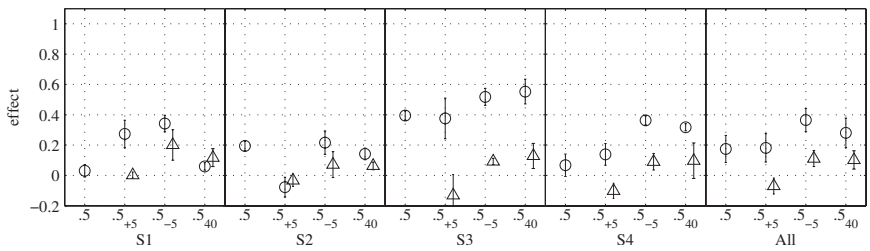

FIG. 7. Effect of ITD. Mean effects of individual subjects and the across-subject mean effect are shown. The *circles* indicate the conditions with an ITD of 0.5 ms. The *triangles* show the same conditions but *without* an ITD from the experiments in Secs. VIII and V. The subscript +5 indicates the conditions with a spectrum level increase of 5 dB. The condition with subscript −5 had a spectrum level decrease of 5 dB. The condition with subscript 40 had a temporal gap between target and fringe. The error bars indicate the standard error of the mean across the different retests.

TABLE VII. The mean number of perceived objects per condition across subjects. For comparison, also the effect sizes of the corresponding conditions from the previous experiments are shown.

Experiment	Label	$N_{objects}$ perceived	Effect
Baseline	F	1.0	0.00
Gap duration	20^{*}	1.5	0.00
	40^{*}	1.8	0.10
	80^{*}	2.0	0.27
	160^{*}	2.0	0.37
	320^{*}	2.0	0.68
Spectral separation	-1^{*}	2.0	0.41
	1^{*}	1.9	0.40
	2^{*}	2.0	0.69
	3^{*}	2.0	0.73
Bandwidth	$\frac{1}{2}^{*}$	1.5	−0.10
	$\frac{1}{2}_{40}^{*}$	2.0	−0.04
	2^{*}	1.3	0.21
	2_{40}^{*}	2.0	0.41
Level and ILD	+5	1.1	−0.07
	−5	1.0	0.11
	±5	1.1	0.15
	$\pm 5_{40}^{*}$	1.9	0.10
	M	1.8	0.35
ITD	0.5	1.2	0.17
	$.5_{+5}$	1.2	0.18
	$.5_{-5}$	1.3	0.37
	$.5_{40}^{*}$	2.0	0.28

*Conditions that are either spectrally or temporally discontinuous.

tional modest improvement of discrimination ability. Similarly, combining a 40-ms temporal gap with halving the fringe bandwidth also resulted in an additional modest improvement of discrimination ability.

Apparently listeners were able to ignore the uninformative stimulus details in the fringe when it was sufficiently distinguishable from the target. The parameters chosen to make the fringes distinguishable from the targets were known from the literature to contribute to the formation of

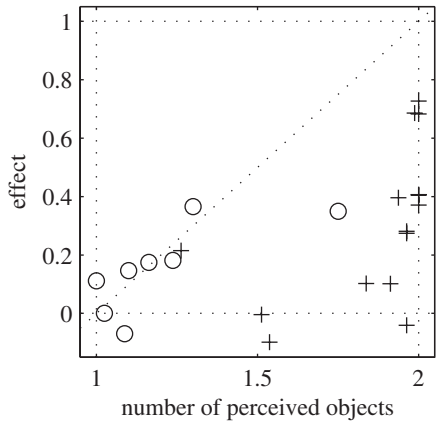

FIG. 8. Scatter plot of the number of perceived objects vs the effect size for all conditions across subjects. Pluses indicate conditions that are either spectrally or temporally discontinuous; circles indicate other conditions.

auditory objects (Yost, 1991). In the last experiment, we have explicitly tested the influence of segregation cues on the number of perceived objects. It appears that the cues indeed influenced the number of perceived objects. It was shown that there was a moderate correlation (R=0.55) between these two measures, but the number of perceived objects was not a close predictor of target discrimination. This is clear, in particular, for the conditions for which the number of perceived objects was approximately 2.

Some fringe alterations (level increase of 5 dB, level decrease of 5 dB, 10-dB ILD, and doubling of the fringe bandwidth) did not lead to improved discrimination of the target tokens. This does not necessarily imply that these cues cannot lead to object formation; however, their effectiveness in creating separate auditory objects may be less than for cues that did lead to improved target discrimination in these experiments.

In this light, the decreased discrimination performance of target tokens with an added fringe without fringe alteration can be explained by assuming that listeners perceived the target plus fringe as a single auditory object and that listeners had a fixed or limited capacity to process or retain an auditory object (Cowan, 2005; Goossens, 2008). In addition, it is assumed that listeners are not able to selectively attend to a subsection of such an auditory object (Goossens, 2008). In the case of a fringed target, the limited resources for retaining or processing the auditory objects need to be distributed over more peripheral information than in the case of a target in isolation. Therefore, the memory or processing for the fringed target is degraded, and discrimination performance is lower.

It has been argued that sensory memory is rich and, in contrast to working memory, perhaps of unlimited capacity (Cowan, 1988, 2005). Therefore, in the case of a discrimination trial where a fringe is appended to the target tokens, the information useful for the discrimination task should be available in sensory memory. In the framework of Cowan (2005), the inability to perform the discrimination when a fringe is appended without a differentiating cue indicates that the *access* to this information is limited. According to Cowan (2005), it is the focus of attention, enabling the listener to draw information from sensory memory into working memory, that is limited. When the fringe is differentiated from the target by introducing a cue, access to the target information can be improved. Arguably, the fringe alteration can enable the listener to direct the focus of attention to the target information within the auditory stimulus containing both target and fringe. It is plausible that the segregation of target and fringe into two *separate* objects is a necessary but not sufficient condition for the listener to direct the focus of attention to the target object.

This auditory object view therefore provides a partial explanation for the effect of introducing fringe alterations on discrimination. When a fringe alteration is introduced that helps to segregate target and fringe into two separate auditory objects, the information in the fringe can be better ignored, and hence, discrimination performance is affected less by the presence of the fringe. According to this view, depending on how well listeners are able to segregate the target

and fringe, the ability to (partly) ignore the fringe increases, and hence, the ability to discriminate the target tokens also increases.

When the results of the experiments are interpreted within this framework, it can be concluded that both spectral and temporal gaps are strong cues for formation of auditory objects. For temporal gaps a similar observation was made by Bregman (1990), (p. 71). In a paragraph describing some of the experiments by van Noorden (1975), he stated that "Apparently, abrupt rises in intensity tell the auditory system that a new sound has joined the mixture and that it should begin the analysis of a new unit."

The experiments on auditory streaming by van Noorden (1975) showed that spectral separation was an important factor in creating segregation in repeated alternating tone-patterns.

In Sec. VII, the bandwidth of the fringes was either double or half the bandwidth of the targets. Thus, their spectra overlapped. The interpretation of these overlapping spectra is ambiguous. For instance, in the condition where the fringe bandwidth doubled, an interpretation of the stimuli is that a new auditory event, the fringe, was presented exactly at the offset of the target. Another interpretation is that the target continues and two flanking noise bands are presented 50 ms after the onset of the target. When the bandwidth of the fringe is halved, a similar line of reasoning could be followed. This ambiguity is a possible explanation why there was no advantage for the bandwidth conditions like there was for the spectral separation conditions. The ambiguous interpretation is not possible for the conditions with discontinuous spectra. For these latter conditions we observe both a higher effect size and a higher number of perceived objects

Throughout the experiments in this study, fringes were added to both targets, except in one of the two baseline conditions where there were no fringes. Another exception was the extra condition in the gap-duration experiments (Sec. V), which replicated a condition of the experiments of Hanna (1984). Here, a fringe was added only to the first target with a temporal gap of 160 ms. On average, performance was worse in the situation with only one fringe compared to the situation with two fringes, although the amount of uninformative stimulus detail was less. Discrimination performance in the two-fringe condition was improved by enlarging the gap from 160 to 320 ms. Apparently the fringes were still influencing discrimination performance for the targets in the condition with a temporal gap of 160 ms. When a fringe was appended to only the first target, the perception of the target was influenced by the presence of the fringe. However, no fringe was added to the second target, and therefore, the perception of the second target was not influenced by a fringe. One interpretation is that adding a fringe to only one target may introduce an asymmetry in the perception of the target tokens, causing performance to be worse than in the two-fringe situation. Possibly, when not sufficiently segregated, the target and fringe are grouped into a larger object (Bregman, 1990, p. 644).

In general, the results from this study suggest that segregation of auditory objects depends strongly on the presence of spectral and temporal separation between stimuli. This has been suggested many times, most notably by van Noorden (1975) and Bregman (1990). Binaural cues can also lead to the segregation of auditory objects, but their importance as segregation cues seems lower than the aforementioned spectral and temporal separation. This is in line with the observation of Bregman (1990), (p. 644) that for the grouping of tones "Humans use spatial origin too, but do not assign such an overwhelming role to it."

In a vowel identification experiment, Drennan *et al.* (2003) found that both ITDs and ILDs can play a role in segregation, but ILDs have a larger impact on segregation (of vowels) than ITDs. This order of impact found for ITDs and ILDs is opposite our findings. A possible explanation for this difference is that their stimuli extended up to 2 kHz, whereas our stimuli for the binaural conditions extended only up to 1.1 kHz. For natural stimuli it is known that ITDs mainly contribute to localization in the low frequency region (below approximately 1500 Hz), and in the high frequency region lateralization is mainly realized through ILDs, although at low frequencies ILDs can be used when present (e.g., Grantham, 1995; Moore, 2003). The different frequency contents in both experiments may have tipped the balance in favor of the ITDs in the current study.

In conclusion, the paradigms used in this paper have indicated a new approach to investigate how auditory object formation is related to the ability to make these objects accessible for cognitive processing. While our data clearly indicate that segregation is required for access, segregation into separate objects does not necessarily imply that relevant information can be drawn into working memory and used for cognitive tasks.

Alain, C., and Arnott, S. R. (**2000**). "Selectively attending to auditory objects," Front. Biosci. **5**, 202–212.

Bregman, A. S. (**1990**). *Auditory Scene Analysis: The Perceptual Organisation of Sound* (MIT, Cambridge, MA).

Buell, T. N., and Hafter, E. R. (**1991**). "Combination of binaural information across frequency bands," J. Acoust. Soc. Am. **90**, 1894–1900.

Cowan, N. (**1988**). "Evolving conceptions of memory storage, selective attention, and their mutual constraints within the human information-processing system," Psychol. Bull. **104**, 163–191.

Cowan, N. (**2005**). *Working Memory Capacity (Essays in Cognitive Psychology)* (Psychology, New York).

Crum, P. A. C., and Bregman, A. S. (**2006**). "Effects of unit formation on the perception of a changing sound," Q. J. Exp. Psychol. **59**, 543–556.

Darwin, C. J., and Carlyon, R. P. (**1995**). In *Hearing*, edited by B. C. Moore (Academic, San Diego), pp. 387–424.

Drennan, W. R., Gatehouse, S., and Lever, C. (**2003**). "Perceptual segregation of competing speech sounds: The role of spatial location," J. Acoust. Soc. Am. **114**, 2178–2189.

Eddins, D. A., Hall, J. W. III, and Grose, J. H. (**1992**). "The detection of temporal gaps as a function of frequency region and absolute noise bandwidth," J. Acoust. Soc. Am. **91**, 1069–1077.

Glasberg, B. R., and Moore, B. C. J. (**1990**). "Derivation of auditory filter shapes from notched-noise data," Hear. Res. **47**, 103–138.

Goossens, T. (**2008**). "Gaussian-noise discrimination and auditory object formation," Ph.D. thesis, Technische Universiteit Eindhoven, Eindhoven, The Netherlands.

Goossens, T., van de Par, S., and Kohlrausch, A. (**2007**). "Processing capacity for perceptual information in Gaussian noise tokens," in 19th International Congress on Acoustics, edited by A. Calvo-Manzano, A. Pérez-López, and S. Santiago.

Goossens, T., van de Par, S., and Kohlrausch, A. (**2008**). "On the ability to discriminate Gaussian-noise tokens or random tone-burst complexes," J. Acoust. Soc. Am. **124**, 2251–2262.

Grantham, D. W. (**1995**). In *Hearing*, edited by B. C. Moore (Academic, San Diego), pp. 297–345.
Hanna, T. E. (**1984**). "Discrimination of reproducible noise as a function of bandwidth and duration," Percept. Psychophys. **36**, 409–416.
Heller, L. M., and Trahiotis, C. (**1995**). "The discrimination of samples of noise in monotic, diotic, and dichotic conditions," J. Acoust. Soc. Am. **97**, 3775–3781.
Moore, B. C. (**2003**). *An Introduction to the Psychology of Hearing* (Academic, London).
Penner, M. J. (**1977**). "Detection of temporal gaps in noise as a measure of the decay of auditory sensation," J. Acoust. Soc. Am. **61**, 552–557.
Royer, F. L., and Robin, D. A. (**1986**). "On the perceived unitization of repetitive auditory patterns," Percept. Psychophys. **39**, 9–18.
van Noorden, L. (**1975**). "Temporal coherence in the perception of tone sequences," Ph.D. thesis, Technische Hogeschool Eindhoven, Eindhoven, The Netherlands.
Woods, W. S., and Colburn, H. S. (**1992**). "Test of a model of auditory object formation using intensity and interaural time difference discrimination," J. Acoust. Soc. Am. **91**, 2894–2902.
Yost, W. (**1991**). "Auditory image perception and analysis: The basis for hearing," Hear. Res. **56**, 8–18.
Yost, W. A., and Sheft, S. (**1993**). In *Human Psychophysics*, edited by W. A. Yost, R. R. Fay, and A. N. Popper (Springer-Verlag, New York), pp. 193–236.

State-space models of head-related transfer functions for virtual auditory scene synthesis

Norman H. Adams[a)]
Applied Physics Laboratory, Johns Hopkins University, Laurel, Maryland 20723

Gregory H. Wakefield
Department of Electrical Engineering and Computer Science, University of Michigan, Ann Arbor, Michigan 48109

(Received 25 June 2008; revised 31 March 2009; accepted 1 April 2009)

This study investigates the use of reduced-order state-space models of collections of head-related transfer functions (HRTFs). Recent head-phone applications have motivated interest in binaural displays that can render multiple simultaneous virtual sound sources, acoustic reflections, and source and listener motion. In the present study, a multi-direction framework is considered that can render such phenomena by filtering source signals with a collection of HRTFs rather than individual HRTFs. The collection of HRTFs is implemented in the state-space, and approximation techniques are applied to construct low-order approximants that are indiscriminable from full-order HRTFs. Two experiments are described in which five observers are asked to discriminate between state-space and full-order renderings. Depending on the stimulus conditions and discrimination task, order thresholds of $7 \leq N \leq 24$ are sufficient for an array of 50 HRTFs surrounding the listener. For comparison, a reference system of truncated minimum-phase impulse responses is also considered. © *2009 Acoustical Society of America.* [DOI: 10.1121/1.3124778]

PACS number(s): 43.66.Pn, 43.60.Qv, 43.66.Yw [JCM] Pages: 3894–3902

I. INTRODUCTION

There is considerable interest in rendering multiple-source, reverberant, time-varying virtual auditory scenes (Shinn-Cunningham and Kulkarni, 1996). Binaural displays have been proposed for reflective environments (for example, Zotkin *et al.*, 2004), source and listener motion (Algazi *et al.*, 2004), and spatially-extended sources (Adams and Wakefield, 2005). In each case, source signals are filtered by multiple pairs of head-related transfer functions (HRTFs), thereby compounding the already steep computational costs associated with direct realization of HRTF-based binaural displays (Blauert, 1997).

Recent studies have introduced state-space techniques for modeling HRTFs (Georgiou and Kyriakakis, 1999; Grantham *et al.*, 2005; Chanda *et al.*, 2006). Adams and Wakefield (2008) describe a low-cost, low-latency state-space system that implements a collection of HRTFs with lower approximation error than direct implementations. However, it is unclear from this research how such a mathematically-defined approximation error translates into a minimum computational cost; the present work estimates this minimum computation cost through a series of listening experiments.

The rest of this paper is organized as follows. In Sec. II, the concept of state-space is introduced, as it pertains to modeling a set of HRTFs, along with methods for reducing the order of the state-space model, and, thereby, the computational cost of the rendering system. Results from two psychophysical experiments are reported in Secs. III and IV. The first experiment reports discrimination thresholds as a function of the order of the state-space approximation for single noise sources. The second experiment reports approximation orders at which listeners report multiple-source virtual auditory scenes to be subjectively equivalent to fully-rendered versions. A preliminary experiment that estimates complete psychometric function for one listener is reported in the Appendix.

II. MODELING COLLECTIONS OF HRTFS

Implementing a collection of HRTFs simultaneously with a separate filter for each transfer function is computationally expensive. For example, suppose each HRTF pair is represented by two 200-tap finite-impulse response (FIR) filters with a sampling rate of 44.1 kHz. Convolving a source with a single pair of impulse responses in real-time requires approximately 17.6×10^6 multiplies per second. This cost scales linearly with the number of directions in the collection and quickly becomes problematic if the number of directions is large. In contrast, the present work considers a system in which each HRTF is modeled by a small set of common *states*, thus reducing the implementation cost of the collection.

A. State-space models of HRTFs

Kistler and Wightman (1992) showed that methods drawn from statistics can be used to model a collection of HRTFs. Principal components analysis (PCA) was employed to model each HRTF as the sum of a collection of principal components. If all of the principal components were re-

[a)]Author to whom correspondence should be addressed. Electronic mail: norman.adams@jhuapl.edu

 0001-4966/2009/125(6)/3894/9/$25.00

tained, then the HRTF was modeled exactly. However, most of the variance in the collection could be retained with only the first five principal components. From this they concluded that HRTFs could be approximated reasonably well with only five components, although this did not necessarily yield a low-cost filter implementation as each component may require a high-order filter.

In an analogous fashion, we draw on methods from the theory of linear, time-invariant systems (Bay, 1999) to model a collection of HRTFs in the state-space. Like PCA, this approach not only enables modeling HRTFs in a low-dimensional space but also provides a convenient method of implementing the entire collection of HRTFs with a single low-order, multiple-input multiple-output (MIMO) system. A state-space system is a type of feedback control system with the property that the collection of transfer functions implemented by the system share the same resonances (spectral peaks) but have independent anti-resonances (spectral notches). Haneda *et al.* (1999) showed that collections of HRTFs also exhibit this property, which suggests that state-space systems may yield an efficient implementation for collections of HRTFs.

Consider an Nth-order MIMO state-space filter with M inputs and P outputs. The input to this filter is a vector $\mathbf{u}[n]$ of length M, and the output is a vector $\mathbf{y}[n]$ of length P. [For example, Grantham *et al.* (2005) considered a state-space filter that implements 17 HRTF pairs arranged with $M=17$ inputs, one for each direction, and $P=2$ outputs, one for each ear. Other arrangements are possible as well.] The order N is the number of states, or internal memory addresses, in the system. The states have no physical acoustic meaning. In general, the computational complexity of a state-space system is $O(N^2)$, hence it desirable that N be small.

In the present work, we consider state-space systems with the following system equations:

$$\mathbf{x}[n+1] = \mathbf{A}\mathbf{x}[n] + \mathbf{B}\mathbf{u}[n],$$

$$\mathbf{y}[n] = \mathbf{C}\mathbf{x}[n], \tag{1}$$

where $\mathbf{x}[n]$ is the state vector of size N, $\mathbf{A}$ is $N \times N$, $\mathbf{B}$ is $N \times M$, and $\mathbf{C}$ is $P \times N$. The output can be related to the input by

$$\mathbf{y}[n] = \sum_{k=1}^{\infty} \mathbf{H}[k]\mathbf{u}[n-k] = \sum_{k=1}^{\infty} \mathbf{C}\mathbf{A}^{k-1}\mathbf{B}\mathbf{u}[n-k], \tag{2}$$

where $\mathbf{H}[n]$ is the $P \times M$ matrix impulse response of the system.

Note that the first equality in Eq. (2) can also describe the input/output relationship of a traditional FIR filterbank, except that the summation is over the finite interval $n=[0,N]$, and the impulse response has length $N+1$ samples. In this case, N is the order of each FIR filter.

B. State-space order reduction

It is straightforward to design a state-space system that models a collection of HRTFs exactly. However, such a system would be computationally prohibitive ($N \approx 500$). The order of the state-space system needs to be reduced, yielding a system that approximates the desired HRTFs. Recent studies that considered state-space models of HRTFs (Georgiou and Kyriakakis, 1999; Grantham *et al.*, 2005; Chanda *et al.*, 2006) employed *balanced model truncation* (BMT) to design low-order systems (Kung, 1978). A related order reduction method is *Hankel-norm optimal approximation* (HOA), which yields low-order systems that minimize the Hankel error (Glover, 1984). In practice, the two methods yield similar performance with HRTFs, although HOA yields a slightly lower maximum spectral error (Adams, 2007). HOA is used throughout the present study. A complete algorithm is described in (Glover, 1984).

In the experiments below, thresholds are reported in terms of system order N for two different system types: state-space and FIR filterbank. The relationship between system order N and computational cost are different for these two system types. Let the computational cost C be defined as the total number of multiplies that need to be performed every sample period. From Eq. (2) it is evident that the cost of an order N_{FIR} FIR filter bank is $C_{\mathrm{FIR}}=PM(N_{\mathrm{FIR}}+1)$. Noting that without loss of generality the $\mathbf{A}$ matrix of a state-space system can be triangularized, it is evident from Eq. (1) that the cost of an order N_{SS} state-space filter is $C_{\mathrm{SS}}=N_{\mathrm{SS}}^2/2+(P+M+1)N_{\mathrm{SS}}$.

In general, $N_{\mathrm{FIR}}/N_{\mathrm{SS}} \neq C_{\mathrm{FIR}}/C_{\mathrm{SS}}$. For example, for a single-input, single-output (SISO) filter $P=M=1$, and an order $N_{\mathrm{SS}}=12$ state-space filter has the same cost as an order $N_{\mathrm{FIR}}=107$ FIR filter. However, the experiments below consider systems with a either a single input and many outputs (SIMO) or many inputs and a single output (MISO). In this case systems of the same order N have similar cost C. In particular, the experiments find state-space order thresholds N_{SS} that are small compared to $\max(P,M)$. Therefore $C \approx \max(P,M)N$ for both system types, and $N_{\mathrm{FIR}}/N_{\mathrm{SS}} \approx C_{\mathrm{FIR}}/C_{\mathrm{SS}}$. As such we report thresholds in terms of system order N. See Adams and Wakefield, 2008 for additional details on state-space approximations of HRTFs and implementation costs.

III. EXPERIMENT I: THRESHOLDS FOR BROADBAND NOISES

The first experiment used an adaptive procedure to determine the minimum order for which a broadband noise rendered by a state-space system cannot be discriminated from a noise rendered by a full-order HRTF. The state-space system was designed to model 50 directions simultaneously, and one of the 50 directions was chosen randomly for each trial. For comparison, an array of truncated minimum-phase FIR representations of HRTFs, for the same 50 directions, was used to generate comparison stimuli.

The 50 directions were selected to be approximately uniformly distributed with an average angular separation between neighboring directions of 30° (Adams, 2007). The azimuths ranged over 360° in 10° increments, and the elevations range from −36° to 90° in 10° increments. The choice of $D=50$ directions was based on practical considerations for virtual auditory scene synthesis. In pilot studies,

we found that this spatial density allowed for smooth interpolation throughout the space of allowed angles.

A. Methods

1. Psychophysical procedure

An adaptive two-interval forced-choice task with flanking cues, similar to that used by Kulkarni and Colburn (2004), was used to measure discrimination threshold. Each trial consisted of a visual warning followed by four observation intervals with an inter-observation interval of 375 ms. The "standard" stimulus was presented during the first and fourth "flanking" intervals; for the second or third "test" intervals, the standard was presented randomly with equal probability and the "comparison" stimulus was presented during the alternate interval. Following the listener's response, visual feedback indicated the interval during which the comparison was presented.

The order of the approximation was adjusted adaptively according to the listener's responses (Levitt, 1971). At the beginning of each block of trials, the system order, N, was set to a value of 6, which, in all test conditions and listeners, rendered a comparison stimulus that was correctly discriminated at least 95% of the time. The system order was adapted using a "2 down, 1 up" stepping rule with equally proportioned steps. For a "down" step, the order was increased by factors of 1.19 and 1.16 for the FIR and state-space systems, respectively, and rounded to the nearest integer. These step sizes were chosen to include 5–7 steps between 60% correct and 90% correct of the psychometric function (see Appendix). The block of trials was terminated after the 12th reversal.

The geometric mean of the last eight reversals of each block of trials was used to estimate the order necessary to achieve 70.7% correct discrimination. Blocks in which the standard deviation of the last eight reversals was larger than twice the adaptive step-size were discarded. Final threshold values are based on the geometric mean of five blocks for each condition.

2. Stimuli

Stimuli were constructed by filtering broadband noise bursts with either full-order HRTFs (standard) or low-order approximants ("comparison"). The noise bursts were 50 ms samples of pseudorandom white noise, gated using a 5 ms raised cosine-squared window. The noise bursts were band-limited from 100 Hz to 16 kHz. The 100 Hz high-pass cutoff frequency was somewhat lower than other studies (for example, Kistler and Wightman, 1992; Kulkarni and Colburn, 1998). Several recent studies suggest that perceptually salient features appear at low frequencies in reflective environments that are not present in free-space, and that these features may be important for externalization (Algazi *et al.*, 2001; Rakerd and Hartmann, 1985; Hartmann and Wittenberg, 1996; Maki *et al.*, 2003). Because one of the experimental conditions involves reflections, we elected to lower the limit of the broadband sources to 100 Hz.

3. Conditions

Three factors were considered: approximation type, noise type, and environment type. With respect to *approximation type*, comparison stimuli were generated by passing the noise source through a single-input, multiple-output (SIMO) state-space system, designed using HOA, or a bank of minimum-phase FIR filters, each of which was designed by truncating the full-order (measured) FIRs (Huopaniemi *et al.*, 1999). For both filter arrays $M=1$ and $P=100$. In either case, the standard was generated by passing the noise source through the bank of full-order FIRs. With respect to *noise type*, a single sample of the pseudorandom noise was used for each trial in the case of "identical" noise; in the case of "independent" noise, different samples of the pseudorandom noise were used in each of the four observation intervals. With respect to *environment type*, a single source was presented at one of the 50 possible directions ("anechoic" case) or at one of the possible directions along with the five first-order reflections of a virtual room ("reverberant" case). A standard image-source method was used to compute the five first-order reflections from the four walls and ceiling of a 6 m wide, 8 m deep and 4 m tall room using a reflection coefficient of $\beta=0.7$. (Allen and Berkley, 1979). The listener was positioned in the center of the room. Nearest-neighbor interpolation was used for the image sources and no diffuse reverberation was included.

4. HRTF collection

A set of HRTFs for a listener, who did not participate in the present experiment, was obtained from the measurement facility at the Naval Submarine Medical Research Laboratory in Groton, CT, using a custom-built apparatus in a 10 m anechoic chamber (Cheng, 2001). HRTFs were measured using Knowles FG3329 microphones mounted in earplugs that blocked the listener's ear canals. Stimuli were presented individually using a stationary vertical array of 15 loudspeakers, and the listener's chair was rotated to measure different azimuths. 512-point Golay codes at 50 kHz were used as measurement stimuli. Ten measurements were taken for each direction to ensure good signal to noise ratio, and to facilitate loudspeaker and converter equalization. HRTFs were measured for 360° in azimuth in 10° increments, and from elevation −36° to +90° in 18° increments. The bandwidth of the measurements was approximately 100 Hz–20 kHz. For the present study 256-point minimum-phase impulse responses at 44.1 kHz were computed for each HRTF, with an appropriate time delay for the contralateral ear (Kulkarni *et al.*, 1999).

5. Participants

Five observers participated in the adaptive-level experiment, one of whom was the first author. The other participants were undergraduates in the Department of Performing Arts Technology in the School of Music, Theatre, and Dance at the University of Michigan, Ann Arbor, each of whom were experienced sound engineers, but none of whom had prior experience in psychoacoustic studies. Four participants were male, and one was female. All participants were be-

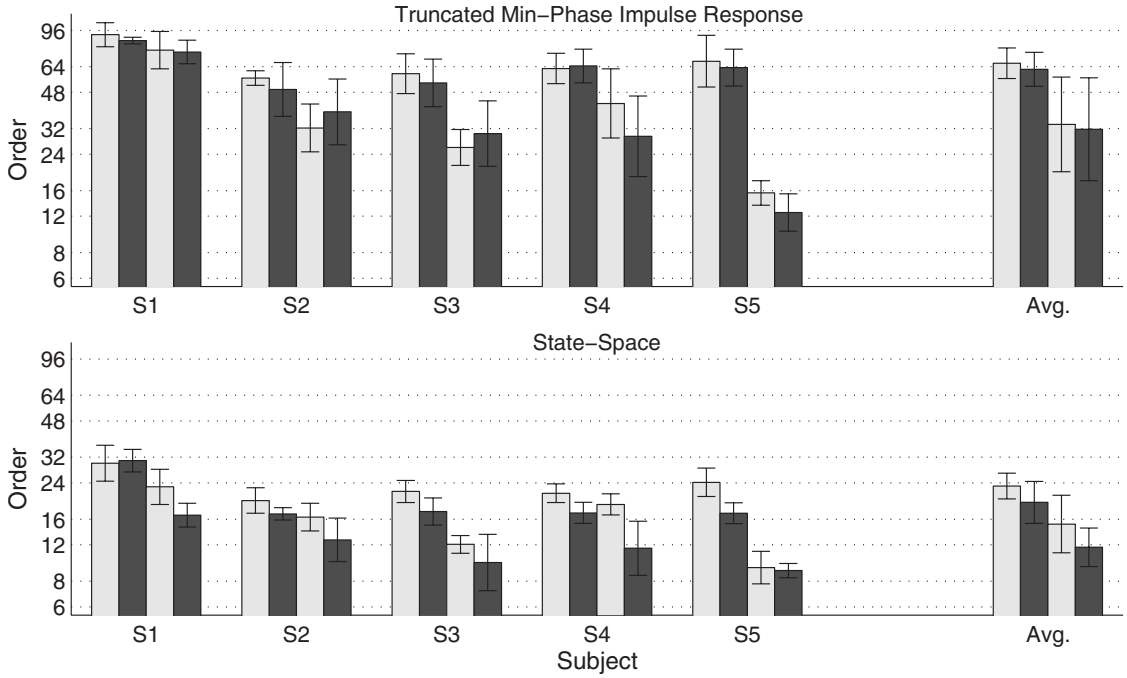

FIG. 1. Thresholds for eight stimulus conditions. Thresholds for all five participants are shown, along with average thresholds to the far right. The thresholds are shown in groups of four, in which the left two bars show thresholds for the identical-noises condition, and the right two bars show thresholds for the independent-noises condition. Thresholds for the anechoic and reflective conditions are shown with light and dark bars, respectively. Thresholds for the truncated min-phase FIRs and state-space system are shown in the top and bottom panels, respectively. Error bars indicated the standard deviation of the threshold estimates.

tween the ages of 19 and 30, and had audiograms that fell within the norms of our laboratory. The experiment required about 14 h of listening time from each participant, divided into 1.5–2 hour sessions.

6. Facility

Stimuli were presented over headphones with the participant seated in a double-walled sound-proof booth (Acoustic Systems, model 19460A) before a liquid crystalline display monitor, keyboard, and computer mouse. The experiment was run in MATLAB on an Apple G5 desktop. The observer indicated their responses by making button presses in the GUI using the computer mouse. Stimuli were delivered over a pair of Beyer-Dynamic DT931 circumaural headphones. Note that circumaural headphones are an appropriate display for this experiment as the measured HRTFs did not include the effect of the ear-canal resonance. Stimuli were not equalized for the headphone transfer function. An M-Audio FireWire410 interface was used for D/A conversion and headphone amplification. The sampling rate was 44.1 kHz. All stimuli were presented at a fixed comfortable listening level.

B. Results

Figure 1 shows threshold estimates for all eight conditions, for each observer as well as the average of all observers. Observers are shown along the abscissa, where S1 is the first author. For the individual observers, the thresholds and error bars show the geometric mean and standard deviation of the five blocks, respectively. For the averages, the thresholds and error bars show the geometric mean and standard deviation of the individual observers, respectively.

FIR thresholds are shown in the top panel and state-space thresholds in the bottom panel. Within each panel, thresholds are shown in groups of four. The left two bars in each group show thresholds for the identical condition and the right two bars show thresholds for the independent condition. Thresholds for the anechoic and reflective conditions are shown with light and dark bars, respectively.

Threshold estimates vary significantly across the five observers. Nonetheless, for all observers the state-space thresholds were lower than the corresponding FIR thresholds. Across all five observers, the state-space thresholds were $9 \leq N \leq 31$, and the FIR thresholds were $13 \leq N \leq 92$. As expected, the independent condition yielded lower thresholds than the identical condition. In contrast, the anechoic versus reflective condition had no affect on the FIR thresholds, but moderately affected the state-space thresholds.

C. Discussion

1. State-space architectures

The bottom panel of Fig. 1 shows that the discrimination state-space thresholds are between 12 and 24. However, Grantham *et al.* (2005) concluded that a minimum order of $N \approx 100$ was necessary for accurate source localization. We believe the disparity between these two results reflects a difference in state-space architecture.

An array of D HRTFs consists of $2D$ total transfer functions. The $2D$ transfer functions can be arrangement into different state-space architectures. Grantham *et al.* (2005) considered a D-input, 2-output MIMO architecture ($M=D$

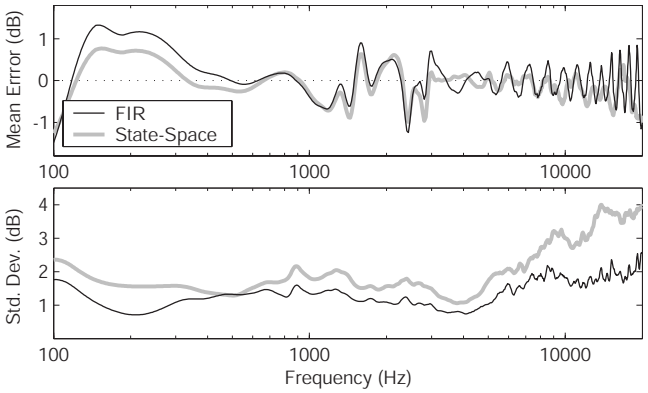

FIG. 2. Decibel error as a function of frequency for an FIR and a state-space system with order $N=34$ and $N=15$, respectively. The top panel gives the mean error, and the bottom panel gives the standard deviation of the error across the $D=50$ directions.

and $P=2$). With this architecture the interaural time delay (ITD) between the two ears must be modeled in the state-space. This places a significant burden on the state-space system and limits the potential for order reduction. Indeed, for $N<80$ the time-delay in the contralateral impulse responses is partially "filled-in."[1]

The ITD distortion would seem to explain, in part, the localization performance reported in (Grantham *et al.*, 2005), which asked listeners to localize virtual sound sources in the horizontal plane. For $N<90$, virtual sources located away from the median plane were localized with positions shifted toward the median. In the present study, a single-input architecture was used for Experiment I and a single-output architecture was used for Experiment II. Both architectures implement the time-delay externally and thus allow the order to be further reduced without distorting the ITD (Adams and Wakefield, 2008).

2. Thresholds for reflective condition

The rightmost bars in Fig. 1 show the average thresholds for all eight conditions. The state-space system yields lower thresholds than the FIR system for all stimulus conditions. However, the type of stimulus conditions affected the thresholds for the two types of systems differently. The independent noises caused the state-space thresholds to drop about 35%, and the FIR thresholds to drop about 50%. The virtual reflections caused the state-space thresholds to drop about 18%, but had no significant effect on the FIR thresholds.

The different trends for anechoic versus reflective condition can be explained by the distribution of spectral error across the 50 directions. Figure 2 shows the mean decibel error (top panel) and standard deviation (bottom panel) for the FIR system with order $N=34$ and state-space system with order $N=15$. These orders are the average thresholds for the independent/anechoic condition (the bars that are second from the right in Fig. 1).

The state-space system yields lower magnitude error for 150–400 Hz and 3–9 kHz, and does not yield higher magnitude error at any frequency. However, the standard deviation of the error is greater with the state-space system at all frequencies. That is, at any fixed frequency the center of the error distribution of the state-space system is closer to zero, yet the distribution is more broad than the distribution of the FIR system. Therefore, if the stimulus consists of several directions added together (as in the reflective condition), then the error at each frequency with the FIR system is more likely to be reinforced than with the state-space system. This trend is strongest in the 150–400 Hz frequency range, where the FIR system yields an average error about 0.5 dB greater than the state-space system, and a standard deviation about 1 dB lower than the state-space system. Overall, this result would seem to favor state-space systems for the display of reflective stimuli.

3. Individual differences

S1 was the first author, and yielded significantly higher thresholds than the other observers for all stimulus conditions. This was likely due to the extended training that this observer received while designing and performing the preliminary experiment described in the Appendix. Nonetheless, the relative trends for different stimulus conditions were similar for S1 and the other observers.

The thresholds for S1 agree with the psychometric functions shown in the Appendix. For the FIR system, S1 yielded thresholds of 92 and 76 for identical and independent noise instances, respectively. Referring to Fig. 4, the psychometric functions cross the 70.7% point at approximately $N=94$ and $N=70$ for the corresponding conditions. For the state-space system, S1 yielded thresholds of 30 and 23 for identical and independent noise instances, respectively. Referring to Fig. 5, the psychometric functions cross the 70.7% point at approximately 28 and 19 for the corresponding conditions.

IV. EXPERIMENT II: THRESHOLDS FOR AUDITORY SCENES

Experiment II assesses the perceptual fidelity of low-order state-space systems for multiple-source stimuli. Whereas Experiment I utilized a single source (noise) presented at one of 50 locations, Experiment II relied upon virtual auditory soundscapes (VAS) comprised of a variety of stationary and moving sources, each of which could be located at an arbitrary position. Observers adjusted the order, N, of the system used to render an approximate VAS to achieve the point of subjective equality with a fully-rendered VAS.

A. Methods

1. Stimulus conditions

Three VASs were constructed. Each VAS was 20–25 s in duration and consisted of several sound sources, some of which occurred simultaneously. All sources were single-channel signals. The sources were taken from a Bang and Olufsen collection of anechoic recordings,[2] a CBS collection of field recordings,[3] and field recordings made by the first author. The sources taken from the Bang and Olufsen collection contain no reverberation, and are labeled "dry" below, whereas the sources taken from the CBS and author field recordings contain natural reverberation, and are labeled reverberant below.

The virtual listener's head was located at the center of the room, and was radius 8.75 cm. The virtual room was 6 m wide and 8 m deep, with no floor or ceiling. For the surfaces to the right and in front of the listener $\beta=0.7$, and for the surfaces to the left and behind the listener $\beta=0.1$. First and second order reflections were rendered. Soundfiles of each VAS are available online.[4]

The first VAS was a recital consisting of a solo trumpet (dry) moving slowly from the left of the stationary listener to the front, followed by four stationary applause sources (reverberant) surrounding the listener in the horizontal plane, followed by three firework whistles (reverberant) moving quickly from either side of the listener to directly above the listener.

The second VAS involved a slowly revolving listener. Three stationary sources were active throughout the duration of the VAS. Two sources (solo speech and solo percussion, both dry) were on either side of the room, at zero elevation. Directly above, and slightly to the side was a field recording of tropical birds (reverberant).

The third VAS was a cross between a barnyard and a zoo. Ten animal sounds were presented in an overlapping sequence: the clucking of chickens, the bleat of a sheep, the roar of a lion, the quack of a duck, the chirping of a small bird, the hoot of an owl, the buzz of a fly, and the ribbets of three frogs. All sources were reverberant. The sounds were distributed approximately uniformly around the listener, with the bird sounds located above the listener, and the others located either in the horizontal plane or below the listener. The bird sounds moved from one side of the listener to the other, whereas the other sounds were stationary.

Each VAS was constructed from a sequence of overlapping static 50 ms frames, with a 5 ms raised-cosine crossfade between frames. For each frame, the location of the direct and image sources relative to the listener were updated and the magnitude and delay adjusted appropriately. Interpolation was performed by mapping each desired source direction to the nearest three HRTF directions included in the state-space system (Pulkki, 1997).

For each condition, an "ideal VAS" was constructed using the full-order HRTFs, and a collection of "Approximate VAS" were constructed using a MISO state-space system for each ear (i.e., two systems with $M=50$ and $P=1$). The order of the state-space systems varied from $N=1$ to $N=89$, with approximately geometric spacing. In total 21 approximations were constructed for each VAS.

2. Psychophysical procedure

The test stimulus was constructed by switching between the "ideal VAS" and the "approximate VAS" every 2.4 s. For each switch, non-overlapping 5 ms raised-cosine squared ramps were used. The observer used a slider to adjust "approximation quality" to find the lowest system order at which he or she perceived no difference. The order N was controlled by a slider that had a random monotonic warp applied to the mapping between slider position and N for each block of the experiment. The three auditory scenes were presented once each in sequence, and the sequence was repeated five times. For each observer a total of 15 blocks were performed, with breaks taken after every 4–6 blocks.

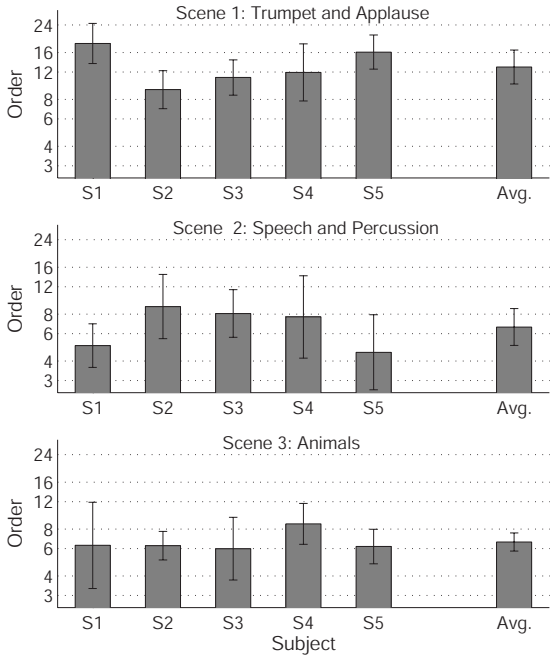

FIG. 3. Discrimination thresholds for three virtual auditory scenes.

3. Participants

The five observers from the previous experiment participated in Experiment II. No training was performed prior to starting Experiment II. The entire experiment required about 1.5 h of listening, and was completed in a single session. The same facility was used as in Experiment I.

B. Results and discussion

Figure 3 shows the average thresholds of subjective equality for the five observers and three auditory scenes. Bar height indicates the geometric mean of five trials, and the error bars indicate the geometric standard deviation. The rightmost bar in each panel shows the geometric mean across observers, and the error bar shows the geometric standard deviation of the observer means.

For the first VAS the average threshold was $N=13$, and for the other two scenes the average threshold was $N=7$. That the thresholds were significantly lower for the second two scenes is likely due to the source signals used to create the scenes. The first VAS contains several recordings of diffuse applause in reverberant environments. The applause signals are the relatively stationary and wideband compared to the other signals used to generate the virtual scenes. As such, the first VAS provides more consistent spectral/temporal cues that aid in discrimination. All five participants reported that they focused their attention upon the applause portion of the first VAS in performing the task.

The second two scenes yielded an average threshold of $N=7$. However, the standard deviation is larger for the second VAS than the third VAS. This may be due to the percussion signal included in the second VAS. The percussion sig-

nal provides sharp impulses that are relatively wideband compared to the other source signals. However, this signal also articulated a clear rhythmic pattern that is invariant to the approximation quality. Hence, the specific timbre of individual percussive hits may have revealed subtle timbral cues that aid discrimination, but only if the observer chose to the concentrate on such timbral minutiae rather than the rhythmic performance. Thus the listening strategy of the observer may have affected thresholds more for the second VAS than the third VAS.

Comparing the thresholds for the two experiments, the thresholds from Experiment I were significantly higher than those from Experiment II. Experiment I allowed the listener to focus on a single, familiar, wideband stimuli. Many practical binaural display applications will not be so demanding on the HRTF approximations. Of the two experiments, the threshold estimates from Experiment II are more likely to be appropriate for practical systems.

V. CONCLUSION

Experiment I yielded state-space thresholds of $12 \leqslant N \leqslant 24$ for a system that models $D=50$ HRTFs. Wideband noises were used as stimuli and an objective adaptive-level procedure was used to estimate the 70.7% discrimination threshold. We included an array of truncated minimum-phase impulse responses for comparison and found that for all conditions the FIR array yield order thresholds that were at least 100% larger than the state-space thresholds (and this trend holds if the thresholds are expressed as net arithmetic cost as well). The use of independent noises instead of identical noises caused the thresholds to drop significantly for both types of system. The inclusion of first-order virtual reflections caused the thresholds to drop for the state-space system, but not the FIR system. This is likely due to the distribution of spectral error across the 50 directions, where the error is more likely to cancel with the state-space system.

Experiment II yielded state-space thresholds of $7 \leqslant N \leqslant 13$ for a system that models $D=50$ directions. Complex and dynamic virtual auditory scenes were used as stimuli, and a subjective method-of-adjustment procedure was used to estimate the threshold of subjective equality. For practical applications, the more optimistic thresholds estimated with Experiment II are probably sufficient.

Next generation binaural displays will be expected to render multiple sources, acoustic reflections, and source and listener motion. The multi-direction framework considered in this study can readily accommodate such phenomena. The cost of this framework can be reduced with a state-space implementation. An order $N=7$ system appears sufficient for most applications and affords a dramatic decrease in computational cost from a full-order implementation. The collection of 50 full-order HRTFs would require approximately 1.13×10^9 multiplies per second in real-time, whereas the $N=7$ state-space system would require about 34×10^6 multiplies per second for the entire collection. In conclusion, we have demonstrated that a state-space approach can yield a low cost and perceptually adequate implementation of a collection of HRTFs.

ACKNOWLEDGMENTS

This work was funded in part by a scholarship from the AFCEA and a fellowship from the Rackham Graduate School. Additional funding was provided by the Office of Naval Research to Dr. Thomas Santoro at the Naval Submarine Medical Research Laboratory, Groton, CT. The authors thank Dr. Jason Corey for his advice on soundscape design.

APPENDIX: PSYCHOMETRIC FUNCTIONS

In order to determine if an adaptive procedure was feasible for Experiment I, and to estimate appropriate steps sizes, the psychometric functions for one observer (the first author) were estimated for several conditions. An additional objective of this experiment was to determine if individualized HRTFs were necessary for Experiments I and II. The procedure was the same as in Experiment I, except that a fixed-level procedure was used instead of an adaptive-level procedure.

1. Methods

Three factors were considered: approximation type, noise type, and HRTF type. The first two factors were the same as those used in Experiment I. With respect to *HRTF type*, stimuli were generated using either a custom HRTF dataset measured for the observer, or the HRTF dataset used in Experiments I and II. That is, the stimuli were generated either from individualized or non-individualized HRTFs. For both the state-space and FIR conditions, seven system orders spanning the range from near-perfect discrimination to near-chance discrimination were tested.

The same four-interval two-alternative forced-choice task as Experiment I was used; however, the order of the approximate system was fixed throughout each block. Trials were presented in blocks of 54 trials. The first four trials of each block were practice. Five blocks for each stimulus condition and approximate order were presented. The eight conditions were divided into four groups. The first two groups tested stimuli generated with individualized HRTFs, and the first and third groups tested identical noises. Within each group, blocks were presented with random system type and system order. Each point in the psychometric functions shown below is the result of 250 responses. The observer performed several hours of training prior to conducting the experiment. The stimulus conditions and psychophysical procedure are described in greater detail in Adams, 2007.

2. Results

Figures 4 and 5 show the psychometric functions for the eight conditions described above. The abscissa plots the system order (N) on a logarithmic scale, and the ordinate plots the observer's percentage correct. The psychometric functions that correspond to the identical condition are shown with solid lines, and the functions that correspond to the independent condition are shown with dashed lines. The individualized HRTF conditions are shown with gray lines, and the non-individualized HRTF conditions are shown with black lines. The FIR conditions are shown in Fig. 4 and the

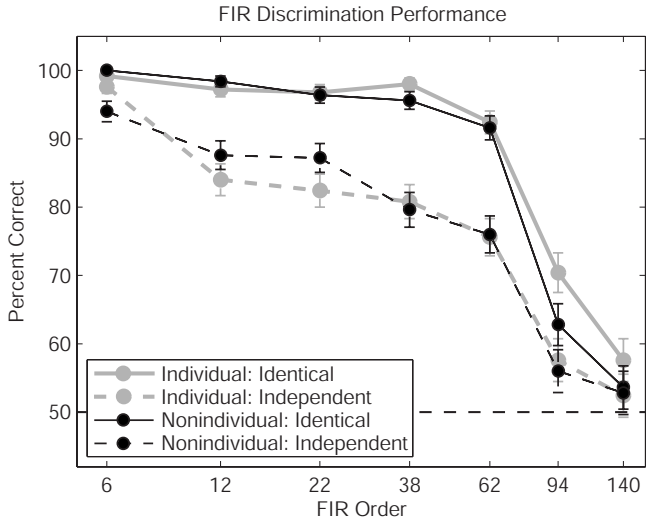

FIG. 4. Psychometric functions showing the observer's percentage correct versus system order (N) for FIR systems. Functions for the identical condition are shown with solid lines, and functions for the independent condition are shown with dashed lines. Functions for the individualized HRTF condition are shown with gray lines, and functions for the non-individualized HRTF conditions are shown with black lines. Each point shows the percent correct of 250 trials. Error-bars show the standard error for each point.

state-space conditions are shown in Fig. 5. Each point of each psychometric function shows the fraction of the 250 trials for which the observer made the correct decision. The standard error was computed assuming a binomial distribution.

For both system types, it is evident that the use of non-individualized HRTFs instead of individualized HRTFs does not significantly change discrimination performance. In contrast, the noise stimuli has a significant effect of discrimination. For the FIR systems, independent noises cause discrimination to drop 10%–20% for $12 \leq N \leq 62$. However, for both noise types, discrimination does not drop to chance until $N > 140$. For the state-space systems, independent noises cause the psychometric function to shift left, and the order at which discrimination falls to change drops from 56 to 42.

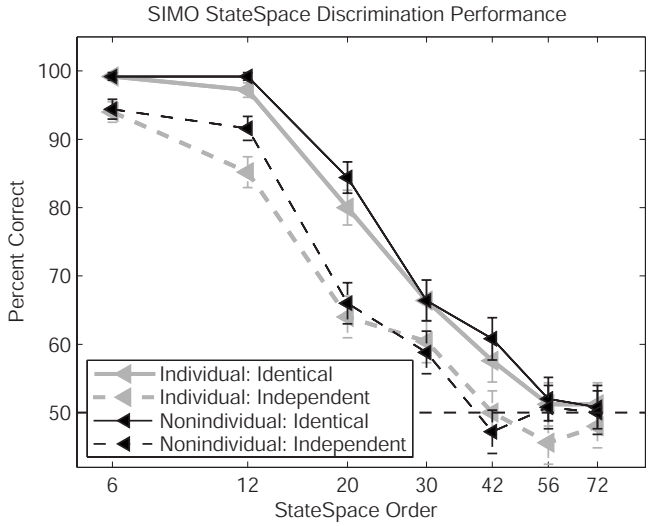

FIG. 5. Psychometric functions for state-space systems.

The fixed-level experiment revealed two important properties that enabled the adaptive-level experiments. First, the psychometric functions are smooth and monotonic. Hence adaptive-level techniques are valid. In particular, in the transition region from 90% to 60%, the psychometric functions are approximately linear in terms of $\log(N)$, permitting geometric step sizes in the adaptive-level experiment.

Second, for the single listener in this experiment, the effect of system order on performance does not depend on whether the subject's own HRTFs, or those of someone else, were used. Whatever stimulus differences exist between an identical-noise signal passed through either an individualized or non-individualized HRTFs, the results suggest that they are small when compared to the variations in the stimulus which are introduced when independent, rather than identical, noise is used as the source. The primary experiments of the present paper report results for non-individualized HRTFs. From the results shown in Figs. 4 and 5, we conclude that an adaptive procedure, properly adjusted in step-size to cover the range of the psychometric function, will yield a consistent estimate of threshold. However, we cannot rule out the possibility that some subjects, when using their own HRTFs, might exhibit higher absolute thresholds.

[1]See Fig. 4 in Grantham *et al.*, 2005 and Fig. 4 in Adams and Wakefield, 2008.
[2]Music for Archimedes (audio CD), Bang and Olufsen, 1992, Catalog No. B&O 101.
[3]New CBS audio-file sound effects (audio CD), Columbia Broadcasting System, 1977, Catalog No. A2 14062/A 14064.
[4]http://www-personal.umich.edu/nhadams/auditoryScenes (Last viewed January, 2009).

Adams, N. (**2007**). "A Model of Head-Related Transfer Functions based on a State-Space Analysis," Ph.D. thesis, University of Michigan, Ann Arbor.
Adams, N., and Wakefield, G. (**2005**). "The binaural display of clouds of point sources," in Proceedings of IEEE Workshop on Application of Signal Processing to Audio and Acoustics, New Paltz, NY.
Adams, N., and Wakefield, G. (**2008**). "State-space synthesis of virtual auditory space," IEEE Trans. Audio, Speech, Lang. Process. **16**, 881–890.
Algazi, V., Avendano, C., and Duda, R. (**2001**). "Elevation localization and head-related transfer functions analysis at low frequencies," J. Acoust. Soc. Am. **109**, 1110–1122.
Algazi, V., Duda, R., and Thompson, D. (**2004**). "Motion tracked binaural sound," J. Audio Eng. Soc. **52**, 1142–1156.
Allen, J., and Berkley, D. (**1979**). "Image method for efficiently simulating small-room acoustics," J. Acoust. Soc. Am. **65**, 943–950.
Bay, J. (**1999**). *Fundamentals of Linear State Space Systems* (McGraw-Hill, Boston, MA).
Blauert, J. (**1997**). *Spatial Hearing: The Psychophysics of Human Sound Localization* (MIT, Cambridge, MA).
Chanda, P., Park, S., and Kang, T. (**2006**). "A binaural synthesis with multiple sound sources Based on spatial features of head-related transfer functions," in Proceedings of IEEE International Joint Conference on Neural Networks.
Cheng, C. (**2001**). "Visualization, measurement, and interpolation of head-related transfer functions (HRTF'S) with applications in electro-acoustic music," Ph.D. thesis, University of Michigan, Ann Arbor.
Georgiou, P., and Kyriakakis, C. (**1999**). "Modeling of head related transfer functions for immersive audio using a state-space approach," in *Proceedings of IEEE Asilomar Conference on Signals, Systems and Computers*, Vol. **1**, pp. 720–724.
Glover, K. (**1984**). "All optimal Hankel-norm approximations of linear multivariable systems and their L^{∞}-error bounds," Int. J. Control **39**, 1115–1193.
Grantham, D., Willhite, J., Frampton, K., and Ashmead, D. (**2005**). "Reduced order modeling of head related impulse responses for virtual acous-

tic displays," J. Acoust. Soc. Am. **117**, 3116–3125.
Haneda, Y., Makino, S., Kaneda, Y., and Kitawaki, N. (**1999**). "Common-acoustical-pole and zero modeling of head-related transfer functions," IEEE Trans. Speech Audio Process. **7**, 188–196.
Hartmann, W., and Wittenberg, A. (**1996**). "On the externalization of sound images," J. Acoust. Soc. Am. **99**, 3678–3688.
Huopaniemi, J., Zacharov, N., and Karjalainen, M. (**1999**). "Objective and subjective evaluation of head-related transfer function filter design," J. Audio Eng. Soc. **47**, 218–239.
Kistler, D., and Wightman, F. (**1992**). "A model of head-related transfer functions based on principal components analysis and minimum-phase reconstruction," J. Acoust. Soc. Am. **91**, 1637–1647.
Kulkarni, A., and Colburn, H. (**1998**). "Role of spectral detail in sound-source localisation," Nature (London) **396**, 747–749.
Kulkarni, A., and Colburn, H. (**2004**). "Infinite-impulse-response models of the head-related transfer function," J. Acoust. Soc. Am. **115**, 1714–1728.
Kulkarni, A., Isabelle, S., and Colburn, H. (**1999**). "Sensitivity of human subjects to head-related transfer-function phase spectra," J. Acoust. Soc. Am. **105**, 2821–2840.
Kung, S. (**1978**). "A new identification and model reduction algorithm via singular value decompositions," in Proceedings of IEEE Asilomar Conference on Signals, Systems and Computers, pp. 705–714.
Levitt, H. (**1971**). "Transformed up-down methods in psychoacoustics," J. Acoust. Soc. Am. **49**, 467–537.
Maki, K., Furukawa, S., and Hirahara, T. (**2003**). "Acoustical cues for sound localization by gerbils in an ecologically realistic environment," Assoc. Res. Otolaryngol. Abstr..
Pulkki, V. (**1997**). "Virtual sound source positioning using vector base amplitude panning," J. Audio Eng. Soc. **45**, 456–466.
Rakerd, B., and Hartmann, W. (**1985**). "Localization of sound in rooms II: The effect of a single reflecting surface," J. Acoust. Soc. Am. **78**, 524–533.
Shinn-Cunningham, B., and Kulkarni, A. (**1996**). "Recent developments in virtual auditory space," in *Virtual Auditory Space: Generation and Applications*, edited by S. Carlile (Springer-Verlag, Berlin, Germany).
Zotkin, D., Duraiswami, R., and Davis, L. (**2004**). "Rendering localized spatial audio in a virtual auditory space," IEEE Trans. Multimedia **6**, 553–564.

Effects of center frequency and rate on the sensitivity to interaural delay in high-frequency click trains

Piotr Majdak[a] and Bernhard Laback
Acoustics Research Institute, Austrian Academy of Sciences, Wohllebengasse 12-14, A-1040 Vienna, Austria

(Received 12 December 2007; revised 28 November 2008; accepted 26 March 2008)

The effects of center frequency and pulse rate on the sensitivity to ongoing envelope interaural time differences (ITDs) were investigated using bandpass-filtered pulse trains. Three center frequencies (4.6, 6.5, and 9.2 kHz) were tested with bandwidths scaled to stimulate an approximately constant range on the basilar membrane. The pulse rate was varied from 200 to 588 pps (pulses per seconds). Five normal-hearing (NH) subjects were tested. Averaged over all rates, the results show a small decrease in sensitivity with increasing center frequency. For all center frequencies, sensitivity decreases with increasing pulse rate, yielding a rate limit of approximately 500 pps. The lack of an interaction between pulse rate and center frequency indicates that auditory filtering was not the rate limiting factor in ITD perception and suggests the existence of other limiting mechanisms, such as phase locking or more central processes. It is concluded that the comparison of the rate limits in ITD perception between cochlear-implant listeners and NH subjects listening to high-frequency bandpass-filtered pulse trains is not confounded by the choice of center frequency of stimulation in NH listeners. © *2009 Acoustical Society of America.* [DOI: 10.1121/1.3120413]

PACS number(s): 43.66.Pn, 43.66.Ts, 43.66.Mk [RYL] Pages: 3903–3913

I. INTRODUCTION

Interaural time differences (ITDs) are important for the localization of sound sources (e.g., Macpherson and Middlebrooks, 2002). It is well known that the ITD information in unmodulated signals can only be processed up to about 1500 Hz (Zwislocki and Feldman, 1956; Blauert, 1997). At higher frequencies, ITD information can be processed from the slowly-varying temporal envelope only. This is supported by various psychoacoustic (Henning, 1974; Nuetzel and Hafter, 1976, 1981; Bernstein, 2001; Bernstein and Trahiotis, 2002) and physiologic studies (Yin *et al.*, 1984; Skottun *et al.*, 2001; Shackleton *et al.*, 2003). The ability to transmit envelope and carrier information in separate paths seems to be a general property of the auditory system (Liang *et al.*, 2002) and was also found in other sensory modalities like visual and electrosensory systems (Middleton *et al.*, 2006).

There is strong evidence that envelope ITD sensitivity depends on the temporal properties of the fast-varying carrier signal. This was shown for sinusoidally amplitude-modulated (SAM) tones (Henning, 1974; Stellmack *et al.*, 2005; Nuetzel and Hafter, 1976), two-tone complexes (McFadden and Pasanen, 1976; Bernstein and Trahiotis, 1994), transposed tones (Bernstein and Trahiotis, 2002), and bandpass-filtered click trains (Hafter and De Maio, 1975; Hafter and Dye, 1983). All these studies found that envelope ITD sensitivity is limited with respect to the rate of the envelope fluctuations. However, ITD sensitivity depends not only on the rate of envelope fluctuations. For example, Bernstein and Trahiotis (2002) found that transposed tones, which have sharper[1] envelopes than SAM tones, yield higher performance for comparable rates. On the physiological basis, it was shown that, under certain conditions,[2] the neural response to transposed tones can even be comparable with the response to low-frequency pure tones (Griffin *et al.*, 2005; Dreyer and Delgutte, 2006).

In cochlear-implant (CI) listeners, Majdak *et al.* (2006) and Laback *et al.* (2007) investigated the sensitivity to ongoing ITD presented at one binaural electrode pair. At least one CI listener tested showed sensitivity up to 800 pps (pulses per second).[3] Further, they compared sensitivity to ongoing *envelope* ITD of normal-hearing (NH) subjects. In NH experiments, they used bandpass-filtered pulse trains to simulate pulsatile stimulation with CIs, similar to McKay and Carlyon (1999). The best NH listeners showed sensitivity up to 600 pps (Majdak *et al.*, 2006) and 400 pps (Laback *et al.*, 2007). Thus, compared to the best performance in electric stimulation, the rate limit of the best NH listeners was lower. Even though only two of five CI listeners showed a higher rate limit than NH listeners, this finding is rather surprising. It has been concluded that the comparison between these two groups may be affected by different properties of electric and acoustic stimulations. In acoustic stimulation the bandpass-filtered pulse train passes through the basilar membrane, where the envelope sharpness can be reduced depending on the stimulation place. This filtering process is bypassed in electric stimulation. Thus, assuming that a sharp envelope is required for ITD sensitivity (Stellmack *et al.*, 2005), the rate limit of the NH listeners may have been affected by auditory filtering in the cochlea. The investigation of a possible limitation in the comparison between NH and CI listeners' results was the main motivation for this study.

If auditory filtering limits ITD perception, then the increase in the stimulus center frequency (CF) should improve performance. This is because the auditory filter bandwidth increases with the CF, causing relatively less reduction in the envelope sharpness (e.g., Patterson *et al.*, 1992), especially at

[a]Author to whom correspondence should be addressed. Electronic mail: piotr@majdak.com

high modulation rates. However, the inversion of that argument is not valid: if performance does not improve with CF, it does not mean that auditory filtering has no effect because auditory filtering may be counteracted by other effects associated with the stimulation of different tonotopic places. Those are (1) changing hearing thresholds, which may result in a change of ITD sensitivity (Nuetzel and Hafter, 1976); (2) stimulating different amounts of peripheral neurons when constant bandwidth stimuli are applied (Buell and Hafter, 1991); and (3) differences in the higher processing stages (e.g., changing number of responding cells in the central nervous system as indicated in Bernstein and Trahiotis, 1994, or differences in the tonotopic specialization of the coincidence detectors as shown in chicks by Kuba *et al.*, 2005). Thus, the ITD sensitivity as a function of CF alone is a misleading indicator for a possible effect of auditory filtering.

However, the question of auditory filtering can be addressed by investigating the effect of CF on the *rate limit*. This is because both increase in rate and decrease in CF can reduce envelope sharpness . Thus, if auditory filtering affects ITD sensitivity, the rate limit should significantly increase with CF. In other words, a significant interaction between CF and rate could indicate that the reduction in the envelope sharpness depends on the tonotopic position and, thus, auditory filtering limits ITD sensitivity. If the interaction is not significant then the rate limit is not affected by the choice of CF and, thus, this limit is probably a result of some more central limitations.

In NH listeners, Hafter and Dye (1983) investigated the detection of ITD in bandpass-filtered click trains as a function of the inter-pulse interval (IPI) and the number of clicks. Although they did not collect data for different CFs, their results indicate that the envelope sharpness reduction due to auditory filtering does not explain the decrease in performance for increasing pulse rate. However, additional data on ITD sensitivity at different CFs are required to substantiate their conclusions.

For other types of stimuli, there are indications that auditory filtering is not the limiting factor in ITD perception, as supported by the results of two studies: Bernstein and Trahiotis (1994) and Bernstein and Trahiotis (2002). For 100% SAM tones and two-tone complexes, Bernstein and Trahiotis (1994) found a general decrease in ITD sensitivity when the CF was increased. They varied the modulation rate as well, showing that the sensitivity to ITD decreased as the rate of envelope fluctuation increased. The comparison of the modulation rate effect between different CFs led to the conclusion that the change in ITD sensitivity is unlikely affected by auditory filtering. For transposed tones, Bernstein and Trahiotis (2002) investigated ongoing ITD sensitivity and compared their results to those obtained with SAM and pure tones. For the lower modulation frequencies (<256 Hz), listeners showed even higher ITD sensitivity to transposed tones than to pure tones with comparable frequency. However, using higher modulation frequencies, JNDs could not be determined for transposed tones. Furthermore, increasing the center frequency of the transposed tones resulted in lower sensitivity as well. From their results, Bernstein and Trahiotis (2002) concluded that for SAM and transposed tones, ITD perception is not primarily limited by the effects of auditory filtering.

Nevertheless, Bernstein and Trahiotis (2002) found large differences in ITD sensitivity between the SAM and transposed tones. Those findings indicate that the relative decrease in ITD sensitivity usually observed for high-frequency stimuli (compared to low-frequency stimuli) is associated with the type of stimuli used, as specified by the center frequency, rate, and sharpness of envelope fluctuation. Hence, conclusions derived for SAM and transposed tones do not automatically apply to other types of stimuli like bandpass-filtered click trains. All these stimuli have different envelope sharpness even for the same CF and rate. Thus the impact of auditory filtering on ITD perception may be different and requires a separate investigation for click trains.

Majdak *et al.* (2006) and Laback *et al.* (2007) used bandpass-filtered click trains because these stimuli appear to be a good approximation of the electric stimulation in CIs when investigating temporal effects (McKay and Carlyon, 1999; Carlyon *et al.*, 2002) in NH listeners. Electric pulse trains presented at one electrode in the cochlea have a very steep onset, which may be best approximated by bandpass-filtered click trains in acoustic stimulation. Of course, when compared to electric pulse trains, the response of an auditory filter to bandpass-filtered click trains results in temporal fluctuations with a clearly reduced envelope sharpness. However, the resulting envelope is still sharper than for SAM or transposed tones. Dreyer and Delgutte (2006) showed that phase locking to transposed tones is better than to SAM tones and for transposed tones, it even reaches levels comparable to pure tones under certain restrictions.[2] Transposed tones clearly have sharper envelopes than SAM tones. Thus, stimuli with even sharper envelopes like bandpass-filtered pulse trains offer the possibility of further improvements in the phase locking effects.

An additional advantage of bandpass-filtered click trains is that the onset slopes do not change with the pulse rate as it is the case for SAM and transposed tones. The amplitude spectrum of a click train is a harmonic series, which can be limited in frequency by applying a bandpass filter. Thus, the bandwidth and the CF are independent, making it possible to systematically stimulate different amounts of neurons at different tonotopic places. In contrast, for both SAM and transposed tones the bandwidth is directly related to the modulation rate and is constant for all CFs. Thus, assuming an approximately logarithmic scaling of the frequency-to-place mapping (Greenwood, 1961), fewer neurons may be stimulated at higher CFs than at lower CFs when SAM and transposed tones are used. Even though the effect of bandwidth on the sensitivity to envelope ITD is still unclear, there are some indications that increasing bandwidth leads to improved envelope ITD perception (Buell and Trahiotis, 1993). Using stimuli with a logarithmically-scaled bandwidth may compensate for the decrease in performance found in the literature for SAM and transposed tones at higher CFs. Thus, for lower rates, co-varying the bandwidth with the CF could lead to high performance across all CFs, which is important in our study in order to limit potential floor effects when

TABLE I. Filter configuration for the conditions CF4.6, CF6.5, and CF9.2. The CF (Hz) is the geometrical CF resulting from the lower and upper edges. The bandwidth (ERB-rate units) is according to Moore and Glasberg (1983). The distance on the basilar membrane (BM) is according to Greenwood (1990).

Code	Center frequency (Hz)	Lower edge (Hz)	Upper edge (Hz)	Bandwidth (Hz)	Bandwidth (ERB-rate units)	Distance on BM (mm)
CF4.6	4589	3900	5400	1500	2.53	2.28
CF6.5	6490	5515	7637	2121	2.35	2.30
CF9.2	9178	7800	10800	3000	2.11	2.32

switching from lower to higher rates. Notice, that in the present study we varied the bandwidth with the CF, however, we do not treat it as an independent variable and its effects are not investigated.

The main focus of this study is to reconsider the comparison between CI and NH listeners performed in Majdak *et al.* (2006) and Laback *et al.* (2007) under the hypothesis that the NH performance was not underestimated because of auditory filtering. The effect of auditory filtering was investigated by systematically varying CF and the pulse rate of bandpass-filtered pulse trains and testing the sensitivity to ongoing envelope ITD in NH listeners. The main hypothesis is tested by comparing the rate limit between three different CFs. This is performed by a statistical analysis of the interaction between CF and pulse rate. Additionally, the results are discussed in the context of the general effects of CF and pulse rate on ITD perception in NH and CI listeners.

II. METHODS

A. Subjects and apparatus

Five NH subjects participated in this study. All subjects were aged between 25 and 35 years and had no indication of hearing abnormalities. One of them (NH2) was an author of this study.

A personal computer system was used to control the experimental task. The stimuli were output via a 24-bit stereo D/A converter (ADDA 2402, Digital Audio Denmark) using a sampling rate of 96 kHz per channel. The analog signals were sent through a headphone amplifier (HB6, TDT) and an attenuator (PA4, TDT), and presented to the subjects via a circumaural headphone (K501, AKG). Calibration of the headphone signals was performed using a sound level meter (2260, Brüel & Kjær) connected to an artificial ear (4153, Brüel & Kjær).

B. Stimuli

The stimuli were 300-ms pulse trains composed of monophasic pulses with a duration of 10.4 μs, corresponding to one sampling interval at a sampling rate of 96 kHz. The pulse rate was varied from 200 to 588 pps. The smallest IPI was 1700 μs. Both of the studies with click trains discussed above, Majdak *et al.* (2006) and Laback *et al.* (2007), showed that for pulse rates above 600 pps ongoing ITD sensitivity degrades to chance rate. Hence, higher pulse rates were not tested.

The ITD was introduced by delaying the temporal position of the pulses at one ear relative to the other ear. To restrict the ITD to the ongoing part of the stimulus only, the position of the first pulse pair (onset) and the last pulse pair (offset) was fixed to a zero ITD (Laback *et al.*, 2007). To minimize the monaural perception of irregularities, half of the ITD was applied to the leading ear and the other half to the lagging ear. Laback *et al.* (2007) showed that these irregularities are not perceptible. The ITD values varied[4] from 20 to 400 μs. The ITD was adapted to account for the subject's sensitivity. According to Majdak *et al.* (2006), ITDs higher than 0.25 IPI can lead to lower performance compared to ITDs lower than 0.25 IPI. This is an effect of the ambiguity in ongoing ITD information provided by the stimulus for ITD=0.5 IPI and results in a nonmonotonic psychometric function. Thus, combinations of ITD and pulse rate resulting in ITD values higher than 0.25 IPI were not tested in this study.

The pulse trains were passed through a digital eighth-order Butterworth filter. Three different CFs were tested: 4589 (CF4.6), 6490 (CF6.5), and 9178 Hz (CF9.2). The lowest CF, CF4.6, was chosen to be identical with the CF used in Carlyon *et al.* (2002); Majdak *et al.* (2006); and Laback *et al.* (2007). The highest CF, CF9.2, is double the frequency of CF4.6 and corresponds to the CF used in Carlyon and Deeks (2002). CF6.5 is the geometrical average of CF4.6 and CF9.2. Using CFs higher than 10 kHz would lead to even shorter impulse responses of auditory filtering. However, we did not test CFs above 10 kHz since Bernstein and Trahiotis (1994) showed that it is hard to retrieve valid data for very high CFs. Also, in electric hearing, the most-basally implanted electrode usually corresponds to frequencies below 10 kHz.

The bandwidth of the stimuli was co-varied with the CF with the aim to obtain an approximately constant stimulation range on the basilar membrane. The bandwidth for CF4.6 is 1500 Hz, which is identical to the bandwidth in previous studies. It corresponds to the ERB-rate of 2.53 (according to Moore and Glasberg, 1983) and a stimulation range of 2.28 mm on the basilar membrane (according to Greenwood, 1990). For CF9.2, the bandwidth is double the bandwidth for CF4.6, which results in 3000 Hz. It roughly corresponds to the ERB-rate of 2.11 and a stimulation range of 2.32 mm on the basilar membrane.[5] Further details about the filter configurations can be found in Table I. By doubling the bandwidth from CF4.6 to CF9.2 and using the geometrical average for CF6.5, we hoped to achieve a similar ITD sensitivity for the three CFs at lower rates. With these bandwidths, the signals clearly stimulate regions outside the critical bandwidth. By doing that we hoped to achieve a good ITD sen-

sitivity at lower rates, which was required to avoid potential floor effects because the performance was expected to decrease with increasing rate.

Given that the sound pressure level (SPL) depends on the pulse rate, the amplitudes of the stimuli were adjusted to maintain a constant *A*-weighted SPL of 66 dB (with reference to 20 μPa), measured at the headphones, for all rates and CFs. We did not compensate for differences in hearing thresholds at different CFs. Despite the filtering of the pulse trains, some artifacts like harmonic distortions or intermodulation at the basilar membrane can cause stimulation outside the desired frequency band. To prevent these artifacts from being heard, a binaurally uncorrelated background noise was continuously played throughout the testing. We used Gaussian white noise ranging from 50 Hz to 20 kHz with the overall *A*-weighted SPL of 52.2 dB. This corresponds to a sound pressure spectrum level of 9.2 dB (with reference to 20 μPa in a 1-Hz band), which is approximately 28 dB below the maximum level of the tonal components in the filtered pulse train. According to Goldstein (1967), with this background noise level the intermodulation components and difference tones, which may potentially transmit ITD information outside the desired frequency band, were masked by either the background noise or the stimulus itself.[6]

C. Procedure

A two-interval, two-alternative forced-choice procedure was used in a lateralization discrimination test. The first interval contained the reference stimulus with zero ITD evoking a centralized auditory image. The second interval contained the target stimulus with the ITD tested. The subjects were requested to indicate whether the second stimulus was perceived to the left or to the right of the first one by pressing an appropriate button. The chance rate was 50%. A score of 100% correct (P_c) responses indicates that all stimuli were discriminated, with lateralization corresponding to the ear receiving the leading signal.

The tests were performed in blocks. Each block contained 70 presentations of four different ITD values[7] for a combination of CF and pulse rate. The ITD values were presented in a randomized order with 35 targets leading to the left and 35 targets leading to the right. The rate and ITD values were varied from block to block with the goal to obtain a good estimation of the 70%-threshold. Thus, in cases where the performance was at chance, blocks with lower ITD values or higher rates were not tested. In cases where the performance was at ceiling, higher ITDs or lower rates were not tested. The initial four ITD values were estimated on the basis of the training results. At least two blocks were completed for a tested condition and the order of blocks was randomized for each subject. Visual response feedback was provided after each trial.

Stimuli with the pulse rate of 200 pps and ITD of 600 μs at CF4.6 were used to train subjects before the main test started. The subjects were trained until they showed a stable performance which was achieved within a few hours.

III. RESULTS

Figure 1 shows the percent correct (P_c) scores as function of the ITD with the pulse rate as parameter. Each panel shows data for one subject and one CF. The dashed horizontal lines show the 70%-threshold used for the JND estimation.

The comparison of the data between the three CFs (columns) suggests a difference in performance. Especially comparing CF9.2 and CF4.6 for subjects NH2, NH7, NH8, and NH9, performance appears to decrease at higher CFs. The effect of the pulse rate seems to be more salient: performance decreases with increasing pulse rate, independent of subject, CF, and ITD.

In Fig. 2, data from Fig. 1 for the ITD of 200 μs were replotted to directly show the effect of the CF. The data are shown as a function of CF and the parameter is rate. Each panel shows data for one listener. It appears that with increasing pulse rate the differences between the CFs become larger, particularly for subject NH8. However, for NH5, the performance appears to be constant for all CFs. Generally, for the highest rate, the performance is in the range of chance, and for the lowest rates, the performance is at ceiling.

The data for all ITD values were statistically analyzed by calculating a multiway repeated-measures analysis of variance (RM ANOVA) with the factors CF, pulse rate, and ITD. The RM ANOVA was chosen because it considers the individual tendencies of each subject in the analysis. To not violate the assumption of homogeneity of variance required for ANOVA, the P_c scores were transformed using the rationalized arcsine transform (Sherbecoe and Studebaker, 2004). The results show that the main effect of CF is highly significant ($p<0.0001$) with decreasing performance for increasing CF. The main effect of the pulse rate is highly significant ($p<0.0001$); performance decreases with increasing pulse rate. As expected, the effect of ITD is highly significant ($p<0.0001$) showing increasing performance for increasing ITD values.

Due to the individual performance of the subjects, for some subjects and conditions there are more extreme P_c scores like 100% or 50% than for others. These extreme values, which represent the tails of the psychometric functions, have an impact on the analysis producing ceiling or floor effects. For example, the Tukey–Kramer *post-hoc* test revealed that the results for the pulse rates of 200, 300, and 400 pps are not significantly different ($p>0.05$), which indicates a possible ceiling effect for pulse rates lower than 400 pps. To reduce this problem, the RM ANOVA was performed again. However, this time we excluded all combinations of ITD$\times$CF$\times$rate$\times$subject for which the P_c was below 60% and above or equal to 90%. The exclusion of these data resulted in a well populated condition matrix and the interactions could be included in the analysis. The main factors were CF, ITD, and pulse rate and the interactions were CF$\times$ITD and CF$\times$pulse rate. The interactions of pulse rate$\times$ITD and pulse rate$\times$ITD$\times$CF were not included.

The results for the main effects did not change ($p=0.002$ for CF; $p<0.0001$ for the effects of ITD and pulse

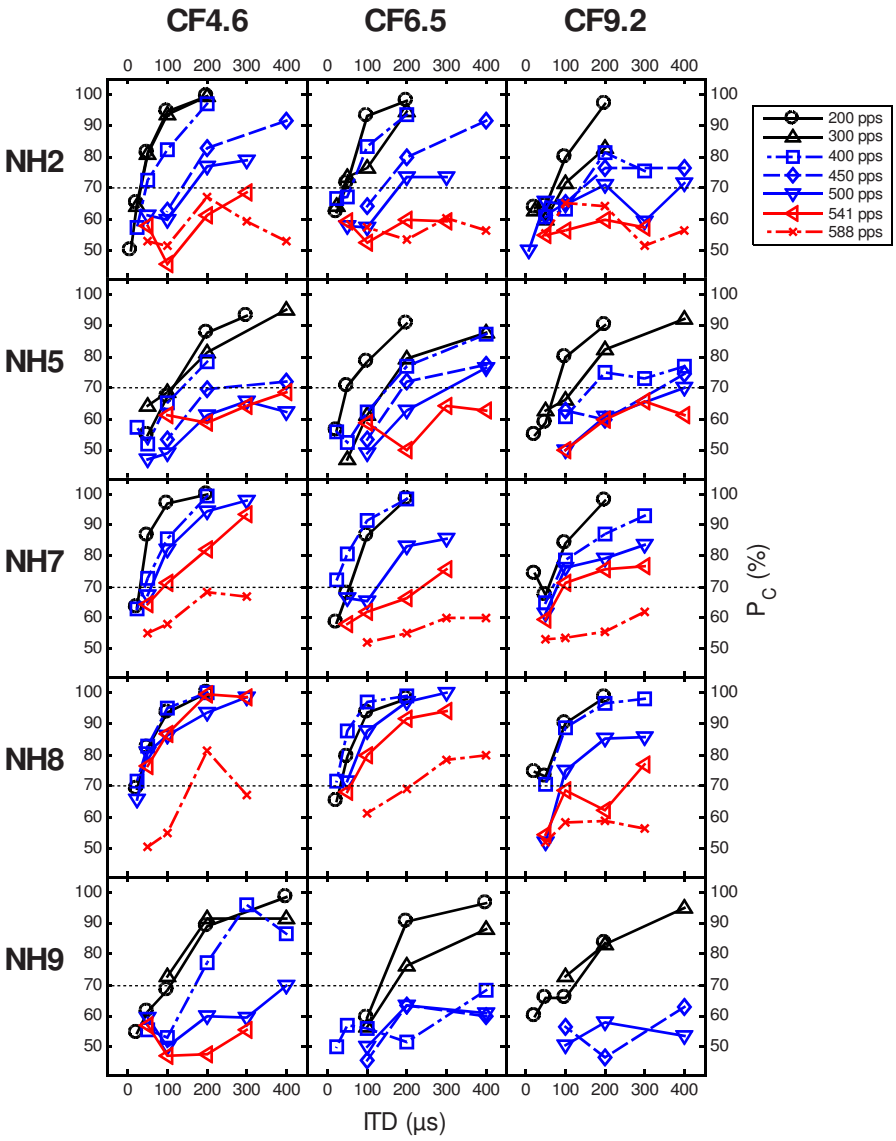

FIG. 1. (Color online) Performance in percent correct (P_c) as a function of the ITD. The parameter is the pulse rate in pps. Each column shows one CF and each row shows results for one subject. The dashed lines show the threshold used for the JND estimation.

rate). Neither interaction was significant ($p=0.1188$ for CF $\times$ ITD; $p=0.4247$ for CF $\times$ pulse rate) showing the independence of the effects of CF, ITD, and pulse rate. The significance of the factor CF is an effect of a decreasing performance with increasing CF as indicated by the P_c averaged over ITD, rate, and subjects for the three CFs (72.7%, 71.5%, and 69.2% for CF4.6, CF6.5, and CF9.2, respectively). For each of the rates from 200 to 541 pps, the Tukey–Kramer *post-hoc* tests revealed a significant decrease in performance between CF4.6 and CF9.2 ($p<0.05$). At the rate of 200 pps, which is least affected by rate limitation effects, the P_c averaged over ITD and subjects are 82.1%

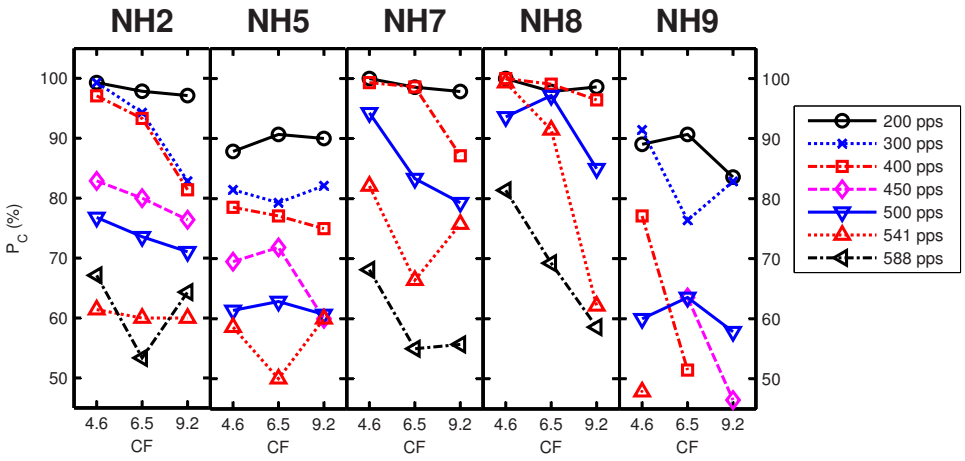

FIG. 2. (Color online) Percent correct (P_c) data from Fig. 1 for ITD of 200 μs as a function of CF. The parameter is the pulse rate. Each panel shows results for one subject.

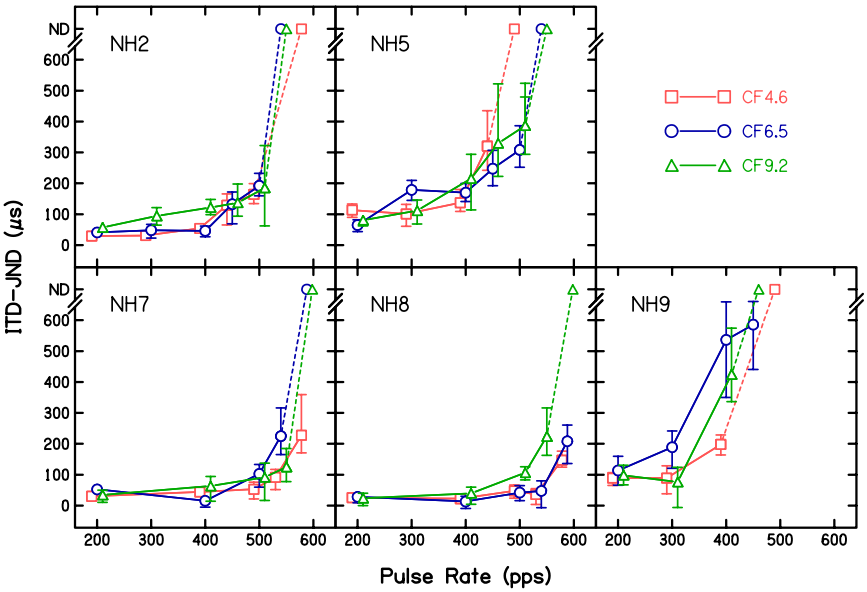

FIG. 3. (Color online) ITD-JNDs as a function of the pulse rate in pps. The parameter is the CF. The vertical bars indicate the 95% confidence intervals. The non-determinable JNDs are drawn at "ND" and are connected with dashed lines.

(CF4.6), 78.7% (CF6.5), and 79.1% (CF9.2). At 588 pps, there was a non-significant effect of CF ($p>0.05$; with an *increase* in performance of 0.98% between CF4.6 and CF9.2). For this rate the data represent results from three subjects only. Notice that the presented average P_c scores are averages over subjects while the statistical analysis takes into account the between-subject variability. These averaged P_c scores are only used to determine the direction of the CF effect. In all cases, the performance decreases with increasing CF.

This comparison may be confounded by the fact that not always the same combination of ITD and rate was tested at different CFs. To strengthen the previous findings, we performed an additional statistical comparison for one ITD only, namely, for the ITD of 200 μs. For this ITD, the results (see Fig. 2) show a good balance between ceiling and floor effects, and the data are available for most combinations of rate $\times$ CF $\times$ subject.[8] Thus, the condition matrix was almost full in this case. An RM ANOVA was performed with factors CF and rate and included the interaction between CF and rate. All main effects were significant ($p<0.0001$) and the interaction was, as in the previous analysis, not significant ($p=0.415$). This supports the previous finding that the rate limit does not change with CF. As in the previous comparison, the effect of CF is due to performance decrease with increasing CF as indicated by the P_c averaged over subjects and rate (85.7%, 80.1%, and 75.9% for CF4.6, CF6.5, and CF9.2, respectively). The Tukey–Kramer *post-hoc* tests revealed a significant decrease in performance between CF4.6 and CF9.2 ($p<0.05$) for 400 pps only. For this rate, the P_c averaged over ITD and subjects are 93.8% (CF4.6), 88.1% (CF6.5), and 82.7% (CF9.2). For all other rates, the P_c averaged over ITD and subjects decreases (not always monotonic) with increasing CF; however, the changes are not statistically significant.

To compare the results to the literature the ITD-JNDs were calculated. Psychometric functions were estimated from maximum-likelihood cumulative Gaussian fits to the raw data (Wichmann and Hill, 2001b).[9] The ITD value yielding 70% of the P_c score along the psychometric function was defined as JND. The estimated JNDs are shown as functions of the pulse rate in Fig. 3, one panel per subject. The parameter is CF. In some cases, mostly for the higher pulse rates, the psychometric functions did not reach 70% and the JNDs could not be determined. These not determinable (ND) JNDs are plotted at "ND." The vertical bars show the 95% confidence intervals of the JNDs and were determined applying a bootstrapping method (Wichmann and Hill, 2001a).

The JNDs for 200 pps, averaged over subjects (± 1 standard deviation) are 57.3 ± 48.9 μs (CF4.6), 59.9 ± 32.9 μs (CF6.5), and 58.7 ± 31.1 μs (CF9.2). By increasing the pulse rate, larger differences in JNDs as a function of CF can be found, especially for subjects NH7, NH8, and NH9. However, no general trend can be revealed just by visual inspection. Many JNDs could not be determined for the higher pulse rates and the consequences of this problem for the statistical analysis are discussed in the Appendix. Thus, the estimated JNDs are only used to further facilitate the interpretation of results and for a comparison to the literature in Sec. IV.

IV. DISCUSSION

In this study, the effect of auditory filtering on ongoing envelope ITD-based perception was tested by varying the CF and the pulse rate of bandpass-filtered pulse trains. The bandwidth of the stimuli was co-varied with the CF to obtain an approximately constant stimulation range on the basilar membrane. In this section, we first generally compare our data to previous studies, and then discuss the effects of CF, rate, and auditory filtering on ITD sensitivity.

A. General comparison

A recent study, which describes effects of subject's variability and training patterns, is Zhang and Wright (2007). They studied ITD sensitivity in eight subjects listening to SAM tones (4-kHz carrier and 300-Hz modulator). After training, the subjects achieved an average JND (± 1 standard

deviation) of approximately 220 ± 50 μs, with 50 μs for the best and 320 μs for the worst subject. Their condition corresponds best to our condition of CF4.6 with the rate of 200 pps, for which the average JND is 57.3 ± 48.9 μs, with 22 μs for the best and 89 μs for the worst subject. Their data can also be compared to our condition CF4.6 with the rate of 300 pps, for which the average JND is 56.3 ± 35.8 μs, with 23.8 μs for the best and 100.8 μs for the worst subject. Thus, the variability of our subjects is similar to that shown in Zhang and Wright, 2007. However, the absolute JND values in our study are much lower, which may result from the different types of stimuli used in both studies. Bernstein *et al.* (1998) tested 19 subjects and showed a JND of 377 ± 191 μs for narrow-band noise stimuli (CF of 4 kHz, bandwidth of 400 Hz). Their variability is much higher than the variability across our subjects. We conclude that the performance variability of our subjects is within a reasonable range and that the conclusions of this study are not likely to be confounded by an accidentally bad sampling of the population.

Bernstein and Trahiotis (2002) studied the sensitivity to ongoing ITD using transposed tones under conditions similar to ours. For 4 kHz and modulation rates of 128 and 256 Hz, they found JNDs of 79 and 100 μs, respectively. These conditions correspond best to our condition CF4.6 and 200 pps, where we found a lower JND of 57 μs. Considering an information integration across frequencies, the larger bandwidth of our bandpass-filtered pulse trains provides a potential explanation for the performance differences. Additionally, our bandpass-filtered click trains, after passing the auditory filters, provide sharper envelopes than SAM or transposed tones. These aspects may explain why bandpass-filtered pulse trains show a higher sensitivity to ITD than transposed tones at the similar rate.

For bandpass-filtered pulse trains at CF4.6 and 200 pps, Laback *et al.* (2007) found a performance, which roughly corresponds to a JND^{10} of 200 μs. This JND is much higher than ours. However, they used four-pulse stimuli, which results in a stimulus duration of 20 ms. The temporal integration effect of the ITD information for our much longer stimuli is the most likely reason for such a large difference. This is supported by findings of Hafter and Dye (1983), who showed that for 200 pps, appending more pulses to a short stimulus improves ITD sensitivity.

B. Effect of the CF

Our results show a significant decrease in ongoing envelope ITD sensitivity as the CF increases. In the following, we try to estimate the size of the sensitivity decrease. The average decrease in P_c scores averaged over subjects, rate, and ITD is 3% when changing from CF4.6 to CF9.2. This difference increases to 10%, when only data for the ITD of 200 μs are considered. However, in both cases, the data contain conditions with rates near the rate limit, which may confound this estimation. Thus, we consider a lower rate, for which there is no evidence for a strong rate limitation due to auditory filtering, namely, a rate of 200 pps. For this particular rate, P_c scores averaged over subjects and ITD show a significant decrease by approximately 3% when CF is increased from CF4.6 to CF9.2. For 200 pps and ITD of 200 μs, for which the condition matrix is well-populated, analysis of the data revealed a non-significant effect of CF. Further, for 200 pps, the estimation of JNDs also shows approximately constant sensitivity for all CFs, with an average JND of about 59 μs. Thus, even though the quantitative comparison of the sensitivity between different CFs depends on the way of analyzing the data, the decrease in ITD sensitivity for increasing CF appears to be small.

Both the statistical analysis and JNDs show results which are contrary to the outcome of Bernstein and Trahiotis (2002). They found a considerable decrease in ITD sensitivity as CF increased for transposed tones; for the modulation rate of 128 Hz, the JNDs increased from 79 to 170 μs when CF was increased from 4 to 10 kHz. Their results for 128-Hz SAM tones showed an even larger effect of CF: the JNDs increased from approximately 150 μs (for 4 kHz) to 350 μs (for 10 kHz). Bernstein and Triahiotis (2002) concluded that the decrease in performance with increasing CF may result from a frequency dependence of central binaural mechanisms which process ITD.

However, the larger CF effect for SAM and transposed tones can also be explained by comparing the envelopes of the auditory filter response to stimuli with the same rate: by increasing the CF, the envelope of SAM or transposed tone response has only a slight increase in the envelope sharpness because of the constant bandwidth. In contrast, for the envelope of our bandpass-filtered click train response, the relative increase in sharpness with increasing CF is even stronger because the bandwidth was increased too. This probably leads to a more compact period histogram of neural discharges (i.e., more neural synchrony), which may contribute to the higher ITD sensitivity. Actually, our stimuli were designed to yield a constant stimulation range on the basilar membrane. By doing this we hoped to stimulate approximately constant amounts of neurons for different CFs. Our results indicate that stimuli with such a bandwidth *almost* compensate for the CF effect observed with SAM and transposed tones. Nevertheless, this is not necessarily at odds with Bernstein and Trahiotis' (2002) conjecture of a frequency dependency in central processing stages. It still may be the case that the sharper envelopes associated with a roughly constant ERB-rate of our stimuli simply compensate for the hypothesized sensitivity decrease in higher ITD processing stages. It is also worth mentioning that the slightly better ITD sensitivity at CF4.6 may be just because the subjects were trained exactly at this CF.

In electric hearing, the place (electrode) has no systematic effect on the width of excitation patterns (Cohen *et al.*, 2003) and therefore, a constant stimulation range is assumed along the tonotopy. With respect to ITD sensitivity, van Hoesel *et al.* (2002) tested in one CI listener at two different tonotopic places and they did not find any difference in JNDs. However, Litovsky *et al.* (2005) showed an effect of place on ITD sensitivity in electric stimulation, although it was not consistent across all subjects and the most plausible explanation may be the place-dependent survival of neurons

(dead regions). Hence, the frequency dependencies in higher processing stages postulated for acoustic hearing could not be shown yet in electric hearing.

Carlyon and Deeks (2002) tested the detectability of dynamic ITDs using bandpass-filtered pulse trains at different CFs. Two of their CFs correspond to our CF4.6 and CF9.2 and for these CFs, they used exactly the same bandwidths as we did. They tested with a 300-Hz *alternating* phase complex, which corresponds to our pulse rate of 600 pps. From the point of view of the monaural stimulus configuration, this is the best-comparable study. However, Carlyon and Deeks (2002) tested a different task: at one ear, they presented signals with a fixed rate and, at the contralateral ear, they presented signals with a fixed but different rate. In such a stimulus, the rate difference creates a dynamic ITD, which periodically bounces between the positive and the negative IPI. In that study, the duration and the rate differences were fixed in such a way that the ITD varied from 0 to at least 413 μs (in terms of increase and decrease) depending on the rate difference. This yields a kind of moving, blurred, or diffuse binaural image, depending on the bouncing rate relative to the limit of binaural sluggishness (Blauert, 1972). In particular, such detection of dynamic ITD corresponds to an incoherence detection task, for which the performance is found to be based on the size of interaural fluctuations (Goupell and Hartmann, 2006). An interesting aspect of Carlyon and Deeks (2002) with respect to our study is that they used exactly the same bandwidth as we do, but they obtained a higher performance then we did. For CF4.6, in their study, all four subjects showed sensitivity to ITD ($d' \geqslant 1$), while in our study for 588 pps, all subjects performed primarily at chance. For CF9.2, in their study, one of three subjects still showed sensitivity to ITD, whereas, in our study, for 588 pps, none of the five subjects performed consistently above the chance. However, their better ITD sensitivity may result from the fact that in general, listeners are extremely sensitive to changes from coherent signals to slightly-incoherent signals (Gabriel and Colburn, 1981), which may have been the main cue in their task. Nevertheless, their outcome validates our finding of a high ITD sensitivity even at CFs as high as 9.6 kHz and supports our further findings about auditory filtering (see Sec. IV D).

C. Effect of the pulse rate

The results show a strong effect of pulse rate. The median rate limit, which is the highest rate yielding a valid JND, is 500 pps. For transposed tones, Bernstein and Trahiotis (2002) found a rate limit of 256 Hz at 4 kHz, which decreased to 128 Hz at 10 kHz. The lower rate limit at 10 kHz may result from floor effects in the performance because their JNDs for 10 kHz were generally higher than the JNDs for lower CFs even at the lowest rate (32 Hz). For CF4.6, Laback *et al.* (2007) found a limit of 200 pps, which is, again, lower than ours. This is probably an effect of overall lower performance resulting from using much shorter stimuli. Majdak *et al.* (2006) tested NH subjects for pulse rates of 400, 600, 800, and 938 pps using stimuli of 300 ms duration, which is the same as in our study. From their Fig. 7, JNDs can be estimated by applying a 70%-threshold to their P_c-data. This way, the JND can be determinated for the rate of 400 pps only. For the next higher rate tested, 600 pps, the JND is not determinable. Thus, their rate limit is higher than 400 pps and lower than 600 pps, which is in agreement with the results of the present study.

In CI listeners, according to Majdak *et al.* (2006), the rate limitation varied between 100 and 800 pps, depending on the subject. Laback *et al.* (2007) found similar rate limits in CI listeners, again varying between 100 and 800 pps across the subjects. In van Hoesel and Tyler (2003) and van Hoesel (2007), ITD sensitivity of eight CI listeners in total was tested under several conditions. Their rate limit ranges from 100 to 600 pps.

Generally, it appears that CI listeners show sometimes a lower and sometimes a higher rate limit than NH listeners. However, both van Hoesel (2007) and we found individual rate limits, which are equal or higher than those in NH listeners. It appears that the average rate limit (over the subject group tested) is similar for both groups, with the difference that the CI listeners' data show much higher variability. The origin for the strong subject dependence found in the CI-studies is still unclear. However, the existence of CI listeners who show higher rate limits than NH listeners indicates that the lower rate limit found in other CI listeners is not a general property of electric stimulation. On the contrary, the sometimes higher rate limits in CI listeners suggest the existence of different limiting mechanisms in the two listener groups, for example, a lower degree of phase locking in acoustic hearing (Abbas, 1993).

D. Rate limit: Effect of auditory filtering?

Let us return now to the main question posited in this study: does auditory filtering affect the rate limit in ITD perception? Considering CF as the only parameter, an increase in ITD sensitivity with increasing CF would argue for an effect of auditory filtering. However, this can be overshadowed by the effects of changing bandwidths, changing absolute thresholds, or even differences in neural processing when CF of the stimulus changes. Thus, a decreasing performance with increasing CF does not rule out a possible effect of auditory filtering. The impact of auditory filtering can be revealed by also varying the pulse rate: with increasing pulse rate, auditory filtering smears the timing information more and more and reduces the envelope sharpness. Thus, if auditory filtering is responsible for the rate limit, this limit should increase with CF. In the statistical analysis of our data, a significant interaction between pulse rate and CF would support such an effect. In fact, two different statistical analyses showed no such interaction ($p > 0.415$) between pulse rate and CF, suggesting no effect of auditory filtering. Thus, our data provide no evidence that the choice of the CF affects the rate limit in ITD perception.

This conclusion is in agreement with the study of Carlyon and Deeks (2002), who compared rate discrimination between monaural and binaural conditions at the rate corresponding to our 600 pps (see Sec. IV B.). They concluded that, even for such a high rate, there is sufficient temporal

information in the auditory periphery, which can be used by the binaural system. This implies that auditory filtering is not the rate limiting factor in ITD perception.

However, such a general conclusion is limited by the methods we used. It could still be the case that the power of our statistics was too small to reveal an effect. The across-channel integration may have concealed some differences in performance, preventing us from finding an effect. We tested only five subjects, thus, there is a chance that auditory filtering affects the rate limit in a subpopulation which was not tested in this study. Furthermore, a possible CF dependency in the more central processing stages of the brain may compensate for the effect we are looking for.

An alternative explanation for the rate limit could be a consequence of a limitation in higher stages of auditory processing. It may be explained by neural effects in terms of a binaural adaptation mechanism, which seems to affect ITD sensitivity at higher pulse rates when periodic pulse trains are used (Hafter and Dye, 1983). This topic still requires more investigation. For example, as shown in Laback and Majdak (2008) for CI listeners and in Goupell *et al.* (2008) for NH listeners, the temporal structure of stimuli plays an important role in the rate limitation mechanism in ITD perception at higher rates.

Finally, one of our aims was to validate the comparisons between the electric and acoustic rate limits in Majdak *et al.* (2006) and Laback *et al.* (2007). Based on our results, we conclude that those comparisons were not affected by the particular choice of the CF in the acoustic CI simulation.

V. SUMMARY AND CONCLUSIONS

This study investigated the effects of rate and center frequency on ongoing *envelope* ITD sensitivity. With increasing center frequency, the bandwidth of our stimuli was co-varied, aiming at an almost constant stimulation range on the basilar membrane. The results show a decrease in sensitivity when the CF is increased from 4.6 to 9.2 kHz. Compared to studies with a constant bandwidth, our stimuli yielded a relatively *small* effect of CF on ITD sensitivity. Further, ITD sensitivity decreased with increasing rate, showing a median limit at 500 pps. No interaction between the effects of rate and CF could be found. This suggests that the rate limitation is not caused by the ringing of auditory filters. Thus, there is no indication that the comparison of rate limits between electric stimulation and acoustic CI simulation is affected by auditory filtering. It is conjectured that in both acoustic and electric hearing, different mechanisms such as phase locking or some higher stages in the binaural processing are responsible for the upper rate limit in ITD perception.

ACKNOWLEDGMENTS

We are indebted to our test persons for their patience while performing the longsome tests. We are grateful to Matt Goupell for helpful comments on this manuscript. Also, we thank Bob Carlyon and two anonymous reviewers for their suggestions to improve this manuscript. This study was supported by the Austrian Academy of Sciences and in part by the Austrian Science Fund (P18401-B15).

TABLE II. Results from separate ANOVAs applying different assumptions for ND JND replacements. Significant effects ($p<0.05$) are shown in bold. "ND JND" describes the replacement for a non-determinable JND (see Appendix).

ND JND	p (CF)	p (pulse rate)	p (CF × pulse rate)
Excluded	0.0859	**<0.0001**	0.9826
630 μs	**0.0414**	**<0.0001**	0.5045
$\frac{1}{4}$ IPI	**0.0373**	**<0.0001**	0.8050
max(JND)	0.0545	**<0.0001**	0.9722
10 ms	0.2327	**<0.0001**	0.2776

APPENDIX

In some cases, mostly for the higher pulse rates, the psychometric functions did not reach 70% for all tested ITD values and the JNDs could not be determined. This appendix shows the problem of including conditions with ND JNDs in an RM ANOVA.

The RM ANOVA is usually performed on all data. However, conditions with ND JNDs cannot be included in the analysis. In the ANOVA model, those conditions are treated as "no information given," leading to a condition matrix not of full rank. This results in a lower test power of the ANOVA. To compensate for this problem, the ND JND conditions can be replaced by a hypothetical JND value, forcing the ANOVA to treat these conditions as if they were measured, even though no sensitivity was found. Thus, the ND JND replacement should be of a sufficiently high magnitude.

We analyzed the JND data using the RM ANOVA under different conditions. The different conditions correspond to the results presented in Table II. In the first ANOVA we excluded the ND JND conditions, taking into account having a condition matrix not of full rank (condition *excluded* in Table II). In the following ANOVAs, we included the ND JND conditions and each ANOVA was performed with a different ND JND replacement. In the second ANOVA, the ND JNDs were set to 630 μs (condition 630 μs), which corresponds to the natural ITD for lateral sounds for an average subject (Blauert, 1997). In the third ANOVA, the ND JNDs were set to $\frac{1}{4}$ IPI (condition $\frac{1}{4}$ IPI), assuming that this yields maximal sensitivity for the ongoing ITD cue (Majdak *et al.*, 2006). In the fourth ANOVA, the ND JNDs were set to the highest JND derived for each subject and CF [condition max (JND)]. These values ranged from 125 to 585 μs. In the fifth and last ANOVA, the ND JNDs were set to 10 ms (an approximation of infinity, which could not be used due to technical limitations). This was the condition 10 ms. All ANOVA results are presented in Table II. The effect of CF is just significant and not significant ($0.0373 \leqslant p \leqslant 0.2327$), depending on the choice for the ND JND replacement. The main effect of the pulse rate is always significant ($p<0.0001$) and the interaction between CF and pulse rate is not significant for all analyses ($p>0.2776$). The comparison of different ND JND replacements clearly shows that inclusion of the ND JND conditions in the ANOVA is problematic and the

results depend strongly on the choice of the ND JND replacement.

A straight forward solution is to exclude ND JND conditions from the analysis. However, this leads to a low test power for at least two reasons. First, for the higher pulse rates, only a small amount of data is available for all subjects. Unfortunately, this is the range of pulse rates where we expect an effect of CF and which needs to be well represented by the data. Second, at lower pulse rates, although the data are available for all subjects, the test power of the ANOVA is reduced using the concept of the JND. Performing the ANOVA on JNDs implies comparing only one sample of data per condition and subject. This reduces the test power compared to the analysis based on P_c scores: they are represented by three to five samples per condition and subject.

Furthermore, the concept of the sigmoidal psychometric function is questionable in our study. This model requires a stimulus variable which, under certain conditions, can always be detected (a small observer lapse is allowed; Wichmann and Hill, 2001b). Said another way, the function range should be between 50% and 100% in our discrimination task. This is not always the case: performance in the ND JND conditions never reached 70%. Furthermore, for conditions with determinable JNDs, it cannot be ensured that increasing ITD would lead to $P_c=100\%$ (e.g., NH8, CF4.6, 588 pps). For example, Majdak *et al.* (2006) showed more general results for ongoing ITD, which were above 70%-threshold but never reached 100% (their Fig. 7, left upper panel). These results show that sigmoidal psychometric functions are not an appropriate model for the statistical analysis of such an effect. Thus, given the absence of an adequate model for our ITD data, only the statistical analyses of the P_c data are appropriate. Nevertheless, the estimated JNDs remain important to facilitate the interpretation of the results and for a comparison to the literature.

[1]Besides the rate, various other aspects of the temporal envelope may be important for envelope ITD perception, namely, modulation depth, duty-cycle, and slope steepness. We use the term "sharpness" to refer to all these aspects.

[2]The required condition is between stimulus levels near thresholds with modulation frequencies below 250 Hz and low spontaneous discharge rate.

[3]The five CI listeners from both studies showed rate limits of 100, 100, 400, 800, and 800 pps, respectively.

[4]The actual values for the ITDs were integer multiples of the sampling interval of 10.4 μs. Thus, the lowest ITD value tested was 20.8 μs, and the highest ITD value tested was 395.8 μs.

[5]Notice that, according to Moore and Glasberg (1983), the formula for ERB-rate calculation is based on data collected up to 6.5 kHz only.

[6]More recent study (Wiegrebe and Patterson, 1999) suggests that the level of quadratic distortion products may be higher than the levels of combination tones as suggested by Goldstein (1967).

[7]For one subject, NH9, only three ITDs were tested.

[8]Three exceptions are given for NH9: (1) for 541 pps, he was tested at CF4.6 only because his performance was at chance already for 500 pps at higher CFs; (2) for 400 pps, we have data for CF4.6 and CF6.5 only; and (3) for 450 pps, we have data for CF6.5 and CF9.2 only.

[9]Using PSIGNIFIT version 2.5.41 (see http://bootstrap-software.org/psignifit/), a software package for fitting psychometric functions to psychophysical data (Wichmann and Hill, 2001b).

[10]They calculated 65%-JNDs, while we calculated 70%-JNDs.

Abbas, P. J. (**1993**). "Electrophysiology," in *Cochlear Implants: Audiological Foundations*, edited by R. S. Tyler (Singular, San Diego).

Bernstein, L. R. (**2001**). "Auditory processing of interaural timing information: New insights," J. Neurosci. Res. **66**, 1035–1046.

Bernstein, L. R., and Trahiotis, C. (**1994**). "Detection of interaural delay in high-frequency sinusoidally amplitude-modulated tones, two-tone complexes, and bands of noise," J. Acoust. Soc. Am. **95**, 3561–3567.

Bernstein, L. R., and Trahiotis, C. (**2002**). "Enhancing sensitivity to interaural delays at high frequencies by using "transposed stimuli"," J. Acoust. Soc. Am. **112**, 1026–1036.

Bernstein, L. R., Trahiotis, C., and Hyde, E. L. (**1998**). "Inter-individual differences in binaural detection of low-frequency or high-frequency tonal signals masked by narrow-band or broadband noise," J. Acoust. Soc. Am. **103**, 2069–2078.

Blauert, J. (**1972**). "On the lag of lateralization caused by interaural time and intensity differences," Audiology **11**, 265–270.

Blauert, J. (**1997**). *Spatial Hearing*, 2nd ed. (MIT, Cambridge, MA).

Buell, T. N., and Hafter, E. R. (**1991**). "Combination of binaural information across frequency bands," J. Acoust. Soc. Am. **90**, 1894–1900.

Buell, T. N., and Trahiotis, C. (**1993**). "Interaural temporal discrimination using two sinusoidally amplitude-modulated, high-frequency tones: Conditions of summation and interference," J. Acoust. Soc. Am. **93**, 480–487.

Carlyon, R. P., and Deeks, J. M. (**2002**). "Limitations on rate discrimination," J. Acoust. Soc. Am. **112**, 1009–1025.

Carlyon, R. P., van Wieringen, A., Long, C. J., Deeks, J. M., and Wouters, J. (**2002**). "Temporal pitch mechanisms in acoustic and electric hearing," J. Acoust. Soc. Am. **112**, 621–633.

Cohen, L. T., Richardson, L. M., Saunders, E., and Cowan, R. S. C. (**2003**). "Spatial spread of neural excitation in cochlear implant recipients: comparison of improved ECAP method and psychophysical forward masking," Hear. Res. **179**, 72–87.

Dreyer, A., and Delgutte, B. (**2006**). "Phase locking of auditory-nerve fibers to the envelopes of high-frequency sounds: implications for sound localization," J. Neurophysiol. **96**, 2327–2341.

Gabriel, K. J., and Colburn, H. S. (**1981**). "Interaural correlation discrimination: I. Bandwidth and level dependence," J. Acoust. Soc. Am. **69**, 1394–401.

Goldstein, J. L. (**1967**). "Auditory nonlinearity," J. Acoust. Soc. Am. **41**, 676–689.

Goupell, M. J., and Hartmann, W. M. (**2006**). "Interaural fluctuations and the detection of interaural incoherence: Bandwidth effects," J. Acoust. Soc. Am. **119**, 3971–3986.

Goupell, M. J., Laback, B., and Majdak, P. (**2009**). "Enhancing sensitivity to interaural time differences at high modulation rates by introducing temporal randomness" (in press).

Greenwood, D. D. (**1961**). "Critical bandwidth and the frequency coordinates of the basilar membrane," J. Acoust. Soc. Am. **33**, 1344–1356.

Greenwood, D. D. (**1990**). "A cochlear frequency-position function for several species—29 years later," J. Acoust. Soc. Am. **87**, 2592–2605.

Griffin, S. J., Bernstein, L. R., Ingham, N. J., and McAlpine, D. (**2005**). "Neural sensitivity to interaural envelope delays in the inferior colliculus of the guinea pig," J. Neurophysiol. **93**, 3463–3478.

Hafter, E. R., and De Maio, J. (**1975**). "Difference thresholds for interaural delay," J. Acoust. Soc. Am. **57**, 181–187.

Hafter, E. R., and Dye, R. H. J. (**1983**). "Detection of interaural differences of time in trains of high-frequency clicks as a function of interclick interval and number," J. Acoust. Soc. Am. **73**, 644–651.

Henning, G. B. (**1974**). "Detectability of interaural delay in high-frequency complex waveforms," J. Acoust. Soc. Am. **55**, 84–90.

Kuba, H., Yamada, R., Fukui, I., and Ohmori, H. (**2005**). "Tonotopic specialization of auditory coincidence detection in nucleus laminaris of the chick," J. Neurosci. **25**, 1924–1934.

Laback, B., and Majdak, P. (**2008**). "Binaural jitter improves interaural-time difference sensitivity of cochlear implantees at high pulse rates," Proc. Natl. Acad. Sci. U.S.A. **105**, 814–817.

Laback, B., Majdak, P., and Baumgartner, W. (**2007**). "Lateralization discrimination of interaural time delays in four-pulse sequences in electric and acoustic hearing," J. Acoust. Soc. Am. **121**, 2182–2191.

Liang, L., Lu, T., and Wang, X. (**2002**). "Neural representations of sinusoidal amplitude and frequency modulations in the primary auditory cortex of awake primates," J. Neurophysiol. **87**, 2237–2261.

Litovsky, R., Agrawal, S., Jones, G., Henry, B., and Van Hoesel, R. (**2005**). "Effect of Interaural electrode pairing on binaural sensitivity on bilateral cochlear implant users," presented at the 28th MidWinter Meeting of the

Association for Research in Otolaryngology, New Orleans, LA.
Macpherson, E. A., and Middlebrooks, J. C. (**2002**). "Listener weighting of cues for lateral angle: The duplex theory of sound localization revisited," J. Acoust. Soc. Am. **111**, 2219–2236.
Majdak, P., Laback, B., and Baumgartner, W. (**2006**). "Effects of interaural time differences in fine structure and envelope on lateral discrimination in electric hearing," J. Acoust. Soc. Am. **120**, 2190–2201.
McFadden, D., and Pasanen, E. G. (**1976**). "Lateralization of high frequencies based on interaural time differences," J. Acoust. Soc. Am. **59**, 634–639.
McKay, C. M., and Carlyon, R. P. (**1999**). "Dual temporal pitch percepts from acoustic and electric amplitude-modulated pulse trains," J. Acoust. Soc. Am. **105**, 347–357.
Middleton, J. W., Longtin, A., Benda, J., and Maler, L. (**2006**). "The cellular basis for parallel neural transmission of a high-frequency stimulus and its low-frequency envelope," Proc. Natl. Acad. Sci. U.S.A. **103**, 14596–14601.
Moore, B. C., and Glasberg, B. R. (**1983**). "Suggested formulae for calculating auditory-filter bandwidths and excitation patterns," J. Acoust. Soc. Am. **74**, 750–753.
Nuetzel, J. M., and Hafter, E. R. (**1976**). "Lateralization of complex waveforms: Effects of fine structure, amplitude, and duration," J. Acoust. Soc. Am. **60**, 1339–1346.
Nuetzel, J. M., and Hafter, E. R. (**1981**). "Discrimination of interaural delays in complex waveforms: Spectral effects," J. Acoust. Soc. Am. **69**, 1112–1118.
Patterson, R. D., Robinson, K., Holdsworth, J. W., McKeown, D., Zhang, C., and Allerhand, M. (**1992**). "Complex sounds and auditory images," in *Auditory Physiology and Perception*, edited by Y. Cazals, L. Demany, and K. Horner (Pergamon, Oxford).
Shackleton, T. M., Skottun, B. C., Arnott, R. H., and Palmer, A. R. (**2003**). "Interaural time difference discrimination thresholds for single neurons in the inferior colliculus of Guinea pigs," J. Neurosci. **23**, 716–724.
Sherbecoe, R. L., and Studebaker, G. A. (**2004**). "Supplementary formulas and tables for calculating and interconverting speech recognition scores in transformed arc-sine units," Int. J. Audiol. **43**, 442–448.
Skottun, B. C., Shackleton, T. M., Arnott, R. H., and Palmer, A. R. (**2001**). "The ability of inferior colliculus neurons to signal differences in interaural delay," Proc. Natl. Acad. Sci. U.S.A. **98**, 14050–14054.
Stellmack, M. A., Viemeister, N. F., and Byrne, A. J. (**2005**). "Discrimination of interaural phase differences in the envelopes of sinusoidally amplitude-modulated 4-kHz tones as a function of modulation depth," J. Acoust. Soc. Am. **118**, 346–352.
van Hoesel, R. J. M. (**2007**). "Sensitivity to binaural timing in bilateral cochlear implant users," J. Acoust. Soc. Am. **121**, 2192–2206.
van Hoesel, R. J. M., and Tyler, R. S. (**2003**). "Speech perception, localization, and lateralization with bilateral cochlear implants," J. Acoust. Soc. Am. **113**, 1617–1630.
van Hoesel, R. J., Ramsden, R., and Odriscoll, M. (**2002**). "Sound-direction identification, interaural time delay discrimination, and speech intelligibility advantages in noise for a bilateral cochlear implant user," Ear Hear. **23**, 137–149.
Wichmann, F. A., and Hill, N. J. (**2001a**). "The psychometric function: II. Bootstrap-based confidence intervals and sampling," Percept. Psychophys. **63**, 1314–1329.
Wichmann, F. A., and Hill, N. J. (**2001b**). "The psychometric function: I. Fitting, sampling, and goodness of fit," Percept. Psychophys. **63**, 1293–1313.
Yin, T. C., Kuwada, S., and Sujaku, Y. (**1984**). "Interaural time sensitivity of high-frequency neurons in the inferior colliculus," J. Acoust. Soc. Am. **76**, 1401–1410.
Zhang, Y., and Wright, B. A. (**2007**). "Similar patterns of learning and performance variability for human discrimination of interaural time differences at high and low frequencies," J. Acoust. Soc. Am. **121**, 2207–2216.
Zwislocki, J., and Feldman, R. S. (**1956**). "Just noticeable differences in dichotic phase," J. Acoust. Soc. Am. **28**, 860–864.
Wiegrebe, L., and Patterson, R. D. (**1999**). "Quantifying the distortion products generated by amplitude-modulated noise," J. Acoust. Soc. Am. **106**, 2709–2718.

A recency effect in sound localization?

G. Christopher Stecker[a)]
Department of Speech and Hearing Sciences, University of Washington, 1417 NE 42nd Street, Seattle, Washington 98105

Ervin R. Hafter
Department of Psychology, University of California at Berkeley, 3210 Tolman Hall No. 1650, Berkeley, California 94720

(Received 10 June 2008; revised 17 March 2009; accepted 31 March 2009)

In a free-field pointing task, listeners localized trains of 4–32 spatially distributed Gabor clicks (narrowband impulses) centered at 4-kHz carrier frequency and repeating at an interval of 5 ms. Multiple regression coefficients estimated the perceptual "weight" applied to each click in a train during location judgments. Temporal weighting functions obtained in this way exhibited two key features: onset dominance, as evidenced by high weight on the initial click, and "upweighting" of late-arriving sound, as evidenced by weights that gradually increased over the duration of each click-train. Across all tested click-train durations, and despite randomly varying the durations from trial to trial, the greatest post-onset weights were consistently found for clicks at or near the offset. The results imply a special importance of late-arriving sound rather than feedforward recovery from onset dominance, and are broadly consistent with recency effects resulting from temporal integration. © *2009 Acoustical Society of America.* [DOI: 10.1121/1.3124776]

PACS number(s): 43.66.Qp, 43.66.Pn, 43.66.Mk [RLF] Pages: 3914–3924

I. INTRODUCTION

According to Rayleigh's duplex theory (Strutt, 1907), azimuthal localization of high-frequency ($>\approx$2-kHz) sound relies primarily on interaural level differences (ILDs); sensitivity to interaural time difference (ITD) is reduced at these frequencies, due in part to ambiguous correspondences of tone phase at the two ears. For modulated high-frequency sounds, however, localization may utilize ITD carried by temporal envelopes ("envelope ITD"). Over the past several decades, numerous studies have investigated important questions such as whether sensitivity to envelope ITD is similar or inferior to fine-structure ITD at low frequencies and over what range of modulation frequencies envelope-ITD sensitivity is evidenced (see, e.g., Henning, 1974; McFadden and Pasanen, 1975, 1976; Nuetzel and Hafter, 1976). Two relatively recent findings are of special interest. First, envelope-ITD sensitivity at high frequency can be similar to fine-structure ITD at low frequency, at least for sounds with temporally interrupted modulators, such as trains of filtered impulses (Hafter and Dye, 1983; Hafter and Buell, 1990) or "transposed tones" (van de Par and Kohlrausch, 1997). Second, psychophysical and physiological sensitivity to ongoing envelope ITD in high-frequency sounds is significantly impaired at modulation rates above 150–200 Hz. At these rates, discrimination of ongoing envelope-ITD information becomes difficult or impossible in the absence of onset ITD (e.g., when the stimulus is slowly gated on at both ears; Bernstein and Trahiotis, 2002). When onset cues are available, this rate-limitation manifests as increased reliance on onset ITD and diminished influence of ongoing ITD (Hafter and Dye, 1983; Saberi, 1996). The affected modulation rates and other characteristics of this *onset dominance* (cf. Freyman *et al.*, 1997) call to mind a range of closely related binaural phenomena including binaural adaptation (Hafter and Dye, 1983; Hafter, 1997), the precedence effect (Wallach *et al.*, 1949), and the Franssen effect (Franssen, 1962; Hartmann and Rakerd, 1989).

The relative contributions of onset and ongoing envelope ITD have been assessed using a variety of methods (Tobias and Schubert, 1959; Abel and Kunov, 1983; Buell *et al.*, 1991; Saberi and Perrott, 1995; Buell *et al.*, 2008). A particularly illuminating approach has been to measure the relative sensitivity of listeners' localization responses to alterations of the spatial cues contained in each temporal portion of the stimulus (e.g., each click in a train of clicks). Plotting the relative sensitivity over time gives a temporal weighting function (TWF) for each stimulus. For example, Stecker and Hafter (2002) presented trains of filtered clicks from loudspeakers in the free-field, varying the location randomly from click to click within each presentation. Following previous studies that used similar techniques to estimate spectral and temporal weights in tone detection and discrimination tasks (Berg, 1989; Richards and Zhu, 1994; Lutfi, 1995; Sadralodabai and Sorkin, 1999), the authors used multiple linear regression of listeners' pointing responses onto the individual click locations to estimate TWFs for click-trains varying in rate. Consistent with previous and subsequent reports, the TWFs indicated strong onset dominance (in the form of increased weight on click 1) for click rates at or above 200 Hz (interclick intervals [ICIs] $<=$5 ms). This finding was similar for trains of 2 or 16 clicks and agreed closely with TWFs measured in previous studies of stimuli varying only in ITD (Shinn-Cunningham *et al.*, 1993, 1995;

a)Author to whom correspondence should be addressed. Electronic mail: cstecker@u.washington.edu

 0001-4966/2009/125(6)/3914/11/$25.00

Saberi, 1996; Dizon *et al.*, 1998; Stellmack *et al.*, 1999). Different from those prior studies was the additional finding that late portions of the stimulus (clicks at or near the offset) were weighted more strongly than intermediate portions—although a similar result was recently reported for virtual-space localization in the vertical plane (Macpherson and Wagner, 2008). This upweighting of late-arriving sound is intriguing because it suggests that the temporal integration of auditory spatial information could be sensitive to the nature of that information, the behavioral requirements of the experimental task, or both.

Among several candidate explanations for the upweighting of late-arriving sound, the most straightforward is that upweighting simply reflects recovery from onset dominance. In the current report, we describe an experiment that tests this explanation via two closely related hypotheses: a "fixed-recovery" hypothesis in which the recovery time is fixed to a specific duration or number of clicks and an "anticipatory-recovery" hypothesis in which the recovery time adjusts according to the stimulus context. That might allow the system to anticipate stimulus durations when predictable and recover sensitivity to spatial cues contained in the stimulus offset. Note that "anticipation" of stimulus durations might require durations to be highly predictable (e.g., as when the duration is fixed across blocks of trials) or might instead adjust quickly in response to local trial-by-trial variation in stimulus duration. In the first case (global predictability) anticipation should be thwarted (and upweighting reduced) by sufficient randomization of stimulus durations (condition 1 of the current study), while in the second case (local predictability), recovery would not be completely thwarted by randomization but would vary depending on whether stimulus durations do or do not repeat from trial to trial (condition 2). The current study tests these possibilities by measuring TWFs over a range of stimulus durations that vary from trial to trial.

II. METHODS

Details of the experimental apparatus, configuration, and analysis used here were previously described by Stecker and Hafter (2002). Additional details regarding the apparatus and basic temporal-weighting analysis can be found in that paper.

A. Subjects

Four subjects participated in this experiment. One (CS) was the first author; others were paid subjects naive to the purpose of the experiments. Three of the subjects were tested in condition 1 and two in condition 2 (see Secs. II D and II H, below). All subjects had normal audiograms (pure-tone thresholds $<$10-dB hearing loss (HL)) between 125 and 8000 Hz.

B. Stimuli

Stimuli were trains of narrowband Gabor clicks (Gaussian-windowed tone bursts) sampled at 50 kHz. Each click consisted of a 4-kHz cosine multiplied by a Gaussian temporal envelope with σ equal to 212 μs.[1] The resulting spectral envelope was Gaussian with σ=750 Hz (half-maximal bandwidth $\approx$1.8 kHz). Trains of 4, 8, 16, or 32 such clicks were synthesized with a peak-to-peak ICI of 5 ms. This ICI was chosen for its combination of clear upweighting and similarly clear (though moderate) onset dominance in the data of Stecker and Hafter (2002). Stimulus level, measured from the listener's position with a continuous train of clicks at 5-ms ICI, was approximately 35-dB sound pressure level (SPL) (A-weighted, "fast" setting) and clearly audible for all subjects.

C. Apparatus

Listeners were seated in an anechoic chamber (Eckel Corp., $8.3\times5.4\times4.0$ m^3), facing an array of 12 ear-height loudspeakers (Audax model MHD12P25 FSM-SQ) separated by 5.5° each and spanning 60.5° in listener-centered azimuth. Loudspeakers were equalized through digital inverse-filtering (frequency distortion within $\pm$1 dB over the range 2–6 kHz), delay, and attenuation to eliminate spectral and path-length differences between speakers. Loudspeakers were obscured visually by an acoustically-transparent white curtain 42 in. in front of the listener.

D. Stimulus presentation and listeners' task

On each trial, a location within the loudspeaker array was selected at random. This location defined the center of a group of five adjacent loudspeakers spanning 22° azimuth. (Thus, there were eight unique loudspeaker groups within the 12-loudspeaker array; group centers spanned the central 37.5° of azimuth.) Each of the 4–32 clicks comprising the click-train stimulus was presented from one loudspeaker in the group, selected randomly for each click. This random variation in location across clicks in the train allows the computation of observer weights for each click.

At the beginning of each trial, subjects faced the loudspeaker array with head still as a stimulus was presented from one of the eight potential loudspeaker groups. Next, subjects directed their gaze (without moving their heads) to foveate the perceived location. Next, they recorded a localization response by marking the point of gaze with a hand-directed laser pointer, the orientation of which was recorded digitally and converted to head-centered coordinates for analysis. This procedure was employed in order to maintain a head-centered coordinate system for responses, avoiding confusion related to mapping from laser-pointer orientation to sound-source position in three-dimensional space. In the event that more than one acoustic image was perceived, subjects were instructed to respond to the leftmost image.[2] Following each response, subjects returned the laser spot to "home" position (head-centered elevation $>$28°, azimuth 0° $\pm$ 17°) to initiate the next trial after a 1-s delay. Each experimental run consisted of 100 uninterrupted trials. Subjects were allowed to take breaks between runs and completed between 7 (subject LS) and 16 (all other subjects) runs per condition.

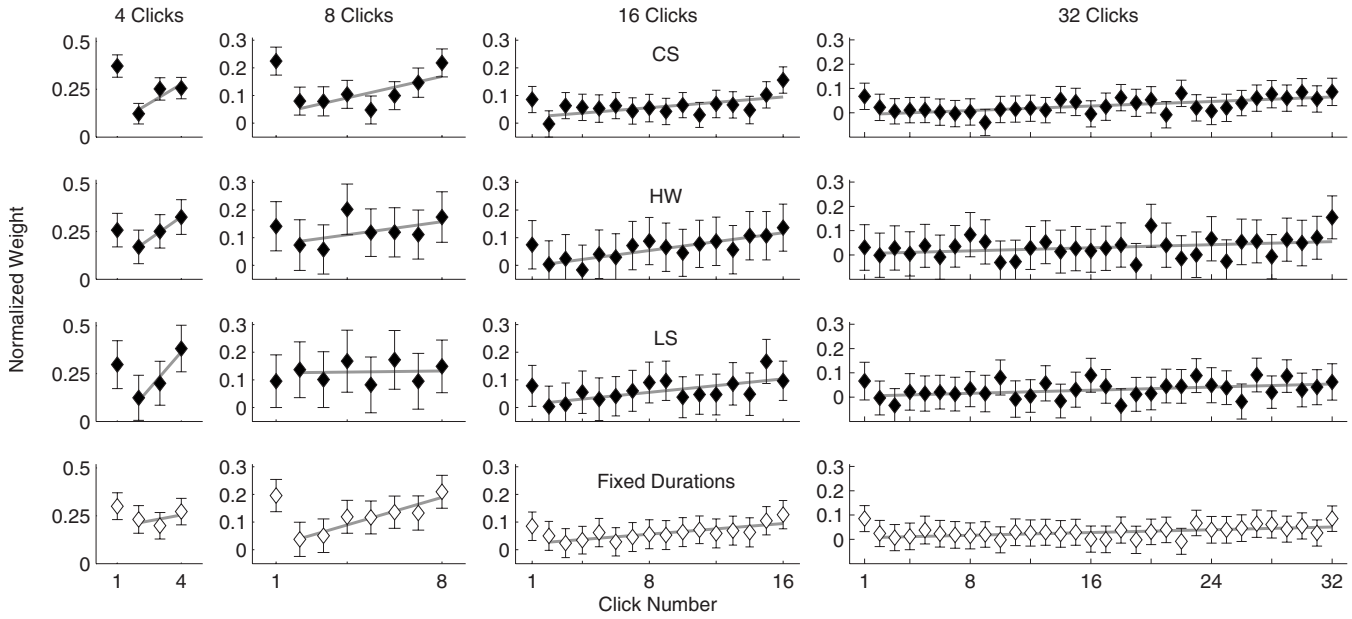

FIG. 1. Normalized weights for click-trains. Upper three rows (filled symbols) plot TWFs for individual subjects, with train length N varied from trial to trial (condition 1). Bottom row (open symbols) plots comparison data obtained with train length N fixed across trials in a block (adapted from Stecker, 2000; Stecker and Hafter, 2002). Columns plot TWFs for trains of 4 (left column), 8, 16, or 32 (right column) clicks. Error bars indicate 95% confidence intervals on weight estimates, and gray lines indicate best linear fit to weights of clicks 2–N.

E. Temporal weighting analysis

The perceptual weights applied to each click in a train were estimated using multiple linear regression of listener response azimuth θ_R onto the azimuths of individual clicks θ_i:

$$\hat{\theta}_R = \sum_{i=1}^{N} b_i \theta_i + k. \tag{1}$$

For comparison across subjects and conditions, regression coefficients b_i were normalized to sum to 1 over each stimulus duration

$$w_i = \frac{b_i}{\sum_{j=1}^{N} b_j} \tag{2}$$

with the resulting normalized weights w_i indicating each click's *relative* influence on the listener's response. Individual weights thus vary from 0 (indicating no linear relationship between click location and response) to 1 (indicating a strong linear relationship). Plots of w_i weights vs click number comprise the TWFs and indicate how click effectiveness varies over the stimulus duration. Figures 1 and 3 plot normalized TWFs for each listener, along with 95% confidence intervals on each normalized weight (Stecker and Hafter, 2002). Figure 5 plots across-subject means of these normalized TWFs.

A reasonable strategy for this task would place equal weight on each click since all clicks are equally informative with regard to the stimulus location. For a discrimination task, such a strategy can be considered *optimal* because the effective variance of a location estimate is reduced by equal averaging across multiple clicks in a train (Saberi, 1996). Unequal weighting, in contrast, is sub-optimal because it reduces this benefit (effectively averaging over a smaller number of clicks). A similar argument for the effectiveness of an equal-weighting strategy can be made for localization in the free-field, although "optimality" is not well-defined for this task.

F. Measures of upweighting

We quantified the degree of upweighting in each TWF in two different ways. The first approach was based on the *average ratio* (AR) originally defined by Saberi (1996) as the ratio of onset click weight to the average of post-onset click weights. We chose to use AR over Saberi's *precedence ratio* (ratio of onset weight to sum of remaining weights) because AR more appropriately facilitates comparison across stimuli differing in click number. For the purposes of this study, we redefined AR as the ratio of onset or offset weight to the mean of intermediate weights (i.e., the mean excluding onset and offset clicks):

$$\mathrm{AR}_{\mathrm{onset}} = \frac{w_1}{\sum_{i=2}^{N-1} w_i/(N-2)} \tag{3}$$

or

$$\mathrm{AR}_{\mathrm{offset}} = \frac{w_N}{\sum_{i=2}^{N-1} w_i/(N-2)}. \tag{4}$$

The second approach we used to quantify upweighting reflects the apparently gradual increase in weights reported by Stecker and Hafter (2002). We used linear regression to fit straight lines through weights 2–N, separately for each subject and condition. Residuals were examined for approximately uniform distribution and did not indicate any clear nonlinear trends. For plotting, slope values were converted to *rise* (slope multiplied by the range of clicks used for fitting), an estimate of the difference between offset and click 2 that

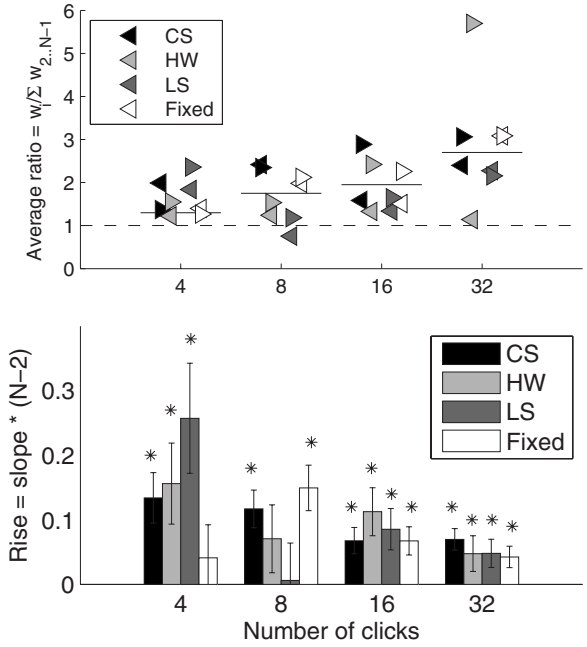

FIG. 2. Top: AR, quantifying the relative influence of onset (left-pointing triangles) and offset (right-pointing triangles) clicks, is plotted for each combination of train-length N (x-axis) and subject tested in condition 1 (filled symbols). Comparison data from fixed-duration studies (Stecker, 2000; Stecker and Hafter, 2002) are plotted with open symbols. The dashed line represents a ratio of 1 (the value that would obtain for equal sensitivity across all clicks in a train); symbols falling above the short solid lines indicate AR significantly greater than 1 at the $p<0.05$ level based on parametric bootstrap testing. Bottom: rise, defined as the expected weight change (based on a linear fit) from click 2 to click N (offset), is plotted for each combination of N and subject tested in condition 1 (filled bars) and for fixed-duration studies (open bars). Positive rise values quantify the trend for weights to increase gradually over the post-onset epoch of the click-train stimulus. Error bars indicate standard error of the rise estimate, while asterisks ($*$) indicate values significantly greater than 0 ($p<0.05$).

would occur given a perfectly linear trend (hence, rise underestimates nonlinear upweighting confined to clicks near the stimulus offset).

G. Null-hypothesis testing

Statistical evaluation of AR and rise employed a parametric bootstrap procedure to evaluate the null hypothesis that AR=1 and rise=0, separately for each combination of subject and condition. Bootstrap weights were generated for each click in a train by random sampling from a normal distribution defined by the original estimate and standard error for that click weight. AR and rise were computed for each of 10 000 bootstrapped TWFs comprised of these weights to generate sampling distributions for each statistic. Sampling distributions for AR were approximately log normal, and the significance level of each AR estimate was computed empirically from the proportion of bootstrapped AR$\leq$1. Sampling distributions for rise were normal. Standard error (e.g., errorbars in Fig. 2) was computed directly from the distribution for each rise estimate and significance levels computed from the proportion of bootstrapped rise$\leq$0. Results of significance testing are displayed in Figs. 2 and 4 for each combination of subject and condition.

A second level of significance testing compared values of AR and rise across subjects and conditions. For this, we used Wilcoxon's one-sample signed-rank test (MATLAB statistics toolbox function "signrank") to evaluate the null hypotheses that (1) median AR equals 1 across subjects and conditions and (2) median rise equals 0. We used the paired-samples version of the same test to compare AR_{onset} and AR_{offset} across subjects and conditions.

H. Train-length manipulation

The length of each click-train was selected randomly on each trial. In condition 1, train length was selected randomly to be 4, 8, 16, or 32 clicks in order to test the hypotheses that (1) weight increases occur after a fixed number of clicks (the "fixed recovery" hypothesis) or (2) weight increases occur at different latency based on "anticipation" of a predictable train offset (the "global anticipatory recovery" hypothesis). In condition 2, train length was constrained to be either 8 or 16 clicks to increase the likelihood of train-length repeats on successive trials so that weighting functions could be reliably computed for both repeated and non-repeated train lengths. This condition tests a "local" anticipatory-recovery hypothesis, in which weight increase occurs at a time matching the duration of the immediately previous trial. Subjects CS, HW, and LS were tested in condition 1, and subjects HW and TL were tested in condition 2.

III. RESULTS

A. Localization accuracy and reliability

The accuracy and reliability of listeners' localization responses were quantified using the multiple regression model responsible for temporal weight estimation [Eq. (1)]. For the current study, this approach offers two key advantages over a more traditional approach in measuring listener performance. First, due to the randomization of individual click locations and the unequal temporal weighting applied to click-trains, it was not possible to compute a "correct" location for each trial outside the context of the regression model. Second, the reliability of localization responses could be computed from the proportion of variance explained by the model (R^2), thus taking into account the effects of individual and condition-specific differences in localization gain, bias, and temporal weighting.

Reliability. R^2 ranged from 0.81 to 0.96, with a mean of 0.89 and standard deviation of 0.04, across subjects and conditions, indicating good reliability of localization responses for all subjects. Note that the quantity $1-R^2$ (proportion of localization variance not explained by the model) estimates the localization error variance[3] as the deviation from expected response given the full model, thus taking account of intersubject and interstimulus differences in localization accuracy.

Accuracy. Because the main focus of the study was on the relative effects of individual click locations on listeners' responses (i.e., TWFs are not affected by gain or bias of listener's responses) and because the task itself was subjective (in the sense that listeners pointed to perceived locations without feedback), absolute accuracy measures are not par-

ticularly meaningful but are included here. Localization gain (the ratio of expected response azimuth to stimulus azimuth) was estimated by the sum of (non-normalized) regression weights b_i over all clicks. Gain ranged from 0.66 to 1.23, with a mean of 0.98 and standard deviation of 0.15, across subjects and conditions. Bias, estimated by the constant term k of the regression equation, ranged from +0.7 to +8.5 (positive value indicates rightward bias), with a median of +3.25° azimuth across subjects and conditions (subject HW exhibited a consistent rightward bias of 6°–8.5° in all conditions; other subjects' biases were generally close to +3°). Gain near 1 and bias near 0 are indicative of accurate (though not necessarily reliable) localization.

B. Temporal weighting functions

Figure 1 plots the TWFs obtained in condition 1 (filled symbols plot normalized weights for each click, with error bars indicating 95% confidence intervals). Although some individual variability is present, key features of the TWFs—specifically, the greater weight for clicks at onset and near offset than for intermediate clicks—appear for most subjects and train lengths. For example, in all but two cases (subject LS at 8 and 32 clicks), the weight applied to click 2 fell below the 95% confidence interval on weight for click N. In all but one case (LS, eight clicks), weights can also be seen to gradually increase over the post-onset duration of each click-train, as reported by Stecker and Hafter (2002) for 16-click-trains. TWFs from that study, along with data for 4-, 8-, and 32-click-trains (adapted from Stecker, 2000) are plotted for comparison in the bottom row of Fig. 1 (open symbols). Those studies measured TWFs for click-train durations that remained fixed across blocks of trials and used a slightly different loudspeaker arrangement, but were otherwise similar to the current study and tested five subjects that included those of the current study. Note that only data for 5-ms ICI are included in the figure. Again, key features of the TWFs (onset dominance and upweighting) appear similar across train lengths and regardless of train-length randomization.

Values of the AR for each subject and condition are plotted in Fig. 2 (top panel). AR values varied somewhat across subjects and train length N, but were consistently and significantly greater than 1 for both onset (Wilcoxon one-sample signed-rank test, $T=4$, $p<0.005$) and offset ($T=0$, $p<0.0005$) clicks, indicating greater influence of these clicks than intermediate clicks. Furthermore, AR of the offset click was slightly but significantly greater than that of the onset click ($T=11$, $p<0.05$). That difference suggests that the magnitude of upweighting is not limited to the magnitude of onset dominance, as would be expected if upweighting were simply recovery from onset dominance.[4]

The lower panel in Fig. 2 plots the rise in weights from click 2 to click N for each combination of train duration and subject, as measured by the slope of best-fitting linear function. Overall, the rise was significantly positive, ($T=0$, $p<0.0005$), similar between subjects, and declined slightly with increasing train length N. The two measures of upweighting (AR and rise) are complementary in that AR is especially sensitive to sharp weight increases near the end of the sound, whereas rise better characterizes gradual weight increases. Both features are present in the data (note in Fig. 1, for example, the tendency for offset clicks to receive weight in excess of the linear trend), however, and the two measures agree. The measures varied slightly, and in opposite ways, with increasing N, suggesting relatively more abrupt weight increase at offset (vs gradual increase) for longer trains. Overall, weights were consistently greater for clicks presented during later portions than middle portions of the train.

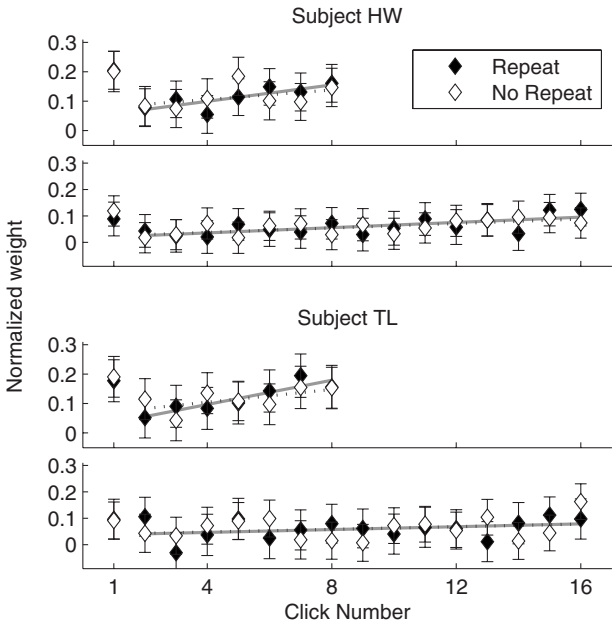

FIG. 3. Normalized weights for click-trains with train-length varied from trial to trial (condition 2). For each subject, upper and lower panels plot functions for 8- and 16-click-trains, respectively. Filled symbols represent weights from trials which repeated the train-length of the immediately-previous trial; open symbols represent weights from trials where train-length differed from the previous trial. Error bars indicate 95% confidence intervals on weight estimates. Lines indicate best linear fit to click weights $2N$ for repeated (gray lines) and non-repeated (dotted lines) trials. There were no significant differences between repeated-length and non-repeated-length trials.

Figure 3 plots TWFs obtained in condition 2; consistent with the findings of condition 1, these exhibited both onset dominance and upweighting of later clicks. TWFs for repeated-length trials (filled symbols) were not significantly different from TWFs for non-repeated trials (open symbols), indicating little if any effect of the local stimulus context on the form of temporal weighting. That result is corroborated by AR values exceeding 1 and rise values exceeding 0 in Fig. 4. Values were similar overall to those measured in condition 1 for both repeated and non-repeated trials. Estimates of rise did not differ significantly between repeated and non-repeated train lengths based on permutation bootstrap testing (8 clicks: $p<0.11$, 16 clicks: $p<0.42$).

IV. DISCUSSION

A. Prior studies indicating recovery from onset dominance

The upweighting effect described in this paper demonstrates one way in which spatial cues contained in the later,

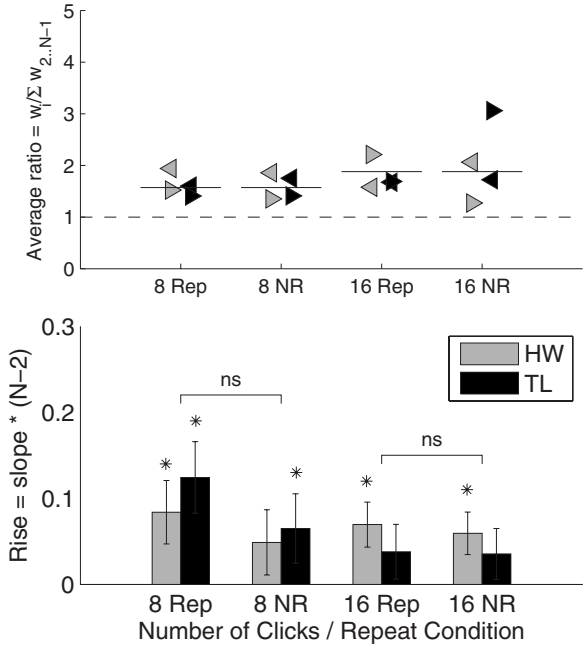

FIG. 4. AR and rise values for data obtained in condition 2. Format identical to Fig. 2, but with AR and rise plotted separately for 8- and 16-click-trains immediately preceded by identical-length trains (Rep="repeat") or by different-length trains (NR="no repeat"). Comparison lines ("ns") indicate lack of significant difference ($p>0.05$) between rise measured with repeated or non-repeated-length trains.

ongoing, portions of a stimulus contribute to sound localization judgments. The role of such ongoing cues has been investigated in several past studies. Tobias and Schubert (1959), for example, studied the duration of ongoing sound necessary to counteract transient cues present at sound onset and offset. Based on their results, Tobias and Schubert (1959) argued that ongoing cues completely dominate the localization of broadband sounds longer than 100 ms in duration; for shorter stimuli, transient and ongoing cues trade. Because the transient cues employed in that study included both onset and offset cues in agreement with each other, the results actually demonstrated a dominance of intermediate over onset and offset cues—contrary to the current results—with long-duration stimuli. The consequent prediction that both onset dominance and upweighting should be eliminated for stimuli over 100 ms in duration is not strongly supported by the current results[5] (Fig. 2), although casual inspection of TWFs plotted in Fig. 1 might suggest somewhat flatter functions for longer stimuli.

Freyman *et al.* (1997) investigated the apparent discrepancy between results like those of Tobias and Schubert (1959) and other studies that demonstrated strong onset dominance (e.g., Kunov and Abel, 1981; Saberi and Perrott, 1995). Based on their results, Freyman *et al.* (1997) argued that onset dominance arises in cases where stimulus periodicity or spectral sparseness renders ongoing cues ambiguous. Note that the high-rate Gabor click-trains used in the current study contain both types of "ambiguous" features and demonstrate strong onset dominance, consistent with the results of Freyman *et al.* (1997). This likely explains the discrepancy between current results and the ongoing-cue dominance reported by Tobias and Schubert (1959).

Zurek (1980) asked listeners to discriminate the lateral positions of pairs of noise bursts and found binaural discrimination to be impaired during a period 2–5 ms following the initial stimulus onset. He suggested that sensitivity to binaural information is transiently reduced following onset and recovers over the subsequent 10 ms. In one experiment, Zurek (1980) inserted a brief (5-ms) dichotic noise "probe" into a longer (50-ms) diotic noise burst (thus introducing a leading and a trailing diotic "fringe"). Discrimination performance was strongly affected by the temporal position of the probe within the background: best near the background onset or offset and worst approximately 2–5-ms post-onset. Discrimination performance improved monotonically with delay beyond this value, reaching near-normal levels only close to the offset of the background noise, somewhat similar to the TWFs measured in the current study. Akeroyd and Bernstein (2001) extended this finding by repeating Zurek's (1980) experiment with added conditions that omitted either the leading or trailing fringe. Consistent with the results of Zurek (1980) and those of the current experiment, they found greatest sensitivity (lowest thresholds) when the probe occurred near the onset or offset of the background noise burst (e.g., when either the leading or trailing burst was omitted).

B. Evaluation of recovery hypotheses

The results of Zurek (1980) provide one candidate explanation for the upweighting effect considered in the current study: that upweighting reflects recovery from the temporary effects of onset dominance. Here, we consider that explanation with respect to results of the current study. Specifically, we consider two sets of hypotheses: (1) the fixed recovery hypothesis, in which recovery takes place over a fixed time course and (2) the anticipatory recovery hypothesis, in which recovery takes place over a time course that is adjusted in a predictive fashion. Two types of anticipatory mechanisms are considered. The "global" anticipatory hypothesis posits that recovery time is adjusted to match the expected stimulus duration when durations are highly predictable (e.g., when they do not change from trial to trial), while the "local" anticipatory hypothesis posits more rapid adjustment of recovery time on a trial-by-trial basis.

Following Zurek (1980), the fixed recovery hypothesis assumes that the post-onset reduction in weights (i.e., onset dominance) reflects a temporary insensitivity to binaural information and that the binaural system recovers sensitivity given sufficient time. The recovery time might reflect the time constant of post-onset inhibition (Zurek, 1980; Lindemann, 1986) or to increasing likelihood of "restarting" the binaural adaptation mechanism (Hafter and Buell, 1990). Previously, Stecker and Hafter (2002) reported recovery of weights to occur near the offsets of 16-click-trains across a range of ICI from 3 to 8 ms and thus a range of train durations spanning 47–122 ms (Stecker and Hafter, 2002). That result supports the view that recovery time should be expressed in number of clicks (16) rather than elapsed time.[6] The fixed-recovery hypothesis predicts recovery to take place at the same point in each train, regardless of train length. Thus, recovery is expected to occur near the midpoint

of 32-click-trains, but remain incomplete for trains of fewer than 16 clicks. The TWFs plotted in Fig. 1 are not consistent with this prediction, as recovery appears consistently near the offset of each tested click-train, regardless of length. A corollary prediction of the fixed-recovery hypothesis is that upweighting should be significantly reduced or eliminated for shorter-duration trains, a prediction that is not supported by either of the summary statistics plotted in Fig. 2.

As an alternative to the fixed-recovery hypothesis, we next consider the anticipatory recovery hypothesis. By this account, upweighting reflects recovery from onset dominance with an adjustable—rather than fixed—recovery time. For example, since echoes act to prolong the proximal stimulus in a room-specific manner, such adjustment could be a means to optimize the temporal extent of onset dominance (echo suppression). Indeed, this trial-to-trial adaptation would be reminiscent of the "buildup" of precedence effects with repeated stimulation (Clifton and Freyman, 1989). The anticipatory-recovery hypothesis predicts recovery to occur at or near the end of each click-train if the duration is predictable from the context of recent stimuli. TWFs measured with duration fixed across blocks of trials (Stecker, 2000; Stecker and Hafter, 2002, lower panels of Fig. 1) appear consistent with that prediction. In the current study, we reduced predictability by randomizing train durations in condition 1 but noted a similar pattern of recovery near the end of each stimulus regardless of duration. Thus, upweighting does not appear to require predictable train lengths, contrary to the prediction of the anticipatory-recovery hypothesis.

While the results obtained in condition 1 argue against an anticipatory recovery mechanism requiring blocks of fixed train durations (a global anticipatory hypothesis), a remaining possibility is for the recovery time to be adjusted on a more rapid, trial-by-trial, basis (a local anticipatory hypothesis). In that case, stimulus durations are predictable when they match the duration of the immediately previous trial ("repeated trials"). TWFs for repeated trials are thus predicted to show recovery near the stimulus offset (as for fixed durations), while TWFs for non-repeated trials should experience recovery at some other time (e.g., reduced recovery if the previous trial was longer in duration, or premature recovery if the previous trial was shorter). In condition 1, repeated trials accounted for 25% of trials, so one might expect some effect of local predictability on TWFs. Casual examination of Fig. 1 suggests that some TWFs exhibited slight weight increases near clicks 4, 8, and 16 in trains of other lengths, possibly consistent with the local hypothesis. Condition 2 separately tested this possibility, however, and found no significant differences between TWFs measured with repeated and non-repeated trials. Thus, despite the suggestive features of condition-1 TWFs, the results are not consistent with either local or global anticipatory recovery.

Overall, TWFs measured in this study showed increased weights near the end of each click-train stimulus, consistent with the observations of Stecker and Hafter (2002). This pattern was observed consistently regardless of click-train duration and despite randomization to reduce the predictability of stimulus duration. These results therefore strongly suggest that upweighting does not reflect a feedforward recovery from onset dominance with either a fixed or anticipatory recovery time. Rather, the weight increases reflect a specific contribution of late-arriving sound, possibly independent of onset dominance. In other words, sound localization reflects a *post hoc* combination of multiple cues (Saberi, 1996) rather than a strictly feedforward accumulation of spatial information.

C. Prior studies that failed to show upweighting

In addition to the current study, a number of other recent studies have also measured TWFs for auditory spatial cues. Although these studies have generally been in agreement with respect to evidence for onset dominance, upweighting has not been consistently reported. Notably, two studies (Saberi, 1996; Dizon *et al.*, 1998) measured TWFs for ITD using headphone presentation, finding strong evidence for onset dominance at fast rates, but no suggestion of upweighting. In contrast, the current study, Stecker and Hafter (2002), and a recent study of TWFs for stimuli varying in median-plane elevation (Macpherson and Wagner, 2008) all reported upweighting of late-arriving sound. What similarities and differences among these studies might account for the differences in findings?

Difference 1: The types of spatial cues presented. Among the most obvious differences are the spatial cues available to listeners in each study. Stecker and Hafter (2002) presented stimuli in the free-field and Macpherson and Wagner (2008) used virtual acoustic space (VAS) recordings based on the acoustic effects of listeners' own ears in the free-field; the studies of Saberi (1996) and Dizon *et al.* (1998) employed headphone presentation, with spatial cues limited to ITD only.[7] Free-field and VAS stimuli possess cues related to ILDs and direction-dependent spectral cues generated by the acoustic effects of the head and outer ears, along with corresponding ITD cues. Varying only ITD, in contrast, places these cues in conflict with one another (ILD and spectral cues indicate a constant, near-midline azimuth). The relative weighting of ITD and ILD cues has been shown to vary with the listening situation (Rakerd and Hartmann, 1985), and ambiguity (as in a cue-conflict situation) may cause listeners to de-emphasize one or the other cue. Two possibilities are suggested by the differences in spatial-cue content. One possible explanation is that upweighting reflects mainly sensitivity to late-arriving ILD and/or spectral cues and somehow does not apply to the temporal integration of ITD. A second possibility is that conflict between cues reduces upweighting by rendering late-arriving cues ambiguous or uninformative (Rakerd and Hartmann, 1985; Freyman *et al.*, 1997).[8]

Difference 2: The nature of tasks involved. Another important difference among these studies is the type of response employed. Dizon *et al.* (1998), for example, used an adjustment technique with acoustic pointer to indicate the perceived lateral positions of stimuli. In that study, test and pointer alternated until subjects were satisfied with the match (a closed-loop procedure in which listeners have multiple opportunities to compare stimuli and minimize adjustment error). Saberi (1996) had subjects discriminate the lateral po-

sitions of stimuli as left or right of midline. In the current study (as in Stecker and Hafter, 2002; Stecker, 2000) subjects made a saccadic eye movement following presentation of a single stimulus (an open-loop procedure with no opportunity for "fine-tuning" the response over multiple presentations). Macpherson and Wagner (2008) had subjects turn their heads in the direction of the perceived location, also in open-loop fashion. The tasks employed in the latter two studies are the most similar; both used orientation (pointing to a location in space) in an open-loop procedure. The discrimination procedure used by Saberi (1996) is most clearly different; discrimination does not necessarily require that subjects be able to report a perceived location, and engages a motor response (button press) that does not require precise positioning within the spatial reference frame of the stimulus representation. The case of Dizon *et al.* (1998) is intermediate; subjects were asked to precisely judge the spatial location of the stimulus, as in the current study, but they did so in the context of a closed-loop task. The various procedures have different memory demands that could explain the difference in upweighting (see Sec. IV D 1). Alternately, we might consider the differences in neural mechanisms responsible for generating the specific motor responses in each task (see Sec. IV D 3): both of the orienting tasks require a response in the same spatial reference frame as the stimulus location, whereas the adjustment and discrimination tasks require a more arbitrary mapping from perception to motor action.

D. Mechanisms that might contribute to upweighting

Although the results clearly suggest a *post-hoc* analysis of late-arriving sound, the mechanisms underlying that *post-hoc* analysis are not clear. Potentially relevant mechanisms, addressed below, relate to the integration of recent information in sensory memory, the perception of apparent motion, and/or the generation of motor responses.

1. Recency in sensory memory

One possible explanation for the relative importance of late-arriving spatial cues may be found in the nature of memory mechanisms involved in integrating these cues over time. Well known from memory tasks (such as free recall of words from a memorized list), for example, are "recency" effects, whereby memory for recent items is better than for prior items (Glanzer and Cunitz, 1966). Within the domain of auditory perception, Sadralodabai and Sorkin (1999) noted clear recency effects in listener weighting of temporal intervals in a tone-pattern discrimination task. Although numerous mechanisms have been considered for recency effects at long time scales (seconds to minutes), one view that is especially amenable to shorter time scales is of recency as a general consequence of temporal integration. For example, a leaky integrator combines new information with a decaying representation of prior information, thus acting as a rudimentary memory that emphasizes the recent over the less-recent.

Similarly, Akeroyd and Bernstein (2001) used temporal integration to account for the dependence of ITD and ILD thresholds on varying-length fringes of diotic noise surrounding a dichotic noise burst (Zurek, 1980). Their model combines a temporal integrator (a "binaural temporal window") with a post-onset weighting function (Houtgast and Aoki, 1994) to model both onset dominance and upweighting-like effects in their discrimination data. Because the temporal window weights prior inputs by a decaying exponential (as in the leaky integrator), its memory-like behavior similarly emphasizes recent input, resulting in increased weight (and reduced thresholds) for binaural information occurring near the offset of a sound.

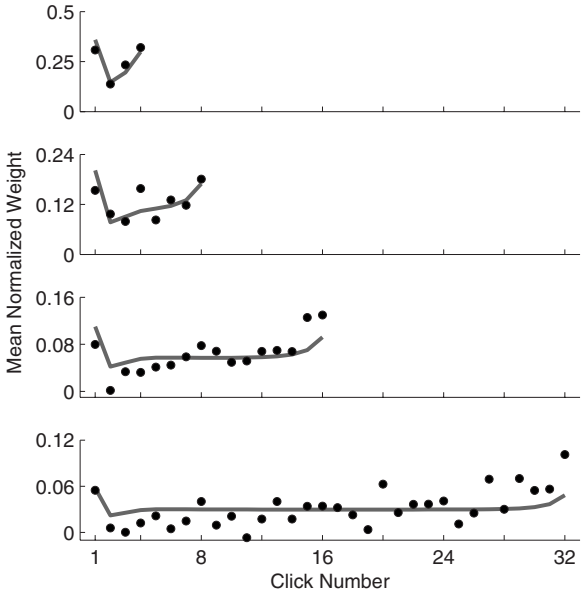

FIG. 5. TWFs predicted by quantitative modeling of binaural temporal integration and post-onset weighting (Akeroyd and Bernstein, 2001). Circles: mean normalized TWFs across subjects for train lengths tested in condition 1. Solid lines: model predictions (see Appendix for modeling details). The combination of post-onset weighting and binaural temporal integration closely matches the measured TWFs for short stimuli (four to eight clicks). For longer durations, the model accounts for the basic TWF shape but appears to underestimate both the magnitude and the duration of upweighting.

In order to quantify the effects of temporal integration on TWFs, we applied the model of Akeroyd and Bernstein (2001) to stimuli as tested in condition 1 of the current study. Details of the model are given in the Appendix. The model predictions are plotted along with cross-subject average TWFs in Fig. 5. The parameters were identical to those used by Akeroyd and Bernstein (2001) to model ITD discrimination thresholds of broadband noise, but still account reasonably well for the narrowband localization-based TWFs of the current study. Both onset dominance and upweighting are apparent in the model predictions. The former is a consequence of the model's post-onset weighting [Eq. (A1)], while the latter reflects temporal integration [Eqs. (A2) and (A3)]. Intermediate weights are reduced due to "dilution" of binaural information by neighboring clicks; this dilution is reduced at stimulus onset and offset when fewer neighbors fall within the limits of the temporal window. Note that for long durations (16–32 clicks), the model TWFs feature constant weights during the middle of the stimulus and a brief increase near the stimulus offset. The temporal extent of the increase reflects the time constant of the binaural temporal window and in this case appears to underestimate the up-

weighting measured in this study. A longer (i.e., more "sluggish;" Grantham and Wightman, 1978) temporal window might have provided a better fit to the present data. If so, that result would be consistent with the view that localization involves relatively slower integrative mechanisms than does binaural discrimination.

Note that the possibility of recency effects in sound localization (due to binaural temporal integration or otherwise) does not speak to the issue of why some studies have reported upweighting (this study, Zurek, 1980; Akeroyd and Bernstein, 2001; Macpherson and Wagner, 2008), while other similar studies have not (Saberi, 1996; Dizon *et al.*, 1998). A satisfactory explanation would require addressing how the use of memory systems differs between these studies. One possibility is that the time constant of temporal integration differs between ILD (or spectral cues) and ITD. Another is that some tasks, such as open-loop orientation, depend on decaying spatial representations that are not utilized in discrimination or closed-loop tasks (see Sec. IV D 3). At this point, however, neither of these possibilities provides a compelling account of the data, insofar as the results of Zurek (1980) and Akeroyd and Bernstein (2001) suggest upweighting for *discrimination* of both ITD and ILD, and the current results demonstrate upweighting for *localization* in the free-field.

2. Apparent motion

Another possibility is that the dynamic locations of stimuli resulted in a perception of apparent motion. While the likelihood of coherent motion of up to 32 clicks is quite low, saltatory motion (e.g., motion caused by displacement of the offset relative to the onset, Grantham, 1997) could produce a sensation of motion in the direction of the displacement. If listeners' judgments were, in turn, biased in the direction of motion, we would expect to observe increased weights at or near the offset of the sound, regardless of duration. These saltatory motion cues thus represent another way in which *post-hoc* analysis of spatial information might produce upweighting. However, the argument for upweighting as a result of apparent motion is a bit circular: if the perceived location of a stimulus is dominated by the onset and offset, then motion may be perceived when onset and offset differ in location. Does the motion enhance the effect of the offset click, or vice versa? Furthermore, it does not explain the differences between studies noted above; all of the referenced TWF studies included dynamic locations that could have introduced apparent motion, unless the types of spatial cues strongly determine the salience of saltatory motion (cf. "binaural sluggishness," Grantham, 1984). Future experiments that directly manipulate perceived motion may be necessary to evaluate this possibility.

3. Response generation

Finally, the *post-hoc* integration of spatial information suggested by the current results could imply a role for decision and/or response aspects of the task. That is, the observed effects might be strongly response-dependent, reflecting nonauditory (cognitive or motor) processes that are not fundamentally involved in the early processing of auditory spatial cues. Could late-arriving cues somehow bias the response representation (e.g., a spatial-motor plan) rather than the sensory representation itself? This view is supported by the apparent failure of upweighting in discrimination and closed-loop adjustment tasks (Saberi, 1996; Dizon *et al.*, 1998), where the two representations are not required to share a common spatial reference frame. Future studies might test this possibility directly by comparing TWFs for identical stimuli across response methods such as open-loop orientation and spatial discrimination.

It is an intriguing possibility that late-arriving cues might affect some tasks and not others, but this explanation requires that response-generation (motor-planning) mechanisms gain access to information about multiple spatial cues (i.e., onset and ongoing cues) *prior to* integration of spatial information across cue type. That is, multiple representations of auditory spatial information (e.g., representations of onset vs ongoing or ITD vs ILD cues) must be separately maintained to relatively high levels within the auditory pathway (that is, at least to those levels involved in generating motor responses). Though difficult to reconcile with a traditional modular view of sensory and motor processing, this interpretation is, in fact, consistent with recent electroencephalographic and lesion-based evidence for separate representations of ITD and ILD within human auditory cortex (Tardif *et al.*, 2006; Yamada *et al.*, 1996; Schroger, 1996; Ungan *et al.*, 2001). The notion that multiple "channels" of spatial information might be integrated at a very late stage of processing is, furthermore, consistent with current views of how auditory space is represented within auditory cortex. Neurophysiological evidence from animal models suggests that auditory spatial codes are distributed across a small number of broadly tuned sub-populations of cortical neurons (Stecker and Middlebrooks, 2003) rather than by sharply tuned individual neurons. Although their aggregate spatial information is sufficient to underlie normal behavior, that information might not be integrated across these sub-populations until the level of multimodal and/or sensorimotor integration (Stecker *et al.*, 2005).

V. SUMMARY AND CONCLUSIONS

The following conclusions can be drawn from the current results.

(1) TWFs for free-field localization of 4000-Hz Gabor click-trains, presented at 5-ms ICI, are characterized by (1) onset dominance, as evidenced by increased weight on the first click, and (2) upweighting of late-arriving sound, evidenced by a gradual increase in weights following the first click and a correspondingly increased weight on the final click.
(2) Upweighting affects most strongly those clicks nearest the offset of the train, regardless of stimulus duration, predictability of duration, or similarity to recent stimuli.
(3) Upweighting of late-arriving sound thus does not reflect a recovery from onset dominance. Among eliminated hypotheses are (1) recovery at a fixed post-onset time, (2) recovery at a variable post-onset time adjusted to match

the (predictable) stimulus duration, and (3) recovery at a variable post-onset time adjusted to the duration of immediately previous stimuli.

ACKNOWLEDGMENTS

The authors thank Miriam Valenzuela and Ephram Cohen for assistance in running this study. Erick Gallun, Bruce Berg, David Wessel, and Frederic Theunissen provided helpful comments during the study design. Erick Gallun, Ewan Macpherson, Andrew Brown, Ian Harrington and Rich Freyman, and three anonymous reviewers provided invaluable comments on earlier versions of the manuscript. Virginia Richards suggested the simplifying term "Gabor click" to describe the Gaussian-filtered impulses used in this and other studies. A portion of this work was previously presented in abstract form [Stecker and Hafter (2002). J. Acoust. Soc. Am. 111, 2355] and in the first author's doctoral dissertation. Work supported by NIH R01 DC00087 (E.R.H.) and R03 DC009482 (G.C.S.).

APPENDIX: MODELING DETAILS

The model of Akeroyd and Bernstein (2001) combines a binaural temporal window of integration with a post-onset weighting function (Houtgast and Aoki, 1994).

Model predictions were computed in the following manner.

(1) Post-onset weights $x(t)$ were computed as a function of post-onset time t of each click in a train, according to the following post-onset weighting function (Houtgast and Aoki, 1994):

$$x(t) = ae^{-t/T_a} + be^{-t/T_b} + 1. \quad \text{(A1)}$$

Parameters for Eq. (A1) were set to the values used by Akeroyd and Bernstein (2001) to model ITD discrimination: $a=3.1$, $T_a=2.8$ ms, $b=-2.1$, and $T_b=5.9$ ms.

(2) Temporally integrated weights $y(t)$ were computed by calculating the ratio of each $x(t)$ weight to the sum of x weights falling within an asymmetric temporal window $\omega(\tau)$ centered on each click time t (Akeroyd and Bernstein, 2001):

$$y(t) = \frac{x(t)}{\int x(t+\tau)\omega(\tau)d\tau}, \quad \text{(A2)}$$

where τ represents time relative to the peak of the binaural temporal window function $\omega(\tau)$:

$$\omega(\tau) = \begin{cases} e^{\pi/T1}, & \tau < 0 \\ e^{-\pi/T2}, & \tau \geq 0, \end{cases} \quad \text{(A3)}$$

and $T1$ and $T2$ are time constants that define the response of the temporal window to prior and subsequent clicks, respectively. As for Eq. (A1), parameters for Eq. (A3) were set to the values used by Akeroyd and Bernstein (2001) to model ITD discrimination: $T1=5.2$ ms and $T2=7.2$ ms.

Model TWFs were computed by normalizing the temporally integrated weights y so that the set of model weights sums to 1 across all clicks in a train. In Fig. 5, normalized model TWFs are plotted along with mean normalized TWFs measured in condition 1 of the current study.

[1]We have previously referred to this duration as "nominally 2 ms," based on the total envelope duration calculated at an amplitude resolution of 16 bits (Stecker and Hafter, 2002). Despite the difference in nomenclature, the stimuli used in the current study are identical to those of the previous study.

[2]This instruction was meant to reduce any effects of listener bias when multiple images were present (for example, by electing to respond to the early-sounding image). Consistent pointing to the leftmost image is expected to flatten TWFs overall when multiple images are perceived rather than to enhance any particular element of the TWF. Subjects were not told to expect multiple images, and in this study, no subjects reported consistent appearances of multiple images. In our previous study (Stecker and Hafter, 2002), the appearance of multiple images was primarily confined to conditions of long ICI (14 ms) and were not reported at 5-ms ICI.

[3]Because $1-R^2$ also includes variance associated with systematic but nonlinear trends in the responses, it estimates an upper bound (rather than an unbiased estimate) on the true localization error.

[4]Note that this result is consistent with the moderate onset dominance observed previously for 5-ms ICI. At shorter ICI, greater onset dominance (and thus greater AR for onset clicks) would be expected.

[5]Note, however, the significant differences between stimuli. Tobias and Schubert (1959) presented broadband noises with amplitude fluctuations reduced by peak limiting, whereas the current study employed narrowband stimuli that were amplitude-modulated at a depth of 100%.

[6]In the current study, ICI was fixed at 5 ms so that duration and click number are perfectly correlated.

[7]Saberi (1996) presented 4000-Hz Gabor click-trains—as used in the current study—with ICI ranging 1.8–12 ms and asked subjects to discriminate the left/right position of trains with ITD varying from click to click. Dizon *et al.* (1998) presented broadband noise bursts divided into four to six temporal "slices" of 2–10 ms duration, each with a randomly selected ITD. Subjects were asked to adjust the ITD of a separate broadband noise pointer—which alternated with the test stimulus—until the lateral positions of test and pointer matched.

[8]On the other hand, the conflicting cue (ILD) might simply impart a center bias to judgments of the main cue (ITD) in these studies. In that case, the cue conflict should not have prevented upweighting.

Abel, S. M., and Kunov, H. (**1983**). "Lateralization based on interaural phase differences: Effects of frequency, amplitude, duration, and shape of rise/decay," J. Acoust. Soc. Am. **73**, 955–960.

Akeroyd, M. A., and Bernstein, L. R. (**2001**). "The variation across time of sensitivity to interaural disparities: Behavioral measurements and quantitative analyses," J. Acoust. Soc. Am. **110**, 2516–2526.

Berg, B. G. (**1989**). "Analysis of weights in multiple observation tasks," J. Acoust. Soc. Am. **86**, 1743–1746.

Bernstein, L. R., and Trahiotis, C. (**2002**). "Enhancing sensitivity to interaural delays at high frequencies using 'transposed stimuli'," J. Acoust. Soc. Am. **112**, 1026–1036.

Buell, T. N., Griffin, S. J., and Bernstein, L. R. (**2008**). "Listeners' sensitivity to 'onset/offset' and 'ongoing' interaural delays in high-frequency, sinusoidally amplitude-modulated tones," J. Acoust. Soc. Am. **123**, 279–294.

Buell, T. N., Trahiotis, C., and Bernstein, L. R. (**1991**). "Lateralization of low-frequency tones: Relative potency of gating and ongoing interaural delays," J. Acoust. Soc. Am. **90**, 3077–3085.

Clifton, R. K., and Freyman, R. L. (**1989**). "Effect of click rate and delay on breakdown of the precedence effect," Percept. Psychophys. **46**, 139–145.

Dizon, R. M., Culling, J. F., Litovsky, R. Y., Shinn-Cunningham, B. G., and Colburn, H. S. (**1998**). "On the development of a post-onset temporal weighting function," Assoc. Res. Otolaryngol. Abstr. **21**, 42.

Franssen, N. V. (**1962**). *Sterophony* (Philips Technical Library, Eindhoven, The Netherlands).

Freyman, R. L., Zurek, P. M., Balakrishnan, Y., and Chiang, Y. C. (**1997**). "Onset dominance in lateralization," J. Acoust. Soc. Am. **101**, 1649–1659.

Glanzer, M., and Cunitz, A. R. (**1966**). "Two storage mechanisms in free recall," J. Verbal Learn. Verbal Behav. **5**, 351–360.

Grantham, D. W. (**1984**). "Discrimination of dynamic interaural intensity differences," J. Acoust. Soc. Am. **76**, 71–76.

Grantham, D. W. (**1997**). "Auditory motion perception: Snapshots revis-

ited," in *Binaural and Spatial Hearing in Real and Virtual Environments*, edited by R. H. Gilkey and T. R. Anderson (Lawrence Erlbaum Associates, Mahwah, NJ), pp. 295–313.
Grantham, D. W., and Wightman, F. L. (**1978**). "Detectability of varying interaural temporal differences," J. Acoust. Soc. Am. **63**, 511–523.
Hafter, E. R. (**1997**). "Binaural adaptation and the effectiveness of a stimulus beyond its onset," in *Binaural and Spatial Hearing in Real and Virtual Environments*, edited by R. H. Gilkey and T. R. Anderson (Lawrence Erlbaum Associates, Mahwah, NJ), pp. 211–232.
Hafter, E. R., and Buell, T. N. (**1990**). "Restarting the adapted binaural system," J. Acoust. Soc. Am. **88**, 806–812.
Hafter, E. R., and Dye, R. H. J. (**1983**). "Detection of interaural differences of time in trains of high-frequency clicks as a function of interclick interval and number," J. Acoust. Soc. Am. **73**, 644–651.
Hartmann, W. M., and Rakerd, B. (**1989**). "Localization of sound in rooms IV: The Franssen effect," J. Acoust. Soc. Am. **86**, 1366–1373.
Henning, G. B. (**1974**). "Detectability of interaural delay in high-frequency complex wave-forms," J. Acoust. Soc. Am. **55**, 84–90.
Houtgast, T., and Aoki, S. (**1994**). "Stimulus-onset dominance in the perception of binaural information," Hear. Res. **72**, 29–36.
Kunov, H., and Abel, S. M. (**1981**). "Effects of rise/decay time on the lateralization of interaurally delayed 1-kHz tones," J. Acoust. Soc. Am. **69**, 769–773.
Lindemann, W. (**1986**). "Extension of a binaural cross-correlation model by contralateral inhibition. II. The law of the first wave front," J. Acoust. Soc. Am. **80**, 1623–1630.
Lutfi, R. A. (**1995**). "Correlation coefficients and correlation ratios as estimates of observer weights in multiple-observation tasks," J. Acoust. Soc. Am. **97**, 1333–1334.
Macpherson, E. A., and Wagner, M. L. (**2008**). "Temporal weighting of cues for vertical-plane sound localization," Assoc. Res. Otolaryngol. Abstr. **31**, 301.
McFadden, D., and Pasanen, E. G. (**1975**). "Binaural beats at high frequencies," Science **190**, 394–396.
McFadden, D., and Pasanen, E. G. (**1976**). "Lateralization of high frequencies based on interaural time differences," J. Acoust. Soc. Am. **59**, 634–639.
Nuetzel, J. M., and Hafter, E. R. (**1976**). "Lateralization of complex waveforms: Effects of fine structure, amplitude, and duration," J. Acoust. Soc. Am. **60**, 1339–1346.
Rakerd, B., and Hartmann, W. M. (**1985**). "Localization of sound in rooms, II: The effects of a single reflecting surface," J. Acoust. Soc. Am. **78**, 524–533.
Richards, V. M., and Zhu, S. P. (**1994**). "Relative estimates of combination weights, decision criteria, and internal noise based on correlation coefficients," J. Acoust. Soc. Am. **95**, 423–434.
Saberi, K. (**1996**). "Observer weighting of interaural delays in filtered impulses," Percept. Psychophys. **58**, 1037–1046.
Saberi, K., and Perrott, D. R. (**1995**). "Lateralization of click-trains with opposing onset and ongoing interaural delays," Acustica **81**, 272–275.
Sadralodabai, T., and Sorkin, R. D. (**1999**). "Effect of temporal position, proportional variance, and proportional duration on decision weights in temporal pattern discrimination," J. Acoust. Soc. Am. **105**, 358–365.
Schroger, E. (**1996**). "Interaural time and level differences: Integrated or separated processing?," Hear. Res. **96**, 191–198.
Shinn-Cunningham, B. G., Zurek, P. M., and Durlach, N. I. (**1993**). "Adjustment and discrimination measures of the precedence effect," J. Acoust. Soc. Am. **93**, 2923–2932.
Shinn-Cunningham, B. G., Zurek, P. M., Durlach, N. I., and Clifton, R. K. (**1995**). "Cross-frequency interactions in the precedence effect," J. Acoust. Soc. Am. **98**, 164–171.
Stecker, G. C. (**2000**). "Observer weighting in sound localization," Ph.D. thesis, University of California, Berkeley, Berkeley, CA.
Stecker, G. C., and Hafter, E. R. (**2002**). "Temporal weighting in sound localization," J. Acoust. Soc. Am. **112**, 1046–1057.
Stecker, G. C., Harrington, I. A., and Middlebrooks, J. C. (**2005**). "Location coding by opponent neural populations in the auditory cortex," PLoS Biol. **3**, e78.
Stecker, G. C., and Middlebrooks, J. C. (**2003**). "Distributed coding of sound locations in the auditory cortex," Biol. Cybern. **89**, 341–349.
Stellmack, M. A., Dye, R. H., and Guzman, S. J. (**1999**). "Observer weighting of interaural delays in source and echo clicks," J. Acoust. Soc. Am. **105**, 377–387.
Strutt, J. W. (**1907**). "On our perception of sound direction," Philos. Mag. **13**, 214–232.
Tardif, E., Murray, M. M., Meylan, R., Spierer, L., and Clarke, S. (**2006**). "The spatio-temporal brain dynamics of processing and integrating sound localization cues in humans," Brain Res. **1092**, 161–176.
Tobias, J. V., and Schubert, E. R. (**1959**). "Effective onset duration of auditory stimuli," J. Acoust. Soc. Am. **31**, 1595–1605.
Ungan, P., Yagcioglu, S., and Goksoy, C. (**2001**). "Differences between the n1 waves of the responses to interaural time and intensity disparities: Scalp topography and dipole sources," Clin. Neurophysiol. **112**, 485–498.
van de Par, S., and Kohlrausch, A. (**1997**). "A new approach to comparing binaural masking level differences at low and high frequencies," J. Acoust. Soc. Am. **101**, 1671–1680.
Wallach, H., Newman, E. B., and Rosenzweig, M. R. (**1949**). "The precedence effect in sound localization," Am. J. Psychol. **62**, 315–336.
Yamada, K., Kaga, K., Uno, A., and Shindo, M. (**1996**). "Sound lateralization in patients with lesions including the auditory cortex: Comparison of interaural time difference (ITD) discrimination and interaural intensity difference (IID) discrimination," Hear. Res. **101**, 173–180.
Zurek, P. M. (**1980**). "The precedence effect and its possible role in the avoidance of inter-aural ambiguities," J. Acoust. Soc. Am. **67**, 952–964.

Controller design and consonantal contrast coding using a multi-finger tactual display[a)]

Ali Israr[b)]
Haptic Interface Research Laboratory, Purdue University, 465 Northwestern Avenue, West Lafayette, Indiana 47907-2035

Peter H. Meckl
Ruth and Joel Spira Laboratory for Electromechanical Systems, 585 Purdue Mall, West Lafayette, Indiana 47907-2088

Charlotte M. Reed
Research Laboratory of Electronics, Massachusetts Institute of Technology, Room 36-751, 77 Massachusetts Avenue, Cambridge, Massachusetts 02139

Hong Z. Tan
Haptic Interface Research Laboratory, Purdue University, 465 Northwestern Avenue, West Lafayette, Indiana 47907-2035

(Received 8 August 2008; revised 24 March 2009; accepted 29 March 2009)

This paper presents the design and evaluation of a new controller for a multi-finger tactual display in speech communication. A two-degree-of-freedom controller consisting of a feedback controller and a prefilter and its application in a consonant contrasting experiment are presented. The feedback controller provides stable, fast, and robust response of the fingerpad interface and the prefilter shapes the frequency-response of the closed-loop system to match with the human detection-threshold function. The controller is subsequently used in a speech communication system that extracts spectral features from recorded speech signals and presents them as vibrational-motional waveforms to three digits on a receiver's left hand. Performance from a consonantal contrast test suggests that participants are able to identify tactual cues necessary for discriminating consonants in the initial position of consonant-vowel-consonant (CVC) segments. The average sensitivity indices for contrasting voicing, place, and manner features are 3.5, 2.7, and 3.4, respectively. The results show that the consonantal features can be successfully transmitted by utilizing a broad range of the kinesthetic-cutaneous sensory system. The present study also demonstrates the validity of designing controllers that take into account not only the electromechanical properties of the hardware, but the sensory characteristics of the human user.
 [DOI: 10.1121/1.3124771]

PACS number(s): 43.66.Wv, 43.66.Ts, 43.66.Gf, 43.60.Ek [ADP] Pages: 3925–3935

I. INTRODUCTION

The motivation for this research is to utilize touch as a sensory substitute for hearing in speech communication for individuals with severe hearing impairments. That such a goal is attainable is demonstrated by users of the Tadoma method who receive speech by placing a hand on the face of a speaker to monitor facial movements and airflow variations associated with speech production. Previous research has documented the speech-reception performance of highly experienced deaf-blind users of the Tadoma method at the segmental, word, and sentence levels (Reed *et al.*, 1985). An analysis of information-transfer (IT) rates for a variety of methods of human communication (Reed and Durlach, 1998) suggests that the communication rates achieved through Tadoma are roughly half of those achieved through normal auditory reception of spoken English. By comparison, the estimated communication rates for speech transmission through artificial tactile aids are substantially below those of the Tadoma method (Reed and Durlach, 1998). The limited success demonstrated thus far with artificial tactual communication systems may be due to a variety of factors, including (1) the homogeneous nature of displays that utilize single or multiple actuators to deliver only high-frequency cutaneous stimulation, and (2) the use of body sites with relatively sparse nerve innervation, such as forearm, abdomen, or neck (Plant, 1989; Waldstein and Boothroyd, 1995; Weisenberger *et al.*, 1989; Galvin *et al.*, 1999; Summers *et al.*, 2005). In contrast, Tadoma users have access to a rich set of stimulus attributes, including kinesthetic movements of the face and jaw, cutaneous vibrations at the neck, airflow at the lips, and muscle tensions in the face, jaw, and neck, which are received through the hands.

To more fully exploit the capabilities of the tactual sensory system that are engaged in the use of the Tadoma

[a)]Part of this work concerning the controller design was presented at the 2004 ASME International Mechanical Engineering Congress and Exposition, Anaheim, CA, Nov. 13-19, 2004.
[b)]Author to whom correspondence should be addressed. Electronic mail: israr@rice.edu

method, an artificial device, the Tactuator, was developed to deliver kinesthetic (motions) as well as cutaneous (vibrations) stimuli through the densely innervated fingertips of the left hand (Tan and Rabinowitz, 1996). Previous research has examined IT rates for multidimensional stimuli delivered through the Tactuator device (Tan *et al.*, 1999, 2003). For example, in Tan *et al.*, 2003, IT rates of up to 21.9 bits/s were achieved using multidimensional synthetic waveforms presented at a single contact site. These rates, which are among the highest reported to date for a touch-based display, are at the lower end of the range of IT rates obtained for auditory reception of speech (Reed and Durlach, 1998).

The present research was concerned with the utilization of the broad kinesthetic-to-cutaneous stimulation range (nearly 0–300 Hz) of the TactuatorII[1] for the display of speech. In particular, this research was designed to extend the work of Yuan (2003) in which speech was encoded for display through the Tactuator device. Yuan (2003) examined the ability to discriminate the voicing cue in consonants using a two-channel speech-coding scheme in which the amplitude envelope of a low-frequency band of speech was used to modulate a 50-Hz waveform delivered to the thumb, and the amplitude envelope of a high-frequency band of speech was used to modulate a 250-Hz waveform at the index finger. Noise-masked normal-hearing participants achieved high levels of performance on the pairwise discrimination of consonants contrasting the feature of voicing through the tactual display alone. This coding scheme was also effective in providing a substantial benefit to lipreading in closed-set consonant identification tasks.

Encouraged by the results of Yuan (2003), the present study investigated consonant discriminability for the features of place and manner of articulation in addition to voicing. A speech-to-touch coding scheme was developed to extract envelope information from three major spectral regions of the speech signal and present them as kinesthetic motional and cutaneous vibrational cues. The three spectral bands included a low-frequency region (intended to convey information about fundamental frequency), a mid-frequency region (intended to convey information about the first formant of speech), and a high-frequency region (intended to convey second-formant information). These bands were somewhat consistent with the assessment of bands of modulated noise required for speech recognition by Shannon *et al.* (1995), as well as those used in previous studies on tactile aids (Weisenberger and Percy, 1995; Clements *et al.*, 1988; Summers, 1992). Amplitude-envelope information from each of these spectral regions was encoded tactually through the use of mid- and high-frequency vibrations at one of the three contactor sites of the TactuatorII (thumb, middle finger, and index finger, respectively). The absolute amplitude of the vibrations at each finger provided information about the energy in the corresponding frequency band. The relative amplitudes of the two vibrations (modulated at 30 and 200 Hz) at each finger channel provided information about energy spread in the corresponding frequency band. In addition to the tactile waveforms, the coding scheme monitored energy peaks within each band and presented this information as low-frequency motional cues—extending the finger for high-frequency contents and flexing the finger for low-frequency contents in the corresponding finger band. These more pronounced representations of formant and formant transition cues were employed in an effort to improve the transmission of cues related to place of articulation, which have been poorly transmitted through previous tactile aids (Clements *et al.*, 1988; Weisenberger *et al.*, 1989; Waldstein and Boothroyd, 1995; Plant, 1989; Summers *et al.*, 2005; Weisenberger and Percy, 1995; Galvin *et al.*, 1999). Acoustical analyses of plosive and fricative consonants have shown that place of articulation is well correlated with the frequency values of the first two formants (spectral peaks in the speech spectrum due to the shape of the mouth), F1 and F2, and their transitions (Ali *et al.*, 2001a, 2001b; Jongman *et al.*, 2000). Therefore, motions indicating changes in F1 and F2 were used to encode information concerning place of articulation. Although the location of the energy peaks was presented as high-frequency vibrations, redundant presentations of the same information as quasi-static positions of the fingers were intended to reduce inter-channel effects that may arise, such as those due to masking. It is well known that masking reduces internal representations of proximal tactual stimuli (Craig and Evans, 1987; Evans, 1987; Tan *et al.*, 2003) and redundant presentation of speech information can lead to improved perceptual performance (Yuan, 2003; Summers *et al.*, 1994).

One challenge associated with the use of broadband signals with an electromechanical system such as the TactuatorII is that the system frequency response is not uniform across its operating range. Therefore, the input signals are distorted spectrally before they are presented to a human user. To solve this problem, a closed-loop two-degree-of-freedom (2DOF) controller was developed to reshape the overall system response. Specifically, the controller compensated for both the frequency response of the TactuatorII and the frequency-dependent human detection-thresholds (HDTs) for tactual stimulation so that when a broadband input signal is applied to the TactuatorII, the relative amplitude of spectral components in the input signal is preserved in terms of perceived intensity when the signal reaches the user's fingers. The 2DOF controller consists of a feedback controller and a prefilter. The feedback controller (referred to as the low-frequency kinesthetic or motion controller) counters the effects of low-frequency disturbances due to a user's finger loading the device, increases the closed-loop bandwidth, and reduces the high-frequency in-line noise. The prefilter (referred to as the broadband cutaneous or vibration controller) shapes the overall system frequency response so that two equal-amplitude spectral components at the reference input would be perceived as equally intense by the human user.

The remainder of this paper describes the controller design and implementation of the TactuatorII system (Sec. II) and the speech-to-touch coding scheme (Sec. III). An experimental study on the pairwise discrimination of consonants with two human observers is reported (Sec. IV) before the paper concludes with a general discussion (Sec. V).

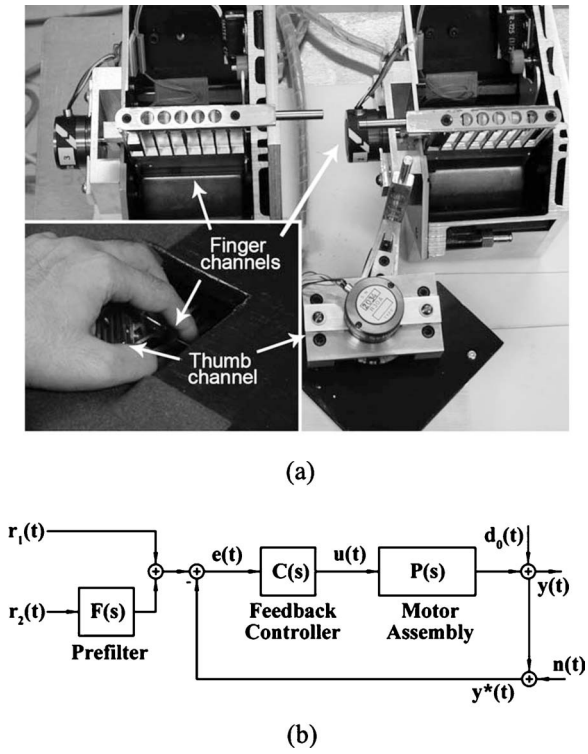

FIG. 1. (a) Three channels of the TactuatorII system and the three hand contact points rested lightly on the "fingerpad interface" rods (inset). (b) The block diagram representation of the 2DOF controller.

II. CONTROLLER DESIGN

A. Apparatus

The TactuatorII consists of three independently-controlled channels interfaced with the fingerpads of the thumb, the index finger, and the middle finger, respectively [Fig. 1(a)]. The range of motion for each digit is about 25 mm. Each channel has a *continuous* frequency response from dc to 300 Hz, delivering stimuli from the kinesthetic range (i.e., low-frequency gross motion) to cutaneous range (i.e., high-frequency vibration) as well as in the mid-frequency range. Across the frequency range of dc to 300 Hz, an amplitude of 0 dB sensation level (SL) (decibels above HDT) to at least 47 dB SL can be achieved at each frequency, thereby matching the dynamic range of tactual perception (Verrillo and Gescheider, 1992). Details of the TactuatorII can be found in Israr *et al.*, 2006 (cf. Sec. II A, on pp. 2790–2791) and Tan and Rabinowitz, 1996.

The frequency response of the motor assembly was obtained by measuring the input-output voltage ratio over the frequency range dc to 300 Hz. It was modeled by a second-order transfer function $P(s)=2875/(s^2+94s+290)$ (see also Tan and Rabinowitz, 1996).

B. Controller design

The main design objective was to shape the frequency response of the TactuatorII so that when driven with a broadband signal (up to 300 Hz), the relative intensities of different spectral components were preserved in terms of the relative sensation levels (SLs) delivered by the TactuatorII. In addition, the controller should be able to reduce the effects of low-frequency finger load disturbance, and achieve fast and stable motion tracking. Because of the similarities among all three channels, controller design for one channel assembly of the TactuatorII is discussed in this paper.

Our approach was to have two main components in the controller: one for the low-frequency kinesthetic movements, and the other for the broadband high-frequency cutaneous region, as explained in Fig. 1(b). The high-frequency broadband reference position signal, $r_2(t)$, was first passed through a prefilter, $F(s)$, and then added to the low-frequency motional reference position, $r_1(t)$. The combined signal was then compared to the measured position signal, $y^*(t)$, to form an error signal, $e(t)$, as the input to the feedback controller, $C(s)$. The output of the feedback controller or the command signal, $u(t)$, was used to drive the motor assembly, $P(s)$, to achieve a position trajectory of $y(t)$ at the point where the fingerpad rests. The effects of finger loading and sensor noise are represented by $d_0(t)$ and $n(t)$, respectively.

Major steps in the design of the feedback controller and the prefilter are outlined below. More details can be found in Israr, 2007 (cf. Chap. 2).

1. Feedback controller for kinesthetic stimulus region

The feedback controller or the motional (kinesthetic) controller $C(s)$ was designed using a lead-lag frequency loop-shaping technique that shaped the frequency response of the open-loop transfer function, $L(s)=C(s)P(s)$, to lie within the constraints determined by the required closed-loop response, $T(s)=C(s)P(s)/[1+C(s)P(s)]$ (Maciejowski, 1989). It consists of an integrator for maintaining the 0 dB closed-loop gain, a pair of zeros for increasing the stability margin, and a high-frequency pole for suppressing inline noise and for the proper structure (causality) of the controller $C(s)$. The final design of the feedback (kinesthetic) controller is given by

$$C(s) = 12.264\frac{s^2 + 111s + 530}{s(s + 260)}.$$

Figure 2 shows the magnitude [panel (a)] and the phase [panel (b)] of the frequency response for the open-loop system (dashed-dotted curve) and the closed-loop system (solid curve). The stability gain and phase margins achieved with the controller $C(s)$ are also shown in Fig. 2. A quantitative analysis of the system showed that the feedback controller was able to reject or reduce unwanted noise. The 60-Hz inline noise was imperceptible by human users due to rapidly falling slope of the closed-loop magnitude frequency response at 60 Hz. The finger load was rejected by keeping the closed-loop response close to the 0 dB line at low frequencies, and by selecting an appropriate bandwidth of about 30 Hz. In the loaded conditions (where the fingerpad was lightly placed on the fingerpad interface), the average deviations of the closed-loop response were 0.34 dB at 1 Hz, 1.43 dB at 8 Hz, 0.64 dB at 40, 0.3 dB at 100, and 0.65 dB at 260 Hz from the unloaded conditions (where the fingerpad interface was displaced with no finger load), measured at four intensity levels.

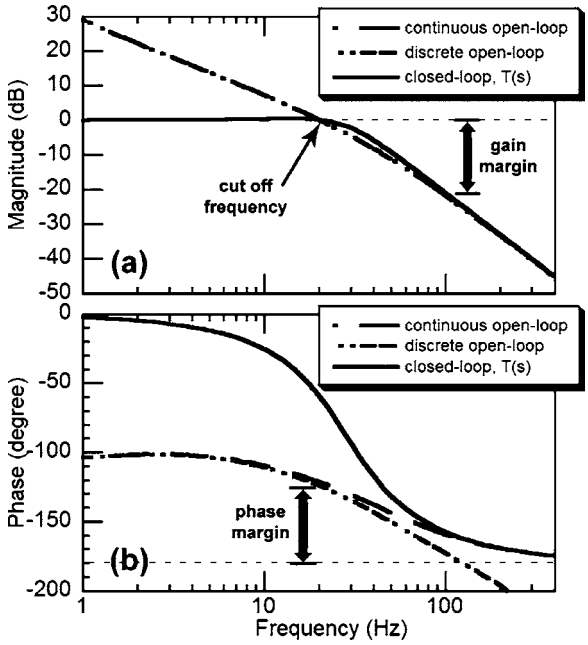

FIG. 2. Comparison of the frequency response of open-loop and closed-loop systems. (a) shows the magnitude response of the open-loop and closed-loop systems. A solid curve shows the input-output transfer function model of the closed-loop TactuatorII assembly. The response of the continuous and discrete open-loop responses overlaps. (b) shows phase response of the open-loop and closed-loop systems. Also shown in the figure are gain and phase margins, which are important criteria for system stability.

2. Prefilter controller for cutaneous stimulus region

For the design of the broadband controller component, i.e., the prefilter $F(s)$, we first considered the typical HDT curve as a function of sinusoidal stimulus frequencies[2] (Bolanowski *et al.*, 1988) (shown as solid curve in Fig. 3). The inverse of this detection-threshold curve was regarded as the sensitivity curve, or equivalently, the "frequency response" of the human user. The *perceived intensity* of a signal, in dB SL, is roughly determined by the distance between the physical intensity of the signal and the detection-threshold at the corresponding frequency (Verrillo and Gescheider, 1992). The effect of the human sensitivity curve on system performance is illustrated in Fig. 4. When a broadband cutaneous

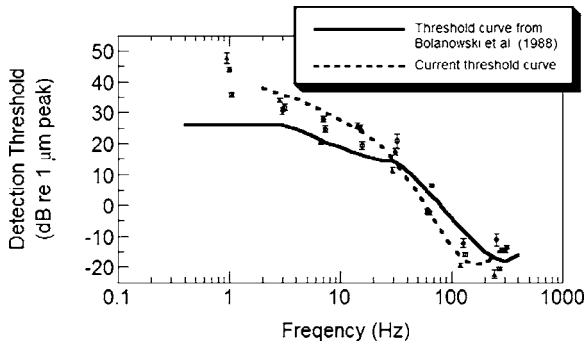

FIG. 3. A typical HDT curve as a function of frequency adapted from Bolanowski *et al.* (1988) (solid curve) and a HDT curve obtained in the present study (dashed curve). Also shown here are data points from three participants (S1—○, S2—□, and S3—△) and the standard errors of their threshold levels. The dashed curve is a first order approximation of the detection-threshold levels for three participants along the frequency continuum.

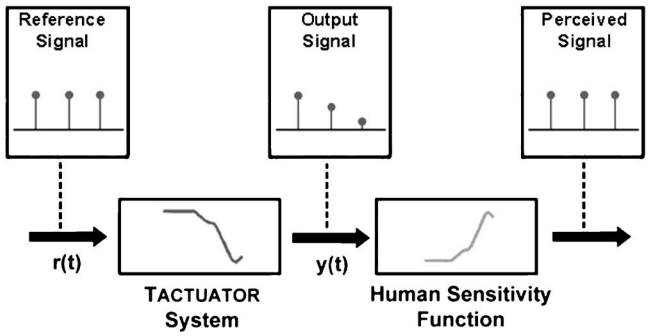

FIG. 4. Graphical illustration of the objectives for the high-frequency cutaneous controller. When the frequency-response function of the mechanical system matches with that of the HDT, the frequency function cancels the effects of variable human sensitivity function and preserves spectral components of the reference input signal.

controller is used to compensate for the human sensitivity function, equal intensities in the input signal (shown as equal intensities in the reference signal, Fig. 4) spectrum will result in equally strong sensations when received by a human user. Therefore, the steady-state response of the overall closed-loop system, $H(s)=F(s)T(s)$, should follow the target frequency function of the HDT curve in the frequency range dc to 300 Hz, i.e., $H(s)=\mathrm{HDT}(s)$.

It was anticipated that the HDT function with the fingerpad interface of the TactuatorII system would differ from that reported in Bolanowski *et al.*, 1988 based on the known

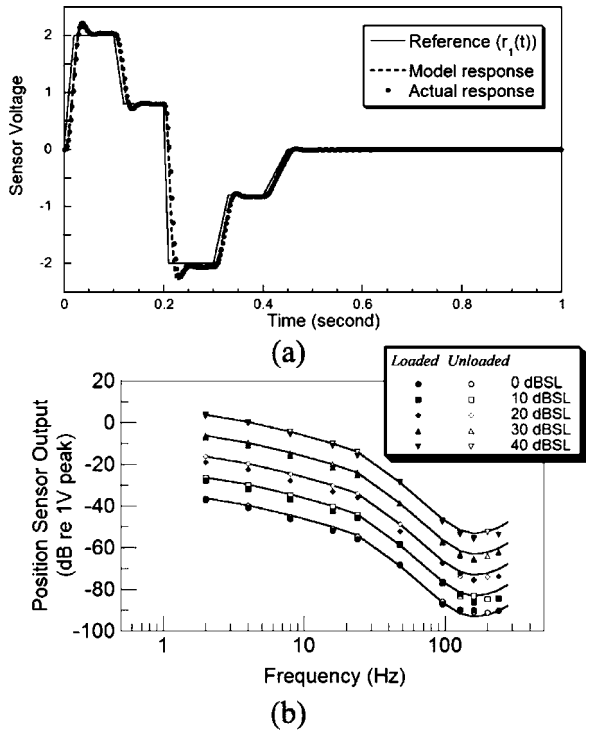

FIG. 5. (a) Response of TactuatorII for ramp signal applied at the reference input, $r_1(t)$, shown as solid line. The response of the model (dashed line) and actual mechanical assembly (dots) showed fast response time and low overshoot. (b) A comparison of the measured sensor outputs (individual data points) and the predicted output levels (solid lines) at 0, 10, 20, 30, and 40 dB SLs without the influence of human finger loading (unloaded condition shown as unfilled symbols) and with the influence of human finger loading (loaded condition as filled symbols).

variation in tactual thresholds with experimental conditions such as contact site, direction of vibrations, use of an annulus surround to restrict penetration of vibrations, etc. (Verrillo and Gescheider, 1992; Brisben *et al.*, 1999). Thus, the detection-thresholds for three highly trained participants were estimated in a psychophysical experiment. Detection-thresholds for 1-s stimulus at nine test frequencies (1, 3, 7, 15, 31, 63, 127, 255, and 300 Hz) were determined with a three-interval forced-choice paradigm combined with a one-up three-down adaptive procedure (Leek, 2001). Thresholds obtained this way corresponded to the 79.4-percentile point on the psychometric function. The results are shown in Fig. 3. Compared with the HDT curve determined by Bolanowski *et al.* (1988), which were measured at the thenar eminence, the newly measured thresholds measured on the index fingerpad followed the same general trend; however, our absolute-threshold measurements were somewhat higher than those of Bolanowski *et al.* (1988) at the lower frequencies and lower than theirs at the higher frequencies. These results were consistent with those found in other studies (Gescheider *et al.*, 1978; Van Doren, 1990; Goble *et al.*, 1996), and those taken earlier with the Tactuator using a Proportional-Integral-Derivative (PID) controller (Tan and Rabinowitz, 1996; Yuan, 2003).

The TactuatorII-specific HDTs were subsequently incorporated into the parameters of the prefilter controller, $F(s)$. A new HDT curve based on the measured data (dashed line in Fig. 3) was obtained and used as the required frequency function $H(s)=F(s)T(s)$. The Laplace transform of the resulting prefilter is

$$F(s) = 0.51\frac{s^4 + 1797s^3 + 1.822 \times 10^6 s^2 + 9.779 \times 10^8 s + 1.955 \times 10^{11}}{s^4 + 1134s^3 + 4.313 \times 10^6 s^2 + 1.337 \times 10^9 s + 1.995 \times 10^{10}}.$$

C. Controller response analysis

The 2DOF controller was implemented on a SBC6711 standalone DSP card (Innovative Integration, Simi Valley, CA) with a 16-bit Analog-to-Digital Converter (ADC) and a 16-bit Digital-to-Analog Converter (DAC) at a sampling rate of 4 kHz. The 2DOF controller design was analyzed by measuring closed-loop reference tracking and overall closed-loop frequency response in unloaded and loaded conditions. In order to readily compare the sensor feedback signal in volts with the threshold levels, the controller input reference was scaled by a factor of 0.003 97. This factor accommodated the magnitude level of the flat portion of the HDT function at lower frequencies (26 dB with regard to 1 μm peak or -34 dB with regard to 1 mm peak in Fig. 3, or equivalently 0.019 95) and the sensor gain of 0.198 98 V/mm.

1. Motion tracking

Figure 5(a) shows the response of the TactuatorII system for ramp trajectories applied at the reference input $r_1(t)$ without the influence of human finger load. Shown are the responses of the model (dashed line) and the actual hardware assembly (dots). The slopes of the reference trajectories were 0.1, -0.06, -0.28, 0.04, and 0.016 V/ms, respectively. The output (position) response of the hardware assembly showed that the low-frequency kinesthetic controller maintained stability of the device, and tracked the reference input with low response time (about 10 ms) and with a small response overshoot.

2. Frequency response

Sinusoidal reference input signals of 2-s duration at various frequencies, $r_2(t)$, were applied to the TactuatorII system, and the position-sensor readings were recorded. The results for unloaded (without finger load) and loaded (with finger placed lightly on the fingerpad interface) conditions are shown in Fig. 5(b). The bottom solid curve corresponds to the HDT curve measured with the TactuatorII (dashed line in Fig. 3), i.e., the 0 dB SL curve. The other four solid curves are at 10, 20, 30, and 40 dB SLs, respectively. The open symbols show the measured outputs at the five SLs with no finger load and the filled symbols show loaded results with a finger resting lightly on the fingerpad interface. There was generally a close match between the measured data points (filled and unfilled symbols) and the expected output levels (solid curves). Deviations at a few frequencies (especially at the highest frequencies) were likely due to signal noise and non-linear finger loading effects at such a low signal level. Therefore, the 2DOF controllers were successful at compensating for the frequency response of the motor assembly and the HDT curve, and the feedback controller was effective at rejecting the low-frequency disturbances caused by the finger load.

The engineering performance measurements presented above indicate that the 2DOF controller met the original design objectives in accurate and fast motion tracking, disturbance rejection, and broadband response shaping. Most importantly, we demonstrated the achievement of the main design objective of preserving the relative intensities of input signal spectral components in terms of dB SLs.

III. SPEECH-TO-TOUCH CODING

Speech features were extracted off-line in MATLAB (The MathWorks, Inc., Natick, MA) from the digitized speech segments and were converted into tactual signals presented through all three channels of the TactuatorII. Before the processing, the speech signal was passed through a pre-emphasis filter that amplified the energy above 1000 Hz at a

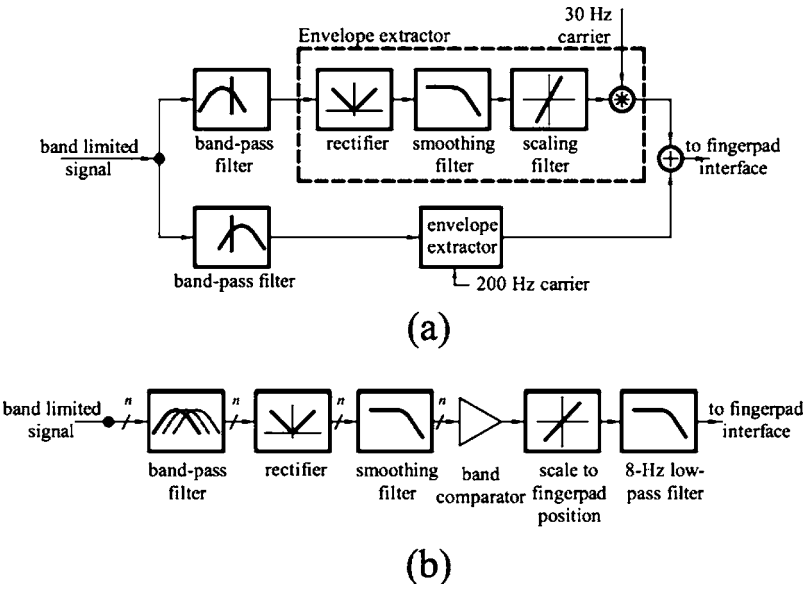

FIG. 6. (a) Block diagram illustration of tactile coding scheme used in the formant bands. (b) Block diagram illustration of motional coding scheme. Spectral features are extracted from three bands of speech signal and presented as motional waveforms.

typical rate of 6 dB/octave in order to compensate for the falling speech spectrum above 1000 Hz. Three major signal processing schemes were used for the extraction of spectral features: (1) low-pass filtering, (2) band-pass filtering, and (3) envelope extraction scheme of Grant *et al.*, (1985). In this scheme, the band-limited signal is rectified and passed through a low-pass filter to extract its temporal envelope, which is then scaled and output with a carrier frequency, as shown in Fig. 6(a). The coding scheme incorporates both high-frequency tactile vibrations and low-frequency motional waveforms.

A. Speech material

The speech materials consisted of C_1VC_2 nonsense syllables spoken by two female speakers of American descent. Each speaker produced eight tokens of each of 16 English consonants (the plosives, fricatives, and affricates: /p, t, k, b, d, g, f, θ, s, ʃ, v, ð, z, ʒ, tʃ, dʒ/) at the initial consonant (C_1) location with medial V = /ɑ/. The final consonant (C_2) was randomly selected from a set of 21 consonants (/p, t, k, b, d, g, f, θ, s, ʃ, v, ð, z, ʒ, tʃ, dʒ, m, n, ŋ, l, r/). The syllables were converted into digital segments and stored as a .mov (QuickTime Movie) file on the hard drive of a desktop computer (see details of conversion in Yuan, 2003). The .mov files were then converted into .wav (waveform audio) files by using CONVERTMOVIE 3.1 (MOVAVI, Novosibirsk, Russia) and with audio format set at a sampling rate of 11 025 Hz and 16-bit mono. The duration of the segments varied from 1.268 to 2.002 s with a mean duration of 1.653 s.

B. Tactile coding scheme

The coding scheme extracted envelopes from three distinct frequency bands (F0-, F1-, and F2-bands) of the speech spectrum and presented them as vibrations (mid- and high-frequency waveforms) through the three channels of the TactuatorII. Table I lists the numerical values for the frequency bands and corresponding finger channels. Spectral energy from the fundamental frequency (F0) region was presented at the thumb channel by passing the low-pass filtered speech signal directly through the 2DOF controller described in Sec. II. Information from the first-formant band (F1) was presented through the middle finger channel and the second-formant band (F2) information through the index finger channel, using processing units described in Fig. 6(a). The formant band-limited signal was processed through two band-pass filters, and amplitude envelopes of these two bands were extracted and modulated with carrier frequencies of 30 and 200 Hz. The 30-Hz waveforms modulated the envelope of the lower-frequency band and the 200-Hz waveforms modulated the higher-frequency band. The two vibratory signals were added and passed through the fingerpad interface. Since the digitized speech segments were normalized to one, the vibrations were scaled to a maximum intensity of 40 dB SL.

Figure 7 illustrates the vibration cues associated with two CVC segments spoken by two female speakers. The top two panels show the 30- and 200-Hz vibrations for segment /bɑC_2/ spoken by speaker 1 and the bottom two panels show the same by speaker 2. Note the similar waveforms at the two fingerpads associated with the same medial vowel /ɑ/. The vowel /ɑ/ has a high first formant and a low second formant. This is indicated by stronger 200-Hz vibrations than the 30-Hz vibrations at the middle fingerpad (see the two left panels in Fig. 7) and significantly stronger 30-Hz vibrations at the index fingerpad (see the two right panels). Cues associated with similar initial consonants are difficult to judge

TABLE I. Speech bands and the corresponding vibrations through the three channels.

TactuatorII channel	Speech bands (Hz)	Envelope bands (Hz)	Carrier frequency (Hz)
Middle finger	F1-band (300–1200)	300–650	30
		650–1200	200
Index finger	F2-band (1150–4000)	1150–1750	30
		1750–4000	200
Thumb	F0-band (80–270)	Low-pass filtered at 270 Hz	

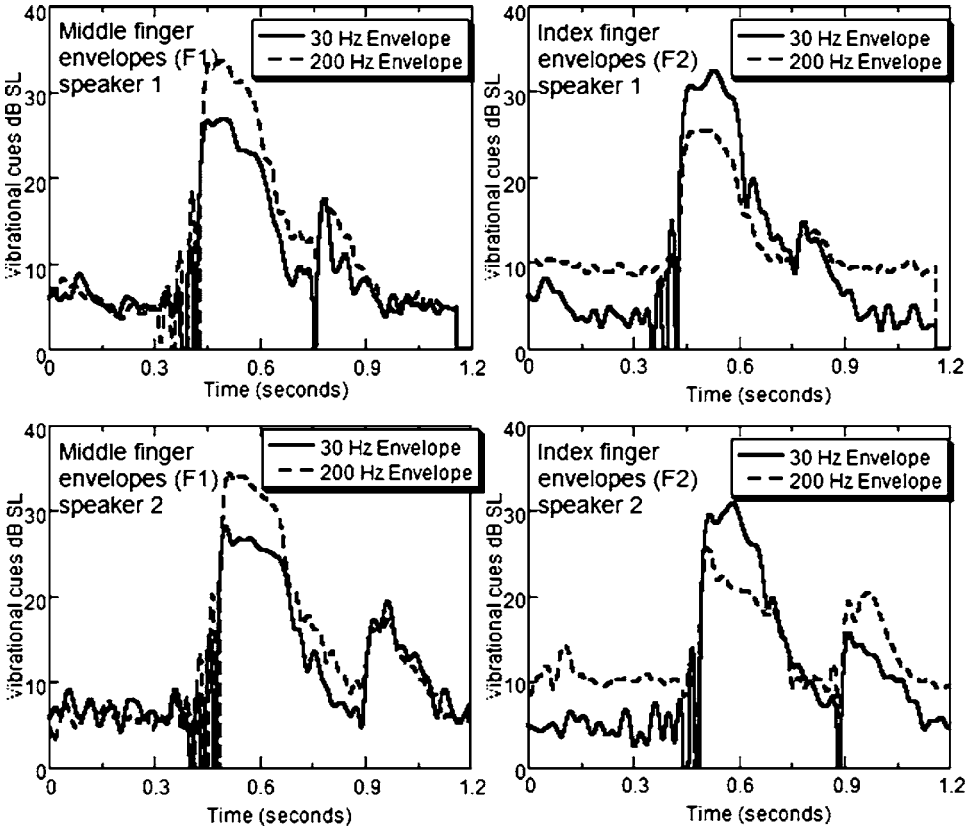

FIG. 7. Illustration of vibration waveforms extracted by using the speech-to-touch coding scheme. The figure shows vibration cues presented on the middle fingerpad (left panel) and on the index fingerpad (right panel). The cues are associated with multiple segments of /baC$_2$/ spoken by two female speakers (Sp1 or Sp2).

because they are not resolved for a small duration of time (either visually or through the tactual sensory system).

C. Motional coding scheme

The coding scheme extracted frequency variations in the F0-, F1-, and F2-bands using processing blocks shown in Fig. 6(b) and presented them through three channels of the TactuatorII. These motion cues indicated variations of spectral energy such as formant transition cues in the consonant-vowel segments and the quasi-static positions of the fingerpad interface redundantly indicated the frequency locations of energy peaks in the frequency band of each channel. As illustrated in Fig. 6(b), the formant band-limited signal was passed through contiguous band-pass filters in parallel and the temporal envelope of each band was obtained. The envelopes were compared and the center frequency of the band with the largest envelope value was noted at each sample instant. The center frequency was linearly mapped to the absolute reference position of the fingerpad interface that ranged ± 12.5 mm from the neutral zero position and was low-pass filtered with a gain crossover at 8 Hz. Thus, the finger extended for high-frequency contents and flexed for the low-frequency contents in the finger band. As with the tactile coding scheme, the features from the F0-, F1-, and F2-bands were presented to the thumb, middle finger, and index finger channels, respectively. The center frequencies and bands of each band-pass filters are shown in Table II. The frequency ranges covered by the middle finger and thumb channels were divided into eight bands, while the larger range encompassed by the index finger channel was divided into ten bands. Illustration of the motion cues associated with two segments of six initial consonants in CVC format spoken by the two speakers is shown in Fig. 8.

IV. PRELIMINARY STUDY OF CONSONANT DISCRIMINATION

A perception study was conducted on the pairwise discriminability of consonants that were processed for display through the three finger-interfaces of the TactuatorII system.

A. Methods

The ability to discriminate consonantal features was tested for 20 pairs of initial consonants that contrasted in voicing, place, and manner features. Each pair contrasted one

TABLE II. Frequency bands for motional cues.

	Frequency band (Hz)		
Filter index	Middle finger	Index finger	Thumb
1	300–400	1150–1300	80–100
2	400–500	1300–1500	100–120
3	500–600	1500–1700	120–140
4	600–700	1700–1900	140–160
5	700–800	1900–2100	170–200
6	800–900	2100–2300	200–220
7	900–1000	2300–2500	220–240
8	1000–1200	2500–3000	240–260
9	N/A	3000–4000	N/A
10	N/A	4000 – 5000	N/A

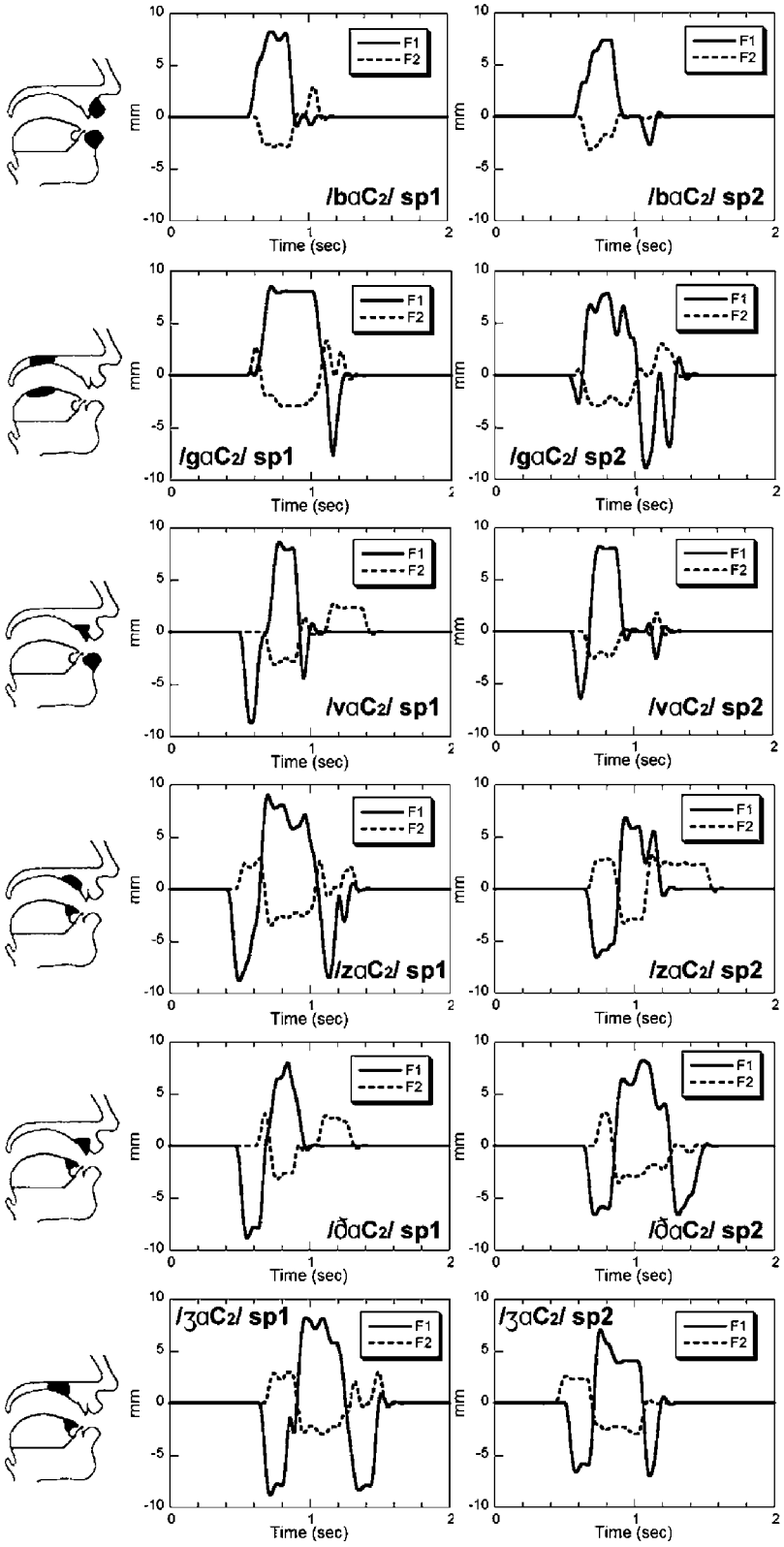

FIG. 8. Illustration of motion waveforms extracted by using the speech-to-touch coding scheme. Each row shows the waveforms associated with two segments of the same initial consonant spoken by two female speakers (sp1 or sp2). The waveforms correspond to the formant location and formant transitions in the first-formant band (solid line, motion waveforms at the middle finger) and in the second-formant band (dashed line, motion waveforms at the index finger). Also shown are the locations of constriction during the production of the initial consonant.

of the three features (and had the same value for each of the other two features). The pairs used in the present study along with their contrasting features are shown in Table III. Out of the 20 pairs, 5 pairs contrasted in voicing, 8 pairs contrasted in place, and 7 pairs contrasted in manner. Two male participants (ages 30 and 22 years old) took part in the experiments. S1, who is one of the authors, was highly experienced with the TactuatorII system, but S2 had not used the device prior to the present study. Both S1 and S2 were research staff members with previous experience in other types of haptic experiments.

The tests were conducted using a two-interval two-alternative forced-choice paradigm (Macmillan and Creelman, 2004). On each trial, the participant was presented with two tactual stimuli associated with a specific pair of consonants. The order of the two consonants was randomized with

TABLE III. Contrasting consonant pairs, associated articulatory and phonetic features, and average evaluation scores in C3.

Pairs	Articulatory features	Contrasting distinction	d'
/p-b/	Bilabial plosives	Voicing	4.65
/k-g/	Velar plosives	Voicing	2.90
/f-v/	Labiodental fricatives	Voicing	2.36
/s-z/	Alveolar fricatives	Voicing	3.78
/tʃ-dʒ	Affricates	Voicing	3.81
/p-t/	Unvoiced plosives-bilabial/alveolar	Place	2.38
/t-k/	Unvoiced plosives-alveolar/velar	Place	1.66
/b-d/	Voiced plosives-bilabial/alveolar	Place	3.80
/d-g/	Voiced plosives-alveolar/velar	Place	2.13
/f-s/	Unvoiced fricatives labiodental/alveolar	Place	1.46
/v-z/	Voiced fricatives labiodental/alveolar	Place	3.80
/θ-ʃ/	Unvoiced fricatives dental/post-alveolar	Place	2.66
/ð-ʒ/	Voiced fricatives dental/post-alveolar	Place	3.60
/p-f/	Unvoiced bilabial plosives/labiodental fricative	Manner	3.12
/b-ð/	Voiced bilabial plosives/dental fricative	Manner	3.47
/t-s/	Unvoiced alveolar plosive/fricative	Manner	3.60
/d-ʒ/	Voiced alveolar plosive/post-alveolar fricative	Manner	4.65
/d-dʒ/	Voiced alveolar plosive/affricate	Manner	2.37
/s-tʃ/	Unvoiced alveolar fricative/affricate	Manner	3.00
/ʃ-tʃ/	Unvoiced post-alveolar fricative/affricate	Manner	3.38

equal *a priori* probability in each trial. The participant was instructed to press a button corresponding to the order of the consonants presented. The duration of each stimulus interval was 2 s with an inter-stimulus-interval of 500 ms. A 150-ms auditory tone and a visual phrase indicating "stimulus 1" or "stimulus 2" were presented 250 ms before the start of each stimulus to mark the beginning of each stimulus interval.

Data were collected for each consonant pair under three different experimental conditions tested in a single session: A 20-trial initial run without any feedback (C1), up to four 20-trial runs with trial-by-trial correct-answer feedback (C2), and a 50-trial final run without feedback (C3). Condition C2 was terminated if a percent-correct score above 90% was obtained in a single run or when the participant had completed all four runs. Conditions C1 and C3 could be viewed as the initial and final assessments of the participants' performance, while C2 provided training as needed (although one could argue that S1 was already "trained" prior to C1). Half of the 256 total speech tokens were used in conditions C1 and C3 and the other half were used in condition C2. Thus, the two sounds associated with each discrimination test were represented by eight tokens apiece (four from each of the two speakers). Each consonant within a pair was presented once or twice to the participant before C1 to familiarize the participant with its tactual cues. The order in which consonant pairs were tested was randomized for each participant. Each participant was tested for no more than two 40–45 min sessions on a single day, and frequent rests were encouraged.

For each experimental run, a 2×2 stimulus-response confusion matrix was obtained, from which the percentage-correct (PC) score, the sensitivity index d', and the response bias β were calculated using signal-detection theory (Macmillan and Creelman, 2004). The sensitivity index was set to 4.65 (corresponding to a hit rate of 0.99 and a false-alarm rate of 0.01) when the performance was perfect.

During the experiment, the TactuatorII was placed to the left of the participant's torso. It was covered by a padded wooden box that served as an armrest for the participant's left forearm. The top of the box had an opening that allowed the participant to place the thumb, the index finger, and the middle finger on the "fingerpad interface" rods (see inset in Fig. 1). Earmuff (Twin-Cup type, H10A, NRR 29, Peltor, Sweden) and pink noise (presented at roughly 80 dB SPL) were used to eliminate possible auditory cues.

B. Results

In general, performance indices increased as the participants gained more experience with the stimuli. Overall, the average sensitivity index of all pairs increased from $d'=2.66$ (PC=83%) in C1 to $d'=3.13$ (PC=91%) in C3. A pairwise two-sided t-test showed that sensitivity scores in C3 were significantly higher than in C1 [$t(39)=2.16$, $p<0.05$]. The sensitivity indices averaged over the two participants for each contrasting consonant in condition C3 are shown in Table III. For consonants contrasting in the voicing, place, and manner of articulation features, the performance levels of the two participants were similar in C3: $d'=3.5$ for S1 and $d'=3.5$ for S2 in voicing, $d'=2.8$ for S1 and $d'=2.6$ for S2 in place, and $d'=3.2$ and $d'=3.6$ for S1 and S2, respectively, in manner distinction. The response bias across the 20 consonant pairs ranged from $\beta=-0.74$ to $\beta=0.63$ and averaged $\beta=0.008$, indicating that the participants generally demonstrated little or no bias in their use of the two response choices. Both participants performed perfectly in discriminating the two consonant pairs /p,b/ and /d,ʒ/. For the remaining pairs, the participants' relative performance levels were mixed as one participant performed better than the other with some pairs but not others. In all cases, d' was greater than 1.0, a typical criterion for discrimination threshold, indicating that the coding scheme succeeded in providing the cues needed for the discrimination of the consonant pairs.

V. DISCUSSION

The coding scheme used in the present study was an extension of the scheme presented in Yuan, 2003, where the envelope of the low-frequency speech band (<350 Hz) was modulated with a 50-Hz vibration at the thumb and the envelope of the high-frequency speech band (>3000 Hz) was modulated with a 250-Hz vibration at the index finger. This scheme was successful in pairwise discrimination of initial consonants that contrasted in voicing only. On average, discriminability of roughly 90% and d' of 2.4 were obtained for eight voiced-unvoiced pairs in four participants. Our coding scheme presented the low-frequency speech band (fundamental frequency band) directly at the thumb and the envelopes of the high-frequency speech band (second-formant band) at the index fingerpad, consistent with the scheme presented in Yuan,2003. The results of the two studies show similar performance: An average discriminability of 94% and d' of 3.5 were obtained in the present study when contrasting

five voiced-unvoiced consonant pairs, indicating that the coding scheme used in Yuan, 2003 was a subset of the scheme used in the present study. The performance level obtained in the present study also appears to compare favorably with the results reported by earlier studies of tactual displays, where discrimination scores were generally less than 75% (Plant, 1989; Clements *et al.*, 1988; Galvin *et al.*, 1999; Waldstein and Boothroyd, 1995; Weisenberger *et al.*, 1989; Summers *et al.*, 2005).

In addition to incorporating the amplitude information from low- and high-frequency speech bands, as in Yuan, 2003, our coding scheme displays energy information from the mid-frequency speech band in the form of temporal envelopes as well as low-frequency motion cues from the three speech bands to the corresponding fingerpads. To the best of our knowledge, this is the first time that low-frequency motion cues have been used to encode speech spectral information. These cues provide both frequency *location* and frequency *transition* information of formants to the receiver's fingerpads. The transition of formants is useful for the distinction of the place of articulation feature in consonants as indicated in Ali *et al.*, 2001a,2001b and Jongman *et al.*,2000. Although some studies have presented contradictory results arguing that formant transitions are not useful for distinguishing place of articulation in consonants [e.g., see a review by Jongman *et al.* (2000)], motion waveforms extracted from the speech-to-touch coding scheme in the present study (see Fig. 8) indicate distinction in transitions as the place of constriction during the production of consonants varies from lips to velum. The cues associated with transition of the second formant can be observed in Fig. 8 (dashed lines). The index finger flexes at the onset of the initial bilabial plosive /b/ and stays flexed for the medial vowel /ɑ/ (first row). The index finger extends at the onset of the initial velar plosive /g/ and flexes at the onset of the medial vowel /ɑ/ (second row). Similarly, for fricatives, the index finger stays at the neutral zero position at the onset of the initial labiodental consonant /v/ (third row) and slightly extends at the onset of the initial dental fricative /ð/ (fifth row). The index finger extends for a longer duration at the onset of the initial alveolar and the post-alveolar fricatives /z/ and /ʒ/ before it flexes at the onset of the medial vowel /ɑ/ (fourth and sixth rows). Thus, as the place of articulation of consonant moves from near lips (bilabials) to near velum, the index finger extends more for the latter initial consonants (corresponding to an increase in F2 associated with an effective shortening of the vocal tract for velar as opposed to labial constrictions). This may explain the better performance level we have achieved in the present study due to the utilization of place of articulation cues.

Results of the pairwise consonantal discrimination experiments in the present study showed that both participants were able to discriminate all eight consonant pairs that differed in the place of articulation feature with an average discriminability of 88% and a d' of 2.7. The results of previous studies with tactual displays indicate poor transmission of place cues. For example, Clements *et al.* (1988) used a 12-by-12 pin tactual matrix display to present acoustic features as vibrations along the two dimensions of the display similar to that in the spectrogram used for speech analysis. The pairwise discrimination performance of the manner of articulation and voicing features was satisfactory (71% for voicing and 80% for manner) but discriminability of place of articulation distinction was poorer, i.e., 66%. Even with the multi-channel spectral display of the Queen's vocoder studied by Weisenberger *et al.* (1989), place of articulation was not discriminated as well as other features (65% for place compared to 75% for manner and 70% for voicing). In other studies, discriminability of place of articulation was at chance level (Waldstein and Boothroyd, 1995; Plant, 1989; Summers *et al.*, 2005; Weisenberger and Percy, 1995; Galvin *et al.*, 1999). Therefore, it appears that the present coding scheme was able to transmit the place of articulation feature more successfully than has been demonstrated previously.

Consonants contrasting manner of articulation have been shown to be well discriminated with the tactile displays of previous studies, i.e., 80% in Clements *et al.*, 1988, 75% in Weisenberger *et al.*, 1989, ≤90% in Weisenberger and Percy, 1995, 70% in Plant, 1989, and <85% in Summers *et al.*, 2005. In the present study, the discriminability of manner of articulation was always greater than 90% except for the /s/-/tʃ/ contrast (88%) by S1 and the /d/-/dʒ/ contrast (84%) by S2. The manner of articulation distinction is associated with coarse spectral variations in speech such as abrupt or smooth temporal variations (e.g., plosives vs fricatives) or the combination of both (as in affricates). The manner discrimination results obtained in the present study are comparable to the best performance obtained with previous tactile speech displays.

A major distinction between the present and previous studies is that the previous displays utilized either the tactile or the kinesthetic sensory system, but not both, to transmit acoustic and phonetic features associated with consonantal and vocalic contrasts (Bliss, 1962; Tan *et al.*, 1997). The two sensory systems are perceptually independent (Bolanowski *et al.*, 1988; Israr *et al.*, 2006) and can be utilized simultaneously to improve the transmission of features associated with speech signals. Tan *et al.* (1999, 2003) formed a set of synthetic waveforms from the two sensory systems and demonstrated that relatively high rates of information could be transmitted through the tactual sense. In the present study, we utilized the entire kinesthetic-cutaneous sensory continuum in an effort to broaden the dynamic range of tactual perception, similar to the Tadoma method, and to improve speech transfer through the human somatosensory system. Our results demonstrate that with the new controller and the coding scheme reported here that engage both the kinesthetic and cutaneous aspects of the somatosensory system, normal-hearing participants were able to discriminate consonantal features at a level that is similar to or higher than those reported by previous studies with other types of tactual speech-information displays.

ACKNOWLEDGMENTS

This research was supported by Research Grant No. R01-DC00126 from the National Institute on Deafness and

Other Communication Disorders, National Institutes of Health.

[1]The first Tactuator was developed at MIT (Tan and Rabinowitz, 1996). A second device, the TactuatorII, was subsequently developed at Purdue University with essentially the same hardware.

[2]The unit "dB with regard to 1 μm peak" is commonly used with HDTs. It is computed as $20 \log_{10}(A/1.0)$ where A denotes the amplitude (in μm) of the sinusoidal signal that can be detected by a human participant at a specific frequency.

Ali, A. M. A., Van der Spiegel, J., and Mueller, P. (**2001a**). "Acoustic-phonetic features for the automatic classification of fricatives," J. Acoust. Soc. Am. **109**, 2217–2235.

Ali, A. M. A., Van der Spiegel, J., and Mueller, P. (**2001b**). "Acoustic-phonetic features for the automatic classification of stop consonants," IEEE Trans. Speech Audio Process. **9**, 833–841.

Bliss, J. C. (**1962**). "Kinesthetic-tactile communications," IRE Trans. Inf. Theory **8**, 92–99.

Bolanowski, S. J., Gescheider, G. A., Verrillo, R. T., and Checkosky, C. M. (**1988**). "Four channels mediate the mechanical aspects of touch," J. Acoust. Soc. Am. **84**, 1680–1694.

Brisben, A. J., Hsiao, S. S., and Johnson, K. O. (**1999**). "Detection of vibration transmitted through an object grasped in the hand," J. Neurophysiol. **81**, 1548–1558.

Clements, M. A., Braida, L. D., and Durlach, N. I. (**1988**). "Tactile communication of speech: Comparison of two computer-based displays," J. Rehabil. Res. Dev. **25**, 25–44.

Craig, J. C., and Evans, P. M. (**1987**). "Vibrotactile masking and the persistence of tactual features," Percept. Psychophys. **42**, 309–371.

Evans, P. M. (**1987**). "Vibrotactile masking: Temporal integration, persistence and strengths of representations," Percept. Psychophys. **42**, 515–525.

Galvin, K. L., Mavrias, G., Moore, A., Cowan, R. S. C., Blamey, P. J., and Clark, G. M. (**1999**). "A comparison of Tactaid II+ and Tactaid 7 use by adults with a profound hearing impairment," Ear Hear. **20**, 471–482.

Gescheider, G. A., Capraro, A. J., Frisina, R. D., Hamer, R. D., and Verrillo, R. T. (**1978**). "The effects of a surround on vibrotactile thresholds," Sens Processes **2**, 99–115.

Goble, A. K., Collins, A. A., and Cholewiak, R. W. (**1996**). "Vibrotactile threshold in young and old observers: The effects of spatial summation and the presence of a rigid surround," J. Acoust. Soc. Am. **99**, 2256–2269.

Grant, K. W., Ardell, L. H., Kuhl, P. K., and Sparks, D. W. (**1985**). "The contribution of fundamental frequency, amplitude envelope, and voicing duration cues to speechreading in normal-hearing subjects," J. Acoust. Soc. Am. **77**, 671–677.

Israr, A. (**2007**). "Tactual transmission of phonetic features," Ph.D. thesis, Purdue University, West Lafayette, IN.

Israr, A., Tan, H. Z., and Reed, C. M. (**2006**). "Frequency and amplitude discrimination along the kinesthetic-cutaneous continuum in the presence of masking stimuli," J. Acoust. Soc. Am. **120**, 2789–2800.

Jongman, A., Wayland, R., and Wong, S. (**2000**). "Acoustic characteristics of English fricatives," J. Acoust. Soc. Am. **108**, 1252–1263.

Leek, M. R. (**2001**). "Adaptive procedures in psychophysical research," Percept. Psychophys. **63**, 1279–1292.

Maciejowski, J. M. (**1989**). *Multivariable Feedback Design* (Addison-Wesley, Reading, MA).

Macmillan, N. A., and Creelman, C. D. (**2004**). *Detection Theory: A User's Guide* (Lawrence Erlbaum Associates, New York).

Plant, G. (**1989**). "A comparison of five commercially available tactile aids," Aust. J. Audiol. **11**, 11–19.

Reed, C. M., and Durlach, N. I. (**1998**). "Note on information transfer rates in human communication," Presence—Teleoperators & Virtual Environments **7**, 509–518.

Reed, C. M., Rabinowitz, W. M., Durlach, N. I., Braida, L. D., Conway-Fithian, S., and Schultz, M. C. (**1985**). "Research on the Tadoma method of speech communication," J. Acoust. Soc. Am. **77**, 247–257.

Shannon, R. V., Zeng, F.-G., Kamath, V., Wygonski, J., and Ekelid, M. (**1995**). "Speech recognition with primarily temporal cues," Science **270**, 303–304.

Summers, I. R. (**1992**). *Tactile Aids for the Hearing Impaired* (Whurr, London).

Summers, I. R., Dixon, P. R., Cooper, P. G., Gratton, D. A., Brown, B. H., and Stevens, J. C. (**1994**). "Vibrotactile and electrotactile perception of time-varying pulse trains," J. Acoust. Soc. Am. **95**, 1548–1558.

Summers, I. R., Whybrow, J. J., Gratton, D. A., Milnes, P., Brown, B. H., and Stevens, J. C. (**2005**). "Tactile information transfer: A comparison of two stimulation sites," J. Acoust. Soc. Am. **118**, 2527–2534.

Tan, H. Z., Durlach, N. I., Rabinowitz, W. M., Reed, C. M., and Santos, J. R. (**1997**). "Reception of Morse code through motional, vibrotactile and auditory stimulation," Percept. Psychophys. **59**, 1004–1017.

Tan, H. Z., Durlach, N. I., Reed, C. M., and Rabinowitz, W. M. (**1999**). "Information transmission with a multifinger tactual display," Percept. Psychophys. **61**, 993–1008.

Tan, H. Z., and Rabinowitz, W. M. (**1996**). "A new multi-finger tactual display," *Proceedings of the International Symposium on Haptic Interfaces for Virtual Environment and Teleoperator Systems*, edited by K. Danai (American Society of Mechanical Engineers, New York), Vol. **58**, pp. 515–522.

Tan, H. Z., Reed, C. M., Delhorne, L. A., Durlach, N. I., and Wan, N. (**2003**). "Temporal masking of multidimensional tactile stimuli," J. Acoust. Soc. Am. **114**, 3295–3308.

Van Doren, C. L. (**1990**). "The effects of a surround on vibrotactile thresholds: Evidence for spatial and temporal independence in the non-Pacinian I (NPI) channel," J. Acoust. Soc. Am. **87**, 2655–2661.

Verrillo, R. T., and Gescheider, G. A. (**1992**). "Perception via the sense of touch," in *Tactile Aids for the Hearing Impaired*, edited by I. R. Summers (Whurr, London), pp. 1–36.

Waldstein, R. S., and Boothroyd, A. (**1995**). "Comparison of two multichannel tactile devices as supplements to speechreading in a postlingually deafened adult," Ear Hear. **16**, 198–208.

Weisenberger, J. M., Broadstone, S. M., and Saunders, F. A. (**1989**). "Evaluation of two multichannel tactile aids for the hearing impaired," J. Acoust. Soc. Am. **86**, 1764–1775.

Weisenberger, J. M., and Percy, M. E. (**1995**). "The transmission of phoneme-level information by multichannel tactile speech perception aids," Ear Hear. **16**, 392–406.

Yuan, H. (**2003**). "Tactual display of consonant voicing to supplement lipreading," Ph.D. thesis, Massachusetts Institute of Technology, Cambridge, MA.

On the relationship between palate shape and articulatory behavior

Jana Brunner[a)]
Humboldt-Universität zu Berlin, 10099 Berlin, Germany; Zentrum für Allgemeine Sprachwissenschaft 10117, Berlin, Germany; and ICP/GIPSA-lab, CNRS, INPG, Université Stendhal and Université Joseph Fourier, Grenoble, France

Susanne Fuchs
Zentrum für Allgemeine Sprachwissenschaft, Berlin, Germany

Pascal Perrier
ICP/GIPSA-lab, CNRS, INPG, 38402 Grenoble, Université Stendhal 38040 Grenoble and Université Joseph Fourier, 38041 Grenoble, France

(Received 14 October 2006; revised 30 March 2009; accepted 1 April 2009)

In this study the acoustic and articulatory variabilities of speakers with different palate shapes were compared. Since the cross-sectional area of the vocal tract changes less for a slight change in tongue position if the palate is domeshaped than if it is flat, the acoustic variability should be greater for flat palates than for domeshaped ones. Consequently, it can be hypothesized that speakers with flat palates should reduce their articulatory variability in order to keep the acoustic output constant. This hypothesis was tested on 32 speakers recorded via electropalatography (EPG) and acoustics. The articulatory and acoustic variability of some of their vowels and /j/ was measured. Indeed, the results show that the speakers with flat palates reduce their variability in tongue height. There is no such trend in acoustic variability. © *2009 Acoustical Society of America.* [DOI: 10.1121/1.3125313]

PACS number(s): 43.70.Bk, 43.70.Mn [CHS] Pages: 3936–3949

I. INTRODUCTION

Since Stevens' seminal paper [Stevens (1972)] it is known that the relationship between articulation and acoustics is nonlinear. In the present study we make use of this nonlinearity in order to investigate speakers' control of variability. Basically, we compare speakers for whom theoretical models of articulatory-acoustic relations predict that they can allow for much articulatory variability without having as much variability in the acoustic output with speakers for whom the models suggest that they cannot allow for so much articulatory variability because then the acoustic output would be too variable. The differences in speakers' variability are assumed to exist because of differences in morphology.

Let us consider two ideal and very different palate shapes in the coronal plane, the one very flat and the other very curved or domeshaped (cf. Fig. 1). Let us also consider for the sake of simplicity and clarity in the demonstration that both palates would have the same distance d_{teeth} between the molars (symbolized as squares). The speaker with the domeshaped palate (right side in the figure) then has to move his or her tongue further up in order to have the same cross-sectional area A as the speaker with the flat palate. The width of the vocal tract at the height of the tongue surface is then d_{tong}, which is smaller than d_{teeth}. For the flat palate d_{tong} would be equal to d_{teeth} and is therefore not given in the figure.

If the tongue is now raised by Δd, the distance between tongue and palate changes to $d_c - \Delta d$ for the domeshaped palate (c stands for *curved*) and $d_f - \Delta d$ for the flat palate. The difference between the original and the new area is for the flat palate

$$\Delta A_f = d_{\text{teeth}} \times \Delta d. \tag{1}$$

For the domeshaped palate, if we approximate the palate sides with straight lines,

$$d_{\text{tong}} = \frac{d_{\text{teeth}} \times d_c}{h_c} \tag{2}$$

the difference in the cross-sectional area is

$$\Delta A_c = d_{\text{teeth}} \Delta d \frac{d_c}{h_c}. \tag{3}$$

Given that h_c (height of the domeshaped palate) is greater than d_c (distance between tongue and domeshaped palate) the fraction d_c / h_c is smaller than 1. Consequently, a comparison between Eqs. (1) and (3) shows that ΔA_c is smaller than ΔA_f. This means that for the same change in articulation the area changes more for the flat palate than for the domeshaped one. Hence, for the same tongue movement, one of the perceptually relevant characteristics of the vocal tract (i.e., the constriction area) will change to a larger extent if the palate is flat than if it is domeshaped.

Under the assumption that speakers should be interested in keeping the acoustic output constant, it is hypothesized that speakers should compensate for these differences in the acoustics caused by differences in palate shape: Speakers

a)Author to whom correspondence should be addressed. Electronic mail: brunner@zas.gwz-berlin.de

 0001-4966/2009/125(6)/3936/14/$25.00

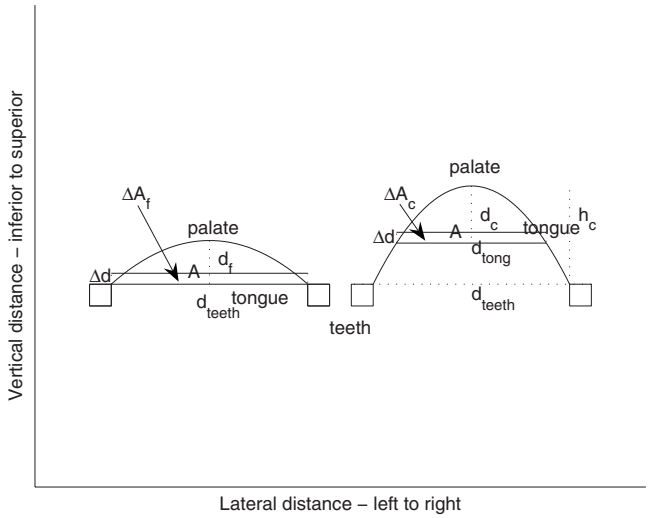

FIG. 1. Schematization of the influence of articulatory variability on the cross-sectional area for speakers with flat palates (left side) and domeshaped palates (right side). Solid lines refer to morphological structures (palate, tongue surface, and teeth). Two tongue positions are given (cf. the two parallel horizontal solid lines). Given the same distance d_{teeth} between the molars (squares), the same variation Δd in the sagittal distance, and the same cross-sectional area A for both palates, ΔA (the wide quadrilateral) is greater for the flat palate than for the domeshaped palate. d_f: cross-sectional distance for flat palate, d_c: cross-sectional distance for domeshaped palate, h_c: height of the domeshaped palate, d_{teeth}: width of the vocal tract at the height of the molars, and d_{tong}: width of the vocal tract at the height of the tongue surface for the domed palate. For the flat palate d_{tong} would be equal to d_{teeth} and is therefore not shown.

with flat palates should reduce their articulatory variability in order to keep the acoustic variability within an acceptable range.

In fact, evidence for differences in articulatory variability associated with these kinds of vocal tract differences has previously been found. Perkell (1997) compared six speakers with different palatal vaults who produced /i/, /ɪ/, and /ɛ/. He found that the speaker with the shallowest vault showed the smallest variability in tongue height for the three vowels. The result has been supported by Mooshammer *et al.* (2004) for the more crowded vowel inventory of German. They compared three speakers, two of them with a domeshaped palate and one with a flat palate, and found that the speaker with a flat palate had a lower articulatory variability as compared to the other speakers.

In this context, the study deals with the following questions. (1) Is the acoustic variability of speakers comparable, no matter what their palate shape is? (2) Is the articulatory variability greater for speakers with domeshaped palates than for speakers with flat palates?

Whereas question (2) deals with the relation between articulatory variability and the palate shape, question (1) deals with the relation between acoustic variability and the palate shape.

In order to investigate these questions 32 speakers were recorded acoustically and via electropalatography (EPG), a method for investigating linguo-palatal contact. The formant variability and the variability of the linguo-palatal contacts were calculated. Furthermore, the shape of the speakers' palates was estimated. If speakers with flat palates turn out to have less articulatory variability but the same acoustic variability as other speakers, this would support the hypothesis that speakers with a flat palate reduce their articulatory variability in order to keep the acoustic variability at a level which the listener can tolerate.

Section II describes the EPG experiment. Section III describes its results. In Sec. IV the results are discussed.

II. METHODS

Section II A gives information about the speakers, their gender, and which language they speak. Section II B describes the variation in palate shape in humans and how we determined the palate shape of our speakers. Section II C describes the recording procedure. Section II D deals with the problem of different crowdedness of the phoneme inventory in the different languages of our speakers, which could influence our measurements of variability. Section II E describes our measurements of articulatory variability. Articulatory variability was assessed in three ways: (1) as the coefficient of variation in the percent of contact (POC) over the complete segment, (2) as the standard deviation of the center of gravity (COG) at the articulatory target, and (3) as the coefficient of variation in the number of contacts in a row. Finally, in Sec. II F we describe how we assessed acoustic variability, i.e., as the standard deviation of the first three formants over the complete segment. Section II G describes the statistics carried out.

A. Speakers

Since the question investigated here is not bound to a certain language but to human speech production in general, 32 speakers of languages featuring different phonological characteristics were recorded:

- 2 speakers of Bulgarian (1 male, 1 female),
- 3 speakers of Polish (1 male, 2 females),
- 11 speakers of English [5 English (2 males, 3 females), 4 Scottish (3 males, 1 female), 1 American (male), and 1 Australian (male)],
- 10 speakers of German (6 males, 4 females),
- 6 speakers of Norwegian (Urban East Norwegian, 2 males, 4 females).

We thus had 15 female and 17 male speakers. Since the gender can be expected to influence at least the acoustic variability we carried out statistical tests for a gender effect in our data.

B. Characterization of the palate shape

Human palates differ considerably both in size and curvature. In the sample of adult palates of Vorperian *et al.* (2005) length variation goes from about 3.7 to 5.2 cm. However, the human palate changes from birth to adulthood. The greatest changes in palate shape take place in very early childhood. Vorperian *et al.* (2005) investigated the growth and restructuring of the vocal tract until the age of 6. They found that the hard palate grows very rapidly until the age of 18 months, where it has reached 80% of its adult mature

size. Cheng *et al.* (2007) showed that there are significant changes in palate shape until the age of 11 which go together with differences in articulatory control (e.g., place of articulation and amount of palatal contact). After age 11 the shape of the palate stays about the same even if the articulatory control develops further. Hiki and Itoh (1986) found that the adult palate is typically deeper than the child's palate.

Fitch and Giedd (1999) showed that from puberty onward there is a gender difference in vocal tract anatomy. These differences are most pronounced in the lips and the pharynx [see also Fant (1966)] which are disproportionately larger in men than in women, and this difference goes beyond the one explainable by body size. Fitch and Giedd (1999), however, did not find changes with regard to palate size between males and females except for those which are due to differences in body size.

Cheng *et al.* (2007) found possible gender differences in palatal contact, which, however, were inconsistent. The authors concluded that "no genuine differences may exist between the sexes" (p. 387).

Since our speakers were all at least 25 years old, one can assume that they have the typical more curved adult palate and adult articulatory patterns. Even if clear gender differences have so far not been found in the literature, we will carry out statistical tests in order to see whether there are gender differences in palatal shape and variability.

In this study we focus on palatal doming. In order to investigate the relationship between palatal doming and variability one needs to determine the curvature of the palate. Measurements were made from the cast of each palate which existed in the form of an EPG palate.

At first the coordinates of each of the 62 electrodes were measured using a caliper. In order to do so the EPG palate was placed on a photocopier and a high quality copy was made on which two dimensions of the placement of each electrode could be seen. A coordinate system was set up on the photocopy with the point of origin in the leftmost, most posterior electrode. The abscissa was set up from the two outermost electrodes on the most posterior row of electrodes. The ordinate was set up perpendicular to the abscissa. Then the x and y values of each electrode were measured with the caliper.

In order to measure the third dimension the artificial palate was put in the dental cast of the subject. A Plexiglas disk with a small hole in it was placed on top. The disk was moved so that the hole was exactly above the electrode to be measured. The caliper was put through the hole, and the distance from the electrode to the Plexiglas disk was measured.

A result of this can be seen in Fig. 2. We selected the sixth row from the front for calculating the coefficient α. This coefficient models the relationship between sagittal distance and area function and gives information about palatal curvature for a constant tongue curvature (cf. Appendix). The sixth row was taken because it presents the middle of the palatal zone. Since the electrode placing of the EPG palate is carried out according to certain anatomical landmarks [Wrench (2007)] the measurement is on the whole comparable for all palates.

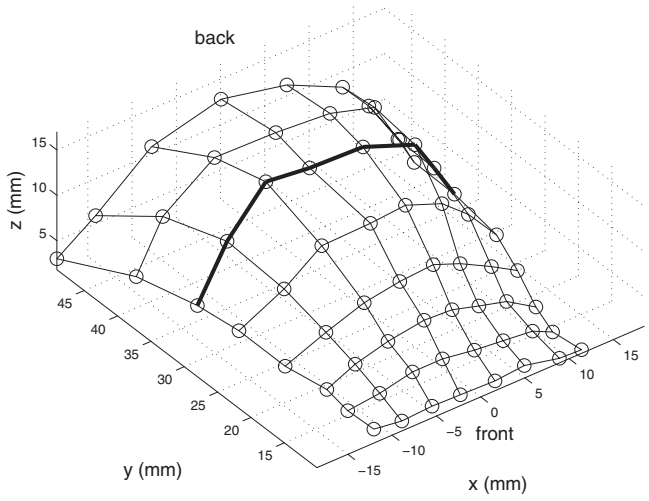

FIG. 2. Coordinates of the palate electrodes (two points were added laterally in the front row). The curvature of the palate was estimated for the sixth row. Distances are in millimeters. α for this palate is 1.8062 (medium palate).

A parabolic approximation with two coefficients was carried out for the measured points of row 6. The palatal shape could now be described by

$$y(x) = ax^2 + b \tag{4}$$

and α was calculated as

$$\alpha = \frac{4}{3\sqrt{|a|}} \tag{5}$$

by assuming that the tongue is flat [cf. Perrier *et al.* (1992) for an explanation]. Assuming that the tongue curvature remains constant, a high α-value corresponds to a flat palate and a low value to a domeshaped palate.

C. EPG recordings

The speakers were recorded via electropalatography (reading system). All speakers were experienced in speaking with an artificial palate and had taken part in several EPG studies before. The experiments started after speakers had become comfortable with the palate and their speech sounded normal to the investigator. The length of this period varied but usually took a couple of minutes. For the Norwegian and all but one of the English subjects the WinEPG was used. The German, Polish, Bulgarian, and English subjects were recorded with EPG 3. A parallel acoustic recording was carried out with a digital audio tape (DAT) recorder for the German, Bulgarian, and Polish subjects and one English subject. For the other subjects the acoustic recording was carried out via WinEPG. The sampling rate of the articulatory data was 100 Hz. During the recording, if an error or dysfluency occurred, additional repetitions were recorded. The speakers produced between 0 and 11 errors per recording, the average error rate was 1.4%.

The sounds to be investigated were the consonant /j/ and the vowels /i/ and /e/ with their lax counterparts /ɪ/ and /ɛ/. In some languages the tense-lax contrast goes together with a length contrast. In German, tense vowels are long in stressed

TABLE I. Number of phonemic contrasts. Leftmost column gives sound class.

	Bulgarian	Polish	English	Norwegian	German
Palatal or velar approximants	1	1	1	1	1
Unrounded front vowels	2	3	4	4	4

position [cf., e.g., Hoole and Mooshammer (2002)] so that the tense vowels in our sample are all long since they occur in stressed position. In Norwegian there is also a tense-lax contrast which is realized by differences in quantity and quality, even if the quality difference is, in contrast to German, predictable from either length or stress [Kristoffersen (2000)]. In English there is also a length contrast; however, the quality contrast is, in comparison to the other two languages, more pronounced [e.g., Peterson and Barney (1952) and Hillenbrand *et al.* (1995) for American English].

The sounds in our sample were chosen because the vocal tract is rather narrow during their production, and consequently an influence of the palate shape can be expected. In order to make the data in the different languages comparable, nonsense words were used rather than real words. Doing so it was possible to take the same items for all the languages. Since some of the sounds do not have phonemic status in all the recorded languages not all the speakers were recorded speaking all items. For Bulgarian and Polish speakers no lax vowels were recorded; for English there was no /e/ (but /ɛ/).

The items in which the sounds were embedded were /'titi/, /'tɪti/, /'tetə/, /'tɛtə/ (for the English speakers /'tɛtər/ or /'tɛtə/) and /'jaja/. The carrier phrases differed from language to language:

- for Bulgarian: *Kazah…na teb*. (I have said…to you.)
- for Polish: *Powiedzialem…do ciebie*. (I said…to you.)
- for German: *Habe…gesagt*. [(I) have said…]
- for English: *Say…please*.
- for Norwegian: *Jeg sa… 'a vet du*. (I said… you know.)

As one can see, the phonetic contexts for the target words differ across the languages. For Bulgarian the test word is preceded by an /x/, for Polish by an /m/, and for the other languages by some kind of centralized vowel. Since carryover effects have been found to spread over two or three segments (Daniloff and Hammarberg, 1973), one could assume that the different preceding sounds could have an influence on the measurements carried out on the target vowel and consonant. However, Daniloff and Hammarberg (1973) found these wide spreadings only for slow speech. Since our speakers spoke with normal speed one can assume that the influence is minor. Additionally, we did not analyze the first phone of the test word, but its presence means that the consonant immediately preceding the target vowel was always the same.

Each sentence was repeated 30 times in randomized order. The beginning and end of each segment of interest was labeled in the acoustic signal using PRAAT 4.2.17 (Boersma and Weenink, 1992):

- sonorant onset and offset for the medial sonorant /j/ as the middle of the formant transitions between the surrounding vowels and the sonorant and
- onset and offset of the second formant for the vowels in stressed position.

D. Influence of the size of the phoneme inventory

There are a couple of studies investigating the influence of the size of the phoneme inventory on token-to-token variability [e.g., Tabain and Butcher (1999) for consonants and Dixon (1980) for vowels]. The basic question behind these studies is whether speakers reduce the variability to a level which allows clear boundaries between the phonemes. Although the results of these studies are not entirely consistent regarding complete phoneme inventories [Tabain and Butcher (1999) found that there is no influence for consonants, but Dixon (1980) found that there is one for vowels] the possibility that this influence exists has to be taken into account in the present study.

In order to find out whether the languages in our study are comparable with respect to the sounds studied here, the phoneme inventories were compared. However, as suggested by the results of Tabain and Butcher (1999) and of Dixon (1980), a more crowded inventory in one domain, e.g., vowels, does not necessarily influence the variability of productions in another domain, e.g., consonants. In order to account for the potential influence of the phoneme inventory on vowel variability, we compared the number of unrounded front vowels in the languages of the study. Rounded front vowels were not counted since we hypothesized that the existence of rounded front vowels in German and Norwegian should not influence the variability of the unrounded front vowels considerably, either articulatorily or acoustically. Indeed, lip rounding and spreading presents an additional degree of freedom and is very likely to provide a clear distinction between the spaces of the articulatory representations of these two vowel categories. Acoustically, lip rounding generates a strong frequency decrease of the lowest front cavity resonance in a way that is very different from the consequence of local tongue displacements. For the approximant /j/, we counted places of articulation for the respective manner of articulation for lingual consonants. The information about the phoneme inventories of Bulgarian and German was taken from The Handbook of the IPA (IPA, 1999). Our sources for the other languages were Kristoffersen (2000) for Norwegian, Gimson and Cruttenden (2001) for British English, and Jassem (2003) for Polish.

All five languages have just one palatal or velar approximant (cf. Table I). With respect to the vowels, English, Norwegian, and German are comparable in terms of the number of places of articulation. Polish and Bulgarian have fewer

unrounded front vowels. We therefore tested if there is an influence of the number of unrounded front vowels on articulatory and acoustic variabilities.

E. Measuring articulatory variability

Articulatory variability was measured in three ways:

(1) as the coefficient of variation in the POC over the complete segment,
(2) as the standard deviation of the COG (a measurement of tongue position variation), and
(3) as the coefficient of variation in the number of contacts at the articulatory target (a measurement of tongue height variation).

1. Coefficient of variation in the percent of contact ("POC-variability")

The POC describes whether there is much or little contact without specifying where the contact occurs. The articulatory variability of this index was calculated as follows:

- calculation of the POC for each EPG frame within the acoustically measured segment,
- temporal alignment of the 30 repetitions for each speaker and each item,
- calculation of a mean and the standard deviation for each sample of the normalized 30 repetitions,
- calculation of a mean of the standard deviations over all samples,
- normalization of this value at the mean POC, and
- calculation of the maximally observed variability.

These steps will now be described in detail.

At first, the POC was calculated for each EPG frame within the measured time interval as

$$p_c = \frac{n_c \times 100}{62}, \tag{6}$$

with n_c is the number of contacts and 62 as the maximal number of contacts (Hardcastle and Gibbon, 1997).

Figure 3 illustrates this method. The left subplot shows the EPG frames of a production of /i/ surrounded by /t/ by speaker E1 (English speaker 1, male). In the beginning there is more contact because the preceding consonant is /t/. The closure, however, cannot be seen anymore since the figure only shows the frames corresponding to the segment of the acoustic signal that has a clear formant structure. Then there is less and less contact. Toward the end there is again more contact because the phoneme following the /i/ is again /t/.

The right subplot in the figure shows the POC for each of the frames in the left subplot. As one can see there is a higher percentage of contact in the beginning (when consonantal characteristics are still present), the POC falls in the middle of the segment (during /i/), and toward the end the POC rises again because of the second /t/. These calculations were carried out for the 30 repetitions of each item.

After this calculation data were split according to speaker and item. As one can imagine, the 30 repetitions of one item usually differed in duration. In order to calculate

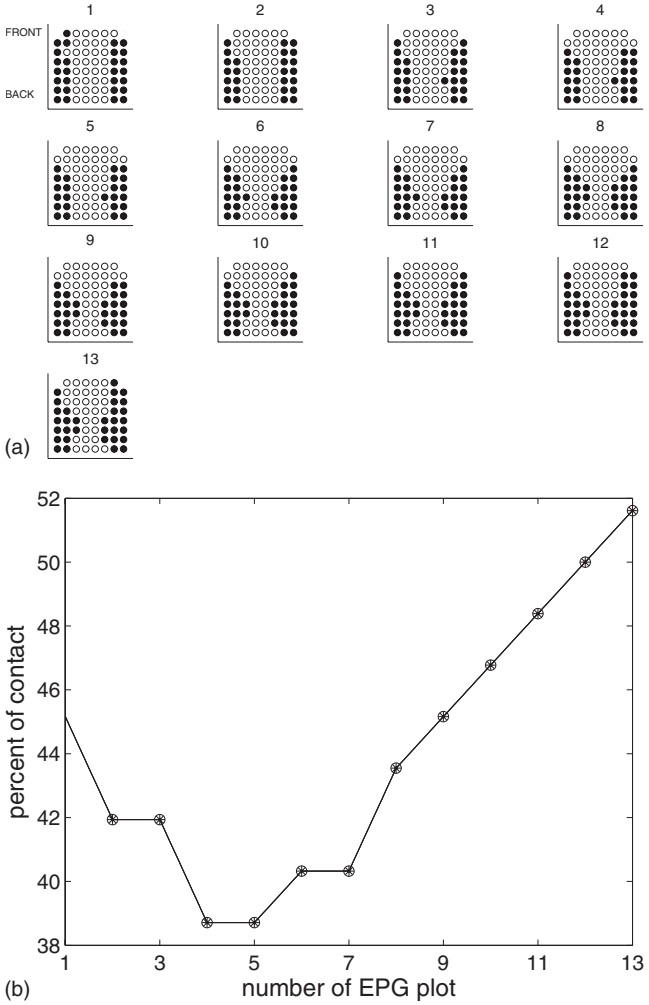

FIG. 3. Left: EPG frames for /i/ surrounded by /t/. Time goes from left to right and from top to bottom. White circles represent electrodes without contact; filled circles electrodes with contact. Right: POC for the EPG frames of /i/ shown on the left (with linear interpolation). Data from speaker E1.

standard deviations over the complete segment, however, they had to be time-aligned. Therefore, they were aligned nonlinearly according to an algorithm proposed by Lucero *et al.* (1997) and Lucero and Koenig (2000). The algorithm aligns beginning, end, maxima, and minima of the POC-signal. The transformation of the time scale is therefore nonlinear.

After this temporal alignment, a mean value and the standard deviation of the 30 repetitions were calculated for each of the sample points of the nonlinearly aligned repetitions. The mean of all the standard deviations (one for each sample point) was calculated separately for each item and each speaker (across the 30 repetitions of one item). When the data were split according to the item (and thus according to the target sound), a significant positive correlation between mean and standard deviation was found for /ɛ/ and /j/. Hence, the standard deviations (one for each sample point) of the POC were normalized by the mean value of the POC. We thereby obtained the coefficient of variation. The resulting value was treated as a measure of the articulatory variability of one item uttered by a speaker and will be called *POC-variability*.

As a final step we calculated the maximally observed variability. This step is grounded in the following reasoning. According to the argumentation in the Introduction, one can expect speakers with flat palates to reduce their articulatory variability. This, however, does not mean that speakers with domeshaped palates should always have a high articulatory variability. For all speakers it is possible that they have less variability than they could allow for. The speakers with domeshaped palates, however, have a greater range of possible levels of variation since the articulatory variability they can allow for without changing the acoustic output considerably is higher.[1] What we are interested in is consequently the maximum possible variability for a certain palate shape. It is therefore important not only to look at the observed variability but at the maximally observed variability for a certain palate shape. In order to do so, we distributed palate shapes across three groups: flat palates, medium palates, and domed palates. The division was carried out linearly: Since the highest observed α was 2.24 and the lowest was 1.23, the border between domed and medium palates was placed at 1.57 and the one separating medium and flat palates at 1.91.

In order to get the maximum possible variability in each palate shape group, for each segment and each palate group, the upper third (rounded to the nearest higher integer) of the observed POC-variability was considered. To give an example for domed palates, for the ten speakers with a domed palate (α between 1.23 and 1.57) the following POC-variabilities were observed for /j/: 0.1139, 0.1194, 0.1239, 0.1254, 0.1279, 0.1736, 0.1783, 0.2199, 0.2223, and 0.3318. The upper third corresponds to the four speakers with the highest variability values: 0.3318, 0.2223, 0.2199, and 0.1783. These four values are the maximally observed articulatory variability for /j/ for speakers with domed palates. This variability will be called *maximally observed POC-variability*.

2. Standard deviation of the center of gravity ("COG-variability")

In contrast to the first measurement which calculated variability over the complete segment, the second measurement is one which corresponds to one moment in time only and not to a complete segment. The reason for doing this was to test whether we would get the same result for canonical tongue positions.

Briefly, the following calculations were carried out:

- determination of an articulatory target for each production,
- calculation of the COG for the target EPG frame,
- calculation of the standard deviation of the mean COG for the 30 repetitions of one item uttered by the same speaker, and
- calculation of the maximally observed COG-variability.

First, in each production we labeled a point in time which could be seen to be the articulatory target position of the sounds. The definition of this articulatory target relies on the assumption that consonants have more linguo-palatal contact than vowels. A transition from a vowel to a consonant will therefore involve an increase in the contact whereas a transition from a consonant to a vowel will involve a reduction in contact. The articulatory target for a vowel was therefore the frame with the least contact within the acoustically measured segment. The articulatory target for a consonant was the frame with the most contact within the acoustically measured segment.

This method is demonstrated in Fig. 3. The articulatory target of the /i/-production shown there would be the fourth and fifth samples in the figure since there is the least contact in this production.

For the EPG frame at this articulatory target position we calculated the COG, which is a measure of the mean location of contact along the anterior-to-posterior axis of the palate [Hardcastle *et al.* (1991)]. If the COG is low this means that there is more contact in the anterior region; if it is high there is more contact in the posterior region of the palate.

The COG was calculated according to the following formula [Cheng *et al.* (2002)]:

$$\mathrm{COG} = \frac{R1 + 2R2 + 3R3 + 4R4 + 5R5 + 6R6 + 7R7 + 8R8}{\Sigma(\mathrm{contacts})}, \tag{7}$$

where $R1-R8$ denote the contacts observed in the horizontal rows of the palate from the most anterior to the most posterior position.

Since there was no correlation between the standard deviation of this coefficient and the mean COG-value we calculated the standard deviation only instead of the coefficient of variation. In order to calculate the highest observed variability we again calculated a mean value of the one-third of speakers with the highest variability in each of our three groups (flat palates, medium palates, and domed palates).

3. Coefficient of variation in the number of contacts in the row with the most contact ("NOC variability")

In order to calculate the variability of the number of contacts we used the articulatory target again. From the EPG frame at the target we took the row with the greatest number of contacts (in Fig. 3 this would be row 6) and calculated the standard deviation of the numbers of contacts within these rows for the 30 repetitions of an item uttered by a speaker. We divided the standard deviation by the mean (and thereby received the coefficient of variation) since there was a correlation between mean and standard deviation. As for all the other parameters, the highest observed variability was calculated. This variability was called *maximally observed NOC-variability*.

The aim of calculating this parameter was to investigate the variability of the groove width which is important for the acoustic output. In contrast to COG-variability the NOC-variability measures tongue height differences instead of differences in tongue position.

F. Measuring acoustic variability

Acoustic variability was calculated on the basis of the frequencies of the first three formants. Section II F 1 de-

scribes how the formants were measured. Section II F 2 describes how the acoustic variability was measured.

1. Formant measurements

For the measurement of the first three formants the data were first downsampled from 48 to 10 kHz. Afterward semi-automatic measurements were carried out in MATLAB with a signal window length of 20 ms (adopized with a Hanning window) and a shift duration of 5 ms (=75% overlap) between neighboring windows.

Two spectral analysis techniques were combined. An LPC[2] analysis with 14 coefficients was calculated. Afterward, upper and lower boundaries in the frequency domain were defined for each formant of each speaker and each vowel. Then the formant detection program looked for true maxima, corresponding to an actual zero crossing of the first derivative of the spectral envelope. It looked for a unique maximum within each of the three frequency ranges that were defined for each of the first three formants.

For example, for most male speakers, F1 was detected in the [200 400 Hz] range for /i/, while F2 was detected in the [1800 2400 Hz] range for /i/. If there was a frequency range within which no true maximum could be found, the program looked for humps on the envelope. Humps correspond to parts of the spectral envelope where the first derivative does not cross zero and has, within an interval of 24 Hz, an amplitude that first reaches a value close to zero and then increases back rapidly (i.e., is multiplied by a factor larger than 10). These parts do not correspond to a true maximum of the spectral envelope since there is no actual velocity zero crossing. However, they show evidence for a local increase in the spectral energy compatible with the existence of a formant.

If at the end of these processing steps the LPC analysis did not propose a solution for each of the formant-specific frequency ranges, the whole process was repeated for the cepstral analysis. The cepstral analysis used the same signal windows (20 ms, Hanning apodization) as the LPC analysis and involved the computation of 256 point Fast Fourier Transforms (FFTs) and inverse FFTs. Liftering in the cepstral domain was 3 ms large for male speakers and 2.3 ms for female speakers. Finally, the results were controlled manually, and the boundaries were reset if necessary.

Formant detection is especially complicated when several formants get closer to form a single peak. To give an example, in German, F2 and F3 of the vowel /i/ are usually very close so that they could be interpreted as one formant by a formant detector. This is the reason why we decided to use a guided semi-automatic detection, and not an automatic one, and to rely on two methods, an LPC analysis and cepstral analysis, in order to compute the spectral envelope.

In order to better illustrate the perceptual influence of a certain variability, the formants were transformed into barks according to the following formula [Schroeder *et al.* (1979)]:

$$F_{\text{bark}} = 7 \times a \sinh(F_{\text{Hz}}/650). \quad (8)$$

For some speakers and some items formants could not be reliably measured, or they could be measured for some repetitions only. If more than 10 repetitions could not be reliably measured, the items were excluded from further acoustic analysis since, judging from our corpus, 20 repetitions are needed for obtaining stable measurements for variability (i.e., the variability stops rising if more repetitions are included). If less than 20 repetitions are taken, variability drops.

Consequently, the following data were excluded from further analysis:

- F2 and F3 of /ɪ/ by male speaker E1 where we usually found three peaks instead of two in the F2-F3 region,
- F2 and F3 of /ɪ/ by female speaker N3 (same problem),
- F2 and F3 of /i/ by female speaker N5 where we often had just one peak instead of two in the F2-F3 region,
- F2 of male speaker E9's /ɪ/ where the formant peak was too small in amplitude,
- F2 and F3 of /e/ by female speaker N4 where the formant peaks were too small in amplitude, and
- F2 of item /ɪ/ by female speaker N6 where the peak was too small in amplitude.

2. Standard deviation of F1, F2, and F3: "F1-variability, F2-variability, and F3 variabilities"

The calculation of acoustic variability was carried out similar to the POC-variability (Sec. II E 1), except that no coefficient of variation was measured. As for the articulatory data, a nonlinear time alignment was carried out for the formant values measured over a complete segment. The mean value and the standard deviation of the bark transformed formants were calculated for each of the samples. Then a mean of the standard deviations was calculated for each sound and each speaker. The coefficient of variation was not calculated since there was no correlation between mean and standard deviation.

G. Statistical analyses

All statistical analyses were carried out in SPSS 15.0. The following tests were carried out.

- In order to investigate whether there is a gender effect in palate size we calculated a one-factorial analysis of variance (ANOVA) with gender as factor and palate shape (α) as dependent variable.
- A possible influence of gender on all the variabilities (POC-variability, COG-variability, NOC-variability, F1-variability, F2-variability, and F3-variability) was assessed with a repeated measures ANOVA with item as within-subject factor and gender as between-subject factor.
- A possible influence of the size of the phoneme inventory on all the variabilities (POC-variability, COG-variability, NOC-variability, F1-variability, F2-variability, and F3-variability) was assessed with a repeated measures ANOVA with item as within-subject factor and vowel inventory type (2 vs 3 vs 4 unrounded front vowels) as between-subject factor.
- In order to see whether there is a significant influence of the palate shape on the maximally observed variabilities the palate shapes were divided into three groups (flat, medium, and domed palates), and the influence of the palate

TABLE II. Results of repeated measures ANOVA with *item* as within-subject factor and *gender* as between-subject factor.

Parameter	Effect	F (p)
POC-variability	Gender	$F(1,30)=2.68$, $p=0.112$
COG-variability	Gender	$F(1,30)=4.820$, $\mathbf{p=0.036}$
NOC-variability	Gender	$F(1,30)=0.037$, $p=0.849$
F1-variability	Gender	$F(1,30)=57.326$, $\mathbf{p=0.000}$
F2-variability	Gender	$F(1,30)=29.688$, $\mathbf{p=0.000}$
F3-variability	Gender	$F(1,30)=2.959$, $p=0.096$

group on the variabilities was assessed via a repeated measures ANOVA with item as within-subject factor and palate group as between-subject factor.

III. RESULTS

This section presents the results for our measurements. At first all the parameters were checked to see if there is a gender effect (Sec. III A). Then the influence of the phoneme inventory on the parameters was investigated (Sec. III B). In Sec. III C the results for the influence of the palate shape on POC-variability, COG-variability, and NOC-variability are presented. Then the influence of the palate shape on the acoustic variability is discussed (Sec. III D). Finally the results of our statistical analysis are presented (Sec. III E).

A. Gender effect

Our corpus included data for 15 female and 17 male speakers. After the calculation of our parameter α we tested whether gender has an influence on the palate shape. A one-factorial ANOVA showed that there was none [$F(31,1)=0.721$, $p=0.403$]. However, as will be seen in Sec. III C 3, although our sample seems to be balanced for gender, all the flat palates belong to males.

Furthermore, we tested all our parameters (POC-variability, COG-variability, and NOC-variability) to see if there is an influence of gender. The results can be found in Table II. As can be seen, there is a significant effect of gender on COG-variability, F1-variability, and F2-variability. The influence of gender on F3-variability is close to reaching significance. In all further analyses of COG-variability, F1-variability, F2-variability, and F3-variability we will therefore split data according to gender.

B. Influence of the size of the phoneme inventory

In Sec. II D we noted that Polish and Bulgarian have fewer unrounded front vowels. The results of a repeated measures ANOVA show that the influence of the size of the phoneme inventory does not reach significance (cf. Table III).

TABLE III. Results of repeated measures ANOVA with *item* as within-subject factor and *vowel inventory type* (number of unrounded front vowels) as between-subject factor.

Parameter	Effect	F (p)
POC-variability	Vowel inventory type	$F(2,29)=1.460$, $p=0.249$
COG-variability	Vowel inventory type	$F(2,29)=0.141$, $p=0.869$
NOC-variability	Vowel inventory type	$F(2,29)=0.138$, $p=0.871$
F1-variability	Vowel inventory type	$F(2,29)=2.012$, $p=0.152$
F2-variability	Vowel inventory type	$F(2,29)=0.027$, $p=0.973$
F3-variability	Vowel inventory type	$F(2,29)=1.594$, $p=0.220$

C. Relationship between palate shape and articulatory variability

1. General findings

Figure 4 shows as an example the relation between POC-variability and the palate shape found for /ɪ/. On the abscissa the α values of the speakers are displayed and on the ordinate the POC-variability.

As can be seen from the crowdedness of the points in the middle of the figure, the sample is not entirely well balanced with regard to the palate shape. Whereas there are just a couple of speakers with a very curved (low α) or a very flat palate (high α), the majority of the speakers clusters around the middle.

Furthermore, as expected, the variability varies more in the left half of the figure (for low α and domed palates) than in the right half (for high α and flat palates). In the left half one can find speakers with both high and low variabilities. On the right side, however, there are only speakers with low variability. This is consistent with the hypothesis that the speakers with a flat palate all reduce their articulatory variability in order to preserve the acoustic output. For the other speakers, the amount of articulatory variability is more variable: It can be significantly larger than for speakers with a flat palate, but this is not systematically the case.

In general, the expected relation can be seen quite clearly: The maximally observed variability for a certain range of palate shapes decreases from left to right. We will therefore go on looking at the results for the maximally observed variability.

Figure 5 shows the percentage of activation of each elec-

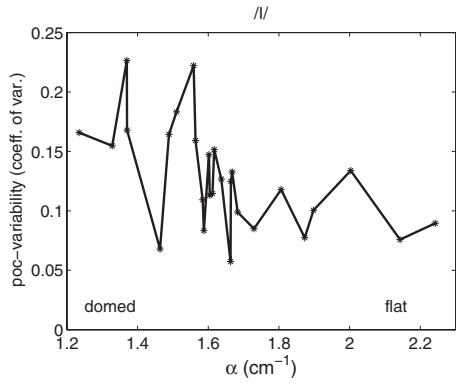

FIG. 4. Relationship between articulatory variability (ordinate) and α (abscissa) for /ɪ/.

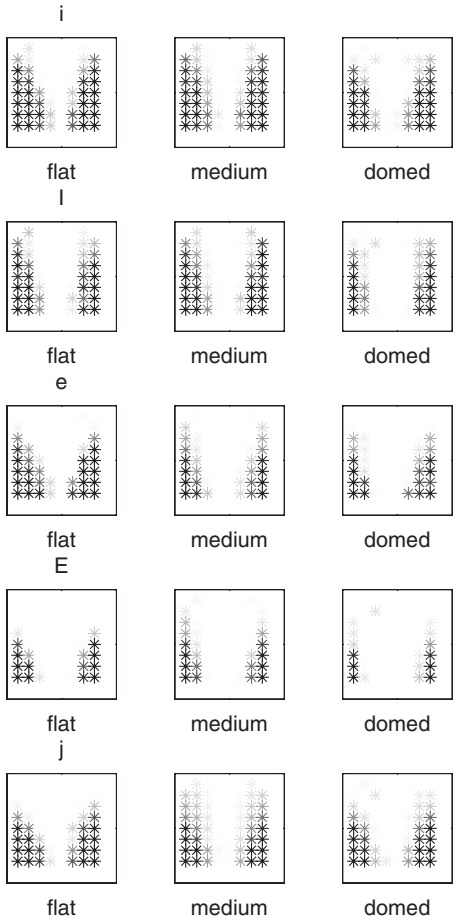

FIG. 5. Mean contact patterns for the five items (rows) and palate types (columns). Black asterisks denote 100% contact (contact over all repetitions of all speakers in that palate group); white asterisks denote 0% contact.

trode at the articulatory target for the three groups of palates and each item. Flat palates are shown in the left column, medium palates in the middle, and domed palates in the right. Each line shows a different item. White asterisks mean "no contact" over all trials of all speakers with this kind of palate and black asterisks mean "always contact" in all trials of all speakers with this kind of palate. Gray asterisks denote an intermediate activation, dark gray means more than 50%, and light gray less than 50%.

One can see that the most gray asterisks (denoting that this contact is sometimes active, sometimes it is not), and therefore the most variability in contacts, are around the groove in the middle and in the most anterior rows. The variability in groove width is probably due to differences in tongue height: When the tongue is lowered, contact in the middle of the palate disappears first. The variability in the front rows is certainly due to differences in tongue position: When the tongue is moved posteriorily, contact in the anterior rows disappears.

2. Percent of contact ("POC-variability")

Figure 6 shows all the POC-variability values as a function of the palate shape. Each small letter gives the value of one measurement of the variability for one sound and one subject. The vertical lines mark the borders of the three groups of palates needed for the calculation of the maximally observed POC-variability. The domed palates are on the left, the medium palates in the middle, and the flat palates on the right. Comparable to Fig. 4 one can see that the variability varies for speakers with a domed palate but tends to be low for the speakers with a flat palate.

Plotted on top of these values bold letters connected by lines can be seen. These are the mean values of the maxi-

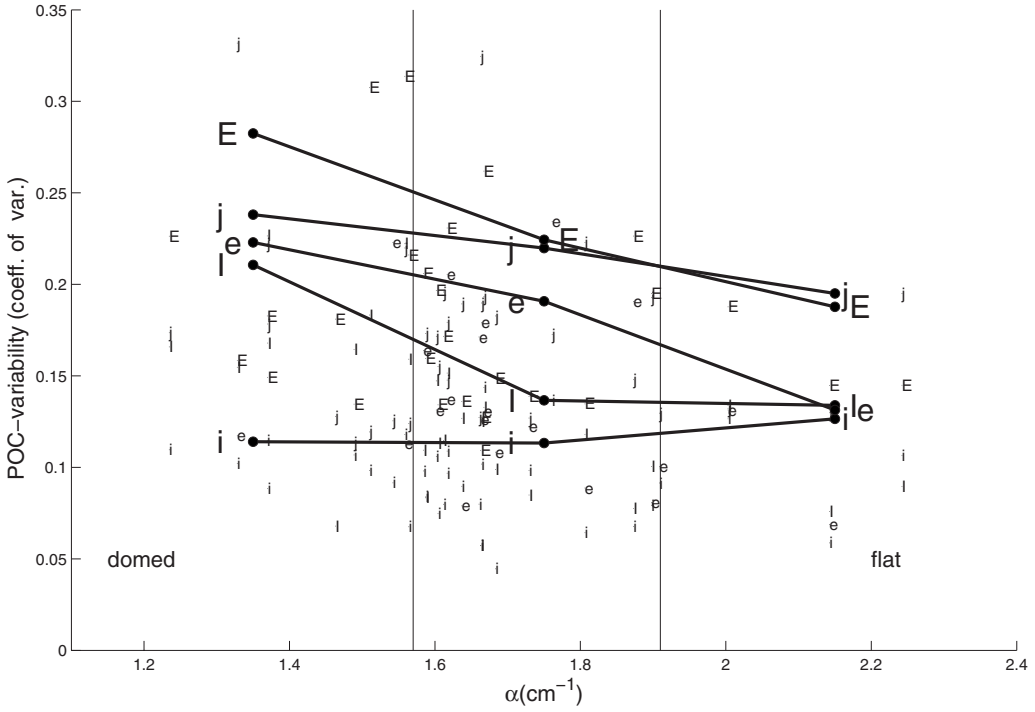

FIG. 6. Relationship between α (abscissa) and POC-variability (ordinate). Small letters show results of single measurements. The lines connecting big letters show maximally observed POC-variability. Vertical lines show borders between palate groups.

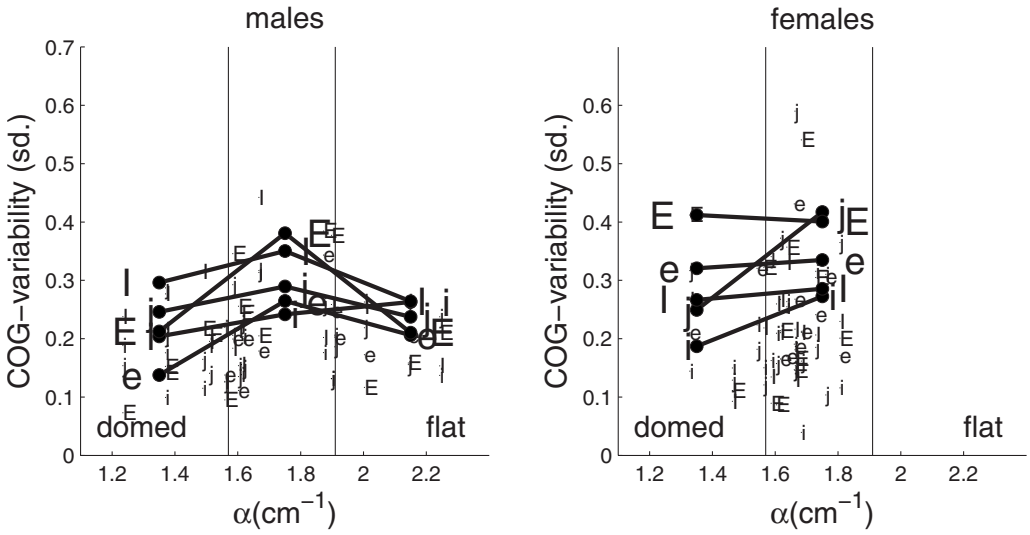

FIG. 7. As Fig. 6, but for COG-variability.

mally observed POC-variability in each group. All the lines, except the one for /i/, are falling from left to right. This means that, even if there are speakers with a domeshaped palate exhibiting low variability, the maximally observed variability in the group of speakers with domeshaped palates is higher than the maximally observed variability in the group of speakers with a flat palate.

3. Center of gravity ("COG-variability")

Figure 7 shows the results for our measurements of COG-variability. Since there was a significant effect of gender, data are split according to gender. As one can see, our small sample of subjects does not contain female subjects with flat palate.

The results do not show the same tendency as for the POC-variability. It rather seems that there is no tendency at all, but that the maximally observed variability is connected to the number of subjects in the group: There are many subjects with a medium palate so there is a high maximally observed COG-variability.

The different results for POC and COG could be due to the fact that the COG measures differences in the front-back dimension whereas the POC measures differences in both dimensions (front-back and laterality).

As can be seen in Fig. 5, variability occurs both in tongue height and tongue position. So the fact that we do not find results for COG but for POC variability could indicate that only the variability in tongue height is connected to the palate shape.

4. Number of contacts in the row with most contact ("NOC-variability")

Figure 8 shows the results of the third method to calculate articulatory variability. The figure shows the coefficient of variation for the contacts in the row with the highest number of contacts at the target position.

As one can see, a similar tendency as for the POC-variability can be observed, even if the details vary. For /ɪ/, /j/, and /ɛ/ one can see that the highest observed variability shown by the big letters and the lines connecting them is highest for the speakers with a domed palate, a little lower for the speakers with a medium palate, and lowest for speakers with a flat palate. For the two tense vowels /i/ and /e/ this tendency cannot be observed.

D. Acoustic variability

According to our rationale in the beginning, speakers with flat palates should have more acoustic variability if they have the same articulatory variability as speakers with a domeshaped palate. Since, however, these speakers have less articulatory variability, they can be expected to have about the same acoustic variability as speakers with domed palates.

Figures 9–11 give the results for the variability of the formants. Since a gender effect was found, data were split by gender. Same as for COG-variability, it is hard to see a tendency, except for the dependence of the variability on the sample size. Most importantly, however, the acoustic variability of speakers with flat palates is never greater than that of speakers with domeshaped palates. As discussed in the

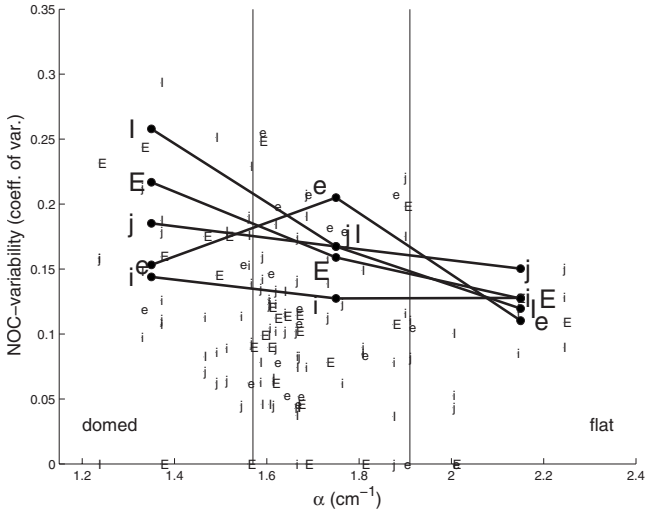

FIG. 8. As Fig. 6, but for NOC-variability.

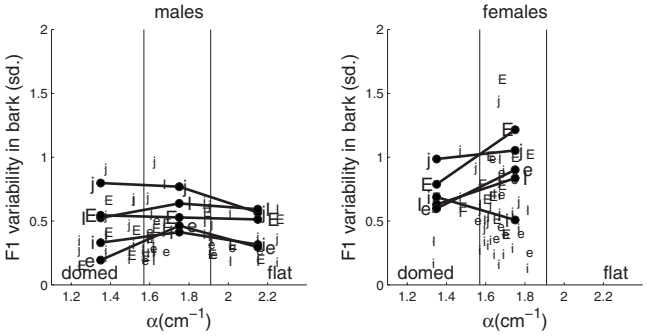

FIG. 9. As Fig. 6, but for F1-variability and maximally observed F1-variability.

Introduction, there should be higher acoustic variability in speakers with flat palates if speakers ignored the differences in acoustic variability resulting from different palate shapes.

E. Statistical analysis

The results of our statistical analysis in Table IV show that for the maximally observed POC- and NOC-variabilities there is a significant effect of the form of the palate on the articulatory variability. None of the acoustic parameters showed a significant effect; neither did maximally observed COG-variability.

IV. DISCUSSION

The aim of the current study was to investigate how morphology influences motor strategies in order to reach an acoustic target.

As has been explained in the Introduction, the starting point of our study was the assumption that, without adjustments by the speaker, a given amount of articulatory variability should result in less acoustic variability if the palate is domeshaped than if it is flat since the constriction area should be modified to a higher degree by articulatory variability in the second case than in the first.

By this reasoning, let us hypothesize that speakers should compensate for the shape of their palate in order to counteract the impact of the palate shape on the acoustic variability and to keep this variability within a range compatible with the correct perception of the phoneme. More precisely, speakers with flat palates should reduce their articulatory variability, and there should be a relationship between palate shape and articulatory variability.

In this theoretical framework, articulatory and acoustic variability of 32 speakers of various languages has been measured. In order to assess articulatory variability we calculated the coefficient of variation in the percent of contact (POC-variability), the standard deviation of the center of gravity (COG-variability), and the coefficient of variation in the number of contacts in the row with most contact (NOC-variability). The first one of these measures assesses overall variability, the second variability in the horizontal dimension (tongue position), and the third the variability in the vertical direction (tongue height).

The first main finding of this experimental study is that for three of the five phonemes that were analyzed, namely, /ɪ, ɛ, j/, there is clearly a relationship between maximal POC- and NOC-variabilities and palate shape. For a fourth item, /e/, there is one for POC-variability. Indeed, for these sounds, speakers with flat palates show reduced articulatory variability. Large articulatory variability is observed for some speakers with domeshaped palates, while small articulatory variability is systematically observed for speakers with a flat palate. For NOC-variability no consistent results could be found. We therefore conclude that there is a systematic relationship between variability in vertical tongue position but not in horizontal tongue position. This is consistent with our rationale from the beginning which predicted a relation between vertical variability and palate shape.

For one sound, /i/, no trend in either POC- or NOC-variability could be observed. This could be due to the generally low articulatory variability of this sound. Fujimura and Kakita (1979) showed that synchronous activity of the different parts of the genioglossus in /i/ leads to a stable articulatory pattern ("stabilization effect") and low acoustic variability ("saturation effect"). Similarly, Perkell (1990, p. 269f)

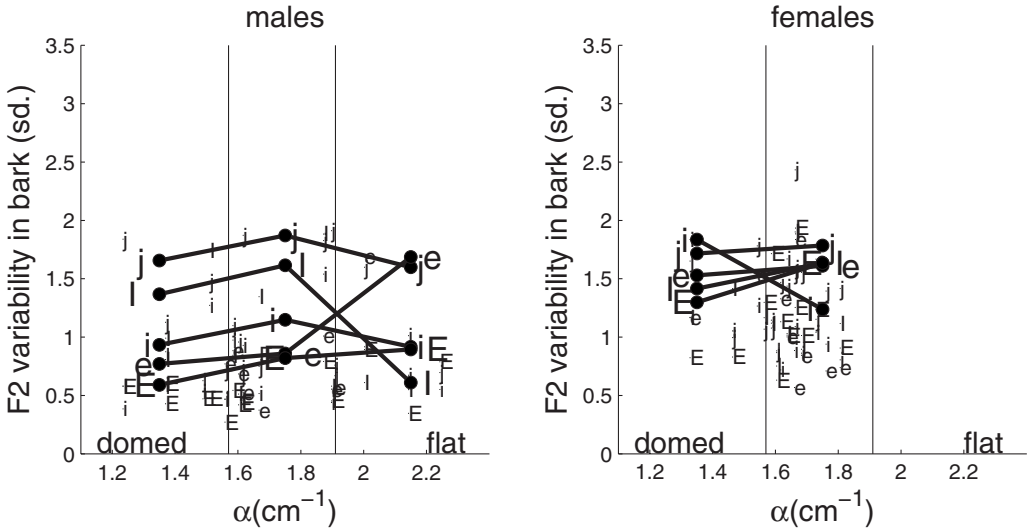

FIG. 10. As Fig. 6, but for F2-variability and maximally observed F2-variability.

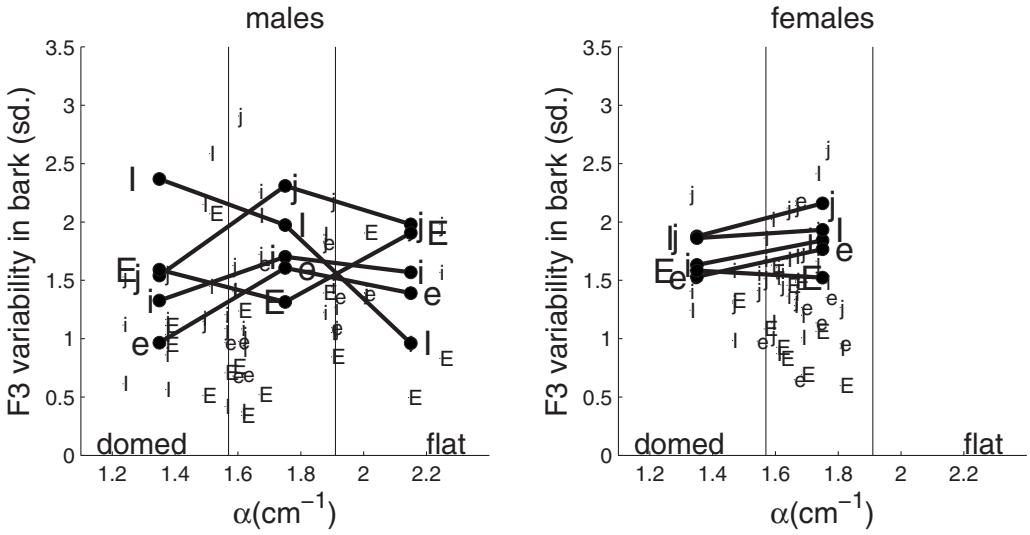

FIG. 11. As Fig. 6, but for F3-variability and maximally observed F3-variability.

described this generally low articulatory variability of high tense vowels as a saturation effect. The tongue blade is stiffened and grooved and pushed against the hard palate by genioglossus posterior activity. In this position the tongue stays rather stable even if activation levels of the genioglossus posterior vary. According to Perkell (1990) this saturation effect would strongly simplify the control of the stability of the tongue positioning for high front vowels, and it would ensure that the acoustic variability remains within a range compatible with a correct perception of the phoneme. This hypothesis is supported by the fact that, in spite of its low articulatory variability, /i/ shows about the same amount of maximal acoustic variability as compared to the other sounds [but see criticisms of the saturation effect hypothesis in Buchaillard *et al.* (2008)].

The second main finding is that the acoustic variability was experimentally never found to be greater for speakers with flat palates than for speakers with domeshaped palates. This shows that the impact of the palate shape on the amount of articulatory variability counteracts the natural influence of palate flattening in the acoustics, namely, the increase in acoustic variability.

TABLE IV. Results of repeated measures ANOVA with *item* as within-subject factor and *palate group* as between-subject factor.

Parameter	Effect	F (p)
POC-variability	Palate group	$F(2,9)=5.698$, $\boldsymbol{p=0.025}$
COG-variability, females	Palate group	$F(1,4)=0.014$, $p=0.293$
COG-variability, males	Palate group	$F(2,3)=3.842$, $p=0.149$
NOC-variability	Palate group	$F(2,9)=4.262$, $\boldsymbol{p=0.05}$
F1-variability, females	Palate group	$F(1,4)=1.813$, $p=0.249$
F1-variability, males	Palate group	$F(2,3)=1.747$, $p=0.314$
F2-variability, females	Palate group	$F(1,4)=0.015$, $p=0.909$
F2-variability, males	Palate group	$F(2,3)=0.177$, $p=0.846$
F3-variability, females	Palate group	$F(1,4)=0.926$, $p=0.390$
F2-variability, males	Palate group	$F(2,3)=0.588$, $p=0.609$

Consequently, we interpret the experimental findings of this study as supporting the hypothesis that, in order to preserve the acoustic correlates of the perception of these phonemes, speakers specifically adapt their articulatory variability to their morphology. More precisely, speakers control the accuracy of their tongue positioning in relation to their palate shape in order to make sure that the acoustic variability remains within a range compatible with the correct perception of the phoneme. For some speakers, i.e., those for whom the amount of acoustic variability is very sensitive to changes in the amount of articulatory variability, the reduction in the articulatory variability even generated a reduction in the acoustic variability which was stronger than the one imposed by perceptual accuracy requirements (i.e., the acoustic variability was below the one measured for speakers with other palate shapes).

ACKNOWLEDGMENTS

This work was supported by a grant from the German Research Council (PO 334/4-1) and by the POPAART P2R program. We would like to thank Olessia Panzyga and Anke Busler at the Zentrum für Allgemeine Sprachwissenschaft for acoustical labeling and for carrying out palate measurements. We furthermore thank Jim Scobbie, Alan Wrench, and Inger Moen for enabling recordings in Edinburgh and Oslo. We are indebted to Jorge C. Lucero who provided a program for the calculation of the temporal alignment. Thanks to Christian Geng and Tine Mooshammer for statistical advice. We are grateful to Laura Koenig, Tine Mooshammer, four anonymous reviewers, and the editor Christine Shadle for comments on earlier versions of this paper. Thanks to Jörg Dreyer and Daniel Pape for technical support. Thanks to Marzena Zygis, Dora Tonneva, Hristo Velkov, and Inger Moen for help during the development of the speech material. Furthermore, many thanks to the subjects at the Zentrum für Allgemeine Sprachwissenschaft in Berlin, at the QMUC Edinburgh, and at the University of Oslo.

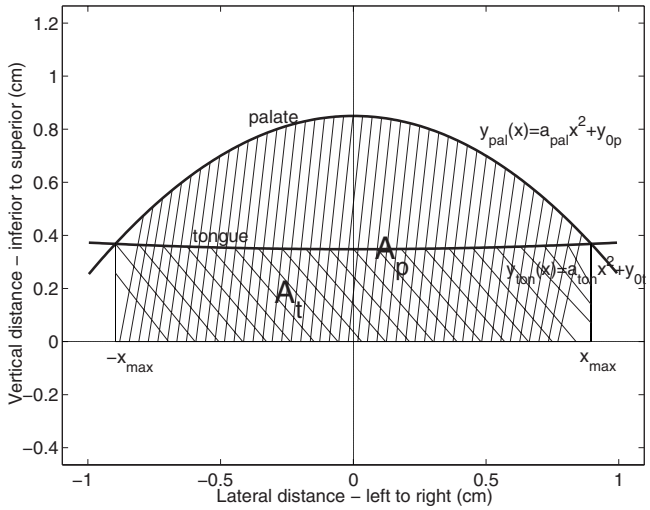

FIG. 12. Calculation of the cross sagittal area and the coefficient α. The tongue and the palate are represented by biparabolic equations. The cross-sectional area is calculated as the difference between the area under the palate and the area under the tongue. α can then be calculated from the area and the cross-sectional distance as $\alpha=4/3\sqrt{a_{ton}-a_{pal}}$ (Perrier *et al.*, 1992).

APPENDIX: COMPUTATION OF THE CROSS-SECTIONAL AREA AND THE COEFFICIENT α IN THE MODEL

In order to represent the palate and tongue shape we use a double-parabola model. In the following we will describe how the alpha coefficient is derived for this general model and then how it is derived in our special case where we have no information on the tongue surface and therefore assume that the tongue is flat. The double-parabola model was used because it gives a good fitting with the contact electrodes measured and allows to gain a single parameter for the description of palatal doming.

For the computation of the cross-sectional area in the model, the palate and the tongue are represented as (cf. Fig. 12)

$$y_{pal}(x) = a_{pal}x^2 + y_{0p}, \tag{A1}$$

$$y_{ton}(x) = a_{ton}x^2 + y_{0t} \tag{A2}$$

for $a_{pal}<0$, with y_{0p} being the midsagittal point of the palate and y_{0t} the midsagittal point of the tongue surface. a_{ton} could be positive or negative and still be articulatorily meaningful. For our calculations we chose $a_{ton}=0$. The area below the palate is

$$A_p = \int_{-x_{max}}^{x_{max}} (a_{pal}x^2 + y_{0p})dx \tag{A3}$$

$$= \tfrac{1}{3}a_{pal}(x_{max}^3 + x_{max}^3) + y_{0p}(x_{max} + x_{max}) \tag{A4}$$

$$= \tfrac{2}{3}a_{pal}x_{max}^3 + 2y_{0p}x_{max}, \tag{A5}$$

with x_{max} and $-x_{max}$ being the x-values of the intersection points of tongue and palate. The area below the tongue is

$$A_t = \tfrac{2}{3}a_{ton}x_{max}^3 + 2y_{0t}x_{max}. \tag{A6}$$

The resulting cross-sectional area is the difference between A_p and A_t.

$$A = \tfrac{2}{3}(a_{pal} - a_{ton})x_{max}^3 + 2(y_{0p} - y_{0t})x_{max}. \tag{A7}$$

One can now introduce the cross-sectional distance d_{sagit} as the difference between y_{0p} and y_{0t}.

$$A = \tfrac{2}{3}(a_{pal} - a_{ton})x_{max}^3 + 2d_{sagit}x_{max}. \tag{A8}$$

Since

$$y_{pal}(x_{max}) = y_{ton}(x_{max}) \tag{A9}$$

and

$$x_{max} > 0 \tag{A10}$$

$$a_{pal}(x_{max})^2 + y_{0p} = a_{ton}(x_{max})^2 + y_{0t} \tag{A11}$$

$$x_{max} = \sqrt{\frac{y_{0p} - y_{0t}}{a_{ton} - a_{pal}}} \tag{A12}$$

for $(a_{ton}-a_{pal})>0$; otherwise there will be no intersection between tongue and palate. Since the sagittal distance is

$$d_{sagit} = y_{0p} - y_{0t}, \tag{A13}$$

$$x_{max} = \left(\frac{d_{sagit}}{a_{ton} - a_{pal}}\right)^{1/2}. \tag{A14}$$

By replacing x_{max} in formula (A8) one gets

$$A = -\frac{2(d_{sagit})^{3/2}}{3(a_{ton} - a_{pal})^{1/2}} + \frac{2(d_{sagit})^{3/2}}{(a_{ton} - a_{pal})^{1/2}}, \tag{A15}$$

$$A = \frac{4(d_{sagit})^{3/2}}{3(a_{ton} - a_{pal})^{1/2}}, \tag{A16}$$

$$A = \alpha d_{sagit}^{1.5}, \tag{A17}$$

with

$$\alpha = \frac{4}{3\sqrt{a_{ton} - a_{pal}}}. \tag{A18}$$

If $a_{ton}=0$,

$$\alpha = \frac{4}{3\sqrt{0 - a_{pal}}}, \tag{A19}$$

which, since $a_{pal}<0$, is equivalent to Eq. (5).

[1]Thanks to Phil Hoole for raising this idea.
[2]Linear predictive coding, a spectral analysis method based on an autoregressive model of the signal.

Boersma, P., and Weenink, D. (**1992**). "Praat, a system for doing phonetics by computer," www.praat.org (Last viewed January **2008**).
Buchaillard, S., Perrier, P., and Payan, Y. (**2008**). "Muscle saturation effect in /i/ production: Counterevidence from a 3D biomechanical model of the tongue," J. Acoust. Soc. Am. **123**, 3321.
Cheng, H., Murdoch, B., Goozé, J., and Scott, D. (**2007**). "Electropalatographic assessment of tongue-to-palate contact patterns and variability in children, adolescents, and adults," J. Speech Lang. Hear. Res. **50**, 375–392.

Daniloff, R., and Hammarberg, R. (**1973**). "On defining coarticulation," J. Phonetics **1**, 239–248.
Dixon, R. M. W. (**1980**). *The Languages of Australia* (Cambridge University Press, Cambridge).
Fant, G. (**1966**). "A note on vocal tract size factors and non-uniform F-pattern scalings," Speech Transm. Lab. Q. Prog. Status Rep. **4**, 22–30.
Fitch, W., and Giedd, J. (**1999**). "Morphology and development of the human vocal tract: A study using magnetic resonance imaging," J. Acoust. Soc. Am. **106**, 1511–1522.
Fujimura, O., and Kakita, K. (**1979**). "Remarks on quantitative description of the lingual articulation," in *Frontiers of Speech Communication Research*, edited by B. Lindblom and S. Ohman (Academic Press, London, New York), pp. 17–24.
Gimson, A. C., and Cruttenden, A. (**2001**). *Pronunciation of English* (Arnold, London).
Hardcastle, W. J., and Gibbon, F. (**1997**). "Electropalatography and its clinical applications," in *Instrumental Clinical Phonetics*, edited by M. J. Ball and C. Code (Whurr, London), pp. 149–193.
Hardcastle, W. J., Gibbon, F. E., and Jones, W. (**1991**). "Visual display of tongue-palate contact: Electropalatography in the assessment and remediation of speech disorders," Br. J. Disord. Commun. **26**, 41–74.
Hiki, S., and Itoh, H. (**1986**). "Influence of palate shape on lingual articulation," Speech Commun. **5**, 141–158.
Hillenbrand, J., Getty, L. A., Clark, M. J., and Wheeler, K. (**1995**). "Acoustic characteristics of American English vowels," J. Acoust. Soc. Am. **97**, 3099–3111.
Hoole, P., and Mooshammer, C. (**2002**). "Articulatory analysis of the German vowel system," in *Silbenschnitt und Tonakzente*, edited by P. Auer, P. Gilles, and H. Spiekermann (Niemeyer, Tübingen), pp. 129–152.
IPA (**1999**). *Handbook of the International Phonetic Association: A Guide to the Use of the International Phonetic Alphabet* (Cambridge University Press, Cambridge).
Jassem, W. (**2003**). "Polish," J. Int. Phonetic Assoc. **33**, 103–107.
Kristoffersen, G. (**2000**). *The Phonology of Norwegian* (Oxford University Press, Oxford).
Lucero, J. C., and Koenig, L. L. (**2000**). "Time normalization of voice signals using functional data analysis," J. Acoust. Soc. Am. **108**, 1408–1420.
Lucero, J. C., Munhall, K. G., Gracco, V. L., and Ramsay, J. O. (**1997**). "On the registration of time and the patterning of speech movements," J. Speech Lang. Hear. Res. **40**, 1111–1117.
Mooshammer, C., Perrier, P., Fuchs, S., Geng, C., and Pape, D. (**2004**). "An EMMA and EPG study on token-to-token variability," AIPUK **36**, 47–63.
Perkell, J. (**1990**). "Testing theories of speech production: Implications of some detailed analyses of variable articulatory data," in *Speech Production and Speech Modelling*, edited by W. J. Hardcastle and A. Marchal (Kluwer Academic, Dordrecht, The Netherlands), pp. 263–288.
Perkell, J. S. (**1997**). "Articulatory processes," in *The Handbook of Phonetic Sciences*, edited by W. J. Hardcastle and J. Laver (Blackwell, Oxford and Cambridge, MA), pp. 333–370.
Perrier, P., Boë, L. J., and Sock, R. (**1992**). "Vocal tract area function estimation from midsagittal dimensions with CT scans and a vocal tract cast: Modelling the transition with two sets of coefficients," J. Speech Hear. Res. **35**, 53–67.
Peterson, G., and Barney, H. (**1952**). "Control methods used in the study of vowels," J. Acoust. Soc. Am. **24**, 175–184.
Schroeder, M., Atal, B., and Hall, J. (**1979**). "Objective measure of certain speech signal degradations based on masking properties of human auditory perception," in *Frontiers of Speech Communication*, edited by B. Lindblom and S. Ohman (Academic, London).
Stevens, K. N. (**1972**). "The quantal nature of speech: Evidence from articulatory-acoustic data," in *Human Communication: A Unified View*, edited by E. E. Davis and P. B. Denes (McGraw-Hill, New York), pp. 51–66.
Tabain, M., and Butcher, A. (**1999**). "Stop consonants in Yanyuwa and Yindjibarndi: A locus equation perspective," J. Phonetics **27**, 333–357.
Vorperian, H., Kent, R., Lindstrom, M., Kalina, C., Gentry, L., and Yandell, B. (**2005**). "Development of vocal tract length during early childhood: A magnetic resonance imaging study," J. Acoust. Soc. Am. **117**, 338–350.
Wrench, A. A. (**2007**). "Advances in EPG palate design," International Journal of Speech-Language Pathology **9**, 3–12.

The acquisition of Korean word-initial stops[a)]

Minjung Kim[b)] and Carol Stoel-Gammon
Department of Speech and Hearing Sciences, University of Washington, 1417 N.E. 42nd Street, Seattle, Washington 98105-6246

(Received 29 January 2008; revised 22 January 2009; accepted 26 March 2009)

A number of studies have investigated acquisition of stop voicing contrast in various languages by voice onset time measurement. Korean stops, however, are all voiceless word-initially and are differentiated by multiple acoustic-phonetic parameters resulting in a three-way contrast (fortis, aspirated, and lenis). The present study examines developmental patterns of Korean word-initial stops produced by 40 Korean children aged 2;6 (year; month), 3;0, 3;6, and 4;0 years, and compare the children's productions to those of 10 female adults. Voice onset time, fundamental frequency, and amplitude difference between the first and second harmonics of the post-stop vowel are obtained from monosyllabic near-minimal triplets at three places of articulation (labial, alveolar, and velar). Acoustic measures of children's productions reveal both universal phonetic patterns and phonetic variation associated with articulatory complexity specific to Korean. Language-specific fundamental frequency variation begins to emerge as early as 2;6, but appears to be mastered later than the voice onset time distinction. In comparison to the adults, young Korean children exhibit greater overlap across stop categories, and the acoustic overlap decreases over age. Results suggest that language-specific phonetic details as well as universal patterns should be examined to provide a better understanding of the speech sound development of a given language.
 [DOI: 10.1121/1.3123402]

PACS number(s): 43.70.Ep, 43.70.Fq [RYL] Pages: 3950–3961

I. INTRODUCTION

This paper presents an acoustic study of stops produced by young children acquiring Korean. Most instrumental studies of the acquisition of "voicing" have focused on measures of voice onset time (VOT), and it is well documented that VOT is a common feature for differentiating stops across languages (e.g., Lisker and Abramson, 1964). Korean stops differ by place and have a three-way laryngeal contrast in word-initial position; moreover the stops are all described as voiceless and often overlap in VOT ranges (Han and Weitzman, 1970; Hardcastle, 1973; Kim, 1965; Lisker and Abramson, 1964). As a result, multiple acoustic-phonetic parameters are required to distinguish three types of Korean stops. At present, very little is known about how young Korean children learn the multiple phonetic features of this stop system. In the study that follows, acoustic-phonetic properties of initial stops produced by young Korean children are examined and compared with previous cross-linguistic research on the acquisition of stops. In addition, the phonetic patterns in child speech are compared with those in adult speech to provide a basis for examining developmental aspects of children's speech.

A. Literature review

1. VOT and f_0 as acoustic correlates of stop consonant voicing or aspiration

Most research focuses on three modal values of VOT corresponding to voiced, voiceless unaspirated, and voiceless aspirated categories (Cho and Ladefoged, 1999; Henton *et al.*, 1992). Among the three types, voiceless unaspirated (short-lag) stops are known to be most common in the world's languages and are considered to be the "easiest" to produce in terms of articulation and aerodynamics (Westbury and Keating, 1986).

The preference for this stop type is seen in child data at both prelinguistic and early linguistic stages. Eilers *et al.* (1984) reported that both English and Spanish infants in the pre-meaningful stage of development predominantly produced short-lag stops. In the early linguistic stage, children learning different languages acquire short-lag stops before long-lag stops or prevoiced stops (see Gilbert, 1977; Kewley-Port and Preston, 1974; Macken and Barton, 1980a for English; Allen, 1985 for French; Clumeck *et al.*, 1981 for Cantonese; Davis, 1995 for Hindi; Gandour *et al.*, 1986 for Thai; Eilers *et al.*, 1984; and Macken and Barton, 1980b for Spanish).

Cross-linguistic studies have revealed that a contrast between short-lag vs. long-lag stops is acquired earlier than one between lead vs. short lag. While American English learners demonstrated a short- and long-lag contrast at least by 2;6 (Gilbert, 1977), Mexican Spanish-learning children did not exhibit a lead and short-lag contrast until age 4 (Macken and Barton, 1980b). The late acquisition of initial prevoiced stops has been explained in part by children's learning strategy. It

[a)]This study is based on the doctoral dissertation of the first author. A portion of this work was presented at the Fourth Joint Meeting of the Acoustical Society of America and Acoustical Society of Japan, Honolulu, HI, November 2006.
[b)]Author to whom correspondence should be addressed. Electronic mail: minjungk@u.washington.edu

 0001-4966/2009/125(6)/3950/12/$25.00

is reported, for example, that children learning Mexican Spanish produce spirantized voiced stops as found, to a more limited extent, in word-initial stops of the adult language (cf. Macken and Barton, 1980b). Young French-learning children aged 2;6, on the other hand, showed avoidance of initial prevoiced stops by adding voiced segments prior to voiced stops (Allen, 1985). Gandour *et al.* (1986) suggested that children learning Thai, which has a three-way stop contrast, acquire prevoiced stops latest because of articulatory difficulty. It has been also reported that young children exhibit a wider range of VOT for long-lag stops compared to short-lag stops and need more time to acquire adult-like VOT values following emergence of contrastive VOT distribution (Clumeck *et al.*, 1981; Gandour *et al.*, 1986; Gilbert, 1977).

Another acoustic correlate of the voicing contrast is differences in the fundamental frequency at the onset of the following vowel; specifically, f_0 at the onset of voicing is reported to be higher after voiceless stops than after voiced stops (e.g., House and Fairbanks, 1953; Lehiste and Peterson, 1961; Silverman, 1987 for English; Hombert *et al.*, 1979 for French; and Löfqvist *et al.*, 1989 for Dutch). This f_0 difference is described as either a universal phonetic phenomenon or a language-dependent property. The former perspective is that f_0 perturbation results from aerodynamic and/or physiological factors (cf. Hombert *et al.*, 1979). Based on electromyographic data showing greater laryngeal muscle activity for a voiceless stop relative to a voiced stop, Löfqvist *et al.* (1989) suggested that the higher f_0 following a voiceless stop is associated with vocal fold tension, and that f_0 variation occurs as a by-product of the different laryngeal gestures for voicing. Kingston and Diehl (1994), on the other hand, argued that f_0 variation, which occurs regardless of the presence or absence of vocal fold vibration in different languages, is "controlled" to enhance the contrastiveness of phonological voicing.

Research on f_0 perturbation in child speech is very limited. Robb and Smith (2002) reported that 4-year-old children exhibited a high f_0 falling pattern after voiceless consonants although the pattern was not adult-like; unfortunately, their study did not measure f_0 at voice onset after voiced consonants. Ohde (1985) compared VOT and f_0 perturbation pattern of 8- to 9-year-old children with those of adults, and reported that the children showed similar but more variable f_0 variation compared to adults. He suggested that f_0 is a secondary feature of voicing distinction and is mastered later than the primary phonetic feature, VOT.

2. Korean stop consonants

In Korean, three types of stops, referred to as fortis (or tense), aspirated, and lenis (or lax), are produced at three places of articulation: labial /p*,p,p^h/, alveolar /t*,t,t^h/, and velar /k*,k,k^h/ stops all are voiceless phrase-initially, and word-initially in words produced in isolation. In phrase-initial position, including single-word productions, *fortis stops* are described as unaspirated and laryngealized, *aspirated stops* as strongly aspirated, and *lenis stops* as slightly aspirated and breathy (e.g., Cho *et al.*, 2002).

The three types of stops can be distinguished by three acoustic properties: VOT, fundamental frequency (f_0) of the following vowel, and voice quality at the onset of the following vowel (Cho *et al.*, 2002; Kim *et al.*, 2002). In general, mean VOT values are shortest for fortis stops, intermediate for lenis stops, and longest for aspirated stops; however, VOT ranges often overlap (Han and Weitzman, 1970; Hardcastle, 1973; Kim, 1965). Whereas the VOT values markedly distinguish fortis stops from aspirated stops, f_0 differences serve to distinguish lenis stops from fortis or aspirated stops: f_0 at the onset of the vowels following lenis stops is generally lower than that following fortis or aspirated stops (Ahn, 1999; Cho *et al.*, 2002). Jun (1996) reported that the f_0 difference in Korean stops persists until the end of the vowel and is much greater in magnitude than that found in English and French. Jun (1996) suggested that the f_0 differences serve to "enhance a phonological contrast," thus making lenis stops perceptually more salient. Jun's (1996) argument may be related to Kingston and Diehl's (1994) theory of emphasizing phonological contrasts in that Korean speakers tend to manipulate the voice onset f_0 in order to make a phonological distinction.

Korean word-initial stops are also characterized by the voice quality of the following vowel: the voice onset after a lenis stop has a breathy voice, and the voice onset after a fortis stop has a creaky (or pressed) voice. The difference in amplitude between the first and second harmonics ($H1-H2$) at the onset of voicing is greater for lenis stops and aspirated stops relative to fortis stops in Korean (Ahn, 1999; Cho *et al.*, 2002).

There are few investigations of the acoustic-phonetic properties of consonants produced by young Korean children. Kang (1998) measured several phonetic properties of Korean obstruents spontaneously produced by a Korean child aged 2;8, and found a greater overlap of VOT values between the aspirated and lenis stops. With respect to the fundamental frequency (f_0), the f_0 difference was less distinct when compared to adult speech. More recently, Jun's (2006) longitudinal diary study demonstrated that a child learning the Chonnam dialect of Korean acquired adult-like fortis stops first and began to exhibit an f_0 difference at the onset of voicing between aspirated and lenis stops at 18 months while VOT values remained similar for both categories. The primary limitation of these studies is that they each reported findings for a single child and the words in the analyses were not controlled in terms of the number of syllables and phonetic context.

B. Predictions regarding the acquisition of Korean three-way stop contrast

In light of findings in literature, some predictions can be made with regard to development of phonetic properties distinguishing Korean initial stops. Young Korean children are predicted to first manifest the "universal" patterns reported for young children acquiring a range of languages, and then begin to develop language-specific phonetic patterns. The following "stages" in the development of acoustic-phonetic features are predicted. Initially, Korean children will produce short-lag stops, with VOT values that correspond to the fortis stop category in the adult form. In the next stage, Korean

TABLE I. Target words with Korean stops in word-initial position.

Fortis	Aspirated	Lenis
/p*aŋ/ "bread"	/p^{h}al/ "arm"	/pal/ "foot"
/t*ʌk/ "rice cake"	/t^{h}ʌk/ "chin"	/tak/ "hen"
/k*ot/ "flower"	/k^{h}oŋ/ "bead"	/koŋ/ "ball"

children will exhibit a bimodal VOT distribution (presumably fortis vs. aspirated or lenis stops) by using VOT as a primary phonetic attribute prior to voice onset f_0, which may be more susceptible to prosodic contexts. In the third stage, Korean children will begin to differentiate the long-lag categories (aspirated and lenis stops) using language-specific f_0 variation. It is also predicted that children will exhibit more overlap among contrastive stop categories compared to adults as seen in young children learning other languages (e.g., Gandour *et al.*, 1986; Zlatin and Koenigsknecht, 1976); the degree of overlap would decrease over age.

II. METHODS

A. Participants

Forty typically developing monolingual Korean children participated in this study. All children lived in Seoul or Gyounggi province, where Seoul dialect is used, and their mothers were speakers of the Seoul dialect. The participants were divided into four groups based on age, with ten children per group at ages 2;6 (year; month), 3;0, 3;6, and 4;0. Each age group had an equal number of male and female children. The age range from 2;6 to 4;0 was selected based on the reports that Korean children begin to distinguish three types of Korean initial stops around 2;6 and that errors across different stop categories decrease considerably after 4;0 (cf. Kim and Pae, 2005; Kim, 1996; Kim and Shin, 1992). According to parent report, the participants had no speech, language, hearing, and cognitive problems; they scored above the 16th percentile on a Korean version (Kim *et al.*, 2004) of the Peabody Picture Vocabulary Test–Revised (Dunn *et al.*, 1979). Adult speech samples were collected from ten women randomly selected among the child participants' mothers in order to compare children's productions with those of adults. All adult participants were Seoul dialect speakers with no history of speech, language, and hearing impairment.

B. Speech materials

As shown in Table I, target words were monosyllabic near-minimal triplets for word-initial fortis, aspirated, and lenis stops at each place of articulation. All these words were selected from McArthur Communicative Development Inventory-Korean (Pae *et al.*, 2004), and therefore were familiar words to children at the target ages. In order to increase the number of tokens for some of the younger children, a small set of additional words such as /pɑm/ "chestnut," /tɑl/ "moon," and /t^{h}ʌl/ "fur" was also included for analysis when needed.

To minimize possible effects of vowels or final consonants on the VOT of prevocalic stops (Klatt, 1975; Weismer, 1979) and of intrinsic f_0 effects of vowels (Lehiste and Peterson, 1961; Whalen and Levitt, 1995), an effort was made to choose triplets with the same neighboring segments. However, because of the limited size of young children's vocabulary, the triplets include words with different vowels or final consonants (see Table I). For comparison of $H1-H2$ differences, a low vowel like [a], which has the highest first formant frequency, is generally used to prevent the first formant energy from affecting the amplitude of $H1$ and $H2$. In this study, however, the mid vowel /o/ and mid-low vowel /ʌ/ were included for the same reason. In any case, the vowel identity or neighboring segment factors would not be a significant problem in comparisons of phonetic patterns across age groups because all participants produced the same target words with almost equal number of tokens. To avoid influences of phrase- or sentence-level factors, only single-word utterances were analyzed.

C. Procedures

Child data were collected in a quiet room at the participants' homes. A 40- to 60-min recording session occurred within 10 days of the target age. Children's speech samples were audiotaped using a Sony digital audio tape recorder. Children wore a vest with an Azden WMS-PRO wireless microphone attached approximately 10 cm from the mouth, along with a small transmitter placed in a pocket inside the vest. During the session, children were engaged in naming activities with toys, objects, or picture cards. The experimenter interacted with most of the children, but for some of the youngest children who were not cooperative, the mother was also involved in the activities as instructed by the experimenter. Most of the target words were produced in response to questions such as "what is this?" During the session, children were given multiple opportunities to produce target words provided through the repeated use of the materials.

The goal was to obtain at least five tokens for each stop consonant: p*, p^h, p, t*, t^h, t, k*, k^h, and k. Adult participants were recorded using the same equipment with the wireless microphone attached on their clothes. Index cards containing both targeted words and untargeted words in Korean orthography were presented repeatedly in a random order. The mothers were instructed to say each word in isolation as naturally as possible.

All speech samples were re-digitized at a 44.1 kHz sampling rate using COOL EDIT PRO 2, and then tokens of words with target phonemes word-initially were identified. Five tokens for each stop consonant were randomly selected for acoustic analysis; only tokens that were produced as stops at correct places were chosen. A total of eight tokens were excluded due to place or manner errors. Tokens that were extremely elongated, too loud or soft, or had ambient noise were also excluded.

A total of 2233 CVC (consonant + vowel + consonant) tokens (5 groups × 10 participants × 9 stops × mostly 5 tokens) were analyzed. Over 99% of the tokens were spontaneous or elicited productions in isolation; a few imitations ($n=18$) were included to increase the number of tokens. Although a minimum of five tokens per stop consonant was

desired, a few tokens ($n=10$) were rejected due to inappropriateness for spectral and temporal measures; for a few of the youngest children's data sets, the number of productions of a certain stop consonant was insufficient ($n=7$).

D. Acoustic analysis

VOT, fundamental frequency (f_0), and the amplitude difference between the first and second harmonics ($H1-H2$) were obtained using speech analysis software, PRAAT 4. 4. 13 (Boersma and Weenink, 2006). VOT measures were made by marking the interval between the beginning of the stop burst and the onset of the periodic glottal vibrations as displayed in the waveform and the 200 Hz broad bandwidth spectrogram with a 6-kHz range. The voice onset was determined directly from the waveform, supplemented by the signal of the voice bar from the spectrogram, in order to identify the voice onset more accurately in the presence of aspiration or breathy voicing (cf. Francis *et al.*, 2003), as often is the case of the voice onset after Korean lenis stops. In the cases of prevoicing, the offset of the negative VOT was identified by the stop burst since vocal fold vibrations were sustained through the burst into the following vowel.

f_0 values were taken at the onset of the following vowel, that is, the end point of VOT. However, some tokens with breathy or creaky phonation did not display a pitch track at the onset of the vowel. In such cases, f_0 was measured at near points within 10 ms (i.e., within one time step of the analysis program) from the true onset. About 40 tokens for which the pitch track of the voice onset was not captured using PRAAT were given f_0 values through additional speech software, TF32 (Milenkovic, 2001). Nevertheless, f_0 values of 13 tokens were unable to be determined.

Amplitudes (dB) of the first ($H1$) and the second ($H2$) harmonics were measured based on the 2048-point fast Fourier transform (FFT) spectrum with a 25 ms window sliced from the voice onset, and the difference of the amplitudes ($H1-H2$) was calculated. Three tokens, which presented unreliable harmonic peak values probably due to extreme roughness or creakiness at voice onset, were given no energy values.

Approximately 10% of the total 2233 tokens, randomly selected from all participants at all ages, were re-measured for the three acoustic parameters by the same analyzer and a second analyzer to determine intra- and inter-analyzer reliabilities. The intra-analyzer reliability was done approximately 5 months after the initial measurement has been completed, and the average values of VOT, f_0, and $H1-H2$ differed in absolute mean values by 2 ms, 3 Hz, and 0.9 dB, respectively. The mean differences between measures of the first and the second analyzers were 5 ms, 5 Hz, and 1.9 dB for the three parameters.

E. Statistical analysis

General linear model repeated measures analysis of variance (ANOVA) was conducted for VOT, f_0, and $H1-H2$, respectively, with stop category as a within-subject factor and age as a between-subjects factor. To avoid violating the sphericity assumption associated with repeated measures designs, a Huynh–Feldt corrected degree of freedom was adopted for all F tests. All pairwise *post hoc* comparisons were carried out with Bonferroni adjustment of the alpha level ($\alpha=0.05$) for each individual test. A linear discriminant analysis (DA) was performed to assess how well each age group distinguishes the three types of Korean stops with the combinations of the acoustic measures. All acoustic measures were entered using a stepwise procedure based on minimizing Wilks' lambda at each step. The significance level for each variable's entry into discriminant functions was set at 0.05 for an F test, and the prior probabilities were calculated from the number of stop productions in each stop category. All statistical analyses were done using the SPSS version 10 (SPSS Inc., 1999).

III. RESULTS

A. Voice onset time (VOT)

Results of repeated measures ANOVA (stop category by place by age) revealed significant main effects of stop category [$F(2,378)=2443.65$, $p<0.001$], place [$F(2,378)=169.38$, $p<0.001$], and age [$F(4,189)=48.02$, $p<0.001$], and a significant interaction of stop category and age [$F(8,378)=25.78$, $p<0.001$], and stop category and place [$F(4,756)=16.79$, $p<0.001$]. Because it is of greater interest to examine how different types of stops are differentiated by VOT in each age group, VOT differences among three stop categories were assessed per group. The results of repeated measures ANOVAs showed that there was a significant stop category effect for all age groups: 2;6-year-olds [$F(2,70)=217.16$, $p<0.001$], 3;0-year-olds [$F(2,76)=512.99$, $p<0.001$], 3;6-year-olds [$F(2,72)=509.31$, $p<0.001$], 4;0-year-olds [$F(2,80)=541.49$, $p<0.001$], and adults [$F(2,80)=1475.54$, $p<0.001$].

Multiple comparisons with a Bonferroni adjustment showed that VOT for the adult group was significantly shortest for fortis stops, intermediate for lenis stops, and longest for aspirated stops at all places of articulation ($p<0.001$ for each comparison), in agreement with previous studies. For the children, 2;6-year-olds produced significantly longer aspirated and lenis stops than fortis stops, with no significant difference between aspirated and lenis stops at all places of articulation ($p<0.001$). The 3-year-olds, on the other hand, demonstrated significant differences for all stop categories ($p<0.001$ for all comparisons except for $p<0.05$ for velar and $p<0.01$ for labial aspirated and lenis comparisons). For the 3;6-year- and 4-year-old children, VOT was significantly shortest for fortis stops, intermediate for lenis stops, and longest for aspirated stops only at labial place; for alveolar and velar stops, there was a significant difference in fortis stops vs. aspirated or lenis stops, with no significant difference between the two long-lag stops.

Group means and standard deviations for VOT values for each place of articulation are displayed in Table II. It can be seen that VOT values for aspirated and lenis stops produced by the 3;6-year-olds were the longest of all groups, while those produced by the 2;6-year-olds were the shortest. Table II also reveals the presence of negative VOT values in

TABLE II. Means and standard deviations (in parentheses) of VOT (ms), f_0 (Hz), and $H1-H2$ (dB) for each age group.

Measure		VOT				
Age group	Stop category	Labial	Alveolar	Velar	f_0	$H1-H2$
2;6	Fortis	−3.9 (15.9)	1.7 (12.8)	22.4 (14.2)	381.4 (62.1)	−6.4 (8.3)
	Aspirated	49.2 (41.7)	50.8 (46.9)	58.8 (37.5)	387.9 (98.4)	1.5 (10.1)
	Lenis	50.0 (41.5)	39.9 (34.3)	63.0 (39.8)	363.0 (77.7)	2.1 (8.0)
3;0	Fortis	−5.7 (17.9)	−1.3 (17.0)	18.5 (21.4)	354.5 (62.0)	−5.7 (7.6)
	Aspirated	74.5 (48.7)	62.2 (37.9)	86.1 (34.8)	370.2 (62.6)	5.5 (8.0)
	Lenis	58.8 (31.9)	43.3 (28.3)	72.6 (28.0)	326.0 (50.3)	6.0 (6.6)
3;6	Fortis	−4.5 (19.2)	0.9 (11.8)	15.8 (13.0)	371.8 (68.8)	−3.8 (7.5)
	Aspirated	89.6 (27.9)	69.0 (34.3)	99.3 (29.1)	396.2 (82.2)	6.1 (8.5)
	Lenis	75.2 (30.2)	71.9 (34.9)	83.7 (37.5)	316.5 (57.6)	7.0 (6.8)
4;0	Fortis	−4.8 (23.0)	1.3 (11.5)	15.2 (13.3)	346.2 (60.3)	−6.6 (7.2)
	Aspirated	85.4 (31.6)	62.0 (28.1)	85.2 (27.2)	358.2 (48.3)	6.2 (7.4)
	Lenis	68.1 (34.7)	64.2 (35.2)	76.9 (32.0)	301.6 (43.9)	6.5 (7.8)
Adult	Fortis	5.4 (4.4)	6.2 (2.7)	23.7 (9.0)	252.4 (29.2)	−3.7 (4.6)
	Aspirated	71.6 (16.3)	59.3 (14.4)	84.8 (14.1)	285.5 (30.1)	7.8 (6.9)
	Lenis	57.9 (18.2)	48.1 (15.6)	59.9 (15.0)	218.9 (18.9)	6.2 (7.7)

children's productions of fortis stops; this finding was not expected given that lead voicing is not a characteristic of adult Korean. In the adult data set, lead voicing occurred in only one token, classified as an extreme outlier. The occurrence of prevoicing is examined in more detail in Table III showing the percentage of productions with lead stop voicing for each stop consonant in each child group. The table shows that a majority of children at all ages produced lead voicing for labial stops and about half the children produced lead voicing for alveolar fortis stops.

Some tokens with lead voicing also exhibited evidence of nasalization during stop closure. Although the nasal feature was not measured instrumentally, it was perceptually identified in many of the stop productions with lead VOT, and there was some spectrographic evidence of strong energy in the voice bars. Four tokens excluded from this study revealed substitutions of nasals for target fortis stops.

Even though mean values of acoustic measures are often used to determine emergence of phonetic categories in child speech, mean values in children's productions may not be representative for certain phonetic categories. Because of potential skewed distributions in child data, the degree of overlap may be a more appropriate measure to evaluate developmental patterns of phonemic categories (cf. Koenig, 2001). In order to explore the degree of overlap in VOT among stop categories in these data, box plots exhibiting VOT distributions for each place of articulation are presented in Fig. 1(a) (labial stops), Fig. 1(b) (alveolar stops), and Fig. 1(c) (velar stops). In each figure, the box contains values between the 25th and the 75th percentile, i.e., the middle half of the distribution. The line in the middle of the box corresponds to the median: half of all values are greater than median and the other half are smaller than median. The lower and upper brackets in the box plots represent the 10th and 90th percentile values: 80% of the values fall within two brackets. Outliers with values between 1.5 and 3 times the box length are represented by a circle (○), and extreme outliers, with values greater than 3 times the box length, are indicated by an asterisk (*).

TABLE III. Percentage (%) of tokens realized as lead voicing stops for each child age group (number of children, out of 10 per group, in parentheses).

	Age group			
Stop	2;6	3;0	3;6	4;0
p*	39 (8)	38 (8)	42 (7)	38 (7)
p^h	2 (1)	0	0	0
p	4 (1)	0	0	0
t*	17 (3)	28 (7)	17 (4)	22 (7)
t^h	2 (1)	0	0	0
t	4 (2)	2 (1)	0	0
k*	2 (1)	6 (1)	2 (1)	2 (1)
k^h	0	0	0	0
k	0	0	0	0

The box plots reveal different VOT distributions between child and adult groups. While adult data explicitly differentiate fortis stops from aspirated or lenis stops by VOT, except for some overlap between fortis and lenis stops for velars, children's productions exhibit some overlap in VOT between fortis stops and aspirated or lenis stops at all places of articulation. This overlapping trend is most prominent in the data from 2;6-year-olds. Nonetheless, even at this age, the box areas corresponding to the center half of the distributions for fortis and the other two types of stops do not overlap, indicating that VOT serves to distinguish fortis stops from aspirated or lenis stops. The VOT ranges for aspirated and lenis stops, in contrast, substantially overlap in the children's productions as well as those of the adults, although the

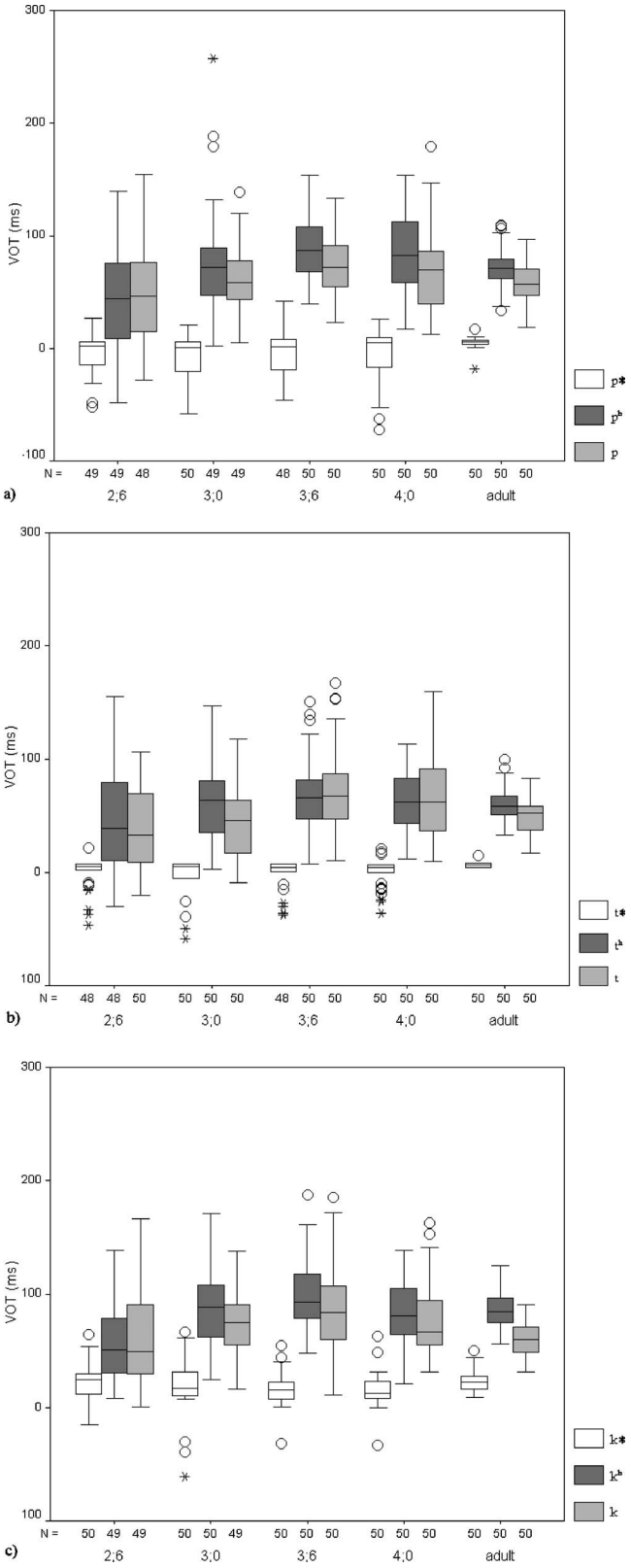

FIG. 1. Box plots of VOT (ms) production for three types of stops (white squares=fortis, dark gray squares=aspirated, and light gray squares =lenis) by each age group for (a) labial, (b) alveolar, and (c) velar places of articulation. The box area contains the middle 50% of the distribution, each line within boxes denotes median, and two brackets mark 80% of the distribution. Outliers (values between 1.5 and 3 times the box length) are represented by circles (○), and extremes (values over 3 times the box length) by asterisks (*).

median values tend to be greater for aspirated stops. This finding highlights the necessity of other acoustic parameters to separate these categories, presumably the fundamental frequency of the following vowel.

The figures show that a majority of productions for fortis stops fall within the short-lag region of the VOT continuum (i.e., 0 to +20 ms for labials and alveolars, and 0 to +40 ms for velars; cf. Macken and Barton, 1980a) at all places in adult speech. For the children, velar fortis stops are within the short-lag region, while many labial and alveolar fortis stops vary from lead (39.1% at labial place and 20.9% at alveolar place) to short-lag VOT values. On the other hand, stop productions for aspirated and lenis categories tend to fall within the long-lag region, mostly with 40–150 ms at all places except for the 2;6-year-olds who demonstrated a high percentage of short-lag stops (approximately 35% for each place of articulation). Further examination of the 10 children in the 2;6 group revealed that 3 children produced most of their words with short-lag VOT, regardless of the type of stop. Table IV shows the VOT values for these three children (referred to in the table as the "early stage-2;6" subgroup) compared with the values for the seven other children in the age group. Although the mean for labial fortis stops was smaller relative to the means for other types of stops on account of the presence of some prevoiced tokens, there were no significant differences in the means for each place of articulation for this group. Because these three children produced primarily short-lag stops, they were considered to be in the earliest stages of VOT development and are referred to as early stage-2;6. The figures also show wider VOT ranges in children's productions when compared with the adults. As reported for children learning other languages (Clumeck *et al.*, 1981; Gandour *et al.*, 1986; Gilbert, 1977), this pattern was noticeable particularly in aspirated and lenis stop categories corresponding to long-lag stops, and also in children's /p*/ productions with lead VOT values.

B. Fundamental frequency (f_0)

Given the substantial overlap in VOT ranges in both adult and child speech, primarily between aspirated stops and lenis stops, f_0 is expected to play an important role in differentiating these two types of stops. The results of repeated measures ANOVAs showed significant main effects of stop category [$F(2,1322)=345.95$, $p<0.001$], and age [$F(4,661)=543.15$, $p<0.001$], and an interaction of stop category and age [$F(8,1322)=11.61$, $p<0.001$]. The stop category effect was significant for all age groups: 2;6-year-olds [$F(2,262)=10.864$, $p<0.001$], 3;0-year-olds [$F(1.97,266.20)=31.27$, $p<0.001$], 3;6-year-olds [$F(2,266)=109.47$, $p<0.001$], 4;0-year-[$F(2,254)=117.31$, $p<0.001$], and adults [$F(1.99,269.20)=634.28$, $p<0.001$].

Pairwise comparisons showed that f_0 for the adult group was significantly lowest for lenis stops, intermediate for fortis stops, and highest for aspirated stops ($p<0.001$ for each comparison) as reported in prior studies. For the children, all age groups demonstrated significantly higher f_0 for fortis and aspirated stops compared to lenis stops ($p<0.01$ for 2;6-

TABLE IV. Means and standard deviations (in parentheses) of VOT (ms), f_0 (Hz), and $H1-H2$ (dB) for the early stage-2;6 subgroup (2;6a; $n=3$) and the subgroup excluding early stage-2;6 children (2;6b; $n=7$).

Measure		VOT				
Age group	Stop category	Labial	Alveolar	Velar	$f0$	$H1-H2$
2;6a	Fortis	0.4 (11.6)	5.6 (9.6)	27.8 (10.6)	354.2 (72.8)	−6.2 (7.1)
	Aspirated	4.8 (16.3)	5.0 (11.4)	24.4 (12.9)	343.3 (62.4)	−6.5 (7.7)
	Lenis	9.5 (16.8)	4.9 (10.3)	36.1 (17.4)	345.0 (46.2)	−4.6 (5.4)
2;6b	Fortis	−5.7 (17.2)	0.3 (13.6)	20.0 (15.1)	392.3 (53.9)	−6.4 (8.7)
	Aspirated	66.9 (35.0)	67.8 (43.5)	73.9 (34.7)	406.0 (104.6)	4.8 (9.2)
	Lenis	66.7 (36.9)	54.9 (29.6)	74.9 (41.2)	370.8 (86.9)	4.9 (7.2)

year-olds and $p<0.001$ for children in the other age groups). For the fortis vs. aspirated stop contrast, only the 3;6-year-olds produced significantly higher f_0 for aspirated stops than fortis stops ($p<0.001$), conforming to the adult pattern.

Table II shows group mean and standard deviation for f_0 values. It is apparent that the children's f_0 at the voice onset following every type of stop is much higher than that of adults, as predicted by a general pattern of high f_0 in children's productions. The absolute f_0 values tend to decrease over age for each stop category except for the 3;6 group. Children in this age group exhibit highest f_0 values after aspirated stops, which make a greater distinction from lenis stops; these children also produced the longest VOTs for aspirated and lenis stops.

In terms of f_0 ranges, Fig. 2 shows the presence of overlap among the three types of stops in both adult and child speech. Nevertheless, adult productions exhibit nonoverlapping box areas for each stop category and apparent distinctions of aspirated vs. lenis stops for the majority of tokens. The older children, ages 3;6 and 4;0, produce a greater f_0 distinction between aspirated and lenis stops relative to the younger children, ages 2;6 and 3;0. In addition, the three children classified as early stage-2;6 (i.e., the children who produced mostly short-lag stops for all stop categories) demonstrated no significant f_0 differences among three stop categories, suggesting that the f_0 distinction may emerge after a phonetic contrast by VOT is present (see Table IV for mean f_0 values).

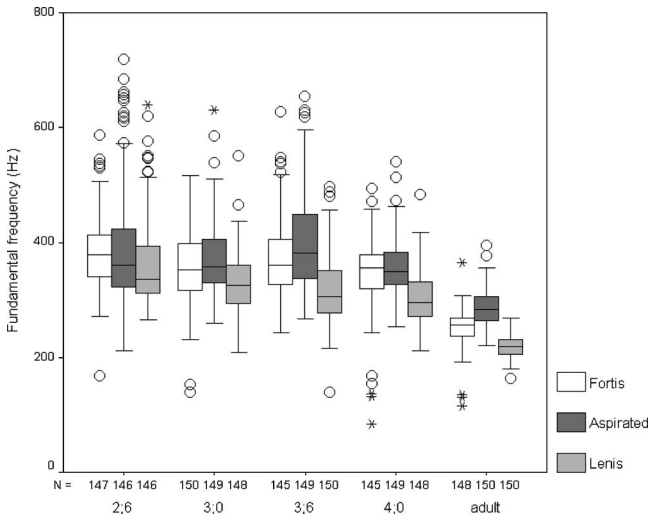

FIG. 2. Box plots of fundamental frequency (Hz) by stop category for each age group.

As in the case of VOT, the children show a greater range of f_0, especially for aspirated stops, and a greater number of extremely high f_0 values relative to adults. At the same time, some noticeably low values were noted in both adult and child speech, due to creaky voice onset following fortis stops.

C. $H1-H2$

On the basis of previous studies in which VOT and $H1-H2$ for Korean stops tend to co-vary to some degree (e.g., Ahn, 1999), it was expected that fortis stops with lead or short VOT would be separated from aspirated or lenis stops with long VOT by $H1-H2$ as well. The results of repeated measures ANOVAs revealed a significant effect of stop category [$F(2,1366)=756.64$, $p<0.001$] and of age [$F(4,683)=22.68$, $p<0.001$], and an interaction of stop category and age [$F(8,1366)=5.17$, $p<0.001$]. The stop category effect was significant for all age groups: 2;6-year-olds [$F(2,266)=65.73$, $p<0.001$], 3;0-year-olds [$F(2,274)=177.18$, $p<0.001$], 3;6-year-olds [$F(2,270)=125.36$, $p<0.001$], 4;0-year-olds [$F(2,276)=200.77$, $p<0.001$], and adults [$F(2,280)=306.77$, $p<0.001$].

Pairwise comparisons indicated that $H1-H2$ was significantly smallest for fortis stops with negative values, intermediate for lenis stops, and greatest for aspirated stops ($p<0.01$ for aspirated vs. lenis stops and $p<0.001$ for the other comparisons) in adult productions. The results indicate that the voice onset after fortis stops has creaky voicing while the voice onset after lenis and aspirated stops has breathy voicing as reported in previous studies (e.g., Ahn, 1999). The children showed a significant $H1-H2$ differentiation between fortis stops and aspirated or lenis stops ($p<0.001$) at all ages, but no significant difference between the aspirated and lenis categories. The amplitude difference between the first and second harmonics ($H1-H2$) appears to co-vary with VOT. When compared to adults, children appear to produce more creaky voice after fortis stops.

With regard to age-related differences, 2;6-year-olds displayed relatively small values for aspirated and lenis stops compared to other adult and child groups, as reported in Table II. The pattern may be affected by individual differ-

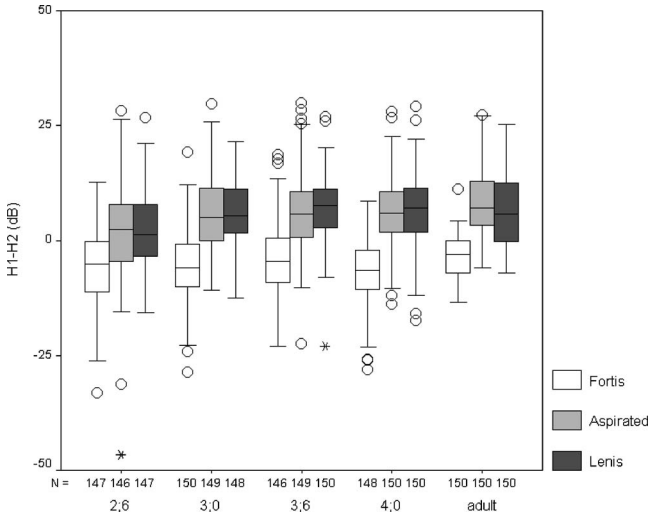

FIG. 3. Box plots of $H1-H2$ (dB) by stop category for each age group.

ences in this age group as in the case of VOT. That is, the consistent short-lag stop productions of the three early stage-2;6 children may have reduced the mean values of $H1-H2$, as shown in Table IV. There were no significant mean differences among the three types of stops in early stage-2;6 children; in contrast, $H1-H2$ of fortis stops in the other 2;6 children was significantly smaller relative to those of lenis and aspirated stops.

The box plots for $H1-H2$ in Fig. 3 manifest a similar pattern in adult and child groups with observable overlap between fortis stops and aspirated or lenis stops. It can be seen, however, that greater overlap occurs in the 2;6 group whereas the 4-year-olds exhibit a greater distinction between these categories, as evidenced by a separation of box areas. In addition, the children show more variability relative to adults as evidenced by brackets denoting the range for energy values of most productions.

D. Discriminant analysis

A stepwise linear DA was conducted for each age group and each place of articulation. In every analysis for all places and age groups, two discriminant functions accounted for a significant portion of the variance. Except for the 2;6 group, VOT, f_0, and $H1-H2$ were significant variables for stop category classification. In the case of 2;6-year-olds, only VOT and f_0 were significant for labials, and only VOT and $H1-H2$ for alveolars and velars. For classification of each case in the analysis, the "leave-one-out cross-validation technique" (the "jackknife") was carried out. This technique computes the discriminant functions derived from all cases but that case.

The classification results in Table V provide an indication of how well children differentiate among the three types of stops using the three acoustic parameters. The three-way matrices based on place and age show the percentage of stop productions classified correctly or incorrectly. "Overall percent" corresponds to correct classification across the three stop categories. As expected, most of the adult stop productions were correctly classified (92%–100%), indicating that the three stop categories are well differentiated by the three acoustic parameters. In the children's productions, however, a substantial number of productions were misclassified into different stop categories. While fortis stops were classified most accurately (85%–98%) for all child groups, aspirated and lenis stops were often misclassified in the 2;6 and 3;0 age groups. In the 3;6 and 4;0 groups, misclassification oc-

TABLE V. Classification results based on DA: Percentage of stop productions classified correctly (in bold) or incorrectly is presented in three-way matrices with regard to place and age, respectively, with original stop categories listed in the second column. "Overall" corresponds to the percentage of correct classification across stop categories at each place of articulation.

	% stop productions classified													
		Labial					Alveolar					Velar		
Age group		/p*/	/p^h/	/p/	Overall		/t*/	/t^h/	/t/	Overall		/k*/	/k^h/	/k/	Overall
2;6	/p*/	**93.9**	4.1	2.0		/t*/	**85.4**	0.0	14.6		/k*/	**88.0**	6.0	6.0	
	/p^h/	26.5	**28.6**	44.9		/t^h/	31.3	**33.3**	35.4		/k^h/	30.6	**40.8**	28.6	
	/p/	20.8	27.1	**52.1**	**58.2**	/t/	24.0	16.0	**60.0**	**59.6**	/k/	32.7	22.4	**44.9**	**58.1**
3;0	/p*/	**88.0**	0.0	12.0		/t*/	**94.0**	0.0	6.0		/k*/	**90.0**	4.0	6.0	
	/p^h/	12.2	**63.3**	24.5		/t^h/	16.0	**62.0**	22.0		/k^h/	14.0	**62.0**	24.0	
	/p/	12.2	24.5	**63.3**	**71.6**	/t/	24.0	24.0	**52.0**	**69.3**	/k/	18.4	20.4	**61.2**	**71.1**
3;6	/p*/	**97.9**	0.0	2.1		/t*/	**93.6**	4.3	2.1		/k*/	**94.0**	2.0	4.0	
	/p^h/	2.0	**69.4**	28.6		/t^h/	6.0	**60.0**	34.0		/k^h/	0.0	**74.0**	26.0	
	/p/	4.0	16.0	**80.0**	**82.3**	/t/	2.0	24.0	**74.0**	**75.5**	/k/	8.0	18.0	**74.0**	**80.7**
4;0	/p*/	**97.9**	0.0	2.1		/t*/	**98.0**	2.0	0.0		/k*/	**95.8**	0.0	4.2	
	/p^h/	0.0	**79.6**	20.4		/t^h/	4.0	**62.0**	34.0		/k^h/	6.0	**58.0**	36.0	
	/p/	2.0	18.0	**80.0**	**85.6**	/t/	2.1	33.3	**64.6**	**74.8**	/k/	6.0	22.0	**72.0**	**75.0**
Adult	/p*/	**100.0**	0.0	0.0		/t*/	**100.0**	0.0	0.0		/k*/	**96.0**	0.0	4.0	
	/p^h/	0.0	**92.0**	8.0		/t^h/	0.0	**98.0**	2.0		/k^h/	0.0	**92.0**	8.0	
	/p/	6.0	2.0	**92.0**	**94.6**	/t/	0.0	8.0	**92.0**	**96.7**	/k/	4.0	4.0	**92.0**	**93.3**

TABLE VI. Percent correct classification based on the adult model for each stop consonant in each age group

	Labial				Alveolar				Velar			
Age group	Overall	/p*/	/p^h/	/p/	Overall	/t*/	/t^h/	/t/	Overall	/k*/	/k^h/	/k/
2;6	51.4	83.7	69.4	0.0	54.1	91.7	72.9	0.0	51.7	76.0	69.4	8.3
3;0	63.5	98.0	85.7	6.1	60.0	92.0	86.0	2.0	60.4	80.0	94.0	6.1
3;6	63.3	89.6	98.0	4.0	61.9	85.1	98.0	4.0	60.7	74.0	100.0	8.0
4;0	67.8	93.6	98.0	14.0	68.0	95.9	100.0	6.3	69.6	89.6	100.0	20.0

curred between aspirated and lenis categories. The correct classification rate for these two categories was lowest for the youngest group, in which only two significant acoustic measures were used for classification. The low correct classification rate may be related to substantial overlap in all acoustic measures of these two categories. The probability rates with which stop productions were correctly classified were also much lower in the 2;6-year-olds' productions, and were lower in child speech compared to adult speech, indicating the weak discriminating power of acoustic variables in children. In general, the overall classification rate increased as a function of age, indicating that older children's stop productions are more contrastive to one another.

Because children are capable of making phonetic contrasts before they produce adult-like phonetic values (e.g., Gilbert, 1977), an additional DA was performed to examine developmental patterns of child speech compared with adult productions; in this case, the child data were classified based on classification functions derived from adult data using STATA 10 (StataCorp LP, 2007). The results are summarized in Table VI. In general, overall classification rates improved with age, and the percentage of correct classification for both fortis and aspirated stops was relatively high, although the correct classification rate of aspirated stops was somewhat low in the youngest group.

Unlike the pattern for fortis and aspirated stops, the classification of lenis stops was remarkably poor in most children (0%–8.3% in the 2;6, 3;0, and 3;6 groups), although the 4;0 group shows a higher rate (6.3%–20.0%). Lenis stops produced by the 2;6-year-old children were misclassified as either fortis (28.0%–39.0%) or aspirated (52.1%–72.0%). The 3;0-year-olds also produced some lenis stops that were misclassified as fortis (10.2%–20.0%), based on the adult classification model. In contrast, in the 3;6 and 4;0 groups, the misclassifications were predominantly in the direction of aspirated stops. The results suggest that the phonetic realizations of children's productions aged 2;6 to 4 years are quite different from those of adults.

IV. DISCUSSION

The present study examined the development of acoustic-phonetic properties of Korean stops in word-initial position; these stops exhibit a three-way contrast differentiated by VOT, fundamental frequency (f_0), and the amplitude differences between the first and second harmonics ($H1-H2$) of the following vowel. Findings from this study show that Korean children aged 2;6 to 4;0 demonstrated both universal phonetic patterns and phonetic variation associated with articulatory complexity specific to Korean.

Among the younger children in the study, stops were differentiated primarily by VOT. Only later did fundamental frequency (f_0) of the following vowel play a distinctive role. As predicted, in the earliest stage of acquisition, the children showed no contrast among stop types, producing most stops with short VOT values and no difference between f_0 and $H1-H2$. This pattern was found in the subgroup of three children of 2;6 group (the early stage-2;6 children). In the next stage, most children exhibited a bimodal VOT distribution for the distinction between fortis stops and aspirated or lenis stops, although there was some evidence of shorter VOT values for lenis stops relative to aspirated stops. Along with the presence of short-lag and long-lag stops exhibiting a large range of VOT values, the children began to use a language-specific feature to make another contrast: they varied fundamental frequency of the following vowel to differentiate between aspirated and lenis categories.

It is interesting to note that f_0 variation emerges around 2;6 years when both aspirated and lenis stops are realized as long-lag stops with no VOT or $H1-H2$ differences. This finding indicates that young Korean children are using a laryngeal gesture (i.e., slack mode of vocal folds) to produce a low f_0 that can differentiate between aspirated and lenis stops. The results provide evidence that f_0, a language-specific feature, is manipulated by young Korean children as a phonological component when a phonemic distinction is required. This finding supports the claim that f_0 variation at the level of the phonetic segment is controlled by language users in order to boost phonological contrastiveness (cf. Kingston and Diehl, 1994).

The f_0 difference, however, was not as distinctive as VOT, which separated fortis stops from aspirated or lenis stops in most productions at 2;6 (except for the three early stage-2;6 children). By comparison, f_0 values of aspirated and lenis stop categories overlapped a great deal, even though there was a significant difference in mean values. In addition, unlike the acquisition of the non-overlapping two-way VOT distinction before age 4;0, the f_0 distinction only gradually improved over age and was not adult-like in the productions of the oldest group of children, age 4;0. This finding may be attributed to later stabilization of f_0 vs. segmental duration because of laryngeal changes due to physiological and anatomical development in children (Lee *et al.* 1999; Ohde, 1985). It is also possible that the phonetic contrast created by f_0 develops later because f_0 may be percep-

tually less salient, due to more variation in different prosodic positions, compared to VOT. For Korean stops, the f_0 variation is absent in phrase-medial position being overridden by overall intonation contour (Jun, 1996).

Although the Korean children's productions support the presence of the universal VOT patterns predicted for phonetic development of stop consonants, there were also language-specific aspects of acquisition associated with Korean stops. As predicted, the fortis category emerged earliest, with short VOT values; however, this category did not become adult-like until 4 years of age. It is intriguing to note that the majority of children in all age groups produced a high proportion of lead voicing for this stop category particularly for labial and alveolar stops where as many as 40% of the tokens were prevoiced (see Table III). The presence of stops with lead voicing in children learning a language with no prevoicing phonemic category has been noted in other studies. For example, Clumeck *et al.* (1981) reported that Cantonese-learning children produced a small number of short-lag stops with lead VOT, even though prevoiced stops never occurred in the productions of Cantonese adult speakers. Given the report that a Korean fortis stop is similar to a Cantonese short-lag stop in that both are produced with short VOT and high f_0 (Francis *et al.*, 2006), it is possible that prevoicing for this type of stop is associated with the difficulty children have in controlling the laryngeal activities (e.g., vocal fold tension) specific to these languages. Alternatively, as in the case of long-lag stops, the presence of prevoicing could simply be a consequence of general temporal variation associated with neuromuscular immaturity in children (Kent and Forner, 1980; Smith, 1992). A VOT range ranging across lead to short-lag regions for short-lag stops is also found in Spanish and Thai child data (Macken and Barton, 1980b, for Spanish; Gandour *et al.*, 1986, for Thai).

The Korean data also showed the presence of nasalization during stop closure of lead voicing stop productions. One plausible interpretation for pre-nasalization in lead voicing stop productions is related to intrinsic laryngeal activities that are involved in fortis stop production. It has been reported that fortis stops are produced with laryngeal and supralaryngeal articulatory tension and high intraoral air pressure (Cho *et al.*, 2002; Dart, 1987), and that Korean adult speakers tend to lower the larynx to decrease the supraglottal pressure for initiating voicing almost simultaneously with the stop release (Fujimura, 1972; Hardcastle, 1973; Kagaya, 1974). Young Korean children appear to expand the supraglottal cavity by opening nasal passage, which leads to reduction in oral air pressure. Thus, the prevoicing with nasalization in Korean child speech can be regarded as a coping strategy for the physiological constraints in achieving this articulatorily complex speech sound production.

A similar articulatory maneuver occurs in children learning prevoiced stops in some other languages. It is reported that Greek-learning children acquire word-initial prevoiced stops relatively early by realizing pre-nasalization that can occur in adult word-medial stops (Kong *et al.*, 2007). In the case of French-learning toddlers, voiced segments, most commonly nasals, were often placed prior to initial voiced stops to enhance continuation of voicing (Allen, 1985).

In comparison with the adults in this study, the children showed greater overlap among the three types of stop categories, and displayed more variability as evidenced by the range of acoustic measures. (It is possible, however, that lower variability in adult speech compared to child speech might be partly due to the different elicitation methods that were used to collect the data.) When all three acoustic parameters were utilized, most fortis stops in the children's productions were well separated from long-lag stops, as in adult speech. In contrast, there was still substantial overlap between aspirated and lenis categories, and decreasing overlap over age was observed. When the child data were classified by an adult classification model (Table VI), the very low rate of correct classification for lenis stops was notable. This result suggests that the phonetic features used by the children to distinguish among the three types of stops differ from those of adults. Although the children exhibited a phonetic contrast between aspirated and lenis categories, they used only f_0, which was still unstable, while adults' productions of lenis stops were differentiated by all three acoustic parameters. Therefore, lenis stop productions with long VOT and relatively high f_0 in child speech were often classified as aspirated stops based on the adult model.

The late acquisition of lenis stops might be explained by some phonetic characteristics inherent to this stop category. First, lenis stops are articulatorily weaker than the other types of stops: Kim (1965) stated that lenis stops differ from their aspirated and fortis counterparts by exhibiting less energy for the burst and aspiration period, a smaller linguopalatal contact, and less lip muscle activity in bilabials. It may be that lenis stops with weak articulations are perceptually less salient, and therefore require more time to master. Second, the phonetic realization of lenis stops is known to be context-sensitive relative to other types of stops (Cho *et al.*, 2002). Lenis stops are slightly aspirated in utterance-initial position, but can be voiced in intervocalic position. The intervocalic voicing is gradient, being affected by the level of the preceding prosodic boundary. The variability due to phonetic context may make this type of stop more difficult to master. Lastly, the production of lenis stops may be articulatorily more complex than that of fortis or aspirated stops because these stops may involve additional laryngeal adjustment for lowering f_0. According to Löfqvist *et al.* (1989), typically, the laryngeal state for voiceless stops leads to high f_0.

Some researchers have suggested that the order of phonemic acquisition is related to lexical effects, specifically frequency of occurrence of the phonemes in the ambient language (Stoel-Gammon, 1998; Stokes and Surendran, 2005). In the case of Korean, lexical effects of the ambient language (i.e., the frequency of occurrence of the phonemes in child and adult speech of Korean) do not seem to explain the observed order of stop acquisition. The McArthur Communicative Development Inventory-Korean (Pae *et al.*, 2004), a receptive and expressive vocabulary checklist designed for 17–30 month-old toddlers, shows that the lenis category is the most frequent in words beginning with stop consonants. In the vocabulary list, the percentages of stop-initial words with fortis, aspirated, and lenis stops are 18.7%, 13.7%, and 67.6%, respectively. Shin (2005) reported a similar finding in

an analysis based on token frequency, rather than type. Examination of 5851 spontaneous utterances produced by 49 Korean children aged 3–8 years revealed that lenis stops were the most common type of stop in word-initial position in all age groups. The percentage ranges for word-initial fortis, aspirated, and lenis stops in all phrase-initial words were 6.7%–12.6%, 10%–17.2%, and 29.8%–32.7% across ages. Little is known regarding frequency in child-directed speech for Korean.

Although the present study did not focus on the effects of place of articulation on VOT, it was found that VOT is significantly longer for velar stops than for other places of articulation in all age groups (a pattern that may be universal), whereas VOT differences at labial and alveolar places were inconsistent. Prevoicing of Korean stops was most common for labial stops, as with previous studies (e.g., Zlatin and Koenigsknecht, 1976). In addition, only at the labial place of articulation at ages 3;0, 3;6, and 4;0 were VOT values significantly different across all three types of stops. This finding indicates that young Korean children attempt to make adult-like phonetic distinctions using VOT when the phonetic values are widely dispersed.

The present investigation has certain limitations that should be acknowledged. First, the developmental patterns of stops were examined based on a small set of words and limited phonetic contexts. Target words were selected based on two primary criteria: (a) they formed near-minimal triplets with restricted vowel environments to control variables that would affect acoustic analyses, and (b) they were likely to be present in the vocabularies of young Korean children. In the future, investigations of stop consonants in the context of various word types with different vowels are needed. Second, as with all cross-sectional studies, developmental patterns are inferred from data gathered from groups of children at different ages. It is possible that some children show more distinctive phonetic contrasts at earlier ages relative to others. In addition, the large overlap in phonetic measures from group data can be partly due to different ranges of phonetic values among children. Longitudinal studies are needed to provide information on the child-specific patterns in the acquisition of Korean stops.

In conclusion, this study suggests that language-specific phonetic details as well as universal patterns should be examined to provide a better understanding of the speech sound development of a given language. Findings showed the presence of phonological universals associated with stop acquisition based on data from a language using multiple phonetic-acoustic features for stop contrasts. As found in children learning other languages, young Korean children first produced the short-lag stops and then exhibited a bimodal VOT contrast. Results from this study also indicate the presence of phonetic markers associated with the acquisition of language-specific laryngeal gestures. In addition, fundamental frequency, which is considered as a redundant or a secondary phonetic feature in other languages, is independently utilized in the acquisition of Korean initial stops.

ACKNOWLEDGMENTS

This study was supported by the University of Washington Graduate School Fund. We would like to thank the families who participated in this study and acknowledge the helpful comments of Ruth Litovsky and two anonymous reviewers.

Ahn, H. (**1999**). "Post-release phonatory processes in English and Korean: Acoustic correlates and implications for Korean phonology," Ph.D. thesis, University of Texas at Austin, Austin, TX.

Allen, G. D. (**1985**). "How the young French child avoids the pre-voicing problem for word-initial voiced stops," J. Child Lang. **12**, 37–46.

Boersma, P., and Weenink, D. (**2006**). "PRAAT: Doing phonetics by computer (version 4.4.13)," Computer program, University of Amsterdam.

Cho, T., Jun, S.-A., and Ladefoged, P. (**2002**). "Acoustic and aerodynamic correlates of Korean stops and fricatives," J. Phonetics **30**, 193–228.

Cho, T., and Ladefoged, P. (**1999**). "Variation and universals in VOT: Evidence from 18 languages," J. Phonetics **27**, 207–229.

Clumeck, H., Barton, D., Macken, M. A., and Huntington, D. A. (**1981**). "The aspiration contrast in Cantonese word-initial stops—Data from children and adults," J. Chin. Linguist. **9**, 210–225.

Dart, S. N. (**1987**). "An aerodynamic study of Korean stop consonants—Measurements and modeling," J. Acoust. Soc. Am. **81**, 138–147.

Davis, K. (**1995**). "Phonetic and phonological contrasts in the acquisition of voicing—Voice onset time production in Hindi and English," J. Child Lang. **22**, 275–305.

Dunn, L. M., Dunn, L. M., Robertson, G. J., and Eisenberg, J. L. (**1979**). *The Peabody Picture Vocabulary Test—Revised* (American Guidance Service, Circle Pines, MN).

Eilers, R. E., Oller, D. K., and Benitogarcia, C. R. (**1984**). "The acquisition of voicing contrasts in Spanish and English learning infants and children—A longitudinal study," J. Child Lang. **11**, 313–336.

Francis, A. L., Ciocca, V., Wong, V. K. M., and Chan, J. K. L. (**2006**). "Is fundamental frequency a cue to aspiration in initial stops?," J. Acoust. Soc. Am. **120**, 2884–2895.

Francis, A. L., Ciocca, V., and Yu, J. M. C. (**2003**). "Accuracy and variability of acoustic measures of voicing onset," J. Acoust. Soc. Am. **113**, 1025–1032.

Fujimura, O. (**1972**). "Acoustics of Speech," in *Speech and Cortical Functioning*, edited by J. H. Gilbert (Academic, New York), pp. 107–161.

Gandour, J., Petty, S. H., Dardarananda, R., Dechongkit, S., and Mukngoen, S. (**1986**). "The acquisition of the voicing contrast in Thai—A study of voice onset time in word-initial stop consonants," J. Child Lang. **13**, 561–572.

Gilbert, J. H. V. (**1977**). "Voice onset time analysis of apical stop production in 3-year-olds," J. Child Lang. **4**, 103–110.

Han, M. S., and Weitzman, R. S. (**1970**). "Acoustic features of Korean /P, T, K, p, t, k,/ and /p^h,t^h,k^h/ ," Phonetica **22**, 112–128.

Hardcastle, W. J. (**1973**). "Some observations of the tense-lax distinction in initial stops in Korean," J. Phonetics **1**, 263–271.

Henton, C., Ladefoged, P., and Maddieson, I. (**1992**). "Stops in the world's languages," Phonetica **49**, 65–101.

Hombert, J. M., Ohala, J. J., and Ewan, W. G. (**1979**). "Phonetic explanations for the development of tones," Language **55**, 37–58.

House, A. S., and Fairbanks, G. (**1953**). "The influence of consonant environment upon the secondary acoustical characteristics of vowels," J. Acoust. Soc. Am. **25**, 105–113.

Jun, S.-A. (**1996**). "Influence of microprosody on macroprosody: A case of phrase initial strengthening," UCLA Working Papers in Phonetics **92**, 97–116.

Jun, S.-A. (**2006**). "Phonological development of Korean: A case study," UCLA Working Papers in Phonetics **105**, 51–65.

Kagaya, R. (**1974**). "A fiberscopic and acoustic study of the Korean stops, affricates and fricatives," J. Phonetics **2**, 161–180.

Kang, K.-S. (**1998**). "On phonetic parameters in the acquisition of Korean obstruents: A case study," in *The Panels*, edited by C. Gruber, D. Higgins, K. S. Olson, and T. Wysocki (Chicago Linguistic Society, Chicago, IL), pp. 311–326.

Kent, R. D., and Forner, L. L. (**1980**). "Speech segment durations in sentence recitations by children and adults," J. Phonetics **8**, 157–168.

Kewley-Port, D., and Preston, M. S. (**1974**). "Early apical stop production: A voice onset time analysis," J. Phonetics **2**, 195–210.

Kim, C.-W. (**1965**). "On the autonomy of the tensity feature in stop classification," Word **21**, 339–359.
Kim, M.-J., and Pae, S.-Y. (**2005**). "The study on the percentage of consonants correct and the ages of consonantal acquisition for Korean-test of articulation for children," Speech Sciences (Korean Association of Speech Sciences, Seoul, Korea), **12**, 139–149.
Kim, M.-R., Beddor, P. S., and Horrocks, J. (**2002**). "The contribution of consonantal and vocalic information to the perception of Korean initial stops," J. Phonetics **30**, 77–100.
Kim, Y.-T. (**1996**). "Study on articulation accuracy of preschool Korean children through picture consonant articulation test," Korean J. Commun. Disord. **1**, 7–33.
Kim, Y.-T., Jang, H.-S., Yim, S.-S., and Paik, H.-J. (**2004**). *Picture Vocabulary Test* (Seoul Rehabilitation Center, Seoul, Korea).
Kim, Y.-T., and Shin, M.-J. (**1992**). "The phonological processes of Korean children (II): Focused on substitution," Korean J. Speech Hear. Disord. **2**, 29–51.
Kingston, J., and Diehl, R. L. (**1994**). "Phonetic knowledge," Languagee **70**, 419–454.
Klatt, D. H. (**1975**). "Voice onset time, frication, and aspiration in word-initial consonant clusters," J. Speech Hear. Res. **18**, 686–706.
Koenig, L. L. (**2001**). "Distributional characteristics of VOT in children's voiceless aspirated stops and interpretation of developmental trends," J. Speech Lang. Hear. Res. **44**, 1058–1068.
Kong, E. J., Beckman, M., and Edwards, J. (**2007**). "Fine-grained phonetics and acquisition of Greek voiced stops," in Proceedings of the 16th International Congress of Phonetic Sciences, edited by J. Trouvain and W. J. Barry, pp. 865–868.
Lee, S., Potamianos, A., and Narayanan, S. (**1999**). "Acoustics of children's speech: Developmental changes of temporal and spectral parameters," J. Acoust. Soc. Am. **105**, 1455–1468.
Lehiste, I., and Peterson, G. E. (**1961**). "Some basic considerations in the analysis of intonation," J. Acoust. Soc. Am. **33**, 419–425.
Lisker, L., and Abramson, A. (**1964**). "A cross-language study of voicing in initial stops: Acoustical measurements," Word **20**, 384–422.
Löfqvist, A., Baer, T., McGarr, N. S., and Story, R. S. (**1989**). "The cricothyroid muscle in voicing control," J. Acoust. Soc. Am. **85**, 1314–1321.
Macken, M. A., and Barton, D. (**1980a**). "The acquisition of the voicing contrast in English: A study of voice onset time in word-initial stop consonants," J. Child Lang. **7**, 41–74.
Macken, M. A., and Barton, D. (**1980b**). "The acquisition of the voicing contrast in Spanish—A phonetic and phonological study of word-initial stop consonants," J. Child Lang. **7**, 433–458.
Milenkovic, P. H. (**2001**). "Time-frequency analyzer (TF32)," Computer program, University of Wisconsin-Madison.
Ohde, R. N. (**1985**). "Fundamental frequency correlates of stop consonant voicing and vowel quality in the speech of preadolescent children," J. Acoust. Soc. Am. **78**, 1554–1561.
Pae, S., Chang, Y., Kwak, K., Sung, H., and Sim, H. (**2004**). "MCDI-K referenced expressive word development of Korean children and gender differences," Korean J. Commun. Disord. **9**, 45–56.
Robb, M. P., and Smith, A. B. (**2002**). "Fundamental frequency onset and offset behavior: A comparative study of children and adults," J. Speech Lang. Hear. Res. **45**, 446–456.
Shin, J. (**2005**). "Phoneme frequency of 3 to 8 year-old Korean children," Korean Linguistics **27**, 163–200.
Silverman, K. (**1987**). "The structure and processing of fundamental frequency contours," Ph.D. thesis, University of Cambridge, Cambridge.
Smith, B. L. (**1992**). "Relationships between duration and temporal variability in children's speech," J. Acoust. Soc. Am. **91**, 2165–2174.
Stoel-Gammon, C. (**1998**). "Sounds and words in early language acquisition: The relationship between lexical and phonological development," in *Exploring the Speech-Language Connection*, edited by R. Paul (Paul H. Brookes, Baltimore, MD), pp. 25–52.
Stokes, S. F., and Surendran, D. (**2005**). "Articulatory complexity, ambient frequency, and functional load as predictors of consonant development in children," J. Speech Lang. Hear. Res. **48**, 577–591.
Weismer, G. (**1979**). "Sensitivity of voice-onset time (VOT) measures to certain segmental features in speech production," J. Phonetics **7**, 197–204.
Westbury, J. R., and Keating, P. A. (**1986**). "On the naturalness of stop consonant voicing," J. Linguist. **22**, 145–166.
Whalen, D. H., and Levitt, A. G. (**1995**). "The universality of intrinsic F0 of vowels," J. Phonetics **23**, 349–366.
Zlatin, M. A., and Koenigsknecht, R. A. (**1976**). "Development of voicing contrast—Comparison of voice onset time in stop perception and production," J. Speech Hear. Res. **19**, 93–111.

Acoustic characteristics of clearly spoken English fricatives

Kazumi Maniwa[a] and Allard Jongman
Department of Linguistics, The University of Kansas, Lawrence, Kansas 66044

Travis Wade
Posit Science Corporation, 7th Floor, 225 Bush Street, San Francisco, California 94104

(Received 28 August 2006; revised 4 June 2008; accepted 1 September 2008)

Speakers can adopt a speaking style that allows them to be understood more easily in difficult communication situations, but few studies have examined the acoustic properties of clearly produced consonants in detail. This study attempts to characterize the adaptations in the clear production of American English fricatives in a carefully controlled range of communication situations. Ten female and ten male talkers produced fricatives in vowel-fricative-vowel contexts in both a conversational and a clear style that was elicited by means of simulated recognition errors in feedback received from an interactive computer program. Acoustic measurements were taken for spectral, amplitudinal, and temporal properties known to influence fricative recognition. Results illustrate that (1) there were consistent overall style effects, several of which (consonant duration, spectral peak frequency, and spectral moments) were consistent with previous findings and a few (notably consonant-to-vowel intensity ratio) of which were not; (2) specific acoustic modifications in clear productions of fricatives were influenced by the nature of the recognition errors that prompted the productions and were consistent with efforts to emphasize potentially misperceived contrasts both within the English fricative inventory and based on feedback from the simulated listener; and (3) talkers differed widely in the types and magnitude of all modifications.
 [DOI: 10.1121/1.2990715]

PACS number(s): 43.70.Fq [CHS] Pages: 3962–3973

I. INTRODUCTION

Language users can alter their speech productions in order to speak more or less "clearly" in response to the communicative needs of different listeners in different situations. Deliberately clarified speech has been seen to yield intelligibility advantages of 3–38 percentage points relative to "normal" conversational speech for hearing-impaired listeners in quiet (Picheny *et al.*, 1985; Uchanski *et al.*, 1996) and in noise or reverberation (Payton *et al.*, 1994; Schum, 1996), normal-hearing listeners in noise or reverberation (Ferguson, 2002; Ferguson and Kewley-Port, 2002; Helfer, 1997; Krause and Braida, 2004; Payton *et al.*, 1994) or with simulated hearing loss or cochlear implants (Gagné *et al.*, 1994; Iverson and Bradlow, 2002; Liu *et al.*, 2004), elderly listeners with or without hearing loss (Helfer, 1998; Schum, 1996), cochlear-implant users (Iverson and Bradlow, 2002; Liu *et al.*, 2004), children with or without learning disabilities (Bradlow *et al.*, 2003), and (to a lesser extent) non-native listeners (Bradlow and Bent, 2002).

Acoustic descriptions of clear speech have generally been dominated by global (sentence-level) patterns; reduced speaking rate, more and longer pauses, increased mean and range of fundamental frequency (f0), a shift in energy to higher frequency regions in long-term spectra, and deeper temporal amplitude modulations have been observed in clear speech (Bradlow *et al.*, 2003; Krause and Braida, 2004; Liu *et al.*, 2004; Picheny *et al.*, 1986; Smiljanić and Bradlow, 2005). At a phonological level, clear speech seems to involve less frequent vowel reduction, burst elimination, alveolar flapping, and more frequent schwa insertion (Bradlow *et al.*, 2003; Krause and Braida, 2004; Picheny *et al.*, 1986). Previous study on the fine-grained acoustic-phonetic characteristics of clear speech has mainly considered vowels, noting increases in vowel durations, expanded F1 × F2 space area, tighter within-category clustering, and more dynamic formant movements (Bradlow *et al.*, 2003; Chen, 1980; Ferguson, 2002; Ferguson and Kewley-Port, 2002; Johnson *et al.*, 1993; Moon and Lindblom, 1994; Picheny *et al.*, 1986; Smiljanić and Bradlow, 2005). Since clear speech is by definition produced in order to increase intelligibility and since a vast majority of perceptual errors result from consonant confusions [e.g., see Miller and Nicely (1955)], it is surprising that clearly produced consonants have not been examined as thoroughly. Previous analyses have been limited to a few temporal and amplitudinal parameters including segmental duration, voice onset time (VOT), and consonant-to-vowel amplitude ratio (CVR) (Bradlow *et al.*, 2003; Chen, 1980; Krause and Braida, 2004; Picheny *et al.*, 1986). Chen (1980) and Picheny *et al.* (1986) found overall longer plosive, fricative, nasal, and semivowel durations; longer VOT for voiceless plosives; and increased CVR for plosives and some fricatives. Larger word-initial CVR was also reported by Bradlow *et al.* (2003). Picheny *et al.* (1986) reported increased peak frequency and overall intensity at higher frequencies in /t/ and /s/ productions, although these changes were not consistently found for consonants produced clearly at faster rates (Krause and Braida, 2004).

[a]Present address: FB Sprachwissenschaft, Raum F521A, Universität Konstanz, 78457 Konstanz, Germany; electronic mail: kazumi.maniwa@uni-konstanz.de

It is particularly unfortunate that clearly produced fricative consonants have not been the subject of more observation, since previous consonant confusion analyses have reported that fricatives, especially nonsibilants, contribute a large source of errors for hearing-impaired listeners and for normal-hearing listeners in noise [e.g., see Bilger and Wang (1976), Miller and Nicely (1955), and Wang and Bilger (1973)]. A few studies have considered vocal effort and rate modifications and hyperarticulation in describing fricative acoustics and perception, but clear production was not the primary focus of these studies, which were therefore inconclusive with respect to specific clear speech alterations. Jesus and Shadle (2002) reported that fricative amplitude and spectral slope increased with vocal effort but did not offer a statistical analysis of these results or consider other properties of the sounds. Perkell *et al.* (2004) observed that average (voiceless) sibilant duration increased from fast-rate speech to normal speech to "clear speech" (obtained by asking talkers to pronounce words carefully without increasing loudness). They also measured the spectral center of gravity but did not find differences related to speaking style. Feijóo *et al.* (1998) investigated the intelligibility of Spanish nonsibilant fricatives in "hyperarticulated" and "hypoarticulated" speech, but acoustic data were provided only for duration and energy level and without statistical analysis, and it was unclear how the two styles were elicited. In any case, hyperarticulated speech did not lead to better intelligibility. This study was designed to provide a comprehensive acoustic description of adaptations that occur in the clear production of English fricatives.

A. Acoustic properties of English fricative sounds

Several studies have attempted to delineate stable acoustic correlates of the fricative place of articulation and voicing. Parameters that seem to influence identification include gross spectral shapes and peak frequencies (Behrens and Blumstein, 1988; Hughes and Halle, 1956; Jongman *et al.*, 2000; Strevens, 1960), the first four moments of the spectral energy distribution (Forrest *et al.*, 1988; Jongman *et al.*, 2000; Nissen and Fox, 2005; Nittrouer, 1995; Nittrouer *et al.*, 1989; Shadle and Mair, 1996), the slopes of lines fitted to spectra in lower and higher frequency regions (Evers *et al.*, 1998; Jesus and Shadle, 2002), formant transition information (Jongman *et al.*, 2000; McGowan and Nittrouer, 1988; Nittrouer *et al.*, 1989; Soli, 1981), overall amplitude (Behrens and Blumstein, 1988; Jongman *et al.*, 2000; Stevens, 1971; Strevens, 1960), amplitude relative to the neighboring vowel in specific frequency regions (Hedrick and Ohde, 1993; Jongman *et al.*, 2000; Stevens, 1985), and duration (Baum and Blumstein, 1987; Crystal and House, 1988; Jongman, 1989; Jongman *et al.*, 2000). Briefly, alveolar fricatives (/s/, /z/) are characterized by spectral energy [above 4 kHz, Hughes and Halle (1956)] and major peaks [3.5–5 kHz, Behrens and Blumstein (1988); 6–8 kHz, Jongman *et al.* (2000)] at higher frequencies compared to palato-alveolars (/ʃ/, /ʒ/; 2–4 kHz; [Hughes and Halle (1956), Behrens and Blumstein (1988)], which display larger overall relative amplitudes. Dental (/θ/, /ð/) and labio-dental (/f/, /v/) fricatives show relatively flat spectra below 10 kHz with no dominating peaks, while alveolar and palato-alveolar fricatives have well-defined peaks. Nonsibilants (/θ/, /ð/, /f/, /v/) show higher standard deviations (SDs), lower overall amplitudes, and shorter durations than sibilants (/s/, /ʃ/, /z/, /ʒ/). Thus, these parameters clearly distinguish sibilants from nonsibilants and from each other but are less effective at determining the place of articulation for nonsibilants. However, it was observed that the onset of F2 at the fricative-vowel boundary was significantly higher for dental fricatives than for labiodental fricatives (Jongman *et al.*, 2000; Nittrouer, 2002) and higher for palato-alveolar fricatives than for alveolar fricatives (Jongman *et al.*, 2000; McGowan and Nittrouer, 1988; Nittrouer *et al.*, 1989). Fewer studies have reported on the voicing distinction in fricatives (Baum and Blumstein, 1987; Crystal and House, 1988; Jesus and Shadle, 2002; Jongman *et al.* 2000). These studies suggest that voiceless fricatives are characterized by higher spectral mean and peak values, more defined peaks, less variance, negative skewness, larger overall amplitude, and longer duration compared to their voiced counterparts.

B. Contrastive effects in clear speech

A secondary question of this study was whether talkers exhibit more specific fricative-dependent, segmental contrast-enhancing changes. It has been suggested that clear speech modifications are inventory dependent (that is, related to the specific phonetic contrasts that must be maintained within a language) and effectively increase the auditory distance between neighboring sound categories. For example, VOT for voiceless stop consonants increases in clear speech but is unchanged for voiced stops (Chen, 1980; Krause and Braida, 2004; Ohala, 1994; Picheny *et al.*, 1986). Similarly, English tense vowels are lengthened to a greater extent than lax, maximizing the inherent duration difference between the two vowel categories (Ferguson and Kewley-Port, 2002; Picheny *et al.*, 1986; Uchanski *et al.*, 1996). Talkers also enlarge the distance between vowels in the F1 × F2 space, producing more extreme, distinct categories (Bradlow *et al.*, 2003; Chen, 1980; Ferguson, 2002; Ferguson and Kewley-Port, 2002; Johnson *et al.*, 1993; Moon and Lindblom, 1994; Picheny *et al.*, 1986; Smiljanić and Bradlow, 2005). Thus, clear speech may reflect knowledge of the contrasts in a phonetic inventory and a general effort to maintain these contrasts. We will refer to such efforts as *inventory-level* contrast-enhancing modifications.

It is less clear whether talkers may also attempt to preserve contrast at a more local level, adapting online in response to perception errors that are likely to occur in specific contexts. According to Lindblom's H and H theory (1990, 1996), speakers constantly assess the listeners' needs for explicit signal information and modulate their speech along a continuum from hypo- to hyperspeech in response to communicative constraints. Along these lines, a speaker's task and goals during clear speech production are quite variable depending on the information needs associated with perhaps each individual segment (depending on cues from the listener, knowledge of the language and lexicon, etc.). We pre-

dicted that explicit feedback from a listener, in particular, might affect clear speech acoustics under these assumptions. For example, when a talker repeats a sequence containing some speech sound after it has been mistaken for another similar sound, is the talker likely to make specific adjustments that are not predictable based on general clear speech patterns or inventory-level contrast-enhancing manipulations? A few previous studies have touched on this issue. Ohala (1994) employed an elicitation method in which speakers received pseudomisrecognitions from the experimenter as feedback to their productions and were asked to repeat target stimuli as clearly as possible. This method was designed to test whether speakers make an effort not only to improve the intelligibility of a target stimulus but also to make it sound more unlike the sound it was mistaken for. Contrary to expectations, there were no differences in VOT, vowel duration, or the first three formants of vowels as a function of this feedback. Thus there was no evidence of locally "contrastive" variation in speech, so it was suggested that clear speech is "stable" and guided more by general principles reflecting the phoneme inventory of a language than by microscopic context information like anticipation of specific errors. Some caution is warranted, however, in interpreting Ohala's (1994) null result. Most notably, while the study considered some 70,000 measurements, this data set was used to account for a very large number of vowel and consonant contrasts and was therefore underpowered with respect to many of the critical comparisons. The present study extends Ohala's (1994) elicitation method for a much more targeted analysis of nearly 500,000 measurements relating to fricative voicing and place of articulation in a single vowel context, namely, /ɑ/. Naturally, including only this context does not allow us to examine differences in phonetic context influences on fricative production [or perception, e.g., Mann and Repp (1980), Mann and Soli (1991), Soli (1981), Yeni-Komshian and Soli (1981), and Whalen (1981)] as a function of speaking style or even to generalize our findings conclusively to other vowel contexts. However, it allows for maximal control in documenting fundamental aspects of (1) how clear speech influences the acoustics of fricatives in general and (2) how successfully listeners can enhance acoustic distance in terms of place of articulation, sibilance, and voicing and the distance between an intended target fricative and an anticipated misperception. As discussed above, we will refer to efforts of the latter type specifically as *local context-dependent* modifications.

An elicitation method somewhat similar to the one used in this study (Maniwa, 2006; Maniwa *et al.*, 2006) was also recently employed to examine the effects of linguistic focus on the production of fricatives in a contrastive context. Silbert and de Jong (2008) measured the duration, first four spectral moments, and power of fricatives produced in the carrier sentence "No, I said [target]," where the target was a fricative-/a/ syllable that the production was intended to disambiguate from a syllable differing in fricative voicing or place of articulation. As in the Ohala (1994) study, no specific disambiguation effects were observed, although the focused productions exhibited some general characteristics of clear speech (increased duration, for example) compared to unfocused productions. Again, it is difficult to make generalizations based on this null result since only a small number of talkers (4), productions (576 total), fricatives (palatoalveolars were not included), and measurements were considered and since elicitation involved a somewhat explicit request for focus that might not have captured the speakers' ability to adapt spontaneously.

C. Talker differences in clear speech production

Studies have shown that different talkers employ different techniques during clear speech production (Bradlow *et al.*, 2003; Chen, 1980; Ferguson, 2002; Krause and Braida, 2004; Liu *et al.*, 2004; Picheny *et al.*, 1986). For example, one speaker in the corpus of Picheny *et al.* increased VOTs for both voiceless and voiced plosives in clear speech, while the other two increased VOTs only for the voiceless one. This speaker also decreased the intensity for fricatives in clear speech, while the other two speakers showed the opposite pattern. The female talker from the study of Bradlow *et al.* (2003) decreased her speaking rate in clear speech to a far greater degree than the male talker. These two talkers also differed noticeably in the f0, vowel space, and CVR differences between clear and conversational speeches. The female talker from the database of Liu *et al.* (2004) also increased the mean and variability of overall sentence durations more than the male talker. Chen's (1980) three talkers varied in complex ways in the degree to which the syllable, VOT, vowel, and formant transition durations changed. The speakers also differed in terms of within-vowel F1×F2 space variability and the magnitude of the increase in the f0 mean in clear speech. Changes in f0 were also inconsistent across two talkers in the study by Krause and Braida (2004).

In short, the acoustics of clear speech are highly talker dependent. However, most of the research that examined talker differences in acoustic modifications recorded small numbers of talkers [$n=2$ for Bradlow *et al.* (2003), Krause and Braida (2004), and Liu *et al.* (2004); $n=3$ for Chen (1980) and Picheny *et al.* (1986); *cf*, $n=12$ for Ferguson (2002)]. With data from only a few speakers, it is unclear whether the patterns of variability observed across speakers and gender would be maintained more generally, or if still other strategies would emerge. This study examined the productions of 20 speakers (10 females and 10 males) to address these questions more conclusively.

D. Hypotheses

This study was designed to answer three questions concerning the production of clear fricatives. First, what (if any) systematic changes are made in clear fricative productions? Based on previous findings, we predicted (henceforth hypothesis 1) that clear fricatives would be (i) longer, (ii) amplified relative to neighboring vowels, and (iii) higher in spectral content, including peak frequencies, spectral mean values, and related measures. Second, are clear speech modifications dependent on the nature of the contrasts in a fricative inventory and/or more local context information provided by "listener" feedback? We expected that, in general (hypothesis 2), clear productions would be influenced by the

perceived likelihood of different misidentification patterns. More specifically, we predicted that on average (i) fricative categories would differ more from minimally contrastive categories in clear than in conversational speech (inventory-level modifications) and (ii) fricatives repeated after misapprehension for similar sounds would be most different from the sounds they were mistaken for (local context-dependent modifications). Finally, in what ways do talkers vary in the production of clear fricatives? We predicted (hypothesis 3) that cross-talker differences would be seen both in the types of modifications that are made and in the extent of these changes.

II. METHOD

A. Participants

Twenty talkers (ten females and ten males) aged between 19 and 34 were recruited from the University of California, Berkeley and the University of Kansas, Lawrence communities. Participants were native speakers of Upper Midwest or Pacific Southwest American English. Talkers reported normal hearing and no history of speech or language disorders. They volunteered for the experiment without monetary compensation.

B. Materials

The eight English fricatives /f/, /θ/, /s/, /ʃ/, /v/, /ð/, /z/, and /ʒ/ and the vowel /ɑ/ were combined to form vowel-fricative-vowel (VCV) syllables. The production of each VCV token was recorded in isolation in conversational and clear speaking styles.

C. Procedures and apparatus

The participants' speech was recorded digitally at a 44.1 kHz sampling rate (16 bit resolution) in a sound-attenuating booth in the Phonology Laboratory, UC Berkeley, using a Marantz PMD670 recorder and a Shure SM-10 A headset microphone (frequency responses of 50–15 000 Hz). The microphone was placed 2.5 cm away from the corner of a talker's mouth at a 45° angle. Participants were seated at a comfortable distance from a visual display of prompt, instruction, and feedback on a computer screen. Before recording began, participants were provided with a list explaining the pronunciation of each sound. Items were written as follows: "afa," "atha," "asa," "asha," "ava," "adha," "aza," and "azha." Participants first read these syllables aloud a few times to become familiar with uniquely spelled syllables. A pronunciation key was available for reference during the session.

The recording session was divided into two parts: warmup and experiment. Programs to provide prompts and feedback were designed using MATLAB 7.0.0.1 (The Mathworks, Inc., 2000). During warmup, talkers produced five repetitions of each VCV in each of two blocks, in response to prompts appearing on a monitor. In the first block, talkers read VCV syllables in a manner approximating the way they spoke in everyday conversation; in the second block, they were instructed to speak more carefully, as if talking to a hearing-impaired or elderly person. This warmup served to familiarize talkers with the interface and materials, to allow them to rehearse the two styles, and to provide a "baseline" recording of speech produced before talkers became aware of the rate and types of misperceptions that would be encountered during the experiment. Speakers were not explicitly instructed or coached on stress type or placement since this might have created a bias toward one style or the other or caused speakers to imitate the experimenter instead of producing clear speech modifications spontaneously.

The elicitation method for the experimental session resembled the one used by Ohala (1994). Before the session, a participant was told that he/she would produce speech as part of an interaction with a computer program that would be recorded. They were instructed to speak first as naturally as possible, as if in casual conversation, when prompted by a VCV stimulus on the screen. Productions in response to these initial prompts served as the "conversational speech" in our acoustic analyses. Participants were told that the program would "guess" which syllables were spoken and would indicate its guess on the screen and that it would frequently misperceive sounds, simulating a hearing-impaired listener. If a participant indicated that a guess was correct (by clicking a box on the screen), the trial was terminated and the program moved on to the next stimulus. If a guess was scored as incorrect, the speaker was given a chance to repeat the target stimulus, doing his or her best to deliver it as intelligibly as possible. These repeated productions served as clear speech in acoustic analyses. The program's guesses were, in fact, unrelated to the speaker's production pattern and represented either (1) the correct response, (2) the voicing-matched but place-unmatched incorrect responses (e.g., /θ/, /s/, and /ʃ/, for /f/), (3) the voicing-unmatched, place-matched incorrect responses (e.g., /v/ for /f/, and (4) the "???" ("don't know") responses. Each response occurred five times for each VCV during the experiment. Thus, there were 30 conversational ($5\times$ one following correct response, three place errors, one voicing error, one ???) and 25 total clear ($5\times$ three preceding place errors, one voicing error, one ???) productions of each fricative by each talker. The order of prompts was randomized separately for each talker, as was the pattern of pseudo-responses. After the participant's second production, a second guess was displayed, which was correct 75% of the time and random otherwise; the participant scored this guess before finally continuing to the next trial. The purpose of this second guess was to encourage optimal effort in clear productions by giving the impression that (1) the program's guesses were actually based on a speaker's productions, (2) recognition performance improved for clear productions, and (3) this performance was actually being recorded for analysis instead of predetermined by the elicitation program. Recording sessions lasted 60–70 min, including the warmup and a 10 min break halfway through the main experiment.

D. Data processing and acoustic measurements

Recordings were hand annotated into VCV segments using the PRAAT speech analysis software (Boersma and Weenink, 2000), equalized for the total rms amplitude, and

further segmented and analyzed using PRAAT and MATLAB. Semiautomatic fricative segmentation was achieved following previous studies (Behrens and Blumstein, 1988; Jongman *et al.*, 2000; Yeni-Komshian and Soli, 1981), in which the fricative was defined as a region of elevated zero-crossings due to the turbulent source in the following manner. Each production was high-pass filtered at 300 Hz using a second order Butterworth filter to minimize voicing and other low-frequency perturbations that might obscure zero-crossings resulting from the turbulent source. The production was then converted into a time series in which each sample was labeled as either differing in sign from the previous sample [1] or not [0], and a zero-crossing envelope was created by low-pass filtering this series at 30 Hz. We found that good identification was achieved by (1) normalizing the log of this envelope to the range $[-1,1]$ and (2) taking the single continuous region closest to the center of the production for which the resulting sequence was above zero corresponding to the fricative. Upon hand checking the segmentation based on visual inspection of the spectrogram and waveform, it was found that 91% of fricatives were accurately labeled; the remaining 9% were labeled by hand.

The acoustic analysis considered 14 spectral, amplitudinal, and duration parameters that previous studies indicate may work in combination with signal fricative contrasts. Spectral measures included the discrete Fourier transform (DFT) spectral peak frequency (1), the first four spectral moments (M1–M4; 2–5), F2 onset transitions (6), spectral slopes below (7) and above (8) peak frequencies, and the average fundamental frequency (f0) of adjacent vowels (9). Amplitudinal measures included normalized rms amplitude (10) and a measure previously referred to [e.g., see Hedrick and Ohde, (1993)] as the "relative amplitude," the amplitude of a fricative relative to the following vowel in the F3 region for sibilants and the F5 region for nonsibilants (since these regions contain important prominences for the two fricative types). To distinguish this measure from the overall normalized amplitude (10), we will refer to it here as the *frequency-specific relative amplitude* (FSRA) (11). Other amplitude-related measures included harmonics-to-noise ratio (HNR) (12) and energy below 500 Hz (13). Finally, we considered the total fricative duration (14). As described in Sec. I A, these 14 measures seem to be the most important for distinguishing fricative place and voicing contrasts. A few measures that had been previously employed but either yielded inconsistent, contradictory, or unreliable results for these contrasts (e.g., F2 range, F3 transition, and locus equations) or are not yet fully understood with respect to fricative production and perception [i.e., fricative noise modulation and "dynamic amplitude"—e.g., see Jackson and Shadle (2000), Jesus and Shadle (2002), Pincas and Jackson (2006), Shadle and Mair (1996)] were not considered.

Except where noted otherwise, all analyses considered 20 ms Hamming windowed segments at five locations (W1–W5), centered over the fricative onset (25%, 50%, and 75% points;) and offset. All spectral measures were based on a 44 100-point DFT of this (zero padded to 1s) segment. Ensemble averaging across tokens within a given speaker/fricative/style condition was used to reduce error in spectral estimates; each spectrum $X(f)$ considered below, then, represents an average of 5–20 (depending on the comparison; see Sec. II E for analysis details) $|\mathrm{DFT}|^2$ values at frequencies of 50–15 000 Hz (the frequency response of the microphone) in 1 Hz increments. In the case of spectral peak and slope measures, the windowed segment was first pre-emphasized with a factor of 0.98. The spectral peak was defined as the frequency bin corresponding to the largest value in $X(f)$. M1 was defined as the center of gravity of the spectrum (the mean frequency weighted by $X(f)$). The remaining three moments (M2–M4) were obtained by first calculating the sum $(\mathrm{M}n=(\Sigma(f-\mathrm{M1})^n X(f))/\Sigma X(f)$ and then normalizing by the variance (M2) as follows. The SD a measure of the diffuseness of the spectrum around the center of gravity, was taken as the square root of the raw M2 measurement. Skewness, an indicator of spectral tilt, measuring asymmetry in the spectrum toward frequencies far above (positive values) or below (negative values) the center of gravity was obtained by dividing the raw M3 value by the 1.5 power of M2. Finally, kurtosis, a measure of the peakedness of the distribution, was obtained by dividing M4 by the square of M2 and subtracting 3. For space reasons, henceforth we use the notation M1–4 to refer to the normalized mean, SD, skewness, and kurtosis values.

F2 values were estimated using a linear prediction-based method [the Burg algorithm; Childers (1978), as implemented in PRAAT], derived at the fricative onset and offset and each vowel midpoint from an analysis that found at most five formants below 5000 Hz (male speakers) or 5500 Hz (female speakers).

Spectral slopes were computed following the procedures described by Evers *et al.* (1998) and Jesus and Shadle (2002). Lines were fit by least squared error to $\log(X(f))$ across two regions defined by the average peak frequency (across talkers and productions) for a place of articulation (8000 Hz for alveolars, 3300 Hz for alveo-palatals, and 6500 Hz for all nonsibilants). A low-frequency slope (dB/kHz) was derived from the spectral values below this peak, and a high-frequency slope was derived from the peak to 15 kHz.

The fundamental frequency was derived using an autocorrelation-based algorithm (Boersma, 1993). It was averaged across the vowels preceding and following the target fricative. The normalized amplitude was taken as the rms amplitude ratio (dB) between the same five windowed fricative segments described above and the average of the two surrounding vowels. The use of both vowels for the f0 and amplitude analysis was necessary because some speakers tended to place emphasis on the first vowel, some placed it on the second, and some placed emphasis inconsistently within and across speaking styles or produced ambiguous patterns with both or neither vowels appearing stressed. FSRA was measured as described in Hedrick and Ohde (1993) and Jongman *et al.* (2000). DFTs (ensemble averaged as described above) were taken of one 23.3 ms Hamming window centered on the fricative midpoint, and one beginning at the onset of the following vowel. For sibilants the peak in the region corresponding to F3 of the frication noise was compared to the peak of the vowel onset in the same

frequency region; for nonsibilants the peak at F5 was used. The relative amplitude was then expressed as the difference (dB) between fricative and vowel amplitudes. HNR was obtained by taking the amplitude difference (dB) between the periodic part of the fricative, estimated using a cross-correlation algorithm [Boersma (1993), as implemented in PRAAT], and the remaining (noise) part. An intensity below 500 Hz was obtained similarly to normalized amplitude, except that the VCV was first low-pass filtered at 500 Hz.

E. Statistical analysis

As discussed in Sec. II D, most acoustic measures were considered at several separate time points across fricatives. This was considered important in general because dynamic patterns and not absolute values seem to drive human perception of speech sounds and also because it seems possible that specific clear speech modifications might disproportionally affect different regions of the sounds or might be dynamic in nature. However, based on previous research, we were only able to make specific hypotheses regarding overall style/fricative differences for each of the 14 acoustic measures and not on time-dependent patterns. For this reason, statistical analyses considered only a single value for each measure. For the ten measures that were observed at five time points, this value was the mean of the measurements for the central three (25%, 50%, and 75%) window locations; this tended to reduce error further by time-averaging measurements over the more stable portion of the fricative. For F2, the value was the mean formant transition distance toward the fricative [i.e., ((onset−V1 midpoint)+(offset −V2 midpoint))/2].

For each metric then, a mixed-model analysis of variance (ANOVA) with speaking style (clear versus conversational), fricative as a within-subject factor, and gender as a between-subject factor was used to address hypothesis 1 (that clear fricatives would be longer, louder, and higher in frequency content) and hypothesis 2 (that inventory-level and contrast-dependent fricative-to-fricative distances in the 14-dimensional acoustic space would be larger in clear speech).

Two additional analyses addressed hypothesis (2) more directly. First, distances between each of the 16 targeted fricative pairs (pairs differing in place or voicing) were calculated for the 14 acoustic measures and were compared depending on whether the sounds were produced in (1) a clear fricative-to-fricative contrastive context, (2) a clear but noncontrastive context, or (3) conversationally. For example, /s/-/ʃ/ distances were considered (1) between productions of /s/ that were produced specifically in response to a "misidentification" as /ʃ/ / (we will represent this with the notation s|ʃ) and /ʃ/ productions produced after identification as /s/ (ʃ|s), (2) between clear /s/ productions that were produced in response to misidentifications of sounds other than /ʃ/ (represented s|~ʃ) and ʃ|~s productions, and (3) initial conversational productions of the two sounds (s|ø, ʃ|ø). As described above, it was predicted that distances would be generally greater in clear than conversational tokens and greatest in contrastive contexts. A one-way ANOVA with style as a within-subject factor was used to compare the distances, averaged across the 16 targeted pairs.

Second, a linear discriminant analysis was used to measure whether fricatives were actually better separated along the measures that were considered. For each place or voicing pair, a set of 14 predictors was constructed, each consisting of 120 (20 speakers×2 fricatives×3 styles) possible training points. For each style (contrastive, noncontrastive, and conversational), a jack-knife verification method was used, in which the classification was run separately for each speaker and style (with the two relevant points for the speaker used as test data and the remaining 118 points as training data), and results were averaged within style conditions.

Finally, hypothesis 3 (which speakers would differ in type and/or extent of acoustic modifications) was addressed using a two-way mixed-model ANOVA with style as a within-subject factor and talker as a between-subject factor. Analyses made use of the R statistical package (v. 2.0.4) (Venables and Ripley, 2002; Balakrishnama and Ganapathiraju, 1998).

III. RESULTS AND DISCUSSION

All 20 participants seemed to have followed the instructions regarding speaking style and, in particular, were able to produce truly "conversational" tokens throughout the experiment despite the laboratory setting and the frequency of recognition errors. This was verified both informally by the first author during the experiment and by acoustically comparing clear and conversational tokens from late in the experimental session, with the samples produced during warmup and earlier in the experiment. For example, fricative duration (usually considered a robust indicator of speaking style) was compared with the sequential order of productions in the experiment (1–440) using Pearson's correlation. For clear fricatives, a small but reliable positive relationship was found ($r=0.095$, $p<0.001$), revealing a tendency for longer clear productions as the experiment progressed. For conversational productions, on the other hand, a small *negative* relationship was seen ($r=-0.090$, $p<0.001$), indicating that conversational productions became slightly *shorter* over the course of the experiment, in complying with the instructions (and possibly resulting from boredom or impatience) and despite the frequency of recognition errors.

Since the productions in response to recognition errors are being referred to as clear, it is also important to verify that they are actually more intelligible for human listeners and not just produced with greater effort. To date, we have observed significant intelligibility advantages for the clear over the conversational tokens discussed here for young normal-hearing listeners, listeners with simulated hearing impairment, and non-native listeners (Maniwa, 2006; Maniwa *et al.*, 2008; Kabak and Maniwa, 2007). By measuring babble thresholds for the same minimal pair distinctions targeted in the elicitation method described here (i.e., place and voicing contrasts), we have verified that each fricative category is more intelligible on average in clear speech. For

TABLE I. Summary of ANOVA results (see Sec. III E) for the style (S) ×fricative (F) ×Gender (G) comparison (left), the one-way comparison of mean fricative-to-fricative distance across styles (center), and the speaker (Sp) ×style comparison (right). F values are given; values in bold are statistically significant after FDR alpha correction.

	G	F	F×G	S	S×G	F×S	F×S×G	S (distance)	Sp	Sp×S
(*df*)	(1, 18)	(7, 126)	(7, 126)	(1, 18)	(1, 18)	(7, 126)	(7, 126)	(2, 56)	(19, 133)	(19, 133)
peak	0.224	**50.6**	**3.19**	**16.6**	1.72	**7.45**	0.878	3.77	**2.53**	1.75
M1	**12.3**	**128**	**4.77**	**65.6**	1.87	**11.6**	2.41	2.01	**4.25**	1.03
M2	0.169	**82.5**	**2.86**	**41.3**	1.38	**11.8**	1.35	2.11	**2.19**	0.927
M3	0.0212	**85.1**	**2.55**	**40.9**	0.704	**8.54**	0.673	1.32	**1.96**	1.27
M4	0.676	**29**	0.815	**20.1**	0.0016	**14.7**	0.879	3.33	1.58	1.91
FSRA	0.66	**40.5**	1.88	**11.3**	0.0827	**5.5**	0.269	4.21	**8.15**	**3.99**
Slope below	1.44	**269**	0.995	**27.2**	0.532	**3.77**	0.964	0.0392	**2.93**	**4.79**
Slope above	1.01	**234**	1.52	2.12	0.681	**5.07**	0.798	2.46	**6.49**	**2.14**
Duration	0.0188	**100**	1.35	**57.2**	0.0465	**18.4**	0.715	**12.3**	**88.6**	**92.2**
f0	**82.8**	**12.4**	**7.03**	**9.14**	3.26	1.31	2.06	1.23	**357**	**5.69**
amp	0.126	**107**	1.15	6.03	0.0014	**6.95**	0.533	**6.72**	**12**	**4.54**
amp500	1.73	**53.5**	1.68	**30.4**	0.0922	**14.8**	0.247	**13.7**	**9.4**	**7.08**
F2	5.83	**52.8**	1.82	**23.7**	0.0545	6.51	0.204	4.45	**10.3**	**4.61**
HNR	6.41	**88.2**	**6.69**	3.83	1.64	**11.7**	0.889	2.02	1.52	1.32

some populations (Maniwa *et al.*, 2008; also see Sec. III C), we have also been able to relate intelligibility differences to average acoustic modifications at the speaker level. While additional study is needed to determine, for example, the relative effects of different overall, inventory-level, and local contrast-enhancing strategies on intelligibility, it thus seems reasonable to refer to the present data as clear speech.

Figures 1–11 show the results of the analyses described in Sec. II D across fricatives, styles, and (where relevant) measurement locations. Table I summarizes the results of the analyses of variance described in Sec. II E. In the following sections, we describe in some detail the significance of these results with respect to our three hypotheses. A more comprehensive descriptive analysis of the data can be found in Maniwa (2006).

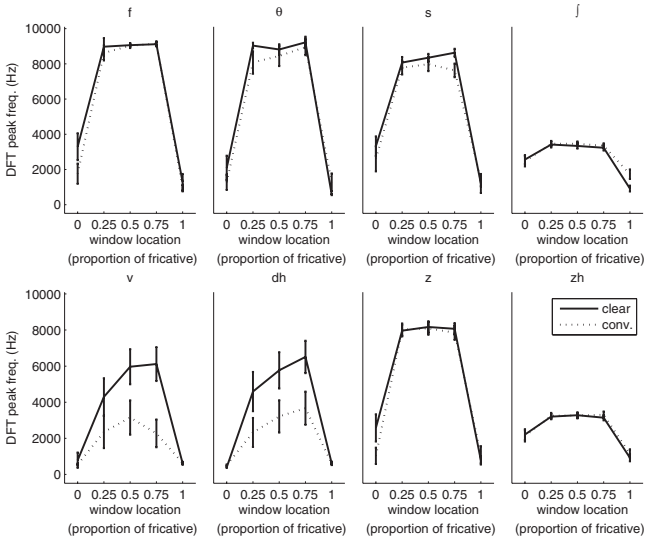

FIG. 1. Mean (and standard error) DFT peak frequency for each fricative as a function of speaking style. The horizontal axis indicates the location of the analysis window, ranging from 0 (fricative onset) to 1 (fricative offset). dh refers to the voiced interdental fricative and zh to the voiced palato-alveolar.

A. Overall clear speech modifications (hypothesis 1)

The leftmost columns in Table I summarize the results of the style×fricative×gender ANOVA. Because 14 separate analyses were conducted across measures that were in several cases highly correlated, a critical alpha level of 0.0073, based on the false discovery rate (FDR) estimate for a 5% false positive rate for the style main effect, was adopted.

As shown in Figs. 1–11, clear and conversational fricatives differed systematically along nearly every dimension we considered. Across speakers and fricatives, duration increased (Fig. 11, 187 ms longer in clear speech), and spectral measures including peak frequency (Fig. 1, on average 818 Hz higher in clear speech), mean (Fig. 2, 668 Hz higher in clear speech), and skewness (Fig. 4, 0.96 lower in clear speech) showed energy concentration in higher frequency re-

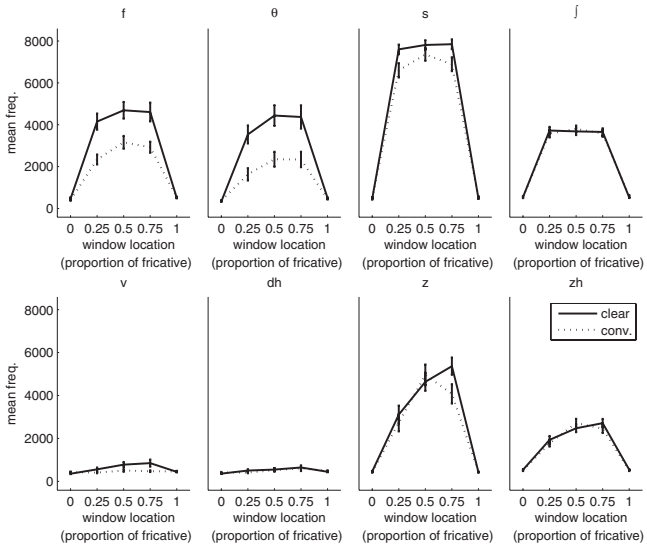

FIG. 2. Mean (and standard error) moment 1 values (center of gravity) for each fricative as a function of speaking style.

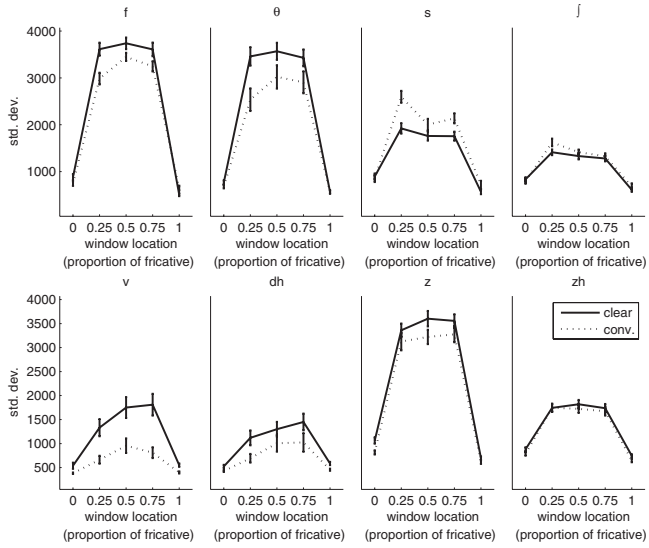

FIG. 3. Mean (and standard error) moment 2 values (SD) for each fricative as a function of speaking style.

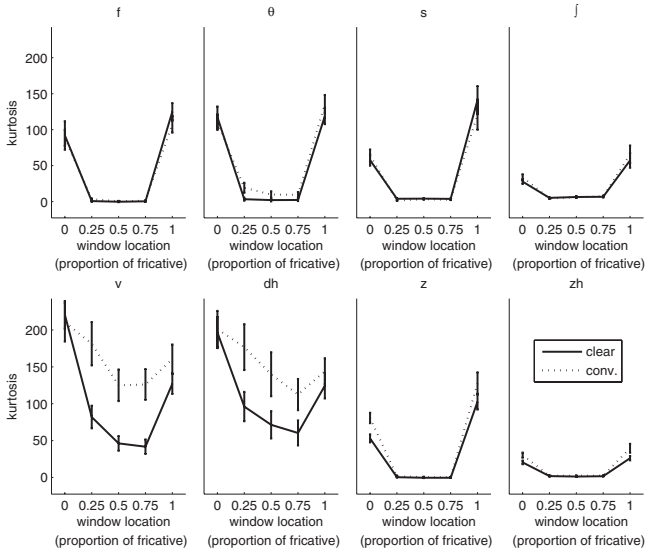

FIG. 5. Mean (and standard error) moment 4 values (kurtosis) for each fricative as a function of speaking style.

gions in clear speech. In general, these effects were seen most clearly at central windows, where there was less variability relating to neighboring vowels or the fricative constriction release. F2 transitions also covered greater frequency ranges in clear speech (Fig. 6, 85 Hz difference on average). Steeper spectral slopes (Fig. 7, on average 1.8 dB/kHz steeper) below the peak frequency also suggest more defined peaks and greater noise source strength for clear speech, consistent with previous reports on fricatives produced with elevated vocal effort (Jesus and Shadle, 2002). Slopes above peak frequencies were more variable, with sibilants (with better defined peaks and steeper slopes overall) showing larger negative values (steeper slopes) but nonsibilants (with near-zero slopes overall) showing, on average, *smaller* values in clear compared to conversational speech. The averaged neighboring vowel f0 was also higher in clear speech (Fig. 11, 4.72 Hz higher on average). These results are in general agreement with previous studies [e.g., see Chen (1980) and Picheny *et al.* (1986)] and are consistent with increased vocal effort in clear speech.

On the other hand, a main effect of style for rms amplitude was found at all five locations, with clear fricatives significantly *lower* in amplitude (Fig. 8, on average 1.08 dB lower in clear speech; that it was higher in W5 is due to the onset of the following vowel). FSRA also decreased in clear speech (Fig. 10, 4.8 dB lower). Clear fricatives also had significantly less energy below 500 Hz (Fig. 9, on average 4.18 dB lower). Lower amplitude measures compared to neighboring vowels were somewhat unexpected considering reports of increased CVR in clear speech [e.g., see Bradlow *et al.* (2003) and Chen (1980)] but not completely surprising. Previous studies have not concentrated on fricatives and, in general, have shown that changes in CVR are stimulus, context, and talker dependent; decreases have even been seen for some fricatives (mostly nonsibilants) for some speakers (Picheny *et al.*, 1986; Krause and Braida, 2004). The present

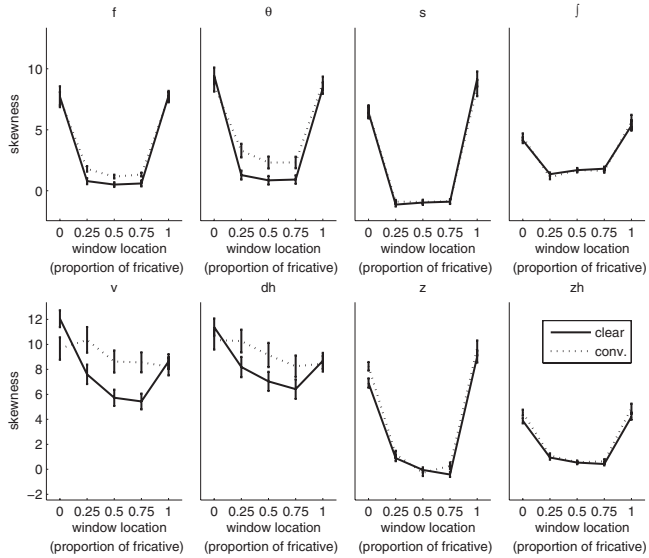

FIG. 4. Mean (and standard error) moment 3 values (skewness) for each fricative as a function of speaking style.

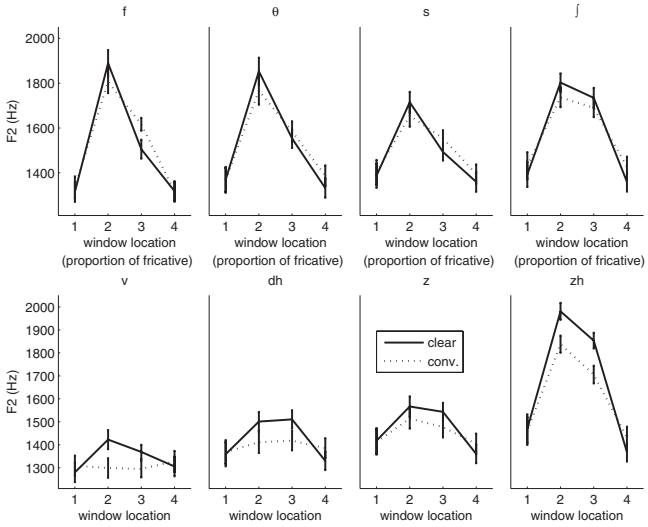

FIG. 6. Mean (and standard error) F2 values (Hz) for each fricative at four window locations (W1=midpoint of the preceding vowel, W2=vowel-fricative onset, W3=fricative-vowel offset, and W4=midpoint of the following vowel) as a function of style.

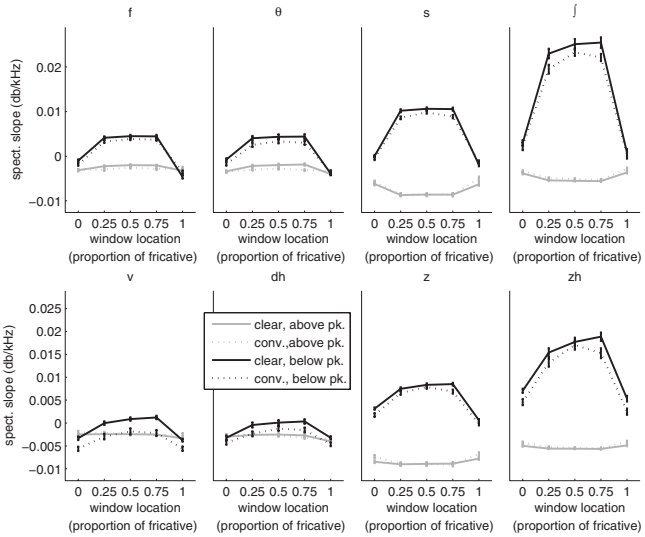

FIG. 7. Mean (and standard error) slope values below and above the peak frequencies for each fricative as a function of speaking style.

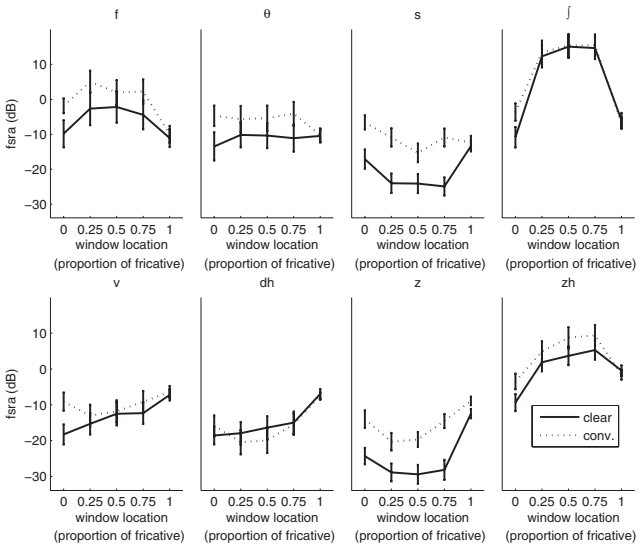

FIG. 9. Mean (and standard error) frequency-specific relative amplitude (FSRA) values as a function of fricative and style.

results are probably best explained in terms of articulatory effort. Since the volume velocity required to increase the level of fricative sounds—particularly nonsibilants—is much greater than that required to increase vowel intensity by a similar amount, it is not surprising that for a similar increase in effort across a word (or even slightly more effort on a fricative), intensity would increase more for vowels than for fricatives (especially nonsibilants).

Thus, hypothesis 1 was clearly confirmed; robust overall changes were seen in the durations, spectra, and probably amplitude of clear fricatives that are consistent with increased vocal effort.

B. Inventory-level and local contrastive patterns (hypothesis 2)

1. Overall tendencies

Style × fricative interactions for several measures were consistent with efforts to maintain contrasts within the English fricative inventory. The place of articulation contrasts, in particular, seemed to be enhanced in clear speech. For example, palato-alveolars are defined by energy concentration at low frequencies; DFT peaks and M1 for palato-alveolars increased much less than for other fricatives (even decreasing in some cases) in clear speech, and skewness generally decreased less (increasing in some cases) for other places of articulation. Differences between sibilants and nonsibilants were also emphasized in clear speech. Nonsibilants, with inherently more diffuse spectra, showed increases in M2 in clear speech, while sibilants decreased (+573 Hz versus −49 Hz). Nonsibilants also decreased in kurtosis in clear speech, whereas voiceless sibilants did not. Acoustic distances between sibilants and nonsibilants also increased in terms of amplitude (see comments in Sec. III A regarding the overall vocal effort for a complementary account of the differences); a significant decrease in the normalized rms amplitude in clear speech was seen only for nonsibilant fricatives; voiceless sibilants actually increased slightly. The F2

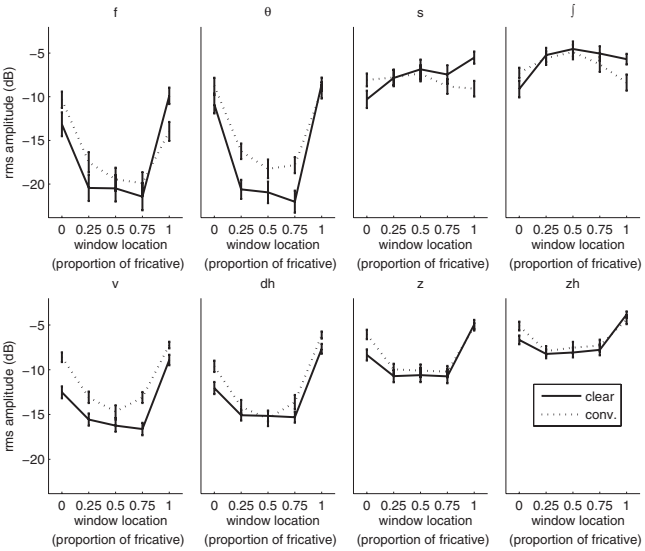

FIG. 8. Mean (and standard error) normalized rms amplitude for each fricative as a function of speaking style.

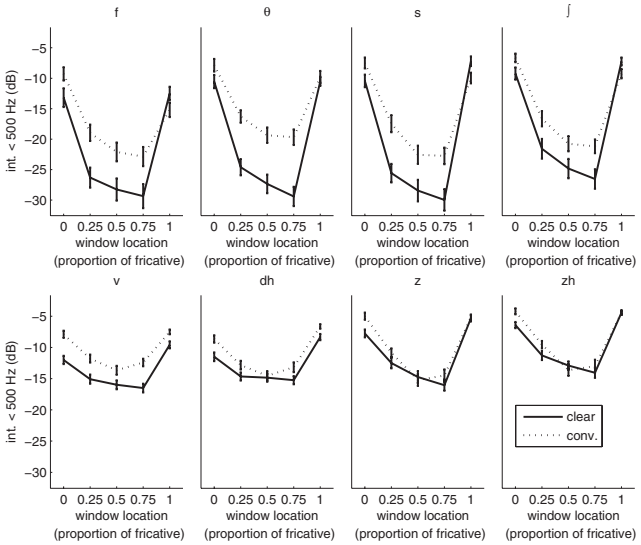

FIG. 10. Mean (and standard error) normalized intensity below 500 Hz for each fricative as a function of speaking style.

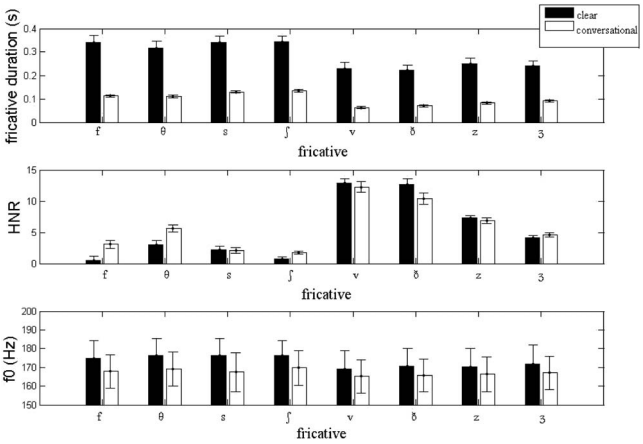

FIG. 11. Mean (and standard error) noise duration as a function of fricative and style (top), HNR averaged across speakers as a function of fricative and style (middle), and f0 values as a function of fricative and style (bottom).

transition distance increased more for palato-alveolars (with inherently higher F2) than alveolars, and dentals (with inherently higher F2) than labio-dentals in clear speech, increasing fricative-to-fricative distance in both cases. This is particularly important for the nonsibilants, for which F2 may be a critical cue (Jongman *et al.*, 2000; Nittrouer, 2002).

Enhanced voicing contrasts were also seen. A style × fricative interaction for duration revealed that inherently longer voiceless fricatives increased more in length than voiced fricatives in clear speech (213 ms versus 159 ms), increasing the distance between the two classes of sounds in terms of duration. The style × fricative interaction was also seen for M2, showing greater increases for voiced than voiceless fricatives (and decreases for voiceless sibilants) in clear speech. These results are in accordance with those from Jongman *et al.* (2000), which showed that voiced fricatives had a significantly greater variance than voiceless ones and similarly increased the average M2 distance between voiced and voiceless sounds in clear speech. A larger decrease (5.24 dB larger) in intensity below 500 Hz for voiced fricatives, an increase in HNR for voiced fricatives (+0.48), and a decrease for voiceless (−0.73) and an increase in f0 in adjacent vowels only for voiceless fricatives (3.24 Hz larger increase for voiceless fricatives) were also consistent with efforts to maintain voicing contrasts in clear speech.

Thus, while it cannot be shown that these changes were a direct result of knowledge of the fricative inventory and its critical contrasts and while the actual results of the changes on the effectiveness of the contrasts must be evaluated through perceptual study, the pattern of results seen was consistent with the notion that clear speech acts to maximize contrast within a language [e.g., see Bradlow *et al.* (2003), Chen (1980), Krause and Braida (2004), Ohala (1994), Picheny *et al.* (1986), Smiljanić and Bradlow (2005)]. These findings support the first (inventory-level contrast) part of hypothesis 2.

2. Distance comparisons

Differences between similar pairs of sounds and the acoustic characteristics of fricative productions, in general, were influenced not only by the speaking style overall but by the specific misidentifications that prompted clear productions as well. An examination of clear productions as a function of misidentification seemed to suggest that context-dependent contrastive efforts (that is, attempts to make sounds more unlike the sounds they had been mistaken for) were responsible for some of the effects that were seen. For example, when speakers repeated the sound /ʃ/ in response to a misidentification of the sound as /s/ (/ʃ|s/), they produced the fricative with significantly lower DFT peak frequencies than when they produced the same sound in response to a misidentification as /ʒ/ (/ʃ|ʒ/; 3356 Hz versus 3504 Hz). This suggests that speakers tried to differentiate the sound /ʃ/ from neighboring sounds in clear speech since it has a typical peak frequency between /ʒ/ and /s/. Similarly, M1 was lower, and M3 higher, in /ʃ|s/ compared to /ʃ|ʒ/ productions.

The one-way ANOVA comparing fricative-to-fricative distances for each measure in contrastive (e.g., /ʃ|s/), noncontrastive (/ʃ|~s/), and conversational (/ʃ|Ø/) contexts was designed to quantify these differences, as well as the inventory-level distance-enhancing manipulations discussed in Sec. III B. We first considered the mean distance across acoustic dimensions (after normalizing all measures to have a SD of 1.0 so that measures were weighted equally). A significant effect of style (F) $F(2,56)=4.02$; $p=0.023$) revealed precisely what we predicted: distances were largest for contrastive productions (0.952 SD units), followed by noncontrastive clear productions (0.948), and smallest for conversational tokens (0.939). Results considering the 14 measures separately are summarized in the center columns of Table I. For nearly every dimension, the predicted order (contrastive > noncontrastive > conversational) was observed, although it reached significance only for duration, amplitude, and low-frequency amplitude ($\alpha=0.0024$, based on the FDR analysis of observed p values). The robustness of the distance enhancement for these measures may be related to the fact that duration varied so much with style (Fig. 10) and that the amplitude measures were relevant to (and therefore may have been adjusted to emphasize) both place and voicing distinctions.

In summary, the comparison of acoustic distances between fricative pairs across measures and misidentification prompts revealed that speakers tended to repeat sounds such that they differed maximally from neighboring sounds and especially from those for which they were initially mistaken. This demonstrates the range of levels at which talkers are sensitive to the communicative demands of a speaking situation and is consistent with the notion that talkers are able to adjust the details of productions based on relatively local fine-grained information (hypothesis 2).

3. Discriminant analysis

Although fricative-to-fricative distances tended to be enhanced in clear speech and by local contrastive efforts, this does not necessarily mean that the speech manipulations introduced in these contexts actually made fricatives easier to identify. For example, increased variability in clear speech could have made the productions of individual speakers more confusable with one another even though mean values for each measure were further apart. The discriminant analy-

sis described in Sec. II E was designed to address this issue directly. Although there was some variability across styles from pair to pair, performance on average was, in accordance with overall distance measures, as predicted: noncontrastive clear productions were more discriminable than conversational ones (94.8% versus 93.9%), and classification was best in contrastive contexts (95.2%). In particular, difficult pairs such as /f/-/θ/ improved substantially in clear styles (0.65 conversation vs. 0.8 clear). Thus, again, consistent with hypothesis 2, clear and contrastive fricatives were more distinct from similar sounds when specific effort was made to reduce confusions.

C. Talker and gender effects (hypothesis 3)

Results of the style × talker ANOVA are shown in the rightmost columns of Table I. Significant talker effects ($\alpha = 0.014$) were seen for every measure except for kurtosis and HNR, and the style × talker interaction was seen for 8 of the 14 measures. This indicates that talkers varied significantly in the magnitude—and sometimes the direction—of acoustic modifications in clear speech. Spectral peak frequency, amplitude, slope above the peak, and FSRA, in particular, showed speaker variability in the direction of clear speech modifications, with SDs of (clear-minus-conversational) differences greater than the respective mean values. In short, hypothesis 3 was supported; talkers differed in their production strategies when they attempted to increase intelligibility; some increased duration more, while others shifted energy distributions toward higher frequency regions more or amplified frication noise relative to the neighboring vowels. Extensive intelligibility experiments will be necessary to determine exactly which of these combinations were most successful at enhancing fricative contrasts. Intelligibility results thus far (Maniwa *et al.*, 2008) seem to suggest that at least for normal-hearing native listeners, the greatest benefits were seen for speakers whose productions involved a relatively large increase in energy at higher frequencies (increased peak, M1, etc.).

One variable that did not seem to contribute to clear-to-conversational acoustic differences was speaker gender. No style × gender or fricative × style × gender interaction was observed for any of the measures (see Table I). This indicates that female and male speakers did not reliably differ in the extent or direction of any acoustic modifications in clear speech. This was somewhat unexpected considering previous reports that female speakers modified their speech to a greater extent than males [e.g., see Bradlow *et al.* (2003) and Liu *et al.* (2004)]. However, since these earlier studies considered a limited number of speakers [e.g., $n=2$ for Bradlow *et al.* (2003)], it was not clear whether the differences observed derived from gender differences or simply talker differences.

D. Dynamic patterns

Figures 1–10 show spectral and amplitude measures over the course of the fricative and not just at one point where the clearest prediction regarding style-related differences could be made. As discussed in Sec. II E, these data were included partly because it was considered possible that differences in different measures might be more prominent at different locations or might be dynamic in nature. To the extent that this possibility can be addressed with the present data, it seems for the most part not to have been the case. Contours representing measures for clear and conversational tokens appear to be roughly parallel over the three central windows, with differences that were generally in the expected directions and that sometimes narrowed or changed direction at fricative-vowel boundaries.

IV. CONCLUSIONS

In sum, this study demonstrates that there are systematic acoustic-phonetic modifications in the production of clear fricatives. Some overall clear speech effects were straightforwardly predictable based on previous findings (e.g., longer duration and energy at higher frequencies), and some were more surprising (especially lower relative amplitude). Across a variety of measures, the acoustic distances between minimally contrasting sounds were enlarged in clear speech, indicating that talkers attempt to maintain contrast between category distributions across the inventory of English fricatives. In addition, talkers were sensitive to specific listener feedback, adjusting repeated productions to be more unlike sounds for which they had been misapprehended. Individual talkers varied widely in the magnitude—and sometimes the direction—of these changes; these differences were not related to talker gender.

Balakrishnama, S., and Ganapathiraju, A. (**1998**). "Linear discriminant analysis: A brief tutorial," available at http://www.zemris.fer.hr/predmeti/kdisc/bojana/Tutorial-LDA-Balakrishnama.pdf (Last viewed May 24, 2007).

Baum, S. R., and Blumstein, S. E. (**1987**). "Preliminary observations on the use of duration as a cue to syllable-initial fricative consonant voicing in English," J. Acoust. Soc. Am. **82**, 1073–1077.

Behrens, S. J., and Blumstein, S. E. (**1988**). "Acoustic characteristics of English voiceless fricatives: A descriptive analysis," J. Phonetics **16**, 295–298.

Bilger, R. C., and Wang, M. D. (**1976**). "Consonant confusions in patients with sensorineural hearing loss," J. Speech Hear. Res. **19**, 718–748.

Boersma, P. (**1993**). "Accurate short-term analysis of the fundamental frequency and the harmonics-to-noise ratio of a sampled sound," IFA Proceedings, Vol. **17**, pp. 97–110.

Boersma, P., and Weenink, D. (**2000**). "Praat, a system for doing phonetics by computer, version 4.406," Institute of Phonetic Sciences, University of Amsterdam, available at http://www.fon.hum.uva.nl/praat/ (Last viewed May 24, 2007).

Bradlow, A. R., and Bent, T. (**2002**). "The clear speech effect for non-native listeners," J. Acoust. Soc. Am. **112**, 272–284.

Bradlow, A. R., Kraus, N., and Hayes, E. (**2003**). "Speaking clearly for children with learning disabilities: Sentence perception in noise," J. Speech Lang. Hear. Res. **46**, 80–97.

Chen, F. R. (**1980**) "Acoustic characteristics and intelligibility of clear and conversational speech at the segmental level," MS thesis, Massachusetts Institute of Technology, Cambridge, MA.

Childers, D. G. (**1978**). *Modern Spectrum Analysis* (IEEE, New York), pp. 252–255.

Crystal, T. H., and House, A. S. (**1988**). "A note on the durations of fricatives in American English," J. Acoust. Soc. Am. **84**, 1932–1935.

Evers, V., Reetz, H., and Lahiri, A. (**1998**). "Crosslinguistic acoustic categorization of sibilants independent of phonological status," J. Phonetics **26**, 345–370.

Feijóo, S., Fernández, S., and Balsa, R. (**1998**). "Context effects in the auditory identification of Spanish fricatives /f/ and /θ/: Hyper and hypospeech," J. Acoust. Soc. Am. **103**, 2982.

Ferguson, S. H. (**2002**). "Vowels in clear and conversational speech: Talker differences in acoustic features and intelligibility for normal-hearing listeners," Ph.D. dissertation, Indiana University, Bloomington, IN.
Ferguson, S. H., and Kewley-Port, D. (**2002**). "Vowel intelligibility in clear and conversational speech for normal-hearing and hearing-impaired listeners," J. Acoust. Soc. Am. **112**, 259–271.
Forrest, K., Weismer, G., Milenkovic, P., and Dougall, R. N. (**1988**). "Statistical analysis of word-initial voiceless obstruents: Preliminary data," J. Acoust. Soc. Am. **84**, 115–123.
Gagné, J. P., Masterson, V. M., Munhall, K. G., Bilida, N., and Querengesser, C. (**1994**). "Across talker variability in auditory, visual, and audiovisual speech intelligibility for conversational and clear speech," J. Acad. Rehabil. Audiol. **27**, 135–158.
Hedrick, M. S., and Ohde, R. N. (**1993**). "Effect of relative amplitude of frication on perception of place of articulation," J. Acoust. Soc. Am. **94**, 2005–2026.
Helfer, K. (**1997**). "Auditory and auditory-visual perception of clear and conversational speech," J. Speech Lang. Hear. Res. **40**, 432–443.
Helfer, K. (**1998**). "Auditory and auditory-visual recognition of clear and conversational speech by older adults," J. Am. Acad. Audiol **9**, 234–242.
Hughes, G. W., and Halle, M. (**1956**). "Spectral properties of fricative consonants," J. Acoust. Soc. Am. **28**, 303–310.
Iverson, P., and Bradlow, A. R. (**2002**). "The recognition of clear speech by adult cochlear implant users," ICSA Workshop*Temporal Integration in the Perception of Speech*, Aix-en Provence, France, 8–10 April.
Jackson, P. J. B., and Shadle, C. H. (**2000**). "Frication noise modulated by voicing, as revealed by pitch-scaled decomposition," J. Acoust. Soc. Am. **108**, 1421–1434.
Jesus, L. M. T., and Shadle, C. H. (**2002**). "A parametric study of the spectral characteristics of European Portuguese fricatives," J. Phonetics **30**, 437–464.
Johnson, K., Flemming, E., and Wright, R. (**1993**). "The hyperspace effect: Phonetic targets are hyperarticulated," Language **69**, 505–528.
Jongman, A. (**1989**). "Duration of frication noise required for identification of English fricatives," J. Acoust. Soc. Am. **85**, 1718–1725.
Jongman, A., Wayland, R., and Wong, S. (**2000**). "Acoustic characteristics of English fricatives," J. Acoust. Soc. Am. **108**, 1252–1263.
Kabak, B., and Maniwa, K. (**2007**). "L2 perception of English fricatives in clear and conversational speech: The role of phonetic similarity and L1 interference," ICPhS XVI, Saabrücken.
Krause, J. C., and Braida, L. D. (**2004**). "Acoustic properties of naturally produced clear speech at normal speaking rates," J. Acoust. Soc. Am. **115**, 362–378.
Lindblom, B. (**1990**). "Explaining phonetic variation: A sketch of the H & H theory," in *Speech Production and Speech Modeling*, edited by W. J. Hardcastle and A. Marchal (Kluwer Academic, Dordrecht), pp. 403–439.
Lindblom, B. (**1996**). "Role of articulation in speech perception: Clues from production," J. Acoust. Soc. Am. **99**, 1683–1692.
Liu, S., Del Rio, E., Bradlow, A. R., and Zeng, F.-G. (**2004**). "Clear speech perception in acoustic and electric hearing," J. Acoust. Soc. Am. **116**, 2373–2383.
Maniwa, K. (**2006**). "Acoustical and perceptual properties of clearly produced fricatives," Ph.D. dissertation, University of Kansas, Lawrence, KS.
Maniwa, K., Jongman, A., and Wade, T. (**2006**). "Acoustic characteristics of clearly produced fricatives," J. Acoust. Soc. Am. **119**, 3301.
Maniwa, K., Jongman, A., and Wade, T. (**2008**). "Perception of clear English fricatives by normal-hearing and simulated hearing-impaired listeners," J. Acoust. Soc. Am. **123**, 1114–1125.
Mann, V. A., and Repp, B. H. (**1980**). "Influence of vocalic context on perception of the [ʃ]-[s] distinction," Percept. Psychophys. **28**, 213–228.
Mann, V. A., and Soli, S. D. (**1991**). "Perceptual order and the effect of vocalic context on fricative perception," Percept. Psychophys. **49**, 399–411.
McGowan, R., and Nittrouer, S. (**1988**). "Differences in fricative production between children and adults: Evidence from an acoustic analysis of /ʃ/ and /s/," J. Acoust. Soc. Am. **83**, 229–236.
Miller, G. A., and Nicely, P. A. (**1955**). "An analysis of perceptual confusions among some English consonants," J. Acoust. Soc. Am. **27**, 338–352.
Moon, S.-J., and Lindblom, B. (**1994**). "Interaction between duration, context, and speaking style in English stressed vowels," J. Acoust. Soc. Am. **96**, 40–55.
Nissen, S. L., and Fox, R. A. (**2005**). "Acoustic and spectral characteristics of young children's fricative productions: A developmental perspective," J. Acoust. Soc. Am. **118**, 2570–2578.
Nittrouer, S. (**1995**). "Children learn separate aspects of speech production at different rates: Evidence from spectral moments," J. Acoust. Soc. Am. **97**, 520–530.
Nittrouer, S. (**2002**). "Learning to perceive speech: How fricative perception changes, and how it stays the same," J. Acoust. Soc. Am. **112**, 711–719.
Nittrouer, S., Studdert-Kennedy, M., and McGowan, R. S. (**1989**). "The emergence of phonetic segments: Evidence from the spectral structure of fricative-vowel syllables spoken by children and adults," J. Speech Hear. Res. **32**, 120–132.
Ohala, J. J. (**1994**). "Acoustic study of clear speech: A test of the contrastive hypothesis," Proceedings of the International Symposium on Prosody, Pacific Convention Plaza Yokohama, Japan, pp. 75–89.
Payton, K. L., Uchanski, R. M., and Braida, L. D. (**1994**). "Intelligibility of conversational and clear speech in noise and reverberation for listeners with normal and impaired hearing," J. Acoust. Soc. Am. **95**, 1581–1592.
Perkell, J. S., Matthies, M. L., Tiede, M., Lane, H., Zandipour, M., Marrone, N., Stockmann, E., and Guenther, F. H. (**2004**). "The distinctiveness of speakers' /s/-/ʃ/ contrast is related to their auditory discrimination and use of an articulatory saturation effect," J. Speech Lang. Hear. Res. **47**, 1259–1269.
Picheny, M. A., Durlach, N. I., and Braida, L. D. (**1985**). "Speaking clearly for the hard of hearing. I: Intelligibility differences between clear and conversational speech," J. Speech Hear. Res. **28**, 96–103.
Picheny, M. A., Durlach, N. I., and Braida, L. D. (**1986**). "Speaking clearly for the hard of hearing II: Acoustic characteristics of clear and conversational speech," J. Speech Hear. Res. **29**, 434–446.
Pincas, J., and Jackson, P. J. B. (**2006**). "Amplitude modulation of turbulence noise by voicing in fricatives," J. Acoust. Soc. Am. **120**, 3966–3977.
Schum, D. (**1996**). "Intelligibility of clear and conversational speech of young and elderly talkers," J. Am. Acad. Audiol **7**, 212–218.
Shadle, C. H., and Mair, S. J. (**1996**). "Quantifying spectral characteristics of fricatives," Proceedings from the International Conference on Spoken Language Processing (ICSLP), Philadelphia, pp. 1521–1524.
Silbert, N., and de Jong, K. (**2008**). "Focus, prosodic context, and phonological feature specification: Patterns of variation in fricative production," J. Acoust. Soc. Am. **123**, pp. 2769–2779.
Smiljanić, R., and Bradlow, A. R. (**2005**). "Production and perception of clear speech in Croatian and English," J. Acoust. Soc. Am. **118**, 1677–1688.
Soli, S. D. (**1981**). "Second formants in fricatives: Acoustic consequences of fricative-vowel coarticulation," J. Acoust. Soc. Am. **70**, 976–984.
Stevens, K. N. (**1971**). "Airflow and turbulence for noise for fricative and stop consonants: Static consideration," J. Acoust. Soc. Am. **50**, 1182–1192.
Stevens, K. N. (**1985**). "Evidence for the role of acoustic boundaries in the perception of speech sounds," in *Phonetic Linguistics: Essays in Honor of Peter Ladefoged*, edited by V. Fromkin (Academic, New York), pp. 243–255.
Strevens, P. (**1960**). "Spectra of fricative noise in human speech," Lang Speech **3**, 32–49.
Uchanski, R. S., Choi, S. S., Braida, L. D., Reed, C. M., and Durlach, N. I. (**1996**). "Speaking clearly for the hard of hearing IV: Further studies of the role of speaking rate," J. Speech Hear. Res. **39**, 494–509.
Venables, W. N., and Ripley, B. D. (**2002**). *Modern Applied Statistics*, edited by S. Fourth (Springer, New York).
Wang, M. D., and Bilger, R. C. (**1973**). "Consonant confusions in noise: A study of perceptual features," J. Acoust. Soc. Am. **54**, 1248–1266.
Whalen, D. H. (**1981**). "Effects of vocalic formant transitions and vowel quality on the English [s]-[š] boundary," J. Acoust. Soc. Am. **69**, 275–282.
Yeni-Komshian, G. H., and Soli, S. D. (**1981**). "Recognition of vowels from information in fricatives: Perceptual evidence of fricative-vowel coarticulation," J. Acoust. Soc. Am. **70**, 966–975.

Individual talker differences in voice-onset-time: Contextual influences[a)]

Rachel M. Theodore,[b)] Joanne L. Miller, and David DeSteno
Department of Psychology, Northeastern University, Boston, Massachusetts 02115

(Received 29 January 2008; revised 24 February 2009; accepted 25 February 2009)

Previous research indicates that talkers differ in phonetically relevant properties of speech, including voice-onset-time (VOT) in word-initial stop consonants; some talkers have characteristically shorter VOTs than others. Previous research also indicates that VOT is robustly affected by contextual influences, including speaking rate and place of articulation. This paper examines whether these contextual influences on VOT are themselves talker-specific. Many tokens of alveolar /ti/ (experiment 1) or labial /pi/ and velar /ki/ (experiment 2) were elicited from talkers across a range of rates. VOT and vowel duration (a metric of rate) were measured for each token. Hierarchical linear modeling analyses showed that (1) VOT increased as rate decreased for all talkers, but the magnitude of the increase varied significantly across talkers; thus the effect of rate on VOT was talker-specific; (2) the talker-specific effect of rate was stable across a change in place of articulation; and (3) for all talkers VOTs were shorter for labial than velar stops, and there was no significant variability in the magnitude of this displacement across talkers; thus the effect of place on VOT was not talker-specific. The implications of these findings for how listeners might accommodate talker differences in VOT during speech perception are discussed.
 [DOI: 10.1121/1.3106131]

PACS number(s): 43.70.Fq, 43.70.Gr, 43.71.Es [AL] Pages: 3974–3982

I. INTRODUCTION

The past 50 years of research in speech acoustics have yielded substantial information on the acoustic parameters that specify individual speech segments. One consistent finding in this domain is that there is considerable variability in the acoustic-phonetic information produced for individual consonants and vowels, such that there is no one-to-one mapping between the acoustic signal and speech segment. Many sources of acoustic-phonetic variability have been examined, including variability that results from differences in pronunciation across individual talkers. Talker differences have been observed for a host of speech sound classes including vowels (Hillenbrand *et al.*, 1995; Peterson and Barney, 1952), fricatives (Newman *et al.*, 2001), stops (Allen *et al.*, 2003; Byrd, 1992; Zue and Laferriere, 1979), and liquids (Espy-Wilson *et al.*, 2000; Hashi *et al.*, 2003). The goal of the current work is to further characterize such talker differences.

Our primary motivation for examining talker differences in detail stems from recent findings in the speech perception literature indicating that listeners retain fine-grained information about how a talker implements speech segments (Goldinger, 1996; Goldinger, 1998; Palmeri *et al.*, 1993) and that this information can be used to facilitate subsequent processing (Bradlow and Bent, 2008; Bradlow and Pisoni, 1999; Clarke and Garrett, 2004; Nygaard and Pisoni, 1998; Nygaard *et al.*, 1994). In order to provide a theoretical account of speech perception that describes the role of talker-specific phonetic detail, comprehensive data on the acoustic-phonetic consequences of talker differences in speech production are necessary.

In this paper we examine talker differences for one phonetically relevant property of speech, voice-onset-time (VOT). VOT is a primary cue marking the linguistic contrast of voicing in word-initial English stops. In word-initial position, English voiced stops (/b/, /d/, and /g/) are typically produced with short VOTs (or, in some cases, with prevoicing), and English voiceless stops (/p/, /t/, and /k/), which are aspirated, are produced with longer VOTs (Lisker and Abramson, 1964). Recent research has shown that this property is subject to individual talker differences (Allen *et al.*, 2003). Focusing on voiceless stops, Allen *et al.* (2003) compared word-initial VOTs for many monosyllabic words across eight talkers. Their results showed that even after statistically controlling for contextual factors such as speaking rate (using both syllable duration and, in separate analyses, vowel duration as metrics of speaking rate), a statistically significant amount of variability in VOT was accounted for by stable differences across individual talkers. In other words, the talkers differed in their characteristic VOTs, with some talkers producing longer VOTs compared to other talkers. Here we build on this finding by examining the role of contextual influences on VOT at the level of individual talkers.

Two contextual factors that have been examined extensively with respect to VOT, and that are the focus of the

[a)]Portions of this work were presented at the 152nd meeting of the Acoustical Society of America, Honolulu, HI, December 2006; the 153rd meeting of the Acoustical Society of America, Salt Lake City, UT, June 2007; and the XVIth International Congress of Phonetic Sciences, Saarbrücken, Germany, August 2007.

[b)]Author to whom correspondence should be addressed. Present address: Department of Cognitive and Linguistic Sciences, Brown University, Providence, Rhode Island 02912. Electronic mail: rachel_theodore@brown.edu

current research, are place of articulation and speaking rate (e.g., Klatt, 1975; Lisker and Abramson, 1967; Picheny *et al.*, 1986; Robb *et al.*, 2005). First consider place of articulation. It is well established that, in general, VOT increases as place moves from an anterior to posterior point of constriction in the vocal tract (e.g., Cho and Ladefoged, 1999; Lisker and Abramson, 1964; Volaitis and Miller, 1992). In the current paper we examine whether talkers systematically vary in the magnitude of this effect.

Next consider speaking rate. At a global level, rate is a complex variable that encompasses the rate at which speech itself is produced as well as the number and duration of pauses and aspects of higher-level prosodic structure. There is evidence that the specific way in which a change in speaking rate is implemented may vary in numerous respects across individual talkers (e.g., Crystal and House, 1982; Kuehn and Moll, 1976; Matthies *et al.*, 2001; McClean, 2000). Nonetheless, it appears that for all talkers a change in overall rate involves a change in the rate of speech itself (and is not solely due to a change in pausing) (Miller *et al.*, 1984), and this is the focus of the current study. Specifically, we examine how the rate at which a given syllable was produced (defined in terms of its syllable or vowel duration) influences VOT. We know from previous research that, in general, VOT systematically increases as speaking rate decreases (and syllables become longer), especially for voiceless aspirated stops such as English /p/, /t/, and /k/ (e.g., Kessinger and Blumstein, 1997; Miller *et al.*, 1986; Nagao and de Jong, 2007). In the current paper we examine whether talkers exhibit systematic variability in the extent to which changes in rate affect VOT.

We report two experiments. Experiment 1 is centered on the effect of speaking rate on VOT in the context of the alveolar voiceless stop /t/. In experiment 2, we extend the findings of experiment 1 to the labial (/p/) and velar (/k/) voiceless stops, as well as examine the effect of place of articulation *per se* on VOT. To preview our results, we find evidence that the magnitude of the speaking rate effect, but not of the place effect, is talker-specific. The implications of these distinct patterns of results for accounts of speech perception are considered in Sec. IV.

II. EXPERIMENT 1

The primary goal of experiment 1 was to extend the investigation of talker differences in word-initial VOT for voiceless stop consonants by examining the effect of speaking rate on VOT at the level of individual talkers. Specifically, we examined whether the magnitude of the increase in VOT as speaking rate decreases systematically differs across talkers. A secondary goal of experiment 1 was to replicate Allen *et al.*, 2003 using a different methodology. They observed talker differences in VOT when speaking rate was statistically controlled; we examined whether such differences are also observed when comparing syllables produced at the same rate of speech.

A. Method

1. Subjects

Ten talkers (five males, E1M1–E1M5; five females, E1F1–E1F5) were recruited from the Northeastern University community for this experiment. The talkers were native speakers of American English between 18 and 31 years of age with no history of speech or language disorders, and were either paid or received partial course credit for their participation.

2. Recordings

A magnitude-production procedure (e.g., Adams *et al.*, 1993; Lane and Grosjean, 1973; Miller *et al.*, 1986; Volaitis and Miller, 1992) was used to elicit multiple repetitions of the syllable /ti/ that span a wide range of syllable durations. The alveolar stop was recorded in a constrained phonetic environment in order to control for factors that can influence VOT and syllable duration (e.g., vowel identity and final consonant, Port and Rotunno, 1979; Weismer, 1979); such factors could introduce extraneous variability, making it difficult to isolate talker-specific effects of rate on VOT. In the magnitude-production procedure, talkers were directed to produce clear tokens of the syllable /ti/ at their normal speaking rate and at rates relative to their normal speaking rate. Each talker was recorded producing eight "runs" of syllables. A run consisted of six repetitions of /ti/ at each of the following speaking rates: normal, twice as fast, four times as fast, as fast as possible, normal, twice as slow, four times as slow, as slow as possible. Thus, each run yielded syllables produced at eight speaking rates—seven unique speaking rates and two blocks of repetitions produced at a "normal" speaking rate. Note that this procedure was used as a tool for acquiring syllables that exhibited variation in overall duration and not as a means to compare the duration of syllables across individuals produced, for example, at a normal speaking rate. The extreme rate prompts (e.g., "as fast as possible") were provided to encourage duration variation, and talkers were told that these prompts should reflect the variation found in natural speech and not, for example, the direction to speak as fast as humanly possible. Talkers were given a practice run prior to the recording session and were also given a short break after the first four runs. All recordings took place in a sound-attenuated booth. Speech was recorded via microphone (AKG C460B) onto digital audiotape.

In total, 3840 syllables (6 repetitions $\times$ 8 speaking rates $\times$ 8 runs $\times$ 10 talkers) were recorded. All recordings were digitized at a sampling rate of 20 kHz using the CSL system (KayPENTAX). Syllables produced in the first block of the normal speaking rate for each run were excluded from further analyses to help ensure that, at least to a first approximation, tokens were evenly distributed across the measured range of syllable (and vowel) duration. In addition, the final repetition at each speaking rate was excluded from further analyses because this token may have been subject to a phrase-final lengthening effect (Klatt, 1976). Excluding these tokens left 2800 possible syllables (5 repetitions $\times$ 7 speaking rates $\times$ 8 runs $\times$ 10 talkers) for acoustic analysis.

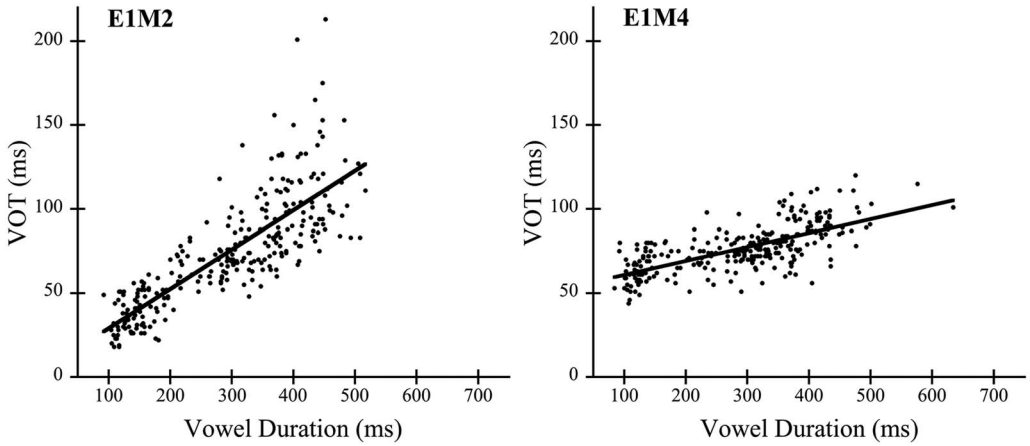

FIG. 1. VOT (ms) as a function of vowel duration (ms) for talkers E1M2 (left panel) and E1M4 (right panel). In both panels, each filled circle represents one token of /ti/ and the solid line represents the linear function relating VOT to vowel duration.

3. Acoustic measurements

The PRAAT speech analysis software (Boersma, 2001) was used to generate a waveform for each syllable. On each waveform, three points in time were located: the onset of the release burst, marked by the onset of low amplitude, aperiodic noise; voicing onset, marked by the onset of high amplitude, periodic energy; and voicing offset, marked by the offset of the last visible glottal pulse. From these three points in time, three durations were calculated. VOT was calculated as the latency between the release burst and voicing onset. Vowel duration was calculated as the latency between voicing onset and voicing offset. Syllable duration was calculated as the latency between the onset of the release burst and voicing offset. In line with numerous studies examining the effect of speaking rate at the segmental level, vowel duration and syllable duration were used as metrics of rate (e.g., Allen *et al.*, 2003; Kessinger and Blumstein, 1997; Nagao and de Jong, 2007; Port, 1981). Vowel duration was used as the primary metric because the statistical analyses used in the current research require that the metric of speaking rate and VOT be mathematically independent. (Because the syllable duration measurement for a particular token includes VOT for that token, syllable duration is not mathematically independent of VOT.) However, syllable duration was also considered, as a secondary metric, in accord with the traditional definition of speaking rate as number of syllables produced per unit time. For all analyses presented in this paper, two versions were conducted; one that used vowel duration as the metric of rate and one that used syllable duration as the metric of rate. Analogous results were found in all cases. For ease of explication, we describe all analyses and results only using the vowel duration metric.

For the 2800 syllables measured, two exclusionary criteria were used to select a final set for statistical analysis. First, a token was excluded if there were production anomalies or if a clear burst onset and vowel offset could not be determined; 2.4% of the tokens were excluded on this basis. Second, a token was excluded if its syllable duration was greater than 799 ms. This criterion, which was established through informal listening, was intended to exclude tokens that were perceived as unnaturally long; 2.8% of the tokens were excluded on this basis. As a result of this selection process, 2654 syllables that spanned durations from 125 to 798 ms were used in subsequent analyses.

4. Reliability

One trained experimenter conducted all acoustic measurements. In order to determine cross-experimenter reliability, a different trained experimenter measured approximately 13% of the syllables (one randomly determined run from each talker). Correlations (Pearson's *r*) between the two experimenters' measurements were 0.99 for both VOT and vowel duration. The mean absolute differences between the experimenters' measurements were 2 ms (SD=2) for VOT and 12 ms (SD=16) for vowel duration.

B. Results

For each of the ten talkers, a linear function relating VOT to vowel duration was calculated using a least squares prediction method. To illustrate, Fig. 1 shows VOT (ms) as a function of vowel duration (ms) for two of the ten talkers; in this figure, each filled circle represents a single token of /ti/ and the solid lines represent the linear functions relating VOT to vowel duration. For both talkers, the tokens span a wide range of vowel durations, and VOT systematically increases as speaking rate decreases.[1]

Table I shows the slopes and intercepts of the ten individual talker functions, as well as the correlations (Pearson's *r*) between the functions and observed values as an index of goodness-of-fit. Slopes are shown as the increase in VOT (ms) per 100 ms increase in vowel duration and the intercepts are shown as VOT at the mean vowel duration produced across all talkers, which was 319 ms. The slopes of the individual talker functions measure the effect of speaking rate on VOT. The intercepts of the individual talker functions represent VOT at a given vowel duration; in other words, the intercepts of the individual talker functions measure VOT at a single speaking rate.

Consider first the slopes of the individual talker functions. Across the ten talkers, the slopes show wide variability. For example, given a 100 ms change in vowel duration, VOT

TABLE I. Slope, intercept, and correlation (Pearson's r) of the alveolar functions for individual talkers. Slopes are shown as VOT (ms)/100 ms vowel duration. The intercepts reflect VOT (ms) at 319 ms vowel duration. Experiment 1.

	Alveolar		
Talker	Slope	Intercept	r
E1M1	21	91	0.78
E1M2	23	79	0.81
E1M3	14	62	0.67
E1M4	8	78	0.69
E1M5	7	62	0.50
E1F1	16	77	0.68
E1F2	10	82	0.71
E1F3	22	86	0.70
E1F4	14	71	0.71
E1F5	12	87	0.74

TABLE II. Intercepts of the alveolar functions for individual talkers, defined as VOT (ms) at 200, 300, 400, and 500 ms vowel durations. Experiment 1.

	Alveolar intercepts			
	Vowel duration			
Talker	200	300	400	500
E1M1	66	87	108	129
E1M2	51	74	97	120
E1M3	45	59	73	87
E1M4	69	77	85	93
E1M5	54	61	68	75
E1F1	58	74	90	106
E1F2	71	81	91	101
E1F3	60	82	104	126
E1F4	54	68	82	96
E1F5	73	85	97	109

for talker E1M2 increases approximately three times as much as VOT for talker E1M4 (also shown in Fig. 1). Turning to the intercepts of the individual talker functions, VOT also varies considerably, spanning values from 62 to 91 ms. Inspection of these parameters suggests that the magnitude of the effect of rate on VOT does vary across talkers, and that talker differences in VOT are present for syllables produced at the same speaking rate.

A hierarchical linear modeling (HLM) analysis (Bryk and Raudenbush, 1992) was used in order to test the statistical significance of the variability in talkers' slopes and intercepts. One benefit of using an HLM analysis is that it allows us to compare the slope and intercept parameters across talkers while taking into account the entire set of data, which consisted of 2654 tokens. (A complete description of the HLM structure for all models presented in this paper is provided in the Appendix.) In terms of the talkers' slopes, results showed that the mean slope across talkers was non-zero [$t(9)=8.11$, $p<0.001$], confirming that VOT systematically increased as vowel duration increased (i.e., rate decreased) across the group of talkers. Critically, the results also showed that there was significant variability in the talkers' slopes [$\chi^2(9)=374.78$, $p<0.001$], indicating that how much VOT increased as rate decreased was not the same for all talkers. In terms of the talkers' intercepts, results confirmed that the mean intercept across talkers was non-zero [$t(9)=25.43$, $p<0.001$], and showed that there was significant variability in the talkers' intercepts [$\chi^2(9)=776.23$, $p<0.001$]. This finding indicates that talkers differed in their characteristic VOTs for utterances produced at the same speaking rate.

An additional set of analyses was performed in order to examine whether talker differences in VOT would be observed across a range of vowel durations, and not solely at the mean vowel duration produced across all talkers. The motivation for these analyses stems from the finding that there was significant variability in the slopes of the individual talker functions, with some functions intersecting within the measured range of vowel duration. As a consequence, even though talker differences in VOT were observed at the mean vowel duration, they will not necessarily be observed across a range of vowel durations. For these analyses, four intercepts (shown in Table II) were calculated for each talker corresponding to VOT (ms) at 200, 300, 400, and 500 ms vowel durations, these values span the range of greatest intersection among the individual functions. HLM analyses (see Appendix) confirmed that there was significant variability in talkers' intercepts at each vowel duration [in all cases; $\chi^2(9)>311.00$, $p<0.001$], indicating that the presence of talker differences in VOT is not contingent on speaking rate.

III. EXPERIMENT 2

Experiment 2 extends the findings from experiment 1 in three ways. First, we attempt to replicate the findings from the first experiment for the other two voiceless stops in English, labial /p/ and velar /k/. Second, we examine whether the effect of rate for a particular talker is stable across a change in place of articulation by comparing the slopes of the functions relating VOT to vowel duration for the labial and velar voiceless stops. Third, experiment 2 examines whether the contextual influence of place of articulation on VOT is itself talker-specific. As noted earlier, previous research has shown that, in general, VOT increases as place moves from front to back in the vocal tract (e.g., Lisker and Abramson, 1964). In the current experiment we examine whether the magnitude of the difference in VOT between /p/ and /k/ varies across individual talkers.

A. Method

1. Subjects

Ten talkers (five males, E2M1–E2M5; five females, E2F1–E2F5) who did not participate in experiment 1 were recruited from the Northeastern University community for this experiment. The talkers were native speakers of American English between 18 and 22 years of age with no history of speech or language disorders, and were either paid or received partial course credit for their participation.

TABLE III. Slope, intercept, and correlation (Pearson's r) of the labial and velar functions for individual talkers. Slopes are shown as VOT (ms)/100 ms vowel duration. The intercepts reflect VOT (ms) at 374 ms vowel duration. Experiment 2.

	Labial			Velar		
Talker	Slope	Intercept	r	Slope	Intercept	r
E2M1	9	60	0.55	6	103	0.32
E2M2	5	37	0.48	10	91	0.55
E2M3	25	83	0.80	20	99	0.81
E2M4	10	55	0.74	7	95	0.53
E2M5	3	30	0.42	4	86	0.48
E2F1	10	78	0.51	13	111	0.44
E2F2	10	64	0.77	9	93	0.71
E2F3	12	77	0.48	13	126	0.61
E2F4	3	57	0.30	6	81	0.58
E2F5	16	81	0.41	23	113	0.59

2. Recordings

The magnitude-production procedure described in experiment 1 was used to elicit multiple repetitions of the syllables /pi/ and /ki/ across a range of syllable durations. As in experiment 1, talkers produced eight runs of each syllable, with each run consisting of six repetitions at eight speaking rates. The order of the labial and velar syllables was counterbalanced across talkers. All recordings followed the procedure outlined for experiment 1.

In total, 7680 syllables (6 repetitions $\times$ 8 speaking rates $\times$ 8 runs $\times$ 10 talkers $\times$ 2 places of articulation) were recorded. All recordings were digitized at a sampling rate of 20 kHz using the CSL system. As in experiment 1, all syllables produced in the first block of the normal speaking rate for each run and the final repetition at each speaking rate were excluded from further analyses. Excluding these tokens left 5600 possible syllables (5 repetitions $\times$ 7 speaking rates $\times$ 8 runs $\times$ 10 talkers $\times$ 2 places of articulation) for acoustic analysis.

3. Acoustic measurements

The PRAAT speech analysis software was used to generate a waveform for each of the 5600 syllables. As in experiment 1, VOT, vowel duration, and syllable duration were calculated for each waveform, and two exclusionary criteria were used to select a final set of syllables for statistical analysis. First, a token was excluded if there were production anomalies or if a clear burst onset and vowel offset could not be determined; 7.4% of the tokens were excluded on this basis. Second, a token was excluded if its syllable duration was greater than 799 ms; 9.6% of the tokens were excluded on this basis. As a result of this selection process, 4646 syllables that spanned durations from 115 to 799 ms were used in subsequent analyses.[2]

4. Reliability

Two trained experimenters, who each measured a subset of the recorded tokens, conducted all acoustic measurements. To determine cross-experimenter reliability, a third trained experimenter measured one randomly determined run of /pi/ and /ki/ for each talker (approximately 13% of the tokens). Correlations (Pearson's r) between the two experimenters' measurements were 0.98 for VOT and 0.99 for vowel duration. The mean absolute differences between the experimenters' measurements were 4 ms (SD=6) for VOT and 29 ms (SD=27) for vowel duration.

B. Results

For each of the ten talkers, two linear functions relating VOT to vowel duration were calculated using a least squares prediction method, one for the labial syllables and one for the velar syllables.[3] Table III shows the slopes and intercepts of the individual talker functions, as well as the correlations (Pearson's r) between the functions and observed values as an index of goodness-of-fit. Slopes are shown as the increase in VOT (ms) per 100 ms increase in vowel duration and the intercepts are shown as VOT at the mean vowel duration produced across all talkers for the labial and velar tokens, which was 374 ms. Three sets of analyses were performed on the parameters specifying the individual talker functions. In the first set of analyses, we attempted to extend findings from experiment 1 to labial and velar voiceless stops. The second set of analyses examined whether, for a given talker, the magnitude of the effect of speaking rate on VOT is stable across place of articulation. The third set of analyses examined whether the contextual influence of place of articulation itself is talker-specific.

1. Replication

Following the structure used for experiment 1, HLM analyses were applied to the labial data (2481 tokens) and, separately, to the velar data (2165 tokens). As expected, the results showed that for both the labial and velar functions, the mean slope across talkers was significantly different from zero [$t(9)=5.05$, $p<0.001$ and $t(9)=5.74$, $p<0.001$; respectively] and the mean intercept across talkers was significantly different from zero [$t(9)=10.94$, $p<0.001$ and $t(9)=22.92$, $p<0.001$; respectively]. Moreover, there was significant variability in the slopes [$\chi^2(9)=481.47$, $p<0.001$ and $\chi^2(9)=332.37$, $p<0.001$; respectively] and intercepts

TABLE IV. Intercepts of the labial and velar functions for individual talkers, defined as VOT (ms) at 200, 300, 400, and 500 ms vowel durations. Experiment 2.

	Labial intercepts				Velar intercepts			
	Vowel duration				Vowel duration			
Talker	200	300	400	500	200	300	400	500
E2M1	44	53	62	71	93	99	105	111
E2M2	28	33	38	43	74	84	94	104
E2M3	40	65	90	115	64	84	104	124
E2M4	37	47	57	67	83	90	97	104
E2M5	24	27	30	33	79	83	87	91
E2F1	60	70	80	90	88	101	114	127
E2F2	47	57	67	77	77	86	95	104
E2F3	57	59	81	93	103	116	129	142
E2F4	51	54	57	60	71	77	83	89
E2F5	53	69	85	101	73	96	119	142

$[\chi^2(9)=1559.82, p<0.001$ and $\chi^2(9)=957.19, p<0.001$; respectively] of the individual talker functions. These results extend the findings from experiment 1 to labial and velar voiceless stops, confirming not only the presence of talker differences in VOT at a single speaking rate, but also that the effect of speaking rate on VOT varied significantly across talkers. As in experiment 1, we also tested for talker differences in VOT across a range of vowel durations (i.e., speaking rates) for both the labial and velar stops (see Table IV). HLM analyses showed that there was significant variability in talkers' intercepts at each vowel duration [in all cases; $\chi^2(9)>274.00, p<0.001$].

2. Stability of the effect of speaking rate on VOT for individual talkers

Results reported above indicate that the magnitude of the effect of speaking rate on VOT varies across talkers for a given voiceless stop. This finding highlights a source of systematic variability in the speech signal in that how much VOT increases as rate decreases can vary from talker to talker. Here we examine a potential source of stability in the speech signal by comparing the effect of rate on VOT for a given talker across a change in place of articulation. In this analysis, we considered the slopes of the labial and velar functions for individual talkers. If, for a given talker, the effect of rate on VOT is stable across a change in place of articulation, then the slopes of the labial and velar functions will be approximately the same. Inspection of the labial and velar slopes, shown in Table III, suggests that this may be the case in that the difference between the labial and velar slopes for any given talker is quite small. To illustrate, Fig. 2 displays VOT (ms) as a function of vowel duration (ms) at both places of articulation for one of the ten talkers. VOT increases as speaking rate decreases for both the labial and velar tokens, and does so to approximately the same degree.

In order to examine the statistical significance of the difference between the labial and velar slopes for individual talkers, we conducted an additional HLM analysis nesting the labial and velar slopes within talkers. Results from this analysis revealed that there was no significant variability across talkers in the difference between the labial and velar slopes $[\chi^2(9)=1.60, p>0.50]$, which indicates that the effect of speaking rate on VOT for a given talker is the same for labial and velar voiceless stops.

3. Effect of place of articulation on VOT for individual talkers

In this set of analyses, we examined whether the magnitude of the difference between labial and velar VOTs varies significantly across talkers. To quantify the effect of place of articulation on VOT for each talker, we used the difference between the labial and velar intercepts, with the intercept defined as VOT at 374 ms vowel duration (shown in Table III). Because the results reported above indicate that the slopes of the labial and velar functions within a given talker are not statistically different (and thus the functions are approximately parallel), using a single point on each function as the basis of comparison is valid in that the difference between labial and velar VOTs will be the same for any value along the *x*-axis.

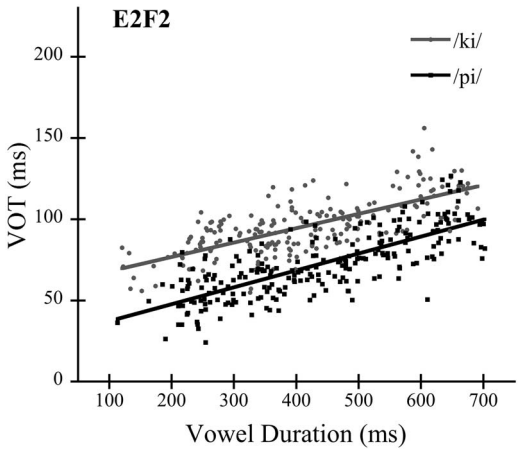

FIG. 2. (Color online) VOT (ms) as a function of vowel duration (ms) for talker E2F2 at two places of articulation, labial /pi/ and velar /ki/. Each black square represents one token of /pi/ and each gray circle represents one token of /ki/. The solid lines represent the calculated function relating VOT to vowel duration at each place of articulation.

As expected, the labial intercept was located at a shorter VOT than the velar intercept for each talker, resulting in a reliable effect of place of articulation on VOT for the group of talkers [mean difference=37.60 ms; $t(9)=9.06$, $p<0.001$]. To examine the central question of whether the magnitude of the difference in labial and velar intercepts varied significantly across talkers, an HLM analysis was used to nest the labial and velar intercepts within talkers. The HLM results showed that there was no significant variability in the difference between the labial and velar intercepts across individual talkers [$\chi^2(9)=2.97$, $p>0.50$]. These results indicate that the effect of place of articulation on VOT does not vary across individual talkers.

IV. DISCUSSION

Previous research has provided evidence for talker-specific variability in the acoustic-phonetic information used to convey individual speech segments (e.g., Espy-Wilson *et al.*, 2000; Newman *et al.*, 2001; Peterson and Barney, 1952; Zue and Laferriere, 1979). As a case in point, recent findings indicate that talkers differ in VOTs produced for voiceless stop consonants; some talkers produce characteristically shorter VOTs than other talkers (Allen *et al.*, 2003). The results from the current research confirm this finding and, most importantly, extend it by examining potential talker specificity in how two contextual variables, speaking rate and place of articulation, influence VOT.

In terms of speaking rate, previous research has shown that as speaking rate decreases (and syllables become longer), VOT systematically increases (e.g., Kessinger and Blumstein, 1997; Volaitis and Miller, 1992). The current results replicated this finding for all three voiceless stops, /p/, /t/, and /k/. However, the results also showed that for each stop, the magnitude of the increase in VOT for a given change in speaking rate varied significantly across talkers. This finding, which indicates that the effect of speaking rate on VOT is talker-specific, highlights a source of systematic variability in the speech signal. Further, the results from experiment 2, which compared /p/ and /k/, showed that for a given talker, the magnitude of the rate effect on VOT remained constant across a change in place of articulation. This finding highlights a source of stability in the speech signal at the individual talker level, in that how rate influences VOT for one voiceless stop is the same for a different voiceless stop.

In terms of place of articulation, the results from experiment 2 showed that for each talker VOTs for /p/ were shorter than VOTs for /k/, in line with previous research (e.g., Lisker and Abramson, 1964). Critically, the results also indicated that the magnitude of displacement between VOTs for /p/ and /k/ did not vary significantly across talkers. Thus, unlike speaking rate, the contextual influence of place of articulation on VOT appears not to be talker-specific.

Taken together, these findings have implications for theoretical accounts of speech perception. It has been established that listeners retain talker-specific acoustic-phonetic information in memory (e.g., Goldinger, 1998) and that familiarity with a particular talker's speech can facilitate word recognition (e.g., Nygaard *et al.*, 1994). Furthermore, findings from literature on perceptual learning in speech suggest that the benefits of talker familiarity observed at the word level might result, at least in part, from talker-specific effects at a prelexical level of representation (e.g., Eisner and McQueen, 2005; Kraljic and Samuel, 2007). Of particular relevance to the current research, Allen and Miller (2004) showed that listeners could learn that one talker produces a particular voiceless stop with characteristically short VOTs and a different talker produces the same stop with characteristically long VOTs.

This finding raises the possibility that listeners may customize stop voicing categories based on individual talkers' characteristic VOTs. However, given contextual influences on VOT, listeners would need to consider a talker's characteristic VOTs not in an absolute manner, but with respect to context. Indeed, it is well established that at a general level, listeners do process VOT in relation to numerous contextual factors, including both speaking rate and place of articulation. These contextual influences systematically affect both the boundaries between phonetic categories and the best exemplars of a given phonetic category (e.g., Lisker and Abramson, 1970; Miller and Volaitis, 1989; Summerfield, 1981; Volaitis and Miller, 1992). We do not yet know whether such context-dependent processing is tuned to the speech of individual talkers, but the results of the current experiments place constraints on the type of exposure listeners might require for such perceptual tuning.

Specifically, the current data suggest that exposure to a talker's VOTs for a voiceless stop at one speaking rate would not optimally inform the listener as to that talker's VOTs for the stop at a novel speaking rate. Because the magnitude of the rate effect systematically varies across talkers, in order to accommodate the contextual influence of rate on VOT listeners would need to learn, for a given talker, how much VOT changes as a function of speaking rate; that is, ascertain the slope of the function relating VOT to rate. However, because the magnitude of the rate effect on VOT for a given talker is stable across a change in place of articulation, tracking the contextual influence of rate in the context of one voiceless stop could potentially inform the listener as to how this contextual influence operates for other voiceless stops in similar phonetic environments.

The current data also suggest that listeners might not need to track the contextual influence of place of articulation *per se* on VOT at the level of individual talkers. Because the magnitude of the place effect does not systematically differ across individual talkers, listeners could rely on more general knowledge, perhaps specific to their language (e.g., Cho and Ladefoged, 1999), to inform them as to how VOT shifts as a function of place of articulation. As a consequence, for a given speaking rate and a similar phonetic environment, learning a particular talker's characteristic VOTs for one voiceless stop may inform the listener as to that talker's VOTs for voiceless stops with a different place of articulation.

In sum, the present data provide basic information on how two contextual factors influence VOT at a talker-specific level and, in so doing, point to constraints on how listeners

might accommodate such contextual variation when customizing phonetic categories for an individual talker's speech. Future research is aimed at examining the nature and extent of such perceptual fine-tuning.

ACKNOWLEDGMENTS

This research was supported by NIH Grant No. R01 DC000130 to J.L.M. and by NIH Grant No. F31 DC009114 (Ruth L. Kirschstein NRSA for Individual Predoctoral Fellows) to R.M.T., and formed the basis for part of the doctoral dissertation of R.M.T. at Northeastern University. We thank Eliza Floyd, Katrina Smith, and Janelle LaMarche for assistance with the acoustic measurements, and we thank the reviewers for their helpful comments and suggestions.

APPENDIX

HLM analyses (Bryk and Raudenbush, 1992) were used in the current research because they allow examination of stable individual differences around group level patterns. HLM analyses are based on linear regression techniques; however, unlike standard regression models, HLM analyses are well suited for examination of data from repeated-measures designs. All of the analyses reported in this paper are based on two HLM structures. The first HLM structure was used to compare slope and intercept parameters within a single place of articulation. This model was used in experiment 1 to compare the slopes and intercepts of the alveolar functions and in experiment 2 to compare the slopes and intercepts of the labial functions and, separately, the velar functions. The second HLM structure was used to compare the slope and intercept parameters across place of articulation. This structure was used in experiment 2 to compare the slopes of the labial functions to the slopes of the velar functions, and, separately, to compare the intercepts of the labial functions to the intercepts of the velar functions. The details of each type of model are presented in turn.

In order to test the statistical significance of the variability in talkers' slopes and intercepts within a single place of articulation, all of the tokens for the particular analysis were nested within each of the ten talkers as follows.

For the level-1 model,

$$\mathrm{VOT}_{ij} = \beta_{0j} + \beta_{1j}\ (\text{vowel duration}) + r_{ij}.$$

For the level-2 model,

$$\beta_{0j} = \gamma_{00} + u_{0j},$$

$$\beta_{1j} = \gamma_{10} + u_{1j}.$$

With this structure, VOT is specified as a function of vowel duration, while incorporating the fact that sets of individual tokens are associated with specific talkers. Importantly, the level-2 model allows the intercepts (β_{0j}) and slopes (β_{1j}) of the level-1 model to vary across talkers. That is, the level-2 model estimates the mean intercept (γ_{00}) and mean slope (γ_{10}) values across talkers while also testing if significant variability exists in these parameters (u_{0j} and u_{1j}, respectively) as a function of stable talker differences.

In order to examine the slopes (or intercepts) across place of articulation, the labial and velar slopes (or intercepts) were nested within talkers as follows.

For the level-1 model,

$$\text{slope (or intercept)}_{ij} = \beta_{0j} + \beta_{1j}\ (\text{place of articulation}) + r_{ij}.$$

For the level-2 model,

$$\beta_{0j} = \gamma_{00},$$

$$\beta_{1j} = \gamma_{10} + u_{1j}.$$

With this structure, slope (or intercept) is specified as a function of place of articulation, while incorporating the fact that pairs of individual values are associated with specific talkers. In order to allow place of articulation to be examined as a linear variable, labial and velar were coded as 0 and 1, respectively. Using this method, the slope parameter of the HLM (β_{1j}) does not indicate the absolute slope (or intercept) for either the labial or velar functions; rather, it represents the difference between the labial and velar slopes (or intercepts). The level-2 model allows the slope (β_{1j}) of the level-1 model to vary across talkers; accordingly, the model estimates the mean difference between the labial and velar slopes (or intercepts) across talkers (γ_{10}) while also testing if significant variability exists in this parameter (u_{1j}).

[1]As described in the main text, one assumption of the statistical analyses used in the current research is that VOT and the metric of speaking rate (e.g., vowel duration) are mathematically independent. An additional assumption is that the relationship between VOT and the metric of speaking rate can be adequately described as linear. For the range of speaking rates that occur in typical speech, there is no established theoretical relationship between VOT and speaking rate. To ensure that a linear function would adequately describe the relationship between VOT and speaking rate for each of the ten talkers in the current study, we compared three different functions using both vowel duration and syllable duration as the metric of speaking rate: a linear function, an exponential function (with VOT on a linear scale and speaking rate on a log scale), and a power function (with both VOT and speaking rate on a log scale). In all 20 cases (10 talkers $\times 2$ metrics of speaking rate), the correlation coefficient (Pearson's r) associated with the linear function was statistically significant, and, critically, was greater than or statistically equal to the correlation coefficient of the exponential and power functions.

[2]As is apparent, a larger percentage of tokens was excluded from statistical analysis in experiment 2 than experiment 1, due both to an increased proportion of anomalous/immeasurable tokens and to an increased proportion of extremely long tokens. The underlying reason for the difference across experiments is not known. Importantly, even with the exclusion, the number of tokens available for statistical analysis in both experiments was very large.

[3]As in experiment 1, we confirmed that the relationship between VOT and the metric of speaking rate could be adequately described as linear for the ten talkers examined here. For each place of articulation, we examined the correlation coefficient (Pearson's r) of three different functions (linear, exponential, and power) using both vowel duration and syllable duration as the metric of speaking rate. In all 40 cases (10 talkers $\times 2$ places of articulation $\times 2$ metrics of speaking rate), the correlation coefficient of the linear function was statistically significant and, critically, was better than or statistically equal to the correlation coefficient of the exponential and power functions.

Adams, S. G., Weismer, G., and Kent, R. (**1993**). "Speaking rate and speech movement velocity profiles," J. Speech Hear. Res. **36**, 41–54.

Allen, J. S., and Miller, J. L. (**2004**). "Listener sensitivity to individual talker differences in voice-onset-time," J. Acoust. Soc. Am. **115**, 3171–3183.

Allen, J. S., Miller, J. L., and DeSteno, D. (**2003**). "Individual talker differ-

ences in voice-onset-time," J. Acoust. Soc. Am. **113**, 544–552.
Boersma, P. (**2001**). "Praat, a system for doing phonetics by computer," Glot International **5**, 341–345.
Bradlow, A. R., and Bent, T. (**2008**). "Perceptual adaptation to non-native speech," Cognition **106**, 707–729.
Bradlow, A. R., and Pisoni, D. B. (**1999**). "Recognition of spoken words by native and non-native listeners: Talker-, listener-, and item-related factors," J. Acoust. Soc. Am. **106**, 2074–2085.
Bryk, A. S., and Raudenbush, S. W. (**1992**). *Hierarchical Linear Models: Applications and Data Analysis Methods* (Sage, Newbury Park, CA).
Byrd, D. (**1992**). "Preliminary results on speaker-dependent variation in the TIMIT database," J. Acoust. Soc. Am. **92**, 593–596.
Cho, T., and Ladefoged, P. (**1999**). "Variations and universals in VOT: Evidence from 18 languages," J. Phonetics **27**, 207–229.
Clarke, C. M., and Garrett, M. F. (**2004**). "Rapid adaptation to foreign-accented English," J. Acoust. Soc. Am. **116**, 3647–3658.
Crystal, T. H., and House, A. S. (**1982**). "Segmental durations in connected speech signals: Preliminary results," J. Acoust. Soc. Am. **72**, 705–716.
Eisner, F., and McQueen, J. M. (**2005**). "The specificity of perceptual learning in speech processing," Percept. Psychophys. **67**, 224–238.
Espy-Wilson, C. Y., Boyce, S. E., Jackson, M., Narayanan, S., and Alwan, A. (**2000**). "Acoustic modeling of American English /r/," J. Acoust. Soc. Am. **108**, 343–356.
Goldinger, S. D. (**1996**). "Words and voices: Episodic traces in spoken word identification and recognition memory," J. Exp. Psychol. Learn. Mem. Cogn. **22**, 1166–1183.
Goldinger, S. D. (**1998**). "Echoes of echoes? An episodic theory of lexical access," Psychol. Rev. **105**, 251–279.
Hashi, M., Honda, K., and Westbury, J. R. (**2003**). "Time-varying acoustic and articulatory characteristics of American English [ɹ]: A cross-speaker study," J. Phonetics **31**, 3–22.
Hillenbrand, J., Getty, L. A., Clark, M. J., and Wheeler, K. (**1995**). "Acoustic characteristics of American English vowels," J. Acoust. Soc. Am. **97**, 3099–3111.
Kessinger, R. H., and Blumstein, S. E. (**1997**). "Effects of speaking rate on voice-onset time in Thai, French, and English," J. Phonetics **25**, 143–168.
Klatt, D. H. (**1975**). "Voice onset time, frication, and aspiration in word-initial consonant clusters," J. Speech Hear. Res. **18**, 686–706.
Klatt, D. H. (**1976**). "Linguistic uses of segmental duration in English: Acoustic and perceptual evidence," J. Acoust. Soc. Am. **59**, 1208–1221.
Kraljic, T., and Samuel, A. G. (**2007**). "Perceptual adjustments to multiple speakers," J. Mem. Lang. **56**, 1–15.
Kuehn, D. P., and Moll, K. L. (**1976**). "A cineradiographic study of VC and CV articulatory velocities," J. Phonetics **4**, 303–320.
Lane, H., and Grosjean, F. (**1973**). "Perception of reading rate by speakers and listeners," J. Exp. Psychol. **97**, 141–147.
Lisker, L., and Abramson, A. S. (**1964**). "A cross-language study of voicing in initial stops: Acoustical measurements," Word **20**, 384–422.
Lisker, L., and Abramson, A. S. (**1967**). "Some effects of context on voice onset time in English stops," Lang Speech **10**, 1–28.
Lisker, L., and Abramson, A. S. (**1970**). "The voicing dimension: Some experiments in comparative phonetics," in *Proceedings of the Sixth International Congress of Phonetic Sciences* (Academia, Prague), pp. 563–567.
Matthies, M., Perrier, P., Perkell, J. S., and Zandipour, M. (**2001**). "Variation in anticipatory coarticulation with changes in clarity and rate," J. Speech Lang. Hear. Res. **44**, 340–353.
McClean, M. D. (**2000**). "Patterns of orofacial movement velocity across variations in speech rate," J. Speech Lang. Hear. Res. **43**, 205–216.
Miller, J. L., and Volaitis, L. E. (**1989**). "Effect of speaking rate on the perceptual structure of a phonetic category," Percept. Psychophys. **46**, 505–512.
Miller, J. L., Green, K. P., and Reeves, A. (**1986**). "Speaking rate and segments: A look at the relation between speech production and speech perception for the voicing contrast," Phonetica **43**, 106–115.
Miller, J. L., Grosjean, F., and Lomanto, C. (**1984**). "Articulation rate and its variability in spontaneous speech: A reanalysis and some implications," Phonetica **41**, 215–225.
Nagao, K., and de Jong, K. (**2007**). "Perceptual rate normalization in naturally produced rate-varied speech," J. Acoust. Soc. Am. **121**, 2882–2898.
Newman, R. S., Clouse, S. A., and Burnham, J. L. (**2001**). "The perceptual consequences of within-talker variability in fricative production," J. Acoust. Soc. Am. **109**, 1181–1196.
Nygaard, L. C., and Pisoni, D. B. (**1998**). "Talker-specific learning in speech perception," Percept. Psychophys. **60**, 355–376.
Nygaard, L. C., Sommers, M. S., and Pisoni, D. B. (**1994**). "Speech perception as a talker-contingent process," Psychol. Sci. **5**, 42–46.
Palmeri, T. J., Goldinger, S. D., and Pisoni, D. B. (**1993**). "Episodic encoding of voice attributes and recognition memory for spoken words," J. Exp. Psychol. Learn. Mem. Cogn. **19**, 309–328.
Peterson, G. E., and Barney, H. L. (**1952**). "Control methods used in a study of the vowels," J. Acoust. Soc. Am. **24**, 175–184.
Picheny, M. A., Durlach, N. I., and Braida, L. D. (**1986**). "Speaking clearly for the hard of hearing II: Acoustic characteristics of clear and conversational speech," J. Speech Hear. Res. **29**, 434–446.
Port, R. F. (**1981**). "Linguistic timing factors in combination," J. Acoust. Soc. Am. **69**, 262–274.
Port, R. F., and Rotunno, R. (**1979**). "Relation between voice-onset time and vowel duration," J. Acoust. Soc. Am. **66**, 654–662.
Robb, M., Gilbert, H., and Lerman, J. (**2005**). "Influence of gender and environmental setting on voice onset time," Folia Phoniatr Logop **57**, 125–133.
Summerfield, Q. (**1981**). "Articulatory rate and perceptual constancy in phonetic perception," J. Exp. Psychol. Hum. Percept. Perform. **7**, 1074–1095.
Volaitis, L. E., and Miller, J. L. (**1992**). "Phonetic prototypes: Influence of place of articulation and speaking rate on the internal structure of voicing categories," J. Acoust. Soc. Am. **92**, 723–735.
Weismer, G. (**1979**). "Sensitivity of voice-onset time (VOT) measures to certain segmental features in speech production," J. Phonetics **7**, 197–204.
Zue, V. W., and Laferriere, M. (**1979**). "Acoustic study of medial /t,d/ in American English," J. Acoust. Soc. Am. **66**, 1039–1050.

General perceptual contributions to lexical tone normalization

Jingyuan Huang[a] and Lori L. Holt
Department of Psychology and the Center for the Neural Basis of Cognition, Carnegie Mellon University, 5000 Forbes Avenue, Pittsburgh, Pennsylvania 15213

(Received 3 November 2008; revised 1 April 2009; accepted 5 April 2009)

Within tone languages that use pitch variations to contrast meaning, large variability exists in the pitches produced by different speakers. Context-dependent perception may help to resolve this perceptual challenge. However, whether speakers rely on context in contour tone perception is unclear; previous studies have produced inconsistent results. The present study aimed to provide an unambiguous test of the effect of context on contour lexical tone perception and to explore its underlying mechanisms. In three experiments, Mandarin listeners' perception of Mandarin first and second (high-level and mid-rising) tones was investigated with preceding speech and non-speech contexts. Results indicate that the mean fundamental frequency (*f*0) of a preceding sentence affects perception of contour lexical tones and the effect is contrastive. Following a sentence with a higher-frequency mean *f*0, the following syllable is more likely to be perceived as a lower frequency lexical tone and vice versa. Moreover, non-speech precursors modeling the mean spectrum of *f*0 also elicit this effect, suggesting general perceptual processing rather than articulatory-based or speaker-identity-driven mechanisms. © *2009 Acoustical Society of America.*
[DOI: 10.1121/1.3125342]

PACS number(s): 43.71.An, 43.66.Ba, 43.71.Hw [RSN] Pages: 3983–3994

I. INTRODUCTION

A. Speaker normalization effects in phonetic categorization

The acoustics of speech are notoriously variable across speakers. Some of this variability is the result of anatomical and physiological differences in the instrument of speech production, such as larger (and differently-proportioned) vocal tracts of male vs female speakers. Other variability such as foreign accent and dialect stems from linguistic and sociolinguistic experience. A result of all this variability is that phonetic categories and decision bounds founded on experience across a variety of talkers may produce miscategorization in application to any *particular* talker. Thus, it has long been suggested that speech categories must be tuned dynamically to the speech of the current talker, for example, by shifting the representation of the individual sounds or by influencing the relevant phonetic category space to which sounds are mapped (Ladefoged and Broadbent 1957). Within the field of speech perception, the accommodation of talker-specific characteristics is referred to as "talker" or "speaker" normalization (e.g., Johnson and Mullennix, 1997).

One of the most influential experiments testing speaker normalization comes from Ladefoged and Broadbent (1957), who demonstrated that manipulating the voice in which a precursor sentence is spoken has a major effect on how listeners categorize a following vowel. Using speech synthesis, Ladefoged and Broadbent (1957) manipulated the frequencies of the first two formants of the sentence "Please say what this word is," resulting in six sentences that sounded like they were spoken by different talkers. Following these context sentences, participants heard synthesized "bVt" target syllables varying in their first two formant frequencies and approximating "bit," "bet," "bat," or "but." Listeners' vowel categorization was influenced by the characteristics of the preceding sentence context. For example, a vowel that was identified as "bit" by 88% of participants in context of the original sentence was identified as "bet" by 90% of participants when the sentence was manipulated to have a lower F1 frequency. In all, these results suggest that extrinsic context interacts with the intrinsic acoustic properties of a speech segment to tune how listeners categorize acoustic speech signals.

Ladefoged and Broadbent (1957) proposed that listeners recover talkers' vocal tract dynamics from context sentences and use this information to scale speech perception, mapping phonetic information available from the vowels of the context sentence onto a F1 × F2 space, and using this information to identify the target vowels by their relative position in this space. Further, Ladefoged and Broadbent (1957) proposed that this re-mapping be considered a speech-specific calibration, "best understood by the reference to the articulatory process in speech" (p. 103). In other words, listeners extract a speaker's vocal tract information from context and normalize perception according to the perceived vocal tract.

A series of subsequent experiments by Watkins and Makin (1994, 1996) calls into question the necessity of a speech-specific interpretation. Watkins and Makin (1994, 1996) conducted several variants of the Ladefoged and Broadbent (1957) task, substituting the "Please say what this word is" with noise analogs and context sentences played backwards. Critically, the effect of context persisted even when contexts did not preserve vocal tract or articulatory information, suggesting that the link between articulatory in-

[a]Author to whom correspondence should be addressed. Electronic mail: jingyuan@andrew.cmu.edu

formation and speaker normalization effects, as posited by Ladefoged and Broadbent (1957), may be tenuous.

One specific alternative interpretation for the shifts in speech categorization described as speaker normalization is that listeners tune perception according to the general distributional characteristics of preceding acoustic context. To make this concrete, it is helpful to consider again the effect reported by Ladefoged and Broadbent (1957). In general, productions of the vowels /I/ and /ɛ/ differ in F1 frequency with /I/ having a lower-frequency F1 (Peterson and Barney, 1952). Presumably, listeners have formed categories for these vowels based on regularities across speakers (or at least the typical values that define the contrasts in relation to other vowels). As a result, when a vowel is encountered with a low F1 it is categorized more often as /I/ as in "bit." However, the actual value that corresponds to a "low F1" appears to be relative to speech produced by a particular talker. As Ladefoged and Broadbent (1957) demonstrated, when the range of F1 in the context sentence is lowered, the same F1 value encourages /ɛ/ as in "bet" categorization. Considering the results of Watkin and Makins (1994, 1996), it is possible that the spectral change in mean frequency of F1, rather than its influence on perceived speaker identity or the articulatory information it may convey, is responsible for the observed effects on speech categorization. If so, effects of speaker normalization potentially may arise from general perceptual processes.

Some recent results investigating the influence of distributions of spectral energy on phonetic categorization support this possibility. Holt (2005) found that sentence-length sequences of non-speech sine-wave tones have a strong influence on categorization of subsequent speech. In these experiments, the sine-wave tone sequences sample a region of spectral energy defined with a particular mean acoustic frequency and variability about this mean; stimuli vary on every trial but sample a consistent region of the spectral space and respect the distributional characteristics that define a condition. Therefore, idiosyncracies of acoustic sampling cannot drive any observed effects of context. For these non-speech "acoustic histories" to impact speech categorization, the long-term distribution characteristics of the acoustic spectra must play a role. Much like the increments and decrements to F1 frequency that Ladefoged and Broadbent (1957) used to manipulate perceived talker in their synthesized context sentences, Holt (2005) made conditions in which the non-speech tone distributions sampled higher- and lower-frequency spectral regions. The resulting stimuli sound something like a higher- and lower-frequency melodies followed by a speech token. Listeners simply identified the speech sound. Holt (2005, 2006a, 2006b) found that the mean frequency of the preceding spectral distribution of non-speech tones exerts a strong influence on speech categorization.

Intriguingly, the speech categorization shifts produced by these simple sine-wave tone sequences mirror the directionality of the influence of acoustic manipulations to sentence contexts and their corresponding influence on speech categorization reported by Ladefoged and Broadbent (1957; see also Watkins and Makin, 1994). Specifically, they are contrastive. A lower frequency context, whether produced by decrementing the mean F1 frequency of a sentence or by shifting the mean frequency of a distribution of non-speech sine-wave tones to lower frequencies, influences listeners' speech categorization by pushing it toward higher-frequency alternatives [e.g., from /I/ to /ɛ/ in the case of the Ladefoged and Broadbent (1957) results]. Despite the commonality in their influence on speech categorization, it is important to highlight the differences in the information available in these two sets of contexts. Unlike the sentence contexts of Ladefoged and Broadbent (1957), the acoustic histories of Holt (2005, 2006a, 2006b) were composed entirely of non-speech stimuli, providing no information about vocal tract characteristics of the speaker, no sampling of the English phonetic space, and no reference to a human voice whatsoever. Nevertheless, they strongly influenced speech categorization. Listeners thus have proven to be very sensitive to the longer-term characteristics of the acoustic signal and adjust perception of speech in relation to statistical regularity in prior acoustic input, even when that input is non-speech. Whatever the mechanisms involved (see Holt, 2006b for speculation on mechanism), they must be rather broadly operative.

The prospect that general auditory processes not specific to speech and not requiring information about articulatory gestures or human vocal tracts may account for effects described as speaker normalization invites the possibility that the commonalities among the effects observed thus far might be applied to make predictions for other normalization challenges in speech perception. From these prior experiments (Holt, 2005, 2006a, 2006b), we would predict spectrally (or temporally, Wade and Holt, 2005) contrastive effects. In addition, they may be elicited by non-speech, as well as speech, precursors. Moreover, given the proposed generality of the auditory processing involved, we should expect effects to generalize beyond English to be present among native listeners of other languages.

In the present work, we exploit the perceptual challenges of lexical tone normalization in Mandarin Chinese listeners' perception to investigate these predictions. We first review the literature of lexical tone normalization in light of the possibility that contrastive general mechanisms may play a role. We then present three experiments to test the predictions outlined above.

B. Speaker normalization in lexical tones

Tone languages use pitch to contrast meaning. For example, Mandarin Chinese has four different lexical tones: high-level tone (tone 1), mid-rising tone (tone 2), low-falling-rising tone (tone 3), and high-falling tone (tone 4) (Ladefoged and Maddieson, 1996). As can be seen in Fig. 1, the *f*0 of Mandarin words changes mean *f*0 frequency (height) and contour (change in frequency) to shift word identity. The *f*0 trajectories are plotted in Fig. 1 for a single isolated syllable spoken by one talker. The large *f*0 differences across lexical tones in these circumstances belie the variability present in more natural utterances. In fact, the exact nature of the *f*0 characteristics of Mandarin words is highly variable across utterances and speakers. Thus, some

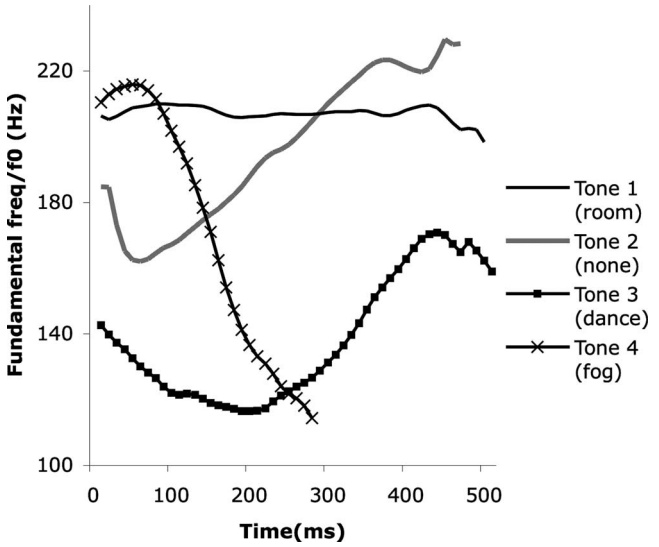

FIG. 1. *F*0 contour of Mandarin tones in the isolated syllable /wu/, measured from the speaker recorded to create stimuli for the present experiments. Changes in tone change the meaning of the syllable, as indicated by the English translations in the figure legend.

of the same perceptual challenges exist for distinguishing lexical tones across speakers and contexts that exist for phonetic categorization across talkers. For example, a lexical tone with a low frequency (like tone 3) that is produced by a higher-frequency voice might have an *f*0 similar to a higher-frequency lexical tone (like tone 2) produced by a lower-frequency voice. In addition, contours are relatively flatter and less distinguishable in fluent speech. Production studies demonstrate that Mandarin tones vary according to the adjacent tones in running speech, and the amount of deviation depends on the nature of the tonal context (Xu, 1994, 1997). The perceptual challenge for listeners is to uncover the intended lexical tone in the face of this acoustic variability. Mirroring the literature for phonetic categorization, several studies have investigated how the perceptual system might "normalize" lexical tones across voices.

In an early study exploring tone normalization, Leather (1983) tested perception of syllables produced with Mandarin's tone 1 and tone 2 following natural sentences spoken by two different speakers. Native Mandarin Chinese listeners labeled acoustically identical target syllables with different lexical tones when targets were preceded by sentence contexts from different speakers, leading Leather (1983) to suggest that perception of lexical tones depends on perceived speaker identity. However, the descriptive data analysis showed that the influence of context was inconsistent across listeners and no inferential statistical analysis was applied because of the small ($N=5$) sample. In addition, little information of the direction of perceptual shift was provided, making it difficult to judge the directionality of any potential influence of context on lexical tone perception from these data.

More recent studies have examined the effect of context on Mandarin tone perception in paired syllables (Lin and Wang, 1985; Fox and Qi, 1990). In Lin and Wang's (1985) study, the *f*0 of the first syllable was held constant with a typical tone 1 *f*0 value (high-level) while the onset *f*0 of second syllable was manipulated across frequencies. Native Mandarin Chinese participants identified the tone of first syllable as tone 1 (high-level) or tone 2 (mid-rising). Results showed that as the onset *f*0 of the second syllable increased, participants were more likely to label the first syllable as tone 2. Using a similar paradigm, Fox and Qi (1990) examined perception of a series of Mandarin Chinese syllables that varied in *f*0 onset frequency from tone 1 to tone 2 in isolation and paired with a preceding syllable with a fixed *f*0 typical of tone 1 or tone 2. Native Chinese and native English listeners identified the tone category of second syllable.[1] Contrasting with Lin and Wang's (1985) findings, there was only a small and inconsistent difference between perception of syllables in isolation and in context and the effect was assimilatory, not contrastive.[2] Interestingly, the observed perceptual pattern was similar for both native (Mandarin) and non-native (English) participant groups.

These early studies examined perception of contour tones, which varied in both *f*0 frequency (height) and *f*0 contour (the change of *f*0) across the syllable. Since the results provided fairly inconsistent evidence for context-dependence, some researchers have suggested that listeners may rely mostly on intrinsic *f*0 contour information of the target syllable and much less on extrinsic information from context in perceiving contour lexical tones (Moore and Jongman, 1997).

Effects of context are much more evident among level tones that vary in *f*0 height but have similar contours. Two studies (Wong and Diehl, 2003; Francis *et al.*, 2006) have provided clear demonstrations of context-dependence in Cantonese level lexical tone perception. Wong and Diehl (2003) examined three level tones from Cantonese (tone 1: high-level tone, tone 3: mid-level tone, and tone 6: low-level tone; with relatively flat *f*0 contours and differentiated primarily by mean *f*0 frequency) as target stimuli. When listeners judged the identity of these tones in manipulated natural speech contexts, the same target stimuli were identified as tone 1 (high-level) 99.5% of the time with a low-frequency context and tone 6 (low-level) 95.8% of the time with a higher-frequency context. The same stimuli were identified as mid-level tone 3 91.9% of the time when the context had an intermediate mean *f*0 frequency. Francis *et al.* (2006) used a similar paradigm and also found that target stimuli were more likely to be perceived as a low level tone with a high-frequency synthesized context whereas the same stimuli were perceived as a high level tone with a lower-*f*0 synthesized context.

In Mandarin tones, Moore and Jongman (1997) examined perception of syllables varying from tone 2 (mid-rising) to tone 3 (low-falling-rising). When spoken in isolation, these tones have similar *f*0 contours, but differ in *f*0 height, the mean *f*0 frequency across the syllable. Preceding sentences recorded from two different speakers with different mean *f*0s, *f*0 turning points (the duration from syllable onset to the point of change in *f*0 direction) and Δf0s (the difference in *f*0 from onset to turning point) exerted a strong influence on Mandarin tone perception. Specifically, whereas perception of target stimuli varying only in *f*0 turning point was not influenced by preceding sentences, perception of tar-

gets varying in $\Delta f0$ was strongly context-dependent. Moreover, the effect was contrastive with respect to mean $f0$.[3] Stimuli were identified as tone 2 (mid-rising) in a low $f0$ speaker context and identification shifted to tone 3 (low-falling-rising) when there was a high $f0$ context. Since context sentences were recorded from two different talkers, Moore and Jongman (1997) argued that listeners use extrinsic $f0$ information from the context sentence to identify a speaker and this information exerts an influence on lexical tone identification. By this view, context-dependence in tone perception arises as a talker-contingent process, presumably mediated through a representation of speaker identity. Another possibility, motivated by analogy to the spectrally-contrastive shifts in phonetic categorization reviewed above and investigated in the present work, is that the different mean $f0$ frequencies of the speakers' voices can exert a contrastive influence on lexical tone perception independent of perception of speaker identity.

In summary, there are clear speaker normalization effects of level lexical tones for which $f0$ frequency is relatively constant little across the syllable (Wong and Diehl, 2003; Francis, *et al.*, 2006). The available evidence also suggests that the directionality of the influence of context on perception of level lexical tones is contrastive. As is observed for phonetic categorization in context, the spectra of preceding context affect perception of targets in a contrastive manner; higher-frequency contexts shift perception to lower frequencies whereas lower-frequency contexts cause the same targets to be perceived as a higher-frequency alternatives (Moore and Jongman, 1997; Wong and Diehl, 2003; Francis *et al.*, 2006).

In comparison to the perceptual results with level lexical tones, observations of the influence of context on perception of contour lexical tones (distinguished by both $f0$ height and contour) have been much more mixed (Leather, 1983; Lin and Wang, 1985; Fox and Qi, 1990). Perception of contour tones could be much more dependent on intrinsic $f0$ information and much less affected by context than perception of level lexical tones. However, as noted above, there are some limitations in previous research investigating the effects of context on contour tones.

C. Research aims

The present research had several aims. Given the contradictory results in previous studies of lexical tone normalization for contour tones, we aimed to provide an unambiguous test of the influence of precursor context on contour tone perception. Here, we exploit paradigms similar to those used in studying effects of context on *level* tones (Wong and Diehl, 2003; Francis *et al.*, 2006) and stimuli similar to those of earlier studies of Mandarin *contour* tones (Leather, 1983; Lin and Wang, 1985; Fox and Qi, 1990). If perception of contour tones does rely on extrinsic information (i.e., it is sensitive to context), we expect to observe shifts in native Mandarin Chinese listeners' contour tone categorization as a function of preceding sentence contexts.

Another aim was to examine potential mechanisms of the pattern of perception that has been described as lexical tone normalization. Observing that natural precursor sentences recorded from different speakers shift tone perception, Moore and Jongman (1997) argued that the acoustic information of the context is used as a cue to identify the speaker and listeners' perception of lexical tones is calibrated via a representation of speaker identity. The pattern of perception thus is posited to be a result of talker-contingent processing. However, in light of the results reviewed above for context-dependent phonetic categorization, it is possible that these results arise not from perceived speaker identity but instead from spectral differences inherent in different speakers' utterances.

One possibility is that the effects may be a product of auditory, rather than phonetic or speaker-identity-specific, processing. Intriguingly, the context effects observed for lexical tones are contrastive in most studies: when there is a $f0$ context with a higher-frequency mean $f0$, the target is more likely to be labeled as a lower-frequency lexical tone and vice versa (Lin and Wang, 1985; Moore and Jongman, 1997; Wong and Diehl, 2003; Francis *et al.* 2006). The contrastive directionality of these effects complements a wide range of studies of phonetic categorization whereby higher-frequency contexts shift perception toward a lower-frequency phonetic alternative (Ladefoged and Broadbent, 1957; Mann, 1980; Lotto *et al.*, 1997; Holt *et al.*, 2000; Holt and Lotto, 2002; Holt, 2005; see Lotto and Holt, 2006 for a brief review). In phonetic categorization, the effects of context are observed for single-syllable contexts (e.g., Mann, 1980; Lotto and Kluender, 1998; Holt *et al.*, 2000; Holt and Lotto, 2002) and also across sentence-length contexts (Ladefoged and Broadbent, 1957; Watkins and Makin, 1994, 1996; Holt, 2005, 2006a, 2006b) mirroring the temporal course of level tone context effects for syllables and sentences observed in the tone normalization literature (Lin and Wang, 1985; Moore and Jongman, 1997; Wong and Diehl, 2003; Francis *et al.*, 2006). General auditory, rather than phonetic, mechanisms have been implicated in phonetic context effects because non-speech contexts mimicking the spectral properties of the speech contexts (but eliminating phonetic and articulatory information) produce similar context effects on speech targets (e.g., Lotto and Kluender, 1998; Holt, 1999, 2005, 2006a, 2006b; Fowler *et al.*, 2000; Holt *et al.*, 2000; Holt and Lotto, 2002; Coady *et al.*, 2003; Lotto *et al.*, 2003; Aravamudhan *et al.*, 2008). Further implicating general perceptual, rather than speech-specific mechanisms, such effects have been observed for a nonhuman animal species (Lotto *et al.*, 1997). The spectrally-contrastive directionality of context effects on lexical tone perception invites the possibility that general auditory processes may play a role in producing the patterns of perception that have been described as tone normalization.

Previous research does provide some clues to mechanism. Fox and Qi (1990) demonstrated that native Mandarin and non-native English listeners exhibit similar effect patterns for Mandarin tone perception. Wong (1998) also found that the effect of context could be observed with an English precursor (varying in $f0$ frequencies but not in lexical $f0$ information) for Cantonese and English bilinguals, although the effect was smaller than that elicited by the Cantonese

precursor contexts. Thus, it appears that linguistic experience with lexical tone may not be essential to these effects and that the influence of context does not rely on *f*0 conveying lexical information in context. Each of these findings is compatible with a spectral contrast account of lexical tone normalization, but they are not definitive. Francis *et al.* (2006) found that listeners' tonal judgments were proportional to the mean *f*0 frequency shifts of context sentences, consistent with predictions from spectral contrast. However, they also reported little effect of context on lexical tone perception using an unintelligible context precursor created by extracting the *f*0 contour of a sentence and using a "hummed" neutral vocal tract, a result that is unexpected from predictions of spectral contrast but that may be understood by more direct understanding of the spectral characteristics of precursor and target and their interactions.

In the present experiments, we sought to test directly whether patterns of perception considered to be examples of lexical tone normalization can be elicited with non-speech precursors. Drawing from the patterns of perception observed for context-dependent phonetic categorization (e.g., Holt, 2005), we predict that if general auditory processing plays a role in what has been described as speaker normalization of lexical tone, speech and nonspeech contexts that share energy in the region of *f*0, but eliminate speaker-specific and speech-specific information, should elicit similar context effects on Mandarin tone perception. Testing this hypothesis allows us to extend investigation of the role of spectral contrast in speech perception beyond English (e.g., Lotto and Kluender, 1998; Holt, 2005) to native Mandarin listeners and beyond segmental categorization to suprasegmental perception.

II. EXPERIMENT 1

The purpose of the first experiment is to extend the findings of speaker normalization of level tones (Wong and Diehl, 2003; Francis *et al.*, 2006) to perception of contour tones differing in both *f*0 height and contour. Mandarin's tone 1 (high-level) and tone 2 (mid-rising) differ in *f*0 height and contour and have been investigated in previous studies of tone normalization with mixed results (Leather, 1983; Lin and Wang, 1985; Fox and Qi, 1990). Whereas previous studies of tone normalization have used speech recorded from different speakers as contexts, the current study examines Mandarin listeners' perception of tone 1 and tone 2 in the context of a preceding Mandarin sentence from a single talker for which *f*0 has been manipulated. This approach to manipulating context holds all potential acoustic cues to speaker identity, other than mean *f*0, constant.

A. Method

1. Participants

Sixteen adult native Mandarin Chinese speakers participated in the experiment for a small payment. Participants did not learn any other Chinese dialects until 2 years old and had been in the United States for fewer than 5 years at the time the experiment was conducted. None reported any speech or hearing disability. Previous studies have shown that lexical tone processing is lateralized (Wang *et al.*, 2001; Wang *et al.*, 2004), so participants were given the Edinburgh handedness inventory before the experiments (Oldfield, 1971). Only right-handed listeners (inventory scores are no less than 40 out of 50) were included in the experiment to increase participant homogeneity.

2. Stimuli

The context stimuli were derived from a digital recording of a male native Mandarin speaker who spoke no other Chinese dialects (22050 Hz sampling rate, 16 bit resolution) uttering the Mandarin sentence: 请说这词/qing3 shuo1 zhe4 ci2 (please say this word). This semantically-neutral sentence was chosen because it possesses all four Mandarin tones.[4] Across five recorded utterances, the speaker's mean *f*0 was 159 Hz with an average range 117 Hz–211 Hz; a single sentence was chosen based on its clarity as judged by the first author, a native speaker of Mandarin Chinese. This sentence had a natural mean *f*0 of 162 Hz with a range 114–217 Hz. Two versions of the sentence were created by shifting the entire *f*0 contour of the sentence such that the average *f*0 of the high-frequency context stimuli was 200 Hz and the average *f*0 frequency of low-frequency context was 165 Hz (PRAAT 4.0, Boersma and Weenink, 2009). These two *f*0 frequencies were the onset *f*0 frequency values measured from recordings of the same speaker uttering tone 1 and tone 2 target stimuli (see below).

Three Mandarin syllables, /wu/, /yi/, /yü/, were used as target syllables. These syllables were chosen because they have different meanings when spoken in tone 1 and tone 2[5] (tone 1: room, cloth, dull; tone 2: none, wonder, fish). The target stimuli were derived from natural recordings of the same speaker who recorded the context sentences. One utterance per syllable was selected from five recorded tone 1 utterances, based on duration (around 450 ms) and clarity. An eight-step series varying perceptually from tone 1 to tone 2 was created for each syllable by manipulating the onset *f*0 frequency from 200 to 165 Hz in 5 Hz steps (PRAAT 4.0, Boersma and Weenink, 2009). From these onset values, *f*0 frequency transitioned linearly to an offset frequency of 200 Hz.[6]

Context sentences and target syllables were matched in rms amplitude. Each target stimulus was concatenated with each context sentence using MATLAB 7.0.1 (Matworks, Inc.), creating 48 stimuli, each with a total duration of 1750 ms. Figure 2(a) depicts the construction of stimuli and Fig. 2(b) gives a representative spectrogram for one stimulus (high frequency, 200 Hz mean *f*0, context and /wu/ target with lowest onset *f*0, 165 Hz).

3. Procedure

Each listener participated in two experiment sessions. In the experiment 1a, participants identified isolated target stimuli with no context. Each of the 24 (eight-step series $\times 3$ syllables) target stimuli was presented ten times in a random order. On each trial, a 500 ms fixation was shown on the screen before syllable presentation. Participants categorized the syllable by pressing "1" or "2" (tone 1 or tone 2) on

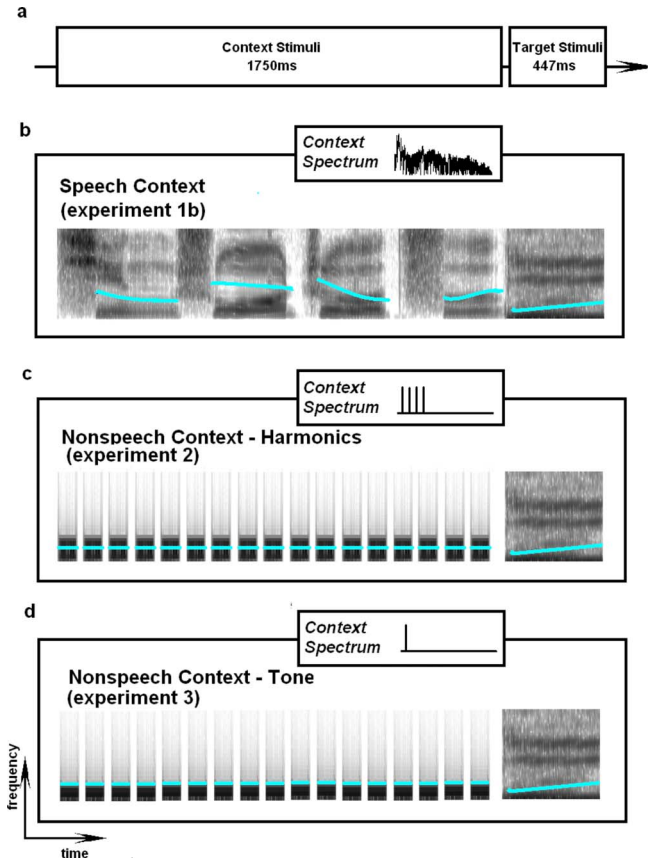

FIG. 2. (Color online) Schematic illustration of stimulus components (a) and representative spectrograms in time × frequency scales for high mean conditions of Experiment 1b (b), Experiment 2 (c), and Experiment 3 (d). The insets in panels (b)–(d) illustrate the spectra of the context sounds in frequency × amplitude axes. The spectrum of each experiment is showed in the inset in a frequency × amplitude scale.

the keyboard using the right hand. Experiment 1b followed Experiment 1a after a short break. The procedure was the same except syllable targets were preceded by context sentences varying in mean $f0$ frequency.

Acoustic presentation was under the control of E-prime (Schneider *et al.*, 2002); stimuli were presented diotically over linear headphones (Beyer DT-150) at approximately 70 dB SPL(A). Participants were tested in individual sound-attenuated booths. The experiment lasted approximately 1 h.

B. Results

Experiment 1a ensures that native Mandarin Chinese participants are able to categorize the syllable targets as Mandarin tone 1 and tone 2. Categorization was very regular across the three syllable series, so for this experiment and those that follow the data were collapsed across the /wu/, /yi/, /yü/ syllables. Average categorization responses as a function of target $f0$ onset frequency are shown in Fig. 3. A repeated measures analysis of variance (ANOVA) revealed a significant main effect for $f0$ onset frequency across the target-syllable series, $F(7,15)=326.74$, $p<0.01$, indicating that tone 1 and tone 2 were well categorized and demonstrating that manipulation of $f0$ onset frequency was sufficient to reliably shift Mandarin tone perception of isolated syllables.

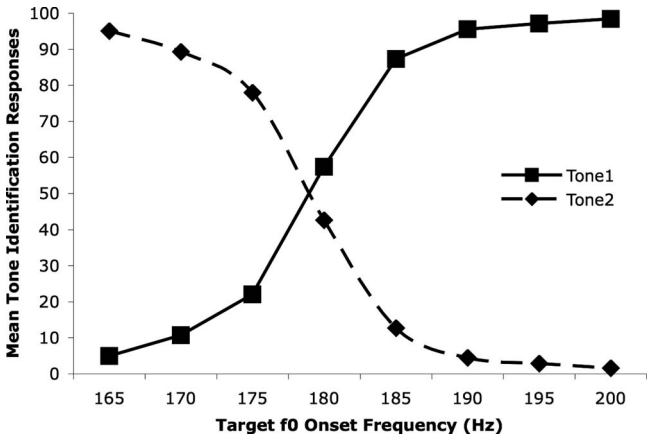

FIG. 3. Results of Experiment 1a. The tone stimuli were well-categorized across the tone 1 to tone 2 series.

Examination of individual's data ensured that each participant exhibited regular categorization across the $f0$ onset frequency series.

Results of Experiment 1b are presented in the Fig. 4(a) (top panel) as a function of target $f0$ onset frequency across participants. The solid line illustrates responses to the target in the context of higher-$f0$ precursor sentences whereas the dashed line represents the lower-$f0$ context. A 2 (speech context mean $f0$ frequency) × 8 (target $f0$ onset frequency) repeated measures ANOVA reveals a significant main effect of mean context $f0$, $F(1,15)=13.34$, $p<0.01$. There was also a main effect of target syllable $f0$ onset frequency, $F(7,15)=268.71$, $p<0.01$, as would be expected for orderly categorization across the tone series. The interaction between average context $f0$ frequency and target $f0$ onset frequency was significant, $F(7,15)=7.26$, $p<0.01$, indicating that the effect of context was exerted mainly in the middle of the tone series where the target stimuli were most perceptually ambiguous.

As expected from previous results and from parallels to context-dependence observed in phonetic context effects, the influence of context is contrastive: the high-frequency context (200 Hz mean $f0$) leads to more tone 2 responses (low onset $f0$), whereas the low-frequency context (165 Hz mean $f0$) leads to fewer tone 2 responses (more tone 1, high-frequency onset $f0$, responses). The significant influence of context indicates that Mandarin listeners do make use of context in contour tone perception. Contour tones, even though they can be distinguished by both $f0$ height and contour, are also context-dependent such that categorization is influenced by the mean $f0$ across a preceding context sentence. The context stimuli of the present experiment differ from those of many previous investigations of the influence of context on lexical tone (Leather, 1983; Moore and Jongman, 1997) because mean $f0$ frequency was manipulated independently of other speaker-specific acoustic variation. Mean $f0$ frequency therefore appears to drive the observed context effect observed here.

It is interesting to note that although the context sentences were manipulated so that they sampled different ranges of $f0$, few participants reported perceiving them as two different speakers. Yet, the contexts exerted an effect on

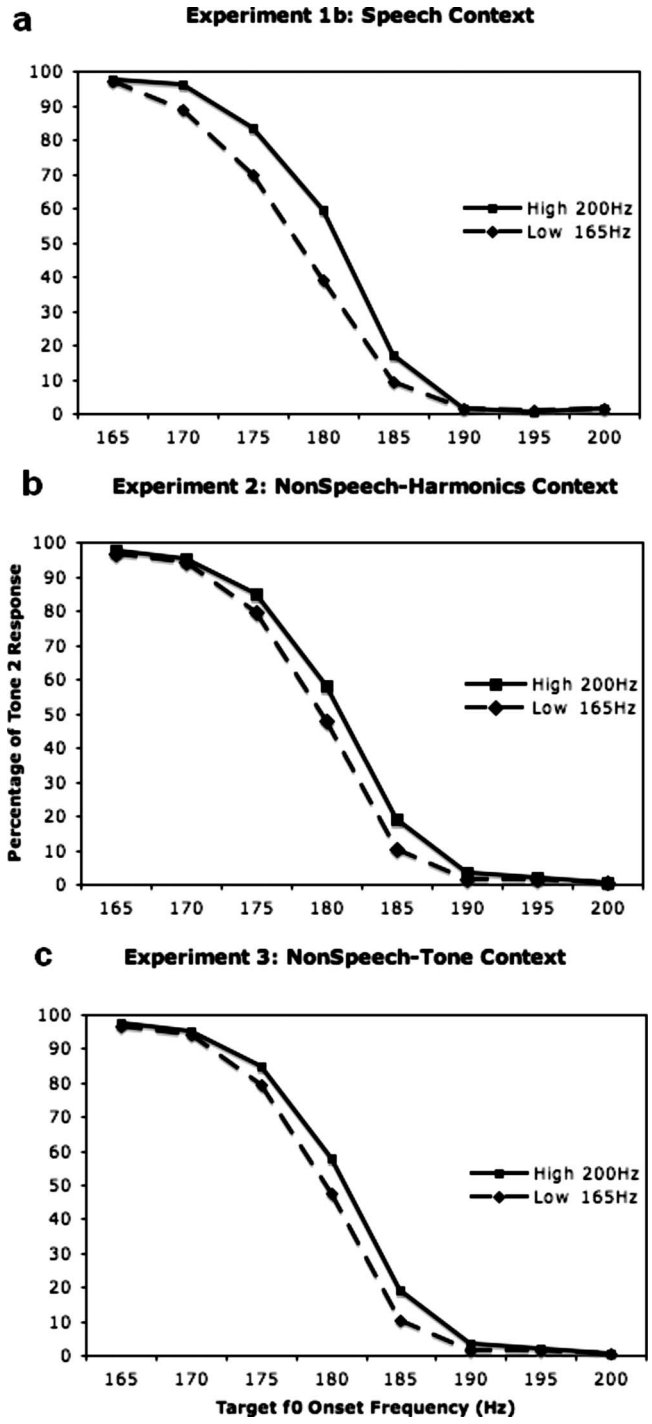

FIG. 4. Mean percentage of tone 2 responses for Experiment 1b (top panel), Experiment 2 (middle panel), and Experiment 3 (bottom panel).

tone perception. The data from 3 participants who reported perceiving different speakers were not qualitatively different from the remaining participants who heard the contexts as instances from the same speaker. These qualitative responses invite the question of whether it is necessary to perceive differences in speaker identity to normalize tone perception, as proposed by Moore and Jongman (1997). Moreover, the contrastive direction of the effect supports the possibility that patterns of perception described as speaker normalization for lexical tones may arise from general auditory mechanisms, as demonstrated for phonetic context effects (e.g., Lotto and Kluender, 1998; Holt, 2005).

III. EXPERIMENT 2

Experiment 2 tests this possibility by investigating Mandarin listeners' tone perception for syllables preceded by non-speech contexts that mimic some of the spectral characteristics of the sentence contexts used in Experiment 1. If general auditory processing accounts for context effects in lexical tones, non-speech contexts should elicit an influence on perception of tone in Mandarin syllables that parallels the sentence *f*0 contours they model. However, if speaker-contingent processing is important, there should be no observed effects of context because the non-speech context stimuli carry no information for speaker identity.

Previous studies (Holt, 2005, 2006a, 2006b) showed that the mean frequency of a sequence of non-speech acoustic stimuli exerts a spectrally-contrastive influence on subsequent speech categorization. In Experiment 1, manipulating the mean *f*0 of the precursor sentence was sufficient to shift listeners' tone 1 versus tone 2 perception, supporting the findings of previous studies of context-dependent lexical tone perception (Francis *et al.*, 2006) and verifying that such context-dependence exists for contour lexical tone. In another study suggestive of an influential role for mean *f*0 in tone perception, Francis *et al.* (2006) examined Cantonese tone perception in the context of monotone speech synthesized by setting *f*0 to a constant frequency, creating a "robot-like" timbre. The monotone contexts differing in mean *f*0 exerted a significant influence on Cantonese tone perception, strongly suggesting that listeners do not require the whole range of variation of speakers' *f*0, but rather rely on average *f*0. Experiment 2 further investigates the role of mean *f*0 in tone perception by utilizing complex *non-speech* stimuli composed of four sine-wave harmonics sharing the same *f*0 as the sentence contexts of Experiment 1b. Using these complex non-speech stimuli that do not possess speaker-identity information or information from which to recover speech gestures provides the opportunity to investigate the possibility that general auditory processing plays a role in tone normalization.

A. Method

1. Participants

The same group of 16 native Mandarin speakers from Experiment 1 was recruited to participate for a small payment. Participants returned for Experiment 2 at least 10 days after Experiment 1.

2. Stimuli

Two non-speech context stimuli were created using MATLAB 7.0.1 (Matworks, Inc.). The stimuli possessed the same mean *f*0 frequency as the sentence contexts in Experiment 1b. The high-frequency context had a 200 Hz *f*0 and the low-frequency context had a 165 Hz *f*0. Each non-speech context was a sequence of 17 tone complexes composed of four equal-amplitude sine-waves with frequencies at the first four multiples of the *f*0. Each of the 17 stimuli was 70 ms, with 5 ms linear amplitude ramps at onset and offset. The 17 non-speech tone complexes were separated by 30 ms silent intervals [see Fig. 2(c)].

These non-speech contexts preceded the target syllables from Experiment 1 with a 50 ms silence separating non-speech contexts and speech targets. The overall duration of the non-speech contexts was 1750 ms, the same duration as the speech contexts of Experiment 1b. Nonspeech context stimuli were matched in rms amplitude to the same value as speech context stimuli and target stimuli of Experiment 1.

3. Procedure

Experimental procedures were identical to those of Experiment 1b.

B. Results

Results are presented in the Fig. 4(b). A 2 (non-speech context $f0$) $\times$ 8 (speech target $f0$ onset frequency) repeated measures ANOVA analysis revealed a significant main effect of context $f0$: $F(1,15)=10.86$, $p<0.01$. As in Experiment 1b, there was a significant main effect of target $f0$ onset frequency, $F(7,15)=186.41$, $p<0.01$, indicating orderly categorization across the tone 1 to tone 2 target syllable series. There was also a significant interaction between context $f0$ frequency and target $f0$ onset frequency, $F(7,15)=2.49$, $p<0.05$, as expected for effects of context that exert the greatest influence on more perceptually-ambiguous targets. Again, the effect of context was contrastive: the non-speech context with a high $f0$ shifted listeners' lexical tone responses to tone 2 (lower-frequency $f0$ onset) whereas there were more tone 1 (higher-frequency $f0$ onset) responses when the non-speech context had a lower-frequency fundamental. Thus, stimuli that eliminate all potential speaker-specific and speech-specific information, but preserve spectral energy in the region of $f0$, are sufficient to shift Mandarin listeners' tone categorization when $f0$ frequency changes in the context. This finding suggests that general auditory processes may play a role in explaining what has been considered to be "speaker normalization" in lexical tones. Information about linguistic structure, speaker identity, or articulatory gestures does not appear to be necessary to account for the speaker normalization effect of sentence context observed in Experiment 1b.

IV. EXPERIMENT 3

The auditory system can extract pitch via the frequency of the fundamental and also via the intervals between higher-frequency harmonics of the fundamental (Bendor and Wang, 2005); the latter may be a more important manner of determining pitch in speech (Plack, 2005). The non-speech contexts in Experiment 2 possessed both types of information. Experiment 3 decouples these sources of pitch information to examine the influence of the first harmonic alone. Thus, this experiment is also an attempt to replicate the influence of non-speech context observed in Experiment 2 using an even simpler non-speech analog that is acoustically even less similar to the speech sentence contexts of Experiment 1b, yet preserves spectral energy in the region of $f0$. If such stimuli elicit a context effect on Mandarin listeners' tone perception, it provides stronger evidence for a role for general auditory processes in patterns of perception attributed to speaker normalization in lexical tone perception.

A. Method

1. Participants

The same group of sixteen native Mandarin speakers from Experiment 1 was recruited to participate for a small payment. They completed Experiment 3 after taking a short break following Experiment 2.

2. Stimuli

Two non-speech context stimuli were created using MATLAB 7.0.1 (Mathworks, Inc.). The stimuli had the same $f0$ frequency as the speech contexts of Experiment 1b and the non-speech four-harmonic stimuli of Experiment 2: the high-frequency context was composed of sine-waves of 200 Hz and the low-frequency context was made up of 165 Hz sine-waves. There were no high-frequency harmonics in the contexts of Experiment 3, leaving only a single sine-wave at the frequency of the first harmonic ($f0$), in contrast to the four-harmonic tone complexes of Experiment 2. Each context stimulus was composed of a sequence of 17, 70 ms sine-wave tones, each with the same frequency, with 30 ms silent intervals separating them [see Fig. 2(d)]. Each of the tones had linear 5 ms amplitude ramps at onset and offset.

These non-speech contexts preceded the speech syllable targets from Experiment 1 with 50 ms of silence separating speech and non-speech. As in the previous experiments, overall context stimulus duration was 1750 ms. Non-speech context stimuli were matched in rms amplitude to the value of speech context stimuli and target stimuli used in Experiment 1.

3. Procedure

Experimental procedures were identical to those of Experiment 1b.

B. Results

Data were scored as a function of target $f0$ onset frequency, collapsed across syllables. Results are plotted in the Fig. 4(c). A 2 (non-speech context $f0$ frequency) $\times$ 8 (speech target $f0$ onset frequency) repeated measures ANOVA revealed a significant main effect of non-speech context frequency on speech target categorization, $F(1,15)=14.21$, $p<0.01$. As expected, there was also a significant main effect of target $f0$ onset frequency, $F(7,15)=333.89$, $p<0.01$, indicating orderly categorization of targets and a significant interaction between context $f0$ frequency and target $f0$ onset frequency, $F(7,15)=4.55$, $p<0.01$, consistent with context exerting the greatest influence on perceptually-ambiguous mid-series targets. Once again, the observed effect was contrastive: the non-speech context with a higher-frequency $f0$ predicted more tone 2 (low $f0$ onset frequency) responses whereas the non-speech contexts with a lower-frequency $f0$ predicted more tone 1 (high $f0$ onset frequency) responses. Providing further evidence for a general auditory account of

what has been considered speaker normalization for tone perception, single sine-waves repeated across a sentence-length duration were sufficient to shift Mandarin listeners' tone perception. The directionality of the effect of the non-speech contexts mirrors the influence of the sentences they model in mean *f*0 frequency. Moreover, it appears that pitch information conveyed by the frequency interval between harmonics, present in the context stimuli of experiment 2 and absent in experiment 3 contexts, is not necessary to elicit an effect of non-speech context on speech. Thus, the spectral energy in the region of the mean fundamental frequency appears to be a key characteristic predicting the influence of context on identification of lexical tones.

V. GENERAL DISCUSSION

There were two main purposes for the present work. First, this study sought to determine whether there is evidence for context-dependent perception of contour tones. Previous research had provided strong evidence for context-dependence with level lexical tones that possess very similar *f*0 contours (Wong and Diehl, 2003; Francis *et al.*, 2006), but there were mixed results for tones differing along both *f*0 height and contour dimensions (Leather, 1983; Lin and Wang, 1985; Fox and Qi, 1990). Moore and Jongman (1997) suggested in their introduction that contour tones are perceived more according to their intrinsic *f*0 characteristics than level tones and are therefore being less susceptible to the influence of preceding speech context. Experiment 1b provides clear evidence that contour tones, in fact, are susceptible to the influence of context. Mandarin listeners do appear to use context in shaping their perception of contour tones, even when the tones may be distinguished by both *f*0 height and contour dimensions. Moreover, since the context sentences of Experiment 1b were created by manipulating the mean *f*0 of a sentence spoken by a single talker, all acoustic characteristics to speaker identity were held constant except for mean *f*0. This provides support for the possibility raised by Francis *et al.* (2006) that the average *f*0 of speech contributes to effects on tone perception more than does the range of variation of *f*0.

The current findings support Leather's (1983) argument that contour tones are context dependent. However, the context effect observed for Mandarin contour tones in Experiment 1b is much smaller than those observed for Cantonese level tones in previous studies. Identification of level tones can be almost completely (nearly 100%) shifted between two tone labels as a function of context (Wong and Diehl, 2003; Francis *et al.*, 2006). Previously-observed context-dependent shifts of Mandarin contour tone identification were also very reliable, but more modest than those found for Cantonese level tones. Moore and Jongman (1997) observed the largest average perceptual shift around 40% across contexts. The current experiment exposed an identification shift of around 20% for the most ambiguous target stimulus (*f*0=180 Hz) across contexts. It is interesting to note that stimuli in the Cantonese studies (Wong and Diehl, 2003; Francis *et al.*, 2006) had nearly identical tone contours whereas Moore and Jongman (1997) used similar, but not completely identical, tone contours. The *f*0 contours of stimuli in the current experiment are very different across targets. Thus, it seems that effects of context may be greater across target stimuli with more similar *f*0 contours. Although the current data provide strong support for context-dependence in perception of contour tones, the results should be interpreted in light of this pattern of observations. Perception of lexical tones, which may be distinguished by both *f*0 height and contour, appears to make use of both intrinsic and extrinsic context information and the degree of context-dependence may rely on the similarity among existing tones in the language. The reason for the observed pattern might come from the multidimensional nature of contour tones (e.g., Chandrasekaran *et al.* 2007; Barrie, 2007). If target tones can be well distinguished by *f*0 contours, context may be less necessary in establishing the percept. In other words, although contour tones exhibit significant speaker normalization or context-dependence, perception of them may be less susceptible to effects of context than level tones. On the other hand, it is possible that in the current study, listeners relied on the static cue (i.e., onset *f*0) more than the dynamic cue (i.e., contour) to make the tone decisions. If this were the case, the relatively smaller context-dependent perceptual effects for contour lexical tones compared to level tones (e.g., in Cantonese) may have arisen because level tones are better-differentiated by static acoustic cues like onset or offset *f*0 frequency than are contour tones. It is still unclear whether perception of onset *f*0 or *f*0 contour was influenced by context in current study. Further studies will be needed to address this question.

The second purpose of the present work was to examine the underlying mechanisms of patterns of perception described as speaker normalization effects in lexical tones. Most previous studies (Lin and Wang, 1985; Moore and Jongman, 1997; Wong and Diehl, 2003; Francis *et al.*, 2006) observed a contrastive effect of speech context on lexical tone perception. With high-frequency *f*0 speech contexts, target stimuli were more likely to be perceived as a low-frequency tone and vice versa. The data from Experiment 1b replicated this finding for the influence of speech contexts on Mandarin contour tone perception. Experiments 2 and 3 found that two different types of non-speech contexts with spectral energy in the region of *f*0 exert contrastive context effects mirroring those observed for speech contexts in Experiment 1b after which they were modeled. Even single sine waves with frequencies at the mean *f*0 of the sentence contexts of Experiment 1b were sufficient to elicit an effect of context on lexical contour tone perception. These results suggest that linguistic information is not necessary in producing the kinds of context-dependent shifts in lexical tone categorization that have been called speaker normalization. This is consistent with the previous finding that an English precursor sentence elicited a context effect in labeling Cantonese lexical tones for Cantonese and English bilinguals (Wong, 1998). Contrary to speaker-contingent accounts (Moore and Jongman, 1997), it does not appear necessary to preserve information about speaker identity to observe these effects. Moreover, gestural information about vocal tract source appears not to be necessary to context-dependent patterns of percep-

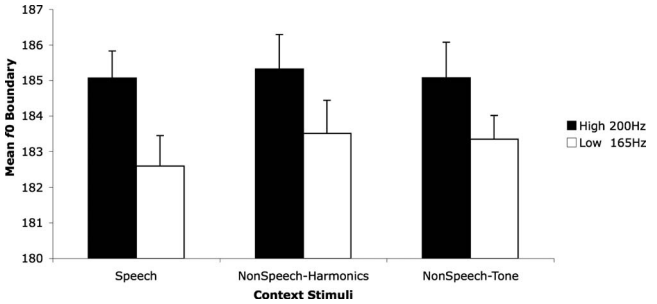

FIG. 5. Probit results for three context experiments (Experiment 1b, Experiment 2, and Experiment 3). A higher frequency $f0$ boundary indicates more tone 2 responses. Error bars indicate standard error of the mean.

tion thought be instances of normalization for lexical tone (see Lotto and Holt, 2006). Given that the only similarity across the contexts of Experiments 1b, 2, and 3 was the spectral energy in the region of $f0$, general auditory mechanisms are implicated.

To give a clear overview of the data across the experiments, Fig. 5 summarizes the results using probit analysis, a model of estimation for discrete decision variables (Finney, 1971), to estimate the identification boundaries and their shifts as a function of preceding context. To calculate the probit boundaries, a cumulative normal curve was used by transforming the percentage of "tone 2" responses to z-scores and finding the best fitting line via linear regression. The boundary was taken to be the $f0$ onset frequency of the target syllable corresponding to 50% on this line.

Since the three experiments share the same group of participants, a 3 (context stimulus type: speech, non-speech harmonics, non-speech single tones) $\times 2$ (context frequency: high, low) repeated measures ANOVA was conducted on the probit boundary values. The analysis confirms a significant context effect, $F(2,15)=46.242$, $p<0.001$ of the high vs low $f0$ contexts, with no significant main effect across the three types of context stimuli, $F(2,15)=0.651$, $p=0.53$. Each of the three context types produced a contrastive context effect whereby the high-frequency context led to a higher $f0$ boundary (i.e., a greater proportion of tone 2, low-frequency onset $f0$, responses) and vice versa. Of note, there was no significant interaction, $F(2,15)=1.305$, $p=0.35$, indicating that the influence of context on lexical tone identification was statistically indistinguishable in magnitude across the speech, non-speech harmonic; and non-speech tone context types. In sum, the probit analysis supports the prospect that the context-dependent shifts in lexical tone identification that have been attributed to speaker normalization may have their bases in general auditory mechanisms that produce spectral contrast.

Moore and Jongman (1997) suggested that because the contexts in their studies were recordings of natural speech from two speakers, tone perception might be mediated through a representation of speaker identity. However, there was no explicit test to verify that listeners indeed perceived the sentences as originating from two different talkers and there were no explicit tests of whether perceived speaker identity was key to eliciting the pattern of perception described as speaker normalization. Given the absence of information about speaker identity in the non-speech contexts of Experiments 2 and 3, it appears unlikely that speaker identity is a necessary factor in producing the kinds of categorization shifts that have been attributed to speaker normalization. Interestingly, the results of Francis *et al.* (2006) suggest that continuity of speaker identity is not necessary for tone normalization; evidence of context-dependent tone perception was even stronger when target and context stimuli came from different speakers, compared to when they were matched.

Other work suggests a role for influences of speaker identity in perception. Magnuson and Nusbaum (2007), for example, found that there were performance costs of adjusting to speaker variability when participants expect multiple speakers, whereas participants did not show this kind of performance when they heard the same materials but were expecting a single speaker. However, the present results demonstrate that auditory interactions of the spectra of context and target are sufficient to produce the kinds of identification shifts that have been taken as evidence of speaker-identity-driven mechanisms in previous research (e.g., Moore and Jongman, 1997).

If general auditory processes are primarily culpable, then one would expect commonality across languages. However, Jongman and Moore (2000) reported different patterns of normalization for Mandarin tone 2 and tone 3 for Mandarin and English listeners. Whereas Mandarin listeners' perception was influenced by preceding sentence contexts when context and target stimuli varied in the same acoustic dimension ($\Delta f0$ or $f0$ contour turning point), context only influenced English listeners when target stimuli varied in both $\Delta f0$ and $f0$ contour turning points. Jongman and Moore (2000) argued that language background aided Mandarin listeners in disambiguating phonemic contrasts, but normalization was the consequence of acoustic discriminability for English listeners. These results would seem to run counter to the present findings.

A major difference between Jongman and Moore (2000) and other cross-language studies in tone normalization (Fox and Qi, 1990; Wong, 1998) is that the former used lexical tones varying in both spectral ($\Delta f0$) and temporal ($f0$ contour turning point) dimensions. The current studies provide a strong support that tone normalization in spectral dimension may have its basis in general auditory processing. Of note, Wade and Holt (2005) showed that rate normalization effects can also be driven by sequences of sine-wave tones varying in their temporal characteristics. A possible explanation for the discrepancy between Jongman and Moore (2000) and other studies may be the interaction of spectral and temporal cues for lexical tone. English participants in Jongman and Moore's (2000) received short training in categorizing Mandarin tone 2 and tone 3. With covariance of $\Delta f0$ and $f0$ contour turning points as they learned these non-native categories, it is possible that English listeners could not separate these two dimensions. On the other hand, with much richer Mandarin lexical tone experience including using all four Mandarin tones, native speakers may be better able to use the cues independently. In other words, the influence of context that has been described as normalization may be driven by

common processes, but operative on very lexical tone categories with very different properties. This is an intriguing prospect that might be further tested.

The direction of the current work was motivated, in part, by previous studies of the influence of context on phonetic categorization. Those studies have produced three working conclusions: (1) Context-dependent phonetic categorization is contrastive in nature: higher frequency contexts shift perception toward lower-frequency targets and vice versa (Mann, 1980; Lotto *et al.*, 1997; Holt and Lotto, 2002; Holt, 2005; 2006a, 2006b; see Wade and Holt, 2005; Diehl and Walsh, 1989 for examples of temporally contrastive context-dependent phonetic categorization). (2) These effects can be elicited with non-speech stimuli modeling spectral/temporal characteristics of the speech contexts; thus, general contrastive perceptual mechanisms, rather than phonetic modules, gestural processing, or speaker-identity-driven mechanisms are implicated (e.g., Lotto and Kluender, 1998; Lotto and Holt, 2006). (3) In sentence-length acoustic materials for which the distribution of spectral energy varies, the key acoustic feature of context that influences the perception of a target sound is the mean frequency (Holt, 2005, 2006b).

The results of the current studies are consistent with each of these conclusions. As such, the present results extend findings of the influence of spectral contrast on speech perception cross-linguistically; previous studies have examined English whereas the present study investigates native Mandarin perception. Moreover, the present results broaden findings of spectral contrast to include suprasegmental, lexical tone. Most generally, the current studies suggest that contour lexical tones are not independent of extrinsic context and non-speech contexts influence lexical contour tone perception in a manner that mirrors the speech contexts they model with their spectra. Patterns of lexical tone perception that have been considered to be instances of speaker normalization may be driven, at least in part, by general auditory mechanisms that serve to perceptually exaggerate acoustic change, rather than speaker-identity-driven or articulatory-based processing.

ACKNOWLEDGMENTS

This work was supported by Grant No. R01DC004674 from the National Institutes of Health. J.H. received support from the Center for the Neural Basis of Cognition.

[1]English listeners were instructed to describe Tone 1 as high, unchanged (i.e., level) pitch and Tone 2 as a mid-rising pitch.

[2]The discrepant results between Lin and Wang (1985) and Fox and Qi (1990) may arise from methodology. See Moore and Jongman (1997) for a possible explanation.

[3]Moore and Jongman (1997) did not distinguish $\Delta f0$ and mean $f0$ in their studies. Context sentences from two speakers differed in both $\Delta f0$ and mean $f0$. Target stimuli had fixed onset and offset $f0$, but differed in both $\Delta f0$ and mean $f0$ because it is impossible to control mean $f0$ without varying $\Delta f0$. Other researchers have argued that the covariance of $\Delta f0$ and mean $f0$ is a weakness of this study (Wong and Diehl, 2003). However, although the influences of $\Delta f0$ and mean $f0$ cannot be decoupled in this study, it is the case that together they produced a significant, contrastive effect of context on lexical tone perception.

[4]Since it is impossible to rule out all contour information in the context, the current study used the context sentence 请说这词 which consisted of all four tones in Mandarin.

[5]Level tones are distinguished from contour tones in Cantonese because they have similar "level contour" and only the overall frequency distinguishes them. However, tone 1 is the only level tone in Mandarin so listeners can use both the level contour and overall frequency to distinguish tone 1 from other tones. In this case, "level" is considered as one of the types of $f0$ contours in Mandarin.

[6]Note that since the offset $f0$ frequency remains constant across target stimuli, changes in onset $f0$ frequency influence the slope of $f0$ frequency change across time.

Aravamudhan, R., Lotto, A. J., and Hawks, J. (**2008**). "Perceptual context effects of speech & non-speech sounds: The role of auditory categories," J. Acoust. Soc. Am. **124**, 1695–1703.

Barrie, M. (**2007**). "Contour tones and contrast in Chinese languages," J. East Asian Linguist. **16**(4), 337–362.

Bendor, D., and Wang, X. (**2005**). "The Neuronal representation of pitch in primate auditory cortex," Nature (London) **436**, 1161–1165.

Boersma, P, and Weenink, D.,

(**2009**). "Praat: doing phonetics by computer," (Version 4.0). http://www.praat.org/, (last accessed May 8, 2009)..

Chandrasekaran, B., Krishnan, A., and Gandour, J. (**2007**). "Mismatch negativity to pitch contours is influenced by language experience," Brain Res. **1128**, 148–156.

Coady, J. A., Kluender, K. R., and Rhode, W. S. (**2003**). "Effects of contrast between onsets of speech and other complex spectra," J. Acoust. Soc. Am. **114**, 2225–2235.

Diehl, R. L., and Walsh, M. A. (**1989**). "An auditory basis for the stimulus-length effect in the perception of stops and glides," J. Acoust. Soc. Am. **85**, 2154–2164.

Finney, D. J. (**1971**). *Probit Analysis* (Cambridge University Press, Cambridge, MA).

Fowler, C. A., Brown, J. M., and Mann, V. A. (**2000**). "Contrast effects do not underlie effects of preceding liquids on stop-consonant identification by humans," J. Exp. Psychol. Hum. Percept. Perform. **26**, 877–888.

Fox, R., and Qi, Y. (**1990**). "Contextual effects in the perception of lexical tone," J. Chin. Linguist. **18**, 261–283.

Francis, A., Ciocca, V., Wong, N., Leung, W., and Chu, P. (**2006**). "Extrinsic context affects perceptual normalization of lexical tone," J. Acoust. Soc. Am. **119**, 1712–1726.

Holt, L. L. (**1999**). "Auditory constraints on speech perception: An examination of spectral contrast," Ph.D. thesis, University of Wisconsin at Madison, Madison, WI.

Holt, L. L. (**2005**). "Temporally nonadjacent nonlinguistic sounds affect speech categorization," Psychol. Sci. **16**, 305–312.

Holt, L. L. (**2006a**). "Speech categorization in context: Joint effects of nonspeech and speech precursors," J. Acoust. Soc. Am. **119**, 4016–4026.

Holt, L. L. (**2006b**). "The mean matters: Effects of statistically-defined nonspeech spectral distributions," J. Acoust. Soc. Am. **120**, 2801–2817.

Holt, L. L., and Lotto, A. J. (**2002**). "Behavioral examinations of the level of auditory processing of speech context effects," Hear. Res. **167**, 156–169.

Holt, L. L., Lotto, A. J., and Kluender, K. R. (**2000**). "Neighboring spectral content influences vowel identification," J. Acoust. Soc. Am. **108**, 710–722.

Johnson, K. J., and Mullennix, J. W. (**1997**). *Talker Variability in Speech Processing* (Academic, San Diego).

Jongman, A., and Moore, C. (**2000**). "The role of language experience in speaker and rate normalization processes," in Proceedings of the sixth International Conference on Spoken Language Processing, Vol. **I**, pp. 62–65.

Ladefoged, P., and Broadbent, D. E. (**1957**). "Information conveyed by vowels," J. Acoust. Soc. Am. **29**, 98–104.

Ladefoged, P., and Maddieson, I. (**1996**). *Sounds of the World's Languages* (Blackwell, Oxford).

Leather, J. (**1983**). "Speaker normalization in perception of lexical tone," J. Phonetics **11**, 373–382.

Lin, T., and Wang, W. (**1985**). "Tone perception," J. Chin. Linguist. **2**, 59–69.

Lotto, A. J., and Holt, L. L. (**2006**). "Putting phonetic context effects into context: A commentary on Fowler (2006)," Percept. Psychophys. **68**, 178–183.

Lotto, A. J., and Kluender, K. R. (**1998**). "General contrast effects in speech perception: Effect of preceding liquid on stop consonant identification," Percept. Psychophys. **60**, 602–619.

Lotto, A. J., Kluender, K. R., and Holt, L. L. (**1997**). "Perceptual compensation for coarticulation by Japanese quail (Coturnix coturnix japonica)," J. Acoust. Soc. Am. **102**, 1134–1140.
Lotto, A. J., Sullivan, S. C., and Holt, L. L. (**2003**). "Central locus for non-speech effects on phonetic identification," J. Acoust. Soc. Am. **113**, 53–56.
Magnuson, J. S., and Nusbaum, H. C. (**2007**). "Acoustic differences, listener expectations, and the perceptual accommodation of talker variability," J. Exp. Psychol. Hum. Percept. Perform. **33**, 391–409.
Mann, V. A. (**1980**). "Influence of preceding liquid on stop-consonant perception," Percept. Psychophys. **28**, 407–412.
Moore, C., and Jongman, A. (**1997**). "Speaker normalization in the perception of Mandarin Chinese tones," J. Acoust. Soc. Am. **102**, 1864–1877.
Oldfield, R. C. (**1971**). "The assessment and analysis of handedness: The Edinburgh inventory," Neurophysiology **9**, 97–113.
Peterson, G. E., and Barney, H. L. (**1952**). "Control methods used in the study of vowels," J. Acoust. Soc. Am. **24**, 175–184.
Plack, C. J. (**2005**). *The Sense of Hearing* (Lawrence Erlbaum Associates, Inc., London).
Schneider, W., Eschman, A., and Zuccolotto, A. (**2002**). "E-Prime user's guide," Psychology Software Tools Inc., Pittsburgh.
Wade, T., and Holt, L. L. (**2005**). "Perceptual effects of preceding non-speech rate on temporal properties of speech categories," Percept. Psychophys. **67**, 939–950.
Wang, Y., Jongman, A., and Sereno, J. (**2001**). "Dichotic perception of mandarin tones by Chinese and American listeners," Brain Lang **78**, 332–348.
Wang, Y., Behne, D., Jongman, A., and Sereno, J. (**2004**). "The role of linguistic experience in the hemispheric processing of lexical tone," Appl. Psycholinguist. **25**, 449–466.
Watkins, A. J., and Makin, S. J. (**1994**). "Perceptual compensation for speaker differences and for spectral-envelope distortion," J. Acoust. Soc. Am. **96**, 1263–1282.
Watkins, A. J., and Makin, S. J. (**1996**). "Effects of spectral contrast on perceptual compensation for spectral-envelope distortion," J. Acoust. Soc. Am. **99**, 3749–3757.
Wong, P. C. M. (**1998**). "Speaker normalization in the perception of Cantonese level tones," MS thesis, University of Texas at Austin, Austin, TX.
Wong, P. C. M., and Diehl, R. L. (**2003**). "Perceptual normalization for inter- and intratalker variation in Cantonese level tones," J. Speech Lang. Hear. Res. **46**, 413–421.
Xu, Y. (**1994**). "Production and perception of coarticulated tones," J. Acoust. Soc. Am. **95**, 2240–2253.
Xu, Y. (**1997**). "Contextual tonal variations in Mandarin," J. Phonetics **25**, 61–83.

Effects of envelope discontinuities on perceptual restoration of amplitude-compressed speech

Deniz Başkent,[a] Cheryl Eiler, and Brent Edwards
Starkey Hearing Research Center, 2150 Shattuck Avenue, Suite 408, Berkeley, California 94704

(Received 19 January 2008; revised 23 March 2009; accepted 5 April 2009)

An interrupted signal may be perceptually restored and, as a result, perceived as continuous, when the interruptions are filled with loud noise bursts. Additionally, when the signal is speech, an improvement in intelligibility may be observed. The perceived continuity of interrupted tones is reduced when the signal level is ramped down and up before and after the noise burst, respectively—an effect that has been attributed to envelope discontinuities at the tone-noise interface [Bregman, A. S., and Dannenbring, G. L. (1977). Can. J. Psychiatry **31**, 151–159]. The hypothesis of the present study was that the perceptual restoration of speech would also be reduced with similar envelope discontinuities that may occur in real life due to the release time constants of hearing-aid compression. In an effort to make the conditions more relevant to hearing aids, speech was amplitude-compressed and normal-hearing listeners of varying ages were recruited. Envelope amplitude ramps were placed at the onsets/offsets of speech segments of interrupted sentences and the restoration effect was measured in two ways: objectively as the improvement in intelligibility when noise was added in the gaps and subjectively through the perceived continuity measured by subjects' own reporting. Both measures showed a reduction as the ramp duration increased—a trend observed for subjects of all ages and for all ramp configurations. These findings can be attributed to envelope discontinuities, with an additional contribution from reduced speech information due to ramping and temporal masking from loud noise bursts.
 [DOI: 10.1121/1.3125329]

PACS number(s): 43.71.An, 43.66.Mk, 43.66.Ts [RSN] Pages: 3995–4005

I. INTRODUCTION

In everyday listening, sounds of interest are commonly masked by more intense sounds in the background. One way the auditory system deals with this difficulty is through the perceptual restoration of the incomplete signal using context information, as well as linguistic knowledge and syntactic and semantic constraints if the signal is speech (Miller and Licklider, 1950; Warren, 1970; Dannenbring, 1976). One consequence of this restoration is the perception of an interrupted signal as continuous once the interruption is filled with a louder sound (continuity illusion; Thurlow, 1957; Thurlow and Elfner, 1959; Warren *et al.*, 1972). For speech, in addition to perceived continuity, an improvement in intelligibility may also be observed through this restoration (phonemic restoration; Cherry and Wiley, 1967; Wiley, 1968; Warren, 1970; Warren and Obusek, 1971; Powers and Wilcox, 1977; Verschuure and Brocaar, 1983; Bashford and Warren, 1987; Bashford *et al.*, 1988, 1996).

One requirement for the intervening loud sound to induce perceptual restoration of the interrupted signal is that there be no perceptual evidence of a change in the signal. It helps when the inducer sound has the appropriate spectral, temporal, or spatial acoustic characteristics, as well as sufficient intensity, to mask the missing signal (had the signal been present during the interruption). It also helps when the signal onsets and offsets around the interruptions are not perceptible (Huggins, 1964; Warren *et al.*, 1972; Bregman and Dannenbring, 1977; Bashford and Warren, 1979; Verschuure and Brocaar, 1983; Bashford and Warren, 1987; Bregman, 1990; Bashford *et al.*, 1992). Under these conditions, the combination of interrupted signal with the inducer sound produces an ambiguous input to the auditory system, which cannot readily infer whether portions of the signal are masked or missing behind the louder sound. One possible explanation is, following the Gestalt principles, the system tends to decide that the signal should be continuous and the audible speech segments should be part of one speech stream (Bregman, 1990; Woods *et al.*, 1996; Assmann and Summerfield, 2004; Husain *et al.*, 2005; Srinivasan and Wang, 2005). This situation seems to facilitate a filling in of the missing speech with the help of top-down processes by using redundancies and context in speech as well as linguistic knowledge and constraints (Warren, 1970; Bashford and Warren, 1979; Samuel, 1981, 1996; Bashford *et al.*, 1996; Assmann and Summerfield, 2004; Sivonen *et al.*, 2006).

The requirement that there be no evidence for a change in the signal, however, may be violated in real-life listening situations. As a result, perceptual restoration may be negatively affected and the potential benefit of improved speech understanding reduced. Such violations may occur, for example, with front-end processing of hearing aids (Edwards, 2004). Let us hypothetically consider an example stimulus of an interrupted tone combined with a loud noise burst, as shown in the top left corner of Fig. 1. A typical feature used in hearing aids is amplitude compression where low-level portions of the input signal are amplified more than high-

[a]Author to whom correspondence should be addressed. Electronic mail: deniz_baskent@starkey.com

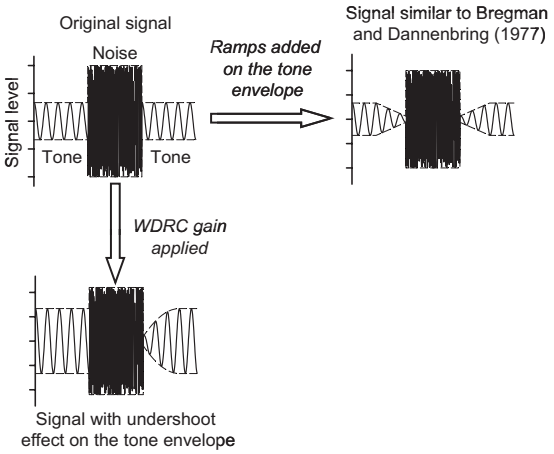

FIG. 1. A signal comprised of a low-intensity interrupted tone combined with a high-intensity noise burst, shown in the upper left corner. The dashed lines indicate the envelope of the combined signal. The upper right corner shows the same combination signal after amplitude ramps were added on the tone envelope preceding and following the noise burst, similar to stimuli used by Bregman and Dannenbring (1977). The lower left corner shows the combination signal after a WDRC gain was applied. Due to the release time constant of compression, a recovery ramp—namely, the undershoot distortion—may be observed on the tone envelope following the noise burst.

level portions. As a result, in a typical compression scenario, tones with a low intensity are amplified with substantial gain. When the signal switches from a low-intensity tone to high-intensity noise, compression is activated and the gain setting changes from substantial to minimal. The reduction in gain due to the activation of compression is the "attack" portion of the compression, which usually happens very fast. By contrast, when the signal switches from a high to low-intensity noise, the gain setting returns from minimal to substantial. This increase in gain is the "release" portion of compression and usually happens slowly, with a pace governed by the release time constant of compression. This slow adjustment in gain may generate an undershoot distortion, that is, an increasing ramp on the tone envelope as shown in the lower left corner of Fig. 1 (Edwards, 2004). Significantly, the distortion between the tone-noise boundary can be harmful for perceptual restoration. Bregman and Dannenbring (1977) produced similar envelope manipulations by adding amplitude ramps on the signal envelope before and after the noise inducer, as shown in the top right corner of Fig. 1. As the duration of the ramps increased, it became difficult for the listeners to perceive the interrupted tone as continuous.

In this study, we hypothesized that the perceptual restoration of speech could also be reduced with similar envelope manipulations—a finding that would have important practical consequences for fitting hearing aids. Based on the previous findings with interrupted tones and as a direct consequence of the violation of the evidence of the continuity rule, we expected three interacting factors. Firstly, envelope discontinuities generated by the ramps were expected to make perceptual restoration of interrupted speech more difficult. Unlike tonal signals, however, speech contains linguistic information that is crucial to its restoration. As a consequence, a second factor potentially affecting the results was a loss in speech information due to the addition of the ramps. A third factor possibly affecting restoration was the potential masking from loud noise bursts onto the speech segments. While the noise level must be high to induce the restoration, this high level then increases the possibility of temporal masking.

Two methods were used to test our hypothesis: an objective measurement of improvement in speech intelligibility due to the addition of noise (Powers and Wilcox, 1977) and a subjective measure in which listeners reported the perceived continuity of interrupted sentences combined with noise. Three different ramp configurations were implemented: one simulating the undershoot distortion, another similar to that used by Bregman and Dannenbring (1977), and one complementing the preceding two and helping to tease out the effects of different factors.

II. METHODS

The first type of ramp configuration simulated the undershoot distortion that can occur with hearing-aid compression (Fig. 1, lower left panel). Ideally, the effect of this configuration should be measured with hearing-impaired listeners who are the real users of these devices. However, the effect of hearing impairment on perceptual restoration is still under investigation and as yet, unknown (Başkent *et al.*, 2007). We therefore decided to focus on the effect of simulated undershoot without the interference from hearing impairment—recruiting normal-hearing listeners for the present study. To make both conditions more realistic and the results more relevant to real hearing-aid users, we (1) made an effort to select listeners of varying ages to more closely parallel the elderly user population, and (2) amplitude-compressed speech before applying the experimental conditions. As a result, in addition to the simulated undershoot in the envelope, other potential perceptual changes due to compression were included in the processed signal.

A. Listeners

A total of 26 normal-hearing listeners participated in the study—all native speakers of American English whose ages varied from 18 to 79 years (with an average age of 37). All subjects' hearing thresholds were better than 20 dB Hearing Level (HL) at audiometric frequencies of 250–4000 Hz. Twenty- two listeners participated in both objective and subjective tests, three only in the objective test, and one in the subjective test alone. Subject participation was determined by their availability for testing.

B. Stimuli

Sentences from the Hearing in Noise Test (HINT) database (Nilsson *et al.*, 1994) and Harvard database (IEEE, 1969) were used for training and data collection sessions, respectively. Although the IEEE sentences have fewer contextual cues (Rabinowitz *et al.*, 1992), this database has the advantage of having a large number of stimuli, which enabled multiple measurements without re-using the sentences with each subject. All sentences were spoken by a single male speaker. The filler noise was a speech-shaped steady noise produced from the long-term speech spectrum of the IEEE sentences.

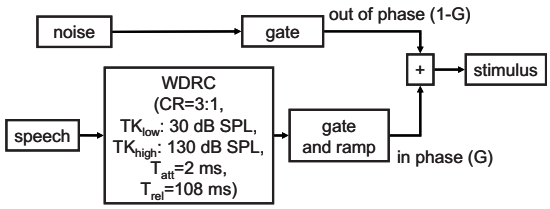

FIG. 2. Summary of the signal processing.

Figure 2 shows a summary of the signal processing; the following sections provide further details.

1. Amplitude compression of speech

The first step of the signal processing involved the compression of sentences with wide-dynamic range compression (WDRC), with a compression ratio of 3:1. The low and high knee points (the levels between which the compression was applied) were set to 30 and 130 dB Sound Pressure Levels (SPLs), respectively. This range was wider than what is typically used in hearing aids, but was chosen so that all speech amplitude components were inside the compression region. The *RC* time constants for the attack and release times were 1 and 30 ms, respectively, measured to be equivalent to the ANSI time constants of 1.7 and 108.4 ms, respectively (ANSI, 2003).

2. Gating

In the next step, the amplitude-compressed sentences and the noise were interrupted periodically by using a gating function of 50% duty cycle and a period of 450 ms, which corresponded to an interruption rate of 2.2 Hz. There were several reasons for selecting this rate. (1) Perceptual restoration of speech is robust with this rate (Warren *et al.*, 1972; Houtgast, 1974; Powers and Wilcox, 1977). (2) Restoration was best when the interruption duration was less than the average word length (Bashford *et al.*, 1988). 2.2 Hz produces interruptions of 225 ms in duration, smaller than the average word durations measured at 378 and 383 ms for HINT and IEEE sentences, respectively. (3) Performance during the pilot study was in the mid-range of the psychometric function for most listeners, minimizing ceiling and floor effects. (4) Speech segments (225 ms in duration) were long enough to implement a range of ramp durations, including the values used by Bregman and Dannenbring (1977).

The gating function started with the *on phase* for speech and *off phase* for noise (Fig. 2) while the rise/fall time of 5 ms was implemented with a cosine ramp. Speech and noise segments overlapped at the transition, as shown in Fig. 3(a), to prevent a reduction in level that could be detected by listeners. Figure 3(b) shows a sample stimulus after interrupted speech was combined with interrupted noise, but before the amplitude ramps were added. Stimuli similar to these (with no ramps) were used to measure baseline performance.

3. Amplitude ramps

In the final step, the amplitude ramps were implemented with cosine ramps that were applied to the gating function

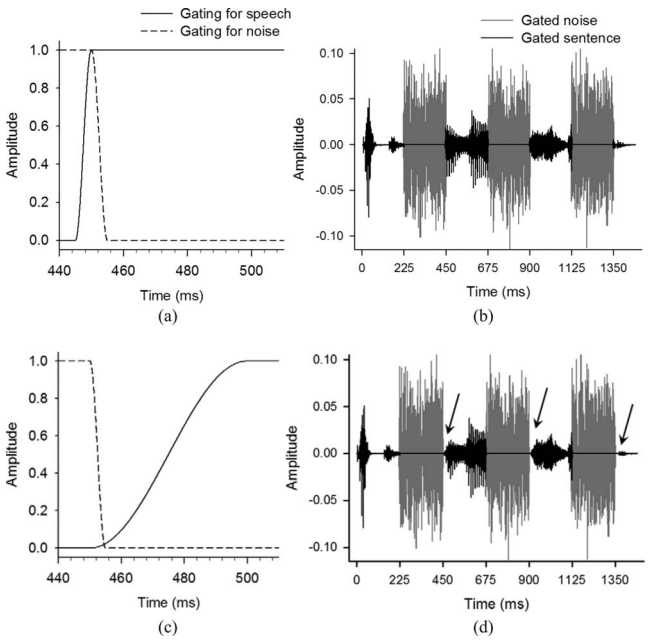

FIG. 3. (a) The envelopes of speech and noise shown at the transition point before an amplitude ramp was added. Note that there is no level discontinuity due to the overlap between the signals. (b) An example stimulus before the amplitude ramps were added. Speech and noise are shown in black and gray, respectively. (c) The same transition from (a), shown after an amplitude ramp of 50 ms added on the speech envelope at the onset of the speech segment. (d) The effect of the amplitude ramp is shown on the stimulus from (b), as indicated by the arrows.

for speech. An example of an envelope ramp at the transition from noise to speech is shown in Fig. 3(c), while the effect of adding this ramp to the overall stimulus is shown in Fig. 3(d).

Ramp durations of 10, 50, and 100 ms simulated time constants comparable to those of syllabic compression systems (Van Tasell, 1993; Souza, 2002) and covered the range of values used by Bregman and Dannenbring (1977).

The ramps were implemented in three different configurations.

(1) *Onset*. Ramps were placed at the onset of the speech segments following the noise bursts—simulating the undershoot (as shown in the top two rows of Fig. 4).
(2) *Both*. Ramps were placed both at the onset and offset of the speech segments—similar to those used by Bregman and Dannenbring (1977) (as shown in the middle rows of Fig. 4).
(3) *Offset*. Ramps were at the offset of the speech segments before the noise bursts (as shown in the bottom rows of Fig. 4).

4. Presentation of the stimuli

The stimuli were presented binaurally using the TDT System III with Sennheiser HD 580 headphones in a soundproof booth. The system was calibrated using a B&K $\frac{1}{2}$ in. microphone mounted in an artificial ear coupler to measure the frequency response of white noise at the output of the headphones. The absolute level of the noise was determined using a reference tone of 96 dB SPL. This noise level was later used to determine the maximum dB SPL for the stimuli

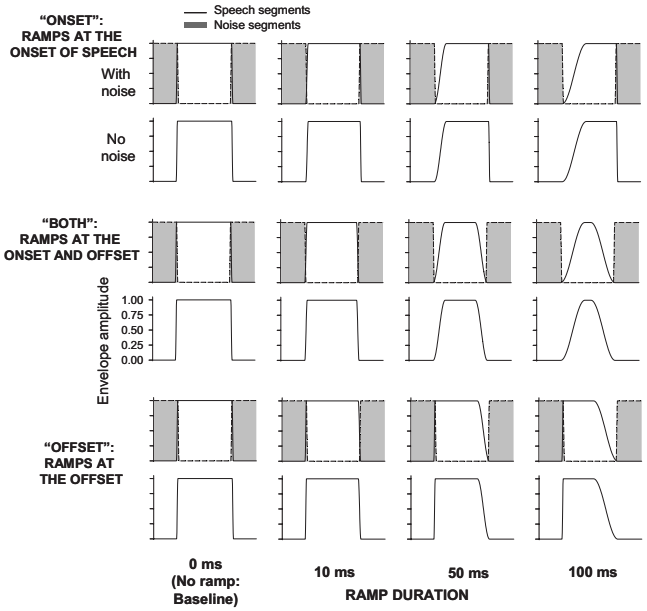

FIG. 4. A summary of the amplitude ramp conditions. The top rows show the envelopes with amplitude ramps added at the onset of speech segments, while the middle rows show the envelopes where the ramps were added both at the onset and offset of the speech segments. The bottom rows show the envelopes where the ramps were added at the offset only. In each row, the left panel shows the baseline condition with no ramp (0 ms) with the ramp duration increasing as one moves toward the right.

at the headphone output. A TDT attenuator was used to adjust the presentation levels with reference to these calculated maximum levels.

Speech was presented at 65 dB SPL. A 1-kHz tone 0.5 s in duration and presented at 60 dB SPL was used to cue the listeners to the beginning of each stimulus. The level of the noise varied during the training whereas a fixed level of 75 dB SPL (again determined by the pilot study) was used during the data collection.

The rms levels of speech stimuli at all stages of signal processing were equalized to 65 dB SPL, the presentation level of the original unprocessed sentence. The motivation for this equalization was to maintain similar energy and loudness levels for speech across all conditions. However, due to this equalization, speech peak levels were most likely higher during the longer-duration ramps.

C. Experimental procedure

The procedure consisted of three sequential stages: Training (to familiarize subjects with the procedure), an objective and subjective test. For listeners who participated in only one of the tests, testing followed the training. The entire procedure was completed in one to three sessions, with a total duration of 2–6 h.

1. Training

Training was similar to the objective test, except that in the training, (1) feedback was provided, (2) sentences were simpler and had more contextual cues, and (3) conditions within the training changed from easy to difficult by a gradual shortening of the speech duty cycle and a speeding up of the interruption rate (both different from those used during actual data collection). A list of ten HINT sentences was used for each training condition. Identical training was given to each subject by keeping the order of both the conditions and the sentences the same. Table I summarizes the conditions used for training and percent correct scores measured within each condition.

2. Objective measure of perceptual restoration

In the objective test, recognition of interruption sentences was measured with and without noise; the increase in intelligibility by the addition of noise was the metric for the perceptual restoration benefit. Subjects were instructed to listen to the processed sentences and verbally repeat as many words as possible. When uncertain, they were encouraged to guess in order to increase the influence of the top-down mechanism. The experimenter judged the accuracy of the repeated words (excluding the articles "the," "a," and "an") and recorded the correct words using the MATLAB GUI. The

TABLE I. Summary of the training conditions and the results obtained with these conditions. The scores denoted by "*" indicated a significant ($p < 0.05$) improvement in intelligibility.

Compression condition for speech segments	Duration of speech segments (ms)	Duration of noise segments (ms)	Speech level (dB SPL)	Noise level (dB SPL)	Raw percent correct scores (average score ± one standard deviation) (%)	Percent correct scores for benefit from perceptual restoration—measured as the difference between no-noise and noise-added conditions (average score ± one standard deviation) (%)
Uncompressed	500	200	65	No noise	94.1 ± 4.9	1.0 ± 5.8
				65	95.1 ± 3.7	
Compressed	300	300	65	No noise	74.6 ± 11.6	8.4* ± 10.0
				70	83.0 ± 7.9	
Compressed	400	200	65	No noise	90.5 ± 5.3	3.3* ± 4.6
				75	93.9 ± 3.3	
Compressed	200	200	65	No noise	62.2 ± 17.4	28.6* ± 19.1
				75	90.8 ± 4.7	

MATLAB program automatically calculated the percent correct scores from the number of the correct words in relation to the total number of words in the sentence, and stored the results in log files for each subject. The experimenter did not know which conditions were being tested, except for an occasional leakage of sound at very high noise levels through the headphones. Each stimulus was presented only once with no repetition and no feedback was provided.

Measurements were repeated twice. Twenty conditions were tested in each round: 2 baseline conditions with no ramp (0 ms) $\times 2$ noise levels (no noise and 75 dB SPL) and 18 ramp conditions with 3 ramp configurations (onset, both, offset) $\times 3$ ramp durations (10, 50, 100 ms) $\times 2$ noise levels (no noise and 75 dB SPL). The order of the conditions was randomized for both each round and each listener. A list of ten IEEE sentences was used in each condition, making a total of 400 sentences (20 conditions $\times 2$ repetitions) used for the entire objective test with each subject.

3. Subjective measure of perceived continuity

In the subjective test, the perceived continuity was measured with interrupted sentences that were combined with the noise bursts. The listeners were instructed to decide if they heard the sentence as interrupted or continuous, and then themselves entered their response using the MATLAB GUI. The MATLAB program automatically calculated the percentage of the sentences heard as continuous and stored the scores in log files.

To help listeners understand the instructions, the test started with ten sentences, half of which were more likely to be perceived as continuous since the noise level was high (75 dB SPL) and half of which were more likely to be perceived as interrupted since the noise level was low (65 dB SPL). After the ten initial sentences, the orders of both the conditions and the sentence lists were randomized.

There were two rounds of measurements. Ten conditions were tested in each round: one baseline condition with no ramp (0 ms) and nine ramp conditions with 3 ramp configurations (onset, both, offset) $\times 3$ ramp durations (10, 50, 100 ms). A list of ten IEEE sentences was used in each condition, making a total of 200 sentences (10 conditions $\times 2$ repetitions) used for the entire subjective test with each subject.

III. RESULTS

Figure 5 shows the average objective and subjective scores as a function of ramp duration. The leftmost score in each panel shows the baseline performance with no ramps (indicated by the ramp duration of 0 ms). The results in the top row are for the "onset" ramp configuration that simulated undershoot (also shown in the top rows of Fig. 4). The results in the middle row are for the "both" configuration, similar to the setting used by Bregman and Dannenbring (1977) (also shown in the middle rows of Fig. 4). The results in the bottom row are for the third "offset" ramp configuration (also shown in the bottom rows of Fig. 4). The two left columns show the objective measures of speech intelligibility. In the leftmost column, the open circles and squares

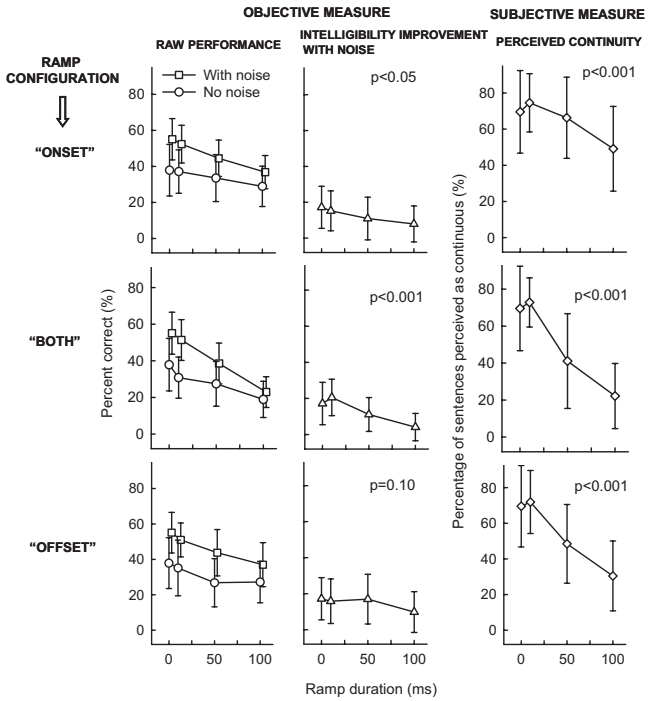

FIG. 5. Average scores from the objective and subjective tests shown as a function of the ramp duration. The panels from top to bottom show the results with the onset, both, and offset ramp configurations, respectively (also shown in Fig. 4). The two left columns show the objective scores. In the leftmost column, the open circles show the performance with interrupted sentences and the open squares show the performance after the noise was added to the interrupted sentences. The difference between these two scores, plotted with open triangles in the middle column, shows the intelligibility benefit. The percentage scores from the subjective measure of perceived continuity are shown in the right column with open diamonds. The significance level of the effect of the ramp duration on the objective and subjective measures is indicated by the p numbers in each panel.

show the raw percent correct scores with the interrupted sentences without and with the noise bursts, respectively. The difference between the two raw scores was attributed to the benefit from perceptual restoration, explicitly shown in the middle column. The right column shows the percentage scores from the subjective measure of perceived continuity.

A. Baseline performance with no ramps

In the baseline condition there were no amplitude ramps on the speech envelope and no discontinuity in the level of the combined signals [Figs. 3(a) and 3(b), and the leftmost column of Fig. 4]. The leftmost scores in each panel of Fig. 5 show the baseline performance. The average restoration benefit was 17.19%, with a standard deviation of 11.71%. Three listeners had negative restoration scores. Despite the difference of using compressed speech in the present study, both mean and variance values were similar to those observed by Powers and Wilcox (1977). The percentage of sentences perceived as continuous was on average 68.10%, with a standard deviation of 22.94%.

B. Effects of the amplitude ramps

Figure 5 shows that in general all scores dropped from the baseline levels as the duration of the ramps increased. First, let us examine the raw percent correct scores in the left

TABLE II. Scores for intelligibility benefit and perceived continuity compared for baseline and 100-ms duration ramp conditions. Superscript letters indicate a significant reduction in the scores due to the ramp, as determined by a posthoc Tukey test.

Ramp configuration	Baseline objective score of restoration benefit (percent correct)	Objective benefit score with the 100-ms ramps (percent correct)	Baseline subjective score of perceived continuity (percentage)	Subjective score with the 100-ms ramp (percentage)
Onset		7.92[a]		49.13[b]
Both	17.19	4.14[b]	69.57	22.17[b]
Offset		9.81		30.43[b]

[a]$p<0.05$.
[b]$p<0.001$.

panels of Fig. 5. Scores both with and without noise dropped as a function of the ramp duration. However, the performance with noise was better than without for almost all ramp durations. A two-factor repeated measures (RM) Analysis of Variance (ANOVA) with the factors of ramp duration and noise was conducted with the scores; both factors had significant main effects on performance for all three ramp configurations [ramp duration, $F(3,72)\geq 37.17$, $p<0.001$ and noise, $F(1,24)\geq 103.80$, $p<0.001$]. Now let us examine the difference in the raw scores between no-noise and noise conditions, an effect that was attributed to the perceptual restoration (shown more explicitly in the middle columns of Fig. 5). The drop in raw scores with the noise (open squares) was more pronounced than the drop in raw scores with no noise (open circles) as the ramp duration increased; hence the restoration benefit decreased. This reduction was significant for onset and both ramp configurations (middle panels of the first and second rows, respectively, in Fig. 5). The significance level was determined by the interaction of the factors of ramp duration and noise [$F(3,72)\geq 3.79$, $p<0.05$ and $p<0.001$, for onset and both configurations, respectively]. Next, let us examine the subjective scores presented in the right column of Fig. 5. These data show that perceived continuity diminished as the ramp duration increased. The main effect of the ramp duration was significant for all three ramp configurations [one-factor RM ANOVA; $F(3,66)\geq 14.83$, $p<0.001$].

For both objective and subjective measures, the strongest effects among ramp configurations were observed with the both configuration and among ramp durations with the longest ramp duration of 100 ms. As a sample comparison, the objective and subjective scores at 100 ms ramp duration are presented in Table II.

C. Analysis of data for age factor

To explore the effects of age on the results, we reanalyzed the data from Fig. 5 re-plotting the individual baseline scores with no ramps as a function of listener age (see Fig. 6). Regression lines (shown by dashed or solid lines) were superimposed on the data to indicate the trend. The correlation coefficients (r_s) and corresponding p values were calculated with the Spearman rank order correlation since we did not know if the correlations were linear. These data show that recognition of interrupted speech (with or without the noise) decreased as the listener's age increased (left panel in Fig. 6). However, perceptual restoration ability seemed to be independent of age; the changes in the intelligibility benefit (see middle panel in Fig. 6) and the perceived continuity (right panel in Fig. 6) as a function of age were minimal and non-significant.

Figure 7 shows another analysis for age, this time for the amplitude ramp conditions. We divided the listeners into two subgroups (using the age of 40 as the threshold) and averaged the scores separately for each. This division was based on the study by Bergman *et al.* (1976) who reported a clear difference in the intelligibility of interrupted speech between listeners younger and older than 40. With this separation, the objective test had 15 younger and 10 older listeners; and the subjective test had 14 younger and 9 older listeners. Similar to Fig. 5, Fig. 7 shows the results with the ramp configurations of onset, both, and offset, in the panels from top to bottom. The panels from left to right show the raw scores with interrupted speech with or without noise, the objective scores of restoration benefit, and subjective scores of perceived continuity, respectively. The only difference from Fig. 5 is that open symbols with solid lines show the results averaged across younger listeners while the gray symbols with dashed lines show the results averaged across listeners older than 40. Similar to the observations from Fig. 6 with the interrupted speech, the raw scores by the older group were

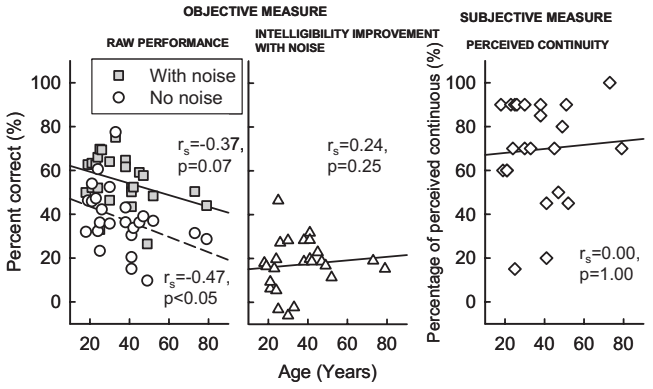

FIG. 6. Individual baseline scores (no ramps) re-plotted from Fig. 5 as a function of age. The dashed and the solid lines superimposed on individual data show the linear regression lines. The correlation coefficients (r_s) and p values, calculated using the Spearman rank order correlation, are indicated in each panel.

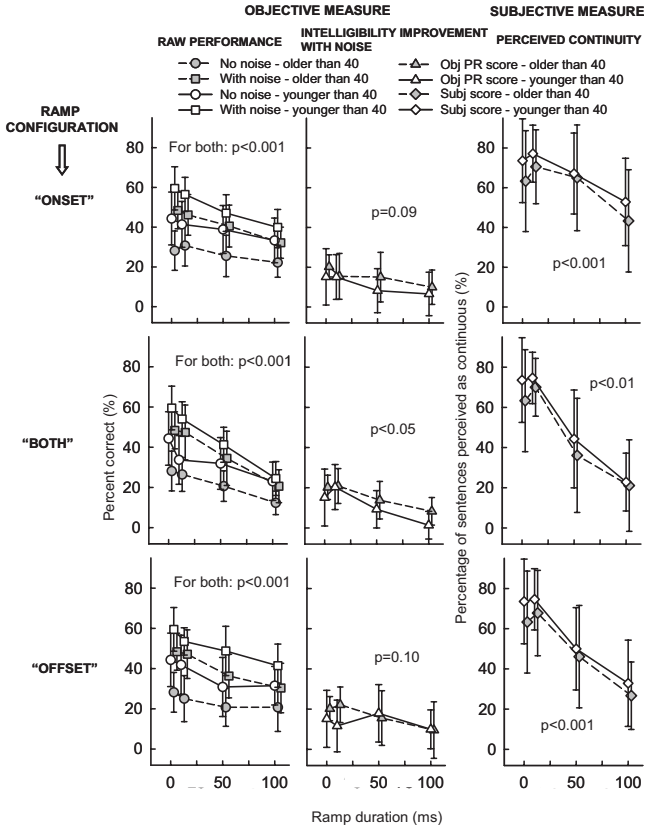

FIG. 7. Data from Fig. 5, averaged for listeners younger and older than 40 years. The p values in each panel indicate a statistically significant difference between the scores of the younger and older listener groups.

substantially lower than the younger group, with or without noise for all ramp configurations (left column of Fig. 7). A two-factor mixed-design ANOVA with the factors of ramp duration and subject group showed that this difference was significant $[F(1,92) \geq 11.82,\ p < 0.001]$. Despite this difference in the raw scores, once the objective scores for the restoration benefit were calculated (as shown in the middle column of Fig. 7) there was no significant difference in performance by the younger and older subject groups for the onset and offset configurations. For the both configuration, the performance by the older group was slightly but significantly better than that by the younger group $[F(1,92)=4.62,\ p<0.05]$, although a posthoc Tukey test did not identify a significant difference for any specific ramp duration. With the subjective measures (shown in the right column of Fig. 7) scores of the older listeners were significantly lower than those of the younger listeners for all three configurations $[F(1,84) \geq 7.24,\ p < 0.01]$. Overall, the scores of the older listeners were lower than those of the younger listeners for the perception of interrupted speech with or without noise and perceived continuity. On the other hand, the restoration benefit was comparable or slightly better for the older listeners. Despite these differences, there was no significant interaction between the main factors of ramp duration and subject group, implying that a similar trend was observed in the data as a function of the ramp duration between the two subject groups.

IV. CONCLUSIONS AND DISCUSSION

A. Effects of amplitude ramps on the perceptual restoration of speech

Baseline scores of the objective and subjective measures of perceptual restoration showed that adding noise to the interruptions increased intelligibility and perceived continuity of interrupted compressed speech, similar to results from earlier studies with interrupted uncompressed speech (Cherry and Wiley, 1967; Wiley, 1968; Warren, 1970; Powers and Wilcox, 1977; Verschuure and Brocaar, 1983; Bashford and Warren, 1987; Bashford *et al.*, 1996). When the amplitude ramps were added on the onsets/offsets of speech segments, both objective and subjective scores decreased significantly from the baseline level as the ramp duration increased.

There are three factors that have potentially contributed to the results observed with the ramps.

(1) *Reduced speech information*. The right panels of Fig. 3 show that one of the direct consequences of adding ramps on the speech envelope was a reduction in speech information—possibly also reducing the linguistic content and context of speech. Both objective and subjective measures of perceptual restoration could have been affected by the loss of speech information, but possibly to different degrees. The increase in intelligibility with intervening noise depends on the filling in by the top-down mechanisms that use speech information and context (Verschuure and Brocaar, 1983; Bashford and Warren, 1987; Bashford *et al.*, 1992, 1996), but these may not be as important for perceived continuity. Continuity illusion works with all signals regardless of linguistic factors, as long as the requirements for perceptual restoration listed in the Introduction are satisfied (Warren *et al.*, 1972; Bregman and Dannenbring, 1977; Bashford and Warren, 1979; Verschuure and Brocaar, 1983; Warren, 1984; Bashford and Warren, 1987; Bregman, 1990; Bashford *et al.*, 1992). Earlier studies indicated that linguistic factors may affect objective and subjective measures of perceptual restoration differently. Intervening noise causes interrupted monosyllables and words (speech with no context) to be perceived as continuous, but usually with no improvement in intelligibility (Miller and Licklider, 1950; Hopkinson, 1967; Kreul, 1971; Samuel, 1981). Improvement is observed with speech that has rich linguistic content and context, such as with sentences or running speech (Schubert and Parker, 1955; Powers and Wilcox, 1977; Verschuure and Brocaar, 1983). Bashford and Warren (1979) showed that it was not necessary to understand speech to perceive it as continuous. The illusion worked even with speech played backwards, although the perceived continuity was more robust with speech played normally rather than backwards. From these observations, loss of speech information would be expected to affect the objective measure more than the subjective. In our study, however, both measures decreased significantly with increasing ramp duration, indicating that there may be factors other than pure information loss that further affected the results. This idea is supported by the results presented in Fig. 5: The average

scores with the interrupted speech with and without the noise (left panels of Fig. 5, open squares and open circles, respectively) showed that both performances dropped as the ramp duration increased; the reduction in scores with the noise, however, was faster. Since theoretically, the information loss is the same between the no-noise and with-noise conditions, the effect of speech information loss should have been similar between the two curves. As it was not, there must have been an additional factor that further reduced the scores with the noise conditions.

(2) *Level discontinuities due to envelope changes*. Our main hypothesis was that the envelope discontinuities due to the ramps would affect the perceptual restoration of speech negatively. Bregman and Dannenbring (1977) previously showed that envelope manipulations similar to ours reduced the perceived continuity of an interrupted tone combined with a noise burst. In their experiment, because of the nature of the stimulus, a tone, there was no linguistic content and, consequently, no effect due to loss of information. Therefore, the reduced continuity illusion must have been mainly due to the level changes in the tone envelope at the temporal edges with the noise. As the basic principles for perceptual restoration of verbal and nonverbal stimuli seem to be similar (Warren *et al.*, 1972; Bregman and Dannenbring, 1977; Bashford and Warren, 1979; Verschuure and Brocaar, 1983; Warren, 1984; Bashford and Warren, 1987; Bregman, 1990; Bashford *et al.*, 1992), the detrimental effects of the ramps observed on perceived continuity of interrupted tones should also apply to perceived continuity of interrupted speech. This reasoning would explain the ramp effects observed on the subjective scores of perceptual restoration. It is not clear, however, how this factor could affect the restoration benefit observed with the objective measure. For example, it is possible that perceived continuity is required in order to benefit from restoration. As explained in the Introduction, the common understanding about improvement in speech intelligibility as a result of noise is that with its addition, the auditory system cannot tell with certainty whether the speech is being interrupted or is continuous and simply masked by the noise. This ambiguity seems to be useful: The system assumes that the speech is continuous but masked—activating top-down mechanisms to fill in missing speech and improve intelligibility (Repp, 1992; Woods *et al.*, 1996; Srinivasan and Wang, 2005). Bashford *et al.* (1992) and Bregman (1990) suggested a two-stage model of perceptual restoration of speech with intervening noise: The primitive first stage works for all signals (verbal or nonverbal) and simply decides whether the signal continues behind the masker from the available cues (the "whether" question). The knowledge-driven second stage then finds a plausible answer to what the missing parts might be (the "what" question). In a later study, Shinn-Cunningham and Wang (2008) reported anecdotal observations, which seemingly contradict the two-stage model by observing an improvement in intelligibility under conditions where speech would not have been perceived as continuous. Yet, they also added that were the perceived continuity induced, improvement might have been more robust. While identification of the specific mechanisms of perceptual restoration is beyond the scope of the present study, generally, perceived continuity and improved intelligibility appear to be closely related for the perceptual restoration of speech (Verschuure and Brocaar, 1983). Therefore, a reduction in perceived continuity could result in the reduction in the objective benefit from restoration.

(3) *Masking*. Loss of speech information and envelope discontinuities seem to be sufficient to explain the general pattern of the results of the present study. However, a third factor should also be considered: masking due to the intense loud noise bursts. To mask interruptions and speech onsets/offsets (in order to induce robust perceptual restoration), the intervening noise has to be a broadband signal of relatively high intensity. Using a broadband and/or intense noise for this purpose, however, has the adverse effect of increased temporal masking (forward or backward) of speech segments (Dirks and Bower, 1970; Bashford *et al.*, 1992, 1996). The various effects of temporal masking are noteworthy for this study.

(a) *For the baseline condition with no ramps*. Masking from noise bursts can theoretically reduce the audibility of speech segments and decrease the linguistic content, which in turn can affect perceptual restoration negatively. The leftmost scores in the left panels of Fig. 5 show the scores with the baseline conditions. Due to the potential masking, there could have been less speech information available to listeners with the noise conditions than the no-noise conditions. Dirks and Bower (1970), however, showed that temporal masking of speech from loud noise bursts was ignorable at slow interruption rates of noise. While at high rates (such as 100 Hz) they observed substantial masking, at the slow rate of 1 Hz (close to the 2.2 Hz rate of the present study) the masking effect was minimal. These results raise the possibility that the effect from masking may not have been substantial in the baseline conditions.

(b) *For conditions with the ramps*. In this instance there could be an opposite (and positive) effect—the partial inaudibility of the ramps compensating for their detrimental effects, especially for shorter ramp durations. An example of this positive effect was observed in the present study with the 10-ms ramp. Scores with this ramp were almost identical to those of the no-ramp baseline, implying that this ramp was not noticed, possibly in response to the temporal masking from noise. The negative effects of the amplitude ramps occurred with the longer-duration ramps of 50 and 100 ms, which in not being (entirely) masked, produced a perceptual effect.

As the effects of forward masking are generally more pronounced than those of backward masking (Gaskell and Henning, 1999) the present study used different ramp configurations to tease out possible differences. The results, however, showed no clear difference in data with onset and

offset configurations—the configurations that would have reflected effects of forward and backward masking separately—raising the possibility that the difference between the two masking mechanisms may have been too small to be reflected in the scores.

Overall, the data indicate that the short duration ramp of 10 ms was not perceptible and did not have any noticeable effect on perceptual restoration. The longer-duration ramps of 50 and 100 ms were not masked, at least not entirely, as they produced a reduction in the scores.

One interesting observation about the overall findings is that both objective and subjective measures decreased monotonically as the ramp duration increased, instead of either measure completely falling apart. Even at the longest ramp duration of 100 ms, there were still positive scores for both measures, albeit much smaller as compared to the baseline. The conventional understanding of continuity illusion sees it as an all-or-none phenomenon. For example, Houtgast (1972) used the threshold between perceived continuity and discontinuity of a signal as a measure for masking experiments. In a later study, however, Warren *et al.* (1994) showed that perceived continuity with nonverbal signals was not all-or-none, but instead worked on a continuum. The results of the present study extend this finding to speech signals. Thus both the intelligibility benefit and perceived continuity of speech do not seem to work as all-or-none mechanisms, but instead, according to a graded effect.

B. Implications for hearing-aid processing: Effects of simulated undershoot

One of the main motivations for the study was to explore the possible effects of undershoot distortion simulated by the onset ramp configuration [shown in Fig. 3(c) and in the lower left corner of Fig. 1]. With this configuration, there was a significant reduction in both the intelligibility benefit and perceived continuity as the ramp duration, i.e., the simulated release time constant, increased. The results imply that in listening environments with fluctuating background noise, compression release times may affect perceptual restoration of speech and hence its intelligibility negatively, depending on the settings of the hearing aid. Note that the configuration used in the present study was an attempt to simulate an extreme case of what may happen with hearing-aid processing in order to observe the effects fully; the results may differ in real-life applications depending on the compression settings used. For example, in the present experiments, the envelope amplitude of speech was reduced to zero immediately after the noise burst at the onset of the amplitude ramp, simulating the greatest change that can theoretically occur in the speech envelope. For a change in that order to happen, the gain applied during the noise and during the speech should differ by 65 dB SPL or more. It is likely that the change in the speech envelope will be less with a more realistic compression system under real-life conditions, and as a result, the disruptive effects of these smaller ramps may be less pronounced than reported here. Additionally, multiband compression where the input stimulus is compressed only at the frequency regions where the listener has reduced dynamic range is commonly used in real-life settings (e.g., Moore *et al.*, 1985; Kuk, 1999; Hansen, 2002). In the present study, the ramps were applied to the overall envelope of broadband speech, as if a single-band compression system was used. If the ramps were applied only to high-frequency bands of speech to simulate multiband compression, the results could again be less dramatic.

C. Applicability of the results to hearing-aid users: Potential effects of age and hearing impairment

As the aforementioned effects of simulated undershoot have been observed with normal-hearing listeners, it is unclear how these results would apply to actual users of hearing aids. Two main factors, advanced age and hearing impairment, could change the results significantly for hearing-aid users. To explore the effects of age, the present study analyzed the data in two different ways: first for the baseline conditions (shown in Fig. 6) and then for the ramp conditions (shown in Fig. 7). The results indicated that the intelligibility of interrupted speech, with or without noise, was negatively correlated, i.e., decreased as the listener's age increased—an expected effect that has previously been observed and attributed to the reduced temporal processing by elderly listeners (Bergman *et al.*, 1976; Gordon-Salant and Fitzgibbons, 1993; Stuart and Phillips, 1996). What was not expected, however, was the lack of change in the restoration benefit scores as a function of age (as seen in the middle panels of Figs. 6 and 7). Previous studies have shown that elderly listeners have difficulty accessing speech information in the dips of a fluctuating background noise (Stuart and Phillips, 1996), again presumably due to reduced temporal processing. We therefore had assumed that the limited access to the speech information in the dips would also make perceptual restoration more difficult for older listeners. Despite the difficulties understanding speech with interruptions, with or without noise, older listeners seemed to make use of the added noise to improve intelligibility as well as younger listeners. A similar observation was made by Madix *et al.* (2005) who, using a different paradigm to measure perceptual restoration, found no difference in performance between younger (19–28 years old) and older (41–62 years old) listeners. A possible explanation for the lack of a decrement in the restoration benefit by elderly listeners might be a compensation by better use of linguistic information (Barrett and Wright, 1979; Wingfield and Tun, 2001). Older listeners may benefit more from context information (Pichora-Fuller *et al.*, 1995) and/or use this information more efficiently (Wingfield *et al.*, 1991) than younger listeners.

The right panel of Fig. 6 showed no effect of age on the baseline subjective scores. However, once analyzed for all conditions, including both the baseline and the ramps (as shown in the right panel of Fig. 7), the scores of the older subjects were significantly lower than those of the younger group. Regardless of this shift in scores, however, the trend in subjective data was almost identical between the subject groups, implying that the negative effects of the ramps were similar for both groups of listeners.

Overall, this analysis established that (1) elderly listeners also benefit from perceptual restoration, and (2) this benefit, as well as perceived continuity, is reduced by level dis-

continuities in a pattern similar to that present with younger listeners. As a result, the findings of the present study would not be expected to differ with hearing-aid users due specifically to their increased age.

The remaining question involved the impact of hearing impairment on the current findings. Earlier studies have shown that, even after audibility was ensured with proper amplification, hearing-impaired listeners had more difficulty in extracting speech from fluctuating background noise (Festen and Plomp, 1990; Eisenberg *et al.*, 1995). One possible explanation is increased forward masking. Nelson and Pavlov (1989) demonstrated longer time constants for forward masking with moderately impaired listeners and Dubno *et al.* (2003) later found a negative correlation between forward masking thresholds and speech intelligibility in fluctuating background noise. This factor, combined with the loss in speech redundancy due to other potential suprathreshold deficits, might make it more difficult for hearing-impaired listeners to have access to speech segments between loud noise bursts—therefore reducing the benefits of perceptual restoration. On the other hand, stronger masking from noise segments might be an advantage for hearing-aid users since the undershoot ramps might be less detectible and therefore less disruptive. We are aware of only one study that has explored perceptual restoration with hearing-impaired listeners (Başkent *et al.*, 2007). The preliminary results showed that while some hearing-impaired listeners benefited from perceptual restoration, this benefit disappeared as the severity of the hearing loss increased. With large variability in the results and compromised audibility as possible confounding factors, however, more data are needed before drawing conclusive results.

V. SUMMARY

The mean and the variance of the baseline restoration benefit and perceived continuity with compressed interrupted speech were similar to values published for uncompressed interrupted speech in previous studies.

All three ramp configurations reduced both objective and subjective scores as the ramp duration increased. One ramp configuration was similar to the configuration used by Bregman and Dannenbring (1977) who showed that perceived continuity of interrupted tones reduced with similar amplitude ramps. They attributed this effect to the discontinuities in the tone envelope due to the ramps. We hypothesized that similar level discontinuities would reduce perceptual restoration of speech as well. Our data supported this hypothesis, with the potential contribution of two additional factors, speech information loss and temporal masking from loud noise bursts, to the results.

The reduction in the scores as a function of ramp duration was graded and the perceptual restoration effect did not entirely disappear even at the longest ramp durations. This observation supports the idea that perceptual restoration benefit and perceived continuity of speech are not an all-or-none mechanism.

One ramp configuration simulated the undershoot distortion. The reduction in perceptual restoration with this configuration indicated the potentially negative effect of hearing-aid processing. The applicability of these results with normal-hearing listeners to actual users of hearing aids would depend on two main factors, hearing impairment and the advanced age of hearing-aid users. An analysis for age showed that the trends for the perceptual restoration data were similar between younger and older listeners, ruling out age as a potential factor that would affect the applicability of the results. The effect of hearing impairment remains unknown at this point. If future research shows that hearing impairment does not prevent benefiting from perceptual restoration, the findings of the present study could have important implications for hearing-aid users.

ACKNOWLEDGMENTS

The authors would like to thank John Galvin and Qian-Jie Fu from House Ear Institute for providing the recordings for the IEEE sentences, Bill Woods for constructive suggestions, the subjects for their efforts, and Anastasios Sarampalis, Nancy Robinson-Kime, and the anonymous reviewers for their comments on a previous version of the manuscript.

ANSI (**2003**). Specification of hearing aid characteristics, S3.22 (American National Standards Inst., New York).

Assmann, P. F., and Summerfield, Q. (**2004**). "The perception of speech under adverse acoustic conditions," *Speech Processing in the Auditory System*, Springer Handbook of Auditory Research Vol. **18**, edited by S. Greenberg, W. A. Ainsworth, A. N. Popper, and R. R. Fay (Springer-Verlag, New York).

Barrett, T. R., and Wright, M. (**1979**). "Age-related facilitation in recall following semantic processing," J. Gerontol. **36**, 194–199.

Bashford, J. A., and Warren, R. M. (**1979**). "Perceptual synthesis of deleted phonemes," J. Acoust. Soc. Am. **65**, 423–426.

Bashford, J. A., and Warren, R. M. (**1987**). "Multiple phonemic restorations follow the rules for auditory induction," Percept. Psychophys. **42**, 114–121.

Bashford, J. A., Myers, M. D., Brubaker, B. S., and Warren, R. M. (**1988**). "Illusory continuity of interrupted speech: Speech rate determines durational limits," J. Acoust. Soc. Am. **84**, 1635–1638.

Bashford, J. A., Riener, K. R., and Warren, R. M. (**1992**). "Increasing the intelligibility of speech through multiple phonemic restorations," Percept. Psychophys. **51**, 211–217.

Bashford, J. A., Warren, R. M., and Brown, C. A. (**1996**). "Use of speech-modulated noise adds strong 'bottom-up' cues for phonemic restoration," Percept. Psychophys. **58**, 342–350.

Başkent, D., Eiler, C., and Edwards, B. (**2007**). "Effects of amplitude ramps on phonemic restoration of compressed speech with normal-hearing and hearing-impaired listeners," Proceedings of the First International Symposium on Auditory and Audiological Research (ISAAR), Helsingør, Denmark, pp. 585–593.

Bergman, M., Blumenfeld, V. G., Cascardo, D., Dash, B., Levitt, H., and Margulies, M. K. (**1976**). "Age-related decremenet in hearing for speech. Sampling and longitudinal studies," J. Gerontol. **31**, 533–538.

Bregman, A. S. (**1990**). *Auditory Scene Analysis: The Perceptual Organization of Sound* (MIT, Cambridge).

Bregman, A. S., and Dannenbring, G. L. (**1977**). "Auditory continuity and amplitude edges," Can. J. Psychiatry **31**, 151–159.

Cherry, C., and Wiley, R. (**1967**). "Speech communications in very noisy environments," Nature (London) **214**, 1164.

Dannenbring, G. L. (**1976**). "Perceived auditory continuity with alternately rising and falling frequency transitions," Can. J. Psychiatry **30**(2), 99–114.

Dirks, D. D., and Bower, D. (**1970**). "Effect of forward masking and backward masking on speech intelligibility," J. Acoust. Soc. Am. **47**, 1003–1008.

Dubno, J. R., Horwitz, A. R., and Ahlstrom, J. B. (**2003**). "Recovery from prior stimulation: Masking of speech by interrupted noise for younger and older adults with normal hearing," J. Acoust. Soc. Am. **113**, 2084–2094.

Edwards, B. (**2004**). "Hearing aids and hearing impairment," *Speech Pro-*

cessing in the Auditory System, Springer Handbook of Auditory Research Vol. **18**, edited by S. Greenberg, W. A. Ainsworth, A. N. Popper, and R. R. Fay (Springer-Verlag, New York).
Eisenberg, L. S., Dirks, D. D., and Bell, T. S. (**1995**). "Speech recognition in amplitude-modulated noise of listeners with normal and listeners with impaired hearing," J. Speech Hear. Res. **38**, 222–233.
Festen, J. M., and Plomp, R. (**1990**). "Effects of fluctuating noise and interfering speech on the speech-reception threshold for impaired and normal hearing," J. Acoust. Soc. Am. **88**, 1725–1736.
Gaskell, H., and Henning, G. B. (**1999**). "Forward and backward masking with brief impulsive stimuli," Hear. Res. **129**, 92–100.
Gordon-Salant, S., and Fitzgibbons, P. J. (**1993**). "Temporal factors and speech recognition performance in young and elderly listeners," J. Speech Hear. Res. **36**, 1276–1285.
Hansen, M. (**2002**). "Effects of multi-channel compression time constants on subjectively perceived sound quality and speech intelligibility," Ear Hear. **23**, 369–380.
Hopkinson, N. T. (**1967**). "Combined effects of interruption and interaural alternation on speech intelligibility," Lang Speech **10**, 234–243.
Houtgast, T. (**1972**). "Psychophysical evidence for lateral inhibition in hearing," J. Acoust. Soc. Am. **51**, 1885–1894.
Houtgast, T. (**1974**). "Lateral suppression in hearing: A psychophysical study on the ear's capability to preserve and enhance speech contrasts," Ph.D. thesis, Free University of Amsterdam, Amsterdam, The Netherlands.
Huggins, A. W. F. (**1964**). "Distortion of the temporal pattern of speech: Interruption and alternation," J. Acoust. Soc. Am. **36**, 1055–1064.
Husain, F. T., Lozito, T. P., Ulloa, A., and Horwitz, B. (**2005**). "Investigating the neural basis of the auditory continuity illusion," J. Cogn Neurosci. **17**, 1275–1292.
IEEE (**1969**). "IEEE recommended practice for speech quality measurements," IEEE Trans. Audio Electroacoust. **AU-17**, 225–246.
Kreul, E. J. (**1971**). "Speech intelligibility for interaural alternated speech with and without intervening noise for words and nonsense," Lang Speech **14**, 99–107.
Kuk, F. K. (**1999**). "Theoretical and practical considerations in compression hearing aids," Trends Amplif. **1**, 5–39.
Madix, S. G., Thelin, J. W., Plyler, P. N., Hedrick, M., and Malone, J. (**2005**). "The effects of age and context on phonemic restoration in young adult females," American Academy of Audiology Annual Conference, Washington, D.C., poster presentation.
Miller, G. A., and Licklider, J. C. R. (**1950**). "The intelligibility of interrupted speech," J. Acoust. Soc. Am. **22**, 167–173.
Moore, B., Laurence, R., and Wright, D. (**1985**). "Improvements in speech intelligibility in quiet and in noise produced by two-channel compression hearing aids," Br. J. Audiol. **19**, 175–187.
Nelson, D. A., and Pavlov, R. (**1989**). "Auditory time constants for off-frequency forward masking in normal-hearing and hearing-impaired listeners," J. Speech Hear. Res. **32**, 296–306.
Nilsson, M., Soli, S., and Sullivan, J. (**1994**). "Development of the hearing in noise test for the measurement of speech reception thresholds in quiet and noise," J. Acoust. Soc. Am. **95**, 1085–1099.
Pichora-Fuller, K. M., Schneider, B. A., and Daneman, M. (**1995**). "How young and old adults listen to and remember speech in noise," J. Acoust. Soc. Am. **97**, 593–608.
Powers, G. L., and Wilcox, J. C. (**1977**). "Intelligibility of temporally interrupted speech with and without intervening noise," J. Acoust. Soc. Am. **61**, 195–199.
Rabinowitz, W. M., Eddington, D. K., Delhorne, L. A., and Cuneo, P. A. (**1992**). "Relations among different measures of speech reception in subjects using a cochlear implant," J. Acoust. Soc. Am. **92**, 1869–1881.
Repp, B. H. (**1992**). "Perceptual restoration of a "missing" speech sound: Auditory induction or illusion?," Percept. Psychophys. **51**, 14–32.
Samuel, A. G. (**1981**). "Phonemic restoration: Insights from a new methodology," J. Exp. Psychol. Gen. **110**, 474–494.
Samuel, A. G. (**1996**). "Does lexical information influence the perceptual restoration of phonemes?," J. Exp. Psychol. Gen. **125**, 28–51.
Schubert, E. D., and Parker, C. D. (**1955**). "Addition to Cherry's finding on switching speech between the two ears," J. Acoust. Soc. Am. **27**, 792–794.
Shinn-Cunningham, B. G., and Wang, D. (**2008**). "Influences of auditory object formation on phonemic restoration," J. Acoust. Soc. Am. **123**, 295–301.
Sivonen, P., Maess, B., Lattner, S., and Friederici, A. D. (**2006**). "Phonemic restoration in a sentence context: Evidence from early and late ERP effects," Brain Res. **1121**, 177–189.
Srinivasan, S., and Wang, D. (**2005**). "A schema-based model for phonemic restoration," Speech Commun. **45**, 63–87.
Stuart, A., and Phillips, D. P. (**1996**). "Word recognition in continuous and interrupted broadband noise by young normal-hearing, older normal-hearing, and presbyacusic listeners," Ear Hear. **17**, 478–489.
Souza, P. (**2002**). "Effects of compression on speech acoustics, intelligibility, and sound quality," Trends Amplif. **6**, 131–165.
Thurlow, W. R. (**1957**). "An auditory figure-ground effect," Am. J. Psychol. **70**, 653–654.
Thurlow, W. R., and Elfner, L. F. (**1959**). "Continuity effects with alternately sounding tones," J. Acoust. Soc. Am. **31**, 1337–1339.
Van Tasell, D. J. (**1993**). "Hearing loss, speech and hearing aids," J. Speech Hear. Res. **36**, 228–244.
Verschuure, J., and Brocaar, M. P. (**1983**). "Intelligibility of interrupted speech with and without intervening noise," Percept. Psychophys. **33**, 232–240.
Warren, R. M. (**1970**). "Perceptual restoration of missing speech sounds," Science **167**, 392–393.
Warren, R. M. (**1984**). "Perceptual restoration of obliterated sounds," Psychol. Bull. **96**, 371–383.
Warren, R. M., and Obusek, C. J. (**1971**). "Speech perception and phonemic restorations," Percept. Psychophys. **9**, 358–362.
Warren, R. M., Obusek, C. J., and Ackroff, J. M. (**1972**). "Auditory induction: Perceptual synthesis of absent sounds," Science **176**, 1149–1151.
Warren, R. M., Bashford, J. A., Jr., Healy, E. W., and Brubaker, B. S. (**1994**). "Auditory induction: Reciprocal changes in alternating sounds," Percept. Psychophys. **55**, 313–322.
Wiley, R. (**1968**). "Speech communication using the strongly voiced components only," Ph.D. thesis, Imperial College, University of London, London, UK.
Wingfield, A., and Tun, P. A. (**2001**). "Spoken language comprehension in older adults: Interactions between sensory and cognitive change in normal hearing," Semin. Hear. **22**, 287–302.
Wingfield, A., Aberdeen, J. S., and Stine, E. A. (**1991**). "Word onset gating and linguistic context in spoken word recognition by young and elderly adults," J. Gerontol. **46**, 127–129.
Woods, W. S., Hansen, M., Wittkop, T., and Kollmeier, B. (**1996**). "A scene analyzer for speech processing," *Proceedings of the ESCA Workshop on the Auditory Basis of Speech Perception, ABSP-1996* (International Speech Communication Association (ISCA), Keele, U.K.), pp. 232–235.

Multitalker speech perception with ideal time-frequency segregation: Effects of voice characteristics and number of talkers

Douglas S. Brungart[a)]
Air Force Research Laboratory, Human Effectiveness Directorate, 2610 Seventh Street, Wright-Patterson AFB, Ohio 45433

Peter S. Chang
Department of Computer Science and Engineering, The Ohio State University, Columbus, Ohio 43210

Brian D. Simpson
Air Force Research Laboratory, Human Effectiveness Directorate, 2610 Seventh Street, Wright-Patterson AFB, Ohio 45433

DeLiang Wang
Department of Computer Science and Engineering and Center for Cognitive Science, The Ohio State University, Columbus, Ohio 43210

(Received 11 December 2007; revised 6 March 2009; accepted 23 March 2009)

When a target voice is masked by an increasingly similar masker voice, increases in energetic masking are likely to occur due to increased spectro-temporal overlap in the competing speech waveforms. However, the impact of this increase may be obscured by informational masking effects related to the increased confusability of the target and masking utterances. In this study, the effects of target-masker similarity and the number of competing talkers on the energetic component of speech-on-speech masking were measured with an ideal time-frequency segregation (ITFS) technique that retained all the target-dominated time-frequency regions of a multitalker mixture but eliminated all the time-frequency regions dominated by the maskers. The results show that target-masker similarity has a small but systematic impact on energetic masking, with roughly a 1 dB release from masking for same-sex maskers versus same-talker maskers and roughly an additional 1 dB release from masking for different-sex masking voices. The results of a second experiment measuring ITFS performance with up to 18 interfering talkers indicate that energetic masking increased systematically with the number of competing talkers. These results suggest that energetic masking differences related to target-masker similarity have a much smaller impact on multitalker listening performance than energetic masking effects related to the number of competing talkers in the stimulus and non-energetic masking effects related to the confusability of the target and masking voices. [DOI: 10.1121/1.3117686]

PACS number(s): 43.71.Gv, 43.66.Dc [RLF] Pages: 4006–4022

I. INTRODUCTION

Speech perception in multitalker listening environments is limited by two very different types of masking. The first is energetic masking, which occurs when the acoustic elements of the target and masking signals overlap in time and frequency in such a way that portions of the target signal are rendered undetectable in the combined audio mixture. The second type of masking, often referred to as informational masking, occurs when the acoustic characteristics of the target and masking voices are perceptually similar and the listener is unable to successfully extract or segregate acoustically detectable target information from the multitalker mixture (Brungart, 2001; Carhart and Tillman, 1969; Freyman *et al.*, 1999; Kidd *et al.*, 1998; Pollack, 1975).

Because both types of masking occur in all multitalker listening tasks, it is often very difficult to tease apart the relative impacts that energetic and informational masking have in even the simplest multitalker listening environments. For example, consider the case of a target talker who is masked either by a similar-sounding talker of the same sex or a very different sounding talker of the opposite sex. Intuitively, it seems quite obvious that performance would be better with a different-sex masker than with a same-sex masker, and many experiments have shown this to be the case (Brokx and Nooteboom, 1982; Bird and Darwin, 1998; Assman and Summerfield, 1994; Darwin *et al.*, 2003; Brungart *et al.*, 2001; Festen and Plomp, 1990). However, the underlying reason for this improvement in performance is not at all easy to identify. In part, it could be the result of reduced spectro-temporal overlap between the target and masking signals. Female voices typically have F0 values about one octave higher than those of males, and they have formant values roughly 16% higher than those of typical

[a)]Author to whom correspondence should be addressed. Electronic mail: douglas.brungart@wpafb.af.mil

 0001-4966/2009/125(6)/4006/17/$25.00

male talkers (Peterson and Barney, 1952). This should lead to some reduction in spectro-temporal overlap between male and female voices, and thus an improvement in intelligibility due to a reduction in energetic masking.

However, it is quite likely that some improvement in intelligibility will also occur simply because the different-sex talkers are much more distinct and less confusable than same-sex talkers. The difficulty lies in determining the relative contributions that reduced spectral overlap and reduced confusability make to the improvement in performance that occurs with a different-sex masker versus a same-sex masker. The most direct results addressing this issue come from a paper by Festen and Plomp (1990) that compared the speech reception thresholds (SRTs) for speech masked by a same or different-sex talker under a variety of conditions. In the baseline condition, where normal speech was used for both the target and masking voices, the SRT was 7–11 dB lower for a different-sex masking voice than for a same-sex masking voice. However, when the same- or different-sex masking voice was replaced by a noise signal that was shaped to have the same long-term spectrum as the masking talker, the SRT advantage in the different-sex condition dropped to less than 2 dB. This suggests that differences in long-term spectrum can account for very little of the release from masking that occurs with a different-sex masking voice. Of course, such an analysis ignores the fact that the spectra of the target and masking voices vary constantly over the course of the utterance. Festen and Plomp (1990) attempted to capture this effect by dividing the signal into two bands (above and below 1 kHz) and separately modulating the amplitudes of the bands to match the envelopes of the corresponding bands of the original masking speech utterances. Again, the results of this condition showed very little release from masking ($<$2 dB) in the different-sex conditions.

The Festen and Plomp (1990) results suggest that energetic factors related to reduced spectro-temporal overlap can account for very little of the improvement in SRT found for different-sex maskers. However, their technique cannot fully account for the release from energetic masking that is likely to occur with a different-sex masker. At low frequencies, the larger differences in F0 that occur for different-sex talkers might lead to a reduction in the instantaneous overlap in the resolved harmonics of the speech signal that would not be captured in the long-term average spectrum of the masking speech (Qin and Oxenham, 2003). At higher frequencies, the two-band modulation is simply insufficient to capture the true spectral fluctuations of the same and different-sex voices. Increasing the number of modulation bands is problematic as well: as the number of bands increases, the masking speech becomes increasingly speech-like, and there is an ever increasing possibility that performance will be limited by the confusability of the target and masking voices and not by the loss of information incurred due to spectro-temporal overlap in the target and masking waveforms.

Another possible approach for isolating the energetic component of speech on speech masking involves the spatial separation of the target and masking signals. Previous research has shown that spatial separation in the perceived locations of the target and masking signals reduces the potential confusability of the two signals and thus results in a substantial reduction in the informational masking caused by the interfering speech stimulus (Freyman *et al.*, 1999). Earlier studies have also shown that the performance differences between same-sex and different-sex maskers are much smaller when the masking voices are spatially separated from the target voice than when they originate from the same location as the target talker (Brungart and Simpson, 2002). Indeed, in the largest spatial separation conditions tested, where the target was located just outside the listener's right ear and the masker was located 1 m away or vice versa, Brungart and Simpson (2002) found almost no difference in performance with same-sex and difference-sex interfering talkers. If one hypothesizes that the energetic component of speech-on-speech masking from a same- or different-sex talker can be approximated by the amount of residual masking that occurs when a speech masker is perceived to be spatially separated from a target speech signal (Freyman *et al.*, 2007), then this result seems to confirm the results of the Festen and Plomp (1990) study showing that there is only a modest difference in energetic masking between same-sex and different-sex interfering voices.

However, the use of spatial separation as a means to isolate energetic masking effects in multitalker speech stimuli is potentially problematic in two important ways. The first is that it is based on the assumption that informational masking is largely eliminated when two speech signals appear to originate from different locations in space. This assumption contrasts with the results of Arbogast *et al.* (2002), which showed that an interfering speech signal can still produce a substantial amount of informational masking even when it is spatially separated 90° apart from the target speech. That experiment used a sinewave vocoding procedure to produce target and masking speech signals that had little or no spectral overlap but were highly intelligible when they were presented individually. The results of the experiment showed that the spatially-separated speech masker produced roughly 7 dB more masking than a spatially-separated random-phase noise masker with the same spectral content. This 7 dB difference suggests that some residual informational masking may remain even when the perceptual locations of the target and masking talkers are clearly separated.

The second potential problem with the use of spatial separation as a means to isolate energetic masking effects in multitalker listening is that the spatial separation itself will lead to a substantial reduction in the energetic masking component of the stimulus. Spatial separation typically results in an increase in signal-to-noise ratio (SNR) at one of the listeners ears (the so-called "better ear advantage") and an additional release from masking due to low-frequency interaural phase differences in the competing stimuli (the "binaural interaction" effect). Thus, to the extent that spatial separation eliminates the informational component of speech-on-speech masking, it will only provide an indication of the effects of energetic masking for a spatially-separated target-masker pair. In cases where there is a desire to explicitly determine the effects of energetic masking for co-located talkers, or in cases such as those involving monaural listeners where spa-

tial separation of the talkers is not an option, alternative methods of isolating the energetic components of speech-on-speech masking are required.

One possible alternative method for evaluating the impact of spectro-temporal overlap on speech-on-speech masking for same-sex and different-sex masking speech is ideal time-frequency segregation (ITFS), a recently proposed technique that attempts to simulate the effects of energetic masking by removing those spectro-temporal regions of the acoustic mixture where the target signal is dominated by the masker waveform (Brungart *et al.*, 2006). ITFS is a signal processing technique that removes time-frequency (T-F) regions of a mixture where target energy would be rendered undetectable by a more intense masker; at the same time, it retains all the T-F regions of the mixture where the target would remain detectable despite the presence of the masker. The term ITFS comes from the fact that the processed signal represents an "ideal" segregation of the acoustic elements that potentially contain useful information about the target signal from a background that contains only information about the masker. Because it eliminates the T-F regions of the stimulus where the local SNR is negative, the ITFS technique presumably removes the same target information from the stimulus that would ordinarily be irretrievably lost due to spectro-temporal overlap with the masker. The advantage of the technique is that the removal of the masked portions of the stimulus eliminates any acoustic portions of the masker that might be confused with the target and thus cause informational masking. While there are clearly some potential areas (forward/backward masking, T-F resolution, etc.) where the ITFS technique may fail to accurately capture all aspects of energetic masking in speech perception (Brungart *et al.*, 2006), the general framework of the ITFS technique provides a means to examine the energetic masking effects that influence the detection of a target signal in an acoustic mixture without potentially confounding effects that might occur due to informational masking.

Brungart *et al.* (2006) showed that the application of the ITFS technique to an acoustic mixture had very different results on the intelligibility of the target signal for noise maskers and speech maskers. When the masking signal was noise, the application of the ITFS technique resulted in a modest (2–5 dB) improvement in the SRT of the target speech. However, when the masking signal was a 1-, 2-, or 3-talker speech signal, the application of the ITFS technique resulted in a much larger release from masking (22–25 dB). The size of the release from masking obtained for the speech masking stimuli in the 2006 study is an indicator of how effectively the ITFS technique is able to eliminate the speech-on-speech masking component that is related to the potential confusability of the target and masking voices. By comparing the residual masking remaining after the application of ITFS, it should be possible to assess the relative differences in masking that occur due to spectro-temporal overlap in two competing speech signals. Thus, one should be able to use ITFS to determine the extent to which a same-talker masker produces more energetic masking than a same-sex or different-sex masker. However, the 2006 study only used same-talker maskers, so no such comparison is possible.

In this paper, we apply the ITFS technique developed in the 2006 study to examine the impact that differences in target and masker voice characteristics have on the energetic component of masking in multitalker speech perception. In a second experiment, we extend the technique to examine how energetic masking effects vary with the number of competing talkers in the stimulus. Section II describes the ITFS technique in more detail.

II. ITFS

ITFS is closely related to the notion of ideal binary mask originated in computational auditory scene analysis (Wang and Brown, 2006, pp. 22–23). Assuming a two-dimensional T-F representation where elements are called T-F units, an ideal binary mask is defined as a binary matrix where 1 indicates that the target energy in the corresponding T-F unit exceeds the interference energy by a predefined local SNR criterion (LC) and 0 indicates otherwise. The mask is called ideal because its construction requires *a priori* knowledge of the spectral content of the target and masking signals, and the selection of a LC value of 0 dB is known to be optimal in terms of the theoretical SNR gain of the processed output mixture (see Wang, 2005; Li and Wang, 2009).

Figure 1 illustrates the ideal binary masks for two-talker mixtures where the target is a male utterance and the masker is a sentence uttered by the same talker, a different male talker, or a female talker. In the figure, mixtures SNR and LC are both set to 0 dB. The top row of Fig. 1 shows the cochleagram of the target. Similar to a spectrogram, a cochleagram is a T-F representation produced by filtering a signal using an auditory filterbank and then windowing each filter response into time frames (Wang and Brown, 2006, pp. 15–19). Aside from the target cochleagram, the same-talker masker condition is shown in the left column, the same-sex masker condition in the middle column, and the different-sex masker condition in the right column. The second row shows the masker cochleagrams in the three conditions, the third row shows the corresponding ideal binary masks where 1 is indicated by white and 0 by black, the fourth row shows the corresponding cochleagrams of the mixtures, and the bottom row shows the ITFS processed mixtures. There is general similarity among the three ideal masks, reflecting the fact that the same target utterance is used and all the masker utterances correspond to the same sentence. However, the ideal masks are different, and the difference is quite noticeable between the same-talker and different-sex talker conditions. For example, the right ideal mask has extended white regions at the bottom which are missing from the left ideal mask, because the first harmonic of the female masker occurs in a higher frequency range than the first harmonic of the male masker.

A visual inspection reveals a resemblance between the ITFS-processed stimuli in the bottom row of Fig. 1 and the original target signal in the top row. Because the ITFS technique removes energy from the masking speech without sig-

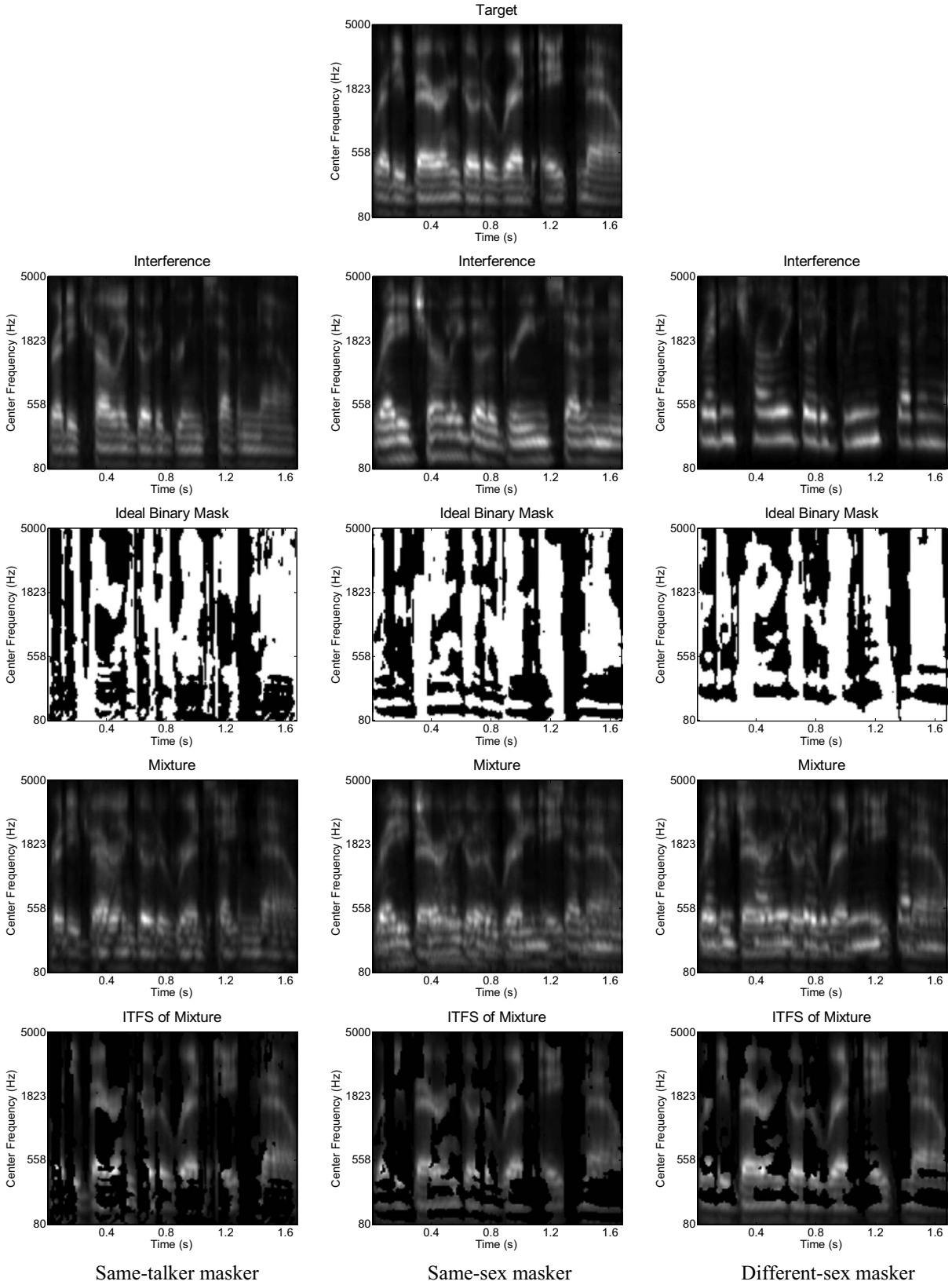

FIG. 1. ITFS illustration for mixtures of two utterances of the same talker, same-sex talkers, and different-sex talkers. Top row: Cochleagram of a target male utterance ("Ready Baron go to red eight now"). The figure displays the responses of the 128-channel gammatone filterbank, where the response energy at each T-F unit is raised to the $\frac{1}{4}$ power for better display. Second row: Cochleagrams of an interfering utterance ("Ready Charlie go to green seven now") spoken by the same talker (left), a same-sex talker (middle), and a different-sex talker (right). Third row: Corresponding ideal binary masks with 0 dB LC, where white pixels indicate 1 and black pixels indicate 0. Fourth row: Corresponding cochleagrams of the mixtures. Bottom row: Corresponding ITFS processed mixtures.

nificantly distorting the spectro-temporal pattern of the original target speech, it often produces large improvements in intelligibility when it is applied to a multitalker acoustic mixture. Brungart *et al.* (2006) reported that ITFS processing produced an intelligibility improvement that was approximately equivalent to a 22–25 dB decrease in the SRT of a multitalker speech signal.

Since ITFS processing does not divide the mixture energy within a T-F unit into target and masker portions but rather makes a binary, all-or-none decision on the mixture energy, it would be interesting to know whether the noise energy in a retained unit hinders speech intelligibility. Drullman (1995) examined a similar question by comparing speech intelligibility in two conditions using an auditory filterbank. In the first condition, noise was kept in the mixture where the noise level in a filter response was lower than the speech level; in the second condition, the noise was removed from the mixture. He found that removing noise that is below the speech level has no effect on intelligibility. On the other hand, a different comparison showed that substituting noise for speech that is below the noise level elevates the SRT by 2 dB (Drullman, 1995). This suggests that there is some useful speech information in T-F units where local SNR is negative, and this is consistent with the observation that a performance plateau with nearly perfect intelligibility centers at the LC value of −6 dB rather than the 0 dB LC (Brungart *et al.*, 2006)—the former LC retains more T-F units where local SNR is between 0 and −6 dB.

Although ideal binary masking techniques have been used for some time in computational auditory scene analysis, they have only recently begun to be applied as a psychophysical tool for measuring human auditory perception. Anzalone *et al.* (2006) tested the effects of processing with a related version of ideal binary mask, defined not in terms of a comparison between target energy and interference energy but a comparison between target energy and a predefined threshold. More specifically, a mask value of 1 was applied if and only if the corresponding target level exceeded a fixed threshold. They used mixtures of speech and speech-shaped noise, and documented the results in terms of SRT. The results show that ideal binary masking leads to substantial SRT reductions: more than 7 dB for normal-hearing listeners and more than 9 dB for hearing impaired listeners. Another intelligibility study by Li and Loizou (2007) used the ideal binary mask to generate "glimpses," or T-F regions with stronger target energy, to study several factors that impact glimpsing of speech in a mixture signal. Their results show that glimpses in the low- to mid-frequency range (up to 3 kHz) containing the first and the second formant of speech are particularly important for speech perception. They also showed that high intelligibility does not require perception of the entire utterance: glimpsing information in a majority of time frames (60%) seems to be sufficient for most intelligibility tasks.

III. EXPERIMENT 1: EFFECTS OF VOICE CHARACTERISTICS ON MULTITALKER LISTENING WITH ITFS

As stated earlier, differences in voice characteristics of competing talkers, in particular, the differences that exist between male and female voices, can increase speech perception performance (relative to the baseline case where the same talker is used for both the target and masking phrases) by as much as an equivalent increase of 7–11 dB in the SNR of the target speech (Festen and Plomp, 1990). In part, this improvement in performance occurs because reduced spectro-temporal overlap between the different-sex talkers allows the listener to "glimpse" a larger portion of the target speech. However, many other non-energetic factors also may contribute to this performance difference. In order to examine the influence of target and interferer similarity on the energetic component of speech-on-speech masking, an experiment was conducted that used the ITFS approach to compare multitalker listening performance with three levels of similarity between target and masking voices: a same-talker condition, where the target and interfering phrases were spoken by the same talker; a same-sex condition, where target and masking phrases were spoken by different talkers of the same sex; and a different-sex condition, where interfering phrases were spoken by talkers who were of the opposite sex of the target talker.

A. Methods

1. Stimuli

As in the previous study of Brungart *et al.* (2006), the speech stimuli used in this experiment were drawn from the publicly available coordinate response measure (CRM) speech corpus for multitalker communications research (Bolia *et al.*, 2000). The CRM corpus is based on a speech intelligibility test first developed by Moore (1981). The corpus contains phrases of the form "Ready (call sign) go to (color) (number) now." There are eight possible call signs ("Arrow," "Baron," "Charlie," "Eagle," "Hopper," "Laker," "Ringo," and "Tiger"), four possible colors ("blue," "green," "red," and "white"), and eight possible numbers (1–8). An example utterance is "Ready Baron go to blue five now." Eight talkers, four male and four female, were used to record each of the 256 possible phrases, resulting in a total of 2048 phrases in the corpus.

For each trial in the experiment, the target signal was a CRM phrase randomly selected from all the phrases containing the target call sign "Baron." The interference consisted of one, two, or three different phrases randomly selected from the CRM corpus that were spoken by the same talker, a different talker of the same sex, or a different talker of the opposite sex, depending on the particular condition of the experiment. Interfering phrases contained call-signs, color coordinates, and number coordinates that were different from the target phrase and different from each other. Each of the interfering phrases was scaled to have the same overall rms power as the target phrase, and then all the interfering

phrases were summed together to produce the overall interference used for ITFS. The target phrase and the interference were added to form the mixture signal.

Note the distinction between the target-to-masker ratio (TMR) and SNR, the former referring to the ratio of the target speech level to the level of each interfering talker and the latter to the ratio of the target talker level to the overall interference level. Hence, TMR was set to 0 dB in this experiment while SNR could be 0 dB or negative depending on how many competing talkers were included in the interference.

2. Listeners

Nine paid subjects participated in the experiment. The listeners all had normal hearing and their ages ranged from 18 to 54 years. Most had participated in previous auditory experiments, and all were familiarized with the CRM corpus and the experimental task prior to conducting this experiment.

3. ITFS segregation processing

Given a target signal, an interference signal, and a LC value, an ideal binary mask was constructed and used to resynthesize the mixture to generate a single ITFS stimulus (see Brungart *et al.*, 2006). Specifically, an input signal was first decomposed using a bank of 128 fourth-order gammatone filters with overlapping passbands (Patterson *et al.*, 1988) and with center frequencies ranging from 80 to 5000 Hz. Each filter response was further divided into 20 ms time frames with 10 ms overlap. Hence, the input signal was transformed into a matrix of T-F units. Within each T-F unit, the local SNR was calculated. If the local SNR was greater than or equal to the LC value, the ideal binary mask was assigned the value of 1 for this T-F unit and the mixture signal within the unit was included in the ITFS signal; if the local SNR was less than the LC value, the binary mask was assigned the value of 0 for the unit and the mixture signal within the unit was excluded from the ITFS signal. For further details on resynthesis from a binary mask, see Brungart *et al.* (2006) and Wang and Brown (2006, pp. 23–25).

Fourteen LC conditions were tested in the experiment, including values ranging from −48 to +30 dB. The LC values were chosen so that more values were tested in the range of 12–24 dB where speech intelligibility is known to drop sharply with increasing LC (Brungart *et al.*, 2006). An unsegregated control condition was also included, where the stimulus was generated by applying ITFS processing to a mixture signal with an all-1 mask. Hence, the control condition amounted to presenting the mixture to a listener after equalizing for any possible distortion that might be introduced by ITFS processing. In all cases, the overall presentation level of the stimulus was kept approximately constant (roughly 65 dB sound pressure level) across all LC values by scaling the maximum value of the ITFS-processed mixture waveform to a fixed level prior to presentation of the stimulus.

4. Procedure

During the experiment, a listener was seated at a control computer in a quiet listening room. The stimuli were generated by a sound card in the control computer (Soundblaster Audigy) and presented to the listener diotically over headphones (Sennheiser HD-520). On each trial, the listener was instructed to use the mouse to select the colored digit corresponding to the color and number of the target phrase (containing the call sign "Baron") on an eight-column, four-row array of colored digits corresponding to the response set of the CRM task.

The experiment was divided into three sub-experiments, with each sub-experiment examining performance with two, three, or four competing talkers over a specific range of LC values. Because some LC values were repeated across sub-experiments, this resulted in an uneven distribution of data collection across the 15 LC conditions tested in the experiment, with some additional trials collected at LC values that overlapped across the sub-experiments. The stimuli for each listener were selected randomly prior to the start of the experiment, processed off-line, and stored on a personal computer (PC) for later presentation to the listeners.

Seven subjects participated in a complete set of trials across the three sub-experiments, resulting in a total of 4500 trials, divided into blocks of 50 trials. The different numbers of talkers and the different characteristics of the interfering talker(s) were evenly distributed across all the trials. Thus, for these subjects, there were 500 trials for each of the nine configurations (2-, 3-, and 4-talkers by same-talker, same-sex, and different-sex configurations). Two additional subjects completed only part of the experiment (3000 trials and 600 trials, respectively). Data from these subjects were included in the overall data analysis, but they were excluded from analyses that required the calculation of separate thresholds for the individual subjects.

B. Results and discussion

Figure 2 shows the percentage of correct color and number identifications as a function of the LC value used to generate the ITFS stimulus for all the configurations in the experiment. The figure is divided into three panels to separate the results for 2, 3, and 4 simultaneous talkers. Within each panel, the three curves show performance for three different levels of similarity between the target and the interfering voices: same-talker, same-sex, and different-sex. Each data curve was generated by fitting with two logistic functions: one for LC values greater than 0 dB, and one for LC values less than 0 dB (Cavallini, 1993). The data in the curves were averaged across listeners, and the error bars in the figure represent the 95% confidence interval for each data point.

The leftmost points of each curve in Fig. 2 show the results from the unsegregated control condition where all of the T-F units in the original mixture were retained in the processed speech. In the same-talker conditions, the listeners correctly identified both the color and number in the target phrase in 8% of the trials in the 4-talker condition, 23% in the 3-talker condition, and 45% in the 2-talker condition.

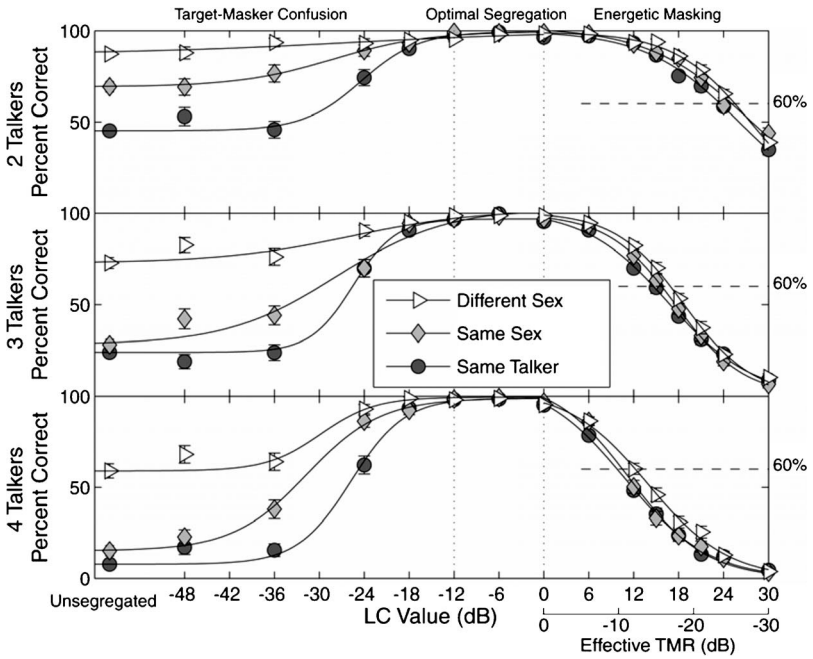

FIG. 2. Percentage of correct color and number identifications in Experiment 1 as a function of LC. The top panel shows results for the 2-talker conditions, the middle panel shows results for the 3-talker conditions, and the bottom panel shows results for the 4-talker conditions. The error bars represent 95% confidence intervals (±1.96 standard errors, calculated from the pooled response data across all listeners) in each condition. Horizontal dashed lines indicate the 60% threshold levels of performance at positive LC values.

This level of performance is comparable to that achieved in the unsegregated conditions of our previous study examining the effect of ITFS processing on same-talker speech (Brungart *et al.*, 2006). Switching from same-talker interfering voices to same-sex interfering voices improved performance substantially in the 2-talker condition but produced a relatively modest improvement in performance in the 3- and 4-talker conditions. Switching from same-sex interfering voices to different-sex interfering voices, however, produced substantial performance improvements in all the configurations tested. These results are consistent with those that have been obtained in other experiments that examined the effect of target-interferer similarity on 2-, 3-, and 4-talker listening at a 0 dB TMR (Brungart *et al.*, 2001).

1. ITFS regions

As was the case in the earlier ITFS study by Brungart *et al.* (2006), the experimental results show that there are three distinct regions of intelligibility performance: an "optimal segregation" region with 0 dB≥LC≥−12 dB, a "target-masker confusion" region with LC<−12 dB, and an "energetic masking" region with LC>0 dB. In the optimal segregation region, performance was nearly perfect in all conditions tested. In this region, the application of the ITFS processing essentially removed all the audible elements of the masking signals from the stimuli, thus eliminating informational masking related to target-masker confusion. At the same time, the processing preserved enough of the target information to allow near perfect color-number intelligibility in the CRM task. It is clear from these results that, even in extreme cases where an acoustic mixture contains four simultaneous voices spoken by the same talker, there are enough T-F units dominated by the target voice to allow a listener to almost perfectly extract the meaning of the target message.

When the LC value was reduced below −12 dB, performance began to steadily decrease. In this target-masker confusion region, the LC value was increasingly negative, which means that the stimulus included an increasing number of T-F units where the masker was more powerful than the target speech. This did not remove any acoustic information from the target speech signal, per se, although it is possible that in some cases the addition of a relatively high-level masker-dominated T-F unit may have obscured some portions of the target signal due to non-simultaneous masking, either upward or downward in frequency or forward or backward in time. The more profound impact that the addition of these masker-dominated T-F units had on performance was an increased probability of incorrectly grouping the interferer-dominated T-F units retained in the ITFS stimulus with the T-F units in the target speech. These confusions resulted in a dramatic increase in the number of trials where the listener incorrectly responded with the number and color keywords contained in the masking phrase. In our earlier study, we showed that, in the 2-talker condition, nearly 100% of the incorrect responses in the target-masker confusion region matched the color and number keywords spoken by the interfering talker (Brungart *et al.*, 2006). In this experiment, this trend was seen across all the target-masker similarity conditions with 2-, 3-, or 4-talkers, with more than 96% of the incorrect color responses and more than 94% of the incorrect number responses in this region matching the keywords spoken by one of the interfering talkers.

The breakpoint in the LC-performance function at −12 dB represents the point where the interferer-dominated T-F units retained in the ITFS stimulus began to resemble an intelligible masking talker. At LC values greater than −12 dB, the interferer-dominated T-F units introduced into the mixture occurred in T-F regions where the target speech also has relatively significant energy, reducing the probability that those units will be interpreted as an additional masking voice. When the LC value was less than −12 dB, the ITFS stimulus included T-F units where the target speech has relatively very weak energy, and the inclusion of these T-F

TABLE I. Threshold effective TMR values for 60% performance in Experiment 1. These values are obtained from the secondary scale at the lower right of Fig. 2.

	Interferer(s) voice characteristics					
	Same-talker	Same-sex		Different-sex		Mean
2 Talkers	−23.68 dB	−25.14 dB	Δ=−1.46 dB	−25.51 dB	Δ=−0.37 dB	−24.78 dB
3 Talkers	−13.73 dB	−15.14 dB	Δ=−1.41 dB	−16.44 dB	Δ=−1.30 dB	−15.10 dB
4 Talkers	−8.88 dB	−9.58 dB	Δ=−0.70 dB	−10.68 dB	Δ=−1.10 dB	−9.72 dB
Δ Mean			Δ=−1.19 dB		Δ=−0.93 dB	

units appeared to produce a substantial amount of informational masking, particularly in the same-talker and same-sex conditions where the masking voices were qualitatively similar to the target voice. In the limit, where the LC value was set to −48 dB, the stimulus essentially contained both the target and masking speech signals in their entirety, and performance asymptoted at the same level as the unsegregated control condition.

For the purposes of this study, the most informative region of Fig. 2 is the energetic masking region, where the LC value was systematically increased above 0 dB. In this region, overall performance decreased with increasing LC value because an increasingly large proportion of the target speech signal failed to meet the threshold SNR value and thus was eliminated from the stimulus. To the extent that the ITFS methodology captures the temporal and spectral resolution of the auditory system (see Brungart *et al.*, 2006), one would expect performance in this region to be directly related to the amount of energetic masking caused by the spectro-temporal overlap between the target and masking signals. From the results in the figure, it is clear that target-masker similarity had a much smaller impact on performance in the energetic masking region than it did in the target-masker confusion region, where performance was limited by the ability to separate the T-F units associated with target and masker voices rather than by the absence of target-dominated T-F units due to the spectro-temporal overlap in the competing signals. However, it is clear that there was a small but consistent advantage for the different-sex speech in the energetic masking region of Fig. 2.

In order to quantify the magnitude of this advantage, it is helpful to take advantage of the close relationship that exists between LC value and TMR in the energetic masking region (Brungart *et al.*, 2006). In that region, each 1 dB increase in LC value removes the same T-F units from the target speech that would be lost due to the increased spectro-temporal overlap caused by a 1 dB decrease in the SNR of the acoustic mixture, or equivalently a 1 dB decrease in the TMR. Thus, for example, an acoustic mixture with a TMR value of 0 dB that is ITFS processed with a LC value of 6 dB retains exactly the same set of target-dominated T-F units as an acoustic mixture with a TMR value of −6 dB processed with a LC value of 0 dB. Therefore, each data point in the energetic masking region can be viewed as an estimate of optimally segregated ITFS performance for an acoustic mixture with an effective TMR value equal to the negative of the LC value plotted in the figure. These effective TMR values are shown in the secondary scale at the lower right of Fig. 2.

In order to calculate the overall thresholds in each condition, the curves in each panel of Fig. 1 were fitted separately for each of the seven listeners who completed the entire experiment and used to calculate individual thresholds for 60% correct performance for each combination of target-interferer similarity and number of interfering talkers. The resulting mean threshold values are presented in Table I. If the threshold values for each target-masker condition are averaged across the number of talkers, it is apparent that changing from same-talker interfering voices to same-sex interfering voices produced, on average, only a 1.19 dB decrease in the 60% threshold TMR value, and changing from same-sex interfering voices to different-sex interfering voices only produced an additional 0.93 dB decrease in the 60% threshold. In order to evaluate the statistical significance of these differences, the individual 60% thresholds were subjected to a two-factor, within-subject analysis of variance (ANOVA). The results of this ANOVA show that the main effects of target-interferer similarity $[F(2,12)=883.357]$ and number of competing talkers $[F(2,12)=28.418]$ were both significant at the $p<0.001$ level, but that their interaction was not significant $[F(4,24)=0.395,\ p=0.740]$. Thus, on the basis of these results, it seems that target-interferer similarity does have a significant impact on energetic masking in multitalker listening, but that it can account for no more than a 2–3 dB change in the energetic masking effectiveness of an interfering speech signal.

These values can be compared to the results of previous experiments that have used different methods to estimate the differences in the energetic masking efficiency of same- and different-sex voices. As noted in Sec. I, Festen and Plomp (1990) used speech-shaped noise to estimate the energetic masking component of same- and different-sex talkers, and found a difference of less than 2 dB across the two types of masking voices, versus a 7–11 dB difference for normal speech maskers. Thus the results obtained with a speech-shaped noise masker are roughly comparable to those obtained with the ITFS method, despite the substantial differences in methodology.

2. Comparison to statistical analyses of ITFS-processed speech

From the psychoacoustic results shown in Fig. 2, it is clear that there is a small but systematic increase in energetic masking when an interfering voice is made more similar to the target talker, and a large increase in energetic masking when the number of interfering talkers increases. Certainly

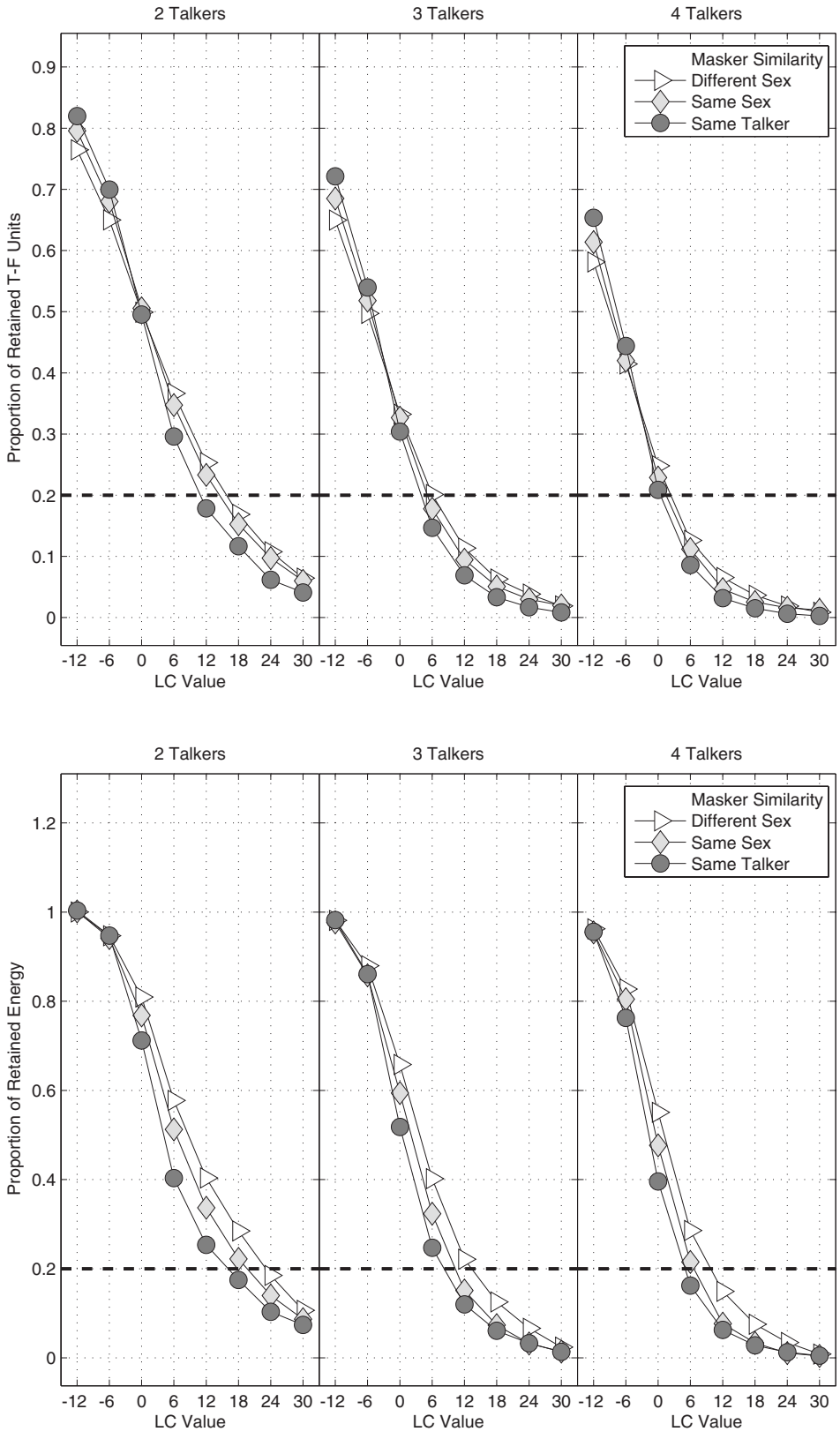

FIG. 3. Acoustic analysis of ITFS-processed stimuli in each masking condition. The top panel shows the proportion of T-F units retained in each stimulus as a function of the LC value. The bottom panel shows the proportion of total energy retained in the target stimulus as a function of the LC value. See text for details.

an interesting question related to these results is the extent to which these psychometric results correlate with the acoustical properties of the target signal that was retained in the ITFS stimulus in each condition. Figure 3 shows two analytical measures of the proportion of the target signal retained after the ITFS processing at each LC value for each masker condition tested in the experiment. The top panel shows the proportion of retained T-F units in each condition. These values were obtained by randomly generating roughly 400 stimuli for each data point using the same procedure used in the psychophysical experiment, and simply counting the number of T-F units retained after the ITFS processing. The

TABLE II. Threshold effective TMR values for retention of 20% of the total T-F units within each type of ITFS-processed stimulus.

	Interferer(s) voice characteristics				
	Same-talker	Same-sex		Different-sex	
2 Talkers	−11.21 dB	−14.29 dB	Δ=−3.08 dB	−15.44 dB	Δ=−1.15 dB
3 Talkers	−3.81 dB	−5.26 dB	Δ=−1.45 dB	−6.22 dB	Δ=−0.96 dB
4 Talkers	−0.45 dB	−1.32 dB	Δ=−0.87 dB	−2.18 dB	Δ=−0.86 dB
Δ Mean			Δ=−1.80 dB		Δ=−0.99 dB

bottom panel shows the proportion of *energy* retained in the stimulus, calculated simply by applying the ideal binary mask for the trial to the target *only* (not the mixture) and determining how much of the target energy was contained in the T-F units that were retained in the ITFS stimulus.

The overall trends of the retained unit and retained energy curves in Fig. 3 are similar to those for the psychoacoustic data in the energetic masking region of Fig. 2, with an increase in the retained portion of the target signal as the similarity between the target and masker decreased. This can be clearly seen in Tables II and III, which show the threshold effective TMR values for 20% retained units and 20% retained energy, respectively, using the same procedure used to calculate the 60% correct individual thresholds in Table I. The overall effects of target-masker similarity were most similar to the psychoacoustic results in the retained-bin metric, where there was a 1.8 dB shift in the threshold for 20% retained units between the same-talker and same-sex conditions (compared to 1.2 dB for the psychoacoustic data), and an additional 1.0 dB difference in the threshold for 20% retained units between the same-sex and different-sex conditions (compared to 0.9 dB for the psychoacoustic data). The shifts for 20% retained energy thresholds shown in Table III were also similar in direction but slightly larger in magnitude than the corresponding shifts in the psychoacoustics results, with a 2.5 dB shift between the same-talker and same-sex conditions and a 3.1 dB shift between the same-sex and different-sex conditions.

Another notable feature shown in the upper panel of Fig. 3 is a reversal in the ordering of the proportion of retained units for the different target-masker similarity conditions when the LC value was less than 0 dB. Indeed, at negative LC values, there were actually more retained units in the same-talker conditions than in the different-sex conditions. This result reflects a fundamental relationship between spectro-temporal overlap and the proportion of retained units in the ideal binary mask paradigm. When the LC value is positive, there is a tendency to eliminate target units in T-F regions where both the target and the masker contain energy, so there is generally a reduction in retained units when the spectro-temporal overlap in the target and masking signals increases. However, when the LC value is negative, this trend is reversed, and there is a general tendency to retain T-F units where the target and masker overlap. Thus, at negative LC values, the proportion of retained target units actually *increases* as the target and masker become more similar. As an illustration of this principle, consider two extreme cases, one where the target and masker have exactly the same energy distribution, and one where they are completely non-overlapping (each occupying 50% of the T-F units). In the completely overlapping case, the proportion of retained units will go from 0% to 100% as the LC value changes from positive to negative, because the local SNR value is exactly 0 dB in every T-F unit. In contrast, in the non-overlapping case, the proportion of retained units remains at 50% independent of the LC value.

In the retained energy proportions shown in the lower panel of Fig. 3, there is no evidence of a reversal in the relative ordering of the different target-masker similarity conditions at negative LC values. This seems to be at least partially related to a ceiling effect in the results. Even in the 4-talker conditions, most of the energy was already retained in the stimulus when the LC value was −6 dB.

If the top and bottom panels are carefully compared across the three different columns of Fig. 3, it is apparent that the ratio of the percentage of retained energy to the percentage of retained units systematically increased as the number of competing talkers increased. This result is most likely related to the changes in the distribution of the energy in the masker. As the number of competing talkers in the stimulus increased, the spectro-temporal distribution of energy in the maskers became more uniform, which reduced the probability of retaining T-F units that contained only a

TABLE III. Threshold effective TMR values for retention of 20% of the total target energy within each type of ITFS-processed stimulus.

	Interferer(s) voice characteristics				
	Same-talker	Same-sex		Different-sex	
2 Talkers	−15.01 dB	−18.76 dB	Δ=−3.75 dB	−21.93 dB	Δ=−3.17 dB
3 Talkers	−7.80 dB	−9.96 dB	Δ=−2.16 dB	−13.14 dB	Δ=−3.18 dB
4 Talkers	−4.68 dB	−6.36 dB	Δ=−1.68 dB	−9.39 dB	Δ=−3.03 dB
Δ Mean			Δ=−2.53 dB		Δ=−3.13 dB

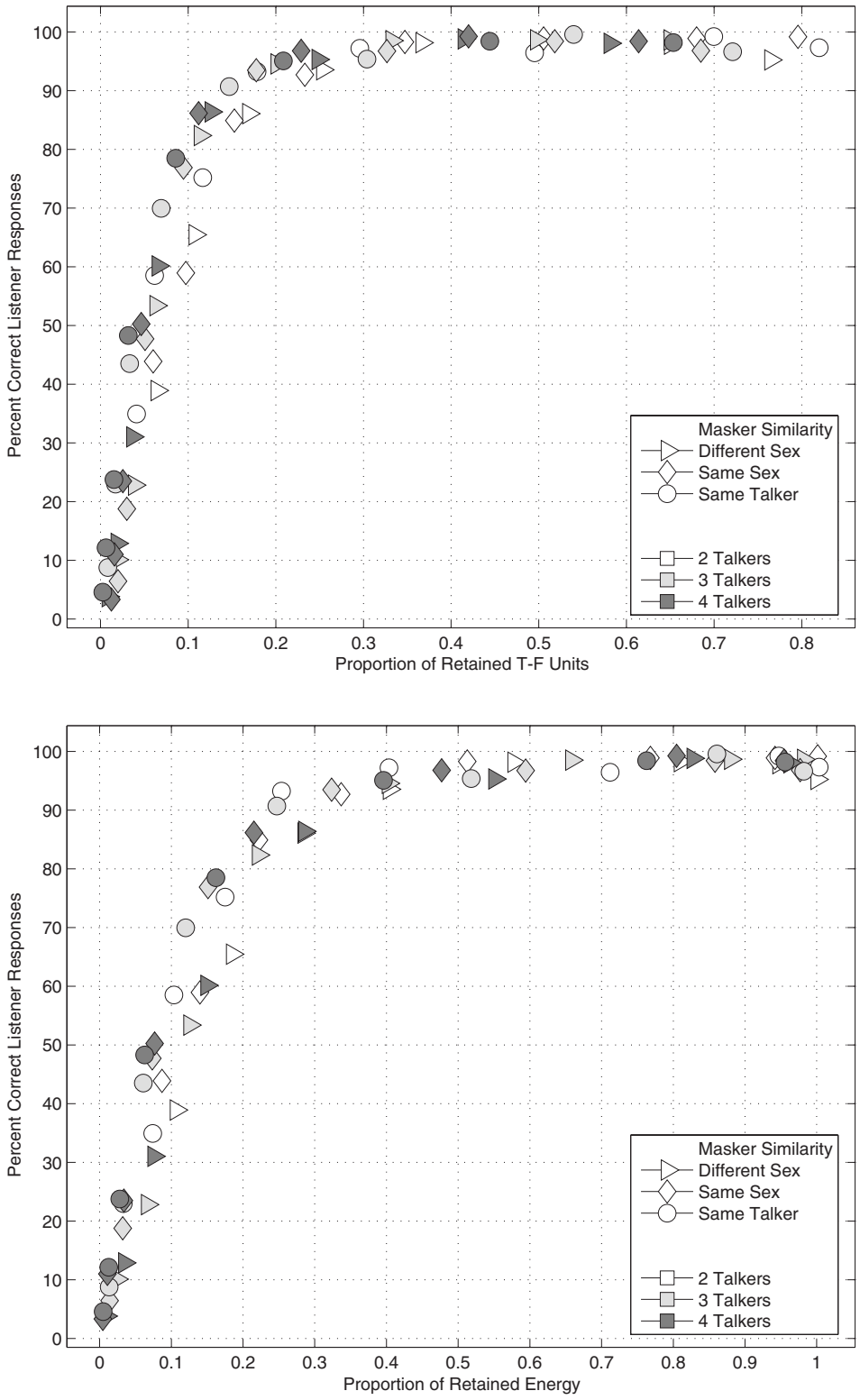

FIG. 4. Scatter plot showing the percentage of correct color and number responses in Experiment 1 as a function of the average proportion of retained T-F units (top panel) and average proportion of retained target energy (bottom panel), in each stimulus condition.

small amount of target energy. This had the net effect of increasing the average amount of target energy per unit in the ITFS stimulus.

The proportions of retained units and retained energy also appeared to do a good job of predicting the overall intelligibility of an ITFS stimulus across different numbers of talkers and different LC values in Experiment 1. This can be seen from Fig. 4, which shows scatter plots of the percentage of correct listener responses in each masker configuration as a function of the proportion of retained units (upper plot) and the proportion of retained target energy (lower plot). In general, the relatively tight distributions of data points in these two scatter plots show that listener performance was similar across all the stimulus conditions that resulted in a similar proportion of retained units or a similar proportion of retained target energy. However, there are two notable trends in the data. In the retained unit plot (upper panel), there was a general tendency for performance in the 2-talker condition

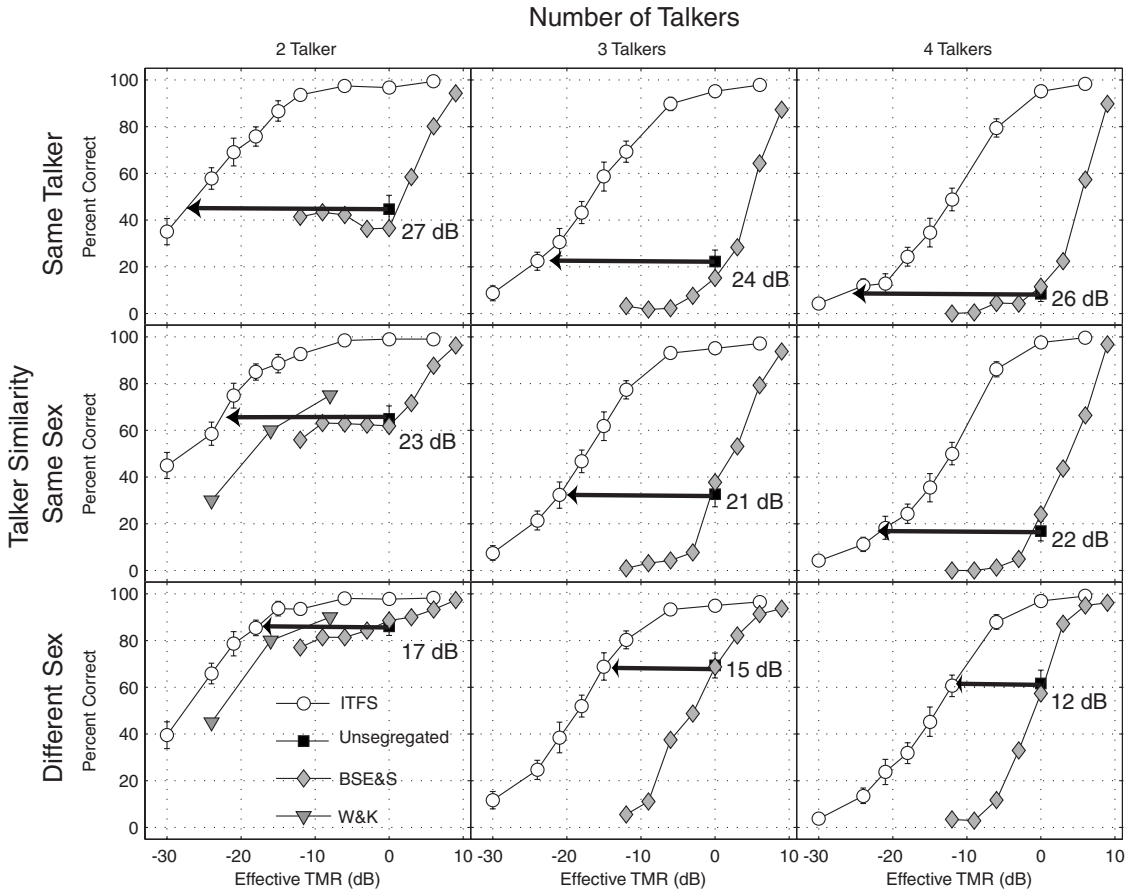

FIG. 5. Comparison of performance with ITFS-processed and unsegregated stimuli as a function of the effective TMR value of the stimulus. The open circles, which are re-plotted from Fig. 2, show performance in the ITFS-processed conditions of the experiment as a function of the effective TMR value of each data point. The filled squares show performance in the unsegregated condition of the experiment. The filled diamonds and filled triangles show performance from two earlier studies that measured multitalker listening performance with unsegregated CRM stimuli as a function of TMR (Brungart *et al.*, 2001, and Wightman and Kistler, 2005, respectively). The black arrows show in decibels the release from masking obtained in the ITFS condition relative to the unprocessed condition at a TMR value of 0 dB.

(white symbols) to fall slightly below performance in the same-talker and same-sex conditions (light and dark gray symbols) with the same proportion of retained units, especially in the range from 0.1 to 0.2 retained units. Similarly, in the retained energy plot (lower panel), there was a general tendency for performance in the different-sex condition (triangles) to fall slightly below performance in the same-sex and same-talker conditions (diamonds and circles) with the same proportion of retained energy.

3. Evaluation of non-energetic masking effects

By comparing the results in Fig. 2 to previous psychophysical results that have measured the effect of TMR on speech perception with the CRM corpus, it is possible to calculate a rough estimate of the amount of non-energetic masking that occurs in each condition. The open circles in Fig. 5 redraw a subset of the data from Fig. 2 in a nine-panel figure, with each row of the figure corresponding to a different level of target-masker voice similarity and each column corresponding to a different number of talkers in the stimulus. Within each panel, the black square at a TMR value of 0 dB shows the level of performance achieved in the unsegregated control condition of this experiment. For comparison, the gray diamonds in the figure show unsegregated performance as a function of TMR from a study that used the same CRM materials used in this experiment (Brungart *et al.*, 2001). These results are nearly identical to the unsegregated results collected at a TMR value of 0 dB in the present experiment. In the 2-talker same-sex and different-sex conditions, shaded triangles have been used to plot the results of another study (Wightman and Kistler, 2005) that examined performance in monaural presentations of the CRM stimuli to adult listeners as a function of TMR value at lower TMR values than those used in the Brungart *et al.* (2001) study. This experiment used only two of the eight talkers in the CRM corpus, and this resulted in generally higher performance levels that are probably not directly comparable to the present study, but the data do provide some insights into the psychometric function for 2-talker CRM listening tasks at very low TMR values.

In all cases, it is clear that the ITFS processing resulted in a substantial improvement in performance over the unsegregated condition conducted at the same effective TMR value. The black arrows show the decrease in effective TMR value required to bring performance with the ITFS-processed mixture down to the same level achieved with the original (unprocessed) mixture at a TMR value of 0 dB. The size of this shift, which is indicated by the number shown to the

right of the arrow, can be viewed as a crude quantitative estimate of the amount of non-energetic masking in each listening condition. Across the nine conditions tested in this experiment, the advantage of the ITFS processing ranged from 12 dB in the 4-talker, different-sex condition to 27 dB in the 2-talker, same-talker condition. These results suggest that, in contrast to the amount of energetic masking, the amount of non-energetic masking is influenced more by the target-masker similarity than by the number of competing talkers in the stimulus. Across all conditions, the amount of non-energetic masking was 6–10 dB higher in the same-sex condition than in the different-sex condition, and an additional 3–4 dB higher in the same-talker condition than in the same-sex condition.

Although the main focus of Experiment 1 was an examination of the effects of target-masker similarity on energetic and non-energetic masking for a fixed number of talkers, the relatively modest variations in non-energetic masking that occurred when the number of interfering talkers was increased at a fixed level of target-masker similarity are also noteworthy. These effects can be seen by looking across the arrows from left to right in each row of Fig. 5. In the same-talker and same-sex conditions, the amount of non-energetic masking was almost constant across the 2, 3, and 4-talker conditions, varying only from 24 to 27 dB in the same-talker masker condition and from 21–23 dB in the same-sex masker condition. In the different-sex masking condition, the amount of non-energetic masking decreased more substantially (from 12 to 17 dB) as the number of interfering talkers increased from 2–4, but this change was still quite modest in comparison to the much larger 9–14 dB changes seen with variations in the target-masker similarity of the stimulus.

Qualitatively, these systematic changes in non-energetic masking with the number of competing talkers appear to be smaller than those reported by Freyman *et al.* (2004), who reported roughly a 5 dB decrease in non-energetic masking as the number of same-sex interfering talkers increased from 2 to 3, and by Simpson and Cooke (2005), who did not use a decibel-based measure but reported an apparent *increase* in non-energetic masking as the number of interfering talkers increased from 1 to 3. However, direct comparisons of non-energetic masking across different measurement methodologies and, in particular, across different speech perception tests should only be made with caution: many factors will influence the amount of non-energetic masking, including the underlying confusability of the target and masking stimuli (relatively high with the CRM stimuli) and the underlying sensitivity of the speech perception test to energetic masking (relatively low with the CRM stimuli). The method for estimating non-energetic masking shown in Fig. 5 is a useful method because it provides a consistent means for comparing informational masking effects across a broad range of different stimulus types. However, it would be a mistake to assume that all speech perception tests will produce the same results obtained with the CRM stimuli. Furthermore, it is difficult to extrapolate the results shown in Fig. 5 to those that would be obtained with a larger number of competing talkers. Experiment 2 was conducted to more fully examine how energetic and non-energetic masking varied as a function of the number of competing talkers in the CRM test.

IV. EXPERIMENT 2: EFFECTS OF NUMBER OF COMPETING TALKERS WITH ITFS

One interesting aspect of the results from Experiment 1 is that none of the conditions tested indicates that any significant amount of energetic masking occurs in a CRM task with a TMR of 0 dB. Even in the most difficult condition tested where the target CRM phrase was masked by three interfering phrases spoken by the same talker who produced the target speech, performance was near 100% when the LC value was set to 0 dB (as compared to about 12% correct in the "unsegregated" condition that included the effects of both informational and energetic masking). This raises the interesting question of how many simultaneous overlapping equal-level speech signals really are necessary to produce a considerable amount of energetic masking in the CRM listening task. In order to explore this question, a second experiment was conducted to examine performance as a function of the number of competing talkers when the LC value was fixed at 0 dB.

A. Methods

The procedures used in Experiment 2 are similar to those used in Experiment 1. For each trial, the target and interfering phrase(s) were randomly selected from the CRM corpus, scaled to have the same overall rms levels, and summed together to produce target, interferer, and mixture signals. The procedures outlined in Sec. III were then used to generate an ideal binary mask with LC set to 0 dB, and this binary mask was used to resynthesize an output signal that was stored off-line on a PC for later presentation to the listeners. The primary difference between Experiment 2 and Experiment 1 was the number of interfering talkers: in Experiment 2, the number of interfering talkers in each trial was randomly selected from 1 of 10 values ranging from 1 to 18 (1, 2, 4, 6, 8, 10, 12, 14, 16, and 18), with all of the interfering phrases spoken by the same talker (randomly selected on each trial) who spoke the target phrase.

Due to the large number of simultaneous voices for some cases, as well as the limiting variety of unique call-sign/color/number combinations in the CRM corpus, extra care was taken to ensure that the phrases presented within each trial differed in terms of call-sign, color, and number to the greatest extent possible. Previously, call signs, colors, and numbers could not repeat within the same trial. In this experiment, while the target call sign remained unique with "Baron," the interferer call signs, colors, and numbers could duplicate within each trial. The distribution of these conditions within each trial was assigned to minimize such duplication. The same nine listeners who participated in Experiment 1 also participated in Experiment 2, with each subject conducting 10 blocks of 50 trials.

B. Results and discussion

The overall results from Experiment 2 are shown by the shaded circles in Fig. 6. In this figure, each shaded circle

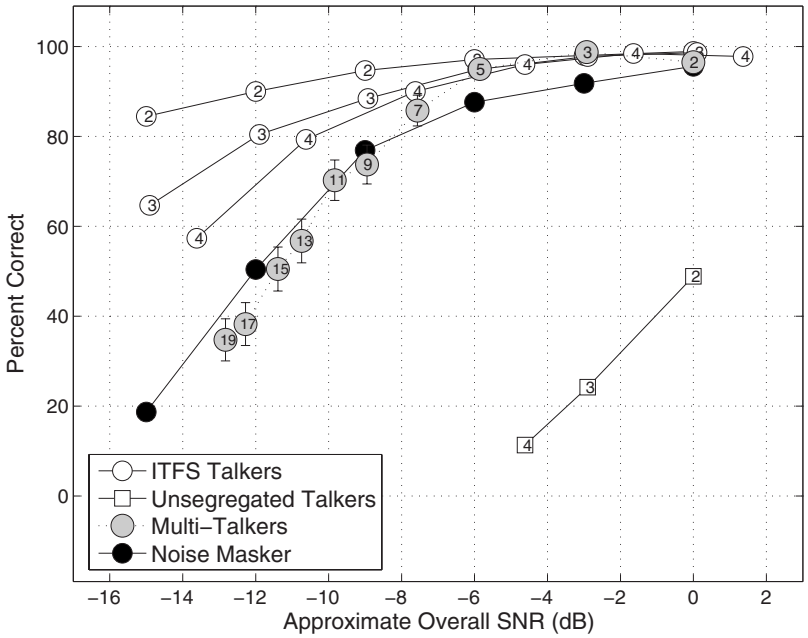

FIG. 6. Percentage of correct color and number identifications in Experiment 2 as a function of the overall SNR. The shaded circles show the performance for each of the ten different numbers of simultaneous talkers tested in Experiment 2, with the number of simultaneous talkers in each condition indicated in the center of each data point. In each case, the data have been plotted as a function of the mean overall SNR. The error bars show the 95% confidence intervals around each data point. For comparison purposes, the open and numbered circles re-plot the data obtained for 2-, 3-, or 4-talkers at different positive LC values to show performance as a function of the approximate overall SNR in a stimulus containing a fixed number of interfering talkers. The open squares show results from the unsegregated conditions with 2-, 3-, or 4-talkers and a TMR value of zero (plotted here as a function of SNR). The closed symbols show performance for a CRM stimulus with an ITFS-processed continuous noise masker (replotted from Brungart *et al.*, 2006).

represents a different number of competing talkers, as indicated by the number at the center of each data point. In each case, the data have been plotted as a function of the mean overall SNR of the original stimulus, calculated from the ratio of the total rms energy in the target phrase to the total rms energy in the interference of a multitalker mixture. For example, in the 3-talker case of Experiment 2 (shaded circles), the two interfering talkers were presented at the same level as the target speech, so the total mixture of interfering signals in that condition is roughly 3 dB more intense than the target and thus produces an overall SNR of approximately −3 dB. In the 19-talker condition, the 18 interfering talkers produce a combined rms interference energy level roughly 13 dB higher than the target phrase, so it is plotted at a SNR value of approximately −13 dB.

As in Experiment 1, these results show that the color and number identification performance is near 100% when the stimulus contained a small number of competing talkers (≤4). As the number of competing talkers is increased beyond 4, there was a steady decrease in performance. However, even in the worst condition tested, where the target speech signal was masked by 18 different competing speech signals each spoken at the same level by the same talker, the application of ITFS with 0 dB LC resulted in a performance level that was well above chance (35% versus 3% for chance performance). These results suggest that the difficulties listeners have in understanding signals containing a large number of competing talkers are largely due to informational, not energetic, masking effects. Put another way, it seems that even extremely dense multitalker babbles often contain enough glimpses of the individual talkers to make it theoretically possible to comprehend a single voice, but without some way to conclusively group the glimpses produced by a single talker together into a cohesive auditory image, the listener has no hope of successfully understanding any of the individual talkers in a complex multitalker environment.

The results from Experiment 2 also provide an opportunity to further explore the energetic masking efficiency of an interfering speech signal. A number of previous researchers have commented that masking signals containing more than one interfering talker generally produce lower intelligibility than masking signals containing a single interfering talker at the same overall SNR. This is believed to occur because the multiple competing speech signals "fill in the gaps" that listeners could ordinarily use to obtain a glimpse of the target speech (Simpson and Cooke, 2005; Freyman *et al.*, 2004; Bronkhorst and Plomp, 1992; Festen and Plomp, 1990; Miller, 1947). To this point, however, it has been difficult to accurately measure this effect because of the complications involved in distinguishing the increased energetic masking caused by filling in the gaps from any change in informational masking that might occur when more voices are added to the stimulus. The ITFS approach used in this study allows us to make a direct comparison of the effects of energetic masking as a function of the number of interfering talkers in the stimulus and the effective overall SNR of the signal.

The open circles in Fig. 6 re-plot the data obtained at the different positive LC values tested in Experiment 1 of Brungart *et al.* (2006) to show performance as a function of the approximate effective overall SNR in a stimulus containing a fixed number of interfering talkers (these data were collected with the same nine listeners used in this study; they are plotted here because the earlier study tested more LC values in the same-talker condition) For example, in the 4-talker condition of that experiment, the ITFS processing with a LC value of 0 dB produces results that roughly simulate the energetic masking that occurs from a 3-talker interfering speech signal presented at a TMR of 0 dB. Such an interfering signal, which contains three speech signals with the same rms power as the target speech, has a combined rms power that is approximately 4.8 dB higher than the target. Consequently, the 4-talker condition with a 0 dB LC value is plotted at an SNR value of −4.8 dB in Fig. 6. Similarly, the 4-talker data collected with a LC value of +3 dB corresponds to a 4-talker signal with a mixture SNR reduced by 3 and 0 dB LC, giving an overall SNR of approximately −7.8 dB.

Thus, the 4-talker data with a LC value of +3 dB from Experiment 1 of Brungart *et al.* (2006) is re-plotted in Fig. 6 at an SNR value of −7.8 dB. Similar procedures are used to plot performance from the 2-, 3-, and 4-talker conditions of that experiment as a function of overall effective SNR for all SNR values from 0 to −13 dB.

For comparison purposes, data are also shown for unsegregated speech maskers and for ITFS-processed noise maskers. The open squares in Fig. 6 re-plot the data from the unsegregated 2-, 3-, and 4-talker conditions of Brungart *et al.* (2006) as a function of stimulus SNR. Finally, the closed symbols in Fig. 6 show performance for the ITFS processed continuous noise masker from Experiment 2 of Brungart *et al.* (2006) as a function of the effective stimulus SNR. In theory, this type of speech-shaped noise masker is equivalent to a masking signal comprised of an infinite number of interfering talkers.

Comparing the different curves in Fig. 6, it is first apparent that performance in the unsegregated condition (open squares) dropped off much more dramatically with an increase in the number of competing talkers than any of the ITFS-processed conditions. Indeed, when the number of unsegregated talkers increases to 4, performance dropped to near chance level, even though the effective SNR value in that condition is greater than −5 dB. In comparison, performance in the ITFS conditions of Experiment 2 remained well above chance level even when there were 19 simultaneous talkers and the SNR was less than −12 dB. Thus one can conclude that non-energetic masking effects related to the confusability of the target and masking voices tend to dominate overall performance in CRM tasks involving more than one simultaneous talker.

Next, it is apparent that the effects of energetic masking indeed increase substantially when additional interfering voices are added to a stimulus in which the overall SNR is held constant—for instance, compare the percent correct values of the curves at the overall SNR of −10 dB. The 2-, 3-, and 4-talker lines show a systematic increase in energetic masking with the number of competing talkers, and the "multitalker" line from Experiment 2 shows considerably worse performance than the 4-talker line for all conditions containing more than four competing talkers. In the most extreme case tested, the 19-talker point from Experiment 2 shows performance dropping to roughly 35% correct responses when the overall SNR is −13 dB, compared to performance levels of approximately 60%, 75%, and 85% in the 4-, 3-, and 2-talker conditions, respectively, at the equivalent overall SNR. These results conclusively demonstrate that the effects of energetic masking increase substantially when additional interfering talkers are added to a multitalker stimulus at a fixed overall SNR.

The results in Fig. 6 also provide some insight into how many simultaneous talkers are necessary for a multitalker speech stimulus to produce the same amount of masking as a speech-shaped noise signal at the same overall SNR value. Comparing the multitalker line to the continuous noise line, we see that the multitalker stimulus generally produced less energetic masking than the noise interferer when it contained seven or fewer simultaneous talkers, but that it actually produced slightly more energetic masking than the noise interferer when it contained nine or more simultaneous talkers. This result suggests that roughly six to eight interfering talkers are required to fill in the gaps in a multitalker stimulus to the point that it will produce the same amount of energetic masking as a continuous noise signal. Note that this is roughly consistent with the results of Simpson and Cooke (2005), which showed that the amount of energetic masking caused by a babble-modulated noise increased sharply as the number of competing talkers used to generate the babble increased from 1 to 6 but began to level off as the number of talkers increased beyond 6. However, Simpson and Cooke (2005) also showed that as many as 512 actual speech signals (as opposed to modulated noises) were required to produce a masker equivalent to speech-shaped noise, suggesting that the composition of the audible portion of the masker plays an important role in determining how well listeners can extract a target speech signal from a complex acoustic mixture. This result provides further evidence that performance in multitalker tasks is limited by the ability to extract usable target information from a mixture containing similar masker information than by a complete loss of target information due to spectro-temporal overlap with a more powerful masker.

V. CONCLUDING REMARKS

The experiments reported in this study extend our previous investigation where ITFS was introduced to remove or largely reduce informational masking effects (Brungart *et al.*, 2006). In Experiment 1, we have applied ITFS to multitalker mixtures where interfering talkers are either the same as or different from the target talker and the number of competing talkers is systemically varied. As in the previous study, the results show that performance is almost perfect when the ITFS method is applied to a multitalker signal with a TMR of 0 dB. As the effective TMR of the stimulus decreases below 0 dB, performance does eventually decrease. However, the vocal similarity of the target and masking signals had relatively little effect on performance for the ITFS stimuli. Changing from a stimulus with interfering phrases spoken by the target talker to a stimulus with masking phrases spoken by different same-sex talkers than the target talker resulted in a large release from non-energetic masking (as indicated by the large improvement in performance in Fig. 2 for ITFS-processed stimuli at LC values less than −6 dB) but only about a 1.19 dB release from energetic masking (as indicated by the relatively small improvement in performance in Fig. 2 for LC values greater than 0 dB). Changing from same-sex interfering talkers to different-sex interfering talkers produced only an additional 0.93 dB release from energetic masking. Thus it seems that energetic masking due to spectro-temporal overlap between the target and masking voices can account for only a tiny fraction of the release from masking that occurs when a same-sex masking voice is replaced with a voice spoken by a different-sex interfering talker.

Conceptually, the non-energetic masking values shown in Fig. 5 are closely related to the notion of informational

masking as it has been applied in the context of multitalker listening (Brungart, 2001; Carhart and Tillman, 1969; Freyman *et al.*, 1999; Kidd *et al.*, 1998; Pollack, 1975). In the context of ITFS, non-energetic masking refers to the release from masking that occurs when the acoustically detectable elements of the target signal are preserved but the acoustically detectable components of the masker are artificially removed from the stimulus. Thus, one would expect non-energetic masking to increase in cases where the target and masker are perceptually similar, and thus hard to distinguish from one another, and decrease in cases where the target and masker are perceptually different. In the most extreme case of masker dissimilarity, where the target signal is speech and the masker is Gaussian noise, Brungart *et al.* (2006) showed that ITFS processing resulted in only a 2–5 dB release from masking. In contrast, the application of ITFS processing in this experiment always produced at least a 12 dB release from masking. This suggests that non-energetic masking effects contribute substantially to the segregation of speech from a speech masker even when that masker is easily distinguished from the target speech by an obvious difference in talker sex. The results also showed a 9–14 dB release from non-energetic masking when switching from same-talker maskers to different-sex maskers. Again, these results are consistent with the notion that informational masking increases when target and masking voices are made progressively more similar to one another.

In Experiment 2, the ITFS technique was applied to a speech signal that was masked by up to 19 simultaneous competing speech signals. Remarkably, the results show that listeners could still perform well above chance when the ITFS procedure was applied to a mixture with 18 simultaneous interfering speech signals, even when all the competing phrases were spoken by the same talker. In contrast, performance was near chance (8%) with just four competing talkers when no ITFS processing was applied. These results show that there are enough target-dominated T-F regions to extract some information about a target speech signal even in extremely dense acoustic mixtures, and suggest that poor performance in multitalker tasks is probably more due to the inability to successfully identify and segregate the target acoustic information in the mixture than to a complete loss of all acoustic information related to the target speech.

ACKNOWLEDGMENTS

This research was supported in part by an AFRL grant via Veridian and an AFOSR grant (LRIR HE-01-COR-01). We thank Y. Li and Z. Jin for their assistance in figure preparation, and Richard Freyman for his helpful comments in the review process.

Anzalone, M. C., Calandruccio, L., Doherty, K. A., and Carney, L. H. (**2006**). "Determination of the potential benefit of time-frequency gain manipulation," Ear Hear. **27**, 480–492.

Assmann, P. F., and Summerfield, A. Q. (**1990**). "Modelling the perception of concurrent vowels: Vowels with different fundamental frequencies," J. Acoust. Soc. Am. **88**, 680–697.

Arbogast, T., Mason, C., and Kidd, G. (**2002**). "The effect of spatial separation on information and energetic masking of speech," J. Acoust. Soc. Am. **112**, 2086–2098.

Bird, J., and Darwin, C. J. (**1998**). "Effects of a difference in fundamental frequency in separating two sentences," in *Psychophysical and Physiological Advances in Hearing*, edited by A. R. Palmer, A. Rees, A. Q. Summerfield, and R. Meddis (Whurr, London), pp. 263–269.

Bolia, R., Nelson, W. T., Ericson, M., and Simpson, B. (**2000**). "A speech corpus for multitalker communications research," J. Acoust. Soc. Am. **107**, 1065–1066.

Brokx, J. P. L., and Nooteboom, S. G. (**1982**). "Intonation and the perceptual separation of simultaneous voices," J. Phonetics **10**, 23–36.

Bronkhorst, A., and Plomp, R. (**1992**). "Effects of multiple speechlike maskers on binaural speech recognitions in normal and impaired listening," J. Acoust. Soc. Am. **92**, 3132–3139.

Brungart, D. (**2001**). "Informational and energetic masking effects in the perception of two simultaneous talkers," J. Acoust. Soc. Am. **109**, 1101–1109.

Brungart, D. S., and Simpson, B. D. (**2002**). "The effects of spatial separation in distance on the informational and energetic masking of a nearby speech signal," J. Acoust. Soc. Am. **112**, 664–676.

Brungart, D., Simpson, B. D., Ericson, M., and Scott, K. (**2001**). "Informational and energetic masking effects in the perception of multiple simultaneous talkers," J. Acoust. Soc. Am. **110**, 2527–2538.

Brungart, D., Chang, P. S., Simpson, B. D., and Wang, D. L. (**2006**). "Isolating the energetic component of speech-on-speech masking with ideal time-frequency segregation," J. Acoust. Soc. Am. **120**, 4007–4018.

Cahart, R., and Tillman, T. (**1969**). "Perceptual masking in multiple sound backgrounds," J. Acoust. Soc. Am. **45**, 694–703.

Cavallini, F. (**1993**). "Fitting a logistic curve to data," Coll. Math. J. **24**, 247–253.

Darwin, C. J., Brungart, D. S., and Simpson, B. D. (**2003**). "Effects of fundamental frequency and vocal-tract length changes on attention to one of two simultaneous talkers," J. Acoust. Soc. Am. **114**, 2913–2922.

Drullman, R. (**1995**). "Speech intelligibility in noise: Relative contribution of speech elements above and below the noise level," J. Acoust. Soc. Am. **98**, 1796–1798.

Festen, J., and Plomp, R. (**1990**). "Effects of fluctuating noise and interfering speech on the speech reception threshold for impaired and normal hearing," J. Acoust. Soc. Am. **88**, 1725–1736.

Freyman, R., Helfer, K., McCall, D., and Clifton, R. (**1999**). "The role of perceived spatial separation in the unmasking of speech," J. Acoust. Soc. Am. **106**, 3578–3587.

Freyman, R. L., Balakrishnan, U., and Helfer, K. S. (**2004**). "Effect of number of masking talkers and auditory priming on informational masking in speech recognition," J. Acoust. Soc. Am. **115**, 2246–2256.

Freyman, R. L., Helfer, K., and Balakrishnan, U. (**2007**). "Variability and uncertainty in masking by competing speech," J. Acoust. Soc. Am. **121**, 1040–1046.

Kidd, G., Mason, C., Rohtla, T., and Deliwala, P. (**1998**). "Release from informational masking due to the spatial separation of sources in the identification of nonspeech auditory patterns," J. Acoust. Soc. Am. **104**, 422–431.

Li, N., and Loizou, P. C. (**2007**). "Factors influencing glimpsing of speech in noise," J. Acoust. Soc. Am. **122**, 1165–1172.

Li, Y., and Wang, D. L. (**2009**). "On the optimality of ideal binary time-frequency masks," Speech Commun. **51**, 230–239.

Miller, G. (**1947**). "Sensitivity to changes in the intensity of white Gaussian noise and its relation to masking and loudness," J. Acoust. Soc. Am. **191**, 609–619.

Moore, T. (**1981**). "Voice communication jamming research," in AGARD Conference Proceedings 331: Aural Communication in Aviation, Neuilly-SurSeine, France, pp. 2:1–2:6.

Patterson, R. D., Holdsworth, J., Nimmo-Smith, I., and Rice, P. (**1988**). "SVOS final report, Part B: Implementing a gammatone filterbank," Report No. 2341, MRC Applied Psychology Unit, Cambridge, UK.

Peterson, G. H., and Barney, H. L. (**1952**). "Control methods used in a study of the vowels," J. Acoust. Soc. Am. **24**, 175–184.

Pollack, I. (**1975**). "Auditory informational masking," J. Acoust. Soc. Am. **57**(S1), S5.

Qin, M. K., and Oxenham, A. J. (**2003**). "Effects of simulated cochlear-implant processing on speech reception in fluctuating maskers," J. Acoust. Soc. Am. **114**, 446–454.

Simpson, S., and Cooke, M. (**2005**). "Consonant identification in N-talker babble is a nonmonotonic function of N," J. Acoust. Soc. Am. **118**, 2775–2778.

Wang, D. L. (**2005**). "On ideal binary mask as the computational goal of auditory scene analysis," in *Speech Separation by Humans and Machines*, edited by P. Divenyi (Kluwer Academic, Norwell, MA), pp. 181–197.

Wang, D. L., and Brown, G. J. (**2006**). *Computational Auditory Scene Analysis: Principles, Algorithms, and Applications*, Wiley, New York/IEEE, Hoboken, NJ.

Wightman, F. L., and Kistler, D. J. (**2005**). "Informational masking of speech in children: Effects of ipsilateral and contralateral distracters," J. Acoust. Soc. Am. **118**, 3164–3176.

Effects of spectral smearing and temporal fine structure degradation on speech masking release

Dan Gnansia[a)]
Laboratoire de Psychologie de la Perception, Université Paris Descartes, UMR CNRS 8158, Ecole Normale Supérieure, Paris, France; MXM Neurelec, 2720 Chemin St Bernard, 06224 Vallauris Cedex, France; and GDR CNRS 2967 GRAEC, 29 rue d'ulm, 75005 Paris, France

Vincent Péan
MXM Neurelec, 2720 Chemin St Bernard, 06224 Vallauris Cedex, France; and GDR CNRS 2967 GRAEC, 29 rue d'ulm, 75005 Paris, France

Bernard Meyer
Assistance Publique-Hôpitaux de Paris, Hôpital St-Antoine, Université Pierre et Marie Curie, 27 rue Chalingny, 75012 Paris, France and GDR CNRS 2967 GRAEC, 29 rue d'ulm, 75005 Paris, France

Christian Lorenzi
Laboratoire de Psychologie de la Perception, Université Paris Descartes, UMR CNRS 8158, Ecole Normale Supérieure, Paris, France and GDR CNRS 2967 GRAEC, 29 rue d'ulm, 75005 Paris, France

(Received 12 June 2008; revised 8 April 2009; accepted 9 April 2009)

This study assessed the effects of spectral smearing and temporal fine structure (TFS) degradation on masking release (MR) (the improvement in speech identification in amplitude-modulated compared to steady noise observed for normal-hearing listeners). Syllables and noise stimuli were processed using either a spectral-smearing algorithm or a tone-excited vocoder. The two processing schemes simulated broadening of the auditory filters by factors of 2 and 4. Simulations of the early stages of auditory processing showed that the two schemes produced comparable excitation patterns; however, fundamental frequency (F0) information conveyed by TFS was degraded more severely by the vocoder than by the spectral-smearing algorithm. Both schemes reduced MR but, for each amount of spectral smearing, the vocoder produced a greater reduction in MR than the spectral-smearing algorithm, consistent with the effects of each scheme on F0 representation. Moreover, the effects of spectral smearing on MR produced by the two schemes were different for manner and voicing. Finally, MR data for listeners with moderate hearing loss were well matched by MR data obtained for normal-hearing listeners with vocoded stimuli, suggesting that impaired frequency selectivity alone may not be sufficient to account for the reduced MR observed for hearing-impaired listeners. [DOI: 10.1121/1.3126344]

PACS number(s): 43.71.Gv, 43.71.Es, 43.66.Mk, 43.71.Ky [BCM] Pages: 4023–4033

I. INTRODUCTION

Speech intelligibility improves—sometimes considerably—when a background masker fluctuates in amplitude compared to when unmodulated noise is used. Among the different auditory mechanisms supposed to be involved in this so-called "speech masking release (MR)" effect (see Füllgrabe *et al.*, 2006; George *et al.*, 2006; or Rhebergen *et al.*, 2006, for recent reviews), the ability of normal-hearing listeners to use "glimpses"—i.e., specific spectrotemporal regions where the target speech energy exceeds that of the masker by a given amount—to identify speech in fluctuating backgrounds may play a critical role (e.g., Miller and Licklider, 1950; Howard-Jones and Rosen, 1993; Cooke, 2006).

Several studies indicate that MR is substantially degraded or abolished for listeners with moderate to severe cochlear hearing loss (e.g., Duquesnoy, 1983; Festen and Plomp, 1990; Gustafsson and Arlinger, 1994; Bacon *et al.*, 1998; Peters *et al.*, 1998; Nelson *et al.*, 2003; Nelson and Jin, 2004; Stickney *et al.*, 2005; George *et al.*, 2006; Lorenzi *et al.*, 2006a, 2006b). Among the different basic sensory deficits that may contribute to this reduction in MR, impaired frequency selectivity (see Moore, 2007, for a review) and impaired perception of temporal fine structure (TFS) cues (the rapid oscillations with a rate close to the center frequency (CF) of the band; e.g. Lorenzi *et al.*, 2006b, 2009; Hopkins *et al.*, 2008; see Moore, 2008, for a review) seem to be of particular importance. It has been suggested that both sensory deficits degrade the ability to glimpse speech in fluctuating background noise by impairing voice pitch (pitch contour and pitch disparities) and formant perception (e.g., Stickney *et al.*, 2004; Binns and Culling, 2007; Moore, 2008). Consistent with this idea, a recent study by Hopkins and Moore (2009) using speech and noise mixtures processed to contain variable amounts of TFS indicates that, for normal-hearing listeners, the greatest benefit of TFS informa-

[a)]Present address: Equipe CNRS Audition, Département d'Etudes Cognitives, Ecole Normale Supérieure, 29 rue d'Ulm, 75005 Paris, France. Electronic mail: dan.gnansia@ens.fr

tion to MR is observed for frequency channels covering the voice fundamental frequency (F0) and its low harmonics.

The effects of both sensory deficits on MR have been demonstrated by simulation studies conducted using normal-hearing listeners, showing that MR is strongly reduced and sometimes disappears when spectral and TFS cues are physically degraded in the speech+noise mixture using various speech-processing schemes. In one set of studies, the degradation of spectral cues was achieved using spectral-smearing techniques that simulated broadening of the auditory filters (e.g., ter Keurs *et al.*, 1993; Baer and Moore, 1994). In another set of studies using vocoders, the degradation of TFS cues was achieved by replacing the carrier signal with noise or by a sine tone within each channel of a bank of analysis frequency channels (e.g., Nelson *et al.*, 2003; Qin and Oxenham, 2003; Fu and Nogaki, 2005; Stickney *et al.*, 2005; Zeng *et al.*, 2005; Füllgrabe *et al.*, 2006; Hopkins *et al.*, 2008; Gnansia *et al.*, 2008).

Any change in the power spectrum of speech and background stimuli produced by spectral-smearing algorithms modifies their TFS, even though the phase spectrum of the stimuli was explicitly preserved by the sequence of operations in such processing schemes. Conversely, any change in the TFS of speech and background stimuli produced by vocoders modifies their power spectrum. Thus, the speech-processing schemes used in previous studies degraded *both* spectral and TFS cues. Deficits in frequency selectivity and TFS processing are likely to occur jointly in most cases of moderate and severe hearing loss. For instance, broader auditory filters result in more complex and more rapidly varying TFS for speech signals, which may make the TFS less usable (e.g., Moore, 2008). However, a recent study suggests that impaired perception of TFS cues may occur in the absence of impaired frequency selectivity (Lorenzi *et al.*, 2009). This warrants further investigation of the contribution of impaired perception of TFS to MR, in combination with impaired frequency selectivity.

It is important to note that vocoders and spectral-smearing algorithms are not equivalent in the time domain. Although the wave shape is altered by the spectral smearing process in Baer and Moore's (1993, 1994) algorithm, the harmonic structure and basic periodicities are preserved. As a consequence, when voiced speech sounds are processed by this algorithm, the resulting output signals still sound voiced. This is not the case for vocoders, which severely degrade the harmonic structure and fundamental periodicity of speech stimuli. Thus, spectral-smearing techniques and vocoders may be set to yield comparable amounts of spectral smearing at the outputs of the auditory filters (i.e., comparable smearing of "place of excitation" cues), while producing different amounts of degradation of TFS cues.

The goal of the present study was to compare MR for normal-hearing listeners using speech and noise stimuli processed to simulate: (i) broadening of auditory filters by factors of 2 and 4, and (ii) different amounts of degradation of TFS cues. Consonant identification was measured using nonsense vowel-consonant-vowel (VCV) stimuli embedded in steady or sinusoidally amplitude-modulated speech-shaped noise maskers presented at a fixed, global signal-to-noise ratio (SNR) yielding 50%-correct identification for steady noise. Amplitude-modulation rate and depth were fixed at 8 Hz and 100%, respectively. These parameters were chosen to get maximum MR with sinusoidally amplitude-modulated speech-shaped noise maskers (Füllgrabe *et al.*, 2006; Lorenzi *et al.*, 2006a; Gnansia *et al.*, 2008). The speech and noise stimuli used in these experiments were degraded using (i) a spectral-smearing technique (Baer and Moore, 1993, 1994) based on the overlap-add method, or (ii) a 32-band tone-excited vocoder (TV) (e.g., Gnansia *et al.*, 2008). In the present paper, these two algorithms will be referred to as Baer and Moore (1993) (B&M) and TV, respectively. Both speech-processing schemes were used to simulate broadening of auditory filters by factors of 2 and 4, which is representative of moderate and severe hearing loss, respectively (e.g., Tyler *et al.*, 1984; Glasberg and Moore, 1986; Dubno and Dirks, 1989; Peters and Moore, 1992; Stone *et al.*, 1992; see also Moore, 2007 for a review). In each experimental condition, MR was quantified as the difference in identification scores or phonetic information received using modulated and steady noise backgrounds. The MR data for normal-hearing listeners were compared to MR data obtained in identical conditions with unprocessed speech and noise maskers for listeners with flat, moderate cochlear hearing loss (Lorenzi *et al.*, 2006a).

In addition, computer simulations of two models of the early stages of auditory processing were conducted using the same speech stimuli and speech-processing schemes to quantify the degradation of (i) place (pattern of excitation) cues and (ii) pitch cues conveyed by TFS. Both models were based on the same front end, which consisted of a model of the peripheral auditory system. The output of this front end was used to compute spectrotemporal excitation patterns (STEPs) (e.g., Cooke, 2006) in the first model and summary autocorrelograms (e.g., Meddis and Hewitt, 1992; Meddis and O'Mard, 1997) in the second one.

II. MATERIAL AND SPEECH-PROCESSING SCHEMES

A. Stimuli

Forty-eight VCV stimuli were recorded digitally via a 16-bit Analog/Digital converter at a 44.1-kHz sampling frequency and equalized in rms power (Lorenzi *et al.*, 1999, 2006a, 2006b; Füllgrabe *et al.*, 2006; Gilbert and Lorenzi, 2006; Gnansia *et al.*, 2008). The stimuli consisted of 3 exemplars of 16 /aCa/ utterances (C=/p,t,k,b,d,g,f,s,ʃ,v,z,ʒ,m,n,r,l/) read by a female native French speaker in quiet (mean VCV duration=648 ms; standard deviation =46 ms). The F0 of the female voice was estimated as 221 Hz using the YIN algorithm (de Cheveigné and Kawahara, 2002). A speech-shaped noise, refreshed in each interval, was added to each utterance. The noise was gated on and off with the target speech item. The noise was digitally generated at a sampling frequency of 44.1 kHz and spectrally shaped to match the long-term power spectrum of the speech material. This noise was either steady or modulated in amplitude by a sine-wave modulator with a modulation depth m of 100%, and a modulation frequency of 8 Hz. The starting phase of the modulation was randomized in each interval.

Each stimulus was presented monaurally to the right ear via headphones (Sennheiser HD 250) at an average sound pressure level (SPL) of 75 dB (root mean square) for continuous speech in noise. Output levels at the headphones were measured using a Brüel and Kjær artificial ear (type 4153) and microphone (type 4192).

B. Spectral-smearing algorithm

Spectrally smeared stimuli were constructed from the unprocessed speech stimuli in quiet or in noise using the B&M algorithm. The algorithm was based on an overlap-and-add procedure (Allen, 1977): For each analysis/synthesis frame (2048 points), the short-term spectrum was calculated using a Hanning window and a fast Fourier transform (FFT). Spectral smearing by a factor of 2 or 4 was then performed on the power spectrum, using a smearing matrix based on 2-ERB_N or 4-ERB_N-wide auditory filters (ERB_N: average equivalent rectangular bandwidth of the auditory filter as determined using young normally hearing listeners tested at moderate sound levels; Moore, 2007). The auditory filters were assumed to have the form of the roex(p) filter suggested by Patterson *et al.* (1982). The smeared power spectrum was then combined with the non-modified phase spectrum, and transformed back into the time domain using an inverse FFT. Waveforms obtained from overlapping analysis frames (50% overlapping) were added to produce the final output. Spectral smearing by a factor of 1 was also performed to produce a set of stimuli with intact spectral cues (signal processing resulting in perfect stimulus reconstruction in that case). A preliminary experiment indicated that, in agreement with Baer and Moore (1993), all listeners reached 100%-correct identification with spectrally smeared speech stimuli presented in quiet, for both values of the smearing factor.

C. Tone-excited vocoder

Vocoded stimuli were constructed from the unprocessed speech stimuli in quiet or in noise, using a TV similar to that described by Gnansia *et al.* (2008). Each digitized signal was passed through a bank of 32, fourth-order gammatone (Patterson, 1987) filters (also called "analysis filters" thereafter), each 1-, 2-, or 4-ERB_N-wide with CFs uniformly spaced along an ERB_N-number scale (one filter per ERB_N) ranging from 80 to 8583 Hz. In each frequency band, the temporal envelope was extracted using full-wave rectification and lowpass filtering at 64 Hz with a zero-phase, sixth-order Butterworth filter. The resulting envelopes were used to amplitude modulate sine-wave carriers with frequencies at the CF of the gammatone filters, and with random starting phase. Impulse responses were peak-aligned for the envelope (using a group delay of 16 ms) and the TFS across frequency channels (Hohmann, 2002). The modulated signals were finally weighted and summed over the 32 frequency bands. The weighting compensated for imperfect superposition of the bands' impulse responses at the desired group delay. The weights were optimized numerically to achieve a flat frequency response (Hohmann, 2002). A preliminary experiment indicated that all listeners reached 100%-correct identification with processed speech stimuli presented in quiet for 1- and 2-ERB_N-wide analysis filters, and about 90%-correct identification in quiet for 4-ERB_N-wide analysis filters.

D. Quantitative assessment of speech-processing schemes

Two computational models of the early stages of auditory processing were used to quantify the degradation produced by each speech-processing scheme for (i) place of excitation cues, and (ii) F0 cues conveyed by TFS. These models were based on the same front end, that is, a four-stage model of peripheral auditory processing consisting of (i) middle ear (bandpass) filtering (first-order Butterworth filter; −3-dB cutoff frequencies: 450–8500 Hz), (ii) cochlear filtering (100, 1-ERB_N-wide gammatone filters with CF logarithmically spaced between 80 and 8000 Hz), (iii) half-wave rectification, and (iv) logarithmic compression. Simulations were conducted using the whole set of 48 VCV stimuli of the present study, presented in quiet.

1. Model I (STEPs)

This model aimed to quantify and compare the smearing effects produced by each speech-processing scheme on place of excitation cues. In both cases, STEPs were obtained by lowpass filtering the output of the 100 channels of the front end using a time constant of 8 ms (Butterworth filter, cutoff frequency=20 Hz; rolloff: 12 dB/octave) and downsampling the filtered stimuli to 900 Hz. In the first simulations (aiming to *quantify* the spectral smearing effects produced by each scheme), the mean correlation coefficient was computed between the STEPs evoked by the processed VCVs (using B&M or TV schemes) and the STEPs evoked by the original (unprocessed) VCVs. The mean correlation coefficient was computed for each VCV stimulus and each amount of spectral smearing used. In the second simulations (aiming to *compare* smearing effects across schemes), the mean correlation coefficient was computed between the STEPs evoked by the B&M-processed VCVs and the STEPs evoked by the TV-processed VCVs for an identical amount of spectral smearing. Again, the mean correlation was computed for each VCV stimulus and each amount of spectral smearing used in this study. The final correlation coefficient used to quantify STEP similarity was obtained by computing the mean correlation coefficient across the 48 VCV stimuli.

The results are presented in Fig. 1 for each amount of spectral smearing. The results of the first simulations are shown by open (TV) and filled (B&M) squares. Mean correlation coefficients are almost the same for each amount of smearing, indicating that the B&M and TV schemes degrade place of excitation cues similarly. The results of the second simulations are shown by stars. Correlations were never perfect; nevertheless, they were high ($\geq$0.9) and similar across smearing conditions, suggesting—again—that the two speech-processing schemes produced similar excitation patterns and spectral-smearing effects.

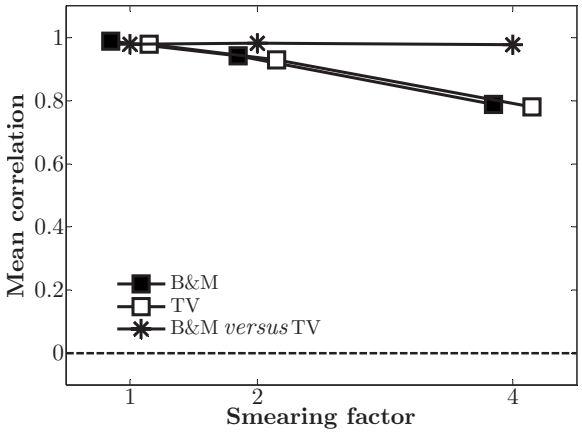

FIG. 1. Mean correlation coefficients showing the effects of the spectral-smearing algorithm developed by B&M and TV on STEPs evoked by VCV stimuli at the output of a model of auditory processing. VCVs were presented in quiet. Open and filled squares show the mean correlation coefficients computed between the STEPs evoked by the processed VCVs using B&M (filled squares) or TV schemes (open squares) and the STEPs evoked by the original (unprocessed) VCVs, as a function of the smearing factor. Stars show the mean correlation coefficients computed between the STEPs evoked by the B&M-processed VCVs and the STEPs evoked by the TV-processed VCVs for an identical amount of spectral smearing. Again, the mean correlations were computed for each amount of spectral smearing used in this study.

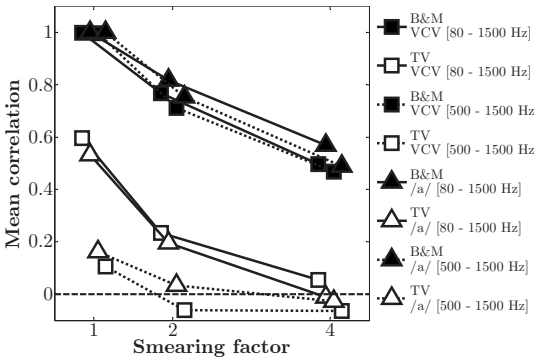

FIG. 2. Mean correlation coefficients showing the effects of the B&M and TV schemes on summary autocorrelograms computed at the output of a model of auditory processing in response to speech stimuli [VCV (squares) or vowel /a/ (triangles)] presented in quiet. The delays considered in the output of the autocorrelograms were restricted to the voice pitch region, that is, between 2 ms (500 Hz) and 12.5 ms (80 Hz). Summary autocorrelograms were computed for a subset of frequency channels of the peripheral processing stage, centered between either 80 and 1500 Hz (continuous lines) or 500 and 1500 Hz (dotted lines). Open and filled symbols show the mean correlation coefficients computed between the summary autocorrelograms evoked by the processed VCVs using B&M (filled symbols) or TV schemes (open symbols) and the summary autocorrelograms evoked by the original (unprocessed) VCVs, as a function of the smearing factor.

2. Model II (summary autocorrelograms)

This second model aimed to quantify the effects produced by each speech-processing scheme in the time (and especially TFS) domain. Stimuli passed through the front end were lowpass filtered at 1.5 kHz (FIR filter; −3 dB cutoff=1.5 kHz; 100-dB attenuation at 5 kHz) to simulate the loss of neural phase-locking to TFS cues above this frequency. For each amount of spectral smearing, summary autocorrelograms (that is across-channel aggregations of autocorrelograms; e.g., Meddis and Hewitt, 1992; Meddis and O'Mard, 1997) were calculated for each type of processed stimulus, and compared to the summary autocorrelograms evoked by the unprocessed versions of the VCV stimuli. Autocorrelation functions were computed over the whole VCV duration and over a shorter segment of 100 ms, corresponding to the second vowel of the VCV stimulus. In each case, autocorrelation functions were restricted to the "periodicity-pitch" region (80–500 Hz) to assess the fidelity of transmission of the fundamental periodicity, a cue potentially important for MR according to previous work (e.g., Stickney *et al.*, 2004; Hopkins and Moore, 2009). In other words, the delays considered in the outputs of the autocorrelograms were restricted between 2 ms (500 Hz) and 12.5 ms (80 Hz). Summary autocorrelograms were calculated by aggregating autocorrelation functions for peripheral channels tuned to low-order (<eighth harmonic), resolved harmonics only (that is, for a subset of gammatone filters in the peripheral processing stage, corresponding to the lowest 56 gammatone filters). This restriction in the calculation of summary autocorrelograms aimed to minimize the contribution of periodic temporal-envelope cues at F0 at the output of auditory filters to the estimate of periodicity pitch. However, it is important to note that TFS cues may also convey useful periodicity-pitch information for partially resolved harmonics (between the 8th and 11th harmonics; e.g., Moore and Moore, 2003a, 2003b; Hopkins and Moore, 2007).

The results are presented in Fig. 2 for each speech-processing scheme and each amount of spectral smearing. Highly similar correlation values were obtained for the whole VCV (squares) and the shorter segment (/a/; triangles). For each speech-processing scheme, correlation values dropped with increasing amount of spectral smearing, consistent with the notion that spectral smearing degrades TFS cues. However, for each amount of spectral smearing (that is, for similar STEPs), much higher correlation values were obtained with the B&M algorithm (filled symbols with continuous lines: correlations between 0.5 and 1) than with the TV scheme (open symbols with continuous lines: correlations between 0 and 0.59). This was particularly clear for smearing by a factor of 2 where the correlation values obtained with the B&M algorithm ranged between 0.77 and 0.82, whereas those obtained with the TV scheme ranged between 0.2 and 0.29. An even greater difference between the B&M algorithm (filled symbols with dotted lines: correlations between 0.49 and 1) and TV scheme (open symbols with dotted lines: correlations between 0 and 0.16) was obtained when summary autocorrelograms were restricted to the mid-frequency range, that is, when summary autocorrelograms were calculated for channels tuned between 0.5 and 1.5 kHz. This revealed that the relatively high correlation value of 0.59 initially obtained with the TV scheme using 1-ERB_N-wide analysis filters (i.e., when no spectral smearing was applied to the stimuli) was mainly driven by the analysis filters tuned to or close to the speaker's F0 (221 Hz).

Taken together, these results confirmed that both processing schemes degraded TFS cues, but the TV scheme degraded pitch-related TFS cues more severely than the B&M algorithm. Maximum degradation of F0 information (corre-

lation values close to zero) was observed when speech was processed by the TV scheme using 4-ERB$_N$-wide analysis filters.

III. METHOD

A. Listeners

Two groups of six normal-hearing listeners participated. The first group was tested with the B&M algorithm. The second one was tested with the TV scheme. Participants were all native French speakers, with normal audiometric thresholds (Hearing Level (HL) less than 20 dB) at octave frequencies between 250 and 8000 Hz, and no history of any hearing difficulties. Ages ranged from 21 to 29 years [mean =25 years; standard deviation (SD)=3 years] and from 22 to 46 years (mean=29 years; SD=9 years) for the first and second groups, respectively. All listeners were fully informed about the goal of the study and provided written consent before their participation. This study was carried out in accordance with the Declaration of Helsinki, and was approved by the French "Regional Ethics Committee" CPP Ile de France VI (07018-ID RCB: 2007-A00343-50).

B. Procedure

Listeners were tested individually in a sound-attenuating booth using a single-interval, 16-alternative procedure without feedback. A PC controlled the course of the experiment. In a typical experimental session, 4 complete and identical sets of the 48 VCV utterances corresponding to a given experimental condition were presented in random order. Each listener was instructed to identify the consonant presented within a single observation interval. The 16 possible responses were displayed orthographically on a computer screen, and the listener entered his/her choice by selecting one response using a computer mouse. The percentage correct identification was calculated and a 16×16 confusion matrix was compiled from the 192 VCV (4×48) utterances for this experimental condition. Chance level corresponded to 6.25%-correct responses (1/16). For each experimental condition and listener, the reception of three speech features (voicing, manner, and place of articulation) was evaluated by information transmission analysis (Miller and Nicely, 1955) of the confusion matrix (see Table I for the assignment of the consonant features in French).

Prior to data collection, listeners received practice for about 30 min to familiarize them with the speech material and different speech-processing conditions. Each listener completed a run using the steady masker and then the modulated masker. The two noise maskers (steady or modulated) were initially equated in rms power. In all experimental conditions, the noise masker was added to each utterance at given global SNR (i.e., calculated over the whole speech and noise duration) determined individually in a preliminary experiment so as to yield consonant identification performance of about 50%-correct in the presence of the steady noise masker. In each interval, the utterance and noise had the same duration, although the duration of the utterances varied. All maskers were shaped using a raised-cosine function with 10-ms rise/fall times. In each experimental condition, estimates of the global SNR satisfying the performance criterion were relatively consistent across listeners.

TABLE I. Phonetic features of the 16 French consonants used in this study (Martin, 1996).

Consonant	Voicing	Manner	Place
p	Unvoiced	Occlusive	Front
t	Unvoiced	Occlusive	Middle
k	Unvoiced	Occlusive	Back
b	Voiced	Occlusive	Front
d	Voiced	Occlusive	Middle
g	Voiced	Occlusive	Back
f	Unvoiced	Constrictive	Front
s	Unvoiced	Constrictive	Middle
ʃ	Unvoiced	Constrictive	Back
v	Voiced	Constrictive	Front
z	Voiced	Constrictive	Middle
ʒ	Voiced	Constrictive	Back
l	Voiced	Constrictive	Middle
r	Voiced	Constrictive	Back
m	Voiced	Occlusive	Front
n	Voiced	Occlusive	Middle

Mean data for steady noise are presented in Table II for each speech-processing scheme. For intact stimuli (B&M algorithm with spectral smearing=1), the global SNR was, on average, equal to −7.3 dB. This is consistent with the SNR obtained by Gnansia *et al.* (2008) in similar conditions. For stimuli processed using the B&M algorithm, the global SNR was, on average, equal to −5 dB for a smearing factor of 2, and −0.3 dB for a smearing factor of 4. This result is comparable with the effects of spectral smearing on speech intelligibility in steady noise reported by Baer and Moore (1993). For stimuli processed with the TV scheme, the global SNR was on average equal to −0.8 dB for 1-ERB$_N$-wide analysis filters, 0.8 dB for 2-ERB$_N$-wide analysis filters, and 2.5 dB for 4-ERB$_N$-wide analysis filters. SNRs obtained with 1-ERB$_N$-wide analysis filters were consistent with those obtained by Gnansia *et al.* (2008) in comparable conditions.

TABLE II. Mean SNR (in dB) and overall identification scores (in % correct) in steady noise for each speech-processing scheme. SDs are given in parentheses.

	Smearing factor=1		Smearing factor=2		Smearing factor=4	
	SNR in dB	% correct	SNR in dB	% correct	SNR in dB	% correct
Spectral smearing	−7.3(1.8)	52(2.6)	−5(1.2)	51(2.7)	−0.3(0.6)	52(2.70)
Tone vocoder	−0.8(1.6)	50(3.9)	0.8(1.6)	46(4.9)	2.5(2.3)	48 (4)

For each amount of spectral smearing, SNRs obtained with the TV scheme were higher than those obtained using the B&M algorithm.

IV. RESULTS

A. Spectral-smearing algorithm

Mean data for stimuli processed by the B&M algorithm are presented in Fig. 3 (filled symbols). The left panels show data for steady (circles) and modulated noise (triangles). The right panels (squares) show MR data corresponding to the improvement in scores for modulated relative to stationary noise. Note that a smearing factor of 1 leaves stimuli intact.

1. Overall identification scores

Consistent with previous studies using identical speech and noise material (Füllgrabe *et al.*, 2006; Lorenzi *et al.*, 2006a; Gnansia *et al.*, 2008), the results show a clear release from masking for intact stimuli, amounting to 35% for overall identification scores. MR decreased when stimuli were spectrally smeared, by 6% and 16% for smearing factors of 2 and 4, respectively. An analysis of variance (ANOVA) conducted on the arcsine-transformed identification scores confirmed the visual impressions. The main effects of masker type [$F(1,5)=823.93$; $p<0.00001$], amount of spectral smearing [$F(2,10)=13.911$; $p<0.005$], and the interaction between the two [$F(2,10)=29.937$; $p<0.0001$] were all significant. Post-hoc comparisons (Scheffé test) showed that overall identification scores for steady noise were not significantly different across spectral-smearing conditions (all $p>0.99$). This was expected because the SNRs at which the signals were presented had been chosen to yield 50% correct identification for steady noise. Scores for modulated noise were significantly better than those for steady noise for each amount of spectral smearing (all $p<0.00005$). Moreover, scores obtained with modulated noise decreased significantly with increasing spectral smearing (all $p<0.01$).

2. Phonetic information received

In agreement with previous studies (e.g., Lorenzi *et al.*, 2006a; Gnansia *et al.*, 2008), the results presented in Fig. 3 show MR for intact stimuli equal to 51%, 48%, and 44% when MR is based on the relative information received for voicing, place of articulation, and manner, respectively. MR decreased with increasing spectral smearing for voicing and especially for place, MR being reduced by 20% and 31%, respectively, with smearing by a factor of 4. Spectral smearing by factors of 2 and 4 had little effect ($\leq$2%) on MR for manner. For voicing, the effects of masker type [$F(1,5)=313.709$; $p<0.00005$] and spectral smearing [$F(2,10)=4.184$; $p<0.05$], and the interaction between the two [$F(2,10)=7.50$; $p<0.05$] were significant. For place of articulation, the main effects of masker type [$F(1,5)=439.32$; $p<0.00001$] and spectral smearing [$F(2,10)=17.319$; $p<0.001$], and the interaction between the two [$F(2,10)=23.345$; $p<0.0005$] were also significant. For manner, the effect of masker type [$F(1,5)=290.26$; $p<0.00005$] was significant, but the effect of spectral smearing [$F(2,10)=0.141$; $p=0.87$] and the interaction between the two [$F(2,10)=0.679$; $p=0.53$] were not. Post-hoc comparisons indicated that, for each phonetic feature and each amount of spectral smearing, phonetic information received for modulated noise was significantly greater than that received for steady noise (all $p<0.05$), confirming the existence of significant MR for each condition of spectral smearing.

B. Tone-excited vocoder

Mean data across listeners for stimuli processed by the TV scheme are also presented in Fig. 3 (open symbols). In each panel, the data are shown as a function of the amount of spectral smearing produced by widening the analysis filters.

1. Overall identification scores

Consistent with previous studies (e.g., Gnansia *et al.*, 2008), a clear decrease in MR (by 15%) occurred when stimuli were vocoded so as to degrade TFS cues within 1-ERB_N-wide frequency bands (smearing factor=1). Figure 3 also shows a decrease in MR when the vocoded stimuli were spectrally smeared by widening the analysis filters. Relative to the MR obtained for unprocessed stimuli (35%), MR dropped by 24% and 27% when the analysis filters were broadened by factors of 2 and 4, respectively. An ANOVA conducted on the arcsine-transformed identification scores showed significant main effects of masker type [$F(1,5)=62.895$; $p<0.01$] and spectral smearing [$F(2,10)=6.142$; $p<0.05$], and a significant interaction between the two [$F(2,10)=7.497$; $p<0.05$]. Post-hoc comparisons showed that scores for steady noise were not significantly different across spectral-smearing conditions (1-, 2-, and 4-ERB_N-wide analysis filters) (all $p>0.58$), whereas those obtained with modulated noise decreased significantly when the analysis filters were broadened by a factor of 2 ($p<0.005$). Further broadening of the analysis filters (by a factor of 4) did not significantly affect scores for modulated noise ($p=0.99$). For 1- and 2-ERB_N-wide analysis filters, scores for modulated noise were significantly higher than those for steady noise ($p<0.05$). However, scores for modulated noise did not differ significantly from those for steady noise for 4-ERB_N-wide analysis filters. Thus, MR was abolished when TFS cues were degraded and analysis filters were broadened by a factor of 4. This result could not be due to a floor effect imposed by the performance criterion for steady noise (50%-correct), because overall identification scores measured using modulated noise could range from chance level (6.25%) to 100%-correct (scores lower than 50%-correct—and thus, negative MR—would then reveal the presence of "interference" effects caused by the modulation applied to the masking noise; e.g. Füllgrabe *et al.*, 2006).

2. Phonetic information received

The results in Fig. 3 show a clear decrease in MR (by 30%, 30%, and 8% for voicing, place, and manner, respectively) when stimuli were vocoded so as to degrade TFS cues within 1-ERB_N-wide frequency bands. MR for voicing, place, and manner reception decreased with increasing spec-

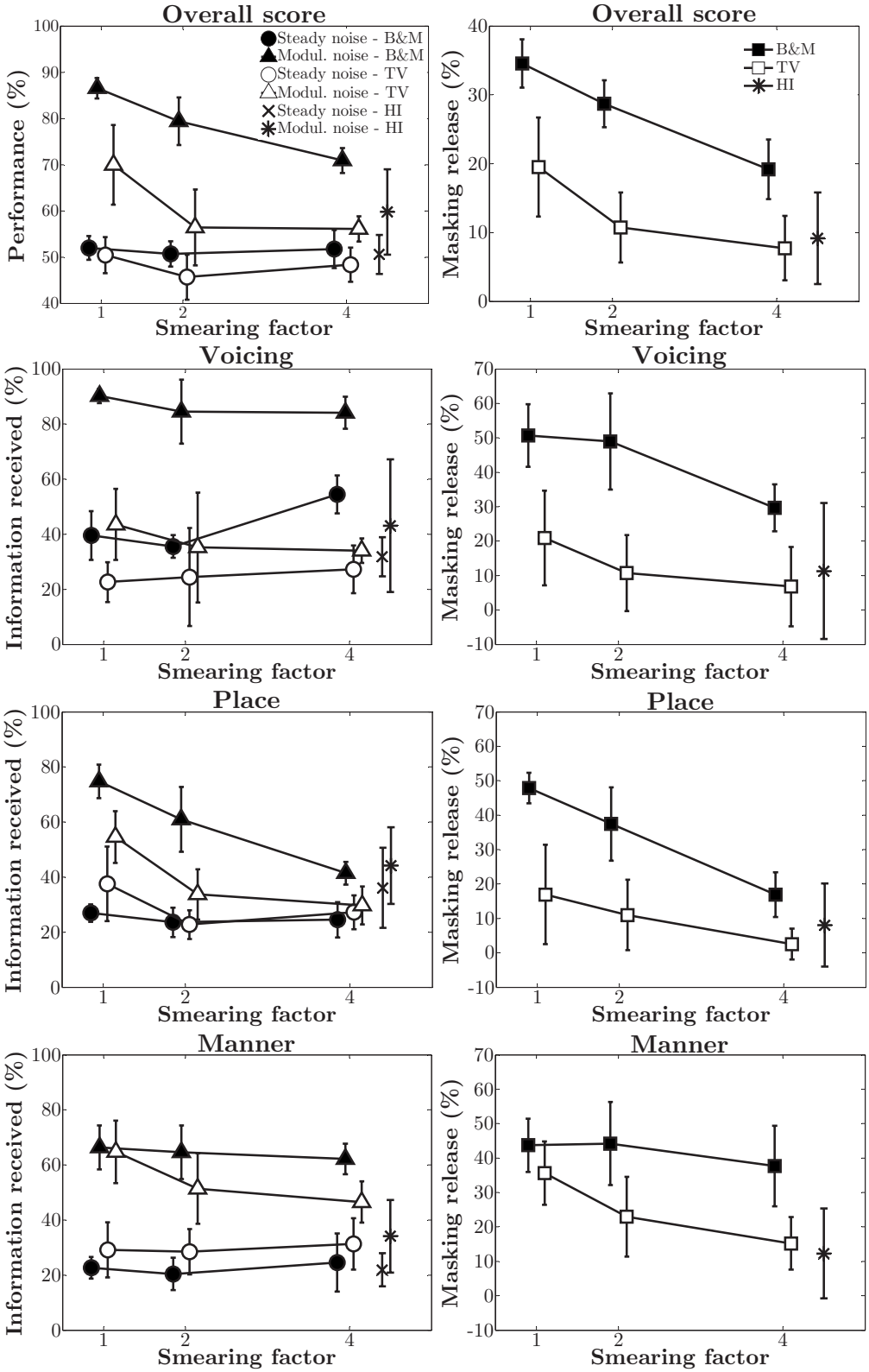

FIG. 3. Mean data for stimuli processed using the B&M algorithm (filled symbols) and TV scheme (open symbols). The left panels show data for steady (circles) and modulated (triangles) noise. The right panels (squares) show MR data, quantified as the difference between identification scores or phonetic information for modulated and for steady noise. From top to bottom panels, the data are presented for overall identification scores, voicing, place of articulation, and manner reception. In each panel, data are shown as a function of the amount of spectral smearing. The mean data for four listeners with flat, moderate hearing loss with unprocessed speech and noise stimuli (Lorenzi *et al.*, 2006a) are also shown (HI; stars). Error bars represent ±1 SD about the mean across listeners.

tral smearing. For voicing, MR decreased by 10% and 14% for broadening by factors of 2 and 4, respectively. In comparison, MR decreased by 6% and 14% for place, and by 13% and 20% for manner. Three ANOVAs showed significant main effects of masker type [voicing: $F(1,5)=53.665$; $p<0.001$; manner: $F(1,5)=171.53$; $p<0.00005$; place:

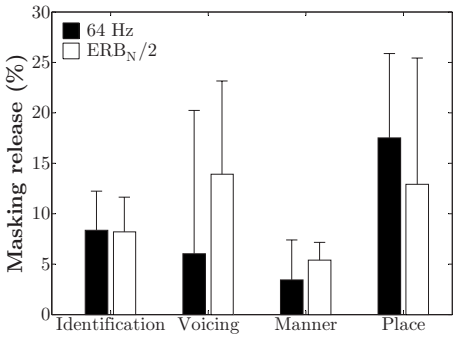

FIG. 4. Mean MR data for overall identification scores, voicing, manner, and place. Speech+noise mixtures were processed by a 32-band, 4-ERB$_N$-wide TV and envelope cues were either lowpass filtered at 64 Hz in each analysis filter (filled bars), or lowpass filtered at ERB$_N$/2 for analysis filters whose bandwidth was greater than 128 Hz (open bars). Error bars represent ±1 SD about the mean across listeners.

$F(1,5)=8.843$; $p<0.05$]. The main effect of spectral smearing was not significant for voicing [$F(2,10)=0.198$; $p=0.82$], marginally significant for manner [$F(2,10)=3.83$; $p=0.058$] and significant for place of articulation [$F(2,10)=12.54$; $p<0.005$]. The interaction between the two factors was significant for manner and place [manner: $F(2,10)=5.951$; $p<0.05$; place: $F(2,10)=5.021$; $p<0.05$] but not for voicing [$F(2,10)=1.64$; $p=0.24$]. It is noteworthy that, in the experiment using the B&M algorithm, the interaction between the factors' masker type and spectral smearing was not significant ($p=0.53$) for manner and significant ($p<0.05$) for voicing.

Post-hoc comparisons for TV data indicated that information received for modulated noise was significantly greater than for steady noise (all $p<0.05$) for spectral-smearing factors of 1 and 2 in the case of manner, and for a smearing factor of 1 in the case of place. No significant MR was found for place and manner when the analysis filters were broadened by a factor of 4.

3. Effect of envelope filtering

The TV processing included envelope lowpass filtering at 64 Hz. This processing scheme degraded fast temporal-envelope cues as well as TFS cues and could have contributed to some of the observed reduction in MR (Stone *et al.*, 2008). The contribution to MR of temporal-envelope cues at rates above 64 Hz was therefore investigated in an additional experiment conducted with four out of the six initial participants. Speech+noise mixtures were processed by a 32-band, 4-ERB$_N$-wide vocoder in which the envelopes were lowpass filtered at ERB$_N$/2 (instead of 64 Hz) for analysis filters whose bandwidths were greater than 128 Hz. This applied to analysis filters tuned above 80 Hz. Otherwise, the envelope was lowpass filtered at 64 Hz. The mean MR data are presented in Fig. 4. The results and ANOVAs showed that increasing the cutoff frequency of the vocoder's lowpass filter did not affect MR significantly for this amount of spectral smearing (all $p>0.3$), except for voicing reception, where a modest (8%) and marginally significant effect [$F(1,3)=9.05$; $p=0.057$] of envelope filtering was observed.

V. DISCUSSION

A. Comparison between speech-processing schemes

The results show that both speech-processing schemes had deleterious effects on MR. However, for each amount of spectral smearing, the TV produced a greater reduction in MR than the B&M algorithm, with a complete abolition of MR when the analysis filters of the TV were broadened by a factor of 4. These findings are consistent with the simulation data showing that the TV degraded F0 information conveyed by TFS cues more than the B&M algorithm, with maximum degradation when stimuli were processed by the TV using 4-ERB$_N$-wide analysis filters.[1]

Information transmission analysis revealed that the effects of spectral smearing on MR produced by the two speech-processing schemes were different for manner and voicing. Spectral smearing using the B&M algorithm gave a significant and substantial decrease in MR for place reception, consistent with a previous investigation of the effects of spectral smearing on consonant identification in quiet and in steady noise (Boothroyd *et al.*, 1996). A smaller effect was observed for voicing. Spectral smearing had no significant effect on MR for manner. In comparison, spectral smearing produced by the TV scheme had a significant deleterious effect on MR for manner and place, but no significant effect on MR for voicing.

Taken together, these results indicate that the two speech-processing schemes had different effects on MR, and that the effects of spectral smearing on the various auditory/phonetic processes underlying MR depended on the severity of TFS degradation.

B. Comparison between data for simulated and real hearing impairment

Figure 3 compares the current data obtained with normal-hearing listeners with the mean of the data obtained for four hearing-impaired (HI) listeners by Lorenzi *et al.* (2006a) (stars in the right-most part of each panel). These four listeners ranged in age between 54 and 62 years and showed sensorineural, bilateral, symmetrical, and flat hearing losses (see Table III). The absolute threshold variation across frequency (0.25–4 kHz) ranged from 5 to 10 dB HL. Pure tone average (PTA) thresholds (mean of audiometric thresholds at 0.25, 0.5, 1, 2, and 4 kHz on the tested ear) ranged from 44 to 46 dB HL. A broadening of auditory-filter bandwidths by a factor of about 2 was expected in these listeners, according to previous psychoacoustical assessments of frequency selectivity as a function of hearing loss (e.g., Moore, 2007). For each HI listener, MR was assessed using the same unprocessed stimuli (speech and noise maskers) and method (SNR being individually determined so as to yield an identification score of 50%-correct for steady noise) as in the current study, except that stimuli were presented at a comfortable listening level of 85 dB SPL (rms) to compensate for reduced audibility, and a different signal-processing technique was used to generate the speech-shaped noise masker.[2]

Figure 3 shows that MR for impaired listeners was generally smaller than that obtained for normal-listeners using the B&M algorithm. This was particularly the case for over-

TABLE III. Age (in years), pure-tone audiometric thresholds, and PTA (in dB HL) of the four HI listeners from the study of Lorenzi *et al.* (2006a).

		Frequency (Hz)						
Listener	Age	250	500	1000	2000	3000	4000	PTA
HI1	59	40	40	45	50	50	50	45
HI2	61	45	45	45	45	40	45	45
HI3	62	40	45	50	45	50	40	44
HI4	54	50	45	45	45	45	45	46

all identification scores and manner reception. For voicing and place reception, the MR data for the HI listeners did, however, overlap with those obtained for normal-listeners when stimuli were spectrally smeared by a factor of 4. Overall, the MR data of the impaired listeners matched the data for normal-hearing listeners obtained with stimuli processed by the TV scheme with a smearing factor between 2 and 4. This match is roughly consistent with the broadening of auditory-filter bandwidths expected from the PTA hearing loss of the four impaired listeners. This was confirmed by planned comparisons indicating that MR expressed in terms of overall identification scores, voicing, place, and manner reception was not significantly different for HI listeners and normal-hearing listeners tested with stimuli processed by the TV scheme with smearing factors of 2 and 4 (all $p > 0.2$). MR was significantly smaller for HI listeners than for normal-hearing listeners tested with the B&M algorithm (all $p < 0.01$, except for voicing and place reception when the smearing factor was 4, all $p > 0.2$).

Taken together, these data suggest that impaired frequency selectivity alone may not be sufficient to *fully* account for the reduced MR observed for listeners with moderate sensorineural hearing loss. This was particularly clear for manner reception, where simulated impaired frequency selectivity using the B&M algorithm had little effect on MR, whereas cochlear hearing loss reduced it substantially. In other words, combined sensory deficits (i.e., impaired frequency selectivity and disrupted perception of TFS cues) seem to be required to account for the limited ability to listen in the temporal dips of background noise observed for listeners with cochlear damage.

VI. CONCLUSIONS

The goal of this study was to assess the combined effects of spectral smearing and TFS degradation on MR. This was achieved by processing nonsense syllables and noise stimuli using either a spectral-smearing algorithm or a vocoder. The two processing schemes simulated broadening of auditory filters by factors of 2 and 4. Computer simulations of the early stages of auditory processing indicated that the TV degraded more severely F0 conveyed by TFS than the B&M algorithm. Overall, the results showed the following.

(1) Both speech-processing schemes reduced MR. However, for each amount of spectral smearing, the TV scheme produced a greater reduction in MR than the B&M algorithm, consistent with the idea that MR depends at least partly on the use of TFS information.
(2) MR was abolished when stimuli were processed by a TV simulating a broadening of auditory filters by a factor of 4, consistent with the severe degradation of F0-related information produced by this processing scheme.
(3) The effects of the two speech-processing schemes on MR were different for manner and voicing. Spectral smearing produced by the B&M algorithm significantly decreased MR for place and voicing reception, but did not have any significant effect on MR for manner. In contrast, the TV processing had a significant, deleterious effect on MR for manner and place, but no significant effect on MR for voicing.
(4) MR data for listeners with moderate flat hearing loss were well matched by MR data obtained for normal-hearing listeners tested with the TV simulating broadening of auditory filters by factors of 2 and 4.

These results show that two speech-processing schemes producing comparable smearing of place of excitation cues but different degradations of pitch-related TFS cues have different effects on MR. The results suggest that both impaired frequency selectivity and impaired perception of TFS cues contribute to the limited ability to glimpse speech in the temporal dips of background noise observed for most HI listeners.

ACKNOWLEDGMENTS

This research was supported by a CIFRE grant to D. Gnansia, and GDR GRAEC CNRS Grant No. 2967. The authors wish to thank Shihab Shamma, Brian C. J. Moore, and three reviewers for valuable comments on a previous version of this manuscript.

[1]It is noteworthy that a good predictor of MR may also be the SNR required for 50%-correct (cf. Table II), regardless of what kind of processing is used (e.g., Bernstein and Grant, 2008). For instance, the TV-processed stimuli with no smearing were tested at about the same SNR as the stimuli processed by the B&M algorithm with a smearing factor of 4. Indeed, MR in those two conditions is quite similar. However, correlations computed from summary autocorrelograms restricted to the voice pitch region (cf. Fig. 2) also predict similar MR for the TV scheme with no smearing and the B&M algorithm with a smearing factor of 4 (the correlation index being about 0.6 in both cases).

[2]In Lorenzi *et al.*, 2006a, the speech-shaped noise was generated by processing white noise with a digital filter whose magnitude response was equal to the long-term average spectrum of the entire set of unprocessed

target VCVs. In the present study, the power spectrum of the entire set of unprocessed target VCVs was computed via FFT, and the speech-shaped noise masker was generated from this power spectrum and a random phase spectrum via inverse FFT. In Lorenzi *et al.*, 2006a, the SNRs used with normal-hearing and HI listeners ranged between −3 and −12 dB for impaired listeners (mean across listeners: −7.5 dB), and between −9 and −15 dB for normal-hearing listeners (mean across listeners: −12 dB). The SNRs used by Lorenzi *et al.* (2006a) for normal-hearing listeners are thus 4.7 dB lower than those used in the present study for intact speech stimuli. The SNRs used by Lorenzi *et al.* (2006a) for HI listeners were on average 4.5 dB higher than those used for the control normal-hearing listeners. This degradation in SNR seems more consistent with the effects of spectral smearing simulated by the B&M algorithm than with those produced by the TV scheme (see Table II). This may be in line with previous work suggesting that the poorer speech reception threshold for a steady noise background observed in HI listeners is better explained by supra-threshold distortions in the spectral domain than supra-threshold distortions in the temporal or intensity domains (e.g., van Schijndel *et al.*, 2001).

Allen, J. (**1977**). "Short term spectral analysis, synthesis, and modification by discrete Fourier transform," IEEE Trans. Acoust., Speech, Signal Process. **25**, 235–238.

Bacon, S. P., Opie, J. M., and Montoya, D. Y. (**1998**). "The effects of hearing loss and noise masking on the masking release for speech in temporally complex backgrounds," J. Speech Lang. Hear. Res. **41**, 549–563.

Baer, T., and Moore, B. C. J. (**1993**). "Effects of spectral smearing on the intelligibility of sentences in noise," J. Acoust. Soc. Am. **94**, 1229–1241.

Baer, T., and Moore, B. C. J. (**1994**). "Effects of spectral smearing on the intelligibility of sentences in the presence of interfering speech," J. Acoust. Soc. Am. **95**, 2277–2280.

Bernstein, J. G., and Grant, K. W. (**2008**). "The role of temporal fine structure in speech source segregation," J. Acoust. Soc. Am. **123**, 3711.

Binns, C., and Culling, J. F. (**2007**). "The role of fundamental frequency contours in the perception of speech against interfering speech," J. Acoust. Soc. Am. **122**, 1765.

Boothroyd, A., Mulhearn, B., Gong, J., and Ostroff, J. (**1996**). "Effects of spectral smearing on phoneme and word recognition," J. Acoust. Soc. Am. **100**, 1807–1818.

Cooke, M. (**2006**). "A glimpsing model of speech perception in noise," J. Acoust. Soc. Am. **119**, 1562–1573.

de Cheveigné, A., and Kawahara, H. (**2002**). "YIN, a fundamental frequency estimator for speech and music," J. Acoust. Soc. Am. **111**, 1917–1930.

Dubno, J. R., and Dirks, D. D. (**1989**). "Auditory filter characteristics and consonant recognition for hearing-impaired listeners," J. Acoust. Soc. Am. **85**, 1666–1675.

Duquesnoy, A. J. (**1983**). "Effect of a single interfering noise or speech source upon the binaural sentence intelligibility of aged persons," J. Acoust. Soc. Am. **74**, 739–743.

Festen, J. M., and Plomp, R. (**1990**). "Effects of fluctuating noise and interfering speech on the speech-reception threshold for impaired and normal hearing," J. Acoust. Soc. Am. **88**, 1725–1736.

Fu, Q. J., and Nogaki, G. (**2005**). "Noise susceptibility of cochlear implant users: The role of spectral resolution and smearing," J. Assoc. Res. Otolaryngol. **6**, 19–27.

Füllgrabe, C., Berthommier, F., and Lorenzi, C. (**2006**). "Masking release for consonant features in temporally fluctuating background noise," Hear. Res. **211**, 74–84.

George, E. L., Festen, J. M., and Houtgast, T. (**2006**). "Factors affecting masking release for speech in modulated noise for normal-hearing and hearing-impaired listeners," J. Acoust. Soc. Am. **120**, 2295–2311.

Gilbert, G., and Lorenzi, C. (**2006**). "The ability of listeners to use recovered envelope cues from speech fine structure," J. Acoust. Soc. Am. **119**, 2438–2444.

Glasberg, B. R., and Moore, B. C. J. (**1986**). "Auditory filter shapes in subjects with unilateral and bilateral cochlear impairments," J. Acoust. Soc. Am. **79**, 1020–1033.

Gnansia, D., Jourdes, V., and Lorenzi, C. (**2008**). "Effect of masker modulation depth on speech masking release," Hear. Res. **239**, 60–68.

Gustafsson, H. A., and Arlinger, S. D. (**1994**). "Masking of speech by amplitude-modulated noise," J. Acoust. Soc. Am. **95**, 518–529.

Hohmann, V. (**2002**). "Frequency analysis and synthesis using a gammatone filterbank," Acust. Acta Acust. **88**, 433–442.

Hopkins, K., and Moore, B. C. J. (**2007**). "Moderate cochlear hearing loss leads to a reduced ability to use temporal fine structure information," J. Acoust. Soc. Am. **122**, 1055–1068.

Hopkins, K., and Moore, B. C. J. (**2009**). "The contribution of temporal fine structure to the intelligibility of speech in steady and modulated noise," J. Acoust. Soc. Am. **125**, 442–446.

Hopkins, K., Moore, B. C. J., and Stone, M. A. (**2008**). "Effects of moderate cochlear hearing loss on the ability to benefit from temporal fine structure information in speech," J. Acoust. Soc. Am. **123**, 1140–1153.

Howard-Jones, P. A., and Rosen, S. (**1993**). "Uncomodulated glimpsing in "checkerboard" noise," J. Acoust. Soc. Am. **93**, 2915–2922.

Lorenzi, C., Berthommier, F., Apoux, F., and Bacri, N. (**1999**). "Effects of envelope expansion on speech recognition," Hear. Res. **136**, 131–138.

Lorenzi, C., Debruille, L., Garnier, S., Fleuriot, P., and Moore, B. C. J. (**2009**). "Abnormal auditory temporal processing for frequencies where absolute thresholds are normal," J. Acoust. Soc. Am. **125**, 27–30.

Lorenzi, C., Gilbert, G., Carn, H., Garnier, S., and Moore, B. C. J. (**2006b**). "Speech perception problems of the hearing impaired reflect inability to use temporal fine structure," Proc. Natl. Acad. Sci. U.S.A. **103**, 18866–18869.

Lorenzi, C., Husson, M., Ardoint, M., and Debruille, X. (**2006a**). "Speech masking release in listeners with flat hearing loss: Effects of masker fluctuation rate on identification scores and phonetic feature reception," Int. J. Audiol. **45**, 487–495.

Martin, P. (**1996**). *Eléments de Phonétique, Avec Application au Français* (Les presses de l'Université Laval, Sainte-Foy, France).

Meddis, R., and Hewitt, M. J. (**1992**). "Modeling the identification of concurrent vowels with different fundamental frequencies," J. Acoust. Soc. Am. **91**, 233–245.

Meddis, R., and O'Mard, L. (**1997**). "A unitary model of pitch perception," J. Acoust. Soc. Am. **102**, 1811–1820.

Miller, G. A., and Licklider, J. C. A. (**1950**). "The intelligibility of interrupted speech," J. Acoust. Soc. Am. **22**, 167–173.

Miller, G. A., and Nicely, P. E. (**1955**). "An analysis of perceptual confusions among some English consonants," J. Acoust. Soc. Am. **27**, 338–352.

Moore, B. C. J. (**2007**). *Cochlear Hearing Loss: Physiological, Psychological and Technical Issues* (Wiley, Chichester).

Moore, B. C. J. (**2008**). "The role of temporal fine structure processing in pitch perception, masking, and speech perception for normal-hearing and hearing-impaired people," J. Assoc. Res. Otolaryngol. **9**, 399–406.

Moore, B. C. J., and Moore, G. A. (**2003a**). "Discrimination of the fundamental frequency of complex tones with fixed and shifting spectral envelopes by normally hearing and hearing-impaired subjects," Hear. Res. **182**, 153–163.

Moore, G. A., and Moore, B. C. J. (**2003b**). "Perception of the low pitch of frequency-shifted complexes," J. Acoust. Soc. Am. **113**, 977–985.

Nelson, P. B., and Jin, S. H. (**2004**). "Factors affecting speech understanding in gated interference: cochlear implant users and normal-hearing listeners," J. Acoust. Soc. Am. **115**, 2286–2294.

Nelson, P. B., Jin, S. H., Carney, A. E., and Nelson, D. A. (**2003**). "Understanding speech in modulated interference: Cochlear implant users and normal-hearing listeners," J. Acoust. Soc. Am. **113**, 961–968.

Patterson, R. D. (**1987**). "A pulse ribbon model of monaural phase perception," J. Acoust. Soc. Am. **82**, 1560–1586.

Patterson, R. D., Nimmo-Smith, I., Weber, D. L., and Milroy, R. (**1982**). "The deterioration of hearing with age: Frequency selectivity, the critical ratio, the audiogram, and speech threshold," J. Acoust. Soc. Am. **72**, 1788–1803.

Peters, R. W., and Moore, B. C. J. (**1992**). "Auditory filter shapes at low center frequencies in young and elderly hearing-impaired subjects," J. Acoust. Soc. Am. **91**, 256–266.

Peters, R. W., Moore, B. C. J., and Baer, T. (**1998**). "Speech reception thresholds in noise with and without spectral and temporal dips for hearing-impaired and normally hearing people," J. Acoust. Soc. Am. **103**, 577–587.

Qin, M. K., and Oxenham, A. J. (**2003**). "Effects of simulated cochlear-implant processing on speech reception in fluctuating maskers," J. Acoust. Soc. Am. **114**, 446–454.

Rhebergen, K. S., Versfeld, N. J., and Dreschler, W. A. (**2006**). "Extended speech intelligibility index for the prediction of the speech reception threshold in fluctuating noise," J. Acoust. Soc. Am. **120**, 3988–3997.

Stickney, G. S., Nie, K., and Zeng, F. G. (**2005**). "Contribution of frequency modulation to speech recognition in noise," J. Acoust. Soc. Am. **118**, 2412–2420.

Stickney, G. S., Zeng, F. G., Litovsky, R., and Assmann, P. (**2004**). "Co-

chlear implant speech recognition with speech maskers," J. Acoust. Soc. Am. **116**, 1081–1091.
Stone, M. A., Fullgrabe, C., and Moore, B. C. J. (**2008**). "Benefit of high-rate envelope cues in vocoder processing: Effect of number of channels and spectral region," J. Acoust. Soc. Am. **124**, 2272–2282.
Stone, M. A., Glasberg, B. R., and Moore, B. C. J. (**1992**). "Simplified measurement of impaired auditory filter shapes using the notched-noise method," Br. J. Audiol. **26**, 329–334.
ter Keurs, M., Festen, J. M., and Plomp, R. (**1993**). "Effect of spectral envelope smearing on speech reception. II," J. Acoust. Soc. Am. **93**, 1547–1552.
Tyler, R. S., Hall, J. W., Glasberg, B. R., Moore, B. C. J., and Patterson, R. D. (**1984**). "Auditory filter asymmetry in the hearing impaired," J. Acoust. Soc. Am. **76**, 1363–1368.
van Schijndel, N. H., Houtgast, T., and Festen, J. M. (**2001**). "Effects of degradation of intensity, time, or frequency content on speech intelligibility for normal-hearing and hearing-impaired listeners," J. Acoust. Soc. Am. **110**, 529–542.
Zeng, F. G., Nie, K., Stickney, G. S., Kong, Y. Y., Vongphoe, M., Bhargave, A., Wei, C., and Cao, K. (**2005**). "Speech recognition with amplitude and frequency modulations," Proc. Natl. Acad. Sci. U.S.A. **102**, 2293–2298.

Modeling the dynamics of a compliant piano action mechanism impacting an elastic stiff string

Chandrika P. Vyasarayani, Stephen Birkett,[a] and John McPhee
Department of Systems Design Engineering, University of Waterloo, Waterloo, Ontario N2L 3G1, Canada

(Received 26 August 2008; revised 2 April 2009; accepted 5 April 2009)

A realistic model of the piano hammer-string interaction must treat the action mechanism and string as a single system. In this paper an elastic stiff string model is integrated with a dynamic model of a compliant action mechanism with flexible hammer shank. Action components represented as rotating bodies interact through felt-lined interfaces for which a specialized contact model with hysteretic damping and tangential friction was developed. The motion of the hammer during string contact is governed by the dynamics of the action mechanism, thereby providing a more sophisticated hammer-string interaction than a simple transverse impact hammer model with fixed contact location. Simulations have been used to compare mechanism response for impact on the elastic string as compared to a rigid stop. Hammer head scuffing along the string and time in contact were predicted to increase, while hammer shank vibration amplitude and peak contact force were decreased. Introducing hammer-string friction decreases the duration of contact and reduces the extent of scuffing. Finally, significant differences in hammer and string motion were predicted for a highly flexible hammer shank. Initial contact time and location, length of contact period and peak force, hammer vibration amplitude, scuffing extent, and string spectral content were all influenced. © *2009 Acoustical Society of America.* [DOI: 10.1121/1.3125343]

PACS number(s): 43.75.Mn, 43.40.Cw [NHF] Pages: 4034–4042

I. INTRODUCTION

The action mechanism in a piano converts a mechanical input at the key into motion of the hammer which impacts the string for tone generation. A typical configuration of a modern grand (horizontal) piano action is shown in Fig. 1, consisting of five main components: key, whippen, repetition lever, jack, and hammer.[1] The components of this mechanism interact through felt-lined interfaces providing compliant, and possibly intermittent, contact locations with friction and damping. Some of these contacts are perfectly transverse, and some are oblique. The mechanical properties of felt[2–4] will influence the damping of vibrations present in the action components due to their flexibility, as well as the transient vibrations which arise when components separate and re-contact during the operation of the mechanism.

The driving force on the hammer is transmitted through the jack under the knuckle. Immediately before its impact with the string, the jack is mechanically forced to lose contact (called escapement or let off), so the hammer may freely leave the string, and vibrations generated on the string through the impact will not be immediately damped by the hammer. Many authors[5–14] exploited this fact and modeled the hammer as a single-degree-of-freedom translating mass with nonlinear compliance, thus assuming perfect normal impact between the string and the hammer. In reality, the hammer shank (on which the hammer is mounted) is a rotating slender beam, so the hammer follows a circular, not linear, trajectory. Moreover, small vibrations are superimposed on its motion due, in part, to the flexibility of the shank and the compressibility of the felt contacts. The effects of these on string motion,[15] contact force,[16] and action mechanism dynamics[17] have been emphasized in the literature.

The hammer-string contact modeling literature[5–14] ignores any effects due to hammer shank flexibility and action compressibility; the only simulation model which includes hammer shank flexibility[17] neglects string dynamics, substituting a rigid stop for the hammer to impact. In this paper we investigate the dynamic significance of flexibility by integrating models of an action mechanism with flexible hammer shank[17] and an elastic stiff piano string.

Hirschkorn *et al.*[18] developed a multibody dynamic model of the action mechanism considering all the components as rotating rigid bodies. A detailed review of earlier action mechanism models was also reported, with the conclusion that none of the existing models is sufficiently realistic nor mechanistic enough to be useful for simulations for prototyping. Parameters in the earlier models were tuned to obtain the observed hammer motion and could not be associated with physical measurements of action components. Izadbakhsh *et al.*[17] extended the Hirschkorn model by including hammer shank flexibility. In both these models, string dynamics are neglected and the hammer impacts a rigid obstacle in place of a string. The development of a simulation model for analysis and design of piano actions, one of the goals of our research, demands a complete multibody dynamic model of the mechanism with string contact. In order to include a realistic hammer-string interaction, the action mechanism and string must be dealt with as a single system. This is necessary so that the effect on system response due to changing physical parameters of the mechanism and/or string may be examined. In general there will be tonal changes, characterized by different partials generated

[a]Author to whom correspondence should be addressed. Electronic mail: sbirkett@real.uwaterloo.ca

 0001-4966/2009/125(6)/4034/9/$25.00

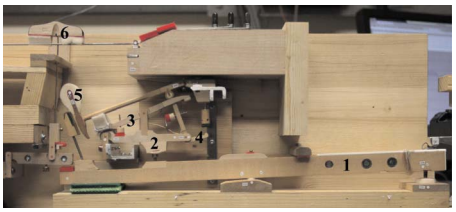

FIG. 1. (Color online) Typical modern grand piano action mechanism: key (1), whippen (2), repetition lever (3), jack (4), hammer (5), and damper (6).

on the string, as well as changes in the dynamic behavior of the components of the mechanism. In this paper we integrate the stiff string model proposed by Fletcher[19] with the flexible action mechanism model presented in Izadbakhsh *et al.*,[17] thus filling the gap between the single-degree-of-freedom hammer-string interaction models[5–14] and dynamic piano action mechanism models with rigid contact.[17,18]

II. MATHEMATICAL MODELING

A. Action mechanism dynamic model

A procedure for constructing a multibody dynamic model of a piano action mechanism with rigid components was presented in Hirschkorn *et al.*;[18] this model was extended to allow a flexible hammer shank in Izadbakhsh *et al.*[17] Further details, including the results of detailed experimental validation, have also been previously published.[20–22] The basic structure of the model is shown in Fig. 2. Bodies representing the action components rotate on pin joints (with friction) representing their bushed pivots connecting them either to ground or to a reference frame attached to another body, for instance, the jack pinned to the whippen. The key, driven by a time dependent force (force profile) applied vertically downward at a location on the front surface, is assumed to rotate on a pin joint at the balance rail (key pivot). A contact detection methodology is followed to determine the dynamic interaction between the components coupled through compliant contact interfaces.

Graph-theoretic methods[23] are used to formulate the equations of motion for the rotation of the five component bodies. Due to the complexity of the equations and in order to avoid manual errors, the entire equation formulation procedure was systematically implemented using computational symbolic algebra, with the aid of the multibody dynamic modeling package DYNAFLEXPRO (Ref. 24) in Maple.[25] One advantage of this graph-theoretic approach is that user-defined coordinates may be freely chosen for each body, allowing the convenience of a purely joint-coordinate formulation. For the rigid component action mechanism, the system is governed by five ordinary differential equations (ODEs).

Hammer shank flexibility is included in the model by splitting the rigid hammer into three components, a rigid head and base, linked by weld joints to the ends of a flexible shank, as shown in Fig. 2. We define two useful measures related to flexibility for the hammer: (i) Hammer head tip displacement with respect to the ground reference frame is an indication of the absolute motion of the string contact point of the hammer head, incorporating both the large-scale rotation on the base pivot, as well as effects on the head motion due to shank vibrations and string contact. (ii) Hammer shank tip deflection is a measure of shank bending defined as the displacement of the tip away from the equilibrium axis of the shank. Wherever hammer head tip displacement is reported in this paper, the undeformed position of the felt will be assumed; in reality, the actual physical tip of the hammer head may be compressed due to its interaction with the strings during contact. The flexible beam model used for the shank is based on the theory developed by Shi *et al.*,[26,27] which considers shear deformation (Rayleigh) and uses Taylor, Legendre, or Chebyshev polynomials

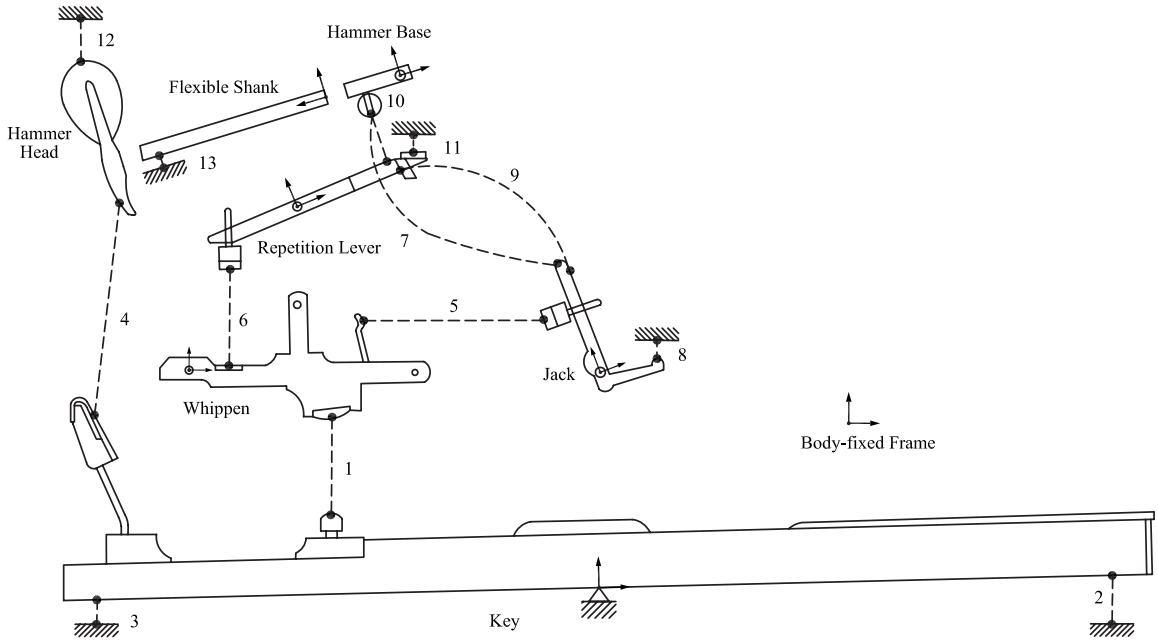

FIG. 2. Components and the 13 contact locations between them (dashed lines) represented in the dynamic piano action mechanism model.

to discretize the governing partial differential equation. A convergence study[17] concluded that three elastic coordinates are sufficient to accurately capture the flexible behavior of the hammer shank. Therefore, the equations of motion for the rigid component action are supplemented by three additional coupled ODEs, two of which represent the dynamics of shank bending, and the third the axial dynamics of the hammer.

Graph-theoretic modeling of multibody systems is a well established methodology,[28] and the exact procedure followed in generating the equations of motion for the dynamic action model has been explicitly and fully described previously. Equations generated in symbolic form have the following general structure:[29]

$$\mathbf{M}\ddot{q} = \mathbf{F}, \tag{1}$$

where $\mathbf{M}$ is the mass matrix and $q=[A_k, A_w, A_j, A_r, A_h, u_{f1}, v_{f1}, v_{f2}]^T$ is the vector of generalized coordinates, consisting of the angular positions of key, whippen, jack, repetition lever, and hammer base, as well as the elastic coordinates that describe the state of the flexible hammer shank. The first five coordinates in q are angles measured counter-clockwise from the ground reference frame (or from the reference frame attached to the whippen, in the case of A_j, A_r) to the body-fixed reference frame attached to the corresponding component. The last three coordinates in q correspond to the axial deformation and the two transverse modes of the flexible shank, respectively. The right-hand force vector $\mathbf{F}$ in Eq. (1) includes quadratic velocity terms and contact forces.

B. Contact modeling

The contact model representing the compliant felt interfaces between components will be described in some detail, as this same approach is used in the present paper to provide a simple model of the hammer-string interaction (contact 12 in Fig. 2). Contact detection is based on geometric proximity, with each of the two contacting surfaces defined as a line, circle, or hybrid shape, which reflects the actual geometry of the component. A phenomenological model defining force vs compression characteristics was obtained empirically for each individual contacting pair of components in the action mechanism.[17,18] The approach can be interpreted as an extension of the contact model proposed by Hunt and Crossley.[30] The experimentally obtained loading and unloading curves determine an average fit curve,

$$f_{\text{fit}}(x) = ax^3 + bx^2 + cx, \tag{2}$$

giving the normal force at a contact based on the interpenetration x of the contact surfaces of the two bodies. Hysteresis is introduced to the contact model by including damping dependent on penetration velocity in the expression for the normal force f_n as follows:

$$f_n = f_{\text{fit}}(x)(1 - d\dot{x}). \tag{3}$$

The damping coefficient d is defined by

$$d = \left(\frac{f_n(x)}{f_{\text{fit}}(x)} - 1\right) \Big/ \dot{x}_{\text{av}}, \tag{4}$$

where x is chosen as the penetration giving the maximum difference between loading and unloading curves, and $\dot{x}_{\text{av}}$ is the average velocity of the penetration observed in experiments with a real action mechanism.

Friction at the contacting interfaces has been represented using a Coulomb friction model proposed by Cull and Tucker,[31] accounting for both static and dynamic friction effects. The expression for frictional force is shown below:

$$f_t = \mu f_n, \tag{5}$$

where the coefficient of friction (CoF) μ is given by the following expression:

$$\mu = A\left(\tanh(s_t/v_t) + \frac{B_1 s_t/v_t}{1 + B_2(s_t/v_t)^4}\right). \tag{6}$$

In this smoothed version of the standard piecewise linear friction model, parameters A, B_1, and B_2 are determined through the static and kinetic friction coefficients while s_t is the relative and v_t is the threshold velocity at which the slipping starts. Details on how these parameters were obtained can be found in the published model.[17,18]

It should be emphasized that an empirical force-compression fit curve as described above implicitly incorporates the contact surface geometry of both bodies involved and consequently cannot be interpreted as characterizing a unique force-compression curve for the felt interface material itself. If the contact geometry of either body is changed, the force-compression curve will, in general, be different, even though the compliant properties of the felt interface are maintained. This observation is of particular importance in understanding the rationale for selecting hammer-string contact parameters in the next section.

C. Hammer-string interaction

In this section we discuss the process of integrating a string model into the action mechanism, in place of the rigid stop used previously[17,18] for hammer contact (location 12 in Fig. 2). This stop was a steel plate fixed to ground and mounted above the hammer, which impacted its narrow edge (3 mm) as if it were a completely rigid string. The equation governing the transverse dynamics of an elastic stiff string, as proposed by Fletcher,[19] is given by the following:

$$\rho\frac{\partial^2 y}{\partial t^2} + EI\frac{\partial^4 y}{\partial x^4} - T\frac{\partial^2 y}{\partial x^2} = f_n(t)\,\delta(x - x_{hc}), \tag{7}$$

where y is the deformation of the string, x is the coordinate along the length of the string, L is the speaking length of the string, T is the tension in the string, ρ is the linear density, I is the area moment of inertia of the cross section, E is the Young's modulus, and δ is the Dirac delta function.

The hammer impact is modeled as an external force on the above string model. In Eq. (7) x_{hc} is the x component of the displacement $\underline{r}_{hc}$ of a point P on the hammer resolved in a frame attached at the boundary of the string, as shown in Fig. 3. The point P is chosen such that the contact surface

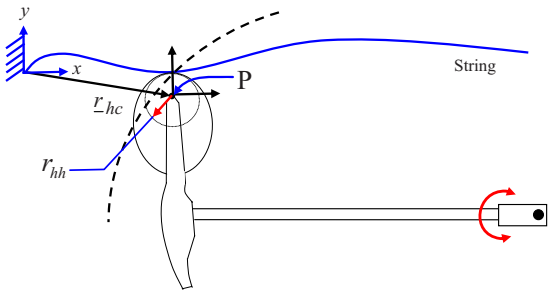

FIG. 3. (Color online) Schematic representation of hammer-string during contact.

geometry of the hammer head can be represented with a circle, which then is used for contact detection with the string represented as a line. The position x_{hc} is governed by the dynamics of the action mechanism, thereby providing a more sophisticated hammer-string interaction than the transverse impact hammer models[5–14] in which impact location does not change during the contact. Boundary conditions for pinned-pinned supports are as follows:

$$y(0,t) = y(L,t) = 0 \quad \text{and} \quad y_{xx}(0,t) = y_{xx}(L,t) = 0. \tag{8}$$

The normal contact force during hammer-string impact can be represented by the general contact model described above:

$$f_n(t) = \psi(a\alpha^3 + b\alpha^2 + c\alpha)(1 + d\dot{\alpha}), \tag{9}$$

where $\alpha = y_{hc} + r_{hh} - y(x_{hc},t)$ is the dynamic compression of felt during contact, parameters a,b,c define the empirical fit curve, d is the damping coefficient for (a compromise) average penetration velocity, and the contact condition ψ is defined by

$$\psi = \begin{cases} 1 & \text{if } y_{hc} + r_{hh} \geqslant y(x_{hc},t) \\ 0 & \text{if } y_{hc} + r_{hh} < y(x_{hc},t). \end{cases} \tag{10}$$

As noted above, neither the hammer nor the felt is characterized by a unique empirical fit curve since an identical hammer contacting different target bodies will, in general, determine different force-compression curves according to the different contact areas pertained to during the stages of compression.[32]

The frictional force at the interface can be obtained as follows:

$$f_t(t) = \mu f_n(t), \tag{11}$$

with μ obtained from Eq. (6) as described above for the general contact model. Previously, friction between hammer and the rigid stop was ignored;[17,18] in this paper we consider some implications of including friction in the hammer-string contact.

A solution to the string equation (7) is assumed to be of the following form:

$$y(x,t) = \sum_{j=1}^{\infty} w_j(x)\,\eta_j(t), \tag{12}$$

where $w_j(x)$ is the jth undamped mass normalized mode shape of the string and $\eta_j(t)$ is the jth mode to be solved.

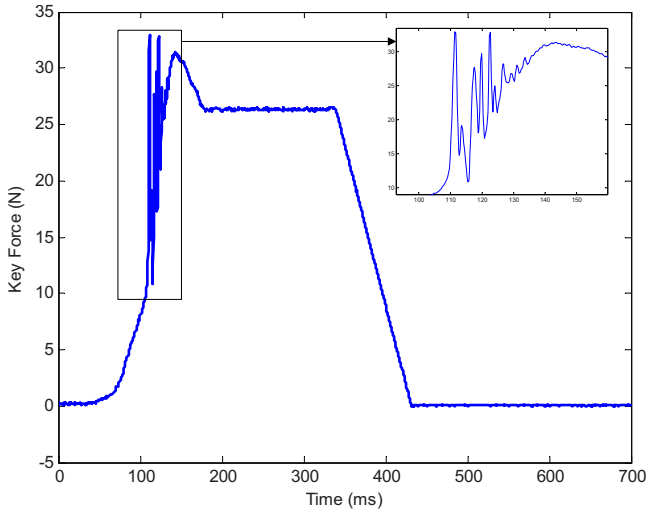

FIG. 4. (Color online) Force profile from a forte blow recorded at the key surface and used for model input.

Substituting the above solution and assuming the damping to be of Rayleigh's form with ξ_j being the modal damping, Eq. (7) can be reduced using orthogonality relations to an infinite number of second order ODEs of the form

$$\ddot{\eta}_j + 2\xi_j\omega_j\dot{\eta} + \omega_j^2\eta = w_j(x_{hc})f_n(t). \tag{13}$$

The closed-form expressions for natural frequencies and mass normalized mode shape given by Fletcher[19] are as follows:

$$\omega_j = \frac{\pi}{L}\sqrt{\frac{T}{\rho}}(1 + \varepsilon\pi^2 j^2), \tag{14}$$

$$w_j(x) = \sqrt{\frac{2}{\rho L}}\sin\left(j\pi\frac{x}{L}\right), \tag{15}$$

where $\varepsilon = \pi d^4 E/64L^2T$ is the inharmonicity index and can be interpreted as the perturbation in the natural frequencies due to the introduction of the small stiffness term in the equation of motion [Eq. (7)].

III. RESULTS AND DISCUSSION

The equations of motion [Eq. (1)] were solved numerically in MATLAB (Ref. 33) along with Eq. (13) discretized considering the first 40 string modes and the customized hammer-string contact model given by Eqs. (9)–(11). The contact force asymptotically converged near 35 modes within a maximum difference of 0.05 N when 35 modes were retained in the solution instead of 40 modes. We have considered 40 modes as it covers the audible frequency range. The stiff solver ODE15s was used with absolute and relative tolerance of 10^{-5}. Action parameters relate to note 52 (C5) of a Boston GP-178 grand piano. All geometric and material properties, dynamic and contact parameters, initial conditions, and key input were the same as those used previously.[34,35] The force profile from a forte blow recorded at the key surface[36] was used to provide the input function shown in Fig. 4; values were linearly interpolated as required because the variable time steps of the solver did not corre-

TABLE I. Physical parameters of the string.

Physical parameter	Value
Length of the string (L)	0.341 m
String tension (T)	703 N
Linear density (ρ)	0.0058 kg/m

spond to the fixed sampling rate of force measurement.

The soundboard bridge termination of the string (on the left side in all illustrations in this paper) is the origin of the (horizontal) string axis; the agraffe termination is at position L on this axis. A fixed geometric relation between string and action is determined by the positions of the string terminations with respect to the action ground points. This is defined by placing the nominal (pseudo-static) hammer-string contact location at 0.88 L on the string axis. (As will be seen, the dynamic hammer-string contact location can vary according to the flexing of the hammer shank.) Hammer blow distance (vertical distance from the hammer at rest to the underside of the string) is a standard 47 mm. The action mechanism is arranged as shown in Fig. 1, with the key front and hammer pivot to the right side of the string contact location.

String parameters used in the present simulations, as given in Table I, were obtained for note 52 (C5) of a Boston GP-178 grand piano; the hammer strikes three such identical parallel strings (a trichord unison) simultaneously. We wish to examine the effect of changing only the target (rigid stop vs trichord strings) while keeping all other factors, including the hammer, identical in the simulations. However, as noted previously, hammer-string contact parameters will be different, in general, for the same hammer striking different targets. This problem has been circumvented by (i) representing the trichord target as a single equivalent string model with linear density and tension both increased by a factor of 3, instead of three individual strings; and (ii) assuming that the stop and the triple-string present the same geometric profile to the hammer. These assumptions ensure that the same hammer force-compression characteristics can be used in each case. The hammer contact fit curve parameters in the present simulations, as well as the damping coefficient, are the same as those used previously.[17,18]

A. Model validation

The action mechanism model being used in these simulations has previously been experimentally validated.[17] The modal string model was validated by comparing simulation results to those of Bensa *et al.*[13] in which a space and time finite difference method (FDM) was used to solve the governing PDE. The comparison in this case was for a simple transverse impact between a single-degree-of-freedom hammer model and the string. A modal damping of ξ_j=0.04 was used in the simulation, with string parameters the same as those used by Bensa *et al.*[13] for validating their FDM (derived originally from Chaigne and Askenfelt[12]). With 30 modes for the string model, simulated hammer-string contact force was seen to be in very close agreement to the FDM results.

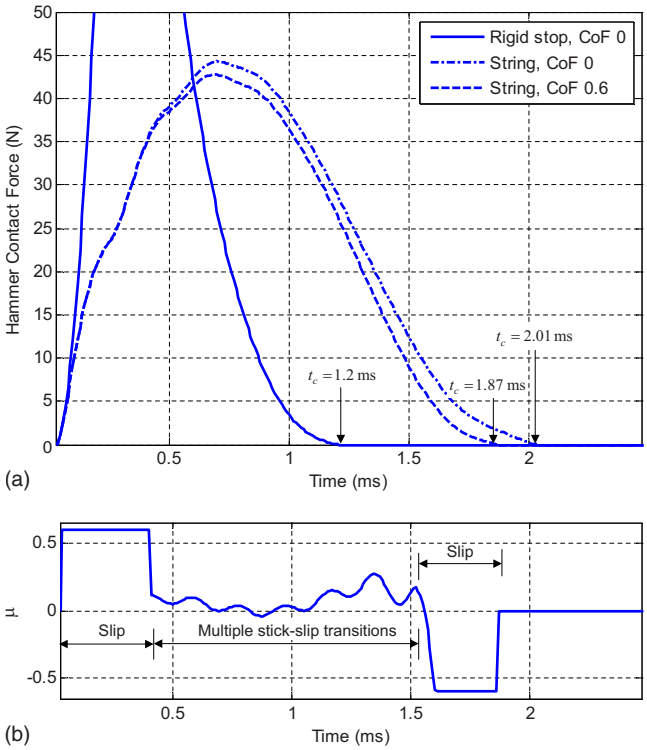

FIG. 5. (Color online) (a) Hammer contact force for rigid stop and string for varying contact CoF. Peak force with rigid stop impact is 95 N. Time zero corresponds to initiation of impact. (b) Variation of CoF during hammer-string impact for A=0.6.

B. Effect of string flexibility on mechanism dynamics

In this section, the behavior of the piano action model with flexible hammer shank is compared for string and rigid stop impact. Friction is not included here since it was not considered previously with the rigid stop.[17] In the simulations the hammer impact occurs about 109 ms after the force profile input begins. The post-impact response of the string is governed by the displacement and velocity immediately after the hammer-string contact.

The time-varying contact force between the hammer and the string is shown in Fig. 5(a). Hammer contact duration (t_c) with the string is 2 ms, about 1.5 times longer than that with the rigid stop (1.2 ms); peak contact force of 44 N with the string is about 50% of that with the rigid stop (95 N). Fluctuations seen in the hammer-string force profile are caused by pulses initiated on the string by the hammer contact, reflected off the boundaries, and returning to interact with the hammer.

The rotation of the hammer base shows a considerable difference for the two impact targets. Deflection of the string in the transverse direction results in an increase in both the hammer-string contact duration and the post-impact angular velocity, as well as a significant reduction in the vibration of the hammer base about its pivot. The position of the hammer head is determined by the angular rotation of the hammer base as well as the flexural configuration of the hammer shank. Figure 6 shows that shank vibration amplitude at the tip is reduced to about 75% of that with the rigid stop (comparing the frictionless cases). Inspection of Fig. 6 provides the lowest mode frequency of about 280 Hz for shank vibra-

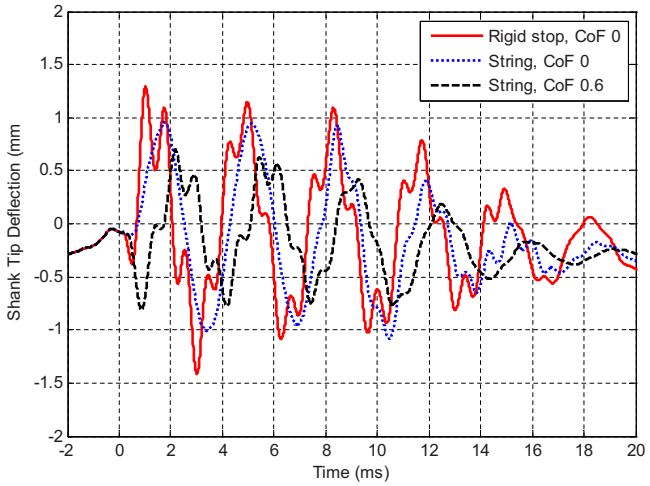

FIG. 6. (Color online) Vibration of flexible hammer shank after hammer head impact with string or rigid stop, expressed by shank tip deflection from equilibrium, for varying contact CoF. Time zero corresponds to initiation of impact.

tions; combining this with the contact times from Fig. 5 shows that the hammer shank executes one-half cycle of oscillation while the hammer is in contact with the string. The lack of high frequency ripples for the string contact in Fig. 6 can be explained as follows. The hammer experiences the same normal force as the string, and it can be seen from Fig. 5 that with a rigid stop the hammer force more closely approximates an ideal impulse, thus exciting more of the higher modes in the response. With the flexible string, the impulse (contact force) is quite smooth, and only the first vibration mode of the hammer is excited during hammer-string interaction. However, the modes are coupled due to geometrical nonlinearity in the beam model, and higher frequency oscillations eventually appear after two cycles of oscillation of hammer shank.

The scuffing motion of the hammer head along the string during hammer-string contact can be seen in the trajectory of the hammer head tip of Fig. 7, as viewed from a reference

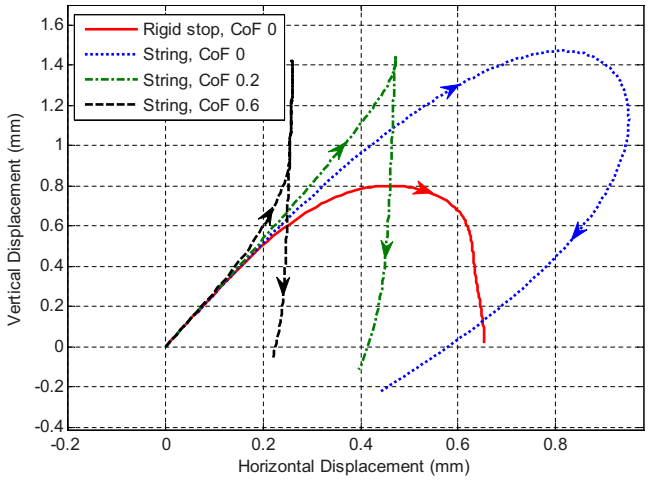

FIG. 7. (Color online) Hammer head tip trajectory during contact period for string and rigid stop, for varying contact CoF. The origin is chosen to represent the initial contact point. Arrows indicate time evolution. It should be noted that the horizontal and vertical scales are not similar.

frame attached to the string boundary. The origin in this trajectory plot is selected as the initial contact point between hammer head tip and string or stop. As mentioned previously, the undeformed position of the hammer head tip is always reported, and thus the vertical displacement of the string will be somewhat less than that implied by the vertical hammer head tip displacement as seen in the trajectory plots since the hammer head felt will have been compressed by the string during contact; in the case of the rigid stop, the implied vertical hammer head tip motion is, in reality, all associated with felt compression as the stop does not move.

C. Effect of hammer-string friction on mechanism dynamics

As previously mentioned, the results above do not include friction between the hammer head and the string or stop. Friction creates a force along the axis of the string, exciting longitudinal modes of vibration. However, the present study neglects the longitudinal motion of the string so this cannot be modeled. Nevertheless, it is interesting to study the effect of friction on the dynamics of the mechanism and, in particular, the amplitude of hammer shank vibration and scuffing of the hammer on the string. In this section this is done using the friction model presented in Sec. II B. The model parameters were taken to be $A=\mu$, where μ is the static CoF, with a slipping velocity of $v_t=0.001$ m/s, $B_1=0$, and $B_2=0$; that is, we consider only a smoothed static friction model in these simulations. A parametric study varying CoF from zero to 0.8 was carried out, covering the full range of potential realistic values. For clarity of presentation, only the extreme cases are included in the following plots. There was also little difference between results for CoF of 0.6 and 0.8.

The variation of friction during the hammer-string contact is shown in Fig. 5 for the case $A=0.6$. During the first 0.4 ms of contact, the hammer slides on the string; it then sticks to the string until 1.55 ms, after which time slipping again occurs until the end of the contact period at 1.8 ms. Due to the vibratory nature of the hammer-string contact, multiple slip-stick transitions occur between 0.4 and 1.55 ms; during this time the relative velocity between hammer and string is below the stick-slip transition velocity of 0.001 m/s and can therefore be regarded as sticking motion [Eq. (6)].

Figure 7 shows the hammer head tip trajectory during its contact with the string for different hammer-string CoFs. It is clear that the amount of hammer head scuffing is reduced with increased CoF, as the frictional force generated at the interface prevents the hammer tip from sliding freely along the string. The scuffing footprint on the string is 0.9, 0.4, and 0.25 mm for CoFs of 0, 0.2, and 0.6, respectively. Predicted normal contact force on the hammer is slightly reduced with increasing CoF, as shown in Fig. 5, and hammer-string contact time is slightly reduced, possibly due to frictional energy loss in the hammer. Different CoFs determine different boundary conditions at the interface of the hammer and string, thus affecting energy transferred to the hammer to excite its modes of vibration, as shown by the shank tip deflection for CoF of 0.6 shown in Fig. 6.

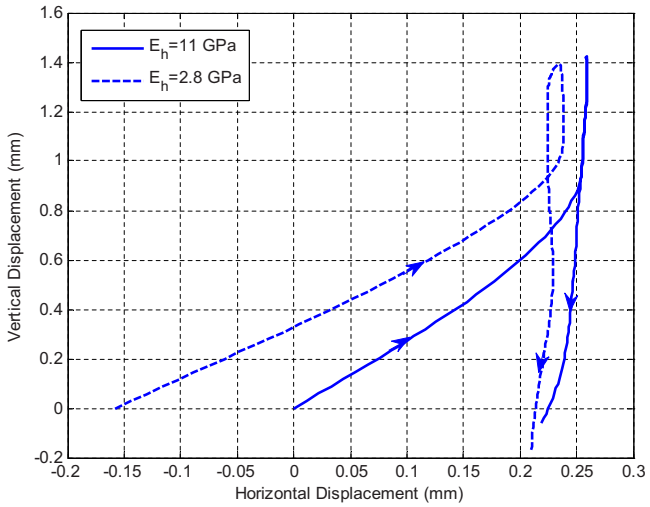

FIG. 8. (Color online) Hammer head tip trajectories during string contact for normal (E_h=11 GPa) and highly flexible (E_h=2.8 GPa) hammer shanks. The origin is chosen as the initial hammer-string contact point for the normally flexible shank. Arrows indicate time evolution. CoF of 0.6. It should be noted that the horizontal and vertical scales are not similar.

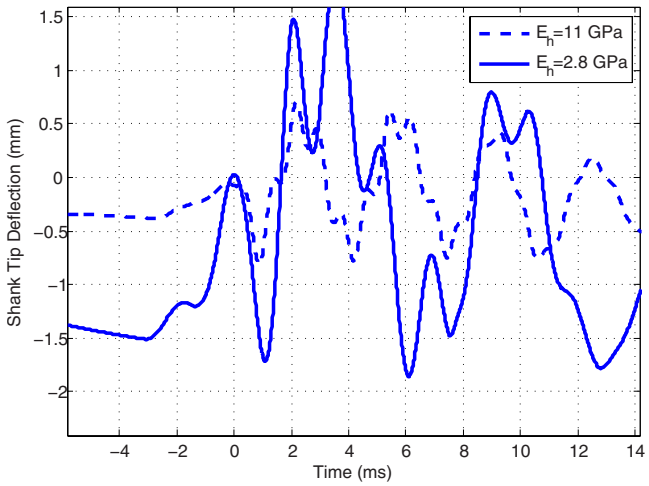

FIG. 9. (Color online) Vibration of hammer shank for normal (E_h =11 GPa) and highly flexible (E_h=2.8 GPa) hammer shanks. CoF of 0.6. Zero time corresponds to impact event in both cases.

D. Effect of hammer shank flexibility on string spectra

The influence of hammer shank flexibility on piano tone is well known to piano professionals who routinely select hammer shanks for different locations from treble to bass according to tap frequencies. It is also common practice to adjust the stiffness of hammer shanks, particularly thinning the treble shanks, as a means to achieve a voicing objective. Wolfenden[37] noted that "in respect to the recoil of hammers from string, the elasticity of the shank is of prime importance." He also pointed out that "the bending of the shank induces a stroking action of the head upon the strings." These effects on hammer-string contact due to hammer shank flexibility have been investigated experimentally;[38] they have also been proposed as a potential mechanism whereby variation in tone (string spectrum) may be achieved with different types of touch at the same dynamic level.[15]

In order to study the effect of hammer-shank flexibility on string spectra, the results of simulations above with the flexible hammer shank have been compared to those in which the stiffness of the shank is reduced by a factor of 4. For simplicity, the increase in shank flexibility was achieved by using a Young's modulus of 2.8 GPa instead of the original realistic value of 11 GPa for a hard maple shank.[39] This highly flexible shank would have equivalent stiffness to one for which the diameter of the original shank has been reduced from 6.4 to 4.5 mm with no change to the Young's modulus; this is a significant, though by no means unrealistic, reduction in shank diameter. No other changes were made in the action and string model parameters, or key force profile input. String damping was neglected in this comparison since the objective was to study the spectral content of the string, and a hammer-string CoF of 0.6 was used.

For the highly flexible shank, an increased hammer head scuffing motion (0.43 vs 0.25 mm footprint) during string contact can be seen in the hammer head tip trajectories shown in Fig. 8. It can also be seen that the initial contact locations are different, the highly flexible shank first touching the string about 0.2 mm closer to the bridge termination (to the left in the diagrams) as compared to the normally flexible shank; in previous simulations (for instance, Fig. 4.7 of Ref. 34), compared to a rigid shank this contact point for the normally flexible shank was already seen to be shifted about 0.1 mm toward the bridge termination. This shift in the contact location can be explained from the shank tip deflection shown in Fig. 9. The highly flexible hammer shank is bent downward away from the string before impact, thus changing the initial contact location of the hammer head. As anticipated, the vibration amplitude of the highly flexible shank is greater than that of the normally flexible shank. Finally, contact time for the highly flexible shank is delayed by 0.2 ms, and the hammer remains in contact with the string for about 0.1 ms longer, the contact period being 1.97 ms as compared to 1.87 ms for the normally flexible shank. The magnitude of these predicted responses for the highly flexible hammer is consistent with reported observations in experiments with a highly flexible hammer shank.[38]

Hammer shank flexibility has been seen to affect many aspects of the hammer-string contact event: contact force, initial time and location, scuffing motion, and duration of contact; consequently, it can be anticipated that the string shape (spectral content) after the hammer contact ends will also be affected by the hammer shank flexibility. This is demonstrated in the time domain plot of Fig. 10 showing simulated string motion during and after impact for the two different shank flexibilities. To further demonstrate the effect of flexibility on spectral content of the string, an explicit plot of modal participation factors $\eta_j(t)$ taken immediately after hammer contact ends is given in Fig. 11. The spectra in decibel calculated as the logarithm of the normalized absolute values $20\log(|\eta_j|/\max|\eta_j|)$ is shown for each of the 40 modes simulated in the string. As anticipated from the time domain string response in Fig. 10, there are significant differences in the spectral content due to variation in the hammer shank flexibility. The fifth partial of the string is found to be very sensitive to highly flexible hammer shank. A differ-

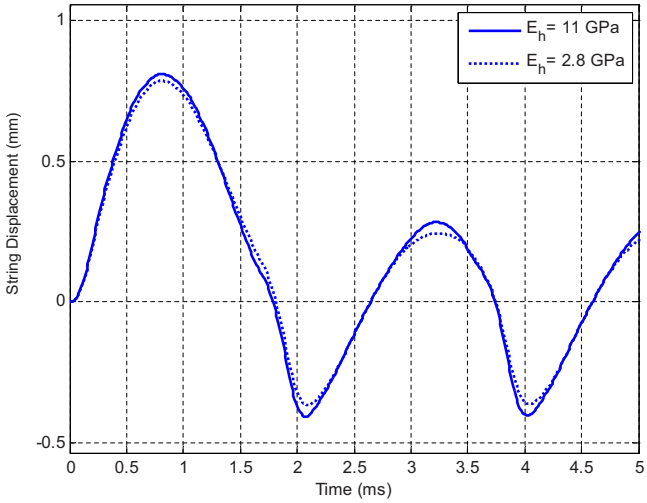

FIG. 10. (Color online) Transverse string displacement at $0.88L$ (close to the strike point) during and after hammer-string contact for normal (E_h =11 GPa) and highly flexible (E_h=2.8 GPa) hammer shanks. Time scales have been shifted for comparison, so contact is initiated at the same t=0 for both hammer shanks. String damping is excluded. CoF of 0.6.

ence of 20 dB can be seen in Fig. 10 with respect to normal shank. The hammer shank vibration during the hammer string interaction can influence the string shape at the end of hammer-string interaction, thus changing its spectral content. It will be interesting to study in future the causal relationship between hammer shank flexibility and its influence on string spectra. Whether the observed differences in spectra would be audible cannot be ascertained from the simulated results, due to the absence of damping and other relevant effects (nonlinear string motion, coupling effects between trichord strings and soundboard design) that could alter perceived tonal quality in listening tests. The psycho-acoustic question of spectral sensitivity is complex.[40] Differences in spectrum occurring in the lower frequency portion of the response (where a distinct effect from hammer shank flexibility is observed in the simulations) are known to be more significant to perception of tone quality.[41]

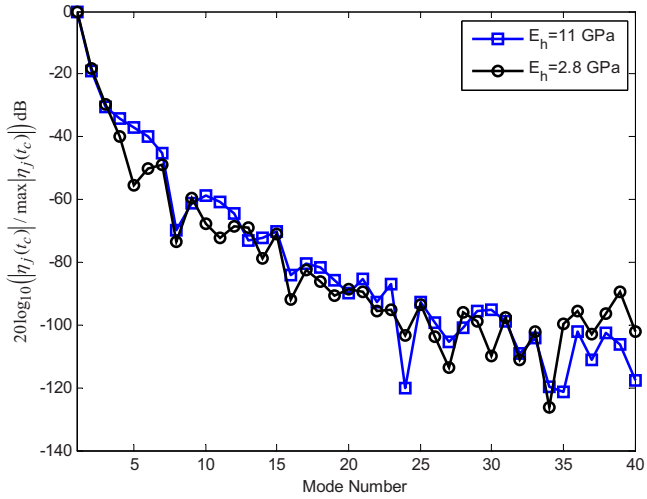

FIG. 11. (Color online) Normalized modal participation factors for the string immediately after contact for normal (E_h=11 GPa) and highly flexible (E_h=2.8 GPa) hammer shanks. CoF of 0.6.

This result also gives some insight into understanding the potential influence of touch on tone, which may be possible without overall change in dynamic level by manipulating the flexural state of the hammer prior to contact. This proposed mechanism would require a reasonable degree of hammer shank flexibility and the ability to control hammer shank vibrations by touch variation.

IV. CONCLUSIONS AND FUTURE WORK

A dynamic model of a piano action mechanism with flexible hammer shank and realistic compliant contacts between components has been integrated with an elastic stiff string model. The effect of string motion on the mechanism has been investigated and compared to previously published results in which the hammer strikes a rigid stop. It was found that replacing the stop by the string in the model increased the extent of hammer scuffing during contact, as well as reduced the predicted vibration of the hammer shank. Hammer shank tip deflection amplitude during contact was also reduced, while peak contact force decreased and hammer-string contact time increased. Introducing hammer-string friction into the simulations decreased the duration of contact and hammer head scuffing. Finally, simulations in which the hammer shank flexibility was increased by a factor of 4 without making any other changes to the model showed significant differences in the behavior of the hammer and string. For the highly flexible hammer shank, there were predicted differences in contact time, force, duration, hammer shank vibration, and scuffing motion on the string. Moreover, these differences were responsible for corresponding changes in the predicted spectral content initiated in the string by hammer impact.

By directly including the action mechanism in the hammer-string interaction model, the possibility is created to simulate subtle effects that may be significant in terms of influencing tone through touch. In order to investigate these, as well as study the effect of felt properties and hammer design parameters on tone, a more detailed and mechanistic compression model is being developed to apply to the hammer-string contact, and the string model replaced with a more sophisticated three dimensional vibrating string. The latter will also allow for the prediction of effects such as longitudinal string vibrations generated by hammer scuffing and friction between hammer and string, as well as coupling between these and the transverse vibration modes. These factors are known to be important components of piano tone.

ACKNOWLEDGMENTS

The authors gratefully acknowledge the financial support of this research by the Natural Sciences and Engineering Research Council of Canada, as well as Steinway Pianos New York.

[1]Note that we have excluded the damper component from the mechanism in this paper. Unless the damper pedal has been engaged, which lifts all the dampers in the piano independently of the keys, the damper lifter is raised by the tail of the key about halfway through the key stroke. Consequently it will have a significant effect on the dynamic response of an

action mechanism, as is well known to pianists. Reported results in the literature are not always clear on the status of the dampers in experimental studies.
[2]J. Dunlop, "Nonlinear vibration properties of felt pads," J. Acoust. Soc. Am. **88**, 911–917 (1990).
[3]A. Stulov, "Experimental and computational studies of piano hammers," Acta. Acust. Acust. **91**, 1086–1097 (2005).
[4]W. Stamm, S. Birkett, and J. McPhee, "Modelling felt compression for contact dynamics simulations," ASME J. Appl. Mech. Submitted.
[5]D. E. Hall, "Piano string excitation in the case of small hammer mass," J. Acoust. Soc. Am. **79**, 141–147 (1986).
[6]H. Suzuki, "Model analysis of a hammer-string interaction," J. Acoust. Soc. Am. **82**, 1145–1151 (1987).
[7]D. E. Hall, "Piano string excitation II: General solution for a hard narrow hammer," J. Acoust. Soc. Am. **81**, 535–546 (1987).
[8]D. E. Hall, "Piano string excitation III: General solution for a soft narrow hammer," J. Acoust. Soc. Am. **81**, 547–555 (1987).
[9]D. E. Hall and A. Askenfelt, "Piano string excitation V: Spectra for real hammers and strings," J. Acoust. Soc. Am. **83**, 1627–1638 (1988).
[10]D. E. Hall, "Piano string excitation VI: Nonlinear modelling," J. Acoust. Soc. Am. **92**, 95–105 (1992).
[11]A. Chaigne and A. Askenfelt, "Numerical simulations of piano strings I. A physical model for a struck string using finite difference methods," J. Acoust. Soc. Am. **95**, 1112–1118 (1994).
[12]A. Chaigne and A. Askenfelt, "Numerical simulations of piano strings II. Comparisons with measurements and systematic exploration of some hammer-string parameters," J. Acoust. Soc. Am. **95**, 1631–1640 (1994).
[13]J. Bensa, O. Gipouloux, and R. K. Martinet, "Parameter fitting for piano sound synthesis by physical modelling," J. Acoust. Soc. Am. **118**, 495–504 (2005).
[14]B. Bank and L. Sujbert, "Generation of longitudinal vibrations in piano strings: From physics to sound synthesis," J. Acoust. Soc. Am. **117**, 2268–2278 (2005).
[15]A. Askenfelt and E. V. Jansson, "From touch to string vibrations II: The motion of the key and hammer," J. Acoust. Soc. Am. **93**, 2181–2196 (1993).
[16]N. Giordano and J. P. Winans, "Piano hammers and their force compression characteristics: Does a power law make sense?," J. Acoust. Soc. Am. **97**, 2577–2585 (1995).
[17]A. Izadbakhsh, J. McPhee, and S. Birkett, "Dynamic modelling and experimental testing of piano action mechanism with a flexible hammer shank," ASME J. Comput. Nonlinear Dyn. **3**, 1–10 (2008).
[18]M. Hirschkorn, J. McPhee, and S. Birkett, "Dynamic modelling and experimental testing of piano action mechanism," ASME J. Comput. Nonlinear Dyn. **1**, 47–55 (2006).
[19]H. Fletcher, "Normal vibration frequencies of a stiff piano string," J. Acoust. Soc. Am. **36**, 203–209 (1964).
[20]M. Hirschkorn, J. McPhee, and S. Birkett, "Dynamic model of a piano action mechanism," in Proceedings of the Fifth International Conference on Multibody Systems, Nonlinear Dynamics and Control (MSNDC), Long Beach, CA (2005) Paper No. DETC2005-84511.
[21]A. Izadbakhsh, J. McPhee, and S. Birkett, "Dynamic modelling of a piano action mechanism with a flexible hammer shank," in Proceedings of the Fifth CCToMM Symposium on Mechanisms, Machines and Mechatronics (CSME Forum), Calgary, AB (2007).
[22]A. Izadbakhsh, J. McPhee, and S. Birkett, "Dynamic modeling and experimental testing of a piano action mechanism with a flexible hammer shank," in Proceedings of the Sixth International Conference on Multibody Systems, Nonlinear Dynamics, and Control (MSNDC), Las Vegas, NV (2007), Paper No. DETC2007-35351.
[23]J. McPhee, "Unified modelling theories for the dynamics of multidisciplinary multibody systems," *Advances in Computational Multibody Systems* (Springer-Verlag, New York, 2005), pp. 129–158.
[24]DynaFlexPro User Manual, Maplesoft, Waterloo, Canada, http://www.maplesoft.com/products/thirdparty/dynaflexpro/index.aspx (Last viewed February 12, 2009).
[25]MAPLE is a trademark of Maplesoft, Waterloo, Ontario, Canada.
[26]P. Shi, J. McPhee, and G. Heppler, "Polynomial shape functions and numerical methods for flexible multibody dynamics," Int. J. Robust Nonlinear Control **29**, 43–64 (2000).
[27]P. Shi, J. McPhee, and G. Heppler, "A deformation field for Euler–Bernoulli beams with applications to flexible multibody dynamics," Multibody Syst. Dyn. **5**, 79–104 (2001).
[28]J. McPhee, "Virtual prototyping of multibody systems with linear graph theory and symbolic computing," *Virtual Nonlinear Multibody Systems*, (Kluwer Academic, Dordrecht, 2003), pp. 37–56.
[29]The equations of motion of a multibody system contain complicated expressions due to kinematic nonlinearities and cannot be shown explicitly in this paper as they would occupy multiple pages of the manuscript. They may be reproduced by following the formulation technique that has been fully described in detail in the previous publications.
[30]K. H. Hunt and F. R. E. Crossley, "Coefficient of restitution interpreted as damping in vibroimpact," ASME J. Appl. Mech. **42**, 440–445 (1975).
[31]S. Cull and R. Tucker, "On the modelling of coulomb friction," J. Phys. A **32**, 2103–2113 (1999).
[32]The compression properties of piano hammer felt may be characterized, however, by a stress-strain curve which is independent of the properties of the target. It is difficult to use this to derive analytically a force-compression curve for a hammer impacting a particular non-planar target, such as a string trichord, on account of the complex local loading involved as the target embeds in the hammer felt.
[33]MATLAB is a trademark of Mathworks, Inc.
[34]A. Izadbakhsh, "Dynamics and control of a piano action mechanism," MS thesis, University of Waterloo, Canada (2006).
[35]M. Hirschkorn, "Dynamic model of a piano action mechanism," MS thesis, University of Waterloo, Canada (2004).
[36]In this case, a pressed touch with the finger resting on the key initially was used. The character of the finger motion is actually not relevant to the model simulations, which use only the recorded force profile at the key surface.
[37]S. Wolfenden, *A Treatise on the Art of Pianoforte Construction* (Gresham Books, Henley-on-Thames, Oxfordshire, 1916).
[38]A. Askenfelt, "Measuring the motion of the piano hammer during string contact," STL-QPSR Quarterly Progress and Status Report, Department of Speech, Music and Hearing, KTH, Sweden, 1991.
[39]In practice, a change in shank stiffness is achieved by altering geometry, in particular shank cross section, for instance, by removing material from the sides of the shank. This will, in general, also affect the inertial properties of the shank.
[40]A. Caclin, S. McAdams, B. K. Smith, and S. Winsberg, "Acoustic correlates of timbre space dimensions: A confirmatory study using synthetic tones," J. Acoust. Soc. Am. **118**, 471–482 (2005).
[41]D. Gunawan and D. Sen, "Spectral envelope sensitivity of musical instrument sounds," J. Acoust. Soc. Am. **123**, 500–506 (2008).

Influence of a gradient of material properties on ultrasonic wave propagation in cortical bone: Application to axial transmission

Guillaume Haïat
CNRS, Laboratoire de Recherches Orthopédiques, UMR CNRS 7052 B2OA, Université Paris 7, 75010 Paris, France

Salah Naili[a)]
Laboratoire de Mécanique Physique, Université Paris12-Val de Marne, 61 Avenue du Général de Gaulle, 94010 Créteil Cédex, France

Quentin Grimal and Maryline Talmant
Laboratoire d'Imagerie Paramétrique, UMR CNRS 7623, Université Pierre et Marie Curie, 75006 Paris, France

Christophe Desceliers and Christian Soize
Laboratoire de Modélisation et Simulation Multi-Echelle, FRE CNRS 3160, Université Paris-Est, 77454 Marne la Vallée Cédex 2, France

(Received 25 November 2008; revised 10 March 2009; accepted 18 March 2009)

The aim of this work is to evaluate the effect of a spatial gradient of material properties (mass density and stiffness coefficients) of cortical bone on its ultrasonic response obtained with an axial transmission device. Therefore, a two-dimensional finite element time-domain method is derived to model transient wave propagation in a three-layer medium composed of an inhomogeneous transverse isotropic solid layer sandwiched between two acoustic fluid layers and excited by an acoustic linear source located in one fluid layer, delivering broadband ultrasonic pulses. The model couples the acoustic propagation in both fluid media with the elastodynamic response of the solid layer. A constant spatial gradient of material properties is considered for two values of bone thicknesses corresponding to relatively thick and thin bone widths. For a thin bone (0.6 mm) compared to wavelength (around 4 mm at 1 MHz), the results are in good agreement with a S_0 Lamb wave assuming a homogeneous material with spatially averaged material properties. For a thick bone (4 mm), the results are in agreement with the propagation of a lateral wave and allow the derivation of an equivalent contributing depth in the case of a transverse isotropic inhomogeneous solid layer. [DOI: 10.1121/1.3117445]

PACS number(s): 43.80.Ev, 43.20.Mv, 43.20.Px, 43.40.Rj [FD] Pages: 4043–4052

I. INTRODUCTION

Osteoporosis is a systemic disease of the skeleton (WHO Study Group, 1994) characterized by a decrease in bone mass and micro-architectural deterioration of bone tissue, implying a consequent increase in bone fragility and susceptibility to fracture. Early studies were devoted to the most porous component of the skeleton (cancellous bone). However, the investigation of cortical bone (Rico, 1997) is important since it accounts for about 80% of the skeleton, supports most of the load of the body, and is mainly involved in osteoporotic fractures (Seeley *et al.*, 1991) of many kinds. Moreover, cortical bone has recently been shown to be determinant for bone mechanical stability (Mayhew *et al.*, 2005) at the femur. Cortical bone is the main component of the diaphysis of long bones such as radius and femur.

The so-called axial transmission (AT) technique has been shown particularly suitable for cortical bone evaluation. In AT technique, both ultrasound emitter and receivers are placed in the same side of the investigated skeletal site along a direction close to the long bone axis. The earliest event or wavelet [usually called first arriving signal (FAS)] of the multicomponent signal recorded at the receivers has been the most often investigated and its velocity measured in the time domain was shown to be able to discriminate healthy subjects from osteoporotic patients in several studies. Therefore, the FAS velocity is now considered as a relevant index of bone status (Barkmann *et al.*, 2000; Hans *et al.*, 1999; Stegman *et al.*, 1995). *In vitro* measurements and predictions using simplified bone models provided at least partial explanations to clinical measurements. Both experimental (Bossy *et al.*, 2004c; Raum *et al.*, 2005) and simulation studies (Bossy *et al.*, 2004b) have indicated that the FAS velocity was related to bone mineral density, to cortical thickness, and to bone elastic properties. From a physical point of view, it has been shown by means of simulations that when the wavelength is comparable or smaller than the cortical thickness, the type of wave contributing to the FAS corresponds to a lateral wave, whereas when the wavelength is large com-

[a)]Author to whom correspondence should be addressed. Electronic mail: naili@univ-paris12.fr

pared to the cortical thickness divided by 4, the received signal corresponding to the FAS comes from the first symmetric Lamb wave mode (noted S_0 in what follows) guided by the whole cortical thickness (Bossy *et al.*, 2002).

Most models of AT developed in the past have considered cortical bone as a homogeneous material. However, bone is heterogeneous at several scales. Its elastic behavior has been described as transverse isotropic in different works [see, for example, Dong and Guo (2004)]. At the macroscopic scale, porosity in the radial direction (which is associated with the cross section of the bone) is heterogeneous at all ages and for both genders (Bousson *et al.*, 2001; Thomas *et al.*, 2005): the mean porosity in the endosteal region (inner part of the bone) is significantly higher than in the periosteal region (outer part of the bone). Moreover, cortical bone is affected by age-related bone resorption and osteoporosis. It undergoes a thinning of the cortical shell, as well as an increase in porosity, mainly from the endosteal region (Bousson *et al.*, 2001). Therefore, porosity in the radial direction may become more heterogeneous with aging and/or osteoporosis. An increase in porosity is likely to affect bone material properties (mass density and elasticity) (Fritsch and Hellmich, 2007), which may in turn impact bone quality (Ammann and Rizzoli, 2003). Similarly, a thinning of the cortical shell is an important indicator of decreasing bone strength and of fracture risk (Turner, 2002).

Modeling the FAS in AT experiment is a time-domain elasto-acoustic problem. Time-domain analytical methods have been used in the past to solve the elasto-acoustic wave system in simple AT models (Grimal and Naili, 2006; Macocco *et al.*, 2005, 2006). However, such methods cannot account for an arbitrary heterogeneity of materials. On the other hand, numerical methods such as finite elements or finite differences allow to account for continuous variations in material elastic properties, which is relevant to model the heterogeneity of bone. In this paper, a finite element code is used (COMSOL MULTIPHYSICS, 2005).

Bossy *et al.* (2004b) assessed the influence of a gradient of longitudinal wave velocity due to a heterogeneous distribution of porosity on the FAS velocity. Their computations were made in the framework of an isotropic behavior of bone and for cortical thickness larger than the wavelength in bone, which corresponds to the case where the FAS comes from the lateral wave. However, a better understanding of the impact of a gradient of material properties in the framework of an anisotropic model of bone may have potential implications in the improvement of AT devices and, in a longer term, in the solution of the inverse problem.

The aim of this paper is to assess the effect of the heterogeneous nature of cortical bone on its ultrasonic response obtained with an AT device. Bone is modeled as an anisotropic material (transverse isotropic), and a gradient of material properties in the radial direction is considered. More specifically, we aim at investigating the potentiality of a two-dimensional (2D) finite element numerical simulation tool to assess the sensitivity of the FAS velocity to independent spatial variations in each stiffness coefficient as well as of mass density. Therefore, a 2D finite element model briefly described in Sec. II is used to compute the dependence of the FAS velocity on the heterogeneous nature of cortical bone at the organ level. Moreover, the models of gradients of material properties and porosity are presented and discussed. Section III describes (i) the sensitivity of the FAS velocity to changes in each stiffness coefficient and in mass density for homogeneous material properties and (ii) the effect of a constant gradient of mass density and of each stiffness coefficient affecting the FAS velocity. The results are then discussed in Sec. IV by comparing them with analytical models.

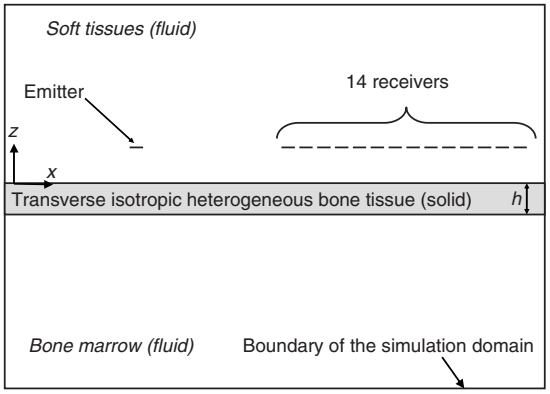

FIG. 1. Schematic representation of the simulation domain corresponding to a three-phase medium. The emitter and receivers are indicated by indents.

II. METHOD

A. Axial transmission configuration

Bone is modeled as a 2–D multilayer medium composed of one elastic transverse isotropic solid layer (corresponding to cortical bone) sandwiched between two acoustic fluid layers, as shown in Fig. 1. The upper medium ($z>0$) corresponds to soft tissues and the lower medium ($z<-h$) corresponds to bone marrow. Both soft tissue and bone marrow are modeled by the same fluid with an acoustic wave velocity of 1500 m s^{-1} and a mass density of 1 g cm^{-3}. The cortical thickness is denoted h and direction z corresponds to the bone radial direction. The other sizes of all domains have been chosen in order to avoid any effect of the wave reflected by the boundaries of the domain on all recorded radiofrequency signals. The boundary conditions at the limits of the simulation box are identical to the one used in Desceliers *et al.* (2008), i.e., stress-free for the solid layer and Neumann conditions for the fluid layers.

In the simulation, a pressure source with a spatial length of 0.75 mm is positioned in the fluid at 4 mm from the upper interface of the solid layer. The excitation signal is a Gaussian pulse with a center frequency of 1 MHz identical to the one given in Desceliers *et al.* (2008). Once the numerical simulation of wave propagation has been performed, the signal is formed for each of the 14 receivers by summing the pressure over the length of each sensor. The 14 receivers are regularly spaced with a pitch of 0.8 mm and a distance of emitter to closest receiver equal to 11 mm. The geometrical arrangement attempts to represent the geometrical arrangement of an actual probe developed by the "Laboratoire d'Imagerie Paramétrique" (France) (Bossy *et al.*, 2004a). The FAS velocity is then determined following the procedure

used in experiments with the actual probe. Signals are collected for each one of the 14 receivers. The first maximum of the FAS is measured for each signal, and intersensor delays are then evaluated by computing the time difference between adjacent sensors (Bossy *et al.*, 2004a). The FAS velocity estimate is then given by the slope of the position of each sensor versus time delays, obtained through a least-square linear regression analysis.

B. 2-D finite element model

In what follows, all viscoelastic or viscous dissipation effects are neglected in the multilayer medium mimicking bone, soft tissues, and marrow. The acoustic wave propagation equation is solved in both fluid media where the formulation is written in terms of pressure. Conversely, the formulation in the solid layer is given in terms of displacement, and the elastodynamic (nondissipative) wave propagation equation is solved using the stiffness tensor which writes for a 2D transverse isotropic medium:

$$\mathbb{C} = \begin{pmatrix} C_{11}(z) & C_{13}(z) & 0 \\ C_{13}(z) & C_{33}(z) & 0 \\ 0 & 0 & C_{55}(z) \end{pmatrix}, \tag{1}$$

where all stiffness coefficients, written using the Voigt notation, only depend on z. The plane of isotropy corresponds to the (y,z) plane in Fig. 1. Note that in this present work, the transverse isotropy imposes the relation $C_{13}=C_{12}$. Subscripts 1, 2, and 3 are associated with x-, y-, and z-axes, respectively.

A continuous variation in the material property S (which corresponds to any stiffness coefficient C_{ij} or to mass density) is considered by the variational formulation of the problem in the simulation code so that a continuous variation in S as a function of z is taken into account. Therefore, no discretization corresponding to spatial variation in S is introduced in our model, and bone is not divided into finite-sized layers of different properties, as it was done in Bossy *et al.* (2004b).

At both interfaces between the fluid layers and the solid layer, the boundary conditions in terms of displacement and normal stresses are taken into account. The model therefore fully describes the fluid-structure interaction between the three sub-domains, accounting for all reflection, refraction, and mode conversion effects. For each computation, around 186 000 triangular elements are used, resulting in about 393 000 degrees of freedom. The simulation software is the 3.3 version of COMSOL MULTIPHYSICS (2005). Accurate discretization of the geometrical space is important when simulating wave propagation. The internodal distance in both directions is chosen at least smaller than 0.15 mm in the fluid and 0.25 in the solid so that it is lower than the smallest wavelength divided by 6 in all directions and both media. This condition leads to a spatially resolved wave propagation (Moser *et al.*, 1999). We verified that decreasing the maximum size of the elements in the solid layer down to 0.2 mm does not modify the results obtained in the present study. Note that there is no artifacts corresponding to the discretization of the spatial variation in the material property S as its variation is continuous. The time step used in the computation is of the order of 10^{-3} μs and one computation takes about 5 h on a desk workstation.

C. Determination of a realistic range of variation in elastic bone properties

In order to define numerical values for a realistic value of the gradient of the different material properties (see Sec. III A), it is necessary to determine the limiting values reached by each elastic property. Our approach consists in considering *in vitro* measurements published in Dong and Guo (2004) and performed in 18 samples. It is assumed that these limiting values for elastic properties are relevant for physiological ranges of variations. Furthermore, the elastic coefficients of the stiffness tensor are constrained to fully verify the thermodynamical conditions of stability.

We assume that cortical bone is transverse isotropic. Transverse isotropy has been shown experimentally by different authors (Dong and Guo, 2004; Reilly and Burnstein, 1974; Rho, 1996) to be a realistic approximation degree of anisotropy in cortical bone and has been extensively used in the simulation of ultrasonic wave propagation (Bossy *et al.*, 2004b; Protopappas *et al.*, 2007).

Dong and Guo (2004) measured the homogenized bone properties by performing tensile and torsional tests with a mechanical testing system on 18 different human femoral bone specimens. The authors measured the values of the longitudinal and transverse Young's moduli (E_L and E_T, respectively) as well as of the longitudinal shear modulus G_L. From these measurements and by assuming constant values of Poisson's ratio, the values of the different components of the stiffness tensor corresponding to the values of E_L, E_T, and G_L measured in Dong and Guo (2004) were obtained following the relationships (Royer and Dieulesaint, 2000)

$$C_{11} = \frac{E_L^2(1-\nu_T)}{(E_L - E_L\nu_T - 2E_T\nu_L^2)},$$

$$C_{33} = \frac{E_T(E_L - E_T\nu_L^2)}{(1+\nu_T)(E_L - E_L\nu_T - 2E_T\nu_L^2)}, \tag{2}$$

$$C_{12} = \frac{E_T E_L \nu_L}{(E_L - E_L\nu_T - 2E_T\nu_L^2)}, \quad C_{55} = G_L. \tag{3}$$

The value of longitudinal Poisson's ratio ν_L is taken equal to 0.37 for all computations because it corresponds to the average value found in Dong and Guo (2004). The value of transverse Poisson's ratio ν_T is taken equal to 0.45, following Eq. (3). The values of the stiffness coefficients corresponding to the mean values of the bone mechanical properties are referred to as "reference" set of parameters in what follows. The maximum and minimum values of the stiffness coefficients are obtained by considering, respectively, the maximum and minimum values of E_L and E_T within the range of variation measured in Dong and Guo (2004), which is a simple mean of obtaining a realistic range of variation for the stiffness coefficients in cortical bone. Furthermore, the elastic properties deduced from the approach reported

above were constrained to verify the thermodynamical stability conditions given by Royer and Dieulesaint (2000):

$$C_{12} < \inf\left(\frac{C_{11}}{2\nu_L}, 2C_{33}\nu_L\right), \tag{4}$$

where $\inf(R)$ is defined to be the smallest real number in R.

We choose a mean value of mass density ρ equal to 1.722 g cm^{-3}, following the value taken in Macocco *et al.* (2006). This value is chosen for the reference mass density. In order to derive a realistic range of variation for mass density, we assume that the reference value is given by a porosity of 7%, which corresponds approximately to the mean porosity at the radius (Baron *et al.*, 2007). The porosity was assumed to vary between 3% and 15% (Bousson *et al.*, 2001; Dong and Guo, 2004), and a rule of mixture leads to the range of variation in mass density.

D. Lamb wave and bulk longitudinal wave

In previous analyses of wave propagation in idealized bone shapes (plate or tube) made of a transversely isotropic material (Bossy *et al.*, 2002, 2004b), the FAS velocity was explicitly related to elastic properties in the limit of large and short wavelength. When the thickness h is smaller than the wavelength λ (typically $h/\lambda < 0.25$), the FAS velocity tends toward the so-called plate velocity which is the phase velocity of the S_0 Lamb wave in the large wavelength limit with the expression

$$v_p = \sqrt{\frac{C_{11}}{\rho} \times \left(1 - \frac{C_{12}^2}{C_{11} \times C_{33}}\right)}. \tag{5}$$

When the thickness h is large compared to wavelength, the FAS velocity tends toward the bulk longitudinal wave velocity inside the material constituting the solid layer:

$$v_b = \sqrt{\frac{C_{11}}{\rho}}. \tag{6}$$

In the present study, simulations were performed with two different solid layer thicknesses, $h=0.6$ mm and $h=4$ mm. Considering the dominant frequency of the broadband ultrasonic pulse and the range of variation in C_{11}, it means that h/λ varies in the intervals defined from 0.14 to 0.19 and from 0.96 to 1.25, respectively, for the thin and thick solid layers.

For the thinnest layer, the effect of a gradient of material property in the solid layer is analyzed on the basis of the propagation of a S_0 wavemode in an immersed homogeneous plate after adjustment of the material properties. Therefore, roots associated with the characteristic equation of the S_0 wave for homogeneous transverse isotropic plate are calculated in the limit of large wavelength.

E. Modeling a gradient of material property

The impact of a controlled gradient vector $\boldsymbol{\delta}$ of any investigated material property S on the FAS velocity is assessed. The scalar S corresponds to one of the stiffness coefficients C_{ij} of $\mathbb{C}$ or to mass density ρ. In each set of simulations, all the material properties are constant and equal to their reference value while S is subjected to the defined gradient. The influence of a spatial gradient of all material property (each stiffness coefficient C_{ij} and mass density) is assessed using the numerical simulation tool. In other words, only one of the different material properties is graded while the others are kept constant during a simulation in order to assess the influence of a gradient of each material property independently. Therefore, no comparison will be made between the different simulations as we aim at assessing the influence of a gradient of each material property independently.

The gradient vector $\boldsymbol{\delta}=\text{grad}\, S=\delta\mathbf{z}$ is assumed to be independent of x in all cases, where $\mathbf{z}$ is a unit vector along z-axis and grad is the gradient operator acting on a scalar field. The quantity δ is always taken positive because the porosity is known to be higher in the endosteal part than in the periosteal part of the bone. Moreover, only the simple situation of affine spatial variations in S is considered, corresponding to a constant value of δ. This affine spatial variation in S is chosen because the actual physiological spatial dependence of S remains unknown.

The minimum and maximum values S_m and S_M of the physiological range corresponding to the material property S defined in Sec. II C using the work of Dong and Guo (2004) are chosen in order to define the extremum possible values of S; this assumption will be discussed in Sec. IV C. The assignment of S_M at the upper surface ($z=0$) and of S_m at the lower surface ($z=-h$) leads to the definition of a maximum value δ_M of δ given by

$$\delta_M = \frac{(S_M - S_m)}{h} > 0 \tag{7}$$

for each value h of the cortical bone width.

Two different affine spatial dependencies of the studied material property are considered and are illustrated in Fig. 2. Associated gradient δ will be referred to as type 1 or 2.

Type 1. The gradient of type 1 is such that the physical property S takes the same value S_M at the upper interface $z=0$ of the solid plate for all values of the gradient δ. The quantity $S(z)$ is therefore given by

$$S(z) = S_M + \delta \times z, \tag{8}$$

where S_M is given by the maximal value of the material property S considered. The maximal value of δ is given by Eq. (7) so that all values of $S(z)$ are always comprised between S_m and S_M.

Type 2. The gradient of type 2 is such that the material property S takes the same value in the middle of the solid plate ($z=-h/2$) for all values of gradient δ. Furthermore, the mean value of the property S is identical for all δ. The quantity $S(z)$ is given by

$$S(z) = \frac{(S_m + S_M)}{2} + \delta \times \left(z + \frac{h}{2}\right). \tag{9}$$

The maximal value of δ is also given by Eq. (7) so that all values of $S(z)$ are again always comprised between S_m

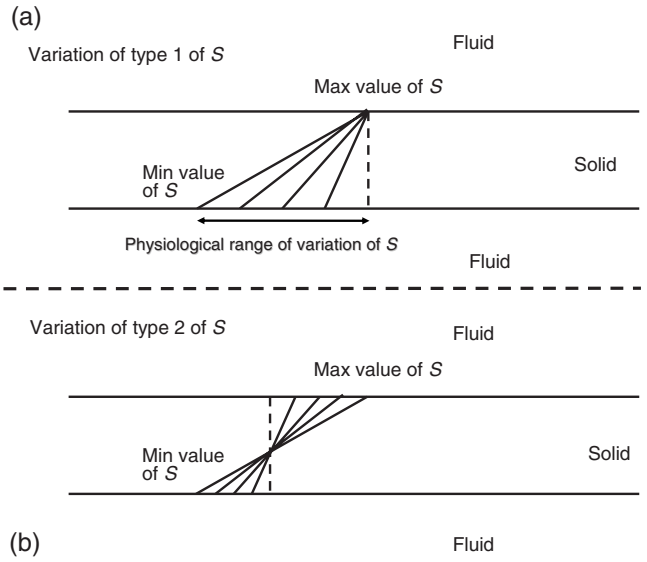

FIG. 2. Schematic representation of the two types of spatial variation considered for the material property S corresponding to the stiffness coefficient and to mass density. The solid lines in the solid layer indicate the spatial dependence of S. The dotted line in the solid layer indicates homogeneous material properties corresponding to the reference material properties. The variation in type 1 shown in (a) corresponds to a constant value at the bone-soft tissue interface. The variation in type 2 shown in (b) corresponds to a constant value in the middle of the bone.

and S_M. Again, the maximal value δ_M of δ is given by Eq. (7). Gradient of type 2 leads for all magnitudes of δ to a constant value of the spatial average of S.

For both types of spatial variation, five different values of δ regularly distributed between 0 and δ_M (included) are arbitrarily considered for each layer thickness, leading to a set of five numerical simulations.

In what follows, the notations δ_{11}, δ_{12}, δ_{33}, and δ_ρ correspond to δ when S is defined by C_{11}, C_{12}, C_{33}, and ρ, respectively.

F. Modeling a gradient of porosity

In the case of bone, all homogenized material properties are expected to exhibit coupled spatial variations because they are all related to porosity, which increases from the periosteal to the endosteal part (Bousson *et al.*, 2001). When porosity increases, the values of the homogenized elastic constants and of mass density are expected to decrease, having opposite and competing effects on the wave velocity. Here, spatial variations in types 1 and 2 are considered for the porosity (noted P), with the minimum and maximum values of porosity P_m and P_M equal, respectively, to 3% and 15%. In the case of spatial variations in types 1 and 2, the porosity P writes, respectively,

$$P(z) = P_M + \delta_P \times z, \tag{10}$$

$$P(z) = \frac{(P_m + P_M)}{2} + \delta_P \times \left(z + \frac{h}{2}\right). \tag{11}$$

Following a simple rule of mixture, a variation in porosity induces an affine variation in mass density given by

$$\rho(z) = \rho_m + \delta_\rho \times (P - P_m). \tag{12}$$

Here, we choose ρ_m in order to obtain a variation in mass density from 1.753 to 1.66 g cm^{-3} when P varies from 3% and 15%, which leads to $\delta_\rho = 7.7 \times 10^{-3}$ g cm^{-3}. These values correspond to a mass density equal to 1.722 g cm^{-3} when $P = 7\%$.

The variations in the elastic coefficients with porosity are taken from the literature. Affine dependence of diagonal components of $\mathbb{C}$ with porosity was derived from Baron *et al.* (2007) where a variation in porosity between 3% and 15% corresponds approximately to a change in C_{11} and C_{33} of 7.8 and 4 GPa, respectively,

$$\begin{aligned} C_{11}(z) &= C_{11}^m + \delta_C \times (P - P_m), \\ C_{33}(z) &= C_{33}^m + \delta_C' \times (P - P_m). \end{aligned} \tag{13}$$

The variations in C_{11} and C_{33} are centered on their reference value. Therefore, C_{11}^m and C_{33}^m are, respectively, equal to 19.7 and 16.85 GPa; the quantities δ_C and δ_C' are, respectively, equal to 0.65 and 0.33 GPa. Note that taking into account a slight non linear variation in C_{11} and C_{33} as a function of porosity should not significantly modify our results. We did not consider any variation of C_{12} which was taken equal to its reference value.

G. Equivalent depth for thick solid layer

In the case of a thick bone width, which corresponds to the propagation of a lateral wave, the ultrasonic response recorded by AT devices does not depend on bone width (Bossy *et al.*, 2002); this result indicates that the ultrasonic response is not sensitive to the material properties within the entire bone width, but only in the vicinity of the upper surface. The estimation of the spatial extent of the region below the surface influencing the ultrasonic response is important for the clinician since this region corresponds to the anatomical location investigated by the device. The penetration depth H estimated in what follows corresponds physically to the average depth investigated by the AT device. The variation in the FAS velocity in presence of a spatial gradient of material property is analyzed in the case of a thick layer ($h > \lambda$) and allows the estimation of the equivalent depth H introduced following Bossy *et al.* (2004b).

In what follows, a simple method aiming at estimating the value of this equivalent depth H in the case of a spatial variation in a given material property S is derived. The equivalent depth H is defined as the depth at which the rate of variation in v_b computed at the depth H and of the FAS velocity (obtained numerically) versus δ is equal. This condition writes

$$\alpha \equiv \frac{dv_F}{d\delta}(\delta) = \frac{\partial v_b}{\partial \delta}(\delta, H), \tag{14}$$

where v_b denotes the longitudinal bulk wave velocity in the axial direction taken at the appropriate depth z and v_F denotes the FAS velocity. The quantity α in the left hand side of Eq. (14) is determined from the numerical results. The term in the right hand side of Eq. (14) is determined analytically. Specifically, for a spatial variation in C_{11} of type 1, combining Eq. (14) together with Eqs. (6) and (8) yields

TABLE I. Mean, maximum, and minimum values of the homogenized longitudinal and transversal Young moduli of the four elastic constants and of mass density affecting the ultrasonic propagation in the framework of the 2D model of Fig. 1. These values are taken from Dong and Guo (2004).

Mechanical quantity	E_L (GPa)	E_T (GPa)	C_{11} (GPa)	C_{12} (GPa)	C_{33} (GPa)	$C_{55}=G_L$ (GPa)	ρ (g cm^{-3})
Mean value (reference)	16.6	9.5	23.1	8.7	15.1	4.7	1.722
Minimum	13.4	6.5	17.6	5.1	9.1	3.3	1.66
Maximum	20.6	12.8	29.6	15.9	25.9	5.5	1.753

$$H_C^1 = -2\alpha\rho v_F^M, \tag{15}$$

where H_C^1 is the equivalent depth for a spatial variation in C_{11} corresponding to a variation in type 1 and v_F^M denotes the mean FAS velocity obtained numerically for the different values of δ investigated, which corresponds to a first order approximation. Similarly, for a spatial variation in C_{11} of type 2, combining Eq. (14) together with Eqs. (6) and (9) yields

$$H_C^2 = -2\alpha\rho v_F^M + \frac{h}{2}, \tag{16}$$

where H_C^2 is the equivalent depth for a spatial variation in C_{11} corresponding to a variation in type 2.

The value of α is determined graphically as the slope of the FAS velocity versus δ for each type of variation assuming a linear variation in the FAS velocity as a function of δ.

Similarly, for a spatial variation in ρ corresponding to variations in types 1 and 2, Eq. (14) yields

$$H_\rho^1 = \frac{2\alpha\rho^M}{v_F^M}, \quad H_\rho^2 = \frac{2\alpha\rho^M}{v_F^M} + \frac{h}{2}, \tag{17}$$

where H_ρ^1 and H_ρ^2 are the equivalent depths for a spatial variation in ρ corresponding to a variation in types 1 and 2, respectively. The quantity ρ^M denotes the mean mass density at the surface ($z=0$) obtained, which corresponds to a first order approximation.

In case of porosity gradient, the equivalent depths can be calculated in a similar way following the detailed expressions

$$H_P^1 = \frac{2\alpha v_F^M \rho^M}{(\delta_\rho \times (v_F^M)^2 - \delta_C)}, \quad H_P^2 = \frac{2\alpha v_F^M \rho^M}{(\delta_\rho \times (v_F^M)^2 - \delta_C)} + \frac{h}{2}, \tag{18}$$

where H_P^1 and H_P^2 are the equivalent depths for a spatial variation in porosity corresponding to a variation in types 1 and 2, respectively.

III. RESULTS

A. Range of realistic material properties

Table I recalls the maximum, minimum, and mean measured values of E_L, E_T, and G_L, as given by Dong and Guo (2004). Table I also shows the maximum, minimum, and mean values of the four components (C_{11}, C_{12}, C_{33}, and C_{55}) of the stiffness tensor $\mathbb{C}$ affecting wave propagation derived from Eqs. (2) and (3).

B. Variation in FAS velocity to changes in bone mechanical properties

From the analysis of numerical simulations, the variation in the FAS velocity due to changes in material properties within a realistic range was assessed for $h=0.6$ and 4 mm and for homogeneous material properties. The minimal (m) and maximal (M) values of each material property are tested, the other material properties remaining equal to their reference values. Table II shows the corresponding FAS velocity variations.

According to the value of h and to the considered material property S, two situations may be distinguished: the difference of the FAS velocities obtained when considering the maximum and minimum values of S may be relatively "large" (above 91 m s^{-1}) or relatively "small" (lower than 20 m s^{-1}). Considering the thick solid layer ($h=4$ mm), Table II shows that small differences of the FAS velocity are obtained when C_{12}, C_{33}, and C_{55} take their minimum or maximum value defined above. On the contrary, the FAS velocity varies significantly when C_{11} or ρ varies within the limits defined above. When considering the thin solid layer ($h=0.6$ mm), changes in C_{55} hardly affect the FAS velocity while changes in C_{11}, C_{12}, C_{33}, and ρ lead to larger changes in the FAS velocity.

C. Qualitative effect of a gradient of material property

Typical snapshots of wave propagation in the multiple layer domain corresponding to the case of a thick solid layer ($h=4$ mm) are shown in Fig. 3, where the grayscale codes the normalized amplitude of the pressure in the fluid and the trace of the stress tensor in the solid. These two quantities are represented in a logarithmic normalized scale for visualization purposes at time $t=8$ μs. Figures 3(a) and 3(b) correspond, respectively, to homogeneous and heterogeneous bones with a gradient δ_{11} of C_{11} equal to 30 GPa cm^{-1}. In the homogeneous solid layer [Fig. 3(a)], the orientation of the fastest wave front is approximately perpendicular to the bone surface, whereas in the heterogeneous solid, this orientation is inclined compared to the bone surface, which is an effect of the gradient of C_{11}. The difference between the two patterns of wave propagation illustrates qualitatively the influence of a gradient of C_{11}.

TABLE II. Sensitivity of the FAS velocity to changes in different stiffness coefficients and in mass density for two values of the cortical thickness and homogeneous bone material properties. The computed FAS velocity is indicated for the minimal and maximal values of each variable corresponding to the realistic range of variation obtained (i) by considering the reference values of Table I and (ii) by verifying that the thermodynamical stability conditions are fulfilled. Values resulting from the stability conditions are marked with an asterisk.

Material property S	C_{11} (GPa)		C_{12} (GPa)		C_{33} (GPa)		$C_{55}=G_L$ (GPa)		ρ (g cm^{-3})	
Realistic range $[S_m,S_M]$ (reference)	[17.6, 29.6]		[5.1, 11.1*]		[11.8*, 25.9]		[3.3, 5.5]		[1.66, 1.753]	
Cortical thickness h (mm)	0.6	4	0.6	4	0.6	4	0.6	4	0.6	4
FAS velocity for S_m (m s^{-1})	2920	3182	3599	3633	3348	3618	3435	3628	3499	3688
FAS velocity for S_M (m s^{-1})	3968	4101	3244	3655	3500	3610	3435	3631	3408	3591

D. Case of thick solid layer

Let us consider first the thick solid layer (h=4 mm). Figure 4 shows the dependence of the FAS velocity on the gradient of C_{11} and of density. As only C_{11} and the density have an effect on the FAS velocity when the solid layer is homogeneous and the thickness h=4 mm, only gradients δ_{11} and δ_ρ with respect to C_{11} and density were considered.

When the gradient is of type 1, the FAS velocity decreases when δ_{11} increases while it increases with δ_ρ. When gradient is of type 2, the FAS velocity increases with δ_{11} and slightly decreases with δ_ρ.

The dashed lines of Fig. 4 show the velocity given from Eq. (6) where the values of C_{11} and ρ are taken at the surface (z=0). For homogeneous bone tissue (δ=0), the FAS velocity is slightly overestimated by v_b.

Due to the near field effect, the FAS velocity is expected to be lower than v_b of about 1.5% (about 60 m s^{-1}) for the distances between emitter and receivers considered (Bossy *et al.*, 2004b).

The difference between the dependence of the FAS velocity on δ and the behavior of v_b at the upper interface may

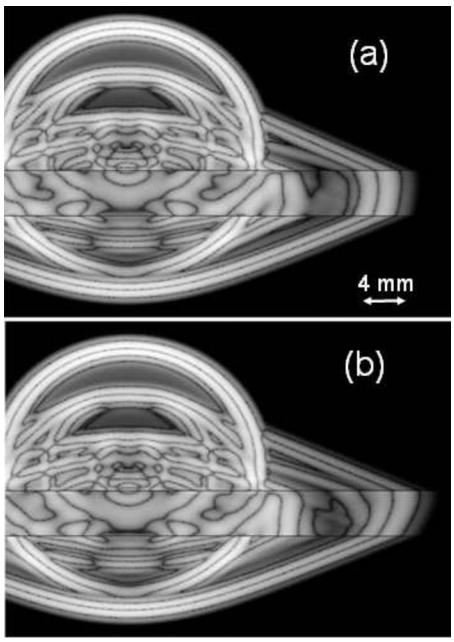

FIG. 3. Snapshot of the ultrasonic propagation a time t=8 μs in the three-layer medium composed of a transverse isotropic solid medium of 4 mm sandwiched between two identical fluid media. (a) The solid layer is homogeneous. (b) The solid layer is heterogeneous with a constant gradient δ_{11} of C_{11} equal to 30 GPa cm^{-1}.

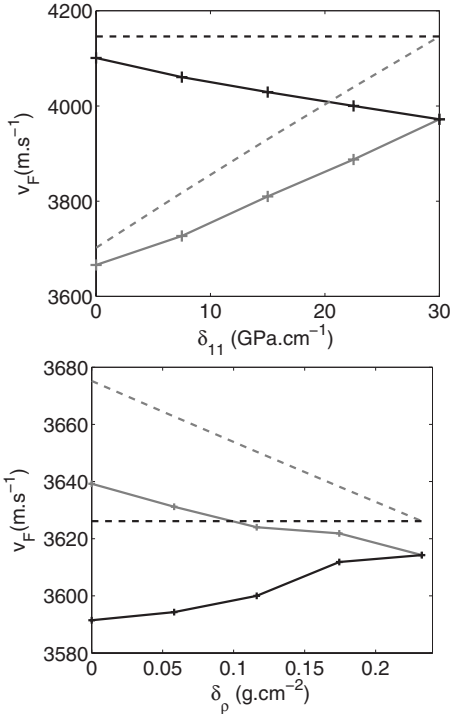

FIG. 4. Case of thick solid layer (h=4 mm). Variation in v_F versus (a) δ_{11} and (b) δ_ρ. The black lines correspond to the variation in type 1 [constant value of (a) C_{11} and (b) ρ at z=0] and the gray lines correspond to the variation in type 2 [constant value of (a) C_{11} and (b) ρ at z=−0.5h]. The continuous lines indicate the results obtained from the finite element model. The dashed lines correspond to the longitudinal bulk wave velocity in the material at the upper interface.

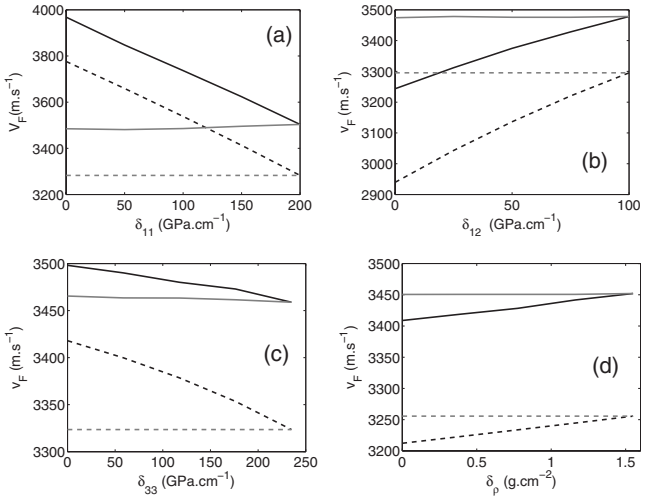

FIG. 5. Case of thin solid layer (h=0.6 mm). Variation in v_F versus (a) δ_{11}, (b) δ_{13}, (c) δ_{33}, and (d) mass density. The black lines correspond to the variation in type 1 (constant value of the considered material property at z=0) and the gray lines correspond to the variation in type 2 (constant value of the considered material property at z=−0.5h). The continuous lines indicate the results obtained from the finite element model. The dashed lines correspond to the longitudinal bulk wave velocity in the material at the upper interface. The dashed lines correspond to solutions to the characteristic equation derived from the works of Nayfeh and Chimenti (1988, 1989).

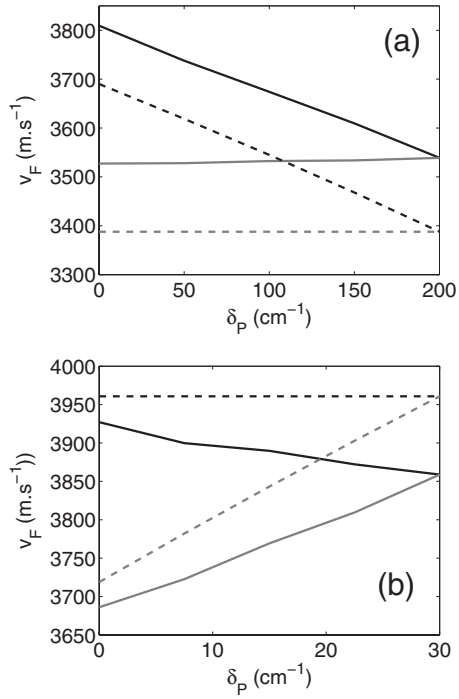

FIG. 6. (a) Case of a thin solid layer (h=0.6 mm) and (b) case of a thick solid layer (h=4 mm). Variation in v_F versus the gradient of porosity δ_P. (a) Same caption as that of Fig. 5 with δ_P and (b) same caption as that of Fig. 4 with δ_P.

be explained by the fact that in the case of a large bone thickness, the FAS velocity is influenced by the material properties within a certain "equivalent depth" (Bossy *et al.*, 2004b). Note that if $v_b(\delta,H)$ was plotted in Fig. 4 (H corresponding to the equivalent depth) as a function of δ, it would by definition have the same slope as that of the solid lines (which corresponds to the FAS velocity).

For a spatial variation in C_{11}, the values of H_C^1 and H_C^2 found using Eqs. (15) and (16) are, respectively, equal to 0.59 and 0.66 mm. The difference may be explained by the slightly nonlinear variation in the FAS velocity as a function of δ and to the first order approximation [see Eq. (14)]. In the case of spatial variations in ρ, the values of H_ρ^1 and H_ρ^2 found using Eq. (17) are, respectively, equal to 1.03 and 1.04 mm. Of note is that the equivalent depth depends on the type of gradient considered. As shown by Bossy *et al.* (2004b), it also depends on the frequency and on the distance between the emitter and receivers.

E. Case of thin solid layer

When considering the thin solid layer (h=0.6 mm), the effect of a gradient of C_{11}, C_{12}, C_{33}, and ρ was investigated according to the results presented in Sec. III B. The results are shown in Fig. 5 corresponding to the gradients of C_{11}, C_{12}, C_{33}, and ρ, respectively. When the gradient is of type 1, the FAS velocity is shown to be a decreasing function of both δ_{11} and δ_{33}, but an increasing function of both δ_{12} and δ_ρ.

If the gradient is of type 2, the FAS velocity stays approximately constant for different values of δ_{11}, δ_{12}, δ_{33}, and δ_ρ.

When the ratio of thickness over wavelength is small, the FAS velocity was found to tend toward the plate velocity v_p (Bossy *et al.*, 2002, 2004b). Therefore, based on the works of Nayfeh and Chimenti (1988, 1989), the characteristic equation for a transverse isotropic solid layer immersed in liquid was solved for the S_0 mode of Lamb wave of a thin layer ($f \times h = 10^{-3}$ mm MHz, where f is the frequency). In Fig. 5, the dashed lines correspond to the phase velocity of the S_0 mode of Lamb wave. The material properties used to obtain the curves with dashed lines in Fig. 5 correspond to the spatially averaged values of the elastic properties and density, respectively. In all cases, the gray dashed line is horizontal since the material property in the middle of the solid layer does not depend on δ for a variation in type 2.

F. Case of a gradient of porosity

Figure 6 shows the results obtained for h=0.6 and 4 mm, respectively, with a gradient of porosity δ_P. The black and gray solid lines show the FAS velocity obtained numerically for a gradient of porosity of types 1 and 2, respectively. The dashed lines of Fig. 6(a) correspond to the phase velocity derived from the characteristic equation defined in Nayfeh and Chimenti (1988, 1989) assuming spatially averaged (reference) material properties. The dashed lines of Fig. 6(b) are obtained using Eq. (6) and considering the material properties at the surface (z=0). Similarly as in the case of a thin bone corresponding to Fig. 5, the results displayed in Fig. 6(a) show that the approach by "the characteristic equation" applied with the spatially averaged material properties is able to account for the variation in the FAS velocity as a function of changes in gradient of porosity. Moreover, for a thick as well as a thin bone thickness, the variation in the FAS velocity as a function of a porosity gradient is qualitatively similar to the variation in the FAS velocity as a function of a gradi-

ent of C_{11} (see Fig. 4). These last results show that in the cases of a small or large bone thickness, the variation in C_{11} induced by a change in porosity seems to impact more importantly the FAS velocity compared to the variation in mass density induced by the same change in porosity. In the case of spatial variations in the porosity, the values of H_P^1 and H_P^2 found using Eq. (18) are, respectively, of 0.46 and 0.63 mm. These last values are different but remain of the same order of magnitude. The difference obtained in the case of a gradient of porosity may be explained by the first order approximation performed to compute H_P^1 and H_P^2, which is not valid when all material properties vary simultaneously.

IV. DISCUSSION

To the best of our knowledge, this study is the first one to focus on the effect of a spatial dependence of transverse isotropic material properties on the FAS velocity estimated with an AT configuration for different solid layer thicknesses.

A. Case of thick solid layer

Bossy *et al.* (2004b) used finite-difference time-domain simulation tools in order to determine the effect of a gradient of longitudinal wave velocity by considering isotropic bone material properties. They focused on the behavior of the lateral wave as the cortical thickness was equal to about three wavelengths. Bossy *et al.* (2004b) found that when a gradient of longitudinal wave velocity of 100 m s^{-1} mm^{-1} is considered in bone tissue, the FAS velocity decreases by about 200 m s^{-1} for a 1 MHz signal compared to the case of a homogeneous material. We found that the decrease in the FAS velocity induced by the same gradient is of 198 m s^{-1}, which is of the order of magnitude of the results found by Bossy *et al.* (2004b). In the case treated in the present study, the thickness to wavelength ratio is about 1, which is relevant on the physiological level.

B. Case of thin solid layer

Several simulation works have predicted that when the ratio h/λ tends to be small, the FAS velocity tends to the S_0 wave velocity (plate velocity) [Fig. 11 of Bossy *et al.* (2004b)]. In the present work for $h=0.6$ mm, the values of the FAS velocity found using the finite element model are always underestimated by a value comprised between 112 and 195 m s^{-1} (according to the values of the stiffness coefficients considered) compared to the phase velocity of the S_0 wave. However, this discrepancy is essentially due to the fact that a thickness of $h=0.6$ mm is not small enough in order to observe a close convergence with the plate velocity. This point is supported by the results of an additional finite element computation for a thinner homogeneous plate ($h=0.3$ mm, $C_{11}=23.1$ GPa). In that case, the FAS velocity was found to be 3320 m s^{-1} compared to 3435 m s^{-1} for a plate with same material properties and $h=0.6$ mm, closer to the plate velocity (3236 m s^{-1}).

As shown in Fig. 5, the relative variations in the FAS velocity as a function of δ show the same trend as the variations in the plate velocity. Accordingly, our results indicate that in the case of a rather small thickness ($h=0.6$ mm), the FAS velocity is essentially sensitive to the *mean value* of the stiffness coefficients within the solid layer. In the case of a gradient of material properties, the plate velocity can account to a certain extent for the mean variations in elasticity. This last result may be explained by the fact that, at the first order, S_0 wave modes are mostly sensitive to geometrical effects of the plate rather than to the variations in material properties.

C. Limitations

This study has a number of limitations. First, no absorption effects were accounted for in cortical bone (Lakes *et al.*, 1986; Sasso *et al.*, 2007, 2008), in soft tissue, or in marrow. Second, the determination of homogenized material properties of cortical bone is a complex problem due to the multiscale nature of bone. Bone material properties depend on the microstructure (e.g., porosity, shape, and distribution of the pores) as well as on the material properties of the bone matrix at smaller scales (e.g., mineralization, orientation of collagen fibrils, etc.). Both porosity and material properties of bone tissue may depend on the radial position in bone and result in a gradient of elasticity. Therefore multiscale models coupled with structural and stiffness measurements at lower scales are needed in order to derive more realistic spatial variations in homogenized material properties. In addition, the gradients of the different stiffness coefficients may be coupled, which was not considered in the present study. Nevertheless, similar trends of the evolution of the FAS velocity as a function of gradients of elasticity should be obtained in more general cases. Third, rough approximations were employed in order to determine the value and the gradient of bone material properties. Our approach was to use the results obtained by Dong and Guo (2004) together with the thermodynamical stability conditions in order to determine a physiological range of variation for each material property. Then, the maximum gradient of each material property S is assumed to correspond to a spatial variation in S, where S takes (i) the maximum value of physiological range determined using the aforementioned approach in the periosteal part and (ii) the minimum value of physiological range at the endosteal part. This method of determination of the spatial variation in the bone material properties constitutes a simple approach but relevant to approximate their complex spatial variation. Real variations in material properties are likely to be significantly more complex. However, for large cortical thickness, the range of variation in δ_{11} (0–30 GPa cm^{-1}) is comparable with that determined from numerical simulations of wave propagation by Bossy *et al.* (2004b) (about 15 GPa cm^{-1}). In addition, our results do not depend on the choice of the physiological range of variation in each material property and changing the values of the bone properties would not modify the main conclusion of this study since linearity is assumed at all stages of the computation.

In this paper, the effect of a gradient of porosity on cortical bone, which may be due to aging and/or to osteoporosis, is investigated. However, whereas C_{12} has been shown to play a role in the propagation in the case of thin bone, its variations were not accounted for since its dependence of porosity was not given in Baron *et al.* (2007).

In the framework of a virtual osteoporosis approach (Haïat *et al.*, 2007), it would be enlightening to derive realistic scenarios of cortical bone alteration and to include them into our model using appropriate homogenization procedures. It has been shown that bone tissue aging leads to an increased mineralization (Grynpas, 1993). Hypermineralized tissues have a tendency to be stiffer as shown in studies using nano-indentation (Hoc *et al.*, 2006) or acoustic microscopy (Raum *et al.*, 2006). Therefore, a combined effect of an increased mineralization together with an increase in porosity as well as in the gradient of porosity would be of great interest to predict the evolution of bone ultrasonic response with age or thickness.

ACKNOWLEDGMENT

This study was supported by the "Agence Nationale de la Recherche" (Contract BoneChar No. BLAN06-2_144779).

Ammann, P., and Rizzoli, R. (**2003**). "Bone strength and its determinants," Osteoporosis Int. **14**, S13–S18.

Barkmann, R., Kantorovich, E., Singal, C., Hans, D., Genant, H. K., Heller, M., and Gluer, C. C. (**2000**). "A new method for quantitative ultrasound measurements at multiple skeletal sites," J. Clin. Densitometry **3**, 1–7.

Baron, C., Talmant, M., and Laugier, P. (**2007**). "Effect of porosity on effective diagonal stiffness coefficients (c_{ii}) and anisotropy of cortical at 1 MHz: A finite-difference time domain study," J. Acoust. Soc. Am. **122**, 1810–1817.

Bossy, E., Talmant, M., and Laugier, P. (**2002**). "Effect of bone cortical thickness on velocity measurements using ultrasonic axial transmission: A 2D simulation study," J. Acoust. Soc. Am. **112**, 297–307.

Bossy, E., Talmant, M., and Laugier, P. (**2004a**). "Bi-directional axial transmission can improve accuracy and precision of ultrasonic velocity measurement in cortical bone: A validation on test material," IEEE Trans. Ultrason. Ferroelectr. Freq. Control **51**, 71–79.

Bossy, E., Talmant, M., and Laugier, P. (**2004b**). "Three-dimensional simulations of ultrasonic axial transmission velocity measurement on cortical bone models," J. Acoust. Soc. Am. **115**, 2314–2324.

Bossy, E., Talmant, M., Peyrin, F., Akrout, L., Cloetens, P., and Laugier, P. (**2004c**). "An *in vitro* study of the ultrasonic axial transmission technique at the radius: 1-MHz velocity measurements are sensitive to both mineralization and intracortical porosity," J. Bone Miner. Res. **19**, 1548–1556.

Bousson, V., Meunier, A., Bergot, C., Vicaut, E., Rocha, M. A., Morais, M. H., Laval Jeantet, A. M., and Laredo, J. D. (**2001**). "Distribution of intracortical porosity in human midfemoral cortex by age and gender," J. Bone Miner. Res. **16**, 1308–1317.

COMSOL MULTIPHYSICS (**2005**). "Model library," Grenoble, France.

Desceliers, C., Soize, C., Grimal, Q., Haïat, G., and Naili, S. (**2008**). "Three dimensional transient elastic waves in multilayer semi-infinite media solved by a time-space-spectral numerical method," Wave Motion **45**, 383–399.

Dong, X. N., and Guo, X. E. (**2004**). "The dependence of transversely isotropic elasticity of human femoral cortical bone on porosity," J. Biomech. **37**, 1281–1287.

Fritsch, A., and Hellmich, C. (**2007**). "'Universal' microstructural patterns in cortical and trabecular, extracellular and extravascular bone materials: Micromechanics-based prediction of anisotropic elasticity," J. Theor. Biol. **244**, 597–620.

Grimal, Q., and Naili, S. (**2006**). "A theoretical analysis in the time-domain of wave reflection on a bone plate," J. Sound Vib. **298**, 12–29.

Grynpas, M. (**1993**). "Age and disease-related changes in the mineral of bone," Calcif. Tissue Int. **53**, S57–S64.

Haïat, G., Padilla, F., Peyrin, F., and Laugier, P. (**2007**). "Variation of ultrasonic parameters with microstructure and material properties of trabecular bone: A three-dimensional model simulation," J. Bone Miner. Res. **22**, 665–674.

Hans, D., Srivastav, S. K., Singal, C., Barkmann, R., Njeh, C. F., Kantorovich, E., Gluer, C. C., and Genant, H. K. (**1999**). "Does combining the results from multiple bone sites measured by a new quantitative ultrasound device improve discrimination of hip fracture?," J. Bone Miner. Res. **14**, 644–651.

Hoc, T., Henry, L., Verdier, M., Aubry, D., Sedel, L., and Meunier, A. (**2006**). "Effect of microstructure on the mechanical properties of Haversian cortical bone," Bone (N.Y.) **38**, 466–474.

Lakes, R. S., Yoon, H. S., and Katz, J. L. (**1986**). "Ultrasonic wave propagation and attenuation in wet bone," J. Biomed. Eng. **8**, 143–148.

Macocco, K., Grimal, Q., Naili, S., and Soize, C. (**2005**). "Probabilistic modelling of an ultrasonic setup: Calculation of the dispersion on wave speed measurements," C. R. Mec. **333**, 565–573.

Macocco, K., Grimal, Q., Naili, S., and Soize, C. (**2006**). "Elastoacoustic model with uncertain mechanical properties for ultrasonic wave velocity prediction: Application to cortical bone evaluation," J. Acoust. Soc. Am. **119**, 729–740.

Mayhew, P. M., Thomas, C. D., Clement, J. G., Loveridge, N., Beck, T. J., Bonfield, W., Burgoyne, C. J., and Reeve, J. (**2005**). "Relation between age, femoral neck cortical stability, and hip fracture risk," Lancet **366**, 129–135.

Moser, F., Jacobs, L., and Qu, J. (**1999**). "Modeling elastic wave propagation in waveguides with the finite element method," NDT & E Int. **32**, 225–234.

Nayfeh, A. H., and Chimenti, D. E. (**1988**). "Ultrasonic wave reflection from liquid-coupled orthotropic plates with application to fibrous composites," J. Appl. Mech. **55**, 863–870.

Nayfeh, A. H., and Chimenti, D. E. (**1989**). "Free wave propagation in plates of general anisotropic media," J. Appl. Mech. **56**, 881–886.

Protopappas, V. C., Kourtis, I. C., Kourtis, L. C., Malizos, K. N., Massalas, C. V., and Fotiadis, D. I. (**2007**). "Three-dimensional finite element modeling of guided ultrasound wave propagation in intact and healing long bones," J. Acoust. Soc. Am. **121**, 3907–3921.

Raum, K., Cleveland, R. O., Peyrin, F., and Laugier, P. (**2006**). "Derivation of elastic stiffness from site-matched mineral density and acoustic impedance maps," Phys. Med. Biol. **51**, 747–758.

Raum, K., Leguerney, I., Chandelier, F., Bossy, E., Talmant, M., Saied, A., Peyrin, F., and Laugier, P. (**2005**). "Bone microstructure and elastic tissue properties are reflected in QUS axial transmission measurements," Ultrasound Med. Biol. **31**, 1225–1235.

Reilly, D. T., and Burnstein, A. H. (**1974**). "The mechanical properties of cortical bone," J. Bone Jt. Surg., Am. Vol. **56**, 1001–1022.

Rho, J. Y. (**1996**). "An ultrasonic method for measuring the elastic properties of human tibial cortical and cancellous bone," Ultrasonics **34**, 777–783.

Rico, H. (**1997**). "The therapy of osteoporosis and the importance of cortical bone," Calcif. Tissue Int. **61**, 431–432.

Royer, D., and Dieulesaint, E. (**2000**). *Elastic Waves in Solids. I: Free and Guided Propagation* (Springer-Verlag, Berlin).

Sasso, M., Haïat, G., Yamato, Y., Naili, S., and Matsukawa, M. (**2007**). "Frequency dependence of ultrasonic attenuation in bovine cortical bone: An in vitro study," Ultrasound Med. Biol. **33**, 1933–1942.

Sasso, M., Haïat, G., Yamato, Y., Naili, S., and Matsukawa, M. (**2008**). "Dependence of ultrasonic attenuation on bone mass and microstructure in bovine cortical bone," J. Biomech. **41**, 347–355.

Seeley, D. G., Browner, W. S., Nevitt, M. C., Genant, H. K., Scott, J. C., and Cummings, S. R. (**1991**). "Which fractures are associated with low appendicular bone mass in elderly women? The study of osteoporotic fractures research group," Ann. Intern Med. **115**, 837–842.

Stegman, M. R., Heaney, R. P., Travers-Gustafson, D., and Leist, J. (**1995**). "Cortical ultrasound velocity as an indicator of bone status," Osteoporosis Int. **5**, 349–533.

Thomas, C. D., Feik, S. A., and Clement, J. G. (**2005**). "Regional variation of intracortical porosity in the midshaft of the human femur: Age and sex differences," J. Anat. **206**, 115–125.

Turner, C. H. (**2002**). "Biomechanics of bone: Determinants of skeletal fragility and bone quality," Osteoporosis Int. **13**, 97–104.

WHO Study Group (**1994**). "Assessment of fracture risk and its application to screening for postmenopausal osteoporosis," WHO Technical Report No. 843, World Health Organization, Geneva, Switzerland, http://www.who.int/reproductive-health/publications/ageing.html (Last viewed April, 2008).

Sound source segregation by goldfish: Two simultaneous tones

Richard R. Fay[a)]
Parmly Hearing Institute, Loyola University Chicago, 6525 N. Sheridan Road, Chicago, Illinois 60626

(Received 11 October 2008; revised 31 March 2009; accepted 31 March 2009)

The perception of two simultaneous tones was investigated in goldfish using classical respiratory conditioning and a stimulus generalization paradigm. Pairs of tones were used to make up a mixture of 150 Hz and a higher harmonic or a mistuned harmonic. Fish were conditioned to the two-tone mixture and then tested for generalization to several pure tones. The simultaneous tones tended to be segregated in perception, with the generalization gradient for single tones having two peaks corresponding to the frequencies of the tone pairs. There were no consistent differences in the generalization gradients following conditioning to harmonic or inharmonic tone pairs. In addition, experiments were carried out in which the two tones of the pair were heard on alternate trials, always as single tones, followed by generalization tests to single tones. There was more generalization in this experiment, reflecting the fact that conditioning and generalization test stimuli were both single tones. However, the shapes of the generalization gradients were similar to those in which fish were conditioned to two simultaneous tones, indicating that the simultaneity of the tones did not make them harder to segregate. As the frequency separation between the two components narrowed, segregation tended to fail.
 [DOI: 10.1121/1.3124777]

PACS number(s): 43.80.Lb [MCH] Pages: 4053–4059

I. INTRODUCTION

In 1964, van Bergeijk (1964) asked the following question about the structure of a fish's auditory experience: "Given that a fish can discriminate between two sounds A and B when they are presented separately, can he still discriminate either one when both are presented simultaneously? Or do the two sounds blend to form a new entity (such as a chord)?" (p. 296). At that time, the concepts of analytic and synthetic listening, sound source segregation, and auditory scene analysis were not yet defined, so van Bergeijk's question seems prescient as well as intelligent. But neither were there obvious methods for answering such a question, and, in fact, there was a general bias against the notion that a fish had any "auditory experience" at all. van Bergeijk (1964) went on to state that if fishes were not able to segregate source A from source B, then vocal communication among fishes would be of very limited use. Actually, it would seem that if fishes were not able to segregate sources, hearing itself would be of very limited use.

The source segregation question for fishes has recently been answered in the affirmative several times, both with respect to single-tone components (Fay, 1992) and more temporally and spectrally complex sources (Fay, 1998, 2000). But unanswered questions remain. For example, first, what is the role of harmonicity? In general, harmonic relationships play a role in human source segregation, and this formed an element of van Bergeijk's question when he suggested that the two sources might "blend" to form a chord. Second, what are the limitations of source segregation with respect to frequency differences? Fay (1992) demonstrated that goldfish behaved as if they had segregated two simultaneous tones of 166 and 724 Hz, but it is not known how the animal performs in segregating more closely spaced tones. The 166–724 Hz segregation could have essentially a simple peripheral explanation in that these two frequencies activate differently tuned auditory nerve channels with center frequencies near these frequencies (Fay and Ream, 1984; Fay, 1997). What happens to segregation, and is it still possible when the two components fall essentially within the same channel? These and other questions were the motivations for the present experiments. The segregation of two simultaneous components was evaluated with respect to the harmonic or inharmonic relations between the components, and as a function of the frequency separation between a low-frequency component (150 Hz) and the higher harmonic component to be possibly segregated.

II. MATERIALS AND METHODS

A. Animals

The subjects were 96 common goldfish (*Carassius auratus*), about 8 cm in standard length, maintained in communal aquaria for from 2 weeks to over 1 year. The fish were obtained from commercial suppliers.

B. Acoustics and stimuli

The experimental test chamber was a water-filled plexiglass cylinder 23 cm in diameter and 28 cm high. A University Sound UW-30 underwater pool speaker projected upward from the bottom of the tank, and was buried in water-saturated sand with the speaker diaphragm about 2 cm below the sand surface.

In general, the acoustic conditioning and test stimuli were either pure tones between 50 and 900 Hz, or two simultaneous (mixed) tones consisting of 150 Hz plus a higher

[a)]Electronic mail: rfay@luc.edu

component at either harmonics of 150 Hz (300, 450, 600, or 750 Hz) or at near or mistuned harmonics (310, 460, 610, or 760 Hz). The two-tone mixtures were called harmonic when the higher frequencies were integer multiples of the 150 fundamental frequency component and were called inharmonic when the harmonics were mistuned by 10 Hz. In all cases, the tones were presented at a level about 40 dB above absolute threshold for the component(s) (Fay, 1969). During conditioning (40 trials), the level of the tone(s) was varied from trial to trial by ± 10 dB. During generalization testing, all stimuli were presented at a constant 40 dB sensation level.

In all experiments, conditioning and test stimuli were 6 s duration signals with 20 ms rise-fall times synthesized in advance, stored on disk, and read out of a 16 bit digital-to-analog converter (DAC1) from Tucker Davis Technologies (TDT) at 5 kHz. The DAC1 output was low-pass filtered at 1500 Hz, led to a TDT programmable attenuator, and then to a Crown 100 W power amplifier and the UW-30 loudspeaker.

The acoustic signals were measured by a Bruel and Kjaer 8103 calibrated miniature hydrophone placed in the fish restrainer (described below). The hydrophone output was amplified, bandpass filtered between 10 and 2500 Hz, and digitized at 5 kHz. Samples were spectrally analyzed using the fast Fourier transform. Levels (in decibels with regard to 1 μPa) at selected frequencies were also measured using an HP 3040A wave analyzer. The experimental tank rested on a vibration-isolated limestone slab inside an Industrial Acoustics single-walled audiometric booth.

C. Experimental design

A total of 12 experiments were carried out, with eight animals per experiment. In each experiment, animals received 40 conditioning trials, and then 40 generalization test trials without shock, but in which every fifth trial was the conditioning stimulus terminated by shock. These reinforced trials served to maintain the conditioned response in the face of the generalization testing procedure that tended to extinguish the conditioned response. In experiments 1–4, animals were conditioned to a two-tone mixture and tested for generalization to eight single tones between 50 and 900 Hz. The two-tone mixtures always had a 150 Hz, fundamental frequency component plus a higher, harmonic frequency component at 300, 450, 600, or 750 Hz. Experiments 5–8 had identical stimuli except that the higher of the two conditioning components were mistuned with respect to perfect harmonics by 10 Hz (310, 460, 610, or 760 Hz). A comparison of generalization behavior between experiments 1–4 and 5–8 helped to evaluate the role that harmonicity might play in two-tone segregation. In experiments 9–12, the conditioning stimuli were two harmonic tones presented alternating with one another on successive trials, rather than simultaneously. Generalization testing stimuli were as in experiments 1–4. This last group of experiments helped to evaluate what was to be expected if the simultaneous tones in experiments 1–4 were perceived as segregated as possible.

D. Conditioning and generalization testing

For respiratory conditioning, a goldfish was restrained in a cloth bag about 2 cm from the water surface, centered in the test tank. Slits in the bag allowed respiratory movements of the gill covers and mouth. A thermistor near the mouth measured respiration. Water flow cooled the thermistor producing a fluctuating voltage proportional to respiration. This waveform was filtered between 1 and 4 Hz and digitized at 5 kHz. Respiratory activity was calculated by summing the piecewise lengths of the respiratory waveform in arbitrary units minus the length expected without respiratory activity (i.e., a flat line) over the same period of time. The response (suppression ratio) during a 6 s conditioning or test stimulus was defined as the ratio of the respiratory activity during the last 4 s of the stimulus to the sum of the latter and the respiratory activity 4 s preceding the stimulus. Complete respiratory suppression results in a suppression ratio (SR) of zero, and no change in respiration results in a SR of 0.5.

Respiratory suppression lasting several seconds was an unconditioned response to a 100 ms ac electric shock delivered through steel electrodes placed near the animal's head and tail. A single conditioning trial included a 4 s pretrial period during which respiration was measured, and a 6 s stimulus presentation that terminated with the shock. Conditioned responses to sound tend to occur after 10–15 trials.

Animals were conditioned and tested in two separate sessions that were between 30 min and 24 h apart. A conditioning session consisted of 40 conditioning trials (random intertrial intervals averaging 3 min). Generalization testing consisted of 40 test trials (average intertrial interval of 1.5 min) of eight test stimuli presented four times each in random order without shock. The conditioning stimulus was presented with shock every fifth trial in order to maintain the conditioned response. Shock voltage was adjusted occasionally in order to maintain the conditioned response. Often, conditioning and testing was suspended for 20–40 min in order to aerate the test tank water and maintain slow respiration. Animals failing to show robust, sustained respiratory suppression during the conditioning period were eliminated as subjects.

A median SR was calculated for each of the stimuli presented four times during each generalization testing session. Generalization was normalized with respect to the median SR to the conditioned stimulus measured during the test session (eight trials) and expressed as a percentage. Percentage generalization was defined as $((0.5-\text{med}_T)/(0.5-\text{med}_C)) \times 100$, where med_T is the median SR to the test stimulus and med_C is the median SR to the conditioning stimulus obtained from eight conditioning stimulus presentations (with shock) during generalization testing. Generalization values above 100% occurred when suppression to a test stimulus was greater than that to the conditioning stimulus. Values below 0% occurred when the SR was greater than 0.5, indicating an acceleration of respiratory activity during the stimulus.

The care and use of animals in this work was approved by the Institutional Animal Care and Use Committee of Loyola University Chicago, and was supported by the NIH

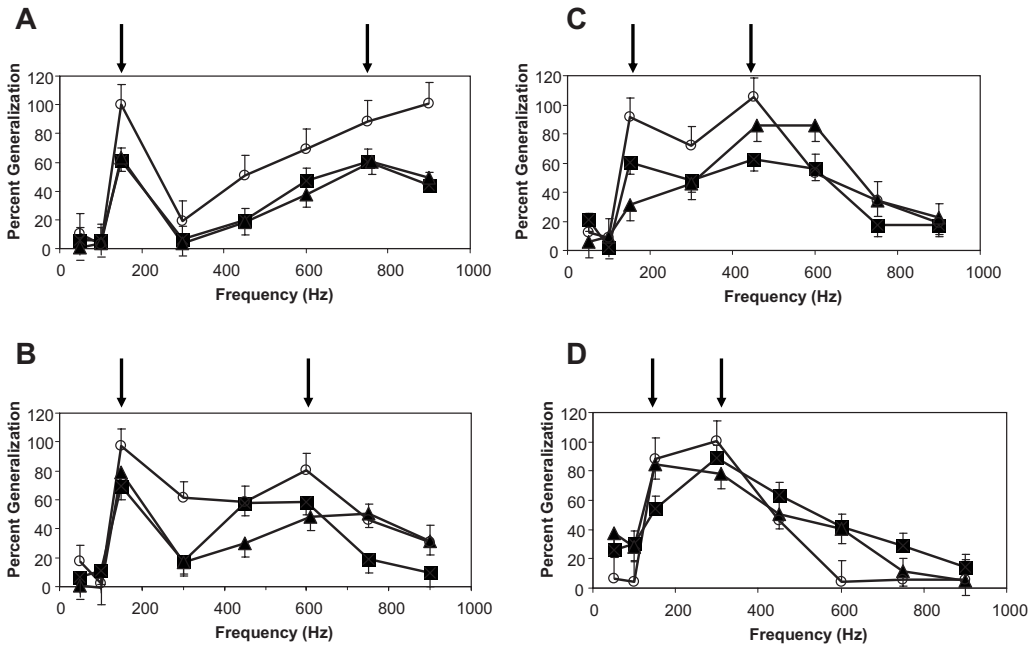

FIG. 1. Group mean generalization gradients for 12 independent groups of eight animals conditioned to two tones. (A) 150+750 Hz, (B) 150+600 Hz, (C) 150+450 Hz, and (D) 150+300 Hz. For all panels, filled squares: two-tone, harmonic complexes; filled triangles: two-tone mistuned complexes; and open circles: two single tones presented on alternate trials. Vertical error bars indicate ±1 standard error at each mean. The two large arrows in each panel indicate the two frequencies making up the conditioning stimuli.

NIDCD Grant No. 1 R01 DC005970 "Sound source segregation and determination," R. Fay P.I.

III. RESULTS

The group mean generalization gradients for all 12 experiments are shown in Fig. 1. As an example, Fig. 1(a) shows the gradients for animals conditioned to 150 and 750 Hz (harmonic)—filled squares, animals conditioned to 150 and 760 Hz (inharmonic)—filled triangles, and animals conditioned to 150 and 750 Hz tones alternating on successive trials—open circles. These three groups were always tested identically using single tones. All groups produced the greatest response at 150 and 750 Hz, suggesting that these two components had been segregated in perception. The maximum amount of generalization for the two groups conditioned to the tonal mixtures reached about 60%, indicating that no single tone used in generalization testing was fully equivalent to the two-tone mixture on which the fish were conditioned. The gradient for the inharmonic test stimuli is essentially identical to that for the harmonic group, suggesting that source segregation for tones does not depend on strict harmonic relationships, at least for these two most widely spaced tones. The gradient for the group conditioned to the two tones presented successively on alternate trials is generally higher (reaching 100%) than for the other two groups, indicating that the single test tones were judged to be essentially equivalent to the single tones used in initial conditioning. There are no other obvious differences between the generalization behavior of the simultaneous and alternating conditioning groups.

In general, the other panels in Figs. 1(b)–1(d) can be described similarly. However, as the two-tone separation narrows, the evidence for source segregation also declines. Figure 1(d) shows that at the smallest component separation (150 and 300 Hz), there is no sign of source segregation. This is due to the limited resolution of the generalization test and the limited resolution of generalization behavior as a sign of source segregation (see Sec. IV). However, the amount of generalization after conditioning to the tonal mixtures is higher in this group (80%–90%), suggesting that the response to the two-tone complex (150 and 300 Hz) was nearly equivalent to the response to the single tones used in the generalization test. Also notice that at this small separation, there is still little sign of the influence of harmonic versus mistuned components on generalization behavior, and no obvious differences between the gradient shapes for simultaneous or successive tone conditioning.

The degree of tone source segregation as revealed by the generalization gradients can be estimated using a peak-valley contrast metric. Contrast was defined as P-T, where P is the average generalization response at the two frequencies used in conditioning and T is the lowest single generalization value that fell between the two peaks. Figure 2 shows this contrast for the four groups and indicates that contrast declines approximately equally and linearly as the frequency separation between the two components declines for both the harmonic and mistuned groups and regardless of whether the goldfish were conditioned to simultaneous or successive tones.

IV. DISCUSSION

These results are generally consistent with the results of a previous experiment (Fay, 1992) on tonal source segregation in goldfish. This and the earlier experiment suggest that two-tone mixtures are naturally analyzed by the goldfish into their individual tonal components and do not tend to be per-

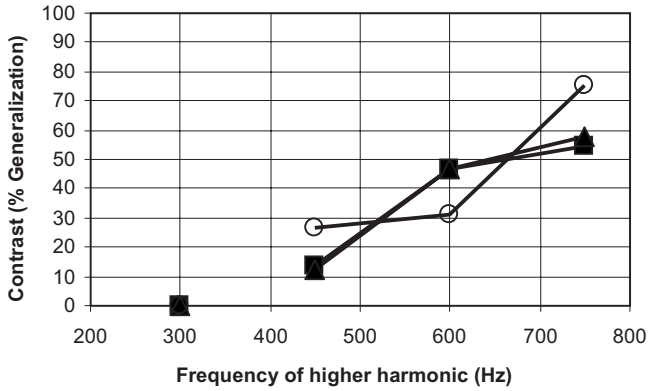

FIG. 2. The degree of segregation indicated by a contrast metric. Contrast (see text) as a function of the frequency of the higher harmonic. Filled squares: two-tone, harmonic complexes; filled triangles: two-tone mistuned complexes; and open circles: two single tones presented on alternate trials.

ceived synthetically as a unique chord or auditory "chimera." Rather, the goldfish auditory system tends to operate analytically and forms a "scene" made up of the collection of individual auditory components or sources. This ability to segregate sources, even those with no obvious biological significance, is presumed to be an adaptation of all auditory systems for analyzing the soundscape for general orientation purposes (Slabbekoorn and Bouton, 2008).

The generalization gradients for the simultaneous and successive groups are substantially similar, indicating that the simultaneous occurrence of the two components did not affect or reduce the source segregation behavior to a greater degree that occurs when the components are heard separately or as single tones. Therefore, there appears to be little or no effect of simultaneity itself on source segregation as measured by this generalization procedure. The frequency selectivity revealed by these generalization experiments seems to be quite acute, and the results are generally consistent with previous generalization experiments using single tones (Fay, 1969, 1970a, 1992).

In order to compare single-tone generalization behavior with the present gradients after conditioning to mixtures, Fig. 3 was constructed. The present gradients for the harmonic mixtures (filled triangles connected by lines) are plotted along with results abstracted from the single-tone gradients (Fay, 1970a, see also Fig. 4). Since the exact frequencies used presently (150, 300, 450, 600, 750 Hz) were not tested with single tones previously, a procedure was developed to predict what these generalization gradients would likely have been if centered on the frequencies used in the present experiments. First, the upper and lower frequencies of each single-tone generalization gradient corresponding to 50% generalization were measured and were plotted as a function of center frequency. The frequencies at 50% generalization corresponding to the present center frequencies were determined by linear interpolation. Then the predicted gradients were plotted in Fig. 3 as three points—the interpolated lower and upper frequencies at 50% generalization, and the center frequency. It can be seen that for the two widest tone separations (panels A and B), the lower leg of the 150 Hz gradients and the upper leg of the higher harmonic gradients are

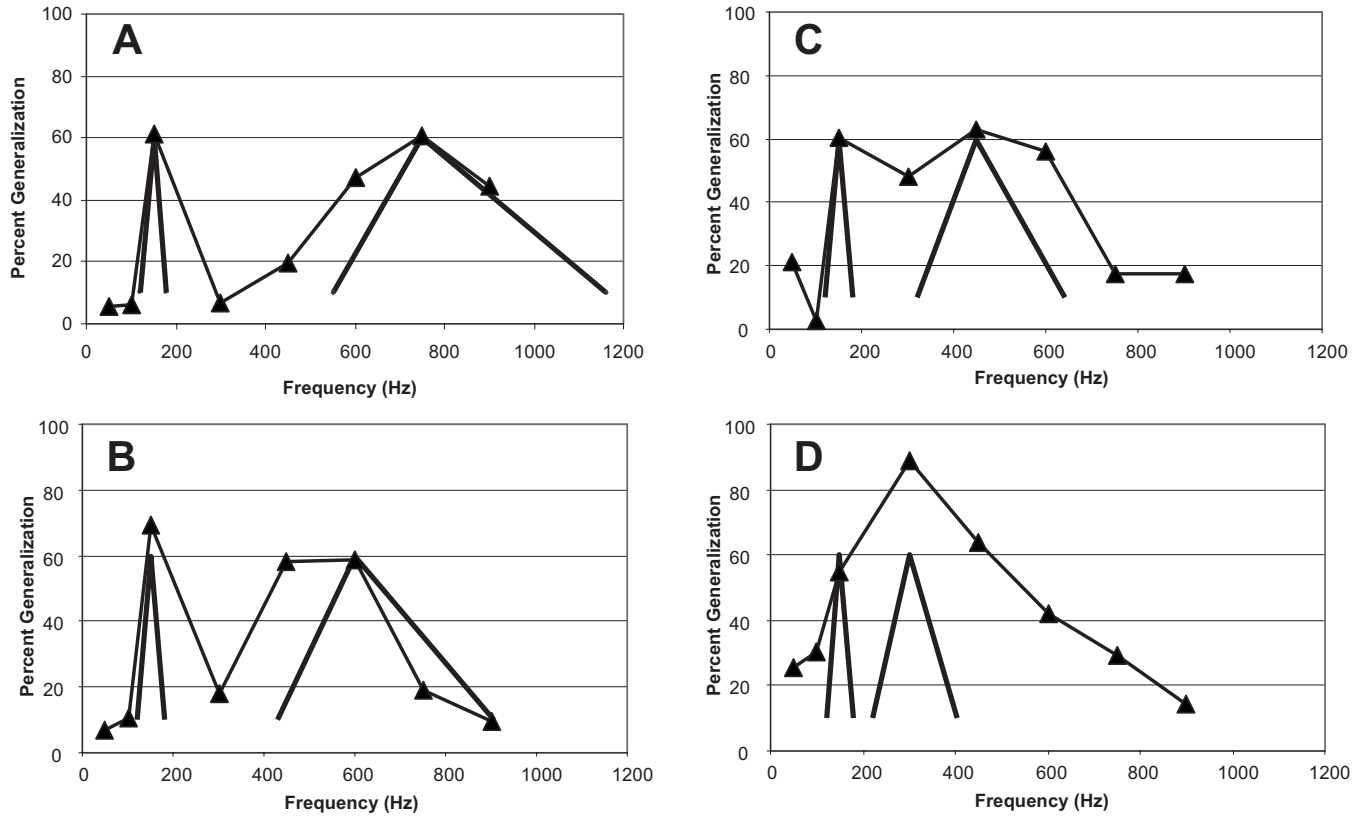

FIG. 3. Generalization gradients for harmonic complexes (filled triangles) along with predictions for generalization gradients to single tones (the two, inverted "V" shapes in each panel—see text). (A) Generalization gradient following conditioning to 150+750 Hz with predicted single-tone gradients to these same frequencies. (B) 150+600 Hz, (C) 150+450 Hz, and (D) 150+300 Hz.

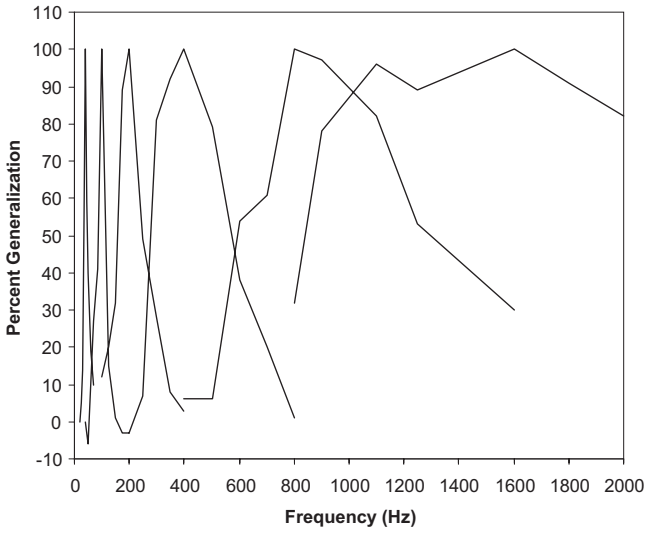

FIG. 4. Single tone generalization gradients for goldfish replotted from Fay, 1970a on a linear frequency scale.

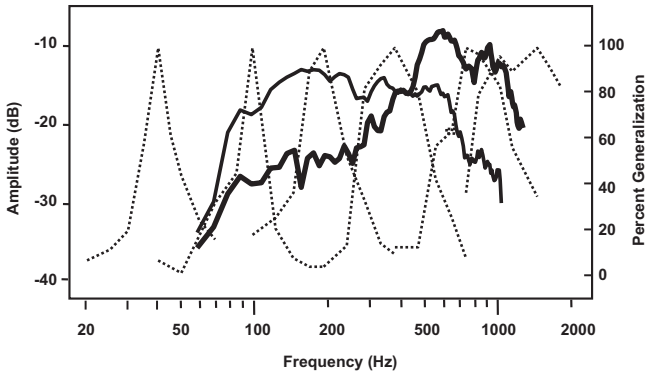

FIG. 5. The gradients of Fig. 4 (dotted lines) along with the two fundamental filter shapes determined for single cells of the goldfish saccular nerve using the revcor method (Fay, 1997). The low-frequency filter (lighter solid line) and the high-frequency filter (heavier solid line).

coincident with those for single tones and the present two-tone mixtures. At test frequencies between the two components, the mixture gradients lie well above the single-tone gradients. For the two narrowest frequency separations (panels C and D), there is more excess generalization, especially above the center frequencies of the higher, single-tone gradients. Thus, we conclude that for the 150 Hz plus 600 and 750 Hz gradients, the generalization behavior is predicted from the single-tone gradients at frequencies above and below the respective tonal frequencies, but between them generalization is greater than predicted. This means that the two-tone mixtures were well analyzed, but this analysis tends to be degraded or uncertain at frequencies between the two mixed tones. As noted above, this uncertainty is not due to the simultaneous presentation of the two tones, but rather with the performance in recalling two, rather than one, tone in the generalization test. For the other two gradients (panels C and D), analysis of the mixtures generally declines and fails completely for the 150+300 Hz gradients. The failure to demonstrate segregation in these cases is due, at least in part, to the combination of the limited resolution of the generalization procedure as a definition of source segregation and the limited resolution of the frequencies chosen for the generalization test.

Figure 4 plots the pure tone generalization gradients that have been obtained from goldfish previously (Fay, 1970a). These gradients are remarkable in suggesting that frequency analysis is very acute, and that it deteriorates monotonically with frequency between 40 and 1600 Hz. For example, the left-most gradient indicates that a 5 Hz deviation from the 40 Hz conditioning frequency results in a significant failure to generalize. Not only is this a discriminable change of frequency (Fay, 1970b) but it is a meaningful one to the goldfish in that it easily controls behavior. What are the mechanisms for this high degree of frequency selectivity, and for the degree of source segregation revealed by these generalization gradients? In other words, what evidence permits the goldfish to decide that there are two sinusoids that make up the mixture stimuli used here, or that a 100 Hz sinusoid has little in common with a 150 Hz sinusoid (see Figs. 4 and 5)?

The first hypothesis that comes to mind is that the segregation behavior is based on peripheral filters (the tuning curves of primary afferents). This hypothesis, in its simplest form, can be quickly rejected. Fay (1978a, 1997) and Fay and Ream (1986) investigated the frequency selectivity of saccular afferents in goldfish and concluded that the hearing range is divided into 2–4 wide-band frequency channels. Figure 5 shows the two major peripheral frequency channels revealed using the reverse correlation (revcor) method in goldfish (Fay, 1997), superimposed on the generalization gradients of Fig. 4. These two channels are quite wide and overlapping, and cannot account in any simple way for the behaviorally determined frequency selectivity, especially at the lowest frequencies. Thus, the hypothesis that the two-tone source segregation behavior of goldfish (Fay, 1992) is simply based on the selective and independent analysis of the two mixed components in peripheral channels can also be rejected.

The remaining possibilities include that this frequency selectivity and source segregation behavior are a result of computations in the brain, begun either with the place-coded peripheral selectivity of Fig. 5 or with the temporally coded waveform, presumably based on phase-locking in the periphery. Computations based on the timing of spikes in the auditory nerve is the hypothesis that has received the most experimental and theoretical attention (e.g., Fay, 1978b; De Cheveigné, 2005).

The temporal coding hypothesis is relevant to the present question of the effects of harmonicity on source segregation. There appears to be no apparent effect of harmonicity on segregation: the generalization gradients are substantially similar for harmonically related and for mistuned components. For human listeners, the mistuning of a harmonic within a harmonic complex tends to make the mistuned component stand out as a separate entity (enhances segregation or analytic listening) (Hartmann, 1988). This phenomenon is often discussed in the context of pitch theory; the frequency of a mistuned harmonic is not consistent with the pitch or fundamental frequency of the rest of the complex and thus is perceptually segregated. Goldfish exhibit a sort of

pitch perception for harmonic complexes (Fay, 2005) but differ from humans in apparently not demonstrating repetition noise pitch (Yost *et al.*, 1978), and in their perceptions that, for example, a 100 Hz pure tone and a harmonic complex with a fundamental frequency (f0) of 100 Hz have no perceptual elements in common (Fay, 2005). The evidence so far is that the goldfish is well aware of the acoustic spectrum but unaware of a spectrum's periodicity or internal structure that can determine pitch for human listeners. Guttman (1963) came to a similar conclusion about the visible spectrum after studying stimulus generalization across single wavelengths in pigeons.

It is noteworthy that in Fay, 2005, goldfish did not generalize at all between a single tone of 100 Hz and a harmonic complex with 20 successive harmonics having a f0 of 100 Hz or vice versa. But in the present experiment, there was significant generalization between a two-tone harmonic complex with f(0)=150 Hz and a 150 Hz single tone. We could predict, therefore, that as the number of higher harmonics of a complex increases, the magnitude of generalization to a single tone at the fundamental frequency declines, in spite of the fact that the 100 Hz periodicity of the complex's waveform becomes better and better defined as more harmonics are added. Apparently, a signal consisting of many successive harmonics is difficult to analyze for the goldfish and is perceived synthetically as quite distinct from a single tone. In any case, the often-stated conclusion that organisms tend to analyze the low-frequency acoustic waveform in the time domain (e.g., Capranica, 1992) may be true to some extent, but fundamental structural features such as waveform periodicity do not appear to strongly determine the resultant perceptions in goldfish. It is not yet clear whether this tentative conclusion applies as well to all fish species or may apply only to hearing specialists (e.g., otophysans) such as goldfish and zebrafish that have a wide hearing range extending to several thousand hertz.

For human listeners, the pitch of complex tones is determined primarily by higher-frequency harmonic components that are not resolved by the peripheral auditory system (the "residue"). Perhaps for goldfish, this unresolved residue (comprised of the fundamental and all audible harmonics) determines aspects of perception, but there may be no pitch or periodicity pattern processor to make sense out of it. Perhaps for goldfish (and other fishes), complex pitch, per se, is not an important aspect of hearing or source segregation.

The present study contributes to this issue by revealing the frequency selectivity of the internal processes (e.g., filtering computations) that perform this segregation. Lu and Fay (1995, 1996) demonstrated the existence of complex and selective tuning curves in the goldfish midbrain (torus semicircularis) and thalamus (central posterior nucleus). Some single-unit tuning curves showed responses to narrow frequency bands in an "island" pattern, where excitatory responses were flanked by suppressive bands, apparently caused by inhibitory interactions. Thus, narrow frequency selectivity of central units appears to be synthesized through excitatory and inhibitory interactions among frequency-selective inputs, ultimately originating in the periphery. Therefore, we tentatively conclude that the segregation behavior revealed here can be best understood in terms of the frequency selectivity synthesized in the brain and ultimately derived from peripheral filtering.

Regardless of the specific mechanisms, however, these experiments indicate an essential similarity between goldfish and human auditory perception. Both species easily segregate many sources in mixtures, and for both species, the spectrum plays a dominant role. For humans and some other vertebrates, the analysis of the spectrum at the periphery seems to be adequate to account for many aspects of source segregation. For goldfish (and possibly other fishes), it appears to be central computations based on a rather crude peripheral frequency selectivity that accounts for the fundamental aspects of source segregation. The absence of a fine peripheral frequency selectivity and tonotopicity in fishes has not been an important limitation on the sense of hearing or its performance in source segregation.

ACKNOWLEDGMENTS

This research was supported by R01 research grant no. DC005970 from the NIH (NIDCD). Thanks are due to Monica Micek for expertly maintaining and running the animals in these experiments.

Capranica, R. R. (**1992**). "The untuning of the tuning curve: Is it time?" Semin. Neurosci. **4**, 401–408.

De Cheveigné, A. (**2005**). "Pitch perception models," in *Pitch: Neural Coding and Perception*, Springer Handbook of Auditory Research Vol. **24**, edited by C. Plack, D. Oxemham, R. Fay, and A. Popper (Springer-Verlag, New York).

Fay, R. R. (**1969**). "Behavioral audiogram for the goldfish," J. Aud Res. **9**, 112–121.

Fay, R. R. (**1970a**). "Auditory frequency generalization in the goldfish (*Carassius auratus*)," J. Exp. Anal. Behav. **14**, 353–360.

Fay, R. R. (**1970b**). "Auditory frequency discrimination in the goldfish (*Carassius auratus*)," J. Comp. Physiol. Psychol. **73**, 175–180.

Fay, R. R. (**1978a**). "Coding of information in single auditory-nerve fibers of the goldfish," J. Acoust. Soc. Am. **63**, 136–146.

Fay, R. R. (**1978b**). "Phase-locking in goldfish saccular nerve fibres accounts for frequency discrimination capacities," Nature (London) **275**, 320–322.

Fay, R. R. (**1992**). "Analytic listening by the goldfish," Hear. Res. **59**, 101–107.

Fay, R. R. (**1997**). "Frequency selectivity of saccular afferents of the goldfish revealed by revcor analysis," in *Diversity in Auditory Mechanics*, edited by E. R. Lewis, G. R. Long, R. F. Lyon, P. M. Narins, C. R. Steele, and E. Hecht-Poinar (World Scientific, Singapore), pp. 69–75.

Fay, R. R. (**1998**). "Auditory stream segregation in goldfish (*Carassius auratus*)," Hear. Res. **120**, 69–76.

Fay, R. R. (**2000**). "Frequency contrasts underlying auditory stream segregation in goldfish," J. Assoc. Res. Otolaryngol. **1**, 120–128.

Fay, R. R. (**2005**). "Perception of pitch by goldfish," Hear. Res. **205**, 7–20.

Fay, R. R., and Ream, T. J. (**1986**). "Acoustic response and tuning in saccular nerve fibers of the goldfish (*Carassius auratus*)," J. Acoust. Soc. Am. **79**, 1883–1895.

Guttman, N. (**1963**). "Laws of behavior and facts of perception," in *Psychology: A Study of a Science*, edited by S. Koch (McGraw-Hill, New York), Vol. **5**, pp. 114–178.

Hartmann, W. M. (**1988**). "Pitch perception and the segregation and integration of auditory entities," in *Auditory Function: Neurological Bases of Hearing*, edited by G. M. Edelman, W. E. Gall, and W. M. Cowan (Wiley, New York), pp. 623–645.

Lu, Z., and Fay, R. R. (**1995**). "Acoustic response properties of single units in the central posterior nucleus of the thalamus of the goldfish (*Carassius auratus*)," J. Comp. Physiol. **176**, 747–760.

Lu, Z., and Fay, R. R. (**1996**). "Two-tone interaction in auditory nerve fibers

and midbrain neurons of the goldfish, *Carassius auratus*," Aud. Neurosci. **2**, 257–273.
Slabbekoorn, H., and Bouton, N. (**2008**). "Soundscape orientation: A new field in need of sound investigation," Anim. Behav. **76**, e5–e8.
van Bergeijk, W. A. (**1964**). "Directional and nondirectional hearing in fish," in *Marine Bio-acoustics*, edited by W. N. Tavolga (Pergamon, Oxford), pp. 281–299.
Yost, W. A., Hill, R., and Perez-Falcon, T. (**1978**). "Pitch and pitch discrimination of broadband signals with rippled power spectra," J. Acoust. Soc. Am. **63**, 1166–1173.

Temporary shift in masked hearing thresholds in a harbor porpoise (*Phocoena phocoena*) after exposure to seismic airgun stimuli

Klaus Lucke and Ursula Siebert
Forschungs- und Technologiezentrum Westküste, Christian-Albrechts-Universität zu Kiel, 25761 Büsum, Germany

Paul A. Lepper
Department of Electronic and Electrical Engineering, Advanced Signal Processing Group, Loughborough University, Loughborough LE11 3TU, United Kingdom

Marie-Anne Blanchet
Fjord & Baelt, Margrethes Plads 1, 5300 Kerteminde, Denmark

(Received 26 September 2008; revised 17 March 2009; accepted 17 March 2009)

An auditory study was conducted to derive data on temporary threshold shift (TTS) induced by single impulses. This information should serve as basis for the definition of noise exposure criteria for harbor porpoises. The measurements of TTS were conducted on a harbor porpoise by measuring the auditory evoked potentials in response to amplitude-modulated sounds. After obtaining baseline hearing data the animal was exposed to single airgun stimuli at increasing received levels. Immediately after each exposure the animal's hearing threshold was tested for significant changes. The received levels of the airgun impulses were increased until TTS was reached. At 4 kHz the predefined TTS criterion was exceeded at a received sound pressure level of 199.7 dB_{pk-pk} re 1 μPa and a sound exposure level (SEL) of 164.3 dB re 1 μPa^2 s. The animal consistently showed aversive behavioral reactions at received sound pressure levels above 174 dB_{pk-pk} re 1 μPa or a SEL of 145 dB re 1 μPa^2 s. Elevated levels of baseline hearing sensitivity indicate potentially masked acoustic thresholds. Therefore, the resulting TTS levels should be considered masked temporary threshold shift (MTTS) levels. The MTTS levels are lower than for any other cetacean species tested so far.
 [DOI: 10.1121/1.3117443]

PACS number(s): 43.80.Nd, 43.80.Lb [WWA] Pages: 4060–4070

I. INTRODUCTION

Anthropogenic sound resulting from shipping, industrial and military activities and many other sources has led to a substantial increase in the underwater background noise in the oceans over the past decades (Hildebrand, 2004). The North and Baltic Seas are among the most intensively used and consequently noisiest marine areas (OSPAR Commission, 2000). Seismic surveys are one of the most prominent contributors to the overall noise budget in these areas, as in almost all oceans. Consequently, these surveys moved into the focus of interest of scientists as well as policy makers due to the intensity of the emitted sounds and spatiotemporal scale of these activities. Seismic surveys are conducted covering vast areas while searching for hydrocarbon deposits—in the central North Sea the most recent campaign was conducted at the Doggerbank area in spring/summer 2007. The total source level of airgun arrays used as sound source during these surveys depends on size, number, and timing of the individual airguns. With source levels ranging from 225 to 255 dB re 1 μPa_{peak} (Richardson *et al.*, 1995), seismic surveys are routinely conducted continuously over several weeks, with repetition rates of several signals per minute.

The acoustic emissions produced during these programs may reach intensities with a potential of causing a variety of effects in the marine fauna at considerable distances—from behavioral reactions (McCauley *et al.*, 2000; Tougaard *et al.*, 2003) and potential stress to physiological effects (Finneran *et al.*, 2002), injury (McCauley *et al.*, 2003), and possibly death (Ketten *et al.*, 1993).

Most odontocete species are known to produce, and be sensitive to, sound (see review in Richardson *et al.*, 1995; Wartzok and Ketten, 1999). They are represented in the central and southern North Sea, the Baltic Sea, and especially in German waters by the harbor porpoise (*Phocoena phocoena*) as the only resident cetacean species. Harbor porpoises have a very acute sense of hearing underwater (Andersen, 1970; Kastelein *et al.*, 2002) and have been shown to use echolocation to find their prey (Busnel *et al.*, 1965) as well as for spatial orientation and navigation underwater (Verfuß *et al.*, 2005). Their acoustic sense has evolved to be their likely dominant sense vital to their survival. Any impairment or damage to their auditory system may have deleterious consequences for the affected individuals.

Auditory studies on terrestrial animals have shown that the exposure to intense impulsive sounds could exceed the tolerance of their auditory system and lead to an increased

hearing threshold (Ahroon *et al.*, 1996; Kryter, 1994; Yost, 2000). Such a noise-induced threshold shift (TS) can either be temporary (TTS) or permanent (PTS), depending on the hearing system's capacity for recovery once the sound has ceased. A similar cause-effect relationship has been found in odontocetes as TTS has been demonstrated in bottlenose dolphins (*Tursiops truncatus*) and belugas (*Delphinapterus leucas*) (Schlundt *et al.*, 2006; Finneran *et al.*, 2002; Nachtigall *et al.*, 2003, 2004) after exposure to intense intermittent or continuous noise. The TTS data obtained so far indicated that the energy flux density [i.e., the acoustic energy over time or sound exposure level (SEL)] of a signal can be used in combination with a maximum peak pressure to determine noise exposure criteria for marine mammals. As SEL is calculated by integrating the squared pressure over a standard unit of time, the duration of a signal plays an important role with regard to TTS. It is still unclear whether the dose-response function follows an "equal-energy rule" in marine mammals, but in the absence of specific data it can be used as a first-order approximation, as pointed out by Southall *et al.* (2007).

Based on these TTS data, a peak pressure of 224 dB_{peak} re 1 μPa and a SEL of 195 dB re 1 μPa^2 s were initially proposed as noise exposure criteria for mid-frequency cetaceans (e.g., bottlenose dolphins and belugas) for exposures to pulsed sounds (Ketten and Finneran, 2004). With the noise exposure criteria proposed by Southall *et al.* (2007), the focus of marine mammal policy has shifted toward PTS and the onset of behavioral disruption. They proposed appropriate interim noise exposure criteria for all toothed whale species based on the dose-response functions found in the two cetacean species tested for their TTS limit so far (see above). The relevant PTS level for single impulses is set for all toothed whale species to a peak pressure of 230 dB_{peak} re 1 μPa and a SEL of 198 dB re 1 μPa^2 s. A criterion for SEL has also been set for the first time for multiple exposures to impulsive sounds, which are likely to lead to a reduced tolerance of the auditory system (Ahroon *et al.*, 1996). This threshold (198 dB re 1 μPa^2 s) is identical to the SEL criteria for single impulses. The subjects from former TTS studies are categorized as mid-frequency cetaceans with the main energy of their echolocation clicks and their range of best hearing sensitivity <100 kHz. Harbor porpoises, in contrast, are categorized as high-frequency cetaceans (Ketten, 2000; Southall *et al.*, 2007), with a best hearing sensitivity at frequencies above 100 kHz (Andersen, 1970; Kastelein *et al.*, 2002) and an energy maximum of their echolocation signals in the range 110–140 kHz (Verboom and Kastelein, 1995). There are no TTS data available for this species, or for any other high-frequency cetacean species. These differences in their acoustic and auditory characteristics may also be reflected in differences in the overall tolerance of their auditory systems to intense noise. Accordingly, a transfer of the first-order approximated auditory dose-response function to the harbor porpoise could be questionable. The same applies to an application of the noise exposure criteria proposed by Southall *et al.* (2007) to assess effects of pile driving impulses on harbor porpoises (as generated, e.g., during the construction of wind turbines).

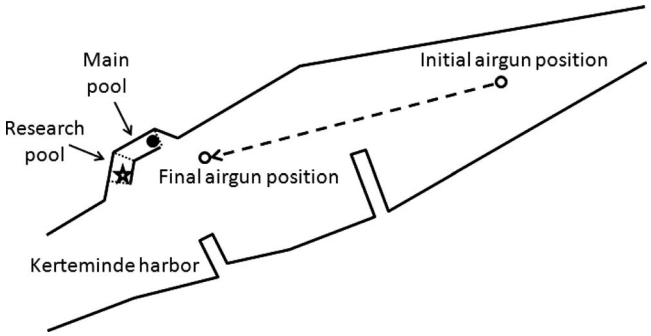

FIG. 1. Schematic overhead view of the experimental setup. Symbols indicate the approximate position of the harbor porpoise during the exposures to the airgun impulses in the main pool (filled circle), its position during the hearing tests (star), and the initial as well as the final location of the airgun (open circles) within the harbor of Kerteminde.

To base the assessment of acoustic effects of impulsive noise on species-specific data, a dedicated TTS study was conducted on one harbor porpoise. A key element for the planned study was access to a harbor porpoise trained to participate in experiments so that the experiments could be conducted under controlled conditions and definitive information on the dose-response function gathered. The aim of this acoustic study was to define the tolerance limit of the auditory system of the harbor porpoise to single impulsive sounds. Such data would enable regulatory agencies to define "zones of impact" (Richardson *et al.*, 1995) around the construction sites. At the same time, such data could be applied as a more robust baseline in the definition of noise exposure criteria for other high-frequency cetacean species [see outline by Southall *et al.* (2007)].

II. METHODS

A. Subject and facility

A male harbor porpoise held under human care in the Fjord & Bælt Centre (F&B) in Kerteminde, Denmark was chosen as subject for the studies. This animal, named *Eigil*, was estimated to be between 9 and 10 years old, with a length of 143 cm and an average weight of 40 kg in 2005 when the study began. A comprehensive medical record of all treatments exists for Eigil for almost his entire life. He was held in this facility with two female harbor porpoises at that time. The older female was pregnant twice during the study period from 2005 until 2007 and gave birth to a female calf right after the end of the studies in summer 2007. The design of the auditory experiments was altered due to the pregnancies and thus they are relevant for discussion of the results.

The animals were held together at the F&B in a semi-natural outdoor pool of 30×20 m^2 and an average depth of 4 m. Their enclosure stretches along the entrance from the Baltic Sea to a small fjord on one side of the busy fishing harbor of Kerteminde. It has a natural sea bottom and solid walls of concrete and steel on the two long sides. It is separated from the harbor on its narrow ends by nets, thereby providing a constant water exchange with the Baltic Sea (Fig. 1).

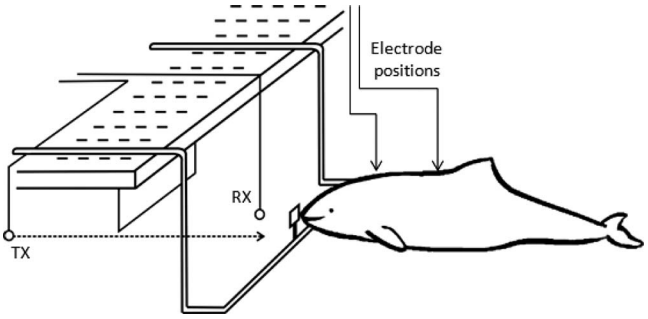

FIG. 2. Schematic plot of the research setup for the AEP measurements with the animal positioning itself at 1.5 m water depth in front of its underwater station and with its body in a straight line with the sound path of the incoming AEP stimuli. The direct sound path is indicated by a dashed line between sound source (TX) and monitoring hydrophone (RX) and the animal's position.

The enclosure is divided into two compartments ("main pool" and "research pool"), allowing separation of the animals for experiments. A floating pen ($4.5 \times 4.5 \times 1.5$ m^3) in the research pool was wrapped with sound absorbing foam, providing an acoustic shelter for the two females during the planned exposures to intense sound in the later stage of the study.

All experiments were conducted with Eigil, who was separated temporarily from the two females to avoid behavioral or acoustic interference between the animals during the research. Eigil was trained to accept the electrodes that were attached to his head and back with suction cups and to dive on command to an underwater station at 1.5 m water depth. The training method used was based on operant conditioning and positive reinforcement (Pryor, 1984; Ramirez, 1999). No food deprivation was used during these experiments. He stationed himself actively at the setup with his rostrum touching a 4×4 cm^2 polyvinylchloride (PVC) plate in front of the sound transducers (Fig. 2) for the hearing tests. He stayed there for 100 s on average until he was called back to the surface by the trainer to receive reinforcement. This experimental sequence was called a "send." A complete research session was comprised of four sends on average. The number of research sessions per day depended on weather conditions and varied between one and four during the study period with an average of two sessions, ideally one in the morning and one in the afternoon.

B. Study design

The study was divided into two modules: The first consisted of measurements of the animal's absolute hearing thresholds over almost its entire functional frequency spectrum, thus providing a baseline for the second module, a tolerance test of the animal's hearing. This TTS test was designed to follow the same procedural structure as the experiments conducted by Finneran *et al.* (2002). The animal's hearing thresholds were measured in half octave steps over ~5.5 octaves with the lower-frequency limit set by the methodological parameters of the auditory evoked potential (AEP) stimulation. The threshold measurements were repeated several times at three selected frequencies (representing the low, mid-, and high frequencies of its functional hearing range) to measure normal variation. This would subsequently allow definition of a frequency-specific TTS criterion.

C. Measurement of auditory sensitivity (AEP method)

The measurement of AEPs (AEP method) was chosen to measure the hearing thresholds in the harbor porpoise as it allows a comparatively rapid data acquisition and is noninvasive. For this reason the technique has been widely adopted in human patients and is also used for screening newborns (Hall, 2006). This technique is based on the presentation of acoustic stimuli, which will generate neuronal potentials in the acoustic system upon perception of these stimuli (Picton, 1987). Two surface electrodes are placed on the animal's skin using suction cups—one near the blowhole and the other near the dorsal fin—to record the neural responses evoked within the auditory system (Supin *et al.*, 2001). These potentials are generated within neuronal nuclei at different positions in the auditory system, thereby forming an electric field, which can be detected and recorded even on the skin surface. AEPs are useful for measuring the functioning of the auditory system and examining important aspects of auditory processing. To distinguish these comparatively small electric potentials from the overall neuronal activity—i.e., electric activity of the animal's musculature, other sensory inputs, etc.—the acoustic test stimuli are presented at a high repetition rate. By coherently averaging the evoked potentials (e.g., more than 500 AEPs), non-acoustic neuronal signals and incoherent acoustic signals not associated with the acoustic stimuli are reduced or eliminated.

A refined methodological approach is based on the use of rhythmic sound modulations. By sinusoidally modulating the amplitude of carrier tone or sound pulse sequence, it is possible to elicit a neuronal response, which includes a specific frequency component correlated with the modulation frequency used. This effect occurs because the auditory system is capable of following the envelope of a sinusoidal signal and producing corresponding neuronal potentials, called an envelope-following response (EFR). By applying a fast-Fourier transformation (FFT) analysis, the modulation frequency component can be identified and quantified. The resulting amplitude of the EFR represents the energy content of the neuronal response at the given modulation frequency. The strength of this EFR can simultaneously be taken as a relative measure for the perception of the carrier frequency of the amplitude-modulated (AM) signal. At each frequency, the stimuli were presented in decreasing intensity, starting at a clearly audible level, until a (neuronal) response was no longer detected. The resulting data were statistically tested for significance by using an F-test to identify EFRs from arbitrarily occurring noise at the given AM frequency (cf. Finneran *et al.*, 2007).

D. Sound generation and data acquisition

The animal's hearing was tested at frequencies between 4 and 160 kHz with sinusoidally amplitude-modulated (modulation rate: 1.2 kHz; duration: 25 ms) signals as AEP stimuli. The signals were of 25 ms duration with a modula-

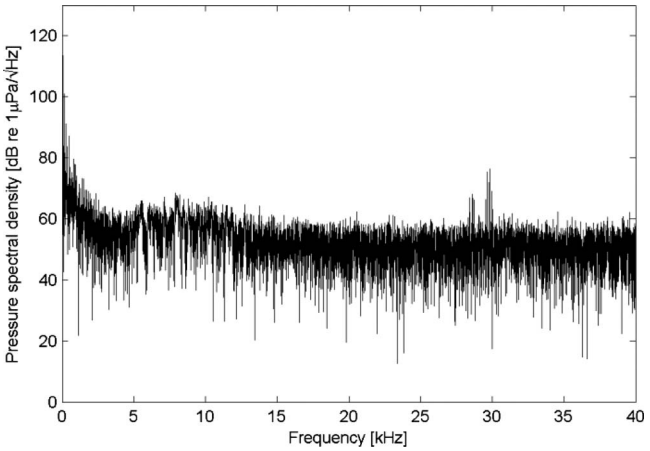

FIG. 3. Background noise level (plotted as pressure spectral density) recorded in the research pool at F&B during quiet conditions. (Analysis carried out on a 2.62 s sequence sampled at 400 kS/s using a Hanning window. The 0.38 Hz FFT bin size was then normalized to a 1 Hz power spectral density band.)

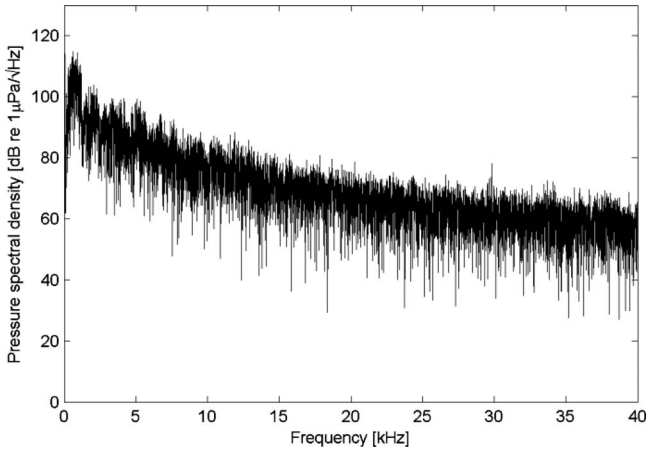

FIG. 4. Background noise level (plotted as pressure spectral density) recorded in the research pool at F&B recorded at the same position as in Fig. 2 during noisy conditions. (Analysis carried out on a 2.62 s sequence sampled at 400 kS/s using a Hanning window. The 0.38 Hz FFT bin size was then normalized to a 1 Hz power spectral density band.)

tion depth of factor 1. A custom-made software application was used to program all acoustic stimuli transmitted to elicit the AEPs during the hearing threshold tests. The signal generation system consisted of a data acquisition card (National Instruments DAQ 6062 E) and two function generators (Thurlby Thandar TG 230 and Agilent 33220A—with the first triggering the latter). At frequencies between 4 and 8 kHz all signals were amplified by a power amplifier PA 100E (Ling Dynamic Systems Ltd., Royston, UK) and transmitted via an underwater transducer USRD J-9. At higher frequencies a power amplifier Brüel&Kjaer 2713 was used to amplify the signals. Due to differences in their transmit response and the geometry of the pool, five different sound transducers had to be used to transmit the acoustic stimuli during the AEP tests: Signals at 4 and 8 kHz were transmitted via an underwater transducer USRD J-9, at 16 and 80 kHz via a Reson TC 4033, at 22.4 kHz via a SRD Ltd. 4 in. ball hydrophone, at 44.8 kHz via a SRD HS70, and all remaining frequencies were transmitted via a SRD HS150 hydrophone. All transmitted and received signals were constantly observed in real time at an oscilloscope and recorded for post-analysis via a monitoring hydrophone (Reson TC 4014) and a preamplifier (Etec B1501) for received level, signal quality, and undesired signal artifacts using software packages SEAPRODAQ (Pavan *et al.*, 2001) and custom software LU-DAQ. The evoked potentials were fed into a custom-built input station consisting of an amplifier (20 dB gain) and an optical separation unit (including 20 dB gain). Additionally, the signals were band-pass filtered (high-pass frequency: 300 Hz, low-pass frequency: 10 kHz, NF Electronic Instruments FV-665) to avoid artifacts. Each sequence of 500 successive potentials was averaged and displayed online as well as stored for post-hoc analysis.

The background noise in Kerteminde harbor is dominated by shipping noise from a variety of boat traffic ranging from recreational and small fishing boats passing the enclosure to fishing boats turning into the unloading area on the opposite side of the harbor and supply vessels for a nearby island (see comparison: Figs. 3 and 4). The background noise was thus dominated by low-frequency noise at varying levels and frequencies, depending on the size, speed, and activity of the respective boats.

E. Sound exposure procedure

A TS was defined as a difference of twice the standard deviation from the average hearing threshold at the particular frequency applied. The TTS criterion of 6 dB as proposed by Southall *et al.* (2007) was used as a second, frequency-independent criterion in this study. The tolerance of the animal's auditory system was then tested by first exposing the animal to a sound impulse as a fatiguing stimulus and then immediately re-measuring the hearing threshold. Any reduction in the animal's hearing sensitivity exceeding the preset TTS criteria would be regarded as evidence of an actual TS. Subsequent measurements of the animal's hearing threshold at the affected frequency would provide information about the recovery function of the auditory system.

The animal's hearing sensitivity was tested at three frequencies (4, 32, and 100 kHz) separately for TTS at a given exposure level of the fatiguing stimulus; i.e., only one hearing frequency was tested after each exposure. As long as the hearing threshold was shown to remain within its normal variation at all three frequencies, the subsequent exposure level of the fatiguing stimulus would be elevated and this procedure repeated until a TS is detected. This precautionary approach was chosen to avoid any risk of permanent hearing loss.

Various metrics have been used for both peak and energy amplitude, hearing threshold, spectral level, and spectral density, many discussed by Madsen (2005). A summary of calculation methodology is given below. Where possible, reported units are provided in formats used in other relevant studies to allow comparison with previous results.

For a specific pulse, the peak-to-peak pressure ($P_{\text{pk-pk}}$) was calculated. Since the peak may have a negative pressure, the peak-to-peak pressure is equivalent to the sum of the magnitudes of the peak positive and peak negative pressures.

Peak pressure is defined as the maximum magnitude of peak positive or peak negative pressure. The value is expressed as the peak-to-peak sound pressure level (SPL) in dB re 1 μPa. This is calculated from

$$\mathrm{SPL}_{\mathrm{pk\text{-}pk}} = 20 \log\left[\frac{P_{\mathrm{pk\text{-}pk}}}{P_0}\right]$$

where P_0 is the reference pressure of 1 μPa (peak-to-peak).

The SEL for a single pulse is the integral of the square of the pressure waveform over the duration of the pulse using a 90% energy criterion. The duration of the pulse is defined as the region of the waveform containing the central 90% of the energy of the pulse. Given by

$$E_{90} = \int_{t_5}^{t_{95}} p^2(t)dt$$

The value is then expressed in dB re 1 μPa^2 s and is calculated from

$$\mathrm{SEL} = 10 \log\left[\frac{E_{90}}{E_0}\right]$$

where E_0 is the reference value of 1 μPa^2 s, t_5 is the time of a 5% increase in energy for the total pulse energy, and t_{95} is the time of 95% of the total energy of the pulse. The pulse duration is therefore defined as the time taken from 5% to 95% of the total pulse energy.

The root mean square (rms) pressure was calculated by taking the square root of the average of the square of the pressure waveform over the duration of the pulse, again using a 90% energy criteria, with the pulse duration defined as above. This is given as

$$P_{\mathrm{rms}} = \sqrt{\frac{1}{T_{90}}\int_{t_5}^{t_{95}} P^2(t)dt}$$

F. Sound source for the fatiguing stimulus

A small sleeve airgun (20 in^3) was used as sound source to produce the fatiguing sound stimuli during the second module. This device was pressurized with nitrogen at a pressure of 137 bar (2000 psi) and was operated at a depth of 2 m (i.e., in mid-water) from a small inflatable boat (source boat) in Kerteminde harbor at varying positions between the F&B and the eastern exit of the harbor area. The exact position of the source boat was determined by GPS, and this information, along with time, weather conditions, and other relevant information on the sound source, was documented for further analysis. An intensive calibration of the airgun had been conducted prior to the study using calibrated hydrophones at the receiving position at the F&B to predict the received levels of the airgun stimuli as a function of its distance to the receiving position in the main pool at the F&B.

The sudden release of pressure from the airgun during a "shot" results in an oscillating air bubble, which projects a short (less than 50 ms), intense impulse (Fig. 5) into the water and across adjacent boundaries (ground wave; audibility of airgun shot in air). The main acoustic energy of this impulse is centered below 500 Hz but considerable energy can also be detected up to above 20 kHz, well above background noise in quieter periods (Fig. 6).

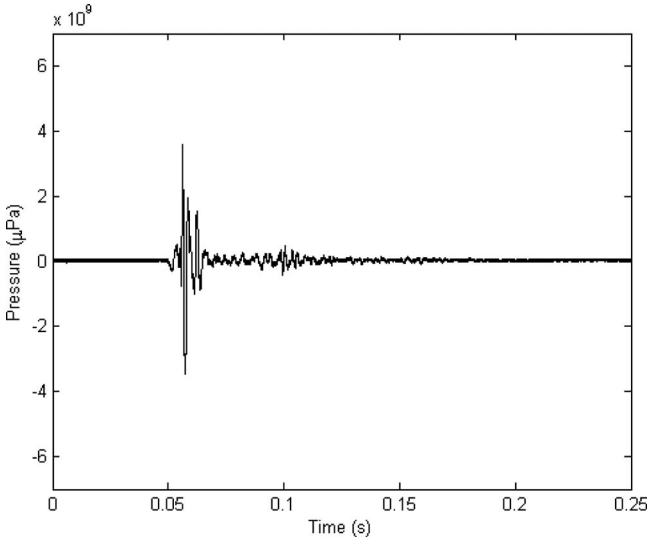

FIG. 5. Time domain representation of an airgun impulse. The airgun was fired at 2 m water depth in Kerteminde harbor and the impulse was recorded at a distance of 14 m to the receiving hydrophone.

Both high- and low-frequency components of the airgun emissions are likely to be attenuated over greater distance in a waveguide. The pulse recorded at the closest range from the airgun to the receiving position used in this study (shown in Fig. 6) therefore has the broadest observed spectrum and was felt to represent the worst case with regard to the potential auditory effects.

Prior to each airgun shot, the two female harbor porpoises were separated into the sound-insulated floating pen. Their general behavior and breathing rates were observed for the period of the sound exposure and compared with baseline data previously obtained under normal conditions. Eigil remained in the main pool. A receiving hydrophone was positioned at 1.5 m water depth at a position at the narrow end of

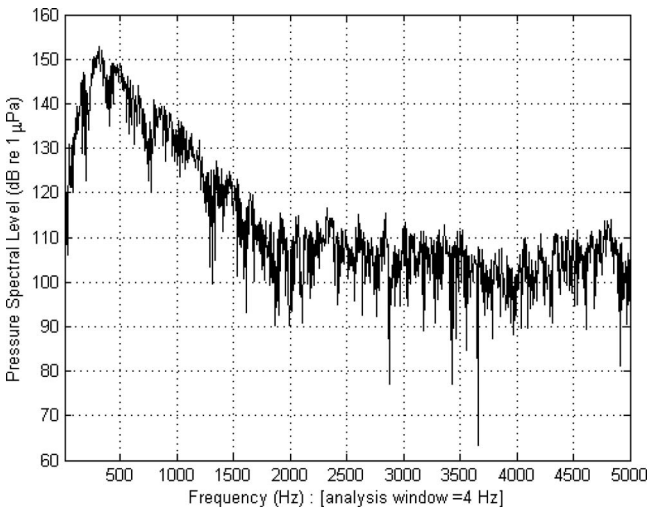

FIG. 6. Frequency spectrum analysis of the recorded airgun impulse (Fig. 4) showing the pressure spectral level (dB re 1 μPa). The frequency spectrum is plotted in hertz, and the spectrum levels are based on a 4 Hz analysis band.

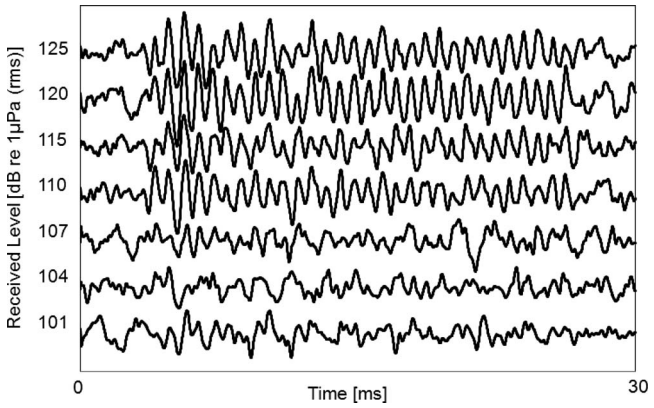

FIG. 7. Examples of EFRs in a harbor porpoise in response to acoustic stimulation with AM signals (averaged over 500 presentations); sampling duration was 30 ms, carrier frequency was 100 kHz, modulation rate was 1.2 kHz, and modulation depth was factor 1. Received levels descended from 125 dB re 1 μPa (rms) in 5-dB steps to 110 dB re 1 μPa (rms) and then in 3-dB steps to 101 dB re 1 μPa (rms).

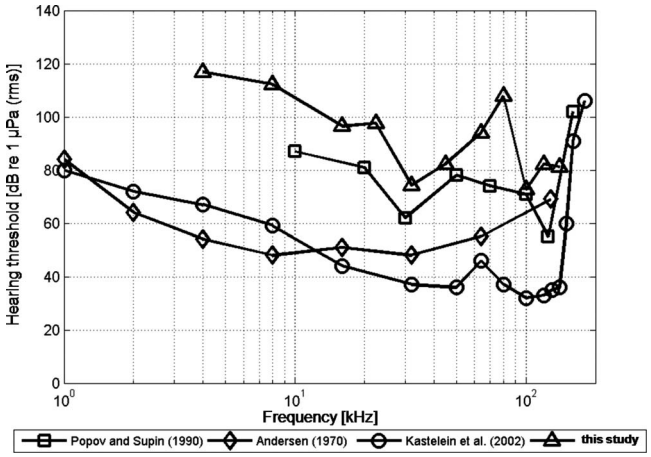

FIG. 8. Harbor porpoise hearing threshold data from different studies. The triangles represent the threshold values achieved in this study. Data from another AEP study (Popov and Supin, 1990) as well as from two behavioral auditory studies (Andersen, 1970; Kastelein *et al.*, 2002) are given for comparison.

the pool facing the eastern exit of Kerteminde harbor. This position had proven to receive the most intense signals during the airgun calibration. The airgun was triggered as soon as Eigil was within approximately 1 m of the receiving hydrophone with his body fully underwater. Control experiments were repeatedly made by conducting the complete procedure except for the exposure to the fatiguing stimulus. The animal's behavior was monitored and video recorded for further analysis. Immediately after each exposure to the fatiguing stimulus, the animal was then led into the research pool where the AEP setup was located. The post-exposure AEP measurements began less than 4 min after the exposure and typically were concluded within 12 min. Within this period his hearing sensitivity could be determined at a single frequency. During this second module, Eigil's hearing sensitivity was tested at 4, 32, and 100 kHz. These frequencies were chosen as representative frequencies for the low, mid-, and high ranges of the animal's functional hearing spectrum.

III. RESULTS

A. Hearing threshold

Eigil's baseline audiogram was determined based on the AEP measurements (Fig. 7) at frequencies between 4 and 140 kHz. At the highest frequency tested, 160 kHz, no AEP responses were detected. The measurements of Eigil's auditory sensitivity at the remaining frequencies resulted in elevated thresholds compared to hearing data published for other harbor porpoises (Fig. 8).

The shape of Eigil's hearing curve with its two minima at the mid- and high-frequency ranges is in good accordance with the previously published data. However, a clear rise in threshold was measured compared to data obtained by Kastelein *et al.* (2002) in a behavioral hearing study, with the maximum difference at 80 kHz. At the higher frequencies Eigil's threshold values are still elevated by 10–20 dB, but the difference is not as pronounced compared to the thresholds obtained by Andersen (1970). Compared to the results from the AEP study by Popov and Supin (1990), Eigil's thresholds are elevated by roughly 10 dB. The mean hearing thresholds at 4, 32, and 100 kHz, respectively, were at 116.9, 74.2, and 72.7 dB re 1 μPa (rms). Based on the variation of the hearing thresholds measured during the first module, the TTS criteria were defined as 122.9 dB re 1 μPa (rms) at 4 kHz, 79.0 dB re 1 μPa (rms) at 32 kHz, and 85.7 dB re 1 μPa (rms) at 100 kHz.

B. TTS tests

Over a period of 4.5 months, Eigil was exposed to a total of 24 airgun impulses. The received peak pressure of the pulses ranged from 161.2 dB_{pk-pk} re 1 μPa to 202.2 dB_{pk-pk} re 1 μPa, with an acoustic energy (SEL) ranging from 140.5 dB re 1 μPa^2 s to 167.2 dB re 1 μPa^2 s. These levels were achieved using source ranges between 150 and 14 m from the animal's position during the exposure.

1. Threshold shifts

A TTS was first measured after Eigil had been exposed to an airgun impulse at a peak pressure of 200.2 dB_{pk-pk} re 1 μPa with corresponding SEL of 164.5 dB re 1 μPa^2 s. The TS was measured when the animal hearing was tested after the exposure for its sensitivity at 4 kHz. Since this TS was only 1.8 dB above the predefined TTS criterion, the exposure was repeated several days later with a received peak pressure level of 202.1 dB_{pk-pk} and a SEL of 165.5 dB re 1 μPa^2 s. The resulting TS at 4 kHz was 9.1 dB above the TTS criterion and hence a clear support of TTS. Another verification of this effect was achieved 2 days later, after an exposure at a peak pressure level of 201.9 dB_{pk-pk} re 1 μPa with a SEL of 165.8 dB re 1 μPa^2 s, when Eigil's hearing revealed a TS at 4 kHz of 15 dB (Fig. 9). No significant elevation of hearing threshold at 32 kHz was observed at a comparable exposure level to the 4 kHz test case. The received energy was similar to the 4 kHz case, but a slightly lower received peak-to-peak pressure was observed (Fig. 10). No statistical change in hearing sensitivity was observed after an exposure to similar source levels

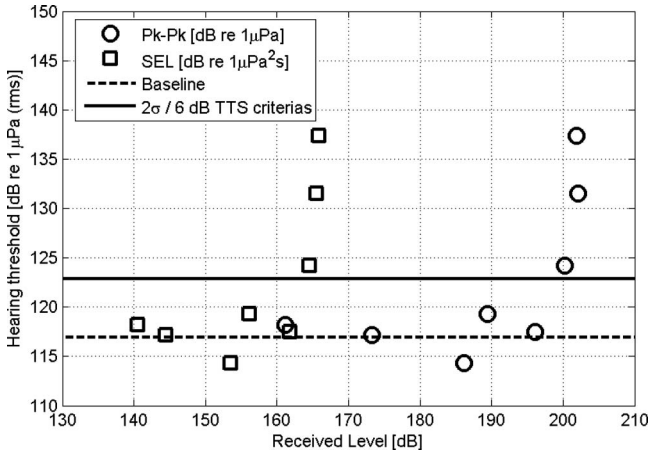

FIG. 9. Hearing threshold at 4 kHz for a harbor porpoise after exposure to airgun stimuli (i.e., post-exposure) at different received levels plotted in relation to the animal's pre-exposure hearing sensitivity. Each post-exposure hearing threshold is plotted twice—circles indicating the received peak-to-peak pressure of the fatiguing stimuli and squares the equivalent received SELs of the same exposure impulses. The dashed line represents the normal hearing threshold and the solid line the two TTS criteria used for comparison (which are identical at 4 kHz). Symbols above the solid line indicate a TS of hearing threshold.

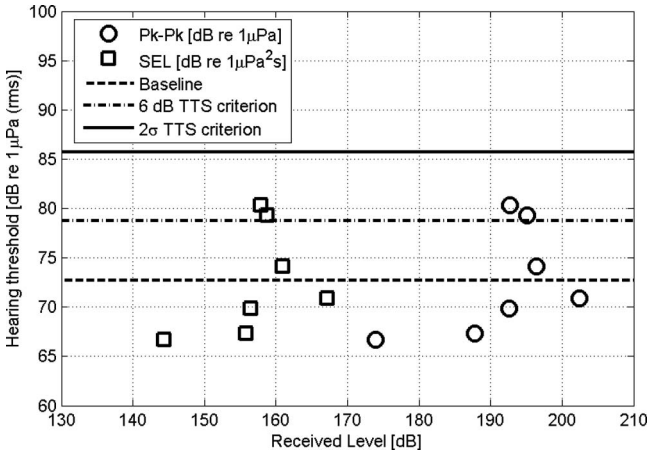

FIG. 11. Hearing threshold at 100 kHz for a harbor porpoise after exposure to airgun stimuli (i.e., post-exposure) at different received levels plotted in relation to the animal's pre-exposure hearing sensitivity. Each post-exposure hearing threshold is plotted twice—circles indicating the received peak-to-peak pressure of the fatiguing stimuli and squares the equivalent received SELs of the same exposure impulses. The dashed line represents the normal hearing threshold. The other lines (dotted-dashed line and solid line) indicate the two different TTS criteria used for comparison; symbols above both these lines indicate a temporary shift of hearing threshold.

for the 100 kHz test case—as regards both received peak pressure and energy (Fig. 11). It should be noted that the airgun source itself creates less energy at the mid- and high-frequency ranges than at 4 kHz.

2. Recovery

An important factor for the assessment of this noise-induced effect is the recovery of the animal's auditory system. After the first clear TS had been measured, a series of AEP measurements was conducted over the following days to follow the further development of Eigil's hearing sensitivity at the affected frequency. 178 min after the initial exposure his hearing had recovered only partially from its TS. It was reduced by 2.9 dB but still being elevated above the TTS criterion. Eigil's sensitivity at 4 kHz improved by 3.5 dB, 269 min post-exposure but only by another 1.4 dB, 29 h post-exposure (Fig. 12).

Assuming a linear recovery from TTS, the animal's hearing sensitivity would have reached the TTS criterion level again in 12 h for the 202.1 dB exposure. However, a log-fitted curve provides a better fit to the data (i.e., the highest regression coefficient) for calculating Eigil's auditory recovery function. By applying this function the animal's hearing sensitivity would have recovered back to the level of the TTS criterion in 55.0 h.

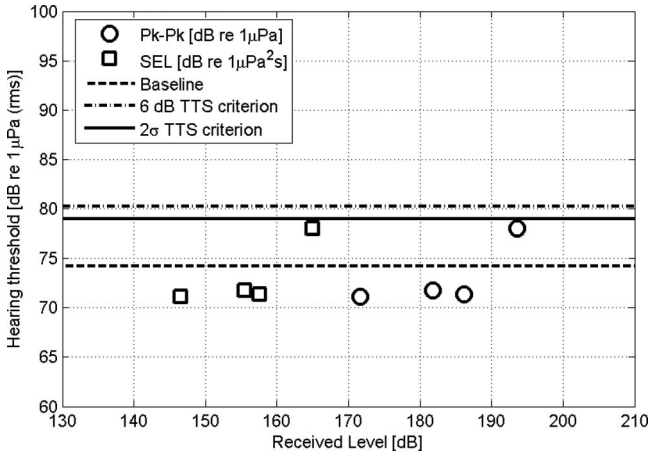

FIG. 10. Hearing threshold at 32 kHz for a harbor porpoise after exposure to airgun stimuli (i.e., post-exposure) at different received levels plotted in relation to the animal's pre-exposure hearing sensitivity. Each post-exposure hearing threshold is plotted twice—circles indicating the received peak-to-peak pressure of the fatiguing stimuli and squares the equivalent received SELs of the same exposure impulses. The dashed line represents the normal hearing threshold. The other lines indicate the two different TTS criteria used for comparison.

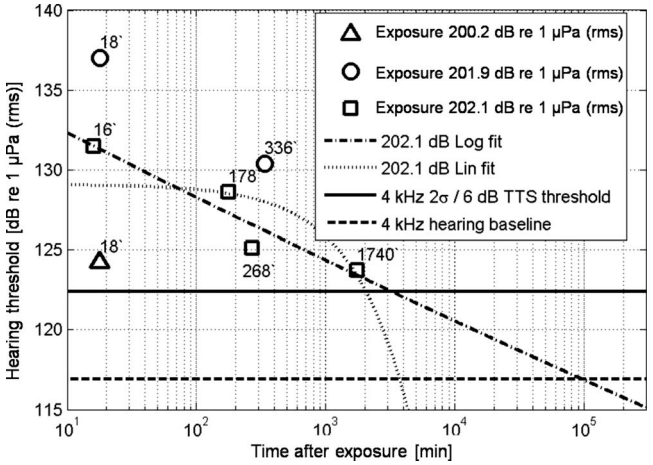

FIG. 12. Recovery function of a harbor porpoise's hearing threshold at 4 kHz after sound-induced TSs. Hearing thresholds measured subsequent to the exposures after different times (given in minutes next to the symbols) are indicated by different shapes for every exposure to the fatiguing stimulus. The recovery function for the exposure at 202,1 dB re 1 μPa (rms) is indicated by the diagonal and curved lines. The dashed line represents the normal hearing threshold and the solid line the two TTS criteria used for comparison (which are identical at 4 kHz).

3. Behavioral reactions

Eigil showed no behavioral reaction during the first exposures when he was exposed to a received pressure level of less than 174 dB_{pk-pk} re 1 μPa or a SEL of 145 dB re 1 μPa^2 s. At higher received levels, the animal showed repeatedly a typical aversive reaction at the time of the sound exposure and behavioral avoidance in the direction of the location of the source. Subsequently the animal avoided approaching the exposure station prior to further exposures as well as during control experiments. It should be noted that the exposure station was deliberately placed at a point of maximum received level within the total available enclosure. After a TTS had been documented and confirmed, the received levels were not raised any higher and no further trials were conducted.

Because one of the female harbor porpoises was pregnant during the exposure period, special measures were taken to protect her and the other animals from unnecessary sound exposures. Both females were kept in a sound-insulated pool and their behavior was continuously monitored during the sound exposures. None of them showed any obvious behavioral reactions during the airgun experiments. The attenuation of the airgun impulses inside their pool was at the order of 30–40 dB lower than at the exposure station. Correspondingly, the two females were never exposed to peak-to-peak pressure levels of more than 160 dB re 1 μPa.

IV. DISCUSSION

The TSs documented in this study represent the first data of its kind for harbor porpoises. Up to now all assessments of potential effects of anthropogenic sounds on harbor porpoises had to be made based on data from other odontocete species, or even terrestrial animals. Thus, the results of this study provide the first reliable information for the harbor porpoise for airgun (or impulse) exposures. These data, and more from future studies, could serve as a basis not only for defining noise exposure criteria for this species but also for deriving group-specific noise exposure criteria for all high-frequency cetaceans. The TS levels for the harbor porpoise differ strongly from data on the bottlenose dolphin or the beluga. This study provides more empirical data for high-frequency echolocating species than was available for Southall *et al.* (2007). Thus, the authors suggest that the proposed thresholds should be adapted accordingly.

The analysis of the animal's observed behavioral reactions to the fatiguing stimuli for the first time provides quantitative clues of a behavioral threshold in harbor porpoises. The fact that Eigil was swimming away from the location of the sound source after exposure to the airgun stimulus but not in control experiments infers avoidance or flight behavior. In a free-ranging animal this reaction might have lasted over a longer period of time than observed in Eigil, who calmed down and was back under behavioral control of the trainers after a few seconds when he was sent to subsequent hearing tests. It also remains questionable whether or not the level of 174 dB_{pk-pk} re 1 μPa pressure or a SEL of 145 dB re 1 μPa^2 s can be applied as threshold limit for behavioral reactions to impulsive sounds in harbor porpoises in general as Eigil was rewarded for tolerating the intense sound exposures and reactions might occur even at lower levels. It seems more likely that this limit varies individually and may be context-specific. So far, the only available data on behavioral reactions of harbor porpoises to impulsive sound have come from observations during the construction of wind turbines at Horns Rev, Denmark (Tougaard *et al.*, 2003) where at a distance of up to 15 km a movement directed away from the sound source was observed in the animals. In the BROMMAD study (Gordon *et al.*, 2000), by contrast, no obvious behavioral reactions were observed in free-ranging harbor porpoises in response to airgun exposures at an estimated received level of 176 dB_{0-pk} re 1 μPa. In this context, the results of the present study constitute the first behavioral threshold in harbor porpoises that was measured under controlled acoustic conditions. The resulting data may be used as a first indication of a threshold range for behavioral reactions of harbor porpoises. The disturbing nature of this sound to harbor porpoises at the given intensities is emphasized by the avoidance behavior observed in Eigil prior to exposures after the exposure level had passed his behavioral threshold for the first time. The fact that Eigil was actively avoiding the monitoring hydrophone showed that he was sensitized. It was a lasting effect as he showed no signs of habituation during the remaining exposures.

The rate of recovery from TTS slowed during recovery period, suggesting a log-correlation in the recovery function. These first data would suggest that recovery rates are different between harbor porpoises and the previously tested mid-frequency cetaceans. The latter usually recover within minutes or, at a maximum, within 2 h from a comparable amount of TS (Finneran *et al.*, 2002; Nachtigall *et al.*, 2003, 2004). Such a slow recovery of the harbor porpoise's hearing sensitivity would also indicate that the third exposure to the airgun stimulus at levels over 200 dB re 1 μPa (received level, RL of 201.9 dB re 1 μPa) may have been premature as the TS was not yet fully recovered. The documented shift of 15 dB above the TTS criterion therefore could then be considered as a cumulative effect from the two consecutive exposures. The level for onset of TTS should accordingly be calculated based on the first two TS values, i.e., a peak-to-peak pressure of 199.7 dB_{pk-pk} re 1 μPa and a SEL of 164.3 dB re 1 μPa^2 s. These levels depend of course on the TTS criterion chosen and would be altered accordingly. Nevertheless, due to the comparatively strong variability within the experimental conditions, a frequency-specific definition of the TTS criterion for this type of fatiguing stimuli seems most appropriate.

The AEP method is the only available method to conduct comparable studies on wild animals. Those studies are relevant to validate the results from a single captive animal in a larger number of animals at a later stage. The results of this study show, on the one hand, that the AEP method can be successfully applied for auditory studies on harbor porpoises even if the animals are unrestrained like Eigil, who was actively swimming and free to leave the experiments at any time. His constant movement during the experiments, on the other hand, caused strong myogenic potentials, which

were recorded along with the auditory potentials during the experiments. These myogenic potentials are strong enough to raise the overall neuronal noise level of the recorded potentials. Any masking of the lowest levels of the auditory potentials by other electrophysiological signals, such as the myogenic potentials, could obscure the real lower end of the regression line, hence leading to a zero-crossing of the regression at a higher threshold value. Consequently the resulting hearing threshold would be elevated.

Probably the most prominent factor that may have influenced the hearing thresholds is the level of background noise in Kerteminde harbor. It is most likely that this broadband noise masked perception of the AEP stimuli by Eigil. A similar effect has been found in auditory studies in humans (Parker *et al.*, 1976) and also in harbor porpoises (Lucke *et al.*, 2007). Acoustic events, such as boats passing at close distance to the research station, were avoided during the experiments by pausing the session. Nevertheless, it was impossible to conduct the experiments at a consistently low level of background noise. As these conditions varied within each research session, and with extreme noise events excluded, one may assume that roughly the same overall noise conditions applied for all sessions.

Despite these physical factors affecting the baseline hearing thresholds, the results may also reflect a genuine hearing deficit that Eigil either developed due to an unnoticed infection of his auditory system or as a result of previously unmonitored exposure to intense sound or a long-term exposure to sounds, e.g., from the nearby harbor. However, it can be ruled out that the elevated thresholds are the result of ototoxic drugs as Eigil is known to have never received such treatments. An age-related hearing deficit is also unlikely as it usually only occurs at high frequencies. The elevated baseline hearing thresholds stretch over both the high and low frequencies. Further aspects leading to error in estimation of Eigil's hearing threshold are the comparatively conservative statistical analysis of the resulting EFR data (F-test) and the use of AEP stimuli, which are likely to be shorter than the auditory integration time of the animal's hearing system.

As a consequence of this physiological and physical masking, the measured baseline hearing thresholds cannot be regarded as absolute but should be defined as masked thresholds, and, accordingly, the documented TSs have to be regarded as masked temporary threshold shifts. The presence of masking noise may have reduced the amount of TTS measured, as indicated by TTS studies on humans (Humes, 1980) and chinchillas (Ades *et al.*, 1974), simulating a pre-exposure reduction in hearing sensitivity. Nevertheless, the onset level of TTS itself, as defined in this study, is likely to be unaffected by the masking noise (Finneran *et al.*, 2005; Southall *et al.*, 2007), presumably due to its comparatively low acoustic energy in comparison to the intense airgun stimuli.

Whether the differences in TTS levels between harbor porpoises and the marine mammal species tested so far are species-specific or representative of the functional hearing groups, as defined by Southall *et al.* (2007), remains unclear. More harbor porpoises, as well as other high-frequency toothed whale species, need to be tested to elucidate this correlation. As for terrestrial animals (Henderson, 2008), the large difference in acoustic tolerance in toothed whales is likely to be attributable to the physical differences in the conductive apparatus rather than to systematic differences in the inner ear. Anatomical differences in the fine structure of the inner ear (Wartzok and Ketten, 1999; Ketten, 2000) and correlated differences in stiffness of the basilar membrane could account for a lower acoustic tolerance to intense sounds in harbor porpoises compared to the toothed whale species tested so far. Moreover, differences in metabolic processes in the inner ear could potentially mediate the high TTS growth rate as well as the long recovery time in harbor porpoises. In the absence of more detailed information it may be valid to generalize and describe this correlation best by means of a mass dependency in the dose-response function for acoustic effects in toothed whales, as documented by Ketten (2006) for the effects of blast impacts.

The TTS data defined in this study are applicable as baseline for the assessment of all activities that go along with the emission of short, impulsive sounds with regard to harbor porpoises. This includes seismic surveys as well as piling construction, both of which show strong acoustic commonalities despite the complexity of their sound emissions. Underwater explosions, however, should be treated separately in this context due to their specific acoustic characteristics of the shock wave, which may yield strong auditory effects irrespective of the peak pressure or energy of the impulse.

Seismic surveys, piling operations, and several other anthropogenic activities at sea involve the repeated emission of intense impulses at varying repetition rates (e.g., 10–15 s interval for seismic surveys and 2–30 s interval for piling). Marine mammals in the vicinity of these operations will consequently be exposed to multiple impulses. While the TTS values determined in this study apply only to a single exposure to a pulsed signal, the auditory effects will accumulate with repeated exposures to such signals if the interval between subsequent exposures is shorter than the recovery time of the hearing system. So far there is no information available on the underlying summation procedure for marine mammals. For harbor porpoises it seems unlikely that they will stay in the area of such intense sound emissions. Nevertheless, if these operations are started without sufficient time for animals to leave the area where received levels will be above or near the TTS levels (as determined in this study), there is an increased risk of TTS or even PTS. The comparatively high TTS growth factor, in combination with the slow recovery rate, worsens this scenario drastically for harbor porpoises compared to mid-frequency odontocetes.

The results emphasize the need for dedicated studies on the cumulative effects of multiple exposures.

ACKNOWLEDGMENTS

This project was supported by the German Federal Ministry for the Environment, Nature Conservation and Nuclear Safety as part of the research project MINOS$^+$ (Grant No. Fkz 0329946B). We would like to acknowledge CGG Veritas, France for providing the airgun and Alain Regnault for his patient support with this device. Wolfgang Voigt, FTZ

Westküste in Büsum, provided valuable support in this respect, too. The staff of the Fjord & Bælt was exceptionally helpful and patient over the whole study period, and special thanks go to Kirstin Anderson Hansen and Gwyneth Shepard who conducted the initial training. Kristian Beedholm and Lee Miller from the University of Southern Denmark, Odense generously provided ongoing logistic and intellectual support. We thank Gianni Pavan (CIBRA, University of Pavia, Italy) for his SEAPRODAQ software, T. Rawlings (Loughborough University, UK) for the LU-DAQ software, and Kristian Beedholm for the AEP software. The authors would also like to thank the source boat team, Jacob Rye Hansen, Cecilia Vanman, Mario Acquarone, Heiko Charwat, and all volunteers. Important parts of the equipment used in these experiments were provided by the Wehrtechnische Dienststelle der Bundeswehr für Schiffe und Marinewaffen (Grant No. WTD 71) in Eckernförde and the Plön measurement site, as well as by the GKSS Forschungszentrum in Geesthacht. Their support is greatly appreciated. The experiments were conducted under permit from the Danish Forest and Nature Agency, Denmark.

Ades, H. W., Trahiotis, C., Kokko-Cunningham, A., and Averbuch, A. (**1974**). "Comparison of hearing thresholds and morphological changes in the chinchilla after exposure to 4 kHz tones," Acta Oto-Laryngol. **78**, 192–206.

Ahroon, W. A., Hamernik, R. P., and Lei, S.-F. (**1996**). "The effect of reverberant blast waves on the auditory system," J. Acoust. Soc. Am. **100**, 2247–2257.

Andersen, S. (**1970**). "Auditory sensitivity of the harbour porpoise *Phocoena phocoena*," *Investigations in Cetacea* (G. Pilleri, Bern), Vol. **2**, pp. 255–259.

Busnel, R. G., Dziedzic, A., and Andersen, S. (**1965**). "Rôle de l'impédance d'une cible dans le seuil de sa détection par le système sonar du marsouin *P. phocaena* (Role of the target strength on the detection threshold by the sonar system of the harbour porpoise)," C.R. Séances Soc. Biol. **159**, 69–74.

Finneran, J. J., Carder, D. A., Schlundt, C. E., and Ridgway, S. H. (**2005**). "Temporary threshold shift (TTS) in bottlenose dolphins (*Tursiops truncatus*) exposed to mid-frequency tones," J. Acoust. Soc. Am. **118**, 2696–2705.

Finneran, J. J., Houser, D. S., and Schlundt, C. E. (**2007**). "Objective detection of bottlenose dolphin (*Tursiops truncatus*) steady-state auditory evoked potentials in response to AM/FM tones," Aquat. Mamm. **33**, 43–54.

Finneran, J. J., Schlundt, C. E., Dear, R., Carder, D. A., and Ridgway, S. H. (**2002**). "Temporary shift in masked hearing thresholds in odontocetes after exposure to single underwater impulses from a seismic watergun," J. Acoust. Soc. Am. **111**, 2929–2940.

Gordon, J., Freeman, S., Chappell, O., Pierpoint, C., Lewis, T., and MacDonald, D. (**2000**). "Investigations of the effects of seismic airguns on harbour porpoises: Experimental exposures to a small source in inshore waters," in *Behavioural and Physiological Responses of Marine Mammals to Acoustic Disturbance (BROMMAD)*, edited by D. Thompson (University of St. Andrews, St. Andrews, UK).

Hall, J. W., III (**2006**). *New Handbook for Auditory Evoked Responses* (Allyn and Bacon, Boston, MA).

Henderson, D. (**2008**). "Creation for noise standards for man: 50 years of research," Bioacoustics **17**, 10–12.

Hildebrand, J. (**2004**). "Sources of anthropogenic sound in the marine environment," International Policy Workshop on Sound and Marine Mammals, London, UK, 28–30 September.

Humes, L. E. (**1980**). "Temporary threshold shift for masked pure tones," Audiology **19**, 335–345.

Kastelein, R. A., Bunskoek, P., Hagedoorn, M., and Au, W. W. L. (**2002**). "Audiogram of a harbour porpoise (*Phocoena phocoena*) measured with narrow-band frequency-modulated signals," J. Acoust. Soc. Am. **112**, 334–344.

Ketten, D. R. (**2000**). "Cetacean Ears," in *Springer Handbook of Auditory Research*, edited by W. W. L. Au, A. N. Popper, and R. R. Fay (Springer, New York, NY), Vol. **12**, pp. 43–108.

Ketten, D. R. (**2006**). "Experimental measures of blast and acoustic trauma in marine mammals," Final Report, Office of Naval Research.

Ketten, D. R., and Finneran, J. J. (**2004**). "Noise exposure criteria: Injury (PTS) criteria," Presentation at the Second Plenary Meeting of the Advisory Committee on Acoustic Impacts on Marine Mammals, Arlington, VA.

Ketten, D. R., Lien, J., and Todd, S. (**1993**). "Blast injury in humpback whale ears: Evidence and implications," J. Acoust. Soc. Am. **94**, 1849–1850.

Kryter, K. D. (**1994**). *The Handbook of Hearing and the Effects of Noise* (Academic, New York).

Lucke, K., Lepper, P. A., Hoeve, B., Everaarts, E., van Elk, N., and Siebert, U. (**2007**). "Perception of low-frequency acoustic signals by a harbour porpoise (*Phocoena phocoena*) in the presence of simulated offshore wind turbine noise," Aquat. Mamm. **33**, 55–68.

Madsen, P. T. (**2005**). "Marine mammals and noise: Problems with root mean square sound pressure levels for transients," J. Acoust. Soc. Am. **117**, 3952–3957.

McCauley, R. D., Fewtrell, J., Duncan, A. J., Jenner, C., Jenner, M.-N., Penrose, J. D., Prince, R. I. T., Adhitya, A., Murdoch, J., and McCabe, C. (**2000**). "Marine seismic surveys: Analysis and propagation of air-gun signals and effects of air-gun exposure on humpback whales, sea turtles, fishes and squid," Report on research conducted for The Australian Petroleum Production and Exploration Association.

McCauley, R. D., Fewtrell, J., and Popper, A. N. (**2003**). "High intensity anthropogenic sound damages fish ears," J. Acoust. Soc. Am. **113**, 638–641.

Nachtigall, P. E., Pawloski, J. L., and Au, W. W. L. (**2003**). "Temporary threshold shifts and recovery following noise exposure in the Atlantic bottlenose dolphin (*Tursiops truncatus*)," J. Acoust. Soc. Am. **113**, 3425–3429.

Nachtigall, P. E., Supin, A. Ya., Pawloski, J. L., and Au, W. W. L. (**2004**). "Temporary threshold shifts after noise exposure in the bottlenose dolphin (*Tursiops truncatus*) measured using auditory evoked potentials," Marine Mammal Sci. **20**, 673–687.

OSPAR Commission (**2000**). "Quality Status Report 2000, Region II–Greater North Sea," OSPAR Commission, London.

Parker, D. E., Tubbs, R. L., Johnston, P. A., and Johnston, L. S. (**1976**). "Influence of auditory fatigue on masked pure-tone thresholds," J. Acoust. Soc. Am. **60**, 881–885.

Pavan, G., Manghi, M., and Fossati, C. (**2001**). "Software and hardware sound analysis tools for field work," *Proceedings of the 2nd Symposium on Underwater Bio-Sonar and Bioacoustic Systems*, Proc. I.O.A., Vol. **23**, pp. 175–183.

Picton, T. W. (**1987**). "Evoked potentials, auditory, human," in *Encyclopedia of Neuroscience*, Vol. **1**, edited by G. Adelmann (Birkhäuser, Boston).

Popov, V. V., and Supin, A. Ya. (**1990**). "Electrophysiological studies of hearing in some cetaceans and manatee," in *Sensory Abilities of Cetaceans: Laboratory and Field Evidence*, edited by J. A. Thomas and R. A. Kastelein (Plenum, New York), pp. 405–415.

Pryor, K. (**1984**). *Don't Shoot the Dog: The New Art of Teaching and Training* (Bantam Books, New York).

Ramirez, K. (**1999**). *Animal Training: Successful Animal Management Through Positive Reinforcement* (Shedd Aquarium, Chicago, IL).

Richardson, W. J., Greene, C. R., Jr., Malme, C. I., and Thomson, D. H. (**1995**). *Marine Mammals and Noise* (Academic, San Diego, CA).

Schlundt, C. E., Dear, R. L., Carder, D. A., and Finneran, J. J. (**2006**). "Growth and recovery of temporary threshold shifts in a dolphin exposed to midfrequency tones with durations up to 128 s," J. Acoust. Soc. Am. **120**, 3227.

Southall, B. L., Bowles, A. E., Ellison, W. T., Finneran, J. J., Gentry, R. L., Greene, C. R., Jr., Kastak, D., Ketten, D. R., Miller, J. H., Nachtigall, P. E., Richardson, W. J., Thomas, J. A., and Tyack, P. L. (**2007**). "Marine mammal noise exposure criteria: Initial scientific recommendations," Aquat. Mamm. **33**, 411–414.

Supin, A. Ya., Popov, V. V., and Mass, A. (**2001**). *The Sensory Physiology of Aquatic Mammals* (Kluwer, Boston, MA).

Tougaard, J., Carstensen, J., Henriksen, O. D., Skov, H., and Teilmann, J. (**2003**). "Short-term effects of the construction of wind turbines on harbour porpoises at Horns Reef," Technical Report No. HME/362-02662, TechWise A/S, Hedeselskabet, Roskilde.

Verboom, W. C., and Kastelein, R. A. (**1995**). "Acoustic signals by harbour

porpoises (*Phocoena phocoena*)," in *Harbour Porpoises—Laboratory Studies to Reduce Bycatch*, edited by P. E. Nachtigall, J. Lien, W. W. L. Au, and A. J. Read (De Spil, Woerden, The Netherlands), pp. 1–39.
Verfuß, U. K., Miller, L. A., and Schnitzler, H.-U. (**2005**). "Spatial orientation in echolocating harbour porpoises (*Phocoena phocoena*)," J. Exp. Biol. **208**, 3385–3394.
Wartzok, D., and Ketten, D. R. (**1999**). "Marine mammal sensory systems," in *Biology of Marine Mammals*, edited by J. E. Reynolds III and S. A. Rommel (Smithsonian Institution Press, Washington, London), pp. 117–175.
Yost, W. A. (**2000**). *Fundamentals of Hearing: An Introduction* (Academic, New York).

Characterization of the trabecular bone structure using frequency modulated ultrasound pulse

Wei Lin, Yi Xia, and Yi-Xian Qin
Department of Biomedical Engineering, Stony Brook University, Stony Brook, New York 11794-2580

(Received 19 August 2008; revised 23 January 2009; accepted 10 April 2009)

The objective of this study was to investigate the efficacy of modulated ultrasound signals in the measurement of bone properties as an early indicator of osteoporosis. Twenty-one trabecular bone cubes were harvested from sheep femoral condyles and the cube axes corresponded to the anatomic superior-inferior (SI), antero-posterior (AP), and medio-lateral (ML) orientations. Micro-CT measurements were made on those samples to obtain bone volume fraction (BV/TV), trabecular thickness (Tb.Th), and trabecular separation (Tb.Sp). Ultrasound tests were performed in the three orthogonal orientations using pulse and frequency modulated ultrasound. The comparison of the frequency modulated attenuation (FMA) with the broadband ultrasound attenuation (BUA) was made within the frequency band between 300 and 700 kHz. Results showed that FMA demonstrated higher correlations to the trabecular structure properties in the SI orientation (R^2=0.84 for BV/TV, R^2=0.77 for Tb.Th, R^2=0.7 for Tb.Sp) than BUA (R^2=0.30 for BV/TV, R^2=0.27 for Tb.Th, R^2=0.33 for Tb.Sp). In the AP orientation, FMA had higher correlation to Tr.Sp (R^2=0.64) than BUA (R^2=0.48), and relatively lower correlation to BV/TV (R^2=0.48) and Tb.Th (R^2=0.31) than BUA (R^2=0.64 for BV/TV and R^2=0.58 for Tb.Th). The results suggested that FMA could be a new ultrasound index for bone properties assessment.
 [DOI: 10.1121/1.3126993]

PACS number(s): 43.80.Qf, 43.80.Vj, 43.80.Sh [TDM] Pages: 4071–4077

I. INTRODUCTION

Osteoporosis is characterized as the loss of bone mass and weaken trabecular structures that consequently causes non-traumatic fractures in bones.[1] It is a major health threat to the elderly population. Currently, dual energy x-ray absorptiometry (DXA) is the most commonly used diagnostic tool for osteoporosis, which measures the bone mineral content or bone mineral density (BMD). However, the DXA derived BMD is based on the attenuation of X-ray through bone tissue. It is not the true volume density but a plane density in the unit of g/cm^2, and is the projection of the two-dimensional (3D) volume onto a two-dimensional (2D) plane. Since 1980s, ultrasound has become an alternative, non-radioactive physical modality in the assessment of bone properties because it has the potential to measure not only the bone quantity but also the bone quality.[2–7] Currently, commercialized quantitative ultrasound (QUS) devices have been used as a preliminary diagnostic tool for osteoporosis in clinic, for example, the Achilles Express from GE healthcare and UBIS 5000 Ultrasound Bone Sonometer from by Diagnostic Medical Systems in France.

The QUS measurements are based on two fundamental ultrasonic parameters, the ultrasound velocity (UV) and the broadband ultrasound attenuation (BUA). UV is determined by Young's modulus and density of the ultrasound medium. A simple equation exists to denote the relationship if the medium is a long uniform bar,

$$C = \sqrt{\frac{E}{\rho}}, \tag{1}$$

where C is the ultrasound wave velocity, and E and ρ are Young's modulus and density of the long bar, respectively. Although ultrasound propagation in bone is much more complicated than in a uniform bar, experimental data have shown that UV has high linear correlation to BMD and modulus.[8–12] Ultrasound attenuation is the energy loss during its propagation through the medium. It is mainly caused by the acoustic scattering from the porous trabecular structure and the heat dissipation due to the viscosity of the bone. The attenuation is frequency dependent on bone and, in particular, linearly proportional to the frequency from 300 to 700 kHz.[13] The slope of this linear segment of the attenuation is defined as BUA. nBUA is the BUA normalized to the width of the bone sample to minimize the width effect. BUA has been reported to be a good indicator of mechanical and structural properties of bone.[14–17]

Ultrasound attenuation is, in fact, the frequency response of bone to the transmission ultrasound. Since the past decade, the ultrasound backscatter has become the focus as an alternative tool to assess bone properties, especially the structural properties of trabecular bone such as porosity and trabecular thickness.[18–22] It is also the frequency response of reflected ultrasound from the bone sample normalized to the frequency spectrum of ultrasound reflected from the reference phantom surface.[19,23,24] The ultrasound backscatter measurement uses the pulse-echo mode and has the advantage over the transmission mode in the attenuation measurement because it enables ultrasound to access critical anatomic locations such as femoral neck and spine where transmission attenuation measurement is difficult to perform. Theoretic and experimental studies also showed that the ultrasound backscatter was promising in identifying the trabecular structure such as trabecular thickness and porosity.[25,26]

Both ultrasound attenuation and backscatter demonstrated that the ultrasonic frequency response from bone was the good indicator of the trabecular bone structure. In those studies, ultrasound pulse was generated by applying an electric pulse with high amplitude and short duration to the ultrasound transducer. This electric pulse has a broad uniform power spectrum much wider than the frequency response of the transducer. Thus the waveform and frequency spectrum of the ultrasound pulse were mainly determined by the transducer and may not be optimal to measure the frequency response of bone. This paper presents an alternative approach to improve the efficacy of the ultrasound measurement of bone properties with the emphasis on the modulated ultrasound signal as the primary measurement signal. The electric signal driving the ultrasound transducer can be predefined to obtain the desired ultrasound waveform and frequency spectrum within the frequency response of the transducer. Modulated ultrasound has been successfully used in medical ultrasound, mostly in medical imaging as a technique to enhance signal to noise ratio.[27–30] However, it is still a new signal modality in bone measurement. Literatures search showed that only a few studies used ultrasound signals other than broadband pulse in the bone measurement. Nowicki *et al.*[31] explored the feasibility of using modulated ultrasound excitation in the estimation of ultrasound attenuation in bone. They found that the modulated ultrasound signal had improved signal to noise ratio, deep penetration into bone tissue, and highly reduced peak pressure amplitudes of the transmitted ultrasound. The work reported in this paper employed frequency modulated ultrasound signal to interrogate the structure of trabecular bone from sheep femoral condyle. The structure parameters such as BV/TV, trabecular thickness, and trabecular space were measured using micro-CT measurement. The correlation analysis was performed to study relationship between the ultrasound attenuation from the modulated ultrasound signal and the structural parameters. The results were compared to the correlation of BUA to the trabecular structure to demonstrate the efficacy of the new ultrasound parameter.

II. MATERIALS AND METHOD

Twenty-one trabecular bone samples of 1 cm^3 were harvested from sheep femoral condyles using a low-speed diamond blade saw (Microslice, Metals Research Limited, Cambridge, England) with continuous water irrigation. Prior to cutting, the femoral shaft was placed at a 45° angle to the blade such that the axes of the cube corresponded to the physiologic superior-inferior (SI), antero-posterior (AP), and medio-lateral (ML) directions. Figure 1 is the illustration of the location of the bone sample in femoral condyle. The SI orientation was considered as major trabecular orientation because it was weight bearing. The choice of sample from sheep femoral condyle instead of human calcaneus was due to the tissue availability.

The trabecular structure parameters were measured using μCT[32] (SCANCO μ40, SCANCO, Bassersdorf, Switzerland). For each sample, a series of cross-sectional 2D gray-scale images were obtained and visualized at the resolution

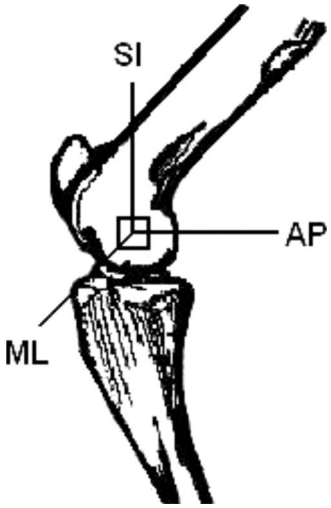

FIG. 1. The anatomic position of the cubic trabecular bone from sheep femoral condyle and the three orthogonal orientations of the cubed sample.

of 30 μm. The gray-scale images were then processed using a local thresholding method into binary images. Pixels with intensity equal or larger than the threshold were considered to be bone pixels of value 1, while those with intensities lower than the threshold were considered to be background with value 0. The threshold was determined as the binary image after thresholding best matched trabecular bone pattern from the original gray-scale image where the area for bone tissue was preserved. This process was performed on at least four samples and the average of the threshold values from those samples was set as the standard threshold for the entire sample set. An $8\times8\times8$ mm^3, region of interest was then selected for each image to calculate the trabecular structural parameter.

Structural indices were assessed from the 3D μCT images rendered from the 2D cross-sectional images. The volume of the trabeculae (BV) was calculated using tetrahedrons representing the enclosed volume of the triangulated surface used for the surface area calculation. BV was also normalized to the total volume of the sample (TV) to obtain the relative bone volume (BV/TV). Mean trabecular thickness (Tb.Th) was determined from the local thickness at each voxel representing bone. With this technique, thickness can be estimated without a model assumption. Trabecular separation (Tb.Sp) was calculated applying the same technique as used for the direct thickness calculation to the non-bone sections of the 3D image.

Ultrasound attenuation measurement was performed using insertion method.[6] As a comparison, both BUA and the frequency modulated attenuation (FMA) were measured on each sample. Two identical broadband unfocused ultrasound transducers of 12.7 mm in diameter with a center frequency at 1 MHz (Olympus NDT, MA) were mounted on opposite sides of a $10\times10\times15$ cm^3 water tank (Fig. 2). The separation of the transducers was approximately 10 cm. The bone sample was positioned in the ultrasound path using a sample holder. There are two signal sources for the ultrasound transmitter, a high voltage pulse from the pulser/receiver (PR 5800, Olympus NDT, MA) for BUA measurement and fre-

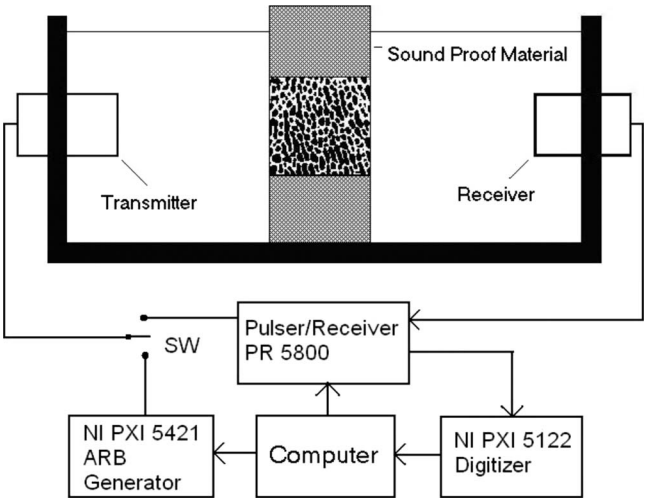

FIG. 2. The ultrasound device setup for bone structural properties measurement using broadband pulse and frequency modulated signals. The pulser/receiver generated broadband pulse and served as the ultrasound receiver for both pulse and frequency modulated signals. The arbitrary waveform generator (NI PXI 5421) generated the frequency modulated signals. The received ultrasound signals were digitized by high speed digitizer (NI PXI 5122). The entire setup was controlled by a desktop computer through LABVIEW.

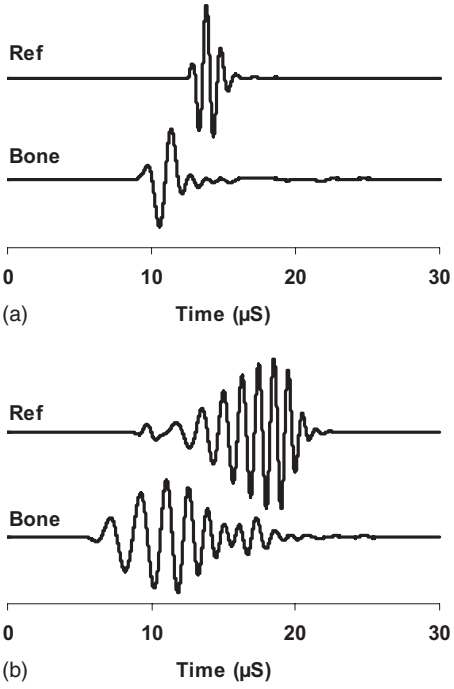

FIG. 3. These were the examples of ultrasound broadband pulses (a) and frequency modulated signals (b). The reference signals (Ref) were directly from the transmitter to the receiver and the bone signals (Bone) were the signals from the transducer, through the bone sample to the receiver.

quency modulated signal from arbitrary waveform generator (PX 5421, National Instruments, TX) for FMA measurement. The modulated ultrasound signal in this study was linear frequency sweep signal between 300 and 700 kHz to match the same frequency band where BUA was calculated. A switch was used to select the signal according to the type of attenuation measurements. The ultrasound signal from the receiver was amplified by the pulser/receiver and sent to the high speed digitizer (PXI 5122, National Instruments) to be digitized for further analysis. The entire device was automated by a personal computer (Dimension 8100, Dell, TX) using LABVIEW (National Instruments, TX) as the software platform for the control and measurement. Both the arbitrary waveform generator and the high speed digitizer were connected to the computer through PXI bus, an industrial version of the PCI bus in personal computers. The computer also adjusted the pulse energy and the amplifier gain of the pulser/receiver (Olympus 5800PR, MA) via GPIB bus. In BUA measurement, the ultrasound transmitter was driven by the pulser/receiver at the energy level of 50 μJ. Based on the equipment specification, the peak to peak amplitude of the driving signal was 265 V at this energy level. In FMA measurement, the modulated signal waveform was first created by the computer and downloaded to the arbitrary waveform generator to drive the ultrasound transmitter. The amplitude of the modulated signal to drive the ultrasound transducer was 10 V peak to peak and the duration of the signal was 10 μs. The sampling frequency of the high speed digitizer was set at 100 MHz and 5000 data point or 50 μs of signal was recorded for each signal.

The insertion method requires measuring two ultrasound signals. One is the reference signal where the bone sample is not in the ultrasound path. The other signal is the bone signal where the bone sample is inserted in the ultrasound path. Figure 3 shows the reference signals and bone signals in pulse [Fig. 3(a)] and frequency modulation [Fig. 3(b)]. The ultrasound energy is proportional to the square of the acoustic pressure and consequently the voltage of the electric signal from the ultrasound receiver. Therefore, we used the square of voltage to represent the ultrasound energy and the coefficient that converts the voltage back to acoustic pressure was canceled out during the attenuation calculation because it was the ratio of reference signal energy to the bone signal energy. During the measurement of FMA, the frequency modulated signal envelope was first extracted using Hilbert transformation. The signal energy was then calculated from the envelope using the following equation:

$$E = \int f^2(t)dt, \tag{2}$$

where E was the acoustic energy and $f(t)$ was the signal envelope. The integration represented the time average of the acoustic energy and was independent to the transfer function of the transducers. The FMA was then calculated as shown in

$$\text{FMA} = 10 \log\left(\frac{E_r}{E_b}\right), \tag{3}$$

where E_r is the ultrasound energy of the reference signal and E_b is the ultrasound energy of the bone signal.

The BUA measurement was performed using the ultrasound pulse. Fast Fourier transform was applied to both reference and bone signals to calculate the frequency spectra. The attenuation function as frequency was obtained by dividing the frequency spectrum of the reference signal to the frequency spectrum of the bone signal between 300 and 700 kHz. The linearity was further verified by checking the attenuation vs frequency curve. The slope of the attenuation

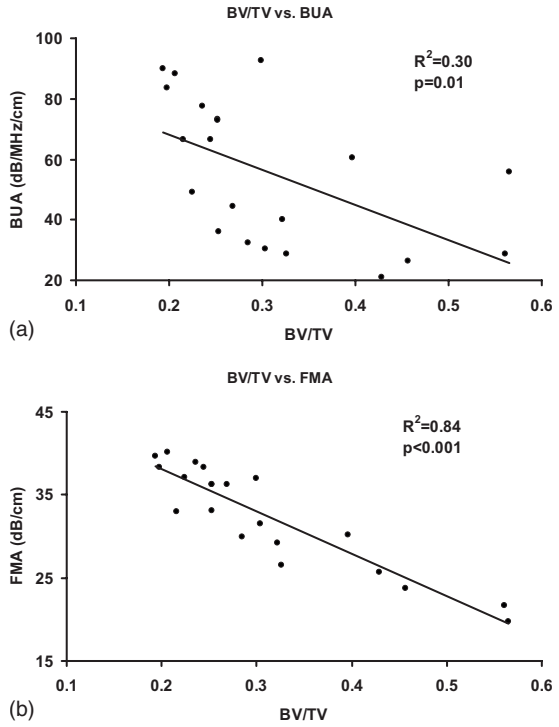

FIG. 4. Correlation between BV/TV to BUA (a) and FMA measured in SI orientation. The correlation was higher between BV/TV and FMA (R^2 =0.84) than between BV/TV and BUA (R^2=0.3).

function was calculated as the BUA. To minimize the effect of sample thickness, both FMA and BUA were normalized to the sample thickness in the orientation of ultrasound measurement. Due to the anisotropy of the ultrasound response to the trabecular bone, ultrasound measurement was done in all three orthogonal orientations, i.e., SI, ML, and AP shown in Fig. 1.

III. RESULTS

Correlation analysis was performed between ultrasound parameters and the structure properties of the trabecular samples. FMA and BUA were the ultrasound parameters and BV/TV, trabecular thickness (Tb.Th), and trabecular separation (Tb.Sp) were the trabecular structure properties. Results showed that both FMA and BUA were sensitive to the anisotropy of the trabecular structure and thus, their values were dependent on the orientation of the ultrasound measurement. For each bone structural parameter, Pearson correlation was done with respect to FMA and BUA in the predetermined SL, AP, and ML orientations using SPSS software (Chicago, IL). Figure 4 illustrates the linear correlation of BUA in SI orientation to BV/TV [Fig. 4(a)] and FMA in SI orientation to BV/TV [Fig. 4(b)], respectively. It showed that BUA and FMA behaved differently in the prediction of BV/TV through linear regression. Table I is the summary of the R^2 value and the corresponding p values from all the correlations of BUA in three orthogonal orientations and their average value to BV/TV, trabecular thickness (Tb.Th), and trabecular separation (Tb.Sp). Table II is the summary of the R^2 value and the corresponding p values from all correlations of FMA in three orthogonal directions and their average value to BV/TV, trabecular thickness, and trabecular separation.

TABLE I. The R^2 value of the correlation of BUA in three orientations and their average to BV/TV, Th, and Tb.Sp. The p-values were also listed.

US direction	BV/TV	Tb.Th	Tb.Sp
SI	0.30	0.27	0.33
	p=0.010	p=0.015	p=0.006
AP	0.64	0.58	0.48
	$p<0.001$	p=0.001	p=0.001
ML	0.01	0.04	0.00
	p=0.759	p=0.369	p=0.783
AVG	0.58	0.47	0.58
	$p<0.001$	p=0.001	$p<0.001$

BUA and FMA have demonstrated modest to excellent correlations to the structure properties if they were measured in either SI or AP direction. In SI orientation, FMA had higher correlations to BV/TV, trabecular thickness, and trabecular space than BUA with the R^2 values more than doubled. In AP orientation, BUA had higher correlation (R^2=0.64) to BV/TV than FMA (R^2=0.48) and higher correlation (R^2 =0.58) to trabecular thickness than FMA (R^2=0.31). However, the differences of those R^2 values were much smaller than those in the SI orientation. Also in the AP orientation, FMA was superior in the correlation to the trabecular space to BUA with R^2 value of 0.64 vs 0.33. In the ML orientation, Both FMA and BUA failed to correlate to the structure properties of the trabecular bone. The average BUA and FMA values from the three directions were also calculated and correlation analysis was performed. The average process may reduce the sensitivity of the FMA and BUA to the structural anisotropy of the trabecular bone. The results showed that the average FMA has higher correlation to BV/TV and trabecular space than the averaged BUA and similar correlations to the trabecular thickness as the average BUA.

Further analysis was done to identify if the correlations of FMA to the bone structural properties was significantly different from those of BUA to the same bone properties. In the previous analysis, it has been demonstrated that both FMA and BUA were linearly correlated to the bone structural properties and those ultrasound parameters are dependent on BV/TV, trabecular thickness, and trabecular space. Analysis of covariance (ANCOVA) was the statistical tool to examine the statistical difference between FMA and BUA when their dependence on the bone properties was considered. For each ANCOVA test, only one bone property was considered as the covariate to the FMA and BUA. Table III shows the p-value

TABLE II. The R^2 value of the correlation of FMA in three orientations and their average to BV/TV, Tb.Th, and Tb.Sp. The p-values were also listed.

US direction	BV/TV	Tb.Th	Tb.Sp
SI	0.84	0.77	0.70
	$p<0.001$	$p<0.001$	$p<0.001$
AP	0.48	0.31	0.64
	p=0.001	p=0.009	$p<0.001$
ML	0.00	0.02	0.06
	p=0.844	p=0.573	p=0.293
AVG	0.63	0.44	0.74
	$p<0.001$	p=0.001	$p<0.001$

TABLE III. The p-values of the ANCOVA analysis of the correlation of FMA and BUA to one of bone structure properties, BV/TV, Tb.Th, and Tb.Sp. The three parameters were chosen as the covariates, respectively.

	AP	ML	SI	AVG
BV/TV	<0.001	<0.001	<0.001	<0.001
Tb.Th	<0.001	<0.001	<0.001	<0.001
Tb.Sp	0.001	<0.001	<0.001	<0.001

of the ANCOVA test. The p values were all less than 0.001, which indicated that the linear correlations of FMA to BV/TV, trabecular thickness, and trabecular space are significantly different from those of BUA to the respective bone properties.

IV. DISCUSSION

FMA and BUA are the indices derived from ultrasound attenuation. It was expected that both indices had the similar performance in the assessment of bone properties. The results clearly demonstrated that FMA was a potential ultrasound index for the assessment of bone quantity and trabecular structure. Both FMA and BUA measured in SI and AP orientations were the good indicators of the bone properties if linear regression was employed. The correlations of FMA to the trabecular structural properties such as BV/TV, trabecular thickness, and trabecular space were similar or even better than those of BUA. They also showed little correlation to the same bone properties if measured in ML orientation.

Even though FMA and BUA were derived from the ultrasound attenuation, they have fundamental difference in how the attenuation data were analyzed. BUA is defined as the slope of the linear section of the attenuation vs frequency curve and often normalized to the sample width to minimize its effect on attenuation. Human calcaneus has been reported to have a good linear dependence of ultrasound attenuation on frequency.[33] Chaffai *et al.*[34] further showed that a nonlinear power fit $\alpha(f)=\alpha_0+\alpha_1 f'$ would be a good representation of the relationship. The mean value of n was close to 1 (1.09) but had a substantial variation (0.4-2.2). Thus, BUA was dependent on the frequency range if n was away from 1 and the attenuation lost the linear frequency dependency. When the linear dependency disappeared, the value BUA was meaningless. Figure 5 shows a typical relationship between the ultrasound attenuation and the frequency of the tested samples. Linear correlation was observed to be between 250 and 700 kHz. However, the slope between 250 and 650 kHz (82.6 dB/MHz) was 12% different from the slope between 300 and 700 kHz (94.2 dB/MHz). BUA was equivalent to the derivative of ultrasound attenuation to frequency and thus was very sensitive to the variations of the attenuation. Therefore, the slight deviation from linearity of the ultrasound attenuation can easily be amplified in BUA. On the contrary, FMA took a different approach to analyze the ultrasound attenuation. It was derived from the time average of the ultrasound energy. It was the integration process that was suppressive to the variations such as noise from the measurement. Therefore, FMA should be more stable than BUA.

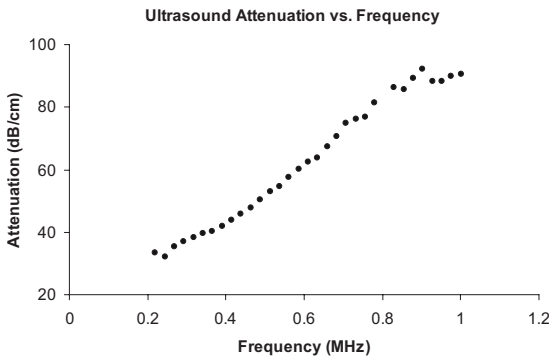

FIG. 5. The dependence of ultrasound attenuation on frequency of the bone samples. Linearity was observed between 250 and 700 kHz.

When ultrasound waves travel through bone, the bone can be considered as a filter to the ultrasound signal. Ultrasound attenuation is the direct measurement of such frequency response determined by the trabecular architecture. It is still promising that the frequency response to ultrasound can be used to derive the bone properties even though the true mechanism of how such response is determined by the trabecular architecture is still not clear. BUA is the slope of the linear relationship of ultrasound attenuation to frequency within a certain frequency band. It is one of the prominent features of the ultrasound response but not a conclusive index that can represent all types of bone responses to ultrasound. It is not sufficient to use BUA as the only ultrasound attenuation index to characterize bone properties. FMA employs frequency modulated ultrasound signal to measure the ultrasound attenuation within an interested frequency band. In this study, the ultrasound signals, also called frequency sweep signals, were linearly modulated between 300 and 700 kHz within the period of 10 μs. The choice of this particular frequency band was for the comparison between BUA and FMA in their capacity of bone properties assessment. Frequency sweep signal has been widely used in the measurement of the frequency response of electronic systems. It is a sinusoid function by nature with its frequency increasing linearly with time. It was equivalent to multiple sinusoidal signals in time sequence within one signal. The envelope of the frequency sweep signal represents the amplitudes of those sinusoidal signals and can be considered as the frequency spectrum of the frequency sweep signal, i.e., at a specific time instant, the envelope is the amplitude of the sinusoidal signal at that instant frequency. By changing the lower and upper bounds of the swept frequency, the frequency sweep signal can examine the details of the ultrasonic attenuation at any specified frequency band. Thus, FMA is considered as the ultrasound attenuation within a specified frequency band. When the lower and upper bounds approach to one frequency, FMA will be the ultrasound attenuation at that frequency. Compared to BUA, FMA is more flexible and can reveal the attenuation details that are most sensitive to bone properties.

One of the prominent features of the trabecular structure is quasi-periodic. When ultrasound wave interacts with this type of structure, the scattered ultrasound wave also becomes quasi-periodic and its quasi-frequency is related to the mean scatterer spacing (MSS). Pereira *et al.*[26] employed the singu-

lar spectrum analysis to estimate the MSS from backscattered ultrasound signals from human trabecular bone. They compared MSS with the trabecular separation of the same bone sample and found good agreement between the two parameters. The frequency related to MSS was around 600 kHz. FMA can be a good candidate for searching such frequency. Although FMA was derived from the transmitted ultrasound, the same principle can be readily used in the analysis of backscattered ultrasound signals. Therefore, FMA is promising in bone properties assessment when it is tuned to a specific frequency band that is the most sensitive to the bone properties of interest. This unique advantage over BUA can make FMA a more favorable ultrasound parameter for the assessment of bone properties.

Another advantage of FMA over BUA is energy efficiency. The broadband ultrasound pulse in BUA measurement has a wide frequency range only limited by the frequency response of the transducer. However, if the interested band was narrower than its frequency response, it is surely not energy efficient because some of the energy outside the interested frequency band is wasted. In addition, the excitation voltage to the transducer has to be very high, usually hundreds of volts, in order to deliver enough energy to penetrate bone samples in a very short period of the pulse. Further, the maximum ultrasound energy allowed for clinic diagnosis is low and it is important to focus the limited energy within the targeted frequency band. The frequency modulated ultrasound has a unique property that its energy is always contained within the predetermined frequency band. Its longer duration (10 μs) than the broadband pulse (<1 μs) allows the same amount of ultrasound energy to be delivered at low power and reduces the driving voltage to the transducer. It was showed that 10 V peak was sufficient in this study for bone measurement. FMA uses the energy efficient frequency modulated ultrasound for the bone property measurement.

The poor correlation of FMA and BUA in the ML orientation to the trabecular bone properties was contradictory to the findings in two other orientations. Ultrasound attenuation in this orientation was also linearly dependent on frequency. This confirmed that the BUA values were valid. Since both FMA and BUA measurements had the same conclusion, it was unlikely that this phenomenon was due to the experimental error. Current data did not support the assumption that the lack of correlation was solely due to the anisotropic structure of the samples. Although the real mechanism of this phenomenon is not known, it can be suggested that the trabecular architecture of the tested samples viewed from the ML orientation interacted with the incoming ultrasound wave in a complete different way that invalidated the assumption of linear correlation of ultrasound attenuation to bone structural properties.

Future work is required to improve the performance of the FMA. First, it is crucial to identify the optimal frequency bands that are most sensitive to the bone properties of interest. Narrow frequency bands will be more efficient because it can minimize the average effect of FMA over the frequency band. This requires a screening of a series of narrow frequency bands that cover a broader frequency spectrum. It is expected that those optimal frequency bands are specific to the anatomic locations of the bone. Second, the adjustment of the ultrasound signal is preferred before driving the transducer to compensate the frequency response of the transducer for the best performance of the FMA. In this study, the electric signal that drove the transducer had uniform amplitude. However, the amplitude of the generated ultrasound also had an amplitude modulation due to the frequency response of the transducer. This effect was minimized by the normalization of the energy of reference signal to bone signal because both signals included the same frequency response of the transducers. However, it is optimal to generate frequency sweep ultrasound signal with uniform amplitude. This requires the addition of amplitude modulation prior to driving the transducer to compensate its frequency response. Lastly, FMA is one of many parameters that can be derived from the new signal modality. Other parameters such as the frequency at the peak of the waveform envelope are also potential candidates for bone property measurements. The frequency modulated signal can also be modified for the measurement of ultrasound backscatters from bone to improve its performance.

ACKNOWLEDGMENTS

This work is kindly supported by the National Osteoporosis Foundation, the National Space Biomedical Research Institute (Grant Nos. TD00207 and TD00405, Y.-X.Q.) through NASA Cooperative Agreement No. NCC 9-58 and New York Advanced Center for Biotechnology.

[1] R. Marcus, D. Feldman, and J. Kelsey, *Osteoporosis* (Academic, San Diego, 2001), p. 32.
[2] J. Behari and S. Singh, "Ultrasound propagation in 'in vivo' bone," Ultrasonics **19**, 87–90 (1981).
[3] K. Firoozbakhsh and S. C. Cowin, "An analytical model of Pauwels' functional adaptation mechanism in bone," J. Biomech. Eng. **103**, 246–252 (1981).
[4] W. Bonfield and A. E. Tully, "Ultrasonic analysis of the Young's modulus of cortical bone," J. Biomed. Eng. **4**, 23–27 (1982).
[5] R. B. Ashman, S. C. Cowin, W. C. Van Buskirk, and J. C. Rice, "A continuous wave technique for the measurement of the elastic properties of cortical bone," J. Biomech. **17**, 349–361 (1984).
[6] C. M. Langton, S. B. Palmer, and R. W. Porter, "The measurement of broadband ultrasonic attenuation in cancellous bone," Eng. Med. **13**, 89–91 (1984).
[7] R. B. Ashman, J. D. Corin, and C. H. Turner, "Elastic properties of cancellous bone: Measurement by an ultrasonic technique," J. Biomech. **20**, 979–986 (1987).
[8] J. A. Evans and M. B. Tavakoli, "Ultrasonic attenuation and velocity in bone," Phys. Med. Biol. **35**, 1387–1396 (1990).
[9] C. H. Turner and M. Eich, "Ultrasonic velocity as a predictor of strength in bovine cancellous bone 85," Calcif. Tissue Int. **49**, 116–119 (1991).
[10] S. Han, J. Rho, J. Medige, and I. Ziv, "Ultrasound velocity and broadband attenuation over a wide range of bone mineral density," Osteoporosis Int. **6**, 291–296 (1996).
[11] R. Hodgskinson, C. F. Njeh, J. D. Currey, and C. M. Langton, "The ability of ultrasound velocity to predict the stiffness of cancellous bone in vitro," Bone (Osaka) **21**, 183–190. 1997.
[12] W. Lin, E. Mittra, and Y. X. Qin, "Determination of ultrasound phase velocity in trabecular bone using time dependent phase tracking technique," ASME J. Biomech. Eng. **128**, 24–29 (2006).
[13] K. A. Wear, "The effect of phase cancellation on estimates of calcaneal broadband ultrasound attenuation in vivo," IEEE Trans. Ultrason. Ferroelectr. Freq. Control **54**, 1352–1359 (2007).
[14] D. C. Bauer, C. C. Gluer, J. A. Cauley, T. M. Vogt, K. E. Ensrud, H. K. Genant, and D. M. Black, "Broadband ultrasound attenuation predicts

fractures strongly and independently of densitometry in older women. A prospective study," Arch. Intern Med. **157**, 629–634 (1997).
[15]M. L. Bouxsein, B. S. Coan, and S. C. Lee, "Prediction of the strength of the elderly proximal femur by bone mineral density and quantitative ultrasound measurements of the heel and tibia," Bone (Osaka) **25**, 49–54 (1999).
[16]C. C. Gluer, C. Y. Wu, and H. K. Genant, "Broadband ultrasound attenuation signals depend on trabecular orientation: An in vitro study," Osteoporosis Int. **3**, 185–191 (1993).
[17]C. M. Langton, C. F. Njeh, R. Hodgskinson, and J. D. Currey, "Prediction of mechanical properties of the human calcaneus by broadband ultrasonic attenuation," Bone (Osaka) **18**, 495–503 (1996).
[18]S. Chaffai, F. Peyrin, G. Berger, and P. Laugier, "Relationships between ultrasonic attenuation, velocity and backscatter and cancellous bone micro-architecture," J. Bone Miner. Res. **14**, S376 (1999).
[19]M. A. Hakulinen, J. Toyras, S. Saarakkala, J. Hirvonen, H. Kroger, and J. S. Jurvelin, "Ability of ultrasound backscattering to predict mechanical properties of bovine trabecular bone," Ultrasound Med. Biol. **30**, 919–927 (2004).
[20]K. A. Wear and D. W. Armstrong, "The relationship between ultrasonic backscatter and bone mineral density in human calcaneus," IEEE Trans. Ultrason. Ferroelectr. Freq. Control **47**, 777–780 (2000).
[21]K. A. Wear and A. Laib, "Relationship between ultrasonic backscatter and trabecular thickness in human calcaneus: Theory and experiment," J. Bone Miner. Res. **17**, S419 (2002).
[22]K. A. Wear, "The effect of trabecular material properties on the frequency dependence of backscatter from cancellous bone," J. Acoust. Soc. Am. **114**, 62–65 (2003).
[23]C. Roux, V. Roberjot, R. Porcher, S. Kolta, M. Dougados, and P. Laugier, "Ultrasonic backscatter and transmission parameters at the os calcis in postmenopausal osteoporosis," J. Bone Miner. Res. **16**, 1353–1362 (2001).
[24]K. A. Wear and A. Laib, "The dependence of ultrasonic backscatter on trabecular thickness in human calcaneus: Theoretical and experimental results," IEEE Trans. Ultrason. Ferroelectr. Freq. Control **50**, 979–986 (2003).
[25]P. H. Nicholson, R. Strelitzki, R. O. Cleveland, and M. L. Bouxsein, "Scattering of ultrasound in cancellous bone: Predictions from a theoretical model," J. Biomech. **33**, 503–506 (2000).
[26]W. C. A. Pereira, S. L. Bridal, A. Coron, and P. Laugier, "Singular spectrum analysis applied to backscattered ultrasound signals from in vitro human cancellous bone specimens," IEEE Trans. Ultrason. Ferroelectr. Freq. Control **51**, 302–312 (2004).
[27]T. Misaridis and J. A. Jensen, "Use of modulated excitation signals in medical ultrasound. Part I: Basic concepts and expected benefits," IEEE Trans. Ultrason. Ferroelectr. Freq. Control **52**, 177–191 (2005).
[28]T. Misaridis and J. A. Jensen, "Use of modulated excitation signals in medical ultrasound. Part II: Design and performance for medical imaging applications," IEEE Trans. Ultrason. Ferroelectr. Freq. Control **52**, 192–207 (2005).
[29]T. Misaridis and J. A. Jensen, "Use of modulated excitation signals in medical ultrasound. Part III: High frame rate imaging," IEEE Trans. Ultrason. Ferroelectr. Freq. Control **52**, 208–219 (2005).
[30]M. H. Pedersen, T. X. Misaridis, and J. A. Jensen, "Clinical evaluation of chirp-coded excitation in medical ultrasound," Ultrasound Med. Biol. **29**, 895–905 (2003).
[31]A. Nowicki, J. Litniewski, W. Secomski, P. A. Lewin, and I. Trots, "Estimation of ultrasonic attenuation in a bone using coded excitation," Ultrasonics **41**, 615–621 (2003).
[32]A. Nazarian, B. D. Snyder, D. Zurakowski, and R. Muller, "Quantitative micro-computed tomography: A non-invasive method to assess equivalent bone mineral density," Bone (Osaka) **43**, 302–311 (2008).
[33]K. A. Wear, "Ultrasonic attenuation in human calcaneus from 0.2 to 1.7 MHz," IEEE Trans. Ultrason. Ferroelectr. Freq. Control **48**, 602–608 (2001).
[34]S. Chaffai, F. Padilla, G. Berger, and P. Laugier, "In vitro measurement of the frequency-dependent attenuation in cancellous bone between 0.2 and 2 MHz," J. Acoust. Soc. Am. **108**, 1281–1289 (2000).

Subharmonic analysis using singular-value decomposition of ultrasound contrast agents

Jonathan Mamou[a] and Jeffrey A. Ketterling
Frederic L. Lizzi Center for Biomedical Engineering, Riverside Research Institute, 156 William Street, New York, New York 10038

(Received 16 October 2008; revised 12 March 2009; accepted 13 March 2009)

Ultrasound contrast agents (UCAs) are designed to be used below 10 MHz, but interest is growing in studying the response of agents to high-frequency ultrasound. In this study, the subharmonic response of polymer-shelled UCAs with a mean diameter of 1.1 μm excited with 40-MHz tone-bursts of 1–20 cycles was analyzed. UCAs were diluted in water and streamed through a flow phantom that permitted single-bubble backscatter events to be acquired at peak-negative pressures from 0.75 to 5.0 MPa. At each exposure condition, 1000 single-bubble-backscatter events were digitized. Subharmonic content at 20 MHz was screened using a conventional and a singular-value-decomposition (SVD) method. The conventional method evaluated each event spectrum individually while the SVD method treated the 1000-event data set at one time. A subharmonic score (SHS) indicative of how much subharmonic content a 1000-event data set contained was computed for both methods. Empirical-simulation results indicated that SHSs obtained from the two methods were linearly related. Also, experimental data with both methods indicated that subharmonic likelihood increased with pulse duration and peaked near 2 MPa. The SVD method also yielded quantitative information about subharmonic events not available with the conventional method. © *2009 Acoustical Society of America.* [DOI: 10.1121/1.3117384]

PACS number(s): 43.80.Vj, 43.80.Qf, 43.25.Yw, 43.60.Cg [FD] Pages: 4078–4091

I. INTRODUCTION

Conventional ultrasound contrast agents (UCAs) are designed for clinical use at frequencies below 10 MHz. Typical UCAs usually have a mean diameter of 2–4 μm where a larger bubble typically has a lower resonance frequency.[1] Only recently, UCAs specifically designed for high-frequency ultrasound (HFU) (>20 MHz) have started to become available. For example, VisualSonics (Toronto ON, Canada) now has three types of commercially-available UCAs called MicroMarker™, and studies are being conducted to investigate angiogenesis in animal models of cancers.[2,3] Nevertheless, many existing and experimental UCAs originally designed for conventional frequencies are currently under investigation for use with HFU. Interest is growing in this field because high-frequency UCAs can be valuable for clinical and pre-clinical studies where HFU is routinely used. For example, high-frequency UCAs could allow evaluating microcirculation for ophthalmic disease diagnosis.[4] UCAs could also be used in small-animal imaging applications to evaluate the normal and abnormal cardiovascular development of genetically-engineered mouse embryos.[5]

The earliest HFU studies of UCAs were conducted using broad-band excitations,[6,4,7] but the results typically showed backscatter centered at the transducer center frequency and no significant harmonic content was detected. The lack of harmonic content makes clinical use of UCAs with HFU limited because conventional non-linear imaging methods cannot be used to separate UCA echoes from tissue echoes. More recently, Goertz *et al.*[8,9] reported generation of harmonic and subharmonic backscatter components for Definity® (Bristol-Myers Squibb, New York, NY) when excited with narrow-band HFU signals. Specifically, Definity® was excited with a tone-burst consisting of 4–10 cycles at either 20 or 30 MHz. The observation of harmonics was unexpected because few UCAs in the submicron size range are expected to exist in a given dose, and, from the theory of free bubbles, the expectation is that relatively high pressures would be required to excite a bubble nonlinearly with HFU. In subsequent studies, Goertz *et al.*[10,11] also observed harmonic backscatter from Optison™ (GE Healthcare, Chalfont St. Giles, UK) and a Bracco agent (Princeton, NJ), although at a much weaker pressure level than observed with Definity®. Theoretical work by Allen *et al.*[12] suggested that shell waves may contribute to high-frequency backscatter components in lipid-shelled UCAs. The apparent unexpected strong harmonic backscatter produced by Definity® and the lack of similar observations for other agents point to the need to better understand UCA response to HFU excitation. In particular, the physical origin of the subharmonic emissions is still unclear and, more importantly, the optimal excitation conditions to generate them are therefore difficult to determine.

More recently, subharmonic responses of Definity® were used for intravascular ultrasound (IVUS) imaging.[13] The results of this study indicated that because subharmonic signals can originate only from UCAs, subharmonic contrast IVUS has potential as a new method for vasa vasorum imaging. The same property was also exploited in a pulse-wave Doppler study using UCAs and HFU[14] to suppress tissue

[a]Author to whom correspondence should be addressed. Electronic mail: mamou@rrinyc.org

echo signals by appropriate band-pass filtering in the subharmonic band of the UCA response. Such filtering was shown to allow higher frame rates and better sensitivity to microvascular flow.

In a previous study,[15] we reported experimental and theoretical results for three types of polymer-shelled UCAs [POINT Biomedical (POINT Biomedical is no longer in operation), San Carlos, CA] with mean diameters of 0.56, 1.1, and 3.4 μm.[16,17] UCAs were excited with tone-bursts from 1 to 20 cycles using a 40-MHz, spherically-focused transducer. Results showed that subharmonic responses could be observed for the three types of UCAs.

In the present study, we investigate new methods and report new results for the polymer-shelled UCAs having a mean diameter of 1.1 μm. The UCAs were excited with tone-bursts from 1 to 20 cycles using the same 40-MHz, spherically-focused transducer, and peak-rarefactional pressure was varied from 0.7 to 5 MPa. A new experimental system was developed to allow acquiring backscatter signals from a single UCA under controlled conditions. Single-bubble-backscatter signals were examined for subharmonic content with two different methods. The first, or conventional, method consisted of screening the spectrum of the backscattered signals for energy near 20 MHz, and the second, or singular-value-decomposition (SVD), method used advanced statistical methods.

The rationale for SVD is that under the same experimental conditions (i.e., UCA, peak-rarefactional pressure, excitation duration, etc.) single-bubble events can be interpreted as the realizations of a random process (i.e., bubble oscillations under the same exposure conditions). Therefore, this study proposes implementing SVD to analyze and classify the subharmonic response of UCAs in a statistically optimal fashion.[18–20] We investigated whether SVD could serve as a valuable tool for understanding bubble dynamics because of its ability to decompose bubble events into an optimal orthonormal base of eigenvectors. The decomposition of UCA echoes onto this SVD-derived base is statistically optimal in the sense that the greatest variance by any projection of the data comes to lie on the first eigenvector, the second greatest variance on the second eigenvector, and so on. The rationale will be to examine the first few eigenvectors for their spectral content and we anticipate that the first eigenvector will correspond to the linear, or normal, response of the bubble. The remaining eigenvectors will be analyzed for the presence of strong spectral content at 20 MHz. We expect SVD processing to be very robust because it will be applied to data sets composed of 1000 events (i.e., realizations). In particular, unwanted data (e.g., adjacent bubbles, moving bubble, excitation failures, etc.) can be easily discarded because these events, unlike the valid events, will have very low energy in the first (and most significant) eigenvector.

The aim of this study was to validate the SVD method as a tool to detect and characterize subharmonic emissions from HFU excitation of UCAs. While the proposed SVD method could be applied at any frequency and for the detection of higher-order harmonics, we are interested in HFU because of the fine-scale image resolution that HFU provides and in subharmonics because tissue generates significant levels of high-order harmonics which makes it difficult to distinguish between UCA and tissue harmonics. Subharmonics are not generated in tissue and, therefore, any subharmonic emissions are related to the nonlinear oscillations of UCAs.

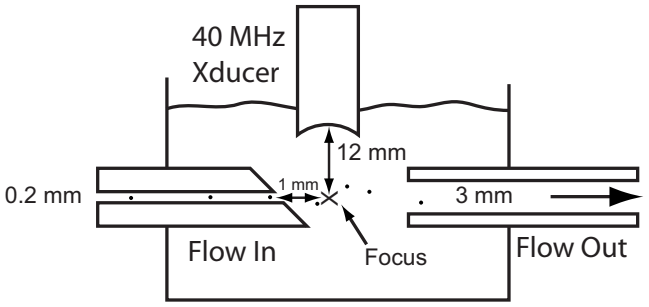

FIG. 1. Flow phantom schematic. The input port had a 200-μm ID and the output port had a 3-mm ID. A tubing pump controlled the flow in and out of the phantom. The input channel was cut at an angle to facilitate alignment of the transducer focal zone with the opening.

II. MATERIAL AND METHODS

A. Contrast agents

The UCAs used in this study were nitrogen-filled, polycaprolactone-shelled agents with a mean diameter of 1.1 μm (POINT Biomedical, model No. 1466). These agents were termed P2 in the previous study.[15] The UCAs were received in a dry form, and a small amount of agent was reconstituted in water for each experiment. Therefore, the gas content of the agents diffused into air over time because the agents were not stored with a nitrogen head after the vial was opened. Experiments were performed by mixing a small amount of agent into 100 ml of deionized, filtered water. The mass of the agents utilized for each experiment was not quantified, but was chosen to provide a consistent rate of single-agent-backscatter events. The water had been briefly degassed by gently stirring 1 l under vacuum for 1 min. The 1-l solution was then returned to atmospheric pressure for at least 12 h. The purpose was not to achieve partial saturation, but to ensure normal 100% gas saturation without the buildup of bubbles on surfaces that typically occurs when water is poured into a container. During experiments, the water was stirred with a magnetic stirring bar to ensure mixing and to reduce the likelihood of the agents sorting themselves by size over time due to buoyancy effects.

B. Flow system

Contrast agents were passed through a flow system and injected into the focal zone of the transducer. The intent of the system was to excite the contrast agents under unconstrained conditions in open fluid. The flow system consisted of a dual-channel tubing pump (REGLO Digital MS-2/8, Ismatec, Glattbrugg, Switzerland) and a flow phantom (Fig. 1). The flow phantom measured $55 \times 77 \times 38$ mm^3 and had an input and output channel separated by 5 mm. The tubing pump was used with 2.06-mm inner diameter (ID) tubing (CP-95608-42, Cole-Parmer, Vernon Hills, IL) in a push-pull configuration, and the flow volume was set to the minimum value of 0.328 ml/min. One line of the pump drew

the diluted mixture of contrast agent from a 100-mL reservoir and injected agents into the flow phantom through a 3-cm-long, 200-μm ID channel (Masterflex Tygon EW-95609-10, Cole-Parmer). The input channel was cut at an angle to provide a specular surface that could be aligned with the transducer focal zone. The flow velocity within the 200-μm channel was 174 mm/s (assuming plug flow), but the actual flow velocity after injection into the bulk fluid would be lower. A second line of the pump drew liquid out of the phantom into a waste reservoir.

C. Exposure conditions

The contrast agents were exposed to 40-MHz tonebursts of 1, 3, 5-10, 15, and 20 cycles. Experiments were conducted with a 40-MHz transducer (PI 50-2 Panametrics, Waltham, MA) having a focal length of 12 mm and an aperture of 6 mm. The depth-of-field (~1 mm) and lateral beamwidth (~70 μm) were measured by scanning a 12-μm-diameter tungsten wire using a pulser/receiver (Panametrics 5900, Olympus NDT, Waltham, MA). The transducer was excited by the output of a power amplifier (1040L ENI, Rochester, NY) driven by an arbitrary-waveform generator (Tabor 1281, Tel Hanan, Israel). The transducer was used for pulse and receive measurements by employing a custom transmit/receive transmit having an inline crossed-diode pair (1N4148, Fairchild Semiconductor Corp., South Portland, ME) between the power amplifier and transducer, and a crossed-diode pair to ground between the receive amplifier and transducer.[21] The receive echo was digitized at 500 MHz with an 8-bit peripheral component interconnect (PCI)-based digitizer (DP110, Acqiris, Monroe, NY) after undergoing 46 dB of amplification (AU-1313, Miteq, Hauppauge, NY). The transducer was calibrated for the various exposure settings using a 40-μm hydrophone (HPM04/1, Precision Acoustics Ltd., Dorset, UK). The transducer was mounted to a motorized positioning system in order to align the transducer with the 200-μm flow channel accurately. After alignment, the transducer was displaced downstream by 1 mm.

While the −6-dB depth-of-field of the transducer (1 mm) was much larger than the 200-μm injection channel, the −6-dB lateral beamwidth of the transducer (70 μm) was smaller than the injection channel. Thus, the axial location of the agent may not necessarily coincide with the peak pressure of the sound field. However, this uncertainty exists for any experiment that uses tightly focused transducers or experiments that wait for a random UCA to pass through the transducer focal zone. We have reduced this uncertainty by carefully injecting UCAs into the transducer focal zone and increasing the acquisition rate of single-agent backscatter events. We also acquired large sets of data for each exposure condition in order to assist in identifying statistical trends.

D. Data acquisition

The data-acquisition system was controlled using a custom software package (LabVIEW, National Instruments, Austin, TX) and was configured to screen consecutively acquired M-mode data sets for valid backscatter events. Once the transducer was aligned with the 200-μm input channel and moved downstream, M-mode data sets of 20 lines with 1000 points/line were acquired at a pulse-repetition frequency (PRF) of 4 kHz and a sampling rate of 500 MHz. The center of the data window was placed at the focal length of the transducer. Figure 2 displays a typical 20-line M-mode data set containing a valid event. With this data-acquisition approach, each UCA was exposed to about six to eight pulses (eight pulses in case of Fig. 7). Multiple exposures per agent guaranteed capturing a backscatter event as the UCA moved through a local maximum pressure whereas a single backscatter event per agent could represent any of the eight lines in Fig. 7. However, even with multiple exposures per agent, we had no guarantee that the agent had passed directly through the peak pressure at the geometric focus.

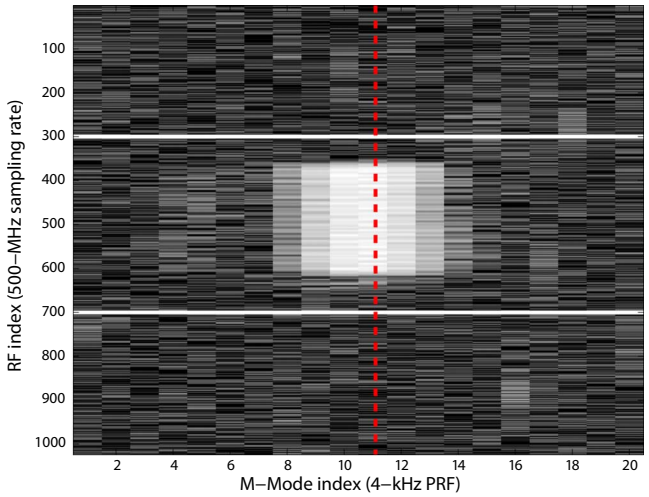

FIG. 2. (Color online) M-mode image of a valid event. The image contains 20 A-lines acquired with a PRF of 4 kHz. In this example, the excitation toneburst was a 20-cycle pulse with a peak-rarefactional pressure of 2.1 MPa. A-lines 8–14 contain echoes from the same agent. The valid event is symbolized by the dashed line. The solid lines symbolize the 400-rf points centered at the focus of the transducer.

The M-mode data were initially scanned in real time to determine whether (1) the maximum value of the M-mode signal was above a noise threshold, (2) the maximum value was below saturation, and (3) the M-mode line with the maximum value was not the first or last M-mode line. In the example of Fig. 2, these conditions are all true and the M-mode with the maximum value (dashed line) was the 11th M-mode line. If conditions (1)–(3) were true, then the line with the maximum value was correlated with an ideal excitation waveform (i.e., number of 40-MHz cycles convolved with the transducer impulse response). If a single correlation peak occurred and that peak was within ±200 points (solid lines in Fig. 2) of the data window center (i.e., the geometric focus), then the processed M-mode line was logged, along with a time stamp, as a valid single-agent backscatter event. This screening process was repeated until 1000 valid backscatter events were acquired for an individual data run. A typical data run would yield valid events for roughly 10–20% of all M-mode acquisitions.

Experiments were performed by selecting a set of drive voltages and excitations; then all aspects of data collection and processing were automated. In order to optimize the voltage range of the digitizer as the drive voltages were in-

cremented during experiments, the peak values of all M-modes above the noise threshold were logged along with a running tally of the total number of acquired M-mode sets. These parameters were used to determine whether the voltage range of the digitizer should be altered. If $<0.5\%$ of all acquired M-modes led to a valid backscatter event, then the voltage scale of the digitizer was reduced. If $>5\%$ of the cases with a peak above the noise threshold were saturated, then the voltage range was increased. If $>95\%$ of the cases with a peak above the noise threshold used only 7 of the available 8 bits, then the voltage range was decreased. Each time a voltage range was changed by the software, the data collection was re-initiated starting at a zero count. In addition, as the voltage range changed, the noise threshold was appropriately scaled to maintain a constant voltage threshold rather than a constant binary threshold.

E. Conventional and SVD subharmonic detection

In this study, two methods were investigated for detecting subharmonic events. The first method, the conventional method, decides whether each event (of a 1000-event data set) was a valid subharmonic event independent of the other events. The second method, the SVD method, does not individually select subharmonic events but processes the 1000-event data set at one time. Both subharmonic detection methods are described below.

1. Conventional method

Data sets were post-processed to screen for subharmonic components in the backscatter. In the conventional subharmonic detection method, the data lines were correlated with an ideal excitation waveform (S) in order to window only the backscatter component of the data. The correlation scores were recorded, and events having a correlation that was below the average correlation minus one standard deviation were discarded as outliers. This screening procedure usually led to the discard of about 10% of the events. The windowed backscatter event was then passed through a Hamming window, zero padded to 2048 points, and a power spectrum was calculated. Finally, three qualitative comparisons were employed to determine whether the spectrum contained a subharmonic component (Fig. 3).

(1) The 40-MHz sub-band of the backscatter event and S were normalized to ± 1, and the mean-square error (MSE) between the two curves was calculated. If the MSE was <0.1, then the fit was declared good. This check provided a simple means to determine if the duration of the backscatter event was less than the ideal excitation waveform. A shorter-duration signal would have resulted in a wider bandwidth and an increase in the MSE. A shorter-duration backscatter signal could have resulted from the destruction of the agent during the acoustic excitation or from an agent that moved out of the sound field during the exposure.
(2) The 20-MHz sub-band of the backscatter event was fitted to a second-order polynomial after normalizing the sub-band to ± 1. If the MSE was <0.1, then the fit was declared good. This check ensured that the 20-MHz band had structure consistent with a subharmonic signal.
(3) The difference in decibels between the 20-MHz peaks of S and the backscatter power spectrum was calculated after normalizing the 40-MHz components of the two signals to the same value. If the difference between the 20-MHz components was >25 dB, then the backscatter spectrum was declared to contain a subharmonic component. This check ensured that a significant 20-MHz component existed in the backscatter signal.

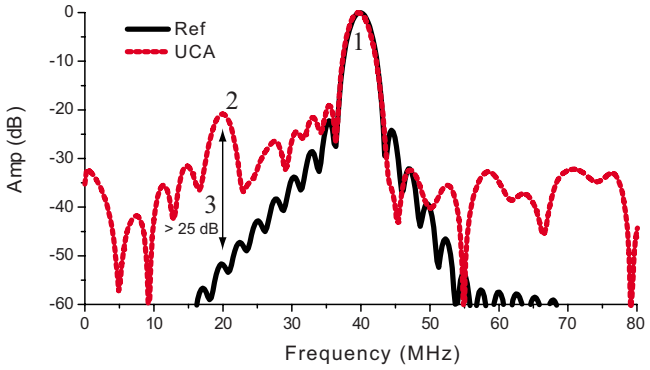

FIG. 3. (Color online) Criteria to determine if a subharmonic was present. (1) 40-MHz sub-band was a good fit to sub-band of S, (2) 20-MHz sub-band was a good fit to a second-order polynomial, and (3) 20-MHz backscatter value was >25 dB of S peak after the 40-MHz components were normalized. The example shows a 10-cycle reference spectrum (solid) compared to a valid backscatter event (dashed).

The screening method that we employed led to some false-positives and false-negatives, but it provided a consistent and uniform approach to screening acquired data. Visual inspection of some test cases showed that this approach was fairly robust at identifying subharmonic events.

2. SVD method

The SVD detection approach is fundamentally different from the conventional method for two reasons. First, each 1000-event data set is processed at one time (i.e., events are not screened individually). Second, the SVD approach does not produce a yes/no answer for subharmonic presence for each individual event whereas the conventional method does.

The outliers of the 1000-event data set were discarded using the same approach as in the conventional method; then, a preprocessing step was conducted to synchronize the remaining events precisely so that their start time was at the same radio-frequency (rf) point. Synchronization was done by equaling the phases of the Fourier transforms of all events at 40 MHz. The synchronization step was necessary because otherwise the SVD processing would consider the lack of synchronization as a property of the agent response, which would be misleading for physical interpretation. Following the synchronization, the events were divided by their respective peak-envelope magnitudes. Then, a matrix, M, was constructed by filling each column with the rf data of each synchronized, normalized, and gated event. (The events were gated by correlation with S just as in the conventional method.) The resulting matrix M had a size $m \times n$, where n was the number of rf points of each gated event and m

(<1000) was the number of remaining events after discarding outliers. The SVD of M was then computed:

$$M = U\Sigma V', \tag{1}$$

where U was of size $m \times m$, Σ was of size $m \times n$, and V was of size $n \times n$. The $'$ symbol refers to the matrix-transposition operation. The matrix Σ was diagonal and its non-zero elements are termed "singular values;" the singular values are real and positive. While it is not directly implied by the SVD definition of Eq. (1), singular values are assumed to be ordered by decreasing order in Σ (i.e., the top-left element of Σ is the largest). The matrix V contains the eigenvectors, and U can be considered to contain the coordinates of the events in the new basis defined by the eigenvectors divided by their corresponding singular values. Note that the eigenvectors corresponding to the largest singular values contain the most information about the complete data set in a minimum-variance sense.

Based on these observations, we interested ourselves in two eigenvectors: the "normal-response" and "subharmonic-response." The normal-response eigenvector, V_1, can be physically interpreted as the normal-response of the agent and it contained the most information about the complete data set. The subharmonic-response eigenvector is hypothesized to contain the most information about the subharmonic events in the data set. To find this eigenvector, the spectrum of each eigenvector was computed and the first eigenvector (i.e., corresponding to the largest singular value) whose spectrum peaked between 19.5 and 20.5 MHz was selected as the most significant eigenvector to describe the subharmonic response of the UCAs within this specific data set. This eigenvector (V_l) was termed the "subharmonic-response eigenvector," and its index was denoted by l ($l > 1$).

3. Subharmonic scores

From each data set of 1000 events and for both subharmonic detection methods, a subharmonic score (SHS), indicative of "how much" subharmonic occurrences were present, was computed. SHS_C, the SHS computed using the conventional method, was defined to be the percentage (between 0 and 100) of events detected as valid subharmonic events. $\mathrm{SHS}_{\mathrm{SVD}}$, the SHS computed using the SVD method, was defined as the peak amplitude of the spectrum of the subharmonic-response eigenvector multiplied by the mean of the absolute value of the scaling coefficient of each event on the subharmonic-response eigenvector. Visually,

$$\mathrm{SHS}_{\mathrm{SVD}} = \Sigma(l,l)\max|\mathrm{FT}\{V_l\}|^2\overline{|U_l|}, \tag{2}$$

where $\Sigma(l,l)$ is the lth diagonal element of Σ, FT is the Fourier transform operator, the overbar represents the ensemble mean, and V_l and U_l are the lth columns of matrices V and U, respectively. V_l is the subharmonic response of the data set and U_l is the coefficient of each event on the subharmonic response. Therefore, from Eq. (2), $\mathrm{SHS}_{\mathrm{SVD}}$ represents the mean "energy" of the entire data set in the specific subharmonic band defined only by the subharmonic response. During preprocessing, the events are normalized to unit amplitude and because V_l is part of the orthonormal basis deduced by SVD, all the terms in Eq. (2) are unitless making $\mathrm{SHS}_{\mathrm{SVD}}$ unitless. (SHS_C is also unitless because it is defined as a percentage.)

F. Empirical simulations

Ideally, the rationale behind the computations of SHS_C and $\mathrm{SHS}_{\mathrm{SVD}}$ is to give physical understanding to the more intricate SVD processing. In particular, the following empirical simulations should help with the physical interpretation of the subharmonic- and normal-response eigenvectors. The conventional method is easier to understand because each event is classified independent of the others, and the selection criteria all have physical meaning, whereas in the SVD method, the entire data set is processed at once and Eqs. (1) and (2) are more difficult to physically interpret. Therefore, we designed simulations to investigate whether SHS_C and $\mathrm{SHS}_{\mathrm{SVD}}$ could be linearly related, i.e., the expression $\mathrm{SHC}_{\mathrm{SVD}} \approx a\mathrm{SHS}_C + b$ valid for some constants a and b.

For these simulations, and for each exposure condition (i.e., time-duration and peak-rarefactional pressure), we built two libraries of events. One library contained only subharmonic events detected by the conventional method and the other contained no subharmonic events. Then, for each value of SHS_C, we built a 1000-event data set by randomly selecting events of both libraries to reach the prescribed value for SHS_C. Then, the SVD method was conducted on the simulated 1000-event data set and $\mathrm{SHS}_{\mathrm{SVD}}$ was computed. For each prescribed value of SHS_C, 20 data sets with 1000 events were simulated to compute mean and standard deviations of $\mathrm{SHS}_{\mathrm{SVD}}$. Afterward, $\mathrm{SHS}_{\mathrm{SVD}}$ values were obtained for SHS_C values ranging from 1 to 25 with 0.5 increments, and a least-squares straight-line fit was computed.

G. Time-durations and subharmonic delay

Several quantities were estimated based on the normal-response and subharmonic-response eigenvectors. These quantities were hypothesized to be related to the physical nature of subharmonic emissions occurring when UCAs are under HFU insonification. The rationale here was to exploit the results of the SVD processing and to understand how a single UCA behaves in a HFU field.

The first two quantities are the time-duration of the normal (τ_{NR}) and subharmonic (τ_{SH}) responses. They were estimated using the following equations:

$$\tau_{\mathrm{NR}} = \frac{\alpha}{B^{\mathrm{NR}}_{6\ \mathrm{dB}}(40\ \mathrm{MHz})}, \tag{3}$$

$$\tau_{\mathrm{SH}} = \frac{\alpha}{B^{\mathrm{SH}}_{6\ \mathrm{dB}}(20\ \mathrm{MHz})}, \tag{4}$$

where $B^{\mathrm{NR}}_{6\ \mathrm{dB}}$ (40 MHz) and $B^{\mathrm{SH}}_{6\ \mathrm{dB}}$ (20 MHz) are the −6-dB bandwidths of the Fourier transform of the normal-response (i.e., column vector V_1) and subharmonic-response (i.e., column vector V_l) eigenvectors centered at 40 and 20 MHz, respectively. The constant α was equal to 1.976 and was found by multiplying the actual known duration of a Hanning-weighted tone-burst by its −6-dB bandwidth.

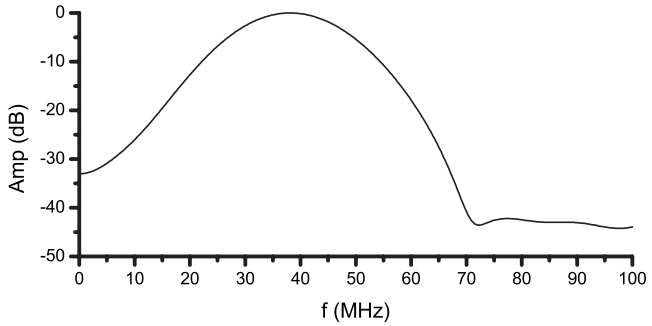

FIG. 4. Glass-plate pulse/echo spectrum. The 20-MHz sensitivity is 12 dB below the peak sensitivity at 40 MHz.

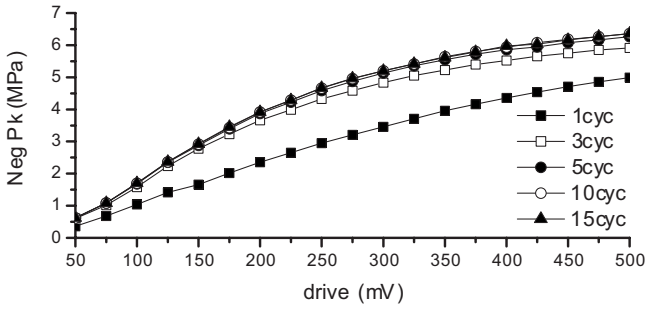

FIG. 5. Peak negative pressures as a function of drive voltage for 1–15-cycle pulse durations.

(Based on this estimation method, α is independent of frequency.) We used Eqs. (3) and (4) to estimate time-durations instead of a more straightforward time-domain-based method because the noise level in the subharmonic-response eigenvector always was much greater than the level in the normal-response eigenvector.

The next quantity estimated was the subharmonic delay, d_{SH}. The subharmonic delay was meant to quantify whether a delay existed between the initiation of the subharmonic response and the normal response. It was estimated as the difference between the time stamps at which the envelope of filtered versions of the subharmonic- and the normal-response eigenvector envelopes reached 75% of their maximal value the first time. The filters were pass-band with identical design except for the pass-band center frequencies of 40 and 20 MHz for the normal and subharmonic responses, respectively. The use of linear filters was necessary because of the significant noise in the subharmonic-response eigenvector.

The final quantity estimated was the time-duration difference, $\Delta = \tau_{NR} - \tau_{SH}$. It was computed to determine whether the subharmonic response was shorter or longer than the normal response. Also, Δ could be compared to d_{SH} to indicate whether the time-duration difference could be associated with a delay in subharmonic response.

III. RESULTS

A. Transducer characterization

The transmit/receive frequency response of the transducer for an impulse excitation (Panametrics 5900, Olympus, Waltham, MA) is shown in Fig. 4. Echo-signal data were acquired from the surface of a quartz plate positioned normal to and in the focal plane of the transducer. The peak sensitivity of the transducer was at 40 MHz and the 20-MHz sensitivity was 12 dB lower. The peak negative pressures at the transducer geometric focus versus drive voltage for a series of tone-bursts are shown in Fig. 5. The pressure showed an initial linear increase with drive signal, but it tended to plateau at high drive voltages. As the number of cycles increased from 1 to 5 cycles, the peak pressure increased slightly for a fixed drive signal. For tone-bursts beyond 5 cycles, the peak pressure remained constant for a fixed drive signal.

B. Illustrative results

In this section, the results obtained using the conventional and SVD methods on an illustrative 1000-event data set are presented. In this illustrative data set, UCAs were excited with 15-cycle tone-bursts with a peak-rarefactional pressure of 2.1 MPa. The conventional subharmonic detection method yielded $SHS_C = 4.23$ (i.e., 4.23%, or 37 out of 874 events; 126 events were discarded as outliers). Figure 6(a) displays the spectra of ten randomly-selected subharmonic events detected by the conventional method. For comparison, Fig. 6(b) displays the spectra of ten non-subharmonic events. Comparing these two figures, the spectra of Fig. 6(a) clearly have significant spectral energy near 20 MHz while the spectra of Fig. 6(b) clearly do not. Furthermore, Fig. 6(a) also gives a hint of ultra-harmonic energy near 60 MHz.

The same data set then was processed using the SVD method, which yielded $SHS_{SVD} = 5.95$. The subharmonic-response eigenvector was V_6 (i.e., $l=6$). Figure 6(c) displays the spectra of the ten events with the largest coefficients on V_6 in absolute value. These events correspond to the ten greatest elements of $|U_6|$. Therefore, based on our interpretation of the SVD-method results, these ten events are the "most subharmonic." For comparison, Fig. 6(d) displays the spectra of the ten events with the smallest coefficients on V_6; therefore, these events can be interpreted as being the "least subharmonic" and correspond to the ten smallest elements of $|U_6|$. The spectra shown in Figs. 6(c) and 6(d) share similarities with those shown in Figs. 6(a) and 6(b), but some differences also are apparent. The ultra-harmonic energy at 60 MHz, which was arguably hinted at in Fig. 6(a), is clearly visible in Fig. 6(c). Also, a second-harmonic frequency component at 80 MHz is visible. Figure 6(d) shows essentially the same spectral content as Fig. 6(b); the difference is in the level of the noise plateau. A simple estimation concluded that the average signal-to-noise ratio (SNR) of the spectra of Fig. 6(d) was about 9 dB greater than the average SNR of the spectra of Fig. 6(b). Overall, these small differences start to illustrate the strength of the SVD method over the conventional method. With the SVD method, we were able to separate the "most" and "least" subharmonic events easily. The conventional method did not provide any means of doing that accurately.

Figures 6(e) and 6(f) display the normalized time waveforms of the most- and least-subharmonic events of the data

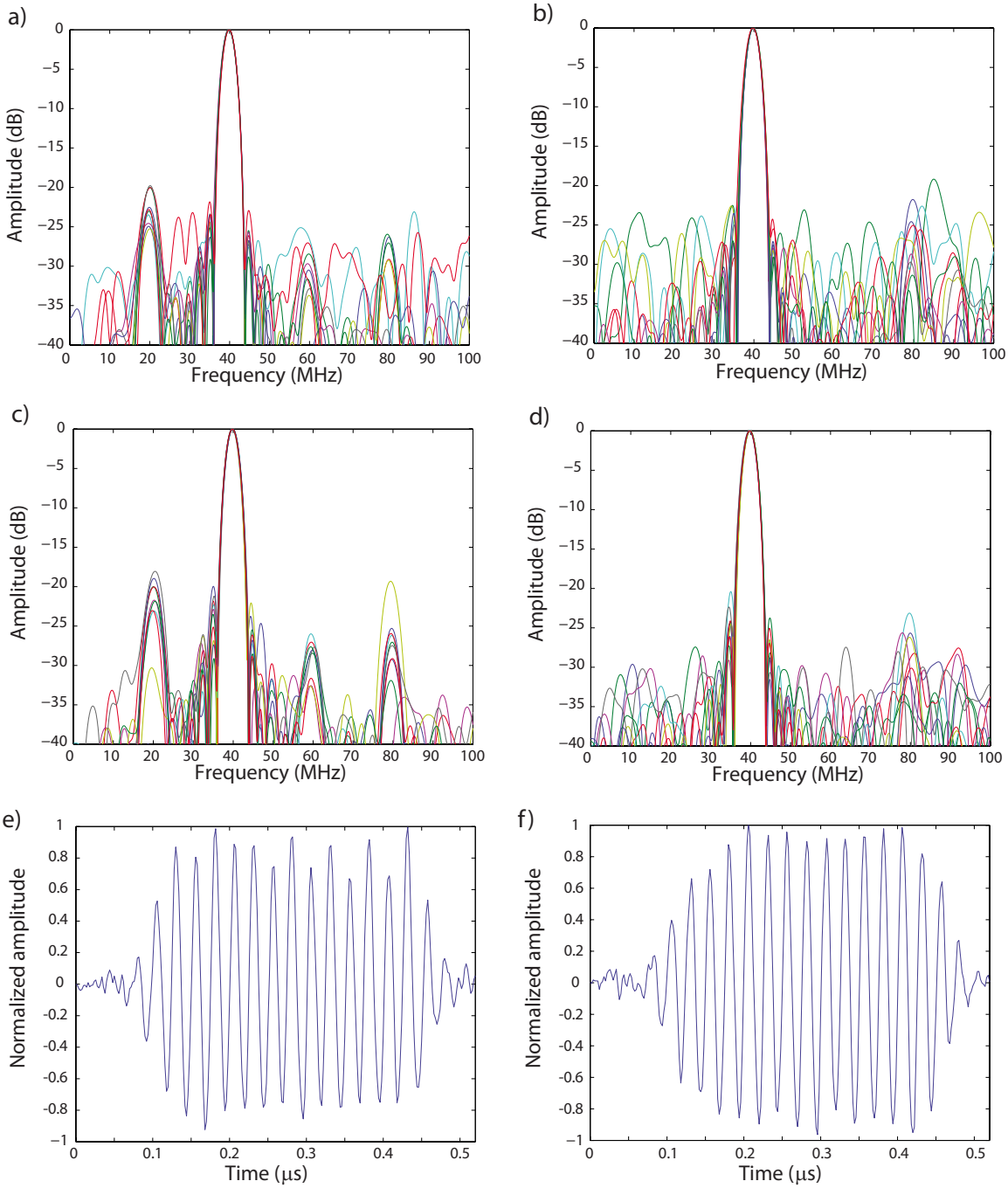

FIG. 6. (Color online) Illustration of the conventional and SVD methods applied to a 1000-event data set acquired with 15-cycle tone-bursts with a peak-rarefactional pressure of 2.1 MPa. Spectra of ten randomly-selected subharmonic events (a) and non-subharmonic events (b) based on the conventional method. Spectra of the ten most (c) and ten least (d) subharmonic events based on the SVD method. Time signals of the most (e) and least (f) subharmonic events based on the SVD method.

set based on the results provided by the SVD method. The subharmonic content of the waveform in Fig. 6(e) is visible after 0.25 μs where the peak positive amplitudes periodically alternate between about 0.7 and 0.9. The waveform in Fig. 6(f) does not show the variation in peak amplitudes.

Figure 7 provides a deeper insight into the SVD method and also further illustrates its strength over the conventional method. Figures 7(a) and 7(b) display the spectra of the subharmonic-response eigenvector (i.e., V_6) and of the normal-response eigenvector (i.e., V_1), respectively. These figures illustrate how τ_{SH} and τ_{NR} were estimated from Eqs. (3) and (4). In this case, the estimation results yielded a slightly longer time-duration for the normal response, specifically, τ_{NR}=0.476 μs and τ_{SH}=0.456 μs (and Δ=20.1 ns). These spectra demonstrated that the normal-response frequency content was strongly concentrated near 40 MHz. The normal-response spectrum also displayed a weak second-harmonic component centered at 80 MHz with a relative amplitude of −32 dB. The spectrum of V_6 was more structured with a strong component near 20 MHz, but with energy in the harmonics of 20 MHz (i.e., 40, 60, and 80 MHz with relative amplitudes of −5, −8, and −7 dB, respectively). This type of spectrum is typical of a finite-duration signal that is nearly periodic with a period of 50 ns (i.e., 1/20 MHz). In

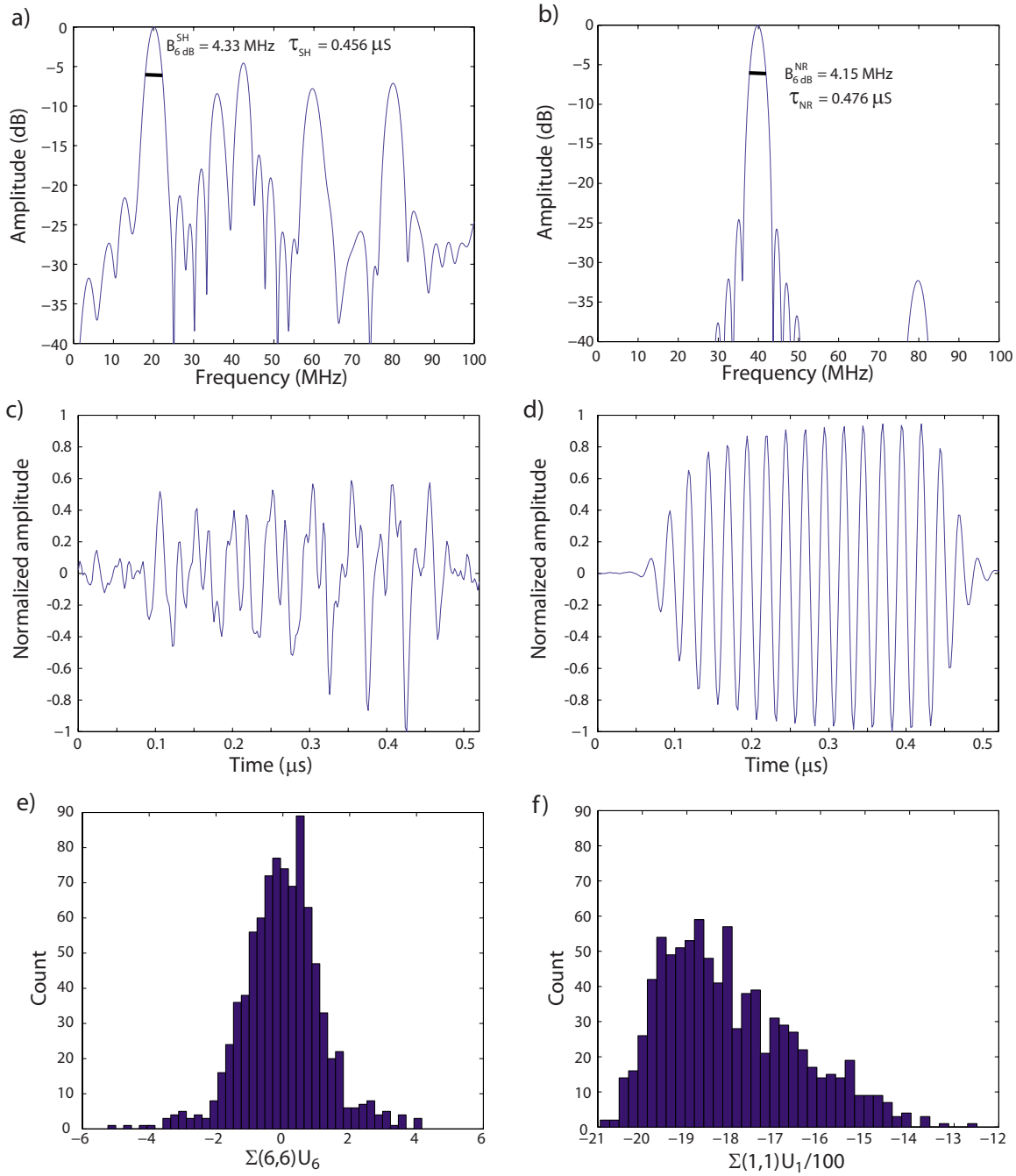

FIG. 7. (Color online) Spectra of the subharmonic (a) and normal-response (b) eigenvectors. Time waveforms of the subharmonic (c) and normal-response (d) eigenvectors. Histograms of the coefficients of the events on the subharmonic (e) and normal-response eigenvectors (f).

addition, the spectra revealed that the SNRs of V_1 and V_6 were very different. The normal-response SNR was at least 40 dB, whereas a crude SNR estimate for the subharmonic response would be 28 dB based on the spectra between 90 and 100 MHz.

Figures 7(c) and 7(d) display the time signals of V_6 and V_1, respectively. V_6 appears noisy but arguably periodic. For example, the last four negative peaks (first one at 0.28 μs) and the last five positive peaks (first one at 0.25 μs) were evenly spaced by 50 ns from each other. The positive peaks have almost-equal amplitudes near 0.55 whereas the negative-peak amplitudes increased from −0.52 to −1.0 (which explains the spectral components at 40, 60, and 80 MHz). Figure 7(c) also illustrates why τ_{SH} was estimated in the spectral domain and not in the time domain. Figure 7(d) shows a noiseless signal, very similar to what would be expected in a linear regime from a glass-plate reflection when the transducer is excited by a 15-cycle tone-burst. The modest non-linear content of this waveform is visible in the slightly asymmetric first cycles of the waveform.

Finally, Figs. 7(e) and 7(f) display the histograms of $\Sigma(6,6)U_6$ and $\Sigma(1,1)U_1$, respectively. The distribution of $\Sigma(6,6)U_6$ was very narrow and centered around 0. The actual mean value was virtually 0 (i.e., $\approx -3.5\times10^{-3}$) and the standard deviation was 1.18. Furthermore, 88% of the ele-

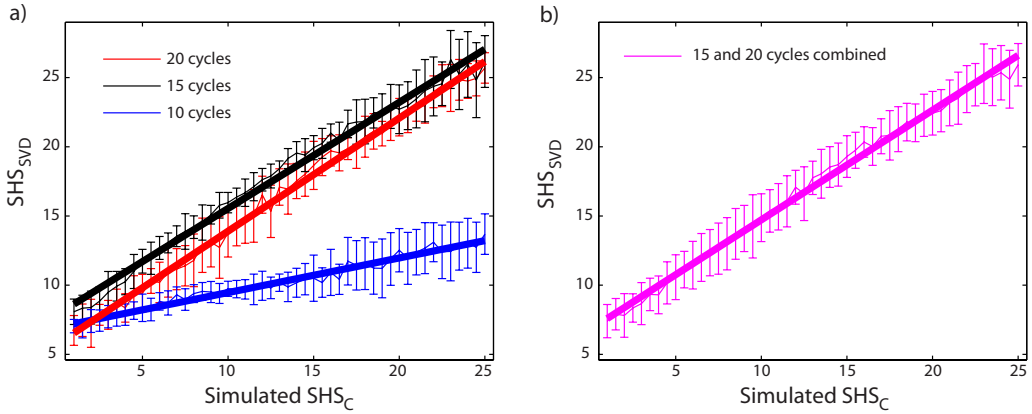

FIG. 8. (Color online) Empirical-simulation results: (a) SHS_{SVD} as a function of simulated SHS_C for 10-, 15-, and 20-cycle excitations. Each data-point is the mean of 20 simulations, and error bars represent standard deviations. (b) SHS_{SVD} as a function of simulated SHS_C for combined 15- and 20-cycle excitations. Each data-point is the mean of 40 simulations (20 with 15-cycle excitation and 20 with 20-cycle excitation). Bold lines represent least-squares straight-line fits to the results.

ments were between −1.18 and 1.18. This distribution indicates that most of the bubble events had a small subharmonic content. An interesting observation was that events can contain either a positive or negative subharmonic component; this property is physically interesting and is discussed further in Sec. III E. The distribution of $\Sigma(1,1)U_1$ was fundamentally different; its mean value was -1.80×10^3 and its standard deviation was 150 and all the values had the same sign. Therefore, each event had a strong component on V_1 which was expected because it was the first eigenvector returned by the SVD processing. Also, eigenvectors have unit norm; therefore, a coefficient of -1.80×10^3 on V_1 is effectively 340 times greater than a coefficient of −5.3 [i.e., the smallest values of $\Sigma(6,6)U_6$] in V_6. This difference corresponded to the subharmonic component being about 25 dB below the fundamental component for the most subharmonic events of the data set. This value was consistent with the spectra in Fig. 6(c).

Another element of information given by the SVD method is d_{SH}. For this specific example, d_{SH}=48 ns, suggesting that the subharmonic response initiated itself about 48 ns after the normal response. Interestingly, 48 ns was about 1 cycle at 20 MHz or 2 cycles at 40 MHz. Also, results led to Δ=20.1 ns, suggesting that the subharmonic response outlasted the normal response by about 27.9 ns (i.e., about 1 cycle at 40 MHz).

C. Empirical-simulation results

In this section, the relationship between SHS_C and SHS_{SVD} is investigated. The conventional method is fairly intuitive to understand and SHS_C is physically interpretable as the probability of a subharmonic event under certain excitation conditions. Therefore, using empirical simulations, we investigated whether SHS_{SVD} and SHS_C can be related in a straightforward fashion.

Figure 8(a) displays the results of the empirical simulations for prescribed SHS_C values ranging from 1 to 25 by 0.5 increments. For each duration, the data-point is the mean of 20 simulations and error bars represent standard deviations. Solid lines symbolize the optimal least-squares fit by a straight line to the data, and Table I provides optimal fit parameters. For all three pulse durations, SHS_{SVD} increased with SHS_C. This is a strong indication that SHS_{SVD} is a reliable means of quantifying subharmonic likelihood and content within a 1000-event data set. Furthermore, the MSEs quoted in Table I indicate that straight-line fits were able to track data accurately for the three different pulse durations.

The results obtained for 15- and 20-cycle excitations were fairly similar: the values for SHS_{SVD} greatly overlap, and the optimal least-squares-fit parameters were nearly identical (Table I). These results suggest that for 15- and 20-cycle excitations, SHS_{SVD} could be reliably inverted to estimate SHS_C with the same formula. Figure 8(b) displays the empirical-simulation results and optimal straight-line fit when simulation results for 15 and 20 cycles were combined. Again, Fig. 8(b) and the last row of Table I suggest that SHS_{SVD} can be modeled accurately as an affine function of SHS_C. Nevertheless, the MSE value for the 15- and 20-cycle combined cases was about 30% greater than the MSE value for each pulse-duration alone.

The 10-cycle results were different than the 15- and 20-cycle results. SHS_{SVD} only increased from about 7 to 13 when SHS_C was varied from 1 to 25. This slight increase of 6 is about double the average standard deviation. Also, the slope of the optimal least-squares fit was only 0.250 and much smaller than that of the 15- and 20-cycle pulse durations (Table I). These results might suggest that only modest subharmonic activity exists for 10-cycle excitations.

Overall, the empirical-simulation results allowed us to conclude that SHS_{SVD} was a valid quantifier of subharmonic

TABLE I. Straight-line least-squares-fit parameters for empirical simulations. (The numbers in Table I are unitless.)

Duration cycles	Slope	Intercept	Mean-squared error
10	0.250	6.96	1.67
15	0.767	7.87	2.14
20	0.817	5.73	2.13
15 and 20	0.792	6.80	2.72

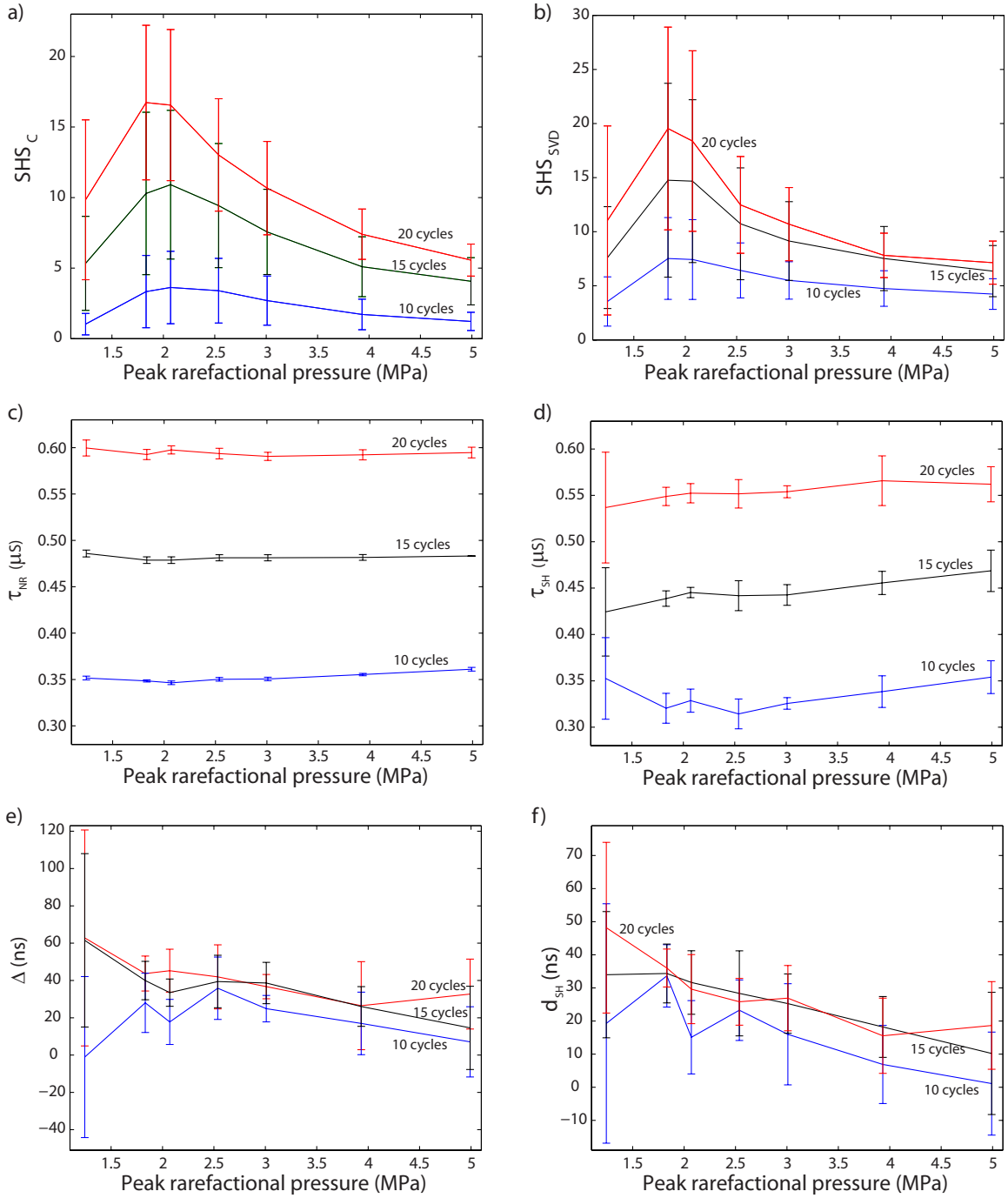

FIG. 9. (Color online) Conventional- and SVD-method results. In all the panels, data-points are the means and error bars represent standard deviations. Results are presented as a function of peak-rarefactional pressure for 10-, 15-, and 20-cycle excitations. (a) SHS_C and (b) SHS_{SVD}. (c) τ_{NR} and (d) τ_{SH}. (e) Δ and (f) d_{SH}.

activity because its trend was the same as that of SHS_C. Furthermore, straight-line fits provided very good fit to the data for the three pulse durations. However, the results also indicated that a different formula should be used for a 10-cycle excitation than for 15- and 20-cycle excitations to predict SHS_C based on values obtained from SHS_{SVD}.

D. Pressure threshold

The next step of the study was to determine the optimal exposure conditions to obtain subharmonic events and whether both methods provide essentially the same answer. Knowledge of these conditions will be critical for *in vivo* studies because UCA echoes could be separated from tissue echoes easily by using a band-pass filter centered in the subharmonic band.

Figures 9(a) and 9(b) display SHS_C and SHS_{SVD} as a function of peak-rarefactional pressure for 10-, 15-, and 20-cycle tone-bursts. Each exposure condition experiment was repeated 11 times (except 9 times for 3.9 and 5 MPa); data-points represent means and error bars symbolize standard deviations. Figure 9(a) indicates that SHS_C increased with pulse duration independent of the peak-rarefactional

pressure. Further, for all pulse durations, the trend of the curves was the same: SHS_C was low at low (<1.5 MPa) and high (>3 MPa) pressures and reached its maximum near 2 MPa. Overall, SHS_C remained small, with a peak value of 17 for 20-cycle tone-bursts with 1.9 MPa. In particular, 10-cycle tone-bursts produced no mean value of SHS_C greater than 3.5 whereas 15- and 20-cycle tone-bursts produced no mean value of SHS_C smaller than 5. Also, 8- and 9-cycle results (not shown) always led to SHS_C values smaller than 1.5. All these results tend to indicate that a 10-cycle pulse duration was the "turn-on" point for significant subharmonic generation which is consistent with the empirical-simulation results (Fig. 8). Finally, Fig. 9(a) illustrates the inherent randomness of the results because of the large standard deviations. The data were collected from the same vial of contrast agents on four different days over 4 months and results showed the same trends every day. (We did not report the results obtained between 0.7 and 1.2 MPa peak-rarefactional pressure because no subharmonic activity was seen for any exposure conditions.)

The results presented in Fig. 9(b) were very similar to those of Fig. 9(a). SHS_{SVD} increased with pulse duration at all pressures, peaked near 2 MPa for all pulse durations, and large standard deviations were observed. Overall, Figs. 9(a) and 9(b) add to the argument that the SVD method provides reliable results because SVD results show the same trends as the conventional method.

Figures 9(c) and 9(d) display estimates of τ_{NR} and τ_{SH} as a function of pressure and pulse duration, respectively. Estimates of τ_{NR} showed no variation as a function of pressure, but naturally increased with pulse duration and the standard deviation of the estimates remained small (<8 ns). The situation was slightly different for the estimates of τ_{SH}. With the exception of the unreliable estimates at 1.1 MPa (i.e., large standard deviations) and of the estimates at 2.1 MPa where SHS_{SVD} reached its maximum, estimates of τ_{SH} indicated a small trend of increase with peak-rarefactional pressure. Standard deviations were larger than that of τ_{NR}. Finally, comparing Figs. 9(c) and 9(d) indicates that overall $\tau_{NR} > \tau_{SH}$, i.e., the normal response lasts longer than the subharmonic response.

To quantify this observation more carefully, Fig. 9(e) displays estimates of $\Delta = \tau_{NR} - \tau_{SH}$ as a function of pressure and pulse duration. Estimates of Δ were overall positive (because $\tau_{NR} > \tau_{SH}$) and showed a decreasing trend with increasing peak-rarefactional pressure (because estimates of τ_{SH} showed an increasing trend). However, estimates of Δ provided new information: estimates of Δ did not vary significantly with pulse duration and numerical values decreased from about 45 ns at 1.8 MPa to about 20 ns at 5 MPa (estimates at 1.1 MPa appear to be unreliable). Physically, this decreasing trend indicated that as pressure increases, the subharmonic-response time-duration becomes closer to the normal-response time-duration (independent of the pulse duration of the excitation).

Finally, Fig. 9(f) displays estimates of d_{SH}. These estimates showed a decreasing trend with increasing peak-rarefactional pressure. In addition, there was arguably no dependence on pulse duration. Physically, this behavior means that as peak-rarefactional pressure increases, the subharmonic response initiates itself quicker after the normal response initiates itself (independent of the pulse duration of the excitation).

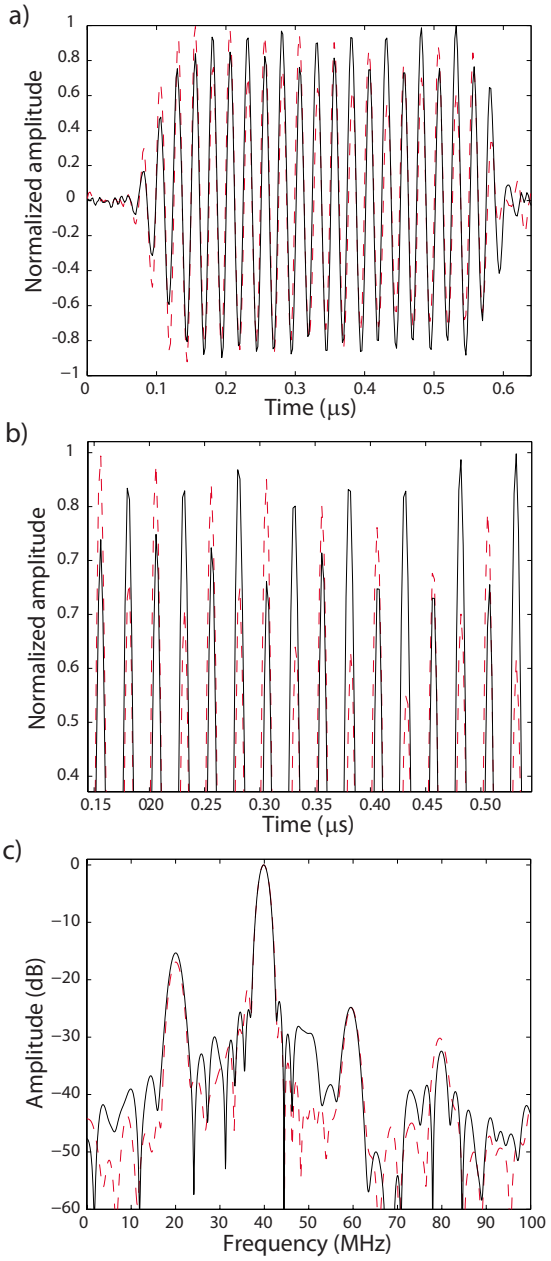

FIG. 10. (Color online) Illustration of positive and negative subharmonic events. (a) Time waveform of the most-positive (dash) and most-negative (solid) subharmonic events of a 1000-event data set obtained with 20-cycle excitation and a peak-rarefactional pressure of 2.1 MPa. (b) Magnified version of (a). (c) Spectra of the most-positive (dash) and most-negative (solid) subharmonic events.

E. Positive and negative subharmonic responses

Figures 7(e) and 7(f) indicate that for the presented example, the coefficients of the decomposition on the normal-response eigenvector always have the same sign while those on the subharmonic-response eigenvector could be positive or negative. Figure 10 displays two recorded events of a data set obtained with a 20-cycle excitation at 2.1-MPa peak-

rarefactional pressure. The waveforms were normalized for easier comparison. The dashed curve corresponds to the "most-positive" (i.e., largest positive coefficient on the subharmonic response) and the solid curve to the "most-negative" (i.e., largest negative coefficient on the subharmonic response) subharmonic events of the data set. Figure 10(a) indicates that the two events had similar waveforms and were well synchronized with positive peaks, negative peaks, and zero-crossings occurring at nearly the same time points. Furthermore, the amplitudes of the positive peaks were periodic for both waveforms, indicating, as in Fig. 6(e), a strong subharmonic content. Nevertheless, a striking difference was apparent in the positive-peak amplitudes of the two waveforms: they seemed to alternate with the dashed curve peaking when the solid curve was at its lowest, as can be better observed in Fig. 10(b). Figure 10(b) clearly indicates that the peak amplitudes were achieved alternatively by the most-positive and most-negative subharmonic events. Although differences between the two events could be observed in the time domain, only small differences were apparent in the frequency domain [Fig. 10(c)]. The spectra of both events had strong components at 40 and 20 MHz and some energy at 60 and 80 MHz. The only difference was the presence of a small component at 50 MHz for the most-negative subharmonic event, but not for the most-positive subharmonic event.

Figure 10 again emphasizes the strength of the SVD method over the conventional method. Based on the conventional-method criteria of Sec. II E 1, both waveforms would be detected by the conventional method as valid subharmonic events. However, only the SVD method gives us the information necessary to track positive and negative subharmonic events.

IV. DISCUSSION AND CONCLUSION

This study investigated a SVD method of analyzing large data sets of single-bubble-backscatter events in order to draw physical insights about bubbles in HFU fields and to provide an approach to detecting and quantifying subharmonic events. The SVD method was compared to a conventional method that utilized individual-event spectra. The conventional method was easier to interpret from a physical standpoint and was used as a baseline reference to evaluate the effectiveness of the SVD method. The experimental [Figs. 9(a) and 9(b)] and empirical-simulation [Figs. 8(a) and 8(b)] results confirmed that the SVD method had performance similar to the conventional method. The SVD method also provided information about the bubble oscillation properties that were not available with the conventional method. For example, the SVD method showed that the subharmonic response of the bubble initiated itself after, and had a shorter time-duration, than the normal response.

The SVD method also provided means of finding the events with the most- and least-subharmonic contents. The conventional subharmonic detection method only provided a yes/no qualitative evaluation and therefore did not provide a means to quantify how much an event was subharmonic. The SVD approach was fundamentally quantitative because it yielded the coefficient of each event on the subharmonic-response eigenvector. For physicists studying bubble oscillations in a HFU field, quantifying the subharmonic events is invaluable. Therefore, the results of this study indicated that the SVD method is a valid and useful tool to study and quantify single-bubble oscillations.

The focus of this study was on the development and the validation of the SVD method. Physical interpretation of the results, to date, is limited and is under current investigation. In particular, we are designing simulations using previous models.[15] The simulations will be conducted to generate 1000-event data sets by varying simulation parameters following experimentally-derived distributions of experimental parameters such as UCA size, incident pressure, and other UCA properties. Size distributions can be obtained from measurements, and pressure distributions can be obtained by estimating the distance of the UCA from the focus of the transducer. In particular, we hope to determine optimal excitation conditions for generating strong subharmonic events and then evaluating these conditions experimentally using the SVD method. If the simulations were able to match the experimental results, then exposure conditions could be further optimized for subharmonic generation. Also, finding only positive subharmonic events based on the SVD processing of the simulations could indicate that the bubble oscillations were not spherical and, thus, a model that assumed spherical oscillation would not be appropriate.

The shell of the UCAs used in this study was stiffer than that of lipid-shelled agents (e.g., Definity®) for which subharmonic events have been reported for much lower pressures and larger bandwidths (i.e., shorter excitation durations).[8,9] Stiffer-shell UCAs typically require higher pressures and longer time-duration exposures to break. The observations of subharmonics at higher pressures and exposure durations that we observed for polymer-shelled agents are consistent with the hypothesis that the polymer-shelled agents need to break before generating subharmonics. It is not clear whether the SVD approach would work as well for lipid-shelled UCAs when they are excited with broadband emissions (e.g., time-durations shorter than 10 cycles). Theoretically, the SVD approach will be able to accurately separate the normal and subharmonic responses of the UCAs as long as they correspond to different singular values.

One of our interests is to evaluate the SVD method when the UCAs are insonified at pressures high enough to lead to inertial cavitation and the resulting broadband backscatter emissions. The conventional method or a band-pass filtering method would be unable to differentiate the subharmonic signal from the part of the broadband emission in the subharmonic band. However, we anticipate that the SVD method could potentially outperform the conventional method because the nature of the subharmonic signal in the time and frequency domains is fundamentally different from the broadband noise. Therefore, the broadband emission and noise should correspond to different singular values and eigenvectors of the SVD and be easily separable. Even in this more challenging situation, the normal-response and subharmonic-response eigenvectors would be correctly sepa-

rated. Furthermore, the SVD is statistically more robust because it uses the complete 1000-event data set to derive the eigenvectors used for characterization.

Similarly, we are investigating how a band-pass filtering approach would perform compared to the SVD method to estimate τ_{NR}, τ_{SH}, d_{SH}, and Δ. For this task, we also anticipate the SVD method to perform better because it should be able to differentiate actual subharmonic emissions from noise and other contributors to the subharmonic band. A band-pass filter approach would use the entire energy in the subharmonic band to estimate time-durations and time delays which would result in errors. Also, the SVD method should be more robust because the SVD eigenvectors used for the estimation of τ_{NR}, τ_{SH}, d_{SH}, and Δ are deduced from the 1000-event data set automatically. Many parameters would need to be carefully adjusted to design a satisfactory band-pass filter, and each set of parameters would lead to different and somewhat arbitrary estimates of τ_{NR}, τ_{SH}, d_{SH}, and Δ.

The next stages of this study will focus on better monitoring of valid events. We propose to accomplish this by combining acoustical and optical methods. The acoustical method will utilize a passive-cavitation detector (PCD) very similar to that of a previous study[22] except that the passive transducer will have a center frequency approximately half that of the exciting transducer. The PCD will provide better selectivity to valid events by guaranteeing in real time that both transducers receive valid signals. Furthermore, better sensitivity in subharmonic detection should be achieved because the receiving transducer will be more sensitive in the subharmonic band. The optical method will use a high-magnification digital camera triggered at the same PRF as the exciting transducer. The focal plane of the camera will be aligned with the focal region of the transducer. The camera will provide a real-time means of estimating the size of UCAs. Therefore, we anticipate that we will be able to link bubble size and subharmonic content and to answer important questions about which sizes are most likely to produce strong subharmonic events.

One of the potential clinical applications of UCAs at high frequencies is imaging of circulation in small veins and arteries (i.e., microcirculation imaging) for ophthalmologic and small-animal applications. SVD studies could determine optimal conditions to excite a non-linear response from UCAs. Then, SVD-based detection methods could permit a more-powerful approach to localizing UCAs and imaging flow when UCAs are nonlinearly excited. Microcirculation typically involves slow-moving, low-volume blood flow and is difficult to detect with current Doppler and HFU instrumentation.

In the eye, conventional ultrasonic instrumentation operating at or below 10 MHz is able to visualize and measure flow in the major orbital vessels supplying the eye,[23–25] but such systems are unable to detect microcirculatory flow in the anterior or posterior segments of the eye. UCA-SVD imaging could prove to be a valuable fine-resolution means to detect this microcirculation using HFU. In developmental biology, the study of vascular development is critical for normal embryonic maturation and currently is the focus of numerous research efforts using a variety of genetically-engineered mouse models. Genetic mechanisms that have gone awry are involved in a number of vascular pathologies, including tumor angiogenesis, so that understanding embryonic vascular development has a broad range of important clinical implications. Direct *in vivo* visualization of the developing embryonic vascular system is an attractive option for analyzing the complex three-dimensional patterns of vessel growth and patterning in normal mouse embryos and in mice with mutations in genes that affect vascular development. We anticipate that UCAs combined with SVD-based detection methods would be extremely valuable for studying vascular-system development in mouse embryos, potentially in three dimensions.

ACKNOWLEDGMENTS

This research was supported in part by NIH Grant No. EB006372 and the Riverside Research Institute Fund for Biomedical Engineering Research. The authors wish to thank POINT Biomedical and T. Ottoboni for making available the polymer-shelled agents used in these studies. The authors thank S. Ramachandran for her assistance in data collection and Dr. E. J. Feleppa for his help in preparing the manuscript.

[1] C. X. Deng and F. L. Lizzi, "A review of physical phenomena associated with ultrasonic contrast agents and illustrative clinical applications," Ultrasound Med. Biol. **28**, 277–286 (2002).
[2] A. Lyshchik, A. C. Fleischer, J. Huamani, D. E. Hallahan, M. Brissova, and J. C. Gore, "Molecular imaging of vascular endothelial growth factor receptor 2 expression using targeted contrast-enhanced high-frequency ultrasonography," J. Ultrasound Med. **26**, 1575–1586 (2007).
[3] J. K. Willmann, R. Paulmurugan, K. Chen, O. Gheysens, M. Rodriguez-Porcel, A. M. Lutz, I. Y. Chen, X. Chen, and S. S. Gambhir, "US imaging of tumor angiogenesis with microbubbles targeted to vascular endothelial growth factor receptor type 2 in mice," Radiology **246**, 508–518 (2008).
[4] C. X. Deng, F. L. Lizzi, R. H. Silverman, R. Ursea, and D. J. Coleman, "Imaging and spectrum analysis of contrast agents in the in vivo rabbit eye using very-high-frequency ultrasound," Ultrasound Med. Biol. **24**, 383–394 (1998).
[5] D. H. Turnbull and F. S. Foster, "Ultrasound biomicroscopy in developmental biology," Trends Biotechnol. **20**, S29–S33 (2002).
[6] K. Morgan, P. Dayton, A. Klibanov, G. Brandenburger, S. Kaul, K. Wei, and K. Ferrara, "Properties of contrast agents insonified at frequencies above 10 MHz," Proc.-IEEE Ultrason. Symp. **2**, 1127–1130 (1996).
[7] P. M. Moran, M. M. Al-Uzri, J. Watson, and M. A. Reveley, "Reduced kamin blocking in non paranoid schizophrenia: Associations with schizotypy," J. Psychiatr. Res. **37**, 155–163 (2003).
[8] D. E. Goertz, E. Cherin, A. Needles, R. Karshafian, A. S. Brown, P. N. Burns, and F. S. Foster, "High frequency nonlinear B-scan imaging of microbubble contrast agents," IEEE Trans. Ultrason. Ferroelectr. Freq. Control **52**, 65–79 (2005).
[9] D. E. Goertz, A. Needles, P. N. Burns, and F. S. Foster, "High-frequency, nonlinear flow imaging of microbubble contrast agents," IEEE Trans. Ultrason. Ferroelectr. Freq. Control **52**, 495–502 (2005).
[10] D. E. Goertz, M. E. Frijlink, N. de Jong, and A. F. van der Steen, "High frequency non-linear scattering from a micrometer to submicrometer sized lipid encapsulated contrast agent," Ultrasound Med. Biol. **32**, 569–577 (2006).
[11] D. E. Goertz, M. E. Frijlink, N. de Jong, and A. F. van der Steen, "Nonlinear intravascular ultrasound contrast imaging," Ultrasound Med. Biol. **32**, 491–502 (2006).
[12] J. S. Allen, D. E. Kruse, and K. W. Ferrara, "Shell waves and acoustic scattering from ultrasound contrast agents," IEEE Trans. Ultrason. Ferroelectr. Freq. Control **48**, 409–418 (2001).
[13] D. E. Goertz, M. E. Frijlink, D. Tempel, V. Bhagwandas, A. Gisolf, R. Krams, N. de Jong, and A. F. van der Steen, "Subharmonic contrast intravascular ultrasound for vasa vasorum imaging," Ultrasound Med. Biol. **33**, 1859–1872 (2007).

[14]A. Needles, D. E. Goertz, R. Karshafian, E. Cherin, A. S. Brown, P. N. Burns, and F. S. Foster, "High-frequency subharmonic pulsed-wave Doppler and color flow imaging of microbubble contrast agents," Ultrasound Med. Biol. **34**, 1139–1151 (2008).
[15]J. A. Ketterling, J. Mamou, J. S. Allen, O. Aristizábal, R. G. Williamson, and D. H. Turnbull, "Excitation of polymer-shelled contrast agents with high-frequency ultrasound," J. Acoust. Soc. Am. **121**, EL48–EL53 (2007).
[16]D. Patel, P. Dayton, J. Gut, E. Wisner, and K. W. Ferrara, "Optical and acoustical interrogation of submicron contrast agents," IEEE Trans. Ultrason. Ferroelectr. Freq. Control **49**, 1641–1651 (2002).
[17]D. N. Patel, S. H. Bloch, P. A. Dayton, and K. W. Ferrara, "Acoustic signatures of submicron contrast agents," IEEE Trans. Ultrason. Ferroelectr. Freq. Control **51**, 293–301 (2004).
[18]J. E. Gentle, *Numerical Linear Algebra for Applications in Statistics*, Statistics and computing (Springer, New York, 1998).
[19]D. Di Pietro Paolo, H. P. Muller, G. Nolte, and S. N. Erne, "Noise reduction in magnetocardiography by singular value decomposition and independent component analysis," Med. Biol. Eng. Comput. **44**, 489–499 (2006).
[20]P. Van Baren and E. S. Ebbini, "Multipoint temperature control during hyperthermia treatments: Theory and simulation," IEEE Trans. Biomed. Eng. **42**, 818–827 (1995).
[21]G. R. Lockwood, J. W. Hunt, and F. S. Foster, "The design of protection circuitry for high-frequency ultrasound imaging systems," IEEE Trans. Ultrason. Ferroelectr. Freq. Control **38**, 48–55 (1991).
[22]A. Y. Ammi, R. O. Cleveland, J. Mamou, G. I. Wang, S. L. Bridal, and W. D. O'Brien, "Ultrasonic contrast agent shell rupture detected by inertial cavitation and rebound signals," IEEE Trans. Ultrason. Ferroelectr. Freq. Control **53**, 126–136 (2006).
[23]D. S. Greenfield, P. A. Heggerick, and T. R. Hedges, "Color Doppler imaging of normal orbital vasculature," Ophthalmology **102**, 1598–605 (1995).
[24]W. E. Lieb, "Color Doppler imaging of the eye and orbit," Radiol. Clin. North Am. **36**, 1059–1071 (1998).
[25]F. Tanquart, O. Berges, P. Koskas, S. Arsene, C. Rossazza, P. Pisella, and L. Pourcelot, "Color Doppler imaging of orbital vessels: Personal experience and literature review," J. Clin. Ultrasound **31**, 258–273 (2003).

Erratum: Acoustic beam scattering and excitation of sphere resonance: Bessel beam example [J. Acoust. Soc. Am. 122, 247–252 (2007)]

Philip L. Marston
Department of Physics and Astronomy, Washington State University, Pullman, Washington 99164-2814

(Received 16 March 2009; accepted 18 March 2009)
[DOI: 10.1121/1.3117446]

PACS number(s): 43.40.Fz, 43.20.Fn, 43.80.Qf, 43.10.Vx

Concerning Appendix B of this paper,[1] a reader kindly pointed out the following error of transcription in the partial-wave denominator shown for evacuated shells. The expression for d_{52} should have been printed: $d_{52}=2[j_n(U) - Uj_n(U)']$. This change brings the expression in agreement with the referenced derivation[2] and it is derivable from expressions given by various other authors. The computations shown here and in the subsequent publications[3,4] pertaining to spherical shells used the correct expression.

[1]P. L. Marston, "Acoustic beam scattering and excitation of sphere resonance: Bessel beam example," J. Acoust. Soc. Am. **122**, 247–252 (2007).
[2]S. G. Kargl and P. L. Marston, "Acoustic beam scattering and excitation of sphere resonance: Bessel beam example," J. Acoust. Soc. Am. **85**, 1014–1028 (1989).
[3]P. L. Marston, "Negative axial radiation forces on solid spheres and shells in a Bessel beam," J. Acoust. Soc. Am. **122**, 3162–3165 (2007).
[4]P. L. Marston, "Scattering of a Bessel beam by a sphere: II. Helicoidal case and spherical shell example," J. Acoust. Soc. Am. **124**, 2905–2910 (2008).

 0001-4966/2009/125(6)/4092/1/$25.00

ACOUSTICAL NEWS—USA

Elaine Moran
Acoustical Society of America, Suite 1NO1, 2 Huntington Quadrangle, Melville, NY 11747-4502

Editor's Note: *Readers of this journal are encouraged to submit news items on awards, appointments, and other activities about themselves or their colleagues. Deadline dates for news and notices are 2 months prior to publication.*

New Fellows of the Acoustical Society of America

Douglas S. Brungart—For contributions to the perception of multiple talkers

2008-09 F.V. Hunt Postdoctoral Research Fellowship awarded to Todd Hay

Todd Hay

The 2008-09 F. V. Hunt Postdoctoral Research Fellowship in Acoustics has been awarded to Todd A. Hay. During his Hunt Fellowship year, Dr. Hay has undertaken a research program at the University of Twente in the Netherland. The subject of his research is on the investigation of bubble interaction dynamics in therapeutic ultrasound. Dr. Hay received BSEE and MSEE degrees in Electrical Engineering from the University of Texas at Austin and a Ph.D. in Electrical Engineering from Penn State University. His Ph.D. thesis is titled "A model of the interaction of bubbles and solid particles under acoustic excitation."

The Hunt Fellowship is granted each year to an ASA member who has recently received his or her doctorate or will be receiving the degree in the year in which the fellowship is to be granted. The recipient of the fellowship is that individual who, through personal qualifications and a proposed research topic, is judged to exhibit the highest potential for benefiting any aspect of the science of sound and promoting its usefulness to society. Further information about the fellowship is available from the Acoustical Society of America, Suite 1NO1, 2 Huntington Quadrangle, Melville, NY 11747-4502. Phone: 516-576-2360; fax: 516-576-2377; E-mail: asa@aip.org; Web: asa.aip.org/fellowships.html.

Advanced Degree Dissertation in Acoustics

Editor's Note: Abstracts of Doctoral and Master's theses will be welcomed at all times. Please note that they must be limited to 200 words, must include the appropriate PACS classification numbers, and formatted as shown below. If sent by postal mail, note that they must be double spaced. The address for obtaining a copy of the thesis is helpful. Submit abstracts to: Acoustical Society of America, Thesis Abstracts, Suite 1NO1, 2 Huntington Quadrangle, Melville, NY 11747-4502, e-mail: asa@aip.org.

Bone-conduction auditory steady-state responses [43.66 Yw, 43.64 Ri,43.66.Sr]—Susan Anne Small, *School of Audiology & Speech Sciences, University of British Columbia, Vancouver, BC, Canada April, 2007 (Ph.D.)*. This research investigated whether multiple auditory-state responses (ASSRs) to bone-conduction stimuli could be used to assess bone-conduction hearing. Infant bone-conduction testing methods, maturation of bone-conduction hearing, and ipsilateral/contralateral asymmetries in ASSRs were also assessed. Results show that bone-conduction ASSRs can estimate thresholds in normal-hearing subjects. Choice of EEG recording parameters can avoid spurious ASSRs due to aliasing; however, non-auditory spurious ASSRs (probably vestibular) can also be recorded. Investigation of infant testing methods on bone-conduction threshold shows that bone-oscillator coupling method and placement location on the temporal bone have no effect; however, a forehead placement results in elevated thresholds. Results show that bone-conducted signals are more effective for infants compared to adults across frequency, especially at low frequencies and that infants do not appear to have an occlusion effect. Normal levels for bone-conduction hearing in young and older infants are proposed. Ipsilateral/contralateral asymmetries in air- and bone-conduction ASSRs are present more often and are larger in infants compared to adults (potentially useful for isolating cochlea contributing to response in infants). The results of these studies indicate that infants can be screened for normal bone-conduction hearing with ASSRs; however, infants with hearing loss must be tested before elevated thresholds can be interpreted.

Supervisor: David R. Stapells

USA Meetings Calendar

Listed below is a summary of meetings related to acoustics to be held in the U.S. in the near future. The month/year notation refers to the issue in which a complete meeting announcement appeared.

24–28 June	5th International Middle-Ear Mechanics in Research and Otology (MEMRO), Stanford University, Stanford, CA [http://memro2009.stanford.edu].

 0001-4966/2009/125(6)/4093/2/$25.00

26–30 October	158th Meeting of the Acoustical Society of America, San Antonio, TX [Acoustical Society of America, Suite 1NO1, 2 Huntington Quadrangle, Melville, NY 11747-4502; Tel.: 516-576-2360; Fax: 516-576-2377; Email: asa@aip.org; WWW: http://asa.aip.org].

2010

19–23 April	Joint Meeting: 158th Meeting of the Acoustical Society of America and Noise Con 2010, Baltimore, MD [Acoustical Society of America, Suite 1NO1, 2 Huntington Quadrangle, Melville, NY 11747-4502; Tel.: 516-576-2360; Fax: 516-576-2377; Email: asa@aip.org; WWW: http://asa.aip.org].
15–19 November	2nd Iberoamerican Conference on Acoustics (Joint Meeting of the Acoustical Society of America, Mexican Institute of Acoustics, and Iberoamerican Federation on Acoustics), Cancun, Mexico [Acoustical Society of America, Suite 1NO1, 2 Huntington Quadrangle, Melville, NY 11747-4502; Tel.: 516-576-2360; Fax: 516-576-2377; Email: asa@aip.org; WWW: http://asa.aip.org].

Cumulative Indexes to the Journal of the Acoustical Society of America

Ordering information: Orders must be paid by check or money order in U.S. funds drawn on a U.S. bank or by Mastercard, Visa, or American Express credit cards. Send orders to Circulation and Fulfillment Division, American Institute of Physics, Suite 1NO1, 2 Huntington Quadrangle, Melville, NY 11747-4502; Tel.: 516-576-2270. Non-U.S. orders add $11 per index.

Some indexes are out of print as noted below.

Volumes 1–10, 1929–1938: JASA, and Contemporary Literature, 1937–1939. Classified by subject and indexed by author. Pp. 131. Price: ASA members $5; Nonmembers $10

Volumes 11–20, 1939–1948: JASA, Contemporary Literature and Patents. Classified by subject and indexed by author and inventor. Pp. 395. Out of Print

Volumes 21–30, 1949–1958: JASA, Contemporary Literature and Patents. Classified by subject and indexed by author and inventor. Pp. 952. Price: ASA members $20; Nonmembers $75

Volumes 31–35, 1959–1963: JASA, Contemporary Literature and Patents. Classified by subject and indexed by author and inventor. Pp. 1140. Price: ASA members $20; Nonmembers $90

Volumes 36–44, 1964–1968: JASA and Patents. Classified by subject and indexed by author and inventor. Pp. 485. Out of Print.

Volumes 36–44, 1964–1968: Contemporary Literature. Classified by subject and indexed by author. Pp. 1060. Out of Print

Volumes 45–54, 1969–1973: JASA and Patents. Classified by subject and indexed by author and inventor. Pp. 540. Price: $20 (paperbound); ASA members $25 (clothbound); Nonmembers $60 (clothbound)

Volumes 55–64, 1974–1978: JASA and Patents. Classified by subject and indexed by author and inventor. Pp. 816. Price: $20 (paperbound); ASA members $25 (clothbound); Nonmembers $60 (clothbound)

Volumes 65–74, 1979–1983: JASA and Patents. Classified by subject and indexed by author and inventor. Pp. 624. Price: ASA members $25 (paperbound); Nonmembers $75 (clothbound)

Volumes 75–84, 1984–1988: JASA and Patents. Classified by subject and indexed by author and inventor. Pp. 625. Price: ASA members $30 (paperbound); Nonmembers $80 (clothbound)

Volumes 85–94, 1989–1993: JASA and Patents. Classified by subject and indexed by author and inventor. Pp. 736. Price: ASA members $30 (paperbound); Nonmembers $80 (clothbound)

Volumes 95–104, 1994–1998: JASA and Patents. Classified by subject and indexed by author and inventor. Pp. 632, Price: ASA members $40 (paperbound); Nonmembers $90 (clothbound)

Volumes 105–114, 1999–2003: JASA and Patents. Classified by subject and indexed by author and inventor. Pp. 616, Price: ASA members $50; Nonmembers $90 (paperbound)

ACOUSTICAL NEWS—INTERNATIONAL

Walter G. Mayer
Physics Department, Georgetown University, Washington, DC 20057

International Meetings Calendar

Below are announcements of meetings and conferences to be held abroad. Entries preceded by an * are new or updated listings.

June 2009

2–5 **XXI Session of the Russian Acoustical Society**, Moscow, Russia (www.akin.ru/main.htm).

17–19 **3rd International Conference on Wind Turbine Noise**, Aalborg, Denmark (www.windturbinenoise2009.org)

21–25 **13th International Conference "Speech and Computer,"** St. Petersburg, Russia (www.specom.nw.ru).

22–26 **3rd International Conference on Underwater Acoustic Measurements: Technologies and Results**, Nafplion, Peleponnese, Greece (www.uam2009.gr).

July 2009

5–9 **16th International Congress on Sound and Vibration**, Krakow, Poland (www.icsv16.org).

19–23 **15th International Conference on Photoacoustics and Photothermal Phenomena**, Leuven, Belgium (www.icppp15.be).

August 2009

12–16 **7th Triennual Conference of the European Society for Cognitive Science of Music (ESCOM2009)**, Jyväskylä, Finland (www.fyu.fi/hum/laitokset/musikki/en/escom2009).

23–28 **Inter-noise 2009**, Ottawa, Ont., Canada (www.internoise2009.com).

September 2009

6–10 **InterSpeech 2009**, Brighton, UK (www.interspeech2009.org).

9–11 **9th International Conference on Theoretical and Computational Acoustics**, Dresden, Germany (Ictca2009.com).

14–18 **5th Animal Sonar Symposium**, Kyoto, Japan (cse.fra.affrc.go.jp/akamatsu/AnimalSonar.html).

15–17 **Autumn Meeting of the Acoustical Society of Japan**, Koriyama, Japan (www.asj.go.jp/index-en.html).

18–22 ***International Conference on Auditory Display 2009 (ICAD)**, Copenhagen, Denmark (www.icad09.dk).

19–23 **IEEE 2009 Ultrasonics Symposium**, Rome, Italy (e-mail: pappalar@uniroma3.it).

21–23 **10th Western Pacific Acoustics Conference (WESPAC)**, Beijing, China (www.wespacx.org).

23–25 **Pacific Rim Underwater Acoustics Conference (9pruac)**, Xi'an, China (e-mail: lfh@mail.ioa.ac.cn).

23–25 **TECNIACUSTICA2010**, Cádiz, Spain (www.sea-acustica.es).

October 2009

5–7 **International Conference on Complexity of Nonlinear Waves**, Tallinn, Estonia (www.ioc.ee/cnw09).

26–28 **Euronoise 2009**, Edinburgh, UK (www.euronoise2009.org.uk).

June 2010

9–11 **14th Conference on Low Frequency Noise and Vibration**, Aalborg, Denmark (www.lowfrequency2010.org).

13–16 **INTERNOISE2009**, Lisbon, Portugal, (www.internoise2009.org).

August 2010

23–27 **20th International Congress on Acoustics (ICA2010)**, Sydney, Australia (www.ica2010sydney.org).

September 2010

15–18 ***Alps-Adria-Acoustics-Association Meeting joint with EAA**, Ljubljana, Slovenia (e-mail: mirko.cudina@fs.uni-lj.si).

26–30 **Interspeech 2010**, Makuhari, Japan (www.interspeech2010.org).

June 2011

27–1 **Forum Acusticum 2011**, Aalborg, Denmark. (www.fa2011.org).

August 2011

27–31 **Interspeech 2011**, Florence, Italy (www.interspeech2011.org).

September 2011

4–7 **International Congress on Ultrasonics**, Gdansk, Poland.

4–7 **Internoise 2011**, Osaka, Japan

November 2011

16–18 ***2nd American/Iberian Meeting on Acoustics**, Cancun, Mexico.

June 2013

2–7 **21st International Congress on Acoustics (ICA2013)**, Montréal, Canada (www.ica2013montreal.org).

Regional Chapter News

Madras Regional Chapter

The Madras Regional Chapter of the Acoustical Society of America (MIRC-ASA) held three meetings in 2008, on 21 June, 19 July and 23-24 December. The December meeting was held jointly with the Acoustical Society of India (ASI).

On 21 June, V. Rajendran, Vice-President of ASI and Director, Research and Development and Center for Nano Science and Technology, K.S. Rangasamy College of Technology, KSR Kalavi Nagar, Triuchengode, delivered an invited lecture titled "Biomedical Application of Micro-electro-mechanical System" and Sri J. Jayapandian, Head, Design Development & Service Section, Material Science Division, IGCAR, Jalpakkam, delivered a lecture for students titled "Applications of Ultrasonics in Science and Technology" at Tamil Nadu Science and Technology Centre (TNSTC). As a result, a large number of students participated in the meeting.

FIG. 1. (l to r): Jesse Hamar, M. Kelvin, and R. Dhilsha, H. S. Paul, and A. Athaullah.

 0001-4966/2009/125(6)/4095/2/$25.00

The Acoustics Fair ceremony of the MIRC-ASA and the International Research Institute for the Deaf (IRID) was conducted at TNSTC on 19 July. The following three students under 20 years of age received awards from H. S. Paul, Chapter Representative of MIRC-ASA and President of Acoustical Foundation for Education and Charitible Trust (AFECT) and IRID) and R. Dhilsha, Vice President of MIRC-ASA: Jesse L. Hamar (First), Sri A. Athaullah, and Sri M. Kelvin (see Fig. 1).

On 23 December, M. Kumaresan Secretary of MIRC-ASA and AFECT and Director of IRID, delivered the Mira Paul Memorial Distinguished Lecture on "Bernoulli Effect and Voice Therapy" and S. S. Agrawal, Past President of ASI and Adviser of AFECT and Adviser of Centre for Development of Advanced Computing, Nodia and Executive Director of KIIT College of Engineering, Gurgang, delivered the Mira Paul Memorial Distinguished Lecture on "Development of Resources and Technologies for Breaking Communication Barriers in the Context of Indian Spoken Languages" at Naval Science and Technology Lab. (NSTL), Visakhapatanam.

The award ceremony of MIRC-ASA and IRID (AFECT) was conducted during the joint meeting between MIRC-ASA & ASI held in December 2008. The chief guest was Vice Admiral Nirmal Verama. At the end of the inaugural function, H.S. Paul presented the Mira Paul Memorial Gold Medal to S. S. Agrawal and M. Kumaresan. On 24 December V. Bhujanga Rao (President of AFECT & Director of NSTL) presented the Silver Medal to A. Ramachandraiah, Treasurer of MIRC-ASA & Trustee of AFECT, Professor Civil Engineering, IIT Madras. (See Figs. 2–5).

FIG. 2. (l to r): V. Bhujanga Rao presenting memento to H. S. Paul.

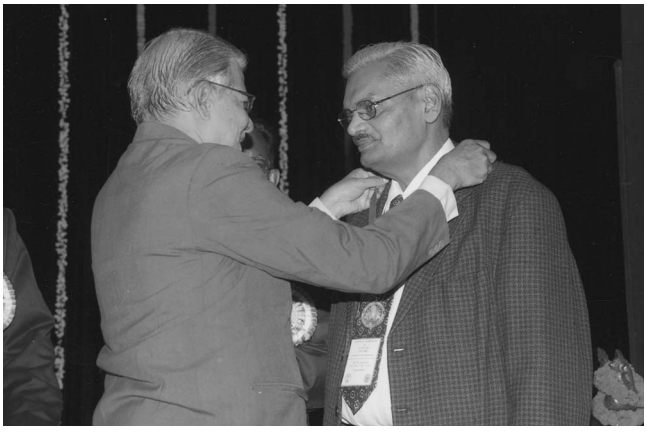

FIG. 3. (l to r): H. S. Paul presents the Mira Paul Memorial Gold Medal to S. S. Agrawal.

The following students won the best paper awards presented by H. S. Paul, Chapter representative of MIRC-ASA: M. Vamsikanth; R. Kalai Selvi; Maneesh V. Kunte, K. Bhavani, P. Santhi and G. Padmanabhan. (see Fig. 6).

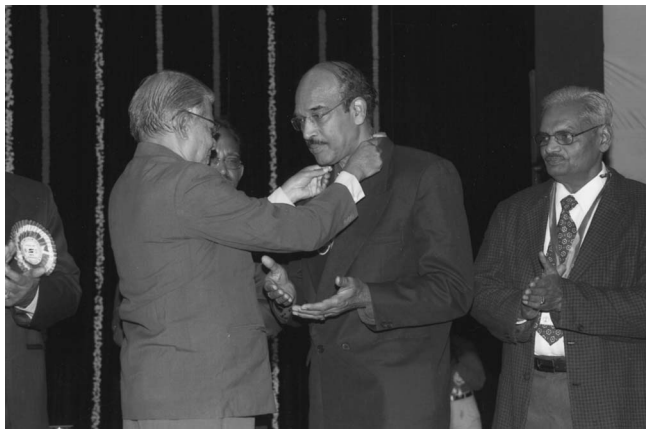

FIG. 4. (l to r) H. S. Paul presents the Mira Paul Memorial Gold Medal to M. Kumaresan.

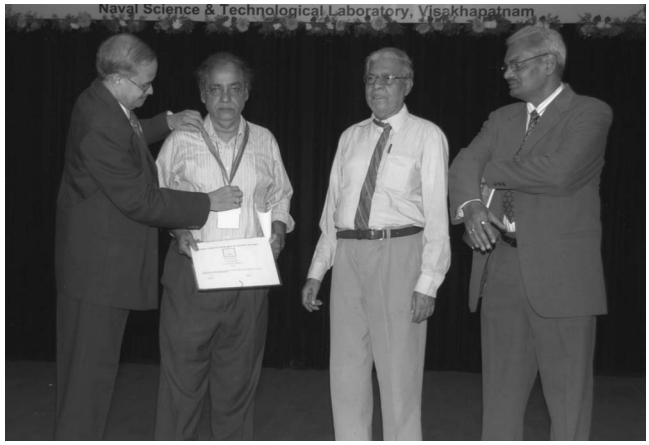

FIG. 5. (l to r) V. Bhujanga Rao presents the Silver Medal to A. Ramachandraiah.

FIG. 6. (l to r) V. Bhujanga Rao, M. Vamsikanth, R. Kalai Selvi, K. Bhavani, H. S. Paul.

BOOK REVIEWS

P. L. Marston
Physics Department, Washington State University, Pullman, Washington 99164

These reviews of books and other forms of information express the opinions of the individual reviewers and are not necessarily endorsed by the Editorial Board of this Journal.

Mechanical Sound: Technology, Culture, and Public Problems of Noise in the Twentieth Century (Inside Technology)

Karin Bijsterveld

The MIT Press, 350 pp. Price: $40,00 (hardcover). ISBN: 978-0-262-02639-0

An exciting and interesting book! Karin Bijsterveld, the author, gives a socio-historical description of industrial noise, traffic noise, noise from neighborhood radios and gramophones, as well as aircraft noise for the period of time between 1875 and today, offering a detailed outline about sounds and sound sources in Europe and the USA.

Once you have started reading you will find it difficult to put the book down: It comprises information on noise and sounds using Murray Schafer's categories and depicts "repertoires of dramatizing sound," "the ongoing charge of industrial noise," and "traffic noise as an instrument of torture." Furthermore, the author discusses "the celebration and control of mechanical sound in music" and the introduction of a "practical aircraft noise index." At the end, she describes the "sound history of technological culture."

This is a special book in which the author describes and analyzes acoustics in its social context. *Mechanical Sound: Technology, Culture, and Public Problems of Noise in the Twentieth Century* is a book for anyone who has interests in acoustics in some way: engineers, sound designers, city planners, and sociologists. The reader receives well-described and detailed information about what has influenced the history of noise.

As a professional acoustician, however, you can easily get lost in the detailed information once you start trying to find specific background information and explanations. Furthermore, there are hardly any references to renowned acousticians and established acoustical methods.

Otherwise, the author succeeds in regarding and discussing acoustics under new and relevant aspects: social relevance, rules for the perception of noise and the communication about noise in laboratories and committees, attempts to find appropriate definitions for annoyance and pleasantness of sounds, discussions about appropriate and inappropriate measuring methods, discussions about the use of test persons, as well as irritations about the paradox phenomenon of experiencing objectively quiet places as noisy and objectively noisy places as acceptable.

"Public concerns should be distinguished from private ones:" This is the author's main claim which she consistently follows through her complete work. There are hundreds of organizations and institutions which are engaged with "public problems" caused by noise. They deal with the questions of noise abatement and aim to find the correct answers and appropriate regulations. By contrast, "private problems" with noise are of different origin and connected to people's individual history in a complex way.

Noise can be seen as a conflict between economic progress, increasing population and social mobility on the one hand and public health on the other hand. The author integrates noise into the context of the historical development of technology and culture. According to the author, the challenge is to historicize sensory perceptions and to focus on the impairment of single persons as well as the dramatization of sound experiences by noise. This finally leads from a private to a public problem. However, the "public solutions" found in regulations do not solve this problem and often even prevent workers from perceiving important sound information. The so-called objective noise evaluations of road noise do not take into account what is at the center of people's complaints about noise.

By the way, it is definitely worth mentioning the graphics and photos chosen by the author to illustrate the worldwide resistance against noise historically.

Karin Bijsterveld refers to the city noise problem as well as to "the celebration and control of mechanical sound in music" which serve as important sound elements of societies. Lifestyles of the 20th and 21st centuries in combination with new product sounds lead to acceptance on the one hand and dilemma on the other hand and demands new attitudes and ways of behaving in societies and neighborhoods.

The European Harmonization in 2000, which aims to "harmonize noise indicators and assessment methods for environmental noise and to use these standards for the development of noise maps," is explored with regard to its use as a "practical aircraft noise index." The author skillfully refers to the past and discusses the many different measuring methods using much historical detail.

The reader is given the feeling of experiencing the historical development himself. Despite going into too much detail from time to time, the author still comes to an interesting result: "This as well as previous work on the history of standardization suggest that there is a world to gain after standards have been considered." Consequently, the author concludes that there is a "putative opposition between economic progress and environmental concerns." Furthermore, she discusses the "sound history of technical culture" with regard to noise and the different subjective evaluations under the aspect of the "paradox of control and the spatial focus of noise abatement." In this final chapter the discussion about public and private noise problems reaches a crucial point. The author puts emphasis on regulations and private arrangements concerning noise in everyday life; she claims that "feeling of being in or out of control is highly significant for the perception of sound."

The dilemma of appropriate evaluation remains. However, according to Karin Bijsterveld there are three alternative approaches in noise abatement—"ecological modernization, sensibility in law, and complaining in style"—which could contribute to the separation of private and public noise problems. These three approaches could serve as a new form of interdisciplinary strategies.

As a whole, the author does not offer any solutions to the reader which is no surprise because such expectations cannot be fulfilled. However, she involves the reader in the process of finding solutions for noise annoyance and gives him the opportunity to reflect about indices for impairment and noise like experts for acoustics. Moreover, the reader is invited to participate in the search for appropriate overall solutions which may induce him to develop problem solving strategies himself.

Altogether a remarkable book, *Mechanical Sound: Technology, Culture, and Public Problems of Noise in the Twentieth Century*, does not only show the complexity of dealing with acoustics but it allows the reader to sense and experience acoustics.

BRIGITTE SCHULTE-FORTKAMP
Institute of Fluid Mechanics and Engineering Acoustics,
Technische Universität Berlin,
10578 Berlin, Germany

Microphone Array Signal Processing

Jacob Benesty, Jingdong Chen, and Yiteng Huang

Springer, Berlin, 2008. 240 pp. price $119 (hardcover). ISBN: 3540786112

Conducting face-to-face conversation is a task typically performed without any great effort. Why is it becoming such a challenging task when the conversation is aided by a communication system? Although the book

 0001-4966/2009/125(6)/4097/1/$25.00

"Microphone Array Signal Processing" by Benesty, Chen, and Huang does not aim to answer this question directly, it does prompt the difficulties arising in applications such as teleconferencing, human-machine interfaces, and hands-free communication, and presents some of the state-of-the-art solutions using microphone arrays and acoustic signal processing.

JASA readers with interest in the areas of acoustic signal processing, speech processing and communication systems, acoustical measurements and instrumentation, and architectural acoustics may find the book relevant and useful. Throughout the book, signal processing methods for microphone arrays are presented that aim to combat *noise* and *reverberation*, two major disturbing factors of speech communion systems. This may not be a simple task, as evident from the large number of methods presented in the book. Although the book tackles the problem from a signal processing perspective, the fundamental problems are acoustic in nature, which is why JASA readers may find this book relevant.

The book is especially written for graduate students and research engineers working on microphone arrays, as the authors suggest, but also for those who would like an update on the state-of-the-art in the area of noise reduction and de-reverberation using microphone arrays. Although the book requires a good background in signal processing, the authors do include throughout the book their insight into the problems at hand, the factors limiting performance, and other practical aspects of the methods, which may benefit those who are interested in an overview of the methods and their features.

The book contains ten chapters. After an introduction in Chap. 1, classical optimal filters such as Wiener, Frost, and Kalman are presented in Chap. 2. The chapter highlights the differences between the various filters and shows that by incorporating different objective functions and constraints, filters can optimize noise reduction, speech distortion, or a mixture of the two. This theme continues to the following chapters.

Chapter 3 presents filtering in the space domain, or beamforming, in a way suitable for those unfamiliar with the topic. Delay-and-sum, minimum-variance distortionless response, null-steering, and other methods are discussed. Chapter 4 follows with the method of linearly-constrained minimum variance for combating both noise and reverberation. It is argued that both can indeed be eliminated, but this requires knowledge of the room impulse responses, which is difficult to estimate in practice when speakers are recorded in a room, for example. The spatio-temporal approach is presented that avoids the need to estimate room impulse responses by employing frequency response functions relative to one of the microphones rather than the actual source. This leads to noise reduction capability, but without the capacity to perform de-reverberation.

Chapter 5 focuses on the task of noise reduction from a multiple-channel view-point using a range of methods, some previously presented, highlighting their ability to reduce noise, maintain the signal without distortion, and exploit the spatial information. Chapter 6 continues with the method of frequency-domain optimal filtering, where by weighting each frequency an improvement in the overall signal-to-noise ratio can be achieved. The method is appropriate for broadband signals such as speech, and various strategies are presented for balancing noise reduction and signal distortion.

Chapter 7 presents a multiple-input–multiple-output model for the problem at hand, analyzing performance with respect to system parameters such as filter lengths. In Chap. 8, further insight into the problem is attained by developing a two-stage solution, namely, source separation and de-reverberation, facilitating de-reverberation methods such as equalization.

Chapter 9 presents the important topic of direction-of-arrival estimation, discussing methods such as multiple signal classification and generalized cross-correlation. Chapter 10 concludes the book with some unaddressed problems, arguing that many aspects of the problems at hand are still open.

To summarize, the book presents in a clear manner a wealth of signal processing methods to combat noise and reverberation using microphone arrays, providing insight into their performance and limitations. JASA readers, including myself, may have liked to see more acoustics incorporated into these methods, e.g., room acoustics, hearing, speech perception, as the disturbances are, after all, acoustic in nature. Perhaps the appropriate combination of signal processing with acoustics may facilitate the desired progress?

BOAZ RAFAELY
Department of Electrical and Computer Engineering,
Ben-Gurion University of the Negev,
Beer-Sheva 84105, Israel

Engineering the Guitar: Theory and Practice

Richard Mark French

Springer, 2008. 284 pp. Price: $49.95 (hardcover). ISBN: 0387743685.

String instruments of the cavity-enclosing, ported shell type are a veritable vibro-acoustic goldmine that encompasses a remarkable range of acoustics just to gain a basic understanding of their overall character. These instruments can be viewed as relatively simple objects excited in a straightforward manner by a player and judged by perceptions, as a craft device requiring many years of experience to properly construct and extract the best sound, or as a system requiring the best contemporary technology just to comprehend some physical aspects of the perceived quality. And just to make matters all the more difficult the modifications and tweaks performed in the mechanical world to enhance perceived quality rely on final judgments mainly in the acoustical world. Compound all this with the reality that there is no direct trail back from sound to mechanics, and it seems astonishing that we are able to create fine sounding string instruments at all.

Although my area of expertise is the violin, many of the concerns in making, playing, and judging bowed string instruments are relevant to the guitar, probably the most popular stringed instrument of all, with commercial USA production nominally 1×10^6 units per year according to the author. While there is considerable material online about engineering applied to the guitar (URLs for a few introductory sites: http://www.guitarengineer.com and http://www.home.agilent.com/agilent/editorial.jspx?cc=AW&lc=eng&ckey=866697&id=866697) and much in the way of published articles (see the Guild of American Luthiers Journal as one example) there does not appear to be another book that deals with the engineering aspects. Thus this book serves a real purpose for scientifically-oriented guitar makers and aficionados as well as those interested in a broad overview of the world of guitars, including materials, introductory acoustics, the neck as cantilever beam, finite and boundary element analyses, guitar electronics, individual and industrial construction techniques, a primer on human hearing, etc., a veritable manifold of matters concerning this very popular instrument. (However, anyone interested in just the craft of building guitars—solid body, acoustic, arch top, etc.—would be better served by one of the many craft-oriented books presently available.)

Of course broad coverage in an ~250 page book must consequently be somewhat shallow on any individual topic, but such a presentation has significant virtues in providing a broad introduction as well as a guide to individuals interested in following up on any topic via over 130 references. *Engineering the Guitar* offers many interesting practical insights although some of these might be difficult for a typical maker to utilize. As an example of the latter, consider the problem of shape; chapter 5 offers a useful analytic parametrization of guitar shape in polar coordinates after conversion from rectangular coordinates (Fig. 5.12 would benefit from R and θ labels as coordinate system origin choice is discussed). What is missing though is a software roadmap for the curve fitting of the geometry data using the rational polynomial series employed. Can this be done in a readily available spreadsheet program, or does it need specialized math software?

The author's personal building experience and his knowledge of a wide variety of guitar construction techniques are put to good use in this book. Its overall broad view is very good reading for those interested in the myriad of details involved in constructing a string instrument and then evaluating it scientifically. The range of references is wide-ranging, although I miss the very first application of nearfield acoustical holography to a musical instrument [W. Strong *et al.*, "Studying a guitar's radiation properties with nearfield holography," J. Guitar Acoust. **6**, 50–59 (1982)] showing

 0001-4966/2009/125(6)/4098/1/$25.00

how important the sound hole radiation is to the overall radiation from the guitar. The weakest part of the book lies in its discussion of the vibration-radiation metamorphosis, where some comprehensive vibration-radiation experiments to get a handle on such matters as radiation efficiency and effective critical frequency would be highly beneficial. Overall, however, the author is to be commended for providing a significant addition to the guitar literature in his broad-ranging book on a very important string instrument.

The review author, with over 35 years of experience in violin research, maintains a comprehensive violin acoustics research facility at East Carolina University, where he is emeritus professor of physics.

GEORGE BISSINGER
Department of Physics,
East Carolina University,
Greenville, NC 27858

 0001-4966/2009/125(6)/4098/1/$25.00

BOOK REVIEWS

P. L. Marston
Physics Department, Washington State University, Pullman, Washington 99164

These reviews of books and other forms of information express the opinions of the individual reviewers and are not necessarily endorsed by the Editorial Board of this Journal.

Mechanical Sound: Technology, Culture, and Public Problems of Noise in the Twentieth Century (Inside Technology)

Karin Bijsterveld

The MIT Press, 350 pp. Price: $40,00 (hardcover). ISBN: 978-0-262-02639-0

An exciting and interesting book! Karin Bijsterveld, the author, gives a socio-historical description of industrial noise, traffic noise, noise from neighborhood radios and gramophones, as well as aircraft noise for the period of time between 1875 and today, offering a detailed outline about sounds and sound sources in Europe and the USA.

Once you have started reading you will find it difficult to put the book down: It comprises information on noise and sounds using Murray Schafer's categories and depicts "repertoires of dramatizing sound," "the ongoing charge of industrial noise," and "traffic noise as an instrument of torture." Furthermore, the author discusses "the celebration and control of mechanical sound in music" and the introduction of a "practical aircraft noise index." At the end, she describes the "sound history of technological culture."

This is a special book in which the author describes and analyzes acoustics in its social context. *Mechanical Sound: Technology, Culture, and Public Problems of Noise in the Twentieth Century* is a book for anyone who has interests in acoustics in some way: engineers, sound designers, city planners, and sociologists. The reader receives well-described and detailed information about what has influenced the history of noise.

As a professional acoustician, however, you can easily get lost in the detailed information once you start trying to find specific background information and explanations. Furthermore, there are hardly any references to renowned acousticians and established acoustical methods.

Otherwise, the author succeeds in regarding and discussing acoustics under new and relevant aspects: social relevance, rules for the perception of noise and the communication about noise in laboratories and committees, attempts to find appropriate definitions for annoyance and pleasantness of sounds, discussions about appropriate and inappropriate measuring methods, discussions about the use of test persons, as well as irritations about the paradox phenomenon of experiencing objectively quiet places as noisy and objectively noisy places as acceptable.

"Public concerns should be distinguished from private ones:" This is the author's main claim which she consistently follows through her complete work. There are hundreds of organizations and institutions which are engaged with "public problems" caused by noise. They deal with the questions of noise abatement and aim to find the correct answers and appropriate regulations. By contrast, "private problems" with noise are of different origin and connected to people's individual history in a complex way.

Noise can be seen as a conflict between economic progress, increasing population and social mobility on the one hand and public health on the other hand. The author integrates noise into the context of the historical development of technology and culture. According to the author, the challenge is to historicize sensory perceptions and to focus on the impairment of single persons as well as the dramatization of sound experiences by noise. This finally leads from a private to a public problem. However, the "public solutions" found in regulations do not solve this problem and often even prevent workers from perceiving important sound information. The so-called objective noise evaluations of road noise do not take into account what is at the center of people's complaints about noise.

By the way, it is definitely worth mentioning the graphics and photos chosen by the author to illustrate the worldwide resistance against noise historically.

Karin Bijsterveld refers to the city noise problem as well as to "the celebration and control of mechanical sound in music" which serve as important sound elements of societies. Lifestyles of the 20th and 21st centuries in combination with new product sounds lead to acceptance on the one hand and dilemma on the other hand and demands new attitudes and ways of behaving in societies and neighborhoods.

The European Harmonization in 2000, which aims to "harmonize noise indicators and assessment methods for environmental noise and to use these standards for the development of noise maps," is explored with regard to its use as a "practical aircraft noise index." The author skillfully refers to the past and discusses the many different measuring methods using much historical detail.

The reader is given the feeling of experiencing the historical development himself. Despite going into too much detail from time to time, the author still comes to an interesting result: "This as well as previous work on the history of standardization suggest that there is a world to gain after standards have been considered." Consequently, the author concludes that there is a "putative opposition between economic progress and environmental concerns." Furthermore, she discusses the "sound history of technical culture" with regard to noise and the different subjective evaluations under the aspect of the "paradox of control and the spatial focus of noise abatement." In this final chapter the discussion about public and private noise problems reaches a crucial point. The author puts emphasis on regulations and private arrangements concerning noise in everyday life; she claims that "feeling of being in or out of control is highly significant for the perception of sound."

The dilemma of appropriate evaluation remains. However, according to Karin Bijsterveld there are three alternative approaches in noise abatement—"ecological modernization, sensibility in law, and complaining in style"—which could contribute to the separation of private and public noise problems. These three approaches could serve as a new form of interdisciplinary strategies.

As a whole, the author does not offer any solutions to the reader which is no surprise because such expectations cannot be fulfilled. However, she involves the reader in the process of finding solutions for noise annoyance and gives him the opportunity to reflect about indices for impairment and noise like experts for acoustics. Moreover, the reader is invited to participate in the search for appropriate overall solutions which may induce him to develop problem solving strategies himself.

Altogether a remarkable book, *Mechanical Sound: Technology, Culture, and Public Problems of Noise in the Twentieth Century*, does not only show the complexity of dealing with acoustics but it allows the reader to sense and experience acoustics.

BRIGITTE SCHULTE-FORTKAMP
Institute of Fluid Mechanics and Engineering Acoustics,
Technische Universität Berlin,
10578 Berlin, Germany

Microphone Array Signal Processing

Jacob Benesty, Jingdong Chen, and Yiteng Huang

Springer, Berlin, 2008. 240 pp. price $119 (hardcover). ISBN: 3540786112

Conducting face-to-face conversation is a task typically performed without any great effort. Why is it becoming such a challenging task when the conversation is aided by a communication system? Although the book

 0001-4966/2009/125(6)/4097/1/$25.00

"Microphone Array Signal Processing" by Benesty, Chen, and Huang does not aim to answer this question directly, it does prompt the difficulties arising in applications such as teleconferencing, human-machine interfaces, and hands-free communication, and presents some of the state-of-the-art solutions using microphone arrays and acoustic signal processing.

JASA readers with interest in the areas of acoustic signal processing, speech processing and communication systems, acoustical measurements and instrumentation, and architectural acoustics may find the book relevant and useful. Throughout the book, signal processing methods for microphone arrays are presented that aim to combat *noise* and *reverberation*, two major disturbing factors of speech communion systems. This may not be a simple task, as evident from the large number of methods presented in the book. Although the book tackles the problem from a signal processing perspective, the fundamental problems are acoustic in nature, which is why JASA readers may find this book relevant.

The book is especially written for graduate students and research engineers working on microphone arrays, as the authors suggest, but also for those who would like an update on the state-of-the-art in the area of noise reduction and de-reverberation using microphone arrays. Although the book requires a good background in signal processing, the authors do include throughout the book their insight into the problems at hand, the factors limiting performance, and other practical aspects of the methods, which may benefit those who are interested in an overview of the methods and their features.

The book contains ten chapters. After an introduction in Chap. 1, classical optimal filters such as Wiener, Frost, and Kalman are presented in Chap. 2. The chapter highlights the differences between the various filters and shows that by incorporating different objective functions and constraints, filters can optimize noise reduction, speech distortion, or a mixture of the two. This theme continues to the following chapters.

Chapter 3 presents filtering in the space domain, or beamforming, in a way suitable for those unfamiliar with the topic. Delay-and-sum, minimum-variance distortionless response, null-steering, and other methods are discussed. Chapter 4 follows with the method of linearly-constrained minimum variance for combating both noise and reverberation. It is argued that both can indeed be eliminated, but this requires knowledge of the room impulse responses, which is difficult to estimate in practice when speakers are recorded in a room, for example. The spatio-temporal approach is presented that avoids the need to estimate room impulse responses by employing frequency response functions relative to one of the microphones rather than the actual source. This leads to noise reduction capability, but without the capacity to perform de-reverberation.

Chapter 5 focuses on the task of noise reduction from a multiple-channel view-point using a range of methods, some previously presented, highlighting their ability to reduce noise, maintain the signal without distortion, and exploit the spatial information. Chapter 6 continues with the method of frequency-domain optimal filtering, where by weighting each frequency an improvement in the overall signal-to-noise ratio can be achieved. The method is appropriate for broadband signals such as speech, and various strategies are presented for balancing noise reduction and signal distortion.

Chapter 7 presents a multiple-input–multiple-output model for the problem at hand, analyzing performance with respect to system parameters such as filter lengths. In Chap. 8, further insight into the problem is attained by developing a two-stage solution, namely, source separation and de-reverberation, facilitating de-reverberation methods such as equalization.

Chapter 9 presents the important topic of direction-of-arrival estimation, discussing methods such as multiple signal classification and generalized cross-correlation. Chapter 10 concludes the book with some unaddressed problems, arguing that many aspects of the problems at hand are still open.

To summarize, the book presents in a clear manner a wealth of signal processing methods to combat noise and reverberation using microphone arrays, providing insight into their performance and limitations. JASA readers, including myself, may have liked to see more acoustics incorporated into these methods, e.g., room acoustics, hearing, speech perception, as the disturbances are, after all, acoustic in nature. Perhaps the appropriate combination of signal processing with acoustics may facilitate the desired progress?

BOAZ RAFAELY
Department of Electrical and Computer Engineering,
Ben-Gurion University of the Negev,
Beer-Sheva 84105, Israel

Engineering the Guitar: Theory and Practice

Richard Mark French

Springer, 2008. 284 pp. Price: $49.95 (hardcover). ISBN: 0387743685.

String instruments of the cavity-enclosing, ported shell type are a veritable vibro-acoustic goldmine that encompasses a remarkable range of acoustics just to gain a basic understanding of their overall character. These instruments can be viewed as relatively simple objects excited in a straightforward manner by a player and judged by perceptions, as a craft device requiring many years of experience to properly construct and extract the best sound, or as a system requiring the best contemporary technology just to comprehend some physical aspects of the perceived quality. And just to make matters all the more difficult the modifications and tweaks performed in the mechanical world to enhance perceived quality rely on final judgments mainly in the acoustical world. Compound all this with the reality that there is no direct trail back from sound to mechanics, and it seems astonishing that we are able to create fine sounding string instruments at all.

Although my area of expertise is the violin, many of the concerns in making, playing, and judging bowed string instruments are relevant to the guitar, probably the most popular stringed instrument of all, with commercial USA production nominally 1×10^6 units per year according to the author. While there is considerable material online about engineering applied to the guitar (URLs for a few introductory sites: http://www.guitarengineer.com and http://www.home.agilent.com/agilent/editorial.jspx?cc=AW&lc=eng&ckey=866697&id=866697) and much in the way of published articles (see the Guild of American Luthiers Journal as one example) there does not appear to be another book that deals with the engineering aspects. Thus this book serves a real purpose for scientifically-oriented guitar makers and aficionados as well as those interested in a broad overview of the world of guitars, including materials, introductory acoustics, the neck as cantilever beam, finite and boundary element analyses, guitar electronics, individual and industrial construction techniques, a primer on human hearing, etc., a veritable manifold of matters concerning this very popular instrument. (However, anyone interested in just the craft of building guitars—solid body, acoustic, arch top, etc.—would be better served by one of the many craft-oriented books presently available.)

Of course broad coverage in an ~250 page book must consequently be somewhat shallow on any individual topic, but such a presentation has significant virtues in providing a broad introduction as well as a guide to individuals interested in following up on any topic via over 130 references. *Engineering the Guitar* offers many interesting practical insights although some of these might be difficult for a typical maker to utilize. As an example of the latter, consider the problem of shape; chapter 5 offers a useful analytic parametrization of guitar shape in polar coordinates after conversion from rectangular coordinates (Fig. 5.12 would benefit from R and θ labels as coordinate system origin choice is discussed). What is missing though is a software roadmap for the curve fitting of the geometry data using the rational polynomial series employed. Can this be done in a readily available spreadsheet program, or does it need specialized math software?

The author's personal building experience and his knowledge of a wide variety of guitar construction techniques are put to good use in this book. Its overall broad view is very good reading for those interested in the myriad of details involved in constructing a string instrument and then evaluating it scientifically. The range of references is wide-ranging, although I miss the very first application of nearfield acoustical holography to a musical instrument [W. Strong *et al.*, "Studying a guitar's radiation properties with nearfield holography," J. Guitar Acoust. **6**, 50–59 (1982)] showing

 0001-4966/2009/125(6)/4098/1/$25.00

how important the sound hole radiation is to the overall radiation from the guitar. The weakest part of the book lies in its discussion of the vibration-radiation metamorphosis, where some comprehensive vibration-radiation experiments to get a handle on such matters as radiation efficiency and effective critical frequency would be highly beneficial. Overall, however, the author is to be commended for providing a significant addition to the guitar literature in his broad-ranging book on a very important string instrument.

The review author, with over 35 years of experience in violin research, maintains a comprehensive violin acoustics research facility at East Carolina University, where he is emeritus professor of physics.

GEORGE BISSINGER
Department of Physics,
East Carolina University,
Greenville, NC 27858

 0001-4966/2009/125(6)/4098/1/$25.00

REVIEWS OF ACOUSTICAL PATENTS

Sean A. Fulop
Dept. of Linguistics, PB92
California State University Fresno
5245 N. Backer Ave., Fresno, California 93740

Lloyd Rice
11222 Flatiron Drive, Lafayette, Colorado 80026

The purpose of these acoustical patent reviews is to provide enough information for a Journal reader to decide whether to seek more information from the patent itself. Any opinions expressed here are those of reviewers as individuals and are not legal opinions. Printed copies of United States Patents may be ordered at $3.00 each from the Commissioner of Patents and Trademarks, Washington, DC 20231. Patents are available via the internet at http://www.uspto.gov.

Reviewers for this issue:

GEORGE L. AUGSPURGER, *Perception, Incorporated, Box 39536, Los Angeles, California 90039*
SEAN A. FULOP, *California State University, Fresno, 5245 N. Backer Avenue M/S PB92, Fresno, California 93740-8001*
JEROME A. HELFFRICH, *Southwest Research Institute, San Antonio, Texas 78228*
DAVID PREVES, *Starkey Laboratories, 6600 Washington Ave. S., Eden Prairie, Minnesota 55344*
CARL J. ROSENBERG, *Acentech Incorporated, 33 Moulton Street, Cambridge, Massachusetts 02138*
NEIL A. SHAW, *Menlo Scientific Acoustics, Inc., Post Office Box 1610, Topanga, California 90290*
ERIC E. UNGAR, *Acentech, Incorporated, 33 Moulton Street, Cambridge, Massachusetts 02138*
ROBERT C. WAAG, *Department of Electrical and Computer Engineering, University of Rochester, Rochester, New York 14627*

7,471,027

43.35.Cg ELASTIC BOUNDARY WAVE DEVICE

Hajime Kando, assignor to Murata Manufacturing Company, Limited
30 December 2008 (Class 310/313 A); filed in Japan 10 February 2003

There seems to be a recent surge of interest in boundary wave (as opposed to surface wave) filters in electronics, and this patent certainly helps explain why. The authors describe very clearly the relative merits and drawbacks of shear horizontal boundary wave devices as opposed to conventional surface acoustic wave devices, and then go on to show how one can construct good devices from $LiNbO_3$ and SiO_2 sandwiches like that shown in the figure. To summarize, boundary wave devices are preferable because they do not need hermetic packaging, so they can be made smaller. In addition, their temperature coefficients can be manipulated rather easily to get near zero values. A couple of case studies are given, as well as nearly all the design information relevant to boundary waves on lithium niobate/silicon dioxide substrates.—JAH

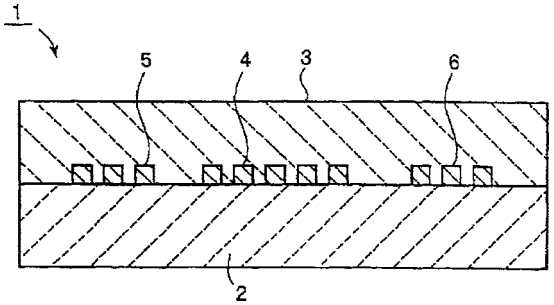

7,475,970

43.35.Zc PIEZOELECTRIC ACTUATOR HAVING PIEZOELECTRIC LAYER AND VIBRATION PLATE WITH GROOVE AND LIQUID TRANSPORTING APPARATUS

Hiroto Sugahara, assignor to Brother Kogyo Kabushiki Kaisha
13 January 2009 (Class 347/70); filed in Japan 31 August 2004

The authors disclose the design of a piezoelectrically operated (as opposed to thermally operated) ink-jet printer head element utilizing flexural wave isolation between the various ink chambers in the form of channels that are formed in the piezoelectric material. The purpose of their design is to reduce the incidence of two different failure types: cracking and chipping during manufacture, and de-lamination during use. First, they claim greater manufacturing yield because the piezoelectric driver material is formed with channels (such as 37 in the figure) in its green state so that they do not need to be formed by dicing or other processes applied when the material has been fired and is brittle. Second, they claim that the use of pressure formed channels in the green material results in lower incidence of failure due to de-lamination of the material over the lifetime of the printer head. Referring to the figure, the ink sits in a reservoir defined by layers of material 2 (presumably silicon) fed from a tank via manifold 17. The reservoir is connected to the orifice 20 formed in polyimide via a channel 21 that is pumped by piezoelectric plate 32. As the volume of the channel is modulated, the ink is pumped to the orifice where it exits. This patent gives a glimpse of the details involved in ink-jet printing technology, at the individual reservoir level as well as at the scale of an entire print head.—JAH

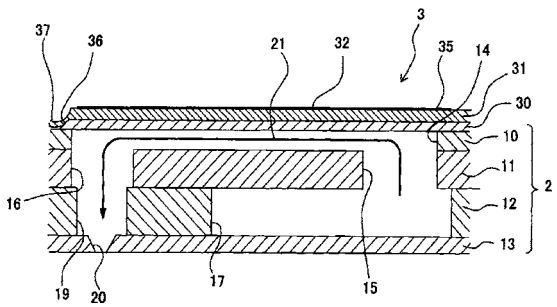

 0001-4966/2009/125(6)/4100/10/$25.00

7,466,839

43.38.Ja WATERPROOF VIBRATION PLATE FOR SPEAKER

Kichiro Yasugahira and Ken Takahashi, assignors to OG Corporation
16 December 2008 (Class 381/426); filed in Japan 26 December 2003

Loudspeakers in automobiles are often mounted in door panels where, according to this patent, they may be exposed to rain or carwash shampoo when the door is opened. The patent discloses a formula and method for adding a water-repellent layer to a felted paper loudspeaker cone during its fabrication.—GLA

7,477,755

43.38.Ja SPEAKER SYSTEM

Shuji Saiki *et al.*, assignors to Panasonic Corporation
13 January 2009 (Class 381/349); filed in Japan 13 April 2004

This is an additional embodiment of the loudspeaker system disclosed in U.S. Patent No. 7,463,747. The goal is to increase the effective volume of a vented speaker enclosure by including a block of activated carbon 34, yet prevent moisture from entering the box. A passive radiator 37 (or a combination of passive radiator and vent) provides the desired air seal and also allows for variations in internal static pressure.—GLA

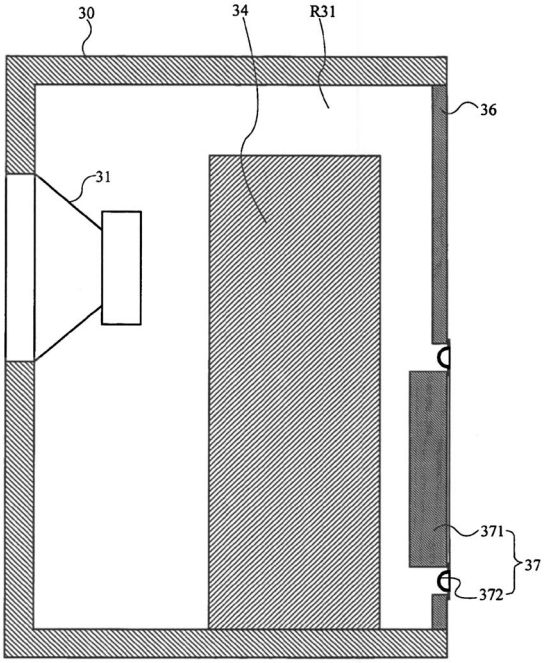

7,477,751

43.38.Kb METHOD AND APPARATUS FOR SOUND TRANSDUCTION WITH MINIMAL INTERFERENCE FROM BACKGROUND NOISE AND MINIMAL LOCAL ACOUSTIC RADIATION

Richard H. Lyon *et al.*, assignors to RH Lyon Corporation
13 January 2009 (Class 381/96); filed 22 April 2004

This patent contains more than a dozen pages of speculative theory but not a hint that the device described has ever been tested. The diagram shows a basic version of a noise-cancelling microphone/speaker. Signals from microphones 210a and 210b are electronically processed to achieve a cardioid pickup pattern. Loudspeaker 212 is located close to the microphone array in the null pickup zone. The talker's mouth 202 is also close to the array on the axis of major sensitivity. The patent argues that if the loudspeaker acts to counteract the sound pressure produced by the talker (as in an active noise cancelling system) then the sound level in the far field will be correspondingly reduced. In effect, the talker will be negatively amplified in the far field even though the sensitivity of the microphone array to the talker's voice is increased rather than reduced. This all involves some fairly sophisticated signal processing. The concept is interesting if it can be made to work.—GLA

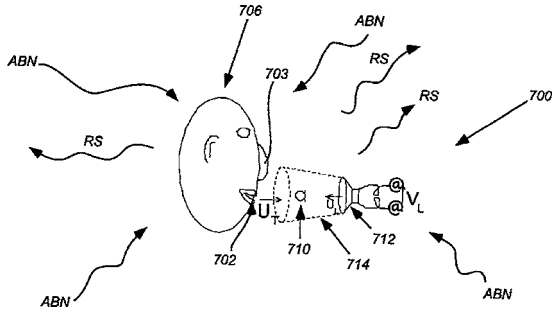

7,474,536

43.38.Lc AUDIO SOUND QUALITY ENHANCEMENT APPARATUS AND METHOD

Ray B. Ridley, Roswell, Georgia
6 January 2009 (Class 361/760); filed 8 July 2005

Makers of high-end audiophile electronic products often advise a warmup period of 15 min or so before transcendent purity is achieved. This patent teaches that heat itself is part of the process, and describes an insulated, temperature-controlled chamber to house critical semiconductors. The crystal oven has been reinvented.—GLA

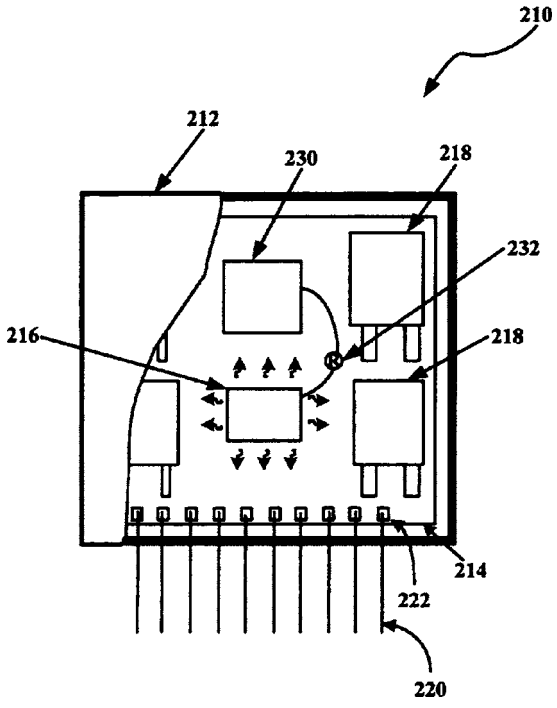

7,466,833

43.38.Si BONE VIBRATING SPEAKER USING THE DIAPHRAGM AND MOBILE PHONE THEREBY

Oug-Ki Lee and Joo-Bae Kim, assignors to Phicom Corporation
16 December 2008 (Class 381/151); filed in Republic of Korea 2 October 2002

This subminiature assembly houses two moving-coil transducers that share a single magnet 32. Pillow-shaped piston 18 serves as a bone conduction transducer, and diaphragm 40 operates as a conventional loudspeaker. The goal is to enable a person with substantial hearing loss to use a mobile telephone by switching to the bone conduction transducer.—GLA

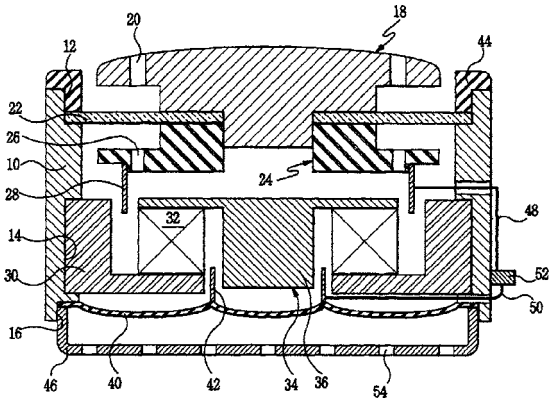

7,474,754

43.38.Si METHOD FOR CANCELING UNWANTED LOUDSPEAKER SIGNALS

Ronaldus Maria Aarts and Daniel Willem Elisabeth Schobben, assignors to Koninklijke Philips Electronics N.V.
6 January 2009 (Class 381/71.6); filed in the European Patent Office 3 October 2001

Conventional noise-cancelling headphones isolate the wearer from all external sounds. But consider the following hypothetical situation: Little Jimmy wants to watch a music video with the sound turned up really loud while his parents try to carry on a conversation in the same room. They might insist that Jimmy use headphones, but that would defeat the purpose of this invention. Instead, the parents wear special headphones that attenuate only the signal from the audio system. In all fairness, there may be legitimate military and industrial applications for such a device.—GLA

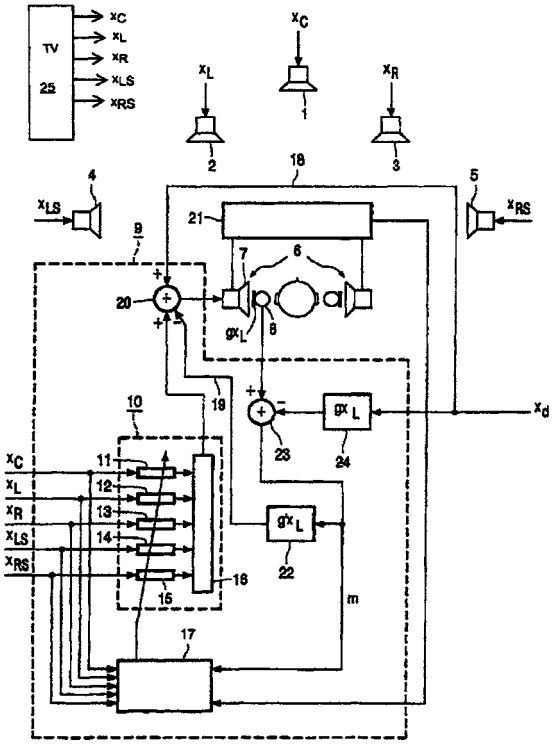

7,442,134

43.40.Kd BALL BAT INCLUDING AN INTEGRAL SHOCK ATTENUATION REGION

William B. Giannetti *et al.*, assignors to Easton Sports, Incorporated
28 October 2008 (Class 473/567); filed 11 March 2005

The walls 12, 14, and 16 of some ball bats 10 can be comprised of multiple layers using a variety of materials. When the bat connects with a ball at the "sweet spot," which is the primary vibration node, also known as the center of percussion (COP), of the assembly, the bat experiences little or no vibration. When the area of contact is not in the vicinity of the COP, the bat can deform into its fundamental and harmonic mode shapes. This vibration can cause shock waves that can "sting" a player's hands. If some layers in wall 14 have lower axial stiffness and/or lower Young's modulus than that of other ply layers, an "integral shock attenuation" (ISA) region is created that has significantly lower axial stiffness than the neighboring regions. These ISAs can be located in transition region 16 or at both ends of barrel 14. ISA materials can include, but are not limited to, aramid fibers (Kevlar and the like), PBO (Zylon), ultra-high weight molecular polyethylene, or other materials that have a relatively low axial Young's modulus at various ply orientations.—NAS

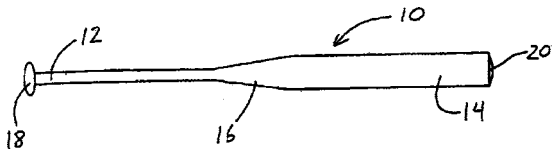

7,438,070

43.40.Tm ARCHERY BOW HAVING IMPROVED DESIGN TO ABSORB SHOCK AND REDUCE VIBRATION

Ralph J. Mancini, Danbury, Connecticut
21 October 2008 (Class 124/25.6); filed 11 January 2006

The patent is a discussion of how molding an energy absorbing and/or dampening material to the bow riser and/or the bow limbs, or coating these with such material, or using a sleeve made from such material, can reduce the vibration, shock, and/or noise generated when said bow converts the stored "kinetic" energy to the arrow via the bowstring. The patent also discusses how a "camo" or color tint pattern can be applied to the coating, molding, and/or sleeve that contains a ultraviolet suppressing material and/or pigments to make the bow less visible to deer, who are said to be able to discern UV light/brighteners. The text reads more like a marketing proposal than a patent description, of which many are cited in the text.—NAS

7,445,173

43.40.Tm DEVICE FOR REDUCING VIBRATIONS AND NOISES OF A PAPER SHREDDER

Tie-Chun Wang, assignor to Michilin Prosperity Company, Limited
4 November 2008 (Class 241/236); filed in China 11 December 2006

A paper shredder core assembly, composed of frames 1, cutting assembly, gear set 3, and motor 4, are attached to housing base 5 using buffer devices, comprised of springs 51 which are "disposed" around rubber cylinders 61 which fit over rods 51, using screws 71 and washers 72, to reduce

noise and vibration. The patent is clear, concise, and to the point.—NAS

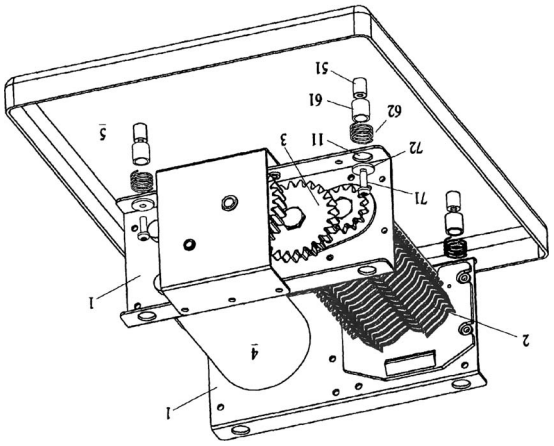

7,445,563

43.40.Tm VIBRATION DAMPING FOR HOLLOW GOLF CLUB HEADS

Frank Werner, assignor to Origin, Incorporated
4 November 2008 (Class 473/332); filed 24 April 2007

In order to reduce the coupling between the crown wall 15 and sole wall 14 of a hollow metal head driver-type golf club, and so mitigate the "strong and often objectionable, sharp ringing sound" generated when the club face strikes the golf ball, a resilient coupling method is used between the crown and sole, comprised of screw 19, rubber or elastomeric washers 13–16, and anchor nut 17 and other similar embodiments, instead of more common rigid methods.—NAS

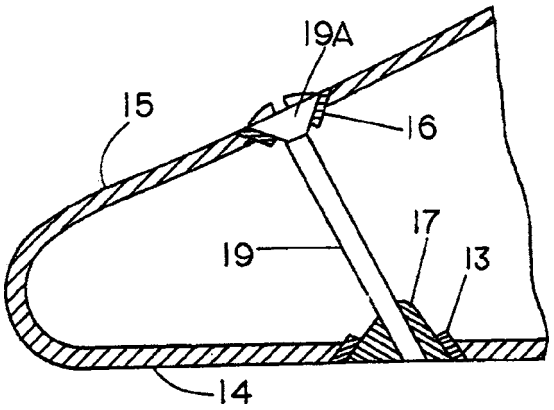

7,464,810

43.40.Tm PLATE-LINK CHAIN

Aurel Vietoris, assignor to Luk Lamellen und Kupplungsbau Beteiligungs KG
16 December 2008 (Class 198/850); filed in Germany 11 May 2006

A plate-link chain (somewhat like a bicycle chain) is made up of parallel plate elements arranged in rows and connected to adjacent elements at hinge joints. Elastically deformable damping plates extend parallel to the chain plates and interconnect adjacent chain links to each other so as to contribute damping as the chain deforms.—EEU

7,464,918

43.40.Tm LIQUID SEALING TYPE VIBRATION CONTROL DEVICE

Shingo Hatakeyama *et al.*, assignors to Toyo Tire & Rubber Company, Limited
16 December 2008 (Class 267/140.13); filed in Japan 4 April 2003

This automotive engine mount includes elastomeric elements and liquid-filled chambers that communicate with each other via orifices. Large low-frequency disturbances are damped due to the liquid flowing between the chambers and small, higher-frequency, disturbances are damped by deformation of the elastic elements.—EEU

7,471,801

43.40.Tm DEVICE FOR THE GENERATION OF OR MONITORING OF VIBRATIONS

Bo Håkansson, assignor to Osseofon AB
30 December 2008 (Class 381/326); filed in Sweden 10 May 2002

This patent relates to an electromagnetic vibrator of the variable reluctance type with applications in hearing aids and the like. It is claimed to provide high efficiency and great compactness by having the magnetic signal flux generated by the coil closed through a bobbin body and one or more yokes, with the bobbin body and yokes made of laminated sheet metal with good magnetic properties. A capacitative impedance may be connected in parallel, so that a parallel resonance occurs in a frequency band where the vibrator is not to consume energy, e.g., at a switch frequency or carrier frequency. Also, a capacitative impedance may be connected in series so that a series resonance is obtained in a frequency band where efficient transformation from electrical to mechanical energy is desired.—EEU

7,468,046

43.40.Vn IMPEDANCE-MATCHED VIBRATION MASSAGER

Mitsuru Takashima, assignor to M.I. Laboratories Corporation
23 December 2008 (Class 601/46); filed 1 February 2005

This hand-held massager includes a closed-loop control system intended to generate vibrations at the resonance of the body part being massaged. The massager includes a hollow cup-shaped contact piece, whose open end is to be placed against the body part being massaged and whose closed end is connected to an electropneumatic vibration generator. A pressure sensor mounted in the side wall of the contact piece senses the oscillatory pressure in the cup's cavity; its signal is fed to a controller that adjusts the frequency of the vibrator to the resonance of the body part.—EEU

7,475,761

43.40.Vn APPARATUS FOR VIBRATION DAMPING IN A MOTOR VEHICLE

Jochem Fischer, assignor to Benteler Automobiltechnik GmbH
13 January 2009 (Class 188/266.7); filed in Germany 25 June 2004

This patent describes a vibration control element that consists of a hollow cylindrical casing with force-transmitting end-plates. Near the wall of the cylinder and in contact with the end-plates are distributed three or more actuators, preferably of the piezoelectric type. These actuators are controlled so as to induce bending in the cylindrical casing in order to counteract unwanted vibrations. Neither the sensors nor the control system are described in this patent.—EEU

7,440,580

43.55.Br ROOM MODE BASS ABSORPTION THROUGH COMBINED DIAPHRAGMATIC AND HELMHOLTZ RESONANCE TECHNIQUES

Anthony Grimani and Evan Reiley, assignors to Performance Media Industries, Limited
21 October 2008 (Class 381/353); filed 16 January 2004

To reduce the pressure difference in small rooms due to the inevitable modes that develop in same, a bass absorber that uses both a Helmholtz cavity absorber and a tympanic diaphragm absorber is described. The Helmholtz resonator mass is defined by opening 24 (to which a cardboard tube is affixed that one assumes resides in the cabinet volume), and the volume is approximately defined by the height of cabinet 10, sides 12, panel 14, and gaskets 22. Panel resonator 14 is defined by panel 14 and springs 18. Both resonators are tuned to the same frequency. The material between spring supports 20 and the apex of the device 10 is neither defined nor described, but following good engineering design and current industry practice is probably a material with a flow resistivity similar to that of fiberglass. The patent provides a good review of the basic design of the devices and references texts that the reviewer is familiar with. The device is one of several marketed by the first inventor for use in home theaters and home studios.—NAS

7,467,498

43.55.Ev FLEXIBLE SHEET MATERIALS FOR TENSIONED STRUCTURES, A METHOD OF MAKING SUCH MATERIALS, AND TENSIONED FALSE CEILINGS COMPRISING SUCH MATERIALS

Marc Fontaine, assignor to Newmat, SA
23 December 2008 (Class 52/145); filed 5 April 2005

The patent discusses the absorptive properties of a thin (less than half a millimeter) micro-perforated, tensioned (stretched) vinyl and how well it works. Variable factors in its sound absorptive performance are the height of the micro-projections, the location of these micro-perforations, and such.—CJR

7,464,790

43.55.Rg SOUND INSULATION/ABSORPTION STRUCTURE, AND STRUCTURE HAVING THESE APPLIED THERETO

Hidekazu Kodama *et al.*, assignors to Rion Company, Limited
16 December 2008 (Class 181/295); filed in Japan 29 May 2003

The structure described in this patent comprises a frame, surface layers of polymer film or metal foil, and absorptive filler between the layers. The surface layers are formed into a curved shape (such as a dome, a barrel, or a cove), the stiffness and related rigidity are alterable by pressurizing the cavity. This in turn affects its transmission loss properties.—CJR

7,467,687

43.55.Ti THERMAL-ACOUSTIC ENCLOSURE

Stephen Craig Mitchell *et al.*, assignors to General Electric Company
23 December 2008 (Class 181/200); filed 12 November 2004

Here is an enclosure for a noisy machine (such as a turbine engine). It has an inner panel (perforated inside, with absorption, of course), another outer panel (might be a honeycomb, with porous filler), and a frame that supports the panels through a vibration isolation mounting.—CJR

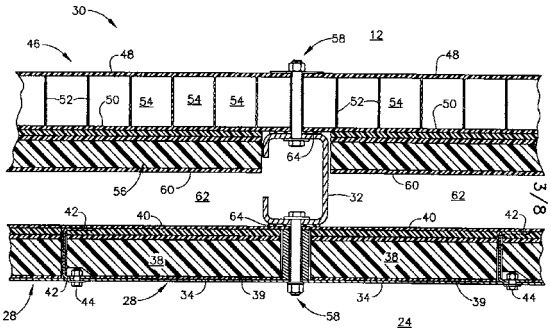

7,467,688

43.55.Vj MULTI-COMPOSITE ACOUSTIC PANEL

Robert Ducharme, assignor to Royal Mat Incorporated
23 December 2008 (Class 181/294); filed in Canada 31 January 2003

This patent gives some recipes for an impact isolation panel using particles of wood fibers from sawdust, crumbs of rubber, and a polyurethane or elastomeric binder.—CJR

7,467,542

43.60.Lq ALIGNMENT-TOLERANT LENS STRUCTURES FOR ACOUSTIC FORCE ACTUATION OF CANTILEVERS

Scott A. Elrod, assignor to Palo Alto Research Center Incorporated
23 December 2008 (Class 73/105); filed 28 September 2005

This patent discloses an interesting form of acoustic imaging that is little discussed in the literature, at least to this reviewer's knowledge. The authors describe a system for implementing atomic force microscopy in liquids utilizing a radiation pressure-driven cantilever. Apparently the idea dates back to papers published in the years 2000–2002, and is designed to

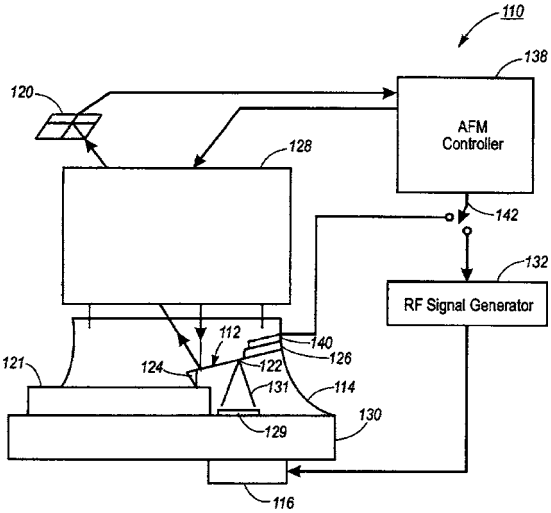

overcome the very high losses involved in oscillating a typical atomic force microscope cantilever in water. The high losses generally mean that piezoelectric excitation of the cantilever motion is ineffective, and something with more force acting over a larger area of the cantilever is needed to get it moving. The idea explored here is to use frequency-spread focused ultrasound to actuate the tip with radiation pressure and to focus the beam of ultrasound in a way that generates an elliptical spot on the cantilever, so as to match its shape fairly well. They go into a number of the details of the

signal properties, the acoustic lens properties, etc., but one wonders what it is used for—perhaps imaging live cells?—JAH

7,467,022

43.66.Ts METHOD FOR FABRICATING A HEARING AID SHELL AND MOLD INCORPORATING TEST FITTING BY THE USER

Vijaykiran Bhagwat and Steven Owens, assignors to Siemens Aktiengesellschaft
16 December 2008 (Class 700/98); filed 6 April 2006

The following occurs during a single visit by a prospective hearing aid wearer at an audiology clinic or dispensing office: an ear impression is made and scanned into a computer terminal. A three-dimensional (3D) model of a custom hearing aid shell is developed and is used to determine whether the hearing aid components will fit. The model is modified accordingly so that everything fits, and a dummy shell is made and evaluated in the wearer's ear for physical fit. After any necessary modifications, when the fit is good, the final 3D data set is sent to the factory site to manufacture the hearing aid.—DAP

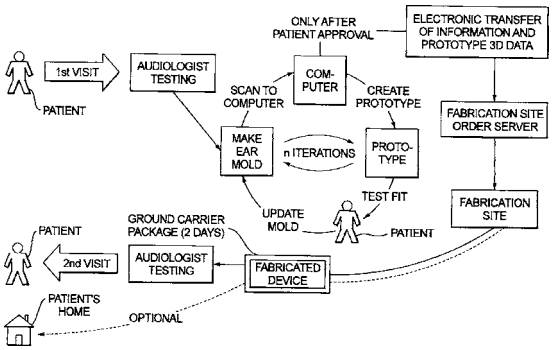

7,469,435

43.66.Ts PILLOW ADAPTED TO RECEIVE SOUND

Bryan C. Cullifer, Norfolk, Virginia
30 December 2008 (Class 5/636); filed 19 January 2008

At first glance this appears to be one of those horseshoe-shaped pillows sold in airline terminals. However, the wedge shape is intended to support the head of a person lying sideways while allowing both ears to receive sound. Potential users may want to try a simple mockup before ordering a pillow; the sensation is certainly different than a conventional pillow, but also different from lying on one's back with both ears exposed.—GLA

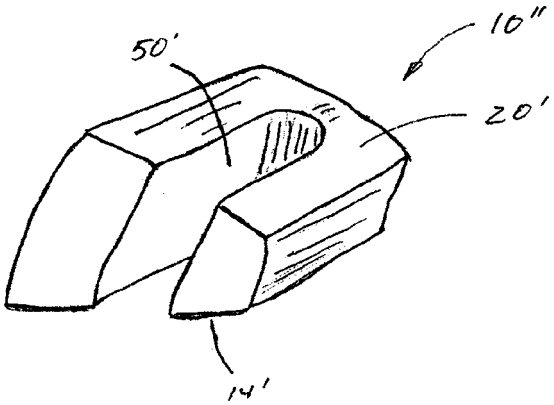

7,471,800

43.66.Ts WAX BARRIER SYSTEM

Mark A. Neilson, assignor to In'Tech Industries, Incorporated
30 December 2008 (Class 381/325); filed 29 March 2004

A wax guard system consists of a permanently-affixed insert mounted into the sound output of an earmold shell, a selection of cerumen guard types, and a number of interchangeable caps covering the ear canal aperture with mesh. Each cap has a cerumen-spreading device insertable into a chamber adjacent to the mesh. The modular wax guard system is said to be customizable for the type of ear wax present in the hearing aid wearer's ear canal.—DAP

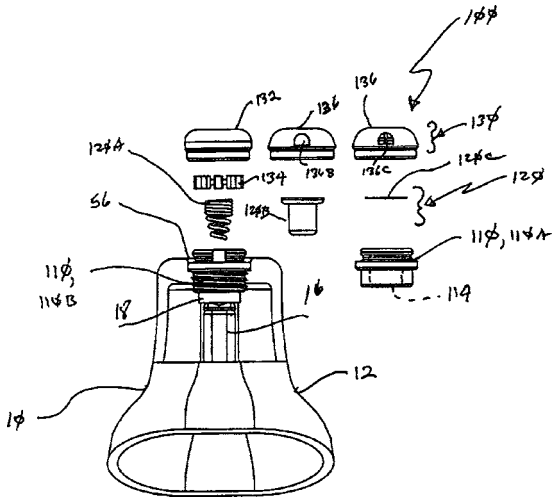

7,471,805

43.66.Ts HEARING AID MECHANISM

Josh Goldberg, assignor to Central Coast Patent Agency, Incorporated
30 December 2008 (Class 381/415); filed 7 December 2006

A hearing aid has a speaker component comprising a coil wrapped around a compartment containing a magnet and a ferrous metal composite diaphragm suspended in a fluid filled with magnetic particles, e.g., a ferrofluid. The magnet is excited when the coil is driven with a voltage, resulting in the diaphragm vibrating.—DAP

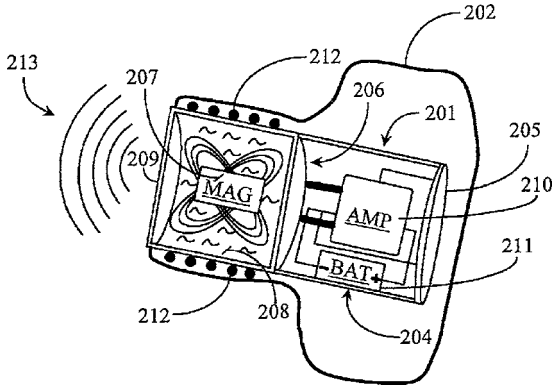

7,474,758

43.66.Ts DIRECTIONAL HEARING GIVEN BINAURAL HEARING AID COVERAGE

Frank Beck and Gerhard Sporer, assignors to Siemens Audiologische Technik GmbH
6 January 2009 (Class 381/313); filed in Germany 26 June 2002

Unaided interaural level difference (ILD) and interaural time difference (ITD) relationships are said to be preserved while wearing hearing aids. The signal transit time through one device of a binaural hearing aid fitting is calculated and, together with its amplification, transmitted wirelessly to the other device. The amplification provided by the second device is adjusted to preserve the ILD. Depending on whether the first or second device has the shorter transit time, the shorter processing delay is modified accordingly to preserve the natural ITD.—DAP

7,477,753

43.66.Ts HEARING AID PROTECTIVE PACKAGING ASSEMBLY

James P. Buckley *et al.*, assignors to InSound Medical, Incorporated
13 January 2009 (Class 381/312); filed 5 January 2006

A tube-shaped metallic container with a removal cap hermetically seals in a hearing aid with enough oxygen and water vapor so that its metal-air battery is activated during storage. The hearing aid, which contains a non-volatile memory, operates in a low-power mode during storage. As soon as the hearing aid is removed from the container and exposed to ambient air, it shifts to a higher power mode. The container also functions as a shock absorber and is electrically conductive to provide protection against electrostatic discharge damage.—DAP

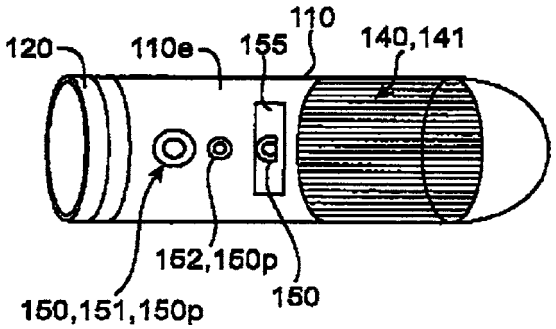

7,477,754

43.66.Ts METHOD FOR COUNTERACTING THE OCCLUSION EFFECTS

Karsten Bo Rasmussen and Søren Laugesen, assignors to Oticon A/S
13 January 2009 (Class 381/317); filed in Denmark 2 September 2002

Some hearing aid users are bothered by the altered "side tone" of the wearer's own voice. This insertable hearing aid includes a sensing microphone inside the ear cavity. Intelligent electronic circuitry modifies the earphone signal to provide appropriate equalization for signals from the sensing microphone but not for other signals picked up by the external microphone.—GLA

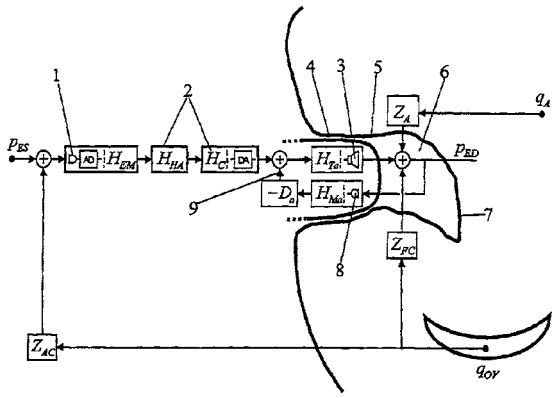

7,477,756

43.66.Ts ISOLATING DEEP CANAL FITTING EARPHONE

Timothy K. Wickstrom *et al.*, assignors to Knowles Electronics, LLC
13 January 2009 (Class 381/380); filed 2 March 2006

This insert earphone contains a tiny receiver 118 located in close proximity to the wearer's eardrum. Damper plug 102 includes an acoustic resistor that also protects the receiver from debris.—GLA

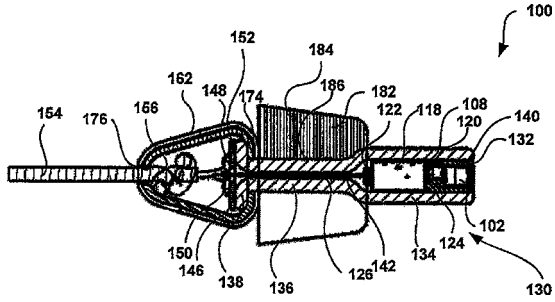

7,465,277

43.66.Yw SYSTEM AND METHODS FOR CONDUCTING MULTIPLE DIAGNOSTIC HEARING TESTS

Christopher L. Wasden *et al.*, assignors to Tympany, LLC
16 December 2008 (Class 600/559); filed 15 May 2003

Self-administered audiometric, tympanogram, acoustic reflex, and otoacoustic emission tests can be conducted by one integrated instrument using a single probe for each ear that contains multiple microphones and loudspeakers, a bone vibrator, and a reversible compressor. The system determines whether ambient noise levels are within acceptable levels during testing.—DAP

7,260,521

43.72.Gy METHOD AND DEVICE FOR ADAPTIVE BANDWIDTH PITCH SEARCH IN CODING WIDEBAND SIGNALS

Bruno Bessette *et al.*, assignors to Voiceage Corporation
21 August 2007 (Class 704/219); filed in Canada 27 October 1998

This patent proposes a new more thorough method of finding and coding the pitch of a wideband speech signal, which accommodates the

greater voicing level variations inherent in wideband speech. The basic idea involves checking a few pitch codebook values and their associated signal paths, and selecting the one offering the least pitch prediction error. The envisioned application involves code-exicited linear prediction.—SAF

7,469,209

43.72.Gy METHOD AND APPARATUS FOR FRAME CLASSIFICATION AND RATE DETERMINATION IN VOICE TRANSCODERS FOR TELECOMMUNICATIONS

Nicola Chong-White *et al.*, assignors to Dilithium Networks Pty Limited
23 December 2008 (Class 704/229); filed 14 August 2003

A frame classification and rate decision module uses source codec parameters from the current and previous frames to determine frame class, rate, and classification feature parameters for the destination codec. A subset of codec parameters is selected for the following frame and rate classification from line spectral frequencies, pitch lag, pitch gains, fixed codebook gains and vectors, rate, and frame energy. Coefficients of the frame classification and rate decision module are pre-computed and stored.—DAP

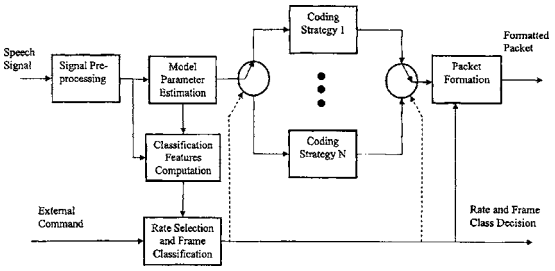

7,472,057

43.72.Gy DETECTOR FOR USE IN VOICE COMMUNICATIONS SYSTEMS

Darwin Rambo, assignor to Broadcom Corporation
30 December 2008 (Class 704/212); filed 17 October 2003

To ensure that the proper decoding algorithm is utilized by the receiver in a communication system, a testing tool is used to identify whether a voice data stream is encoded using a linear, μ-law, or A-law G.711-type algorithm. Six sets of words in the voice data stream are determined that fit into six ranges of values of μ-law equivalents.—DAP

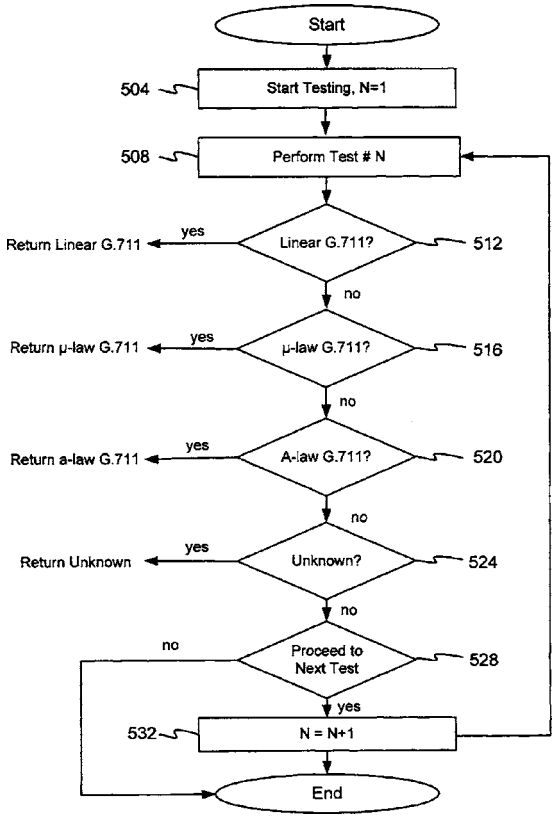

7,472,059

43.72.Gy METHOD AND APPARATUS FOR ROBUST SPEECH CLASSIFICATION

Pengjun Huang, assignor to QUALCOMM Incorporated
30 December 2008 (Class 704/220); filed 8 December 2000

The objective is to improve the classification accuracy in background noise of voiced and unvoiced speech for multi-mode variable rate coders. Background noise and silence can then be coded at lower bit rates. Internal classification parameters are generated from at least one externally-generated input parameter. A normalized auto-correlation coefficient function threshold is determined for voiced speech, transitional speech, and unvoiced speech, and a parameter analyzer is selected according to signal environment. External parameters include speech samples and their signal-to-noise ratio and a voice activity decision.—DAP

7,477,735

43.72.Gy SYSTEM AND METHOD FOR ENHANCED STEREO AUDIO

Trygve Frederik Marton *et al.*, assignors to Tandberg Telecom AS
13 January 2009 (Class 379/406.04); filed in Norway 23 December 2003

To maintain good lip sync with stereo audio signals without causing echo problems, a stereo detector is included with the echo canceller. When stereo at the far end is detected, converging an adaptive echo model to minimize the monaural part of the echo is suspended. When stereo is not detected, converging an echo model to minimize the stereo part of the echo is suspended. Signals with a large stereo component may be attenuated, and stereo images may be removed entirely if they contribute too much echo.—DAP

7,478,040

43.72.Gy METHOD FOR ADAPTIVE FILTERING

Jes Thyssen and Juin-Hwey Chen, assignors to Broadcom Corporation
13 January 2009 (Class 704/228); filed 20 October 2004

To improve perceptual quality of a speech signal by reducing perceived audio coding noise, long-term adaptive post-filtering is used to increase the periodicity of voiced portions of speech by attenuating spectral valleys between harmonics. In order to disable long-term post-filtering during non-periodic signals to prevent the erroneous introduction of excessive periodicity, the instantaneous periodicity is measured and smoothed by low pass filtering. The instantaneous and smoothed periodicities are compared to preset thresholds and the two comparator outputs determine the amount of periodicity added.—DAP

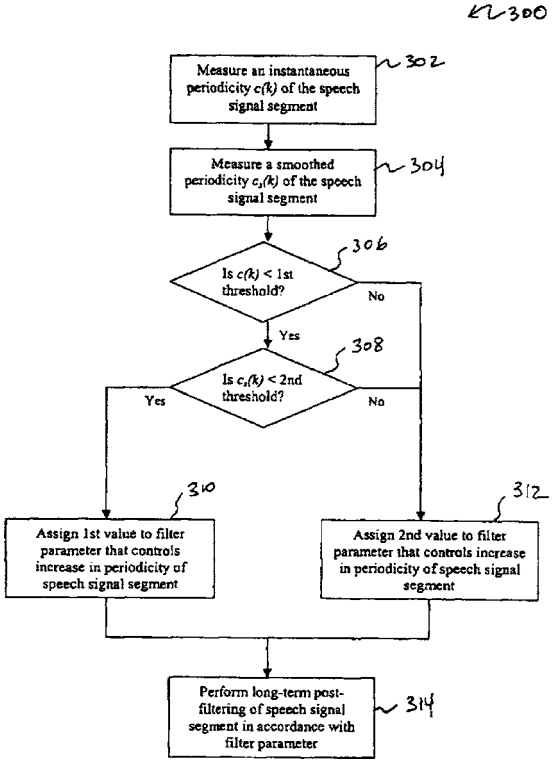

7,478,309

43.72.Gy TRANSMISSION LINE CODING METHOD, TRANSMISSION LINE DECODING METHOD, AND APPARATUS THEREFOR

Yutaka Banba, assignor to Panasonic Corporation
13 January 2009 (Class 714/774); filed in Japan 10 July 2002

The goal is to suppress degradation in a decoded audio signal without adding redundant bits and having to increase bit rate. The importance of each bit in a classification unit of a transmission line coder is determined based on the decoding quality in the presence of a transmission error and a bit classification is assigned accordingly. The encoder selects one of three types of encoding processing for each transmission frame, ranging from no coding to convolution coding with the addition of cyclic redundancy check codes.—DAP

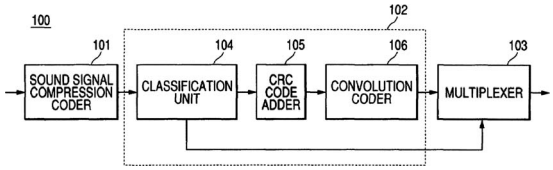

7,251,601

43.72.Ja SPEECH SYNTHESIS METHOD AND SPEECH SYNTHESIZER

Takehiko Kagoshima and Masami Akamine, assignors to Kabushiki Kaisha Toshiba
31 July 2007 (Class 704/268); filed in Japan 26 March 2001

This patent appears to present a method for synthesizing speech by representing each formant as a specially windowed sine wave. The method is not presented clearly, but it seems that each sinusoid representing a formant is windowed so that it resembles the damped resonance excited by a single vocal cord pulse. Then, a pitch function is used to repeat these "damped" sinusoids at a fundamental frequency of voicing. The diagrams are generally more informative than the patent text, which is a shame, because the method seems interesting.—SAF

7,257,534

43.72.Ja SPEECH SYNTHESIS SYSTEM FOR NATURALLY READING INCOMPLETE SENTENCES

Natsuki Saito and Takahiro Kamai, assignors to Matsushita Electric Industrial Company, Limited
14 August 2007 (Class 704/260); filed in Japan 21 July 2004

This patent discusses a general text reading system, such as might be used to read out emails. Such texts often include "incomplete parts-of-sentences" or strings of nonlinguistic information. It is proposed that when an incomplete part-of-sentence is detected (in view of its having a "missing character string"), such an ungrammatical unit can be "obscured" during the read out. The synthesizer is thus encouraged to mumble its way through linguistically incomplete strings.—SAF

7,260,533

43.72.Ja TEXT-TO-SPEECH CONVERSION SYSTEM

Hiroki Kamanaka, assignor to Oki Electric Industry Company, Limited
21 August 2007 (Class 704/260); filed in Japan 25 January 2001

This patent presents a Japanese text-to-speech system that combines presumably standard concatenative synthesis output with prerecorded sounds stored in a "waveform dictionary." In this way, such items as onomatopeic words, song lyrics, or background noises can be directly interpolated into the conventional synthesizer read-out at appropriate locations,

"thereby adding a sense of realism to the output of the synthesized speech." Somehow, 49 claims arise from this.—SAF

7,251,603

43.72.Ne AUDIO-ONLY BACKOFF IN AUDIO-VISUAL SPEECH RECOGNITION SYSTEM

Jonathan H. Connell *et al.*, assignors to International Business Machines Corporation
31 July 2007 (Class 704/270); filed 23 June 2003

This patent relates to a speech recognition system which uses both audio and visual data. Sometimes, visual data might be corrupted or otherwise useless, and under these conditions it is probably a good idea to perform the recognition by relying solely on the audio. Apparently this notion is not sufficiently obvious because it has been patented here.—SAF

7,254,538

43.72.Ne NONLINEAR MAPPING FOR FEATURE EXTRACTION IN AUTOMATIC SPEECH RECOGNITION

Hynek Hermansky *et al.*, assignors to International Computer Science Institute
7 August 2007 (Class 704/256.1); filed 16 November 2000

In the prior art, speech recognition systems that apply a "hybrid neural net hidden Markov model" normally replace the Gaussian mixture acoustic models of a standard hidden Markov model with some kind of neural network that is trained to model each acoustic unit. This patent presents a means of using both a neural net approach to the acoustic modeling and Gaussian mixture modeling in the same system. The general idea is to train the neural network to generate the acoustic unit "probability posteriors," and to then use transformations of these as base features for training of Gaussian mixture models. Large (up to 35%) reductions in recognition error rate are claimed for this kind of combination system.—SAF

7,466.848

43.80.Vj METHOD AND APPARATUS FOR AUTOMATICALLY DETECTING BREAST LESIONS AND TUMORS IN IMAGES

Dimitris N. Metaxas and Anant Madabhushi, assignors to Rutgers, The State University of New Jersey
16 December 2008 (Class 382/128); filed 15 December 2003

Contrast in an ultrasound image of the breast is enhanced. Intensity and texture classifiers that indicate the probability of a pixel corresponding to a tumor are applied. A seed point is identified and a region is grown around a point to indicate the presence or absence of a tumor.—RCW

7,472,597

43.80.Vj ULTRASONIC IMAGING DEVICE AND THE INFORMATION PROCESSING METHOD THEREOF

Liguo Zhang *et al.*, assignors to Shenzhen Mindray Bio-Medical Electronics Company, Limited
6 January 2009 (Class 73/606); filed in China 26 June 2005

Pulse-echo ultrasound signals are analyzed. The analysis is used to control a digital video disk recording unit. Encoded and compressed signals are recorded according to the controls.—RCW

7,473,225

43.80.Vj ULTRASONIC IMAGING SYSTEM AND METHOD

Takashi Azuma *et al.*, assignors to Hitachi Medical Corporation
6 January 2009 (Class 600/442); filed in Japan 25 September 2002

The phase of a beamformer output is corrected to compensate for phase shifts in the lateral direction of the beam and for frequency-dependent attenuation. After phase correction, a derivative operation is used to determine the spatial change of acoustic impedance. A processed version of the differentiated signal is displayed.—RCW

7,473,226

43.80.Vj ULTRASONOGRAPHIC DEVICE AND ULTRASONOGRAPHIC METHOD

Takashi Azuma *et al.*, assignors to Hitachi Medical Corporation
6 January 2009 (Class 600/443); filed in Japan 6 August 2003

Correlation between images is computed to achieve a balance between improved contrast resolution and improved spatial resolution. When the displacement between images is large, envelope-detected signals are synthesized. When the amount of displacement is small, rf signals are synthesized. Alternatively, the system mixing frequency is varied according to the amount of displacement to achieve the desired balance.—RCW

7,474,778

43.80.Vj ULTRASONOGRAPH

Ryuichi Shinomura *et al.*, assignors to Hitachi Medical Corporation
6 January 2009 (Class 382/131); filed in Japan 12 March 2002

A set of elements in a two-dimensional array is selected to produce an image from one direction. Another set of elements is selected to produce an image from another direction. The first image and the second image are combined.—RCW